CODEN: JASMAN 4966

THE JOURNAL of the Acoustical Society of America

Vol. 106, No. 2 August 1999

SOUNDINGS SECTION

GENERAL LINEAR ACOUSTICS [20]

NONLINEAR ACOUSTICS [25]

UNDERWATER SOUND [30]

ULTRASONICS, QUANTUM ACOUSTICS, AND PHYSICAL EFFECTS OF SOUND [35]

(Continued)

CONTENTS—*Continued from preceding page*

(Continued)

CONTENTS—*Continued from preceding page*

PHYSIOLOGICAL ACOUSTICS [64]

PSYCHOLOGICAL ACOUSTICS [66]

SPEECH PRODUCTION [70]

SPEECH PERCEPTION [71]

(Continued)

CONTENTS—*Continued from preceding page*

SPEECH PROCESSING AND COMMUNICATION SYSTEMS [72]

MUSIC AND MUSICAL INSTRUMENTS [75]

BIOACOUSTICS [80]

LETTERS TO THE EDITOR

ERRATA

ACOUSTICS RESEARCH LETTERS ONLINE

CUMULATIVE AUTHOR INDEX

A broadband omnidirectional barrel-stave flextensional transducer

D.F. Jones and D.A. Christopher

Defence Research Establishment Atlantic, P.O. Box 1012, Dartmouth, Nova Scotia, Canada B2Y 3Z7
jones@drea.dnd.ca

Abstract: The piezoelectric Class III barrel-stave flextensional transducer is an underwater acoustic source that is capable of generating sound over a wide frequency band. This broadband performance is achieved through coupling the fundamental flexural and longitudinal modes of vibration. Near the low frequency flexural resonance, the Class III transducer is small compared to a wavelength, and its radiation is omnidirectional. However, at frequencies in the vicinity of the longitudinal resonance, the radiation is directional. In this article, we show through the use of a finite element model that the Class III transducer can be designed for omnidirectional radiation over the entire band.
PACS numbers: 43.38.Fx, 43.38.Ar

1. Introduction

Barrel-stave flextensional transducers have been classified into three distinct categories based on the shapes of their external radiating staves[1-3]. The Class I barrel-stave transducer is primarily operated at its low-frequency fundamental flexural mode, which is well separated from modes at higher frequencies. A Class II design can be used to achieve higher acoustic power at the same flexural resonance frequency as its Class I counterpart. This high-power transducer is a modified Class I design that can accommodate a longer driver, which extends beyond the extremities of the curved staves. A Class III design is basically an end-to-end graft of two Class I transducers. This dual-shell design is capable of broadband radiation due to multimode coupling between the fundamental flexural resonance of the staves and the longitudinal resonance of the driver. The Class III transducer is the subject of this article.

Although the Class III barrel-stave flextensional transducer can radiate sound over a wide band, the directional characteristics of the acoustic radiation change with frequency. For those applications that require broadband omnidirectional sources, a common solution is to use spherical transducers. However, the transducer designer may wish to take advantage of a high energy density material like magnetostrictive rare earth Terfenol-D[4], which is ideal for longitudinal driver elements (e.g., discs and rings) but not easily formed into or driven as hemispherical elements. Thus, it is useful to examine longitudinally-driven transducers with the purpose of extending the omnidirectional frequency band. In this work, finite element analysis techniques were used to investigate the directional characteristics of a Class III barrel-stave flextensional transducer design.

2. Finite element model

The axisymmetric finite element program MAVART was used to analyze a piezoelectric Class III transducer. The geometry of the model is shown in Fig. 1. Two stacks, each consisting of six Navy Type I piezoceramic rings, are used as drivers. Each ring has an outside diameter of 5.06 cm, an inside diameter of 3.94 cm, and a thickness of 1.02 cm. The steel 1020 end and center plates have an outside diameter of 6.96 cm and a thickness of 2.00 cm. The concave aluminum 7075 staves are 4.0 mm thick, and their radius of curvature

(ROC), the key geometrical parameter of interest, is either 20.0 cm or 6.0 cm. The tangential elastic constants for the aluminum stave material are reduced by a factor of 1000 to simulate individual staves mounted on polygonal plates,[5] or a slotted shell mounted on circular plates.[6] The transducer was analyzed in a surrounding sphere of seawater.

3. Predicted results

The performance parameters of interest in this study are the transmitting voltage response (TVR) curves in the axial (Z) and radial (R) directions as well as the XZ directivity patterns. The finite element predictions are shown in Figs. 2-5.

When the radius of curvature of the staves was set to 20 cm, the fundamental flexural and longitudinal resonance frequencies obtained from the peaks in Fig. 2 were 2.65 kHz and 6.31 kHz, respectively. A third peak occurs at 9.57 kHz and corresponds to a second flexural resonance. The TVR curves in the axial and radial directions begin to diverge just beyond the 2.65 kHz peak, indicating a departure from omnidirectionality. This can be seen more clearly in Fig. 3, where the predicted XZ directivity pattern at 2.1 kHz is essentially omnidirectional but elongated in the axial direction at 3.9 kHz.

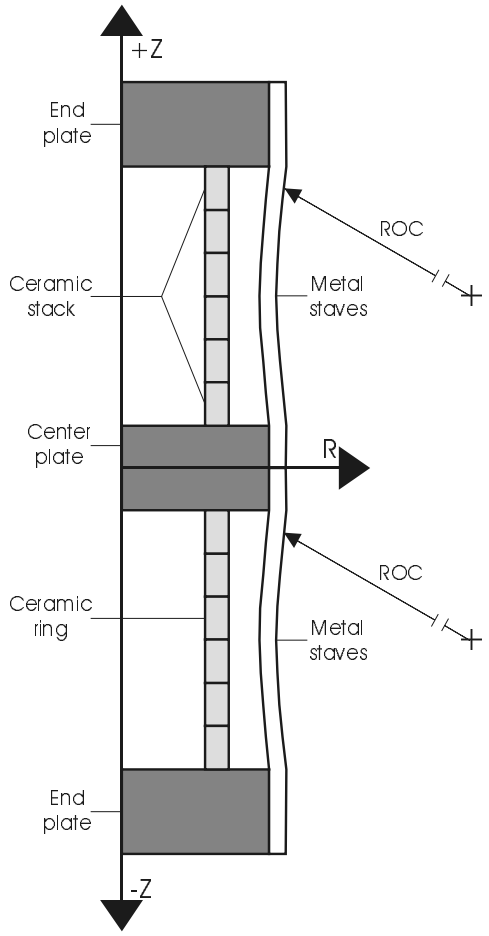

Fig. 1. Class III barrel-stave flextensional transducer geometry.

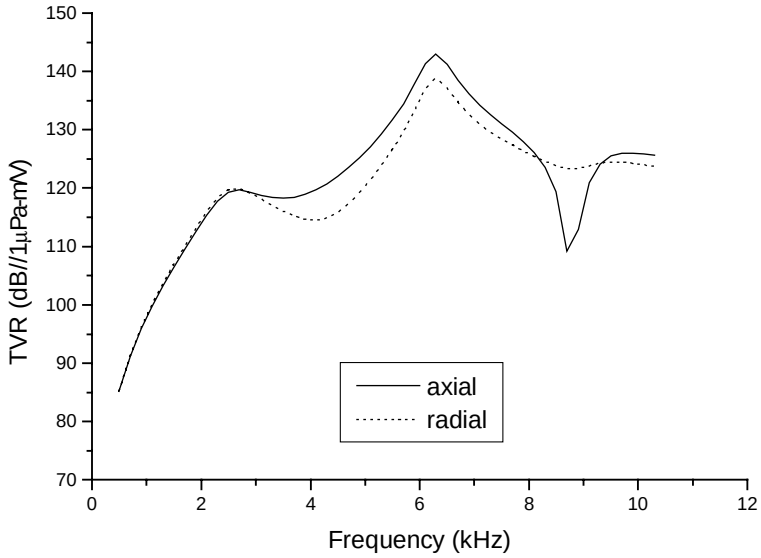

Fig. 2. Predicted TVR curves for the 20 cm ROC configuration.

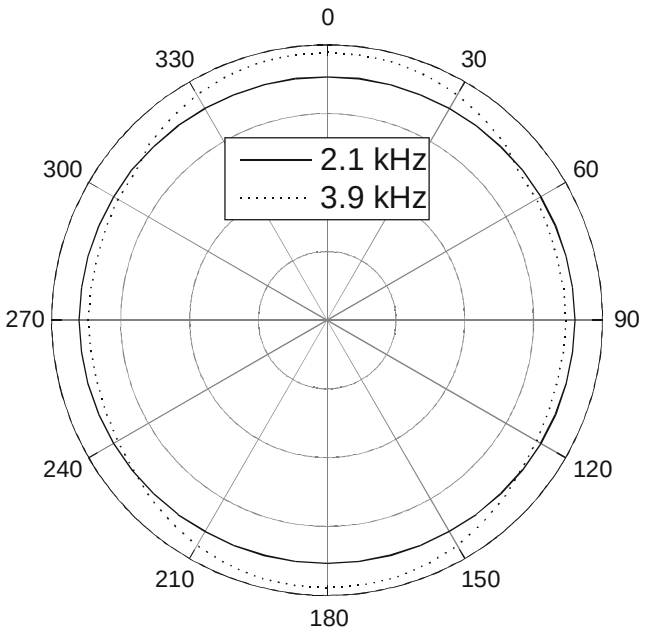

Fig. 3. Predicted XZ directivity patterns for the 20 cm ROC configuration. Center to circumference is 40 dB.

When the radius of curvature of the staves was reduced to 6 cm (i.e., the staves are curved deeper into the transducer), the fundamental flexural resonance increased to 3.98 kHz as shown in Fig. 4. A second flexural resonance is visible at 10.1 kHz, and the longitudinal resonance, which should lie between these flexural modes, does not appear.

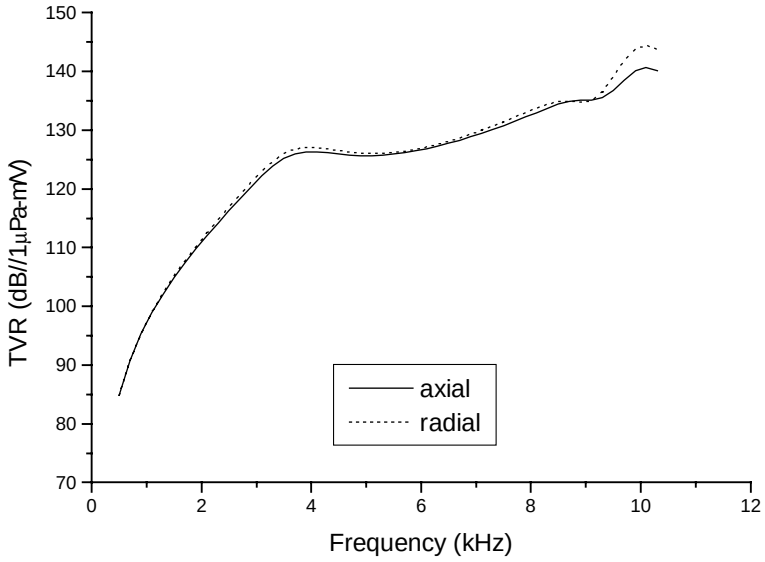

Fig. 4. Predicted TVR curves for the 6 cm ROC configuration.

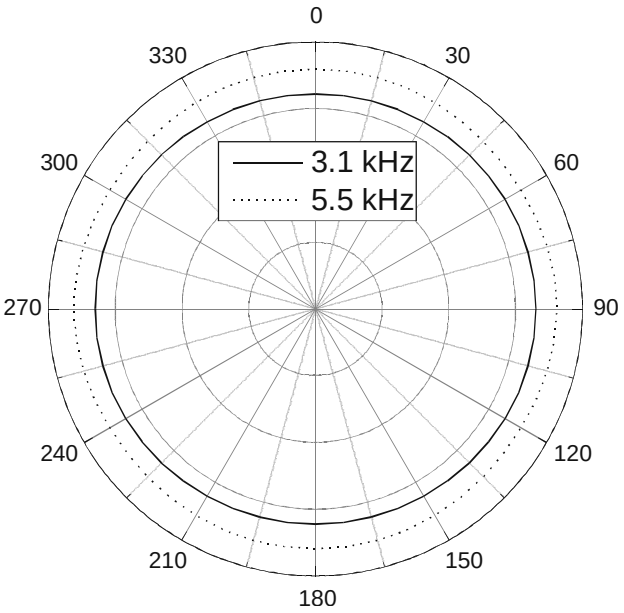

Fig. 5. Predicted XZ directivity patterns for the 6 cm ROC configuration. Center to circumference is 40 dB.

In this case, the axial and radial TVR curves do not significantly deviate from each other over most of the band, indicating omnidirectional radiation extending beyond 8.2 kHz, where the length of the transducer equals a wavelength. Fig. 5 shows two XZ omnidirectional directivity patterns at 3.1 kHz and 5.5 kHz, in agreement with the TVR data.

Two further finite element predictions of note for the 6 cm ROC design concern the electroacoustic efficiency and the directivity index. The former parameter exceeds 65% over the entire 2-9 kHz frequency band, whereas the latter parameter is less than 1.5 dB for all frequencies up to 8.8 kHz.

4. Conclusions

The Class III barrel-stave flextensional transducer has been modelled using finite element analysis techniques. When the concave staves have a shallow curved profile (the 20 cm ROC case), the fundamental flexural mode and the longitudinal mode are clearly evident, and the radiation pattern becomes directional starting at frequencies just above the flexural mode. On the other hand, deeply-curved concave staves (the 6 cm ROC case) cause the fundamental flexural mode to shift to higher frequencies and the longitudinal mode to be suppressed. In addition, the radiation patterns of the deeply-curved design are essentially omnidirectional over the entire 0.5-9 kHz frequency band studied in this work.

References and links

[1]G.A. Brigham and L.H. Royster, "Present status in the design of flextensional underwater acoustic transducers," J. Acoust. Soc. Am. **46**, 92 (abs) (1969).
[2]L.H. Royster, "The flextensional concept: A new approach to the design of underwater acoustic transducers," Appl. Acoust. **3**, 117-126 (1970).
[3]D.F. Jones, D.J. Lewis, C.G. Reithmeier, and G.A. Brownell, "Barrel-stave flextensional transducers for sonar applications," DE-Vol. 84-2, in *Proceedings of the 1995 Design Engineering Technical Conferences*, Vol. 3, Part B (American Society of Mechanical Engineers, New York, 1995), pp. 517-524.
[4]D.F. Jones and J.F. Lindberg, "Recent transduction developments in Canada and the United States," in *Proceedings of the Institute of Acoustics*, Vol. 17, Part 3 (Institute of Acoustics, St. Albans, U.K., 1995), pp. 15-33.
[5]D.F. Jones, "Research and development of the 800 Hz barrel-stave flextensional transducer at the Defence Research Establishment Atlantic," Defence Research Establishment Atlantic Report 98/101, January 1998.
[6]D.F. Jones and D.J. Lewis, "The effects of shell wall thickness and number of slots on the performance of the Merchant slotted-shell flextensional projector," Defence Research Establishment Atlantic Technical Memorandum 95/203, February 1995.

Phoneme recognition by cochlear implant users as a function of signal-to-noise ratio and nonlinear amplitude mapping

Qian-Jie Fu and Robert V. Shannon

Department of Auditory Implants and Perception, House Ear Institute, 2100 West Third Street, Los Angeles, CA 90057
qfu@hei.org *shannon@hei.org*

Abstract: The present study measured phoneme recognition as a function of signal-to-noise levels when different nonlinear loudness mapping functions were implemented in three cochlear implant users using a 4-channel continuous interleaved sampler (CIS) strategy. Results show that phoneme recognition scores in quiet vary only slightly when different amplitude mappings from highly compressive to weakly compressive are applied. As the level of background noise is increased, recognition scores decrease more rapidly for the strongly compressive mapping than for the weakly compressive mapping. Results indicate that, although a strongly compressive mapping between acoustic and electric amplitude produces slightly better performance in quiet, a less compressive mapping may be beneficial for implant listeners in noisy listening conditions.

PACS numbers: 43.71.Es, 43.71.Ky, 43.66.Ts

1. Introduction

In quiet laboratory testing conditions, many cochlear implant users with the latest implant devices can achieve high levels of open-set sentence recognition. However, performance deteriorates significantly in noisy listening conditions (Hochberg et al., 1992; Müller-Deiler et al., 1995) for even the best cochlear implant users. Several explanations for the noise susceptibility of cochlear implant listeners have been proposed recently. One of the most obvious factors is the limited spectral resolution in cochlear implants. In a recent study, Fu et al. (1998) measured phoneme recognition in five normal-hearing listeners as a function of the number of spectral channels. Results showed that as the spectral information was reduced, speech recognition deteriorated only slightly in quiet, but significantly in noise. Phoneme recognition performance of the best cochlear implant users was similar to that of normal-hearing subjects listening to a similar level of spectral reduction. A similar result was reported by Dorman and colleagues (1998a, 1998b). These results indicate that the limited spectral resolution in cochlear implant listeners is a key factor causing noise susceptibility. However, one interesting observation from the Fu et al. and Dorman et al. studies is that some implant listeners had performance comparable to normal-hearing listeners in quiet but significantly poorer performance in noise. One factor that may have contributed to this difference is the loudness mapping function between acoustic amplitude and electric current.

Instantaneous amplitudes in normal speech range over a 30 to 60 dB range (Boothroyd et al., 1994). However, implant listeners typically have dynamic ranges of only 6 to 15 dB in electric current, requiring the acoustic range to be compressed into the electric range. Fu and Shannon (1998) investigated the effect of nonlinear amplitude mapping on vowel and consonant recognition in cochlear implant users and normal-hearing listeners. They found that for both acoustic and implant listeners, the best performance was obtained

when normal loudness was preserved, which, for electrical stimulation, was obtained when a compressive power-law mapping (p=0.22) was applied. A traditional power-law, cross-modality model indicated that this mapping best restored the loudness growth in cochlear implant users. Performance deteriorated only slightly in both acoustic and implant listeners when the amplitude mapping function was either more compressive or more expansive. Thus, instantaneous amplitude nonlinearity has only a minor effect on phoneme recognition in quiet.

Fu and Shannon (1999) investigated the effects of nonlinear amplitude mapping on the recognition of spectrally degraded speech in noise by normal-hearing subjects. They measured vowel and consonant recognition in five normal-hearing listeners as a function of signal-to-noise ratio (S/N) with the exponent of the amplitude-mapping power function as a parameter. The results showed that nonlinear amplitude mapping produced only a mild decrement in speech recognition in quiet but could produce a large decrement in noise. Expansive nonlinear mapping provided better overall performance than linear or compressive mapping in low signal-to-noise ratio conditions.

The goal of the present study is to investigate the effect of nonlinear amplitude mapping on phoneme recognition in cochlear implant users.

2. Methods

2.1 Subjects

Cochlear implant subjects were three postlingually deafened adults using the Nucleus-22 device. All had at least four years experience utilizing the SPEAK speech processing strategy and all were native speakers of American English. The Nucleus processor with the SPEAK strategy divides an input acoustic signal into 20 frequency bands, extracts the amplitude envelope from all 20 bands, and stimulates the electrodes corresponding to the 6 to 10 bands with the maximal amplitude (McDermott et al, 1992). The frequency allocation table specifies the frequency range covered by the speech processor. Two subjects (N4 and N7) used frequency allocation table 9 (150-10,823 Hz) in their clinical implant processor, and one subject (N3) used frequency allocation table 7 (120 Hz - 8,658 Hz). All implant subjects had 20 active electrodes available for use. All implant participants had extensive experience in speech recognition experiments. Table 1 contains relevant information for the three subjects, including their most recent scores on the HINT sentence test and a multitalker, 12-vowel recognition test with their 20-electrode SPEAK processor.

Table 1. Subject information on three Nucleus-22 cochlear implant listeners who participated in the present study.

Subject	Age	Gender	Cause of Deafness	Duration of use	Freq. Table	Score (HINT)	Vowel Score
N3	56	M	Trauma	7 years	7	96.2%	69.5%
N4	40	M	Trauma	5 years	9	100.0%	81.1%
N7	55	M	Unknown	5 years	9	100.0%	64.5%

2.2 Test materials and procedures

Speech recognition was assessed for medial vowels and consonants. Vowel recognition was measured in a 12-alternative identification paradigm, including 10 monophthongs (/i ɪ ɛ æ ɑ ɔ ʊ u ʌ ɝ/) and 2 diphthongs (/e o/), presented in a /h/-vowel-/d/ context. The tokens for these closed-set tests were digitized natural productions from 5 males, 5 females, and 5 children, drawn from the material collected by Hillenbrand et al. (1995). Consonant recognition was measured in a 16-alternative identification paradigm for the consonants /b d g p t k l m n f s ʃ v z j θ/ presented in an /a/-consonant-/a/ context. Two repetitions of each of the 16 consonants were produced by three speakers (1 male, 2 female) for a total of 96 tokens (16 consonants * 3 talkers * 2 repeats).

 0001-4966/99/106(2)/L18/6/$15.00

Each test block included 180 tokens for vowel recognition or 96 tokens for consonant recognition. A stimulus token was randomly chosen from all 180 tokens in vowel recognition and from 96 tokens in consonant recognition and presented to the subject. Following the presentation of each token, the subject responded by pressing one of 12 buttons in the vowel test or one of 16 buttons in the consonant test, each marked with one of the possible responses. The response buttons were labeled in a /h/-vowel-/d/ context (heed, hawed, head, who'd, hid, hood, hud, had, heard, hoed, hod, hayed) for the vowel recognition task and a /a/-consonant-/a/ context followed by an example word for the consonant recognition task.

All signals were presented at comfortable audible levels through a custom implant interface system (Shannon et al., 1990). Subjects had been well familiarized with the test materials and the test procedure from prior experiments. All subjects started with a training session. Speech sounds without noise were used as training conditions. Each training session included 8 consecutive test blocks with the same mapping condition and the same speech material. Feedback was provided. Subjects started the test sessions either after 8 consecutive runs or the performance had been stabilized in three consecutive runs. In the test sessions, the order of signal-to-noise ratio conditions was randomized. The order of the five mapping conditions and the order of the vowel and consonant tests were counterbalanced across subjects. No feedback was provided in test sessions.

2.3 Signal processing

The speech signal was mixed with simplified speech spectrum-shaped noise (constant spectrum level below 800 Hz and 10-dB/octave role-off above 800 Hz). The signal-to-noise ratio (S/N) was defined as the difference in decibels between the root-mean-square (RMS) levels of the whole speech token and the noise.

The 4-channel Continuous Interleaved Sampler (CIS) processor (Wilson et al., 1991) was implemented as follows. The signal was first pre-emphasized using a first-order Butterworth high-pass filter with a cutoff frequency of 1200 Hz and then band-pass filtered into four broad frequency bands using 8^{th} order Butterworth filters. The five corner frequencies (-3 dB down points) of the four bands were at 300 Hz, 713 Hz, 1509 Hz, 3043 Hz, and 6000 Hz. The envelope of the signal in each band was extracted by half-wave rectification and low-pass filtering (8^{th} order Butterworth) with a 160 Hz cutoff frequency. The amplitude histogram in each band was computed for the test materials presented at 70 dB SPL. The maximum amplitude used (A_{max}) was set to the 99^{th} percentile of all amplitude levels in all channels, and the minimal amplitude (A_{min}) was set to the noise floor in the absence of sound input in all channels. The current level (E) of electric stimulation in the i^{th} band was set to the acoustic envelope value (A) raised to a power (Fu and Shannon, 1998). The exponent of the power function was systematically changed from 0.05 to 0.8. This transformed amplitude was used to modulate the amplitude of a continuous, 500 pulse/sec. biphasic pulse train with a 100 μs/phase pulse duration. The stimulus order of the 4 channels was 1-3-2-4 for electrode pairs (16,22), (11,17), (6,12), and (1,7), respectively.

3. Results

Figure 1A and 1B show the mean and individual scores of vowel and consonant recognition as a function of the power function exponents in the quiet condition. The dotted lines show the individual scores from three listeners, and the solid line shows the mean scores from these three subjects. The vowels were consistently recognized at about 50% correct when the exponent of the power function was increased from 0.05 to 0.4 and dropped slightly to 41.7% as the exponent of the power function further increased to 0.8. Similarly, consonant recognition changed slightly from 70% when the value of the exponent of the amplitude mapping function was 0.05, to 73% when p was 0.2, and dropped to 46% when the exponent was increased to 0.8.

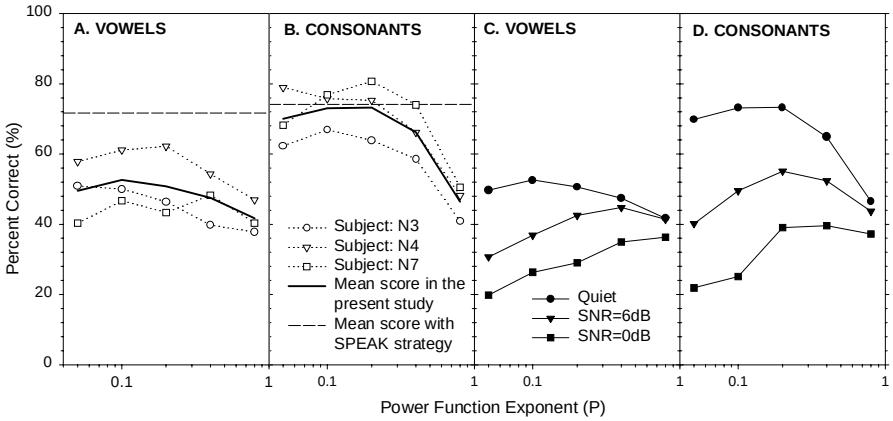

Fig. 1. Recognition scores of vowels and consonants as a function of the power function exponents in quiet and in noise. (A) Vowels (in quiet condition), (B) Consonants (in quiet condition); (C) Vowels (mean scores); (D) Consonants (mean scores).

Figures 1C and 1D show the mean vowel and consonant recognition scores as a function of the exponent of the power function in quiet and in noise. For weak compression (p=0.8), only a slight drop of speech performance was observed at both +6 dB SNR and 0 dB. However, a much larger reduction in performance was observed as the noise level increased for the strongly compressive conditions. When the exponent was 0.05, a 20% reduction occurred in vowel recognition and a 30% reduction in consonant recognition was observed going from quiet conditions to +6 dB SNR.

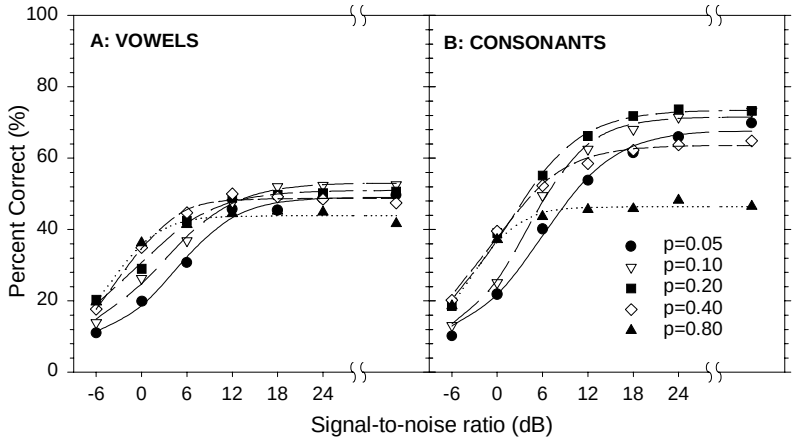

Fig. 2. Recognition scores of vowels and consonants as a function of signal-to-noise ratio. (A) Vowels; (B) Consonants. The lines represent the fitting curve based on a sigmoidal model.

Figures 2A and 2B show the mean scores of vowel and consonant recognition, respectively, as a function of S/N ratio with different amplitude mappings. Both vowel and consonant scores gradually increased as signal-to-noise (S/N) ratio increased for all mapping conditions. The phoneme recognition threshold (PRT) was defined as the S/N level that produced 50% of the performance level in quiet. The lines represent the best fit of a simple sigmoidal model (Fu et al., 1998; Fu and Shannon, 1999) with three parameters: PRT, the slope of the function at PRT (β), and the performance level in quiet.

Figure 3 shows the PRT and slope as a function of the power function exponents. The PRT for both vowels and consonants improved significantly as the mapping function changed

from a strong compression (p=0.05) to a weak compression (p=0.8). However, the slopes of the vowel and consonant functions at PRT were relatively constant.

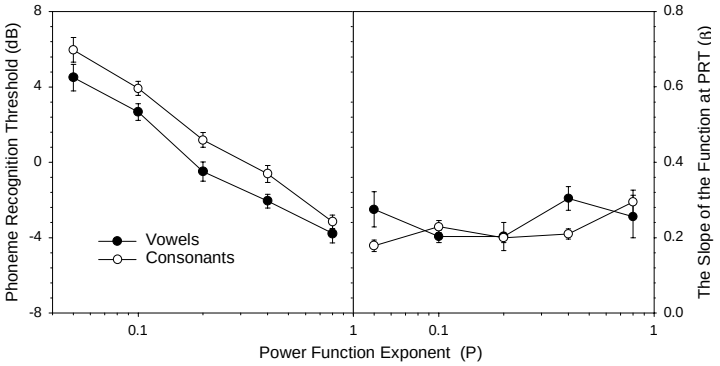

Fig. 3. Phoneme recognition threshold and the slope of vowel and consonant recognition as a function of the power function exponent. Error bars represent +/- one standard deviation.

4. Discussion and conclusions

The present results demonstrate that nonlinear acoustic-to-electric amplitude mappings have only a minor effect on phoneme recognition in quiet, and are consistent with the previous finding in normal-hearing listeners (Fu and Shannon, 1998). However, as the S/N level decreases, the effect of nonlinear amplitude mapping becomes dramatic and asymmetric: performance with weakly compressive mappings declines mildly in noise, but performance declines dramatically in noise with a strongly compressive amplitude mapping.

Two factors have possibly contributed to the differential effect of nonlinear amplitude mapping on speech performance in quiet and noise. One is the loudness-related effect (altered loudness growth function), and the other is the effective S/N ratio after compression. From an information transmission viewpoint, one would expect to obtain the highest vowel and consonant recognition scores when the normal loudness growth was preserved in electric stimulation, as demonstrated in the previous study (Fu and Shannon, 1998). The curve of performance in quiet could be used to roughly estimate the loudness-related effect. Vowel and consonant scores dropped only slightly when the amplitude mapping function was either more compressive or less compressive than the optimal mapping function, indicating that only a moderate degradation was caused by the loudness-related factor. Because the noise was introduced in addition to the loudness-related distortion, different amplitude mapping functions also result in a different effective S/N ratio at the output of the power function compressor. In other words, the effective S/N level will be dependent on the power function exponents. A linearly shifted PRT and a relatively constant slope as a function of power function exponents suggest that the differential effect of nonlinear amplitude mapping in noise was due to the change of the effective S/N ratio caused by compression.

One observation worth mentioning is the difference between the performance in the present study and the performance with the SPEAK strategy. Although the consonant scores for the 4-channel CIS strategy were comparable to those for the SPEAK strategy, the vowel scores for the SPEAK strategy (dashed line in Figure 1) were about 20% higher than the highest scores in Fig. 1 for the 4-channel CIS strategy. Two factors may contribute to this significant difference in vowel recognition. One is the processing strategy itself. The 20-electrode SPEAK strategy provides significantly better spectral resolution than the 4-channel CIS strategy (Fu and Shannon, 1998). The other possible factor is long-term learning because the present results are based on an “acute” study, where no adjustment time for the new speech processor was provided. It is quite possible that the difference will become smaller after significant exposure to the new speech processor with the 4-channel CIS strategy.

The present results also show an interesting similarity between vowel and consonant recognition. In quiet, neither vowel nor consonant recognition was strongly affected by amplitude compression, although consonant recognition did deteriorate more than vowel recognition for most linear mapping ($p=0.8$). Further analysis showed that performance on manner cues (Miller and Nicely, 1955) suffered most in this condition. The amplitude mapping exponent had a similar effect on the PRT for vowels and consonants (Figure 3).

The data in the present study showed that the PRT was highly dependent on amplitude mapping. This suggests that at least part of the large variability in performance across cochlear implant users may be due to nonoptimal amplitude mapping. Implant listeners who have an amplitude mapping function that is too compressive are at a disadvantage in noise compared with implant listeners with less compressive mappings. One implication of the results is that less compressive mappings may be better overall for mixed quiet and noisy conditions. Amplitude mappings that are more linear than the optimal loudness mapping may be slightly poorer in quiet conditions, but would still allow reasonably good speech recognition in noise. In contrast, strongly compressive mappings would allow a similar level of speech recognition in quiet, but would be considerably worse in noise.

Acknowledgments

We wish to thank Prof. James Hillenbrand for allowing us to use the multitalker vowel test materials. The research was supported by grants R03-DC-03861, R01-DC-01526, and contract N01-DC-92100 from NIDCD.

References and links:

Boothroyd, A., Erickson, F.N., and Medwetsky, L. (**1994**). "The hearing aid input: a phonemic approach to assessing the spectral distribution of speech," Ear and Hearing **15**, 432-442.

Dorman, W.F., Loizou, P.C., and Fitzke, J. (**1998a**). "The identification of speech in noise by cochlear implant patients and normal-hearing listeners using 6-channel signal processors," Ear and Hearing **19**, 481-484.

Dorman, W.F., Loizou, P.C., Fitzke, J., and Tu, Z. (**1998b**). "The recognition of sentences in noise by normal-hearing listeners using simulations of cochlear-implant signal processors with 6-20 channels," J. Acoust. Soc. Am. **104**, 3583-3585.

Fu, Q.-J., and Shannon, R.V. (**1998**). "Effects of amplitude nonlinearity on speech recognition by cochlear implant users and normal-hearing listeners," J. Acoust. Soc. Am. **104**, 2571-2577.

Fu, Q.-J., Shannon, R.V., and Wang, X. (**1998**). "Effects of noise and spectral resolution on vowel and consonant recognition: Acoustic and electric hearing," J. Acoust. Soc. Am. **104**, 3586-3596.

Fu, Q.-J. and Shannon, R.V. (**1999**). "Recognition of spectrally degraded speech in noise with nonlinear amplitude mapping," Proceedings of 1999 IEEE International Conference of Acoustics, Speech, and Signal Processing, Vol. 1, 369-372.

Hillenbrand J., Getty, L.A., Clark, M.J., and Wheeler K. (**1995**). "Acoustic characteristics of American English vowels," J. Acoust. Soc. Am. **97**, 3099-3111.

Hochberg, I., Boothroyd, A., Weiss, M., Hellman, S. (**1992**). "Effects of noise and noise suppression on speech perception by cochlear implant users," Ear and Hearing **13**, 263-271.

McDermott, H.J., McKay, C.M., and Vandali, A.E. (**1992**). A new portable sound processor for the University of Melbourne/Nucleus Limited Multichannel cochlear implant, J. Acoust. Soc. Amer., **91**, 3367-3371.

Miller, G. and Nicely, P. (**1955**). "An analysis of perceptual confusions among some English consonants." J. Acoust. Soc. Am. **27**, 338-352.

Müller-Deiler, J., Schmidt, B.J., and Rudert, H. (**1995**). "Effects of noise on speech discrimination in cochlear implant patients," Ann. Otol. Rhinol. Laryngol. **166**, 303-306.

Shannon, R.V., Adams, D.D., Ferrel, R.L., Palumbo, R.L., and Grantgenett, M. (**1990**). "A computer interface for psychophysical and speech research with the Nucleus cochlear implant," J. Acoust. Soc. Am. **87**, 905-907.

Wilson. B. S., Finley, C. C, Lawson, D. T., Wolford, R. D., Eddington, D. K., & Rabinowitz, W. M. (**1991**). New levels of speech recognition with cochlear implants, Nature, **352**, 236-238.

Acoustic scintillations and angle-of-arrival fluctuations observed outdoors with a large planar vertical microphone array

D. Keith Wilson and Calandra R. Tate

Information Science and Technology Directorate, U.S. Army Research Laboratory, Adelphi, Maryland 20783

dkwilson@arl.mil

David C. Swanson and Karl M. Reichard

Applied Research Laboratory, Pennsylvania State University, State College, Pennsylvania 16804

Abstract: A vertical planar array of 32 microphones (eight elements in the vertical direction and four in the horizontal; overall dimensions approximately 6 m by 3 m) was used to image the scintillations and angle-of-arrival fluctuations from a source 770 m distant. Data sets of 20-min duration were collected in a variety atmospheric conditions. On a windy afternoon, the source image underwent dramatic scintillations and fluctuations in its apparent position. For still nighttime conditions, the image was much more stable, although deep fading still occurred.

PACS numbers: 43.28.Fp, 43.60.Gk

1. Introduction

Arrays of microphones can be used to track acoustic sources moving through the atmosphere [Ferguson and Criswick, 1996; Pham and Sadler, 1996]. The atmosphere is hardly a passive participant in the process: random fluctuations in the wind and temperature fields drive random variations in the intensity and orientation of acoustic wave fronts impinging on the array. Although analogous problems have been studied in other areas of wave propagation (see, for example, the discussion in Flatte *et al.* [1979] regarding ocean acoustics), there have been few systematic observations of wave front angle-of-arrival variability for acoustic propagation in the atmosphere. Earlier related experiments have characterized sound-field statistics such as phase and amplitude structure functions [Bass *et al.*, 1991] and spatial coherence [Havelock *et al.*, 1995]. In this study we observe angle-of-arrival variability for near-ground propagation using a 32-element, planar vertical microphone array. Images of the acoustic beamformer output during 20-min trials conducted in three distinct meteorological conditions are presented in MPEG format.

2. Description of the experiment

In June 1998 we assembled a planar vertical array of 32 microphones at Rock Springs, Pennsylvania, on agricultural land maintained by the Pennsylvania State University Agronomy Research Center. The microphones in the array were arranged in eight horizontal rows and four vertical columns. The spacing between the rows was 0.75 m, and the spacing between columns was 0.98 m. The array was supported with four vertical fiberglass beams, which were anchored in cement. The structure is shown in Fig. 1.

Fig. 1. Left: Fiberglass beams and anchors used to support the microphone array. Right: Close-up view of a microphone and the mounting bracket. Readers of the print version should refer to the color version of these pictures in the online archival version.

The on-axis beam pattern of the array at 250 Hz is shown in Fig. 2. The initial nulls occur at $\theta \simeq \pm 13^\circ$ and $\phi \simeq \pm 20^\circ$, where θ is the elevation angle, and ϕ the azimuthal angle. The initial sidelobes are at $\theta \simeq \pm 19^\circ$ and $\phi \simeq \pm 31^\circ$, with the corresponding levels being -13 and -12 dB.

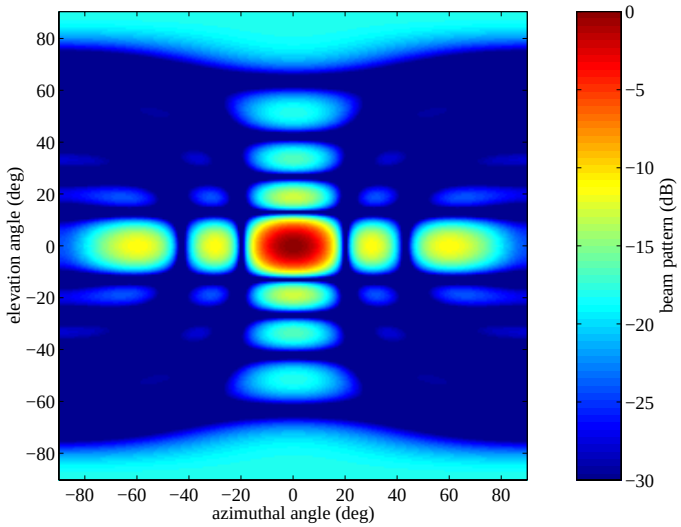

Fig. 2. Beam pattern of the array at $f = 240$ Hz, as a function of the azimuthal and elevation angles (both defined relative to normal incidence). Readers of the print version should refer to the color version of this figure in the online archival version.

The acoustic source in our experiment consisted of a pair of 18-in. woofers, each driven by a 200-W amplifier. The speakers were pointed toward each other and separated by 10 in., with the axis of the speakers perpendicular to the propagation path. By driving the speakers with opposite phases, a monopole-like radiation pattern in the far field was produced. Tones at 50, 100, 150, 200, and 250 Hz were broadcast. The height of the source above the ground was 1.2 m, and the distance from the microphone array was 770 m.

The signals from each of the 32 microphones were digitally sampled at 8000 Hz, thereby generating about 0.5 megabytes of data per second and a total of 585 megabytes per 20-min trial. The analog-to-digital conversion was accomplished using a dedicated PC board, model ADC64 by Innovative Integration. The data were transferred in real time to a PC hard disk. Upon completion of each trial, the data were saved to a recordable CD.

A total of six 20-min trials were run, encompassing several distinct meteorological conditions. The trials are summarized in Table 1. Three of these trials were selected for analysis here: 1738 and 2220 on 18 June, and 1033 on 19 June. The first of these trials took place on a moderately windy evening. Propagation was marginally downwind. The second trial was on a clear, still night, with a strong temperature inversion. The third was on a cloudy morning with light winds, shortly after a rain shower. The temperature gradient was very small for this final trial; in meteorological terminology such conditions are called *nearly neutral*.

Table 1. Summary of the six experimental trials. Time of day is in local daylight savings time. Direction is the angle between the propagation path and the wind vector (0° is downwind propagation, 180° is upwind). Temperature difference is the temperature at 2 m height minus the temperature at 10 m.

Date	Time of Day	Wind Speed (m/s)	Wind Dir. (deg off Array Axis)	Temperature Diff. (°C)
18 June 1998	1536–1556	4.4	51	0.13
18 June 1998	1738–1758	2.3	61	−0.05
18 June 1998	2116–2136	0.3	149	−1.28
18 June 1998	2220–2240	0.1	169	−1.17
19 June 1998	0817–0837	0.8	116	−0.03
19 June 1998	1033–1053	0.4	160	0.10

3. Signal processing

Intensity and angle-of-arrival variability can be visualized by generating sequences of the beamformed array signals. By adjusting the phase of the signals prior to combining them, the main response axis of the array can be steered in different azimuthal and elevational directions. Scanning the main response axis over a large number of azimuthal and elevational directions yields a planar image of the energy arriving at the array. The process of combining the signals with various phase delays (beamforming) can be accomplished efficiently using a two-dimensional fast Fourier transform (2-D FFT). In this study we have chosen to use the 250-Hz component of the signal for imaging, because the ratio of array aperture to wavelength is most favorable for this frequency. Our signal processing method for constructing the images, which is based on common signal-processing techniques, is the following:

1. Load concurrent 80,000-point time series (10 s of data) for each of the microphones.
2. Partition each 80,000-point series into 10 segments. Apply a Hann window to the 8000-point segments and transform (1-D complex FFT) them to the frequency domain.
3. Select the 250 Hz frequency component from each FFT, thereby creating 8×4 complex matrices (representing the magnitude and phase at each microphone) for each of the 10 segments.
4. Average the 10 matrices to obtain a single 8×4 matrix representative of the 10-s interval.
5. Zero-pad the 8×4 matrix to 128×64 points and take the 2-D inverse FFT to create the image.
6. Repeat the process until the end of each 20-min time series is reached. The result is a total of 120 2-D images for each 20-min record.

Given the 8000-Hz sampling rate, the binwidth of each 8000-point FFT is exactly 1 Hz. Therefore the 250 Hz tone (like other integer frequencies) falls in the center of a bin. In actuality there is some modulation in the received frequency caused by atmospheric scattering. By using a longer FFT, we determined this modulation to be less than 0.1 Hz; therefore it does not significantly affect our results.

The padding procedure in Step 5 interpolates the image to a finer angular resolution. Equivalently, it artificially extends the vertical aperture of the array to $128\Delta z = 96$ m, where $\Delta z = 0.75$ m is the vertical sensor spacing. Therefore the 2-D inverse FFT has a vertical wavenumber axis $k_z = [-64, -63, \ldots, 63]\Delta k_z$, where the wavenumber resolution is $\Delta k_z = 2\pi/(96\,\mathrm{m}) = 0.0654\,\mathrm{m}^{-1}$. Similarly, the horizontal aperture is $64\Delta y = 62.7$ m, where $\Delta y = 0.98$ m, and the horizontal wavenumber axis is $k_y = [-32, -31, \ldots, 31]\Delta k_y$, where $\Delta k_y = 0.102\,\mathrm{m}^{-1}$. For small arrival angles, $k_z \simeq k_0\theta$ and $k_y \simeq k_0\phi$ (where $k_0 = 2\pi f/c_0$ is the free-space wavenumber, c_0 is the approximate sound speed, and f is the frequency). Therefore, at 250 Hz (with $c_0 = 335$ m/s), the reconstructed image has interpolated angular resolution $\Delta\theta = 0.799^\circ$ and $\Delta\phi = 1.25^\circ$.

4. Acoustic images

MPEG files containing the sequences of beamformer images are presented in Mm. 1–3. For the session recorded on a windy afternoon (Mm. 1, starting at 1738 on 18 June), the source image was found to undergo dramatic scintillations. The fluctuations in received power have a dynamic range of about 20 dB and occur rapidly relative to the 10-s interval between images. The scintillations are much slower for the data recorded during still nighttime conditions (Mm. 2, 2220 on 18 June); however, a deep fade of about 8 dB, lasting several minutes, was still observed. The data recorded during light winds (Mm. 3, 1033 on 19 June) exhibit somewhat slower fluctuations than the previous windy afternoon, with the wave fronts arriving nearly vertically at the array. (In the sequences for both 1738 and 2220 on 18 June, faint sidelobes from the beamformer are occasionally evident near the bottom of the image. Note that the axes in Mm. 1–3 are $\pm 10^\circ$ elevation and $\pm 15^\circ$ azimuth, as opposed to the entire hemisphere shown in Fig. 2.)

Mm. 1. Beamformer image sequence for the trial beginning at 1738 on 18 June (906 Kb).

Mm. 2. Beamformer image sequence for the trial beginning at 2220 on 18 June (483 Kb).

Mm. 3. Beamformer image sequence for the trial beginning at 1033 on 19 June (894 Kb).

The signal level and angle-of-arrival fluctuations can be quantified using the peak (maximum) intensity in the images. Figures 3–5 show time series of the peak intensity for each of the three datasets and the arrival angles corresponding to the peak. The curves are broken off for records where the estimated SNR falls below 10 dB. (SNR was estimated from the difference between the power spectrum at 250 Hz and the average of 249 and 251 Hz) The intensity for the windy afternoon case (Fig. 3) underwent fluctuations with standard deviation 5.1 dB, close to the value of 5.6 dB characteristic of a strongly scattered wave [Flatté *et al.*, 1979]. The fluctuations occured very rapidly, on time scales comparable to the 1 min. interval between images. The standard deviations of the elevation and azimuthal angles were 1.2° and 1.4°, respectively. These angular deviations are equivalent to displacements of 17 m in the vertical position and 18 m in the horizontal position of the virtual source. The mean elevation angle of the image was 3.7°, corresponding to a virtual source height of 50 m. Because our actual source was not this high, most of the energy reaching the array was likely refracted or scattered from above. The

mean azimuthal offset of 2.4° was approximately the same for all trials and therefore was likely due to imperfect alignment between the array axis and source bearing.

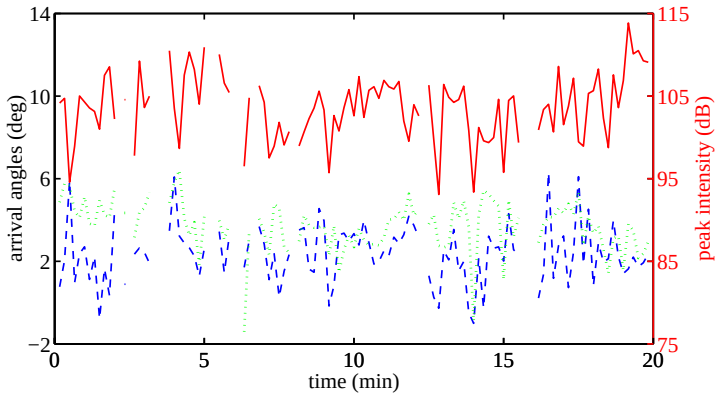

Fig. 3. Wave front angles of arrival and peak intensity at 250 Hz for the trial beginning at 1738 on 18 June 1998. Dotted line (green) is the elevation angle, dashed line (blue) is the azimuthal angle, and solid line (red) is the intensity.

The trial recorded during still nighttime conditions (Fig. 4) exhibited much more gradual changes in the intensity and angles of arrival. During the deep fade late in the trial, the elevation angle also decreased. Quite interestingly, a variation in the azimuthal angle was also observed during this event, indicating that the sound wave underwent significant refraction out of the vertical plane. The mean elevation angle was 6.1° (virtual source height of 83 m). Given the highly stable atmospheric conditions during this trial, clearly there must have been strong downward refraction of sound energy.

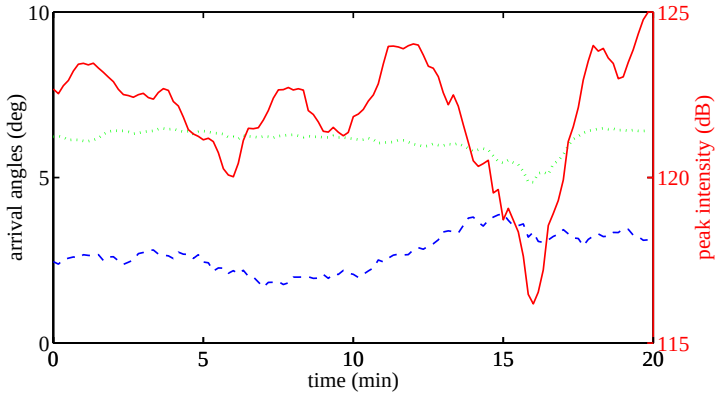

Fig. 4. Wave front angles of arrival and peak intensity for the trial beginning at 2220 on 18 June 1998. Legend is the same as Fig. 3.

The appearance of the trial recorded during light wind conditions (Fig. 5) is similar to the previous windy afternoon. The intensity fluctuations were only 1.6 dB, however, indicating that the wave was not strongly scattered. The standard deviations in the elevation and azimuthal angles were 0.47° and 0.56°, respectively. The center of the image was very close to the horizon (mean elevation angle 0.23°).

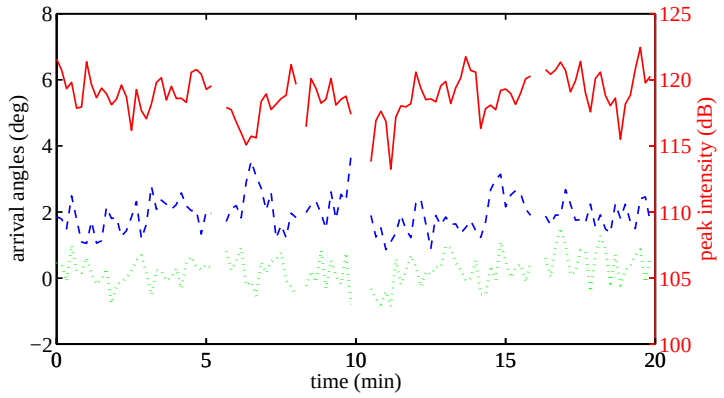

Fig. 5. Wave front angles of arrival and peak intensity for the trial beginning at 1033 on 19 June 1998. Legend is the same as Fig. 3.

5. Conclusion

The sequences of beamformer images in this study vividly demonstrate the dependence of acoustic scintillations and angle-of-arrival fluctuations on atmospheric conditions. On a windy afternoon, the fluctuations were rapid and characteristic of a strongly scattered wave. On a very still night, the image was much more stable, although an episode of deep fading lasting several minutes was still observed. Despite these differences, the windy afternoon and still night had in common that the source image was elevated several degrees above the horizon. On a cloudy morning with light winds, the image scintillated weakly and was positioned nearly on the horizon. The variability observed for the two daytime cases was driven by atmospheric turbulence of differing levels of intensity, whereas the nighttime variability likely resulted from gravity waves, which occur in temperature inversion layers of the atmosphere.

Acknowledgments

This work was funded through the U.S. Army Research Laboratory Director's Research Initiative Program. Jason Estep and Brian Magill (ARL/Penn State) helped build the array and assisted during execution of the experiment. Dr. Chenning Tong and Richard Thompson (Dept. of Meteorology/Penn State) maintained the atmospheric measurement systems.

References and links

Bass, H. E., Bolen, L. N., Raspet, R., McBride, W., and Noble, J. (**1991**). "Acoustic propagation through a turbulent atmosphere: Experimental characterization," *J. Acoust. Soc. Am.* **90**, 3307–3313.

Ferguson, B. G., and Criswick, L. G. (**1996**). "Variability in the bearing and range estimates of acoustic sources in air," *J. Acoust. Soc. Am.* **100**, 2636(A).

Flatté, S. M., *et al.* (**1979**). *Sound Transmission Through a Fluctuating Ocean* (Cambridge University Press, Cambridge, England).

Havelock, D. I., Di, X., Daigle, G. A., and Stinson, M. R. (**1995**). "Spatial coherence of a sound field in a refractive shadow: Comparison of simulation and experiment," *J. Acoust. Soc. Am.* **98**, 2289–2302.

Pham, T., and Sadler, B. M. (**1996**). "Incoherent and coherent aeroacoustic wideband direction-finding algorithms for ground vehicles," *J. Acoust. Soc. Am.* **100**, 2636(A).

SOUNDINGS

Section Editor: Richard Stern

This front section of the *Journal* includes acoustical news, views, reviews, and general tutorial or selected research articles chosen for wide acoustical interest and written for broad acoustical readership.

ACOUSTICAL NEWS—USA

Elaine Moran
Acoustical Society of America, Suite 1NO1, 2 Huntington Quadrangle, Melville, NY 11747-4502

Editor's Note: *Readers of this Journal are asked to submit news items on awards, appointments, and other activities about themselves or their colleagues. Deadline dates for news items and notices are 2 months prior to publication.*

New Fellows of the Acoustical Society of America

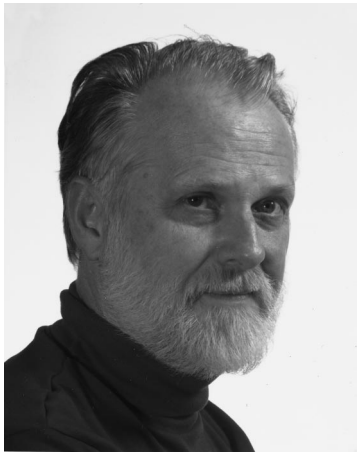

James W. Beauchamp—For contributions to computer analysis and synthesis of musical tones.

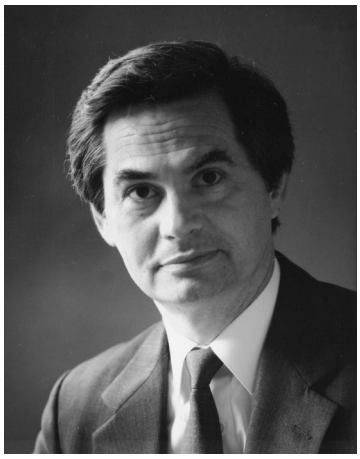

R. Lawrence Kirkegaard–For contributions to acoustics in facilities for the performing arts.

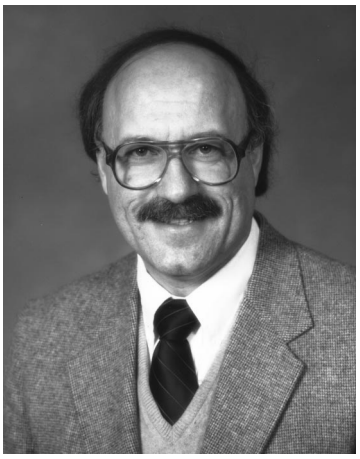

Kenneth P. Roy—For contributions to architectural acoustics and acoustical building materials.

F. V. Hunt Postdoctoral Research Fellowship awarded to Penelope Menounou

The 1999–2000 F. V. Hunt Postdoctoral Research Fellowship in Acoustics was awarded to Penelope Menounou. Under the Fellowship Dr. Menounou will undertake a research program at the University of Texas at Austin. The subject of her research is on aircraft noise propagation through real atmosphere.

Dr. Menounou holds a Diploma from the National Technical University of Athens and a Ph.D. from the University of Texas at Austin. Her Ph.D. thesis was on ''Theoretical study of diffraction by straight and ragged edge noise barriers.''

The Hunt Fellowship is granted each year to an ASA member who has recently received his or her doctorate or will be receiving the degree in the year in which the fellowship is to be granted. The recipient of the fellowship is that individual who, through personal qualifications and a proposed research topic, is judged to exhibit the highest potential for benefiting any aspect of the science of sound and promoting its usefulness to society. Further information about the Fellowship is available from the Acoustical Society of America, Suite 1NO1, 2 Huntington Quadrangle, Melville, NY 11747-4502, Tel: 516-576-2360; Fax: 516-576-2377; E-mail: asa@aip.org.

Pranab Saha named 1999 MSPE Engineer of the Year

Dr. Pranab Saha, P.E., a Member of the Acoustical Society of America, has been selected the 1999 Michigan Society of Professional Engineers (MSPE) ''Engineer of the Year.'' MSPE recognized Dr. Saha at their 52nd Annual Conference held in May for his contributions to the engineering profession, to the MSPE Organization and to the Oakland Chapter of MSPE.

Dr. Saha is a Principal Consultant and Co-owner of Kolano and Saha Engineers, Inc. in Waterford, Michigan. He earned a Ph.D. in Mechanical Engineering from the Georgia Institute of Technology.

Regional Chapter News

Greater Boston

January Meeting

Boston ASA and AES Joint Concert/Meeting at Historic Faneuil Hall

[Editor's note: This review by Eric Reuter is reprinted from the AES Boston Section, February 1999 Newsletter. Mr. Reuter is a member of both the Greater Boston Chapter of ASA and the Boston Section of AES. He is a graduate of the Worcester Polytechnic Institute, where he studied with Dr. Richard Campbell. He is a member of the consulting staff of Cavanaugh Tocci Associates in Sudbury, Massachusetts (E-mail: ereuter@cavtocci.com).]

Approximately forty members of both the Boston AES section and the Greater Boston section of the Acoustical Society of America (ASA) attended a joint meeting on 10 January at Boston's Faneuil Hall. The main

 0001-4966/99/106(2)/523/5/$15.00

event was a public concert by the Boston Classical Orchestra (BCO), which the AES and ASA had been invited to record using several experimental multichannel techniques. Following the concert, most members continued the meeting with dinner and a discussion of classical music recording.

For comparative purposes, three separate surround recording techniques were implemented, using a total of 16 microphones. Since the orchestra anticipated a sold-out hall, all microphones were suspended, keeping the floor and aisles free of stands and cables. Thanks to pre-rigged cables placed during the week before, the recording crew was able to set up in three hours before the concert.

The first microphone array consisted of four omnidirectional microphones hung in a trapezoidal pattern about four meters above the audience. The main pair was just above the first row of audience seating, spaced about one meter left and right of the center line. The rear pair, four meters further into the hall, was spaced about two meters on either side of the center line.

The second technique was a coincident ''quad-cardioid'' microphone array built by Dick Campbell, consisting of four horizontal cardioid capsules oriented every 90 degrees, effectively creating four coincident pairs facing the front, rear, right and left. The array was hung about 2 meters behind the conductor and 3 meters above the floor. An additional cardioid microphone was pointed straight up for use as an overhead channel with these first two techniques.

The third approach was provided by guest Michael Godfrey, an independent researcher working with George Wong under a grant from the Canadian National Research Council. Godfrey brought a seven channel wireless ''space sampling'' microphone array of his own design, which was hung about 3 meters behind the conductor and 2.5 meters above the floor. Seven miniature capsules (one each for front left, center and right, surround left and right, overhead and low frequency) were mounted flush with the surface of a hard plastic dummy-head shape. Seven belt pack transmitters at the array sent the individual mike signals to receivers for amplification, mixing and recording. All of the signals were routed through a Mackie console and recorded on a pair of synchronized Tascam DA-38s.

As part of a pre-concert lecture offered by the orchestra, engineer David Moulton spoke to the audience on the basics of surround sound and the recording techniques being employed. The concert itself, conducted by Steven Lipsitt, consisted of works by Mozart, Haydn and Schnittke, and the recording was overseen by David Moulton and Michael Crici. The Schnittke work should be especially interesting to hear in surround sound, as it concluded with the musicians roaming around the hall.

At dinner after the concert, BAES and ASA members were joined by BCO principal bassoon player Tom Stephenson (also of Emmanuel Recording), timpanist Dennis Sullivan and maestro Harry Ellis Dickson. Additional contributors were Bose acoustic engineer (and trumpet player) Jeff Hoefler and Torben Paulsen, a Danish researcher who is visiting Northeastern University and has extensively studied hearing loss in musicians.

Amongst a number of humorous anecdotes, the discussion focused on musical acoustics and performance issues as seen from the unique perspective of classical musicians.

Mr. Dickson shared a number of opinions, including the point that good recordings provide valuable income and prestige to orchestras and that players, and often conductors, don't know how an ensemble really sounds to an audience. Therefore, musicians are sometimes astonished to hear playbacks and may wonder out loud if they actually made that nice sound.

This was a very successful AES/ASA joint meeting and an example of how our respective societies can come together and enjoy a wonderful day of acoustics and audio engineering. A mixing session using these recordings will be the subject of a future joint meeting.

ERIC REUTER

May Meeting

Associate Professor Torben Poulsen from the Department of Acoustic Technology at the Technical University of Denmark recently visited Professor Mary Florentine's laboratory at Northeastern University for two months. While in Boston, he gave a talk to the Greater Boston Chapter on hearing protector testing. The talk covered hearing protectors in general with an overview of the most common types and the test methods. Emphasis was on recent investigations on the problems involved in testing of hearing protectors. The attenuation is determined by measuring the hearing thresholds for a number of test subjects with and without the use of the hearing protector. The measurements are made in a diffuse sound field and one of the investigations was a Nordic comparison of attenuation data from different implementations of the diffuse sound field. Another investigation mentioned in the talk was related to the recent American standard (ANSI S12.6-1997) which includes two different options for fitting of the hearing protector on the test subject: the ''experimenter supervised fit'' and the ''subject fit'' methods. Especially for ear plugs these two fitting methods lead to very different results. The results of the investigations will be part of the background material for the revision of the ISO 4869-1 standard.

MARY FLORENTINE

Central Pennsylvania Chapter

The Central Pennsylvania Chapter of the Acoustical Society of America (CPCASA) organized two seminars this past academic year. The first was held on January 21 and was given by David J. Miller from the Electrical Engineering Department at Penn State. Professor Miller's talk was entitled, ''Ensemble Classification by Critic-driven Combining.'' Professor Miller described a new method for combining estimates obtained from each classifier in an ensemble. Although this critic-driven method is a general technique, it has applications in speech recognition and other types of pattern recognition and signal classification.

The second seminar was held on April 30 and was sponsored by both the CPCASA and the Acoustics Department at Penn State. The seminar was given by Roman Sepiejewski from Bose Corporation. The title of Roman's talk was ''Active Noise Reduction Technology in Headphone Applications.'' The focus of the seminar was an overview of some of the different design considerations of noise canceling aviation headsets.

A demonstration of active noise reduction headsets was included as part of the seminar. Members of the audience were given a chance to hear the noise cancellation ability of Bose's newest aviation headset.

The CPCASA also sponsors a student award each year. The award this year was actually a prize given to the winner of a contest. The objective of the contest was to find the most errors in a specified acoustics textbook. Ray Wakeland was the winner of the contest and was awarded a cash prize.

DAVID KASPER

USA Meetings Calendar

Listed below is a summary of meetings related to acoustics to be held in the U.S. in the near future. The month/year notation refers to the issue in which a complete meeting announcement appeared.

1999

30 Sept.–2 Oct.	Seventh Annual Conference on the Management of the Tinnitus Patient, Iowa City, IA [Rich Tyler, Dept. of Otolaryngology, Head and Neck Surgery, The University of Iowa, 200 Hawkins Dr., #E230 GH, Iowa City, IA 52242-1078; Tel.: 319-356-2471; Fax: 319-353-6739; E-mail: rich-tyler@uiowa.edu; WWW: http://www.medicine.uiowa.edu/otolaryngology/news/news.html].
7–10 Oct.	Symposium on Occupational Hearing Loss, Philadelphia, PA [American Institute for Voice and Ear Research, Attn: Barbara-Ruth Roberts, 1721 Pine St., Philadelphia, PA 19103; Tel.: 215-545-2068; Fax: 215-735-2725]. Deadline for submission of abstracts: 1 May.
1–5 Nov.	138th meeting of the Acoustical Society of America, Columbus, OH [Acoustical Society of America, Suite 1NO1, 2 Huntington Quadrangle, Melville, NY 11747-4502; Tel.: 516-576-2360; Fax: 516-576-2377; E-mail: asa@aip.org; WWW: asa.aip.org].
2–4 Dec.	ACTIVE 99, Fort Lauderdale, FL [Institute of Noise Control Engineering, P.O. Box 3206 Arlington Branch, Poughkeepsie, NY 12603; Tel.: 914-462-4006; Fax: 914-463-020; E-mail: INCEUSA@aol.com;/users.aol.com/inceusa/ince.html].
6–8 Dec.	INTER-NOISE 99, Fort Lauderdale, FL [Institute of Noise Control Engineering, P.O. Box 3206 Arlington Branch, Poughkeepsie, NY 12603; Tel.: 914-462-4006; Fax: 914-463-020; E-mail: INCEUSA@aol.com;/users.aol.com/inceusa/ince.html].

2000

29 May–2 June	139th meeting of the Acoustical Society of America, Atlanta, GA [Acoustical Society of America, Suite 1NO1, 2 Huntington Quadrangle, Melville, NY 11747-4502; Tel.: 516-576-2360; Fax: 516-576-2377; E-mail: asa@aip.org; WWW: asa.aip.org].

4–8 Dec. 140th meeting of the Acoustical Society of America, Newport Beach, CA [Acoustical Society of America, Suite 1NO1, 2 Huntington Quadrangle, Melville, NY 11747-4502; Tel.: 516-576-2360; Fax: 516-576-2377; E-mail: asa@aip.org; WWW: asa.aip.org].

Revisions to Membership List

New Associates

Arnold, Jim H., GT Exhaust Systems, Inc., 4121 NW 37th Street, Lincoln, NE 68524

Baird, P. David, EDO Corporation, 2645 South 300 West, Salt Lake City, UT 84115

Beck, Steven D., Signal and Image Processing Dept., Tracor, 6500 Tracor Lane, Austin, TX 78725

Belyaeva, Irina Yu., Inst. of Applied Physics, Russian Academy of Sciences, Hydrophysics and Hydroacoustics, 46 Uljanova Str., Nizhny, Novgorod 603600 Russia

Bhattacharya, Bhaskar, Glenayre R&D, Inc., 1570 Kootenay Street, Vancouver, BC V5K 5B8, Canada

Biru, Lu, Electrical Engineering Dept., Acoustics Research Lab., National Univ. of Singapore, 10 Kent Ridge Crescent, 119260 Singapore

Boone, Marinus M., Voorweg 105-A, Zoetermeer 2715NG, The Netherlands

Boucher, Michael F., 7927 Farnifold, Apt. 2, Germantown, TN 38138

Brown, Daniel V., Allied Signal Engines, Acoustics Engineering, 111 South 34th Street, Phoenix, AZ 85034-2802

Casey, Ross H., Preco, 415 North Maple Grove, Boise, ID 83704

Cheenne, Dominique J., Radio/Sound, Columbia College Chicago, 676 North La Salle, #300, Chicago, IL 60610

Chojar, Sunil, 46 Molasses Hill Road, Lebanon, NJ 08833-3207

Chun, Kay O., 1130 East Broadway, #269, Glendale, CA 91204

Corl, Paul D., 3883 El Centro Street, Palo Alto, CA 94306

Coyette, Jean-Pierre G., Rue Point Des Brebis 18, Chaumont-Gistoux B1325 Belgium

Cunningham, Glen B., 2 Dock Square, Rockport, MA 01966

Daggett, John E., J. D. Edwards & Associates, 4370 La Jolla Village Drive, 4th Floor, San Diego, CA 92122

Dawe, Lloyd A., School of Graduate and Professional Studies, Cameron University, 2800 West Gore Boulevard, Lawton, OK 73505

Douaze, Etienne, National Univ. of Singapore, Tropical Marine Science Inst., 14 Kent Ridge Road, 119223 Singapore

Edgecock, Trevor M., 16 Robinson Heights, Stalbridge, Dorset DT10 2PA, U.K.

Fabian, Martin J., R. W. Beckett Corporation, Product Engineering, 38251 Center Ridge Road, North Ridgeville, OH 44039

Faltys, Michael A., 19235 Celtic Street, Northridge, CA 91326

Farag, Hania H., 11 Syria Str., Roushdy, Alexandria, Egypt

Fast, N. Douglass, Johns Maville, 10100 West Ute Avenue, Littleton, CO 80127

Freeman, Angelina M., 8055 La Salle Avenue, Baton Rouge, LA 70806

Frieda, Elaina M., Bussenstr. 32, Stuttgart 70184 Germany

Fujioka, Chieko N., Ridge Corporation, 7808 Bryn Mawr Drive, Dallas, TX 75225

Garces, Milton A., P.O. Box 1599, Kailua-Kona, HI 96745-1599

Goeggelmann, Thomas, Nokia Mobile Phones, Produktions gesellschaft mbH, Wilhelm-Runge Strabe 11, Ulm 89081 Germany

Goodlin, Ruth A., Electro-Craft Motion Control, 250 McCormick Road, Gallipolis, OH 45631

Gorog, Sylvie, ISAT, Univ. of Dijon, 49 Rue Mademoiselle Bourgeois, BP 31, Nevers 58000 France

Grealy, Philip J., John Collings Engineers, PC, 11 Bradhurst Avenue, Hawthorne, NY 10532

Hair, Hugh A., 6941 Lymekiln Road, Fayetteville, NY 13066

Han, Wei, Halliburton Energy Services, 2135 Highway 6, South, Houston, TX 77077

Hao, Xinwei, 5606 Bissonnet, #76, Houston, TX 77081

Hassell, Gregory M., Test and Evaluation Ranges, DERA, Building A22, Winfrith Tech. Center, Dorchester, Dorset DT2 8XJ, U.K.

Heise, Ulrich, Hartwigstr 44, Bremen 28209 Germany

Holt, Nigel J., Psychology, Univ. of Reading, Whiteknights Campus, Early Gate, Reading, Berkshire RU6 6AL, U.K.

Hong, Seung B., 466 Foothill Boulevard, #323, La Canada Flintridge, CA 91011

Honge, Sseung S., 2708 Foothill Boulevard, #407, La Crescenta, CA 91214

Honkalehto, Taina, Alaska Fisheries Science Center, NOAA Fisheries, 7600 Sand Point Way, NE, Building 4, Seattle, WA 98115

Jang, Jaehee, R&D Center, SK Engineering & Construction, 192-18 Kwanhun-Dong, Chongro-gu, Seoul 110-300 Korea

Janker, Peter M., Geisteswissenschaatliche Zentren Berlin, Zentrum Fuer Allgemeine Sprachnissenschaft, Jaeger Strasse 10/11, Berlin D-10117 Germany

Kellermann, Walter L., Lehrstuhl fuer Nachrichtentechnik, Telecommunications Inst., Cauerstr 7, Erlangen 91058 Germany

Kim, Yoon H., 264 South La Cienega Boulevard, #1290, Beverly Hills, CA 90211

Koch, Robert M., 18 McIntosh Drive, Portsmouth, RI 02871

Kushibiki, Jun-Ichi, Dept. of Electrical Engineering, Tohoku University, 05 Aoba, Aramaki-Aza, Aoba-Ku, Sendai 980-8579 Japan

Lacefield, James C., Electrical and Computer Eng., Univ. of Rochester, Ultrasound Research Lab., 601 Elmwood Avenue, Box 648, Rochester, NY 14642

Lizana, Pablo R., Antonia #15 Casa 9, Col. San Jeronimo Lidile, Mexico DF 10200

Long, Lyle N., 908 Bayberry Drive, State College, PA 16801

LoVetri, Joe, Dept. of Electrical & Computer Eng., Univ. of Western Ontario, London, ON N6A 5B9, Canada

Lucas, Michael J., Rotary Compressor Division, Ingerooll-Rand, P.O. Box 1600, Davidson, NC 28036

Luo, Henry Y., Unitron Industries, Ltd., R&D Dept., 20 Beasley Drive, P.O. Box 9017, Kitchener, ON N2G 4X1, Canada

Mattei, Pierre-Olivier, Lab. de Mecanique et d'Acoustique, Centre National de la Recherche Scientifique, 31 chemin Joseph-Aiguier, Marseille, Cedex 20, 13402 France

McAteer, James A., Anatomy, Indiana University School of Medicine, 635 Barnhill Drive, Indianapolis, IN 46202-5120

McCoy, Priscilla C., 1232 Milvia Street, Berkeley, CA 94709

Min, Jung H., 289 South Robertson Boulevard, #461, Beverly Hills, CA 90211

Minasyan, Georgiy R., 2042 Spring Mill Road, Lafayette Hill, PA 19444

Miranda, Frances J., ENT/Audiology, 1011 Baldwin Park Boulevard, Baldwin Park, CA 91706

Mochida, Takemi, Information Science Research Dept., NTT Basic Research Laboratories, 3-1 Morinosato-wakamiya, Atsugi-shi, Kanagawa-ken, 243-0198 Japan

Moore, Matthew J., 47 Walsh Street, Apt. 4, Framingham, MA 01701

Moroney, Richard M., 3 Kensington Court, Princeton, NJ 08540

Murray, Rachel V., Meyer Sound Laboratories, 2832 San Pablo Avenue, Berkeley, CA 94702

Nadi, Mustapha, Lab. d'Instrumentation Electronique, Univ. of H. Poincare-Nancy, Lien, BP 239, Vandoeuvre 54506 France

Negreira, Carlos A., Inst. de Fisica, Facultad de Caelones, P.O. Box 16120, Distrito 6, Montevideo, Uruguay

O'Brien, Daniel N., 516 Hudson Street, Apt. 3, Hoboken, NJ 07030

Pallayil, Venugopalan, Acoustic Research Lab., National Univ. of Singapore, 10 Kent Ridge Crescent, 119260 Singapore

Parry, Steve P., 9431B Noblewood Street, Anchorage, AK 99515

Parssinen, Carol E., 277 Broadway, Apt. 8, Arlington, MA 02474-5313

Pastore, Thomas J., 416 Forward Street, La Jolla, CA 92037

Phelps, Andy D., Nokia R&D Ltd., Research & Technology, Nokia House, Summit Avenue, Southwood, Farnborough, Hampshire GU14 0NZ, U.K.

Pietrzyk, Andrzej, Tire-Vehicle Technology, Goodyear Technical Center, Colmar-Berg L-7750 Luxembourg

Potter, David C., NOAA/NMFS, Protected Species Branch, 166 Water Street, Woods Hole, MA 02543

Pressnitzer, Daniel, Centre for the Neural Basis of Hearing, Dept. of Physiology, Downing Street, Cambridge CB2 3EG, U.K.

Preston, Jon M., Quester Tangent Corp., 99-9865 West Saanich Road, Sidney, BC V8L 3S1, Canada

Roy, Charles C., CCR Associates LLC, 12 Dennisin Road, P.O. Box 159, Essex, CT 06426-0159

Sapoval, Bernard, Physique de la Matiere Comdemsee, Ecole Polytechnique, Palaiseau 91128 France

Scales, John A., Dept. of Geophysics, Colorado School of Mines, Golden, CO 80401

Sekiyama, Kaoru, Dept. of Psychology, Faculty of Letters, Kanazawa University, Kanazawa, Ishikawa, 920-1192 Japan
Shin, Jung O., 428 Hawthorne Street, #212, Glendale, CA 91204
Silveira, Marcio, Embraco S/A Empresa Brasileira de Compressores S/A, Acoustical Lab, Rua Rui Barbosa 1020, Joinville SC 89219-901 Brazil
Simard, Yvan, Maurice Lamontagne Institute, 850 Route de la Mer, Mont-Joli, PQ G5H 3Z4, Canada
Somek, Branko, Martikaneecka 10, Zagreb 10000 Croatia
Sonnenschein, Elazar, Divecom Ltd., 9 Dmarim Street, Industrial Park, Omer, 84965 Israel
Tan, Paul L., 5167 North Oak Street Trafficway, Kansas City, MO 64118-4622
Tello, Lucio N., 3905 Horizon Place, Ft. Worth, TX 76133
Ting, Carina M., 12 Berkshire Road, Framingham, MA 01702
Tomilina, Tatiana M., Lab. of Structural Acoustics, Mechanical Engineering Research Inst., M. Kharitonjevski 4, Moscow 101830 Russia
Tsushima, Teruaki, Foreign Language Center, Ryutsu Kagaku University, 3-1, Gakuen-Nishi-Machi, Nishi-Ku, Kobe, Hyogo 651-2188 Japan
van den Honert, Chris, Cochlear Corp., 61 Inverness Drive, East, Englewood, CO 80112
Viveiros, Elvira B., Rua Joao P. Duarte Silva 480/403.B, Florianopolis SC 88037-001 Brazil
Walsh, Michael R., Industrial Acoustics Company, 1160 Commerce Avenue, Bronx, NY 10462
Wilcox, Thomas E., Marine Sonic Technology, Ltd., 5508 George Washington Memorial Highway, White Marsh, VA 23183
Wong, Colman, Flat C, 17/F PoShing Building, Kau Yuk Road, Yuen Long, N. T., Hong Kong
Yam, Shek T., Dept. of Mechanical Engineering, Hong Kong Polytechnic University, Kowloon, Hong Kong
Zhou, Wei, Aeroacoustics and Vibration, United Technologies Carrier Corporation, Carrier Parkway, P.O. Box 4808, Syracuse, NY 13221
Zimmer, Karin, Inst. fuer Kognitiousforschung, Univ. Oldenburg, FB 5/A6, P.O. Box 2503, Oldenburg 26111 Germany

New Students

Abrams, Robert J., Otopathology, Kresge Hearing Research Inst., Ann Arbor, MI 48104
Atkinson, John D., 117 Main Street, Apt. 6, Brattleboro, VT 05301
Bartsch, Mark A., 128 Plumwood Road, Dayton, OH 45409
Billerey, Roger, 1626 Armacost Avenue, #7B, Los Angeles, CA 90025
Bourland, Candace D., 1506 Amberwood Circle, Nashville, TN 37221
Boyczuk, Jeff P., School of Communication Sciences & Disorders, McGill University, 1266 Pine Avenue, West, Montreal, PQ H3G 1A4, Canada
Carter, Jennifer C., 233 Linden Street, Boylston, MA 01505
Christianson, Caryn J., Univ. of Wisconsin Eau Claire, 404 Katherine Putnam Hall, Eau Claire, WI 54701
Couche, Jerome C., 1003 Colley Avenue, #12, Norfolk, VA 23507
Coughlin, Maureen P., Speech and Hearing Sciences, Indiana University, 200 South Jordan Avenue, Bloomington, IN 47405
Diaz, Armand M., 33-27 201st Street, Bayside, NY 11361
Epstein, Melissa A., Linguistics, UCLA, 3125 Campbell Hall, Los Angeles, CA 90095-1543
Fernandes, Luis L., Civil Environmental and Architectural Engineering, Univ. of Colorado at Boulder, Campus Box 428, Boulder, CO 80309-0428
Ferrini, Vicki L., Marine Sciences Research Center, State University of New York, Stony Brook, NY 11794-5000
Fine, Peninah S., 2 City View Road, Brookline, MA 02446
Franklin, Jonathan B., Apt. 20A, Escondido Village, Stanford, CA 94305
Gallegos, Jr., Jose A., 1068 North Gage Avenue, Los Angeles, CA 90063
Gibbons, Christopher M., 1333 Neil Avenue, Columbus, OH 43201
Gonzalez, Jorge E., 604-A Cabell Avenue, Charlottesville, VA 22903
Gordon, Matthew K., Linguistics, Univ. of California, Los Angeles, 405 Hilgard Avenue, Los Angeles, CA 90095-1543
Gottinger, Bernd, 920 Stubblefield Lane, Baltimore, MD 21202
Gregory, Joseph W., 5103 Benson Road, Angier, NC 27501
Holobinko, Anastasia, 1435 Bennett Road, Madison, OH 44057
Hood, Adrian A., 5686 Stevens Forest Road, #36, Columbia, MO 21045
Huang, Jun, 2137 Beckman Inst., 405 North Mathews Avenue, Urbana, IL 61801
Huber, Jessica E., 368 1/2 Linwood Avenue, Buffalo, NY 14209
Im, Jong-In, 107-603 Daedong Wooband, Apt. 94-8, Woohyun-dong, Bukgu, Pohang, Kyung-buk 791-220 Korea
Johnstone, Jain T., Psychology, Univ. of Geneva, 9 Route de Drize, Geneva CH-1227 Switzerland
Karlsson, Fredrik, Alvans vag 92 Qtr., Umea 90750 Sweden
Khilnani, Kamlesh T., 571 State Road, #148, North Dartmouth, MA 02747
Kim, Hea-Won, P.O. Box 42, Closter, NY 07624
King, John E., 604A Cabell Avenue, Charlottesville, VA 22903
Kitahara, Mafuyu, Dept. of Linguistics, Cognitive Science Program, Indiana University, 1021 East 3rd Street, Memorial Hall #322, Bloomington, IN 47405-7005
Klem, David W., 5031 Ponce De Leon Boulevard, Coral Gables, FL 33146
Lackpour, Jahan A., 5 Sunnyside Lane, Yardley, PA 19067
Li, Tang-Chun, 3620 Lorne Crescent, #902, Montreal, PQ H2X 2B1, Canada
Lieuwen, Tim C., 785 Bellemeade Avenue, Atlanta, GA 30318
Lindeman, Stephanie A., 213 West Mosley Street, Apt. 6, Ann Arbor, MI 48103
Maceira Isorna, Jacobo, Republica de Arxentina Street 43, 2A, Santiago de Compostela, A Coruna, 15706 Spain
Marino, Viviane C., Oral Biology, Craniofacial Center, Room D8-30, Dental Science Building, P.O. Box 100424, Gainesville, FL 32610-0424
Matlo, Matyas M., 464 Huntington Avenue, #512, Boston, MA 02115
Miele, Joshua A., 1331 Bonita Avenue, Apt. #2, Berkeley, CA 94709
Murphy, Patrick E., 206 Reservoir Road, Newport, NY 13416
Murray, Siobhan E., 23G Westridge Road, Portswood, Southampton SO17 2HP, England
Nakamoto, Kyle T., 2320 West 239th Street, Torrance, CA 90501
Namasivayam, Aravind K., Dept. of Speech-Language Pathology, University of Toronto, Tanz Neuroscience Building, 8 Queens Park Crescent West, Toronto, ON M5S 3H2, Canada
Odgaard, Eric C., Psychology Dept., Univ. of Nebraska, Lincoln, 238 Burnett Hall, Lincoln, NE 68588-0308
Park, Christopher D., Mechanical Engineering and Materials Science, Duke University, Box 90300, Hudson Hall Research Drive, Durham, NC 27708-0300
Philip, Trudy L., 600 East Pollock Road, Apt. 3504C, State College, PA 16801
Plauche, Madelaine C., Linguistics, Univ. of California, Berkeley, 1203 Dwinelle Hall, Berkeley, CA 94720
Prasad, Daryl S., 86A Norfolk Street, Ponsonby, Auckland 1001 New Zealand
Radhakrishnan, Sreedivya, Speech Pathology and Audiology, Kent State University, P.O. Box 5190, Kent, OH 44242-0001
Ries, Dennis T., 8308 Kimball Drive, Eden Prairie, MN 55347
Romond, Rachel A., Occidental College, 1600 Campus Road, Box 504, Los Angeles, CA 90041
Schram, David J., 428 Lorraine, Glen Ellyn, IL 60137
Seiger, Liat, 120 West 44th Street, New York, NY 10036
Silver, David J., 2955 Hickory Court, Palm Harbor, FL 34683
Sokolov, Dahlia L., Applied Physics Lab., Dept. of Bioengineering, Univ. of Washington, 1013 NE 40th Street, Seattle, WA 98105
Steeve, Roger W., 6516 21st Drive, NE, Marysville, WA 98271
Stimac, Alan, Sortina 41, Zagreb HR-10000 Croatia
Sundara, Megha, School of Communication Sciences and Disorders, McGill University, 1266 Pine Avenue, West, Montreal, PQ H3G 1A8, Canada
Suzuki, Ryuji, Center for Marine Science and Technology, Univ. Massachusetts Dartmouth, 706 South Rodney French Blvd., New Bedford, MA 02744-1221
Tzanetakis, George, Computer Science, Princeton University, 35 Olden Street, Princeton, NJ 08544
Vaynshteyn, Irina, 8320 Bay Parkway, Apt. C34, Brooklyn, NY 11214
Wang, Lugen, Welding Engineering, Ohio State University, 1248 Arthur E. Adams Drive, Columbus, OH 43221
Zeller, Sarah E., Theoretical & Applied Mechanics, Univ. of Illinois, 104 South Wright Street, MC-262, Urbana, IL 61801

Members Elected Fellows

J. W. Beauchamp, A. E. Bowles, J. C. Brown, R. Carre, H. A. Conklin, R. E. Green, Jr., R. D. Hellweg, Jr., R. L. Kirkegaard, S. E. McAdams, P. B. Nagy, K. P. Roy, N. S. Timmerman, S. Ueha, S. Yoshikawa

Reinstated

A. B. Coppens—*Fellow*
J. C. Gimendez de Paz, B. Schnitta—*Members*
W. Han, S. Koshigoe, A. D. Phelps, R. M. Stern, G. Zhang—*Associates*

Associates Elected Members

H. A. Alter, S. Asvadurov, K. Akamatsu, G. H. Berndtsson, L. D. Blomberg, M. Bouchard, G. L. Bullock, R. W. Chan, J. T. Christoff, L. M. Cross, S. M. Connolly, D. D. G. Efthymiatos, W. B. England, N. J. Felgate, R. L. Gentry, G. P. Gibbs, P. N. Hodgson, D. C. Hurley, S. M. Jaeger, H. E. Jones, J. J. Kelly, R. J. Korneliussen, E. W. Kreamer, R. A. Lester, R. M. Lilkendey, C. W. Lim, J-Y. Lu, K. Lucke, H. H. M. Miedema, S. N. Nittrouer, M. Pavlidou, B. Pedersen, J. S. Popovics, W. Qiao, M. L. Readhead, M. Recuero, J. R. Richardson, W. Rongqing, P. H. Scarbrough, R. A. Schmidt, B. M. Shield, N. Sugimoto, J. Tian, J. A. Utman, G. L. Wojcik, A. N. Woodger, E. H. Waterman

Students to Associates

J. Auriemmo, M. M. Campbell, W. A. Castleman, K. M. Cienkowski, J. S. Dembowski, S. D. Duncan, R. Eyraud, K. D. Frampton, R. B. Gampert, C. A. Gentry, T. Gmeiner, M. Gordon, R. Gunda, B. Halberstam, E. R. Jensen, J. Lentz, J. A. Lightfoot, A. J. S. Locke, R. C. Loftman, P. Menounou, A. D. Munro, A. T. Neel, M. P. Olivieri, J. W. Parkins, D. V. Rabinkin, J. G. Rasimas, R. Ratnam, W. M. Sanders, M. A. Whitley III

Associate to Student

L. A. L. Souza

Resigned

V. A. Del Grosso—*Fellow*

J. E. Breeding, Jr., W. A. Conrad, J. J. Gilheany, J. B. Gubelmann, S. L. Losiewicz, M. Paping, J. C. Risset, A. Rupert, D. Sonderquist, S. Tazaki, M. M. P. Weydert, R. M. Wilmotte, J. E. Zeile, Jr.—*Members*

C. R. Bradley, K. A. Petersen, P. J. T. Filippi, P. J. Flynn, C. T. Gomez-Fernandini, A. M. Hepfer, K. Hutchenson, W. H. Martin, A. Maurudis, L. A. Rammage, H. Truckenbrodt, D. West—*Associates*

A. Cote, P. C. Debergue, D. T. Dieken, B. Patry, M. J. Richer, U. Sundberg, M. A. Tournour, J. Voix—*Students*

Deceased

J. E. Cole III, R. O. Fehr, R. N. Lane, H. B. Miller—*Fellows*

H. J. Naake—*Member*

K. Denning—*Associate*

Fellows	835
Members	2784
Associates	2795
Students	832
	7246

ACOUSTICAL NEWS—INTERNATIONAL

Walter G. Mayer
Physics Department, Georgetown University, Washington, DC 20057

Institute of Acoustics (UK)—25th Anniversary Conference

An anniversary meeting on 13 May 1999 at the Barbican Centre, London, marked the Silver Jubilee of the Institute of Acoustics. Keynote lectures, reviewing the current status of the various Specialist Groups of IOA, were delivered in the morning. After a Celebration Luncheon, a number of parallel sessions were scheduled for the afternoon, followed by the Annual General Meeting in the late afternoon. The festive day came to a close with the President's reception. Happy Anniversary!

Acoustical Society of Lithuania—10th Anniversary

After the collapse of the Soviet Union, the Baltic States regained their independence and with it, the Lithuanian Acoustical Society was founded. The 10th anniversary of this event will be celebrated by the society next year when the First International Conference of the Lithuanian Acoustical Society will be held in Vilnius. Happy Anniversary!

Professor Leif Bjørnø receives Hartmann Prize

Professor Bjørnø was selected to receive the 1999 Hartmann Prize. This award was established about 20 years ago and is presented every year to a person in music, literature, art, medicine, or science and technology for outstanding contributions to the Danish Community and to his or her profession at large. The Hartmann Prize, being the most prestigious Danish award, is accompanied by a substantial amount of money. In its citation, the 1999 Hartmann Prize Committee and the Hartmann Foundation emphasized Professor Bjørnø's many contributions to underwater acoustics and to ultrasonics, reflected in over 300 publications, and, in particular, his contributions to industry in Denmark and other countries through his efforts to create a bridge between university research and industrial development and progress.

Papers published in JASJ(E)

A listing of Invited Papers and Regular Papers appearing in the latest issue of the English language version of the *Journal of the Acoustical Society of Japan*, JASJ(E), was published for the first time in the January 1995 issue of the Journal. This listing is continued below.

The May issue of JASJ(E), Vol. 20, No. 3 (1999) contains the following contributions.

K. Ozeki, Y. Ishigami, and K. Takagi, ''Performance comparison of recognition systems: A Bayasian approach''
I. Dawa, S. Okawa, and K. Shirai, ''Design of Mongolian speech database considering dialectal characteristics''
V. Sornlertlamvanich, N. Takahashi, and H. Isahara, ''Building a Thai part-of-speech tagged corpus (ORCHID)''
K. Itou, M. Yamamoto, K. Takeda, T. Takezawa, T. Matsuoka, T. Kobayashi, K. Shikano, and S. Itahashi, ''JNAS: Japanese speech corpus for large vocabulary continuous speech recognition research''
K. Itou, K. Akiba, O. Hasegawa, S. Hayamizu, and K. Tanaka, ''A Japanese spontaneous speech corpus collected using automatically interferencing Wizard of Oz system''
C. Tseng and F. Chou, ''Machine readable phonetic transcription system for Chinese dialects spoken in Taiwan''
S. Nakamura, K. Hiyane, F. Asano, and T. Endo, ''Sound scene data collection in real acoustical environments''

International Meetings Calendar

Below are announcements of meetings to be held abroad. Entries preceded by an * are new or updated listings with full contact addresses given in parentheses. Month/year listings following other entries refer to meeting announcements, with full contact addresses, which were published in previous issues of the *Journal*.

August 1999

2–6 **International Symposium on High-Power Ultrasonics**, Vitebsk. (Fax: +375 212 24 39 53; e-mail: 1pm@ita.belpak.vitebsk.by) *2/99*

September 1999

1–4 **15th International Symposium on Nonlinear Acoustics (ISNA-15)**, Göttingen. (Fax: +49 551 39 77 20; Web: www.physik3.gwdg.de/isna/) *10/97*

15–17 **British Society of Audiology Annual Conference**, Buxton. (Fax: +44 0118 935 1915; Web: www.b-s-a.demon.co.uk) *8/98*

30–2 ***Acoustical Society of Japan Autumn Meeting**, Matsue, Japan. (Acoustical Society of Japan, Ikeda-Building, 2-7-7, Yoyogi, Shibuya-ku, Tokyo, 151-0053 Japan; Fax: +81 3 3379 1456; e-mail: kym05145@nifty.ne.jp)

October 1999

9–10 ***INCE/Japan Annual Meeting**, Tokyo, Japan. (INCE c/o Kobayasi Institute, 3-20-41 Higashimotomachi, Kokobunji, Tokyo, 185-0022 Japan; Fax: +81 42 327 3847)

18–19 ***Acoustics Week in Canada 1999**, Victoria, BC, Canada. (S. Dosso, Centre for Earth and Ocean Research, University of Victoria, P.O. Box 3055, Victoria, BC V8W 3P6, Canada; Fax: +1 250 472 4100; e-mail: sdosso@uvic.ca)

20–22 **Iberian Meeting of the Spanish and the Portuguese Acoustical Societies**, Avila. (Fax: +34 91 411 7651; e-mail: ssantiago@fresno.csic.es) *12/98*

28–29 **Swiss Acoustical Society Fall Meeting**, Biel. (Fax: +41 1 823 4783; e-mail: beat.hohmann@compuserve.com) *6/99*

November 1999

17–18 ***Institute of Acoustics (UK) Autumn Conference on Environmental Noise Issues**, Stratford upon Avon, UK. (IOA, 77A St. Peter's Street, St. Albans, Herts, AL1 3BN, UK; Fax: +44 1727 850 553; e-mail: acoustics@clus1.ulcc.ac.uk)

18–21 ***Reproduced Sound 15**, Stratford upon Avon, UK. (IOA, 77A St. Peter's Street, St. Albans, Herts, AL1 3BN, UK; Fax: +44 1727 850 553; e-mail: acoustics@clus1.ulcc.ac.uk)

24–26 **Australian Acoustical Society Conference**, Melbourne. (Fax: +61 3 9720 6952; e-mail: acousticdes@bigpond.com) *6/99*

March 2000

15–17 ***Acoustical Society of Japan Spring Meeting**, Tokyo, Japan. (Acoustical Society of Japan, Ikeda-Building, 2-7-7, Yoyogi, Shibuya-ku, Tokyo, 151-0053 Japan; Fax: +81 3 3379 1456; e-mail: kym05145@nifty.ne.jp)

20–24 **Meeting of the German Acoustical Society (DAGA)**, Oldenburg. (Fax: +49 441 798 3698; e-mail: dega@aku.physik.uni-oldenburg.de) *10/98*

 0001-4966/99/106(2)/531/2/$15.00

April 2000

3–4 *__Structural Acoustics 2000, Zakopane__, Poland. (AGH, Al.Mickiewicza 30, 30-059 Krakow, Poland; Fax: +48 12 423 3163; Web: www.cyf-kr.edu.pl/ghpanusz)

May 2000

17–19 **9th International Meeting on Low Frequency Noise & Vibration**, Aalborg. (Fax: +44 1277 223453) *6/99*

June 2000

5–9 **International Conference on Acoustics, Speech and Signal Processing (ICASSP-2000)**, Istanbul. (Fax: +1 410 455 3969; Web: icassp2000.sdsu.edu) *6/99*

6–9 **5th International Symposium on Transport Noise and Vibration**, St. Petersburg. (Fax: +7 812 1279323; e-mail: noise@mail.rcom.ru) *6/99*

July 2000

4–7 **7th International Congress on Sound and Vibration**, Garmisch-Partenkirchen. (Fax: +49 531 295 2320; Web: www.iiav.org/icsv7.html) *12/98*

August 2000

28–30 **INTER-NOISE 2000**, Nice. (Fax: +33 1 47 88 90 60; Web: www.inrets.fr/services/manif) *6/99*

31–2 **International Conference on Noise & Vibration Pre-Design and Characterization Using Energy Methods (NOVEM)**, Lyon. (Fax: +33 4 7243 8712; Web: www.insa-lyon.fr/laboratoires/lva.html) *6/99*

September 2000

3–6 **5th French Congress on Acoustics**—Joint Meeting of the Swiss and French Acoustical Societies, Lausanne. (Fax: +41 21693 26 73) *4/99*

17–21 *__Acoustical Society of Lithuania First International Conference__, Vilnius, Lithuania. (Acoustical Society of Lithuania, Kriviu 15-2, 2007 Vilnius, Lithuania; Fax: +370 2 223 451; e-mail: daumantas.ciblys@ff.vu.lt)

October 2000

3–5 **WESTPRAC VII**, Kumamoto. (Fax: +81 96 342 3630; Web: cogni.eecs.kumamoto-u.ac.jp/others/westprac7) 6/98

16–18 **2nd Iberoamerican Congress on Acoustics, 31st National Meeting of the Spanish Acoustical Society, and EAA Symposium**, Madrid. (Fax: +34 91 411 7651; e-mail: ssantiago@fresno.csic.es) *12/98*

16–20 **6th International Conference on Spoken Language Processing**, Beijing. (Fax: +86 10 6256 9079; e-mail: mchu@plum.ioa.ac.cn) *10/98*

August 2001

28–30 **INTER-NOISE 2001**, The Hague. (e-mail: secretary@internoise2001.tudelft.nl; Web: internoise2001.tudelft.nl) *6/99*

September 2001

2–7 **17th International Congress on Acoustics (ICA)**, Rome. (Fax: +39 6 4424 0183; Web: www.uniromal.it/energ/ica.html) *10/98*

BOOK REVIEWS

James F. Bartram
94 Kane Avenue, Middletown, Rhode Island 02842

These reviews of books and other forms of information express the opinions of the individual reviewers and are not necessarily endorsed by the Editorial Board of this Journal.

Editorial Policy: *If there is a negative review, the author of the book will be given a chance to respond to the review in this section of the Journal and the reviewer will be allowed to respond to the author's comments. [See ''Book Reviews Editor's Note,'' J. Acoust. Soc. Am.* ***81****, 1651 (May 1987).]*

Testing Loudspeakers

Joseph D'Appolito

Audio Amateur Press, Peterborough, NH 03458-0876. x+174 pp. Price: $34.95.

Joseph D'Apploito is a well-known loudspeaker designer, whose most notable design is the MTM configuration, a vertical arrangement consisting of a tweeter placed between two lower-frequency drivers. The publisher of this soft-cover book also puts out the *Speaker Builder*, a magazine aimed at do-it-yourselfers who represent the current generation of the Dynaco-Heathkit crowd. D'Appolito is listed in the masthead as a contributing editor.

I wish I had *Testing Loudspeakers* a bit more than a year ago when I was constructing a ''super monitor'' system. As the author correctly pointed out, there is no shortage of texts on loudspeaker design and construction but there is no single tutorial reference on loudspeaker testing for the seasoned hobbyist or technician. Hence the *raison d'êtr*e for this useful book.

As the author explained in the first chapter, the book is divided into two broad areas, one area dealing with techniques without the use of computers and the second area describing digital techniques of measurement. The text subdivides into seven chapters. The first chapter summarizes the contents of each chapter. Chapter 2 contains a short history of the evolution of low-frequency direct radiator loudspeaker design, commencing with Kellogg and Rice's invention in the 1920s of the direct radiator loudspeaker; then proceeding to Olson's introduction of electric circuit analogue techniques for analysis of low-frequency speakers; Thiel's 1961 landmark paper describing selection of driver parameters, enclosure volume, and tuning so as to align the frequency response of a vented box with the frequency response of established electrical filters; Benson's expansion of Thiel's work; and Small's application to closed-box and passive radiator designs as well as vented-box versions.

The second chapter continues on with the development of a driver electromechanical model from fundamentals, and the model is applied to explain the shape of the impedance curve. Three techniques are outlined for measuring the driver impedance curve and thereby the Thiel–Small parameters. These three methods—namely the voltage-divider method, the constant current method, and the constant voltage procedure—require relatively simple analog test instruments. They are described clearly, step-by-step, and examples are given to illustrate the outcome of each step. Wisely, the author gives us the benefit of his vast experience by making recommendations for precluding errors and optimizing the accuracy of the measurements.

Chapter 3 deals with impedance characteristics of drivers mounted in enclosures. It begins with a discussion of the theory underlying the mass reactance loading on a driver cone, that exists when the driver is mounted on a large baffle or in an enclosure, thereby causing a downward shift in the driver's resonant frequency. The procedures for measuring the mass reactance loading, determining the downward shift in driver resonance, establishing the driver/enclosure resonant frequency and compliance ratio α, along with the mechanical and electrical Q's are given here with the use of a real example. The effect of filling material (such as fiberglass or Dacron®) in closed-box systems is explained in terms of simple gas dynamics, particularly with respect to the increases in the effective enclosure volume, mass reactance, and system losses and the lessening of box Q and system efficiency. Single-tuned vented systems are described in terms of impedance curves, along with the procedures for determining driver resonance frequency, mass reactance in a vented box, tuning frequency of the box, the driver-box compliance ratio, and the Q's of driver and box. Two examples, including one for a dual woofer system, are demonstrated. The transmission-line enclosure with and without filling material is also examined. The conclusion of the chapter discusses anomalous behavior of the impedance curve, interpretations of such anomalies that arise from structural vibrations of the enclosure, presence of internal standing waves, or occurrence in vented boxes of ''organ pipe'' resonances.

Acoustical testing of single drivers constitutes the topic of Chapter 4. The chapter opens with a discussion of the factors that affect the accuracy of frequency-response tests of individual drivers mounted in enclosures. Microphone types are described in terms of their transduction principles, polar response, and sensitivity. The omnidirectional pressure microphone calibrated for free-field response is shown to rank as the best for loudspeaker frequency-response measurements. The remainder of the chapter deals with the effect of the environment on loudspeaker measurements and the means of obtaining accurate measurements in listening rooms, which should be beneficial to those not fortunate enough to have access to anechoic chambers (the ideal environment for testing). Equations are given to predict the standing wave modes in rectangular rooms, with due regard given to dominant floor reflection and the resultant comb-filter response. Equations are given to predict the dips and peaks caused by such reflection. Three testing techniques (far-field, near-field, and ground-plane measurements) and two test signals (pink noise and warble tones) are described as means of minimizing the impact of standing waves and reflections on measurement accuracy. The effect of baffle geometry on frequency response also enters into consideration, particularly edge diffraction and spreading loss. Simple equations are listed for predicting the frequencies or frequency ranges over which the diffraction effects will be apparent. Two examples conclude Chapter 4, one on how the frequency-response curves of multiple drivers can be used to establish a crossover frequency and the other outlining a more accurate technique for determining the tuning frequency of a vented box through near-field measurement of the woofer acoustic output.

Chapter 5 treats acoustical testing of multiple-driver systems. The methodologies of Chapter 4 are extended to include frequency-response measurements of multiple-driver systems. Due regard is given to the fact that the acoustic centers of the individual drivers do not coincide, so microphone placement becomes a problem. Too close placement of the microphone to the loudspeaker does not allow proper integration of the individual drivers, and excessively far placement subjects the measurements to contamination by room reflections and ambient noise. Crossovers in themselves also produce changes in response variations with respect to microphone placement. The effect of floor bounce in multi-driver systems is shown to be augmented by the differing heights of the individual drivers from the floor. Several speaker designs are used as examples of frequency-response and impedance measurements to highlight different but important aspects of the measurement process and to provide insight on interpreting the results. Polar response patterns are described for different types of speakers, with the ribbon-type being an especially interesting case. All of this type of measurement can be achieved with relatively simple instruments, namely a sine-wave oscillator, which can be frequency-modulated to provide 1/3-octavewise warble tones, a calibrated laboratory microphone, and a wide-band preamplifier.

The increasing versatility of personal computers lends itself nicely to measurements of loudspeaker performance. With the help of data-acquisition systems and analytical programs, one can now rather easily measure transient behavior in the time domain, interdriver time delay, phase response, and driver acoustic phase centers, among other things. Chapter 6 concentrates on the use of the time domain through the use of data acquisition systems acting as the digital equivalents of an oscilloscope. Here, data are displayed on a time axis rather than a frequency axis used in the ana-

 0001-4966/99/106(2)/539/2/$15.00

logue methods of the earlier chapters. Advantage is taken of the fact that there is a direct relationship between time-domain data and frequency-domain data. The concept of the Fourier transform is explained, with emphasis on the importance of having a thorough understanding of the Fourier transform and other concepts in digital signal processing in order to be able to properly interpret and utilize the data obtained by digital means. The quality of data depends on the sampling time resolution of data processing in order to obtain loudspeaker impulse function. Five sections in this chapter alone are used to explain how to obtain valid representations of impulse response and frequency response from sampled data. The Fourier series of representing continuous-time periodic signals, the sampling process converting a continuous-time signal into discrete-time signal, the problem of signal aliasing, the Discrete Fourier Transform (DFT), the Fast Fourier Transform (FFT) algorithm, and a technique for measuring Maximum Length Sequence (MLS) are all described. Phase and phase response are defined, with examples cited to show that phase angles exceeding a few hundred degrees are possible in some networks and loudspeaker systems. Other concepts are also introduced, e.g., minimum phase response, excess phase, and acoustic phase center of a driver.

Chapter 7 concentrates on loudspeaker testing, principally with the MLSSA and the CLIO PC-based electrical and acoustical data-acquisition systems. While the principal stimulus for the MLSSA technique is the MLS sequence, CLIO not only uses the MLS signal but also provides pink noise, sine waves, swept sine waves, tone bursts, and multi-tone signals. The chapter contains examples of measuring impedance, capacitance, inductance, and Thiel–Small parameters in both systems. A discussion follows on the use of the more common measurements for loudspeaker design and evaluation. It is pointed out that measurement capabilities apply somewhat differently for two different areas: loudspeaker system design and loudspeaker system performance evaluation. In the design process, applicable data include voice coil impedance magnitude and phase for individual drivers, driver on-axis frequency and phase response, and the relative location of driver acoustic phase centers. A two-way design serves as an example showing the full data collection process with a follow-up of the design to completion, including the intermediate measurement results and the final system response. Measurements for loudspeaker performance design, however, differ from those for design purposes and are more extensive. These entail system impedance magnitude and phase. On-axis frequency response, system sensitivity, cumulative spectral decay, step response, excess group delay, horizontal and vertical polar response, power response, and harmonic and intermodulation distortion. A full sequence of these tests is reported for a two-way MTM system, and the implications of the results are explained. Three more examples close out the last chapter to further illustrate the versatility of PC-based techniques.

A 30-page section follows the final chapter, consisting of advertisements by vendors of loudspeaker parts, testing equipment, and computer programs for design and/or testing loudspeaker systems. This section can be very useful to designers and experimenters seeking parts or equipment that are somewhat more exotic than can be found in a local Radio Shack.

The author obviously took care in organizing and writing the material, which is easy to learn from, particularly if one is familiar with the fundamentals of electric circuitry. The mathematics given in the text generally does not go beyond high school level but does suffice very well for the purpose of evaluating loudspeaker systems.

In summary, *Testing Loudspeakers* is a valuable guide for those who wish to test their loudspeaker designs as well as for those who wish to brush up or upgrade their testing techniques.

DANIEL R. RAICHEL
CUNY Graduate School
Mechanical and Aerospace Engineering Department and
School of Architecture and Environmental Studies
The City College of the City University of New York
New York, New York 10031

Elastic wave propagation and scattering in heterogeneous, anisotropic media: Textured polycrystalline materials

Joseph A. Turner
Department of Engineering Mechanics, W317.4 Nebraska Hall, University of Nebraska-Lincoln, Lincoln, Nebraska 68588-0526

(Received 23 September 1998; accepted for publication 3 May 1999)

The propagation of elastic waves through heterogeneous, anisotropic media is considered. Appropriate ensemble averaging of the elastic wave equation leads to the Dyson equation which governs the mean response of the field. The Dyson equation is given here in terms of anisotropic elastic Green's dyadics for the medium with and without heterogeneities. The solution of the Dyson equation for the mean response is given for heterogeneities that are weak. The formalism is further specified for the case of equiaxed cubic polycrystalline metals with a single aligned axis. The Green's dyadics in this case are those for a transversely isotropic medium. Simple expressions for the attenuations of the shear horizontal, quasicompressional, and quasishear waves are given in terms of integrations on the unit circle. The derived expressions are limited to frequencies below the geometric optics limit, but give the attenuations in a direct manner. Comparisons with previous results are also discussed. It is anticipated that a similar approach is necessary for the study of wave propagation in complex anisotropic materials such as fiber-reinforced composites. In addition, the results are applicable to diffuse ultrasonic inspection of textured polycrystalline media. © *1999 Acoustical Society of America.* [S0001-4966(99)04008-4]

PACS numbers: 43.20.Bi, 43.20.Gp, 43.35.Cg [DEC]

INTRODUCTION

The study of wave propagation and scattering of elastic waves in heterogeneous, anisotropic media is related to nondestructive testing, materials characterization and acoustic emission of many important materials. Examples include polycrystalline media with texture, fiber-reinforced composites, and extruded metal-matrix composites. Elastic waves which propagate through such media lose energy due to scattering from the heterogeneous structure of the material. This scattering may be characterized by the attenuation of the medium. If the medium is statistically isotropic, the attenuation is independent of propagation direction. In an anisotropic medium the scattering attenuation is a function of propagation direction. The analysis of this scattering attenuation is, therefore, more complicated than that of the isotropic case. The study of statistically isotropic media and the corresponding scattering attenuation has received considerable attention. The problem of wave propagation in textured polycrystalline materials has, however, received lesser attention. Stanke and Kino[1] briefly discuss the applicability of the Keller approximation[2] to the case of polycrystalline media with texture, although they provide no specific results. Hirsekorn was one of the first to carefully examine the scattering in textured polycrystals as a function of frequency.[3] The use of a single-sized, spherical grain resulted in unphysical oscillations at higher frequencies. She then extended her theory, using the same perturbation approach, to determine the directional dependence of the phase velocity and attenuation of the three wave types.[4] The problem was considered more recently by Ahmed and Thompson.[5] They also examined the case of polycrystalline grains with an aligned axis and developed algebraic equations governing the wave number. The roots of these equations, found numerically, determined the phase velocity and scattering attenuation. Their results were applicable for all frequencies from the Rayleigh limit to the geometric optics limit due to their use of the Keller approximation alone without additional approximations. They have also examined correlations defined by both equiaxed grains and grains with elongation.[5,6] They further noted the relations between the diffuse backscatter and the presence of texture.[7]

The general scattering problem as discussed by these authors and others involves a scattering integral with a Green's function as its kernel. If the medium is statistically isotropic, this Green's function clearly takes the form of the Green's function for the isotropic medium. In the case of statistically anisotropic media this choice is less clear. Stanke and Kino argue that the isotropic Green's function may be used in the analysis for polycrystalline materials with texture.[1] This argument was the basis of the work by Ahmed and Thompson.[5] They used the isotropic Green's function as given by Lifshitz and Parkhamovski[8] to describe the scattering in textured media. In addition, they simplified the analysis by using the polarization directions for the isotropic waves. Examination of the Keller approximation indicates that the choice of Green's function is not so clear. In the original discussion,[2] a small variable ε was defined as a measure of the departure of the medium from homogeneity. The Green's function within the scattering integral corresponded to that for the medium for which the heterogeneity was zero. For textured polycrystalline materials, the homogeneous medium is anisotropic. Thus, an anisotropic Green's function may be more appropriate for this and other similar problems. Comparisons between these different solution methods (e.g., isotropic Green's function with and without anisotropic polarizations and anisotropic Green's function) in terms of the

strength of the anisotropy will not be addressed here.

The use of an anisotropic Green's function for modeling the scattering in statistically anisotropic media is the subject of this article. Here, the problem is formulated in terms of the Dyson equation as discussed by Frisch[9] and Weaver.[10] The Dyson equation is easily solved in the spatial Fourier transform domain within the limits of the first-order smoothing approximation (FOSA), or Keller[2] approximation. A further approximation is also made which restricts the results to frequencies below the high-frequency geometric optics limit. The problem is further specified for the case of cubic polycrystalline grains with one aligned axis and with the other two axes randomly oriented. In this case, the anisotropy reduces to that of transverse isotropy. The result is the attenuation as a function of direction and frequency for the shear horizontal, quasicompressional, and quasishear waves. In particular, the angular dependence of the attenuations in the Rayleigh limit is obtained explicitly. Outside the Rayleigh limit, simple expressions for the attenuations of the shear horizontal, quasicompressional, and quasishear waves are derived in terms of integrations on the unit circle. The results are quantitatively similar to those of Ahmed and Thompson,[5] but are given here in a more direct manner. Differences in the angular dependence are also seen due to the use of the anisotropic Green's function here.

The present formulation also allows the extension to the full multiple scattering problem to be made in a straightforward manner. Such an extension in terms of radiative transfer and diffusion has been discussed previously for the statistically isotropic case using similar methods.[10–13] Although the present application is for textured metals, the formalism is sufficiently general to be applied to other heterogeneous media with statistical anisotropy such as fiber-reinforced composites and extruded metal-matrix composites.

In the next section, the Dyson equation is discussed in terms of the appropriate Green's dyadics. The formalism is developed for a general anisotropic material without reference to a particular symmetry class. The solution of the mean response is further reduced in the succeeding section for the case of a transversely isotropic medium. The elastic modulus tensor is specified for this case and expressions for the attenuation of each wave type are given. Finally, the covariance tensor of the elastic moduli fluctuations is further specified for that of cubic polycrystals with texture and solutions for the case of stainless steel with aligned [001] axes are given.

I. PRELIMINARY ELASTODYNAMICS

The equation of motion for the elastodynamic response of an infinite, linear-elastic material to deformation is given in terms of the Green's dyadic by

$$\left\{-\delta_{jk}\frac{\partial^2}{\partial t^2}+\frac{\partial}{\partial x_i}C_{ijkl}(\mathbf{x})\frac{\partial}{\partial x_l}\right\}G_{k\alpha}(\mathbf{x},\mathbf{x}';t) = \delta_{j\alpha}\delta^3(\mathbf{x}-\mathbf{x}')\,\delta(t). \tag{1}$$

The second-rank Green's dyadic, $G_{k\alpha}(\mathbf{x},\mathbf{x}';t)$, defines the response at location $\mathbf{x}$ in the kth direction to a unit impulse at location $\mathbf{x}'$ in the αth direction. The moduli are spatially variable and density is assumed uniform throughout. The units in Eq. (1) have been chosen such that the density is unity. The moduli are assumed to be spatially heterogeneous and of the form $C_{ijkl}(\mathbf{x})=C^0_{ijkl}+\delta C_{ijkl}(\mathbf{x})$. Thus, the moduli have the form of average moduli, $C^0_{ijkl}=\langle C_{ijkl}(\mathbf{x})\rangle$, plus a fluctuation about this mean, $\delta C_{ijkl}(\mathbf{x})$. The fluctuations are assumed to have zero mean, $\langle \delta C_{ijkl}(\mathbf{x})\rangle=0$. The mean moduli are not necessarily isotropic—the material may have global anisotropy. The covariance of the moduli is represented by an eighth-rank tensor

$$\Lambda(\mathbf{x}-\mathbf{y})^{ijkl}_{\alpha\beta\gamma\delta}=\langle \delta C_{ijkl}(\mathbf{x})\,\delta C_{\alpha\beta\gamma\delta}(\mathbf{y})\rangle. \tag{2}$$

The covariance, $\mathbf{\Lambda}$, is given as a function of the difference between two vectors, $\mathbf{x}-\mathbf{y}$. This assumption implies that the medium is statistically homogeneous. However, the additional assumption of statistical isotropy (that $\mathbf{\Lambda}$ is a function of $|\mathbf{x}-\mathbf{y}|$) is not made here. The power spectral density of the moduli fluctuations, $\tilde{\mathbf{\Lambda}}$, is given by the Fourier transform of the covariance

$$\tilde{\Lambda}(\mathbf{p})^{ijkl}_{\alpha\beta\gamma\delta}=\int \Lambda(\mathbf{r})^{ijkl}_{\alpha\beta\gamma\delta}e^{-i\mathbf{r}\cdot\mathbf{p}}\,d^3r. \tag{3}$$

Defining a temporal Fourier transform pair for the functions $f(t)$ and $\tilde{f}(\omega)$ by

$$\tilde{f}(\omega)=\int f(t)e^{i\omega t}\,dt, \tag{4}$$

$$f(t)=\frac{1}{2\pi}\int \tilde{f}(\omega)e^{-i\omega t}\,d\omega, \tag{5}$$

allows Eq. (1) to be transformed as

$$\left\{\omega^2\delta_{jk}+C^0_{ijkl}\frac{\partial}{\partial x_i}\frac{\partial}{\partial x_l}+\frac{\partial}{\partial x_i}\delta C_{ijkl}(\mathbf{x})\frac{\partial}{\partial x_l}\right\}G_{k\alpha}(\mathbf{x},\mathbf{x}',\omega) = \delta_{j\alpha}\delta^3(\mathbf{x}-\mathbf{x}'). \tag{6}$$

The random nature of the medium suggests that the Green's function, $\mathbf{G}$, is of little value as it will also be a random function. The interesting quantities are instead those related to the statistics of the response. These statistics include the mean response, $\langle\mathbf{G}\rangle$, and the covariance of the response, $\langle\mathbf{GG}^*\rangle$, with the * denoting a complex conjugate. This article is devoted to examination of the mean response with corresponding phase velocities and attenuations.

Wave propagation and scattering problems of this sort do not lend themselves to solution by perturbation methods. As Frisch points out, these solutions do not converge.[9] Instead Frisch used diagrammatic methods for solution of the mean response.[9] The mean response, $\langle\mathbf{G}\rangle$, is governed by the Dyson equation which is given by[9,10]

$$\langle G_{i\alpha}(\mathbf{x},\mathbf{x}')\rangle=G^0_{i\alpha}(\mathbf{x},\mathbf{x}')+\int\int G^0_{i\beta}(\mathbf{x},\mathbf{y})M_{\beta j}(\mathbf{y},\mathbf{z}) \times\langle G_{j\alpha}(\mathbf{z},\mathbf{x}')\rangle\,d^3y\,d^3z. \tag{7}$$

In Eq. (7), the quantity $\mathbf{G}^0$ is the bare Green's dyadic. It defines the response of the medium without

heterogeneities—the solution of Eq. (6) with $\delta C_{ijkl}(\mathbf{x})=0$. The second-rank tensor $\mathbf{M}$ is the mass or self-energy operator.[9] The Dyson equation, Eq. (7), is easily solved in Fourier transform space under the assumption of statistical homogeneity. The spatial Fourier transform pair for $\mathbf{G}^0$ is given by

$$G^0_{i\alpha}(\mathbf{p})\,\delta^3(\mathbf{p}-\mathbf{q})=\frac{1}{(2\pi)^3}\int\int G^0_{i\alpha}(\mathbf{x},\mathbf{x}') \times e^{-i\mathbf{p}\cdot\mathbf{x}}e^{i\mathbf{q}\cdot\mathbf{x}'}\,d^3x\,d^3x', \tag{8}$$

$$G^0_{i\alpha}(\mathbf{x},\mathbf{x}')=\frac{1}{(2\pi)^3}\int\int G^0_{i\alpha}(\mathbf{p})\,\delta^3(\mathbf{p}-\mathbf{q}) \times e^{i\mathbf{p}\cdot\mathbf{x}}e^{-i\mathbf{q}\cdot\mathbf{x}'}\,d^3p\,d^3q. \tag{9}$$

The Fourier transforms which define $\langle\mathbf{G}(\mathbf{p})\rangle$ and $\tilde{\mathbf{M}}(\mathbf{p})$ are given by expressions similar to that defining $\mathbf{G}^0(\mathbf{p})$. The assumption of statistical homogeneity ensures that they are functions of a single wave vector in Fourier space. The Dyson equation can then be spatially Fourier transformed and solved for $\langle\mathbf{G}(\mathbf{p})\rangle$. The result is

$$\langle\mathbf{G}(\mathbf{p})\rangle=[\mathbf{G}^0(\mathbf{p})^{-1}-\tilde{\mathbf{M}}(\mathbf{p})]^{-1}, \tag{10}$$

where $\tilde{\mathbf{M}}$ is the spatial transform of the self-energy. The Dyson equation is exact and describes the mean response of the medium. The main difficulty in the solution of Eq. (10) is the representation of $\mathbf{M}$. Approximations of $\mathbf{M}$ are often necessary to obtain closed-form solutions of Eq. (10). The self-energy, $\mathbf{M}$, can be written as an expansion in powers of moduli fluctuations. Approximation of $\mathbf{M}$ can then be made to first order using the first term in such an expansion. Frisch discusses the equivalence of this technique, which he called the first-order smoothing approximation (FOSA),[9] and the Keller approximation.[2] The FOSA expression for $\mathbf{M}$ is given by[10]

$$M_{\beta j}(\mathbf{y},\mathbf{z})\approx\left\langle\frac{\partial}{\partial y_\alpha}\,\delta C_{\alpha\beta\gamma\delta}(\mathbf{y}) \times\frac{\partial}{\partial y_\delta}\,G^0_{\gamma k}(\mathbf{y},\mathbf{z})\,\frac{\partial}{\partial z_i}\,\delta C_{ijkl}(\mathbf{z})\,\frac{\partial}{\partial z_l}\right\rangle. \tag{11}$$

Such an approximation is assumed valid as long as the fluctuations, $\delta\mathbf{C}$, are not too large. The spatial Fourier transform, as defined by Eq. (8), of the self-energy, $\mathbf{M}$, is then formulated. Manipulation of this integration allows it to be reduced to[10]

$$\tilde{M}_{\beta j}(\mathbf{p})=\int d^3s\,G^0_{\gamma k}(\mathbf{s})\,p_\alpha p_l s_\delta s_i\tilde{\Lambda}(\mathbf{p}-\mathbf{s})^{ijkl}_{\alpha\beta\gamma\delta}. \tag{12}$$

Thus, the transform of the self-energy can be written as a convolution between the bare Green's dyadic and the Fourier transform of the covariance of the moduli fluctuations. This expression, Eq. (12), and the Dyson equation, Eq. (10), are the primary results of this section which are used in the remainder of the article. The components of $\tilde{\mathbf{M}}$, as discussed in Sec. III, are used to calculate the phase velocity and attenuation of the various propagation modes. Equation (12) is identical to that given by Weaver for a statistically isotropic medium. However, the use of an anisotropic Green's dyadic for representing $\mathbf{G}^0$, which is discussed below, is the main new result here. The abbreviated presentation given in this section serves as a reminder of the general procedure for the description of the mean response. The Dyson equation, Eq. (10), and the expression for the self-energy, Eq. (12), will be used below for the derivation of the attenuations. Readers interested in further details of the scattering theory are referred to the articles of Karal and Keller,[2] Frisch,[9] Stanke and Kino,[1] and Weaver.[10]

II. GREEN'S DYADIC FOR TRANSVERSELY ISOTROPIC MEDIA

The solution of the Dyson equation, Eq. (10), for the mean response requires the Green's dyadic for the bare medium. The bare Green's dyadic, $\mathbf{G}^0$, is defined as the solution of the equation of motion, Eq. (6), without heterogeneities $[\delta C_{ijkl}(\mathbf{x})=0]$. The emphasis here is on anisotropic media with heterogeneities. Thus, the $\mathbf{G}^0$ required is that for an anisotropic medium. The lowest possible anisotropic symmetry class to be considered is that of a medium with a single symmetry axis. Although this is the simplest case of global anisotropy, relevant transversely isotropic or uniaxial materials include fiber-reinforced composites and polycrystalline media with fiber textures. These types of media have a single symmetry axis defined here by the unit vector, $\hat{\mathbf{n}}$. This direction is termed the ''fiber'' direction although the medium may not be composed of any fibers. The fourth-rank elastic moduli tensor, $\mathbf{C}$, in a transversely isotropic medium is a function of $\hat{\mathbf{n}}$ and is written

$$\begin{aligned}C_{ijkl}=&\lambda_\perp\delta_{ij}\delta_{kl}+\mu_\perp(\delta_{ik}\delta_{jl}+\delta_{il}\delta_{jk})+A(\delta_{ij}\hat{n}_k\hat{n}_l\\&+\delta_{kl}\hat{n}_i\hat{n}_j)+B(\delta_{ik}\hat{n}_j\hat{n}_l+\delta_{il}\hat{n}_j\hat{n}_k+\delta_{jk}\hat{n}_i\hat{n}_l\\&+\delta_{jl}\hat{n}_i\hat{n}_k)+D\hat{n}_i\hat{n}_j\hat{n}_k\hat{n}_l.\end{aligned} \tag{13}$$

The above elastic constants are defined as $A=\nu-\lambda_\perp$, $B=\mu_\parallel-\mu_\perp$, and $D=\lambda_\perp+2\mu_\perp+\lambda_\parallel+2\mu_\parallel-2(\nu+2\mu_\parallel)$. The elastic moduli, $\lambda_\parallel+2\mu_\parallel$, $\lambda_\perp+2\mu_\perp$, $\mu_\perp$, $\mu_\parallel$, and ν can be defined alternatively as C_{11}, C_{33}, C_{44}, C_{66}, and C_{13}, respectively.[14]

Substitution of this form for $\mathbf{C}$ into the equation of motion, Eq. (6), gives in direct notation

$$\begin{aligned}\{\omega^2\mathbf{I}-p^2[&(\mu_\perp+B(\hat{\mathbf{p}}\cdot\hat{\mathbf{n}})^2)\mathbf{I}+\hat{\mathbf{p}}\hat{\mathbf{p}}(\lambda_\perp+\mu_\perp)\\&+\hat{\mathbf{n}}\hat{\mathbf{n}}(B+D(\hat{\mathbf{p}}\cdot\hat{\mathbf{n}})^2)+(A+B)(\hat{\mathbf{p}}\cdot\hat{\mathbf{n}})\\&\times(\hat{\mathbf{p}}\hat{\mathbf{n}}+\hat{\mathbf{n}}\hat{\mathbf{p}})]\}\cdot\mathbf{G}^0(\mathbf{p},\hat{\mathbf{n}})=\mathbf{I},\end{aligned} \tag{14}$$

where $\mathbf{p}$ is the wave vector with magnitude, p, and direction $\hat{\mathbf{p}}$.

The above equation can be written in terms of the wave matrix, $\mathbf{N}$, by[14]

$$N_{jk}G_{k\alpha}(\mathbf{p},\omega)=\delta_{j\alpha}. \tag{15}$$

The eigenvectors of $\mathbf{N}$ define the polarization directions for the propagating waves.[14] These eigenvectors can be found directly from the wave matrix, $\mathbf{N}$. Explicit expressions

of the directions of these eigenvectors are required for the results which follow. For this reason, an alternative method of determining the eigenvectors is given here.

The shear horizontal wave in a transversely isotropic medium is known to be polarized perpendicular to the plane defined by $\hat{\mathbf{p}}$ and $\hat{\mathbf{n}}$. This vector, $\hat{\mathbf{u}}_1$, is given by

$$\hat{\mathbf{u}}_1=\frac{\hat{\mathbf{p}}\times\hat{\mathbf{n}}}{|\hat{\mathbf{p}}\times\hat{\mathbf{n}}|}=\frac{\hat{\mathbf{p}}\times\hat{\mathbf{n}}}{\sin\Theta}, \tag{16}$$

where Θ defines the angle between the $\hat{\mathbf{p}}$ and $\hat{\mathbf{n}}$. The identity dyadic can then be expanded as $\mathbf{I}=\hat{\mathbf{u}}_1\hat{\mathbf{u}}_1+(\mathbf{I}-\hat{\mathbf{u}}_1\hat{\mathbf{u}}_1)$. Use of the identity[15]

$$(\hat{\mathbf{p}}\cdot\hat{\mathbf{n}})(\hat{\mathbf{p}}\hat{\mathbf{n}}+\hat{\mathbf{n}}\hat{\mathbf{p}})$$
$$=\hat{\mathbf{u}}_1\hat{\mathbf{u}}_1(1-(\hat{\mathbf{p}}\cdot\hat{\mathbf{n}})^2)-\mathbf{I}(1-(\hat{\mathbf{p}}\cdot\hat{\mathbf{n}})^2)+\hat{\mathbf{n}}\hat{\mathbf{n}}+\hat{\mathbf{p}}\hat{\mathbf{p}}, \tag{17}$$

allows the last term in Eq. (14) to be expanded. The result is

$$\{\hat{\mathbf{u}}_1\hat{\mathbf{u}}_1[g^0_{\mathrm{SH}}(\mathbf{p})]^{-1}+(\mathbf{I}-\hat{\mathbf{u}}_1\hat{\mathbf{u}}_1)\omega^2$$
$$-p^2[(\mathbf{I}-\hat{\mathbf{u}}_1\hat{\mathbf{u}}_1)Q+P\hat{\mathbf{p}}\hat{\mathbf{p}}+E\hat{\mathbf{n}}\hat{\mathbf{n}}]\}\cdot\mathbf{G}^0(\mathbf{p},\hat{\mathbf{n}})=\mathbf{I}, \tag{18}$$

where the shear horizontal dispersion relation is

$$[g^0_{\mathrm{SH}}(\mathbf{p})]^{-1}=\omega^2-p^2(\mu_\perp+B(\hat{\mathbf{p}}\cdot\hat{\mathbf{n}})^2). \tag{19}$$

The quantities Q, P, and E in Eq. (18) are defined by

$$Q=\mu_\perp+B(\hat{\mathbf{p}}\cdot\hat{\mathbf{n}})^2-(A+B)(1-(\hat{\mathbf{p}}\cdot\hat{\mathbf{n}})^2),$$
$$P=\lambda_\perp+\mu_\perp+A+B=\nu+\mu_\parallel, \tag{20}$$
$$E=A+2B+D(\hat{\mathbf{p}}\cdot\hat{\mathbf{n}})^2.$$

The quasi P and SV waves are polarized in directions defined by $\hat{\mathbf{u}}_2$ and $\hat{\mathbf{u}}_3$ both of which lie in the $\hat{\mathbf{p}}$-$\hat{\mathbf{n}}$ plane. They form an orthonormal basis with $\hat{\mathbf{u}}_1$ such that $\hat{\mathbf{u}}_3=\hat{\mathbf{u}}_1\times\hat{\mathbf{u}}_2$. The vector $\hat{\mathbf{u}}_2$ is directed at an angle ψ from the propagation direction $\hat{\mathbf{p}}$. Use of the directions $\hat{\mathbf{u}}_2$ and $\hat{\mathbf{u}}_3$ allows $\mathbf{G}^0$ to be diagonalized. Thus $\mathbf{I}-\hat{\mathbf{u}}_1\hat{\mathbf{u}}_1=\hat{\mathbf{u}}_2\hat{\mathbf{u}}_2+\hat{\mathbf{u}}_3\hat{\mathbf{u}}_3$. The vectors $\hat{\mathbf{p}}$ and $\hat{\mathbf{n}}$ are then written in terms of $\hat{\mathbf{u}}_2$ and $\hat{\mathbf{u}}_3$ as

$$\hat{\mathbf{p}}=\hat{\mathbf{u}}_2\cos\psi+\hat{\mathbf{u}}_3\sin\psi, \tag{21}$$

$$\hat{\mathbf{n}}=\hat{\mathbf{u}}_2\cos(\psi+\Theta)+\hat{\mathbf{u}}_3\sin(\psi+\Theta). \tag{22}$$

Substitution into Eq. (18) gives

$$\{\hat{\mathbf{u}}_1\hat{\mathbf{u}}_1[g^0_{\mathrm{SH}}(\mathbf{p})]^{-1}+\hat{\mathbf{u}}_2\hat{\mathbf{u}}_2[\omega^2-p^2(Q+P\cos^2\psi$$
$$+E\cos^2(\Theta+\psi))]+\hat{\mathbf{u}}_3\hat{\mathbf{u}}_3[\omega^2-p^2(Q+P\sin^2\psi+E\sin^2$$
$$\times(\Theta+\psi))]-(\hat{\mathbf{u}}_2\hat{\mathbf{u}}_3+\hat{\mathbf{u}}_3\hat{\mathbf{u}}_2)[E\sin(\Theta+\psi)\cos(\Theta+\psi)$$
$$+P\sin\psi\cos\psi]\}\cdot\mathbf{G}^0(\mathbf{p})=\mathbf{I}. \tag{23}$$

The vectors $\hat{\mathbf{u}}_2$ and $\hat{\mathbf{u}}_3$, which define the polarizations of the quasi-P and quasi-SV waves, respectively, are eigenvectors of $\mathbf{N}$ and diagonalize $\mathbf{G}^0$. Thus, the term in Eq. (23) containing $\hat{\mathbf{u}}_2\hat{\mathbf{u}}_3+\hat{\mathbf{u}}_3\hat{\mathbf{u}}_2$ must be zero. This fact establishes a criterion for the angle ψ given by

$$\tan 2\psi=\frac{-E\sin 2\Theta}{P+E\cos 2\Theta}. \tag{24}$$

The directions of $\hat{\mathbf{u}}_2$ and $\hat{\mathbf{u}}_3$ are defined in terms of ψ for later convenience. The above equation for ψ, Eq. (24), must be used with care when numerical methods are employed. The value of ψ which satisfies Eq. (24) may correspond to either the quasi-P or quasi-SV wave. It should also be kept in mind that the vectors $\hat{\mathbf{u}}_2$ and $\hat{\mathbf{u}}_3$ are functions of the direction of propagation, $\hat{\mathbf{p}}$, relative to the fiber direction, $\hat{\mathbf{n}}$. This dependence, $\psi=\psi(\Theta)$, which is evident in Eq. (24), will remain implicit throughout.

The bare Green's dyadic may now be written

$$\mathbf{G}^0(\mathbf{p})=g^0_{\mathrm{SH}}(\mathbf{p})\hat{\mathbf{u}}_1\hat{\mathbf{u}}_1+g^0_{\mathrm{qP}}(\mathbf{p})\hat{\mathbf{u}}_2\hat{\mathbf{u}}_2+g^0_{\mathrm{qSV}}(\mathbf{p})\hat{\mathbf{u}}_3\hat{\mathbf{u}}_3. \tag{25}$$

The dispersion relations for the bare response of the SH, qP, and qSV waves are given by

$$g^0_{\mathrm{SH}}(\mathbf{p})=[\omega^2-p^2(\mu_\perp+B\cos^2\Theta)]^{-1}=[\omega^2-p^2c^2_{\mathrm{SH}}]^{-1},$$
$$g^0_{\mathrm{qP}}(\mathbf{p})=[\omega^2-p^2(Q+P\cos^2\psi+E\cos^2(\Theta+\psi))]^{-1}$$
$$=[\omega^2-p^2c^2_{\mathrm{qP}}]^{-1}, \tag{26}$$
$$g^0_{\mathrm{qSV}}(\mathbf{p})=[\omega^2-p^2(Q+P\sin^2\psi+E\sin^2(\Theta+\psi))]^{-1}$$
$$=[\omega^2-p^2c^2_{\mathrm{qSV}}]^{-1},$$

where the angle ψ is defined by Eq. (24) and Q, P, and E are defined in Eq. (20). The above expressions also describe the phase velocity, c_β, as a function of propagation direction for each wave type, β. The imaginary parts of these expressions will be used below and are given by

$$\mathrm{Im}g^0_\beta(\mathbf{p})=-\pi\,\mathrm{sgn}(\omega)\,\delta(\omega^2-p^2c^2_\beta). \tag{27}$$

The mean response of the heterogeneous medium is now given by solution of the Dyson equation.

III. MEAN RESPONSE

The mean response, $\langle\mathbf{G}(\mathbf{p})\rangle$, is given by solution of the Dyson equation, Eq. (10), above. The solution of $\langle\mathbf{G}(\mathbf{p})\rangle$ is expressed in terms of $\mathbf{G}^0(\mathbf{p})$ and $\tilde{\mathbf{M}}(\mathbf{p})$. Like $\mathbf{G}^0$, the mean response and self-energy may be expanded in terms of the orthonormal basis defined by $\hat{\mathbf{u}}_1$, $\hat{\mathbf{u}}_2$, and $\hat{\mathbf{u}}_3$. Thus,

$$\langle\mathbf{G}(\mathbf{p})\rangle=g_{\mathrm{SH}}(\mathbf{p})\hat{\mathbf{u}}_1\hat{\mathbf{u}}_1+g_{\mathrm{qP}}(\mathbf{p})\hat{\mathbf{u}}_2\hat{\mathbf{u}}_2+g_{\mathrm{qSV}}(\mathbf{p})\hat{\mathbf{u}}_3\hat{\mathbf{u}}_3,$$
$$\tilde{\mathbf{M}}(\mathbf{p})=m_{\mathrm{SH}}(\mathbf{p})\hat{\mathbf{u}}_1\hat{\mathbf{u}}_1+m_{\mathrm{qP}}(\mathbf{p})\hat{\mathbf{u}}_2\hat{\mathbf{u}}_2+m_{\mathrm{qSV}}(\mathbf{p})\hat{\mathbf{u}}_3\hat{\mathbf{u}}_3, \tag{28}$$

where it is again emphasized that the directions $\hat{\mathbf{u}}_1$, $\hat{\mathbf{u}}_2$, and $\hat{\mathbf{u}}_3$ are dependent upon the propagation direction $\hat{\mathbf{p}}$.

The dispersion relations for the mean response are then given by the solution of the Dyson equation, Eq. (10), as

$$g_\beta(\mathbf{p})=[g^0_\beta(\mathbf{p})^{-1}-m_\beta(\mathbf{p})]^{-1}$$
$$=[\omega^2-p^2c^2_\beta-m_\beta(\mathbf{p})]^{-1}, \tag{29}$$

for each wave type, β. This expression for the dispersion relation of the mean response defines the phase velocity and attenuation of each wave type. Solution of

$$\omega^2 - p^2 c_\beta^2 - m_\beta(\mathbf{p}) = 0, \tag{30}$$

for the wave vector p, is required given $\tilde{\mathbf{M}}$ defined in Eq. (12). The inverse Fourier transform of $\langle \mathbf{G}(\mathbf{p}) \rangle$ will be dominated by the poles of the dispersion relations. The phase velocity is given by the real part of p and the attenuation by the imaginary part. Such solutions of Eq. (30) are usually done numerically using root finding techniques.[5] However, explicit expressions for the attenuation can be determined using an approximation valid below the high-frequency geometric optics limit. In this case, the wave vector $\mathbf{p}$ within the self-energy is approximated as being equal to the bare wave vector. Such an approximation, $m_\beta(\mathbf{p}) \approx m_\beta[(\omega/c_\beta)\hat{\mathbf{p}}]$, is sometimes called a Born approximation.[1,10] This approximation allows the imaginary part of $\mathbf{p}$ to be calculated directly from Eq. (30). The attenuation of each wave type is given by

$$\alpha_\beta(\hat{\mathbf{p}}) = -\frac{1}{2\omega c_\beta(\hat{\mathbf{p}})} \mathrm{Im} m_\beta\left(\frac{\omega}{c_\beta}\hat{\mathbf{p}}\right). \tag{31}$$

The final step in this derivation now lies in the expression for the imaginary part of the self-energy. The definition of the self-energy was given by Eq. (12). The form of the self-energy given by Eq. (28) is substituted into Eq. (12). Appropriate inner products allow each component of the self-energy to be determined independently. The wave numbers which appear in Eq. (12) are approximated to the same degree of the Born approximation discussed above. The integration over the magnitude of the wave vector is easily done due to the delta-function form of $\mathbf{G}^0(\mathbf{s})$. The delta functions are the result of consideration of the imaginary parts of the dispersion relations given by Eq. (27). The attenuations for the three wave types, each defined by Eq. (31), are finally given by

$$\alpha_{\mathrm{SH}}(\hat{\mathbf{p}}) = \frac{1}{c_{\mathrm{SH}}^3(\hat{\mathbf{p}})}\left\{ \frac{\pi}{4}\int d^2\hat{s}\frac{\omega^4}{c_{\mathrm{SH}}^5(\hat{\mathbf{s}})}\tilde{\Lambda}\left(\frac{\omega}{c_{\mathrm{SH}}(\hat{\mathbf{p}})}\hat{\mathbf{p}} - \frac{\omega}{c_{\mathrm{SH}}(\hat{\mathbf{s}})}\hat{\mathbf{s}}\right)_{\cdots\hat{\mathbf{u}}_1\hat{\mathbf{p}}\hat{\mathbf{s}}\hat{\mathbf{v}}_1}^{\cdots\hat{\mathbf{u}}_1\hat{\mathbf{p}}\hat{\mathbf{s}}\hat{\mathbf{v}}_1} + \frac{\pi}{4}\int d^2\hat{s}\frac{\omega^4}{c_{\mathrm{qP}}^5(\hat{\mathbf{s}})}\tilde{\Lambda}\left(\frac{\omega}{c_{\mathrm{SH}}(\hat{\mathbf{p}})}\hat{\mathbf{p}} - \frac{\omega}{c_{\mathrm{qP}}(\hat{\mathbf{s}})}\hat{\mathbf{s}}\right)_{\cdots\hat{\mathbf{u}}_1\hat{\mathbf{p}}\hat{\mathbf{s}}\hat{\mathbf{v}}_2}^{\cdots\hat{\mathbf{u}}_1\hat{\mathbf{p}}\hat{\mathbf{s}}\hat{\mathbf{v}}_2}$$
$$+ \frac{\pi}{4}\int d^2\hat{s}\frac{\omega^4}{c_{\mathrm{qSV}}^5(\hat{\mathbf{s}})}\tilde{\Lambda}\left(\frac{\omega}{c_{\mathrm{SH}}(\hat{\mathbf{p}})}\hat{\mathbf{p}} - \frac{\omega}{c_{\mathrm{qSV}}(\hat{\mathbf{s}})}\hat{\mathbf{s}}\right)_{\cdots\hat{\mathbf{u}}_1\hat{\mathbf{p}}\hat{\mathbf{s}}\hat{\mathbf{v}}_3}^{\cdots\hat{\mathbf{u}}_1\hat{\mathbf{p}}\hat{\mathbf{s}}\hat{\mathbf{v}}_3}\Bigg\}, \tag{32}$$

$$\alpha_{\mathrm{qP}}(\hat{\mathbf{p}}) = \frac{1}{c_{\mathrm{qP}}^3(\hat{\mathbf{p}})}\left\{ \frac{\pi}{4}\int d^2\hat{s}\frac{\omega^4}{c_{\mathrm{SH}}^5(\hat{\mathbf{s}})}\tilde{\Lambda}\left(\frac{\omega}{c_{\mathrm{qP}}(\hat{\mathbf{p}})}\hat{\mathbf{p}} - \frac{\omega}{c_{\mathrm{SH}}(\hat{\mathbf{s}})}\hat{\mathbf{s}}\right)_{\cdots\hat{\mathbf{u}}_2\hat{\mathbf{p}}\hat{\mathbf{s}}\hat{\mathbf{v}}_1}^{\cdots\hat{\mathbf{u}}_2\hat{\mathbf{p}}\hat{\mathbf{s}}\hat{\mathbf{v}}_1} + \frac{\pi}{4}\int d^2\hat{s}\frac{\omega^4}{c_{\mathrm{qP}}^5(\hat{\mathbf{s}})}\tilde{\Lambda}\left(\frac{\omega}{c_{\mathrm{qP}}(\hat{\mathbf{p}})}\hat{\mathbf{p}} - \frac{\omega}{c_{\mathrm{qP}}(\hat{\mathbf{s}})}\hat{\mathbf{s}}\right)_{\cdots\hat{\mathbf{u}}_2\hat{\mathbf{p}}\hat{\mathbf{s}}\hat{\mathbf{v}}_2}^{\cdots\hat{\mathbf{u}}_2\hat{\mathbf{p}}\hat{\mathbf{s}}\hat{\mathbf{v}}_2}$$
$$+ \frac{\pi}{4}\int d^2\hat{s}\frac{\omega^4}{c_{qSV}^5(\hat{\mathbf{s}})}\tilde{\Lambda}\left(\frac{\omega}{c_{\mathrm{qP}}(\hat{\mathbf{p}})}\hat{\mathbf{p}} - \frac{\omega}{c_{qSV}(\hat{\mathbf{s}})}\hat{\mathbf{s}}\right)_{\cdots\hat{\mathbf{u}}_2\hat{\mathbf{p}}\hat{\mathbf{s}}\hat{\mathbf{v}}_3}^{\cdots\hat{\mathbf{u}}_2\hat{\mathbf{p}}\hat{\mathbf{s}}\hat{\mathbf{v}}_3}\Bigg\}, \tag{33}$$

$$\alpha_{\mathrm{qSV}}(\hat{\mathbf{p}}) = \frac{1}{c_{\mathrm{qSV}}^3(\hat{\mathbf{p}})}\left\{ \frac{\pi}{4}\int d^2\hat{s}\frac{\omega^4}{c_{\mathrm{SH}}^5(\hat{\mathbf{s}})}\tilde{\Lambda}\left(\frac{\omega}{c_{\mathrm{qSV}}(\hat{\mathbf{p}})}\hat{\mathbf{p}} - \frac{\omega}{c_{\mathrm{SH}}(\hat{\mathbf{s}})}\hat{\mathbf{s}}\right)_{\cdots\hat{\mathbf{u}}_3\hat{\mathbf{p}}\hat{\mathbf{s}}\hat{\mathbf{v}}_1}^{\cdots\hat{\mathbf{u}}_3\hat{\mathbf{p}}\hat{\mathbf{s}}\hat{\mathbf{v}}_1} + \frac{\pi}{4}\int d^2\hat{s}\frac{\omega^4}{c_{\mathrm{qP}}^5(\hat{\mathbf{s}})}\tilde{\Lambda}\left(\frac{\omega}{c_{\mathrm{qSV}}(\hat{\mathbf{p}})}\hat{\mathbf{p}} - \frac{\omega}{c_{\mathrm{qP}}(\hat{\mathbf{s}})}\hat{\mathbf{s}}\right)_{\cdots\hat{\mathbf{u}}_3\hat{\mathbf{p}}\hat{\mathbf{s}}\hat{\mathbf{v}}_2}^{\cdots\hat{\mathbf{u}}_3\hat{\mathbf{p}}\hat{\mathbf{s}}\hat{\mathbf{v}}_2}$$
$$+ \frac{\pi}{4}\int d^2\hat{s}\frac{\omega^4}{c_{\mathrm{qSV}}^5(\hat{\mathbf{s}})}\tilde{\Lambda}\left(\frac{\omega}{c_{\mathrm{qSV}}(\hat{\mathbf{p}})}\hat{\mathbf{p}} - \frac{\omega}{c_{\mathrm{qSV}}(\hat{\mathbf{s}})}\hat{\mathbf{s}}\right)_{\cdots\hat{\mathbf{u}}_3\hat{\mathbf{p}}\hat{\mathbf{s}}\hat{\mathbf{v}}_3}^{\cdots\hat{\mathbf{u}}_3\hat{\mathbf{p}}\hat{\mathbf{s}}\hat{\mathbf{v}}_3}\Bigg\}. \tag{34}$$

The integrals in the above equations are over the unit sphere defined by $\hat{\mathbf{s}}$. The direction $\hat{\mathbf{p}}$ defines the propagation direction, $\hat{\mathbf{s}}$ is the scattered direction, and the polarization directions, $\hat{\mathbf{u}}$ and $\hat{\mathbf{v}}$. In the above expressions the dependence of the vectors $\hat{\mathbf{u}}$ on $\hat{\mathbf{p}}$ and of $\hat{\mathbf{v}}$ on $\hat{\mathbf{s}}$ is implicit. The argument of the autocorrelation is the difference between the incoming and outgoing propagation directions. The inner products on the autocorrelation of the moduli fluctuations are given in terms of four unit vectors. This inner product is given explicitly by $\tilde{\Lambda}(\mathbf{q})_{\cdots\hat{\mathbf{u}}\hat{\mathbf{p}}\hat{\mathbf{s}}\hat{\mathbf{v}}}^{\cdots\hat{\mathbf{u}}\hat{\mathbf{p}}\hat{\mathbf{s}}\hat{\mathbf{v}}} = \tilde{\Lambda}(\mathbf{q})_{\alpha\beta\gamma\delta}^{ijkl}\hat{u}_\beta\hat{u}_k\hat{p}_\alpha\hat{p}_l\hat{s}_i\hat{s}_\delta\hat{v}_\gamma\hat{v}_j$.

The above expressions for the attenuation are more complicated than those for a statistically isotropic medium considered by Weaver.[10] They reduce to the forms given there in the case of statistical isotropy. The dependence of wave speed and polarization direction on propagation direction greatly complicates the integrations. In the next section, the covariance is specified for equiaxed cubic polycrystals with texture.

IV. EQUIAXED POLYCRYSTALLINE MEDIA WITH TEXTURE

The above formalism is now specified for the particular problem of equiaxed cubic polycrystalline media with one aligned axis. This particular grain structure arises during welding or solidification. In this case the transverse isotropy is the result of alignment of one grain axis in all grains. The other axes are randomly oriented about that axis. Two assumptions are made about the fluctuations of the elastic moduli. The tensorial and spatial components of covariance are first assumed independent. This assumption implies

$$\tilde{\Lambda}(\mathbf{p})^{ijkl}_{\alpha\beta\gamma\delta} = \Xi^{ijkl}_{\alpha\beta\gamma\delta}\tilde{W}(\mathbf{p}), \tag{35}$$

where $\tilde{W}$ $(\mathbf{p})$ is the Fourier transform of the spatial correlation function. The grains are also assumed to be equiaxed such that $W(\mathbf{r}) = e^{-r/L}$. The correlation length, L, is of the order of the grain radius. The Fourier transform is then given by

$$\tilde{W}(\mathbf{q}) = \frac{L^3}{\pi^2(1+L^2q^2)^2}. \tag{36}$$

The forms of the attenuation given above contain the difference of two vectors, $\tilde{W}(\mathbf{q}) = \tilde{W}([\omega/c_1(\Theta)]\hat{\mathbf{p}} - [\omega/c_2(\Theta')]\hat{\mathbf{s}})$ as the argument for $\tilde{\Lambda}(\mathbf{p})$. The form of correlation function is dependent upon magnitude of this vector. Trigonometry reduces the magnitude of this difference to

$$q^2 = \left|\frac{\omega}{c_1(\Theta)}\hat{\mathbf{p}} - \frac{\omega}{c_2(\Theta')}\hat{\mathbf{s}}\right|^2 = \frac{\omega^2}{c_1^2(\Theta)} + \frac{\omega^2}{c_2^2(\Theta')} - \frac{2\omega^2}{c_1(\Theta)c_2(\Theta')}(\hat{\mathbf{p}}\cdot\hat{\mathbf{s}}). \tag{37}$$

The form of the eighth-rank tensor, $\Xi^{ijkl}_{\alpha\beta\gamma\delta}$, is now discussed with regard to cubic crystallites.

A. Statistics of textured cubic polycrystalline media with aligned [001] axis

The average medium is characterized by the average elastic modulus tensor, $\langle C_{ijkl}\rangle$. For a statistically transversely isotropic medium, the average modulus is a fourth-rank tensor which is a function of the unit vector $\hat{\mathbf{n}}$. The most general form for this tensor is

$$\begin{aligned}\langle C_{ijkl}(\mathbf{x})\rangle \equiv C^0_{ijkl} &= \lambda_\perp \delta_{ij}\delta_{kl} + \mu_\perp(\delta_{ik}\delta_{jl} + \delta_{il}\delta_{jk}) \\ &+ A(\delta_{ij}\hat{n}_k\hat{n}_l + \delta_{kl}\hat{n}_i\hat{n}_j) \\ &+ B(\delta_{ik}\hat{n}_j\hat{n}_l + \delta_{il}\hat{n}_j\hat{n}_k + \delta_{jk}\hat{n}_i\hat{n}_l + \delta_{jl}\hat{n}_i\hat{n}_k) \\ &+ D\hat{n}_i\hat{n}_j\hat{n}_k\hat{n}_l. \end{aligned} \tag{38}$$

The elastic modulus tensor for a single cubic crystal is given by

$$C_{ijkl}(\mathbf{x}) = c_{12}\delta_{ij}\delta_{kl} + c_{44}(\delta_{ik}\delta_{jl} + \delta_{il}\delta_{jk}) + \eta\sum_{n=1}^{3} a_i^n a_j^n a_k^n a_l^n, \tag{39}$$

where $\eta = c_{11} - c_{12} - 2c_{44}$ is the single-crystal anisotropy. The elements a_i^n define the rotation matrix in terms of the Euler angles. Each grain is assumed to have a different orientation such that the last term in Eq. (39) is dependent upon $\mathbf{x}$. The ensemble average for this medium is defined by rotation about the aligned axis of the grains. This average is given by

$$\langle f\rangle = \frac{1}{2\pi}\int_0^{2\pi} f(\phi)\,d\phi, \tag{40}$$

where the dummy variable ϕ is defined in the plane perpendicular to the direction of the aligned axis.

Carrying out the average for Eq. (39) and equating like terms with Eq. (38) gives

$$\lambda_\perp = c_{12} + \frac{\eta}{4}, \quad \mu_\perp = c_{44} + \frac{\eta}{4}, \quad A = B = -\frac{\eta}{4}, \quad D = \frac{7\eta}{4}. \tag{41}$$

The average modulus tensor is then

$$\begin{aligned}\langle C_{ijkl}\rangle = &\left(c_{12} + \frac{\eta}{4}\right)\delta_{ij}\delta_{kl} + \left(c_{44} + \frac{\eta}{4}\right)(\delta_{ik}\delta_{jl} + \delta_{il}\delta_{jk}) \\ &- \frac{\eta}{4}(\delta_{ij}\hat{n}_k\hat{n}_l + \delta_{kl}\hat{n}_i\hat{n}_j) - \frac{\eta}{4}(\delta_{ik}\hat{n}_j\hat{n}_l + \delta_{il}\hat{n}_j\hat{n}_k \\ &+ \delta_{jk}\hat{n}_i\hat{n}_l + \delta_{jl}\hat{n}_i\hat{n}_k) + \frac{7\eta}{4}\hat{n}_i\hat{n}_j\hat{n}_k\hat{n}_l. \end{aligned} \tag{42}$$

The eighth-rank covariance, $\Xi^{ijkl}_{\alpha\beta\gamma\delta}$, is also a function of the single vector $\hat{\mathbf{n}}$. It can therefore be constructed of Kronecker deltas and pairs of $\hat{\mathbf{n}}$'s. The symmetry of the cubic crystal also implies that this tensor must be invariant to permutation of Latin or Greek indices and exchange of all Latin for all Greek indices. Thus, the covariance of moduli fluctuations may be written in terms of 14 independent tensors as

$$\Xi^{ijkl}_{\alpha\beta\gamma\delta} = \langle C_{ijkl}C_{\alpha\beta\gamma\delta}\rangle - \langle C_{ijkl}\rangle\langle C_{\alpha\beta\gamma\delta}\rangle = \eta^2\left\langle\left(\sum_{n=1}^{3} a_i^n a_j^n a_k^n a_l^n\right)\left(\sum_{n=1}^{3} a_\alpha^n a_\beta^n a_\gamma^n a_\delta^n\right)\right\rangle - \eta^2\left\langle\sum_{n=1}^{3} a_i^n a_j^n a_k^n a_l^n\right\rangle\left\langle\sum_{n=1}^{3} a_\alpha^n a_\beta^n a_\gamma^n a_\delta^n\right\rangle$$

$$
\begin{aligned}
&= b_0(\delta_{ij}\delta_{kl}+\delta_{ik}\delta_{jl}+\delta_{il}\delta_{jk})(\delta_{\alpha\beta}\delta_{\gamma\delta}+\delta_{\alpha\gamma}\delta_{\beta\delta}+\delta_{\alpha\delta}\delta_{\beta\gamma})+d_0(\delta_{LL}\delta_{GG}\delta_{GL}\delta_{GL}-72 \text{ terms})\\
&+h_0(\delta_{GL}\delta_{GL}\delta_{GL}\delta_{GL}-24 \text{ terms})+b_2(\delta_{LL}\delta_{LL}\delta_{GG}\hat{n}_G\hat{n}_G+\delta_{GG}\delta_{GG}\delta_{LL}\hat{n}_L\hat{n}_L-36 \text{ terms})+c_2(\delta_{GL}\delta_{GL}\delta_{LL}\hat{n}_G\hat{n}_G\\
&+\delta_{GL}\delta_{GL}\delta_{GG}\hat{n}_L\hat{n}_L-144 \text{ terms})+d_2(\hat{n}_G\hat{n}_L\delta_{GL}\delta_{GG}\delta_{LL}-144 \text{ terms})+h_2(\hat{n}_G\hat{n}_L\delta_{GL}\delta_{GL}\delta_{GL}-96 \text{ terms})\\
&+b_4[\hat{n}_i\hat{n}_j\hat{n}_k\hat{n}_l(\delta_{\alpha\beta}\delta_{\gamma\delta}+\delta_{\alpha\gamma}\delta_{\beta\delta}+\delta_{\alpha\delta}\delta_{\beta\gamma})+\hat{n}_\alpha\hat{n}_\beta\hat{n}_\gamma\hat{n}_\delta(\delta_{ij}\delta_{kl}+\delta_{ik}\delta_{jl}+\delta_{il}\delta_{jk})]\\
&+c_4(\delta_{GG}\delta_{LL}\hat{n}_G\hat{n}_G\hat{n}_L\hat{n}_L-36 \text{ terms})+d_4(\delta_{LL}\delta_{GL}\hat{n}_L\hat{n}_G\hat{n}_G\hat{n}_G+\delta_{GG}\delta_{GL}\hat{n}_L\hat{n}_L\hat{n}_L\hat{n}_G-96 \text{ terms})\\
&+h_4(\delta_{GL}\delta_{GL}\hat{n}_L\hat{n}_L\hat{n}_G\hat{n}G-72 \text{ terms})+b_6(\delta_{GG}\hat{n}_G\hat{n}_G\hat{n}_L\hat{n}_L\hat{n}_L\hat{n}_L+\delta_{LL}\hat{n}_L\hat{n}_L\hat{n}_G\hat{n}_G\hat{n}_G\hat{n}_G-12 \text{ terms})\\
&+d_6(\delta_{LG}\hat{n}_L\hat{n}_L\hat{n}_L\hat{n}_G\hat{n}_G\hat{n}_G-16 \text{ terms})+d_8\hat{n}_i\hat{n}_j\hat{n}_k\hat{n}_l\hat{n}_\alpha\hat{n}_\beta\hat{n}_\gamma\hat{n}_\delta. \qquad (43)
\end{aligned}
$$

The above terms not explicitly given are written in terms of G and L. This notation implies the form of the terms given by Greek or Latin indices. All possible permutations of the particular form are implied and the number of terms of each form is also given. For example, the factor c_4 contains terms such as $\delta_{\alpha\beta}\delta_{ij}\hat{n}_\gamma\hat{n}_\delta\hat{n}_k\hat{n}_l$ and $\delta_{\alpha\gamma}\delta_{ik}\hat{n}_\beta\hat{n}_\delta\hat{n}_j\hat{n}_l$ plus all other permutations of Greek and Latin indices for a total of 36 terms.

The 764 terms in Eq. (43) completely define the covariance in a coordinate-free manner. The averages given in terms of the Euler angles can be carried out and compared with the results of the covariance given by the general form. The coefficients are found to be

$$
\begin{aligned}
&d_8=b_6=-d_6=\frac{9\eta^2}{288},\\
&b_4=-d_4=-h_2=h_0=\frac{3\eta^2}{288},\\
&d_2=c_2=b_0=-d_0=-b_2=-c_4=\frac{\eta^2}{288},\\
&h_4=\frac{5\eta^2}{288}.
\end{aligned} \qquad (44)
$$

The forms of the attenuations given in Eqs. (32)–(34) above require various inner products on the covariance tensor. These inner products have the general form of $\Xi^{\cdots\hat{\mathbf{q}}\hat{\mathbf{p}}\hat{\mathbf{s}}\hat{\mathbf{r}}}_{\cdots\hat{\mathbf{q}}\hat{\mathbf{p}}\hat{\mathbf{s}}\hat{\mathbf{r}}}$, where the vectors $\hat{\mathbf{p}}$ and $\hat{\mathbf{s}}$ represent the incoming and outgoing and propagation directions, respectively, and the vectors $\hat{\mathbf{q}}$ and $\hat{\mathbf{r}}$ are vectors defining the polarization directions of the particular wave. These vectors are perpendicular to the plane defined by $\hat{\mathbf{s}}$ or $\hat{\mathbf{p}}$ and $\hat{\mathbf{n}}$ (for SH waves) or they lie in this plane (for qP and qSV). This general inner product can be written in terms of various combinations of inner products of the vectors involved. The most general form is given explicitly elsewhere.[16]

Specific inner products required for the calculation of the attenuations are now determined. The attenuations will vary angularly only within the plane defined by the propagation direction and the fiber direction. Therefore, without loss of generality, a reference plane is defined as the $\hat{\mathbf{p}}$-$\hat{\mathbf{n}}$ plane. The following vectors are then defined with respect to a general xyz coordinate system as

$$
\begin{aligned}
&\hat{\mathbf{n}}=\hat{\mathbf{z}},\\
&\hat{\mathbf{p}}=\hat{\mathbf{y}}\sin\Theta+\hat{\mathbf{z}}\cos\Theta,\\
&\hat{\mathbf{s}}=\hat{\mathbf{x}}\sin\Theta'\cos\phi'+\hat{\mathbf{y}}\sin\Theta'\sin\phi'+\hat{\mathbf{z}}\cos\Theta'.
\end{aligned} \qquad (45)
$$

The polarization vectors are then defined with respect to these angles and ψ [Eq. (24)] as

$$
\begin{aligned}
&\hat{\mathbf{u}}_1=\hat{\mathbf{x}},\\
&\hat{\mathbf{u}}_2=\hat{\mathbf{y}}\sin\gamma+\hat{\mathbf{z}}\cos\gamma,\\
&\hat{\mathbf{u}}_3=-\hat{\mathbf{y}}\cos\gamma+\hat{\mathbf{z}}\sin\gamma,
\end{aligned} \qquad (46)
$$

and

$$
\begin{aligned}
&\hat{\mathbf{v}}_1=\hat{\mathbf{x}}\sin\phi'-\hat{\mathbf{y}}\cos\phi',\\
&\hat{\mathbf{v}}_2=\hat{\mathbf{x}}\sin\gamma'\cos\phi'+\hat{\mathbf{y}}\sin\gamma'\sin\phi'+\hat{\mathbf{z}}\cos\gamma',\\
&\hat{\mathbf{v}}_3=-\hat{\mathbf{x}}\cos\gamma'\cos\phi'-\hat{\mathbf{y}}\cos\gamma'\sin\phi'+\hat{\mathbf{z}}\sin\gamma',
\end{aligned} \qquad (47)
$$

where the angles γ and γ' used above are defined by

$$
\gamma=\Theta+\psi(\Theta), \quad \gamma'=\Theta'+\psi(\Theta'). \qquad (48)
$$

These angles, γ and γ', define the orientation angle of the qP wave with respect to the $\hat{\mathbf{n}}$ direction in the $\hat{\mathbf{p}}$-$\hat{\mathbf{n}}$ and $\hat{\mathbf{s}}$-$\hat{\mathbf{n}}$ planes, respectively.

Using these definitions of the relevant unit vectors, the required inner products simplify considerably. The inner products are for α_{SH},

$$\Xi^{\cdots\hat{\mathbf{u}}_1\hat{\mathbf{p}}\hat{\mathbf{s}}\hat{\mathbf{v}}_1}_{\cdots\hat{\mathbf{u}}_1\hat{\mathbf{p}}\hat{\mathbf{s}}\hat{\mathbf{v}}_1}=\frac{\eta^2}{32}\sin^2\Theta'\sin^2\Theta,$$

$$\Xi^{\cdots\hat{\mathbf{u}}_1\hat{\mathbf{p}}\hat{\mathbf{s}}\hat{\mathbf{v}}_2}_{\cdots\hat{\mathbf{u}}_1\hat{\mathbf{p}}\hat{\mathbf{s}}\hat{\mathbf{v}}_2}=\frac{\eta^2}{32}\sin^2\Theta'\sin^2\gamma'\sin^2\Theta, \tag{49}$$

$$\Xi^{\cdots\hat{\mathbf{u}}_1\hat{\mathbf{p}}\hat{\mathbf{s}}\hat{\mathbf{v}}_3}_{\cdots\hat{\mathbf{u}}_1\hat{\mathbf{p}}\hat{\mathbf{s}}\hat{\mathbf{v}}_3}=\frac{\eta^2}{32}\sin^2\Theta'\cos^2\gamma'\sin^2\Theta,$$

for α_{qP},

$$\Xi^{\cdots\hat{\mathbf{u}}_2\hat{\mathbf{p}}\hat{\mathbf{s}}\hat{\mathbf{v}}_1}_{\cdots\hat{\mathbf{u}}_2\hat{\mathbf{p}}\hat{\mathbf{s}}\hat{\mathbf{v}}_1}=\frac{\eta^2}{32}\sin^2\Theta'\sin^2\gamma\sin^2\Theta,$$

$$\Xi^{\cdots\hat{\mathbf{u}}_2\hat{\mathbf{p}}\hat{\mathbf{s}}\hat{\mathbf{v}}_2}_{\cdots\hat{\mathbf{u}}_2\hat{\mathbf{p}}\hat{\mathbf{s}}\hat{\mathbf{v}}_2}=\frac{\eta^2}{32}\sin^2\Theta'\sin^2\gamma'\sin^2\gamma\sin^2\Theta, \tag{50}$$

$$\Xi^{\cdots\hat{\mathbf{u}}_2\hat{\mathbf{p}}\hat{\mathbf{s}}\hat{\mathbf{v}}_3}_{\cdots\hat{\mathbf{u}}_2\hat{\mathbf{p}}\hat{\mathbf{s}}\hat{\mathbf{v}}_3}=\frac{\eta^2}{32}\sin^2\Theta'\cos^2\gamma'\sin^2\gamma\sin^2\Theta;$$

and, for α_{qSV},

$$\Xi^{\cdots\hat{\mathbf{u}}_3\hat{\mathbf{p}}\hat{\mathbf{s}}\hat{\mathbf{v}}_1}_{\cdots\hat{\mathbf{u}}_3\hat{\mathbf{p}}\hat{\mathbf{s}}\hat{\mathbf{v}}_1}=\frac{\eta^2}{32}\sin^2\Theta'\cos^2\gamma\sin^2\Theta,$$

$$\Xi^{\cdots\hat{\mathbf{u}}_3\hat{\mathbf{p}}\hat{\mathbf{s}}\hat{\mathbf{v}}_2}_{\cdots\hat{\mathbf{u}}_3\hat{\mathbf{p}}\hat{\mathbf{s}}\hat{\mathbf{v}}_2}=\frac{\eta^2}{32}\sin^2\Theta'\sin^2\gamma'\cos^2\gamma\sin^2\Theta, \tag{51}$$

$$\Xi^{\cdots\hat{\mathbf{u}}_3\hat{\mathbf{p}}\hat{\mathbf{s}}\hat{\mathbf{v}}_3}_{\cdots\hat{\mathbf{u}}_3\hat{\mathbf{p}}\hat{\mathbf{s}}\hat{\mathbf{v}}_3}=\frac{\eta^2}{32}\sin^2\Theta'\cos^2\gamma'\cos^2\gamma\sin^2\Theta,$$

where γ and γ' are defined in Eq. (48). The expressions given by Eqs. (49)–(51) are also directly related to the diffuse propagation including backscatter.[11–13]

Using the above inner products, the attenuations reduce to

$$\alpha_{\mathrm{SH}}(\Theta)=\frac{\omega^4\sin^2\Theta}{c^3_{\mathrm{SH}}(\Theta)}\,\frac{\eta^2\pi}{128}\int_0^{2\pi}d\phi'\int_0^{\pi}\left[\frac{\tilde{W}_{\mathrm{SH-SH}}(\hat{\mathbf{p}},\hat{\mathbf{s}})\sin^3\Theta'}{c^5_{\mathrm{SH}}(\Theta')}+\frac{\tilde{W}_{\mathrm{SH-qP}}(\hat{\mathbf{p}},\hat{\mathbf{s}})\sin^3\Theta'\sin^2\gamma'}{c^5_{\mathrm{qP}}(\Theta')}+\frac{\tilde{W}_{\mathrm{SH-qSV}}(\hat{\mathbf{p}},\hat{\mathbf{s}})\sin^3\Theta'\cos^2\gamma'}{c^5_{\mathrm{qSV}}(\Theta')}\right]d\Theta', \tag{52}$$

$$\alpha_{\mathrm{qP}}(\Theta)=\frac{\omega^4\sin^2\gamma\sin^2\Theta}{c^3_{\mathrm{qP}}(\Theta)}\,\frac{\eta^2\pi}{128}\int_0^{2\pi}d\phi'\times\int_0^{\pi}\left[\frac{\tilde{W}_{\mathrm{qP-SH}}(\hat{\mathbf{p}},\hat{\mathbf{s}})\sin^3\Theta'}{c^5_{\mathrm{SH}}(\Theta')}+\frac{\tilde{W}_{\mathrm{qP-qP}}(\hat{\mathbf{p}},\hat{\mathbf{s}})\sin^3\Theta'\sin^2\gamma'}{c^5_{\mathrm{qP}}(\Theta')}+\frac{\tilde{W}_{\mathrm{qP-qSV}}(\hat{\mathbf{p}},\hat{\mathbf{s}})\sin^3\Theta'\cos^2\gamma'}{c^5_{\mathrm{qSV}}(\Theta')}\right]d\Theta', \tag{53}$$

$$\alpha_{\mathrm{qSV}}(\Theta)=\frac{\omega^4\cos^2\gamma\sin^2\Theta}{c^3_{\mathrm{qSV}}(\Theta)}\,\frac{\eta^2\pi}{128}\int_0^{2\pi}d\phi'\times\int_0^{\pi}\left[\frac{\tilde{W}_{\mathrm{qSV-SH}}(\hat{\mathbf{p}},\hat{\mathbf{s}})\sin^3\Theta'}{c^5_{\mathrm{SH}}(\Theta')}+\frac{\tilde{W}_{\mathrm{qSV-qP}}(\hat{\mathbf{p}},\hat{\mathbf{s}})\sin^3\Theta'\sin^2\gamma'}{c^5_{\mathrm{qP}}(\Theta')}+\frac{\tilde{W}_{\mathrm{qSV-qSV}}(\hat{\mathbf{p}},\hat{\mathbf{s}})\sin^3\Theta'\cos^2\gamma'}{c^5_{\mathrm{qSV}}(\Theta')}\right]d\Theta'. \tag{54}$$

These expressions are now nondimensionalized and simplified. Reference wave speeds are needed for the nondimensionalization. Rather than using the Voigt average wave speeds, wave speeds characteristic of the anisotropic medium are used. Average wave speeds are defined as

$$\overline{c}_\beta=\frac{1}{2}\int_0^{\pi}c_\beta(\Theta)\sin\Theta\;d\Theta, \tag{55}$$

for each wave type, β. The three nondimensional frequencies are then defined as $x_\beta=\omega L/\overline{c}_\beta$. Finally, dimensionless quantities which describe the slowness surface for each wave type are defined by $r_\beta(\Theta)=\overline{c}_\beta/c_\beta(\Theta)$.

The expressions for the spatial correlation functions must now be discussed. Using the form of the spatial Fourier transform of the correlation function, given by Eq. (36), the functions $\tilde{W}_{\beta-\gamma}(\hat{\mathbf{p}},\hat{\mathbf{s}})$ are determined. In terms of the above dimensionless quantities, we find

$$\tilde{W}_{\beta-\gamma}(\hat{\mathbf{p}},\hat{\mathbf{s}})=\frac{L^3}{\pi^2(1+x_\beta^2r_\beta^2(\Theta)+x_\gamma^2r_\gamma^2(\Theta')-2x_\beta x_\gamma r_\beta(\Theta)r_\gamma(\Theta')\hat{\mathbf{p}}\cdot\hat{\mathbf{s}})^2} \tag{56}$$

for the incoming wave type β and outgoing wave type γ. The inner product, $\hat{\mathbf{p}}\cdot\hat{\mathbf{s}}=\cos\Theta\cos\Theta'+\sin\Theta\sin\Theta'\sin\phi'$. The integration over ϕ' in Eqs. (52)–(54) can be done in closed form. The resulting dimensionless attenuations are then

$$\alpha_{\mathrm{SH}}(\Theta)L = x_{\mathrm{SH}}^4 \frac{\eta^2}{64\rho^2 \overline{c}_{\mathrm{SH}}^4} r_{\mathrm{SH}}^3(\Theta)\sin^2\Theta \times \left[I_{\mathrm{SH-SH}} + I_{\mathrm{SH-qP}} \left(\frac{\overline{c}_{\mathrm{SH}}}{\overline{\overline{c}}_{\mathrm{qP}}} \right)^5 + I_{\mathrm{SH-qSV}} \left(\frac{\overline{c}_{\mathrm{SH}}}{\overline{\overline{c}}_{\mathrm{qSV}}} \right)^5 \right], \tag{57}$$

$$\alpha_{\mathrm{qP}}(\Theta)L = x_{\mathrm{qP}}^4 \frac{\eta^2}{64\rho^2 \overline{c}_{\mathrm{qP}}^4} r_{\mathrm{qP}}^3(\Theta)\sin^2\Theta\sin^2\gamma \times \left[I_{\mathrm{qP-SH}} \left(\frac{\overline{c}_{\mathrm{qP}}}{\overline{\overline{c}}_{\mathrm{SH}}} \right)^5 + I_{\mathrm{qP-qP}} + I_{\mathrm{qP-qSV}} \left(\frac{\overline{c}_{\mathrm{qP}}}{\overline{\overline{c}}_{\mathrm{qSV}}} \right)^5 \right], \tag{58}$$

$$\alpha_{\mathrm{qSV}}(\Theta)L = x_{\mathrm{qSV}}^4 \frac{\eta^2}{64\rho^2 \overline{c}_{\mathrm{qSV}}^4} r_{\mathrm{qSV}}^3(\Theta)\sin^2\Theta\cos^2\gamma \times \left[I_{\mathrm{qSV-SH}} \left(\frac{\overline{c}_{\mathrm{qSV}}}{\overline{\overline{c}}_{\mathrm{SH}}} \right)^5 + I_{\mathrm{qSV-qP}} \left(\frac{\overline{c}_{\mathrm{qSV}}}{\overline{\overline{c}}_{\mathrm{qP}}} \right)^5 + I_{\mathrm{qSV-qSV}} \right], \tag{59}$$

with the density, ρ, now included.

The above terms within the square brackets represent integrals which are given by the general forms

$$I_{\beta-\mathrm{SH}} = \int_0^{\pi} \frac{r_{\mathrm{SH}}^5(\Theta')X_{\beta-\mathrm{SH}}\sin^3\Theta'}{(X_{\beta-\mathrm{SH}}^2 - Y_{\beta-\mathrm{SH}}^2)^{3/2}} d\Theta',$$

$$I_{\beta-\mathrm{qP}} = \int_0^{\pi} \frac{r_{\mathrm{qP}}^5(\Theta')X_{\beta-\mathrm{qP}}\sin^2(\Theta'+\psi(\Theta'))\sin^3\Theta'}{(X_{\beta-\mathrm{qP}}^2 - Y_{\beta-\mathrm{qP}}^2)^{3/2}} d\Theta', \tag{60}$$

$$I_{\beta-\mathrm{qSV}} = \int_0^{\pi} \frac{r_{\mathrm{qSV}}^5(\Theta')X_{\beta-\mathrm{qSV}}\cos^2(\Theta'+\psi(\Theta'))\sin^3\Theta'}{(X_{\beta-\mathrm{qSV}}^2 - Y_{\beta-\mathrm{qSV}}^2)^{3/2}} d\Theta',$$

with

$$X_{\beta-\gamma} = 1 + x_\beta^2 r_\beta^2(\Theta) + x_\gamma^2 r_\gamma^2(\Theta') - 2x_\beta x_\gamma r_\beta(\Theta) r_\gamma(\Theta')\cos\Theta\cos\Theta',$$
$$Y_{\beta-\gamma} = 2x_\beta x_\gamma r_\beta(\Theta) r_\gamma(\Theta')\sin\Theta\sin\Theta', \tag{61}$$

for the different wave types, β and γ.

In the Rayleigh limit, these integrals simplify considerably. They become independent of incident direction and frequency and are given by

$$I_{\beta-\mathrm{SH}} = \int_0^{\pi} r_{\mathrm{SH}}^5(\Theta')\sin^3\Theta'\, d\Theta',$$

$$I_{\beta-\mathrm{qP}} = \int_0^{\pi} r_{\mathrm{qP}}^5(\Theta')\sin^2(\Theta'+\psi(\Theta'))\sin^3\Theta'\, d\Theta', \tag{62}$$

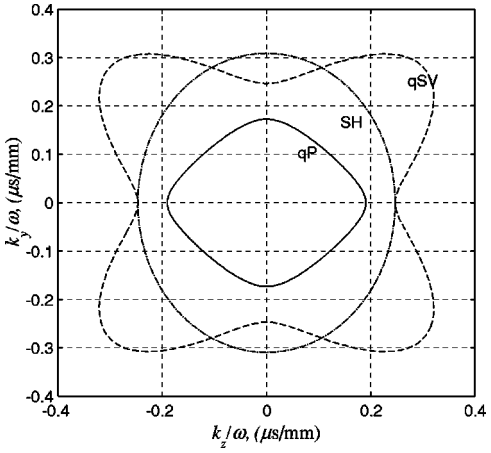

FIG. 1. Slowness surfaces for stainless steel with texture.

$$I_{\beta-\mathrm{qSV}} = \int_0^{\pi} r_{\mathrm{qSV}}^5(\Theta')\cos^2(\Theta'+\psi(\Theta'))\sin^3\Theta'\, d\Theta',$$

for all incoming wave types β. Thus, the angular dependence of the attenuations in the Rayleigh limit is seen explicitly. The attenuations are dependent upon the cube of the slowness multiplied by a factor related to the polarization type. The attenuation α_{SH} varies as $r_{\mathrm{SH}}^3(\Theta)\sin^2\Theta$, α_{qP} varies as $r_{\mathrm{qP}}^3(\Theta)\sin^2(\Theta+\psi(\Theta))\sin^2\Theta$, and α_{qSV} varies as $r_{\mathrm{qSV}}^3(\Theta)\cos^2(\Theta+\psi(\Theta))\sin^2\Theta$.

B. Results for stainless steel

Numerical results are now presented for the specific case of stainless steel with aligned [001] axes. The material properties used are[5]

$$c_{11} = 2.16\times10^{11}\ \mathrm{Pa}, \quad c_{12} = 1.45\times10^{11}\ \mathrm{Pa}, \quad c_{44} = 1.29\times10^{11}\ \mathrm{Pa}, \quad \rho = 7860\ \mathrm{kg/m^3}. \tag{63}$$

The slowness surfaces calculated using the dispersion relations for the bare medium, Eqs. (26), are shown in Fig. 1. These results agree well with those of previous authors.[5]

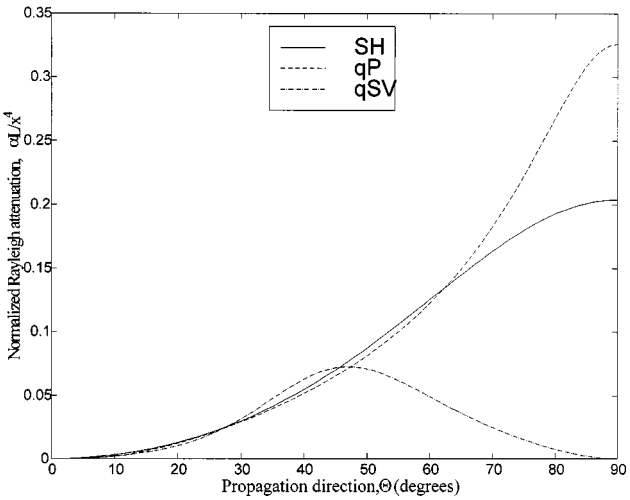

FIG. 2. Dimensionless attenuation in the Rayleigh limit as a function of direction for the SH, qP, and qSV waves. The dimensionless attenuation αL has been normalized by the fourth power of the dimensionless frequency for the respective wave type: $\alpha_{\mathrm{SH}}L/x_{\mathrm{SH}}^4$, $\alpha_{\mathrm{qP}}L/x_{\mathrm{qP}}^4$, and $\alpha_{\mathrm{qSV}}L/x_{\mathrm{qSV}}^4$.

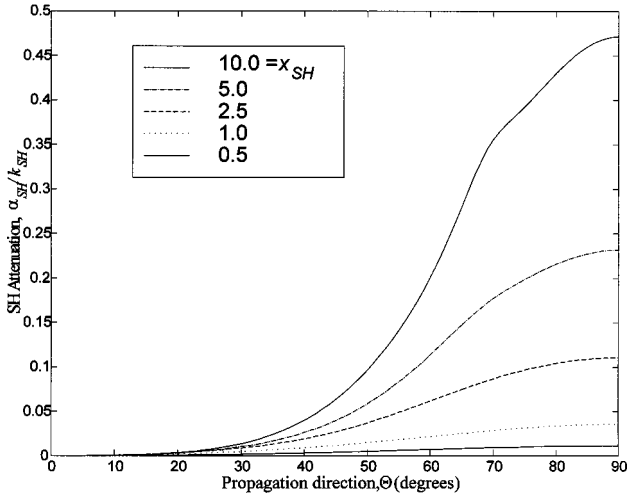

FIG. 3. Angular dependence of the normalized SH attenuation, $\alpha_{\mathrm{SH}}/k_{\mathrm{SH}}$, for various frequencies, x_{SH}.

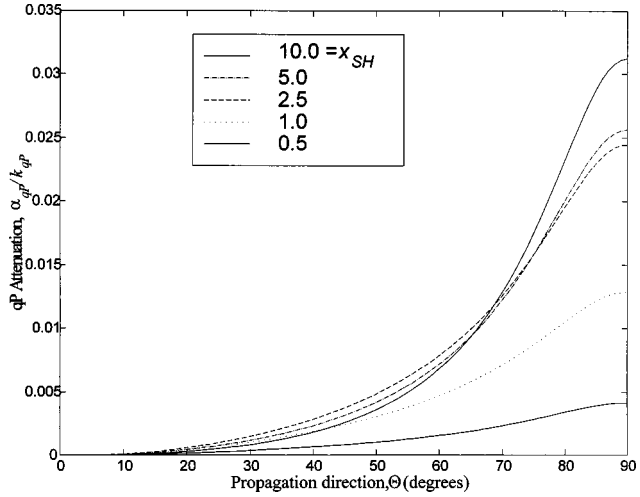

FIG. 4. Angular dependence of the normalized qP attenuation, $\alpha_{\mathrm{qP}}/k_{\mathrm{qP}}$, for various frequencies, x_{SH}.

Attenuation results, using Eqs. (57)–(59) are given in terms of the single dimensionless frequency $x_{\mathrm{SH}} = \omega L/\bar{c}_{\mathrm{SH}}$. The calculations are primarily limited to $x_{\mathrm{SH}} < 10$ corresponding to the onset of the geometric optics limit observed by Ahmed and Thompson.[5] (Their dimensionless frequency, $\chi = kd$, is based on the grain diameter. Here, this quantity contains the grain radius.) The required integrals were calculated numerically using a Newton–Cotes quadrature function *quad8* available in the software package Matlab.[17]

In the Rayleigh limit, the integrals in Eqs. (60) reduce to those given by Eqs. (62). For the case considered here, with parameters given by Eq. (63), these integrals are $I_{\beta-\mathrm{SH}} = 1.623$, $I_{\beta-\mathrm{qP}} = 1.068$, and $I_{\beta-\mathrm{qSV}} = 0.6271$. In the Rayleigh regime the attenuation depends on the fourth power of frequency. Thus, the angular dependence of the three attenuations is described by the quantity $\alpha L/x^4$. This parameter for each wave type is shown in Fig. 2. The *SH* and qP waves have their maxima perpendicular to the fiber direction. All wave types have zero attenuation in the fiber direction—the material properties do not vary in that direction. The qSV wave is seen to have zero attenuation in the fiber direction and perpendicular to the fiber direction. This result is the same as previous work.[4,5] Here, however, the same symmetry is not seen. The qSV attenuation actually peaks at 47.1° rather than 45°. The qSV attenuation greater than the peak is slightly higher than that for propagation directions below the peak as well. Thus, the inclusion of the wave polarizations through the anisotropic Green's dyadic results in slight differences from the case without.

Results outside the Rayleigh regime are calculated using the complete integrals, Eqs. (60). The directional dependence of the attenuation as a function of frequency is presented first. Figure 3 shows the normalized SH attenuation, $\alpha_{\mathrm{SH}}/k_{\mathrm{SH}}$, as a function of propagation direction for five different frequencies. These results may be contrasted with the results in the Rayleigh limit. As the frequency increases we see that the attenuation in the cross-fiber direction increases more than in other directions. The results for the normalized qP attenuation, $\alpha_{\mathrm{qP}}/k_{\mathrm{qP}}$, are shown in Fig. 4. These results are similar to the SH attenuation. The cross-fiber attenuation increases more rapidly than other directions as the frequency increases. Similar results were seen by Hirsekorn[4] and Ahmed and Thompson.[5]

The normalized qSV attenuation, $\alpha_{\mathrm{qSV}}/k_{\mathrm{qSV}}$, is shown in Fig. 5 at the same frequencies as Figs. 3 and 4. The attenuation in the fiber and cross-fiber directions is zero as expected from the form of the modulus fluctuations. The direction of maximum α_{qSV}, as observed in Fig. 5, is seen to be a function of frequency. This result is shown more explicitly in Fig. 6 in which the direction of maximum α_{qSV} is plotted versus x_{SH}. This direction is 47.1° in the Rayleigh limit as was seen in Fig. 2. The direction of maximum α_{qSV} then increases with increasing frequency. The peak in this maximum occurs at a frequency of about $x_{\mathrm{SH}} = 1.8$ at an angle of 51.8°. The direction of maximum α_{qSV} then decreases for larger values of x_{SH}. The result presented here differs from that presented by Ahmed and Thompson.[5] Their maximum α_{qSV} occurs at 45° in the Rayleigh regime. At higher frequencies they noted an increase in the angle of maximum α_{qSV}, although the shift from 45° is not as dra-

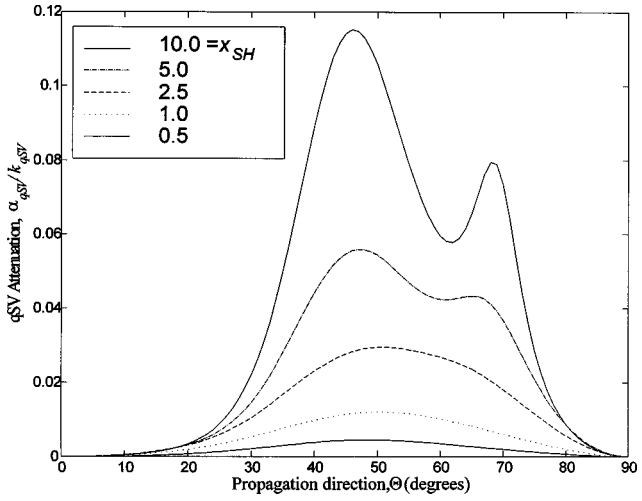

FIG. 5. Angular dependence of the normalized qSV attenuation, $\alpha_{\mathrm{qSV}}/k_{\mathrm{qSV}}$, for various frequencies, x_{SH}.

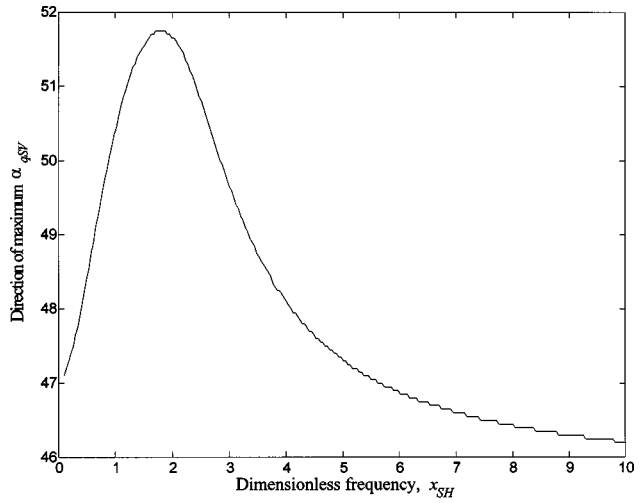

FIG. 6. Direction of maximum qSV attenuation as a function of frequency, x_{SH}. This angle is about 47.1° in the low-frequency limit, peaks at about 51.8° at $x_{\mathrm{SH}}=1.8$ and then decreases for higher frequencies.

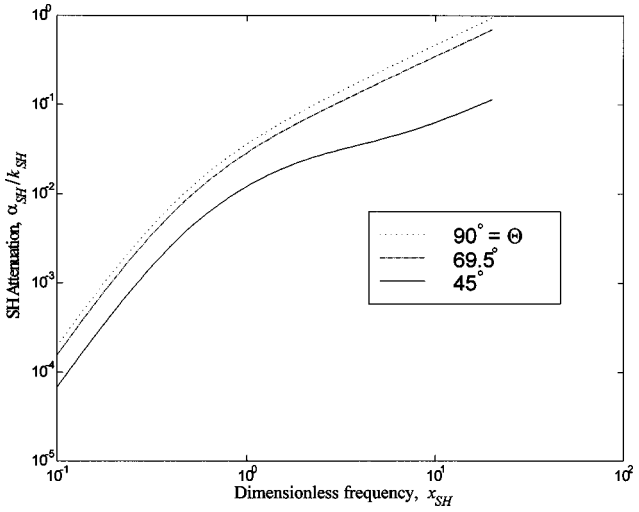

FIG. 7. Normalized SH attenuation, $\alpha_{\mathrm{SH}}/k_{\mathrm{SH}}$, as a function of dimensionless frequency, x_{SH}, for propagation directions of 45°, 69.5°, and 90°.

matic as that seen here. This difference is also attributed to the inclusion of polarization direction in the present results.

The appearance of the additional peak in the SV attenuation at about 69° is observed. The presence of such a peak at the same angle was also observed by Ahmed and Thompson. They suggested that this phenomenon was related to the stochastic-geometric transition. However, the presence of this peak in the present results shows that this is not the case—the above derivation is limited to frequencies excluding the high-frequency geometric limit. The above forms of the attenuation allow this phenomenon to be examined more closely. The integrals $I_{\mathrm{SH-qSV}}$ and $I_{\mathrm{qSV-SH}}$ in the equations for attenuation, Eqs. (60), have peaks at about 69°. This peak is the result of the form of the spatial correlation function between the SH and qSV modes. The term $X_{\mathrm{SH-qSV}}(X^2_{\mathrm{SH-qSV}}-Y^2_{\mathrm{SH-qSV}})^{-3/2}$ determines the specific direction of this peak and is a function of the angular phase velocities and propagation direction. Closer examination shows that this peak occurs at the angle corresponding to the intersection of the SH and qSV slowness surfaces of 69.3°. The appearance of a similar peak is seen in the angular plot of SH attenuation, Fig. 3, at $x_{\mathrm{SH}}=10$.

Finally, results are presented for the normalized attenuations as a function of frequency for several propagation directions. In Figs. 7 and 8 the normalized SH and qP attenuations are plotted versus dimensionless frequency, x_{SH}, for propagation directions of 45°, 69.5°, and 90°. The SH attenuation in the cross-fiber direction is seen to increase more rapidly than other directions for increasing frequency. The qP attenuation has a local maximum which is a function of propagation direction. Similar results were given by Ahmed and Thompson.[5] The normalized qSV attenuation is plotted versus frequency, x_{SH}, for propagation directions of 45° and 69.5° in Fig. 9. The attenuation at 69.5° increases more rapidly than that at 45°. However, at higher frequencies the ratio between the two appears to be constant. Thus, the peak at 69.5° observed in the angular plots, Fig. 5, is not expected to become larger than that of 45°, within the frequency limits used here.

V. DISCUSSION

The propagation and scattering of elastic waves in heterogeneous, anisotropic media has been examined. Appropriate ensemble averaging of the elastic wave equation resulted in the Dyson equation, governing the mean field. The problem was further specified for the case of transverse isotropy. The Green's dyadic for a transversely isotropic medium was used to derive expressions for the attenuation of the shear horizontal, quasicompressional, and quasishear waves. The covariance of moduli fluctuations were determined in coordinate-free form for cubic polycrystalline materials with aligned [001] axes. The final forms of the attenuations for the three wave types were given by simple expressions involving integrations over the unit circle. The integrands are dependent upon inner products on the convariance of modulus fluctuations and factors of phase velocity. The simple form of the results makes them particularly useful for nondestructive testing and materials characterization research and for inclusion of attenuation in numerical models of elastic wave propagation such as those by Spies.[14,18,19] The results pre-

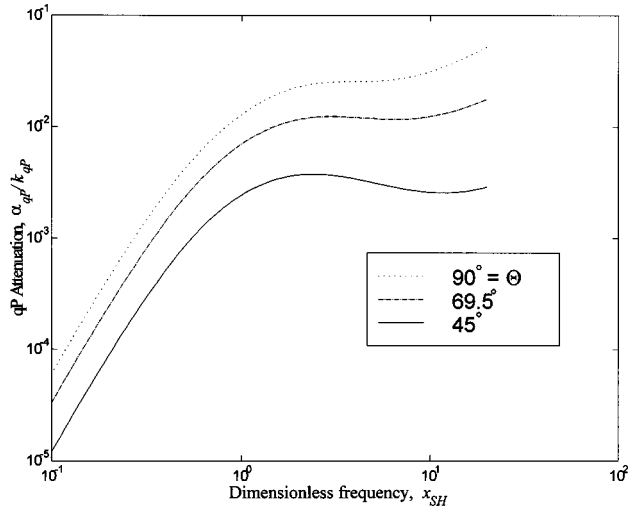

FIG. 8. Normalized qP attenuation, $\alpha_{\mathrm{qP}}/k_{\mathrm{qP}}$, as a function of dimensionless frequency, x_{SH}, for propagation directions of 45°, 69.5°, and 90°.

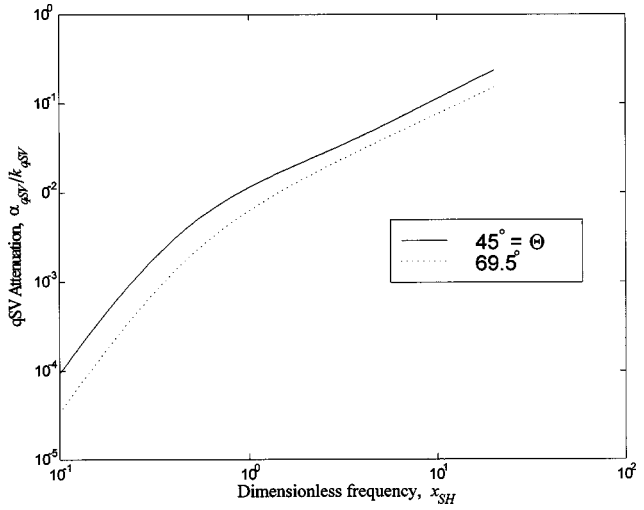

FIG. 9. Normalized qSV attenuation, $\alpha_{\mathrm{qSV}}/k_{\mathrm{qSV}}$, as a function of dimensionless frequency, x_{SH}, for propagation directions of 45° and 69.5°. The attenuation at 69.5° is initially much smaller than that at 45°. It then increases more quickly than that at 45°. The ratio between the two appears to then be constant at higher frequencies.

sented here are also directly related to diffuse field methods such as backscatter techniques. In addition, the above formalism holds for other forms of global anisotropy. The bare Green's dyadic may be expanded in a similar fashion. The main difficulty will then lie in the determination of the form of the covariance of elastic moduli fluctuations.

ACKNOWLEDGMENTS

The Alexander von Humboldt Foundation and the Fraunhofer-Institut für zerstörungsfreie Prüfverfahren (IzfP), in Saarbrücken, Germany are both gratefully acknowledged for support during a portion of this work. The author also thanks M. Spies for conversations regarding this work.

[1] F. E. Stanke and G. S. Kino, ''A unified theory for elastic wave propagation in polycrystalline materials,'' J. Acoust. Soc. Am. **75**, 665–681 (1984).

[2] F. C. Karal and J. B Keller, ''Elastic, electromagnetic, and other waves in a random medium,'' J. Math. Phys. **5**, 537–547 (1964).

[3] S. Hirsekorn, ''The scattering of ultrasonic waves in polycrystalline materials with texture,'' J. Acoust. Soc. Am. **77**, 832–843 (1985).

[4] S. Hirsekorn, ''Directional dependence of ultrasonic propagation in textured polycrystals,'' J. Acoust. Soc. Am. **79**, 1269–1279 (1986).

[5] S. Ahmed and R. B. Thompson, ''Propagation of elastic waves in equiaxed stainless-steel polycrystals with aligned [001] axes,'' J. Acoust. Soc. Am. **99**, 2086–2096 (1996).

[6] S. Ahmed and R. B. Thompson, in *Effects of Preferred Grain Orientation and Grain Elongation on Ultrasonic Wave Propagation in Stainless Steel*, edited by D. O. Thompson and D. E. Chimenti (Plenum, New York, 1992), Vol. 11B, pp. 1999–2006.

[7] S. Ahmed and R. B. Thompson, ''Influence of Columnar Microstructure on Ultrasonic Backscattering,'' in *Review of Progress in QNDE*, edited by D. O. Thompson and D. E. Chimenti (Plenum, New York, 1995), Vol. 14, pp. 1617–1624.

[8] E. M. Lifshits and G. D. Parkhamovski, Zh. Eksp. Teor. Fiz. **20**, 175–182 (1950).

[9] U. Frisch, ''Wave Propagation in Random Media,'' in *Probalistic Methods in Applied Mathematics*, edited by A. T. Barucha-Reid (Academic, New York, 1968), Vol. 1, pp. 75–198.

[10] R. L. Weaver, ''Diffusion of Ultrasound in Polycrystals,'' J. Mech. Phys. Solids **38**, 55–86 (1990).

[11] J. A. Turner and R. L. Weaver, ''Radiative transfer and multiple scattering of diffuse ultrasound in polycrystalline media,'' J. Acoust. Soc. Am. **96**, 3675–3683 (1994).

[12] J. A. Turner and R. L. Weaver, ''Time dependence of multiply scattered diffuse ultrasound in polycrystalline media,'' J. Acoust. Soc. Am. **973**, 2639–2644 (1995).

[13] J. A. Turner and R. L. Weaver, ''Ultrasonic radiative transfer theory: Effects of a fluid–solid interface,'' J. Acoust. Soc. Am. **98**, 2801–2808 (1995).

[14] M. Spies, ''Elastic waves in homogeneous and layered transversely isotropic media: Plane waves and Gaussian wave packets. A general approach,'' J. Acoust. Soc. Am. **95**, 1748–1760 (1994).

[15] F. I. Fedorov, *Theory of Elastic Waves in Crystals* (Plenum, New York, 1968).

[16] J. A. Turner, ''Elastic wave propagation and scattering in heterogeneous, anisotropic media: Textured polycrystalline materials,'' Dept. of Engineering Mechanics Technical Report EM1.998 (September 1998).

[17] Matlab, *The Language of Technical Computing* (The Math Works, Natick, MA, 1996).

[18] M. Spies, ''Elastic wave propagation in general transversely isotropic media. I. Green's functions and elastodynamic holography,'' J. Acoust. Soc. Am. **96**, 1144–1157 (1994).

[19] M. Spies, ''Elastic wave propagation in transversely isotropic media. II. The generalized Rayleigh function and an integral representation for the transducer field. Theory,'' J. Acoust. Soc. Am. **97**, 1–13 (1995).

Anderson (1950) revisited

C. Feuillade
Naval Research Laboratory, Stennis Space Center, Mississippi 39529-5004

C. S. Clay
Geophysical and Polar Research Center, University of Wisconsin-Madison, 1215 West Dayton Street, Madison, Wisconsin 53706

(Received 5 November 1998; accepted for publication 5 May 1999)

The Anderson fluid sphere scattering model [J. Acoust. Soc. Am. **22**, 426–431 (1950)] is reexamined to clarify three issues which have been the source of misunderstanding among underwater acousticians. First, the accuracy of the Morse large range approximation for the spherical Hankel functions is investigated. It is shown that the minimum range for use of the approximation is strongly mode number dependent, and should be carefully evaluated in short range and/or high frequency applications. Second, the precise characterization of the forward scatter region is studied. When the scattered field and the incident plane wave are combined, it is shown that little advantage is obtained in detection and localization applications by using forward scattering, rather than backscattering. Third, the translational response, or ''rebound,'' of the sphere under the action of the incident field is examined. By demonstrating that Anderson's theory is a limiting case of Faran's scattering model [J. Acoust. Soc. Am. **23**, 405–418 (1951)] for an elastic sphere, which contains the rebound response, it is shown that the response is completely explainable within Anderson's theory, and is consistent with a description which uses a normal mode expansion around a fixed origin. © *1999 Acoustical Society of America.* [S0001-4966(99)05808-7]

PACS numbers: 43.20.Fn, 43.20.Ks, 43.30.Gv [DLB]

INTRODUCTION

Many objects of interest to the marine acoustician are characterized well by spherical forms. For this reason, the radiation and scattering of sound from spheres has attained great importance, and has been closely studied. A general method for determining the acoustic behavior of spheres is offered by the axially symmetric spherical mode solution, as described by Morse.[1a] This basic approach has provided the starting point for many investigations in underwater sound, including the properties of transducers, mines, shells, bubbles, and biological organisms. An updated overview of the theory, together with several of the more important applications, has recently been presented by Medwin and Clay.[2a]

In 1950, Anderson[3] published a study of sound scattering by a fluid-filled sphere entrained within a fluid. In what has since become a classic and seminal paper, he represented the spherical mode method in an elegant form which is particularly amenable to several important underwater acoustics applications, and convenient for numerical computations. For instance, the ability to independently vary the density and sound speed in the internal and external fluids allows his theory to be used successfully to describe scattering from water-entrained objects as different, e.g., as air bubbles (high contrast),[2b] and zooplankton (low contrast),[4] over a broad frequency range.

The concepts and results of Anderson's paper have rightfully become accepted currency among underwater acousticians; but some aspects of his work can easily be misunderstood, particularly in relation to some currently emerging transmission, detection and multiple scattering applications. After almost half a century it seems timely and reasonable to reexamine Anderson's theoretical-numerical methodology, in order to elucidate the remaining difficulties and, thereby, avoid potentially serious errors.

Specifically, in this present paper, we use new numerical calculations to explore three issues arising from Anderson's work. First, we investigate the accuracy of the Morse approximation for the spherical Bessel and Neumann functions,[1b] which was used to convert the sum on partial waves or modes to the large range approximation and thereby determine the scattering length or form function. In applications, for instance, where the purpose is to find the backscattered target strength of a single remotely located object, such that the incident field is a plane wave and the scattered field is calculated at large range, the Morse approximation is quite good. However, if an accurate determination of the scattered field close to the object is needed, as, for example, in the investigation we present here of the actual pressure fields in the forward scatter region when the incident wave is included, then it becomes necessary to use the correct analytical forms for the Bessel and Neumann functions. In the forward direction, Anderson states: ''... the quantity R_θ [i.e., the scattering length] does not give directly the diffraction pattern due to a spherical obstacle; it represents only the pressure amplitude in the spherically scattered wave and must be combined with the incident plane wave to give the true diffraction pattern.'' He recognizes that the incident and diffracted waves must be coherently summed to give the true pressure field behind the object. This operation requires accurate phases and amplitudes for the diffracted wave and the incident plane wave. This issue also arises when it becomes necessary to correctly incorporate radiative interactions between many closely spaced objects in multiple

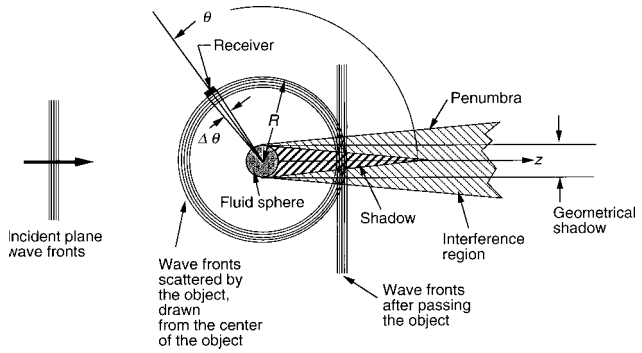

FIG. 1. Scattering geometry. This cartoon depicts a plane wave, traveling in the $+z$ direction, incident upon a fluid sphere (radius a, density ρ_1 and sound speed c_1), entrained in a second fluid (density ρ, sound speed c). For simplicity, the scattered waves are shown as spherical, which they are in time, although not generally in phase and amplitude. In the forward region, the scattered field and incident field interfere, and may produce a shadow. (This figure is adapted from Fig. 7.1.1, Medwin and Clay, Ref. 2.)

scattering problems. We show that the minimum range for use of the approximation is strongly mode number dependent, and should be carefully evaluated in short range and/or high frequency applications.

The second issue we investigate in this paper is the precise characterization of the forward-scatter region. The necessity of combining the forward-scattered field and the incident plane wave is easily overlooked, and this mistake often results in the misleading impression that there is a very large forward scattered field due to the diffracted component alone. Contrarily, the forward diffracted component and the incident field actually add coherently to create a ''shadow'' or ''null'' region. What physically happens can be understood by thinking about how experimental measurements of directional sound scatter would be made. For example, let a transmitter transmit a ping towards the scatterer (see Fig. 1). Then, simple time domain measurements could be used to separate the scattered sound from the incident ping when they do not arrive at the same time. As the receiver is moved from the back-scatter direction into the forward-scatter direction, the scattered sound and incident ping would arrive at nearly the same time, so that the two waves interfere. If one were to use very long pings, or continuous wave transmissions and a directional receiver, the receiving transducer would have to be large relative to the wavelength. The transducer would average the diffracted components over the angles subtended by the transducer. For incident plane waves, the amplitude of the incident field does not change with range. However, to a reasonable approximation, the amplitude of the scattered sound waves decreases in proportion to the inverse range from the sphere. Since the total sound pressure outside the sphere is the sum of the incident and scattered sound, at very large ranges in the forward direction the sound pressure tends to the incident plane wave field. Close to the sphere, the sum of the incident and scattered waves give a representation of the shadow region. Actually, large objects and very short wavelengths are required to display a proper shadow. We show that the depth of the shadow region is also strongly dependent upon the density and sound speed ratios between the two fluids.

The third issue we examine in this paper is the question of the translational response, or ''rebound,'' of the sphere as it is bodily displaced by the action of the incident field. In his paper, Anderson represented scattering from a fixed rigid sphere by allowing the density and sound speed ratios between the inner and outer fluids to approach infinity. The sphere is described as ''fixed'' because, when its density is made infinitely large, it becomes too inertially massive to move in response to the incident field. Clearly, the scattering behavior in this case is of limited interest, since it is not representative of any physical object likely to be found in the marine environment. In 1965, Hickling and Wang[5] determined the scattering response of a rigid movable sphere, which allowed the behavior of rigid objects of finite density to be described. The essential difference between their theory and that of Anderson occurs in the scattering coefficient for the dipole term. Apparently, it is the dipole component of the incident field which induces the translational motion of the sphere, and this must be properly incorporated into the theory in order to correctly prescribe the physical behavior. The apparent failure of Anderson's theory to completely specify the scattering coefficient for the dipole term for the rigid sphere case has, subsequently, led to some confusion as to whether it gives a sufficient description of the translational response for the general fluid sphere case itself. A question is sometimes posed in the following manner: ''If the sphere moves, as a whole, in reaction to the incident field; can its behavior then be accurately described in terms of normal modes expanded around a fixed origin?'' In this paper we show that concerns about the adequacy of Anderson's theory to describe the fluid sphere case are unfounded. We demonstrate that both Anderson's theory, and that of Hickling and Wang, are limiting cases of a more general theory, i.e., that of Faran[6] for the scattering response of an elastic sphere. Since Faran's theory can be shown to incorporate the translational response mechanism, then Anderson's theory contains it also. We also show, by examination of the variable radial displacement at the surface of a fluid sphere, that the translational body response is completely explainable within Anderson's theory, and that it is therefore perfectly consistent with a description which uses a normal mode expansion around a fixed origin.

In Sec. I of this paper we present a short statement of Anderson's fluid sphere theory. Section II is a study of the Morse approximation for the spherical Hankel functions. In Sec. III we discuss the total pressure field around the sphere, and especially the behavior in the forward scatter direction. Section IV considers the translational response question. This is followed by a summary of conclusions.

I. BASIC EQUATIONS AND GEOMETRY

The theory for describing scattering by a fluid sphere is given by Anderson,[3] and may also be found in Medwin and Clay.[2c] We will present only a brief recapitulation here and will, for convenience, assume that the incident field is propagating in the $+z$ direction.[7] The measurement geometry for axially symmetric sound scatter is indicated in Fig. 1. The fluid surrounding the sphere has density ρ, sound speed c; and the propagation wave number $k=\omega/c$, where ω is the

angular frequency of the incident field. The fluid sphere has density ρ_1, sound speed c_1; and the wave number $k_1 = \omega/c_1$. The ratios of these parameters are expressed using g and h as follows:

$$g=\frac{\rho_1}{\rho}, \quad h=\frac{c_1}{c}, \quad \text{and} \quad k_1=\frac{k}{h}. \tag{1}$$

The solutions are expressed in terms of spherical normal modes consisting of products of Legendre polynomials (P_m) and spherical Bessel (j_m) and spherical Neumann (n_m) functions, e.g.,

$$P_m(\mu)[j_m(kR)+in_m(kR)], \tag{2}$$

where $\mu=\cos\theta$. Due to the axial symmetry, there is no ϕ dependence. An incident plane wave traveling in the $+z$ direction (such that the backscatter is seen at $\theta=\pi$) is written

$$p_{\text{inc}}=P_{\text{inc}}e^{i(kz-\omega t)}$$

$$=P_{\text{inc}}\sum_{m=0}^{\infty} i^m(2m+1)\,P_m(\mu)\,j_m(kR)\,e^{-i\omega t}, \tag{3}$$

where P_{inc} is the sound pressure amplitude factor, and $\cos\theta=z/R$. The pressure field inside the sphere ($R\leqslant a$) is written

$$p_{\text{int}}=\sum_{m=0}^{\infty} B_m\,P_m(\mu)\,j_m(k_1R)\,e^{-i\omega t}, \tag{4}$$

and the scattered pressure ($R>a$) is written

$$p_{\text{scat}}=\sum_{m=0}^{\infty} A_m\,P_m(\mu)\,[j_m(kR)+in_m(kR)]\,e^{-i\omega t}. \tag{5}$$

Two boundary conditions are satisfied at the surface of the sphere ($R=a$): (a) the continuity of pressure; and (b) the continuity of the radial component of particle velocity, which is given by

$$u_R=\frac{-i}{\rho c}\frac{\partial p}{\partial(kR)}. \tag{6}$$

Application of these two boundary conditions at the surface of the sphere allows the coefficients A_m and B_m to be calculated. For each mode, evaluation at $R=a$ leads to a pair of equations:

$$P_{\text{inc}}i^m(2m+1)\,j_m(ka)+A_m\,h_m(ka)=B_m\,j_m(k_1a);$$

$$\frac{1}{\rho c}[P_{\text{inc}}i^m(2m+1)\,j_m'(ka)+A_m\,h_m'(ka)]=\frac{B_m}{\rho_1c_1}\,j_m'(k_1a),$$

where h_m is the spherical Hankel function of the first kind defined by

$$h_m(kR)=j_m(kR)+in_m(kR). \tag{7}$$

The parameters may be rearranged by defining

$$A_m=-P_{\text{inc}}i^m(2m+1)\,D_m; \tag{8a}$$

$$B_m=-P_{\text{inc}}i^m(2m+1)\,E_m, \tag{8b}$$

so that D_m and E_m are given by

$$D_m=\frac{j_m'(k_1a)j_m(ka)-gh\,j_m(k_1a)j_m'(ka)}{j_m'(k_1a)h_m(ka)-gh\,j_m(k_1a)h_m'(ka)}; \tag{9a}$$

$$E_m=\frac{gh[h_m'(ka)j_m(ka)-h_m(ka)j_m'(ka)]}{j_m'(k_1a)h_m(ka)-gh\,j_m(k_1a)h_m'(ka)}. \tag{9b}$$

Substituting A_m from Eq. (8a) into Eq. (5) gives an expression for p_{scat}, i.e.,

$$p_{\text{scat}}=-P_{\text{inc}}\sum_{m=0}^{\infty} i^m(2m+1)D_mP_m(\mu)h_m(kR)e^{-i\omega t}, \tag{10}$$

which is the general partial wave solution (for all kR, $R>a$) describing acoustic scattering by a fluid sphere in a fluid medium. Anderson represents scattering from a rigid sphere by letting gh in Eq. (9a) become infinite. Scattering from a gas-filled sphere is described by letting the density ρ_1 and the sound speed c_1 be those of the gas at its local pressure and temperature. The scattering parameters for the partial waves, and the range-dependent spherical Hankel functions, are products in the summation. An approximation is needed to write the summation as the product of a range-dependent term and a summation of the scattering parameters.

The total acoustic field external to the sphere, p_{tot}, is given exactly by the sum of the incident field p_{inc} [Eq. (3)] and the scattered field p_{scat} [Eq. (10)], i.e.,

$$p_{\text{tot}}=p_{\text{inc}}+p_{\text{scat}}$$

$$=P_{\text{inc}}\sum_{m=0}^{\infty} i^m(2m+1)P_m(\mu)[j_m(kR)$$

$$-D_mh_m(kR)]e^{-i\omega t}. \tag{11}$$

We will be particularly interested later in the behavior of p_{tot} in the forward scatter direction.

Substituting B_m from Eq. (8b) into Eq. (4) gives the solution for the internal field in the sphere for all k_1R, $R\leqslant a$:

$$p_{\text{int}}=-P_{\text{inc}}\sum_{m=0}^{\infty} i^m(2m+1)E_m\,P_m(\mu)\,j_m(k_1R)e^{-i\omega t}. \tag{12}$$

This expression will be used later, in combination with Eq. (6), when we investigate the translational response of the sphere under the action of the incident field.

II. THE MORSE LARGE RANGE APPROXIMATION FOR THE SPHERICAL HANKEL FUNCTIONS

The range dependence is usually factored out of the general summation Eq. (10) for very large ratios of R/a by using Morse's Hankel function approximation for kR tending to infinity.[1b] Morse's approximation for the spherical Bessel and Neumann functions is

$$\text{for } kR\gg 1, \quad j_m(kR)\to\frac{1}{kR}\cos\left[kR-\frac{(m+1)\pi}{2}\right];$$

$$\text{for } kR\gg 1, \quad n_m(kR)\to\frac{1}{kR}\sin\left[kR-\frac{(m+1)\pi}{2}\right], \tag{13}$$

so that

$$i^m h_m(kR) \approx \frac{i^m}{kR} e^{i[kR-(m+1)\pi/2]} = \frac{-i}{kR} e^{ikR}. \quad (14)$$

The substitution of Eq. (14) into Eq. (10) gives the familiar form of the separated scattering equation for the sound pressure at range R, i.e.,

$$p_{\text{scat}} = P_{\text{inc}} \frac{i}{kR} e^{i(kR-\omega t)} \sum_{m=0}^{\infty} P_m(\mu)(2m+1)D_m. \quad (15)$$

This form of the scattering equation can be written as the product of a scattering length and the incident pressure at the sphere:

$$p_{\text{scat}} = P_{\text{inc}} \frac{1}{R} e^{i(kR-\omega t)} \mathscr{L}, \quad (16)$$

where the acoustic scattering length, $\mathscr{L}$, is given by

$$\mathscr{L} = \frac{ia}{ka} \sum_{m=0}^{M-1} P_m(\mu)(2m+1)D_m, \quad (17)$$

and $M \geqslant ka+3$. The scattering length is also commonly expressed as the ''form function''

$$F_\infty(ka) = |\mathscr{L}|/(a/2), \quad (18)$$

or in terms of the scattering cross section, i.e.,

$$\Delta\sigma_{bs} = |\mathscr{L}|^2. \quad (19)$$

Accurate phases and amplitudes are needed for computations of single scattering, and of multiple scattering from an array of spheres. Our purpose here is to compare the exact Hankel function (via the Bessel and Neumann functions) and the Morse large kR approximation. The approximation is best for low modes, because the condition, ''large'' kR, depends on the mode number. For example, Eq. (14) is exact for $m=0$. Figure 2(a) compares the exact $j_1(kR)$ and $n_1(kR)$ with their Morse approximations for $m=1$. The errors are small for $kR>3$, indicating that the approximation should, in most cases, be good for low mode scattering calculations. The results for $m=5$ [Figs. 2(b) and 2(c)] show that the envelopes of the amplitudes of the exact and approximate $j_5(kR)$ and $n_5(kR)$ are about the same. However, the phases of the exact $j_5(kR)$ and $n_5(kR)$ differ from those predicted by their corresponding approximations. The phase difference decreases as kR increases. Further trials (results not shown) at $m=0$, 1, 5, and 10, indicate that $kR>5m$ prescribes a reasonable lower kR limit for application of the approximation. In the summations contained in Eqs. (10) and (12), the modes are added coherently, and the phase differences between the modes are important. The Morse approximation is used to write the familiar sonar scattering equations [Eqs. (15)–(19)]. The computations of the exact Bessel and Neumann functions here, and all those used in the examples discussed below, were performed using the double precision intrinsic Bessel and Neumann function routines of MATLAB.

III. TOTAL PRESSURE FIELD AROUND A SPHERE

In the acoustics literature the common practice, over many years, has been to graphically depict the angular and

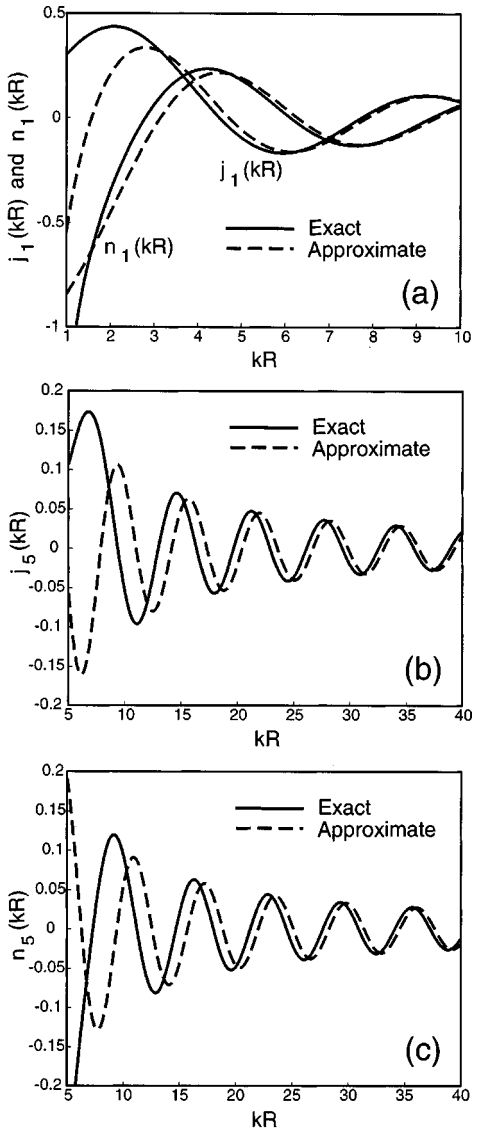

FIG. 2. Comparisons of exact and approximate Hankel functions. The approximate functions are from Morse (Ref. 1, p. 317). $h_m(kR)=j_m(kR)+in_m(kR)$. (a) $j_1(kR)$ and $n_1(kR)$ Exact solid line and approximate dashed line. (b) $j_5(kR)$ Exact solid line and approximate dashed line. (c) $n_5(kR)$ Exact solid line and approximate dashed line.

frequency variations of the scattered field *independently of the incident field* by means of the form function (see, for example, Fig. 80 of Ref. 1, and Figs. 7.5.5 and 7.5.6 of Ref. 2). As a result, the fact that the observed acoustic field external to a scattering object is actually the coherent sum of the incident and scattered components is sometimes overlooked. For incidence frequencies greater than $ka \sim 1-2$, spheres of all acoustic compositions typically begin to scatter more sound in the forward direction than in the backward direction. At higher frequencies, the forward scattering lobe becomes very strongly pronounced, and it is quite easy to get the mistaken impression that there may be considerable advantages obtained by using forward scatter, rather than backscatter, for various detection and localization applications. In fact, the full character of the acoustic field in the forward direction is much less simple, and can only be properly understood and quantified in terms of the coherent summation

of the forward scattered field and the incident field, which varies both with the acoustic properties of the sphere and with frequency. To investigate this issue, we present results here for three types of scatterers. The first two cases are high contrast objects, i.e., a fixed rigid sphere and an air bubble in water. The third case is a low contrast sphere.

A. Fixed rigid sphere

In Anderson's paper, scattering from a fixed rigid sphere is represented by allowing the ratios g and h [Eq. (1)] to approach infinity. In this case, the coefficients D_m [Eq. (9a)] appearing in the expansion Eq. (10) for the scattered field have the following asymptotic form:

$$D_m \underset{g,h\to\infty}{\to} \frac{j_m'(ka)}{h_m'(ka)}. \tag{20}$$

Figure 3(a) shows the angular variation of the resulting form function Eq. (18) for a fixed rigid sphere for $ka=20$. The strong lobe in the forward scatter direction ($+z$ axis) is clearly seen. Figure 3(b) is a 2-D gray scale plot showing the amplitude of the scattered pressure field [derived from Eq. (10), with $P_{\text{inc}}=1$] for the same case. Again, the high degree of forward scatter is quite evident, with the amplitude at some points along the $+z$ axis attaining values more than twice that of the incident field. Figure 3(c) is a 2-D gray scale plot of the amplitude of the total pressure field [this time derived from Eq. (11), again with $P_{\text{inc}}=1$] for the same case. The gray scale range is identical for both Fig. 3(b) and (c). Comparison of Fig. 3(b) and (c) shows that the incident field and the scattered field combine in the forward direction in such a way as to produce a total field with a significantly smaller maximum amplitude than that observed for the scattered field alone. The total field amplitude decreases with range, so that at only 10 radii from the sphere along the $+z$ axis, the amplitude is only slightly greater than that of the incident field. Its angular variation is also very rapid. For $\theta \sim$ a few degrees from the $+z$ axis, the total field amplitude falls well below that of the incident field, and it then oscillates minimally about the incident field value as a function of angle.

How do the scattered field and the total field vary as a function of frequency? Figure 4(a)–(f) shows: (a) the variation of the total field amplitude along the $+z$ axis (solid line); (b) the variation of the forward scatter field amplitude along the $+z$ axis (dashed line); (c) the variation of the backscatter field amplitude along the $-z$ axis (but plotted along the same axis with the other curves, for comparison: dot-dashed line), for frequencies $ka=1$, 5, 10, 20, 40, and 80. (Note also, in Fig. 4, the logarithmic scale in range, which extends to 1000 radii; the variable amplitude scale; and the dotted lines, which represent the amplitude of the incident field, i.e., unity.) For $ka=1$, the forward and backscatter amplitudes decrease at about the same rate with range, both reaching zero at about 100 radii. The forward scatter field combines constructively with the incident field to produce a small enhancement of the total field along the $+z$ axis, which again disappears beyond about 100 radii. When the frequency is increased to $ka=5$, the forward scatter field

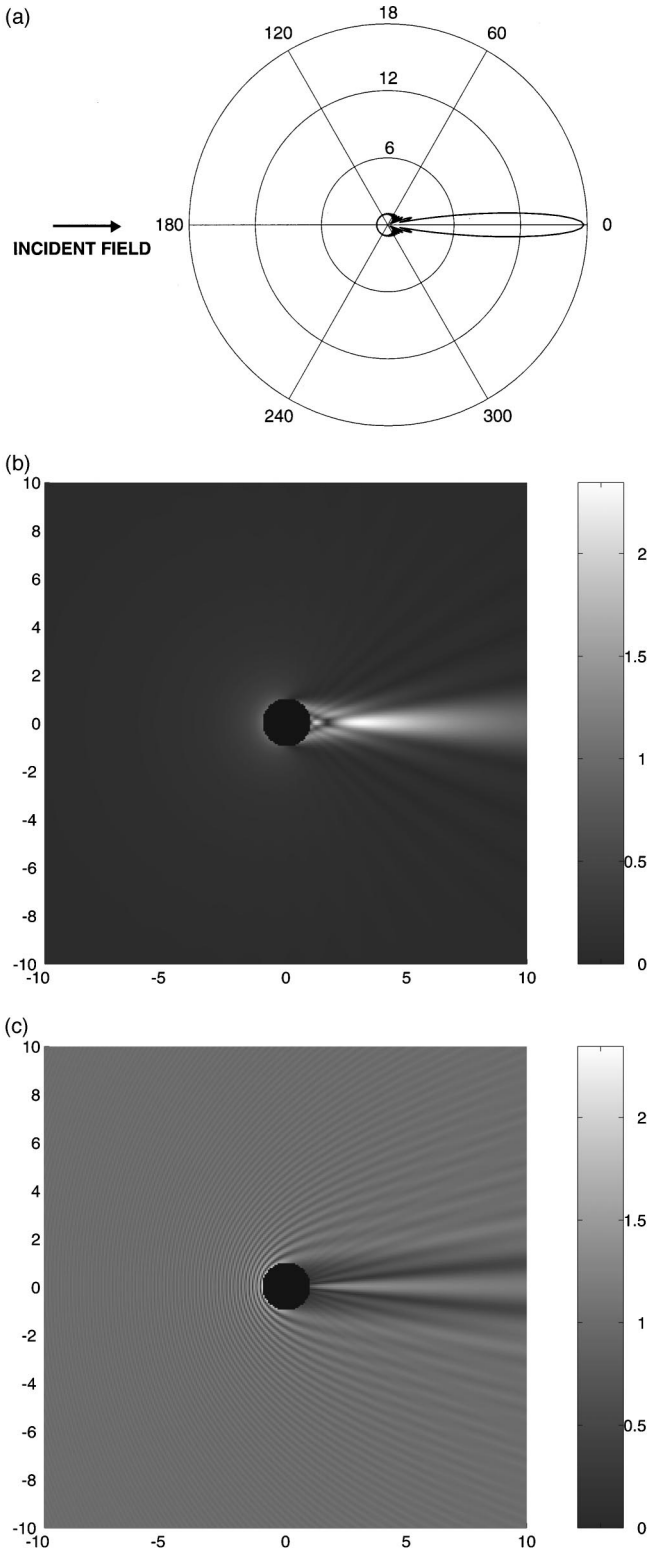

FIG. 3. Scatter from a fixed rigid sphere, as a function of direction, for $ka=20$. (a) Conventional form function. (b) Gray scale plot of the scattered field amplitude only. The external field is incident from the left. The x and y axes in the plot denote distance from the center of the sphere, scaled in radii. (c) Gray scale plot of the total field amplitude.

begins to predominate over the backscatter, and combines with the incident field to produce a slightly stronger enhancement of the total field along the $+z$ axis. As the frequency is further increased, two main trends may be discerned. First,

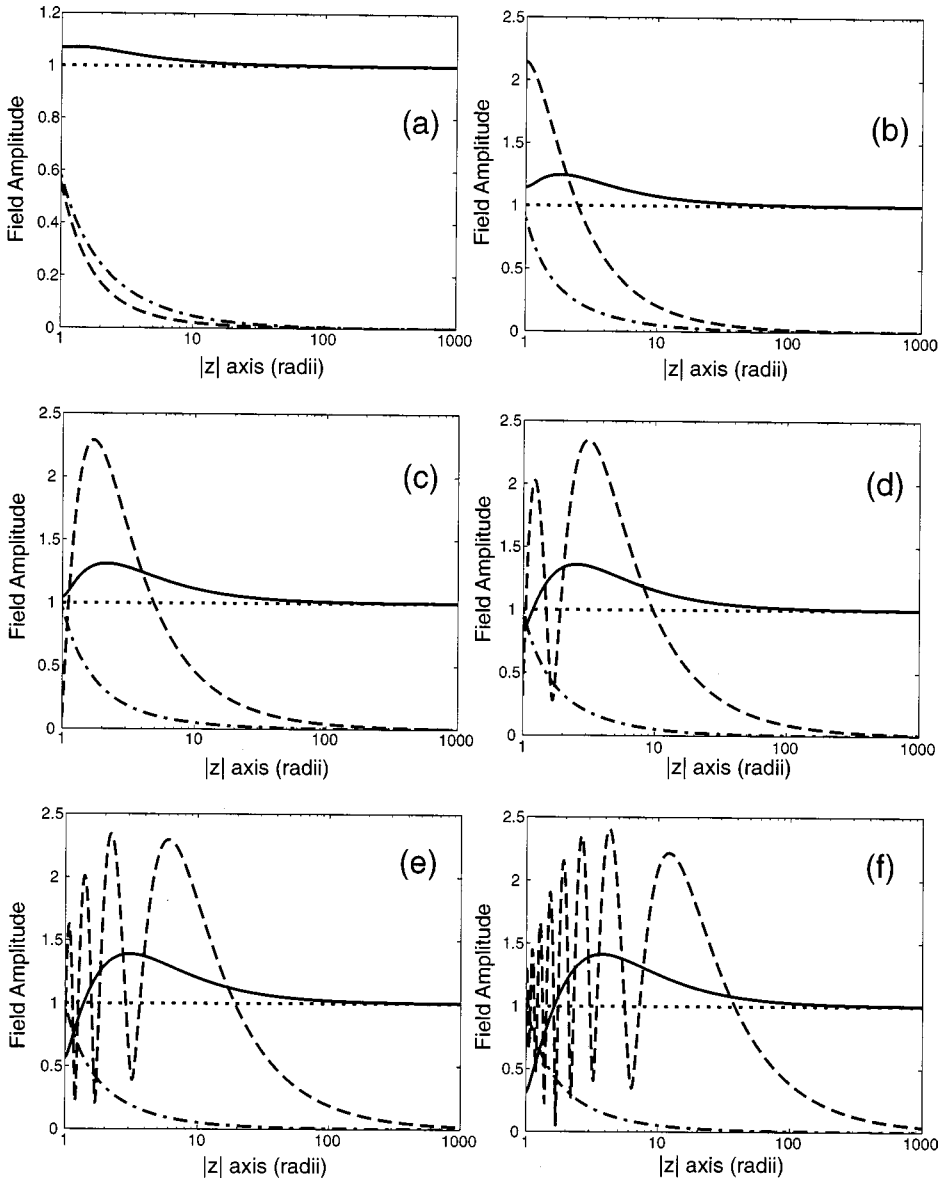

FIG. 4. Scatter from a fixed rigid sphere along the $|z|$ axis. Note the log scale along the $|z|$ axis, and the variable field amplitude scale. Key: Solid line: total field amplitude $(+z)$, dotted line: incident field amplitude, dashed line: forward scatter amplitude $(+z)$, and dot-dash line: backscatter amplitude $(-z)$. Distance is R/a (i.e., it is scaled in radii). (a) $ka=1$; (b) $ka=5$; (c) $ka=10$; (d) $ka=20$; (e) $ka=40$; and (f) $ka=80$.

the forward scatter amplitude begins to oscillate as a function of range along the $+z$ axis. Second, the total field amplitude develops a progressively deeper shadow zone immediately adjacent to the sphere, followed by a steadily increasing, although still small, enhancement which decays away with range.

Two main conclusions may be drawn from the sequence of Fig. 4(a)–(f). First, since the total field amplitude along the $+z$ axis (which is formed by the coherent sum of the forward scattered field and the incident field) changes quite smoothly with range, and does not show the same rapid variations as the forward scattered field, then the forward scattered field must oscillate with basically the same period as, but in relative antiphase to, the incident field. Second, for all the cases examined, the enhancement of the total field at a range of 100 radii is <1 dB. With regard to this second point, a very instructive lesson may be learned by looking at the case for (say) $ka=80$, in Fig. 4(f). Inspection of this figure shows that the amplitude of the forward scattered field at a range of 100 radii is much higher than that of the backscattered field. If it were indeed possible to observe the forward scatter independently of the incident field, then a great advantage could be gained in various applications by using forward scattering, rather than backscattering, techniques. In fact it is the total field that is observed, and this has a much smaller enhancement, as Fig. 4(f) shows.

B. Air bubble in water

Figure 5(a) shows the angular variation of the form function Eq. (18) for an air bubble in water for $ka=20$, as given by Anderson's model with $g=0.001\,26$ and $h=0.22$. A strong forward scatter lobe (with maximum extension greater than for the rigid sphere) may again be clearly seen. Figure 5(b) is a 2-D gray scale plot showing the amplitude of the scattered field for the same case. At some points along the $+z$ axis, the amplitude is almost twice that of the incident field. Figure 5(c) is a 2-D gray scale plot of the corresponding total field amplitude. In this case, the incident field and the scattered field combine along the $+z$ axis to produce a total field with amplitude consistently less than the incident field, with a deep shadow close to the sphere. The develop-

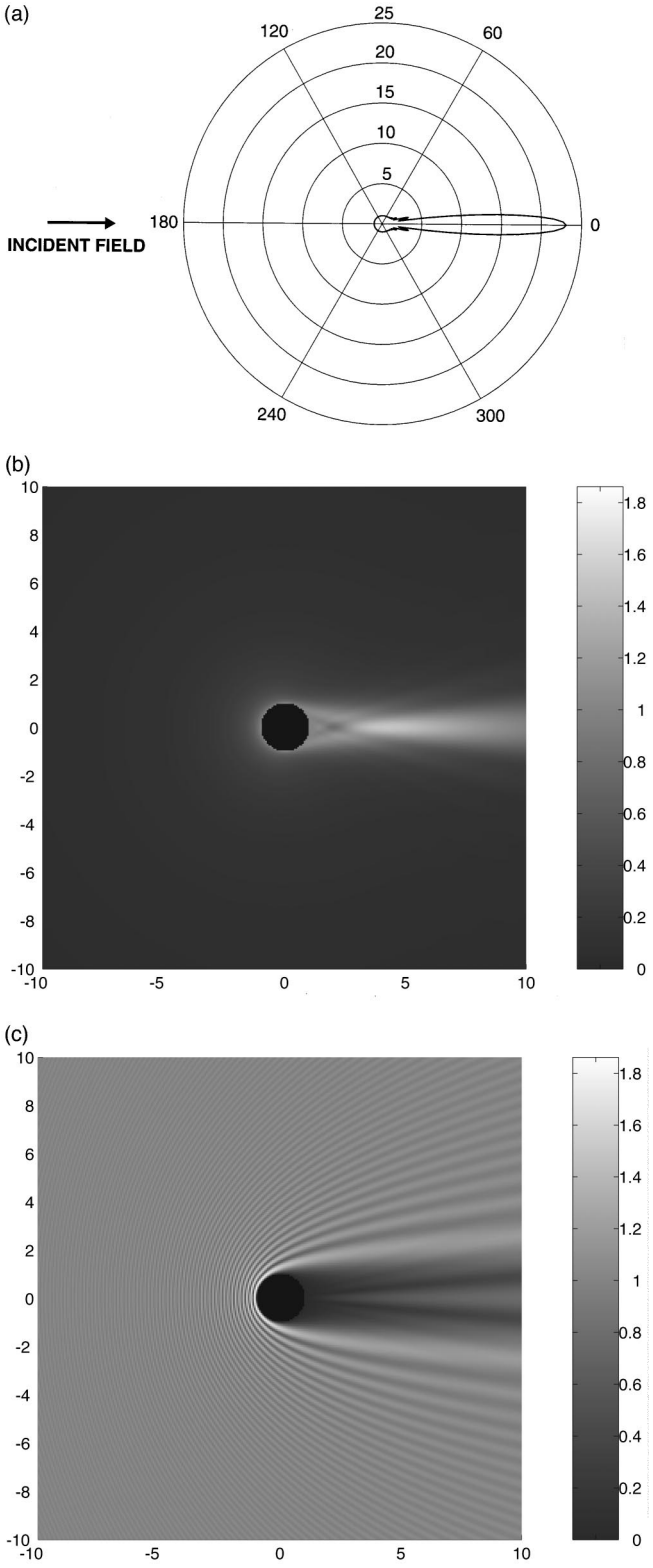

FIG. 5. Scatter from an air-filled sphere as a function of direction, for $ka=20$. $g=0.001\,26$ and $h=0.22$. (a) Conventional form function. (b) Gray scale plot of the scattered field amplitude only. The external field is incident from the left. The x and y axes in the plot denote distance from the center of the sphere, scaled in radii. (c) Gray scale plot of the total field amplitude.

ment of this phenomenon may be seen in Fig. 6(a)–(f), which shows the range variation of the different field amplitudes for the same sequence of frequencies used in Fig. 4. For $ka=1$, the forward and backscatter amplitudes decrease at about the same rate with range, as for the rigid sphere. In this case, however, even at this relatively low frequency, the total field along the $+z$ axis indicates a deep shadow adjacent to the sphere, which extends beyond 100 radii. As the frequency is increased, features begin to appear which are similar to the rigid sphere case. The forward scatter field predominates over the backscatter, and begins to oscillate as a function of range along the $+z$ axis. The total field amplitude develops a progressively deeper shadow region but, in this case, never shows any enhancement over the incident field amplitude. Conclusions similar to the rigid sphere case can also be drawn. The forward scattered field must oscillate with the same period and in antiphase to the incident field, because the two must interfere destructively to produce the shadow region; and the change in the observed field amplitude (at 100 radii) is very small (i.e., the absolute value of the change is <0.5 dB).

C. Low contrast sphere

Figure 7(a) shows the angular variation of the form function Eq. (18) for a low contrast sphere for $ka=20$. To obtain this result, values of $g=1.06$ and $h=1.02$ were used in Eq. (9a) (values like these are typically used in the Anderson model to represent scattering from zooplankton[4]). While the forward scatter is still clearly evident, comparison with Figs. 3(a), 5(a) shows that the maximum lobe extension is about half that of the two previous cases. Also, the degree of backscatter is very small indeed. Figure 7(b) is a 2-D gray scale plot showing the amplitude of the scattered field for the same case. Inspection of the scale on the right hand side shows that the maximum forward scattered amplitude is not much greater than that of the incident field. Figure 7(c) is a 2-D gray scale plot of the corresponding total field amplitude, and shows some features different from the two high contrast cases. For example, the sphere seems to act as an acoustic lens, focusing the sound into a ''bright'' spot a few radii from the sphere along the $+z$ axis. Beyond this spot, further along the $+z$ axis, the incident field and the scattered field interfere to produce a long shadow zone.

Further differences may be observed by examining Fig. 8(a)–(f). First, while the forward and backscatter are both of similar amplitude (and very small) at $ka=1$, the forward scatter increases quite rapidly with frequency, while the degree of backscatter remains practically unchanged over the whole frequency range. The low backscatter is presumably due to the small change in acoustic impedance at the boundary between the sphere ($g=1.06$, $h=1.02$) and the surrounding medium ($g=1$, $h=1$). Second, as oscillations begin to appear in the forward scatter amplitude as a function of range along the $+z$ axis, corresponding oscillations, *with practically the same phase*, appear in the total field amplitude. This must again be due to the similarity of the two acoustic media, such that sound travels with essentially the same phase velocity both through the sphere and around it. Further along the $+z$ axis from the sphere, the scattered field and the incident field eventually become antiphased, since they interfere destructively to produce a shadow region. The range at which this occurs moves further from the sphere as the fre-

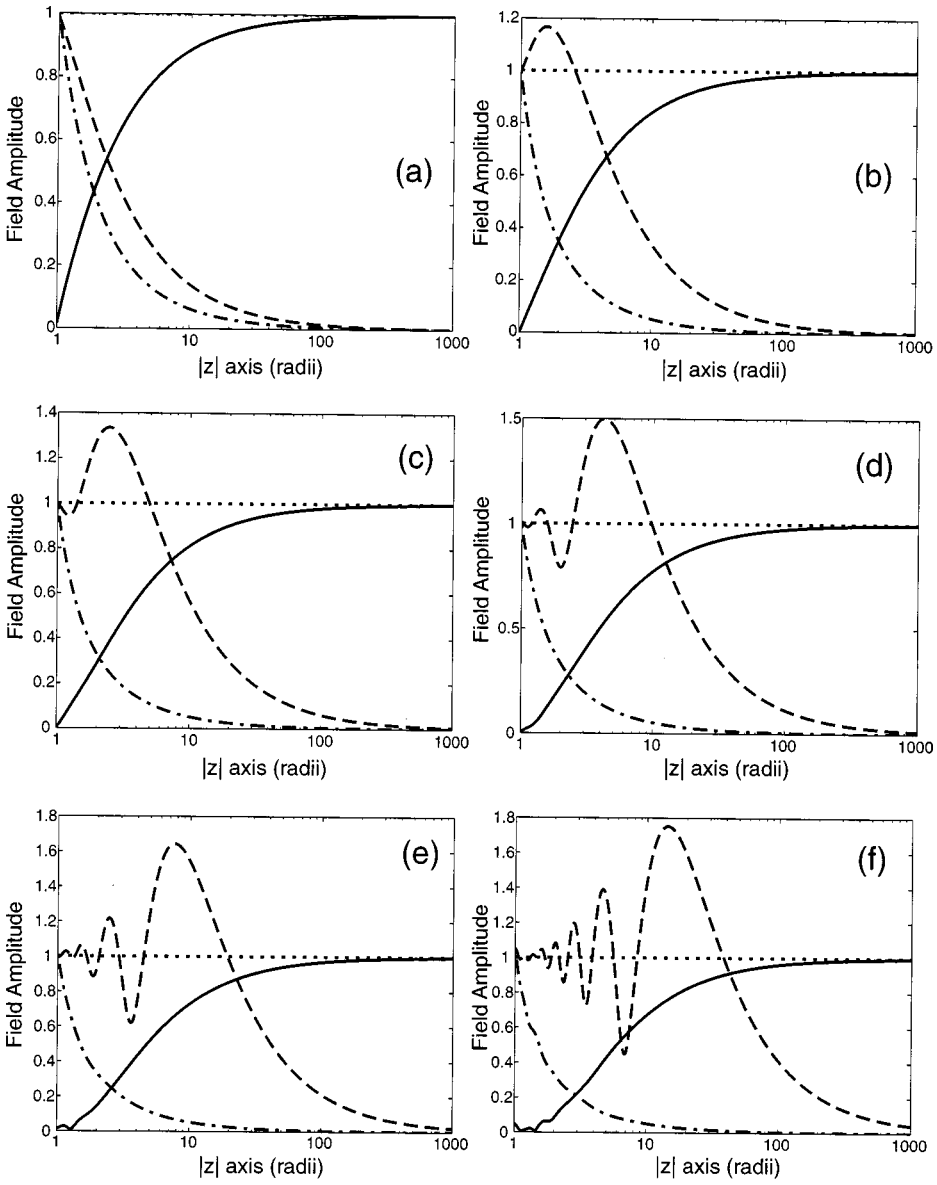

FIG. 6. Scatter from an air-filled sphere along the $|z|$ axis, for $ka=20$. $g=0.001\,26$ and $h=0.22$. Note the log scale along the $|z|$ axis, and the variable field amplitude scale. Key: Solid line: total field amplitude $(+z)$, dotted line: incident field amplitude, dashed line: forward scatter amplitude $(+z)$, and dot-dash line: backscatter amplitude $(-z)$. Distance is R/a (i.e., it is scaled in radii). (a) $ka=1$; (b) $ka=5$; (c) $ka=10$; (d) $ka=20$; (e) $ka=40$; and (f) $ka=80$.

quency is increased. This can give rise to a change in the total field amplitude in the forward scatter direction which is apparently greater than for the two previous high contrast cases, but is still quite small (i.e., the absolute value of the change is <1.0 dB at 100 radii for $ka=80$).

IV. THE TRANSLATIONAL RESPONSE MECHANISM OF THE ANDERSON SPHERE

The description of scattering from a rigid sphere given in Anderson's paper has limited applicability. Since the density of the inner fluid is allowed to approach infinity [see Eq. (20)], the sphere becomes too massive to react to the incident field (i.e., it is ''fixed'') and, therefore, physically unrealistic. An attempt to remove this limitation was made in 1965 by Hickling and Wang,[5] who determined the scattering response of a rigid *movable* sphere, and thus allowed the behavior of rigid objects of finite density to be described. They showed that the incorporation of the translational response mechanism, or ''rebound,'' of the rigid sphere in reaction to the incident field made a difference only to the dipole term in expansion Eq. (10) for the scattered field. Their prescription for the coefficients D_m of the expansion is

$$D_m=\begin{cases}\dfrac{g\,ka\,j_m'(ka)-j_m(ka)}{g\,ka\,h_m'(ka)-h_m(ka)} & (m=1)\\[2ex] \dfrac{j_m'(ka)}{h_m'(ka)} & (m\neq 1)\end{cases}, \tag{21}$$

which reduces to (20) as $g\to\infty$, or when ka becomes very large. In practice, the modifications to the Anderson theory introduced by Hickling and Wang are important only at relatively low frequencies. For $g\geqslant 1$, $ka\geqslant 10$, the two methods give almost identical results.

While the inclusion of the translational response for a rigid sphere is only of practical significance in low frequency and/or low density cases, the very fact that the mechanism is not intrinsically predicted by the original Anderson theory has led to some confusion about this theory's inherent correctness. A misunderstanding has arisen about whether a

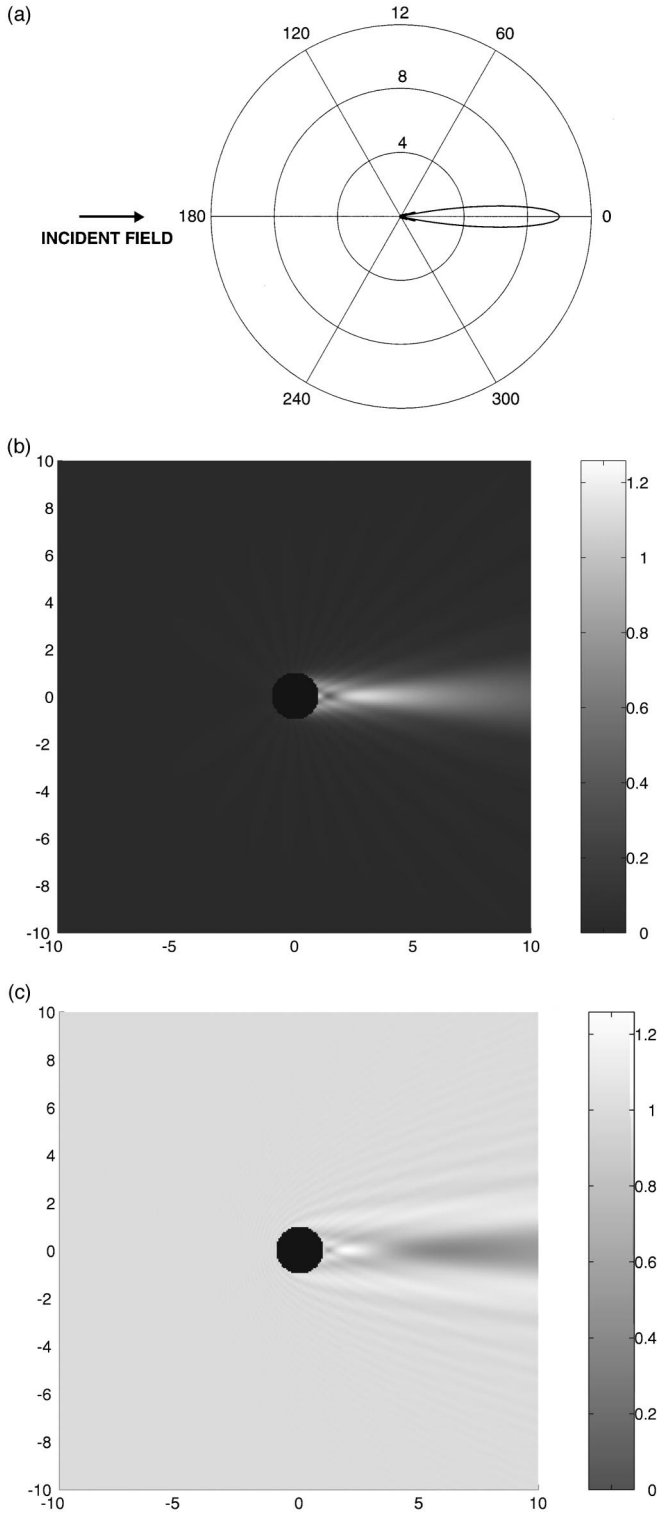

FIG. 7. Scatter from a low contrast fluid-filled sphere as a function of direction, for $ka=20$. $g=1.06$ and $h=1.02$. (a) Conventional form function. (b) Gray scale plot of the scattered field amplitude only. The external field is incident from the left. The x and y axes in the plot denote distance from the center of the sphere, scaled in radii. (c) Gray scale plot of the total field amplitude.

theory which uses a fixed coordinate system to describe physical motion can properly be used to describe a phenomenon in which a discrete translation of the body center is a principal element. We will now attempt to clarify this issue and, as we do so, will find that it leads to some interesting insights into the distinctions between the physical ideas of ''rigidity,'' ''fluidity,'' and ''elasticity.''

Hickling and Wang[5] introduced the characteristics of rigidity into their theory when they specified the displacement of the sphere under the action of the incident field. They argued that, since the sphere is perfectly rigid, it should be displaced along the line of the incident field *without changing its spherical shape*. To accommodate this rigid body behavior they allowed the geometrical center of the sphere to shift away from the origin of coordinates, and it is the implementation of appropriate boundary conditions to incorporate this linear motion which gives rise to the modification of the coefficient D_1 [see Eq. (21)] for the dipole term in the expansion of the scattered field. Why then does not Anderson's theory also predict the translational rebound motion of a rigid sphere? As we examine this question, it is critically important to keep in mind that Anderson's theory is specifically designed to describe acoustic scattering from a general *fluid* sphere. Since, by definition, it is not the physical nature of fluids (even dense and highly incompressible fluids) to respond to external forces by moving in a rigid manner, we should not necessarily expect Anderson's theory to predict rigid body motion such as that described by Hickling and Wang. Indeed, we shall see that Anderson's theory does the job it was intended to do (i.e., predict scattering from a fluid sphere) very well. Only when an attempt is made to force it to describe a completely foreign, unfluidlike object (i.e., a rigid sphere), does it fail.

To demonstrate the behavior of the Anderson sphere, let us first consider the displacement of the surface of a fluid sphere as it scatters sound. When the incident field impinges on the sphere, each point on the fluid surface responds by expanding outward, or contracting inward, according to whether the local pressure decreases, or increases, respectively. Typically, the pressure distribution around the sphere is a function of θ, in which case the surface is fluidly deformed and becomes nonspherical in shape. The displacement of the surface is directly related to the radial particle velocity, and an expression for this quantity for all k_1R, $R \leqslant a$, can be readily obtained by combining Eqs. (6) and (12):

$$u_{\text{int}} = i\frac{P_{\text{inc}}}{\rho_1 c_1}\sum_{m=0}^{\infty} i^m(2m+1)\,E_m\,P_m(\mu)\,j_m'(k_1R)e^{-i\omega t}. \quad (22)$$

It is convenient to scale this quantity to the particle velocity associated with the incident field in the external fluid medium (i.e., $u_{\text{inc}} = P_{\text{inc}}/\rho c$) to give

$$\frac{u_{\text{int}}}{u_{\text{inc}}} = i\frac{\rho c}{\rho_1 c_1}\sum_{m=0}^{\infty} i^m(2m+1)\,E_m\,P_m(\mu)\,j_m'(k_1R)e^{-i\omega t}, \quad (23)$$

and, at the surface of the sphere, define a quantity:

$$\nu_a = \left.\frac{u_{\text{int}}}{u_{\text{inc}}}\right|_{R=a} = \frac{i}{gh}\sum_{m=0}^{\infty} i^m(2m+1) \times E_m\,P_m(\mu)\,j_m'(k_1a)e^{-i\omega t}. \quad (24)$$

We then compute the z-component of this quantity ($\nu_z = \nu_a \cos\theta$) at each point on the surface of the sphere, and

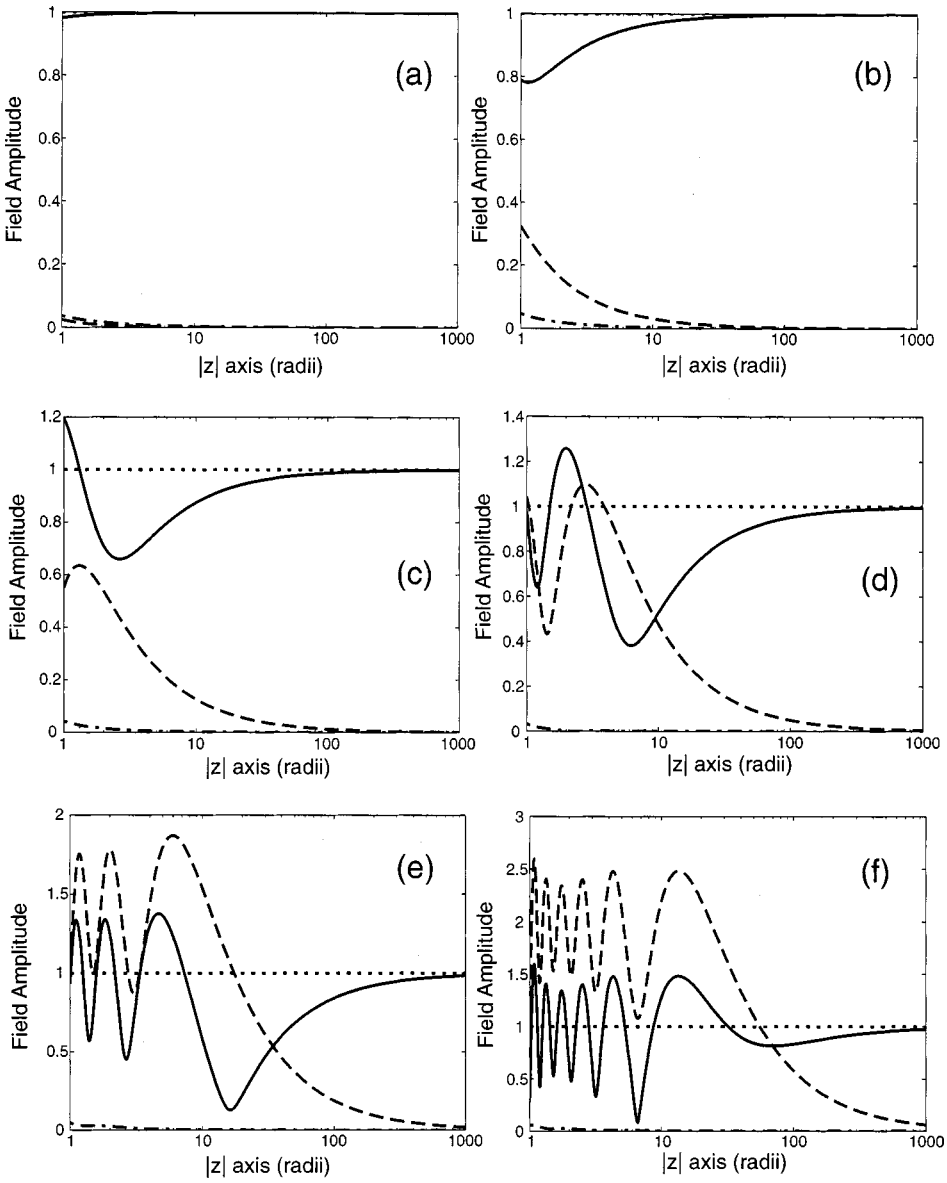

FIG. 8. Scatter from a low contrast fluid-filled sphere along the $|z|$ axis, for $ka=20$. $g=1.06$ and $h=1.02$. Note the log scale along the $|z|$ axis, and the variable field amplitude scale. Key: Solid line: total field amplitude $(+z)$, dotted line: incident field amplitude, dashed line: forward scatter amplitude $(+z)$, and dot-dash line: backscatter amplitude $(-z)$. Distance is R/a (i.e., it is scaled in radii). (a) $ka=1$; (b) $ka=5$; (c) $ka=10$; (d) $ka=20$; (e) $ka=40$; and (f) $ka=80$.

integrate over the surface of the sphere to find the average velocity ''flux'' $\langle \nu_z \rangle$:

$$\langle \nu_z \rangle = \frac{1}{2} \int_0^{\pi} \nu_z \sin\theta \, d\theta. \tag{25}$$

Figure 9 depicts the frequency variation of both the real and imaginary parts of $\langle \nu_z \rangle$ for water-entrained fluid spheres with four different combinations of density and sound speed properties. The parameters for these four cases represent: (a) air ($g=0.001\,26$, $h=0.22$, $gh=2.77\times10^{-4}$); (b) low contrast fluid ($g=1.06$, $h=1.02$, $gh=1.08$); (c) sedimentary rock ($g=2.4$, $h=2$, $gh=4.8$); and (c) stainless steel ($g=7.9$, $h=3.73$, $gh=29.47$). [N.B. A complete physical description of rock and steel actually requires an elastic scattering model, such as that of Faran,[6] which is discussed below. Our purpose here is to study the behavior of the Anderson model, which incorporates only the density and compressional sound speed of materials. It might be helpful to think of cases (c) and (d) as representing ''fluid'' rock, and ''fluid'' steel.] Figure 9 indicates two principal features.

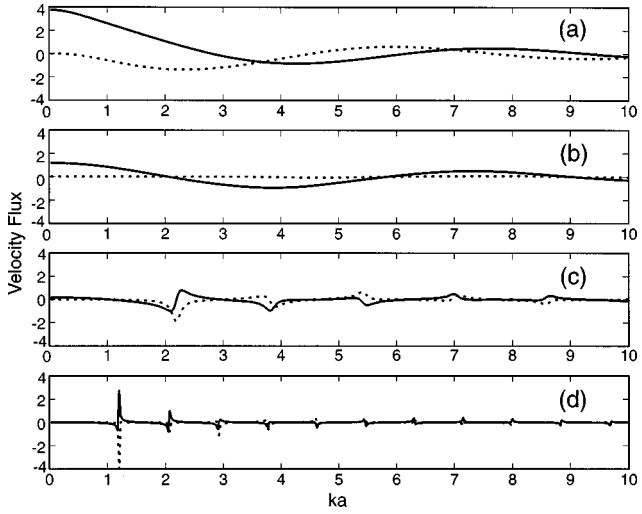

FIG. 9. Average velocity flux through the surface of the sphere along the z axis. Velocities are relative to the velocity amplitude of the incident wave. The velocities were computed at $t=0$. The solid line is the real component and the dotted line is the imaginary component. (a) Air: $g=0.001\,26$ and $h=0.22$. (b) Low contrast fluid: $g=1.06$ and $h=1.02$ (almost water). (c) Fluid ''rock'': $g=2.4$ and $h=2$. (d) Fluid ''steel'': $g=7.9$ and $h=3.73$.

First, the velocity flux $\langle \nu_z \rangle$ varies with frequency, and can take both negative and positive values. This shows that the Anderson model does typically predict a net nonzero translation of the scatterer body away from its original rest position, as it moves in response to the incident field. Second, the $\langle \nu_z \rangle$ variations decrease in amplitude with increasing frequency, and they also indicate an overall decreasing trend as the values of g and h (and, hence, gh) are increased. Since gh appears in the denominator of Eq. (24), it is clear that if gh were allowed to approach infinity, $\langle \nu_z \rangle$ would tend to zero for all frequencies. This is the behavior noted earlier, i.e., the Anderson model does not predict the translational response of a rigid sphere (as realized by allowing gh to approach infinity). Taken together, the results shown in Fig. 9 are consistent, and give no indication that the Anderson model does not correctly describe the motion of a fluid sphere. A translational response of the fluid sphere via *body deformation* is observed, suggesting that the question raised above, about whether fixed coordinates can be used to describe scattering from a rebounding object, is ill-posed.

The next step in this study is to examine the effect of variable rigidity, which necessitates the investigation of scattering from an elastic sphere. The theory of scattering from an elastic sphere was introduced by Faran.[6] His approach, like Anderson's, uses field expansions around a fixed origin. The incident and scattered fields are again given by Eqs. (3) and (10) but, in this case, the acoustic wave inside the elastic sphere consists of both compressional and shear components, and a third boundary condition is necessary at the surface of the sphere. We will not reproduce the theory here, but refer the reader to Faran's paper. To facilitate later discussion, we simply note the following expressions for the speed of propagation of compressional waves (c_L) and shear waves (c_T) in the internal elastic medium, i.e.,

$$c_L = \left(\frac{\lambda_1 + 2\mu_1}{\rho_1} \right)^{1/2}; \quad c_T = \left(\frac{\mu_1}{\rho_1} \right)^{1/2}, \tag{26}$$

where ρ_1 is again the density of the sphere, and λ_1 and μ_1 are the elastic Lamé constants. The inclusion of elastic properties in the sphere leads to a different expression for the coefficients D_m of the scattered field Eq. (10), as detailed in Eqs. (28)–(30) of Ref. 6 and also in Eqs. (6)–(8) of Ref. 8.

The rigidity, or stiffness, of an elastic solid is determined by μ_1, the shear rigidity modulus. To study the effect of variable rigidity on acoustic scattering from an elastic sphere, we will use the Faran model to investigate the variation of the form function $F_\infty(ka)$ [see Eq. (18)], as a function of frequency and of μ_1, for an air bubble. Figure 10(a) shows the variation of the form function (to $ka=10$) for an air bubble ($\rho_1 = 0.001\,26\ \mathrm{g\,cm^{-3}}$; $c_1 = 33\,000\ \mathrm{cm\,s^{-1}}$) in water ($\rho = 1\ \mathrm{g\,cm^{-3}}$; $c = 150\,000\ \mathrm{cm\,s^{-1}}$). Air is a fluid, of course, and curve 1 (the solid line) shows the form function predicted by the Anderson fluid sphere model. The characteristic monopole resonance at $ka \approx 0.0135$ is clearly evident, together with many higher frequency, higher order, resonances. Curve 2 (the dashed line) shows the form function for the same object predicted by the Hickling and Wang movable rigid sphere model. The object represented by the latter case is obviously unnatural (i.e., an infinitely stiff air bubble which rebounds without change of shape), but is close to one of the examples considered by Hickling and Wang (they actually used $g=0$, see Fig. 1 of Ref. 5). Figure 10(b) shows related results obtained with the Faran model. Curve 1 (the solid line) in Fig. 10(b) shows the form function for a sphere of ''elastic'' air, with: $c_L = c_1 = 33\,000\ \mathrm{cm\,s^{-1}}$; $c_T = 100\ \mathrm{cm\,s^{-1}}$; $\rho_1 = 0.001\,26\ \mathrm{g\,cm^{-3}}$. The shear rigidity modulus corresponding to $c_T = 100\ \mathrm{cm\,s^{-1}}$ [i.e., $\mu_1 = 12.6\ \mathrm{dyne\,cm^{-2}}$, as calculated from Eq. (26)] is very small, so that the internal elastic medium is practically the same as fluid air. The corresponding value of $\lambda_1 = 1.37 \times 10^5\ \mathrm{dyne\,cm^{-2}}$. Comparison of curve 1 of Fig. 10(b) with curve 1 of Fig. 10(a) shows that the Faran model predicts the same form function as the Anderson model. Curve 2 (the

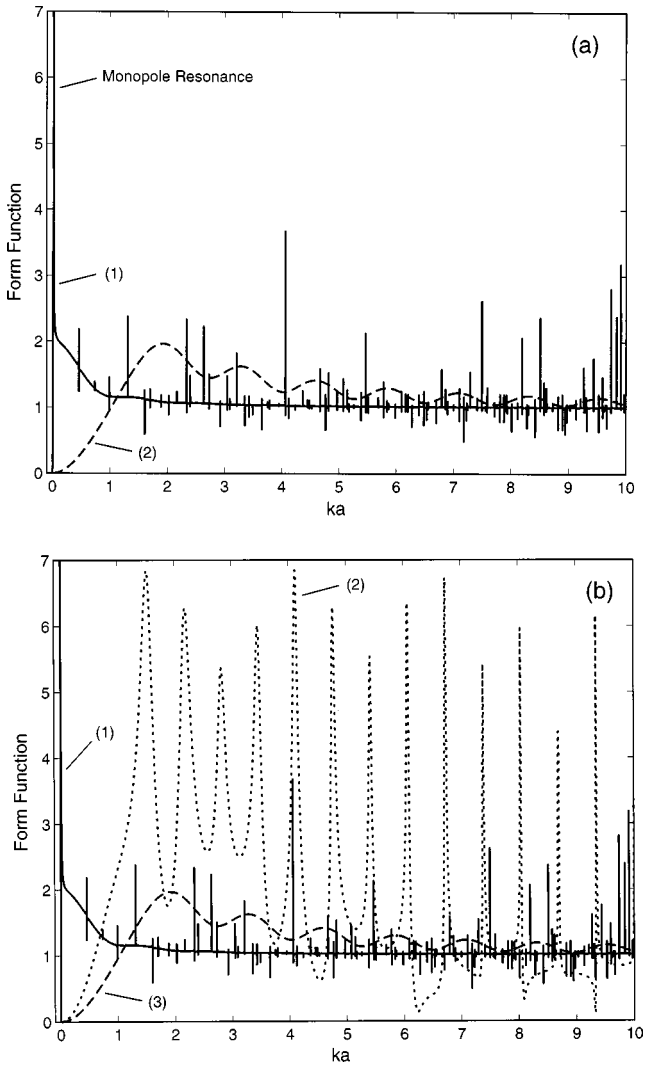

FIG. 10. Backscatter form functions for spheres as a function of *ka*. (a) Curve 1 was calculated using Anderson's model (Ref. 3) for an air bubble ($\rho_1 = 0.001\,26\ \mathrm{g\,cm^{-3}}$; $c_1 = 33\,000\ \mathrm{cm\,s^{-1}}$) in water ($\rho = 1\ \mathrm{g\,cm^{-3}}$; $c = 150\,000\ \mathrm{cm\,s^{-1}}$). Curve 2 shows the form function for the same object predicted by the movable rigid sphere model (Ref. 5). (b) All three curves in this figure were calculated using Faran's model (Ref. 6). Curve 1 shows the form function for a sphere of ''elastic'' air in water, with $c_L = 33\,000\ \mathrm{cm\,s^{-1}}$; $c_T = 100\ \mathrm{cm\,s^{-1}}$. Curve 2 is for an elastic sphere with $c_L = 4.47 \times 10^6\ \mathrm{cm\,s^{-1}}$; $c_T = 3.16 \times 10^6\ \mathrm{cm\,s^{-1}}$. This was achieved by increasing the shear rigidity modulus μ_1, but keeping λ_1 unchanged. Curve 3 is for an elastic sphere with $c_L = 4.47 \times 10^8\ \mathrm{cm\,s^{-1}}$; $c_T = 3.16 \times 10^8\ \mathrm{cm\,s^{-1}}$. This was achieved by further increasing μ_1, but still keeping λ_1 unchanged.

dotted line) in Fig. 10(b) shows the form function when the shear rigidity modulus is increased to $\mu_1 = 12.6 \times 10^8$ dyne cm^{-2} (thus making the internal medium very rigid) while keeping λ_1 unchanged. This causes the values of the compressional and shear sound speeds to increase by large amounts [see Eqs. (26)], to $c_L = 4.47 \times 10^6$ cm s^{-1} and $c_T = 3.16 \times 10^6$ cm s^{-1}, respectively. The resulting form function now has a distinctively different resonance structure from that of fluid air. Curve 3 (the dashed line) in Fig. 10(b) shows the form function when the shear rigidity modulus is increased to $\mu_1 = 12.6 \times 10^{12}$ dyne cm^{-2} (making the medium extremely rigid) while still keeping λ_1 unchanged. The values of the compressional and shear sound speeds become $c_L = 4.47 \times 10^8$ cm s^{-1} and $c_T = 3.16 \times 10^8$ cm s^{-1}, respectively. Comparison of curve 3 of Fig. 10(b) with curve 2 of Fig. 10(a) shows that the Faran model now predicts the same form function as the Hickling and Wang model.

What conclusions are to be drawn from Fig. 10? The first conclusion is that both the Anderson model and the movable rigid sphere model are implicitly contained within the Faran model as limiting cases, but in *opposite senses* as far as rigidity is concerned. Figure 10 shows that, depending on which way the shear rigidity modulus μ_1 is varied, the Faran model is capable of reproducing the behavior of either the Anderson model or the movable rigid sphere. The interrelationship of the three models agrees with what we would expect from basic physical reasoning: (a) a fluid medium is an elastic medium with very low, or vanishing, rigidity; (b) a rigid medium is an elastic medium with very high rigidity.

The second conclusion is that the Faran model predicts the translational rebound of an elastic scatterer as it responds to the incident field and, therefore, that the Anderson model must do so also. The fact that the Faran model predicts the rebound can be seen by comparing Fig. 10(a) and 10(b). When the value of the shear rigidity modulus μ_1 is greatly increased, the air bubble responds identically to a rigid movable sphere of the same density. However, no change is engendered in the inherent nature of the Faran theory merely by varying μ_1, so the theory must also predict the rebound for a normal elastic sphere. Furthermore, when μ_1 is greatly *decreased*, the Faran model reproduces exactly the response of the Anderson model so, by the same reasoning, the Anderson model must correctly predict the rebound for a fluid sphere.

As a corollary to the second conclusion, both the Faran and Anderson theories show that there is no problem associated with using a normal mode expansion around fixed coordinates to describe scattering from a rebounding sphere. Figure 9 shows that, for a fluid sphere, the rebound motion is accomplished by a deformation of the spherical shape, resulting in a net translation of the body mass. For an elastic object, the motion must also occur by this means. Only in the case of a perfectly rigid sphere (a physically unrealizable object) must the motion be achieved by a discrete translation without change of shape.

V. CONCLUSIONS

The Anderson fluid sphere scattering model has been reexamined to clarify three issues which have been the source of misunderstanding among underwater acousticians. First, the accuracy of the Morse approximation for the spherical Hankel functions, commonly used to convert the sum on partial waves to the large range approximation, was investigated. It was shown that the minimum range for use of the approximation is strongly mode number dependent, and should be carefully evaluated in short range and/or high frequency applications. Second, the precise characterization of the forward scatter region was studied. By combining the scattered field and the incident plane wave in the forward direction, it was shown that little advantage is obtained in detection and localization applications by using forward scattering, rather than backscattering. Third, the translational response, or ''rebound,'' of the sphere under the action of the incident field was examined. By demonstrating that Anderson's theory is a limiting case of Faran's scattering model for an elastic sphere, which contains the rebound response, it was shown that the response is completely explainable within Anderson's theory, and is consistent with a description which uses a normal mode expansion around a fixed origin.

ACKNOWLEDGMENT

This work was supported by the U.S. Office of Naval Research.

[1] P. M. Morse, *Vibration and Sound* (reprinted by American Institute of Physics, New York, 1981), 2nd ed.: (a) pp. 311–326; (b) p. 317, Eqs. 27.11.

[2] H. Medwin and C. S. Clay, *Fundamentals of Acoustical Oceanography* (Academic, San Diego, 1998): (a) pp. 276–280; (b) pp. 289–291; (c) pp. 284–286.

[3] V. C. Anderson, ''Sound scattering from a fluid sphere,'' J. Acoust. Soc. Am. **22**, 426–431 (1950).

[4] D. C. McNaught, M. Buzzard, and S. Levine, ''Zooplankton production in Lake Ontario as influenced by environmental perturbations,'' Environ. Prot. Agency (U.S.) EPA-660/3-75-021, 40-63 (1975); R. K. Johnson, ''Sound scattering from a fluid sphere revisited,'' J. Acoust. Soc. Am. **61**, 375–377 (1977), and Erratum, *ibid.* **63**, 626(E) (1978).

[5] R. Hickling and N. M. Wang, ''Scattering of sound by a rigid movable sphere,'' J. Acoust. Soc. Am. **39**, 276–279 (1966).

[6] J. J. Faran, Jr., ''Sound scattering by solid cylinders and spheres,'' J. Acoust. Soc. Am. **23**, 405–418 (1951).

[7] While Morse uses the $+z$ direction for the incident field (see Ref. 1, p. 354, Eq. 29.8), Anderson uses the $-z$ direction. The practical difference between these two conventions is that the term i^m appearing in the plane wave expansion (for $+z$) is replaced by $(-i)^m$ (for $-z$, see Ref. 3, Eq. 5). Also, rather than the backscattered field being observed at $\theta = \pi$ (for $+z$), it is observed instead at $\theta = 0$ (for $-z$). We chose to adopt the $+z$ convention because this seems to accord most with current practice in the scattering theory literature.

[8] R. Hickling, ''Analysis of echoes from a solid elastic sphere in water,'' J. Acoust. Soc. Am. **34**, 1582–1592 (1962).

An axisymmetric poroelastic finite element formulation

Yeon June Kang
School of Mechanical and Aerospace Engineering, Seoul National University, San 56-1 Shinlim-Dong, Kwanak-Ku, Seoul 151-742, Korea

Bryce K. Gardner[a)]
Automated Analysis Corporation, 2805 S. Industrial, Suite 100, Ann Arbor, Michigan 48104

J. Stuart Bolton
1077 Ray W. Herrick Laboratories, School of Mechanical Engineering, Purdue University, West Lafayette, Indiana 47907-1077

(Received 20 November 1998; accepted for publication 5 April 1999)

In the past, various two- and three-dimensional Cartesian, poroelastic finite element formulations have been proposed and demonstrated. Here an axisymmetric formulation of a poroelastic finite element is presented. The intention of this work was to develop a finite element formulation that could easily and efficiently model axisymmetric sound propagation in circular structures having arbitrary, axially dependent radii, and that are lined or filled with elastic porous sound absorbing materials such as foams. The formulation starts from the Biot equations for an elastic porous material expressed explicitly in axisymmetric form. By following a standard finite element development, a **u-U** formulation results. Procedures for coupling the axisymmetric elements to an adjacent acoustical domain are described, as are the boundary conditions appropriate for unfaced foams. Calculations described here show that the present formulation yields predictions as accurate as a Cartesian, three-dimensional model in much reduced time. Predictions made using the present model are also compared with measurements of sound transmission through cylindrical foam plugs, and the predicted results are shown to agree well with the measurements. Good agreement was also found in the case of sound transmission through a conical foam plug. [S0001-4966(99)03308-1]

PACS numbers: 43.20.Gp, 43.20.Mv [DEC]

INTRODUCTION

The work reported here relates to the modeling of axisymmetric structures lined or filled with elastic porous materials such as polyurethane foams: e.g., lined circular ducts or simple silencers. This article is the fourth in a series dealing with various aspects of finite element modeling of elastic porous noise control materials.[1–3] The poroelastic finite element formulation described in Refs. 1–3, and further developed here, is based on the Biot theory for wave propagation in elastic porous media.[4,5]

The development of a Cartesian finite element representation of homogeneous elastic porous materials was described in the first of the three articles, as were the procedures required to couple poroelastic finite elements to adjacent acoustical domains.[1] The application of a finite element model to calculate the normal incidence absorption coefficient of finite-sized, plane foam treatments (either constrained at their edges, as if placed in a standing wave tube, or unconstrained) was demonstrated. In the second article, the extension of the finite element treatment to the prediction of sound transmission through plane, finite-depth porous layers that were used either by themselves or as linings of finite, double panel systems, was described.[2] In the third article, boundary conditions were described that allow foam elements to be coupled to acoustical domains at arbitrarily angled interfaces.[3] By using the latter conditions together with the sound transmission prediction capability developed previously, it was shown, for example, that the transmission loss of a wedge-shaped foam treatment is higher in certain frequency ranges than that of a plane treatment of the same volume. A similar effect had been noted previously with respect to the normal incidence sound absorption offered by a foam wedge.[6]

Recently, several poroelastic, finite element formulations have been described: see, for example, Refs. 1, 7, 8, and 9. All of these formulations are based on the Biot model,[4] and all were presented in Cartesian form. Note that axisymmetric calculations are described in Ref. 7, but no details of the axisymmetric element formulation or implementation are given. An axisymmetric finite element model of sound propagation along an axisymmetric lined duct has been presented by Kagawa *et al.*[10] However, they considered the case of a locally reacting duct lining, in which case wave propagation within the lining material is not modeled. In contrast, Easwaren *et al.* considered wave propagation in a foam-filled duct of constant, circular cross section.[11] However, the objective of that work was to solve an eigenvalue problem in the axial wave number, and Cartesian finite elements were used to formulate the problem. Vigran *et al.* used an axisymmetric finite element implementation of the Biot model to study the effect of sample edge constraint on the measured values of the surface normal impedance and absorption coefficient of elastic porous materials placed in standing wave tubes.[12] However, no description of the axi-

[a)]Now at M/S 157-410, Jet Propulsion Laboratory, California Institute of Technology, 4800 Oak Drive, Pasadena, CA 91109-8099.

symmetric finite element implementation was given. The conclusions they drew regarding the stiffening effect of the edge constraint and the shifting of resonances related to frame motion are similar to those reported earlier in Ref. 1. Finite element models of wave propagation along rectangular ducts lined with extended or locally reacting porous materials that may be considered to be effective fluids have also been extensively studied by Astley and Cummings: see, for example, Ref. 13.

In the present article, a poroelastic finite element based on the Biot equations, expressed explicitly in axisymmetric form, is described. Also presented are the boundary conditions and coupling procedures that must be applied when axisymmetric poroelastic elements are coupled to adjacent axisymmetric acoustic finite elements. The accuracy and efficiency of the axisymmetric poroelastic finite-element formulation is first demonstrated by comparing predictions made using the axisymmetric formulation with those made using a three-dimensional, Cartesian formulation. Predictions made using the axisymmetric formulation are here also compared with measurements of normal incidence sound transmission through cylindrical foam plugs in two configurations. Finally, predictions made using the present model have been compared with measurements of sound transmission through a conical foam plug in order to explore the acoustical effect of lining shape.

I. FINITE ELEMENT FORMULATIONS

A. Foam element

The present formulation of an axisymmetric, elastic porous finite element model is based on the elastic porous material theory and procedures that have been described extensively in Refs. 1–3. The work described in those references was itself based on the Biot theory for wave propagation in elastic porous materials.[4,5]

Consider a physical arrangement that can be conveniently described in terms of the cylindrical coordinates (r,θ,z). When the geometry, material properties, boundary conditions, and loading of the problem are independent of the circumferential angle, θ, the problem solution must itself be independent of θ. Thus under those conditions a three-dimensional problem can be reduced to a two-dimensional one in the (r,z) coordinates. The latter is the case considered here.

By combining the stress-strain relations and the dynamic equations that describe the motions of both the solid and fluid phases of an elastic porous material, it is possible to obtain two coupled, differential equations that govern wave propagation in poroelastic media. When a harmonic time dependence of the form $e^{j\omega t}$ is assumed, those two equations can be written as

$$N\nabla^2\mathbf{u}+\nabla[(A+N)e_s+Q\epsilon]=-\omega^2(\rho_{11}\mathbf{u}+\rho_{12}\mathbf{U}) + j\omega b(\mathbf{u}-\mathbf{U}), \quad (1)$$

$$\nabla[Qe_s+R\epsilon]=-\omega^2(\rho_{12}\mathbf{u}+\rho_{22}\mathbf{U})-j\omega b(\mathbf{u}-\mathbf{U}). \quad (2)$$

In Eqs. (1) and (2), e_s and ϵ are, respectively, the solid and fluid volumetric strains, the vector solid and fluid displacement fields are denoted by $\mathbf{u}$ and $\mathbf{U}$, respectively, N is the elastic shear modulus, and A is the first Lamé constant. The coefficients R and Q quantify the stiffness of the interstitial fluid and the coupling between volume changes of the solid and fluid phases of the material, respectively. The inertias of the solid and fluid phases, and the effects of momentum transfer between the two phases resulting from pore tortuosity are accounted for by the mass coefficients, ρ_{11}, ρ_{12}, and ρ_{22}. Finally, the viscous coupling force that is proportional to the relative velocity of the two phases is modeled by using an equivalent viscous coupling factor, b, that can be related to the macroscopic flow resistivity of the porous material.[1] When written explicitly in axisymmetric form, the solid and fluid volumetric strains become, respectively,

$$e_s=\nabla\cdot\mathbf{u}=\frac{\partial u_r}{\partial r}+\frac{u_r}{r}+\frac{\partial u_z}{\partial z}$$

and

$$\epsilon=\nabla\cdot\mathbf{U}=\frac{\partial U_r}{\partial r}+\frac{U_r}{r}+\frac{\partial U_z}{\partial z},$$

where u_r, u_z, U_r, and U_z are the radial and axial components of the solid and fluid phase displacements, respectively. Note that an axisymmetric radial displacement induces an axisymmetric circumferential strain (i.e., the terms u_r/r and U_r/r): see, for example, Ref. 14.

In the development of the weak form, it is necessary to consider an arbitrary, typical element. It is assumed that Ω^e is such an element of the finite element mesh. The finite element model based on Eqs. (1) and (2) is then developed over Ω^e. First, Eqs. (1) and (2) are multiplied by appropriate weighting functions, $\psi_i\,(i=1,2,3,4)$, which are themselves assumed to be once differentiable with respect to r and z. The resulting equations are then integrated by parts over the element domain Ω^e so as to distribute the differentiation equally over the weighting functions and displacement variables. The weak form of the differential equations (1) and (2) is thus obtained as

$$\begin{aligned}0=&2\pi\int_{\Omega^e}\Bigg[r\frac{\partial\psi_1}{\partial r}\left(2N\frac{\partial u_r}{\partial r}+A\nabla\cdot\mathbf{u}+Q\nabla\cdot\mathbf{U}\right)\\&+\psi_1\left\{2N\frac{u_r}{r}+A\nabla\cdot\mathbf{u}+Q\nabla\cdot\mathbf{U}\right\}+r\frac{\partial\psi_1}{\partial z}\\&\times N\left(\frac{\partial u_z}{\partial r}+\frac{\partial u_r}{\partial z}\right)-\omega^2\rho_{11}^*r\psi_1u_r-\omega^2\rho_{12}^*r\psi_1U_r\Bigg]dr\,dz\\&-2\pi\int_{B^e}\psi_1r(n_{fr}\sigma_r+n_{fz}\tau_{zr})dB,\end{aligned} \quad (3)$$

$$\begin{aligned}0=&2\pi\int_{\Omega^e}\Bigg[r\frac{\partial\psi_2}{\partial r}N\left(\frac{\partial u_z}{\partial r}+\frac{\partial u_r}{\partial z}\right)\\&+r\frac{\partial\psi_2}{\partial z}\left\{2N\frac{\partial u_z}{\partial z}+A\nabla\cdot\mathbf{u}+Q\nabla\cdot\mathbf{U}\right\}\\&-\omega^2\rho_{11}^*r\psi_2u_z-\omega^2\rho_{12}^*r\psi_2U_2\Bigg]dr\,dz\\&-2\pi\int_{B^e}\psi_2r(n_{fr}\tau_{zr}+n_{fz}\sigma_z)dB,\end{aligned} \quad (4)$$

$$0=2\pi\int_{\Omega^e}\left[r\frac{\partial\psi_3}{\partial r}(R\nabla\cdot\mathbf{U}+Q\nabla\cdot\mathbf{u})+\psi_3(R\nabla\cdot\mathbf{U}+Q\nabla\cdot\mathbf{u})\right.$$
$$\left.-\omega^2\rho_{12}^*r\psi_3u_r-\omega^2\rho_{22}^*r\psi_3U_r\right]dr\,dz$$
$$-2\pi\int_{B^e}\psi_3r(n_{fr}s)dB, \tag{5}$$

$$0=2\pi\int_{\Omega^e}\left[r\frac{\partial\psi_4}{\partial r}(R\nabla\cdot\mathbf{U}+Q\nabla\cdot\mathbf{u})-\omega^2\rho_{12}^*r\psi_4u_z\right.$$
$$\left.-\omega^2\rho_{22}^*r\psi_4U_z\right]dr\,dz-2\pi\int_{B^e}\psi_4r(n_{fz}s)dB. \tag{6}$$

In Eqs. (3)–(6), essential and natural boundary conditions appear in the various boundary integrals. The functions ψ_1, ψ_2, ψ_3, and ψ_4 that appear in the boundary integrals indicate that the essential boundary conditions are the displacement components: i.e., u_r, u_z, U_r, and U_z. The parenthetic terms within the boundary integrals, on the other hand, represent the natural boundary conditions. In this case, the natural boundary conditions constitute the force boundary conditions. The force terms, σ_r, σ_z, and τ_{rz}, are the normal and shear forces per unit material area acting on the solid phase of the foam, and s is the normal force per unit material area acting on the foam's fluid component. The terms n_{fr} and n_{fz} are the r- and z-components of the outward unit normal vector, $\mathbf{n}_f$, on the boundary B^e of the foam system, and dB is the arc length of an infinitesimal line element along the boundary. Also in Eqs. (3)–(6), $\rho_{11}^*=\rho_{11}+b/j\omega$, $\rho_{12}^*=\rho_{12}-b/j\omega$, $\rho_{22}^*=\rho_{22}+b/j\omega$, and they correspond respectively to ρ_{11}, ρ_{12}, and ρ_{22} when they are modified to allow for both inertial and viscous coupling between the solid and fluid phases.[5]

Next, it is assumed that the displacement components u_r, u_z, U_r, and U_z can be approximated by basis functions of the form:

$$u_r(r,z)\approx u^e(r,z)=\sum_{j=1}^{m}u_j^e\phi_j(r,z), \tag{7a}$$

$$u_z(r,z)\approx w^e(r,z)=\sum_{j=1}^{m}w_j^e\phi_j(r,z), \tag{7b}$$

$$U_r(r,z)\approx U^e(r,z)=\sum_{j=1}^{m}U_j^e\phi_j(r,z), \tag{7c}$$

$$U_z(r,z)\approx W^e(r,z)=\sum_{j=1}^{m}W_j^e\phi_j(r,z). \tag{7d}$$

In Eqs. (7), u_j^e, w_j^e, U_j^e, and W_j^e are, respectively, the values of u^e, w^e, U^e, and W^e at the jth node, (r_j,z_j), of the element, and the ϕ_j's are Lagrange basis functions of order $m-1$. Note that it has been assumed *a priori* that the solid and fluid displacements exhibit a zero-order circumferential variation.

When Galerkin's weighted-residual approximation is applied to an element, the weighting functions are set to

$$\psi_1=\psi_2=\psi_3=\psi_4=\phi_i \quad (i=1,2,3,...m). \tag{8}$$

By substituting Eqs. (7) and (8) into Eqs. (3)–(6), the axisymmetric foam finite element model may be obtained in elemental matrix form: i.e.,

$$\begin{bmatrix}[\mathbf{K^{11}}] & [\mathbf{K^{12}}] & [\mathbf{K^{13}}] & [\mathbf{K^{14}}]\\ [\mathbf{K^{21}}] & [\mathbf{K^{22}}] & [\mathbf{K^{23}}] & [\mathbf{K^{24}}]\\ [\mathbf{K^{31}}] & [\mathbf{K^{32}}] & [\mathbf{K^{33}}] & [\mathbf{K^{34}}]\\ [\mathbf{K^{41}}] & [\mathbf{K^{42}}] & [\mathbf{K^{43}}] & [\mathbf{K^{44}}]\end{bmatrix}^{\mathbf{e}}\begin{Bmatrix}\{\mathbf{u}\}\\ \{\mathbf{w}\}\\ \{\mathbf{U}\}\\ \{\mathbf{W}\}\end{Bmatrix}^{\mathbf{e}}=\begin{Bmatrix}\{\mathbf{F^1}\}\\ \{\mathbf{F^2}\}\\ \{\mathbf{F^3}\}\\ \{\mathbf{F^4}\}\end{Bmatrix}^{\mathbf{e}}. \tag{9}$$

Here $[\mathbf{K^{ij}}]$ is the dynamic stiffness matrix for the axisymmetric foam element ($[\mathbf{K^{ij}}]=[\mathbf{K^{ji}}]^T$, $i,j=1,2,3,4$), and the elements of that matrix are listed in the Appendix. In Eq. (9), the partitioned submatrices $\{\mathbf{F^1}\}$ are force vectors related to the normal and shear stresses acting on the solid and fluid phases of the foam, and they are:

$$F_i^1=2\pi\int_{B^e}r\phi_i(n_{fr}\sigma_r+n_{fz}\tau_{zr})dB, \tag{10a}$$

$$F_i^2=2\pi\int_{B^e}r\phi_i(n_{fr}\tau_{zr}+n_{fz}\sigma_z)dB, \tag{10b}$$

$$F_i^3=2\pi\int_{B^e}r\phi_i(n_{fr}s)dB, \tag{10c}$$

$$F_i^4=2\pi\int_{B^e}r\phi_i(n_{fz}s)dB. \tag{10d}$$

When the elemental Eqs. (9) are assembled based on the continuity of primary variables (the displacement components of the foam) and the balance of secondary variables (the normal and shear stresses acting on the solid and fluid phases of the foam) at the connecting nodes, the axisymmetric global foam system equations that govern wave propagation in the foam are obtained. The global foam system equations will then be of the form

$$[\mathbf{K_f}]\begin{Bmatrix}\{\mathbf{u}\}\\ \{\mathbf{w}\}\\ \{\mathbf{U}\}\\ \{\mathbf{W}\}\end{Bmatrix}=\begin{Bmatrix}\{\mathbf{F^1}\}\\ \{\mathbf{F^2}\}\\ \{\mathbf{F^3}\}\\ \{\mathbf{F^4}\}\end{Bmatrix}, \tag{11}$$

where $[\mathbf{K_f}]$ is the global dynamic stiffness matrix of the axisymmetric foam treatment.

B. Acoustical element

The axisymmetric, acoustical finite element formulation for ideal fluids such as air can be established easily: its derivation will only be outlined here. In a homogeneous acoustical medium, the wave equation in axisymmetric form is

$$\frac{1}{r}\frac{\partial}{\partial r}\left(r\frac{\partial p}{\partial r}\right)+\frac{\partial^2p}{\partial z^2}+k^2p=0, \tag{12}$$

where p is the sound pressure and k is the wave number. The axisymmetric global acoustical system equations can be expressed in the same form as those for the foam: i.e.,

$$[\mathbf{K_a}]\{\mathbf{p}\}=\{\mathbf{Q}\}, \tag{13}$$

where $\{\mathbf{p}\}$ is the vector of unknown nodal pressures and $\{\mathbf{Q}\}$ is the normal volume velocity flux vector. In Eq. (13), the matrices $[\mathbf{K_a}]$ and $\{\mathbf{Q}\}$ are, respectively, defined as

$$K_{ij}=2\pi\int_{\Omega^e}\left[r\frac{\partial\phi_i}{\partial r}\frac{\partial\phi_j}{\partial r}+r\frac{\partial\phi_i}{\partial z}\frac{\partial\phi_j}{\partial z}-k^2r\phi_i\phi_j\right]dr\,dz, \tag{14a}$$

$$Q_i=-j\omega\rho_0 2\pi\int_{B^e}r\phi_i(n_{ar}\nu_r+n_{az}\nu_z)dB. \tag{14b}$$

Here ν_r and ν_z are, respectively, the radial and axial components of the acoustic particle velocity vector in the air, $\mathbf{v_a}$, and n_{ar} and n_{az} are the corresponding components of the outward unit normal vector, $\mathbf{n_a}$, on the boundary.

II. BOUNDARY CONDITIONS AND COUPLING PROCEDURES

A. Boundary conditions

To couple a foam system to a neighboring acoustical system at an arbitrary orientation with respect to the global coordinates in the axisymmetric space, appropriate boundary conditions, which are conceptually the same as those for a Cartesian space, must be enforced at each node along the interface. At an open interface there are force and normal volume velocity conditions to be satisfied in the r and z directions. Those conditions are

$$hp\mathbf{n_a}=s\mathbf{n_t}, \tag{15a}$$

$$(1-h)p\mathbf{n_a}=(\sigma_r n_{fr}+\tau_{zr}n_{fz})\mathbf{i}+(\tau_{zr}n_{fr}+\sigma_z n_{fz})\mathbf{k}, \tag{15b}$$

$$\mathbf{v_a}=j\omega(1-h)\mathbf{u}+j\omega h\mathbf{U}, \tag{15c}$$

where h is the surface porosity (and the surface porosity is here assumed to be equal to the volume porosity), and $\mathbf{i}$ and $\mathbf{k}$ are, respectively, the unit vectors in the r and z directions. The first of these equations requires that force per unit material area acting on the fluid component of the poroelastic medium be equal to the porosity times the pressure in the adjoining acoustic field. The second equation expresses a similar relationship for the force acting on the solid phase of the poroelastic material. The last condition represents the compatibility of the normal volume velocity at the interface.

When the foam is placed adjacent to a hard surface, the boundary conditions are simpler. Specifically, when the elastic porous material is solidly connected to the hard surface, i.e., when it is considered to be ''bonded'' or glued to the adjacent surface,[5] for example, it is assumed that the displacements of both the foam's solid and fluid phases normal to the hard surface are zero. In addition, the tangential component of the solid phase motion must also be set equal to zero when the foam is considered to be bonded to the hard surface. However, the tangential displacement of the fluid component displacement within the foam is unconstrained at the hard surface: i.e., the fluid phase of the foam may ''slip'' at the boundary. When the foam is not solidly attached to the hard surface, but simply rests loosely against it or is separated from the surface by a small air gap, the situation is different. In that case, the normal component of the foam's volume velocity at the interface, i.e., the right hand side of Eq. (15c), is set equal to zero: that is, no individual conditions are placed on the normal components of the displacements of the solid or fluid phases.[5] In addition, in this ''unbonded'' configuration, the tangential components of the foam's fluid and solid phases are unconstrained at the interface: i.e., both the solid and fluid phases may ''slip'' under these conditions.

B. Coupling procedures

To couple poroelastic and acoustical systems, it is necessary to substitute the set of boundary conditions Eqs. (15a)–(15c) into Eqs. (10a)–(10d) and (14b). In that way one obtains

$$F_i^1=2\pi n_{ar}(1-h)\int_B r\phi_i p\,dB \approx 2\pi n_{ar}(1-h)\sum_{j=1}^{m}p_j\int_B r\phi_i\phi_j\,dB, \tag{16a}$$

$$F_i^2=2\pi n_{az}(1-h)\int_B r\phi_i p\,dB \approx 2\pi n_{az}(1-h)\sum_{j=1}^{m}p_j\int_B r\phi_i\phi_j\,dB, \tag{16b}$$

$$F_i^3=2\pi n_{ar}h\int_B r\phi_i p\,dB\approx 2\pi n_{ar}h\sum_{j=1}^{m}p_j\int_B r\phi_i\phi_j\,dB, \tag{16c}$$

$$F_i^4=2\pi n_{az}h\int_B r\phi_i p\,dB\approx 2\pi n_{az}h\sum_{j=1}^{m}p_j\int_B r\phi_i\phi_j\,dB, \tag{16d}$$

$$\begin{aligned}Q_i&=2\pi\omega^2\rho_0\int_B r\phi_i[(1-h)\mathbf{n_a}\cdot\mathbf{u}+h\mathbf{n_a}\cdot\mathbf{U}]dB\\&\approx 2\pi n_{ar}\omega^2\rho_0(1-h)\sum_{j=1}^{m}u_j\int_B r\phi_i\phi_j\,dB\\&\quad+2\pi n_{az}\omega^2\rho_0(1-h)\sum_{j=1}^{m}w_j\int_B r\phi_i\phi_j\,dB\\&\quad+2\pi n_{ar}\omega^2\rho_0 h\sum_{j=1}^{m}U_j\int_B r\phi_i\phi_j\,dB\\&\quad+2\pi n_{az}\omega^2\rho_0 h\sum_{j=1}^{m}W_j\int_B r\phi_i\phi_j\,dB.\end{aligned} \tag{16e}$$

In Eqs. (16a)–(16e), the components of the outward unit normal vector of the acoustical system are evaluated at the interface.

Since all the flux vectors at the interface nodes are now expressed in terms of nodal unknowns, it is possible to place those terms within the coupled dynamic stiffness matrix in a systematic way. The final axisymmetric acoustic-poroelastic system equations have the form

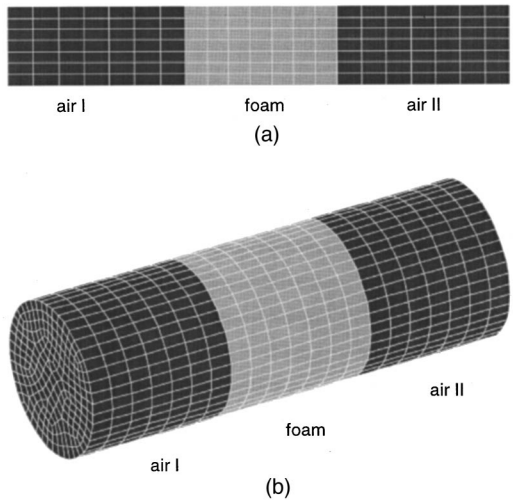

FIG. 1. Configurations for: (a) two-dimensional axisymmetric air/foam/air standing wave tube model; (b) three-dimensional air/foam/air standing wave tube model.

$$\begin{bmatrix} [\mathbf{K_a}] & \vdots & [\mathbf{K_{af1}}] \\ \cdots & \vdots & \cdots \\ [\mathbf{K_{af2}}] & \vdots & [\mathbf{K_f}] \end{bmatrix} \begin{Bmatrix} \{\mathbf{p}\} \\ \{\mathbf{u}\} \\ \{\mathbf{w}\} \\ \{\mathbf{U}\} \\ \{\mathbf{W}\} \end{Bmatrix} = \begin{Bmatrix} \{\mathbf{Q}\} \\ \{\mathbf{F^1}\} \\ \{\mathbf{F^2}\} \\ \{\mathbf{F^3}\} \\ \{\mathbf{F^4}\} \end{Bmatrix}, \tag{17}$$

where $[\mathbf{K_{af1}}]$ and $[\mathbf{K_{af2}}]$ are the matrices resulting from the coupling of the acoustical and poroelastic finite elements.

III. COMPARISON WITH THREE-DIMENSIONAL CARTESIAN SOLUTION

The axisymmetric formulation was first verified by comparison with a previously validated, three-dimensional code based on earlier work:[1] The models that were used in the validation study are described in this section. The particular configuration considered was a cylindrical plug of foam that filled part of the length of a cylindrical duct and that was placed between air-filled upstream and downstream sections; see Fig. 1. The transmission loss of the foam plug was calculated using both three-dimensional and axisymmetric formulations, and the results of the axisymmetric formulation were also compared with experimental results to be described in Sec. IV. The material properties used in the computations presented here, and which were intended to represent the foam used in the transmission loss measurement, are listed in Table I. Note that the porosity was estimated based on the material's measured bulk density, and that the flow resistivity was measured. The tortuosity and stiffness factors were chosen based on previous experience and were adjusted to give good agreement between the measured and predicted transmission loss; see Sec. IV.

TABLE I. Poroelastic material properties used in calculations.

Porosity	Tortuosity	Flow resistivity (MKS Rayls/m)	Young's modulus (Pa)	Loss factor	Poisson ratio	Bulk density (kg/m^3)
0.98	3.0	25×10^3	6.15×10^5	0.15	0.45	30

The axisymmetric finite element model is shown in Fig. 1(a). The light gray elements represents a plug of foam 0.028 m in length and 0.0145 m in radius, and the dark gray elements represent the up- and downstream air spaces (i.e., air regions I and II) that were each 0.033 m in length and 0.0145 m in radius. The lower edge of the model represents the axis of symmetry, while the upper edge represents the outer circumference of the duct. The model comprised 49 foam elements and 98 air elements for a total of 147 elements having 192 nodes. All of the elements in the axisymmetric model were linear, four-node, quadrilateral elements.

The equivalent three-dimensional model is shown in Fig. 1(b). Again the light gray elements represent the foam material and the dark gray elements represent the adjacent air spaces. The three-dimensional model represented exactly the same volume of foam and air as the axisymmetric model illustrated in Fig. 1(a). However, the three-dimensional model comprised 1456 foam and 2912 air elements for a total of 4368 elements having 5082 nodes. The mesh density in the axial direction was identical in the two models. In each radial slice of the three-dimensional model there were 208 elements, which compares with 7 elements in each slice of the axisymmetric model. The average lengths of the radial edges of the elements in the three-dimensional model were approximately the same as those of the axisymmetric elements. All of the elements in the three-dimensional model were linear, eight-node, hexahedral elements.

The same boundary conditions were applied in both the axisymmetric and the three-dimensional cases. The duct circumference was itself assumed to be a rigid. Thus in the air spaces, a zero normal velocity condition applied at the duct wall. In the axisymmetric case the radial displacement of both the solid and fluid phases of the foam were set to zero at the duct circumference to model the hard wall boundary condition. In the three-dimensional case, the components of the solid phase displacements normal to the duct circumference were constrained to be zero along with the corresponding components of the fluid phase motion. The open surface boundary conditions described in Sec. II A were applied to couple the air and foam domains. Note that this set of boundary conditions corresponds to an unconstrained-edge case: i.e., the foam's solid phase may slip axially with respect to the duct wall. This case should give transmission loss results identical to those for normal incidence plane wave transmission through a laterally infinite, plane foam layer of the same thickness as the foam plug. In both cases, the normal incidence plane wave excitation and the absence of edge constraints cause the in-plane (i.e., radial in the axisymmetric case) displacements of both the solid and fluid phases to be zero.[2]

A unit amplitude axial velocity was applied to the left side of air region I in both cases to simulate a plane piston. The right hand end of air space II was terminated by a $\rho_0 c$ impedance (i.e., a normalized impedance of unity), thus creating an anechoic termination. In this case the power transmission coefficient, τ, of the foam plug was calculated as the

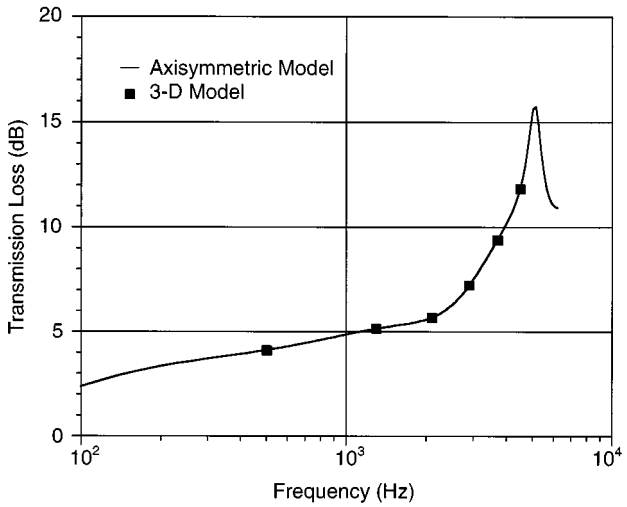

FIG. 2. Comparison of sound transmission losses predicted using axisymmetric and three-dimensional finite element models.

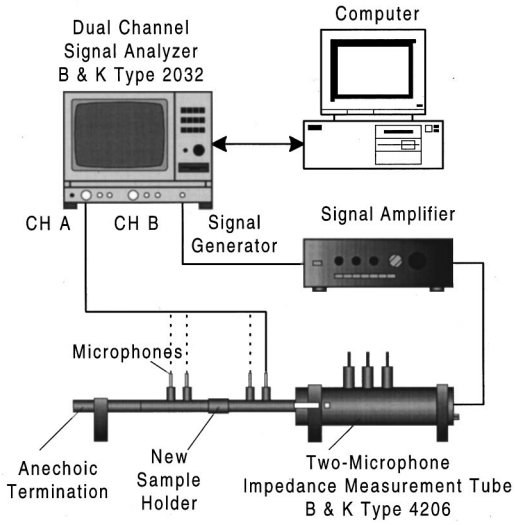

FIG. 3. Experimental setup for measurements of sound transmission loss through foam plugs in standing wave tube.

ratio of the sound power leaving the duct through the $\rho_0 c$ termination to the sound power delivered to the duct by the piston. The transmission loss (TL) was then $10 \log(1/\tau)$. Results are presented here for the frequencies from 100 Hz to 5 kHz: i.e., up to a frequency below the cut on of the first higher order mode in the air spaces.

The transmission losses predicted by using the two models are shown in Fig. 2: For practical purposes, the results are identical. Note that results were calculated at a relatively small number of frequencies in the three-dimensional case owing to the lengthy computation times required in that case. Indeed, it took approximately 5500 times longer to solve the problem at each frequency when using the three-dimensional model as when using the axisymmetric formulation. Note that the recently proposed **u**-p poroelastic finite element implementation offers a speed advantage with respect to the present **u-U** formulation since the number of nodal degrees-of-freedom are reduced from six to four within the poroelastic domain.[15] The reduction in computation time would apply equally to Cartesian and axisymmetric implementations.

IV. COMPARISON WITH EXPERIMENTAL RESULTS

A. Experimental procedure

Several measurements of the normal incidence transmission loss of cylindrical foam samples were conducted to provide data with which predictions made using the axisymmetric formulation could be compared. The measurement procedure used in the present work[16] was based on the transfer function method for measuring in-duct acoustical properties,[17,18] and it may be considered to be an extension of the two-microphone standing wave tube method for measuring normal incidence absorption.[19,20]

The two-microphone standing wave tube method for absorption measurement involves the use of a test apparatus comprising a tube of constant cross section with a loudspeaker at one end and provision for holding a sample at the other end. The loudspeaker is used to generate a plane standing wave field in the tube. While a broadband signal is radiated from the loudspeaker, the transfer function is measured between two microphones flush mounted to the interior surface of the tube. From knowledge of that transfer function and the positions of the microphones with respect to the sample, it is possible to determine the plane wave reflection coefficient of the sample, from which the surface normal impedance and the normal incidence absorption coefficient can also be calculated.

In the measurement procedure followed here, the two-microphone procedure was modified to allow the measurement of the normal incidence transmission loss. The foam samples under test were placed in a new sample holder attached to the end of a standard ASTM E 1050 tube (a Brüel and Kjær Two-Microphone Impedance Measurement Tube Type 4206). The test section comprised a 50-mm-long section of stainless steel tubing having the same inner diameter, 2.9 cm, as the standing wave tube. Downstream of the sample holder provision was made for flush mounting two additional microphones, and an anechoic termination was attached to the downstream section of the tube. A schematic representation of the experimental apparatus is shown in Fig. 3. The anechoic termination was fabricated from 13 layers of loosely packed 3M Thinsulate TAI 6000 to form a layer approximately 66 cm deep. The termination was designed to have an absorption coefficient larger than 0.97 at all frequencies above 500 Hz.[16] The surface normal impedance of the termination is shown in Fig. 4.

By making measurements of the complex sound pressure at four locations, two upstream and two downstream of the sample, it is possible to decompose the sound field into plane wave components propagating up- and downstream. The broadband random signal delivered to the loudspeaker was used as a reference signal to establish the phase of the sound pressure at the four microphone locations. The pressure transmission coefficient, T, was calculated as the ratio of the plane wave component propagating away from the sample in the downstream tube section to the incident component in the upstream section. The transmission loss was then calculated as $20 \log_{10}(1/|T|)$. Note that the provision of

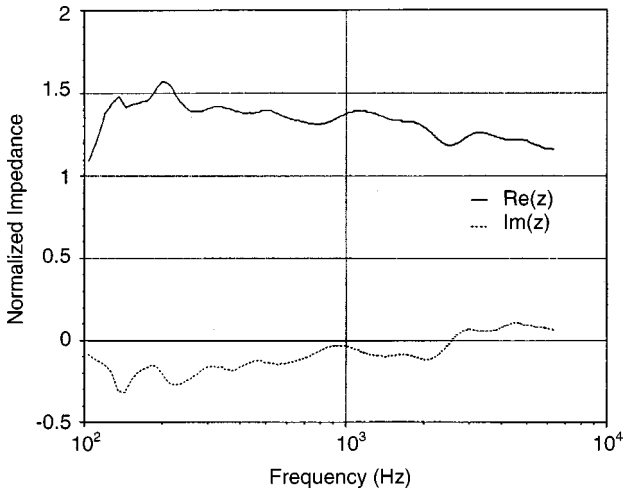

FIG. 4. Normalized surface normal impedance of the standing wave tube termination.

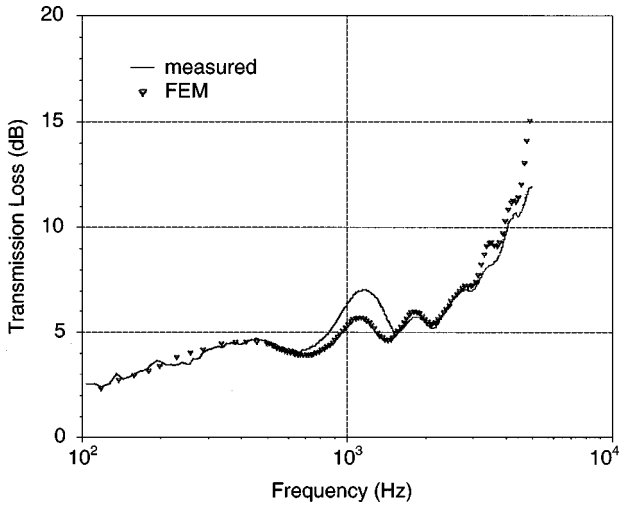

FIG. 5. Sound transmission loss of uniform foam plug when its circumferential edge was unconstrained in the axial direction.

anechoic termination is required to allow the configuration used here to satisfy approximately the assumption usually made in theoretical calculations of transmission loss: i.e., that the transmitted field consists only of sound propagating away from the transmitting surface. As will be seen, the reflection from the termination used in the present experiments had a small but noticeable effect on the results. That effect can be easily reproduced in the theoretical calculations when the termination impedance is known, as was the case here.

Note that the Brüel and Kjær Apparatus Type 4206 is normally supplied with sample holders suitable for both low-frequency (100 Hz–1600 Hz) and high-frequency (500 Hz–6400 Hz) measurements. The work presented here entailed the use of the high-frequency tube only. The results are thus considered to be accurate in the 500 Hz–6400 Hz range; it is believed that the results at lower frequencies are also accurate in this case, however, owing to the low reactivity of the sound fields in the up- and downstream sections.

B. Results

The first sample tested was a piece of polyurethane foam having the same outer diameter as the inner diameter of the sample holder and a length of 0.028 m.

Sound transmission through the cylindrical foam plug was modeled using the axisymmetric elements developed in this study: The model used to make the predictions in this case was the same as that used in the validation study described in Sec. III. In the model, the radius of the foam plug was made 0.0145 m, its length was set to 0.028 m, and the length of the air on each side of the foam plug was made 0.033 m. Unit velocities were prescribed at the nodes on the left-hand face of air space I in order to generate a plane wave traveling toward the foam section. The measured termination impedance was imposed at the right-hand face of acoustical system II. Since the length of the finite element model was not the same as that of the impedance tube used in the experiment, the measured impedance data were phase corrected when applied to the model. The elastic porous material properties that were used to make the predictions are shown in Table I. In a manner similar to that used in the experimental measurement, the complex amplitudes of the incident and transmitted wave components were estimated from the pressures at two adjacent nodes (separated in the z-direction) in air spaces I and II, respectively, that were obtained by solving Eq. (17). From those components, the plane wave transmission coefficient, and thus the normal incidence transmission loss, could then be calculated.

Two different cylindrical cases were considered: i.e., ''free'' and ''glued.'' In the free case the foam was assumed to be just in contact with the duct circumference. Thus it was assumed that the solid phase of the foam was free to move in the axial direction but was constrained to have zero displacement in the radial direction. In the glued case, the foam was assumed to be bonded to the duct interior so that the foam's solid phase displacement was constrained to be zero in both the axial and radial directions. In the experimental realization of the free case, the foam sample was cut carefully so that it fit smoothly into the interior of the sample holder while at the same time there were no visible gaps around the sample's circumference. In the glued case, an adhesive was applied to the outer surface of the foam plug before it was inserted into the sample holder. Care was taken so that the sample was not compressed in this process: i.e., the length of the sample was determined to be the same in both cases. The measured and predicted results for the free and glued cases are shown in Figs. 5 and 6, respectively.

It may be seen that the finite element prediction for the free case is in generally good agreement with the measurements, although the predicted transmission loss is overestimated in the high-frequency limit. Note that the ''ripple'' in the transmission loss results, in part, from reflections from the ''anechoic'' termination: This effect will be considered further in the next sub-section.

In the glued case, the agreement is not quite as good as in the free case, particularly at low frequencies, perhaps because the foam plug was not perfectly bonded all the way around its circumference. The latter effect might account for the overestimate of the transmission loss at low frequencies. Nevertheless, bonding of the sample evidently enhances the transmission loss peak in the neighborhood of 2000 Hz by

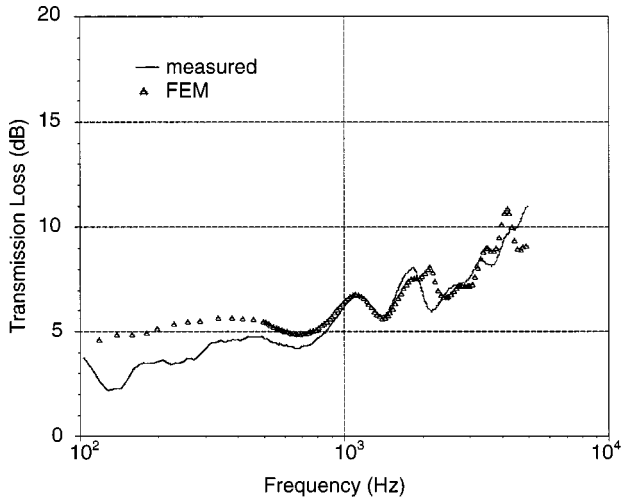

FIG. 6. Sound transmission loss of uniform foam plug when its circumferential edge was glued to the wall of the standing wave tube.

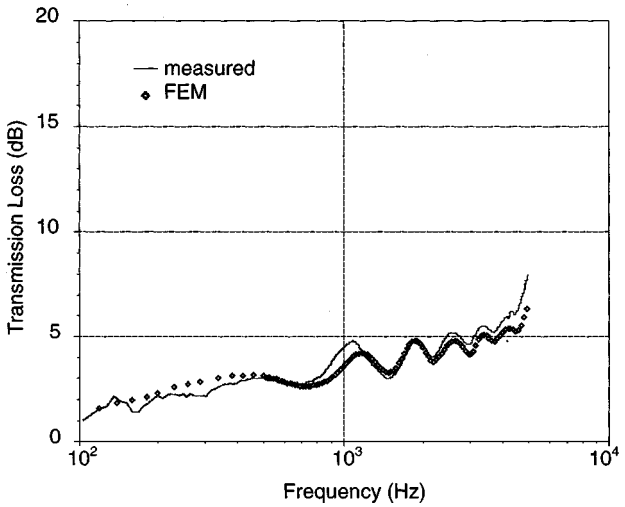

FIG. 8. Sound transmission loss of conical foam plug when its circumferential edge was free to move in the axial direction.

comparison with the peak near 1000 Hz, and this feature is successfully reproduced by the finite element predictions. In addition, the direct attachment of the sample to the duct wall causes the transmission loss to be decreased at high frequencies compared to the free case, perhaps because of the increased significance of the frame wave in this configuration. The latter feature is reproduced in character by the finite-element results.

Measurements were also conducted using a conical foam plug that was created by carefully ''shaving'' a cylindrical foam plug that was 0.028 m in length. Only the free configuration was tested in this case, and the axisymmetric model for this configuration is shown in Fig. 7 where the conical plug is shown to scale. It may be seen from the results plotted in Fig. 8 that the finite element prediction is in excellent agreement with the measurements over the entire frequency range. The results also show that shaping the foam into a cone resulted in a significant reduction of the transmission loss compared to the free cylindrical plug case (see Fig. 5). The decrease in transmission loss in this case presumably results from the decrease in the total treatment volume and hence mass.

C. Effect of finite termination impedance

Finally, it is interesting to explore the effect of the ''anechoic'' termination. As noted earlier, the termination had an absorption coefficient greater than 0.97 at all frequencies above 500 Hz and so might have been expected to have a rather small effect on the measured transmission loss. Nonetheless, both earlier measurements of sound transmission through an orifice plate[16] and the present results have indicated that ripples having an amplitude of 1 dB or more are superimposed on the transmission loss by the effect of reflection from the termination. To demonstrate this effect,

FIG. 7. Configurations for axisymmetric air/conical foam plug/air standing wave tube model.

finite element predictions were made for the free and glued cylindrical plugs and for the conical plug when the duct was assumed to be terminated either by the measured impedance or by a unity normalized impedance, i.e., $\rho_0 c$, and the results are shown in Fig. 9. The effect of the termination impedance may be easily seen in each case, and the effect diminishes at high frequencies as the performance of the termination approaches the ideal case. Thus it may be concluded that the ripple visible in the measured transmission losses presented here is an effect of the measurement procedure and apparatus rather than of the foam itself.

V. CONCLUSIONS

In this article, the formulation of an axisymmetric, poroelastic finite element has been described. It has been shown that that formulation can be used to reproduce results obtained by using a three-dimensional poroelastic finite element formulation in cylindrical geometries. In addition, it has been shown that predictions made using the axisymmet-

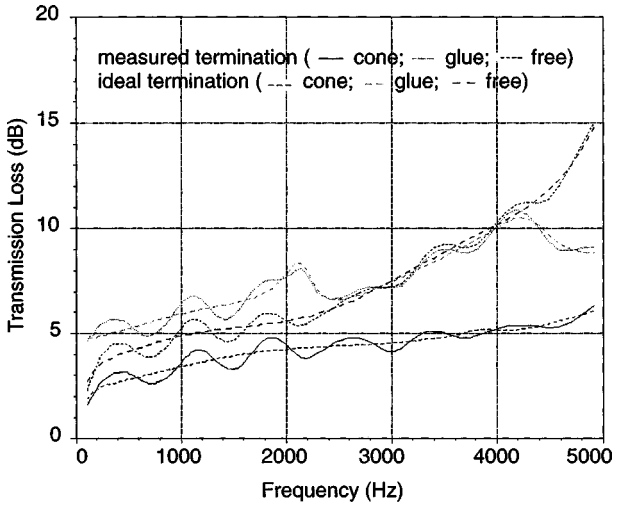

FIG. 9. Effect of termination impedance on sound transmission loss.

ric elements agree well with measurements of sound transmission through cylindrical foam systems in a number of different configurations.

Although a rigorous comparison between the computational speed of the axisymmetric and the three-dimensional formulations has not been attempted, it is clear that the use of the former elements results in greatly increased speed when considering systems that may be approximated as being cylindrical. That efficiency makes it feasible, for example, to perform iterative design exercises to identify optimal duct linings.

The elements described here will also make it straightforward to examine the effect of various types of edge constraints on the measured acoustical properties of samples placed in cylindrical standing wave tubes: thus the present formulation may serve as a useful adjunct to standard experimental techniques. In the same vein, the bulk stiffness of poroelastic materials is sometimes estimated by measuring the mechanical impedance of cylindrical samples of materials. The relation between the stiffness properties measured in that way and the bulk stiffness properties of the material is sometimes not clear owing to the effects of both finite sample size and the traction conditions at the interface of the sample and the drive and support surfaces. The present work makes it possible to model those measurements in an efficient manner, and so will make it possible to relate unequivocally the measured mechanical impedance of finite samples to the stiffness properties of the bulk material.

Finally, in the present work only axisymmetric forcing disturbances and boundary conditions have been considered. In future work, methods to account for nonaxisymmetric forcing of cylindrical systems having either axisymmetric or nonaxisymmetric boundary conditions will be considered.

ACKNOWLEDGMENTS

The authors are grateful to Richard J. Yun, now at Hughes Aerospace Corporation and formerly a Graduate Research Assistant at the Ray W. Herrick Laboratories, for making the transmission loss measurements described in Sec. IV. This article was completed while the third author was visiting the Center for Noise and Vibration Control (NOVIC), Department of Mechanical Engineering, Korea Advanced Institute of Science and Technology. He is grateful to the faculty, students, and staff of NOVIC for their hospitality, and to the Korea Research Foundation (KRF) for providing financial support. The work described in this article was made possible by funding from the National Aeronautics and Space Administration.

APPENDIX: STIFFNESS MATRIX ELEMENTS

$$K_{ij}^{11}=2\pi\int_{\Omega^e}\left[(2N+A)\left(r\frac{\partial\phi_i}{\partial r}\frac{\partial\phi_j}{\partial r}+\frac{1}{r}\phi_i\phi_j\right)+A\left(\frac{\partial\phi_i}{\partial r}\phi_j+\phi_i\frac{\partial\phi_j}{\partial r}\right)+Nr\frac{\partial\phi_i}{\partial z}\frac{\partial\phi_j}{\partial z}-\omega^2\rho_{11}^{*}r\phi_i\phi_j\right]dr\,dz,$$

$$K_{ij}^{12}=2\pi\int_{\Omega^e}\left[A\left(r\frac{\partial\phi_i}{\partial r}\frac{\partial\phi_j}{\partial z}+\phi_i\frac{\partial\phi_j}{\partial z}\right)+Nr\frac{\partial\phi_i}{\partial z}\frac{\partial\phi_j}{\partial z}\right]dr\,dz,$$

$$K_{ij}^{13}=2\pi\int_{\Omega^e}\left[Q\left(r\frac{\partial\phi_i}{\partial r}\frac{\partial\phi_j}{\partial r}+\frac{\partial\phi_i}{\partial r}\phi_j+\phi_i\frac{\partial\phi_j}{\partial r}+\frac{1}{r}\phi_i\phi_j\right)-\omega^2\rho_{12}^{*}r\phi_i\phi_j\right]dr\,dz,$$

$$K_{ij}^{14}=2\pi\int_{\Omega^e}\left[Q\left(r\frac{\partial\phi_i}{\partial r}\frac{\partial\phi_j}{\partial z}+\phi_i\frac{\partial\phi_j}{\partial z}\right)\right]dr\,dz,$$

$$K_{ij}^{22}=2\pi\int_{\Omega^e}\left[Nr\frac{\partial\phi_i}{\partial r}\frac{\partial\phi_j}{\partial r}+(2N+A)r\frac{\partial\phi_i}{\partial z}\frac{\partial\phi_j}{\partial z}-\omega^2\rho_{11}^{*}r\phi_i\phi_j\right]dr\,dz,$$

$$K_{ij}^{23}=2\pi\int_{\Omega^e}\left[Q\left(r\frac{\partial\phi_i}{\partial z}\frac{\partial\phi_j}{\partial r}+\frac{\partial\phi_i}{\partial z}\phi_j\right)\right]dr\,dz,$$

$$K_{ij}^{24}=2\pi\int_{\Omega^e}\left[Qr\frac{\partial\phi_i}{\partial z}\frac{\partial\phi_j}{\partial z}-\omega^2\rho_{12}^{*}r\phi_i\phi_j\right]dr\,dz,$$

$$K_{ij}^{33}=2\pi\int_{\Omega^e}\left[R\left(r\frac{\partial\phi_i}{\partial r}\frac{\partial\phi_j}{\partial r}+\frac{\partial\phi_i}{\partial r}\phi_j+\phi_i\frac{\partial\phi_j}{\partial r}+\frac{1}{r}\phi_i\phi_j\right)-\omega^2\rho_{22}^{*}r\phi_i\phi_j\right]dr\,dz,$$

$$K_{ij}^{34}=2\pi\int_{\Omega^e}\left[R\left(r\frac{\partial\phi_i}{\partial r}\frac{\partial\phi_j}{\partial z}+\phi_i\frac{\partial\phi_j}{\partial z}\right)\right]dr\,dz,$$

$$K_{ij}^{44}=2\pi\int_{\Omega^e}\left[Rr\frac{\partial\phi_i}{\partial z}\frac{\partial\phi_j}{\partial z}-\omega^2\rho_{22}^{*}r\phi_i\phi_j\right]dr\,dz.$$

[1] Yeon June Kang and J. Stuart Bolton, ''Finite element modeling of isotropic elastic porous materials coupled with acoustical finite elements,'' J. Acoust. Soc. Am. **98**, 635–643 (1995).
[2] Yeon June Kang and J. Stuart Bolton, ''A finite element model for sound transmission through foam-lined double panel structures,'' J. Acoust. Soc. Am. **99**, 2755–2765 (1996).
[3] Yeon June Kang and J. Stuart Bolton, ''Sound transmission through elastic porous wedges and foam layers having spatially graded properties,'' J. Acoust. Soc. Am. **102**, 3319–3332 (1997).
[4] M. A. Biot, ''Theory of propagation of elastic waves in a fluid-saturated porous solid I. Low frequency range. II. Higher frequency range,'' J. Acoust. Soc. Am. **28**, 168–191 (1956).
[5] J. S. Bolton, N.-M. Shiau, and Y. J. Kang, ''Sound transmission through multi-panel structures lined with elastic porous materials,'' J. Sound Vib. **191**, 317–347 (1996).
[6] Y. J. Kang and J. S. Bolton, ''Optimal design of acoustical foam treatments,'' Trans. ASME J. Vib. Acoust. **181**, 498–504 (1996).
[7] T. F. Johansen, J.-F. Allard, and B. Brouard, ''Finite element method for predicting the acoustical properties of porous samples,'' Acta Acust. (China) **3**, 487–491 (1995).
[8] J. P. Coyette and H. Wynendaele, ''A finite element model for predicting the acoustic transmission characteristics of layered structures,'' in *Proceedings of INTER-NOISE 95* (Noise Control Foundation, Poughkeepsie, NY, 1995), Vol. 2, pp. 1279–1282.
[9] N. Atalla and R. Panneton, ''The effects of multilayer sound absorbing treatments on the noise field inside a plate-backed cavity,'' Noise Control Eng. J. **44**, 235–243 (1996).

[10] Y. Kagawa, T. Yamabuchi, and A. Mori, ''Finite element simulation of an axisymmetric acoustic transmission system with sound absorbing wall,'' J. Sound Vib. **53**, 357–374 (1977).
[11] V. Easwaran, W. Lauriks, and J. P. Coyette, ''Displacement-based finite element method for guided wave propagation problems: Application to poroelastic media,'' J. Acoust. Soc. Am. **100**, 2989–3002 (1996).
[12] T. E. Vigran, L. Kelders, W. Lauriks, and P. Leclaire, ''Prediction and measurements of the influence of boundary conditions in a standing wave tube,'' Acust. Acta Acust. **83**, 419–423 (1997).
[13] R. J. Astley and A. Cummings, ''A finite element scheme for attenuation in ducts lined with porous material: Comparison with experiment,'' J. Sound Vib. **116**, 239–263 (1987).
[14] R. D. Cook, D. S. Malkus, and M. E. Plesha, *Concepts and Applications of Finite Element Analysis*, 3rd ed. (Wiley, New York, 1989), see pp. 294–298.
[15] N. Atalla, R. Panneton, and P. Debergue, ''Numerical modeling of the vibroacoustic behavior of multilayer structures with poroelastic materials,'' in *Proceedings of NOISE-CON 98* (Noise Control Foundation, Poughkeepsie, NY, 1998), pp. 611–614.
[16] J. S. Bolton, R. J. Yun, J. Pope, and D. Apfel, ''Development of a new sound transmission test for automotive sealant materials,'' Society of Automotive Engineers 1997 Transactions **106**, Journal of Passenger Cars (section 6), 2651–2658 (1998).
[17] J. Y. Chung and D. A. Blaser, ''Transfer function method of measuring in-duct acoustic properties. I. Theory,'' J. Acoust. Soc. Am. **68**, 907–913 (1980).
[18] Chung and D. A. Blaser, ''Transfer function method of measuring in-duct acoustic properties. II. Experiment,'' J. Acoust. Soc. Am. **68**, 914–921 (1980).
[19] ASTM Standard E 1050-90, ''Impedance and absorption of acoustical materials using a tube, two microphones, and a digital frequency analysis system.''
[20] ISO 10534-2, ''Acoustics—Determination of sound absorption coefficient and impedance in impedance tubes—Part 2 Transfer function method.''

Theory of compressional and transverse wave propagation in consolidated porous media

Michael J. Buckingham[a)]
Marine Physical Laboratory, Scripps Institution of Oceanography, University of California, San Diego, 9500 Gilman Drive, La Jolla, California 92093-0213

(Received 3 December 1997; accepted for publication 22 February 1999)

A theory of compressional and shear wave propagation in consolidated porous media (rocks) is developed by extending ideas already introduced in connection with unconsolidated marine sediments. The consolidated material is treated as an elastic medium which exhibits a specific form of stress relaxation associated with grain boundaries and microcracks. The stress relaxation, which is linear in the sense that it obeys superposition, shows hysteresis, as characterized by a material response function. Two linear wave equations are derived, one for compressional and the second for shear waves, from which expressions for the wave speeds and attenuations are established. In both cases, the attenuation is found to scale with the first power of frequency, consistent with many observations of attenuation in sandstones, limestones, and shales; the wave speeds show weak logarithmic dispersion. These expressions for the wave speeds and attenuations satisfy the Kronig–Kramers dispersion relationships, as they must if the response of the medium to disturbances is to be causal. Some comments are offered on the nature of the material response, notably that it appears to be primarily associated with grain-boundary interactions occurring at a molecular level, rather than being related to the macroscopic properties of the material, such as density or porosity. [S0001-4966(99)02106-2]

PACS numbers: 43.20.Jr, 43.30.Ky, 43.30.Ma, 43.35.Mr [DEC]

LIST OF SYMBOLS

c_p	compressional wave speed (m/s)
c_s	shear wave speed (m/s)
c_{p0}	compressional wave speed in absence of intergranular stress relaxation (m/s)
c_{s0}	shear wave speed in absence of intergranular stress relaxation (m/s)
α_p	compressional attenuation coefficient (nepers/m)
α_s	shear attenuation coefficient (nepers/m)
β_p	compressional loss tangent
β_s	shear loss tangent
Q_p	quality factor, compressional waves
Q_s	quality factor, shear waves
χ_p	compressional dissipation coefficient
χ_s	shear dissipation coefficient
μ	dynamic rigidity modulus of skeletal frame
μ_p	compressional stress relaxation rigidity modulus
μ_s	shear stress relaxation rigidity modulus
ω	angular frequency
t	time
p	pressure fluctuation
$\underline{s}$	particle displacement
$\underline{v}$	particle velocity
ρ	density fluctuation
$\psi(t)$	velocity potential, compressional wave
$\psi_s(t)$	velocity potential, shear wave
$\underline{A}(t)$	vector potential
$\Psi(j\omega)$	Fourier transform of $\psi(t)$
$\Psi_s(j\omega)$	Fourier transform of $\psi_s(t)$
$h(t)$	compressional material response function
$h_s(t)$	shear material response function
$H(j\omega)$	Fourier transform of $h(t)$
$H_s(j\omega)$	Fourier transform of $h_s(t)$
n	compressional material response exponent ($0<n<1$)
m	shear material response exponent ($0<m<1$)
N	fractional porosity
ρ_0	bulk density of medium
ρ_f	density of pore fluid
$\underline{\rho_s}$	density of mineral solid
κ	bulk modulus of skeletal frame
κ	bulk modulus of medium
κ_f	bulk modulus of pore fluid
κ_s	bulk modulus of mineral solid

INTRODUCTION

A theoretical treatment of compressional and shear wave propagation in saturated, solid porous media such as rocks and consolidated marine sediments was developed in two classic papers by Biot.[1,2] Essentially, he considered that the pore fluid can move relative to the skeletal mineral frame, and found that two compressional waves are admissible, the so-called fast and slow waves, as well as a shear wave. The fast wave corresponds to the situation where the pore fluid and the solid material move essentially in phase, whereas they are in opposite phase in the slow wave. Although the slow wave is a propagating wave, it is very heavily attenuated relative to the fast wave.

Biot included dissipation in his theory, which he attrib-

[a)]Also affiliated with: Institute of Sound and Vibration Research, The University, Southampton SO17 1BJ, England.

uted to viscosity of the pore fluid. As with any viscous medium, this gives rise to an attenuation coefficient that depends on frequency, f, scaling as f^2 at low frequencies and as $f^{1/2}$ above some threshold frequency. Correspondingly, his wave speeds are dispersive, increasing as $f^{1/2}$ at higher frequencies. Dissipation associated with the mineral frame, occurring for instance at grain boundaries, is not included in Biot's original model.

The question of the frequency dependence of the attenuation coefficient of waves in rocks is of considerable interest to the geophysics community. Many measurements of attenuation have been performed, both *in situ* and under laboratory conditions,[3] which provide strong evidence that the attenuation scales essentially as the first power of frequency, f^1, over the very broad frequency range from 10^{-2} to 10^7 Hz.[4] A discussion of these attenuation measurements, including a bibliography, is given by Johnston *et al.*[5] It has also been reported[6,7] that dispersion is negligible in rocks up to frequencies as high as 1 MHz, that is, the wave speed is essentially independent of frequency.

These experimental observations are not in accord with the predictions of the Biot theory.[1,2] The disparity stems from Biot's assumed loss mechanism, the viscosity of the pore fluid. Two alternative dissipation mechanisms are intrinsic loss in the minerals constituting the skeletal frame, although this is almost certainly negligible, and some form of dissipation arising from the relative movement between grain boundaries or crack surfaces. The latter type of dissipation cannot be identified as Coulomb friction, since this is a nonlinear mechanism for which there is no evidence[8] at the very low level of strain (10^{-6} or less) associated with wave propagation.

The purpose of this article is to develop a theory of seismic wave propagation in consolidated porous materials in which the dissipation, although arising from the relative movement of grain boundaries, is distinctly different from Coulomb friction. The loss mechanism in question was introduced recently by Buckingham[9–11] in connection with wave propagation in unconsolidated marine sediments. The new mechanism, which is strictly linear in that the principle of superposition is obeyed, takes account of stress relaxation occurring at grain-boundary contacts and leads to an attenuation that scales almost exactly as the first power of frequency and a phase speed that shows weak logarithmic dispersion. Both features are in accord with observations in saturated sediments and in rocks. Moreover, the predicted phase speed and attenuation satisfy the Kronig–Kramers[12,13] relationships, which must hold if the medium is to be causal, regardless of the physical mechanism responsible for the propagation.

An interesting outcome of the Biot theory[1,2] is the prediction of the slow compressional wave. Such a wave has been observed under controlled experimental conditions in consolidated porous media consisting of lightly fused glass beads saturated with water.[14,15] In unconsolidated media, it appears that the slow wave is either absent or negligible.[15] Since the slow wave is very difficult to detect, even in consolidated media, it is neglected entirely in the present analysis. In effect, this means that the pore fluid and the skeletal mineral frame are assumed to move together, which leads to a significant simplification in the theoretical development. This situation is, in fact, a special case of the Biot theory. Clearly, the slow wave could be included in the analysis by adopting the full formalism of the Biot theory, but with the new grain-boundary stress relaxation mechanism replacing the viscosity of the pore fluid. From a practical point of view, this more general approach would not lead to significantly different properties for the two primary waves, the fast wave and the shear wave, which is why it is not pursued here.

I. THE EQUATION OF MOTION

The analysis of wave propagation in a consolidated porous medium developed below follows lines similar to Buckingham's[9,10] treatment of waves in unconsolidated materials. Now, of course, the elasticity of the mineral frame must be included in the analysis, which is the main departure from the previous theoretical developments.

The porous medium is treated as a (macroscopically) homogeneous, isotropic elastic solid with shear modulus μ. Since the elasticity is associated exclusively with the mineral frame, μ is independent of the properties of the pore fluid. Thus, if the pore fluid were removed and replaced by a vacuum, μ could be measured directly using a standard laboratory technique. In fact, the shear modulus of most rocks is already available in the literature.[16] In setting up the wave equations, it is implicit that elements of volume are being considered in a way which is standard for a homogeneous medium. The dimensions of such volume elements are assumed to be small compared with the wavelengths of interest, but large in relation to the size of the pores. For most granular media of interest here, this treatment is valid for frequencies below several hundred kHz.

To begin, suppose that all dissipation is neglected. The composite material may then be treated as a simple elastic solid, the (linearized) equation of motion for which is[17]

$$\rho_0 \frac{\partial^2 \underline{s}}{\partial t^2} = \left(\kappa + \frac{4}{3}\mu\right) \text{grad div } \underline{s} - \mu \text{ curl curl } \underline{s}, \tag{1}$$

where ρ_0 is bulk density and κ is the bulk modulus of the medium, t is time, and the vector $\underline{s}$ is displacement. When the displacements are small, as is the case with wave propagation, the velocity, $\underline{v}$, can be expressed as the partial derivative of $\underline{s}$

$$\underline{v} = \frac{\partial \underline{s}}{\partial t}, \tag{2}$$

and the equation of motion can be expressed in terms of the velocity as

$$\rho_0 \frac{\partial^2 \underline{v}}{\partial t^2} = \left(\kappa + \frac{4}{3}\mu\right) \text{grad div } \underline{v} - \mu \text{ curl curl } \underline{v}. \tag{3}$$

Turning now to the question of dissipation, the stress relaxation terms are formulated exactly as in the treatment of compressional and shear waves in an unconsolidated medium.[10] Thus, the full equation of motion, including stress relaxation terms, is proposed as

$$\rho_0 \frac{\partial^2 \underline{v}}{\partial t^2} = \left(\kappa + \frac{4}{3}\mu\right) \text{grad div } \underline{v} - \mu \text{ curl curl } \underline{v} + \lambda_f \text{ grad div } \frac{\partial}{\partial t}[h(t) \otimes \underline{v}(t)] + \frac{4}{3}\eta_f \text{ grad div} \frac{\partial}{\partial t}[h_s(t) \otimes \underline{v}(t)] - \eta_f \text{ curl curl} \frac{\partial}{\partial t}[h_s(t) \otimes \underline{v}(t)], \quad (4)$$

where $h(t)$ and $h_s(t)$ are material response functions for compressional and shear disturbances, respectively, and the symbol $\otimes$ denotes a temporal convolution. The stress relaxation terms in Eq. (4) will be familiar as representing viscous losses when the response functions are Dirac delta functions, since $\delta(t) \otimes \underline{v}(t) = \underline{v}(t)$. In this special case, η_f and λ_f would be the coefficients of shear and bulk viscosity, respectively. Now, viscosity is simply a form of internal friction that arises when layers of a fluid medium slide against one another. In such a medium the stress and strain rate follow each other instantaneously. By extension, the convolutions in Eq. (4) may be thought of as representing a generalized viscosity, or internal friction, that occurs in granular materials as particles move in relation to one another. In this situation, the stress–strain rate relationship depends on the history of the loading process, as represented by the response functions $h(t)$ and $h_s(t)$. With appropriate forms for the response functions, propagation behavior is obtained that differs significantly from that encountered in a viscous medium.

Although the stress relaxation terms in Eq. (4) are postulated as representing dissipation and dispersion associated with the relative motion of grain boundaries[18] in granular media, we still consider the material to be homogeneous and continuous as far as the wave analysis is concerned. This is consistent with the fact that the wavelengths of interest are very much greater than the size scale of the heterogeneities in the medium. As in the theoretical treatment of compressional and shear waves in unconsolidated materials,[10] the response functions are assigned the forms

$$h(t) = u(t) \frac{t_0^{n-1}}{t^n}, \quad 0 < n < 1, \quad (5)$$

and

$$h_s(t) = u(t) \frac{t_1^{m-1}}{t^m}, \quad 0 < m < 1, \quad (6)$$

where the unit step function, $u(t)$, ensures that the response of the medium is causal. The temporal coefficients t_0 and t_1 maintain the correct units of inverse time for the response functions, giving the convolutions the dimensions of velocity, as required.

The choice of an inverse-time power law for the response functions is not entirely arbitrary. Certain polymeric materials exhibit a form of stress relaxation that varies as t^{-n}, where n is positive, and in fact such behavior has been empirically represented by Nutting's equation.[19,20] As with granular materials, the polymers also show a constant-Q,[21] or equivalently, an attenuation that scales as the first power of frequency, suggesting that the granular media may show the same form of stress relaxation as the plastics, namely, t^{-n}.

II. WAVE EQUATIONS

The equation of motion [Eq. (4)] may be decomposed into two wave equations, one representing compressional and the other transverse disturbances, by expressing the velocity as the sum of the gradient of a scalar potential, ψ, and the curl of a zero-divergence vector potential $\underline{A}$. For shear waves of vertical polarization, $\underline{A}$ itself may be expressed in terms of a scalar shear potential ψ_s.

The argument is fairly standard and is the same as that followed by Buckingham,[10] except that now the elastic terms must be included in the equations. Rather than repeat the details of the derivation, the resultant wave equations are simply stated here:

$$\nabla^2 \psi - \frac{1}{c_{p0}^2} \frac{\partial^2 \psi}{\partial t^2} + \frac{\lambda_f}{\rho_0 c_{p0}^2} \frac{\partial}{\partial t} \nabla^2 [h(t) \otimes \psi(t)] + \frac{4\eta_f}{3\rho_0 c_{p0}^2} \frac{\partial}{\partial t} \nabla^2 [h_s(t) \otimes \psi(t)] = 0 \quad \text{(compressional)}, \quad (7)$$

and

$$\nabla^2 \psi_s - \frac{1}{c_{s0}^2} \frac{\partial^2 \psi_s}{\partial t^2} + \frac{\eta_f}{\rho_0 c_{s0}^2} \frac{\partial}{\partial t} \nabla^2 [h_s(t) \otimes \psi_s(t)] = 0 \quad \text{(shear)}. \quad (8)$$

In these expressions, c_{p0} and c_{s0} are, respectively, the phase speeds that the compressional and shear waves would have if the stress relaxation were somehow turned off. Thus, c_{p0} and c_{s0} are given by the usual expressions for an elastic medium

$$c_{p0} = \sqrt{\frac{\kappa + \frac{4}{3}\mu}{\rho_0}}, \quad (9)$$

and

$$c_{s0} = \sqrt{\frac{\mu}{\rho_0}}. \quad (10)$$

As discussed below, the actual phase speeds differ from c_{p0} and c_{s0} because of the effective stiffness introduced into the medium by the grain-to-grain stress relaxation mechanism.

It is important to note that Eqs. (9) and (10) are expressed in the time domain, implying that the various elastic and dissipation coefficients appearing in these equations are real constants. That is to say, these coefficients are not permitted to be complex nor may they show any dependence on frequency.

To convert to the frequency domain, the wave equations must be Fourier transformed with respect to time. The resulting reduced wave equations are

$$\nabla^2 \Psi + \frac{\omega^2}{c_{p0}^2} \Psi + \frac{j\omega}{\rho_0 c_{p0}^2} [\lambda_f H(j\omega) + \tfrac{4}{3}\eta_f H_s(j\omega)] \nabla^2 \Psi = 0, \quad (11)$$

and

$$\nabla^2\Psi_s+\frac{\omega^2}{c_{s0}^2}\Psi_s+j\omega\frac{\eta_f}{\rho_0 c_{s0}^2}H_s(j\omega)\nabla^2\Psi_s=0, \tag{12}$$

where $j=\sqrt{-1}$, ω is angular frequency, and (Ψ,Ψ_s) are the Fourier transforms of the compressional and shear potentials (ψ,ψ_s). The transforms of the response functions (H,H_s) are the following standard forms:[22]

$$H(j\omega)=\frac{\Gamma(1-n)}{(j\omega t_0)^{1-n}}, \tag{13}$$

and

$$H_s(j\omega)=\frac{\Gamma(1-m)}{(j\omega t_1)^{1-m}}, \tag{14}$$

where $\Gamma(...)$ is the gamma function, which is essentially unity when n and m are very small numbers, as is the case for granular media.

By substituting Eqs. (13) and (14) into (11) and (12), the reduced wave equations may be expressed in the form

$$\nabla^2\Psi+\frac{\omega^2}{c_{p0}^2[1+(j\omega t_0)^n\chi_p+(j\omega t_1)^m(c_{s0}/c_{p0})^2\chi_s]}\Psi=0, \tag{15}$$

and

$$\nabla^2\Psi_s+\frac{\omega^2}{c_{s0}^2[1+(j\omega t_1)^m\chi_s]}\Psi_s=0, \tag{16}$$

where the dimensionless coefficients χ_p and χ_s are

$$\chi_p=\frac{\lambda_f\Gamma(1-n)}{\rho_0 c_{p0}^2 t_0}=\frac{4\mu_p}{3\rho_0 c_{p0}^2} \tag{17}$$

and

$$\chi_s=\frac{\eta_f\Gamma(1-m)}{\rho_0 c_{s0}^2 t_1}=\frac{\mu_s}{\rho_0 c_{s0}^2}. \tag{18}$$

Notice that these expressions define two new coefficients, μ_p and μ_s, which are stress relaxation rigidity moduli describing the additional stiffness of the medium that arises from the grain boundary interactions.

III. WAVE SPEEDS AND ATTENUATIONS

The phase speeds and attenuations of the compressional and shear waves are easily deduced from Eqs. (15) and (16), and in fact the former has already been discussed at some length in this context by Buckingham.[9] Since both equations have exactly the same form, only the latter is addressed here in the interest of brevity.

The solution of Eq. (16) for one-dimensional shear wave propagation in the x-direction is

$$\Psi_s=\Psi_{s0}\exp-j\frac{\omega}{c_{s0}\sqrt{1+(j\omega t_1)^m\chi_s}}|x|, \tag{19}$$

where Ψ_{s0} is the amplitude of the wave. It follows that the phase speed is

$$c_s=c_{s0}/\mathrm{Re}[1+(j\omega t_1)^m\chi_s]^{-1/2}, \tag{20}$$

and the attenuation coefficient is

$$\alpha_s=\frac{\omega}{c_{s0}}\mathrm{Im}[1+(j\omega t_1)^m\chi_s]^{-1/2}. \tag{21}$$

These expressions for the phase speed and attenuation are exact, since no approximations have yet been introduced (apart from linearizing the equation of motion). Notice that in the low frequency limit ($\omega\to 0$) the phase speed reduces to c_{s0}, the speed in the absence of stress relaxation, and the attenuation is zero.

Since m is small compared with unity, the expressions in Eqs. (20) and (21) may be accurately approximated to first order in m. Based on an argument described by Buckingham,[9,10] the results are

$$c_s\approx c_{s0}\sqrt{1+\chi_s}\left[1+\frac{m\chi_s}{2(1+\chi_s)}\ln(|\omega|t_1)\right], \tag{22}$$

and

$$\alpha_s\approx\frac{m\pi}{4}\frac{\chi_s}{(1+\chi_s)^{3/2}}\frac{|\omega|}{c_{s0}}. \tag{23}$$

Thus, to this order of approximation, the attenuation coefficient scales as the first power of frequency and the phase speed shows very weak logarithmic dispersion, both in accord with observations of wave propagation in rocks.[7,23]

Now, the attenuation may alternatively be expressed in terms of the loss tangent, β_s, representing the imaginary part of the complex wave number relative to the real part. ($\beta_s=1/2Q_s$, where Q_s, is the quality factor, a parameter that is commonly used as a measure of attenuation in rock geophysics.) It is easily shown that

$$\beta_s=\frac{\alpha_s c_s}{\omega}\approx\frac{m\pi}{4}\frac{\chi_s}{1+\chi_s}, \tag{24}$$

from which it follows that the wave speed in Eq. (22) can be written as

$$c_s\approx c_{s0}\sqrt{1+\chi_s}\left[1+\frac{2\beta_s}{\pi}\ln(|\omega|t_1)\right]. \tag{25}$$

Similar results hold for the compressional wave:[9,10]

$$\beta_p\approx\frac{(\chi_p n\pi/4)+\chi_s(m\pi/3)(c_{s0}/c_{p0})^2}{1+\chi_p+\chi_s(4/3)(c_{s0}/c_{p0})^2} \tag{26}$$

and

$$c_p\approx c_{p0}\sqrt{1+\chi_p+\frac{4}{3}\left(\frac{c_{s0}}{c_{p0}}\right)^2\chi_s}\times\left[1+P\frac{2\beta_p}{\pi}\ln(|\omega|t_0)+S\frac{2\beta_p}{\pi}\ln(|\omega|t_1)\right], \tag{27}$$

$$P=\left[1+\frac{4m\chi_s}{3n\chi_p}\left(\frac{c_{s0}}{c_{p0}}\right)^2\right]^{-1}, \tag{27a}$$

$$S=\left[1+\frac{3n\chi_p}{4m\chi_s}\left(\frac{c_{p0}}{c_{s0}}\right)^2\right]^{-1}. \tag{27b}$$

These results for the phase speed and attenuation pairs are interesting because they satisfy the Kronig–Kramers relationships identically,[24] which is required if the response of the medium is to be causal. Although the question of causality is important in connection with pulse propagation, it has long been an unresolved issue in the context of materials

which show an attenuation that scales as the first power of frequency.[25] Buckingham,[9] however, has shown that the impulse response of a dissipative medium of the type described above is strictly causal; that is to say, no anomalous behavior is observed in the received pulse around the origin in time.

If the weak frequency dispersion is neglected, the wave speeds in Eqs. (25) and (27) are approximated as

$$c_p \approx c_{p0}\sqrt{1+\chi_p+\frac{4}{3}\left(\frac{c_{s0}}{c_{p0}}\right)^2\chi_s} = \sqrt{\frac{\kappa+\frac{4}{3}[\mu+\mu_p+\mu_s]}{\rho_0}}, \tag{28}$$

and

$$c_s \approx c_{s0}\sqrt{1+\chi_s} = \sqrt{\frac{\mu+\mu_s}{\rho_0}}. \tag{29}$$

The loss tangents in Eqs. (24) and (26) can also be expressed in terms of the stress relaxation moduli μ_p and μ_s as follows:

$$\beta_p = \frac{\pi}{3}\frac{(n\mu_p+m\mu_s)}{[\kappa+\frac{4}{3}(\mu+\mu_p+\mu_s)]}, \tag{30}$$

and

$$\beta_s = \frac{m\pi}{4}\frac{\mu_s}{\mu+\mu_s}. \tag{31}$$

In the absence of a skeletal frame (i.e., $\mu=0$), Eqs. (28) to (31) reduce identically to the corresponding expressions for an unconsolidated sediment. According to Eqs. (28) and (29), the stress relaxation mechanism has the effect of raising the phase speeds above the values c_{p0} and c_{s0} that they would have had if the medium were lossless. This occurs because the stress relaxation terms lead, not only to attenuation, but also to a stiffening of the material, as is apparent from Eqs. (28) and (29), where the effective shear modulus is seen to be $(\mu+\mu_p+\mu_s)$ for compressional waves and $(\mu+\mu_s)$ for shear waves.

Mathematically, the additional stress relaxation stiffness, represented by the moduli μ_p and μ_s introduced in Eqs. (17) and (18), is characteristic of response functions that follow an inversetime power law. Such behavior would not occur if the stress relaxation were in the form of an exponential decay, nor, of course, would the attenuation scale as the first power of frequency. Note that, in the limiting case when n and m become vanishingly small, the attenuation [Eqs. (30) and (31)] goes to zero and the sole effect of the stress relaxation terms in the equation of motion is to raise the wave speeds by increasing the stiffness of the medium.

The approximations in Eqs. (25) and (24) have been compared[9] with the exact expressions in Eqs. (20) and (21), using values of the parameters that are representative of geophysical materials. It is difficult to distinguish the approximations from the exact forms over some 12 decades of frequency.

IV. EVALUATION OF THE GEOACOUSTIC PARAMETERS

Equations (28) to (31) for the compressional and shear wave speeds and attenuations contain two elastic moduli (κ, μ), four stress relaxation coefficients (μ_p, μ_s, n, m), and the density of the porous material, ρ_0. The values of the bulk modulus and the density may be derived from straightforward arguments, but the remaining five parameters are rather more difficult to evaluate, for reasons discussed below.

The density, ρ_0, is simply the weighted mean of the densities of the fluid and mineral components constituting the medium:

$$\rho_0 = N\rho_f + (1-N)\rho_s, \tag{32}$$

where ρ_f and ρ_s are the densities of the pore fluid and the mineral solid, respectively, and N is the porosity of the material. The bulk modulus, κ, of the porous medium depends on the bulk modulus of the mineral solid, κ_s, the bulk modulus of the pore fluid, κ_f, and the bulk modulus of the evacuated skeleton, $\bar{k}$. Based on the assumption that the skeletal frame and the pore fluid move together, Gassmann[26] derived the following expression[27] for the bulk modulus of the medium:

$$\kappa = \kappa_s\frac{\bar{\kappa}+q}{\kappa_s+q}, \quad q = \frac{\kappa_f(\kappa_s-\bar{\kappa})}{N(\kappa_s-\kappa_f)}. \tag{33}$$

The concept of a ''frame bulk modulus'' has been employed by Gassmann[26] and others to account for the ''softening'' effect on the overall bulk modulus of the contacts between grains. If the cementation forming the contact regions were as hard as the grains themselves, then the frame bulk modulus would equal the grain bulk modulus. If, on the other hand, the contact regions were extremely soft, then the frame bulk modulus would be close to zero. Generally, the effect of the contacts is quite different from either of these two extreme cases. In particular, the contacts appear to exhibit stress relaxation, that is, they are neither purely elastic nor purely dissipative, which of course is the basis of the wave theoretic analysis developed above.

The effect of the intergranular stress relaxation has already been taken into account in the wave theory through the terms involving λ_f and η_f in Eq. (4). These two coefficients are embedded, respectively, in the compressional and shear stress relaxation rigidity moduli, μ_p and μ_s, which appear in the expressions for the wave speeds and loss tangents. Since the compressional effect of the grain contacts is included in the wave theory, the frame bulk modulus, $\bar{k}$, is redundant and should be set to zero in Gassmann's expression for the bulk modulus of the medium. In this case, Gassmann's equation reduces to the familiar weighted mean for the bulk modulus of a two-phase medium:

$$\frac{1}{\kappa} = N\frac{1}{\kappa_f} + (1-N)\frac{1}{\kappa_s}. \tag{34}$$

Equation (34) in conjunction with the stress-relaxation wave theory imply that the composite medium is being treated as a fluid in which the grains are in suspension, with the compressional effects of the intergranular interactions being represented by the convolution involving the material response

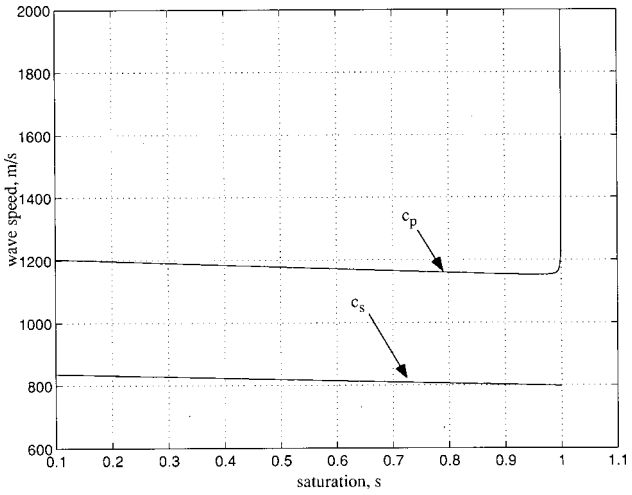

FIG. 1. Compressional and shear wave speeds computed from Eqs. (28), (29) and (32) to (35). The following parameter values, appropriate to the Murphy's Massillon sandstone, were used: $N=0.23$; $\rho_s=2660$ kg/m^3; $\rho_a=1$ kg/m^3; $\rho_w=998$ kg/m^3; $\kappa_s=3.6\times10^{10}$ Pa; $\kappa_a=1.16\times10^5$ Pa; $\kappa_w=2.19\times10^{10}$ Pa; $\bar{k}=0$.

function $h(t)$ in Eq. (4). Thus, this convolution term may, in a sense, be regarded as a substitute for the frame bulk modulus.

Incidentally, the elastic rigidity modulus, μ, representing the shear strength of the mineral frame cannot be set to zero because μ governs the shear-wave speed at very low frequencies [see Eq. (20)]. Since, in a consolidated material, the shear wave speed remains finite as the frequency is reduced, the rigidity modulus, μ, representing purely elastic interactions at the grain boundaries, must also be non-zero. To summarize, in a consolidated porous medium, the grain contacts give rise to stress relaxation, which introduces rigidity and dissipation, as well as effectively raising the bulk modulus of the two-phase medium, and they also provide elastic rigidity, which manifests itself as the stiffness of the mineral frame. In an unconsolidated medium such as sand or silt the only difference is that the elastic rigidity modulus is zero,[9,10] the implication being that in such materials there is no elastic frame. The lack of an elastic frame is consistent with the fact that an unconsolidated medium is incapable of supporting a tensile stress because the grains are, by definition, not bonded together. In the unconsolidated case, the rigidity that supports the propagation of shear waves is provided entirely by the stress relaxation occurring at the grain contacts.[10]

Returning to the consolidated case, in the event that some air is present in the pores, that is, the medium is not fully saturated, the density, ρ_f, and bulk modulus, κ_f, may be represented in terms of the fractional saturation, s, as follows:

$$\frac{1}{\kappa_f}=s\frac{1}{\kappa_w}+(1-s)\frac{1}{\kappa_a} \tag{35}$$

and

$$\rho_f=s\rho_w+(1-s)\rho_a, \tag{36}$$

where the subscripts ''a'' and ''w'' denote ''air'' and ''water,'' respectively. The effect of the level of saturation on the compressional and shear wave speeds is found by substituting the above expressions for the bulk modulus, κ, and the density, ρ_0, into Eqs. (28) and (29). Taking parameter values appropriate to Massilon sandstone, the material used by Murphy[28] in his experiments on wave speeds and attenuations, the curves shown in Fig. 1 are obtained. These curves are independent of n and m, but they do depend on μ, μ_p, and μ_s. These three parameters, which are independent of the saturation, have been chosen to fit the theoretical wave speeds to Murphy's measurements,[28] as presented in his Fig. 5. To obtain the fit, which is almost perfect, we have set $(\mu+\mu_s)=1.45\times10^{10}$ Pa and $\mu_p=8\times10^8$ Pa. Note that, from the wave speed data, it is not possible to assign values to μ and μ_s individually. In other words, the quantity $(\mu+\mu_s)$ plays the role of an effective elastic rigidity modulus as far as the wave speeds (and also the attenuations) are concerned.

It can be seen in Fig. 1 that both wave speeds show a gentle negative slope over most of the saturation range, which is due solely to the slight increase in the density, ρ_0, with decreasing gas content in the pores. As the saturation approaches 100%, nothing spectacular happens to the shear wave speed, but the compressional speed increases rapidly as a direct result of the dramatic increase in the bulk modulus of the pore fluid that occurs as the gas content is reduced to zero. These density and bulk modulus effects are well known and are consistent with Murphy's own interpretation[28] of his wave speed versus saturation data.

Murphy[28] also measured the attenuation (his Fig. 6) of the compressional and shear wave in Massilon sandstone. In principle, by fitting the theoretical expressions for the attenuation [Eqs. (29) and (30)] to these data, it should be possible to evaluate n and $m\mu_s$ (but not m and μ_s individually). Since all the rigidity moduli are independent of the level of saturation, it is evident from Murphy's Fig. 6 that n and m must both vary significantly with s. At present, as no physical model exists for the dependence of the material response indices on the saturation level, there is little to be gained by simply choosing empirical forms for n and m that match Murphy's attenuation data. In other types of rock, the attenuation behavior could be quite different.

A final comment on the two stress relaxation rigidity moduli is perhaps in order. It has been stated above that μ_p and μ_s, are independent of the level saturation, which is true provided sufficient moisture is present to lubricate the grain contacts. This will be the case when the saturation level is above approximately 2%. For lower levels of saturation, however, as found in moon rocks or vacuum-outgassed rocks, not even a monolayer layer of water is present on the surfaces of the pores and no lubrication exists at grain contacts. As a result, in an extremely dry, unlubricated material, μ_p and μ_s may be expected to take values that are significantly greater than those for the same material but with a higher moisture content. Moreover, since sliding at grain boundaries is strongly inhibited in such dry, unlubricated rocks, the material response indices, m and n, must decrease dramatically. In other words, the attenuation of compressional and shear waves in these extremely dry specimens is essentially zero.

V. CONCLUDING REMARKS

The internal stress relaxation mechanism proposed in this article has the potential for explaining much of the observed behavior of consolidated porous media (rocks). It differs from Coulomb friction[29] in that the new mechanism is linear, in the sense of obeying superposition, although the stress is not proportional to the rate of strain. Moreover, the theory leads naturally to an attenuation of compressional and shear waves that is proportional to the first power of frequency (i.e., a constant Q), as observed in wet and dry rocks. Since the stress relaxation is assumed to arise at grain boundaries and microcracks in the mineral frame, the theory provides a possible means of interpreting the effects of pore-fluid lubrication on wave speeds and attenuation. Similarly, the effects of both partial saturation and confining-pressure variations may also be investigated.

Numerous measurements of the geoacoustic properties of rocks, particularly sandstones, limestones, and oil-bearing shales, have been reported, many of which were taken under controlled laboratory conditions. Nevertheless, it would be very helpful to have available more comprehensive data sets containing direct measurements of wave speeds (compressional and shear) and attenuations, taken under varying dry and saturated conditions. As summarized by Johnston,[30] the attenuation is known to be less in air-dry rocks than in fully or partially saturated rocks; it is very much less in vacuum-outgassed rocks (e.g., lunar samples) than in air-dry rocks. It seems that the presence of one or two monolayers of water, corresponding to the air-dry condition, leads to a significant increase in the attenuation compared to an absence of water, obtained by vacuum outgassing.[31,32]

Interestingly, the introduction of benzene vapor instead of water to vacuum-outgassed sedimentary rocks produces little change in the attenuation.[32] Johnston[30] tentatively identifies the polar nature of water as being responsible for the observed rapid increase in attenuation when monolayers of water are introduced into the vacuum-outgassed rock. If this is so, it suggests that bonding forces on a molecular level give rise to the attenuation, which is consistent with the idea that the indices n and m, characterizing the material response functions in Eqs. (5) and (6), depend on microscopic interactions occurring at grain boundaries, rather than on macroscopic properties such as density or porosity. A similar suggestion has been made by Buckingham[9] in connection with attenuation in unconsolidated marine sediments. Based on these observations, it would appear that much information on the indices, n and m, and the stress relaxation moduli, μ_p and μ_c, could be obtained by further measurements of the attenuations and velocities in vacuum-outgassed rocks *vis-à-vis* air-dry rocks containing minute quantities of fluid.

[1] M. A. Biot, ''Theory of propagation of elastic waves in a fluid-saturated porous solid: I. Low-frequency range,'' J. Acoust. Soc. Am. **28**, 168–178 (1956).

[2] M. A. Biot, ''Theory of propagation of elastic waves in a fluid-saturated porous solid: II. Higher frequency range,'' J. Acoust. Soc. Am. **28**, 179–191 (1956).

[3] M. N. Toksöz and D. H. Johnston (eds.), ''Seismic Wave Attenuation,'' *Geophysics Reprint Series, No. 2* (Society of Exploration Geophysicists, Tulsa, OK, 1981), p. 459.

[4] L. Peselnick and W. F. Outerbridge, ''Internal friction in shear and shear modulus of Solenhofen limestone over a frequency range of 10^7 cycles per second,'' J. Geophys. Res. **66**, 581–588 (1961).

[5] D. H. Johnston, M. N. Toksöz, and A. Timur, ''Attenuation of seismic waves in dry and saturated rocks. II. Mechanisms,'' Geophysics **44**, 691–711 (1979).

[6] M. R. Wyllie, A. R. Gregory, and L. W. Gardner, ''Elastic wave velocities in heterogeneous and porous media,'' Geophysics **21**, 41–70 (1956).

[7] F. J. McDonal, F. A. Angona, R. L. Mills, R. L. Sengbush, R. G. Van Nostrand, and J. E. White, ''Attenuation of shear and compressional waves in Pierre shale,'' Geophysics **23**, 421–439 (1958).

[8] K. Winkler, A. Nur, and M. Gladwin, ''Friction and seismic attenuation in rocks,'' Nature (London) **277**, 528–531 (1979).

[9] M. J. Buckingham, ''Theory of acoustic attenuation, dispersion and pulse propagation in granular materials including marine sediments,'' J. Acoust. Soc. Am. **102**, 2579–2596 (1997).

[10] M. J. Buckingham, ''Theory of compressional and shear waves in fluid-like marine sediments,'' J. Acoust. Soc. Am. **103**, 288–299 (1998).

[11] M. J. Buckingham, ''On the phase speed and attenuation of an interface wave in an unconsolidated marine sediment,'' J. Acoust. Soc. Am. (in press).

[12] R. Kronig, ''On the theory of dispersion of X-rays,'' J. Opt. Soc. Am. **12**, 547–557 (1926).

[13] H. A. Kramers, ''La diffusion de la lumiere par les atomes,'' in *Atti Congr. Intern. Fisica*, pp. 545–557 (1927).

[14] T. J. Plona, ''Observation of a second bulk compressional wave in a porous medium at ultrasonic frequencies,'' Appl. Phys. Lett. **36**, 259–261 (1980).

[15] D. L. Johnson and T. J. Plona, ''Acoustic slow waves and the consolidation transition,'' J. Acoust. Soc. Am. **72**, 556–565 (1982).

[16] R. S. Carmichael, *CRC Practical Handbook of Physical Properties of Rocks and Minerals* (CRC Press, Boca Raton, 1989), p. 741.

[17] P. M. Morse and H. Feshbach, *Methods of Theoretical Physics: Part I* (McGraw-Hill, New York, 1953).

[18] L. Peselnick and I. Zietz, ''Internal friction of fine grained limestones at ultrasonic frequencies,'' Geophysics **24**, 285–296 (1959).

[19] P. G. Nutting, ''A study of elastic viscous deformation,'' Proc. Am. Soc. Testing Mat. **21**, 1162–1171 (1921).

[20] R. Bachdahl and L. E. Nielsen, ''The application of Nutting's equation to the viscoelastic behavior of certain polymeric systems,'' J. Appl. Phys. **22**, 1344–1349 (1951).

[21] D. E. Weston, ''On the frequency independence of the acoustic loss factor in earth materials,'' Geophys. J. R. Astron. Soc. **8**, 269–271 (1963).

[22] A. Erdélyi, *Tables of Integral Transforms, Volume 1* (McGraw-Hill, New York, 1954), p. 391.

[23] M. N. Toksöz, D. H. Johnston, and A. Timur, ''Attenuation of seismic waves in dry and saturated rocks, I. Laboratory measurements,'' Geophysics **44**, 681–690 (1979).

[24] M. O'Donnell, E. T. Jaynes, and J. G. Miller, ''Kramers–Kronig relationship between ultrasonic attenuation and phase velocity,'' J. Acoust. Soc. Am. **69**, 696–701 (1981).

[25] J. E. White, *Underground Sound: Application of Seismic Waves* (Elsevier, Amsterdam, 1983), p. 253

[26] F. Gassmann, ''Über die elastizität poröser medien,'' Vierteljahrsscher. Naturforsch. Ges. Zürich **96**, 1–23 (1951).

[27] E. L. Hamilton, ''Elastic properties of marine sediments,'' J. Geophys. Res. **76**, 579–604 (1971).

[28] W. F. Murphy, III, ''Effects of partial water saturation on attenuation in Massilon sandstone and Vycor porous glass,'' J. Acoust. Soc. Am. **71**, 1458–1468 (1982).

[29] J. B. Walsh, ''Seismic wave attenuation in rock due to friction,'' J. Geophys. Res. **71**, 2591–2599 (1966).

[30] D. H. Johnston, ''Attenuation: A state-of-the-art summary,'' in *Seismic Wave Attenuation* (Society of Exploration Geophysicists, Tulsa, OK, 1981), pp. 123–135.

[31] B. I. Pandit and M. S. King, ''The variation of elastic wave velocities and quality factor of a sandstone with moisture content,'' Can. J. Earth Sciences **16**, 2187–2195 (1979).

[32] V. A. Clark, T. W. Spencer, B. R. Tittman, L. A. Ahlberg, and L. T. Coombe, ''Effect of volatiles on attenuation (Q^{-1}) and velocity in sedimentary rocks,'' J. Geophys. Res. **85**, 5190–5198 (1980).

Development of dispersion curves for two-layered cylinders using laser ultrasonics

Markus Kley
School of Civil and Environmental Engineering, Georgia Institute of Technology, Atlanta, Georgia 30332

Christine Valle
G. W. Woodruff School of Mechanical Engineering, Georgia Institute of Technology, Atlanta, Georgia 30332

Laurence J. Jacobs[a)]
School of Civil and Environmental Engineering, Georgia Institute of Technology, Atlanta, Georgia 30332

Jianmin Qu and Jacek Jarzynski
G. W. Woodruff School of Mechanical Engineering, Georgia Institute of Technology, Atlanta, Georgia 30332

(Received 17 November 1998; accepted for publication 16 April 1999)

In this paper, laser-ultrasonic techniques are employed to develop a quantitative understanding of the underlying principles of the propagation of guided circumferential waves in two-layered cylindrical components. The high-fidelity, broad-bandwidth, point source/receiver and noncontact nature of these optical techniques are critical elements to the success of this work. The experimental procedure consists of measuring a series of transient, circumferentially propagating waves in a cylindrical waveguide and then operating on these transient waveforms with signal-processing techniques to develop the dispersion relationship for that waveguide; this procedure extracts the steady-state behavior from a series of transient measurements. These dispersion curves are compared to theoretical values. There is good agreement between the experimental and theoretical results, thus demonstrating the accuracy and effectiveness of using laser-ultrasonic techniques to study the propagation of guided circumferential waves. © *1999 Acoustical Society of America.* [S0001-4966(99)05707-0]

PACS numbers: 43.20.Mv [DEC]

INTRODUCTION

There exists a widespread need for methodologies that can nondestructively evaluate cylindrical components such as a helicopter rotor hub. Of particular interest is a geometry which consists of a hollow outer cylinder with either a solid or hollow inner-cylindrical shaft. With this specific two-layered geometry, fatigue cracks usually develop at the interface (at the outer surface of the inner shaft and the inner surface of the outer hollow cylinder) and grow in the radial direction. Unfortunately, conventional ultrasonic methodologies (such as pulse–echo) are difficult to implement in these components, mainly because of accessibility issues. A promising new methodology uses guided circumferential waves to examine cylindrical components. The primary advantage with using these guided waves is that they are capable of interrogating the entire component, including inaccessible regions of a complex structure. On the other hand, the main difficulty with the application of guided waves for the evaluation of cylindrical components is the inherent complexity of the waveforms, making interpretation difficult.

This research employs a laser-ultrasonic technique to develop a quantitative understanding of the underlying principles of the propagation of guided circumferential waves in two-layered cylindrical components. The high-fidelity, broad-bandwidth, and noncontact nature of the optical technique are critical for the success of this work. In addition, laser ultrasonics allows for measurements with a point source and a point receiver, thus enabling spatial sampling techniques such as the two-dimensional Fourier transformation (2D-FFT). By using these state-of-the-art laser-ultrasonic methodologies, it is possible to experimentally measure transient waves in a variety of cylindrical specimens without any of the frequency biases present in, for example, piezoelectric transducers.

It is important to note that the proposed experimental procedure makes measurements of *transient* waveforms in cylindrical waveguides. While these transient waveforms provide valuable information about the propagation of guided circumferential waves, they are not in themselves sufficient to quantitatively understand the propagation of guided waves in cylindrical waveguides; this comprehension requires an understanding of the *steady-state* (*time harmonic*) behavior of wave propagation in cylindrical waveguides. Steady-state behavior of guided waves is best interpreted in terms of dispersion curves, which present the relationship between frequency and phase velocity (or wave number) for each of the infinite number of modes possible in a particular waveguide. In order to experimentally model (and understand) steady-state behavior, this research consists of measuring a series of transient waveforms and operating on them with signal-processing techniques to infer the dispersion

a)Author to whom correspondence should be addressed.

curves of the waveguide. There are two signal-processing techniques used in this research: the 2D-FFT and the Prony method. Each of these signal-processing techniques requires multiple transient waveforms (generated with exactly the same source), each having a different propagation distance, separated by an equally spaced increment. In this study, these multiple, equally spaced measurements are made with a repeatable optical source, the pulse of an Nd-YAG laser. By using a fiber-optic delivery system to launch this laser pulse, it is possible to provide a repeatable source at equally spaced increments.

There has been extensive research into the propagation of guided waves in flat, layered components (Chimenti[1]), but there is much less information on the propagation of guided waves in cylindrical, layered components. Valle *et al.*[2] recently developed an analytical model to obtain the dispersion relationship for guided waves that propagate in the circumferential direction of a two-layered cylinder; one motivation for the current research is to obtain an experimental comparison that endorses the theoretical results developed in Ref. 2. Hutchins and Lundgren[3] and Schumacher *et al.*[4] used laser-ultrasonic techniques to study the propagation of transient Lamb waves in (flat) layered materials. Kawald *et al.*[5] examined circumferential surface waves in a thin layer bonded to a solid cylinder, while Liu and Qu[6] studied guided circumferential waves in a circular structure. Note that solutions exist for propagation in the axial direction of a hollow cylinder (e.g., Gazis[7]), but this paper addresses propagation in the circumferential direction.

The objective of the present study is to develop and evaluate laser techniques for the noncontact generation and detection of transient, broadband ultrasonic signals in layered cylindrical structures. The experimental procedure measures ultrasonic waveforms over an array of closely spaced points, and signal-processing techniques are then applied to this array data to determine dispersion curves over a wide frequency range (200 kHz to 10 MHz). In future work, this system will be used to study the effects of imperfections (such as fatigue cracks) on the propagation of circumferential waves in cylindrical structures.

I. EXPERIMENTAL PROCEDURE

Guided waves are generated with the pulse of a *Q*-switched Nd:YAG laser that is launched into an optical fiber. Laser generation of ultrasound in a metal creates a repeatable, broadband ultrasonic waveform; see Scruby and Drain[8] for details. The Nd:YAG laser (1064 nm) used in this study emits a 450-mJ, 4–6-ns pulse with a spatially Gaussian profile. The beam is attenuated and focused before it is launched into the optical fiber. The other end of the optical fiber is mounted on a rotation stage with a fine micrometer adjustment with a graduation of 0.013 283° that allows for a minimum circumferential (arc) increment of 14.721 μm at a radius of 63.5 mm (the outer radius of each specimen being interrogated). The specimen is mounted in the center of the rotation stage to ensure that the fiber end is kept at a constant distance (about 1 mm) from a specimen's surface throughout each experiment (see Fig. 1). This setup provides a laser source that generates exactly the same ultrasonic signal, at multiple, equally spaced locations, throughout each experiment. Note that this setup does not guarantee that the laser source is exactly the same (spot size of approximately 1 mm) for all the specimens (or for a specimen that is removed and reinstalled), just that the laser source remains constant as the fiber is rotated to different source locations on the same specimen.

Laser detection of these guided waves is accomplished with a dual-probe, heterodyne interferometer that is a modified version of the instrument described in detail in Bruttomesso *et al.*[9] This optical device uses the Doppler shift to simultaneously measure out-of-plane surface velocity (particle velocity) at two points on the specimen's surface. The interferometer works by measuring frequency changes in the light reflected off the specimen surface. In a heterodyne interferometer, a frequency shift is initially imposed (using an acousto-optic modulator) to create a reference and a probe beam. The probe beam is reflected off the specimen surface and is recombined with the reference beam at a photodiode. This creates a beat frequency equal to the initially imposed frequency shift. Frequency shifts in the light reflected from the specimen surface result in proportional shifts in the beat frequency. As a result, the beat-frequency signal acts as a carrier that is demodulated in real time (with an FM discriminator) to obtain the surface velocity. The interferometer makes high-fidelity, absolute measurements of surface velocity (particle velocity) over a bandwidth of 200 kHz to 10 MHz.

It is important to note that the proposed experimental procedure requires only a single ultrasonic receiver (probe). However, this work uses the second receiver (probe) as a redundant check on the consistency of the optical source. An additional use of the signals measured with the second probe is for the development of dispersion relationships with the two-point phase method.[10] Another study[11] showed that the two-point phase method is not as robust and quantitative in determining dispersion relationships for these cylindrical specimens.

Note that all of the waves presented are low-pass filtered at 10 MHz. In addition, in order to increase the signal-to-noise ratio (SNR), each waveform presented represents a collection of averages, sometimes as many as 100. This signal-averaging procedure works because noise is random, while the ''real'' signal is repeatable; SNR is improved by the square root of N, where N is the number of averages.

Three different aluminum specimens are examined in this study. The first specimen is a hollow cylinder with an outer diameter of 127 mm and a wall thickness of 4 mm. The second specimen consists of the same hollow aluminum cylinder with an inner aluminum (solid) shaft (119-mm diameter). A thin layer of 10W-40 motor oil provides a slip-boundary condition at the interface between the inner shaft and the outer cylinder. The third specimen combines the original outer, hollow-aluminum cylinder with an inner hollow-aluminum cylinder (119-mm outer diameter and a wall thickness of 4 mm) and the same slip interface. Note that all three specimens have the same outer cylinder, and that the surface of this cylinder is sanded and polished with a polishing paste. This surface preparation enables true non-

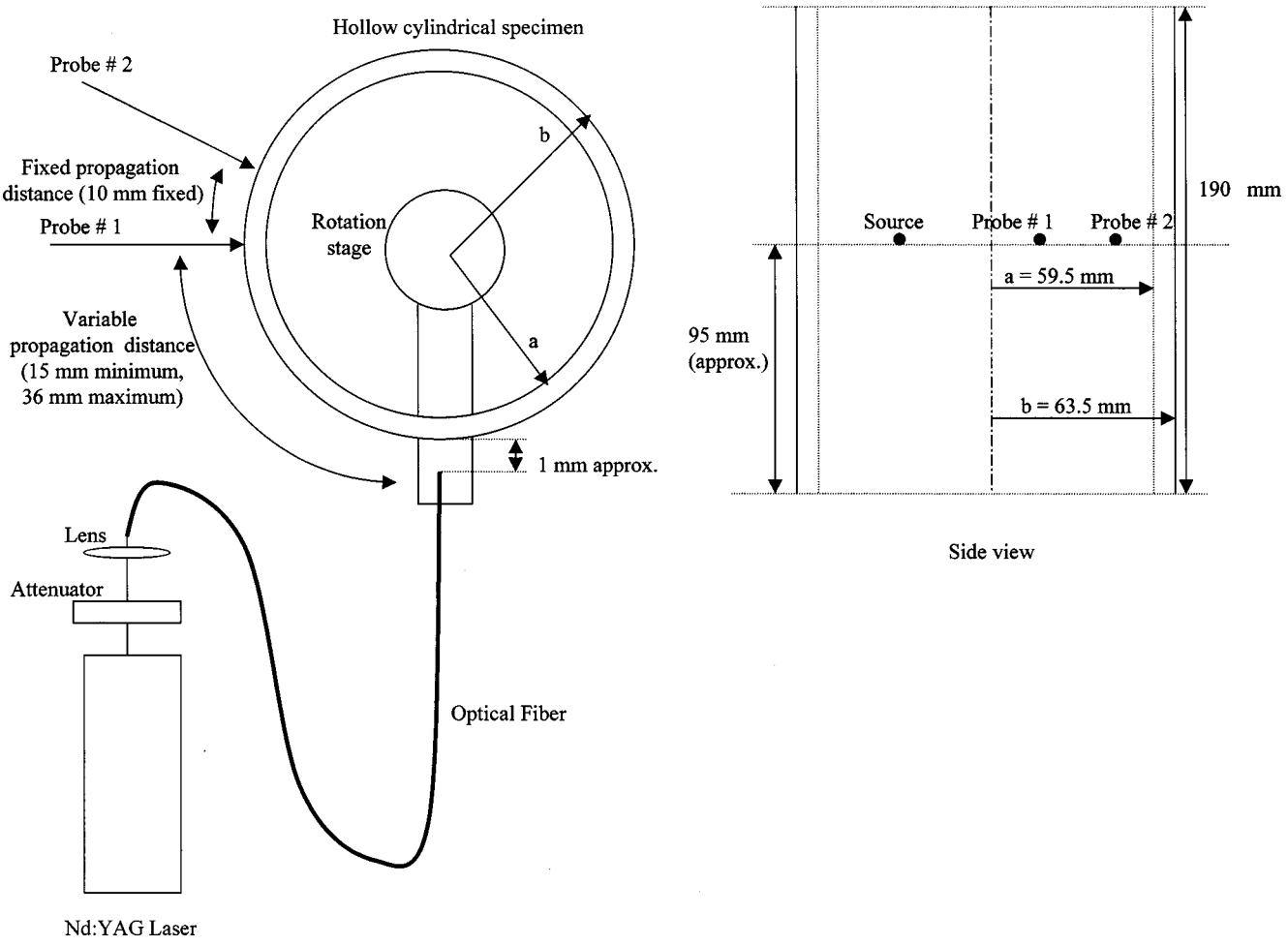

FIG. 1. Schematic of optical-fiber delivery system and hollow specimen.

contact detection (there are no artificial surface treatments such as reflective tape) and provides a consistent surface for guided wave propagation. The length of each specimen is 190 mm and all measurements are made in the vicinity of the center line (see Fig. 1). As a result, these specimens are treated as infinitely long cylinders—reflections from the ends arrive well after the signal of interest.

II. EXPERIMENTALLY MEASURED TRANSIENT WAVEFORMS

While the receiver is kept in a fixed position, the source is placed at 49 equally spaced locations. Incremental (circumferential) distances of 0.4 mm separate these multiple source locations. Note that the closest source-to-receiver (propagation) distance is 15 mm, while the farthest propagation distance is 36 mm. This results in the (generation and) detection of 49 waveforms, each with a different propagation distance and each generated with exactly the same laser source.

Figure 2 shows three typical transient waveforms with the same propagation distance (15 mm), but measured in the three different specimens (the hollow cylinder, the hollow cylinder with a solid inner shaft, and the hollow cylinder with a hollow inner cylinder). Note that the amplitudes of all three waveforms are normalized to enable a representative comparison and consider the outstanding SNR exhibited in these waveforms; high SNR is critical for the success of the next step—development of dispersion curves. A qualitative analysis of these three waveforms shows identical *arrival times* for both the beginning of the signal (the first nonzero disturbance at 2 μs) and the Rayleigh wave (mode), but significant differences between the shapes of each signal. The identical arrival times of the Rayleigh waves is not surprising, since they all propagate along the same outer cylinder. The variances in shape are due to differences between the three specimens (the presence of the inner shaft and inner cylinder), as well as the presence of the slip boundary (interface). Unfortunately, besides matching arrival times and making generic comments about changes in shape, no other analysis is possible. As a result, it is impossible to quantitatively interpret these transient waveforms. However, it is possible to develop dispersion curves and then quantitatively interpret these results.

III. DEVELOPMENT OF DISPERSION CURVES

This research uses two different signal-processing techniques to develop dispersion curves from each set of (experimentally measured) equally spaced, transient waveforms: the 2D-FFT and the Prony method. Implementation of the 2D-FFT is fairly straightforward—perform a temporal Fourier

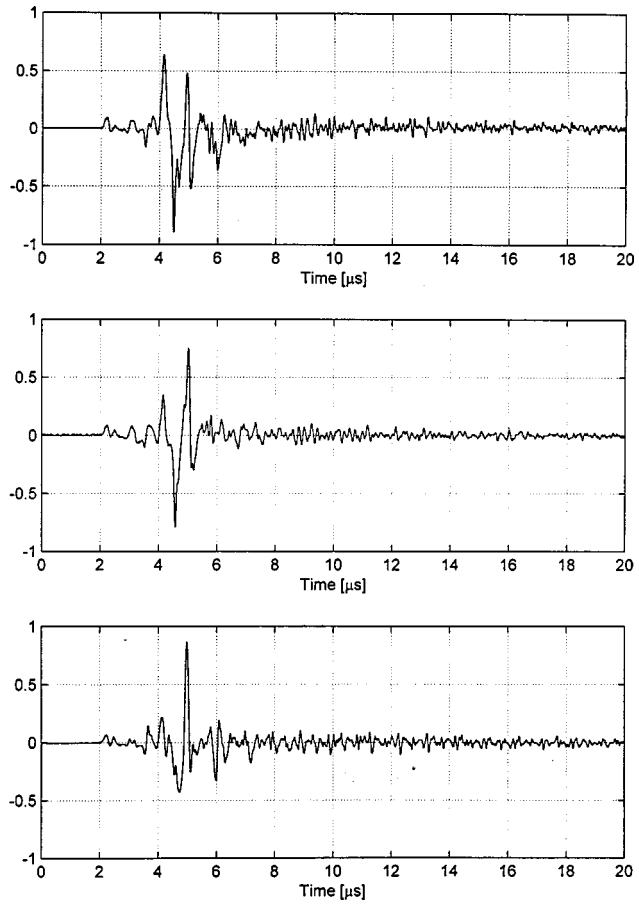

FIG. 2. Comparison of three typical guided circumferential waves with the same propagation distance (15 mm), but measured in the hollow cylinder, the hollow outer cylinder with a solid inner shaft, and the hollow outer cylinder with a hollow inner cylinder (top, middle, and bottom, respectively).

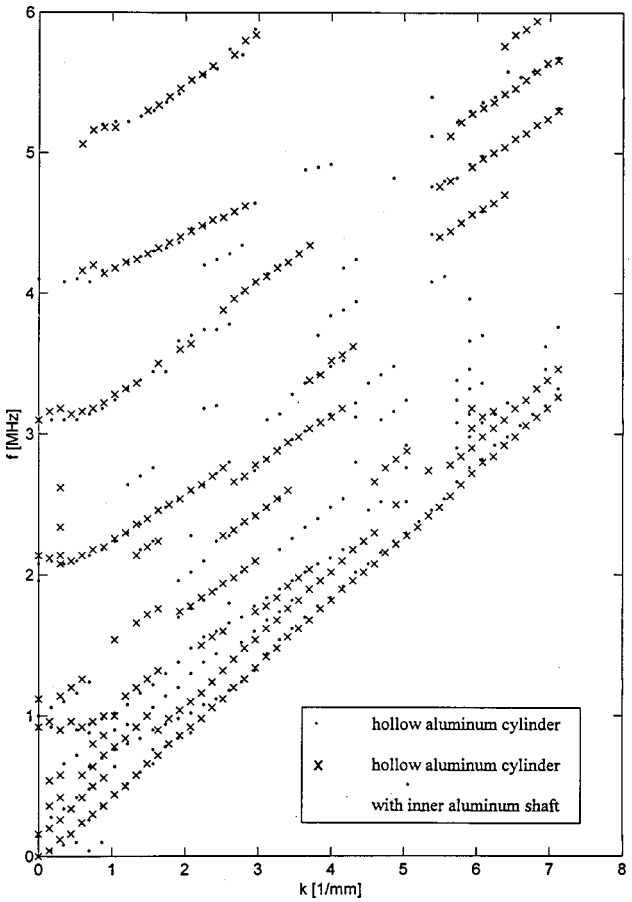

FIG. 3. Comparison of $k-f$ spectrum for hollow cylinder with spectrum of hollow outer cylinder with solid inner shaft (2D-FFT).

transform (going from the time to the frequency domain) followed by a spatial Fourier transform (going from the spatial to the wave number domain). The resulting frequency (f) versus wave number (k) spectrum shows a series of peaks that represents individual modes (see Alleyne and Cawley[12] or Moser *et al.*[13]). In order to be effective, the 2D-FFT requires a large number of broadband, transient signals measured with a small (incremental) spatial sampling distance. Note that the 2D-FFT does not require (or use) any prior knowledge concerning the waveguide being modeled.

In contrast, the Prony method requires knowledge of the propagating modes in a waveguide. If the number of modes at a specific frequency is known *a priori*, the Prony method fits that number of modes to the transient data (see Glandier *et al.*[14]). The objective of the Prony method is to find a set of p exponentials of arbitrary complex amplitude (magnitude and phase) and complex wave number (wave number and attenuation) that best approximates the real, spatial data. The Prony algorithm is particularly appropriate when the signal is indeed a sum of exponentials, and when the order of the model (i.e., the number of exponentials) is known (or estimated) *a priori*. The Prony method (like the 2D-FFT) requires waveforms from equispaced sources. Unfortunately, noise in a signal has more of a negative effect on the Prony method than on the 2D-FFT. Although the Prony method can theoretically identify a number of modes that is equal to half of the number of spatially sampled signals, the presence of noise will severely reduce this limit.[14] The procedure described in Ref. 14 and used in the present study is a basic Prony method that is relatively simple to apply. Recently, an extended Prony method[15] has been developed which includes a systematic procedure for discriminating against spurious peaks in the wave number spectrum due to noise.

The Prony method is implemented with a two-step process. First, perform a spatial Fourier transform (from the spatial to the wave number domain) and second, determine the amplitudes for these wave numbers by implementing a linear, least-squares fit to a model of the data (see Refs. 11 or 14 for details).

IV. EXPERIMENTALLY CALCULATED DISPERSION CURVES

The 2D-FFT is used to calculate the dispersion curves for each of the specimens; the results indicate that certain $k-f$ combinations have significant amplitudes (peaks), and these combinations are solutions to the specimens' dispersion relationships (the specimens' individual modes). The local maxima in the vicinity of each peak for both the hollow cylinder and the cylinder with solid shaft are plotted in Fig. 3, while Fig. 4 is a comparison of the $k-f$ peaks for the hollow cylinder and the cylinder with an inner hollow cylinder.

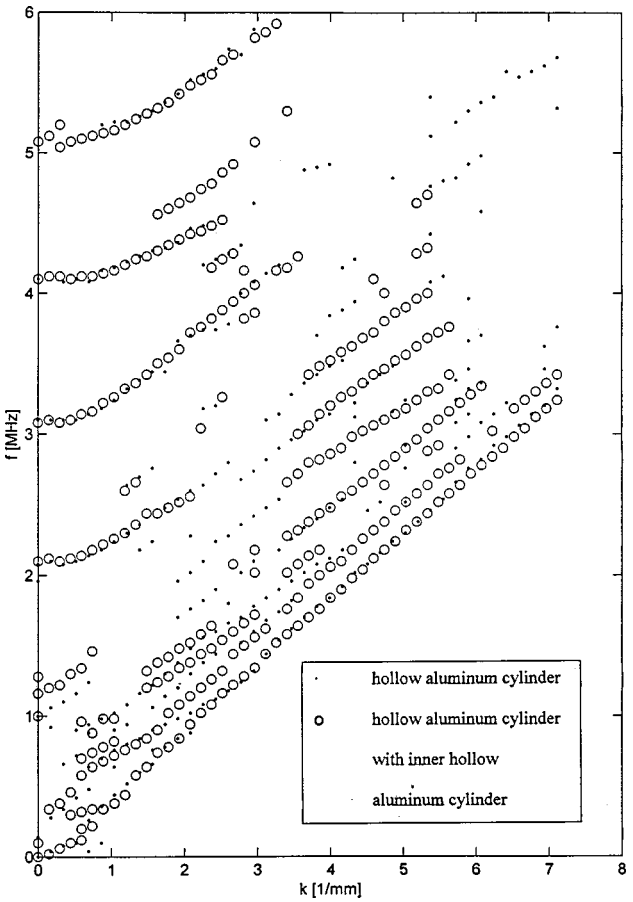

FIG. 4. Comparison of $k-f$ spectrum for hollow cylinder with spectrum of hollow outer cylinder with hollow inner cylinder (2D-FFT).

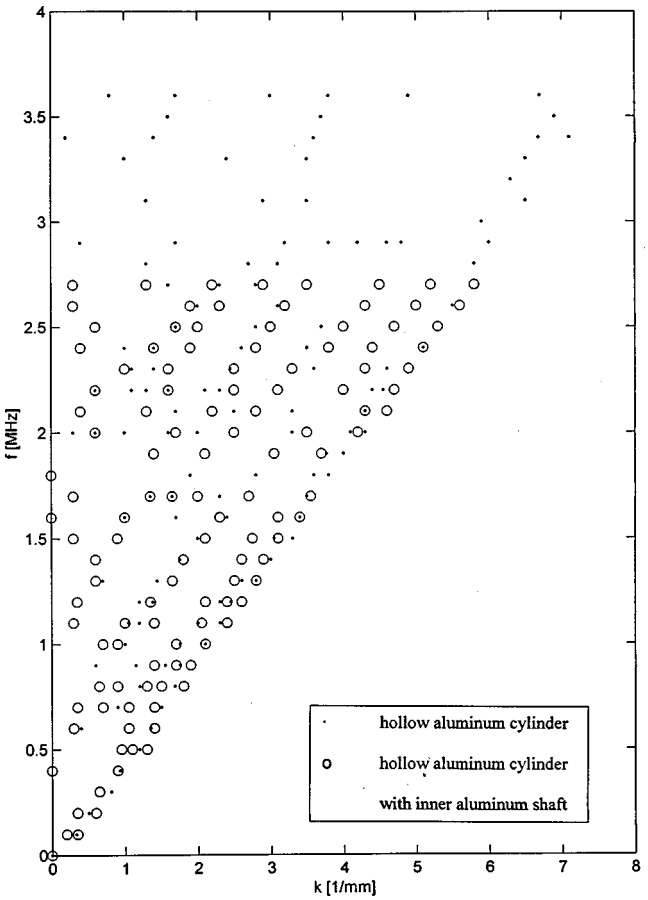

FIG. 5. Comparison of $k-f$ spectrum for hollow cylinder with spectrum of hollow outer cylinder with solid inner shaft (Prony method).

These figures show that all three specimens have the same first mode—the Rayleigh mode; the Rayleigh mode is nearly a straight line, so it is (effectively) nondispersive. There is a series of higher modes that have clear and definitive cutoff frequencies, indicating that these higher modes exist only above a specific lower-frequency value. In addition, dispersion is clearly visible in these higher modes; they follow a curve in the beginning, and turn into straight lines at higher wave numbers (or frequencies). Overall, the results from the 2D-FFT provide excellent definition and clarity of the individual modes that are present in each specimen.

Next, the Prony method is used to operate on the same set of transient waveforms. For example, Fig. 5 shows the $k-f$ spectra for the hollow cylinder and the hollow cylinder with the inner shaft. These spectra are very similar to those developed with the 2D-FFT, each exhibiting the same general trends. Note that the Prony method allows for more ''control'' over the selection of each mode than is possible with the 2D-FFT. For example, the Prony method involves an iterative process, with a large amount of user flexibility to eliminate (or ignore) certain spectrum points. As a result, it is *possible* to exert a deliberate bias and create artificially good results; this level of control is not possible with the 2D-FFT. However, an advantage of the Prony method is that the dispersion curves are calculated on a frequency-by-frequency basis, which enables a high degree of refinement in frequency ranges of interest. As a result, the Prony method is capable of separating closely spaced modes.

The fact that all three specimens have the same first (Rayleigh) mode is not surprising since they all correspond to a surface wave that propagates on the same outer surface. The second modes show differences between the hollow cylinder and the other two specimens. For example, in the hollow cylinder, the first and second modes approach each other at around 1 MHz; they are effectively inseparable (above 1 MHz) in the 2D-FFT results. In contrast, the second modes in each of the other two specimens remain well separated from their respective first modes, and continue on a parallel slope equal to the Rayleigh wave-phase velocity. Valle *et al.*[2] theoretically determined the effects of an inner shaft on the first five modes and showed that for a layered cylinder at higher frequencies, the second mode is actually an additional Rayleigh wave that propagates along the free-sliding interface. Next, consider the differences between each specimen in the vicinity of 1 MHz. The hollow cylinder has two modes with a cutoff frequency of 1 MHz, while the other two specimens each show one mode starting below 1 MHz and one mode starting above 1 MHz. However, there is much overlap and not many significant differences when comparing the higher modes (those with cutoff frequencies above 2 MHz) for all three specimens. The similarities for these higher modes show that the inner cylinder (or shaft) has little effect on the experimentally measured dispersion

curves above a certain frequency (2 MHz for this configuration).

It is important to note that all of these dispersion relationships are calculated from transient waveforms that are measured with a receiver (the heterodyne interferometer) that only measures the out-of-plane component of surface velocity. As a result, there is a certain bias in this frequency spectrum since it only contains modes that excite significant out-of-(the radial)-plane (or flexural) motion. This experimental procedure does not identify modes that primarily excite in-plane (longitudinal) motion. Consequently, the frequency spectra presented in Figs. 3–5 are not necessarily the complete spectra—certain in-plane portions of the modes are missing. However, there are no ''pure'' flexural or longitudinal modes for circumferential waves that propagate in a cylinder,[2] so Figs. 3–5 provide a very good representation of the dispersion curves for these cylinders.

V. COMPARISON WITH THEORY

The accuracy and validity of these experimentally obtained dispersion curves is determined by comparing them with the theoretical results developed in Ref. 2. Valle *et al.*[2] uses two-dimensional linear elasticity to develop the dispersion relationship for time harmonic, circumferential waves in (infinitely long) two-layered cylinders. This work uses potential functions that represent guided waves that propagate in the circumferential direction, which is a natural extension of Lamb waves in a flat plate. The boundary conditions are as follows: (1) zero traction at the outer surface; (2) slip-boundary condition at the interface (continuous radial tractions and displacements, plus zero shear stress at the interface); and (3) zero traction at the inner surface (when the second cylinder is hollow). The potentials are written in terms of Bessel functions of the first and second kind. The resulting system of six homogeneous equations is written in matrix form, and the condition that the determinant of this matrix must vanish yields a characteristic equation that is solved numerically. The numerical solution involves selecting a specific (nondimensional) wave number, and using a bisection root-finding scheme to solve the characteristic equation for the corresponding (nondimensional) frequency. Implementation of the numerical solution requires extreme care, since the determinant experiences rapid changes in the vicinity of its roots.[2]

For example, Fig. 6 compares the first eight theoretical modes of the hollow cylinder with those obtained experimentally (with the 2D-FFT). As a more detailed comparison between these theoretical and experimental data, Fig. 7 isolates the results for the second through fifth modes only. Next, Fig. 8 compares the first three theoretical modes (with the experimental results from the 2D-FFT) for the hollow cylinder with the solid inner shaft. There is good agreement between the spectra of both these specimens; these figures clearly demonstrate the accuracy of the experimentally measured dispersion curves. The main disparities occur in the second mode in the hollow cylinder (where the experimental data is inseparable from the first mode above 1 MHz) and the lack of separation between the second and third modes in the

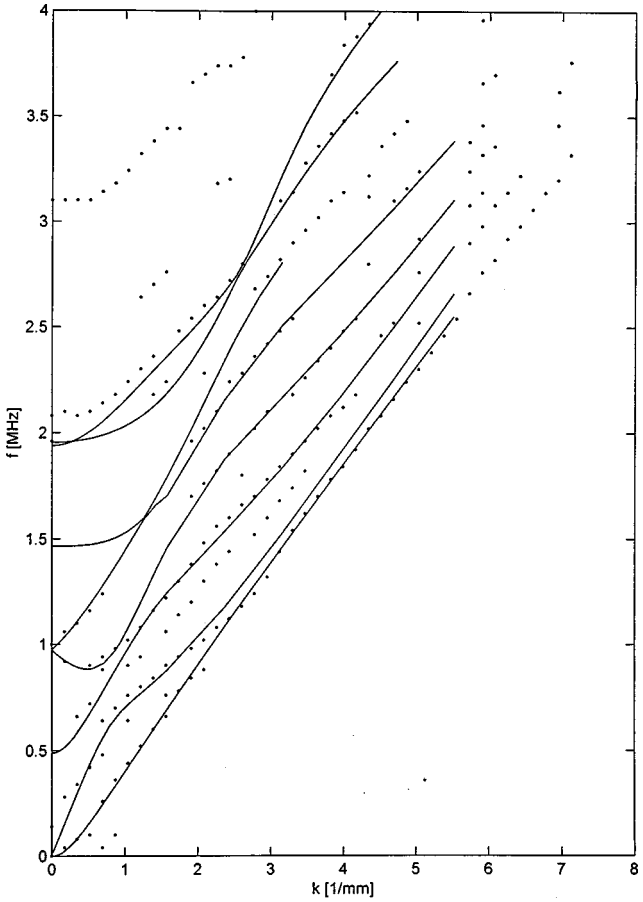

FIG. 6. Comparison of experimental $k-f$ spectrum (2D-FFT) and first eight theoretical modes for hollow cylinder.

hollow cylinder with solid shaft. These disparities are ascribed to difficulties in using the 2D-FFT to extract closely spaced modes.

It should be noted that a theoretical flat-plate model would not completely capture the physics of the high-frequency circumferential waves that propagate in the relatively thin cylinder of this study. Liu and Qu[6] showed that

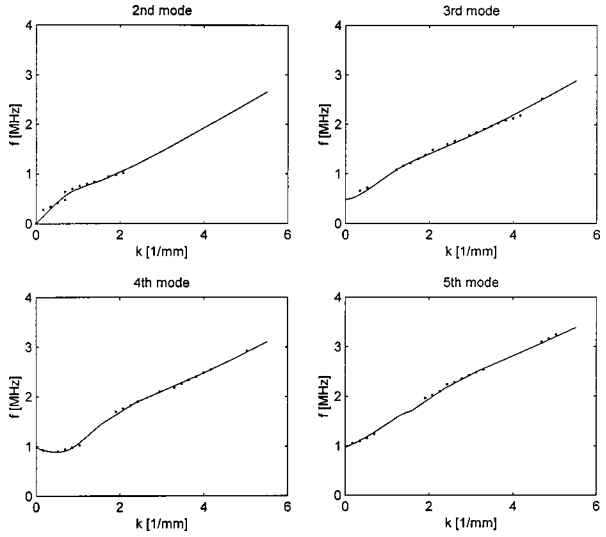

FIG. 7. Detailed comparison of experimental $k-f$ spectrum (2D-FFT) and second through fifth modes (theoretical) for hollow cylinder.

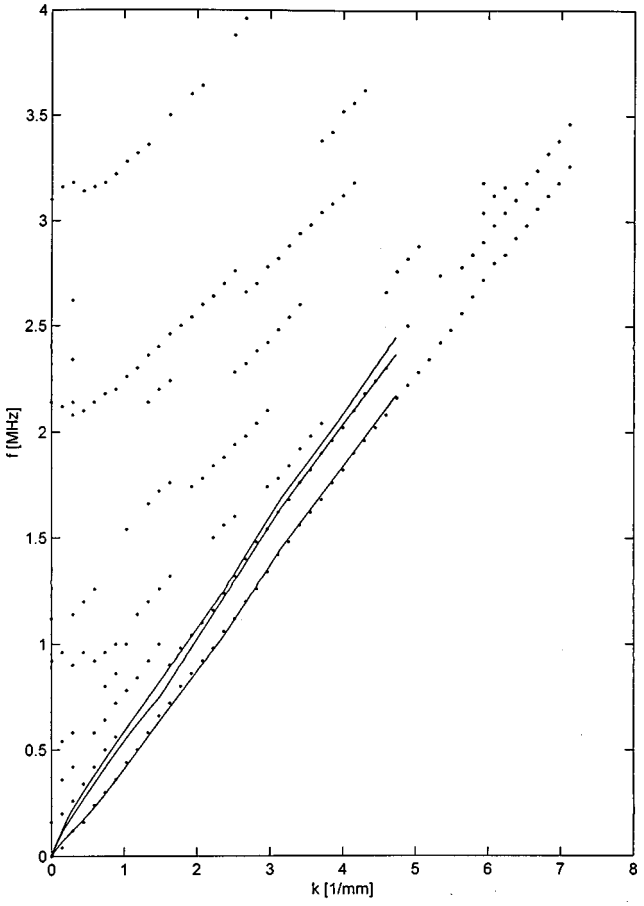

FIG. 8. Comparison of experimental $k-f$ spectrum (2D-FFT) and first three theoretical modes for hollow outer cylinder with solid inner shaft.

the propagating wave fields in a thin shell and a flat plate are quite different, even though their dispersion curves might be similar.

VI. CONCLUSION

This paper demonstrates the effectiveness of using laser-ultrasonic techniques to study the propagation of guided waves in layered cylinders. By using this innovative technique, it is possible to experimentally measure transient waves in a variety of cylindrical specimens and to study the influence of a number of geometric features on these guided waves. It is critical to note that these experimental measurements are possible only because of the high-fidelity, unbiased, broadband, point source/point receiver and noncontact nature of laser ultrasonics.

One objective fulfilled by this research is to increase the understanding of the underlying principles of the propagation of guided circumferential waves by making benchmark, high-fidelity measurements of transient waves in two-layered cylinders. Another specific accomplishment of this research is a demonstration that it is possible to use a fiber-optic delivery system, coupled with a heterodyne interferometer, to generate and detect guided waves from multiple, equally spaced source locations, with an excellent SNR.

As a direct result of the high SNR of these experimentally measured transient waveforms, it is possible to use signal-processing techniques to calculate dispersion curves, and thus determine the steady-state behavior of cylindrical waveguides. This work achieves success with two different signal-processing techniques: the 2D-FFT and the Prony method. Since each of these signal-processing techniques can operate on exactly the same set of equally spaced transient waveforms, it is possible to compare the accuracy and robustness of each technique. This research shows that while both methods are extremely effective, the 2D-FFT is more suitable in identifying well-spaced modes, while the Prony method is better at separating a large number of closely spaced modes.

A final motivation for the current research is to experimentally validate the theoretical model developed in Ref. 2. A comparison of theoretical and experimental results demonstrates the fidelity and accuracy of the experimental measurements made in this research, and there is good agreement.

ACKNOWLEDGMENTS

This work is supported by the Office of Naval Research M-URI Program ''Integrated Diagnostics'' (Contract No. N00014-95-1-0539). In addition, the Duetscher Akademischer Austausch Dienst (DAAD) provided partial support to Markus Kley.

[1] D. E. Chimenti, ''Guided waves in plates and their use in materials characterization,'' Appl. Mech. Rev. **50**, No. 5, 247–284 (1997).
[2] C. Valle, J. Qu, and L. J. Jacobs, ''Guided circumferential waves in layered cylinders,'' Int. J. Eng. Sci. (to be published).
[3] D. A. Hutchins and K. Lundgren, ''A laser study of transient Lamb waves in thin materials,'' J. Acoust. Soc. Am. **85**, 1441–1448 (1989).
[4] N. A. Schumacher, C. P. Burger, and P. H. Gien, ''A laser-based investigation of higher-order modes in transient Lamb waves,'' J. Acoust. Soc. Am. **93**, 2981–2984 (1993).
[5] U. Kawald, C. Desmet, W. Lauriks, C. Glorieux, and J. Thoen, ''Investigation of the dispersion relations of surface acoustic waves propagating on a layered cylinder,'' J. Acoust. Soc. Am. **99**, 926–930 (1996).
[6] G. Liu and J. Qu, ''Guided circumferential waves in a circular annulus,'' J. Appl. Mech. **65**, 424–430 (1998).
[7] D. Gazis, ''Three dimensional investigation of the propagation of waves in hollow circular cylinders, I. Analytical and II. Numerical results,'' J. Acoust. Soc. Am. **31**, 568–578 (1959).
[8] C. B. Scruby and L. E. Drain, *Laser Ultrasonics: Techniques and Applications* (Hilger, New York, 1990).
[9] D. A. Bruttomesso, L. J. Jacobs, and R. D. Costley, ''Development of an interferometer for acoustic emission testing,'' J. Eng. Mech. **119**, 2303–2316 (1993).
[10] W. Sachse and Y.-H. Pao, ''On the determination of phase and group velocities of dispersive waves in solids,'' J. Appl. Phys. **49**, 4320–4327 (1978).
[11] M. Kley, ''Development of Dispersion Relationships for Layered Cylinders using Laser Ultrasonics,'' M.S. thesis, Georgia Institute of Technology, Atlanta, Georgia, 1998.
[12] D. Alleyne and P. Cawley, ''A two-dimensional Fourier transform method for measurement of propagating multimode signals,'' J. Acoust. Soc. Am. **89**, 1159–1168 (1991).
[13] F. Moser, L. J. Jacobs, and J. Qu, ''Modeling elastic wave propagation in wave guides with the finite element method,'' NDT & E Int. **32,** 225–234 (1999).
[14] Y. G. Glandier, Y. H. Berthelot, and J. Jarzynski, ''Wave-vector analysis of the forced vibrations of cylindrical shells of finite length,'' J. Acoust. Soc. Am. **92**, 1985–1993 (1992).
[15] K. Grosh and E. G. Williams, ''Complex wave-number decomposition of structural vibrations,'' J. Acoust. Soc. Am. **93**, 836–848 (1993).

Singular perturbation analysis of an acoustically levitated sphere: Flow about the velocity node

Hong Zhao and S. S. Sadhal
Department of Aerospace & Mechanical Engineering, University of Southern California, Los Angeles, California 90089-1453

Eugene H. Trinh
Jet Propulsion Laboratory, 4800 Oak Grove Drive, Pasadena, California 91109

(Received 14 May 1997; accepted for publication 21 March 1999)

This analysis consists of the development of the fluid flow about a spherical particle placed at the velocity node of a standing wave. High-frequency acoustic fields are being used to levitate particles in Earth gravity, and to stabilize particles in low-gravity situations. While a standing wave in an infinite medium may be purely oscillatory with no net flow components, the interaction with particles or solid walls leads to nonlinear effects that create a net steady component of the flow. In the present development, the perturbation method is employed to derive the flow field for the situation when a spherical particle is positioned at the velocity node. As found in an earlier analysis [Riley, Q. J. Mech. Appl. Math **19**, 461 (1966)] applicable to a solid sphere at the velocity antinode, there is a thin shear-wave region adjacent to the spherical boundary. However, this thin Stokes layer does not cover the entire sphere in the same manner as in the previous case. In the polar regions flow reversal takes place but the Stokes layer opens to the surrounding field. On an equatorial belt region there are closed streamlines. [S0001-4966(99)05807-5]

PACS numbers: 43.25.Uv [MAB]

NOMENCLATURE

a	radius of the sphere
i	$\sqrt{-1}$
k	wave number
M^2	frequency parameter, $ia^2\omega/\nu$
p	acoustic pressure
p'	pressure
r	radial coordinate
R	Reynolds number, $U_\infty a/\nu$
t	time
U_∞	velocity amplitude in the sound wave
z	coordinate along the polar axis

Greek letters

δ	Stokes layer thickness, $\sqrt{2\nu/\omega}$
ϵ	perturbation parameter, $\epsilon = U_\infty/\omega a$
η	normal boundary-layer coordinate [Eq. (32)]
θ	angular coordinate
λ	wavelength of the sound field, viscosity ratio
$\bar{\mu}$	$\cos\theta$
ν	kinematic viscosity of the fluid
ρ	acoustic density
ρ'	density
ϱ	radial cylindrical coordinate, $\varrho = r\sin\theta$
τ	dimensionless time, ωt
φ	velocity potential
ψ	stream function
ω	angular frequency

Subscripts

c	undisturbed quantities
0	leading order quantities
1	first order quantities
∞	far field

Superscripts

b	boundary layer quantities
*	nondimensional quantities

INTRODUCTION

In an Earth-gravity field, containerless processing is possible with acoustic and/or electrostatic levitation. With the application of the principle of radiation pressure, ultrasound levitators have been in use for many years in ground based experiments.[1–4] Recent advances in single-particle levitation technology have rekindled scientific interest in the determination of the bulk and surface physical properties of liquids in the metastable supercooled, supersaturated, or superheated states. The capability of indefinitely suspending in a host fluid or vacuum, a high-purity liquid in the form of a free drop, without inducing large scale translational or oscillatory motion has created the opportunity to accurately determine the temperature dependence of a number of its thermodynamic properties. It has also become possible to observe and to quantify the rates of transport processes involving its free surface and the surrounding fluids, and to examine the details of phase transformations such as melting and solidification, evaporation, and condensation.

The acoustic field provides the radiation pressure necessary to levitate a liquid drop in a gravitational field. Studies

on the effects of radiation pressure on spheres and disks go as far back as 1930, when some of the earliest theoretical studies were conducted by King.[5,6] Subsequently, many investigations[1,2,7–10] on the radiation force have been conducted for both drops and bubbles. With the application of this principle, ultrasound levitators have been in use for many years in ground-based experiments. Electrostatic levitation is another way for containerless processing. In zero gravity, the acoustic field can be used to stabilize a fluid particle.

Acoustic streaming is generally classified as two common types. One happens because of the spatial attenuation of a wave in free space. This type of streaming is usually associated with a high Reynolds number flow. The second mechanism arises from the friction between the medium and a solid wall when the former is vibrating in contact with the latter, e.g., a wave traveling down a waveguide, a standing wave in a resonant chamber, or a wave scattering off a solid object. Unlike the spatial attenuation mentioned earlier, this effect is largely confined to a thin viscous boundary layer of thickness $\delta=(2\nu/\omega)^{1/2}$ on the surface, where ν is the kinematic viscosity of the medium and ω is the angular frequency of the wave. It is also a significant dissipation mechanism, and provides a strong force in driving acoustic streaming. While the medium outside the layer vibrates irrotationally as in a sound field, the one within the layer has vorticity because its motion has to conform to the no slip condition on wall. We are now interested in this second mechanism of streaming.

If a body of typical dimension a oscillates with velocity, say, $U_\infty\cos(\omega t)$ in a viscous fluid and $\epsilon=U_\infty/\omega a\ll 1$, then, although the leading order solution is oscillatory, higher order terms include not only higher harmonics but steady contributions to the velocity. Mathematically, this can be explained by the existence of the nonlinear terms which may have steady nonzero component. Physically, the condition $\epsilon\ll 1$ implies that the amplitude of the oscillation is small compared with the particle radius a. The existence of this steady streaming was first pointed out by Rayleigh[11] in his work on Kundt's dust tube and was later studied in a boundary-layer context by Schlichting[12] who considered flows with the additional constraint $|M|^2=\omega a^2/\nu\gg 1$, where ν denotes the kinematic viscosity of the fluid. For such a flow it is now well-established that the first order fluctuation vorticity is confined to a shear-wave region of thickness $O(\nu/\omega)^{1/2}$ beyond which steady velocities $O(\epsilon U_\infty)$ persist. Riley[13] has considered the case of an oscillating sphere for both $|M|\gg 1$ and $0<|M|<1$. This result is applicable to the streaming around the sphere which is at the velocity antinode of the wave that vibrates vertically. Further analyses for a torsionally oscillating sphere and for combined linear-rotational oscillations have been given by Gopinath.[14,15] For thermal oscillations in tune with the acoustic field, effects similar to steady streaming have been shown for convective transport by Gopinath and Mills.[16] Deformations of acoustically levitated drops have been studied in several investigations,[17–21] both experimentally and theoretically. Most of the theoretical developments have been based on inviscid fluid dynamics.

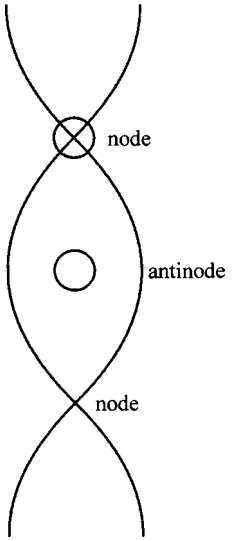

FIG. 1. Velocity node and antinode identification.

In the analytical investigations to date, little consideration has been given to the viscous effects when a particle is placed at the velocity node of the wave. The velocity node and antinode are identified in Fig. 1. The results from the investigation of the flow field will provide information about the characteristics of the levitation process. The theory will be very useful in overcoming some of experimental problems by providing suitable direction. For example, presently with acoustic levitation there is a residual flow field, including solid-body rotation for drops. Such instabilities interfere with, for example, the steady application of thermal stimuli which would serve as a means for the measurement of thermophysical properties. This problem needs to be solved and detailed understanding of the flow studies would be beneficial. Furthermore, very little is known about the pressure field. The flow calculations together with experimental measurements of the drop position can be used to predict the pressure field which is difficult to measure. For levitation under zero-gravity conditions, the drop assumes an equilibrium position at the velocity antinode when the external medium is a gas, or if the particle is very small. When the particle phase has higher compressibility than the external phase (e.g., a gas bubble in a liquid) the equilibrium position is at the velocity node. While the antinode solution has been available from Riley's[13] work, the node solution is a new development. While Riley's[13] solution is valid in the incompressible flow regime for the low Mach number approximation, in the present development some compressibility effects have to be accounted for.

In the discussion here, the focus is on analysis of the solid sphere being placed at the velocity node of the wave. Besides the direct application to such physical cases, the analysis about the velocity node leads to an important result for calculating the streaming when the sphere is placed between the velocity node and antinode of the wave. Eventually, the analysis will be used to obtain the flow field for a sphere levitated at a position between the node and the antinode. In this proposed development, use will be made of the existing antinode solution of Riley[13] and the present node

solution through a nonlinear combination. Although Lee and Wang[22] have considered this kind of problem, their result depends on an algorithm for calculating the tangential velocity on the edge of the recirculating shear layer. Detailed flow field in the shear layer for such situations is yet unavailable. A more rigorous development of the flow field is necessary to fully understand the fluid mechanics, and the present calculations provide an additional component for the complete development.

Riley[13] gave the solution for an oscillating sphere in an otherwise quiescent infinite fluid medium. This solution is applicable to a small sphere positioned at the velocity antinode of a standing wave provided $a \ll \lambda$, i.e., the size of the sphere is small compared to the wavelength. We briefly discuss Riley's[13] solution since it forms a basis for further development. The following dimensionless parameters are relevant:

$$R=\frac{U_\infty a}{\nu}, \quad M^2=\frac{i\omega a^2}{\nu}, \quad \text{and} \quad \frac{R}{|M|^2}=\epsilon=\frac{U_\infty}{\omega a}\ll 1, \tag{1}$$

where U_∞ is a characteristic velocity and R is the Reynolds number. While Riley[13] considered both $|M|\ll 1$ and $|M| \gg 1$, the latter case (high frequency) is the one relevant to ultrasound levitation.

For a standing wave with velocity

$$u_z=U_\infty \cos k(z+Z_0)e^{i\omega t}, \tag{2}$$

the local velocity in the neighborhood of the node ($kZ_0 = \frac{1}{2}\pi$) is

$$u_z=-U_\infty \sin(kz)e^{i\omega t}=-U_\infty\left(kz-\frac{k^3z^3}{3!}\ldots\right)e^{i\omega t}. \tag{3}$$

With a small particle at the node, the surrounding field may just be taken as the first term

$$u_z=-U_\infty kze^{i\omega t}. \tag{4}$$

While the medium inside the boundary layer near the sphere vibrates rotationally to meet the no slip boundary condition on the wall, the medium outside the layer vibrates irrotationally as in a sound field. Therefore, the far field flow can be written as a potential function,

$$\varphi_\infty=\frac{U_\infty}{k}\cos(kz)e^{i\omega t}=\frac{U_\infty}{k}\left(1-\frac{1}{2}k^2r^2\cos^2\theta+\ldots\right)e^{i\omega t}. \tag{5}$$

I. EQUATIONS OF MOTION

The equations of motion are as follows:

- Continuity:

$$\frac{\partial \rho'}{\partial t}+\nabla\cdot(\rho'\mathbf{u})=0, \tag{6}$$

- Momentum:

$$\rho'\frac{\partial \mathbf{u}}{\partial t}+\rho'\nabla\cdot\mathbf{u}=-\nabla p'+\mu\nabla^2\mathbf{u}, \tag{7}$$

where c is the speed of sound, and ρ' and p' are the density and pressure, respectively. Here, we follow the standard procedure and consider these parameters to be disturbances to time-independent values in the form

$$\rho'=\rho_c+\rho, \tag{8}$$

$$p'=p_c+p. \tag{9}$$

The quantities ρ and p are known as the acoustic density and acoustic pressure, respectively.

We first scale the flow parameters as follows:

$$\mathbf{u}^*=\frac{\mathbf{u}}{U_\infty}, \quad \psi^*=\frac{\psi}{U_\infty a^2}, \quad \mathbf{x}^*=\frac{\mathbf{x}}{a},$$

$$\varphi^*=\frac{\varphi}{U_\infty a}, \quad \tau=\omega t, \tag{10}$$

$$p^*=\frac{p}{\rho_c U_\infty \omega a}, \quad \rho^*=\frac{\rho c^2}{\rho_c U_\infty \omega a}, \quad \text{and} \quad \nabla^*=a\nabla,$$

and drop the asterisks.

Using adiabatic relation $\rho=p/c^2$, the dimensionless parameters p and ρ are equal, i.e.,

$$p=\rho. \tag{11}$$

In dimensionless form, the continuity equation becomes

$$k^2a^2\frac{\partial \rho}{\partial \tau}+\nabla\cdot\mathbf{u}+\epsilon(k^2a^2)\nabla\cdot(\rho\mathbf{u})=0, \tag{12}$$

where $k=\omega/c$ is the wave number, and ϵ is defined in Eq. (1). The momentum equation becomes

$$(1+\rho\epsilon(ka)^2)\frac{\partial \mathbf{u}}{\partial \tau}+\epsilon(1+\rho\epsilon(ka)^2)\mathbf{u}\cdot\nabla\mathbf{u}$$

$$=-\nabla p+\frac{1}{|M|^2}\nabla^2\mathbf{u}. \tag{13}$$

On the surface of the particle the boundary conditions are the usual no-slip type, i.e.,

$$\mathbf{u}=\mathbf{0} \quad \text{on} \quad r=1. \tag{14}$$

The far field conditions take the form

$$u_z=-kaze^{i\tau}=-kar\cos\theta e^{i\tau}, \tag{15}$$

and

$$\varphi_\infty=\frac{1}{ka}\left[1-\frac{1}{3}(ka)^2r^2P_2(\bar{\mu})-\frac{1}{6}(ka)^2r^2\right]e^{i\tau}, \tag{16}$$

where $P_n(\bar{\mu})$ represents Legendre polynomials, and $\bar{\mu}=\cos\theta$.

II. SOLUTION

Applying perturbation method, we seek a solution for the outer flow by writing

$$\mathbf{u}=\mathbf{u}_0+\epsilon\mathbf{u}_1+O(\epsilon^2), \tag{17}$$

$$p=p_0+\epsilon p_1+O(\epsilon^2), \tag{18}$$

and

$$\rho=\rho_0+\epsilon\rho_1+O(\epsilon^2). \tag{19}$$

A. The leading-order solution

Upon inserting Eqs. (17), (18), and (19) into the momentum equation (13), we find that the leading-order velocity of outer flow satisfies

$$\frac{\partial \mathbf{u}_0}{\partial \tau} = -\nabla p_0. \tag{20}$$

The above Eq. (20) shows that the leading-order outer flow is irrotational. Then $\mathbf{u}_0$ can be written in the form of a potential function,

$$\mathbf{u}_0 = \nabla \varphi_0, \tag{21}$$

whereupon Eq. (20), as usual, becomes

$$p_0 = -\frac{\partial \varphi_0}{\partial \tau}. \tag{22}$$

Since we already know the far-field potential in Eq. (16), the far-field pressure and density can be written as

$$p_\infty = \rho_\infty = -\frac{i}{ka}\left[1 - \frac{1}{3}(ka)^2 r^2 P_2(\bar{\mu}) - \frac{1}{6}(ka)^2 r^2\right] e^{i\tau}. \tag{23}$$

The first term $(-i/(ka))e^{i\tau}$ contains information about compressibility. From the continuity equation (12), the leading-order solution $\mathbf{u}_0$ satisfies

$$(ka)^2 \frac{\partial \rho_0}{\partial \tau} + \nabla \cdot \mathbf{u}_0 = 0. \tag{24}$$

To keep proper order, only the term $(-i/(ka))e^{i\tau}$ in ρ_0 is needed here, and therefore,

$$(ka)e^{i\tau} + \nabla \cdot \mathbf{u}_0 = 0. \tag{25}$$

By rewriting Eq. (25) in the form of a potential function, we obtain

$$\nabla^2 \phi_0 + (ka) = 0, \tag{26}$$

where

$$\varphi_0 = \phi_0(r,\theta) e^{i\tau}. \tag{27}$$

On the surface of the sphere, normal velocity is zero, i.e.,

$$u_{r0} = \frac{\partial \varphi_0}{\partial r} = 0 \quad \text{at} \quad r = 1. \tag{28}$$

With the boundary condition (28) and the far-field condition (16), we find that

$$\varphi_0 = \left\{\frac{1}{ka} - \frac{ka}{3}\left(\frac{r^2}{2} + \frac{1}{r}\right) - \frac{ka}{3}\left(r^2 + \frac{2}{3r^3}\right) P_2(\bar{\mu})\right\} e^{i\tau}, \tag{29}$$

and

$$p_0 = \rho_0 = -i\left\{\frac{1}{ka} - \frac{ka}{3}\left(\frac{r^2}{2} + \frac{1}{r}\right) - \frac{ka}{3}\left(r^2 + \frac{2}{3r^3}\right) P_2(\bar{\mu})\right\} e^{i\tau}. \tag{30}$$

In the boundary layer, we let the velocity be

$$\mathbf{u}^b = u_r^b \hat{\mathbf{r}} + u_\theta^b \hat{\boldsymbol{\theta}}, \tag{31}$$

where u_r^b is the normal velocity and u_θ^b is the tangential velocity. As we know, when $|M|^2 \gg 1$, the vorticity generated at the surface of the sphere, is confined to a thin shear-wave layer of thickness $O(|M|^{-1})$ (see Riley[13]). We may, therefore, scale the inner variables inside the shear-wave layer as

$$\eta = (r-1)\frac{|M|}{\sqrt{2}}, \tag{32}$$

and

$$u_\eta^b = \frac{|M|}{\sqrt{2}} u_r^b. \tag{33}$$

Again, we seek a perturbation solution by expanding velocity, pressure, and density as powers in ϵ so that

$$\mathbf{u}^b = \mathbf{u}_0^b + \epsilon \mathbf{u}_1^b + O(\epsilon^2), \tag{34}$$

$$p^b = p_0^b + \epsilon p_1^b + O(\epsilon^2), \tag{35}$$

and

$$\rho^b = \rho_0^b + \epsilon \rho_1^b + O(\epsilon^2). \tag{36}$$

By inserting Eqs. (34), (35), and (36) into momentum equation (13), we have

$$\frac{\partial u_{r0}^b}{\partial \tau} = -\frac{\partial p_0^b}{\partial r} = -\frac{|M|}{\sqrt{2}} \frac{\partial p_0^b}{\partial \eta} \tag{37}$$

for the leading-order normal velocity, and

$$\frac{\partial u_{\theta 0}^b}{\partial \tau} = -\frac{\partial p_0^b}{\partial \theta} + \frac{1}{2} \frac{\partial^2 u_{\theta 0}^b}{\partial \eta^2} \tag{38}$$

for the leading-order tangential velocity in the boundary layer. Since the frequency parameter $|M| \gg 1$, we may deduce from Eq. (37) that the leading-order acoustic pressure p_0^b in the boundary layer is a function of θ and τ only, i.e.,

$$\frac{\partial p_0^b}{\partial \eta} = 0. \tag{39}$$

Then, from Eq. (30), it is found that

$$p_0^b = \rho_0^b = p_0|_{r=1} = -\frac{i}{ka}\left\{1 - \frac{1}{2}(ka)^2 - \frac{5}{9}(ka)^2 P_2(\bar{\mu})\right\} e^{i\tau}. \tag{40}$$

With the insertion of Eq. (40) and the boundary condition

$$u_{\theta 0}^b = 0 \quad \text{at} \quad \eta = 0, \tag{41}$$

we find

$$u_{\theta 0}^b = \tfrac{5}{3}(ka)\sin\theta\cos\theta(1 - e^{-(1+i)\eta}) e^{i\tau}. \tag{42}$$

From the continuity equation (12), we obtain the equation for the leading-order normal velocity in the boundary layer $u_{\eta 0}^b$ as

$$(ka)^2 \frac{\partial \rho_0^b}{\partial \tau} + \frac{\partial u_{\eta 0}^b}{\partial \eta} + \frac{1}{\sin\theta} \frac{\partial}{\partial \theta}(u_{\theta 0}^b \sin\theta) = 0. \tag{43}$$

With the boundary condition

$$u^b_{\eta 0}=0 \quad \text{at} \quad \eta=0, \tag{44}$$

the solution of $u^b_{\eta 0}$ is found to be

$$u^b_{\eta 0}=\{-ka\,\eta+\tfrac{10}{3}(ka)[-\eta+\tfrac{1}{2}(1-i) \times(1-e^{-(1+i)\eta})]P_2(\bar{\mu})\}e^{i\tau}, \tag{45}$$

where the first term $-ka\,\eta e^{i\tau}$ represents the compressibility in the boundary layer.

B. The first-order solution [$O(\epsilon)$]

The first-order solution is much more complex than the leading order. As we are more interested in the steady streaming outside the sphere, we only consider the steady state solutions here. In this section, all the first order variables are time-independent.

By carrying out the perturbation expansion to order of ϵ, the continuity equation in the boundary layer becomes

$$\nabla\cdot\mathbf{u}^b_1+(ka)^2\langle\nabla\cdot(\rho^b_0\mathbf{u}^b_0)\rangle=0, \tag{46}$$

in which $\langle\ \rangle$ denotes the time-averaged mean of the corresponding term. As we already know the solutions of ρ^b_0 and $\mathbf{u}^b_0$ in Sec. II A, we can prove that the term $\langle\nabla\cdot(\rho^b_0\mathbf{u}^b_0)\rangle$ is zero. Therefore,

$$\nabla\cdot\mathbf{u}^b_1=0. \tag{47}$$

Equation (47) proves that the first-order steady flow in the boundary layer is incompressible. Inserting Eqs. (34), (35), and (36) into the momentum equation (13), and equating both sides to order ϵ, we have

$$\left\langle \rho^b_0(ka)^2\frac{\partial u^b_{\eta 0}}{\partial\tau}\right\rangle+\left\langle u^b_{\eta 0}\frac{\partial u^b_{\eta 0}}{\partial\eta}\right\rangle+\left\langle u^b_{\theta 0}\frac{\partial u^b_{\eta 0}}{\partial\theta}\right\rangle =-\frac{|M|^2}{2}\frac{\partial p^b_1}{\partial\eta}+\frac{\partial^2 u^b_{\eta 1}}{\partial\eta^2}, \tag{48}$$

for the first-order normal velocity in the boundary layer, and

$$\left\langle \rho^b_0(ka)^2\frac{\partial u^b_{\theta 0}}{\partial\tau}\right\rangle+\left\langle u^b_{\eta 0}\frac{\partial u^b_{\theta 0}}{\partial\eta}\right\rangle+\left\langle u^b_{\theta 0}\frac{\partial u^b_{\theta 0}}{\partial\theta}\right\rangle =-\frac{\partial p^b_1}{\partial\theta}+\frac{1}{2}\frac{\partial^2 u^b_{\theta 1}}{\partial\eta^2}, \tag{49}$$

for the first-order tangential velocity in the boundary layer. Because of the condition $|M|^2\gg 1$, we may deduce from Eq. (48) that

$$\frac{\partial p^b_1}{\partial\eta}=0, \tag{50}$$

which means that the first-order time-independent pressure in the boundary layer is a function of θ only. As the steady flow in the boundary layer is incompressible, the stream function ψ^b_1 can be introduced such that

$$u^b_{r1}=\frac{1}{r^2\sin\theta}\left(\frac{\partial\psi^b_1}{\partial\theta}\right), \tag{51}$$

and

$$u^b_{\theta 1}=-\frac{1}{r\sin\theta}\left(\frac{\partial\psi^b_1}{\partial r}\right). \tag{52}$$

Inserting Eq. (52) into Eq. (49), with the limit $\psi^b_1=o(\eta^2)$, and the boundary conditions

$$\psi^b_1=0 \quad \text{at} \quad \eta=0,$$

$$\frac{\partial\psi^b_1}{\partial\eta}=0 \quad \text{at} \quad \eta=0,$$

we obtain the solution for ψ^b_1 as

$$\psi^b_1=-\frac{\sqrt{2}}{|M|}(ka)^2\Bigg\{\left(\frac{25}{72}e^{-2\eta}+\frac{10}{3}e^{-\eta}\cos\eta +\frac{35}{18}e^{-\eta}\sin\eta+\frac{5}{9}\eta e^{-\eta}\sin\eta+\frac{25}{12}\eta-\frac{265}{72}\right) \times\bar{\mu}(1-\bar{\mu}^2)+\left(-\frac{25}{36}e^{-2\eta}-\frac{100}{9}e^{-\eta}\cos\eta -\frac{125}{18}e^{-\eta}\sin\eta-\frac{25}{6}\eta e^{-\eta}\sin\eta-\frac{50}{9}\eta+\frac{425}{36}\right) \times\bar{\mu}^3(1-\bar{\mu}^2)\Bigg\}. \tag{53}$$

The perturbation solution Eq. (53) may only be regarded as an inner solution, appropriate to the shear-wave layer, and we must seek an additional asymptotic series in the outer region where

$$(r-1)=O(1).$$

By carrying out the perturbation expansion to order ϵ, the continuity equation outside the boundary layer becomes

$$\nabla\cdot\mathbf{u}_1+(ka)^2\langle\nabla\cdot(\rho_0\mathbf{u}_0)\rangle=0. \tag{54}$$

Again, from Sec. II A we can prove that $\langle\nabla\cdot(\rho_0\mathbf{u}_0)\rangle$ is zero, and thus

$$\nabla\cdot\mathbf{u}_1=0, \tag{55}$$

which means the first-order steady flow outside the boundary layer is incompressible. Then, just as we introduced the inner variable ψ^b_1, we introduce the outer stream function ψ_1 such that

$$u_{r1}=\frac{1}{r^2\sin\theta}\left(\frac{\partial\psi_1}{\partial\theta}\right) \quad \text{and} \quad u_{\theta 1}=-\frac{1}{r\sin\theta}\left(\frac{\partial\psi_1}{\partial r}\right). \tag{56}$$

Equating coefficients of powers of ϵ in the momentum equation (13), and using the above stream function relationship, we obtain the Stokes flow equation

$$D^4\psi_1=0, \tag{57}$$

where D^2 is defined as

$$D^2=\frac{\partial^2}{\partial r^2}+\frac{(1-\bar{\mu}^2)}{r^2}\frac{\partial^2}{\partial\bar{\mu}^2}. \tag{58}$$

Equation (57) indicates that the first-order steady streaming outside the boundary layer is Stokes flow. The appropriate solution, taking account of the matching requirement and the condition $\psi_1=o(r^2)$ as $r\to\infty$, is

$$\psi_1=(D_2r^{-2}+F_2)\bar{\mu}(1-\bar{\mu}^2)$$
$$+(D_4r^{-4}+F_4r^{-2})(1-\bar{\mu}^2)(7\bar{\mu}^3-3\bar{\mu}). \quad (59)$$

Now by letting $r\to 1$ and introducing the inner variable η defined in Eq. (32), we have

$$\psi_1\sim\left\{(D_2+F_2-3D_4-3F_4)+(-2D_2+12D_4+6F_4)\frac{\sqrt{2}}{|M|}\eta\right\}\bar{\mu}(1-\bar{\mu}^2)+\left\{(7D_4+7F_4)+(-28D_4-14F_4)\frac{\sqrt{2}}{|M|}\eta\right\}\bar{\mu}^3(1-\bar{\mu}^2). \quad (60)$$

Upon matching to this order with Eq. (53) as $\eta\to\infty$, we find

$$D_2+F_2-3D_4-3F_4=0, \quad (61)$$

$$-2D_2+12D_4+6F_4=-\tfrac{25}{12}(ka)^2, \quad (62)$$

$$7D_4+7F_4=0, \quad (63)$$

$$-28D_4-14F_4=\tfrac{50}{9}(ka)^2, \quad (64)$$

from which we deduce that

$$D_2=-\tfrac{25}{168}(ka)^2, \quad F_2=\tfrac{25}{168}(ka)^2,$$

$$D_4=-\tfrac{25}{63}(ka)^2, \quad F_4=\tfrac{25}{63}(ka)^2.$$

With these constants determined, the expression for ψ_1 is found to be

$$\psi_1=(ka)^2\,\tfrac{25}{168}(-r^{-2}+1)\bar{\mu}(1-\bar{\mu}^2)+(ka)^2\times\tfrac{25}{63}(-r^{-4}+r^{-2})(7\bar{\mu}^3-3\bar{\mu})(1-\bar{\mu}^2). \quad (65)$$

The existence of ψ_1 proves that steady part of the first-order velocity in the boundary layer persists outside the layer and induces a steady streaming velocity $O(\epsilon)$ outside that region.

III. DISCUSSION

The inner and outer solutions both have time-independent components which exhibit the steady streaming motion. The flow field exhibits symmetry about the polar axis and the equatorial plane. This symmetry is to be expected since the problem, as defined, is symmetric. The streamlines have been plotted for one quadrant in Fig. 2. The detailed flow near the sphere is shown in Fig. 3 where the radial scale is highly stretched. Some interesting flow patterns have been predicted. While there is a thin layer on the surface of the particle, as in the case a particle at the velocity antinode, the streamlines are not closed. Flow reversal within the layer is seen in two segments: the polar regions, $0°<\theta<46°$, $134°<\theta<180°$, and the equatorial belt, $46°<\theta<134°$. Closed recirculating streamlines only exist in the equatorial belt. Outside this range, the streamlines merge with the exterior flow. Mathematically, this behavior results because the Stokes layer solution consists of two components corresponding to the first and the third spherical harmonics. These solutions add up with two guaranteed zeros in the radial direction only for a limited region over the sphere as discussed.

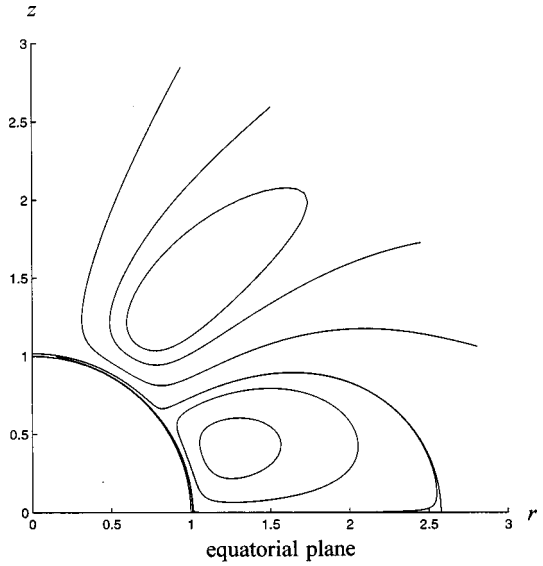

FIG. 2. Steady streaming flow streamlines about a sphere at the velocity node. The fluid motion is clockwise in the upper vortex, and anticlockwise in the lower one.

These results have some important implications for experimental studies relating to particle levitation. For example, for a particle levitated in a gravity field, it is displaced from the antinode or the node of a standing wave. We would therefore need to expand the standing wave velocity u_z such that

$$u_z=A\cos[k(z+Z_0)]e^{i\tau}$$
$$=[A\cos kZ_0-A(kz)\sin kZ_0+O(k^2z^2)]e^{i\tau} \quad (66)$$

for small ka, in which Z_0 is the displacement of the sphere from the antinode, and $k=\omega/c$. Here, the first term of Eq. (66) is just the far-field velocity for Riley's[13] problem, and the second term is the far-field velocity for the problem we have just discussed. That means the problem in which the

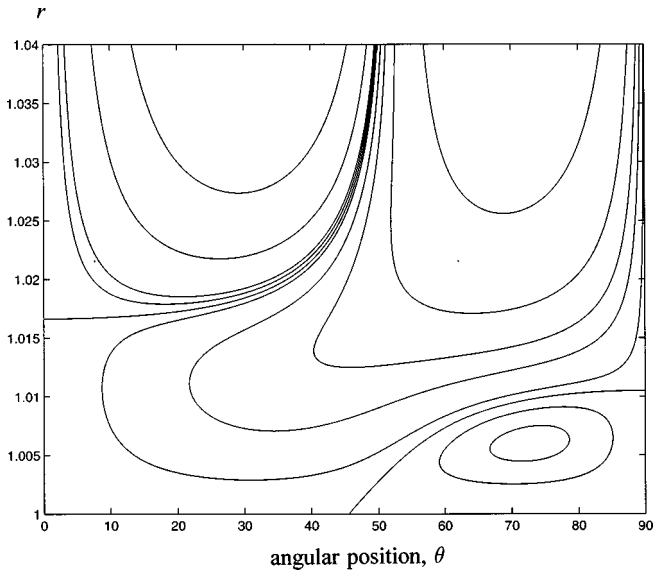

FIG. 3. Detailed flow field near the sphere with a stretched radial scale. The motion is clockwise in the upper left region and the lower closed streamlines, and anticlockwise elsewhere.

sphere is displaced from the antinode is the combination of the two problems we just discussed, together with some additional nonlinear terms. This is presently under investigation.

ACKNOWLEDGMENTS

The authors are very grateful to Dr. Alexei Rednikov for the many discussions on this paper, and to the U.S. National Aeronautics and Space Administration for the support of this work under Grant No. NAG3-1842.

[1] R. E. Apfel, ''Technique for measuring the adiabatic compressibility, density, and sound speed of a submicroliter liquid sample,'' J. Acoust. Soc. Am. **59**, 339–343 (1976).
[2] A. I. Eller, ''Force on a bubble in a standing acoustic wave,'' J. Acoust. Soc. Am. **43**, 170–171 (1968).
[3] A. R. Hanson, E. G. Domich, and H. S. Adams, ''Acoustic liquid drop holder,'' Rev. Sci. Instrum. **35**, 1031–1034 (1964).
[4] P. L. Marston and R. E. Apfel, ''Acoustically forced shape oscillations of hydrocarbon drops levitated in water,'' J. Colloid Interface Sci. **68**, 280–286 (1979).
[5] L. V. King, ''On the acoustic radiation pressure on spheres,'' Proc. R. Soc. London, Ser. A **147**, 212–240 (1934).
[6] L. V. King, ''On the theory of the inertia and diffraction corrections for the Rayleight disc,'' Proc. R. Soc. London, Ser. A **153**, 17–40 (1935).
[7] T. J. Asaki and P. L. Marston, ''Acoustic radiation force on a bubble driven above resonance,'' J. Acoust. Soc. Am. **96**, 3096–3099 (1994).
[8] C. P. Lee and T. G. Wang, ''Acoustic radiation force on a bubble,'' J. Acoust. Soc. Am. **93**, 1637–1640 (1993).
[9] J. Wu and G. Du, ''Acoustic force on a small compressible sphere in a focused beam,'' J. Acoust. Soc. Am. **87**, 997–1003 (1990).
[10] K. Yosioka and Y. Kawasima, ''Acoustic radiation pressure on a compressible sphere,'' Acustica **5**, 167–173 (1955).
[11] J. W. S. Rayleigh, ''On the circulation of air observed in Kundt's tubes, and on some allied acoustical problems,'' Philos. Trans. R. Soc. London **175**, 1–21 (1884) [Lord Rayleigh, *Scientific Papers*, Vol. II, article 108, pp. 239–257, Dover, 1964].
[12] H. Schlichting, ''Berechnung ebener periodischer grenzchichtströmungen,'' Phys. Z. **23**, 327–335 (1932).
[13] N. Riley, ''On a sphere oscillating in a viscous liquid,'' Q. J. Mech. Appl. Math. **19**, 461–472 (1966).
[14] A. Gopinath, ''Steady streaming due to a small-amplitude torsional oscillations of a sphere in a viscous fluid,'' Q. J. Mech. Appl. Math. **46**, 501–520 (1993).
[15] A. Gopinath, ''Steady streaming due to small-amplitude superposed oscillations of a sphere in a viscous fluid,'' Q. J. Mech. Appl. Math. **47**, 461–480 (1994).
[16] A. Gopinath and A. F. Mills, ''Convective heat transfer from a sphere due to acoustic streaming,'' ASME J. Heat Transfer, **115**, 332–341 (1993).
[17] H. W. Jackson, M. Barmatz, and C. Shipley, ''Equilibrium shape and location of a liquid drop acoustically positioned in a resonant rectangular chamber,'' J. Acoust. Soc. Am. **84**, 1845–1862 (1988).
[18] T. Shi and R. E. Apfel, ''Oscillations of a deformed liquid drop in an acoustic field,'' Phys. Fluids **95**, 1545–1552 (1995).
[19] T. Shi and R. E. Apfel, ''Deformation and position of acoustically levitated drops,'' J. Acoust. Soc. Am. **96**, 1545–1552 (1996).
[20] Y. Tian, R. G. Holt, and R. E. Apfel, ''Deformation and location of an acoustically levitated drop,'' J. Acoust. Soc. Am. **93**, 3096 (1993).
[21] E. H. Trinh and C.-J. Hsu, ''Equilibrium shapes of acoustically levitated drops,'' J. Acoust. Soc. Am. **79**, 1335–1338 (1986).
[22] C. P. Lee and T. G. Wang, ''Outer acoustic streaming,'' J. Acoust. Soc. Am. **88**, 2367–2375 (1990).

General perturbative solution to wave scattering from a soft random cylindrical surface

Nikolaos C. Skaropoulos and Dimitrios P. Chrissoulidis
Department of Electrical and Computer Engineering, Faculty of Technology, Aristotle University of Thessaloniki, Mail: P.O. Box 1562, GR-54006 Thessaloniki, Greece

(Received 24 June 1998; accepted for publication 5 May 1999)

A perturbative solution to the problem of plane-wave scattering from a soft, randomly rough, cylindrical surface is obtained by use of the Rayleigh hypothesis and the assumption that coupled radiation modes can be present in the scattered wave. The wave amplitudes of the cylindrical-wave expansion of the scattered field are expressed as an asymptotic series in the root-mean-square of surface irregularities. The end result of the analysis is a concise recursive formula for the coefficients of that series. The solution is energy consistent up to fourth-order in the smallness parameter. Specific information about the validity and applicability of the solution is given by use of the mean boundary condition error, which is defined in this paper with a view to assessing the conformity of near-field results with the boundary condition. The numerical results show that the fourth-order approximation is more accurate than the second-order one, but it may, under certain conditions, exhibit higher mean boundary condition error. © *1999 Acoustical Society of America.* [S0001-4966(99)05708-2]

PACS numbers: 43.30.Hw, 43.40.Kf, 43.20.Fn [DLB]

INTRODUCTION

Wave scattering from rough cylindrical surfaces is a problem of both theoretical and practical interest; this problem has been addressed with a variety of methods.[1–5] Yeh[1] and Erma[2] used a Rayleigh perturbation method to treat electromagnetic wave scattering from deterministic rough cylinders. Eftimiu[3,4] used an extinction-theorem perturbation method to formulate electromagnetic wave scattering from random rough cylinders with angular or axial corrugations. Ogura and Nakayama[5] applied the stochastic functional method to wave scattering from a random rough cylindrical surface with Gaussian statistics.

The common feature of the aforementioned methods is that the boundary condition and/or the scattered wave field are formulated as a power series in the root-mean-square of surface irregularities, which serves as smallness parameter. Approximate solutions, accurate, at most, to second order in that parameter, were thus obtained and are generally deemed good, if the ratio of the smallness parameter to the wavelength is very small. Yet, the domain of applicability of second-order perturbation solutions is still not precisely known; this is due to the lack of higher-order results and to the absence of a quantitative error criterion.

In this paper, a Rayleigh perturbation method is applied to wave scattering from a soft, random rough, cylindrical surface with Gaussian statistics. This method can be applied to other scattering surfaces and boundary conditions; yet, more complicated cases are deferred to future work. Interest is focused on the validity and the domain of applicability of this method. To this end, theoretical expressions are obtained for the general perturbation term and numerical results are presented for the second- and fourth-order approximate solutions. Furthermore, a numerical error criterion is defined, which is indicative of eventual violations of the boundary condition on the random rough surface. Comparisons between second- and fourth-order results,[6–9] albeit for other scattering surfaces, have shown that, in most cases, inclusion of the fourth-order term improves the accuracy of the perturbative solution.

The first step of the analytical formulation is the decomposition of the incident plane wave into cylindrical waves, which allows a termwise treatment of the problem in hand. The scattered wave field consists of outgoing cylindrical waves, which can be coupled to one another as a result of the incomplete cylindrical symmetry. The wave amplitudes of the scattered field are expressed as an asymptotic power series in the root-mean-square of surface irregularities; the coefficients of that series are determined through a Taylor series expansion of the Dirichlet boundary condition on the random surface. The end result is a concise recurrence formula for the general perturbation term.

The second- and fourth-order approximate solutions are validated by means of two error criteria: (a) that they should be energy consistent, and (b) that they should be in conformity with the boundary condition on the random surface. On the one hand, criterion (a) is analytically checked through the forward-scattering theorem. On the other hand, criterion (b), which consists in examining whether the mean field vanishes on the rough surface, is checked numerically. This criterion is associated with errors due to the truncation of the infinite perturbation series and errors due to the Rayleigh hypothesis[10] itself; the latter may not be valid in the near field, especially when the indentations on the scattering surface are very deep.[11–15]

The numerical results indicate that, as far as the boundary condition is concerned, the fourth-order solution is generally more accurate than the second-order one. Yet, as roughness increases, the former deteriorates faster than the

latter, which is a sign of limited radius of convergence of the perturbation series on the scattering surface. The domain of applicability of these solutions depends on the correlation radius of surface roughness, extending as the latter increases. The maximum allowable value of the smallness parameter is determined by use of the boundary condition criterion. Calculations of far-field scatter are also presented; the difference from the reference case of a smooth cylindrical surface is generally small, the impact of roughness on the incoherent part of the field being most significant in the backscattering direction.

The paper is organized as follows: the scattering surface is introduced in Sec. I, the wave field is formulated in Sec. II, the wave amplitudes are determined in Sec. III, and far-field expressions are given in Sec. IV. Checks, numerical results, and discussions follow in Sec. V. Some useful formulas are available in Appendices A and B.

I. RANDOM ROUGH SCATTERING SURFACE

The random rough scattering surface S is two dimensional (2-D) and circular in the mean (Fig. 1). With regard to the cylindrical coordinate system $(O;r\theta)$, any point on S is determined by $r_s=a(1+\epsilon f(\theta,\omega))$, where a is the radius of the mean surface S_2, ϵ is a smallness parameter, and $f(\theta,\omega)$ is a normalized (i.e., zero mean, unit variance) homogeneous Gaussian random field on S_2; the variable ω, suppressed from this point onward, stands for any point of the sample space Ω.

Because of the homogeneity of the random field $f(\theta)$ on S_2, the covariance function $R(\theta_1,\theta_2)=\langle f(\theta_1)f(\theta_2)\rangle$ is periodically dependent on $\theta=\theta_2-\theta_1$, which suggests the following spectral representation:

$$R(\theta)=\sum_{n=-\infty}^{\infty} C_n e^{in\theta}. \tag{1}$$

A spectral representation can be written for $f(\theta)$ itself:[5]

$$f(\theta)=\sum_{n=-\infty}^{\infty} e^{in\theta}F_n B_n. \tag{2}$$

Equation (2) involves the deterministic spectral coefficients F_n and the random variables

$$B_n=\frac{1}{2\pi}\frac{1}{F_n}\int_0^{2\pi} e^{-in\theta}f(\theta)d\theta, \tag{3}$$

which are zero mean and Gaussian because $f(\theta)$ is zero mean and Gaussian, too. Since $f(\theta)$ is real valued, the equalities $B_{-n}=\overline{B_n}$ and $F_{-n}=\overline{F_n}$ must hold, where $\overline{B_n}$ and $\overline{F_n}$ stand for the complex conjugate of B_n and F_n, respectively.

It can easily be verified by use of Eqs. (1), (2), and (3) that, because of the homogeneity of $f(\theta)$, the random variables B_n are mutually orthogonal. Moreover, B_n can be made mutually orthonormal, if $C_n=|F_n|^2$; the latter has no effect on generality. The orthonormality of B_n is expressed by $\langle\overline{B_n}B_m\rangle=\delta_{m,n}$, where $\delta_{m,n}$ is the Kronecker delta. Thus the deterministic spectral coefficients F_n, actually the squared magnitude thereof, constitute the power spectrum of $f(\theta)$. The assumption that the latter is of unit variance amounts to $\Sigma_{n=-\infty}^{\infty}|F_n|^2=1$.

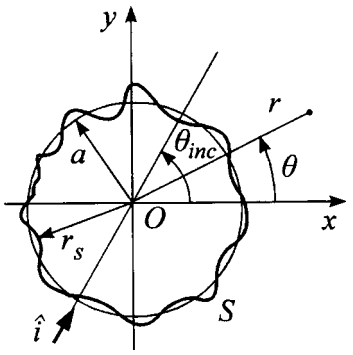

FIG. 1. Geometric configuration.

II. WAVE FIELD FORMULATION

The random wave field $\psi(kr,\theta)$ outside S (i.e., for $r\geqslant r_s$) obeys the 2-D Helmholtz equation

$$(\nabla^2+k^2)\psi(kr,\theta)=0, \tag{4}$$

where k is the wave number of the supporting medium. By use of the shorthand notation $\rho=kr$, the Dirichlet boundary condition on S is expressed by $\psi(\rho_s,\theta)=0$, where $\rho_s=kr_s$.

The wave field $\psi=\psi^{\rm inc}+\psi^{\rm sca}$ comprises the incident wave and the scattered wave. The former, which is assumed to be a plane wave propagated in the direction $\hat{i}=\hat{x}\cos\theta_{\rm inc}+\hat{y}\sin\theta_{\rm inc}$, is expressed as follows:

$$\psi^{\rm inc}(\rho,\theta)=\sum_{m=-\infty}^{\infty} i^m\psi_m^{\rm inc}(\rho,\theta)e^{-im\theta_{\rm inc}}, \tag{5}$$

where $\psi_m^{\rm inc}(\rho,\theta)=J_m(\rho)e^{im\theta}$ is a cylindrical wave function of order m and $J_m(\cdot)$ is the mth-order cylindrical Bessel function of the first kind.[16] The scattered wave is formulated accordingly:

$$\psi^{\rm sca}(\rho,\theta)=\sum_{m=-\infty}^{\infty} i^m\psi_m^{\rm sca}(\rho,\theta)e^{-im\theta_{\rm inc}}. \tag{6}$$

Thus excitation of S by $\psi_m^{\rm inc}$ gives rise to $\psi_m^{\rm sca}$, and $\psi^{\rm sca}$ is obtained by superposition of $\psi_m^{\rm sca}$ for all $m\in Z$.

Interest is, therefore, focused on the scattered wave function $\psi_m^{\rm sca}$, which may be written as a sum of appropriate cylindrical wave functions:

$$\psi_m^{\rm sca}(\rho,\theta)=\sum_{n=-\infty}^{\infty} A_{mn}H_n^{(1)}(\rho)e^{in\theta}. \tag{7}$$

$H_n^{(1)}(\rho)$ is the nth-order cylindrical Hankel function of the first kind,[16] which acquires the form of an outgoing cylindrical wave for $\rho\gg 1$. The cylindrical wave function $H_n^{(1)}(\rho)e^{in\theta}$ obeys the 2-D Helmholtz equation as well as the radiation condition at infinity, hence so does $\psi_m^{\rm sca}$, as expanded in Eq. (7). The unknown wave amplitudes A_{mn} are random variables, statistical properties of which are determined in Sec. III. It should be noted that the above formula-

tion makes use of the Rayleigh hypothesis,[10] since ψ_m^{sca} is assumed to be composed of only outgoing waves even in the region $\rho_s(\theta) \leqslant \rho \leqslant \max\{\rho_s(\theta)\}$.

Specific reference should be made to the presence of coupled wave functions, namely radiation modes corresponding to $n \neq m$, in Eq. (7). Such modes would not exist if S were smooth, in which case both Eq. (4) and the Dirichlet boundary condition would be invariant under rotations; therefore, ψ_m^{sca} and ψ_m^{inc} would belong to the same 1-D irreducible invariant subspace of the vector space of functions on S_2 with respect to the group of rotations in 2-D space.[5,17,18] Thus if $S \equiv S_2$, it should be expected that $A_{mn} = 0$ for $n \neq m$. The situation is more complicated if S is randomly rough, since then the invariance under rotations of the boundary condition only holds in a probabilistic sense[5] and, therefore, coupled modes with wave amplitudes A_{mn}, $n \neq m$, should be taken into account. As shown in Sec. III, $\langle A_{mn} \rangle = 0$, if $n \neq m$; hence, coupled modes do not contribute to the coherent part of the scattered wave field.

III. DETERMINATION OF WAVE AMPLITUDES

The wave amplitudes A_{mn} are expressed as an asymptotic power series in the smallness parameter ϵ:[2,19]

$$A_{mn} = \sum_{p=0}^{\infty} \epsilon^p A_{mn}^p. \tag{8}$$

A_{mn}^0 corresponds to the marginal case $S \equiv S_2$, obtained in the limit $\epsilon \to 0$, and A_{mn}^p, $p \geqslant 1$, are corrections to A_{mn}^0 of order p in ϵ.

The scattered wave function ψ_m^{sca} comprises the primary scattered wave $\psi_m^{1,\mathrm{sca}}(\rho,\theta) = \Sigma_{n=-\infty}^{\infty} A_{mn}^0 H_n^{(1)}(\rho) e^{in\theta}$, which represents scattering from S_2, and the secondary scattered wave $\psi_m^{2,\mathrm{sca}}(\rho,\theta) = \Sigma_{n=-\infty}^{\infty} \Sigma_{p=1}^{\infty} A_{mn}^p H_n^{(1)}(\rho) e^{in\theta}$, which is associated with roughness on S. Thus $\psi_m^{\mathrm{sca}} = \psi_m^{1,\mathrm{sca}} + \psi_m^{2,\mathrm{sca}}$ and, evidently, A_{mn}^0 are only used by $\psi_m^{1,\mathrm{sca}}$, whereas A_{mn}^p, $p \geqslant 1$, are only used by $\psi_m^{2,\mathrm{sca}}$.

The Dirichlet boundary condition $\psi(\rho_s,\theta) = 0$ on S evidently amounts to $\psi_m^{\mathrm{inc}}(\rho_s,\theta) + \psi_m^{\mathrm{sca}}(\rho_s,\theta) = 0$ for any $m \in Z$. The latter, if expanded into a Taylor series around $\rho_0 = ka$, yields

$$\sum_{p=0}^{\infty} \epsilon^p \frac{[\rho_0 f(\theta)]^p}{p!} \left[J_m{}^{(p)}(\rho_0) e^{im\theta} + \sum_{n=-\infty}^{\infty} A_{mn} H_n^{(1)(p)}(\rho_0) e^{in\theta} \right] = 0, \tag{9}$$

where $Z_\nu^{(p)}(\rho_0) = d^p Z_\nu(\rho)/d\rho^p|_{\rho=\rho_0}$, $\nu \in Z$, and Z_ν represents either J_ν or $H_\nu^{(1)}$. By use of Eq. (8) and of the identity $\Sigma_{p=0}^{\infty} \epsilon^p A_p \Sigma_{p=0}^{\infty} \epsilon^p B_p = \Sigma_{p=0}^{\infty} \epsilon^p \Sigma_{q=0}^{p} A_q B_{p-q}$,[2] Eq. (9) is written as follows:

$$\sum_{p=0}^{\infty} \epsilon^p \left[\frac{[\rho_0 f(\theta)]^p}{p!} J_m{}^{(p)}(\rho_0) e^{im\theta} + \sum_{q=0}^{p} \frac{[\rho_0 f(\theta)]^q}{q!} \sum_{n=-\infty}^{\infty} A_{mn}^{p-q} H_n^{(1)(q)}(\rho_0) e^{in\theta} \right] = 0. \tag{10}$$

The coefficient of ϵ^p in the left-hand side of Eq. (10) must be equal to zero for any $p \in Z_0^+$.[2,19] Hence,

$$\frac{[\rho_0 f(\theta)]^p}{p!} J_m{}^{(p)}(\rho_0) e^{im\theta} + \sum_{q=0}^{p} \frac{[\rho_0 f(\theta)]^q}{q!} \times \sum_{n=-\infty}^{\infty} A_{mn}^{p-q} H_n^{(1)(q)}(\rho_0) e^{in\theta} = 0, \tag{11}$$

and, if the first term of the sum over q is singled out, Eq. (11) is written as follows:

$$\sum_{n=-\infty}^{\infty} A_{mn}^p H_n^{(1)}(\rho_0) e^{in\theta} = -\frac{[\rho_0 f(\theta)]^p}{p!} J_m{}^{(p)}(\rho_0) e^{im\theta} - \sum_{q=1}^{p} \frac{[\rho_0 f(\theta)]^q}{q!} \times \sum_{n=-\infty}^{\infty} A_{mn}^{p-q} H_n^{(1)(q)}(\rho_0) e^{in\theta}. \tag{12}$$

If both sides of Eq. (12) are multiplied by $e^{-i\nu\theta}$, $\nu \in Z$, and then integrated with respect to θ in the range $[0,2\pi]$, the following recurrence equation is obtained:

$$2\pi A_{m\nu}^p H_\nu^{(1)}(\rho_0) = -\frac{{\rho_0}^p}{p!} I_{m-\nu}^p J_m{}^{(p)}(\rho_0) - \sum_{q=1}^{p} \frac{{\rho_0}^q}{q!} \sum_{n=-\infty}^{\infty} A_{mn}^{p-q} I_{n-\nu}^q H_n^{(1)(q)}(\rho_0), \tag{13}$$

where $I_\nu^p = \int_0^{2\pi} f^p(\theta) e^{i\nu\theta} d\theta$. The right-hand side of Eq. (13) involves known quantities and wave amplitudes $A_{mn}^{p'}$ of order $0 \leqslant p' < p$; if the latter were known, A_{mn}^p would readily be determined.

The above recurrence equation, if initialized with $p = 0$, yields

$$A_{mn}^0 = -\delta_{m,n} \frac{J_m(\rho_0)}{H_m^{(1)}(\rho_0)}. \tag{14}$$

The next step is taken with $p = 1$:

$$2\pi A_{m\nu}^1 H_\nu^{(1)}(\rho_0) = -\rho_0 J_m{}^{(1)}(\rho_0) I_{m-\nu}^1 - \rho_0 \times \sum_{n=-\infty}^{\infty} A_{mn}^0 I_{n-\nu}^1 H_n^{(1)(1)}(\rho_0). \tag{15}$$

By use of Eqs. (2) and (14), and of the Wronski relation,[16] Eq. (15) is eventually reduced to the following:

$$A_{mn}^1 = \frac{2iF_{n-m}B_{n-m}}{\pi H_n^{(1)}(\rho_0) H_m^{(1)}(\rho_0)}. \tag{16}$$

This procedure can be extended to $p > 1$ by use of the following identity:

$$I^p_{m-n}=2\pi\sum_{n_1=-\infty}^{\infty}\sum_{n_2=-\infty}^{\infty}\cdots\sum_{n_{p-1}=-\infty}^{\infty}F_{n-n_1}F_{n_1-n_2}\cdots F_{n_{p-1}-m}B_{n-n_1}B_{n_1-n_2}\cdots B_{n_{p-1}-m}, \quad (17)$$

which is obtained from Eq. (2). The end result is a concise expression for A^p_{mn}, $p\geqslant 1$:

$$A^p_{mn}=\frac{1}{H^{(1)}_n(\rho_0)}\sum_{n_1=-\infty}^{\infty}\sum_{n_2=-\infty}^{\infty}\cdots\sum_{n_{p-1}=-\infty}^{\infty}G_p(m,n_1,\ldots,n_{p-1})F_{n-n_1}F_{n_1-n_2}\cdots F_{n_{p-1}-m}B_{n-n_1}B_{n_1-n_2}\cdots B_{n_{p-1}-m}. \quad (18)$$

The deterministic function $G_p(m,n_1,\ldots,n_{p-1})$ is defined through the recurrence equation

$$G_p(m,n_1,\ldots,n_{p-1})=-\frac{{\rho_0}^p}{p!}W_m{}^{(p)}(\rho_0)-\sum_{q=1}^{p-1}\frac{{\rho_0}^q}{q!}\frac{H^{(1)^{(q)}}_{n_q}(\rho_0)}{H^{(1)}_{n_q}(\rho_0)}\times G_{p-q}(m,n_{q+1},\ldots,n_{p-1}), \quad (19)$$

where $W_m(\cdot)=J_m(\cdot)+A^0_{mn}H^{(1)}_m(\cdot)$ and $G_1(m)=2i/\pi H^{(1)}_m(\rho_0)$.

The above results are most general, since, apart from the spectral representation of Eq. (2) for the random field $f(\theta)$, no other assumption has been used in the analysis that led to Eq. (18). Still, the determination of statistical moments of A^p_{mn}, as well as joint statistical moments thereof, calls for the determination of joint statistical moments of the random variables B_n, $n\in Z$, which can be facilitated by use of the assumption that $f(\theta)$ is homogeneous, zero mean, and Gaussian. The latter, according to the discussion of Sec. I, suggests that B_n, $n\in Z$, are mutually orthogonal, zero mean, and Gaussian. Hence, the following formula can be applied:[20]

$$\langle B_{n_1}B_{n_2}\cdots B_{n_l}\rangle=0 \quad \text{for } l \text{ odd}, \quad (20a)$$

$$\langle B_{n_1}B_{n_2}\cdots B_{n_l}\rangle=\sum_{j_1,j_2,\ldots,j_l}\langle B_{j_1}B_{j_2}\rangle\cdots\langle B_{j_{l-1}}B_{j_l}\rangle \quad \text{for } l \text{ even}, \quad (20b)$$

and the summation in Eq. (20b) is taken over all distinct combinations of $l/2$ pairs of $B_{n_1},B_{n_2},\ldots,B_{n_l}$. For example, if $l=4$, Eq. (20b) yields $\langle B_{n_1}B_{n_2}B_{n_3}B_{n_4}\rangle=\langle B_{n_1}B_{n_2}\rangle\langle B_{n_3}B_{n_4}\rangle+\langle B_{n_1}B_{n_3}\rangle\langle B_{n_2}B_{n_4}\rangle+\langle B_{n_1}B_{n_4}\rangle\langle B_{n_2}B_{n_3}\rangle$.

As verified in Sec. IV, second- and fourth-order moments of ψ^{sca} can be expressed in terms of second-order joint moments of B_n. Furthermore, it follows from the orthogonality of B_n, $n\in Z$, that $\langle B_{n_1}B_{n_2}\cdots B_{n_l}\rangle=0$ unless $n_1+n_2+\cdots+n_l=0$. Therefore, in view of Eq. (18), $\langle A_{mn}\rangle=0$ if $m\neq n$, which proves that coupled modes do not contribute to the coherent part of the scattered wave field.

IV. CHARACTERISTICS OF FAR-FIELD SCATTER

The scattered wave far from the origin of coordinates (i.e., for $\rho\gg 1$) may be expressed as a diverging cylindrical wave $\psi^{\text{sca}}(\rho,\theta)=\Phi(\theta)e^{i\rho}/\sqrt{\rho}$; the direction-dependent factor $\Phi(\theta)$ is the scattering amplitude. By use of Eqs. (6)–(8) and of the asymptotic expansion of Hankel functions of the first kind for large arguments,[16] it can be shown that

$$\Phi(\theta)=\sqrt{\frac{2}{\pi i}}\sum_{p=0}^{\infty}\epsilon^p\sum_{m=-\infty}^{\infty}\sum_{n=-\infty}^{\infty}i^{(m-n)}A^p_{mn}e^{in\theta}. \quad (21)$$

The expression of Eq. (21) has been obtained by use of the assumption $\theta_{\text{inc}}=0$ which has no effect on generality. The coherent part of the scattering amplitude is obtained from Eq. (21) by averaging:

$$\langle\Phi(\theta)\rangle=\sqrt{\frac{2}{\pi i}}\sum_{p=0}^{\infty}\epsilon^p\sum_{m=-\infty}^{\infty}\langle A^p_{mm}\rangle e^{im\theta}. \quad (22)$$

The coherent differential scattering cross section is defined as $\sigma_c(\theta)=|\langle\Phi(\theta)\rangle|^2$ and the coherent scattering cross section σ_c can be obtained from $\sigma_c(\theta)$ by integration with respect to θ in the range $[0,2\pi]$. Accordingly, the incoherent differential scattering cross section is defined as $\sigma_{ic}(\theta)=\langle|\Phi(\theta)|^2\rangle-|\langle\Phi(\theta)\rangle|^2$ and the incoherent scattering cross section is $\sigma_{ic}=\int_0^{2\pi}\sigma_{ic}(\theta)d\theta$. The following expressions for $\sigma_c(\theta)$, σ_c, $\sigma_{ic}(\theta)$, and σ_{ic}, which are accurate up to fourth order in ϵ, have been obtained by use of Eqs. (21) and (22):

$$\sigma_c(\theta)\approx\frac{2}{\pi}\text{Re}\sum_{m=-\infty}^{\infty}\sum_{m'=-\infty}^{\infty}e^{i(m-m')\theta}[A^0_{mm}\overline{A^0_{m'm'}}+2\epsilon^2\langle A^2_{mm}\rangle\overline{A^0_{m'm'}}+2\epsilon^4\langle A^4_{mm}\rangle\overline{A^0_{m'm'}}+\epsilon^4\langle A^2_{mm}\rangle\overline{A^2_{m'm'}}], \quad (23a)$$

$$\sigma_c\approx 4\sum_{m=-\infty}^{\infty}[|A^0_{mm}|^2+2\epsilon^2\,\text{Re}\{\langle A^2_{mm}\rangle\overline{A^0_{mm}}\}+2\epsilon^4\,\text{Re}\{\langle A^4_{mm}\rangle\overline{A^0_{mm}}\}+\epsilon^4|A^2_{mm}|^2], \quad (23b)$$

$$\sigma_{ic}(\theta)\approx\frac{2}{\pi}\text{Re}\sum_{m=-\infty}^{\infty}\sum_{n=-\infty}^{\infty}\sum_{m'=-\infty}^{\infty}\sum_{n'=-\infty}^{\infty}\frac{i^{(m-m')}}{i^{(n-n')}}\times e^{i(n-n')\theta}[\epsilon^2\langle A^1_{mn}\overline{A^1_{m'n'}}\rangle+\epsilon^4(\langle A^2_{mn}\overline{A^2_{m'n'}}\rangle-\delta_{mn}\delta_{m'n'}\langle A^2_{mn}\rangle\overline{\langle A^2_{m'n'}\rangle}+2\langle A^3_{mn}\overline{A^1_{m'n'}}\rangle)], \quad (24a)$$

$$\sigma_{ic}\approx 4\,\text{Re}\sum_{m=-\infty}^{\infty}\sum_{n=-\infty}^{\infty}[\epsilon^2\langle|A^1_{mn}|^2\rangle+\epsilon^4(\langle|A^2_{mn}|^2\rangle-\delta_{mn}|\langle A^2_{mn}\rangle|^2+2\langle A^3_{mn}\overline{A^1_{mn}}\rangle)]. \quad (24b)$$

The statistical moments of the wave amplitudes that appear in Eqs. (23) and (24) are determined in Appendix A.

V. RESULTS AND DISCUSSION

The approximate solutions presented above have been validated by means of two error criteria; first, that the solution must be energy consistent and, second, that the mean

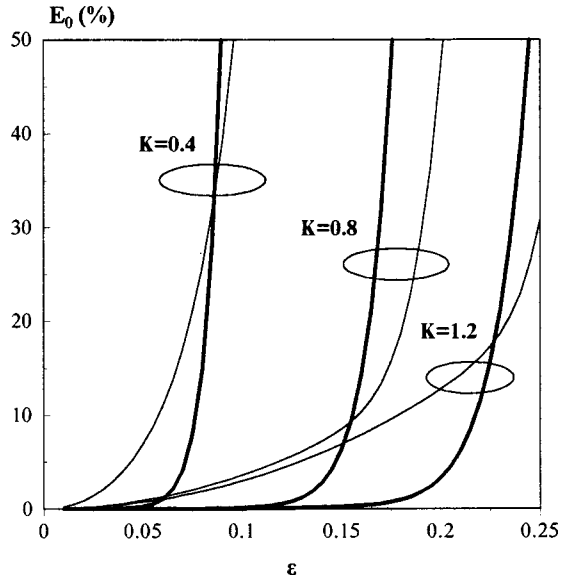

FIG. 2. Relative mean boundary condition error versus smallness parameter for zero-order cylindrical-wave excitation; $ka=1$. E_0 should be equal to 0 for an accurate solution. Second- and fourth-order results are shown by thin and thick curves, respectively.

field on S must conform with the boundary condition. Calculations of the wave amplitudes have been made by use of Eq. (18) with the infinite summations truncated; at least three-digit accuracy has been achieved in all cases. The following coefficients,[5]

$$|F_n|^2=\frac{e^{-K^2n^2/2}}{\sum_{\nu=-\infty}^{\infty} e^{-K^2\nu^2/2}}, \tag{25}$$

have been used for the power spectrum of $f(\theta)$; K is a measure of the correlation distance of surface roughness.

Energy consistency has been checked analytically by application of the forward-scattering theorem,[5] which states that $\sigma_c+\sigma_{ic}=\sqrt{8\pi}\,\mathrm{Im}\{\langle\Phi(0)\rangle/\sqrt{i}\}$. Zero-, second-, and fourth-order approximations of this equation have been obtained by use of Eqs. (22), (23b), and (24b):

$$|A^0_{mm}|^2=-\mathrm{Re}\{A^0_{mm}\}, \tag{26a}$$

$$2\,\mathrm{Re}\{\langle A^2_{mm}\rangle\overline{A^0_{mm}}\}+\sum_{n=-\infty}^{\infty}\langle|A^1_{mn}|^2\rangle=-\mathrm{Re}\{\langle A^2_{mm}\rangle\}, \tag{26b}$$

$$2\,\mathrm{Re}\{\langle A^4_{mm}\rangle\overline{A^0_{mm}}\}+\sum_{n=-\infty}^{\infty}\langle|A^2_{mn}|^2\rangle+2\sum_{n=-\infty}^{\infty}\mathrm{Re}\{\langle A^3_{mn}\overline{A^1_{mn}}\rangle\}=-\mathrm{Re}\{\langle A^4_{mm}\rangle\}. \tag{26c}$$

It can be shown after long but straightforward algebra that Eqs. (26) hold identically and, therefore, the perturbative solution proposed herein is energy consistent, at least up to the fourth order in ϵ.

Conformity with the boundary condition has been checked numerically through comparisons of the mean unperturbed field $\langle\psi^{\mathrm{inc}}+\psi^{1,\mathrm{sca}}\rangle$ to the mean perturbed field $-\langle\psi^{2,\mathrm{sca}}\rangle$, both at $\rho=\rho_s$. The difference between them, if any, amounts to violation of the Dirichlet boundary condition on S by the mean field and it can be attributed either to the truncation of the asymptotic series of Eq. (8) for A_{mn} or to the assumption that $\psi^{2,\mathrm{sca}}$ consists of only outgoing waves.

As a result of the above consideration, the relative mean boundary condition error for cylindrical-wave excitation has been defined as follows:

$$E_m=\frac{\langle(\psi^{\mathrm{inc}}_m+\psi^{1,\mathrm{sca}}_m+\psi^{2,\mathrm{sca}}_m)_{\rho=\rho_s}\rangle}{\langle(\psi^{\mathrm{inc}}_m+\psi^{1,\mathrm{sca}}_m)_{\rho=\rho_s}\rangle}=\frac{\sum_{l=0}^{\infty}\frac{(2l+1)!!}{(2l+1)!}(\rho_0\epsilon)^{2l}V^{(2l)}_m(\rho_0)}{\sum_{l=0}^{\infty}\frac{(2l+1)!!}{(2l+1)!}(\rho_0\epsilon)^{2l}W^{(2l)}_m(\rho_0)}, \tag{27}$$

where

$$V^{(2l)}_m(\rho_0)=W^{(2l)}_m(\rho_0)+2l\rho_0^{-2}R^{(2)}_{m,l-1}(\rho_0) \tag{28}$$

for the second-order solution, whereas

$$V^{(2l)}_m(\rho_0)=W^{(2l)}_m(\rho_0)+2l\rho_0^{-2}R^{(2)}_{m,l-1}(\rho_0)+4l(l-1)\rho_0^{-4}R^{(4)}_{m,l-2}(\rho_0) \tag{29}$$

for the fourth-order solution; $R^{(2)}_{ml}(\rho_0)$ and $R^{(4)}_{ml}(\rho_0)$ are defined in Appendix B. Accordingly, the relative mean boundary condition error for plane-wave excitation has been defined as follows:

$$E(\theta)=\frac{\langle(\psi^{\mathrm{inc}}+\psi^{1,\mathrm{sca}}+\psi^{2,\mathrm{sca}})_{\rho=\rho_s}\rangle}{\langle(\psi^{\mathrm{inc}}+\psi^{1,\mathrm{sca}})_{\rho=\rho_s}\rangle}=\frac{\sum_{m=-\infty}^{\infty}i^m e^{im\theta}\sum_{l=0}^{\infty}\frac{(2l+1)!!}{(2l+1)!}(\rho_0\epsilon)^{2l}V^{(2l)}_m(\rho_0)}{\sum_{m=-\infty}^{\infty}i^m e^{im\theta}\sum_{l=0}^{\infty}\frac{(2l+1)!!}{(2l+1)!}(\rho_0\epsilon)^{2l}W^{(2l)}_m(\rho_0)}. \tag{30}$$

Both E_m and $E(\theta)$ may provide information about the consistency of the approximate solution under test. As the 2-D Helmholtz equation has been obeyed, the only remaining requisite for a solution to be acceptable is that the boundary condition be satisfied. It should be mentioned, though, that, by use of E_m and $E(\theta)$, only the mean field at S can be checked; the behavior of higher-order statistical moments of the field as well as the relationship between the boundary condition error and the far-field error are beyond the scope of this paper.

Plots of E_0 against the smallness parameter ϵ are shown in Fig. 2. Evidently, E_0 increases rapidly with ϵ, especially for small values of K. The fourth-order solution is more accurate than the second-order one up to a certain value of ϵ, deteriorating faster beyond that value. Hence, depending on K and ϵ, the series expansion $A_{0n}=\Sigma_{p=0}^{\infty}\epsilon^p A^p_{0n}$ may not converge as expected and it may even diverge. Figure 2 suggests that the radius of convergence of the above series expansion is finite and proportional to K.

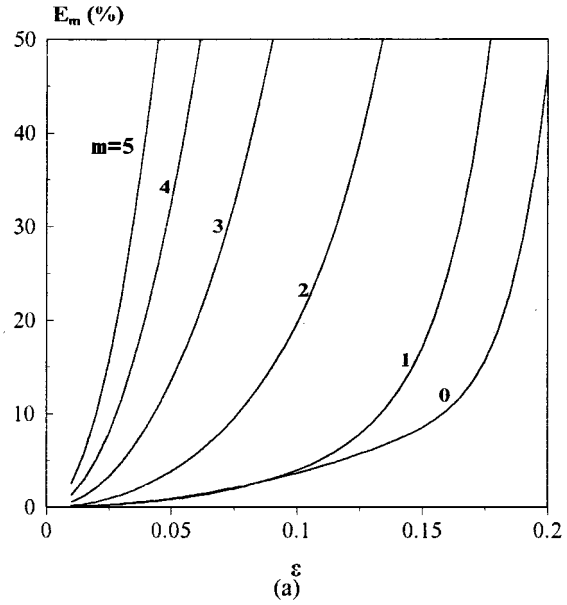

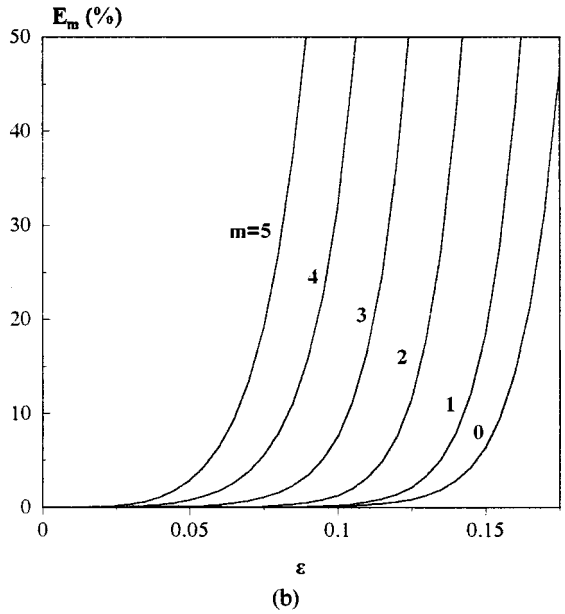

FIG. 3. Relative mean boundary condition error versus smallness parameter for higher-order cylindrical-wave excitation; $ka=1$; $K=0.8$ rad. Second- (a) and fourth-order (b) results.

The conclusions about E_0, drawn from Fig. 2, also apply to E_m, $m \in Z^+$ (Fig. 3). Moreover, Fig. 3 indicates that the mean boundary condition error increases with the order of the exciting cylindrical wave and that the advantage of the fourth-order solution over the second-order one is more pronounced for greater *m*.

Plane-wave excitation has also been considered. Plots of $E(\theta)$ are presented (Fig. 4) for $\theta=0°$, viz. opposite to incidence; other results, not shown in this paper, indicate that $E(\theta)$ is generally smaller than $E(0)\equiv E$. It is evident that, although E roughly behaves as E_0, it is somewhat greater; this can be attributed to the greater mean boundary condition error associated with higher-order cylindrical-wave excitation. Furthermore, it may be inferred from Figs. 3 and 4 that E is proportional to ka, since more terms have to be taken into account in Eq. (28) as ka increases.

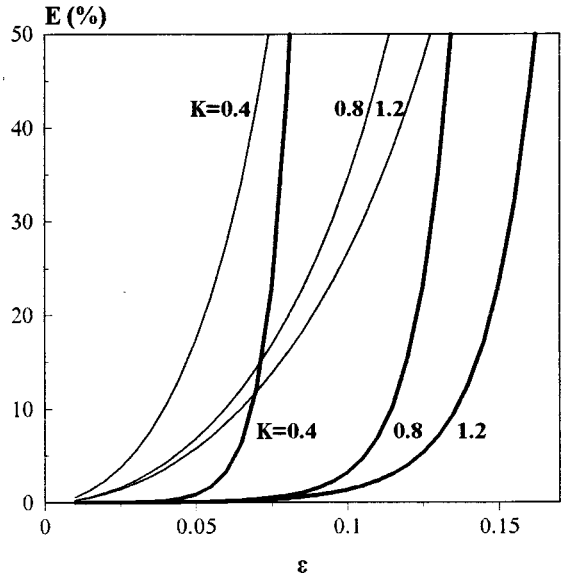

FIG. 4. Relative mean boundary condition error versus smallness parameter for plane-wave excitation; $ka=1$; $\theta=0°$. Second- and fourth-order results are shown by thin and thick curves, respectively.

The dependence of the accuracy of the proposed solution on the roughness parameters K and ϵ is probed further by Fig. 5, which provides information about the applicability of the approximate solution in the $K-\epsilon$ plane; the limit of applicability has been set by the, more or less arbitrary, requirement $E\leqslant 10\%$. Thus restrictions on the maximum allowable value of ϵ can easily be determined for any given K. The area between the two curves of Fig. 5 represents the advantage of the fourth-order solution over the second-order one.

The numerical results for the characteristics of far-field scatter from the random surface S use as reference the corresponding results for the smooth cylindrical surface S_2. Calculations have been made by use of the fourth-order approximation to A_{mn}; the roughness parameters K and ϵ have

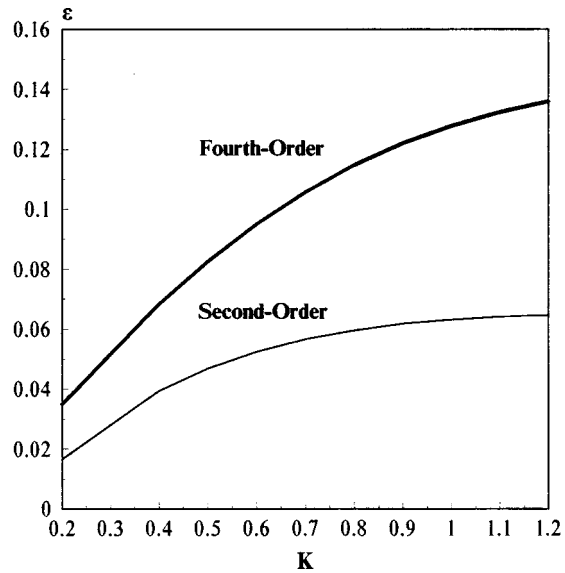

FIG. 5. Applicability limit of the second- and fourth-order solution in the $K-\epsilon$ plane; the limit has been set by the requirement $E\leqslant 10\%$.

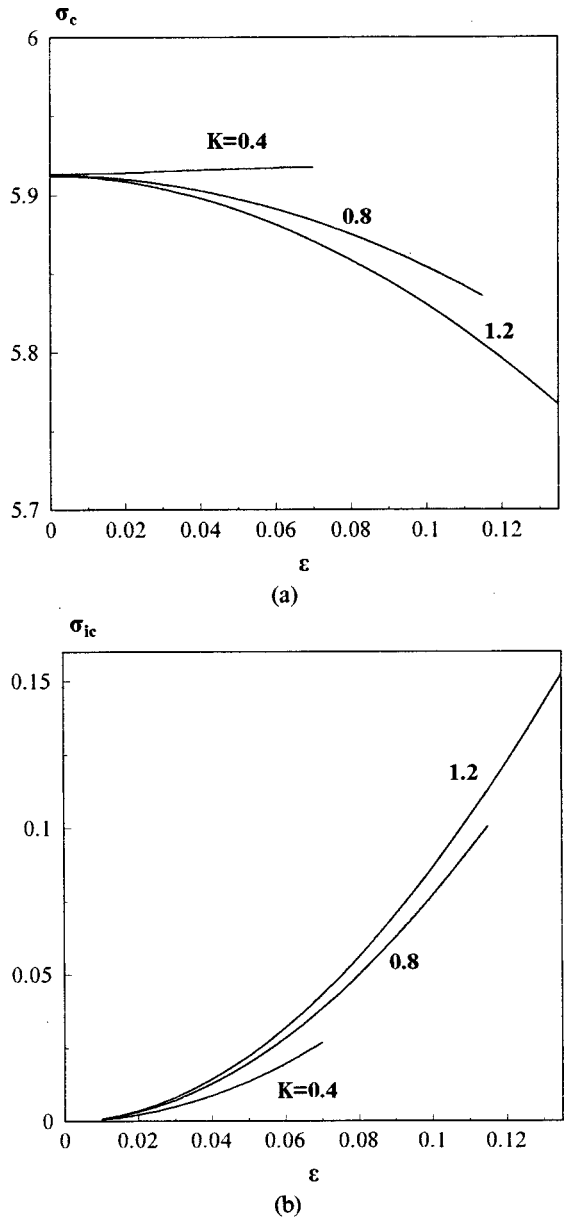

FIG. 6. Coherent (a) and incoherent (b) scattering cross section versus smallness parameter; $ka=1$.

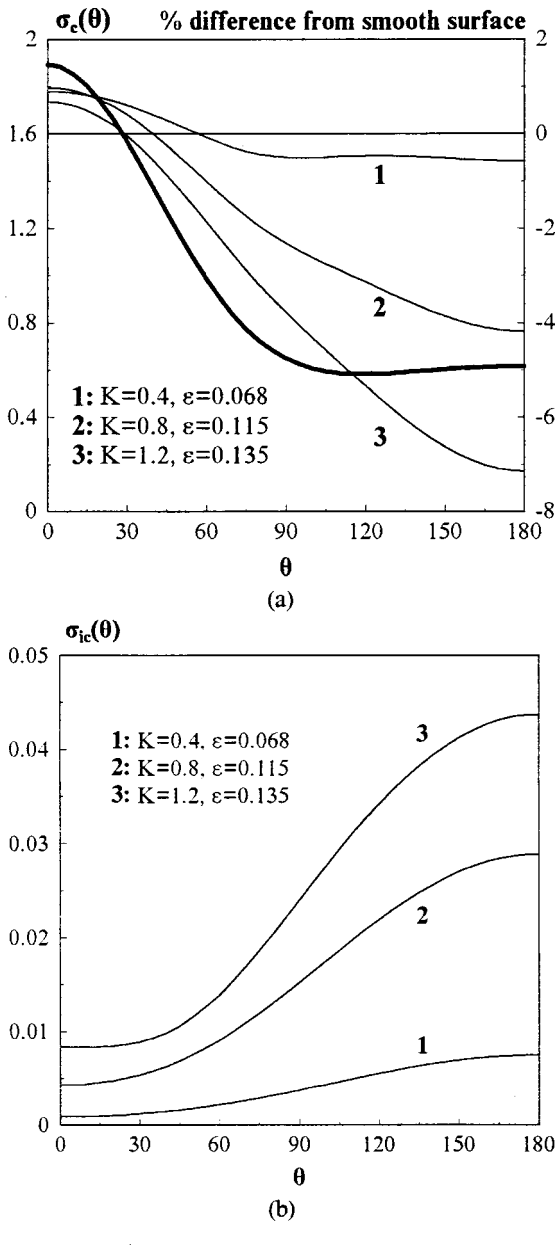

FIG. 7. Angular distribution of far-field scatter; $ka=1$. (a) Coherent differential scattering cross section versus scattering angle. The thick curve (left-hand vertical axis) corresponds to scattering from a smooth cylindrical surface ($\epsilon=0$); curves 1, 2, and 3 (right-hand vertical axis) display the percentage difference in $\sigma_c(\theta)$ of a random cylindrical surface from the corresponding smooth surface. (b) Incoherent differential scattering cross section.

been chosen so that the applicability limit, as defined above, is never exceeded.

The dependence of σ_c and σ_{ic} on ϵ is examined first. According to Fig. 6(a), the coherent part of the scattering cross section decreases as ϵ increases, this trend being more pronounced for greater K. Still, the absolute value of the deviation of σ_c from the value that corresponds to the smooth cylindrical surface (i.e., $\epsilon=0$) is less than 2.5%, the maximum occurring for $K=1.2$, $\epsilon=0.135$. The incoherent part of the scattering cross section [Fig. 6(b)] increases with ϵ, as expected, but it is considerably weaker than the coherent part.

Finally, the angular distribution of scatter, coherent and incoherent, is examined. As a result of surface roughness [Fig. 7(a)], the coherent part of forward scatter ($\theta=0°$) is slightly enhanced, whereas the coherent part of backward scatter ($\theta=180°$) is reduced; compared to the reference case of a smooth cylindrical surface, the maximum reduction of $\sigma_c(180°)$ is 7% and it occurs for $K=1.2$, $\epsilon=0.135$. As far as incoherent scatter is concerned [Fig. 7(b)], $\sigma_{ic}(\theta)$ is maximum in the backscattering direction ($\theta=180°$) and it is at least an order of magnitude weaker than $\sigma_c(\theta)$.

VI. CONCLUSIONS

The perturbative analysis of this paper leads to a recurrence equation which yields corrections of any order to the wave amplitudes of the scattered field. An essential feature of this formulation is the existence of coupled radiation

modes in the series expansion of the scattered wave field; roughness gives rise to coupling of radiation modes, which is shown to affect only the incoherent part of the field.

The second- and fourth-order approximate solutions are analytically proven to be energy consistent for any value of the smallness parameter. Their domain of applicability is determined through calculations of the mean boundary condition error, which is defined herein. The numerical results indicate that the fourth-order solution is more accurate than the second-order one up to a certain value of the smallness parameter, deteriorating faster beyond that value. The limit of applicability is dependent on the correlation radius of surface roughness. The mean boundary condition error, which is a near-field criterion, incorporates eventual shortcomings of the Rayleigh hypothesis. Its connection to the far-field error, which is of interest in practice, will be investigated in future work.

APPENDIX A

The statistical moments of the wave amplitudes A_{mn}^{p} can be obtained by use of Eqs. (18) and (20) and by use of the orthogonality properties of the Gaussian random variables B_n, $n \in Z$. In particular, the following statistical moments of A_{mn}^{p} are required for second- and fourth-order expressions of coherent scatter:

$$\langle A_{mm}^{2} \rangle = \frac{1}{H_m^{(1)}(\rho_0)} \sum_{n_1=-\infty}^{\infty} |F_{n_1}|^2 G_2(m,m+n_1), \tag{A1}$$

$$\langle A_{mm}^{4} \rangle = \frac{1}{H_m^{(1)}(\rho_0)} \sum_{n_1=-\infty}^{\infty} \sum_{n_2=-\infty}^{\infty} |F_{n_1}|^2 |F_{n_2}|^2 [G_4(m,m+n_1, m,m+n_2) + G_4(m,m+n_2, m+n_1, m+n_1+n_2, m+n_2) + G_4(m,m+n_1, m+n_1, m+n_1+n_2, m+n_2)]. \tag{A2}$$

Second- and fourth-order expressions of incoherent scatter involve the following statistical moments of A_{mn}^{p}:

$$\langle A_{mn}^{1} \overline{A_{m'n'}^{1}} \rangle = \frac{\delta_{n-m,n'-m'}}{H_n^{(1)}(\rho_0) \overline{H_{n'}^{(1)}(\rho_0)}} |F_{n-m}|^2 G_1(m) \overline{G_1(m')}, \tag{A3}$$

$$\langle A_{mn}^{2} \overline{A_{m'n'}^{2}} \rangle = \frac{\delta_{n-m,n'-m'}}{H_n^{(1)}(\rho_0) \overline{H_{n'}^{(1)}(\rho_0)}} \sum_{n_1=-\infty}^{\infty} |F_{n_1-m}|^2 |F_{n_1-n}|^2 \times G_2(m,n_1) [\overline{G_2(m', n_1+m'-m)} + \overline{G_2(m', n+m'-n_1)}], \tag{A4}$$

$$\langle A_{mn}^{3} \overline{A_{m'n'}^{1}} \rangle = \frac{\delta_{n-m,n'-m'}}{H_n^{(1)}(\rho_0) \overline{H_{n'}^{(1)}(\rho_0)}} |F_{n-m}|^2 \overline{G_1(m')} \times \sum_{n_1=-\infty}^{\infty} [|F_{n_1-m}|^2 G_3(m,m,n_1) + |F_{n_1-m}|^2 G_3(m,n_1+n-m,n_1) + |F_{n_1-n}|^2 G_3(m,n_1,n)]. \tag{A5}$$

APPENDIX B

The abbreviations $R_{ml}^{(2)}(\rho_0)$ and $R_{ml}^{(4)}(\rho_0)$, which have been used in Eqs. (28) and (29), are defined as follows:

$$R_{ml}^{(2)} = \sum_{j_1=-\infty}^{\infty} \sum_{j_2=-\infty}^{\infty} k^4 |F_{j_1}|^2 |F_{j_2}|^2 [\rho_0 Q(2l+1,m+j_1) G_1(m) + Q(2l,m) G_2(m,m+j_1) + 2l Q(2l,m+j_1+j_2) G_2(m,m+j_1)], \tag{B1}$$

$$R_{ml}^{(4)} = \sum_{j_1=-\infty}^{\infty} \sum_{j_2=-\infty}^{\infty} \sum_{j_3=-\infty}^{\infty} \sum_{j_4=-\infty}^{\infty} k^8 |F_{j_1}|^2 |F_{j_2}|^2 |F_{j_3}|^2 |F_{j_4}|^2 [Q(2l,m) A(m,j_1,j_2) + \rho_0 Q(2l+1,m+j_1) B(m,j_1,j_2) + 2l Q(2l,m+j_1+j_2) C(m,j_1,j_2,j_3) + 2l(2l-2) Q(2l,m+j_1+j_2+j_3+j_4) G_4(m,m+j_1+j_2+j_3,m+j_1+j_2,m+j_1) + 2l\rho_0 Q(2l+1,m+j_1+j_2+j_3) G_3(m,m+j_1+j_2,m+j_1)]. \tag{B2}$$

Equation (B1) and (B2) use the following abbreviations:

$$A(m,j_1,j_2) = G_4(m,m+j_1,m,m+j_2) + G_4(m,m+j_1,m+j_1+j_2,m+j_2) + G_4(m,m+j_1,m+j_1+j_2,m+j_1), \tag{B3}$$

$$B(m,j_1,j_2) = G_3(m,m,m+j_2) + G_3(m,m+j_1+j_2, m+j_1) + G_3(m,m+j_1+j_2,m+j_2), \tag{B4}$$

$$C(m,j_1,j_2,j_3) = G_4(m,m+j_1+j_2+j_3,m+j_1+j_2, m+j_1) + G_4(m,m+j_1+j_2+j_3, m+j_1+j_3,m+j_1) + G_4(m,m+j_1+j_2+j_3,m+j_2+j_3,m+j_3), \tag{B5}$$

$$Q(p,j) = \frac{H_j^{(1)^{(p)}}(\rho_0)}{H_j^{(1)}(\rho_0)}. \tag{B6}$$

[1] C. Yeh, ''Perturbation method in the diffraction of electromagnetic waves by arbitrarily shaped penetrable obstacles,'' J. Math. Phys. **6**, 2008–2013 (1965).
[2] V. A. Erma, ''An exact solution for the scattering of electromagnetic waves from conductors of arbitrary shape I. Case of cylindrical symmetry,'' Phys. Rev. **173**, 1243–1257 (1968).
[3] C. Eftimiu, ''Electromagnetic scattering by rough conducting circular cylinders—I: Angular corrugation,'' IEEE Trans. Antennas Propag. **AP-36**, 651–658 (1988).
[4] C. Eftimiu, ''Electromagnetic scattering by rough conducting circular cylinders—II: Axial corrugation,'' IEEE Trans. Antennas Propag. **AP-36**, 659–663 (1988).
[5] H. Ogura and H. Nakayama, ''Scattering of waves from a random cylindrical surface,'' J. Math. Phys. **29**, 851–860 (1988).
[6] M. Chen and A. Fung, ''A numerical study of the regions of validity of the Kirchhoff and small-perturbation rough surface scattering models,'' Radio Sci. **23**, 163–170 (1988).
[7] E. Thorsos and D. Jackson, ''The validity of the perturbation approximation for rough surface scattering using a Gaussian roughness spectrum,'' J. Acoust. Soc. Am. **86**, 261–277 (1989).
[8] J. Soto-Crespo, M. Nieto-Vesperinas, and A. Friberg, ''Scattering from slightly rough random surfaces: A detailed study on the validity of the small perturbation method,'' J. Opt. Soc. Am. A **7**, 1185–1201 (1990).
[9] P. Jansson, ''Acoustic scattering from a rough sphere,'' J. Acoust. Soc. Am. **93**, 3032–3042 (1993).
[10] J. W. Strutt (Lord Rayleigh), *The Theory of Sound* (Dover, New York, 1945).
[11] W. C. Meecham, ''Variation method for the calculation of the distribution of energy reflected from a periodic surface. I,'' J. Appl. Phys. **27**, 361–367 (1956).
[12] P. M. van den Berg and J. T. Fokkema, ''The Rayleigh hypothesis in the theory of diffraction by a cylindrical obstacle,'' IEEE Trans. Antennas Propag. **AP-27**, 577–583 (1979).
[13] V. I. Tatarskii, ''Relation between the Rayleigh equation in diffraction theory and the equation based on Green's formula,'' J. Opt. Soc. Am. A **12**, 1254–1260 (1995).
[14] L. Cazandjian, ''Identity of the Rayleigh–Fourier and extinction theorem method solutions for scattering and transmission of sound at a rough fluid–solid interface,'' J. Acoust. Soc. Am. **90**, 416–425 (1991).
[15] J.-M. Chesneaux and A. Wirgin, ''Reflection from a corrugated surface revisited,'' J. Acoust. Soc. Am. **96**, 1116–1129 (1994); L. Cazandjian, ''Comments on 'Reflection from a corrugated surface revisited' [J. Acoust. Soc. Am. **96**, 1116–1129 (1994)],'' *ibid.* **98**, 1813–1814 (1995); J.-M. Chesneaux and A. Wirgin, ''Response to ''Comments on 'Reflection from a corrugated surface revisited' [J. Acoust. Soc. Am. **96**, 1116–1129 (1994)],'' '' *ibid.* **98**, 1815–1816 (1995).
[16] *Handbook of Mathematical Functions*, edited by M. Abramowitz and I. Stegun (Dover, New York, 1970).
[17] N. Ja. Vilenkin, *Special Functions and the Theory of Group Representations*, English Translation (American Mathematical Society, Providence, 1968).
[18] I. M. Gel'fand, R. A. Minlos, and Z. Ya. Shapiro, *Representation of the Rotation and Lorentz Groups and their Applications*, English Translation (Pergamon, London, 1963).
[19] M. Van. Dyke, *Perturbation Methods in Fluid Mechanics* (Academic, New York, 1964).
[20] T. T. Soong, *Random Differential Equations in Science and Engineering* (Academic, New York, 1973), Chap. 2, pp. 26–28.

Multiaspect identification of submerged elastic targets via wave-based matching pursuits and hidden Markov models

Paul Runkle and Lawrence Carin[a)]
Department of Electrical and Computer Engineering, Duke University, Durham, North Carolina 27708-0291

Luise Couchman and Joseph A. Bucaro
Naval Research Laboratory, Physical Acoustics, Code 7130, Washington, DC 20375-5000

Timothy J. Yoder
SFA, Inc., Largo, Maryland 20785

(Received 26 June 1998; revised 19 January 1999; accepted 20 April 1999)

This paper investigates classification of submerged elastic targets using a sequence of backscattered acoustic signals corresponding to measurements at multiple target-sensor orientations. Wavefront and resonant features are extracted from each of the multiaspect signals using the method of matching pursuits, with a wave-based dictionary. A discrete hidden Markov model (HMM) is designed for each of the target classes under consideration, with identification of an unknown target effected by considering which model has the maximum likelihood of producing the observed sequence of feature vectors. HMMs are stochastic models which are well suited to describing piecewise-stationary processes, and are appropriate for multiaspect classification due to the strong aspect dependence of the scattered fields for most realistic targets. After establishing the physical and geometric correspondence between multiaspect sensing and the HMM parameters, performance is assessed through consideration of measured acoustic data from five similar submerged elastic targets. Results are presented with and without additive noise. © *1999 Acoustical Society of America.* [S0001-4966(99)03208-7]

PACS numbers: 43.30.Vh, 43.30.Gv [AN]

INTRODUCTION

We are interested in using the backscattered acoustic fields from a limited set of target-sensor orientations to effect the identification of a concealed or distant submerged target, without forming an acoustic image. Nonimaging acoustic identification approaches offer many advantages over acoustic imaging systems for applications such as mine countermeasures[1] and active antisubmarine sonar. This target identification approach exploits both the geometric (utilized by imaging systems) and elastic (ignored in imaging theory) components of the backscattered acoustic fields. We assume that a possible target has been detected, and that it is now to be identified as one of a finite number of known, expected targets; if it is not well matched to any of the catalogue of expected targets, the unknown object is deemed a false target.

The acoustic fields scattered from a general submerged elastic target are often a strong function of the target-sensor orientation. A matched-filter-based identification scheme is computationally expensive, as it requires storage and manipulation of a large set of representative multiaspect backscattered waveforms. Moreover, such algorithms are generally inflexible to random variations in the scattering phenomenology (e.g., due to changes in the background environment). Consequently, researchers have investigated the use of scattering *features* to effect target identification, rather than the entire scattered waveform itself. For example, there has been significant interest in the use of target resonances[2] and scattering from traveling waves[3–5] (helical, Bloch, flexural, etc.). Acoustic fields scattered from most elastic targets may also be characterized in part by nonresonant features, such as wavefronts.[6,7] While resonances are characterized by localized behavior in frequency and extended support in time, wavefronts have localized support in time and extended support in frequency. Signal-processing methods have been developed which are dedicated to extracting resonance-like features,[8,9] or wavefont-like features[10–12] with such features subsequently used to develop statistical models for target detection and identification.

Although algorithms have been developed for processing resonant- and wavefront-like data, there remains a need for methods that can exploit both feature types simultaneously. In this context, there has been significant interest in the development of signal-processing algorithms that adapt to the waveform of interest. This has resulted in adaptive wavelet methods[13] as well as best-basis[14] algorithms. Moreover, a matching-pursuits algorithm has been developed[15] that utilizes a dictionary of time-frequency atoms that are well matched to the target of interest. By exploiting knowledge of the aforementioned fundamental scattering phenomenology, we have developed such a wavefront-resonance matching-pursuits dictionary.[16] While this matching-pursuits paradigm has been examined by us previously in the context of target detection,[12] here our focus is on the problem of statistically coupling the matching-pursuits features extracted

[a)]Electronic mail: lcarin@ee.duke.edu

from multiaspect observations to effect target discrimination, after detection has already occurred.

The identification approach presented here characterizes the sequence of feature vectors as a doubly stochastic process, and is motivated by the observed multiaspect interrogation paradigm employed by mammals, such as bats.[17] We assume that the target is distant or concealed, and therefore that the absolute multiple target-sensor orientations are ''hidden.'' Furthermore, based on prior knowledge of the scattering physics, it is assumed that the extracted features are statistically stationary over relatively small changes in target-sensor orientations, but may vary significantly for large changes in orientation. In this context we exploit a hidden Markov model (HMM).[18,19] The HMM accounts for the relatively slowly varying statistical variation of the features (wavefronts and resonances) for small changes in target-sensor orientation. Moreover, it explicitly exploits the sequential changes in the feature statistics when the target is viewed from a large range of orientations. Hidden Markov models are widely used in speech processing[18,19] and, as discussed, we exploit the vast literature on HMMs available from that community.

The remainder of the paper is organized as follows. In Sec. I the wave-based matching-pursuits algorithm is summarized. In anticipation of HMM identification, the continuous parameters extracted via matching pursuits are quantized in terms of a finite number of parameter vectors, which constitute a ''codebook.'' Thus, in Sec. I we also describe how matching pursuits is used to ''populate'' the codebook and subsequently how matching-pursuits parameter-vector quantization is performed. The HMM is detailed in Sec. II, where it is demonstrated as a natural consequence of a maximum-likelihood classifier, after making reasonable assumptions and approximations. Example results for the measured multiaspect acoustic-scattering data are presented in Sec. III, followed in Sec. IV by conclusions and suggested future work.

I. WAVE-BASED MATCHING PURSUITS AND VECTOR QUANTIZATION

A. Algorithm basics

The matching pursuits algorithm[15,16] utilizes a dictionary of fundamental elements $\boldsymbol{e}(\gamma)$, where γ represents the associated vector parameters. The dictionary is initially discretized into N normalized vectors $\boldsymbol{e}(\gamma_n)$, where the γ_n represent N realizations of the general parameter vector γ. Given a sampled waveform $\boldsymbol{f}$, we form the inner product $\langle \boldsymbol{f}|\boldsymbol{e}(\gamma_n)\rangle$ with each discretized element $\boldsymbol{e}(\gamma_n)$ in the finite-size dictionary D. The inner product of vectors $\boldsymbol{f}$ and $\boldsymbol{e}(\gamma_n)$ is defined as $\langle \boldsymbol{f}|\boldsymbol{e}(\gamma_n)\rangle \equiv \boldsymbol{f}[\boldsymbol{e}(\gamma_n)]^H$, where superscript H represents the Hermitian transpose, and $|\boldsymbol{f}|^2 \equiv \langle \boldsymbol{f}|\boldsymbol{f}\rangle$. We select that $\boldsymbol{e}(\gamma_n)$ for which $|\langle \boldsymbol{f}|\boldsymbol{e}(\gamma_n)\rangle| \geqslant |\langle \boldsymbol{f}|\boldsymbol{e}(\gamma_k)\rangle| \forall \boldsymbol{e}(\gamma_k) \in D$. A gradient search in the continuous γ space is then performed in the vicinity of γ_n, from which we find the γ that maximizes the inner product $|\langle \boldsymbol{f}|\boldsymbol{e}(\gamma)\rangle|$, defining the associated vector $\hat{\boldsymbol{e}}_1$. We now have the representation

$$\boldsymbol{f} = \langle \boldsymbol{f}|\hat{\boldsymbol{e}}_1\rangle \hat{\boldsymbol{e}}_1 + \boldsymbol{R}_1, \tag{1}$$

where $\boldsymbol{R}_1$ is the remainder after the first iteration ($\langle \boldsymbol{R}_1|\hat{\boldsymbol{e}}_1\rangle = 0$). This process is now repeated, but instead of operating on $\boldsymbol{f}$, we perform inner products of the elements in D with $\boldsymbol{R}_1$, followed by the associated gradient search in the γ space. After K such matching-pursuits iterations, we have

$$\boldsymbol{f} = \sum_{k=1}^{K} \langle \boldsymbol{R}_{k-1}|\hat{\boldsymbol{e}}_k\rangle \hat{\boldsymbol{e}}_k + \boldsymbol{R}_K, \quad \boldsymbol{R}_o \equiv \boldsymbol{f}. \tag{2}$$

If the vectors represented by D, with the associated gradient search, constitute a complete set, then $|\boldsymbol{R}_K| \to 0$ as $K \to \infty$. However, for our purposes we are not interested in a complete decomposition of the signal $\boldsymbol{f}$; rather, we wish to use a relatively small number of iterations K to extract the principal constituents $\acute{\boldsymbol{e}}_k$ most representative of $\boldsymbol{f}$.

B. Wave-based dictionary

The algorithm discussed above can be utilized with a general dictionary D.[15,16] However, for acoustic scattering applications, it is natural to tailor the dictionary to the underlying wave physics. To this end, we introduce the discrete-time dictionary elements

$$\begin{aligned} \boldsymbol{e}(i;p,l,q,\phi) = {} & \cos[2\pi(i - q2^{p-1})l2^{-p} + \phi] \\ & \times \exp[-(i - q2^{p-1})2^{-p}]U(i - q2^{p-1}), \\ & p = \log_2 N_i, \ldots, \log_2(\xi N_i) \\ & l = 0, \ldots, 2^p - 1, \\ & q = 0, \ldots, N_s 2^{1-p}, \end{aligned} \tag{3}$$

where $U(\beta) = 0$ for $\beta < 0$ and $U(\beta) = 1$ for $\beta \geqslant 0$, N_s represents the number of samples in the data under investigation, N_i is the nominal number of meaningful (nonzero) time samples in the incident pulse, and ξN_i represents the largest expected length for a resonant waveform (typically, we utilize $\xi = 8$). In (3), p and q take on integer values, and therefore the logarithms and quotients in (3) are rounded off accordingly, if necessary. The sampling paradigm for p, l, and q is analogous to that applied in Ref. 15 for a Gabor dictionary, but here, in the context of our wave-based dictionary, we assure that the minimum envelope width is no smaller than the width of the incident excitation and the maximum width is consistent with the longest-duration resonance or resonance-like feature that may be realistically excited. Note that (3) is in its un-normalized form, while in the actual matching-pursuits implementation all vectors in D are normalized appropriately.

For the finite dictionary D used in the initial matching-pursuits search (before performing gradient optimization of the parameters γ), we utilize the *complex* vectors

$$\begin{aligned} \boldsymbol{e}_c(i;p,l,q) = {} & \exp[j2\pi(i - q2^{p-1})l2^{-p}] \\ & \times \exp[-(i - q2^{p-1})2^{-p}]U(i - q2^{p-1}), \end{aligned} \tag{4}$$

where $j = (-1)^{1/2}$. In a manner similar to that discussed in Ref. 15, the phase ϕ is estimated while forming inner products with the initial coarsely sampled $\boldsymbol{e}_c$, and then p, l, q, and ϕ (i.e., the parameters γ) are refined subsequently via the gradient search [performed using the *real* vectors $\boldsymbol{e}$, in (3)].

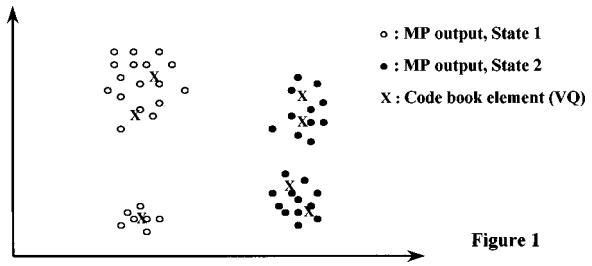

FIG. 1. Qualitative demonstration of vector quantization (VQ) of the parameter vector extracted via matching pursuits. Each circle corresponds to a parameter vector, projected onto a two-dimensional subspace. The darkened and open circles symbolize scattered waveforms characterized by different wave physics (as seen in this two-dimensional parameter subspace), and the ''x'' symbols denote possible quantized vectors used to constitute the codebook.

C. Codebook development and vector quantization

For target identification, we are interested in the generation of a codebook that is representative of the variability in the parameters extracted via matching pursuits. In particular, after K matching-pursuits iterations on a given scattered waveform, we extract the parameter vector $\boldsymbol{u}=\{\omega_1,\alpha_1,t_2-t_1,\omega_2,\alpha_2,\ldots,t_K-t_1,\omega_K,\alpha_K\}$. This vector stores the angular frequency and decay constant extracted on each matching-pursuits iteration ($\omega=2\pi/\alpha$ and $\alpha=2^p$), as well as the timing ($t=q2^{p-1}$) relative to t_1. The parameters t_i, ω_i, α_i correspond to the wave-object extracted on the ith matching-pursuit iteration, and in $\boldsymbol{u}$ *relative* times are used because such are only dependent upon the target geometry (and the target-sensor orientation), while the absolute arrival times are dependent on the (variable) target-sensor distance. The vector $\boldsymbol{u}$ essentially represents a parsing of the scattered waveform in terms of the wavefront-resonance, wave-based matching-pursuits dictionary. This compact representation, in terms of $3K-1$ parameters, should be contrasted with storage of the original waveform of N_s samples (in most examples, $N_s \gg 3K-1$).

The vector $\boldsymbol{u}$ resides in the $3K-1$ dimensional space. To determine the regions in that space of importance for scattering from a given target, we perform wave-based matching pursuits on all scattered waveforms available from the target (sampling the range of target-sensor orientations expected in practice). For Λ observation angles, we obtain Λ vectors $\boldsymbol{u}_1,\boldsymbol{u}_2,\ldots,\boldsymbol{u}_\Lambda$, which constitute the distribution of the $3K-1$ parameters for the target of interest. Subsequently, we define a codebook of elements (in the same $3K-1$ dimensional space) that adequately represents the distribution defined by the Λ vectors, across all targets, where the number of codebook elements N_c is designed such that $N_c \ll \Lambda$. This procedure is demonstrated schematically in Fig. 1, for a two-dimensional slice in the $3K-1$ dimensional space. Each clustered set of vectors $\boldsymbol{u}$ with similar parameters is representative of angular regions over which the scattering physics is relatively invariant.

There are two related issues that need to be addressed: (i) determination of the optimal codebook $\hat{\boldsymbol{u}}_1,\hat{\boldsymbol{u}}_2,\ldots,\hat{\boldsymbol{u}}_{Nc}$ for representation of the variability in the training data $\boldsymbol{u}_1,\boldsymbol{u}_2,\ldots,\boldsymbol{u}_\Lambda$ and (ii) after the codebook is so defined, the mapping from a general measured parameter vector $\boldsymbol{u}$ to the appropriate codebook element $\hat{\boldsymbol{u}}_k$. Both of these issues fall within the domain of vector quantization (VQ), whereby a general vector $\boldsymbol{u}$, the elements of which can take on any real value, is mapped into a vector $\hat{\boldsymbol{u}}_k$, the elements of which can take on a set of discrete real values. Issue (i) is termed ''populating the codebook,'' [20,21] implemented during the training phase; and (ii) addresses how each codebook element is assigned, during the testing phase (i.e., when the scattered waveform from an unknown target is used in the context of target identification). There is a vast VQ literature,[20–22] while here, for completeness, we only address the fundamental issues.

We begin by defining a distortion or distance metric $d(\boldsymbol{u},\hat{\boldsymbol{u}})$, where we utilize the Mahalanobis distance[23]

$$d(\boldsymbol{u},\hat{\boldsymbol{u}})=(\boldsymbol{u}-\hat{\boldsymbol{u}})^T\boldsymbol{C}^{-1}(\boldsymbol{u}-\hat{\boldsymbol{u}})$$
$$\text{with}\quad \boldsymbol{C}=E[(\boldsymbol{u}-\overline{\boldsymbol{u}})(\boldsymbol{u}-\overline{\boldsymbol{u}})^T], \tag{5}$$

where $\boldsymbol{C}$ is the covariance matrix and $\overline{u}=E(\boldsymbol{u})$ (each of which we estimate through averaging over the available vectors $\boldsymbol{u}$). The expression in (5) is termed a distortion measure because it represents a non-negative cost associated with quantizing the vector $\boldsymbol{u}$ with the representative vector $\hat{\boldsymbol{u}}$. While (5) is a popular metric, there are several alternatives in the literature.[22] Moreover, from our discussion of the matching-pursuits algorithm, the vectors $\boldsymbol{u}$ and $\hat{\boldsymbol{u}}$ in (5) are assumed to be of length $3K-1$.

For a codebook of vectors $\hat{\boldsymbol{u}}_1,\hat{\boldsymbol{u}}_2,\ldots,\hat{\boldsymbol{u}}_{Nc}$, a general vector $\boldsymbol{u}$ is quantized via the quantization operator $g(\cdot)$, where

$$\hat{\boldsymbol{u}}_k=g(\boldsymbol{u}) \quad \text{iff} \quad d(\boldsymbol{u},\hat{\boldsymbol{u}}_k)\leqslant d(\boldsymbol{u},\hat{\boldsymbol{u}}_i) \quad \forall 1\leqslant i\leqslant N_c, \tag{6}$$

which is essentially a ''nearest-neighbor'' mapping. While this solution to issue (ii) is relatively straightforward and intuitive, there are several different algorithms available for generation of the codebook itself. The interested reader is referred to Ref. 22 for an excellent summary of the various methods available for codebook generation. The algorithm applied here, referred to as K-means,[21] is implemented by defining an initial codebook of N_c vectors, and then using the metric in (6) to cluster (associate) each of the training vectors $\boldsymbol{u}_1,\boldsymbol{u}_2,\ldots,\boldsymbol{u}_\Lambda$ with a particular codebook element. The codebook elements are then updated, with the new codebook vector $\hat{\boldsymbol{u}}_k'$—associated with cluster C_k—defined by the cluster centroid

$$\boldsymbol{u}_k'=\frac{1}{N_k}\sum_{\boldsymbol{u}_\mathbf{n}\in C_k}\boldsymbol{u}_\mathbf{n}, \tag{7}$$

with the number of training vectors in C_k represented by N_k. This processed is iterated, until convergence is reached at the final codebook.

II. HIDDEN MARKOV MODEL TARGET IDENTIFICATION

The target-identification paradigm employed here assumes that a putative target has been detected and is being interrogated to effect discrimination. The target position is therefore assumed known, but the target is concealed or sufficiently distant that its identity and orientation are unknown.

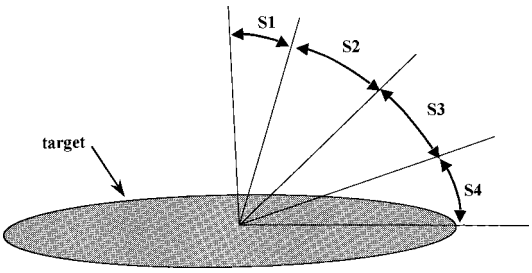

FIG. 2. Angular sectors, or ''states,'' relative to a target center. The wave physics characteristic of a state varies slowly with varying target-sensor orientation, as long as the angle of observation remains in a given state. In this example the target is characterized by four distinct states, S1–S4.

During interrogation, the backscattered fields are observed from M different target-sensor orientations; since the target orientation (and identity) are unknown, the relative angles between the M measurements are known, but the absolute target-sensor orientations are unknown (or ''hidden''). Wave-based matching pursuits is applied to each of the M scattered waveforms, realizing M parameter vectors $\boldsymbol{u}_1, \boldsymbol{u}_2, \ldots, \boldsymbol{u}_M$. Vector quantization is performed for the M continuous parameter vectors, after which the M scattered waveforms are mapped to the M-dimensional observation vector $\boldsymbol{O}=\{O_1, O_2, \ldots, O_M\}$, where each discrete observation O_m represents one of the codebook elements. Therefore, through matching pursuits and vector quantization, we have mapped M aspect-dependent time-domain scattered waveforms into M discrete elements, each of which is a member of an N_c-element codebook.

Maximum-likelihood discrimination[23] is effected by selecting that target T_i for which

$$p(\boldsymbol{O}|T_i) \geqslant p(\boldsymbol{O}|T_k) \quad \forall T_k \in \boldsymbol{T}, \tag{8}$$

where T_k denotes the kth target, $\boldsymbol{T}$ represents the set of all targets anticipated, and $p(\boldsymbol{O}|T_k)$ represents the probability of observing $\boldsymbol{O}$ for target T_k; we have assumed equal prior probabilities for observing each target. Even for noise-free data, $\boldsymbol{O}$ must be treated as a random process, since the underlying physics $\boldsymbol{O}$ represents is a function of the *hidden* target-sensor orientation—while the *relative* target-sensor orientations of the sequence of scattered waveforms are known, the absolute target-sensor orientation is assumed unknown, and treated stochastically.

We now consider in greater detail the evaluation of $p(\boldsymbol{O}|T_k)$. We assume that there are angular sectors, characterized by a limited range of target-sensor orientations, over which the underlying wave physics is slowly varying. Such regions are schematized in Fig. 2, and are termed ''states.'' We therefore have

$$p(\boldsymbol{O}|T_k) = \sum_{\text{all } \boldsymbol{S_n}} p(\boldsymbol{O}|\boldsymbol{S_n}, T_k) p_S(\boldsymbol{S_n}|T_k), \tag{9}$$

where $\boldsymbol{S}_n$ denotes the nth possible realization of $\boldsymbol{S}$, with $\boldsymbol{S}$ an M-dimensional vector that represents the sequence of states sampled by the M scattered waveforms under test. Note that in (9) we assume that the underlying state sequence $\boldsymbol{S}$ is hidden, and therefore sum over all possible realizations of $\boldsymbol{S}$, weighted by the probability of each, given by $p_S(\boldsymbol{S}_n|T_k)$. For a target with M_s states (M_s angular sectors over which the underlying wave physics is relatively slowly varying), there are M_s^M discrete possibilities for $\boldsymbol{S}_n$, constituting the range of the sum in (9).

If we assume that the probability of observing a codebook element in a given state is independent of what happens in any other state, with the symbol $B_i(O_m)$ representing the probability of observing codebook element O_m in state S_i, then (2) becomes

$$p(\boldsymbol{O}|T_k) = \sum_{m=1}^{M_s} B_m(O_1) \sum_{i=1}^{M_s} B_i(O_2) \sum_{n=1}^{M_s} B_n(O_3) \cdots \sum_{q=1}^{M_s} B_q(O_M) p_S[\boldsymbol{S}=(S_m, S_i, S_n, \cdots, S_q)|T_k]. \tag{10}$$

Further, we make the assumption that the M state transitions, for the M target-sensor orientations, can be modeled by a Markov process. Consequently, the probability of transitioning into a given state is dictated only by the previous state occupied, with A_{ij} representing the probability of transitioning from state i to state j. With these assumptions, (10) becomes

$$p(\boldsymbol{O}|T_k) = \sum_{m=1}^{M_s} \pi_m B_m(O_1) \sum_{i=1}^{M_s} A_{mi} B_i(O_2) \times \sum_{n=1}^{M_s} A_{in} B_n(O_3) \cdots \sum_{q=1}^{M_s} A_{pq} B_q(O_M), \tag{11}$$

where π_m represents the probability that the first observed scattered waveform is measured in state m.

Before proceeding, we summarize the assumptions that lead to (11). First, it was assumed that the target-sensor orientations can be segmented into a set of sectors or states, over which the underlying scattering physics is slowly varying. Consequently, in each state one can define a function that characterizes the probability of observing each codebook element. Further, along these same lines, we have assumed that the probability of selecting a particular codebook element is only dependent on the state within which the associated scattered waveform resides, independent of which codebook elements were selected at previously processed target-sensor orientations. This assumption simplifies the subsequent evaluation of $p(\boldsymbol{O}|T_k)$, and its implications are discussed further below. Finally, we have assumed that the sequence of state transitions can be represented by a Markov model (actually, a *hidden* Markov model, or HMM,[18,19] since the underlying states are assumed hidden from the sensor). As discussed below, while this assumption is reasonable for many applications, it can be relaxed without significant changes to the overall signal-processing paradigm.

The HMM is characterized by the matrices $\boldsymbol{A}$ and $\boldsymbol{B}$ and the vector π. The $N_s \times N_s$ matrix $\boldsymbol{A}$, represents the aforementioned state-transition probabilities, for a model with N_s states; the $N_c \times N_s$ matrix $\boldsymbol{B}$ represents the probability of observing each codebook element, as a function of the state occupied, for a codebook of N_c elements, with $B_{mi} = B_i(O_m)$; and the K-dimensional vector π gives the initial-

state probabilities, with π_i representing the probability that the first scattered waveform under test resides in state *i*. The parameters $\boldsymbol{A}$ and π can be estimated using simple geometric considerations. In particular, if φ_i represents the angular extent of the *i*th state, and if we assume that the probability of observing any angle is uniformly likely, then

$$\pi_i = \frac{\varphi_i}{\sum_{k=1}^{M_s} \varphi_k}. \tag{12}$$

Analogously, if $\Delta\varphi \leqslant \varphi_i \forall i \in [1, M_s]$,

$$A_{i,i+1} = A_{i,i-1} = \frac{\Delta\varphi}{2\varphi_i}, \quad A_{i,i} = \frac{\varphi_i - \Delta\varphi}{\varphi_i}, \tag{13}$$

with all other $A_{ij} = 0$. Therefore, $\boldsymbol{A}$ is a tri-diagonal matrix, with components derivable directly from geometry.

Having defined the state-transition probabilities and the initial-state probabilities, represented by $\boldsymbol{A}$ and π, respectively, it remains to define the matrix $\boldsymbol{B}$. This matrix is defined during a ''training'' phase, after the states have been delineated, using all the data available from the target in question. If n_i represents the number of scattered waveforms available from state *i*, and n_{mi} represents the number of times matching pursuits followed by VQ resulted in the selection of codebook element *m*, then

$$B_{mi} = B_i(O_m) = \frac{n_{mi}}{n_i}. \tag{14}$$

From the above discussion, we see that reasonable assumptions have justified the evaluation of the probabilities $p(\boldsymbol{O}|T_k)$ via an HMM. Moreover, simple geometric considerations as well as a training phase allow direct computation of the HMM parameters $\boldsymbol{A}$, $\boldsymbol{B}$, and π. Upon consideration of (12)–(14), it is seen that the accuracy of the HMM parameters is dictated principally by an accurate and meaningful state decomposition, with each state representative of an angular sector over which the wave physics is slowly varying. While such a state decomposition can often be effected by considering the aspect-dependent characteristic of the fields scattered from a given target, or *a priori* physical insight, there are likely to be target classes for which such a decomposition will be less than obvious (or unique). To accommodate such scenarios, researchers have developed algorithms that optimize $\boldsymbol{A}$, $\boldsymbol{B}$, and π (and, implicitly, the underlying states). In particular, the Baum–Welch[18,19] and Viterbi[24] algorithms adjust $\boldsymbol{A}$, $\boldsymbol{B}$, and π such that $p(\boldsymbol{O}|T_k)$ is maximized when $\boldsymbol{O}$ is representative of target T_k. Therefore, the expressions in (12)–(14) can be viewed as starting points for the HMM parameters, which we have refined here via the Baum–Welch[18,19] method. Consequently, our final $\boldsymbol{A}$, $\boldsymbol{B}$, and π are not explicitly tied to our initial state segmentation, thereby allowing robustness for targets with complex aspect-dependent scattering behavior.

After having derived $\boldsymbol{A}$, $\boldsymbol{B}$, and π, one still must implement the summations in (11) for evaluation of $p(\boldsymbol{O}|T_k)$. Here, the assumptions that lead to the form in (11)—that the state transitions are characterized by a Markov model and that the probabilities $B_{mi} = B_i(O_m)$ are dependent only on the properties of state *i*—yield a technique by which the multiple summations can be evaluated efficiently. In particular, the ''forward–backward'' algorithm[18,19] capitalizes on the redundancies in (3), resulting in a tremendous acceleration in the rate with which the multiple state sequences and associated probabilities are evaluated.

From the above discussions, we have explained how the probabilities $p(\boldsymbol{O}|T_k)$ required for target identification can be evaluated efficiently via an HMM construct. Moreover, through exploitation of existing literature, primarily in speech processing,[18,19] the requisite HMM parameters are readily evaluated. The simplifying assumptions with regard to the Markov state transitions and codebook-observation probabilities are also utilized ubiquitously in speech processing,[18,19] where HMMs have met with remarkable success. However, it is recognized that there are inherent inaccuracies expected with such a paradigm, which will be explored and modified in future research. For example, the state-transition probabilities are not always rigorously characterized by a Markov model. For example, if state *i* has an angular extent of $2\Delta\varphi < \varphi_i < 3\Delta\varphi$, and one is in this state for two consecutive scattered waveforms, then the probability of transitioning out of this state is 100% for the third scattered waveform. This is a simple example that reflects that the state-transition probabilities are modeled more accurately by including history beyond the previous state occupied.

Finally, we note that the basic paradigm utilized here assumes that vector quantization is performed, during which the generally continuous parameter vector extracted via matching pursuits is mapped to one element in a codebook. Alternatively, instead of using vector quantization (and, implicitly, the discrete set of codebook probabilities represented by $\boldsymbol{B}$), one could envision development of an HMM that exploits the continuous matching-pursuits parameters directly. Such continuous HMMs have also been exploited in the context of speech processing,[18,19] and will be the subject of future research in the application of interest here.

III. EXAMPLE RESULTS

A. Measurement system and targets considered

To test the (matching-pursuits)-HMM target-identification paradigm, we have considered measured acoustic backscattering data from five submerged elastic targets: (1) a cylindrical air-filled shell; (2) a duplicate shell, stiffened with equally spaced ring stiffeners; (3) a duplicate shell, stiffened with unequally spaced ring stiffeners and augmented by resiliently mounted, elastic internal rods; (4) a slightly larger, nearly periodically ribbed shell; and (5) a duplicate of shell 4, with a large number ($\sim$1000) of attached internal oscillators. Schematics of the targets are shown in Fig. 3. The first three targets are visually indistinguishable, as are the last two slightly larger targets. As might be expected from the geometrical similarity represented in Fig. 3, the backscattered acoustic waveforms from these targets are very similar (demonstrated below), with the majority of the differences between the total waveforms resulting from the internal structure. This constitutes close to an impossible task for an image-based target-identification algorithm, as well as

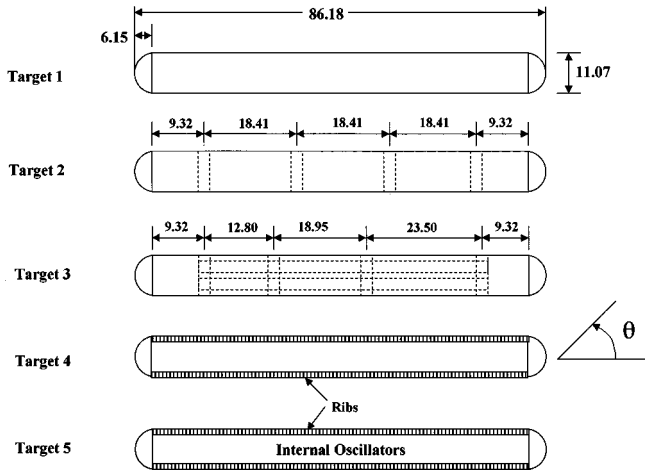

FIG. 3. Schematics of the five targets considered in the measurements, the backscattering data from which is utilized to test the identification algorithm. All units shown are in meters, and the shell thickness of each target is 0.53 mm. (a) target 1, (b) target 2, (c) target 3, (d) target 4, (e) target 5. The two inserts in (e) depict one of the ~1000 internal oscillators in target 5 and how the oscillator is typically mounted to a rib. A 0 deg incidence angle corresponds to excitation along the target axis, with 90 deg corresponding to broadside incidence.

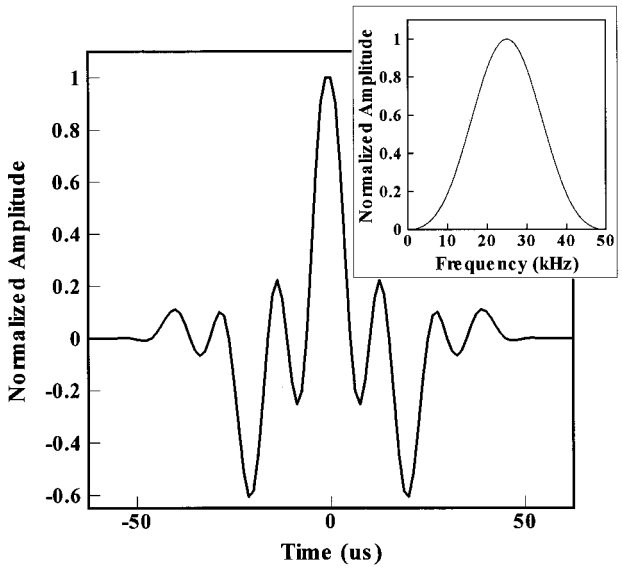

FIG. 4. Incident pulse shape and associated spectrum, used for the backscattered waveforms.

a challenging test for our non-image-based target-identification algorithm. Specifics on the measurement system and further details on the targets measured by the target facility section at the Naval Research Laboratory can be found in Refs. 5, 25 and 26. In particular, targets 1 and 3 are described in Ref. 25, target 4 in Ref. 5, and targets 4 and 5 in Ref. 26. The (matching pursuits)-HMM architecture is relatively efficient during identification: all results presented here were implemented on a Pentium II personal computer, with a few seconds required for the processing of the multiple waveforms (here, from $M=1$ to $M=10$). The required training time using multiple noisy realizations is significantly slower, largely due to the fact that matching pursuits is a greedy search algorithm.[15] Since the HMM itself is transparent to feature selection, we are currently investigating the use of autoregressive techniques which are well suited to modeling resonances, but are computationally more efficient than matching pursuits.

Each of the targets was ensonified by an acoustic waveform with bandwidth from approximately 11–40 kHz, corresponding to relative target dimensions of $2.9 \leqslant ka \leqslant 10.4$, where k is the wave number and a is the average radius of the targets (see Fig. 3). To realize waveforms that approximate a minimum time-bandwidth product, we have deconvolved the spectrum of the incident waveform, and have synthesized scattered waveforms assuming the incident-pulse shape in Fig. 4 (representative of a Blackman pulse[27]). This step is not necessary, but we find it convenient to utilize an incident pulse with minimum temporal support. In Fig. 5 we plot the frequency-dependent backscattered signature of each target, as a function of the incidence angle, assuming the incident spectrum in Fig. 4. As expected from the similarity of the target geometries, depicted in Fig. 3, the angle and frequency dependence of the backscattered fields are very similar for all targets.

All of the backscattered fields contain the dominant geometric feature, specular scattering from the target broad side (near 90 deg ensonification) and have much smaller specular reflections from the target ends. The differences and similarities in the elastic components of scattering can best be appreciated by comparing the scattering from the more-complicated shells to that from the most simple and well-understood shell, target 1. The scattering from the empty target 1 shell contains three ''ring resonances'' [28] superimposed on the broadside scattering. These resonance features are seen in all five targets, although they are less pronounced in the targets with complicated internal structures (targets 2, 3, and 5) and they are shifted to lower frequencies for the larger-diameter targets (targets 4 and 5). The scattering from target 1 also contains the well-defined traveling-wave dispersion highlights (within 30 deg of broadside), which are attributed to the helical membrane waves traveling down the simple shell.[3] This well-defined dispersion is evident in target 4, the simple, periodically ribbed shell, but transforms into a confused region of increased scattering strength for the targets with more complicated internal structures (targets 2, 3, and 5).[25,26] In addition to the simple elastic mechanisms supported in target 1, target 4 also has a noticeable elastic attribute with broad support in ensonification angle and localized support in frequency (with the frequency varying with angle), which is attributed to a Bloch wave[4,5] excited by the flexural wave interacting with the internal periodic structure characteristic of this target. The angle-dependent frequency dependence of such a feature has been investigated in detail.[4,5] The Bloch-wave highlight is not clearly visible in the other ribbed target (target 5) because of the dominant scattering associated with the nonperiodic oscillators attached to its ribs.[26] The nature of the changes in the scattering from the five targets constitutes a challenging test for the target-identification algorithm.

B. Vector quantization

After performing K matching-pursuits iterations, we generate a $3K-1$ dimensional parameter vector $\boldsymbol{u}$. In Fig. 6

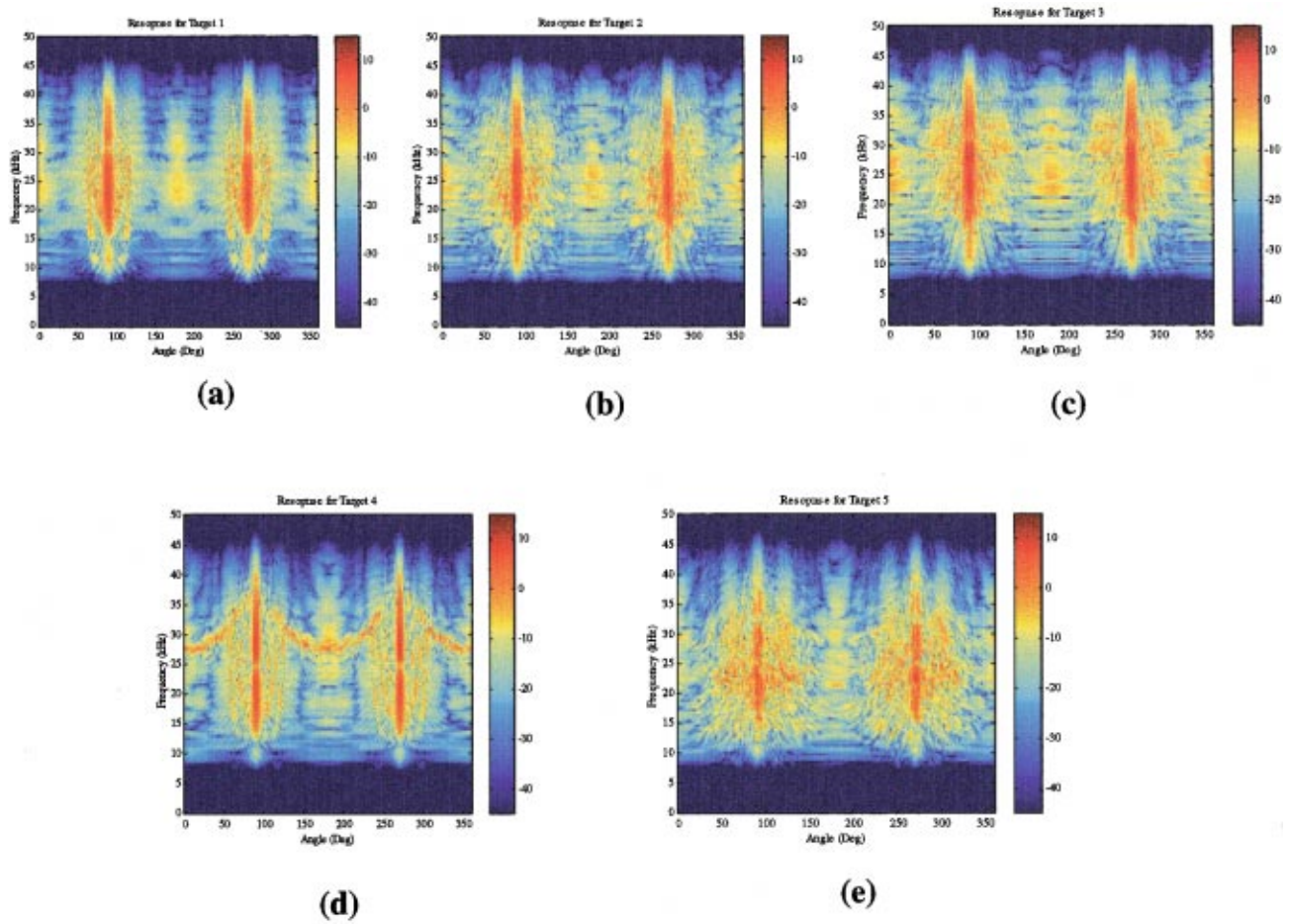

FIG. 5. Frequency and angle-dependent acoustic fields, backscattered from the five elastic targets considered in Fig. 3. The incident spectrum is as in Fig. 4. (a) target 1, (b) target 2, (c) target 3, (d) target 4, (e) target 5.

we demonstrate the distribution of this vector, projected onto the two-dimensional $(\omega_1, \tau_2 - \tau_1)$ phase space; each point $\boldsymbol{u}$ represents a particular target and backscatter angle, and here we have considered $K=3$ matching-pursuits iterations. The data in Fig. 6 correspond to all five targets and observation angles (1 deg sampling was used in the measurements), and the associated codebook elements are also shown in this reduced phase space (marked by the ''x'' symbols). In this example, we utilize a 32-element codebook, defined by the algorithm described in (7). We see from Fig. 6 that the codebook does a reasonable job of representing the parameter distribution. A larger codebook will generally represent this distribution better, but may ultimately yield poorer estimates for the $\boldsymbol{B}$ matrix (for a fixed set of training data). This is a particular problem for noise-free data, like that considered in Fig. 6, for which the number of independent target-sensor realizations is limited. However, if the noise statistics are known, they could be used to produce enough waveform realizations to provide an accurate estimate of $\boldsymbol{B}$, while also better representing the distribution of $\boldsymbol{u}$. As discussed below, when considering noisy data we have found it effective to utilize a larger codebook.

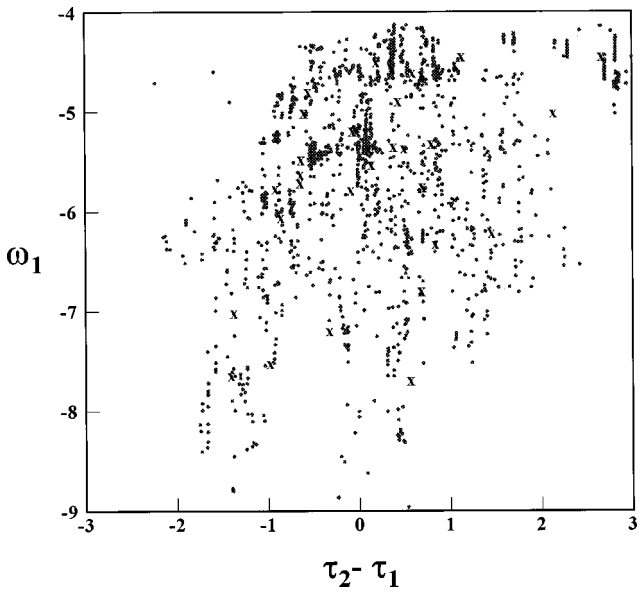

FIG. 6. Distribution of the matching-pursuits parameter vector, projected onto the $(\omega_1, \tau_2 - \tau_1)$ subspace. Results (points) are shown for all the scattering data shown in Fig. 5, using $K=3$ matching-pursuits iterations.

In Fig. 6, we have shown the distribution of the parameter vector $\boldsymbol{u}$ for *all* targets and observation angles, these being used to generate the codebook; the same codebook is applied to the HMM for each target. It is of interest, however, to examine the target-dependent distribution of $\boldsymbol{u}$, the intertarget differences in such ultimately dictating the algorithm's effectiveness as a discriminator. For example, in Fig. 7 we plot the distribution of $\boldsymbol{u}$ for target 1 and target 4,

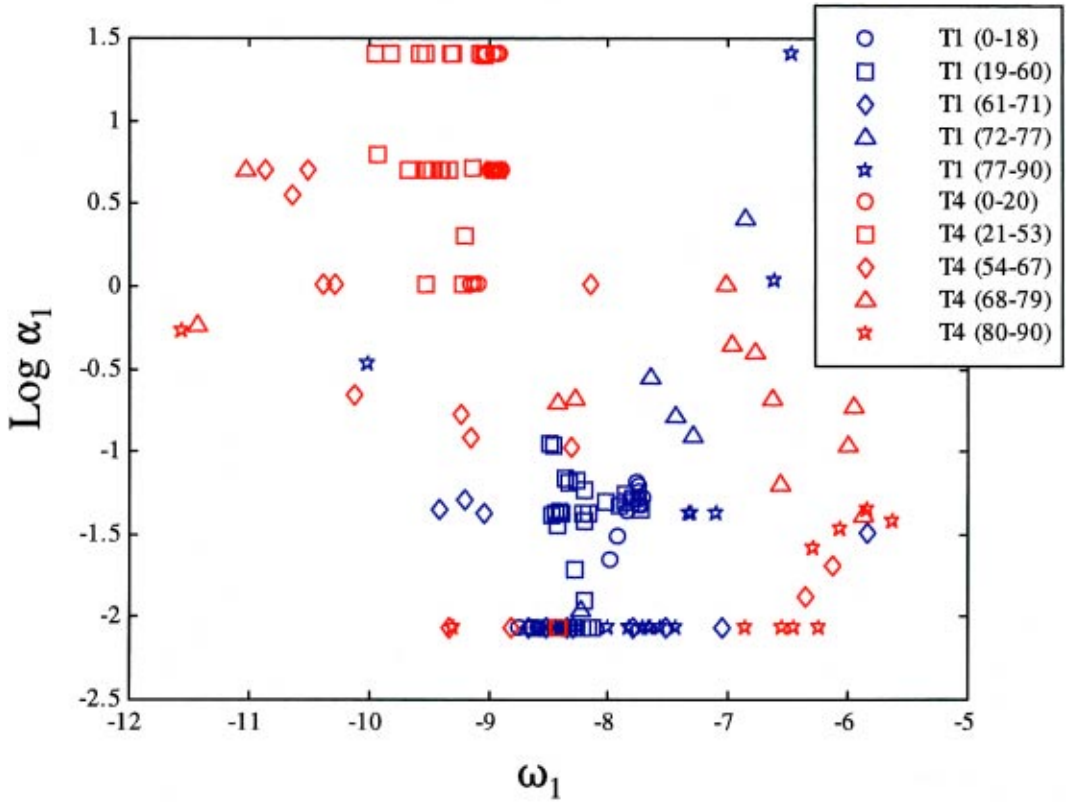

FIG. 7. Distribution of the matching-pursuits parameter vectors, for target 1 and target 4 (see Figs. 3 and 5), projected onto the (ω_1, α_1) subspace. As in Fig. 6, $K=3$ matching-pursuits iterations are used. The parameter vectors are identified in terms of the state in which the associated backscattered waveform resided. T1 and T4 correspond to targets 1 and 4, respectively, and also shown are the angular sectors characteristic of the five-state decomposition used for each target (before Baum–Welch reestimation). Considering target 1 (T1), the 0 deg–18 deg state corresponds to specular diffraction from the ends of the shell; the 19 deg–60 deg sector is absent elastic scattering, characterized primarily by diffractive compressional scattering; in the 61 deg–71 deg state the compressional wave travels straight down the shell (phase matched); the 72 deg–77 deg state is dominated by helical membrane waves; and the 77 deg–90 deg state is principally characterized by scattering from the target broadside. Each of the five targets has a similar five-state decomposition.

projected onto the two-dimensional (ω_1, α_1) phase space. The results in Fig. 7 are plotted as a function of the orientation-dependent state in which the backscattered waveform resides, using our initial state decomposition (recall that the Baum–Welch algorithm[18,19] refines the initial state decomposition, if necessary). Several issues are evident through consideration of Fig. 7. For example, we see that the features are well mapped into orientation-dependent sectors, over which the wave physics is slowly varying, justifying the state decomposition. Moreover, the features due to target 1 and target 4 have noticeable differences, the latter being influenced strongly by the aforementioned Bloch wave. Finally, we reiterate that Figs. 6 and 7 depict only two dimensions of the 8-dimensional phase space in which the parameter vectors $\boldsymbol{u}$ reside $(K=3)$; Figs. 6 and 7 only demonstrate a very incomplete (two-dimensional) subset of the total information exploited by the HMM.

C. Discrimination performance: Noise-free data

We first consider noise-free data, as presented in Fig. 5. We utilized $K=3$ matching-pursuits iterations, for each target and all available angles of observation, from which a 32-element codebook was defined. After defining the initial state decompositions, with five states for each target, initial estimates for $\boldsymbol{A}$, $\boldsymbol{B}$, and π were defined as in (12)–(14), with these refined via Baum–Welch.[18,19] For the data considered here, we witnessed noticeable changes in $\boldsymbol{A}$, $\boldsymbol{B}$, and π after reestimation, which we attribute to the difficulty of estimating the state decompositions from two-dimensional projections (e.g., Figs. 6 and 7) of an 8-dimensional space.

For the results presented here, we utilize a 5 deg angular sampling rate, and consider initial angles ranging from 0–180 deg (see Fig. 3). Clearly, when testing the HMM we know all of the backscattering angles used to constitute the data under test, but this information is assumed hidden from the model, wherein such information is not utilized. In Fig. 8 we plot $-\ln[p(\boldsymbol{O}|T_k)]$, where, as discussed above, $\boldsymbol{O}$ is an M-dimensional vector representing the sequence of M codebook elements extracted after applying matching pursuits and vector quantization to the M angular-dependent backscattered waveforms. In Fig. 8, we consider data from each of the five targets. If the data correspond to target T_i, correct discrimination occurs when $-\ln[p(\boldsymbol{O}|T_i)] < -\ln[p(\boldsymbol{O}|T_k)]$ $\forall k \neq i$. Considering the results in Fig. 8, in which $M=10$ scattered waveforms were used (covering in total 45 deg variation in the target-sensor orientation), we see that very good discrimination is achieved, despite the similarity of the targets and corresponding data (Figs. 3 and 5, respectively).

The results in Fig. 8 are summarized in Table I, in which we tabulate the probability of misidentification, for each of

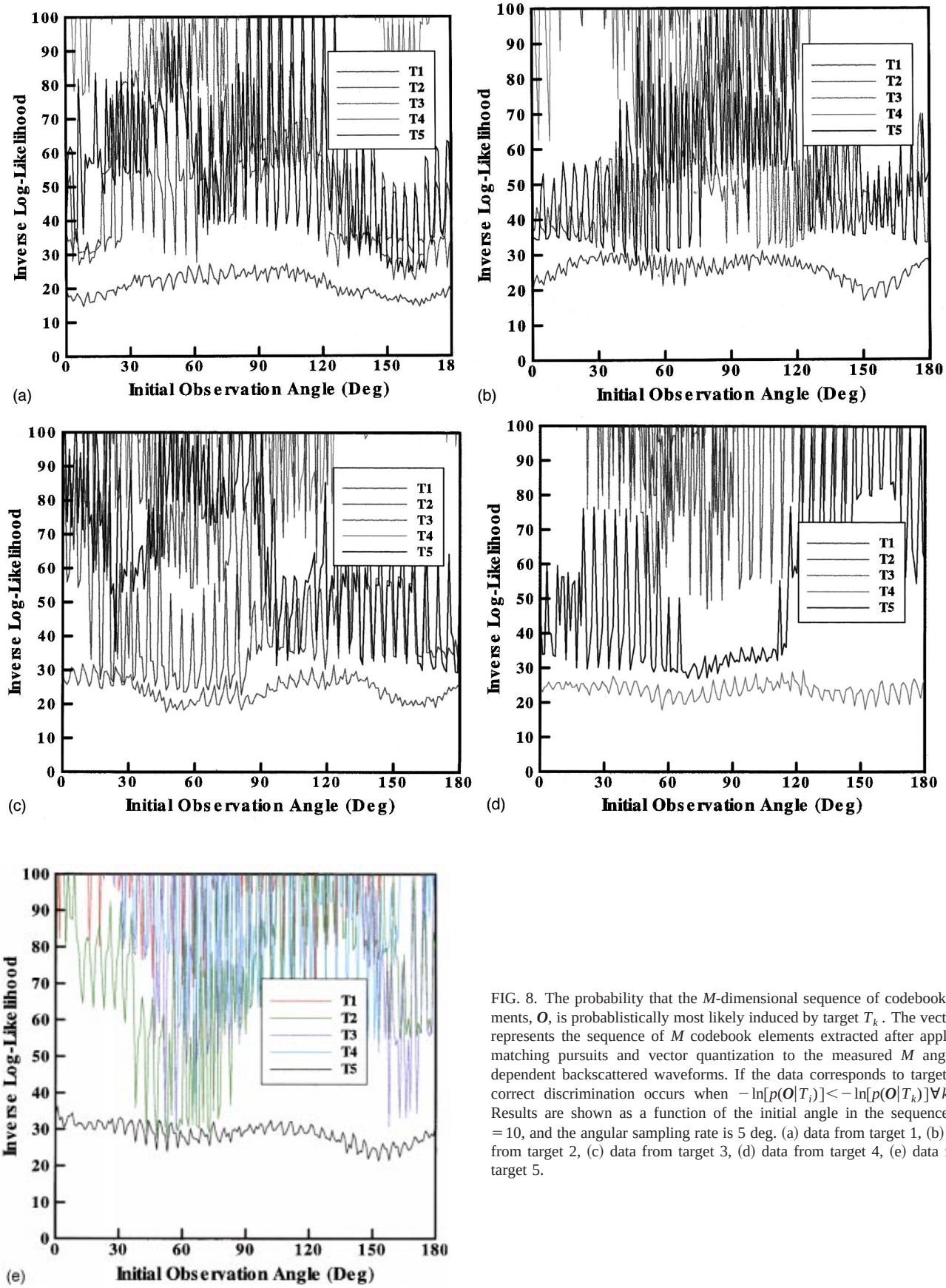

FIG. 8. The probability that the M-dimensional sequence of codebook elements, $\boldsymbol{O}$, is probablistically most likely induced by target T_k. The vector $\boldsymbol{O}$ represents the sequence of M codebook elements extracted after applying matching pursuits and vector quantization to the measured M angular-dependent backscattered waveforms. If the data corresponds to target T_i, correct discrimination occurs when $-\ln[p(\boldsymbol{O}|T_i)] < -\ln[p(\boldsymbol{O}|T_k)] \forall k \neq i$. Results are shown as a function of the initial angle in the sequence, $M = 10$, and the angular sampling rate is 5 deg. (a) data from target 1, (b) data from target 2, (c) data from target 3, (d) data from target 4, (e) data from target 5.

the five targets. We see that, for the noise-free case, four of the five targets had no misidentifications, while target 2 only had one misidentification. When we reduce the number of scattered waveforms to $M=5$ (total angular span of 20 deg, with 5 deg sampling), the misidentification probability increases noticeably. Except for target 2, which was consistently misidentified as target 3 (its closest physical match), the probability of correct identification is in excess of 91%. As expected, when the number of waveforms sampled reduces to $M=2$, the probability of misidentification increases markedly. This corresponds to only 5 deg of angularly sampled data (at the 5 deg sampling rate used). These latter results underscore the need for a multiaspect identification paradigm to distinguishing targets with highly similar elastic properties. An additional observation concerning the features best suited for small-angular-sampling identification can be made from these results. Targets 1 and 4 have average misidentification rates of 2.2% and 14.4% for 20 deg and 5 deg angular sectors, respectively. The remaining targets have an average misidentification rate of 10.3% and 43.3% for the same angular sampling. This implies that the well-defined traveling wave dispersion highlights in targets 1 and 4 (target 1 has helical membrane wave dispersion highlights, and target 4 has both helical membrane and Bloch wave dispersion highlights) are being exploited by the algorithm for identification based on limited angular sampling.

D. Discrimination performance: Noisy data

In the next set of examples, we consider additive noise, initially white Gaussian noise, and subsequently colored Gaussian noise. For a waveform $\boldsymbol{f}=\boldsymbol{s}+\boldsymbol{n}$, where $\boldsymbol{s}$ is the underlying scattered signal and $\boldsymbol{n}$ represents the additive noise, the signal-to-noise ratio (SNR) is generally defined as $\langle \boldsymbol{s}|\boldsymbol{s}\rangle/\sigma^2$, where σ^2 is the noise variance. For the matching-pursuits algorithm utilized here, it is important to also consider the signal-component SNR, or SC-SNR. In particular, if the *noise-free* waveform is decomposed via matching pursuits in the representation (after K iterations)

$$\boldsymbol{s}\cong\sum_{k=1}^{K}\langle \boldsymbol{s}|\hat{\boldsymbol{e}}_k\rangle\hat{\boldsymbol{e}}_k, \tag{15}$$

then the SC-SNR for the kth matching-pursuits component is defined (in the presence of additive noise) as $|\langle \boldsymbol{s}|\hat{\boldsymbol{e}}_k\rangle|^2/\sigma^2$. We have demonstrated[12] that the SC-SNR must be in excess of approximately 5 dB to assure reliable matching-pursuits performance in noisy data. For the noisy data considered here, the noise variance has been selected such that the *minimum* SC-SNR for *all* scattered waveforms (using $K=3$ matching-pursuits iterations) is in excess of 5 dB. To demonstrate such noise realizations, in Fig. 9 we show example waveforms from each of the five states characteristic of target 1: 15 deg corresponds to the specular scattering from the end of the target, 45 deg corresponds to the weak geometric diffraction at quartering angles, 65 deg corresponds to the helical membrane waves traveling down the length of the target, 75 deg corresponds to the helical membrane near beam where they form a tight spiral around the cylinder, and 85 deg corresponds to the beam and ring resonance scattering. This figure dramatizes the fact that the waveform backscattered from a complex target has a strength (and shape) which is a strong function of the target-sensor orientation. While the noise level considered is sufficient to cause significant contamination to the waveforms at 15 deg and 45 deg, the other three waveforms are characterized by a relatively large SNR (and SC-SNR). In Table II we tabulate the average SNR for each of the five states, for all five targets. The SNR is minimum for states near the target axis, at which the scattered fields are characterized principally by relatively weak diffraction at the front and rear of the target. The other, stronger scattering phenomena, such as helical membrane waves, ring resonance, and beam specular scattering are excited in states S3–S5, away from this axis. As expected, state S5, at or near broadside, is characterized by the largest scattered amplitude, and hence the largest SNR. The data presented in Fig. 9 and Table II are representative of white Gaussian noise, and similar properties hold for the colored noise discussed below.

In Table III are presented the misidentification results for the white-Gaussian noise case, considering $M=10$, 5, and 2 scattered waveforms, at a 5 deg angular sampling rate. As expected, relative to the noise-free case of Table I, the misclassfication probability is increased. However, for the $M=10$ case, proper identification occurred over 90% of the

TABLE I. Probability of misidentification, for each of the five targets in Fig. 3. Results are shown for noise-free data, considering $M=10$, 5, and 2 scattered waveforms, at a 5 deg sampling rate.

	10 Obs	5 Obs	2 Obs
$T1$	0.00	0.55	14.36
$T2$	0.55	16.02	43.09
$T3$	0.00	8.83	42.54
$T4$	0.00	3.86	14.36
$T5$	0.00	6.62	44.20
Mean	0.11	7.18	31.71

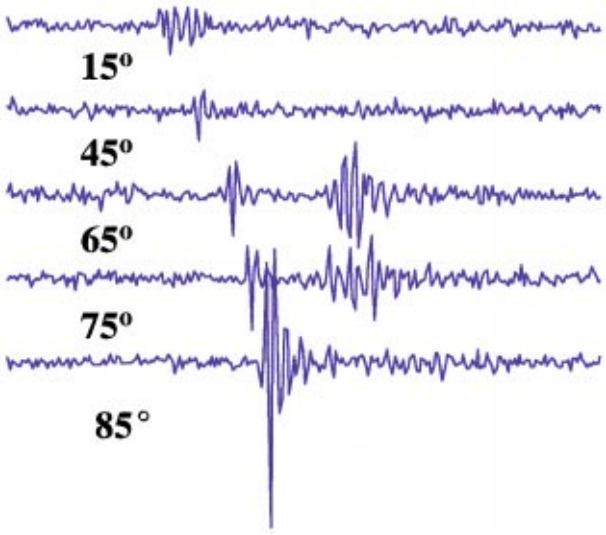

FIG. 9. Example scattered waveforms from target 1, taken from each of the states used in the HMM to describe that target. The waveforms are shown with example noise realizations, for the noise variance utilized here. These waveforms are shown with white Gaussian noise, while an additional set of results (not shown) considers colored noise as well.

TABLE II. Average SNR for each of the five states, for all five targets in Fig. 3. Results are shown for white Gaussian noise, at the noise level displayed in Fig. 9.

	$S1$	$S2$	$S3$	$S4$	$S5$
$T1$	12.7	9.8	19.7	20.3	26.0
$T2$	13.0	14.3	19.1	20.7	26.5
$T3$	15.5	15.4	20.6	20.9	26.5
$T4$	15.9	15.8	19.7	19.3	25.8
$T5$	17.5	14.2	21.1	20.6	25.2

time, except for target 2, which, like in the noise-free case considered in Table I, was characterized by the highest probability of misidentification. The algorithm performance drops sharply as the number of observation angles M is reduced.

For the noisy examples tabulated in Table III, we used $K=3$ matching-pursuits iterations and a codebook of 64 elements. To accelerate the matching-pursuits computations, we first applied matching pursuits to each of the noise-free scattered waveforms, with the set of elements selected used to define a reduced dictionary D', which was then applied to the noisy data. This approach has two advantages: The reduced dictionary is more closely matched to the underlying scattered signals than the original dictionary, thereby enhancing algorithm robustness to noise. Further, the reduced (smaller) dictionary dramatically increases the speed at which the matching-pursuits algorithm can search through its dictionary. The initial dictionary described in (4) had 234 elements, while the reduced dictionary consisted of only 105 elements. Finally, we note that the HMM algorithm was trained using all initial angles from 0 deg–180 deg, considering 15 noise realizations for each of the scattered waveforms. The algorithm was tested in the same manner, using four *different* noise realizations for each scattered waveform. In this manner, unlike the noise-free case, for the noisy data the algorithm was trained and tested on different data.

The final set of results considers nonwhite Gaussian noise. In particular, the noise was generated by filtering the white-Gaussian noise considered in Fig. 9 and Tables II and III through a linear filter with impulse response defined in Fig. 4, descriptive of the incident pulse shape. In this manner, the colored noise is defined to have a correlation length consistent with the incident-pulse width, with this phenomenon expected of clutter. The results for this case are presented in Table IV, in the manner of Tables I and III. Even for this colored-noise example, the (matching-pursuits)-HMM algorithm provides robust identification performance, despite the high degree of similarity between the five targets considered. In fact, comparing Tables III and IV, we see the

TABLE III. As in Table I, for the case of additive white Gaussian noise (at the levels depicted in Table 2).

	10 Obs	5 Obs	2 Obs
$T1$	6.08	26.10	44.75
$T2$	13.54	33.56	59.53
$T3$	5.52	24.03	39.23
$T4$	2.90	5.66	15.47
$T5$	5.11	22.10	47.51
Mean	6.63	22.20	41.30

TABLE IV. As in Table III, but considering colored additive Gaussian noise. The noise is generated by passing the white Gaussian noise considered in Fig. 9 and in Tables II and III through a filter characterized by the incident-pulse spectrum, shown in Fig. 4.

	10 Obs	5 Obs	2 Obs
$T1$	5.11	18.65	44.61
$T2$	9.12	27.62	52.90
$T3$	3.45	21.27	36.60
$T4$	2.35	3.73	13.67
$T5$	9.67	26.52	48.36
Mean	5.94	19.55	39.31

results for the colored noise are actually slightly better than those for the white noise. This is a consequence of the manner in which the noise was generated: The total noise energy is lower for the colored noise than for the white noise, the spectrum of the former having been windowed to match the spectrum of the incident pulse in Fig. 4 (the white noise has a flat spectrum). For the colored-noise examples, the HMM algorithm was trained and tested in the same manner as for the white noise. Note that, in Tables III and IV, target 4 has a probability of misidentification that is markedly better than that of any of the other targets; we attribute this to the unique Bloch wave only visible on this target, a feature being observable from almost all incidence angles (see Fig. 5).

IV. CONCLUSIONS AND FUTURE WORK

The (matching-pursuits)-HMM algorithm represents a new target-identification tool, tested here using measured acoustic backscattering data from five very similar submerged elastic targets. The algorithm explicitly exploits data from multiple target-sensor positions, with the realistic assumption that the target and its orientation are unknown. The accuracy of the technique appears to be very promising, based on results from both the noise-free and noisy data.

There are several areas that warrant further research. That of particular interest involves elimination of the vector-quantization step applied in the discrete HMMs utilized here. After applying matching pursuits to the M scattered waveforms under test, we have M matching-pursuits parameter vectors $\boldsymbol{u}_1, \boldsymbol{u}_2, \ldots, \boldsymbol{u}_M$. Rather than applying vector quantization and mapping these vectors to M codebook elements, a continuous HMM can be derived, in which the vectors $\boldsymbol{u}_1, \boldsymbol{u}_2, \ldots, \boldsymbol{u}_M$ are exploited directly. In the continuous HMM, we directly define the probability of extracting the matching-pursuits parameter vector $\boldsymbol{u}$ for a given state, with $\boldsymbol{u}$ residing in a continuous $3K-1$ dimensional space (for K matching-pursuits iterations). There is a vast continuous-HMM literature, developed for speech processing,[18,19] which can be transferred to the target-identification problem of interest here. In addition to continuous HMMs, in future research we will apply the Viterbi[24] training algorithm, which has several features which make it preferable to the Baum–Welch[18,19] algorithm applied here.

Finally, the HMM construct requires a training phase, to learn the state-dependent codebook probabilities, as well as the state-transition probabilities. Artificial neural networks[29] (ANNs) also require training, and therefore ANNs are related

to the HMMs considered here. However, we have developed a close relationship between the HMMs and the scattering physics/sensor motion, resulting in an intuitively satisfying interpretation of the model parameters which is often lacking with ANNs. Nevertheless, a worthwhile direction of future research would involve a comparison of ANN and HMM performance, using the same matching-pursuits feature parsing.

ACKNOWLEDGMENTS

The portion of this work undertaken at Duke has been supported in part by the Office of Naval Research, under Grant No. N00014-96-1-0861 and by the Naval Research Laboratory, code 7130. The authors would like to thank Brian Houston at the Target Facility Section at the Naval Research Laboratory for providing the experimental data used throughout this paper.

[1] T. J. Yoder, J. A. Bucaro, B. H. Houston, and H. J. Simpson, ''Long-range detection and identification of underwater mines using very low frequencies (1–10 KHz),'' *Proceedings of the SPIE AeroSense Conference*, Orlando, FL, April 1998 (paper 3392-27).

[2] L. Flax, G. C. Gaunaurd, and H. Uberall, ''Theory of resonant scattering,'' in *Physical Acoustics XV* (Academic, New York, 1981).

[3] M. L. Rumerman, ''Contribution of membrane wave reradiation to scattering from finite cylindrical steel shells in water,'' J. Acoust. Soc. Am. **93**, 5–14 (1993).

[4] D. M. Photiadid, J. A. Bucaro, and B. H. Houston, ''Scattering from flexural waves on a ribbed cylindrical shell,'' J. Acoust. Soc. Am. **96**, 2785–2793 (1994).

[5] B. H. Houston, J. A. Bucaro, and D. M. Photiadis, ''Broadband acoustic scattering from a ribbed shell,'' J. Acoust. Soc. Am. **98**, 2851–2861 (1995).

[6] J. B. Keller, ''Geometrical theory of diffraction,'' J. Opt. Soc. Am. **52**, 116–130 (1962).

[7] I. T. Lu and L. B. Felsen, ''Ray, mode, and hybrid options for source excited propagation in an elastic plate,'' J. Acoust. Soc. Am. **78**, 223–233 (1985).

[8] M. R. Azimi-Sadjadi, J. Wilbur, and G. J. Dobeck, ''Isolation of resonance in acoustic backscatter from elastic targets using adaptive estimation schemes,'' IEEE J. Ocean Eng. **20**, 346–353 (1995).

[9] A. J. Poggio, M. L. Van Blaricum, E. K. Miller, and R. Mittra, ''Evaluation of a processing technique for transient data,'' IEEE Trans. Antennas Propag. **26**, 165–173 (1978).

[10] M. McClure, R. C. Qiu, and L. Carin, ''On the superresolution identification of observables from swept-frequency scattering data,'' IEEE Trans. Antennas Propag. **45**, 631–641 (1997).

[11] R. A. Atles, ''Sonar for generalized target description and its similarity to animal echolocation systems,'' J. Acoust. Soc. Am. **59**, 97–105 (1976).

[12] M. McClure and L. Carin, ''Wave-based matching-pursuits detection of submerged elastic targets,'' J. Acoust. Soc. Am. **104**, 937–946 (1998).

[13] C. Herley and M. Vetterli, ''Orthogonal time-varying filter banks and wavelet packets,'' IEEE Trans. Signal Process. **42**, 2650–2663 (1994).

[14] M. V. Wickerhauser and R. R. Coifman, ''Entropy based algorithms for best basis selection,'' IEEE Trans. Inf. Theory **32**, 712–718 (1992).

[15] S. G. Mallat and Z. Zhang, ''Matching pursuits with time-frequency dictionaries,'' IEEE Trans. Signal Process. **41**, 3397–3415 (1993).

[16] M. McClure and L. Carin, ''Matching pursuits with a wave-based dictionary,'' IEEE Trans. Signal Process. **45**, 2912–2927 (1997).

[17] J. A. Simmons, P. A. Saillant, and S. P. Dear, ''Through a bat's ear,'' IEEE Spectr. , 46–48 (1992).

[18] L. R. Rabiner and B. H. Juang, ''An introduction to hidden Markov models,'' IEEE Acoust. Speech Signal Proc. Mag. **3**, 4–16 (1986).

[19] L. R. Rabiner, ''A tutorial on hidden Markov models and selected applications in speech recognition,'' Proc. IEEE **77**, 257–285 (1989).

[20] J. Makhoul, S. Raucos, and H. Gish, ''Vector quantization in speech coding,'' Proc. IEEE **73**, 1551–1558 (1985).

[21] Y. Linde, A. Buzo, and R. M. Gray, ''An algorithm for vector quantizer design,'' IEEE Trans. Commun. **28**, 84–95 (1980).

[22] J. Deller, J. Proakis, J. Hansen, *Discrete-Time Processing of Speech Signals* (Prentice-Hall, Englewood Cliffs, NJ, 1993).

[23] L. L. Scharf, *Statistical Signal Processing, Detection, Estimation, and Time Series Analysis* (Addison-Wesley, Reading, MA, 1990).

[24] A. Viterbi, ''Error bounds for convolutional codes and an asymptotically optimum decoding algorithm,'' IEEE Trans. Inf. Theory **13**, 260–269 (1967).

[25] J. E. Bondaryk and H. Schmidt, ''Array processing for the analysis of stiffened, fluid-loaded, cylindrical shells,'' J. Acoust. Soc. Am. **97**, 1067–1074 (1995).

[26] D. M. Photiadis, J. A. Bucaro, and B. H. Houston, ''The effect of internal oscillators on the acoustic response of a submerged shell,'' J. Acoust. Soc. Am. **101**, 895–995 (1997).

[27] R. B. Blackman and J. W. Tukey, *The Measurement of Power Spectra* (Dover, New York, 1958), Appedix B.5, pp. 95–100.

[28] D. Dragonette, D. M Drumheller, C. F. Gaumond, D. H. Hughes, B. T. O'Connor, N. Yen, and T. Yoder, ''The application of two-dimensional signal transformations to the analysis and synthesis of structural excitations observed in acoustical scattering,'' Proc. IEEE **84**, 1249–1264 (1996).

[29] J. H. L. Hansen and B. Womack, ''Feature analysis and neural network based classification of speech under stress,'' IEEE Trans. Speech Audio Process. **4**, 307–313 (1996).

Acoustic attenuation in very shallow water due to the presence of bubbles in rip currents

J. W. Caruthers, S. J. Stanic, and P. A. Elmore
Naval Research Laboratory, Stennis Space Center, Mississippi 39529

R. R. Goodman[a)]
Applied Research Laboratory, University of Pennsylvania, State College, Pennsylvania 16804

(Received 1 May 1998; accepted for publication 9 April 1999)

An experiment was performed just off the research pier at the Scripps Institute of Oceanography to determine the acoustic effects of small bubbles in very shallow water (~6 m depth). The distance offshore was ~300 m. The propagation lengths were 2–10 m, and the frequency range was from 39 to 244 kHz. During the experiment, rip currents passed through the field of measurement instruments. These rip currents were laden with bubbles created in the surf between the instruments and the shore. The effects of these rip currents on the spatial distributions of the resulting acoustic attenuation are discussed. From the attenuation data, the bubble distributions are calculated using a new iterative approach [Caruthers *et al.*, in press, J. Acoust. Soc. Am.] that is based on the well-known resonant bubble approximation. Calculated bubble distributions varied from an essentially uniform lack of bubbles during quiescent periods to highly inhomogeneous and dense bubbly regions within rip events. Such observed distributions were consistent with measurements made by other investigators during the experiment. [S0001-4966(99)05307-2]

PACS numbers: 43.30.Es, 43.30.Pc, 43.35.Bf [SAC-B]

INTRODUCTION

The Naval Research Laboratory (NRL) performed an acoustics experiment just off the beach at Panama City, Florida, in the Spring of 1995.[1] One objective of that experiment was to determine the relative effects of bubbles that may be generated locally by wind waves and those of bubbles generated by the surf and swept out to deeper water by rip currents and other near-shore dynamics. During a three-day period in the course of the experiment, a day of very calm weather prevailed, providing a good baseline measurement. A day of severe stormy weather and then a day of settling conditions followed this. The effects of bubbles, as noted in the dispersion of sound velocities over frequencies from 20 to 200 kHz under these varying conditions, was significant and suggested that small bubble diameters were important.

To further the study into these effects, an experiment was planned for the region offshore from the beach and north of the pier at Scripps Institution of Oceanography (SIO). That experiment was conducted in the Spring of 1997.[2] For this new experiment, a wide array of measurements was taken by several organizations to study the near-shore effects of bubbles more closely than the 1995 Panama City Experiment. Figure 1 shows the layout of the field of various sensors for what might be termed the ''Coordinated Core Measurements'' of the experiment. The institutions participating in these core measurements were NRL, SIO, the Institute for Ocean Sciences (IOS), British Columbia, Canada, and the Applied Physics Laboratory, University of Washington (APL/UW).

We deployed a specially made triangular array (called the delta frame) of two sources and eight hydrophones to improve upon measurements we felt were important as indicated in the Panama City Experiment. In particular, it was important that we insure that the baselines of propagation were firmly fixed, that there be a reciprocal path in the direction of wave motion, and that there be an ability to measure horizontal spatial inhomogeneities. In this paper, we report on the attenuation produced by the migration and inhomogeneity of bubble concentrations carried across the delta frame by the action of rip currents as noted during the Scripps Pier Experiment.

The nearshore dynamics off the Scripps beach have been discussed in a number of papers.[3–5] Rip currents are an ubiquitous feature of those dynamics. A rip current is essentially a jet of water streaming offshore that is the release of potential energy created in the beach zone by the nonlinearity of the breaking swell. The phenomenon we observed at the delta frame appeared more like a plume of turbulent water at the head of the jet. This plume tended to migrate offshore slower that the current at its core. To distinguish it from the core current itself, we will call the overall phenomenon a ''rip event.'' As examples of how rip events appear on the surface, Fig. 2 shows two events occurring just north of the pier at SIO. The plumes appear as clouds of sediment-laden water with a foamy boundary on the surface and, sometimes, slightly choppy waves contained by the boundary. Figure 3 shows the details of a sediment and bubble-laden rip event over the delta frame. Also characteristic of some rip events is a breaking of the incoming swell further offshore within the rip current itself due to its opposing motion. An example of

[a)]Currently at the Naval Research Laboratory, Stennis Space Center under an Intergovernmental Personnel Agreement.

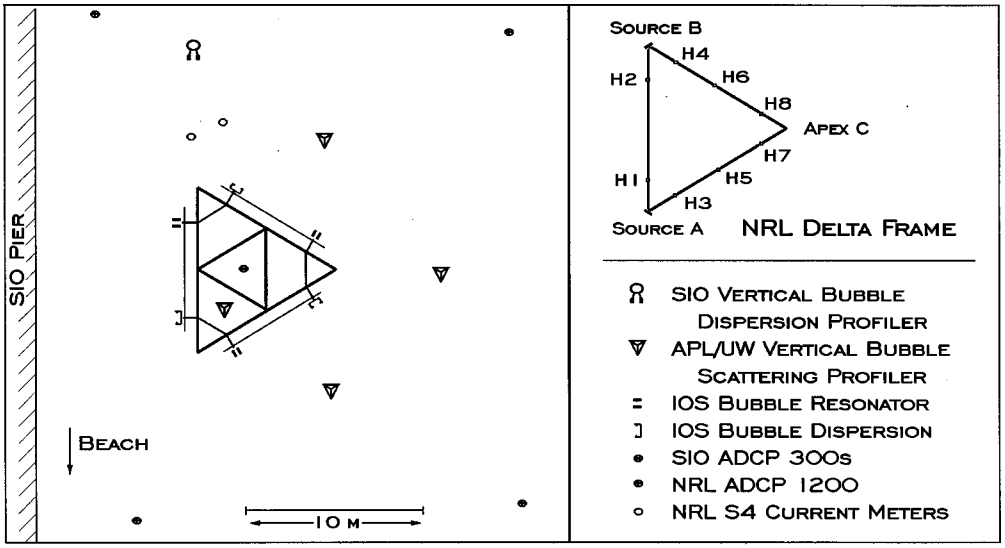

FIG. 1. The field of Coordinated Core Measurement systems used in the Scripps Pier Bubble Experiment in the Spring of 1997. [Symbols legend: H, hydrophone number (e.g., H1); ADCP, Acoustic Doppler Current Profiler; NRL, SIO, IOS, APL/UW, institutions named in text.]

the foamy remnants of such breaking can be seen in the right hand picture in Fig. 2.

An earlier sector-scan sonar study of rips at the SIO pier found clear evidence of rip currents and described their character, which includes strong acoustic backscatter.[5] The study suggests the backscatter is due to microbubbles rather than the sediment load they also carry. The bubble content of rip events is one of their least understood characteristics.

Bubble distributions produced by wind waves in deep water have been studied extensively[6–8] and are, to some extent, understood, except in terms of their smaller bubble radii. If the bubble distributions carried offshore by a rip current are remnants of what was generated in the active surf and if they took several minutes to reach offshore, then we expect that only the smaller bubble radii will remain entrained. It is the purpose of this paper to examine the bubble content of rip events to investigate the expectation that they are laden with bubbles of smaller radii.

I. THE DELTA-FRAME MEASUREMENT SYSTEM

Figure 4 is a picture of the delta frame while being deployed off the Scripps pier. The frame was placed just north of the pier about 10 m away. The acoustic paths were about 4 m deep and about 2 m off the bottom. The two sources (A and B) and the eight hydrophones (H1–H8) were placed about 1 m above the frame to reduce reflections from the frame. The sources had narrow vertical beam patterns to further reduce the effects of reflections from the frame and to eliminate reflections from the surface and bottom.

Eight frequencies (39, 59, 78, 98, 117, 146, 186, and 244 kHz) were emitted from the sources. Each frequency component had a 0.1-ms duration with a modified Hanning envelope. The frequency components and the sequence of their emissions were specially coded to ensure that the various components did not overlap at any hydrophone and that all transmissions would occur within a 12-ms period in order to fit into an active ping schedule which included emissions from other experiments. The received signals were sampled at 625 kHz in 12 bits. The cycle of eight transmissions from each of the two sources was made once a second for 1 h and 28 min. During periods of concentrated measurements, two runs per day were made: one at low tide and one at high tide. Ten runs over a course of ten days were made.

The various arrivals in each transmission were sorted out and their decibel magnitudes were determined using the following procedure. The received digitized signals were

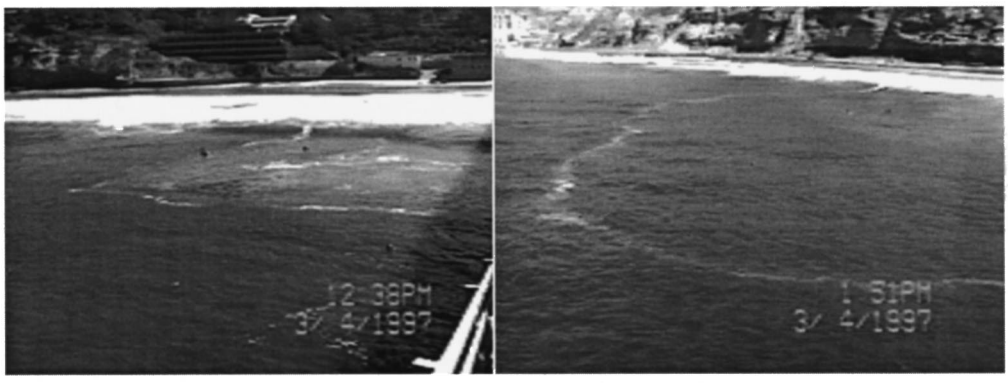

FIG. 2. Typical surface expression of two rip events observed off the Scripps Pier, March 1997.

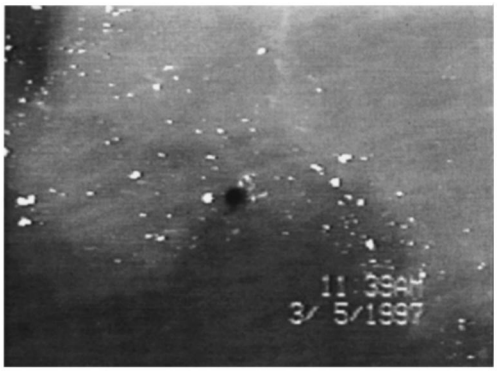

FIG. 3. Detailed view of rip events directly over the delta frame. Sediment-laden water and the foamy surface boundary are clearly depicted.

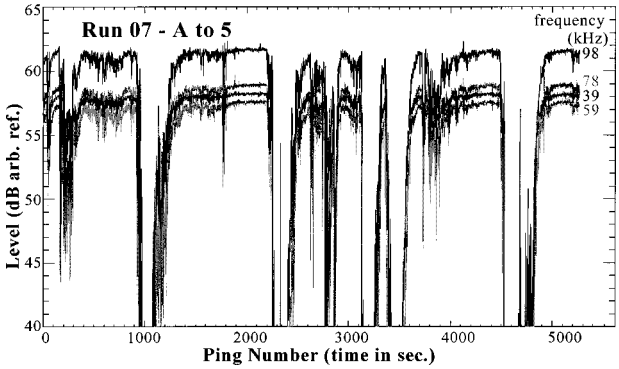

FIG. 5. Attenuation data for propagation from source A to hydrophone 5 (A5) for the four lowest frequencies during run 7.

squared, smoothed over 30 points and converted to decibels. The center two-thirds of the resulting envelope was averaged to give the final decibel value, which ranged in arbitrary units around 60 dB (but varied depending on the source/hydrophone pair). The time scale for deterministic changes in these magnitudes was observed to be of the order of 10 s, so we ensemble averaged 10 pings to give the final values for study. (Throughout the paper we refer to this average by the first ping number in the group.)

When rip events enveloped the delta frame, dramatic effects on sound attenuation occurred. Dispersion of sound speed also occurred, but it was more subtle for the short path lengths in the delta-frame configuration. In this study, we concentrate on attenuation. The conditions that prevailed for most of run 6 provided a very stable baseline of signals. For source A, the standard deviation of the signal level (averaged as described above) varied by less than 0.02 dB and for source B less than 0.05 dB during quiescent periods. Early in run 6, beginning around ping 200, there was an especially stable period of some of the strongest signals observed (although over the entire run they varied by only a few hundredths of a decibel). This highly stable period lasted several minutes. We concluded that this was probably the most bubble-free water observed during the experiment and used an average of 100 pings during this period to establish a baseline for all runs. It happened that this coincided with a period of the highest tide and some of the lowest swell during the experiment, suggesting the surf was breaking the least and the farthest from the delta frame. Over the course of the ten days of measurements, numerous periods occurred that matched the data of run 6 within 0.1 dB (equating to rms errors of less than 0.05 dB/m), and no period occurred in which losses were less than the data of run 6 by more than the expected error. This baseline, therefore, calibrates the ''no loss'' case, which we interpret as a ''no bubble'' case and all values of loss are referenced to it.

During run 6 and other high-tide runs (e.g., runs 4 and 8) no rips were observed to cross the frame and all losses were minor. These small variations in transmission properties are to be compared with the attenuation due to bubbles that was determined to be 5–30 dB when rip events prevailed at low tide (e.g., runs 5 and 7). (Some losses were deemed to be far greater than 30 dB, but we set our reliable measurement limit here to ensure adequate signal-to-noise.) The remainder of this work will discuss the spatial and temporal variations in attenuation during segments of run 7 as compared to the baseline.

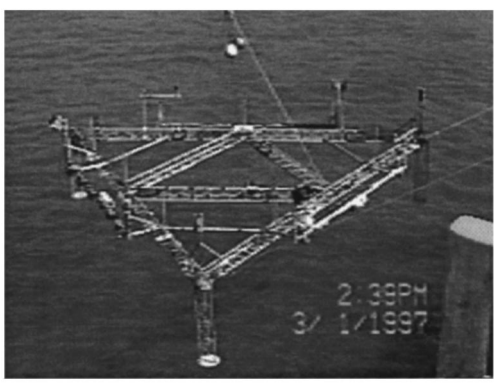

FIG. 4. Delta frame being deployed off the Scripps pier.

II. ATTENUATION MEASUREMENTS

Run 7 occurred in a period of especially low tide with surf breaking just shoreward of the delta frame. Figure 5 shows the received levels for the four lowest frequencies emitted by source A and received on hydrophone 5 (symbolically A5) as they evolved in time (seconds after the start of run or ping number). Before discussing the dramatic dropouts in the received levels seen in this figure, we should point out the approaches to quiescent periods (e.g., around pings 2100, 4400, and 5100). These losses approach 0 dB as compared to the baseline and represent periods in this very active run when quiescence was being approached after the passage of a rip event.

Now note the deep drops in the signal levels in run 7. Visual observations of the surface correlate these losses with the onset and evolution of rip events at the delta frame. The onset of the dropouts appear to be rapid (in less than 1 min) but the return to quiescence is more extended (greater than 3 min). This is consistent with an intuitive notion of the passage an abrupt front containing bubbly water followed by a slower rise in received level of bubbles as the bubbles purge from the medium.

Figure 6 provides a more complete snapshot of the data for run 7 than Fig. 5. The figure includes all the data from the

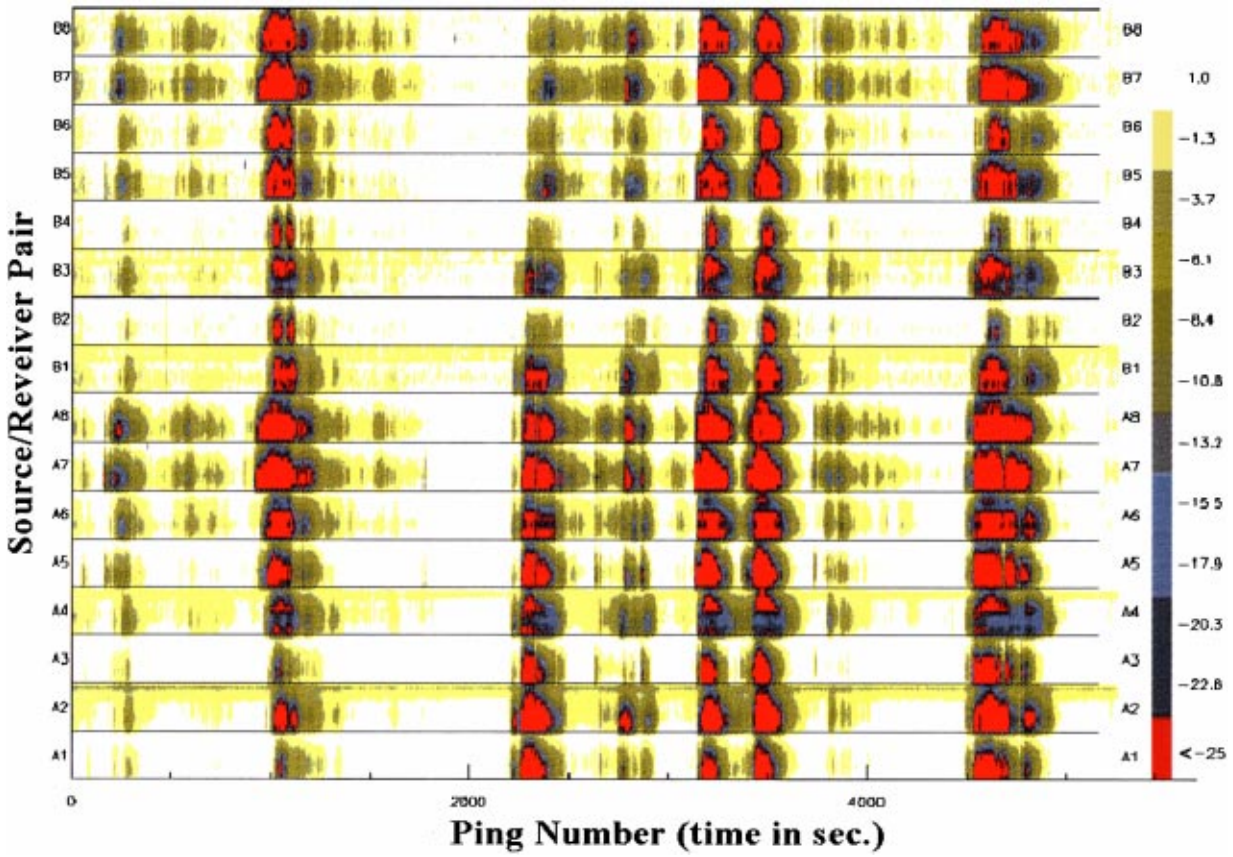

FIG. 6. Attenuation data in 16 image bars for each source (A,B) and hydrophone (1–8) pair and all frequencies during run 7. (Source/Hydrophone labels are shown on both sides of images.)

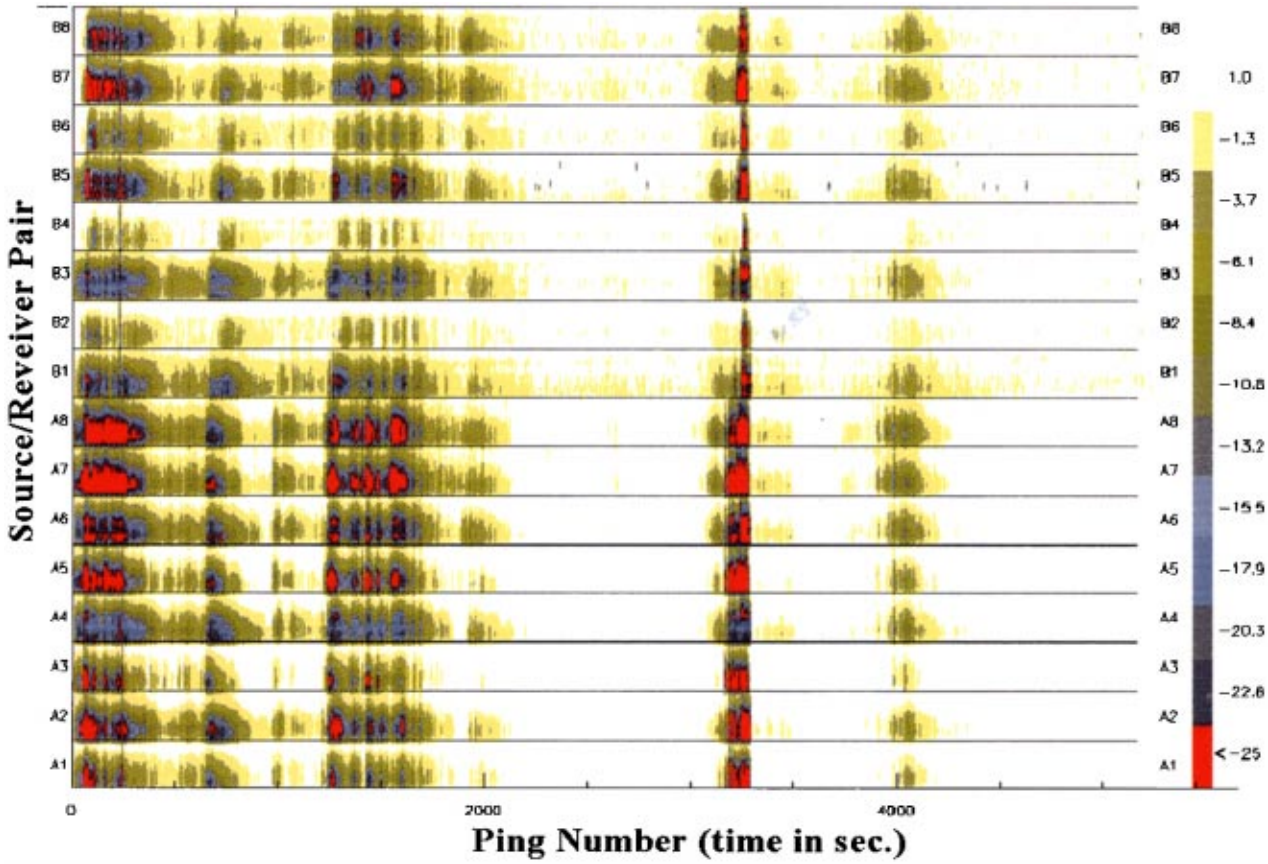

FIG. 7. Attenuation data in image form (similar to Fig. 6) for run 5.

run, but requires additional explanation. Like Fig. 5 the abscissa is time (or ping number). Vertically arrayed are 16 image plots, one horizontal bar for each of the source/receiver pairs (e.g., A5) as labeled on both sides of the bars. Within each bar, the ordinate is frequency from 39 kHz to 244 kHz. To improve the visualization of trends, the data were smoothed in time and frequency (over the adjacent points in both cases). The color chart of the losses (as referenced to the baseline value for each source/receiver pair) is given at the right. (To help orient the reader to the relationship between Figs. 5 and 6, we point out that the lower half of the A5 bar in Fig. 6 is an image display of the line graphs in Fig. 5.) Figure 7 is a similar representation of all the data in run 5. In addition to providing a qualitative picture of all the data for these runs, these images offer an opportunity to see delays in the movements of bubble clouds through the frame and frequency (bubble radius) differences within the clouds.

Before discussing specific aspects of selected pings in greater detail in the next two subsections, we first comment on observation errors as they relate to our measurement process, automated processing, and detailed analyses. Because of the volume of data processed and displayed in the last three figures, the procedures were automated and losses were limited to a fixed threshold of about -25 dB. Although some measured losses were valid to only -20 dB and others to as much as -40 dB, the quality of the measurements generally diminished with greater loss due to noise in the environment and cross-talk in the cables. Since such effects are dependent upon frequency and the performance and separation of specific source/receiver pairs, they are not easily quantified, and a single threshold for maximum meaningful loss cannot be set except with individual and detailed analyses. This is not a reasonable approach in the face of the large volume of data displayed in the previous figures. However, setting the specific thresholds for meaningful loss measurements can be done for detailed analyses of a limited number of specific pings. Therefore, in the next two subsections we analyze only a few ping sets from run 7 in greater detail.

The two points to be made in the following subsections are (a) the strong horizontally inhomogeneous effects of the rip events in terms of the attenuation due to the bubble fields they carry and (b) the bubble distributions that their frequency dependencies imply. Similar effects produced by the rip events are clear in data of the various sensors of other investigators in the Coordinated Core Measurements.[9] Also, video footage of the surface expressions of the rip events available for run 7 can be matched with the attenuation events to within 1 min.

A. Spatial inhomogeneities of bubble concentration

Spatial patterns of bubble distribution inhomogeneities and their magnitudes can be illustrated with simple graphical displays. Figure 8 is such a presentation of the numerical values of the losses across the frame from the two sources and for three frequencies and two pings (2823 and 2255). The pairs of triangles arrayed in the vertical are for the designated sources (A below, B above), and the triplets in the horizontal are for the designated frequencies (58, 117, and 244 kHz). These diagrams show clearly that the bubble effects are strong and that they tend to be inhomogeneous in space and bubble sizes (by virtue of their differences in frequency dependencies). These regions correlate well with the passage of rip events as they migrate over the frame. The scale of the inhomogeneities within the rips are of the order of a few meters in many cases. For all the cases presented here, the greatest effects occurred in the lower frequency ranges. For ping 2823, the strongest loss region appears to be between hydrophones 1 and 2 (along leg AB) and extending out to the right across the C apex. For ping 2255, there is a very strong bubble field right at the A apex. For this ping, it is clear that attenuation is weak only at the lowest and highest frequencies. The spatial distributions suggested by the above analysis has also been analyzed tomographically.[10]

Two aspects of the diagrams for ping 2255 require further comment. First, since there is such a strong loss around the A apex, the loss out to the more distant phones exceeds the measurement limits as discussed above. And, as discussed above, we arrive at these limits by individual detailed analysis of the received signals in relation to the noise. Therefore, in those cases where the loss limit has been exceeded, we show the maximum measurable loss. (Note that we cannot measure as great attenuation losses for the hydrophones further from the source apexes than for the nearer ones because of the additional losses due to spreading.)

The second point to be made here is that, in some cases, there appears to be less attenuation out to greater range than in close. We believe that measurement errors cannot explain this. Currently our working hypothesis is that, given such a strong attenuation region around the A apex, and essentially no attenuation beyond (note the propagation from source B in the diagrams), there is a potential for the attendant strong sound-speed gradients to promote focusing. The present data are not sufficient to test this hypothesis.

Figure 9 is a spatial display of attenuation for pings 0979 and 3445. These two pings represent stronger events than those in pings 2255 and 2823, as evidenced by the greater losses and the greater number of threshold excedences. Similarly to ping 2255, the bubbles appear to be very strong and close to the A apex for ping 3445. For ping 0979, a region of high bubble content occurs over the right half of the delta frame near the C apex.

B. Frequency dependence of attenuation

Attenuation as a function of frequency can readily be obtained when given a bubble density distribution, but the inverse operation entails the solution of an ill-conditioned integral equation. An algebraic relationship, called the ''resonant bubble approximation,'' exists that approximates the solution of the integral equation in the zeroth order to provide a bubble distribution that corresponds to measured attenuation data. However, measurable error occurs in attenuation values recovered from a bubble distribution approximated in this manner. An iterative procedure has been developed that allows for a first-order improved estimate of the bubble distribution and a closer match between the re-

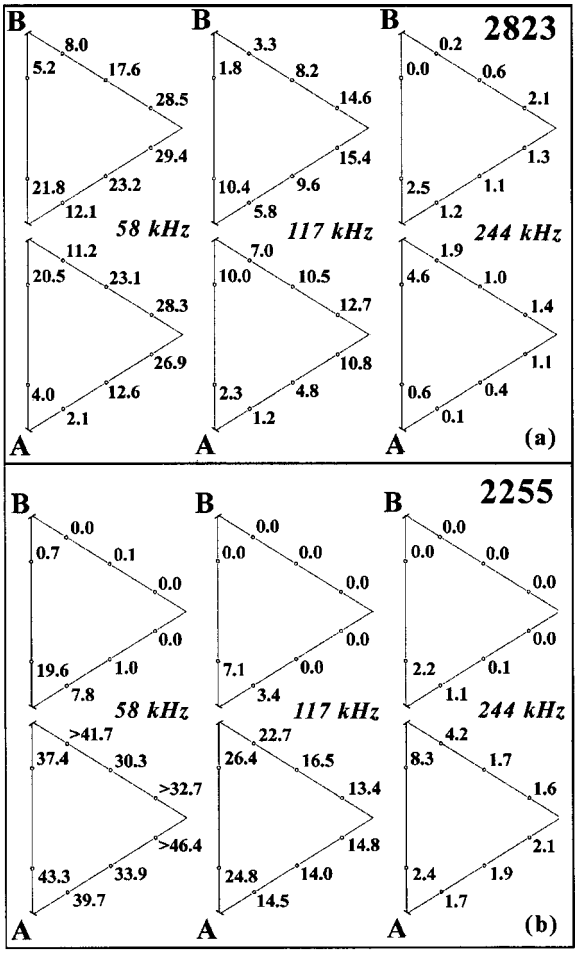

FIG. 8. Spatial display of losses for run 7, (a) ping 2823, (b) ping 2255. (In each figure set the following scheme is used: The bottom row of triangles represent losses from source A to hydrophone locations in dB and the top row from source B. The horizontal triad of the A/B pairs represent losses for the given frequencies, 58, 117, and 244 kHz.)

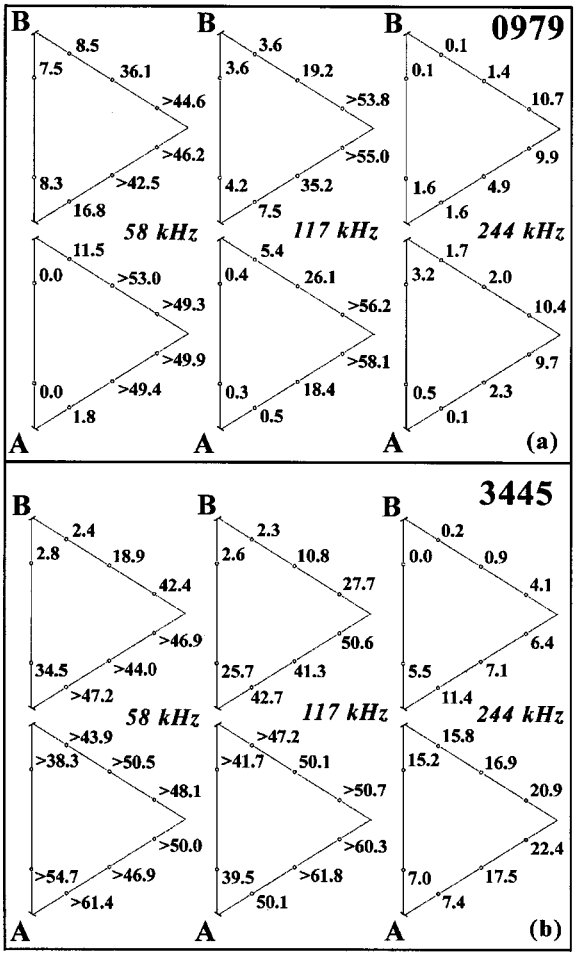

FIG. 9. Spatial display of losses for run 7, (a) ping 0979, (b) ping 3445. (Form similar to Fig. 8.)

covered attenuation using this improved distribution and the original attenuation data.[11] That procedure is used here to evaluate the improved bubble distributions.

Because each set of pings produces a large volume of attenuation data, we limit our discussion of the frequency dependence of attenuation and bubble distributions to a single ping set, run 7, ping 2823. A review of many pings in which there are rip effects reveals a great deal of similarity in the resulting attenuation curves and in the bubble distributions they imply. We will discuss pings from the two sources (A and B) to selected hydrophones, but for all eight frequencies in each case. Figures 10 to 15 show examples for source/hydrophone pairs A1, A3, B2, B4, A8, and B7, respectively. (See Fig. 1 for source/hydrophone labels.) The (a) diagram in each is for the attenuation curve and the (b) diagram is for the corresponding bubble distribution. Referring to Fig. 8 (ping 2823) reveals the spatial distributions of losses and the paths of propagation.

For each of the figures (Figs. 10–15), the iterative procedure was used to compute the bubble distribution from the attenuation data. To account for the off-resonance effects that enter through the integral equation in the iterative procedure, extrapolation and interpolation of the attenuation data were required.[11] The data were extrapolated beyond the limits of the actual data (39–244 kHz) down to 30 kHz on the lower end and up to 276 kHz on the upper end. The validity of the extrapolated ''data'' was checked by the degree to which the results could recover the measured attenuation at the actual limits. A simple linear interpolation was made in Log(attenuation) versus frequency. This scheme tended to reduce scalloping in the bubble distribution between data values over that which occurred if interpolation were done linearly in attenuation (although some residual scalloping can be seen in the figures). The improvements obtained by the iterative approach can be seen in the closer match of the attenuation computed from the standard integral equation applied to the first-order improvement in the bubble population, versus that computed from the integral equation applied to the bubble population calculated from the standard resonant bubble approximation.

III. DISCUSSION OF RESULTS

Although different in magnitude, attenuation appears to be fairly consistent in shape between each of the source/hydrophone pairs. The small differences in shapes can be attributed to small spatial inhomogeneities in the bubble field for ping 2823. Generally, the observed attenuation had a broad maximum from 50 to 90 kHz. For all pings studied so

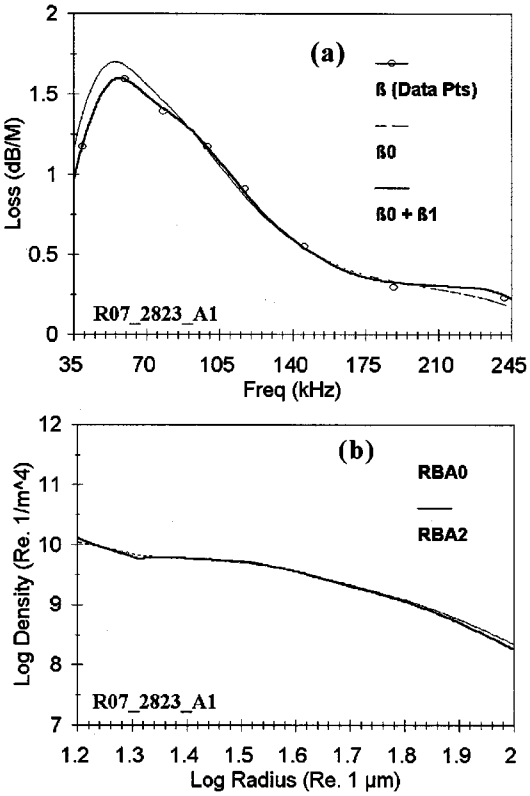

FIG. 10. Run 7, ping 2823, source/hydrophone pair A1: (a) Attenuation and (b) Bubble population. (In addition to the attenuation data points (β), the results of successive iterations between attenuation and bubble population[11] are shown. The solid curves in each represent the final answers.)

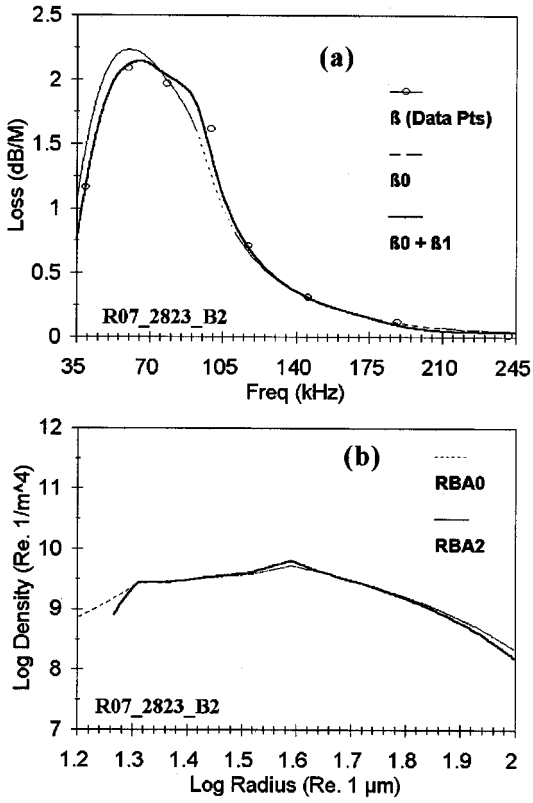

FIG. 12. Run 7, ping 2823, source/hydrophone pair B2: (a) Attenuation and (b) Bubble population. (Same as Fig. 10.)

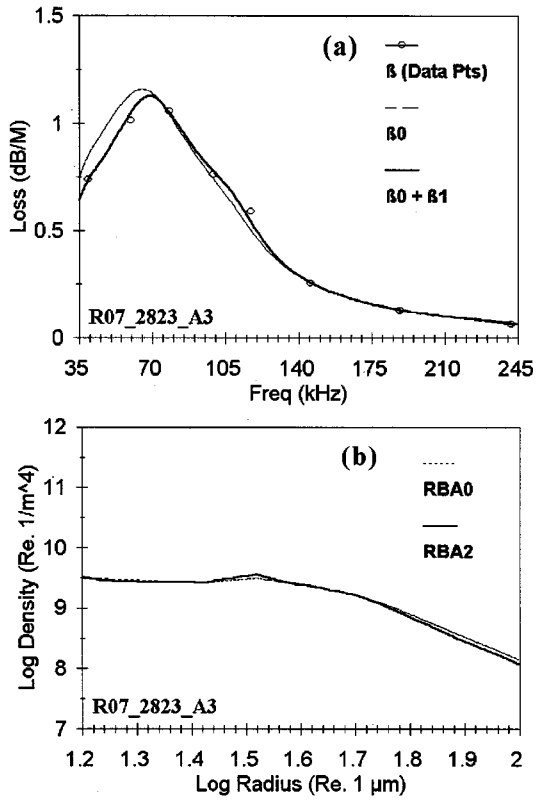

FIG. 11. Run 7, ping 2823, source/hydrophone pair A3: (a) Attenuation and (b) Bubble population. (Same as Fig. 10.)

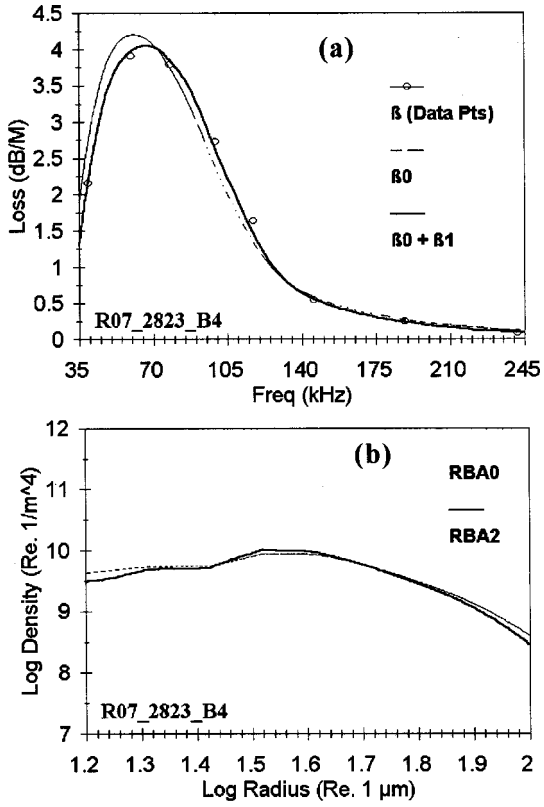

FIG. 13. Run 7, ping 2823, source/hydrophone pair B4: (a) Attenuation and (b) Bubble population. (Same as Fig. 10.)

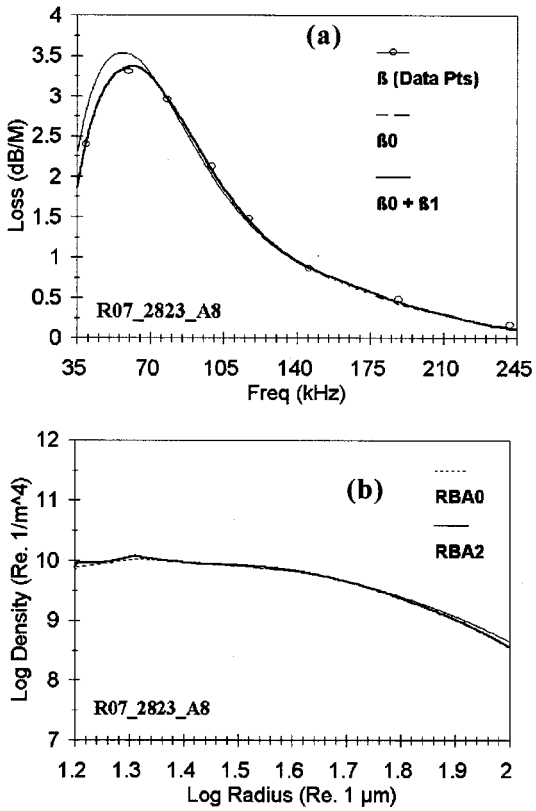

FIG. 14. Run 7, ping 2823, source/hydrophone pair A8: (a) Attenuation and (b) Bubble population. (Same as Fig. 10.)

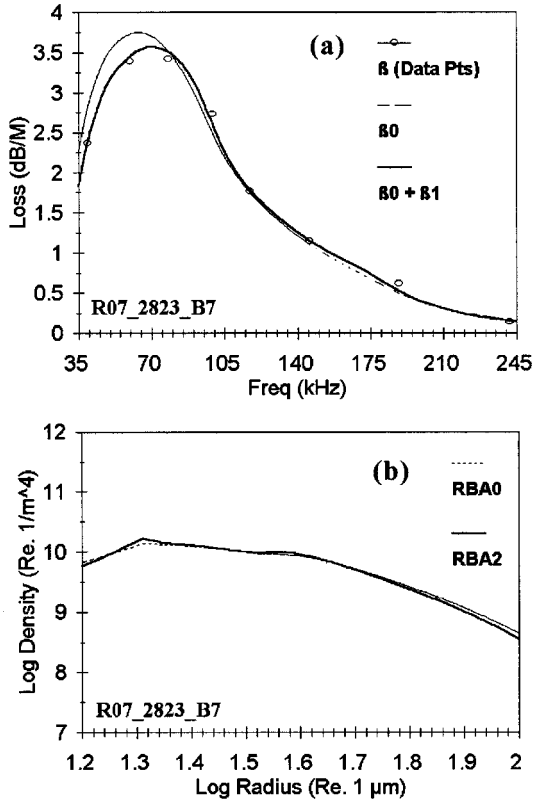

FIG. 15. Run 7, ping 2823, source/hydrophone pair B7: (a) Attenuation and (b) Bubble population. (Same as Fig. 10.)

far, this broad maximum occurs, indicating the presence of a preponderance of bubbles in the radius range from 80 to 40 μm. Generally, there was a power-law-type falloff for bubbles with radii between 80 μm and 100 μm, with an exponent near -4. The low attenuation below 39 kHz, and extrapolated to 30 kHz, suggests that bubbles with radii above 130 μm were negligible. The occasional small, but finite attenuation at frequencies as high as 240 kHz [e.g., Fig. 10(a)] implies the presence of bubbles with radii as small as 16 μm. The waters around the B source appear to have fewer bubbles of smaller radii. The details of these resulting bubble distributions can be seen in Figs. 10(b)–15(b).

The high concentrations of bubbles in the 40–80 μm range requires additional discussion. The Panama City Experiment suggested the presence of a preponderance of bubbles with radii smaller than 20 μm in surf conditions similar to the Scripps Pier Experiment. It appears that, in each case, bubbles were generated in the surf and carried off shore by rip currents. For the Scripps Pier Experiment it took about 10 min for the rip event to reach the delta frame. (We did not have as clear an indication of prominent rip events in the Panama City data, nor did we observe surface indications of such events as we saw at Scripps Pier.) We would expect only the finest bubbles to have remained entrained, because experience with bubbles in deep water suggests that the larger bubbles purge very quickly. There are, however, several hydrodynamic phenomena that could account for ''younger'' water at the head of the rip event than the evolution time of the event itself would account for. First, the core current is carrying the bubble laden water offshore faster than the movement of the foam line at the head of the event. Second, because of the opposing direction of the current to the incoming swell, breaking occurs further offshore than otherwise. Finally, the added and younger turbulence of the closer breaking could keep the larger bubbles down deeper.

IV. SUMMARY AND CONCLUSIONS

It is clear that bubbles carried seaward by rip events near breaking surf on a beach produce dramatic effects on the acoustics of shallow water. During the Scripps Pier Experiment, there were extended periods in which no bubble effects were discernable (e.g., all of run 6), while, at other times, rip events occurred frequently within the run (e.g., runs 5 and 7). Runs 6 and 7 represent the extremes in the data collected. The primary distinctions between them were the strength of the breaking surf and its proximity to the delta frame. Run 6 occurred during the high end of the Spring Tide of 8 March 1997, coincident with the New Moon, and run 7 occurred at the low end.

The bubble effects over the delta frame were clearly inhomogeneous and had scales that, to some degree, were contained within the frame ($\sim$10 m) and resolvable by the frame ($\sim$2 m). Generally, the effects appeared to begin at the point nearest the beach (A apex) and progress across the frame to the B apex. Generally, short paths ($\sim$2 m) from a single source to receivers separated in horizontal angle by 60 degrees showed very similar results, and were sometimes different from the opposite source and receiver pair.

The acoustic effects of the bubble-laden waters of the rip events appeared abruptly for sets of source/hydrophone pairs and tended to move across the delta frame in an orderly manner. Following some rip events, there were slow evolutions back to quiescent periods which approached the baseline conditions. For this analysis, we looked only at isolated strong events and paid little attention to their evolution. Later analyses will address the movement of the events across the frame and their decay toward background. This may reveal more details on the purging of bubbles or the homogeneous mixing of the aging turbulence.

ACKNOWLEDGMENTS

The authors of this report wish to thank the Office of Naval Research and its program managers, Dr. Jeffery Simmen and Edward Chaika, for supporting this project and the technical and fiscal help provided by the NRL High-Frequency Program managed by Dr. Dan Ramsdale. We also express our appreciation for the dedicated work of Roger Meredith, Ted Kennedy, and Robert Fisher of NRL and Richard Smith and Robert Brown of Neptune Sciences who helped make this work a success. We also thank Dr. Jorge Novarini for theoretical discussions. Dr. P. A. Elmore is funded by ONR and NRL through a postdoctoral fellowship from the American Society of Engineering Education.

[1] R. R. Goodman, S. J. Stanic, and J. W. Caruthers, ''Observations of high-frequency sound propagation in shallow water with bubbles induced by storm and surf,'' IEEE J. Oceanic Eng. (submitted).
[2] J. W. Caruthers, P. A. Elmore, S. J. Stanic, and R. R. Goodman, ''The Scripps Pier Bubble Experiments of 1997,'' Proceedings of the 16th Int. Congress on Acoustics and the 135th Mtg. of the Acoust. Soc. of Am., pp. 697–698 (1998).
[3] D. L. Inman and B. M. Bush, ''The coastal challenge,'' Science **181**, 20–32 (1973).
[4] C. D. Miller and A. Barcilon, ''The dynamics of the Littoral zone,'' Rev. Geophys. **14**, 81–91 (1976).
[5] J. A. Smith and J. L. Largier, ''Observations of nearshore circulation: Rip currents,'' J. Geophys. Res. **100**, 10967–10975 (1995).
[6] G. B. Crawford and D. M. Farmer, ''On the spatial distribution of ocean bubbles,'' J. Geophys. Res. **92**, 8231–8243 (1987).
[7] H. Medwin and N. D. Breitz, ''Ambient and transient bubble spectral densities in quiescent seas and under spilling breakers,'' J. Geophys. Res. **94**, 12751–12759 (1989).
[8] S. Vagle and D. M. Farmer, ''The measurement of bubble-size distributions by acoustical backscatter,'' J. Atmos. and Oceanic Tech. **9**, 630–644 (1992).
[9] Discussions with Dr. Peter Dahl, Dr. David Farmer, Dr. Kenneth Melville, and Dr. Eric Terrill.
[10] D. Rouseff, F. S. Henyey, P. A. Elmore, and J. W. Caruthers, ''Tomographic Reconstruction of Evolving Bubble Fields in the Scripps Pier Bubble Experiment,'' Proceedings of the 16th Intern'l Congress on Acoustics and the 135th Mtg. of the Acoust. Society of Am., Seattle, WA, pp. 707–708, 20–26 June 1998.
[11] J. W. Caruthers, P. A. Elmore, J. C. Novarini, and R. R. Goodman, ''An iterative approach for approximating bubble distributions from attenuation measurements,'' J. Acoust. Soc. Am. **106**, 185 (1999).

Waves in rotating conducting piezoelectric media

J. Wauer
Institut für Technische Mechanik, Universität Karlsruhe, D-76128 Karlsruhe, Germany

(Received 1 June 1998; accepted for publication 16 April 1999)

The propagation of waves in a conducting piezoelectric solid is studied for the case when the entire medium rotates with a uniform angular velocity. For comparison, both the conventional electrically quasistatic theory and the fully dynamic Maxwell equations are taken into consideration. In completion, a generalized thermoelastic theory of piezoelectric bodies is incorporated. The governing dispersion relations are obtained to determine the effects of moderate rotation, thermal, and constant electrical conductivity on the finite phase velocity of the waves. Analysis is carried out for plane waves in an infinite medium but also for surface waves of a half-space. Finally, the radial vibrations of a hollow cylinder are addressed. The evaluations are specified for hexagonal crystals of (6 mm) class and a simple arrangement of the direction of wave propagation and the crystal and rotational axes. © *1999 Acoustical Society of America.* [S0001-4966(99)01708-7]

PACS numbers: 43.30.At [PJR]

INTRODUCTION

In recent years, considerable attention has been given to the study of wave propagation and free vibrations in piezoelectric crystals. The approach usually adopted in treating piezoelectric solids is simplification of Maxwell's equations by neglecting magnetic effects, conduction, displacement currents, and free charges. This classical, electrically quasistatic theory of piezoelectric bodies, which is sufficient for nearly all engineering applications, is clearly fomulated in a book by Tiersten[1] based on earlier contributions by Toupin[2] or Berlincourt *et al.*[3] Surface waves in piezoelectrics were studied by Coquin and Tiersten[4] and Ingebrigtsen[5] and wave propagation in planar layers of finite thickness by Paul *et al.*[6] In the same context, Mindlin[7] developed the conventional theory of thermo-piezoelectricity which leads to the drawback of an infinite heat propagation speed. Concrete two-dimensional dynamic problems of this category of thermo-piezoelectricity were treated by Paul and Renganathan[8] and Yang and Batra.[9] As a contribution examining the wave propagation in laminated piezoelectric media, the study by Pauley and Dong[10] will be mentioned.

The present work will deal with piezoelectric solids in a broader sense. Not only the classical electrostatic theory but also the complete electrodynamic equations as considered in great detail by Kyame first[11] for a lossless medium and later[12] including a constant electric conductivity will be included in the discussion. An extension to piezoelectric semiconductors considered by Hutson and White[13] will not be followed up here. Surface waves in piezoelectrics based on this general theory were discussed for example, by Tseng and White.[14] Taking thermal effects into consideration, a generalized theory originating from Lord and Shulman[15] and applied to piezoelectric bodies by Chandrasekharaiah[16] will be used.

In all the related papers, structural members at rest were considered. The main objective of the present contribution is to focus attention on rotating media (similar as that by Chaudhuri and Debnath[17] for magneto-thermo-elastic wave propagation). For convenience, a moderate angular speed and no additional bias fields are assumed, so that a linear theory is adequate from the beginning. The propagation of plane waves in a rotating piezoelectric material is analyzed in detail. The work is applied to the concrete examples of infinite crystals of special symmetry and a corresponding half-space in which surface waves are of particular interest. The problem of the radial oscillations of a hollow thin-walled cylinder is also addressed. Several limiting cases of interest are discussed.

I. FORMULATION

Let x_1, x_2, and x_3 be orthogonal body-fixed axes arbitrarily oriented with respect to the crystal axes of the piezoelectric solid. The usual definition of the infinitesimal Green strain tensor ϵ_{ij} in terms of the displacements u_i is

$$2\epsilon_{ij}=\frac{\partial u_i}{\partial x_j}+\frac{\partial u_j}{\partial x_i}. \tag{1}$$

Any solution for wave propagation in the piezoelectric medium must simultaneously satisfy Maxwell's field equations

$$\nabla\times\mathbf{H}=\frac{\partial\mathbf{D}}{\partial t}+\mathbf{J}, \tag{2}$$

$$\nabla\times\mathbf{E}=\mathbf{0}\Rightarrow\mathbf{E}=-\nabla\phi \tag{3a}$$

or

$$\mathbf{E}=-\frac{\partial\mathbf{B}}{\partial t}-\nabla\times[\mathbf{B}\times(\boldsymbol{\Omega}\times\mathbf{r})], \tag{3b}$$

$$\nabla\cdot\mathbf{B}=0, \tag{4a}$$

$$\nabla\cdot\mathbf{D}=0, \tag{4b}$$

the law of conservation of energy

$$\rho T_0\frac{\partial s}{\partial t}+\nabla\cdot\mathbf{q}=0, \tag{5}$$

and Newton's law of force

$$\rho\left[\frac{\partial^2\mathbf{u}}{\partial t^2}+\boldsymbol{\Omega}\times(\boldsymbol{\Omega}\times\mathbf{u})+2\boldsymbol{\Omega}\times\frac{\partial\mathbf{u}}{\partial t}\right]=\boldsymbol{\nabla}\cdot\mathbf{T} \tag{6}$$

in the rotating reference frame (rotative speed $\boldsymbol{\Omega}$), so that two additional terms due to centripetal acceleration and Coriolis acceleration appear. In these equations, ρ is the mass density, $\mathbf{T}$ is the Cauchy stress tensor, s is the entropy, $\mathbf{E}$ and $\mathbf{H}$ are the electric and magnetic field intensity, respectively, $\mathbf{B}$ is the magnetic flux intensity, $\mathbf{J}$ is the electrical current density, and $\mathbf{D}$ is the electrical displacement. Further, $\mathbf{q}$ and $\mathbf{r}$ are, respectively, the heat flux vector in the material and the position vector to a general material particle, and T_0 is the initial uniform temperature of the body. Obviously, the electrically quasistatic approximation and fully dynamic description in Maxwell's equations is expressed by the different formulations of Faraday's law Eq. (3). A significant consequence is that within the quasistatic theory, the magnetic effects expressed by the magnetic densities $\mathbf{H}$ and $\mathbf{B}$ are separated so that Eqs. (2) and (4a) need not to be considered. Within the general theory, the modification of the dynamic relation Eq. (3b) due to the rigid body velocity $\Omega\times\mathbf{r}$ as mentioned for such cases by Pao[18] or Schmidt[19] is remarkable.

The constitutive equations can be written (with repeated indices as summation indices) as

$$T_{ij}=c_{ijkl}\epsilon_{kl}-\beta_{ij}\theta-e_{kij}E_k, \tag{7a}$$

$$\rho s=c\,\theta+\beta_{ij}\epsilon_{ij}+p_iE_i, \tag{7b}$$

$$\left(1+\tau\frac{\partial}{\partial t}\right)q_i=-k_{ij}\frac{\partial\theta}{\partial x_j}, \tag{7c}$$

$$D_i=p_i\theta+e_{ijk}\epsilon_{jk}+\alpha_{ij}E_j, \tag{7d}$$

and

$$B_i=\mu_0H_i, \tag{8}$$

$$J_k=\sigma_{ik}E_k \tag{9a}$$

or

$$J_k=\sigma_{ik}\{E_k+[(\boldsymbol{\Omega}\times\mathbf{r})\times\mathbf{B}]_k\}. \tag{9b}$$

Here c_{ijkl} is the isothermal elastic tensor for constant electric field, e_{ijk} is the piezoelectric tensor, α_{ij} is the electric permittivity tensor, p_i are the pyroelectric moduli, β_{ij} are the thermal stress moduli, and k_{ij} is the thermal conductivity tensor, all referred to the axes x_i. τ is the thermal relaxation time and cT_0 represents the specific heat at constant strain. μ_0 denotes the permeability and σ_{ij} is the electric conductivity tensor. It should be noticed that within the quasistatic theory, the constitutive equation (8) is unimportant and Ohm's law Eq. (9) has no consequence; only if a semiconducting material is considered (see Wauer and Suherman[20]), it will become significant. Within the fully dynamic formulation, Ohm's law Eq. (9) has to be modified again due to the rigid body velocity $\Omega\times\mathbf{r}$ (see Chaudhuri and Debnath[17] or Schmidt[19]).

Eliminating s and q_i from Eqs. (7b), (7c), and (5), one obtains a generalized heat conduction wave equation

$$-k_{ij}\frac{\partial^2\theta}{\partial x_i\partial x_j}+T_0\left(1+\tau\frac{\partial}{\partial t}\right)\left(c\frac{\partial\theta}{\partial t}+\beta_{ij}\frac{\partial^2u_i}{\partial x_j\partial t}-p_i\frac{\partial^2\phi}{\partial x_i\partial t}\right)=0, \tag{10}$$

where within the electrically dynamic theory $-(\partial\phi/\partial x_i)$ has to be replaced by E_i. Analogously, eliminating T_{ij} from Eqs. (7a) and (6) and using Eq. (1), one obtains a set of mechanical wave equations

$$\rho\left[\frac{\partial^2\mathbf{u}}{\partial t^2}+\boldsymbol{\Omega}\times(\boldsymbol{\Omega}\times\mathbf{u})+2\boldsymbol{\Omega}\times\frac{\partial\mathbf{u}}{\partial t}\right]_j-c_{ijkl}\frac{\partial^2u_k}{\partial x_l\,\partial x_i}+\beta_{ij}\frac{\partial\theta}{\partial x_i}-e_{kij}\frac{\partial^2\phi}{\partial x_k\,\partial x_i}=0. \tag{11}$$

Again, substituting E_k for $-(\partial\phi/\partial x_k)$ leads to the fully dynamic formulation. To obtain the completing set of electrical wave equations, the procedure depends on which theory is applied. Within the classical piezoelectric theory, substitute Eq. (7d) using Eq. (3) into Eq. (4b) and obtain

$$-\alpha_{ij}\frac{\partial^2\phi}{\partial x_i\,\partial x_j}+e_{kij}\frac{\partial^2u_i}{\partial x_j\,\partial x_k}+p_i\frac{\partial\theta}{\partial x_i}=0. \tag{12}$$

Within the general theory, the Ampére–Maxwell equation (2) and Faraday's law Eq. (3) using the constitutive Eqs. (7d)–(9) form the system of six wave equations:

$$-(\boldsymbol{\nabla}\times\mathbf{H})_i+p_i\frac{\partial\theta}{\partial t}+e_{ijk}\frac{\partial^2u_j}{\partial x_k\,\partial t}+\alpha_{ij}\frac{\partial E_j}{\partial t}+\sigma_{ij}\{E_j+\mu_0[(\boldsymbol{\Omega}\times\mathbf{r})\times\mathbf{H}]_j\}=0, \tag{13}$$

$$\boldsymbol{\nabla}\times\mathbf{E}+\mu_0\left\{\frac{\partial\mathbf{H}}{\partial t}+\nabla\times[\mathbf{H}\times(\boldsymbol{\Omega}\times\mathbf{r})]\right\}=0. \tag{14}$$

If the influence of the rigid body motion is neglected, i.e., $\Omega\times\mathbf{r}\approx\mathbf{0}$, take the curl of the remaining Eq. (3), replace $\mathbf{B}$ by $\mathbf{H}$ using Eq. (8), and combine Eq. (2) with Eqs. (7d), (9), and (1) to result in a shortened set of three equations:

$$\frac{\partial^2E_j}{\partial x_i\,\partial x_j}-\frac{\partial^2E_i}{\partial x_j\,\partial x_j}+\mu_0\left(\alpha_{ij}\frac{\partial^2E_j}{\partial t^2}+e_{ijk}\frac{\partial^3u_j}{\partial x_k\,\partial t^2}+p_i\frac{\partial^2\theta}{\partial t^2}+\sigma_{ij}\frac{\partial E_j}{\partial t}\right)=0. \tag{15}$$

The complete system of five, ten, or seven wave equations must be solved in general, under appropriate boundary and initial conditions.

Neglecting within general theory the rotation and both the thermal influences and the electrical conductivity, the equations simplify to a case formulated by Eringen and Maugin[21] based on Kyame's[11] work. Neglecting only the rotational speed and applying the convential electrically quasistatic approximation, one ends in a set of equations formulated within the classical thermo-piezoelectricity by Yang and Batra.[9]

II. PLANE WAVE PROPAGATION IN AN INFINITE MEDIUM

Consider thermo-electric-elastic wave propagation in the x_1 direction. Derivatives with respect to x_2 and x_3 are then zero.

Under such plane wave conditions, B_1 and H_1 are constant in space and time and $(\nabla\times\mathbf{H})_1=0$, which yields the conservation of the current density J_1 upon differentiating with respect to x_1. The constitutive equations (7) simplify to

$$T_{1j}=c_{1j1k}S_{1k}-\beta_{1j}\theta-e_{k1j}E_k, \tag{16a}$$

$$\rho s=c\,\theta+\beta_{1j}S_{1j}+p_iE_i, \tag{16b}$$

$$\left(1+\tau\frac{\partial}{\partial t}\right)q_i=-k_{i1}\frac{\partial\theta}{\partial x_1}, \tag{16c}$$

$$D_i=p_i\theta+e_{i1k}S_{1k}+\alpha_{ij}E_j. \tag{16d}$$

Instead of the strain tensor ϵ_{ij} Eq. (1), for the present plane wave conditions a modified strain

$$S_{1j}=\frac{\partial u_j}{\partial x_1}, \tag{17}$$

is preferred in Eq. (16).

Heat conduction equation (10) reduces to

$$-k_{11}\frac{\partial^2\theta}{\partial x_1^2}+T_0\left(1+\tau\frac{\partial}{\partial t}\right)\left(c\frac{\partial\theta}{\partial t}+\beta_{j1}\frac{\partial^2u_j}{\partial x_1\partial t}-p_1\frac{\partial^2\phi}{\partial x_1\partial t}\right)=0, \tag{18}$$

and the set of wave equations (11) is

$$\rho\left[\frac{\partial^2\mathbf{u}}{\partial t^2}+\boldsymbol{\Omega}\times(\boldsymbol{\Omega}\times\mathbf{u})+2\boldsymbol{\Omega}\times\frac{\partial\mathbf{u}}{\partial t}\right]_j-c_{1j1k}\frac{\partial^2u_k}{\partial x_1^2}+\beta_{1j}\frac{\partial\theta}{\partial x_1}-e_{11j}\frac{\partial^2\phi}{\partial x_1^2}=0. \tag{19}$$

For further consideration of this chapter, the conventional thermo-piezoelectric theory and the fully dynamic formulation neglecting the rigid body velocity (as Chaudhuri and Debnath[17] did for a thermo-magnetoelastic medium) will be discussed. It will be noticed that assuming this simplified dynamic theory is critical: for an infinite solid, there exist particles with $\mathbf{r}\to\infty$, i.e., the far-field wave propagation cannot be described correctly. The solutions obtained by neglecting the rigid body velocity are only useful in the neighborhood of the rotational axis.

Within the conventional theory which does not possesses this drawback, the governing equation (12) reduces to

$$-\alpha_{11}\frac{\partial^2\phi}{\partial x_1^2}+e_{1i1}\frac{\partial^2u_i}{\partial x_1^2}+p_1\frac{\partial\theta}{\partial x_1}=0 \tag{20}$$

and completes Eqs. (18) and (19). By assuming plane wave solutions of the form

$$\theta(x_1,t)=\theta^0e^{j(kx_1-\omega t)},\quad u_i(x_1,t)=u_i^0e^{j(kx_1-\omega t)},\quad \phi=\phi^0e^{j(kx_1-\omega t)}, \tag{21}$$

one obtains, after dropping the common factor $e^{j(kx_1-\omega t)}$,

$$k^2k_{11}\theta^0-T_0(1-j\omega\tau)(j\omega c\,\theta^0-k\omega\beta_{i1}u_i^0+k\omega p_1\phi^0)=0,$$

$$\rho[-\omega^2\mathbf{u}^0+\boldsymbol{\Omega}\times(\boldsymbol{\Omega}\times\mathbf{u}^0)-2j\omega\boldsymbol{\Omega}\times\mathbf{u}^0]_i+k^2c_{1i1l}u_l^0+jk\beta_{1i}\theta^0+k^2e_{11i}\phi^0=0, \tag{22}$$

$$k^2\alpha_{11}\phi^0-k^2e_{1i1}u_i^0+jkp_1\theta^0=0.$$

A nontrivial solution of these five linear homogeneous equations for θ^0, u_i^0, and ϕ^0 exists only if the determinant of the coefficients vanishes. Invoking from now on the additional assumption that the rotational axis is perpendicular to the x_1 direction of wave propagation and even more specific, $\Omega_1=\Omega_3=0$ and $\Omega_2=\Omega\neq0$, yields the governing dispersion relation

$$\det\mathbf{G}=0, \tag{23}$$

where the elements g_{ij} $(i,j=1,...,5)$ of the matrix $\mathbf{G}$ are

$$\begin{aligned}
&g_{11}=k_{11}-\frac{j\omega T_0c}{k^2}(1-j\omega\tau);\\
&g_{1i}=\frac{T_0\omega\beta_{(i-1)1}}{k}(1-j\omega\tau),\quad i=2,3,4;\\
&g_{15}=-\frac{\omega T_0p_1}{k}(1-j\omega\tau);\quad g_{21}=\frac{j\beta_{11}}{k\rho};\\
&g_{22}=\frac{c_{1111}}{\rho}-\frac{\omega^2+\Omega^2}{k^2};\quad g_{23}=\frac{c_{1112}}{\rho};\\
&g_{24}=\frac{c_{1113}}{\rho}-2j\frac{\omega\Omega}{k^2};\quad g_{25}=\frac{e_{111}}{\rho};\\
&g_{31}=\frac{j\beta_{12}}{k\rho};\quad g_{32}=\frac{c_{1211}}{\rho};\quad g_{33}=\frac{c_{1212}}{\rho}-\frac{\omega^2}{k^2};\\
&g_{34}=\frac{c_{1213}}{\rho};\quad g_{35}=\frac{e_{112}}{\rho};\\
&g_{41}=\frac{j\beta_{13}}{k\rho};\quad g_{42}=\frac{c_{1311}}{\rho}+2j\frac{\omega\Omega}{k^2};\quad g_{43}=\frac{c_{1312}}{\rho};\\
&g_{44}=\frac{c_{1313}}{\rho}-\frac{\omega^2+\Omega^2}{k^2};\quad g_{45}=\frac{e_{113}}{\rho};\\
&g_{51}=\frac{jp_1}{k};\quad g_{5i}=-e_{1(i-1)1},\quad i=2,3,4;\quad g_{55}=\alpha_{11}.
\end{aligned} \tag{24}$$

Inspection shows that Eq. (23) leads to an algebraic equation of the eighth degree in ω/k. Several of the individual elements are complex and there is an additional dependence on the frequency. Thus in general, the roots of the equation will be both complex and frequency dependent. It follows that the resulting waves will propagate with frequency-dependent phase velocities and, further, that damping of the waves will occur. In special cases, some of the complex roots may degenerate to purely imaginary values (see the example at the end of this chapter) describing a creep motion and not an oscillation. If the thermal conduction is neglected, purely real roots will occur on characterizing undamped oscillations.

Within the simplified fully dynamic theory, taking into consideration the mentioned wave conditions in wave equations (15), it is sufficient (following Hutson and White[12]) to take the equations for E_2 and E_3 only:

$$-\frac{\partial^2 E_p}{\partial x_1^2}+\mu_0\left(\alpha_{pj}\frac{\partial^2 E_j}{\partial t^2}+e_{pj1}\frac{\partial^3 u_j}{\partial x_1\,\partial t^2}+p_p\frac{\partial^2\theta}{\partial t^2}+\sigma_{pj}\frac{\partial E_j}{\partial t}\right)=0, \tag{25}$$

where $i,j,k=1$, 2, or 3, but $p,q=2$ or 3. Equations (18), (19) [in which $-p_1(\partial\phi/\partial x_1):=p_iE_i$ and $-e_{11j}(\partial^2\phi/\partial x_1^2):=e_{k1j}(\partial E_k/\partial x_1)$], and (25) are six coupled wave equations in the seven variables θ, u_i, and E_i. However, E_1 can be expressed as a function of the other six variables using $(\nabla\times\mathbf{H})_1=0$ and Eqs. (16d) and (8):

$$\left(\sigma_{11}E_1+\gamma_{11}\frac{\partial E_1}{\partial t}\right)+e_{1j1}\frac{\partial^2 u_j}{\partial x_1\,\partial t}+p_1\frac{\partial\theta}{\partial t}+\left(\sigma_{1q}E_q+\alpha_{1q}\frac{\partial E_q}{\partial t}\right)=0. \tag{26}$$

By assuming plane wave solutions analogous to Eq. (21) where $E_i(x_1,t)$ with its amplitude E_i^0 replaces ϕ with ϕ^0 and eliminating E_1 from Eqs. (18), (19), and (25) using (26), one now obtains

$$\begin{aligned}
&k^2k_{11}\theta^0-T_0(1-j\omega\tau)(j\omega c'\theta^0-k\omega\beta'_{j1}u_j^0+j\omega p''_qE_q^0)=0,\\
&\rho[-\omega^2\mathbf{u}^0+\boldsymbol{\Omega}\times(\boldsymbol{\Omega}\times\mathbf{u}^0)-2j\omega\boldsymbol{\Omega}\times\mathbf{u}^0]_j+k^2c'_{1j1k}u_k^0\\
&\quad+jk\beta'_{1j}\theta^0+jke'_{q1j}E_q^0=0,\\
&k^2E_p^0-\mu_0\omega^2[\alpha'_{pq}E_q^0+jke'_{pj1}u_j^0+p'_p\theta^0]=0,
\end{aligned} \tag{27}$$

where

$$\begin{aligned}
c'_{1j1k}&=c_{1j1k}+\frac{e_{1j1}e_{1k1}}{\gamma_{11}+\dfrac{j\sigma_{11}}{\omega}},\\
e'_{q1j}&=e_{q1j}-\frac{e_{1j1}\left(\alpha_{1q}+\dfrac{j\sigma_{1q}}{\omega}\right)}{\alpha_{11}+\dfrac{j\sigma_{11}}{\omega}},\\
\alpha'_{pq}&=\alpha_{pq}+\frac{j\omega_{pq}}{\omega}-\frac{\left(\alpha_{p1}+\dfrac{j\sigma_{p1}}{\omega}\right)\left(\alpha_{1q}+\dfrac{j\sigma_{1q}}{\omega}\right)}{\alpha_{11}+\dfrac{j\sigma_{11}}{\omega}},\\
p'_p&=p_p-\frac{p_1\left(\alpha_{p1}+\dfrac{j\sigma_{p1}}{\omega}\right)}{\alpha_{11}+\dfrac{j\sigma_{11}}{\omega}},\\
p''_q&=p_q-\frac{p_1\left(\alpha_{1q}+\dfrac{j\sigma_{1q}}{\omega}\right)}{\alpha_{11}+\dfrac{j\sigma_{11}}{\omega}},
\end{aligned} \tag{28}$$

$$\begin{aligned}
\beta'_{j1}&=\beta_{j1}-\frac{e_{1j1}p_1}{\alpha_{11}+\dfrac{j\sigma_{11}}{\omega}},\qquad \beta'_{1j}=\beta_{1j}-\frac{e_{1j1}p_1}{\alpha_{11}+\dfrac{j\sigma_{11}}{\omega}},\\
c'&=c-\frac{p_1^2}{\alpha_{11}+\dfrac{j\sigma_{11}}{\omega}}.
\end{aligned}$$

Earlier argumentation leads to the governing dispersion relation

$$\det\mathbf{C}=0, \tag{29}$$

where the elements c_{ij} $(i,j=1,...,6)$ of the matrix $\mathbf{C}$ are

$$\begin{aligned}
&c_{11}=k_{11}-\frac{j\omega T_0c'}{k^2}(1-j\omega\tau);\\
&c_{1j}=\frac{T_0\omega\beta'_{(j-1)1}}{k}(1-j\omega\tau),\quad j=2,3,4;\\
&c_{1j}=-\frac{j\omega T_0p''_{j-3}}{k^2}(1-j\omega\tau),\quad j=5,6;\\
&c_{21}=\frac{j\beta'_{11}}{k\rho};\quad c_{22}=\frac{c'_{1111}}{\rho}-\frac{\omega^2+\Omega^2}{k^2};\quad c_{23}=\frac{c'_{1112}}{\rho};\\
&c_{24}=\frac{c'_{1113}}{\rho}-2j\frac{\omega\Omega}{k^2};\quad c_{2j}=\frac{je'_{(j-3)11}}{k\rho},\quad j=5,6;\\
&c_{31}=\frac{j\beta'_{12}}{k\rho};\quad c_{32}=\frac{c'_{1211}}{\rho};\quad c_{33}=\frac{c'_{1212}}{\rho}-\frac{\omega^2}{k^2};\\
&c_{34}=\frac{c'_{1213}}{\rho};\quad c_{3j}=\frac{je'_{(j-3)12}}{k\rho},\quad j=5,6;\\
&c_{41}=\frac{j\beta'_{13}}{k\rho};\quad c_{42}=\frac{c'_{1311}}{\rho}+2j\frac{\omega\Omega}{k^2};\quad c_{43}=\frac{c'_{1312}}{\rho};\\
&c_{44}=\frac{c'_{1313}}{\rho}-\frac{\omega^2+\Omega^2}{k^2};\quad c_{4j}=\frac{je'_{(j-3)13}}{k\rho},\quad j=5,6;\\
&c_{51}=\frac{\omega^2}{k^2}p'_2;\quad c_{5j}=\frac{j\omega^2}{k}e'_{2(j-1)1},\quad j=2,3,4;\\
&c_{55}=\frac{\omega^2}{k^2}\alpha'_{22}-\frac{1}{\mu_0};\quad c_{56}=\frac{\omega^2}{k^2}\alpha'_{23};\\
&c_{61}=\frac{\omega^2}{k^2}p'_3;\quad c_{6j}=\frac{j\omega^2}{k}e'_{3(j-1)1},\quad j=2,3,4;\\
&c_{65}=\frac{\omega^2}{k^2}\alpha'_{32};\quad c_{66}=\frac{\omega^2}{k^2}\alpha'_{33}-\frac{1}{\mu_0}.
\end{aligned} \tag{30}$$

In this case, Eq. (29) yields an algebraic equation of the twelfth degree in ω/k. All the coefficients of the individual terms will be complex and frequency dependent in general. Thus the consequences for the roots of the equation and the characteristics of the propagating waves are the same (in a more general form) as within the quasistatic theory.

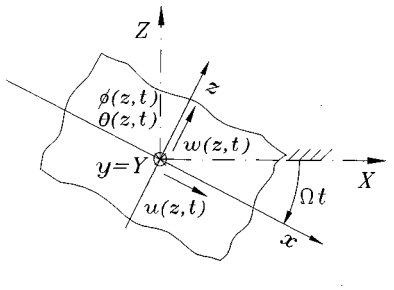

FIG. 1. Geometry of rotating medium and reference frames.

If the piezoelectric tensor is zero, Eq. (25) splits into a fourth-order thermo-elastic wave determinant and second-order electromagnetic wave determinant.

As shown by Kyame[11] and Hutson and White,[13] the piezoelectricity may be taken into account in the propagation of the thermo-elastic waves to a very good approximation by solving only the fourth-order thermo-acoustic determinant with the piezoelectric conductivity modified thermal and elastic constants β'_{1j}, β'_{j1}, and c'_{1j1k}, neglecting the coupling with the electromagnetic waves. But it has to be noticed that this approximation does not yield the same results as an direct evaluation of the dispersion relation Eq. (23).

Since no boundary conditions are involved, only one determinantal equation, (23) or (29), has to be evaluated. By using one of the available program packages for symbolic manipulation, this is straight forward. The evaluation can be simplified if piezoelectric bodies of special symmetry are considered, e.g., for hexagonal (6 mm) class,[3] and the crystal axes x, y, z are parallel to the reference axes x_i.

Exactly this example will be discussed in the following (see Fig. 1). For convenience, only the electrically quasistatic theory is applied but thermal influences are taken into account. To obtain a case for which an interesting coupling appears, an arrangement $x_1 := z$, $x_2 := y$ and $x_3 := -x$ is chosen. As appropriate, the displacement coordinates are also replaced as u, v, w corresponding to x, y, z. Finally Voigt's notation is used (see for instance, Paul and Renganathan[8]) so that the wave propagation is governed by the five differential equations

$$
\begin{aligned}
&-k_{33}\theta_{,zz}+T_0\left(1+\tau\frac{\partial}{\partial t}\right)[c\theta_{,t}+\beta_3 w_{,zt}-p_3\phi_{,zt}]=0,\\
&\rho(u_{,tt}-\Omega^2 u+2\Omega w_{,t})-c_{44}u_{,zz}=0,\\
&\rho v_{,tt}-c_{44}v_{,zz}=0,\\
&\rho(w_{,tt}-\Omega^2 w-2\Omega u_{,t})-c_{33}w_{,zz}-e_{33}\phi_{,zz}+\beta_3\theta_{,z}=0,\\
&e_{33}w_{,zz}-\alpha_{33}\phi_{,zz}+p_3\theta_{,z}=0,
\end{aligned}
\tag{31}
$$

where $(.)_{,t}$ and $(.)_{,z}$ replaces $\partial(.)/\partial t$ and $\partial(.)/\partial z$, respectively. Obviously, there is a pure elastic wave $v(z,t)$ decoupled from the other field quantities and thermo-piezoelectric waves described by the remaining coupled wave equations in $\theta(z,t)$, $u(z,t)$, $w(z,t)$, and $\phi(z,t)$. It follows that also the resulting dispersion relation Eq. (24) simplifies taking the final form

$$
\begin{vmatrix}
g'_{11} & g'_{12} & g'_{13} & g'_{14}\\
g'_{21} & g'_{22} & g'_{23} & g'_{24}\\
g'_{31} & g'_{32} & g'_{33} & g'_{34}\\
g'_{41} & g'_{42} & g'_{43} & g'_{44}
\end{vmatrix}=0,
\tag{32}
$$

where

$$
\begin{aligned}
&g'_{11}=k_{33}-\frac{j\omega T_0 c}{k^2}(1-j\omega\tau),\quad g'_{12}=0,\\
&g'_{13}=\frac{T_0\omega\beta_3}{k}(1-j\omega\tau),\quad g'_{14}=-\frac{\omega T_0 p_1}{k}(1-j\omega\tau),\\
&g'_{21}=0,\quad g'_{22}=\frac{c_{44}}{\rho}-\frac{\omega^2+\Omega^2}{k^2},\quad g'_{23}=-2j\frac{\omega\Omega}{k^2},\\
&g'_{24}=0,\quad g'_{31}=\frac{j\beta_3}{k\rho},\quad g'_{32}=+2j\frac{\omega\Omega}{k^2},\\
&g'_{33}=\frac{c_{33}}{\rho}-\frac{\omega^2+\Omega^2}{k^2},\quad g'_{34}=\frac{e_{33}}{\rho},\\
&g'_{41}=\frac{jp_3}{k},\quad g'_{42}=0,\quad g'_{43}=-e_{33},\quad g'_{44}=\alpha_{33}.
\end{aligned}
\tag{33}
$$

For the quantitative evaluation, the piezoceramics $BaTiO_3$ is considered[22] introducing the same nondimensional variables and parameters as in that reference. In addition, the relaxation parameter τ is included here in which the used dimensionless notation is denoted τ_0. The elements of the dispersion relation Eq. (32) turn into

$$
\begin{aligned}
&g'_{11}=1-j\frac{\omega T_T}{k^2}(1-j\omega\tau_0),\quad g'_{12}=0,\\
&g'_{13}=\frac{\alpha_{\theta\omega}}{k}(1-j\omega\tau_0),\quad g'_{14}=-\frac{\varepsilon_{\theta\phi}\omega}{k}(1-j\omega\tau_0),\\
&g'_{21}=0,\quad g'_{22}=\gamma_{44}-\frac{\omega^2+\Omega^2}{k^2},\quad g'_{23}=-2j\frac{\omega\Omega}{k^2},\\
&g'_{24}=0,\quad g'_{31}=j\frac{\varepsilon_{w\theta}}{k},\quad g'_{32}=+2j\frac{\omega\Omega}{k^2},\\
&g'_{33}=1-\frac{\omega^2+\Omega^2}{k^2},\quad g'_{34}=\varepsilon_{w\phi},\\
&g'_{41}=\frac{j}{k},\quad g'_{42}=0,\quad g'_{43}=-1,\quad g'_{44}=1.
\end{aligned}
\tag{34}
$$

The nondimensional wave number k and the speed parameter Ω are varied. Figure 2 shows for the same parameter values as used by Wauer[22] and $\tau_0=0.2$ the real and the imaginary part of the frequency parameter ω versus the wave number k (which is assumed to be real valued here) for three different Ω values. Even for the nonrotating case, the waves become dispersive due to the accompanying thermal conduction process. With increasing rotational speed, this effect strengthens. In general, there are six circular frequencies ω for a fixed parameter set and given values of k and Ω recalling the fact that the remaining field equations in Eq. (31) are of sixth order in time. One pair of them yielding two purely negative

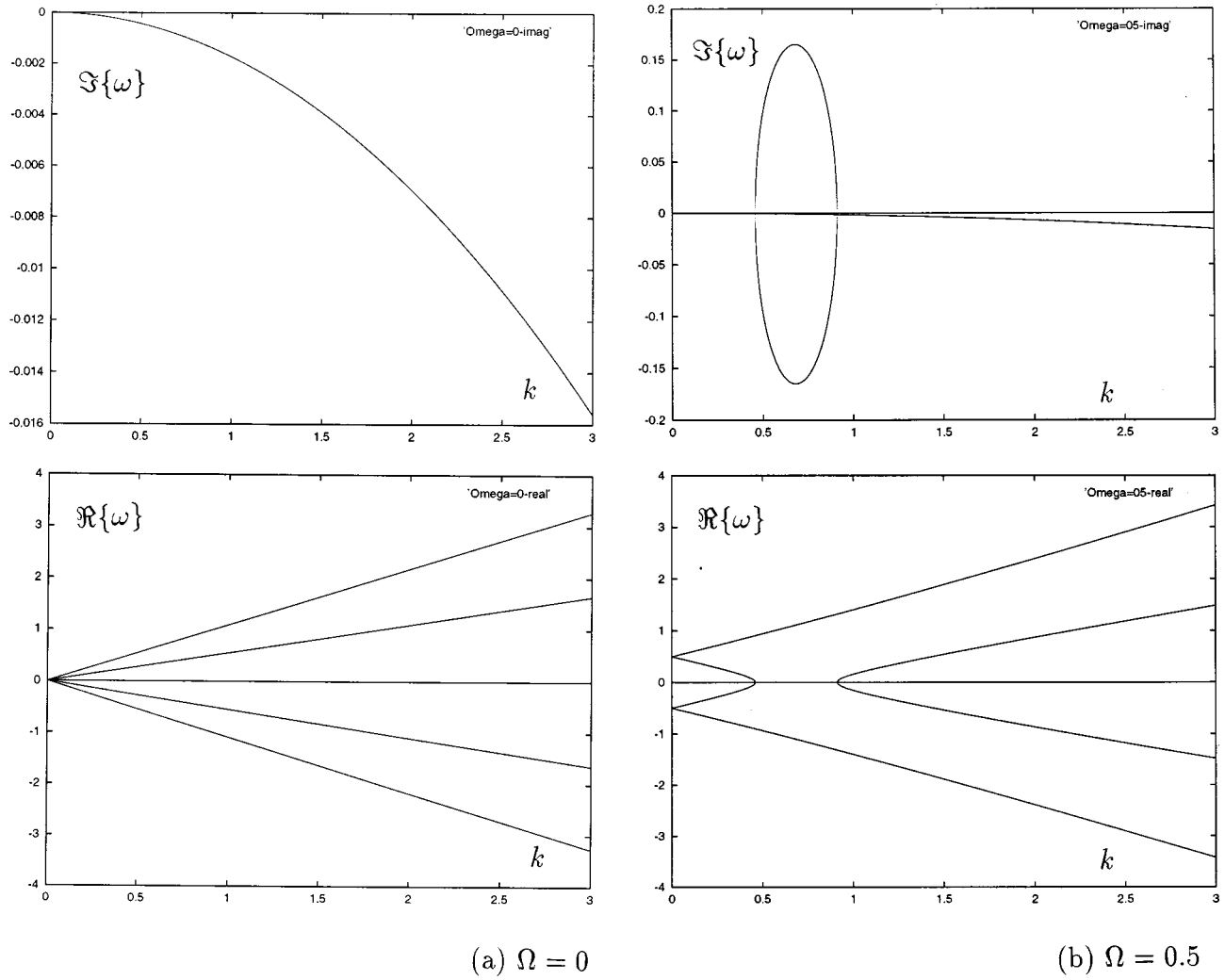

FIG. 2. Frequency wave number diagram. (a) $\Omega=0$; (b) $\Omega=0.5$; (c) $\Omega=1.0$.

exponents $-j\omega$ in Eq. (21) corresponds to the thermal creep motion, while the other two complex pairs are associated with the piezoelectric waves which are damped but much less than the first one. Within the used scaling (for $\Im\{\omega\}$), the larger value of the first pair (in the order of -10^3) is beyond the graphical illustration and the other two (in the order of -10^{-7}) cannot be visualized. An interesting feature is the fact that, with increasing speed, instabilities may occur (characterized by positive imaginary part $\Im\{\omega\}$). For rotating disks, this phenomenon is well-known if the disk is clamped at the outside surface (see Seemann and Wauer[23]). But it is also known that for a traction-free outside boundary with a clamped center, there is a stiffening effect and the structural member is stable for this case in the whole speed range. Therefore, the results obtained here can be guaranteed only for sufficiently low speeds; for higher angular velocities, they have to be checked by a computation embedded in a geometrically nonlinear theory of piezoelectricity.

III. SURFACE WAVES

If there is a bounding surface, surface waves may occur. Piezoelectric surface waves can be studied in an approach parallel to that for Rayleigh waves of elastodynamics. Such studies, in fact exist (see Coquin and Tiersten[4] or Ingebrigtsen[5] within the classical theory and Tseng and White[14] applying the full Maxwell equations), and are modifications of elastic surface waves for anisotropic bodies. Here, attention is focused on the effect of angular speed where thermal influences are also incorporated. For convenience, only the classical theory for pyroelectric media will be applied.

Equations (10)–(12) represent the governing field equations; appropriate boundary conditions at the surface have to be added. The following prescribed homogeneous boundary conditions are chosen:

$$\begin{aligned} &\theta=0 \ \text{ on } \ S_\theta, \quad q_i n_i=0 \ \text{ on } \ S_q, \\ &u_i=0 \ \text{ on } \ S_u, \quad T_{ij} n_j=0 \ \text{ on } \ S_T, \\ &\phi=0 \ \text{ on } \ S_\phi, \quad D_i n_i=0 \ \text{ on } \ S_D. \end{aligned} \tag{35}$$

The smooth regular surface S with the unit outward normal n_i is partitioned as

$$S_\theta \cup S_q = S_u \cup S_T = S_\phi \cup S_D = S. \tag{36}$$

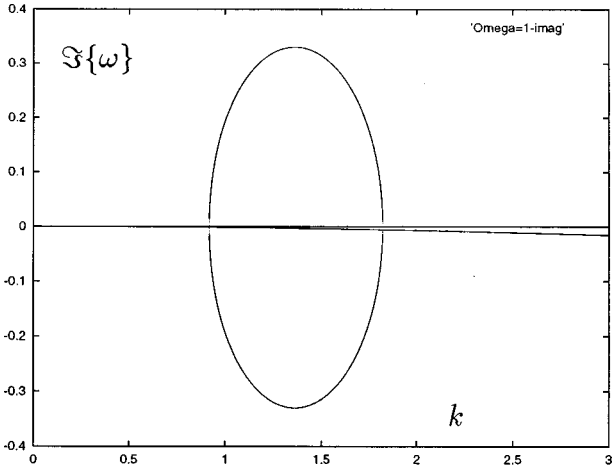

(c) $\Omega = 1.0$

FIG. 2. (*Continued.*)

As a specific situation, the surface is located at the x_1, x_2 plane and is kept at the initial uniform temperature, traction free, and at a vanishing potential:

$$\theta = 0, \quad T_{i3} n_3 = 0, \quad \phi = 0. \tag{37}$$

Using the constitutive equations (7), the stress T_{i2} can also be expressed by the state variables θ, u_i, and ϕ. Additionally, the temperature θ, the displacements u_i, and the potential ϕ are assumed to approach zero if $x_3 \to \infty$.

A propagation of surface waves in the x_1 direction is considered. Solutions of Eqs. (10)–(12) which are independent of x_2 and vanish at $x_3 = \infty$, have the form

$$\begin{aligned} \theta(x_1, x_3, t) &= C^{\theta} e^{-\lambda x_3} e^{j(kx_1 - \omega t)}, \\ u_i(x_1, x_3, t) &= C^{u_i} e^{-\lambda x_3} e^{j(kx_1 - \omega t)}, \\ \phi(x_1, x_3, t) &= C^{\phi} e^{-\lambda x_3} e^{j(kx_1 - \omega t)}, \end{aligned} \tag{38}$$

where λ is the so-called decay factor. Substituting Eqs. (38) successively into Eqs. (10)–(12), one obtains

$$\begin{aligned} &(k^2 k_{11} - \lambda^2 k_{33}) C^{\theta} - T_0 (1 - j\omega\tau)[j\omega c C^{\theta} \\ &\quad + (j\lambda \beta_{i3} - k\beta_{i1}) \omega C^{u_i} - (\lambda_{p_3} - k p_1) \omega C^{\phi}] = 0, \\ &\rho[-\omega^2 \mathbf{C}^u + \boldsymbol{\Omega} \times (\boldsymbol{\Omega} \times \mathbf{C}^u) - 2j\omega \boldsymbol{\Omega} \times \mathbf{C}^u]_i \\ &\quad + [c_{1i1l} k^2 + j\lambda k (c_{1i3l} + c_{3i1l}) - \lambda^2 c_{3i3l}] C^{u_l} \\ &\quad + (jk\beta_{1i} - \lambda \beta_{3i}) C^{\theta} + [e_{11i} k^2 \\ &\quad + jk\lambda (e_{13i} + e_{31i}) - \lambda^2 e_{33i}] C^{\phi} = 0, \\ &[k^2 \alpha_{11} + (\alpha_{13} + \alpha_{31}) jk\lambda - \alpha_{33} \lambda^2] C^{\phi} - [k^2 e_{1i1} \\ &\quad + (e_{1i3} + e_{3i1}) jk\lambda - \lambda^2 e_{3i3}] C^{u_i} + (jkp_1 - \lambda p_3) C^{\theta} = 0. \end{aligned} \tag{39}$$

The vanishing determinant

$$\det \mathbf{A} = 0 \tag{40}$$

is the dispersion relation which leads to a polynomial equation for the decay factor λ as a function of wave number k and circular frequency ω. Introducing the earlier assumption $\Omega_1 = \Omega_3 = 0$ and $\Omega_2 = \Omega \neq 0$, elements a_{ij} $(i,j = 1,...,5)$ of the matrix $\mathbf{A}$ in Eq. (40) read

$$\begin{aligned} a_{11} &= k_{11} - \frac{\lambda^2}{k^2} k_{33} - \frac{T_0}{k^2} (1 - j\omega\tau) j\omega c; \\ a_{1i} &= \frac{T_0}{k^2} (1 - j\omega\tau)(k\beta_{(i-1)1} - j\lambda \beta_{(i-1)3}) \omega, \quad i = 2,3,4; \\ a_{15} &= -\frac{T_0}{k^2} (1 - j\omega\tau)(kp_1 - \lambda p_3) \omega; \\ a_{21} &= \frac{jk\beta_{11} - \lambda \beta_{31}}{\rho k^2}; \\ a_{22} &= \frac{c_{1111}}{\rho} - \frac{\omega^2 + \Omega^2}{k^2} + \frac{j\lambda}{\rho k} (c_{1131} + c_{3111}) - \frac{\lambda^2}{\rho k^2} c_{3131}; \\ a_{23} &= \frac{c_{1112}}{\rho} + \frac{j\lambda}{\rho k} (c_{1132} + c_{3112}) - \frac{\lambda^2}{\rho k^2} c_{3132}; \\ a_{24} &= \frac{c_{1113}}{\rho} - 2j \frac{\omega\Omega}{k^2} + \frac{j\lambda}{\rho k} (c_{1133} + c_{3113}) - \frac{\lambda^2}{\rho k^2} c_{3133}; \\ a_{25} &= \frac{e_{111}}{\rho} + \frac{j\lambda}{\rho k} (e_{131} + e_{311}) - \frac{\lambda^2}{\rho k^2} e_{331}; \\ a_{31} &= \frac{jk\beta_{12} - \lambda \beta_{32}}{\rho k^2}; \\ a_{32} &= \frac{c_{1211}}{\rho} + \frac{j\lambda}{\rho k} (c_{1231} + c_{3211}) - \frac{\lambda^2}{\rho k^2} c_{3231}; \\ a_{33} &= \frac{c_{1212}}{\rho} - \frac{\omega^2}{k^2} + \frac{j\lambda}{\rho k} (c_{1232} + c_{3212}) - \frac{\lambda^2}{\rho k^2} c_{3232}; \\ a_{34} &= \frac{c_{1213}}{\rho} + \frac{j\lambda}{\rho k} (c_{1233} + c_{3213}) - \frac{\lambda^2}{\rho k^2} c_{3233}; \\ a_{35} &= \frac{e_{112}}{\rho} + \frac{j\lambda}{\rho k} (e_{132} + e_{312}) - \frac{\lambda^2}{\rho k^2} e_{332}; \\ a_{41} &= \frac{jk\beta_{13} - \lambda \beta_{33}}{\rho k^2}; \end{aligned} \tag{41}$$

$$a_{42}=\frac{c_{1311}}{\rho}+2j\,\frac{\omega\Omega}{k^2}+\frac{j\lambda}{\rho k}(c_{1331}+c_{3311})-\frac{\lambda^2}{\rho k^2}c_{3331};$$

$$a_{43}=\frac{c_{1312}}{\rho}+\frac{j\lambda}{\rho k}(c_{1332}+c_{3312})-\frac{\lambda^2}{\rho k^2}c_{3332};$$

$$a_{44}=\frac{c_{1313}}{\rho}-\frac{\omega^2+\Omega^2}{k^2}+\frac{j\lambda}{\rho k}(c_{1333}+c_{3313})-\frac{\lambda^2}{\rho k^2}c_{3333};$$

$$a_{45}=\frac{e_{113}}{\rho}+\frac{j\lambda}{\rho k}(e_{133}+e_{313})-\frac{\lambda^2}{\rho k^2}e_{333};$$

$$a_{51}=\frac{jkp_1-\lambda p_3}{k^2};$$

$$a_{5i}=-e_{1(i-1)1}-(e_{1(i-1)3}+e_{3(i-1)1})\frac{j\lambda}{k}+\frac{\lambda^2}{k^2}e_{3(i-1)3},\quad i=2,3,4;$$

$$a_{55}=\alpha_{11}+(\alpha_{13}+\alpha_{31})\frac{j\lambda}{k}-\alpha_{33}\frac{\lambda^2}{k^2}.$$

In general, there are ten solutions λ_n but only five of them have a positive real part to satisfy the boundary conditions at $x_3=\infty$. For each of these values λ_n $(n=1,2,...,5)$, there exists a set of amplitudes C_n^{θ}, $C_n^{u_i}$, and C_n^{ϕ} in Eq. (39). The ratio of these amplitudes can be found from any four of the five equations in Eq. (39). Let these ratios be

$$P_{in}=\frac{C_n^{u_i}}{C_n^{\phi}},\quad Q_n=\frac{C_n^{\theta}}{C_n^{\phi}}. \tag{42}$$

Then the solutions in Eq. (38) can be rewritten depending only on the five constants C_n^{ϕ}. In a last step, they are subject to the five surface conditions in Eq. (37). For nontrivial solutions to exist, the determinant of the resulting system of algebraic equations

$$\mathbf{FZ}=\mathbf{0},\quad \mathbf{Z}=[C_1^{\phi},C_2^{\phi},\ldots,C_5^{\phi}]^T \tag{43}$$

must be zero, i.e.,

$$\det\mathbf{F}=0, \tag{44}$$

where the elements f_{ij} of the 5×5 system matrix $\mathbf{F}$ in Eq. (42) are not written down explicitly. This is the characteristic equation determining the phase velocity ω/k. After the velocity and the decay constants are found solving both determinantal equations (38) and (42) simultaneously, the temperature, the displacements, and the electrical potential can be found expressing in a final step the remaining constants C_n^{ϕ} by one of them using any four of the five equations (43). In general, a completely numerical evaluation is required.

For neglecting thermal influences and looking to inplane motions, a significant problem reduction results as illustrated in Fig. 3 for a half-space $x_3\geqslant0$ corresponding to the plate problem considered by Paul *et al.*[6] For comparison, $x_1:=x$, $x_2:=y$ and $x_3:=z$ are chosen and again, Voigt's notation is introduced. The components $u_1:=u$ and $u_3:=w$ of the displacement field and the electric potential ϕ are assumed to be independent of $x_2:=y$ so that the wave equations (10)–(12) simplify to

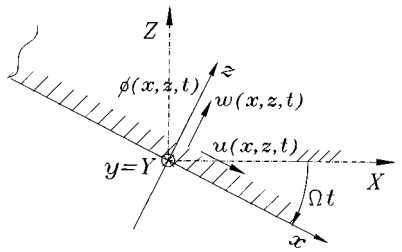

FIG. 3. Geometry of rotating half-space and reference frames.

$$\begin{aligned}
&\rho(u_{,tt}-\Omega^2u+2\Omega w_{,t})-c_{11}u_{,xx}-(c_{13}+c_{44})w_{,xz}\\
&\quad-c_{44}u_{,zz}-(e_{31}+e_{15})\phi_{,xz}=0,\\
&\rho(w_{,tt}-\Omega^2w-2\Omega u_{,t})-c_{44}w_{,xx}-c_{33}w_{,zz}\\
&\quad-(c_{13}+c_{44})u_{,zx}-e_{15}\phi_{,xx}-e_{33}\phi_{,zz}=0,\\
&e_{15}w_{,xx}+(e_{15}+e_{31})e_{,zx}-\alpha_{11}\phi_{,xx}+e_{33}w_{,zz}-\alpha_{33}\phi_{,zz}=0.
\end{aligned} \tag{45}$$

The corresponding surface conditions in Eq. (37) have to be added, i.e.,

$$\begin{aligned}
&c_{13}u_{,x}+c_{33}w_{,z}+e_{33}\phi_{,z}=0,\\
&c_{44}(w_{,x}+u_{,z})+e_{15}\phi_{,x}=0,\quad \phi=0
\end{aligned} \tag{46}$$

at $z=0$. For further analysis, the same dimensionless formulation as mentioned in Sec. II is introduced, here for the governing boundary value problem Eqs. (45), (46):

$$\begin{aligned}
&-\gamma_{11}u^{**}-(\gamma_{13}+\gamma_{44})w^{*\prime}-(\delta_{31}+\delta_{15})\varepsilon_{w\phi}\phi^{*\prime}\\
&\quad-\gamma_{44}u''+\ddot{u}+2\Omega\dot{w}-\Omega^2u=0,\\
&-\gamma_{44}w^{**}-w''-(\gamma_{13}+\gamma_{44})u^{*\prime}-\delta_{15}\varepsilon_{w\phi}\phi^{**}-\varepsilon_{w\phi}\phi''\\
&\quad+\ddot{w}-2\Omega\dot{u}-\Omega^2w=0,\\
&(\delta_{15}+\delta_{31})u^{*\prime}+\delta_{15}w^{**}+w''-\epsilon\phi^{**}-\phi''=0,
\end{aligned} \tag{47}$$

and

$$\begin{aligned}
&\delta_{13}u^{*}+w'+\varepsilon_{w\phi}\phi'=0,\\
&\gamma_{44}(w^{*}+u')+\delta_{15}\varepsilon_{w\phi}\phi'=0,\quad \phi=0
\end{aligned} \tag{48}$$

at $z=0$.

While for a piezoelectric body at rest the resulting dispersion relation becomes a cubic equation in λ^2 so that analytical solutions for $\lambda_n^2(k,\omega)$ $(n=1,2,3)$ can be computed, it remains of fully sixth order in λ_n under the influence of rotation. It follows that still a completely numerical procedure is required.

Since it can be assumed that the qualitative effect of angular speed can be seen also for an elastic isotropic solid, this further simplified problem will be examined finally. The dispersion relation Eq. (40) simplifies drastically:

$$\begin{vmatrix} k^2-\gamma_{44}\lambda^2-\omega^2-\Omega^2 & -2j\omega\Omega+(1-\gamma_{44})jk\lambda \\ +2j\omega\Omega+(1-\gamma_{44})jk\lambda & \gamma_{44}k^2-\lambda^2-\omega^2-\Omega^2 \end{vmatrix}=0. \tag{49}$$

The decay factor can be calculated analytically:

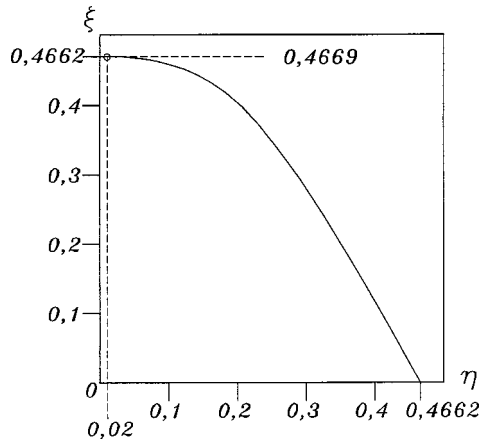

FIG. 4. Rayleigh wave speed versus angular speed.

$$\kappa_{1,2}^2 = 1 - \frac{1+R}{2}(\xi^2+\eta^2) \pm \sqrt{(1+R)^2(\xi^4+\eta^4)+2(1+6R+R^2)\xi^2\eta^2}, \tag{50}$$

where

$$R=\frac{1}{\gamma_{44}}, \quad \kappa=\frac{\lambda}{k}, \quad \xi=\frac{\omega}{k}, \quad \eta=\frac{\Omega}{k}. \tag{51}$$

Analogous to Eq. (42), the ratio C_u/C_w can be computed for each positive value $\sqrt{\kappa_1}$ and $\sqrt{\kappa_2}$ so that the solutions u and w according to Eq. (38) are determined. Then, the remaining two boundary conditions in Eq. (48)

$$(1-2\gamma_{44})u^* + w' = 0, \quad w^* + u' = 0 \tag{52}$$

at $z=0$ can be applied leading to the characteristic equation (44) where the elements f_{ij} of matrix $\mathbf{F}$ read

$$\begin{aligned} f_{11} &= 2(1-2R)\xi\eta - \kappa_1[(\gamma_{44}-1)(1-2R)+\xi^2+\eta^2 - \gamma_{44}+\kappa_1^2], \\ f_{12} &= 2(1-2R)\xi\eta - \kappa_2[(\gamma_{44}-1)(1-2R)+\xi^2+\eta^2+1 - \gamma_{44}+\kappa_1^2], \\ f_{21} &= 2\xi\eta R\kappa_1 - 1 + R(\xi^2+\eta^2) - \kappa_1^2(1-2R), \\ f_{22} &= 2\xi\eta R\kappa_2 - 1 + R(\xi^2+\eta^2) - \kappa_2^2(1-2R). \end{aligned} \tag{53}$$

Figure 4 shows the characteristic wave speed parameter ξ versus angular velocity parameter η for a fixed value of γ_{44}. It can be seen clearly that with increasing η, the characteristic ξ value first increases slightly before it decreases monotonically. For a critical value η_c, it becomes zero. Similar as for the wave propagation in an unbounded medium, the results become obviously useless for larger rotational speeds.

It should be noticed that the corresponding antiplane motion which is governed by the u_2 component of the displacement field is not effected by the angular speed; due to the choice of crystal and rotational axes, it is a pure elastic wave not related with Bleustein's problem.[24]

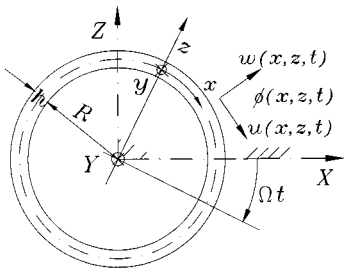

FIG. 5. Geometry of rotating annulus and reference frames.

IV. WAVES IN BOUNDED WAVEGUIDES

The elegance of the analysis of waves in unbounded media does not extend to bodies of finite dimensions. In general, the wave propagation problem is much more complicated due to the reflections of the wave motion at the bounding surfaces. There are boundary conditions [similar to the surface conditions in Eqs. (35) or (37)] or transition conditions to a surrounding medium involved so that a considerable computing expense may be expected which in many cases is even greater than for the study of surface waves.

Applying the conventional electrically quasistatic theory, the complete problem is described by the field equations (10), (11), and (12), and boundary conditions Eqs. (35) or (37) on a surface S Eq. (36) enclosing the body. Within the simplified dynamic theory, Eq. (15) and the components of the electric field intensity E_i, respectively, replace Eq. (12) and the electric potential ϕ (the corresponding part of surface is called S_E) while in the general dynamic case, the electric field quantities E_i are accompanied by magnetic field quantities H_i. It follows instead that Eq. (15), the set of wave equations (13), (14) becomes relevant and the surface S Eq. (36) has to be modified into

$$S_\theta \cup S_q = S_u \cup S_T = S_E \cup S_D = S_H \cup S_B = S \tag{54}$$

so that magnetic boundary conditions have to be added:

$$H_i = 0 \ \text{ on } \ S_H, \quad B_i n_i = 0 \ \text{ on } \ S_B. \tag{55}$$

In practical cases, instead of a bounding surface with fixed boundary conditions a surrounding medium, e.g., vacuum, has to be taken into consideration. Then a second set of field equations with appropriate transition conditions of the governing field quantities between solid and vacuum would appear.

If all components of the field variables and a finite axial wave number are taken into consideration, even cases of simple geometry with fixed boundary conditions are complicated. Here a coupled motion independent of the axial coordinate (x_2) will be treated, often based to studies on the dynamics of infinitely long slabs or cylinders. Such problems have recently been discussed by the author[22,25] following Paul *et al.*[6] and as well Paul and Renganathan[8] as Yang and Batra[9] who analyzed a piezoelectric and a pyroelectric slab, respectively, with surfaces which are (x_1,x_2) planes separated by a distance d, and which rotates about an axis which is parallel to the surfaces in the x_2 direction through the midplane. A further simplification appears for a thin-walled circular annulus (see Fig. 5) with inner radius R and thick-

ness of wall h. It can be considered in such an approximation that the governing boundary value problem will be formulated in quasi-Cartesian coordinates, i.e., approximately, there is a circumferential coordinate $x_1 := x = [R + (h/2)]\varphi$ $(0 \leqslant \varphi \leqslant 2\pi)$ and a radial one, $-(h/2) \leqslant x_3 := z \leqslant +(h/2)$. In the case of problems of cylindrical symmetry further to be addressed, all the considered variables become functions of z and t only. The piezoelectric vibrations will be examined within the fully dynamic theory. The displacement vector will be taken of the form

$$u_1 := u \neq 0, \quad u_2 := v \equiv 0, \quad u_3 := w \neq 0. \tag{56}$$

The induced magnetic field $\mathbf{H}$ will have one component H in the axial direction y while the induced electric field $\mathbf{E}$ will have one component E in the circumferential direction $[R + (h/2)]\varphi$. Finally, it will be assumed that at the two surfaces, not only the thermal and mechanical field quantities but also the appearing electric and magnetic field variables can be fixed at constant values, e.g., to be zero there. An interaction with the electric and magnetic field variables outside the solid (in the surrounding vacuum, for example) does not appear under this assumption.

Checking the governing field equations (10), (11), (13), and (14), it becomes obvious that for the case considered the rigid body terms have no influence in Maxwell's equations, i.e., they shorten to the equation set (15). Therefore, the resulting boundary value problem reads

$$\begin{aligned}
&-k_{33}\frac{\partial^2\theta}{\partial z^2} + T_0\left(1+\tau\frac{\partial}{\partial t}\right)\left(c\frac{\partial\theta}{\partial t} + \beta_{13}\frac{\partial^2 u}{\partial z\,\partial t} + \beta_{33}\frac{\partial^2 w}{\partial z\,\partial t}\right.\\
&\qquad \left. + p_1\frac{\partial E}{\partial t}\right) = 0,\\
&\rho\left(\frac{\partial^2 u}{\partial t^2} - \Omega^2 u + 2\Omega w_{,t}\right) - c_{3113}\frac{\partial^2 u}{\partial z^2} - c_{3133}\frac{\partial^2 w}{\partial z^2} + \beta_{31}\frac{\partial\theta}{\partial z}\\
&\qquad + e_{131}\frac{\partial E}{\partial z} = 0,\\
&\rho\left(\frac{\partial^2 w}{\partial t^2} - \Omega^2 w - 2\Omega u_{,t}\right) - c_{3333}\frac{\partial^2 w}{\partial z^2} - c_{3313}\frac{\partial^2 u}{\partial z^2}\\
&\qquad + \beta_{33}\frac{\partial\theta}{\partial z} + e_{133}\frac{\partial E}{\partial z} = 0,\\
&\frac{\partial^2 E}{\partial z^2} + \mu_0\left(\alpha_{11}\frac{\partial^2 E}{\partial t^2} + e_{113}\frac{\partial^3 u}{\partial z\,\partial t^2} + e_{133}\frac{\partial^3 w}{\partial z\,\partial t^2} + p_1\frac{\partial\theta}{\partial t}\right.\\
&\qquad \left. + \sigma_{11}\frac{\partial E}{\partial t}\right) = 0
\end{aligned} \tag{57}$$

and

$$\theta = u = w = E = 0 \tag{58}$$

at $z \pm (h/2)$.

In general, there will be a discrete spectrum of wave numbers k corresponding with the waves running back and forth along the z direction, and for a fixed set of different parameters (rotational speed and material properties) there are eight distinct eigenfrequencies. One pair of them characterizes the thermal creep motion, two pairs are associated with the mechanical vibrations, and the last pair corresponds to the electromagnetic waves (which would obtain infinitely high values within the conventional electrically quasistatic theory). The specific values of the wave number k are determined by the thickness of the annulus and the boundary conditions at $z = \pm(h/2)$.

Qualitatively, the results can be taken for certain values of k from a recent paper[25] by the author. Quantitatively, the computation of the eigenvalues is more complicated because the governing determinant to be zero leads to characteristic eigenvalue equation of eighth and not of fifth degree. It is important that, with increasing speed, for the present problem instabilities may occur which might be possible for a fixed outside and a traction-free inner surface.

V. CONCLUSIONS

By taking the Maxwell equations in two different formulations and both additional thermal as well electric conductivity effects, the propagation of waves in rotating piezoelectric solids has been analyzed.

A linear theory is assumed so that all considerations are restricted to small speed rates because all pre-deformations due to steady-state centrifugal forces are neglected.

It has been shown that, depending on the assumptions in Maxwell's equations, a linear boundary value problem of different order in space and time results which is examined here for some basic cases of space-independent coefficients. It follows that, basically, an analytical or semi-analytical computation of the wave characteristics is possible.

The obtained results verify that, even though no mechanical damping influences are taken into account, the circular frequencies for the waves in unbounded media or the eigenvalues characterizing surface waves or the dynamics of an annulus are complex in general, i.e., there is thermal damping. For real problems this damping is very small. In addition, there is a thermal wave which is a creep motion for realistic data.

The rotational speed influences the wave characteristics significantly. The most interesting phenomenon is a destabilizing effect which for an annulus with a clamped outside boundary seems to be plausible, while for the wave propagation in an infinite medium, for surface waves in rotating half-spaces or for waves in bounded piezoelectrics with stress free outside surfaces, the results must be checked by a calculation which takes into consideration centrifugal stiffening effects. For finite bodies of cylindrical symmetry such a study is in preparation.

ACKNOWLEDGMENTS

In some parts, the present work originates from a six-month visit at Virginia Polytechnic Institute and State University. The author thanks Professors Daniel J. Inman and Raymond H. Plaut for their invitation. Financial support was provided by the Volkswagen Foundation.

[1] H. F. Tiersten, *Linear Piezoelectric Plate Vibrations* (Plenum, New York, 1969).
[2] R. A. Toupin, ''A dynamical theory of piezoelectrics,'' Int. J. Eng. Sci. **1**, 101–126 (1963).
[3] D. A. Berlincourt, D. R. Curran, and H. Jaffe, ''Piezoelectric and piezomagnetic materials and their function as transducers,'' in *Physical Acoustics*, edited by W. P. Mason (Academic, New York, 1964), p. 14.
[4] G. A. Coquin and H. F. Tiersten, ''Rayleigh waves in linear elastic dielectrics,'' J. Acoust. Soc. Am. **41**, 921–939 (1967).
[5] K. A. Ingebrigtsen, ''Surface waves in piezoelectrics,'' J. Appl. Phys. **40**, 2681–2686 (1969).
[6] H. S. Paul, D. P. Raju, and T. R. Balakrishnan, ''Free vibrations of a piezoelectric layer of hexagonal (6 mm) class, Int. J. Eng. Sci. **21**, 691–704 (1983).
[7] R. D. Mindlin, ''On the equations of motion of piezoelectric crystals,'' in *Problems of Continuum Mechanics*, N. I. Muskhelishvili 70th Birthday Volume (SIAM, Philadelphia, 1961), pp. 282–290.
[8] H. S. Paul and K. Renganathan, ''Free vibrations of a pyroelectric layer of hexagonal (6 mm) Class,'' J. Acoust. Soc. Am. **78**, 395–397 (1985).
[9] J. S. Yang and R. C. Batra, ''Free vibrations of a linear thermopiezoelectric body,'' J. Therm. Stresses **18**, 247–262 (1995).
[10] K. E. Pauley and S. B. Dong, ''Analysis of plane waves in laminated plates,'' Wave Electron. **1**, 265–285 (1974/76).
[11] J. J. Kyame, ''Wave propagation in piezoelectric crystals,'' J. Acoust. Soc. Am. **21**, 159–167 (1949).
[12] J. J. Kyame, ''Conductivity and viscous effects on wave propagation in piezoelectric crystals,'' J. Acoust. Soc. Am. **26**, 990–993 (1954).
[13] A. R. Hutson and D. L. White, ''Elastic wave propagation in piezoelectric semiconductors,'' J. Appl. Phys. **33**, 40–47 (1962).
[14] C.-C. Tseng and R. M. White, ''Propagation of piezoelectric and elastic surface waves on the basal plane of hexagonal piezoelectric crystals,'' J. Appl. Phys. **38**, 4274–4280 (1967).
[15] H. W. Lord and Y. Shulman, ''A generalized dynamical theory of thermoelasticity,'' J. Mech. Phys. Solids **15**, 299–309 (1967).
[16] D. S. Chandrasekharaiah, ''A generalized linear thermoelasticity theory for piezoelectric media,'' Acta Mech. **71**, 39–49 (1988).
[17] S. K. R. Chaudhuri and L. Debnath, ''Magneto-thermo-elastic plane waves in rotating media,'' Int. J. Eng. Sci. **21**, 155–163 (1983).
[18] Y.-H. Pao, ''Electromagnetic forces in deformable continua,'' in *Mechanics Today, Vol. 4*, edited by S. Nemath-Nasser (Pergamon, New York, 1978), pp. 209–305.
[19] R. Schmidt, ''Entwicklung und Anwendung einer Theorie der Magneto-Elasto-Dynamik von Schalen,'' Dr. sc. tech. Thesis, Technical University of Dresden (1980).
[20] J. Wauer and S. Suherman, ''Thickness vibrations of a piezosemiconducting plate layer,'' Int. J. Eng. Sci. **35**, 1387–1404 (1997).
[21] A. C. Eringen and G. A. Maugin, *Electrodynamics of Continua I* (Springer, New York, 1990), pp. 290–303.
[22] J. Wauer, ''Wave propagation in rotating thermo-piezoelectric solids,'' in *Modern Practice in Stress and Vibration Analysis*, edited by M. D. Gilchrist (Balkema, Rotterdam, 1997), pp. 127–136.
[23] W. Seemann and J. Wauer, ''Vibration of high speed disk rotors,'' in *Dynamics of Rotating Machinery, Part II*, edited by J. H. Kim and W.-J. Yang (Hemisphere, New York, 1990), pp. 35–50.
[24] J. L. Bleustein, ''A new surface wave in piezoelectric materials,'' Appl. Phys. Lett. **13**, 412–413 (1969).
[25] J. Wauer, ''Zur Dynamik rotierender pyroelektrischer Körper mit Rechteckquerschnitt,'' Z. Angew. Math. Mech. **78**, S801–S802 (1998).

Yellow Shark Spring 1995: Inversion results from sparse broadband acoustic measurements over a highly range-dependent soft clay layer

Martin Siderius and Jean-Pierre Hermand
SACLANT Undersea Research Centre, Viale S. Bartolomeo 400, 19138 La Spezia, Italy

(Received 11 May 1998; accepted for publication 22 February 1999)

In May 1995, SACLANTCEN performed broadband (200–800 Hz) acoustic measurements in the Giglio basin off the coast of Italy as part of the Yellow Shark inversion experiments. In this paper, inversion of sparse, broadband transmission loss (TL) measurements is investigated to determine bottom properties in strongly range-dependent (RD) situations commonly encountered in shallow water. The data are from the Elba–Formiche transect where water depth varies from 65 m at the acoustic projector location, to approximately 120 m at the 4-element vertical arrays deployed at ranges of 8, 16, 24, 32, and 40 km along the transect. The experimental site has a soft clay-layer bottom which varies in thickness from 3 to 10 m with a sound speed less than the water column. A modal analysis including coupling effect is given to explain the frequency bands for which high TL was observed as a function of range and depth. The TL measurements were inverted by matching the RD fields with model results. Using parabolic equation modeling, bottom geoacoustic parameters were varied in a marching search to fit the TL measured at the five ranges. The experimental results demonstrate that RD bottom properties such as sound speed and thickness of the slow clay layer can be obtained from broadband TL measurements sparsely distributed in range and depth. [S0001-4966(99)04907-3]

PACS numbers: 43.30.Pc, 43.30.Zk, 43.30.Ma [DLB]

INTRODUCTION

In shallow water, the strong dependence of acoustic propagation on bottom type has led to environmental inversion methods which exploit this relationship. In matched-field processing (MFP)-based inversions, acoustic fields are computed for many hypothetical bottom types in a search for suitable agreement between observed and modeled data. A number of papers have been published in recent years on determining properties of the environment by MFP using efficient search algorithms.[1–5] Inversion using MFP produces an estimate of the environment which, in the model, will best reproduce the observed acoustic field. Recently, experimental MFP inversion results have been published for nearly range-independent sites, based on narrow-band processing of shot data recorded on a vertical array.[6–8] Full-field inversion results from the Yellow Shark 1994 sea trials demonstrated that broadband measurements and processing were both required to obtain bottom parameters estimates that had low bias and variance with respect to *in situ* standard geoacoustic measurements.[9,10] Other inversion methods have been proposed which use horizontal hydrophone arrays with model-based processing[11] or form synthetic horizontal arrays to estimate wave number spectra.[12–14] A review of the acoustic inversion literature can be found in Ref. 9 and a collection of papers on these and other ocean acoustic inversion methods are presented in Ref. 15. The present paper differs from previous work as sparse, broadband transmission loss (TL) measurements from a strongly range-dependent (RD) site are used to invert for bottom properties. Added constraints are put on the sparse receiver inversion by forcing a match between observed and modeled data in absolute level over a broadband of frequencies.

The observed strong frequency dependence of TL on bottom type has led to studies on optimal frequencies of propagation in shallow-water environments. TL measurements have been made which demonstrate optimum frequencies of propagation depending on bottom type, water-column sound-speed profile (seasonal), and experimental geometry.[16–18] These demonstrations involved silt and/or sand bottoms with speeds greater than the water column. The analytic expressions for the frequency dependence of TL assumed a two-layer model with a fast sub-bottom. In contrast to low-loss frequencies of propagation, high-loss frequencies can occur when the upper layer of the sea floor has a compressional wave sound speed less than the water. By applying ray theory and assuming very small grazing angles for the bottom interaction, an analytic expression for the reflection coefficients was derived which shows selected frequencies of poor propagation under these conditions.[19]

The Yellow Shark sea trials conducted in the Fall of 1994 and the Spring of 1995 in the Giglio basin, off the west coast of Italy, were designed to develop and validate inversion techniques based on broadband propagation measurements.[9,10,20,21] Preliminary data/model comparison showed that frequency-dependent TL could be exploited to infer RD geoacoustic properties of the bottom.[22] In this paper, an approach is outlined to invert calibrated acoustic measurements taken along a 40-km transect between the islands of Elba and Formiche di Grosseto. The feasibility of using sparse TL data to determine important properties of the RD bottom are addressed. Broadband frequency-averaged

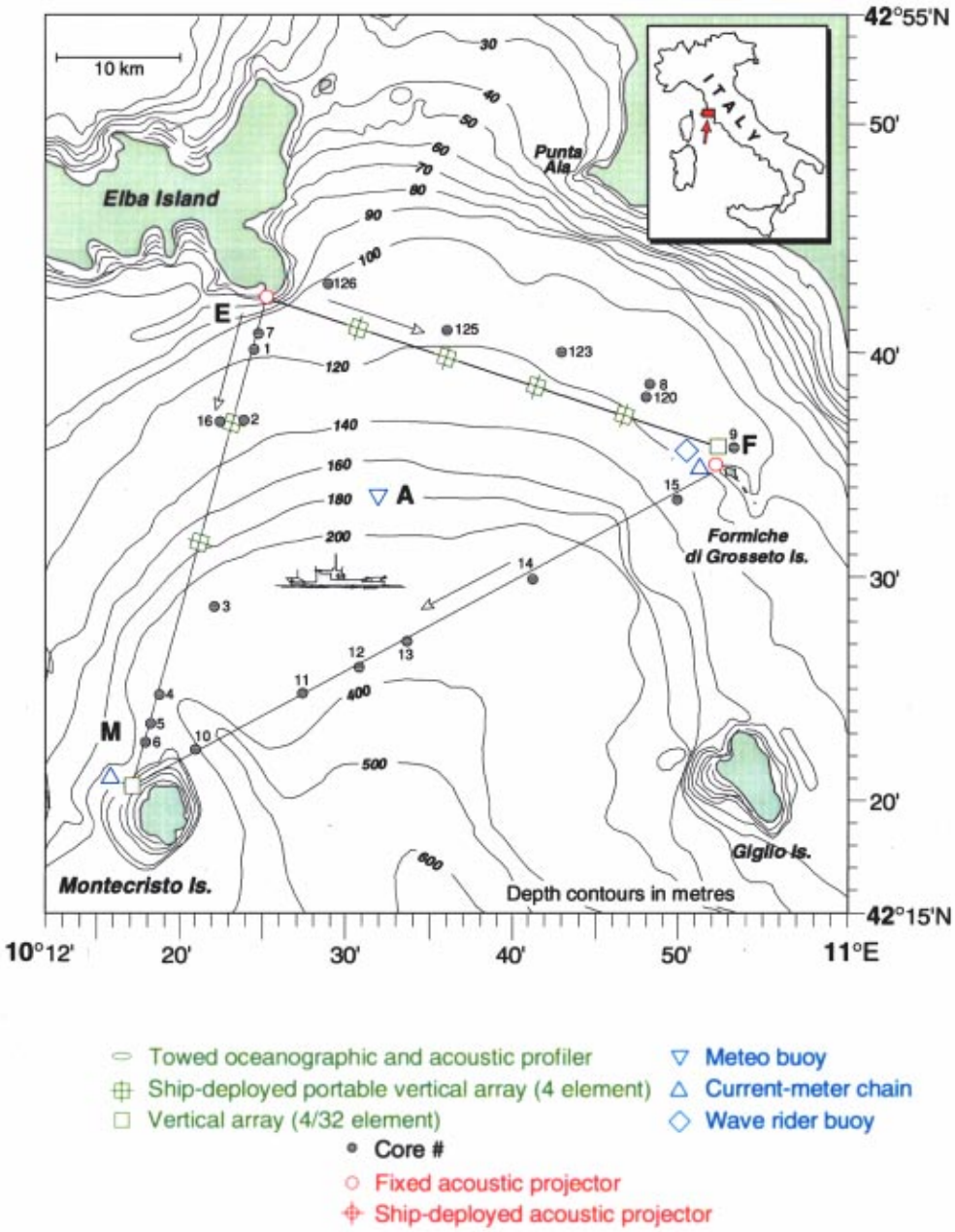

FIG. 1. Area of the Yellow Shark 95 experiments. Cores 1–16 are taken from Ref. 21, and cores 120, 123, 125, and 126 are taken from Ref. 27. The arrows indicate the direction of acoustic propagation. The 40-km transect between Elba (E) and Formiche di Grosseto (F) islands is considered in this paper.

TL is used as the acoustic observable because of its robustness against experimental or environmental uncertainty, and its low sensitivity, compared to narrow-band signals, to random fluctuations that occur due to a rough surface or bottom.[23]

The Yellow Shark Spring 1995 experimental geometry and environmental measurements are described in Sec. I. The site has a slow clay layer with variable thickness and compressional sound speed less than in the water column. The TL measurements show a frequency dependence which is especially strong on the hydrophone located near the bottom. The center frequency of the high-loss band is different from that expected using the above-mentioned analytic expression for propagation over a slow layer. Modal analysis is applied in Sec. II to explain the measured TL and depth-dependent location of the high-loss frequencies of propagation. Also presented in Sec. II is a mode-coupling analysis showing the effect of the strong range dependence upon propagation. A study of the sensitivity of the acoustic measurements to various bottom parameters is given in Sec. III. In Sec. IV a range-marching MFP inversion method is applied to TL data for determining RD bottom properties. The experimental inversion results show good agreement with direct geophysical measurements.

I. YELLOW SHARK 1995

During the Yellow Shark 95 experiments, extensive acoustic and environmental measurements were performed along three RD transects in the Giglio basin between the islands of Elba, Formiche di Grosseto, and Montecristo (transects 2, 3, and 4 in Fig. 1 in Ref. 9). Large time-

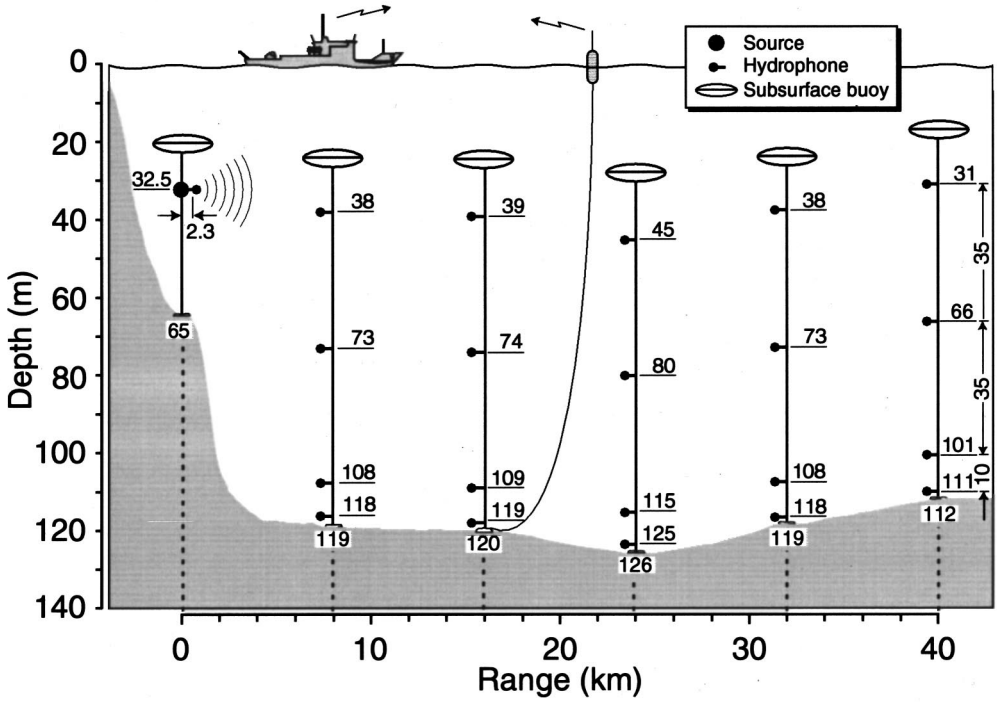

FIG. 2. Sound source and vertical arrays geometry for the runs on 2 May 1995, and bathymetry along the EF transect.

bandwidth-product signals spanning the frequency band 200–1600 Hz were transmitted with a repetition rate of 1 min for a period of 12 days. The propagation distances ranged from 8 to 55 km.

A. Experimental configuration

A map of the experimental area is shown in Fig. 1. The acoustic and oceanographic moorings deployed for the whole experiment are indicated. The TL data analyzed in this paper were obtained on 2 May 1995 along the 40-km Elba–Formiche (EF) transect. Figure 2 shows the experimental geometry. A sound source was bottom-moored in 65-m water depth and suspended at mid-water depth off the southeast point of Elba Island and connected to driving amplifiers on the shore. The sound source consisted of two flextensional projectors covering the frequency bands 200–800 and 800–1600 Hz. A 4-element vertical array was bottom-moored in 112-m water depth near the Formiche di Grosseto islands and connected to the shore. Another similar array (portable) with radio telemetry was deployed and bottom-moored by R/V ALLIANCE every 8 km along the EF transect. The hydrophones were positioned at $H-1$ m, $H-11$ m, $H-46$ m, and $H-81$ m where H is the local water depth. The hydrophone depths were slightly different from point to point as a result of the bathymetry. The water depth along the EF transect was nominally 120 m after a rapid decline from 65 m at the source location.

B. Acoustic data and processing

The probe signals consisted of 12-s duration pulses linear-frequency modulated over the bands 200–800 Hz (LF) and 800–1600 Hz (HF), transmitted every 2 min during the day from Elba (even minute) and Formiche (odd minute) stations. The electrical signals applied to the acoustic projectors were equalized to obtain a flat spectrum from the high-Q projectors. The resulting acoustic waveforms were measured in the far field (2.3 m) of the source from a pole-mounted reference hydrophone. The recorded waveforms were used to correct for the projector distortions and to calibrate the measured frequency-dependent transmission loss. Only the LF signals received from Elba station are considered in this paper (Table I).

Figure 3 shows the measured TL as a function of range and depth. The following description outlines the method for determining the TL.[22] The received signals were cross-correlated with the transmitted waveforms measured on the source reference hydrophone. One-sided cross spectra were calculated from fast Fourier transform using lag weighting. The transfer functions of the reference and vertical array hy-

TABLE I. Acoustic data selected from the Yellow Shark (LF) runs between Elba and Formiche di Grosseto islands on 2 May 1995. The runs are all documented in Ref. 21.

Run number	Time (UTC)	Ranges (km)	Pings
28	0606–0628	8	13
		40	13
32	0952–1028	16	19
		40	19
33	1031–1209	40	49
34	1212–1256	24	22
		40	23
36	1358–1416	24	15
		40	5
37	1420–1610	40	56
38	1624–1710	32	23
		40	16

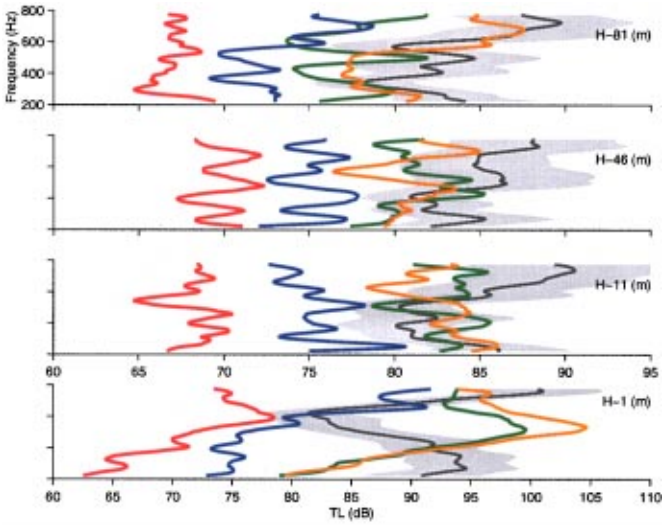

FIG. 3. Broadband transmission loss (TI) calculated from frequency response measurements at ranges of 8 (red), 16 (blue), 24 (green), 32 (orange), and 40 km (gray) on four hydrophones at $H-81$ m (top), $H-46$ m, $H-11$ m, and $H-1$ m (bottom) water depths. The TL scale is different for the $H-1$ m hydrophone. The light-gray area represents the variability of the measurements taken at 40 km (± 1 standard deviation).

drophone chains were included in the processing. At 40-km range, the broadband frequency responses were ensemble averaged (181 pings) over the whole day, whereas at the intermediate ranges of 8, 16, 24, and 32 km the averaging period corresponded to half the period of deployment (LF runs in Table I). The TL data were further smoothed using a moving average over 50-Hz-wide frequency bands for later comparison with model results averaged similarly. The variability of the TL at 40 km is also shown in Fig. 3.

C. Oceanographic data

The hydrological conditions along the EF transect were measured during the acoustic transmissions. Figure 4 shows the sea-surface temperature over the experimental area. This infrared image taken by the NOAA14 satellite at 1230 UTC on the day after the TL measurements and other images taken on following days showed that the surface was consistently 0.5–1.0 °C warmer near Elba island. CTD casts taken during the TL measurements and other days showed simultaneous temperature and salinity changes in the upper meters of the water column near the midpoint of the transect. Figure 5 shows the ocean sound-speed profile (SSP) as function of time and range calculated from CTD data at 4, 11, and 28 km ranges from Elba station. Other CTD profiles were collected every hour at Formiche station.[21] The surface temperature distribution and CTD data indicated two different water bodies in the upper layer, each extending over half the length of the EF transect. The resulting spatial and temporal variability of the ocean SSP affected acoustic propagation especially at frequencies above 400 Hz. This was concluded since the source/receiver geometry was fixed and the sea was calm. The variability is evident by the gray shaded area for the 40-km TL in Fig. 3. The gray area represents $\pm$ one standard deviation of the TL measurements taken over the entire day of the experiment.

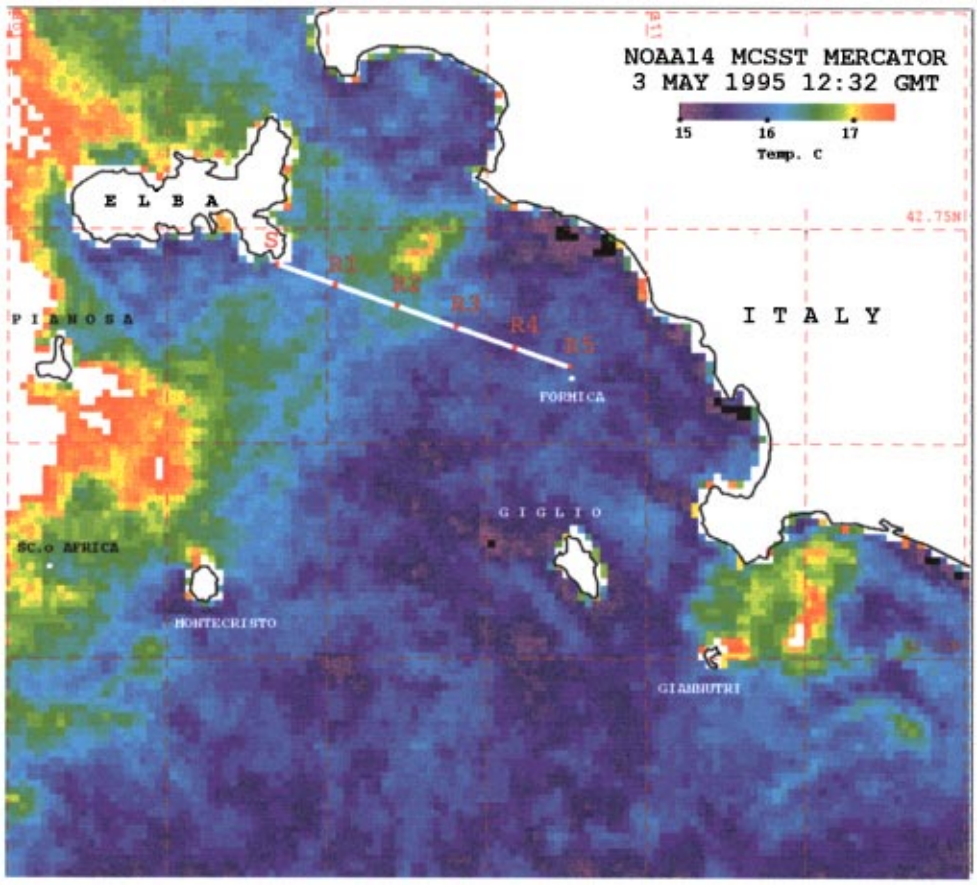

FIG. 4. Infrared NOAA14 satellite image showing sea-surface temperature over the Yellow Shark 95 experimental region on 3 May 1995.

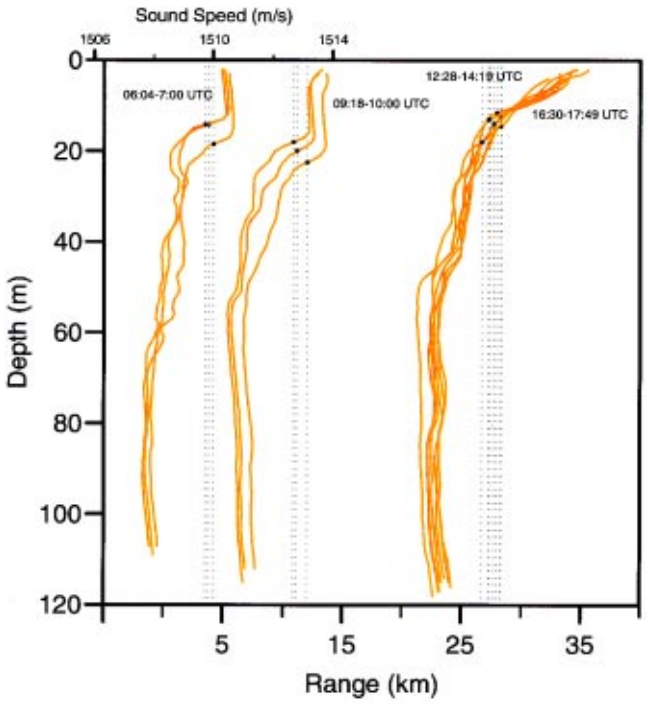

FIG. 5. Ocean sound-speed profiles collected on 2 May 1995 along the EF transect. The range is referred to the sound source at Elba Island. For each profile, the dot and vertical line indicate the midvalue of the sound speed scale.

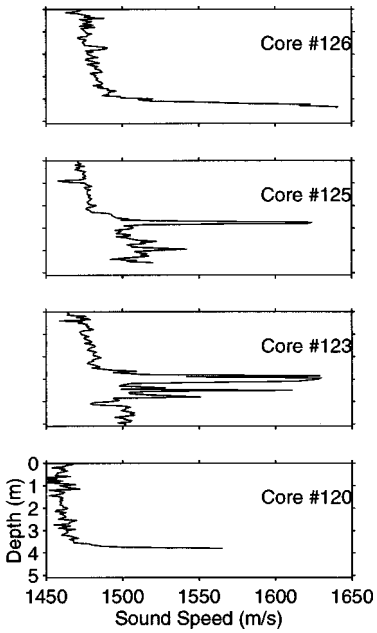

FIG. 7. Compressional wave sound-speed profiles measured on sediment cores. The selected cores are close to the receiving arrays as shown in Fig. 1.

D. Geophysical data

The sea bottom in the Giglio basin platform is characterized by a low-speed clay layer of variable thickness (several meters) overlying a higher-speed silty clay bottom with grain stone at the interface; the sub-bottom is made of similar consolidated sediments.[9] From the Yellow Shark experiments in the summer of 1994, broadband full-field inversion of 32-element vertical-array data estimated an upper sound speed of 1465–1475 m/s and a gradient of 2.5–4.5 s^{-1} for the top sediment layer and a sound speed of 1530–1540 m/s for the silt sub-bottom northwest of Formiche di Grosseto islands.[9,10] The sound speed and gradient in the top layer were mildly range dependent. The inferred density of 1.5 g/cm^3 and attenuation of 0.04–0.06 decibels per wavelength (dB/λ) of the top layer, and respectively, 1.8 g/cm^3 and 0.10–0.15 dB/λ of the sub-bottom, were consistent with early results in Ref. 24. Seismic profiling, sediment coring, and historical data were used to build a geoacoustic model of the Giglio basin platform (Fig. 15 in Ref. 9). Geological interpretation of seismic profiles and sediment cores showed that the geoacoustic model and above ranges of parameter values were applicable to the whole platform.[25,26,10] Henceforth, this will be referred to as the YS geoacoustic model. The digitized seismic profile in Fig. 6 shows the range-dependent top-layer thickness (3–10 m) along EF transect.[22] Figure 1 shows the locations of sediment cores collected during Yellow Shark 95[21] and of previously collected samples.[27] Figure 7 shows the variability of sound speed in the top clay layer along the EF transect. The coring locations were close to the vertical arrays ranges. See cores 8 and 9 in Fig. 12 of Ref. 9 for comparison with core 120 at 32-km range and core 9 at 40-km range, respectively.

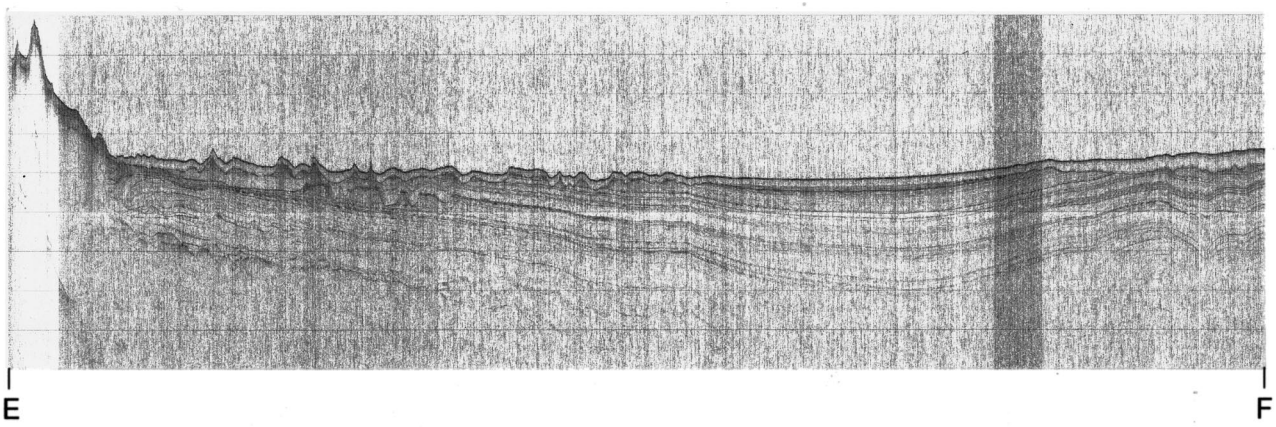

FIG. 6. High-resolution seismic profile of the EF transect. The sound source was at the Elba station (E) and the stationary VA was at Formiche (F).

II. PROPAGATION OVER THE ELBA–FORMICHE TRANSECT

Important acoustic propagation anomalies take place when the environment is that given by the YS geoacoustic model described in the previous section. From the YS model, two RD models of the Elba–Formiche (EF) transect will be derived, EF-A and EF-B. A modal analysis is applied to EF-A and EF-B which describes the response of low frequency (200–800 Hz) acoustic propagation in these environments.

Assuming the ocean waveguide is driven by a time-harmonic $\exp(-i\omega t)$ point source at range $r=0$ and depth $z=z_s$, and neglecting a constant scaling factor, the adiabatic approximation predicts the acoustic pressure to be given by

$$P(\omega;r,z) = \sum_m \frac{1}{\sqrt{\phi_m(\omega)}} \Psi_m(\omega;0,z_s)\Psi_m(\omega;r,z)\exp[i\phi_m(\omega)], \tag{1}$$

where Ψ_m is the local normal mode and ϕ_m is the integration of the local eigenvalues, k_m, between source and receiver.[28] The local normal modes and eigenvalues satisfy the depth equation for each range

$$\rho(z)\frac{d}{dz}\left[\frac{1}{\rho(z)}\frac{d}{dz}\Psi_m(\omega;z)\right] + \left[\frac{\omega^2}{c(z)^2} - k_m(\omega)^2\right]\Psi_m(\omega;z) = 0, \tag{2}$$

where $\rho(z)$ is density and $c(z)$ is the sound speed. Under the assumption of range independence, $\phi_m = k_m r$. If the medium is slightly lossy, a perturbation approach can be used; to first order $\Psi_m(\omega;z)$ remains real and $k_m(\omega) = k'_m(\omega) + i\alpha_m(\omega)$.

A. EF-A model: Propagation over a lossy clay layer

The slow clay layer overlying a fast sub-bottom forms a secondary waveguide with a cutoff frequency above which acoustic modes are supported. This layer acts as a bandstop filter, attenuating selected frequencies which infuse significant energy from the water into the clay. The frequency bands of high loss can be observed in long-range acoustic measurements, and the degree of loss will depend on the attenuation of the clay. In a modal representation, the nulls in broadband TL correspond to the frequencies which strongly excite modes which travel in the clay waveguide.

This filtering effect of the clay layer was simulated using the range-dependent, finite-element, parabolic equation code RAM.[29] The EF-A model simplifies the EF transect by using a range-averaged environment. Constant bathymetry with range is taken ($H=120$ m) with the first 22 km having a clay layer thickness of $T_{\text{clay}}=4$ m followed by a 1-km transition region to $T_{\text{clay}}=6$ m for the remainder of the 40 km. The source is located at midwater depth and the water column has a constant sound speed of $C_{\text{water}}=1509$ m/s (the average of all the CTD measurements); the clay layer is homogeneous with sound speed $C_{\text{clay}}=1480$ m/s, density $\rho_{\text{clay}}=1.5$ g/cm^3, and attenuation $\alpha_{\text{clay}}=0.06$ dB/λ. The sub-bottom is also homogeneous with sound speed $C_{\text{silt}}=1560$ m/s, density $\rho_{\text{silt}}=1.8$ g/cm^3, and attenuation $\alpha_{\text{silt}}=0.15$ dB/λ. Constant hydrophone distances from the bottom are maintained at $H-1$ m, $H-11$ m, $H-46$ m, and $H-81$ m, as was the experimental configuration. EF-A is useful for illustrating the main features of the acoustic propagation in a simplified setting without the complicated realism which will be later incorporated into the EF-B model in Secs. II B and IV.

In Fig. 8, frequency-averaged TL plots are presented for the EF-A model. Strong frequency-dependent features of the TL are evident. In the top three hydrophones, bands of high loss occur near 260 and 800 Hz. The $H-1$ m (bottom) hydrophone has a slightly different response. A high-loss band is developing near 580 Hz over the first 22 km and two bands begin to develop at 300 and 800 Hz for propagation between 23 and 40 km. The bands of high loss are weak up to 20-km range, which is consistent with measurements (shown in Fig. 3). The bottom phone's strong bands of high loss are also consistent with the measured TL—although the EF-A model fails to match at all ranges due to the oversimplified model.

The results of Fig. 8 can be interpreted using normal modes. As the large-scale features of the propagation loss are of primary interest, the frequency-averaged TL is approximated by an incoherent calculation[28]

$$\mathrm{TL}(\omega;r,z) = -10\log\frac{1}{\rho(z_s)}\sum_m \left|\frac{1}{\sqrt{k_m r}}\Psi_m(\omega;0,z_s) \times \Psi_m(\omega;r,z)\exp(ik_m r)\right|^2. \tag{3}$$

Considering the first 22 km where $T_{\text{clay}}=4$ m, the low frequencies (below 200 Hz) do not support modal propagation in the clay and mode 1 is waterborne. At higher frequencies (above 300 Hz), mode 1 is contained mostly in the clay layer and has little energy in the water column. As a result, for a source positioned at midwater depth, mode 1 is poorly excited at high frequencies and at low frequencies, is a low-loss waterborne mode. At the transition frequencies (200–300 Hz), a source at midwater depth excites energy into the clay layer, which is consequently attenuated after long-range propagation. To see the filtering effect, several conditions must occur: the clay-layer waveguide must support acoustic modes, the clay-layer modes must be excited either directly by the source or through mode coupling, and the clay must be lossy. Figure 9 shows the propagation of mode 1 only, propagation summing all M discrete modes and propagation summing modes 2,...,M. The high-frequency TL is not affected by the absence of mode 1 mainly because the midwater source does not excite this mode. In contrast, the low frequencies are dominated by this low-loss mode. The band of high TL is developed in the frequency transition region centered around that predicted, using the analytic expression derived using a ray model.[19] Modal group velocity curves show that the mode filtering transition region occurs at the frequencies in which the modes move from traveling in the water to the clay.[22]

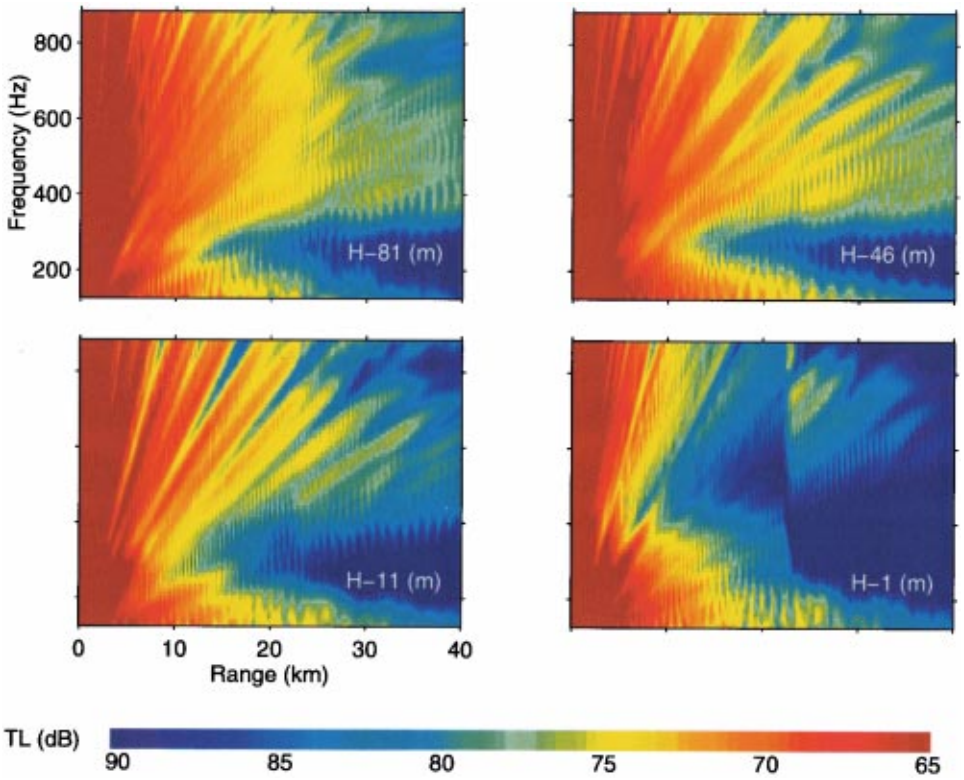

FIG. 8. Transmission loss for EF-A model at the four depths indicated. Bands of high loss can be seen near 200 and 800 Hz. Note the strong influence of the local value of T_{clay} on the $H-1$ hydrophone as it increases from 4 to 6 m between 22 and 23 km ranges.

For receivers near the bottom, a second, stronger effect dominates the TL curves. In Fig. 10, the TL is shown for hydrophones at three depths. The appearance of a second band of high loss is evident on the H—1 m hydrophone at 580 Hz. The reason for the high-loss band at 580 Hz is the lack of modal energy at the H—1 m position. That is, the sum of mode functions [in Eq. (1)] evaluated at depth of H—1 m approaches zero at 580 Hz. The minimum is a consequence of the local normal modes and hence the local environment. This effect causes the local environmental conditions to strongly influence the measured TL at the H—1 m hydrophone position.

Another band of high loss develops at the frequencies in which the clay-layer thickness also supports mode 2. In the case of $T_{clay}=6$ m, as for the 23–40-km section of the EF-A model, the mode 2 transition region is at 800 Hz, as seen in Fig. 11. The mode 1 transition region has moved down to 170 Hz.

The high TL band due to mode 1 filtering can be seen in the first 22 km of the EF-A model, and the weaker mode 2 loss starts to develop at ranges 23–40 km where $T_{clay}=6$ m (Fig. 8). Mode 1 filtering in the 23–40-km section is shifted down in frequency and this ''smears'' the high-loss band towards the lower frequencies. The localized behavior of the H—1 hydrophone is evident in Fig. 8, as a shifting in frequency of the high-loss band occurs between 22- and 23-km

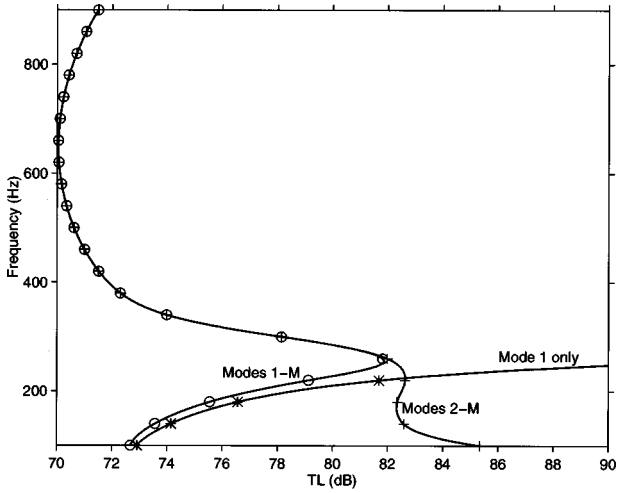

FIG. 9. Effect of mode 1 on propagation; summation over all modes $1-M$ (○), modes $2-M$ (+) and mode 1 only (*). Response is at midwater depth and bottom properties are the same as defined for the first 22 km of the EF-A model.

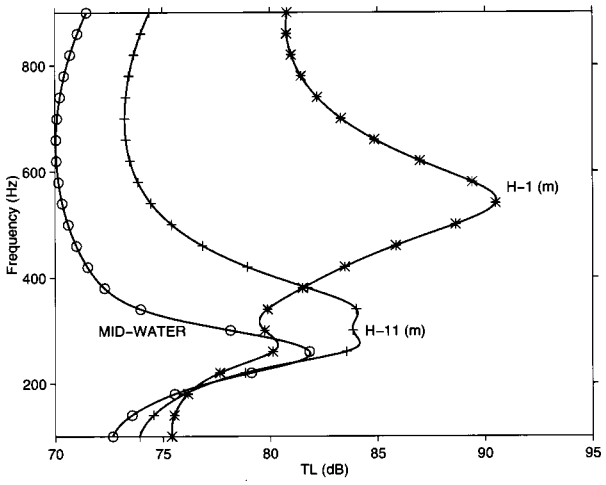

FIG. 10. Depth dependence of high-loss band for $T_{clay}=4$ m. Only mode 1 filtering is within the band of frequencies shown. Midwater hydrophone (○), $H-11$ m (+), and $H-1$ m (*). Bottom properties are the same as defined for the first 22 km of the EF-A model.

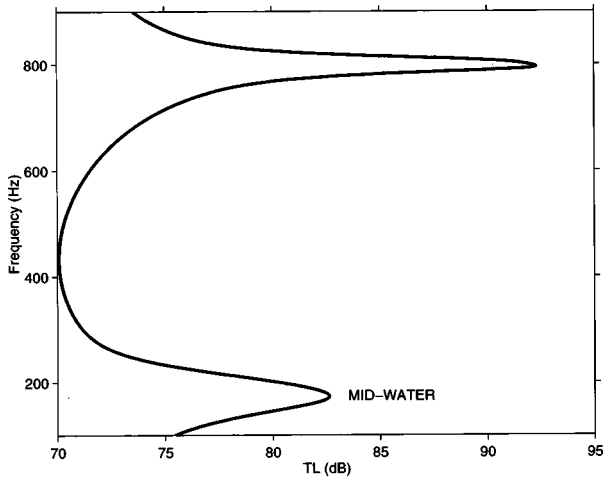

FIG. 11. Two bands of high loss for $T_{clay}=6$ m. Mode 2 filtering is evident near 800 Hz. Bottom properties are the same as defined for the 23–40-km section of the EF-A model.

range, where T_{clay} has a transition from 4 to 6 m. In contrast to the upper hydrophones, the strong frequency-band shifting can only be seen on the bottom hydrophone.

B. EF-B model

The EF-A model gives insight into the filtering effect caused by the clay layer. The EF-B model considered here has the same water and bottom properties as the EF-A model with an added level of complexity as the range-dependent bathymetry and clay-layer thickness obtained from a digitized seismic profile are included. In this section, a mode-coupling analysis is used to determine the exchange of energy between propagating modes.

Ocean acoustic models that assume little or no variability in the environment with respect to range allow application of the adiabatic approximation which implies no transfer of energy between the acoustic modes. That is, the acoustic modes propagate independently and do not couple energy to each other. The validity of the adiabatic approximation depends on environmental factors as well as frequency.[30–32] Referring to (1), a more general expression for the pressure field is formulated in Ref. 33,

$$P(\omega;r,z)=\sum_m a_m(\omega;r)\Psi_m(\omega;r,z), \tag{4}$$

where $a_m(\omega;r)$ is the complex coefficient for mode m and depends on the source depth and environment. For adiabatic propagation,

$$a_m(\omega;r)=\frac{1}{\sqrt{\phi_m(\omega)}}\Psi_m(\omega;0,z_s)\exp[i\phi_m(\omega)]. \tag{5}$$

In (5), $|a_m(\omega,r)|$ varies in range by the geometrical spreading and by a weakly mode-dependent attenuation. For strong range dependence, modes exchange energy as they propagate causing the modal coefficients to differ from the expression given by (5). At any range, using the orthogonality property of the modes, both sides of (4) can be multiplied by the local-mode function $\Psi_m(\omega;r,z)$ and integrated over depth, decomposing the pressure field into the modal coefficients. The parabolic equation (PE) code RAM was used to determine propagation for the EF-B model and verified with coupled, normal-mode code CSNAP.[34] For convenience, as a starting field (source function), each of the discrete modes was excited with unity amplitude and the resulting field launched into the waveguide. The normal-mode code KRAKEN was used to compute the local modes.[35] The pressure field was decomposed at 100-m intervals in range, to extract the modal amplitudes. Figure 12 shows the modal amplitudes as a function of range at 500 Hz along with the

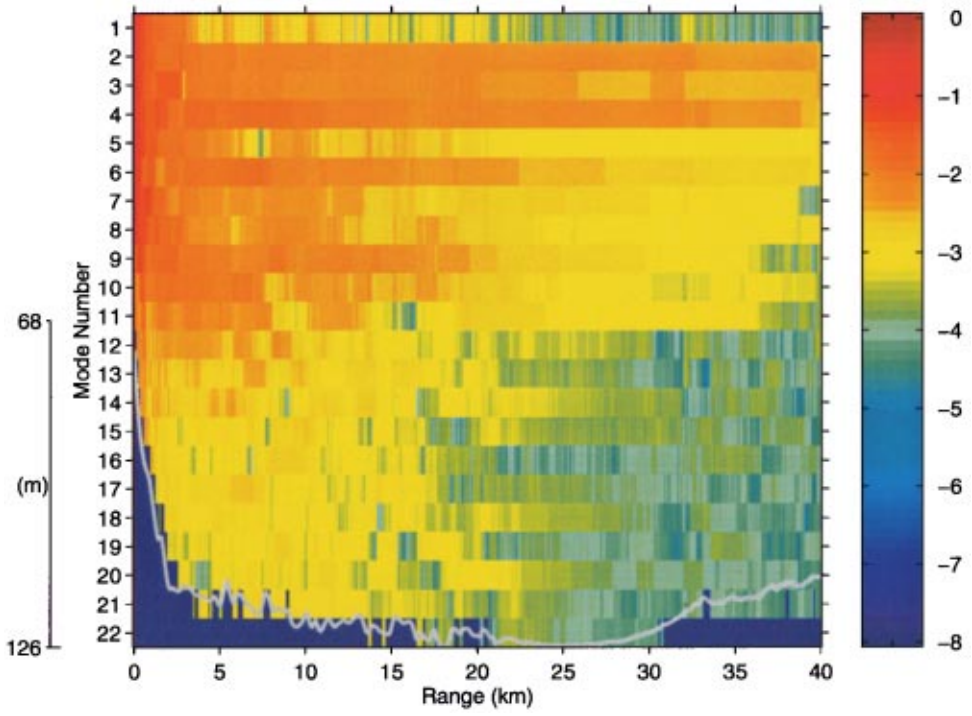

FIG. 12. Modal amplitudes ($\log|a_m|$) for the EF-B model with changing bathymetry and clay-layer thickness. Bathymetry is shown as a gray line with scale on the left.

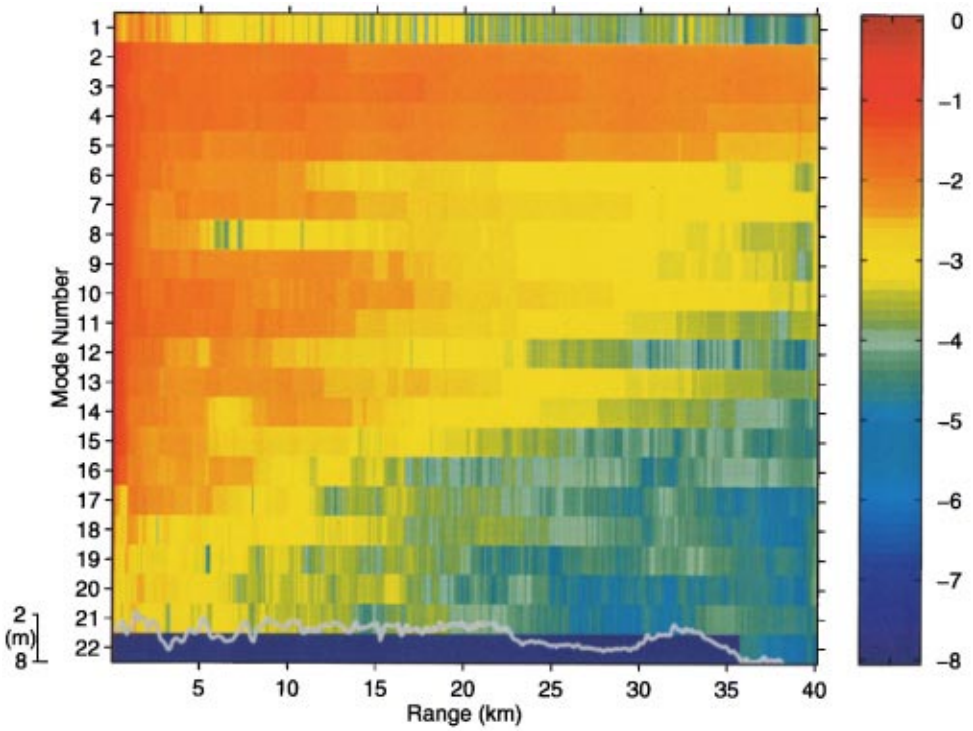

FIG. 13. Modal amplitudes ($\log|a_m|$) using EF-B model with range-dependent clay-layer thickness but holding the water depth constant. The gray line indicates the local value of clay-layer thickness with scale on the left.

bathymetry. At the source location, 11 modes are supported. In the first 5 km of propagation, there is the addition of new, strongly energized modes as the water depth increases and more modes are supported. Throughout the EF transect, modes appear and disappear according to the changing H and T_{clay}. The increase and decrease in the modal amplitudes is an indication of the exchange of energy between the modes, as there is coupling throughout the transect.

To isolate the effect of bathymetry and clay layer on mode coupling, a second case was simulated keeping the depth constant at $H=120$ m, but still using the range-dependent T_{clay}. The modal amplitudes and T_{clay} are shown in Fig. 13. Note the change of some modal amplitudes as the range dependence of T_{clay} only causes modes to couple. A newly energized mode (number 22) appears at range 36 km due to the increase in T_{clay} from 3 to 8 m.

This analysis shows there is significant exchange of energy between the modes caused by both the range-dependent H and T_{clay}. A PE model such as RAM with range steps of about a wavelength and capable of including mode-coupling effects is well suited for range-dependent environments such as the EF-B model.

III. SENSITIVITY ANALYSIS

Range-independent numerical simulations are used (with KRAKEN) to identify the relationship between bottom properties and frequency response. Six bottom properties are varied to determine the effect on TL 20 km down range. This is not an exhaustive study, but will illustrate the sensitivity of the acoustic field to a slow clay layer over a faster sub-bottom.

For a baseline, a test case is used with the same properties as the first 22 km of the EF-A model. The parameters varied are $T_{\text{clay}}, C_{\text{clay}}, \alpha_{\text{clay}}, C_{\text{silt}}$, the sound-speed gradient in the clay layer, ΔC_{clay}, and the density ratio, $\rho_{\text{clay}}/\rho_{\text{water}}$. When a single parameter is varied, the others are maintained at baseline values: $T_{\text{clay}}=4$ m, $C_{\text{clay}}=1480$ m/s, $\alpha_{\text{clay}}=0.06$ dB/λ, $C_{\text{silt}}=1560$ m/s, $\Delta C_{\text{clay}}=0\ \text{s}^{-1}$, $\rho_{\text{clay}}/\rho_{\text{water}}=1.5$ and $\rho_{\text{silt}}/\rho_{\text{water}}=1.8$. Because of the depth dependence in the pressure field described previously, sensitivity results will be presented at midwater depth and at 1 m from the bottom. For convenience, these will be referred to as the top and bottom hydrophones. In Figs. 14 and 15, the TL is shown as a function of parameter value and frequency. For each plot, the corresponding baseline value is indicated by a vertical line.

As clay thickness is varied, the top and bottom hydrophone TL curves appear very sensitive over the range $0.5\ \text{m} \leqslant T_{\text{clay}} \leqslant 9$ m. The top hydrophone shows a high TL band moving from near 800 Hz at $T_{\text{clay}}=0.5$ m to under 200 Hz at $T_{\text{clay}}=9$ m. For T_{clay} between 5 and 6 m, the second notch frequency due to mode 2 filtering begins to appear. The bands corresponding to modes 1 and 2 filtering are evident for the top and bottom hydrophones. The bottom hydrophone shows even higher TL bands centered at frequencies in which the mode functions all approach zero, as described previously in Sec. II A.

The TL resulting from varying the sound speed in the clay shows the top hydrophone as having a marked band of high loss, which shifts upward in frequency as C_{clay} is increased. For $C_{\text{clay}}=1460$ m/s, the band of high loss appears near 200 Hz and is approaching 800 Hz as $C_{\text{clay}}=1510$ m/s. The TL level also increases as the sound speed is increased. The bottom hydrophone shows a similar band of high loss at the same location as the top hydrophone, but shows a band of higher TL, which again is a result of the depth-dependent frequency response as described in Sec. II A.

Also shown in Figs. 14 and 15 is the TL for the top and

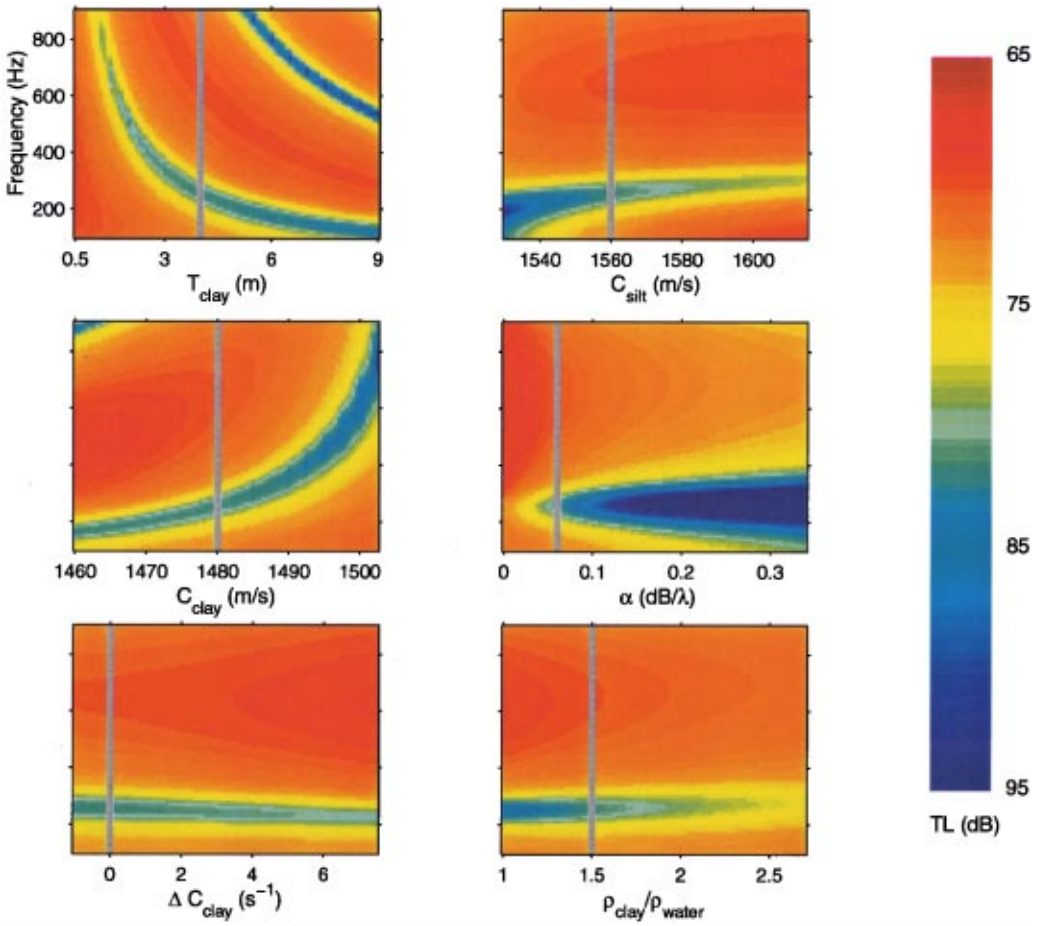

FIG. 14. Midwater hydrophone sensitivity to varying environmental parameters. The plots show simulated TL at 20 km using the EF-A geoacoustic model. The solid vertical line indicates the baseline value held fixed while the other parameters are varied.

bottom hydrophones as ΔC_{clay} is varied from -1 s^{-1} to $+7$ s^{-1} maintaining the average sound speed at 1480 m/s. The high-loss band shifts slightly with frequency as the gradient changes. The different bands of high TL between the top and bottom hydrophones are again evident, but neither is greatly affected by the sound-speed gradient.

Varying C_{silt} from 1530 to 1610 m/s has a modest effect on TL for both the top and bottom hydrophones. A slight shifting up in frequency of the high-loss band occurs with increasing C_{silt}. As the sound speed is increased, the level of loss decreases slightly, due to less penetration.

The effect on the top and bottom hydrophones as α_{clay} is varied from 0 to 0.32 dB/λ shows the bands of high loss increasing nearly uniformly across frequency with attenuation. For attenuation levels near 0 dB/λ, the top hydrophone does not have a distinctive band of frequencies with high loss, but at 0.32 dB/λ the loss near 300 Hz is greater than 20 dB. The bottom hydrophone shows the two bands of high loss even more clearly as the attenuation is increased. Also, the bottom hydrophone shows a band of high loss even when the attenuation in the clay is zero, which is consistent with the notion that the bottom hydrophone high-loss band is not entirely a result of long-range propagation and attenuation.

The density of the clay seems to be a relatively insensitive parameter to the type of measurements considered here. Varying the ratio $\rho_{\text{clay}}/\rho_{\text{water}}$ from 1 to 2.75 does not greatly impact the location of the high-loss frequency bands. The bottom hydrophone appears slightly more sensitive to this parameter than does the top hydrophone.

The results of the sensitivity study show that the main properties of the bottom affecting the frequency-dependent acoustic fields down range are T_{clay}, C_{clay}, and C_{silt}. The α_{clay} acts to emphasize the high-loss bands without shifting them in frequency; ΔC_{clay} and ρ_{clay} are the least sensitive of the parameters considered here. For determining properties of the ocean bottom by acoustic inversion, this sensitivity study also provides an estimate of reasonable bounds for the search spaces for each unknown quantity. The shapes of the bands of high loss for T_{clay} and C_{clay} suggest a coupling between these parameters. A thinner clay layer with a faster sound speed may produce a high TL at the same frequency. This coupling is apparent when trying to determine, through inversion of the acoustic data, both T_{clay} and C_{clay}. This can be seen from the inversion results described in the next section.

IV. INVERSION OF THE ELBA–FORMICHE ACOUSTIC DATA

In Fig. 3, the experimentally observed TL data are presented as a function of frequency for the five measurement ranges. The ensemble-averaged data show large scale fea-

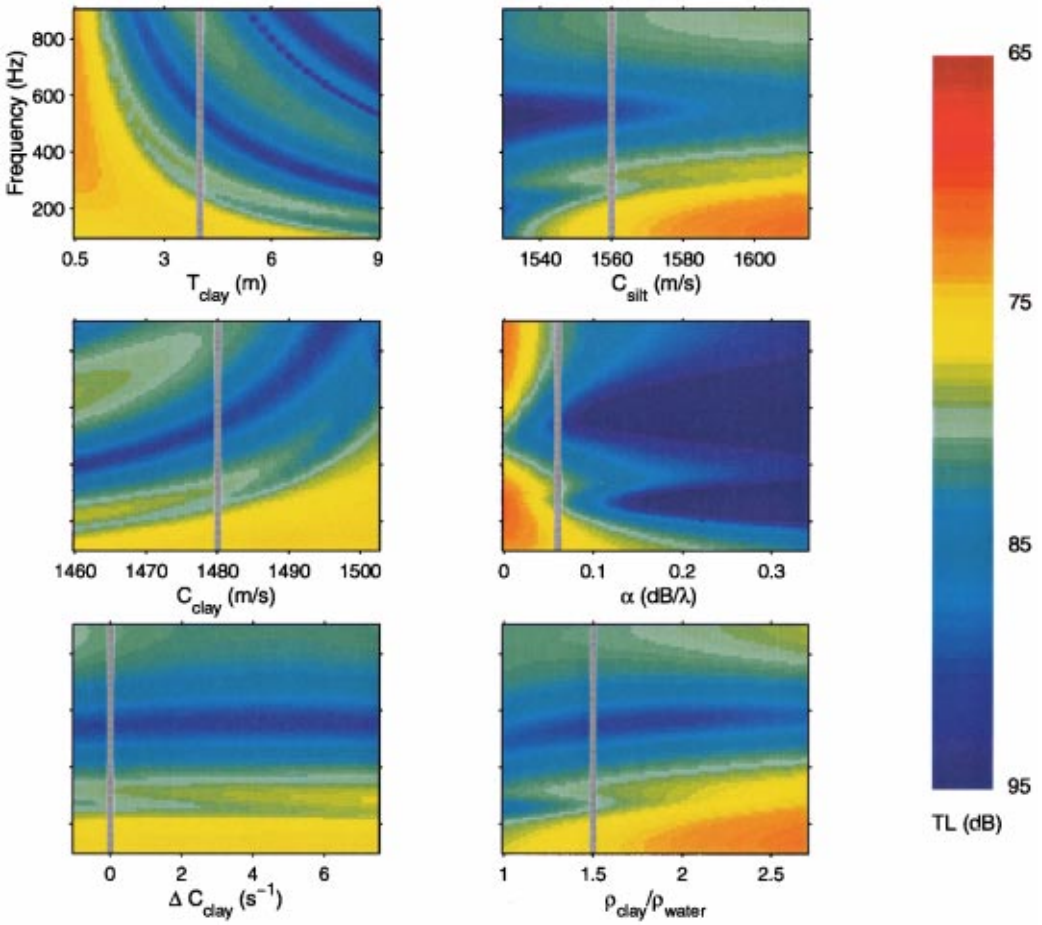

FIG. 15. Bottom hydrophone sensitivity to varying environmental parameters. The plots show simulated TL at 20 km using the EF-A geoacoustic model. The solid vertical line indicates the baseline value held fixed while the other parameters are varied.

tures which vary with range and are particularly strong on the $H-1$ hydrophone. Note the measured data for the $H-1$ hydrophone at 24 km where $T_{\text{clay}} \approx 4$ m, in which the high-loss frequency band is near 580 Hz as compared to the EF-A modeled TL at 20 km where the clay layer has nearly the same value (Fig. 10). The strong TL features on the $H-1$ hydrophone appear even using the simpler EF-A model. However, the EF-B model with RD bottom properties needed to be included in the inversion models to match the measured data at all ranges. Although the frequency-averaged TL simulations did not show a high sensitivity to the ocean sound speed, the RD profiles were included in the inversion models and linearly interpolated between (CTD casts 38, 39, and 40 on 2 May 1995 in Ref. 21 were used). In Secs. IV A and B, the inversion models, method, and results are described.

A. Inversion method

The inversion approach was as follows: RAM was used to simulate the RD propagation and the most sensitive bottom parameters were varied searching for the best match (in the least mean-squared-error sense) between modeled and experimentally measured TL. The simulations were performed in 10-Hz increments in the band from 200–800 Hz. As with the measured data, the simulated data were smoothed using a moving average of 50-Hz width. A march-

TABLE II. Estimated bottom properties for the 40-km Yellow Shark 95 experimental region Elba to Formiche transect. For T_{clay}, in parentheses are the measured average values over the segment using seismic profile data. Inversions 2 used measured T_{clay} from the seismic profile.

Parameter	0–8 (km)	8–16 (km)	16–24 (km)	24–32 (km)	32–40 (km)
C_{clay} (m/s)					
Inversion 1	1484 s.d. 5.6	1484 s.d. 6.7	1484 s.d. 4.5	1467 s.d. 7.0	1463 s.d. 3.9
Inversion 2	1478 s.d. 2.5	1484 s.d. 1.3	1493 s.d. 1.0	1463 s.d. 1.0	1486 s.d. 1.4
C_{silt} (m/s)					
Inversion 1	1554 s.d. 9.8	1585 s.d. 15.1	1551 s.d. 15.7	1586 s.d. 22.3	1563 s.d. 24.2
Inversion 2	1553 s.d. 5.2	1584 s.d. 5.9	1557 s.d. 17.8	1582 s.d. 8.2	1583 s.d. 5.2
T_{clay} (m)					
Inversion 1	4.8 s.d. 0.3 (4.7)	4.4 s.d. 0.9 (3.8)	3.1 s.d. 0.2 (4.0)	4.2 s.d. 0.4 (5.5)	5.6 s.d. 0.3 (6.5)

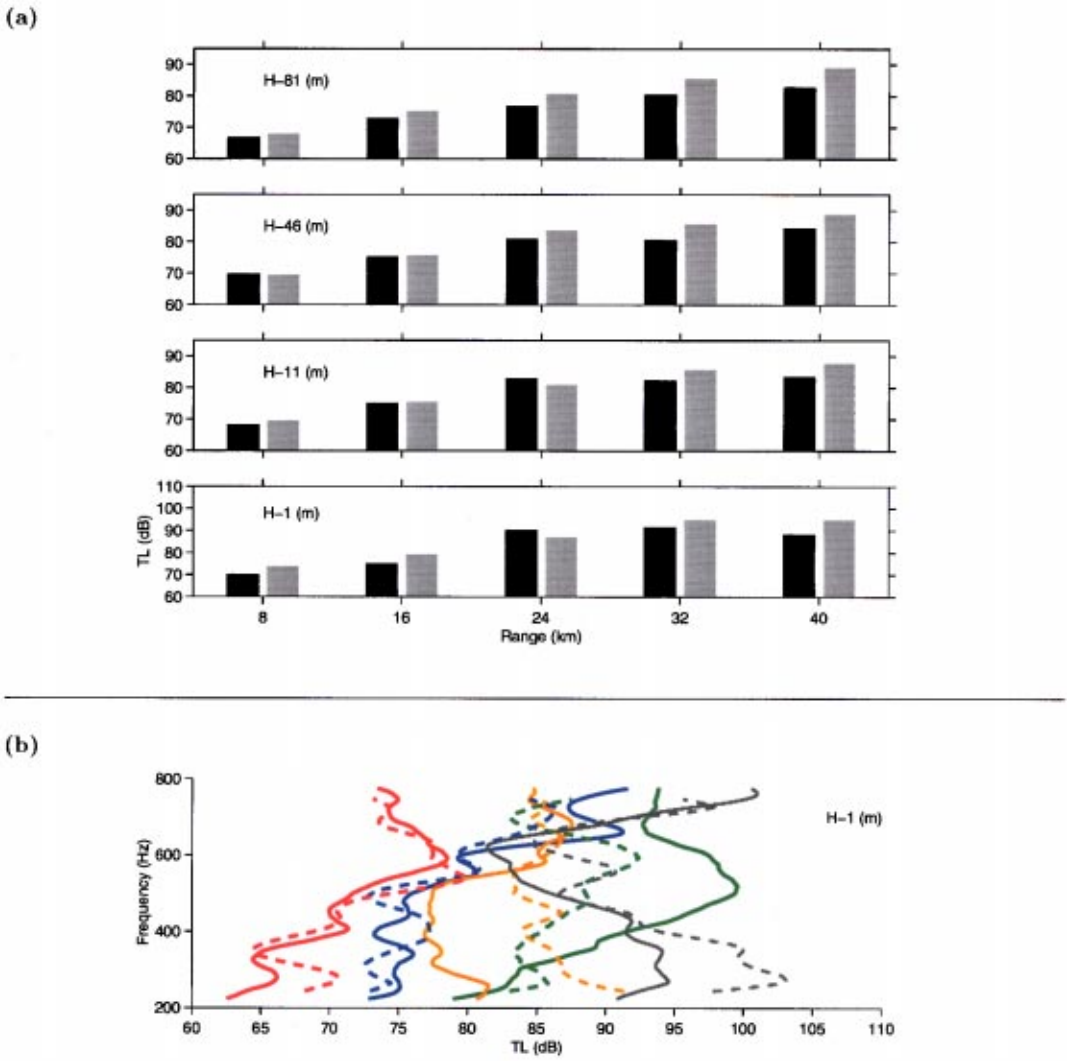

FIG. 16. At the top (a), averaged TL over frequency for model (light gray) and measured (black) hydrophones located at $H-81$ m, $H-46$ m, $H-11$ m, and $H-1$ m. Note the TL scale change on the $H-1$ hydrophone. Bottom plot (b) is measured (solid) and modeled (dashed) TL vs frequency for $H-1$ m hydrophone for inversion 2 at ranges of 8 (red), 16 (blue), 24 (green), 32 (orange), and 40 km (gray).

ing technique in range was used in which the bottom parameters giving the best fit to the measured data were determined at each array location before proceeding down range. The EF transect was divided into five range segments: 0–8, 8–16, 16–24, 24–32, and 32–40 km. The final ranges of each segment correspond to the locations of the vertical arrays. The simulated pressure field with the best fit was stored and the PE was restarted from that range when searching for the bottom parameters of the next segment. The marching provides a computational advantage in that searching for the bottom properties of the last range segment between 32–40 km requires the same computation time as the first segment between 0–8 km. Simulation run times were lengthy, making it impractical to use global optimization methods such as simulated annealing or genetic algorithms, which require computing several thousand forward models.

B. Inversion results

The first inversion used a search space consisting of: $T_{\text{clay}}=3-9$ m, $C_{\text{clay}}=1460-1500$ m/s, and $C_{\text{silt}}=1540-1600$ m/s. The second inversion used T_{clay} from the measured seismic profile and searched over $C_{\text{clay}}=1460-1500$ m/s and $C_{\text{silt}}=1540-1600$ m/s. The search increment for C_{clay} was 5 m/s, C_{silt} was 10 m/s, and T_{clay} was 0.5 m. The results are summarized in Table II with an estimate of the uncertainty. The estimates of the bottom parameters and uncertainty were made by taking the mean and standard deviation of the top 5% of the inversion models. That is, out of all the possible models, the 5% with the least mean-squared error was used for the estimates. The hydrophones located at $H-81$ m, $H-46$ m, and $H-11$ m had relatively flat TL responses across frequency in contrast to the $H-1$ m hydrophone, which had strong features. The inversion showed sensitivity to the averaged TL values over frequency for the upper three hydrophones, but to the TL features of the bottom hydrophone.

These results are summarized in Fig. 16, where model and experimental TL are presented for inversion 2. The differences between modeled and measured TL might be caused by structure in the sound speed, not included in the models, or to the simplifying assumptions built into the geoacoustic model.

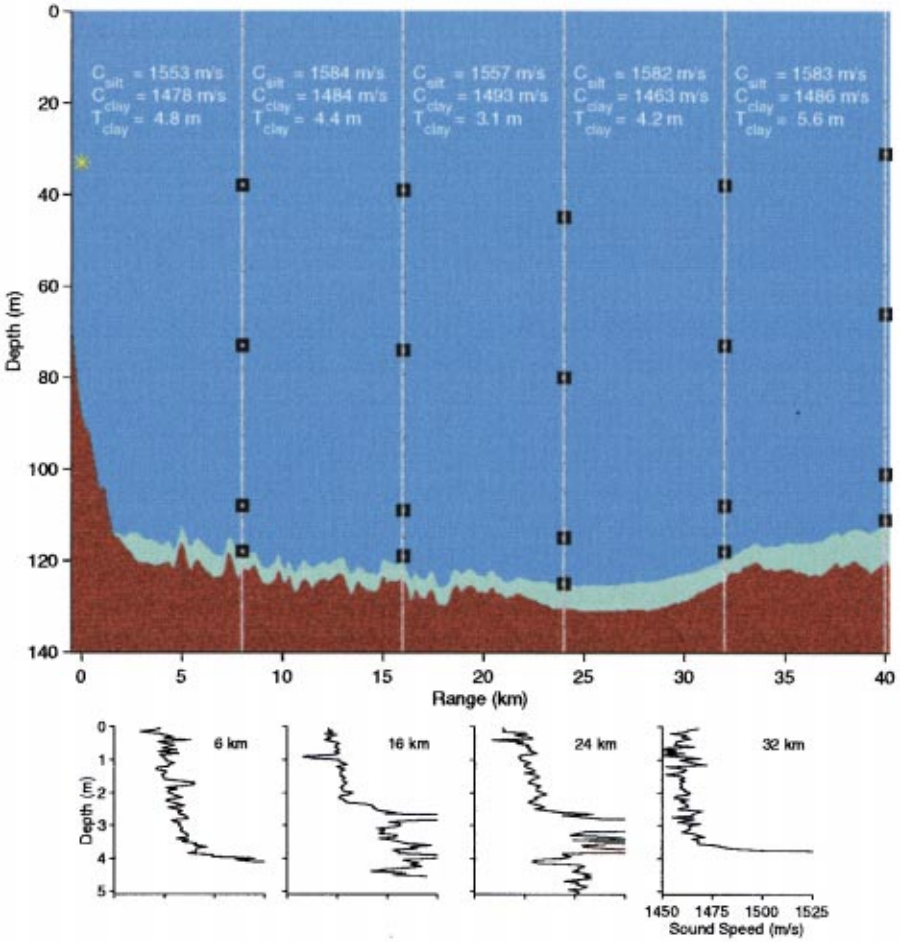

FIG. 17. Bathymetry, clay layer (green), and silt sub-bottom (brown) along the EF transect with the parameter values from the inversions. Range 0 is referenced to the source location (*) near the island of Elba and receivers are shown as black squares. The inverted bottom properties agree well with clay-layer thickness measured from a seismic profile and sound speed measured from core samples. The ranges of the cores samples are shown (also shown in Fig. 1).

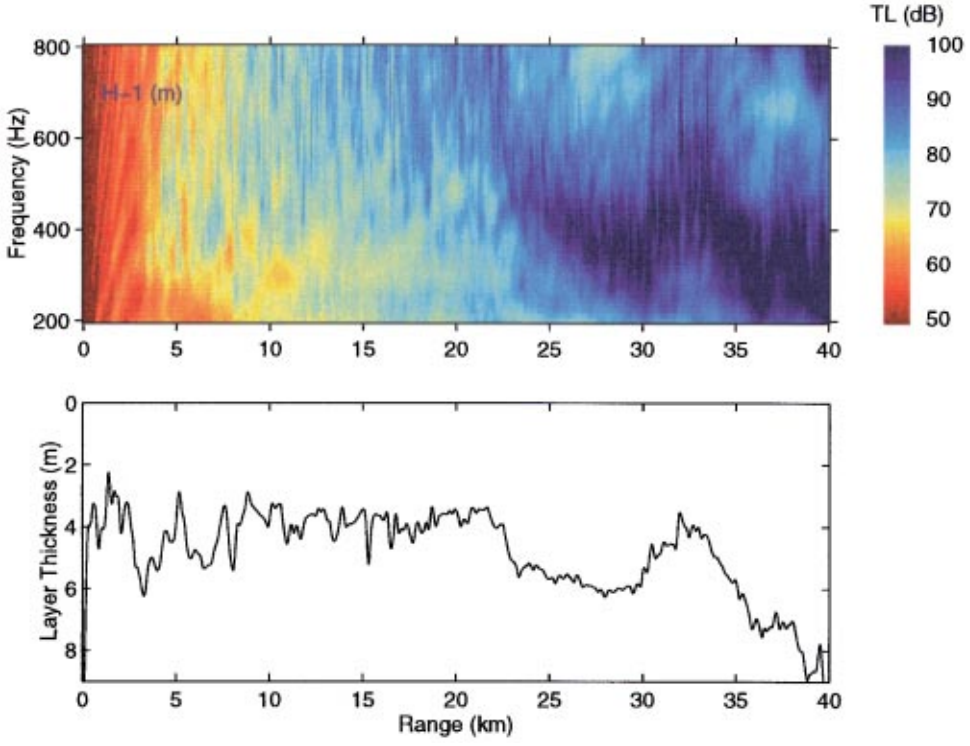

FIG. 18. The top panel shows the modeled TL data for the $H-1$ hydrophone and the lower panel shows the measured T_{clay}. Note the high TL band which follows the clay layer thickness curve.

V. DISCUSSION AND CONCLUSIONS

The inversion results should be interpreted carefully since only a subspace of possible bottom properties was considered. However, there is good agreement with the direct measurements. In Fig. 17, the parameter estimates are shown for T_{clay} taken from inversion 1, for C_{clay} and C_{silt} from inversion 2. The inverted value of T_{clay} corresponds well with the stratigraphy indicated in the seismic profile. When a range-dependent T_{clay} is taken from the seismic profile data and used for inversion 2, the sound speeds in the clay show a range dependence that closely follows the core sample measurements, which were taken near each of the acoustic stations. Note the inversion results at range 32 km for $C_{\text{clay}} = 1463$ m/s, which is a sudden drop in the sound speed compared to the other regions and the consistency of this value with the nearby core sample. There is a coupling between T_{clay} and C_{clay} which is difficult to separate from the types of measurements considered here. This was evident in the sensitivity study and supported by the inversion results. As the band of high-loss TL has a strong influence on the inversion results, in cases where T_{clay} may be estimated too large, to compensate, C_{clay} will likely be estimated too low. This may not always hold, as many factors can contribute to the inversion results but, in general, this was the case as shown in Table II.

The bottom hydrophone shows a high sensitivity to the local conditions of the seafloor. This can be illustrated by looking at Fig. 18, where simulated TL on the bottom hydrophone is presented as a function of range, compared to the range-dependent T_{clay} from the seismic profile. The geoacoustic parameters from inversion 2 are used. There is a clear tracking between the local clay-layer thickness and the band of high TL. This high sensitivity of the bottom hydrophone was also evident in the sensitivity analysis and suggests that a single hydrophone near the seafloor may be sufficient for this type of geoacoustic inversion.

The Yellow Shark 95-measured TL along the EF transect shows strong frequency-dependent features that can be matched in numerical simulation using a range-dependent geoacoustic model. Sparse measurements were used as the receiving arrays contained just four elements. The model/data fit obtained demonstrates that frequency-response measurements can be used as an acoustic observable for inversion of bottom properties. The range dependence was shown to induce mode coupling and requires use of an appropriate forward model. The clay layer causes a frequency response with bands of high loss which depend on the thickness and sound speed of the layer. High-loss bands are strongest at the hydrophone near the seafloor. The upper hydrophones do not show as clear a development of the frequency bands of high TL. This is due to the smearing of the high TL bands as the clay-layer thickness, bathymetry, and water-column sound speed all vary with range. The sensitivity study showed that although the smoothed TL data do not provide information about fine details of the bottom, they can be used to identify important properties of the slow clay layer and the faster sub-bottom. Overall, the inversion results agree well with the seismic data and core samples.

[1] M. D. Collins and W. A. Kuperman, ''Focalization: Environmental focusing and source localization,'' J. Acoust. Soc. Am. **90**, 1410–1422 (1991).
[2] M. D. Collins, W. A. Kuperman, and H. Schmidt, ''Nonlinear inversion for ocean bottom properties,'' J. Acoust. Soc. Am. **92**, 2770–2783 (1992).
[3] C. E. Lindsay and N. R. Chapman, ''Matched field inversion for geophysical parameters using adaptive simulated annealing,'' IEEE J. Ocean Eng. **18(3)**, 224–231 (1993).
[4] S. E. Dosso, M. L. Yeremy, J. M. Ozard, and N. R. Chapman, ''Estimation of ocean bottom properties by matched-field inversion of acoustic field data,'' IEEE J. Ocean Eng. **18(3)**, 232–239 (1993).
[5] P. Gerstoft, ''Inversion of seismo-acoustic data using genetic algorithms and *a posteriori* probability distributions,'' J. Acoust. Soc. Am. **95**, 770–782 (1994).
[6] G. Haralabus and P. Gerstoft, ''Source localization in shallow water using multi-frequency processing of shot data,'' SR-253, SACLANT Undersea Research Centre, La Spezia, Italy, 1996.
[7] N. R. Chapman and C. E. Lindsay, ''Matched-field inversion for geoacoustic model parameters in shallow water,'' IEEE J. Ocean Eng. **21**, 347–354 (1996).
[8] A. Tolstoy, ''Using matched-field processing to estimate shallow-water bottom properties from shot data taken in the Mediterranean Sea,'' IEEE J. Ocean Eng. **21(4)**, 471–479 (1996).
[9] J. P. Hermand and P. Gerstoft, ''Inversion of broadband multi-tone acoustic data from the Yellow Shark summer experiments,'' IEEE J. Ocean Eng. **21**, 324–346 (1996).
[10] J. P. Hermand, ''Broad-band geo-acoustic inversion in shallow water from waveguide impulse response measurements on a single hydrophone: Theory and experimental results,'' IEEE J. Ocean Eng. **24**, 41–66 (1999).
[11] A. Caiti, S. M. Jesus, and A. Kristensen, ''Geoacoustic seafloor exploration with a towed array in a shallow water area of the Strait of Sicily,'' IEEE J. Ocean Eng. **21**(4), 347–354 (1996).
[12] G. V. Frisk and J. F. Lynch, ''Shallow water waveguide characterization using the Hankel Transform,'' J. Acoust. Soc. Am. **76**, 205–216 (1984).
[13] G. V. Frisk, J. F. Lynch, and S. D. Rajan, ''Determination of compressional wave speed profiles using modal inverse techniques in a range-dependent environment in Nantucket Sound,'' J. Acoust. Soc. Am. **86**, 1928–1939 (1989).
[14] S. D. Rajan, J. F. Lynch, and G. V. Frisk, ''Perturbative inversion methods for obtaining bottom geoacoustic parameters in shallow water,'' J. Acoust. Soc. Am. **82**, 998–1017 (1987).
[15] O. Diachok, A. Caiti, P. Gerstoft, and H. Schmidt, editors, *Full field Inversion Methods in Ocean and Seismo-acoustics* (Kluwer Academic, Dordrecht, 1995).
[16] T. Akal, ''Sea floor effects on shallow-water acoustic propagation,'' in *Bottom Interacting Ocean Acoustics* (Plenum, New York, 1980), pp. 557–575.
[17] F. B. Jensen and W. A. Kuperman, ''Optimum frequency of propagation in shallow water environments,'' J. Acoust. Soc. Am. **73**, 813–819 (1983).
[18] D. A. Gershfeld and A. I. Eller, ''Geometric considerations in determining the optimum frequency of acoustic propagation in a shallow water waveguide,'' J. Acoust. Soc. Am. **78**, 632–641 (1985).
[19] O. F. Hastrup, ''Some bottom-reflection loss anomalies near grazing and their effect on propagation in shallow water,'' in *Bottom Interacting Ocean Acoustics* (Plenum, New York, 1980), pp. 135–152.
[20] J. P. Hermand, W. Roderick, P. Guerrini, L. Gualdesi, and F. De Strobel, ''Phase speed and pressure field measurements with a towed oceanographic and acoustic profiler: Yellow shark 95 geo-acoustic inversion results,'' in *Proceedings of the Fourth European Conference on Underwater Acoustics*, Rome, Italy, 1998 (Italian National Research Council, Instituto di Acustica), pp. 339–346.
[21] J. P. Hermand, F. Spina, P. Nardini, and E. Baglioni, ''Yellow Shark broadband inversion experiment: Environmental data 1994–1995,'' SACLANTCEN CD-ROM Yellow Shark series YS-2, 1996.
[22] J. P. Hermand and R. J. Soukup, ''Broadband inversion experiment Yellow Shark '95: Modelling the transfer function of a shallow-water environment with range-dependent soft clay bottom,'' in *Proceedings of the Third European Conference on Underwater Acoustics*, Vol. II (Heraklion, Crete, Greece, 1996. Foundation for Research and Technology-Hellas Institute of Applied and Computational Mathematics), pp. 931–936.
[23] D. Rouseff and T. E. Ewart, ''Effect of random sea surface and bottom roughness on propagation in shallow water,'' J. Acoust. Soc. Am. **98**, 3397–3404 (1995).

[24] F. B. Jensen, ''Comparison of transmission loss data for different shallow-water areas with theoretical results provided by a three-fluid normal-mode propagation model,'' in *Sound Propagation in Shallow Water*, Vol. II (SACLANTCEN CP-14, La Spezia, Italy, 1974), pp. 79–92.
[25] E. Michelozzi, ''Quaternary sediments in the Elba–Formiche islands basin,'' Tech. Rep. IN-678, SACLANT Undersea Research Centre, La Spezia, Italy, 1994.
[26] E. Michelozzi, P. Guerrini, R. Chiarabini, B. Tonarelli, and M. C. Mori, ''Yellow Shark core data analysis,'' Tech. Rep. Unpublished document, SACLANT Undersea Research Centre, La Spezia, Italy, 1996.
[27] T. Akal, C. Gehin, B. Matteucci, and B. Tonarelli, ''Measured and computed physical properties of sediment cores Island of Elba zone,'' SM-82, SACLANT Undersea Research Centre, La Spezia, Italy, 1972.
[28] F. B. Jensen, W. A. Kuperman, M. B. Porter, and Henrik Schmidt, *Computational Ocean Acoustics* (American Institute of Physics, Inc., New York, 1994).
[29] M. D. Collins and E. K. Westwood, ''A higher-order energy conserving parabolic equation for range-dependent ocean depth, sound speed, and density,'' J. Acoust. Soc. Am. **89**, 1068–1075 (1991).
[30] A. O. Williams, Jr., ''Mode interaction in an isovelocity ocean of uniformly varying depth,'' J. Acoust. Soc. Am. **67**, 177–185 (1980).
[31] S. T. McDaniel, ''Mode coupling due to interaction with the seabed,'' J. Acoust. Soc. Am. **72**, 916–923 (1982).
[32] S. T. McDaniel and D. F. McCammon, ''Mode coupling and the environmental sensitivity of shallow-water propagation loss predictions,'' J. Acoust. Soc. Am. **82**, 217–223 (1987).
[33] R. B. Evans, ''A coupled mode solution for acoustic propagation in a waveguide with stepwise depth variations of a penetrable bottom,'' J. Acoust. Soc. Am. **74**, 188–195 (1983).
[34] M. C. Ferla, M. B. Porter, and F. B. Jensen, ''C-SNAP: coupled SACLANTCEN normal mode propagation loss model,'' SM-274, SACLANT Undersea Research Centre, La Spezia, Italy, 1993.
[35] M. P. Porter, ''The KRAKEN normal mode program,'' SM-245, SACLANT Undersea Research Centre, La Spezia, Italy, 1991.

Measurements and predictions of the phase velocity and attenuation coefficient in suspensions of elastic microspheres

Joel Mobley, Kendall R. Waters, Christopher S. Hall, and Jon N. Marsh
Laboratory for Ultrasonics, Department of Physics, Washington University, St. Louis, Missouri 63130-4899

Michael S. Hughes and Gary H. Brandenburger
Mallinckrodt, Inc., 675 McDonnell Boulevard, Hazelwood, Missouri 63042

James G. Miller
Laboratory for Ultrasonics, Department of Physics, Washington University, St. Louis, Missouri 63130-4899

(Received 18 August 1998; revised 16 February 1998; accepted 13 May 1999)

The phase velocities and attenuation coefficients for suspensions of narrowly sized polymer microspheres are reported over a broadband spectrum from 3 to 30 MHz. The six suspensions used in this work contain microspheres with respective average diameters near 40 μm, 50 μm, 60 μm, 70 μm, 80 μm, and 100 μm. The results of these measurements are compared with theoretical expressions for the phase velocity and attenuation coefficient derived from the scattering properties of an elastic sphere in water using the weak scattering limit of the Waterman and Truell dispersion relation [J. Math. Phys. **2**, 512–537 (1961)]. This single-scattering limit of the theory is found to be sufficient for predicting the ultrasonic transport properties of these suspensions to a considerable degree of accuracy. © *1999 Acoustical Society of America.* [S0001-4966(99)05608-8]

PACS numbers: 43.35.Bf, 43.20.Bi, 43.20.Hq, 43.80.Vj [HEB]

INTRODUCTION

The scattering of sound from solid elastic spheres suspended in a liquid has applications in a variety of areas in acoustics.[1–5] A significant portion of this research has been built upon experimental and theoretical work performed in the 1950's and 1960's concerning the scattering of sound from individual spheres.[6–8] In addition, Resonant Scattering Theory (RST) has provided insightful interpretations of the scattered sound from an individual scatterer.[9] These foundations have proven useful for investigations of suspensions of elastic particles based on a single-scattering approach.[1,3,4,10] A multiple-scattering framework[10–14] has also been used to interpret the results of measurements of the properties of suspensions.

In recent years, the scattering of sound from suspensions of particles has played an important role in areas such as the study of sonic transport through sedimentation in the marine environment[4] as well as the use of ultrasonic contrast agents in diagnostic medicine.[15] In addition, suspensions of elastic spheres have been proposed as acoustic calibration standards.[16] We also consider this work as further validation of the use of agitation techniques in the course of measuring the properties of suspensions.[5,15,16]

In this paper we measure the attenuation coefficients and phase velocities for six suspensions of solid plastic microspheres with narrow size distributions. We compare experimental results with predictions developed using the dispersion relation of Waterman and Truell[14] in the limit of weak scattering density. This single-scattering limit of the theory is sufficient for predicting the velocity and attenuation properties of these suspensions to a considerable degree of accuracy.

In Sec. I of the paper, expressions for the phase velocity and attenuation coefficient for a suspension of solid elastic spheres are obtained using the multiple-scattering dispersion relation in the limit of weak scattering density. In Sec. II, we describe the experimental arrangement and data acquisition methods. Section III follows with the comparisons between experimentally determined and theoretically predicted phase velocities and attenuation coefficients.

In addition to the main portion of the text, two appendices are included. In Appendix A, the theoretical expressions for the phase velocity and attenuation coefficient are derived from a straightforward single-scattering model. Appendix B provides details of the error analyses.

I. THEORY

In this section, expressions are derived for the phase velocity and attenuation coefficient for solid elastic spheres suspended in a liquid which are uniformly and randomly distributed within a plane of finite thickness. The derivation uses the multiple-scattering dispersion relation of Waterman and Truell[14] in the limit of weak scattering density and the solution by Faran[6] for the scattering from an elastic sphere in a fluid.

The phase velocity and attenuation coefficient for a suspension are connected to the scattering properties of the individual suspended particles by the Waterman and Truell dispersion relation,[14]

$$K_s = k_w \sqrt{\left(1 + \frac{\eta 2\pi}{k_w^2} f(0)\right)^2 - \left(\frac{\eta 2\pi}{k_w^2} f(\pi)\right)^2}, \qquad (1)$$

where ω is the angular frequency, $K_s = [\omega/c_s(\omega)] - i\alpha_s(\omega)$ is the complex wave number of the suspension, $c_s(\omega)$ and

$\alpha_s(\omega)$ are the phase velocity and attenuation coefficient of the suspension, $k_w=\omega/c_w$ is the wave number in the host medium (which is taken to be water), η is the number density of the scatterers, and $f(0)$ and $f(\pi)$ are the single-particle amplitudes for forward and backward scattering, respectively. This relation was derived by considering a uniform distribution of scatterers suspended in an otherwise homogeneous host material with the approximation that the exciting pressure field incident on a scatterer is the total field that would exist in the neighborhood of the scatterer if it were not present (see Ref. 13, Section 2.4).

The nature of the multiple-scattering processes can be seen by expanding the right hand side of Eq. (1) as a power series in $(\eta 2\pi c_w^2)/\omega^2$:

$$k_w\sqrt{1+2\frac{\eta 2\pi c_w^2}{\omega^2}f(0)+\left(\frac{\eta 2\pi c_w^2}{\omega^2}\right)^2(f(0)^2-f(\pi)^2)}$$
$$=k_w\Bigg[1+\frac{\eta 2\pi c_w^2}{\omega^2}f(0)-\frac{1}{2}\left(\frac{\eta 2\pi c_w^2}{\omega^2}\right)^2 f(\pi)^2$$
$$+\frac{1}{2}\left(\frac{\eta 2\pi c_w^2}{\omega^2}\right)^3 f(0)f(\pi)^2$$
$$-\frac{1}{8}\left(\frac{\eta 2\pi c_w^2}{\omega^2}\right)^4(f(\pi)^4+4f(0)^2f(\pi)^2)+\cdots\Bigg]. \quad (2)$$

In this form one can interpret each term in the series as representing the number of interactions of the scatterers and the scattered field; the term $[(\eta 2\pi c_w^2)/\omega^2]f(0)$ represents a wave scattered only once as it passes through the suspension while the term $\frac{1}{2}(\eta 2\pi c_w^2/\omega^2)^2 f(\pi)^2$ is due to a wave backscattered twice in the suspension. A term with coefficient $(\eta 2\pi c_w^2/\omega^2)^n$ is the contribution of a wave scattered n times as it crosses the suspension. Note that the dispersion relation suggests multiple-scattering events that ultimately direct the wave in the forward direction of the incident field are of concern, since the backscattering amplitude always appears in even powers.

The material properties and shape of the particles are implicitly accounted for by the scattering amplitudes. The scattering of sound from a plane wave by an elastic sphere can be solved by determining general solutions to the relevant equations both inside and outside the sphere and satisfying the boundary conditions at the surface. In this work, we use the solution of Faran[6] with some minor notational differences. The sphere has radius a and its center is taken as the origin of the coordinate system as diagrammed in Fig. 1. By applying the boundary conditions on the stresses and displacements at the surface of the sphere, an expression for the expansion coefficients for the scattered field in the fluid is derived.

The total pressure field in the fluid at $\mathbf{r}$ due to one spherical scatterer centered at $\mathbf{r}'$ is written as follows:

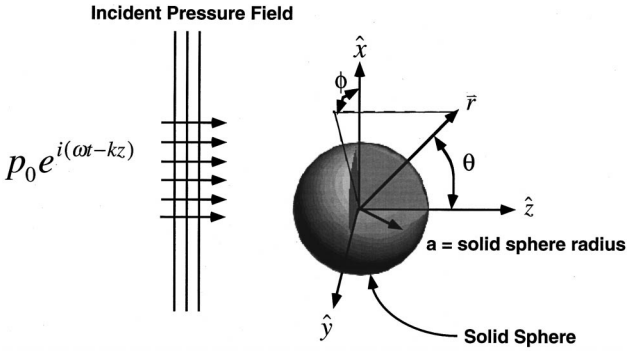

FIG. 1. The geometry for the scattering problem of a solid sphere in an inviscid fluid. This diagram shows the physical model used for deriving the properties of the plastic microsphere suspensions.

$$p_{\text{total}}(\mathbf{r})=p_{\text{inc}}(\mathbf{r})+p_{\text{scatt}}(\mathbf{r}) \quad (3a)$$
$$=p_0\exp(-ik_wz)+p_0\exp(-ik_wz')$$
$$\times\sum_{n=0}^{\infty}(-i)^n(2n+1)D_nh_n^{(2)}(k_w|\mathbf{r}-\mathbf{r}'|)$$
$$\times P_n[\cos\theta(\mathbf{r}-\mathbf{r}')], \quad (3b)$$

where p_0 is the amplitude of the incident plane wave, $h_n^{(2)}(x)$ the spherical Hankel functions of the second kind, $P_n(x)$ the Legendre polynomials, and D_n the expansion coefficients. [The expansion coefficients $\{D_n\}$ used here are related to those of Faran's $\{c_n\}$ by $D_n=c_n/p_0(2n+1)(-i)^n$.] The unique scattering behavior of this system is encompassed in the expansion coefficients $\{D_n\}$, which depend on the physical properties of the sphere (density ρ_s, radius a, shear and longitudinal speed of sound of bulk material c_T and c_L), fluid (density ρ_w and sound speed c_w), and incident pressure field (frequency ω), that is,

$$D_n=D_n(\omega,c_w,c_L,c_T,a,\rho_w,\rho_s) \quad (4a)$$
$$=D_n(k_wa,k_La,k_Ta,\rho_w,\rho_s). \quad (4b)$$

The scattering amplitudes and the expansion coefficients are related by

$$f(\theta)=\frac{i}{k_w}\sum_{n=0}^{\infty}(2n+1)D_nP_n(\cos\theta). \quad (5)$$

For the suspensions examined in this work we find that the following condition holds:

$$\frac{\eta 2\pi c_w^3}{\omega^3}\left|\sum_n(2n+1)D_nP_n(\cos\theta)\right|$$
$$=\frac{\eta 2\pi}{k_w^2}|f(\theta)|\ll 1, \quad (\theta=0 \text{ or } \pi). \quad (6)$$

Thus we can approximate the dispersion relation by its first order expansion:

$$\frac{\omega}{c_s(\omega)} - i\alpha_s(\omega) \cong \frac{\omega}{c_w} + \frac{\eta 2\pi c_w}{\omega} f(0) \tag{7a}$$

$$= \frac{\omega}{c_w} + i\frac{\eta 2\pi c_w^2}{\omega^2} \sum_{n=0}^{\infty} (2n+1) D_n . \tag{7b}$$

Of course, keeping only the first two terms of the expansion [Eq. (2)] is physically equivalent to limiting the sonic field to a single interaction with the suspended scatterers. This limit can be achieved by any combination of factors (e.g., weak scattering amplitude, small number density of particles, high frequency) that satisfy the condition in Eq. (6). This lowest order approximation is also an exact result of the Waterman and Truell approach if one assumes the excitation field each scatterer sees is only the incident plane wave. Equating real and imaginary parts, the phase velocity and attenuation coefficient are given by

$$c_s(\omega) = \frac{c_w}{1 - \frac{\eta 2\pi c_w^3}{\omega^3} \sum_{n=0}^{\infty} (2n+1) \mathrm{Im}[D_n(\omega)]}, \tag{8}$$

$$\alpha_s(\omega) = -\frac{\eta 2\pi c_w^2}{\omega^2} \sum_{n=0}^{\infty} (2n+1) \mathrm{Re}[D_n(\omega)]. \tag{9}$$

These same results can also be derived straightforwardly using an independent scatterer model of the suspension. This derivation is provided in Appendix A.

II. METHODS

A. Ultrasonic spectroscopy

Broadband ultrasonic spectroscopic methods use the Fourier transforms of time-localized (i.e., broadband) signals to derive material parameters over a range of frequencies. In this work, the phase velocities and attenuation coefficients from 3 to 30 MHz were determined from through-sample and reference (waterpath-only) signals by comparing the magnitudes and phases of their Fourier coefficients. The measurement procedure is diagrammed in Fig. 2(a) and 2(b). Based on the ultrasonic spectroscopy technique in the context of a through-transmission substitution measurement method,[17] the phase velocity relation can be shown to be

$$c_s(\omega) = \frac{c_w}{1 - \frac{c_w}{\omega d}(\Delta\phi(\omega) + \phi_c(\omega,h))}, \tag{10}$$

where

$$\phi_c(\omega,h) \equiv 2\omega h\left(\frac{1}{c_p(\omega)} - \frac{1}{c_w}\right) \tag{11}$$

is the phase shift due to the plastic windows (Saran Wrap™) of the sample chamber, $c_p(\omega)$ is the speed of sound in the plastic windows, $\Delta\phi(\omega) \equiv \phi_s(\omega) - \phi_w(\omega)$ is the difference in the phase spectra of the through-sample and reference traces, d is the sample thickness, and h is the thickness of the plastic window. Multiple reverberations in the sample chamber itself are not an issue, and so their effects are not included in Eq. (10).

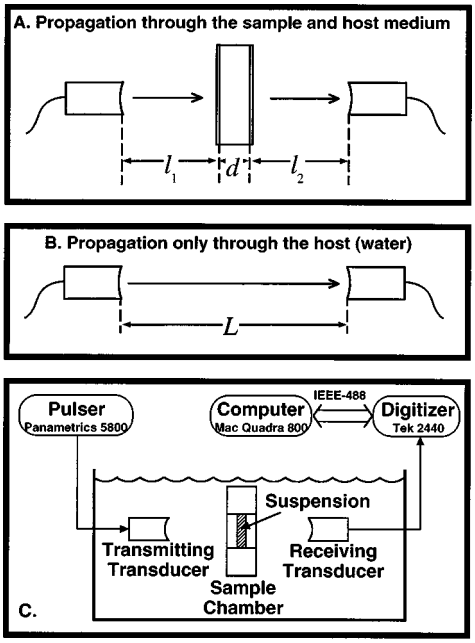

FIG. 2. Diagram of measurement procedure to obtain (a) the through-sample signal and (b) the reference signal. (c) Experimental setup.

Compensating Eqs. (3), (4), and (7) of Ref. 18 for the effects of the sample chamber walls, the Fourier transforms of the two signals can be written as

$$F_s(\omega) = |T(\omega,h)||F(\omega)| \times \exp(-\alpha_w(\omega)[L-d-2h] - \alpha_s(\omega)d) \times \exp\left(-i\omega\left[\frac{L-d-2h}{c_w} + \frac{d}{c_s(\omega)} + \frac{2h}{c_p(\omega)}\right] + i\phi_0\right) \tag{12}$$

and

$$F_w(\omega) = |F(\omega)|\exp(-\alpha_w(\omega)L)\exp\left(-i\omega\frac{L}{c_w} + i\phi_0\right), \tag{13}$$

where $F_s(\omega)$ is the Fourier transform of the through-sample trace, $F_w(\omega)$ is the Fourier transform of the waterpath-only trace, $T(\omega,h)$ is transmission factor taking into account the sample interfaces and plastic windows, L is the transducer separation, $\alpha_w(\omega)$ is the attenuation coefficient for water, $|F(\omega)|$ is the magnitude of the Fourier transform of the transmitted pulse, and ϕ_0 is the phase of the Fourier transform of the transmitted pulse. Solving for the attenuation coefficient of the sample results in the following relation:

$$\alpha_s(\omega) = \alpha_w(\omega)\left(1 + \frac{2h}{d}\right) - \frac{\ln\frac{|F_s(\omega)|}{|F_w(\omega)|} - \ln|T(\omega,h)|}{d}. \tag{14}$$

B. Microsphere suspensions

The solid microspheres (Duke Scientific Corporation, Palo Alto, CA) are manufactured for the calibration of particle-sizing instruments. According to the manufacturer the particles are made from polystyrene and/or polystyrene divinylbenzene. The microspheres, as packaged, are sus-

pended in Isoton® (a saline solution) with a small amount of dispersant added to prevent particle aggregation. Data were acquired for six individual suspensions. Throughout this paper, we refer to the individual suspensions by the approximate mean diameter of the microspheres they contain (40 μm, 50 μm, 60 μm, 70 μm, 80 μm, and 100 μm, respectively). The distribution of the microsphere diameters in each suspension was measured using an optical particle sizer (Accusizer 770A). The full width at half-maximum of each distribution is about 5% of the mean diameter. Further details on the size distributions of these particles can be found in Hall *et al.*[5] The volume concentration of microspheres was about 1% in each suspension.

C. Data acquisition

The data were acquired at Mallinckrodt, Inc. using a through-transmission broadband immersion system [see Fig. 2(c)]. The ultrasound was generated and received by two focused PVDF transducers (Panametrics, 3.25 in. nominal focus and 0.4 in. nominal active diameter) immersed in a water bath and separated by 6.5 in. The transmitter was excited by a broadband pulser/receiver unit (Panametrics 5800). The received signals were fed to a digital oscilloscope (Tektronix 2440) where they were digitized to 8-bits at a rate of 250 MSamples/s. The data were then downloaded to a computer for off-line storage and analysis.

The suspensions were contained in a custom designed sample chamber.[15] To ensure spatial homogeneity, the suspensions were agitated during acquisition via pipette mixing. This method of mixing has proven to be effective in obtaining stable and reliable measurements for suspensions of polymer microspheres[5] and Albunex® microbubbles.[15] The walls of the sample chamber were oriented normal to the direction of ultrasonic propagation and formed by single layers of Saran Wrap (approximately 25 μm thick).

For each suspension, 1000 time traces of through-transmitted ultrasound were acquired. In addition to the through-sample acquisitions, a minimum of 100 waterpath-only traces were captured to serve as the reference data in the analysis. Data were also acquired with the sample chamber filled only with Isoton to compensate for the plastic windows of the chamber. Each time trace consisted of 1024 samples with a time interval of 0.004 μs between points. The oscilloscope was triggered by the pulser while the data acquisition delay time was set manually on the oscilloscope to position the received signal within the acquisition window. The traces were acquired and downloaded to the computer at a rate of approximately 30 per s. Figure 3 displays a waterpath-only signal and a signal from the propagation through the 100-μm suspension.

D. Data reduction and analysis

After storage to disk, the recorded waveforms from the through-transmitted acquisitions were averaged in sets of 50 before further processing. The waterpath (reference) signals were averaged in sets of at least 10. These averaged signals were discrete Fourier transformed (using the FFT algorithm) and their magnitude and unwrapped phase spectra were determined. These phase and magnitude spectra were averaged and the results employed in Eqs. (10) and (14) to determine the phase velocity and attenuation coefficient for the given sample. The velocity in water was assumed to be dispersionless and determined by the temperature of the water using the formula of Del Grosso and Mader (Table III, combined fit).[19] The attenuation coefficient of water was taken to be proportional to ω^2.[20,21] The compensations to the phase velocity (ϕ_c) and attenuation coefficient ($|T|$) due to the chamber windows were determined with data from the acquisi-

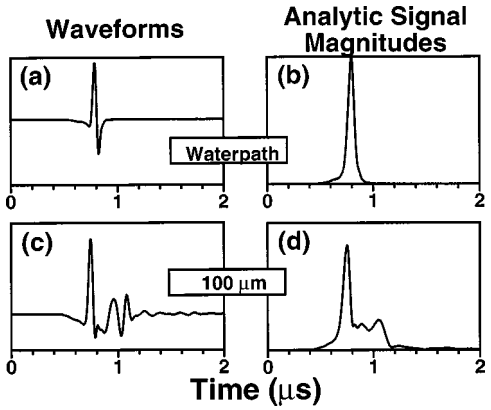

FIG. 3. Waveforms from the microsphere data acquisitions and their analytic signal envelopes. Frames (a) and (b) are the waterpath-only waveform and envelope. Frames (c) and (d) are from the propagation through the 100-μm suspension. These waveforms represent the average of 1000 captured oscilloscope traces.

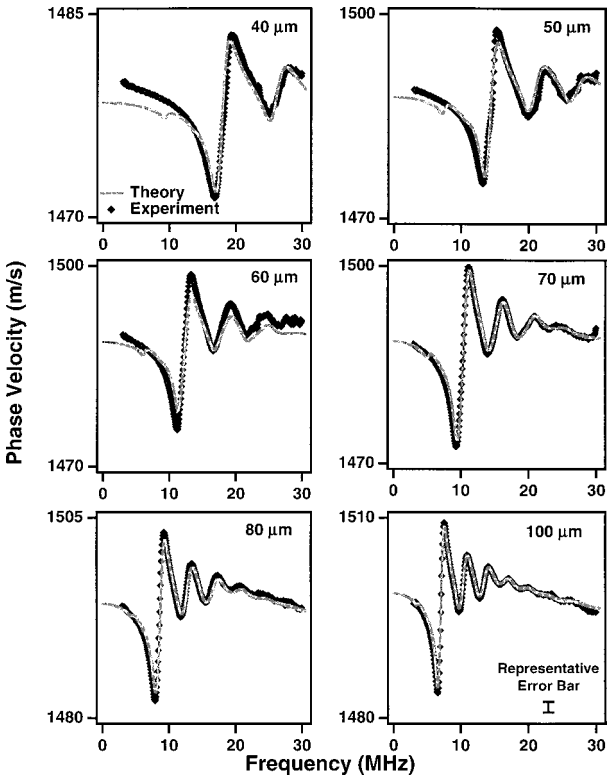

FIG. 4. The experimentally measured and theoretically predicted phase velocities for each suspension of microspheres. A representative error bar is included.

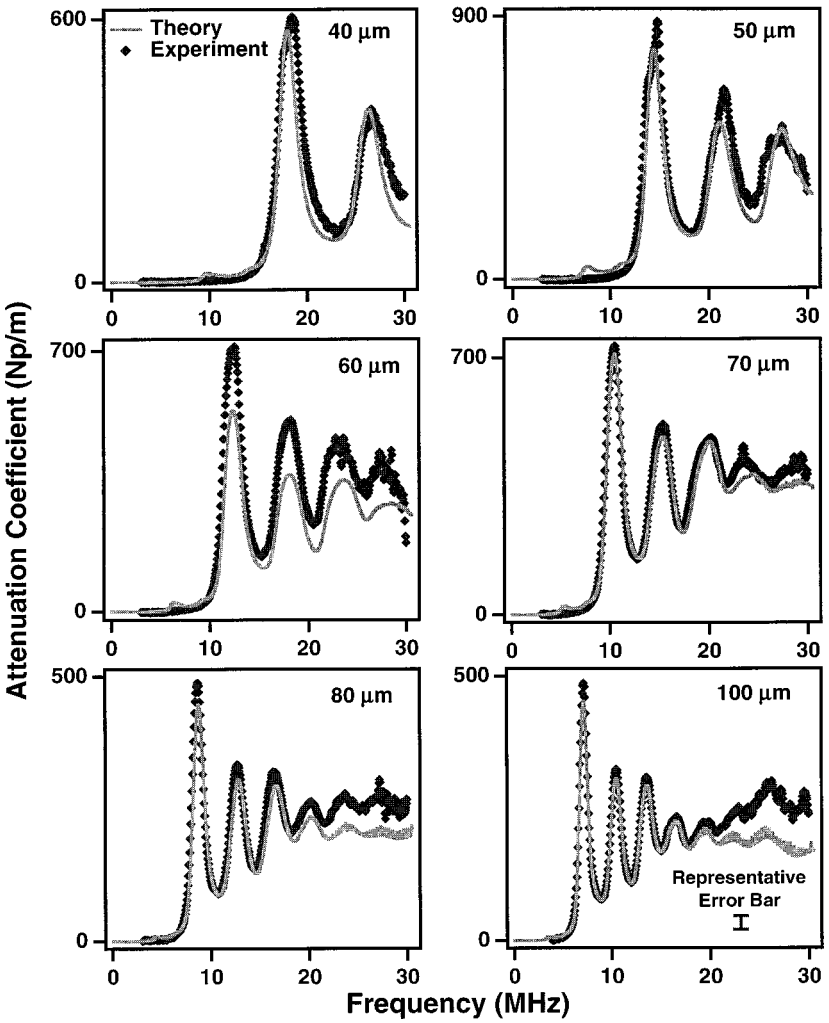

FIG. 5. The experimentally measured and theoretically predicted attenuation coefficients for each suspension of microspheres. A representative error bar is included.

tions involving both the waterpath-only and the ''empty'' (i.e., filled with Isoton but no microspheres) sample chamber.

E. Theoretical predictions

The theoretical results were calculated using the properties of polystyrene for the spheres ($c_L = 2380$ m/s, $c_s = 1180$ m/s, $\rho_s = 1.06$ g/mL) and water (c_w ranging from 1488 to 1491 m/s depending on the temperature during the acquisition, $\rho_w = 1.0$ g/mL) for the host medium. Note that some reported values for the shear velocity in polystyrene are near 1100 m/s; however, in previous work[5] predicting the backscatter coefficients for these suspensions it was found that the value 1180 m/s obtained the best fit to the observed frequency dependence. In this work, no further attempts were made to adjust the material parameters of the spheres. For each suspension the calculations were performed by summing over the size distribution measured by the Accusizer. These calculations employ the first 15 expansion coefficients, $D_0 - D_{14}$. For the attenuation coefficient calculations, Eq. (9) was extended for a distribution of sphere sizes,

$$\alpha_s(\omega) = -\frac{2\pi c_w^2}{\omega^2} \sum_q \left[\eta(a_q) \sum_{n=0}^{14} (2n+1) \mathrm{Re}[D_n(\omega, a_q)] \right], \tag{15}$$

where $\eta(a_q)$ is the number density distribution of microspheres. In calculating the phase predictions, we used a modified form of Eq. (8):

$$\frac{1}{c_s(\omega)} - \frac{1}{c_0} = -\frac{2\pi c_w^2}{\omega^3} \times \sum_q \left[\eta(a_q) \sum_{n=0}^{14} (2n+1) \mathrm{Im}[D_n(\omega, a_q)] \right]. \tag{16}$$

The parameter c_0 was adjusted to match the absolute levels of the theoretically predicted phase velocities to the experimentally measured values. In all cases, the adjustable parameter agreed to better than 1% with the expected value for the speed of sound in water.

III. RESULTS AND DISCUSSION

Figures 4 and 5 compare the measured values with the predictions for the phase velocity and attenuation coefficient, respectively. Note that the vertical scales differ for each of the six suspensions. The uncertainties for each measurement were calculated from the first order error propagations of Eqs. (10) and (14) (see Appendix B). Figure 6 displays only the measured values of the phase velocity and attenuation

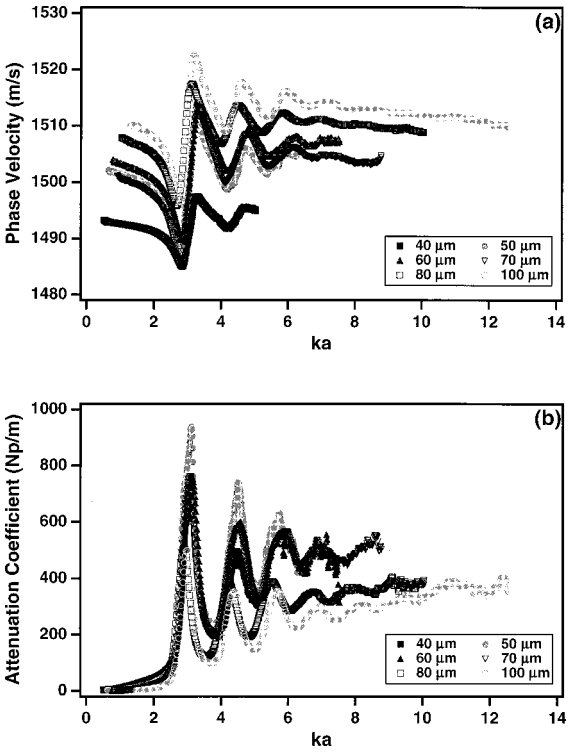

FIG. 6. (a) Experimentally measured phase velocity for each suspension of microspheres as a function of $a/\lambda(=ka/2\pi)$. (b) Experimentally measured attenuation coefficient for each suspension of microspheres as a function of $a/\lambda(=ka/2\pi)$.

coefficient, respectively, for all six of the suspensions as a function of the mean circumference to wavelength ratio $(2\pi a/\lambda)=ka$. This figure illustrates that the frequency dependence of the scattering coefficients $\{D_n\}$ (which govern the local structure of the propagation parameters) is correctly expressed in terms of dimensionless frequency variables as noted in Eq. (3).

Overall, the predicted shapes of the phase velocity and attenuation curves track the experimental results closely. For five of the six suspensions, the differences between theory and experiment are only apparent under close inspection. The only large discrepancy occurred for the 60-μm results. Here the predicted dispersion and attenuation values are clearly too small. If the predicted dispersion and attenuation coefficient curves are increased by a factor of 1.33 they come into close agreement with the measurements. This suggests that the measured volume concentration of microspheres in the 60-μm suspension may have been underestimated by about 25%.

For a more quantitative comparison, we looked at the magnitude of dispersion (i.e., $\Delta c \equiv c_s^{\max} - c_s^{\min}$), peak value in the attenuation coefficient $\alpha_{\max}$, and the positions of the local extrema in the attenuation and velocity. In general the predictions always underestimate Δc and $\alpha_{\max}$. For the 100-μm suspension, the predicted magnitude of dispersion was within the error bounds of the measured value. For the 40-μm, 70-μm, and 80-μm suspensions, the predicted and measured Δc's agreed to better than 10%. In all but two cases, the predicted and measured $\alpha_{\max}$'s also agreed to better than 10%. The positions of the peaks and nadirs in the results were also predicted reasonably accurately. For the 100-μm suspension, the positions of the local maxima and minima were predicted correctly or at most off by one point of the frequency axis (i.e., the sampling resolution). The same held true for the three largest peaks in the attenuation coefficient. For all of the suspensions, the positions of the first three peaks and nadirs for both phase velocity and attenuation coefficient were predicted to better than 0.5 MHz.

To understand the sensitivity of the theoretical model to small changes in the inputs, we performed the calculations (for a single size of sphere) by varying each input individually by $\pm 10\%$. For three of the inputs, sphere radius a, speed of sound in the host liquid c_w, and shear wave velocity of the sphere's bulk material c_T, 10% changes resulted in at least 20% changes in Δc and $\alpha_{\max}$. Of course, 10% changes in the number density η also resulted in 10% changes in the results. For the remaining inputs ρ_w, ρ_s, and c_L, the variations had at most an 8% impact. For the inputs a, c_w, η, and ρ_w, an increase (decrease) in their respective value also led to an increase (decrease) in Δc and $\alpha_{\max}$. For c_T, ρ_s, and c_L an increase (decrease) caused a decrease (increase) in the outcomes. The positions of the peaks were most sensitive to changes in the sphere radius a where 10% changes led to approximately 10% shifts. An increase (decrease) in a or ρ_w led to a shift of the peaks to lower (higher) frequencies. Changes in the shear velocity c_T shifted the peaks by about 8%. For c_T, ρ_s, c_L, and c_w, an increase led to a shift to higher frequencies and vice versa.

In order to examine the consequences of ignoring multiple scattering effects, we performed the calculations for the 100-μm suspension using the full multiple-scattering dispersion relation. We found the differences between the exact relation and the single-scattering approximation were on the order of 0.01% for the phase velocity and 1% for the attenuation coefficient. The contributions of the full dispersion relation over the first order expansion can almost entirely be accounted for by the second order scattering term in Eq. (2), $2(\eta^2\pi^2 c_w^3/\omega^3) f(\pi)^2$. We also looked at the impact of limiting the summations of the scattering coefficients D_n to the first 15 terms by extending the calculations out to 100 terms for the 100-μm suspension. This had no noticeable impact on the predictions over the bandwidth of interest.

IV. CONCLUSION

In this work, the phase velocity and attenuation coefficients of suspensions of plastic microspheres in saline were measured from 3 to 30 MHz using a broadband technique. Each suspension contained a narrow distribution of sphere diameters. Using a single-scattering approximation to the dispersion relation, theoretical predictions of the phase velocity and attenuation coefficient were calculated. The predictions matched the frequency dependencies of the measurements well. The sensitivity of the predictions to the small changes in the inputs is discussed.

APPENDIX A: ALTERNATE DERIVATION OF THE SINGLE-SCATTERING DISPERSION RELATION

In the single-scattering limit, the expressions for the phase velocity [Eq. (8)] and attenuation coefficient [Eq. (9)] for a suspension of spheres can be derived in a straightforward manner. In this approximation, each sphere interacts only with the incident field and therefore the scattered field is simply given as the superposition of the singly scattered fields of the individual particles. The procedure followed is similar to that used to calculate the index of refraction for the propagation of electromagnetic waves through matter.[22]

The derivation of the velocity and attenuation expressions for a suspension of particles starts by calculating the field scattered from a plane wave incident on a sheet of spheres. The spheres, each of radius a, are uniformly and randomly distributed within a sheet of thickness Δz embedded in a fluid (see Fig. A1). The number of spheres in any cross-sectional area A of the sheet is given by $A\Delta z\,\eta$. Using Eq. (3) the field at point $Q(\rho=0,\theta,z)$ (as defined in Fig. A1) due to scatterers at a distance $|\mathbf{r}-\mathbf{r}'|=\sqrt{\rho'^2+(z-z')^2}$ in the differential volume element $dV'=\rho'\,d\phi'\,d\rho'\,dz'$ is given by

$$dp_{at\,Q}^{\text{scatt}}=\eta\rho'\,d\phi'\,d\rho'\,dz'p_0\exp(-ik_wz')\times\sum_{n=0}^{\infty}(-i)^n(2n+1)D_nh_n^{(2)}(k_w|\mathbf{r}-\mathbf{r}'|)\times P_n[\cos\theta(\mathbf{r}-\mathbf{r}')],\tag{A1}$$

where $\cos\theta(\mathbf{r}-\mathbf{r}')=z-z'/|\mathbf{r}-\mathbf{r}'|$ and $|\mathbf{r}-\mathbf{r}'|^2=\rho'^2+(z-z')^2$ in our coordinate system and $p_0\exp(-ik_wz')$ is the incident field. The total field from the scatterers is then calculated by integrating over the volume of the entire sheet,

$$p_{at\,Q}^{\text{scatt}}=\eta2\pi p_0\sum_{n=0}^{\infty}(-i)^n(2n+1)D_n\times\int_0^{\Delta z}\int_0^{\infty}\exp(-ik_wz')h_n^{(2)}(k_w|\mathbf{r}-\mathbf{r}'|)\times P_n[\cos\theta(\mathbf{r}-\mathbf{r}')]\rho'\,dz'\,d\rho'.\tag{A2}$$

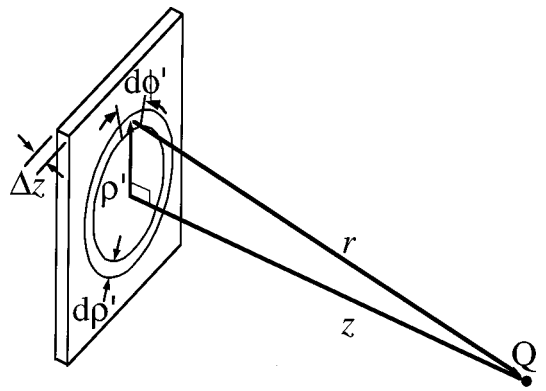

FIG. A1. The geometry for the determination of the total field at Q due to a uniform distribution of scatterers in an unbound plane of thickness Δz. This diagram defines the coordinates used in Appendix A.

The integral over ρ' can be rewritten using the substitution $u^2=|\mathbf{r}-\mathbf{r}'|^2$

$$\int_0^{\infty}h_n^{(2)}(k_w|\mathbf{r}-\mathbf{r}'|)P_n[\cos\theta(\mathbf{r}-\mathbf{r}')]\rho'\,d\rho'=\int_{z-z'}^{\infty}h_n^{(2)}(k_wu)P_n\left[\frac{z-z'}{u}\right]u\,du.\tag{A3}$$

It can then be shown that[23]

$$\int_{z-z'}^{\infty}h_n^{(2)}(k_wu)P_n\left[\frac{z-z'}{u}\right]u\,du=i^n\frac{\exp[-ik_w(z-z')]}{k_w^2}.\tag{A4}$$

The total scattering contribution to the pressure field at Q is

$$p_{at\,Q}^{\text{scatt}}=p_0\exp(-ik_wz)\frac{\eta2\pi}{k_w^2}\sum_{n=0}^{\infty}(2n+1)D_n\times\int_0^{\Delta z}\exp(-ik_wz')\exp(ik_wz')dz'\tag{A5a}$$

$$=p_0\exp(-ik_wz)\frac{\eta2\pi\Delta z}{k_w^2}\sum_{n=0}^{\infty}(2n+1)D_n.\tag{A5b}$$

The total field is the superposition of the incident and scattered fields:

$$p_{at\,Q}^{\text{total}}(\mathbf{r})=p_{\text{inc}}(\mathbf{r})+p_{at\,Q}^{\text{scatt}}(\mathbf{r})\tag{A6a}$$

$$=p_0\exp(-ik_wz)+p_0\exp(-ik_wz)\Delta z\frac{\eta2\pi}{k_w^2}\times\sum_{n=0}^{\infty}(2n+1)D_n\tag{A6b}$$

$$=p_0\exp(-ik_wz)\left(1+\Delta z\frac{\eta2\pi}{k_w^2}\sum_{n=0}^{\infty}(2n+1)D_n\right).\tag{A6c}$$

Now consider the modeling of the suspension as a linear elastic medium. The transmission of the plane wave across the sheet is given by a transfer function $H(\Delta z)$ which can be written in terms of the complex wave number K_s:

$$p_{at\,Q}^{\text{total}}=p_0\exp[-ik_w(z-\Delta z)]H(\Delta z)\tag{A7a}$$

$$=p_0\exp[-ik_w(z-\Delta z)]\exp[-iK_s\Delta z]\tag{A7b}$$

$$=p_0\exp[-ik_wz]\exp[-i(K_s-k_w)\Delta z].\tag{A7c}$$

When the thickness of the layer can be made small enough (the minimum thickness must be at least as large as the diameter of a particle to make physical sense) that

$$|K_s-k_w|\Delta z\ll1,\tag{A8}$$

the transmitted field in the linear response model is given by

$$p_{at\,Q}^{\text{total}}\cong p_0\exp(-ik_wz)(1-i(K_s-k_w)\Delta z).\tag{A9}$$

By comparing the linear elastic model and the scattering solution [Eq. (A6c)] of the suspension,

$$-i(K_s-k_w)=\frac{\eta2\pi}{k_w^2}\sum_{n=0}^{\infty}(2n+1)D_n.\tag{A10}$$

Rearranging, we arrive at Eq. (7b)

$$\frac{\omega}{c_s(\omega)} - i\alpha_s(\omega) = \frac{\omega}{c_w} + i\frac{\eta 2\pi c_w^2}{\omega^2}\sum_{n=0}^{\infty}(2n+1)D_n(\omega). \tag{7b,A11}$$

from which the expressions for the phase velocity and attenuation coefficient [Eqs. (8) and (9)] are recovered.

APPENDIX B: PROPAGATION OF ERRORS

The velocity determination essentially requires the measurement of three quantities: temperature (determines the speed of sound in the water), length (sample chamber and chamber wall thicknesses), and time (delay intervals given by $\Delta\phi/\omega$ and ϕ_c/ω); and the knowledge of the velocity and thickness of the window material. The fractional error equation [as derived from Eq. (10)] is

$$\frac{\delta c_s}{c_s} = \left[\frac{c_s^2}{c_w^4}\left(\frac{\partial c}{\partial \vartheta}\right)^2 \delta\vartheta^2 + \left(\frac{c_s}{c_w}-1\right)^2\left(\frac{\delta d}{d}\right)^2 + \left(\frac{c_s}{d}\right)^2\left(\delta\frac{\Delta\phi}{\omega}(t)\right)^2 + \left(\frac{c_s}{d}\right)^2\left(\delta\frac{\phi_c}{\omega}(t)\right)^2\right]^{1/2}. \tag{B1}$$

For these experiments, the individual terms in Eq. (B1) were all found to be of the same order of magnitude.

The first order uncertainties in the attenuation coefficient for normal incidence are given by

$$\delta\alpha_s = \sqrt{\left(\frac{\partial\alpha_s}{\partial\alpha_w}\frac{\partial\alpha_w}{\partial c_w}\delta\alpha_w\right)^2 + \frac{1}{d^2}\left(\left(\frac{\delta|F_w|}{|F_w|}\right)^2 + \left(\frac{\delta|F_s|}{|F_s|}\right)^2 + (\alpha_s-\alpha_w)^2\delta d^2 + \left(\frac{\delta|T|}{|T|}\right)^2\right)}. \tag{B2}$$

The uncertainties in the Fourier amplitude terms $\delta|F_w|$ and $\delta|F_s|$ were determined from the standard deviations of the magnitude spectra. For these measurements, the dominant terms in the attenuation uncertainty were those of the through-transmitted Fourier amplitudes $(1/d)(\delta|F_s|/|F_s|)$, and the sample thicknesses $|\alpha_s-\alpha_w|(\delta d/d)$.

[1] J. R. Allegra and S. A. Hawley, ''Attenuation of sound in suspensions and emulsions: Theory and Experiments,'' J. Acoust. Soc. Am. **51**, 1545–1564 (1972).
[2] A. E. Hay and D. G. Mercer, ''On the theory of sound scattering and viscous absorption in aqueous suspensions at medium and short wavelength,'' J. Acoust. Soc. Am. **78**, 1761–1771 (1985).
[3] A. E. Hay and A. S. Schaafsma, ''Resonance scattering in suspensions,'' J. Acoust. Soc. Am. **85**, 1124–1138 (1989).
[4] P. D. Thorne and S. C. Campbell, ''Backscattering by a suspension of spheres,'' J. Acoust. Soc. Am. **92**, 978–986 (1992).
[5] C. S. Hall, J. N. Marsh, M. S. Hughes, J. Mobley, K. D. Wallace, J. G. Miller, and G. H. Brandenburger, ''Broadband measurements of the attenuation coefficient and backscatter coefficient for suspensions: A potential calibration tool,'' J. Acoust. Soc. Am. **101**, 1162–1171 (1997).
[6] J. J. Faran, ''Sound scattering by solid cylinders and spheres,'' J. Acoust. Soc. Am. **23**, 405–418 (1951).
[7] R. Hickling, ''Analysis of echoes from a solid elastic sphere in water,'' J. Acoust. Soc. Am. **34**, 1582–1592 (1962).
[8] R. Hickling, ''Analysis of echoes from a hollow metallic sphere in water,'' J. Acoust. Soc. Am. **36**, 1124–1137 (1964).
[9] L. Flax, G. C. Gaunard, and H. Überall, ''Theory of resonance scattering,'' in *Physical Acoustics: Volume XV*, edited by W. P. Mason and R. N. Thurston (Academic, New York, 1981), Vol. XV, pp. 191–294.
[10] C. A. Farrow, L. W. Anson, and R. C. Chivers, ''Multiple scattering of ultrasound in suspensions,'' Acustica **81**, 402–411 (1995).
[11] L. L. Foldy, ''The multiple scattering of waves,'' Phys. Rev. **67**, 107–119 (1945).
[12] M. Lax, ''Multiple scattering of waves,'' Rev. Mod. Phys. **23**, 287–310 (1951).
[13] V. Twersky, ''On scattering of waves by random distributions. I. Free-space scatterer formalism,'' J. Math. Phys. **3**, 700–715 (1962).
[14] P. C. Waterman and R. Truell, ''Multiple scattering of waves,'' J. Math. Phys. **2**, 512–537 (1961).
[15] J. N. Marsh, C. S. Hall, M. S. Hughes, J. Mobley, J. G. Miller, and G. H. Brandenburger, ''Broadband through-transmission signal loss measurements of Albunex® suspensions at concentrations approaching *in vivo* doses,'' J. Acoust. Soc. Am. **101**, 1155–1161 (1997).
[16] T. L. Rhyne, K. B. Sagar, S. L. Wann, and G. Haasler, ''The myocardial signature: Absolute backscatter, cyclical variation, frequency variation, and statistics,'' Ultrason. Imaging **8**, 107–120 (1986).
[17] W. Sachse and Y.-H. Pao, ''On the determination of phase and group velocities of dispersive waves in solids,'' J. Appl. Phys. **49**, 4320–4327 (1978).
[18] J. Mobley, J. N. Marsh, C. S. Hall, M. S. Hughes, G. H. Brandenburger, and J. G. Miller, ''Broadband measurements of phase velocity in Albunex® suspensions,'' J. Acoust. Soc. Am. **103**, 2145–2153 (1998).
[19] V. A. Del Grosso and C. W. Mader, ''Speed of sound in pure water,'' J. Acoust. Soc. Am. **52**, 1442–1446 (1972).
[20] R. J. Urick, *Principles of Underwater Sound*, 3rd ed. (McGraw-Hill, New York, 1983).
[21] L. A. Davidovich, S. Makhkamov, L. Pulatova, P. K. Khabibullaev, and M. G. Khaliulin, ''Acoustical properties of certain organic liquids at frequencies from 0.3 to 3 GHz,'' Sov. Phys. Acoust. **18**, 264–266 (1972).
[22] J. D. Jackson, *Classical Electrodynamics* (Wiley, New York, 1975), pp. 310–312.
[23] R. J. Urick and W. S. Ament, ''The propagation of sound in composite media,'' J. Acoust. Soc. Am. **21**, 115–119 (1949).

Contactless mode-selective resonance ultrasound spectroscopy: Electromagnetic acoustic resonance

Hirotsugu Ogi
Graduate School of Engineering Science, Osaka University, Machikaneyama 1-3, Toyonaka, Osaka 560-8531, Japan and Materials Science and Engineering Laboratory, NIST, Boulder, Colorado 80303

Hassel Ledbetter and Sudook Kim
Materials Science and Engineering Laboratory, NIST, Boulder, Colorado 80303

Masahiko Hirao
Graduate School of Engineering Science, Osaka University, Machikaneyama 1-3, Toyonaka, Osaka 560-8531, Japan

(Received 15 December 1998; accepted for publication 12 May 1999)

A noncontacting resonant-ultrasound-spectroscopy (RUS) method for measuring elastic constants and internal friction of conducting materials is described, and applied to monocrystalline copper. This method is called electromagnetic acoustic resonance (EMAR). Contactless acoustic coupling is achieved by energy transduction between the electromagnetic field and the ultrasonic vibrations. A solenoidal coil and static magnetic field induce Lorentz forces on specimen surfaces without using a coupling agent. By changing the field direction, a particular set of vibration modes can be selectively excited and detected, an advantage in identifying the vibration modes of the observed resonance peaks. Contactless coupling allows the measure of intrinsic internal friction free from energy loss associated with contact coupling. The elastic constants and internal friction measured by EMAR are compared with those by the usual RUS method for a rectangular-parallelepiped copper monocrystal. Both methods yielded the same elastic constants despite fewer resonant peaks in the EMAR case. The two methods gave essentially the same shear-mode internal friction, but the RUS method gave higher volume-mode internal friction. © *1999 Acoustical Society of America.* [S0001-4966(99)05208-X]

PACS numbers: 43.35.Cg, 43.35.Yb [HEB]

INTRODUCTION

Resonant ultrasound spectroscopy (RUS) is recognized as a useful method to determine elastic constants of solids, even for a crystal of lower symmetry. The usual RUS configuration uses a sphere, cylinder, or rectangular-parallelepiped specimen, whose dimensions are typically 10 to 1 mm, and two sandwiching transducers that touch the specimen at opposite corners. One transducer generates a continuous wave (cw) oscillation and the other detects ultrasonic oscillation. Sweeping through frequency, one obtains the frequency response of the received amplitude, which consists of a spectrum of resonance peaks. The resonance frequencies are then used in an inverse calculation to find the complete set of elastic constants. Good overviews of RUS were given by Maynard[1] and Migliori and Sarrao.[2]

To make full use of the attractive feature of RUS that one can obtain all independent elastic constants with a single frequency scan on a single specimen, many efforts have been made both for measurement development and numerical calculation of the resonance frequencies. Concerning technical study and application, Migliori and his co-workers[3] made large contributions. They developed instrumentation for acquiring the resonance spectrum of very small specimens ($\sim$0.001 cm^3) as a function of temperature (20–400 K). Kuokkala and Schwarz[4] used a deposited nickel film for noncontact ultrasonic transduction and measured internal friction of an $Ni_{80}P_{20}$ alloy up to 520 K. Ledbetter *et al.*[5] applied RUS to measure elastic constants of a boron–aluminum fiber-reinforced composite. More recently, Tanaka *et al.*[6–8] measured elastic constants of monocrystals of intermetallic compounds, including γ-TiAl. Isaak *et al.*[9] used it to measure the shear-modulus pressure derivative of fused silica and discussed the effect of mass density of pressurizing gases. Concerning numerical calculation, Holland[10] used a Fourier series to approximate deformation in a cubic specimen. Demarest[11] used Legendre polynomials and obtained a good solution with a smaller number of harmonic functions. Ohno[12] also used Legendre functions and established an effective method for obtaining free-vibration resonant frequencies.

A key to the successful determination of elastic constants is the correct correspondence between the observed and calculated resonance frequencies. Because the identification of the observed resonance modes is not straightforward, one needs to know beforehand a set of elastic constants near real values. Otherwise, the inversion fails to converge or converges to a false minimum. This forces us to supplement RUS with other methods such as a pulse–echo or rod resonance. To reduce these troubles, several efforts have been made for resonance-peak mode identification. Ohno[12] used different rates of changes of resonant frequencies by varying the specimen size. Maynard[13] switched assignments of frequencies during the iteration calculation for finding the best fit. Migliori *et al.*[3] changed the sample orientation relative to

 0001-4966/99/106(2)/660/6/$15.00

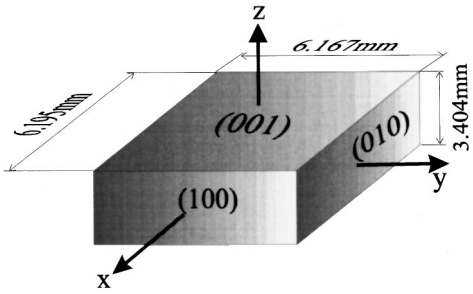

FIG. 1. Rectangular-parallelepiped specimen of copper monocrystal (6.159 $\times$6.167$\times$3.404 mm^3).

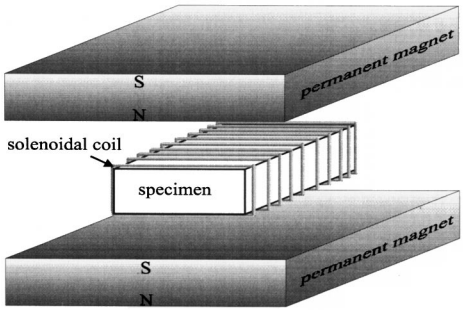

FIG. 2. Typical setup for electromagnetic–acoustic transduction.

the transducers and monitored the signal amplitude. Okamoto *et al.*[14] used multiple detectors attached to different points on the surface to evaluate the vibration symmetry using the multiple outputs. These methods are laborious and sometimes inapplicable for a solid having larger internal friction because broad resonant peaks usually overlap one another. The best way to identify the mode is to independently produce only one group of vibrations, filtering others out. No one reported a method realizing this goal for RUS method.

In the present study, we present a new noncontacting RUS method to selectively excite and detect only one group of vibrations; electromagnetic acoustic resonance (EMAR).[15–19] A specimen is inserted in a solenoidal coil where a uniform static magnetic field is applied. By driving the coil with a high-power rf burst, electromagnetic body forces occur directly on the specimen surfaces. The same coil works as a receiver. Because the direction and symmetry of the body forces can be easily controlled by changing the geometrical configuration of the static field and the coil, we can generate and detect only a selected subgroup of resonances. The acoustically contactless coupling has an especially important advantage in measuring internal friction. Little energy loss to transducers occurs, which helps us measure intrinsic internal friction. Another outstanding aspect of EMAR is its contactless feasibility at elevated temperatures. The authors[19] made a noncontact monitoring of internal friction evolution in an SiC/Ti composite up to 1000 K. The present study demonstrates the usefulness of EMAR to determine elastic constants and internal friction with a rectangular-parallelepiped copper monocrystal.

I. MODE-SELECTION METHOD

Figure 1 shows the shape and size of the copper monocrystal used in the present study. The *x*, *y*, and *z* axes are defined as shown. Archimedes-method mass density was 8.94 g/cm^3. The dimension fluctuation was within 0.3%. Measurements were made at ambient temperature.

Figure 2 shows a typical measurement setup. The specimen was inserted into a thin plastic sheet in a solenoidal coil fixed between two permanent-magnet blocks. The solenoidal coil is loose and the specimen is unconstrained. Mechanical specimen-plastic coupling is weak because of no applied force, just specimen mass, and because of large acoustic-impedance mismatch. Thus, this situation can be considered as acoustically noncontacting. The permanent magnets provide the static magnetic field needed for Lorentz-force coupling. The magnetic field was 0.15 T. Driving the coil with a high-power rf burst causes eddy currents on the surfaces, which interact with the magnetic field and generate Lorentz forces. These forces are the sources of the ultrasonic vibration. The reverse mechanism works in the receiving process. Details of the electromagnetic coupling into the acoustic wave can be found elsewhere.[17–20]

We measured the three configurations shown in Fig. 3: magnetic field parallel to *x* axis and the resultant Lorentz forces normal to *x* axis (case I); magnetic field parallel to *z* axis and Lorentz forces parallel to *x* axis (case II); and magnetic field parallel to *z* axis and Lorentz forces parallel to *y* axis (case III). Considering *x*-, *y*-, and *z*-components of displacement on the surfaces, *u*, *v*, and *w*, respectively, we notice that in case I *w* on $x-y$ faces can be detected by the reversed-Lorentz-force mechanism only when it is an odd function about *z* and an even function about *x* and *y*, and also *v* on $z-x$ faces can be detected only when it is an odd function about *y* and an even function about *x* and *z*. Similarly, in case II and case III, the Lorentz-force mechanism

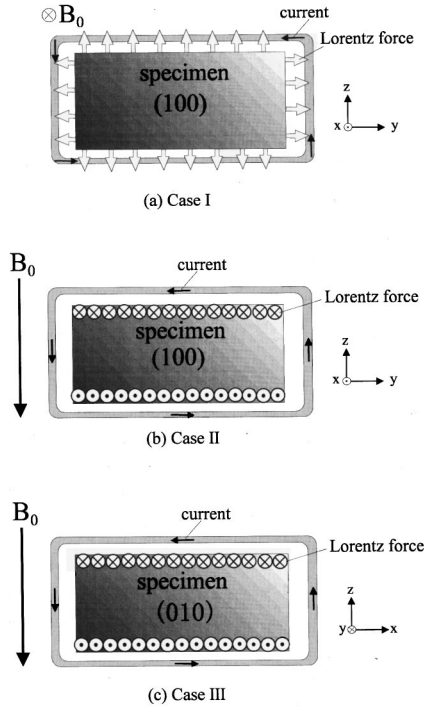

FIG. 3. Three configurations of the coil and static field for generating (a) OD group, (b) OY group, and (c) OX group.

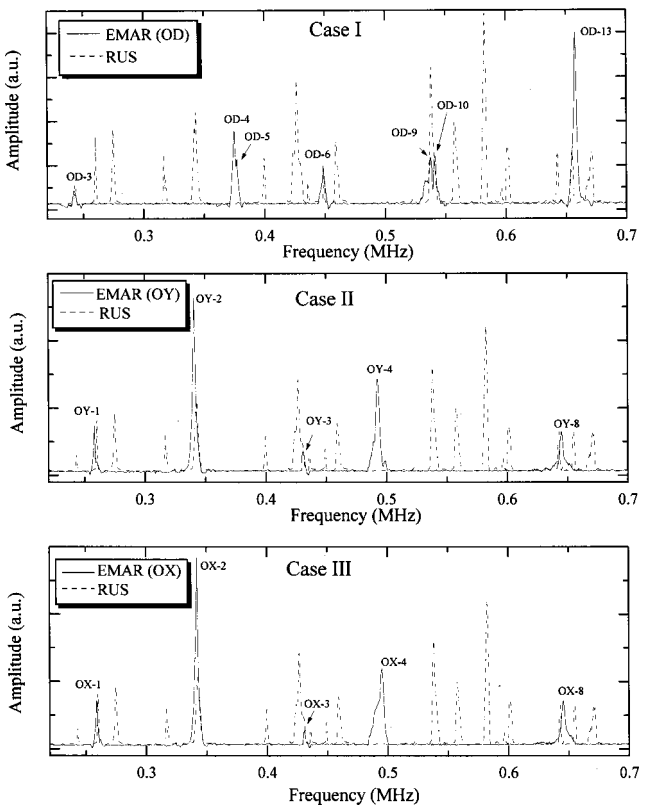

FIG. 4. Resonance spectrum for the three cases. RUS results are shown as a broken line.

works responding to u and w on $x-y$ faces, respectively. To detect them with the same coil, they must be odd functions about z and even functions about x and y. For a rectangular-parallelepiped crystal with symmetry orthorhombic or higher, the vibration modes fall into eight groups, depending on the deformation symmetry.[11,12] Among them, only the OD group (breathing vibration) satisfies the condition of the deformation symmetry of case I. Similar analysis shows that only the OY group (torsional vibration about the y-axis) can be detected in case II, and the OX group (torsional vibration about the x-axis) in case III. Thus, we can easily select the vibration group by changing the configuration of the measurement setup.

II. THE ELASTIC CONSTANTS

We show the resonance spectra in Fig. 4 for the three cases. For comparison, we made the usual RUS measurement using the same specimen. The detailed configuration of the RUS measurement in the present study is found in Ref. 5. The RUS result is shown in Fig. 4 with a dashed line, which demonstrates detection of many groups of vibration other than the above three. Different EMAR configurations led to different spectra, as expected. We determined the resonance frequencies by fitting the Lorentzian function to a peak and calculating its center. Although the number of the resonant peaks observed with EMAR is fewer than that with RUS, the determination of a set of elastic constants is straightforward. This is because mode identification is much easier in EMAR. For example, the OX-2 and OY-2 resonances occur at close frequencies, and they overlap in RUS measurement as shown

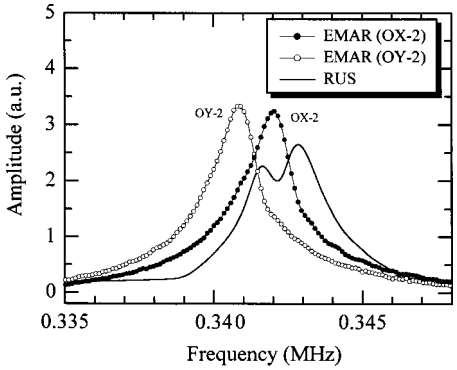

FIG. 5. Resonance spectra measured by EMAR and RUS.

in Fig. 5. However, because EMAR can select either of them, the distinction is easy, giving no ambiguity. We made the inverse calculation developed in previous studies,[5,12] using the EMAR resonance frequencies, and we obtained the three cubic-symmetry elastic constants. Measured and calculated resonance frequencies are shown in Table I. (Equipment limitations prevented our detecting the lower-frequency modes OD-1 and OD-2.) Measured and calculated frequencies agreed within 0.4%, which is comparable with the fractional error of the specimen dimensions. This iterative calculation needs a first guess of elastic constants. We started the iteration with several sets of elastic constants covering a wide range (C_{11}:100–230 GPa, C_{12}:70–150 GPa, C_{44}:50–150 GPa) and we obtained the same results. We also deduced the elastic constants with the RUS frequencies using a larger number of resonances. In this case, to get correct convergence, we needed better guesses ($C_{11}=168$ GPa, $C_{12}=120$ GPa, $C_{44}=74$ GPa). The measured and calculated frequencies also showed a difference of 0.4%.

Table II shows the elastic constants deduced from the

TABLE I. Measured (f_{meas}) and calculated (f_{calc}) resonance frequencies for EMAR case.

Mode	f_{meas} (MHz)	f_{calc} (MHz)	Difference (%)
OD-1	···	0.183 706	···
OD-2	···	0.211 36	···
OD-3	0.242 323	0.242 549	0.09
OD-4	0.374 916	0.373 805	−0.3
OD-5	0.375 139	0.374 833	−0.08
OD-6	0.448 678	0.450 268	0.35
OD-7	···	0.472 787	···
OD-8	···	0.494 272	···
OD-9	0.535 587	0.533 39	−0.41
OD-10	0.542 134	0.543 198	0.2
OD-11	···	0.567 346	···
OD-12	···	0.643 16	···
OD-13	0.657 429	0.657 74	0.05
OX-1	0.258 849	0.258 944	0.04
OX-2	0.341 657	0.341 765	0.03
OX-3	0.429 726	0.428 519	−0.28
OX-4	0.492 967	0.494 452	0.3
OY-1	0.257 887	0.258 572	0.27
OY-2	0.340 418	0.340 449	0.01
OY-3	0.430 686	0.429 46	−0.28
OY-4	0.492 49	0.493 67	0.24

TABLE II. Elastic constants and internal friction of a copper monocrystal determined by EMAR and RUS.

	C_{ij} (GPa)				$Q_{ij}^{-1}(\times 10^{-3})$	
	EMAR	RUS	Ref. 21	Ref. 22	EMAR	RUS
C_{11}	167.0	168.7	169.7	168.4	1.14	1.74
C_{12}	120.9	121.6	122.6	121.4	0.30	1.34
C_{44}	74.64	75.46	74.49	75.40	2.59	2.46
$B=(C_{11}+2C_{12})/3$	136.2	137.3	137.3	137.1	0.64	1.50
$C'=(C_{11}-C_{12})/2$	23.05	23.52	23.35	23.50	3.34	2.80
$C_{110,110}=(C_{11}+C_{12}+2C_{44})/2$	218.6	220.6	220.6	220.3	1.40	1.87
$C_{111,111}=(C_{11}+2C_{12}+4C_{44})/3$	235.7	237.9	237.6	237.7	1.47	1.90
$C_{111,\,\mathrm{arb}}=(C_{11}-C_{12}+C_{44})/3$	40.25	40.84	40.54	40.80	2.88	2.59
C_L	199.6	201.6	⋯	⋯	1.34	1.84
G	47.54	48.22	⋯	⋯	2.83	2.57
E	127.8	129.5	⋯	⋯	2.60	2.46
ν	0.3437	0.3428	⋯	⋯	⋯	⋯

two methods and those obtained previously,[21,22] including other useful elastic-constant combinations obtained from C_{11}, C_{12}, and C_{44}. Using Kröner's method,[23] we calculated the usual isotropic-material averaged-over-direction elastic constants: shear modulus G, longitudinal modulus C_L, Young's modulus E, and Poisson ratio ν. EMAR provided slightly smaller stiffness constants than those measured by the RUS method. This may be caused by the mechanical coupling of RUS, even if it is weak; that is, RUS does not achieve ideal free vibration. To obtain the resonance frequencies of free vibration with RUS, one should minimize the forces from the sandwiching piezoelectric transducers. Applied load partially constrains the sample deformation and increases the resonant frequencies (see Fig. 5), leading to larger elastic constants in general.[24] We noticed this influence during measurements when the force was changed. However, since we did our best to minimize the force in the RUS measurement (it may be slightly larger than the sample mass), the influence on the elastic constants should be insignificant.

EMAR does not detect all vibration modes expected for a given configuration (see Fig. 3). For example, OD-11 and OD-12 were missing in case I. These absences occur because the solenoidal coil detects the integral displacement over the specimen faces. If this value is too small, EMAR fails to detect that mode. It would be most useful to develop a model that predicts vibration-mode amplitudes. Then, we could predict low-amplitude modes and further facilitate mode identification.

Another configuration between the coil and static field will make it possible to generate other vibration groups. For example, designing a solenoidal coil where the direction of the driving current is reversed at the center of the sample, one can change the deformation symmetry that can be detected by the coil. Considering that the axial direction of such a coil is along the x axis and the static field is applied along the x axis, displacement w on $x-y$ faces can be detected only if it is an odd function about z, an even function about y, and an odd function about x. This is known as the EX mode[12] (symmetric flexure vibration along the x axis). In principle, one can select one of seven classes of vibration modes with the present method. Not excitable is the EV mode (asymmetric flexure mode).

III. THE INTERNAL FRICTION

EMAR has the important advantage that no energy loss occurs from mechanical contact. Thus, it is ideal for measuring internal friction. The measurement is never affected by uncertain changes of mechanical-coupling conditions, which are accompanied by varying temperature and pressure (or stress). Thus, together with the applicability to *in situ* monitoring, intensive studies have been made using EMAR to detect the evolution of internal friction at elevated temperatures,[18,19] during deformation,[25] recovery,[26] and fatigue.[27]

Here, we compare the internal friction measured by EMAR and RUS. In RUS measurements, internal friction is usually obtained from the resonance peak width: $Q^{-1}=\Delta f/f_r$, where Δf denotes the peak width at the half-power amplitude and f_r resonance frequency. We determined Q^{-1} by fitting a Lorentzian function to the resonance peak and calculating Δf. In EMAR, internal friction can be measured from the resonance ringdown.[16] After an excitation with a burst signal at a resonance frequency, the reverberation exponentially decays with time. This ringdown curve provides the attenuation coefficient α by fitting an exponential function. Figure 6 shows an example of the measured ringdown curve and the fitted exponential function for the OX-2 mode. We show the same measurements on a logarithmic scale. Departure from the fitted curve at low-amplitude region is caused by the background noise. Q^{-1} and α are related by

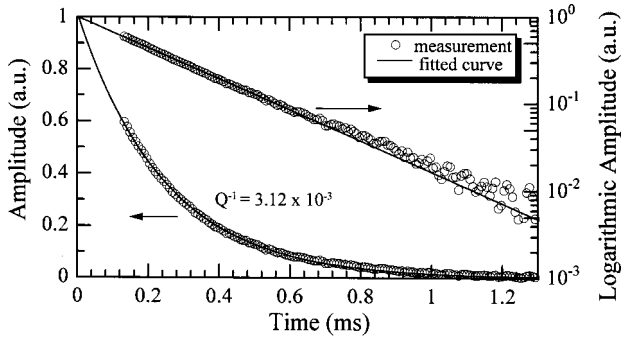

FIG. 6. Measured ringdown curve of OX-2 mode with EMAR. Solid line is a fitted exponential function. Logarithmic-scale amplitude for the same data is also shown.

TABLE III. Internal friction measured by EMAR (Q^{-1}_{EMAR}) and RUS (Q^{-1}_{RUS}).

Mode	$Q^{-1}_{\mathrm{EMAR}}(\times 10^{-3})$	$Q^{-1}_{\mathrm{RUS}}(\times 10^{-3})$	Difference (%)
OD-1	···	2.63	···
OD-2	···	1.36	···
OD-3	2.73	3.52	−29
OD-4	4.46	2.68	39
OD-5	4.33	2.80	35
OD-6	2.10	3.00	−43
OD-7	···	···	···
OD-8	···	···	···
OD-9	3.01	3.04	−1
OD-10	1.44	1.51	−5
OD-11	···	3.38	···
OD-12	···	1.71	···
OD-13	1.55	1.74	−12
OX-1	2.20	2.38	−8
OX-2	3.12	3.78	−21
OX-3	1.94	1.83	6
OX-4	4.01	···	···
OY-1	2.42	2.82	−17
OY-2	3.16	3.43	−9
OY-3	2.03	2.06	−1
OY-4	3.87	···	···

$Q^{-1}=\alpha/(f_r\pi)$. In the EMAR case, $\Delta f/f_r$ should not be used for Q^{-1} because at a slightly off-resonance frequency the burst wave cannot cancel the ringdown signal adequately, unlike the cw signal, resulting in a broader resonance peak width.

Table III compares Q^{-1} measured by RUS and EMAR. For most modes, Q^{-1} from RUS exceeded that from EMAR. OD-4 and OD-5 modes showed larger Q^{-1} in the EMAR measurement. RUS Q^{-1} values for these modes are not reliable because of the very low resonance intensity (see Fig. 4). Because we can calculate the contribution of each elastic constant to the resonant frequencies, we can also calculate the internal friction for each elastic constant; that is, the internal friction tensor Q^{-1}_{ij}.[28,29] Q^{-1}_{ij} is useful because one can calculate the internal friction of any oscillation mode. We show Q^{-1}_{ij} thus calculated in Table II. Internal friction for the bulk modulus B was considerably smaller. Because in monocrystal copper a large part of the internal friction is caused by dislocation damping, this observation is easily understood because of the lower mobility of dislocations during hydrostatic loading. The larger internal friction of shear waves (internal friction for C_{44}, C', $C_{111,\mathrm{arb}}$, and G) than those of longitudinal waves (C_{11}, $C_{110,110}$, $C_{111,111}$, and C_L) indicates that shear waves more effectively cause dislocation vibration about their pinning points than do longitudinal waves. This is supported by a simultaneous measurement of shear wave and longitudinal wave internal friction on deforming polycrystalline copper.[25] The ratio of internal friction for longitudinal modulus (C_L) and shear modulus (G) was 2.1 for EMAR. The ratio for RUS was 1.4, which is comparable with a ratio 1.6 found by Ledbetter and co-workers[28] in studying polycrystalline copper using RUS. Comparing EMAR and RUS, we find a larger RUS Q^{-1}_{ij} for longitudinal waves and, especially, for the bulk modulus; the Q^{-1}_{ij} for shear waves were comparable. This indicates that vibration modes accompanying volume change cause energy losses into the sandwiching transducers in an RUS measurement, even when the loading force is minimized.

The only possible extra energy loss in EMAR is eddy-current loss in the specimen. Ultrasonic vibration in a uniform magnetic field generates eddy currents within the specimen. This loss is estimated by[16]

$$Q^{-1}_{\mathrm{ed}}=\frac{\sigma B_0^2}{\omega\rho}. \tag{1}$$

Here, σ denotes electric conductivity, B_0 flux density of the static field, ω angular frequency, and ρ mass density. Taking $\sigma=6\times10^7$ S/m, $\rho=8.94$ g/cm^3, $f=0.2$ MHz, and $B_0=0.15$ T, we have $Q^{-1}_{\mathrm{ed}}=1.2\times10^{-4}$, which is small compared with the measured Q^{-1}. One may consider that Q^{-1}_{ed} has to be compensated for a material of low Q^{-1} and high conductivity. Fortunately, such a material shows good electromagnetic–acoustic transduction efficiency and we can lower the static magnetic field and thus also Q^{-1}_{ed}.

IV. CONCLUSIONS

(1) Electromagnetic acoustic resonance (EMAR) works well in measuring elastic constants, even with a smaller number of resonant peaks than in RUS. By changing the geometrical configuration of the coil and static field, one can selectively generate and detect a particular group of vibration modes. This helps identify vibration modes for the elastic-constant determination.

(2) The inverse calculation using the mode-identified resonant frequencies with EMAR provided one set of elastic constants, being independent of the initial guessed values for iteration. The RUS method can be extremely sensitive to the first guess.

(3) Elastic constants measured by EMAR were generally smaller than those by RUS with contacting transducers by approximately 1%.

(4) Except for the pure-shear modes, internal friction measured by EMAR was lower than that by RUS for all useful elastic constant combinations. The difference was substantial for the breathing modes because the RUS method involves energy loss into the transducers, even for minimum coupling load.

[1] J. Maynard, ''Resonant ultrasound spectroscopy,'' Phys. Today **49**, 26 (1996).

[2] A. Migliori and J. Sarrao, *Resonant Ultrasound Spectroscopy* (Wiley, New York, 1997).

[3] A. Migliori, J. Sarrao, M. W. Visscher, T. Bell, M. Lei, Z. Fisk, and R. Leisure, ''Resonant ultrasound spectroscopic technique for measurement of the elastic moduli of solids,'' Physica B **183**, 1 (1993).

[4] V.-T. Kuokkala and R. B. Schwarz, ''The use of magnetostrictive film transducers in the measurement of elastic moduli and ultrasonic attenuation of solids,'' Rev. Sci. Instrum. **63**, 3136 (1992).

[5] H. Ledbetter, C. Fortunko, and P. Heyliger, ''Orthotropic elastic constants of a boron-aluminum fiber-reinforced composite: An acoustic-resonance-spectroscopy study,'' J. Appl. Phys. **78**, 1542 (1995).

[6] K. Tanaka, T. Ichitsubo, H. Inui, M. Yamaguchi, and M. Koiwa, ''Single-crystal elastic constants of γ-TiAl,'' Philos. Mag. A **73**, 71 (1996).

[7] K. Tanaka and M. Koiwa, ''Single-crystal elastic constants of intermetallic compounds,'' Intermetallics **4**, 29 (1996).

[8] K. Tanaka, K. Okamoto, H. Inui, Y. Minonishi, M. Yamaguchi, and M.

Koiwa, ''Elastic constants and their temperature dependence for the intermetallic compound Ti_3Al,'' Philos. Mag. A **73**, 1475 (1996).
[9] D. Isaak, J. Carnes, O. Anderson, and H. Oda, ''Elasticity of fused silica spheres under pressure using resonant ultrasound spectroscopy,'' J. Acoust. Soc. Am. **104**, 2200 (1998).
[10] R. Holland, ''Resonant properties of piezoelectric ceramic rectangular parallelepipeds,'' J. Acoust. Soc. Am. **43**, 988 (1968).
[11] H. Demarest, Jr., ''Cube-resonance method to determine the elastic constants of solids,'' J. Acoust. Soc. Am. **49**, 768 (1971).
[12] I. Ohno, ''Free vibration of a rectangular parallelepiped crystal and its application to determination of elastic constants of orthorhombic crystals,'' J. Phys. Earth **24**, 355 (1976).
[13] J. Maynard, ''The use of piezoelectric film and ultrasound resonance to determine the complete elastic tensor in one measurement,'' J. Acoust. Soc. Am. **91**, 1754 (1992).
[14] K. Okamoto, K. Tanaka, and M. Koiwa, *Proceedings of the Second Pacific Rim International Conference on Advanced Materials and Processing*, edited by K. S. Shin, J. K. Yoon, and S. J. Kim (Korean Institute of Metals and Materials, 1995), p. 1153.
[15] M. Hirao, H. Ogi, and H. Fukuoka, ''Resonance EMAT system for acoustoelastic stress evaluation in sheet metals,'' Rev. Sci. Instrum. **64**, 3198 (1993).
[16] H. Ogi, M. Hirao, and T. Honda, ''Ultrasonic attenuation and grain size evaluation using electromagnetic acoustic resonance,'' J. Acoust. Soc. Am. **98**, 458 (1995).
[17] M. Hirao and H. Ogi, ''Electromagnetic acoustic resonance and materials characterization,'' Ultrasonics **35**, 413 (1997).
[18] W. Johnson, ''Ultrasonic damping in pure aluminum at elevated temperature,'' J. Appl. Phys. **83**, 2462 (1998).
[19] H. Ogi, G. Shimoike, M. Hirao, K. Takashima, H. Ohtani, and H. Ledbetter, *Review of Progress in QNDE*, Vol. 18, edited by D. O. Thompson and D. E. Chimenti (Plenum, New York, 1999), p. 1337.
[20] H. Ogi, ''Field dependence of coupling efficiency between electromagnetic field and ultrasonic bulk waves,'' J. Appl. Phys. **82**, 3940 (1997).
[21] H. Ledbetter and S. Kim, Personal communication, unpublished.
[22] R. Hearmon, ''Elastic constants of anisotropic materials-II,'' Adv. Phys. **5**, 323 (1956).
[23] E. Kröner, ''Self-consistent scheme and graded disorder in polycrystal elasticity,'' J. Phys. F **8**, 2261 (1978).
[24] Y. Sumino, I. Ohno, T. Goto, and M. Kumazawa, ''Measurement of elastic constants and internal friction in single-crystal MgO by rectangular parallelepiped resonance,'' J. Phys. Earth **24**, 263 (1976).
[25] H. Ogi, N. Suzuki, and M. Hirao, ''Noncontact ultrasonic spectroscopy on deforming polycrystalline copper; dislocation damping and acoustoelasticity,'' Metall. Mater. Trans. A **29**, 2987 (1998).
[26] H. Ogi, A. Tsujimoto, M. Hirao, and H. Ledbetter (unpublished).
[27] H. Ogi, M. Hirao, and K. Minoura, ''Noncontact measurement of ultrasonic attenuation during rotating fatigue test of steel,'' J. Appl. Phys. **81**, 3677 (1997).
[28] H. Ledbetter, C. Fortunko, and P. Heyliger, ''Elastic constants and internal friction of polycrystalline copper,'' J. Mater. Res. **10**, 1352 (1995).
[29] P. Heyliger and H. Ledbetter, in *Mechanical Spectroscopy*, edited by L. Magalas (Elsevier, Amsterdam, 1999) (unpublished).

Theoretical and experimental studies of surface waves on solid–fluid interfaces when the value of the fluid sound velocity is located between the shear and the longitudinal ones in the solid

Frédéric Padilla, Michel de Billy, and Gérard Quentin
Groupe de Physique de Solides–CNRS UMR 7588, Tour 23, Université Paris 7–Denis Diderot, 2 place Jussieu, 75251 Paris, France

(Received 12 May 1998; accepted for publication 31 March 1999)

The existence of two surface waves propagating on a plane solid–fluid interface is demonstrated when the value of the fluid sound velocity is located between the shear and the longitudinal ones in the solid. First, the Scholte–Stoneley dispersion equation is studied analytically and numerically to find the roots corresponding to the Stoneley and the Rayleigh waves. The anatomy of each one is then described with the formalism of the evanescent plane waves: both waves are unleaky. Finally, the results are confirmed experimentally by measuring the times of flight on a Plexiglas–water interface and on a PVC–water interface. © *1999 Acoustical Society of America.*
[S0001-4966(99)02607-7]

PACS numbers: 43.35.Pt [HEB]

INTRODUCTION

Two surface waves may propagate on a plane solid–liquid interface: the generalized Rayleigh wave and the Stoneley wave.[1,2] Results are well established when the fluid sound velocity c_F is lower than the velocities of the bulk shear wave c_S and the bulk longitudinal wave c_L in the solid. In that case the generalized Rayleigh wave propagates with a phase velocity slightly lower than c_S and radiates energy into the fluid. The Stoneley wave phase velocity is lower than the velocities in the three medium.

The main objective of this paper is to study the existence of such surface waves on interfaces when the fluid sound velocity is larger than the velocity of the bulk shear wave in the solid: $c_S \leqslant c_F \leqslant c_L$. We may call these types of interfaces ''plastic–fluid'' interfaces by opposition to the ''metal–fluid'' interface as described in the previous paragraph.

It seems that few works are concerned with the plastic–fluid interface. Following the results of Brower *et al.*,[3] if such surface waves exist, they would be unleaky, because their phase velocities are close or lower than c_S. Consequently, it should be very difficult to generate them from the fluid. This may be the reason why the existence of these waves was not detected with the study of plastic plates by reflection or transmission coefficient.[4–6] Nevertheless, the Stoneley wave has been recently observed experimentally on a PVC–water (PVC: polyvinyl chloride) interface, with a highly viscoelastic type of PVC.[7] Favretto-Anrès showed that a decaying Stoneley wave could propagate on this interface, but didn't study the Rayleigh wave.

Numerical studies of the dispersion equation for plane interfaces may be found in the domain of geophysics. Some authors searched the roots of the equation to describe the pulse which could propagate along the interface with an integral method. They were interested in the roots which should have a physical significance.

Gilbert and Laster[8] studied the solid–solid problem and relaxed one of the solids to a fluid, but only with $c_F \leqslant c_S$. Pilant[9] did the same for all fluid sound velocities. But he predicted that only the Stoneley wave should exist when $c_S \leqslant c_F \leqslant c_L$. Phinney[10] treated the solid–fluid interface, but, in the real root corresponding to the Stoneley wave, he looked only for complex roots. Now as we might see further, when $c_S \leqslant c_F$, the Rayleigh root becomes real.

Our purpose is to show numerically and experimentally that a Rayleigh wave and a Stoneley wave may propagate on a general plastic–fluid interface. To carry out this work, we use the formalism of the evanescent plane waves[11,12] coupled with an analysis of the Scholte–Stoneley dispersion equation. For this last point we follow the approach of Ansell,[13] who studied all the solutions of the equation. Each of these solutions is located on a Riemann sheet and the anatomy of the corresponding surface wave is described. By comparing with the metal–fluid case, the numerical study is limited to the roots which become the Rayleigh root of the plastic–vacuum interface as the density of the fluid decreases to zero. When these two roots are found it is then possible to show that the two corresponding surface waves are not leaky. Finally, the results are confirmed experimentally by measuring the times of flight on a Plexiglas–water interface and on a PVC–water interface.

Section I is devoted to a brief survey of the general properties of the evanescent plane waves. It is a very useful tool to understand the structure of waves as was done for the generalized Rayleigh wave,[14] the circumferential Rayleigh wave,[15] and the Lamb waves.[16]

In Sec. II, we study analytically the Scholte–Stoneley equation and its different solutions. Particular attention is brought to the roots corresponding to the Rayleigh and Stoneley surface waves.

In Sec. III, these solutions are calculated as the density of the fluid decreases to zero. It is shown that on a plastic–

fluid interface a Rayleigh wave may be defined which propagates with no loss.

Finally we present in Sec. IV experimental results concerning the existence of these waves and we show that good agreement exists between the numerical predictions and the experimental measurements.

I. FORMALISM OF THE EVANESCENT PLANE WAVES

In the solid and in the fluid, we shall describe the waves with the formalism of the evanescent plane waves as presented in Refs. 11 and 12. We set out here briefly the main properties that we shall use in the next sections.

Let the acoustic displacement vector **d** (or any other acoustical disturbances) be

$$\mathbf{d}(\mathbf{r},t)=\mathbf{D_0}\exp i(\mathbf{K}\cdot\mathbf{r}-\omega t), \tag{1}$$

where $\mathbf{D_0}$ is the complex amplitude vector; $\mathbf{K}=\mathbf{K}'+\mathbf{K}''$ is the complex wave vector where $\mathbf{K}'$ stands for the wave vector and $\mathbf{K}''$ for the attenuation vector; $\mathbf{r}$ is the spatial coordinate; ω is the angular frequency and t is the time. The wave propagates in the $\mathbf{K}'$ direction and is exponentially damped in the $\mathbf{K}''$ direction.

In a free isotropic medium, the acoustic displacement **d** must satisfy the Helmholtz equation, and so the wave vector **K** obeys the dispersion equation:

$$\mathbf{K}\cdot\mathbf{K}=\mathcal{K}_i^2, \tag{2}$$

where the subscript i will differentiate the three types of homogeneous waves, i.e., $i=F$ designates the longitudinal wave in the fluid, $i=L$ the longitudinal wave in the solid and $i=S$ the shear wave in the solid. $\mathcal{K}_i$ is the wave number of the homogeneous plane wave i and $\mathcal{K}_i=\omega/c_i$ where c_i is the phase velocity of the homogeneous plane wave i. Separating real and imaginary parts of Eq. (2) leads to the system:

$$K'^2=\mathcal{K}_i^2+K''^2, \tag{3}$$

$$\mathbf{K}'\cdot\mathbf{K}''=0, \tag{4}$$

where $K'=\|\mathbf{K}'\|$. We deduce from Eq. (4) that the propagation direction of the evanescent plane wave is always orthogonal to its damping direction. The phase velocity in the direction of propagation is $c_{ph}=\omega/K'$. Because of the inequality $K'\geqslant\mathcal{K}_i$, which comes from Eq. (3), the evanescent plane wave propagates in medium i with a velocity c_{ph} lower than the velocity c_i.

II. THE SCHOLTE–STONELEY EQUATION

The presentation of the Scholte–Stoneley equation in this section is based on the work of Ansell.[13] Some of these results are developed and physical interpretations are given with the formalism used in the previous section.

A. Analysis of the equation

The plane solid–fluid interface may be treated as a two-dimensional problem without loss of generality. A coordinate system attached to the interface is noted $(\mathbf{x},\mathbf{z})$. The z axis is normal to the boundary $z=0$ and the x axis is parallel to it. The dispersion equation for a wave propagating at the solid–fluid interface is obtained by writing the continuity of the normal acoustic displacement and the continuity of the normal stress tensor on the plane $z=0$.[1] The Scholte–Stoneley equation for the wave number K_x along the interface is obtained by writing the acoustic displacement in the fluid and in the solid as in the relation Eq. (1):

$$S(K_x)=K_{Fz}[4K_x^2K_{Sz}K_{Lz}+(K_S^2-2K_x^2)^2]-\rho K_S^4K_{Lz}=0, \tag{5}$$

where the dimensionless parameter $\rho=\rho_F/\rho_S$ is the ratio between the fluid density and the solid density; and:

$$K_{iz}=\sqrt{\mathcal{K}_i^2-K_x^2} \tag{6}$$

is the z component of the complex wave vector $\mathbf{K}_i$ $(i=F,L,S)$ which satisfies the dispersion Eq. (2).

A surface wave as the generalized Rayleigh wave[14] or the Stoneley wave[17] can be decomposed as a set of three evanescent plane waves: a longitudinal wave in the fluid, a longitudinal wave and a shear wave in the solid. Each of the three complex wave vector $\mathbf{K}_i$ has a projection K_x on the interface which is the solution of Eq. (5). This component verifies the generalized Descartes–Snell laws.[18]

The component K_{iz} is a complex square root. It may be written on two Riemann sheets which correspond to the square root with a positive real part and the square root with a negative real part. The top Riemann sheet is defined by:

$$-\frac{\pi}{2}\leqslant\arg[K_{iz}]\leqslant\frac{\pi}{2}$$

and is noted with a + sign.

Equation (5) contains three square roots K_{iz}. The Riemann surface for the function S also has eight sheets which are designated by a group of three signs $(\pm,\pm,\pm)$. Each of the signs stands for the Riemann sheet of (K_{Fz},K_{Sz},K_{Lz}). And so the function S gives rise to eight separate functions, noted S_j and S_{-j} with $j=1,2,3,4$. These functions are written in Table I.

TABLE I. The four functions S_j when K_{Fz} is on the top Riemann sheet, i.e., when $K'_{Fz}\geqslant 0$. The functions S_{-j} are obtained by replacing K_{iz} by $-K_{iz}$.

Function	Sign of K'_{Fz}	Sign of K'_{Sz}	Sign of K'_{Lz}
$S_1(K_x)=K_{Fz}[4K_x^2K_{Sz}K_{Lz}+(K_S^2-2K_x^2)^2]+\rho K_S^4K_{Lz}$	+	−	−
$S_2(K_x)=K_{Fz}[4K_x^2K_{Sz}K_{Lz}+(K_S^2-2K_x^2)^2]-\rho K_S^4K_{Lz}$	+	+	+
$S_3(K_x)=K_{Fz}[-4K_x^2K_{Sz}K_{Lz}+(K_S^2-2K_x^2)^2]-\rho K_S^4K_{Lz}$	+	−	+
$S_4(K_x)=K_{Fz}[-4K_x^2K_{Sz}K_{Lz}+(K_S^2-2K_x^2)^2]+\rho K_S^4K_{Lz}$	+	+	−

The product of the four functions S_j is a polynomial of degree eight in K_x^2 with real coefficients. This polynomial may be solved with a classical procedure (here the Bairstow's method). Each root K_{x_0} is the solution of one of the four equations $S_j(K_{x_0})=0$. To assign the root to its corresponding equation, each function S_j is tested with the different solutions. If K_{x_0} is a zero of the polynomial, the conju-

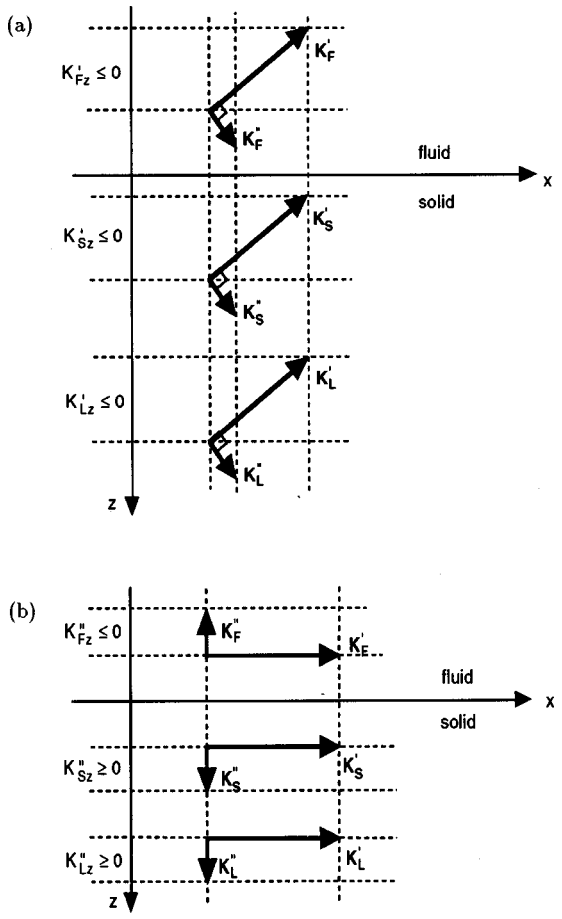

FIG. 1. (a) Structure of a surface wave corresponding to a complex root which is on the Riemann sheet $(-,-,-)$. It is the structure of the Rayleigh wave on a ''metal–fluid'' interface. (b) Structure of a surface wave corresponding to a real root which is greater than $\mathcal{K}_i$ in the three medium and solution for $K''_{Fz} \leqslant 0$, $K''_{Sz} \geqslant 0$ and $K''_{Lz} \geqslant 0$. It is the structure of the Stoneley wave on a ''metal–fluid'' interface.

gate value $\overline{K}_{x_0}$ and the opposite $-K_{x_0}$ are also zeroes. So it is possible to restrain the study in the first quadrant of the complex K_x plane. It means that the solutions of Eq. (5) with $K'_x \geqslant 0$ and $K''_x \geqslant 0$ may be studied only.

B. Location of the roots

There are three branch points in the complex K_x plane for the function S at $K_x = \mathcal{K}_i$ where K_{iz} is zero. There are also three branch cuts on the real axis, the intersection between two Riemann sheets, which are:

$$[\mathcal{K}_i ; +\infty[.$$

On these intervals, K_{iz} is purely imaginary, and $K'_{iz} = 0$. The problem of the choice of the sign of the square roots remains. In that case, the two possible values of K''_{iz}, i.e., $K''_{iz} \geqslant 0$ and $K''_{iz} \leqslant 0$, are tested for the numerical computation, and the sign of K''_{iz} for which K_x is a zero of Eq. (5) is then determined.

In the next section we study the values of the roots of Eq. (5) as the current parameter ρ decreases from ρ_F/ρ_S to zero. Indeed, computations have been done from $\rho_F = 1$ to $\rho_F = 0$ to study the limit procedure from the solid–water interface to the solid–vacuum interface. In this situation, the

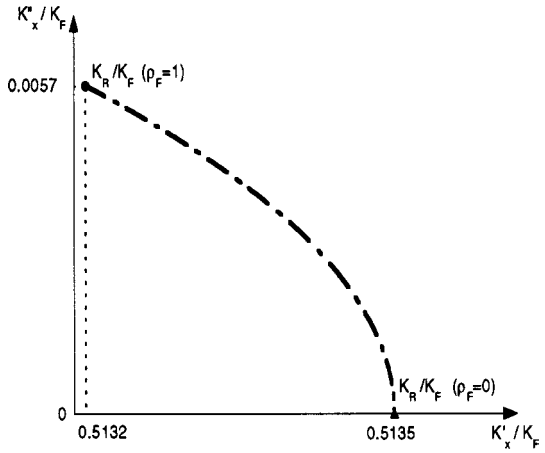

FIG. 2. The normalized Rayleigh root $K_R/\mathcal{K}_F$ in the complex K_x plane, when ρ_F decreases from 1 to 0 (the origin of the abscissa is $K'_x/\mathcal{K}_F = 0.5132$). The black point is the solution K_R for the metal–fluid interface, the black triangle is the solution K_{R_0} for the metal–vacuum interface. The materials used are steel ($\rho_S = 7.8$; $c_L = 5740$ m/s; $c_S = 3112$ m/s) and water ($\rho_F = 1$; $c_F = 1480$ m/s).

roots of Eq. (5) move in the complex K_x plane and the root of one function $S_j(K_x) = 0$ may become the root of another function $S_{n \neq j}(K_x) = 0$ as it crosses a branch cut. But as noticed by Ansell this occurs only at $K_x = \mathcal{K}_S$ or $K_x = \mathcal{K}_S/2$.

With this analysis, we know on which Riemann sheet is located each solution K_{x_0} of Eq. (5). The structure of the corresponding interface wave is also completely defined: The propagation and the damping direction of the waves in the fluid and in the solid are fixed by the signs of K'_{iz} and K''_{iz} as illustrated by Fig. 1.

III. NUMERICAL STUDY OF THE SCHOLTE–STONELEY EQUATION

We focus here on the differences between the solutions of the Scholte–Stoneley equation for the generalized Rayleigh wave and the Stoneley wave on two types of interface: first the ''metal–fluid'' interface ($c_F \leqslant c_S \leqslant c_L$) and then the ''plastic–fluid'' interface ($c_S \leqslant c_F \leqslant c_L$). For each solution, the structure of the wave is detailed.

A. Metal–fluid interface

1. Rayleigh wave

The particular complex zero of Eq. (5) which is called the Rayleigh zero K_R is defined by the limit procedure when the density of the fluid decreases to zero. The Scholte–Stoneley equation becomes the Rayleigh equation and the generalized Rayleigh wave becomes a free Rayleigh wave. When $\rho_F = 0$, the imaginary part of K_R vanishes and its real part is the real Rayleigh zero for the solid–vacuum interface K_{R_0} as illustrated by the curve in Fig. 2.

This solution is located on the Riemann sheet $(-,-,-)$. The structure of the wave is the one of a leaky surface wave. As shown in Fig. 1(a), its amplitude is exponentially damped in the directions normal to the interface and along the interface during the propagation. As the leaky Rayleigh wave propagates, energy is radiated into the liquid. The in-

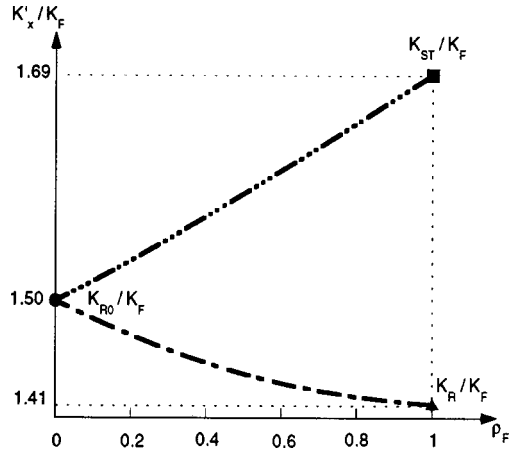

FIG. 3. The two normalized real roots $K_x'/\mathcal{K}_F$ as a function of ρ_F. The black square is the Rayleigh root, the black triangle the Stoneley root at the plastic–fluid interface. The black point is the Rayleigh root at the plastic–vacuum interface. Characteristics of the materials used are for PVC ($\rho_S=1.56$; $c_S=1050$ m/s; $c_L=2380$ m/s) and for water ($\rho_F=1$; $c_F=1480$ m/s).

crease of amplitude in the liquid away from the interface can be explained by taking into account the effect of bounded beams present in real experimental situations. A decomposition of a bounded beams into plane waves shows that the wave is limited in space and that its amplitude is finite.[14]

The existence of this leaky surface wave is submitted to certain conditions.[3] As the phase velocity along the interface c_R is always close to c_S, the velocity c_S must be greater than the velocity c_F in the fluid. If not, the Rayleigh angle of radiation would be an imaginary angle.

2. Stoneley wave

The Stoneley zero K_{ST} is defined as the greatest real root of Eq. (5). It has been tabulated by Strick and Ginzbarg in Ref. 19. K_{ST} is greater than $\mathcal{K}_i$ in the three medium, and so the phase velocity of the surface wave along the boundary is lower than the velocities c_F, c_S and c_L.

Consequently the components K_{iz} are purely imaginary, and the solution is found when $K''_{Fz}\leqslant 0$, $K''_{Sz}\geqslant 0$ and $K''_{Lz}\geqslant 0$. Therefore the structure of the wave is different than the structure of the generalized Rayleigh wave.[17] The direction of propagation is along the interface and the direction of damping is normal to it as plotted in Fig. 1(b). Its amplitude decreases in both media away from the interface. The Stoneley wave is lossless in its direction of propagation.

B. Plastic–fluid interface

When compared to the metal–fluid interface case, the plastic–fluid interface case is rather tricky. They are two real roots of the Scholte–Stoneley equation which go to K_{R_0} in the limit $\rho_F=0$, as illustrated by the curve in Fig. 3. As we shall see, these two roots may be related to a Stoneley wave and a Rayleigh wave.

1. Stoneley wave

The greatest of the two real roots of Eq. (5) is also greater than $\mathcal{K}_i$ in the three medium. As we have seen in the previous Subsection III A 2, this root is related to the Stoneley wave. Again the solution is found when $K''_{Fz}\leqslant 0$, $K''_{Sz}\geqslant 0$ and $K''_{Lz}\geqslant 0$. Therefore the corresponding wave has the same structure as on the metal–fluid interface.

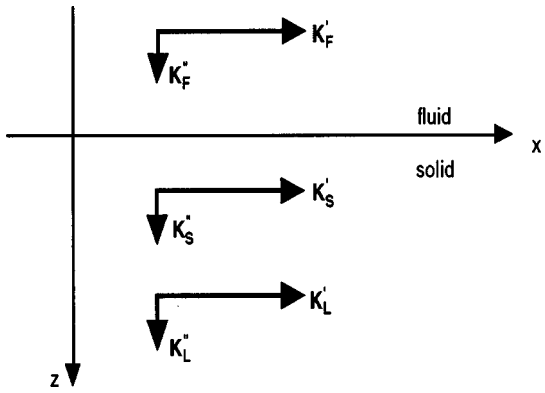

FIG. 4. The structure of the Rayleigh wave on a PVC–water interface as a set of three evanescent plane waves.

2. Rayleigh wave

The second real root K_R exhibits two different types of numerical behavior as ρ_F decreases to zero. It depends on the relative values of the parameter ρ and the factor ρ_c given by the relationship[13]

$$\rho_c=\sqrt{\frac{1-(K_F/K_S)^2}{1-(K_L/K_S)^2}}. \tag{7}$$

The parameter ρ may be greater or lower than ρ_c resulting from the density of the ''plastic'' material. We propose an example for each situation. Note that in every case, K_R is greater than $\mathcal{K}_i$ in the three medium. Consequently, the components K_{iz} are purely imaginary like for the Stoneley wave.

a. PVC–water interface: $\rho\leqslant\rho_c$. In the case of the PVC-water interface, ρ is lower than ρ_c. For any values of ρ, the solution is found when $K''_{Fz}\geqslant 0$, $K''_{Sz}\geqslant 0$ and $K''_{Lz}\geqslant 0$. Hence, the structure of the wave is different from the structure of the Stoneley wave because the attenuation vector in the fluid is directed toward the interface as shown in Fig. 4. This structure is coherent with the one at the metal–fluid interface. It comes to a limit when the Rayleigh angle of radiation increases to 90 degrees.

b. Plexiglas–water interface: $\rho\geqslant\rho_c$. With the Plexiglas–water interface, where ρ is greater than ρ_c, a change of determination is found in the numerical behavior of the root as ρ_F decreases to zero. It can be decomposed into three steps, as illustrated by the curve in Fig. 5. At first, for $\rho\geqslant\rho_c$, the solution is found when $K''_{Fz}\geqslant 0$, $K''_{Sz}\leqslant 0$ and $K''_{Lz}\geqslant 0$. Next, at the point $\rho=\rho_c$, K_R equals $\mathcal{K}_S$ and $K''_{Sz}=0$. For this particular value of ρ, the surface wave is a shear wave propagating along the interface. Thereafter, for $\rho\leqslant\rho_c$, a change of the sign of K''_{Sz} occurs: K_R becomes a solution for $K''_{Fz}\geqslant 0$, $K''_{Sz}\geqslant 0$ and $K''_{Lz}\geqslant 0$. It is then the same determination as for the PVC-water interface.

c. Synthesis for the ''plastic–fluid'' interface. On both types of plastic-fluid interface, the Stoneley wave and the Rayleigh wave have a phase velocity along the boundary which verifies the following relation:

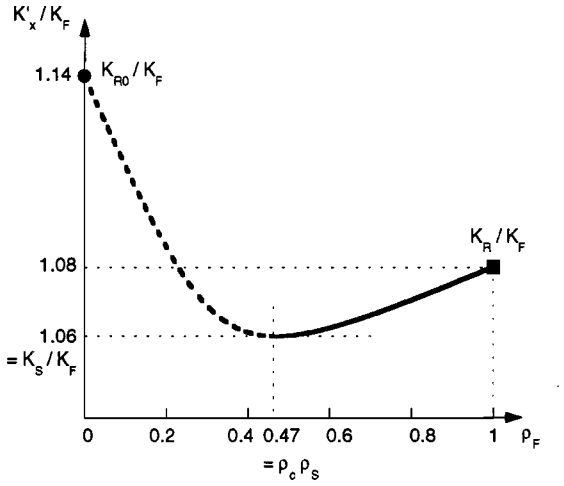

FIG. 5. The normalized real Rayleigh root $K_R/\mathcal{K}_F$ as a function of ρ_F. The three steps are: full line for $\rho_F=1$ to $\rho_F=\rho_c\rho_S$; particular point $\rho_F=\rho_c\rho_S$ when $K_R/\mathcal{K}_F=\mathcal{K}_S/\mathcal{K}_F$; dashed line for $\rho_F=\rho_c\rho_S$ to $\rho_F=0$.

$$c_{\mathrm{ST}}\leqslant c_R\leqslant c_S\leqslant c_F\leqslant c_L\,. \tag{8}$$

As we have seen, it seems possible to define a Rayleigh wave on solid–liquid interfaces even when the sound velocity in the fluid is larger than the shear wave velocity in the solid. Unlike the case when $c_S\geqslant c_F$, such a surface wave is unleaky.

To our knowledge, it is the first time that this Rayleigh wave is mentioned, even if it has been predicted numerically by Ansell.[13] This is not surprising if we consider that most of the former experimental studies of surface waves (and Lamb waves) with plastic materials have been made on reflection and transmission coefficients.[4,5] As this wave is not a leaky wave, it should be very difficult to generate it from the fluid.

These results have to be compared with the works about pseudo-Rayleigh waves. As in geophysics in the references we have cited,[8–10] the propagation of surface waves on plane interfaces has been treated with integral methods. In this context, there is one sheet of integration wherein lies the Stoneley root of the dispersion equation for solid–fluid interfaces. By deformation of the branch line contours onto lower Riemann surfaces, the contribution of the roots lying on these lower sheets may be underscored. It is the case of the generalized Rayleigh wave, which is also called pseudo-Rayleigh waves: The corresponding root of the dispersion equation is located on a different sheet from the integration sheet. However, only the complex roots have been studied, which correspond to leaking pseudo-surface waves.

In a way, we can say that we study here a ''pseudo-Rayleigh wave,'' but in a particular case where this wave is not leaky. This was made possible by a direct study of the Scholte–Stoneley dispersion equation which leads to a different approach of the problem. The interpretation using the formalism of the evanescent plane waves induced us to think on a different interpretation of the structure of the waves. An experimental confirmation of their existence is presented in the next section.

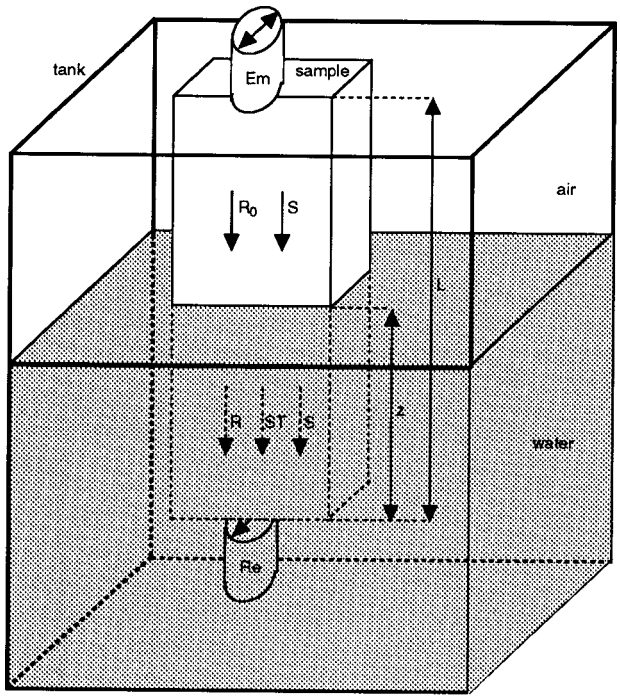

FIG. 6. Schematic diagram of the experimental device. (Em) emitter transducer, (Re) receptor transducer, (S) bulk shear wave, (R_0) free Rayleigh wave, (R) generalized Rayleigh wave, (ST) Stoneley wave.

IV. EXPERIMENTAL RESULTS

The purpose of the experiments is to measure arrival times for the two surface waves. The phase velocities deduced from the numerical computations for K_R and K_{ST} might then be compared to the experimental ones deduced from the times of flight on the sample.

A. Experimental device

These experiments are based on the technique used by de Billy[20] to generate surface waves on wedges. The plane interface may be considered as the limit case of a 180 degrees apex wedge. Two shear contact transducers (Em, Re) are coupled with the extremities of the faces of a rectangular sample (Fig. 6). The emitter is driven with short pulses of 1 MHz central frequency. The direction of the polarization of the transmitters is perpendicular to the interface. At the beginning, the sample is in air and is then partially immersed in water in steps of 4 mm. The experiments are realized at room temperature ($c_F\approx 1480\pm 5$ m/s).

The emitter generates simultaneously a bulk shear wave (S) and a free Rayleigh surface wave (R_0) at the solid–air interface (considered as a solid–vacuum interface). When the sample is immersed in water, the free Rayleigh wave gives rise to a generalized Rayleigh wave (R) and a Stoneley wave (ST) as described in Refs. 21 and 22.

B. Recorded wavetrains

The recorded wavetrains obtained with a Plexiglas sample of 140 mm long for different lengths of immersion z are presented in Fig. 7. At the Plexiglas–vacuum interface, only the bulk shear wave (S) and the free Rayleigh wave (R_0) are present. The arrival time of the bulk shear wave is

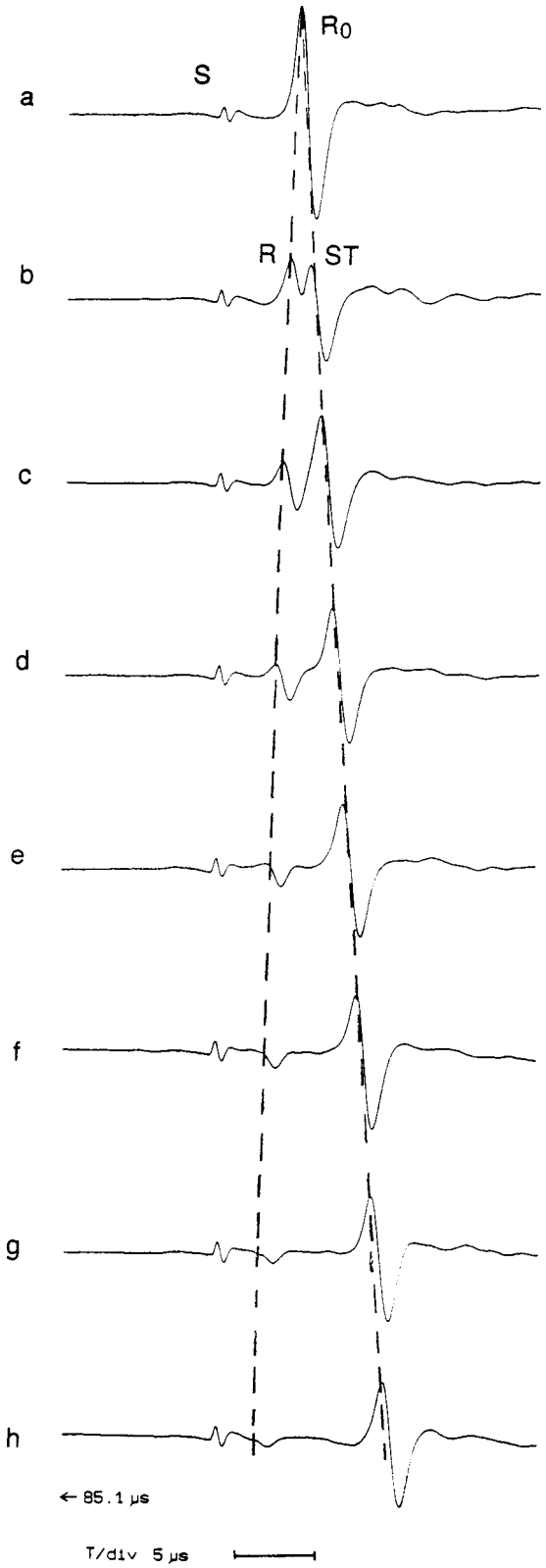

FIG. 7. Wavetrains obtained at the Plexiglas–water interface (140 mm long) for different lengths of immersion. (a) Free sample; (b) $z=8$ mm; (c) $z=16$ mm; (d) $z=24$ mm; (e) $z=32$ mm; (f) $z=40$ mm; (g) $z=48$ mm; (h) $z=56$ mm.

independent of the presence of the fluid and its amplitude remains constant. A generalized Rayleigh wave (R) and a Stoneley wave (ST) appear when the solid is immersed. It is interesting to notice that the echoes of the two surface waves move apart one from the other. As the velocity of the Stoneley wave is clearly below the velocity of the free Rayleigh wave (numerical values are presented in the next Subsection IV C), the corresponding echo arrives later as z increases. On the contrary, the velocity of the generalized Rayleigh wave is greater than the one of the free Rayleigh wave, and is close to c_S. As the immersed distance increases, the echo of this surface wave arrives earlier and earlier and becomes indistinguishable from the echo of the shear bulk wave. The same kind of echoes have been recorded with the PVC sample.

TABLE II. Characteristics of the solids and of the surface waves. Longitudinal and transverse velocities c_L and c_S have been measured with an accuracy of $\pm 0.1\%$.

Material	ρ_S	c_L (m/s)	c_S (m/s)	c_{R_0} (m/s)	c_R (m/s)	c_{ST} (m/s)
Plexiglas	1.18	2745	1390	1295	1363	1058
PVC	1.56	2236	1112	1040	1110	914

C. Arrival times

The arrival times have been calculated and measured on a Plexiglas sample ($L=140$ mm) and on a PVC sample ($L=100$ mm). When a length z of the solid is immersed, the arrival times correspond to the propagation of a free Rayleigh wave on the distance $L-z$, and the propagation of a generalized Rayleigh wave or a Stoneley wave on the distance z. Thus the theoretical arrival times t_R of the Rayleigh wave and t_{ST} of the Stoneley wave are, respectively:

$$t_R=\frac{L-z}{c_{R_0}}+\frac{z}{c_R}=\frac{L}{c_{R_0}}-z\left(\frac{1}{c_{R_0}}-\frac{1}{c_R}\right), \tag{9}$$

$$t_{\mathrm{ST}}=\frac{L-z}{c_{R_0}}+\frac{z}{c_{\mathrm{ST}}}=\frac{L}{c_{R_0}}-z\left(\frac{1}{c_{R_0}}-\frac{1}{c_{\mathrm{ST}}}\right), \tag{10}$$

where c_{R_0} designates the celerity of the free Rayleigh wave. The calculated values of the velocities are given in Table II. The corresponding variations are linear with a negative slope for the Rayleigh wave (because $c_R \geqslant c_{R_0}$), and with a positive slope for the Stoneley wave (because $c_{R_0} \geqslant c_{\mathrm{ST}}$) as seen in Fig. 8 where the theoretical and experiment arrival times are plotted. For the bulk shear wave, $t_S=L/c_S$. The comparison between the theoretical predictions and the experimental values is good. The differences do not exceed 2%. A better agreement is observed for the Rayleigh wave. It comes certainly from the fact that the beginning of the Stoneley echo is not clearly defined, which produces consequently an inaccuracy on the experimental measurement.

One could imagine that a longitudinal wave is generated at the air–water boundary, and that the Rayleigh echo detected is an artifact. The arrival times t_F of this expected wave have also been plotted in Fig. 8 as a function of z. These have been supposed for the calculations as due to the propagation of a free Rayleigh wave on a distance $L-z$ and of a longitudinal wave in the fluid on distance z. So we have

$$t_F=\frac{L-z}{c_{R_0}}+\frac{z}{c_F}=\frac{L}{c_{R_0}}-z\left(\frac{1}{c_{R_0}}-\frac{1}{c_F}\right). \tag{11}$$

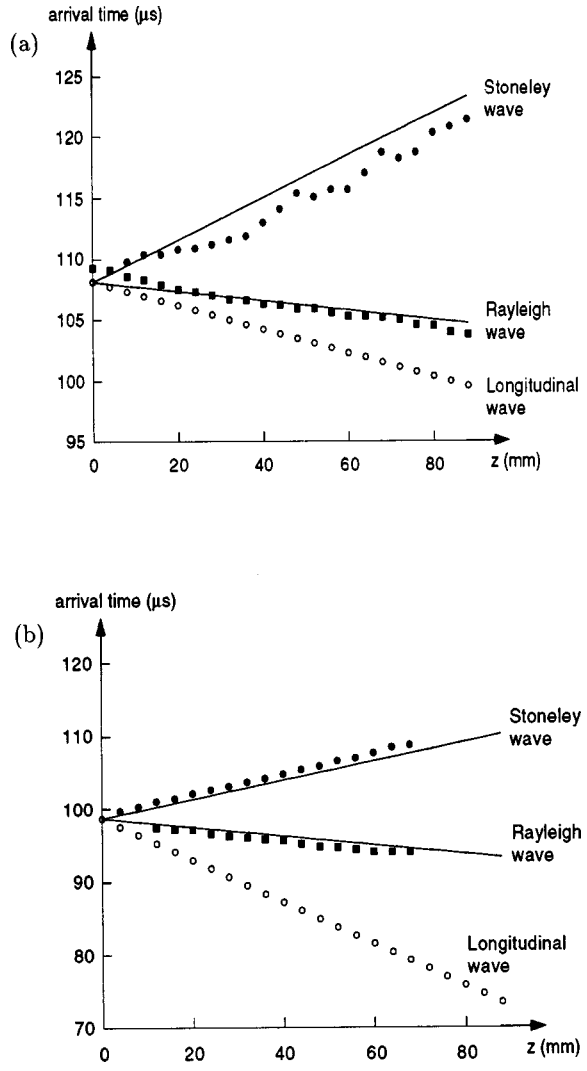

FIG. 8. Variation of the arrival times of the Rayleigh wave and the Stoneley wave as a function of the immersed length z on Plexiglas–water (a) interface and PVC–water interface (b). Theoretical arrival times (full lines) are compared with the measured arrival times for the Stoneley wave (black points) and for the Rayleigh wave (black squares). Empty circles indicate the calculated arrival times of a longitudinal wave in the fluid.

As c_F is greater than c_{R_0}, the corresponding variations are linear and show a negative slope. The calculated values of t_F are quite different from these of t_R. It can be concluded that no mistake was made concerning the Rayleigh echo. These results establish that the echo may be identified as due to a Rayleigh wave.

From the records, it is seen that as the immersed length increases, the amplitude of the Stoneley waves remains constant. It propagates with no loss on the plastic–fluid interface. On the other side, the Rayleigh echo decreases as z increases. This effect has not yet been explained and is not consistent with the theory: The surface waves are supposed to be lossless. Computations have been made with a model of viscoelastic solid to take account of a dissipation, but it misreads the observed phenomena. Indeed, these computations show that the attenuation which is due to viscoelasticity should be greater on the Stoneley wave than on the Rayleigh wave. But, as seen in Fig. 7, only the Rayleigh wave is attenuated. This case is different from the one observed by Favretto,[7] which dealt with a viscoelastic PVC sample of a different type. The author showed that, for this type of material, the Stoneley wave is actually attenuated during its propagation. But the material is not the same as used in our experiments. Other hypothesis are studied.

V. CONCLUSION

The Stoneley and the Rayleigh roots of the Scholte–Stoneley equation are studied analytically and numerically. With the analytical approach, it is possible to locate each root on the Riemann surface of the Scholte–Stoneley equation, and so to describe the anatomy of the corresponding wave by using the formalism of the evanescent plane waves.

The main objective of this paper is to know if surface waves could exist on plastic–fluid interfaces, where the fluid sound velocity is larger than the shear wave velocity in the solid. To determine numerically the proper roots of the equation, a comparison is made with the case of the metal–fluid interface. Two roots are found, which go to the Rayleigh root of the solid–vacuum interface as the density of the fluid decreases to zero. One of the two is the Stoneley root, and so the second may be defined as the Rayleigh root. The study of the corresponding anatomy shows that these two surface waves are not leaky and propagate with no loss in their direction propagation along the boundary.

To verify experimentally these conclusions, times of flight are measured on a Plexiglas and on a PVC sample. They are found to be in very good agreement with the theoretical predictions. Therefore, the existence of the two waves is confirmed. A problem appears with the decay of amplitude of the Rayleigh wave as the immersed length of the sample increases, which is not consistent with the theory. A test is made with a viscoelastic model, but the results are not conclusive. This question still awaits answers.

[1] I. A. Viktorov, *Rayleigh and Lamb Waves* (Plenum, New York, 1967).
[2] L. M. Brekhovskikh, *Waves in Layered Media* (Academic, New York, 1980).
[3] N. G. Brower, D. E. Himberger, and W. G. Mayer, ''Restrictions on the existence of leaky Rayleigh waves,'' IEEE Trans. Sonics Ultrason. **SU-26**, 306–308 (1979).
[4] T. J. Plona, M. Behravesh, and W. G. Mayer, ''Rayleigh and Lamb waves at liquid solid boundaries,'' Ultrasonics **13**, 171–175 (1975).
[5] W. Madigosky and R. Fiorito, ''Modal resonance analysis of acoustic transmission and reflection losses in viscoelastic plates,'' J. Acoust. Soc. Am. **65**, 1105–1115 (1979).
[6] P. Chevée and M. Deschamps, ''Interactions d'ondes planes hétérogènes au sein d'une lame à faces parallèles dissipative: Confrontation théorie expérience (in French),'' Acustica **76**, 224–230 (1992).
[7] N. Favretto-Anrès, ''Theoretical study of the Stoneley-Scholte wave at the interface between an ideal fluid and a viscoelastic solid,'' Acustica **82**, 829–838 (1996).
[8] F. Gilbert and S. J. Laster, ''Excitation and propagation of pulses on a interface,'' Bull. Seismol. Soc. Am. **52**, 299–319 (1962).
[9] W. L. Pilant, ''Complex roots of the Stoneley-wave equation,'' Bull. Seismol. Soc. Am. **62**, 285–299 (1972).
[10] R. A. Phinney, ''Propagation of leaking interface waves,'' Bull. Seismol. Soc. Am. **51**, 527–555 (1961).
[11] B. Poirée, ''Les ondes planes évanescentes dans les fluides parfaits et les solides élastiques (in French),'' J. Acoust. **2**, 205–216 (1989).
[12] Ph. Boulanger and M. Hayes, *Bivectors and Waves in Mechanics and Optics* (Chapman & Hall, London, 1993).
[13] J. H. Ansell, ''The roots of the Stoneley wave equation for liquid-solid interfaces,'' Pure Appl. Geophys. **94**, 172–188 (1972).
[14] G. Quentin, A. Derem, and B. Poirée, ''The formalism of the evanescent

plane waves and its importance in the study of the generalized Rayleigh wave,'' J. Acoust. **3**, 321–336 (1990).
[15] F. Padilla, B. Poirée, G. Quentin, and M. Talmant, Rayleigh circumferential wave and evanescent plane waves (in preparation).
[16] O. Poncelet and M. Deschamps, ''Lamb waves generated by complex harmonic inhomogeneous plane waves,'' J. Acoust. Soc. Am. **102**, 292–300 (1997).
[17] B. Poirée and F. Luppé, ''Evanescent plane waves and the Scholte-Stoneley interface wave,'' J. Acoust. **4**, 575–588 (1991).
[18] M. Deschamps, ''Reflection and refraction of the evanscent plane wave on plane interfaces,'' J. Acoust. Soc. Am. **96**, 2841–2848 (1994).
[19] E. Strick and A. S. Ginzbarg, ''Stoneley-wave velocities for a fluid-solid interface,'' Bull. Seismol. Soc. Am. **46**, 281–292 (1956).
[20] M. de Billy, ''On the scattering of antisymetric edge modes,'' J. Acoust. Soc. Am. **101**, 3261–3269 (1997).
[21] M. de Billy, ''Influence of the wetting and the angle of immersion on the generation of a Scholte wave: Experimental investigation,'' Phys. Lett. **96A**, 85–87 (1983).
[22] M. de Billy and G. Quentin, ''Experimental study of the Scholte wave propagation on a plane surface partially immersed in a liquid,'' J. Appl. Phys. **54**, 4314–4322 (1983).

The oscillation of gas bubbles in tubes: Experimental results

X. Geng, H. Yuan, H. N. Oğuz, and A. Prosperetti[a)]
Department of Mechanical Engineering, The Johns Hopkins University, Baltimore, Maryland 21218

(Received 5 October 1997; accepted for publication 15 April 1999)

An experimental study is presented of the frequency dependence and damping of the forced volume oscillations of gas bubbles in liquid-filled tubes. The bubbles occupy the entire section of the tube and are driven by a needle attached to a loudspeaker cone. The liquids used were water, a water–surfactant solution, and silicon oil, and the tube diameters were 1 and 3 mm. The results are in excellent agreement with the theory developed in two earlier papers. This work is motivated by the possibility of using gas bubbles as actuators in fluid-handling microdevices. © *1999 Acoustical Society of America.* [S0001-4966(99)04807-9]

PACS numbers: 43.35.Pt, 43.20.Ks, 47.55.Dz [HEB]

INTRODUCTION

In two recent papers, a theory was presented for the natural frequency[1] and damping[2] of the oscillations of gas bubbles in liquid-filled tubes. In the present study, we describe an experimental investigation that is in excellent agreement with the theoretical predictions.

While an extensive literature exists on the small-amplitude volume oscillations of gas bubbles in unbounded liquids (reviewed, for instance, in Refs. 3–6), the physics of bubbles confined in channels and tubes presents such substantial differences that a specific investigation is necessary. This statement is especially applicable to the bubbles considered here, which are large enough to occupy an entire section of the tube. Indeed, in this case, the inertia of the system is entirely dependent on the length of the liquid columns on either side of the bubble, rather than being proportional to the bubble volume. Furthermore, the liquid flow in the tube can be strongly affected by viscosity which, for free bubbles, is usually unimportant except for very small radii.

This work is motivated by the possibility to use gas bubbles as actuators in the small fluid-handling systems that advances in silicon manufacturing technology render possible (see, e.g., Refs. 7–9). One of the attractive features of such an application is that gas bubbles can be powered remotely by ultrasonic sources with no need for direct contact between the actuator and the power supply.

I. EXPERIMENT

Glass tubes with a diameter of 1 and 3 mm were used with water, silicon oil, and a surfactant solution of 50 ppm Triton-X-100 in water. This amount is about 37% of the critical micellar concentration. A drop of liquid was placed in the desired position in the upper part of the tube by means of a hypodermic syringe. A second drop was introduced so as to fill the lower part of the tube, leaving an air gap between its upper surface and the lower surface of the first drop. A stainless-steel needle of suitable size, cut perpendicularly to the axis and plugged with silicon glue, was filed so as to fit snugly, and then inserted into the lower end of the tube leaving no air gap between its tip and the lower liquid region. The length of the liquid column separating the needle tip from the lower surface of the bubble was of the order of 10–20 mm. The needle was attached to a loudspeaker driven by an amplifier and function generator while the glass tube was mounted in a fixed plexiglass plate (Fig. 1).

The objective of the experiment was to determine the amplitude of oscillation of the gas volume as a function of frequency. For this purpose, a charge-coupled device (CCD) camera was used to take digital snapshots of the bubble at equally spaced time intervals. Since the speed of the camera was not sufficient to record the necessary number of pictures during a single cycle, pictures were taken at time intervals $nT+\Delta t$, with T the period of the needle oscillations, n a suitable integer (such that $nT \simeq 500$ ms), and $\Delta t = 0.1$ ms, which gives 30 to 100 frames per cycle depending on the driving frequency. Sample sequences of the pictures acquired in this way are shown in Figs. 2–5.

The digital images produced by the CCD camera were scanned to determine the position of the surface bounding the gas space. From this digitized version of the bubble surface, with the assumption of axial symmetry, the instantaneous bubble volume $V(t)$ could be computed. The image processing was carried out automatically in real time during

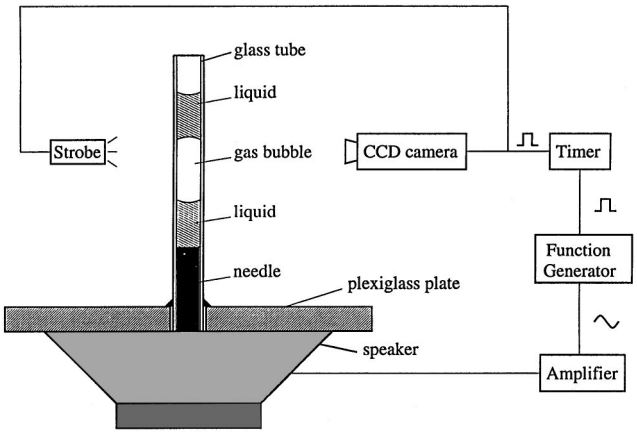

FIG. 1. Sketch of the experimental apparatus. The tube containing the two liquid columns separated by the air bubble is inserted onto a needle fastened to a loudspeaker cone. The loudspeaker is driven by a function generator connected through an amplifier.

[a)]Electronic mail: prosper@titan.me.jhu.edu

the course of the experiment, and there was no need to store the images.

The bubble volume was converted to an effective length L_e by

$$L_e(t) = V(t)/S, \tag{1}$$

where S is the tube cross-sectional area. Since we did not correct for refraction, the CCD images are distorted. However, by comparing the needle image when inside the liquid-filled tube and in air, we established that the distortion was a constant independent of the distance from the tube axis, much in the same way as the effect produced by a lens. Since S in Eq. (1) was also measured from the same images, the final value of L_e is therefore unaffected by the optical distortion. Before running the experiment, the initial value L_0 of the effective bubble length was measured in the same way.

For all frequencies, we took 200 data points and least-squares fitted them to an expression of the form

$$L(t) = A_B \cos(\omega t + \phi) + ct + L', \tag{2}$$

where ω is the angular frequency of the driver and A_B, ϕ, c, and L' are determined from the fit. The largest difference between the value of L' obtained from the fit and the initial value L_0 was about 1%. The term ct was included to account for any drift due, e.g., to loss of liquid leaking past the needle, but in all cases it was found to be very small, with a contribution of the order of 1% or less. After the determination of the parameters in (2), an error ϵ_B was computed from

$$\epsilon_B = \sqrt{\frac{1}{N-1}\sum_{k=1}^{N}[L(t_k) - L_e(t_k)]^2}, \tag{3}$$

with L calculated from (2) and L_e the measured data; the sum is over all the data points.

The same process was carried out to determine the oscillation amplitude A_N of the needle and the corresponding error ϵ_N. The total error ϵ affecting the normalized oscillation amplitude

$$Z = A_B/A_N, \tag{4}$$

was compounded quadratically

$$\epsilon = \frac{\sqrt{\epsilon_B^2 + Z^2\epsilon_N^2}}{A_N}. \tag{5}$$

This is the length of the error bars shown in the comparison of data and theory in the following figures.

We found that, if the absolute amplitude of the volume oscillations was too large, surface instabilities [see, e.g., the right surface of the bubble in frame 5 of Fig. 2(b)] tended to disrupt the bubble and to cause significant error in the data. Also at large amplitudes, sometimes the bubble surface loses its definition [see, e.g., the left surfaces in frame 4 of Fig. 2(a) and frames 4 and 5 of Fig. 2(b)] and the edge-detection algorithm fails. (This situation was only encountered in the 1-mm-diameter tube with water, which is the reason we also used the surfactant solution in this tube.) Similarly, when the drive was too weak, the quality of the data was also poor. For this reason, as the frequency was varied, the driving amplitude was continuously adjusted so as to avoid these two extreme conditions. To test for hysteresis effects, the experiment was run by starting the frequency sweeps both from below and above the resonance frequency of the bubble. The results were, however, the same with the two procedures.

II. THEORY

As in Ref. 2, the bubble is schematized as a cylinder the length of which varies in the course of the oscillations. It was shown in Ref. 1 that, as far as the effective ''mass'' and ''spring'' of the equivalent oscillator are concerned, this is an excellent approximation even for bubbles that do not quite occupy the entire cross section of the tube, provided the length of the liquid columns is not too small. As far as thermal effects are concerned, the neglect of the curvature of the liquid–gas interface has the effect of slightly underestimating the area available for heat transfer. This might by undesirable for very short bubbles, but not here, where most of the bubble surface area actually consists of the lateral tube surface. Thus, we believe the model to be applicable, which, as will be seen later, is confirmed by the comparison with the data.

The situation considered here exhibits minor differences with respect to that of Ref. 2, and it is therefore necessary to modify slightly the relations derived there.

Let $x(t)$ denote the position of the liquid column separating the bubble from the ambient, and $x_N(t)$ the position of the liquid column forced by the needle, both measured from the respective equilibrium positions. The instantaneous length of the bubble is

$$x(t) - x_N(t) = L_0[1 + X(t)], \tag{6}$$

where L_0 is the undisturbed initial length and $X(t)$ the dimensionless amplitude of oscillation. The pressure in the bubble can be assumed spatially uniform and is written as

$$p(t) = p_0[1 - \Phi X(t)], \tag{7}$$

where p_0 is the equilibrium (ambient) pressure and Φ a complex quantity, explicitly given in Ref. 2, dependent on the ratio γ of the gas specific heats and on the parameters

$$\mathcal{A} = 1 + \frac{L_0}{R}, \quad \Omega = \frac{\omega}{4D(1/L_0 + 1/R)^2}, \tag{8}$$

in which $\omega = 2\pi f$ is the angular frequency of the driver, R the radius of the tube, and D the gas thermal diffusivity. The real and imaginary parts of Φ are shown as functions of Ω in Fig. 12 for $\gamma = 1.4$ and for aspect ratios $\mathcal{A} = 6$ and 12, which are close to those occurring in the experiments.

Let l be the length of the liquid column above the bubble. The equation of motion of this liquid column is

$$m\ddot{x} = -2\beta_v\dot{x} - p_0 S\Phi X, \tag{9}$$

where $m = lS\rho$ (with ρ the liquid density) is the mass of the liquid, S the cross-sectional area of the tube, and β_v the viscous damping parameter specified below. Upon substituting (6), we then have

$$L_0 m\ddot{X} + 2\beta_v L_0\dot{X} + p_0 S\Phi X = -m\ddot{x}_N - 2\beta_v\dot{x}_N. \tag{10}$$

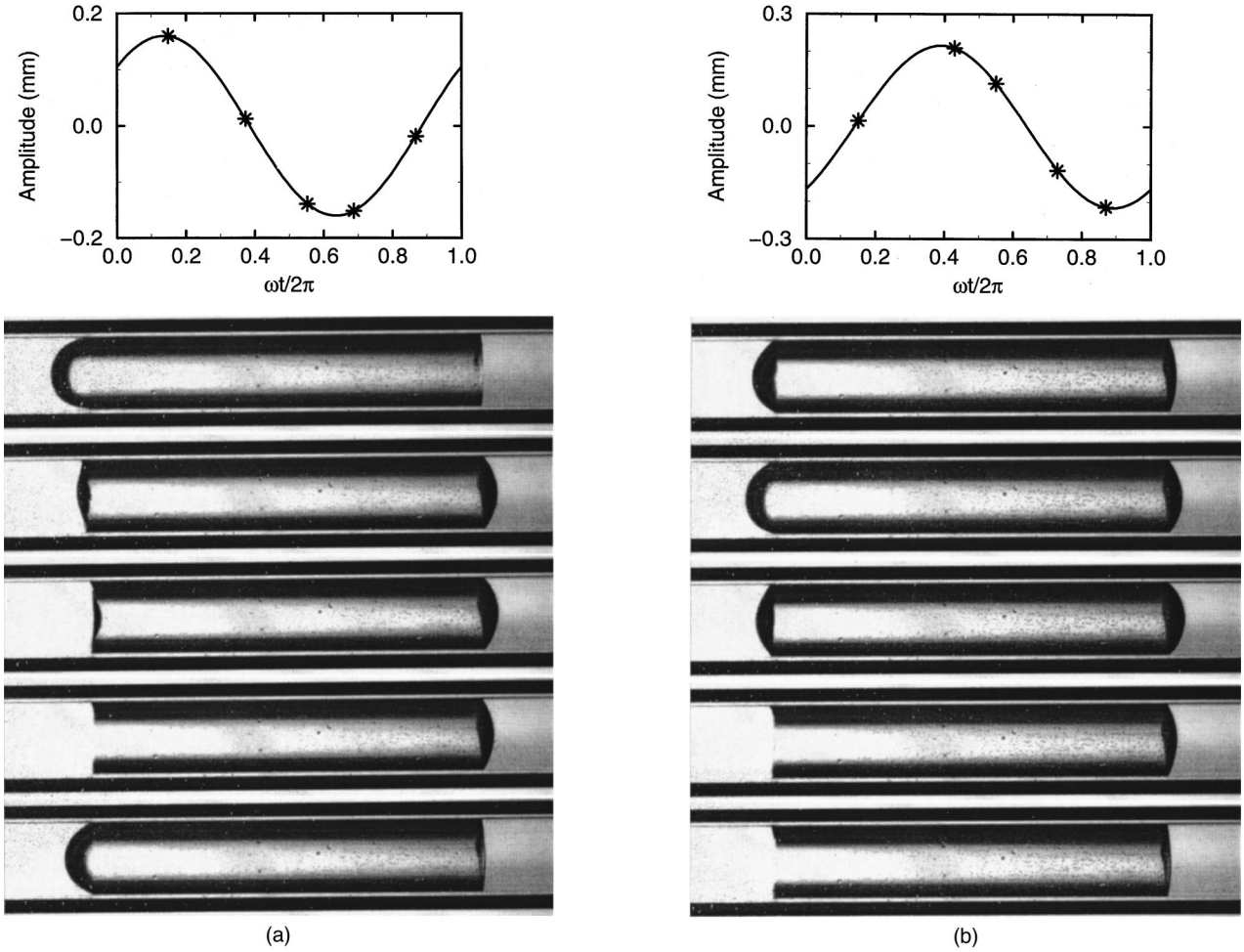

FIG. 2. Sample sequences of gas-bubble oscillations at 150 Hz (a) and 200 Hz (b) for pure water in the 1-mm-diameter tube. The bubble resonance frequency is 173 Hz. Other parameter values are given in Table I. The graphs above the photographic sequences show the position of each frame in the oscillation cycle. The data presented below are based on 200 such images. Time $t=0$ corresponds to the maximum upward displacement of the needle. Gravity acts from left to right. The needle is outside the frame to the right. The position of the contact line is clearly visible. Note the small drops on the glass surface, indicating that it is not covered by a liquid film. The bright bands along the sides of the tube are due to refraction in the glass.

The viscous damping parameter β_v is discussed in Ref. 2, where it is argued that it can be approximately calculated from

$$\beta_v = \frac{\nu m}{S}\left\langle \int_S \left[\frac{\partial}{\partial r}\left(\frac{u}{\dot{x}}\right)\right]^2 dS \right\rangle, \tag{11}$$

where ν is the liquid kinematic viscosity, the angle brackets denote the average over a cycle, the integration is over the cross section of the tube, r is the radial coordinate, and u is given by the solution of the Navier–Stokes equations for fully developed oscillatory flow (see, e.g., Ref. 10). The integral cannot be evaluated in closed form and it is graphed in Fig. 8 of Ref. 2. Asymptotic approximations are readily available for conditions in which the viscous penetration length, $\sqrt{\nu/\omega}$, is either much smaller or much larger than the tube radius R. In the former case (high frequency), dissipation occurs in a thin boundary layer and the result is

$$\beta_v = m\sqrt{\frac{\pi\nu\omega}{2S}}, \tag{12}$$

which is accurate for $R\sqrt{\omega/\nu}>30$, approximately. At low frequency ($R\sqrt{\omega/\nu}<3$), on the other hand, one finds

$$\beta_v = 4\frac{\nu m}{R^2}, \tag{13}$$

in agreement with the result for Poiseuille flow.

It should be noted that viscosity is not the only dissipative mechanism affecting the oscillations. The phase lag between the volume pulsations and the temperature oscillations in the gas causes a thermal damping that enters Eq. (10) through the imaginary part of Φ. As will be seen in the next section, this contribution to the damping can be far more significant than the viscous one.

For steady sinusoidal forcing $x_N = A_N \exp i\omega t$, Eq. (10) is readily solved. The dimensionless oscillation amplitude Z defined in (4) is found to be

$$Z = \frac{L_0 m(\omega^2 - 2i\beta_v\omega)}{p_0 S\Phi + 2iL_0\beta_v\omega - L_0 m\omega^2}. \tag{14}$$

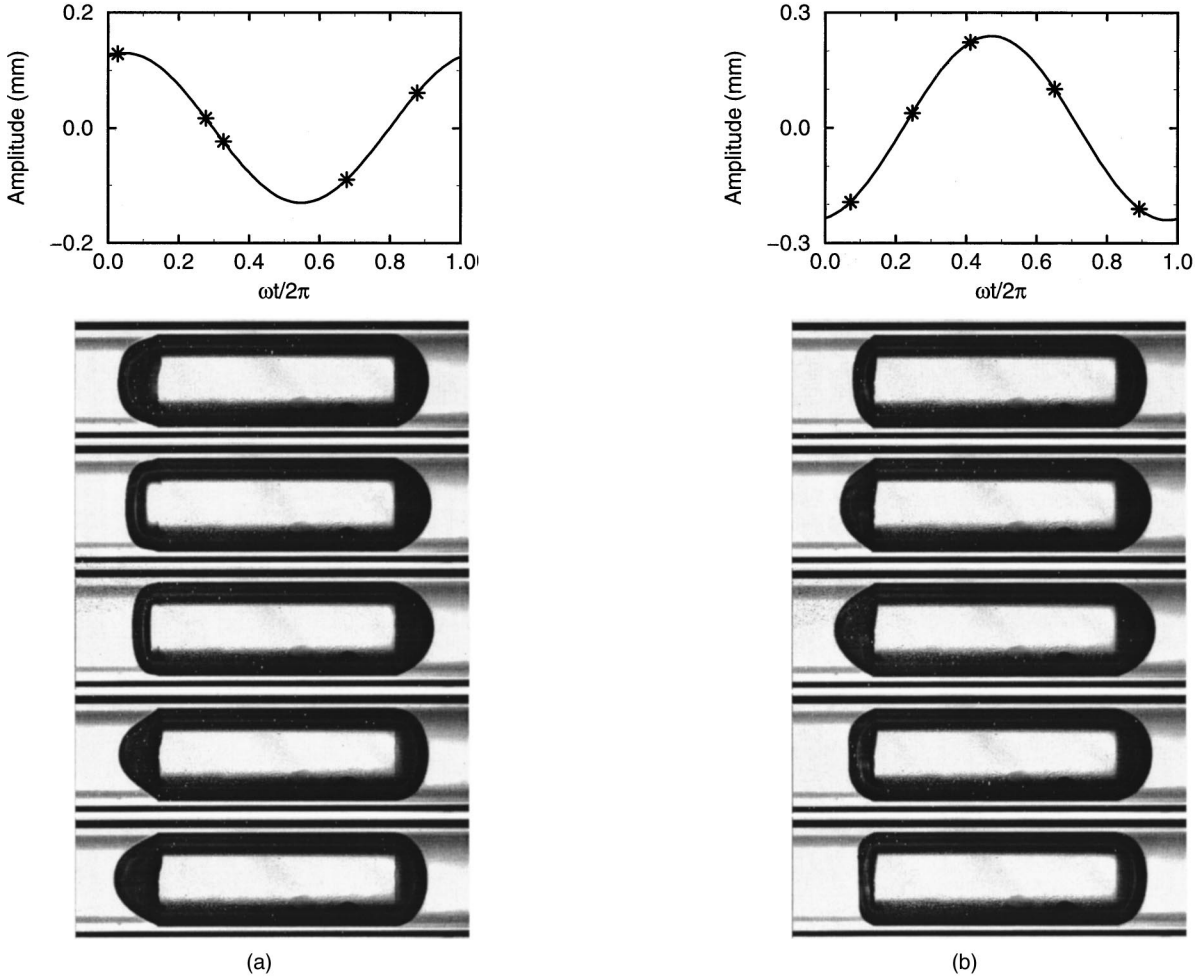

FIG. 3. Sample sequences of gas-bubble oscillations at 100 Hz (a) and 150 Hz (b) for pure water in the 3-mm-diameter tube. The bubble resonance frequency is 124 Hz. Other parameter values are given in Table I. The graphs above the photographic sequences show the position of each frame in the oscillation cycle. Time $t=0$ corresponds to the maximum upward displacement of the needle. Gravity acts from left to right. The needle is outside the frame to the right. The position of the contact line is clearly visible. Note the capillary waves on the left (upper) surface of the bubble.

III. RESULTS

Typical sequences of the pictures on which our data are based are shown in Figs. 2–5. The needle is on the right outside the field of view and the graph above each photographic sequence shows the position of each frame in the oscillation cycle. In these graphs, $t=0$ corresponds to the maximum upward displacement of the needle.

In interpreting these images, it should be kept in mind that the white stripes along the cylindrical body of the bubbles are not a residual liquid film, but an artifact due to refraction in the glass. The lateral boundary of the bubbles always appears to be the inner surface of the tube. For the case of water, this fact is confirmed by the tiny liquid drops visible in Figs. 2 and 3 on the tube surface. In some images of the water cases (Figs. 2, 3, and 4) the liquid–glass contact line is quite evident. The situation is not as clear for the silicon oil case of Fig. 5. As a matter of fact, we were unable to take data with silicon oil in the larger tube, because a thin liquid film was observed to flow from the upper to the lower bubble surface along the tube wall. The effect, if present at all, was much smaller for the 1-mm-diameter tube shown in Fig. 5 as no difference between the length of the liquid column above the bubble before and after the experiment could be measured.

In the pictures of Fig. 2 one can observe a very slight movement of the contact line. The effect is due to an excitation amplitude larger than that normally used to take data so as to illustrate more clearly the oscillation cycle. In all the other experiments, the amplitude of oscillation was small enough that the (dynamic) advancing and receding contact angles were not exceeded and the contact line was not observed to move.

Figures 2(a) and (b) have been taken with water in the 1-mm-diameter tube, below and above the resonance frequency of the bubble, respectively. This circumstance is evident from the fact that the liquid surfaces in Fig. 2(a) move in phase, while they have opposite phase in Fig. 2(b). A similar pattern is visible in Fig. 3 taken in the 3-mm-diameter tube. Several frames of Fig. 3 show evidence of the appearance of capillary waves on the bubble upper surface (on the left of the pictures). These waves are probably the result of a Faraday-type parametric amplification mechanism.

A striking qualitative difference between the two water

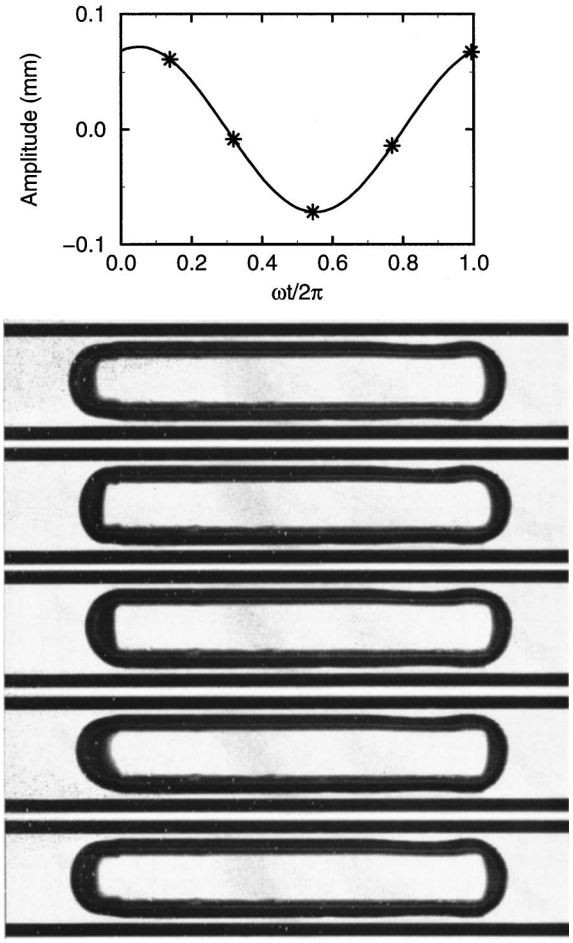

FIG. 4. Sample sequences of gas-bubble oscillations at 150 Hz for the water–Triton-X-100 solution in the 1-mm-diameter tube. The bubble resonance frequency is 189 Hz. Other parameter values are given in Table I. The graphs above the photographic sequences show the position of each frame in the oscillation cycle. Time $t=0$ corresponds to the maximum upward displacement of the needle. Gravity acts from left to right. The needle is outside the frame to the right. The position of the upper contact line is clearly visible on the left in frames 1, 2 , and 5. The slight curvature on the tube wall (upper right in the picture) is an optical artifact from an imperfection of the glass tube.

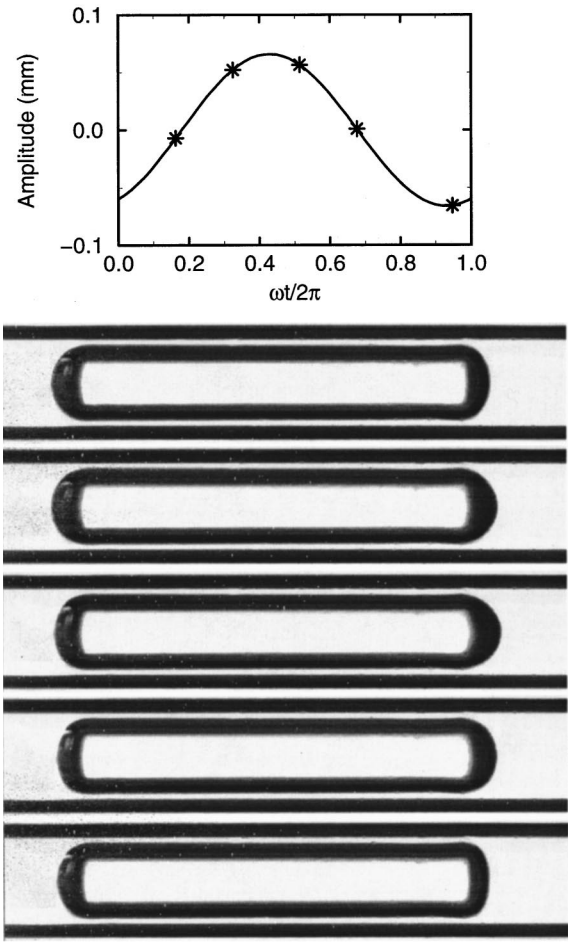

FIG. 5. Sample sequences of gas-bubble oscillations at 180 Hz for silicon oil in the 1-mm-diameter tube. The bubble resonance frequency is 235 Hz. Other parameter values are given in Table I. The graphs above the photographic sequences show the position of each frame in the oscillation cycle.

cases (Figs. 2 and 3) and the water–Triton and silicon ones (Figs. 4 and 5) is that, on average, the surface curvature seems to be much larger for the latter. This feature is a consequence of the difference in advancing and receding contact angles between the two systems. To illustrate the point, for pure water and the surfactant solution in the 1 mm-diameter tube, we show in Figs. 6 and 7 pairs of images: the upper one shows the bubble pushed into the tube by insertion of the needle, and the bottom one the equilibrium bubble shape before the sound is turned on. It is seen here, e.g., that the receding contact angle (at the top of the bubble, i.e., on the left of the images) is much larger for pure water than for the solution. It is therefore clear that, when the bubble stops (lower image in each pair), the pure water is much less curved than the Triton–water one. These static bubble shapes are essentially the average interface shape around which the bubble oscillates, and explain therefore the qualitative difference between the curvatures observed in Figs. 2, 4, and 5. Another interesting remark to be made, especially in connection with Fig. 6, is the strong difference between the (apparent) contact angles at the leading and trailing edges of the bubble. This is graphic evidence of the prevalence of a strong contact-angle hysteresis, which explains why the contact line does not move in the course of the oscillations.

Typical experimental results for the normalized oscillation amplitudes are compared with theory in Figs. 8 and 9

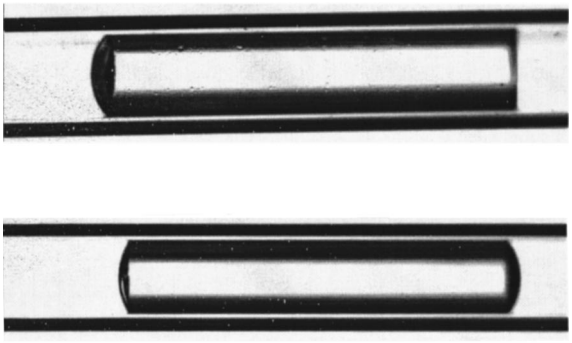

FIG. 6. The upper frame shows an air bubble as it is being pushed by the needle into the 1-mm-tube for pure water. The lower image is the same bubble at equilibrium. Note the marked difference between the advancing and receding contact angles in the upper image.

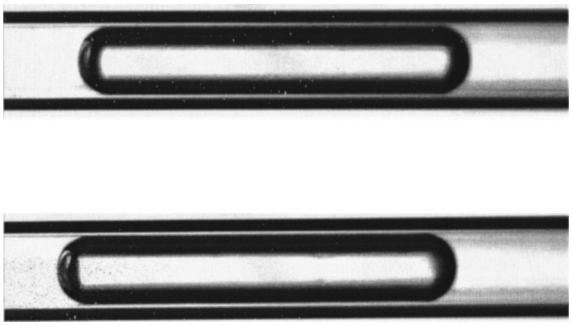

FIG. 7. The upper frame shows an air bubble as it is being pushed by the needle into the 1-mm-tube for the water–triton solution. The lower image is the same bubble at equilibrium. The difference between the advancing and receding contact angles is less in this case, but they are both smaller than in the pure-water case of the previous figure.

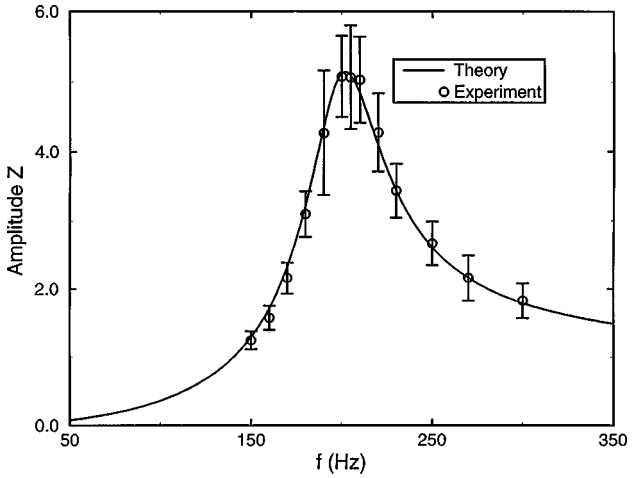

FIG. 8. Comparison between theory (solid line) and experiment for pure water in the 1-mm-tube. The normalized amplitude Z is defined in (4).

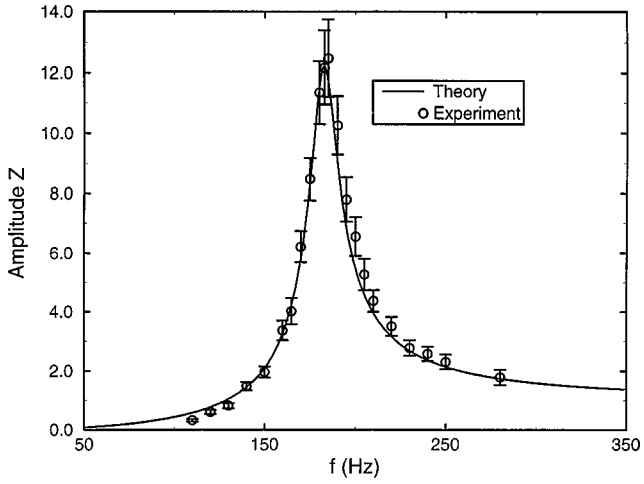

FIG. 9. Comparison between theory (solid line) and experiment for pure water in the 3-mm-tube. The normalized amplitude Z is defined in (4).

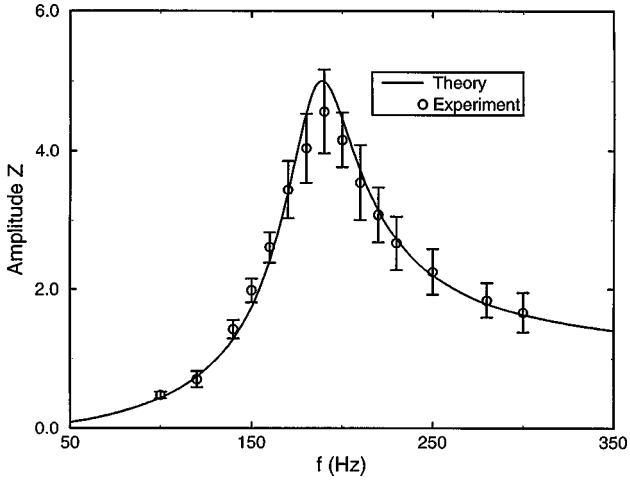

FIG. 10. Comparison between theory (solid line) and experiment for the water–Triton-X solution in the 1-mm-tube. The normalized amplitude Z is defined in (4). Note that, in contrast to the previous two cases, the maximum falls below the theoretical prediction, indicating the presence of additional dissipation due to surface effects not included in the theory.

(water), 10 (Triton-X-100 solution), and 11 (silicon oil). The relevant parameter values are given in Table I. It may be observed here that the experiments cover a range of the dimensionless frequency Ω where thermal effects in the bubble are significant, as can be seen from Fig. 12. Furthermore, while the high- and low-frequency approximations (12) and (13) are applicable to the 3-mm-diameter tube and the silicon oil cases, the range of dimensionless viscous penetration lengths for water and the surfactant solution in the 1-mm-diameter tube falls outside the limits of validity of the approximations, and the complete expression must be used. Thus, we feel that the present experiments constitute a meaningful test of the theory.

The two water cases of Figs. 8 and 9 display an excellent agreement with theory. Data acquisition is easier for the larger tube (Fig. 9), which accordingly has smaller error bars.

A very simplified theory of the phenomenon under consideration can be formulated neglecting thermal effects altogether and assuming an isothermal or adiabatic behavior of the gas. We show in Fig. 13 a comparison between the exact

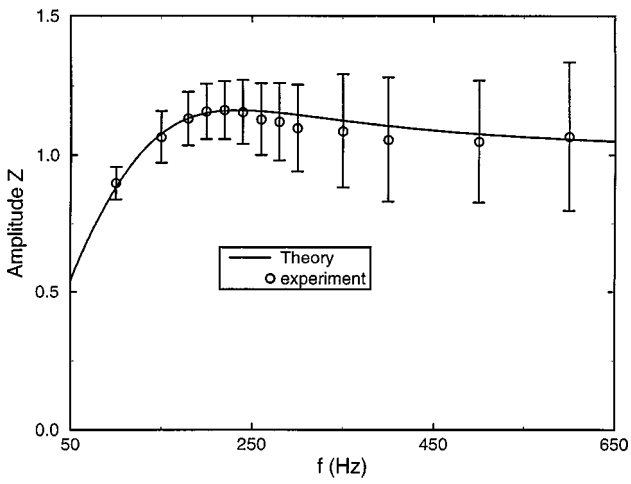

FIG. 11. Comparison between theory (solid line) and experiment for the silicon oil in the 1-mm-tube. The normalized amplitude Z is defined in (4).

TABLE I. Parameter values for the cases illustrated in the figures; l is the length of the upper liquid column, L_0 the undisturbed bubble length, and the dimensionless frequency Ω is defined in (8).

Figure no.	l (mm)	L_0 (mm)	$\mathcal{A}$	Res. freq. (Hz)	$\Omega_{\min}$	$\Omega_{\max}$	$R\sqrt{\omega_{\min}/\nu}$	$R\sqrt{\omega_{\max}/\nu}$
2(a),(b)	16.5	6.30	13.6	173	⋯	⋯	⋯	⋯
3(a),(b)	20.0	11.0	8.33	124	⋯	⋯	⋯	⋯
9	14.7	5.23	11.5	202	0.74	4.4	8.86	21.7
10	14.5	7.0	5.67	183	5.4	32.4	26.6	65.1
4, 11	15.0	5.85	12.7	189	0.75	4.5	8.86	21.7
5, 12	22.0	5.85	12.7	235	0.75	4.5	1.25	3.07

theory of Sec. II with three versions of a simplified theory for the case of Fig. 9. The solid line is the same as that shown in Fig. 9 and represents the complete theory. The dotted and dot-and-dash lines show the results obtained by neglecting thermal dissipation and assuming the gas to behave isothermally or adiabatically, respectively. The dashed line neglects thermal dissipation, but includes thermal effects in the calculation of the gas stiffness. It can be seen here that thermal effects play a substantial role not only in limiting the peak response through their effect on dissipation, but also in determining the gas stiffness and therefore the position of the resonance frequency.

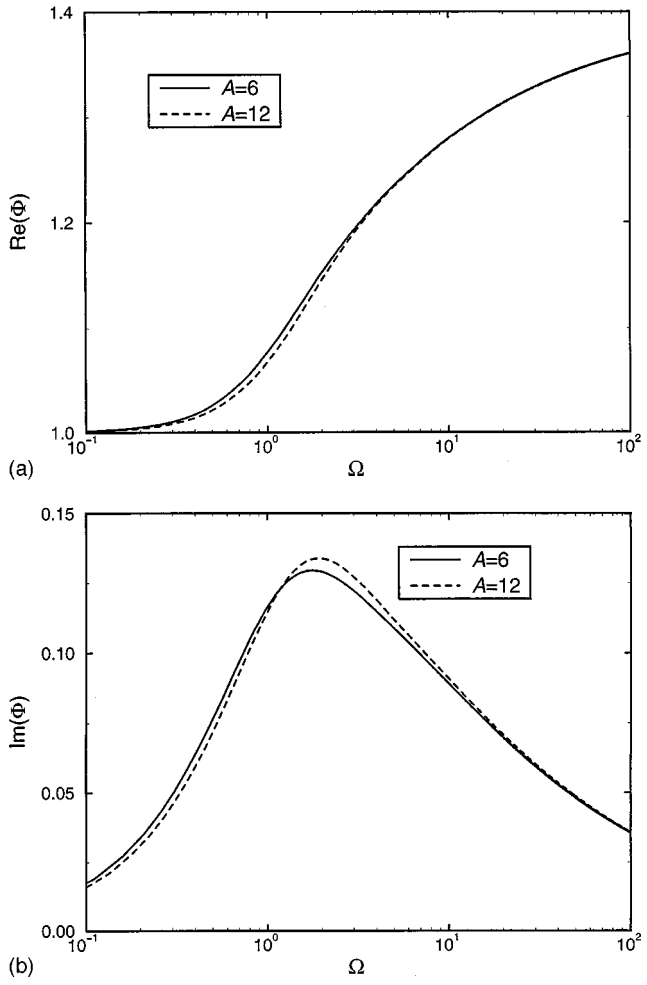

FIG. 12. Graph of the real (a) and imaginary (b) parts of the function Φ defined in Eq. (27) of Ref. 2 for $\gamma=1.4$ and aspect ratios $\mathcal{A}=6$ (solid) and 12 (dashed). The dimensionless frequency Ω is defined in (8).

Figure 10 is for the 50-ppm Triton-X-100 solution. In plotting the theoretical result, no account was taken of the presence of the surfactant and the same theory as for water was used. It is seen that, while this theory agrees with the data away from resonance, it overpredicts the resonant response. If one tries to fit the data by adjusting the liquid viscosity, a viscosity value about 40% greater than that of water would be necessary. This is completely unrealistic for the small concentrations used in the experiment. The Marangoni stresses set up by the inability of the surfactant concentration to follow the surface motion[11] at these relatively high frequencies are probably responsible for the additional dissipation encountered here. A more detailed investigation of this phenomenon falls outside the scope of the present study.

The bubble response in the highly viscous silicon oil is much smaller than in the water cases. The error bars appear therefore bigger, although in relative terms, around the maximum, they are comparable to those in the other figures. It may be observed that the model captures correctly the marked change of behavior between the low- and high-viscosity cases.

IV. CONCLUSIONS

In the present paper, we have compared experimental results for the forced oscillations of gas bubbles in tubes with

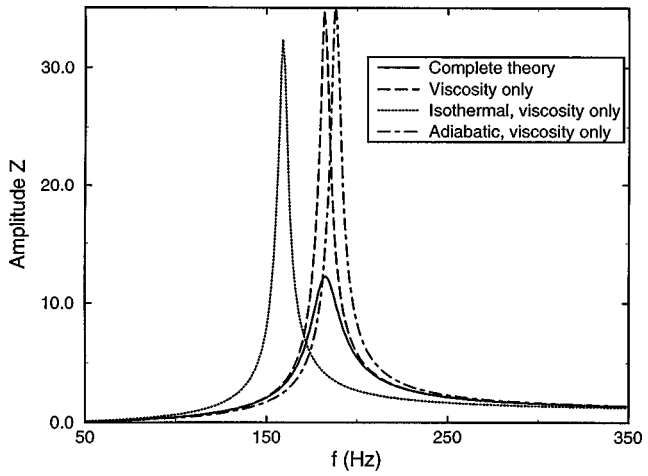

FIG. 13. Normalized oscillation amplitude as predicted by several theories. The solid line is the same one as shown in Fig. 9 and is the prediction of the complete theory. The dotted and dot-and-dash lines show the results obtained by neglecting thermal dissipation and assuming the gas to behave isothermally or adiabatically, respectively. The dashed line includes thermal effects in the calculation of the bubble stiffness, but neglects their contribution to energy dissipation.

a theory developed in two earlier studies. An excellent agreement has been found which, among other features, illustrates the importance of thermal phenomena in determining the bubble response.

An interesting side observation that can be made from the photographs taken in the course of the experiment is the graphic illustration of contact-angle hysteresis and its role in determining the equilibrium bubble shape and the lack of motion of the gas–liquid–glass contact line.

ACKNOWLEDGMENTS

We are grateful to Professor Kathleen Stebe for some useful comments. This study has been supported by AFOSR under Grant No. F49620-96-1-0386.

[1] H. N. Oğuz and A. Prosperetti, ''The natural frequency of oscillation of gas bubbles in tubes,'' J. Acoust. Soc. Am. **103**, 3301–3308 (1998).
[2] X. M. Chen and A. Prosperetti, ''Thermal processes in the oscillations of gas bubbles in tubes,'' J. Acoust. Soc. Am. **104**, 1389–1398 (1998).
[3] M. S. Plesset and A. Prosperetti, ''Bubble dynamics and cavitation,'' Annu. Rev. Fluid Mech. **9**, 145–185 (1977).
[4] R. E. Apfel, ''Acoustic cavitation,'' *Methods of Experimental Physics—Vol. 19 Ultrasonics*, edited by P. D. Edmonds (Academic, New York, 1981), pp. 355–411.
[5] A. Prosperetti, ''Bubble phenomena in sound fields: Part one,'' Ultrasonics **22**, 69–77 (1984).
[6] A. Prosperetti, ''Bubble phenomena in sound fields: Part two,'' Ultrasonics **22**, 115–124 (1984).
[7] H. Fujita and K. J. Gabriel, ''New opportunities for micro actuators,'' in *Transducers '91* (I.E.E.E., New York, 1991), pp. 14–20.
[8] L. Lin, A. P. Pisano, and A. P. Lee, ''Microbubble powered actuator,'' in *Transducers '91* (I.E.E.E., New York, 1991), pp. 1041–1044.
[9] P. Gravesen, J. Branebjerg, and O. S. Jensen, ''Microfluidics-a review,'' J. Micromech. Microeng. **3**, 168–182 (1993).
[10] L. G. Leal, *Laminar Flow and Convective Transport Processes* (Butterworth-Heinemann, Boston, 1992).
[11] C. D. Eggleton and K. J. Stebe, ''An adsorption–desorption controlled surfactant on a deforming droplet,'' J. Colloid Interface Sci. **208**, 68–80 (1998).

Experimental verification of the calculated diffraction field generated by inhomogeneous waves obliquely incident on a periodically rough liquid–solid boundary

R. Briers[a] and O. Leroy
Interdisciplinary Research Center, K. U. Leuven Campus Kortrijk E. Sabbelaan 53, B-8500 Kortrijk, Belgium

O. Poncelet and M. Deschamps
Laboratoire de Mécanique Physique, Université de Bordeaux I Cours de la Libération 351, 33405-Talence Cedex, France

(Received 18 May 1998; revised 16 November 1998; accepted 6 April 1999)

In this paper, the diffraction of an inhomogeneous plane bulk wave at a corrugated liquid–solid boundary is considered. The classical diffraction law of Bragg for homogeneous plane waves is generalized for incident inhomogeneous bulk waves, and the obtained results are verified experimentally. The solution of the generalized diffraction law is not unique. Depending on the chosen solution, the reflection (and transmission) coefficients of the diffracted inhomogeneous waves have a different modulus and phase. An illustration is given for the zeroth-order reflection and compared with experimental results. A reflection coefficient greater than unity is observed. This effect agrees with the inhomogeneous wave theory. © *1999 Acoustical Society of America.* [S0001-4966(99)00408-7]

PACS numbers: 43.35.Pt [HEB]

INTRODUCTION

The diffraction of ultrasonic bulk waves at periodic rough surfaces has been studied by quite a number of scientific groups using different approximations. A detailed overview of all methods to study diffraction gratings and a nearly complete list of the most important references on this subject is given in the book of Maystre[1] and the review of Bishop and Smith.[2] However, a survey of the literature brings to light that most theoretical and experimental work deals with the case of incident homogeneous plane waves.[3,4] In recent years, we have been convinced both by theoretical and experimental evidence that a study of inhomogeneous plane waves generally reveals much more information about the scanned medium. For instance, the mathematical representation of any type of surface wave (Rayleigh, Lamb, Stoneley wave, etc.) is locally a combination of such inhomogeneous waves, and they cannot be described in terms of homogeneous plane waves. Therefore, it may not seem surprising at all that, in general, only inhomogeneous waves are the real stimuli of surface waves for nondestructive testing-material investigation.[5,6] A systematic study of the anatomy of inhomogeneous plane waves and its applications in linear acoustics can be found in Refs. 7–10. In the past, we studied the excitation of surface waves due to inhomogeneous bulk wave interaction with periodic rough surfaces.[11,12] Therefore, the diffraction models[13,14] developed for incident homogeneous plane waves were generalized for incident inhomogeneous plane waves. The assumptions that were made in these works (reflection coefficient greater than unity and diffraction angles greater than 90°) have now been verified experimentally for the first time. Instead of using the classical Fourier approximation, bounded ultrasonic beams can be described in terms of inhomogeneous plane waves.[15,16] So, the study of the diffraction of one inhomogeneous plane wave at a grating is important in view of understanding the diffraction effects of bounded ultrasonic beams at corrugated surfaces.

I. DESCRIPTION OF THE INCIDENT AND DIFFRACTED ULTRASONIC FIELDS

Let the liquid–solid boundary be given by $z=f(x)$ in the global coordinate system (x,z) as shown in Fig. 1, with

$$f(x+\Lambda)=f(x), \tag{1}$$

where Λ is the spatial periodicity of the rough surface. Liquid and solid are assumed to be lossless. Consider a bulk inhomogeneous plane wave with heterogeneity coefficient β_i incident from the liquid upon the corrugated boundary at an angle θ_i. In the local coordinate system (x_i,z_i), in which the z_i-axis is normal to the local surface, this wave can be represented by the velocity potential

$$\varphi_i(x_i,z_i,t)=\exp(\beta_i x_i)\exp[i(k_i' z_i-\omega t)], \tag{2}$$

which is the mathematical description of a harmonic wave propagating with a phase velocity ω/k_i' in the z_i-direction and, if β_i is positive, exponentially decaying in the negative x_i-direction; $\omega=2\pi f$ with f the frequency. The planes of constant phase ($z_i=$constant) are orthogonal to the planes of constant amplitude ($\beta_i x_i=$constant), which is the definition of a bulk inhomogeneous plane wave. For a fixed angular frequency, the dispersion equation links the inhomogeneous plane-wave features β_i and k_i' to the sound velocity v_r in the liquid

[a]Postdoctoral Fellow of the Fund for Scientific Research—Flanders (Belgium) (F.W.O). Electronic mail: Rudy.Briers@kulak.ac.be

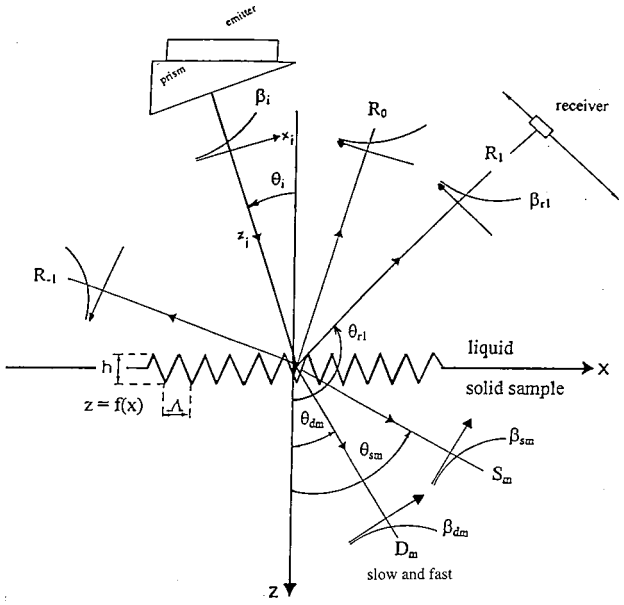

FIG. 1. The diffraction of an inhomogeneous bulk wave incident at a liquid–solid corrugated boundary. Definition of the parameters.

$$(k_i')^2-(\beta_i)^2=\left(\frac{\omega}{v_r}\right)^2. \tag{3}$$

In the global coordinate system (x,z), the velocity potential (2) takes the form

$$\varphi_i(x,z,t)=\exp[i(k_i x+K_i z-\omega t)], \tag{4}$$

with

$$k_i=k_i' \sin\theta_i+i\beta_i\cos\theta_i, \tag{5a}$$

$$K_i=k_i' \cos\theta_i-i\beta_i\sin\theta_i. \tag{5b}$$

Due to the periodic character of the corrugation, the velocity potentials of the reflected and transmitted ultrasonic fields can be represented by a Fourier series[17] in the coordinate along the interface $z=0$. This means that the incident energy will be scattered in several inhomogeneous plane waves having different directions in reflection and transmission. This assumption corresponds to Rayleigh's basic idea and, although its validity is questioned by many scientists,[18] its simplicity opens perspectives for a straightforward understanding of the physics behind the problem. The Fourier expansions for the velocity potentials $\varphi_r,\varphi_d,\varphi_s$ of, respectively, the reflected, the transmitted dilatational, and shear ultrasonic fields are

$$\varphi_r(x,z,t)=\sum_{m=-\infty}^{m=+\infty} R_m \exp[i(k_m x+K_{rm} z-\omega t)], \tag{6a}$$

$$\varphi_d(x,z,t)=\sum_{m=-\infty}^{m=+\infty} D_m \exp[i(k_m x+K_{dm} z-\omega t)], \tag{6b}$$

$$\varphi_s(x,z,t)=\sum_{m=-\infty}^{m=+\infty} S_m \exp[i(k_m x+K_{sm} z-\omega t)], \tag{6c}$$

with

$$k_m=k_{\sigma m}' \sin\theta_{\sigma m}+i\beta_{\sigma m}\cos\theta_{\sigma m}, \tag{7a}$$

$$K_{\sigma m}=k_{\sigma m}' \cos\theta_{\sigma m}-i\beta_{\sigma m}\sin\theta_{\sigma m}, \tag{7b}$$

and

$$(k_{\sigma m}')^2-(\beta_{\sigma m})^2=\left(\frac{\omega}{v_\sigma}\right)^2=(k_\sigma)^2, \quad \sigma=r,d,s. \tag{8}$$

R_m, D_m, and S_m are the unknown reflection and transmission coefficients of the mth diffraction order. Note that for each diffraction order m, the reflected and transmitted waves have the same x-component k_m [Eq. (7a)]. The angles of diffraction $\theta_{\sigma m}$ in expressions (7a) and (7b) are measured from the positive z-axis; $m>0$ corresponds to forward scattering, while $m<0$ corresponds to backward scattering. In the dispersion Eq. (8), v_r, v_d, and v_s are, respectively, the sound velocity in the liquid, and the dilatational and shear sound velocity in the solid.

II. GENERALIZED DIFFRACTION EQUATION

In this section, the generalized diffraction equation for inhomogeneous plane waves is presented and discussed. In order to find the heterogeneity coefficient $\beta_{\sigma m}$, the angle of diffraction $\theta_{\sigma m}$, and the phase velocity $\omega/k_{\sigma m}'$ (in the direction $\theta_{\sigma m}$) of the mth-order diffracted inhomogeneous plane wave, the dispersion Eq. (8) is combined with the classical diffraction equation of optics[19] (Bragg's law)

$$k_m=k_i+m\frac{2\pi}{\Lambda}, \tag{9}$$

wherein the x-components of the complex wave vectors of the incident and diffracted waves are substituted. Equating the real and imaginary parts in both members of Eq. (9) results in a set of nonlinear equations in the unknown parameters $\beta_{\sigma m}$, $\theta_{\sigma m}$, and $k_{\sigma m}'$ that has to be solved numerically

$$k_{\sigma m}' \sin\theta_{\sigma m}=k_i' \sin\theta_i+m\frac{2\pi}{\Lambda}, \tag{10a}$$

$$\beta_{\sigma m}\cos\theta_{\sigma m}=\beta_i\cos\theta_i. \tag{10b}$$

The validity of the generalized diffraction Eq. (10) has been verified experimentally. The technique to generate a bulk inhomogeneous plane wave is described in detail in Ref. 20. This technique is based upon the transmission of a homogeneous and attenuated plane wave through a prism made of a lossy material (PVC) immersed in a lossless liquid. In accordance with Snell's law, the amplitude of the transmitted wave through the prism decreases exponentially in a direction orthogonal to its propagation direction. The inhomogeneous waves that were generated for the present work have heterogeneity coefficients $\beta_i=0.028$ 1/mm and $\beta_i=0.037$ 1/mm at, respectively, 2 and 3 MHz. The sample in the experimental setup (see Fig. 1) is a sawtooth corrugated-aluminum plate with the following acoustic and grating parameters: dilatational sound velocity $v_d=6387$ m/s, shear sound velocity $v_s=3189$ m/s, density $\rho=2680$ kg/m^3, height of the grating $h=150\,\mu$m, periodicity of the grating $\Lambda=900\,\mu$m.

A goniometer supports the corrugated sample immersed in water. The sample rotation θ_i corresponds to the angle of incidence. The inhomogeneous plane-wave emitter is in a

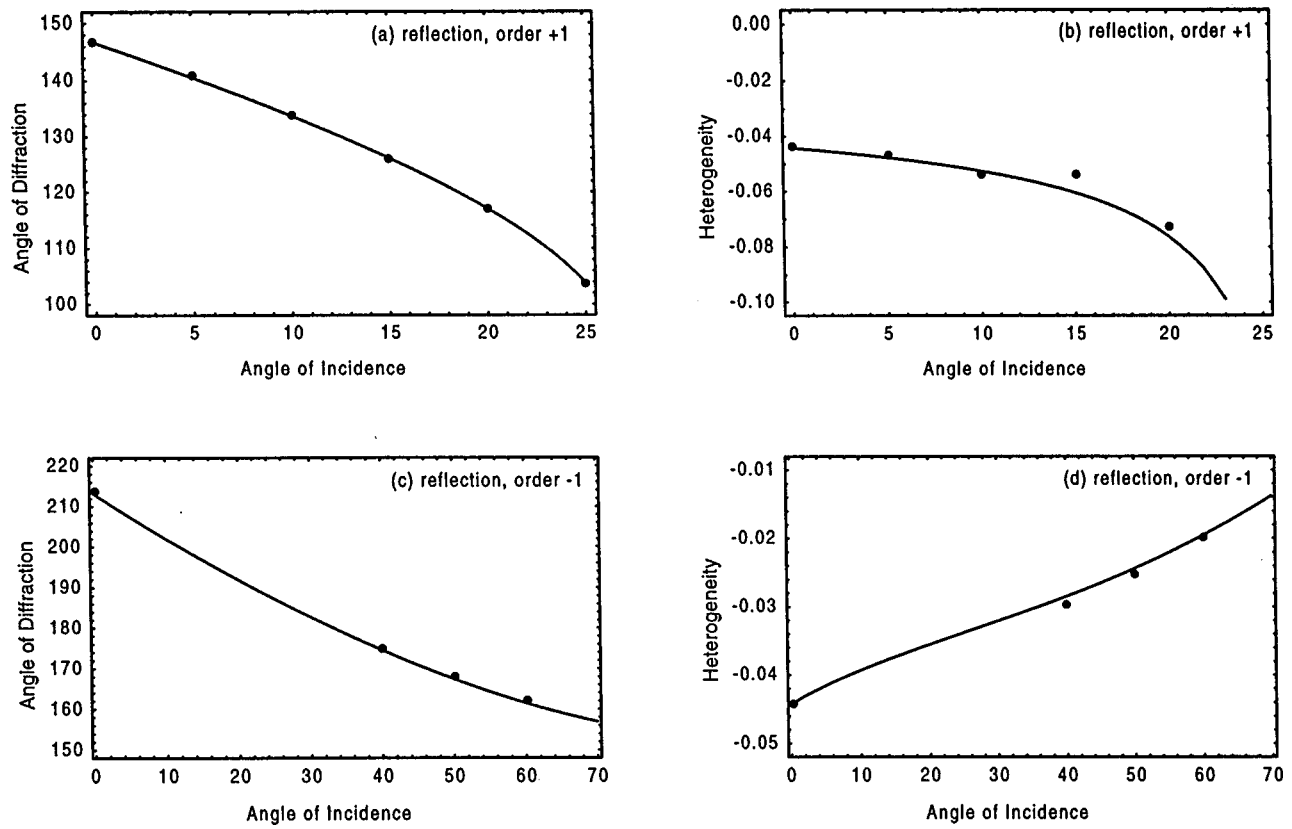

FIG. 2. Comparison between the theoretically calculated (line) and experimentally measured (circles) diffraction angle (deg) and heterogeneity coefficient (1/mm) for an inhomogeneous bulk wave ($\beta_i = 0.037$ 1/mm, $f = 3$ MHz) incident at an angle θ_i (degrees) on a grating with spatial periodicity $\Lambda = 900\ \mu$m. (a), (b): θ_{r1} and β_{r1}, (c), (d): $\theta_{r(-1)}$ and $\beta_{r(-1)}$.

fixed position. The receiver is the usual 3/4 in. transducer and is supported by a second goniometer which is concentric with the first. Analyzing the mth diffraction order in reflection, the second goniometer imposes a rotation in agreement with the theoretically calculated diffraction angle θ_{rm}. In order to obtain the wave profile (or heterogeneity coefficient), the receiver can scan the direction which is orthogonal to the direction of diffraction defined by the angle θ_{rm}.

Using the pulsing technique,[10] the effects of standing waves between the interfaces of the sample are eliminated. The central frequency of the pulse is 2.5 MHz. The sample thickness (2 cm) is greater than 4 wavelengths so that the dilatational and shear modes generated in the sample are space- and time separated. In this way, overlapping contributions due to mode conversions do not exist in the temporal window. The temporal responses of the receiver are captured and a fast Fourier transform (FFT) is performed. The number of points is 128 and the sampling frequency is 25 MHz. The amplitude is then taken equal to the value of the amplitude spectrum at a fixed frequency.

Figure 2(a) and (c) show the comparison between the calculated and the measured diffraction angle of the plus first (θ_{r1}) and the minus first ($\theta_{r(-1)}$) diffraction order in reflection when changing the angle of incidence at a frequency of 3 MHz. In Fig. 2(b) and (d), the modulus of the corresponding heterogeneity coefficients β_{r1} and $\beta_{r(-1)}$ is plotted. It is pointed out that the measurements are in good agreement with the theoretical predictions. Figure 3 shows the wave profile of the minus first diffraction order in reflection for two fixed angles of incidence (0 deg and 60 deg). The width L_1 of the diffracted beam corresponding to normal incidence (0 deg) is smaller than the width L_2 of the diffracted beam corresponding to an angle of incidence of 60 deg (the beamwidth of an inhomogeneous wave is determined by the position along the wavefront where a sudden drop in amplitude occurs).[10] On the other hand, the former has a greater heterogeneity coefficient than the latter (for $\theta_i = 0$ deg, the value of $|\beta_{r(-1)}| = 0.044$, while for $\theta_i = 60$ deg, the value of

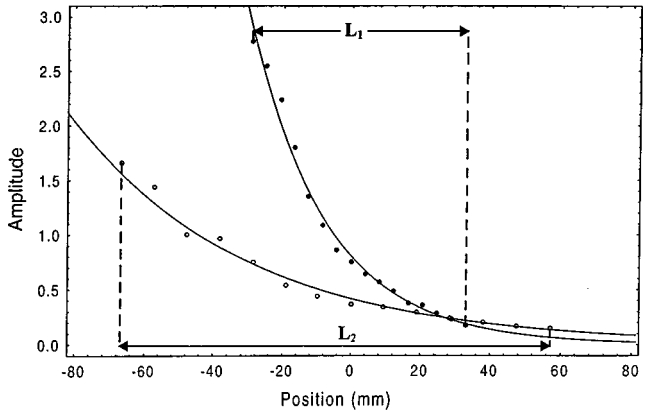

FIG. 3. Comparison between the theoretically calculated (line) and experimentally measured (circles) wave profile of the minus first diffraction order in reflection at two different angles of incidence θ_i ($\beta_i = 0.037$ 1/mm, $f = 3$ MHz) on a grating with spatial periodicity $\Lambda = 900\ \mu$m. ●: $\theta_i = 0$ deg, $\theta_{r(-1)} = 214$ deg, $\beta_{r(-1)} = -0.044$ 1/mm. ○: $\theta_i = 60$ deg, $\theta_{r(-1)} = 162.5$ deg, $\beta_{r(-1)} = -0.019$ 1/mm.

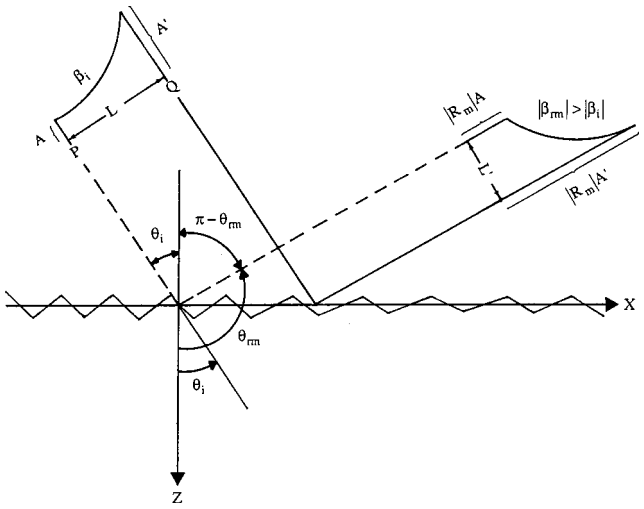

FIG. 4. A geometrical interpretation of the generalized diffraction law of Bragg for the situation when the angle of incidence θ_i is smaller than $|\pi - \theta_{rm}|$ (θ_{rm} measured from the positive z-axis).

$|\beta_{r(-1)}| = 0.019$). Generally, one may conclude that if the angle of incidence θ_i is smaller than $|\pi - \theta_{rm}|$, the modulus of the heterogeneity coefficient β_{rm} of the inhomogeneous wave diffracted in the direction θ_{rm} is greater than the modulus of the heterogeneity coefficient β_i of the incident wave, and vice versa. A geometrical interpretation of the generalized diffraction law for inhomogeneous plane waves gives a simple explanation (see Fig. 4). After diffraction, the amplitudes A and A' of the points P and Q will be multiplied by the same factor $|R_m|$, but simultaneously the width L' of the beam diffracted in the direction θ_{rm} is reduced and given by $L' = |\cos(\pi - \theta_{rm})/\cos\theta_i| L$ with L the width of the incident beam. Consequently, the heterogeneity coefficient of the diffracted wave profile must increase.

III. THE AMPLITUDES OF DIFFRACTED INHOMOGENEOUS WAVES

A. The system of coupled equations for the unknown amplitudes

The velocity potentials (4) and (6a)–(6c) must satisfy the continuity conditions at the boundary $z = f(x)$, similar to the case of a plane boundary:[21]

$$\mathbf{u}^1 \cdot \operatorname{grad} \xi = \mathbf{u}^2 \cdot \operatorname{grad} \xi, \quad \text{on} \quad \xi(x,z) = 0, \tag{11}$$

for the continuity of the normal displacements and

$$\sum_{j=1}^{3} T_{ij}^1 (\operatorname{grad} \xi)_j = \sum_{j=1}^{3} T_{ij}^2 (\operatorname{grad} \xi)_j, \quad \text{no} \quad \xi(x,z) = 0, \tag{12}$$

for the continuity of stresses, where

$$\xi(x,z) = f(x) - z = 0, \tag{13}$$

$$\mathbf{u}^1 = \operatorname{grad}(\varphi_i + \varphi_r), \tag{14}$$

$$\mathbf{u}^2 = \operatorname{grad} \varphi_d + \operatorname{rot}(\varphi_s \mathbf{e}_y), \tag{15}$$

and $\mathbf{e}_y$ is the unit vector along the y-axis. The superscripts 1 and 2 are used to indicate the liquid and the solid. The boundary conditions (11) and (12) are periodic functions in x. Consequently, a sufficient condition for the solution is to demand that the Fourier coefficients are equal over one period Λ,[14] leading to the following infinite system of coupled complex equations in the unknown amplitudes or scattering coefficients R_m, D_m, and S_m:

$$\sum_{m=-\infty}^{+\infty} (k_m k_n - k^2) R_m I_{mn}^r + \sum_{m=-\infty}^{+\infty} (k_d^2 - k_m k_n) D_m I_{mn}^d + \sum_{m=-\infty}^{+\infty} k_n K_{sm} S_m I_{mn}^s = (k^2 - k_i k_n) I_{0n}, \tag{16}$$

$$\sum_{m=-\infty}^{+\infty} (k_m - k_n) R_m I_{mn}^r - \rho \sum_{m=-\infty}^{+\infty} \left(k_m - k_n + 2k_n \frac{K_{dm}^2}{k_s^2} \right) \times D_m I_{mn}^d + \rho \sum_{m=-\infty}^{+\infty} K_{sm} \left(1 - \frac{2}{k_s^2} k_m k_n \right) S_m I_{mn}^s = (k_n - k_i) I_{0n}, \tag{17}$$

$$\sum_{m=-\infty}^{+\infty} K_{rm} R_m I_{mn}^r - \rho \sum_{m=-\infty}^{+\infty} K_{dm} \left(1 - \frac{2}{k_s^2} k_m k_n \right) D_m I_{dm}^d - \rho \sum_{m=-\infty}^{+\infty} \left(k_m - k_n + 2k_n \frac{K_{sm}^2}{k_s^2} \right) S_m I_{mn}^s = -K_i I_{0n}, \tag{18}$$

where n, running from $-\infty$ to $+\infty$, is the index of the Fourier coefficient. The symbols I_{mn}^{σ} and I_{0n} stand for the integrals

$$I_{mn}^{\sigma} = \frac{1}{K_{\sigma m}} \int_0^{\Lambda} \exp\{i[K_{\sigma m} f(x) + (k_m - k_n)x]\} dx,$$
$$I_{0n} = \frac{1}{K_i} \int_0^{\Lambda} \exp\{i[K_i f(x) + (k_i - k_n)x]\} dx, \tag{19}$$

which account for the shape function $f(x)$ of the corrugation.

In order to implement the above system numerically, one is obliged to truncate it to a finite order m, neglecting all reflected and transmitted scattered orders with indices in absolute value of $m+1$ or larger.

B. Comparison between theory and experiment

In this section, the theoretical predictions for the modulus and phase of the zeroth-order reflected inhomogeneous bulk wave at a corrugated surface are verified experimentally. The phase measurements of the zeroth-order reflection coefficient are carried out assuming that the spectral phase $\phi(f)$ is described by a linear curve in terms of the frequency f, such that

$$\phi(f) = 2\pi\tau f + \phi_0, \tag{20}$$

where ϕ_0 is the constant phase due to the reflection at the interface and τ stands for the time of flight. The slope is directly connected with the delay due to wave propagation, and the origin value provides the measurement of the phase. This measurement is obtained simply by exploiting the relation (20) at the frequency of measurement f_0 and at the sampled frequencies on both sides of f_0.

In Fig. 5(a) and (b), respectively, the modulus and the phase of the reflection coefficient for the zeroth-order dif-

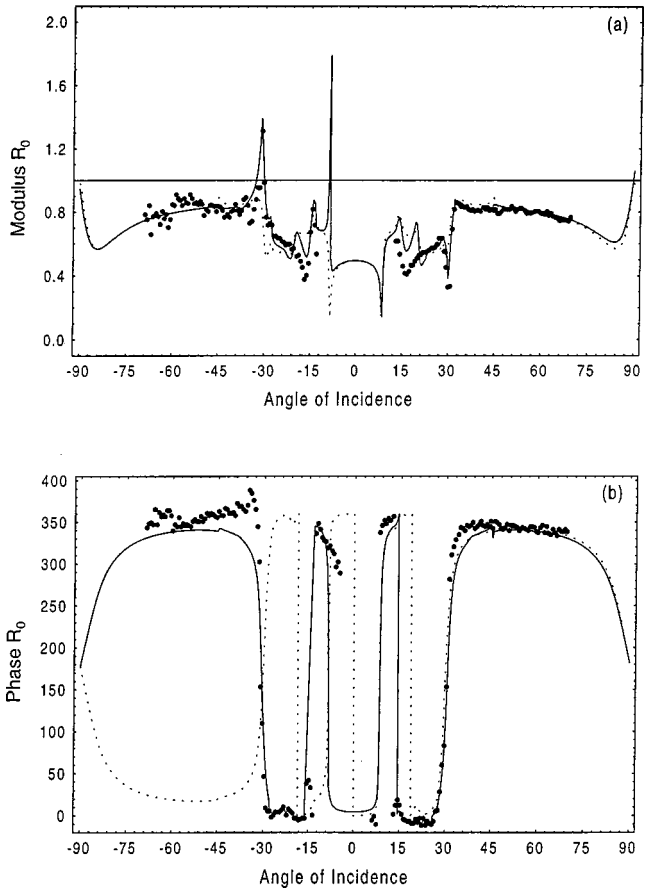

FIG. 5. Comparison between theory and experiment for the modulus (a) and phase (b) of the zeroth-order reflectioncoefficient for an inhomogeneous bulk wave ($\beta_i = 0.028$ 1/mm, $f = 2$ MH) incident at an angle θ_i (deg) on a sawtooth corrugated-aluminum sample with periodicity $\Lambda = 900\ \mu$m and height $h = 150\ \mu$m. Dotted line: theoretical curve based on solution I of the generalized diffraction law; solid line: theoretical curve based on a combination of solutions I and II of the generalized diffraction law, circles: experimental curve.

fracted inhomogeneous wave are plotted as a function of the angle of incidence. To obtain the zeroth-order reflection coefficient, the system (16)–(18) was truncated and solved. In this work, an approximation to order $m = 8$ was found to be sufficient, since the influence of higher orders in the calculations of the diffraction coefficients was not greater than 1 dB.

In this system the quantities k_m and $K_{\sigma m}$ appear, which are calculated according to the relations (7a) and (7b), wherein we have to substitute the solutions $\beta_{\sigma m}$, $\theta_{\sigma m}$, and $k'_{\sigma m}$ of the generalized diffraction law (10). At this point, it is important to remark that the solution of the generalized diffraction law is not unique. Indeed, if for fixed values of β_i, θ_i, and k'_i the triplet $(\beta_{\sigma m}, \theta_{\sigma m}, k'_{\sigma m})$ is a solution (hereafter referred to as *solution I*), then a second solution is defined by the triplet $(\beta^*_{\sigma m}, \theta^*_{\sigma m}, k'^*_{\sigma m}) = (-\beta_{\sigma m}, \pi - \theta_{\sigma m}, k'_{\sigma m})$ (hereafter referred to as *solution II*). The solution II implies reflection angles θ_{rm} in the *first* and *fourth* quadrant and transmission angles θ_{dm}, θ_{sm} in the *second* and *third* quadrant (see Fig. 6).

The dotted curve in Fig. 5 was obtained on the basis of solution I. In this case, for all angles of incidence θ_i, the

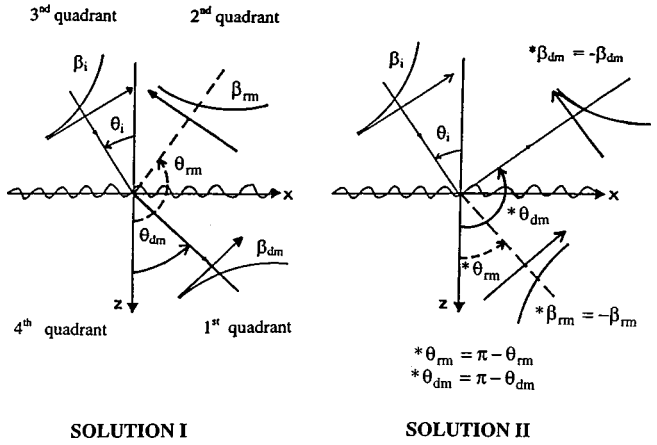

FIG. 6. The two solutions I and II of the generalized diffraction law illustrated for the reflection angle θ_{rm} and the transmission angle θ_{dm} (same reasoning for θ_{sm}).

angles of reflection θ_{rm} are chosen in the second and third quadrant, while the angles of transmission $\theta_{\sigma m}$ $(\sigma = d, s)$ are chosen in the first and fourth quadrant. In fact, this is the same procedure that is followed when studying the diffraction of homogeneous plane waves at a rough surface.

However, in order to obtain the solid curve in Fig. 5, we first had to define critical angles of incidence. To this end, the diffraction law that is classically used for *homogeneous* plane-wave diffraction at a grating is introduced [a particular case of the generalized diffraction law (10) whereby $\beta_i = 0$]

$$\sin\theta_{\sigma m} = \frac{v_\sigma}{v}\sin\theta_i + m\frac{2\pi v_\sigma}{\Lambda f}. \tag{21}$$

Now, the following choice was made. If the angle of incidence θ_i is such that

$|\sin\theta_{\sigma m}| \leqslant 1$: use solution I,

$|\sin\theta_{\sigma m}| \geqslant 1$: use solution II.

In the latter case (solution II), for several diffraction orders the reflection angle can be situated in the first or fourth quadrant while the transmission angles are located in the second and third quadrant. Solution II may seem to be a peculiar mathematical solution. However, the good agreement between the theoretical results obtained on the basis of solution II and the performed measurements indicates that only solution II admits a correct description of the diffraction problem. Note that these observations are quite similar to those for the reflection of an inhomogeneous bulk wave at a plane interface.[22] A modulus for the zero-order reflection coefficient greater than 1 in Fig. 5(a) may be interpreted as a lateral shift of the specular reflected wave, and is not in contradiction with the energy balance.[23] The peak around the Rayleigh angle (30 deg) is related to the generation of a Rayleigh surface wave along the rough surface.

IV. CONCLUSION

From the theoretical and experimental investigation of the diffraction of one inhomogeneous plane wave at a rough surface, different and interesting results have been obtained.

First, it has been shown that the classical diffraction law as used for homogeneous plane waves can be generalized for inhomogeneous plane waves. The diffracted inhomogeneous bulk waves all have a different exponential decay (heterogeneity coefficient) from the incident inhomogeneous wave. Second, a correct choice of the solutions of the generalized diffraction law is important to obtain the correct modulus and phase of the scattering coefficients of the diffracted orders. The zeroth-order reflection coefficient can be greater than unity for certain angles of incidence. The minimum at the positive Rayleigh angle of incidence is for a negative Rayleigh angle of incidence converted into a peak with an amplitude greater than 1. As shown, to explain this phenomenon the generalized diffraction law leads to unexpected solutions. The minimum and maximum at Rayleigh angle incidence can be interpreted as a shift of the reflected inhomogeneous wave to the left or to the right in comparison with the specular reflection. In that way, the energy conservation laws hold true and a very good agreement is found between the theoretical and experimental results.

[1] D. Mayste, *Selected Papers on Diffraction Gratings*, SPIE Milestone Series Vol. MS 83 (SPIE, Washington, DC, 1993).

[2] G. C. Bishop and J. Smith, ''A scattering model for nondifferentiable periodic surface roughness,'' J. Acoust. Soc. Am. **91**, 744–770 (1992).

[3] A. Jungman, L. Adler, J. D. Achenbach, and R. Roberts, ''Reflection from a boundary with periodic roughness: theory and experiment,'' J. Acoust. Soc. Am. **74**, 1025–1032 (1983).

[4] J. T. Fokkema, ''Reflection and transmission of acoustic waves by the periodic interface between a solid and a liquid,'' Wave Motion **3**, 145 (1981).

[5] K. Van Den Abeele and O. Leroy, ''Complex harmonic wave scattering as the framework for investigation of bounded beam reflection and transmission at plane interfaces and its importance in the study of vibrational modes,'' J. Acoust. Soc. Am. **93**, 308–323 (1993).

[6] O. Poncelet and M. Deschamps, ''Lamb waves generated by complex harmonic inhomogeneous plane waves,'' J. Acoust. Soc. Am. **102**, 292–300 (1997).

[7] B. Poirée, ''Complex harmonic waves,'' in *Proceedings of the Symposium on Physical Acoustics: Fundamentals and Applications*, Kortrijk, Belgium, edited by O. Leroy and M. Breazeale (Plenum, New York, 1990), pp. 99–117.

[8] B. Poirée, ''Les ondes planes evanescentes dans les fluides parfaits et les solides elastiques,'' J. Acoust. **2**, 205–216 (1989).

[9] M. Deschamps, ''L'onde plane hétérogène et ses applications en acoustique linéaire,'' J. Acoust. **4**, 269–305 (1991).

[10] M. Deschamps, ''Reflection and refraction of the inhomogeneous plane wave,'' in *Acoustic Interaction with Submerged Elastic Structures*, Part I, edited by A. Guran, J. Ripoche, and F. Ziegler (World Scientific, Singapore, 1997), pp. 164–206.

[11] R. Briers, ''Contributions to the study of acoustic scattering and conversion phenomena in discontinuous structures by introducing a mode theory and by applying the inhomogeneous wave theory,'' Ph.D. thesis, K. U. Leuven Campus Kortrijk, 1995, Prom. Professor Dr. O. Leroy.

[12] W. Huang, R. Briers, S. I. Rokhlin, and O. Leroy, ''Experimental study of inhomogeneous wave reflection from a solid-air periodically rough boundary using leaky Rayleigh waves,'' J. Acoust. Soc. Am. **96**, 363–369 (1994).

[13] J. M. Claeys, O. Leroy, A. Jungman, and L. Adler, ''Diffraction of ultrasonic waves from periodically rough liquid-solid surface,'' J. Appl. Phys. **54**, 575–5662 (1983).

[14] K. Mampaert and O. Leroy, ''Reflection and transmission of normally incident ultrasonic waves on periodic solid–liquid interfaces,'' J. Acoust. Soc. Am. **83**, 1390–1398 (1988).

[15] J. M. Claeys and O. Leroy, ''Reflection and transmission of bounded sound beams on half spaces and trough plates,'' J. Acoust. Soc. Am. **72**, 585–590 (1982).

[16] K. Van Den Abeele and O. Leroy, ''On the influence of frequency and width of an ultrasonic bounded beam in the investigation of materials: study in terms of heterogeneous plane waves,'' J. Acoust. Soc. Am. **93**, 2688–2699 (1993).

[17] J. L. Uretsky, ''The scattering of plane waves from periodic surfaces,'' Ann. Phys. **33**, 400–427 (1965).

[18] R. F. Millar, ''The Rayleigh hypothesis and a related least-squares solution to scattering problems for periodic surfaces and other scatterers,'' Radio Sci. **8**, 785–796 (1973).

[19] J. Lekner, *Theory of Reflection of Electromagnetic and Particle Waves* (Martinus Nyhoff, Dordrecht, 1987), p. 207.

[20] M. Deschamps and B. Hosten, ''Génération de l'onde hétérogène de volume dans un liquide non absorbant,'' Acustica **68** No. 2, 92–95 (1989).

[21] B. Poiree, ''Les discontinuités en acoustique et en électromagnétisme,'' Rev. Cethedec **39**, 21–34 (1974).

[22] M. Deschamps, ''Reflection and refraction of the evanescent plane wave on plane interfaces,'' J. Acoust. Soc. Am. **96**, 2841–2848 (1994).

[23] O. Leroy, G. Quentin, and J. M. Claeys, ''Energy conservation for inhomogeneous plane waves,'' J. Acoust. Soc. Am. **84**, 374–378 (1988).

Thermoacoustics in a single pore with an applied temperature gradient

G. Petculescu and L. A. Wilen[a)]
Department of Physics and Astronomy, Ohio University, Athens, Ohio 45701

(Received 10 September 1998; accepted for publication 6 May 1999)

Thermoacoustic effects in a circular pore with an applied temperature gradient are investigated. A volume-modulation technique is employed to measure the compressibility of a gas in the pore directly. When a temperature gradient is imposed on the pore, the compressibility is sensitive to thermoacoustic effects which depend on both thermal and viscous properties of the gas. Experimental results for argon and nitrogen covering a wide range of temperature gradients are presented and compared with theoretical predictions. Good agreement is found. Viscous dissipation is shown to be negligible in the arrangement studied, and the effect of viscosity is to modify the velocity profile in a way which enhances thermoacoustic gain. The measurements characterize certain thermoacoustic properties of the pore and the technique can be extended to study novel stack geometries such as stacked screens, pin arrays with varying pin orientations, reticulated vitreous carbon (RVC), or others. © *1999 Acoustical Society of America.* [S0001-4966(99)04108-9]

PACS numbers: 43.35.Ud, 43.20.Mv, 43.20.Ye [HEB]

INTRODUCTION

The efficiency of a thermoacoustic device depends critically upon properties of the stack. New and unusual stack geometries have the potential to increase the efficiency of such devices. Arnott, Bass, and Raspet,[1] and also Stinson,[2] performed theoretical calculations which laid the groundwork for comparing uniform stacks of arbitrary cross-sectional geometries. Swift and Keolian[3] calculated that stacks using the ''pin array'' geometry would be more efficient than those of other cross-sectional geometries. Their calculations were later verified experimentally by Hayden and Swift.[4]

A departure from stacks which are uniform in cross section may prove to have similar advantages. Rott and Zouzoulas[5] have calculated the effect of a flaring or conical-shaped tube on the stability equation for a Sondhauss tube. This work was later considered by Lightfoot,[6] who showed that it may be possible to improve the efficiency of refrigerators with parallel plate stacks by varying the plate spacing along the direction of the temperature gradient. Raspet *et al.*[7] have studied resonators with extreme cross-sectional variations approaching the Helmholtz limit.

More complex porous structures have also been investigated. Recent work by Adeff *et al.*[8] to look at reticulated vitreous carbon (RVC) stacks, and earlier work by Reed and Hofler[9] on stacked screens, showed that these geometries can produce good efficiency. They have a number of other advantages as well, such as simplicity of construction. These studies tested RVC and screen stacks empirically by measuring their performance in thermoacoustic prime movers and refrigerators.

We have been working to develop new techniques to evaluate stacks of arbitrary geometry by direct measurements of the thermoviscous functions which characterize the stack. In earlier work, we proposed the use of a simple method which allows the thermal response function $F(\lambda_T)$ to be measured directly for single pores.[10] $F(\lambda_T)$ measures the dynamic thermal coupling of a gas to the pore walls. Later work employing this technique yielded results for pores of rectangular, circular, and coaxial geometries which agreed very well with theoretical predictions.[11] We also measured $F(\lambda_T)$ for two stacked-screen geometries.

For a pore of uniform cross section which is oriented along the temperature gradient, a measurement of $F(\lambda_T)$ completely determines the thermoacoustic behavior because the differential equations and boundary conditions which describe the thermal and viscous coupling of the gas to the pore walls are identical.[1] In contrast, for pores of other geometries, thermal *and* viscous terms in the equations must be measured independently to characterize the thermoacoustic behavior of the pore.

In an extension of our earlier technique, we measure here the thermoacoustic response of gas in a circular pore with an applied temperature gradient. As the gas moves back and forth in the gradient, there is an added contribution to the pressure oscillations which depends explicitly on the viscosity. The validity of the technique is tested with circular pores because the theory can be calculated exactly. Measurements are performed for argon and nitrogen with temperature differences across the pore varying from 0 ° to 400 °C. We demonstrate that these measurements accurately account for the thermal *and* viscous behavior of the gas in the pore. This technique will be applied to the study of stacks with more exotic geometries to understand how they will operate in a thermoacoustic device.

I. EXPERIMENTAL TECHNIQUE

The experimental technique is similar to the one used in an earlier experiment designed to measure the thermoacoustic function $F(\lambda_T)$ for single pores of various geometries.[11] The setup is shown in Fig. 1. One side of a circular brass

a)Electronic mail: wilen@helios.phy.ohiou.edu

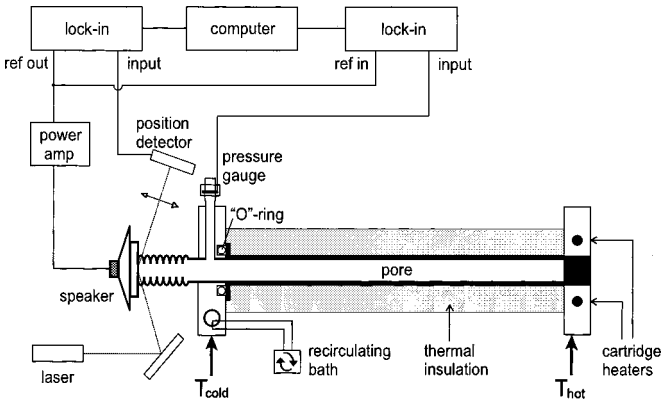

FIG. 1. Schematic diagram of the experimental setup.

pore of inner diameter 0.161 in. and length 3.240 in. was attached to a bellows modulated by a loudspeaker. The motion of the bellows was monitored by bouncing a laser beam off a mirror on the speaker cone onto a position-sensitive detector. The resulting pressure oscillations were sensed with a differential silicon pressure gauge (Honeywell Microswitch model 24PCAFA1G). The position and pressure signals were detected with two vector lock-in amplifiers (Stanford Research Systems models SR850 and SR830) as the drive frequency, f, was stepped from 0.5 to 96 Hz in 71 equal increments of $f^{1/2}$.

Different gases could be metered into the cell and sealed off under approximately one atmosphere. The static pressure in the cell was determined by measuring the outside pressure with a capacitance manometer (MKS Baratron model 622A 13T ED), and also the pressure difference between the inside and outside using the silicon pressure gauge.

One side of the pore was held at room temperature (23 °C) by circulating water through a copper plate in good thermal contact with the pore. The opposite side was controlled to any temperature from 23 °C up to 430 °C by two cartridge heaters mounted in a second copper plate also in good contact with the pore. The temperatures of both sides were measured with *K*-type thermocouples and were actively controlled to within a precision of 0.1 °C and absolute accuracy of approximately 2 °C.

The cell was designed so that the uniform pore could be replaced by a plate which essentially blanked off the bellows and pressure-gauge section of the cell. For this case, the cell was always controlled at a uniform temperature of 23 °C. These ''no pore'' measurements were used to subtract out the effect of the nonuniform part of the cell consisting of the bellows and pressure gauge. Thus, from measurements with and without the pore, the complex compressibility of the uniform pore section alone could be determined.

For the pore used in the experiment, the acoustic wavelength in the gas is much longer than the length of the pore. It is therefore a reasonable approximation to consider the pressure response to be spatially uniform. To first order, the pressure and volume of the cell can then be written as

$$P(t)=P_0+P_1(\omega)\exp(-i\omega t),$$
$$V(t)=V_0+V_1(\omega)\exp(-i\omega t), \tag{1}$$

where P_0 and V_0 are the equilibrium values and P_1 and V_1 are the acoustic variations. The quantities measured directly in the experiment are $P_0, P_1(\omega)$, and the displacement of the bellows, denoted by $X_1(\omega)$. $X_1(\omega)$ is related to $V_1(\omega)$ by $X_1(\omega)=V_1(\omega)/A_{\text{eff}}$ where A_{eff} is the effective cross-sectional area of the bellows. In the absence of a temperature gradient, and in the limit of zero frequency, the pressure oscillations are strictly isothermal, and therefore $P_0V_1(0)+V_0P_1(0)=0$ (assuming an ideal gas). This allows us to determine the equilibrium volume of the cell in terms of experimentally measured quantities as

$$V_0=-\left.\frac{P_0V_1(0)}{P_1(0)}\right|_{T_{0z}=0}, \tag{2}$$

where T_{0z} is the temperature gradient along the pore. From the above relation, we determine the volume of the cell with and without the pore inserted. For runs with a temperature gradient, we apply a correction to the volume due to the thermal expansion of the pore.

The complex compressibility is defined as

$$C(\omega)=-\frac{1}{V}\frac{V_1(\omega)}{P_1(\omega)}. \tag{3}$$

Rather than working with the compressibility directly, it will prove more convenient to work with the dimensionless quantity, $P_0C(\omega)$

$$P_0C(\omega)=-\frac{P_0}{V_0}\frac{V_1(\omega)}{P_1(\omega)}. \tag{4}$$

This quantity has a natural interpretation because, in the absence of a temperature gradient, it is equal to 1 at zero frequency (isothermal oscillations) and approaches $1/\gamma$ at high frequencies (adiabatic oscillations). For convenience, we will refer to this quantity simply as the compressibility. Note that the compressibility is completely determined by the experimentally measured quantities. Note also that, because it depends on the volume ratio $V_1(\omega)/V_0$, A_{eff} drops out, and need not actually be measured.

The measured compressibility represents an average of the thermoacoustic properties of the pore and the end including the bellows and the pressure gauge. However, by measuring the pressure and displacement signals with and without the pore in place, the end effects can be subtracted out to give the compressibility which would be measured for the pore alone. Such a subtraction procedure has been discussed in similar contexts previously,[10,11] and here we simply present the result. Let the functions $[P_0C(\omega)]_{\text{p}}$ and $[P_0C(\omega)]_{\text{wp}}$ correspond to the compressibility, and V_{p} and V_{wp}, correspond to the volume, measured for runs with and without the pore, respectively. The compressibility for the pore alone is then given by

$$[P_0C(\omega)]_{\text{pore alone}}=\frac{V_p}{(V_p-V_{wp})}[P_0C(\omega)]_p - \frac{V_{wp}}{(V_p-V_{wp})}[P_0C(\omega)]_{wp}. \quad (5)$$

Strictly speaking, this result is only correct if the two runs were made at the same static pressure. If they were not, we correct the no pore run by realizing that the compressibility is a universal function (depending only on the cell geometry) when expressed as a function of the thermal penetration depth.[10,12] Hence, the results for two runs made at different static pressures P_a and P_b are functionally related by

$$P_aC(\omega)=P_bC(\omega P_b/P_a). \quad (6)$$

After correcting the no pore run for the pressure, Eq. (5) can be applied. Hereafter, when we refer to the compressibility of the pore, we intend the quantity described in Eq. (5) for the ''pore alone'' after the appropriate subtraction has been performed.

II. THEORY

The theory for the compressibility of a pore with an imposed temperature gradient can be written down explicitly. The basic starting equation is easily derived from the thermoacoustic theory[13]

$$\frac{-i\omega}{P_0}\left[1-\frac{\gamma-1}{\gamma}F(\lambda_T)\right]P_1+\frac{T_{0z}}{T(z)}\left[\frac{F(\lambda_T)-F(\lambda)}{(1-N_p)F(\lambda)}\right]v_z(z) + \frac{d}{dz}v_z(z)=0. \quad (7)$$

γ is the ratio of specific heats, T_{0z} is the temperature gradient along the pore, $T(z)$ is the absolute temperature at position z along the pore, and v_z is the cross-sectional average of the velocity. λ, λ_T, and N_p are defined by

$$\lambda=R\sqrt{\frac{\rho_0\omega}{\eta}}, \quad \lambda_T=R\sqrt{\frac{\rho_0\omega c_p}{\kappa}}, \quad N_p=\frac{\eta c_p}{\kappa}, \quad (8)$$

where ρ_0 is the density, η is the viscosity, c_p is the specific heat per unit mass at constant pressure, and κ is thermal conductivity. R is the hydraulic radius of the pore. For a circular pore, the function F is given by[1]

$$F(\lambda)=1-(2/\sqrt{i}\lambda)[J_1(\sqrt{i}\lambda)/J_0(\sqrt{i}\lambda)]. \quad (9)$$

Physically, Eq. (7) expresses the fact that pressure oscillations (first term) result from both the compression of the gas (third term) and the motion of the gas in the gradient (second term). The first term accounts for dissipation due to thermal effects and the second is responsible for thermoacoustic gain. As will be discussed later, our experiment is not sensitive to dissipation due to purely viscous effects. To solve Eq. (7), it is useful to cast it into dimensionless form. We define dimensionless variables as follows:

$$\alpha=\frac{z}{L}, \quad D(\alpha)=\frac{-v_z(\alpha L)/i\omega L}{P_1/P_0}, \quad (10)$$

where L is the length of the pore. We assume that the temperature gradient is constant along the length of the pore. With these assumptions, the differential equation takes the form

$$\left[1-\frac{\gamma-1}{\gamma}F(\lambda_T)\right] + \frac{T_H-T_C}{T_C+\alpha(T_H-T_C)}\left[\frac{F(\lambda_T)-F(\lambda)}{(1-N_p)F(\lambda)}\right]D(\alpha) + \frac{d}{d\alpha}D(\alpha)=0, \quad (11)$$

where T_H and T_C are the temperatures of the hot and cold sides of the pore, respectively. λ_T, λ, γ, and N_p are all functions of α via their dependence on temperature, and hence position, along the pore. We find functional forms for each of these quantities using polynomial fits to literature values[14] for the viscosity, thermal conductivity, c_P and c_v, versus temperature. The density is given by the ideal gas equation, $\rho_0=P_0/RT$. For specified values of T_H, T_C, P_0, and ω, the differential equation is solved numerically using the NDSolve routine in MATHEMATICA. The boundary condition that the velocity must vanish at the closed end of the pore is given by $D(1)=0$. The function $D(\alpha)$ is evaluated at $\alpha=0$ for values of the frequency ranging from 0 to 100 Hz. $D(0)$ can be identified with $P_0C(\omega)$, the compressibility of the pore, by noting that $-v_z(z=0)/i\omega L=V_1(\omega)/V_0$.

Equation (11) can also be solved analytically in certain limits as a check of the numerical calculation. For $T_{0z}=0$, $D(0)=1-F(\lambda_T)\gamma/(\gamma-1)$. For arbitrary temperature gradients, $D(0)=[T_C\ln(T_H/T_C)]/(T_H-T_C)$ in the limit of $\omega=0$, and $D(0)=\gamma^{-1}$ in the limit $\omega\to\infty$.

III. RESULTS

In Fig. 2(a) and (b), we plot the experimental results for the compressibility versus $f^{1/2}$, along with the theory, for nitrogen and argon at five values of temperature difference across the pore. The measurements agree well with the theory in all cases. The small differences observed are consistent with the errors present in the experiment, as discussed below. The data are plotted versus $f^{1/2}$ rather than λ_T because λ_T depends on temperature, and hence varies over the length of the pore. For reference, we have plotted $\lambda_T/f^{1/2}$ and $\lambda/f^{1/2}$ as a function of temperature for both nitrogen and argon (Fig. 3).

Statistical errors in the measured displacement result from the noise in the signal conditioning electronics for the position detector, as well as noise in the power amplifier circuit driving the loudspeaker. Noise in the pressure signal is due principally to the Johnson noise of the sensor at frequencies >10 Hz, but at lower frequencies is dominated by fluctuations in atmospheric pressure. (Recall that the pressure gauge is open to the atmosphere on one side.) The combined statistical errors result in error bars roughly the size of the plotted points below 2 Hz, decreasing to much smaller at higher frequencies.

Systematic errors can arise from a number of sources. The quantity P_0C depends only on the ratios of pressures and displacements, and therefore is not sensitive to the absolute calibration of either of the sensors. There can be system-

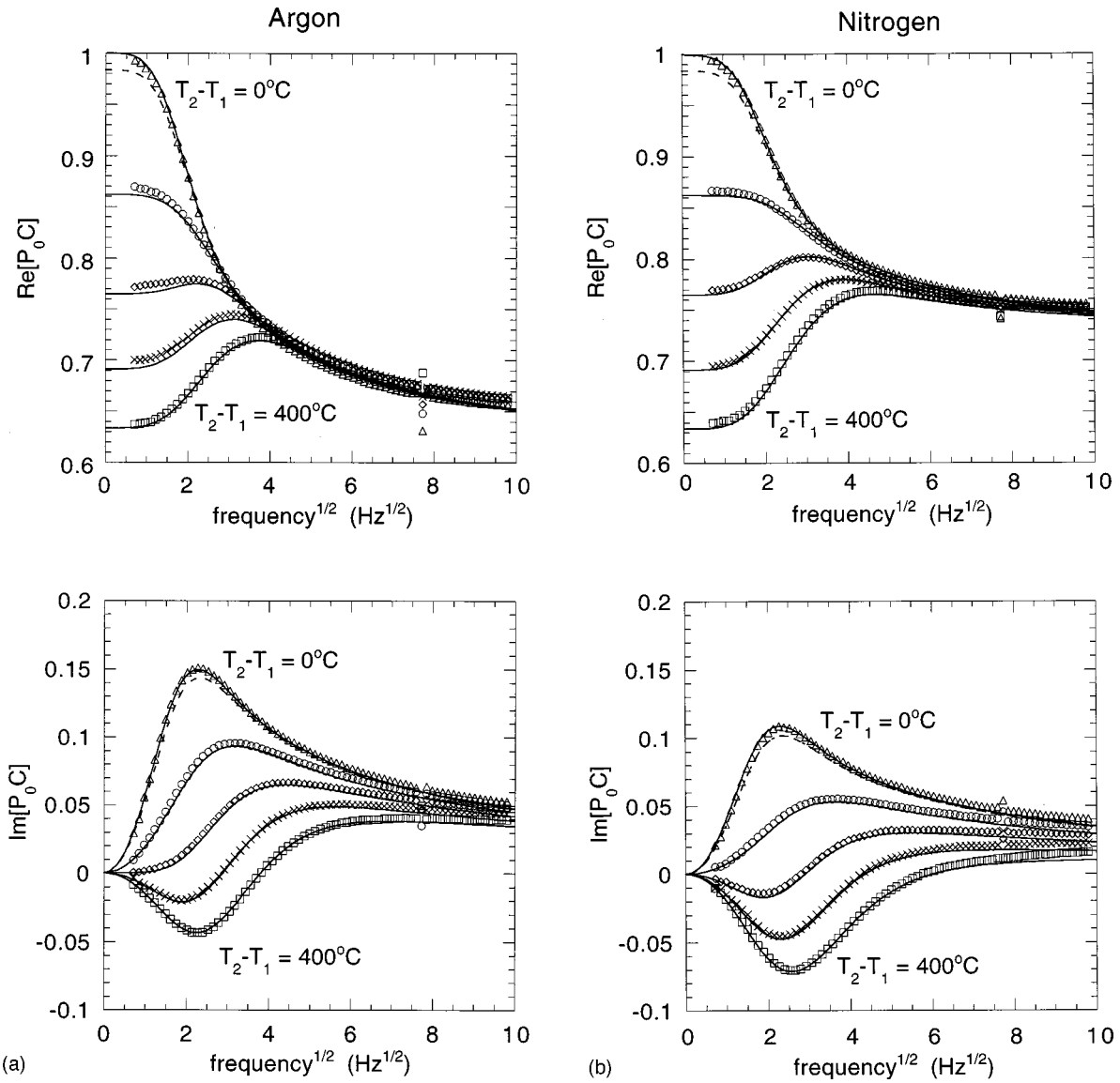

FIG. 2. P_0C vs $f^{1/2}$ plotted for the results from (a) argon and (b) nitrogen. For each gas, measurements were taken at temperature differences of 0 °C (triangles), 100 °C (circles), 200 °C (diamonds), 300 °C (crosses), and 400 °C (squares). The solid lines are the corresponding results of the theory. The dashed line is the theory for a temperature difference of 10 °C.

atic errors, however, due to nonlinearities in the sensors, or due to a nontrivial frequency response. We calibrated both sensors, and found that they were linear to $<0.5\%$ over the range in which the measurements were taken. The frequency response of the pressure gauge is set by the resonant frequency of the silicon diaphragm from which it is made, estimated to be >50 KHz. For the displacement measurements, the frequency response is limited by the signal conditioning circuit, which is flat to well over 100 KHz. Consequently, for the frequency range employed in the experiment (0–100 Hz), frequency-dependent effects are negligible. The largest source of systematic errors was due to small shifts in the sensitivity of the pressure gauge and/or position sensor which occurred between (and to a lesser extent, during) runs. Such shifts translate into an error in the equilibrium volume of the pore, which has the effect of producing a small multiplicative error in the curves (before subtraction). By repeating runs several times under the same conditions, we determined that the maximum systematic uncertainty (in absolute units) is 0.005 for the imaginary component and 0.015 for the real component.

Errors in the temperature measurements can also result in systematic disagreement between the experiment and theory. In Fig. 2(a), we have included the theoretical result (dashed lines) for a temperature difference of 10 °C to exhibit the sensitivity of the theory to such errors.

The small glitch observed in the experimental curves is due to pickup at 60 Hz. The disagreement at the upper end of the frequency range (>40 Hz) is due to the finite length of the pore relative to the wavelength of sound.[11]

IV. DISCUSSION

The boundary conditions for this system are different than for a stack in a thermoacoustic engine because here the particle velocity vanishes at one end. Nevertheless, many aspects of its behavior are similar. Consider the time-averaged power produced by the pore, given by

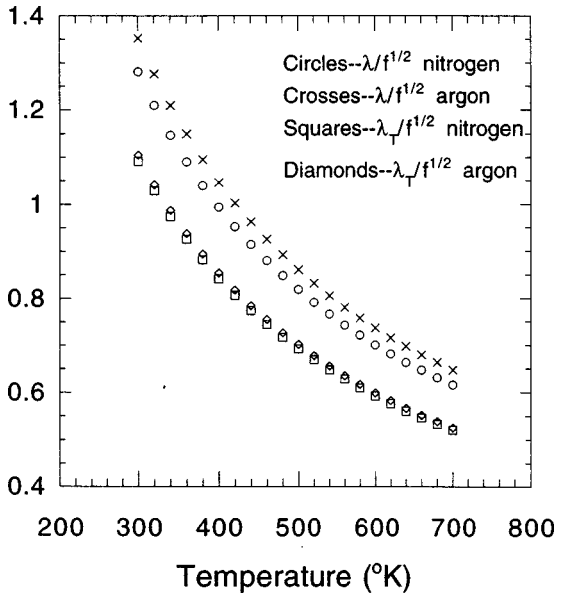

FIG. 3. $\lambda_T/f^{1/2}$ and $\lambda/f^{1/2}$ as a function of temperature for nitrogen and argon.

$$\dot{W}=\frac{1}{\tau}\int_0^{\tau}\left(P\frac{dV}{dt}\right)dt=\frac{1}{2}\mathrm{Re}\left[\tilde{P}_1\frac{dV_1}{dt}\right]$$
$$=-\frac{1}{2}\omega\frac{V_0|P_1|^2}{P_0}\mathrm{Im}[P_0C(\omega)]. \qquad (12)$$

In the absence of a gradient, the effects of thermal conductivity and viscosity are always dissipative, the imaginary part of the compressibility is positive, and work is being done on the system. At a particular temperature gradient, analogous to the critical gradient defined for prime movers, the imaginary part of the compressibility becomes negative (for some range of frequencies), and the system does positive work on its surroundings. Note that the critical gradient for nitrogen is lower than that for argon, consistent with the value of γ for each gas.[15]

The viscosity plays an unusual role in the thermoacoustic behavior of the gas for this system. To illustrate this point, we have plotted the experimental results for argon (Fig. 4) along with the theoretical curves which were obtained by assuming a vanishing viscosity. Note that the effect of viscosity is actually to *decrease* the onset temperature of the system, despite the fact that it is usually associated with purely dissipative effects. Also, for a temperature difference of 400 °C, the maximum power produced by the pore is more than twice as big when viscosity is included.

To understand this effect, it is first important to realize that in this short single-pore geometry, the effects of viscous dissipation are extremely small. Using the formalism in Swift[15] or that developed by Arnott and co-workers,[1,16,17] it is not difficult to show that in the expression for work flow, the terms due to viscous dissipation are smaller than those due to thermal effects by the factor $(\omega L/c)^2$, where c is the speed of sound. For the frequency of interest ($\approx$7 Hz), this factor is less than 5×10^{-5}.

Following Swift,[15] one can show that the power per unit

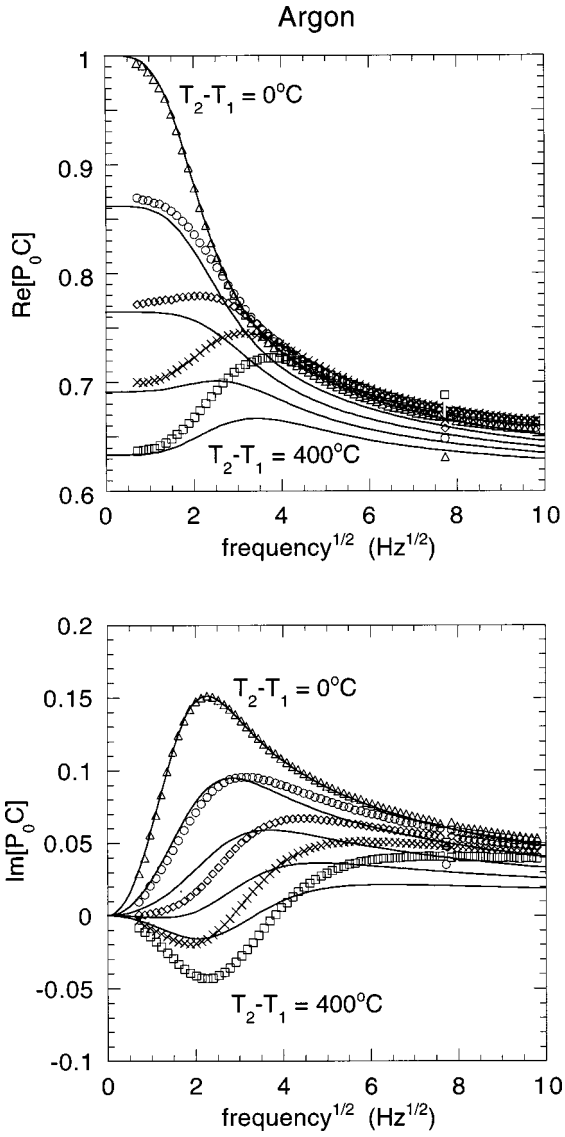

FIG. 4. P_0C vs $f^{1/2}$ plotted for the results from argon, along with the theory calculated assuming that the gas has zero viscosity.

volume due to thermal effects at the position specified by the cylindrical coordinates r and z is given by

$$\dot{w}_2=-\frac{1}{2}\frac{\omega|P_1|^2}{P_0}\mathrm{Im}\left[\frac{T_1^{\mathrm{LG}}(r,z)/T(z)}{P_1/P_0}\right]. \qquad (13)$$

T_1^{LG} denotes the complex temperature oscillations of a gas parcel in the pore as a function of the position of the parcel. The superscript LG indicates that the temperature oscillations are to be calculated in the Lagrangian frame. In other words, these are the temperature oscillations in the moving frame of the parcel of gas as it oscillates back and forth, as opposed to a fixed point in space.

Following the results in Arnott *et al.*,[1] one can show that the normalized displacement and temperature-oscillation profiles in the pore at the cold end ($z=0$) are given by

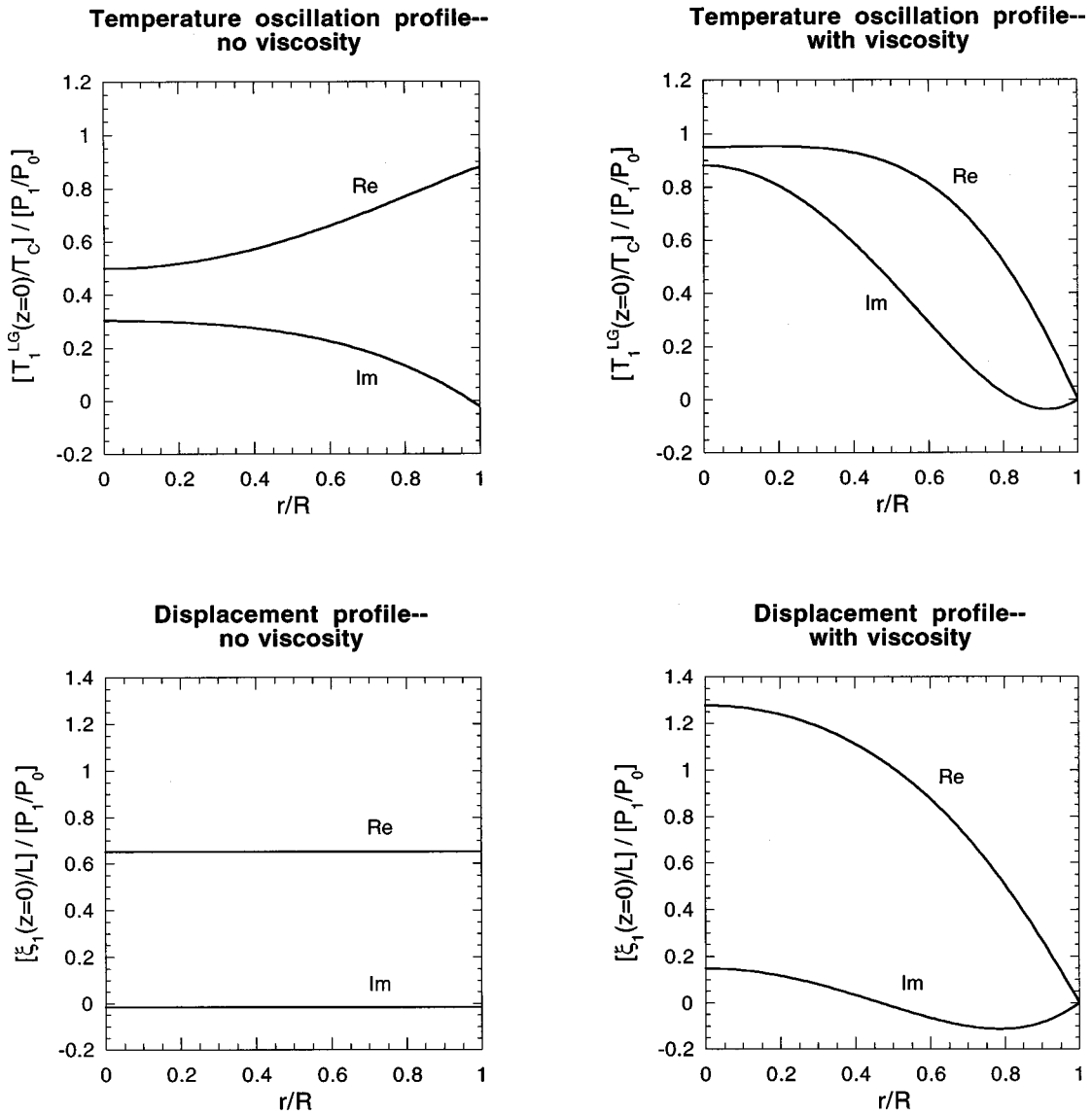

FIG. 5. The normalized temperature oscillations and displacement oscillations at the cold end of the pore for a frequency of 7 Hz plotted as a function of the radius (normalized by the pore radius) for argon. The temperature oscillations are calculated in the Lagrangian frame of reference.

$$\frac{T_1^{\mathrm{LG}}(r,z=0)/T_{\mathrm{C}}}{P_1/P_0}=\left[\frac{\gamma-1}{\gamma}F(r,\lambda_T)\right] - \frac{T_{\mathrm{H}}-T_{\mathrm{C}}}{T_{\mathrm{C}}}\left[\frac{F(r,\lambda_T)-F(r,\lambda)}{(1-N_p)F(\lambda)}\right]D(0), \tag{14}$$

$$\frac{\xi_1(r,z=0)/L}{P_1/P_0}=\left[\frac{F(r,\lambda)}{F(\lambda)}\right]D(0), \tag{15}$$

where $F(r,\lambda)$ is defined by

$$F(r,\lambda)=1-\frac{J_0(\sqrt{i}\lambda r/R)}{J_0(\sqrt{i}\lambda)}. \tag{16}$$

ξ_1 refers to the displacement oscillations of a gas parcel at the cold end of the pore as a function of the radius r of the parcel. We evaluated T_1^{LG} and ξ_1 for argon at a frequency of 7 Hz and a temperature difference of 400 °C, both including and neglecting viscosity. The results are shown in Fig. 5.

Referring to Eq. (13), along with the plots in Fig. 5, we can now give an explanation for the viscous enhancement effect as follows: The presence of viscosity changes the particle displacement profile in the pore. In the viscous case, the gas near (within one viscous penetration depth) the wall does not move. By continuity, the gas in the center of the pore must have a higher displacement (and velocity) relative to the inviscid case. In both the viscous and nonviscous cases, the gas near the wall is pinned to the temperature of the wall, hence, the imaginary (out of phase) part of the temperature oscillations is small there. (Note that for the nonviscous case, the real part of the temperature oscillations is nonvanishing at the wall because, in the Lagrangian frame, the gas parcel sees an oscillatory wall temperature.) Therefore, it is principally the gas in the center of the pore, whose temperature fluctuations are significantly out of phase with the pressure, which contributes to the thermoacoustic power. These fluctuations are bigger in the viscous case because the displacement is larger in the center (relative to the inviscid case), and

hence the gas sees a larger temperature swing as it moves to and fro.

V. CONCLUSIONS

We have presented measurements for a simple, and yet somewhat unusual, thermoacoustic device consisting of a single circular pore with an imposed temperature gradient. With the imposed gradient, the device is sensitive to thermoacoustic gain as well as thermal dissipation effects, in contrast to previous measurements which probed thermal dissipation effects only. The results compare very well with the exact theory. The device shows behavior similar to more traditional thermoacoustic devices by exhibiting a well-defined critical temperature gradient at which it produces a net time-averaged power. Here, though, viscous dissipation is negligible and the effect of viscosity is to modify the velocity profile in a way which *enhances* thermoacoustic gain.

By extending this measurement technique to stacks of other geometries, we hope to better characterize how such stacks will operate in any thermoacoustic device.

ACKNOWLEDGMENTS

The authors gratefully acknowledge discussions with Rich Raspet and Pat Arnott which led to a deeper understanding of viscous effects. The authors would also like to thank the reviewers for many helpful comments and suggestions. This work was supported by the Office of Naval Research and Ohio University Research and Sponsored Programs.

[1] W. P. Arnott, H. E. Bass, and R. Raspet, ''General formulation of thermoacoustics for stacks having arbitrarily shaped pore cross sections,'' J. Acoust. Soc. Am. **90**, 3228–3237 (1991).
[2] M. R. Stinson, ''The propagation of plane sound waves in narrow and wide circular tubes, and the generalization to uniform tubes of arbitrary cross-sectional shape,'' J. Acoust. Soc. Am. **89**, 550–558 (1991).
[3] G. W. Swift and R. M. Keolian, ''Thermoacoustics in pin-array stacks,'' J. Acoust. Soc. Am. **94**, 941–943 (1993).
[4] M. E. Hayden and G. W. Swift, ''Thermoacoustic relaxation in a pin array stack,'' J. Acoust. Soc. Am. **102**, 2714–2722 (1997).
[5] N. Rott and G. Zouzoulas, ''Thermally driven oscillations, Part IV: Tubes with variable cross-section,'' Z. Angew. Math. Phys. **27**, 197 (1976).
[6] J. A. Lightfoot, ''Thermoacoustic engines in alternate geometry resonators,'' Ph.D. dissertation, Physics Department, University of Mississippi, 1997.
[7] R. Raspet, J. A. Lightfoot, J. R. Belcher, and H. E. Bass, ''Thermoacoustic sound source in the Helmholtz limit,'' J. Acoust. Soc. Am. **S96**, 3221 (1994).
[8] J. A. Adeff, T. J. Hofler, A. A. Atchley, and W. C. Moss, ''Measurements with reticulated vitreous carbon stacks in thermoacoustic prime movers and refrigerators,'' J. Acoust. Soc. Am. **104**, 32 (1998).
[9] M. S. Reed and T. J. Hofler, ''Measurements with wire mesh stacks in thermoacoustic prime movers,'' J. Acoust. Soc. Am. **S99**, 2559 (1996).
[10] L. A. Wilen, ''Measurements of scaling properties for acoustic propagation in a single pore,'' J. Acoust. Soc. Am. **101**, 1388–1397 (1997).
[11] L. A. Wilen, ''Measurements of thermoacoustic functions for single pores,'' J. Acoust. Soc. Am. **103**, 1406–1412 (1998).
[12] J. R. Olson and G. W. Swift, ''Similitude in thermoacoustics,'' J. Acoust. Soc. Am. **95**, 1405–1412 (1991).
[13] This result can be derived using Eqs. (13), (25), and (26) in Ref. 1 above. See also R. Raspet, J. Brewster, and H. E. Bass, ''A new approximation method for thermoacoustic calculations,'' J. Acoust. Soc. Am. **103**, 2395 (1998).
[14] *CRC Handbook of Chemistry and Physics*, 75th ed., edited by D. R. Lide (CRC Press, Boca Raton, 1994); *Thermophysical Properties of Matter*, edited by Y. S. Touloukian (IFI/Plenum, New York, 1970).
[15] G. W. Swift, ''Thermoacoustic engines,'' J. Acoust. Soc. Am. **84**, 1145–1180 (1988).
[16] W. P. Arnott, J. R. Belcher, R. Raspet, and H. E. Bass, ''Stability analysis of a helium filled thermoacoustic engine,'' J. Acoust. Soc. Am. **96**, 370–375 (1994).
[17] W. P. Arnott, J. A. Lightfoot, R. Raspet, and H. Moosmüller, ''Radial wave thermoacoustic engines: Theory and examples for refrigerators and high-gain narrow-bandwidth photoacoustic spectrometers,'' J. Acoust. Soc. Am. **99**, 734–745 (1996).

A new theoretical approach to photoacoustic signal generation

C. G. A. Hoelen and F. F. M. de Mul[a)]
University of Twente, Department of Applied Physics, P.O. Box 217, 7500 AE Enschede, The Netherlands

(Received 26 August 1998; accepted for publication 26 April 1999)

From the various mechanisms of photoacoustic (PA) signal generation, the one due to local thermal expansion in aqueous media is treated here in detail. This mechanism is also referred to as thermoelastic PA signal generation. A new physical explanation of the spherical PA profile is presented, from which the signals generated by other source geometries and temporal profiles can be deduced. The characteristic PA signal profiles are discussed for some fundamental and practical source geometries. Also the PA signal attenuation and deformation due to viscous and thermoelastic losses is discussed. The analytic result for the transient generated by a spherical Gaussian spatiotemporal PA source is presented. Experimental PA signals are shown for several geometries and source diameters. © *1999 Acoustical Society of America.* [S0001-4966(99)00208-8]

PACS numbers: 43.35.Ud [HEB]

INTRODUCTION

Photoacoustic (PA) signal generation is generally the result of photothermal heating effects. Several mechanisms[1–7] are possible with various generation efficiencies, including absorption processes like electrostriction, thermal expansion, ablation, plasma formation, and cavitation, or nonabsorption processes like radiative pressure and Brillouin scattering. PA techniques may be used for material characterization, for trace detection or for imaging of the surface or the interior of a sample. A new application is the imaging of soft biological tissues. While optical imaging techniques suffer from strong scattering in dermal and subdermal tissue, this has relatively little influence on PA imaging.

Thermal expansion is the process of the absorption of light in a restricted volume followed by thermal relaxation. The induced temperature increase produces a stress that will propagate through the sample. For short laser pulses the pressure is linearly proportional to the absorbed energy density. The shape of the PA transient depends on the absorption distribution, but in general a bipolar signal is generated by spherical or cylindrical sources. The initial compression amplitude of the acoustic transient is about half the initially generated amplitude. This originates from the fact that half the disturbance starts to propagate outward from the center of the source volume and the other half propagates inward. Most times this factor is forgotten in simple phenomenological descriptions. In general the acoustic amplitude is measured, and the output of a detector is proportional to the absorbed optical energy. Thermoelastic expansion is the most dominant mechanism at radiant power densities below the vaporization threshold. In liquids[7] the conversion efficiency is typically below 10^{-4}.

Electrostriction is a process where the volume of the sample changes proportionally to the radiant intensity due to the polarizability of the sample. For the relative amplitudes of the electrostrictive pressure and the thermal expansion pressure it has been shown[1] that for a cylindrical source in liquids like water $|P_{el}|/|P_{th}| \approx k(\mu_a \tau_0)^{-1}$ where $k = 10^{-9}$ s/m, μ_a is the absorption coefficient and τ_0 is the width of the PA pulse. Using the cylindrical model as an approximation for other cases, it follows that for $\tau_0 > 10$ ns and $\mu_a > 10\ \mathrm{m}^{-1}$ the electrostrictive pressure is negligible compared to the thermal expansion pressure.

The maximum radiation pressure, caused by the change of momentum upon light reflection, is $P_{\mathrm{rad}} = 2\psi/c$, where ψ is the radiant fluence rate and c the light velocity. In nearly all cases, compared to the other interaction mechanisms, radiation pressure is negligible.

In liquids, at high radiant intensities (absorption above a threshold of about 2.2 kJ/cm^3) vapor bubbles may be generated.[3] Bubbles generated by ps–μs laser pulses are known to produce shock waves with pressure amplitudes in the kilobar range at their collapse.[8] These shock waves are able to destroy hard biological tissues, which is used in laser-induced lithotripsy. A laser fluence threshold for bubble formation of 40 J/cm^2 has been observed[8] for 230 μs laser pulses delivered to an absorber with $\mu_a = 30\ \mathrm{cm}^{-1}$. Cavitation around absorbing microparticles, induced by 30 ns laser pulses, may generate relatively small (<1 kPa) peak pressures.[9] The dependence on the laser pulse energy was about quadratic, while for low energies this was linear. For weakly absorbing particles, no bubble formation was observed up to the laser induced break down. The properties of the PA signals seem to give a clear indication of the occurrence of vapor bubble formation.

At very high laser intensities ($>10^{11}$ W/cm^2) dielectric breakdown of the sample may occur, also called optical breakdown or plasma-induced ablation.[10] At 3 mm from a focused laser beam in water, transient pressure amplitudes of the order of 50 MPa have been detected.[4]

The thermal expansion mechanism is interesting for application in medical diagnosis because it is nondestructive and noninvasive. Because tissue has many characteristics close to those of water, PA signal generation in aqueous solutions is of great importance for the development of PA tissue imaging. Compared with the applications in solids (materials characterization) or gases (spectroscopy, gas tracing), the applications in liquids are not much discussed, ex-

[a)]Corresponding author; electronic mail: mul@tn.utwente.nl

cept for material characterization.[1–7,11] Both modulated CW and pulsed PA signals are used extensively for the determination of material parameters of gases and liquids.[3,5] The PA signal generation in liquids differs in two ways from that in solids or gases: first, solids support the propagation of shear, surface and sheet waves, and second, the source geometries are most times very different. In metals and most semiconductors the source volume is essentially disklike. Significant mode conversion may occur. This is of importance for the interpretation of signals in nondestructive testing[12,13] but is of minor importance for low viscous liquids. In tissue, pulsed PA signals may be used to image the spatial distribution of optical absorbers. Accurate localization of the (micro-) vascular system should be possible because of the large optical differences between blood and dermis. Reconstruction algorithms such as the synthetic delay-and-sum focus forming[14–16] can be applied to the PA signals generated by small elementary source volumes.[17–19] Based on the PA signal generated by a homogeneous spherical source the signals that may be generated by several spherical and cylindrical sources are deduced and discussed.

PHOTOACOUSTIC THEORY

In most theoretical treatments of PA signal generation, one of two extremes is considered: the laser pulse duration τ_L is short compared to the acoustic transit time $\tau_a = 1/v$ across the characteristic length l of the source with longitudinal acoustic phase velocity v, or vice versa. Hu[20] developed a theory concerning spherical PA pulse generation in liquids. This theory does not take into account τ_a, and therefore may be applied to small sources only. For short illumination time, this theory was improved by Sigrist and Kneubühl[21] for spherical Gaussian sources, and this was experimentally confirmed. For long light pulses, Diebold *et al.*[22,23] showed that the time profiles of the PA pulses in one-, two- and three-dimensional symmetrical geometry is proportional to, respectively, the zeroth, the so called one-half and the first time derivative of the laser pulse $\Theta(\tau)$, i.e., the PA signals are proportional to $\Theta(\tau)$, $(d/d\tau)^{1/2}(\Theta(\tau))$, and $(d/d\tau)(\Theta(\tau))$ where τ is the retarded time. For cylindrical geometry, Lai and Young[24] and Heritier[25] solved the wave equations taking into account the laser pulse duration as well as the source diameter. They showed that, for Gaussian temporal and spatial distributions, the important parameter for the temporal profile of the PA pulse is the effective time τ that is related to τ_l and τ_a according to the relation

$$\tau_e = \sqrt{\tau_l^2 + \tau_a^2}, \tag{1}$$

where τ_l is half the pulse duration between the $1/e$-points of the temporal amplitude distribution, and τ_a is half the acoustic transit time between the $1/e$-points of the radial amplitude distribution. For spherical geometry, this relation has not yet been derived analytically. However, from qualitative considerations it follows that a similar relation should hold in this case, as was already suggested by Hutchins.[4] Apart from the source dimensions and the laser pulse duration, the relaxation time of the absorbed energy should be taken into account when calculating the photoacoustic signal shape.[26] If the relaxation time is fast compared to the laser pulse and the acoustic propagation time across the PA source diameter, the relaxation time is masked by the acoustic propagation time in the medium, and thus is not observable in the shape of the ultrasonic waves. In the other case the heating function should be described as a combined function of the laser pulse width and the relaxation (in particular as a convolution of the temporal laser pulse profile and the exponentially decaying heat deposition that describes the relaxation process). Numerical calculations for a cylindrical Gaussian PA source showed an amplitude decrease and an increase in pulse width for relevant decay times while the signal profile was not much affected. In this paper this effect is not taken into account explicitly. The quantitative calculations concerning cylindrical photoacoustic waves based on the theoretical results that have been reported are complicated and impractical to use in imaging applications with variable source geometries and source dimensions. Furthermore, an extended source distribution can be sub-divided into small elementary source volumes that all contribute to the signal in a point of observation by superposition of the individual signals. Thus the PA signal generated by a small spherical source volume is of more importance for imaging applications of photoacoustics. A rigorous comparison of experimental PA signals with theoretical results for the interesting range of relevant PA source geometries is not present yet.

For PA signal generation in gases and nonviscous liquids, local stress is rotationally symmetric and therefore can be represented by the (scalar) excess pressure P. For small strains the stress-strain relation is characterized by the bulk modulus B, also called the coefficient of incompressibility: $P = -B\Delta_V$, which is the first term of a Taylor series in Δ_V, and where Δ_V is the dilatation or fractional volume change $\Delta V/V$. For nonviscous media the shear rigidity modulus is zero and the bulk modulus B equals the expression for the elastic stiffness constant c of solid materials. The bulk modulus B is related to the density ρ and the longitudinal acoustic phase velocity v according to[27] $B = \rho v^2$. The isobaric fractional volume change due to a temperature change is expressed by $\Delta_V = \beta \Delta T$, where β is the thermal volume expansion coefficient. For instantaneous heating the resulting pressure P_0 can then be expressed as

$$P_0 = \beta \rho v^2 \Delta T_0. \tag{2}$$

If the heating is induced by a short laser pulse and the heat diffusion is slow compared to the pulse duration, the temperature rise ΔT is proportional to the absorbed energy density E_a':

$$\Delta T = E_a'/(\rho c_p), \tag{3}$$

and the absorbed energy is determined by the radiant fluence rate and the absorption coefficient of the medium at the specified location.

The requirement of a small fractional volume change for the applicability of the first order approximation of the stress-strain relation is equivalent to the requirement of a small excess pressure amplitude relative to the hydrostatic or

internal pressure P_0 of the medium.[7] For water, P_0 is about 3100 bar, and in most cases the PA amplitudes are much smaller.

SPHERICAL PHOTOACOUSTIC SOURCES

The temperature distribution originating from a heat pole taken at time $t=\tau$, which is a Gaussian spatial distribution with the e^{-1} value located at $r=(4\kappa_T\tau)^{1/2}$, where $\kappa_T[\mathrm{m}^2/\mathrm{s}]$ is the thermal diffusivity, was used by Sigrist *et al.*[21] to describe the temperature distribution at $t=0$ for the case of laser heating of some finite source volume. If E_a represents the laser pulse energy absorbed by the source volume in a ''short'' time, then the spatial and temporal temperature distribution after the heating at $t=0$ is described by

$$\Delta T(r,t)=\frac{E_a}{\rho c_p \pi^{3/2}(r_0^2+4\kappa_T t)^{3/2}}\exp\left(-\frac{r^2}{r_0^2+4\kappa_T t}\right). \quad (4)$$

At $t=0$, this corresponds to a Gaussian distribution in space with $1/e$ radius r_0. The assumption of a short laser pulse implies that the temperature profile of the PA source does not change significantly during the laser heating, and that the duration of the heating, which equals the laser pulse duration, is much smaller than the duration of the generated acoustic pulse. The characteristic time of the signal is r_0/v and if this is much smaller than r_0^2/κ_T the heat diffusion is slow compared to the duration of the PA signal. This results in a minimum value for $r_0: r_0 \gg \kappa_T/v = 9.3\times10^{-11}$ m for water or 6.4×10^{-11} m for soft tissue.[28] For all practical cases this will be true. With these assumptions and using the initial Gaussian temperature distribution as given by Eq. (4) at time zero for spherically symmetric geometry the solution of the wave equation (valid for small amplitudes) was found:[21]

$$P(r,t)=-P_{\max}\frac{\sqrt{2e}v}{r_0}\left(t-\frac{r}{v}\right)\exp\left\{-\left[\frac{v}{r_0}\left(t-\frac{r}{v}\right)\right]^2\right\};$$
$$P_{\max}=-P_{\min}=\frac{\beta E_a v^2}{(2\pi)^{3/2}\sqrt{e}c_p r_0^2 r}, \quad (5)$$

where the pressure is given in the form of an amplitude factor $P_{\max}$ times a normalized function. This function is equivalent to the first derivative of a Gaussian function with the retarded time $t-r/v$ as the variable, thus consisting of a positive (compression) pulse followed by a negative (rarefaction) peak; see Fig. 1. The flex point of a normal distribution is located at $x=\sigma$, the square root of the variance. The peak amplitudes of the spherical PA pulse are located at $t=r/v \pm \tau_{pp}/2$, where $\tau_{pp}=2\sigma=2^{1/2}r_0/v$. So the position of the maxima corresponds with the maxima of the gradient of the absorption distribution. The PA pulse generated by an instantaneously heated spherical source has been shown to be perfectly anti-symmetric as a function of time relative to the acoustic transit time $t=r/v$ from the center of the source to the point of observation. The pulse does not show this symmetry as a function of the spherical coordinate r, due to the r^{-1} dependence of the pressure pulse amplitudes. For a cylindrical source, a wider but smaller rarefaction peak follows the compression peak. The rarefaction peak of the PA pulse is not caused by cooling of the source because heat diffusion is negligible on the time scale of the pulse. Hu[20] assumed the rarefaction to be caused by the inertia of mass, while many authors after him did not mention a physical interpretation at all, among them Sigrist and Kneubühl,[21] Lai and Young[24] as well as Heritier,[25] and authors of reviews on photoacoustic and photothermal signal generation like Hutchins[4] and Tam.[1] Because it is easily demonstrated that in the one-dimensional case (in particular a plane PA source of finite thickness embedded in a medium of infinite extent with an identical acoustic impedance) two compression pulses are generated which propagate in opposite directions, inertia of mass does not explain the rarefaction explicitly. On the other hand, the boundary conditions for PA pulse generation by a plane, cylindrical or spherical source are nearly identical if the source is not located near an interface of different acoustic impedance. It is the geometry of the PA source that must be regarded as the crucial factor. In principle with the solution of the wave equation for a temporal and spatial delta pulse heating function all other PA sources can be constructed by the superposition principle.

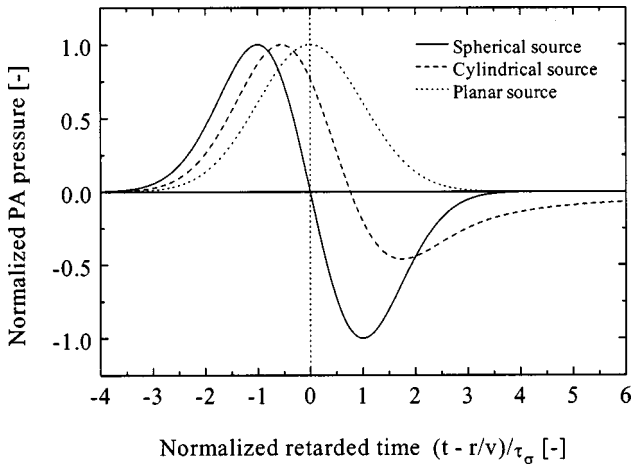

FIG. 1. Temporal profiles of the normalized PA pulses generated by (A) a 3D-, (B) a 2D-, and (C) a 1D-Gaussian source distribution for a temporal delta pulse heating function. The time is retarded with the acoustic transit time from the center of the source to the point of observation.

Figure 1 shows three characteristic, theoretical, geometry-dependent, normalized PA pulses as a function of time. The spherical signal corresponds with the theory of Sigrist and Kneubühl.[21] The cylindrical signal is numerically generated by a line source composed of overlapping Gaussian spherical sources. Relative to the spherical signal, for the cylindrical signal the maximum compression, the zero crossing point, and the maximum rarefaction arrive later, while the rarefaction peak has widened and decreased in amplitude. This result is in good agreement with the theory of Lai and Young[24] for a Gaussian cylindrical source; the peak locations show less than 2% deviation from this theory, and the ratio of the peak amplitudes less than 4%. Pulse C is the pulse generated by a plane source composed of spherical sources as predicted by integration of the expression for the spherical pulse, yielding the Gaussian distribution that was used for the temperature distribution of the source, in agreement with the simple solution of the one-dimensional equation of motion.

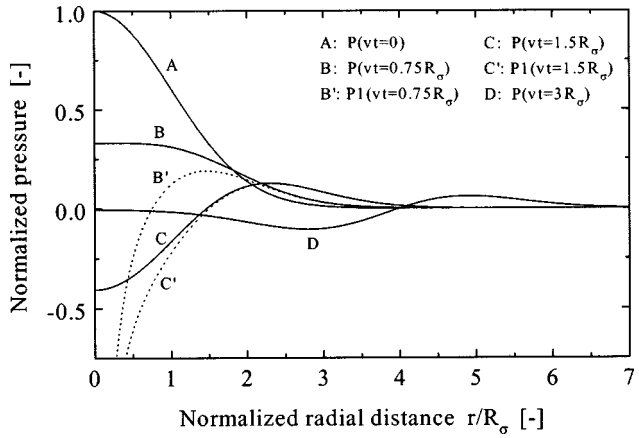

FIG. 2. Spatial pressure distribution, with the time as a parameter, as the result of an initially spherical Gaussian distribution. The solid curves (A–D) show the distribution as described by Eq. (16). The dotted curves show the distribution as described by Eq. (5) or by the first term of Eq. (16), where part of the contributions from the source are neglected and a singularity at the origin is present.

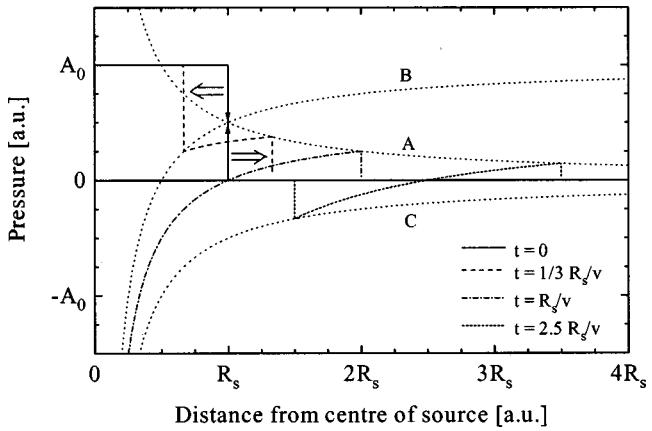

FIG. 3. Development of a spherical pressure transient. At $t=0$ the pressure is increased instantaneously and homogeneously in a sphere with radius R_S. Curves A and B indicate the amplitude for respectively the inward and outward propagating disturbance. Curve C indicates the amplitude for the outward propagating disturbance after reflection at the origin of the initially inward propagating disturbance.

Although Sigrist and Kneubühl did not take into account the (inverting) reflection of the PA pulse at the water–air interface in the comparison of their theory with experiments, from simple considerations it follows that the rarefaction peak should exist. A plane pressure pulse would not be able to propagate undisturbed (with finite longitudinal extent) if a spherical pulse would be monopolar, because the plane source can be thought to consist of many spherical sources, and in that case, at any point of observation, at every time after passage of the front of the pulse, pressure contributions originating from certain locations in the plane of generation would be present that do not interfere destructively.

The spatial distribution of the laser-induced stress at various times after instantaneous heating according to the spherical model of Sigrist and Kneubühl is shown in Fig. 2 as the dotted curves. It shows the generation of a negative delta peak at the center of the source, immediately after heating. The resulting outgoing pressure pulse evolves to the well known bipolar PA pulse. Recently, the physical interpretation of the rarefaction peak was mentioned again by Diebold *et al.*[22] They presented an alternative theoretical treatment of PA signal generation for plane, cylindrical and spherical sources. An important difference between the one- and three-dimensional waves, they state, is that ''a spherical wave launched in the direction of the origin undergoes a reflection at the origin and reappears at the field point with an inverted amplitude.'' In this way the minus sign introduced in the resulting expression for the PA pressure is justified, by which the temporal profile becomes anti-symmetric bipolar. However, the assumption of an inverting reflection leads to unacceptable consequences; an incoming compression pulse, for example, would return as rarefaction pulse, leaving behind a higher mass density at the origin without affecting the pressure. When trying to find a physical interpretation for the generation of the rarefaction peak for spherical (and cylindrical) symmetry, one should realize that the propagating pressure disturbances arise from the locations where the gradient of the pressure distribution is unequal to zero, supposing that all particles have zero velocity at $t=0$, the moment of instantaneous heating. Trying to explain the existence of the rarefaction pulse by assuming that a generated PA pulse at $t=0$ consists of two compression pulses with equal amplitudes but propagating in opposite directions, as is so easy for the one-dimensional case due to the undisturbed amplitudes during propagation, may be formally correct, but is physically rather artificial. Using the one-dimensional model to predict pulse shapes in two- and three-dimensional cases easily yields misleading results.

To explain the PA pulse shape, it is instructive to consider a spherical source with a homogeneous pressure distribution at $t=0$, which is not equal to the equilibrium pressure of the medium. Then the outgoing pressure disturbance, i.e., the local increase in pressure, has to decrease inversely proportional to the radius (distance between the center of the source and the point of observation), due to the conservation of energy. The pressure disturbance which propagates toward the center of the source, i.e., the local decrease in pressure, has to increase according to the same $1/r$ dependence. In this interpretation, there is no inverting reflection of an incoming compression pulse, but an incoming decrease in pressure, resulting in an infinite negative peak in the origin at $t=R_S/v$, after which the pressure in the origin returns to its equilibrium value. Immediately after heating, the temporary equilibrium pressure is the average local pressure, and half of the pressure step will propagate as a pressure decreasing step function into the region with the higher pressure, while the other half of the step will propagate as a pressure increasing step function into the region with the lower pressure. The propagation of the pressure disturbance is visualized in Fig. 3 for a spherical step function of the form

$$P_0(r)=A_0U(R_S-r), \tag{6}$$

where $U(x)$ is the Heaviside unit step function and R_S is the radius of the source. If the pressure is generated by instantaneous absorption of light and the source volume is optically thin, then according to Eqs. (2) and (3) the amplitude A_0 can be expressed as

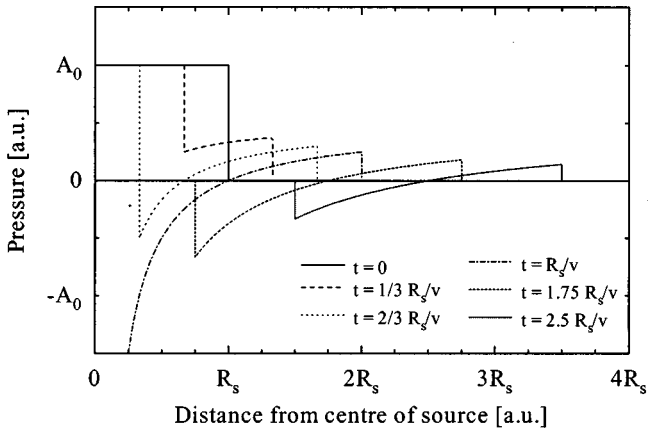

FIG. 4. Propagation of a spherical pressure pulse after instantaneous and homogeneous heating of a sphere with radius R_S. The radial pressure distribution is shown for various values of the time t after the heating.

$$A_0 = \beta v^2 E_a' c_p^{-1}, \tag{7}$$

where $E_a' = \mu_a \Phi$ is the energy absorbed per unit volume, μ_a is the optical absorption coefficient and Φ is the radiant fluence. Curve A represents the $1/r$ dependence of the outgoing compression pulse amplitude. Curve B shows the $1/r$ dependence of the resulting pressure inside the source due to the inward propagating decrease in pressure, relative to the initially induced pressure inside the source. These curves are described by

$$P_A(r) = \frac{A_0}{2}\frac{R_S}{r}; \quad P_B(r) = A_0\left(1 - \frac{R_S}{2r}\right). \tag{8}$$

Curve C again represents the $1/r$ dependence of the minimum of the outgoing rarefaction peak as will be shown hereafter. Figure 4 shows the resulting pressure pulse shape at various time intervals after the heating. At any location, the disturbance has not yet arrived for $t < |r - R_S|/v$, and has passed for $t > (r + R_S)/v$ as will be shown. If a disturbance is present, it originates from the pressure step at $r = R_S$ and $t = 0$, and has been propagating during an interval t. The front of the outgoing disturbance has moved during an interval t to $r = R_S + vt$ and has an amplitude given by $P_A(r)$. Outside the source and for $t > (r - R_S)/v$ the disturbance originates from a location r_i inside the source determined by

$$2(R_S - r_i) + r - R_S = vt, \tag{9}$$

where the amplitude (at arrival of the inwards propagating disturbance) was $P_B(r_i)$. This is the amplitude of the outgoing disturbance P_D from this location at that particular time, which then decreases according to the $1/r$-dependence:

$$P_D(r,t) = P_B(r_i(r,t))\left(\frac{r_i(r,t)}{r}\right). \tag{10}$$

This expression is valid for $r - R_S < vt < r + R_S$. Conservation of energy will show that for $vt > r + R_S$ no deviation from the equilibrium pressure can be present. For small volume changes, i.e., for $A_0 \ll B$, the initial potential (mechanical) energy E_0 directly after the heat deposition can be expressed as

$$E_0 = \tfrac{1}{2} V_S A_0^2 / B, \tag{11}$$

where V_S is the source volume. For any location outside the source, the front of the transient arrives at $t = (r - R_S)/v$. At $t = (r + R_S)/v$ the energy E that has been transported outward by the PA transient is given by

$$E = 4\pi r^2 \int_{\text{pulse}} -P_D(r,t)\frac{\partial u(r,t)}{\partial t}\,dt$$
$$= \frac{4\pi r^2 v}{B}\int_{r - R_S/v}^{r + R_S/v} P_D^2(r,t)\,dt = \frac{2}{3}\pi R_S^3 \frac{A_0^2}{B}, \tag{12}$$

where u is the particle displacement, B is the elastic bulk modulus, and use has been made of the relations $\partial u/\partial t = v \nabla u$ and $\nabla u = -P/B$. So for small amplitudes ($A_0 \ll B$) the energy of the transient as described by Eq. (10) is equal to the initial potential energy of the pressure distribution, showing that the bipolar pulse contains all of the generated mechanical energy. This means that for $t > (r + R_S)/v$, the pressure is equal to the equilibrium value. Combining the expressions for the initially generated pressure at $t = 0$ [Eq. (6)] and the propagation of the pressure disturbance for $t > 0$ [Eqs. (9) and (10)] with the appropriate step functions gives the complete expression $P_{HS}(r,t)$ for the transient generated by instantaneous homogeneous heating of a sphere:

$$P_{HS}(r,t) = A_0\Bigg(U\{R_S - vt - r\} + \left(\frac{r - vt}{2r}\right)$$
$$\times U\{r - |R_S - vt|\}U\{R_S + vt - r\}\Bigg)U(t). \tag{13}$$

The first term represents the pressure in the region of the sphere where the inward propagating disturbance (originating from the pressure step at $r = R_S$) has not yet arrived. This term plays a role in the source volume until $t = R_S/v$. The second term represents the region where a pressure disturbance is present. As long as the inward propagating wavefront has not yet arrived at the center of the source (i.e., for $t < R_S/v$), this region expands from $r = R_S$ (where a pressure gradient was induced) with the speed of sound both inward and outward. As soon as the inward propagating wavefront has reached the center, the spatial width of the transient stays constant ($2R_S$) and the transient moves only outward. Outside the source for $t < (r - R_S)/v$ it has not yet arrived at the distance r, and for $t > (r + R_S)/v$, valid for all values of r, the transient has passed, and the pressure is again at its equilibrium value. The pressure minimum of the outward traveling transient occurs at $t = (r + R_S)/v$ with a value of $-P_A(r)$, indicated in Fig. 3 by curve C.

With respect to the acoustic transient, the instantaneous generation of a local pressure disturbance by deposition of heat is equivalent to an instantaneous isothermal increase of mass in the source volume. In the latter case, conservation of mass requires conservation of the induced pressure surplus. Analogously this also holds for the pressure surplus P_S induced by heat deposition:

$$P_S(t) = \int_0^\infty 4\pi r^2 P_{HS}(r,t)\,dr = \text{constant}. \tag{14}$$

Directly after the heat deposition, the induced pressure surplus is $P_{S,0}=V_S A_0$. For the outgoing transient is found

$$P_S(t)=\int_{vt-R_S}^{vt+R_S} 4\pi r^2 \frac{A_0}{2}\left(\frac{r-vt}{r}\right)dr=P_{S,0}, \tag{15}$$

which shows that Eq. (13) satisfies the conservation of mass. The total mass surplus (compared to the equilibrium situation) is transported outward by the bipolar pulse. Of course this is only valid on a time scale where heat conduction is negligible. Upon cooling down of the source, the mass moves back again to the equilibrium situation as it was before the deposition of heat. However, this process is much slower and, relative to the PA transient, the corresponding pressures are negligible.

The expression derived for $P_{HS}(r,t)$ can be generalized for sources with a temperature distribution depending on r, by regarding this distribution as a superposition of step functions. If the pressure distribution is a continuous function of r, the pressure step equals $-\nabla P_0(r)$. Then the resulting spherically symmetric pressure disturbance $P_{\delta t}(r,t)$ is described by the summation of all the step function contributions:

$$\begin{aligned}P_{\delta t}(r,t)&=\int_0^\infty -\nabla P_0(r')\Bigg[U\Big\{(r'-vt-r\}+\left(\frac{r-vt}{2r}\right)\\&\quad\times U\{r-|r'-vt|\}U\{r'+vt-r\}\Bigg]U(t)dr'\\&=\left[\left(\frac{r-vt}{2r}\right)P_0(|r-vt|)+\left(\frac{r+vt}{2r}\right)P_0(r+vt)\right]U(t).\end{aligned} \tag{16}$$

If we examine the pressure $P_{\delta t}(r,t)$ at a specific location r as a function of the time t we see that the first term represents both the initially outward propagating contributions and the initially inward propagating contributions that are reflected at the origin, while the second term represents the inward propagating contributions from locations at distances larger than the distance at which the pressure is evaluated. For a Gaussian distribution the evolution of the PA transient is shown in Fig. 4 for several time intervals after the heating. The dotted curves show the distribution as described by the first term of Eq. (16) or, equivalently, by Eq. (5). Now it is clear why according to the model of Sigrist and Kneubühl a singularity at the origin is present. This expression is only valid for locations outside the source volume. For evaluation inside the source volume, Eq. (16) should be used. This result is equivalent to the result obtained by Diebold and Sun.[23] The expression also shows that $P_{\delta t}(r,t)$ due to an instantaneous heating is temporally anti-symmetric bipolar relative to $t=r/v$ only if the point of observation is outside the source volume.

If the temporal shape of the heating function is not a delta function but a continuous function $T(t)$, then $P(r,t)$ is described by the convolution (denoted in the text with $*$) of $P_{\delta t}(r,t)$ with $T(t)$:

$$P(r,t)=\int_{-\infty}^{\infty} P_{\delta t}(r,t-\tau)T(\tau)d\tau. \tag{17}$$

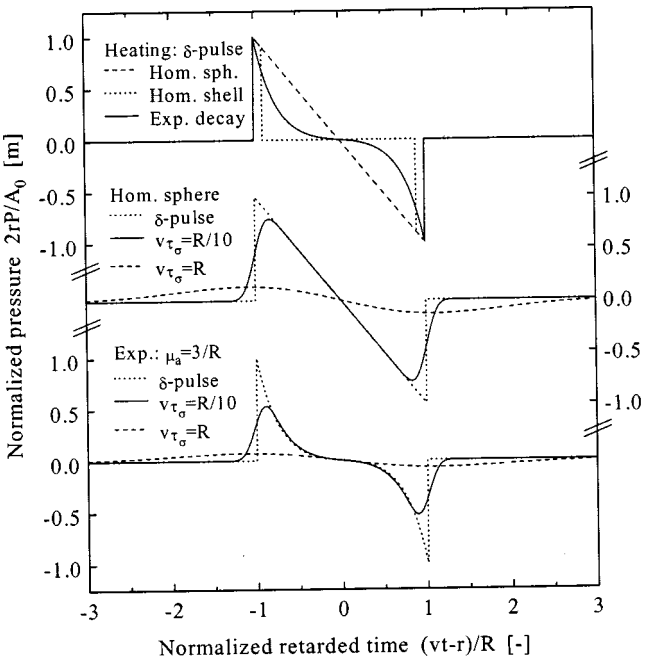

FIG. 5. Theoretical PA signals generated by spherically symmetric sources. The upper traces are for instantaneous heating of a homogeneous sphere, a spherical shell and an inward exponentially decaying absorption in a sphere. The middle traces show the PA signals from a homogeneous sphere for several Gaussian heating functions. The lower traces show these signals for the exponentially decreasing absorption distribution.

$P_{\delta t}(r,t)$ can be expressed as $P_e(r,t)U(t)$, where $P_e(r,t)=P_{\delta t}(r,t)+P_{\delta t}(r,-t)$ is an even function of t. For $t>T_L$, where T_L is the half width of a pulsed heating function $T(t)$, $P(r,t)=P_e(r,t)*T(t)$. This result is often much better accessible because of the absence of the step function and is valid for all values of r. For Gaussian distributions this is valid for $t\gg\tau_l$. However, the pressure outside the source volume, being valid for all values of t, is more interesting. So we can, alternatively, express $P_{\delta t}$ as $(P_1(r,t)+P_1(r,-t))U(t)$ where

$$P_1(r,t)=\frac{r-vt}{2r}P_0(|r-vt|). \tag{18}$$

Then for $r>R_S$, where R_S is the radius of the source, $P(r,t)=P_1(r,t)*T(t)$. For Gaussian distributions this is valid for $r\gg R_\sigma$.

SPHERICAL, CYLINDRICAL AND PLANAR ABSORPTION DISTRIBUTIONS

An absorber that is irradiated from outside will show an exponentially decaying absorption distribution. For strong absorption this may be approximated by a thin absorbing shell. From Eq. (18) the pressure generated by instantaneous homogeneous absorption in a spherical shell and by inward exponentially decaying absorption in a sphere are obtained immediately for any location outside the source volume. These signals are shown as the upper traces in Fig. 5. The pressure A_0 generated at the outer boundary of the source was taken equal for all absorption distributions. The thickness of the shell was taken as $R/10$ for clarity, where R is the radius of the sphere. For the case of diffuse irradiation of an

homogeneous absorbing sphere, the absorption coefficient was taken such that the radius corresponds with three optical lengths, i.e., $\mu_a = 3/R$. Irradiation of the sample with a light pulse of finite duration will broaden the PA signal according to Eq. (17). The numerical evaluation of the convolution is shown in Fig. 5 for the homogeneous spherical PA source (middle traces) and for the exponentially decaying absorption in a sphere (lower traces). The heating functions were taken as normal distributions with identical total energy and with $\tau_\sigma = R/(10v)$ and $\tau_\sigma = R/v$, respectively, while the δ-pulse heating function (corresponding with $\tau_\sigma = 0$) was taken for reference. Although for the widest light pulse the characteristic duration is comparable to the characteristic acoustic transit time of the source, we see that the signal shape hardly reflects the spatial absorption distribution any more while the signal amplitude has decreased significantly. This holds for all absorption distributions. It becomes clear from the graphs that the signal amplitudes decrease strongly with increasing light pulse duration. In the limit of a small geometrical source diameter compared to the acoustic propagation during the light pulse, the pressure amplitude is inversely proportional to the square of the light pulse duration as will be shown later.

Taking the limit of a vanishing spherical source radius gives the PA signal generated by a photoacoustic point source. Integration over the source volume and convolution with the temporal heating function yields the signal generated by any other PA source. For integration it is advantageous to express the pressure as a temporal derivative of a potential function:

$$P_\delta(r,vt) = \lim_{R\to 0} A_0 \frac{r-vt}{2r} U(R-|r-vt|)$$

$$= A_0 \frac{\partial}{\partial(vt)} \Phi_\delta(r,vt), \tag{19}$$

where $\Phi_\delta(r,vt) = k_0 \delta(r-vt)/r$ which is a potential function with $\delta(x)$ as the Dirac delta function. Because the signal from a homogeneous sphere is known, integration over a sphere gives for the constant k_0 a value of $1/(4\pi)$. An instantaneously generated pressure distribution can be expressed as a sum of point sources, so $P(r,t)$ can be expressed as a sum of contributions from acoustic point sources. Then the pressure can also be expressed as the derivative with respect to (vt) of the sum of point source potential functions:

$$P(\mathbf{r},t) = \frac{\partial}{\partial(vt)} \Phi(\mathbf{r},vt);$$

$$\Phi(\mathbf{r},vt) = \int P_0(\boldsymbol{\rho}) \Phi_\delta(|\boldsymbol{\rho}-\mathbf{r}|,vt)\, d\boldsymbol{\rho}, \tag{20}$$

where P_0 is the instantaneously generated initial pressure.

Integration of Φ_δ over a plane results in a simple step function:

$$\Phi_p(x,vt) = k_0 U(vt-|x|), \tag{21}$$

where x is the distance from the plane. In this way we arrive immediately at the expression for the acoustic transient generated by an instantaneously heated planar source:

$$P_P(x,t) = \frac{\partial}{\partial(vt)} \int_{-\infty}^{\infty} P_0(\xi - x) \times \int_0^\infty 2\pi\rho \Phi_\delta(\sqrt{(\xi-x)^2+\rho^2},t)\, d\rho\, d\xi$$

$$= \tfrac{1}{2}[P_0(x+vt) + P_0(x-vt)], \tag{22}$$

where $P_0(x)$ is the initially generated one-dimensional pressure distribution. This is the well known simple summation of two planar waves propagating in opposite directions. For a temporally extended heating function $T(t)$ this expression should be convolved with $T(t)$.

Integration of Φ_δ along a line yields for the potential function $\Phi_l(r,vt)$ of a line source under delta pulse illumination:

$$\Phi_l(r,vt) = \frac{k_0}{\sqrt{(vt)^2 - r^2}} U(vt-r). \tag{23}$$

From the integration of this line source potential function across the diameter of a cylindrical source the pressure generated by any cylindrical source can be evaluated numerically. With the far field approximation $(r \gg R)$, the potential function for a homogeneous cylinder with initial pressure amplitude A_0 can easily be expressed as

$$\Phi_{HC}(R,r,vt) = A_0 k_0 \int_{r-R}^{b} \sqrt{\frac{R^2-(x-r)^2}{(vt)^2-x^2}}\, dx\, U(vt-(r-R)), \tag{24}$$

where $b = vt$ if $r-R < vt < r+R$, and $b = r+R$ if $vt > r+R$. For $vt < r-R$ the acoustic transient has not yet arrived at the point of observation and the potential is zero. The potential for any continuous cylindrical heat distribution can be expressed as the superposition of potential functions for homogeneous cylinders with amplitudes determined by the gradient of the initial pressure distribution:

$$\Phi_{\mathrm{cyl}}(r,vt) = \frac{1}{4\pi} \int_0^\infty -\nabla P_0(r') \Phi_{HC}(r',r,vt)\, dr', \tag{25}$$

where r should be far outside the source volume and discontinuities are easily handled with help of the expression for Φ_{HC}. For the cylindrical equivalent of the absorption distributions as used before for the spherical sources, the potential functions are shown in Fig. 6. The corresponding photoacoustic signals, obtained by taking numerically the derivative of Φ with respect to vt, are shown as the upper traces in Fig. 7. The PA signals for the homogeneous cylinder and the cylindrical shell are in agreement with the ones presented by Diebold and Sun.[23] From these results the relative amplitudes of the PA signals generated by instantaneous heating of a homogeneous cylinder $P_{HC,\max}$ and a homogeneous sphere $P_{HS,\max}$ are given by

$$P_{HC,\max}/P_{HS,\max} = 0.250\sqrt{r/R}. \tag{26}$$

The convolution with a temporal heating function was calculated for two Gaussian functions [with $\tau_\sigma = R/v$ and $\tau_\sigma = R/(10v)$]. The results for the homogeneous absorption and the inward exponentially decaying absorption are shown in

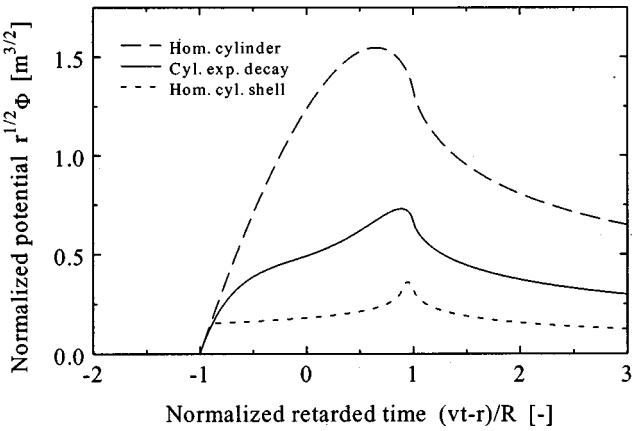

FIG. 6. The potential function as a function of time for several cylindrical sources from which the PA signals are obtained by taking the temporal derivative. The curves are for instantaneous heating and, respectively, for homogeneous absorption in a cylinder and in a thin cylindrical shell, and for absorption that decays exponentially from the surface of a cylinder inward. For the latter the radius corresponds with an optical length of 3.

Fig. 7, the middle and lower traces, respectively. The results for the homogeneous cylinder with a Gaussian temporal heating function are in qualitative agreement with the results presented by Lai and Young.[24] We see that the character of the PA signal from a homogeneous cylindrical absorption is bipolar, while it is tripolar for a shell-like absorption distribution as long as the light pulse duration is short compared to the acoustic transit time through the source. For $\tau_\sigma = R/v$ the PA signal mainly reflects the characteristics of the heating pulse. For shell-like absorption distributions it is the

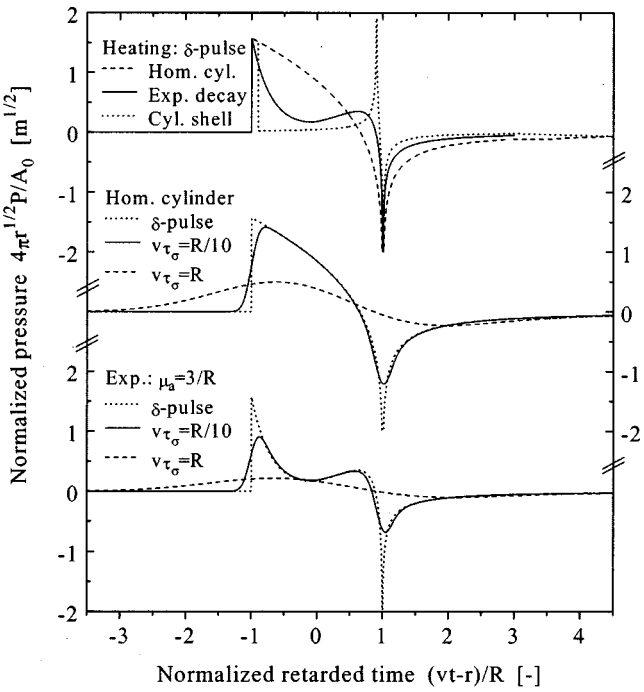

FIG. 7. Theoretical PA signals generated by cylindrically symmetric sources. The upper traces are for instantaneous heating of a homogeneous cylinder, a thin cylindrical shell and for absorption that decays exponentially from the boundary of a cylinder inward. The middle traces show the PA signals from a homogeneous cylinder for several Gaussian heating functions. The lower traces show these signals for the exponentially decreasing absorption distribution.

acoustic transit time through the thickness of the shell that should be compared with the light pulse duration to explain the PA pulse shape. Again we see that the signal amplitude decreases rapidly with increasing heating pulse duration. This means that for efficient PA pulse generation the light pulse duration should be short relative to the acoustic transit time through the optical penetration depth in the source.

ANALYTIC RESULT FOR SPHERICAL AND TEMPORAL NORMAL HEAT DISTRIBUTIONS

For a spherical Gaussian source, the initial pressure rise $P_0(r)$ is given by

$$P_0(r) = \frac{\beta v^2 E_a}{c_p (2\pi)^{3/2} R_\sigma^3} \exp\left\{ -\frac{1}{2}\left(\frac{r}{R_\sigma} \right)^2 \right\}, \tag{27}$$

where E_a is the total absorbed energy. In the far field ($r \gg R_\sigma$), the acoustic transient $P_\delta(r,t)$ generated by instantaneous heating of this spatial absorption distribution is given by Eq. (29) with $\tau_l = 0$. A Gaussian heating function $T(t)$ is described by

$$T(t) = (\sqrt{2\pi}\tau_l)^{-1} \exp\{ -\tfrac{1}{2}(t/\tau_l)^2 \}. \tag{28}$$

For $r \gg R_\sigma$ the contribution to the PA signal originating from the source volume outside the sphere with radius r can be neglected, and the convolution of $P_\delta(r,t)$ with $T(t)$ is given by

$$P(r,t) = -P_{\max}(r) \sqrt{e} \frac{t-\tau}{\tau_e} \exp\left\{ -\frac{1}{2}\left(\frac{t-\tau}{\tau_e} \right)^2 \right\};$$

$$P_{\max}(r) = \frac{\beta E_a}{2\sqrt{e}(2\pi)^{3/2} c_p \tau_e^2 r}; \quad \tau = \frac{r}{v};$$

$$\tau_e = \sqrt{\tau_a^2 + \tau_l^2}; \quad \tau_a = \frac{R_\sigma}{v}. \tag{29}$$

This expression is a far field approximation. To obtain a correct expression that includes the near field, a second term should be added as indicated by Eq. (16), i.e., the same expression evaluated at the negative time should be added. For $\tau_l \ll \tau_a$ this far field approximation is identical to the expression derived by Sigrist and Kneubühl. In the opposite case where $\tau_l \gg \tau_a$ it was shown before that the time profile of the PA wave is proportional to the first time derivative of the intensity profile of the exciting light pulse evaluated at the retarded time.[22,23,29] This is exactly what follows from Eqs. (29) and (28) for $\tau_l \gg \tau_a$. Equation (29) shows that, for a Gaussian spatial and temporal heat deposition, the effective time constant that describes the spherical PA pulse is the same weighting of the acoustic transit time and the laser pulse duration as given previously for cylindrical sources. The peaks of the PA signal are at $t = r/v \pm \tau_e$, and the peak–peak interval $\tau_{\rm pp}$ can be expressed as

$$\tau_{\rm pp} = 2\tau_e = \sqrt{T_{\rm fl}^2 + \left(\frac{D_{\rm fl}}{v} \right)^2}, \tag{30}$$

where $T_{\rm fl}$ is the interval between the flex points of the temporal profile of the heating function and $D_{\rm fl}$ is the distance between the flex points of the spatial heat distribution.

The initial PA source pressure is proportional to the temperature rise of the source volume which is proportional to the absorbed energy. Because the acoustic energy is proportional to the square of the amplitude, the efficiency of the thermoelastic photoacoustic conversion is proportional to the absorbed light energy. This shows again that this description of the process is valid only for relatively small deviations of the relevant parameters from their equilibrium values.

For longitudinal acoustic waves in aqueous media the main sources of signal attenuation are thermoelastic or thermal conduction losses and relaxation absorption or viscous losses.[27] Both mechanisms of acoustic attenuation are proportional to the square of the frequency. In materials possessing large molecular chains the attenuation due to hysteresis absorption or change-of-state losses is proportional to the frequency. For water, the frequency dependent sound absorption coefficient α for the pressure amplitude is proportional to the square frequency and is given by[27] $\alpha=\gamma f^2$, where $\gamma=25\times10^{-15}\,\mathrm{s^2/m}$ and f [Hz] is the frequency of the acoustic wave. Fourier transformation of the PA pulse as described by the Gaussian source model gives the amplitude spectrum of the undisturbed pulse, which should be multiplied by the frequency dependent sound absorption and then transformed back to the time domain to find the PA pulse deformation in the time domain due to absorption. The amplitude spectrum of the theoretical PA pulse in the presence of sound absorption (proportional to f^2) is given by

$$|P_A(r,f)|=\frac{\beta E_a}{2c_p r} f \exp\{-(2(\pi\tau_e)^2+\gamma r)f^2\}. \tag{31}$$

After inverse Fourier transformation of $P_A(r,f)$, the time dependent attenuated PA pulse $P_A(r,t)$ is again described by Eq. (29), except that the effective time constant τ_e should be replaced by a distance-dependent effective time constant $\tau_e(r)$ defined by

$$\tau_e(r)=\sqrt{\tau_l^2+\tau_a^2+\frac{\gamma r}{2\pi^2}}, \tag{32}$$

where τ_a and τ_l are defined as before and γ is the spectral amplitude attenuation coefficient. In Fig. 8 the temporal profiles of a spherical PA pulse are shown for some propagation distances r, relative to the corresponding signals in absence of sound absorption. The source radius R_σ is 5 μm, simulating a group of several red blood cells as the smallest possible source volume, and the laser pulse duration $2\tau_l$ is 8 ns. For larger PA source radii or longer laser pulse durations, the distortion of the PA pulse is less prominent due to the lower mean frequency of the PA signal. In cases where $\gamma r<\tau_e$ the influence of the sound absorption can be neglected. This means that in practical cases where $r<5$ mm and $\tau_{pp}>20$ ns the signal distortion is negligible. For most soft tissues the absorption coefficient is linearly proportional to the frequency[30] and the signal distortion will be less pronounced than for propagation in water, although the amplitude attenuation is somewhat larger. Using as an example the same time constant τ_e of 5.2 ns, corresponding with the peak spectral amplitude at 30 MHz, for water $\alpha=2.25\,\mathrm{cm^{-1}}$ and for soft tissue $\alpha=3.6\,\mathrm{cm^{-1}}$ at 30 MHz.

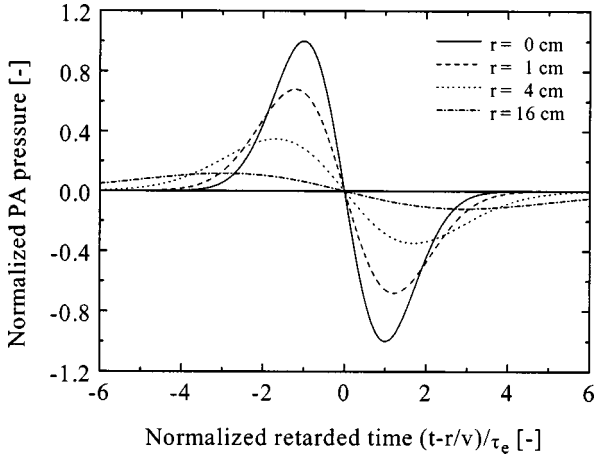

FIG. 8. The influence of sound absorption in water on the theoretical PA signal generated by a spherical normal source distribution. The curves correspond with different propagation distances. The signals are normalized with respect to the signal at the point of observation for absorption-free propagation.

EXPERIMENTAL PA SIGNALS

The experimental setup used for the generation and detection of PA signals is shown in Fig. 9. A *Q*-switched frequency doubled Nd:YAG laser (PL) provides 8 ns wide (FWHM) light pulses at 532 nm wavelength and at 10 Hz repetition rate. A 50 μm core diameter glass fiber (GF) is used to illuminate the sample. An FND 100 photo diode (PD) is used to provide the trigger for the Tektronix TDS 220 oscilloscope. Schott neutral density filters (F) are used to adjust the intensity. The signals are detected with a 200 μm diameter piezoelectric PVdF hydrophone (H).[31] Signal detection in liquids with a piezoelectric polymer sensor[32] give better correspondence between theory and experiment (for Gaussian cylindrical sources) than with a piezoelectric ceramic sensor,[33] although the latter may have a higher sensitivity. With translation stages (TS) the position of the transducer is adjusted. Absorbing polymer spheres, strands and absorber filled nylon tubing were used as PA sources (A). The microspheres were embedded in a slice of transparent silicon resin, while the strands and tubes were mounted directly in the water filled container (C). For local irradiation of cylindrical absorbers the glass fiber facet was located di-

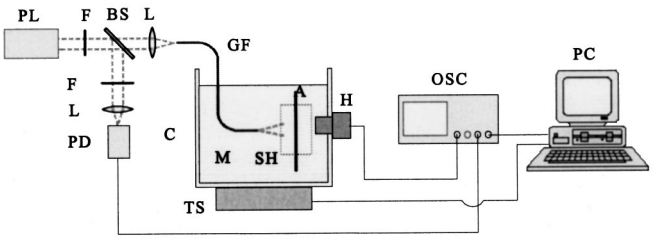

FIG. 9. Experimental setup for the generation and detection of PA signals in an aqueous medium *M*. Upon irradiation with 8-ns laser pulses the absorber A generates a photoacoustic signal that is detected with the hydrophone H. See the text for more details.

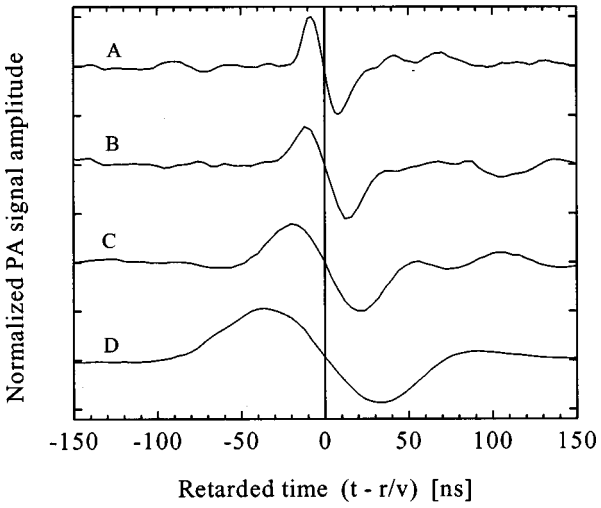

FIG. 10. Several spherical PA transients as a function of the retarded time. Characteristic dimension of the sources are: A: 8 μm; B: 13 μm; C: 100 μm; D: 200 μm. Polystyrene spheres and locally irradiated polymer strands acted as PA source. The transit times are, respectively, 1.0, 1.0, 4.5, and 6.5 μs.

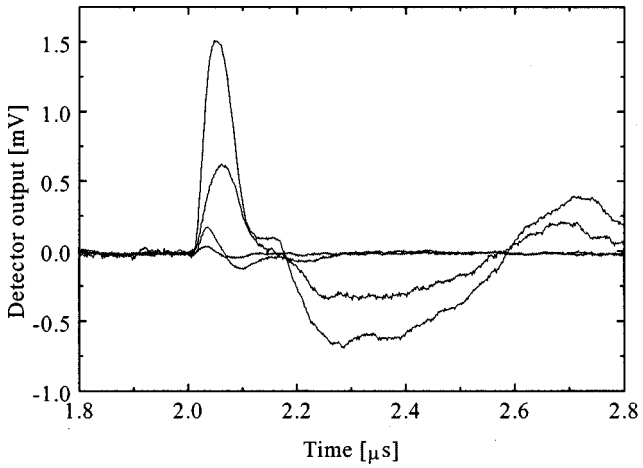

FIG. 11. Distortion of the PA signal shape at high absorbed energies due to nonthermoelastic effects. The laser beam is focused on an 8-μm diameter carbon fiber surrounded by water. The relative energies are 1, 1.7, 2.4, and 7. The signals were recorded with a 1 mm diameter, 28-μm-thick piezoelectric PVdF element at 3-mm distance and were averaged 500 times.

rectly near the absorber. Figure 10 shows several spherically propagating PA signals generated by sources with various diameters. The characteristic dimensions of the sources are 8, 13, 100 and 200 μm. In all experiments the irradiance was well below 10 MW/cm^2 and the maximum dose well below 10 J/cm^3, so the occurrence of vapor bubble formation, ionization or dielectric breakdown was very unlikely. To prevent destructive acoustic interference on the transducer surface the detection distance was increased with increasing source diameter. The detection distances were 1.5, 1.5, 6.8, and 9.8 mm for curves A–D, respectively. The peak-to-peak interval τ_{pp} of the corresponding signals are 16, 24, 42 and 68 ns which are in reasonable agreement with the theoretical values of 12, 18, 47 and 75 ns. For the smaller sources the laser pulse duration τ_l contributes significantly to the acoustic pulse duration τ_{pp}. The signal amplitudes were found to be inversely proportional to the detection distance as is expected for spherical propagation with relatively low acoustic losses. Estimation of the temperature rise of the sources based on the light absorption and on the pressure amplitudes showed that the induced temperature rises are limited to several degrees.

For high local radiant fluences the transients are not only generated by the thermoelastic mechanism any more and in this regime nonlinear effects may be observed. For various laser pulse energies Fig. 11 shows the PA signals generated by an 8 μm diameter carbon fiber in water with the laser beam focused (from aside) directly on it. For the low energy region a relatively fast bipolar pulse is observed. For higher energies both the compression and rarefaction peaks broaden, but relative to the compression peak, the rarefaction peak broadens dramatically while it increases less in amplitude. These results seem to indicate that the shape of the signal already shows whether the signal generation is beyond the thermoelastic regime.

With the help of the theoretical results for cylindrical sources the experimental transient generated by the irradiation of an absorbing cylinder can be understood. The PA signal generated by an absorbing fluid (Evans Blue) in a nylon vessel with an inner diameter of 150 μm is shown in Fig. 12. The absorption coefficient was chosen such that the radius of the cylinder corresponds with three optical lengths. The optical penetration depth is 24 μm. For the laser pulse, τ_σ was about 5 ns which corresponds with $R/(10v)$. The vessel was mounted in a highly scattering Intralipid dilution and irradiated with a glass fiber from a distance of several mm. The acoustic transient was detected at the opposite side at 1.6 mm distance with a 0.2 mm diameter piezoelectric PVdF hydrophone. The dashed lines in Fig. 12 indicate the virtual positions of the vessel walls (i.e., the acoustic transit times from the vessel walls to the transducer). The theoretical PA signal for homogeneous diffuse irradiation of the ab-

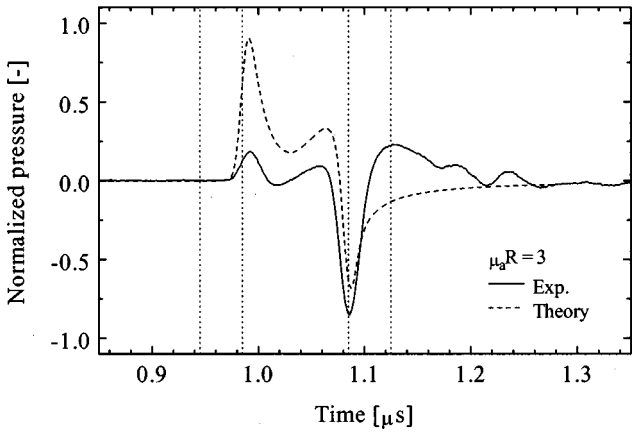

FIG. 12. Experimental PA signal generated upon irradiation with a glass fiber of a nylon vessel (inner diameter 150 μm, outer diameter 350 μm) filled with an Evans Blue dilution ($\mu_a = 400\,\mathrm{cm}^{-1}$) and mounted in an optically scattering medium. Laser pulse duration: 10 ns. Acoustic detection opposite to the irradiating fiber. The irradiance at the side of the fiber was ca. 2.5 times larger than at the side of the detector. For comparison the predicted signal for homogeneous irradiance has also been plotted in the graph.

sorbing cylinder is also shown in the graph. The tripolar pulse shape is present in the experimental signal, but there are also some differences. The vessel walls are 75 μm thick. Because of different acoustic impedances, the acoustic amplitude reflection at the water-nylon interface is about 23% and causes signal distortions, especially for $vt > r + R$. The irradiance at the side of the vessel facing the glass fiber was about 2.5 times higher than at the opposite side. As a consequence the signal amplitude in the first part of the signal is significantly smaller than for homogeneous irradiation. However, there is a reasonable correspondence between the theoretical and experimental signals.

CONCLUSIONS

From first principles the acoustic transient generated by instantaneous and homogeneous heating of a sphere has been derived. From this signal the fundamental shape of a temporally and spatially δ-pulse shaped, thermoelastically generated PA signal was shown to be bipolar. This can be expressed as the temporal derivative of a delta pulse function. With this function the transients generated by extended spatial and temporal heating functions can be derived. For a spherical source, the peak-to-peak time interval is determined by the laser pulse duration and the acoustic transit time through the source in the direction of observation. A physical explanation for this fundamental PA signal shape has been presented. The PA signal generated by various spherical and cylindrical absorption distributions and temporal heating functions has been presented. In this way the signal generated by irradiation of a spherical or cylindrical homogeneous absorber distribution was presented for several light pulse durations. Experimental PA signals from irradiated transparent tubes containing an absorbing fluid show reasonable correspondence with the theoretical signal shape. The front and rear of an optically thick cylinder correspond with the largest signal amplitudes, as long as the light pulse is short compared to the acoustic transit time. Sound absorption causes signal broadening and signal attenuation, but in aqueous media these effects are negligible for frequencies up to about 30 MHz and detection distances up to about 1 cm. For spherical Gaussian spatiotemporal sources it is possible to express the PA signal as a simple analytical function, even in the presence of acoustic losses due to thermal conduction and viscosity of the medium. Experimental results for sources with various diameters between 10 and 200 μm are in reasonable agreement with the theory, where for the smallest sources the duration of the heating pulse (about 10 ns) contributes significantly to the acoustic pulse duration. These results can be used for random PA source distributions to derive the average radial absorption distribution from the detected pressure. This may lead to an efficient reconstruction algorithm for PA imaging of absorption distributions in optically scattering media. For long laser pulse durations the distribution is blurred by the acoustic propagation distance during the heating pulse. This significantly reduces the signal amplitudes and the pulse duration should be limited to about one-tenth of the characteristic acoustic transit time of the source for optimal signal generation.

[1] A. C. Tam, ''Applications of photoacoustic sensing techniques,'' Rev. Mod. Phys. **58**, 381–431 (1986).
[2] S. J. Davies, C. Edwards, G. S. Taylor, and S. B. Palmer, ''Laser-generated ultrasound: Its properties, mechanisms and multifarious applications,'' J. Phys. D **26**, 329–348 (1993).
[3] C. K. N. Patel and A. C. Tam, ''Pulsed optoacoustic spectroscopy of condensed matter,'' Rev. Mod. Phys. **53**, 517–550 (1981).
[4] D. A. Hutchins, ''Mechanisms of pulsed photoacoustic generation,'' Can. J. Phys. **64**, 1247–1264 (1986).
[5] D. A. Hutchins and A. C. Tam, ''Pulsed photoacoustic materials characterization,'' IEEE Trans. Ultrason. Ferroelectr. Freq. Control **UFFC-33**, 429–449 (1986).
[6] V. E. Gusev and A. A. Karabutov, *Laser Optoacoustics* (American Institute of Physics, New York, 1993).
[7] M. W. Sigrist, ''Laser generation of acoustic waves in liquids and gases,'' J. Appl. Phys. **60**, R83–R121 (1986).
[8] T. Asshauer, K. Rink, and G. Delacrétaz, ''Acoustic transient generation by holmium-laser-induced cavitation bubbles,'' J. Appl. Phys. **76**, 5007–5013 (1994).
[9] S. S. Alimpiev, Y. O. Simanovski, S. V. Egerev, and A. E. Pashin, ''Optoacoustic detection of microparticles in liquids at laser fluences below the optical breakdown threshold,'' Laser Chem. **16**, 63–73 (1995).
[10] M. H. Niemz, *Interaction Mechanisms* (Springer, Berlin, 1996), Chap. 3, pp. 45–148.
[11] A. C. Tam, ''Signal enhancement and noise suppression considerations in photothermal spectroscopy,'' in *Photoacoustic and Photothermal Phenomena III*, edited by D. Bićanić, Springer Series in Optical Sciences (Springer, Berlin, 1992), Vol. 69, pp. 447–462.
[12] D. A. Hutchins, F. Nadeau, and P. Cielo, ''A pulsed photoacoustic investigation of ultrasonic mode conversion,'' Can. J. Phys. **64**, 1334–1340 (1986).
[13] L. F. Bresse and D. A. Hutchins, ''Transient generation by a wide thermoelastic source at a solid surface,'' J. Appl. Phys. **65**, 1441–1446 (1989).
[14] J. A. Evans, ''Pulse-echo ultrasound,'' in *Practical Ultrasound*, edited by R. Lerski (IRL Press, Oxford, 1988), pp. 15–29.
[15] D. E. Dudgeon, ''Fundamentals of digital array processing,'' Proc. IEEE **65**, 898–904 (1977).
[16] D. H. Johnson and D. E. Dudgeon, ''Array Signal Processing: Concepts and Techniques,'' (PTR Prentice Hall, Englewood Cliffs, NJ, 1993), Chap. 4, pp. 111–190.
[17] C. G. A. Hoelen, R. Pongers, G. Hamhuis, F. F. M. de Mul, and J. Greve, ''Photoacoustic blood cell detection and imaging of blood vessels in phantom tissue,'' Proc. Optical and Imaging Techniques for Biomonitoring, edited by H. J. Foth and R. Marchesini, SPIE **3196**, 142–153 (1997).
[18] C. G. A. Hoelen, R. Pongers, A. Dekker, and F. F. M. de Mul, ''3D-photoacoustic imaging of blood vessels,'' in Advances in Optical Imaging and Photon Migration, edited by J. Fujimoto and M. S. Patterson, OSA TOPS **21**, 386–390 (1998).
[19] C. G. A. Hoelen, F. F. M. de Mul, R. Pongers, and A. Dekker, ''Three-dimensional photoacoustic imaging of blood vessels in tissue,'' Opt. Lett. **23**, 648–650 (1998).
[20] C.-L. Hu, ''Spherical model of an acoustical wave generated by rapid laser heating in a liquid,'' J. Acoust. Soc. Am. **46**, 728–736 (1969).
[21] M. W. Sigrist and F. K. Kneubühl, ''Laser generated stress waves in liquids,'' J. Acoust. Soc. Am. **64**, 1652–1663 (1978).
[22] G. J. Diebold, T. Sun, and M. I. Khan, ''Photoacoustic waveforms generated by fluid bodies,'' in *Photoacoustic and Photothermal Phenomena III*, edited by D. Bićanić, Springer Series in Optical Sciences (Springer, Berlin, 1992), Vol. 69, pp. 263–269.
[23] G. J. Diebold and T. Sun, ''Properties of photoacoustic waves in one, two and three dimensions,'' Acustica **80**, 339–351 (1994).
[24] H. M. Lai and K. Young, ''Theory of the pulsed optoacoustic technique,'' J. Acoust. Soc. Am. **72**, 2000–2007 (1982).
[25] J.-M. Heritier, ''Electrostrictive limit and focusing effects in pulsed photoacoustic detection,'' Opt. Commun. **44**, 267–272 (1983).
[26] C.-Y. Kuo, M. M. F. Vieira, and C. K. N. Patel, ''Transient optoacoustic pulse generation and detection,'' J. Appl. Phys. **55**, 3333–3336 (1984).
[27] V. M. Ristic, *Principles of Acoustic Devices* (Wiley, New York, 1983).
[28] D. L. Balageas, J. C. Krapez, and P. Cielo, ''Pulsed photothermal modelling of layered materials,'' J. Appl. Phys. **59**, 348–357 (1986).
[29] M. I. Khan and G. J. Diebold, ''The photoacoustic effect generated by an isotropic solid sphere,'' Ultrasonics **33**, 265–269 (1995).

[30] J. A. Evans, ''Physics—The nature of ultrasound,'' in *Practical Ultrasound*, edited by R. Lerski (IRL Press, Oxford, 1988), pp. 1–13.
[31] C. G. A. Hoelen, F. F. M. de Mul, and J. Greve, ''Non-destructive photoacoustic subsurface tissue imaging: A feasibility study,'' Proc. Optical and Imaging Techniques for Biomonitoring, edited by H. J. Foth and R. Marchesini, SPIE **2628**, 308–318 (1995).
[32] S. J. Komorowski and E. M. Eyring, ''Pulse shapes of nanosecond photoacoustic signals in liquids detected by piezoelectric foil,'' J. Appl. Phys. **62**, 3066–3069 (1987).
[33] K. M. Quan, H. A. MacKenzie, P. Hodgson, and G. B. Christison, ''Photoacoustic generation in liquids with low optical absorption,'' Ultrasonics **32**, 181–186 (1994).

An alternative stack arrangement for thermoacoustic heat pumps and refrigerators

J. Bösel and Ch. Trepp
Institute for Process Engineering, Swiss Federal Institute of Technology (ETH) Zürich, 8092 Zürich, Switzerland

J. G. Fourie
Vortek Industries, 1820 Pandora Street, Vancouver, British Columbia V5L 1M5, Canada

(Received 20 May 1998; accepted for publication 6 April 1999)

One major setback of thermoacoustic engines—when comparing them with ''conventional'' heat-engines or refrigerators—is their low power density. In this work a new attempt for achieving higher power densities was undertaken. The stack of a thermoacoustic engine, which usually consists of parallel plates much longer than the acoustic displacement amplitude, was substituted by parallel-plate segments, which were only a fraction of the displacement amplitude long and randomly orientated to each other. This alternative stack arrangement was expected to benefit from improved heat transfer characteristics and an anisotropic thermal conductivity. A simplified numerical model confirmed these expectations. Experiments with a thermoacoustic heat pump were carried out. The experimental results qualitatively agreed with the numerical model. At most, the power density was raised by approximately 50%. The coefficient of performance—defined as useful heat output divided by work input—increased by approximately one-third. © *1999 Acoustical Society of America.* [S0001-4966(99)00308-2]

PACS numbers: 43.35.Ud [HEB]

INTRODUCTION

Thermoacoustic effects have been known for a long time. The generation of sound by an imposed temperature gradient, for example, was observed by glassblowers more than 200 years ago. However, the reverse process, i.e., pumping heat against a substantial temperature gradient with sound, has only been utilized in the past 15 years.

Heat pumping occurs when a suitable rigid, porous structure is properly placed in a fluid which maintains an acoustic standing wave. For small acoustic amplitudes and a regular porous geometry an exact linear theory was developed by Rott[1] and expanded by Wheatley,[2] Swift[3] and others.[4–6]

Even though thermoacoustic refrigerators have some inherent, theoretical benefits—e.g., simplicity and very long lifetime—they are not very efficient and have low power densities (defined for a refrigerator as the useful refrigeration power per resonator volume) when comparing them to ''conventional'' machines like Stirling-type refrigerators. Recently, there have been proposals[7] to increase the acoustic amplitudes for achieving higher power densities. Unfortunately this reduces the efficiency even further (because of nonlinearities like turbulence or streaming) and causes the linear acoustic theory to be no longer applicable.

Another attempt to improve the behavior of thermoacoustic engines has been made by substituting the ''stack'' of parallel plates, which usually constitute the solid medium, with other structures like pins, leading to slightly larger acoustic amplitudes and higher efficiencies.[8] Also, random structures, e.g., wire mesh screens, have been discussed and experimentally tested.[9]

In the following sections, an alternative ''stack'' design for achieving higher power densities is presented. Numerical calculations and experiments with a thermoacoustic heat pump are discussed.

I. THEORETICAL BACKGROUND

A. Thermoacoustic heat pumps and refrigerators

A thermoacoustic heat pump, or refrigerator, consists of a plane wave resonator, two heat exchangers and a porous structure in-between (Fig. 1). A driver, in most cases a loudspeaker, supplies the acoustic energy necessary to pump heat from the low temperature side to the high temperature side of the porous structure. The porous structure is usually made of a stack of thin parallel plates much longer than the acoustic displacement amplitude. This arrangement is referred to as a *Continuous Stack* (CS), shown in Fig. 2. During operation, fluid interacts thermally with the plates within a penetration depth δ_κ from the surface of the plates. This leads to a net energy flux parallel to the plate alignment up the temperature gradient (cp. Swift[3]). Heat is conducted from ''hot'' to ''cold'' in the plates in the opposite direction to the thermoacoustically activated heat flow in the fluid, thus reducing the stack's overall ability to pump heat.

B. An alternative stack arrangement

The power density of the stack shown in Fig. 2 could be enhanced by any one of the following ways. First, the heat transfer rate between the fluid and the plate could be improved. Second, if the thermal penetration depth could be reduced then the plates could be spaced closer together, allowing more surface area for heat transfer. Third, a stack could be introduced with a high material thermal conductiv-

 0001-4966/99/106(2)/707/9/$15.00

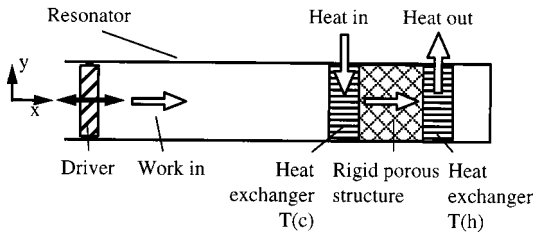

FIG. 1. Principle parts of a thermoacoustic heat pump or refrigerator. Heat is pumped from the low-temperature $[T(c)]$ heat exchanger to the high-temperature $[T(h)]$ heat exchanger.

ity normal to the direction of oscillating flow and a low overall thermal conductivity in the direction of oscillating flow.

These enhancements are realized with an alternative stack arrangement, referred to as an *Intermittent Stack* (IS),[10] which is shown in Fig. 3. It is accomplished by cutting a continuous stack into short segments. The plates in each segment can then be aligned at a 90 degree angle to those in the adjacent sections or randomly to each other.

In each section, thermal boundary layers develop anew with large temperature gradients at the leading edges of the plates. This improves the efficiency of the heat transfer process at the solid/fluid interface. Since boundary layers do not completely develop (because the segments are ''short'') the thermal and viscous penetration depths become smaller, allowing the plates to be stacked closer together. The point contacts between consecutive sections of plates reduce the cross-sectional plate area available for conduction. This yields a lower overall thermal conductivity in the direction of oscillating flow.

C. Numerical analysis

1. Assumptions

The purpose of the numerical solution was to give an idea on how the intermittent stack might perform. It was not intended to accurately predict the behavior of a complete thermoacoustic engine. The following assumptions were used: Only *randomly* aligned stack segments were considered. Heat exchangers, resonator walls, etc. were not taken into account. The effect of viscosity was not considered. The velocity component normal to the plate was assumed to be zero. The plates had an infinitely large heat capacity. The

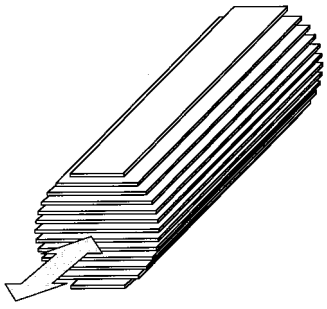

FIG. 2. ''Stack'' of long parallel plates.

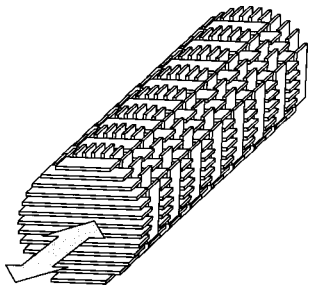

FIG. 3. Regular **I**ntermittent **S**tack (IS) arrangement: each segment is aligned at a 90 degree angle to the neighboring segments. The text treats the more general case where the segments are aligned randomly to each other.

fluid was assumed an ideal gas. At a given position in streamwise direction the mean temperature T_m and the mean temperature gradient ∇T_m are the same in plate and fluid and constant in time. Only a small number of segments with an overall length much shorter than the wavelength was considered. This allows the assumption of a standing-wave phase relation between pressure and velocity (short-stack approximation, cp. Swift[3]). At the same time the overall length of the intermittent stack was chosen to be long enough for end effects not to influence thermal behavior in the middle of the stack.

Finally, the three dimensional problem was reduced to two dimensions. To explain this, two randomly orientated plates, (A) and (B), are considered (Fig. 4). For both plates the mean temperature T_m is assumed to be constant in space and time and the starting temperature profile above plate (A) is uniform. At the downstream edge of plate (A) a smooth temperature profile has evolved. The starting temperature profile above plate (B) is uniform perpendicular to the plate surface and is now dependent on the position y. For example, at y_1 the difference $T_{\mathrm{Fluid}}(y_1)-T_m$ is smaller than the difference $T_{\mathrm{Fluid}}(y_2)-T_m$ at y_2. Consequently, the heat flux from the fluid to the plate is larger at y_2. By averaging the finishing profile of plate (A) along the y-axis (a sudden cross-mixing of the fluid is assumed) the starting temperature profile above plate (B) becomes independent of the position y. However, the averaged heat flux from the fluid to the plate remains the same as before. It then becomes sufficient to

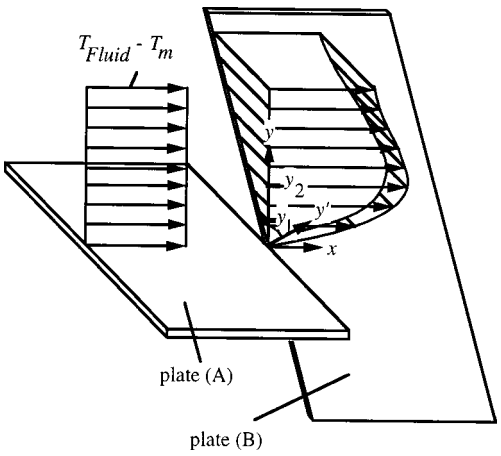

FIG. 4. Temperature profiles above a plate (A) in the intermittent arrangement: T_m is the plate temperature and T_{fluid} the fluid temperature.

calculate only the 2D temperature distribution in the x-y-plane [plate (A)] and in the x-y'-plane [plate (B)].

To compare the numerical approach with the well-known analytical solution,[3] the temperature field and heat fluxes for a continuous stack, with the same geometrical characteristics as the intermittent stack, were calculated. In this case, only one segment had to be considered with a length equal to the overall length of all the consecutive segments of the intermittent stack. Numerically and analytically calculated temperature fields and heat fluxes should roughly agree in the middle of a ''long'' segment.

The model did not allow any predictions concerning the acoustic power required by a heat pump, or that released by a prime mover, nor did it allow any predictions concerning the overall thermodynamic performance of either. However, it was suitable for estimating the performance of the intermittent stack relative to that of the continuous stack.

2. Governing equations

With the short-stack approximation and by excluding friction the flow field is known and there is no need to solve the momentum equation. For a standing wave directed along the x-direction, the pressure p in the fluid is (using the complex notation)

$$p = p_m + p_1^s e^{i\omega t}, \tag{1}$$

where p_m is the mean pressure, p_1^s is the pressure amplitude of the standing wave $p_1^s = P_A \sin(2\pi x/\lambda)$, P_A is the pressure amplitude at the pressure antinodes of the wave, λ is the wavelength, ω is the angular frequency of the wave, and t is time.

The acoustic velocity u in the stack is

$$u = i u_1^s e^{i\omega t}, \tag{2}$$

where u_1^s is the velocity amplitude of the standing wave $u_1^s = (1 + l/y_0)(P_A/\rho_m a)\cos(2\pi x/\lambda)$, l is the plate half-thickness, y_0 is the plate half-gap, ρ_m is the mean density and a is the sonic speed of the fluid. By integrating Eq. (2) with respect to time, the fluid displacement can be calculated and the displacement amplitude X_A becomes

$$X_A = (1 + l/y_0)(P_A/\rho_m a^2)\lambda/2\pi. \tag{3}$$

The continuity equation and the energy equation remain to be solved. By applying the assumptions mentioned above the energy equation reduces to[11]

$$\frac{\partial}{\partial t}(\rho T) + \frac{\partial}{\partial x}(\rho u T) = \frac{k}{c_P}\left(\frac{\partial^2 T}{\partial x^2} + \frac{\partial^2 T}{\partial y^2}\right) + \frac{1}{c_P}\left(\frac{\partial p}{\partial t} + u\frac{\partial p}{\partial x}\right), \tag{4}$$

where ρ is the fluid's density, T is temperature, k is the thermal conductivity that is assumed to be independent of temperature, and c_p is the fluid's isobaric specific heat. The four terms in Eq. (4) are identified as: (from left to right) the unsteady term, the convection term, the diffusion term and the source term.

With the ideal gas law, $p = \rho R T$, where R is the specific gas constant, density in Eq. (4) can be expressed as a function of pressure and temperature.

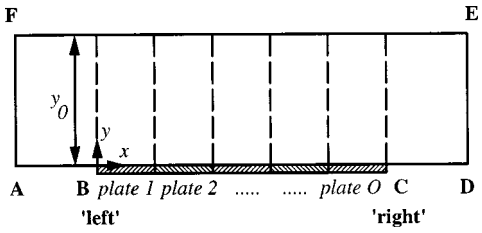

FIG. 5. Computation domain for the intermittent stack arrangement.

3. Numerical method

The numerical solution of the nonlinear Eq. (4) allows predictions concerning the performance of the intermittent stack also at larger pressure amplitudes. It is based on the implicit solution algorithm of Patankar,[12] who proposes that for a given flow field the convection and diffusion terms in the discretized form of Eq. (4) can be related by a Power Law Scheme.[13]

A schematic of the computation domain with O segments in the arrangement is shown in Fig. 5. The y-coordinate starts at the plate surface and implies that the plate has negligible thickness. The half-width between two plates is represented by y_0. To solve Eq. (4) several boundary conditions must be known.

First, there is reflection symmetry on the boundaries AB, CD and EF, thus

$$\left.\frac{\partial T}{\partial y}\right|_{AB} = \left.\frac{\partial T}{\partial y}\right|_{CD} = \left.\frac{\partial T}{\partial y}\right|_{y0} = 0. \tag{5}$$

Second, the mean temperature T_m and temperature gradient ∇T_m in the fluid, which are both independent of time, corresponded to the mean temperature and gradient in the plates. Therefore, the boundary condition on BC is

$$T|_{BC} = T_m(x), \quad \left.\frac{\partial T}{\partial x}\right|_{BC} = \nabla T_m. \tag{6}$$

Finally, for flow in the positive x-direction the boundary conditions on AF and DE are

$$T|_{AF} = T_m|_{AF} + \left(T_m|_{AF}\frac{C_1 - 1}{C_1 + 1} - \nabla T_m \frac{u_1^s|_{AF}}{\omega}\right)e^{i\omega t},$$
$$\left.\frac{\partial T}{\partial x}\right|_{DE} = 0, \tag{7}$$

and for flow in the negative x-direction

$$T|_{DE} = T_m|_{DE} + \left(T_m|_{DE}\frac{C_2 - 1}{C_2 + 1} - \nabla T_m \frac{u_1^s|_{DE}}{\omega}\right)e^{i\omega t},$$
$$\left.\frac{\partial T}{\partial x}\right|_{AF} = 0. \tag{8}$$

The constants C_1 and C_2 are

$$C_1 = \left(\frac{1 + p_1^s|_{AF}/p_m}{1 - p_1^s|_{AF}/p_m}\right)^{(\gamma-1)/\gamma},$$
$$C_2 = \left(\frac{1 + p_1^s|_{DE}/p_m}{1 - p_1^s|_{DE}/p_m}\right)^{(\gamma-1)/\gamma}, \tag{9}$$

where γ is the ratio of the isobaric to the isochoric specific heat. The computation domain was selected large enough so that the presence of the plate does not thermally effect the upstream boundary. The temperature there changes due to the pressure and displacement oscillations in an adiabatic process [Eqs. (7), (8)]. At the same time, the distance between the plate edge and the downstream boundary is large enough so that the temperature in the *x*-direction there can be assumed to be constant.

4. Heat flux

Heat is carried along *x* by the hydrodynamic transport of entropy, given by

$$\dot{Q}_{\mathrm{hydr}}=\overline{\langle \dot{m}Ts\rangle}=\Pi\overline{\int_0^{y_0}\rho uTs\,dy}=\Pi\overline{\int_0^{y_0}\frac{p}{R}us\,dy}, \quad (10)$$

where $\dot{m}$ is mass flow, s is specific entropy, and Π is plate perimeter. The overbar denotes time average over an integer number of periods and $\langle\ \rangle$ denotes the spatial average over y between the plates.

With $s=s_m+c_p\ln(T/T_m)-R\ln(p/p_m)$ the hydrodynamic heat flux per unit length becomes

$$\frac{\dot{Q}_{\mathrm{hydr}}}{\Pi}=\overline{\int_0^{y_0}pu(c_p/R\ln(T/T_m)-\ln(p/p_m))dy}. \quad (11)$$

Heat is also conducted down the temperature gradient in both the fluid and the plate. The net heat flux is therefore given by

$$\frac{\dot{Q}}{\Pi}=\frac{\dot{Q}_{\mathrm{hydr}}}{\Pi}-(y_0k+lk_s)\nabla T_m, \quad (12)$$

where k_s is the thermal conductivity of the plate material. In this case, the finite thickness of the plates is considered.

In the short-stack approximation, the heat flux between the plate and the fluid is independent of *x* as long as end effects do not play a role. In this analysis, the heat flux was calculated at the center position of the plate, located in the middle of the stack. The absolute value of the heat flux is directly proportional to the power density of the thermoacoustic engine. Therefore, heat flux may serve as a measure for power density.

5. Analytical solution for the single, infinitely long plate

For frictionless flow of an ideal gas in a low-amplitude standing wave field, Swift[3] presents the analytical solution of the energy equation for a single, infinitely long plate. Similarly, for a stack consisting of infinitely long plates the temperature in the gas can be calculated as a function of the space coordinate y and time t [see Swift,[3] Eq. (A10)]:

$$T=T_m+T_1e^{i\omega t}=T_m+\left(\frac{p_1^s}{\rho_mc_p}-\nabla T_m\frac{u_1^s}{\omega}\right)\times\left(1-\frac{\cosh((1+i)(y_0-y)/\delta_\kappa)}{\cosh((1+i)y_0/\delta_\kappa)}\right)e^{i\omega t}, \quad (13)$$

where T_1 is temperature amplitude and $\delta_\kappa=\sqrt{2k/\rho_mc_p\omega}$ is the thermal penetration depth.

Considering only first order quantities the hydrodynamic heat flux is[3]

$$\dot{Q}_{\mathrm{hydr}}=\Pi\int_0^{y_0}T_m\rho_m\overline{s_1u_1}\,dy=\frac{\Pi}{2}\rho_mc_pu_1^s\int_0^{y_0}\mathrm{Im}[T_1]dy. \quad (14)$$

Using Eq. (13), and with $\eta_0=y_0/\delta_\kappa$, the heat flux per unit length becomes

$$\frac{\dot{Q}_{\mathrm{hydr}}}{\Pi}=-\frac{1}{4}\rho_mc_pu_1^s\delta_\kappa\left(\frac{p_1^s}{\rho_mc_p}-\nabla T_m\frac{u_1^s}{\omega}\right)\times\frac{\sin 2\eta_0-\sinh 2\eta_0}{\cos 2\eta_0+\cosh 2\eta_0}. \quad (15)$$

Considering heat conduction in the fluid as well as the plate, the net heat flux per unit length can be calculated using Eq. (12).

II. EXPERIMENTAL SETUP

A. Background

In order to compare the performance of the intermittent stack to that of the continuous stack, a thermoacoustic heat pump was designed. The apparatus corresponded in principle to the schematic sketch in Fig. 1.

For practical reasons (such as high reliability, robustness and high drive ratios) an oil free, hermetically sealed piston compressor with continuous-adjustable piston speed (maximum 3000 rpm) was used as a driver. Due to the modest rotating speeds and relatively short resonator (see below), the oscillations were not driven at resonance. Consequently, the pressure amplitude was nearly independent of position *x* in the resonator and the volumetric velocity was an almost linear function of position. The driver had to be placed to the ''cold'' end of the resonator. Since this was a rather disadvantageous configuration for a refrigerator, a heat pump with the driver at ambient temperature was utilized.

B. Apparatus

At first, a heat pump consisting of a cylindrical resonator with a continuous stack was designed and built. The design was based on Rott's linear theory.[1,3] Pure helium gas was used to a maximum mean pressure of 20 bar. The maximum frequency of the gas oscillation was 50 Hz. An intermittent stack was then designed and built with a plate thickness and gap width that corresponded to that of the continuous stack. The heat exchangers also consisted of parallel plates similar to those of the stacks, but with smaller gaps between them. The characteristics of the resonator, stacks and heat exchangers are summarized in Table I. The piston of the compressor had a diameter of 5 cm and a stroke of 2 cm. The segments in the intermittent stack had to be shorter than two times the acoustic displacement amplitude anywhere between the two heat exchangers. A length of 2 mm met this requirement ($<25\%$ of $2X_A$). The segment disks were cut by laser from a

TABLE I. Characteristics of several components of the experimental apparatus.

	Resonator	Stack	Heat exchangers
Length	38 cm	18 cm	2 cm
Diameter	4 cm	4 cm	4 cm
Gap width	-	1.1 mm	0.4 mm
Plate thickness	-	0.3 mm	0.3 mm
Material	stainless steel	stainless steel	copper

2 mm thick stainless steel sheet. They were stacked inside the resonator tube and were separated from each other by 0.05 mm thick paper rings.

In the low-temperature-(ambient-) side heat exchanger, heat was supplied by electrical resistance heaters. The heat at the high-temperature-end heat exchanger was removed by synthetic oil flowing in six tubes through the heat exchanger matrix. By measuring the oil's mass flow rate and inlet and outlet temperatures this amount of heat could be calculated.

Since the low-temperature-end heat exchanger was thermally anchored to ambience, the heat flow into the resonator could not be accurately determined. It was therefore necessary to measure the acoustic power delivered by the piston. With the acoustic power being calculated from the equation $I=\overline{pu}$ $(=\dot{W}/A$, where $\dot{W}$ is the work done and A the cross-sectional area), the pressure p and gas velocity u directly above the piston had to be measured. Since the velocities of the gas and the piston are the same, it was sufficient to determine the piston position and its phase relation to the pressure signal by an optical method. Hot-side and ambient-side temperatures, as well as several other temperatures, were measured using thermocouples. For maximum thermal insulation, the whole apparatus was placed into a vacuum vessel and wrapped with several radiation shields.

C. Experiments

In the experiments, the mean He-gas pressure p_m was varied between 10 and 19 bar and the frequency of oscillation f was varied between 35 and 50 Hz. Also, the gas temperature in the hot-side heat exchanger T_H was varied by changing the secondary fluid inlet temperatures. The cold-side gas temperature T_C was kept constant at ambient temperature (20 °C). The temperature difference between the hot side and the cold side, $\Delta T=T_H-T_C$, varied between approximately 60 and 120 K. Due to geometric constraints the drive ratio (P_A/p_m) was constant at 0.07 in all the experiments.

Experiments were carried out with both stacks at exactly the same operating conditions. Only a comparison between the performance of the two stack types was of interest, therefore, the overall performance of the complete engine was not considered.

III. RESULTS

A. Numerical calculations

Numerical calculations were carried out for the same geometry and operating conditions (p_m, P_A, f) used in the experimental setup.

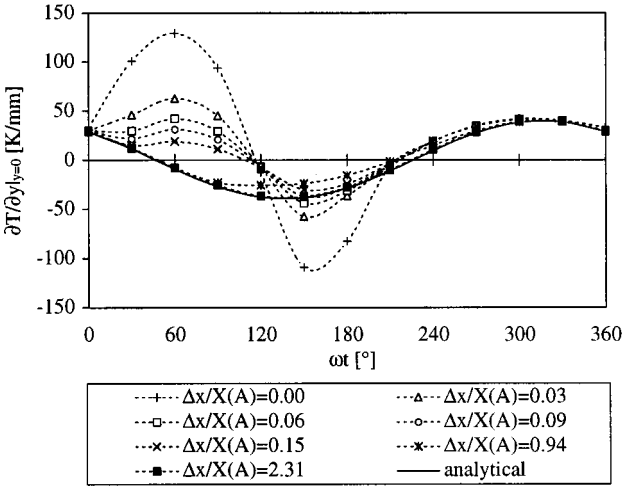

FIG. 6. Temperature gradients $\partial T/\partial y$ at the plate surface of a ''long'' plate with the distance from the plate edge Δx [normalized with the displacement amplitude $X(\mathrm{A})=5.2$ mm] as parameter ($p_m=14.5$ bar; $P_A/p_m=0.07$, $f=42.5$ Hz, $\nabla T_m=0$ K/m, $y_0=0.55$ mm).

1. Continuous stack

A numerical investigation of the behavior of a stack consisting of long plates allowed first for the numerical scheme to be evaluated against an analytical solution, second for a minimum plate length to be identified (such that plate edge thermal effects do not influence the thermal behavior in the middle of the plate), and third for the magnitude and direction of temperature gradients normal to the plate surface, experienced during an acoustic cycle, to be determined at the plate's edge and other positions.

The 24 mm long plates ($\approx 4.6X_A$) were positioned in the middle of the (otherwise empty) resonator, similar to the ''thermoacoustic couple'' described by Wheatley.[2] The mean pressure p_m was 14.5 bar and the frequency f was 42.5 Hz. The plate temperature was assumed to be constant at 20 °C ($\nabla T_m=0$). For a regular grid the spacing between grid points in the x-direction was 3% of the gas displacement amplitude X_A. In the y-direction this spacing was 6% of the thermal penetration depth δ_κ, with reference to a mean temperature T_m of 20 °C.

Figure 6 shows the temperature gradient normal to the plate surface $(\partial T/\partial y)$ as a function of time with the relative distance from the right plate edge $(\Delta x/X_A)$ (cp. Fig. 5) as a parameter. The flow is negative during the first half-cycle and positive during the last half-cycle [cp. Eq. (2)].

The following conclusions were drawn: (1) In the middle of the plate $(\Delta x/X_A=2.31)$ the numerically computed temperature gradient normal to the plate surface agrees to within 5% with the analytical solution for a stack consisting of infinitely long plates. The plates are therefore assumed long enough for thermal boundary layers to develop completely. (2) The temperature gradient at the leading plate edge is larger than on the rest of the plate. It approaches that of an infinitely long plate within $x=1.5X_A$ (not shown in Fig. 6). A segment in the intermittent stack should therefore not be longer than $1.5X_A$. (3) There is a phase shift in time of the temperature gradient normal to the plate surface $(\partial T/\partial y)$ between the edge and the middle of the plate. Since

TABLE II. Heat flux at the middle position of the thermoacoustic couple, calculated numerically and analytically.

∇T_m [K/m]	0	411	633
$\dot{Q}/\Pi$ numerical [W/m]	13.7	10.6	8.9
$\dot{Q}/\Pi$ analytical [W/m]	14.1	11.0	9.3
Ratio	0.97	0.96	0.95

the direction of heat flow between the gas and the plate is proportional to $-\partial T/\partial y$, there are times when the direction of heat flow at the edge of the plate is different from that in the middle of the plate. (4) Since the absolute value of the temperature gradient $\partial T/\partial y$ is larger near the leading edges, more heat is transferred between the plate and the gas in these regions.

In the middle of the plate the net heat flux into and out of the plate is zero over the period of an acoustic cycle. Over the same period, there is a net heat flux into the plate at the right hand edge and a net heat flux out of the plate at the left hand edge. The right hand edge therefore serves as a heat sink while the left hand edge becomes a heat source. Heat is hydrodynamically transported from left to right, i.e., from the open to the closed end of the resonator, while it is conducted in the opposite direction in the plate. Cao *et al.*[14] also observed the existence of large temperature gradients normal to the plate surface at the plate edges in a detailed numerical study of a thermoacoustic couple.

Finally, the heat flux at the center position of the stack was calculated numerically according to Eq. (11), and compared to the analytical solution given by Eq. (15). The results are summarized for different temperature gradients ∇T_m in Table II and the agreement is good.

The numerical method was sufficiently accurate to describe the behavior of a stack consisting of long plates.

2. Intermittent stack

The behavior of 11 2-mm-, 7 3-mm-, and 5 4-mm-long segments was investigated. The segments were positioned in the center of the resonator. Calculations were carried out at four different operating conditions: at mean pressures p_m of 10 and 19 bar, with frequencies f of 35 and 50 Hz at each of the pressures. The displacement amplitude was kept constant at 6.7 mm (due to the fixed stroke of the piston used in the experiments). Figures 7–10 show the ratio of the heat fluxes of the intermittent stack ($\dot{Q}_{\mathrm{IS}}$) to that of the continuous stack ($\dot{Q}_{\mathrm{CS}}$), as a function of segment length and with the temperature gradient as parameter. The heat fluxes are taken at the center position of the segment in the middle of the stack. The empty symbols represent the hydrodynamic heat flux only, given by Eq. (11). The filled symbols represent the overall heat flux, which includes heat conduction losses in the gas and the plate, and which is given by Eq. (12). The lines act as visual guides only.

Several conclusions were drawn: (1) For the given geometry and operating conditions, a maximum power density increase of approximately 50% was observed. (2) The increase in power density is larger for shorter segments, for which temperature gradients are larger and boundary layers smaller. The more often boundary layers must develop anew

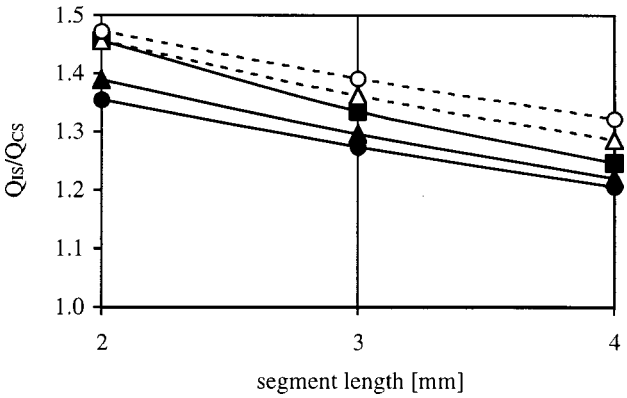

FIG. 7. Ratio of heat fluxes parallel to the plates for the intermittent (IS) and continuous (CS) arrangement as a function of segment length with the temperature gradient in the plates as parameter: overall heat flux [Eq. (12)] at $\nabla T_m = 0$ K/m (■), 411 K/m (▲), 633 K/m (●) and hydrodynamic heat flux [Eq. (11)] at $\nabla T_m = 411$ K/m (△), 633 K/m (○) ($p_m = 19.0$ bar; $P_A/p_m = 0.07$, $f = 50.0$ Hz, $y_0 = 0.55$ mm).

(i.e., the more often the flow is ''interrupted''), the higher the power density will be. Since in these calculations the shortest segments were 2 mm long (≈30% of the displacement amplitude), it is not clear whether there is a minimum or optimum length for the given geometry and operating conditions. However, from the calculations it can be concluded that the segment length should be at least shorter than one-third of the displacement amplitude. (3) When the intermittent stack is assumed to have the same heat conduction losses as the continuous arrangement, the relative increase of the overall heat flux is larger at smaller temperature gradients. The intermittent stack performs even better (with one exception, see Fig. 10) if it had the same conduction losses because of the improved heat transfer. (4) Not accounting for heat conduction (i.e., assuming that the stack has an anisotropic conductivity), the relative increase of the (hydrodynamic) heat flow is even larger and the stack performs better at higher temperature gradients ∇T_m. The anisotropic thermal conductivity of the intermittent stack is therefore desirable. (5) At $p_m = 19$ bar and $f = 50$ Hz the plate gap is about four times the penetration depth ($4\delta_\kappa$), and at $p_m = 10$ bar

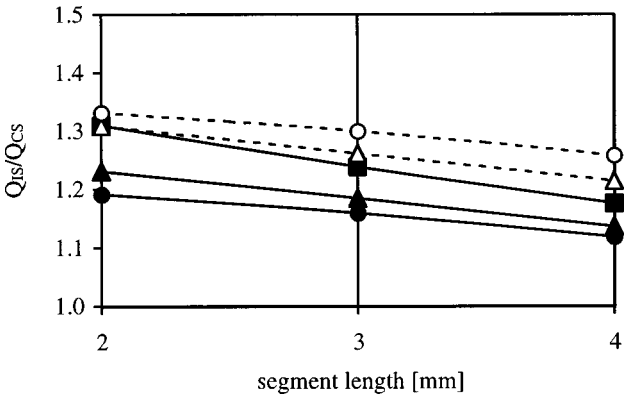

FIG. 8. Ratio of heat fluxes parallel to the plates for the intermittent (IS) and continuous (CS) arrangement as a function of segment length with the temperature gradient in the plates as parameter: overall heat flux [Eq. (12)] at $\nabla T_m = 0$ K/m (■), 411 K/m (▲), 633 K/m (●) and hydrodynamic heat flux [Eq. (11)] at $\nabla T_m = 411$ K/m (△), 633 K/m (○) ($p_m = 19.0$ bar; $P_A/p_m = 0.07$, $f = 35.0$ Hz, $y_0 = 0.55$ mm).

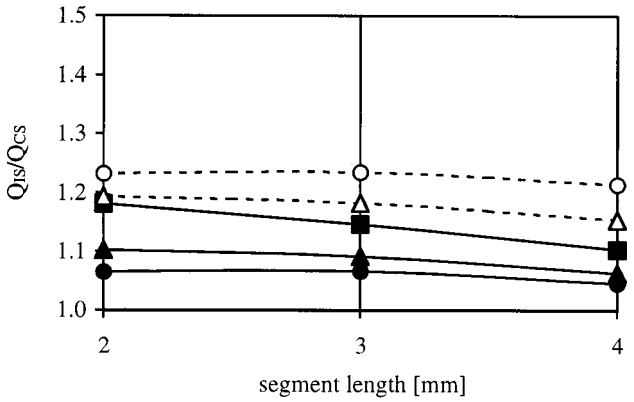

FIG. 9. Ratio of heat fluxes parallel to the plates for the intermittent (IS) and continuous (CS) arrangement as a function of segment length with the temperature gradient in the plates as parameter: overall heat flux [Eq. (12)] at $\nabla T_m = 0$ K/m (■), 411 K/m (▲), 633 K/m (●) and hydrodynamic heat flux [Eq. (11)] at $\nabla T_m = 411$ K/m (△), 633 K/m (○) ($p_m = 10.0$ bar; $P_A/p_m = 0.07$, $f = 50.0$ Hz, $y_0 = 0.55$ mm).

and $f = 35$ Hz it is only $2.5\delta_\kappa$. Since the optimum plate gap for the continuous stack is approximately $3-4\,\delta_\kappa$, the plates are spaced either too far apart or too close together for these two operating conditions. Surprisingly, higher increases in power density were observed for plates stacked further than $3\,\delta_\kappa$ apart. Like in the experiments, the gap between the plates was kept constant while the penetration depth δ_κ was varied by changing the operating conditions (p_m and f). This way, other factors with favorable and adverse effects on the heat flux were introduced. The results from these calculations therefore did not yield an optimum plate gap width for the intermittent stack.

B. Experiments

Figures 11–14 compare the power densities of the continuous stack (CS) and the intermittent stack (IS) at four different operating conditions. In each figure, the heat removed at the hot-side heat exchanger $\dot{Q}_H$, which is a measure of power density, is plotted against the gas-temperature

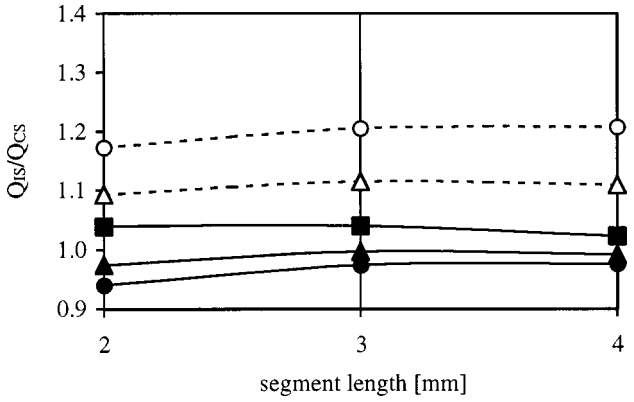

FIG. 10. Ratio of heat fluxes parallel to the plates for the intermittent (IS) and continuous (CS) arrangement as a function of segment length with the temperature gradient in the plates as parameter: overall heat flux [Eq. (12)] at $\nabla T_m = 0$ K/m (■), 411 K/m (▲), 633 K/m (●) and hydrodynamic heat flux [Eq. (11)] at $\nabla T_m = 411$ K/m (△), 633 K/m (○) ($p_m = 10.0$ bar; $P_A/p_m = 0.07$, $f = 35.0$ Hz, $y_0 = 0.55$ mm).

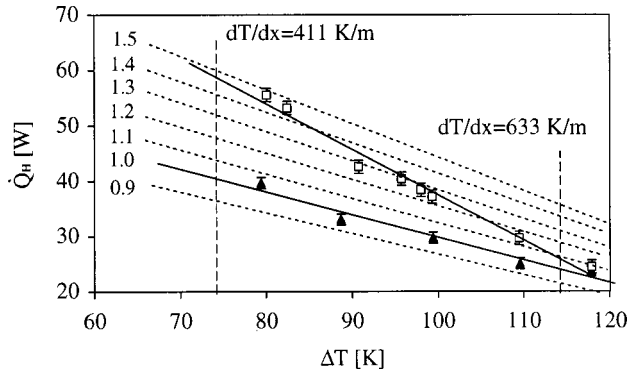

FIG. 11. Heat flow at the hot-side heat exchanger versus temperature difference between hot- and cold-side exchangers for the continuous (▲) and the intermittent stack (□) arrangement ($p_m = 19.2$ bar; $P_A/p_m = 0.07$, $f = 50.0$ Hz).

difference between the hot- and cold-side heat exchanger. For comparison between results from the numerical solution (Sec. III A) and the experimental results, it is helpful to note that a temperature difference ΔT of 74 K yields a mean temperature gradient ∇T_m of 411 K/m and a ΔT of 114 K yields a ∇T_m of 633 K/m. The triangles represent data points of the continuous stack, while the squares represent those of the intermittent stack. Figures 11 and 12 show continuous, straight lines, fitted through the data points of both stack types. Broken lines represent the straight-line fit through the continuous stack data, multiplied by a factor indicated next to each broken line. So the improvement (or deterioration) obtained with the intermittent stack relative to the continuous stack can be directly read from the diagrams. The straight-line fit through the continuous stack data approximates the theory of Rott.[1,3]

The experiments confirmed that power density increases when using an intermittent stack in place of a continuous stack. This increase depended on operating conditions ($p_m, f, \nabla T_m$). No increase was observed at low pressures and frequencies. This observation was consistent with the predictions of the numerical model (see Sec. III A), but a convincing explanation could not be found. Again, it can be speculated that varying the operating conditions has other,

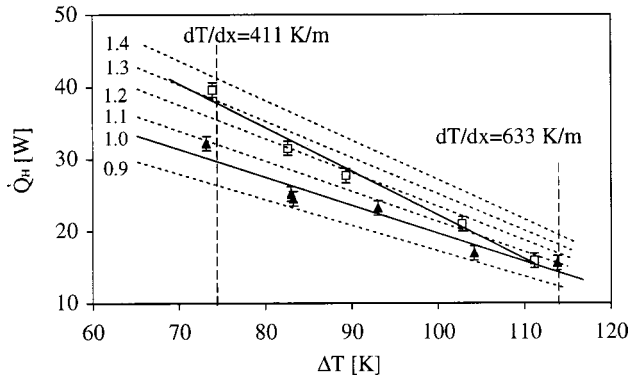

FIG. 12. Heat flow at the hot-side heat exchanger versus temperature difference between hot- and cold-side exchangers for the continuous (▲) and the intermittent stack (□) arrangement ($p_m = 19.2$ bar; $P_A/p_m = 0.07$, $f = 35.0$ Hz).

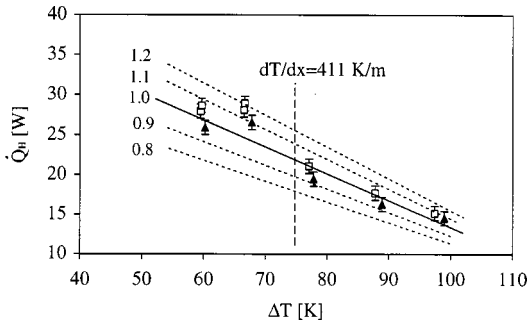

FIG. 13. Heat flow at the hot-side heat exchanger versus temperature difference between hot- and cold-side exchangers for the continuous (▲) and the intermittent stack (□) arrangement ($p_m = 10.0$ bar; $P_A/p_m = 0.07$, $f = 50.0$ Hz).

unfavorable effects than varying the plate gap. At high pressures and frequencies, $\dot{Q}_H$ was, approximately 1.4 to 1.5 times higher. The highest improvements occurred at small temperature differences and temperature gradients.

The improvements in power density obtained in these experiments qualitatively agree with results from the numerical solution. The quantitative agreement is good for small temperature gradients, but poor at larger temperature gradients. However, it could not be expected that the experiments and the numerical results would quantitatively agree, because the numerical approach had some restricting limitations—as stated above.

Quite surprisingly, the intermittent stack also yielded a higher coefficient of performance, defined as COP $= \dot{Q}_H / \dot{W}$. Only 6% more work was required by the resonator when the continuous stack was substituted by the intermittent stack. The additional work may be a consequence of higher viscous shear and hydrodynamic form drag across each plate section—among other reasons like additional acoustic attenuation due to added heat transfer. At the operating conditions for which the best results were obtained, i.e., $p_m = 19.2$ bar and $f = 50$ Hz, Fig. 15 shows that at $\Delta T = 80$ K the COP was approximately 30% higher. At $\Delta T = 100$ K there was still an improvement of approximately 20%. This tendency could be attributed to the fact that at modest frequencies, for which the flow was mostly laminar, viscous dissipation did not increase significantly. However, it must be stated again that this conclusion could not be proved by the theoretical model.

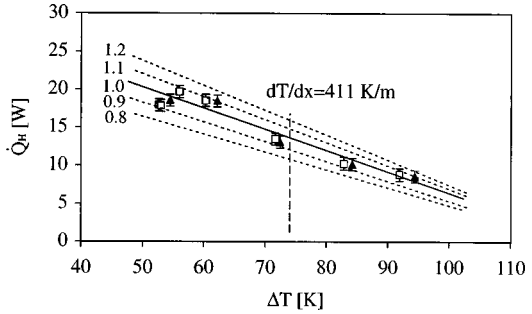

FIG. 14. Heat flow at the hot-side heat exchanger versus temperature difference between hot- and cold-side exchangers for the continuous (▲) and the intermittent stack (□) arrangement ($p_m = 10.0$ bar; $P_A/p_m = 0.07$, $f = 35.0$ Hz).

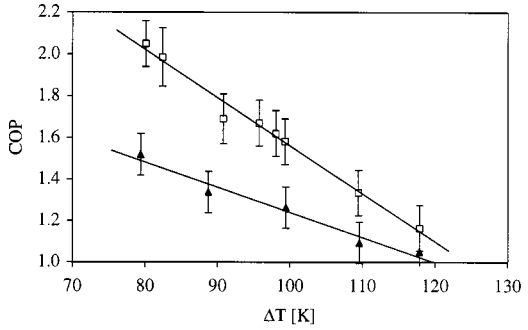

FIG. 15. Coefficient of performance (COP) versus temperature difference between hot- and cold-side exchangers for the continuous (▲) and the intermittent stack (□) arrangement ($p_m = 19.2$ bar, $P_A/p_m = 0.07$, $f = 50.0$ Hz).

IV. CONCLUSIONS

It was theoretically and experimentally shown that using an intermittent stack in place of a continuous stack in a thermoacoustic engine leads to higher power densities and an improved coefficient of performance. In experiments conducted, the power density of a thermoacoustic heat pump was raised by a factor of 1.4 to 1.5 and the COP improved by approximately one-third.

It is important to carefully design the segments of the intermittent stack. The following can be used as guidelines. First, even though an optimum segment length was not identified for the operating conditions at which the stacks were compared, a segment length not longer than one-third of the acoustic displacement amplitude is suggested (e.g., $1/10 X_A$). It is possible to use different segment lengths in the same stack, with their lengths depending on their position in the resonator. Second, it is not clear whether a regular pattern of orientation of the segments will lead to higher improvements. A random orientation is probably sufficient. Third, in order to reduce the overall thermal conductivity of the stack in the streamwise direction, neighboring segments should have a minimum of contact points. The use of thin spacers of low thermal conductivity between the segments is recommended.

Using the thermoacoustic engine as a prime mover, where high temperatures eliminate the use of plastics as a low thermal conductivity stack material, the anisotropic thermal conductivity of the intermittent stack allows the use of higher thermal conductivity stack materials without adversely effecting its overall performance.

The segments used were quite expensive to fabricate. Other similar (and cheaper) structures like wire mesh screens might be as successful (cp. Hofler[9]). However, even though similar physical effects are present (smaller boundary layers, largely reduced conductivity in streamwise direction), the results of this study cannot be directly used in describing the behavior of screens, because they are geometrically quite different from segments of parallel plates.

ACKNOWLEDGMENT

This work was supported by the Swiss Federal Institute of Technology (ETH), Zürich, Switzerland.

[1] N. Rott, ''Damped and thermally driven acoustic oscillations in wide and narrow tubes,'' J. Appl. Math. Physics **20**, 230 (1969).
[2] J. C. Wheatley, T. Hofler, G. W. Swift, and A. Migliori, ''An intrinsically irreversible heat engine,'' J. Acoust. Soc. Am. **74**, 153 (1983).
[3] G. W. Swift, ''Thermoacoustic engines,'' J. Acoust. Soc. Am. **84**, 1145 (1988).
[4] W. P. Arnott, H. E. Bass, and R. Raspet, ''General formulation of thermoacoustics for stacks having arbitrarily shaped pore cross sections,'' J. Acoust. Soc. Am. **90**, 3228 (1991).
[5] R. Raspet, H. E. Bass, and J. Kordomenos, ''Thermoacoustics of traveling waves: Theoretical analysis for an inviscid ideal gas,'' J. Acoust. Soc. Am. **94**, 2232 (1993).
[6] H. Luck and Ch. Trepp, ''Thermoacoustic oscillations in cryogenics,'' Cryogenics **32**, 690 (1992).
[7] G. W. Swift and D. L. Gardner, ''Thermoacoustics at high power density,'' J. Acoust. Soc. Am. **100**, 2814 (1996).
[8] G. W. Swift and R. M. Keolian, ''Thermoacoustics in pin-array stacks,'' J. Acoust. Soc. Am. **94**, 941 (1993).
[9] T. J. Hofler and M. S. Reed, ''Measurements with wire mesh stacks in thermoacoustic prime movers,'' J. Acoust. Soc. Am. **99**, 2559 (1996).
[10] J. G. Fourie and J. P. du Plessis, ''Analysis of an intermittent stack arrangement,'' Technical Report, TW9501, University of Stellenbosch, South Africa (1995).
[11] J. Bösel, ''Untersuchungen zur Erhöhung der Leistungsdichte thermoakustischer Maschinen,'' Ph. D. dissertation, Swiss Federal Institute of Technology, Diss. ETH Nr. 12530 (1998).
[12] S. V. Patankar, *Numerical Heat Transfer and Fluid Flow* (Hemisphere, New York, 1980).
[13] S. V. Patankar, ''A calculation procedure for two-dimensional elliptic situation,'' Num. Heat Transfer **4**, 409 (1981).
[14] N. Cao, J. R. Olson, G. W. Swift, and S. Chen, ''Energy flux density in a thermoacoustic couple,'' J. Acoust. Soc. Am. **99**, 3456 (1996).

Time-reversal mirrors and rough surfaces: Theory

James H. Rose[a)]
Department of Physics and Astronomy and Ames Laboratory, Iowa State University, Ames, Iowa 50011

Mehmet Bilgen
Department of Radiology, University of Kansas Medical Center, Kansas City, Kansas 66160

Philippe Roux[b)] and Mathias Fink
Laboratoire Ondes et Acoustique, ESPCI, Université Paris VII, 10 Rue Vauquelin, 75005, Paris, France

(Received 11 May 1998; revised 2 November 1998; accepted 25 March 1999)

A systematic study is presented of the sensitivity of acoustic time-reversal mirrors (TRMs) to errors. One result is a novel acoustic method for determining the root-mean-square, rms, height and the surface-height autocorrelation function of rough surfaces. In particular, the effects of misregistering a TRM are studied with respect to a rough surface—the reflected wavefield is recorded in one place, time reversed, and then rebroadcast in a second place. This displacement causes the signal to depend importantly on the surface's rms height and autocorrelation function. Simple closed-form formulas are presented for determining the rms height and the normalized surface-height autocorrelation function for both deterministic and randomly rough surfaces. Also presented is a numerical study that illustrates the statistical uncertainty in and the spatial resolution of the proposed method. An accompanying experimental article tests the proposed method with measurements made on a number of different rough surfaces.
[S0001-4966(99)02107-4]

PACS numbers: 43.35.Yb [HEB]

INTRODUCTION

Consider a simple localized pulse of sound incident on a strongly heterogeneous, nondissipative, linear acoustic medium that consequently scatters the sound widely over space and time. A simple question, ''Given the medium and the wave field measured over some bounding surface, what is the initial impulse?'' At first blush, this question seems very difficult, perhaps impossible. However, there is a simple and apparently robust method for finding the answer. Namely, time reverse the sound field at each point on a bounding surface (last-in, first-out) and retransmit the result into the medium. The time-reversed wave field, initially widely dispersed in space and time, is matched to the medium and evolves into the time-reversed initial impulse. Thus, the time-reversal process can be said to be a correlator—it takes complicated fields and makes them simple.

The correlating properties of time reversal for acoustic waves are seemingly robust. Fink and collaborators pioneered time-reversal methods for ultrasonic waves in the context of propagation in linear and nondissipative materials.[1–6] Surprisingly, they found that the recovery of the initial impulse was not very sensitive to the experimental setup. For example, they found that it was not necessary to retransmit the time-reversed wave over the entire bounding surface.[5] In fact, for most of the systems studied experimentally, useful results were obtain using a *linear array* of piezoelectric transducers combined with the appropriate technology for recording, time reversing, and then reemitting the signals. These systems, which have angular apertures that are much less than 4π, are called time-reversal mirrors (TRMs).[1,3–5]

Since the time-reversal process appears to act as a relatively robust correlator, a number of questions naturally arise having to do with the breakdown of the correlation as the conditions for the validity of the time-reversal experiment are violated. First question: ''How does the estimate for the recovered initial pulse change—if either the measurement system or the sample is deformed before the time-reversed field is retransmitted?'' That is, ''Just how robust is the time-reversal process and how does it break down?'' Second question, ''Can one use time reversal to simplify the measurement of the autocorrelation functions that are often used to describe the statistics of complicated heterogeneous media?'' These are deep questions and we will begin an initial exploration of these ideas and show, as an example, that they lead to a new technique for characterizing rough surfaces. A simple theory for characterizing rough surfaces with a TRM will be developed in this article, while experimental measurements will be reported in the companion paper.[7] There are many applications where ultrasound is the most natural and sometimes the only way of determining the rms height and the surface-height autocorrelation function of rough surfaces. Examples are the measurement of atherosclerosis *in vivo*, exploration of the sea floor, and the determination of interfacial roughness between two solids.

We propose a new method that uses the TRM to measure the surface-height autocorrelation function and the rms height for a certain class of rough surfaces. This new method is based on the general idea of introducing a perturbation into the time-reversal process. The reflected wavefield is recorded in one place, time reversed, and then rebroadcast after displacing the TRM a certain distance **d** parallel to the rough

[a)]Electronic mail: jhrose@iastate.edu
[b)]Electronic mail: philippe.roux@espci.fr

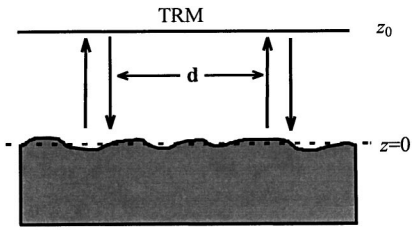

FIG. 1. Shows the hypothetical experiment. The TRM is indicated by the line marked z_0, while the dark curvy line indicates the rough surface. The mean plane of the surface is indicated by the dashed line. The initial transmission and reflection as well as the transmission and reflection after time reversal are indicated by the arrows, while the translation of the surface is indicated by **d**.

surface—see Fig. 1. The surface-height autocorrelation function and the rms height are determined from the decorrelation of the TRM's signal with this displacement.

The structure of this paper is as follows. In Sec. I, we derive simple closed form analytic formulas for the normalized surface autocorrelation function and the rms height of two-dimensional rough surfaces. The cost is a number of idealizations: restricting the roughness to very low aspect ratios, assuming a spatially infinite TRM, and using elementary ray theory. These formulas are tested in the companion experimental paper. In Sec. II, we find a series solution for the restricted case of a one-dimensional rippled surface. This calculation includes both the finite size of the TRM as well as the wave nature of sound. The resulting series solution, although notably more complicated, remains computable and illustrates the utility and limitation of the simple analytic formulas of Sec. I. Finally, the paper is concluded with a summary and discussion in Sec. III.

I. TRM MEASUREMENT OF ROUGH-SURFACE PARAMETERS

We derive the formulas needed to characterize rough surfaces using a TRM. In Sec. I A we present a time-domain approach that solves the forward problem—that is, given the rough surface, determine the TRM's signal. In Sec. I B we discuss the sensitivity of the TRM to the rms height and surface autocorrelation function, while in Sec. I C we solve the inverse problem—that is, given the TRM's signal, characterize the surface.

A. Simple model for TRM surface characterization

A technique is proposed for measuring the rms height and reconstructing the surface-height autocorrelation function of a rough plate immersed in water. The technique is motivated by a very simple model, which, however, retains the essence of the problem. A number of nonessential approximations have been made for simplicity and the removal of these approximations is discussed at the end of the subsection.

The roughness may be either random or deterministic. For the random case, we assume that the surface consists of very low rolling hills and valleys on an otherwise flat surface. The sample's mean surface is defined to the plane $z=0$, while the surface height at each point $\mathbf{r}$ of this plane is denoted by an isotropic, zero-mean, spatially stationary, random variable $z=h(\mathbf{r})$. The behavior of the roughness parallel to the surface will be characterized by the normalized surface-height autocorrelation function

$$C(\mathbf{r}-\mathbf{r}')\equiv\langle h(\mathbf{r})h(\mathbf{r}')\rangle/h^2. \tag{1}$$

Here, in an abuse of notation, h denotes the rms height. In many cases, an autocorrelation length, L, may be extracted from $C(\mathbf{r})$, and the random surfaces considered are assumed to have a very small aspect ratio, i.e., $h\ll L$.

The TRM is assumed to be infinite and thus to cover the entire plane $z=z_0$ as shown in Fig. 1. It is further assumed that one may transmit, measure, record, and time reverse arbitrary pressure pulses on this plane. We use ray acoustics and further assume that all rays propagate normal to the mean surface; straight up or down.

The basic experiment is idealized as follows. At time $t=0$, a delta-function pressure pulse, $\delta(t+(z-z_0)/c_w)$, is launched downwards from the TRM toward the surface, where c_w is the velocity of sound in water. This pulse is idealized as a set of parallel rays. Each ray reflects from the surface and returns to its point of origin. The resulting pressure, p, is measured and recorded at the TRM:

$$p(t,\mathbf{r},z_0)=R\,\delta(t+2h(\mathbf{r})/c_w-2z_0/c_w). \tag{2}$$

Here, R denotes the normal-incidence reflection coefficient. Next the received signal is ''time reversed,''

$$p(t,\mathbf{r},z_0)=R\,\delta(t-2h(\mathbf{r})/c_w+2z_0/c_w). \tag{3}$$

That is, for each point $\mathbf{r}$ on the plane $z=z_0$, one reverses the time order of the pressure recorded there. Next, the idealized TRM is translated parallel to the plane by **d**, which changes the time-reversed pressure on the plane $z=z_0$ to

$$p(t,\mathbf{r},z_0)=R\,\delta(t-2h(\mathbf{r}-\mathbf{d})/c_w+2z_0/c_w). \tag{4}$$

This shifted pressure field is then retransmitted, propagates to the surface, is reflected, and propagates back to the TRM at $z=z_0$. (In the actual experiment there is an arbitrary time delay between recording the signal and retransmitting the pressure pulse. We ignore this unimportant delay in order to keep the formulas as simple as possible.) The final pressure measured at the TRM after this second reflection is

$$p(t,\mathbf{r},z_0)=R^2\,\delta(t-2h(\mathbf{r}-\mathbf{d})/c_w+2h(\mathbf{r})/c_w). \tag{5}$$

One may interpret Eq. (5) as follows. The roughness modifies the reflected pulse by an overall reflection coefficient and a time delay. The reflection coefficient appears squared because the measurement involves two reflections from the surface. The time delay arises because of surface roughness; a ray returns at a later time if it strikes a valley (a time delay) or at an earlier time if it strikes a peak (a time advance). Suppose some particular ray is time delayed. Time reversal (i.e., reversing the time order of the recorded pressure pulse) *changes this time delay into a time advance*. Suppose that this time-reversed pressure pulse is rebroadcast with no change in position. The ray propagated from this point is again subject to the same time delay that was experienced initially. This second delay exactly *cancels the time advance created by time reversal* and the original incident pulse is recovered—the normal course of events for TRM

operation. However, suppose that the TRM is displaced by $\mathbf{d}$ prior to retransmission. Now the time advance, $2h(\mathbf{r}-\mathbf{d})/c_w$, and the time delay, $2h(\mathbf{r})/c_w$, do not necessarily cancel unless $\mathbf{d}=0$. Clearly, the final measured pressure field, Eq. (5), depends on both the rms height and the surface-height autocorrelation function.

The signal is defined to be the average of the final received pressure over the surface of the TRM:

$$\mathrm{Sig}(t,\mathbf{d}) \equiv \frac{R^2}{\mathrm{Area}} \int d^2\mathbf{r}\, \delta(t-2h(\mathbf{r}-\mathbf{d})/c_w + 2h(\mathbf{r})/c_w). \tag{6}$$

Here, Area denotes the area of the TRM taken in the limit that it covers the entire xy plane at $z=z_0$. Because it is defined to be the final received pressure pulse averaged over the plane of the TRM (at time t and for displacement $\mathbf{d}$), the signal has a definite fixed value. Consequently, the signal and its mean value are the same thing, $\mathrm{Sig}=\langle \mathrm{Sig} \rangle$ and the terms ''signal'' and ''average signal'' are used indistinguishably in this section. However, in Sec. II, a finite transducer is considered. There, the signal depends on the particular part of the rough surface investigated and the signal will differ from its average.

The signal can be evaluated in more explicit form using the assumption that $h(\mathbf{r})$ is a zero-mean, spatially isotropic and stationary, random variable (not necessarily Gaussian). With this assumption one may replace the area average by the ensemble average, denoted by $\langle ... \rangle$,

$$\mathrm{Sig}(t,\mathbf{d}) \equiv R^2 \langle \delta(t-2h(\mathbf{r}-\mathbf{d})/c_w + 2h(\mathbf{r})/c_w) \rangle. \tag{7}$$

The signal can be further evaluated if we assume that $h(\mathbf{r})$ is not only a random variable as described above, but also Gaussianly distributed [see Eq. (A2) of the Appendix). In this case

$$\mathrm{Sig}(t,\mathbf{d}) = \frac{R^2}{4\sqrt{\pi}} \frac{c_w}{h\sqrt{1-C(\mathbf{d})}} \times \exp(-c_w^2 t^2/(16h^2(1-C(\mathbf{d})))), \tag{8}$$

our basic result for the forward problem. Note that the transient signal has the same functional form as the Gaussian surface-height distribution function. The signal, within our simplified model, depends solely on the rms height h and the normalized autocorrelation function, $C(\mathbf{d})$.

Experimental tests of the proposed method were carried out using broadband time-domain pulses, but then interpreted in the frequency domain.[7] The frequency-domain signal is obtained for the general case by Fourier transforming Eq. (6),

$$\mathrm{Sig}(\omega,\mathbf{d}) = \frac{R^2}{\mathrm{Area}} \int d^2\mathbf{r} e^{2ik_w(h(\mathbf{r}-\mathbf{d})-h(\mathbf{r}))}. \tag{9}$$

Here, k_w denotes the wave number in water. Both time-domain and frequency-domain signals will be denoted by Sig; they are to be distinguished by the argument. For $k_w h$ sufficiently small, Eq. (9) can be expanded to second order in the surface height and evaluated:

$$\mathrm{Sig}(\omega,\mathbf{d}) \approx R^2(1-4k_w^2h^2(1-C(\mathbf{d}))). \tag{10}$$

The frequency-domain signal for the Gaussian random surface defined above is obtained by taking the Fourier transform of Eq. (8). One finds

$$\mathrm{Sig}(\omega,\mathbf{d}) = R^2 e^{-4k_w^2h^2(1-C(\mathbf{d}))}. \tag{11}$$

This formula is particularly simply for very large displacements $\mathbf{d}$, since $C(\infty)=0$ for a Gaussian autocorrelation function. The asymptotic limit $R^2\exp(-4k_w^2h^2)$ is just the result of combining two *incoherent* reflections from the surface.

The assumption of ray propagation simplifies the problem more than necessary but yields what is probably the simplest derivation possible. In fact, one may derive the equations given in this section while accounting for the wave nature of sound propagation. That derivation proceeds as follows. The reflection from the surface is treated in the phase-screen approximation.[8–10]—the frequency-domain analog of the time delays introduced above, see Eq. (20) below. The propagation of the incident and reflected pressure fields in the water bath can be accurately treated by expanding these pressure fields in plane waves and propagating them according to the Fresnel (paraxial) approximation, see Eq. (19) below.

B. Sensitivity of the TRM to roughness

The signal, calculated for a variety of rough surfaces, illustrates the sensitivity of the proposed method to surface roughness. Consider a surface whose rms height is much less than the wavelength, $k_w h \ll 1$. In this case, the difference $\mathrm{Sig}(\omega,\mathbf{d}) - \mathrm{Sig}(\omega,\infty)$ is linearly proportional to the normalized autocorrelation function. The change in signal strength with displacement is relatively weak, being proportional to $(k_w h)^2$.

The variation of the signal with displacement is more complicated for rougher surfaces, where $k_w h$ can be greater than one. Figure 2(a) shows the predicted signal for Gaussian random rough surfaces, calculated using Eq. (11) for $k_w h = 0.5$, 1.0, 2.0, and 3.0 for a Gaussian autocorrelation function. Figure 2(b) shows the predicted signal for an exponential autocorrelation function. Note that the shape of the curves are rather different for the two cases. Hence, the TRM is not only sensitive to the autocorrelation length, but also to the shape of the autocorrelation functions.

The signal changes rapidly on the scale of L if the surface is very rough, i.e., $k_w h$ is large. First, consider an exponential autocorrelation function, $\exp(-x/L)$. Upon expanding the exponential, substituting in Eq. (11), and keeping the leading term one obtains

$$\mathrm{Sig}(\omega,\mathbf{d}) \approx R^2 e^{-4k_w^2h^2d/L}. \tag{12}$$

That is, the signal decorrelates with a smaller and smaller characteristic distance $L/(4k_w^2h^2)$ as $k_w h$ increases. The same analysis can be made for a Gaussian autocorrelation function, $\exp(-x^2/L^2)$ and one finds that the signal decorrelates over a characteristic distance $L/(2k_w h)$. For very rough surfaces, the signal decorrelates more rapidly for exponential autocorrelation functions.

The signal for deterministic rough surfaces can also be calculated using simple ray analysis—Eq. (6). Consider a

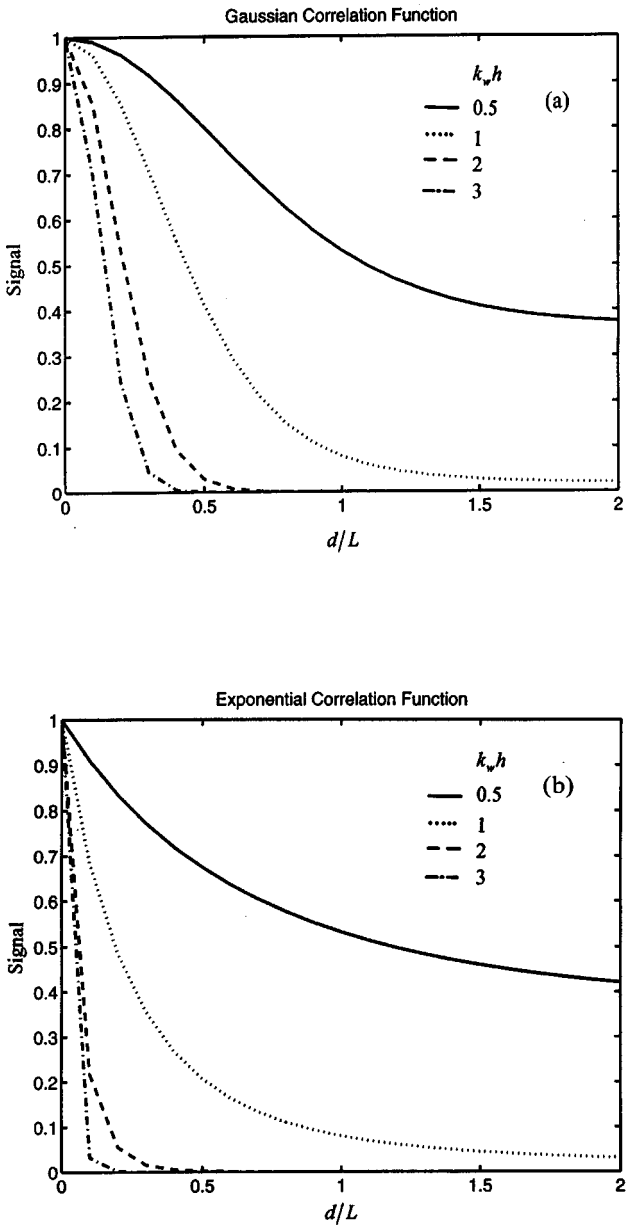

FIG. 2. Shows the different TRM signals predicted for a Gaussian (a) and an exponential (b) autocorrelation function for $k_w h = 0.5$, 1, 2, and 3. The signal is normalized by setting $R = 1.0$.

one-dimensional periodic surface with steps of height $2h$ and repeat distance $2L$. The signal after Fourier transform is given by the sawtooth pattern

$$\mathrm{Sig} = R^2[1 - \sin^2(2k_w h)(1 - C(d))] \tag{13}$$

for all values of $k_w h$. Here, $C(x)$ is the normalized autocorrelation function for the surface and is given by $1 - 2x/L$ for $0 < x < L$ and $-3 + 2x/L$ for $L < x < 2L$ and then repeated periodically over the whole line. The signal is linearly related to the autocorrelation function at each frequency. Finally, the fact that the signal repeats periodically for $k_w h = n\pi$, where n is an integer, introduces an ambiguity in finding the rms height from the signal.

C. Estimating the normalized surface autocorrelation function

The normalized surface autocorrelation function and the rms height can be derived from the signal. For the purposes of experiment, it is often more convenient to analyze the measurements in the frequency domain. Equations (9)–(11) will be used and are expected to be valid as long as the array's diffraction limited spot is much less than L and $h \ll L$. The change in wave number at the surface is given $\Delta k = 2k_w$.

We consider first a general rough surface, supposing that $\Delta k h \ll 1$, and obtain $C(\mathbf{d})$ by solving Eq. (10). Upon using the fact that the signal for $|\mathbf{d}| = 0$ is given by

$$\mathrm{Sig}(\omega, 0) = R^2, \tag{14}$$

one obtains

$$C(d) = \frac{1}{\Delta k^2 h^2}[\mathrm{Sig}(\omega, d)/\mathrm{Sig}(\omega, 0) + \Delta k^2 h^2 - 1]. \tag{15}$$

If $C(d)$ vanishes for large $|\mathrm{d}|$, one finds both $C(d)$ and h independently from Eq. (15).

The most useful formulas are obtained if we assume that the surface height is Gaussianly distributed. In this case, the signal is related to the normalized autocorrelation function via Eq. (11). For these surfaces h can be smaller than, comparable to or greater than the wavelength, but both the wavelength and h must be much less than L. A simple formula for h follows immediately by considering the signal for zero and for infinite displacement:

$$h = \frac{1}{\Delta k}\sqrt{\ln[\mathrm{Sig}(\omega, 0)/\mathrm{Sig}(\omega, \infty)]}. \tag{16}$$

Finally, one arrives at the following formula for the normalized surface autocorrelation length:

$$C(d) = 1 - \frac{\ln[\mathrm{Sig}(\omega, \mathbf{d})/\mathrm{Sig}(\omega, 0)]}{\ln[\mathrm{Sig}(\omega, \infty)/\mathrm{Sig}(\omega, 0)]}. \tag{17}$$

Equations (15)–(17) also apply to an experiment of the same kind but carried out in transmission. See the companion experimental paper for details of the setup. The only difference in the formulas is that $\Delta k = k_w - k_s$, where k_s denotes the wave number in the solid.

II. FINITE SIZE, RESOLUTION AND VARIANCE

The finite size of the transducer importantly modifies the simple picture used so far. The effects of diffraction and scattering become essential. The analysis of these complicating factors is simpler in the frequency domain, which will be used exclusively in this section. The effects of finite size are twofold. First, if the surface is random, the signal itself becomes a random variable and must be characterized statistically—we use the mean value and the variance. Second, the spatial resolution now depends on the size of the aperture as well as on the frequency and the distance of the TRM from the surface. In this section, we explore these effects by developing and numerically evaluating a simple approximate model for a finite sized one-dimensional (1D) TRM above a randomly rippled 1D surface. Approximate

formulas for the average signal are given in Sec. III A, while approximate formulas for the average of the squared signal are given in Sec. III B. Finally, in Sec. III C, we show how the resolution of the method and the statistical uncertainty of the signal depend on the parameters of the problem.

The TRM is assumed to be finite in the x direction, but to extend to infinity in the y direction. Similarly, the surface is randomly rippled; that is, it is rough but varies only in the x direction. The dependence on the y direction is trivial and plays no real role in our analysis. The essential new feature is that the TRM is finite in the x direction. We assume that the surface height is a random Gaussian variable, as described in the first section. The incident field due to the TRM is defined by

$$u_I(\omega,x,z_0)\equiv\exp(-x^2/A^2), \tag{18}$$

at z_0 where A denotes the half-width of the transducer. The variable x denotes the coordinate parallel to the surface and (x,z) denotes the general two-dimensional coordinate. The propagation of the incident wavefield in water from the transducer to the surface is described by the 1D Fresnel approximation

$$u_I(\omega,x,0)\approx\sqrt{\frac{-ik_w}{2\pi z_0}}e^{ik_w z_0}\int ds u_I(\omega,x,z_0)\times\exp\left(\frac{ik_w}{2z_0}(s-x)^2\right). \tag{19}$$

The interaction of the incident wavefield with the rough surface is described by the phase-screen approximation—the frequency-domain analog of the time shifts introduced in Sec. I. Briefly, in the phase-screen approximation, the rough surface is replaced by a plane at $z=0$ with a spatially varying reflection coefficient

$$R\exp(2ik_w h(\mathbf{r})). \tag{20}$$

A. Calculation of the average TRM signal

The signal was defined above as the area average of the pressure field over the TRM. Explicitly, upon using Eqs. (19) and (20), we find that the signal is given by the following random process

$$\mathrm{Sig}(h,L,A,z_0,\omega)\equiv\frac{1}{\mathrm{Area}}\left(\frac{k_w}{2\pi z_0}\right)^2\int\int\int\int\int ds_1\,ds_2 ds_3\,ds_4\,ds_5 u_I^*(\omega,s_1,z_0)u_I^2(\omega,s_3,z_0)u_I(\omega,s_5,z_0)\times\exp\left(\frac{ik_w}{2z_0}((s_5-s_4)^2+(s_4-s_3)^2-(s_3-s_2)^2-(s_2-s_1)^2)\right)\exp(i2k_w(h(s_4-d)-h(s_2))). \tag{21}$$

The signal results from two transmissions and two receptions, each contributing a term proportional to u_I. The propagation of the waves is accounted for using the Fresnel approximation—first line of Eq. (21)—while the effects of roughness appear in the second line. Upon substituting Eq. (18) into Eq. (21) and integrating over s_3, s_1, and s_5, we find

$$\mathrm{Sig}(h,L_s,A,z_0,\omega)=\frac{1}{\mathrm{Area}}\left(\frac{k_w}{2\pi z_0}\right)^2\frac{\pi^{3/2}}{p|p_1|^2}\int\int ds_2\,ds_4\times\exp(-c_1(s_2^2+s_4^2)+c_5(s_4^2-s_2^2)-(c_3+ic_4)(s_2-s_4)^2)\times\exp(i2k_w(h(s_4-d)-h(s_2))), \tag{22}$$

where

$$p^2=\frac{2}{A^2}, \tag{23a}$$

$$p_1^2=\frac{1}{A^2}+\frac{ik_w}{2z_0}, \tag{23b}$$

$$c_1+ic_2=\frac{(k_w/2z_0)^2}{p_1^2}, \tag{23c}$$

$$c_3+ic_4=\frac{(k_w/2z_0)^2}{p^2}, \tag{23d}$$

$$c_5=i\left(\frac{k_w}{z_0}+c_2\right). \tag{23e}$$

Note that c_4 is identically zero.

Next, we calculate the *average* TRM signal, $\langle\mathrm{Sig}\rangle$, by making the ergodic hypothesis that equates spatial and ensemble averages, and taking the ensemble average of the random signal given by Eq. (22). The evaluation of the ensemble average requires an explicit expression for $\langle\exp(i2k_w(h(s_4-d)-h(s_2)))\rangle$. We use the coordinate transformation

$$s_2=(q_1+q_2)/2,\quad s_4=(-q_1+q_2)/2, \tag{24}$$

to evaluate Eq. (22). Recall that the surface height distribution, h, is described by a spatially uniform zero-mean Gaussian random process. It follows from the Appendix that

$$\langle\exp(i2k_w(h(s_4-d)-h(s_2)))\rangle=\exp(-\sigma^2(1-C(q_1-d))), \tag{25}$$

where $\sigma=2k_w h$ is the rms value of the phase change due to surface roughness, while $C(.)$ is the autocorrelation function.

The assumption of a Gaussian autocorrelation function allows one to expand the exponential in Eq. (25) in an infi-

nite series, substitute the result in Eq. (22) and then evaluate the integrals in the transformed coordinates to find the average TRM signal

$$\langle \mathrm{Sig} \rangle = \frac{1}{4\ \mathrm{Area}} \left(\frac{k_w}{2z_0} \right)^2 \frac{\sqrt{2\pi}}{p|p_1|^2\sqrt{c_1}} e^{-\sigma^2} \sum_{n=0}^{\infty} \frac{(\sigma^2)^n}{n!\sqrt{q_3}} \times \exp\left(-\left(1 - \frac{n}{L^2 q_3} \right) \frac{nd^2}{L^2} \right), \tag{26}$$

where

$$q_3 = 0.5c_1 - 0.5\frac{c_5^2}{c_1} + c_3 + ic_4 + \frac{n}{L^2}. \tag{27}$$

B. Calculation of the TRM signal power

The power of the TRM's signal for one realization of the surface is defined by

$$\mathrm{Sig\ Sig}^* = \frac{1}{\mathrm{Area}^2} \left(\frac{k_w}{2z_0} \right)^4 \frac{1}{\pi|p|^2|p_1|^4} \int\int\int\int ds_1\, ds_2\, ds_3\, ds_4\ \exp(-c_1(s_1^2+s_2^2+s_3^2+s_4^2) - c_3((s_1-s_3)^2 + (s_2-s_4)^2)) \exp(ic_4((s_1-s_3)^2-(s_2-s_4)^2) + c_5(s_1^2-s_2^2-s_3^2+s_4^2)) \times \exp(i2k_w(h(s_1)-h(s_2)-h(s_3-d)+h(s_4-d))). \tag{28}$$

Next, we calculate the ensemble average of the signal power. Since the surface-height distribution, h, is described by a spatially uniform zero-mean Gaussian random process, we can write the following

$$\langle \exp(i2k_w(h(s_1)-h(s_2)-h(s_3-q)+h(s_4-q))) \rangle = \exp\,(-\sigma^2 H(s_1,s_2,s_3,s_4)), \tag{29}$$

where we used Eq. (A1) of the Appendix. Here, H is defined by

$$H(s_1,s_2,s_3,s_4) \equiv 2 - C(s_1-s_2) - C(s_3-s_1-d) + C(s_4-s_1-d) + C(s_3-s_2-d) - C(s_4-s_2-d) - C(s_3-s_4). \tag{30}$$

We make the coordinate transformation

$$\begin{aligned} s_1 &= (x_1+x_2+x_3+x_4)/2, \\ s_2 &= (-x_1-x_2+x_3+x_4)/2, \\ s_3 &= d+(x_1-x_2-x_3+x_4)/2, \\ s_4 &= d+(-x_1+x_2-x_3+x_4)/2. \end{aligned} \tag{31}$$

In the new coordinates, the integrand becomes independent of x_4 and the integral over that coordinate is completed trivially. Next, we obtain the series solution by (1) expanding the exponential $\exp(-\sigma^2 H(x_1,x_2,x_3))$ in an infinite series, (2) changing the order of the summations and integrations, and finally (3) evaluating the resulting integrals. After evaluating the integrals over x_1, x_2, x_3, the average TRM signal power is obtained in series form

$$\langle \mathrm{Sig\ Sig}^* \rangle = \frac{1}{\mathrm{Area}^2} \left(\frac{k}{2z_0} \right)^4 \frac{\pi e^{-2\sigma^2}}{|p|^2|p_1|^4} \times \sum_{\substack{a,b,c,\\ d,e,f=0}}^{\infty} \left(\frac{(-\sigma^2)^{a+b}(\sigma^2)^{c+d+e+f}}{a!b!c!d!e!f!} \times \frac{\exp\,(c_{12}d^2)}{\sqrt{c_1c_6c_7c_{10}}} \right), \tag{32}$$

where

$$c_6 = c_1 + \frac{a+b+c+d}{L^2}, \tag{33a}$$

$$c_7 = c_1 + 2c_3 + \frac{c+d+e+f}{L^2} - \frac{(c-d)^2}{L^4 c_6}, \tag{33b}$$

$$c_8 = c_5 - i2c_4 + \frac{c_5(c-d)}{L^2 c_6}, \tag{33c}$$

$$c_9 = i2c_4 - \frac{(e-f)}{L^2} + \frac{(a-b-L^2c_5)(c-d)}{L^4 c_6}, \tag{33d}$$

$$c_{10} = c_1 + 2c_3 + \frac{(a+b+e+f)}{L^2} + \frac{(a-b-L^2c_5)^2}{L^2} - \frac{c_9^2}{c_7}, \tag{33e}$$

$$c_{11} = c_1 + 2c_3 + \frac{(a-b-L^2c_5)c_5}{L^2 c_6} + \frac{c_8 c_9}{c_7}, \tag{33f}$$

$$c_{12} = -c_1 - 2c_3 + \frac{c_5^2}{c_6} + \frac{c_8^2}{c_7} + \frac{c_{11}^2}{c_{10}}. \tag{33g}$$

C. Resolution and normalized variance

The dependence of the TRM's resolution on the size of the TRM, as well as its distance from the surface, will be illustrated using the equations derived above. The following parameters are used in the plots, unless otherwise indicated: radius, $A = 12.7$ mm, off-set $z_0 = 50$ mm, frequency, f

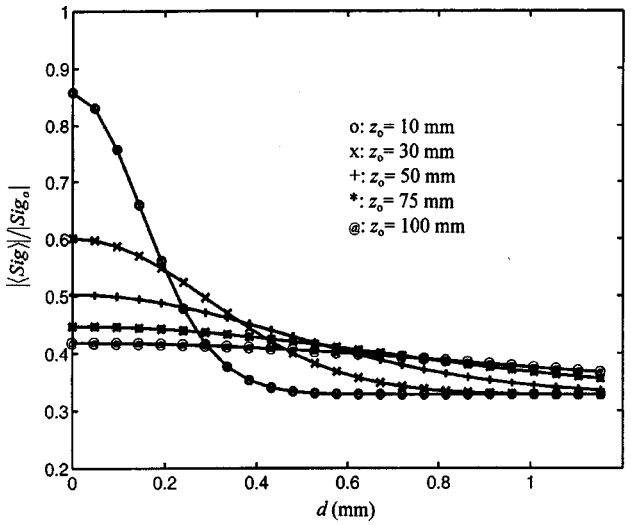

FIG. 3. Shows the average signal as a function of displacement d for $f=3$ MHz, $A=12.7$ mm, $L=0.2$ mm, and $h=0.042$ mm. The different curves correspond to different off-set distances z_0. Note the striking similarity to the next figure, Fig. 4.

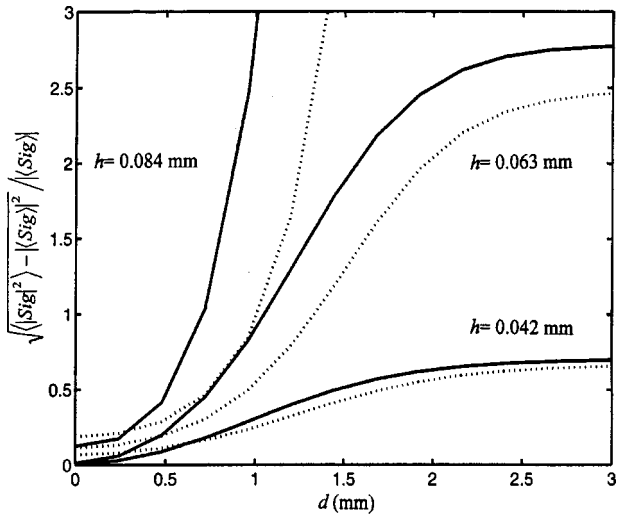

FIG. 5. Shows the uncertainty in the signal plotted against the displacement d for $f=3$ MHz, $A=12.7$ mm, $L=1.0$ mm, and $h=0.042$ mm. The solid lines correspond to $z_0=10$ mm, while the dashed lines correspond to $z_0=50$ mm.

$=3$ MHz, sound velocity, 1.5 mm/μs, rms height, $h=0.042$ mm, and autocorrelation length, $L=1$ mm.

The resolution is expected to decrease when we move the TRM further from the surface, since the angular aperture decreases and consequently more and more high spatial frequencies are lost. Figure 3 plots the magnitude of the average signal versus the displacement for different off-set distances $z_0=10$, 30, 50, 75, and 100 mm. The signal for $z_0=10$ mm has the largest dynamic range, decreasing from 0.85 for $d=0$ to 0.34 for $d=1$ mm. Furthermore, this signal is the narrowest, falling to half its peak value at roughly 0.20 mm; i.e., the resolution is enough to display the autocorrelation length of 1 mm. On the other hand, the signal for the $z_0=100$ mm is nearly flat over the entire range, varying from 0.42 to 0.40 and the decrease is over a range of 1 mm, giving little hint of the autocorrelation length. In general, the curves for larger off-sets show less dynamic range and become broader and broader as the off-set increases.

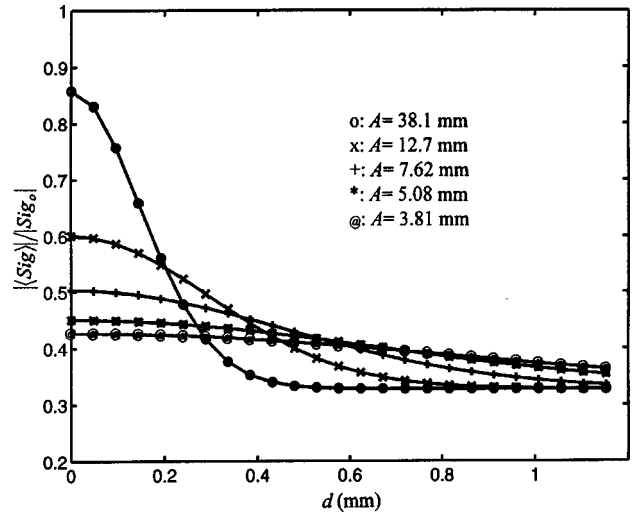

FIG. 4. Shows the average signal as a displacement d for $f=3$ MHz, $z_0=30$ mm, $L=0.2$ mm, and $h=0.042$ mm. The different curves correspond to different TRM radii A. Note the striking similarity to the previous figure, Fig. 3.

The resolution is expected to be better for larger TRM's at a fixed distance from the surface—depending primarily on the angular aperture. Figure 4 plots the magnitude of the average signal versus displacement for different TRM radii. The curves are calculated for a TRM with radii of 3.81, 6.08, 7.62, 12.7, and 38.1 mm at an off-set distance of 30 mm. These value of the radii were chosen so that the angular aperture θ were the same as those used in Fig. 3 for signal versus offset. We see that Figs. 3 and 4 are nearly identical. This confirms our expectations that the angular aperture and the frequency are the most important variables for determining the resolution.

The finite size of the TRM leads to a signal that is a random variable. The randomness is reduced by spatial averaging in the experiments reported in Ref. 7. Here, we attempt to indicate the degree of uncertainty for each realization of the signal—by calculating the square root of the variance normalized by the signal. The uncertainty is defined by

$$U\equiv\sqrt{\frac{\langle|\mathrm{Sig}|^2\rangle-|\langle\mathrm{Sig}\rangle|^2}{|\langle\mathrm{Sig}\rangle|^2}}. \tag{34}$$

Figure 5 shows U as a function of displacement for three different rms heights and for $z_0=10$ and 50 mm. The uncertainty in the signal increases very rapidly with rms height. For each case, it is small for small misregistrations and increases on the scale of the autocorrelation length, 1 mm. This behavior is expected from the nature of the time-reversal process. For small misregistrations time reversal nearly cancels the effects of roughness, which then has little effect on the signal. For larger misregistrations, the random nature of the signal becomes increasingly important and the uncertainty increases. Figure 6 shows U as a function of displacement for five different autocorrelation lengths and for a rms height of 0.042 mm. For large d the uncertainty is least for

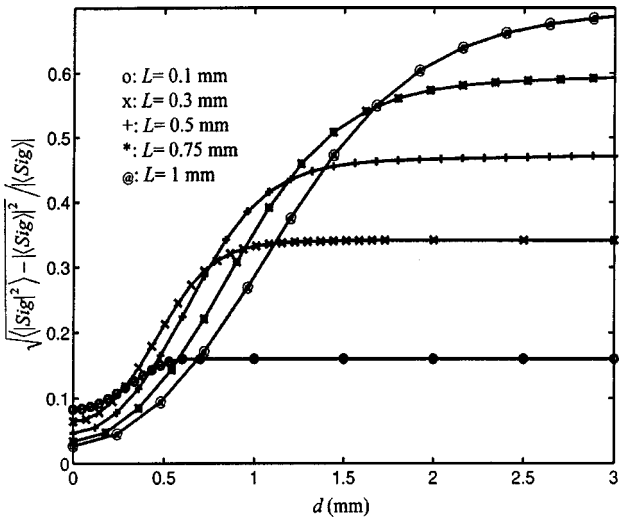

FIG. 6. Shows the uncertainty in the signal plotted against the displacement for $f=3$ MHz, $A=12.7$ mm, $z_0=25$ mm, and $h=0.042$ mm for different L's. The curves separate at large d and there the uncertainty is larger for larger L's.

the surfaces with the smallest autocorrelation length—as might be expected, since, in this case, the number of independent scattering sites is relatively large.

III. DISCUSSION AND SUMMARY

In this paper, we started with a general question: ''How does the time-reversal process degrade if the medium is perturbed after the first reflection but before the time-reversed wave is retransmitted?'' We have considered a particularly simple change in the medium—a translation with respect to the TRM. One might imagine many other perturbations such as removing individual scatterers from a complicated medium that exhibits strong multiple-scattering. Or, one might consider media that vary in time. One interesting application that follows from this idea is to use the TRM as a dark-field detector. One records the signal at some time and periodically thereafter interrogates the sample with the time-reversed waves. As long as there has been no significant change, one finds the time-reversed incident impulse, which can then be canceled to obtain a null response. Changes in the sample with time cause the TRM signal to vary from this null response and in this sense the TRM becomes a dark-field detector.

The study of surface roughness was significantly simplified by assuming an infinite TRM with infinitely fine elements. It can be shown rather straightforwardly[11] that, in this case, the decorrelation of the TRM's signal depends on the autocorrelation function of the singly reflected wave field at the surface of the transducer. The scattering is often modeled using a single-scattering approximation (Born approximation, phase screen approximation, etc.). For such systems, the autocorrelation functions that describe the material properties of the medium can sometimes be inferred from the measured autocorrelation function of the pressure field at the TRM. We examined this latter idea throughout this paper for the particular case of rough surfaces.

In summary, we have studied the decorrelation of the TRM's signal upon translation of the sample using the simplest model that retained the essence of the problem. The TRM's signal was found to depend simply on the surface autocorrelation function, which led to elementary closed-form formulas for the rms height and the autocorrelation function. The limitations of these simple analytic formulas were explored numerically for a simple model of a finite-sized TRM and a one-dimensional randomly rippled surface. The resulting series solutions were then used to study the variance in the results and the resolution of the TRM when used in this way. Experimental results and their comparison with theory are contained in a companion article—Ref. 7.

APPENDIX: STATISTICAL IDENTITIES

We have used certain statistical identities in this paper. We start with the following well-known identity[12] for a real, Gaussian, zero-mean random variable f

$$\langle e^{ikf}\rangle = e^{-k^2\langle f^2\rangle/2}. \tag{A1}$$

Here, k denotes any real number. Next we take the Fourier transform of both sides of Eq. (A1) with respect to k and obtain

$$\langle \delta(t-f)\rangle = \frac{1}{\sqrt{2\pi\langle f^2\rangle}}\exp\left(-\frac{t^2}{2\langle f^2\rangle}\right). \tag{A2}$$

[1] M. Fink, C. Prada, F. Wu, and D. Cassereau, ''Self-focusing in inhomogeneous media with time-reversal acoustic mirrors,'' Proc. IEEE Ultrason. Symp. (1989), pp. 681–686.
[2] D. Cassereau, F. Wu, and M. Fink, ''Limits of self-focusing using closed time-reversal cavities—Theory and experiment,'' Proc. IEEE Ultrason. Symp. (1990), pp. 1613–1618.
[3] M. Fink, ''Time reversed acoustics,'' Phys. Today **50**, 34–40 (March 1997).
[4] M. Fink, ''Time reversal in acoustics,'' Contemp. Phys. **37**, 95–109 (1996).
[5] D. Cassereau and M. Fink, ''Focusing with plane time-reversal mirrors: an efficient alternative to closed cavities,'' J. Acoust. Soc. Am. **94**, 2373–2386 (1993).
[6] M. Fink, ''Time-reversal of ultrasonic fields-Part I: Basic principles,'' IEEE Trans. Ultrason. Ferroelectr. Freq. Control **39**, 555–556 (1992).
[7] Ph. Roux, J. De Rosny, M. Fink, and J. H. Rose, ''Time reversal mirrors and rough surfaces: Experiment,'' J. Accoust. Soc. Am. **106**, 724–732 (1999).
[8] C. Eckhart, ''The scattering of sound from the sea surface,'' J. Acoust. Soc. Am. **25**, 556 (1953).
[9] P. B. Nagy and L. Adler, ''Surface roughness induced attenuation of reflected and transmitted ultrasonic waves,'' J. Acoust. Soc. Am. **82**, 193–197 (1987).
[10] P. B. Nagy and J. H. Rose, ''Surface roughness and the ultrasonic detection of subsurface scatterers,'' J. Appl. Phys. **73**, 566–580 (1993).
[11] J. H. Rose, P. Roux, and M. Fink (unpublished).
[12] A. Papoulis, *Probability, Random Variables and Stochastic Processes* (McGraw–Hill, New York, 1991).

Time-reversal mirrors and rough surfaces: Experiment

Philippe Roux, Julien De Rosny, and Mathias Fink
Laboratoire Ondes et Acoustique, ESPCI, Université Paris VII, 10 Rue Vauquelin, 75005, Paris, France

James H. Rose[a)]
Department of Physics and Astronomy and Ames Laboratory, Iowa State University, Ames, Iowa 50011

(Received 11 May 1998; revised 2 November 1998; accepted 25 March 1999)

A novel acoustic time-reversal technique has been tested for determining the surface-height autocorrelation function and rms height of rough surfaces. A time-reversal mirror (TRM) was used to insonify periodically and ''randomly'' rough surfaces of otherwise flat samples immersed in water. The standard use of the TRM is as follows: transmit an initial planar pulse, record the signals at each array element, digitally time reverse each signal, and then retransmit the time-reversed signal. As expected from time-reversal symmetry, one approximately recovers the incident planar pulse after the reflection of the retransmitted wave. The new technique is a simple modification of this procedure. Namely, as before, we record and time reverse the initial reflection. However, we next translate the transducer a fixed distance parallel to the surface before retransmitting. For very small displacements, little change is observed in the TRM's signal. For larger and larger translations, the TRM's signal decorrelates, i.e., it less and less resembles the incident pulse. The signal's decorrelation as a function of displacement is directly related to the autocorrelation function of the rough surface—within the limits set by the system's point response function. The TRM was used both in reflection mode and in transmission mode. Samples consisted of ''randomly'' rough surfaces of metal and plastic plates, as well as metal plates machined to have periodically rough surfaces. Evidence is provided that the time-reversal mirror is sensitive to the surface-height autocorrelation and, in favorable cases, determines the autocorrelation function and rms height. [S0001-4966(99)02207-9]

PACS numbers: 43.35.Yb [HEB]

INTRODUCTION

Recently, new experimental acoustic techniques[1–3] based explicitly on time-reversal invariance have been introduced. These techniques depend on the experimental observation that the retransmission of time-reversed acoustic waves recovers the incident wave field. Wave fields that have been widely scattered in space and time become simple again after being recorded on a measurement surface, time reversed, and retransmitted. Thus, the time-reversal process acts as a correlator. Furthermore Fink *et al.*[4,5] have introduced a new type of acoustic equipment, the time-reversal mirror (TRM), that consists of a linear array whose elements are connected to electronics that digitally record the received signal, time reverse it, and rebroadcast it into the medium. Perhaps surprisingly, the experimental reconstruction of the incident pulse using TRM's is generally found to be robust.

Here, we propose and test the idea that time-reversal mirrors can be useful for estimating the autocorrelation functions of complicated scattering systems. Details of the proposal are found in the companion theory paper.[6] The basic idea is that the reconstruction of the incident pulse is disturbed if the medium is perturbed prior to the retransmission of the time-reversed wave field. Furthermore, it is supposed that (in most cases) the signal will decorrelate more as the medium is perturbed more. Various autocorrelation functions of the system can be estimated by measuring the increased decorrelation of the signal as the medium is increasingly perturbed. In this paper, we test the proposed measurement technique by estimating the surface-height autocorrelation function and the root-mean-square (rms) height, h, of rough surfaces and comparing them with independent profilometric measurements.

The characterization of rough surfaces is a problem of considerable interest, both in general and in the realm of acoustics. There is a well-developed pulse-echo technique for measuring the rms height using a single unfocused broadband phase-sensitive transducer.[7,8] One immerses the sample in a water bath and insonifies the surface with a normally incident planar pulse. The rough surface introduces phase variations in the wave front and the resulting interference reduces the signal produced by the specular reflected wave. The higher the frequency, the larger the phase variations and the greater the reduction of the signal. Consequently, the rms height can be determined by measuring the attenuation of the spatially averaged specular beam as a function of frequency. This technique is well developed and produces accurate estimates for the rms height, being primarily limited by the number of independent measurements needed to estimate the average of the specular signal.

Acoustic techniques for measuring the normalized surface-height autocorrelation function, $C(\mathbf{r})$, or the autocorrelation length, L, of rough surfaces are less developed. One may, of course, use an acoustic microscope and map out the surface height distribution, $h(\mathbf{r})$, point by point—in the manner of a profilometer. The autocorrelation function can then

a)Electronic mail: jhrose@iastate.edu

be calculated numerically. This technique is generally rather slow. Another technique measures the acoustic power diffusely backscattered as a function of angle.[9] The angular distribution is directly related to the slopes of the various protuberances ($\sim h/L$) and can be used to estimate L given h. However, the measurement and inference are difficult due to the weakness of the diffusely scattered waves and the need for spatial averaging. More recently, a double-reflection technique has been introduced that permits one to estimate the autocorrelation length from the specular wave after two reflections from the surface.[10] In this technique, one prepares a transducer with a long quartz buffer rod, which also acts as an acoustic mirror. One insonifies the surface with a broadband pulse and generates a reflected wave. The resulting wave next reflects from the acoustic mirror and some little time later reflects a second time from the rough surface. Finally, the wave field generated by the second reflection is measured at the transducer. The size of the signal depends on the phase shifts and their degree of correlation. If the transducer is sufficiently near the surface, the phase shifts (induced by the two different reflections) are correlated on a scale governed by the autocorrelation length of the surface, and the wave field is relatively strongly attenuated. Crudely, a given acoustic ray bounces from the same bump on the surface twice and the phase shifts add coherently. If, however, the transducer is sufficiently far from the rough surface, the wave field diffracts causing the phase shifts induced by the two different reflections to become uncorrelated, and the wave field is relatively weakly attenuated. Again crudely, diffraction causes the incident sound to bounce from two statistically independent bumps on the surface and the independent phase shifts cause the waves to add incoherently. Since the degree of phase correlation alters the amplitude of the signal, it turns out that one can infer the autocorrelation function of the rough surface—by measuring the signal as a function of *the transducer's distance from the surface*. This technique was demonstrated for special samples. It has the advantage of inferring the autocorrelation function from the relatively large specular reflection, rather than the weak diffusely scattered waves. Further, it introduces the idea of using two reflections from the surface in order to introduce correlations in the wave field, which can then be used to infer the correlation function.

Time-reversal mirrors, when applied to rough surfaces, also measure two reflections: the direct reflection from the surface and the reflection of the time-reversed wave. The use of a TRM builds in strong correlations between the phase shifts engendered by the two reflections. The basic hypothesis is that one can determine the rms height and surface autocorrelation function by experimentally altering the extent of these correlations. Theoretical details are provided in the companion paper.[6] Here, we present an experimental study of the use of a time-reversal mirror (TRM) with rough surfaces. We tried to answer two questions. First, ''How well does the time-reversal mirror work for very rough random surfaces?'' Second, ''To what degree can the time-reversal mirror be used to infer the properties of rough surfaces?'' That is, we tested the hypothesis that one can measure both the rms height and the autocorrelation function of the rough surface *by translating the TRM parallel to the surface* prior to the retransmission of the time-reversed signal.

The paper is structured as follows. In Sec. I, we describe the setup of the experiment and briefly describe our equipment. We present experimental results that demonstrate the essential features of our the new technique. In Sec. II, we present and analyze measurements made on periodically rough surfaces. In Sec. III, we report and analyze measurements made on ''randomly'' rough surfaces. Autocorrelation lengths and rms heights are estimated and compared to independent measurements for four different samples. We conclude the paper with a summary and discussion of the advantages and disadvantages of measuring the autocorrelation function and rms height with a TRM.

I. TIME REVERSAL AND ROUGH SURFACES

In this section, we first describe the experimental setup and our equipment. We then present measurements that test the essential features of the new technique.

A. Setup and equipment

The TRM consists of a linear transducer array with 128 elements excited at a central frequency of 3.5 MHz (the wavelength in water is equal to 0.42 mm). The center-to-center spacing between two neighboring elements is 0.205 mm along the x axis, resulting in a total aperture in the x direction of approximately 26 mm. Each transducer element extends 20 mm in the y direction. The array is prefocused at 60 mm in water in the y direction. Each element of the array has its own amplifier, an 8-bit A/D converter, a storage memory and a 8-bit D/A converter working at a 20-MHz sampling rate. When the elements of the TRM are fired at the same time, the result is an incident locally plane wave field with a duration of a few periods at 3.5 MHz. The usable bandwidth of the TRM extends from 2.4 to 4.3 MHz. See Ref. 2 for a more detailed description of the experimental setup used with TRMs.

A schematic of the experiments is shown in Fig. 1(a) for reflection geometry and in Fig. 1(b) for transmission geometry. The reflection geometry is described first. We immerse an otherwise flat roughened plate in a water bath and insonify it with a broadband, phase-sensitive, linear acoustic array. The array is oriented with its axis normal to the mean surface of the sample. The array elements are pulsed simultaneously and identically to produce a locally plane wave that propagates to the surface and reflects. The resulting backscattered waves are recorded on each transducer. Next, the array is translated along its length parallel to the surface by a distance $\mathbf{d}$. The recorded reflected signals at each transducer element are time reversed digitally. Next, the time-reversed signals are rebroadcast; that is, the electric signal received by the ith element is time reversed and then used to drive a signal generator, which in turn pulses that element. The rebroadcast wave propagates to the surface interacts and reflects. Finally, the signal, $S(\mathbf{d})$, is the summed response of all the elements of the array in plane-wave reception, time gated for the reception of the reflection from the time-reversed wave. Some of our samples have very complicated rough surfaces that we will refer to as ''randomly'' rough.

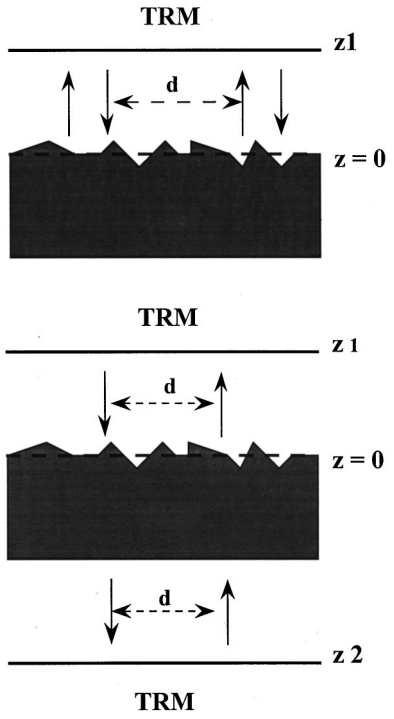

FIG. 1. Schematic setup for measurements made in (a) reflection geometry and (b) transmission geometry.

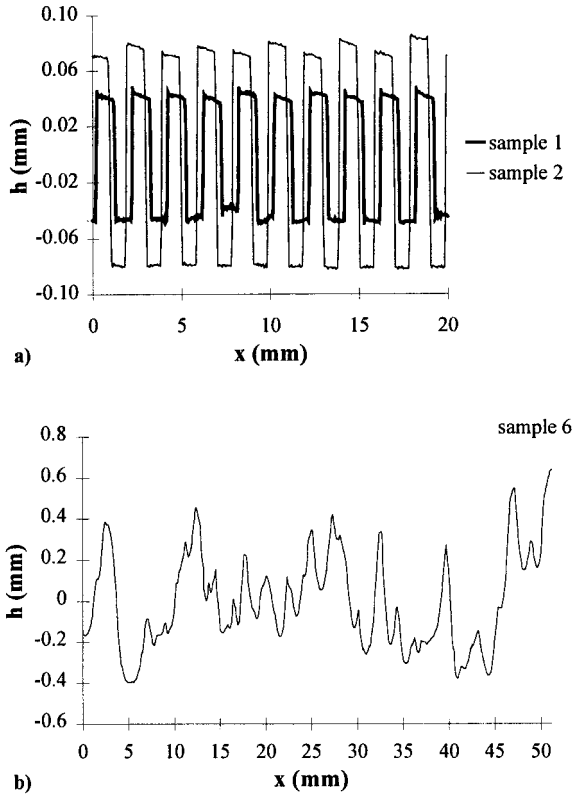

FIG. 2. Profilometer trace for (a) periodic rough surfaces and (b) a random rough surface.

For these samples, we obtained estimates of the spatially averaged signal, $\mathrm{Sig}(\mathbf{d}) \equiv \langle S(\mathbf{d}) \rangle$ and the variance of $S(\mathbf{d})$ that were obtained by averaging the signal over a number of spatial positions.

Measurements were also made in what we call transmission geometry; see Fig. 1(b). These measurements were made using two TRMs, although only one is strictly necessary. We again consider a thin, flat rectangular plate roughened on one side and placed in a water bath. The TRMs are placed in the water bath on opposite sides of the plate and aligned with each other. The array on the roughened side of the plate emits a locally planar wave that transmits through the water, the roughened surface of the plate, the smooth surface of the plate, and then through the water to the second TRM. The second TRM digitally stores and time reverses the wave field. Next, we translate the sample a distance **d** and transmit the time-reversed signal using the second TRM. The retransmitted wave propagates through the water, through the plate's smooth surface, its rough surface, and then through the water to the first TRM. Finally, the signal, $S(\mathbf{d})$, is the summed response of all the elements of the first array in plane-wave reception, time gated for the reception of the transmission of the time-reversed wave. As above, the spatially averaged signal is denoted by $\mathrm{Sig}(\mathbf{d})$. Finally, notice that the time-reversal capability of the first TRM was never used, its only function was as a conventional phased array.

We will report normalized measurements in this paper in order to reduce the effects of the transducer. In particular, we divide the signal for displacement d by the signal for zero displacement. We define the normalized signal by

$$NS(\omega,d) \equiv S(\omega,d)/S(\omega,0), \tag{1}$$

and the normalized spatially averaged signal by

$$N\mathrm{Sig}(\omega,d) \equiv \mathrm{Sig}(\omega,d)/\mathrm{Sig}(\omega,0). \tag{2}$$

From now on, we will only consider displacements where the transducer is moved parallel to its long axis, and we will denote the length of such translations by d.

Two types of samples with rough surfaces were used in the experiments: deterministic and random. The two deterministic samples were made by machining periodically parallel slots on the surface of brass plates. The slots for sample 1 were 43 μm in depth, with a width of 1 mm and with a spacing between slots of 1 mm. Sample 2 was the same except that the depth of the slots was 79 μm. Figure 2(a) plots the surface height of each sample as measured using a mechanical profilometer. There was a variation of approximately 10% in the depth of the individual cuts, which was ignored when making comparisons with theory.

''Randomly'' rough surfaces with nominally planar mean surfaces were produced by (1) peening the surfaces of brass and aluminum plates and (2) by partially melting coarse plastic particles and casting them. The surface-height profile of each sample was measured using a mechanical profilometer. Figure 2(b) shows one surface-height profile for a plastic plate—sample 6. The velocity of longitudinal sound in the plastic plates was approximately 2050 m/s. The rms height, the autocorrelation length, and the autocorrelation function were extracted from the profilometry measurements for each of the four ''random'' surfaces. Table I summarizes the profilometric measurements for all the samples. The normalized autocorrelation function was defined in terms of the surface height function, $h(\mathbf{r})$, as

TABLE I. Specifies the samples used in the experiments and compares profilometric and TRM measurements of the rms height and the autocorrelation length.

			Profilometry		Acoustics	
Sample	Surface	Material	L (mm)	h (μm)	L (mm)	h (μm)
1	periodic	brass	1	43	1	41.2
2	periodic	brass	1	79	1	84.2
3	random	brass	~0.4	~45	0.90	40.1
4	random	aluminum	1.27	21.5	1.37	21.9
5	random	plastic	3.03	133.6	3.0	136.6
6	random	plastic	1.2	268.4	1.3	270.4
7	random	plastic	~0.8	~450	···	···

$$C(d)=\langle h(\mathbf{d}-\mathbf{r})h(\mathbf{r})\rangle/\langle h(\mathbf{r})h(\mathbf{r})\rangle, \quad (3)$$

and is one of the primary objects of our study. In deriving Eq. (3), we assumed that the roughness is described by a spatial stationary random process.

B. Basic elements of the proposed technique

The basic elements of the experimental technique are discussed below. We discuss the use of the time-reversal mirror for both smooth and rough surfaces with and without translation. Received signals are plotted as B-scans, i.e., gray-scale representations of the signal received at each element of the array are shown as a function of time. In order to orient the reader, we begin by considering the signal for a TRM oriented with its axis normal to a smooth planar sample. First the array was used to produce a locally plane wave that propagated to the smooth surface and was reflected. The resulting signal is shown in Fig. 3(a). Next this signal was recorded, time reversed, and rebroadcast. Figure 4(a) shows the result—with a changed time scale. The planar wave front was recovered as expected. The major difference is that the time-reversed signal shows more oscillations than the singly reflected signal, since the transducer response function enters twice in the case of time reversal.

Next consider a very rough (''random'') plastic plate—sample 7. Here $k_w h=5.4$, where k_w denotes the acoustic wave number in water and h the rms height of the surface. First, the array is used to launch a locally plane wave that is oriented normal to the mean surface. The resulting B-scan is shown in Fig. 3(b). Roughness has caused the response to become random looking and to be dispersed over approximately 10 μs. Second, these signals were time reversed and rebroadcast with the array in its initial position. The resulting signals are shown in Fig. 4(b). Despite the severe roughness of the surface, the reflected wave is clearly planar. Thus the TRM is able to reverse the gross distortions introduced into the wave field—even for a surface with $k_w h=5.4$.

The TRM correlated the waves generated by reflection from a rough surface. This correlation arose because the retransmitted wave field was ''matched to the roughened surface'' by time reversal. If the array is moved prior to retransmission, the ''matching'' will be reduced. Figure 4(c) shows the result of translating the array by a distance of 0.25 mm ($\approx\lambda/2$) along its length before broadcasting the time-reversed signal. The plane wave nature of the response is still evident but considerably distorted. Figure 4(d) shows the same except that the array was translated by a distance of 0.50 mm ($\approx\lambda$). The plane wave is no longer evident. Upon comparing Fig. 4(b)–(d), it is evident that the signal becomes more random looking and dispersed over time with increasing translation of the array. It is this decorrelation, quantified via the normalized spatially averaged signal, $N\mathrm{Sig}(\mathbf{d})$, that we use to characterize the rms height and the autocorrelation function.

A method for determining h, L, and $C(\mathbf{d})$ is given in the companion theoretical paper. Here, we reproduce the equations that we will use to reduce our data. For randomly rough surfaces, our method first assumes that the surface-height distribution is representative of a Gaussian random process. Our ''randomly'' rough samples are largely consistent with this approximation—see Fig. 5(a) and (b) for the surface-height distributions obtained from the profilometry measure-

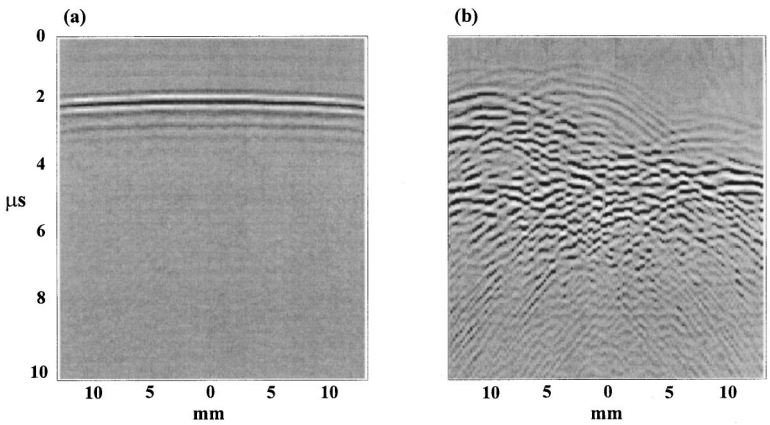

FIG. 3. Spatial-temporal representation (B-Scan) of the field received on the array: (a) after reflection from a smooth surface, and (b) after reflection from a rough random surface.

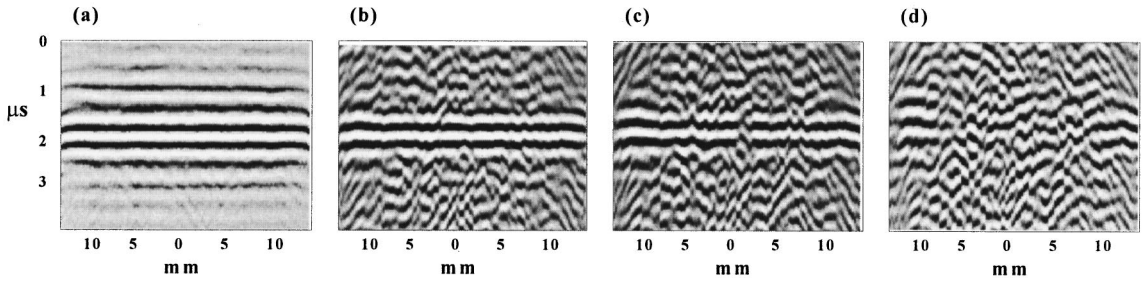

FIG. 4. Spatial-temporal representation (B-scan) of the field received on the array after reflection of the time-reversed field from (a) a smooth surface, (b) a random rough surface, (c) the rough surface after translating the array by $d=0.25$ mm, and (d) the rough surface after translating the array by $d=0.50$ mm.

ments of samples 5 and 6. Second, it is assumed that the spatial and ensemble averages are the same. Third, the phase-screen approximation (or equivalently, the simple ray model) is used to characterize the effects of roughness on the reflected wave. That is, it is assumed that the rms height is small compared to the correlation length. No such restriction is placed on the wavelength and the wavelength can be comparable to or greater than h. Finally, we assume that the effects of diffraction may be neglected. Under these assumptions, we find that the normalized autocorrelation function for randomly rough surfaces is given

$$C(\mathbf{d}) \approx 1 - \frac{\ln[N\mathrm{Sig}(\omega,\mathbf{d})]}{\ln[N\mathrm{Sig}(\omega,\infty)]}, \tag{4}$$

for both reflection and transmission geometry. The rms height is given by

$$h \approx \frac{1}{2k_w}\sqrt{-\ln[N\mathrm{Sig}(\omega,\infty)]} \tag{5a}$$

for reflection geometry, and by

$$h \approx \frac{1}{(k_w - k_s)}\sqrt{-\ln[N\mathrm{Sig}(\omega,\infty)]} \tag{5b}$$

for transmission geometry.

The phase-screen approximation (or equivalently, the simple ray model) was also used to calculate the signals for the one-dimensional periodic surfaces described above. One finds, upon neglecting diffraction, that the deterministic normalized signal, $NS(\omega,d)$, is given by

$$NS(\omega,d) = 1 - \sin^2(2k_w h)(1 - C(d)). \tag{6}$$

Here, $C(x)$ is the normalized autocorrelation function for the surface-height distribution and it is given by $C(x)=1-2x/L$ for $0<x<L$ and $-3+2x/L$ for $L<x<2L$, which is then repeated periodically over the whole line. Note that no spatial average is taken for the periodic samples.

II. PERIODICALLY ROUGH SURFACES

Periodically rough surfaces were studied for several reasons. First, it is relatively easy to machine such samples with a specified slot height and repeat distance. Second, periodic surfaces often appear in various acoustic inspection problems. They are also of interest as diffraction gratings. Third, the signal can be obtained, in the phase-screen approximation, as a simple closed-form expression if the effects of diffraction are neglected. Thus, periodic samples provide a straightforward and easily controlled test of some of the important approximations used in the analysis presented in the companion article.

The critical variables that describe the periodic surfaces are the repeat distance, L, and the rms height, h. The critical equipment variables are the array's aperture and distance from the surface, as well as the frequency. The simple formula for the signal, Eq. (6), was calculated assuming that the loss of high-spatial frequencies due to diffraction and scattering can be neglected. This condition can be met if the frequency is sufficiently high, and, for a fixed distance from the surface, the array has a sufficiently large aperture. Essentially, we need to ensure that the system-limited spot size is smaller than the repeat distance of the surface.

Reflection measurements were made for the periodically machined samples 1 and 2 described in the last section. The

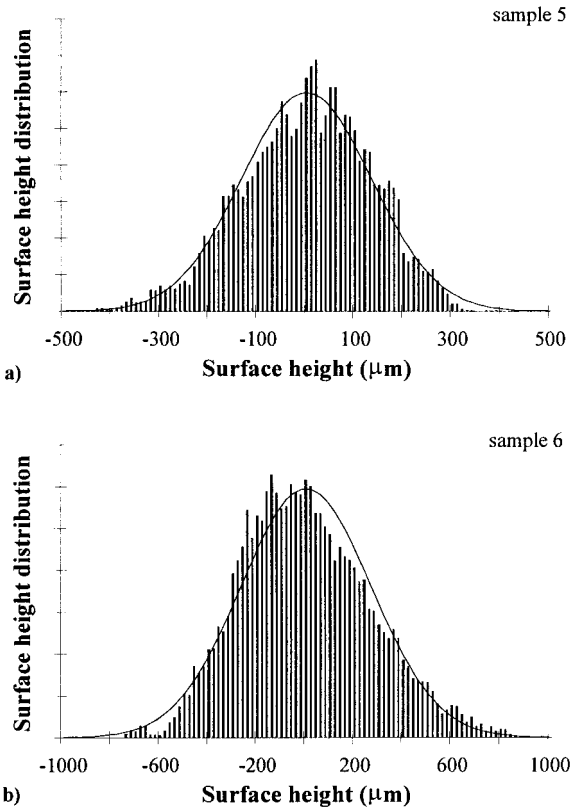

FIG. 5. Surface height distribution for (a) sample 5 and (b) sample 6.

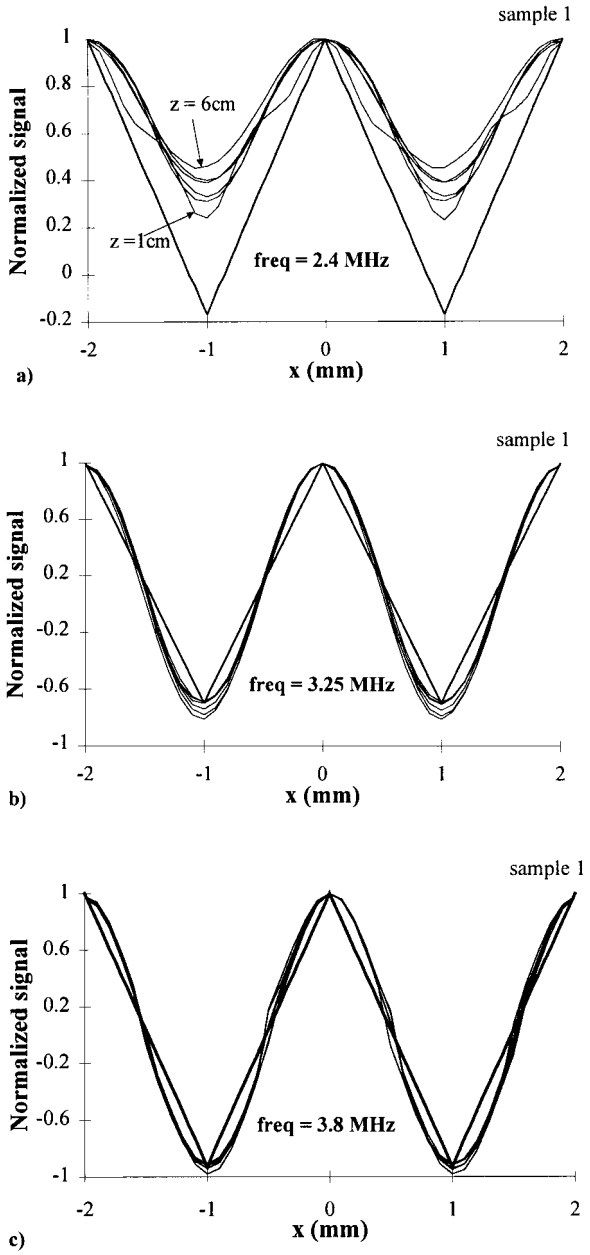

FIG. 6. Normalized signal measured for sample 1 for $z=1$ cm to $z=6$ cm (a) at $f=2.4$ MHz, (b) at $f=3.25$ MHz, and (c) at $f=3.8$ MHz. The full line corresponds to the nondiffracting theory calculated using the nominal features of the surface as measured by profilometry.

samples were oriented with the x axis chosen to be perpendicular to the grooves. The linear array was also oriented with its length along the x axis. Measurements were first made at $x=0$ and then as the array was moved to a series of points along the x axis. Since the theory neglects the loss of high spatial frequencies, it is important to measure the conditions under which diffraction can be neglected for our particular experimental set-up. Figure 6(a)–(c) shows the normalized signal obtained at three frequencies from sample 1 (slot depth 43 μm). Each figure plots the normalized signal versus the displacement (x) for five distances (z) of the transducer from the surface. The results are compared with theory calculated using the profilometric measurements given in Table I, neglecting the effects of diffraction. As can be seen, the agreement between theory and experiment is good for $z=1-6$ cm at $f=3.8$ and 3.2 MHz. The experimental curves are rounded due to diffraction, while the theory curves are sharply triangular. However, measurement and theory do not agree at $f=2.4$ MHz. In this case, the normalized signal $NS(\omega,x)$ depends on the transducer's distance from the surface, since the size of the focal spot is comparable to the width of the periodic slots at this frequency and diffraction cannot be ignored.

The normalized signal for sample 1 (slot depth 43 μm) measured at eight different frequencies ranging between 2.55 and 4.3 MHz for $z=2$ cm is shown in Fig. 7. The normalized signal is nearly periodic with a maximum of 1.0 (by construction) and minima ranging from 0.2 to -1.05. The repeat distance is 1 mm. Note that the minimum becomes more negative with increased frequency from 2.55 to 4.05 MHz (until it reaches the value of -1.0) and then becomes less negative at 4.3 MHz, as predicted by Eq. (6).

The surface parameters were extracted by comparing Eq. (6) to the measured normalized signal at each frequency. Figure 8 plots the minimum value of the measured normalized signal as a function of each frequency and compares it with Eq. (6) calculated for three different rms heights. The thin line corresponds to the value of the rms height that provides the best least-square fit. A comparison of the measurement and the model shows that the fit is degraded at the lowest frequency by the effect of diffraction. Table I compares the estimated surface profile parameters with those measured with the profilometer. The overall agreement between theory and experiment is good.

III. CORRELATION FUNCTIONS OF ''RANDOMLY'' ROUGH SURFACES

Complicated surfaces occur ubiquitously in nature due to fractures, due to erosion by small particles, and due to aggregation of particles into larger structures. Consequently, there is intense interest in finding novel and effective methods of characterizing such surfaces. If the surfaces are sufficiently complicated, it is often desirable to describe the surfaces in terms of a few statistical measures. Consequently, we studied the use of the TRM to characterize the specially prepared ''random'' surface described in Sec. I. These samples were designed to have surface-height profiles (about a mean plane) that could be modeled by a zero-mean spatially stationary Gaussian random process. We tested the hypothesis that the TRM can be used to infer the rms height and autocorrelation function of this special class of samples.

Measurements (using the reflection geometry) are reported for a roughened aluminum plate—sample 4. For a given center frequency, the reflection method is good for relatively small rms heights. The distance from the array to the surface was held fixed at 1.0 cm. The array was translated parallel the surface in increments of 0.02 cm. The measurement was repeated at 110 different places on the surface and the results were combined to obtain the spatially averaged signal. The measurements were made using broadband pulses. The results were Fourier transformed to obtain the spatially averaged signal at four equally spaced frequencies

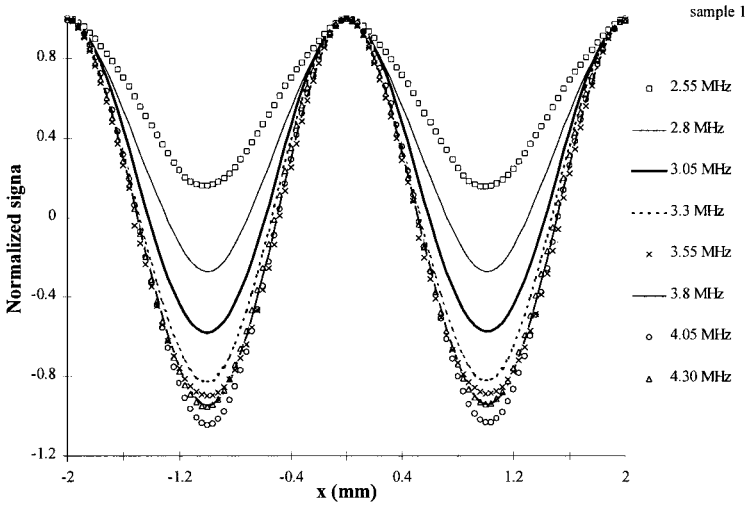

FIG. 7. $NS(\omega,d)$ measured with periodic surface 1 for $z=2$ cm at eight frequencies from $f=2.55$ MHz to $f=4.3$ MHz.

ranging from 2.6 to 4.1 MHz (see Fig. 9). Equations (4) and (5a) were used to obtain estimates of the rms height and the normalized autocorrelation function. The rms height was estimated to be 21.9 μm with a standard deviation of ± 1 μm, compared to 21.5 μm measured with the profilometer. The normalized surface-height autocorrelation function was estimated as a function of frequency from the TRM data and is shown in Fig. 10(a). The dark line shows the surface-height autocorrelation function obtained using a mechanical profilometer. We see that the TRM estimates for the normalized autocorrelation function depend rather weakly on the frequency (as they should) and are close to the results of profilometry. Next, we obtained a final TRM estimate by averaging the results found at different frequencies. The average is shown and compared to profilometry in Fig. 10(b). The error bars indicate the range of estimates—obtained by calculating the autocorrelation function at each frequency.

Measurements were also made in reflection mode for a brass plate—sample 3. This sample was included to show a case where our method for measuring the autocorrelation function cannot be expected to work, since the autocorrelation length is less than the wavelength ($\lambda \sim 0.5$ mm) and thus adequate resolution is precluded by diffraction. The experimental conditions were the same as for the aluminum samples. This sample was obtained from one of the authors of Ref. 9 and is not simple. M. de Billy noted in a private communication that measurements were made with a profilometer along lines oriented in three different directions. Values for the rms height were estimated for each of these lines and found to be 59, 48, and 22 μs, while estimates for the autocorrelation length were 38, 400 and 210 μs (Ref. 11) (no independent profilometric measurements were carried out in our laboratory). For our purposes, the important thing is that the estimates for L are less than the wavelength. We proceeded to estimate the normalized autocorrelation function from Eqs. (4) and (5a). Figure 11(a) shows the estimated normalized autocorrelation function for four different frequencies. We found that the estimates of the autocorrelation function were no longer independent of frequency. The estimated normalized autocorrelation function narrows significantly as the frequency increases. This indicates that the method has failed since the actual surface-height autocorrelation function obviously has nothing to do with the acoustic system or its frequency. Our results were probably more closely connected to the diffraction limited resolution of the system than to the surface height autocorrelation function. Figure 11(b) shows the estimate for the normalized autocorrelation function averaged over frequency. The autocorrelation length estimated from this graph is roughly 1 mm compared to the nominal value of less than 0.40 mm. The rms

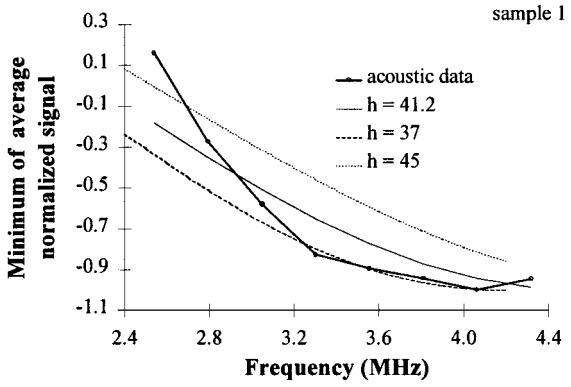

FIG. 8. Minimum of $NS(\omega,d)$ versus frequency. The full line corresponds to the acoustic measurement. The thin line corresponds to the best least-squares fit of Eq. (6), $h=41.2$ μm. The two other lines correspond to Eq. (6) with $h=41.2$ μm$\pm 10\%$. The nominal value of h, obtained from profilometry measurements, is $h=43$ μm.

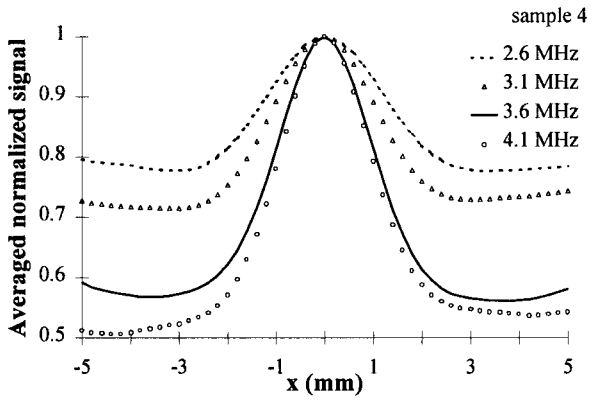

FIG. 9. $N\mathrm{Sig}(\omega,d)$ measured with ''random'' rough surface 4 for $z=1$ cm, at four frequencies from $f=2.6$ MHz to $f=4.1$ MHz.

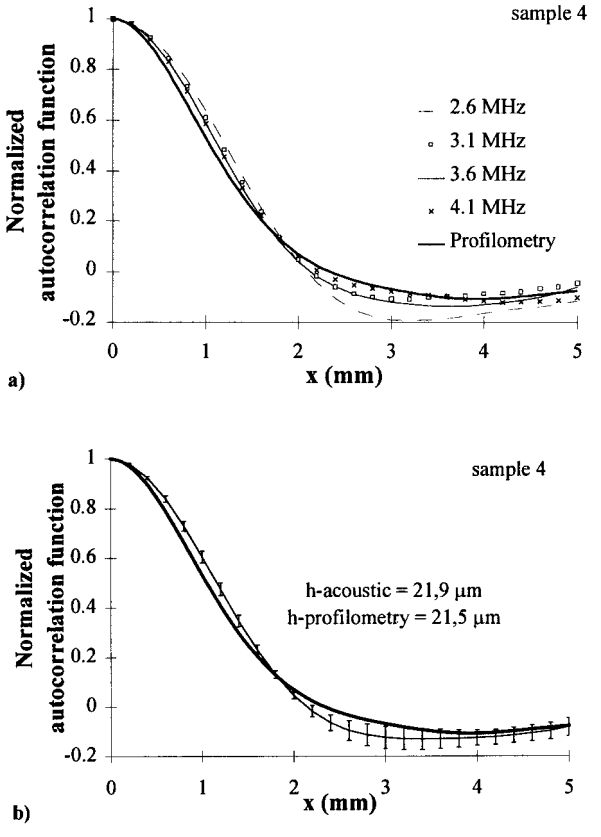

FIG. 10. The TRM estimate for the normalized autocorrelation function for sample 4: (a) for four different frequencies, and (b) averaged over the whole frequency bandwidth. The error bars indicate the range of values found. The full line corresponds to the normalized autocorrelation function obtained from profilometric measurements.

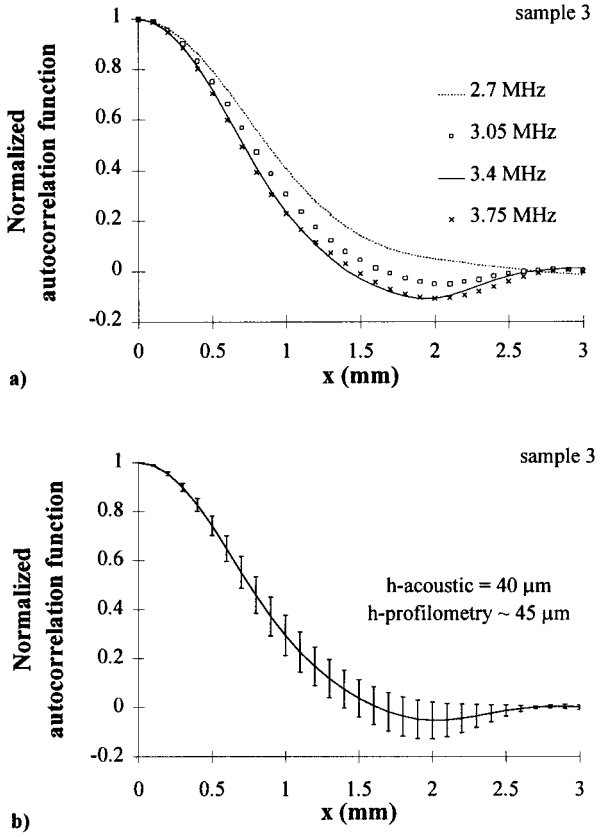

FIG. 11. Normalized autocorrelation function estimated for rough surface 3 for $z=1$ cm: (a) at four frequencies ranging from $f=2.7$ MHz to $f=3.75$ MHz, and (b) averaged over the whole frequency bandwidth. The error bars indicate the range of values found.

height was estimated to be 40 μm from the acoustic data, which is in, probably fortuitously, good agreement with the nominal value of 20–60 μm.

Transmission measurements were used to estimate the rms height and autocorrelation length for two roughened plastic plates—samples 5 and 6. TRM 1 was oriented normally to the roughened surface at a distance of 5.5 cm, while TRM 2 was aligned and oriented normally on the opposite side of the sample at a distance of 2.0 cm from its smooth surface. The TRMs were translated together parallel to the surface in increments of 0.04 cm. The measurements were repeated at 142 different places for sample 5 and at 50 different places for sample 6. The results were combined to obtain the spatially averaged signal. The measurements were made using broadband pulses. The results were Fourier transformed to obtain the spatially averaged signal at four equally spaced frequencies ranging from 2.6 to 4.1 MHz (see Fig. 12), which shows the results for sample 5. Equations (4) and (5) were then used to obtain estimates of the rms height and the normalized autocorrelation function. Figure 13(a) shows the frequency-averaged TRM estimate for the normalized autocorrelation function of sample 5, while Fig. 13(b) shows the same for sample 6. The error bars indicate the range of values obtained at different frequencies. The rms height of sample 5 was estimated acoustically to be 137 ± 4 μm, which should be compared to 134 μm measured with the profilometer. The acoustic estimate for sample 6 is $h=270\pm 17$ μm compared to 268 μm measured with the profilometer. The rms heights are obviously in good agreement with the nominal measurements. The overall agreement between the acoustically estimated autocorrelation functions and the results of profilometry is good.

IV. DISCUSSION AND SUMMARY

A novel method to characterize rough surfaces using time-reversal mirrors was tested. In particular, we examined two hypotheses: (1) that the incident wave field can be reconstructed using a TRM even for very rough surfaces; and

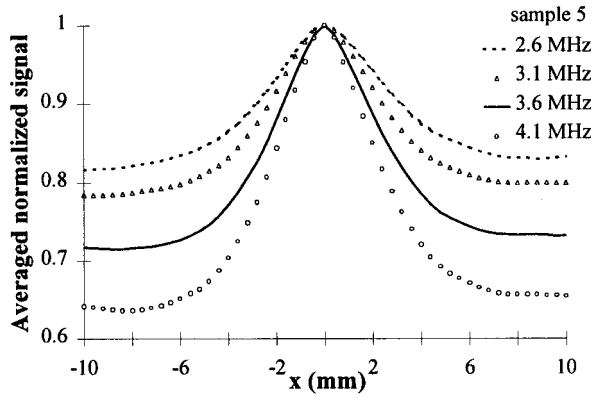

FIG. 12. $N\mathrm{Sig}(\omega,d)$ measured in transmission geometry with rough surface of sample 5 at four frequencies ranging from $f=2.6$ MHz to $f=4.1$ MHz.

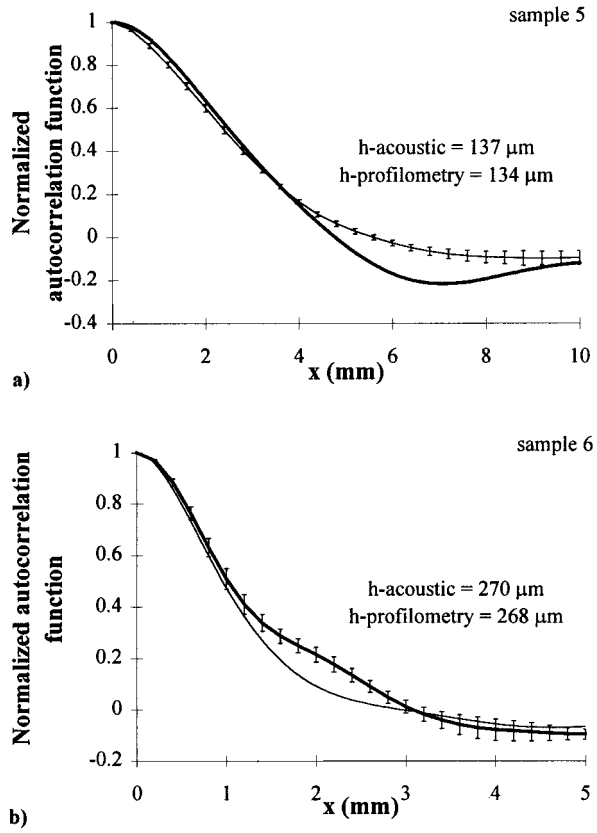

FIG. 13. Frequency-averaged estimate for the normalized autocorrelation function (a) of sample 5 and (b) of sample 6. The full line corresponds to the normalized autocorrelation function obtained from profilometry measurements for each sample. The error bars indicate the range of values found at different frequencies.

(2) that the rms height and the normalized surface-height autocorrelation function can be reconstructed using a TRM, supposing that the point response function of the array is smaller than the characteristic lengths of the autocorrelation function. We found that the initial wave field could be recovered even for a very rough surface. Within the resolution of the system, our measurements were consistent with the recovery of the rms height and the autocorrelation length for several samples that had $h \ll L$.

The proposed method is, in principle, sensitive to the shape of the autocorrelation function as well as to the autocorrelation length. Our reconstructions hints that this may, in fact, be true. However, the present set of samples and data analysis are too limited to come to a definite conclusion. It would be interesting to test the proposed method against samples with different types of well-characterized autocorrelation functions, e.g., Gaussian, exponential, and fractal.

Our work suggests that TRM measurements combined with Eqs. (4) and (5) provide a rapid and effective method for determining the rms height and autocorrelation length of random rough surfaces under the following conditions. First, the mean surface must be flat enough over the region of interest. Second, the type of roughness should not vary appreciably over a region of interest. Third, the region of interest must be large enough to obtain adequate signal-to-noise in the spatially averaged signal. That is, we should be able to model the roughness locally as a spatially stationary Gaussian random process. Fourth, the TRM must have adequate bandwidth; that is, the point response function of the TRM must be smaller than the characteristic features of the autocorrelation function.

Two different geometries were used in the measurements: reflection and transmission. The wave number transfer, δk, times the rms height, $\delta k h$, determines the frequency range in which these methods will be useful. Reflection geometry, which has the larger δk, is preferred if the roughness is relatively small. Transmission geometry, which has a smaller δk, is more appropriate if the rms height is relatively large. Calculation indicates that these methods should be able to determine the rms height and reconstruct the autocorrelation function for surfaces that vary in the rms height by more than a factor of 10. Using our current limited set of samples, we have measured rms heights ranging from 40 to 270 μm and autocorrelation lengths ranging from 0.9 to 3.0 mm.

ACKNOWLEDGMENTS

We would like thank Michel De Billy, Jean Schmitbuhl, and Benoit Roman for their help in providing the samples and profilometry measurements.

[1] M. Fink, ''Time reversed acoustics,'' Phys. Today **50**, 34–40 (March 1997).
[2] D. Casserau, F. Wu, and M. Fink, ''Limits of self-focusing using closed time-reversal cavities-Theory and experiment,'' Proc. IEEE Ultrason. Symp. (1990), pp. 1613–1618.
[3] W. A. Kuperman, W. S. Hodgkiss, H. C. Song, T. Akai, C. Ferla, and D. Jackson, ''Phase conjugation in the ocean: Experimental demonstration of an acoustic time-reversal mirror,'' J. Acoust. Soc. Am. **103**, 25–40 (1998).
[4] D. Casserau and M. Fink, ''Focusing with plane time-reversal mirrors: an efficient alternative to closed cavities,'' J. Acoust. Soc. Am. **94**, 2373–2386 (1993).
[5] M. Fink, C. Prada, F. Wu, and D. Cassier, ''Self-focusing in inhomogeneous media with time-reversal acoustic mirrors,'' Proc. IEEE Ultrason. Symp. (1989), pp. 681–686.
[6] J. H. Rose, M. Bilgen, P. Roux, and M. Fink, ''Time reversal mirrors and rough surfaces: Theory,'' J. Acoust. Soc. Am. **106**, 716–723 (1999).
[7] P. B. Nagy and L. Adler, ''Surface roughness induced attenuation of reflected and transmitted ultrasonic waves,'' J. Acoust. Soc. Am. **82**, 193–197 (1987).
[8] P. B. Nagy and J. H. Rose, ''Surface roughness and the ultrasonic detection of subsurface scatterers,'' J. Appl. Phys. **73**, 566–580 (1993).
[9] M. De Billy and G. Quentin, ''Backscattering of acoustic waves by random rough surfaces immersed in water,'' J. Acoust. Soc. Am. **72**, 591 (1982).
[10] J. H. Rose, M. Bilgen, and P. Nagy, ''Acoustic double reflection and transmission at a rough water-solid interface,'' J. Acoust. Soc. Am. **95**, 3242–3251 (1994).
[11] M. de Billy, private communication (1998).

Porous piezoelectric ceramic hydrophone

Stefano Marselli and Vittorio Pavia
Whitehead Alenia Sistemi Subacquei S.p.A., via di Levante 48, I-57128, Livorno, Italy

Carmen Galassi and Edoardo Roncari
CNR, Istituto di Ricerche Tecnologiche per la Ceramica, via Granarolo 64, I-48018, Faenza, Italy

Floriana Craciun[a] and Guido Guidarelli
CNR, Istituto di Acustica ''O. M. Corbino,'' Area di Ricerca Roma-Tor Vergata, via del Fosso del Cavaliere 100, I-00133, Roma, Italy

(Received 26 December 1998; accepted for publication 23 April 1999)

The construction and evaluation of a hydrophone based on porous piezoelectric ceramics with high $d_h g_h$ figure of merit (FOM) is described. It has been shown that, in order to improve the hydrophone signal-to-noise ratio, a piezoelectric material with a high FOM should be employed. A porous piezoelectric material has been prepared by mixing calcined lead zirconate titanate (PZT) powder with fine particle starch powder. Square plate samples have been cold pressed from this material, which were then heated to eliminate the organic component, sintered, electroded, and poled in a high electric field. An optimum pore volume fraction of approximately 40% has been selected in order to obtain materials with high piezoelectric coefficients and reasonably good mechanical resistance. For this composition a hydrostatic figure of merit of approximately 10^{-11} m^2/N has been obtained that is a few orders of magnitude higher than traditional piezoceramics. Square plate elements were assembled in a planar hydrophone which was made watertight with polyurethane resin. The hydrophone was characterized by different measurements performed in a water tank, by using a pulsed sound technique. Results on acoustical sensitivity measurements, directivity, equivalent noise pressure level, and sensitivity variation with pressure are presented and discussed.
 [S0001-4966(99)01608-2]

PACS numbers: 43.38.Fx, 43.38.Ar [SLE]

INTRODUCTION

Increasing of the signal-to-noise ratio is a crucial task of an acoustic receiving system. It has been shown by Young[1] that an important factor for the signal-to-noise ratio of a hydrophone is the mean-squared spectral noise pressure $\overline{p_H^2}$ defined by the relationship

$$\overline{p_H^2} = \frac{4kT|Z_H|R_\theta \tan\delta}{M^2}, \tag{1}$$

where k is Boltzmann's constant ($k=1.38\times10^{-23}$ J/K), T the absolute ambient temperature, Z_H the complex impedance of the hydrophone, R_θ the directivity factor, $\tan\delta$ the dielectric loss factor, and M the hydrophone sensitivity. $\overline{p_H^2}$ is an inverse FOM of the hydrophone, in the sense the lower its value the better the system performance.

For the simplest case of a hydrophone based on a hydrostatic-drive piezoelectric ceramic element, which is in contact with the acoustic pressure field on all faces, the sensitivity is

$$M = g_h l, \tag{2}$$

where $g_h = g_{33} + 2g_{31}$ is the hydrostatic piezoelectric coefficient and l is the length in the x_3-direction. Moreover, in the low-frequency approximation, when the piezoelectric hydrophone is small compared to the acoustic wavelength and is operating well below mechanical resonance, the hydrophone is almost omnidirectional ($R_\theta=1$) and its electrical impedance is $Z_H = 1/(\omega C_H)$, where C_H is the hydrophone capacitance ($C_H = \epsilon_{33}^T A/l$, with ϵ_{33}^T the free permittivity and A the electrode area). In this case the Eq. (1) can be written as

$$\overline{p_H^2} = \frac{4kT\tan\delta}{\omega V d_h g_h}, \tag{3}$$

where V is the volume of the ceramic material, $d_h = d_{33} + 2d_{31}$ is the hydrostatic charge piezoelectric constant and the relation $d_h = \epsilon_{33}^T g_h$ between the piezoelectric charge and voltage coefficients has been used. It can be observed that for a given volume of ceramic material the hydrophone mean-squared spectral noise pressure $\overline{p_H^2}$ can be minimized if both d_h and g_h are as high as possible. Therefore a FOM of the piezoelectric material can be defined as the product $d_h g_h$ (if only the electroded faces are in contact with acoustic pressure field and the other faces are isolated, $M = g_{33} l$ and FOM$= d_{33} g_{33}$). It can therefore be seen that dense PZT-type piezoelectric ceramic materials, which are generally used in underwater applications, are not appropriate for hydrostatic sensing applications, due to their low hydrostatic FOM. Indeed, as d_{31} is nearly 1/2 of d_{33} and is opposite in sign, d_h is very small; the piezoelectric voltage constant g_h is very small, too, in these materials. Moreover, the stiff and dense PZT also has the disadvantage of poor acoustic coupling to water. Therefore in the last decades new materials with improved piezoelectric properties and good qualities for hydro-

[a]Electronic mail: floriana@idac.rm.cnr.it

phone applications, obtained by introducing soft material inhomogeneities (e.g., voids) into piezoelectric ceramics and polymers, have been investigated and tested in hydrophones.[2–20] In porous piezoelectric materials, a partial decoupling between transversal and longitudinal effects avoids canceling, therefore d_h increases. Moreover, due to the lower dielectric constant, g_h is furthermore increased. Theoretical[21] and experimental[7,14,15,17] investigations have shown that their elastic, dielectric, and piezoelectric properties vary with porosity with power laws typical for percolation systems.[22] The hydrostatic FOM of porous piezoelectric materials can reach values a few orders of magnitude higher than in dense materials. Therefore we expect to obtain better hydrophones by using piezoelectric materials with higher figures of merit.

I. POROUS PIEZOCERAMIC SAMPLES PREPARATION AND CHARACTERIZATION

Porous piezoelectric ceramics were prepared by mixing PZT powder of composition $Pb_{0.988}(Zr_{0.52}Ti_{0.48})_{0.976}Nb_{0.024}O_3$, calcined at 850 °C, with starch rice powder, in 50% volume ratio.[19] The starch of rice was chosen for its narrower particle size distribution and its easier blending without agglomerate formation. The two component powders were dry mixed in a jar for 20 h, then standard shape samples (for piezoelectric characterization) as well as square plate samples (for hydrophone construction) have been pressed at 50 MPa.

The critical step of the sample preparation process was the heat treatment, in particular the heating rate during starch decomposition which could produce breaking of the samples if too high, therefore thermogravimetric analysis has been previously performed in order to determine the best heating cycle. Analysis shows that starch completely burns out between 250 °C and 450 °C. Therefore the heating rate was initially 50 °C/h until 200 °C and 30 °C/h until 450 °C, to assure a complete burn out of the organic additive; then it was increased to 100 °C/h until 600 °C and 200 °C/h thereafter, up to the sintering temperature of 1150 °C, when a soaking time of 30 min was allowed. The sintering was performed in closed alumina crucibles in lead atmosphere, given by a $PbZrO_3$ source. The final density of the samples was approximately 4.8 g/cm^3 (total porosity 39%). The sintered samples were ground to remove surface layers, silver electroded, and poled into silicone oil at 120 °C under a dc field of 3 kV/mm for 40 min. After poling, they have been thoroughly cleaned in acetone in order to eliminate the oil. The crystallographic structure was identified by x-ray diffraction (XRD) and microstructure was investigated by scanning electron microscopy (SEM) performed on sample fracture.[19] Piezoelectric, elastic, and dielectric properties were measured on standard shape samples as recommended by IEEE standards. The piezoelectric d_{33} charge coefficient was also measured by a direct method on a d_{33} meter.

Measurements of the sensitivity of samples in the receiving mode in air at 250-Hz frequency and in condition of hydrostatic load were carried out with the equipment shown in Fig. 1. Porous piezoelectric ceramic samples together with a reference microphone were subjected to the same acoustic field produced by a loudspeaker and their electrical output signals were measured and compared by an impedance analyzer HP4194A. As a result the calibrated sensitivity of the samples, thereafter used to calculate the hydrostatic voltage coefficient, was obtained.

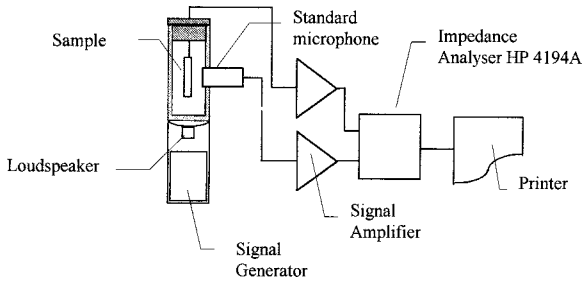

FIG. 1. Experimental setup for measuring the sensitivity of piezoelectric samples in air.

II. HYDROPHONE CONSTRUCTION AND EVALUATION

Square samples with dimensions $27\times27\times5$ mm^3 (active electrode area 26.2×26.2 mm^2) were used to assemble a planar hydrophone (Fig. 2).[18] The elements have been electrically connected and the array was embedded in polyurethane resin and surrounded with a fine metal grid. A cable of length 3 m and capacity of 150 pF/m was used for the electrical connection. The final dimensions of the hydrophone were $110\times110\times20$ mm^3 and its total capacity was 5517 pF.

The admittance was measured with an impedance bridge HP4194A, with the hydrophone immersed in a large water tank, in order to assure free-field conditions.[23] In order to measure the hydrophone free-field voltage sensitivity, defined as the ratio of the open-circuit output voltage to the free-field plane wave pressure, a comparison method [23] has been used, based on the experimental setup presented in Fig. 3. It consists of subjecting the unknown and standard hydrophones to the same free-field pressure and then comparing their electrical output voltages. As the two hydrophones are simultaneously immersed in the same sound field produced by the projector in a limited water tank, some precautions (like applying proximity criteria[23] and using a pulsed sound technique[23]) have been taken in order to assure as much as possible true free-field plane-wave conditions. In our measurement a standard B&K8100 hydrophone has been used for calibration. A rotating device allowed the hydrophone to change the orientation with respect to the wave normal.

The same experimental setup as that presented in Fig. 3 was used for measuring the directivity patterns (the variation

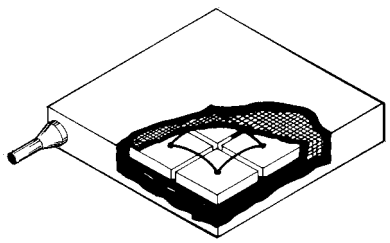

FIG. 2. Schematic drawing of the constructed planar hydrophone, made of 3×3 square plate porous piezoceramic elements. The dimensions are $110\times110\times20$ mm^3.

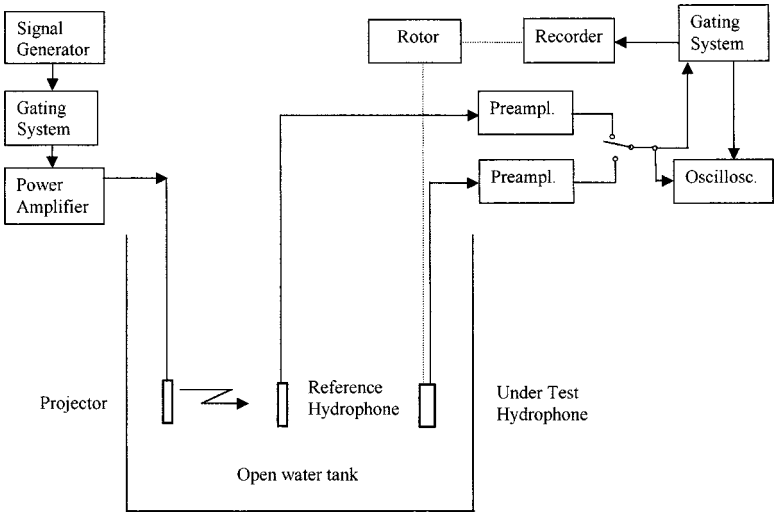

FIG. 3. Experimental setup for measuring hydrophone sensitivity by comparison with a standard hydrophone.

of the free-field sensitivity as a function of direction) at different frequencies. The hydrophone was rotated by the mechanical positioning device about its vertical axis with fine angular steps and the corresponding output voltage registered. An average of few different readings was taken at each step in order to obtain more reliable results.

The sensitivity variation as a function of hydrostatic pressure was measured with the experimental setup shown in Fig. 4. A smaller hydrophone formed by three elements was assembled for the measurement. The hydrophone was introduced in a pressure vessel and the pressure was varied between the ambient value and 60 bars; the measurements were carried out with filtered noise in the frequency range between 2 kHz and 20 kHz.

III. RESULTS AND DISCUSSION

The XRD patterns of the prepared material show the presence of a rhombohedral perovskitic phase together with the tetragonal phase. The mean value density of the samples was 4.78 g/cm^3. When comparing with the density of the dense PZT samples ($\rho_{\mathrm{PZT}}=7.82$ g/cm^3), this corresponds to a total porosity of about 39%. A similar value was already obtained using other organic additives like methyl-hydroxyethil-cellulose[16] showing that the dry mixing of PZT powder with organic powder used as porosity agent is a suitable way to realize materials with high porosity and high piezoelectric coefficients.

SEM investigation of the fracture surface of the samples showed the presence of isotropically distributed interconnected pores of different dimensions, with diameters ranging between fractions of a micrometer and a few micrometers.[19]

The main physical properties of the porous samples obtained from the measurements performed on single elements (as described in the previous section) are reported in Table I, together with the corresponding properties of PZT-5A material, widely used in receiving systems. A more extensive comparison with other piezoelectric materials is given in Ref. 20, where hydrophones based on these materials are also presented and compared. The free permittivity ϵ_{33}^{T} was obtained from the measured capacity, by taking into account the effective geometry of the plates and electrodes. The piezoelectric voltage constant g_h was calculated from Eq. (2) by dividing the value of sensitivity measured in air by the thickness of sample, while the piezoelectric charge constants d_h and d_{31} were given by the relationships $d_h=g_h\epsilon_{33}$ and $d_{31}=1/2(d_{33}-d_h)$, respectively. It can be observed that the hydrostatic FOM of the porous material is a few orders of magnitude higher than that corresponding to PZT-5A.

The admittance versus frequency curve of the hydrophone evidenced two main peaks, attributed to the length resonance (approximately 35 kHz) and thickness resonance (approximately 167 kHz) of the piezoelectric elements.

The free-field voltage sensitivity of the constructed planar hydrophone (measured without preamplifier) is shown in Fig. 5 for the frequency range between 1 kHz and 40 kHz. It can be observed that the hydrophone is characterized by a high sensitivity of approximately 193 dB $re{:}1$ V/μPa, with almost neglectable level variations within ± 1 dB, up to 22 kHz. The sudden increase in level, at approximately 35 kHz, is due to the first resonance mode of the piezoelectric elements.

Figure 6(a)–(d) shows polar plots of hydrophone horizontal (and vertical) directivity patterns measured at six different frequencies: 5, 10, 15, 20, 30, and 40 kHz. The three

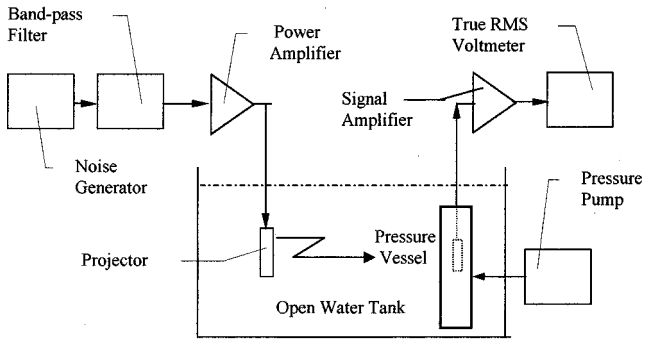

FIG. 4. Experimental setup for under pressure sensitivity measurement.

TABLE I. Main physical characteristics of the porous PZT samples, compared to those corresponding to PZT 5A.

	ρ (g/cm^3)	ρ/ρ_{PZT}	$\epsilon_{33}^T/\epsilon_0$	$\tan\delta$	s_{11}^E (10^{-12} m^2/N)	s_{33}^E (10^{-12} m^2/N)	k_{31}	k_{33}	d_{31} (10^{-12} C/N)	d_{33} (10^{-12} C/N)	d_h (10^{-12} C/N)	g_{31} (10^{-3} Vm/N)	g_{33} (10^{-3} Vm/N)	g_h (10^{-3} Vm/N)	$d_h g_h$ (10^{-15} m^2/N)
Porous PZT	4.78	0.61	500	0.03	58	75	−0.08	0.5	−39	295	217	−8.8	66.6	49	10 600
PZT5A	7.75	1	1700	0.02	16.4	18.8	−0.34	0.7	−171	374	32	−11.4	24.8	2	64

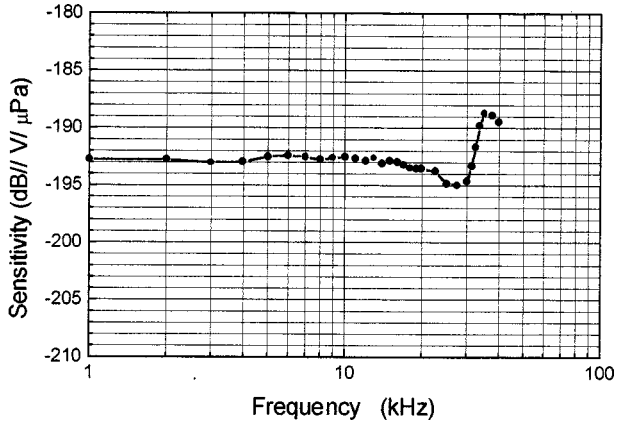

FIG. 5. Measured free-field sensitivity of planar hydrophone versus frequency.

patterns in Fig. 6(a) have been obtained at 5 kHz, 10 kHz, and 15 kHz, with the frequency increasing toward the center. The 0° point on all diagrams corresponds to the hydrophone acoustic axis pointing to the projector. Since the hydrophone was symmetrically loaded on each face, the beam patterns are bidirectional. At frequencies below 5 kHz the wavelength is much higher than hydrophone dimensions, therefore it becomes omnidirectional (within ± 1.5 dB). A simple calculation following well known directivity formula[23] shows that the measured directivity patterns of the constructed hydrophone correspond to those expected from a 86-mm line.

The equivalent noise pressure of the hydrophone has been estimated by using the measured values of sensitivity $M=-193\,\mathrm{dB}\,re{:}\,1\,\mathrm{V}/\mu\mathrm{Pa}$, capacity $C_H=5517\,\mathrm{pF}$, loss factor $\tan\delta=0.03$ and ambient temperature $T=286\,\mathrm{K}$ in Eq. (1). The results are plotted as curve 3 in Fig. 7, for the frequency range 0.1–10 kHz. The influence of the directivity factor R_θ has been neglected in Eq. (1) in the frequency range below 10 kHz. Indeed, an estimation of the directivity index $DI=10\log R_\theta$ following the theoretical approach of Ref. 24 gives at 5 kHz $DI\cong 0.9\,\mathrm{dB}$ and at 10 kHz $DI\cong 3.5\,\mathrm{dB}$, which does not significantly alter the results. The inherent noise pressure of a typical preamplifier stage (such as AD475 from Analog Devices) has been also included, by hypothesizing a noise voltage source of 4 nV/$\sqrt{}$Hz together with a noise current source of 7 fA/$\sqrt{}$Hz and a 10-MΩ input impedance. A software program for analysis of analogical networks (SPICE) has been used for simulating the preamplified hydrophone and for calculating its total noise pressure. The total equivalent noise pressure of the hydrophone including preamplifier should be lower than the noise pressure corresponding to Knudsen sea state zero,[23] which is the lowest noise field that the hydrophone would be expected to measure. This is evident in Fig. 7, when comparing the total hydrophone noise pressure (curve 2) with the noise level at sea state zero (curve 1).

The variation of the sensitivity as a function of the pressure is shown in Fig. 8. The results are obtained by making the average of the measured values for the various frequency ranges. It can be observed that the sensitivity has a very small increasing, within 0.7 dB, when the static pressure is

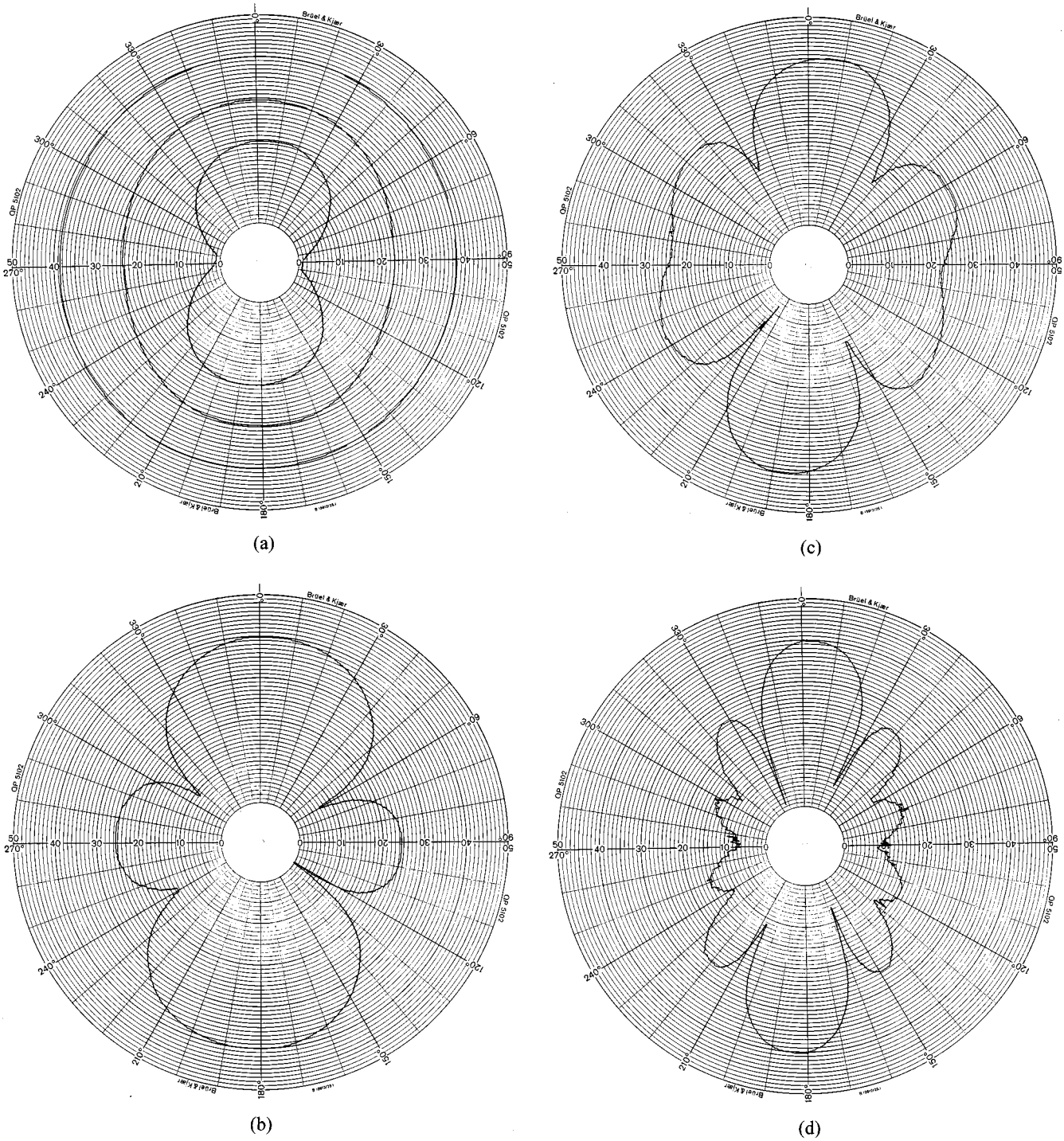

FIG. 6. (a) Experimental directivity patterns of the constructed planar hydrophone measured at 5, 10, and 15 kHz (frequency increasing toward the center). One division on the radial scale corresponds to 1 dB; (b), (c), and (d) the same as in (a), but at the frequencies 20, 30, and 40 kHz, respectively.

increased up to 60 bar. One can therefore conclude that the hydrophone based on porous piezoelectric ceramics can successfully operate even at a depth of 600 m.

IV. CONCLUSIONS

A new porous piezoelectric material with enhanced hydrostatic FOM has been prepared by mixing Nb-doped PZT calcined powder with fine particle starch powder. A planar hydrophone based on this material has been constructed and evaluated. The hydrophone was characterized by measurements of acoustic sensitivity, directivity, equivalent noise pressure level, and sensitivity variation with static pressure. The results of these measurements showed that porous piezoelectric ceramics can be successfully used in hydrophones, allowing one to obtain high acoustic sensitivity, low noise pressure level, and high signal-to-noise ratio. Testing of sensitivity variation with static pressure demonstrated that, in spite of the porosity of the active elements, the hydrophone can be safely operated at a relatively high depth levels, without damage or significant response variation.

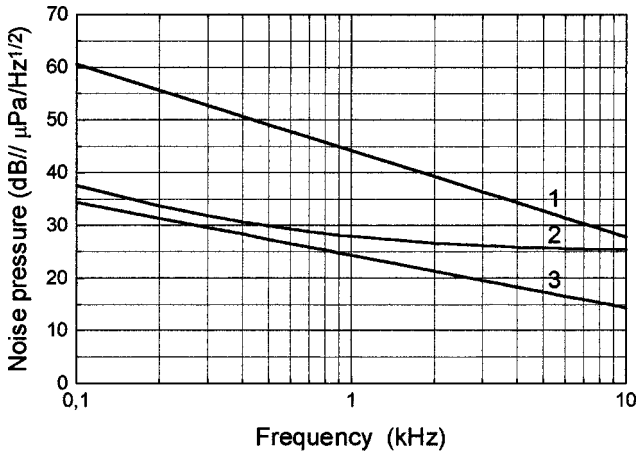

FIG. 7. Equivalent noise pressure level of hydrophone with (curve 2) and without (curve 3) preamplifier stage, compared with the noise level at Knudsen sea state zero (curve 1).

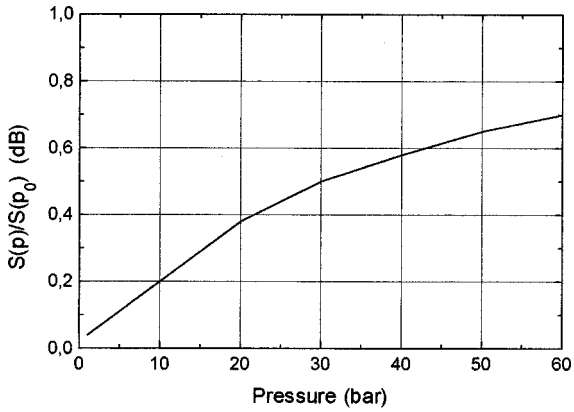

FIG. 8. Variation of the hydrophone sensitivity as a function of the static pressure.

[1] J. W. Young, ''Optimization of acoustic receiver noise performance,'' J. Acoust. Soc. Am. **61**, 1471 (1977).

[2] K. Hikita, K. Yamada, M. Nishioka, and M. Ono, ''Piezoelectric properties of the porous PZT and porous PZT composite with silicone rubber,'' Ferroelectrics **49**, 265 (1983).

[3] R. Y. Ting, ''Piezoelectric properties of a porous PZT ceramic,'' Ferroelectrics **65**, 11 (1985).

[4] M. B. Moffett and J. M. Powers, ''A ρc hydrophone,'' J. Acoust. Soc. Am. **80**, 375 (1986).

[5] M. B. Moffett, J. M. Powers, and W. L. Clay, Jr., ''Ultrasonic microprobe hydrophones,'' J. Acoust. Soc. Am. **84**, 1186 (1988).

[6] U. Bast and W. Wersing, ''The influence of internal voids with 3-1 connectivity on the properties of piezoelectric ceramics prepared by a new planar process,'' Ferroelectrics **94**, 229 (1989).

[7] C. Gaillard-Groleas, M. Lagier, and D. Sornette, ''Critical behavior in piezoelectric ceramics,'' Phys. Rev. Lett. **64**, 1577 (1990).

[8] T. Hayashi, S. Sugihara, and K. Okazaki, ''Processing of porous 3-3 PZT ceramics using capsule-free O_2-HiP,'' Jpn. J. Appl. Phys. **30**, 2243 (1991).

[9] K. Mizumura, Y. Kurihara, H. Ohashi, S. Kumamoto, and K. Okuno, ''Porous piezoelectric ceramic transducer,'' Jpn. J. Appl. Phys. **30**, 2271 (1991).

[10] S. Kumamoto, K. Mizumura, Y. Kurihara, H. Ohhashi, and K. Okuno, ''Experimental evaluation of cylindrical ceramic tubes composed of porous $Pb(ZrTi)O_3$ ceramics,'' Jpn. J. Appl. Phys. **30**, 2292 (1991).

[11] M. L. Dunn and M. Taya, ''Electromechanical properties of porous piezoelectric ceramics,'' J. Acoust. Soc. Am. **76**, 1697 (1993).

[12] O. Lacour, M. Lagier, and D. Sornette, ''Effect of dynamic fluid compressibility and permeability on porous piezoelectric ceramics,'' J. Acoust. Soc. Am. **96**, 3548 (1994).

[13] P. Loebmann and W. Glaubitt, ''Densification and crystallization of lead titanate aerogels,'' J. Am. Ceram. Soc. **80**, 2658 (1997), and references therein.

[14] F. Craciun, G. Guidarelli, C. Galassi, and E. Roncari, ''Critical behavior of ultrasonic wave velocities in porous piezoelectric ceramics,'' in 1997 IEEE Ultrasonics Symposium Proceedings (IEEE, New York, 1997), p. 573.

[15] F. Craciun, G. Guidarelli, C. Galassi, and E. Roncari, ''Elastic wave propagation in porous piezoelectric ceramics,'' Ultrasonics **36**, 427 (1998).

[16] F. Craciun, C. Galassi, E. Roncari, A. Filippi, and G. Guidarelli, ''Electroelastic properties of porous piezoelectric ceramics obtained by tape casting,'' Ferroelectrics **205**, 49 (1998).

[17] F. Craciun, C. Galassi, and E. Roncari, ''Experimental evidence for similar critical behavior of elastic modulus and electric conductivity in porous ceramic materials,'' Europhys. Lett. **41**, 55 (1998).

[18] S. Marselli, V. Pavia, C. Galassi, E. Roncari, F. Craciun, and G. Guidarelli, ''Characteristics of hydrophones based on porous piezoelectric materials, Proc. 4th European Conference on Underwater Acoustics, edited by A. Alippi and G. B. Cannelli (CNR-IDAC, Rome, Italy, 1998), p. 921.

[19] E. Roncari, C. Galassi, F. Craciun, G. Guidarelli, S. Marselli, and V. Pavia, ''Ferroelectric ceramics with included porosity for hydrophone applications,'' Proc. ISAF XI (ISAF XI, Montreux, 1998), to be published.

[20] S. Marselli, F. Silvano, C. Galassi, E. Roncari, F. Craciun, and G. Guidarelli, ''Use of porous lead zirconate titanate ceramics in piezoelectric hydrophones,'' Proceedings of Sonar Transducer '99 Conference (Birmingham, 1999), in print.

[21] D. Sornette, M. Lagier, S. Roux, and A. Hansen, ''Critical piezoelectricity in percolation,'' J. Phys. (France) **50**, 2201 (1989).

[22] M. Sahimi, *Applications of Percolation Theory* (Taylor and Francis, London, 1994).

[23] R. J. Bobber, *Underwater Electroacustic Measurements* (Naval Research Laboratory, U.S. Government Printing Office, Washington, DC, 1970).

[24] R. J. Urick, *Principles of Underwater Sound for Engineers* (McGraw-Hill, New York, 1967), pp. 47–49.

A low-frequency feedback-controlled audio system

Joe H. Mullins[a)]
Department of Mechanical Engineering, University of New Mexico, Albuquerque, New Mexico 87131

(Received 26 December 1998; accepted for publication 21 April 1999)

A novel closed-loop low-frequency speaker system has been designed, built, and tested which provides the control signal through the use of a single pressure-sensitive sensor internal to the speaker enclosure. This technique allows the use of one or more passive radiators in the same radiating system while ensuring that the control signal accurately reflects the total radiation from all elements. The nature of the sensor used also tends to correct for nonlinear distortion caused by finite cabinet volume, and the use of a passive radiator allows the production of a power level well beyond that produced by the same speaker in a sealed-box alignment. Feedback factors of 30 to 50 dB have been achieved using conventional speaker elements and active analog correcting networks. The effects of acoustical delay, placement of speaker and sensor, and direct acoustical radiation on the sensor are discussed, and results described. For purposes of subjective evaluation, conventional mid-range and high-frequency elements have been added to the system, and a stereo pair has been constructed and measured acoustically.
[S0001-4966(99)01308-9]

PACS numbers: 40.38.Ja, 43.38.Ar [SLE]

INTRODUCTION

A number of audio systems have been patented, proposed, and sold commercially that use some form of motional feedback. Many of these have been created for the purpose of replacing the last bastion of the open loop in high-fidelity audio systems with one that is controlled by way of a feedback system.

None, it would seem, has been universally successful; that is, successful in the sense of largely replacing the conventional directly driven loudspeaker in its many configurations. These include sealed-box systems, ported systems, those using passive as well as active radiators, and multiple speaker systems. Many of these are quite good, having been designed and redesigned, over and over, for many years, until they have become acoustically quite accurate.

Nevertheless, the idea of closing the loop around this element to bring the transduction of sound into the realm of feedback control systems retains its appeal, allowing us to focus on a single element, the sensor, as the principal determiner of audio fidelity. The system discussed below is one that takes an approach different from that of previous work, making it possible to use conventional loudspeaker elements in a configuration that has the attractive features described above. We believe it to be completely novel, although it is still an experimental (noncommercial) system.

This is a low-frequency audio system that uses a woofer and passive radiator in a feedback arrangement that includes all radiating members in a single feedback loop. This system uses a sensor that not only measures all of the radiation, but also provides some correction for nonlinearity arising from the finite size of the enclosure or other sources such as loudspeaker nonlinearity. It also allows feedback factors of 30 to 50 dB and unity gain crossover points of 300 to 1000 Hz.

The use of the passive radiator, in a particularly inexpensive and simple form, makes possible the production of very low frequencies at high power beyond the capability of the loudspeaker in a simple sealed-box alignment. The use of the large feedback and accurate sensor also allows us to drive the loudspeaker beyond its normal linear range and still maintain good acoustic accuracy and low distortion at high power.

I. THE FUNDAMENTAL OPERATING PRINCIPLES

A. The low-frequency limit

There are several fundamental considerations that underpin the approach to this system. We first consider just a sealed enclosure, with one or more portions of the walls capable of motion or flexing. They could be loudspeaker cones, passive radiators, or even flexible walls. We consider first the limit of low frequencies; that is, the regime in which the wavelength of sound is very long compared to the dimensions of the box.

In such a case the enclosure itself can be considered to be a ''simple'' sound source, and the radiation of sound will be given as follows:[1]

$$p=\frac{\rho}{4\pi r}Q'\left(t-\frac{r}{c}\right),$$

where p is the acoustic pressure (differential), ρ is the density of air, r is the radial distance from source, Q is the rate of change of volume element (prime denotes differentiation), t is time, and c is the velocity of sound.

If we now make a common assumption that the volume change is a sinusoid, we may write the far-field sound pressure p as

$$p=i\omega\frac{\rho}{4\pi r}Q_0e^{-ik(r-ct)}, \tag{1}$$

a)Electronic mail: JoeHMull@aol.com

where $k=\omega/c$, the propagation constant; ω is the angular frequency (rad/s); and Q_0 is the peak volume rate of change.

If we now compute the total acoustic power radiated, assuming the source is suspended in free space, we find that the power W is

$$W=4\pi R^2\left\langle\frac{p^2}{\rho c}\right\rangle=\frac{\rho\omega^2Q_0^2}{8\pi c},$$

where we have observed that $\langle p^2\rangle$ (average value of pressure) is $(p\ \text{peak})^2/2$.

The above expression is valid for radiation into an unobstructed sphere. If we use a more common assumption, radiation into a hemisphere (such as, for example, a piston in an infinite hemispherical baffle), this expression is doubled as

$$W=\frac{\rho\omega^2Q_0^2}{4\pi c}=\frac{\rho\omega^4U_0^2}{4\pi c}, \tag{2}$$

where U_0 is the amplitude of the volume change (not the rate of change, Q_0). It is therefore clear that if we measure and control the volume change (specifically as the inverse square of the frequency) we can control the acoustic power, independent of the source of that volume change, whether from the loudspeaker, passive radiator, or other. This suggests that the measurement of pressure in the enclosure would be a good method to control the volume change, and thus the radiated power. Measurement of pressure in the enclosure as method of evaluating the characteristics of the radiating system (e.g., a sealed or vented enclosure) is not a new idea, of course, having been observed by others[2,3] and treated extensively by D. B. Keele.[4]

It is the method of this control that is a key part of the system we are describing. In the low-frequency range, the pressure in the enclosure, which is sealed, obeys the adiabatic PV relationship

$$P/P_0=(V_0/V)^\gamma,$$

where P and P_0 are variable and fixed absolute pressures, respectively, V and V_0 are the corresponding volumes, and γ is the ratio of specific heats at constant pressure and constant volume.

This relationship is nonlinear, so that very high power levels and/or very low frequencies can begin to introduce nonlinear distortion in the pressure/volume relationship. However, if the sensor used is also a small sealed box, with a moving element (cone or membrane) that has a suspension whose compliance is high compared to that afforded by the small air volume in the sensor enclosure and the mass of the moving element sufficiently small, then the PV relationship in the enclosure mimics that of the larger system. That is, if the compliance of the sensor device is sufficiently large, the pressure inside the sensor enclosure for low frequencies is essentially the same as the pressure outside the sensor, which is the pressure inside the main enclosure. Then, since the two pressure relationships are the same, we find that

$$\frac{P}{P_0}=\left[\frac{V_0}{V}\right]^\gamma=\left[\frac{\nu_s}{\nu}\right]^\gamma,$$

where ν is the variable volume of the sensor and ν_s is the fixed volume of sensor.

This leads to the relationship

$$\frac{\nu}{\nu_s}=\frac{V}{V_0},$$

or that the sensor volume is exactly proportional to the main enclosure volume. Given that the moving element of the sensor is measured as a displacement, this implies that the motion of the sensor element accurately measures the main system volume displacement and thus the acoustic radiation.

In the system we are describing, the sensor consists of a small, high-compliance, long-throw woofer, mounted in a very small enclosure. The stiffness represented by the air in the small enclosure completely dominates the native stiffness of the sensor speaker, and so fulfills the conditions described above. This also places the resonance frequency of the moving element well above the primary range of interest. This resonance is also easily compensated by a pair of complex conjugate zeros in the electrical circuit, so that the sensor system can operate above its natural resonance for purposes of continuing the feedback loop to frequencies above this resonance. The result is a sensor that has the desired properties to above 1 kHz in the current design.

B. The direct acoustic radiation

As is clear from Eq. (1) the direct acoustic radiation goes as the first derivative of the volume rate of change, or as the second derivative of the volume change. The pressure arising directly from the volume change, however, which is the pressure change felt in the limit of low frequencies, is proportional only to the volume change itself (neglecting nonlinearity for the moment). Assuming that the sensor is exposed to both the gross pressure changes and to that arising from the acoustic radiation of, for example, the loudspeaker, and that there are negligible acoustic reflections, we see that the pressure will have a form similar to

$$p=AU_0-B\omega^2U_0, \tag{3}$$

where A and B are constants and we have omitted the $e^{i\omega t}$.

Obviously, this predicts a zero at some frequency such that $A=B\omega^2$. In the actual system, several processes introduce damping, for the most part because of acoustic absorbing material in the main enclosure, but also because of damping terms in the sensor and radiator. The result is that the pressure assumes the approximate form

$$p=U_0(A-B\omega^2+i\omega C), \tag{4}$$

where C is another constant. The values of the three constants depend upon the geometry, damping, and overall configuration of the sensor and radiators. In general it is obtained by measurement, but in any case has been found to be relatively easy to correct with a single complex conjugate pole pair. This fact is important in obtaining constant acoustic output from the actual system. The relationship of this pressure to the overall radiation has been extensively investigated[4] and is in general quite complex. For our purposes here, however, in the damped internal environment,

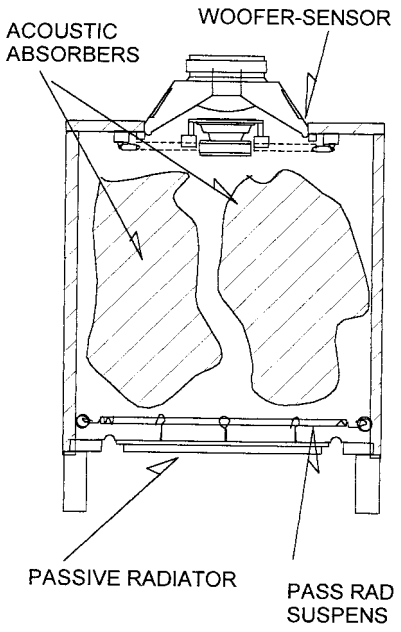

FIG. 1. Low-frequency system assembly, showing placement of the speaker, sensor, and passive radiator. The box horizontal outside dimension is 55.9 cm (22 in.).

the simple frequency dependence described above appears to hold, as shown later in Fig. 5.

II. DESCRIPTION OF THE PHYSICAL SYSTEM

The system is represented schematically in Fig. 1. The loudspeaker (woofer) is a standard, good quality 12-in. model. The loudspeaker used in the most recent implementation is a Swan 305 woofer. Some of the electromechanical parameters for this speaker are given in Table I.

Figure 1 makes obvious one of the critical features of this design. The speaker is mounted in reverse of the conventional way, with the magnet structure, basket, spider, and associated parts *outside* the cabinet, while the conventional radiating surface faces inward. That is, the speaker radiates into the outside environment from its back surface. This arrangement is shown in more detail in Fig. 2.

The reason for this novel arrangement can be understood by noting the placement of the sensor. The latter is placed as close as possible to the radiating surface of the woofer; in fact, the clearance is just enough to avoid mechanical interference during the maximum excursion of the woofer. This close spacing reduces to a minimum the delay between a signal applied to the woofer and its detection by the sensor.

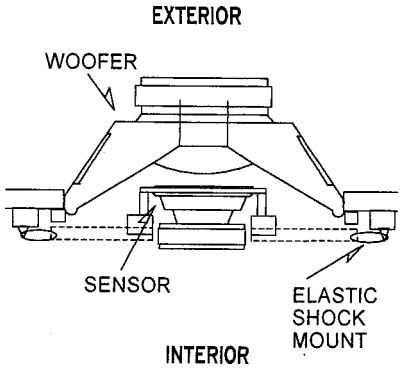

FIG. 2. Detail of the low-frequency speaker and sensor assembly. The woofer speaker is a 30-cm (12-in.) model.

As a consequence, a larger feedback factor can be effected, and the open loop unity gain point can be placed higher in frequency without excessive phase shift. We note that the sensor is substantially smaller than the woofer cone.

The sensor itself is a small, high-compliance woofer. The current version uses a Vifa P11WH-00-08, a high-compliance, long-throw 4 1/2-in. woofer. Some parameters of this loudspeaker are given in Table II. The reason for choosing a long-throw woofer is not for its delivery power, but rather to ensure that it is very linear over the range used.

The ''enclosure'' for the sensor is created by simply sealing off all openings in the basket and the pole-piece vent, as well as adding some additional varnish to better seal the surround. Many surrounds are relatively permeable, a situation that cannot be tolerated in a device that is designed to respond to very low frequencies.

The mounting for the sensor is a damped elastic one, to avoid transmitting mechanical vibrations directly to the sensor. Vibration mechanically coupled to the sensor inserts undesirable noise into the feedback system, and remains a problem that needs additional work. Additional damping is afforded by the filling material for the main enclosure. In fact, this damping material is critical to the operation of the system, since it is very important to avoid excessive reflections from the direct acoustic radiation.

The passive radiator for this system is simply a plate of material of the proper weight, preferably one with some acoustic damping. The surround is a standard 18-in. speaker surround and the suspension consists of two bungee cords stretched across the cabinet, parallel to the plane of the passive radiator. Probably a better solution (avoiding the inevitable aging of the bungee cords) would be the use of long coiled springs with suitable damping cover in place of the

TABLE I. Electromechanical parameters for the speaker used in the low-frequency system. It is a commercially available speaker, the Swan 305 woofer.

Moving mass, g	110.4	g
Suspension stiffness, N/m	2246	N/m
do coil resistance, Ω	5.2	
Force constant, N/A	14.74	N/A
Mechanical ''*Q*''	9.654	
Xmax (max linear amplitude), mm	7.3	
Effective radiating area, m^2	0.0531	

TABLE II. Electromechanical parameters for the speaker used as a sensor in the low-frequency system. It is a commercially available speaker, the Vifa P-11WH-00-08.

Moving mass, g	5	g
Suspension stiffness, N/m	534	N/m
dc coil resistance, Ω	5.4	
Force constant, N/A	5.8	N/A
Mechanical ''*Q*''	1.1	
Xmax (max linear amplitude), mm	3	
Effective radiating area, m^2	0.0062	

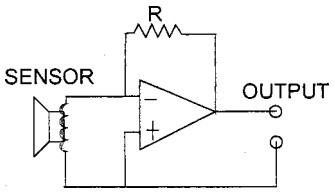

FIG. 3. The sensor preamplifier, shown in a simplified single-ended form. The transimpedance, resistor *R*, is 100 ohms.

bungee cords. As one of the major advantages of this system, it is not necessary for the passive radiator, speaker, and damping elements to be tuned in a way so as to produce an acoustically ''flat'' system. Instead, we have chosen the weight and size of the passive radiator to maximize the power output of the system (primarily by constraining the speaker excursion) down to its lowest rated frequency; that is, the lowest frequency for full power output. In this version that frequency is 21 Hz. The cabinet volume is approximately 142 liters (5 cubic ft).

We have chosen this configuration, with passive radiator on the bottom and woofer on the top, for convenience in combining this low-frequency radiator with a mid- and high-frequency portion. Placing the woofer (which is the dominant radiator at the woofer/midrange crossover point) at the top of the cabinet puts it in the closest possible proximity to the mid-range speaker. This makes for a much cleaner crossover. The short legs, of course, are necessary to raise the passive radiator off the floor.

There are two other advantages to this configuration. One, it is a more or less axial arrangement, making it easy to merge with a system designed to approximate a radiating tower. Two, it causes the reaction forces from the rather heavy passive radiator to be vertical, substantially reducing the cabinet vibration that would be present were the passive radiator placed on the side of the enclosure.

III. THE SIGNAL AND POWER SYSTEMS

To take maximum advantage of the potentially very low noise of the sensor, we feed the output coil into a low-input impedance transimpedance amplifier. A single-ended version of this amplifier is shown in Fig. 3. In the actual case we use a balanced version, reducing the stray noise pickup such as ac hum. This arrangement gives the sensor a signal-to-noise ratio in excess of 100 dB.

The system block operation is shown schematically in Fig. 4. The overall operation is as follows. The input signal passes through a variable gain stage and a filter stage. The purpose of both is to avoid the application of excessive signals to the feedback system, which by its nature will drive the system to destruction if the signal so demands. In particular, the filter contains a very sharp (8th-order maximally flat) low-frequency cutoff to avoid the introduction of subsonic signals that, because of the very high feedback factor, are capable of driving the loudspeaker to excessive excursions. The variable gain amplifier is activated only if the output signal to the speaker exceeds safe values, at which point it reduces the input signal temporarily. It thus acts as a limiter. The filter stage also has the crossover network to the

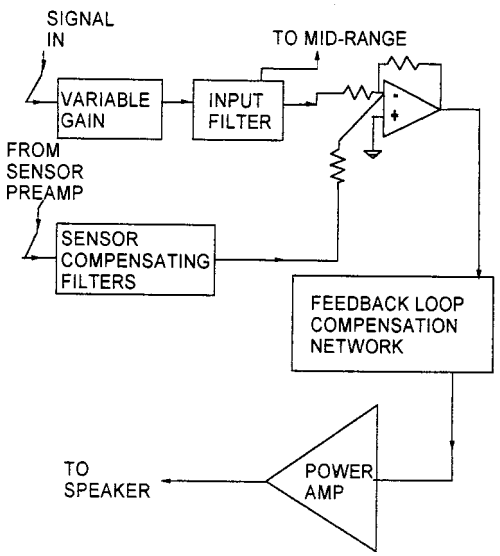

FIG. 4. Block diagram of the low-frequency portion of the electronic system. The mid-range and high-frequency portion, not shown, is a conventional-powered speaker system.

mid- and high-frequency portions of the system. All filters used in this implementation are active analog filters.

After amplification, the signal is conditioned by the feedback loop compensation network to provide the appropriate frequency response for the feedback loop. The action of the network is discussed in more detail below. The output of the network is then fed to the power amplifier for driving the speaker.

The output of the sensor is conditioned electronically in several ways. In the first place, there is correction for the natural resonance of the sensor, as discussed above. There is also a complex conjugate pole pair to correct for the mixing of the gross pressure changes with the direct acoustic radiation, resulting in the behavior shown in Eq. (4).

Finally, it is necessary to correct the final output so that the signal is proportional to acoustic intensity. As can be seen from Eq. (2), this implies that the signal should be proportional to the volume displacement times the frequency squared, or twice differentiated. One derivative occurs automatically since the sensor coil responds to velocity, not displacement. It is necessary only to insert a single zero below the frequency range of interest to produce the proper signal. First, the (linearized) response E_S of the sensor is given to a good approximation by

$$E_S = \frac{i\omega p\,\eta a\,\kappa g}{1-(\omega/\omega_0)^2 + i\omega/(\omega_0 Q_s)}, \tag{5}$$

where η is the overall compliance of the sensor element, including enclosure, a is the area of the sensor moving element, κ is the sensor force constant, g is the gain of the sensor preamplifier, Q_s is the ''Q'' of the sensor assembly, ω_0 is the resonance frequency of the sensor assembly, and p is the differential pressure incident on the sensor.

The incident pressure is given by Eq. (4). Substitution of this expression yields

$$E_S = \frac{i\omega U_0 \alpha \eta \kappa g (A - B\omega^2 + iC\omega)}{1 - (\omega/\omega_0)^2 + i\omega/(\omega_0 Q_S)}. \quad (6)$$

We correct this signal with the network, given by

$$N_S = \frac{\{1 + i\omega/\omega_L\}\{1 - (\omega/\omega_0)^2 + i\omega/(\omega_0 Q_S)\}}{A - B\omega^2 + iC\omega}, \quad (7)$$

where ω_L is a frequency well below the acoustical range of interest.

The product E_C of N_S and E_S is then given by

$$E_C = i\omega U_0 a \eta \kappa g (1 + i\omega/\omega_L), \quad (8)$$

that becomes, for $\omega \gg \omega_L$

$$E_C \approx -\omega^2 U_0 a \eta \kappa g/\omega_L, \quad (9)$$

which is the necessary condition for the signal to represent accurately the radiated power.

The constants *A*, *B*, and *C*, as well as the constants in the sensor resonance equation, are determined by measurement, although good approximations can be obtained by careful modeling. The sensor network, as all the other networks in this implementation, is realized with active filters. They are stable and relatively simple.

Primarily, the feedback loop compensation network determines the stability and the performance of the feedback loop. It is selected to bring the gain to unity at low frequencies and at high frequencies with reasonable phase margins and with large open-loop gain in the center of the range. Recall that the overall loop gain includes the transfer function between the acoustic radiating elements and the sensor. This is difficult to model over the entire frequency range and in practice has been determined by direct measurement. With this function in hand, however, the rest of the network design, although complex, is relatively straightforward (for a typical open-loop gain, see Fig. 8).

To give some idea of the values involved, in the current design the resonance frequency of the sensor is around 275 Hz and the apparent ''zero'' caused by the interference between the gross cabinet pressure and the acoustic radiation is around 65 Hz. These can be seen in Fig. 5. We have found that it requires around 20 poles and zeros, not counting the sensor correcting network or the input filters, to make a reasonably comfortable feedback loop.

This system was designed to put out approximately 450 mW of acoustic power throughout its range, assuming radiation into a hemisphere (resulting in about 900 mW into a quadrant of a sphere, a better approximation to a large room). Its low point is 21 Hz, and its high point is determined, of course, by the crossover to the mid-range system. In order to supply this much acoustic power, approximately 150 W of electrical output power is required at the most inefficient point.

IV. STABILITY OF THE FEEDBACK LOOP

An important consideration for this type of system is the stability of the loop. In particular, as remarked before, the gain at high frequencies must be brought to unity gain and below before the phase shift has equaled 180 deg, and preferably considerably less than that. The high-frequency phase

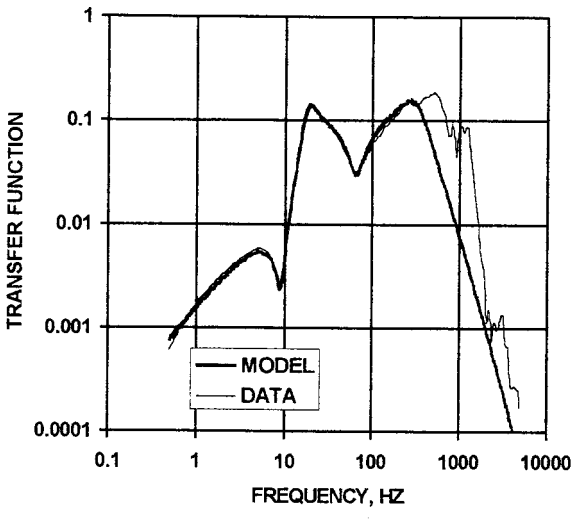

FIG. 5. A comparison of the modeled and measured transfer function between voltage applied to the woofer and the output from the sensor preamp.

shift comes partly from the gain slope, and partly from the nonminimal phase portion, the delay. We have discussed the manner of addressing the high-frequency part by means of the physical proximity of the sensor. The low-frequency unity gain point is another matter.

Since the transfer function at very low frequencies between radiation and sensor is primarily determined by the gross pressure changes in the enclosure, it is important that this be reasonably well behaved. The pressure/displacement relationship is well behaved for a sealed box, of course, the pressure being simply proportional to the displacement. The system we have described uses a passive radiator that, although sealed, has a finite compliance by way of the suspension illustrated in Fig. 1. Therefore, at sufficiently low frequencies the pressure/displacement relationship is still proportional (independent of frequency), although the proportionality constant is different, determined primarily by the area of the passive radiator and its suspension compliance. Under these circumstances it is easy to effect a stable unity gain crossover.

Were the passive radiator an open vent, as in a normal ''bass reflex'' cabinet, this relationship would not be so simple, and the transfer function would fall off much more rapidly at very low frequencies. In fact, at frequencies below the Helmholtz resonance the pressure drops as the square of the frequency for fixed excursion of the speaker, making the velocity fall as the third power. This makes the achievement of a good gain crossover very difficult, if not impossible, without the introduction of significant low-frequency noise because of the very large gains needed at low frequencies. This approach was in fact attempted before the current model, and was shown to have extremely poor performance. Therefore, it is critical to this design to use a solid passive radiator that is sealed and suspended with a relatively stable compliance.

V. OTHER SENSOR APPROACHES

There are other arrangements that could be used to approximate the results described above, assuming the use of a

solid passive radiator instead of a vent. For example, accelerometers could be placed on the passive radiator and speaker, or a moving-coil sensor could be used on one or both, assuming the passive radiator was equipped with a magnet structure and coil. This approach is described in an earlier patent by the author;[5] an appropriate combination of sensors on these two elements could accomplish the same purpose as the sealed-box moving-coil sensor described above. This implies that the main radiator and passive radiator are acting essentially as pistons, or at least with electronically correctable deviations from piston behavior. The method described in this paper requires no such assumption, but does introduce some acoustic delay and the added complication of the direct acoustic radiation. Neither of these drawbacks appears to be serious, however.

VI. MEASURED RESULTS AND COMPARISON TO MODEL

In order to test the various aspects of the system described above, we have constructed a set of two of the systems. Since it is difficult to do subjective tests as well as quantitative ones with a single low-frequency system or even a pair of them, we have also added a high-frequency component to each. This high-frequency component is a Dynaudio ''Gemini'' kit, which is designed as a full-range system using two small, high-quality woofers and vents along with an excellent tweeter. It would appear to be able to handle the full power level for which the low-frequency system is designed, although not at the lower end of its range. However, the electronic crossover employed rolls off the Gemini at lower frequencies, so this is not a problem. This is described in more detail in the results that follow.

A. Woofer-sensor transfer function

The transfer function is shown in Fig. 5. Two results are plotted there: the measured values and the values predicted by the model. The model is essentially that of a modified ''lumped constant'' with the direct radiation component added. In order to obtain the fit shown, the attenuation coefficient of the absorbing material in the box was adjusted empirically, and some adjustment had to be made to the radiation coefficient of the speaker. It was also necessary to adjust the compliance and damping of the passive radiator empirically, since no accurate objective measurements were made. Masses of speaker and passive radiator, all speaker parameters, enclosure volume, and sensor parameters were measured independently.

The measurements of the sensor were carried out at the output of the sensor preamplifier, which is a very-low-noise device with an effective input impedance of zero and a transimpedance of 100 ohms. All measurements, including the acoustical ones described below, were carried out at a relatively high power level, with a fixed 25 volts peak across the main speaker.

These measurements show a relatively good fit except at the highest frequencies. Since the model did not take into account either speaker cone mode breakup or box resonances, it is not surprising that the measurements and model disagree at high frequencies. For the most part, however, these deviations are at frequencies well outside the designed range of the woofer system.

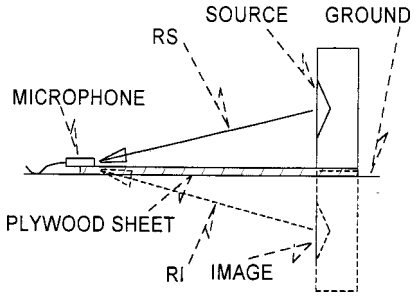

FIG. 6. The arrangement used to make acoustical measurements on the speaker elements. The measurements were made in the open.

From a practical point of view, whether or not the model and measurements agree is unimportant, since only the measured values are used in the design of the feedback system. However, the agreement adds some confidence that we are dealing with behavior that is reasonably well understood.

Principal features of this behavior are seen in the dip at approximately 9 Hz, which is caused by the resonance of the mass of the passive radiator with its suspension, and the dip at approximately 65 Hz. The latter is the result of the interference between the volume pressure changes and the acoustic radiation described in the foregoing.

B. Acoustical measurements

In order to verify the basic elements of the system and to get some data for the design of the crossover network, we have done acoustical measurements on both the low-frequency and the Gemini systems. Because we were interested particularly in the low-frequency range of the speaker, and because no anechoic chamber with adequate low-frequency behavior was available at the time, we conducted the measurements in the open.

Since we were interested in measuring the system in a way that would allow us to predict the behavior in a fixed (albeit hypothetical) environment of radiation into a hemisphere, we used a ground-plane technique. In an open, paved area, with no structures close enough to cause problems with reflections, we placed a sheet of plywood, to create a hard, smooth, reflecting surface. Placed on this sheet were the microphone and the speaker assembly, with the speaker placed with the radiating area as close as possible to the plywood sheet. In the case of the woofer, this necessitated placing the system on its side.

The arrangement is shown schematically in Fig. 6. As can be seen, assuming the reflecting surface is flat and perfectly reflective, the distance from the microphone to the source is nearly the same as the distance from the microphone to the image of the source. Therefore, they add in phase, giving a result that, except for a small correction that amounts to increased radial distance (**RS** and **RI** in the figure), the measurements are those that would be obtained for the idealized hemisphere. The primary deviation to be expected is the misalignment of the microphone from the ideal

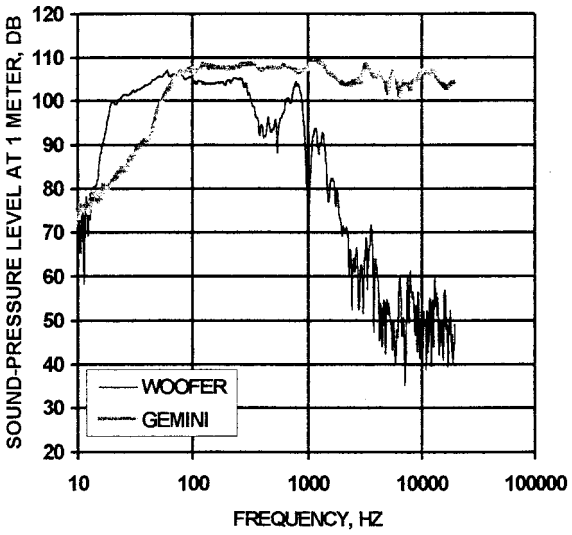

FIG. 7. Acoustical measurements of the low-frequency (woofer) and high-frequency (Gemini) elements with no feedback. The measurements are normalized to the sound-pressure level in dB relative to 20 mPa at 1 m from the center of the radiator. In both cases, the drive level is 25 V (peak).

plane represented by the plywood sheet. In our case, the geometry indicates that this would occur only for frequencies near the upper end (above 15 kHz). The use of such ground-plane acoustical measurements was investigated extensively by M. R. Gander,[6] and although it is not as convenient, for obvious reasons, as the internal environment provided by an anechoic chamber, the low-frequency measurements can often be much better.

It must be recognized that the equivalence of ground plane and idealized hemisphere radiation is strictly true only for the low frequencies, since at higher frequencies one cannot avoid the effect of the geometry of the speaker enclosures, as compared to an infinite wall. However, it is free of low-frequency anomalies. All measurements discussed below are based on the ground-plane technique. As usual, in a normal room the actual response of the system will be considerably stronger in the bass than shown by these results. We will refer to these as ''pseudo'' hemisphere quantities.

Measurements of one of the woofer systems and one of the Gemini systems are shown in Fig. 7 (the other in each case is very similar). These are open-loop measurements, with the same 25 V peak driving the speaker system. To maintain a comparable normalization, all acoustic data are expressed as dB, in this case SPL at 1 m with the 25 V peak drive, radiating into a (pseudo) hemisphere.

The microphone used in the measurements was a B&K 4190 Falcon series with a 2669 preamplifier. The frequency flatness should be better than ± 0.25 dB. All measurements were performed using an Ariel Corporation SYSid system.

VII. CONTROL SYSTEM AND FEEDBACK CHARACTERISTICS

The feedback loop correcting network and the network that corrects the sensor output discussed in the foregoing were designed using the actual measurements rather than the model. All are active filters, since the complexity of this

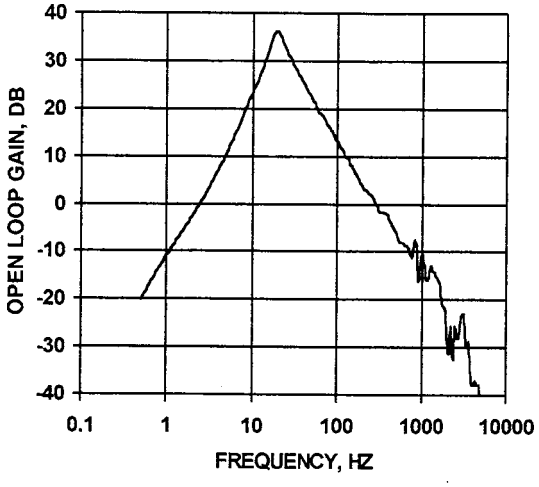

FIG. 8. Typical open-loop gain of the low-frequency system, including the speaker-sensor transfer function, all networks, and power amplifier. The peak gain is approximately 36 dB.

design makes the use of active filters greatly preferred. This extends to the crossover network as well, since separate power amplifiers, all contained within the same housing, are used for all four components. This makes it relatively easy to configure a superior crossover network.

A typical open-loop gain is shown in Fig. 8, and the corresponding Nyquist plot in Fig. 9. The peak open-loop gain is about 35 dB, and it occurs near the low end of the design range, where the driver and passive radiators have the greatest amplitude. A greater gain here could easily be achieved, but it is not necessary and only complicates the task of obtaining good phase and gain margins at the high-frequency gain crossover points.

The details of the gain near the unity gain points at high and low frequency are shown in Fig. 10. We can see that the phase margins are excellent at low frequency, somewhat less so at high frequency (note the critical point at minus 1 on the horizontal axis).[7] The reason, of course, is primarily because of the acoustic delay, which is negligible at low frequency but becomes a significant factor at high frequencies.

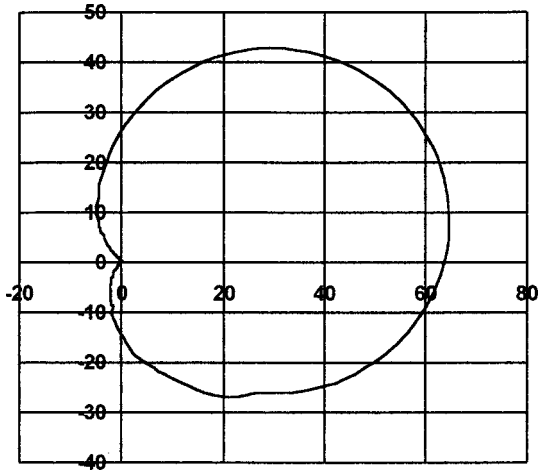

FIG. 9. Nyquist diagram of the open-loop gain, showing behavior pertinent to feedback stability. The real axis is horizontal and the imaginary axis (real frequency) is vertical. The diagram proceeds clockwise as frequency increases.

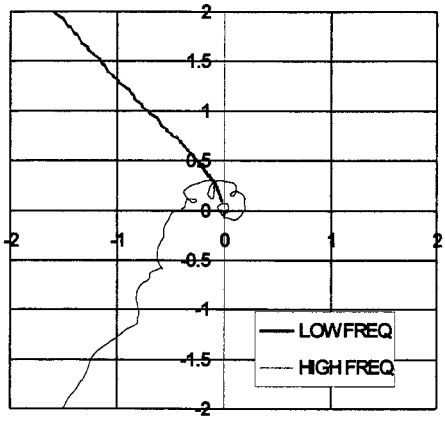

FIG. 10. Detail of the Nyquist diagram, showing behavior at very low and very high frequencies. Note that the critical point is at minus 1 on the horizontal (real) axis, and that the diagram shows an acceptable margin for high- and low-frequency gain crossover.

This uses the network of about 20 poles and zeros mentioned earlier. In operation the system is extremely stable and well behaved. The low-frequency cutoff and variable gain input amplifier are effective in preventing the system from being overdriven, which could easily happen with an unrestricted input.

VIII. PERFORMANCE OF THE SYSTEM WITH FEEDBACK AND CROSSOVER NETWORK

The closed-loop output of the woofer and the open-loop output of the mid-range/tweeter system have been used to design a crossover system for the two. The data shown in Fig. 11 are from acoustical measurements modified by the feedback. A small correction has been applied to account for the fact that the passive radiators (in the Gemini case, a vent) are displaced somewhat from the main radiator, and thus add somewhat differently at different locations. The corrections are actually quite small, but for completeness they have been applied so that the data in the figure are correct for a distance of 3 m from the main radiator of the woofer and at the same height (approximately 0.76 m).

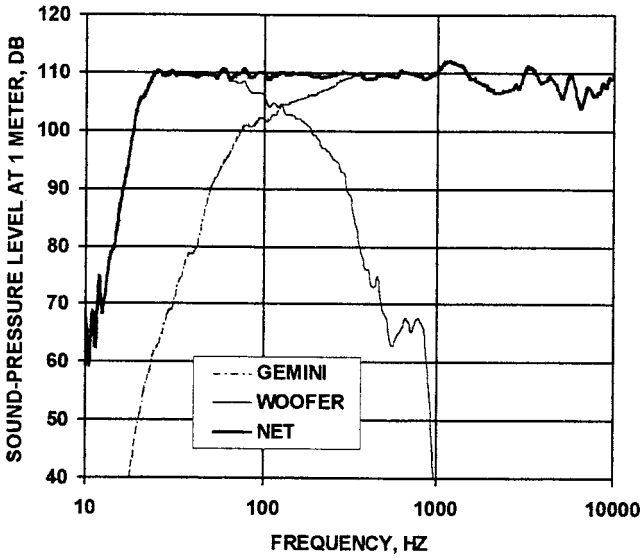

FIG. 11. Closed-loop output of the combined system. The measurements are normalized to the sound-pressure level in dB relative to 20 mPa at 1 m from the center of the low-frequency radiator, assuming radiation into a pseudo hemisphere. A small correction has been applied, however, because of the separation of the vent in the Gemini system from the primary radiator, to make these results apply strictly at a distance of 3 m. The chart represents the output at maximum designed power level.

The absolute value of the output, however, is normalized to SPL at 1 m (not 3), at maximum designed output power of the system, radiating into our pseudo hemisphere. The measurements from which these data were derived were taken at an altitude of approximately 6250 ft (1905 m) and a temperature of 73 F. The atmospheric pressure here is approximately 603 mm Hg. At sea level, the output power would be appropriately greater.

The crossover network is relatively simple compared to the feedback correcting networks. The high-frequency portion consists of a single first-order, low-frequency rolloff (the Gemini system). The woofer crossover is more complex, with a first-order, high-frequency rolloff, a single complex conjugate zero and three complex conjugate pole sets. The Gemini crossover could have been accomplished with passive elements, but it was very simple to do it with active elements.

IX. CONCLUSIONS

We have designed and constructed a novel low-frequency, feedback-controlled speaker system, using a single internal pressure-sensitive detector as the sensor. This system allows the use of one or more passive radiators whose contribution to the total radiation is automatically and correctly added to the sensor signal, while correcting for inherent nonlinearity of the enclosure pressure–volume relationship. The use of a solid passive radiator is important for low-frequency stability and low noise, but this radiator can be a simple plate with conventional speaker surround, provided that the suspension compliance is relatively stable. This allows the design to optimize other parameters, such as power output, rather than frequency flatness, since the sensor and the feedback correct the latter. The placement of the sensor to minimize acoustic delay from the primary speaker necessitates mounting the primary radiator facing inward, the reverse of the conventional mounting. A feedback factor of 30 to 50 dB at the lowest frequencies is attainable with relatively straightforward networks. The system uses only conventional loudspeaker elements.

ACKNOWLEDGMENTS

Early work focused on the feedback arrangement using a solid passive radiator and accelerometers (as cited in the 1974 patent[5]) was done while the author was a member of the California Institute of Technology faculty. The collaboration of Ronald A. Emerling and James D. Van Putten at this time is happily acknowledged. The current work was done while the author was a professor and later an emeritus professor in the Department of Mechanical Engineering at the University of New Mexico. The Ariel SYSid system is the property of the Health Sciences Center at the University

of New Mexico. The author gratefully acknowledges the support of the Department of Mechanical Engineering in this work.

[1] P. M. Morse, *Vibration and Sound* (2nd ed.) (McGraw-Hill, New York, 1948), pp. 312–313.
[2] L. L. Beranek, *Acoustics* (McGraw-Hill, New York, 1954), Chap. 8, Pt. XX, pp. 239–258.
[3] R. H. Small, ''Simplified Loudspeaker Measurements at Low Frequencies,'' J. Audio Eng. Soc. **20**(1), 28–33 (1972).
[4] D. B. Keele, Jr., ''Low-Frequency Loudspeaker Assessment by Nearfield Sound-Pressure Measurement,'' J. Audio Eng. Soc. **22**(3), 154–162 (1974).
[5] J. H. Mullins, US Patent 3,821,473, June 1974.
[6] M. R. Gander, ''Ground-Plane Acoustic Measurements of Loudspeaker Systems,'' J. Audio Eng. Soc. **30**(10), 723–731 (1982).
[7] For the classic discussion of stability criteria in feedback systems see, for example, H. W. Bode, *Network Synthesis and Feedback Amplifier Design* (Van Nostrand, New York, 1952). A more readable modern text is, for example, C. L. Phillips, and R. D. Harbor, *Basic Feedback Control Systems*, Alternate 2nd ed. (Prentice–Hall, Engelwood Cliffs, NJ, 1991).

Three-dimensional vibrations of hollow cones and cylinders with linear thickness variations

Jae-Hoon Kang
School of Constructional and Environmental System Engineering, Kyongju University, Kyongju, Kyongbook, South Korea

Arthur W. Leissa
Applied Mechanics Program, The Ohio State University, Columbus, Ohio 43210-1181

(Received 8 October 1998; revised 23 January 1999; accepted 12 May 1999)

A three-dimensional method of analysis is presented for determining the free vibration frequencies and mode shapes of hollow cones and cylinders with variable thickness. Displacement components u_s, u_z, and u_θ in the meridional, normal, and circumferential directions, respectively, are taken to be sinusoidal in time, periodic in θ, and algebraic polynomials in the s and z directions. Potential (strain) and kinetic energies of the cones and cylinders are formulated, and upper bound values of the frequencies are obtained by minimizing the frequencies. As the degree of the polynomials is increased, frequencies converge to the exact values. Novel numerical results are presented for thick, linearly tapered, hollow cones and cylinders with completely free boundaries. Convergence to four-digit exactitude is demonstrated for the first five frequencies of the cones and cylinders. The method is applicable to thin cones and cylinders, as well as thick and very thick ones. © *1999 Acoustical Society of America.* [S0001-4966(99)04808-0]

PACS numbers: 43.40.Ey [CBB]

INTRODUCTION

Three-dimensional (3D) analysis of structural elements has long been a goal of those who work in the field. With the current availability of computers of increased speed and capacity, it is now possible to perform 3D structural analyses of bodies to obtain accurate values of static displacements, free vibration frequencies and mode shapes, and buckling loads and mode shapes. Conical shells play an important role in many industrial fields and are used as structural components for loudspeakers, aircraft, space vehicles, and so on. Therefore, their dynamic behavior has drawn the attention of numerous researchers. However, the vibration of truncated conical shells has been studied to a lesser extent than that of cylindrical shells because of the greater mathematical complexity involved in characterizing their geometry and dynamic behavior, and the greater difficulty in solving the governing equations. Sufficient engineering data have not been obtained since the analysis requires considerable analytical labor and computational time even when the conical shells have uniform thickness and the analysis is based on two-dimensional classical thin shell theory.

The only analysis of truncated conical shells based upon a 3D method was made by Leissa and So[1] in 1995. They presented a procedure for determining the free vibration frequencies and corresponding mode shapes of truncated hollow cones of arbitrary thickness and having arbitrary boundary conditions by applying the Ritz method. The method was then used to obtain accurate and extensive frequencies for two sets of completely free, truncated hollow cones, one set consisting of thick conical shells, and the other being tori having square-generating cross sections. However, all the given numerical results were only for uniform thickness and completely free boundaries.

Three groups of researchers studied the conical shell with variable thickness using 2D shell theory. In 1977, Penzes and Padovan[2] analyzed a tapered cone by an approximate closed-form solution. In 1982, Irie[3] *et al.* treated the free vibration of a truncated conical shell having a meridional thickness expressed by an arbitrary function, in which the transfer matrix approach was used. The natural frequencies and the mode shapes of truncated conical shells with linearly, parabolically, or exponentially varying thickness were calculated numerically. The third group that studied variable thickness conical shells was Professor Takahashi and his coworkers. In one series of papers[4–6] they developed a 2D theory for moderately thick conical shells of variable thickness. This theory assumed a normal displacement component which does not vary through the thickness, and tangential displacements varying linearly, along with bending rotations, as in the well-known Mindlin plate theory. The vibration equations of motion reduced to a set of ordinary differential equations for which exact solutions could be found by the Frobenius power series method. Frequencies were found for shells having linear thickness variation with one circular and clamped, and the other either clamped or free. The analysis was generalized by Takahashi *et al.* in a subsequent publication,[7] permitting quadratic variations of the displacement components through the thickness, thereby generating a higher-order, 2D, thick shell theory.

However, none of the above references gave numerical results for completely free truncated hollow conical shells with thickness varying linearly along the meridional direction.

Several researchers have studied the 3D vibrations of hollow circular cylinders,[8–11] which are a special case of the cone. A summary of these studies may be found in the paper by So and Leissa.[11] These works all treated cylinders having uniform wall thickness.

Some references exist which analyze the vibrations of

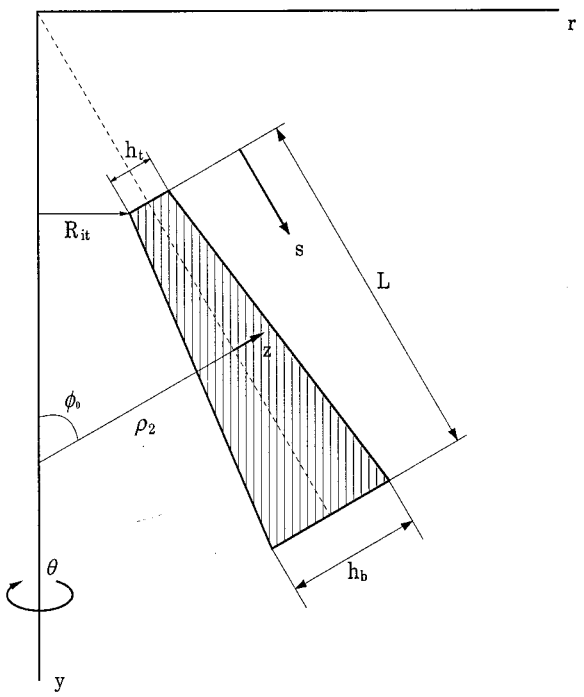

FIG. 1. Cross section of a truncated hollow cone with linearly varying thickness and the coordinates (s,z,θ).

circular cylindrical shells having continuously variable wall thickness by means of 2D shell theory. Early investigations of this type were by Gontkevich[12] and Federhofer.[13] In 1972, Stoneking[14] applied the partition method to formulate a set of equations which is used to calculate the natural frequencies and mode shapes of the cylinder with variable thickness having clamped–clamped boundary conditions. Takahashi[15] *et al.* and Suzuki[16] *et al.* have studied shells with different thickness variation parameters. They did not maintain a constant mass for the shell. Also, very few circumferential modes were analyzed. Radhamohan and Maiti[17] analyzed a shell of linearly varying thickness with a constraint on mass for its free vibration and buckling characteristics. In Refs. 18 and 19, axisymmetric vibration characteristics of cylindrical shells and vessels, with variable thickness in the direction of the generator, were analyzed. Suzuki[20] *et al.* discussed a cylindrical shell with variable thickness and capped with a circular plate. Bergman[21] *et al.* derived the equations for free vibration of a cylindrical shell of variable thickness. Sivadas and Ganesan[22] presented a semianalytical finite-element analysis for determining the natural frequencies of thin circular isotropic cylindrical shells with linear or quadratic thickness variation along the axial direction. Two end conditions, viz., simply supported ends and clamped ends, were considered for analysis using Love's first approximation shell theory to solve the problem. They also analyzed thick circular cylindrical shells with variable thickness for their axisymmetric vibration behavior[23] using a higher-order isoparametric axisymmetric finite-element method with 21 degrees of freedom. A linear variation of thickness along the axial direction, symmetric about the mid-length of the shell, was assumed, with the maximum thickness occurring at the support ends. They used a thick shell theory, which includes the thickness normal strain and transverse shear effect of the shells. The results were compared with two other theories, viz., the thick shell theory without thickness normal strain and Love's first approximation thin shell theory without shear deformation and rotary inertia. Suzuki[24] *et al.* presented an analytical solution procedure for free vibrations of rotating circular cylindrical shells with quadratic thickness variation along the axial direction having both ends clamped. However, none of the above references gave the numerical results for completely free circular cylindrical shells with linearly varying thickness along the axial direction.

In the present 3D analysis, the Ritz method is used to obtain accurate frequencies. Although the method itself does not yield exact solutions, proper use of displacement components in the form of algebraic polynomials permits one to obtain frequency upper bounds that are as close to the exact values as desired. Frequencies presented in this work are thus obtained that are very close to their exact values, being exact to four significant figures.

I. ANALYSIS

Figure 1 shows the cross section of a truncated hollow cone with a slant height L, slope angle ϕ_0, and linearly varying thickness (h) in the meridional coordinate s. The thicknesses at the top $(s=0)$ and bottom $(s=L)$ ends of the cone are denoted by h_t and h_b, respectively. The coordinate system (s,z,θ) is used in the analysis. The meridional (s) and thickness (z) coordinates are measured from the top end and normally from the mid-surface of the cone, respectively, and θ is the circumferential angle. One of the defining dimensions used is R_{it}, which is the radius (r) to the inner, top edge of the cone. Using this, and requiring it to be positive, eliminates the possibility of overlapping corners along this edge. The second principal radius of curvature of the middle surface is denoted by ρ_2, that is to say, the radius of curvature of the middle surface in the plane normal to the meridian. This radius may be expressed as follows (cf. Ref. 25):

$$\rho_2=\frac{s\cos\phi_0+R_{it}}{\sin\phi_0}+\frac{h_t}{2}. \tag{1}$$

Utilizing tensor analysis in the first author's dissertation (Kang[26]), the three equations of motion in the curvilinear coordinate system (s,z,θ) were found to be

$$\begin{aligned}
&\sigma_{sz,z}+\frac{1}{r}[(\sigma_{ss}-\sigma_{\theta\theta})\cos\phi_0+\sigma_{s\theta,\theta}+\sigma_{sz}\sin\phi_0]\\
&\quad+\sigma_{ss,s}=\rho\ddot{u}_s,\\
&\sigma_{zz,z}+\frac{1}{r}[(\sigma_{zz}-\sigma_{\theta\theta})\sin\phi_0+\sigma_{z\theta,\theta}+\sigma_{sz}\cos\phi_0]\\
&\quad+\sigma_{sz,s}=\rho\ddot{u}_z,\\
&\sigma_{z\theta,z}+\frac{1}{r}(2\sigma_{s\theta}\cos\phi_0+2\sigma_{z\theta}\sin\phi_0+\sigma_{\theta\theta,\theta})\\
&\quad+\sigma_{s\theta,s}=\rho\ddot{u}_\theta,
\end{aligned} \tag{2}$$

where r is the distance of an arbitrary point within the shell element from the axis of revolution (y), defined by

$$r \equiv s\cos\phi_0 + \left(z + \frac{h_t}{2}\right)\sin\phi_0 + R_{it}, \tag{3}$$

and the σ_{ij} are the normal ($i=j$) and shear ($i\neq j$) stress components; u_s, u_z, and u_θ are the displacement components in the s, z, and θ directions, respectively; ρ is mass density per unit volume; the commas indicate spatial derivatives; and the dots denote time derivatives.

The well-known relationships between the stress and tensorial strains ε_{ij} of isotropic, linear elasticity are

$$\sigma_{ii} = \lambda(\varepsilon_{ss}+\varepsilon_{zz}+\varepsilon_{\theta\theta}) + 2G\varepsilon_{ii}, \quad \sigma_{ij} = 2G\varepsilon_{ij} (i\neq j), \tag{4}$$

where λ and G are the Lamé parameters[27] expressed in terms of Young's modulus (E) and Poisson's ratio (ν) for an isotropic solid as

$$\lambda = \frac{E\nu}{(1+\nu)(1-2\nu)}, \quad G = \frac{E}{2(1+\nu)}. \tag{5}$$

The three-dimensional tensorial strains are found to be related to the three displacements u_s, u_z, and u_θ, by[26]

$$\begin{aligned}
&\varepsilon_{ss} = u_{s,s},\\
&\varepsilon_{zz} = u_{z,z},\\
&\varepsilon_{\theta\theta} = \frac{1}{r}(u_{\theta,\theta} + u_s\cos\phi_0 + u_z\sin\phi_0),\\
&\varepsilon_{sz} = \tfrac{1}{2}(u_{s,z} + u_{z,s}),\\
&\varepsilon_{s\theta} = \frac{1}{2r}(u_{s,\theta} - u_\theta\cos\phi_0 + ru_{\theta,s}),\\
&\varepsilon_{z\theta} = \frac{1}{2r}(u_{z,\theta} - u_\theta\sin\phi_0 + ru_{\theta,z}).
\end{aligned} \tag{6}$$

Substituting Eqs. (4) and (6) into Eqs. (2), one obtains a set of second-order partial differential equations in u_s, u_z, and u_θ governing free vibrations. Exact solutions are intractable, however, because of the variable coefficients $1/r$ that appear in many terms. Alternatively, one may approach the problem from an energy perspective.

During vibratory deformation of the body, its strain (potential) energy (V) is the integral over the domain (Ω),

$$V = \frac{1}{2}\int_\Omega (\sigma_{ss}\varepsilon_{ss} + \sigma_{zz}\varepsilon_{zz} + \sigma_{\theta\theta}\varepsilon_{\theta\theta} + 2\sigma_{sz}\varepsilon_{sz} + 2\sigma_{s\theta}\varepsilon_{s\theta} + 2\sigma_{z\theta}\varepsilon_{z\theta}) r\,ds\,dz\,d\theta. \tag{7}$$

Substituting Eqs. (4) and (6) into Eq. (7) results in the strain energy in terms of the three displacements,

$$V = \frac{1}{2}\int_\Omega [\lambda(\varepsilon_{ss}+\varepsilon_{zz}+\varepsilon_{\theta\theta})^2 + 2G\{\varepsilon_{ss}^2 + \varepsilon_{zz}^2 + \varepsilon_{\theta\theta}^2 + 2(\varepsilon_{sz}^2 + \varepsilon_{z\theta}^2 + \varepsilon_{s\theta}^2)\}] r\,ds\,dz\,d\theta, \tag{8}$$

where the tensorial strains ε_{ij} are defined in terms of the three displacements by Eqs. (6).

The kinetic energy (T) is simply

$$T = \frac{1}{2}\int_\Omega \rho(\dot{u}_s^2 + \dot{u}_z^2 + \dot{u}_\theta^2) r\,ds\,dz\,d\theta. \tag{9}$$

For convenience, the thickness z and meridional s coordinates are made dimensionless as

$$\zeta \equiv \frac{z}{h_m}, \quad \psi \equiv \frac{s}{L}, \tag{10}$$

where h_m is the average shell thickness, defined by

$$h_m \equiv \frac{h_t + h_b}{2}. \tag{11}$$

For the free, undamped vibration, the time (t) response of the three displacements is sinusoidal and, moreover, the circular symmetry of the conical shell allows the displacements to be expressed by

$$\begin{aligned}
u_s(\psi,\zeta,\theta,t) &= U_s(\psi,\zeta)\cos n\theta\sin(\omega t+\alpha),\\
u_z(\psi,\zeta,\theta,t) &= U_z(\psi,\zeta)\cos n\theta\sin(\omega t+\alpha),\\
u_\theta(\psi,\zeta,\theta,t) &= U_\theta(\psi,\zeta)\sin n\theta\sin(\omega t+\alpha),
\end{aligned} \tag{12}$$

where U_s, U_z, and U_θ are displacement functions of ψ and ζ, ω is a natural frequency, and α is an arbitrary phase angle determined by the initial conditions. That the variable θ is separable from the others (ψ,ζ,t), as used in Eqs. (12), in the correct solution is verified by examining Eqs. (2). The circumferential wave number is taken to be an integer ($n=0,1,2,3...,\infty$) for a closed shell ($0\leqslant\theta\leqslant 360°$) to ensure periodicity in θ. Then Eqs. (12) account for all free vibration modes except for the torsional ones. These modes arise from an alternative set of solutions which are the same as Eqs. (12), except that $\cos n\theta$ and $\sin n\theta$ are interchanged. For $n>0$ this set duplicates the solutions of Eqs. (12), with the symmetry axes of the mode shapes being rotated. But for $n=0$ the alternative set reduces to $u_s = u_z = 0$, $u_\theta = U_\theta^*(s,z)\sin(\omega t+\alpha)$, which corresponds to the torsional modes. The displacements uncouple by circumferential mode number (n), leaving only coupling in s and z.

The Ritz method uses the maximum potential (strain) energy ($V_{\max}$) and the maximum kinetic energy ($T_{\max}$) functionals in a cycle of vibratory motion. The functionals are obtained by setting $\sin^2(\omega t+\alpha)$ and $\cos^2(\omega t+\alpha)$ equal to unity in Eqs. (8) and (9) after the displacements (12) are substituted, and by using the nondimensional coordinates ζ and ψ in Eqs. (10) as follows:

$$V_{\max} = \frac{LG}{2}\int_0^1\int_{-\delta(\psi)/2}^{\delta(\psi)/2}\left[\left\{\frac{\lambda}{G}(K_1+K_2+K_3)^2 + 2(K_1^2+K_2^2+K_3^2) + K_4^2\right\}\Gamma_1 + (K_5^2+K_6^2)\Gamma_2\right] r^* d\zeta\,d\psi, \tag{13}$$

$$T_{\max}^* = \frac{\rho L h_m^2}{2}\int_0^1\int_{-\delta(\psi)/2}^{\delta(\psi)/2}[(U_s^2+U_z^2)\Gamma_1 + U_\theta^2\Gamma_2] r^* d\zeta\,d\psi, \tag{14}$$

where

$$K_1 \equiv \frac{U_s \cos\phi_0 + U_z \sin\phi_0 + nU_\theta}{r^*},$$

$$K_2 \equiv \frac{h_m}{L} U_{s,\psi},$$

$$K_3 \equiv U_{z,\zeta},$$

$$K_4 \equiv \frac{h_m}{L} U_{z,\psi} + U_{s,\zeta}, \tag{15}$$

$$K_5 \equiv \frac{nU_z + U_\theta \sin\phi_0}{r^*} - U_{\theta,\zeta},$$

$$K_6 \equiv \frac{nU_s + U_\theta \cos\phi_0}{r^*} - \frac{h_m}{L} U_{\theta,\psi},$$

and since the shell thickness variation is limited to be linear with s or ψ in this paper, the nondimensional thickness $\delta(\psi)$ can be defined by

$$\delta(\psi) \equiv \frac{h(\psi)}{h_m} = 2(1-h^*)\psi + h^*, \tag{16}$$

where h^* is the thickness ratio, defined by

$$h^* \equiv \frac{h_t}{h_m}, \tag{17}$$

Γ_1 and Γ_2 are constants defined by

$$\Gamma_1 \equiv \int_0^{2\pi} \cos^2 n\theta d\theta = \begin{cases} 2\pi & \text{if } n=0 \\ \pi & \text{if } n \geqslant 1 \end{cases},$$

$$\Gamma_2 \equiv \int_0^{2\pi} \sin^2 n\theta d\theta = \begin{cases} 0 & \text{if } n=0 \\ \pi & \text{if } n \geqslant 1' \end{cases} \tag{18}$$

and r^* is nondimensional, defined by

$$r^*(\psi,\zeta) \equiv \frac{r}{h_m} = \frac{L}{h_m}\psi\cos\phi_0 + \left(\frac{h^*}{2} + \zeta\right)\sin\phi_0 + \frac{R_{it}}{h_m}. \tag{19}$$

It is known that λ and G have the same units as E from Eqs. (5). The nondimensional constant λ/G in Eq. (13) involves only ν, i.e., $\lambda/G = 2\nu/(1-2\nu)$.

The displacement functions U_s, U_z, and U_θ in Eqs. (12) are further assumed as

$$U_s(\psi,\zeta) = \eta_s(\psi,\zeta)\sum_{i=0}^{I}\sum_{j=0}^{J} A_{ij}\psi^i\zeta^j,$$

$$U_z(\psi,\zeta) = \eta_z(\psi,\zeta)\sum_{k=0}^{K}\sum_{l=0}^{L} B_{kl}\psi^k\zeta^l, \tag{20}$$

$$U_\theta(\psi,\zeta) = \eta_\theta(\psi,\zeta)\sum_{m=0}^{M}\sum_{n=0}^{N} C_{mn}\psi^m\zeta^n,$$

and similarly for U_θ^*, where i, j, k, l, m, and n are integers; I, J, K, L, M, and N are the highest degrees of the polynomial terms; A_{ij}, B_{kl}, and C_{mn} are arbitrary coefficients; and the η are functions depending upon the geometric boundary conditions to be enforced. For example,

(1) Completely free: $\eta_s = \eta_z = \eta_\theta = 1$,

TABLE I. Convergence of frequencies $\omega L\sqrt{\rho/G}$ of a completely free, truncated hollow cone for the five lowest frequency modes for $n=2$ with $h_t/h_b = 1/3$, $\phi_0 = 60°$, $R_{it}/L = 1/4$, $h_m/L = 1/4$, and $\nu = 0.3$. (**TZ**=Total number of natural polynomial terms used in the z or ζ direction; **TS**=total number of natural polynomial terms used in the s or ψ direction; **DET**=determinant order.)

TZ	TS	DET	1	2	3	4	5
2	**2**	**12**	0.8686	1.641	3.668	4.759	7.721
2	**4**	**24**	0.8062	1.491	3.277	4.025	4.925
2	**6**	**36**	0.8019	1.481	3.263	3.907	4.830
2	**8**	**48**	0.8018	1.480	3.261	3.897	4.824
2	**10**	**60**	0.8018	1.479	3.261	3.896	4.823
3	**2**	**18**	0.8205	1.606	3.633	4.755	7.637
3	**4**	**36**	0.7792	1.442	3.228	3.945	4.883
3	**6**	**54**	0.7762	1.435	3.217	3.801	4.796
3	**8**	**72**	0.7761	1.434	3.216	3.790	4.791
3	**10**	**90**	0.7761	1.433	3.216	3.789	4.791
4	**2**	**24**	0.8028	1.597	3.619	4.746	7.610
4	**4**	**48**	0.7650	1.427	3.213	3.918	4.870
4	**6**	**72**	0.7623	1.420	3.203	3.760	4.783
4	**8**	**96**	0.7623	1.418	3.202	3.751	4.779
4	**10**	**120**	0.7622	1.418	3.202	3.750	4.778
5	**2**	**30**	0.8022	1.595	3.616	4.746	7.603
5	**4**	**60**	0.7644	1.427	3.213	3.916	4.869
5	**6**	**90**	0.7618	1.419	3.202	3.757	4.782
5	**8**	**120**	***0.7617***	1.418	3.202	3.749	***4.778***
5	**10**	**150**	0.7617	***1.417***	3.201	***3.748***	4.778
6	**2**	**36**	0.8014	1.590	3.612	4.746	7.602
6	**4**	**72**	0.7639	1.426	3.212	3.913	4.868
6	**6**	**108**	0.7618	1.419	3.202	3.756	4.782
6	**8**	**144**	0.7617	1.418	***3.201***	3.749	4.778
6	**9**	**162**	0.7617	1.417	3.201	3.748	4.778

(2) Top end ($s=0$) fixed, remaining boundaries free: $\eta_s = \eta_z = \eta_\theta = \psi$,

(3) Bottom end ($s=L$) fixed, remaining boundaries free: $\eta_s = \eta_z = \eta_\theta = \psi - 1$,

(4) Both ends fixed, remaining boundaries free: $\eta_s = \eta_z = \eta_\theta = \psi(\psi-1)$,

(5) Inner surface ($z=-h/2$) fixed, remaining boundaries free: $\eta_s = \eta_z = \eta_\theta = \zeta + \delta(\psi)/2$,

(6) Outer surface ($z=h/2$) fixed, remaining boundaries free: $\eta_s = \eta_z = \eta_\theta = \zeta - \delta(\psi)/2$,

(7) Both surfaces restrained normally and meridionally, but not circumferentially,

$$\eta_s = \eta_z = [\zeta + \delta(\psi)/2][\zeta - \delta(\psi)/2], \quad \eta_\theta = 1,$$

Both surfaces restrained normally, but not tangentially,

$$\eta_z = [\zeta + \delta(\psi)/2][\zeta - \delta(\psi)/2], \quad \eta_s = \eta_\theta = 1.$$

The functions of η_s, η_z, and η_θ shown above impose only the necessary geometric constraints. Together with the algebraic polynomials in Eqs. (20) they form function sets which are mathematically complete (cf. Ref. 27, pp. 266–268). Thus the function sets are capable of representing any three-dimensional motion of the body with increasing accuracy as the indices I, J, ..., N are increased. In the limit, as sufficient terms are taken, all internal kinematic constraints vanish, and the functions in Eqs. (20) will approach the exact solution as closely as desired.

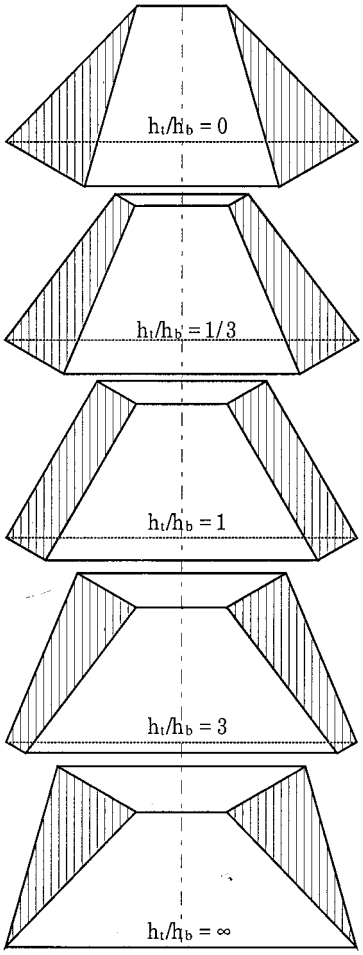

FIG. 2. Cross sections of linearly tapered truncated hollow cones with $\phi_0 = 60°$ and $h_m/L = R_{it}/L = 1/4$.

The eigenvalue problem is formulated by minimizing the free vibration frequencies with respect to the arbitrary coefficients, thereby minimizing the effects of the internal constraints present when the function sets are finite. This corresponds to the equations (cf. Ref. 28),

$$\frac{\partial}{\partial A_{ij}}(V_{\max} - T_{\max}) = 0 \quad (i = 0,1,2,...,I; j = 0,1,2,...,J),$$

$$\frac{\partial}{\partial B_{kl}}(V_{\max} - T_{\max}) = 0 \quad (k = 0,1,2,...,K; l = 0,1,2,...,L), \quad (21)$$

$$\frac{\partial}{\partial C_{mn}}(V_{\max} - T_{\max}) = 0 \quad (m = 0,1,2,...,M; n = 0,1,2,...,N),$$

Equations (21) yield a set of $(I+1)(J+1)+(K+1)(L+1)+(M+1)(N+1)$ linear, homogeneous, algebraic equations in the unknowns A_{ij}, B_{kl}, and C_{mn}. For a nontrivial solution the determinant of the coefficient matrix is set equal to zero, which yields the frequencies (eigenvalues). These frequencies are upper bounds on the exact values. The mode shape (eigenfunction) corresponding to each frequency is obtained, in the usual manner, by substituting each ω back into the set of algebraic equations, and solving for the ratios of coefficients.

TABLE II. Nondimensional frequencies $\omega L\sqrt{\rho/G}$ of completely free, truncated hollow cones with linearly varying thickness for $\phi_0 = 60°$, $R_{it}/L = 1/4$, $h_m/L = 1/4$, and $\nu = 0.3$. (T-torsional mode, A-axisymmetric mode. Numbers in parentheses identify frequency sequences.)

		h_t/h_b				
n	**Mode**	**0**	**1/3**	**1**	**3**	**∞**
0(T)	**1**	4.590	3.915	3.523	3.384	3.711
	2	7.531	6.748	6.497	6.396	6.814
	3	7.806	9.615	9.569	9.456	8.773
	4	10.554	9.738	12.670	10.674	10.043
	5	12.382	12.795	12.804	12.586	12.347
0(A)	**1**	(3) 2.261	(4) 2.081	(4) 1.928	(4) 1.817	(4) 1.786
	2	3.023	2.993	2.956	2.891	2.856
	3	4.648	4.117	3.650	3.241	3.101
	4	6.160	5.643	5.518	5.330	5.257
	5	6.831	6.051	5.661	5.678	6.379
1	**1**	(5) 2.536	(5) 2.330	(5) 2.158	2.040	2.082
	2	3.234	3.064	2.965	2.955	3.076
	3	4.154	3.679	3.476	3.276	3.285
	4	6.045	5.409	5.168	4.875	4.761
	5	6.275	5.783	5.348	5.270	5.352
2	**1**	(1) 0.9728	(1) 0.7617	(1) 0.6184	(1) 0.5770	(1) 0.6802
	2	(2) 1.360	(2) 1.417	(2) 1.468	(3) 1.459	(3) 1.408
	3	3.440	3.201	3.004	2.761	2.754
	4	4.051	3.748	3.696	3.739	3.875
	5	4.895	4.778	4.613	4.451	4.521
3	**1**	(4) 2.312	(3) 1.878	(3) 1.496	(2) 1.256	(2) 1.387
	2	3.049	3.090	3.095	3.034	3.035
	3	4.413	4.419	4.224	3.874	3.504
	4	5.139	4.979	4.791	4.706	4.886
	5	6.495	6.473	6.137	5.664	5.551
4	**1**	3.693	3.127	2.508	(5) 1.970	(5) 1.959
	2	4.683	4.554	4.448	4.225	4.069
	3	5.772	5.799	5.439	5.237	4.837
	4	6.569	6.759	6.497	6.018	5.992
	5	7.789	8.143	7.572	6.713	6.180

II. LINEARLY TAPERED HOLLOW CONES

Table I shows a convergence study made for a completely free, thick cone ($h_m/L = 1/4$) with considerable thickness variation ($h_t/h_b = 1/3$), having a small opening at the top ($R_{it}/L = 1/4$) and an apex angle of 30° ($\phi_0 = 60°$). The second of the five shapes in Fig. 2 is drawn with these ratios. Poisson's ratio (ν) is taken to be 0.3. Table I shows the first five nondimensional frequencies $\omega L\sqrt{\rho/G}$ for two circumferential waves ($n = 2$) in the mode shapes. The number of polynomial terms taken in the thickness (z or ζ) direction is $TZ = J+1 = L+1 = N+1$, and the number in the meridional (s or ψ) direction is $TS = I+1 = K+1 = M+1$. The resulting order of the frequency determinant generated is labeled ''DET'' in Table I.

It is seen that the frequencies have converged monotonically to four significant figures in Table I and, for the reasons given above, these are exact values to four digits. Values given in bold face type and underlined are the converged values for the smallest determinant sizes with which they are achieved. The four-digit convergence for the first five frequencies requires determinants of order 120 to 150. For $TZ = 6$, the largest value of TS which may be used is nine,

TABLE III. Convergence of frequencies $\omega L\sqrt{\rho/G}$ of a completely free, circular cylinder for the five lowest torsional ($n=0$) modes with $h_t/h_b=1/3$, $a/L=3/8$, and $h_m/L=1/4$. (**TZ**=total number of natural polynomial terms used in the z or ζ direction; **TS**=total number of natural polynomial terms used in the s or ψ direction; **DET**=determinant order.)

TZ	TS	DET	1	2	3	4	5
2	**2**	**4**	3.642	12.411	19.147	22.569	⋯
2	**4**	**8**	3.278	7.610	12.257	13.238	16.063
2	**6**	**12**	3.272	6.368	9.618	12.260	15.229
2	**8**	**16**	3.272	6.353	9.469	12.243	12.928
2	**10**	**20**	3.272	6.353	9.465	12.231	12.633
3	**2**	**6**	3.627	12.248	18.929	23.171	33.001
3	**4**	**12**	3.268	7.505	12.105	13.133	15.985
3	**6**	**18**	***3.263***	6.348	9.580	12.124	15.119
3	**8**	**24**	3.263	***6.335***	9.440	12.101	12.865
3	**10**	**30**	3.263	6.335	9.436	12.091	12.601
4	**2**	**8**	3.626	11.183	18.369	23.069	32.097
4	**4**	**16**	3.268	7.501	11.055	13.030	14.778
4	**6**	**24**	3.263	6.348	9.575	11.024	13.959
4	**8**	**32**	3.263	6.335	9.438	11.018	12.838
4	**10**	**40**	3.263	6.335	***9.434***	11.017	12.569
5	**2**	**10**	3.623	11.182	18.198	19.473	31.262
5	**4**	**20**	3.268	7.481	11.055	12.933	14.777
5	**6**	**30**	3.263	6.348	9.570	11.024	13.959
5	**8**	**40**	3.263	6.335	9.437	11.018	12.833
5	**10**	**50**	3.263	6.335	9.434	11.017	***12.568***
6	**2**	**12**	3.623	11.180	18.036	19.432	26.717
6	**4**	**24**	3.268	7.475	11.042	12.884	14.701
6	**6**	**36**	3.263	6.348	9.568	11.020	13.955
6	**8**	**48**	3.263	6.335	9.437	***11.014***	12.832
6	**9**	**54**	3.263	6.335	9.435	11.014	12.576

before numerical ill-conditioning is encountered with the ordinary algebraic polynomial trial functions of Eqs. (20).

It is interesting to note that the solutions presented in Table I for $TZ=2$, even when $TS=10$, are inaccurate when compared with the converged values for higher TZ. Nevertheless, these relatively inaccurate solutions are much more accurate than would be obtained from classical (thin) shell theory for this relatively thick shell, and also more accurate than solutions from a first-order shear deformation theory. The latter theory corresponds to $J=N=1$, but $L=0$, preventing thickness-stretch displacement. The classical theory has additional kinematic constraints between U_s, U_z, and U_θ. Conversely, if three-digit accuracy is needed for the frequencies, then Table I shows that TZ must be at least four.

Extensive additional convergence studies were also made (cf. Ref. 26) for other circumferential mode numbers ($n=0$, axisymmetric and torsional; and $n=1$) for the hollow cone of Table I, as well as for ones having other thickness variations ($h_t/h_b=1$ and 0). Convergence rates for all cases were approximately the same as that seen in Table I.

Table II presents accurate (four significant figure) frequencies for five thickness variations: $h_t/h_b=0$ (sharp edge at the top), $h_t/h_b=1/3$ (the configuration of Table I), $h_t/h_b=1$ (constant thickness), $h_t/h_b=3$, and $h_t/h_b=\infty$ (sharp edge at the bottom). Other parameters are the same as were used in Table I ($\phi_0=60°$, $R_{it}/L=1/4$, $h_m/L=1/4$, and $\nu=0.3$). Figure 2 is drawn with these shapes. Data are given for the axisymmetric, torsional, and $n=1$, 2, 3, 4 modes.

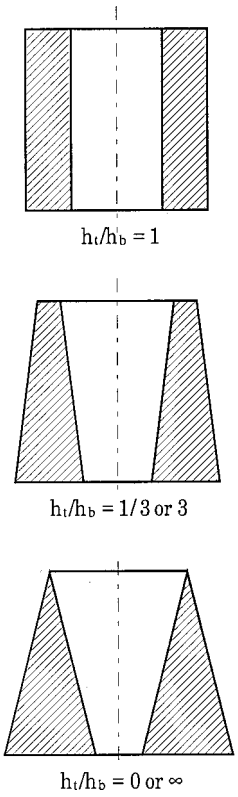

FIG. 3. Cross sections of linearly tapered hollow circular cylinders with $a/L=3/8$ and $h_m/L=1/4$.

Numbers in parentheses in Table II identify the lowest five frequencies for each configuration. It is seen that the lowest frequency is for $n=2$ for all five configurations, and that the lowest torsional frequency for each configuration is at least the twelfth frequency overall. For thin circular cylindrical shells, numerous results in the published literature show clearly that the fundamental frequencies typically occur at higher circumferential wave numbers, but that as the thickness increases the wave numbers decrease, and may be for $n=2$, especially when the ends are free (cf. Ref. 29, pp. 63 and 130), although this trend is not clearly established for thin conical shells. The 3D results of Table II, which are for very thick shells, are in accord with this trend.

III. LINEARLY TAPERED HOLLOW CYLINDERS

The circular cylinder is a special case of the cone which has $\phi_0=90°$, so that ρ_2 and r in Eqs. (1) and (3) become $\rho_2=a$ and $r=a+z$, where a is the radius of the mid-surface.

Table III presents a convergence study made for a completely free, thick ($h_m/L=1/4$) hollow circular cylinder ($a/L=3/8$) with considerable thickness variation ($h_t/h_b=1/3$). This is the second of the shapes seen in Fig. 3. Poisson's ratio (ν) is taken to be 0.3. Table III shows the first five nondimensional frequencies $\omega L\sqrt{\rho/G}$ of torsional modes ($n=0$).

It is seen that the four-digit convergence for the first five frequencies requires determinants of at least order 18 to 50. The first three torsional frequencies converge much more rapidly than those for the $n=2$ mode for the hollow cone seen previously in Table I since only one displacement com-

TABLE IV. Nondimensional frequencies $\omega L\sqrt{\rho/G}$ of completely free, circular cylinders with linearly varying thickness for $a/L=3/8$, $h_m/L=1/4$, and $\nu=0.3$ (T~torsional mode, A~axisymmetric mode. Numbers in parentheses identify frequency sequences.)

n	Mode	h_t/h_b 1	1/3	0
0(T)	**1**	(3) 3.142	(4) 3.263	(5) 3.789
	2	6.283	6.335	6.904
	3	9.425	9.434	9.446
	4	12.567	11.014	10.133
	5	13.628	12.560	12.927
0(A)	**1**	4.085	4.076	3.954
	2	4.303	4.335	4.462
	3	4.609	4.602	4.760
	4	5.786	5.891	6.230
	5	6.183	6.179	6.660
1	**1**	(4) 3.208	(3) 3.217	(4) 3.458
	2	(5) 3.786	3.881	4.258
	3	4.961	4.985	4.896
	4	5.862	5.747	6.016
	5	6.159	6.156	6.201
2	**1**	(1) 1.940	(1) 1.713	(1) 1.700
	2	(2) 2.090	(2) 2.326	(2) 2.592
	3	3.870	(5) 3.749	3.797
	4	4.996	5.128	5.448
	5	6.586	6.487	6.403
3	**1**	4.574	3.875	(3) 3.273
	2	4.695	5.068	4.876
	3	5.607	5.390	5.290
	4	6.954	6.955	6.793
	5	8.398	8.269	8.163
4	**1**	7.319	6.242	4.569
	2	7.357	7.308	6.491
	3	7.901	7.788	7.419
	4	8.963	8.929	8.452
	5	10.317	10.448	9.930

ponent u_θ is involved. One observes that a thick (2D) shell theory, as represented by $TZ=2$, yields frequencies which are significantly different than those from 3D analysis only in the case of the fourth mode.

Additional, accurate frequencies are given in Table IV, not only for the cylinder of Table III, but for two others ($h_t/h_b=1,0$) having the same ratios of mean thickness to height ($h_m/L=1/4$) and mid-surface radius to height ($a/L=3/8$). The three cylinders are depicted in Fig. 3. It is seen that the first two frequencies are both for $n=2$ for all three configurations, which is in accord with the trend for thick circular cylindrical shells explained above (cf. Ref. 29, pp. 63 and 130). It is also interesting to note that, in contrast with the data for the hollow cone (Table II, the lowest torsional frequency for each configuration is the third, fourth, or fifth one.

The correctness of the computer program developed and used in the present analysis was partially substantiated by using it to compare results from it with those presented by So and Leissa[11] for hollow cylinders. This is a special case of the present analysis when $\phi_0=90°$ and the thickness (h) is constant. Using the same numbers of terms in the displacement functions, the present program yielded the same frequencies (six digits) as those reported by So and Leissa (e.g., their Table 1). Moreover, So and Leissa obtained very close agreement (cf. their Table 3) with frequencies published by two other sets of researchers using other 3D method of analysis, one of them employing finite elements.

IV. CONCLUDING REMARKS

Accurate frequency data determined by the 3D Ritz analysis have been presented for thick, hollow cones and cylinders with linearly varying thickness along the meridional direction. The analysis uses the 3D equations of the theory of elasticity in their general forms for isotropic, homogeneous materials. They are only limited to small strains. No other constraints are placed upon the displacements. This is in stark contrast with the classical two-dimensional shell theories, which make very limiting assumptions about the displacement variations through the shell thickness. Although the method has the capability of analyzing accurately very thick shells, which 2D shell theories (thin or thick) cannot, it can also be applied to thin shells, thereby determining conclusively the accuracies of the shell theories.

The method is straightforward, but it is capable of determining frequencies and mode shapes as close to the exact ones as desired. It can therefore obtain benchmark results against which 3D finite-element results may be compared to determine the accuracy of the latter. Moreover, the frequency determinants required by the present method are at least an order of magnitude smaller than those needed by a finite-element analysis of comparable accuracy.

Numerical results were presented for linearly tapered cones and cylinders having all boundaries free. The method may also be applied accurately to cases where one or more of the boundaries are fixed, or partially fixed. This was demonstrated by Leissa and So[30,31] in 3D vibration analyses of circular cylinders having one of the circular end surfaces fixed, and the others free. The method of analysis employed there is a special case of the more general method presented here.

[1] A. W. Leissa and J. So, ''Three-dimensional vibration of truncated hollow cones,'' J. Vib. Control **1**, 145–158 (1995).
[2] L. E. Penzes and J. Padovan, ''Maxielement analysis for free vibrations of orthotropic shells of revolution,'' J. Sound Vib. **54**, 249–263 (1977).
[3] T. Irie, G. Yamada, and Y. Kaneko, ''Free vibration of a conical shell with variable thickness,'' J. Sound Vib. **82**(1), 83–94 (1982).
[4] S. Takahashi, K. Suzuki, E. Anzai, and T. Kosawada, ''Vibrations of conical shells with variable thickness,'' Bull. JSME **25**, 1435–1442 (1982).
[5] S. Takahashi, K. Suzuki, E. Anzai, and T. Kosawada, ''Axisymmetric vibrations of conical shells with variable thickness,'' Bull. JSME **25**, 1771–1780 (1982).
[6] S. Takahashi, K. Suzuki, and T. Kosawada, ''Vibrations of conical shells with variable thickness (continued),'' Bull. JSME **28**, 117–123 (1985).
[7] S. Takahashi, K. Suzuki, and T. Kosawada, ''Vibrations of conical shells with variable thickness (3rd report, analysis by the higher-order improved theory),'' Bull. JSME **29**, 4306–4311 (1986).
[8] R. S. Girgis and S. P. Verma, ''Method for accurate determination of resonant frequencies and vibration behavior of stators of electrical machines,'' IEE Proc. B. Electr. Power Appl. **128**, 1–11 (1981).
[9] G. M. L. Gladwell and D. K. Vijay, ''Natural frequencies of free finite length circular cylinders,'' J. Sound Vib. **42**, 387–397 (1975).
[10] J. R. Hutchinson and El-Azhari, ''Vibrations of free hollow circular cylinders,'' ASME J. Appl. Mech. **53**, 641–646 (1986).
[11] J. So and A. W. Leissa, ''Free vibrations of thick hollow circular cylinders

from three-dimensional analysis,'' ASME J. Vib. Acoust **119**, 89–95 (1995).
[12] V. S. Gontkevich, *Vibrations of Plates and Shells*, edited by A. P. Filipov (Nauk Dumka, Kiev, 1964). (Transl. by Lockheed Missiles and Space Co.).
[13] K. Federhofer, ''Über die Eigenschwingungen der Kreiszylinderschale mit veränderlicher Wanderstärke,'' Öster. Akad. der Wiss., Mat.-Nat. Klasse, Abt. Kka, 161 Bd., June 1952, 89–105.
[14] J. E. Stoneking, ''Free vibrations of shells of revolution with variable thickness,'' Nucl. Eng. Des. **24**, 314–321 (1973).
[15] S. Takahashi, K. Suzuki, T. Kosawada, and E. Anzai, ''Vibration of cylindrical shells with variable thickness,'' Bull. JSME **24**(196), 1826–1836 (1981).
[16] K. Suzuki, E. Anzai, and S. Takahashi, ''Vibrations of cylindrical shells with varying thickness,'' Bull. JSME **25**(205), 1108–1119 (1982).
[17] S. Radhamohan and M. Maiti, ''Vibration of initially stressed cylinders of variable thickness,'' J. Sound Vib. **53**, 267–271 (1977).
[18] K. Suzuki, M. Konno, and S. Takahashi, ''Axisymmetric vibration of cylindrical shell with varying thickness,'' Bull. JSME **24**(198), 2122–2132 (1981).
[19] K. Suzuki, M. Konno, T. Kosawada, and S. Takahashi, ''Axisymmetric vibration of vessel with varying thickness,'' Bull. JSME **25**(208), 1592–1600 (1982).
[20] K. Suzuki, S. Takahashi, E. Anzai, and T. Kosawada, ''Vibration of a cylindrical shell with variable thickness capped by a circular plate,'' Bull. JSME **26**(220), 1775–1782 (1983).
[21] R. M. Bergman, S. A. Sidorin, and P. E. Tovstik, ''Construction of solutions of the equations for free vibration of a cylindrical shell of variable thickness along the directrix,'' Mech. Solids **14**(4), 127–134 (1979).
[22] K. R. Sivadas and N. Ganesan, ''Free vibration of circular cylindrical shells with axially varying thickness,'' J. Sound Vib. **147**(1), 73–85 (1991).
[23] K. R. Sivadas and N. Ganesan, ''Axisymmetric vibration analysis of thick cylindrical shell with variable thickness,'' J. Sound Vib. **160**(3), 387–400 (1993).
[24] K. Suzuki, T. Kosawada, G. Shikanai, and K. Hayashi, ''Vibrations of rotating circular cylindrical shells with varying thickness,'' J. Sound Vib. **166**(2), 267–282 (1993).
[25] Edward Y. W. Tsui, *Stresses in Shells of Revolution* (Pacific Coast, 1968).
[26] Jae-Hoon Kang, ''Three-dimensional vibration analysis of thick shells of revolution with arbitrary curvature and variable thickness,'' Ph.D. dissertation, The Ohio State University, 1997.
[27] L. V. Kantorovich and V. I. Krylov, *Approximate Methods of Higher Analysis* (Noordhoff, Groningen 1958).
[28] W. Ritz, ''Über eine neue Methode zur Lösung gewisser Variationsprobleme der mathematischen Physik,'' J. Reine Angew. Math. **135**, 1–61 (1909).
[29] A. W. Leissa, *Vibration of Shells* (U.S. Government Printing Office, Washington D.C. 1973). (Reprinted by The Acoustical Society of America, 1993).
[30] A. W. Leissa and J. So, ''Comparisons of vibration frequencies for rods and beams from one-dimensional and three-dimensional analyses,'' J. Acoust. Soc. Am. **98**(4), 2122–2135 (1995).
[31] A. W. Leissa and J. So, ''Accurate vibration frequencies of circular cylinders from three-dimensional analysis,'' J. Acoust. Soc. Am. **98**(4), 2136–2141 (1995).

Optimized acoustic properties of cellular solids

Xiaolin Wang and Tian J. Lu
Department of Engineering, University of Cambridge, Cambridge CB2 1PZ, United Kingdom

(Received 18 December 1998; accepted for publication 16 May 1999)

The optimized cell size and shape, cell size variations, sample thickness, and air cavity depth behind the sample for best sound absorption performance of air-filled porous materials having simple cell morphologies are studied in this paper. The focus is on cellular foams that are rigidly framed, e.g., aluminum alloy foams and honeycombs. The governing equations of wave propagation are solved by using the point-matching method, and the predictions are compared with known analytical solutions. The effects of cell size variations are studied for Voronoi polygons. A domain-matching method is introduced to obtain the optimal combination of cell size and shape, sample thickness, and cavity depth for selected ranges of frequency. At given porosity, the effect of cell shape on sound absorption is small. The optimized cell size for best sound absorbers is on the order of ~0.1 mm for practical combinations of sample thickness, cavity depth, and porosity. A random distribution of cell sizes tends to tighten the region where combinations of sample thickness and cavity depth achieve high sound absorption coefficient. © *1999 Acoustical Society of America.*
[S0001-4966(99)06408-5]

PACS numbers: 43.50.Gf, 43.55.Ev, 43.20.Mv, 43.20.Hq [MRS]

INTRODUCTION

Sound absorption in porous media has long been an interest in the industry of noise control. An extensive experimental as well as theoretical literature exists for nonmetallic porous materials.[1–5] A new class of low-density foams, metallic foams, has novel mechanical, thermal, and electrical properties, and is currently under exploitation for a wide range of applications, including structural components for transportation vehicles and heat dissipation media for high power electronic devices. A less known feature of these cellular metals is their capability to absorb sound in applications such as lining of road tunnels, mufflers of cars, and sound silencers of aircrafts.[6,7]

The performance of sound absorbers is evaluated by the sound absorption coefficient, defined as the ratio between the absorbed and the incident sound energy. For a rigid-framed porous material such as metal foam, this absorption is mainly attributed to thermoelastic damping and viscous loss generated while the sound propagates through a large number of small air passages in the material. It is known that the shape and size of these passages, the thickness, and the mounting method of the material will all affect the actual value of the absorption coefficient. Hence in order to achieve best performance of absorption in a porous material such as metal foams, we need to answer questions of whether or not an optimized shape and size of cell exists, how to distribute cells with varying sizes, and how to choose the sample thickness and cavity depth behind a panel absorber.

Sound propagation in a circular tube was solved by Kirchhoff[8] where the simultaneous effects of thermal and viscous forces are accounted for. Zwikker and Kosten[1] later introduced a simpler approach where these two effects are decoupled. More recently, Stinson[9] gave two criteria for the validation of this simplification. It is shown that thermal and viscous effects can be separated when the tube radius r_w is greater than 10^{-3} cm, and the sound frequency f satisfies $r_w f^{3/2} < 10^6\ \mathrm{cm\,s^{-3/2}}$. This means that the frequency can reach as high as 10^6 Hz when $r_w \sim 10^{-3}$ cm, covering the range of frequencies and tube radius in practice. Aluminum foams and honeycombs having cells of size about $10^{-2} \sim 10^{-1}$ cm are currently available. The frequencies audible to the human ear are about 20 Hz~20 kHz. The generalization of this result by Stinson[9] to uniform pores having arbitrary shape of cross section validates the decoupling process for other pore cross-sectional geometries.

Exact solutions for specific cross-sectional shapes of uniform pores are available for circles, rectangles, slits, and triangles.[10] The finite-element method was used to examine the velocity profiles and boundary shear forces for sound propagation in narrow tubes of hexagonal and other cross sections.[11]

In addition to these analytical and numerical solutions for simple pore geometries, a well-known empirical exponential law was developed by Delany and Bazley[4] for a wide range of fibrous materials with porosities near unity. This exponential law does not specify a particular type of pore cross section, all sound propagation properties being functions of a single nonacoustic parameter—the static flow resistance. It leads to erroneous predictions at low frequencies, and is advised not to be extrapolated beyond the range of the experimental data.

Based on the general frequency dependence of the viscous forces, Allard and Champoux[5] developed a new empirical relationship for highly porous rigid-framed fibrous materials. In addition to the static flow resistance, two new parameters are needed, one related to the pore geometry and the other being the ratio of two length scales associated separately with viscous and thermal dissipation processes. A notable feature of Allard and Champoux's approach is that

physically sound predictions at both low and high frequencies are obtained.

Another theoretical approach for sound propagation through porous media is Wilson's relaxation-matched method.[12] In contrast to models based on matching low- and high-frequency asymptotic behaviors, Wilson's relaxation-type model is physically more realistic for all frequencies. It is based on the concept of modal wave modes and the dominance of a particular mode in the description of complex density and compressibility. Three parameters are needed in the relaxation model, i.e., static flow resistance and two relaxation times characterizing the process of wave fields to establish either viscous or thermal equilibrium in the material.

Note that the decoupled sound propagation equations are similar to those for structural membrane vibration, and a number of methods to deal with this type of vibration have already been developed. Solutions for sound propagation in pores of varying cross sections can therefore take this advantage. One of the methods is the point-matching method[13–15] where the boundary conditions are satisfied at a few selected points on the boundary. In this way, a semianalytical solution is achieved to approximate the exact solution.

The point-matching method is used in this paper to solve sound propagation through polygonal ducts such as those in hexagonal and Voronoi honeycombs. The effects of cell shape and size, cell size variations, sample thickness, and cavity depth are examined using a domain-matching method to establish the optimized acoustic properties of cellular foams.

I. BACKGROUND: CHARACTERISTICS OF SOUND ABSORPTION

Two fundamental characteristics describing sound propagation in uniform porous materials are wave impedance Z and propagation constant m.[1,10] Since air-filled metallic foams are concerned, it is assumed that the cell walls are rigid so that the mechanical damping in the material itself is neglected.

A general expression for wave impedance is

$$Z=\left[\frac{\rho}{C}\right]^{1/2}, \tag{1}$$

where ρ, C are the complex density and compressibility of the medium. The real part of the propagation constant m characterizes the attenuation of the wave as it travels across the material while the imaginary part denotes the phase shift of sound propagation. A general expression for this constant is

$$m=i\omega[\rho C]^{1/2}, \tag{2}$$

where ω is the angular frequency and $i=\sqrt{-1}$. Note that both the wave impedance and propagation constant are material properties.

For a sound propagating along a uniform tube, the complex density ρ_x is related to the pressure gradient dp/dz along the tube and the average velocity $\langle v\rangle_x$ of air particles inside the tube by[10]

$$\rho_x(\omega)\equiv\frac{i}{\omega\langle v\rangle_x}\frac{dp}{dz}, \tag{3}$$

where the bracket ''$\langle\cdot\rangle$'' denotes the average over the cross section of the tube and the subscript ''x'' is used to denote quantities associated with a single tube. The complex compressibility is

$$C_x(\omega)=\frac{\gamma-(\gamma-1)[\rho_0/\rho_x(N_{pr}\omega)]}{\gamma P_0}, \tag{4}$$

where P_0, ρ_0, and γ are the pressure, density, and specific heat ratio of air respectively, and N_{pr} is the Prandtl number. The Prandtl number is defined as $N_{\mathrm{pr}}\equiv c_p\mu/\chi$, where χ, μ, and c_p are the thermal conductivity, dynamic viscosity, and specific heat per unit mass at constant pressure of air. The flow resistivity for a stationary current in a single pore is $\sigma_x=\lim_{\omega\to 0} i\omega\rho_x(\omega)$. Generally speaking, it can be written as $\sigma_x=k_0\mu/d^2$, where k_0 is a constant depending on the pore geometry, and d is the hydraulic radius defined by twice the cross-sectional area divided by the circumference of the tube.

The properties of a bulk medium ρ, C, σ and those of a single pore ρ_x, C_x, σ_x are related by[10]

$$\rho=\rho_x\frac{q^2}{\Omega},\quad C=\Omega C_x,\quad \sigma=\sigma_x\frac{q^2}{\Omega}, \tag{5}$$

where q, Ω, and σ are the tortuosity, porosity, and static flow resistance of the bulk medium. For hexagonal honeycombs and cellular metal foams that are of concern here, the tortuosity is approximately unity, hence $q=1$ is assumed below for simplicity. Nevertheless, the effect of q can be taken into account through Eq. (5) after working out effective single pore properties. For porous materials having more tortuous microstructures than those considered here, the effect of tortuosity can be important; then, a more general model such as the Allard–Champoux model may be used to establish the optimum parameter.

Equation (5) indicates that in order to understand a bulk medium one only needs to know the effective single pore properties ρ_x, C_x, provided that Ω,σ can be measured by experiments. Consequently, in the section that follows, the focus is placed on using the point-matching method to establish the effective single pore properties for both regularly and irregularly arranged honeycomb-like structures.

II. SOUND PROPAGATION IN 2D CELLULAR SOLIDS

A. Point-matching method

The idea of the point-matching method is to find a function satisfying both the governing equations and the boundary conditions on a few selected boundary points.[13] The decoupled equation for time-harmonic motion along a tube[9] is

$$\nabla^2 v-\frac{i\rho_0\omega}{\mu}v=\frac{1}{\mu}\frac{dp}{dz}, \tag{6}$$

where v denotes the particle velocity along the tube axis of z and μ is the dynamic viscosity of air. The velocity v on the boundary is zero due to viscosity on the tube walls. Sound propagation through a hexagonal tube is sketched in Fig. 1.

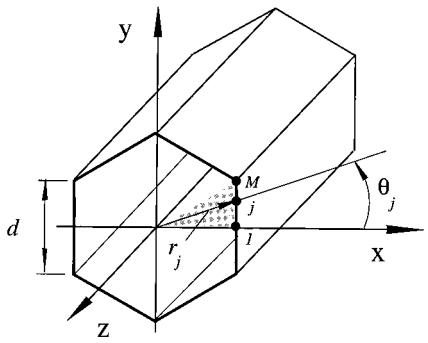

FIG. 1. A regular hexagonal tube, uniform along its axis *z*.

Upon introducing a nondimensional parameter $\beta \equiv [\omega\rho_0/\mu]^{1/2}d$, Eq. (6) can be nondimensionalized as

$$\bar{\nabla}^2\bar{v} - i\beta^2\bar{v} = 1, \tag{7}$$

where variables with a hat bar are nondimensional quantities; $\bar{v} \equiv v\mu/(d^2 dp/dz)$, $\bar{\nabla}^2 \equiv \partial^2/\partial^2\bar{x} + \partial^2/\partial^2\bar{y}$, $\bar{x} \equiv x/d$, $\bar{y} \equiv y/d$. The nondimensional parameter β is related to the quotient of two stresses caused separately by sound pressure and viscosity, so it is referred to as the acoustic Reynolds number.

Equation (7) is solved by using the separation of variables technique. Let the polar coordinates (r, θ) be origined at the center of a tube. For ducts with an *N*-side regular polygonal cross section as shown in Fig. 1, the solutions must be symmetrical in variable θ with a periodicity of $2\pi/N$ and nonsingular at the center $\bar{r} \equiv r/d = 0$. This leads to the drop-out of those terms involving the product of $\sin\theta$ and the Neumann function in the following general solution:

$$\bar{v} = \sum_{n=0,N,2N,3N,\ldots}^{\infty} A_n J_n(\sqrt{-i}\beta\bar{r})\cos n\theta + i\beta^{-2}, \tag{8}$$

where J_n is the Bessel function of the first kind and A_n are constants to be determined by satisfying the boundary conditions $\bar{v} = 0$ at selected boundary points.

B. Periodic structures

Taking advantage of the symmetry and periodicity of an *N*-sided regular polygon, only half a side of the boundary needs to be considered in order to satisfy the boundary conditions. A total of *M* points on this half-side is selected to approximate the exact solution. The boundary conditions become thence

$$\sum_{n=0,N,2N,\ldots}^{(M-1)N} A_n J_n(\sqrt{-i}\beta\bar{r}_j)\cos n\theta_j + i\beta^{-2} = 0$$

$$j = 1,2,\ldots,M. \tag{9}$$

Table I shows the first three coefficients A_0, A_6, A_{12} calculated for a regular hexagonal tube ($N=6$), with the frequency parameter fixed at $\beta=1$ and *M* taking values of 3,4,...9, respectively. Note that these coefficients tend to converge with increasing *M*. The products of these coefficients with their corresponding Bessel and cosine functions averaged over the cross-sectional area of the duct are also listed in Table I for selected values of cardinal number *n*. Observe that the real part of the second product $\mathrm{Re}(\langle A_6 J_6 \cos 6\theta\rangle_x)$ is $\sim 10^{-3}$, two orders of magnitude smaller than that of the first, and the third is much smaller than the second. This suggests that the first few terms in the sum of (8) may be sufficient for calculating $\bar{v}$.

In the limiting case of circular pores, the number of sides is infinite. Then, only one constant A_1 needs to be determined in (8) as the norm of A_n becomes infinitely small when $n \to \infty$. It can be shown that this leads to the analytical solution obtained by Zwikker and Kosten.[1]

Once the velocity field within the tube is known, other properties concerning sound propagation are readily obtained by using Eqs. (1)–(5). The calculated complex density as a function of the frequency parameter β for a hexagonal cross-section tube is shown in Fig. 2, which compares favorably with the result obtained by Craggs and Hilderbrandt[11] based on the finite-element method. Note that at high frequencies, the real part of the complex density approaches the density of free air as it should.

The complex density for an equilateral triangular tube calculated by the point-matching method is also shown in Fig. 2 and compared with the analytical solution of Stinson and Champoux.[10] The two results are nearly indistinguishable, indicating again the accuracy of the present approach. For completeness, Fig. 2 also presents the complex densities for other cross-sectional shapes calculated using existing analytical solutions.[1,10] These solutions are summarized in Table II. It should be pointed out that, in Fig. 2, the hydraulic radii *d* of the circle, hexagon, square, triangle are equal for given values of the acoustic Reynolds number β and frequency ω.

The results obtained from the point-matching method are compared in Fig. 3 with those predicted from three different acoustic models: Delany and Bazley's empirical

TABLE I. Coefficients of series solution (8) for $\beta=1$.

M[a]	A_0	$\mathrm{Re}(\langle A_0 J_0\rangle_x)$	A_6	$\mathrm{Re}(\langle A_6 J_6 \cos(6\theta)\rangle_x)$	A_{12}	$\mathrm{Re}(\langle A_{12} J_{12} \cos(12\theta)\rangle_x)$
3	$-0.195-.710i$	-0.248	$-0.128e3-0.750e3i$	$-0.360e-2$	$0.251e10-0.328e9i$	$-0.551e-3$
4	$-0.195-.710i$	-0.247	$-0.123e3-0.718e3i$	$-0.345e-2$	$0.228e10-0.295e9i$	$-0.499e-3$
5	$-0.195-.710i$	-0.247	$-0.122e3-0.711e3i$	$-0.341e-2$	$0.204e10-0.265e9i$	$-0.447e-3$
6	$-0.195-.710i$	-0.247	$-0.121e3-0.708e3i$	$-0.340e-2$	$0.196e10-0.256e9i$	$-0.430e-3$
7	$-0.195-.710i$	-0.247	$-0.121e3-0.707e3i$	$-0.339e-2$	$0.194e10-0.252e9i$	$-0.424e-3$
8	$-0.195-.710i$	-0.247	$-0.121e3-0.706e3i$	$-0.339e-2$	$0.192e10-0.250e9i$	$-0.420e-3$
9	$-0.195-.710i$	-0.247	$-0121e3-0.706e3i$	$-0.339e-2$	$0.191e10-0.249e9i$	$-0.418e-3$

[a]*M* denotes the number of points selected on half of a side of the boundary. All points are chosen equally spanned.

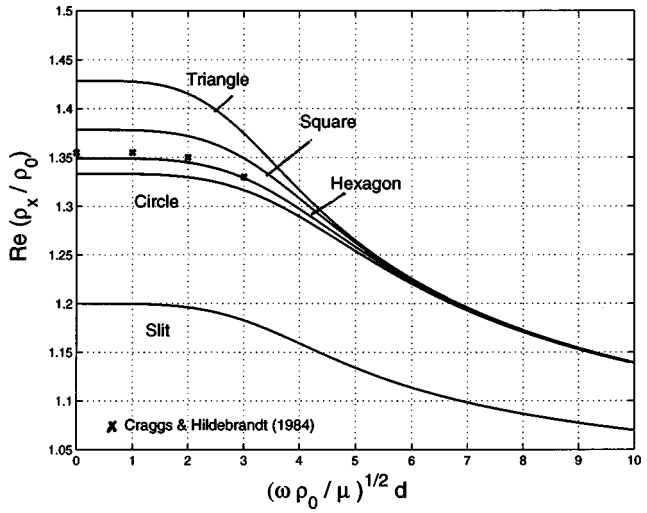

FIG. 2. Complex density as function of frequency parameter $\beta=[\omega\rho_0/\mu]^{1/2}d$ and cross-sectional shape. Results for circular, triangular, and square cross sections are calculated by using formulas listed in Table II. Results for hexagonal cross sections are calculated by the point-matching method. Results for triangular cross sections by the point-matching method coincide with those by the analytical formula of Table II. The cross mark represents the finite-element results of Craggs and Hilderbrandt (Ref. 11).

power laws, Allard and Champoux's semiempirical relationships, and Wilson's relaxation-matched model. A summary of these models is given in Table III.

Comparing the definitions of the acoustic Reynolds number β with that for the static flow resistance σ, one has

$$\beta^2=2\pi\rho_0 k_0\frac{f}{\sigma}. \tag{10}$$

The quotient f/σ is exactly the parameter used by Delany and Bazley.[4] All calculations based on parameter β are thus in Fig. 3 transferred according to this quotient.

It is seen from Fig. 3 that the results for both hexagonal and triangular cross sections by the point-matching method, and those for circular cross sections by Zwikker and Kosten,[1] are well in agreement with the relaxation-matched method by Wilson.[12] At low frequencies, the real component of the characteristic impedance varies as $\omega^{-1/2}$ whilst its imaginary component varies as $\omega^{1/2}$; the real and imaginary components of the propagation constant are equal in magnitude and both vary as $\omega^{1/2}$. These low-frequency limits are correctly predicted by the relaxation-matched solution and Allard and Champoux's semiempirical solution, but not by the equations of Delany and Bazley. At high frequencies, the characteristic impedance approaches q^2/Ω; the real component of the propagation constant varies as $\omega^{1/2}$ but its imaginary component approaches ω/c. We note that, at high frequencies, the relaxation-matched model leads to correct solutions, the Allard–Champoux equations only give approximate solutions, whilst the Delany–Bazley relations provide unphysical predictions. Finally, whilst the relaxation-matched solution is applicable to a wide range of porosities, the other two solutions are developed essentially for highly porous materials with $\Omega\approx 1$.

C. Random structures

Metal foams are typically manufactured by a foaming process where a supersaturated gas is made to separate from the molten metal. If all gas bubbles nucleate simultaneously but randomly in space and grow at the same linear rate, the resulting structure is a space-filling Voronoi model with random morphological microstructures.[6] In a Voronoi structure, nuclei of gas bubbles are randomly distributed with a density specified *a priori*. Nucleation of bubbles occurs at all sites simultaneously and all bubbles grow at the same rate. Practically, to create a 2D Voronoi diagram, randomly generated nucleation points are placed in a 2D domain according to an assumed distribution function. The domain is then divided into Voronoi polygons by drawing lines from each point to the nearest-neighboring points, with normals drawn to bisect these lines. The area surrounding each generation point enclosed by the normals constitutes the Voronoi cell, typically a polygon with four to eight sides. The average number of sides of a Voronoi cell is six, the standard deviation being 1.68.[16] Vonoroi diagrams have been employed to study the elastic and plastic behaviors of 2D random honeycombs[17–19] and the finite elastic deformation of 3D random foams.[20] Their acoustic behaviors are studied below.

For honeycombs having Voronoi cells, the variation of cell size and shape is taken into account by postulating a probability distribution of polygon area A. The area A of the Voronoi polygons is gamma distributed, if no constraint is placed on the minimum distance between neighboring ran-

TABLE II. Analytical formulas of complex density and compressibility for uniform tubes with various cross sections.

Cross section	Complex density ρ_x/ρ_0	Complex compressibility $C_x\gamma P_0$
Triangle[a]	$\epsilon^2/(\epsilon^2-3\epsilon\coth\epsilon+3)$	$\gamma-(\gamma-1)[(N_{pr}\epsilon^2-3N_{pr}^{1/2}\epsilon\coth(N_{pr}^{1/2}\epsilon)+3)/(N_{pr}\epsilon^2)]$
Rectangular[b]	$\frac{\eta a^2b^2}{4i\omega\rho_0}\left[\Sigma_{k=0}^{\infty}\Sigma_{n=0}^{\infty}\frac{1}{\alpha_k^2\beta_n^2(\alpha_k^2+\beta_n^2+i\omega\rho_0/\eta)}\right]^{-1}$	$\gamma-(\gamma-1)4i\omega N_{pr}\rho_0/(\eta^2a^2b^2)\Sigma_{k=0}^{\infty}\Sigma_{n=0}^{\infty}\frac{1}{\alpha_k^2\beta_n^2(\alpha_k^2+\beta_n^2+i\omega\rho_0N_{pr}/\eta)}$
Circle[c]	$1/\left[1-\frac{2}{\sqrt{-i}\beta}\frac{J_1(\sqrt{-i}\beta)}{J_0(\sqrt{-i}\beta)}\right]$	$1+(\gamma-1)\left[\frac{2J_1(\sqrt{-iN_{pr}}\beta)}{J_0(\sqrt{-iN_{pr}}\beta)}\frac{1}{\sqrt{-iN_{pr}}\beta}\right]$
Slit	$[1-\tanh(\sqrt{-i}\beta)/(\sqrt{-i}\beta)]^{-1}$	$1+(\gamma-1)[\tanh(\sqrt{-iN_{pr}}\beta)/(\sqrt{-iN_{pr}}\beta)]$

[a]$\beta\equiv[\omega\rho_0/\mu]^{1/2}d$. For an equilateral triangle, $\epsilon\equiv 9\beta^2/4$.
[b]For a single pore of rectangular cross section with half-width b and half-length a, $\alpha_k=(k+1/2)\pi/a$ and $\beta_n=(n+1/2)\pi/b$.
[c]Function J_n, $n=0,1...$ is the Bessel function of the first kind.

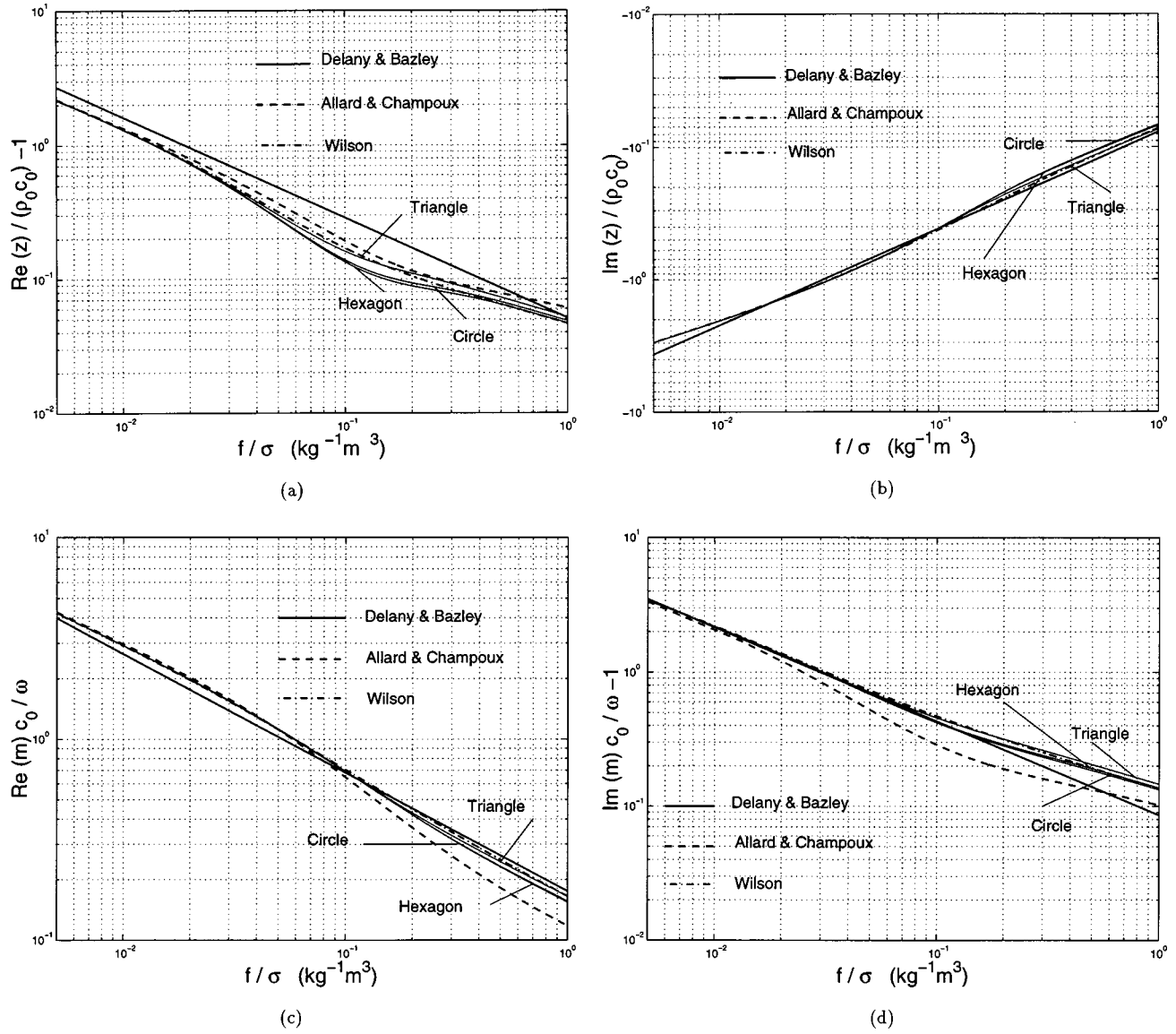

FIG. 3. Comparison of the point-matching method with other acoustic models. (a), (b) Real and imaginary part of the wave impedance Z; (c), (d) real and imaginary part of the wave propagation constant m as functions of the frequency to static flow resistance ratio f/σ.

dom points. The probability $p_v(A)dA$ of A in the interval $A, A+dA$ is[21]

$$p_v(A) = \frac{\alpha^\alpha}{\Gamma(\alpha)} \left(\frac{A}{\langle A \rangle} \right)^{\alpha-1} \exp\left(-\alpha \frac{A}{\langle A \rangle} \right) \frac{1}{\langle A \rangle}, \tag{11}$$

where Γ is the gamma function, $\alpha = 3.61$, and $\langle A \rangle$ is the average value of A.

Following Tarnow,[21,22] each Voronoi polygon is approximated by a circle of radius r. An infinitely thick Γ-distributed Voronoi structure is then replaced by an effec-

TABLE III. Acoustic models.

Models	Impedance $Z/(\rho_0 c_0)$ or density ρ/ρ_0	Propagation constant mc_0/ω or bulk modulus $(C_x \gamma P_0)^{-1}$
[a]	$1+9.08(f/\sigma)^{-0.75}-i11.9(f/\sigma)^{-0.73}$	$10.3(f/\sigma)^{-0.59}+i(1+10.8(f/\sigma)^{-0.70})$
[b]	$1+1/(i2\pi)(\rho_0 f/\sigma)^{-1}[1+i\pi(\rho_0 f/\sigma)]^{1/2}$	$\left[\gamma-\dfrac{\gamma-1}{1+1/(i8\pi N_{pr})(\rho_0 f/\sigma)^{-1}[1+i4\pi N_{pr}\rho_0 f/\sigma]^{1/2}}\right]^{-1}$
[c]	$\dfrac{1}{\Omega}\dfrac{[1-i(\rho_0/(\pi\Omega))(f/\sigma)]^{1/2}}{[1-i(\rho_0/(\pi\Omega))(f/\sigma)]^{1/2}-1}$	$\dfrac{1}{\Omega}\dfrac{[1-i(N_{pr}\rho_0/(\pi\Omega))(f/\sigma)]^{1/2}}{[1-i(N_{pr}\rho_0/(\pi\Omega))(f/\sigma)]^{1/2}+\gamma-1}$

[a]Empirical equations for complex impedance and propagation constant by Delany and Bazley (Ref. 4).
[b]Semiempirical equations for complex density and bulk modulus by Allard and Champoux (Ref. 5), valid for $\Omega \approx 1$, $f/\sigma < 1$ kg^{-1} m^3.
[c]Relaxation-matched equations for complex density and bulk modulus by Wilson (Ref. 12).

tive porous medium comprising uniformly distributed circular tubes of mean size r_v.

Based on the approximation of using circles for Voronoi cells, the probability density of cells having radius r in the interval r, $r+dr$ is $2\pi r p_v dr$. Consequently, from the solution of the volume velocity $\langle \overline{v} \rangle_x$ through a circular tube of radius r, the mean complex density of air in the Voronoi structure can be calculated as

$$\langle \rho_x \rangle = \frac{i\rho_0}{\beta^2} \int_0^\infty \frac{p_v}{\langle \overline{v} \rangle_x} 2\pi \overline{r} d\overline{r}$$

$$= \rho_0 \int_0^\infty \frac{p_v 2\pi \overline{r} d\overline{r}}{1 - \dfrac{2}{\sqrt{-i}\beta\overline{r}} \dfrac{J_1(\sqrt{-i}\beta\overline{r})}{J_0(\sqrt{-i}\beta\overline{r})}}, \tag{12}$$

where $\beta = \sqrt{\omega\rho_0/\mu} r_v$ and $\overline{r} = r/r_v$, while the mean compressibility is given by

$$\langle C_x \rangle = \frac{1}{\gamma P_0} \left[\gamma - (\gamma - 1) \right.$$

$$\left. \times \int_0^\infty \left[1 - \frac{2}{\sqrt{-i}N_{pr}\beta\overline{r}} \frac{J_1(\sqrt{-i}N_{pr}\beta\overline{r})}{J_0(\sqrt{-i}N_{pr}\beta\overline{r})} \right] p_v 2\pi \overline{r} d\overline{r} \right]. \tag{13}$$

The predicted sound absorption behavior of Voronoi structures is discussed later in relation to the effect of cell shape [cf. Fig. 5(a)].

III. OPTIMIZED ACOUSTIC PROPERTIES

It can be shown that, for a layer of uniform medium of thickness L_s having properties m,Z, and backed by an impedance z_r, the specific wave impedance z_s at its free surface is[1]

$$z_s = Z \frac{z_r \cosh mL_s + Z \sinh mL_s}{z_r \sinh mL_s + Z \cosh mL_s}, \tag{14}$$

which is valid for plane waves traveling perpendicular to the layer. The absorption coefficient α of a normal plane wave impinging on a wall of specific impedance z_s is

$$\alpha = 1 - \left| \frac{z_s - Z_0}{z_s + Z_0} \right|^2. \tag{15}$$

Dimensional analysis dictates that the coefficient of sound absorption α for a layer of porous material mounted on a hard wall with a cavity in between is determined by the following nondimensional characteristic parameters:

$$\beta, \Omega, \frac{L_s}{\Lambda}, \frac{L_c}{\Lambda}, \tag{16}$$

where L_s and L_c are separately the sample thickness and cavity depth, respectively, and $\Lambda \equiv c\rho_0 d^2/\mu$ is a characteristic length scale. The first two parameters connect functions associated with a single pore to those of a bulk of parallel pores. The last two characterize the geometry of a sound-absorptive panel and the way of mounting it. This section will first introduce a domain-matching method. The effect of factors such as cell shape, cell size and its variation, sample-thickness, and cavity-depth on sound absorption will then be examined. Finally, numerical examples will be given to demonstrate how to optimize the combination of these factors by the domain-matching method.

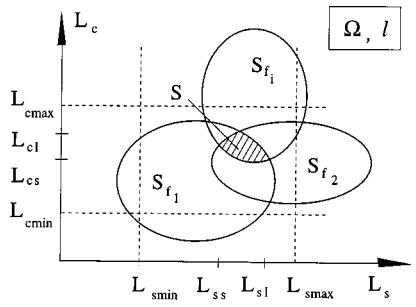

FIG. 4. Sketch of the domain-matching optimization at fixed porosity Ω and cell size ℓ.

A. Domain-matching method

For convenience in practice, the previously derived dimensionless parameters β, Ω, L_s/Λ, L_c/Λ are converted into five physical parameters: frequency, sample thickness, cavity depth, cell size, and porosity. In order to identify the optimal combinations, the following criteria are proposed:

Oa Sound-absorption coefficient greater than a given value α_0 in a given range of frequencies $\{f_i\}$;

Ob Sample thickness as thin as possible.

In addition, constraints due to manufacturing limits and mounting environment are taken as

Ca Possible minimum cell size $\ell_{\min}$;

Cb Ranges of sample thickness and cavity length $L_{\text{smin}} \leqslant L_s \leqslant L_{\text{smax}}$, $0 \leqslant L_c \leqslant L_{\text{cmax}}$.

Here the cell size ℓ is taken as equal to the hydraulic radius of the cell. In general, for a given cell size and porosity, a series of sound-absorption-coefficient contours against sample-thickness and cavity-depth at various frequencies can be drawn and relayed on one another. The common domain of $\alpha \geqslant \alpha_0$ within the range of (Cb), if it exists, will show optimal combinations on which the sound absorption satisfies the above criteria (Oa) and (Ca-b). Repeating this procedure for varying cell sizes, one can carry out further optimization against criterion (Ob).

Specifically, let $\{S_{fi}\}$ denote a set of $\{L_s, L_c\}$ for frequencies $f \in \{f_i\}$, with each subset S_{fi} satisfying $\alpha \geqslant \alpha_0$. For a given level of porosity Ω and a given cell size ℓ, a series of contours corresponding to various frequencies can be drawn and relayed onto each other. This procedure is sketched in Fig. 4. The common domain S can be identified as the intersection of sets $S_{f1}, S_{f2}, \ldots, S_{fi}, \ldots$

$$S = \{L_s, L_c : \cap_i S_{fi}, L_{\text{smin}} \leqslant L_s \leqslant L_{\text{smax}},$$

$$0 \leqslant L_c \leqslant L_{\text{cmin}}, \ell, \Omega\}. \tag{17}$$

All points $\{L_s, L_c\}$ in this common domain satisfy the criterion Oa and the conditions Ca-b. If S exists, there must also exist a smallest possible sample thickness L_{ss}, a largest pos-

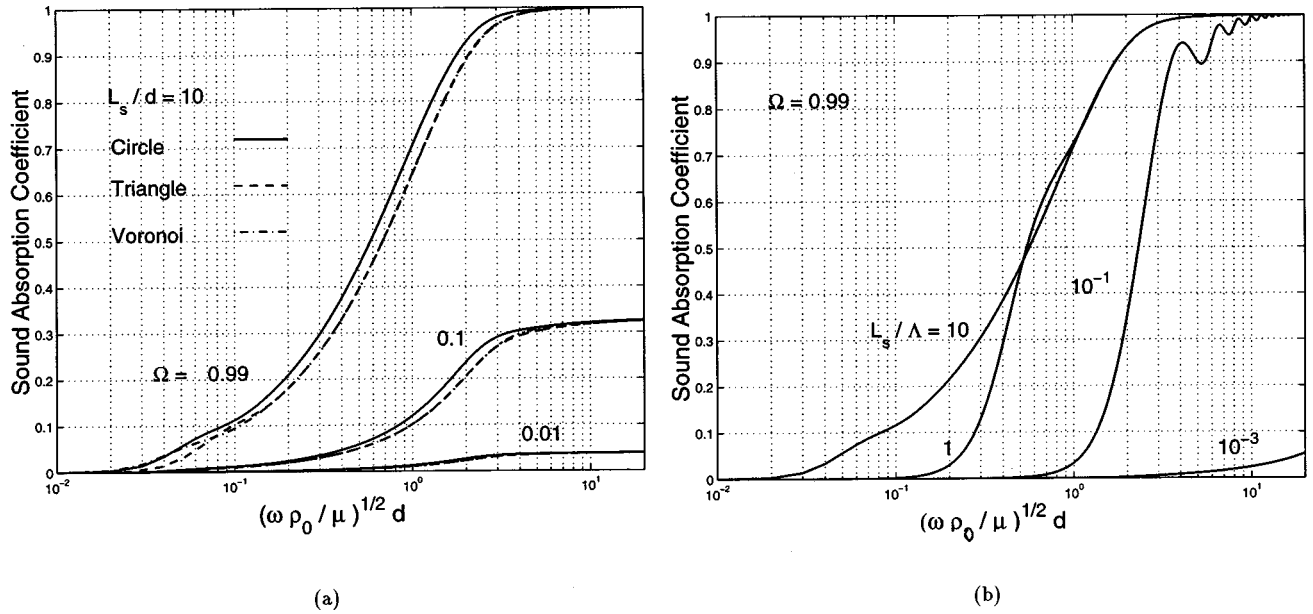

FIG. 5. (a) Sound-absorption coefficient of a rigid wall-backed sample with a fixed thickness ratio $L_s/\Lambda = 10$ as a function of frequency, cell shape (assuming same cross-sectional area), and porosity; (b) sound-absorption coefficient of a rigid wall-backed sample with a fixed porosity level of $\Omega = 0.99$ as a function of sample thickness and frequency.

sible sample thickness L_{sl}, a smallest cavity depth L_{cs}, and a largest cavity depth L_{cl} (Fig. 4). Furthermore, the cell size corresponding to a sample that satisfies criterion Ob is defined here as the optimal cell size ℓ_{opt},

$$L_{ss}|_{\ell=\ell_{\text{opt}}} = \min\{L_{ss}:\ell\}. \tag{18}$$

Practically, an optimal index Q may be introduced as

$$Q \equiv \frac{1}{(1-\alpha_0)\Delta f}\left[\int_{f_{\min}}^{f_{\max}} \alpha df - \alpha_0 \Delta f\right], \tag{19}$$

where $\Delta f = f_{\max} - f_{\min}$ is the bandwidth of frequencies to be absorbed at a level of $\alpha \geqslant \alpha_0$. This is in fact a measure of the area under the absorption curve $\alpha(f)$ between $f_{\min}$ and $f_{\max}$. Those crests on the Q-surface are therefore the locally optimized combinations.

B. Cell shape

To study the effects of cell cross-sectional shape, samples of fixed thickness ratio $L_s/\Lambda = 10$ against a rigid wall are first studied. Note that $\Lambda \sim 10^7 d^2$ for sound propagating in an air-saturated porous medium at room temperature. This implies that for a sample with cell size of ~ 0.1 mm the sample thickness is around 10 cm, given $L_s/\Lambda = 10$. Figure 5(a) presents the sound absorption coefficients as functions of $\beta = \sqrt{\omega \rho_0/\mu}\, d$ for samples having either circular or equilateral triangular pores. Here, L_s/Λ is fixed at 10 and d is taken as the radius of an equivalent circle having the same cross-sectional area for each type of pore. Three sets of lines are drawn according to three porosities $\Omega = 0.01$, 0.1, and 0.99. Note that, for a given frequency, panels with equilateral triangular cells have slightly lower sound absorption coefficients than those of panels with other types of cell, regardless of porosity. Selected calculations show that the results for squares and hexagons fall in between those for triangular and circular pores; the difference is small, about 10% in the range of frequencies concerned. This implies that on the condition of equal cross-sectional area, the ability to absorb sound for circular tubes is slightly higher than that of tubes having other shapes of cross section. From Fig. 5(a) it is also noticed that, in general, honeycombs at higher porosity levels are better sound absorbers. This phenomenon is obvious, as higher porosity means a larger area of surface on which the air passes over with friction, so the influence of viscosity is increased. Also, for the same reason, energy dissipation due to thermal transport is increased as the porosity level is increased.

C. Sample thickness

The effect of sample thickness on sound absorption of honeycombs containing circular cells and backed by rigid wall is shown in Fig. 5(b) for the case of $\Omega = 0.99$. Generally speaking, the sound absorption coefficient increases as the sample becomes thicker, and all absorption curves collapse onto one single limit curve as the thickness ratio L_s/Λ becomes larger than about 10.

However, for certain ranges of thickness ratio, such as $L_s/\Lambda \sim 10^{-1}$, a thinner sample may be a better sound absorber than a thicker sample. For example, Fig. 5(b) shows that, within certain frequency ranges, a 1-cm-thick sample with a cell size of 1 mm can absorb sound better than a 10-cm-thick sample comprising cells of the same size.

D. Cell size and cell size variation

The cell size effect is evident in Figs. 5(a) and 5(b) for honeycombs having uniformly distributed cells. According to the definition of the acoustic Reynolds number, for a given frequency, the larger the cell size, the larger the number becomes. Figures 5(a) and 5(b) hence indicate that, for a given frequency, the sound-absorption coefficient increases with increasing cell size for relatively thick honeycombs, but may

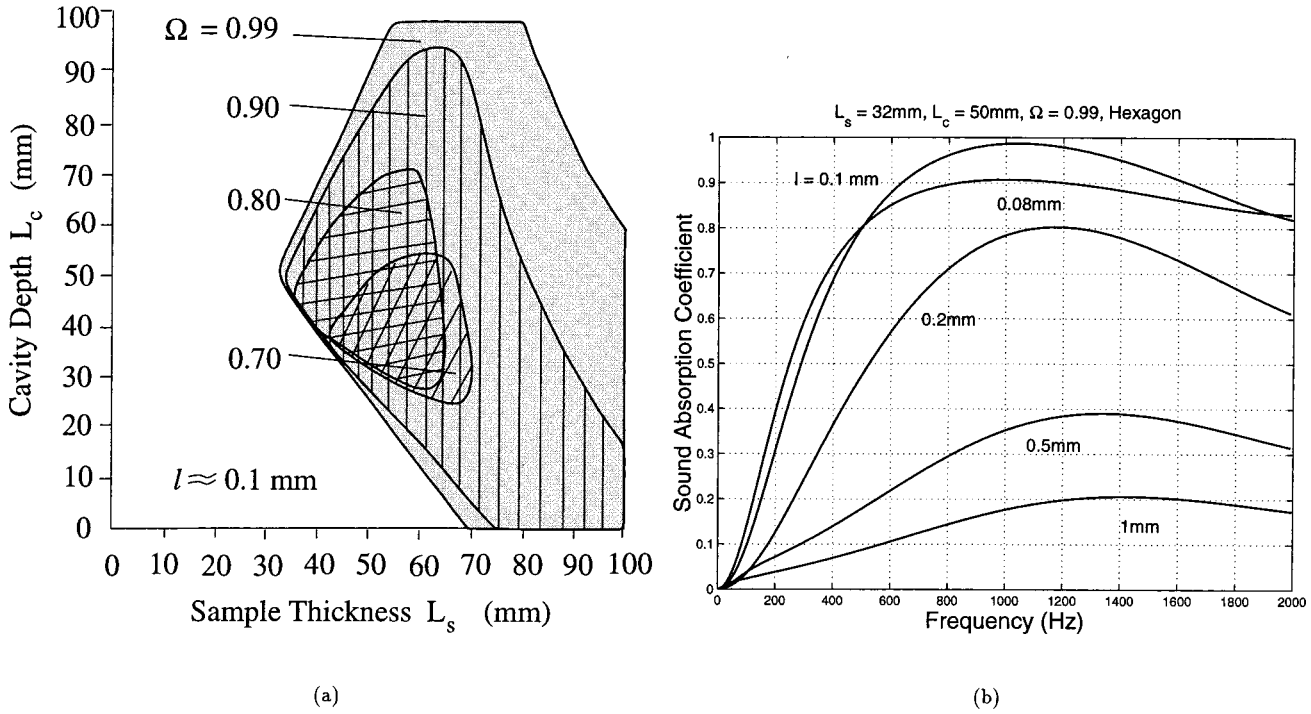

FIG. 6. Optimization of regular hexagonal honeycombs. (a) Shaded domains of optimal absorption $\alpha \geqslant 0.8$ covering $500 \leqslant f \leqslant 2000$ Hz for cell size $\ell \approx 0.1$ mm, porosity $\Omega = 0.7$, 0.8, 0.9, and 0.99, (b) sound-absorption coefficient plotted as function of frequency and cell size at $\{L_s, L_c\} = \{32,50\}$ mm, and $\Omega = 0.99$.

locally decrease for thinner honeycombs. For example, the thickness ratio of 10^{-3} may represent a 1-cm-thick sample having a cell size of 1 mm, and the ratio of 10^{-1} may represent a sample of the same thickness but with a cell size of only 0.1 mm. Figure 5(b) then shows that, within certain frequency ranges, the 1-cm-thick sample having a cell size of 0.1 mm can absorb sound better than a sample of the same thickness but with a larger cell size of 1 mm. Thus an optimal cell size may exist for panels of finite thickness, as shown later in Sec. III E.

Finally, the effect of cell size variations for Voronoi cells is shown in Fig. 5(a) in a way similar to examining uniformly distributed pores. In general, the sound absorption coefficients of Voronoi cells are smaller than those of uniformly distributed circular pores, although the difference is small ($<10\%$).

E. Optimal combinations—numerical examples

Experiments by Lu *et al.*[7] were carried out for metallic foams with porosity around 0.9 and frequencies ranged within 2000 Hz. In order to demonstrate the optimization procedures for such materials, numerical examples are presented for both regular honeycombs and random Voronoi honeycombs. Levels of porosities and ranges of frequencies are therefore chosen to match those in the experiments. In addition, it is expected that if the sound-absorption coefficient of a metallic foam exceeds 0.8 over a fairly wide range of low frequencies (e.g., 500~2000 Hz), it can find attractive applications in transportation vehicles. Consequently, $\{f_i\} \in [500,2000]$ Hz and $\alpha_0 = 0.8$ are assumed in the following examples.

For hexagonal honeycombs with porosities of 0.7, 0.8, 0.9, 0.99 and a fixed cell size of 0.1 mm, Fig. 6(a) illustrates their common domains which satisfy the criteria that $\{f_i\} \in [500,2000]$ Hz, $\alpha_0 = 0.8$, $\ell_{\min} = 0.01$ mm, $L_{s\min} = 0.1$ mm, and $L_{s\max} = L_{c\max} = 10$ cm. Each of these common domains is represented by a shaded area in Fig. 6(a). It is found for $\Omega \leqslant 0.6$ there is no such optimal combination satisfying Oa-b, Ca-b, and $\{f_i\} \in [500,2000]$ Hz. Cases for other values of cell size have also been studied, but the cell size $\ell \approx 0.1$ mm produces the smallest L_{ss}. For optimal performances at high porosities ($\Omega > 0.6$), Fig. 6(a) reveals that the thinnest sample thicknesses are around 3–4 cm while cavity depths are around 4–5 cm. These calculations for different porosities also show that the higher the porosity, the wider the area of the common domain.

As an illustration, the sound absorption coefficient against frequency at a combination of $\{L_s, L_c\} = \{32,50\}$ mm for $\Omega = 0.99$ is plotted in Fig. 6(b). Each line represents a certain cell size ℓ. This figure shows that the area under line $\ell = 0.1$ mm is the largest in [500, 2000] Hz. A best performance of sound-absorption is therefore expected from $\ell = 0.1$ mm for the above combination of sample thickness and cavity depth.

The results for Voronoi polygons are presented Fig. 7 for $\Omega > 0.6$. It is seen that the effective domains are similar to Fig. 6 but with a narrower range of optimal combinations. The optimal thickness is around 4~5 cm, slightly larger than that for regular honeycombs. The optimal cavity depth is around 3~4 cm, slightly smaller than that for uniform hexagonal honeycombs. The optimal average cell size is not changed, around 0.1 mm.

The above analysis also demonstrates that the domain-

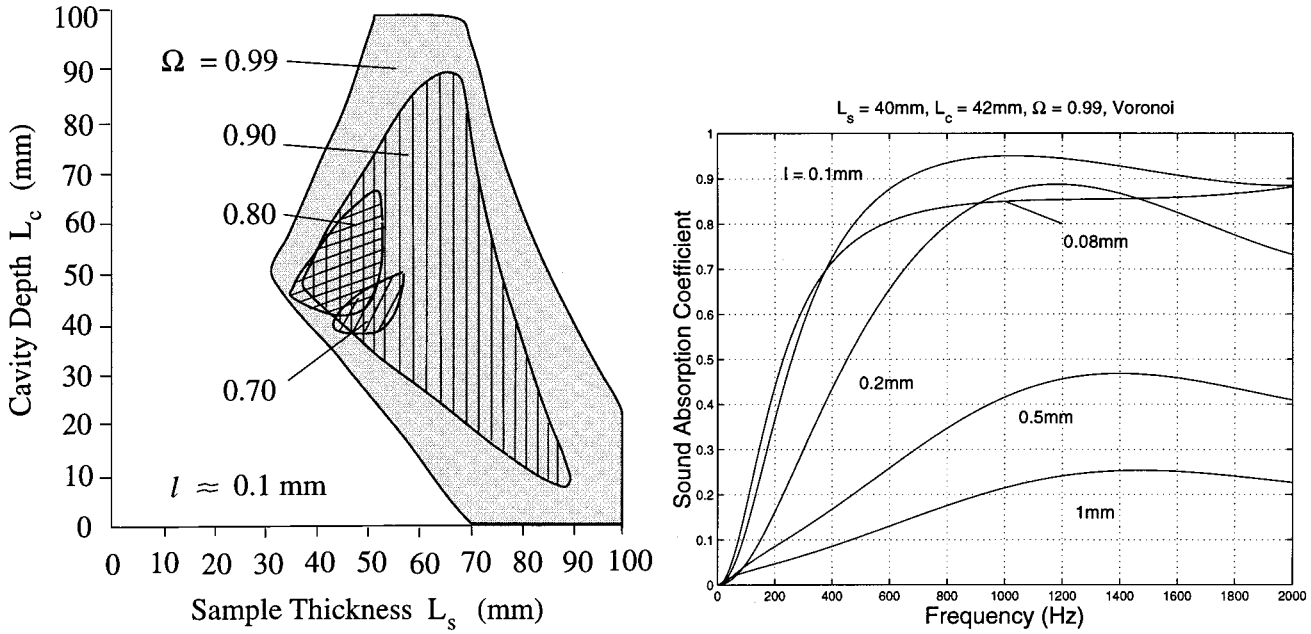

(a) (b)

FIG. 7. Optimization of Voronoi honeycombs. (a) Shaded domains of optimal absorption $\alpha \geqslant 0.8$ covering $500 \leqslant f \leqslant 2000$ Hz for cell size $l \approx 0.1$ mm, porosity $\Omega = 0.7$, 0.8, 0.9, and 0.99, (b) sound-absorption coefficient plotted as function of frequency and cell size at $\{L_s, L_c\} = \{40,42\}$ mm, $\Omega = 0.99$.

matching method can be used in a similar way to find optimal combinations according to various user-defined optimization criteria.

IV. CONCLUSION

The sound-absorption capability of two-dimensional cellular solids is studied using the point-matching method. The results for regular hexagonal honeycombs agree closely with those obtained from the method of finite elements. The effects of cell shape, cell size and its spatial variation, sample thickness, and cavity depth on sound absorption are analyzed systematically.

Cell shapes only have a small effect on sound absorption. The effect of cell size variations is also found to be small for Γ-distributed Voronoi structures. The effect of cell size on sound absorption is more complicated. For a fixed porosity, sound absorption is increased by increasing the cell size if the sample is (infinitely) thick. For thinner panels, the cell size effect is intermingled with the effects of sample thickness and cavity depth. A domain-matching method is developed to locate the optimized combinations of cell size, sample thickness, and cavity depth for efficiently absorbing sound in a given range of frequencies. The optimal cell size for best sound absorbers is on the order of ~0.1 mm for practical combinations of sample thickness, cavity depth, and porosity.

ACKNOWLEDGMENTS

This work was supported by the EPSRC and by the DARPA/ONR MURI program on Ultralight Metal Structures (No. N00014-1-96-1028).

[1] C. Zwikker and C. W. Kosten, Sound Absorbing Materials (Elsevier, New York, 1949).
[2] M. A. Biot, ''Theory of propagation of elastic waves in a fluid-saturated porous solid. I. Low frequency range,'' J. Acoust. Soc. Am. **28**, 168–178 (1956).
[3] M. A. Biot, ''Theory of propagation of elastic waves in a fluid-saturated porous solid. II. Higher frequency range,'' J. Acoust. Soc. Am. **28**, 179–191 (1956).
[4] M. E. Delany and E. N. Bazley, ''Acoustical properties of fibrous absorbent materials,'' Appl. Acoust. **3**, 105–116 (1969).
[5] J. F. Allard and Y. Champoux, ''New empirical equations for sound propagation in rigid frame fibrous materials,'' J. Acoust. Soc. Am. **91**, 3346–3353 (1992).
[6] L. J. Gibson and M. F. Ashby, Cellular Solids: Structure and Properties 2nd ed. (Cambridge University Press, Cambridge 1997).
[7] T. J. Lu, A. Hess, and M. F. Ashby, ''Sound absorption in metallic foams,'' J. Appl. Phys. **85**, 7528–7539 (1999).
[8] G. Kirchhoff, ''On the influence of heat conduction in a gas on sound propagation,'' Annu. Phys. Chem. **134**, 177–193 (1868).
[9] M. Stinson, ''The propagation of plane sound waves in narrow and wide circular tubes, and generalization to uniform tubes of arbitrary cross-sectional shape,'' J. Acoust. Soc. Am. **89**, 550–558 (1991).
[10] M. Stinson and Y. Champoux, ''Propagation of sound and the assignment of shape factors in model porous materials having simple pore geometries,'' J. Acoust. Soc. Am. **91**, 685–695 (1992).
[11] A. Craggs and J. G. Hilderbrandt, ''Effective densities and resistivities for acoustic propagation in narrow tubes,'' J. Sound Vib. **92**, 321–331 (1984).
[12] D. K. Wilson, ''Relaxation-matched modeling of propagation through porous media, including fractal pore structure,'' J. Acoust. Soc. Am. **94**, 1136–1145 (1993).
[13] H. D. Conway, ''The bending, buckling, and flexural vibration of simply supported polygonal plates by point-matching,'' J. Appl. Mech. **28**, 288–291 (1961).
[14] H. Y. Yee and N. F. Audeh, ''Uniform waveguides with arbitrary cross section considered by the point-matching method,'' IEEE Trans. Microwave Theory Tech. **65**, 847–851 (1965).
[15] R. Glav, ''The point-matching method on dissipative silencers of arbitrary cross-section,'' J. Sound Vib. **189**, 123–135 (1996).
[16] K. Mahin, K. Hanson, and J. Morris, Jr., ''Comparative analysis of the cellular and Johnson-Mehl microstructures through computer simulation,'' Acta Mater. **28**, 443–453 (1980).
[17] M. Silva, W. Hayes, and L. Gisbon, ''The effect of non-periodic micro-

structure on the elastic properties of two-dimensional cellular solids,'' Int. J. Mech. Sci. **37**, 1161–1177 (1995).
[18] M. Silva and L. Gisbon, ''The effect of non-periodic microstructure and defects on the compressive strength of two-dimensional cellular solids,'' Int. J. Mech. Sci. **39**, 549–563 (1997).
[19] C. Chen, T. J. Lu, and N. A. Fleck, ''Effect of imperfections on the yielding of 2-d foams,'' J. Mech. Phys. Solids (in press).
[20] A. Kraynik, M. Neilsen, D. Reinelt, and W. Warren, ''Foam micromechanics,'' in Proceedings of the NATO Advanced Study Institute on Foams, Emulsions, and Cellular Materials, Cargese, Corsica, 1997.
[21] V. Tarnow, ''Airflow resistivity of models of fibrous acoustic materials,'' J. Acoust. Soc. Am. **100**, 3706–3713 (1996).
[22] V. Tarnow, ''Calculation of the dynamic air flow resistivity of fibre materials,'' J. Acoust. Soc. Am. **102**, 1680–1688 (1997).

Active control of fan tones radiated from turbofan engines. I. External error sensors

P. Joseph, P. A. Nelson, and M. J. Fisher
Institute of Sound and Vibration Research, University of Southampton, Southampton SO17 IBJ, United Kingdon

(Received 21 November 1996; accepted for publication 31 March 1999)

This paper is the first of two papers dealing with the active control of fan tones radiated from the intake of turbofan engines. The present paper describes an idealized mathematical model for the prediction of the sound transmission and radiation of harmonic sound from a finite-length, unflanged hollow hard-walled circular duct containing a subsonic axial mean flow. The paper proceeds to use this model in computer simulations aimed at assessing the potential for reducing the far-field radiated sound by active means using two rings of discrete secondary sources on the duct wall. Perfect knowledge of the sound field to be controled is assumed throughout. The paper investigates two control objectives. The first is concerned with minimizing the total sound power transmitted along the duct, and hence the total sound power radiated. The other is concerned with minimizing the radiated sound power radiated into a specified band of sideline solid angles. Implicit in this investigation is the assumption of perfect observability of the radiated far field equivalent to a large number of error sensors located in the far field. The corresponding performance for the two control objectives when the observability of the sound field is limited to measurements made by a number of the error sensors situated on the duct wall is the subject of the companion paper. © *1999 Acoustical Society of America.* [S0001-4966(99)03807-2]

PACS numbers: 43.50.Ki [PJR]

INTRODUCTION

A. Background

The new legislation likely to supersede the current FAR 36 stage 3 legal requirements governing aircraft noise emissions is expected to demand an additional reduction of between 5 to 10 dB in EPNL (effective perceived noise level) over current levels. At the same time, the current trend is towards higher by-pass ratio engines with the expected introduction of ultra-high by-pass ratio engines over the next few years. The blade passing frequency of this new generation of engines is lower and the intake duct shorter than those presently in service. It is unlikely, therefore, that in the future, conventional passive treatments will be sufficiently effective as a means of noise suppression and alternative methods must be sought.

Active control has been investigated in recent years as a possible technique for suppressing the fan tones radiated from turbofan engines on an aircraft under approach conditions. Despite the obvious practical difficulties related to the sensing and the control of high-amplitude sound fields in a high-speed and turbulent flow environment, there has recently been considerable interest in this problem. The research dealing with this subject has increased steadily over recent years.

B. Previous work

One of the earliest papers related to this problem is that by Berge *et al.*[1] who describe a boundary element method for predicting the reduction in sound power radiated from a finite-length duct with a bell-mouth termination obtained when eight pistonlike secondary actuators were used to control the radiated field. At roughly the same time, Kraft and Kontos[2] presented an investigation into the active control of a single propagating mode using a number of secondary sources mounted flush with the duct wall. Their objective was the global control of the transmitted sound field and the effect on radiated field in this study was not considered. The paper includes a good discussion on the secondary source and sensor requirements. More recently, a number of very useful papers have originated from researchers at Virginia Polytechnic whose work is centred around the Pratt and Whitney JT15D engine. This work has been a combination of theoretical modeling[3,4] and experimental testing on a fully instrumented, laboratory based engine.[5–7] In parallel to these experiments has been the development of high-power-level, lightweight secondary sources.[6,8,9] This brief survey of the related literature is by no means exhaustive but is meant to convey the scale of interest in this problem.

C. Scope of the present study

This paper is the first of two papers dealing with the active control of fan tones radiated from the intake of turbofan engines. A computer model for the computation of the transmission and radiation of harmonic sound from an unflanged, hard-walled finite-length circular duct containing a subsonic axial mean flow is described that incorporates a number of classical results in duct acoustics. This model is then used in computer simulations aimed at assessing the potential of active control for reducing: (*i*) the total radiated sound power and (*ii*) the sound power radiated into a specified band of angles orientated beneath the engine towards ''the ground.''

In this numerical study, excitation of the sound field is assumed to be due to periodic wake interaction at the blade

passing frequency by the stator vanes from a nearby rotor stage. For simplicity of computation, this source mechanism is modeled by a ring of point axial dipoles collocated with the stator vanes. For the sake of realism, however, additional modes are included in the simulations. These are often observed in practice due to unsteady intake flow. Control of this modal sound field is affected by two rings of 16-point monopole secondary sources located on the wall of the intake duct. The rotor is assumed to comprise of 25 blades and 30 stator guide vanes. Implicit in this investigation is the assumption that the field to be controled is known completely. Even though the practical realization of these computer simulations would involve an unrealistically large number of sensors located in the far field, the simulation results presented here are useful since they identify upper-bound limits on the theoretically achievable performance. The performance degradation resulting from incomplete knowledge of the radiated field by the use of in-duct error sensors is addressed in the companion paper.[10]

I. IDEALIZED MATHEMATICAL MODEL OF THE TRANSMITTED AND RADIATED SOUND FIELD FROM A TURBOFAN ENGINE

A. Features of the turbofan model

A computer model for predicting the transmission and radiation of the tones produced by a fan in a short duct is described below. In the model only the essential features of this duct transmission and radiation problem are included. The main elements of the computer model are listed below:

(i) The duct is assumed to be unflanged, of finite length with hard walls, containing a subsonic axial uniform flow. The importance of including a mean flow is made clear in the companion paper which describes a control strategy for implementing the control using an in-duct error sensor array. For simplicity, the primary source (rotor and stator) is modeled by a ring of point axial dipole sources and the secondary sources as two rings of point monopoles. Their sound fields are computed using the normal mode Green's function solution due to Morfey.[11] This solution requires the modal reflection coefficients at both the inlet and exhaust terminations. The model is restricted to the propagating modes.

(ii) Modal reflection coefficients at the duct openings are computed using the theory due to Zorumski.[12] This theory is only approximately applicable in the model since it relates to a semi-infinite rigid flanged circular duct, whereas the duct in our model is of finite length and unflanged. Identical modal reflection coefficients at the inlet and exhaust are assumed. Modal coupling by the duct opening is neglected; only the reflection coefficient for like-modes are computed. Note that for the range of frequencies of interest here, $ka>1$, the modal reflection coefficients are generally negligible, except in the case of modes close to cut-off where they are close to unity.[12]

(iii) Modal far-field radiation is computed using the classical Wiener–Hopf solution for a semi-infinite, rigid walled, circular unflanged duct.[13–17] The flanged-duct directivity functions due to Tyler and Sofrin[18] obtained in the Kirchhoff approximation are much simpler to compute but are unsatisfactory in the present application. They have been found to be inaccurate at angles greater than about 70° to the duct axis, and are undefined at angles beyond 90°.

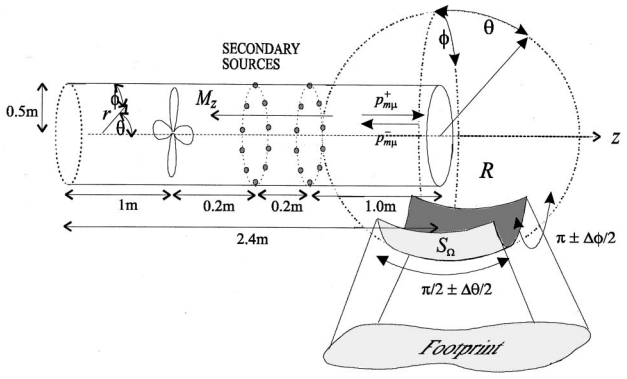

FIG. 1. Finite-length, hard-walled duct containing a mean subsonic intake flow. Two rings of secondary sources are driven to minimize the sound power radiated across the surface S_Ω of a far-field control sector subtending a solid angle Ω_c with polar and azimuthal angular dimensions of $\Delta\theta$ and $\Delta\phi$.

B. Basic relations

Figure 1 depicts a finite-length, hard-walled unflanged hollow circular duct containing an axial mean flow. Two rings of secondary sources located on the duct wall are driven so as to minimize the sound power radiated from the duct intake into a solid angle Ω_c.

The acoustic pressure $p(\mathbf{y},z,t)$ in the duct satisfies the convected wave equation

$$\left(\left(\frac{\partial}{\partial t}+c_0\mathrm{M}_z\frac{\partial}{\partial z}\right)^2-c_0^2\nabla^2\right)p(\mathbf{y},z,t)=0, \tag{1}$$

where c_0 is the speed of sound, M_z is the flow Mach number in the axial direction z which, for subsonic flows in the duct intake, lies in the range $-1\leqslant \mathrm{M}_z\leqslant 0$, and $\mathbf{y}$ is a two-dimensional vector $\mathbf{y}=(\phi,r)$ that specifies the position over a duct cross section. The solution to Eq. (1) for a rotating fan may be expressed as a sum of pressure fields that are harmonically related in frequency to its fan blade passing frequency. The field at each frequency can be expressed as the sum of modal solutions to Eq. (1). The resultant sound field in the duct is therefore of the form

$$p(\mathbf{y},z,t)=\sum_{n=1}^{\infty}\sum_{m=-\infty}^{\infty}\sum_{\mu=1}^{\infty}p_{nm\mu}(\mathbf{y},z,t). \tag{2}$$

In the intake of a cylindrical hard-walled duct excited by a B bladed rotor rotating at an angular frequency Ω, the term $p_{nm\mu}(\mathbf{y},z,t)$ denotes a single mode of circumferential order m and radial order μ, at the nth harmonic of the blade passing frequency. In a uniform flow, a single mode without reflection may be written in the separable form

$$p_{nm\mu}(\mathbf{y},z,t)=\overline{p}_{nm\mu}e^{in\Omega Bt-ik_{znm\mu}z}\Psi_{m\mu}(\mathbf{y}), \tag{3}$$

where $\Psi_{m\mu}(\mathbf{y})$ denotes a set of ortho-normal mode shape functions over the duct cross section,

$$\Psi_{m\mu}(\mathbf{y}) = e^{im\phi} J_m(k_{rnm\mu} r)/N_{m\mu}, \tag{4}$$

and $\overline{p}_{nm\mu}$ and $k_{znm\mu}$ denote its pressure amplitude and axial component of wave number, respectively. The term $N_{m\mu}$ denotes a factor introduced to satisfy the modal normalization condition $S^{-1}\int_S |\Psi_{m\mu}|^2 \, dS = 1$, S being the duct cross-sectional area. For the remainder of this paper the subscript n denoting the harmonic order of the blade passing frequency and the time dependence t will be suppressed. The hard wall boundary condition ensures that the radial particle velocity vanishes at the duct wall. This condition determines the modal eigenvalues (transverse wave number components) as $k_{rm\mu} = j'_{m\mu}/a$, where a is the duct radius and $j'_{m\mu}$ denotes the μth stationary value of the Bessel function of the first kind of order m defined by $J'_m(j'_{m\mu}) = 0$, where the prime denotes differentiation with respect to argument. The axial wave number component $k_{zm\mu}$ is deduced by solving the dispersion relation of Eq. (5) below that is obtained by substituting the single mode solution of Eq. (3) into Eq. (1):

$$k_{rm\mu}^2 + k_{zm\mu}^2 = (k - M_z k_{zm\mu})^2, \tag{5}$$

where k is the free space wave number at the nth harmonic of the fan blade passing frequency (nFBPF), $k = nB\Omega/c_0$. Solving this equation for $k_{zm\mu}$ yields the two solutions

$$k_{zm\mu} = k_{zm\mu}^{\pm} = \frac{(M_z \pm \alpha_{m\mu})}{1 - M_z^2} k, \quad \alpha_{m\mu} = \sqrt{1 - 1/\zeta_{m\mu}^2}, \tag{6}$$

where $\zeta_{m\mu}$ is the cut-off ratio defined by

$$\zeta_{m\mu} = (k/k_{rm\mu})\sqrt{1 - M_z^2}. \tag{7}$$

For subsonic flows $k_{zm\mu}^+$ and $k_{zm\mu}^-$ are the axial wave numbers associated with wave propagation in the directions towards the exit of the duct intake, and a reflected wave in the direction of the flow, respectively. The signs in Eq. (6) do not necessarily relate to the direction of the phase velocities, but refer to the group velocity direction corresponding to sound power transmission.[11] The distinction between modal phase and group velocities will be of importance in the companion paper[10] where a strategy is proposed for controling the radiated field using in-duct sensors. The definition of cut-off in Eq. (7) identifies the propagating modes by $\zeta_{m\mu} \geqslant 1$. Modes of cut-off ratio less than unity are evanescent and their contributions to the far field are generally weak except for fans located close to the duct face. The effects of a uniform flow is to reduce the cut-off ratio by the factor $(1 - M_z^2)^{1/2}$, and hence increase the number of propagating modes by the reciprocal of this factor. The presence of a mean flow is therefore generally detrimental to active control performance. This inference has been confirmed directly by Joseph *et al.*[19] in a study of the effect of a mean flow on the active control of free field source radiation. The effect of varying the mean flow velocity is not investigated, however.

The cut-off ratio $\zeta_{m\mu}$ defined by Eq. (7) is a fundamental parameter in duct acoustics. A number of studies, most notably those due to Rice,[20,21] and more recently by Joseph and Morfey,[17] have demonstrated that the modal indices (m,μ) are generally unimportant since they do not uniquely describe modal behavior. Equations (6) and (7) demonstrate that these modal indices may be combined to determine a single, but nonunique, value of the cut-off ratio $\zeta_{m\mu}$ in terms of which many modal transmission and radiation characteristics may be accurately expressed. The cut-off ratio will be used in Sec. VII as a means of interpreting the control principles involved in total sound power minimization and the minimization of sound power radiation in an axisymmetric band of sideline angles.

C. Modal admittance ratio

A basic quantity in duct acoustics, which allows the computation of the acoustic power in the duct [Eq. (15)], as well as the in-duct Green's function [Eq. (12)], is the modal admittance ratio $\beta_{m\mu}(z)$. It is defined as the ratio of particle velocity to the acoustic pressure in a single mode as a function of axial position along the duct. An expression for $\beta_{m\mu}(z)$ in the intake and exhaust branches of the flow duct may be derived by first obtaining an expression for the modal acoustic pressure and then applying the momentum equation. The acoustic pressure in a single mode is the sum of an incident wave and a wave reflected from the open termination with mode amplitudes $\overline{p}_{m\mu}^+$ and $\overline{p}_{m\mu}^-$,

$$p_{m\mu}(\mathbf{y},z) = (\overline{p}_{m\mu}^+ e^{-ik_{zm\mu}^+} + \overline{p}_{m\mu}^- e^{-ik_{zm\mu}^-})\Psi_{m\mu}(\mathbf{y}). \tag{8}$$

By approximating the duct termination as an impedance boundary (i.e., neglecting modal coupling), the incident and reflected mode amplitudes may be related through a reflection coefficient at the open termination of the duct intake. An expression for the axial particle velocity $\mu_{zm\mu}(\mathbf{y},z)$ then follows by the application of the momentum equation to Eq. (8) from which β may be derived. In the intake duct, the result is[11]

$$\beta_{m\mu}^1(z) = \frac{u_{zm\mu}(\mathbf{y},z)}{p_{m\mu}(\mathbf{y},z)} = -\frac{1}{\rho c_0} \frac{i\alpha_{m\mu}(1 - M_z^2)\tan\varphi_{m\mu}(z) + M_z(1 - \alpha_{m\mu}^2)}{1 - \alpha_{m\mu}^2 M_z^2}. \tag{9}$$

The term $\varphi_{m\mu}(z)$ denotes the complex reflection phase of any arbitrary axial position along the duct intake given by

$$\varphi_{m\mu}(z) = \frac{\alpha_{m\mu} k}{1 - M_z^2}(z_1 - z) + \varphi_{m\mu}(z_1), \qquad e^{2i\varphi_{m\mu}(z_t)} = R_{m\mu}^1, \tag{10}$$

where z_1 denotes the axial position of the duct intake termination and $R_{m\mu}^1$ is the modal reflection coefficient at the duct intake termination. An analogous expression describes the modal admittance $\beta_{m\mu}^E(z)$ in the duct exhaust where the complex reflection phase $\varphi_{m\mu}(z)$ now relates to that at the duct exhaust termination, and the axial coordinate of the exhaust termination z_E replaces z_I. In the computer simulations, the modal reflection coefficients are computed using the theory due to Zorumski[12] for a semi-infinite, flanged circular duct in the absence of flow. Their values at the intake and exhaust terminations are assumed to be identical. For the

range of frequencies of interest here ($5 \leqslant ka \leqslant 24$), the modal reflection coefficient are generally negligible except for the modes close to cut-off which tend to unity in the cut-off frequency limit.[12]

D. In-duct Green's function

In the computer model, the primary and secondary sources are assumed to be axial dipole and monopole sources with dipole moment and volume velocity source strength distributions $q(\mathbf{y},z_s)$ and $f_z(\mathbf{y},z_s)$ respectively. The sources are assumed to be compact in the axial direction, a simplification that allows the acoustic pressure at any point $(\mathbf{y},z)$ in the duct to be written in the form

$$p(\mathbf{y},z)=\sum_{m,\mu} q_{m\mu}\Psi_{m\mu}(\mathbf{y})g_{m\mu}(z|z_s),$$
$$q_{m\mu}=\frac{1}{S}\int_S \Psi_{m\mu}(\mathbf{y}')q(\mathbf{y}',z_s)\,d\mathbf{y}', \tag{11a}$$

$$p(\mathbf{y},z)=\sum_{m,\mu} f_{zm\mu}\Psi_{m\mu}(\mathbf{y})\frac{g_{m\mu}(z|z_s)}{\partial z_s},$$
$$f_{zm\mu}=\frac{1}{S}\int_S \Psi_{m\mu}(\mathbf{y}')f_z(\mathbf{y}',z_s)\,d\mathbf{y}', \tag{11b}$$

where $g_{m\mu}(z|z_s)$ is the single-frequency modal response function, which as indicated, depends only upon the source and receiver axial coordinates z_s and z, respectively. This function for a finite-length, circular duct with an axial mean flow has been derived by Morfey.[11] He argued that the presence of flow did not alter the boundary condition at the source plane of a monopole source distribution without flow at which the net force is zero. The derivation of g therefore proceeds exactly as for when flow is absent and incorporates the solutions for the axial wave number components of Eq. (6), and the modal admittance ratio of Eq. (9) in the two duct branches. The derivation is straightforward, but the algebra lengthy. We shall merely quote the final result which is[11]

$$g_{m\mu}(z|z_s)=\frac{\rho}{\alpha_{m\mu}S}\frac{1}{\tan\varphi^1_{m\mu}(z_s)-\tan\varphi^E_{m\mu}(z_s)}\frac{\varphi^1_{m\mu}(z)}{\varphi^1_{m\mu}(z_s)}$$
$$\times\exp\left[\frac{-ikM_z(z_1-z)}{(1-M_z^2)}\right],\quad z>z_1, \tag{12}$$

where ρ is the ambient mass density. An analogous expression describes the Green's function in the exhaust duct. The modal summations in Eqs. (11) in the general case is taken over mode orders m spinning in both directions. In the present study, however, the propagating modes excited by the primary source [Eq. (11b)] are assumed to spin in one direction only (cf. Sec. II B below), while the modes excited by the secondary source are assumed to spin in both directions.

E. Radiated sound field: In-duct to far-field transfer function

The far-field modal radiation is computed using the modal directivity functions at a semi-infinite, hard-walled, unflanged circular duct. The restriction to semi-infinite ducts precludes the inclusion in the model of mutual loading effects between the inlet and exhaust which are therefore assumed to radiate independently. These modal directivity functions were first derived using the Wiener–Hopf technique by Levine and Schwinger for the plane wave,[13] and by Weinstein[14] and Lansing[15] for the higher-order modes. A form of these equations, more amenable to computation, was summarized by Homicz and Lordi.[16] This paper also includes the form of these no-flow expressions following the application of the Prandtl–Glauert transformation as a means of including the effects of a uniform flow. This is the solution we shall adopt here to compute the modal radiation from the inlet and exhaust, given the mode amplitudes incident upon the duct terminations from Eqs. (8) and (11). This solution is appropriate for computing the radiation from the intake, but it is an approximation at the duct exhaust where vortex shedding occurs at the trailing edge.

Above its cut-off frequency, a single mode incident upon the termination of the duct inlet (or exhaust) is described by $p^+_{m\mu}=\overline{p}^+_{m\mu}e^{-jk_{znm\mu}}\Psi_{m\mu}(\mathbf{y})$. To compute the radiated field due to this mode the dimensionless in-duct to far-field transfer function $H_{m\mu}(ka,\theta)$ is introduced defined by[17]

$$p_{m\mu,f}(R,\theta,\phi)=\frac{a}{R}\overline{p}^+_{m\mu}H_{m\mu}(ka,\theta)e^{-im\phi-ikR}, \tag{13}$$

where $p_{m\mu,f}(R,\theta,\phi)$ denotes the acoustic pressure at any far-field point (R,θ,ϕ) due to the (m,μ)th mode (Fig. 1). Note that the radiated sound field is expressed in terms of the incident-mode amplitude arriving at the open end of the duct. The factor $H_{m\mu}(ka,\theta)$ therefore automatically incorporates the reflection process at the duct termination, unlike the corresponding expressions for a flanged duct derived by Tyler and Sofrin[18] in the Kirchloff approximation.

II. SIMULATION PARAMETERS

A. Duct parameters

Computer simulations presented in this and the companion paper[10] are standardized on a set of duct and fan parameters typical of modern turbofan engines. The computer simulations assume a hard-walled circular duct of length 2.4 m with a 0.5 m radius. The intake flow speed Mach number is assumed to be constant and equal to $M_z=-0.3$.

B. Rotor/stator parameters

The rotor is assumed to comprise of $B=25$ blades, adjacent to a stator stage with $V=30$ intake guide vanes, at an axial distance of 1.4 m from the face of the duct intake. Its effective source distribution is modeled by a ring of 30 axial point dipole sources located at 80% of the duct radius. Each dipole source is modeled by $f_z(\mathbf{y_a},z_s)=f_z(\phi_s,0.8a)\delta(z-z_s)$, where $f_z(\phi_{sj},0.8a)$ denotes the axial dipole moment of constant amplitude, but random phase, and where δ is the Dirac delta function. The modal summation in the computer model is restricted to the circumferential mode indices m satisfying the Tyler and Sofrin[18] criterion $m=nB-pV$, $p=\pm1,\pm2\pm3$. Other possible m values obtained from this expression represent nonpropagating modes since they vio-

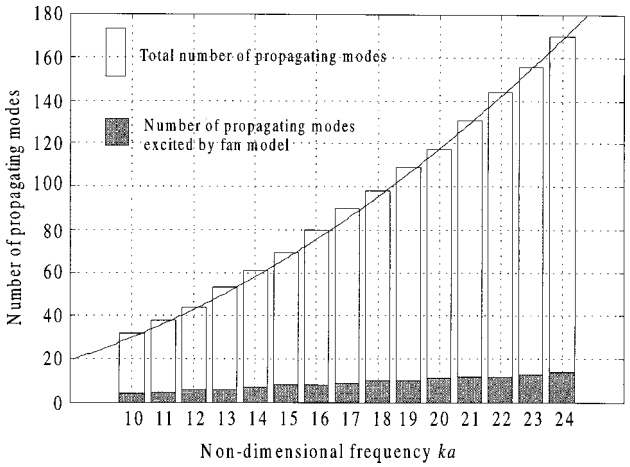

FIG. 2. Number of primary source propagating modes included in the computer model (shaded bars) and the total number of propagating modes (hollow bars), versus frequency. Solid curve denotes the high-frequency asymptotic mode count formula $N(ka,\mathrm{M}_z)=(\frac{1}{2}ka/\beta)^2+\frac{1}{2}ka/\beta$.

late the approximate cut-on condition[22] $|m/nB| \leqslant \mathrm{M}_t/\sqrt{1-\mathrm{M}_z^2}$, where M_t is the blade tip Mach number $\mathrm{M}_t = \Omega a/c_0$. In the simulations, the blade tip speed Mach number M_t is assumed to be subsonic in accordance with $\mathrm{M}_t^2 + \mathrm{M}_z^2 \leqslant 1$ so that ''rotor-alone'' modes are cut-off.[22] Application of the Tyler and Sofrin formula at the blade passing frequency $n=1$ to the choice of B and V given above indicates that only the $m=+5$ mode can propagate, with other modes being cut-off. For the sake of realism, therefore, the computer simulations will also include the $m=+1$ modes which are excited in addition to the $m=+5$ modes generated purely through rotor-stator interaction. Extraneous modes are often present which can be attributed to distorted intake flow, such as ingested turbulence. A prediction of the modes present based entirely on the Tyler and Sofrin formula given above may therefore lead to an underestimate for the number of modes present, and hence an overestimate for the predicted control performance.

The number of propagating modes excited by this hypothetical primary source distribution versus ka is plotted in Fig. 2 below, together with the maximum possible number of modes excited by the secondary sources. Also shown for comparison is the high-frequency asymptotic mode count formula[23] $N(ka,\mathrm{M}_z)=(\frac{1}{2}ka/\beta)^2+\frac{1}{2}ka/\beta$, where $\beta = \sqrt{1-\mathrm{M}_z^2}$.

C. Second sources: Number and location

Control of the radiated field is implemented by the use of 2 rings of 16 uniformly spaced (monopole) secondary sources located at an axial distance of 1.2 and 1 m from the face of the duct intake. This source distribution in each of the two source rings is of the form $q(\mathbf{y_a},z_{sl})=q(\phi_{sj},a)\,\delta(z-z_{sl})$, $l=1,2$. The reason for this choice of secondary source distribution is discussed in Sec. V where three criteria are proposed for selecting the number and arrangement of secondary sources necessary for ensuring good control performance. Control performance in the axisymmetric duct has been found to be insensitive to the angular positions of the secondary sources on the wall, but highly sensitive to the separation distance between the source rings. Comparatively poorer power reductions have been obtained for source rings closer together than $\lambda/2$. This is because the sound fields produced by each source ring are highly correlated, leading to redundant secondary sources and consequently diminished control performance. The axial secondary source ring separation distance of 0.2 m has therefore been chosen on the basis that it is greater than half a wavelength of 0.16 m at the lowest frequency of interest in this investigation of $ka=10$.

III. MINIMUM TRANSMITTED SOUND POWER

A. Minimum total sound power: Theory

The first control objective explored here for reducing the far-field radiation is the minimization of the net transmitted sound power and hence the total radiated power from the duct intake. In the presence of a mean flow, however, the exact classical expressions for acoustic energy in a quiescent medium cease to be valid. The difficulties involved in reaching a definition of acoustic energy in flow are made clear by Morfey[24] whose definition of generalized acoustic intensity and energy density, although to some extent arbitrary, appears to have gained widest acceptance. This definition satisfies a conservation law in any irrotational, constant entropy flow. In a uniform axial flow field, Morfey's expression for the net acoustic intensity I_z in the axial direction of a duct at a single frequency reduces to[11]

$$I_z(z)=\frac{1}{2}\Bigg[\mathrm{Re}\{p^*u_z\}+\frac{\mathrm{M}_z}{\rho c_0}\mathrm{Re}\{p^*p\}+\mathrm{M}_z^2\,\mathrm{Re}\{p^*u_z\} + \rho c_0 \mathrm{M}_z\,\mathrm{Re}\{u_z^*u_z\}\Bigg], \tag{14}$$

where u_z is the axial particle velocity and ''*'' denotes the complex conjugate. In general, scattering by the duct termination causes the modes to become coupled. The column vector of modal axial particle velocities $\mathbf{u}_z$ is therefore related to the column vector of modal pressures $\mathbf{p}$ via a matrix $\mathbf{B}$ of modal admittance ratios with elements β [Eq. (9)]. Putting $\mathbf{u}_z=\mathbf{Bp}/\rho c$, Eq. (14) becomes

$$I_z(z)=\frac{1}{2\rho c_0}\Bigg[\frac{1}{2}(\mathbf{p}^{\mathrm{H}}\mathbf{Bp}+\mathbf{p}^T\mathbf{B}^*\mathbf{p}^*)+\mathrm{M}_z\mathbf{p}^{\mathrm{H}}\mathbf{p} + \frac{1}{2}M_z^2(\mathbf{p}^{\mathrm{H}}\mathbf{Bp}+\mathbf{p}^T\mathbf{B}^*\mathbf{p}^*)+\mathrm{M}_z\mathbf{p}^{\mathrm{H}}\mathbf{B}^{\mathrm{H}}\mathbf{Bp}\Bigg], \tag{15}$$

where ''H'' is the Hermitian transpose operator. When coupling is ignored, only the propagating modes need to be included in the modal summation since the cut-off modes radiate only weakly to the far field. The net axial sound power W_z flowing towards the duct openings is obtained by integrating the net axial intensity over a duct cross section. Making use of the orthogonality property of the mode shape functions in the integration and simplifying the resulting expression gives

$$W_z=\overline{\mathbf{p}}^{\mathrm{H}}\mathbf{Y}\overline{\mathbf{p}}, \tag{16}$$

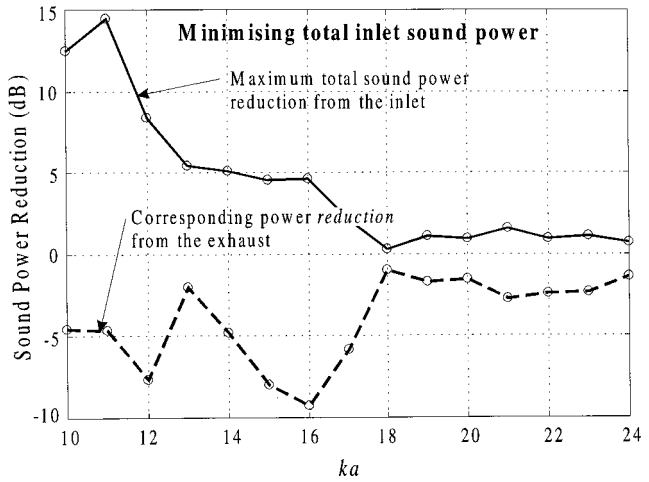

FIG. 3. Maximum total sound power reduction from the duct inlet (in decibels) versus frequency (solid curve) and the corresponding sound power reduction at the exhaust (dashed curve).

where the term $\overline{\mathbf{p}}$ denotes the column vector of modal amplitudes defined by $\overline{\mathbf{p}}=[\overline{p_{00}}\ \overline{p_{01}}\cdots\overline{p_{mn}}]^T$ and $\mathbf{Y}$ denotes the real part of a generalized modal admittance matrix which incorporates convection effects as well as coupling between the modes. From Eq. (15) this matrix is given by

$$\mathbf{Y}=(1+M_z^2)^{\frac{1}{2}}(\mathbf{B}+\mathbf{B}^{\mathrm{H}})+\mathrm{M}_z(\mathbf{I}+\mathbf{B}^{\mathrm{H}}\mathbf{B}). \tag{17}$$

Coupled reflection coefficients for the calculation of $\mathbf{B}$ can be computed directly from the expressions due to Zorumski[12] for the termination of a semi-infinite hard-walled flanged circular duct. Note that $\overline{\mathbf{p}}$ and $\mathbf{Y}$ both depend on the axial position z, although in a lossless duct W_z is independent of z by energy conservation. Even though the effects of modal coupling in the computer simulations are neglected here (so that $\mathbf{B}$ is diagonal), expressing the transmitted sound power in the form of Eqs. (16) and (17) is useful for computational purposes. Furthermore, it proves the existence of a unique set of complex secondary source strengths for which this quadratic function, and hence the transmitted and radiated sound powers, takes a global minimum value. Two properties of the modal admittance matrix $\mathbf{Y}$ ensure that this is the case. First, the matrix is Hermitian, having the symmetry property $\mathrm{Y}=\mathrm{Y}^H$. Second, this matrix is positive definite, i.e., $\overline{\mathbf{p}}^H\mathbf{Y}\overline{\mathbf{p}}\geqslant 0$, for all $\overline{\mathbf{p}}$; a property which has a basis on physical grounds since the direction of net sound power output (if not zero) must be away from the primary–secondary source combination towards the duct openings. The matrix algebra for computing the minimum of this function with respect to the secondary source strengths is presented in Ref. 25.

B. Minimum total sound power: Results

The minimum net sound power transmitted axially along the duct intake for the fan and duct parameters, and the two secondary source rings, described in Sec. II, was computed at integer values of the nondimensional frequency ka between 10 and 24. The results are plotted in Fig. 3 (solid curve). The dashed line represents the *reduction* in the sound power radiated from the exhaust following control of power from the intake.

The control performance indicated in Fig. 3 exhibits a marked sensitivity to frequency. For ka values below 10, typical sound power reductions are many tens of decibels and have therefore not been plotted. At $ka=12$, reductions in sound power from the inlet remain in excess of 10 dB, but diminish significantly as the frequencies increase above this. At $ka=16$, reductions are limited to just 5 dB, dropping to just 1 dB at frequencies above this. An explanation for this general behavior follows from the variation of the total mode count with frequency plotted in Fig. 2.

In Fig. 2, $ka=10$ is the frequency at which the number of secondary sources (2×16) in this example approximately equals the total number of propagating modes. Below this frequency, the control system is overdetermined and perfect control of the radiated field is possible, in principle, providing the secondary sources are able to couple perfectly into all the modes. However, coupling to the duct modes by the wall-mounted secondary sources is seldom perfect which imposes fundamental limits on the theoretically achievable control performance. Below the transition frequency in this example, control performance is substantial nevertheless. The number of secondary sources must therefore be chosen and located for the purpose of providing effective control of not only the modes excited by the fan, but also the generally much larger number of modes excited by the secondary sources themselves. Modal spillover is therefore the most significant factor in limiting control effectiveness, and not the number of primary modes present originally. This explains the striking sensitivity of control performance to frequency in Fig. 3, even though the number of primary modes originally present in the duct increases quite slowly with frequency (Fig. 2). Criteria for choosing the number and arrangement of secondary sources are presented in Sec. III.

Figure 3 indicates an increase in the exhaust sound power output (dashed curve) at all frequencies following the minimization of the total intake sound power. The two curves in Fig. 2 are approximately mirror images suggesting that reductions in sound power at the intake are accompanied by similar increases in sound power radiated from the exhaust duct. The total sound power output (inlet plus exhaust) following control is roughly unchanged. Rather than absorbing sound power, therefore, the secondary sources operate in a predominantly reactive mode by reflecting the flow of sound energy upstream and out from the exhaust.

The changes to the far-field directivity resulting from the minimization of intake radiated sound power is illustrated in Fig. 4. It shows the polar directivity at the intake and exhaust before and after control at $ka=16$, averaged over all azimuthal angles. No attempt has been made to sum the pressures from the two ends. The figure is shown slightly inclined in an attempt to convey an engine ''on approach.''

In this example, the largest intake sound pressure reduction is approximately 10 dB which occurs at about 10° to the duct axis. This is the angle of maximum intensity due to the main radiation lobe of a single, well cut-on, dominant mode. However, sound pressure level reductions in the important sideline directions are limited to less than 3 dB. At the exhaust, the sound pressure level is increased at all angles, with the largest increase appearing in the sideline direction.

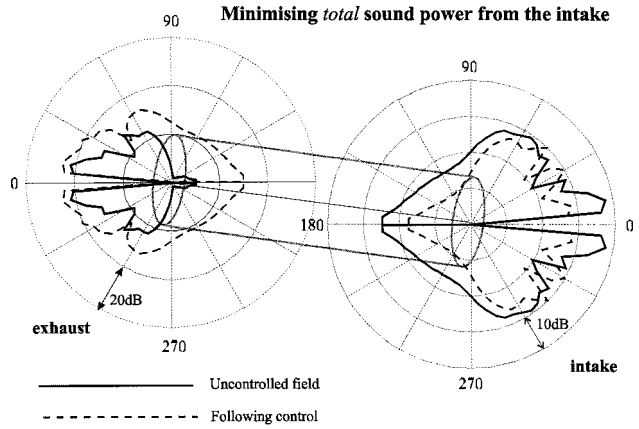

FIG. 4. Sound pressure level (in decibels) versus polar angle before and after the minimization of total intake radiated sound power.

The simulation results in Fig. 4 demonstrate that minimizing the total radiated inlet sound power produces modifications to the far-field directivity that are essentially arbitrary. Naturally, the radiation angles of greatest sound pressure level reductions correspond to those at which the intensity preceding control are greatest. A more strategic control objective is therefore needed to target specifically these important sideline angles. The performance gain obtained by minimizing the sound power in an axisymmetric band of sideline polar angles is now examined. The investigation will then proceed to study the improvement gained by confining the control surface further by reducing the circumferential bandwidth $\Delta\phi$ to 90° (Fig. 1).

IV. MINIMUM RADIATED SOUND POWER ACROSS A BAND OF RADIATION ANGLES

A. Theory

A more effective control strategy for reducing EPLNL than minimizing the total sound power is the minimization of sound power radiated into an appropriate control solid angle $\Omega_c(\Delta\theta,\Delta\phi)$ (Fig. 1), with angular dimensions $\Delta\theta$ and $\Delta\phi$ chosen to correspond roughly to the engine noise footprint. The appropriate cost function in this case is given by the integrated far-field squared pressure over S_Ω,

$$J_{\Omega_c}=\int_{S_\Omega}|p_f(R,\theta,\phi)|^2\sin\theta\,d\theta\,d\phi,\quad R\gg\lambda, \tag{18}$$

where $S_\Omega=R^2\Omega_c$. Note that the calculation of total sound power based on Eq. (18) taken over a surface completely enclosing the duct intake has been found to be in close agreement with that computed from the integration of in-duct intensity [Eq. (15)] over a duct cross section. For ease of computation Ω_c is chosen to be a ''spherical rectangle'' with coordinates given by $\Omega_c=(\pi/2\pm\Delta\theta/2,\pi\pm\Delta\phi/2)$, specifying polar and azimuthal angular bandwidths of $\Delta\theta$ and $\Delta\phi$ from the point $(\pi/2,\pi)$ directly beneath the face of the duct intake (Fig. 1). In practice, the integration is approximated by the sum of squared pressures over a uniform grid of far-field positions. In vector form, this is expressed by

$$J_{\Omega_c}\propto\mathbf{p}_f^H\mathbf{p}_f, \tag{19}$$

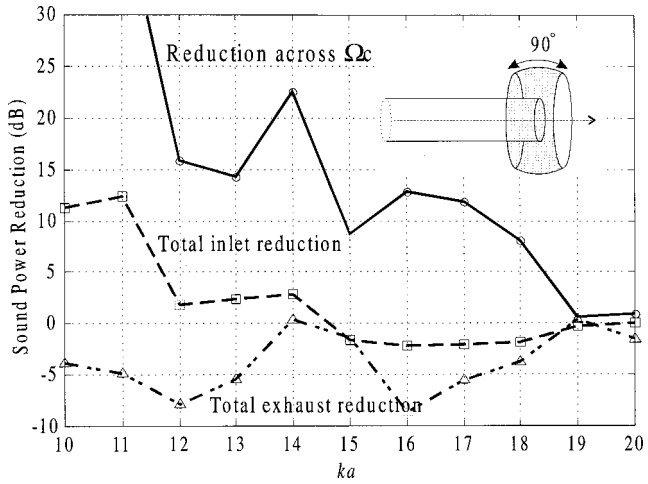

FIG. 5. Sound power reduction (in decibels) across an axisymmetric sector of sideline angles of 90° bandwidth versus frequency (solid curve). Triangles represent the corresponding reductions in total power at the inlet, and diamonds the sound power reductions at the exhaust.

where $\mathbf{p}_f=[p_f(R,\theta_1,\phi_1)p_f(R,\theta_2,\phi_1)p_f(R,\theta_1,\phi_2)p_f(R,\theta_1,\phi_3)\cdots]^T$ with $\{\theta_1,\phi_1\,\theta_2,\phi_2\cdots\}\in\Omega_c$. This cost function, like that of Eq. (16) for the transmitted sound power, may also be expanded to yield a Hermitian quadratic function, thereby establishing the existence of a unique global minimum value of J with respect to the complex secondary source strengths. We begin by investigating sound power minimization over an axisymmetric control region in the sideline direction.

B. Minimum sound power over an axisymmetric control region: Results

Adopting the same duct and fan parameters as those used in Sec. III, the optimum reduction in Eq. (19) versus ka was computed for the axisymmetric ($\Delta\phi=2\pi$) control region Ω_c with $\Delta\phi=\pi/2$. Evaluation of the pressure in Eq. (19) was performed over a uniform grid of points across Ω_c separated by 5° in both polar and azimuthal directions. The results are plotted in Fig. 5.

Sound power reductions in this figure represent an appreciable improvement over the minimization of total radiated sound power plotted in Fig. 3. Reductions in the axisymmetric control bandwidth Ω_c are in excess of 20 dB at ka below 12, falling to around 10 dB at the higher values of ka of between 12 and 16. Compared with the minimization of the total power, this general level of performance gain is approximately consistent with a 6-dB theoretical improvement predicted based on the hypothesis that the reduction in power is inversely proportional to the solid angle Ω_c subtended by the control surface. This speculative scaling principle will be compared with the exact power reduction variation versus $\Delta\phi$ and $\Delta\theta$ in Sec. IV D below.

At values of ka greater than 16, the performance drops sharply with typical reductions in sound power across the control region being less than 5 dB. This poor level of performance at the higher frequencies will diminish even further in a practical active control realization once the error sensors are introduced into the duct wall and the radiated field is inferred indirectly.

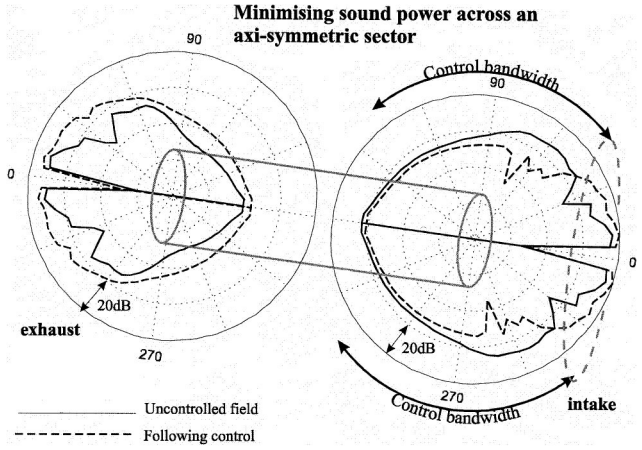

FIG. 6. Sound pressure level (in decibels) versus polar angle at $ka=16$ from the intake and exhaust, before and after minimization of radiated sound power from the inlet across an axisymmetric sector of 90° beamwidth.

The dashed line in Fig. 5 depicts the reduction in the total intake sound power as a function of frequency following sound power minimization across Ω_c. It shows a small overall sound power reduction at most frequencies. At the exhaust, however, the results at all frequencies undergo a greater sound power increase (dotted line), indicating a net increase in radiated sound power from both the intake and exhaust. The effect of this control objective at $ka=16$ on the far-field directivities at the intake and exhaust, averaged over all azimuthal angles, is illustrated in Fig. 6.

Figure 6 may be compared directly with Fig. 4 following total sound power minimization. Within the sideline control region Ω_c, sound pressure level reductions vary between 10 and 15 dB, but drop off sharply outside this region into the rear arc. At angles close to the duct axis, sound pressure level increases are typically about 10 dB. In the exhaust duct the radiated sound power output has increased at all angles, but in the sideline direction are limited to less than 5 dB. Greater EPLNL reductions may therefore be obtained by the simultaneous control of intake and exhaust radiation. This control strategy will not be considered further here.

Figure 7 below depicts the change in sound pressure level as a function azimuthal, as well as polar angle, in the forward arc ($\theta \leqslant 90°$). Polar angles are measured from the duct axis and are plotted linearly against the radial coordinate; variations in azimuthal ϕ are plotted circumferentially. The forward arc boundary $\theta=45°$ of the control region Ω_c is represented by the white line.

External to the control region, the sound pressure level at most angles experiences an increase by approximately 10 dB. Here, the four lobes of the $m=4$ difference ''frequency'' can be observed due to interference between two $m=1$ and $m=5$ modes whose amplitudes have been similarly increased by about 20 dB. A similar pattern can be seen within the control region $\theta>45°$ in which the reduction levels appear reasonable uniform at about 10 dB, but with small, localized regions of very high pressure level reduction (-30 dB) or localized regions of amplification ($+10$ dB). These characteristics are typical of the interference field in a highly coherent sound field involving a large number of modes.

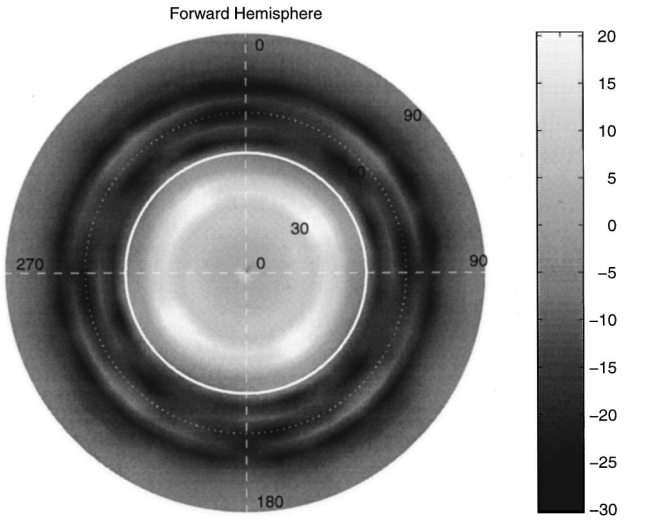

FIG. 7. Sound pressure level variation over the forward are of the duct intake following sound power minimization over an axisymmetric band of angles with polar angle beamwidth equal to 90° (cf. Fig. 6).

C. Minimum sound power over a nonaxisymmetric control region: Results

The computer simulations described in Sec. IV B above were repeated for the nonaxisymmetric control surface Ω_c with azimuthal and polar bandwidths equal to $\Delta\phi=\Delta\theta=\pi/2$ (Fig. 8).

The level of improvement achieved by reducing by a factor of 4 the solid angle of the control region compared with the previous axisymmetric example is, once again, approximately consistent with the 6-dB performance gain predicted from their solid angle ratios. Typical improvements are found at $ka=16$ where the sound power reduction is roughly 20 dB compared with typical reductions of 10 and 5 dB following the minimization of sideline and total sound power output, respectively. Changes to the sound pressure level at $ka=16$ across the entire forward hemisphere following control across Ω_c are presented in Fig. 9.

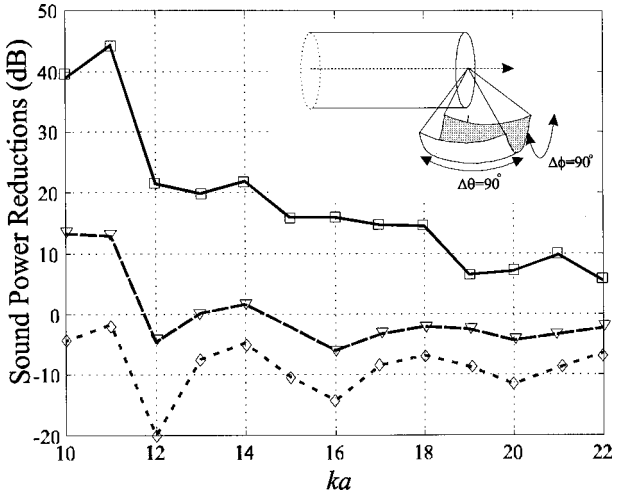

FIG. 8. Maximum sound power reduction (in decibels) (solid line) across a control sector with angular dimensions: $45° \leqslant \theta \leqslant 135°$, $135° \leqslant \phi \leqslant 225°$ versus frequency. Triangles represent the corresponding reductions in total power at the inlet, and diamonds the reductions at the exhaust.

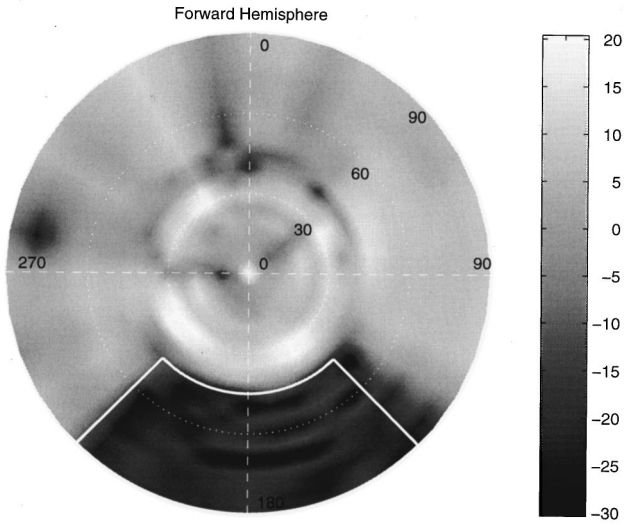

FIG. 9. Sound pressure level variation in the forward arc following sound power minimization over a control zone with angular dimensions equal to $45° \leqslant \theta \leqslant 135°$, $135° \leqslant \phi \leqslant 225°$ (cf. Fig 8).

The distinctive feature of this figure is the exceptional accuracy with which the region of sound pressure level reduction remains within the boundaries of the control region at this frequency. Leakage of the sound pressure level reduction from the control region is found to occur at lower frequencies. At the angles external to Ω_c, the increase in sound pressure level is fairly uniform, with an average value of about 5 dB. Note that control of the radiated field across the polar angles can only be achieved by appropriately reducing the amplitudes of the modes whose principal radiation lobes lie within its beamwidth. Control in the azimuthal directions is achieved by a different process which involves appropriately rotating the various spinning modes $\exp im\phi$ to cause them to destructively interfere in the desired band of azimuthal angles.

D. Variation of control performance with bandwidth dimensions $\Delta\theta$ and $\Delta\phi$

An investigation is now presented into the variation of sound power reduction with the control dimensions $\Delta\theta$ and $\Delta\phi$. The same default parameters as those listed in Sec. IV were used to compute the maximum power reduction for the range of semi-polar $\Delta\phi/2$ angles between 5° and 90° in 5° intervals, and azimuthal half-angles $\Delta\phi/2$ between 10° and 180° in 10° intervals. The results are presented in Fig. 10(a) as contours of constant sound power reduction.

In an attempt to explain the general behavior observed in this figure, it is speculated that the maximum sound power reduction, $\min J(\Omega_c)$, over the far-field region sketched in Fig. 1 is inversely proportional to its subtended solid angle:

$$\min J(\Omega_c)/J_0(\Omega_c) \propto \Omega_c^{-1}; \quad \Omega_c = 2\Delta\phi \sin(\Delta\theta/2), \tag{20}$$

where $J_0(\Omega_c)$ denotes the sound power radiated across Ω_c before control. A prediction of the maximum sound power reduction based upon this conjecture is presented in Fig. 10(b) alongside the exact calculation at $ka = 16$ in Fig 10(a). The empirical model of Eq. (20) is arranged to agree with the model predictions at $\Delta\theta = 100°$, $\Delta\phi = 200°$. Equation (20) can be seen to provide acceptable agreement to the exact values for the 10- and 15-dB reduction contours occurring at large solid angles. At smaller solid angles, however, control performance is considerably better than that predicted by this simplistic model.

V. NUMBER AND POSITION OF SECONDARY SOURCES

This section presents a brief investigation into the variability of control performance with the number and the distribution of secondary sources. Computer simulations of control performance variability with secondary source configurations have demonstrated an absence of a single criterion for determining the number and arrangement of secondary sources necessary to ensure good levels of control performance. These are discussed below. The number of sources and their axial separation distance has been found to affect control performance to a greater extent than their angular position at the duct wall owing to the symmetry properties of the axisymmetric duct.

A. Estimate for the number of sources based on total number of modes

In the active control of enclosed sound fields, good control performance is assured by matching the number of sec-

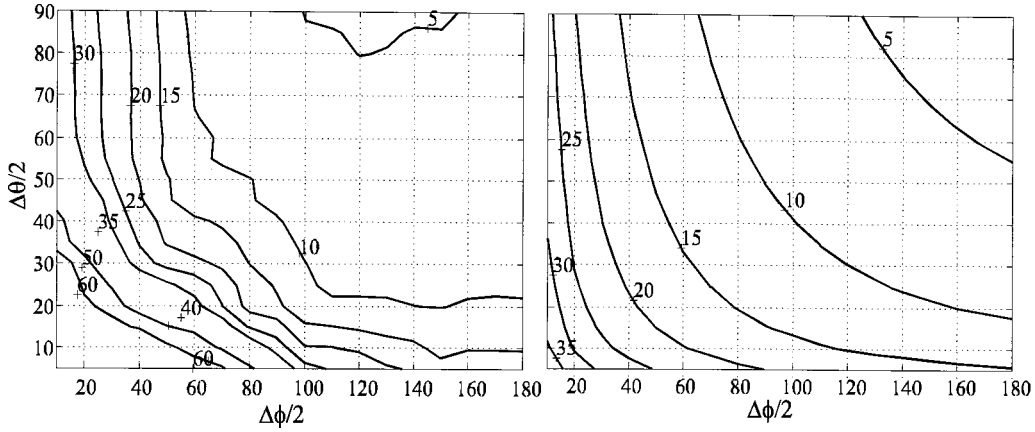

FIG. 10. (a) Contours of constant sound power. (b) Contours of reduction at $ka = 16$ versus half-angle control $-20\log_{10}[2\Delta\phi \sin(\Delta\theta/2)] + 24.6$ bandwidths $\Delta\theta/2$ and $\Delta\phi/2$.

ondary sources to the number of modes to be controled, providing they are sufficiently well coupled. By assuming that *all* the propagating modes must be controled to achieve worthwhile control performance, an approximate upper-bound estimate for the number of secondary sources N_s may be obtained from the expression for the number of modes. In the high-frequency limit, the total number of propagating modes $N(ka,M_z)$, including clockwise and anti-clockwise spinning modes, may be obtained from the asymptotic formula given by[23] $N(ka,M_z)=(\frac{1}{2}ka/\beta)^2+\frac{1}{2}ka/\beta$ (Fig. 2). Conversely, given a number of secondary source N_s, this formula may be inverted to give $ka=\beta\sqrt{4N_s+1}-1$ for the upper frequency limit, above which control performance may begin to diminish.

B. Estimate for the number of sources based on the number of modes contributing to the control region

Restricting the control region to the band of polar angles $\theta_1 \leqslant \theta \leqslant \theta_2$ reduces substantially the number of modes which must be controled for small bandwidths $\theta_2-\theta_1$. An estimate for this number of modes may be deduced from the mode count distribution function across cut-off ratios due to Rice,[23] and by noting that the in-duct axial propagation angle and the angle of the principal radiation lobe in the absence of flow are equal.[20] The number of modes $\delta N(\xi)$ with cut-on ratio (reciprocal of cut-off ratio $\xi=1/\zeta$) between $\xi+\delta\xi$ and ξ is given by $\delta N(\xi)\approx N(ka)n(\xi)\delta\xi$, where n is the normalized, high-frequency asymptotic density function. In terms of cut-on ratio, n is given by[26] $n(\xi)=2\xi$. Putting $\xi=\sin\theta$ in this formula gives $n(\theta)=\sin 2\theta$ for the modal distribution function across the angles θ of the principal radiation lobes. The number of modes at a frequency ka with main radiation lobes falling within $\theta_1 \leqslant \theta \leqslant \theta_2$ is therefore approximated by $N_\theta(ka,\theta_1,\theta_2)=N(ka)\int_{\theta_1}^{\theta_2}\sin 2\theta\, d\theta$. Performing the integration and substituting the expression for $N(ka)$ above leads to

$$N_\theta(ka,\theta_1,\theta_2)=\tfrac{1}{2}N(ka)(\cos 2\theta_1-\cos 2\theta_2). \tag{21}$$

It may be verified that $N_\theta(ka,0,\frac{1}{2}\pi)=N(ka)$. Good levels of control performance are therefore anticipated for numbers of secondary sources $N_s=N_\theta(ka,\theta_1,\theta_2)$ providing that the sources are able to couple fully into these modes and that modal spillover is not excessive. A deficiency with this argument is that it provides no guidelines on the distribution of the sources between the rings, or the number of rings. An alternative criterion for the number and separation distance between the secondary sources, designed to eliminate modal spillover, is based upon the Nyquist sampling criterion.

C. A Nyquist criterion for the number of secondary sources in a single ring, and the number of rings

The Nyquist sampling theorem requires the number of secondary sources in a single ring needed to control (or detect) all the spinning modal orders without aliasing into lower-order modes, and hence prevent modal spillover, to be at least twice the highest spatial frequency m present. This highest (propagating) spinning mode order may be estimated from the approximate cut-off condition[22] $m<ka$. The integer value of ka therefore provides an estimate for the highest spinning mode order present at a frequency ka, so that $2ka$ denotes the approximate number of secondary required in a single ring to eliminate modal spillover.

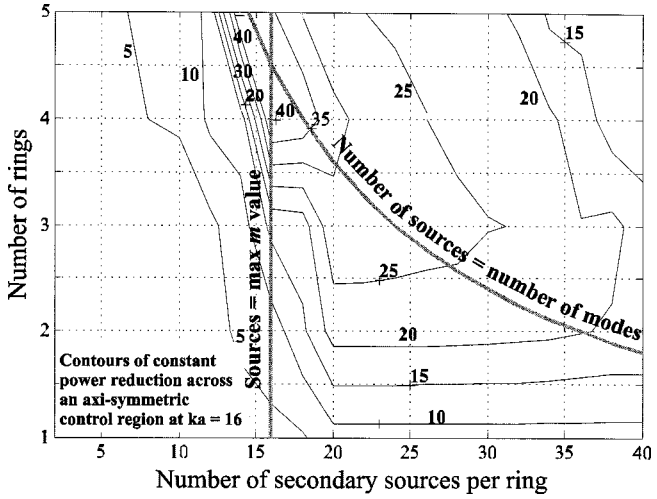

FIG. 11. Contours of constant sound power reduction (in decibels) at $ka=16$ across an axisymmetric band of polar angles $45°\leqslant\theta\leqslant135°$ versus the number of secondary sources per rings, and the number of rings of $0.2m$ axial separation distance.

Perfect control of all the radial mode orders in each circumferential mode order m is achieved by matching the number of secondary source rings to the greatest number of radial mode orders in a single spinning mode. This occurs for the axisymmetric $m=0$ mode which, according to Rice,[25] has approximately $(ka/\beta\pi)+\frac{1}{4}$ radial orders. To satisfy the Nyquist theorem, the source rings are required to be closer together than one-half the wavelength of the highest axial wave number. This occurs for the plane wave mode with axial wave number equal to k/β. The source rings must therefore be further apart than the axial separation distance of $\lambda\beta/2$. Based on these two considerations, the total number of sources is required to be $2(ka/\beta)^2+ka/\beta$, which is approximately a factor of 8 greater than the total number of propagating modes.

D. Control performance versus number and configuration of secondary sources: Simulation results

The relative importance of the three criteria A, B, and C presented in Secs. IV above was investigated by computing the variation in the optimal sound power reduction as a function of the numbers of sources in a single ring, and the number of rings. This calculation was undertaken at $ka=16$ for the axisymmetric control region $45°\leqslant\theta\leqslant135°$. The numbers of secondary sources were varied between 2 and 40 per ring, and for numbers of rings between 1 to 5, separated by 0.2 m. In this example there are a total of 72 propagating modes, of which 36 have principal radiation lobes falling within $45°\leqslant\theta\leqslant90°$ (there are no main lobes in the rear arc). The maximum spinning mode order present at this frequency is $m=15$ and the largest number of radial mode orders is 6 at $m=0$. The results are shown in Fig. 11 as contours of constant sound power reduction.

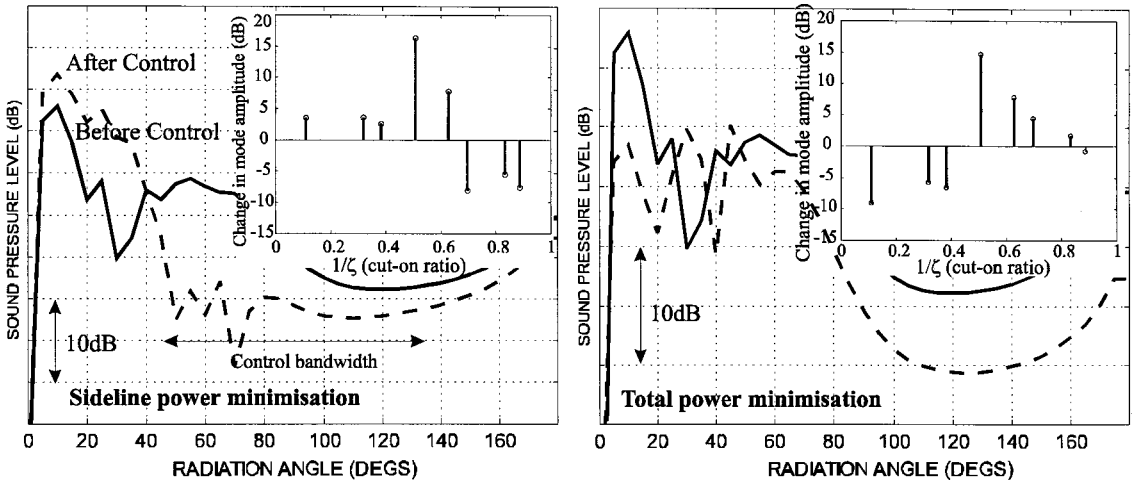

FIG. 12. (a) Sound pressure level (in decibels) before and after the minimization of sound power at $ka=16$ across an axisymmetric band of sideline angles of 90° bandwidth. Inset figure shows the associated change to the mode amplitudes versus cut-on ratio. (b) Sound pressure level (in decibels) before and after the minimization of total sound power at $ka=16$. Inset figure shows the associated change to the mode amplitudes versus cut-on ratio.

These results demonstrate that none of the criteria in Secs. IV alone is able to predict the transition between good and poor control performance as the number of secondary sources is varied. This figure indicates a consistently poor performance when the sources are restricted to a single ring. Poor performance is also obtained when the number of sources is less than the 36 modes with principal radiation lobes lying within the control beamwidth. Similarly poor performance is found for numbers of sources in a single ring less than ten, irrespective of the number of rings. In this case, control of different radial mode orders with the same m value is impossible. For numbers of sources in a single ring exceeding 20, the control performance provided by a fixed number of rings ceases to improve. These findings suggest that most of the energy in the control beamwidth is radiated by the lowest ten spinning mode orders. The remaining six highest m orders each contain only two radial mode orders. Their contribution to the pressure in the control beamwidth is likely to be comparatively small. The Nyquist criterion applied to the effective highest spinning mode order therefore appears to be the appropriate factor in deciding the number of sources in a single ring.

In Fig. 11, employing more sources than the maximum number propagating modes can be seen to result in a deterioration in control performance. This is a result of an inaccurate matrix inversion in these overdetermined examples. Even though choosing the number of sources based exclusively on the Nyquist sampling theorem is the only strategy for eliminating modal spillover, this optimization procedure in a practical realization may be ill conditioned, ultimately leading to poorer performance. Figure 11 indicates that an effective, but efficient, deployment of secondary sources comprises at least as many sources in a single ring as the highest propagating spinning mode order present, and approximately half as many rings as axisymmetric radial mode orders $m=0$. One of the most efficient configurations of the 32 secondary sources assumed in this study is therefore as two rings of 16 sources.

VI. RELATIONSHIP OF REDUCTIONS IN THE RADIATED FIELD TO CHANGES IN IN-DUCT MODE AMPLITUDES

Insight into the mechanism underlying the control objectives described above may be gained by plotting the change in mode amplitudes against cut-on ratio $1/\xi$. Typical results are presented in Fig. 12(a) and (b) following the minimization at $ka=16$ of the total radiated sound power, and the power radiated into an axisymmetric band of sideline angles with beamwidth $\Delta\theta=90°$, respectively. Also shown in these figures are the corresponding changes to their intake far-field directivity pattern.

These results reveal a close correspondence between the far-field pressure reductions versus polar angle, and the reductions in mode amplitudes versus cut-on ratio. This connection arises from the exact equality, in the absence of flow, between the modal axial propagation angle ($=\sin\zeta$), and the angle of the principal radiation lobe of maximum intensity.[20] The presence of a mean flow modifies this relationship, which, at low Mach, is a small effect.[20] At cut-off, for example, the axial propagation angle equal to 90° in zero flow, but reduces to 72° in the present case where $M_z=-0.3$; the principal radiation lobe angle is 90° in both cases.

The minimization of sideline radiated sound power plotted in Fig. 12(b) involves a reduction in the amplitudes of the three modes closest to cut-off (with cut-on ratios closest to unity). The opposite process is observed to be involved in minimizing the total radiated sound power as shown in Fig. 12(a). The modes of greatest amplitude reduction are those that are most cut-on whose radiation angles of maximum intensity are the smallest. These mode amplitude reductions are achieved at the expense of amplifying the modes which radiate the least power, i.e., the modes closest to cut-off. In the limit as the frequency approaches cut-off, the sound power radiated by a single mode tends to zero.[17]

Figure 12(a) and (b) suggests that controling the radiation over an axisymmetric control sector may be accomplished by a reduction in the amplitudes of those dominant

modes whose axial propagation angles, and hence main radiation lobe angles, lie within its beamwidth. Changes to the phase of the mode amplitudes in the axisymmetric case are therefore relatively unimportant. This connection between far-field pressure reductions and the associated changes to the in-duct sound field suggests a method for approximately reproducing this behavior using an in-duct error sensor array. This is the subject of the companion paper. Control of the radiated sound field over a non-axisymmetric region relies upon the precise interference between the far-field radiation due to different modes. Interference between modes is clearly much more difficult to contrive using in-duct error sensors than modifying their mode amplitudes within the duct which may be detected by direct measurement.

VII. CONCLUSIONS

A computer model based on a number of classical results in flow-duct acoustics has been described for predicting the transmission and radiation of single-frequency sound from the inlet of a turbofan engine. Rotor–stator interaction is assumed to be the principal noise-generating mechanism whose excitation of the modes is modeled by a ring of point axial dipole sources and by restricting the circumferential mode orders to those satisfying the Tyler and Sofrin criterion. The number of primary modes included in the model was taken to be typical of those due to rotor–stator interaction, whereas the two rings of 16 secondary sources were assumed to excite all the propagating modes spinning in both directions. This model was then used to assess the potential for reducing the radiated sound field by active means. Two control objectives were explored. The first is the minimization of total intake sound power. The other is the minimization of sound power radiated into a specified solid angle orientated towards ''the ground.'' The important assumption made throughout this paper is that the radiated field under control is completely determined. Control performance is therefore limited only by imperfect controllability of the modes by the wall-mounted secondary sources.

The minimization of total radiated sound power was found to produce greatest sound pressure level reductions at the angles that, before control, were of greatest sound pressure level. The far-field angles of greatest benefit were therefore found to be arbitrary, although a slight improvement of a few decibels to the radiation at sideline angles was also observed at most frequencies. By reducing the solid angle into which the radiated power is to be minimized, improved control performance was obtained that was roughly proportional to the fractional reduction in the control solid angle. The principal advantage of this approach, however, is that the control region may be orientated below the engine to provide greatest benefit for ground-based observers. Sound power reductions in excess of 20 dB were predicted at frequencies ka less than about 15 for a control solid angle with dimensions of 90° by 90°.

The number and configuration of secondary sources necessary for providing effective control was also investigated. No simple criterion could be found for making this decision. However, as a ''rule of thumb,'' it was found that the number of secondary sources in a single ring should be at least equal to the effective highest propagating spinning mode that contributes significantly to the specified control region. The number of rings should be equal to at least half the number of axisymmetric radial mode orders $m=0$.

This paper has found a connection for axisymmetric control bandwidths between the sound pressure level versus polar angle, and the corresponding reduction of in-duct mode amplitudes versus cut-on ratio. Reducing sideline radiation, for example, has been shown to be due to a reduction in the modes closest to cut-off. These are characterized by cut-on ratio close to unity and hence possess the fastest axial phase speeds. The usefulness of this finding is that it suggests a strategy for reproducing this behavior by the use of a number of axial arrays of error sensors located on the duct wall. These allow the estimation of the in-duct axial wave number spectrum, whose energy in the low wave number components may be minimized to achieve the desired reduction in the far-field directivity in the sideline direction.

[1] D. Berge, E. Bouty, and J. M. Cailleau, ''Active Noise Control of a Jet Engine at Low Frequency Radiation: BEM for predicting far field noise reduction,'' Proceedings of the 15th AIAA Aeroacoustics Conference, Long Beach, CA, 25–27 October 1993.

[2] R. E. Kraft and K. B. Kontos, ''Theoretical Implications of Active Noise Control for Turbo Fan Engines,'' Proceedings of the 15th AIAA Aeroacoustics Conference, Long Beach, CA, 25–27 October 1993.

[3] R. A. Burdisso, C. R. Fuller, and S. A. L. Clegg, ''An Analytical Study of Active Control of Narrow Band Turbofan Inlet Noise,'' 16th AIAA Aeroacoustics Conference, Munich, Germany, 1995.

[4] J. D. Risi, R. A. Burdisso, and C. R. Fuller, ''Analytical investigation of active control of radiated inlet fan noise,'' J. Acoust. Soc. Am. **99**, 408–416 (1996).

[5] R. H. Thomas, R. A. Burdisso, C. R. Fuller, and W. F. O'Brien, ''Active control of fan noise from a JT15D turbo fan engine,'' J. Sound Vib. **161**(3), 532–537 (1993).

[6] R. A. Burdisso, C. R. Fuller, and J. P. Smith, ''Experiments on the Active Control of a Turbo Fan Inlet Noise using Compact, Lightweight Inlet Control and Error Transducers,'' 16th AIAA Acroacoustics Conference, Munich, Germany, 1995, CEAS/AIAA-95-028.

[7] J. P. Smith, R. A. Burdisso, and C. R. Fuller, ''Experiments on the Active Control Inlet Noise from a Turbofan Jet Engine using Multiple Circumferential Control Arrays,'' 2nd AIAA/CEAS Aeroacoustics Conference, State College, PA, 6–8 May 1996.

[8] H. Rajiyah and F. Pla, ''Optimal Design of PZT Actuator-Based Acoustic Radiators for Active Control of Aircraft Engine Noise—Part 1: One Dimensional Configurations,'' 2nd AIAA/CEAS Aeroacoustics Conference, State College, PA, 6–8 May 1996.

[9] M. Drzewiecki, R. H. Thomas, C. R. Fuller, R. A. Burdisso, and J. B. Niemczuk, ''Acousto-Fluidic Drivers for Use with Active Noise Control Systems,'' 16th AIAA, Aeroacoustics Conference, Munich, Germany, 1995, CEAS/AIAA-95-028.

[10] P. Joseph, P. A. Nelson, and M. J. Fisher, ''Active control of fan tones radiated from ducted turbofan engines. II. Internal error sensors,'' J. Acoust. Soc. Am. **106**, 779–786 (1999).

[11] C. L. Morfey, ''Sound transmission and generation in ducts with flow,'' J. Sound Vib. **14**(1), 37–55 (1971).

[12] W. E. Zorumski, ''Generalised radiation impedances and reflection coefficients of circular and annular ducts,'' J. Acoust. Soc. Am. **54**, 1667–1673 (1973).

[13] H. Levine and J. Schwinger, ''On the radiation of sound from an unflanged circular pipe,'' Phys. Rev. **74**(4), 383–405 (1947).

[14] L. A. Weinstein, *The Theory of Diffraction and the Factorization Method* (Golem, Boulder, CO, 1969).

[15] D. L. Lansing *et al.*, ''Radiation of Sound from an Unflanged Duct with Flow,'' 79th meeting of the Acoustical Society of America, 21–24 April 1970, Atlantic City, NJ.

[16] G. F. Homicz and J. A. Lordi, ''A note on the radiative directivity patterns of duct acoustic modes,'' J. Sound Vib. **41**(3), 283–290 (1975).

[17] P. Joseph and C. L. Morfey, ''Multimode radiation from an unflanged,

semi-infinite circular duct,'' J. Acoust. Soc. Am. **105**, 2590–2600 (1998).
[18] J. M. Tyler and T. G. Sofrin, ''Axial Compressor Noise Studies,'' SAE Transactions No. 70 (1962).
[19] P. Joseph, C. L. Morfey, and P. A. Nelson, ''Active control of source sound power radiation in uniform flow,'' J. Sound Vib. **212**(2), 357–364 (1998).
[20] E. J. Rice and M. F. Heidmann, ''Modal Propagation Angles in a Cylindrical Duct with Flow and their Relation to Sound Propagation,'' Proceedings of the 17th Aerospace Sciences meeting, New Orleans, 15–17 January 1979, Paper 79-0183.
[21] E. J. Rice, ''Multi-modal far field acoustic radiation pattern using cut-off ratio,'' AIAA J. **16**, 906–911 (1979).
[22] M. E. Goldstein, *Aeroacoustics* (McGraw–Hill, New York, 1976).
[23] E. J. Rice, ''Modal density function and number of propagating modes in ducts,'' NASA TM-73839 (1976).
[24] C. L. Morfey, ''Acoustic energy in non-uniform flows,'' J. Sound Vib. **14**(2), 159–170 (1971).
[25] P. A. Nelson and S. J. Elliott, *Active Control of Sound* (Academic, London, 1991).
[26] This distribution function was originally expressed in terms of cut-off ratio in the form $n(\xi)=2\xi^{-3}$. The present result $n(\xi)=2\xi$ in terms of cut-on ratio is obtained by making the change of variable $\xi=1/\xi$ in this density function.

Active control of fan tones radiated from turbofan engines. II. In-duct error sensors

P. Joseph, P. A. Nelson, and M. J. Fisher
Institute of Sound and Vibration Research, University of Southampton, Southampton SO17 1BJ, United Kingdom

(Received 21 November 1996; accepted for publication 31 March 1999)

This paper continues an earlier companion paper in which the results of active control computer simulations aimed at assessing the potential for reducing the fan tones radiated from the inlet of turbofan engines were presented. The earlier study found that good levels of reductions in the sound power transmitted and sound pressure radiated towards the sidelines could be obtained by using error sensors located in the radiated far field. The present paper is also concerned with these control objectives, but with the important difference that the error sensors are located on the duct wall. The error sensor array described in this paper is comprised of a number of axial line array of discrete sensors uniformly distributed around the duct wall. By applying the appropriate phase delay between the sensor signals in a single axial array and summing, an estimate of the mode amplitudes versus axial propagation angle can be obtained. This in-duct pressure measurement can be related to the far-field radiation pattern. Practical issues are also addressed such as the influence on the array's performance of the in-duct boundary layer and interference from cut-off modes. The basis for the technique is the close relationship between the in-duct ray–mode angles and those of the far-field peak pressure lobe of the radiated field. © *1999 Acoustical Society of America.*
[S0001-4966(99)03907-7]

PACS numbers: 43.50.Ki, 43.60.Bf [PJR]

INTRODUCTION

This paper is the second of two papers dealing with the active control of fan tones radiated from the intake of turbofan engines. The first paper[1] describes a mathematical model for predicting the transmission and radiation of harmonic sound from a finite-length, hard-walled unflanged circular duct containing an axial subsonic mean flow. This model was then used to compute theoretical predictions of the maximum reduction in the transmitted sound power along the duct, and also the maximum reduction in the sound power radiated into a specified solid angle directed towards ''the ground.'' It was found that minimizing the total sound power produced greatest sound pressure level reductions in directions that were not necessarily those for which ''ground-based'' observers could most benefit. Substantially greater sideline pressure reductions were obtained when these radiation angles were targeted specifically. The paper found that worthwhile levels of sound pressure reduction were possible over a wide frequency range by the use of a realistic number of secondary sources mounted at the duct wall

The computer predictions presented in the first paper[1] were made assuming perfect knowledge of the radiated sound field. The implementation of this assumption in practice would require many hundreds of error sensors in the far field which, during flight, is clearly impracticable. The purpose of the present paper is to establish whether comparable levels of performance can be achieved when the input signals to the controller are derived from acoustic pressure measurements made by error sensors located on the duct wall. A typical configuration of wall-mounted secondary sources and error sensors is sketched in Fig. 1 in the form of a number of rings uniformly distributed along the length of the intake duct. The pressure signals from these sensors are input to a controller for the purpose of driving the secondary sources in order to reduce the radiated field across a specified control sector (shaded region), or reduce the total radiated sound power.

A processing scheme for achieving these objectives based entirely on in-duct pressure measurements is described in this paper.[2] The performance obtained by using the in-duct sensor array is compared to the corresponding maximum theoretical reduction obtained by the use of a large number of far-field error sensors. Some practical issues related to the practical implementation of this in-duct error sensing technique are also addressed. In Sec. IV the influence on the array's performance by an idealized aerodynamic boundary layer at the duct wall is discussed. In Sec. V, the contamination of the array response from weakly radiating cut-off modes is briefly examined.

I. RELATIONSHIP BETWEEN IN-DUCT PROPAGATION ANGLE AND THE FAR-FIELD RADIATION ANGLE FOR UNIFORM MACH NUMBER INSIDE AND OUTSIDE THE DUCT

The use of in-duct acoustic pressure measurements for the robust estimation of far-field radiation, and hence as the input to an active controller, is fundamentally dependent on the existence of a unique and simple relationship between the transmitted sound field and the radiated far field in a single mode. This relationship has been investigated by Wright[3] and Candel[4] for semi-infinite rectangular wave guides, and by Homicz and Lordi[5] for circular ducts without flow. One of the most comprehensive treatments of this problem in circu-

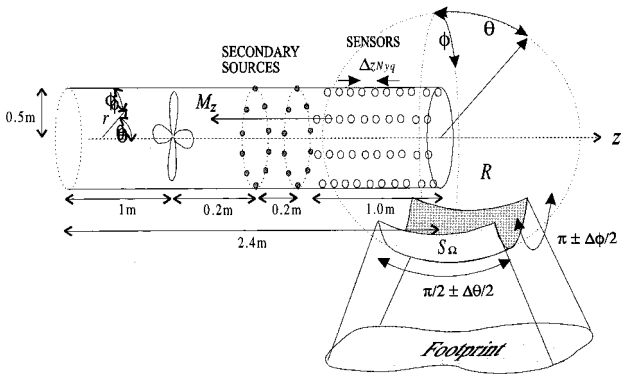

FIG. 1. Rings of secondary sources and error sensors for the active control of far field radiation over an axisymmetric sector (shaded region).

lar ducts with a mean flow is due to Rice[6] from which most of the results presented in this section are taken.

Two angles are important for the characterization of modal sound transmission and radiation from both flanged and unflanged flow ducts. One is the angle $\theta_{m\mu}$ with which the normal component of the phase velocity vector (i.e., the normal to the local wavefront) makes with the duct axis. The other is the angle with which the group velocity vector makes with the duct axis. This second angle is more fundamental in that it specifies the direction of sound power propagation and, in the special case where the flow Mach number is everywhere equal, it is coincident with the angle $\theta_{Pm\mu}$ of peak far-field radiation. The classical expressions for these two angles are derived in Secs. I A and B for the purpose of establishing a simple relationship between them. This relationship may then be used to estimate the forward are radiation pattern from a decomposition within the duct of the transmitted sound field versus axial propagation angle. The design of the array and the processing of its signals for making this measurement is discussed in Sec. II.

A. In-duct axial propagation angle

The acoustic pressure $p(r,\phi,z,t)$ due to a single (m,μ) mode propagating towards the open end of a cylindrical, hard-walled duct at a single frequency ω is given by

$$p_{m\mu}(\mathbf{y},z,t)=\overline{p}_{m\mu}e^{i\omega t-ik_{Zm\mu}(z_s-z)}\Psi_{m\mu}(\mathbf{y}),$$
$$\Psi_{m\mu}(\mathbf{y})=e^{im\phi}J_m(k_{rm\mu}r)/N_{m\mu}, \tag{1}$$

where all the terms have been previously defined in Ref. 1 and $\mathbf{y}$ denotes a position on a duct cross section $\mathbf{y}=(r,\phi)$. From hereon the dependence on the time dependence t will be omitted. Substituting this equation into the convected wave equation in Ref. 1 leads to the dispersion relation,

$$k_{rm\mu}^2+k_{zm\mu}^2=(k-\mathrm{M}_z k_{zm\mu})^2, \tag{2}$$

where k is the free space wave number ω/c, c is the sound speed in the absence of flow, and M_z the Mach number, which for subsonic mean flows in the duct intake lies in the range $-1\leqslant \mathrm{M}_z \leqslant 0$. Recognizing that $k_{r\mu m}$ is the combined radial–circumferential wave number in the transverse $r-\phi$ plane,[6] the wave number combination $k-\mathrm{M}_z k_{zm\mu}$ on the right-hand side of Eq. (2) represents the wave number normal to the local modal wavefront whose angle $\theta_{m\mu}$ to the duct axis given by

$$\cos\theta_{m\mu}=\frac{k_{zm\mu}}{k-\mathrm{M}_z k_{zm\mu}}. \tag{3}$$

It is useful to express $\theta_{m\mu}$ in terms of cut-on ratio (the reciprocal of cut-off ratio) defined by

$$\zeta_{m\mu}=\frac{k\sqrt{1-\mathrm{M}_z^2}}{k_{rm\mu}}. \tag{4}$$

Eliminating in Eq. (3) the explicit dependence on the transverse wave number by the use of Eqs. (2) and (4) allows the axial propagation angle to be expressed as a function of cut-on ratio in the form

$$\cos\theta_{m\mu}=\frac{-\mathrm{M}_z+\sqrt{1-\zeta_{m\mu}^2}}{1-\mathrm{M}_z\sqrt{1-\zeta_{m\mu}^2}}. \tag{5}$$

B. Far-field modal peak pressure lobe angle

Equation (6) below provides an alternative expression of Eq. (3) for the propagation angle $\theta_{m\mu}$. It is expressed in terms of the axial modal phase speed $c_{m\mu}$, and the speed of sound c which may be regarded as a vector normal to the local modal wavefront,

$$\cos\theta_{m\mu}=c_{m\mu}/c. \tag{6}$$

However, the resultant direction of propagation will not be normal to the wavefront, but in the direction of the resultant vector c_R. This vector has the same transverse component as c in the $r-\phi$ plane (since there is zero flow component in these coordinate directions), but a different axial propagation angle that takes account of the drift velocity $c\mathrm{M}_z$. If $c_{gm\mu}$ denotes the axial component of group velocity,

$$c_{gm\mu}=\frac{d\omega}{dk_{zm\mu}}, \tag{7}$$

the principal lobe of far-field radiation $\theta_{Pm\mu}$ may be equated to the angle, relative to the duct axis, of sound power transmission, $\cos\theta_{Pm\mu}=c_{gm\mu}/c_R$. Performing the differentiation on the dispersion relation of Eq. (2) yields the following relationship between the axial phase and axial group velocities:

$$c_{gm\mu}=c_{m\mu}+c\mathrm{M}_z. \tag{8}$$

This equation reveals a simple relationship between the axial speed of sound power transmission and the axial component of phase velocity that involves only an additive ''drift velocity'' $c\mathrm{M}_z$ correction. The angle of the principal radiation lobe $\theta_{Pm\mu}$ is therefore given by

$$\theta_{Pm\mu}=\frac{c_{m\mu}+c\mathrm{M}_z}{c_R}, \tag{9}$$

where c_R is the resultant sound speed in the direction of sound power propagation. A sketch indicating this relationship between the phase and group velocities in this special case is given in Fig. 2.

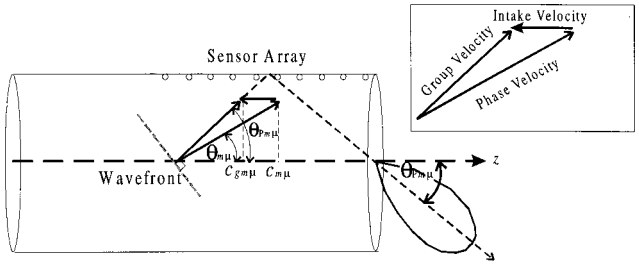

FIG. 2. Relationship between phase velocity, group velocity, and intake axial flow velocity in an intake duct.

Combining Eqs. (2), (4), (8), and (9), the angle $\theta_{Pm\mu}$ of far-field peak radiation in terms of cut-on ratio is of the form[6]

$$\cos\theta_{Pm\mu}=\left(\frac{(1-\mathrm{M}_z^2)(1-\zeta_{m\mu}^2)}{1-\mathrm{M}_z^2(1-\zeta_{m\mu}^2)}\right)^{1/2}, \tag{10}$$

which is in agreement with that, for example, given in Ref. 5 due to Homicz and Lordi whose expressions for the modal far-field directivity functions are used in the computer simulations presented here and in Ref. 1. Eliminating the cut-on ratio between Eqs. (5) and (10) yields a direct relation between the in-duct and radiation angle of peak pressure of the form

$$\cos\theta_{Pm\mu}=\frac{\mathrm{M}_z+\cos\theta_{m\mu}}{\sqrt{1+\mathrm{M}_z^2+2\mathrm{M}_z\cos\theta_{m\mu}}}. \tag{11}$$

Equation (11) reduces to the exact, well-known equality between in-duct and far-field angles $\theta_{Pm\mu}=\theta_{m\mu}$ for $\mathrm{M}_z=0$[5]. Equation (11) has been used to generate the curves in Fig. 2 depicting the variation of peak pressure lobe radiation angle $\theta_{Pm\mu}$ versus the axial propagation angle $\theta_{m\mu}$ for the Mach number: $\mathrm{M}_z=0$, -0.3, -0.5, and -0.7.

Increasing the intake Mach number in Fig. 2 increases the deviation between the two angles, and reduces the maximum propagation angle. For Mach numbers typical of ''approach,'' $\mathrm{M}_z>-0.5$, the angle of far-field modal peak pressure radiation and the axial propagation angle differ by no more than 30°. The relationship between the two angles for the more general case of differing flow speeds inside and outside the duct is also determined by applying the principle of group velocity continuity.[6] Similar agreement between the two angles is found for in-duct and external Mach numbers less than 0.5.

The approximate equality between the in-duct and far-field angles in Fig. 3 suggest that a measurement of the sound field transmitted along the duct as a function of the axial propagation angle $\theta_{m\mu}$ approximately equals the angular distribution of modal peak pressure lobes that dominate the forward-arc far-field radiation pattern. By inputting these pressure measurements to an active controller, it is shown below that far-field pressure reductions may be obtained that are within about 6 dB of the reduction obtained when the radiated field is known perfectly. A limitation with this approach is that control is restricted to axisymmetric sectors since it is unable to control the sound field in the azimuthal direction.

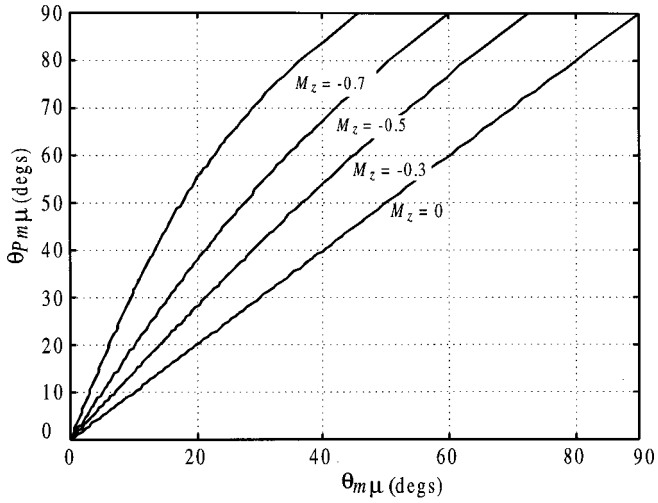

FIG. 3. The function $\cos\theta_{Pm\mu}=(\mathrm{M}_z+\cos\theta_{m\mu})/\sqrt{1+\mathrm{M}_z^2+2\mathrm{M}_z\cos\theta_{m\mu}}$, evaluated for a range of intake Mach numbers, relating the axial propagation angle $\theta_{m\mu}$ to the angle $\theta_{Pm\mu}$ of the peak radiation lobe in the radiated far field for the special case when the flow speed is everywhere the same.

II. PRINCIPLE OF THE IN-DUCT ERROR SENSOR ARRAY

The Fourier transform of the acoustic pressure $p(\mathbf{y},z)$ as a function of axial distance z along the duct provides an estimate for its axial wave number decomposition $\hat{p}(\mathbf{y},k_z)$. Of interest here is the variation of mode pressure amplitude versus propagation angle $\theta_{m\mu}$ in view of the close relationship discussed in Sec. I to the forward arc pressure pattern. The relationship between the axial component of wave number and the axial propagation angle follows directly from Eq. (3) as

$$k_{zm\mu}=k\alpha(\theta_{m\mu});\quad \alpha(\theta)=\frac{\cos\theta}{1+\mathrm{M}_z\cos\theta}. \tag{12}$$

The absence from this expression of the duct radius a suggests that it has general applicability to all circular flow ducts. The axial variation in the acoustic pressure transmitted along the duct wall towards the open end of the duct has the form

$$p(\mathbf{y_a},z)=\sum_{m,\mu}\overline{p}_{m\mu}\Psi_{m\mu}(\mathbf{y_a})e^{-ik\alpha(\theta_{m\mu})(z-z_s)},\quad z\geqslant z_s, \tag{13}$$

where $\overline{p}_{m\mu}$ is the mode amplitude at the source plane $z=z_s$ and $\mathbf{y_a}=(a,\phi)$ is a position vector on the duct wall. An approximate decomposition of the transmitted sound field at position $\mathbf{y_a}$ along the duct wall as a function of the axial propagation angle may be obtained by taking the Fourier transform of the sound field uniformly sampled at less than the Nyquist distance Δz_{Nyq}. This distance is one-half the wavelength at the highest axial component of wave number present; this is due to the plane wave mode $\theta_{00}=0°$, transmitted at the highest frequency $f_{\max}$, and highest free stream intake flow speed $\mathrm{M}_{z\,\max}$ of interest,

$$\Delta z<\Delta z_{\mathrm{Nyq}}=\tfrac{1}{2}(c/f_{\max})(1+\mathrm{M}_{z\,\max}), \tag{14}$$

where $\mathrm{M}_{z\,\max}\leqslant 0$ in the intake duct. Even though the plane wave mode is only weakly excited by rotor–stator interac-

tion, it may be strongly amplified due to the effects of modal spillover by the secondary sources. Aliasing of the plane wave component and other well cut-on modes must therefore be avoided by complying with the sampling criterion of Eq. (14). Equation (14) indicates that the effect of a mean flow in the direction opposing the direction of propagation allows the sensors to be located closer together than if flow was absent. A greater number of sensors separated by Δz_{Nyq} may therefore be located within the duct intake, leading to higher resolution in the measured axial wave number spectrum compared to the no-flow case for the same number of sensors.

An estimate for the acoustic pressure amplitude $\hat{p}(\mathbf{y_a}, \theta_0)$ of the field arriving at an angle θ_0 to the duct wall $r=a$ at circumferential angle ϕ may be obtained by taking the discrete Fourier transform of N pressure measurement $p(\mathbf{y_a}, z_n)$ made along the duct wall at the axial positions: $z_n = z_1 + (n-1)\Delta z,\ n = 1,2,3,...,N$:

$$\hat{p}(\mathbf{y_a}, \theta_0) = \frac{1}{N} \sum_{n=1}^{N} e^{in\psi(\theta_0)} p(\mathbf{y_a}, z_n), \quad \Psi(\theta) = k\Delta z\, \alpha(\theta). \tag{15}$$

Applying Eq. (15) to (13) gives

$$\hat{p}(\mathbf{y_a}, \theta_0) = \sum_{m,\mu} \overline{p}_{m\mu} \Psi_{m\mu}(\mathbf{y_a}) e^{i\varphi_{m\mu}} H(\theta_{m\mu} | \theta_0), \tag{16}$$

where $H(\theta|\theta_0)$ is the nondimensional directivity (sensitivity) function to a plane wave arriving at angle θ_0:

$$H(\theta|\theta_0) = \frac{1}{N} \frac{\sin(\frac{1}{2}N\Delta\Psi)}{\sin(\frac{1}{2}\Delta\Psi)}, \quad \Delta\Psi = \Psi(\theta) - \Psi(\theta_0), \tag{17}$$

and $\varphi_{m\mu}$ is the phase term given by Eq. (18) below that is constant across the array for each mode and which accounts for the phase delay between the source plane and the array sensor closest to it,

$$\varphi_{m\mu} = k(z_1 - z_s - \Delta z)\alpha(\theta_{m\mu}). \tag{18}$$

For realistic values of N, however, (about ten) the array has finite beamwidth θ_B which sets an upper limit on the resolution with which the modal propagation angles may be resolved. An estimate for the array beamwidth for broadside beam-steer angles (close to the propagation angles of the near cut-off modes) may be obtained from $\theta_B = 2(\theta_0 - \theta_{\mathrm{null}})$, where θ_{null} corresponds to the first zero in the receiver's response function away from the beam-steer direction. Putting $\theta_0 = \pi/2$ in Eq. (17), setting the numerator $\sin(\frac{1}{2}N\Delta\Psi)$ to zero, and solving for θ_B yields

$$\theta_B = \pi - 2\cos^{-1}\left(\frac{\lambda}{L - \lambda \mathrm{M}_z}\right), \tag{19}$$

where λ is the zero-flow acoustic wavelength and $L = (N-1)\Delta z$ is the array length. Typical broadside receiver beamwidths for two realistic array lengths and flow Mach numbers is given in Table I.

The effect of an intake flow ($\mathrm{M}_z < 0$) reduces the array beamwidth compared with the no-flow case for the same array length. Note that attempts to improve the array resolution further by the use of high-resolution, non-Fourier-based techniques developed largely for underwater acoustics applications[7] were found to be unsuccessful for fan tones owing to the high level of coherence between the modal arrival signals at the same frequency.

TABLE I. Approximate beamwidths for typical axial sensor array parameters.

$N\Delta z/\lambda$	M_z	θ_B
5	0	23.0°
5	−0.3	21.8°
8	0	14.4°
8	−0.3	13.8°

The connection discussed in Sec. I between the in-duct and far-field radiation angle suggests that in the present application, it is not necessary to completely resolve the different modes, which is impossible in any case by the short array lengths that may be fitted within short intake ducts. For current purposes, it is sufficient to be able to make an approximate estimate of the signal energy in a band of propagation angles on the basis that modes with approximately equal axial propagation angles (and therefore cut-off ratio) have approximately equal peak pressure radiation lobe angles [cf. Eq. (11)]. The level of sidelobe rejection is therefore anticipated to be more important than the beamwidth, suggesting that improved performance may be derived by ''amplitude shading'' of the array sensors.

III. THE ACTIVE REDUCTION IN TOTAL RADIATED SOUND POWER

A. Theory

The active minimization of the total radiated sound power was investigated in Ref. 1 where it was found that the angles of greatest pressure reduction were those of greatest intensity prior to control. These angles were generally found to be well away from the sideline directions and therefore of minimal benefit to ground-based observers. Since there may be occasions when reducing total radiated sound power is a desirable objective, its implementation using in-duct error sensors is now investigated.

The sound power transmitted along the flow duct can be written as the integrated axial intensity taken over a duct cross section[1]

$$W = \int_S I_z(\mathbf{y})\, dS, \quad I_z(\mathbf{y}, z) = \sum_{m,\mu} \gamma_{m\mu}(z) |p_{m\mu}(\mathbf{y}, z)|^2, \tag{20}$$

where $\gamma_{m\mu}(z)$ is the real part of an effective modal admittance in the flow calculated from

$$\gamma_{m\mu}(z) = (1 + \mathrm{M}_z^2)\, \mathrm{Re}\{\beta_{m\mu}\} + \mathrm{M}_z(1 + |\beta_{m\mu}|^2) \tag{21}$$

and $\beta_{m\mu} = \beta_{m\mu}(z)$ is the modal admittance ratio.[1] The use of Eq. (15) allows the expression of Eq. (20) for the axial intensity involving a double summation over the modal indices (m, μ) to be replaced by a single summation taken over axial propagation angle θ, providing a suitable paramaterization on $\theta_{m\mu}$ can be found for the modal admittance ratio $\gamma_{m\mu}$. Evidence for this is provided by Fig. 4 in a plot of $\gamma_{m\mu}/\gamma_{00}$, calculated from the exact expression of Eq. (21) for each of

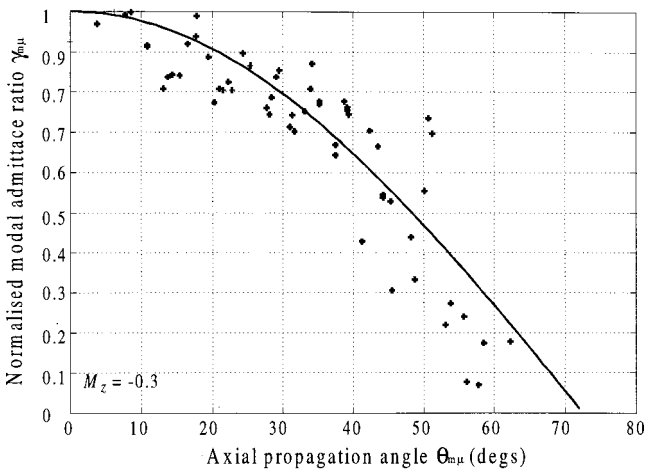

FIG. 4. Typical variation of normalized modal admittance ratio, denoted by ''+'', at an arbitrary distance along a finite length duct with a uniform mean flow of Mach number $M_z=-0.3$ [Eq. (21)] versus axial modal propagation angle $\theta_{m\mu}$ in the duct intake. Solid curve is the approximating function $\cos(\frac{1}{2}\pi\theta/\theta_{z\,\max})$, where $\theta_{z\,\max}=\cos(-M_z)$.

the propagating modes at some arbitrary axial location in the intake duct at $ka=20$ and $M_z=-0.3$, against the axial propagation angle $\theta_{m\mu}$.

The modal admittance ratio plotted in Fig. 4 is observed to approximately collapse on the modal propagation angle $\theta_{m\mu}$, and tends to zero as the mode approaches cut-off, i.e., $\gamma_{m\mu}\rightarrow 0$ as $\theta_{m\mu}\rightarrow\theta_{z\,\max}$. The sound power in a single mode therefore falls to zero as cutoff is approached. By inspection, a good approximation $\hat{\gamma}(\theta)$ to the modal admittance γ versus propagation angle, which also incorporates this cut-off condition, is given by

$$\frac{\hat{\gamma}(\theta)}{\hat{\gamma}(0)}=\Gamma(\theta)=\cos\left(\frac{1}{2}\pi\theta/\theta_{z\,\max}\right);\quad \theta_{z\,\max}=\cos^{-1}(-M_z). \tag{22}$$

Equation (22) plotted in Fig. 4 can be observed to be in acceptable agreement with the exact values at discrete propagation angles. For $M_z=0$, Eq. (22) reduces to $\Gamma(\theta)=\cos\theta$, which is exact for infinite ducts. The final simplifying assumption made here is that most of the energy flow down the duct is concentrated along the duct wall. The integration of the axial intensity over a duct cross section in Eq. (20) can now be approximated by a discrete summation of the estimated intensity from K wall-mounted axial sensor arrays uniformly distributed around the duct wall (Fig. 1).

A cost function $J_{\hat{W}}$ based upon duct wall pressure measurements that is approximately proportional to the transmitted sound power is given by

$$J_{\hat{W}}=\sum_{j=1}^{J}\Gamma(\theta_j)\sum_{k=1}^{K}|\hat{p}(\theta_j,a,\phi_k)|^2,$$
$$\hat{p}(\theta_j,a,\phi_k)=\frac{1}{N}\sum_{n=1}^{N}e^{in\Psi(\theta_j)}p(a,\phi_k,z_n), \tag{23}$$

where the range of beam-steer angles θ_j is taken over the full range propagation angles; $\theta_1=0°$ and $\theta_J=\theta_{z\,\max}$ in some appropriate angle increment.

FIG. 5. Optimal reduction in total radiated sound power (in decibels) obtained when complete knowledge of the transmitted sound field is assumed (solid curve), and the sound power reduction obtained when using the in-duct error sensor array and minimizing the cost function of Eq. (23) (dashed line).

B. Numerical results: A comparison of total sound power reduction using far-field and in-duct error sensors

At each integer value of ka between 10 and 20, Eq. (23) was minimized with respect to the complex strengths of the secondary sources arranged in two rings of 16 sources located at 1.2 and 1 m from the duct inlet termination. Details of the rotor–stator model assumed as the primary source are given in Ref. 1. As illustrated schematically in Fig. 1, the error sensors are arranged in $K=12$ rings, separated axially at the Nyquist distance Δz_{Nyq} such that the number of rings N used in the simulations were varied depending on ka. At the lowest frequency under investigation, $ka=10$ where $a=0.5$ m, Eq. (14) for $M_z=-0.3$ gives $\Delta z_{\mathrm{Nyq}}=11$ cm and at $ka=20$, $\Delta z_{\mathrm{Nyq}}=5.5$ cm. In the 1-m intake duct length assumed in the present study (Fig. 1), $N=9$ sensor rings were used at the lowest frequency and $N=16$ rings at the highest frequency (to reduce computation time, even though 19 rings would fit). The beam-steer angles θ_0 were taken from 0° to 75° in 5° increments. The total radiated sound was computed before and after control. A comparison of the sound power reduction obtained by this means and that obtained with perfect knowledge of the radiated field is assumed[1] is plotted in Fig. 5.

The reduction in total radiated sound power obtained from the in-duct error sensor array is generally is shown to be within 6 dB of the theoretical maximum reduction obtained when the radiated field is completely determined. While these reductions are not particularly good, even with the use of the external sensor array, the agreement between the error sensor strategies confirms the principles underlying the in-duct error array.

IV. SOUND PRESSURE LEVEL REDUCTIONS TOWARDS THE SIDELINE DIRECTION

A. Theory

In the first paper[1] it was found that a more effective strategy for reducing sideline radiation by active means is to

target these radiation angles specifically, rather than minimize a global quantity such as total radiated sound power. The effect that reducing the sound power radiated across an axisymmetric sideline control sector has on the transmitted sound field may be predicted from the close agreement plotted in Fig. 3 between the in-duct and far-field angles. It implies that controling the sound field in these directions produces reductions in the amplitudes of the modes closest to cut-off. Precisely this behavior is observed in Fig. 12(a) and (b) in Ref. 1 by the use of external error sensors. Conversely, reducing the amplitude of the near cut-off modes must reduce the sound field radiated to the sidelines. A cost function for achieving these modifications to the transmitted sound field, and hence reduce sideline radiation, by the use of in-duct pressure measurements is now described.

By analogy with the cost function of Eq. (23) for reducing total sound power, a suitable weighting function on $|\hat{p}(\theta_j, a, \phi_k)|^2$ in a cost function involving only in-duct pressure measurements that amplifies the sensitivity of the sensor array to modes most responsible for sideline radiation is $e^{-\eta(\theta_{z\,\max}-\theta_j)}$, where η is an arbitrary dimensionless constant greater than zero. This function affords maximum weighting to the modes with axial propagation angle closest to the cut-off angle $\theta_{z\,\max}=\cos^{-1}(-M_z)$. A cost function for reducing sideline radiation in terms of in-duct pressure measurements is given by Eq. (24):

$$J_{\Delta\hat{\Omega}}=\sum_{0\geqslant\theta_j>\theta_{z\,\max}}^{\theta_{z\,\max}} e^{-\eta(\theta_{z\,\max}-\theta_j)}\sum_{k=1}^{K}|\hat{p}(\theta_j,a,\phi_k)|^2,$$
$$\hat{p}(\theta_j,a,\phi_k)=\frac{1}{N}\sum_{n=1}^{N} e^{in\Psi(\theta_j)}p(a,\phi_k,z_n). \tag{24}$$

The range of beam-steer angles θ_j over which the cost function is to be taken is now restricted to the range of propagation angles close to $\theta_{z\,\max}$, unlike in Eq. (23) for reducing the total sound power where θ_j is taken over the full range of propagation angles.

B. Numerical results: A comparison between the use of in-duct and far-field error sensors for the active reduction in sound power over an axisymmetric, sideline sector

The cost function of Eq. (24) was minimized with respect to the complex source strengths arranged in two rings of 16 located at 1 and 1.2 m from the duct face (Fig. 1), at integer values of the nondimensional frequencies of ka between 10 to 20. The error sensors were arranged as described previously in Sec. III B. The beam-steer angles θ_0 were taken between 30° and 75° in 5° increments, with a weighting factor equal to $\eta=2$. The sound power radiated into an axisymmetric sector with polar angles from 45° to 135° was then computed and compared with its value before control. The benefit of increasing the sensor array length was examined by repeating this procedure with 16 sensor rings, even though the array now extends beyond the duct inlet termination for most of the frequency range and is therefore impracticable. The results are plotted in Fig. 6, together the maximum sound power reduction obtained across the sideline control sector when the radiated field is completely determined.[1]

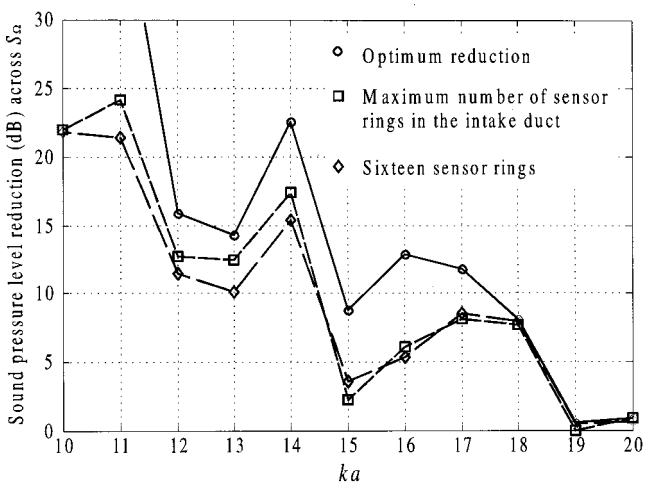

FIG. 6. Sound power reduction (in decibels) across an axisymmetric band of radiation angles from 45° to 135° to the duct axis, versus frequency: − Optimal reduction obtained when radiated field is completely determined (○); reduction obtained with maximum number of sensor rings of 12 in the intake duct separated by Δz_{Nyq} (□), and reduction obtained with 16 rings of 12 sensors which exceed the length of the intake duct (◇).

At nondimensional frequencies of ka less than 12, where the number of propagating modes does not exceed 40 and near-perfect control is possible when the radiated field is known, both in-duct sensor arrays (dashed curves) afford sideline sound power reductions in excess of 20 dB. At frequencies above this, both arrays provide levels of sound power reductions that are within 6 dB of the theoretical maximum (solid curve). This means that in the frequency range $ka\leqslant 18$, where good active control performance is possible in principle, unacceptable performance is observed at only two of the ka values investigated, namely $ka=15$ and 16. For $ka>18$, active control is predicted to afford insignificant axisymmetric control performance, even when the radiated field is completely determined.

The sound pressure level versus radiation angle at $ka=14$ before and after control is plotted in Fig 7. The dashed line corresponds to the radiation pattern obtained with 12 rings each with 12 error sensors, and the dotted curve is the result obtained with the use of a large number of far-field error sensor over the axisymmetric band of radiation angles between 45° and 135°. The two insert figures show the change in mode amplitude versus axial propagation angles following control with the external error sensors (lower figure) and following the use of the in-duct error sensor array (upper figure).

In Fig. 7, the most pronounced effect of sideline control on the radiation pattern is in the direction of the broad radiation lobe which peaks with greatest intensity at approximately 55°. The ideal controller is observed to reduce the amplitude of the single mode of 40° propagation angle responsible for this main radiation lobe by in excess of 20 dB (upper insert figure), thereby exposing the radiation pattern due to less dominant modes beneath it (dashed curve). When

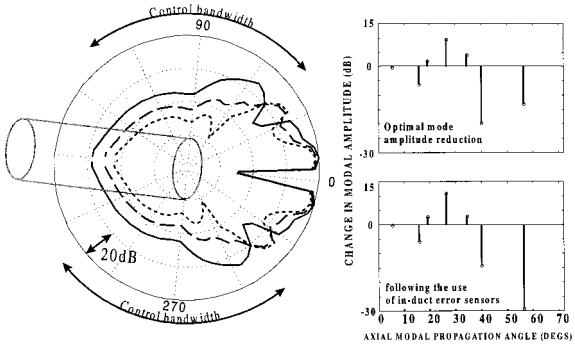

FIG. 7. Sound pressure level reduction (in decibels) versus polar angle at $ka=14$. Before control (solid line), following minimization of sound power radiated across an axisymmetric band of angles between 45 and 135 (dotted curve), and following the minimization of Eq. (24) with 12 rings of 12 sensors with beam steer angles taken between 35°(5°)70° (dashed curve). Inset figures give the change in the mode amplitudes versus axial propagation angles when the radiated field is completely determined (upper), and when using the in-duct sensor array (lower).

the in-duct sensor array is used, this mode is attenuated by only 15 dB (lower figure) so that the radiation pattern remains obscured. Nevertheless, a 10-dB reduction is observed in the pressure pattern in the sideline direction.

V. EFFECT ON ARRAY PERFORMANCE OF CUT-OFF MODES

A potential difficulty with introducing the error sensors into the duct is that the measured signals may become contaminated by weakly radiating cut-off modes, and nonacoustic pressure fluctuations. For sufficiently long arrays, turbulent pressure fluctuations may be uncorrelated over the length of the array and their wave number spectra may occur outside the range of acoustic wave numbers of the propagating modes [cf. Eq. (12)]. Both properties enhance the turbulence rejection capabilities of the array.

Contamination of the measured signals by exponentially decaying cut-off modes may be reduced by locating the sensors as far as possible from the turbomachinery and secondary sources. However, even when this is not possible, for example, in very short intake ducts, some degree of rejection of these unwanted cut-off modes occurs because they have an apparent propagation angle of exactly 90°, whereas the propagating modes are transmitted at angles not exceeding $\theta_{z\,\max}=\cos^{-1}(-M_z)$, which is less than 90° for $M_z<0$. Evanescent, cut-off modes therefore always arrive at the array ''off-beam'' into the sidelobes, leading to some rejection of these weakly radiating pressure contributions.

An illustration of the principles by which cut-off modes are attenuated by the array processing is given by Fig. 8. It shows the output from a ten-sensor array to a unit amplitude mode propagating very close to cut-off at the maximum propagating angle of about 72° at $M_z=-0.3$ versus beam-steer angles from 0° to 90°. Also plotted in this figure is the array output to a unit amplitude mode just below cut-off. Both propagating and cut-off modes therefore have identical amplitudes at the array, and this represents an unlikely worst possible case. The contribution from the cut-off mode to the array output is 30 dB below that due to the propagating mode just below cut-off 72°. Also shown in Fig. 8 is the array

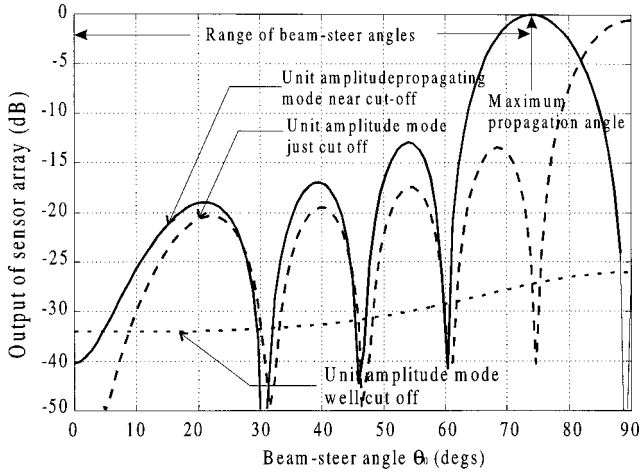

FIG. 8. Output of a ten-element sensor array (in decibels) versus beam-steer angle in response to a propagating mode just before cut-off (solid curve), a mode only just cut-off (dashed curve), and a mode well cut-off (dotted curve).

response to a well cut-off mode whose amplitude at the first sensor is unity. The contribution of this mode to the total output is clearly negligible.

VI. THE EFFECT OF AERODYNAMIC BOUNDARY LAYERS ON SENSOR ARRAY PERFORMANCE

The inference of far-field radiation from pressure measurements at the duct wall may be adversely affected by the aerodynamic boundary layer in which the sensors are situated. This boundary layer is characterized by a lower flow velocity than in the free stream from which most of the sound field is radiated. The effect of an idealized laminar boundary layer on the error sensor array for performing the axial wave number decomposition of an in-duct sound field is now briefly examined.

The sensor array estimates the axial propagation angle indirectly from the modal axial wave number via Eq. (3). At a fixed propagation angle and frequency, the axial component of the wave number along the duct is preserved across the duct cross section of the duct for any flow speed profile that is independent of position along the duct. This is because the axial trace velocity on either side of an arbitrary stratification of different flow speeds along the duct must match exactly. The presence of an aerodynamic boundary layer at the duct wall, and the shear velocity profile across the duct cross-sectional area, therefore presents no fundamental difficulty with the implementation of this technique for detecting the propagating modes.

A beneficial influence of the idealized boundary layer is a shielding property of the unwanted well cut-on modes. Modes arriving at the boundary layer at angles below a critical angle fail to penetrate, but are reflected. The sound field transmitted across the layer at these angles is evanescent. An approximate estimate of the critical angle at which total internal reflection occurs is obtained by equating the trace velocities on either side of a hypothetical boundary layer characterized by a sudden flow speed discontinuity in which the

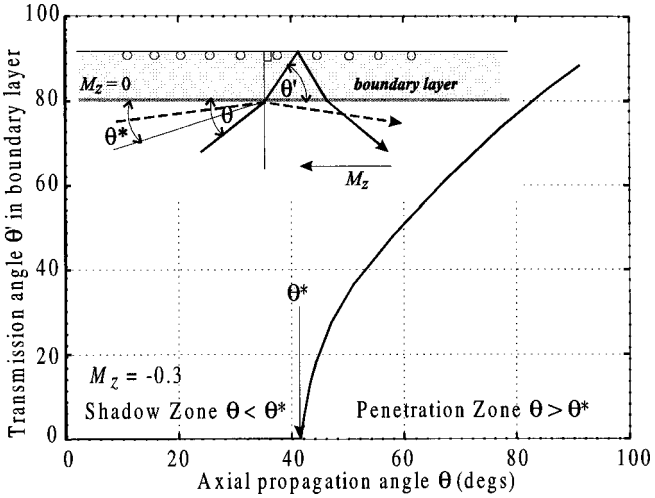

FIG. 9. Plane wave angle of transmission across a hypothetical boundary layer modeled as flow/zero-flow discontinuity, versus the incidence angle. Waves incident at angles less than the critical angle θ^* characteristic of the well cut-on modes undergo total internal reflection.

flow speed is exactly zero. At the boundary layer interface, the axial phase speed is given by

$$\frac{c}{\cos\theta_{m\mu}} + c\mathrm{M}_z = \frac{c}{\cos\theta'_{m\mu}}, \tag{25}$$

where M_z refers to the Mach number of the free stream flow and $\theta'_{m\mu}$ is the modal angle of transmission at the duct wall (Fig. 8). Solving for $\theta'_{m\mu}$ gives

$$\cos\theta'_{m\mu} = \alpha(\theta_{m\mu}) = \frac{\cos\theta_{m\mu}}{1+\mathrm{M}_z\cos\theta_{m\mu}}. \tag{26}$$

The transmission of sound across the boundary layer due to an incident wave is most effective for real value of $\theta'_{m\mu}$, with imaginary values representing waves in the boundary layer that are exponentially decaying. From Eq. (26), $\theta'_{m\mu}$ takes imaginary values for $\theta_{m\mu} \leqslant \theta^*$, where θ^* denotes the critical angle for transmission across the boundary layer given by

$$\alpha(\theta^*) = 1, \quad \theta^* = \cos^{-1}((1-\mathrm{M}_z)^{-1}). \tag{27}$$

This shielding property is illustrated in Fig. 9 which shows a plot of the angle of transmission into the boundary layer θ' versus the axial propagation angle θ incident at the boundary layer. Also shown in this figure is the passage of wavefronts incident upon the idealized boundary layer at less than, and greater than, the critical angle θ^*.

The pressure signals for modal propagation angles below this critical value in the fictitious boundary layer are evanescent and the microphone signals, depending on the boundary layer thickness, will be comparatively weak. The range of angles below θ^* defined by Eq. (27) for which incident waves are internally reflected at the boundary layer are fortuitously those of the well cut-on modes for which the receiver array in the control of sideline radiation was designed to reject.

VII. CONCLUSIONS AND COMMENTS

An in-duct sensor error array has been described which permits the active control of sound radiation from the intake of turbofan engines. Both sideline radiation and total radiated sound power can be controled with only a 6-dB degradation in control effectiveness to that obtained by locating the error sensors in the radiated field for axisymmetric control sectors. The basis for the technique is the close relationship between the mode angles present in the duct and those of the far-field peak pressure lobe of the radiated field.

One of the attractions of this technique is its simplicity since it requires only the frequency and the speed of the free stream flow as input parameters.

The presence of aerodynamic boundary layers at the duct wall, or shear velocity profiles across the duct, are not anticipated to invalidate the technique. The technique works by estimating the axial wave numbers from a number of pressure measurements axially along the duct wall from which the axial propagation angles can be inferred. The axial modal wave numbers remain constant across the duct cross-sectional area since the wave trace velocities on either side of an axial mean velocity stratification down the duct must match exactly. Cut-off modes have also been shown not to be detrimental to the operation of the array as these appear at the sensors at angles outside the range of axial propagation angle in the intake flow. These unwanted contributions are therefore automatically attenuated by the array processing.

[1] P. Joseph, P. A. Nelson, and M. J. Fisher, ''Active control of fan tone radiated from turbofan engines. I. External error sensors,'' J. Acoust. Soc. Am. **106**, 706–778 (1999).
[2] P. Joseph, P. A. Nelson, and M. J. Fisher, ''An In-Duct Sensor Array for the Active Control of Sound Radiated from Circular Flow Ducts,'' UK Patent Application No. 9605739.3 (1996).
[3] S. E. Wright, ''Waveguides and rotating sources,'' J. Sov. Laser Res. **25**, 163–178 (1972).
[4] S. M. Candel, ''Acoustic radiation from the end of a two-dimensional duct—effects of uniform flow and duct lining,'' J. Sound Vib. **28**, 1–13 (1973).
[5] G. F. Homicz and J. A. Lordi, ''A note on the radiative directivity patterns of duct acoustic modes,'' J. Sound Vib. **41**(3), 283–290 (1975).
[6] E. J. Rice and M. F. Heidmann, ''Modal Propagation Angles in a Cylindrical Duct with Flow and their Relation to Sound Propagation,'' Proceedings of the 17th Aerospace Sciences Meeting, New Orleans, 15–17 January 1979, Paper 79-0183.
[7] M. Bouvet and G. Bienvenu (editors), *High-Resolution Methods in Underwater Acoustics*, Lecture Notes in Control and Information Sciences (Springer-Verlag, New York, 1991).

Broadband performance of an active headrest

B. Rafaely,[a] S. J. Elliott, and J. Garcia-Bonito
Institute of Sound and Vibration Research, University of Southampton, Southampton SO17 1BJ, United Kingdom

(Received 18 February 1998; revised 20 October 1998; accepted 2 May 1999)

This paper presents a study of the attenuation of broadband random acoustic disturbances, when using a feedback active headrest system, as originially suggested by Olson and May. Previous studies showed that a practical active headrest can be designed for tonal disturbances using feedforward controllers. However, many applications, such as jet aircraft and cars, require feedback systems to control random disturbances over a wide frequency bandwidth. In this work, robust feedback controllers are designed to control broadband random disturbances in the low-frequency range based on measured data from a laboratory headrest system. The results show that a practically useful performance can be achieved, but only if the controller is designed to minimize the pressure at a ''virtual microphone'' close to the listener's ears, and that the performance is maintained reasonably well with movements of the listener's head. The paper emphasizes the importance of both the acoustics and the control in the design of broadband active headrest systems. © *1999 Acoustical Society of America.* [S0001-4966(99)03908-9]

PACS numbers: 43.50.Ki [MRS]

INTRODUCTION

Active control of sound in enclosures can be achieved either globally, where the sound in the entire enclosure is attenuated, or locally, where the sound is attenuated at isolated zones of quiet. Although global control is more desirable, it is not always practical, due to the complexity of the sound field at high frequencies.[1] In this case, local active control is the more practical alternative. Previous work on local active control of diffuse sound fields[2,3] showed that the zones of quiet are limited in diameter to about a tenth of a wavelength, which implies that local control is only effective at low frequencies. Due to the limited size of the zones of quiet, the most effective way to employ local control is to center the zones of quiet close to the listener's ears, using an active headrest system, for example. Garcia and Elliott[4] showed that the zones of quiet produced by an active headrest system in a pure tone diffuse sound field can be predicted numerically, and are of practical size at low frequencies. To achieve this, a virtual microphone arrangement[5] can be used, where the sound is attenuated at a location remote from the microphone, towards the ears, to increase the attenuation at the listener's ears. In their study, Garcia and Elliott assumed that the secondary field perfectly cancels the primary field at the cancellation point. This was a reasonable assumption for pure tone sound fields, since high attenuation levels of tones can be achieved in practice, using an adaptive feedforward system, for example, as was verified by a later experiment.[6]

Although the studies described above support the feasibility of a practical active headrest system, in many applications, such as passenger seats in jet aircraft and cars, the disturbing sound is typically broadband random and not tonal, and usually originates from several sources. In this case a reference signal that is coherent with the primary disturbance is usually not available, and a feedforward controller cannot be realized. A broadband active headrest system for random disturbances must therefore incorporate a feedback controller, as originally suggested by Olson and May.[7] In this case, the analysis of sound attenuation cannot be performed by assuming perfect control at the cancellation point, since the actual attenuation level at this point will depend on the performance of the control system. Factors such as system delay, disturbance bandwidth, and the controller design objectives can therefore affect the attenuation at the cancellation point, and the extent of the zones of quiet.

The aim and contribution of this paper is the analysis of the performance of a feedback active headrest system for broadband random disturbances, which emphasizes the close and interacting requirements of the acoustic performance limitations and those due to the implementation of the feedback controller. It should be noted that for ''broadband'' disturbances that consist of multiple tones, a simple extension of the single tone analysis would be sufficient, since every frequency can be controlled independently. However, for broadband random disturbances in a feedback control configuration, the various frequencies cannot be controlled independently, and in many cases improving the performance at one frequency range will degrade the performance elsewhere (due to the Bode sensitivity integral or the ''waterbed effect''[8]). The performance is also affected by other factors, such as system delay. The performance analysis for broadband random disturbances must therefore be performed by actually designing a feedback controller, and not by extending the single tone results. This study shows that practical performance can be achieved for random disturbances using a feedback active headset controller, but only if a virtual microphone arrangement is used, and that good performance is maintained with movements of the listener's head.

The paper is presented as follows. The acoustic behavior of an active headrest system is discussed in Sec. I. The feed-

[a]Electronic mail: br@isvr.soton.ac.uk

 0001-4966/99/106(2)/787/7/$15.00

back controller and its design are presented in Sec. II, and in Sec. III the laboratory headrest system is described. The attenuation results calculated for the laboratory system are then presented in Sec. IV.

I. ACOUSTIC ANALYSIS

In this section we present a discussion of the acoustic behavior of active headrest systems. A more detailed analysis can be found in the recent work by Garcia and Elliott[4] and Joseph *et al.*,[2] which involved both analytical analysis and numerical methods to predict the extent of the zones of quiet around a cancellation point in a pure tone diffuse sound field. A fundamental result of Joseph *et al.* is the dependence of the extent of the zones of quiet on the *gradient* of the pressure radiated from the secondary source. Therefore, higher levels of attenuation, and larger zones of quiet, can be achieved if the secondary pressure is spatially more uniform. A formulation was developed for the simple case of a monopole secondary source placed at the origin to cancel the pressure at a radial distance r_0 away from the source, in a pure tone diffuse primary field. Assuming perfect cancellation at the cancellation point, the attenuation at a radial distance Δr from the cancellation point can be written as[1]

$$\varepsilon(r_0+\Delta r)=(1+k^2r_0^2)\left(\frac{\Delta r}{r_0}\right)^2, \tag{1}$$

where k is the wave number and $10\log_{10}(\varepsilon)$ is the attenuation in decibels. The radial distance Δr from the cancellation point at which an attenuation of $10\log_{10}(\varepsilon)$ (dB) is achieved, denoted by Δr_ε, can therefore be calculated by

$$(\Delta r_\varepsilon)^2=\frac{r_0^2\varepsilon}{1+k^2r_0^2}. \tag{2}$$

Although Eq. (2) represents the extent of the zones of quiet in an idealized model, it was found to be a useful guide in understanding the behavior of more practical local control systems. Figure 1 shows the extent of the 10-dB zone of quiet ($2\Delta r_{0.1}$), in centimeters, as a function of the distance between the cancellation point and the secondary source, for tonal excitations at frequencies of 100, 300, and 500 Hz. It can be seen that the zones of quiet are larger at low frequencies, and that a zone of quiet having a practical size (5–10 cm) can only be achieved at frequencies lower than 500 Hz. The extent of the zones of quiet converges to a sphere of diameter $\lambda/10$ as the distance between the secondary source and the cancellation point is increased. Since practical zones of quiet are only achieved below 500 Hz, the design of feedback controllers presented later concentrates on this lower frequency range.

A more realistic headrest system will include a loudspeaker as a secondary source and a listener's head, which will affect the results predicted by the simple model presented above. First, the radiation of a loudspeaker is usually not omni-directional, so the secondary field has larger spatial variability and larger pressure gradient. In general, a loudspeaker with larger vibrating surfaces will produce larger zones of quiet.[2,4] Also, the volume velocity and the pressure gradient very close to a loudspeaker diaphragm are much smaller than those predicted by a point source, so the extent of the zones of quiet very close to a loudspeaker diaphragm is larger than predicted by Fig. 1. The presence of the head also affects the secondary field by imposing zero particle velocity, and thus zero pressure gradient, at the head surface. This causes a ''flattening'' of the secondary field, which increases the extent of the zones of quiet close to the head.[4] Finally, the presence of the head will alter the primary field as well, although the changes are not significant, because the primary field is more uniform than the secondary field.[4]

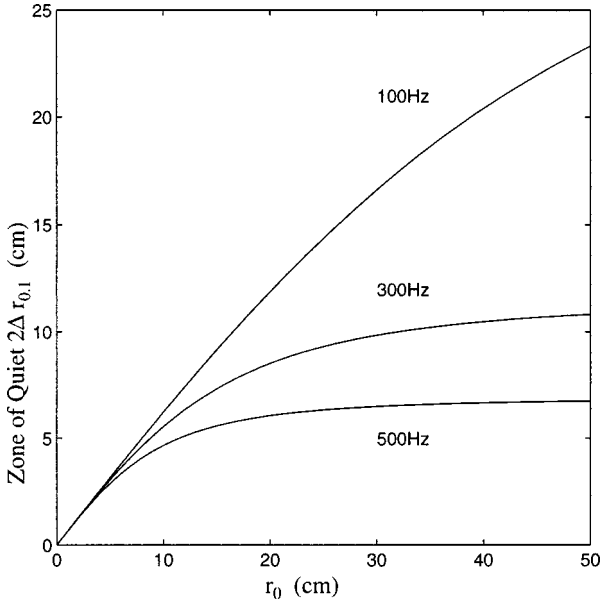

FIG. 1. The spatial extent of the 10-dB zone of quiet, in centimeters, for a monopole secondary source in a pure tone diffuse primary field, cancelling the pressure at a distance r_0 from the secondary source. Given for three different primary excitation frequencies.

II. FEEDBACK CONTROL

The performance achieved when attenuating broadband random sound using a feedback controller is limited not only by the acoustics, as described in the previous section, but also by the control system. Factors such as the frequency response of the ''plant'' (from loudspeaker input to microphone output), the characteristics of the disturbance, and constraints imposed on the control system can greatly affect the performance. Figure 2 illustrates the arrangement of an active headrest system as used in this work. The closely located secondary loudspeaker and microphone (m_1) are connected via a feedback controller, which is designed to attenuate the primary sound at the location of a virtual microphone[5,6] (m_2), nearer the listener's ear. The virtual microphone arrangement is used since in a practical headrest system, the physical microphone is generally placed inside the seat headrest, relatively far from the listener's ear, so designing a controller that attenuates the sound at the location of the physical microphone will usually produce poor attenuation at the listener's ear, as will be shown later.

The active headrest system illustrated in Fig. 2 can be described using a generalized control block diagram,[8] as in Fig. 3. The primary disturbance measured by the physical microphone and by the virtual microphone can generally be

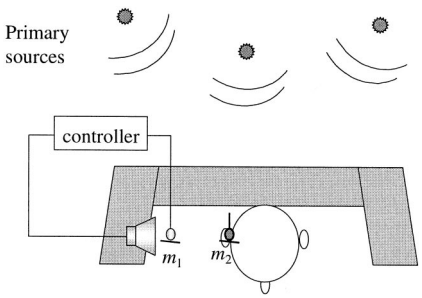

FIG. 2. An active headrest system with a feedback controller, connected to a loudspeaker and a ''physical'' microphone (m_1) located inside the seat headrest. The controller is designed to attenuate the primary sound field at the ''virtual'' microphone location (m_2), at the entrance to the ear canal of a manikin.

modeled as multiple primary noise sources filtered by a vector of shaping filters, denoted by $\mathbf{W}_{1p}$ and $\mathbf{W}_{1v}$, respectively. Because the primary sources of sound which generate the disturbance signals at the physical and virtual microphones are generally remote from the headrest, the primary sound field measured at the two microphone positions is very similar, provided their spacing is small compare to an acoustic wavelength. We can thus simplify the general block diagram under these conditions by assuming that both disturbances are generated by a single white primary source signal, filtered by the scalar transfer functions W_{1p} and W_{1v} which are equal, and which will both be denoted as W_1 below.

The response of the ''physical plant,'' from the loudspeaker input to the physical microphone output, is denoted by P_p, and the response of the ''virtual plant,'' from the loudspeaker input to the output of the virtual microphone, is denoted by P_v. Because of the strong acoustic near field of the secondary loudspeaker it is not generally reasonable to assume that P_p is equal to P_v, and to achieve good performance at the virtual microphone it is important to maintain the distinction between these two plant responses. It is important to note that the output of the physical microphone is used as the control input signal, while the output of the virtual microphone is only used in the off-line design, i.e., the

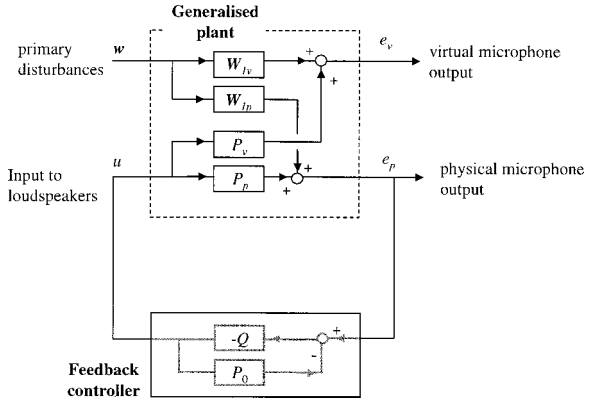

FIG. 3. A generalized control diagram representing the physical and virtual plants, P_p and P_v, and the disturbance shaping filters in the physical and virtual locations, W_{1p} and W_{1v}. An internal model control configuration is used for the feedback controller, with a control filter Q and a plant model P_0.

controller is designed to minimize the output of the virtual microphone, so that the best attenuation is achieved near the listener's ears, as will be shown later.

The control problem illustrated in Fig. 3 can be formulated and solved in various ways. Most controller design methods aim at designing a controller that will produce good disturbance rejection over the control bandwidth, while making the stability or the performance of the controller robust to some uncertainty in the plant model to overcome inaccuracies in the modelling or variations in the plant over time. For example, in linear quadratic Gaussian[8] (LQG) control, a quadratic cost function is formulated, which usually minimizes the mean-square of the error signal, while robustness to plant uncertainty can be achieved by adding a penalty term which is proportional to the control effort. Alternatively, in H_∞ design methods[8,9] a robust performance formulation can be used where desired levels of disturbance rejection and closed-loop stability are achieved for some defined uncertainty in the plant.

Although these and possibly other methods could be used to design the feedback controllers, in this study a mixed H_2/H_∞ method was used based on finite impulse response (FIR) Q-parametrization and convex optimization, originally suggested by Boyd *et al.*[10] to predict the limits of performance of control systems. The method, which was found useful in integrating various design objectives for active control, is described by Boyd[10–12] and was previously used for active control by Titterton and Olkin,[13] Rafaely,[14] and Rafaely and Elliott.[15] It relies on having an internal model of the nominal plant,[17] P_0, as shown in Fig. 3, which ensures that performance objectives and the constraints described below are convex functions of the parameters of the control filter Q.

The controller design in this work is similar to the design method presented by Rafaely and Elliott,[15] only in this work a virtual microphone design is employed. The objective of the control system is to minimize the A-weighted acoustic pressure level at the listener's ears, which is equivalent to minimizing the variance, or the mean-squared value of the virtual error signal, e_v, shown in Fig. 3, filtered by an A-weighting filter. This seems a reasonable performance objective since it is related to the dBA measure, widely used to account for acoustic noise level,[16] although other performance objectives, such as minimizing the ∞-norm, or the peak spectral level of the disturbance, could also be considered. It is also assumed that we know the long-term power spectral density of the pressure signal at the cancellation point due to the primary source, which acts as the disturbance to the feedback controller. Other requirements from a practical active control system include robust stability (the closed-loop system must remain stable for given changes and uncertainties in the plant response), and limited disturbance enhancement (the disturbance should not be significantly enhanced at frequencies outside the control bandwidth).

The design objective used here included both the performance objectives and constraints, and is written as follows:

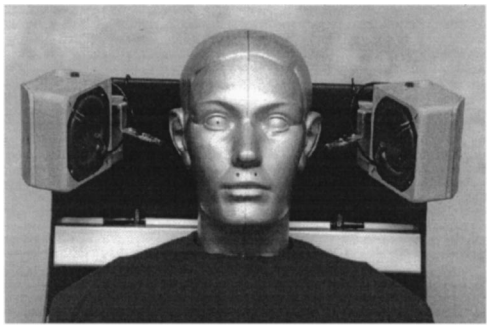

FIG. 4. The experimental headrest system.

$$\begin{aligned}&\text{Minimize:} \quad \|(1-QP_v)W_1A\|_2^2 \\ &\text{(performance at the virtual microphone)} \\ &\text{Subject to:} \quad \|QP_0W_2\|_\infty<1 \quad \text{(robust stability)} \\ &\|(1-QP_v)W_3\|_\infty<1 \quad \text{(disturbance enhancement)},\end{aligned} \tag{3}$$

where A denotes the A-weighting filter, W_1 was defined above, W_2 denotes the multiplicative uncertainty associated with the plant response, which results mainly from the listener's head movements,[15] and $1/W_3$ represents the limit on disturbance enhancement. The problem presented in Eq. (3) is solved by first using frequency discretization of all frequency response functions, and then solving the resulting convex optimization problem to find the coefficients of the FIR filter Q.[15]

It is important to note that the physical plant response (or its model P_0) is used in the robust stability term in Eq. (3), since closed-loop stability depends on the physical loop, as illustrated in Fig. 3. On the other hand, the response of the virtual microphone, P_v, is used in the performance term and the disturbance enhancement term, since these are related to the cancellation point, i.e., the virtual microphone location.

III. EXPERIMENTAL SETUP

The method described above was used to design feedback controllers for an experimental active headrest system, as shown in Fig. 4. The system included a loudspeaker and a ''physical'' control microphone placed 2 cm apart at the side of the headrest, and a manikin placed at the center of the seat. An additional microphone placed at the opening of the manikin's ear canal was used as the ''virtual'' microphone, to measure the frequency response from the secondary loudspeaker to the cancellation point near the manikin's ear, denoted as P_v in Fig. 3. Since this microphone is only used in the design stage prior to control, and not during the controller operation, it is referred to as a ''virtual microphone.''

Figure 5 shows a schematic diagram of the experimental headrest system, where the physical microphone is denoted by ''○'' and the virtual microphone is denoted by ''*.'' The condition with the manikin's head in the central seat position is referred to here as the ''nominal'' condition. The plant model, P_0, as in Fig. 3, is taken to be a measurement of the physical plant under nominal conditions, and the virtual plant, P_v, was also measured under nominal conditions. Therefore, using the nominal performance objective as formulated in Eq. (3), the best performance is achieved under nominal conditions. This is a reasonable objective since the best performance is achieved when the head is in the central seat position, which is assumed to be the most occupied position. Other design methods such as H_∞ robust performance could be used, which will attempt to achieve some desirable disturbance rejection levels for all plants, but these are left as suggestions for future study. Although the control system here is designed with the nominal plant, its performance is analyzed for various head positions to illustrate the fact that performance robustness has been achieved. The symbols ''×'' in Fig. 5 denote different positions of the manikin's ear canal opening as the manikin was moved around, which simulated head movements in a real headrest system.

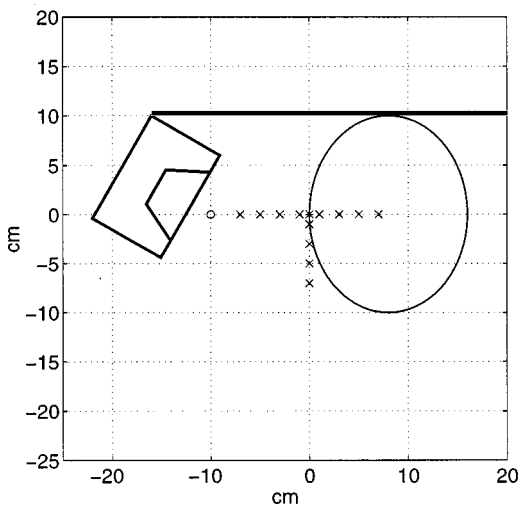

FIG. 5. The geometric arrangement of the headrest, with the control loudspeaker, a physical control microphone marked by ''○'' located 2 cm away from the loudspeaker, and a manikin located at the center of the headrest, with its right ear denoted by ''*'' positioned at the origin of the coordinate system, 10 cm from the control microphone. The manikin was also moved to other positions, for which the right ear was located at the different positions marked ''×.''

IV. RESULTS

Two feedback controllers were designed to attenuate broadband disturbances in the active headrest system. One controller with the filter Q_1 was designed to minimize the output of the physical microphone, which is referred to as the physical microphone controller, and another controller with the filter Q_2 was designed to minimize the output of the virtual microphone, which is referred to as the virtual microphone controller. The performance term in the design of Q_1 included the physical plant under nominal conditions, i.e., $\|(1-Q_1P_p)W_1A\|_2^2$ was used in Eq. (3), so that the sound at the physical error e_p in Fig. 3 is minimized. The performance term in the design of Q_2, however, included the virtual plant under nominal conditions, i.e., $\|(1-Q_2P_v)W_1A\|_2^2$ was used in Eq. (3), so that the sound at the virtual error e_v is minimized. The corresponding disturbance enhancement terms of $\|(1-Q_1P_p)W_3\|_\infty$ and $\|(1-Q_2P_v)W_3\|_\infty$ were used for the design of Q_1 and Q_2, respectively.

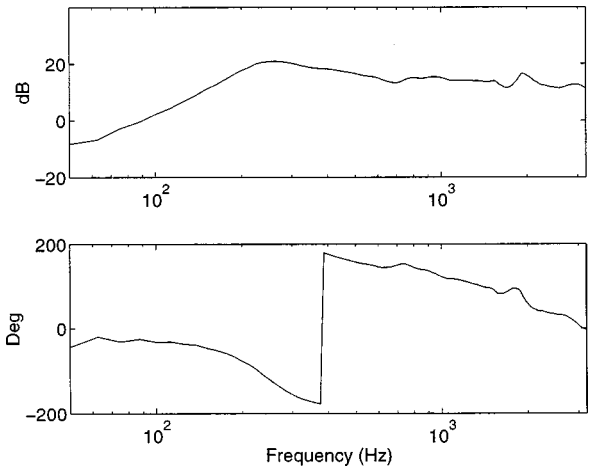

FIG. 6. The frequency response of the headrest physical plant P_p (from loudspeaker input to physical microphone output) with the manikin at the central position, which was also used as the plant model P_0.

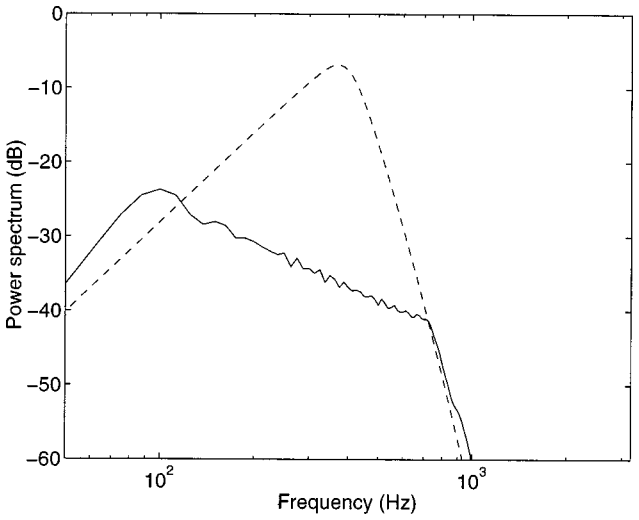

FIG. 7. The power spectral density of the disturbance at the physical microphone location before control (---) and after control (———) with the physical microphone controller Q_1.

The primary disturbance was generated by a remote loudspeaker, driven by a white noise generator which is filtered by a low-pass filter with a cutoff frequency of 400 Hz. This low-frequency range was chosen since at higher frequencies the zones of quiet are too small to be of practical use (as discussed in Sec. I). The disturbance shaping filter W_1 therefore included an eight-pole Butterworth low-pass filter with a cutoff frequency of 400 Hz. The weighting filter denoted by A in Eq. (3) included a two-pole Butterworth high-pass filter with a cutoff frequency of 600 Hz, which modelled the A-weighting filter at low frequencies. This weighting filter prevented high control effort at less audible frequencies. It should be noted that the controllers were designed to perform optimally for this assumed disturbance spectrum, although once the feedback controller is designed, the attenuation achieved at each frequency is completely independent of the disturbance spectrum. If the disturbance spectrum or the disturbance-to-error path were to change, as might happen in practical situations, the performance would no longer be optimal. If these spectral changes are significant, then an adaptive controller, which could concentrate the performance at a narrow frequency range, for example, would probably provide a better solution than the fixed controller considered here.

The frequency response of the nominal physical plant, from the input of the loudspeaker to the output of the physical microphone with manikin in central position, was measured and is shown in Fig. 6. The frequency response of the physical plant with the manikin in all other positions, as illustrated by the symbol ''×'' in Fig. 5, was also measured, and from these measurements the multiplicative plant uncertainty bound W_2 was calculated.[15] The disturbance enhancement bound in Eq. (3) was set to $W_3=0.5$, which constrained the disturbance enhancement to be less than 6 dB at all frequencies. The FIR control filters Q with 128 coefficients were designed, using a sampling frequency of 6400 Hz and a fast Fourier transform (FFT) size of 512 points. Although the resulting control filters were digital FIR filters, the components of a conventional digital control system (low-pass filters and filtering delay) were not included in the plant response. The analysis performed in this work is intended to illustrate the fundamental limits of performance. It is therefore assumed that either an analog controller could be designed which had the same frequency response as that of the controller designed here, or that a digital system with a very high sampling frequency would be used, such that the effect of the low-pass filters and filtering delay will be negligible.

Figure 7 shows the disturbance power spectral density at the physical microphone output, before control (dashed curve) and after control (solid curve) for the physical microphone controller Q_1. Figure 8 shows similar curves for the disturbance at the output of the virtual microphone, for the virtual microphone controller Q_2. In both designs the enhancement and robust stability constraints were maintained. An overall attenuation of 19.1 dB is obtained for the physical microphone controller (Q_1), while an attenuation of only 9.5 dB is achieved by the virtual microphone controller (Q_2).

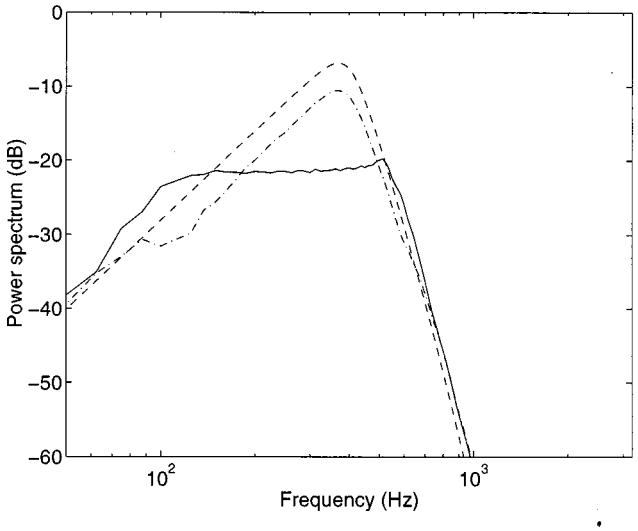

FIG. 8. The power spectral density of the disturbance at the virtual microphone location before control (---), after control with virtual microphone controller Q_2 (———), and after control with physical microphone controller Q_1 (-·-).

The difference can be explained by considering the delay of the physical and virtual plants. Since the physical and virtual microphones are about 10 cm apart, the delay in the virtual plant is about 300 μs longer than that in the physical plant, and since plant delay has a significant effect on the performance bandwidth of a feedback system,[8,17,18] the system with the longer delay has poorer performance. However, when the disturbance attenuation of the physical microphone controller at the *virtual microphone* location is examined, as shown in Fig. 8 (dash–dotted curve), it can be seen that the physical microphone controller achieves a much lower attenuation at the virtual microphone than the virtual microphone controller, i.e., 3.7 dB compared to 9.5 dB. From this result it is clear that good performance at the virtual location, i.e., the listener's ear, requires a controller that is explicitly designed for that cancellation point.

A more detailed analysis of the active headrest performance was then undertaken, by calculating the attenuation at the listener's ear for various head positions. This is important in a practical headrest system, which is expected to perform well for head positions other than the center. To perform this calculation, the frequency responses of the plants P_p and P_v in Fig. 3 were measured for all the various manikin positions in Fig. 5, and these are denoted by $P_p(\mathbf{x})$ and $P_v(\mathbf{x})$, respectively, where $\mathbf{x}$ denotes the vector of lateral and forward positions of the manikin. The disturbance attenuation at the manikin's ear canal opening (the virtual microphone location), for various manikin positions, was then calculated by dividing the power of the virtual microphone output signal after control (without assuming $P_0 = P_p$), with the power of the same signal before control. This can be written as

$$\varepsilon(\mathbf{x}) = \left\| \left(1 - \frac{QP_v(\mathbf{x})}{1 + Q(P_p(\mathbf{x}) - P_0)} \right) W_1 A \right\|_2^2 \Big/ \| W_1 A \|_2^2, \tag{4}$$

from which the overall sound attenuation in dB ($10 \log_{10} \varepsilon$) at the manikin ear was calculated for all manikin positions. It should be emphasized that both the physical microphone controller and the virtual microphone controller were assumed to be fixed for these calculations, with the response of the controllers calculated for the central, i.e., the nominal, head position.

Figure 9 shows the overall attenuation at the manikin's ear for the two controllers, as a function of the lateral position of the manikin. It can be seen that for movements of the head around the central position, 0 cm on the scale in Fig. 9, the virtual microphone controller performs significantly better than the physical microphone controller, as expected, while only for locations very close to the physical microphone does the physical microphone controller perform better. It is interesting to note that the performance is better for lateral movements towards the loudspeaker than away from it, thus creating some lateral asymmetry in the performance. Figure 10 illustrates the variations in the overall attenuation at the ear of the manikin as it is moved forward rather than sideways, showing that the attenuation with the virtual microphone controller is better for all manikin positions in this direction. Overall, an attenuation of 5–10 dB is achieved with the virtual microphone design for lateral head movements of up to about ± 5 cm, and forward head movements of up to 7 cm. These results show that useful attenuation levels can be achieved for broadband random disturbances in the low-frequency range.

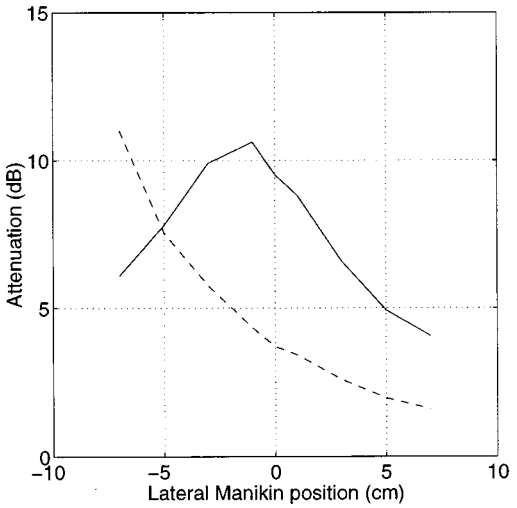

FIG. 9. Overall attenuation at the manikin's ear as a function of the manikin lateral position for the physical microphone controller Q_1 (---), and the virtual microphone controller Q_2 (———).

It is important to note that there is a trade-off between the acoustic requirements for the position of the cancellation point and those of the control system. The control system requires a short plant delay to achieve high attenuation levels for broadband disturbances, so cancellation locations nearer the loudspeaker are preferred. On the other hand, in order to achieve zones of quiet which are large enough to extend to the listener's ears, the cancellation location should be placed some distance from the loudspeaker. It seems from the results presented above that the limited extent of the zone of quiet due to the acoustic limitations has a more dominant effect on performance at the ear than the degradation of the performance due to the additional acoustic delay. In the case

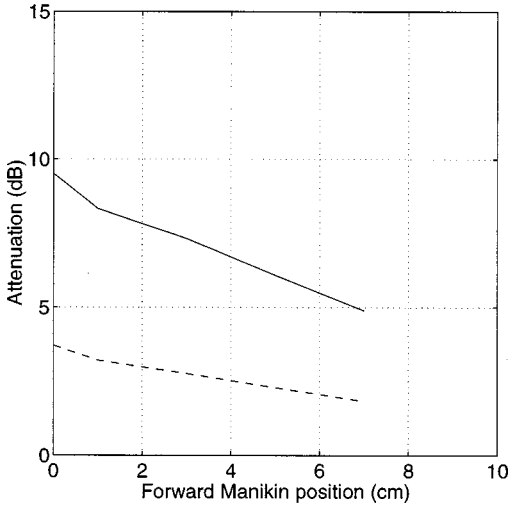

FIG. 10. Overall attenuation at the manikin's ear as a function of the manikin forward position for the physical microphone controller Q_1 (---), and the virtual microphone controller Q_2 (———).

of narrow-band disturbances (e.g., tones), the extra acoustic delay has little effect on performance,[8,17,18] and the performance advantages of having the cancellation point near the ear would be even more clear.

V. CONCLUSIONS

A performance analysis has been presented for an active headrest system which uses feedback to control broadband random disturbances, which included both acoustic and feedback control considerations in the calculation of the sound attenuation. A robust feedback controller was designed to minimize the pressure at a ''virtual microphone'' location near the ear. The results indicate that 5–10 dB of attenuation can be achieved for head movements of up to about 5 cm, which is close to the fundamental physical limit on the zone of quiet at the higher disturbance frequencies. It was also shown that a system designed to minimize the pressure at the control microphone close to the secondary loudspeaker gave an attenuation that was generally below 5 dB for this range of head positions.

Future work is expected to include design methods that will produce more laterally symmetric sound attenuation, and real-time implementation of the feedback active headrest controller. Early results[19] indicate that designing a controller with the cancellation point a few centimeters from the ear also produces good attenuation, since the zones of quiet tend to be attracted to the head, due to the lack of pressure gradient at the side of the head.[4]

ACKNOWLEDGMENTS

The authors are grateful for the support given by The Ian Karten Charitable Trust, the ORS awards scheme, the AJA association, and the Institute of Sound and Vibration Research, who supported this research. The authors are also grateful to the reviewers for their valuable comments.

[1] P. A. Nelson and S. J. Elliott, *Active Control of Sound* (Academic, London, 1992).
[2] P. Joseph, S. J. Elliott, and P. A. Nelson, ''Near field zones of quiet,'' J. Sound Vib. **172**(5), 605–627 (1994).
[3] S. J. Elliott, P. Joseph, A. J. Bullmore, and P. A. Nelson, ''Active cancellation at a point in a pure tone diffuse sound field,'' J. Sound Vib. **117**, 35–38 (1988).
[4] J. Garcia-Bonito and S. J. Elliott, ''Local active control of diffracted diffuse sound fields,'' J. Acoust. Soc. Am. **98**, 1017–1024 (1995).
[5] S. J. Elliott and A. David, ''A virtual microphone arrangement for local active sound control,'' 1st International conference on motion and vibration control, Yokahama, Japan (1992).
[6] J. Garcia-Bonito, S. J. Elliott, and C. C. Boucher, ''Generation of zones of quiet using a virtual microphone arrangement,'' J. Acoust. Soc. Am. **101**, 3498–3516 (1997).
[7] H. F. Olson and E. G. May, ''Electronic sound absorber,'' J. Acoust. Soc. Am. **25**, 1130–1136 (1953).
[8] S. Skogestad and I. Postlethwaite, *Multivariable Feedback Control* (Wiley, Chichester, UK, 1996).
[9] J. C. Doyle, B. A. Francis, and A. R. Tannenbaum, *Feedback Control Theory* (MacMillan, 1992).
[10] P. B. Boyd, V. Balakrishnan, C. H. Barrat, N. M. Khraishi, X. Li, D. G. Meyer, and S. A. Norman, ''A new CAD Method and Associated Architectures for Linear Controllers,'' IEEE Trans. Autom. Control. **33**(3), 268–283 (1998).
[11] S. Boyd and C. Barratt, *Linear Controller Design: Limits of Performance* (Prentice–Hall, Englewood Cliffs, NJ, 1991).
[12] H. Hindi, B. Babak Hassibi, and S. P. Boyd, ''Multiobjective H_2/H_∞—Optimal Control via Finite Dimensional Q-Parametrization and Linear Matrix Inequalities,'' The American Control Conference, June 1998.
[13] P. J. Titterton and J. A. Olkin, ''A practical method for constrained-optimization controller design: H^2 or H^∞ optimization with multiple H^2 and/or H^∞ constraints,'' Proceedings of the 29th IEEE Asilomar conference on Signals, Systems and Computers, October 1995, pp. 1265–1269.
[14] B. Rafaely, ''Feedback control of sound,'' Ph.D. thesis, ISVR, University of Southampton, England, 1997.
[15] B. Rafaely and S. J. Elliott, ''H_2/H_∞ active control of sound in a Headrest: design and implementation,'' IEEE Trans. Control System Technol. **7**, 79–84 (1999).
[16] L. E. Kinsler, A. R. Frey, A. B. Coppens, and J. V. Sanders, *Fundamentals of Acoustics*, 3rd ed. (Wiley, New York, 1982).
[17] M. Morari and E. Zafiriou, *Robust Process Control* (Prentice–Hall, Englewood Cliffs, NJ, 1989).
[18] G. F. Franklin, J. D. Powell, and A. Emamni-Naeini, *Feedback Control of Dynamic Systems*, 3rd ed. (Addison–Wesley Reading, MA, 1994).
[19] B. Rafaely and S. Elliott, ''Feedback control of sound in headrest,'' Proceedings of the ACTIVE'97 conference, Budapest, Hungary, August 1997, pp. 445–456.

Novel acoustic sources from squeezed cavities in car tires

M. J. Gagen
Department of Physics, University of Queensland, Qld 4072, Australia

(Received 10 July 1998; accepted for publication 17 April 1999)

This paper demonstrates that the partial squeezing of car tire cavities at ground impact cannot be adequately modeled by the usual acoustic wave equation. A more complete treatment must begin with the Euler equations for fluid flow in a squeezed cavity to derive a wave equation dependent on cavity wall velocities and accelerations. These can be sizable as ground impact causes the walls of a tire cavity to move with velocities of order 1 m/s and with accelerations of 10^3 m/s^2 over time scales of about 1 ms. Further, the geometry of a typical cavity is such that width compression causes significant increases in pressure and density to occur before the arrival of the rarefaction wave propagating from the open end of the cavity begins to exhaust the full length of the cavity. This causes significant departures from equilibrium density and pressure conditions. These influences are demonstrated both analytically and numerically.
[S0001-4966(99)00708-0]

PACS numbers: 43.50.Lj, 43.25.Ts [MRS]

INTRODUCTION

The loudest component of the far-field noise of cars traveling over 50 km/h and of trucks traveling over 80 km/h is tire noise.[1] Previous treatments examining this area have typically used the low velocities of air movements around the tire/pavement contact point to justify use of the acoustic wave equation and acoustic monopole theory. For instance, monopole theory has long been used to model air pumped from the squeezed cavities in car tires[2] and is well confirmed by experiments showing the dependence of the sound intensity on the second time derivative of volume changes $\ddot{V}$ particularly when the volume changes are simple harmonic. When volume changes depart from being sinusoidal the fit between theory and experiment is not so good.[3] Air pumping noise sources occur as air moves into and out of tire cavities as the tire tread contacts the road and have been modeled by treating the squeezed cavity as an organ pipe with one end closed so as to sustain a $\lambda/4$ resonance. This approach models the air as a piston moving backwards and forwards on a spring.[4–6] Experimental investigations have confirmed the worth of these approaches.[7,8]

Other noise sources include Helmholtz resonances and horn effects between the tire and the road[8,9] as well as from interactions with road pavements[10,11] and bridge grids.[12] Finally, the tire itself possesses certain natural radial and tangential modes of vibration and excitation of these modes generates noise. These modes are usually modeled using variants of circular ring models.[1,13–15]

Jointly, the listed noise sources above are able to explain a significant part of the far-field sound intensity of car tires but cannot be considered a complete explanation. This paper demonstrates that the squeezed cavities in car tires feature large-amplitude pressure and density excursions which lie outside the regime of applicability of small-amplitude acoustic monopole theory and $\lambda/4$ pipe resonance approaches. Rather, we argue that the high accelerations and velocities of the walls of a groove in a car tire can violate the assumptions underlying these approaches. A body of air responds as a damped oscillator to volume changes and pressure differentials[6] and the finite size of the spring constant necessarily means that there is a time delay between a volume change and resulting air movements. In effect, air responds sluggishly to sufficiently fast volume changes. This makes it worthwhile to investigate whether the squeezed cavities of car tires can hit the ground and suffer a volume loss faster than the air within the cavity can evacuate along its length. A typical period over which a cavity undergoes squeezing can be shorter than 0.2 ms and, in this time, a rarefaction wave can only travel about 6 cm. As the lengths of many tire cavities are of this order, it is evident that the volume decrease can occur before the air is able to fully evacuate from the cavity. Then, a decrease in volume by, say, 10% leads to an 11% increase in the density while a 50% volume decrease generates a doubling of the density. These potentially large density fluctuations are well outside the regime of applicability of small-amplitude acoustic theory which explicitly assumes that density and pressure excursions are small. This paper seeks to incorporate the effects of squeezed volume losses within the acoustic wave equation by including cavity wall acceleration and velocity terms.

Some evidence for the plausibility of these claims can be obtained from the literature and this is canvassed in Sec. I. In Sec. II we derive the acoustic wave equation from the Euler equations for adiabatic air flow to examine the underlying acoustic linearization assumptions. We show heuristically in Sec. III that these assumptions are violated in the squeezed cavities of car tires which can generate large pressure and density fluctuations. This motivates us to discard these inapplicable assumptions to give the Euler equations appropriate for squeezed systems in Sec. IV and to rederive a ''squeezed'' acoustic wave equation in Sec. V that contains many sound source terms not included in the usual acoustic wave equation. Subsequently, we discuss approximate analytic solutions to the squeezed Euler equations in Sect. VI and show numerical simulations of a squeezed car tire

groove under typical acceleration and velocity regimes in Sec. VII.

I. EXPERIMENTAL EVIDENCE FOR SQUEEZING EFFECTS

The literature contains some experimental indications that squeezing effects might be important contributions to car tires noise. We canvass this evidence now.

The principle observation implicating squeezing effects in tire noise generation is that of Ejsmont *et al.*[7] where it was noted that there was a nonlinear dependence of emitted sound intensities upon groove width. It was noted that both thin width grooves and large width grooves generate small sound intensities while medium width grooves generate large sound intensities. The width of a groove does not appear in $\lambda/4$ pipe resonance theory which only considers the length of a groove and is not taken into account in monopole theory which only considers time rates of change of the total volume. These observations tend to show that the geometry of a squeezed groove has some influence on sound intensity.

The volume change of a squeezed groove is difficult to observe at high speeds. Estimates of the change in volume range from an assumed 10%[2] to 18% obtained from clay-extrusion measurements.[4] Reference 5 used static measurements to obtain a volume change of 5% and estimated a maximum of 3% at high speeds. These estimates do not take into account the additional loss of volume caused by a bumpy road pavement intruding into the air space of a cavity on ground contact. Typical road pavements might contain gravel fragments of 5 to 8 mm in size which is similar to the groove widths of a typical tire cavity[8] so these gravel fragments might routinely cause additional volume losses greater than those estimated above. It has been well established that the far-field sound intensity depends on highly nonlinear interactions between a tire tread and road pavements with, for example, observations that certain surfaces may be relatively noisy for cars but silent for trucks.[10,16]

These volume deformations occur as the groove moves into contact with the ground at which point the tire wall is subject to radial accelerations of up to 3300 m/s^2 peak to peak and tangential accelerations of about 1000 m/s^2 peak to peak on millisecond timescales. These accelerations are typical of a car traveling at 80 km/h[1,8] and it is these accelerations which cause the volume loss on time scales faster than the air can evacuate from the cavity.

II. ACOUSTIC THEORY

The usual acoustic wave equation is derived in the low velocity and adiabatic limits of the Euler equations for fluid flow. The conservative form of the inviscid and dimensionless Euler equations in two dimensions for perfect gases in the adiabatic limit and with zero conductivity are[17–21]

$$\partial_t U+\partial_x F+\partial_y G=0,$$

$$U=\begin{pmatrix}\rho\\ \rho v_x\\ \rho v_y\end{pmatrix},\quad F=\begin{pmatrix}\rho v_x\\ \rho v_x^2+\rho^{\gamma}/\gamma\\ \rho v_x v_y\end{pmatrix},\quad G=\begin{pmatrix}\rho v_y\\ \rho v_x v_y\\ \rho v_y^2+\rho^{\gamma}/\gamma\end{pmatrix}. \tag{1}$$

Here, we show the mass continuity (top line) and momentum conservation equations in the x and y directions with velocities v_x and v_y, respectively. (We exploit symmetry to constrain fluid motions to this plane.) The adiabatic limit is realized by relating fluid pressure p to fluid density ρ as $p=\rho^{\gamma}$ where $\gamma=1.4$ is the usual ratio of specific heats. All variables are dimensionless with dimensioned (primed) variables being given by $x'=xL$, $v'=va_0$, $p'=pp_0$, $\rho'=\rho\rho_0$, and $t'=tL/a_0$ with L being some convenient length parameter and $a_0^2=\gamma p_0/\rho_0$ being the local speed of sound in ambient pressure and density conditions of p_0 and ρ_0. With these choices a unit velocity equates to the speed of sound in the fluid.

The appearance and propagation of acoustic disturbances is entirely described by Eq. (1) but is usually written as a wave equation[21] after making the small wave approximation. In nondimensional units, a Taylor series expansion in pressure gives

$$p=1+p_1 \tag{2}$$

and

$$\rho=1+\left.\frac{\partial\rho}{\partial p}\right|_0(p-1)+\left.\frac{\partial^2\rho}{\partial p^2}\right|_0\frac{(p-1)^2}{2}$$

$$=1+p_1/\gamma+\frac{1}{2\gamma}\left(\frac{1}{\gamma}-1\right)p_1^2. \tag{3}$$

This Taylor expansion is valid only when $p_1\ll 1$ and we can truncate the expansion at the first term to give small-amplitude acoustic theory. (The error involved in this truncation equates to the second term and is non-negligible when pressure fluctuations are greater than about $p_1>10^{-2}$. In this paper we will show that squeezed systems generate densities of $\rho=1.1$ in dimensionless terms, giving $p_1\approx 0.14$ with a resulting truncation error of 0.002 which cannot be ignored.)

The acoustic wave equation is then obtained by differentiating Eq. (1) or its three-dimensional equivalent to solve for $\partial_{tt}\rho$ with the further assumption of small fluid velocities $v_x, v_y\ll 1$ to give

$$\partial_{tt}p_1-\partial_{xx}p_1-\partial_{yy}p_1-\partial_{zz}p_1=0, \tag{4}$$

where now we explicitly show the third dimension to permit comparisons to the derivations below.

Acoustic monopole theory applies this equation to a vibrating point source modeled as a small spherical emitter of radius R undergoing small oscillations much less than the radius $\dot{R}\delta t\ll R$. The resulting volume changes are then $\dot{V}=4\pi R^2\dot{R}$ which cause spherically symmetric pressure waves to propagate into the surrounding medium. These pressure waves decay as $1/r$ and have the usual functional dependence on $(r-a_0t)$ to satisfy the wave equation and to describe delayed waves traveling outwards from the sphere at speed a_0. Thus, at the point (r,t), the pressure has functional dependence

$$p_1(r,t) \propto \frac{\overline{p}(r-a_0 t)}{r}. \tag{5}$$

In spherical coordinates with approximately constant fluid density the conservation of momentum equation (1) is $\rho \partial_t v_r = -\partial_r p_1/\gamma$ where we set $v_r^2 = 0$ for low fluid velocities. Substituting Eq. (5) here gives

$$\rho \partial_t v_r \propto -\partial_r \frac{\overline{p}(r-a_0 t)}{\gamma r} \propto \frac{\overline{p}}{\gamma r^2} - \frac{\partial_r \overline{p}}{\gamma r}. \tag{6}$$

This solution applies at the surface of the sphere where $r = R$ is small and assumed to be much smaller than the wavelength of sound emitted, allowing us to ignore the second term on the rhs. Noting that $v_r = \dot{R}$ and $\ddot{R} \approx \ddot{V}/(4\pi R^2)$ we have

$$\frac{\rho \ddot{V}}{4\pi R^2} \approx \frac{\overline{p}}{\gamma R^2}. \tag{7}$$

In turn, this allows us to solve for $\overline{p}$ and to substitute this back into Eq. (5) to obtain

$$p_1(r,t) \approx \frac{\gamma \rho \ddot{V}}{4\pi r} \tag{8}$$

relating the pressure wave emitted by a monopole source to the second derivative of the volume change of that source. Dipole and quadropole sources are then constructed from appropriate arrays of monopoles.[21]

Demonstrations of the failure of monopole theory can be easily derived when we consider a small spherical balloon attached by a thin straw to a pump so that its volume can be changed in a controlled manner. We consider two cases where the small balloon undergoes a linear collapse to zero volume with constant acceleration $\ddot{V} = 0$ and where the balloon undergoes a collapse and rebound sequence obtained by setting $\ddot{V} = c$, a positive constant, to obtain a volume quadratic in time.

The linear collapse of the balloon described by $\ddot{V} = 0$ gives volume $V(t) = V_0(1 - t/T)$ for suitable constants V_0 and T and is expected to produce a rarefaction wave in the surrounding medium which should be heard if severe enough. However, this pressure fluctuation makes no appearance in monopole theory which predicts a pressure fluctuation of zero.

Simple experiments can be performed to confirm the inadequacy of the monopole predictions. Clapping your hands together features linear squeezing with $\ddot{V} = 0$ except at the time of impact so monopole theory predicts no sound emission at all prior to this time and claims that the ''clap'' comes only from the instantaneous decelerations and body vibrations caused by impact. This prediction can be shown to be incorrect by first clapping your hands with the fingers together and then clapping with the fingers spread apart. By use of two experiments we create a control which allows us to eliminate the deceleration from consideration as both experiments feature the same decelerations and body vibrations. (The position of the fingers will not change decelerations or vibrations.) The very different magnitudes of the claps generated in these two experiments arising from exactly the same decelerations means sound intensities cannot be entirely explained by monopole theory with its exclusive reliance on volume accelerations as a source of noise.

A clearer failure occurs when we consider a balloon underdoing a volume acceleration $\ddot{V} = c$, a positive constant, to give a volume varying quadratically in time as $V(t) = (V_0 - \delta V)(1 - t/\tau)^2 + \delta V$ where V_0 is the initial volume and δV is the small volume of the balloon at the time τ of smallest radius. Here, the collapse and rebound of the balloon is expected to produce first a rarefaction wave followed by an overpressure wave which should be heard if the movements are severe enough. However, monopole theory predicts an always positive constant pressure wave $p_1 \propto 2(V_0 - \delta V)/\tau^2$.

Monopole theory has a restricted domain of applicability due to the very simplicity which is its principle advantage. As mentioned previously, air responds sluggishly even to local volume changes as a damped oscillator while monopole theory equates local air movements exactly with the volume changes of the system. (This sluggishness is additional to the usual propagation delays of wave motion at finite speed.) Further, simple source monopole theory considers only single frequency, simple harmonic motions.[21] For motions which are not simple harmonic, we should first perform a Fourier decomposition into frequency components before applying monopole theory. When volume changes are linear or quadratic the Fourier decomposition is broad and acoustic emissions are not well modeled by single-frequency monopole theory. We note that Fig. 14 of Ref. 3 shows that monopole theory correctly predicts acoustic intensities when volume changes are approximately simple harmonic and provides poor predictions otherwise.

Any treatment of volumes varying linearly and quadratically in time requires a rederivation of the acoustic wave equation properly taking account of the geometry of the system and allowing for the velocity and acceleration of the groove walls. We heuristically motivate a full examination of such systems in the next section.

III. PRESSURE AND DENSITY FLUCTUATIONS IN TIRE GROOVES

We seek to heuristically consider density (and pressure) fluctuations in a tire groove undergoing squeezing as it enters the contact patch.

Consider a tire traveling forward at linear speed v with a groove etched into its rim that is orientated at angle ϕ to the direction of travel, and suppose that the groove, initially of width d_0, undergoes a compression to width d_1 as it enters the tire–road contact patch. The groove is expected to compress as the surrounding rubber takes the full weight of the vehicle. This situation is shown in Fig. 1. It seems reasonable to assume that the groove is subject to an inflow of air along its length as the rubber side walls (hatched areas) descend onto the road and displace air sideways. This implies that the pressure wave caused by squeezing will dissipate only after the wave has traveled the full length L of the groove.

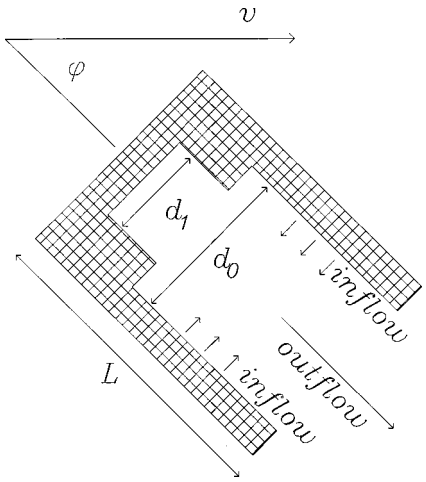

FIG. 1. Squeezed geometry for tire grooves orientated at angle ϕ to the direction of travel.

(Throughout we consider a groove with one end closed—the analysis can be applied to an open ended groove of twice the length.)

The groove of length L has projection $L\cos\phi$ in the direction of travel and undergoes a squeezing along its entire length L in time $L\cos\phi/v$. The compression point on the groove then has velocity of

$$v_c=\frac{v}{\cos\phi}. \tag{9}$$

The groove squeezing causes an increase in the density and pressure of the cavity which propagates to the end of the cavity at the sound speed a_0 (for small fluctuations). To a first approximation, air cannot leave the cavity until this pressure wave has traversed the full length of the cavity which takes a time $\tau=L/a_0$. In this same time the cavity has undergone a volume decrease $\delta V=(d_0-d_1)v_c\tau W$ from its intial volume $V_0=d_0LW$. As no air has escaped to time τ we can immediately write the average density at time τ as

$$\rho=\frac{\rho_0V_0}{V_0-\delta V}, \tag{10}$$

where ρ_0 is the initial density in the groove. In dimensionless terms, the density fluctuation $\delta\rho=(\rho-\rho_0)/\rho_0$ is

$$\delta\rho=\left[\frac{d_0a_0\cos\phi}{(d_0-d_1)v}-1\right]^{-1}. \tag{11}$$

As shown previously, we can ignore pressure and density fluctuations when these fluctuations are small and less than of order 10^{-2}. Conversely, we cannot ignore squeezing effects when $\delta\rho>10^{-2}$ or when

$$\frac{d_0a_0\cos\phi}{(d_0-d_1)v}<10^2. \tag{12}$$

Noting $a_0\approx340$ m/s and typical squeezing volume losses of around $d_0/(d_0-d_1)\approx10$ gives

$$\frac{\cos\phi}{v}<0.03 \tag{13}$$

to indicate when squeezing effects cannot be ignored.

In practical terms, when the forward speed of the car is $v=100$ km/h or $v=28$ m/s we find that all grooves of orientation angle $\phi>33$ degrees will undergo significant fluctuations due to squeezing. Conversely, if grooves are oriented at angles of $\phi=45$ degrees say, then squeezing effects are relevant only above speeds of $v=24$ m/s or $v=85$ km/h. This is precisely the speed range at which unexplained tire noise occurs.

The simple heuristic treatment of this section demonstrates that squeezing effects are expected to cause significant departures from ambiant pressure and density conditions with the magnitude of these departures invalidating the usual first-order Taylor series truncated acoustic theory. A proper analysis of a compression point moving along a groove at arbitrary angle ϕ is difficult and would require spatial- and time-dependent coordinate transforms. This lies outside the scope of this paper. However, by narrowing our focus to consider only squeezed grooves orientated perpendicularly to the direction of travel, we are able to model squeezing effects using only time-dependent coordinate transformations and this is feasible. We turn to consider these methods now.

IV. FLUID DYNAMICS IN SQUEEZED CAVITIES

Most fluid dynamical flow problems are solved in regions defined by stationary boundaries. In contrast, we consider a region with dynamic boundaries chosen to change the nature of the solutions of the system of fluid equations. In effect, the boundary dynamics are described by their own boundary equations which are additional to the usual fluid equations. It is well understood that adding further equations to a given system of equations will usually change the nature of the solution space. A common example of how moving boundaries can modify the acoustic field within a region is the active control of noise in vehicles.[22] Here, loud speakers are used to pump out-of-phase sound across the boundary of the vehicle to cancel pressure fluctuations within that vehicle. Then, the moving boundary ideally forces the solution of the acoustic wave equation to be one of constant density $\rho=1$ and constant pressure $p=1$ everywhere in the vehicle. However, active control approaches typically deal only with small amplitude acoustic waves and boundary movements which are small compared to the size of the vehicle. In this paper we consider large pressure and density excursions which cannot be treated using small wave acoustic theory.

Consider the fluid in a region contracting due to external applied forces as shown in Fig. 2. Here a board of length L is

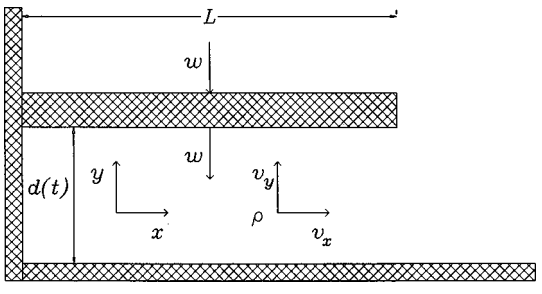

FIG. 2. Squeezed geometry for tire grooves orientated perpendicular to the direction of travel.

descending at velocity w towards a surface. The enclosed fluid is moving with velocity (v_x, v_y) and is expected to be ejected from between the boards into the outside uncompressed region as the internal pressure builds up. (We exploit symmetry to ignore the z direction.) We model the separation distance as $d(t)=d_0 f(t)$ with time-dependent function chosen so that $f(0)=1$ and $w=d_0\dot{f}$.

This system is entirely described by the Euler equations (1) together with dynamical boundary conditions specifying that the fluid velocity is constrained to have $v_y=w$ along the top and bottom surfaces of the descending board and to have $v_x=0$ on the right-most vertical edge of the board. (Here we consider an inviscid fluid.) An entirely identical description of this squeezed physical system can be obtained by making a time-dependent coordinate transformation[19]

$$x=x, \quad y=f(t)\chi+g(t), \quad t=t \tag{14}$$

designed to render the moving board stationary mathematically. This is achieved by choosing $f(t)$ and $g(t)$ so that as the board in real space changes its y position, the functions f and g are varied so as to leave the χ position of the board constant in computational space.

To clarify the physical meaning of this dynamic coordinate transformation consider the case where the board is descending smoothly at constant speed w, and for simplicity consider regions where $g(t)=0$ (the compressed region between the boards). Then, air parcels immediately adjacent to the descending board must have vertical velocity $w=\dot{f}<0$, while air located adjacent to the stationary bottom surface must have zero vertical velocity. Further, for small speeds w it is reasonable to expect that the the air parcels located half way between the descending board and the stationary bottom surface will have vertical speeds of $w/2$ and, in general, that the vertical air speed is linearly proportional to the relative height of an air parcel between the stationary surface and the descending board. This linear velocity dependence (valid only at slow speeds) is realized by having air located initially at height y_0 (where the maximum height is set to unity) moving downwards in physical space with velocity $v_y=y_0\dot{f}$. The initial height at time $t=0$ when $f(0)=1$ satisfies $y_0=\chi$ in Eq. (14) giving $v_y=\dot{f}\chi$ with different χ for different parcels of air. A linear dependence of vertical velocity on initial height is achieved by setting $v_y=\dot{f}\chi$, or as it is convenient to define the parameter $v_\chi=(v_y-\dot{f}\chi-\dot{g})/f$ and we achieve a linear dependence of the vertical velocity on initial height by setting $v_\chi=0$.

Standard change of coordinate methods[23] or consultation of the helpful Ref. 19 then give the computational space fluid equations as

$$\partial_t U+\partial_x F+\partial_\chi G=0,$$

$$U=\begin{pmatrix} f\rho \\ f\rho v_x \\ f\rho v_y \end{pmatrix}, \quad F=\begin{pmatrix} f\rho v_x \\ f(\rho v_x^2+\rho^{\gamma}/\gamma) \\ f\rho v_x v_y \end{pmatrix}, \tag{15}$$

$$G=\begin{pmatrix} f\rho v_\chi \\ f\rho v_x v_\chi \\ f\rho v_y v_\chi+\rho^{\gamma}/\gamma \end{pmatrix}.$$

Here, we mix terms v_y and $v_\chi=(v_y-\dot{f}\chi-\dot{g})/f$ to maximally simplify the equations. These equations reduce to the usual Euler equations (1) in the limit $f=1$, $g=0$, and $y=\chi$.

In real space, the squeezing of the boards compresses the inside air to expel a jet of air while in computational space the board is stationary. Here, squeezing forces have been converted into mass and momentum injection terms proportional to $\dot{f}/f$ with the injection of mass and momentum everywhere into the space between the boards generating the observed jet of air in exactly the same way as a solid-fuel rocket.[17,18] This indicates that whenever we have large wall velocities, $\dot{f}\approx 1$ in dimensionless units, we can expect significant expelled jet flows.

V. SQUEEZED ACOUSTIC WAVE EQUATION

That squeezed systems can violate the assumptions underlying monopole theory in at least two regimes is made apparent by solving for $\partial_{tt}\rho$ using the squeezed fluid equations (15) without making the small wave or low-velocity approximations. The squeezed wave equation with all terms is

$$\begin{aligned} 0=\partial_{tt}\rho-\frac{\partial_{xx}\rho^{\gamma}}{\gamma}-\frac{\partial_{\chi\chi}\rho^{\gamma}}{\gamma f^2}-\partial_{xx}(\rho v_x^2)-\partial_{x\chi}(\rho v_x v_\chi) \\ -\frac{\partial_{\chi x}(\rho v_x v_y)}{f}-\frac{\partial_{\chi\chi}(\rho v_y v_\chi)}{f}+\frac{\ddot{f}}{f}\rho+\frac{2\dot{f}\partial_t\rho}{f} \\ -\frac{\partial_{\chi t}[\rho(\dot{f}\chi+\dot{g})]}{f}-\frac{\dot{f}\partial_\chi(\rho v_y)}{f^2}. \end{aligned} \tag{16}$$

This equation reduces to the usual small amplitude wave equation (4) in the limits $f=1$, $g=0$, v_x, $v_y\ll 1$, $p=1+p_1$ for $p_1\ll 1$, and $\rho=1+p_1/\gamma$.

Here, it is apparent that terms previously left out in the usual wave equation treatment become large in either of two limits. The first is at full closure with $f\to 0$ and $\dot{f}\neq 0$. This case shows a finite-time singularity in the fluid dynamics which places a regular singular point into the fluid equations. Regular singular points in dynamical equations can have the effect of driving solutions to exhibit singularities, and, in other work, we explore how these singularities can drive supersonic expelled jets from squeezed systems[24] and relativistic jets from large astrophysical systems. However, cavities in car tires are not usually squeezed to a singularity and generally have $f\approx 1$.

The second case of interest occurs in the limit of high wall velocities and accelerations when $O(\dot{f})\approx O(\dot{\rho})$ or $O(\ddot{f})\approx O(\ddot{\rho})$. Car tires can approach these regimes.

Consider a typical groove of length $L=7.5$ cm, width $d_0=5$ mm, and depth $W=d_0$ cut into the rim of a tire traveling forward with linear speed v. As the groove moves into the contact patch with the road (to take the full weight of the car) the groove undergoes a squeezing of its volume of around 10% modeled by a compression of the width of $A=0.1d_0=0.5$ mm. The groove uncompresses a time τ_c

$=d_c/v$ later when it leaves the contact patch of length about $d_c=20$ cm. Groove squeezing occurs in a time $\tau\approx d_0/v \approx 0.3$ ms at $v=15$ m/s or about 50 km/h.

Simple estimates of the velocity and acceleration of the groove wall are then $\dot{d}\approx A/\tau\approx 1.5$ m/s and $\ddot{d}\approx A/\tau^2 \approx 4500\,\text{m/s}^2$. These calculations are in accord with observation.[1,8] In this paper, the width of groove is modeled by $d(t)=d_0 f(t)$ so, in nondimensional units, we have

$$\dot{f}=\frac{\dot{d}}{d_0}=\frac{ALv}{a_0 d_0^2}, \quad \ddot{f}=\frac{\ddot{d}}{d_0}=\frac{AL^2v^2}{a_0^2 d_0^3}. \tag{17}$$

We note that the dimensionless acceleration increases quadratically with linear speed v. These simple estimates give $\dot{f}\approx\ddot{f}\approx 0.1$ at $v=25$ m/s, or about 90 km/h, and increasing at higher speeds. These values are compared to $\rho\approx 1$ in dimensionless units, indicating that squeezing can have significant effects on fluid dynamics.

VI. ANALYTIC SOLUTIONS TO SQUEEZED SYSTEMS

In this section we briefly provide indicative solutions for the fluid flow in squeezed systems as we seek to understand the nature of the expelled jet including how its kinetic energy might eventually contribute to the far-field sound intensity via turbulence or vortex generation.

A physical understanding of a squeezed system of Fig. 2 is readily had by considering a constant density approximation which allows equating the loss of internal volume $\delta V = -LWw\,\delta t$ with the gain in volume of the expelled jet $\delta V = Wd(t)v(L,t)\,\delta t$ giving

$$v(L,t)=-\frac{wL}{d(t)}=-\frac{\dot{f}L}{f}. \tag{18}$$

As mentioned previously, simple experiments confirm the importance of the spatial amplification factor L: clap your hands with fingers together ($L\approx 3$ cm) and with fingers apart ($L'=L/4$) noting the different sounds.

Two particular analytic solutions of interest can be obtained for linear squeezing $f(t)=1-t/T$, $\dot{f}=-1/T$, and with $g=0$. Here, T is the closure time of the cavity. We further assume smoothed vertical flows $\partial_\chi\rho=0$, $v_\chi=0$, and $v_y=\dot{f}y$.

The first solution of interest is a squeezed cavity with both ends closed—a piston—obtained by setting all x gradients and v_x equal to zero. This reduces Eq. (15) to $\partial_t(f\rho)=0$ with nondimensional solution

$$\rho(t)=\frac{1}{f}. \tag{19}$$

Here we see that a linear squeezing of 10% immediately generates a commensurate increase in density.

The second solution applies to an open ended cavity with nonzero x gradients and velocities $v_x\neq 0$. We still consider expulsion velocities small enough to satisfy $v_x^2=0$. If we then assume approximately constant density $\rho=1$, then both Eqs. (1) and (15) are satisfied by

$$v_x(x,t)=-\frac{\dot{f}x}{f}, \tag{20}$$

which extends the previous heuristic solution of Eq. (18). This solution is strictly valid only while $v_x<0.3$ where free-flowing air remains approximately uncompressed, but this is expected to be satisfied for car tires.

In time δt, a mass $\delta m=\rho LWd_0\dot{f}\,\delta t$ is expelled at velocity $v(L,t)$ given by Eq. (20) and with kinetic energy $\delta E=(\frac{1}{2})\delta m v^2$. This integrates to give total mass expulsion to time t of

$$m(t)=m_0(1-f) \tag{21}$$

and total kinetic energy of the expelled jet of

$$E(t)=-E_pT^2\int_0^t dt(\dot{f}^3/f^2), \tag{22}$$

where $m_0=\rho LWd_0$ is the initial fluid mass and $E_p=\frac{1}{2}m_0(L/T)^2$ is the kinetic energy of a mass m_0 moving over distance L in closure time T. For the constant-velocity linear squeezing case with loss of volume given by $\delta V/V=t/T=A/d_0$ this gives

$$m=\frac{A}{d_0}m_0, \quad E=\frac{A}{d_0-A}E_p. \tag{23}$$

This last relationship gives the kinetic energy of the jet as proportional to the square of the velocity of the car as

$$E=\frac{\rho WA^3L^3v^2}{2(1-A/d_0)d_0^4}. \tag{24}$$

The velocity solution of Eq. (20) can also be used to suggest the evolution of spatial density concentrations along the length of the expelled jet. Consider a jet with expulsion velocity given by Eq. (20) so that at the open end of the cavity where $x=L$ the horizontal velocity at time t is $v_x(L,t)=-\dot{f}L/f(t)$. We note the velocity of air parcels expelled at different times is different though once any air parcel has escaped from the cavity it is no longer compressed or accelerated (to a first-order approximation). This allows applying a constant velocity approximation to motion outside the cavity to give an estimate of the position of any particular air parcel at later times. Then, the position at closure time T of a particle expelled at the earlier time t is

$$X(t,T)=L+v(L,t)(T-t). \tag{25}$$

For linear squeezing we have $f(t)=(1-t/T)$ giving $X(t,T)=2L$ for all the expelled particles in the air jet, implying an approximate density distribution of

$$\rho(x,T)\propto\delta[x-2L]. \tag{26}$$

Such density concentrations, if large enough, can source the formation of shock fronts within the jet and can contribute to far-field sound intensities.

The above discussions can contribute to understanding sound sources from squeezed cavities in car tires. For instance, the assumption that the velocity of the expelled jet causes turbulence to generate sound waves suggests that the sound intensity will depend on the ratio L/d, or the geometry

of the cavity. This is in accord with observations that both thin width and large width grooves emit less sound than medium width grooves.[7] Evidently, for large grooves $L \approx d$ and velocities are small so no sound from air jets is expected. Medium width grooves have $L > d > 0$, giving a ratio L/d large enough to give significant sound emission. Finally, thin width grooves with $d \approx 0$ have very little air in them so the initial mass $m_0 \approx 0$, meaning that the kinetic energy of the expelled jet is never significant and little sound is expected.

It is beyond the scope of this paper to discuss extreme nonlinearities like the formation of shock fronts in expelled jets, and our inviscid treatment means that we cannot comment about the sound generation role, if any, of vortices in the expelled jet.

VII. NUMERICAL SIMULATIONS

Squeezed cavities are analytically intractable and necessitate a resort to computational fluid dynamics (CFD) and we apply MacCormack's technique to Eq. (15). This standard scheme employs an explicit finite element method which is second order accurate in space and time.[20,25]

Consider a tire moving at approximate speed $v = 25\,\text{m/s}$ with grooves of length $L = 7.5\,\text{cm}$ and width and depth $d_0 = W = 5\,\text{mm}$. The groove undergoes a compression of 10% over a time of about 0.2 ms.

We note that in this time a rarefaction wave can only just travel from the open end of the groove to the closed end of the groove ($L \approx a_0 \tau \approx 6\,\text{cm}$) where pressure and density is building up. Further, sound waves have made about 15 crossings of the width of the groove to equilibrate the pressure and density across the width. Before the arrival of the rarefaction wave at any point, the fluid gradients in the x direction are zero and the piston solution of Eq. (19) is applicable. Thus, we expect that a 10% squeezing of the groove will cause a roughly 11% increase in density near the closed end of the groove. The arrival of the rarefaction wave will then cause a density gradient of about 11% between the closed and open ends of the groove and this gradient will generate velocity gradients of order 0.11 in the x direction leading to expulsion velocities of $v_x \approx 0.11$ at the open end of the cavity. This translates into speeds of about 30 m/s. These simple expectations are met in the simulations below.

The CFD numerical simulation is shown in Fig. 3 which shows the groove walls as the raised sections of the graph. (Only the top edge of the groove is shown for clarity.) The top edge is stationary in computation space but has caused a 4% compression in graph (a) and a 10% compression in graph (b). In graph (a) we see that the compression has equilibrated across the narrow width of the cavity and the density has increased by about 4% in accordance with Eq. (19). The increase in density causes a rarefaction wave to propagate from the open end of the cavity to the left but this wave has only had time to move a limited distance along the cavity. In graph (b) we reach the full compression of 10%, causing the density to increase by approximately 11%. This is also the time at which the rarefaction wave reaches the end of the cavity and all the air begins to exhaust from the cavity.

As previously noted after Eq. (3), a density fluctuation of 11% corresponds to a pressure fluctuation of 14% and the magnitude of this fluctuation lies well outside the validity regime for a linear truncation of the Taylor series expansion underlying small amplitude acoustic theory. It is for this reason that we must use the full Euler equations to derive the squeezed wave equation (16).

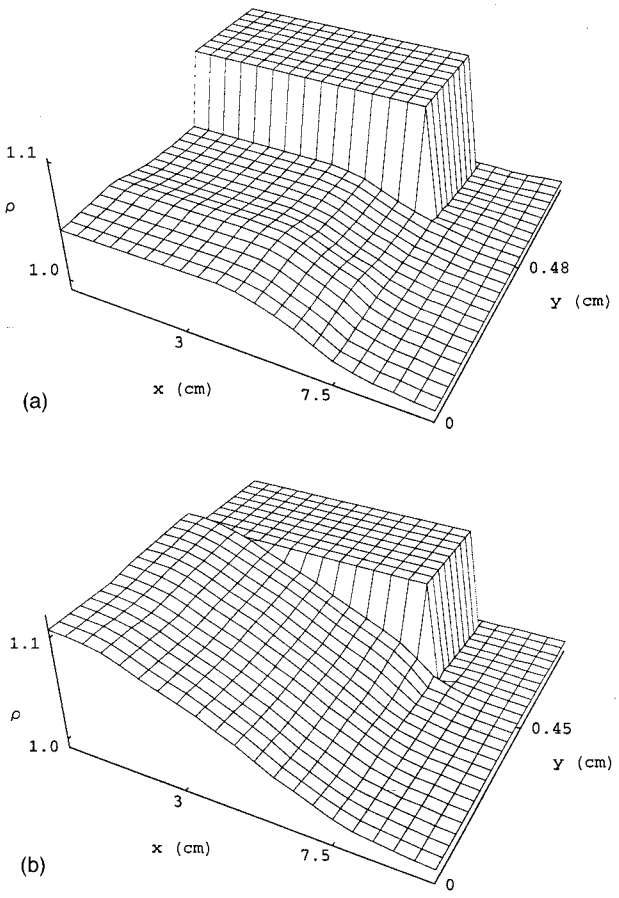

FIG. 3. The density profile of the air contained within the squeezed cavity (with only top wall shown) at times $t = 0.05$ ms with 4% squeezing in graph (a) and at $t = 0.2$ ms with 10% squeezing in graph (b). The density is given in dimensionless units. (Note the changes in the vertical scale as the groove compresses.)

Once the air begins to evacuate, the piston solution is no longer valid and we must consider the velocity solution of Eq. (20) with its linear dependence on position x. The validity of this solution is shown in Fig. 4 at the time of 10% squeezing which clearly shows the expected linear increase of velocity with position. This also confirms our simple ex-

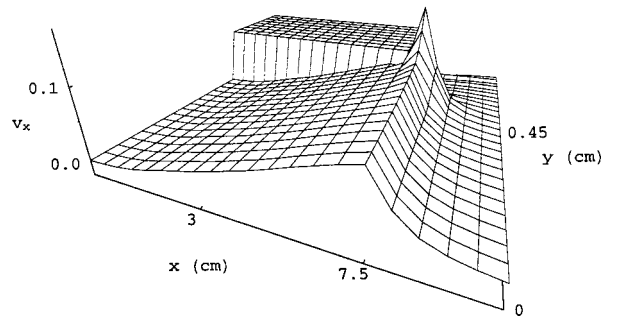

FIG. 4. The linear dependence of expulsion velocity on position x in dimensionless units.

pectation of a maximum velocity of around $v_x \approx 0.1$ in dimensionless units at the open end of the tube.

It is expected that the observed velocity flows will exhaust the cavity back to atmospheric pressure over the 6-ms period during which the cavity passes through the contact patch between the tire and the road. Then, the cavity will uncompress by about 10%, causing a decrease in density and pressure below ambient conditions by about 10%. The cavity will then open along its length and the pressure and density fluctuations are then expected to drive Helmoltz and Horn resonances.

These simulations serve to confirm the relevance of the analytic solutions for density under piston conditions in Eq. (19) and for the expulsion velocity in Eq. (20). However, they do not give insight into the far-field sound intensity emitted from squeezed cavities as the numerical grid is to coarse by a factor of 10 or more while a full simulation of passage through the contact patch (taking about 6 ms) requires an increase in grid area by a factor of 30^2. Thus, a full simulation is about 90 000 times larger than that shown here and is computationally intractable at this time.

VIII. CONCLUSION

In this paper we derived a squeezed acoustic wave equation suitable for application to squeezed fluid systems. The starting point of this derivation was the Euler equations for fluid flow together with the moving boundary conditions specifying a cavity under compression. This derivation demonstrated that the usual assumption of a small-amplitude acoustic wave equation and the acoustic monopole theory derived from this equation is incorrect for squeezed systems.

Approximate analytic solutions were obtained for the fluid flow in squeezed systems and were used to identify a pistonlike increase in density within a squeezed cavity before the cavity begins to exhaust along its full length. These solutions show that the exhaust velocity has a linear dependence on cavity length and can reach significant speeds. The mass and kinetic energy and density structure of the resulting expelled jet were examined using the derived approximate solutions. Finally, we used computational fluid dynamics approaches to directly investigate fluid flow and to confirm the applicability of the approximate analytic solutions.

ACKNOWLEDGMENTS

The author gratefully acknowledges helpful discussions with Ulf Sandberg. Initial stages of this work were completed at the Yukawa Institute of Theoretical Physics, Kyoto University, Japan, with the support of the Japan Society for the Promotion of Science and the Japanese Ministry of Education, Science and Culture (Mombusho).

[1] M. Heckl, ''Tyre noise generation,'' Wear **113**, 157–170 (1986).
[2] R. E. Hayden, ''Roadside noise from the interaction of a rolling tire with road surface,'' in *Proceedings of the Purdue Noise Conference*, West Lafayette, IN, 1971, pp. 62–67.
[3] K. Plotkin, W. Fuller, and M. Montroll, ''Identification of tire noise generation mechanisms using a roadwheel facility,'' in *International Tire/Road Noise Conference 1979*, pp. 127–141.
[4] I. D. Wilken, L. J. Oswald, and R. Kickling, ''Research on individual noise source mechanisms of truck tires: Aeroacoustic sources,'' in *SAE Highway Noise Symposium* (Society of Automobile Engineers, Warrendale, 1976), 762022, pp. 155–165.
[5] M. G. Richards, ''Cross lug tire noise mechanisms,'' in *SAE Highway Noise Symposium* (Society of Automobile Engineers, Warrendale, 1976), Paper 762024, pp. 181–186.
[6] J. F. Hamet, C. Deffayet, and M. A. Pallas, ''Air-pumping phenomena in road cavities,'' in *International Tire/Road Noise Conference 1990*, pp. 19–29.
[7] J. A. Ejsmont, U. Sandberg, and S. Taryma, ''Influence of tread pattern on tire/road noise,'' in *Transactions of the Society of Automotive Engineers* (Society of Automotive Engineers, Warrendale, 1984), pp. 1–9.
[8] M. Jennewein and M. Bergmann, ''Investigations concerning tyre/road noise sources and possibilities of noise reduction,'' Proc. Inst. Mech. Eng., Part C: Mech. Eng. Sci. **199**, 199–205 (1985).
[9] N.-A. Nilsson, ''Air resonant and vibrational radiation—possible mechanisms for noise from cross-bar tires,'' in *International Tire/Road Noise Conference 1979*, pp. 93–109.
[10] U. Sandberg and G. Descornet, ''Road surface influence on tire/road noise,'' in *Proceedings of Internoise 1980: Noise Control Foundation*, 1980, pp. 1–14.
[11] M. C. Bérengier, M. R. Stinson, G. A. Daigle, and J. F. Hamet, ''Porous road pavements: Acoustical characterization and propagation effects,'' J. Acoust. Soc. Am. **101**, 155–162 (1997).
[12] J. M. Cuschieri, S. Gregory, and M. Tournour, ''Open grid bridge noise from grid and tire vibrations,'' J. Sound Vib. **190(3)**, 317–343 (1996).
[13] W. Kropp, ''Structure-borne sound on a smooth tyre,'' Appl. Acoust. **26**, 181–192 (1989).
[14] O. A. Olatunbosun and J. W. Dunn, ''Generalized representation of the low frequency radial dynamic parameters of rolling tyres,'' Int. J. Vehicle Design **12**, 513–525 (1991).
[15] S. C. Huang, ''The vibration of rolling tyres in ground contact,'' Int. J. Vehicle Design, **13**(1), 78–95 (1992).
[16] U. Sandberg, ''Road traffic noise: The influence of the road surface and its characterization,'' Appl. Acoust. **21**, 97–118 (1987).
[17] M. J. Zucrow and J. D. Hoffman, *Gas Dynamics* (Wiley, New York, 1976).
[18] Z. U. A. Warsi, *Fluid Dynamics: Theoretical and Computational Approaches* (CRC, Boca Raton, 1993).
[19] K. A. Hoffmann and S. T. Chiang, *Computational Fluid Dynamics for Engineers* (Engineering Education System, Wichita, KS, 1993).
[20] J. D. Anderson, *Computational Fluid Dynamics: The Basics with Applications* (McGraw–Hill, New York, 1995).
[21] P. M. Morse and K. Uno Ingard, *Theoretical Acoustics* (McGraw–Hill, New York, 1968).
[22] S. J. Elliott, ''Active control of structure-borne noise,'' J. Sound Vib. **177**(5), 651–673 (1994).
[23] S. Weinberg, *Gravitation and Cosmology: Principles and Applications of the General Theory of Relativity* (Wiley, New York, 1972).
[24] M. J. Gagen, ''Expelled jets from squeezed fluid singularities,'' accepted by AIAA J.
[25] R. W. MacCormack, ''The effect of viscosity in hyper-velocity impact cratering,'' AIAA Paper, 69–354 (1969).

A study of damping effects on spatial distribution and level of reverberant sound in a rectangular acoustic cavity

Linda P. Franzoni
Department of Mechanical Engineering and Materials Science, Duke University, Durham, North Carolina 27708-0300

Danielle S. Labrozzi
Ericsson, 7001 Development Drive, Research Triangle Park, North Carolina 27709-3969

(Received 2 December 1998; revised 31 March 1999; accepted 14 April 1999)

Based on computer simulations of sound fields in rectangular enclosures, important observations are made regarding sound pressure levels and the spatial variation of the broadband reverberant field. From these observations an empirical formula is deduced that describes the slow *spatial variation* of the broadband reverberant mean-square pressure in one lengthwise direction. Two room shapes were studied: an elongated rectangular enclosure and an almost cubic enclosure, both with broadband sound source(s) on an endwall. Source position, relative phasing of multiple sources, level, and placement of absorptive material were variables in the study. The numerical results for the spatially averaged mean-square pressure in the reverberant field were often not in very close agreement with values predicted from a traditional Sabine approach. The prediction was improved by accounting for the power absorbed on the first reflection and an approximate formula is given for this correction factor. The reverberant sound field is characterized by a gradual spatial variation in the direction away from the source. This spatial variation scales exponentially with the sidewall absorptivity, as demonstrated by the numerical simulations. An approximate emperical formula is shown to predict this spatial variation fairly well. The computer simulations showed elevated sound pressure levels at the enclosure boundaries, for all cases, and also in the interior, for sound fields excited by a single broadband source on an endwall. These intensification zones occur along a plane in front of the source and along a plane which corresponds to the reflection of the source, whether or not the source is on a line of symmetry.
[S0001-4966(99)00608-6]

PACS numbers: 43.55.Br, 43.55.Ka [JDQ]

INTRODUCTION

Methods for predicting the magnitude and spatial distribution of sound pressure in reverberant spaces include statistical energy analysis, asymptotic modal analysis, classical modal analysis, ray tracing techniques, finite element analysis, and boundary element analysis. Statistical energy analysis and asymptotic modal analysis are particularly suited for systems which have high modal density and are lightly damped (with assumptions of uncorrelated modes, equal distribution of energy, etc.). With the exception of ray tracing, the other methods mentioned are typically applicable in the low-frequency range where there are relatively few modes in the bandwidth of interest, and become computationally cumbersome at higher frequencies.

Many sound fields of practical importance are in the high-frequency range, namely wavelengths are small compared to the enclosure dimensions, have high modal density, and are **not** *lightly* damped. Examples of these types of sound fields are found in vehicle interiors, for example, airplane fuselages. At this time, an efficient theoretical method, like asymptotic modal analysis, does not exist for determining the spatial distribution of sound pressure levels in these types of spaces. It is the ultimate goal of this research program to develop such a method. Toward that end, *exact* computer simulations of the reverberant sound field in two rectangular acoustic cavities (one which is long and narrow, one which is more cubic) have been made. The computer program provides a numerical solution to the three-dimensional wave equation with the appropriate wall impedance and sound source boundary conditions for each configuration studied.

The computer simulations show some unexpected results. The traditional Sabine equation overpredicts the spatially averaged mean-square pressures by 50% or more, in some cases, when compared to the computer simulations. The agreement is slightly better when there are multiple sources on a wall, as opposed to a single point source. The Sabine theory can be modified, by removing the energy absorbed by the first reflection. This adjustment factor improves the results dramatically. An exact and an approximate version of the modification is presented. As expected, both the original Sabine theory and the modified theory break down for increasing levels of absorption and for less homogeneously distributed absorption.

The spatial variation of the sound fields in the lengthwise direction correlates well with an exponentially varying function. The exponent is linearly related to the sidewall absorptivity. This is particularly true for rooms studied with equally distributed absorption, but shows similar behavior when the absorption is distributed less uniformly. From the correlations presented, an approximate equation for the ex-

ponentially varying spatial distribution of the broadband reverberant field is proposed. This equation is shown to work well for the two rooms studied, and is thought to be a good approximation in general.

In addition, intensification zones, i.e., locations with a high level of spatial correlation between modes, are known to occur at the boundaries. When a point source is located along an axis of symmetry, intensification has been observed in the interior as well. The computer simulations show that for any point source location there will be intensification zones in the reverberant field. The locations of the increased sound pressure levels correspond to the source location and the location of an image source. These effects are most pronounced for lightly damped sidewalls, but are also present to a lesser extent when damping is placed on a wall or walls of the cavity.

I. HISTORICAL BACKGROUND

The first predictions of sound pressure levels in rooms with different levels of absorption were based on the experimental work of Wallace Sabine. From his experiments in room acoustics, Sabine was able to develop an analytical formula which related the mean-square pressure in the room to the amount of absorption and physical dimensions of the room. However, several assumptions inherent in the analytical expression limit its accuracy and usefulness. The one which is most important is that the sound field in the room is diffuse. This assumption is valid for lightly damped rooms which have more reverberant characteristics. Other assumptions which affect the applicability of the prediction are: that the propagation of sound in any direction of the enclosure is equally probable, and that the boundaries of the enclosure will provide continuous absorption.[1] Sabine's theory neglects issues of room configuration, damping distribution, and the effect of different angles of incidence on the absorption.[2–7] Sabine's classical work provided the basis for later room acoustics theories, including geometrical acoustics. It has become the foundation for other theories. For example, Eyring based his theory on Sabine's work without the assumption of continuous absorption.[2]

Wave theory is also used to predict sound pressure levels in enclosures. Unlike Sabine's theory, this theory provides an exact solution to the sound field. It incorporates the room configuration and damping distribution through the boundary conditions of the room. The wave theory can only explicitly solve for basic geometries that correspond to 11 coordinate systems which allow separation of variables for the wave equation. It is also more useful in the low-frequency range or in a small volume where the number of waves is small. If a high-frequency or large volume is used, the computation becomes cumbersome and impossible without the aid of a computer.[1,6,8,9] Also the vibration characteristics of the boundaries of buildings, including walls, doors, and windows are not accounted for in this theory.[10]

An approach that was considered by Gibbs and Jones uses the method of images and accounts for a nondiffuse sound field. It also uses the effective power of the image source.[3] The method of images is not a recent method and was, in fact, discussed by Bolt in 1950.[11] Another well-known technique for predicting sound pressure levels is ray tracing, which is computationally intensive since it requires following each sound wave in time and space as it reflects and is absorbed at the surfaces.[12]

A method based on the energy differential equation is applicable for enclosures in which the sound field is not completely diffuse. The differential equation is based on Sabine's equation and Eyring's equation. Related work is presented in a paper by Ohta *et al.*[9] Sergeev combined a geometric and statistical approach in an effort to analyze a nondiffuse rectangular room.[13]

For rooms that are of irregular or complex shape, the finite element method is often used. It can also account for nonuniform distributions of damping. This method is more suited to the low-frequency range since the number of elements required is dependent upon the size of the wavelengths present. At high frequencies, the wavelengths will be short and the method will require a larger number of elements (and therefore, calculations).[14–16]

The prediction of sound fields in an enclosure can also be determined by the boundary element method. An indirect boundary element method has been investigated by Bernhard and Kipp.[17] The advantage of this method is that only the boundaries are modeled. However, element size is still dependent upon wavelength size, and at high frequencies a larger number of elements will be needed. The ineffectiveness of the boundary element method at certain frequencies has been studied by Hussain and Peat.[18] A method similar to the wave theory is classical modal analysis (CMA). The sound pressure is described as a series of coefficients times the normal modes of the system. This method is also restricted to separable geometries. At high frequencies a large computational effort is required, because the contributions of the individual modes are taken into account. Usually the ''hard box'' or ''rigid wall'' modes of the system are used in the expansion. Therefore, when the room deviates from the hard wall conditions it takes more modes to approach the correct result and all the modes become coupled to each other.[19]

Statistical energy analysis (SEA) is used to predict high-frequency sound fields under certain conditions. These conditions are: diffuse sound field, little or no damping, and that the acoustic field behaves stochastically. In SEA the modes of vibration of the room and its boundaries are an integral part of the analysis. The entire system is divided into subsystems which contribute to the resulting sound pressure level. The energy of each subsystem can be solved from a set of linear equations which are derived by relating the power of applied forces to the energy of the coupled systems. The advantage of SEA is the minimal computational effort required since the modes are not considered individually.[10] The disadvantages of SEA are: parameters such as ''coupling loss factors'' are not well determined and may need to be found experimentally; and SEA is not capable of resolving the spatial variation of the sound field since it only predicts average levels. Furthermore, SEA is restricted to the middle- and high-frequency ranges since a large number of modes are required for a diffuse field.[20]

A method similar to SEA is asymptotic modal analysis

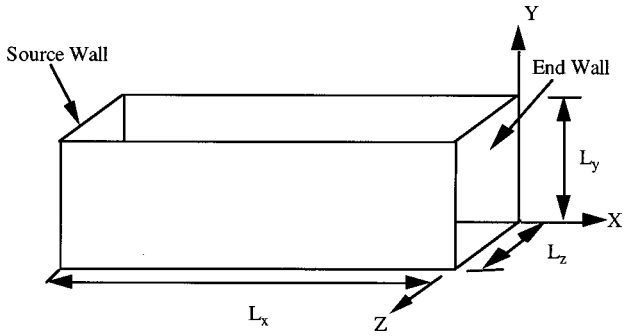

FIG. 1. Room shape and coordinate system.

(AMA). It is derived from classical modal analysis in a formal way and involves the assumption that the number of structural modes or acoustic modes approach infinity. The resulting expression for pressure does not require the summation of the individual modal contributions. In fact, the *spatially averaged* AMA sound pressure level expression is identical to that of SEA. Unlike SEA, asymptotic modal analysis is not restricted to spatial averages, which is one of the advantages of the method. However, uniform distribution of absorbing material is assumed and the method is restricted to low levels of absorption, i.e., ''lightly damped systems.'' [20–22]

II. DESCRIPTION OF THE ACOUSTIC SYSTEM STUDIED

The study presented here is based on a computer simulation of two rooms, one of which could be described as ''long and rectangular'' and one which could be described as ''boxy'' (not quite cubic). A single point source or multiple point sources were placed on an endwall of the room. The source location for single sources, the phase distribution for multiple sources, and the amount and distribution of the absorption were variables in the study.

A. Room configuration

The models used for this study were rectangular enclosures. The first enclosure was a long rectangular room with the dimensions of $L_x = 7.0$ ft, $L_y = 3.0$ ft, $L_z = 2.0$ ft, and a volume of 42 cubic feet. The second enclosure was more cubic, with a volume of 49.35 cubic feet. It had the dimensions $L_x = 3.5$ ft, $L_y = 3.0$ ft, and $L_z = 4.7$ ft. Both enclosures had the same surface area. Although these dimensions do not seem realistic for a room, they correspond to the dimensions of a scale model which will be used in future experimental work. The coordinate system is shown in Fig. 1.

B. Source configuration

Simulations were run for the cases of a single source on an endwall, and for cases where multiple (4) sources with different phase configurations were located on an endwall. For the single source cases, eight different source locations were chosen as shown in Fig. 2. For the multiple source cases, the source strengths were equal with locations fixed as shown in Fig. 3, but the phases varied. Three configurations were studied: all four sources in-phase; sources on a diagonal

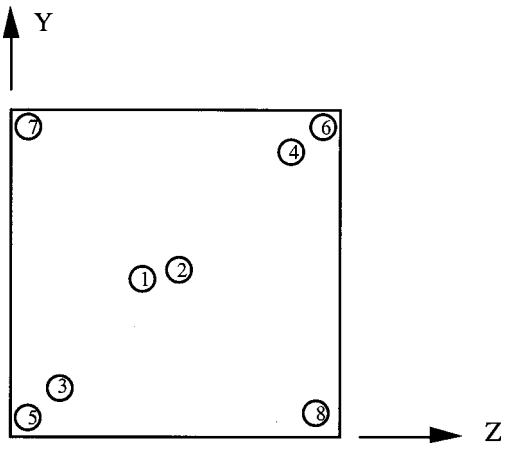

FIG. 2. Source locations on $-L_x$ wall for single source baffled monopoles

were in-phase with each other and out-of-phase with the opposite diagonal; and two sources vertically in-line were in-phase with each other and out-of-phase with the sources next to them.

C. Damping distribution

The damping material covered one or more entire walls, and was modeled mathematically as a real impedance, symbolically z_b or z_w. The different configurations are shown in Fig. 4. The absorptive wall(s) were either: the endwall alone (z_b), two sidewalls only (z_w), or an endwall and two sidewalls (z_b and z_w).

The absorptivity in English sabins was calculated by adding the products of the random incidence absorption coefficient times the covered wall areas. A small wall covered with a very absorptive damping material could have the same absorptivity (sabins) as a larger area covered with less absorptive material. For generality, the results are presented in terms of a ratio of absorptivity to total surface area of the enclosure, i.e., an effective absorption coefficient for the room as a whole.

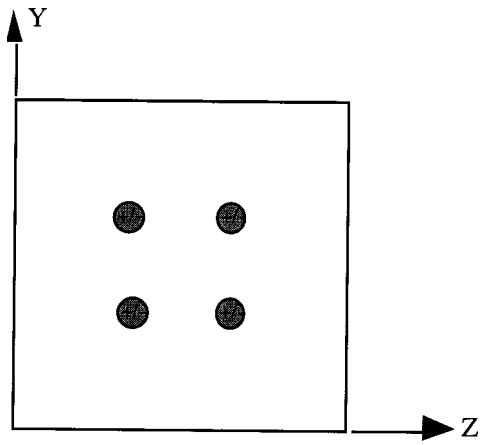

FIG. 3. Source locations for cases with four baffled monopole sources acting together in combinations of pairs which were either in-phase or out-of-phase. If brought close enough together these sources could simulate a dipole or quadrupole.

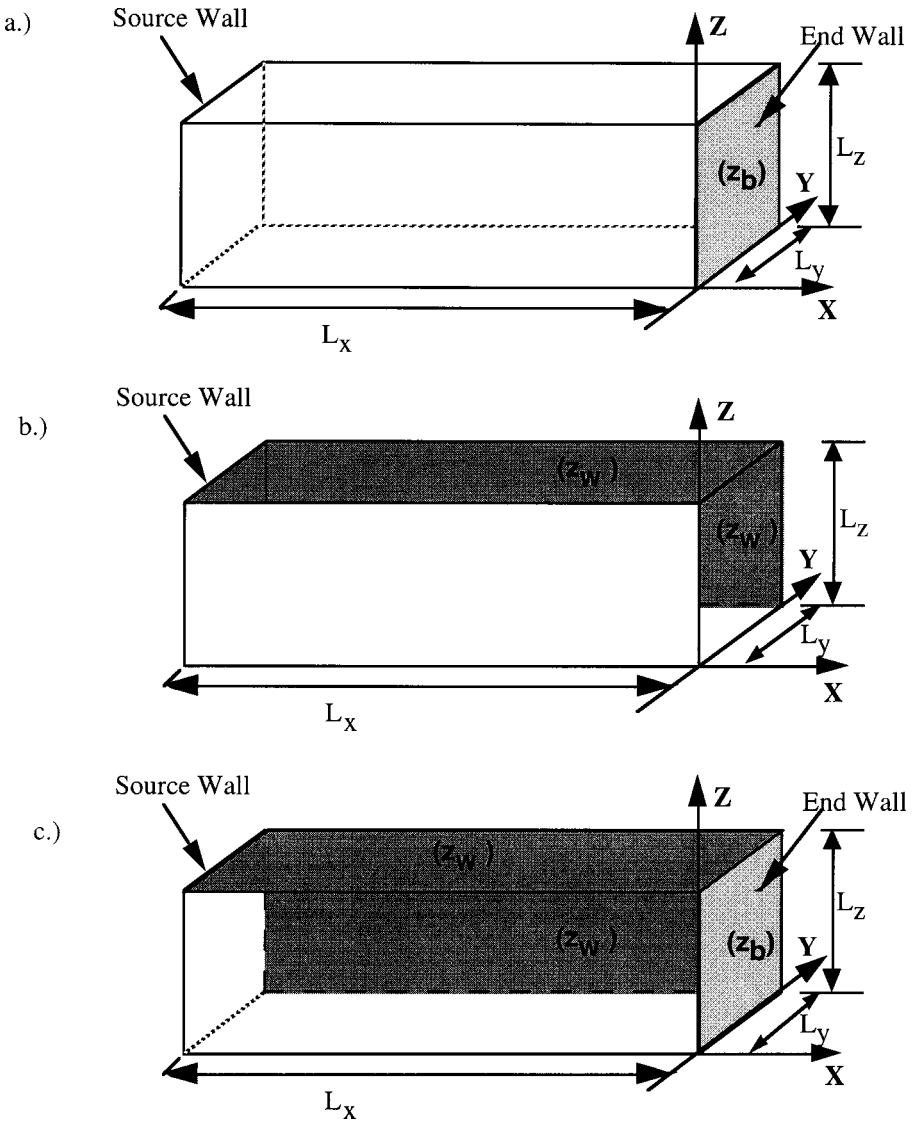

FIG. 4. Configurations of damping distribution: (a) impedance z_b on the $x=0$ endwall, (b) impedance z_w on $y=L_y$ and $z=L_z$ sidewalls, and (c) impedance z_b on the $x=0$ endwall and z_w on $y=L_y$ and $z=L_z$ sidewalls.

III. DEVELOPMENT OF WAVE THEORY

The sound pressure in a rectangular enclosure as shown in Fig. 1 must satisfy the three-dimensional wave equation:

$$\frac{\partial^2 p}{\partial x^2}+\frac{\partial^2 p}{\partial y^2}+\frac{\partial^2 p}{\partial z^2}-\frac{1}{c^2}\frac{\partial^2 p}{\partial t^2}=0. \tag{1}$$

The following impedance boundary conditions apply on the $x=0$, $y=L_y$ and $z=L_z$ walls:

$$\left.\frac{p}{u}\right|_{x=0}=z_b, \quad \left.\frac{p}{v}\right|_{y=L_y}=z_w, \quad \left.\frac{p}{w}\right|_{z=L_z}=z_w, \tag{2}$$

where the acoustic velocity, $\mathbf{q}=u\mathbf{i}+v\mathbf{j}+w\mathbf{k}$. In addition to the impedance boundary conditions, there are also hardwall boundary conditions on two other walls, $y=0$, and $z=0$.

$$\left.\frac{\partial p}{\partial z}\right|_{y=0}=0, \quad \left.\frac{\partial p}{\partial y}\right|_{z=0}=0. \tag{3}$$

The $x=-L_x$ wall, i.e., the source wall, is a hardwall except for a point or points where there is a sound source. The source (or sources) is assumed to be a simple baffled monopole of strength Q, located at y_0, z_0 on the $x=-L_x$ wall. The volumetric strength, Q, is defined as

$$Q\equiv\int_0^{L_y}\int_0^{L_z}\left.u\right|_{x=-L_x}dz\,dy. \tag{4}$$

This provides the final boundary condition. Namely,

$$u|_{x=-L_x}=U_0e^{i\omega t}=Q\,\delta(y-y_0)\,\delta(z-z_0)e^{i\omega t}, \tag{5}$$

which can be extended to include multiple sources by superposition. Invoking the acoustic momentum equation the boundary condition on the source wall becomes

$$-\frac{1}{\rho}\left.\frac{\partial p}{\partial x}\right|_{x=-L_x}=i\omega Q\,\delta(y-y_0)\,\delta(z-z_0)e^{i\omega t}. \tag{6}$$

The mathematical solution for the case of a single monopole source of strength Q located at source location y_0, z_0 results in the following analytical expression for the pressure as a complex quantity:

$$p(x,y,z,t)=\sum_m \sum_n P_{mn}\left(\overline{z}_b\frac{k_x}{k}\cos(k_x x)-i\sin(k_x x)\right)\times(\cos(k_y y)\cos(k_z z))e^{i\omega t}, \quad (7)$$

where

$$P_{mn}=\frac{4Q\rho ck}{L_y L_z k_x}\cos(k_y y_0)\cos(k_z z_0)\times\frac{1}{(\overline{z}_b k_x+k)^2\left(i\overline{z}_b\frac{k_x}{k}\sin k_x L_x+\cos k_x L_x\right)\beta_y(\overline{z}_w)\beta_z(\overline{z}_w)}$$

and

$$\beta_y(\overline{z}_w)=1+i\frac{kL_y\overline{z}_w}{(k_y L_y\overline{z}_w)^2-(kL_y)^2}$$

and

$$\beta_z(\overline{z}_w)=1+i\frac{kL_z\overline{z}_w}{(k_z L_z\overline{z}_w)^2-(kL_z)^2}.$$

The double summation arises because there are an infinite number of wave numbers k_y and k_z, which satisfy the given eigenvalue problem. The complex wave numbers, k_y and k_z, will be discussed in detail in the next section of this paper. The dimensionless impedances $\overline{z}_b$ and $\overline{z}_w$ have been normalized by ρc.

Equation (7) is valid when there is *one* source of strength Q on the $x=-L_x$ endwall. When there are multiple sources, the superposition principle can be applied. For the case of four baffled monopole sources of strengths Q_1, Q_2, Q_3, and Q_4, the term, $Q\cos(k_y y_0)\cos(k_z z_0)$, can be replaced by a summation of the four terms: $\Sigma_{j=1}^4 Q_j\cos(k_y y_j)\cos(k_z z_j)$, assuming that source 1 is located at y_1, z_1 and source 2 is located at y_2, z_2, etc. The sources can be in-phase or out-of-phase by making Q a positive or negative value. The four sources were not placed in close enough proximity to each other (within a wavelength), to simulate a dipole or quadrupole, even though their phases were configured in that way. However, it was thought that having multiple sources would produce a more diffuse sound field after fewer reflections than the rooms with a single point source.

In the numerical studies the pressure was calculated in a one-third octave band about the center frequency of 4000 Hz (corresponding to a dimensionless $k_c L_x=160$ for room 1). The dimensionless transfer function $H(\omega)$ representing the ratio of pressure p (output) to source strength Q (input) was defined as

$$H(\omega)=\frac{pL_y L_z}{Q\rho c}, \quad (8)$$

where $H(\omega)$ is directly obtainable from Eq. (7).

Equation (7) represents the pressure at a *single* frequency and at a single spatial location. In order to calculate the mean-square pressure in a frequency band, the following relationships were used and can be found in Ref. 23. The mean-square level in the band is equal to an integral of the mean-square power-spectral density over the frequency interval, where ω_u and ω_l are the upper and lower frequencies in the band, respectively. Thus

$$\overline{p^2}=\int_{\omega_l}^{\omega_u}\overline{p^2_{psd}}\,d\omega \quad \text{and} \quad \overline{Q^2}=\int_{\omega_l}^{\omega_u}\overline{Q^2_{psd}}\,d\omega. \quad (9)$$

The power-spectral densities of the input and output quantities are related through the transfer function as follows:

$$\overline{p^2_{psd}}=|H(\omega)|^2\overline{Q^2_{psd}}. \quad (10)$$

Assuming $\overline{Q}_{psd}$ is constant in the bandwidth of interest, the mean-square pressure equals:

$$\overline{p^2}=\int_{\omega_l}^{\omega_u}\overline{p^2_{psd}}\,d\omega=\int_{\omega_l}^{\omega_u}|H(\omega)|^2\overline{Q^2_{psd}}\,d\omega=\overline{Q^2_{psd}}\int_{\omega_l}^{\omega_u}|H(\omega)|^2\,d\omega. \quad (11)$$

Or, in terms of mean-square source strength in the band:

$$\overline{p^2}=\frac{\overline{Q^2}}{\omega_u-\omega_l}\int_{\omega_l}^{\omega_u}|H(\omega)|^2\,d\omega. \quad (12)$$

In the numerical studies, the integral was replaced by a summation, and sufficiently small increments in frequency were taken, such that $H(\omega)$ was essentially constant over each $d\omega$. Replacing the integral by a sum, $d\omega$ becomes $(\omega_u-\omega_l)/N$, where N is the number of increments:

$$\frac{\overline{p^2}}{\overline{Q^2}}\frac{(L_y L_z)^2}{(\rho c)^2}=\frac{\Sigma_n|H(\omega)|^2}{N}. \quad (13)$$

This quantity is referred to as ''dimensionless mean-square pressure'' in the results section. When multiple sources were considered, they were assumed to be equal in strength, such that the magnitude could be factored out of the sum and Eqs. (8)–(13) could be applied.

A. Complex wave numbers

Wave numbers k_y and k_z which appear in Eq. (7), and therefore in the transfer function $H(\omega)$, do not correspond to $m\pi/L_y$ and $n\pi/L_z$, as in the hardwall case for which $z_w\to\infty$. Due to the impedance boundary conditions at $y=L_y$ and $z=L_z$, the wave numbers are complex. Applying the impedance boundary condition at $y=L_y$ leads to the following transcendental equation for wave number, k_y:

$$k_y L_y\tan(k_y L_y)=i\omega\rho L_y/z_w. \quad (14)$$

To solve this equation, define: $k_y L_y=m\pi+\epsilon$, and substitute into Eq. (14):

$$(m\pi+\epsilon)\tan(\epsilon)=ikL_y/\overline{z}_w=i\gamma. \quad (15)$$

The overbar denotes that the impedance has been normalized by ρc. Taking the derivative of Eq. (15) with respect to γ, gives a differential equation for $d\epsilon/d\gamma$:

$$\frac{d\epsilon}{d\gamma}=\frac{i\cos^2\epsilon}{\frac{1}{2}(\sin 2\epsilon)+\epsilon+m\pi}. \quad (16)$$

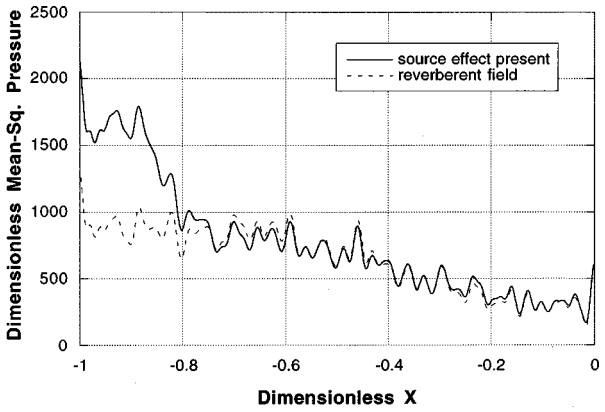

FIG. 5. A single trajectory in the x direction in room 1 with a dimensionless impedance of 22.5 on two sidewalls and 0.5 on the endwall. The sound field is shown, with and without the pressure which comes directly from the source. The source is slightly off-center on the source endwall.

This equation was first numerically integrated for ϵ and then converged to a higher level of accuracy by applying a Newton–Raphson scheme to Eq. (15). Knowing ϵ, wave number k_y is then

$$k_y=(m\pi+\epsilon)/L_y\,. \tag{17}$$

The process is the same for k_z. The wave numbers are guaranteed to be orthogonal by the Sturm–Liouville theory. The wave number in x is found from the dispersion relation:

$$k_x=\pm\sqrt{(\omega/c)^2-k_y^2-k_z^2}. \tag{18}$$

B. Calculation of sound pressure level in the reverberant field

For a harmonic sound source(s), computation of Eq. (7) with the appropriate complex wave numbers results in the total acoustic pressure (as a complex quantity) at any point in the rectangular acoustic cavity as a function of frequency. This pressure includes the pressure directly from the source as well as the reverberant field. In order to study the reverberant field, it was necessary to remove the portion of the complex sound pressure that came directly from the source to the point of evaluation before taking the root-mean-square and the band average. The source on the wall behaves like a simple baffled monopole with harmonic time dependence.[5] As a dimensionless ratio, this can be written as follows:

$$\frac{p_{\text{direct}}L_yL_z}{Q\rho c}=\frac{iL_yL_zk}{2\pi r}e^{-ikr}. \tag{19}$$

The contribution of the direct field is given in Eq. (19) for a single source which is located a distance r from the point where the pressure is being calculated.

Figure 5 shows an example of the dimensionless pressure in the 1/3rd octave band centered at 4000 Hz ($kL_x=160$ for room 1) with and without the direct field. In this plot, a ''numerical microphone'' traversed the more cubic cavity along a line of constant y, z, i.e., on a trajectory moving between the source wall and the endwall. The sound source in this case was a single baffled monopole at source location 1 (slightly off-center; see Fig. 2). All future results presented will be for the *reverberant field only* (i.e., the direct field removed).

C. Volume average of reverberant field

Trajectories were run with the reverberant field computed along a line parallel to the x, y, or z axis. The starting location for each trajectory varied, and many trajectories were run starting from each of the three walls $x=0$, $y=0$, and $z=0$. The x trajectories were averaged to represent a typical spatial distribution in the x direction. The same was done for the y and z directions. Assuming these averages denoted by P_x^{ave}, P_y^{ave}, P_z^{ave} represent a continuous distribution in their respective directions, the trajectories they represent will cross through each other and will only include the elevated boundary levels at the beginning and ending of their own trajectory direction. Therefore by volume averaging these cross-sectional averages, the interior will be counted three times, while the boundaries would be counted once. Interior average values, excluding the boundary and elevated levels in its vicinity (approximately one-third wavelength from each wall) were calculated separately and defined as: P_x^{interior}, P_y^{interior}, P_z^{interior}. Therefore, a more precise volume average can be calculated by subtracting two-thirds of the volume average of P_x^{interior}, P_y^{interior}, P_z^{interior} from the volume average of P_x^{ave}, P_y^{ave}, and P_z^{ave}. This result will only count the interior once and each boundary once.

IV. SPATIALLY AVERAGED REVERBERANT FIELD: MODIFICATION OF SABINE THEORY

According to Sabine, the spatially averaged mean-square reverberant pressure can be calculated from

$$\overline{p}^2_{\text{rev}}=\frac{4\rho c\Pi}{A}, \tag{20}$$

where A (in sabins) is the total absorptivity in the room and Π is the power of the sound source. The power of a baffled monopole[5] can be written as

$$\Pi=\frac{\rho ck^2Q^2}{4\pi}. \tag{21}$$

Note, this implies that if the source strength Q is constant in a band, as was assumed in this study; then the power must vary with frequency. For comparison between the predicted reverberant sound pressure level and the calculated one in the study, the pressures in both cases were nondimensionalized by $(Q\rho c)/(L_yL_z)$.

A. Removal of first reflection

In the Sabine theory, it is assumed that the reverberant field contains sound waves that have undergone many reflections. By using Eq. (21) for the power in Eq. (20) the reverberant field is overestimated since this implies all of the power from the source is present in the reverberant field. In actuality, some of the power from the source is absorbed on the first reflection, additional power is absorbed on the second, etc. In the first few reflections, the sound has not yet

achieved a diffuse character, but rather has a definite nondiffuse form. As suggested by Eyring's early work in this area, a way to compensate for this effect is to adjust the power of the source in the Sabine equation [Eq. (20)] by removing power that is absorbed by the first few reflections. The largest contribution comes from the first reflection. It will be shown that good agreement between the simulations and the theory was obtained when only the first reflection was taken into account.

The incremental power which is absorbed from the first sound wave coming directly from the source onto an incremental area ($\delta\xi\ \delta\eta$) of an impedance-covered wall at an angle θ (measured from the normal to the surface) is

$$\delta\Pi_{\text{absorbed}}=(\overline{p^2}/\rho c)\,\alpha(\theta)\cos(\theta)\,\delta\xi\,\delta\eta, \tag{22}$$

where $\alpha(\theta)$ is the oblique incidence absorption coefficient. The mean-square pressure, which is used to calculate incoherent intensity, is equal to that from a point source of strength Q:

$$\overline{p^2}=\left(\frac{\rho c k}{2\pi}\right)^2\frac{Q^2}{2}\,\frac{1}{r^2}. \tag{23}$$

The power absorbed is then found by integrating Eq. (22) over all the covered surface areas of the enclosure. The ξ, η variables represent a 2-D coordinate system for a covered wall. The variable r in Eq. (23) equals the distance from the point source (for example, at y_0, z_0) to a point on the covered wall (ξ, η). Assuming a normalized real impedance $\overline{r_b}$ on a given wall, the fraction of power absorbed to total power of the source is

$$\frac{\Pi_{\text{absorbed}}}{\Pi_{\text{total}}}=\frac{2}{\pi}\int_0^W\int_0^H\frac{\overline{r_b}z_s^2}{(\overline{r_b}z_s+1)\sqrt{(x-x_s)^2+(y-y_s)^2+z_s^2}}\times dx\,dy, \tag{24}$$

where x_s, y_s, z_s locates the source in a coordinate system referenced to the covered wall, and W and H are the dimensions of the covered wall. This integration must be done for each covered wall, and the results summed to give the total fraction of power absorbed on the first reflection.

The power in Eq. (21) is then multiplied by $(1-(\Pi_{\text{absorbed}}/\Pi_{\text{total}}))$ and the resultant power is used in Eq. (20) to predict the reverberant mean-square pressure averaged throughout the volume. The resulting equation is a modification of the Sabine prediction [Eq. (20)], namely:

$$\overline{p^2}_{\text{rev}}=\frac{4\rho c\Pi_{\text{total}}}{A}\cdot\left(1-\frac{\Pi_{\text{absorbed}}}{\Pi_{\text{total}}}\right). \tag{25}$$

This expression only accounts for the energy absorbed by the first reflection, but improves the agreement considerably. Equation (25) will be referred to as the ''modified Sabine equation.''

As an example, data for source locations 1, 3 and 6 in Room 2 are presented in Fig. 6. For each level of absorptivity, there will be one prediction based on Eq. (20) (the original Sabine equation) regardless of source position. However, after correcting for the first reflection, there will be three different predicted values for each of the three different source positions in the same room with the same amount and configuration of damping. For simplicity, the data presented are for cases where the same amount of impedance is placed on two sidewalls and the endwall opposite the source (as opposed to different impedance values on each of the walls).

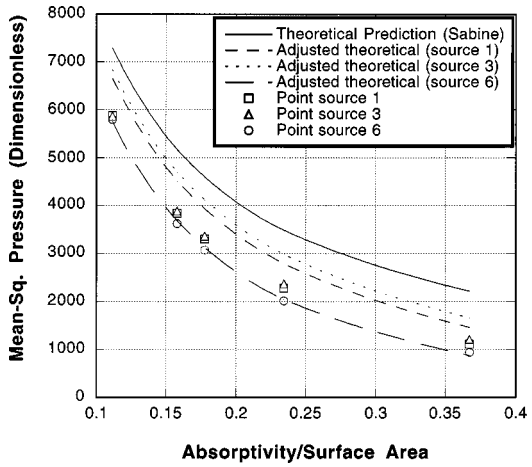

FIG. 6. Dimensionless mean-square pressure for three source locations versus absorptivity level. Theoretical prediction based on original Sabine equation (solid line), three predictions (dashed lines) adjusting the source power to account for losses due to the first reflection (modified Sabine equation), and data from numerical simulations are shown.

In Fig. 6, the predicted values from the modified Sabine equation, the predicted values from the original Sabine equation, and the corresponding values from the computer simulations are shown. Curves are drawn through the predicted values. The numerical data points from the simulations are shown as symbols. Source location 1 is near the center of an end wall, source location 3 is near a hard–hard corner of the enclosure, and source location 6 is near a damped–damped corner. In all cases, the modified Sabine estimate outperforms the original Sabine estimate, although the most substantial improvement occurred for source location 6.

To consider the power absorbed due to subsequent reflections, a similar calculation can be done. Image sources should be included which correspond to each ''hardwall'' reflection. The power absorbed by each impedance wall from each image source should then be calculated. Consideration of subsequent reflections improves the results. However, in most cases reasonable agreement was achieved after removal of the first reflection, and the increased calculation effort required to account for the subsequent reflections could not be justified.

B. Approximate formula for power adjustment

As an alternative to performing the integrals in Eq. (24) over each absorbing surface, an approximation could have been made. However, this approximation does not account for source position. In the approximation, $\overline{\alpha}$ is defined as the effective absorption of the room.

$$\overline{\alpha}\equiv\frac{\alpha_{\text{random}}S_{\text{covered}}}{S_{\text{total}}}. \tag{26}$$

$\overline{\alpha}$ is called ''dimensionless absorptivity'' or equivalently, ''absorptivity/surface area,'' in subsequent plots. The

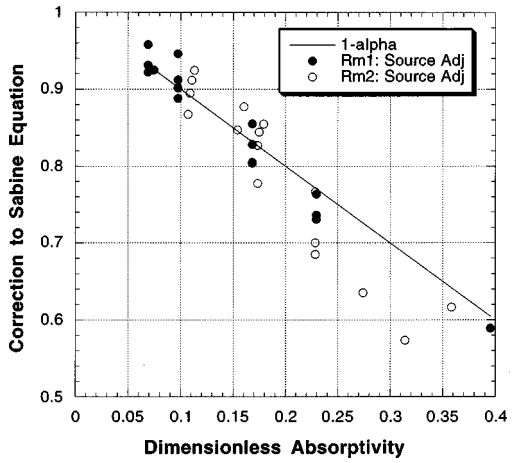

FIG. 7. Comparison between two methods of calculating the fraction of power to be used in the modified Sabine equation, $(1-\Pi_{\text{absorbed}}/\Pi_{\text{total}})$. Circles correspond to calculations for each specific room geometry. The line is an approximate result.

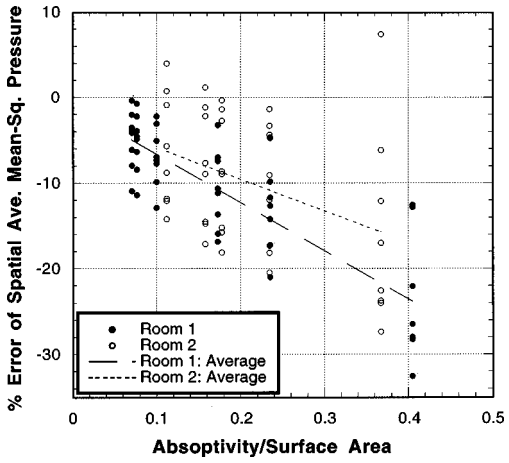

FIG. 8. Sensitivity to source position as shown by the percent error between the modified Sabine equation and the computer simulations for calculating the spatially averaged mean-square pressure of the reverberant field. Results for rooms 1 and 2 are plotted versus the effective absorptivity of the room. Impedances z_b and z_w were equal. Dashed lines correspond to a linear fit through the average error for a given level of effective absorptivity for each room.

amount of power absorbed by incident sound waves directly from the source is approximately equal to

$$\Pi_{\text{absorbed}} \approx \Pi_{\text{total}} \overline{\alpha}. \tag{27}$$

Therefore, an approximate correction factor for the modified Sabine equation could have been

$$1-\frac{\Pi_{\text{absorbed}}}{\Pi_{\text{total}}} \approx 1-\overline{\alpha}, \tag{28}$$

corresponding to an adjusted source power equal to $\Pi_{\text{total}} - \Pi_{\text{absorbed}} \approx \Pi_{\text{total}}(1-\overline{\alpha})$. In Fig. 7, a comparison is shown between the approximate correction factor [Eq. (28)], and the calculated source adjustment, $(1-\Pi_{\text{absorbed}}/\Pi_{\text{total}})$ based on the integrals given in Eq. (24) for both rooms where there are multiple sources on the endwall and z_b (endwall impedance) is not necessarily equal to z_w (sidewall impedance). The cases where $z_b = z_w$ fall closest to the line. Note, for a given absorptivity, several combinations of z_b and z_w values are possible (and are presented). Although this approximation appears to work fairly well, all subsequent results are based on the modified Sabine equation corrected by the source adjustment from integrating the power absorbed over each of the absorbing surfaces (an exact result).

This correction factor is similar to that derived by others, in that it also bears a relationship with absorptivity. In both the Norris and Eyring formula and the Millington–Sette formula for reverberation time there is a factor of $\ln(1-\overline{\alpha_e})$, where $\overline{\alpha_e}$ is the effective random-incidence energy-absorption coefficient.[5]

C. Comparisons between numerical simulations and predicted values

In Figs. 8–10, the percent error between the volume-averaged dimensionless sound pressure levels predicted by the modified Sabine equation and those calculated from the computer simulation are plotted versus the dimensionless absorptivity of the room [English sabins (ft^2)/total surface area (ft^2)]. These errors have been minimized by adjusting the power [using Eq. (24)] to account for losses due to the energy absorbed on the first reflection from an absorbing wall. Without this correction (i.e., the original Sabine equation), predictions were always too high; this correction brought the results into closer agreement as shown by the error plots. For these plots, percent error is given by

$$\%\text{error} = 100 \cdot \frac{\text{calculated}-\text{predicted}}{\text{predicted}}, \tag{29}$$

where ''predicted'' refers to the modified Sabine equation and ''calculated'' refers to the computer simulation results.

The sensitivity to source position is shown in Fig. 8. A single baffled monopole is the sound source, and the damping material has been evenly distributed over two sidewalls and an endwall. For each room, eight different source locations were run, each giving different values for the volume-averaged sound pressure level at a fixed absorptivity. The

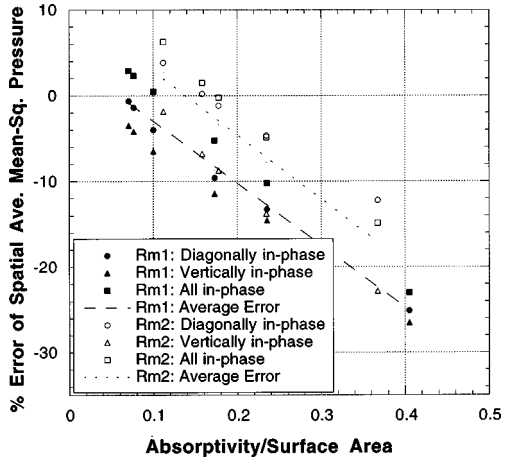

FIG. 9. Sensitivity of relative phasing in the case of multiple sources on the endwall. Percent error in the spatially averaged mean-square pressure of the reverberant field for rooms 1 and 2 are plotted versus the effective absorptivity of the room. Impedances z_b and z_w were equal. Dashed lines correspond to a linear fit through the average error for a given level of effective absorptivity for each room.

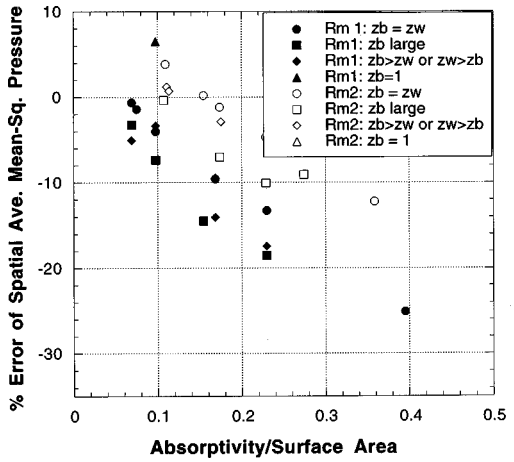

FIG. 10. Sensitivity to damping distribution. Percent error of the spatially averaged mean-square pressure in the reverberant field versus dimensionless absorptivity are shown for rooms 1 and 2 with a fixed source configuration, but with different impedance values on the absorbing walls.

percent error associated with each source position versus dimensionless absorptivity is represented by a circle (solid for room 1, open for room 2). For a particular absorptivity there are eight %error values, one for each source location. A dashed line representing a linear curve fit through the average of the errors at each absorptivity for each room. Two observations can be made: one regarding the average error versus absorptivity level, and the other regarding the spread of the %error around the regression line through the mean values as a function of absorptivity level.

As expected, the average error grows with increasing absorptivity. Comparing the results of the two rooms, for a given absorptivity the overall average error is smaller for the more cubic room. This is an expected result because the more cubic room distributes the energy more evenly. However, the error is more spread out with respect to source position. This is most likely due to the increased surface area of the source wall in the more cubic room (room 2) resulting in larger distances between source positions. In addition, the error appears to have a wider variation with source position as the absorptivity increases (again, more pronounced for room 2). These comparisons are made between the numerical simulation and the Sabine prediction with the *first reflection* removed; at higher absorptivity levels, the removal of subsequent reflections becomes more important.

In Fig. 9, the percent error (calculated as before) is plotted versus dimensionless absorptivity for cases having four sound sources on an endwall. The spatial separation between all sources was several acoustic wavelengths. The relative phasing of the four broadband sound sources was varied, but their positions on the endwall were fixed. The damping configurations were such that the impedance values were equal on the three absorbing walls. Three cases are shown: (1) sources on a diagonal are in-phase with each other and out-of-phase with the diagonally opposing sources; (2) sources vertically in-line are in-phase with each other and out-of-phase with the sources next to them; and (3) all four sources are in-phase.

At each absorptivity level, the predicted level of spatially averaged mean-square pressure (corrected for first reflections) is a constant since the phase information and fixed source positions do not change the modified Sabine equation. However, three different levels are obtained by the numerical simulations for the different source phase relationships. Percent errors were computed based on the differences between the calculated and predicted results [Eq. (29)]. Again, a regression line (dashed) was run through the average of the three errors at each absorptivity value. As expected, the errors grow with increasing absorption due to the failure of the theory to predict the reverberant field in highly damped rooms. When the four sources are in-phase, the highest spatially averaged reverberant mean-square pressures were obtained, whereas when the sources were out-of-phase with the sources beside them (''vertically in-phase'') the lowest spatially averaged reverberant mean-square pressure levels were obtained. This is most likely due to a partial null along the centerline where the sources essentially canceled each other out, causing a reduction in the overall levels.

In Fig. 10, similar error plots are shown for cases where the source phasing was held constant and the damping distribution was varied. The diagonally in-phase configuration was used, since it was closest to the average of the other cases. Of the source configurations studied, it was thought to create the most ideal (diffuse) sound field. The damping configurations were shown in Fig. 4. Different values of endwall impedance (z_b) were used as well as different values of sidewall impedance (z_w) to achieve overall absorptivity levels in the rooms.

Circles (solid for room 1, open for room 2) in Fig. 10 correspond to a damping distribution where $z_b = z_w$, i.e., the same impedance is used on the endwall and the two sidewalls. Since in the previous plot the damping was evenly distributed in this way, these circles are the same as those on the previous plot. Squares represent damping configurations where the endwall impedance is very large, making it essentially a hard wall. In these cases, only the sidewall impedance is used to achieve the desired amount of absorptivity in the room. Cases where the impedance on the endwall is not equal to the impedance on the two sidewalls, and neither the endwall impedance nor the sidewall impedance are large enough to consider them ''hard,'' are represented by a diamond symbol.

A special case was also considered, designated by an triangle, where the endwall impedance was equal to the characteristic impedance of air (ρc). The sidewall impedances could be adjusted to give different values of absorptivity for the room, and these cases gave extremely high errors in the adjusted Sabine equation [Eq. (25)]. Only one of these cases is shown because the other cases have errors so large they are outside the range of the plot. For example, in room 2 an error of 253% at 13 English sabins occurs when (normalized) $\overline{z_b} = 1$ and $\overline{z_w} = 500$, and an error of 71.7% occurs at 14.7 English sabins for a similar case with slightly more absorptive sidewalls ($\overline{z_w} = 100$). In these cases, the presence of a highly absorptive wall (anechoic, at normal incidence) makes the sound field *directional* rather than *diffuse*, since there are relatively few reflections from this wall. This damping configuration causes Sabine's assumption of equal energy in all directions to be violated.

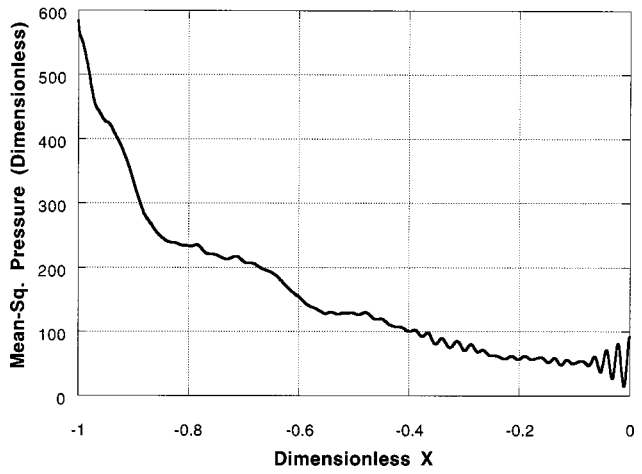

FIG. 11. The spatial variation of mean-square pressure in the lengthwise direction is shown as an average of all trajectories in the x direction for room 1. The source location was 8 and dimensionless impedance of 4.0 distributed on two sidewalls and an endwall.

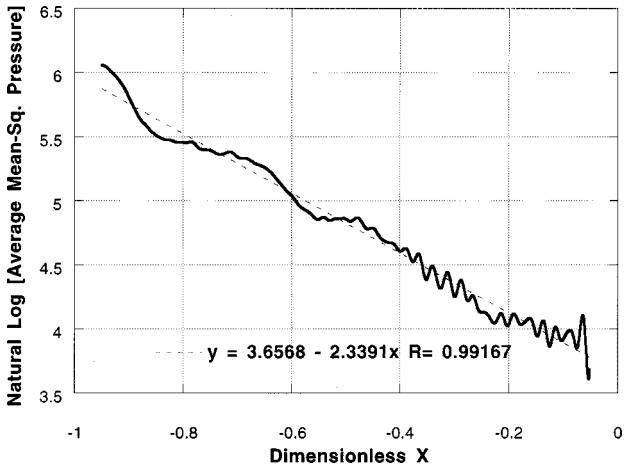

FIG. 12. The natural logarithm of the mean-square pressure in Fig. 11 versus dimensionless distance $\overline{x}$ is shown, along with a linear curve fit through the data. The equation of the line and correlation coefficient (R) are given.

As shown in Fig. 10, the theory predicts the levels more accurately when the impedance is more equally distributed. Other than the special case of an anechoic (at normal incidence) endwall, the largest errors generally occur when the endwall is a hard wall with no absorption (actually a very large real impedance). These errors are more pronounced in the more cubic room because all of the walls contribute equally to the absorption and distribution of sound. In the more rectangular room the *sidwalls* play a more important role in distributing the sound.

V. SPATIAL VARIATION OF THE REVERBERANT FIELD

Plots of sound pressure versus distance have ''fast'' and ''slow'' variations. Over short distances, there are sometimes rapid variations around a mean level, while over larger distances there tends to be a slower change in the mean level. To study the slower changing spatial variation of the sound pressure in a certain direction, cross-sectional averages of the dimensionless mean-square pressure in a one-third octave band centered at 4000 Hz were plotted versus distance away from the source. The cross-sectional averages were taken by averaging the many trajectories in a single direction.

In Fig. 11, a typical spatial variation plot is shown. This plot shows the spatial average at cross sections along the longest dimension of room 1, the elongated rectangular room. There is a single source (at location 8, near a damped/hard corner) on the source wall and impedances are equal on the two sidewalls and the endwall ($\overline{z_b}=\overline{z_w}=4$, corresponding to 32 English sabins). Notice the average reverberant sound pressure levels vary by a factor of 10 from one end of the room to the other. In this case, an error of 27% occurred in the volumetric spatially averaged reverberant pressure predicted by the modified Sabine Theory [Eq. (25), i.e., including the power correction] when compared to that calculated by the computer simulation. This is obviously not a very uniform sound field.

A. Curve-fit analysis

A function of the form

$$\overline{p^2}=Ce^{\mu\overline{x}} \tag{30}$$

was assumed for the spatial variation of the average level in a y-z plane as a function of normalized distance ($\overline{x}=x/L_x$). An exponential curve fit was determined for the data points calculated, or alternatively, the natural logarithm of the spatial average was plotted versus distance and a linear fit was determined which best fit the data. Other curve fits using polynomials of different orders were also tried, but the numerical data had the best correlation using exponential curve-fits.

In Fig. 12, the natural logarithm of the average pressure values (plotted in Fig. 11) is taken and the curve is replotted. A straight line can be fit through these values with a correlation coefficient of 0.992. The slope and intercept of the line are approximately -2.34 and 3.66, respectively. These values are taken from the equation for the line which best fits the data. The slope and intercept of this line have a specific meaning with respect to the spatial variation of the mean-square sound pressure levels in this frequency band.

Taking the natural logarithm of both sides of the assumed form for $\overline{p^2}$ results in the linear equation:

$$\ln(\overline{p^2})=\ln C+\mu\overline{x}. \tag{31}$$

The slope (μ) of this line corresponds to the rate of spatial exponential fall-off of the sound pressure level and the intercept ($\ln C$) is related to both the overall average level and the slope times the distance traversed. It was found empirically that the rate of exponential attenuation, μ, and the amount of absorption *on the sidewalls* of the cavity are linearly related to each other.

One pair of slope and intercept exists for each source location and damping configuration. There are pairs of slope and intercept values for each of the cases which were considered in the study. In Figs. 13 and 14, the slopes (i.e., the exponential decay rate, μ) are plotted versus the absorptivity from the sidewalls only. The intercept values are not plotted

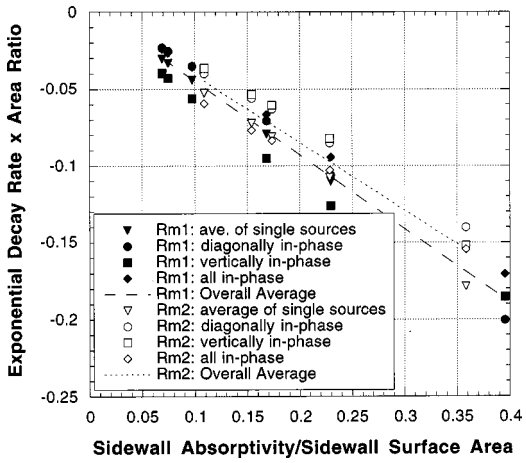

FIG. 13. Effect of source type on the exponential decay rate in rooms 1 and 2. A linear relationship is shown between the quantity: exponential decay rate, μ times the area ratio (cross-sectional area/sidewall surface area) and the effective sidewall absorptivity. The damping distribution is held constant, with impedances z_b and z_w equal.

because no new information is gained from these plots. The overall average sound pressure levels have already been shown to correlate with the total absorptivity, based on the modified Sabine Equation, in previous plots.

Figures 13 and 14 show that there is a *linear relationship* between the amount of absorption on the *sidewalls* of the room and the decay rate, μ, of the reverberant field. When the decay rate is multiplied by the ratio of cross-sectional area to sidewall surface area the results for both rooms collapse nicely onto a single plot. In Fig. 13, the source configurations are varied; both rooms are presented on the same plot. The single source cases have been averaged into a single value at each level of sidewall absorptivity in order to avoid cluttering the plots with many individual data points for each sound source location. A linear relationship between the sidewall absorptivity and the exponential decay rate can be extrapolated from the plots. The line relating μ times the area ratio and the sidewall absorptivity has zero intercept and a slope of approximately $-1/2$.

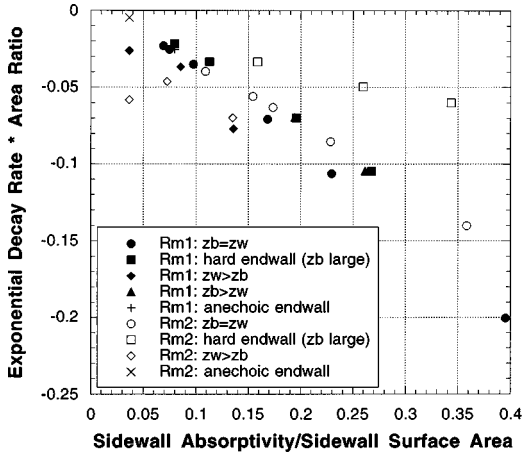

FIG. 14. Effect of damping distribution on the exponential decay rate in rooms 1 and 2. Results are for a single source configuration. An approximate linear relationship is shown between the quantity: exponential decay rate, μ times the area ratio (cross-sectional area/sidewall surface area) and the effective sidewall absorptivity.

In Fig. 14 results of exponential decay rate versus sidewall absorptivity are also shown, but for the cases of different damping configurations. In each of these cases, the sources are the four monopoles whose diagonals are in-phase. For the longer room (room 1), Fig. 14 shows that the values for different damping configurations cluster about a line. However, in the more cubic room, where the lengthwise direction from source to endwall is substantially shorter than in the previous room, the damping distribution makes a bigger difference in the rate of exponential spatial variation, and the plot shows significant ''spread'' in the data.

B. Development of an empirical formula

Assuming that Eq. (30) is an appropriate model for the slow spatial variation of the reverberant mean-square pressure in the lengthwise direction of the enclosure, determination of the constant C and the exponent μ in terms of known quantities leads to a formula for $\overline{p^2}_{\text{rev}}$ as a function of x. The plots of exponential decay rate times the area ratio (cross-sectional area/sidewall surface area) versus dimensionless sidewall absorptivity show an approximately linear relationship between these two quantities. A fairly good approximation for the slope of this line is $-1/2$, in which case, the exponential decay rate can be written as

$$\mu = -\frac{1}{2}\overline{\alpha}_w \frac{S_{\text{sidewall surface}}}{S_{\text{cross-section}}} = -\frac{1}{2}\overline{\alpha}_w \overline{S}, \tag{32}$$

where $\overline{S}$ is the area ratio of the sidewall surface area divided by the cross-sectional area, and $\overline{\alpha}_w$ is the random incidence absorption coefficient associated with the sidewall impedance times the ratio of sidewall surface area covered by the sidewall impedance divided by the total sidewall surface area. In other words,

$$\overline{\alpha}_w = \alpha_{\text{random}} \cdot \frac{S_{\text{covered}}}{S_{\text{sidewall surface}}}. \tag{33}$$

Therefore, $\overline{\alpha}_w$ is an effective wall absorption coefficient (and has been the abscissa for the previous two plots). The constant C can be determined from the volume average of the reverberant mean-square pressure.

The volume average of Eq. (30) is:

$$\langle \overline{p^2}_{\text{rev}} \rangle_{\text{spatial ave}} = \int_{-1}^{0} C e^{\mu \overline{x}} d\overline{x} = \frac{C}{\mu}(1 - e^{-\mu}). \tag{34}$$

From this equation, the constant can be determined from known quantities, assuming the spatial average of the reverberant mean-square pressure is known or can be predicted. It has been shown that when the power has been adjusted to account for that which is absorbed on the first reflection, the spatially averaged reverberant mean-square pressure can be predicted from the modified Sabine formula with some amount of error.

The error (as shown in Figs. 8–10) grows with increasing absorption in an approximately linear manner. Depending upon the variable under consideration, source position, source type/phase, or absorption distribution, the slope of the linear growth in percent error (divided by 100) varies from approximately -0.4 to -0.7 for the cases studied. Choosing

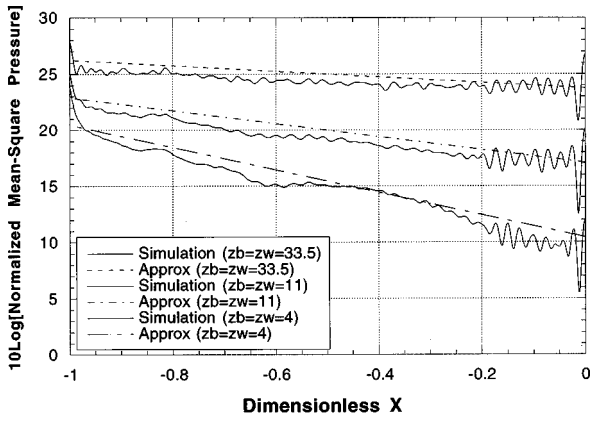

FIG. 15. Room 1, comparison between the numerical simulation and the approximate exponential curve for the spatial variation of the reverberant field in the lengthwise (x) direction. Different curves correspond to different levels of absorption. Also, note intensification at the boundaries.

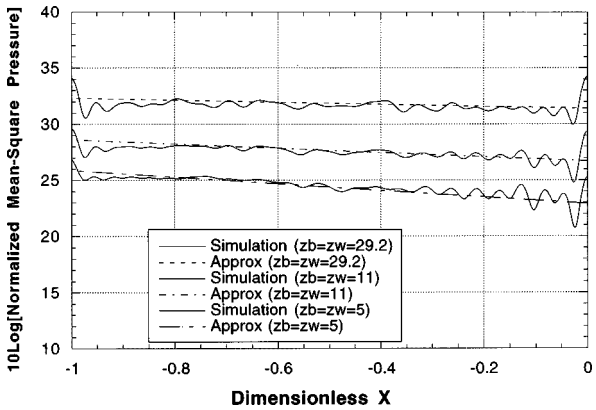

FIG. 16. Room 2, comparison between the numerical simulation and the approximate exponential curve for the spatial variation of the reverberant field in the lengthwise (x) direction. Different curves correspond to different levels of absorption. Also, note intensification at the boundaries.

an intermediate value of -0.5 to represent an average rate of error growth, a correction factor based on the absorption level can be determined. Defining E as the percent error divided by one hundred [from Eq. (29)]:

$$E=\frac{\langle \overline{p}^2_{\text{calculated}}\rangle-\langle \overline{p}^2_{\text{predicted}}\rangle}{\langle \overline{p}^2_{\text{predicted}}\rangle}=-\frac{1}{2}\overline{\alpha}_{\text{total}}, \tag{35}$$

where $\langle \overline{p}^2_{\text{predicted}}\rangle$ is the reverberant mean-square pressure predicted by the modified Sabine equation (corrected for the first reflection's absorbed power). Therefore, a good approximation for $\langle \overline{P}^2_{\text{rev}}\rangle_{\text{spatial ave}}$ would be

$$\langle \overline{p}^2_{\text{rev}}\rangle_{\text{spatial ave}}=\langle \overline{p}^2_{\text{predicted}}\rangle\cdot(1-\tfrac{1}{2}\overline{\alpha}_{\text{total}}). \tag{36}$$

Equation (36) can then be substituted into Eq. (34) to solve for the constant in terms of known quantities, where $\langle \overline{p}^2_{\text{predicted}}\rangle$ is given by Eq. (25). From Eqs. (32), (34), and (36), an approximate expression for the slow spatial variation in the broadband reverberant mean-square pressure as a function of known quantities is

$$\overline{p}^2_{\text{rev}}(\overline{x})=\langle \overline{p}^2_{\text{predicted}}\rangle\cdot\left(1-\frac{1}{2}\overline{\alpha}_{\text{total}}\right)\frac{\tfrac{1}{2}\overline{\alpha}_w\overline{S}}{(e^{(1/2)\overline{\alpha}_w\overline{S}}-1)}\cdot e^{-(1/2)\overline{\alpha}_w\overline{S}\overline{x}}, \tag{37}$$

where $\langle \overline{p}^2_{\text{predicted}}\rangle$ comes from Eq. (25) with Eq. (24) as a correction. Instead, a completely analytical, but more approximate, formula that avoids integrating Eq. (24) to compute the absorbed power can be written as:

$$\overline{p}^2_{\text{rev}}(\overline{x})=\left(\frac{4\rho c\Pi_{\text{total}}}{A}\right)\left[\frac{(1-\overline{\alpha}_{\text{total}})(1-\overline{\alpha}_{\text{total}}/2)}{(1+\overline{\alpha}_w\overline{S}/2)}\right]e^{-(1/2)\overline{\alpha}_w\overline{S}\overline{x}}. \tag{38}$$

This formula uses Eq. (28) rather than Eq. (24), and a three-term Taylor Series expansion for the exponential term in the denominator of Eq. (37). Notice the equation can be grouped into the product of: the original Sabine formula, an absorptivity correction, and an exponential spatial dependence.

In Figs. 15 and 16, plots of the spatial variation for the broadband reverberant mean-square pressure field in the lengthwise direction are shown. The horizontal axis varies from $\overline{x}=-1$ at the source wall to $\overline{x}=0$ at the absorbing endwall. Three sets of curves are shown on each graph, corresponding to different levels of absorption. In these cases, the impedances on the endwall and the absorbing sidewalls were equal. The solid lines correspond to data from the numerical simulations. These are averages of between 8 and 11 parallel trajectories at fixed y, z locations running in the x direction. The dashed lines correspond to the approximate curves based on Eq. (37) (linear due to the logarithmic scale). Note the elevated levels at the boundaries, these will be discussed in the next section. Also, notice that the long rectangular room (room 1) has more spatial variation than room 2.

Overall, the approximate equation does remarkably well compared to an extensive (exact) numerical simulation. The same formula predicts the spatial distribution of the cross-sectional average mean-square pressure in these two very different rooms with errors that are typically 1 dB or less. Further analytical work is underway to more fully develop the predictive formulas presented. Current empirical results are based on the correlations observed in the numerical simulations; specifically, that both the error in the predicted spatially averaged reverberant pressure and the exponential decay rate of the spatial variation scale linearly with absorptivity.

C. Intensification zones

It is well-known that the sound pressure level will have a maximum at a hard wall, edge, or corner of the room due to the spatial correlation at the boundaries. However, on an impedance wall, it is possible to have a local minimum rather than a maximum, particularly for highly absorptive walls. In addition to the special cases of room boundaries, when there is a point source on a wall the sound pressure levels will be elevated along a line in front of the source. In fact, the sound pressure levels will be increased on intersecting planes which pass through the source. These regions of increased sound pressure level, both on boundaries and on interior planes, have been termed ''intensification zones.'' [24]

In the previous figures (Fig. 15 and Fig. 16), the typical intensification zones can be seen at the two ends of each

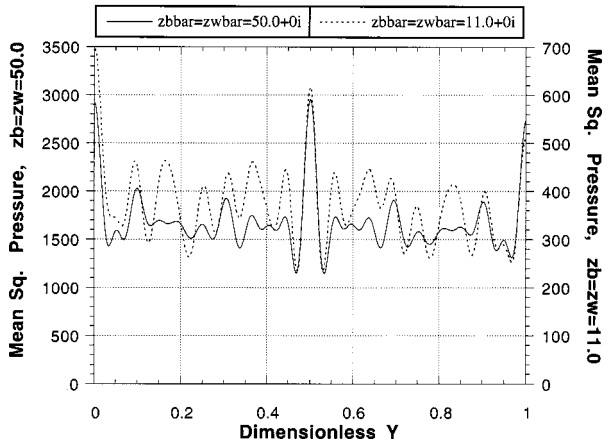

FIG. 17. Average of trajectories in the y direction showing intensification zones at sidewalls and center when the source is in the center. Source location 2 (refer to Fig. 2), room 1. Separate curves for different impedances showing different levels, but intensification present in both cases.

room. While the magnitudes are different, the behaviors are similar. The impedance endwall is at $\overline{x}=0$, and the source is located at dimensionless $\overline{x}=-1$. The peaks at the two endwalls are indicative of intensification zones due to correlation at hard walls, even though the endwalls are absorptive.

Intensification zones corresponding to a source location of a single ''point'' source are shown in Figs. 17 and 18. To demonstrate these intensification zones, trajectories across the cavity are shown. In Fig. 17, the source is in the center of the source wall, and two curves are shown corresponding to different levels of absorption. The intensification peak clearly shows up at the center plane where dimensionless $y=0.5$ for both values of impedance plotted. Adjusting for the different scales in the two cases, it is remarkable how similar the character of the curves appears. These plots are averages of parallel trajectories which were run in the y-direction at various fixed x, z positions. Each of the individual y trajectories that make up one curve on the plot had a substantial peak in the center.

In Fig. 18, the source is at location 4, which is located at a dimensionless $\overline{y}$ coordinate of 0.7 from the $\overline{y}=0$ (hard) wall. There is a peak here due to the correlation of this location with the source position, even though the direct field has been removed. In addition, there is another peak at $\overline{y}=0.3$, which corresponds to a correlation with a reflection off the hard wall. This peak also appears in every trajectory that was run across the room in the y direction, for this source location. These types of intensification phenomena are somewhat surprising, since there is no symmetry involved. It was previously assumed that for this type of reinforcement in a fairly diffuse field, the damping would have to have been symmetrically distributed and/or the source would have needed to have been on a line (plane) of symmetry. However, the intensification effect was detected in most of these numerical simulations (nonsymmetric situations), although it was weaker for more absorptive impedance cases.

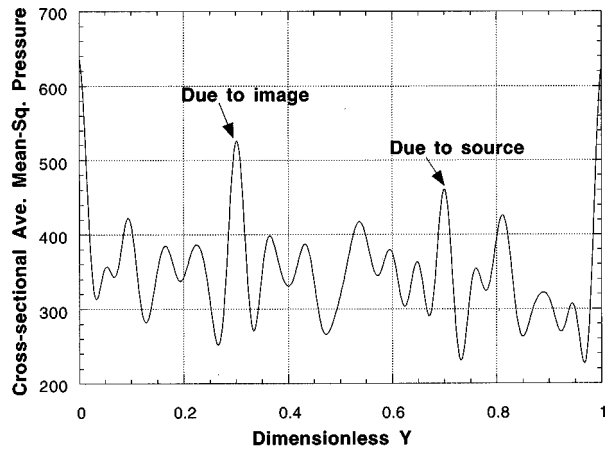

FIG. 18. Intensification due to single source. Source location 4 corresponds to dimensionless $y=0.7$, its image with respect to the hard wall occurs at dimensionless $y=0.3$. The dimensionless impedance is on two walls and the end wall and equals 11.0.

VI. CONCLUDING REMARKS

Numerical simulations of the acoustic sound field in two enclosures were used to study the effects of damping distribution and source location (or phase configuration) on the characteristics of the reverberant field. It was shown that the overall spatial average can be fairly well predicted using classical results based on Sabine's early work. Compared to the numerical results, a better prediction can be obtained when the source strength is diminished by an amount equivalent to that which is absorbed by first reflections from absorbing surfaces, and an approximate formula for this was given. When taken into account, agreement between the predicted spatially averaged sound pressure level, and those which were calculated from the numerical simulations showed the expected trends. Errors in prediction increased as the absorptivity increased, because the sound field became less diffuse.

The Sabine theory (traditional or modified) was better able to predict the spatially averaged sound pressure levels when multiple sources were used to excite the room, than when a single source was used. Multiple sources probably require fewer reflections before the sound field can be described as diffuse. Other than adjusting the power of the source to account for loss due to absorption of the first reflection, the Sabine theory is unable to account for the relative locations of the source and the absorption. This effect is less pronounced when there are multiple sources.

The global spatial variation of the sound pressure levels in the direction from source wall to opposite endwall was best described by an exponentially decaying function. The rate of spatial decay in the lengthwise direction scaled linearly with the sidewall absorptivity. The overall levels scale with total absorptivity, in rough agreement with classical theory. A simple empirical formula for the spatial variation as an exponentially decaying function was shown to agree fairly well with the computer simulations of both rooms, even though the room geometries were very different.

Regions of elevated sound pressure level were observed in the numerical simulations. These regions not only occurred at the boundaries of the room, as expected, but also occurred in the interior of the room in certain cases. These

intensification zones appeared for cases where a single source was present, and were most pronounced for cases with light damping. However, the source did not need to be on a line of symmetry, and the damping did not need to be distributed symmetrically for these intensification zones to occur. Increased sound pressure levels occurred both in front of the source and on a plane which corresponded to a reflection of the source off a hardwall.

ACKNOWLEDGMENT

This work was sponsored by the National Science Foundation under Grant No. CMS-98-96345.

[1] P. M. Morse and R. H. Bolt, ''Sound waves in rooms,'' Rev. Mod. Phys. **16**, 69–150 (1944).
[2] C. F. Eyring, ''Reverberation time in dead rooms,'' J. Acoust. Soc. Am. **1**, 217–241 (1930).
[3] B. M. Gibbs and D. K. Jones, ''A Simple image method for calculating the distribution of sound pressure levels within an enclosure,'' Acustica **27**, 24–32 (1972).
[4] Y. Hirata, ''Geometrical acoustics for rectangular rooms,'' Acustica **43**, 247–252 (1979.)
[5] L. Kinsler *et al.*, *Fundamentals of Acoustics*, 3rd ed. (Wiley, New York, 1950), Chap. 13.
[6] R. B. Lindsay, *Mechanical Radiation* (McGraw-Hill, New York, 1960), Chap. 11.
[7] A. Pierce, *Acoustics: An Introduction to its Physical Principles and Applications* (Acoustical Society of America, New York, 1981), Chap. 6, pp. 250– 312.
[8] K. H. Kuttruff, ''Sound decay in enclosures with nondiffuse sound field,'' Wallace Clement Sabine Centennial Symposium, pages 85–88, 1994.
[9] M. Ohta, H. Iwashige, and K. Nakamura, ''A new trial toward the prediction of a sound field in a incompletely diffused room based on the energy differential equation,'' Acustica **77**, 12–20 (1992).
[10] R. Wentang and K. Attenborough, ''Prediction of sound fields in rooms using statistical energy analysis,'' Appl. Acoust. **34**, 207–220 (1991).
[11] R. H. Bolt, P. E. Doak, and P. J. Westervelt, ''Pulse statistics analysis of room acoustics,'' J. Acoust. Soc. Am. **22**, 328–340 (1950).
[12] A. Krokstad, S. Strom, and S. Sorsdal, ''Calculating the acoustical room response by the use of a ray tracing technique,'' J. Sound Vib. **8**, 118–125 (1968).
[13] M. V. Sergeev, ''Acoustical properties of rectangular rooms of various proportions,'' Sov. Phys. Acoust. **25**, 335–338 (1979).
[14] A. Craggs, ''A finite element method for the free vibration of air in ducts and rooms with absorbing walls,'' J. Vib. Acoust. **173**, 568–576 (1994).
[15] A. Craggs, ''The application of acoustic and absorption finite elements to sound fields in small enclosures,'' *Finite Element Applications in Acoustics* (American Society of Mechanical Engineers, New York, 1981), pp. 1–19.
[16] V. Easwaran and A. Craggs, ''On further validation and use of the finite element method to room acoustics,'' J. Vib. Acoust. **187**, 195–212 (1995).
[17] C. R. Kipp and R. J. Bernhard, ''Prediction of acoustical behavior in cavities using an indirect boundary element method,'' J. Vib. Stress, Reliability in Design, **109**, 22–28 (1987).
[18] K. A. Hussain and K. S. Peat, ''Boundary element analysis of low frequency cavity acoustical problems,'' J. Sound Vib. **168**, 197–209 (1995).
[19] L. P. Franzoni and E. H. Dowell, ''On the accuracy of modal analysis in reverberant acoustical systems with damping,'' J. Acoust. Soc. Am. **97**, 687–690 (1995).
[20] L. F. Peretti and E. H. Dowell, ''Asymptotic modal analysis of a rectangular acoustic cavity excited by wall vibration,'' AIAA J. **30**, 1191–1198 (1992).
[21] Y. Kubota and E. H. Dowell, ''Asymptotic modal analysis for sound fields of a reverberant chamber,'' J. Acoust. Soc. Am. **92**, 1106–1112 (1992).
[22] L. F. Peretti and E. H. Dowell, ''Experimental verification of the asymptotic modal analysis method as applied to a rectangular acoustic cavity excited by structural vibration,'' J. Vib. Acoust. **114**, 546–554 (1992).
[23] J. C. Hardin, ''Introduction to Time Series Analysis,'' NASA Reference Publication 1145. Virginia: Langley Research Center, pp. 31–49, 1986.
[24] L. F. Peretti and E. H. Dowell, ''Study of intensification zones in a rectangular acoustic cavity,'' AIAA J. **30**, 1199–1206 (1992).

Ascertaining confidence within the ray-tracing method

Javier Giner[a)]
Department of Financial Economy and Accounting, University of La Laguna, 38071—La Laguna, Tenerife, Spain

Carmelo Militello
Department of Fundamental and Experimental Physics, University of La Laguna, 38071—La Laguna, Tenerife, Spain

Amando García
Department of Applied Physics, University of Valencia, 46100—Burjassot, Valencia, Spain

(Received 22 July 1998; revised 30 March 1999; accepted 14 April 1999)

The Monte Carlo method is applied to the ray-tracing method to obtain an error measure of the sound energy hitting a receptor during a time interval. Simple geometrical interpretations are introduced to guide the equation development. The variance measurement method introduced a few years ago as an error indicator for the ray-tracing technique is analyzed and compared with the new method. It is shown that the previous method cannot be considered either an error measure or an error estimator, and that the new one provides a consistent answer to many simulation problems. The effects of wall absorption, reverberation time, elapsed time, and integration interval in both formulas are evaluated. © *1999 Acoustical Society of America.* [S0001-4966(99)06007-5]

PACS numbers: 43.55.Ka, 43.55.Br [JDQ]

INTRODUCTION

This paper addresses the problem of error estimation within the pure ray-tracing technique, i.e., a pure ray tracing using a receptor volume to find the reflections of the room. Nowadays, most room acoustic models use a hybrid algorithm, which combines image-source calculations with some kind of ray tracing. When extrapolating the results of this paper to the ray-tracing part of those models, the reader must be certain that the technique used matches the one presented here.

In using a ray-tracing program to simulate the acoustic behavior of a room, the first decision refers to the number of rays to be considered. This number ranges from about 50 000 to millions, depending on the author of the computer program, the shape of the room, the number and size of receptors, and the absorption distribution, among other factors. The change in the computed parameters when the number of rays is duplicated can be used as a guideline. If they do not change, it can be assumed (sometimes wrongly) that the method converges. However, to duplicate a big number is not a straightforward operation from the computer point of view.

In order to discuss this subject, the following points should be mentioned:

(1) The ray tracing technique is valid under the hypothesis of geometrical acoustics.
(2) Convergence produced by increasing the number of rays used in the calculations should not be confused with convergence to the solution of the differential equation that governs sound propagation. The ray-tracing technique is very different from the finite-element method, where a better solution of the original differential equation is obtained on reducing the mesh size and increasing the number of unknown variables.
(3) For rays selected as unbiased samples of all the possible rays departing from the sound source, convergence gives an account of how different the results will be computed with different samples of the same size.
(4) If in a given experiment the confidence of our results can be evaluated as a function of the number of rays used, an estimation of the number of rays needed to reduce the uncertainty to reasonable limits can be carried out.

Points (1) and (2) are a warning to inexperienced pure ray-tracing code users. Points (3) and (4) can be handled by applying the rules of the Monte Carlo method to the ray-tracing technique.

The first application of the Monte Carlo method in acoustics was developed by Allred and Newhouse[1] to compute the mean free path of rays inside a room. Schroeder[2] later used this method to compute reverberation time in room acoustics. None of them addressed the error problem. Haviland and Thanedar[3] applied the method to the impulse response of a room, including an error estimation. As the results of a Monte Carlo experiment are statistical variables, we need to compute their average and standard deviation to define them. If the experiment is repeated M times with a number of rays each time, we can compute the average and the standard deviation. Juricic and Santon[4] also applied this technique. Many authors have studied the use of a large amount of rays to get more reliable results (Santon,[5] Vorländer,[6] Naylor[7]). Nevertheless, to obtain a general formula for the number of rays needed for a given room does not seem a simple task.

This paper is mainly focused on the work of Kullowsky.[8] His work has been referenced by many authors,

a)Electronic mail: jginer@ull.es

such as Naylor[8] and Maercke.[9] Kullowsky proposed the use of the variance as an error indicator of the error, in order to compute the energy arriving to a receptor in a given time interval. Although not explicitly named as an error measure in the above-mentioned paper, this error measure does not depend on the total number of rays involved in the analysis, but on the number of rays that hits the receptor during the time considered and its variance. Consequently, operating in this way, the number of rays needed cannot be predicted. In the next section, it is shown that the Kullowsky error indicator fails in predicting the discretization error in the most simple problems.

I. THE VARIANCE FROM KULLOWSKY

Kullowsky proposed the following expression as an error indicator:

$$s^2_{k(\text{Kullowsky})}=\frac{N_k^2}{N_k-1}\left[\sum_{i=1}^{N_k}(e_{i,k})^2-\frac{1}{N_k}\left(\sum_{i=1}^{N_k}e_{i,k}\right)^2\right], \quad (1)$$

where $e_{i,k}$ is the energy contained in the ith ray that hits the receptor during time interval k, and N_k is the number of rays that hits the receptor during time interval k.

Kullowsky takes the variance of the energy arriving to a given receptor and multiplies it by N_k^2.

In the Monte Carlo method, the variance of the rays that finally hit the receptor is not important, but the variance of all the rays departing from the source looking for the receptor is. The sum has N terms instead of the N_k considered by Kullowsky. Although the remaining rays do not contribute to sound power, they do contribute to the variance value.

Equation (1) fails as an error indicator because it converges to a fixed value, the variance of the energy reaching the receptor. The computed value will not diminish as we increase the number of rays used in the analysis.

II. CALCULATION OF AN ERROR ESTIMATOR BASED ON THE MONTE CARLO METHOD. GEOMETRICAL INTERPRETATION

Let us assume that a clean sphere has a number of stain spots over it with different sizes and shapes. The unknown solid angle subtended by these spots is Ω_k. The objective is to compute the fraction F_k of this solid angle to the total angle 4π. The values of this fraction can be approximated by using the Monte Carlo method (Kalos and Whitlock[10]). A methodology that allows to distinguish among clean and stained points over the sphere surface must be available.

The exact value of F_k is obtained from the following integral:

$$F_k=\int_\Omega g f\, d\Omega, \quad (2)$$

where g is defined as:

$$g=\begin{cases}1 & \text{over the stained surface,} \quad \Omega_k,\\ 0 & \text{over the clean surface,} \quad (\Omega-\Omega_k),\end{cases} \quad (3)$$

and f is uniform probability density function that normalizes the integral to 1

$$f=\frac{1}{4\pi} \quad \text{in } \Omega, \quad \text{and satisfies } \int_\Omega f\, d\Omega=1. \quad (4)$$

With these definitions, the integral (2) results in

$$F_k=\frac{1}{4\pi}\int_{\Omega_k}d\Omega=\frac{\Omega_k}{4\pi}, \quad (5)$$

which is the fraction value we wanted to compute.

The Monte Carlo method establishes that an approximation to (5) can be computed by sampling g uniformly. The samples can be envisioned as rays diverging from the center of the sphere, hitting the surface, and getting their corresponding value. The mean of all the computed values g_i is an approximation, F_k', to the desired integral

$$F_k'=\frac{1}{N}\sum_{i=1}^{N}g_i \quad \text{or} \quad F_k'=\frac{N_k}{N}, \quad (6)$$

where N is the total number of samples and N_k is the number of samples that hits the stained spots ($g_i=1$)

In our case, the variance of the samples is

$$s^2=\frac{1}{N}\sum_{i=1}^{N}g_i^2-\left(\frac{1}{N}\sum_{i=1}^{N}g_i\right)^2 \quad \text{or} \quad s^2=\frac{N_k}{N}-\left(\frac{N_k}{N}\right)^2. \quad (7)$$

The approximation F_k' is a statistical variable. For different experiments, each made of N unbiased samples, different and independent values of F_k' will be obtained. They have an average value $\langle F_k'\rangle$. In the limit, for large enough N, the average value $\langle F_k'\rangle$ approaches the exact value of the integral

$$\lim_{N\to\infty}\langle F_k'\rangle=F_k. \quad (8)$$

The variance of the values F_k' is

$$\text{Var}[F_k']=\frac{\sigma^2}{N}, \quad (9)$$

where σ is the standard deviation of g, as a measure of the variations of the function. Fortunately, for large values of N, it can be approximated by the variance of the samples in one experiment, s^2. Then,

$$\text{Var}[F_k']=\frac{\sigma^2}{N}\approx\frac{s^2}{N}. \quad (10)$$

It must be emphasized that although the value of s^2 converges to a value, the variance of F_k' goes to zero as $1/N$.

The Monte Carlo method tell us that the error in computing F_k' is proportional to the standard deviation. Then, the value of the integral and an error estimation can be obtained as

$$F_k=F_k'\pm\sqrt{\text{Var}[F_k']}\approx F_k'\pm\frac{s}{\sqrt{N}}, \quad (11)$$

where s is computed from (7).

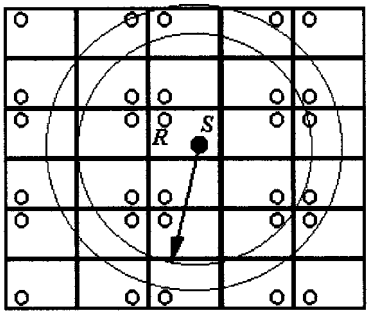

FIG. 1. Images of a receptor in a rectangular room.

III. COMPUTING THE SOUND ENERGY THAT REACHES A RECEPTOR DURING A TIME INTERVAL

As shown by Fig. 1, the sound intensity that reaches a given receptor during a time interval can be computed as the sum of the contributions of a central source to each receptor image, Fig. 1. During the time interval running from t_i to t_i+dt, only the images inside the spherical layer of thickness cdt will be reached by the source.

Figure 2 shows a spherical receptor of radius R, an omnidirectional point source, and three completely reflective walls. At time t_i the sound ray S_1 reaches the center of the receptor after two reflections at $\mathbf{p_1}$ and $\mathbf{p_2}$. At time t_i+dt another sound ray, S_2, hits the center after one reflection at $\mathbf{p_3}$. Taking into account the reflections, the rays can be rectified to obtain the diagram shown in Fig. 3. Then, on departing from the source, the ray is looking for an image of the receptor (compare with Sec. II where the ray was looking for a stain spot over the sphere). For small enough dt it is assured that a ray will hit a receptor image only once. Notice that, as time passes, the solid angle subtended by a receptor reduces proportionally to $1/t^2$. Fortunately, the number of images increases proportionally to t^2. Then, the probability for a sound ray to hit a receptor image during a time interval is constant with time because the solid angle subtended by the receptor images remains constant. This contradicts the assertion that, with time, the initial number of rays becomes insufficient to find all the images. Actually, once we reach the statistical time, the probability remains constant. This point will be further explored in Sec. VI.

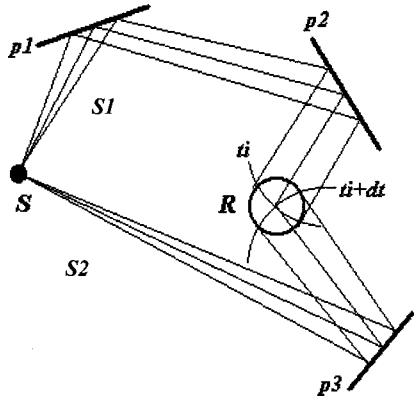

FIG. 2. Two sound rays, S_1 and S_2, with different paths, hitting the same receptor.

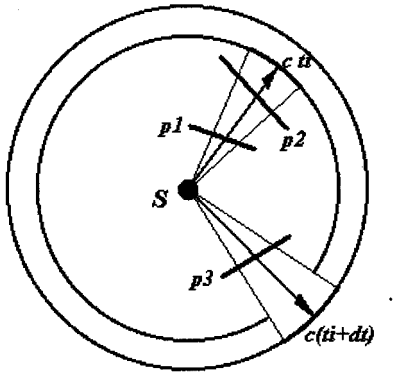

FIG. 3. Figure 2 represented in the receptor images space.

A. Totally reflective walls

In the case that the absorption coefficient of the walls is equal to zero, the computation of the sound power that reaches the receptor during a time interval is equivalent to the evaluation of the ratio of the solid angle subtended by the image receptors to 4π.

The solid angle subtended by each one of the n_r receptor images is Ω_s, where $s=1,...,n_r$. Notice that they do not have to be equal and that their sum is Ω_k. The fraction power P_k that reaches the receptor during the k time interval can be calculated as follows:

$$P_k=\int_\Omega g f\, d\Omega, \tag{12}$$

where, P_0 being the power of source,

$$g=\begin{cases} P_0 \text{ in } \Omega_k \\ 0 \text{ in } (\Omega-\Omega_k) \end{cases} \quad \text{and } f=1/(4\pi) \text{ in } \Omega. \tag{13}$$

The integral (12) becomes

$$P_k=\frac{P_0}{4\pi}\int_{\Omega_k} d\Omega = P_0\frac{\Omega_k}{4\pi}. \tag{14}$$

By using the Monte Carlo method, the integral (14) can be approximated by

$$P_k'=\frac{1}{N}\sum_{i=1}^{N} g_i = P_0\sum_{s=1}^{n_r}\frac{N_s}{N}=P_0\frac{N_k}{N}, \tag{15}$$

where n_r is the number of different images found by the method, N_s is the number of rays that hit the sth image ($s=1,...,n_r$), N_k is the total number of rays that hits the images of the receptor during time interval $k(N_k=\Sigma N_s)$, and N is the total number of rays released from the source.

Consequently, it is concluded that the sound power that reaches a receptor can be computed with the same methodology used in the previous section to evaluate the solid angle subtended by the stain spots. The only difference is that the corresponding integral has to be weighted by the source power.

B. Absorption in the walls

In this case, each image is seen from the source through the images of the walls. The wall images become a filter for the sound rays (Fig. 2). Now, each ray has to be weighted with the reduced power resulting from each wall reflection. After the first reflection the source is no longer isotropic. The anisotropy of the source is constantly changing with each reflection. The fraction of power that reaches a receptor image s is

$$P_s = P_0 \rho_s \frac{\Omega_s}{\Omega}, \tag{16}$$

for $s=1,...,n_r$, where Ω_s is the solid angle subtended by the receptor image and $\Omega = 4\pi$. The reflection coefficient ρ_s is a number smaller than 1. It becomes smaller after each reflection. The values of g and f are defined by

$$g = \begin{cases} P_0 \rho_s & \text{in } \Omega_s \\ 0 & \text{in } (\Omega - \Omega_s) \end{cases} \quad \text{and} \quad f = 1/(4\pi) \text{ in } \Omega. \tag{17}$$

Then, the integral (12) becomes

$$P_k = \int_\Omega g f \, d\Omega = \frac{1}{4\pi} \int_{\Omega_1,...,\Omega_s,...,\Omega_{n_r}} P_0 \rho_s \, d\Omega$$

$$= P_0 \sum_{s=1}^{n_r} \frac{\Omega_s}{4\pi} \rho_s. \tag{18}$$

To complete the calculations, it is assumed that ρ_s is constant within a receptor image. If this is not the case, the terms of the sum will range from 1 to the number of image sectors where ρ_s is constant. To compute each term of the sum (i.e., the ratio of the solid angle subtended by a receptor image to the total solid angle), the results obtained in Sec. (III A) are used. In this way, an approximation to (18) by the Monte Carlo method is

$$P'_k = \frac{1}{N} \sum_{i=1}^{N} g_i = P_0 \sum_{s=1}^{n_r} \frac{\rho_s N_s}{N}. \tag{19}$$

If instead of classifying the rays by the receptor image they hit, it is done by the power p_i they carry on,

$$p_i = \frac{P_0}{N} \rho_i, \tag{20}$$

Eq. (19) can be written

$$P'_k = \sum_{i=1}^{N_k} p_i = \sum_{i=1}^{N_k} \frac{P_0}{N} \rho_i. \tag{21}$$

Once the approximation to the desired integral is computed, by a reasoning parallel to that used in Sec. II, the variance is obtained

$$s_k^2 = \frac{1}{N} \sum_{i=1}^{N_k} (P_0 \rho_i)^2 - \left(\frac{1}{N} \sum_{i=1}^{N_k} P_0 \rho_i \right)^2. \tag{22}$$

This expression can be used to ascertain the error in computing the sound power that reaches a receptor during a given interval time.

C. Power, energy, and intensity

In the previous analysis, it was assumed that the source emitted a pulse of power P_0 during a time dt. This elapsed time must be smaller than the time increment considered for the interval time k. The energy associated to each ray hitting the receptor image is

$$e_i = \frac{P_0 \, dt}{N} \rho_i. \tag{23}$$

Assuming that A is the receptor characteristic area, the sound intensity is

$$I_k^i = \frac{e_i}{A} = \frac{1}{A} \frac{P_0 \, dt}{N} \rho_i. \tag{24}$$

Hence, a sound ray's power, energy, and intensity during a time interval are related by a multiplicative constant. Therefore, the equations obtained in Secs. II, III A, and III B do not need to be reworked.

IV. ABSOLUTE AND RELATIVE ERROR

The previous analysis must be applied to each interval k of the impulse response. The computed intensity during the interval will have a value I'_k and a standard deviation r'_k. The theoretical value can be approximated by

$$I_k = I'_k \pm r'_k, \tag{25}$$

where

$$r'_k = \sqrt{\frac{s_k^2}{N}}. \tag{26}$$

The Pearson relative variation coefficient[10] is

$$m'_k = \frac{r'_k}{I'_k}, \tag{27}$$

which can be considered the statistical relative error.

V. DIFFERENCES BETWEEN BOTH FORMULAS

For the sake of comparison, both variances are rewritten, the one proposed by Kullowsky, Eq. (1), and the one obtained in the previous section, Eq. (22). In the equations, it is assumed that the total number of rays N and the number of rays that reach the receptor N_k are big enough so that $N \cong N-1$ and $N_k \cong N_k - 1$.

$$s_{k(\text{Kullowsky})}^2 = N_k^2 \left[\frac{1}{N_k} \sum_{i=1}^{N_k} (p_{i,k})^2 - \left(\frac{1}{N_k} \sum_{i=1}^{N_k} p_{i,k} \right)^2 \right], \tag{28}$$

$$s_k^2 = \frac{1}{N} \sum_{i=1}^{N_k} (p_{i,k})^2 - \left(\frac{1}{N} \sum_{i=1}^{N_k} p_{i,k} \right)^2. \tag{29}$$

The structure of both equations is the same but, in (29), N appears instead of N_k. Of course, they measure different things. For Kullowsky, the error measure is related to how different the power contributed by each ray is that reaches the receptor. Thus, for a time interval at the beginning of the response, Eq. (28) will compute less error. More than that, if only a wave front is captured the error will be zero, indepen-

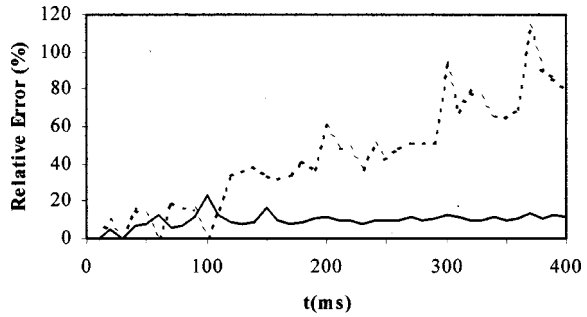

FIG. 4. Relative error for the impulse response of a rectangular room with uniform absorption coefficient, $\alpha=0.273$. Dashed line, Eq. (28) from Kullowsky. Solid line, new Eq. (29). Equation (28) rapidly increases its value as a consequence of the increase in the variance of the energy hitting the receptor. Equation (29) increases more slowly (compare with Fig. 6, where it is represented alone).

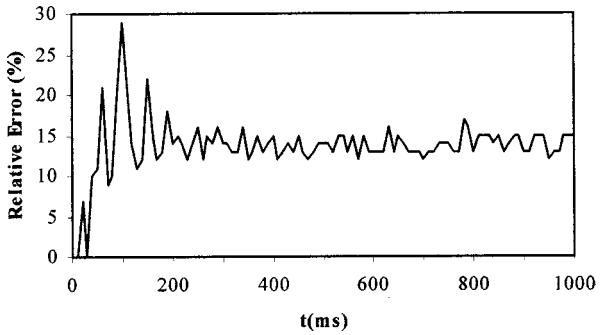

FIG. 5. Relative error with new Eq. (29) for the sound intensity as a function of time in a rectangular room. Perfectly reflecting walls. $N=100.000$ rays. Notice that once the statistical time is reached, the relative error remains constant as predicted in Sec. VI A.

dently of the number of rays used to discretize the front.

This problem can be illustrated by means of a simple numerical example. Suppose that the wave front of an omnidirectional source of 1 W hits a spherical receptor which has a radius of 1 m and its center is placed 10 m from the receptor. The incident power is proportional to the solid angle

$$P_k=\frac{\pi 1^2}{4\pi 10^2}=\frac{1}{400}=0.0025\ \mathrm{W}. \tag{30}$$

Now, 10 000 rays are used to discretize the source. Considering a uniform probability density for the source, the receptor will be impacted by a fraction of rays proportional to the solid angle subtended. Thus, N_k should be around 25 rays. The estimated value for the power, P_k', should be around the value of P_k. The error from (28) will be zero, because all the rays reaching the receptor have the same power. Then, the value of Eq. (28) cannot be considered as an error measure because it does not take into account the quality of the discretization.

Nevertheless, from Eq. (29) we obtain

$$s^2=0.002\,493\,75\ \ \mathrm{W}^2. \tag{31}$$

As the computed variance is required by the Monte Carlo method, the relative error of the approximation can be evaluated as

$$m=\frac{r}{I}=\frac{\sqrt{s^2/N}}{I}=\frac{0.000\,499\,37}{0.0025}\cong 0.20. \tag{32}$$

The resulting relative error is big, 20%, but it seems a logic result. In the example, a few rays, 10 000, are used to sample a sphere of more than 1200 m^2 in order to find an area of 3.14 m^2.

Let us show another example, corresponding to a rectangular room, 30 m long, 20 m wide, and 10 m high ($x\in[0,30]$, $y\in[-10,10]$, $z\in[0,10]$ m). The source has coordinates (4,0,2) m and the receptor (12.5, −2.5, 0) m. The receptor radius is 1 m. A uniform absorption coefficient $\alpha=0.273$ is assumed for the room. In Fig. 4, the error in computing the sound intensity at each interval with formulas (28) and (29), respectively, is shown. The integration time Δt is 10 ms. The number of rays used is $N=100.000$. At the interval running from 20 to 30 ms, both formulas compute zero because there is no energy reaching the receptor. At intervals (50–60) and (90–100), the formula from Kullowsky computes a zero because it is catching rays with the same energy.

VI. THE RELATIVE ERROR AS A FUNCTION OF THE ELAPSED TIME

It is accepted that the error of the ray-tracing technique increases as a function of the elapsed time. In general, Eq. (28) confirms this statement. However, Eq. (28) is a measure of how diffusive (in the sense of nonuniform) the sound field is during the interval of interest. Will the statistical error increase with time? To answer this question, let us analyze two rooms, one with perfectly reflecting walls and the other with a uniform absorbing coefficient.

A. Perfectly reflecting walls

After the statistical time is reached, in a room without absorption in the walls, the sound intensity measured at the receptor must be constant with time. As it was pointed out in Sec. III, the statistical error will be constant because, although the solid angle subtended by a receptor image reduces with time as a function of $1/t^2$, the number of images increases each Δt proportionally to t^2. Following Kuttruff's work[11] the images increment is given by

$$\Delta N_r=4\pi\frac{c^3t^2}{V}\Delta t, \tag{33}$$

where c is the sound speed and V is the room volume. In order to probe this statement, the energy hitting the receptor of the rectangular room during the first 1000 ms with an integration time Δt of 10 ms is evaluated. Figure 5 shows the computed value of m' with new Eq. (29) for each interval. It can be seen that it remains constant. The value of zero is reached when no energy hits the receptor during a time interval. Equation (28) will compute a null relative error, independently of the number of rays used for the analysis.

B. Homogeneous absorption over the walls

Let us consider the same room analyzed in the previous section, but now uniformly covered with a material with absorption coefficient $\alpha=0.273$. The results obtained with Eq. (29) are presented in Fig. 6. It should be observed that the

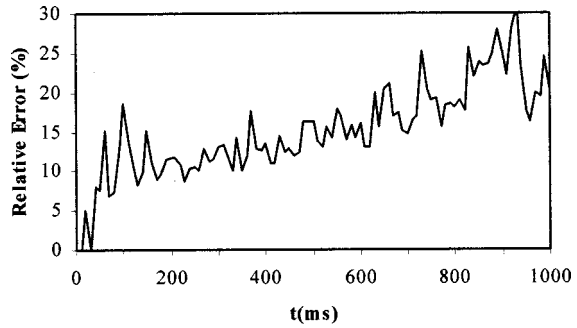

FIG. 6. Relative error for the sound intensity as a function of time in a rectangular room. Homogeneous absorption, $\alpha = 0.273$. $N = 100.000$ rays.

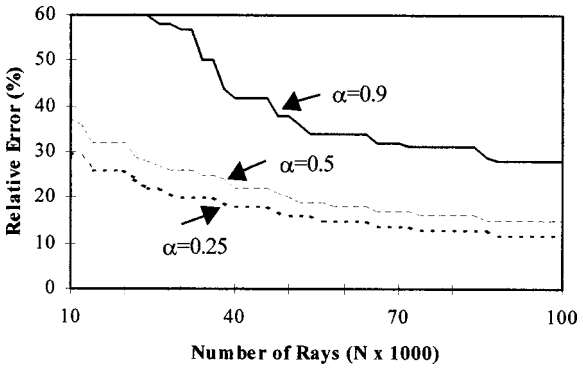

FIG. 7. Relative error computed during the time interval running from 130 to 140 ms, as a function of the absorption coefficient and the ray number used for the analysis.

relative error now increases linearly with time. The increment is due to the fact that the rays with shorter trajectories reduce their energy faster than the others. The energy distribution becomes more irregular with time and we need more rays to sample this irregularity. Equation (28) computes much higher values for the error and is not represented here.

A further case is an ellipsoidal room with uniform absorption. The source is in one focus, the receptor is in the other. Formula (29) will compute a constant error for the interval when the sound energy reaches the receptor, and zero at any other time. The formula of Kullowsky will always compute zero.

VII. THE RELATIVE ERROR AS A FUNCTION OF THE INTEGRATION TIME Δt

It is necessary to define which values of Δt are admissible. For the developments of Sec. III to be valid, the value of Δt should be small enough to ensure that a ray departing in a given direction (Fig. 3) will hit only one receptor image during the interval. Due to this, receptors near a wall or corner can suffer a restriction in their placement. For an integration time of 10 ms, the center of the receptor must be placed at least 2 m from the wall. For admissible time intervals, formula (29) states that the error is lower for large time intervals than for short intervals. When the number of rays that hits the receptor, N_k, increases, the sampling of the changes in the interval is better and the energy average will be more representative, i.e., its value can be easily approximated with different experiments. Therefore, the statistical error is small. If more confidence is necessary for a small Δt, the number of rays used in the analysis must be increased.

Formula (28) establishes that in order to reduce the error, it is necessary to consider smaller time intervals. It stems from the fact that for a small Δt, the energy reaching the receptor will have a lower variance. In the limit, for a very small interval, where an experiment can place only one ray and other experiments none, the maximum confidence is obtained. This result is puzzling, to say the least.

VIII. THE RELATIVE ERROR AS A FUNCTION OF THE ABSORPTION COEFFICIENT

Equations (28) and (29) will compute smaller values for increasing absorption coefficients. This should not lead to the wrong conclusion that rooms with small reverberation time allow us to compute the intensity with a small error. Moreover, it must not be concluded that a smaller number of rays can be used for these cases.

Following Eqs. (22) and (27), the relative error for the sound power reaching a receptor is

$$m(P') = \sqrt{\sum_{i=1}^{N_k} p_i^2 \Big/ \left(\sum_{i=1}^{N_k} p_i \right)^2 - \frac{1}{N}}. \tag{34}$$

If the absorption coefficient increases, the denominator of the first term of the radicand decreases faster than the numerator, increasing the relative error. Of course, this is not the case for a proportional reduction of the power as can be obtained in an elliptical or a cubic room, where all the rays travel the same distance and have almost the same number of reflections. In those particular cases, the ratio remain constant.

Figure 7 shows the results obtained with Eq. (34) as a function of the number of rays used in the analysis, for the same rectangular room described previously, with uniform absorption and three different absorption coefficients. It can be seen that the relative error increases with the absorption coefficient. This can be extended to the reverberation time. Rooms with small reverberation time prompt the use of more rays in order to decrease the relative error.

IX. CONCLUSIONS

In this paper, a simple equation, no more complicated than the existing one, based on the Monte Carlo method, has been developed. It allows us to have an idea of the certainty and repeatability of our results. The formula is consistent and gives a consistent answer for the problems that can be faced within a ray-tracing analysis. Nevertheless, it does not answer the problem of the confidence in computing objective parameters. It can be argued that the error in computing the SPL can be obtained by the addition of the error in computing the sound level during each interval. It is clearly nonsense because by using smaller time intervals, within the same experiment, bigger errors are obtained but the same SPL is always computed. On the other hand, the value of Δt cannot be increased arbitrarily (cf. Sec. VII A). More research is needed in order to develop formulas, within the Monte Carlo method framework, to solve the problem of the confidence in computing the objective parameters.

[1] J. C. Allred and A. Newhouse, ''Application of the Monte Carlo method to architectural acoustics. II,'' J. Acoust. Soc. Am. **30**, 903–904 (1958).
[2] M. R. Schroeder, ''Digital simulation of sound transmission in reverberant spaces,'' J. Acoust. Soc. Am. **47**, 424–431 (1970).
[3] J. K. Haviland and B. D. Thanedar, ''Monte Carlo applications to acoustical field solutions,'' J. Acoust. Soc. Am. **54**, 1442–1448 (1973).
[4] H. Juricic and F. Santon, ''Images et rayons sonores dans le calcul numérique des échogrammes,'' Acustica **28**, 77–89 (1973).
[5] F. Santon, ''Numerical prediction of echograms and of the intelligibility of speech in Rooms,'' J. Acoust. Soc. Am. **59**, 1399–1405 (1976).
[6] M. Vorländer, ''Simulation of the transient and steady-state sound propagation in rooms using a new combined ray-tracing/image-source algorithm,'' J. Acoust. Soc. Am. **86**, 172–188 (1989).
[7] G. M. Naylor, ''ODEON-another hybrid room acoustical model,'' Appl. Acoust. **38**, 131–143 (1993).
[8] A. Kullowsky, ''Error investigation for the ray tracing technique,'' Appl. Acoust. **15**, 263–274 (1982).
[9] D. Van Maercke and J. Martin, ''The prediction of echograms and impulse responses within the Epidaure software,'' Appl. Acoust. **38**, 93–114 (1993).
[10] M. H. Kalos and P. A. Whitlock, *Monte Carlo Methods* (Wiley, New York, 1986).
[11] H. Kuttruff, *Room Acoustics*, 2nd ed. (Applied Science, England, 1979).

Accurate estimation of the mean sound pressure level in enclosures

Albert Schaffner
Austrian Workers Compensation Board (AUVA), Adalbert Stifter Str. 65, 1200 Vienna, Austria

(Received 14 January 1999; accepted for publication 21 April 1999)

The accurate determination of the mean sound pressure level is the basis for the determination of the sound power of a source in enclosures. The relation between the sound power of the source under investigation and the mean sound pressure level to be measured in the room can be derived either by means of wave theory or statistical room acoustics. It is shown that both models yield the same relation in the limiting case of high frequencies. Taking this relation as a starting point, it is first possible to include the modal behavior into the statistical model which is important in order to extend the validity of the statistical model to the low-frequency range. Second, the correction term for the potential energy stored near the room boundaries, which is known as the Waterhouse correction, is improved by taking into account the absorption characteristic of the room walls. The improved relation gives a higher accuracy for the determination of the mean sound pressure level in enclosures especially in the low-frequency range. Experimental data is given to verify the theoretical results. [S0001-4966(99)01508-8]

PACS numbers: 43.58.Fm, 43.55.Br, 43.50.Yw [SLE]

INTRODUCTION

The accurate estimation of the mean sound pressure level is the basis for the determination of the sound power of a source in enclosures. The relation between the sound power of the source under investigation and the mean sound pressure level to be measured in the room can be derived by means of statistical room acoustics assuming a diffuse sound field. This assumption is valid for frequencies beyond the limiting frequency f_1 of the room given by[1]

$$f_1 = 2000\sqrt{T_{60}/V}, \tag{1}$$

where T_{60} is the reverberation time and V is the room volume. In order to extend the validity of the given statistical theory to lower frequencies the effects of the modal behavior have to be considered.

The building up of a diffuse sound field is only possible if a sufficient number of room modes are excited. In rooms with hard walls where the modal density at low frequencies is very poor, it is therefore necessary to broaden the resonances by adequate damping using absorbing material. In order to obtain an accurate estimation of the mean sound pressure level one therefore has to include the absorption characteristic of the room into the correction term representing the modal behavior.

I. SOUND PRESSURE LEVEL DISTRIBUTION IN A RECTANGULAR ROOM

The sound field in an enclosure can be represented by a superposition of standing waves (normal modes) which are set into vibration by a source. Because of the boundary conditions for a room with rigid walls, the allowed normal modes are restricted to wave numbers given by[2]

$$k_{n_x n_y n_z} = \pi\left[\left(\frac{n_x}{L_x}\right)^2 + \left(\frac{n_y}{L_y}\right)^2 + \left(\frac{n_z}{L_z}\right)^2\right]^{1/2}, \tag{2}$$

where the n_i are non-negative integers and the L_i are the linear room dimensions. In the following we will use the abbreviation n for the triple $(n_x n_y n_z)$.

Normal modes for which the propagation is parallel to one of the room edges (i.e., two of the n_i are zero) are referred to as an ''axial mode''. If one of the n_i is zero, the corresponding vibration pattern is called a ''tangential mode'', and if none of the n_i equals zero, we are speaking of an ''oblique mode''. The sound pressure distribution in an enclosure can be calculated by a summation over all normal modes with frequencies $\omega_n = c \cdot k_{n_x n_y n_z}$.

In order to calculate the sound pressure level distribution in a rectangular room we assume a monopole sound source represented by a sphere of average radius r_a which is expanding and contracting so that the radial velocity of its surface is everywhere the same function of time $v_r(t)$. The rate of flow of air away from the surface of the sphere in every direction equals $4\pi r_a^2 v_r(t)$ and is called the source strength $Q(t)$. Assuming a harmonic time dependence $Q(t) = Q_0 \cdot e^{-i\omega t}$, the sound pressure at a position P_1 due to the source mounted at point P_2 in a rectangular room with volume V is given by[3]

$$p(P_1) = \frac{\rho c^2 Q_0}{V} e^{-i\omega t} \sum_n \frac{\varepsilon_{nx}\varepsilon_{ny}\varepsilon_{nz}\Phi_n(P_1)\Phi_n(P_2)}{[2\omega_n/(\tau_n\omega)] + i[(\omega_n^2/\omega) - \omega]}, \tag{3}$$

where $\Phi_n(P_1)$ and $\Phi_n(P_2)$ are the values of the normal modes Φ_n, i.e., the sound pressure at point P_1 and at the source position P_2, $\varepsilon_0 = 1$, $\varepsilon_n = 2$ for $n \neq 0$, ω_n is the frequency of the normal mode and τ_n is a time constant characterizing the damping of Φ_n. According to Morse[3] the mean squared sound pressure averaged over the room and

averaged over a suitable number of source positions may be calculated from Eq. (3):

$$\langle p_{\mathrm{rms}}^2\rangle = \frac{\rho^2 c^4 Q_0^2}{2V^2}\sum_n \frac{1}{[2\omega_n/(\tau_n\omega)]^2+[(\omega_n^2/\omega)-\omega]^2}. \quad (4)$$

The calculation of Eq. (4) is complicated as the number of room modes from zero frequency to an upper limit frequency increases with the third power of the upper limit frequency, each mode having its particular damping constant. For practical purposes one needs an equation which can be evaluated easily. For the limiting case of high frequencies, where only the oblique modes are considered, the time constant τ_n may be regarded equal for all modes

$$\tau_n \approx \tau_0 \quad (5)$$

and can be expressed by[3]

$$\tau_0 = \frac{8V}{cS\alpha}, \quad (6)$$

where α is the mean absorption coefficient of the room boundaries and S is the room surface. The frequency spacing between two normal modes can be neglected and Eq. (4) simplifies to

$$\langle p_{\mathrm{rms}}^2\rangle = \frac{\rho^2 c Q_0^2 \tau_0 \omega^2}{16\pi V} \approx \frac{\rho^2 Q_0^2 \omega^2}{2\pi\alpha S}. \quad (7)$$

Introducing the sound power W in watts radiated by the monopole source,

$$W = \frac{\rho\omega^2 Q_0^2}{8c\pi}, \quad (8)$$

we get

$$\frac{\langle p_{\mathrm{rms}}^2\rangle}{\rho c} = \frac{4W}{\alpha S}, \quad (9)$$

which is the well-known relation between the sound power of the source and the mean-square pressure that is to be measured in a reverberation room. As Eq. (9) can easily be derived by means of statistical room acoustics, wave theory and statistical theory are equivalent at the high-frequency range.

In the following we will take Eq. (9) as a starting point, keeping in mind that we have gained this expression by just taking into account the oblique modes of the sound field. It will be shown that the number of axial and tangential modes at a given frequency can be included in the statistical model by denoting the complete Waterhouse correction which describes the storage of potential energy near the room boundaries in a reverberant sound field. As the Waterhouse correction is derived for rigid boundaries we will be able to further improve our statistical model by thoroughly considering the role of absorption.

II. THE WATERHOUSE CORRECTION

Waterhouse[4] has shown that interference patterns exist at reflecting boundaries in reverberant sound fields. These interference patterns are due to the lack of phase randomness of the plane waves in front of rigid boundaries where the normal component of the sound velocity has to vanish.

According to Waterhouse, the ratio of the mean square pressure in front of a rigid corner $\langle p_r^2\rangle$ to the mean square pressure remote from the corner $\langle p_i^2\rangle$ is given by

$$\frac{\langle p_r^2\rangle}{\langle p_i^2\rangle} = 1 + j_0(2kx) + j_0(2ky) + j_0(2kz) + j_0(2k\rho_1) + j_0(2k\rho_2) + j_0(2k\rho_3) + j_0(2kr),$$

where $j_0(a) = \sin(a)/a$ is the spherical Bessel function, ρ_1, ρ_2, and ρ_3 are the distances from the point (x,y,z) to the edge, and r is the distance from the point to the corner. The first term 1 can be considered due to the incident wave, and the first three Bessel functions represent the interference pattern formed by the incident wave and the image waves due to the walls. The next three Bessel functions represent the interference pattern formed by the incident wave and the image waves due to the edges and the last term is due to the superposition of the incident wave and the image wave of the corner.

In order to obtain the potential energy which is stored in this pattern we have to integrate $\langle p_r^2\rangle$ over the room dimensions according to Appendix A. Collecting the expressions for the mean potential energy stored in the interference patterns at the 6 walls, 12 edges, and 8 corners then results in

$$E_{\mathrm{pattern}} = \frac{\lambda}{8}S + \frac{\lambda^2}{32\pi}L, \quad (10)$$

where S is the room surface $2(L_xL_y + L_xL_z + L_yL_z)$ and L is the sum of the linear dimensions of the room $4(L_x + L_y + L_z)$.

The ratio of the energy in the room to the energy measured in the central portion of the room is therefore

$$W_C = \frac{\lambda S/8 + \lambda^2 L/(32\pi) + abc}{abc} = 1 + \frac{S\lambda}{8V} + \frac{L\lambda^2}{32\pi V}, \quad (11)$$

which is the Waterhouse correction.

It has been pointed out[5] that the Waterhouse correction is identical to a correction factor which is used when the modal density dN/df of a room is described as a function of the room volume V,

$$\frac{dN}{df} = \frac{4\pi f^2}{c^3}V\left(1 + \frac{S\lambda}{8V} + \frac{L\lambda^2}{32\pi V}\right), \quad (12)$$

where f is the frequency and c is the speed of sound. Because at low frequencies the axial and tangential modes are most important, we have to take into account the complete Waterhouse correction for an accurate estimation of the mean sound pressure level in order to represent the modal behavior of the sound field.

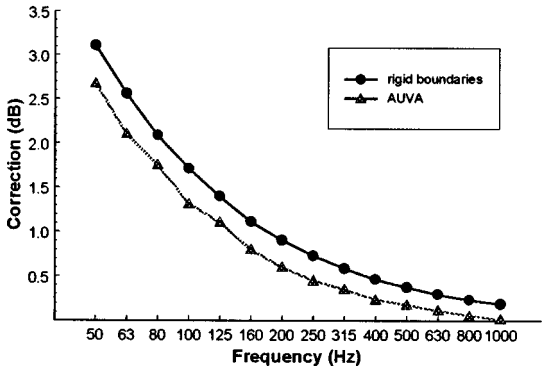

FIG. 1. Comparison of the Waterhouse correction for rigid boundaries and the correction for resilient boundaries.

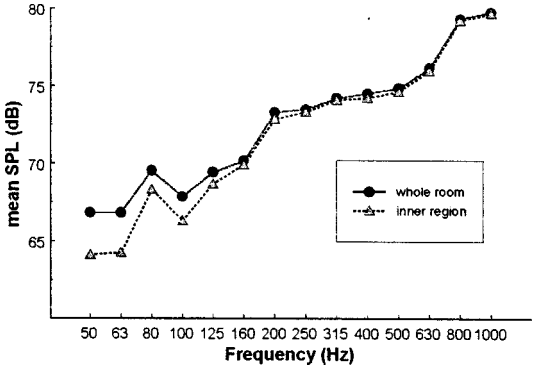

FIG. 2. Mean sound pressure level determined from a sample of the whole room and the inner region of the room.

The correct expression for the mean square sound pressure in a reverberation room follows to be

$$\frac{\langle p_{\mathrm{rms}}^2 \rangle}{\rho c} = \frac{4W}{\alpha S}\left(1 + \frac{S\lambda}{8V} + \frac{L\lambda^2}{32\pi V}\right). \tag{13}$$

III. THE CORRECTION FACTOR FOR RESILIENT BOUNDARIES

Waterhouse has calculated the interference patterns established in a room with rigid boundaries. In real rooms a wave incident on a wall is partly absorbed and partly reflected. The ratio of the amplitude of the reflected wave p_{ref} and the amplitude of the incident wave p_{inc} is given by

$$\frac{p_{\mathrm{ref}}}{p_{\mathrm{inc}}} = \sqrt{1-\alpha}, \tag{14}$$

where α is the mean absorption coefficient determined by reverberation time measurements. If we consequentally consider the interference pattern to be built up by the incident wave and the part of it which is reflected by the wall, we will end up with a correction factor for the energy which depends on α and is lower than the correction for a room with rigid boundaries.

As has been shown in the preceeding, only the interference patterns in front of the walls and the edges give a contribution to the mean room energy. If one follows the derivation of the interference patterns thoroughly by introducing absorption (see derivations in Appendix B), one will find the exact expression for the mean square sound pressure:

$$\begin{aligned}\frac{\langle p_{\mathrm{rms}}^2 \rangle}{\rho c} = \frac{4W}{\alpha S}\cdot\Bigg(&\frac{1}{8}[1+3(1-\alpha)+3(1-\alpha)^2+(1-\alpha)^3] \\ &+ \frac{1}{4}[\sqrt{1-\alpha}+2(1-\alpha)^{3/2}+(1-\alpha)^{5/2}]\cdot\frac{S\lambda}{8V} \\ &+ \frac{1}{2}[(1-\alpha)+(1-\alpha)^2]\frac{L\lambda^2}{32\pi V}\Bigg).\end{aligned} \tag{15}$$

The differences between the Waterhouse correction for rigid boundaries and the correction factor for resilient boundaries [using the data of the reverberation room of the Austrian workers' compensation board (AUVA)] as derived above are illustrated in Fig. 1.

It is evident from Fig. 1 that by disregarding absorption, the error in the correction level is up to 0.5 dB in the low-frequency range. The difference is decreasing for higher frequencies and becomes less than 0.2 dB above 500 Hz.

IV. EXPERIMENTAL CONFIRMATION

In order to confirm the theoretical considerations experimentally accurate measurements of the sound pressure level distribution have been carried out in the reverberation room of the AUVA.[6]

Measurement positions have been defined at a height of 1.5 ± 0.15 m above a grid of 796 measurement points with a distance of 20 cm from one point to the next. A reference sound source Brüel & Kjær type 4204 has been used as noise source, and the measurement time period was 30 s. The time for the field to stabilize before measurement was at least 60 s.

The comparison for the mean sound pressure level of the whole room and the mean sound pressure level of the inner part of the room, which is the region which is at least 1 m apart from any room boundary, are displayed in Fig. 2. The corresponding standard deviations are displayed in Fig. 3.

It is evident that the difference between the mean sound pressure level of the whole room and the inner part of the room increases with decreasing frequency and has its maximum of 2.7 dB at 50 Hz.

The standard deviation increases significantly for frequencies below 100 Hz, which can easily be explained con-

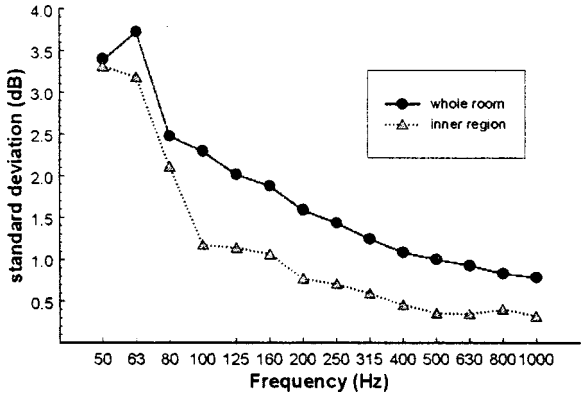

FIG. 3. Standard deviation of a sample of the whole room and the inner region of the room.

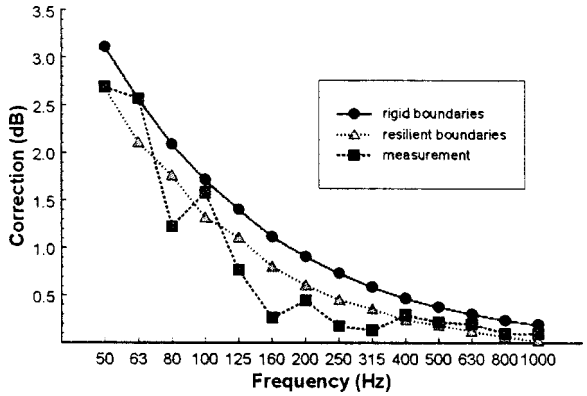

FIG. 4. Experimental verification of the validity of the correction factor for resilient boundaries.

sidering the interference patterns. The deviation of the square of the sound pressure from its value remote from the room boundaries is most significant at the wall and up to a distance of one quarter of the wavelength away from the wall. When we define the inner part of the room as the region at least 1 m from the boundaries this corresponds to a quarter of a wavelength for 85 Hz. Therefore, the sampling procedure is not correct as in the sense of sampling remote from the room boundaries at frequencies below 85 Hz.

The correction for an accurate estimation of the mean sound pressure level of the whole room by measuring the mean sound pressure level in the inner part of the room corresponds to the differences displayed in Fig. 2 and is compared with the Waterhouse correction for a room with rigid boundaries and the correction for resilient boundaries derived in this paper in Fig. 4.

The experimental data shows a very good agreement with the model for resilient boundaries. Using the Waterhouse correction the mean sound pressure level of the whole room at the low frequency range would be overestimated by about 0.4 dB in the average whereas the deviation of the model for resilient boundaries is only about 0.2 dB in the average and is less than 0.1 dB for frequencies above 315 Hz.

V. CONCLUSION

The estimation of the mean sound pressure level in enclosures which is the fundamental quantity to be measured, e.g., in sound power measurements, can be improved by taking into account the interference patterns in front of the room boundaries. The corresponding correction has been derived by Waterhouse and has been established in the relevant standards for the case of rigid walls. The similarity to the expression for the number of room eigenmodes known from wave theory indicates that the complete Waterhouse correction has to be applied for the estimation at low frequencies.

A further improvement has been achieved by extending the model to the real case of resilient boundaries. The validity of this model has been confirmed by accurate measurements of the sound pressure level distribution in a reverberation room.

APPENDIX A: MEAN ENERGY CONTAINED IN INTERFERENCE PATTERNS

The potential energy which is stored in the interference pattern in front of a wall [see Eq. (9)] is given by

$$\int_0^{L_x} j_0(2kx)dx \approx \int_0^{\infty} j_0(2kx)dx = \frac{\lambda}{8}. \tag{A1}$$

The integral in Eq. (A1) is converging, which means that if we measure at a sufficient distance remote from the wall we will be able to avoid the wall pattern.

For the edge pattern we require

$$\begin{aligned}\int_0^{L_x}\int_0^{L_y} j_0(2k\rho')dx\,dy &= \frac{\lambda}{8}\int_0^{\rho}\sin(2k\rho')d\rho' \\ &= -[\lambda^2/(32\pi)]\cdot[\cos(2k\rho')]_0^{\rho} \\ &= -[\lambda^2/(32\pi)]\cdot[\cos(2k\rho)-1],\end{aligned} \tag{A2}$$

where ρ is the distance to the edge.

The integral in Eq. (A2) does not converge. This means that there is a contribution of the edge pattern throughout the whole room. If we are measuring the sound pressure in the room we usually choose several microphone positions which cover a region of several wavelengths.

In order to take into account the edge pattern we therefore have to average the result of the integral given in Eq. (A2) over a number of wavelengths, i.e.,

$$-[\lambda^2/(32\pi)]\frac{1}{\rho}\int_0^{\rho}[\cos(2k\rho')-1]d\rho' = \frac{\lambda^2}{32\pi}, \tag{A3}$$

if the upper integration limit is set to an integer multiple of the wavelength.

The expression for the corner pattern is given by

$$\begin{aligned}\int_0^{L_x}\int_0^{L_y}\int_0^{L_z} j_0(2kr')dx\,dy\,dz &= \frac{\lambda}{8}\int_0^{r} r'\sin(2kr')dr' \\ &= \frac{\lambda^2}{32\pi}\left[\frac{\lambda}{4\pi}\sin\left(\frac{4\pi r'}{\lambda}\right) - r'\cos\left(\frac{4\pi r'}{\lambda}\right)\right]_0^{r},\end{aligned} \tag{A4}$$

where r is the distance to the corner.

Again the integral does not converge. For $r \gg \lambda/4\pi$ we can ignore the sine term and average the remaining expression over a number of wavelengths, i.e.,

$$\begin{aligned}-\frac{1}{r}\int_0^{r}\left[r'\cos\left(\frac{4\pi r'}{\lambda}\right)\right]dr' \\ = -\frac{1}{r}\left[\frac{\lambda}{4\pi}r'\sin\left(\frac{4\pi r'}{\lambda}\right) + \frac{\lambda^2}{16\pi^2}\cos\left(\frac{4\pi r'}{\lambda}\right)\right]_0^{r} = 0.\end{aligned} \tag{A5}$$

When the upper limit of the integration is set to an integer multiple of the wavelength the integral is equal to zero. If we achieve a sufficient space averaging by moving the microphone over a path which extends over a number of wavelengths there will be no contribution of the extra energy contained in the interference pattern due to the corner reflection to the reading of the sound pressure level.

APPENDIX B: DERIVATION OF THE CORRECTION FACTOR FOR RESILIENT BOUNDARIES

The sound pressure in front of a resilient edge is given by the superposition of one incident plane wave and its reflections

$$p = e^{i\omega t}[e^{-i(l+m+n)} + \sqrt{1-\alpha}\cdot(e^{-i(-l+m+n)} + e^{-i(l-m+n)} + e^{-i(l+m-n)}) + (1-\alpha)\cdot(e^{-i(-l-m+n)} + e^{-i(-l+m-n)} + e^{-i(l-m-n)}) + (1-\alpha)^{3/2}\cdot e^{-i(-l-m-n)}], \tag{B1}$$

where $l = kx\cos\theta$, $m = ky\sin\theta\cos\phi$, and $n = kz\sin\theta\sin\phi$ in a polar coordinate system with $r = x\cos\theta + y\sin\theta\cos\phi + z\sin\theta\sin\phi$ being a plane of constant phase whose distance from the origin is r.

The time-averaged mean square pressure $\langle p^2\rangle$ reads

$$\langle p^2\rangle = \tfrac{1}{2}(p\cdot p^*) = \tfrac{1}{2}\cdot[1+3(1-\alpha)+3(1-\alpha)^2+(1-\alpha)^3] + [\sqrt{1-\alpha}+2(1-\alpha)^{3/2}+(1-\alpha)^{5/3}] \cdot[\cos(2l)+\cos(2m)+\cos(2n)] + 2[(1-\alpha)+(1-\alpha)^2] \cdot[\cos(2l)\cos(2m)+\cos(2l)\cos(2n)+\cos(2m)\cos(2n)] + 4(1-\alpha)^{3/2}\cos(2l)\cos(2m)\cos(2n). \tag{B2}$$

In a reverberant sound field the waves are incident from all directions. Space averaging yields

$$\langle p_r^2\rangle = \frac{2}{\pi}\int_0^{\pi/2}\int_0^{\pi/2}\langle p^2\rangle \sin\theta\, d\phi\, d\theta = \tfrac{1}{2}\cdot[1+3(1-\alpha)+3(1-\alpha)^2+(1-\alpha)^3] + [\sqrt{1-\alpha}+2(1-\alpha)^{3/2}+(1-\alpha)^{5/2}][j_0(2kx)+j_0(2ky)+j_0(2kz)] + 2[(1-\alpha)+(1-\alpha)^2][j_0(2k\rho_1)+j_0(2k\rho_2)+j_0(2k\rho_3)] + 4(1-\alpha)^{3/2}j_0(2kr), \tag{B3}$$

where $\rho_1^2 = y^2+z^2$, etc., and $r^2 = x^2+y^2+z^2$.

In order to normalize the mean square sound pressure given in Eq. (B3) to the mean square sound pressure of the incident wave, Eq. (B3) has to be divided by 4 (as the incident wave causes four reflected waves).

The potential energy stored in the interference pattern is calculated following the steps in Appendix A so that

$$\frac{\langle p_r^2\rangle}{4} = \frac{1}{8}\cdot[1+3(1-\alpha)+3(1-\alpha)^2+(1-\alpha)^3] + \tfrac{1}{4}[\sqrt{1-\alpha}+2(1-\alpha)^{3/2}+(1-\alpha)^{5/2}] \cdot\frac{S\lambda}{8V} + \frac{1}{2}[(1-\alpha)+(1-\alpha)^2]\frac{L\lambda^2}{32\pi V} \tag{B4}$$

is the correction factor for the estimation of the mean sound pressure in an enclosure.

[1] M. R. Schroeder and H. Kuttruff, ''On frequency response curves in rooms,'' J. Acoust. Soc. Am. **34**, 76–80 (1962).
[2] H. Kutruff, *Room Acoustics*, 2nd ed. (Applied Science, London, 1979), p. 51.
[3] P. M. Morse, *Vibration and Sound*, 2nd ed. (Acoustical Society of America, New York, 1983), pp. 381–429.
[4] R. V. Waterhouse, ''Interference patterns in reverberant sound fields,'' J. Acoust. Soc. Am. **27**, 247–258 (1955).
[5] S. Uosukainen, ''On The Use of The Waterhouse Correction,'' J. Sound Vib. **186(2)**, 223–230 (1995).
[6] A. Schaffner, ''Measurement of The Sound Pressure Level Distribution in a Reverberation Room—Consequences for Sound Power Measurements,'' Proc. Inter-Noise 97 (1997), pp. 1327–1330.

Coherence estimation for high-frequency narrowband cw pulsed signals in shallow water

Roger W. Meredith
Naval Research Laboratory, Ocean Acoustics Branch, Stennis Space Center, Mississippi 39529-5004

Samuel M. Nagle[a)]
Office of Naval Research, Science and Technology Reserve Det. 822, Naval Reserve Center, Everett, Washington 98207-2900

(Received 22 July 1997; revised 4 February 1999; accepted 3 May 1998)

Signal coherence is an important environmental predictor for sonar performance and is often difficult to estimate. This paper examines different methods for estimating signal coherence from data not amenable to coherence estimation. Methods are compared using narrowband, high-frequency, short pulse length continuous wave signals (cw) that typify those used by mine-hunting sonars in complex shallow-water environments in which the spectral frequency resolution is poor using classical overlapping segments and Fourier techniques. Alternate approaches for the spectral and coherence estimation were the autoregressive parametric based approach, harmonic wavelet approach, and concatenation. These methods provide a statistic similar to coherence that is shown to be useful for specialized data. Low model orders in the parametric method yield results that are difficult to interpret. The wavelet approach is more suited for signals whose frequency spans several wavelet levels. Concatenation via narrowband spectral averaging improves spectral resolution but at the expense of pulse train temporal resolution. Generally, these other methods perform no better than classical Fourier-based techniques; however, they can be useful in a limited sense as a relative measure of the ''spectrum sameness'' between outputs of a single system. © *1999 Acoustical Society of America.* [S0001-4966(99)04508-7]

PACS numbers: 43.60.Gk, 43.30.Re [JCB]

INTRODUCTION

A fundamental requirement in the processing of underwater acoustic signals by sonar arrays is that the signal is coherent across the spatial aperture of the array and over the time duration of the processing. By summing the received responses from a hydrophone array, a sonar system can provide higher signal-to-noise levels than any individual hydrophone. Coherent signals add while incoherent noise cancels and array gain is achieved. Array gain may be degraded when unwanted coherent signals or correlated noises are also present.

In shallow water, high-resolution sonars are often characterized by their small angular beamwidths (<3 deg) and fine range resolution (<1.5 m). In order to achieve such capabilities, high frequencies (>20 kHz) and short pulse lengths (<5 ms) are normally used over relatively short ranges (<1500 m). The shallow-water environment can change significantly over short distances or over small time periods. Storms, tides, currents, and seasonal variations create significant environmental changes in time frames ranging from hourly to seasonally and in spatial frames ranging from a few tens of meters to several miles. Fluctuations in the ocean medium act to decorrelate desired signals, thus reducing array gain. Array gain may be further degraded due to multipath interference and scattering from the boundaries and inhomogeneities in the ocean.

Coherence estimates may be desired from experimental data that are not amenable to coherence determination. In this paper we evaluate different methods for estimating a quantitative measure of signal coherence for high-frequency, short pulse length, narrowband cw pulsed signals in shallow water. These methods may be useful in special circumstances and in a relative fashion to compare environments or signals.

These alternate methods are shown to provide a statistic similar to coherence that can be useful in a limited sense as a relative measure of the ''spectrum sameness'' between outputs of a single system. These methods do not appear to work well in comparing outputs from different systems. Low model orders in the nonlinear parametric method yield results that are not only difficult to interpret but appear to be more susceptible to random phase fluctuations and noise. The wavelet approach is similar to the classical approach; however, simulations suggest that it too is susceptible to errors from random phase fluctuations and noise. The wavelet approach is more suited for signals whose frequency spans several wavelet levels. Concatenation via narrowband spectral averaging improves spectral resolution but at the expense of pulse train temporal resolution. Generally, these other methods perform no better than classical Fourier-based techniques.

I. BACKGROUND

Linear coherence is a statistic that is classically used to measure system linearity, and relates two random processes, one an input process, to an output. It is often used as a

[a)]Current address: Primex Aerospace Company, P.O. Box 97009, Redmond, Washington 98703-9709.

prediction for system input, and for the purposes of this paper is limited to imply a quantitative measure of the common spectral density between two signals. Using the notation from Bendat and Piersol,[1] coherence is defined as follows:

$$\gamma(f)^2_{xy}=\frac{|S_{xy}(f)|^2}{S_{xx}(f)S_{yy}(f)} \quad 0\leqslant\gamma(f)^2_{xy}\leqslant 1, \tag{1}$$

where

$$S_{xx}=\int_{-\infty}^{\infty}R_{xx}(\tau)e^{-j2\pi f\tau}d\tau, \tag{2}$$

$$S_{yy}=\int_{-\infty}^{\infty}R_{yy}(\tau)e^{-j2\pi f\tau}d\tau, \tag{3}$$

are the respective autospectral density functions, and

$$R_{xx}=\frac{1}{T}\int_0^T x(t)x(t+\tau)dt, \tag{4}$$

$$R_{yy}=\frac{1}{T}\int_0^T y(t)y(t+\tau)dt, \tag{5}$$

are the autocorrelation functions. Similarly, the cross spectral density function is given by

$$S_{xy}=\int_{-\infty}^{\infty}R_{xy}(\tau)e^{-j2\pi f\tau}d\tau, \tag{6}$$

where

$$R_{xy}=\frac{1}{T}\int_0^T x(t)y(t+\tau)dt \tag{7}$$

is the cross correlation of the two processes being evaluated.

In an ideal linear system, the coherence will be equal to unity and as the coherence falls below unity, sonar performance will be degraded. Coherence will be less than unity when any one of the following conditions exists:

(1) Extraneous amplitude and phase noise are present in the measurements.
(2) Resolution bias errors are present in the spectral measurements.
(3) The system relating input to output is not linear.
(4) The output is dependent on more that just a single input.

For underwater acoustic signals, conditions 1, 3, and 4 can be affected by the ocean medium, as previously discussed.

This paper examines different methods for estimating signal coherence from data not amenable to strict linear coherence estimation as defined by Eq. (1).

(1) Classical Fourier method,
(2) Autoregressive (Burg method),
(3) Harmonic wavelet,
(4) Concatenation.

These measures are not strict measures of coherence but are a measure of ''spectrum similarity'' in a broad sense that may be useful in a relative fashion for evaluating environmental stability or predicting sonar performance. Two signals are examined using each method,

(1) measured data with high signal-to-noise ratio (SNR)
(2) synthetic data with both linear and random phase fluctuations.

Each method differs in the technique used to evaluate the spectral terms of Eq. (1) that are given by expressions 2, 3, and 6. The first method employs classical spectral estimation based on Fourier transform methodology and is used to develop Eq. (1). Due to the short pulse length and segmentation required for spectral estimation, the spectral frequency bin width was greater than the signal bandwidth. This limitation motivated the search for alternate schemes for the spectral and coherence estimation. The second method employs a parametric model of the received signals (autoregressive model). The third method uses the wavelet transform to extract time-frequency information from each pulse, and develops a statistic akin to coherence from the estimated wavelet transform coefficients. The fourth and last method involves concatenation of successive pulses (by averaging narrowband spectral estimates of individual pulses) to increase the frequency resolution at the expense of the pulse train temporal resolution.

II. MEASUREMENT DATA DESCRIPTION

The measured data used in this study were collected as part of high-frequency acoustic experiments conducted in shallow water in Kiel, Germany. In the experiments, a train of 150 pulses was transmitted at 150 kHz with a pulse length of 1 millisecond, and a repetition rate of one pulse per second. The received signals were modulated so that the center frequency was 5 kHz prior to being low-pass filtered, and quadrature sampled at a 20-kHz rate for post processing.

To evaluate the variations in temporal coherence, a sequence of pulses spanning 150 sec provides a train of input data that can be compared over time as a function of source/receiver spacing. Using the first pulse as a reference, the temporal coherence is then determined by considering each subsequent pulse in the train as an output of a system driven by the reference pulse. Although not done in our study, spatial coherence may also be evaluated using a similar method, where a reference hydrophone may be defined in the receiving array, and the received outputs from other hydrophones within the array can be treated as system outputs.

III. COHERENCE ESTIMATION RESULTS

A. Evaluation of coherence based on Fourier spectral estimates

The key to determining coherence comes in the evaluation of the spectral densities, Eqs. (2), (3), and (6), through periodogram estimation. This is implemented by taking the Fourier transform of the autocorrelations. For discrete data such as these, the power spectrum estimates appear as discrete frequency components separated in frequency by the reciprocal of the record length. Once the auto and cross spectral densities are estimated, coherence is calculated by Eq. (1). The Welch procedure[2] of windowing and averaging was used to obtain estimates of the auto and cross spectral densities. In this procedure, the original data are divided into an

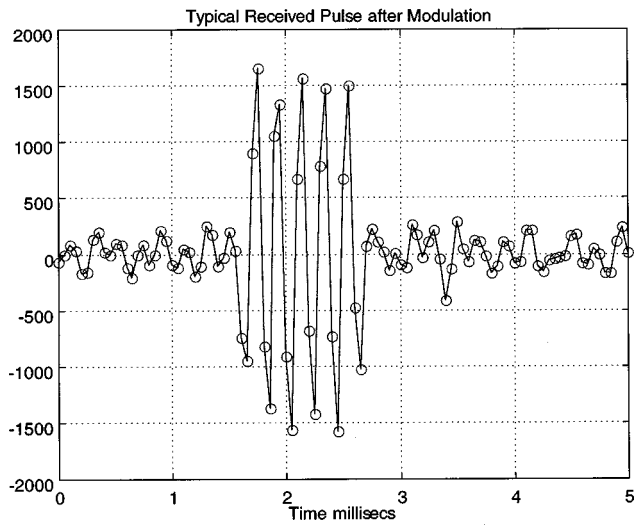

FIG. 1. Typical narrowband, cw pulse signal received at 150 kHz, modulated to 5 kHz, and sampled at 20 kHz.

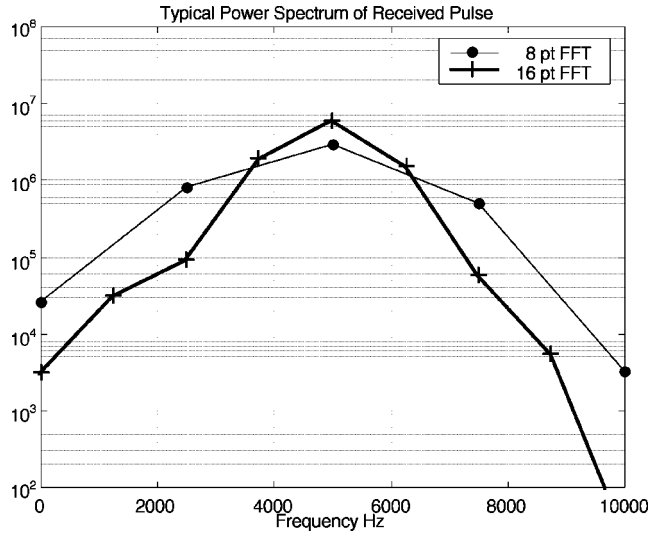

FIG. 2. Power spectral density of received pulsed cw sinusoid using both 8-point and 16-point FFT sizes, 50% overlap, and a Hanning window.

integer number of segments, with 50% overlap between segments. Segmentation and overlapping allow ensemble averaging of spectral estimates, which reduces the variance on each spectral level estimate at the cost of increased computational load due to computing multiple fast Fourier transforms (FFTs). A Hanning window is applied to each segment and the resulting modified periodograms are averaged to obtain an estimate of the power spectral density. This classical method is the baseline coherence estimate used to compare with estimates from the other methods.

To estimate coherence, a trade-off is required between spectral averaging (needed for coherence estimate) and spectral bin width (needed for resolution). To obtain a large number of averages and good resolution, lots of sample points are needed, but high-resolution sonars typically employ short pulse lengths to increase temporal resolution. Thus the number of sample points is small, and they are further reduced in the segmentation process for spectral averaging. If the ocean medium were stationary and ergodic over needed ranges and time scales, then we could ensemble average spectrums over successive pings. This is the basis of concatenation described in Sec. III D, but coherence changes from ping to ping (for example: between pings over the time it might take to form a synthetic aperture) are lost. Since the direct path portion consists of only about 32 points, window lengths of 8 and 16 were used. Such short time windows result in extremely broad spectral bins, but gives us a sufficient number of segments so that a coherence estimate can be achieved by averaging spectrums from a single ping.

Using the above choices for spectral estimation parameters, the autospectral density estimates for the pulse in Fig. 1 are illustrated in Fig. 2, where the results using an 8-point FFT window and a 16-point FFT window are shown. This processing results in spectral frequency bin widths of 2500 and 1250 Hz, respectively. A monochromatic cw is time gated to create each pulse in the data set. For cw signals with a high signal-to-noise ratio (15–20 dB), the spectral level is 3–6 dB higher for the signal frequency bin than for the neighboring bins and can be easily resolved. For lower SNR signals this will not be the case, resulting in larger fluctuations in spectral levels and thus more severe fluctuations in coherence. In addition, active sonar systems are often reverberation limited rather than ambient noise limited, and reverberant returns tend to be more coherent than ambient noise. Accordingly, spectral estimates for short narrowband cw pulses are more difficult to estimate. Spectral frequency bins larger than the original signal bandwidth reduce the signal-to-noise ratio of the coherence estimate. Due to spectral estimation problems, the resulting coherence estimate, as a function of frequency, varies by less than 10% over a large frequency span. SNR is sufficient to resolve the coherence peak, but the relative difference in coherence between the peak frequency and adjacent frequency is less than 3%. By repeatedly calculating the coherence at the signal frequency for each pulse, using pulse number 1 as reference, the temporal coherence over the duration of the data set can be evaluated. Figure 3 illustrates the variability of coherence over the 150-sec run period. Plots are shown for the center frequency bin (at the signal center frequency) and the two adjacent frequency bins. The signal bandwidth is 10 Hz; the spectral bin width is 1250 Hz for the 16-point FFT and 2500 Hz for the 8-point FFT. Notice the high coherence in both adjacent frequency bins where a signal exists due to spectral spreading by the FFT. This indicates a coherent background, and the long-term trends are significantly different for the two adjacent bins.

B. Evaluation of coherence using an autoregressive parametric model

Parametric-model-based power spectral estimators overcome the limitation on spectral resolution bandwidth by extrapolating the signal outside of the analysis window, effectively providing a longer record length for analysis. Several good references are available that provide a detailed description of the underlying mathematics that surrounds these methods,[2–4] only a brief overview is given here.

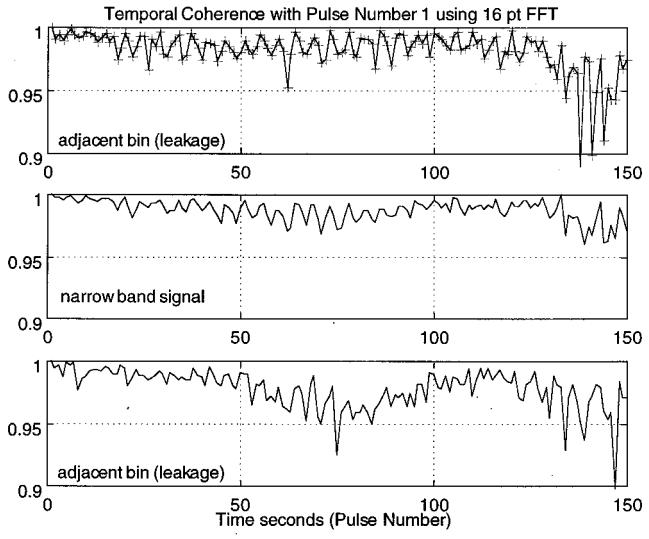

FIG. 3. Coherence as a function of pulse number using pulse 1 as reference. Since the pulse repetition rate is 1 pulse per sec, there is a one-to-one correspondence of pulse number with time in seconds. The center plot is for the signal frequency bin. The + indicates the 1 ping per sec pulse repetition rate.

Parametric methods fall into three subgroups: autoregressive (AR), moving average (MA), and autoregressive moving average (ARMA). Model selection depends on spectral characteristics. Since we are expecting spectral peaks with no sharp nulls we select an all-pole model of order N, which means the system transfer function is modeled by N poles. Using the standard z-transform notation common for sampled data systems, the general system transfer function equation for an AR model is given by

$$H(z)=\frac{1}{a(0)+a(1)z^{-1}+a(2)z^{-2}\ldots a(p)z^{-k}} \quad . \tag{8}$$

We employed the Maximum Entropy Spectral modeling method developed by Burg[5] to derive the polynomial coefficients $a(0)$ through $a(p)$ in the denominator of Eq. (8).

To obtain the autospectral density and the cross spectral density estimates, we first determined the autocorrelation and the cross correlation sequences from the raw data and then used these correlation values as inputs into the Burg algorithm to derive the AR coefficients. The frequency response spectrums for the all-pole models were then used as estimates for the auto and the cross spectrums, respectively.

The power spectrum derived by the AR model is shown in Fig. 4. In this case, a model order of 3 was used, and a data set size of 128 was specified, resulting in spectral bins that are 156.25 Hz wide. Note that the source peak at 5000 Hz is much narrower with respect to the earlier FFT-based spectral estimate, Fig. 2. In general, higher model orders provide more accurate spectral magnitudes. In a paper by Makhoul,[6] it is shown that as the model order is increased, a signal's spectrum can be approximated arbitrarily close by an all-pole model. In our case, we found that using model orders greater than 3 resulted in ill-conditioned covariance matrices. The ill-condition occurrence at such a low model order is most likely due to the large dynamic range of the

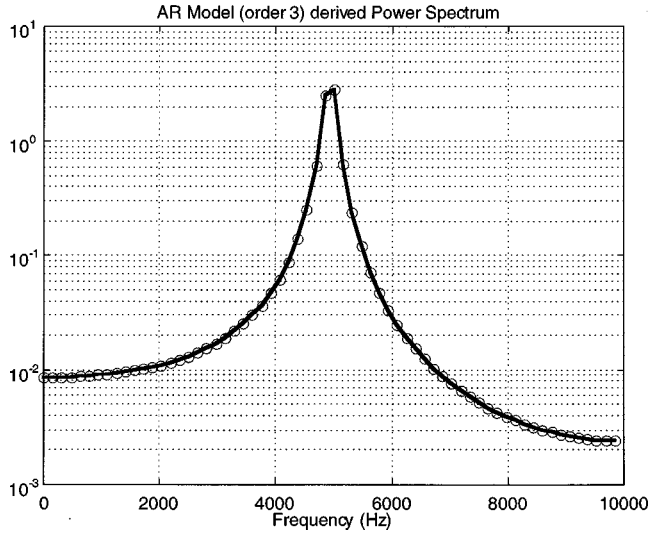

FIG. 4. Power spectral density of received pulse cw sinusoid using AR model for the autocorrelation of the received signal.

signal being modeled, and the limited samples available for generating the correlation matrix necessary to derive the AR coefficients. This limitation results in nonlinearities in the absolute magnitudes of the spectral density estimates used in our calculation of coherence. Thus the coherence formula, Eq. (1), results in values for coherence that may be greater than 1.

This makes interpretation difficult, and accordingly is not a strict measure of linear coherence. However, it is a measure of ''spectrum likeness,'' and it is possible to characterize how this estimate changes as a function of phase, amplitude, and frequency. The signal coherence at 5000 Hz is more clearly resolved than the FFT estimate of coherence, and although not shown, the coherence level in adjacent bins is drastically reduced.

Figure 5 shows the AR estimated temporal coherence for the same 150 pulses computed by the classical method shown in Fig. 3. In order to display the two results on the same plot, the following scaling was applied. The ratio of the variance in the coherence to the y-axis display range is set equal for both methods. Note that both the structure and trends of the AR-based coherence are different than from the classical FFT-based computation. The AR model has sharper

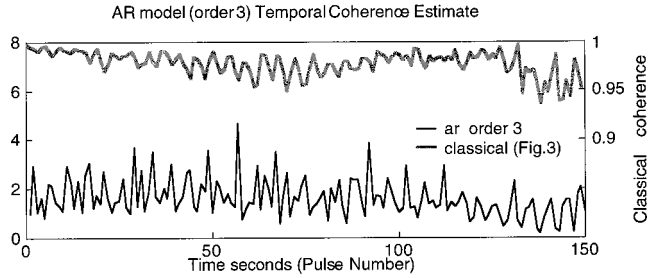

FIG. 5. Coherence estimation as a function of pulse number using pulse 1 as reference and AR spectrum estimation. Pulse repetition rate is 1 pulse per sec. In order to display the two results on the same plot, the ratio of the variance of the coherence to the y-axis display range is set equal for both methods.

and higher amplitude fluctuations as well as a more constant long-term trend.

C. Evaluation of coherence using the discrete wavelet transform

Using wavelet theory as a method for determining coherence is briefly explored. The wavelet transform is similar to the Fourier transform methodology in that it expands a function using a family of basis functions. A signal is decomposed into a set of component parts that when summed together reconstruct the signal. It differs, however, in two aspects from the Fourier transform: (1) the basis functions may be either finite or infinite in length, (2) the basis functions are time shifted as well as time compressed or time dilated versions of a single analyzing base wavelet function. It is not the objective of this paper to describe wavelets in depth. Many references are available[7–10] that provide a good introduction to wavelet theory and its applications in engineering and science.

Using the notation from Newland,[7] the goal of the discrete wavelet transform (DWT) is to decompose an arbitrary signal $f(x)$ into an infinite summation of wavelets at different scales with different coefficients, according to the expansion

$$f(x)=\sum_{j=-\infty}^{\infty}\sum_{k=-\infty}^{\infty} c_{j,k}W(2^j x-k). \tag{9}$$

The analyzing base wavelet is $W(x)$, and $c_{j,k}$ are the transform coefficients. Each of the terms within the double summation of Eq. (9) represents time scaled (either compressed or stretched) and time translated versions of $W(x)$. The index j is an integer commonly referred to as the wavelet ''level'' and can roughly be thought of as being analogous to frequency. With each ascending value of j, the wavelet becomes contracted in time by a factor of 2. The contraction in the time domain results is a doubling of the frequency bandwidth, and thus a constant time-bandwidth product for all wavelet levels is maintained. At a given wavelet level j, $2j$ wavelets are required to span the record length under analysis. The index k in Eq. (9) represents a time translation of a wavelet within the analysis interval for a particular level.

The wavelet basis selected for this analysis is from a family of infinite length wavelet functions that was developed by Newland,[7] and has the characteristic that each wavelet level represents a component from an octave band of frequencies. The wavelets are known as harmonic wavelets, and are defined in the frequency domain by

$$\begin{aligned} W(\omega)&=(1/2\pi)2^{-j}e^{-i\omega k/2^j} \quad \text{for } 2\pi 2j<w<4\pi 2j,\\ &=0 \quad \text{elsewhere,} \end{aligned} \tag{10}$$

where j is the wavelet level. The Fourier transform of the wavelet has constant magnitude within an octave band of frequencies, and 0 outside of this band. The magnitude is set to normalize the enclosed area to unity. When harmonic wavelet decomposition is applied to a set of real sampled data, the coefficients generated are complex conjugate pairs. One means of displaying information from the wavelet transform is to plot the squared wavelet coefficient values, $c_{j,k}$, on a two-dimensional grid base, where one dimension is wavelet level (index j, which is akin to frequency), and the other dimension being wavelet position (index k), a measure of time; in this manner a time-frequency map is formed.

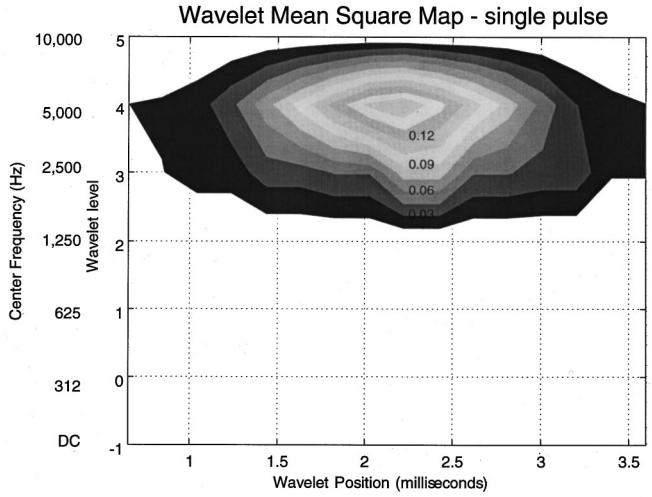

FIG. 6. Contour plot of the resulting wavelet mean-square-energy map displaying wavelet position (time) and wavelet level (frequency) information for the reference pulse, pulse number 1.

The mean-square map for the received acoustic pulse from Fig. 1 is shown in Fig. 6. This map was derived by windowing 64 points around the direct path portion of the signal, resulting in five wavelet levels. Note that the signal energy is concentrated at wavelet level 4: this level corresponds to the octave of frequencies centered about 5 kHz as would be expected, and near the center of the wavelet position. Most of the energy is contained in the single wavelet level. Only the wavelet levels adjacent to this level exhibit spectral spreading, and the lower levels exhibit no energy. The steepness of the contours indicates the high signal-to-noise ratio of the pulse. This is what a very narrowband, noise-free pulse looks like in the wavelet domain.

The harmonic wavelet family and the resulting information provided in the mean-square maps can be used to estimate a numerical analog of coherence using the wavelet coefficients. Whereas a signal's mean-square power can be determined by the area under its power spectral density curve derived from the Fourier transform, in wavelet analysis, the mean-square power of a signal is given by the volume under the two-dimensional wavelet surface of the square values of the wavelet coefficients over the time-frequency plane. Thus, a statistic equivalent to that given in Eq. (1) is formed by substituting wavelet transform derived power terms for the autopower spectrums (denominator factors) and the cross power spectrum (numerator).

To estimate coherence from the wavelet coefficients obtained by the DWT, the autocorrelation functions, Eqs. (4) and (5), were computed, then the cross correlation function, Eq. (7), of the reference pulse and a pulse indexed by i as previously described were computed. The DWT is then applied to each of the correlations separately and the mean-square maps for each of the correlation functions are derived from the coefficients giving $C_{xx}(j,k)$, $C_{yy}(j,k)$ and

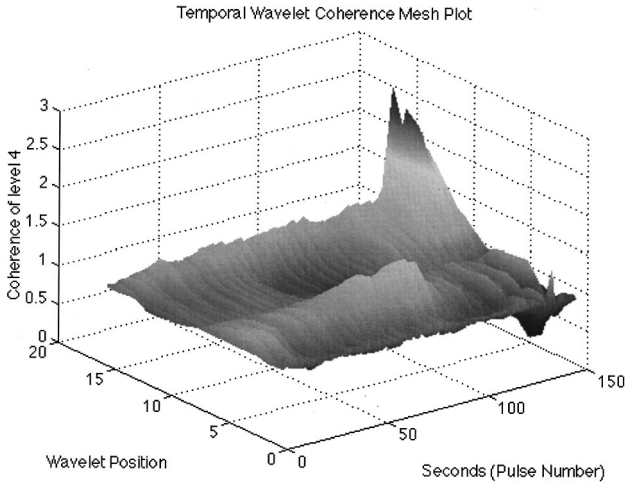

FIG. 7. Three-dimension coherence surface from the wavelet mean-square-energy map for wavelet level 4 as a function of wavelet position and pulse number.

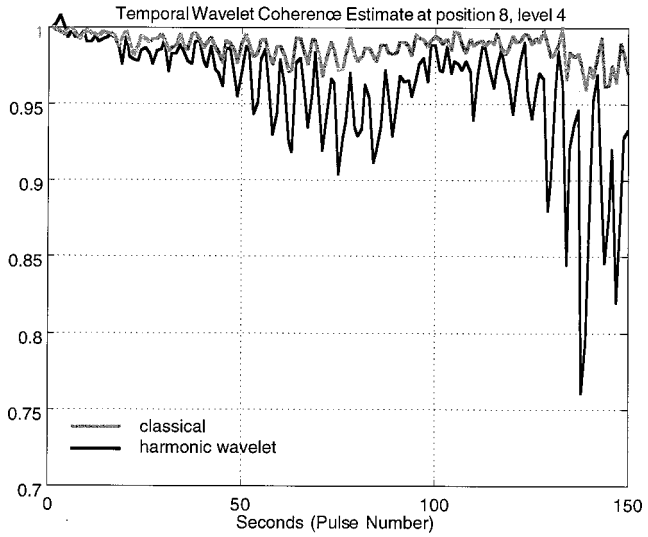

FIG. 8. Coherence estimation as a function of pulse number for wavelet level 4 and wavelet position 8 plotted on the same scale as the coherence from the classical method Fig. 3. This is one slice of the surface in Fig. 7.

$C_{xy}(j,k)$. The array of mean-square map coefficients from each wavelet level of the square of the cross correlation function map is then divided, element by element, by the element by element product of the wavelet coefficients derived from each autocorrelation functions as indicated in Eq. (11). A surface is created of wavelet coherence values that are indexed by *j*, wavelet level, and *k*, wavelet position,

$$\gamma^2_{\mathrm{Wav}_{xy}}(j,k)=\frac{|C_{xy}(j,k)|^2}{|C_{xx}(j,k)||C_{yy}(j,k)|} \quad \text{for all } k \text{ at level } j. \tag{11}$$

For the measured data used herein, the wavelet level where the signal power is predominant occurs in level 4, where the 5-kHz frequency is centered and has 16 wavelets equally spaced across the analysis time interval.

This process generates a wavelet coherence subspace (for each pulse with respect to reference pulse 1) of the 150-ping data set as a function of ping number, wavelet position, *k*, and wavelet level, *j*. Figure 7 illustrates a surface plot of wavelet coherence for wavelet level 4 only, as a function of wavelet position and pulse number for the example data set. Additional information on coherence as a function of pulse length is gained by using wavelets. Figure 7 shows coherence has relative maxima and minima as a function of wavelet position that appears consistent throughout the example data set. How much of this curvature is related to environmental changes in the medium, or processing parameters, or equipment fidelity is not known at this time, but it is new information. The temporal wavelet coherence at a position near the center of the pulse (at wavelet position $k=8$) gives a plot that looks very similar to the temporal coherence derived using the Fourier methods as shown in Fig. 8. Note that the basic shape and structure of the wavelet coherence are much like those of the classical method, but the higher frequency oscillations are more severe. Results obtained with this wavelet transform are similar to those derived with the Fourier methods. There is one drawback, the constant time-bandwidth product characteristic of the wavelet transform prevents a narrowband analysis at the signal frequency, and thus suffers from the same SNR limitations seen when we used Fourier methods.

D. Evaluation of coherence using concatenation of successive pulses

The last method examined for estimating coherence is pulse concatenation. Concatenation of successive pulses can be used to achieve higher spectral resolutions at the expense of reducing the ensemble of pulses. Concatenation presents unique difficulties, but since our interest is in a single frequency, and since the signal is very narrowband, the effect of concatenation on only one frequency need be considered.

Concatenation can be done in the time domain by simply concatenating the time series of successive pulses. The sample length for each pulse in the concatenation group can be predetermined by requiring an integer number of cycles. Each group of concatenated pulses can be processed for coherence using the Fourier spectral estimates identical to that in Sec. III A. Since the time series for the group is much longer than the time series for a single ping, spectral resolution is increased. However, the resulting power spectrum from each group of concatenated pulses may be noisy with high sidelobe levels. The spectrum levels and structure will be very dependent on the starting sample and the total number of samples chosen for concatenation. The more pulses used in the concatenation, the better frequency resolution in both the spectral levels and coherence estimates: however, that leaves fewer groups and less temporal resolution over the total 150-sec time span of the data set. Also, the more concatenation, the higher potential for errors due to possible relative phase differences in the individual pulse alignments. These factors lead to an overall poor estimate of coherence and this method is not shown here.

Concatenation can be better accomplished in the frequency domain by averaging narrowband spectra. The auto and cross correlations are obtained as before. The spectrum

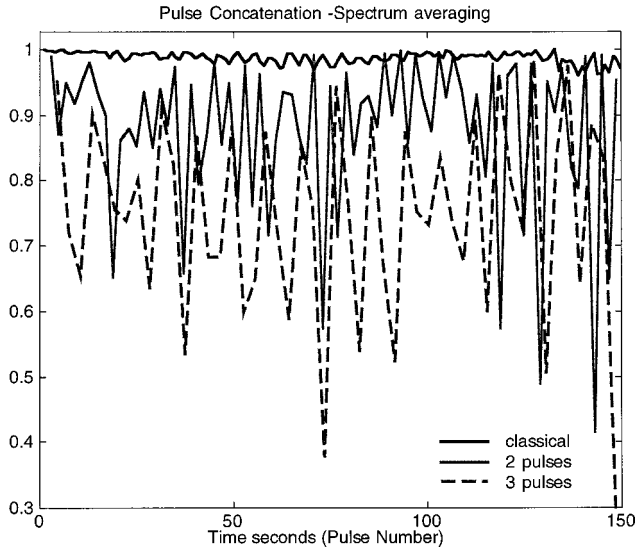

FIG. 9. Coherence as a function of pulse number using groups of two and three concatenated pulses and spectral averaging. The pulse repetition rate is 1 pulse per sec.

is estimated without using segmentation and overlap. This allows a larger size FFT which improves spectral resolution: however, only a single narrowband spectral estimate is obtained for each pulse. This is done for the desired number of successive pulses. The narrowband spectral estimates for the group of pulses is then averaged and coherence is computed. A weighted running average over the pulse group was used to help maintain the temporal resolution as a function of pulse number. For a two-pulse group the weights were [0.5 0.5] and for the three pulse group the weights were [0.33 0.66 0.33]. Figure 9 shows the coherence over the 150-sec-long data set using concatenation group sizes of two and three pulses, respectively.

The long-term trend in these coherence estimates is similar to the classical result; however, the coherence levels are much more erratic, varying by 20% in the concatenation and only by 5% using the classical method. These peaks and nulls are consistent with narrowband spectral estimation of fluctuating signals and are also consistent with the wideband spectral estimates of the classical method. However, as Fig. 9 demonstrates, this method is highly sensitive on the number of pulses in the concatenation. As the number of pulses in the concatenation is increased, the overall coherence is reduced and the variance is increased.

IV. ROBUSTNESS

Two numerical studies were performed to assess something about the robustness of these methods, one study for different types of phase fluctuations and the other for low signal-to-noise ratio pulses. In both methods synthetic signals were created with similar pulse characteristics as the data shown previously.

A. Effects of phase fluctuations

To examine the effects of phase fluctuations, two signals were synthesized, the first is a cw pulse with a 20° linear phase shift from ping to ping, and the second, a cw pulse with a uniformly distributed random phase shift (between 0 and π) from ping to ping. Figure 10 shows the resulting coherence estimates as a function of time (ping number) for both synthesized signals for the four methods.

The classical method result, Fig. 10(a), for a linear phase shift from ping to ping, is just what one would expect, and the random phase result which consists of deep nulls and oscillations is consistent with random phase fluctuations and will be used to benchmark the other methods. The coherence scale is different for each plot to better illustrate the effect of the random phase on the individual methods. Equation (1) implies a coherence value of unity for noise-free signals shifted linearly in phase. These studies agree, indicating that small linear phase changes from pulse to pulse do not degrade coherence estimation by any of the methods. Concatenation by narrowband spectrum averaging yields the highest coherence values for random phase fluctuations. If one compares the variance in the coherence of the random phase estimates with that of the linear phase estimates, the wavelet method has the largest change, indicating that it is more susceptible to random phase fluctuations than either the AR or the concatenation. However, recall that the wavelet method is designed for broad frequency bandwidth signals and here it is being used with narrowband cw signals. Note that the nonlinear AR estimate in the linear phase case shows a peak where the coherence is smallest in the classical method, and is minimum where the classical coherence is maximum.

B. Effects of noise

To evaluate the affect of SNR on each coherence estimation method, synthesized sinusoidal signals, similar to the signal pulses with zero phase change from pulse to pulse, were corrupted with additive, uncorrelated, normally distributed noise, and the signal amplitude was varied to simulate SNR values over the range of -10 to $+40$ dB. At each value of SNR evaluated, 500 pulses were synthesized and then processed using the coherence estimation techniques previously discussed. The mean and standard deviation of the coherence estimates of the simulated pulse train with the first pulse in the set were then determined. The resulting mean coherence, Fig. 11(a), and the standard deviation, Fig. 11(c), about the mean are plotted as a function of SNR in Fig. 11 for the classical, wavelet, and concatenation methods. Because of the nonlinear nature of the AR spectrum estimation, AR results are plotted separately in Figs. 11(b) and 11(d).

In the classical, wavelet, and concatenation cases the mean coherence estimate increases and approaches unity as the SNR increases, Fig. 11(a). This is an expected result as the signal strength overwhelms the decorrelating effects of the noise. Similarly, the standard deviation of the estimates trends downward as shown in Fig. 11(c). The interesting part is the consistent trends at lower SNR values. The wavelet-based coherence estimation method generally exhibits lower coherence values than do the two Fourier-based methods, and larger deviations especially at SNR levels below 10. This is likely due to the wide bandwidth of the wavelet level where the signal frequency resides, allowing a greater decorrelating effect from in-band noise. The coherence esti-

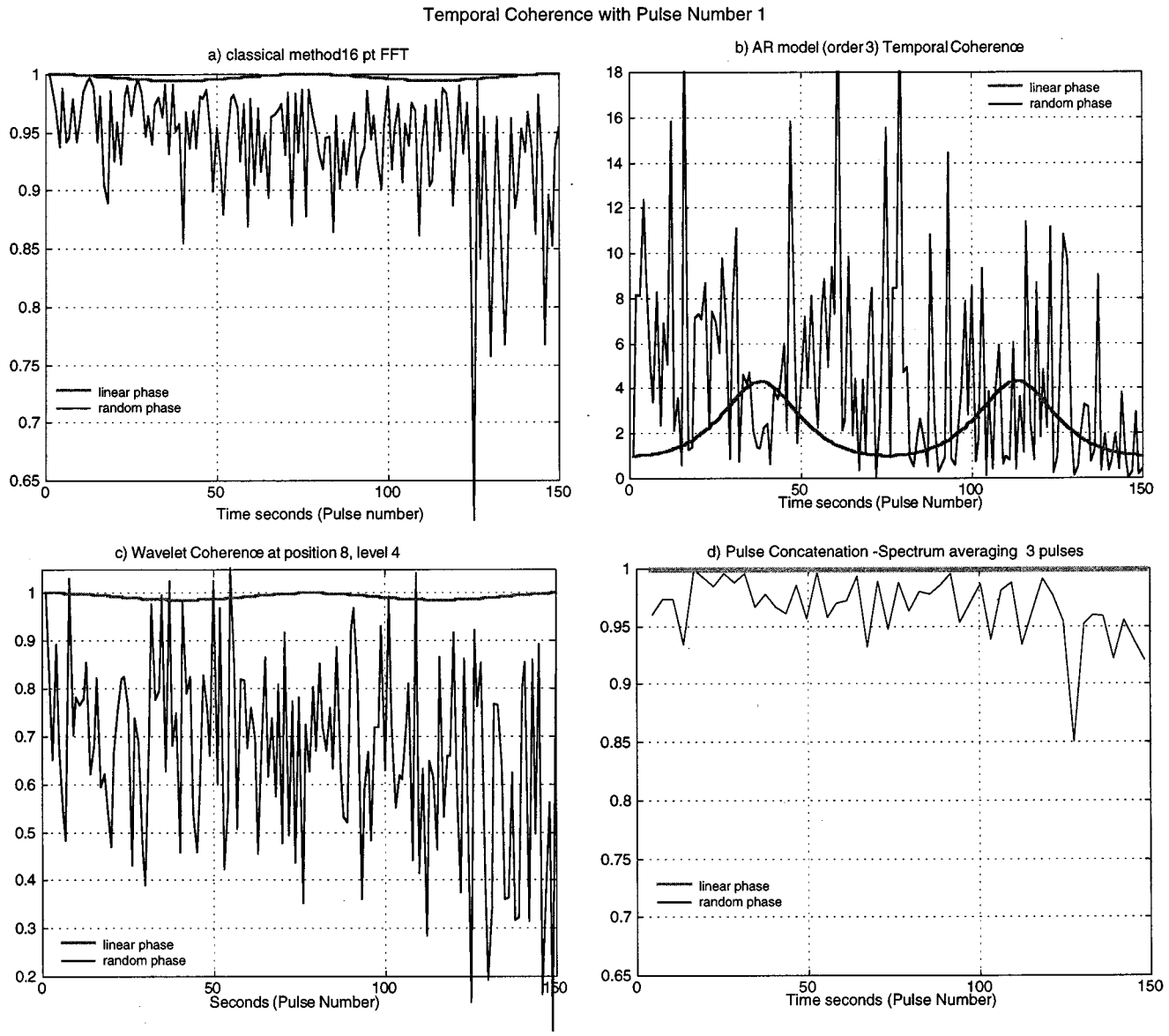

FIG. 10. Coherence estimation as a function of pulse number for synthesized pings with linear phase relationships and with random phase relationships processed by each method, (a) classical, (b) AR model order 3, (c) wavelet, and (d) pulse concatenation via spectral averaging.

mates derived by concatenation with narrowband spectral averaging exhibit the highest coherence values and the lowest standard deviation; however, as previously discussed, these higher coherence levels are achieved at the expense of temporal resolution. Figures 11(b) and 11(d) illustrate the results achieved using the nonlinear AR model approach. Both the mean coherence and standard deviation plots are puzzling and difficult to interpret. Both mean coherence and standard deviations are spiky, particularly at SNR levels below 10. This large variation of estimated coherence as a function of SNR presumably means that the model order used for AR spectral estimation is too low for adequate accuracy in estimating the magnitude of the spectra, regardless of SNR. The inaccuracy must tend to become very exaggerated at the lower SNR levels where the peaks occur. Again, as in the linear phase case, the AR estimate is inverted with respect to the other methods, when the nonlinear AR estimate is low, coherence is high.

V. CONCLUSION AND SUMMARY

Linear coherence has many applications: as a measure of an input/output system's linearity, as a prediction for system output, and as a measure of common spectral density between two signals. We have looked at four different methods for determining coherence. As previously discussed, frequency resolution is constrained to the inverse of the limited observation time, and for the short duration pulsed sinusoids examined in this study, poor frequency resolution results. Application of classical Fourier-based spectral estimation techniques for generating a periodogram result in very broad frequency bins deemed unacceptable for such short duration pulses, but these other methods have generally failed to make better estimates. Fourier transform methods still provide the best method for computing linear coherence for an input/output system.

The frequency resolution is much improved using AR

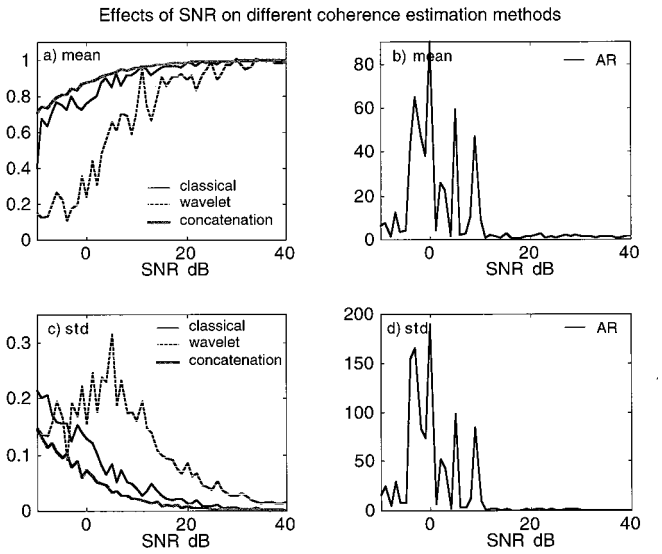

FIG. 11. The mean coherence and the standard deviation about the mean coherence for 500 synthesized pings as a function of SNR processed by each method. Each pulse represents a single pulsed sinusoid corrupted with uncorrelated Gaussian noise and zero phase change from pulse to pulse. The AR result is plotted separately due to the nonlinear nature of spectrum estimation.

methods; however, the spectral magnitude errors imposed by the low model order results in large errors in the spectral magnitudes, and yields coherence results that are difficult to interpret. The AR estimate does not appear useful for array performance prediction or for predicting system output based on the input and the coherence function. It is also not a measure of nonlinearity of the system. Comparing the AR estimates from one system with another system is difficult if not futile. However, the AR coherence estimate can be used in a limited sense as a relative measure of the commonality or ''sameness'' between two signals or as a measure of commonality between outputs of a single system. The AR method also has potential for yielding better results if higher model orders could be achieved without incurring an ill-conditioning of the correlation matrix.

Using orthogonal wavelets, the discrete wavelet transform provides a new method to estimate coherence, and a temporal coherence map can be easily generated that displays the value for the wavelet estimate of coherence in a two-dimensional form. This maps the coherence of both the signal frequency bands and the nonsignal frequency bands as a function of time. The wavelet coherence estimate matches well with both the overall trend and structure of the Fourier-transform-based coherence estimate as shown in Fig. 4, although the actual levels are slightly lower. The constant time-bandwidth characteristic of wavelet decomposition prevents a narrowband analysis at our signal frequency. The selection of the base wavelet is crucial to determining the coherence dependencies on SNR and phase fluctuations.

Both the AR coherence estimate and the wavelet coherence estimate over the 150 sec show more severe high-frequency oscillations than the Fourier-transform-based coherence estimate. For the AR estimate this is most likely due to the errors imposed by using such a low model order for modeling the signal. Unless a way is found to achieve better spectral estimation accuracy through higher model orders, this method is a poor choice for coherence estimation. Both the AR coherence estimate and the wavelet coherence estimate appear more effected by random fluctuations than does the Fourier method. Concatenation gave the highest values of coherence for low SNR synthesized signals.

ACKNOWLEDGMENTS

This work was made possible in part by the United States Naval Reserve while attached to the Office of Naval Research, Science and Technology Reserve detachment 822, and by the Primex Aerospace Company for supporting Reserve training. This work was performed under Naval Research Laboratory Task UW-35-2-05, program element 0602435N. The authors wish to thank the Associate Editor, and the reviewers for their attention to detail and helpful suggestions.

[1] J. S. Bendat and A. G. Piersol, *Engineering Applications of Correlation and Spectral Analysis* (Wiley, New York, 1980), Appendix B.
[2] C. W. Therrien, *Discrete Random Signals and Statistical Signal Processing* (Prentice-Hall, Englewood Cliffs, NJ, 1992), pp 595–596.
[3] S. L. Marple, Jr., *Digital Spectral Analysis with Applications* (Prentice-Hall, Englewood Cliffs, NJ, 1987), Chap. 6 and 7.
[4] S. M. Kay, *Modern Spectral Estimation, Theory and Applications* (Prentice-Hall, Englewood Cliffs, NJ, 1988), Chap. 5–7.
[5] J. P. Burg, ''Maximum entropy spectral analysis,'' in *Proceedings of the 37th Meeting of the Society of Exploration Geophysicists, 1967*.
[6] J. Makhoul, ''Linear prediction: A tutorial review,'' Proc. IEEE **63**(4), 561–580 (1975).
[7] D. E. Newland, *Random Vibrations, Spectral & Wavelet Analysis* (Longman, Harlow, and Wiley, New York, 1993), Chap. 17.
[8] I., Daubechies, *Ten Lectures on Wavelets* (SIAM, 1992).
[9] R. R. Coifman, Y. Meyer, and V. Wickerhauser, *Wavelet Analysis and Signal Processing* (Yale University New Haven, 1991).
[10] S. Mallat, ''A Theory for multiresolution signal decomposition: The wavelet representation,'' IEEE Trans. Pattern. Anal. Mach. Intell. **11**(7), 674–693 (1989).

Locating animals from their sounds and tomography of the atmosphere: Experimental demonstration

John L. Spiesberger[a)]
Department of Meteorology and the Applied Research Laboratory, 512 Walker Building, Pennsylvania State University, University Park, Pennsylvania 16802

(Received 1 October 1997; accepted for publication 21 April 1999)

Calling animals are located using widely distributed receivers, and the sounds from the animals are used to map the sound speed and wind fields by means of tomography. In particular, two Red-Winged Blackbirds *Agelaius phoeniceus* are correctly located within a meter using recordings from five receivers spread over a 20 by 30 m region. The demonstration hinges on two new developments. First, a new algorithm for blindly estimating the impulse response of the channel is shown capable of estimating the differences in the time of first arrivals at two receivers. Since it is known that the first arrivals travel along nearly straight paths, the difference in time constrains the animal's location to a hyperboloid, and the animal is located by intersecting hyperboloids from many pairs of receivers. Second, in order to accurately find the intersection point and map the sound speed and wind fields using tomography, a nonlinear equation is solved. The new algorithm for blindly estimating the impulse response of a channel offers a new way for locating sounds and making tomographic maps of the environment without any requirement for a model for the propagation of sound such as is needed for focalization and matched field processing. © *1999 Acoustical Society of America.* [S0001-4966(99)00108-3]

PACS numbers: 43.60.Gk, 43.60.Rw, 43.60.Pt [JCB]

INTRODUCTION

Measuring and understanding the distributions of animals is a fundamental goal in ecology and conservation. Passive acoustic sensing of calling animals has the potential for estimating distributions by providing locations[1–6] and identifications.[7–11] Because sound propagates through and around visual obstacles, acoustic data are available for locating animals that are difficult to see. Locating animals from their sounds should be possible during the night, under the water, and in dense forests and jungles. Acoustic locations can identify which animal is calling when it is difficult to discern which of several animals in view is vocalizing, such as in a pod of dolphins.[5] Spiesberger and Fristrup[12] explored theoretical limits for locating calling animals. With two additional developments described here, those techniques are shown to work reliably.

The most accurate solutions for the locations of calling animals, or any sounds, can only be approached by simultaneously estimating the sound speed and wind (current) fields using a tomographic technique.[12–17] Acoustic tomography of the ocean, Earth, and atmosphere is usually practiced by recording the signals emitted at known times from known locations at known receiving points.[18–20] The travel times, and possibly the amplitudes of the recordings, are converted to profiles of sound speed and wind (current) fields using a formal inversion technique. In other situations, estimates of the sound speed field are made without *a priori* knowledge of the locations of the sources.[13–17] These focalization and matched field processing techniques can be used when there is a sufficiently reliable model for the propagation of sound. The source's location and the sound speed field are estimated by finding fits of the data with a library of modeled solutions for the propagation of sound through hypothetical source locations and environmental conditions.

The animal location problem addressed here is fundamentally different and more difficult than that for these problems because (1) the location and time of the animal's call are unknown and (2) there is not a model for the propagation of sound so there is no practical way to compare the data with a model to estimate the animal's location and the environmental conditions. For example, the locations of the trees, houses, and the ground are unknown in the experiment discussed in this paper. These obstacles lead to significant aberrations of the transmitted signal because they introduce paths as the sound reflects and interacts with their boundaries.

The theoretical methods for locating animals and estimating the environment with tomography[12] did not work reliably for the two atmospheric experiments carried out by the author. The first experiment used eight receivers in a 30 m by 30 m region in a woods in North Falmouth, MA.[21] The second experiment is reported here. The theories failed because the standard signal processing method for obtaining the acoustic data did not work and because the location and tomographic problem is not as linear as thought. Solutions for these problems are presented in this paper. The problem with the signal processing method is discussed next.

A method for locating the origin of a signal whose initiation time is unknown involves measuring the difference in the signal's travel time between each of several pairs of widely separated receivers. The difference in travel time is used because it is independent of the initiation time of the

[a)]Present address: Department of Earth and Environmental Science, 3440 Market St., Suite 400, U. Pennsylvania, Philadelphia, PA 19104-3325.

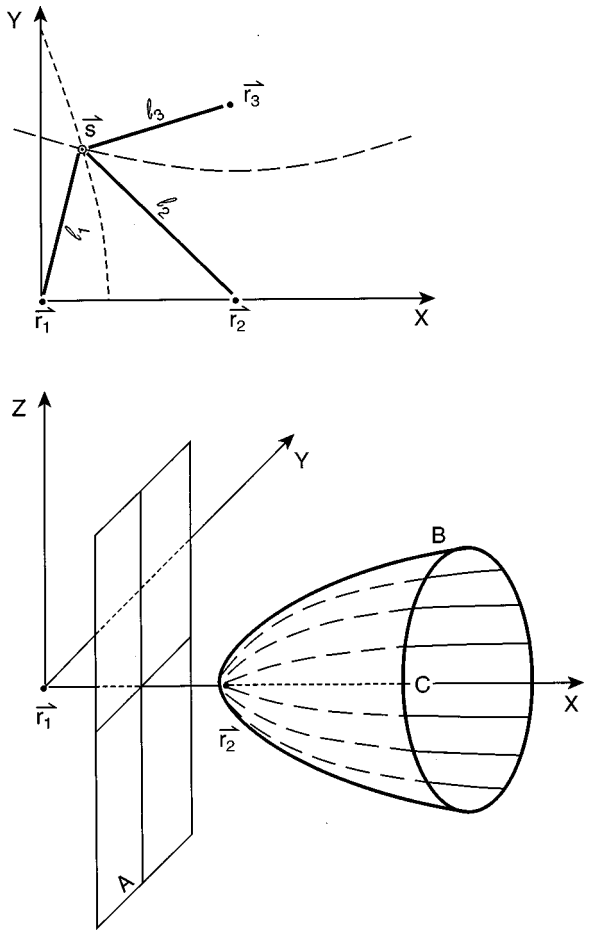

FIG. 1. **Upper**: Locating sources in two dimensions. The three acoustic receivers are at $\mathbf{r}_i$; $i=1,2,3$. The acoustic source is at **s**. The ranges between the source and the receivers are l_i for $i=1,2,3$. The curves are hyperbolas which define the possible positions of the source based on the measured travel time differences for receivers 1 and 2 (short-dashed) and for receiver 2 and 3 (long-dashed). **Lower**: In three dimensions, the difference of the arrival times (receiver 2 minus receiver 1) constrains the source location to the surface of a hyperboloid. If the travel-time difference is zero, the hyperboloid reduces to a plane (A). If the travel-time difference is positive (the signal arrives at receiver 2 first), the hyperboloid looks like surface B. If the travel-time difference is equal to the time required for an acoustic signal to travel from receiver 1 to 2, the hyperboloid reduces to the line segment (C) which starts at $\mathbf{r}_2$ and extends in the positive x direction. After Ref. 12.

signal. When the speed of the signal's propagation is constant and there are no winds, each travel time difference (TTD) confines the signal to the surface of a hyperboloid (Fig. 1). In general, a minimum of five receivers is required to locate the signal when no prior information such as its elevation is known.[12]

Cross-correlation is a standard method for estimating TTDs because its estimates are accurate and it often provides a tremendous gain in the signal-to-noise ratio.[22–24] The gain increases the distance over which animals may be located (Fig. 3 in Ref. 12).

Cross-correlation failed to provide a reliable means for estimating TTDs in the experiment reported by Ref. 21 and the experiment described here. The reason for the failure is due to the way that sound propagates.

At short distances in air and water, sound often propagates between two points along many paths, called multipath. The first arrival propagates along a path that may be nearly straight. The other arrivals are caused either by refraction, due to spatial variations in winds (currents) and the speed of sound, or by reflections from boundaries (Fig. 2). The travel times of sound along the paths are usually different. When there is only one path to each of two receivers, there is one peak in the cross-correlation function. The lag of this peak is the desired TTD. With multipath, there are many peaks in the cross-correlation function. Which peak is chosen if some multipath lead to peaks whose magnitudes are similar to or greater than the peak corresponding to the first arrivals? In many terrestrial and shallow water environments with imprecisely known boundaries, the first arrival may be the only path that is useful for locating animals since the geometry of the other paths may be difficult to estimate. Cross-correlation does not tell us which peak to choose. For example, suppose there are three paths reaching each receiver. The cross-correlation of the acoustic pressure signal between two receivers has up to $3\times3=9$ peaks. If five receivers are used for locating animals, there are four independent cross-correlations that can be formed.[12] One is faced with determining which of the $9^4=6561$ sets of four travel time differences is correct. Freitag and Tyack report a similar problem (p. 2199 in Ref. 5).

A solution to this conundrum has been found using a new signal-processing technique which combines the information in auto- and cross-correlation functions.[25] In general, the technique yields estimates for the relative arrival times of multipath at each receiver without using any knowledge of how the multipath reach the receiver. In this sense, the technique offers a new means for blindly estimating the impulse response of a channel, a subject of current interest in electromagnetic communication systems.[26] Once the relative travel times of multipath are estimated, the source can be located if one knows something about the geometry of at least one of the paths at each receiver. Although the new technique works with realistic simulations, it has not been previously applied to data. Its efficacy is demonstrated here with sounds from birds.

I. PRELIMINARIES

The acoustic pressure fluctuations originating from an animal are $\nu(t)$ where the call begins at time $t=0$. There are N_j multipath reaching receiver j. For tutorial purposes, the received signal is written as

$$\phi_j(t)=\sum_{n=1}^{N_j} a_j[n]\,\nu(t-t_j[n])+e_j(t), \tag{1}$$

where the amplitude and travel time of the nth multipath are $a_j[n]$ and $t_j[n]$, respectively. The noise is $e_j(t)$. In reality, the method used to locate animals allows for aberration of the phase and amplitude of the Fourier components of the emitted signal. Such aberrations occur due to differential absorption in frequency, turbulence, etc. The ability to locate animals only requires that multipath lead to peaks in auto- and cross-correlation functions.[25] The unbiased auto- and cross-correlation functions are defined as

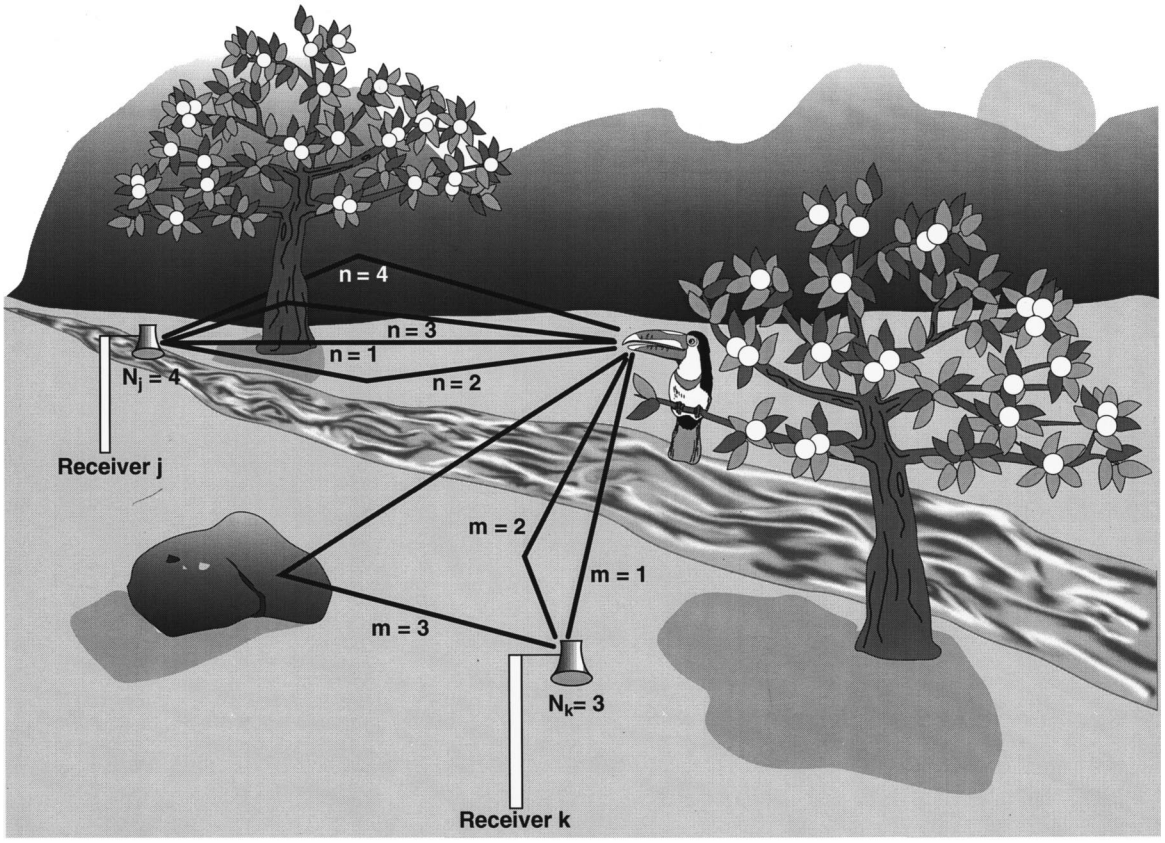

FIG. 2. View of $N_j=4$ and $N_k=3$ acoustic paths between a Toucan and receivers j and k, respectively. The direct paths are $n=1$ and $m=1$. The other paths reflect from the ground, a rock, and a cliff.

$$R_{ij}(\tau)\equiv\frac{1}{t_2-t_1-|\tau|}\int_{t_1}^{t_2}\phi_i(t)\,\phi_j(t-\tau)\,dt, \tag{2}$$

where $i=j$ and $i\neq j$ for auto and cross-correlations respectively. The limits of the integral should bound the signal.

If there is only one path between the animal and all receivers, then the cross-correlation function has a peak at lag

$$\tau_{ij}[1,1]=t_i[1]-t_j[1], \tag{3}$$

which is the desired TTD. However, there is a maximum of N_iN_j signal-related peaks in the cross-correlation function in the presence of multipath. They occur at lags

$$\tau_{ij}[m,n]=t_i[m]-t_j[n], \tag{4}$$

where $m=1,2,3,\cdots N_i$ and $n=1,2,3,\cdots N_j$.

II. DATA

On 4 June 1995, five inexpensive Radio Shack omnidirectional dynamic receivers, catalog number 33-985F, were mounted on PVC pipes with C-clamps a few meters above the ground in a field in Port Matilda, PA. Their relative locations and two benchmarks near trees were measured within ± 0.05 m with surveying equipment (Fig. 3 and Table I). Coaxial cables connected the receivers to Symmetrix preamplifiers which provided 80 dB gain. The signals were recorded on a six-channel analog cassette recorder, model MR-30, manufactured by TEAC. Signals were digitized at a frequency of 16 kHz.

Temperature and relative humidity were measured in the

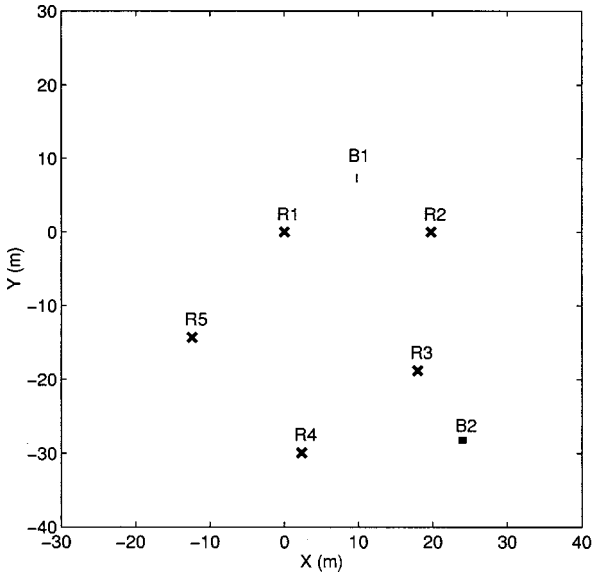

FIG. 3. Locations of five receivers, R1–5, and the locations of two Red-Winged Blackbirds *Agelaius phoeniceus* at B1 and B2. The black regions at B1 and B2 denote the 95% confidence limits for the positions of each bird located using passive acoustic techniques. Tables I and IV list the locations of the receivers and birds.

TABLE I. Cartesian (x,y,z) coordinates for the five receivers shown in Fig. 3.

Receiver	Cartesian coordinate (m)		
	x	y	z
R1	0	0	0
R2	19.76	0	0
R3	17.96	−18.80	0
R4	2.34	−29.92	−0.02
R5	−12.41	−14.35	−0.43

shade within 0.2 °C and 10%, respectively. The data were taken when the temperature and relative humidity were about 19.6 °C and 77%, respectively. The wind was blowing very slowly toward the East, the direction of negative values on the y-axis in Fig. 3. It was partly cloudy. The site is about 300 m above sea level, where atmospheric pressure is about 970 mbar. The corresponding speed of sound is 344 m/s [Eq. (3) in Ref. 12, but p should equal 1013 mbar in that equation, which is 760 mm of mercury].

At 9:20 AM, Eastern Standard Time, a Red-Winged Blackbird, *Agelaius phoeniceus*, called in a tree at B1 (Fig. 3). The recorded signals were noisy. As the call had frequencies between 2000 and 6000 Hz, a bandpass filter was applied to each record to increase its signal-to-noise ratio (Figs. 4 and 5).

The signal-to-noise ratios of the cross-correlations are significantly larger when the time-bandwidth product, TW, is much larger than one (p. 55 in Ref. 27). The duration and bandwidth of the signal are T and W, respectively. For this Red-Winged Blackbird, the estimates for T and W are about 1 s and 3000 Hz, respectively, resulting in a time-bandwidth product of 3000. The peak signal-to-noise ratio after cross-correlation is

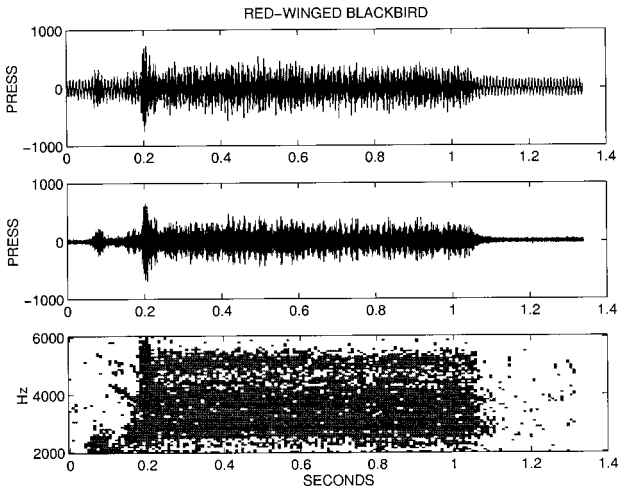

FIG. 4. **Top**: Recorded signal at receiver 1 due to the Red-Winged Blackbird *Agelaius phoeniceus* near B1 in Fig. 3. The ordinate is a linear scale in this and the middle panel, and is proportional to pressure in arbitrary units. **Middle**: Same except the signal is bandpass filtered to suppress frequencies less than 2000 and greater than 6000 Hz. The bird emits frequencies in between. **Bottom**: The spectrogram of the middle panel showing the frequencies from the bird as a function of time in decibels (arbitrary reference). The spectrogram has been clipped to exclude most of the noise. Darker pixels indicate louder sounds. The lightest grays are about 60 dB less than the darkest blacks.

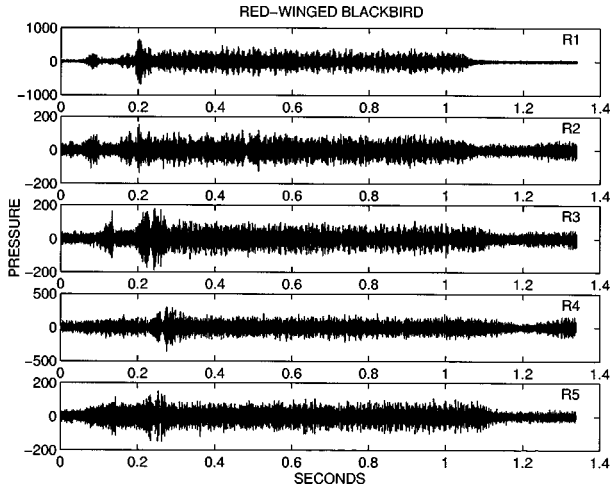

FIG. 5. The pressure fluctuations at five receivers following bandpass filtering between 2 and 6 kHz. The bird is located near B1 in Fig. 3.

$$\mathrm{SN}_{\mathrm{peak}} = 10\log_{10}\frac{(\max[R_{ij}(\tau)])^2}{\sigma_n^2}\ (\mathrm{dB}), \tag{5}$$

where the maximum value in the cross-correlation function is $\max[R_{ij}(\tau)]$ and the variance of the noise in the cross-correlation function is σ_n^2. Peak signal-to-noise ratios vary from 33 to 47 dB (Fig. 6 and Table II). These ratios are large because the time-bandwidth product gives a gain of about $10\log_{10}(3000/2) = 32$ dB over that in the records [Eq. (37) in Ref. 12 where $d_1^2 = d_2^2$ in application of that equation].

The widths of the peaks in the cross-correlation functions are about 1 ms [Fig. 7(a)]. This is the same order-of-magnitude as the inverse bandwidth, namely $W^{-1} \cong 0.0003$ s.

Without noise, there are $\mathcal{R}-1$ independent TTDs given by $\tau_{1j}[1,1]$ where $j = 2,3,\cdots\mathcal{R}$ and the number of receivers is $\mathcal{R}$. For example, the reason that $\tau_{23}[1,1]$ does not provide an independent piece of information is because $\tau_{23}[1,1] = \tau_{13}[1,1] - \tau_{12}[1,1]$. However, data are noisy and one uses all the receiver pairs to obtain the most accurate location. The number of different pairs is

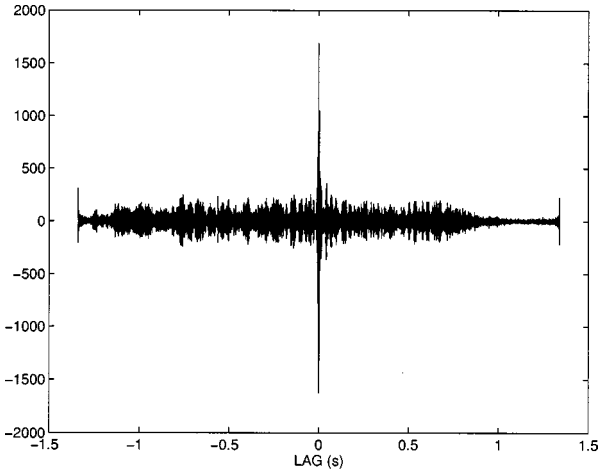

FIG. 6. The cross-correlation function between receivers one and two, $R_{12}(\tau)$, for the Red-Winged Blackbird at B1 (Fig. 3). The signals are bandpassed prior to cross-correlation (Fig. 5). The peak signal-to-noise ratio is 47 dB.

TABLE II. The differences in travel time between the first arriving multipath at the indicated receiver pairs. These lags are indicated with arrows in Fig. 7(a), (b). The peak signal-to-noise ratios are computed from Eq. (5).

Travel-time difference	(s)	Peak S/N ratio (dB)
$\tau_{12}[1,1]$	−0.000 63	47
$\tau_{13}[1,1]$	−0.043 56	44
$\tau_{23}[1,1]$	−0.042 88	35
$\tau_{14}[1,1]$	−0.074 31	42
$\tau_{24}[1,1]$	−0.073 69	33
$\tau_{34}[1,1]$	−0.030 69	39
$\tau_{15}[1,1]$	−0.053 75	42
$\tau_{25}[1,1]$	−0.053 13	35
$\tau_{35}[1,1]$	−0.010 25	36
$\tau_{45}[1,1]$	+0.020 50	35

$$N_{ccfs}=\mathcal{R}(\mathcal{R}-1)/2. \tag{6}$$

For $\mathcal{R}=5$ receivers, there are ten pairs whose TTDs are

$$\begin{pmatrix} \tau_{12}[1,1] & \tau_{13}[1,1] & \tau_{14}[1,1] & \tau_{15}[1,1] \\ & \tau_{23}[1,1] & \tau_{24}[1,1] & \tau_{25}[1,1] \\ & & \tau_{34}[1,1] & \tau_{35}[1,1] \\ & & & \tau_{45}[1,1] \end{pmatrix}. \tag{7}$$

This collection of TTDs is referred to as a TTD set.

Because of multipath, there are hundreds of peaks in the cross-correlation functions [Fig. 7(a), (b)]. It is not always clear that the biggest is the desired TTD. For example, the two highest peaks in $R_{13}(\tau)$ and $R_{14}(\tau)$ have amplitudes within 4% and 0.2% of one another [Fig. 7(a)]. The ambiguity is resolved with a new algorithm.[25] The cross-correlation functions are graphed on a logarithmic scale to show both small and large peaks used in this algorithm. Appendix A summarizes the outputs of this algorithm for the data in Fig. 7(a), (b).

III. MODEL FOR ANIMAL LOCATION AND TRAVEL-TIME DIFFERENCES: NONLINEARITIES

A linear approximation may be used to relate the TTDs with the position of the animal and the fields of sound speed and wind [Eq. (78) in Ref. 12]. This approximation is invalid here because the initial estimate for the animal's location is not close enough to its actual location. If we assume that the nonlinear terms in the TTD, which refer to the actual minus reference position of the animal, contribute no more than a 10% change in the TTDs, then the linear approximation is valid when

$$\delta s \leqslant 0.1L, \tag{8}$$

$$\delta r(j) \leqslant 0.1L, \tag{9}$$

where the corrections to the initial estimates for any Cartesian coordinate of the source and receiver are δs and $\delta r(j)$, respectively, and the typical distance from the animal to the receivers is L [Eqs. (B12), (B13)]. Here, $L\sim 10$ m, so the linear approximation is valid if the corrections are less than a meter. For the receivers, the linear approximation is valid since the relative locations of the receivers are measured within a few centimeters. The linear approximation is invalid for the corrections to the source's location since those corrections are of the order 1 m.

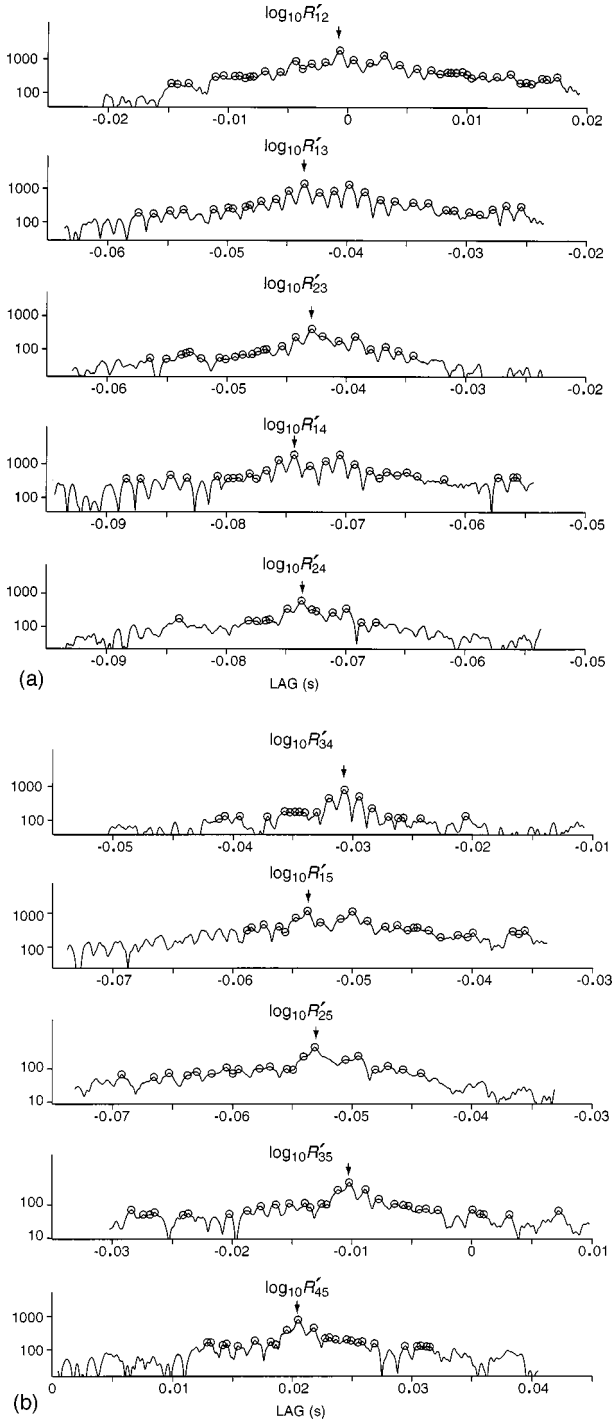

FIG. 7. (a) The logarithms of the envelopes of the ten cross-correlation functions, R'_{ij}, for the indicated receiver pairs i-j. The prime in R'_{ij} means that the envelopes are the amplitude of the Hilbert transform of the cross-correlation function (see Fig. 4 in Ref. 25). The time series being correlated are in Fig. 5. The arrows indicate the peaks corresponding to the differences in travel times between the first arrivals at each pair of receivers (Table II). The ○'s indicate the peaks that are used to estimate these travel-time differences using the correlation equations described by Ref. 25. The top panel shows the peaks in the vicinity of the big peak in Fig. 6. The ordinates are logarithmically scaled to show the range of peaks that are picked for the signal processing algorithm (Ref. 25). (b) Same as (a), but for different cross-correlations.

Consequently, a nonlinear model is used to solve for the animal's position and the fields of sound speed and wind.

Solutions are sought by discretizing values for the position, sound speed, and wind fields, and retaining combinations of these values which fit the measured TTDs. In our case, there is no reliable model for the acoustic receptions except for the direct path which does not reflect from boundaries, so this is not a problem in matched field processing.[28] In order to reduce the number of exhaustive trials to a practical number, the sound speed, c, and each Cartesian component of the wind field, (u,v,w), are taken to be constant throughout the experimental region. If the first arrival travels along a straight path, the TTDs may be related to the positions of the source and receivers through

$$\tau_{ij}[1,1]=\frac{1}{c}(l_i-l_j)-\frac{1}{c_0^2}\{u\cdot[r_x(i)-r_x(j)] + v\cdot[r_y(i)-r_y(j)]+w\cdot[r_z(i)-r_z(j)]\}+e_{ij}. \tag{10}$$

The first term on the right side is the time for the call to propagate from the source-to-receiver i minus the time to propagate from the source-to-receiver j at speed c. The distance from receiver i to the source is

$$l_i=\sqrt{(r_x(i)-s_x)^2+(r_y(i)-s_y)^2+(r_z(i)-s_z)^2}, \tag{11}$$

where the Cartesian coordinates of the receiver and the source are $(r_x(i),r_y(i),r_z(i))$ and (s_x,s_y,s_z), respectively. The second term on the right side gives the effects of winds on the difference in travel time. An estimate for the speed of sound is c_0. The term, e_{ij}, includes the sum of the measurement errors as well as all unmodeled effects such as deviations from a straight line path due to refraction, nonuniform variations of the sound speed and wind fields, and aberrations due to discretizing the space of solutions (Appendix C). Equation (10) is obtained from Eq. (78) of Ref. 12.

IV. SOLUTIONS OF THE NONLINEAR EQUATIONS

Because the bird and receivers are near the same level (Table I), it is illuminating to graph two-dimensional hyperbolas from the data (Table II) for each of the $N_{ccfs}=10$ pairs of receivers. Their intersections give an approximate location for the bird (Fig. 8). For some purposes this location may be sufficiently accurate. A more accurate method is provided below because it is important to find out how accurately an animal can be located.

We seek values of (s_x,s_y,s_z) and (c,u,v,w) which obey Eq. (10) given values of the TTD's in Table II and for c_0 equal to 343 m/s. The intersected hyperbola in Fig. 8 are used to guide an initial guess for the horizontal x-y location of the animal. This rectangular region is subdivided into cells of dimension δx by δy. The center of each cell is taken as a candidate for (s_x,s_y), and s_z may be found analytically given a guess for (c,u,v,w) and a measured value $\tau_{ij}[1,1]$ (Appendix C). The vertical coordinate of the animal, s_z, lies on the surface of a three-dimensional hyperboloid such as shown in Fig. 1. In fact, the analytical solution for s_z may yield no solution, one solution, or two solutions. No solution is found if (s_x,s_y) is outside of the region where the hyperboloid intersects the x-y plane. One solution is found if

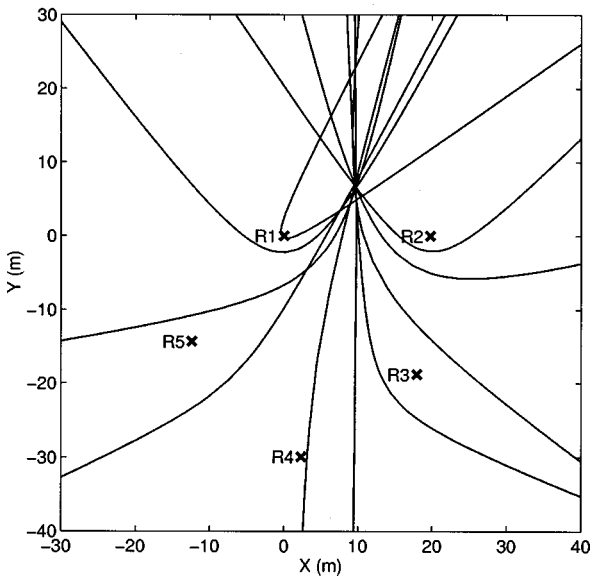

FIG. 8. A two-dimensional approximation for the hyperbolic geometry involved in locating the Red-Winged Blackbird, B1, using ten intersecting hyperbolas. The positions of the receivers are the same as in Fig. 3. Note that the hyperbolas intersect above R1 and R2. This intersection region is near B1 in Fig. 3.

(s_x,s_y) lies on the hyperbola given by the intersection of the horizontal plane with the hyperboloid. Two solutions are found if (s_x,s_y) lies within the region where the horizontal plane intersects the hyperboloid.

Because of the error term $\epsilon_{ij}[1,1]$ in Eq. (10), the vertical location of the animal may span 0, 1, or 2 ranges of values for s_z instead of just 0, 1, or 2 solutions for s_z as described above. With one TTD, namely, $\tau_{ij}[1,1]$, the span of values for s_z is estimated by varying $\tau_{ij}[1,1]$ by two standard deviations in either direction where the standard deviation of ϵ_{ij} is σ [Eq. (C7)]. Varying the data by $\pm 2\sigma$ is equivalent to finding the thickness of the family of hyperboloids which intersect a vertical line through (s_x,s_y). Each of the $N_{ccfs}=10$ TTDs accordingly yields a thick hyperboloid. The animal's vertical coordinate lies within the intersection of these ten thick hyperboloids, if such a solution exists. If there is a solution, then we have a solution for (s_x,s_y), (c,u,v,w), and a minimum and maximum value for s_z. Otherwise, there is no solution for the location of the animal and the sound speed and wind fields.

Contributions to the noise term, ϵ_{ij}, include discretization effects as shown in Eq. (C7). These effects are minimized by using small cell sizes and small steps in the discretization of the sound speed and wind fields. Taking small steps increases the number of times that solutions are sought for Eq. (10). An example is illuminating. The number of times that ten thick hyperboloids are intersected for solutions of s_z is

$$N_{\text{trial}}\equiv\left(1+\frac{X}{\delta x}\right)\left(1+\frac{Y}{\delta y}\right)\left(1+\frac{c_{\max}-c_{\min}}{\Delta_c}\right) \times\left(1+\frac{u_{\max}-u_{\min}}{\Delta_u}\right)\left(1+\frac{v_{\max}-v_{\min}}{\Delta_v}\right), \tag{12}$$

where the initial x-y region for a bird is taken to be X by Y.

TABLE III. Values taken for locating the birds and estimating the sound speed and wind fields. The minimum and maximum values of sound speed and wind used for solution to the nonlinear equation are indicated.

Quantity	Value	Units
δx	0.0297	m
δy	0.0297	m
Δ_c	0.75	m/s
Δ_u	0.375	m/s
Δ_v	0.375	m/s
Δ_w	0.375	m/s
σ_1	0.000 067	s
$dc+du+dv+dw$ in Eq. (C6)	1	m/s
L in Eq. (C6)	10	m
σ_2	0.0001	s
$c_{\min}$	343.2	m/s
$c_{\max}$	345.45	m/s
$u_{\min}$	−2	m/s
$u_{\max}$	2.125	m/s
$v_{\min}$	−2	m/s
$v_{\max}$	2.125	m/s
$w_{\min}$	−0.5	m/s
$w_{\max}$	0.5	m/s

The maximum, minimum, and incremental values taken for (c,u,v) are $(c_{\max},u_{\max},v_{\max})$, $(c_{\min},u_{\min},v_{\min})$, and $(\Delta_c,\Delta_u,\Delta_v)$, respectively. We will see in the next section that we may let the vertical component of the wind vanish to good approximation. For the values given in Table III, and for $X=Y=3$ m, there are $N_{\text{trial}}\sim 43\,000$ trials. These trials were computed in three CPU minutes on a SUN Ultrasparc chip at 160 MHz.

V. RESULTS

The acoustic solution for the location of the Red-Winged Blackbird at B1 falls within the small black line labeled B1 in Fig. 3. This location is consistent with the location of the bird determined using a standard surveying technique (Table IV). The acoustic survey has more accuracy in the horizontal than the vertical plane because the bird and the receivers are all near the same elevation. The vertical location might be as accurate as the horizontal location if the receivers were mounted at elevations that spanned 30 m, about the same distance as the horizontal separation of the receivers (Fig. 3). The acoustic solution for the volume of space which encloses the 95% confidence limits for the bird's location corresponds to the ranges of values of sound speed and winds listed in Table III.

TABLE IV. Cartesian (x,y,z) coordinates plus 95% confidence limits for the locations of the Red-Winged Blackbirds, B1 and B2, in Fig. 3 estimated using acoustic tomography and a standard surveying technique. The standard survey location is obtained by visually estimating the location of the bird relative to a nearby benchmark whose location is determined optically.

Bird	Survey method	Cartesian coordinates (m)		
B1	Tomography	$(9.8\pm0.15,$	$7.3\pm0.64,$	$3.9\pm2.1)$
	Standard	$(9.8\pm0.5,$	$6.8\pm0.5,$	$2.3\pm1)$
B2	Tomography	$(24.0\pm0.6,$	$-28.2\pm0.5,$	$2.3\pm2.6)$
	Standard	$(23.9\pm0.5,$	$-28.3\pm0.5,$	$-0.6\pm1)$

A second Red-Winged Blackbird called at B2 at 9:46 AM EST, 4 June 1995. Before solving Eq. (10), its approximate location was satisfactorily found by intersecting ten hyperbolas in an analogous fashion to that done in Fig. 8 for the other bird. The bird called from the top of a small tree. The ranges of its horizontal coordinates are shown by the filled in rectangular region labeled B2 in Fig. 3. Limits for its location are consistent with that obtained using a standard surveying technique (Table IV).

Triples of acceptable (c,u,v) are displayed for a vertical wind speed of 0 m/s (Fig. 9). The tomographic estimates are similar for other values of w in the run (Table III). The insensitivity to w stems from the fact that the acoustic paths are almost perpendicular to this component of the wind. Tomographic solutions for (c,u,v) show dependencies between sound speeds and winds, but the fields themselves are not accurately estimated. For example, the speed of sound could be anywhere between 343 and 345 m/s for acceptable values of u, v, and the locations of the bird shown by the thin line in Fig. 3. A change of 1 m/s is equivalent to a temperature change of 1.7 °C.

Figure 9 in Ref. 12 showed error maps for the sound speed and wind fields with a linear inverse. In that simulation, four animals called simultaneously with signals recorded on ten receivers. The standard deviations of the sound speed and wind fields had theoretical values of about 0.4 and

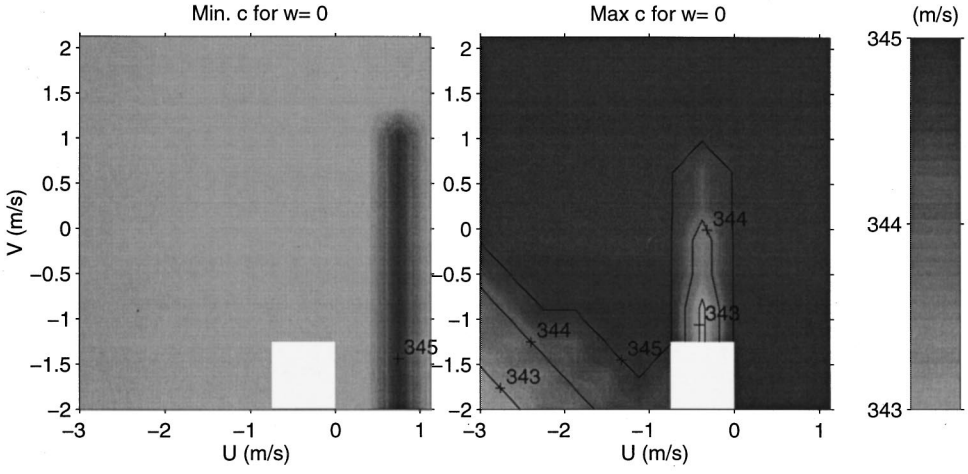

FIG. 9. Tomographic estimates for the minimum and maximum values of the speed of sound as a function of the horizontal components of the winds, u, and v, for the bird calling at B1 in Fig. 3. Values are shown for a vertical wind speed of $w=0$ m/s. The white square at the bottom indicates that there is no solution for the bird's location for any speed of sound between 343 and 345 m/s and for u and v in the white square.

0.3 m/s, respectively. There are several possible reasons why those errors are less than obtained here. First, there are five acoustic paths in this experiment, and the theoretical example had four birds$\times 10$ receivers$=40$ paths. Tomographic maps gain accuracy with increasing numbers of paths. Second, the theoretical example in Ref. 12 sought solutions for the corrections to the initial estimates for the receiver positions and for nonuniform variations of the sound speed and wind fields. Because of computational limitations, the solution to Eq. (10) in this study has to be implemented by including those effects into contributions to the noise term, ϵ_{ij}, in Eq. (10). This decreases the accuracy for the estimates of the sound speed and wind fields.

VI. DISCUSSION

Because the problem of locating animals acoustically is nonlinear, it is not possible to use the linear theory in Ref. 12 to obtain the most accurate estimates for the winds, sound speeds, and animal's position. Further research beyond that considered in this paper will be required to obtain more accurate estimates than obtained with my solution of the nonlinear Eq. (10).

The new signal-processing algorithm selects the correct peaks from the cross-correlation functions. This is the first time that data have been used to validate the algorithm.[25] It is worth noting that the algorithm assumes that the receptions have been pre-filtered to suppress all calls except those from a single animal. This may sometimes be accomplished by bandpass filtering and time windowing. It may be possible to generalize this algorithm to work with multiple calls in the same frequency band which overlap in time at the receivers. A method for this has not been developed. Nonetheless, there are many cases in which time-windowed receptions are dominated by one call in one frequency band. Even in the jungle, there are times when signals would be dominated by a single call. For example, in the tropical rain forest in Suriname, there are many afternoons when the dominant signal is that of a Screaming Piha *Lipaugus vociferans* or a White Bellbird *Procnias alba*. This acoustic location technique needs to be tried in many different environments to evaluate its applicability.

ACKNOWLEDGMENTS

I thank Dr. Kurt Fristrup for introducing me to the marvelous world of a tropical rain forest in Suriname, where we began our collaboration in 1980. I thank Mary, Ari, Maia, and Cleo for making these ideas more enjoyable to contemplate. I thank my colleagues in the Department of Meteorology for providing a warm and intellectually exciting environment in which to think. I thank Andrew Jacobson, Drs. Dennis Lamb, George Young, Craig Bohren, and the reviewers for their comments.

APPENDIX A: ESTIMATING TRAVEL-TIME DIFFERENCES

Reference 25 provides a new algorithm for selecting the peaks in the cross-correlation functions which correspond to the differences in travel times of the first arrivals. A description of this algorithm is beyond the scope of this paper. This Appendix describes the parameters that are used for and from this algorithm for the bird at B1 in Fig. 3. The lag equations [Eq. (9) in Ref. 25] are satisfied when their misfits are less than or equal to 0.000 25 s. There are 118 candidates for the reference-lag sets, called TTD sets here. Of these, one is the best, yielding the best values for all three objective functions $S=29$, $|\mathbf{r}|=0.0157$, and $C=371$ (see Ref. 25 for a definition of the cost functions). The numbers of multipath satisfying the lag equations given by Eq. (9) in Ref. 25 are 12, 2, 8, 3, and 4 at receivers 1–5, respectively.

APPENDIX B: NONLINEARITY OF THE TRAVEL-TIME DIFFERENCES

The travel-time differences are related to the corrections of the initial positions of the source and receivers through the nonlinear Eq. (10). The purpose of this Appendix is to show when the linear approximation for these corrections breaks down. The initial estimates for the locations of the receivers and source are $\mathbf{r}_0(i)=(r_{0x}(i),r_{0y}(i),r_{0z}(i))$ and $\mathbf{s}_0=(s_{0x},s_{0y},s_{0z})$, respectively. Their actual positions are

$$\mathbf{r}(i)=\mathbf{r}_0(i)+\delta\mathbf{r}(i), \tag{B1}$$

$$\mathbf{s}=\mathbf{s}_0+\delta\mathbf{s}. \tag{B2}$$

Substituting these into Eq. (10) yields the sum of two functions. The first is linearly related to the parameters $\delta\mathbf{s}$, $\delta\mathbf{r}(i)$, c, u, v, and w by

$$L(i,j)=c_0^{-1}[F(i)-F(j)]-\frac{1}{c_0^2}\{u[r_{0x}(i)-r_{0x}(j)] + v[r_{0y}(i)-r_{0y}(j)]+w[r_{0z}(i)-r_{0z}(j)]\}+e_{ij}, \tag{B3}$$

and the other, NL, is nonlinearly related to the parameters. $F(i)$ is

$$F(i)=\cos\theta_x(i)[\delta r_x(i)-\delta s_x] + \cos\theta_y(i)[\delta r_y(i)-\delta s_y] + \cos\theta_z(i)[\delta r_z(i)-\delta s_z], \tag{B4}$$

where $\delta\mathbf{s}=(\delta s_x,\delta s_y,\delta s_z)$, $\delta\mathbf{r}(i)=(\delta r_x(i),\delta r_y(i),\delta r_z(i))$, and

$$\cos\theta_x(i)=\frac{r_{0x}(i)-s_{0x}}{|\mathbf{r}_0(i)-\mathbf{s}_0|}, \tag{B5}$$

$$\cos\theta_y(i)=\frac{r_{0y}(i)-s_{0y}}{|\mathbf{r}_0(i)-\mathbf{s}_0|}, \tag{B6}$$

$$\cos\theta_z(i)=\frac{r_{0z}(i)-s_{0z}}{|\mathbf{r}_0(i)-\mathbf{s}_0|} \tag{B7}$$

[Eqs. (78), (79) in Ref. 12].

Equation (B3) is the Taylor series expansion of Eq. (10) to first order, and NL contains higher orders. The second order terms in $\delta r_x^2(i)$ and δs_x^2 are

$$-\frac{1}{2cl_0(i)}\sin^2\theta_x(i)\,\delta r_x^2(i),$$

and

$$\frac{1}{2c}\left(\frac{\sin^2\theta_x(i)}{l_0(i)}-\frac{\sin^2\theta_x(j)}{l_0(j)}\right)\delta s_x^2,$$

respectively. The second order terms in the receiver and source corrections in the y and z coordinates are the same except x is replaced by y or z. There are other cross terms at second order such as $\delta s_x \delta s_y$, but it is unnecessary to write these out for this analysis.

The ratio of the second to first order variation in δs_x is

$$q_x(i,j)=\frac{\delta s_x}{2}\frac{\{[\sin^2\theta_x(i)/l_0(i)]-[\sin^2\theta_x(j)/l_0(j)]\}}{[\cos\theta_x(j)-\cos\theta_x(i)]}, \tag{B8}$$

with similar expressions for the ratios of second to first order terms in δs_y and δs_z. The ratio of the second to first order variation in δr_x is

$$p_x(j)=\frac{1}{2l_0(j)}\frac{\sin\theta_x(j)}{\cos\theta_x(j)}\,\delta r_x(j), \tag{B9}$$

with similar expressions for the y and z components of $\delta\mathbf{r}(j)$. Equations (B8), (B9) are approximately the fraction of the TTD due to nonlinearity in the corrections of the source and receiver locations. They may be solved to obtain estimates for the location corrections leading to a specified fractional nonlinearity as

$$\delta s_x=2q_x(i,j)\frac{\cos\theta_x(j)-\cos\theta_x(i)}{[\sin^2\theta_x(i)/l_0(i)]-[\sin^2\theta_x(j)/l_0(j)]}, \tag{B10}$$

$$\delta r_x(j)=2p_x(j)l_0(j)\frac{\cos\theta_x(j)}{\sin^2\theta_x(j)}. \tag{B11}$$

The order of magnitude for these equations is found using $O(\cos\theta_x)=O(\sin\theta_x)=1$, $O(l_0)=L$, where the typical distance from the animal to the receivers is L. The results for the order of magnitudes of δs_x and $\delta r_x(j)$ in terms of the nonlinearity of the TTDs are,

$$O(\delta s_x)=q_x(i,j)L, \tag{B12}$$

$$O(\delta r_x(j))=p_x(j)L. \tag{B13}$$

APPENDIX C: LOCATIONS AND TOMOGRAPHY

1. Solving for the vertical coordinate of the animal

This section provides an analytical solution for the vertical coordinate(s) of a hyperboloid at the point(s) where it intersects a vertical line that passes through a specified x-y location in the horizontal plane. Specifically, a solution is sought for s_z from Eq. (10) given (s_x,s_y), τ_{ij}, c,c_0, and (u,v,w) by rewriting it as

$$l_i-l_j=a_1, \tag{C1}$$

where,

$$a_1\equiv\frac{\tau_{ij}[1,1]}{n}+\frac{1}{nc_0^2}\{u[r_x(i)-r_x(j)]+v[r_y(i)-r_y(j)]+w[r_z(i)-r_z(j)]\},$$

and the sound slowness is given by

$$n\equiv 1/c.$$

In the solution of Eq. (C1), consider i and j fixed, and let c_0, c, and (u,v,w) be constants. In Eq. (C1), a_1 is independent of s_z. Squaring it yields

$$l_i^2+l_j^2-2l_il_j=a_1^2.$$

Substitute Eq. (11) for l_i and l_j in this and defining

$$a_2\equiv[s_x-r_x(i)]^2+[s_y-r_y(i)]^2+r_z^2(i)+[s_x-r_x(j)]^2+[s_y-r_y(j)]^2+r_z^2(j),$$

leaves

$$a_3+2s_z[s_z-r_z(i)-r_z(j)]=2l_il_j, \tag{C2}$$

where

$$a_3\equiv a_2-a_1^2.$$

Using Eq. (11), the square of the right side of Eq. (C2) can be written as

$$4l_i^2l_j^2=4[a_4+(s_z-r_z(i))^2][a_5+(s_z-r_z(j))^2], \tag{C3}$$

where

$$a_4\equiv(s_x-r_x(i))^2+(s_y-r_y(i))^2,$$

$$a_5\equiv(s_x-r_x(j))^2+(s_y-r_y(j))^2.$$

Equating the square of the right side of Eq. (C2) with the right side of Eq. (C3) yields a quadratic equation for s_z

$$\alpha_1+\alpha_2s_z+\alpha_3s_z^2=0, \tag{C4}$$

where

$$\alpha_1\equiv 4a_4a_5+4a_4r_z^2(j)+4a_5r_z^2(i)+4r_z^2(i)r_z^2(j)-a_3^2,$$

$$\alpha_2\equiv -8a_4r_z(j)-8a_5r_z(i)-8[r_z(i)r_z^2(j)+r_z(j)r_z^2(i)]+4a_3[r_z(i)+r_z(j)],$$

$$\alpha_3\equiv 4(a_4+a_5)+4(r_z^2(j)+r_z^2(i))+16r_z(i)r_z(j)-4a_3-4(r_z(i)+r_z(j))^2.$$

It is fortuitous that the solution for s_z is found from a quadratic equation as the cubic and quartic powers from Eqs. (C2) and (C3) vanish.

2. Estimating the standard deviation of ϵ_{ij} in Eq. (10)

Modeled TTDs are computed with a quantization interval of

$$\Delta_c=\tau_{ij}[1,1]\big|_{n=1/[c_0-(\delta c/2)]}-\tau_{ij}[1,1]\big|_{n=1/[c_0+(\delta c/2)]},$$

due to quantizing the speed of sound at interval δc. Here, $\tau_{ij}[1,1]$ from Eq. (10) is evaluated at the indicated values of the sound slowness. Similarly, modeled TTDs are computed at quantization intervals of

$$\Delta_u = \frac{\delta u}{c_0^2}(r_x(i) - r_x(j)),$$

$$\Delta_v = \frac{\delta v}{c_0^2}(r_y(i) - r_y(j)),$$

$$\Delta_w = \frac{\delta w}{c_0^2}(r_z(i) - r_z(j)),$$

for the three components of the wind. Discretization of the horizontal plane into cells δx and δy leads to a quantization of the modeled TTDs

$$d\tau_{ij} \cong \left|\frac{\partial \tau_{ij}}{\partial s_x}\delta x\right| + \left|\frac{\partial \tau_{ij}}{\partial s_y}\delta y\right|,$$

which is

$$\Delta_{\text{cell}} = c^{-1}\left\{\left|\frac{s_x - r_x(i)}{l_i} - \frac{s_x - r_x(j)}{l_j}\right||\delta x| + \left|\frac{s_y - r_y(i)}{l_i} - \frac{s_y - r_y(j)}{l_j}\right||\delta y|\right\}. \quad \text{(C5)}$$

The errors in the relative locations of the receivers lead to errors in the modeled TTDs by amount Δ_{rec}. This is a function of the location of the animal and the pair of receivers used for the TTD. Δ_{rec} is calculated numerically. The variance of the measured TTD, σ_1^2, due to noise and interference effects in the cross-correlation functions is estimated from the data (Appendix C in Ref. 25). Each of Δ_c, Δ_u, Δ_v, Δ_w, and Δ_{rec} are assumed to be statistically independent uniformly distributed random variables.

The straight path approximation and non-uniform spatial variations of the fields of sound speed and winds lead to a variance of

$$\sigma_2^2 = \sigma_{\text{straight}}^2 + \sigma_{\text{nonhomog}}^2,$$

in the TTDs. σ_{straight} is estimated from Eq. (14) of Ref. 12. Its value is 0.1 μs in this experiment. σ_{nonhomog} is estimated from

$$\delta\tau_{ij} \sim -\frac{L}{c_0^2}[dc + du + dv + dw], \quad \text{(C6)}$$

where the order of magnitude of non-uniform variations of (c,u,v,w) are (dc,du,dv,dw).

The noise term, e_{ij}, in Eq. (10) has zero mean and variance

$$\sigma^2 = \tfrac{1}{12}(\Delta_u^2 + \Delta_v^2 + \Delta_w^2 + \Delta_c^2 + \Delta_{\text{cell}}^2 + \Delta_{\text{rec}}^2) + \sigma_1^2 + \sigma_2^2. \quad \text{(C7)}$$

The factor, 1/12, comes about as the variance of a uniformly distributed random variable on the interval, Δ, is $\frac{1}{12}\Delta^2$.

[1] R. A. Walker, ''Some intense, low-frequency, underwater sounds of wide geographic distribution, apparently of biological origin,'' J. Acoust. Soc. Am. **35**, 1816–1824 (1963).

[2] W. A. Watkins and W. E. Schevill, ''Sound source location by arrival times on a non-rigid three-dimensional hydrophone array,'' Deep-Sea Res. **19**, 691–706 (1971).

[3] I. Magyar, W. M. Schleidt, and D. Miller, ''Localization of sound producing animals using the arrival time differences of their signals at an array of microphones,'' Experientia **34**, 676–677 (1978).

[4] C. W. Clark, ''A real-time direction finding device for determining the bearing to the underwater sounds of southern right whales *Eubalaena australis*,'' J. Acoust. Soc. Am. **68**, 508–511 (1980).

[5] L. E. Freitag and P. L. Tyack, ''Passive acoustic localization of the Atlantic bottlenose dolphin using whistles and echolocation clicks,'' J. Acoust. Soc. Am. **93**, 2197–2205 (1993).

[6] M. A. McDonald, J. A. Hildebrand, and S. C. Webb, ''Blue and fin whales observed on a seafloor array in the Northeast Pacific,'' J. Acoust. Soc. Am. **98**, 712–721 (1995).

[7] C. W. Clark, P. Marler, and K. Beeman, ''Quantitative analysis of animal vocal phonology: An application to swamp sparrow song,'' Ethnology **76**, 101–115 (1987).

[8] K. Bailey, ''The structure and variation of the separation call of the bobwhite quail (*colinus virginianus, Odontophorinae*),'' Anim. Behav. **26**, 296–303 (1978).

[9] D. Symmes, J. D. Newman, G. Talmage-Riggs, and A. K. Leiblich, ''Individuality and stability of isolation peeps in squirrel monkeys,'' Anim. Behav. **27**, 1142–1152 (1979).

[10] J. R. Buck and P. L. Tyack, ''A quantitative measure of similarity for *tursiops truncatus* signature whistles,'' J. Acoust. Soc. Am. **94**, 2497–2506 (1993).

[11] J. R. Potter, D. K. Mellinger, and C. W. Clark, ''Marine mammal call discrimination using artificial neural networks,'' J. Acoust. Soc. Am. **96**, 1255–1262 (1994).

[12] J. L. Spiesberger and K. M. Fristrup, ''Passive localization of calling animals and sensing of their acoustic environment using acoustic tomography,'' Am. Nat. **135**, 107–153 (1990).

[13] M. D. Collins and W. A. Kuperman, ''Focalization: Environmental focusing and source localization,'' J. Acoust. Soc. Am. **90**, 1410–1422 (1991).

[14] J. L. Krolik, ''Matched-field minimum variance beamforming in a random ocean channel,'' J. Acoust. Soc. Am. **92**, 1408–1419 (1992).

[15] S. Li and P. M. Schultheiss, ''Depth measurement of remote sources using multipath propagation,'' IEEE J. Ocean Eng. **18**, 379–387 (1993).

[16] S. Narasimhan and J. L. Krolik, ''Fundamental limits on acoustic source range estimation performance in uncertain ocean channels,'' J. Acoust. Soc. Am. **97**, 215–226 (1995).

[17] A. Kristensen, A. Caiti, F. Ingenito, M. D. Max, J. M. Berkson, M. D. Collins, L. T. Fialkowski, N. C. Makris, E. McDonald, J. S. Perkins, and W. A. Kuperman, ''Environmental confirmation of focalization,'' in *Full Field Inversion Methods in Ocean and Seismo-Acoustics*, edited by Diachok *et al.* (Kluwer Academic, Dordrecht, 1995), pp. 153–158.

[18] B. Cornuelle, C. Wunsch, D. Behringer, T. Birdsall, M. Brown, R. Heinmiller, R. Knox, K. Metzger, W. Munk, J. Spiesberger, R. Spindel, D. Webb, and P. Worcester, ''Tomographic maps of the ocean mesoscale-1: Pure acoustics,'' J. Phys. Oceanogr. **15**, 133–152 (1985).

[19] J. H. Woodhouse and A. M. Dziewonski, ''Mapping the upper mantle: Three-dimensional modeling of Earth structure by inversion of seismic waveforms,'' J. Geophys. Res. **89**, 5953–5986 (1984).

[20] D. K. Wilson and D. W. Thomson, ''Acoustic tomographic monitoring of the atmospheric surface layer,'' J. Atm. Oceanic Technology **11**, 751–769 (1994).

[21] J. L. Spiesberger, ''Passive acoustic localization enhanced with tomography and acoustic thermometry in the ocean,'' J. Marine and Freshwater Behaviour and Physiology **30**, 147–172 (1997).

[22] D. O. North, ''An analysis of the factors which determine signal/noise discrimination in pulsed-carrier system,'' Proc. IEEE **51**, 1016–1027 (1943).

[23] J. H. Van Vleck and D. Middleton, ''A theoretical comparison of the visual, aural, and meter reception of pulsed signals in the presence of noise,'' J. Appl. Phys. **17**, 940–971 (1946).

[24] C. W. Helstrom, *Statistical Theory of Signal Detection* (Pergamon, New York, 1975).

[25] J. L. Spiesberger, ''Linking auto- and cross-correlation functions with correlation equations: Application to estimating the relative travel times and amplitudes of multipath,'' J. Acoust. Soc. Am. **104**, 300–312 (1998).

[26] R. Liu and L. Tong, ''Special issue on blind systems identification and estimation,'' Proc. IEEE **86**, 1903–2089 (1998).

[27] A. W. Rihaczek, *Principles of High-Resolution Radar* (McGraw-Hill, New York, 1969), p. 498.

[28] H. P. Bucker, ''Use of calculated sound fields and matched-field detection to locate sound sources in shallow water,'' J. Acoust. Soc. Am. **59**, 368–373 (1976).

Longitudinal endolymph movements and endocochlear potential changes induced by stimulation at infrasonic frequencies

Alec N. Salt[a] and John E. DeMott
Department of Otolaryngology, Washington University School of Medicine, St. Louis, Missouri 63110

(Received 30 November 1998; revised 18 March 1999; accepted 18 April 1999)

The inner ear is continually exposed to pressure fluctuations in the infrasonic frequency range (<20 Hz) from external and internal body sources. The cochlea is generally regarded to be insensitive to such stimulation. The effects of stimulation at infrasonic frequencies (0.1 to 10 Hz) on endocochlear potential (EP) and endolymph movements in the guinea pig cochlea were studied. Stimuli were applied directly to the perilymph of scala tympani or scala vestibuli of the cochlea via a fluid-filled pipette. Stimuli, especially those near 1 Hz, elicited large EP changes which under some conditions exceeded 20 mV in amplitude and were equivalent to a cochlear microphonic (CM) response. Accompanying the electrical responses was a cyclical, longitudinal displacement of the endolymph. The amplitude and phase of the CM varied according to which perilymphatic scala the stimuli were applied to and whether a perforation was made in the opposing perilymphatic scala. Spontaneously occurring middle ear muscle contractions were also found to induce EP deflections and longitudinal endolymph movements comparable to those generated by perilymphatic injections. These findings suggest that cochlear fluid movements induced by pressure fluctuations at infrasonic frequencies could play a role in fluid homeostasis in the normal state and in fluid disturbances in pathological states. © *1999 Acoustical Society of America.* [S0001-4966(99)00808-5]

PACS numbers: 43.64.Nf, 43.64.Kc [RDF]

INTRODUCTION

Understanding how the endolymph of the inner ear is regulated is relevant to clinical conditions such as Meniere's disease, in which a volume increase (hydrops) of endolymph is believed to play a role. One important and controversial aspect of endolymph homeostasis is the question of whether longitudinal endolymph movements make a significant contribution. Studies using chemical flow markers have shown that longitudinal endolymph flow is exceedingly slow in the normal cochlea (Salt *et al.*, 1986; Sykova *et al.*, 1987; Salt and Thalmann, 1989) and makes little contribution to ion turnover (Salt and Thalmann, 1988). Under normal circumstances, turnover of ions in cochlear endolymph is believed to be dominated by local transport processes. However, recent studies have shown that under some conditions, higher rates of longitudinal endolymph flow occur. Salt and DeMott (1997) demonstrated that when artificial endolymph was injected at low rates into the second cochlear turn, a basally directed flow was induced at a rate which varied with the injection rate. This is consistent with studies which have shown that chemical markers injected into endolymph in volume move towards the endolymphatic sac (Guild, 1927; Lundqvist *et al.*, 1964). In contrast, an apically directed endolymph movement was generated by a reduction of endolymph volume induced by perfusion of the perilymphatic spaces with hypertonic medium (Salt and DeMott, 1995). Histologic studies have also demonstrated hyperosmotically induced morphologic changes of the endolymphatic sac consistent with it taking on a secretory, rather than resorptive, role under these conditions (Takumida *et al.*, 1989). These studies are consistent with extremely low rates of standing flow in the normal animal, and with the endolymphatic sac being a bidirectional site of volume regulation under conditions of volume deficiency or excess, in which longitudinal endolymph movements play a part.

We have recently found that some mechanical disturbances applied to perilymph also induce longitudinal endolymph movements. Salt and DeMott (1998) showed that perfusion of the perilymphatic spaces from scala tympani (ST) to scala vestibuli (SV) resulted in a small displacement of endolymph towards the basal turn by an amount which increased as perfusion rate increased. When the perfusion direction was reversed, with fluid flowing from SV to ST, endolymph was displaced apically. The observation that sustained flow through the perilymphatic spaces resulted in a longitudinal endolymph displacement raised the possibility that oscillating, low-frequency fluctuations applied to perilymph would likely induce cyclical longitudinal displacements of endolymph. Inner ear fluid pressures are not static, but fluctuate with cardiac and respiratory cycles by more than 0.3 mm Hg (Bohmer, 1993), which represents more than 120 dB *re* 20 μPa. Low-frequency pressure pulses up to 20 mm Hg (more than 160 dB) occur in cerebrospinal fluid (CSF) during common activities such as coughing, sneezing and swallowing (Marchbanks and Reid, 1990). The low-frequency component of such pulses is transmitted to the cochlea through the cochlear aqueduct, which in humans is believed to attenuate only frequencies above 20 Hz (Gopen *et al.*, 1997). The present study was therefore designed to investigate cochlear responses to stimulation with infrasonic frequencies. To achieve this goal a transducer was developed which allowed us to apply low-frequency stimulation to the perilymph via a fluid-filled pipette inserted into a scala. The

[a]Electronic mail: salta@msnotes.wustl.edu

present paper reports the effect of such stimulation on the endocochlear potential and on longitudinal endolymph movements measured by ionic marker techniques.

I. METHODS

A. Animal preparation

This study used 21 pigmented guinea pigs weighing 300–500 g, which were anesthetized with Inactin (sodium thiobutabarbital; RBI chemicals, MA), given intraperitoneally at a dose of 100 mg/kg. The left external jugular vein was cannulated and supplementary doses of Inactin were given intravenously as required to maintain deep surgical anesthesia. Body temperature was maintained at 38 °C–39 °C with a thermistor-controlled heating pad. The head was secured in a rigid head-holder and the right cochlea was exposed by a ventrolateral approach. A tracheal cannulation was performed and animals were artificially ventilated, maintaining an end-tidal CO_2 level close to 5%. Unless specified otherwise, animals were given pancuronium bromide prior to recordings (administered intravenously: to effect) as a muscle relaxant.

B. Stimulus delivery

Stimuli in the frequency range from 0.1 to 10 Hz were delivered to the perilymphatic spaces through a fluid-filled pipette placed in the basal turn of SV or ST. The pipette had a tip diameter of 80 to 120 μm, and was inserted into a hole in the bony wall of the scala which had been drilled with a sharpened needle. A bead of paint near the tip of the pipette provided a flexible gasket to aid in sealing the pipette to the bony wall. The pipette was connected by polyethylene tubing to the outer casing from a 60-ml syringe, with the plunger removed and the back sealed with a flexible rubber diaphragm. The syringe, tubing and pipette were filled with an artificial perilymph containing (in mM) NaCl (125), KCl (3.5), $CaCl_2$ (1.3), $NaHCO_3$ (25), $MgCl_2$ (1.2), NaH_2PO_4 (0.75) and glucose (5). After bubbling with 5% CO_2, the *p*H of this solution was close to 7.4. The rubber diaphragm on the syringe casing was driven by a Bruel & Kjaer model 4810 mini-shaker. Pressure in the stimulus delivery line was measured by a MP-15D transducer (Micron Instruments Inc, Los Angeles, CA). Stimuli consisting of five cycles (one cycle linear rise-time, three cycles plateau, one cycle linear fall time) were generated by a Wavetek 275 arbitrary waveform generator, attenuated and delivered to the 4810 mini-shaker by a power amplifier capable of dc output. The frequency response of this system, measured by the pressure transducer in the line, was exceptionally flat, varying by less than 0.5 dB across the range from 0.1 to 20 Hz.

C. Endocochlear potential measurement

In 15 of the experiments where endolymphatic flow was not measured, endocochlear potential (EP) was recorded from a 500 mM KCl-filled pipette. The pipette was inserted into the endolymphatic space of the second turn through an approximately 30 μm access fenestra made in the lateral wall over the stria vascularis. Electrodes were beveled to a tip

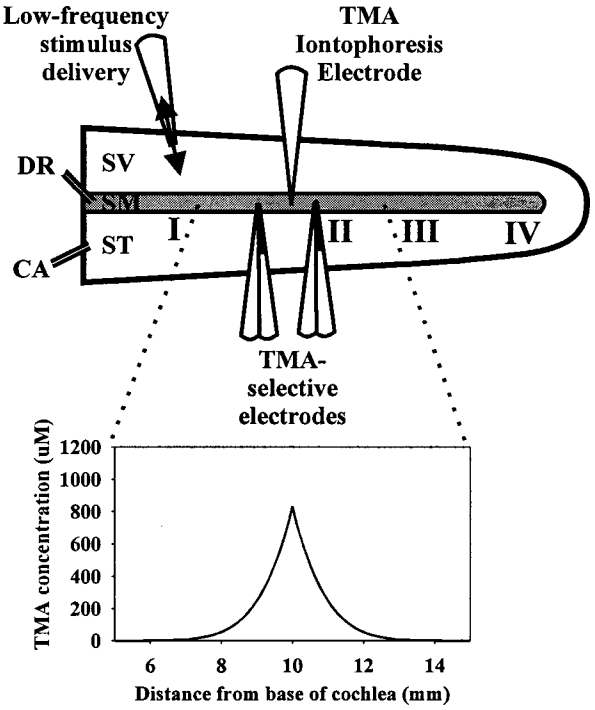

FIG. 1. Schematic representation of the technique for endolymph flow measurement *in vivo*. The upper panel shows the cochlea uncoiled with the three scalae labeled (scala vestibuli: SV; scala media: SM; scala tympani: ST). In addition, the cochlear aqueduct (CA) and ductus reuniens (DR) are shown. The four cochlear turns are indicated by Roman numerals. Low-frequency stimuli were delivered by a fluid-filled pipette inserted into SV. Flow was measured in turn II using an ionic marker system which required up to three electrodes as shown. The flow marker (TMA) was iontophoresed into SM and its concentration measured by two TMA-selective electrodes, one placed 0.5 mm basal and one 0.5 mm apical to the iontophoresis. The distance between electrodes has been exaggerated in the figure for clarity. The lower panel shows the variation of concentration with distance which occurs after the marker has been iontophoresed for 20 min. Longitudinal movements of endolymph will displace this profile, resulting in an increased concentration at one electrode and a decreased concentration at the other, as detailed in the text.

diameter of 2–3 μm. Electrodes were connected by Ag/AgCl junctions to a high input impedance electrometer ($>10^{14}\,\Omega$). No capacitance compensation was employed. Potentials were measured with respect to a Ag/AgCl reference cell, placed under the skin on the muscles of the neck.

D. Endolymph flow and area measurement

Endolymph movements were measured in the second cochlear turn in six experiments. Flow was quantified using tetramethylammonium (TMA^+) as a marker ion, as described in prior publications (Salt and DeMott, 1995, 1997). The experimental design in its most complete form is schematized in Fig. 1. Three electrodes were inserted into endolymph through access fenestras as described above, separated along the lateral wall of the cochlea by approximately 0.5 mm. The middle electrode of the three contained 160 mM TMACl, from which TMA^+ was iontophoresed into endolymph by a current of 50 nA. The other two electrodes, one placed apically and one placed basally to the site of iontophoresis, were each double-barreled TMA^+-selective electrodes, used to monitor the spread of TMA^+ in the apical and basal directions. The method utilizes the fact that marker

spread from the injection site is dominated by diffusion, which results in a highly peaked concentration profile centered on the injection site, as shown in the figure. Once this profile is established, a longitudinal movement of endolymph would give a concentration increase at one electrode and a decrease at the other, depending on the direction of longitudinal movement. The degree of endolymph movement was derived from marker concentration data using a mathematical model as described in previous studies (Salt and DeMott, 1997). In the present study, measurements with two ion-selective electrodes showed that marker changes were dominated by flow effects alone, therefore, later experiments used a technically simplified procedure in which only a single ion-selective electrode was used to record marker changes. In these experiments, the single ion-selective electrode was randomly placed either apical or basal to the injection site. In flow measurement experiments, EP was measured from the potential barrel of one of the ion-selective electrodes.

The TMA^+-selective electrodes were manufactured and calibrated in accordance with methods which are fully described elsewhere (Salt and Vora, 1991; Salt and DeMott, 1997). For the electrodes used in this study we found a mean slope of 74.8 mV/decade TMA change (s.d. 13.3) and a linear response detection limit of 132 μM (s.d. 74), values which were comparable with our prior studies. Iontophoresis pipettes were made from single-barreled glass electrodes with internal fiber, beveled to a tip diameter of 2–3 μm. Electrode tips were filled to the shoulder with 0.5% agarose gel, to prevent volume displacement of the electrolyte. Electrodes were then back-filled with 160 mM TMACl and stored in the same solution to allow the electrolyte to equilibrate with the gel. An optically coupled iontophoresis unit (World Precision Instruments, Sarasota, FL, Model 260) was used to eject TMA into endolymph.

E. Data collection and analysis

The EP, marker ion concentration and pressure responses to low-frequency stimuli were collected using an Analogic Data Precision D6000 under the control of a computer. Peak to peak amplitude measurements were made and logged on line. In addition, waveforms were stored as required for off-line analysis. Statistical significance was determined using Sigmastat software (Jandel Corp, San Rafael, CA).

The care and use of the guinea-pigs used for this study were approved by the Animal Studies Committee of Washington University, St. Louis, MO, Approved protocol nos. 95069 and 98092.

II. RESULTS

A. Stimulus delivery to scala vestibuli

1. Stimulus-induced EP responses

Delivery of 1-Hz stimulation to SV resulted in large changes in the EP measured from the second turn, as shown in Fig. 2. In this experiment, the baseline EP measured in quiet, prior to the delivery of the stimulus sequence, was 72.4 mV. The EP was modulated with 1-Hz stimulation, generating a cochlear microphonic (CM) comparable to that

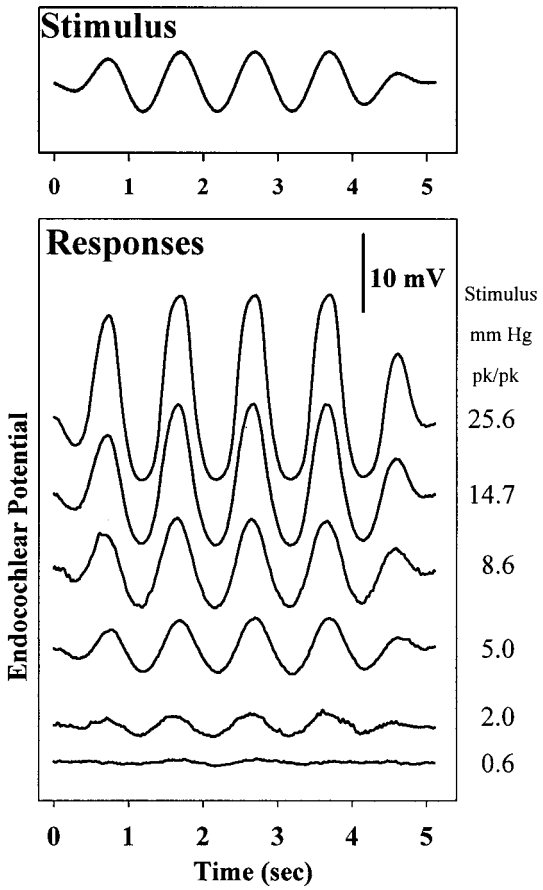

FIG. 2. Endocochlear potential changes (lower panel) in response to a 1-Hz stimulus (upper panel), delivered to scala vestibuli at varying levels. As stimulus level increases large potential changes equivalent to a cochlear microphonic are generated, amounting to 23.7 mV pk/pk at the highest stimulus level used. The baseline EP in quiet was 72.4 mV, a value which was not changed systematically by any of the stimuli delivered.

with stimuli in the auditory range. At the highest level shown, the CM (i.e., the stimulus-induced EP change recorded from the electrode in the endolymphatic space) was 23.7 mV pk/pk. This consisted of an EP depolarization to 64.3 mV and a hyperpolarization to 88.0 mV. The asymmetry of the response is equivalent to the positive summating potential seen in response to low-frequency stimuli in the auditory range. The CM was approximately in-phase with the applied stimulus, with potential increase taking place during the application of positive pressure to SV. None of these stimuli had any sustained effect on the EP value in quiet. For this experiment, the EP measured following the highest stimulus level used was 71.1 mV. The traces show that the cochlea responds to stimulation at infrasonic frequencies in a manner quite comparable to sounds within the auditory range.

One initial concern was the possibility that the CM could be artifactual in origin, since it was large and in-phase with the applied stimulus. To verify the physiological origins of the response, we measured CM amplitude with the stimulus delivery pipette just touching the fluid of SV, but not inserted or sealed into the fenestra, and compared it with the response when the pipette inserted into the scala until a seal was achieved. The response to a 1-Hz stimulus was 17.9 mV pk/pk with the pipette sealed into the fenestra, compared

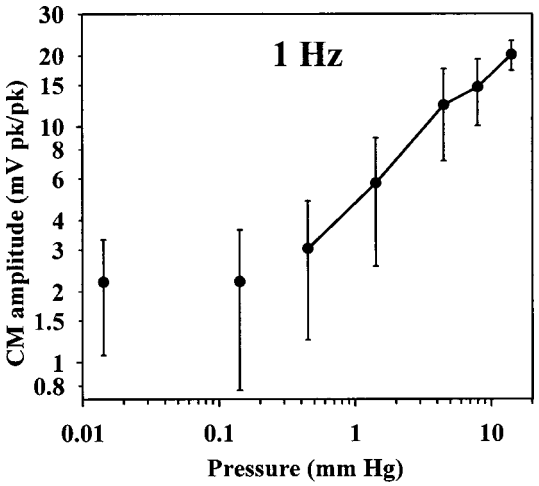

FIG. 3. Mean cochlear microphonic (CM) amplitude in the second cochlear turn of 12 animals during 1-Hz stimulation applied to scala vestibuli. Bars indicate standard deviation. The solid line connects the points which are above the noise floor.

with 1.1 mV pk/pk with the pipette just touching the perilymph. This confirms that the CM originates as a physiologic response to induced pressure change. Subsequent studies with different stimulus delivery conditions (presented below) also support this view.

The mean amplitude of the CM as a function of the applied level of a 1-Hz stimulus in 12 animals is summarized in Fig. 3. The CM shows the characteristic, approximately linear increase when plotted on logarithmic axes. One issue in these input/output curves concerns the noise floor, which amounted to a few millivolts in many animals. The higher background noise in this preparation was generated by EP fluctuations associated with respiration, which were exacerbated by the perforation and pipette insertion into SV, as required for stimulus delivery.

Another difference in this input/output function is that it showed no tendency to decline with increasing levels, after reaching a maximum. For low-frequency stimuli in the audible range, CM input/output functions typically show a broad maximum, with decreasing responses at higher stimulus levels. For 1-Hz stimulation we found the CM amplitude to increase up to the point where damage to the cochlea occurred. Stimulus levels 10 dB higher than those shown here were found to cause sustained EP decrease and were hence avoided. This is demonstrated in Fig. 4, in which the CM amplitude and the EP in quiet after each stimulus were monitored. Each symbol on the upper three panels represents the delivery of a single stimulus, which was increased progressively until EP decrease was observed. The CM input/output function from this experiment shows that it was not possible to establish a response maximum to 1-Hz stimulation without risking damage to the ear. In this respect the responses to stimulation at infrasonic frequencies differ from those to stimuli in the auditory range.

The amplitude of the induced CM varied with stimulus frequency, as summarized in Fig. 5. The CM responses of maximal amplitude were generated with stimuli of 1–3 Hz, although large responses were observed across the entire range of frequencies tested.

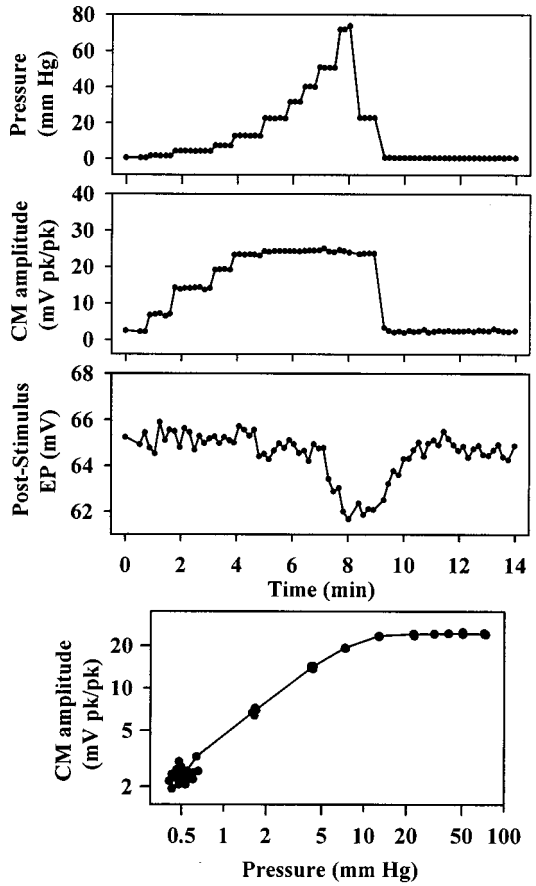

FIG. 4. Example experiment in which stimuli were driven to high levels. In the upper three panels, each point represents a single stimulus delivered at the pressure indicated in panel 1. The CM magnitude is shown in panel 2, and the poststimulus EP, measured in quiet is shown in panel 3. With high stimulus levels, the EP measured in quiet showed a decline which took some minutes to recover. The lower panel shows the input/output function for this animal, based on all stimulus levels used in the upper panels.

2. Endolymph movements

Longitudinal movements of endolymph were quantified using low levels of TMA as a flow marker, as described in the methods. Figure 6 shows an experiment in which flow

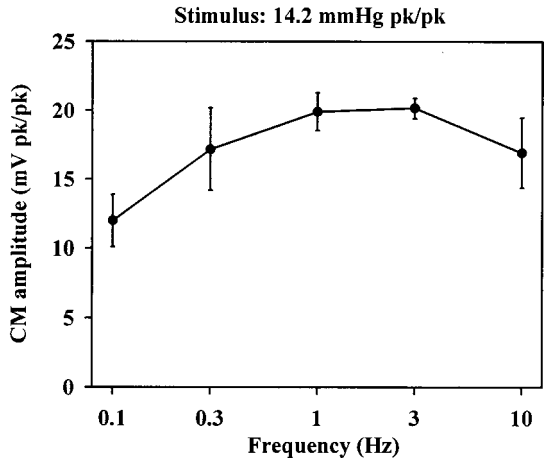

FIG. 5. Dependence of CM amplitude on applied stimulus frequency, averaged in five animals. Largest responses were generated with stimuli of 1–3 Hz. Bars indicate standard deviation.

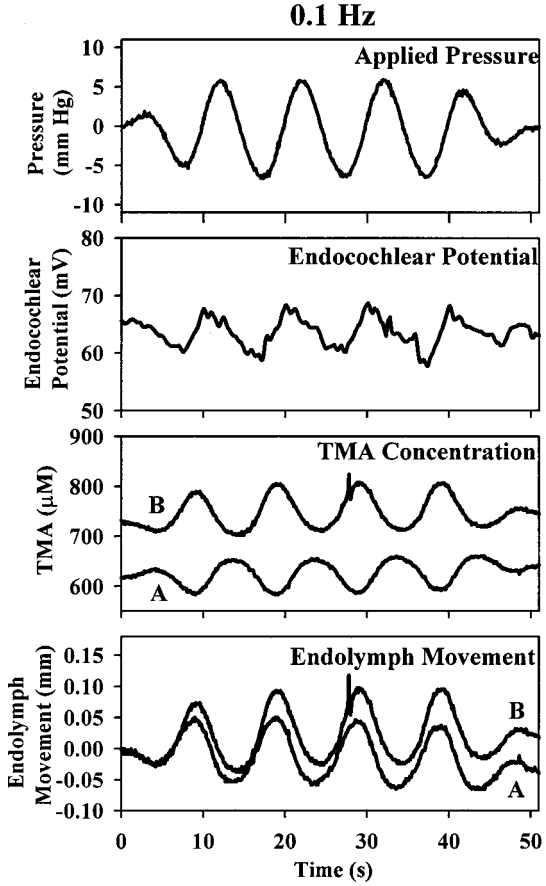

FIG. 6. Measurement of endolymphatic movements induced by 0.1-Hz stimulation. The stimulus applied to scala vestibuli is shown in panel 1, and induced endocochlear potential changes are shown in panel 2. As a result of stimulation, changes of concentration of TMA (the volume flow marker in endolymph) are observed by the TMA-selective electrodes, one placed basally (B) and the other placed apically (A) to the TMA injection site (see Fig. 1 and Sec. I for details of the technique). The observation that concentration changes are opposite in phase at the two sites is consistent with a longitudinal oscillation of endolymph. Based on the calculated concentration profile of marker in endolymph, the amount of endolymph movement can be quantified for the two traces, as given in panel 4.

marker was monitored simultaneously with two recording electrodes, one basal and one apical to the site at which TMA was iontophoresed into endolymph. In this experiment, a longitudinal movement of endolymph would be expected to induce oppositely-directed concentration changes at the two recording electrodes, since the endolymph concentration is maximal at the site of injection (see Fig. 1). This figure shows that delivery of a 0.1-Hz stimulus induces cyclical changes of both the EP and the measured TMA concentration. The TMA changes are seen to be in opposite phase at the two recording locations, demonstrating that they arise as a result of longitudinal movements of endolymph. The two TMA concentration time courses were transformed to longitudinal endolymph movements, based on the TMA profile as a function of distance in the endolymph calculated for the individual experiment. This calculation takes into account the opposite direction of the concentration gradient on the basal and apical sides of the TMA injection, so that the endolymph movement indicated by the two electrodes is comparable (lower panel). In later experiments, the complexity of the experiment was reduced by using only one ion-selective electrode to monitor marker changes.

A summary of the variation of EP changes (CM) and flow as a function of stimulus frequency is given in Fig. 7. To facilitate within cycle comparisons, repeated response cycles within the plateau portion of the stimulus were averaged for each individual response, and then results across the six experiments were averaged. Stimulus, endocochlear potential and longitudinal endolymph displacement waveforms were measured for five frequencies from 10 to 0.1 Hz. Note that the time window varies from 0.1 to 10 s, representing one period of the stimulus. Stimuli were delivered at a constant attenuation setting, resulting in some variation in the applied stimulus pressure (upper row). The EP data in these experiments (middle row) again demonstrates a maximum CM amplitude with stimulus frequencies of 1–3 Hz. The phase the CM was similar to the applied stimulus, except at 10 Hz. At the lower frequencies tested, the CM amplitude was smaller and the waveform became distorted. Induced endolymph displacements were found to be small at 10 Hz but increased systematically as frequency decreased. At 0.1 Hz, the cycle-by-cycle longitudinal displacement of endolymph averaged 0.16 mm. To put this figure in perspective, since the measurement is made in the second turn with approximately 8 mm of endolymph apical to the measurement site, this represents approximately 2% of the endolymph volume being displaced with each cycle. It was also notable that with 0.1-Hz stimulation the measured endolymph displacement was closer to sinusoidal than the CM. The phase of the flow also varied more across frequency than did the CM. At 3 Hz, flow showed a similar response phase to the CM, while at 0.1 Hz, flow was almost in opposite phase to CM. One technical concern in these experiments was the possibility that ion-dependent voltages could be contaminated by the CM, due to the slower response time of the ion electrode relative to the potential recording. In all experiments we therefore delivered stimuli and recorded concentration-dependent potentials from endolymph before volume marker was injected. To exclude the possibility that such changes could contaminate flow measurements, baseline traces in the absence of volume marker, which were dependent on electrode characteristics and therefore very stable with time, were subtracted from responses recorded in the presence of the volume marker. The subtracted component was small at 0.1 Hz (0.013 mV without marker, 0.054 mV with marker for the six experiments in Fig. 7) but increased with stimulus frequency while the amount of flow decreased (corresponding figures at 1 Hz: 0.019 and 0.027 mV, and at 10 Hz: 0.038 and 0.038 mV). This procedure ensured that any waveform component that did not arise from TMA movements was eliminated.

3. Dependence on stimulus delivery conditions

The amplitude of CM responses to infrasonic stimuli was found to vary with the scala into which injection was made and with the presence or absence of an outlet in the opposite perilymphatic scala. All the data presented up to this point were collected for injections into SV with no outlet. Figure 8 shows the variation in CM responses in an ex-

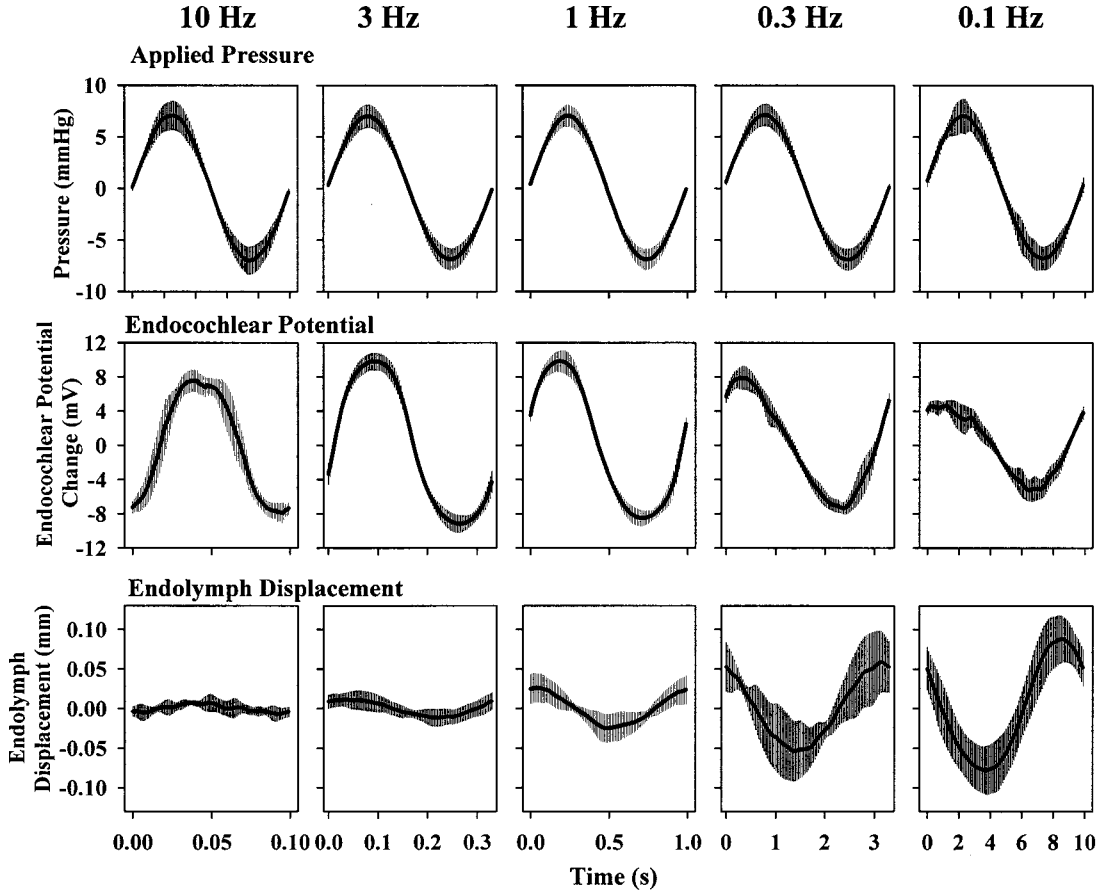

FIG. 7. Summary of mean (±s.d.) endocochlear potential change (middle row) and endolymph displacement (lower row) as stimulus frequency was varied in six experiments. Individual plateau cycles of each response were averaged to generate an averaged single response cycle. Endocochlear potential changes are largest in the 1–3-Hz range. In contrast, endolymph displacement becomes larger as frequency decreases.

periment performed for stimuli applied to SV, with and without an outlet (80–100 μm diameter) made in the basal turn of ST. In the example shown, making the outlet reduced the CM amplitude to low frequency stimulation, especially at frequencies above 1 Hz. However, there was considerable interanimal variation and the CM amplitude reduction with 1-Hz stimulation was not statistically significant (*t*-test, $p = 0.18$).

When stimuli were delivered to ST with no outlet, CM was consistently smaller than with stimulus delivery to SV. Figure 9 shows the response amplitudes as a function of stimulus frequency for one experiment, and a summary across experiments for 1-Hz stimulation. The CM was significantly increased when an outlet is made in SV (*t*-test, $p = 0.002$). The amplitude of cochlear responses to low-frequency stimulation thus depends on the site at which the stimulation is delivered and whether any other perforations of the otic capsule exist. The phase of the response also varies with the site of the applied stimulation, as shown in Fig. 10. For stimuli applied to SV the CM was approximately in phase with the stimulus, while CM generated by stimuli applied to ST was out of phase with the applied stimulus. This further supports the view that the large amplitude responses we record cannot arise as a stimulus-dependent artifact, but instead represent a response of the cochlea to the applied pressure.

4. Spontaneous middle ear muscle contractions

In some guinea pig preparations in which the bulla was opened, but prior to being given muscle relaxant, spontane-

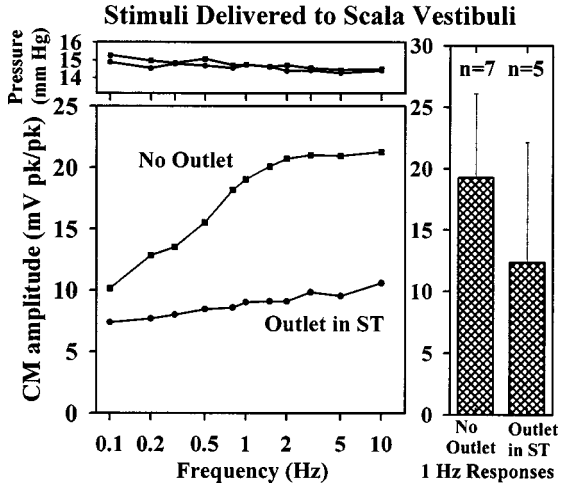

FIG. 8. Left: Example of the dependence of CM magnitude for injections into scala vestibuli for the case when no outlet is present in scala tympani (squares), or when an outlet in ST is present (circles). For each stimulus, the pressure (upper panel) and CM amplitude (lower panel) are given. Right: Summary of CM amplitudes at 1 Hz for the number of experiments indicated. Although the mean response is lower when an outlet is present in ST, the difference between the two groups was not statistically significant (*t*-test, $p = 0.18$).

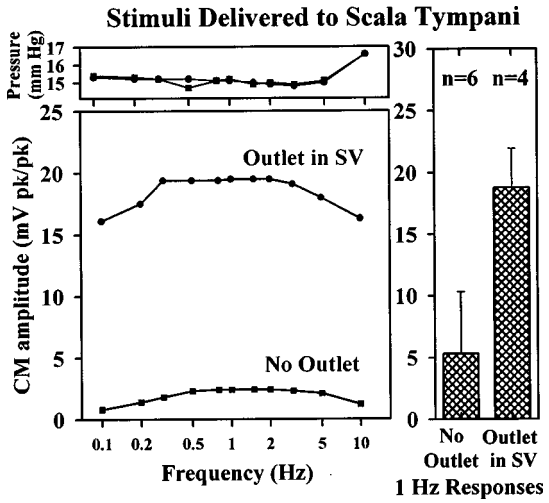

FIG. 9. Left: Example of the dependence of CM magnitude for injections into scala tympani for the case when no outlet is present in scala vestibuli (squares), or when an outlet in SV is present (circles). For each stimulus, the pressure (upper panel) and CM amplitude (lower panel) are given. Right: Summary of CM amplitudes at 1 Hz for the number of experiments indicated. The mean response is significantly higher when an outlet is present in SV (*t*-test, $p = 0.002$).

ous contractions of the middle ear muscles were evident. When viewed through the operating microscope, the tympanic membrane was seen to be transiently displaced medially before returning to its original position. During each contraction, the stapes was displaced into SV and the round window membrane was observed to be displaced outward from the cochlea. Endocochlear potential was recorded from the second turn of two animals which were undergoing spontaneous muscle contractions. In one of these animals, TMA injection and TMA-recording electrodes were placed to

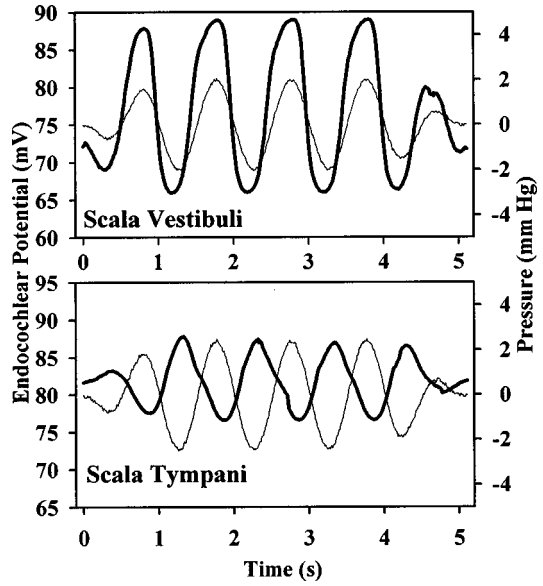

FIG. 10. Comparison of endocochlear potential changes (heavy lines) in response to 1-Hz stimulation applied to scala vestibuli (upper panel) or to scala tympani (lower panel) in different experiments. For scala tympani stimulation, an outlet was present in scala vestibuli. The applied stimuli, measured simultaneously with the response, are shown as thinner lines. Note that the stimulus-induced CM response reverses phase with respect to the stimulus when applied to the opposing perilymphatic scala.

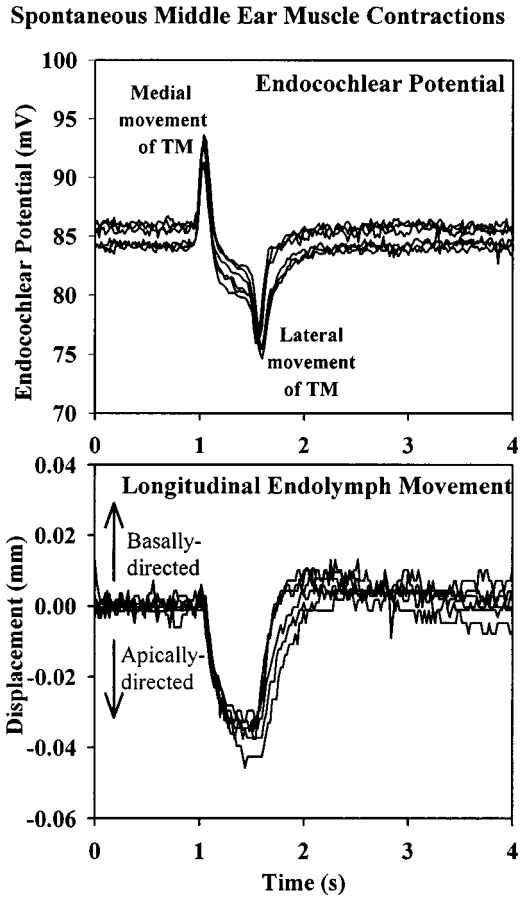

FIG. 11. Upper panel: Endocochlear potential changes resulting from six spontaneous middle ear muscle contractions in one preparation. Data were aligned so the initial peaks were overlaid. The amplitude of EP change averaged 16.9 mV. Lower panel: Longitudinal endolymph movements associated with spontaneous middle ear muscle contractions, as measured by induced flow marker concentration changes. With each contraction, endolymph is displaced apically by an average of 0.034 mm for the duration of the contraction, which in this case averaged 0.54 s.

quantify longitudinal endolymphatic movements. The findings in response to repeated spontaneous contractions observed over a 43-min period are summarized in Fig. 11. Contractions resulted in sizeable, transient EP changes which averaged 16.9 mV pk/pk (s.d. 0.9, $n = 6$) with a contraction duration (assessed by the time difference between positive and negative peaks) which averaged 0.54 s (s.d. 0.03, $n = 6$). Spectral analysis of the EP waveforms showed the response to be dominated by components near 1 Hz. Associated with the EP change was an apically directed displacement of endolymph which averaged 0.034 mm (s.d. 0.003, $n = 6$). In contrast to the EP change, the endolymph displacement was sustained throughout the muscle contraction. Upon release of the contraction, endolymph returned in the basal direction, showing a small overshoot. The magnitude of these observed changes suggests that pressure waves of comparable amplitude to those delivered in the present study may be generated by a physiological process, specifically the contraction of middle ear muscles.

III. DISCUSSION

The present study demonstrates that under some conditions, pressure fluctuations applied to the perilymph gives

rise to substantial EP changes and small longitudinal movements of endolymph. These findings are consistent with an earlier study in which sustained injections into the cochlea were found to induce longitudinal endolymph movements (Salt and DeMott, 1998). In that study, it was found that endolymph displacement varied as a function of the flow rate through the perilymphatic space, with flow directed from SV to ST generating an apically directed endolymph displacement. The present study also found that for infrasonic (0.1 Hz) stimuli, positive pressure applied to SV resulted in apically directed endolymph movement. However, we have further shown that for higher frequencies of stimulation, the phase relationship between applied pressure and endolymph displacement varies, as depicted in Fig. 7. By varying stimulus conditions, we have confirmed that endolymph displacements and EP changes appear to be associated with conditions when longitudinal perilymph flow occurs. This corresponds to periods when a pressure differential is present across the basilar membrane, which is generally regarded as the stimulus for transduction (Voss *et al.*, 1996). Stimulation conditions which produce little perilymph movement along the length of the cochlea, such as stimulus delivery to ST without an outlet, were shown to produce small CM responses in the present study. These findings are in agreement with the small EP changes and longitudinal endolymph movements seen with sustained injections under similar conditions (Salt and DeMott, 1998). Under conditions where larger perilymph movements occur, such as with stimulus delivery to SV (where the round window and cochlea aqueduct provide a compliance and outlet respectively), or delivery to ST with an outlet in SV, then larger CM responses are induced. The physiologic significance of this dependence is that the variety of pressure fluctuations in the CSF, which enter ST of the cochlea through the cochlear aqueduct, will have only minor effects on transduction and the endolymphatic system. Pressure changes associated with postural changes, respiration, coughing, sneezing, heavy lifting, etc., which are transmitted to the cochlea by the CSF, would therefore not be expected to cause endolymphatic disturbance in the normal state.

In contrast, we have shown that high-amplitude, low-frequency movements of the stapes result in significant endolymph disturbances, in the form of EP changes and longitudinal fluid movements. Such movements of the stapes can be induced by sustained or alternating pressures applied to the ear canal (e.g., barometric pressure changes, impedance audiometry, etc.) sustained or alternating pressures applied to the middle ear space (e.g., Valsalva maneuver, sniffing), or may be generated by the middle ear reflex. The spontaneous contractions which we observed in anesthetized guinea pigs have been previously shown by electromyography to originate from contractions of the tensor tympani muscle (Avan *et al.*, 1992). Contraction of the tensor tympani occurs during swallowing (Salen and Zakrisson, 1978), but the role of this contraction in swallowing has remained unexplained since pressure measurements suggested that it does not play a significant role in the ventilation of the middle ear space (Honjo *et al.*, 1983). Indeed, one author has argued that the tensor tympani fulfills no function in the middle ear (Howell, 1984). In the present study, the observation that longitudinal endolymph movements are induced by presumed contractions of the tensor tympani muscle raises the possibility that endolymph homeostasis is not completely a continuous process, as is generally believed, but instead may partially depend on periodic movements of the middle ear structures. In the same manner as the middle ear pressure is only corrected periodically during swallowing, endolymph volume regulation may also depend in some way on periodically occurring stapes movements. While our results do not demonstrate that endolymph volume is affected by middle ear movements, the concept that, in pathological states, endolymph volume regulation is in some manner related to middle ear function is supported by a number of studies. Montandon *et al.* (1989) reported that 82% of patients with Meniere's disease gained relief from vertigo attacks by the insertion of tympanostomy tubes in the affected ear. This observation was supported in animal studies by Kimura and Hutta (1997). They found significantly reduced endolymphatic hydrops in guinea pigs following ablation of the endolymphatic sac if the tympanic membrane was also perforated. In both of these studies, it is not clear whether changes of middle ear pressure, gas composition, or changes in mechanical properties contribute to the cochlear fluid changes. It has also been reported that pressure fluctuations delivered to the middle ear, consisting of sustained pressure with superimposed 9-Hz or 200-Hz sine waves of twice the amplitude (up to a combined total of 2 kP; approximately 15 mm Hg) improved cochlear sensitivity (Densert, 1987) and electrocochlographic responses (Densert *et al.*, 1997) in Meniere's patients. Sakikawa and Kimura (1997) found that guinea pigs following endolymphatic sac ablation developed significantly less hydrops when pressure was applied twice a day to the external ear canal, while hydrops was not affected by overpressure treatment of the animal in a pressure chamber. The mechanism of these effects remains unknown, but the possibility that endolymph volume regulation is influenced by middle ear status remains an intriguing possibility.

Our finding of endolymph movements induced by tympanic membrane displacements may help explain observations that low-frequency (0.1 to 10 Hz) or static pressures applied to the external ear canal results in vestibular stimulation and nystagmus in guinea pigs (Parker *et al.*, 1968; Reschke and Parker, 1970; Parker and von Gierke, 1971). The applied pressure stimuli found to be most effective in one of these studies (Parker *et al.*, 1968) were in the range from 0.1 to 10 Hz, which is comparable with the present study. The possibility that endolymph displacements played a part in this phenomenon was suggested by the authors as a possible explanation of their observations. Our study represents the first direct confirmation that endolymph movements are induced by middle ear movements.

Middle ear pressure changes have been shown to influence vestibular nerve activity in anesthetized cats (Ito *et al.*, 1990). The sensitivity of the vestibular response to middle ear pressure changes has also been shown to be reduced by surgical closure of the cochlear aqueduct (Suzuki *et al.*, 1994). These findings are in accordance with our proposed requirement for perilymph flow along the cochlea to occur in

order to generate endolymph movements. By closing the cochlear aqueduct, which provides an outlet for perilymph movements, endolymphatic movements would be reduced. In humans, visual field displacements have been observed during exposure to intense transient acoustic stimuli at repetition rates of 0.6 to 6 times per second (Parker *et al.*, 1978). This stimulation is likely to induce the acoustic reflex repeatedly, resulting in cyclical, low-frequency movements of the stapes. There is, therefore, considerable accumulated data to support the view that the inner ear is in some manner influenced by middle ear status, in which the findings of the present study are likely to play some part.

The CM response we have observed to infrasonic stimulation is likely to be generated by the hair cells in a manner identical to that for sounds in the auditory range. The response follows the dynamics of the stimulus, inverts when stimulation is applied to the opposite perilymphatic scala, and has growth and saturation properties consistent with the documented nonlinearities of mechanoelectrical transduction by the hair cells. On the other hand, we cannot yet exclude the possibility that voltage-induced changes of other ion transport processes, occurring in tissues other than the hair cells, may contribute to the observed response. An important issue raised by the study concerns the large CM magnitude with infrasonic sounds, to which the ear has generally been regarded as insensitive. Based on sensitivity functions of the CM, Dallos (1970) suggested that low-frequency sensitivity was attenuated by the helicotrema, which shunted pressure differences between SV and ST. This apparent discrepancy is largely explained by the fact that physiologic pressure fluctuations at low frequency, and the stimuli presented here, are at higher levels than those presented within the auditory range. Given the normal pressure fluctuations present in the inner ear of the guinea pig, which are approximately 0.3 mm Hg at a frequency near 1 Hz, a frequency which is established by the respiratory rate (Bohmer, 1993) and the lack of indication of any damage to the cochlear at the applied stimulus levels used here, we believe the levels used are not beyond the physiologic range. Furthermore, the observation that middle ear muscle contractions elicit responses of similar magnitude and frequency confirm that appropriate levels were used for the stimulus frequencies under test. We therefore conclude that the ear does become less sensitive as stimulus frequency is reduced, but the levels of stimulation are typically at a high enough level that, even with the attenuation provided by the helicotrema, large responses are elicited. By an extrapolation of Dallos' data from guinea pigs we can estimate that a stimulus of 100 dB SPL would be required to elicit a 3 μV response at 1 Hz. Comparing our response amplitude to 1 Hz in Fig. 4 of 5.75 mV at 1.42 mmHg (140 dB SPL), we can see that our response is 66 dB greater amplitude with a stimulus of 40 dB higher amplitude, which is a 26-dB difference. This difference may be substantially accounted for by the fact we are comparing airborne delivery of stimuli in Dallos' study with delivery directly to the cochlear fluids in the present study, and the difference may correspond to the pressure gain of the middle ear at acoustic frequencies. Our data provide no compelling evidence for other forms of low-frequency attenuation, such as through adaptive processes of the tip links of hair cell stereocilia. The large responses observed with 1-Hz stimulation confirm the fact that the hair cells are quite capable of transducing such low frequencies. However, there have been few studies of cochlear sensitivity to pressure fluctuations in the infrasonic range. In one study, Konishi and Nielson (1978) blocked helicotrema of guinea pigs and recorded from single afferent fibers using a trapezoid stimulus delivered mechanically to the middle ear ossicles with plateau up to 200 ms. They reported that under these conditions, 39% of afferent fibers exhibited a ''tonic'' (nonadapting) response. These findings are in accordance with a limited capacity for mammalian cochlear hair cells to exhibit adaptation relative to hair cells derived from nonmammalian species (reviewed by Kros, 1996).

ACKNOWLEDGMENT

This study was supported by Research Grant No. RO1 DC01368 from the National Institute on Deafness and Other Communication Disorders, National Institutes of Health.

Avan, P., Loth, D., Menguy, C., and Teyssou, M. (**1992**). ''Hypothetical roles of middle ear muscles in the guinea pig,'' Hearing Res. **59**, 59–69.

Bohmer, A. (**1993**). ''Hydrostatic pressure in the inner ear fluid compartments and its effect on inner ear function,'' Acta Oto-Laryngol. Suppl. **507**, 3–24.

Dallos, P. (**1970**). ''Low-frequency auditory characteristics: Species dependence,'' J. Acoust. Soc. Am. **48**, 489–499.

Densert, B. (**1987**). ''Effects of overpressure on hearing function in Meniere's Disease,'' Acta Oto-Laryngol. **103**, 32–42.

Densert, B., Densert, O., Arlinger, S., Sass, K., and Odkvist, L. (**1997**). ''Immediate effects of middle ear pressure changes on the electrocochleographic recordings in patients with Meniere's disease: a clinical placebo-controlled study,'' Am. J. Otolaryngol. **18**, 726–733.

Gopen, Q., Rosowski, J. J., Merchant, S. N. (**1997**). ''Anatomy of the normal human cochlear aqueduct with functional implications,'' Hearing Res. **107**, 9–22.

Guild, S. R. (**1927**). ''The circulation of the endolymph,'' Am. J. Anat. **39**, 57–81.

Honjo, I., Ushiro, K., Haji, T., Nozoe, T., and Matsui, H. (**1983**). ''Role of tensor tympani muscle in Eustachian tube function,'' Acta Oto-Laryngol. **95**, 329–332.

Howell, P. (**1984**). ''Are two muscles needed for the normal functioning of the mammalian inner ear?'' Acta Oto-Laryngol. **98**, 204–207.

Ito, J., Naito, Y., and Honjo, I. (**1990**). ''The influence of middle ear pressure on the vestibular nerve activity in cats,'' Acta Oto-Laryngol. **110**, 203–208.

Kimura, R. S., and Hutta, J. (**1997**). ''Inhibition of experimentally induced hydrops by middle ear ventilation,'' Eur. Arch. Otorhinolaryngol. **254**, 213–218.

Konishi, T., and Nielson, D. W. (**1978**). ''The temporal relationship between basilar membrane motion and nerve impulse initiation in auditory nerve fibers in guinea pigs,'' Jpn. J. Physiol. **28**, 291–307.

Kros, C. J. (**1996**). ''Physiology of mammalian cochlear hair cells,'' in *The Cochlea*, P. Dallos, A. N. Popper, and R. R. Fay (Springer, New York), pp. 318–385.

Lundquist, P. G., Kimura, R., and Wersall, J. (**1964**). ''Experiments in endolymph circulation,'' Acta Oto-Laryngol. **188**, 194–201.

Marchbanks, R. J., and Reid, A. (**1990**). ''Cochlear and cerebrospinal fluid pressure: their inter-relationship and control mechanisms,'' Br. J. Audiol. **24**, 179–187.

Montandon, P., Guillemin, P., and Hausler, R. (**1989**). ''Treatment of Meniere's disease by minor surgical procedures: sacculotomy, cochleosacculotomy, transtympanic ventilation tubes,'' in *Meniere's Disease*, edited by J. B. Nadol (Kugler and Ghedini, Amsterdam), pp. 503–508.

Parker, D. E., and von Gierke, H. E. (**1971**). ''Vestibular nerve response to pressure changes in the external auditory meatus of the guinea pig,'' Acta Oto-Laryngol. **71**, 456–461.

Parker, D. E., Tubbs, R. L., Littlefield, V. M. (**1978**). ''Visual-field displacements in human beings evoked by acoustical transients,'' J. Acoust. Soc. Am. **63**, 1912–1918.
Parker, D. E., von Gierke, H. E., and Reschke, M. (**1968**). ''Studies of acoustical stimulation of the vestibular system,'' Aerosp. Med. **39**, 1321–1325.
Reschke, M. F., and Parker, D. E. (**1970**). ''Stimulation of the vestibular apparatus in the guinea pig by static pressure changes: Head and eye movements,'' J. Acoust. Soc. Am. **48**, 913–923.
Sakikawa, Y., and Kimura, R. S. (**1997**). ''Middle ear overpressure treatment of endolymphatic hydrops in guinea pigs,'' J. Otorhinolaryngol. Relat. Spec. **59**, 84–90.
Salen, B., and Zakrisson, J. E. (**1978**). ''Electromyogram of the tensor tympani muscle in man during swallowing,'' Acta Oto-Laryngol. **85**, 453–455.
Salt, A. N., and DeMott, J. E. (**1995**). ''Endolymph volume changes during osmotic dehydration measured by two marker techniques,'' Hearing Res. **90**, 12–23.
Salt, A. N., and DeMott, J. E. (**1997**). ''Longitudinal endolymph flow associated with acute volume increase in the guinea pig cochlea,'' Hearing Res. **107**, 29–40.
Salt, A. N., and DeMott, J. E. (**1998**). ''Longitudinal endolymph movements induced by perilymphatic injections,'' Hearing Res. **123**, 137–147.
Salt, A. N., and Thalmann, R. (**1988**). ''Interpretation of endolymph flow results,'' Hearing Res. **33**, 279–281.
Salt, A. N., and Thalmann, R. (**1989**). ''Rate of longitudinal flow of cochlear endolymph,'' in *Meniere's Disease*, edited by J. B. Nadol (Kugler, Amsterdam), pp. 69–73.
Salt, A. N., and Vora, A. R. (**1991**). ''Calibration of ion-selective microelectrodes for use with high levels of interfering ions,'' J. Neurosci. Methods **38**, 233–237.
Salt, A. N., Thalmann, R., Marcus, D. C., and Bohne, B. A. (**1986**). ''Direct measurement of longitudinal endolymph flow rate in the guinea pig cochlea,'' Hearing Res. **23**, 141–151.
Suzuki, M., Kitahara, M., and Kitano, H. (**1994**). ''The influence of vestibular and cochlear aqueducts on vestibular response to middle ear pressure changes in guinea pigs,'' Acta Oto-Laryngol. Suppl. **510**, 16–19.
Sykova, E., Syka, J., Johnstone, B. M., and Yates, G. K. (**1987**). ''Longitudinal flow of endolymph measured by distribution of tetraethylammonium and choline in scala media,'' Hearing Res. **28**, 161–171.
Takumida, M., Bagger-Sjoback, D., and Rask-Andersen, H. (**1989**). ''The endolymphatic sac and inner ear homeostasis I: Effect of glycerol on the endolymphatic sac with or without colchicine pretreatment,'' Hearing Res. **40**, 1–16.
Voss, S. E., Rosowski, J. J., and Peake, W. T. (**1996**). ''Is the pressure difference between the oval and round windows the effective acoustic stimulus for the cochlea?'' J. Acoust. Soc. Am. **100**, 1602–1616.

Medial efferent effects on auditory-nerve responses to tail-frequency tones. I. Rate reduction

Konstantina M. Stankovic
Eaton–Peabody Laboratory of Auditory Physiology, Department of Otolaryngology, Massachusetts Eye and Ear Infirmary, 243 Charles Street, Boston, Massachusetts 02114 and Harvard–MIT Division of Health Sciences and Technology, and Research Laboratory of Electronics, Massachusetts Institute of Technology, Cambridge, Massachusetts 02139

John J. Guinan, Jr.[a)]
Eaton–Peabody Laboratory of Auditory Physiology, Department of Otolaryngology, Massachusetts Eye and Ear Infirmary, 243 Charles Street, Boston, Massachusetts 02114 and Harvard–MIT Division of Health Sciences and Technology, and Research Laboratory of Electronics, Massachusetts Institute of Technology, Cambridge, Massachusetts 02139 and Department of Otology and Laryngology, Harvard Medical School, Boston, Massachusetts 02115

(Received 5 November 1998; revised 15 March 1999; accepted 19 April 1999)

One way medial efferents are thought to inhibit responses of auditory-nerve fibers (ANFs) is by reducing the gain of the cochlear amplifier thereby reducing motion of the basilar membrane. If this is the only mechanism of medial efferent inhibition, then medial efferents would not be expected to inhibit responses where the cochlear amplifier has little effect, i.e., at sound frequencies in the tails of tuning curves. Inhibition at tail frequencies was tested for by obtaining randomized rate-level functions from cat ANFs with high characteristic frequencies (CF$\geqslant$5 kHz), stimulated with tones two or more octaves below CF. It was found that electrical stimulation of medial efferents can indeed inhibit ANF responses to tail-frequency tones. The amplitude of efferent inhibition depended on both sound level (largest near to threshold) and frequency (largest two to three octaves below CF). On average, inhibition of high-CF ANFs responding to 1 kHz tones was around 5 dB. Although an efferent reduction of basilar-membrane motion cannot be ruled out as the mechanism producing the inhibition of ANF responses to tail frequency tones, it seems more likely that efferents produce this effect by changing the micromechanics of the cochlear partition. [S0001-4966(99)00908-X]

PACS numbers: 43.64.Pg, 43.64.Kc, 43.64.Ld [RDF]

INTRODUCTION

Stimulation of medial olivocochlear efferents that synapse on outer hair cells (OHCs) reduces activity in auditory-nerve fibers that contact inner hair cells (IHCs) even though there are no known neuronal connections between medial efferents and these afferents, or between OHCs and IHCs. It is now widely believed that the major mechanism for this inhibition is an efferent-induced reduction of cochlear-amplifier gain that reduces basilar-membrane motion in response to sound (reviewed by Guinan, 1996). If this is the only way in which medial efferents inhibit, then medial efferents would be expected to have little or no effect at sound frequencies in the broadly tuned, insensitive, low-frequency ''tail'' region of tuning curves because active cochlear mechanisms appear to have little or no effect on basilar-membrane motion an octave or more below CF (Rhode, 1973; Ruggero *et al.*, 1991, 1996, 1997; Nuttall and Dolan, 1996).

Earlier investigations left the impression that efferents do not significantly affect responses of auditory-nerve fibers (ANFs) to tail-frequency stimuli, even in fibers that show large inhibitions at the characteristic frequency (CF) (Wiederhold, 1970; Kiang *et al.*, 1970; Guinan and Gifford, 1988c). This impression was further reinforced by the finding that efferent stimulation had little effect on IHC receptor potentials evoked by tail-frequency tones (Brown and Nuttall, 1984). Most recently, this impression was supported by the report that efferent stimulation ''had no apparent effect on the basilar-membrane displacement in response to tones at frequencies more than one-half octave below CF'' (Murugasu and Russell, 1996).

Despite this earlier work, a systematic study of efferent effects on responses to tail-frequency tones is lacking in the literature. All of the studies that reported the small efferent effects at tail frequencies were focused mainly on other aspects of efferent inhibition. The most relevant study—an exploration of efferent effects on ANF tuning curves (Guinan and Gifford, 1988c)—concluded that efferents sometimes significantly elevate tuning-curve tails (see their Fig. 1), but the inhibition at 1 kHz (the approximate center of the tails) was small, averaging only 1 dB. However, there are several limitations of tuning-curve studies. First, these studies measured the efferent effect only at threshold. Second, the prolonged efferent stimulation required to record a whole tuning curve with efferent stimulation (usually more than several minutes) complicates the interpretation because (1) there is adaptation in the effects of efferent stimulation, (2) the effer-

[a)]Electronic mail: jjg@epl.meei.harvard.edu

ent slow effect (Sridhar *et al.*, 1995) may change the results depending on whether the tuning curve is measured by sweeping frequency up or down, and (3) the properties of the stimulating electrode may change with long stimulating runs (Mountain, 1978).

The current study is the first extensive examination of efferent effects at tail frequencies. To overcome the difficulties involved with measuring efferent effects on tuning curves and to extend the sound-level range sampled, we recorded sound level series at specific tail frequencies with and without efferent stimulation. By simultaneously randomizing the presentation of sound level and efferent stimulation—while keeping the sound-on and shocks-on duty cycles low—adaptation was minimized both in the responses of ANFs to sound, and in the effects of efferent stimulation (Guinan and Stankovic, 1996). Our results show that efferents can have an appreciable effect at tail frequencies and therefore that some current conceptions regarding cochlear physiology need revision.

I. METHODS

A. Surgical preparation

Healthy adult cats weighing, 1.5–3.0 kg, with no signs of middle-ear infections, were used. Anesthesia was induced by intraperitoneal injection of 0.15 ml/kg diallyl barbiturate in urethane (100 mg/gl diallyl barbiturate, 400 mg/ml monethyurea, and 400 mg/ml urethane), and maintained by injections of $\frac{1}{10}$ of the original dose, as needed. Treatment of experimental animals was in accordance with protocols approved by the Committees on Animal Care at the Massachusetts Institute of Technology and the Massachusetts Eye and Ear Infirmary.

The surgical approach to the auditory nerve was as in Kiang *et al.* (1965). Briefly, after insertion of a tracheal tube and cannulation of a femoral vein for an intravascular drip of a lactated Ringers, the ear canals were surgically exposed and the auditory bullae opened. The bony septum between the bulla and middle ear was removed and the tendons of the middle ear muscles were cut using cautery or a surgical argon laser with a ''Megabeam Endo-ENT Probe.'' A posterior craniotomy was performed and the medial and lateral parts of the cerebellum were aspirated to expose the floor of the fourth ventricle and the exit of the auditory nerve.

To increase the efficacy of efferent stimulation without evoking motion, some animals were paralyzed with intravenous atracurium in saline and artificially ventilated. Ventilator parameters were adjusted so as to maintain the breathing rate at 15–18 breaths per minute, and expired CO_2 at 3.5%–5%. Every animal's physiological state was continuously monitored using a custom-LabView system for real-time monitoring of electrocardiograms, electroencephalograms, breathing rate, CO_2 content in expired air, and rectal temperature.

Cochlear sensitivity was monitored by recording auditory-nerve compound action potentials (CAPs) with an electrode on or near the round window and using an automated tone-pip audiogram (Guinan and Stankovic, 1996). Sometimes, CAP audiograms were elevated for a few hours after middle-ear-muscle cutting. However, for all animals reported here, CAP audiograms were in the normal range by the time data acquisition started—usually ten or more hours after middle-ear-muscle cutting.

B. Stimulation and recording

Efferents were stimulated along the midline of the floor of the fourth ventricle using a multiprong electrode (Gifford and Guinan, 1987) and shock timing as in (Guinan and Stankovic (1996). Briefly, shocks (0.3-ms pulses at 200/s) were transformer coupled to the pair of adjacent prongs which yielded the greatest inhibition of the click-evoked CAP response without evoking movement. The CAP inhibition (measured as the equivalent reduction in sound level) ranged from 10–20 dB while gathering the data reported here.

Recordings of single ANFs were done as in Kiang *et al.* (1965) with broadband noise bursts as a search stimulus. Based on their spontaneous rate (SR), ANFs were grouped into three categories: low: SR$\leqslant$0.5, medium: 0.5$<$SR$<$18, and high: SR$\geqslant$18 spikes/s (Liberman, 1978). We studied fibers of all SRs but were biased toward high-SR fibers because they have the lowest tail thresholds. This enabled us to record the tuning curve tails and at least a 20-dB portion of the fiber's dynamic range (sound levels at which rate increases with sound level) without causing acoustic trauma.

We concentrated on fibers with CFs$\geqslant$10 kHz because (1) they had clearly defined tips and tails, and (2) most of the tail could be studied without harmonic distortion of the tail-frequency stimulus eliciting a response in the tip region of a tuning curve. Some fibers with CFs$<$10 kHz were also studied and these gave the same qualitative results as fibers with CFs$\geqslant$10 kHz. Since harmonic distortion in the stimulus was an important issue, we determined it for every experiment. In the last four experiments, harmonic distortion was measured directly from Fourier transforms of the sound pressure in the ear canal recorded during spike-data acquisition. For earlier experiments, harmonic distortion was calculated from (1) the driver voltage attenuation, (2) measurements of harmonic distortion in a closed cavity at this attenuation, and (3) the sound pressure versus frequency calibration for the individual experiment. Data were rejected for any run for which the harmonic distortion fell within the tuning-curve tip.

C. Data gathering

After making contact with a fiber, data were gathered in the following sequence: (1) A tuning curve was obtained. In the tip region, standard tuning-curve parameters (30 points per octave, level steps of 3/4 dB) were used, but in the tail region, where threshold is not a strong function of frequency, the point spacing was changed to 6 points per octave to increase the speed. (2) Spontaneous firing was recorded for 20 s, and SR was calculated. (3) Randomized level functions with and without efferent stimulation were run at a tail frequency. Fiber contact time permitting, additional level functions were obtained at the same and/or at different tail frequencies and/or at CF.

Our level-function paradigm randomized both sound level and the presence/absence of efferent stimulation (as in Guinan and Stankovic, 1996) and yielded two rate-level curves—one ''with efferents activated'' and one ''without efferents activated.'' Points were acquired every 3 s, and at each point the firing rate was obtained by averaging responses from ten sequential tone bursts (50 ms on, 50 ms off, 2.5 ms rise/fall time). Spikes were counted within a time window from 6 ms after the beginning of the tone-burst rise to 1 ms after the end of the tone-burst fall. For points ''with efferents activated,'' a train of efferent shocks started 100 ms before the onset of tone bursts and lasted throughout the duration of the tone bursts (i.e., 1.1 s). At tail frequencies, most randomized level functions covered the range from 40–100 dB SPL with 3-dB resolution. Exceptions include the first three experiments where some rate-level curves were 50–100 dB SPL with 2.5-dB resolution, 60–100 dB SPL with 2-dB resolution, or 70–100 dB SPL with 1.5-dB resolution. In the last three experiments, rate-level curves were 40–91 dB SPL with 3-dB resolution in order to minimize exposure to potentially traumatic sounds. At CF, randomized rate-level curves were from 0–100 dB SPL with 5-dB resolution.

Our most commonly used sound frequency was 1 kHz because (1) tuning-curve tails are usually most sensitive around 1 kHz, and (2) the harmonic distortion from an intense 1 kHz stimulus is usually outside of the tuning-curve tip for fibers with CF$\geqslant$10 kHz. Doing many runs up to 100 dB SPL at a single frequency often led to hearing loss (evidenced by elevation of CAP thresholds to tone pips) near that frequency. However, these threshold shifts were for fibers with CFs near the tail frequency and thus are not directly relevant to fibers with CFs$\geqslant$10 kHz. All of the data presented here are from fibers with CFs at frequencies with stable hearing, i.e., at which CAP thresholds remained within 5–15 dB (most commonly within 10 dB) of the initial measurements. Low-frequency hearing was preserved in the last three experiments in which rate-level curves were run only up to 91 dB SPL. The efferent effects in these cats were in agreement with the results from earlier experiments and suggest that the threshold losses near 1 kHz had little or no influence on our results. Because of this, we felt justified in pooling data across all cats (except two, see below), so that this report is based on ANFs from 17 cats. Data from two cats were not included: one because of audible noise associated with the ventilator, the other because the cat had extremely sensitive hearing. In the latter cat, efferent stimulation caused an unusually large ($\approx$80%) reduction of SR, suggesting that ''spontaneous'' activity was in fact a response to animal-generated noise (as suggested by Wiederhold and Kiang, 1970; Guinan and Gifford, 1988b; Kawase *et al.*, 1993). Furthermore, rate-level curves in response to a single tail-frequency tone demonstrated dips characteristic of two-tone suppression (Abbas and Sachs, 1976), providing additional evidence that the cat was responding to sounds not present in the stimulus.

D. Data selection

In addition to the data selection criteria already stated, several other criteria had to be met. Only fibers with tail thresholds that exceeded tip thresholds by at least 35 dB were included. For each data set, peri-stimulus-time histograms locked to the shock times were inspected to detect possible missed or extra triggers due to shock artifacts. Only data free of such artifacts were included.

E. Data analysis

All data analysis was done with Matlab 5 software. For easier data handling in Matlab, the sound-level spacing in all tail runs was ''standardized'' to the most commonly used sound-level spacing of 3 dB. Rate-level curves with level spacing of 1.5 dB were down sampled (every-other point used) and those with 2 or 2.5 dB were linearly interpolated (these only covered ranges of 70–100 dB, 60–100 dB, and 50–100 dB, respectively).

To aid in evaluating data in the figures and for use in statistical tests, standard errors were calculated or estimated for firing rate points. When there were multiple sets of rate-level curves, the standard error (se) of an average rate point was calculated in the usual way as $\mathrm{se}=\sigma/\sqrt{n}$, where σ is the standard deviation of the data and n is the number of rate-level curves. When only a single set of rate-level curves was available, an arbitrary formula for se was used: se=10 spikes/s if the driven firing rate (i.e., firing rate minus SR) was $\leqslant$20 spikes/s; otherwise, se=20 spikes/s (se estimates were needed because se was used as a weighting factor for fitting data with straight lines for statistical tests, see below). This formula was arrived at by selecting fibers for which σ could be calculated from multiple measurements, and then plotting σ as a function of the driven firing rate. In comparison with the data, the simplified formula overestimates se.

To aid detecting trends in scatter plots, a loess fit (also known as local nonparametric regression) was used (Cleveland, 1993). The loess fit is characterized by two parameters: (1) a smoothing parameter that is related to the size of the smoothing window, and (2) the degree of the locally fitted polynomial (here always set to 1). In figures with a loess fit, the smoothing parameter was normally 0.2, which means that the smoothing window included 20% of the data.

We tested for the significance of a statistic, without making any assumptions about underlying statistical distributions (e.g., that the data are normally distributed) by using permutation tests (Efron and Tibshirani, 1993). In a permutation test the actual data are used to provide an estimate of the underlying distribution space of possible data. The probability that a certain value of a statistic might arise from chance is then estimated by repeated trials in which the original data points are shuffled with the statistic calculated on each trial. For example, presume we had obtained data in N fibers and calculated statistic ''S'' which compares low-SR and high-SR fibers (e.g., S might be the difference in slopes of ΔL_n versus sound level plots as in Sec. II B). We want to know if the value of S might have occurred by chance, i.e., how often this value might occur in a population of N fibers

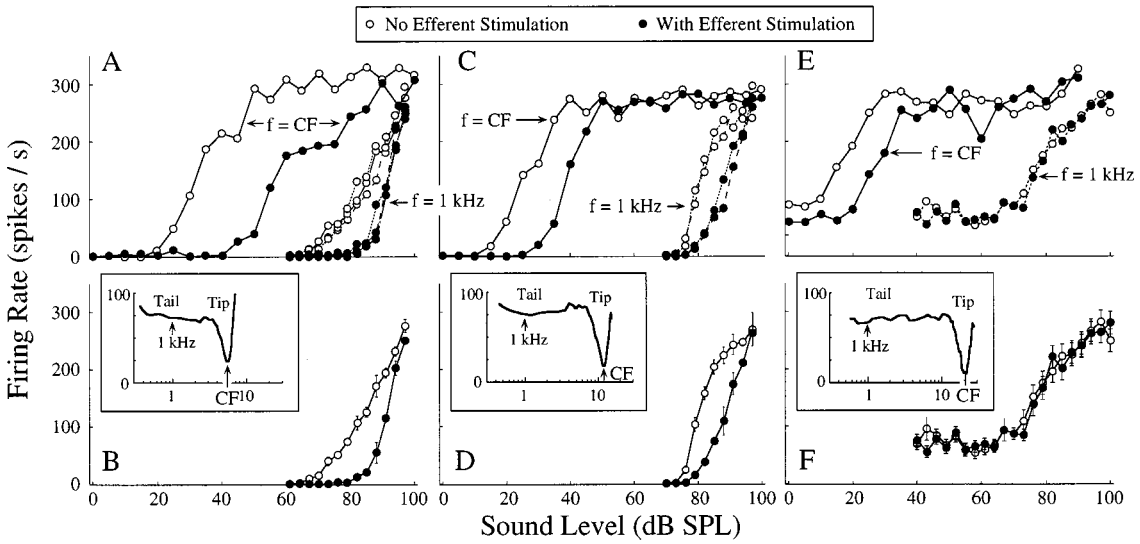

FIG. 1. Examples of level function pairs with (filled circles) and without (open circles) efferent stimulation from three auditory-nerve fibers. The fibers at left and center show clear efferent inhibition at tail frequencies while the fiber at right does not. Top panels: Pairs of rate-level curves in response to tone bursts at CF (left in panel), and in response to tone bursts at 1 kHz (right in panel). At 1 kHz, multiple sets of rate-level curves in (a) and (c) illustrate their reproducibility. Bottom panels: Average rate-level curves at 1 kHz derived from the data at top. Error bars indicate calculated [(b) and (d)] or assigned (f) standard error of the mean (see Sec. I). Insets: Fiber tuning curves with arrows indicating the tone frequencies used and labels indicating tip and tail. Horizontal axis: tone frequency (kHz); vertical axis: sound level (dB SPL). Left: Fiber TS27-76, CF=5.62 kHz, SR=1.60 spikes/s. Center: Fiber TS28-86, CF=11.95 kHz, SR=0.9 spikes/s. Right: Fiber TS46-20, CF=21.26 kHz, SR=71.2 spikes/s.

split arbitrarily into low-SR and high-SR groups. For each trial, the N fibers are randomly sorted (shuffled) into ''pseudo-SR'' groups containing the number of low-SR and high-SR fibers in the original data, and the same statistic (now called ''S_{pseudo}'') is calculated. The results from a large number of trials (we used 1000; this was enough to reach convergence) are expressed as a histogram of {the number of trials with a given S_{pseudo}} vs S_{pseudo}. This histogram provides an estimate of the real distribution of S, *if* low-SR fibers are no different than high-SR fibers in the characteristics that determine S. Finally, the measured S in the original data is compared to this histogram and is considered to be significant at the 0.05 level if it falls further from the mean than 95% of the histogram values.

II. RESULTS

We found that efferents can indeed affect ANF responses to tail-frequency tones and that the effect varied across fibers and stimulation parameters. Typically, the efferent effect at tail frequencies ranged from clear inhibition to no apparent effect, as shown in Fig. 1. This figure shows rate-level functions for tones at a tail frequency (1 kHz) and, for comparison, at fiber CF. Panels (a) and (c) show data from multiple runs at the tail frequency and illustrate the reproducibility of the data. The bottom panels show averages and standard errors derived from these multiple runs [Fig. 1(b) and (d)] or from the firing rate [Fig. 1(f), see Sec I]. The efferent inhibition is a rightward shift of the rate-level curve, meaning that a higher sound level was required with efferent stimulation to produce the same response as in the absence of efferent stimulation. Note that efferent stimulation can also change the slope of the tail-frequency rate-level curves, and the extent of this varies across fibers [compare Fig. 1(a) and (c)]. Figure 1(f) demonstrates that efferents can have a negligible effect at 1 kHz, even in fibers that show a significant shift at CF. Since there was no clear line of demarcation between fibers that showed efferent inhibition at tail frequencies and those that did not, we cannot make a precise statement as to what fraction of auditory-nerve fibers were inhibited at tail frequencies. Nonetheless, at least 80% of the fibers tested appeared to be inhibited [i.e., had tail-frequency rate versus level functions more like Fig. 1(a) and (b) than Fig. 1(c)]. Furthermore, inhibition at tail frequencies was found in every animal that was adequately tested.

In a few fibers (there were 3 clear examples out of 165 fibers), efferent stimulation enhanced the ANF response to tail-frequency tones. Since these three fibers had sensitive tips and high-SR activity, this enhancement is probably due to efferent-induced removal of adaptation, with the adaptation due to fiber responses to animal noise or other unintended stimuli (see Kawase *et al.*, 1993). Thus the atypical efferent-induced enhancement in these three fibers appears to be due to efferent inhibition of sounds that excite the fiber in the tip region of the tuning curve rather than an efferent enhancement that is specific to sound in the tail region. Since the thresholds of almost all of our fibers were above these very sensitive fibers, we presume that efferent-induced removal of adaptation had little role in the responses of most fibers in our sample.

A. Level shift, ΔL

As a measure of the efferent effect on rate-level curves, we used the level shift, ΔL (Fig. 2). Level shift is the amount (in dB) by which the sound level must be increased with efferent stimulation to produce the same response as obtained without efferent stimulation. As noted above, ΔL was usually not constant in the rising phase of the level functions

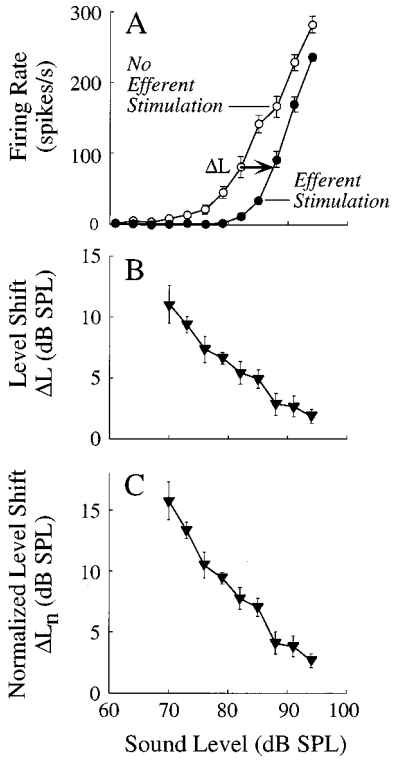

FIG. 2. Computing the level shift, ΔL, and the normalized level shift, ΔL_n. (a) Rate-level curves averaged from five pairs of curves with ΔL illustrated for the point at 82 dB SPL. ΔL was measured from each no-efferent-stimulation point in the rising phase of the response (visually determined) to the point at the same rate in the with-efferent-stimulation curve. The with-efferent-stimulation curve was determined by straight lines point to point and, if necessary, an extension past the highest point by a straight line through the highest three points (as in Guinan and Stankovic, 1996, Fig. 1). (b) ΔL and its standard errors calculated from the rate-level curves in panel (a). The main source of error in ΔL stems from the errors in determination of the firing rate, because errors associated with determination of the sound level are negligible in comparison. The error in ΔL was calculated from the errors in the firing rates taking into account the influence of the slopes of the level functions (Meyer, 1975). Details of the procedure used are given in Stankovic (1997). (c) ΔL normalized to a CAP inhibition of 20 dB by multiplying ΔL from (b) with 20/14. Note that standard errors were also normalized using the same factor (i.e., 20/14). Fiber TS37-17, CF $=10.59$ kHz, SR $=1.2$ spikes/s.

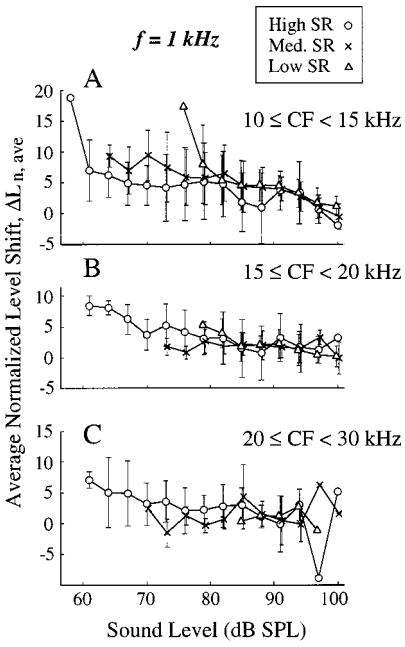

FIG. 3. The normalized efferent-induced level shift, ΔL_n, versus sound level for auditory-nerve fibers from three CF regions (10–15 kHz, 15–20 kHz and 20–30 kHz), stimulated with a tail-frequency tone of 1 kHz. Each curve shows averages from one SR group. Bars indicate standard deviations; points without bars are from one fiber only. Differences in the lowest initial sound level among the SR groups reflect differences in tail thresholds. To clearly show error bars from different SR groups, medium-SR data were shifted to the right by 0.2 dB, and low-SR data were shifted to the left by 0.2 dB. The number of fibers in each SR group are: (a) 24 high, 18 medium, 13 low. (b) 25 high, 7 medium, 9 low. (c) 14 high, 5 medium, 1 low.

[Figs. 1(a) and (c) and 2] so a single number could not be used to characterize the efferent inhibition. Since we wanted to compare ΔL's measured from many fibers but the strength of the efferent inhibition varied across and within experiments, ΔL was normalized to a CAP shift of 20 dB (CAP shift was measured in the same way as ΔL but using CAP level functions). For example, when the CAP shift was 14 dB, the normalized $\Delta L(\Delta L_n)$ was $\Delta L_n = \Delta L \times 20/14$ [e.g., Fig. 2(c)]. This is the same normalization we have used previously and makes the data presented here comparable to our earlier data (Gifford and Guinan, 1987; Guinan and Gifford, 1998a, b, c; Guinan and Stankovic, 1996).

Statistical tests of our data confirm our visual impression that efferent stimulation inhibits responses to tail-frequency stimuli across most fibers. Specifically, *t*-tests were applied to every ΔL (or ΔL_n)—regardless of sound level—from fibers with CFs between 10–30 kHz stimulated with 500 Hz (9 fibers, average $\Delta L_n = 1.5$ dB, 1 kHz (116 fibers, average $\Delta L_n = 3.6$ dB), 2 kHz (28 fibers, average $\Delta L_n = 6.9$ dB), and 3 kHz (10 fibers, average $\Delta L_n = 7.1$ dB). These tests showed that, on average, ΔL (raw or normalized) was different from zero at a very highly significant level ($p < 0.0001$) for each sound frequency. However, these overall statistics ignore dependencies of ΔL_n on other variables such as sound level and the characteristics of individual ANFs (CF and spontaneous rate). These dependencies are summarized in the next two sections.

B. Dependence of ΔL_n on sound level and spontaneous rate

To explore the dependencies of ΔL_n on sound level and spontaneous rate—while controlling for the dependencies on sound frequency and CF—we considered one sound frequency at a time with fibers grouped in CF bands. The bands were determined by the amount of data available for a given sound frequency. The most data was obtained on fibers with CFs $\geqslant 10$ kHz and tones at 1 kHz so three CF bands (10–15, 15–20, and 20–30 kHz) were used for the fibers responding to 1 kHz (Fig. 3). For other tone frequencies we had less data so one CF band (10–20 kHz) was used (2 kHz: Fig. 4; 3 kHz: Fig. 5; 500 Hz: not shown). For these frequencies, CFs above 20 kHz were not included because there were too few data and the efferent effects were considerably less for CFs over 20 kHz.

Figures 3–5 provide a visual appraisal of the dependence of ΔL_n on sound level and spontaneous rate in two ways: plots of averages and scatter plots. All three figures show plots of averages and standard errors for each SR

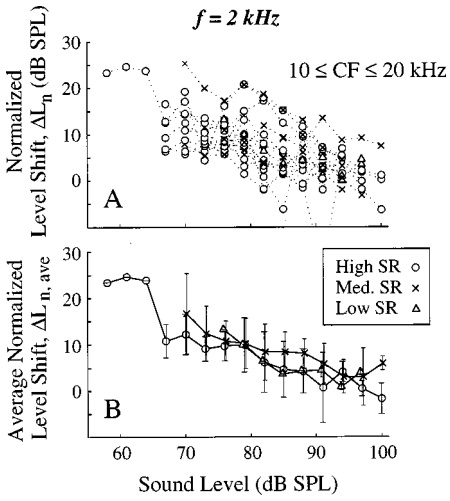

FIG. 4. The normalized efferent-induced level shift, ΔL_n, versus sound level for auditory-nerve fibers with CFs from 10–20 kHz, stimulated with a tail-frequency tone of 2 kHz. (a) Superimposed data from individual fibers. Data from a fiber are connected by dotted lines. Differences in the lowest initial sound level reflect differences in tail thresholds of individual fibers; differences in the highest sound level reflect differences in availability of the data. (b) Averages for each SR group, based on the data in panel (a). Bars indicate standard deviations; points without bars are from one fiber only. As in Fig. 3, medium-SR data were shifted to the right by 0.2 dB, and low-SR data were shifted to the left by 0.2 dB. The number of fibers in each SR group are 12 high, 5 medium, 3 low.

group, a display which allows a visual appraisal of *average* differences. In Figs. 4 and 5, where there are fewer fibers in each group, we have also included scatter plots which allow a better appraisal of the differences across individual fibers and the degree to which averages and standard errors summarize the data. Visual inspection of Figs. 3–5 suggests there is little difference in ΔL_n across SR groups and that ΔL_n depends on sound level.

This visual impression was confirmed by several statistical tests that indicated there were no significant differences in ΔL_n across SR groups. Testing for changes across SR groups was complicated by the fact that the data from individual fibers often did not cover the same range of sound levels. In particular, low-SR fibers had higher thresholds than high-SR fibers and therefore had fewer measures of ΔL_n at low sound levels. To overcome this, a straight line was fit (using a least squares criterion) to the data from each fiber, and the mean slope and intercept were calculated for each SR group. Permutation tests (Efron and Tibshirani, 1993; see Sec. I) were done by shuffling the fibers across SR groups and using the difference in the mean slope (or intercept) of two SR groups as a comparison statistic. Alternatively, fibers were shuffled among SR groups, for each resulting SR group a line was fit to all ΔL_n's, and comparison statistics were calculated from the difference in slope (or intercept) of the lines from two SR groups. In all of these cases, statistically significant differences across SR groups were not detected at the $p=0.05$ level. Because there were no significant differences among SR groups, data were pooled across SR groups for subsequent tests.

Permutation tests also showed that ΔL_n varied significantly with sound level, at least for most fiber groups. Our initial tests were done using the fiber groups in Figs. 3–5 by shuffling the ΔL_n's from each sound level and comparing the slopes of straight lines fitted through the resulting plots of ΔL_n versus sound level. A significant dependence of ΔL_n on sound level ($p<0.05$) was found for 1-kHz tones and CFs of 15–20 kHz, and for 2- or 3-kHz tones and CFs of 10–20 kHz. Although this test did not show a significant variation across all sound levels for 1-kHz tones and CFs of 10–15 kHz, visual inspection suggested that the greatest variation in this group was between 90–100 dB SPL [see Fig. 3(a)]. A permutation test restricted to 90–100 dB SPL for this group showed a very highly significant ($p<0.001$) dependence of ΔL_n on sound level across this limited sound-level range.

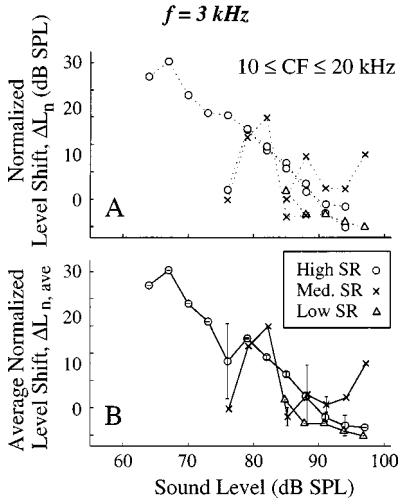

FIG. 5. The normalized efferent-induced level shift, ΔL_n, versus sound level for auditory-nerve fibers with CFs from 10–20 kHz, stimulated with a tail-frequency tone of 3 kHz. Even though there are too few fibers to make strong statements about trends in the data, the figure illustrates that efferents can have a substantial (level-dependent) effect for a tail-frequency stimulus of 3 kHz. Layout as in Fig. 4. The number of fibers in each SR group are 2 high, 2 medium, 1 low.

C. Dependence of ΔL_n on sound frequency

Perhaps the best way to study the dependence of ΔL_n on sound frequency is to obtain level functions from many different tone frequencies on a single fiber. Two examples with particularly extensive data are shown in Figs. 6 and 7. For the fiber in Fig. 6, efferent inhibition was minimal at 500 Hz, small at 1 kHz, larger at 2–2.2 kHz, maximal at 2.5–3 kHz, and again minimal at 4 kHz. This fiber is also interesting because the without-efferent-stimulation rate-level curves at 2–3 kHz seem to have two rising portions separated by a small plateau (these features were shown consistently in multiple runs at each frequency). At these frequencies, efferents appear to inhibit the lower-level portion substantially more than the upper-level portion.[1] For the fiber in Fig. 7 the overall efferent effect was small but the frequency dependence of the efferent inhibition can still be appreciated. Specifically, the inhibition was minimal at 500 Hz, small at 1–1.5 kHz, somewhat bigger at 1.7–2 kHz, and back to minimal at 3 kHz.

We were able to get data at many tone frequencies for only a few fibers, so to provide a more comprehensive view

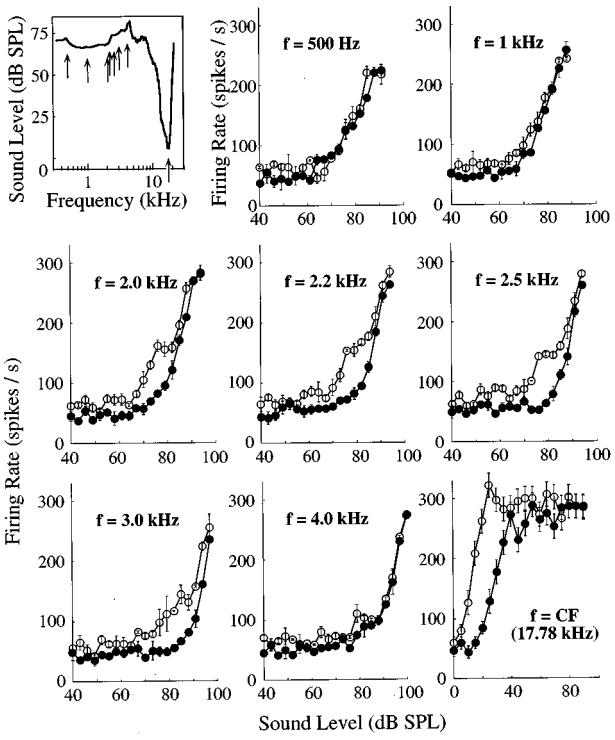

FIG. 6. Data from one auditory-nerve fiber demonstrating that efferent inhibition in the tail depends on tone frequency. Tone frequencies are stated in each panel and indicated by arrows on the tuning curve in the upper left panel. Every pair of rate-level curves in this figure (except the CF run) is an average of multiple runs. Bars on points at tail frequencies are the standard error of the mean calculated from these runs. Note that the sound-level axis is different on the f=CF panel. Fiber TS37-24, CF=17.78 kHz, SR =69.4 spikes/s. The number of runs at each frequency are 2 at 500 Hz, 3 at 1 kHz, 3 at 2 kHz, 3 at 2.2 kHz, 3 at 2.5 kHz, 2 at 3 kHz, 2 at 4 kHz, and 1 at 17.78 kHz.

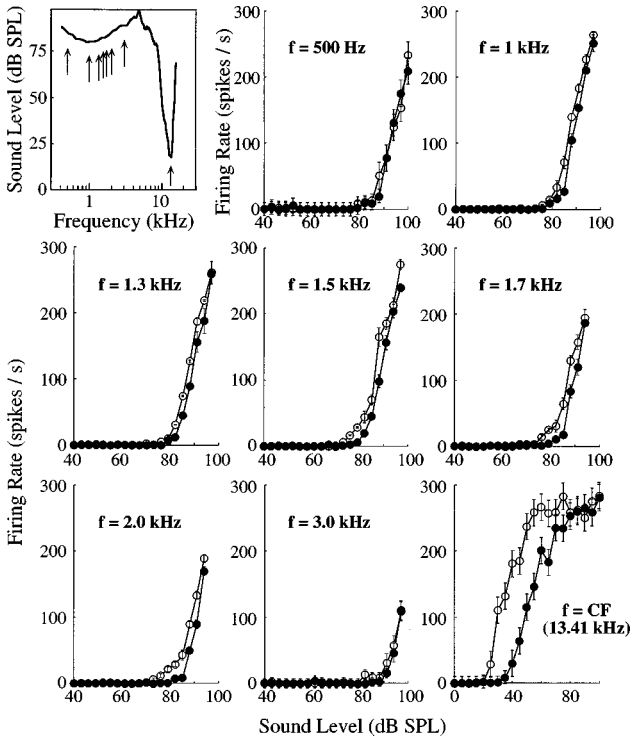

FIG. 7. Data from an auditory-nerve fiber demonstrating that efferent inhibition in the tail depends on tone frequency, even when the inhibition is weak. Layout as in Fig. 6. Again, the rate-level curves in each panel (except f=0.5 and 3 kHz) are averages of multiple runs, and bars on individual points indicate standard errors calculated from these runs (or estimated from the rate for f=0.5 and 3 kHz). Fiber TS37-22, CF=13.41 kHz, SR =0.2 spikes/s. The number of runs at each frequency are 1 at 500 Hz, 3 at 1 kHz, 2 at 1.3 kHz, 3 at 1.5 kHz, 2 at 1.7 kHz, 5 at 2 kHz, 1 at 3 kHz, and 2 at 13.41 kHz.

of the dependence of ΔL_n on sound frequency we used data pooled from many fibers. This has already been done in Figs. 3–5 which show data from fibers in CF bands stimulated at one tone frequency. Visual inspection of these figures suggests that ΔL_n is greater for 2- and 3-kHz tones than for 1-kHz tones across a variety of sound levels. To determine whether there was a statistically significant change in ΔL_n across stimulus-tone frequencies of 1, 2, and 3 kHz at levels of 64–97 dB SPL for fibers with CFs between 10–20 kHz [i.e., using data from Figs. 3(a) and (b), 4, and 5], we used permutation tests (Efron and Tibshirani, 1993; see Sec. I). In these tests, no distinction was made between SR classes since previous statistical tests did not detect significant differences among SR groups. To use data from different sound levels and take into account that ΔL_n varies with sound level, the ΔL_n versus sound-level data for each fiber were fit with a straight line and the ΔL_n value at 70 dB SPL (a level in the middle of the data) was used to characterize the individual fiber. Fiber data were shuffled across tone-frequencies groups and comparison statistics were obtained from the difference in average $\Delta L_{n,70}$ values of two tone frequencies. These permutation tests revealed that the original data show statistically significant differences in ΔL_n across tone frequency: 1 kHz vs 3 kHz ($p<0.001$), 1 kHz vs 2 kHz ($p<0.001$), and 2 kHz vs 3 kHz ($p<0.019$). Only one of these differences across frequency was robust enough to show up when the comparison statistic was obtained by first shuffling the fiber data across tone-frequency groups, then fitting a ΔL_n versus sound-level line to the pooled data of a tone-frequency group and obtaining a $\Delta L_{n,70}$. A significant change was detected between responses at 1 and 3 kHz ($p<0.01$), but not 1 and 2 kHz ($p>0.13$), or 2 and 3 kHz ($p>0.10$). Nonetheless, the first test is sufficient to enable us to say that there are statistically significant differences in ΔL_n across tone frequency.

To focus on the frequency dependence of ΔL_n, we averaged ΔL_n across all sound levels $\leqslant$85 dB SPL and thereby collapsed the level dependence of ΔL_n into a single, average ΔL_n value—the ''average normalized level shift'' or $\Delta L_{n,\mathrm{ave}}$. Averaging was done only up to 85 dB SPL to focus on sound levels for which ΔL_n tended to be large. Since fibers from different SR groups have different tail thresholds, ΔL_n was typically averaged down to lower sound levels for high-SR fibers than for medium-SR and low-SR fibers. Also, since ΔL_n tended to be larger at low sound levels than at high sound levels (Figs. 3–5), the averaging procedure introduced a bias in $\Delta L_{n,\mathrm{ave}}$ across SR groups, thereby precluding comparisons across SR groups. Because of this, the frequency dependence of $\Delta L_{n,\mathrm{ave}}$ was analyzed with fibers of all SRs considered together.

The average normalized level shift, $\Delta L_{n,\mathrm{ave}}$, as a function of tone frequency, is shown in Fig. 8(a) and (b) for fibers with CFs between 10–30 kHz. There is substantial

scatter in values from individual fibers [Fig. 8(a)] but some clear trends in the average across fibers [Fig. 8(b)]. As tone frequency increased, the efferent inhibition grew from 500 Hz to 2–3 kHz, and then declined [Fig. 8(b)]. The downward trend at the highest frequencies should be interpreted with caution because it comes from only few fibers.

The average normalized level shift, $\Delta L_{n,\mathrm{ave}}$, as a function of tone frequency relative to CF, is shown in Fig. 8(c). Expressing tone frequency as f/CF aligns tuning curves at their tips. Plotted this way, the data show a trend similar to that in Fig. 8(a) and (b) with perhaps somewhat less scatter. In Fig. 8(c), $\Delta L_{n,\mathrm{ave}}$ peaks 2–3 octaves below CF. Again the downward trend at the highest frequencies should be interpreted with caution although we note that the trend is consistent with data from single fibers (e.g., Figs. 6 and 7)—data that are included in Fig. 8(c).

III. DISCUSSION

Our data clearly show that efferent stimulation can produce substantial inhibition of auditory-nerve responses to tail-frequency tones. To insure the reliability of the data we applied strict criteria, selecting only data with excellent triggering, free of shock artifacts, and free of contamination from harmonic distortion. To a considerable extent the parametric dependencies in the present data argue against the possibility that these artifacts substantially affected the results. For instance, the efferent inhibition at tail frequencies decreased with sound level, opposite the expected result if harmonic distortion at high sound levels was producing excitation in the tuning-curve tip.

Although the previous literature on efferent inhibition at tone frequencies below CF has emphasized the small size of the effects seen, a close examination shows considerable, but not complete, consistency with our results. Wiederhold (1970) and Brown and Nuttall (1984) tested almost exclusively at tone frequencies within 1 octave of CF and found little or no inhibition at frequencies $\frac{1}{2}$ to 1 octave below CF. We do not have measurements at such frequencies, but an extrapolation of our data suggests that there are small effects at these frequencies (see Fig. 8). A somewhat greater, but mixed, discrepancy exists with efferent effects obtained from tuning curves. Kiang *et al.* (1970) showed one fiber with no efferent inhibition at tail frequencies, and Guinan and Gifford (1988c) showed many tuning curves, some with and some without substantial efferent inhibition at tail frequencies. These data could be considered consistent with our present results except that the average inhibition for threshold tones at 1 kHz was 1 dB in Guinan and Gifford (1988c) but considerably greater here (typically 5–10 dB at the 1-kHz threshold). In the initial work on the present project, we ran tuning curves with and without efferent shocks and found variable results, sometimes from the same fiber. We are not sure of the origin of this problem, but think it may be due either to adaptation in the efferent effect (a possibility suggested by Guinan and Gifford, 1988c and/or inconsistent properties of electrical stimulation over the several minutes of continuous shock stimulation needed to monitor efferent effects on tuning curves. Our present use of short bursts of efferent stimulation (1.1 s) and randomized series produce

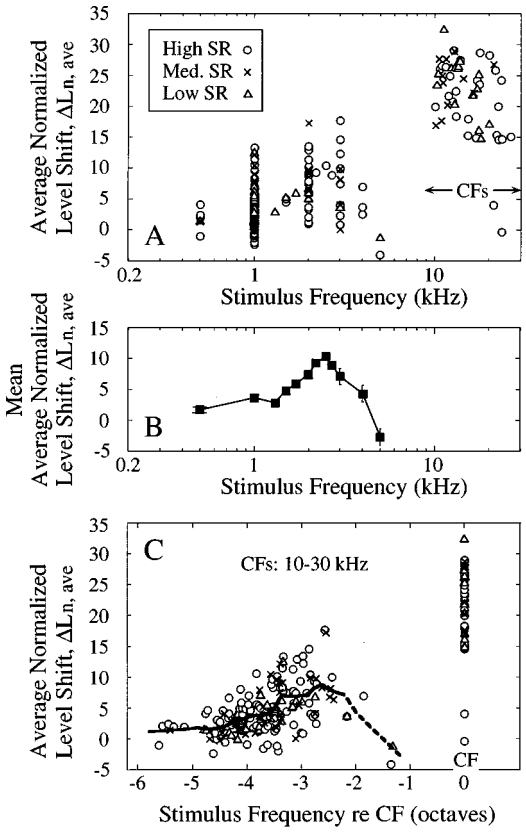

FIG. 8. Efferent inhibition as a function of tone frequency. (a) The average normalized level shift, $\Delta L_{n,\mathrm{ave}}$, versus tone frequency for fibers with CFs between 10–30 kHz. Data from 117 fibers with at least one tail-frequency point per fiber and sometimes one CF point. Each tail-frequency point shows ΔL_n averaged over all relevant data from one fiber for tone levels $\leqslant$85 dB SPL; there are 107 high-SR, 43 medium-SR and 32 low-SR points. Each CF point represents ΔL_n averaged over all data in the rising phase of the CF level function for tone levels $\leqslant$85 dB SPL. (b) The average curve derived from the tail-frequency data in panel (a). Each point is the mean of $\Delta L_{n,\mathrm{ave}}$ at one tone frequency; bars (most are smaller than the points) indicate standard error of the mean for frequencies with more than one point. (c) The average normalized level shift, $\Delta L_{n,\mathrm{ave}}$, versus tone frequency relative to CF. Same data as panel (a). The thick line is a loess fit (smoothing factor$=0.2$) to the data; the dashed part indicates uncertainty in the trend due to paucity of data.

consistent results [e.g., Fig. 1(a) and (c)], and we believe our present results give an accurate picture of efferent effects at tail frequencies.

A. The relation of efferent inhibition to the shape of the tuning-curve tail

A comparison of the frequency dependence of efferent inhibition with that of the tuning-curve tail shows that the inhibition is largest at frequencies above the most sensitive part of the tail (Fig. 9). In Fig. 9 we compare the efferent inhibition from Fig. 8(c) (plotted downward) with tuning curves averaged from three CF bands that span the range of CFs used. Figure 9 shows that the efferent inhibition is broadly tuned, similar to the frequency dependencies of the tuning-curve tails, but the inhibition peaks at a frequency above the most sensitive parts of the tails from each frequency band. Similar results were obtained from individual fibers (e.g., Figs. 6 and 7). Figures 6, 7, and 9 also illustrate

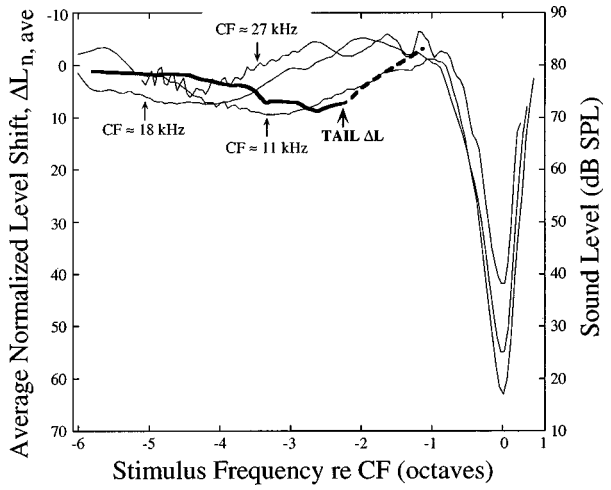

FIG. 9. Comparison of the frequency dependence of $\Delta L_{n,\mathrm{ave}}$ and tails of neural tuning curves. The thick curve is the $\Delta L_{n,\mathrm{ave}}$ curve from Fig. 8(c) plotted upside down (ordinate shown at left). The thin curves are ''averaged'' tuning curves (ordinate shown at right) in three CF bands: $10 \leqslant \mathrm{CF} \leqslant 12$ kHz (labeled 11 kHz, $n=29$); $16 \leqslant \mathrm{CF} \leqslant 20$ kHz (labeled 18 kHz, $n=38$); and $24 \leqslant \mathrm{CF} \leqslant 30$ kHz (labeled 27 kHz, $n=5$). The ''average'' tuning curves were obtained by superimposing tuning curves from the fibers in this study—plotted as a function of f/CF—for each CF group and finding the loess fit (with a smoothing factor of 0.03, see Sec. I).

that efferent inhibition can be very different at tail frequencies with similar thresholds on the upper and lower parts of the tail (e.g., in Fig. 9 compare points at 2.6 and 4 octaves below CF on the tuning curve labeled ''$\mathrm{CF} \approx 11$ kHz''). The net effect of the efferent inhibition shown in Fig. 9 is to raise the threshold in the upper edge of the tail with little effect at the lower edge so that the tail seems to be shifted to lower frequencies.

Two previous papers are consistent with our results in indicating that the higher- and lower-frequency parts of tuning curve tails can be affected differently by various manipulations. Siegel and Relkin (1987) showed that perilymphatic perfusion of Mg^{2+} in chinchillas caused a frequency-dependent elevation of tuning curve tails with the greatest elevation in the region near where the tail meets the tip. Sewell (1984) also found a frequency-dependent elevation of tuning curve tails from intravenous administration of furosemide in cats. These results, together with ours, call into question the idea that the tuning-curve tail is a single entity that is uniform in its properties across its frequency range.

B. The observed results are due to fast inhibition from shock-evoked activity in medial olivocochlear efferents

Before considering mechanisms further, it is important to point out that there are several compelling reasons to believe that the efferent effects reported here are due to medial olivocochlear (MOC) efferents that synapse on outer hair cells, rather than lateral olivocochlear (LOC) efferents that synapse on ANF dendrites contacting inner hair cells: (1) The use of extracellular shocks and high shock rates both strongly favor stimulation of the myelinated MOC fibers over the unmyelinated LOC fibers (Gifford and Guinan, 1987). (2) We recorded from neurons from the cochlear base but only a very low percentage of the crossed LOC fibers (the only ones near our stimulating electrode) go to the cochlear base (Guinan *et al.*, 1984). (3) In an individual fiber, efferent inhibition varied with tone frequency which would not be expected from LOC synapses on the dendrite of an auditory-nerve fiber. (4) The LOC innervation varies considerably across fibers with different SRs (Liberman, 1980b), but the observed inhibition varied little across SR groups. In addition, the effects are not due to middle-ear-muscles because their tendons were cut. We also note that the cats in this study were kept in a deep anesthetic state so that it is unlikely that the efferent inhibition reported here was influenced substantially by sound-evoked efferent activity. As a test of this, in one cat we attempted to measure efferent inhibition evoked by contralateral sound (as in Warren and Liberman, 1989), but could not detect any, despite a prominent inhibition at tail frequencies when efferents were stimulated electrically.

Based on a variety of evidence, our results appear to be attributable to fast efferent effects rather than the slow efferent inhibition described by Sridhar *et al.* (1995). In our data, inhibition was evident on the first tone burst, just 100 ms after the onset of efferent stimulation. In addition, our stimulus paradigm presented efferent stimulation at a low duty cycle (1.1 out of 6 s, on average), about half of that used by Sridhar *et al.* (1995) to evoke efferent slow effects. Also, our randomized stimulation paradigm would average away any differences due to slow effects that lasted much longer than the 3-s trial time.

C. Could the efferent inhibition of ANF responses to tail-frequency tones be due to an efferent reduction of basilar-membrane motion?

There are only two published reports of efferent effects on basilar membrane motion in response to tail-frequency tones, and these provide opposing views (Murugasu and Russell, 1996; Russell and Murugasu, 1997). Murugasu and Russell (1996) reported that efferents did not affect basilar-membrane (BM) motion at frequencies more than $\frac{1}{2}$ octave below CF. However, the major focus of that study was not on tail frequencies and the tail-frequency observations appear to be very limited in scope. Motivated by our preliminary data showing efferent inhibition of ANF responses at tail frequencies (Stankovic and Guinan, 1997), Russell and Murugasu (1997) presented data showing efferent inhibition of BM motion (by 10 dB at 65 dB SPL, decreasing at higher levels) that is very reminiscent of our data (see Figs. 3–5). However, these basilar-membrane data are for only one frequency from one animal (4 kHz with $\mathrm{CF}=15$ kHz). Therefore, it remains to be seen what fraction, if any, of the ANF inhibition at tail frequencies is produced by efferent reduction of basilar-membrane motion. To resolve this issue we need careful measurements of basilar-membrane motion not just at tail frequencies, but also at sound levels near the tail thresholds where we have found the largest efferent effects.

It is useful to make the tentative assumption that an efferent reduction of basilar-membrane motion completely accounts for the inhibition of ANF responses to tail-frequency tones, to see the implications of this assumption.

Since the efferents involved are medial efferents ending on OHCs, one implication would be that OHCs influence basilar-membrane motion at tail frequencies. This would be somewhat surprising since a variety of agents that are presumed to influence basilar-membrane motion primarily through OHCs (e.g., furosemide, acoustic trauma, death; Rhode, 1973; Ruggero *et al.*, 1991, 1996, 1997; Nuttall and Dolan, 1996) have little or no effect on basilar-membrane motion at tail frequencies. In addition, evidence from several species indicates that, in the absence of efferent stimulation, basilar-membrane motion grows linearly with sound level in response to tail-frequency tones (guinea pig: Sellick *et al.*, 1982; Nuttall and Dolan, 1996; chinchilla: Ruggero *et al.*, 1997; cat: Cooper and Rhode, 1992). In particular, Ruggero *et al.* (1997) would have been able to detect systematic deviations from linearity of 2 dB or more. This, with our finding that efferent inhibition changes across sound levels (Fig. 1–7), implies that for tail-frequency tones, BM motion with efferent stimulation would have to grow nonlinearly with a growth rate *faster*, on average, than sound level. Again, while not impossible, this would be surprising. This linearity argument, while weak, appears to us to be the strongest evidence available on this issue. In summary, the hypothesis that an efferent reduction of basilar-membrane motion entirely accounts for the inhibition of ANF responses to tail-frequency tones cannot be ruled out, but it seems more likely that inhibition of basilar-membrane motion accounts for little, if any, of the inhibition of ANF responses to tail-frequency tones.

D. If the inhibition is not due to a reduction of basilar-membrane motion, then what is it due to?

If, in response to tail-frequency tones, efferent stimulation does not change basilar-membrane motion but does change the firing of auditory-nerve fibers, then efferents must affect some stage in between. This implies a divergence between basilar-membrane motion and neural firing when comparing tip versus tail frequencies, but this is not surprising because (1) agents that affect the tips of neural or mechanical tuning curves do not always have the same effect in the tail [e.g., furosemide (Ruggero and Rich, 1991; Sewell, 1984), acoustic trauma (Ruggero *et al.*, 1993; Liberman and Kiang, 1978), and death (Rhode, 1973; Ruggero *et al.*, 1997; Nuttall and Dolan, 1996)]. (2) In the one case where direct measurements of basilar-membrane and auditory-nerve tuning curves were made on the same animal, the tips are very similar but the tails clearly diverge (Narayan *et al.*, 1998). In theory, efferent inhibition which would affect tuning-curve tails of auditory-nerve fibers but not basilar-membrane motion might occur anywhere between basilar-membrane motion and the excitation of auditory-nerve fibers. There are two general mechanisms worth serious consideration for how efferent endings on OHCs might affect other parts of the cochlea: (1) electrical effects through the MOC potential, or (2) mechanical effects that change cochlear micromechanics (specifically, that change the coupling between basilar-membrane motion and the bending of IHC stereocilia).

1. Inhibition from the MOC potential

Activation of MOC efferents produces the MOC potential, an efferent-evoked voltage change that can be measured as a reduction of the endocochlear potential (EP) or as a positive potential within the organ of Corti (Fex, 1967; Brown and Nuttall, 1984; Gifford and Guinan, 1987; Guinan and Stankovic, 1995; see Guinan, 1996 for a review). Although changes in EP that influence OHCs and change the gain of the cochlear amplifier are important for CF stimulation, the effect of this OHC-based change appears to be negligible at tail-frequencies (at least on basilar-membrane motion, see Ruggero and Rich, 1991). One long-considered way that the MOC potential might inhibit auditory-nerve fibers is by reducing IHC transmembrane potential and/or IHC receptor potentials (Geisler, 1974; Guinan and Gifford, 1988b; Guinan and Stankovic, 1995). Brown and Nuttall (1984) found MOC potentials of 0 to $+1.5$ mV in IHCs, $+0.5$ to $+2$ mV in the organ of Corti near IHCs and -2 to -4 mV in scala media. These data suggest that efferents might produce an IHC transmembrane potential of $\frac{1}{2}$ mV, which might be enough to produce a significant effect.

An estimate of the inhibition from the MOC potential can be obtained from the finding that furosemide injections reduced EP and increased auditory-nerve tuning-curve thresholds at tail frequencies by 0.3 dB for every 1-mV decrease in EP (Sewell, 1984). If the same ratio holds for an efferent-induced change in EP, then the 4-mV change in EP in the hook region of the cat (the largest reported; Gifford and Guinan, 1987) would increase tail thresholds by about 1.2 dB. The tail-threshold change for fibers with 10–15 kHz CFs should be larger because medial efferent innervation is larger in the 10–15-kHz CF region than in the hook region (Guinan *et al.*, 1984; Liberman *et al.*, 1990). A relevant index of this innervation difference is the efferent inhibition of spontaneous activity which is thought to be due to the efferent-induced change in EP (ΔEP) (Guinan and Gifford, 1988b; Guinan and Stankovic, 1995). Figure 6 of Guinan and Gifford (1988b) indicates that for 10-kHz CFs (the region with the largest inhibition of spontaneous activity), the inhibition is approximately twice that found for 30-kHz CFs (the CF region used to measure ΔEP). Thus, ΔEP might make tail threshold changes of 2.4 dB for fibers with CFs near 10 kHz. Since we found an average elevation of tail threshold of $\approx$5 dB, occasionally being as large as 25 dB, it seems likely that the efferent-induced reduction of EP plays a role, but perhaps only a minor role, in inhibiting auditory-nerve fiber responses near threshold at tail frequencies. However, ΔEP might be the major factor producing the much smaller inhibition seen at 100 dB SPL.

Another way in which the MOC potential might inhibit auditory-nerve responses is through changes in extracellular potential around IHC-afferent synapses or near the action-potential initiation sites of auditory-nerve fibers (see Russell and Sellick, 1983; Guinan and Gifford, 1988b; Hill *et al.*, 1989; Cheatham and Dallos, 1998; Cody and Mountain, 1989). Such extracellular potential changes might change IHC transmembrane potentials near the IHC-afferent synapse and affect transmitter release, or change the probability of action potentials being initiated for a given transmitter re-

lease. Since the MOC potential can be on the order of 1 mV near IHCs (Brown and Nuttall, 1984), substantial changes in afferent firing might be produced. There is, at present, no direct way of evaluating this hypothesis. However, an important consideration is that auditory-nerve fibers in the different SR groups have synapses at different locations on pillar versus modiolar sides of the IHCs, and with different afferent fiber thicknesses in the region under IHCs (Liberman, 1980a; Liberman and Oliver, 1984). Considering that the MOC potential is due to current flowing into synapses at the bases of OHCs, it seems possible that there would be significant spatial gradients in the MOC potential in the region near and under IHCs. If there are spatial gradients in the MOC potential, and if tail-frequency inhibition is due to effects of the MOC potential in this region, then we might expect substantial changes in tail-frequency inhibition across SR groups. However, our data have not revealed any systematic difference in efferent inhibition at tail frequencies across SR groups. Although the uncertainties in this line of reasoning preclude a definitive conclusion, the lack of difference in the inhibition across SR groups argues against the hypothesis that the tail-frequency inhibition is due to extracellular MOC potential influences in the region around and under IHCs.

At first glance, the fact that the efferent inhibition at tail frequencies depends on tone frequency and level might seem to preclude an origin of the inhibition in the MOC potential because the MOC potential is a d.c. change. However, Fex (1967) found that the amplitude of the MOC potential changed with sound stimulation (presumably because sound produces a change in organ of Corti conductances—Geisler *et al.*, 1977) and this interaction may be dependent on frequency. It therefore remains possible, but unlikely, that the MOC potential accounts for efferent inhibition at tail frequencies.

2. Inhibition from an efferent-induced change in cochlear micromechanics

An alternate mechanism by which efferents might inhibit auditory-nerve fibers at tail frequencies without substantially changing basilar-membrane motion is by changing cochlear micromechanics so that basilar membrane motion is less efficiently coupled to the bending of IHC stereocilia. Although it is conceptually possible that efferents, through the MOC potential, might change mechanical properties at a distant point (e.g., IHC stereocilia), it seems most likely that any mechanical change takes place in the OHCs or the OHC stereocilia. There is good evidence for an efferent-induced mechanical change on a slow time scale in guinea pig OHCs (Sziklai *et al.*, 1996), so an efferent-induced mechanical change on a fast time scale would not be surprising. One appealing mechanism is an efferent-induced reduction of OHC stiffness (perhaps like that found by Sziklai *et al.*, 1996) that leads to reduced motion of the upper part of the organ of Corti relative to the basilar membrane. Another possibility is that efferent activity changes OHC stereocilia stiffness (e.g., by hyperpolarizing the OHCs) and that this ultimately changes the coupling between basilar-membrane motion and the bending of IHC stereocilia. Since the efferent-induced change in auditory-nerve firing rate depends on sound level, the efferent-induced change in cochlear micromechanics must also depend on sound level. This could come about either because efferents produce a nonlinear mechanical change, or because the coupling between basilar-membrane motion and the bending of IHC stereocilia is nonlinear even without efferent modulation. Whatever the actual mechanisms involved, the requirements that the efferent-induced mechanical change reduce the bending of IHC stereocilia without substantially changing basilar-membrane motion, and that the greatest change be at sound levels near the tail threshold and sound frequencies 2–3 octaves below CF, greatly constrains the types of mechanical change that might account for efferent tail-frequency inhibition. All in all, our data indicate that current conceptions that auditory-nerve-fiber tuning-curve tails represent a passive, constant coupling of basilar-membrane motion to IHC stereocilia needs substantial revision.

E. Implications of tail-frequency efferent inhibition for audition

Although the main goal of the present work is to help understand basic cochlear mechanisms, it is worth noting that the efferent inhibition of responses to tail-frequency tones may also have significant implications for signal coding by auditory-nerve fibers. Efferent inhibition at tail frequencies can be substantial (e.g., 15 dB at tail threshold). Furthermore, the sound levels and frequencies at which this inhibition is substantial are important for conversational speech. Thus, efferent inhibition at tail frequencies seems likely to be relevant for all hearing people, but it may be particularly relevant for the hearing impaired who have reduced tuning curve tips.

IV. CONCLUSIONS

(i) Medial efferents can inhibit responses of ANFs to tail-frequency tones even though the cochlear amplifier may have little effect at frequencies far below CF.

(ii) Activation of medial efferents lowers responses more in the higher-frequency part than the lower-frequency part of ANF tuning curves, thus tuning-curve tails should not be regarded as single entities with frequency-independent characteristics.

(iii) Since basilar membrane motion at tail frequencies always appears to be linear but efferent inhibition of auditory-nerve fibers at tail frequencies is strongly dependent on sound level, it seems unlikely that efferent inhibition at tail frequencies is due entirely to a reduction in basilar-membrane motion.

(iv) The efferent-induced reduction of EP probably provides part of the inhibition of auditory-nerve fiber responses at tail frequencies. It seems most likely that the remaining inhibition is due to efferent-induced changes in cochlear micromechanics.

(v) The existence and characteristics of medial-efferent inhibition of responses at tail frequencies provide new constraints on concepts of how the cochlea works.

ACKNOWLEDGMENTS

We thank Dr. M. C. Brown, Dr. M. C. Liberman, and Dr. C. A. Shera for comments on the manuscript, and Dr. D. K. Eddington, Dr. D. C. Mountain, Dr. J. B. Nadol, Jr., and Dr. W. F. Sewell for comments on the thesis that led to this paper. We also thank Dr. C. A. Shera for introducing us to loess fitting and permutation tests. This work was supported (in part) by Research Grant No. 5 RO1 DC 00235, Training Grant No. T32 DC00038 and Medical Scientist Training Program grant T32 MGM07753 from the National Institute on Deafness and Other Communication Disorders, National Institutes of Health.

[1]These data are reminiscent of the efferent inhibition of tone level functions in the tip region of low-CF fibers that also showed a low-level portion that was inhibited substantially by efferent stimulation, and a high-level portion that showed little or no inhibition (Gifford and Guinan, 1983). However, in the present data, the transition from the lower-level to the higher-level portion of the rate-level curves was not accompanied by an abrupt reversal in the response phase (phase of the first Fourier component of a period histogram) as were the transitions found by Gifford and Guinan (1983). Instead, the response phases gradually decreased with sound level and were similarly affected by efferent stimulation across all sound levels.

Abbas, P. J., and Sachs, M. B. (**1976**). ''Two-tone suppression in auditory-nerve fibers: Extension of a stimulus-response relationship,'' J. Acoust. Soc. Am. **59**, 112–122.

Brown, M. C., and Nuttall, A. L. (**1984**). ''Efferent control of cochlear inner hair cell responses in the guinea pig,'' J. Physiol. (London) **354**, 625–646.

Cheatham, M. A., and Dallos, P. (**1998**). ''The level dependence of response phase: observations from cochlear hair cells,'' J. Acoust. Soc. Am. **104**, 356–369.

Cleveland, W. S. (**1993**). *Visualizing Data* (AT&T Bell Laboratories, Murray Hill, NJ, 1993).

Cody, A. R., and Mountain, D. C. (**1989**). ''Low-frequency responses of inner hair cells: evidence for a mechanical origin of peak splitting,'' Hearing Res. **41**, 89–99.

Cooper, N. P., and Rhode, W. S. (**1992**). ''Basilar membrane mechanics in the hook region of cat and guinea-pig cochleae: Sharp tuning and nonlinearity in the absence of baseline position shifts,'' Hearing Res. **63**, 163–190.

Efron, B., and Tibshirani, R. J. (**1993**). *An Introduction to the Bootstrap* (Chapman and Hall, New York).

Fex, J. (**1967**). ''Efferent inhibition in the cochlea related to hair-cell dc activity: Study of postsynaptic activity of the crossed olivo-cochlear fibers in the cat,'' J. Acoust. Soc. Am. **41**, 666–675.

Geisler, C. D. (**1974**). ''Model of crossed olivocochlear bundle effects,'' J. Acoust. Soc. Am. **56**, 1910–1912.

Geisler, C. D., Mountain, D. C., Hubbard, A. E., Adrian, H. O., and Ravindran, A. (**1977**). ''Alternating electrical-resistance changes in the guinea-pig caused by acoustic stimuli,'' J. Acoust. Soc. Am. **61**, 1557–1566.

Gifford, M. L., and Guinan, J. J. (**1983**). ''Effects of crossed-olivocochlear-bundle stimulation on cat auditory nerve fiber responses to tones,'' J. Acoust. Soc. Am. **74**, 115–123.

Gifford, M. L., and Guinan, Jr., J. J. (**1987**). ''Effects of electrical stimulation of medial olivocochlear neurons on ipsilateral and contralateral cochlear responses,'' Hearing Res. **29**, 179–194.

Guinan, Jr., J. J. (**1996**). ''The Physiology of Olivocochlear Efferents,'' in *The Cochlea*, edited by P. J. Dallos, A. N. Popper, and R. R. Fay (Springer-Verlag, New York), pp. 435–502.

Guinan, Jr., J. J., and Gifford, M. L. (**1988a**). ''Effects of electrical stimulation of efferent olivocochlear neurons on cat auditory-nerve fibers. I. Rate-level functions,'' Hearing Res. **33**, 97–114.

Guinan, Jr., J. J., and Gifford, M. L. (**1988b**). ''Effects of electrical stimulation of efferent olivocochlear neurons on cat auditory-nerve fibers. II. Spontaneous rate,'' Hearing Res. **33**, 115–128.

Guinan, Jr., J. J., and Gifford, M. L. (**1988c**). ''Effects of electrical stimulation of efferent olivocochlear neurons on cat auditory-nerve fibers. III. Tuning curves and thresholds at CF,'' Hearing Res. **37**, 29–46.

Guinan, Jr., J. J., and Stankovic, K. M. (**1995**). ''Medial olivocochlear efferent inhibition of auditory-nerve firing mediated by changes in endocochlear potential,'' Assoc. Res. Otolaryngol. Abstr **18**, 172.

Guinan, Jr., J. J., and Stankovic, K. M. (**1996**). ''Medial efferent inhibition produces the largest equivalent attenuations at moderate to high sound levels in cat auditory-nerve fibers,'' J. Acoust. Soc. Am. **100**, 1680–1690.

Guinan, Jr., J. J., Warr, W. B., and Norris, B. E. (**1984**). ''Topographic organization of the olivocochlear projections from the lateral and medial zones of the superior olivary complex,'' J. Comp. Neurol. **226**, 21–27.

Hill, K. G., Stange, G., Gummer, A. W., and Mo, J. (**1989**). ''A model proposing synaptic and extra-synaptic influences on the responses of cochlear nerve fibres,'' Hearing Res. **39**, 75–90.

Kawase, T., Delgutte, B., and Liberman, M. C. (**1993**). ''Anti-masking effects of the olivocochlear reflex, II: Enhancement of auditory-nerve response to masked tones,'' J. Neurophysiol. **70**, 2533–2549.

Kiang, N. Y. S., Moxon, E. C., and Levine, R. A. (**1970**). ''Auditory-nerve activity in cats with normal and abnormal cochleas,'' in *Ciba Foundation Symposium on Sensorineural Hearing Loss*, edited by G. E. W. Wolstenholme and J. Knight (Churchill, London), pp. 241–273.

Kiang, N. Y. S., Watanabe, T., Thomas, E. C., and Clark, L. F. (**1965**). *Discharge Patterns of Single Fibers in the Cat's Auditory Nerve* (MIT, Cambridge, MA).

Liberman, M. C. (**1978**). ''Auditory-nerve response from cats raised in a low-noise chamber,'' J. Acoust. Soc. Am. **63**, 442–455.

Liberman, M. C. (**1980a**). ''Morphological differences among radial afferent fibers in the cat cochlea: An electron-microscopic study of serial sections,'' Hearing Res. **3**, 45–63.

Liberman, M. C. (**1980b**). ''Efferent synapses in the inner hair cell area of the cat cochlea: An electron microscopic study of serial sections,'' Hearing Res. **3**, 189–204.

Liberman, M. C., and Kiang, N. Y. S. (**1978**). ''Acoustic trauma in cats. Cochlear pathology and auditory-nerve activity,'' Acta Oto-Laryngol. Suppl. **358**, 1–63.

Liberman, M. C., and Oliver, M. E. (**1984**). ''Morphometry of intracellularly labeled neurons of the auditory nerve: Correlations with functional properties,'' J. Comp. Neurol. **223**, 163–176.

Liberman, M. C., Dodds, L. W., and Pierce, S. (**1990**). ''Afferent and efferent innervation of the cat cochlea: quantitative analysis with light and electron microscopy,'' J. Comp. Neurol. **301**, 443–460.

Meyer, S. L. (**1975**). *Data Analysis for Scientists and Engineers* (Wiley, New York).

Mountain, D. C. (**1978**). ''A comparison of electrical changes in the cochlea caused by stimulation of the crossed olivocochlear bundle and by d.c. polarization.,'' Ph.D. thesis, Univ. of Wisconsin—Madison.

Murugasu, E., and Russell, I. J. (**1996**). ''The effect of efferent stimulation on basilar membrane displacement in the basal turn of the guinea pig cochlea,'' J. Neurosci. **16**, 325–332.

Narayan, S. S., Temchin, A. N., Recio, A., and Ruggero, M. A. (**1998**). ''Frequency tuning of basilar membrane and auditory nerve fibers in the same cochleae,'' Science **282**, 1882–1884.

Nuttall, A. L., and Dolan, D. F. (**1996**). ''Steady-state sinusoidal velocity responses of the basilar membrane in guinea pig,'' J. Acoust. Soc. Am. **99**, 1556–1565.

Rhode, W. S. (**1973**). ''An investigation of postmortem cochlear mechanics using the Mössbauer effect,'' in *Basic Mechanisms of Hearing*, edited by A. R. Møller (Academic, New York), pp. 49–67.

Ruggero, M. A., and Rich, N. C. (**1991**). ''Furosemide alters organ of Corti mechanics: Evidence for feedback of outer hair cells upon the basilar membrane,'' J. Neurosci. **11**, 1057–1067.

Ruggero, M. A., Rich, N. C., and Recio, A. (**1993**). *Alteration of Basilar Membrane Responses to Sound by Acoustic Overstimulation* (World Scientific, Singapore), pp. 258–265.

Ruggero, M. A., Rich, N. C., and Recio, A. (**1996**). ''The effect of intense acoustic stimulation on basilar-membrane vibrations,'' Aud. Neurosci. **2**, 329–345.

Ruggero, M. A., Rich, N. C., Recio, A., Narayan, S. S., and Robles, L. (**1997**). ''Basilar-membrane responses to tones at the base of the chinchilla cochlea,'' J. Acoust. Soc. Am. **101**, 2151–2163.

Russell, I. J., and Murugasu, E. (**1997**). ''Efferent suppression of basilar membrane vibration depends on tone frequency and level: implications for the active control of basilar membrane mechanics,'' in *Psychophysical and Physiological Advances in Hearing. Proceedings of the 11th International Symposium on Hearing*, edited by A. R. Palmer, A. Rees, and A. Q. Summefield *et al.* (Whurr, London), pp. 18–24.

Russell, I. J., and Sellick, P. M. (**1983**). ''Low-frequency characteristics of intracellularly recorded receptor potentials in guinea-pig cochlear hair cells,'' J. Physiol. (London) **338**, 179–206.
Sellick, P. M., Patuzzi, R., and Johnstone, B. M. (**1982**). ''Measurement of basilar membrane motion in the guinea pig using the Mössbauer technique,'' J. Acoust. Soc. Am. **72**, 131–141.
Sewell, W. F. (**1984**). ''The effects of furosemide on the endocochlear potential and auditory-nerve fiber tuning curves in cats,'' Hearing Res. **14**, 305–314.
Siegel, J. H., and Relkin, E. M. (**1987**). ''Antagonistic effects of perilymphatic calcium and magnesium on the activity of single cochlear afferent neurons,'' Hearing Res. **28**, 131–147.
Sridhar, T. S., Liberman, M. C., Brown, M. C., and Sewell, W. F. (**1995**). ''A novel cholinergic ''slow effect'' of olivocochlear stimulation on cochlear potentials in the guinea pig,'' J. Neurosci. **15**, 3667–3678.
Stankovic, K. M., and Guinan, Jr., J. J. (**1997**). ''Efferent effects on auditory-nerve responses to tail-frequency tones: Inhibition without altering basilar-membrane motion?'' Assoc. Res. Otolaryngol. Abstr. **20**, 155.
Sziklai, I., He, D. Z. Z., and Dallos, P. (**1996**). ''Effect of acetylcholine and GABA on the transfer function of electromotility in isolated outer hair cells,'' Hearing Res. **95**, 87–99.
Warren III, E. H., and Liberman, M. C. (**1989**). ''Effects of contralateral sound on auditory-nerve responses. I. Contributions of cochlear efferents,'' Hearing Res. **37**, 89–104.
Wiederhold, M. L. (**1970**). ''Variations in the effects of electric stimulation of the crossed olivocochlear bundle on cat single auditory-nerve-fiber responses to tone bursts,'' J. Acoust. Soc. Am. **48**, 966–977.
Wiederhold, M. L., and Kiang, N. Y. S. (**1970**). ''Effects of electric stimulation of the crossed olivocochlear bundle on single auditory-nerve fibers in the cat,'' J. Acoust. Soc. Am. **48**, 950–965.

The normalized interaural correlation: Accounting for NoSπ thresholds obtained with Gaussian and "low-noise" masking noise

Leslie R. Bernstein
Surgical Research Center, Department of Surgery (Otolaryngology) and Center for Neurological Sciences University of Connecticut Health Center Farmington, Connecticut 06030

Steven van de Par
Surgical Research Center, Department of Surgery (Otolaryngology) and Center for Neurological Sciences, University of Connecticut Health Center, Farmington, Connecticut 06030 and IPO, Center for Research on User–System Interaction, P.O. Box 513, 5600 MB Eindhoven, The Netherlands

Constantine Trahiotis
Surgical Research Center, Department of Surgery (Otolaryngology) and Center for Neurological Sciences, University of Connecticut Health Center, Farmington, Connecticut 06030

(Received 8 February 1999; revised 30 April 1999; accepted 14 May 1999)

Recently, Eddins and Barber [J. Acoust. Soc. Am. **103**, 2578–2589 (1998)] and Hall *et al.* [J. Acoust. Soc. Am. **103**, 2573–2577 (1998)] independently reported that greater masking of interaurally phase-reversed (Sπ) tones was produced by diotic low-noise noise than by diotic Gaussian noise. Based on quantitative analyses, Eddins and Barber suggested that their results could not be accounted for by assuming that listeners' judgments were based on constant-criterion changes in the normalized interaural correlation produced by adding the Sπ signal to the diotic masker. In particular, they showed that a model like the one previously employed by Bernstein and Trahiotis [J. Acoust. Soc. Am. **100**, 3774–3784 (1996)] predicted an ordering of thresholds between the conditions of interest that was opposite to that observed. Bernstein and Trahiotis computed the normalized interaural correlation subsequent to half-wave, square-law rectification and low-pass filtering, the parameters of which were chosen to mimic peripheral auditory processing. In this report, it is demonstrated that augmenting the model by adding a physiologically valid stage of ''envelope compression'' *prior* to rectification and low-pass filtering provides a remedy. The new model not only accounts for the data obtained by Eddins and Barber (and the similar data obtained by Hall *et al.*), but also does not diminish the highly successful account of the comprehensive set of data that gave rise to the original form of the model. Therefore, models based on the computation of the normalized interaural correlation appear to remain valid because they can account, both quantitatively and qualitatively, for a wide variety of binaural detection and discrimination data. [S0001-4966(99)06108-1]

PACS numbers: 43.66.Ba, 43.66.Dc, 43.66.Pn [DWG]

INTRODUCTION

Recently, Eddins and Barber (1998) and Hall *et al.* (1998) demonstrated that diotic narrow-band masking noise constructed to have minimal fluctuations in amplitude (so-called low-noise noise) produced 2 or 3 dB more masking of interaurally phase-reversed (Sπ), 500-Hz tones than did Gaussian noise of the same nominal bandwidth and power. In addition, Eddins and Barber observed that smaller differences in amounts of masking were produced by the two types of maskers when the measurements were conducted at 4 kHz.

In an effort to account for their results, Eddins and Barber considered an explanation based on differential changes in the normalized interaural correlation that would be produced by the addition of the Sπ signals to each of the two types of diotic masker in their NoSπ masking configuration. Following an approach published recently by Bernstein and Trahiotis (1996), Eddins and Barber computed the normalized interaural correlation subsequent to half-wave, square-law rectification and low-pass filtering of the stimuli. Their low-pass filter, like that of Bernstein and Trahiotis, had a cutoff frequency of 425 Hz and was of a form derived from physiological measures of neural synchrony, as a function of center frequency (Weiss and Rose, 1988). Bernstein and Trahiotis (1996) had demonstrated that they could account quite well for binaural discrimination thresholds obtained in their NoSo vs NoSπ task across a broad range of center frequencies and signal-to-noise ratios by computing the normalized correlation in this manner. Specifically, Bernstein and Trahiotis were able to account for the complex patterning of their data across center frequency by assuming that threshold performance corresponded to that level of Sπ signal that produced a constant-criterion decrease of the normalized interaural correlation of the diotic masker.

The analysis performed by Eddins and Barber (1998) showed that, for behaviorally relevant signal-to-noise ratios, the normalized correlation computed as described above was reduced to a *greater* extent when the Sπ signal was added to

the low-noise masker than when it was added to the Gaussian-noise masker. Therefore, under the assumption that detection at threshold is mediated by a constant-criterion reduction in interaural correlation, thresholds would be predicted to be *lower* for the *low-noise* masker than for the Gaussian-noise masker, exactly the *opposite* of the relation observed by Eddins and Barber. In a separate analysis, Eddins and Barber computed the normalized correlations for the 500-Hz signals in the absence of the low-pass filter and obtained similar predictions. On the basis of these two types of analyses, Eddins and Barber suggested that the listeners' use of changes in the normalized interaural correlation, *per se*, cannot account for the ordering of their behavioral thresholds.

It occurred to us that the relative changes in the normalized interaural correlation that Eddins and Barber computed might depend heavily upon the specific type or types of nonlinearity (including the rectifier) that are incorporated in the modeling, rather than on the specific form of the low-pass filter. Bernstein and Trahiotis (1996) originally chose to employ a square-law rectifier because (1) its effects appear to mimic closely relevant aspects of peripheral auditory processing (Colburn, 1973; Yates *et al.*, 1990), and (2) similar ''expansive'' stages of rectification have previously been incorporated in successful auditory-nerve-based cross-correlation models of binaural hearing (Colburn, 1973; Stern and Colburn, 1978; Saberi, 1995). Quite recently, van de Par and Kohlrausch (1998) demonstrated that they could account for both the frequency dependence of the masking-level difference (MLD) and its dependence on the probability distribution, or degree of fluctuation, of the envelope of the masker by using a model based on the assumption that a stage of ''envelope compression'' precedes square-law rectification. We will demonstrate how incorporating a similar stage of compression of the envelope prior to rectification and low-pass filtering allows one to account quantitatively for $N_0S\pi$ thresholds in low-noise noise and Gaussian noise via the normalized interaural correlation while maintaining a highly successful quantitative account of Bernstein and Trahiotis' (1996) discrimination data. An important aspect of the compressive nonlinearity that we employed is that it affects transduction of stimuli in a manner consistent with physiological observations.

I. MODELING PERIPHERAL AUDITORY COMPRESSION

The results of several physiological investigations (Rhode, 1971; Sellick *et al.*, 1982; Ruggero *et al.*, 1997) have demonstrated ''compression'' in that an increase in the level of the stimulus of 1 dB results in an increase in the response of the basilar membrane of about 0.2 dB. This relation holds for ''medium'' sound-pressure levels of 40–70 dB or so, which are similar to those used in psychoacoustic investigations. In addition, Ruggero *et al.* (1997) observed that basilar-membrane compression appears to be established essentially instantaneously.

One way to model mathematically such an outcome is to apply compression to the stimulus waveform using the fractional power 0.2 and to assume that the transformed signal resembles the motion of the basilar membrane that drives inner hair cells. That form of compression does produce an ''input–output'' function similar to that derived from physiological measures. It should be noted, however, that compressing the waveform in that manner introduces substantial harmonic distortion, producing a second harmonic which is only about 17 dB below the level of the fundamental (see the Appendix). It is the case, however, that such harmonic distortion appears to be highly attenuated by the local bandpass filtering properties of the basilar membrane (see Ruggero *et al.*, 1997).

An alternative manner of implementing peripheral auditory compression was recently described by van de Par and Kohlrausch (1998). They applied compression to only the *envelope* (or magnitude) of the stimulus. As shown in the Appendix, raising the values of only the envelope of the input waveform to the power 0.2 has the virtue of introducing minimal harmonic distortion while producing an input–output function like that observed in the physiological investigations of basilar-membrane motion. Capitalizing on these findings, we were able to employ a computationally efficient means of modeling peripheral auditory compression.

In the computer simulations described below, compression was applied by raising the envelope of the stimulus to a power between 0 and 1 and then recombining the compressed envelope with the fine structure of the original stimulus. The resulting waveform was then subjected to half-wave, square-law rectification and to low-pass filtering in the manner described by Bernstein and Trahiotis (1996). Finally, the normalized interaural correlation of the transformed stimuli was computed and used to predict behavioral thresholds.

II. COMPRESSIVE NONLINEARITY AND MEASURES OF THE NORMALIZED INTERAURAL CORRELATION

Figure 1 shows measurements of the normalized interaural correlation for stimuli presented in the $N_0S\pi$ configuration, as a function of signal-to-noise ratio (S/N), in dB. In order to obtain the measurements, an $S\pi$, tonal signal was added to a 50-Hz-wide band of low-noise noise or Gaussian noise centered at the frequency of the signal. A bandwidth of 50 Hz was chosen because that was the value employed by Eddins and Barber (1998).

The left-hand panels of Fig. 1 contain the values of the normalized interaural correlation computed subsequent to half-wave, square-law rectification and low-pass filtering at 425 Hz as previously described by Bernstein and Trahiotis (1996). That is, the computations in the left-hand panels of Fig. 1 were made without an initial stage of compression. The right-hand panels of Fig. 1 contain the values of normalized correlation obtained when a stage of envelope compression (exponent = 0.2) preceded the same square-law rectifier and low-pass filter. The upper and lower panels of Fig. 1 display the measurements for signal frequencies of 500 Hz and 4 kHz, respectively. Within each panel, the solid line depicts the measures obtained with Gaussian maskers; the dashed line depicts the measures obtained with low-noise maskers.[1]

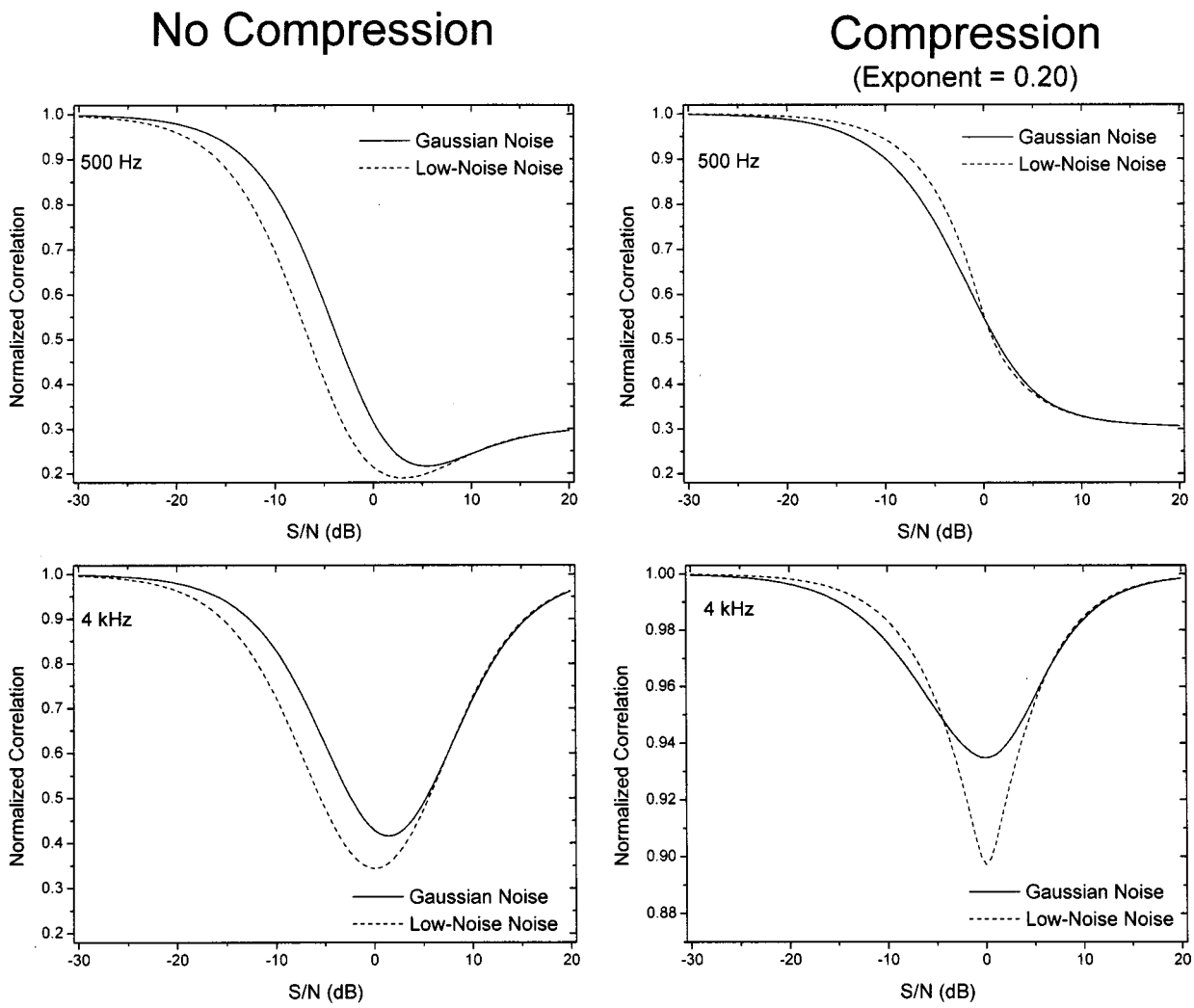

FIG. 1. The normalized correlation as a function of signal-to-noise ratio in dB. The left-hand panels contain the values of the normalized correlation computed subsequent to half-wave, square-law rectification and low-pass filtering at 425; that is, without an initial stage of compression. The right-hand panels contain the values of normalized correlation obtained when a stage of envelope compression (exponent=0.2) preceded the same square-law rectifier and low-pass filter. The upper and lower panels display the measurements for signal frequencies of 500 Hz and 4 kHz, respectively. Solid lines depict measures obtained with Gaussian maskers; dashed lines depict measures obtained with low-noise maskers.

Examination of the left-hand panels of Fig. 1 reveals that, when no compression is included, the model produces uniformly *lower* values of correlation for the low-noise masker, as compared to the Gaussian-noise masker. This is entirely consistent with and replicates the measurements obtained by Eddins and Barber (1998). Examination of the right-hand panels of the figure reveals the opposite outcome for all signal-to-noise ratios of interest (below 0 dB). Note that when a stage of envelope compression is added to the model, the values of the normalized correlation of the transformed stimuli are now *lower* for the *Gaussian-noise* masker than they are for the low-noise masker. This outcome is qualitatively in accord with the behavioral thresholds measured by Eddins and Barber. In the following, we show that this type of model provides a quantitative account of differences in binaural masking produced by low-noise vs Gaussian-noise maskers (Eddins and Barber, 1998; Hall *et al.*, 1998), while still accounting for the data obtained by Bernstein and Trahiotis (1996).

III. QUANTITATIVE ACCOUNTS OF THE DATA VIA THE NORMALIZED INTERAURAL CORRELATION

A. NoSπ thresholds with Gaussian and low-noise maskers

In order to account quantitatively for Eddins and Barber's data, it was first necessary to determine the degree of compression required in the first stage of the model. We began by performing computer simulations in which 500-Hz tones were added to 50-Hz-wide bands of Gaussian noises or to 50-Hz-wide bands of low-noise noise in the NoSπ configuration. The signal-to-noise ratio in each case was adjusted to correspond to the average threshold value obtained by Eddins and Barber (1998) across their seven listeners. We measured the normalized correlation while varying the exponent of compression between 0.05 and 0.6, in steps of 0.05. Average values of normalized correlation were computed across 200 independent, 819-ms-long, tokens of low-noise noise and Gaussian noise, respectively.

The results of the measurements are shown in Fig. 2,

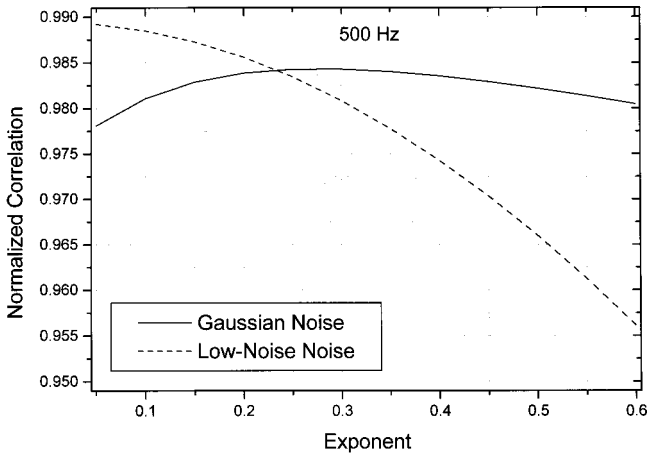

FIG. 2. Normalized correlation as a function of the exponent of compression for 500-Hz, Sπ, tonal signals added to 50-Hz-wide, diotic Gaussian noise (solid line) or to 50-Hz-wide diotic low-noise noise (dashed line). In each case, the signal-to-noise ratio corresponded to the average threshold measured by Eddins and Barber (1998).

where the normalized interaural correlation is plotted as a function of the amount of compression applied to the envelope of the stimulus. The measurements reveal that the normalized correlation corresponding to the average thresholds observed by Eddins and Barber (1998) in the two types of masking conditions is identical when the exponent of the compressive function is approximately 0.23. This value of compression, which was derived from a model and psychophysical data, is quite close to the value of 0.2 which was measured by Sellick *et al.* (1982) and Ruggero (1992) in their physiological studies.

We believe that the virtual equivalence between the physiologically derived and the psychophysically derived magnitudes of compression is not merely coincidental. That belief is bolstered by noting that, when such a form of and amount of compression is followed by a square-law rectifier, the ''total'' compression produced along the peripheral auditory pathway would be 0.46 (0.23×2). This agrees well with the value of compression of 0.4 obtained by Oxenham and Moore (1995), who studied additivity of masking, and by van de Par and Kohlrausch (1998), who measured monaural and binaural masked thresholds. In summary, the average NoSπ thresholds obtained by Eddins and Barber at 500 Hz can be predicted on the basis of a constant-criterion change in the normalized interaural correlation when a stage of physiologically valid envelope compression precedes the rectification and low-pass filtering described by Bernstein and Trahiotis (1996).

An analysis similar to that described above was performed on the data from the four listeners that Eddins and Barber called their ''large-MLD'' group. Their MLDs measured at 500 Hz with Gaussian-noise maskers exceeded 17 dB. In addition, their data revealed a greater disparity between NoSπ thresholds measured with Gaussian noise vs low-noise noise. Despite these differences in the data, the normalized correlation for the two masking conditions was, again, found to be equivalent when the exponent representing the stage of compression was slightly greater than 0.2. Thus, the exponent determining the degree of compression within the first stage of the model appears to be, at least for Eddins and Barber's listeners, ''robust'' against the magnitude of the MLD and the amounts of masking produced by the two types of noises. Therefore, we used an exponent of 0.23 in all subsequent calculations of threshold, which were carried out in order to test the generality of the approach.

We first computed the normalized correlation produced by adding Sπ tones to diotic Gaussian maskers at the signal-to-noise ratios that represented the average threshold measured by Eddins and Barber (1998) and by Hall *et al.* (1998), respectively. The bandwidth of our maskers was either 50 Hz, in order to match the bandwidth employed by Eddins and Barber, or 10 Hz, in order to match the bandwidth employed by Hall *et al.* Then, with these correlations in hand, we found the signal-to-noise ratio (to the nearest 0.25 dB) that produced, in a case-by-case manner, the same normalized correlation for a low-noise (rather than a Gaussian-noise) masker.

Table I contains the results of these analyses for the average of the data obtained by Eddins and Barber (1998) across their seven listeners, the average of the data obtained by Eddins and Barber from their large MLD group, and the average of the data obtained by Hall *et al.* (1998) from their six listeners. The left and right portions of the table contain obtained and predicted thresholds when the frequency of the signal was either 500 Hz or 4 kHz, respectively.

Beginning with the 500-Hz conditions, note that the predicted, like the obtained, NoSπ thresholds for the low-noise masker are *higher* than the thresholds obtained in Gaussian noise. In addition, the predicted low-noise thresholds are within 1 dB of the obtained thresholds. Of course, the accuracy of the prediction of Eddins and Barber's (1998) average data is not new to this analysis, because those data were used earlier in order to determine the exponent of the compressive

TABLE I. Obtained NoSπ thresholds (S/N, in dB) with Gaussian-noise maskers; obtained and predicted NoSπ thresholds with low-noise (LNN) maskers. Predicted values represent the signal-to-noise ratios (to the nearest 0.25 dB) that produced, in a case-by-case manner, the same normalized correlation for a low-noise as that produced at threshold for the Gaussian-noise maskers.

	500 Hz			4 kHz		
	Gaussian	LNN		Gaussian	LNN	
	Obtained	Obtained	Predicted	Obtained	Obtained	Predicted
Eddins and Barber Mean	−19	−16	−16	−11	−10	−8.75
Eddins and Barber ''large MLD'' Group	−23	−19.5	−20.25	−14.5	−14	−12.25
Hall *et al.*	−16.9	−14.7	−14	⋯	⋯	⋯

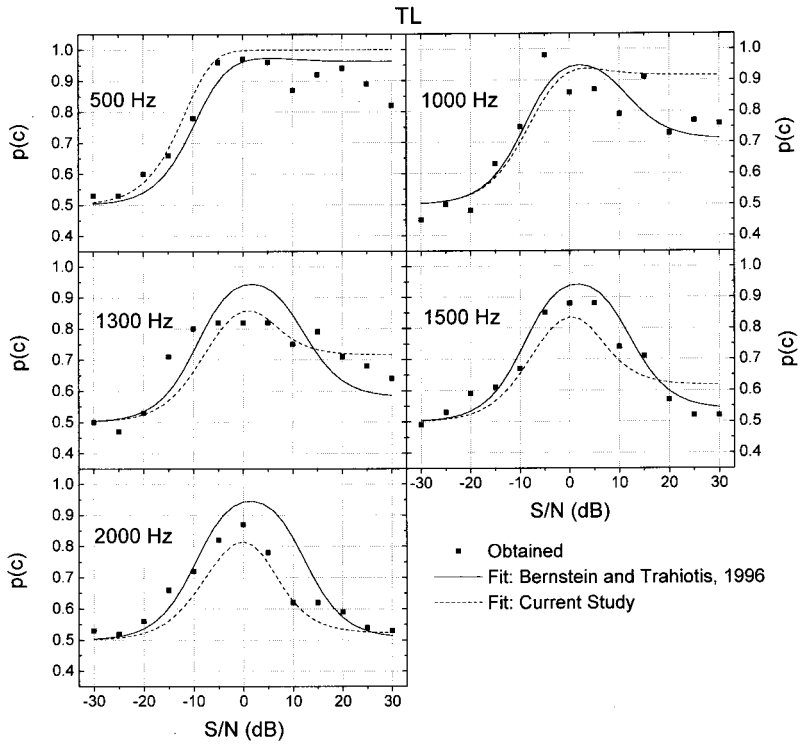

FIG. 3. $p(c)$ as a function of signal-to-noise ratio in dB for Bernstein and Trahiotis' (1996) listener TL. Squares represent the empirical data. Solid lines represent the predictions originally reported by Bernstein and Trahiotis; dashed lines represent the predictions obtained in the current study utilizing compression, rectification, and a low-pass cutoff of 425 Hz. Each panel displays data and predictions for a different center frequency.

nonlinearity. The accuracy of the predictions for the other two groups of listeners attests both to the generality of the model and to the ability to account for binaural detection across Gaussian and low-noise masking conditions at 500 Hz.

Let us now consider the obtained and predicted thresholds for the 4-kHz conditions (right half of the table). Note that Eddins and Barber's masked thresholds are higher than those obtained at 500 Hz and that thresholds at 4 kHz for low-noise and Gaussian-noise maskers differ by only about 1 dB. The model correctly predicts that NoSπ thresholds obtained with the low-noise and Gaussian-noise maskers are higher at 4 kHz than at 500 Hz, but predicts slightly larger (1.25 to 1.75 dB) low-noise thresholds than were actually obtained. We next provide a much more rigorous test of the model's ability to account for changes in binaural thresholds as a function of center frequency by considering the data obtained by Bernstein and Trahiotis (1996).

B. NoSo vs NoSπ discrimination thresholds

Recall that Bernstein and Trahiotis (1996) measured listeners' abilities to discriminate between NoSo and NoSπ conditions across a broad range of signal-to-noise ratios and center frequencies using Gaussian-noise maskers. We reanalyzed their data in the following manner. The normalized interaural correlation was computed subsequent to envelope compression (exponent of 0.23), half-wave, square-law rectification, and low-pass filtering at 425 Hz, for each signal-to-noise ratio and center frequency tested. These normalized correlations were subtracted from 1.0, yielding measures of change in correlation, $\Delta\rho$. Then, for each listener, the measures of $\Delta\rho$ were paired with their corresponding values of percentage correct, $p(c)$. The paired values were then used in order to determine the best-fitting (in the least-squares sense) ''psychometric'' function of the form

$$p(c) = 1 - 0.5e^{-a(\Delta\rho)}. \tag{1}$$

That was the form of psychometric function used by Bernstein and Trahiotis where a was the parameter that was adjusted within the fitting procedure. These psychometric functions were then used to arrive at predicted values of $p(c)$ by entering the $\Delta\rho$ corresponding to each condition.

The amounts of variance in the data accounted for by this procedure, taken across all center frequencies and signal-to-noise ratios, were: 72% for listener BT, 85% for listener MM, and 76% for listener TL. For the same listeners, Bernstein and Trahiotis (1996) found that 86%, 80%, and 80%, respectively, of the variance in the data was accounted for when the computation of the normalized interaural correlation *did not* include compression.

Figure 3 illustrates, for one representative listener, listener TL, how well the predictions of the model capture the differences in the patterning of the data across center frequency. The figure contains the empirical data plotted as squares; the solid lines represent the predictions originally reported by Bernstein and Trahiotis; the dashed lines represent the predictions obtained in the current study utilizing compression, rectification, and a low-pass cutoff of 425 Hz. The individual panels display $p(c)$ as a function of signal-to-noise ratio in dB for each center frequency. Both sets of predictions account for about 80% of the variance in the data. Additional analyses revealed that the predictions could be improved somewhat by decreasing the cutoff of the low-pass filter from 425 to 375 Hz. By doing so, the variance accounted for in the data increased modestly, becoming

76%, 87%, and 82%, for listeners BT, MM, and TL, respectively. Reducing the cutoff of the low-pass filter to 375 Hz had negligible effects (i.e., no more than 0.5 dB) on the predicted NoSπ thresholds obtained with low-noise noise maskers shown in Table I. Overall, it appears that a general model of binaural detection in which the listeners' decisions are based on changes in the normalized interaural correlation computed subsequent to (peripheral) envelope compression, half-wave, square-law rectification, and low-pass filtering in the region of 400 Hz accounts well for data obtained with either low-noise maskers or Gaussian-noise maskers.

IV. SUMMARY AND CONCLUSIONS

In a recent issue of this journal, Eddins and Barber (1998) and Hall *et al.* (1998) independently reported that greater masking was produced by low-noise noise, as compared to Gaussian noise, when the stimuli were presented in the NoSπ configuration. The results of certain analyses conducted by Eddins and Barber led them to suggest that their results could not be accounted for by assuming that listeners' judgments were based on changes in normalized interaural correlation produced by adding the Sπ signal to the diotic masker. In particular, they showed that a model like the one previously employed by Bernstein and Trahiotis (1996) predicted an ordering of thresholds between the conditions of interest that was opposite to that observed. In that model, the normalized interaural correlation is computed subsequent to half-wave, square-law rectification and low-pass filtering like that which characterizes peripheral auditory processing. In this report, we demonstrate that adding a physiologically valid stage of envelope compression *prior* to rectification and low-pass filtering provides a remedy. The new model not only accounts for the data obtained by Eddins and Barber (and the similar data obtained Hall *et al.*), but also accounts for the comprehensive set of NoSo vs NoSπ discrimination thresholds that gave rise to the model suggested by Bernstein and Trahiotis. In conclusion, the normalized interaural correlation, computed subsequent to transformations mimicking peripheral auditory processing (e.g., Blauert and Cobben, 1978; Stern and Colburn, 1978; Stern and Shear, 1996; Bernstein and Trahiotis, 1996; van de Par and Kohlrausch, 1998; 1999), appears to be a useful metric because it accounts both quantitatively and qualitatively for a variety of binaural detection and discrimination data.

ACKNOWLEDGMENTS

The authors thank David Eddins, Quentin Summerfield, and Wes Grantham for their helpful comments and suggestions. The authors also wish to acknowledge their respective institutions for supporting and encouraging the many fruitful collaborations and interactions among members of our respective laboratories that have occurred over the past several years. This research was supported by Research Grant No. NIH DC-00234 from the National Institute on Deafness and Other Communication Disorders, National Institutes of Health.

APPENDIX: MODELING PERIPHERAL COMPRESSION

The essential requirement of a mathematical model of peripheral compression is that an increment in level of 1 dB at the input results in an increment of less than 1 dB at the output. For purposes of illustration, we will use the example in which an increment of 1 dB at the input results in an increment of 0.2 dB at the output. As discussed in the body of the paper, that quantitative relation characterizes several physiological investigations of the basilar membrane (e.g., Rhode, 1971; Sellick *et al.*, 1982; Ruggero *et al.*, 1997).

Such an input–output function can be obtained when the input waveform is raised to a fractional power of 0.2 by using an equation of the form

$$W_o(t) = \max(0, W_i(t))^{0.2} - \max(0, -W_i(t))^{0.2}, \qquad \text{(A1)}$$

where $W_i(t)$ is the input waveform and $W_o(t)$ is the output waveform.

A drawback of this method is that it introduces considerably large amounts of harmonic distortion. This is shown in the top panel of Fig. A1, which displays the power spectrum produced by compressing the waveform of a 50-Hz-wide band of Gaussian noise centered at 500 Hz. Note that the second harmonic is about 17 dB lower in level than the fundamental. This type of harmonic distortion is inconsistent with the virtual absence of harmonic distortion observed by Ruggero *et al.*, 1997 (see p. 2160) when they used tone bursts to measure motions of the basilar membrane.

A computationally useful alternative that produces the required compression, but does not produce harmonic distortion, is to raise to the fractional power of 0.2 *only the envelope* of the waveform (and not the waveform itself). In order to accomplish this, the input waveform $W_i(t)$ is decomposed into its Hilbert envelope, $H_i(t)$, and its fine structure, $F_i(t)$

$$W_i(t) = H_i(t) F_i(t). \qquad \text{(A2)}$$

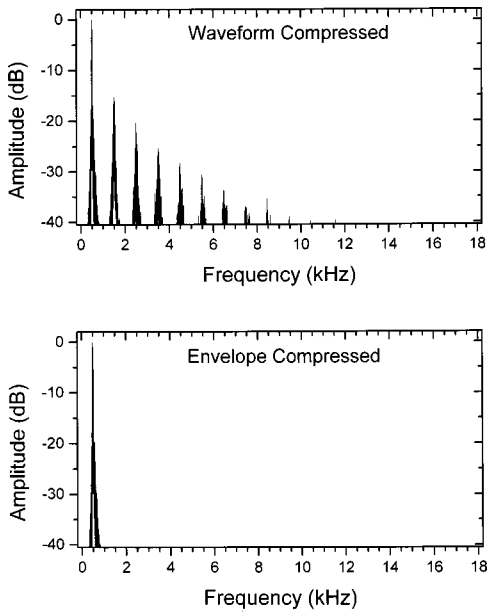

FIG. A1. Power spectrum of a 50-Hz-wide Gaussian noise centered at 500 Hz following compression of the waveform (upper panel) or compression of only the envelope (lower panel). In both cases, compression was achieved by raising the appropriate functions to the power 0.2.

Then, a compression of the envelope of 0.2 will result in the desired output waveform, $W_o(t)$, where

$$W_o(t) = H_i(t)^{0.2} F_i(t). \tag{A3}$$

For practical purposes concerning computational efficiency, we note that Eq. (A3) is equivalent to

$$W_o(t) = H_i(t)^{-0.8} H_i(t) F_i(t)$$

or,

$$W_o(t) = H_i(t)^{-0.8} W_i(t). \tag{A4}$$

Thus, one can achieve compression of the envelope of the waveform of 0.2 by simply multiplying the input waveform by its Hilbert envelope raised to the power -0.8 (i.e., 0.2–1). The spectrum of the output resulting from compression of only the envelope of the input waveform is shown in the lower panel of Fig. A1. Note that, consistent with the physiological findings, the level of harmonic distortion is now more than 40 below the level of the fundamental.

[1]The process of generating a low-noise noise, which was recently described in detail by Kohlrausch *et al.* (1997), began with a Gaussian noise having a rectangular power spectrum of the desired bandwidth. The following two-step procedure was carried out ten times in an iterative fashion. First, the waveform was divided by its Hilbert envelope. Second, the resulting waveform was limited to its original power spectrum by setting to zero the magnitude of all components outside the original passband. The introduction of components outside the original passband is a necessary consequence of altering the ''natural'' relation between the envelope and fine structure of a band of Gaussian noise (see Amenta *et al.*, 1987). In order to evaluate the degree to which low-noise noise generated in this manner approximated the low-noise noise utilized by Eddins and Barber (1998), we computed the mean normalized fourth moment of the envelope (Hartmann and Pumplin, 1988). The computation was performed by averaging the values of the normalized fourth moment of the envelopes of 500 tokens of 819-ms-long, 50-Hz-wide bands of low-noise noise generated with our iterative procedure. We obtained an average value of the normalized fourth moment of the envelope of 1.02, which is extremely close to the value of 1.04 that characterized the low-noise noise utilized by Eddins and Barber. They generated their low-noise noise by adjusting the phase spectrum in a manner shown by Hartmann and Pumplin (1991) to yield minimal fluctuations of the envelope.

Amenta, III, C. A., Trahiotis, C., Bernstein, L. R., and Nuetzel, J. M. (**1987**). ''Some physical and psychological effects produced by selective delays of the envelope of narrow bands of noise,'' Hearing Res. **29**, 147–161.

Bernstein, L. R., and Trahiotis, C. (**1996**). ''The normalized correlation: Accounting for binaural detection across center frequency,'' J. Acoust. Soc. Am. **100**, 3774–3784.

Blauert, J., and Cobben, W. (**1978**). ''Some consideration of binaural cross correlation analysis,'' Acustica **39**, 96–103.

Colburn, H. S. (**1973**). ''Theory of binaural interaction based on auditory-nerve data I. General strategy and preliminary results on interaural discrimination,'' J. Acoust. Soc. Am. **54**, 1458–1470.

Eddins, D. A., and Barber, L. E. (**1998**). ''The influence of stimulus envelope and fine structure on the binaural masking level difference,'' J. Acoust. Soc. Am. **103**, 2578–2589.

Hall, III, J. W., Grose, J. H., and Hartmann, W. M. (**1998**). ''The masking-level difference in low-noise noise,'' J. Acoust. Soc. Am. **103**, 2573–2577.

Hartmann, W. M., and Pumplin, J. (**1988**). ''Noise power fluctuations and the masking of sine signals,'' J. Acoust. Soc. Am. **83**, 2277–2289.

Hartmann, W. M., and Pumplin, J. (**1991**). AIP Document No. PAPS-JASMA-90-1986-15.

Kohlrausch, A., Fassel, R., van der Heijden, M., Kortekaas, R., van de Par, S., and Oxenham, A. J. (**1997**). ''Detection of tones in low-noise noise: Further evidence for the role of envelope fluctuations,'' Acustica **83**, 659–669.

Oxenham, A. J., and Moore, B. C. J. (**1995**). ''Additivity of masking in normally hearing and hearing-impaired subjects,'' J. Acoust. Soc. Am. **98**, 1921–1934.

Rhode, W. S. (**1971**). ''Observations of vibration of the basilar membrane in squirrel monkeys using the Mössbauer technique,'' J. Acoust. Soc. Am. **49**, 1218–1231.

Ruggero, M. A. (**1992**). ''Responses to sound of the basilar membrane of the mammalian cochlea,'' Curr. Opin. Neurobiol. **2**, 449–456.

Ruggero, M. A., Rich, N. C., and Robles, L. (**1997**). ''Basilar-membrane responses to tones at the base of the chinchilla cochlea,'' J. Acoust. Soc. Am. **101**, 2151–2163.

Saberi, K. (**1995**). ''Lateralization of comodulated complex waveforms,'' J. Acoust. Soc. Am. **98**, 3146–3156.

Sellick, P. M., Patuzzi, R., and Johnstone, B. M. (**1982**). ''Measurement of the basilar membrane motion in the guinea pig using the Mössbauer technique,'' J. Acoust. Soc. Am. **72**, 131–141.

Stern, R. M., and Colburn, H. S. (**1978**). ''Theory of binaural interaction based on auditory-nerve data. IV. A model for subjective lateral position,'' J. Acoust. Soc. Am. **64**, 127–140.

Stern, R. M., and Shear, G. D. (**1996**). ''Lateralization and detection of low-frequency binaural stimuli: Effects of distribution of interaural delay,'' J. Acoust. Soc. Am. **100**, 2278–2288.

van de Par, S., and Kohlrausch, A. (**1998**). ''Diotic and dichotic detection using multiplied-noise maskers,'' J. Acoust. Soc. Am. **103**, 2100–2110.

van de Par, S., and Kohlrausch, A. (**1999**). ''The influence of basilar-membrane compression on binaural detection,'' J. Acoust. Soc. Am. (submitted).

Weiss, T. F., and Rose, C. (**1988**). ''A comparison of synchronization filters in different auditory receptor organs,'' Hearing Res. **33**, 175–180.

Yates, G. K., Winter, I. M., and Robertson, D. (**1990**). ''Basilar membrane nonlinearity determines auditory nerve rate-intensity functions and cochlear dynamic range,'' Hearing Res. **45**, 203–220.

Proportional frequency compression of speech for listeners with sensorineural hearing loss

Christopher W. Turner and Richard R. Hurtig
Department of Speech Pathology and Audiology, University of Iowa, Iowa City, Iowa 52242

(Received 23 October 1998; revised 22 January 1999; accepted 20 April 1999)

This study examined proportional frequency compression as a strategy for improving speech recognition in listeners with high-frequency sensorineural hearing loss. This method of frequency compression preserved the ratios between the frequencies of the components of natural speech, as well as the temporal envelope of the unprocessed speech stimuli. Nonsense syllables spoken by a female and a male talker were used as the speech materials. Both frequency-compressed speech and the control condition of unprocessed speech were presented with high-pass amplification. For the materials spoken by the female talker, significant increases in speech recognition were observed in slightly less than one-half of the listeners with hearing impairment. For the male-talker materials, one-fifth of the hearing-impaired listeners showed significant recognition improvements. The increases in speech recognition due solely to frequency compression were generally smaller than those solely due to high-pass amplification. The results indicate that while high-pass amplification is still the most effective approach for improving speech recognition of listeners with high-frequency hearing loss, proportional frequency compression can offer significant improvements in addition to those provided by amplification for some patients. © *1999 Acoustical Society of America.* [S0001-4966(99)02308-5]

PACS numbers: 43.66.Ba, 43.66.Lj, 43.71.An, 43.71.Ky [JWH]

INTRODUCTION

The presence of sensorineural hearing loss can lead to deficits in speech recognition. Damage in the cochlea, which is the usual underlying cause of the hearing loss, can prevent portions of the speech signal from being transmitted accurately to the brain. The vast majority of sensorineural hearing losses involve a greater degree of hearing loss in the higher frequencies than in the low frequencies, associated with a typical pattern of damage in the cochlea that is more severe at the basal end than the apical end. For this reason, the idea of moving speech information from the higher frequencies to the lower frequencies has long been an attractive idea in the search for ways to remediate sensorineural hearing loss. This approach of frequency lowering of speech historically has not, however, lived up to its initial expectations [see Braida *et al.* (1979) for a very complete summary of early work in this area]. There are several developments in the fields of speech processing and the study of hearing loss which suggests that this approach may now begin to provide some benefits to certain patients with high-frequency hearing loss.

If, in the process of frequency-lowering speech, the important cues for speech recognition are transformed into an entirely new form, recognition will be either degraded, or at best, will require large amounts of training for listeners to learn to use the new cues. Several types of devices, frequency transposers, and vocoders have previously been tried, with little success, for hearing-impaired listeners (e.g., Johannson, 1966; Ling, 1968; Guttman and Nelson, 1968). These devices typically shift a band of high frequencies by a fixed number of Hertz to lower frequencies using amplitude modulation techniques, or some other form of nonlinear distortion. Often the shifted band is mixed with the original low-frequency signal. Reed *et al.* (1983, 1985) tested a digital frequency lowering scheme which preserved the fundamental frequency of speech sounds, while shifting the component frequencies of speech downward by various frequency-warping factors. These types of frequency-lowering schemes typically produce an unnatural speech signal. Without extensive training, recognition scores were typically much poorer than the original signal for both normal-hearing and hearing-impaired listeners. And even after training, well-controlled studies have shown no advantage for these types of processed speech over unprocessed speech in hearing-impaired listeners.

On the other hand, human listeners are quite accustomed to recognizing at least one type of frequency-lowered speech. The variation in sizes of the vocal apparatus between various speakers and speaker types (i.e., males, females, and children) produces speech that has different frequency contents. Peterson and Barney (1952) found that the average values of formants for specific vowels produced by male talkers were about 70% of the corresponding average values for children. Yet, most listeners easily adapt to different talkers, and recognition is relatively unaffected. One important unifying acoustic characteristic of speech across various individual speakers is that the ratios between the frequencies of the vocal tract resonances (formant peaks) are relatively constant (Peterson and Barney, 1952). In other words, the proportional relations between the frequencies of formant peaks for a given speech sound across speakers appear to remain approximately constant; each frequency is shifted upward or downward by a fixed multiplicative factor. These ratios between formant peaks serve as a relatively invariant cue for the identity of vowels (Ladefoged and Broadbent, 1957; Neary, 1989), and presumably many other speech sounds have cues which are similarly invariant across the different

 0001-4966/99/106(2)/877/10/$15.00

frequencies present in the speech of different talkers. Hurtig (1991) found excellent recognition of vowels by normal-hearing listeners after only 15 min of practice when proportional frequency shifting was used to lower the frequency of the speech tokens. For this reason, proportional frequency-lowering, or frequency-compression schemes, might offer some promise as a method for remediation of speech perception difficulties of listeners with high-frequency sensorineural hearing loss. Many listeners with sensorineural hearing loss report that they have more difficulty understanding speech produced by female talkers than speech from males, further suggesting that proportionally frequency-lowered speech may have some utility in improving their speech recognition.

As long as proportional frequency compression is not too severe, normal-hearing listeners do quite well at understanding the processed speech. Daniloff *et al.* (1968) found that vowel recognition for normal-hearing listeners remained at very high levels as long as the compression factor was no more severe than 0.7. They also found that the recognition of materials produced by female talkers was somewhat more resistant to frequency compression than that of male talkers. Recognition scores reached asymptotic and high values after only a few hours of practice sessions in their study. Nagafuchi (1976) compressed the frequencies of monosyllables containing both consonants and vowels by various proportionality factors, and also found that the performance of normal-hearing listeners remained high as long as signals were compressed no more severely than 70% of their original bandwidth. Similar findings were reported by Fu and Shannon (1998). Thus the normal auditory system is quite adaptable in its ability to understand speech that is proportionally compressed in frequency up to approximately 70% of its original bandwidth. These findings would seem to suggest a limitation upon the amount of proportional frequency compression that listeners can tolerate without experiencing degradation of speech perception, and this limitation may have some implications for using frequency-compression techniques for listeners with hearing impairment.

Previous work on frequency lowering has, in general, concentrated on patients with severe-to-profound hearing losses across a wide frequency range (the so-called corner audiograms). For example, Beasley *et al.* (1976) presented time-compressed, slow-playback speech to children with losses greater than 90 dB at all frequencies. The frequency range was compressed to 65% of its original range. No advantage of the processed speech over linear amplification was noted. The time-compression aspect of the processing (introduced to restore the original duration of the speech signals following the slow-playback process) involves deleting segments of the speech signal, which may have also contributed to the negative results. In many of the patients of these studies, there had been no response to sound at any level for frequencies above 1000–2000 Hz, and the goal of frequency lowering of speech in those studies was simply to move the speech into a frequency range where the patient had some residual hearing. Thus speech which may have had useful information in frequencies extending upward to 3000–4000 Hz was often processed to fit in a bandwidth only one-quarter to one-half of its original extent. In general, no improvements were seen in patients' recognition scores when such severe compressions of the frequency were applied to the speech signal. Previous work on frequency lowering and frequency compression in normal-hearing listeners provides some insight as to why many of the past attempts to use the technique on hearing-impaired listeners have failed. In general, previous results with normal-hearing listeners suggest that attempts to compress speech into the remaining frequencies of ''corner'' audiogram patients were too ambitious, in that the intelligibility of the speech is highly degraded by such severe frequency compressions and/or shifting.

Some exceptions to the above studies do exist in the literature. Bennett and Byers (1967) used slow-playback speech to proportionally lower the frequency of their test materials which were constructed to test consonant identification. The hearing-impaired listeners had moderate-to-severe hearing losses for frequencies of 2000 Hz and above. Compression factors of 80% resulted in improvements of up to 8 percentage points in speech recognition for a few listeners. The slow-playback technique used in that study changed (lengthened) the temporal patterns of speech in addition to lowering the speech frequencies and may have contributed to the lack of larger improvements in consonant identification. Obviously, a pure slow-playback scheme is impractical for use in a real hearing aid, since the aid could not ''keep up'' with ongoing conversations and the auditory signal would become de-synchronized from the visual cues of speech. Mazur *et al.* (1979) tested patients with moderate hearing losses in the high frequencies using speech processed by a slow-playback, time-compression system. In one condition (80% compression for a female talker) a small improvement of 3 percentage points was noted. In this case, the time-compression aspect of the processing algorithm quite likely introduced some loss of information or distortions of the speech temporal waveform, which may have served to limit the effectiveness of the system. Parent *et al.* (1997) describe results from four patients fitted with a commercially available, wearable frequency transposition device that incorporated a variation of the ''slow-playback'' frequency-compression algorithm (along with a process that changed the frequency-compression factor depending upon the type of speech sound). Two of these patients showed improvements in speech recognition when using the transposition aid as compared to their conventional hearing aids. However, this comparison between conventional and frequency transposition hearing aids also included some advantages for the transposition aids in the amount of amplification gain provided to each patient.

Numerous investigators have reported that providing audible speech (as a typical hearing aid is designed to do) does not always result in a commensurate improvement in speech recognition scores for patients with more severe hearing losses (e.g., Kamm *et al.*, 1985; Pavlovic, 1984). More recent work by Ching *et al.* (1998), Hogan and Turner (1998), and Turner and Cummings (1999) has provided a more detailed quantitative account of the ability of listeners with high-frequency hearing loss to obtain benefit from audible speech information. Several factors appear to be important.

Both the frequency region of the speech information as well as the degree of hearing loss present at that frequency region are important factors in determining whether or not a patient can use audible speech information successfully. Generally, when hearing loss exceeds approximately 60 dB HL for frequencies of 2000–3000 Hz and above, audible speech information provides reduced or minimal benefit to the hearing-impaired listener. These results suggest that the speech information contained in the higher-frequency regions might benefit from being shifted to lower-frequency regions where hearing sensitivity is better than 60 dB HL. One might hypothesize that when hearing loss exceeds 60 dB HL, the auditory system cannot accurately transmit frequency (place of articulation) information, and this type of information is usually associated with higher-frequency regions (over 1000 Hz) of the speech spectrum where cues such as second-formant frequency transitions are located.

In summary, the previous literature points toward some specific improvements in the methods used for frequency lowering of speech which may be desirable, as well as some specific patient characteristics where the technique may prove beneficial. First, it would appear that proportional frequency lowering would have the greatest potential for producing a speech signal that can be easily recognized as opposed to other schemes that result in unnatural speech cues. Second, the normal temporal characteristics and durations of the speech should be preserved as much as possible. Third, the frequency span of the compressed speech should be no less than 60%–70% of the original bandwidth, as more severe compressions will tend to decrease the intelligibility of the signal. Finally, this restriction on the amount of frequency compression allowable, along with the recent findings on the ability of the impaired auditory system to use audible speech, suggests a specific type of patient who is most likely to show benefit from frequency lowering. Those patients with severe or greater hearing losses for frequencies above 2000 Hz (where they cannot use audible speech), yet having usable (i.e., better than 60 dB HL) hearing for frequencies below 2000 Hz would appear to have the potential to benefit from mild amounts of proportional frequency compression. In the present study, we have attempted to address these issues in order to test the effectiveness of frequency compression as an aid to speech recognition one more time.

I. METHODS

A. Listeners

Three normal-hearing listeners took part in the experiments. They were between 19 and 31 years of age and had pure-tone sensitivity thresholds better than 20 dB HL (ANSI, 1996) at audiometric test frequencies.

Fifteen listeners with sensorineural hearing loss were also recruited into the study. In one of these listeners, both ears were tested, yielding a total of 16 ears in this group. All 16 ears exhibited sensorineural hearing losses as indicated by no air-bone gaps in their audiometric thresholds and normal tympanometric results. Listeners were recruited with hearing losses that were generally greater than 40–50 dB HL in the high frequencies and better than 40 dB HL in the lower frequencies. Figure 1 displays the audiograms of the listeners. Their ages ranged from 16 to 78 years of age. Nine of the 15 listeners had recently participated in a previous experiment in our laboratory which used the same speech materials in an unprocessed form.

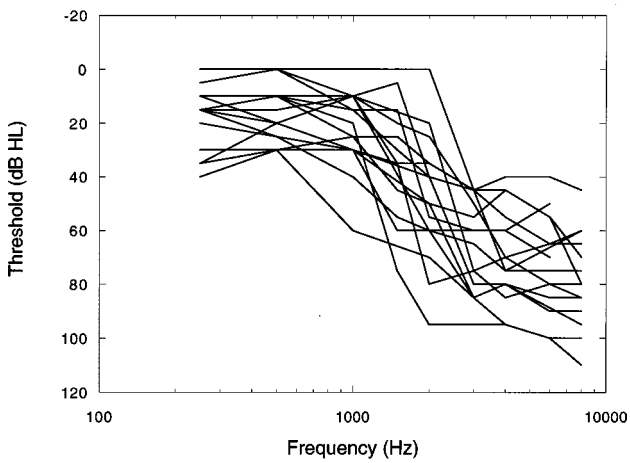

FIG. 1. The audiometric thresholds at standard test frequencies for the 16 hearing-impaired ears tested. Hearing Level (HL) values are in reference to ANSI (1996) standards for audiometers.

B. Speech processing

The speech stimuli used for testing were taken from the UCLA NST (Nonsense Syllable Test) recordings. These speech tokens are monosyllables consisting of a consonant and a vowel. Speech lists consisting of CV (consonant–vowel) syllables were used in the present experiment. Each list consisted of 21 consonants paired with one of three common vowels (a, i, or u) and were spoken by a single male talker or a single female talker. Thus the two possible talkers and the three possible vowels yielded six lists. These stimuli were recorded digitally in 16-bit format and stored on the hard disk of a Macintosh 9500 Computer. For each presentation of a list to a listener, the 21 different tokens of the list were presented in a novel randomized order.

For the unprocessed speech condition (1.0 frequency compression), no modifications of the signals were made. Frequency-compression factors of 0.9, 0.8, 0.7, 0.6, and 0.5 were accomplished using the commercially available music production program Digital Performer 2.1 (Mark of the Unicorn, Inc.). The pitch shift function was set for the standard pitch shifting algorithm, which essentially lowers each component frequency of the complex signal by a given multiplicative factor and does not produce significant alterations of the temporal envelope or duration of the stimuli. Thus the fundamental frequency of the processed stimuli was also lowered by the frequency-compression factor. In Fig. 2(a) the waveform of an unprocessed square wave at 500 Hz (with some intentional variations in the temporal amplitude envelope) is shown, and in Fig. 2(b) the waveform of the same signal processed at a frequency-compression factor of 0.8 is shown, which changes the signal to a 400-Hz square wave, are shown as an example. Note that the same slow amplitude variations in the original waveform (temporal envelope) remain approximately the same in the processed,

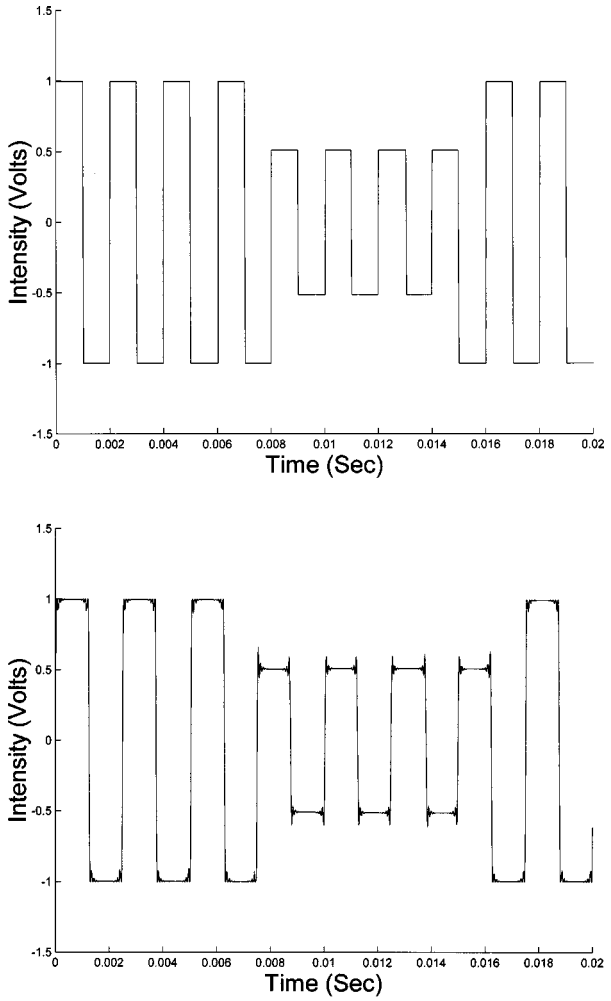

FIG. 2. (a) The unprocessed waveform of a 500-Hz square wave with variation in the overall amplitude over time; (b) The waveform of (a) after processing with the frequency-compression scheme set to a factor of 0.8. The new waveform has a frequency of 400 Hz.

frequency-compressed signal. Thus the algorithm changes the (fine-structure) frequencies present in the original waveform, yet leaves the temporal envelope of the signal relatively unchanged. The algorithm produced a small amount of distortion [visible in Fig. 2(b)], however, this distortion was typically −30 dB relative to the original signal and was not apparent in listening to the stimuli. The processed speech stimuli were computed off-line and stored on the computer. While the proportional frequency compression as performed by this commercial algorithm is not a ''real-time'' process, the process in general is potentially amenable to use in a ''real-time'' digital signal processing hearing aid.

C. Presentation of speech stimuli

The present study was designed to determine if frequency compression could provide benefits to hearing-impaired listeners better than those provided by simple hearing-aid amplification alone. For this reason, all listeners received both processed and unprocessed speech under conditions of high-pass amplification, in order to provide increased audibility of the high-frequency speech components. In addition, for all hearing-impaired listeners except two, unprocessed speech was also presented in a condition without the high-pass amplification, in order to obtain a measure of performance in an ''unaided'' condition.

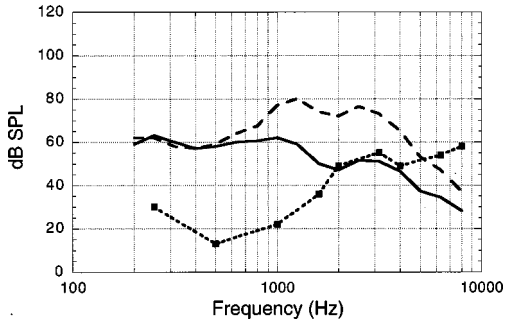

FIG. 3. Example of the long-term rms speech levels (in one-third octave band levels) of the six NST lists plotted along with the sensitivity thresholds of one of the hearing-impaired patients. The upper dashed line represents the speech spectrum under the high-pass spectral shaping condition. The middle solid line represents the speech spectrum without the spectral shaping. The filled squares represent the listener's pure-tone thresholds.

Normal-hearing listeners received the speech materials at an overall level of 70 dB SPL (long-term rms). The presentation levels for each of the hearing-impaired patients were chosen by the experimenter on an individual basis. The levels were chosen to (1) maximize audibility of the entire speech range under the high-pass amplification condition, and (2) not exceed listener discomfort. For the conditions of high-pass amplification and for the conditions without the high-pass amplification, speech presentation levels were equivalent for frequencies of 800 Hz and below; for frequencies above 800 Hz, the high-pass amplification provided up to 30 dB of gain. The levels for the ''unaided'' speech conditions were chosen individually for each patient to provide inaudible or minimally audible speech for frequencies of 2000 Hz and above. An example of a typical patient's thresholds, along with the one-third octave band spectra of the unprocessed speech under the aided and unaided conditions, are shown in Fig. 3.

Speech was output through 16-bit digital-to-analog converters (Audiomedia III, DigiDesign, Inc.), attenuated, and presented under computer control via Sennheiser HD-25 SP headphones. For the high-pass amplified conditions, an Altec-Lansing 1753A one-third octave band graphic equalizer was inserted in the signal path and the presentation levels were adjusted accordingly. When appropriate, speech spectrum masking noise was presented to the contralateral ear of the hearing-impaired listeners to prevent cross-head hearing in a better ear from contaminating the results.

D. Procedures

Speech testing was performed using a closed-set response paradigm, in which the listener heard the speech token, and was then required to press a button corresponding to the consonant heard. Experiment participants were allowed to practice (with trial-by trial feedback) until asymptotic and stable performance was attained in all conditions and lists. This was defined as two consecutive runs of 100 trials on each list in which the percent-correct scores for the two runs were within 6 percentage points of one another. Alterna-

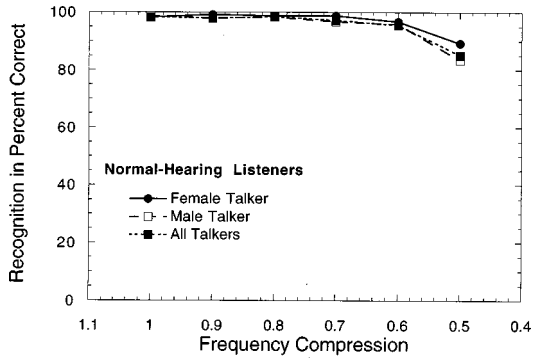

FIG. 4. Recognition scores for the group of normal-hearing listeners as a function of the degree of frequency compression. Scores are shown for the female talker, male talker, and both talkers combined.

tively, for normal-hearing listeners, the asymptotic and stable performance criteria could also be satisfied by a score of 95% or greater on a single 100-trial run on a particular list. All normal-hearing listeners received at least 1200 trials practice (200 trials per speech list) for each condition. The hearing-impaired listeners received at least 2400 trials practice for each condition. Therefore the individual speech tokens were heard approximately nine to ten times each by the listeners during the training sessions. Once stable performance had been reached, final data collection began. Final data consisted of 100 trials per list for each of the 6 lists (600 trials total) with no trial-by-trial feedback. The various frequency-compression conditions were completed in a random order. For the first five hearing-impaired listeners, the experimenter re-ran earlier conditions following the completion of final data collection to check if the additional experimental training served to improve the scores over time. No evidence was found of this, and the re-running of conditions was not included in the remainder of the listeners' protocols. The final condition tested for all hearing-impaired listeners was the control condition in which the speech materials were presented without high-pass amplification. Two of the hearing-impaired participants were unable to complete all conditions of the experiment. One listener provided data for only the high-pass amplified, female-talker speech materials. One other listener with hearing impairment did not complete the condition of no high-pass amplification.

II. RESULTS

A. Normal-hearing listeners

Figure 4 displays the group mean recognition performance for the three normal-hearing listeners for the female and male speakers (three lists each), along with the average across the two speakers (six lists total) as a function of the degree of frequency compression. The three individual listeners performed very similarly to each other, so only the group mean results are shown. The 1.0 condition represents the unprocessed speech. In summary, performance was essentially unaffected for frequency compressions up to 0.7, at compression ratios of 0.6 and 0.5 performance began to drop.

B. Hearing-impaired listeners

For many of the hearing-impaired listeners, speech recognition performance depended upon the degree of frequency compression. Whether the speech was spoken by the male or the female talker was also a factor, with frequency compression being generally more successful at improving the recognition of the female-spoken speech materials. We can define the maximum improvement due to frequency compression as the difference in percentage points between the highest score in any of the compressed speech conditions (0.9 through 0.5) minus the score for the uncompressed (1.0) condition. In terms of the group data, the average maximum improvement showed that frequency compression provided a significant improvement for all the talker conditions. For the female-talker materials, the average improvement across subjects was 7.98% [$t(15)=5.55$, $p<0.05$]. For the male talker, the improvement was smaller at 4.67% [$t(14)=3.53$, $p<0.05$].

The average performance of the group, however, does not adequately describe the range of performances obtained across listeners. In general, the performance across the 16 hearing-impaired ears varied, with some patients showing obvious improvements in speech recognition for the frequency-compressed speech, and some showing little or no improvement. For these reasons, it is more instructive to consider the data in a fashion that displays the results of individual participants in each condition. Ninety-five percent confidence intervals for significant differences between two speech discrimination scores will be used to determine if speech recognition showed a significant improvement with frequency compression, as compared to the unprocessed (1.0) condition. For the final data for recognition of the female- or male-talker materials (3 lists or 300 items), if the unprocessed speech recognition scores are approximately 70%, the critical difference is approximately 8 percentage points (Thornton and Raffin, 1978). For the combined data across the two speakers (6 lists or 600 items), the critical difference is approximately 6 percentage points.

In the two panels of Fig. 5, the recognition scores of the hearing-impaired listeners are shown for the entire six-list set of speech materials (female- and male-talker speech materials combined). In this case, the critical difference is 6 percentage points and the data are divided into two panels in Fig. 5 accordingly. Six ears showed increases greater than the critical difference (panel a), and nine showed less (panel b). Eight of the fifteen ears showed maximum scores for the 0.8 frequency-compression condition, and six showed a maximum at the 0.9 condition. Figure 6(a) shows the distribution of maximum increases for the combined-talker materials in bar graph format. These values range from -4.3 to 11.3 percentage points with a mean of 5.4. The arrow indicates the 6 percentage point critical difference for a significant improvement in speech recognition.

There were some differences in the benefits provided to hearing-impaired listeners by frequency compression between the results obtained with the female versus the male talker materials. The critical difference for these data is 8 percentage points. Figure 6(b) and (c) display the maximum increases for the recognition scores for the female and male

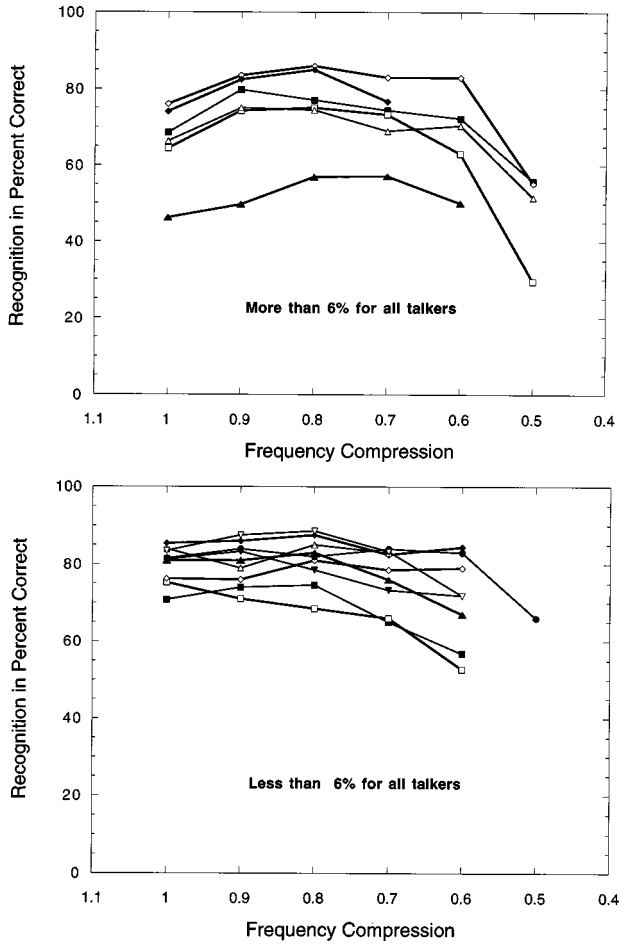

FIG. 5. Recognition scores for the individual hearing-impaired listeners for the combined male- and female-talker materials as a function of the degree of frequency compression. (a) Recognition scores for the six individual hearing-impaired ears that achieved more than an 6 percentage point improvement over the uncompressed speech in any of the frequency-compression conditions. (b) Recognition scores for the nine hearing-impaired ears that achieved less than 6 percentage point improvement in the frequency-compression conditions.

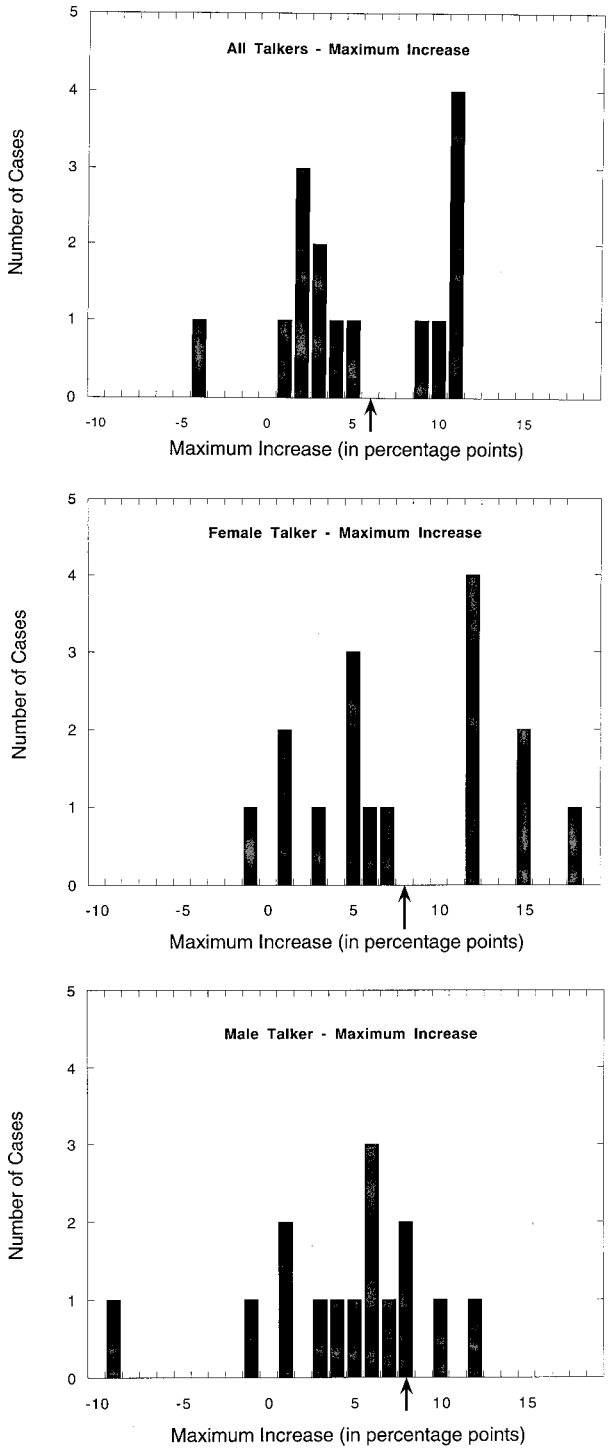

FIG. 6. The distribution of maximum increases in recognition scores for frequency-compression conditions as compared to uncompressed speech for all hearing-impaired ears. Panel (a) shows the distribution of maximum increases for the male- and female-talker lists combined. The arrow at 6% indicates the criterion for statistically significant benefits due to frequency compression. Panels (b) and (c) show the distribution of maximum increases for the female- and male-talker materials, respectively. The arrow at 8% in these panels indicates the criterion for statistically significant benefits due to frequency compression.

talker, respectively. For the female-talker materials, seven ears showed significant improvements in speech recognition, and nine did not, as shown in Fig. 6(b). The maximum increases across all 16 ears ranged from −1 to 18 percentage points, with a mean value of 7.98 percentage points. For 7 of the 16 ears, maximum scores occurred for the 0.8 frequency compression condition for the female-talker materials, and the 0.9 and 0.7 conditions each produced maximum scores for four listeners.

Figure 6(c) displays the maximum increases for the results using the male-talker speech materials. Again the critical difference for significant differences in recognition scores is 8 percentage points. Three of the 15 ears tested showed significant increases for the male talker, and 12 showed less than the critical difference. Maximum scores across subjects occurred approximately equally for the 1.0, 0.9, and 0.8 frequency-compression conditions. The distribution of maximum increases for all ears ranged from −8.6 to 12 percentage points with a mean of 4.67 percentage points.

In summary, frequency compression appears to show real benefits for slightly less than half the listeners when tested with the speech spoken by the female talker. Benefits were less evident for the speech materials spoken by the male talker. It is important to remember here that the speech signals were high-pass amplified for all frequency-compression conditions in these comparisons. Therefore, any

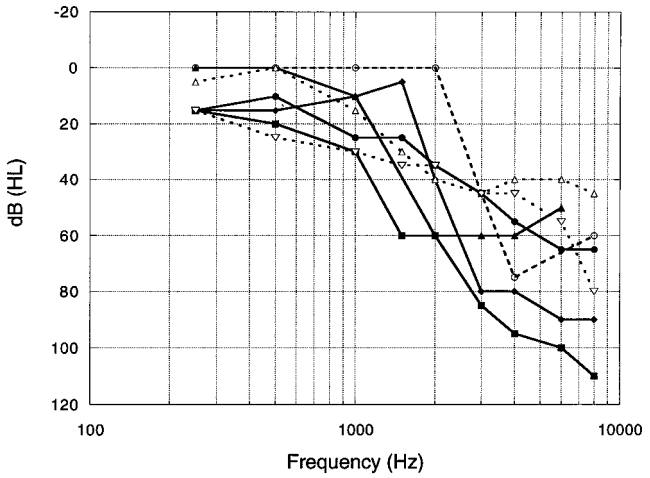

FIG. 7. Audiograms for selected ears from frequency-compression experiment. The dark lines with filled symbols are the audiograms of the four ears showing the largest improvement for the female-talker materials (more than 13 percentage points improvement). The dashed lines with open symbols represent the three ears with the smallest improvement for the female-talker materials (less than 1 percentage point improvement).

changes in score from the 1.0 compression condition represent changes in performance compared to that which might be expected from a traditional hearing aid. In view of the fact that the results were variable across our recruited listeners, it is of interest to determine if there were some listener characteristics that might serve to predict who might be a viable candidate for frequency compression.

C. Predictors of benefit

There was no clear distinction between the audiograms of those ears showing significant increases in speech recognition with frequency compression and those who did not. There was, however, a trend toward those listeners with more severe hearing losses in the higher frequencies to show more benefit from frequency compression as opposed to those listeners with less severe losses in the high frequencies. As an example, Fig. 7 plots the individual audiograms of the four listeners showing the greatest benefit (greater than 13%) from frequency compression of the female-talker materials (solid lines) along with the audiograms of the three listeners with the least benefit (less than 1%) (dashed lines). The thresholds for 2, 3, and 4 kHz show a tendency to support the idea that patients with more severe losses in the high frequencies will be the ones who can benefit most from frequency compression. However, even among these selected extreme cases from our group, there is considerable overlap among the audiograms.

The data supply a range of audiometric thresholds that can be correlated with the range of maximum increases observed in individual patients. All correlations for 2.0, 3.0, and 4.0 kHz were in the correct (positive) direction to support the idea that more severe hearing losses in the high frequencies are associated with greater benefit from frequency compression. However, none of the observed correlations were significantly different from $r=0.0$ at the $p=0.05$ level of confidence, and the amount of variance explained by any of the measures based upon thresholds is very small indeed (the largest correlation coefficient between any audiometric threshold and maximum benefit was $r=0.35$, which would explain only 12% of the variance of the data). In addition, audiometric slope, as calculated by the difference in thresholds between 2.0 kHz and either 3.0 or 4.0 kHz provided no significant correlations with benefit. In summary, individual audiometric thresholds, as well as audiometric slope, were not good predictors of which listeners did or did not benefit for frequency compression.

There was one fairly obvious listener characteristic that did separate individuals fairly well into groups that did or did not show benefit from frequency compression. An examination of Fig. 5 reveals that those listeners who scored (relatively) low on the unprocessed speech were, in general, those who showed benefit from frequency compression. For the combined talker scores, as shown in Fig. 5, the correlation coefficient between listeners' scores for unprocessed speech scores and maximum benefit was significant ($r=-0.61$; $p<0.05$). For the female-talker materials, less than or greater than 70% correct recognition on the 1.0 compression condition divided individuals perfectly into the two groups. Here the linear correlation coefficient between listeners' scores for unprocessed speech scores and maximum benefit was $r=-0.71$ ($p<0.05$). For the male-talker material results, the division is not as clear, due to the fact that only 3 of 15 listeners showed significant benefit. The correlation coefficient between unprocessed speech scores and maximum benefit for the male talker was smaller, but still significant ($r=-0.42$; $p<0.05$). If a listener achieves these relatively high scores for unprocessed speech, then frequency compression probably will not yield additional benefit. On the other hand, if the listener does not achieve scores within these ranges for unprocessed speech, frequency compression would appear to offer a high probability of increasing the recognition performance.

D. Comparisons between amplification benefit and frequency-compression benefit

Up to this point, results have been presented as comparisons between various frequency-compression conditions where, in each case, speech was presented with high-pass amplification to simulate the audibility increases provided by traditional hearing aids. The benefits of frequency compression were calculated as the differences between the uncompressed (1.0) condition under high-pass amplification and the various compression conditions under high-pass amplification. Therefore, the improvements resulting from frequency compression shown so far represent the kind of improvements that would be above and beyond standard amplification. It is also of interest to compare the benefits of frequency compression to the benefits that are realized from conventional amplification. In this case, the comparison benefit value would be recognition scores obtained with high-pass amplification alone (no frequency compression) minus the scores obtained with ''unamplified'' speech recognition (also with no frequency compression). This comparison allows the reader to put the present frequency-compression data into some perspective. In addition, it allows us to examine a hypothesis which would seem to follow from previous

work on the limitations of benefit provided by high-frequency amplification; that those listeners who cannot realize benefit from the increases in audibility provided by standard amplification would be the most likely to receive benefit from a frequency-compression scheme.

Figure 8 shows the benefit received from high-pass amplification alone (unprocessed speech with high-pass amplification minus unprocessed speech without high-pass amplification) plotted against the maximum benefit received from high-pass amplification plus frequency compression (the highest scoring condition of the 1.0–0.5 compression factors with high-pass amplification minus unprocessed speech without high-pass amplification). Thus if a listener's highest score occurred in the 1.0 condition with high-pass amplification (in other words, no benefit from frequency compression), that listener's data point would fall on the diagonal line. The three panels show the results separately for the female-talker, male-talker, and combined-talker materials. In each figure, the thick diagonal line represents the case where the maximum benefit provided by high-pass amplification alone is no more than that provided by high-pass amplification plus frequency compression. Data points lying above this diagonal line represent cases where the individual received additional benefit from frequency compression, and the vertical distance of each point above the diagonal line is the benefit from frequency compression alone.

These comparisons show that frequency compression can provide benefit in addition to that provided by high-pass amplification for many listeners. The data points in each panel are fit by a linear regression line, which, in each panel, has a slope of less than one and is elevated above the heavy diagonal line. The extent that the slopes of the regression lines differ from the diagonal line indicates the support for the hypothesis that those listeners showing the smallest benefit from conventional amplification tend to be the same individuals who stand to gain the most benefit from frequency compression. Although the data do generally conform to this pattern, the slopes of the regression lines were not statistically significantly different from 1.0 (due primarily to the small number of subjects). For example, the slope of the regression line for the female-talker materials condition was 0.86, with a 95% confidence interval surrounding this estimate of plus and minus 0.41.

III. DISCUSSION

The proportional frequency-compression scheme employed in this study, which preserves the natural ratios between the frequency components of speech and also generally preserves the temporal envelopes of the signal, provided significant improvements in speech recognition for many of the hearing-impaired listeners. Because these essential cues for speech recognition are preserved in the transformation, proportional frequency compression which also maintains the temporal characteristics of speech appears to hold more promise for improving speech recognition for hearing-impaired patients than many of the previous attempts at frequency lowering.

Normal-hearing listeners showed no decreases in recognition scores for compression ratios of approximately 0.7 and

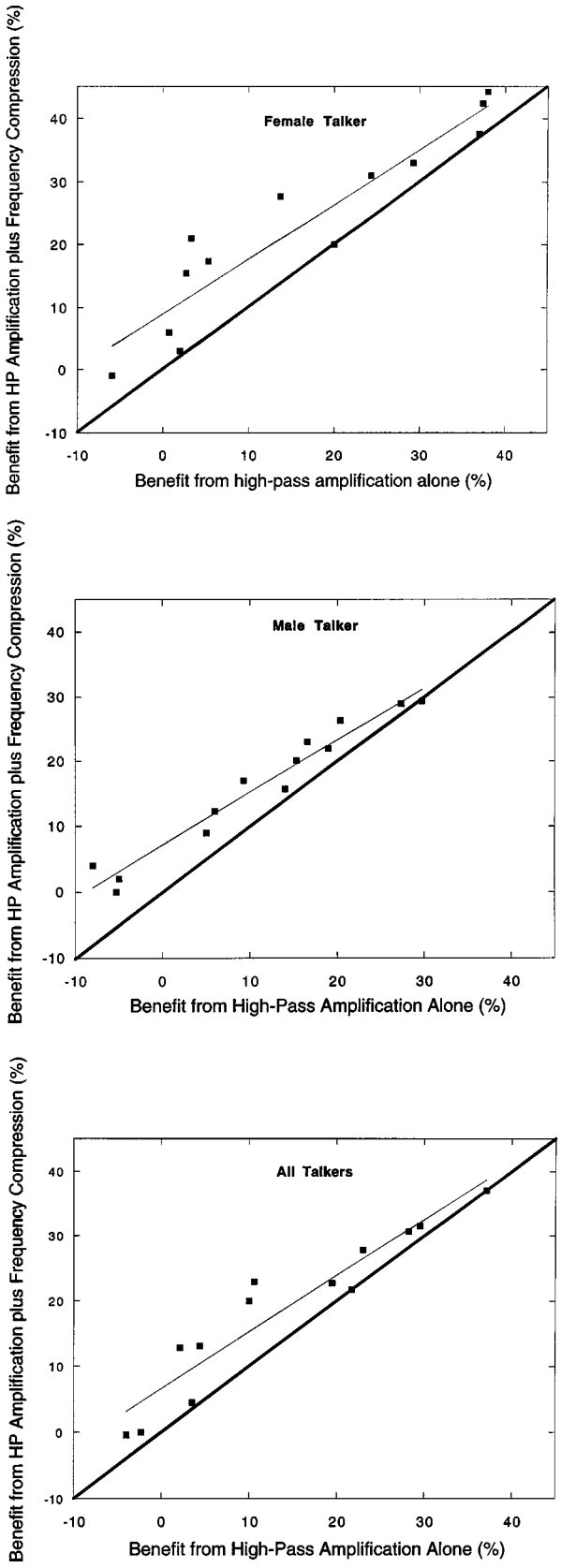

FIG. 8. The amount of benefit from simple high-pass amplification plus the maximum benefit from frequency compression plotted as a function of the amount of benefit from simple high-pass amplification for individual hearing-impaired ears. Benefit is expressed in percentage points. Panels (a), (b), and (c) display the data for female-talker, male-talker, and combined-talker materials. The heavy solid diagonal line represents the function for the case where no additional benefit from compression was obtained. The lighter line is the least squares regression fit to the data points.

greater. These results are entirely consistent with the previous research, as discussed in the Introduction. The NST speech lists are difficult materials for all listeners. The digital frequency compression for the higher compression factor conditions provided by the Digital Performer Software did not decrease scores from their unprocessed values, which were near 100% for the normal-hearing subjects, and is an indication that this type of processing is most likely superior to previous attempts to frequency- and time-compress speech. Qualitatively, the normal-hearing and hearing-impaired listeners reported that frequency-compression processing merely seemed to ''change the gender'' of the talker.

Frequency compression provided significant benefit for nearly 45% of the hearing-impaired ears for the speech materials spoken by the female talker. On the other hand, only 3 of 15 ears showed significant benefit for the male-talker speech. Thus for some situations and some patients, proportional frequency compression can offer real advantages. It was encouraging to note that for most listeners, providing a degree of frequency compression to improve the recognition of female talkers did not actually decrease recognition for the speech of the male talker. In these cases, a fixed degree of frequency compression for all situations would be an appropriate choice. However, there might be some advantage to allowing some individual users to switch this processing on and off for different talkers, since the number of listeners in the present study who showed benefit for all talkers was less than the number showing benefit for only the female talkers. These benefits from frequency compression are in addition to any benefit provided by traditional high-frequency amplification. There was a trend for listeners who showed the smallest improvements from traditional amplification to be the same individuals who showed the largest benefit from frequency compression.

In the present experiment, listeners were trained until asymptotic performance was reached in all conditions before final data were collected. This required only minimal training for all listeners. To a certain extent, this is not too surprising, since proportional frequency compression of the magnitudes used in this study are not too different than the ranges of proportional frequency shifts that listeners encounter in real life across different talkers. Whether more extensive and very long-term training might produce even higher scores for frequency-compressed speech was not tested. A recent report by Rosen *et al.* (1997) tested speech recognition in normal-hearing listeners under conditions of proportional frequency shifting (in an upward direction of approximately 2–3 octaves) over many test sessions. They reported that training did improve scores over time, however, most of the improvement occurred over the first few sessions. Nonetheless, the possibility does exist that the present results might underestimate the eventual benefit provided by frequency compression. On the other hand, since subjects listened to each of the test items at least nine to ten times each during the training sessions, our results do not necessarily generalize to results that might be obtained using completely novel speech tokens.

No strong audiometric predictors of benefit from frequency compression were noted, but some general trends did appear. The sensitivity loss at 2, 3, or 4 kHz or measures of audiometric slope in individual listeners was only weakly correlated with maximum benefit. As shown in Hogan and Turner (1998) and Ching *et al.* (1998), there is a spread in the data points for predicting how much benefit a listener will receive from traditional amplification, even when those listeners have equivalent losses of hearing sensitivity. The present data are in line with these previous findings. Thus the ability to use audible high-frequency speech information in regions of more severe hearing loss is diminished or absent in some listeners, and for these listeners frequency compression may provide benefit. Further research on these techniques in a larger and more heterogeneous listener group may identify some stronger audiometric predictors.

The strongest predictive relation uncovered in the present data was the fact that those listeners who tended to score lowest on unprocessed speech were the same listeners who showed the greatest benefit from frequency compression. Across all listeners, there appeared to be a maximum recognition score that could be attained for each type of speech material. If a listener's score for unprocessed speech was below this maximum, then frequency compression tended to improve their score to this maximum. If their score was already at this maximum for unprocessed speech, then frequency compression did not provide an additional increase. It appears that the proportional frequency-lowering scheme employed in this experiment does not increase the saliency of all phonemes. In particular, some of the fricative sounds, such as /s/ and /f/, sounded unnatural to the authors after frequency compression. This is presumably due to the fact that the size of the oral cavity anterior to the place of constriction is the major factor controlling the spectrum of the fricative, and for fricatives such as these the constriction is at or near the front of the oral cavity (Heinz and Stevens, 1969). The size of this oral cavity would not be expected to change across speakers in the same proportional manner as the other oral cavities, thus a simple proportional scaling of frequency produces an unnatural sound. This implies that proportional frequency compression cannot ''solve'' all of the problems of the hearing-impaired listener. Frequency compression can, however, increase the saliency of some speech cues to bring up the scores of those listeners who seem to be performing at a lower level than might be expected from traditional amplification.

In summary, frequency compression, using modern digital techniques which can preserve the proportional frequency relations of normal speech and also preserve the normal temporal envelopes of speech, appears to offer some promise for remediation of sensorineural hearing loss. There are, however, limits as to how much speech can be compressed without degrading performance, which will translate into a limitation on the kinds of patients for whom frequency compression is beneficial. Patients with more severe hearing losses in the higher frequencies (above 1000–2000 Hz), yet having better hearing levels in the lower frequencies will be most likely to benefit. Traditional amplification to restore audibility will still be the most effective tool for improving speech recognition in nearly all patients, but for those patients who have an inability to effectively use amplified

speech in high-frequency regions, frequency compression may serve to increase the benefit provided by future hearing aids.

ACKNOWLEDGMENTS

This work was supported in part by NIDCD Grant No. RO1 DC 00377. The assistance of Chiemi Tanaka, Jennifer Knapp, Sarah Flock, Beth Wahl, Steve Nash, Bom Jun Kwong, and Maureen Mehr is greatly appreciated.

ANSI (**1996**). ANSI S3.6-1996. ''American National Standard: Specification for Audiometers'' (American National Standards Institute, New York).

Beasley, D. S., Mosher, N. L., and Orchik, D. J. (**1976**). ''Use of frequency-shifted/time-compressed speech with hearing impaired children,'' Audiology **15**, 395–406.

Bennett, D. N., and Byers, V. W. (**1967**). ''Increased intelligibility in the hypacusic by slow-play frequency transportation,'' J. Aud. Res. **7**, 107–118.

Braida, L. D., Durlach, N. I., Lippman, R. P., Hicks, B. L., Rabinowitz, W. M., and Reed, C. M. (**1978**). ''Hearing Aids—A review of past research on linear amplification, amplitude compression, and frequency lowering,'' ASHA Monographs Number 19, American Speech-Language-Hearing Association, Rockville, MD.

Ching, T., Dillon, H., and Bryne, D. (**1998**). ''Speech recognition of hearing-impaired listeners: Predictions from audibility and the limited role of high-frequency amplification,'' J. Acoust. Soc. Am. **103**, 1128–1140.

Daniloff, R. G., Shiner, T. H., and Zemlin, W. R. (**1968**). ''Intelligibility of vowels altered in duration and frequency,'' J. Acoust. Soc. Am. **44**, 700–707.

Fu, Q.-J., and Shannon, R. V., ''Recognition of spectrally degraded and frequency-shifted vowels in acoustic and electric hearing,'' J. Acoust. Soc. Am. (submitted).

Guttman, N., and Nelson, J. R. (**1968**). ''An instrument that creates some artificial speech spectra for the severely hard of hearing,'' Am. Ann. Deaf **113**, 295–302.

Heinz, J. M., and Stevens, K. N. (**1961**). ''On the properties of voiceless fricative consonants,'' J. Acoust. Soc. Am. **33**, 589–596.

Hogan, C. A., and Turner, C. W. (**1998**). ''High-frequency audibility: Benefits for hearing-impaired listeners,'' J. Acoust. Soc. Am. **104**, 432–441.

Hurtig, R. R. (**1991**). ''Perception of spectrally compressed speech,'' Proceedings of the XIIth International Congress of Phonetic Sciences, Vol. 2, pp. 98–101.

Johannson, B. (**1966**). ''The use of the transposer for the management of the deaf child,'' Internat. Audiol. **5**, 362–373.

Kamm, C. A., Dirks, D. D., and Bell, T. D. (**1985**). ''Speech recognition and the articulation index for normal and hearing-impaired listeners,'' J. Acoust. Soc. Am. **77**, 281–288.

Ladefoged, P., and Broadbent, D. E. (**1957**). ''Information conveyed by vowels,'' J. Acoust. Soc. Am. **29**, 98–104.

Ling, D. (**1968**). ''Three experiments on frequency transposition,'' Am. Ann. Deaf. **113**, 283–294.

Mazur, M., Simon, H., Scheinberg, J., and Levitt, H. (**1979**). ''Moderate frequency compression for the moderately hearing impaired,'' J. Acoust. Soc. Am. **62**, 1273–1278.

Miller, G. A., and Nicely, P. E. (**1955**). ''An analysis of perceptual confusions among some English consonants,'' J. Acoust. Soc. Am. **27**, 338–352.

Nagafuchi, M. (**1976**). ''Intelligibility of distorted speech sounds shifted in frequency and time in normal children,'' Audiology **15**, 326–337.

Neary, T. (**1989**). ''Static, dynamic, and relational properties in vowel perception,'' J. Acoust. Soc. Am. **85**, 2088–2113.

Parent, T. B., Chmiel, R., and Jerger, J. (**1997**). ''Comparison of performance with frequency transposition hearing aids and conventional hearing aids,'' J. Am. Acad. Aud. **8**, 355–365.

Pavlovic, C. V. (**1984**). ''Use of the Articulation Index for assessing residual auditory function in listeners with sensorineural hearing impairment,'' J. Acoust. Soc. Am. **75**, 1253–1258.

Peterson, G., and Barney, H. (**1952**). ''Control methods used in a study of vowels,'' J. Acoust. Soc. Am. **24**, 175–184.

Posen, M. P., Reed, C. M., and Braida, L. D. (**1993**). ''Intelligibility of frequency-lowered speech produced by a channel vocoder,'' J. Rehabil. Res. Dev. **30**, 26–38.

Reed, C. M., Hicks, B. L., Braida, L. D., and Durlach, N. I. (**1983**). ''Discrimination of speech processed by low-pass filtering and pitch-invariant frequency lowering,'' J. Acoust. Soc. Am. **74**, 409–419.

Reed, C. M., Schultz, K. I., Braida, L. D., and Durlach, N. I. (**1985**). ''Discrimination and identification of frequency-lowered speech in listeners with high-frequency hearing impairment,'' J. Acoust. Soc. Am. **78**, 2139–2141.

Rosen, S., Faulkner, A., and Wilkonson, L. (**1997**). ''Perceptual adaptation by normal listeners to upward shifts of spectral information in speech and its relevance for users of cochlear implants,'' Speech, Hearing and Language: Work in Progress, Vol. 10, pp. 1–15, University College of London, London.

Thornton, A. R., and Raffin, M. J. M. (**1978**). ''Speech-discrimination scores modeled as a binomial variable,'' J. Speech Hear. Res. **21**, 507–518.

Turner, C. W., and Cummings, K. J. (**1999**). ''Speech audibility for listeners with high-frequency hearing loss,'' Am. J. Audiology (in press).

Wallace, W., and Koury, G. (**1981**). ''Transfer effects from listening to frequency-controlled and frequency-shifted accelerated speech,'' J. Speech Hear. Res. **24**, 185–191.

Pitch shifts of mistuned partials: A time-domain model

Alain de Cheveigné
Laboratoire de Linguistique Formelle, CNRS/Université Paris 7, 2 place Jussieu, 75251, Paris, France and ATR Human Information Processing Research Laboratories, 2-2 Hikaridai, Seika-cho, Soraku-gun, Kyoto 619-0288, Japan

(Received 9 December 1998; revised 17 February 1999; accepted 20 April 1999)

Mistuning one partial of a complex harmonic tone makes that partial easier to hear as a tone separate from the complex. At the same time, two pitch shifts may be observed. First, the low pitch of the complex is shifted in the direction of the mistuning, as if it were ''pulled'' by the partial. Second, the mistuning of the partial is perceptually exaggerated, as if the pitch of the partial were ''pushed'' away from the harmonic series defined by the complex. This paper shows how the latter effect can emerge within a hypothetical neural circuit. The circuit involves a gating neuron fed by three pathways, one direct and excitatory and the other two delayed and inhibitory. The neuron responds to any excitatory input spike unless it is accompanied by an inhibitory input spike on either delayed input, thus acting as a kind of ''anticoincidence counter.'' The first delay is fixed and tuned to the period of the background harmonic complex. Its purpose is to weaken correlates of in-tune components and allow the mistuned partial to stand out. The second delay is variable and used to estimate the period of the mistuned partial, by searching for a minimum output as a function of delay. With an appropriate choice of parameters, the estimate is subject to shifts that are of the same sign as the mistuning and that peak at about 4% mistuning and decrease beyond, as observed experimentally. [S0001-4966(99)02208-0]

PACS numbers: 43.66.Ba, 43.66.Hg, 43.64.Bt [JWH]

INTRODUCTION

Partials of a harmonic complex are difficult to hear unless attention is drawn to them, for example, with the help of a resonator (Helmholtz, 1877). However, if a partial is mistuned it becomes easier to hear as an entity separate from the complex (Hartmann *et al.*, 1986, 1990; Moore *et al.*, 1986). At the same time, both the pitch of the partial and that of the complex are affected by the mistuning. The pitch of the partial varies with mistuning, but more than expected on the basis of its frequency, as illustrated in Fig. 1(a). The difference between measured pitch (symbols) and expected pitch (dotted line) is known as the ''pitch shift of the mistuned partial'' (Hartmann and Doty, 1996). The shift has typically the same sign as the mistuning; it is greatest when the mistuning is about 4%, and it decreases for larger mistunings [Fig. 1(b)].

The low pitch of the complex also changes with the mistuning of the partial. The shift is in the same direction as the mistuning and peaks at a mistuning of about 3% [Fig. 1(c)], beyond which the low pitch starts to move back until at 8% mistuning it regains its original value (Moore *et al.*, 1986; Darwin *et al.*, 1994; Hukin and Darwin, 1995). When plotted, both shifts look alike but their nature is rather different: The low pitch is as it were ''attracted'' by the mistuned partial, whereas the pitch of the partial is ''repulsed'' by the harmonic series. The mutual influence between partial and complex is not symmetrical.

The existence of a low pitch shift is relatively easy to account for. Most pitch models base their estimate of the low pitch on an ensemble of partials, and would respond to a small mistuning of any of them by a proportional shift of the low pitch (Terhardt, 1974; Goldstein, 1973; Meddis and O'Mard, 1997). In percentage, the slope of the shift-vs-mistuning function for any partial is less than one [compare with the dotted line in Fig. 1(c)], and its value can be used as an estimate of the weight of the partial in the pitch calculation (Moore *et al.*, 1985; Moore, 1987). An extra assumption is required to explain why this dependency is limited to mistunings smaller than 3%, beyond which the weight of the partial decreases. For that purpose, Duifhuis *et al.* (1982) proposed a ''harmonic sieve'' to limit the amount of mistuning permitted to partials participating in the pitch. The ''sieve'' may take the form of an arbitrary rule in a pattern matching algorithm, or else it may be attributed to an emergent property of a pitch extraction mechanism. For example, in a model based on histograms of first-order interspike intervals (ISI) pooled across frequency, ISIs evoked by the mistuned partial affected the position of the ''period mode'' at small mistunings, and formed a separate distribution at large mistunings (Moore, 1987).

In contrast, the pitch shift of the mistuned partial is harder to explain. Most pitch models focus on the pitch of the whole stimulus (low pitch) and do not explicitly address the perception of the pitch of individual partials. (Licklider, 1951; Moore, 1977; Goldstein, 1973; Wightman, 1973; Meddis and Hewitt, 1991a, b). Srulovicz and Goldstein (1983) mentioned that neighboring partials might affect the *accuracy* of the representation of a partial's frequency, but said nothing of effects upon its value. Goldstein *et al.* (1978) invoked small biases of the estimates of components of a complex, but did not say how they arose, or how to predict their value. Terhardt (1979) gave precise rules determining how the pitch of a partial (''spectral pitch'') should be affected by the presence of other partials: The fundamental component should shift negatively, and all other components positively.

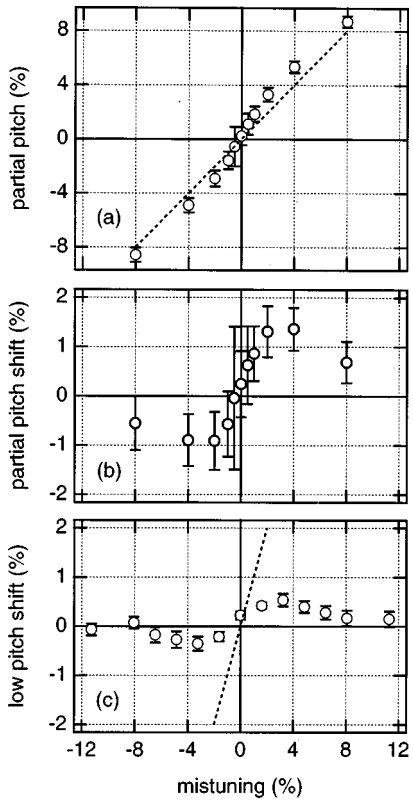

FIG. 1. (a) Pitch of the fifth partial of a complex tone of fundamental 200 Hz as a function of its mistuning. Pitch and mistuning are both expressed as a percentage relative to 1000 Hz. The difference between these data points and the dotted line represents the ''pitch shift of the mistuned partial.'' This shift is replotted in (b). Error bars represent one standard error of the mean (Hartmann and Doty, 1996). (c) Shift of the low pitch of a complex of fundamental 155 Hz as a function of mistuning of the fourth partial (Darwin *et al.*, 1994). The dotted line represents a shift/mistuning slope of one.

However, this description does not match the shifts observed by Hartmann and Doty (1996). The shifts appeared to result not from interactions between neighboring partials, but from the interaction between the partial's frequency, and a *harmonic template* defined by the in-tune partials of the complex (Lin and Hartmann, 1997). A harmonic template was used by the model of Goldstein (1973), to allow noisy estimates of the frequencies of all partials to collectively determine the low pitch of the complex. One might speculate that, in return, such a template somehow affects the pitches of the partials when they are mistuned.

A recent paper proposed a model of such interaction (de Cheveigné, 1997b). A noisy estimate of the partial's frequency determined its pitch, and also the probability of its fusion within the background harmonic complex. This probability varied according to the proximity of the frequency estimate with a harmonic template. If fusion prevents an independent pitch from being heard, it follows that the distribution of pitch matches is biased relative to its distribution in the absence of the complex, and this results in a pitch shift. The model accounted for experimental data quite well, but gave no hint as to the nature of the internal frequency representation, the source of noise, or the nature of the events described by the probability functions. The purpose of the present study is to work out the details of a more concrete model, based on the hypothesis that frequency is represented by the *time-domain* pattern of neural discharge. This hypothesis was supported by Hartmann *et al.* (1990) who found an absolute frequency limit between 2.2 and 3.5 kHz for the segregation of mistuned harmonics, which they interpreted as reflecting a reduction in neural synchrony at high frequencies.

The model described in this paper uses the concept of *harmonic cancellation*, the process by which harmonic (periodic) interference is suppressed to allow targets to be perceived. Harmonic cancellation has emerged experimentally as a principle behind F_0-guided segregation of harmonic sounds (Lea, 1992; Summerfield and Culling, 1992; de Cheveigné *et al.*, 1995, 1997a, 1997b). According to that principle, the auditory system takes advantage of the harmonic structure of interference to get rid of it. Several models of harmonic cancellation have been proposed, among which the channel selection model of Meddis and Hewitt (1992), and the time-domain ''neural cancellation filter'' of de Cheveigné (1993, 1997a). In the latter model, correlates of the interference were suppressed within neural spike trains to allow evidence of the target to emerge. These models explain the improvement in identification observed in ''double-vowel experiments'' when vowels have different fundamental frequencies (F_0) (Scheffers, 1983; Assmann and Summerfield, 1990).

Applied to pitch perception, the ''neural cancellation filter'' allows the period of a stimulus to be estimated from the position of the *minimum* output of an array of such filters, evidence of the best possible cancellation. In this role it is similar to the autocorrelation model of pitch perception (Licklider, 1951; Meddis and Hewitt, 1991a, 1991b), excitatory interaction being replaced by inhibitory interaction, and the search for a maximum by a search for a minimum (de Cheveigné, 1998). The cancellation filter can also assist the estimation of multiple pitches: Tuned to the period of one periodic sound, it suppresses that sound and allows the period(s) of the other sound(s) to be estimated (de Cheveigné, 1993; de Cheveigné and Kawahara, 1999). The present paper is based on the hypothesis that harmonic cancellation is used both in a preprocessing stage, to filter out unwanted components, and in a pitch perception stage to estimate the period. This is shown to result in pitch shifts similar to those observed experimentally.

I. ESTIMATING THE PITCH OF A MISTUNED PARTIAL

The model aims at estimating the pitch of a mistuned partial. It is based on the cancellation model of pitch perception of de Cheveigné (1998) with which it differs in two ways. First, processing is restricted to a single channel (or group of similar channels) tuned to the frequency region of the mistuned partial. Second, an additional branch of neural processing is introduced to weaken correlates of the background harmonic complex and make the mistuned partial easier to estimate. These assumptions are motivated in Sec. I D. Standard and modified cancellation filters are first presented, followed by details of the simulation (spike generation, etc.). They are then applied to the task of pitch perception of a mistuned partial. Finally, the various parameters and assumptions of the model are discussed one after the other.

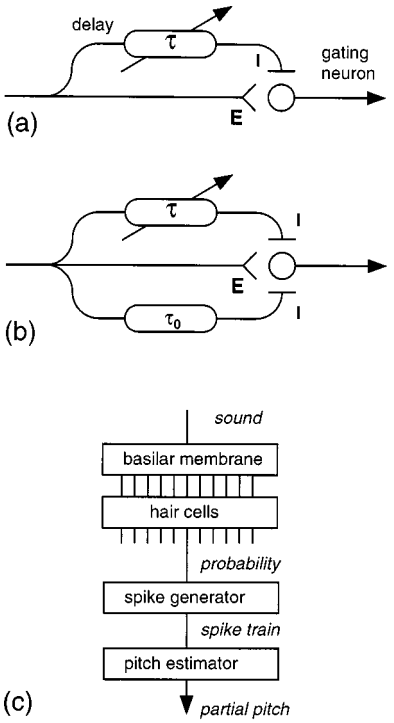

FIG. 2. (a) Standard neural cancellation filter used in the pitch perception model of de Cheveigné (1998). The pitch period is estimated by an array of such filters with delays τ covering the range of expected pitch periods. The delay that produces a minimum output is the period estimate. (b) Modified cancellation filter used in the present model for estimation of a mistuned partial. One delay, τ_0, is fixed and set to the period T_0 of the background harmonic complex. The other, τ, is variable and used to estimate the partial's pitch period T. (c) Schema of the partial pitch perception model. Sound is processed by a gammatone basilar-membrane/haircell model to produce a tonotopic array of auditory-nerve fiber discharge probability functions. A single channel with CF equal to the nominal frequency of the partial is selected to drive a model of spike generation (inhomogenous Poisson process with refractory effects). The spike train is processed by an array of modified cancellation filters (b) to estimate the mistuned partial's pitch.

A. Standard and modified neural cancellation filters

The standard ''neural cancellation filter'' is illustrated in Fig. 2(a). This hypothetical network consists of a gating neuron fed by two pathways, one direct and excitatory, the other delayed and inhibitory. The neuron fires each time a spike arrives along the direct pathway, *unless* a spike arrives simultaneously along the delayed pathway. The neural cancellation filter has been used to account for source segregation on the basis of fundamental frequency (F_0) as observed in ''double-vowel'' experiments (de Cheveigné, 1993, 1997a), and also pitch perception, in a ''negative'' version of the autocorrelation model (de Cheveigné, 1998). To estimate the pitch period, the delay parameter τ is varied until a minimum output is found (equivalently, an array of filters with various τ parameters is scanned). The corresponding delay gives the pitch period estimate. This description applies to a single channel. For the perception of the *low pitch* of a complex, a similar operation is supposed to occur in parallel in all channels emerging from the cochlea. The results of different channels may be combined as suggested by Moore (1997) or Meddis and Hewitt (1991a, 1991b).

For the task of perceiving the pitch of a *single* partial, it is reasonable to suppose that processing is instead restricted to a limited set of channels. In addition, the present model replaces the standard neural cancellation filter of Fig. 2(a) by the ''modified neural cancellation filter'' of Fig. 2(b). In the modified filter, the gating neuron is fed by an extra inhibitory delayed pathway with delay τ_0. Formally, the filter transmits any incoming spike with probability 1 unless the spike is preceded by a spike after an all-order interval in the range $[\tau_0-\Delta\tau_0/2,\tau_0+\Delta\tau_0/2]$ *or* in the range $[\tau-\Delta\tau/2,\tau+\Delta\tau/2]$, in which case transmission probability is 0. Parameters $\Delta\tau_0$ and $\Delta\tau$ determine the width of the ''tolerance windows'' around τ_0 and τ. Particular spikes are removed, and the result is to reduce the density of all-order intervals with durations similar to τ_0 or τ.

When estimating a mistuned partial, the delay τ_0 is set to the period $T_0=1/F_0$ of the background harmonic complex. The motivation for this extra pathway is given in Sec. I D. For now it is sufficient to think of it as a sort of time-domain ''harmonic sieve'' (Duifhuis *et al.*, 1982) that suppresses features in tune with the harmonic series of the background complex, and allows correlates of the mistuned partial to emerge. The second delay, τ, is variable and used to estimate the mistuned partial's period.

B. Simulation

The structure of the model is illustrated in Fig. 2(c). The stimulus waveform (complex with mistuned partial) is filtered by a gammatone filter and hair cell transduction stage (Patterson *et al.*, 1992; Meddis, 1988; Slaney, 1993) that produces an array of discharge probability functions. A single channel is selected, with a characteristic frequency (CF) equal to the nominal frequency of the partial (frequency in the absence of mistuning). It is used to drive a model of auditory nerve fiber discharge production. The resulting spike trains feed the pitch estimation stage that consists of an array of modified cancellation filters with delays covering the range of expected pitch periods.

Stimuli were 16-component complex tones with sine starting phase. The components (partials) followed a 200-Hz harmonic series, with the exception of one partial that could be mistuned by -8% to $+8\%$. Stimuli were generated at a 100-kHz sampling rate and fed to the basilar-membrane/haircell model. Spikes were produced stochastically by an inhomogeneous Poisson process with refractory effects, and stored as interspike intervals with a resolution limited only by the floating point representation. Subsequent calculations used a 10-μs resolution. Refractory effects were modeled as an absolute dead time of 1 ms. Further details and references may be found in de Cheveigné (1998). The average discharge rate was approximately 200 spikes/s. Spikes were produced in parallel for N fibers with similar characteristics ($N=100$). Before pitch estimation, the N spike trains were merged together into a single spike train. This step allows interval statistics to include intervals between spikes of different trains, thus making better use of the available information (de Cheveigné, 1993, 1998). Because of memory limitations, stimuli were shorter than those of Hartmann and Doty (1996): 100 ms vs 400 ms.[1] The first 20 ms of each spike train were discarded to reduce the effects of ringing and haircell adaptation.

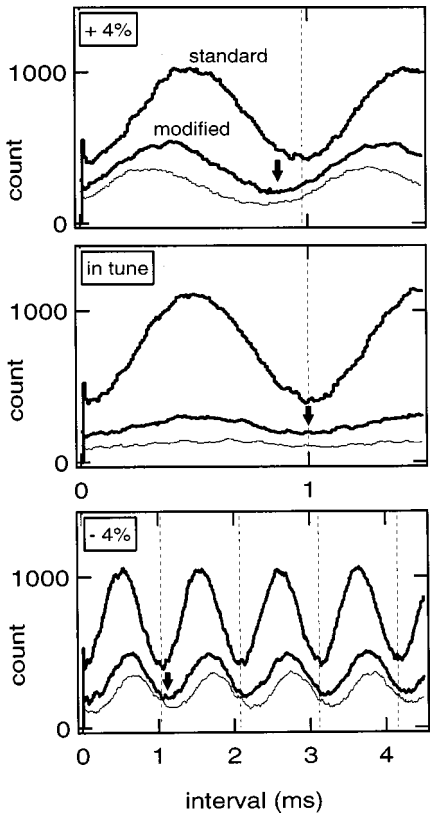

FIG. 3. Top panel, upper thick line: output of a standard cancellation filter as a function of delay, for the fifth partial of a 200-Hz complex. The partial was mistuned by +4%. Lower lines: same for a modified cancellation filter with parameters $\Delta\tau = 50\ \mu$s, and either $\Delta\tau_0 = 50\ \mu$s (thick line) or $\Delta\tau_0 = 100\ \mu$s (thin line). Middle panel: same for a mistuning of 0%. Bottom panel: same, for a mistuning of −4%. The horizontal scale was widened to accommodate higher-order minima. Vertical dotted lines indicate integer multiples of the period of the partial.

The model was applied to the mistuned fifth partial of a 200-Hz complex. Figure 3 shows the output of the standard and modified neural cancellation filters for three values of mistuning. In the top panel the partial is mistuned by +4%. The output of the standard cancellation filter (uppermost thick line) shows a minimum as a function of τ at a delay equal to the period (equivalent to the period peak of the autocorrelation model). The function is subject to random variations, but on average the minimum is centered on the period of the partial (dotted line). In contrast, the response of the modified cancellation filter (lower thick line) shows a minimum (arrow) that is shifted in the direction of greater mistunings. That is the origin of the pitch shift in the present model.

In the middle panel the partial is in tune with the background harmonic complex. Neglecting random fluctuations, the period minima of the standard (upper thick line) and modified (lower thick line) filters are centered on the period of the partial (dotted line and arrow). There is no pitch shift. In the bottom panel the partial is mistuned by −4%. The shift in this case is toward longer delays, exaggerating once again the effects of mistuning (arrow). The horizontal scale was widened to show that higher-order minima undergo shifts of the same *absolute* magnitude as the first. Shifts for higher-order minima are thus smaller in proportion, a fact that is exploited later on.

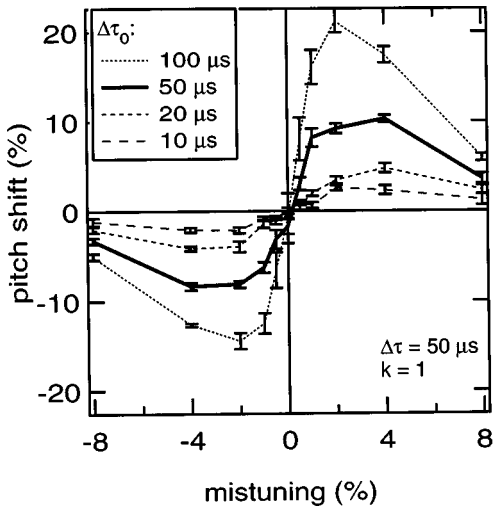

FIG. 4. Pitch shift predicted by the model as a function of mistuning for the fifth partial of a 200-Hz complex, for different values of the $\Delta\tau_0$ parameter. The pitch estimate was based on the position of the first-order minimum ($k = 1$, see text).

Because the extra branch removes more spikes, the output of the modified filter is less than that of the standard filter, particularly when the partial is in tune with the complex (middle panel). The modified filter de-emphasizes in-tune partials. In the simulations that produced the thick lines, $\Delta\tau_0 = \Delta\tau = 0.05$ ms. The thin lines were obtained for $\Delta\tau_0 = 0.1$ ms. With this value, the ''tolerance window'' for removal of intervals equal to T_0 is wider, shifts for the mistuned partials are greater (top and bottom), and the output pattern for the in-tune partial is flatter (middle).

C. Predicted shift patterns

The model was simulated with the same set of mistunings (−8%, −4%, −2%, −1%, −0.5%, 0, 0.5%, 1%, 2%, 4%, 8%) as in the experimental data of Fig. 1(a), (b). For each value of mistuning, the modified cancellation filter was applied to the spike train and τ was varied in a ±40% range around the period of the partial. The array of output spike counts was smoothed by convolution with a 20 point window (0.2 ms) to reduce noise, and the position of the minimum was taken as a period estimate. The simulation was repeated ten times per data point, to refine the averages and estimate their reliability (the purpose was *not* to model the variability of a hypothetical neural process, nor that of subjects responses). Simulations were time and memory consuming, and this limited the range of conditions that could be explored, and the degree to which variability could be reduced by averaging.

Pitch shifts as a function of mistuning for the fifth partial are plotted in Fig. 4. The parameter $\Delta\tau_0$ was given several values, while $\Delta\tau$ was kept fixed at 50 μs. Error bars represent the standard error of the mean over ten simulations. In their *shape*, predicted shift functions are quite similar to the experimental data: Shifts are of the same sign as the mistuning, and they peak at about 4% and decrease beyond. However, predicted shifts are considerably larger than those ob-

served experimentally [Fig. 1(b)]. This problem is addressed in the next section. Shift size varies with $\Delta\tau_0$, which controls the size of the coincidence window for the $\tau_0 = T_0$ branch, and thus indirectly the probability that spikes will be removed by that branch. At $\Delta\tau_0 = 0$ the circuit is equivalent to the standard cancellation filter for which no shifts occur.

D. Questions

So far the model accounts for the shape of the pitch shift function for the fifth partial, but not its magnitude. This section examines that issue and others.

1. Effect size

There are several ways to reconcile the magnitudes of predicted and observed pitch shifts. One is to postulate small values of $\Delta\tau_0$, or a reduced probability of spike suppression in the τ_0 branch of the filter. Another is to suppose that pitch is derived in part from *higher-order* valleys of the pattern (it was seen in Sec. I B that shifts are proportionally smaller for higher-order valleys).

The assumption that higher-order valleys are involved is attractive. The matched filter of Srulovicz and Goldstein (1983) was sensitive to higher-order modes of ISI (first-order interspike interval) histograms. The ''narrowed autocorrelation function'' of Brown and Puckett (1989), which also incorporated information from higher-order modes of the autocorrelation function, was applied to pitch perception by de Cheveigné (1989) and Slaney (1990) to account for the small size of frequency discrimination thresholds and their nearly inverse dependency on frequency and duration (up to 1 kHz and 100 ms, respectively) (Moore, 1973). If this assumption is accepted, simulated shifts can be brought in line with experimental shifts by dividing them by a constant k representing the shift reduction due to the smaller relative shifts of higher-order valleys. With $k = 8$ the match between predicted and experimental data for the fifth partial is good (topmost panel in Fig. 5).

2. Shifts for other partials

Figure 5 shows predicted shifts (lines) for partials 2 to 5, together with experimental data measured by Hartmann and Doty (1996) (symbols). Parameter k was 8, 8, 11, and 8, respectively, for partials 2 to 5. Other model parameters were the same for all partials. Simulated shifts match experimental shifts very well for the fourth and fifth partial, reproducing even the tendency for positive mistunings to produce slightly larger shifts. The match is less good for lower partials, but simulated shifts remain everywhere within experimental error bars. Figure 6 shows similar data for the seventh partial and the fundamental, with k set, respectively, to 8 and 4.

For the seventh partial the experimental data are well predicted for mistunings between -4% and 4%, but not $\pm 8\%$. At -8% the model predicts a *positive* shift. This is logical because the partial (1288 Hz) is actually closer to the sixth harmonic (1200) than to the seventh (1400). The ''repulsive'' effect of the harmonic series thus increases the pitch estimate instead of decreasing it. A similar explanation holds for the negative shift at 8%. Most other data points of Hartmann and Doty (1996) and Lin and Hartmann (1997) are

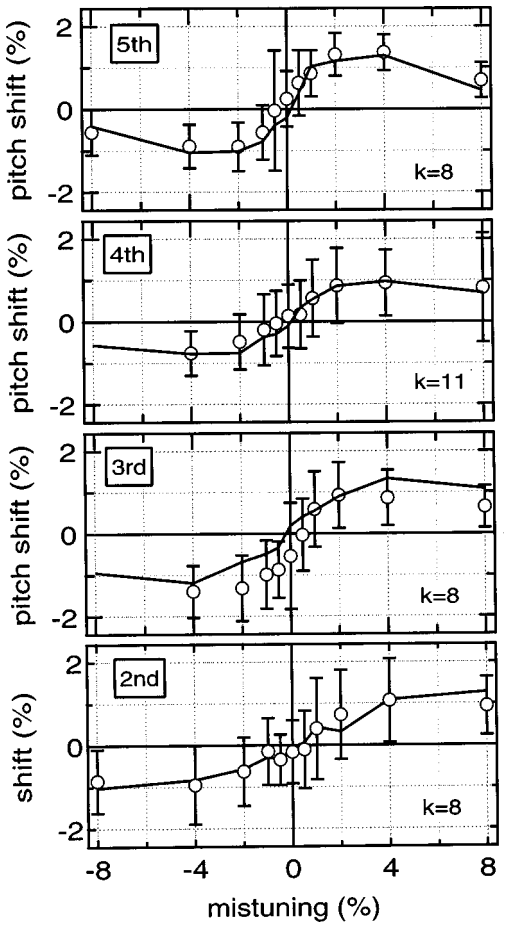

FIG. 5. Lines: pitch shifts predicted by the model as a function of mistuning for partials of various ranks. Symbols: pitch shifts measured experimentally by Hartmann and Doty (1996) for the same partials. Error bars represent one standard error of the mean over experimental data. Parameters $\Delta\tau$ and $\Delta\tau_0$ were the same for all partials. The scaling parameter k was adjusted ''by eye'' to obtain a satisfactory fit.

consistent with the principle of a repulsive effect of the harmonic series, embodied by the model. Experimental data for $\pm 8\%$ mistunings of the seventh partial are exceptions to this principle.

For the fundamental, the simulated shifts fall within error bars despite a sort of ''glitch'' at 1% and 2% mistuning, that may reflect phase effects as discussed later in this section. Apart from this glitch, the monotonic shape of the experimental shift function at the fundamental is reproduced.

3. Why the extra branch?

Why would the auditory system go to the expense of an extra branch in the cancellation filter, particularly if it produces systematic shifts that the standard filter could avoid? One can suggest that it is part of a mechanism to keep the focus on the mistuned partial, without which attention might wander to neighboring in-tune partials, making the task difficult. The modified filter produces outputs that are larger for mistuned than for in-tune partials, and also more strongly modulated as a function of τ (Fig. 3). Channels responding to the mistuned partial are more prominent, and this eases the task of hearing out the partial. Figure 7 illustrates this point by showing the number of spikes that escape removal by the τ_0 branch as a function of CF, for a mistuning of 4%. Chan-

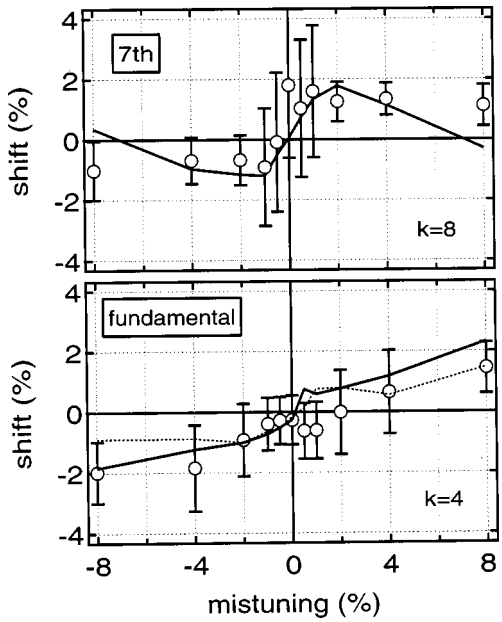

FIG. 6. Same as Fig. 5, for the fundamental and seventh partial. The dotted line in the lower plot (fundamental) is for a stimulus with reversed polarity (180 degree phase shift of all components).

nels responding to the mistuned partial are favored, the contrast being greater for larger values of $\Delta\tau_0$. Such focusing is impossible when the partial is in-tune, which may explain why in-tune partials are harder to hear out.

4. Why not use separate cancellation filters?

The idea of using harmonic cancellation to suppress a competing sound (in this case the background harmonic complex) was put forward in previous studies (de Cheveigné, 1993, 1997a; de Cheveigné and Kawahara, 1999). They assumed, however, that it would take the form of a separate cancellation filter preceding the estimation stage, as illustrated in Fig. 8. Why then postulate the topology of Fig. 2(b)?

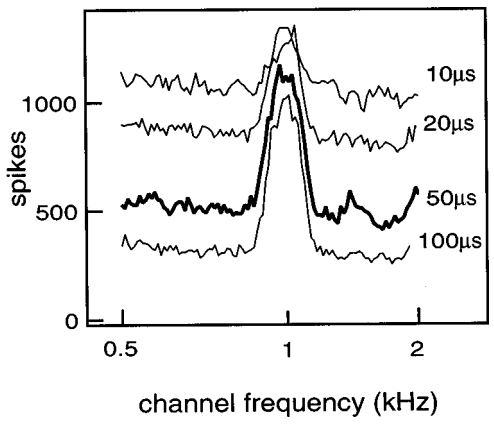

FIG. 7. Number of spikes that escape removal by the τ_0 branch as a function of channel frequency, for various values of the $\Delta\tau_0$ parameter, in response to the 200-Hz complex with a fifth partial mistuned by 4%. More spikes are removed from channels that respond to components in tune with the harmonic complex, than from channels that respond to the mistuned partial. The contrast is greater for larger values of $\Delta\tau_0$.

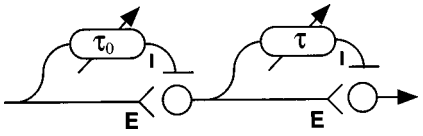

FIG. 8. Two cascaded cancellation filters, as proposed by de Cheveigné and Kawahara (1999) to estimate multiple pitches. The first attenuates components in-tune with one part of the stimulus (for example the harmonic complex), the second is used to estimate the period of the remainder (for example a mistuned partial). This topology is ruled out by the experimental data of Hartmann and Doty (1996), according to the present theory.

It turns out that a model based on the topology of Fig. 8 produces no shifts. To understand why, it is necessary to first understand how shifts were produced by the previous topology. Within a channel tuned to a mistuned partial, spikes tend to occur at peaks of basilar-membrane motion. All-order interspike intervals (ISI) are thus distributed with a maximum corresponding to the period T of the partial. Because of the stochastic nature of spike generation, some spikes occur early within the peak: These tend to be preceded by ISIs that are shorter than T. Likewise, spikes that occur late in the peak tend to be preceded by ISIs that are longer than T. However, both populations are balanced, and the minimum output of a standard cancellation filter is obtained for $\tau = T$.

Consider now the modified cancellation filter [Fig. 2(b)], and suppose that the partial of order n is mistuned positively. In the basilar-membrane region that responds to the partial, peaks of motion occur at intervals T that are shorter than an integer fraction of the period T_0 of the complex. If the τ_0 branch is tuned to T_0, it removes spikes that tend to occur *late* within a peak of basilar-membrane motion. Late-occurring spikes being removed by the τ_0 branch, it is advantageous to mistune the τ branch to remove spikes that occur *early*, because that maximizes spike suppression. The minimum as a function of τ is thus displaced. That is the origin of the shift with the filter of Fig. 2(b).

In the case of cascaded filters as in Fig. 8, the second cancellation filter (tuned to τ) estimates the most common interval in the output of the first. Interval statistics are modified by the first filter, that removes certain spikes, but this does not result in the systematic shifts observed with the other topology. To understand why, notice that every spike determines two populations of intervals—those that *end* on the spike, and those that *begin* on it. If a spike occurs late, one population is biased toward long intervals, but the other is equally biased toward short intervals. The net effect of removing that spike on average interval length is zero. The interval statistics cannot be significantly biased in this way, and that explains the lack of shifts for the topology of Fig. 8.

The lack of shifts for the circuit of Fig. 8 explains why that topology was not chosen for the pitch shift model. It does not explain why the auditory system might have made the same choice. Figure 8 requires an extra relay with high temporal accuracy. Not only that, but each relay requires its own array of delay lines, whereas in Fig. 2(b) both delay lines are chosen from the same array. Considerations of this type may explain why the auditory system adopted the topology of Fig. 2(b), despite the fact that it is conceptually more

complex and produces pitch shifts. In any case, it is remarkable that the psychophysical data of Hartmann and Doty (1996) can be translated into such a precise anatomical constraint.

5. Why cancellation?

Cancellation and autocorrelation are closely related (de Cheveigné, 1998). Autocorrelation being familiar to many, it is reasonable to ask whether the model can be recast in terms of a ''modified autocorrelation,'' by replacing inhibitory by excitatory interaction in the circuit of Fig. 2(b). The answer is yes, in the sense that reversing the sign of the interaction produces a ''modified autocorrelation function'' with maxima that show exactly the same shifts. However, whereas the extra inhibitory branch made sense in terms of cancellation of an unwanted background complex, it is harder to justify the extra branch if it is excitatory. Across channels, the output would be *smaller* in channels tuned to the mistuned partial instead of larger, which makes little sense if the task is to hear out that partial. Cancellation is more logical, but one should not reject the possibility that the shifts occur within a different kind of neural circuit, for example excitatory.

6. How is T_0 estimated?

The T_0 estimate (necessary to set the fixed delay τ_0) may be derived from the period estimation stage of any model of low pitch perception, for example, autocorrelation or cancellation. Judging from the shifts of the low pitch as a function of mistuning [Fig. 1(c)], it would appear that channels responding to the mistuned partial are included in the estimate for small mistunings ($<4\%$) and excluded for large mistunings ($>4\%$). At small mistunings the T_0 estimate might thus be slightly shifted, but this is of little consequence to the model as long as the shift is small relative to the mistuning.

What range of channels must be included in the T_0 calculation? Lin and Hartmann (1997) found shifts for harmonic complexes that lacked many partials, in particular those immediately above and/or below the mistuned partial. This suggests that the estimation of T_0 involves a broad range of channels. On the other hand, Roberts and Brunstrom (1998) found shifts for partials mistuned from a slightly inharmonic complex (derived from a harmonic complex by uniformly ''shifting'' or ''stretching'' it). This suggests instead that the template (or T_0 estimate) is derived from a set of partials neighboring the mistuned partial. More research is needed to resolve this apparent contradiction. The idea of a ''local'' harmonic template parallels the ''modified Equalization Cancellation'' model of Culling and Summerfield (1995; Culling *et al.*, 1998a, 1998b) in which binaural cancellation occurs with parameters local to each channel, rather than common to all channels as in the original EC model of Durlach (1963). Local harmonic templates might also explain monaural segregation data for vowels with formants or partials exchanged between harmonic series in a way that would confuse a mechanism that fits all harmonics of a vowel to a single harmonic series (Culling and Darwin, 1993, 1994).

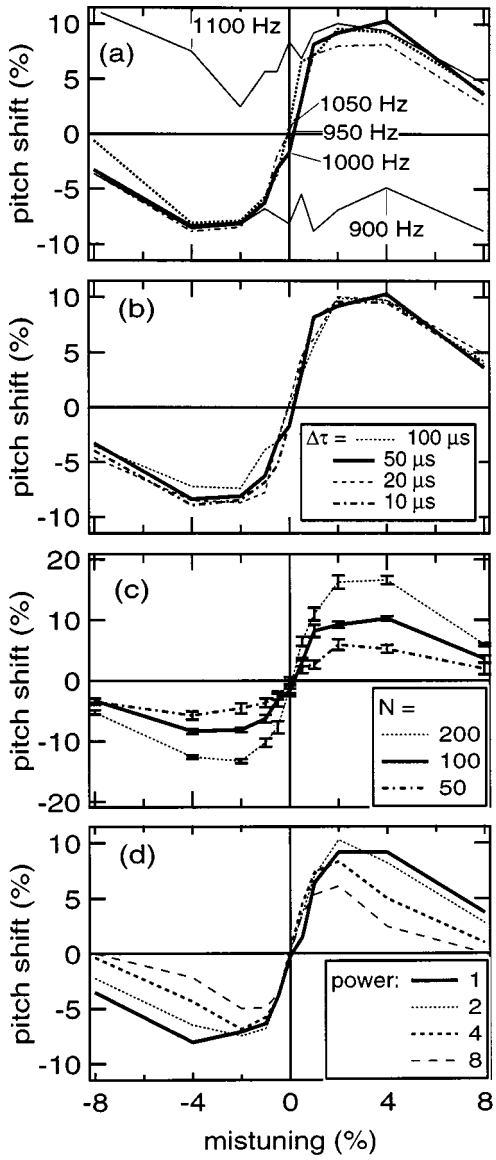

FIG. 9. Effects of various model parameters on the pitch shift as a function of mistuning of the fifth partial of a 200-Hz complex. (a) Effect of the channel frequency. Each line is for a different channel of the basilar-membrane/haircell model ($k=1$, $\Delta\tau=\Delta\tau_0=50$ μs, $N=100$). (b) Effect of $\Delta\tau$ ($k=1$, $\Delta\tau_0=50$ μs, $N=100$). (c) Effect of the number of fibers N ($k=1$, $\Delta\tau=\Delta\tau_0=50$ μs). (d) Effect of adding a sharpening stage, implemented by raising the haircell model output to a power before spike generation. Each line is for a different power (power=1 implies no sharpening) ($k=1$, $\Delta\tau=\Delta\tau_0=50$ μs, $N=100$).

7. Effects of other parameters

Figure 9(a) shows pitch shifts obtained from five different channels of the basilar-membrane/haircell model (900 Hz, 950 Hz, 1000 Hz, 1050 Hz, 1100 Hz), as a function of mistuning of the fifth partial. Estimates are erratic for the two extreme channels, but consistent between the three central channels, and presumably any other channels within this range. Within this range, the estimates do not depend on which set of channels are included in the simulation. Based

on the cochlear frequency map of Greenwood (1990), and an estimated number of 30 000 auditory nerve fibers in man, the cochlear region between 950 and 1050 Hz feeds about 540 fibers, an ample number for the model. With a larger value of $\Delta\tau_0$ (more severe rejection of the background harmonic series), estimates are consistent over an even wider range of channels (not shown).

Figure 9(b) shows the effect of the parameter $\Delta\tau$. $\Delta\tau_0$ was kept constant at 50 μs. The effect of this parameter is small.

Figure 9(c) shows the effect of varying the number N of fibers used in the simulation. Shift size is reduced when N is reduced, but the shape of the shift function hardly changes. A change in discharge rate (for example, due to a change in stimulus level) would have a similar effect.

It has been suggested that pitch perception might involve *temporal sharpening* of neural discharge patterns, for example, by onset cells in the cochlear nucleus. Sharpening was simulated by raising to a power the probability function at the output of the haircell model, and scaling it to obtain an average probability of 200 spikes/s. Effects of sharpening are displayed in Fig. 9(d). Sharpening causes the shift pattern to vary over a narrower range, while the slope near 0% mistuning remains approximately the same. A close match to experimental data was found without sharpening (Fig. 5). It can only be degraded if sharpening is introduced. This argues *against* the hypothesis that auditory nerve fiber discharge patterns undergo temporal sharpening before pitch extraction, at least for this particular task (see also Shofner, 1998).

In summary, the model is remarkably insensitive to changes in parameters, other than the simple scaling effect of changing $\Delta\tau_0$, k, or N. To change the shape of the shift function required a structural change (addition of a sharpening stage) that the experimental data do not support. The fact that the model fits the data *despite* this lack of flexibility can be interpreted as an additional argument in favor of the model.

8. Evidence of phase effects

Mistuning causes the stimulus waveform to beat at a rate of nmF_0, where n is the rank of the mistuned partial, m is the mistuning factor, and F_0 is the fundamental. For the fifth partial of a 200-Hz complex, the beat periods for mistunings of $\pm 0.5\%$, $\pm 1\%$, $\pm 2\%$, $\pm 4\%$, $\pm 8\%$ are, respectively, 200 ms, 100 ms, 50 ms, 25 ms, and 12.5 ms. Beat periods are proportionally longer for mistuned partials of lower ranks (for the fundamental they are, respectively, 1000 ms, 500 ms, 250 ms, 125 ms, and 62.5 ms). The waveform fluctuates with the beat, and the shape of a stimulus thus depends on which part of the beat period it samples, which in turn depends on the relative starting phases of the various components. Phase effects are thus to be expected. They should be small when the beat period is shorter than the stimulus, but possibly relatively large when the beat period is longer. Indeed, Hartmann (1988) found phase effects for the detection of mistuned partials, particularly for short stimuli.

The present simulations used 100-ms stimuli (the first 20 ms of the spike trains produced were removed, so the model operated essentially on the last 80 ms). This is shorter than a beat period for many conditions, particularly for partials of low rank. The minor irregularities visible in Fig. 5 (second harmonic) and Fig. 6 (fundamental) are highly reproducible, and it turns out that they are also phase dependent. The dotted line in Fig. 6 (fundamental) was obtained for a reversal in polarity of the stimulus (180 degree phase shift of all components). There is thus some evidence that the model is phase sensitive. However, no attempt was made to extend it to account for the phase dependency of detection reported by Hartmann (1988).

II. DISCUSSION

A previous paper (de Cheveigné, 1997b) proposed a different model to explain the same phenomena. That model did not suggest what physiological mechanisms were involved. In particular it was neutral on the question of whether pitch is derived from time-domain or spectral (place) representations. The present paper offers a more concrete model based on the hypothesis of time-domain processing of neural spike trains. In the absence of an equally plausible place model, this theory (together with the phenomenon that it explains) can be interpreted as supporting a time-domain model of pitch perception.

The model is congruent with the hypothesis of a time-domain neural cancellation filter that was proposed to explain concurrent voice segregation (de Cheveigné, 1993, 1997a) and pitch perception (de Cheveigné, 1998), and in particular with the hypothesis that harmonic cancellation is used to ease the perception of pitch in the presence of competing harmonic sounds (de Cheveigné and Kawahara, 1999). However, the lack of shifts for the topology of Fig. 8 suggests that the arbitrary levels of cascaded filters imagined by de Cheveigné and Kawahara (1999) might not be available in the auditory system. The theory puts strong constraints on the topology of the neural circuits involved in this task, by ruling out one topology that was *a priori* plausible, and showing that another can account for the shifts. However, it does *not* prove that it is the only one. In particular it was pointed out that replacing inhibitory by excitatory interaction in Fig. 2(b) would result in similar shifts.

The question arises as to what part of the auditory system might house such processing. The auditory system contains circuitry specialized in relaying high-resolution temporal information. Globular and spherical bushy cells in the cochlear nucleus (CN) are fed by axons of the auditory nerve via secure synapses that guarantee little degradation of temporal accuracy. They project to a number of relays in the brainstem: contralateral CN, superior olivary complex, nuclei of the lateral lemniscus (NLL), and inferior colliculus (IC) (Rhode and Greenberg, 1992; Romand and Avan, 1997). Within the superior olivary complex, principal cells in the medial nucleus of the trapezoidal body (MNTB) are fed by thick axons from contralateral globular bushy cells, via specialized synapses called calyces of Held. These neurons, which are inhibitory, project to ipsilateral lateral superior olive (LSO) and are supposed to be involved in the processing of interaural level differences (ILD). ILDs in principle do not involve time, and it is therefore surprising to find time-specialized circuitry involved in their processing. It has been suggested that the LSO also processes onset time disparities

(Batra *et al.*, 1997; Joris and Yin, 1998). One can speculate that this circuitry supports other forms of time-domain processing. In addition to the ipsilateral LSO, principal cells of the MNTB project to the ventral nucleus of the lateral lemniscus (VNLL) and to dorsomedial and ventromedial periolivary nuclei (DMPO and VMPO) (Spangler *et al.*, 1985). Smith *et al.* (1998) cite as an enigma that these regions receive both excitatory and inhibitory input from contralateral bushy cells, an arrangement that makes little sense in terms of binaural processing.

Other projections of the MNTB include the IC, contralateral CN, and even the outer haircells of the (mainly contralateral) cochlea, via the medial olivo-cochlear bundle (MOCB) (Helfert and Aschoff, 1997; Irvine, 1992; Warr, 1992). The hypothesis that cancellation occurs in the mechanical domain, involving reverse transduction of time-domain signals carried by efferent pathways, is attractive given the relative linearity and wide dynamic range of mechanical vibration. Unfortunately that hypothesis seems unlikely, as recordings from the MOCB have failed to reveal any stimulus-locked temporal structure (Guinan, 1996). In brain-slice preparations of the mouse CN, Wickesberg and Oertel (1990) found evidence for delayed inhibitory input to bushy and stellate cells in the anteroventral cochlear nucleus (AVCN) via the dorsal cochlear nucleus (DCN). They suggested that it served for monaural echo suppression, but harmonic cancellation might be another candidate role.

Neurons with the right sort of gating properties have been found in the LSO (lateral superior olive) (Batra *et al.*, 1997; Joris *et al.*, 1998; Sanes, 1990). In those neurons, presynaptic discharges in excitatory afferents produce EPSPs (excitatory post-synaptic potentials) and those in inhibitory afferents produce IPSPs (inhibitory post-synaptic potentials), both of which appear to be of short duration in certain LSO cells (Batra *et al.*, 1997). Supposing that an EPSP is sufficient to reach the neuron's firing threshold, and a well-timed IPSP sufficient to *prevent* the threshold from being reached, the neuron's properties would match those postulated by the neural cancellation filter.

The lack of evidence for delay lines has been pointed out many times. It is, however, possible that such delays might be hard to observe, if they occur within thin axonal fibers that feed the processing neuron. An *array* of neurons ordered according to delay or period might not be observed, if the delays were tuned, for example, by switching afferents.

Maas (1997a, 1997b) gave two theorems that support the thesis that spike-time representations may be used for complex processing in the nervous system (auditory or otherwise). The first demonstrates that any network based on a rate representation processed by ''sigmoidal'' neurons can be simulated by a network of spiking neurons, of comparable size. The second shows that for certain tasks (for example, the ''winner take all'' task) a sigmoidal network requires many more neurons than a spiking network. Together they imply that spiking neurons are more ''powerful'' than sigmoidal neurons. Spike-time processing is also much faster. These considerations argue against the proposition that a temporal code, which is natural in the auditory system, must necessarily be translated to a rate/place code before significant processing can occur. Maas has also suggested that filters of arbitrary impulse response could be ''synthesized'' by combinations of EPSPs and IPSPs, each weighted by the strength of the synapse and time-shifted by the delay of the pathway that feeds it. The circuits of Fig. 2 are simple examples of that idea, but one could speculate on more sophisticated circuits for the processing of vowel timbre, or dynamic features of speech or environmental sounds.

The model is specialized for a particular task. The assumptions it makes (an extra delayed branch, selection of a subset of channels) would make no sense if the task were, say, to match the low pitch of a harmonic complex. The two tasks therefore require different models. One can object that this violates the principle of parsimony, yet it is not unreasonable to imagine that the auditory system might employ different tools to solve different problems. To segregate a high-order partial from a harmonic complex, and match its pitch, is a more complex operation than to simply match the low pitch. There is a striking gap between the complexity of anatomic and physiological descriptions of the auditory system, and the models available to account for them. By maintaining that gap, an overdogmatic defense of parsimony might do a disservice to our understanding. It helps that various models use a uniform set of ingredients: delay, coincidence (whether excitatory or inhibitory), temporal integration, selective weighting (for example, of different tonotopic channels), etc. It would help further still if they could be assembled in a modular fashion, for example, by placing the pitch estimation model at the output of the module that suppresses the background complex. By ruling out the topology of Fig. 8 in favor of that of Fig. 2(b), the present study showed the limits of such modularity.

III. CONCLUSIONS

(1) The systematic shifts in the pitch of a partial that are observed when that partial is mistuned from a harmonic complex can be reproduced within a model based on time-domain processing of auditory nerve fiber discharge patterns.
(2) The model involves a neural circuit with a gating neuron fed by three pathways, one direct and excitatory, and the other two delayed and inhibitory. The delay parameter of one of the delayed pathways is varied in search of a minimum. The delay at the minimum is an estimate of the partial's period, and is used as the cue to the pitch of the partial in the model.
(3) The delay of the second pathway is tuned to the period of the background harmonic complex. Its purpose is to suppress the in-tune correlates of the complex, and thus ease the task of hearing out the mistuned partial.
(4) The pitch shift arises as a result of the stochastic nature of nerve discharge production, and its interaction with the two delayed pathways.
(5) The shifts are absent in a circuit that is *a priori* at least as plausible, consisting of two independent neural cancellation filters. The existence of shifts thus suggests constraints on the topologies of neural processing available for this kind of task.

(6) The fact that a plausible mechanism of time-domain neural processing predicts the same pitch shifts as observed experimentally argues in favor of a time-domain mechanism of pitch perception, at least for the pitch of partials. The weight of this argument depends upon the lack of a similarly detailed model of the spectral (place) variety.

ACKNOWLEDGMENTS

Part of this work was carried out at ATR Human Information Processing Research Laboratories, within a research agreement with the Center National de la Recherche Scientifique and the University of Paris 7. The author thanks ATR for its kind hospitality, and the CNRS for leave of absence. Chris Darwin provided the data for Fig. 1(c) and Bill Hartmann that of Figs. 5 and 6. The simulations relied heavily on Malcolm Slaney's AuditoryToolbox code. Thanks to Bill Hartmann, two anonymous reviewers, and the editor for useful comments on previous versions of the manuscript.

[1]The shorter duration (100 ms instead of 400 ms) increases the sensitivity of the simulation to phase effects that can occur when the stimulus is shorter than a beat period. Phase effects were observed, particularly at the fundamental, as discussed in Sec. I D. Based on simulations with various starting phase spectra, it appears that they are not large enough to affect the major pattern of simulated shifts, or the validity of the conclusions.

Assmann, P. F., and Summerfield, Q. (**1990**). ''Modeling the perception of concurrent vowels: Vowels with different fundamental frequencies,'' J. Acoust. Soc. Am. **88**, 680–697.

Batra, R., Kuwada, S., and Fitzpatrick, D. C. (**1997**). ''Sensitivity to interaural temporal disparities of low- and high-frequency neurons in the superior olivary complex. II. Coincidence detection,'' J. Neurophysiol. **78**, 1237–1247.

Brown, J. C., and Puckette, M. S. (**1989**). ''Calculation of a ''narrowed'' autocorrelation function,'' J. Acoust. Soc. Am. **85**, 1595–1601.

Culling, J. F., and Darwin, C. J. (**1993**). ''Perceptual separation of simultaneous vowels: Within and across-formant grouping by *F*0,'' J. Acoust. Soc. Am. **93**, 3454–3467.

Culling, J. F., and Darwin, C. J. (**1994**). ''Perceptual and computational separation of simultaneous vowels: Cues arising from low frequency beating,'' J. Acoust. Soc. Am. **95**, 1559–1569.

Culling, J. F., and Summerfield, Q. (**1995**). ''Perceptual segregation of concurrent speech sounds: Absence of across-frequency grouping by common interaural delay,'' J. Acoust. Soc. Am. **98**, 785–797.

Culling, J. F., Marshall, D., and Summerfield, Q. (**1998b**). ''Dichotic pitches as illusions of binaural unmasking II: The Fourcin pitch and the dichotic repetition pitch,'' J. Acoust. Soc. Am. **103**, 3527–3539.

Culling, J. F., Summerfield, Q., and Marshall, D. H. (**1998a**). ''Dichotic pitches as illusions of binaural unmasking I: Huggin's pitch and the 'binaural edge pitch,' '' J. Acoust. Soc. Am. **103**, 3509–3526.

Darwin, C. J., Ciocca, V., and Sandell, G. J. (**1994**). ''Effects of frequency and amplitude modulation on the pitch of a complex tone with a mistuned harmonic,'' J. Acoust. Soc. Am. **95**, 2631–2636.

de Cheveigné, A. (**1989**). ''Pitch and the narrowed autocoincidence histogram,'' Proc. ICMPC, Kyoto, 67–70.

de Cheveigne, A. (**1993**). ''Separation of concurrent harmonic sounds: Fundamental frequency estimation and a time-domain cancellation model of auditory processing,'' J. Acoust. Soc. Am. **93**, 3271–3290.

de Cheveigné, A. (**1997a**). ''Concurrent vowel identification III: A neural model of harmonic interference cancellation,'' J. Acoust. Soc. Am. **101**, 2857–2865.

de Cheveigné, A. (**1997b**). ''Harmonic fusion and pitch shifts of inharmonic partials,'' J. Acoust. Soc. Am. **102**, 1083–1087.

de Cheveigné, A. (**1998**). ''Cancellation model of pitch perception,'' J. Acoust. Soc. Am. **103**, 1261–1271.

de Cheveigné, A., and Kawahara, H. (**1999**). ''Multiple period estimation and pitch perception model,'' Speech Commun. **27**, 175–185.

de Cheveigné, A., Kawahara, H., Tsuzaki, M., and Aikawa, K. (**1997a**). ''Concurrent vowel identification I: Effects of relative level and *F*0 difference,'' J. Acoust. Soc. Am. **101**, 2839–2847.

de Cheveigné, A., McAdams, S., and Marin, C. (**1997b**). ''Concurrent vowel identification II: Effects of phase, harmonicity and task,'' J. Acoust. Soc. Am. **101**, 2848–2856.

de Cheveigne, A., McAdams, S., Laroche, J., and Rosenberg, M. (**1995**). ''Identification of concurrent harmonic and inharmonic vowels: A test of the theory of harmonic cancellation and enhancement,'' J. Acoust. Soc. Am. **97**, 3736–3748.

Duifhuis, H., Willems, L. F., and Sluyter, R. J. (**1982**). ''Measurement of pitch in speech: An implementation of Goldstein's theory of pitch perception,'' J. Acoust. Soc. Am. **71**, 1568–1580.

Durlach, N. I. (**1963**). ''Equalization and cancellation theory of binaural masking-level differences,'' J. Acoust. Soc. Am. **35**, 1206–1218.

Goldstein, J. L. (**1973**). ''An optimum processor theory for the central formation of the pitch of complex tones,'' J. Acoust. Soc. Am. **54**, 1496–1516.

Goldstein, J. L., Gerson, A., Srulovicz, P., and Furst, M. (**1978**). ''Verification of the optimal probabilistic basis of aural processing in pitch of complex tones,'' J. Acoust. Soc. Am. **63**, 486–497.

Greenwood, D. D. (**1990**). ''A cochlear frequency-position function for several species—29 years later,'' J. Acoust. Soc. Am. **87**, 2592–2605.

Guinan, J. J. (**1996**). ''Physiology of olivocochlear efferents,'' in *The Cochlea*, edited by P. Dallos, A. N. Popper, and R. R. Fay (Springer Verlag, New York), pp. 435–502.

Hartmann, W. M., McAdams, S., and Smith, B. K. (**1986**). ''Matching the pitch of a mistuned harmonic in a complex tone,'' IRCAM technical report.

Hartmann, W. M. (**1988**). ''Pitch perception and the segregation and integration of auditory entities,'' in *Auditory Function—Neurological Bases of Hearing*, edited by G. M. Edelman, W. E. Gall, and W. M. Cowan (Wiley, New York), pp. 623–645.

Hartmann, W. M., McAdams, S., and Smith, B. K. (**1990**). ''Hearing a mistuned harmonic in an otherwise periodic complex tone,'' J. Acoust. Soc. Am. **88**, 1712–1724.

Hartmann, W. M., and Doty, S. L. (**1996**). ''On the pitches of the components of a complex tone,'' J. Acoust. Soc. Am. **99**, 567–578.

Helfert, R. H., and Aschoff, A. (**1997**). ''Superior olivary complex and nuclei of the lateral lemniscus,'' in *The Central Auditory System*, edited by G. Ehret and R. Romand (Oxford University Press, New York), pp. 193–258.

Helmholtz, H. v. (**1877**). *On the Sensations of Tone* (English translation A. J. Ellis, 1954) (Dover, New York).

Hukin, R. W., and Darwin, C. J. (**1995**). ''Comparison of the effect of onset asynchrony on auditory grouping in pitch matching and vowel identification,'' Percept. Psychophys. **57**, 191–196.

Irvine, D. R. F. (**1992**). ''Physiology of the auditory brainstem,'' in *The Mammalian Auditory Pathway: Neurophysiology*, edited by A. N. Popper and R. R. Fay (Springer Verlag, New York), pp. 153–231.

Joris, P. X., and Yin, T. C. T. (**1998**). ''Envelope coding in the lateral superior olive. III. Comparison with afferent pathways,'' J. Neurophysiol. **79**, 253–269.

Lea, A. (**1992**), ''Auditory models of vowel perception,'' Nottingham University unpublished doctoral dissertation.

Licklider, J. C. R. (**1951**). ''A duplex theory of pitch perception,'' Experientia **7**, 128–134.

Lin, J. L., and Hartmann, W. M. (**1997**). ''The pitch of mistuned harmonics: Evidence for a template model,'' J. Acoust. Soc. Am. **103**, 2608–2617.

Maas, W. (**1997a**). ''Networks of spiking neurons: the third generation of neural network models,'' Neural Networks **10**, 1659–1671.

Maas, W. (**1997b**). ''Fast sigmoidal networks via spiking neurons,'' Neural Comput. **9**, 279–304.

Meddis, R. (**1988**). ''Simulation of auditory-neural transduction: further studies,'' J. Acoust. Soc. Am. **83**, 1056–1063.

Meddis, R., and Hewitt, M. J. (**1991a**). ''Virtual pitch and phase sensitivity of a computer model of the auditory periphery. I: Pitch identification,'' J. Acoust. Soc. Am. **89**, 2866–2882.

Meddis, R., and Hewitt, M. J. (**1991b**). ''Virtual pitch and phase sensitivity of a computer model of the auditory periphery. II: Phase sensitivity,'' J. Acoust. Soc. Am. **89**, 2883–2894.

Meddis, R., and Hewitt, M. J. (**1992**). ''Modeling the identification of concurrent vowels with different fundamental frequencies,'' J. Acoust. Soc. Am. **91**, 233–245.

Meddis, R., and O'Mard, L. (**1997**). ''A unitary model of pitch perception,'' J. Acoust. Soc. Am. **102**, 1811–1820.
Moore, B. C. J. (**1973**). ''Frequency difference limens for short-duration tones,'' J. Acoust. Soc. Am. **54**, 610–619.
Moore, B. C. J. (**1977**). *An Introduction to the Psychology of Hearing* (Academic, London).
Moore, B. C. J. (**1987**). ''The perception of inharmonic complex tones,'' in *Auditory Processing of Complex Sounds*, edited by Y. A. Watson (Laurence Erlbaum, Hillsdale), pp. 180–189.
Moore, B. C. J., Peters, R. W., and Glasberg, B. R. (**1985**). ''Thresholds for the detection of inharmonicity in complex tones,'' J. Acoust. Soc. Am. **77**, 1861–1867.
Moore, B. C. J., Peters, R. W., and Glasberg, B. R. (**1986**). ''Thresholds for hearing mistuned partials as separate tones in harmonic complexes,'' J. Acoust. Soc. Am. **80**, 479–483.
Patterson, R. D., Robinson, K., Holdsworth, J., McKeown, D., Zhang, C., and Allerhand, M. (**1992**). ''Complex sounds and auditory images,'' in *Auditory Physiology and Perception*, edited by Y. Cazals, K. Horner, and L. Demany (Pergamon, Oxford), pp. 429–446.
Rhode, W. S., and Greenberg, S. (**1992**). ''Physiology of the cochlear nuclei,'' in *The Mammalian Auditory Pathway: Physiology*, edited by A. N. Popper and R. R. Fay (Springer Verlag, New York), pp. 94–152.
Roberts, B., and Brunstrom, J. M. (**1998**). ''Perceptual segregation and pitch shifts of mistuned components in harmonic complexes and in regular inharmonic complexes,'' J. Acoust. Soc. Am. **104**, 2326–2338.
Romand, R., and Avan, P. (**1997**). ''Anatomical and functional aspects of the cochlear nucleus,'' in *The Central Auditory System*, edited by G. Ehret and R. Romand (Oxford University Press, New York), pp. 97–191.
Sanes, D. H. (**1990**). ''An in vitro analysis of sound localization mechanisms in gerbil lateral superior olive,'' J. Neurosci. **10**, 3494–3506.
Scheffers, M. T. M. (**1983**). ''Sifting vowels,'' Gröningen unpublished doctoral dissertation.
Shofner, W. P. (**1998**). ''Evidence that primarylike units are the major CN subsystem which encodes pitch related information in their temporal discharge,'' ARO abstract #382.
Slaney, M. (**1990**). ''A perceptual pitch detector,'' Proc. ICASSP-90, pp. 357–360.
Slaney, M. (**1993**). ''An efficient implementation of the Patterson-Holdsworth auditory filter bank,'' Apple Computer technical report, 35.
Smith, P. H., Joris, P. X., and Yin, T. C. T. (**1998**). ''Anatomy and physiology of principal cells of the medial nucleus of the trapezoid body (MNTB) of the cat,'' J. Neurophysiol. **79**, 3127–3142.
Spangler, K. M., Warr, B., and Henkel, C. K. (**1985**). ''The projections of principal cells of the medial nucleus of the trapezoid body in the cat,'' J. Comp. Neurol. **238**, 249–262.
Srulovicz, P., and Goldstein, J. L. (**1983**). ''A central spectrum model: A synthesis of auditory-nerve timing and place cues in monaural communication of frequency spectrum,'' J. Acoust. Soc. Am. **73**, 1266–1276.
Summerfield, Q., and Culling, J. F. (**1992**). ''Periodicity of maskers not targets determines ease of perceptual segregation using differences in fundamental frequency,'' Proc. 124th meeting of the ASA, 2317(A).
Terhardt, E. (**1974**). ''Pitch, consonance and harmony,'' J. Acoust. Soc. Am. **55**, 1061–1069.
Terhardt, E. (**1979**). ''Calculating virtual pitch,'' Hearing Res. **1**, 155–182.
Warr, W. B. (**1992**). ''Organization of olivocochlear efferent systems in mammals,'' in *The Mammalian Auditory Pathway: Neuroanatomy*, edited by D. B. Webster, A. N. Popper, and R. R. Fay (Springer Verlag, New York), pp. 410–448.
Wickesberg, R. E., and Oertel, D. (**1990**). ''Delayed, frequency-specific inhibition in the cochlear nuclei of mice: A mechanism for monaural echo suppression,'' J. Neurosci. **10**, 1762–1768.
Wightman, F. L. (**1973**). ''The pattern-transformation model of pitch,'' J. Acoust. Soc. Am. **54**, 407–416.

Further evaluation of a model of loudness perception applied to cochlear hearing loss

Brian C. J. Moore,[a] Brian R. Glasberg, and Deborah A. Vickers
Department of Experimental Psychology, University of Cambridge, Cambridge CB2 3EB, England

(Received 3 August 1998; revised 8 February 1999; accepted 25 March 1999)

This paper describes further tests of a model for loudness perception in people with cochlear hearing loss. It is assumed that the hearing loss (the elevation in absolute threshold) at each audiometric frequency can be partitioned into a loss due to damage to outer hair cells (OHCs) and a loss due to damage to inner hair cells (IHCs) and/or neurons. The former affects primarily the active mechanism that amplifies the basilar membrane (BM) response to weak sounds. It is modeled by increasing the excitation level required for threshold, which results in a steeper growth of specific loudness with increasing excitation level. Loss of frequency selectivity, which results in broader excitation patterns, is also assumed to be directly related to the OHC loss. IHC damage is modeled by an attenuation of the calculated excitation level at each frequency. The model also allows for the possibility of complete loss of IHCs or functional neurons at certain places within the cochlea (''dead'' regions). The parameters of the model (OHC loss at each audiometric frequency, plus frequency limits of the dead regions) were determined for three subjects with unilateral cochlear hearing loss, using data on loudness matches between sinusoids presented alternately to their two ears. Further experiments used bands of noise that were either 1-equivalent rectangular bandwidth (ERB) wide or 6-ERBs wide, centered at 1 kHz. Subjects made loudness matches for these bands of noise both within ears and across ears. The model was reasonably accurate in predicting the results of these matches without any further adjustment of the parameters. © *1999 Acoustical Society of America.* [S0001-4966(99)01707-5]

PACS numbers: 43.66.Cb, 43.66.Sr, 43.66.Ba [RVS]

INTRODUCTION

In a previous paper (Moore and Glasberg, 1997) we described a model of loudness perception for people with cochlear hearing loss. The model was developed from a model of loudness perception for normal hearing (Moore and Glasberg, 1996), that was in turn developed from a model originally proposed by Zwicker and co-workers (Zwicker, 1958; Zwicker and Scharf, 1965; Zwicker *et al.*, 1984; Zwicker and Fastl, 1990). A similar model was proposed even earlier by Fletcher and Munson (1937). The model is largely based on psychoacoustical data, but it nevertheless uses concepts derived from physiology, and the stages in the model are intended to approximately represent stages of physiological processing.

The model has four stages. The first stage is a fixed filter to account for the transmission of sound through the outer and middle ear. The next stage is the calculation of an excitation pattern for the sound under consideration; for a detailed description of the concept of the excitation pattern, see Moore (1997). Briefly, the excitation pattern can be thought of as representing the distribution of excitation at different points along the basilar membrane (BM), although the calculated patterns do not fully take into account the compression that occurs on the BM; input–output functions on the BM show a strong compressive nonlinearity for mid-range sound levels for frequencies close to the characteristic frequency (CF), but are nearly linear for frequencies well below CF (Sellick *et al.*, 1982; Robles *et al.*, 1976; Ruggero *et al.*, 1997). This difference between tones close to CF and tones well below CF is reflected in the fact that the calculated excitation pattern for a sinusoid grows more rapidly with increasing level on its high-frequency side than around the tip. However, in contrast to physiological measures of BM responses, the excitation pattern grows *linearly* around the tip and *expansively* on the high-frequency side, which reflects the properties of the masking patterns which were originally used to develop the concept of the excitation pattern (Fletcher, 1940; Zwicker, 1956). At a later stage in the model (see below for details), the excitation at each frequency is subjected to a compressive nonlinearity, which is intended to include the effects of the compression on the BM. The model is unrealistic in the sense that the filtering on the BM and the nonlinear input–output function on the BM are not two separate processes. Nevertheless, the end result in the model is probably similar to what would be obtained using a more realistic model of BM responses, such as proposed by Giguère and Woodland (1994).

The excitation patterns are calculated from the outputs of auditory filters, which represent frequency selectivity at specific center frequencies. The auditory-filter shapes are derived from psychoacoustical experiments on masking (Glasberg and Moore, 1990). The frequency scale of the excitation pattern is translated into a scale that is related to how the sound is represented in the auditory system. This scale is based on the equivalent rectangular bandwidth (ERB) of the auditory filter, which is closely related to the ''critical band-

[a]Author to whom correspondence should be addressed. Electronic mail: bcjm@cus.cam.ac.uk

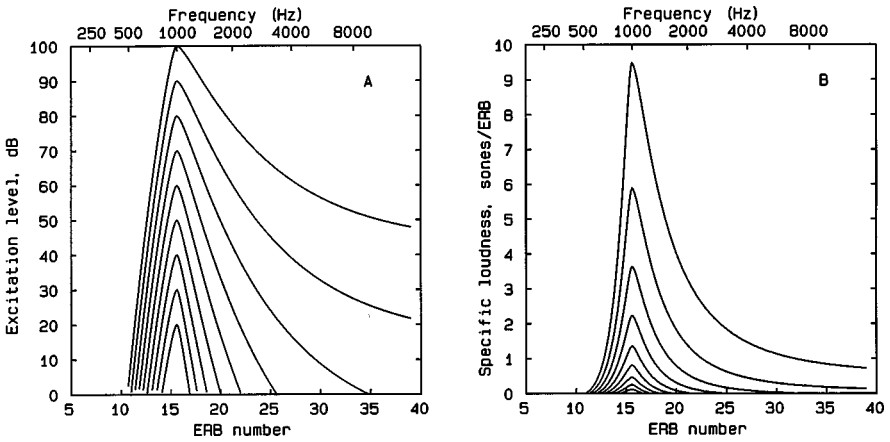

FIG. 1. Panel (A) shows calculated excitation patterns for a 1-kHz tone at levels ranging from 20 to 100 dB in 10-dB steps. The abscissa is plotted with ERB number along the bottom, with the corresponding frequency in Hertz plotted at the top. Panel (B) shows specific loudness patterns corresponding to the excitation patterns shown in panel (A).

width'' Zwicker, 1961; Scharf, 1970); each ERB corresponds roughly to a constant distance of about 0.89 mm along the BM (Greenwood, 1961, 1990; Moore, 1986). Excitation patterns of a 1000-Hz sinusoid for a normal ear are plotted in panel A of Fig. 1 for input levels of the sinusoid from 20 to 100 dB SPL. The scale at the top of the figure shows the frequency corresponding to the ERB number at the bottom of the figure. The frequency of 1000 Hz corresponds to an ERB number of 15.62.

The next stage is a transformation from excitation level to specific loudness, *N*, which is the loudness per ERB. The specific loudness is a kind of loudness density. It represents the loudness that would be evoked by the excitation within a 0.89-mm range on the BM if it were possible to present that excitation alone (without any excitation at adjacent regions on the BM). There is a compressive relationship between excitation and specific loudness; when the excitation is doubled, the specific loudness grows by less than a factor of 2. In fact, for values of the excitation well above the threshold value, the specific loudness grows by a factor of only about 1.15 when the excitation is doubled. The relationship between excitation and specific loudness is plotted in Fig. 2 for a series of values of the excitation level at absolute threshold, L_{ETHRQ}. The value of *N* is plotted on a logarithmic scale as a function of excitation level in decibels (also a log scale). The steepness of the initial part of the curves depends on the value of L_{ETHRQ}; the higher L_{ETHRQ}, the steeper the curve. Thus, the functions show a recruitment-like effect, since higher thresholds are associated with steeper functions.

The compressive nonlinearity in the model can be thought of as representing the overall effects of the transformation from the physical stimulus to neural activity. At least two nonlinearities contribute to this overall effect: the compressive nonlinearity of the BM input–output function, and the nonlinear transformation from BM velocity or amplitude to neural activity (Yates, 1990).

If the specific loudness is plotted as a function of ERB number, the resulting pattern is called a *specific loudness pattern*. Examples of specific loudness patterns are shown in panel (B) of Fig. 1. The overall loudness of a given sound, in sones, is assumed to be equal to the sum of the loudness in each ERB. This is equal to the total area under the specific loudness pattern plotted as *N* versus ERB. Thus, the loudness of any sound, including a single sinusoid, is assumed to depend partly on the spreading of excitation along the BM. Note that the exact neural code corresponding to the specific loudness is not specified. It might correspond to the summed neural activity (for example, total spikes per second) in neurons with CFs within a specific range, in which case the overall loudness would correspond to the total neural activity in the auditory nerve. This has often been assumed in the past, although the validity of the assumption has recently been questioned (Relkin and Doucet, 1997). An alternative possibility is that specific loudness is represented in the relative activity of neurons with different thresholds and dynamic ranges. The model does not require the code to be known. It simply assumes that there is a compressive relationship between excitation and specific loudness and that the overall loudness corresponds to the sum of the specific loudness across frequency.

Consider now the application of the model to cochlear hearing loss. The elevation of absolute threshold due to cochlear hearing loss can occur in two main ways. First, dam-

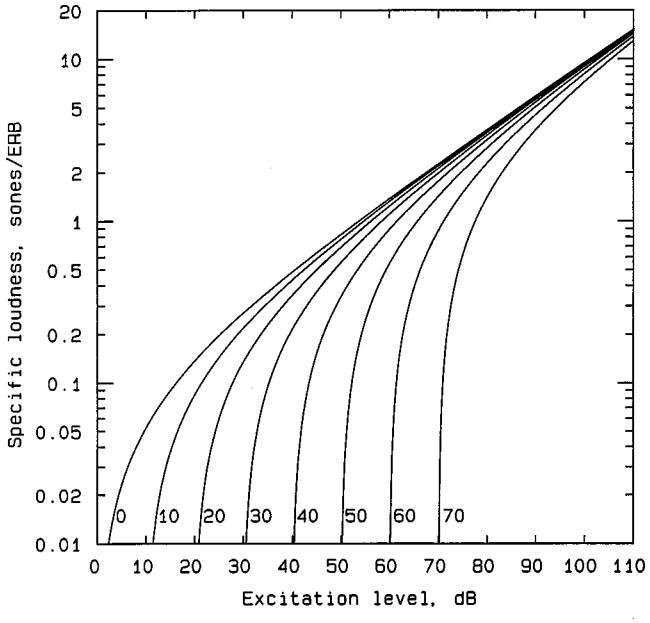

FIG. 2. Functions relating specific loudness (log scale) to excitation level in dB. The parameter is the absolute threshold in dB, which is indicated by a number next to each curve.

age to the OHCs impairs the operation of the ''active mechanism'' that amplifies the BM response to weak sounds (Moore, 1995; Yates, 1995). This results in reduced BM amplitude of vibration for a given low sound level. Hence, the sound level has to be increased to give a just-detectable amount of vibration. Second, IHC damage can result in reduced efficiency of transduction, so the amount of BM vibration needed to reach threshold is higher than normal. In principle, it is possible to partition the overall hearing loss (in dB) at a given frequency into a component due to OHC damage and a component due to IHC (and neural) damage:

$$HL_{TOTAL} = HL_{OHC} + HL_{IHC}. \quad (1)$$

For example, if the total hearing loss at a given frequency is 60 dB, 40 dB of that loss might be due to OHC damage and 20 dB to IHC damage. In the model, it is assumed that HL_{OHC} cannot be greater than 65 dB for frequencies of 2 kHz and above and 55 dB for frequencies below that; these limits are based on physiological estimates of the maximum gain provided by the cochlear active mechanism (Yates, 1995; Ruggero *et al.*, 1997), although it must be acknowledged that there is considerable uncertainty associated with these estimates. Any loss greater than this is assumed to reflect a mixture of OHC loss and IHC loss. Hearing losses less than this may also reflect a mixture of OHC loss and IHC loss. Note that the proportion of a hearing loss that is attributed to OHC or IHC damage is not the same as the proportion of OHCs and IHCs that are damaged or lost. In the above example, 40 dB of the hearing loss was attributed to OHC damage and 20 dB to IHC damage, but this does *not* imply that damage to the OHCs was twice as great as damage to IHCs.

Damage to the OHCs is modeled by increasing the value of L_{ETHRQ}, which results in a steeper growth of specific loudness with increasing excitation level; see Fig. 2. This mimics the reduction in or loss of the compressive nonlinearity in the input–output function of the BM, which is mainly associated with OHC damage (Ruggero and Rich, 1991; Moore, 1995); the perceptual consequence of this is loudness recruitment (Yates, 1990; Moore, 1995). IHC damage is modeled by an attenuation of the calculated excitation level at each frequency, following a suggestion of Launer (Launer, 1995; Launer *et al.*, 1997).

Frequency selectivity is usually reduced in cases of cochlear hearing loss; for reviews, see Tyler (1986) and Moore (1995). For a sinusoidal stimulus, this leads to an excitation pattern which is broader in an impaired ear than in a normal ear. Moore and Glasberg (1997) developed a series of equations that described empirically how the sharpness of the auditory filters varied with input sound level and with hearing loss. The degree of broadening with hearing loss was assumed to depend specifically on HL_{OHC} rather than on HL_{TOTAL}. Excitation patterns calculated using these equations become broader with increasing hearing loss, but the patterns change less in shape with level as the hearing loss increases. These broader excitation patterns are used in the loudness model.

The model also allows for the possibility of complete loss of IHCs, or functional neurons, at certain places within the cochlea. These places are referred to as ''dead regions'' (Moore, 1995; Moore *et al.*, 1997b). In this paper, a dead region is described in terms of the range of characteristic frequencies (CFs) that would normally be associated with that region. Say, for example, that the IHCs are nonfunctioning over a region of the BM having CFs in the range 4000 to 10 000 Hz. This is described as a dead region extending from 4000 to 10 000 Hz. Dead regions are not necessarily easily identified from the pure-tone audiogram. For example, when there is a low-frequency dead region, low frequencies may be detected using the responses of neurons with CFs above the dead region (Thornton and Abbas, 1980; Florentine and Houtsma, 1983) This can lead to a relatively ''flat'' hearing loss at low frequencies. Ways of identifying dead regions are described in Moore and Glasberg (1997) and in Moore (1998). In the loudness model, excitation at places corresponding to dead regions is set to a very low value, which leads to zero specific loudness.

In our previous paper (Moore and Glasberg, 1997), the model was evaluated using data obtained in our laboratory from subjects with unilateral or highly asymmetric hearing losses, who were required to make loudness matches between sinusoids presented alternately to the two ears. An example of the data and of the predictions of the model is shown in Fig. 3. The subject whose data are shown, who also took part in the present experiment, was assumed to have a dead region at low frequencies (up to 280 Hz) in her impaired ear. For the subjects tested by Moore and Glasberg, it was possible to determine precisely the parameters required by the model.

The model was also evaluated using data in the literature on loudness summation. In normally hearing subjects, if the bandwidth of a sound, such as a noise, is varied keeping the *overall* intensity fixed, the loudness remains constant as long as the bandwidth is less than a certain value, called the critical bandwidth (CB) for loudness. If the bandwidth is increased beyond the CB, the loudness increases (Zwicker *et al.*, 1957). The reason for this effect can be understood by considering how specific loudness patterns change with bandwidth. With increasing bandwidth up to the CB, the specific loudness patterns become lower at their tips, but broader; the decrease in area around the tip is almost exactly canceled by the increase on the skirts, so that the total area remains almost constant (Moore and Glasberg, 1986; Moore *et al.*, 1997a). When the bandwidth is increased beyond the CB, the increase on the skirts is greater than the decrease around the tip, and the total area, and hence the predicted loudness, increases. Since the increase depends on the summation of specific loudness at different CFs, the increase in loudness is often described as *loudness summation*.

Loudness summation is usually reduced in people with cochlear hearing loss; the increase in loudness with increasing bandwidth is less than occurs in normally hearing people (Scharf and Hellman, 1966; Bonding, 1979; Florentine and Zwicker, 1979; Bonding and Elberling, 1980). Often, the experiments have involved comparisons of loudness between narrow-band noises and broadband noises. Typically, one sound, the reference sound, is fixed in level, and the other sound, the comparison sound, is adjusted in level to achieve

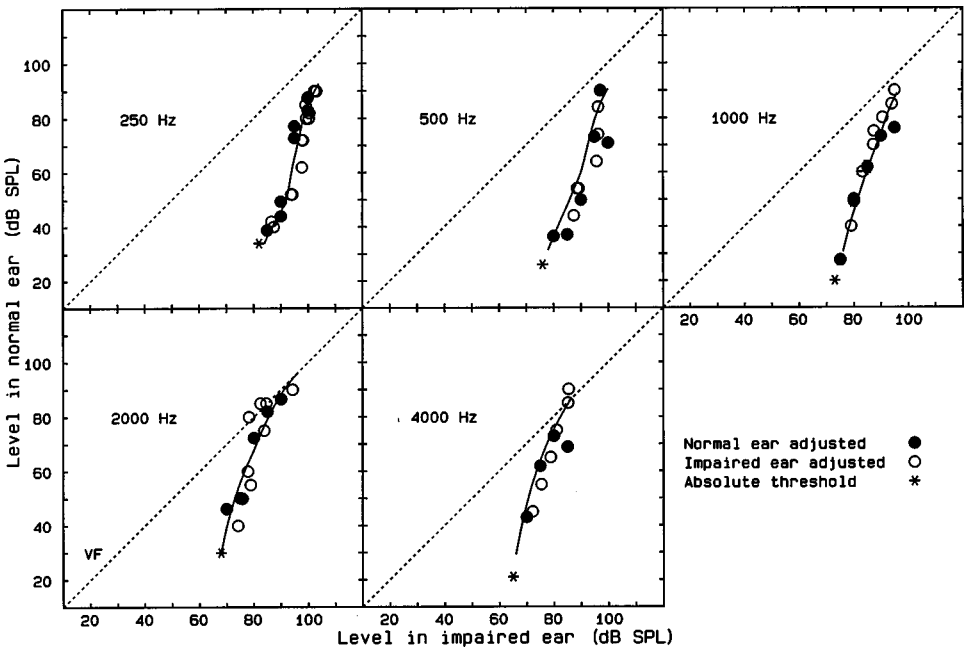

FIG. 3. Loudness-matching functions for subject VF for sinusoidal stimuli with frequencies of 250, 500, 1000, 2000, and 4000 Hz. Each panel shows results for a different signal frequency. Asterisks show the absolute threshold for each ear. The curves show predictions of the loudness model. The diagonal dotted lines indicate equal levels in the two ears. The data are taken from Moore and Glasberg (1997).

equal loudness. The two sounds are alternated. For normally hearing subjects, the level of the sound with the greater bandwidth is usually lower than that of the sound with the narrower bandwidth, at the point of equal loudness. The extent of this level difference, ΔL, varies with overall level, being greatest at moderate sound levels (Zwicker *et al.*, 1957; Zwicker and Scharf, 1965; Bonding, 1979; Bonding and Elberling, 1980; Zwicker and Fastl, 1990). For hearing-impaired subjects, the value of ΔL is usually markedly smaller than normal (Scharf and Hellman, 1966; Bonding, 1979; Florentine and Zwicker, 1979; Bonding and Elberling, 1980).

Previously, we used the model to fit data in the literature on loudness summation in hearing-impaired subjects (Moore and Glasberg, 1997). However, the parameters required by the model could not be determined precisely; we simply chose ''reasonable'' values. The model fitted the data quite well, but there was not independent verification that the parameters used were appropriate for the specific subjects who had been tested.

In the present paper, we provide a more rigorous evaluation of how well the model can account for changes in loudness with bandwidth for subjects with cochlear hearing loss. The earlier data on pure-tone loudness matching obtained for three subjects with unilateral cochlear hearing loss were used to fix the parameters of the model for each subject. Those same subjects took part in an experiment using bands of noise that were either 1- or 6-ERBs wide. Subjects made loudness matches for these bands of noise both within each ear and across ears. We then determined how well the model could predict these data, without any further adjustment of the parameters.

I. THE EXPERIMENT—LOUDNESS MATCHING FOR BANDS OF NOISE

A. Subjects

Three subjects with unilateral or highly asymmetric cochlear hearing loss were used; AW, VF, and DF. Full details of the subjects are given in our earlier paper (Moore and Glasberg, 1997). The absolute thresholds of the subjects are given in Table I. At the time of testing with the noise bands used in the present study, the hearing of AW in his better ear had deteriorated somewhat, relative to that measured at the time of the earlier experiment. For his poorer ear, and for all ears of the other subjects, absolute thresholds were essentially the same as for the earlier experiment. Thresholds are specified in dB HL, but were actually measured in dB SPL using Sennheiser HD 414 earphones and an adaptive two-alternative forced-choice procedure. They were converted to dB HL from the measured frequency response of the HD 414 earphones at the eardrum (Rastronic Portarem 2000 probe microphone measurement system), together with estimates of the minimum audible pressure (MAP) at the eardrum for monaural listening (Killion, 1978).

Table I also shows the values of HL_{OHC} and the frequency limits of the dead region that were assumed for each subject. The values of HL_{OHC} were chosen to give the best fit to the loudness-matching data for sinusoids described in the earlier paper (Moore and Glasberg, 1997). This was not done using a rigorous fitting procedure; rather, the values were adjusted ''by hand'' until good fits were obtained. Generally, the steeper the rate of loudness growth in a given ear at a given frequency, the greater the value of HL_{OHC} for that ear and frequency. Note that values of HL_{OHC} are given even for frequencies within the assumed dead region. This is done since, for stimuli with frequencies falling in the dead region, the spread of excitation to adjacent frequency regions is determined by the values of HL_{OHC}. Evidence for the dead regions was obtained in two ways. First, subjective reports of the subjects indicated that pure tones sounded distorted or noise-like when they fell within the frequency range corresponding to the dead region. Second, measures of psychophysical tuning curves (PTCs) showed that the tips of the tuning curves were shifted away from the frequency of the signal when the signal was presented within the frequency range corresponding to the dead region (Thornton and Ab-

TABLE I. Values of the absolute threshold (HL_{TOTAL}, dB HL) for the impaired (worse) ear of each subject and values of the parameters assumed in the model. The table also shows absolute thresholds for the better ear. Values of HL_{OHC} for the better ear were assumed to be 80% of these values.

			Frequency, kHz							
Subject	Ear		0.125	0.25	0.5	1.0	2.0	4.0	6.0	8.0
VF	Worse	HL_{TOTAL}	62	63	62	63	60	54	47	40
		HL_{OHC}	30	30	30	43	50	45	45	40
		Frequency limits of ''dead'' region, kHz 0.0, 0.28								
	Better	HL_{TOTAL}	15	15	12	9	22	10	18	25
AW	Worse	HL_{TOTAL}	67	67	78	70	61	66	75	81
		HL_{OHC}	35	35	40	40	46	55	55	55
		Frequency limits of ''dead'' region, kHz 0.28, 1.0								
	Better	HL_{TOTAL}	10	10	13	10	26	39	49	60
DF	Worse	HL_{TOTAL}	67	67	75	68	60	55	65	65
		HL_{OHC}	20	20	20	20	30	35	65	65
		Frequency limits of ''dead'' region, kHz 0.1, 0.5								
	Better	HL_{TOTAL}	0	0	10	6	9	14	35	40

bas, 1980; Florentine and Houtsma, 1983; Moore, 1998). The exact frequency limits of the dead region were adjusted so that the model predicted with reasonable accuracy the absolute threshold at frequencies within the dead region; see Moore and Glasberg (1997).

B. Method

The subjects were required to make loudness matches between bands of noise. One sound, the reference sound, was fixed in level, and the other sound, the comparison sound, was varied in level to achieve equal loudness. Each sound was gated with a 200-ms steady-state portion and 10-ms raised-cosine rise and fall times. The two sounds were presented in regular alternation with 500-ms interstimulus intervals. When the reference sound was presented to the normal ear, its level ranged from 20 to 90 or 100 dB SPL. When the reference sound was presented to the impaired ear, its level ranged from 10 to 90 or 100 dB SPL. The starting level of the comparison sound was chosen randomly from within the range of levels from 20 dB above absolute threshold (20 dB SL) to 85 dB SPL for the better ear and 10 dB SL to 95 dB SPL for the poorer ear. Subjects could press one button to increase the level of the comparison sound, and another to decrease its level. If no button was pressed, then the level stayed the same indefinitely. A change from pressing one button to pressing the other was called a turnaround. The step size for the change in level of the comparison sound was 3 dB until two turnarounds had occurred, and was 1 dB thereafter. Subjects were instructed to ''bracket'' the point of equal loudness several times, by making the comparison sound clearly louder than the reference sound and then clearly softer, and then to use the buttons to make the two sounds equal in loudness. When they were satisfied that the two sounds were equally loud, a third button was pressed, which terminated the run. The final adjusted level was taken as the point of equal loudness. A record was kept of the levels visited during a run, to check that subjects had bracketed the match as instructed, and to check that the smaller step size had been reached. If this was not the case, subjects were reinstructed, and additional measurements were taken. For each level of the reference sound, five matches were obtained. Results presented are the means of the five matches. To reduce bias effects, when two sounds, A and B, were being compared, on half of the trials A was the reference sound, and on half the trials B was the reference sound. Subjects were trained for several hours before data collection started.

Loudness recruitment severely limited the range of levels that could be used in the impaired ear. At low sensation levels of the reference sound, subjects complained that when they tried to use the bracketing procedure, the comparison sound sometimes became inaudible. At high levels of the reference sound, subjects were reluctant to use the bracketing procedure because this would require making the comparison sound uncomfortably loud. Results will only be presented for levels of the reference sound for which the bracketing procedure could be used reliably.

Stimuli were digitally generated using a Tucker-Davis Technologies (TDT) AP2 array processor in a host PC connected via an optical interface to a 16-bit digital-to-analog converter (TDT PD1, 32 768-Hz sampling rate). Stimulus levels were controlled by TDT PA4 programmable attenuators. Two noise bands were used, both centered at 1000 Hz, with bandwidths of 1 ERB (934–1066 Hz) and 6 ERBs (602–1398 Hz). ERB values were taken from Glasberg and Moore (1990). The noise bands were initially generated in the frequency domain. Two 16 384-point buffers, representing the real and imaginary parts of the spectrum up to the Nyquist frequency, were loaded with independent Gaussian-distributed random numbers over the range corresponding to the desired band and were set to zero outside this range. The edge frequencies were specified with 1-Hz resolution. An inverse fast Fourier transform (FFT) was then used to give a 1-s noise buffer; the spectral components had a random phase and the envelope had a Rayleigh distribution. The stimulus to be presented on each trial was chosen randomly from within the 1-s buffer, and the 10-ms raised-cosine ramps were applied digitally. A new 1-s noise buffer was generated at the start of each run.

Stimuli were delivered using Sennheiser HD414 earphones. Although these are an ''open-air'' design, the cross-talk between the ears is low. Using a probe microphone in

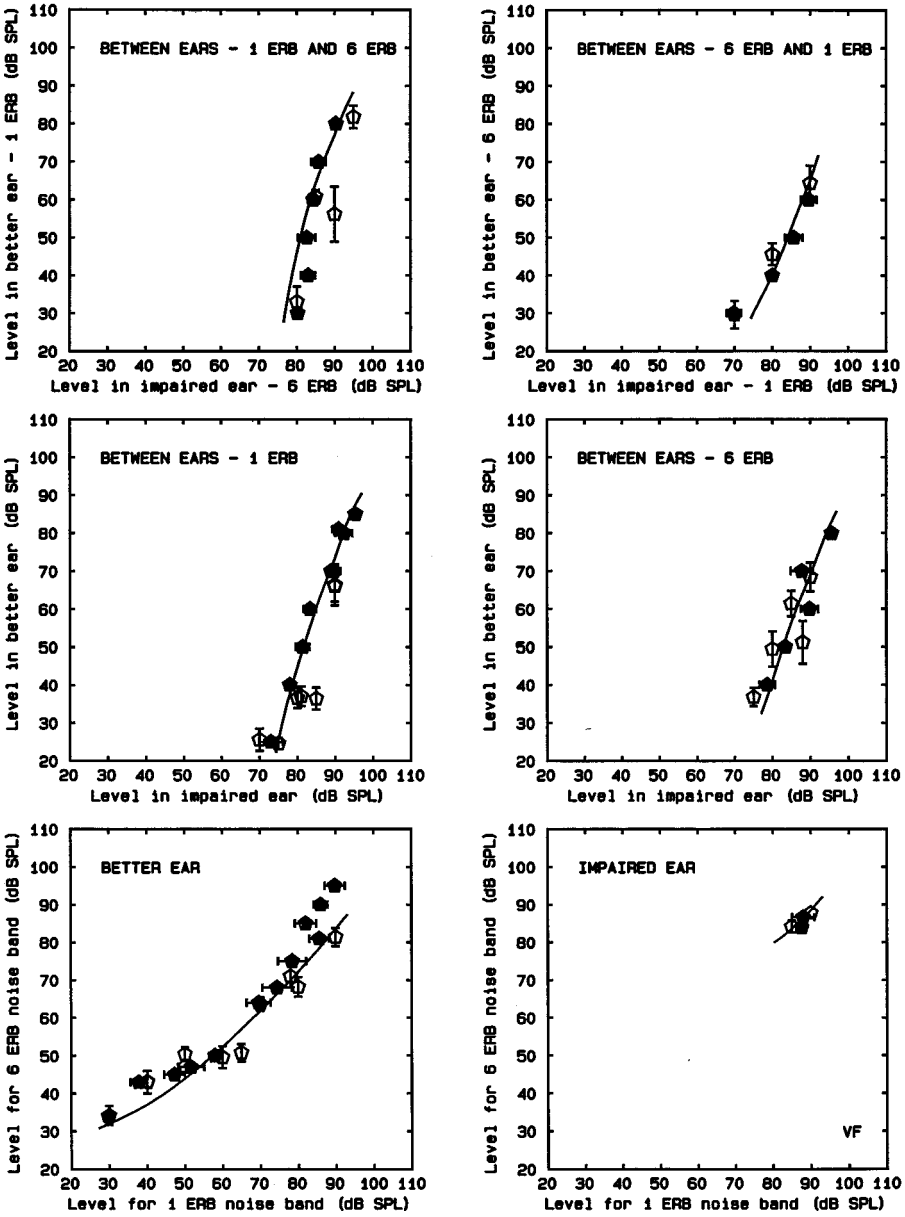

FIG. 4. Loudness-matching functions for noise bands of width either 1 or 6 ERBs for subject VF. Each panel shows results for one of the six conditions described in the text. The stimulus levels are specified as overall level defined in terms of the voltage delivered to the earphone. Open symbols indicate that the sound whose level is plotted on the abscissa was fixed in level (reference sound), while the sound whose level is plotted on the ordinate was varied in level (comparison sound). Filled symbols indicate the reverse. Each point is based on the mean of five matches. Error bars indicate ±one standard deviation. Lines show predictions of the loudness model. The model took into account the frequency response of the earphone.

one ear canal, with a sound delivered via an earphone on the other ear, the cross-talk was measured to be at least 65 dB down at 1 kHz. Of course, some sound would be transmitted to the contralateral ear via bone conduction. However, the interaural cross-talk produced in this way is probably more than 65 dB down (Zwislocki, 1953). Subjects were tested in a double-walled sound-attenuating chamber.

Loudness matches were made both within and across ears. Specifically, the following conditions were used:

(1) 1-ERB wide in the normal ear matched with 1-ERB wide in the impaired ear.
(2) 6-ERBs wide in the normal ear matched with 6-ERBs wide in the impaired ear.
(3) 6-ERBs wide in the normal ear matched with 1-ERB wide in the impaired ear.
(4) 1-ERB wide in the normal ear matched with 6-ERBs wide in the impaired ear.
(5) 6-ERBs wide in the normal ear matched with 1-ERB wide in the normal ear.
(6) 6-ERBs wide in the impaired ear matched with 1-ERB wide in the impaired ear.

When both noises were presented to the impaired ear, a continuous pink noise was presented to the normal ear to prevent ''cross hearing.'' The noise had a spectrum level of 25 dB at 1 kHz (*re* 20 μPa). When the noises were balanced across ears, subjects were asked to confirm that the two noises were heard in opposite ears. This was always the case.

C. Results

The results are shown in Figs. 4, 5, and 6 for subjects VF, AW, and DF, respectively. The curves show predictions of the loudness model, using the parameters derived from the data for pure-tone loudness matching (Moore and Glasberg, 1997). For all subjects, it was assumed that HL_{OHC} for the better ear was 80% of HL_{TOTAL}. The predictions were derived by calculating loudness as a function of overall level for each ear and each noise band. The resulting functions

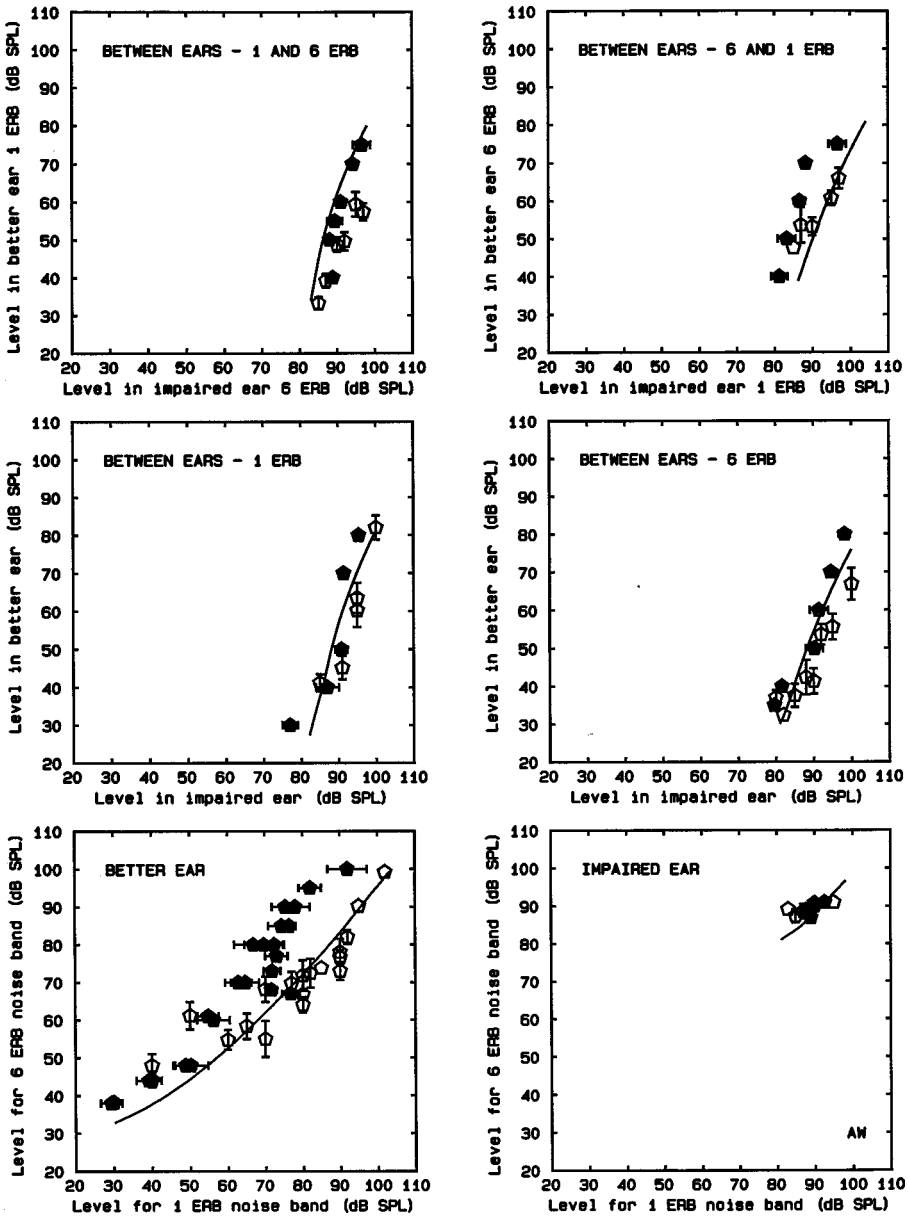

FIG. 5. As Fig. 4, but for subject AW.

were used to determine levels that would give equal loudness for the six conditions that were described earlier.

Subjects reported that the task was more difficult when they were required to match the loudness of two noise bands with different widths (1 ERB versus 6 ERBs) than when they were matching the loudness of the same noise band across ears. This is reflected in the variability of the data, which was greater in the former case, especially for subject AW. Subject AW also showed rather large bias effects, which can be clearly seen in the bottom-left panel of Fig. 5. For the higher levels, results differed markedly depending on which sound was adjusted in level (compare the filled symbols with the open symbols). Generally, this bias can be interpreted as a reluctance to adjust the comparison sound to a higher loudness.

The results for the better ears matching 6-ERBs-wide noise with 1-ERB-wide noise (bottom-left panels) show a pattern broadly consistent with what would be expected from prior work on loudness summation (Zwicker *et al.*, 1957; Zwicker and Fastl, 1990), although the results for AW show quite a lot of scatter. For mid-range sound levels, equal loudness is achieved when the 6-ERBs-wide noise is somewhat lower in overall level than the 1-ERB-wide noise; this is the classical loudness summation effect. The effect is somewhat reduced for very low levels and very high levels. The model reproduces this aspect of the results. However, the data tend to lie slightly above the predictions, perhaps suggesting that the model predicts ''too much'' loudness summation.

The results for the impaired ears matching 6-ERBs-wide noise with 1-ERB-wide noise (bottom-right panels) cover only a small range of levels, owing to the restricted dynamic ranges of the subjects in their impaired ears. The results show less loudness summation than for the normal ears; the 6-ERBs-wide noise matches the loudness of the 1-ERB-wide noise when the overall levels of the noises are roughly equal. This is consistent with previous work on loudness summation in hearing-impaired subjects (Bonding, 1979; Florentine and Zwicker, 1979; Launer, 1995; Launer *et al.*, 1997), and it is predicted by the model.

The results of loudness matches across the two ears for

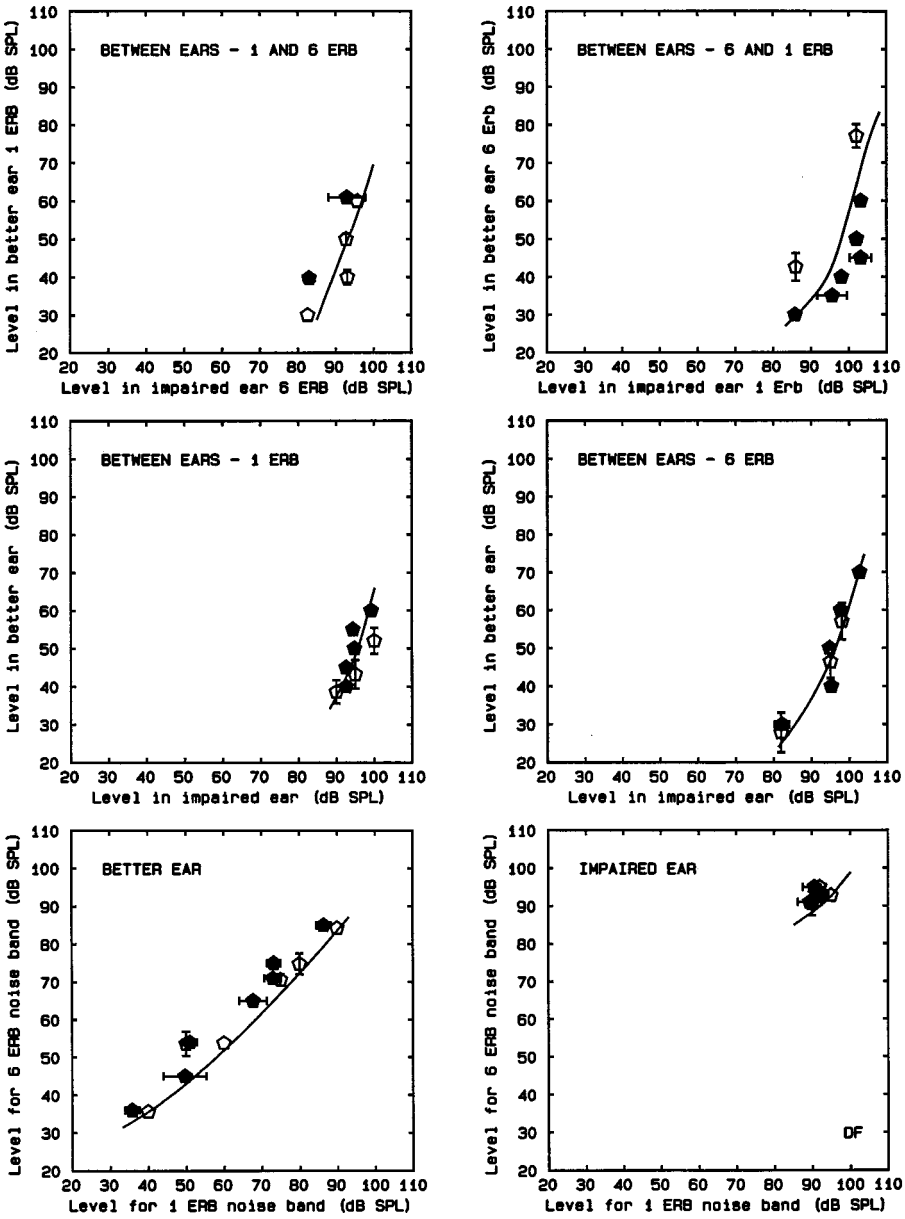

FIG. 6. As Fig. 4, but for subject DF.

1-ERB-wide noise (left column, middle panel) show the expected recruitment effect, although the results for DF show only partial recruitment; even at high levels the level in the better ear required for equal loudness was markedly lower than that in the impaired ear. The data are similar to those obtained using the same subjects with 1-kHz sinusoidal stimuli. The data show a reasonably small scatter, and the predictions of the model fit the data very well. The results of loudness matches across the two ears for 6-ERB-wide noise (right column, middle panel) also show a recruitment effect. Again, the data show a reasonably small scatter, although the results for AW show a clear bias effect relating to which sound was adjusted; the open symbols mostly lie below the filled symbols. The predictions of the model fit the data well.

Subjects reported that matching the loudness of two different noise bands across the two ears (top row, left and right panels) was very difficult. This is reflected in the somewhat larger scatter of the data, especially for subject DF. This subject refused to make more than a few matches in these two conditions, saying that the task was too difficult. Overall, the predictions of the model fit the data reasonably well, especially for subject VF, for whom the scatter in the data was smallest.

II. DISCUSSION

These results provide further validation of the loudness model as applied to cochlear hearing loss. They show that parameters of the model derived from loudness matches between the two ears for pure tones can be used to predict the results of loudness matches for noise bands of different widths, both within and across ears. The validity of the loudness model for complex stimuli is important, since the model has been applied to the initial fitting of both linear and compression hearing aids, based on the calculated specific loudness patterns for speech-shaped noise (Moore and Glasberg, 1998; Moore *et al.*, 1999 a,b).

One limitation of the model is that, in common with other loudness models, it is applicable only to steady sounds of reasonably long duration. The model uses as its input the

power spectrum of the sounds. Loudness calculations based on the long-term power spectrum of sounds might be in error for sounds that are strongly modulated or time varying, such as speech. However, Moore *et al.* (Moore *et al.*, 1998, 1999c) have shown for a variety of amplitude-modulated sounds, including sinusoidally modulated sinusoids, sinusoidally modulated speech-shaped noise, and speech-shaped noise modulated with the envelope of a single talker, that the overall loudness impression for each sound is similar to that produced by a corresponding unmodulated sound when the sounds are matched in terms of their long-term power spectrum. Thus, the model is unlikely to give predictions that are seriously in error for time-varying sounds.

It should be acknowledged that the model is almost certainly wrong in some respects. For example, the model does not take into account the possible effects of suppression on loudness (Houtgast, 1974). This may account for the fact that, when used to predict *partial* loudness for normally hearing subjects, the model underestimates the loudness reduction of a tone produced by background noise with a spectral notch at the signal frequency (Moore *et al.*, 1985). However, the predictions of the model are reasonably accurate for tones, including complex tones, presented in broadband noise backgrounds (Moore and Glasberg, 1996; Moore *et al.*, 1997a). In any case, the model as applied to hearing impairment has not yet been extended to allow the prediction of partial loudness. For predicting the loudness of sounds in quiet, the model appears to be rather accurate, both for normal and for hearing-impaired subjects.

III. SUMMARY

We have described a loudness model which attempts to relate changes in loudness perception produced by cochlear damage to the underlying physiological causes, specifically damage to the OHCs and IHCs. The former is modeled by a raised internal threshold (L_{ETHRQ}), which also leads to a steepening of the function relating specific loudness to excitation. The latter is modeled by an attenuation of the excitation level. The model also incorporates the effects of reduced frequency selectivity and the existence of dead regions within the cochlea. The present paper provided a test of the accuracy with which the model could predict data on loudness summation for three subjects with unilateral or highly asymmetric cochlear hearing loss. The parameters of the model (OHC loss at each audiometric frequency, plus frequency limits of the dead regions) had been determined previously for these subjects using data on loudness matches between sinusoids presented alternately to their two ears. We described further experiments using bands of noise that were either 1-ERB or 6-ERBs wide, centered at 1 kHz. Subjects made loudness matches for these bands of noise both within ears and across ears. The model was reasonably accurate in predicting the results of these matches without any further adjustment of the parameters. We can conclude that the model as applied to cochlear hearing loss can account for the loudness of narrow-band sounds as a function of level, and for changes in loudness with bandwidth.

ACKNOWLEDGMENTS

This work was supported by the Medical Research Council, The European Union, and the British–German Academic Research Collaboration (ARC) Program. We thank Joseph Alcántara for helpful comments on earlier versions of this paper and Tom Baer for writing the computer program to run the experiments. We also thank Chris Turner and an anonymous reviewer for their comments on an earlier version of this paper.

Bonding, P. (**1979**). ''Critical bandwidth in loudness summation in sensorineural hearing loss,'' Br. J. Audiol. **13**, 23–30.

Bonding, P., and Elberling, C. (**1980**). ''Loudness summation across frequency under masking and in sensorineural hearing loss,'' Audiology **19**, 57–74.

Fletcher, H. (**1940**). ''Auditory patterns,'' Rev. Mod. Phys. **12**, 47–65.

Fletcher, H., and Munson, W. A. (**1937**). ''Relation between loudness and masking,'' J. Acoust. Soc. Am. **9**, 1–10.

Florentine, M., and Houtsma, A. J. M. (**1983**). ''Tuning curves and pitch matches in a listener with a unilateral, low-frequency hearing loss,'' J. Acoust. Soc. Am. **73**, 961–965.

Florentine, M., and Zwicker, E. (**1979**). ''A model of loudness summation applied to noise-induced hearing loss,'' Hearing Res. **1**, 121–132.

Giguère, C., and Woodland, P. C. (**1994**). ''A computational model of the auditory periphery for speech and hearing research. I. Ascending path,'' J. Acoust. Soc. Am. **95**, 331–342.

Glasberg, B. R., and Moore, B. C. J. (**1990**). ''Derivation of auditory filter shapes from notched-noise data,'' Hearing Res. **47**, 103–138.

Greenwood, D. D. (**1961**). ''Critical bandwidth and the frequency coordinates of the basilar membrane,'' J. Acoust. Soc. Am. **33**, 1344–1356.

Greenwood, D. D. (**1990**). ''A cochlear frequency-position function for several species-29 years later,'' J. Acoust. Soc. Am. **87**, 2592–2605.

Houtgast, T. (**1974**). ''Lateral suppression and loudness reduction of a tone in noise,'' Acustica **30**, 214–221.

Killion, M. C. (**1978**). ''Revised estimate of minimal audible pressure: Where is the 'missing 6 dB'?,'' J. Acoust. Soc. Am. **63**, 1501–1510.

Launer, S. (**1995**). ''Loudness perception in listeners with sensorineural hearing impairment,'' Ph.D Thesis, Oldenburg, Germany.

Launer, S., Hohmann, V., and Kollmeier, B. (**1997**). ''Modeling loudness growth and loudness summation in hearing-impaired listeners,'' in *Modeling Sensorineural Hearing Loss*, edited by W. Jesteadt (Erlbaum, Mahwah, NJ).

Moore, B. C. J. (**1986**). ''Parallels between frequency selectivity measured psychophysically and in cochlear mechanics,'' Scand. Audiol. Suppl. **25**, 139–152.

Moore, B. C. J. (**1995**). *Perceptual Consequences of Cochlear Damage* (Oxford University Press, Oxford).

Moore, B. C. J. (**1997**). *An Introduction to the Psychology of Hearing*, 4th ed. (Academic, San Diego).

Moore, B. C. J. (**1998**). *Cochlear Hearing Loss* (Whurr, London).

Moore, B. C. J., Alcántara, J. I., Stone, M. A., and Glasberg, B. R. (**1999a**). ''Use of a loudness model for hearing aid fitting. II. Hearing aids with multi-channel compression,'' Br. J. Audiol. **33**, 99–113.

Moore, B. C. J., and Glasberg, B. R. (**1986**). ''The role of frequency selectivity in the perception of loudness, pitch and time,'' in *Frequency Selectivity in Hearing*, edited by B. C. J. Moore (Academic, London).

Moore, B. C. J., and Glasberg, B. R. (**1996**). ''A revision of Zwicker's loudness model,'' Acust. Acta Acust. **82**, 335–345.

Moore, B. C. J., and Glasberg, B. R. (**1997**). ''A model of loudness perception applied to cochlear hearing loss,'' Aud. Neurosci. **3**, 289–311.

Moore, B. C. J., and Glasberg, B. R. (**1998**). ''Use of a loudness model for hearing aid fitting. I. Linear hearing aids,'' Br. J. Audiol. **32**, 301–319.

Moore, B. C. J., Glasberg, B. R., and Baer, T. (**1997a**). ''A model for the prediction of thresholds, loudness, and partial loudness,'' J. Audio Eng. Soc. **45,** 224–240.

Moore, B. C. J., Glasberg, B. R., Hess, R. F., and Birchall, J. P. (**1985**). ''Effects of flanking noise bands on the rate of growth of loudness of tones in normal and recruiting ears,'' J. Acoust. Soc. Am. **77**, 1505–1515.

Moore, B. C. J., Glasberg, B. R., and Stone, M. A. (**1999b**). ''Use of a loudness model for hearing aid fitting. III. A general method for deriving

initial fittings for hearing aids with multi-channel compression,'' Br. J. Audiol. (in press).
Moore, B. C. J., Launer, S., Vickers, D., and Baer, T. (**1998**). ''Loudness of modulated sounds as a function of modulation rate, modulation depth, modulation waveform and overall level,'' in *Psychophysical and Physiological Advances in Hearing*, edited by A. R. Palmer, A. Rees, A. Q. Summerfield, and R. Meddis (Whurr, London).
Moore, B. C. J., Vickers, D. A., Baer, T., and Launer, S. (**1999c**). ''Factors affecting the loudness of modulated sounds,'' J. Acoust. Soc. Am. (in press).
Moore, B. C. J., Vickers, D. A., Glasberg, B. R., and Baer, T. (**1997b**). ''Comparison of real and simulated hearing impairment in subjects with unilateral and bilateral cochlear hearing loss,'' Br. J. Audiol. **31**, 227–245.
Relkin, E. M., and Doucet, J. R. (**1997**). ''Is loudness simply proportional to the auditory nerve spike count?,'' J. Acoust. Soc. Am. **191**, 2735–2740.
Robles, L., Ruggero, M. A., and Rich, N. C. (**1986**). ''Basilar membrane mechanics at the base of the chinchilla cochlea I. Input–output functions, tuning curves, and response phases,'' J. Acoust. Soc. Am. **80**, 1364–1374.
Ruggero, M. A., and Rich, N. C. (**1991**). ''Furosemide alters organ of Corti mechanics: Evidence for feedback of outer hair cells upon the basilar membrane,'' J. Neurosci. **11**, 1057–1067.
Ruggero, M. A., Rich, N. C., Recio, A., Narayan, S. S., and Robles, L. (**1997**). ''Basilar-membrane responses to tones at the base of the chinchilla cochlea,'' J. Acoust. Soc. Am. **101**, 2151–2163.
Scharf, B. (**1970**). ''Critical bands,'' in *Foundations of Modern Auditory Theory*, edited by J. V. Tobias (Academic, New York).
Scharf, B., and Hellman, R. P. (**1966**). ''Model of loudness summation applied to impaired ears,'' J. Acoust. Soc. Am. **40**, 71–78.
Sellick, P. M., Patuzzi, R., and Johnstone, B. M. (**1982**). ''Measurement of basilar membrane motion in the guinea pig using the Mössbauer technique,'' J. Acoust. Soc. Am. **72**, 131–141.
Thornton, A. R., and Abbas, P. J. (**1980**). ''Low-frequency hearing loss: perception of filtered speech, psychophysical tuning curves, and masking,'' J. Acoust. Soc. Am. **67**, 638–643.
Tyler, R. S. (**1986**). ''Frequency resolution in hearing-impaired listeners,'' in *Frequency Selectivity in Hearing*, edited by B. C. J. Moore (Academic, London).
Yates, G. K. (**1990**). ''Basilar membrane nonlinearity and its influence on auditory nerve rate-intensity functions,'' Hearing Res. **50**, 145–162.
Yates, G. K. (**1995**). ''Cochlear structure and function,'' in *Hearing*, edited by B. C. J. Moore (Academic, San Diego).
Zwicker, E. (**1956**). ''Die elementaren Grundlagen zur Bestimmung der Informationskapazität des Gehörs,'' Acustica **6**, 356–381.
Zwicker, E. (**1958**). ''Über psychologische und methodische Grundlagen der Lautheit,'' Acustica **8**, 237–258.
Zwicker, E. (**1961**). ''Subdivision of the audible frequency range into critical bands (Frequenzgruppen),'' J. Acoust. Soc. Am. **33**, 248.
Zwicker, E., and Fastl, H. (**1990**). *Psychoacoustics—Facts and Models* (Springer, Berlin).
Zwicker, E., Fastl, H., and Dallmayr, C. (**1984**). ''BASIC-Program for calculating the loudness of sounds from their 1/3-oct. band spectra according to ISO 532B,'' Acustica **55**, 63–67.
Zwicker, E., Flottorp, G., and Stevens, S. S. (**1957**). ''Critical bandwidth in loudness summation,'' J. Acoust. Soc. Am. **29**, 548–557.
Zwicker, E., and Scharf, B. (**1965**). ''A model of loudness summation,'' Psychol. Rev. **72**, 3–26.
Zwislocki, J. (**1953**). ''Acoustic attenuation between the ears,'' J. Acoust. Soc. Am. **25**, 752–759.

Modulation masking produced by beating modulators

Brian C. J. Moore, Aleksander Sek,[a] and Brian R. Glasberg
Department of Experimental Psychology, University of Cambridge, Downing Street, Cambridge CB2 3EB, England

(Received 18 December 1998; revised 6 April 1999; accepted 30 April 1999)

This study examined whether ''modulation masking'' could be produced by temporal similarity of the probe and masker envelopes, even when the masker envelope did not contain a spectral component close to the probe frequency. Both masker and probe amplitude modulation were applied to a single 4-kHz sinusoidal or narrow-band noise carrier with a level of 70 dB SPL. The threshold for detecting 5-Hz probe modulation was affected by the presence of a pair of masker modulators beating at a 5-Hz rate (40 and 45 Hz, 50 and 55 Hz, or 60 and 65 Hz). The threshold was dependent on the phase of the probe modulation relative to the beat cycle of the masker modulators; the threshold elevation was greatest (12–15 dB for the sinusoidal carrier and 9–11 dB for the noise carrier, expressed as $20 \log m$) when the peak amplitude of the probe modulation coincided with a peak in the beat cycle. The maximum threshold elevation of the 5-Hz probe produced by the beating masker modulators was 7–12 dB greater than that produced by the individual components of the masker modulators. The threshold elevation produced by the beating masker modulators was 2–10 dB greater for 5-Hz probe modulation than for 3- or 7-Hz probe modulation. These results cannot be explained in terms of the spectra of the envelopes of the stimuli, as the beating masker modulators did not produce a 5-Hz component in the spectra of the envelopes. The threshold for detecting 5-Hz probe modulation in the presence of 5-Hz masker modulation varied with the relative phase of the probe and masker modulation. The pattern of results was similar to that found with the beating two-component modulators, except that thresholds were highest when the masker and probe were 180° out of phase. The results are consistent with the idea that nonlinearities within the auditory system introduce distortion in the internal representation of the envelopes of the stimuli. In the case of two-component beating modulators, a weak component is introduced at the beat rate, and it has an amplitude minimum when the beat cycle is at its maximum. The results could be fitted well using two models, one based on the concept of a sliding temporal integrator and one based on the concept of a modulation filter bank.
[S0001-4966(99)03408-6]

PACS numbers: 43.66.Dc, 43.66.Mk, 43.66.Nm, 43.66.Ba [DWG]

INTRODUCTION

In everyday life the amplitude of most sounds changes markedly over time and the pattern of these changes appears to play an important role in conveying auditory information. For example, it has been proposed that the crucial information used to understand speech is derived from the patterns of amplitude modulation in different audio frequency bands (Plomp, 1988; Drullman *et al.*, 1994; Greenberg and Arai, 1998). In the past, the perception of amplitude changes has been modeled by a sequence of stages, including a bank of bandpass filters (the auditory filters). Each filter is followed by a nonlinear device and a ''smoothing'' device. Usually, this smoothing device is thought of as occurring after the auditory nerve; it is assumed to reflect a relatively central process. The output of the smoothing device is fed to a decision device.

The smoothing device has been modeled by a low-pass filter (Viemeister, 1979) or by a sliding temporal integrator (temporal window) (Festen and Plomp, 1981; Moore *et al.*, 1988; Plack and Moore, 1990; Oxenham and Moore, 1994). However, more recently it has been proposed that modulation perception depends on a second stage of filtering in the auditory system (Dau *et al.*, 1997a, b). It is assumed that the envelopes of the outputs of the auditory filters are fed to a second array of overlapping bandpass filters tuned to different envelope modulation rates. This set of filters is usually called a ''modulation filter bank'' (MFB). The concept of the MFB implies that the auditory system performs a limited resolution spectral analysis of the envelope at the output of each auditory filter.

The MFB is assumed to exist in a specialized part of the brain that contains an array of neurons each tuned to a different modulation rate (Martens, 1982; Kay, 1982; Dau *et al.*, 1997a, 1997b). Each neuron can be considered as a filter in the modulation domain. Neurons with appropriate properties have been found in the cochlear nucleus (Møller, 1976) and the inferior colliculus (Rees and Møller, 1983; Schreiner and Langner, 1988; Lorenzi *et al.*, 1995). For a review see Palmer (1995).

Psychoacoustical evidence consistent with the concept of a MFB has come from experiments involving detection of ''probe'' modulation in the presence of masker modulation. Houtgast (1989) performed such experiments using a broadband pink noise carrier. He measured thresholds for detecting sinusoidal amplitude modulation (the probe) in the pres-

[a]Present address: Institute of Acoustics, Adam Mickiewicz University, Matejki 48/49, 60-769 Poznan, Poland.

ence of clearly audible amplitude changes produced by a masking modulator (a half-octave wide band of noise) applied to the same carrier. His results showed a tuning effect which could be interpreted as indicating selectivity in the modulation-frequency domain, analogous to the frequency selectivity observed in the audio-frequency domain. Similar effects were observed by Bacon and Grantham (1989) for a white noise carrier; they showed that ''modulation masking'' was maximal when the frequencies of the masker and signal modulators were close to each other. Dau (1996) showed that his model (based on the concept of the MFB) could account for the data of Houtgast and of Bacon and Grantham. He also showed that it could account for temporal modulation transfer functions (TMTFs) (Viemeister, 1979) for different types of noise carriers (Eddins, 1993). However, in Dau's model, the inherent fluctuations of the noise carrier play a critical role. The model does not account for TMTFs obtained with sinusoidal carriers at high modulation rates (above about 100 Hz).

The MFB concept is not the only way to explain the results of experiments on modulation masking. Most such results can be explained in terms of the similarity between the temporal pattern of the masker and that of the signal; the more similar these patterns, the greater the amount of modulation masking. For example, a sinusoidally modulated signal may be perceived as having a certain rhythm. If a modulated masker is perceived as having a similar rhythm, the masker may have a greater masking effect than when the rhythms of the signal and masker are different. The rhythm could be extracted via some sort of counting mechanism, at least for low envelope modulation rates. Thus it remains unclear whether the auditory system actually performs a spectral analysis of the envelope, as implied by the MFB concept.

One experiment that does seem clearly to support the idea of a MFB was conducted by Dau *et al.* (1997a). They amplitude modulated a 5-kHz sinusoidal carrier with a masker that consisted of the third to seventh harmonics of a 30-Hz fundamental frequency; the phases of the components were random. The lowest component in the masker modulation had a frequency of 90 Hz, but the masker modulation had a repetition rate of 30 Hz. The task was to detect sinusoidal probe modulation in the range 20–120 Hz. The amount of modulation masking increased progressively as the probe frequency was increased from 20 to about 100 Hz. There was no sign of a maximum in the masking function at 30 Hz, even though the temporal pattern of the masker and signal was similar at this frequency. The results are consistent with the idea that the auditory system performs a spectral analysis of the envelope; the masker modulation did not have a spectral component around 30 Hz, and therefore there was no peak in the masking function around 30 Hz.

The present experiment also examined modulation masking for cases where the probe modulation was at a frequency remote from any spectral frequency in the masker modulation, but there was nevertheless a similarity between the temporal pattern of the masker modulation and the probe modulation. This was achieved by using a two-component modulator. The ''beats'' between these two components had a rate that was equal to or close to the probe frequency. A similar method has been used by Sheft and Yost (1997) to examine modulation detection interference (MDI). However, in their experiment the probe modulation was applied to a carrier frequency that was different from the carrier frequency or frequencies of the masker. In our experiment, the masker and probe modulators were applied to a single carrier (either a sinusoid or a noise band). Sheft and Yost found that significant MDI occurred for 4-Hz probe modulation when the masker modulators had a 4-Hz separation, giving 4-Hz beats. The MDI was greater than that produced by the individual components of the masker modulator. They concluded that there was a ''masking effect not predicted by a spectral representation of the probe and masker envelopes.'' We sought to determine if the same was true when the masker and probe modulation were applied to a single narrow-band carrier.

One complication in testing the concept of the MFB is that there may be significant nonlinearity in the auditory system prior to the MFB. This could introduce distortion components, including a component at the beat frequency of a two-component modulator, in the internal representation of the envelope. Examples of such nonlinearity include the compressive input–output function of the basilar membrane (Sellick *et al.*, 1982; Ruggero *et al.*, 1997; Moore and Oxenham, 1998), and the transduction from basilar-membrane vibration to neural activity (Yates, 1990). Sheft and Yost (1997) considered the possibility that a distortion component at the beat frequency could account for their MDI results. They referred to a study of Shofner *et al.* (1996) which measured responses of neurons in the chinchilla cochlear nucleus to carriers at the characteristic frequency that were amplitude modulated by two-component modulators. This study did reveal evidence for a distortion component at the beat rate of the modulators, and the magnitude of this component did not vary with beat rate over the range 4–16 Hz. Sheft and Yost concluded that the distortion component might provide a basis for explaining the MDI effect but that it did not explain why the amount of MDI at the beat rate decreased when the beat rate was increased from 4 to 10 Hz.

Returning to our own experiment, if nonlinearities do introduce an envelope component at the beat frequency of a two-component modulator, this could result in modulation masking around the beat frequency. To test this possibility, we measured thresholds for detecting probe modulation at the beat frequency as a function of the phase of that modulation relative to the phase of the beat. The pattern of results as a function of phase was compared with that obtained when the masker consisted of a single component at the same frequency as the beat frequency of the two-component maskers.

I. METHOD

A. Procedure

Thresholds were measured using an adaptive two-interval forced-choice procedure, with a two-down one-up stepping rule that estimates the 70.7% correct point on the psychometric function. Masker modulation was present in both intervals of a trial, and the probe modulation was pre-

sented in either the first or the second interval, selected at random. The task of the subject was to indicate, by pressing one of two buttons, the interval containing the probe modulation. Feedback was provided by lights following each response. At the start of a run, the probe modulation depth was chosen to be well above the threshold value. Following two correct responses, the modulation depth, m, was decreased, while following one incorrect response it was increased. The step size was 3.5 dB (in terms of $20 \log m$) until four reversals, after which it was decreased to 2 dB and eight more reversals were obtained. The threshold for a given run was taken as the mean value of $20 \log m$ at the last eight reversals. Each threshold reported here is based on the mean of four runs.

To avoid overmodulation, the sum of the modulation indices for all modulators (masker and signal) was not allowed to exceed 1. When the adaptive procedure called for a value of the signal modulation index that would lead to a sum greater than 1, the signal modulation index was limited to the value giving a sum of 1. When thresholds were smaller than -15 dB, the limit was never applied. When thresholds were higher than -15 dB, the limit was sometimes applied during the first four reversals, but rarely (less than 5% of runs) during the last eight reversals.

B. Stimuli

The carrier was either a 4-kHz sinusoid or a 300-Hz-wide noise centered at 4 kHz. This relatively high carrier frequency was chosen so that the spectral sidebands produced by the modulation would not be resolved even for the highest modulation frequency used (65 Hz). We used both sinusoidal and noise carriers so that we could assess the role of the inherent amplitude fluctuations in the carrier; recall that the model of Dau *et al.* (Dau *et al.*, 1997a, 1997b) accounts accurately for data obtained with noise carriers, but is less successful for sinusoidal carriers. The carrier level was 70 dB SPL. The probe modulation frequency was 3, 5, or 7 Hz.

The following masker modulators were used:

(1) Single sinusoidal modulators with frequency 40, 50, or 60 Hz and with $m = 0.3$ or 0.6. The modulation always started in ''sine'' phase, i.e., at a positive-going zero crossing. The equation describing the masker envelope, $E(t)$, is

$$E(t) = 1 + m \sin(2\pi f_m t), \tag{1}$$

where f_m is the modulator frequency.

(2) Pairs of sinusoidal modulators with frequencies separated by 5 Hz. The frequencies of the modulators were 40 and 45 Hz, 50 and 55 Hz, or 60 and 65 Hz. The value of m for each modulator component was 0.3. Each modulator started in sine phase. The equation describing the masker envelope, $E(t)$, is

$$E(t) = 1 + 0.3 \sin(2\pi f_{ml} t) + 0.3 \sin(2\pi f_{mu} t), \tag{2}$$

where f_{ml} and f_{mu} are the modulator frequencies. The pairs of modulators produced beats in the envelope at a 5-Hz rate, as illustrated in the upper panel of Fig. 1, but there was no spectral component in the envelope at 5 Hz. If modulation masking depends on a spectral analysis of the envelope, then there should not be more masking of the 5-Hz probe than of the 3- or 7-Hz probes. On the other hand, if modulation masking depends on similarity in the temporal patterns of the probe and masker modulation, there should be more masking of the 5-Hz probe than of the 3- or 7-Hz probes. For the 5-Hz probe modulation, thresholds were measured for four different phases of the probe modulation, relative to the beat cycle in the masker modulation. The phases were 0, 90, 180, and 270°. For the relative phase of 0°, the peak in the signal modulator coincided with the peak in the beats, as illustrated in the second panel of Fig. 1. This meant that the signal modulator phase was shifted by 90° ($\pi/2$ radians) relative to sine phase. For relative phases of 90, 180, and 270°, the signal modulator phase was shifted by 180, 270, and 0°, respectively. The envelope waveforms resulting from adding the signal modulation to the masker modulation are illustrated in Fig. 1, for relative phases of 0, 90, and 180°. The waveform for 270° phase is simply a time-reversal of that for 90° phase. For the 3- and 7-Hz probe modulation, thresholds were measured only for the probe modulation starting in sine phase. However, pilot experiments showed no effect of starting phase for the 3- and 7-Hz probe modu-

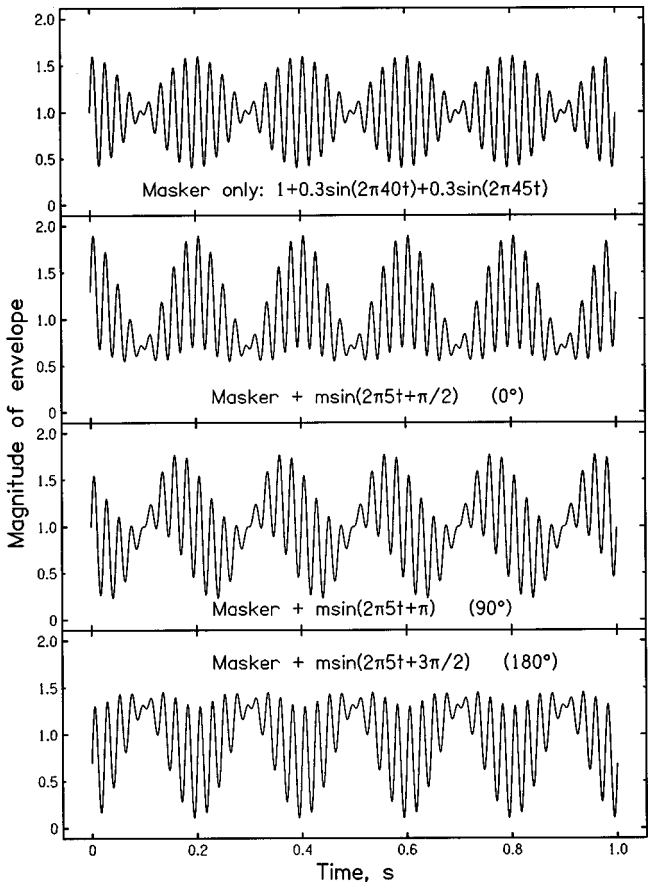

FIG. 1. The top panel shows the envelope of a two-component (beating) masker modulator with component frequencies of 40 and 45 Hz. The other three panels show the envelopes resulting from adding 5-Hz probe modulation (at a suprathreshold depth of 0.3) to the masker modulation, for three different relative phases. For the phase labeled as 0°, the peak amplitude of the probe coincided with the peak in the beat cycle.

lation.

(3) A single sinusoidal modulator with frequency 5 Hz. The masker modulation always started in sine phase. Thresholds were measured for four different starting phases of the 5-Hz probe modulation, relative to the phase of the masker modulation. The phases were 0, 90, 180, and 270°. For the 0° relative phase condition, the probe modulation started in sine phase. The condition with 5-Hz masker modulation was included to assess the pattern of results that would be observed if a nonlinearity prior to the hypothetical MFB introduced a low-level component at 5 Hz in the envelope spectrum of the two-component maskers. The modulation depth of the 5-Hz modulator was 0.1.

Thresholds were also measured for the detection of probe modulation in the absence of any masker modulation, for probe frequencies of 3, 5, and 7 Hz.

On each trial, the carrier was presented in two bursts separated by a silent interval of 300 ms. Each burst had a 20-ms raised-cosine rise and fall, and an overall duration (including rise/fall times) of 1000 ms. The modulation was applied during the whole of the carrier, and the starting phase of the modulation is defined relative to the start of the carrier.

Stimuli were generated using a Tucker-Davis array processor (TDT-AP2) in a host PC, and a 16-bit digital to analog converter (TDT-DD1) operating at a 50-kHz sampling rate. The noise carrier was initially specified in the frequency domain, and was transformed into the time domain via an inverse Fourier transform, using a routine supplied by Tucker-Davis. A new noise sample was generated for every stimulus. The stimuli were attenuated (TDT-PA4) and sent through an output amplifier (TDT-HB6) to a Sennheiser HD414 earphone. Only one ear was tested for each subject. Subjects were seated in a double-walled sound-attenuating chamber.

C. Subjects

Three subjects were tested. One was author AS. The other two subjects were paid for their services. All subjects had absolute thresholds less than 20 dB HL at all audiometric frequencies and had no history of hearing disorders. All had previous experience in psychoacoustic tasks. They were given practice in all conditions until their performance appeared to be stable; this took between 10 and 15 h. The thresholds gathered during the practice sessions were discarded.

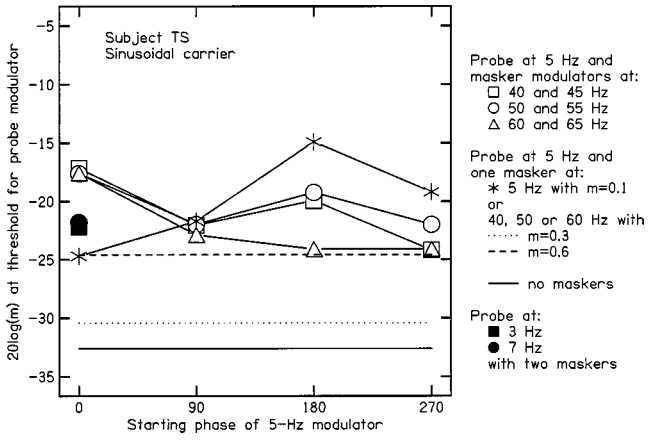

FIG. 2. Results for subject TS for the sinusoidal carrier. Thresholds for detecting the probe modulation are expressed as $20 \log m$, where m is the probe modulation depth. The various conditions are indicated in the key at the side.

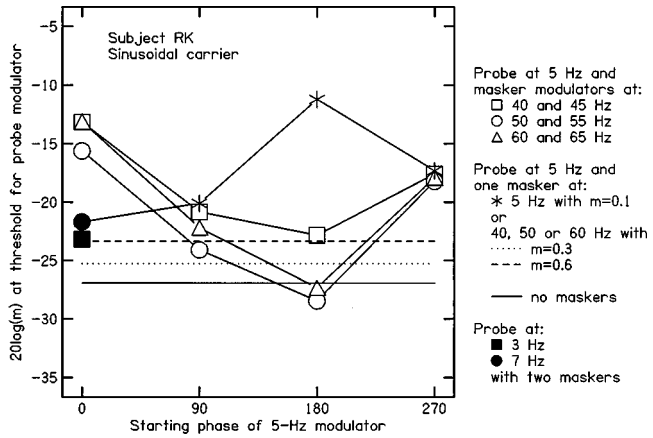

FIG. 3. As Fig. 2, but for subject RK.

II. RESULTS

A. Sinusoidal carrier

The results differed somewhat across subjects, so the individual results for the sinusoidal carrier are shown in Figs. 2–4. The threshold for detecting 5-Hz probe modulation in the absence of masker modulation is shown as the horizontal solid line without symbols. Thresholds were almost the same for the 3- and 7-Hz probe modulators. For each subject, thresholds for detecting 5-Hz probe modulation in the presence of a single masker modulator component (40, 50, or 60 Hz) were almost the same for the three masker modulation rates used. The standard deviation of the thresholds across masker modulation rates was 1.2, 1.6, and 0.5 dB for subjects TS, RK, and AS, respectively. Therefore, these thresholds were averaged across masker modulation rate and are shown as the dotted line ($m=0.3$) and dashed line ($m=0.6$). Thresholds with $m=0.3$ were 2–3 dB higher than when no masker modulation was present, and those with m

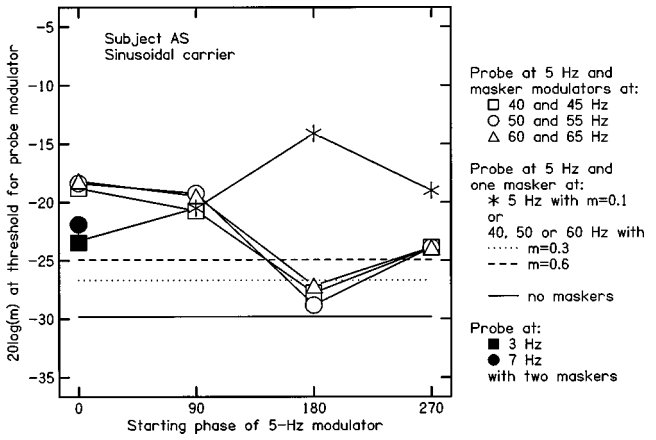

FIG. 4. As Fig. 2, but for subject AS.

$=0.6$ were 3–8 dB higher. These relatively small amounts of modulation masking are as expected from previous work, given the relatively large frequency separation between the probe and masker modulation frequencies.

Results for the 5-Hz probe modulation in the presence of masker modulators consisting of pairs of sinusoids are shown as open symbols. For each subject, the results are very similar for the three pairs of masker modulation frequencies (40 and 45, 50 and 55, or 60 and 65 Hz). There is a clear effect of the relative phase of the probe modulation. For all subjects, thresholds are highest for the relative phase of 0°. The results for the other phases differ somewhat across subjects. For RK and AS, the thresholds are lowest for a phase of 180°. For TS, the thresholds are roughly equal for phases of 90, 180, and 270°. For the phase of 0°, thresholds are clearly higher than those obtained in the presence of a single masker modulator component with $m=0.3$ or 0.6. Furthermore, in the presence of the two-component maskers, thresholds are clearly higher for the 5-Hz modulation with 0° relative phase than for the 3- or 7-Hz modulation; thresholds for the latter two cases are shown by the solid squares and solid circles, respectively (results were similar for the three different masker modulator pairs, so only the mean across masker pairs is shown).

These results are not consistent with the idea that modulation masking depends upon the spectral similarity of the probe and masker envelopes. The two-component masker modulators did not have a spectral component at or close to 5 Hz, but they produced a local maximum in modulation masking at 5 Hz, and they produced more masking than would be produced by the individual components of the maskers.

The concept of the MFB might be salvaged if there were significant nonlinearities before the MFB. If such nonlinearities introduced an envelope component at the beat rate of the two-component modulators, then the pattern of results as a function of the phase of the 5-Hz probe modulator should be similar to that obtained when a 5-Hz masker modulator was actually present.

The asterisks in Figs. 2–4 show thresholds for detecting 5-Hz probe modulation in the presence of a single 5-Hz masker modulator, with modulation depth of 0.1. The pattern of results is similar for all three subjects; thresholds are highest for the modulation phase of 180° and tend to be lowest for the phase of 0°; thresholds for phases of 90 and 270° tend to be slightly above those for 0°.

The pattern of results for the 5-Hz masker modulator can be understood in the following way. In all cases, the probe modulation was probably detected simply as a change in the depth of 5-Hz modulation; for comparable effects of phase using noise carriers, see Bacon and Grantham (1989) and Strickland and Viemeister (1996). For the 0° phase, the probe and masker modulation were in phase, so their amplitudes added. For the 180° phase, the modulation depth in the probe interval was the difference between the modulation depth of the probe modulator and that of the masker modulator. Thus to get a modulation depth in the signal interval that was greater than 0.1 (the masker modulation depth), the modulation depth of the probe modulator had to exceed 0.2; otherwise the modulation depth would have been greater in the nonsignal interval.[1] For the 90 and 270° phases, the *powers* of the masker and probe modulators would have added. For a given modulation depth of the probe, this resulted in a smaller change in modulation depth than for the 0° phase. Thus thresholds were slightly higher for the 90 and 270° phases than for the 0° phase, but markedly lower than for the 180° phase. The change in modulation depth at threshold, averaged across phases, was 0.043, which is similar to the threshold change in modulation depth reported by Schöne (1979) for a 1-kHz carrier and a reference modulation depth of 0.1; see also Ozimek and Sek (1988).

The results obtained using the 5-Hz masker modulator have a similar form to those for the two-component modulators, except for a phase shift of 180°. Thus, in principle, the pattern of results for the two-component modulators might be explained by the presence of a 5-Hz component in the internal representation of the masker envelope. This component would have to be 180° out of phase with the beat in the envelope; in other words, the 5-Hz distortion component would have a minimum in its instantaneous amplitude when the beats were at a maximum. We will return to this point later. On average, the 5-Hz masker modulator produced slightly higher thresholds than the two-component modulators. This implies that, if there was a 5-Hz component in the internal representation of the envelope of the two-component maskers, that component had a relatively low amplitude, less than that produced by an external 5-Hz masker modulator with $m=0.1$.

To assess the statistical significance of the phase effects, a within-subjects analysis of variance (ANOVA) was conducted with factors masker type (40 plus 45 Hz, 50 plus 55 Hz, 60 plus 65 Hz, and 5 Hz alone) and relative phase of the probe modulation. The main effect of masker type was not significant; $F(3,6)=3.25$, $p=0.102$. The main effect of relative phase was also not significant; $F(3,6)=1.78$, $p=0.25$. The interaction of masker type and phase was highly significant; $F(9,18)=15.09$, $p<0.001$. Post hoc tests, based on the least significant differences test (Snedecor and Cochran, 1967) showed that for each phase, results did not differ significantly for the three maskers consisting of pairs of modulators. However, for the relative phase of 0°, the 5-Hz masker modulator gave significantly lower thresholds than for all of the modulator pairs ($p<0.02$), while for the relative phase of 180°, the 5-Hz masker modulator gave significantly higher thresholds than for all of the modulator pairs ($p<0.001$).

In summary, the two-component masker modulators produced more masking of 5-Hz probe modulation than that produced by the individual components of the maskers, when the probe modulation was in phase with the beat produced by the two-component masker modulators. The masking was greater for 5-Hz probe modulation than for 3- or 7-Hz probe modulation. For the 5-Hz probe modulation, the pattern of results as a function of phase was similar for the two-component masker modulators and for a masker modulator with a single component at 5 Hz. However, the phase giving the highest threshold was 180° different for the two-component masker modulators and the 5-Hz masker modu-

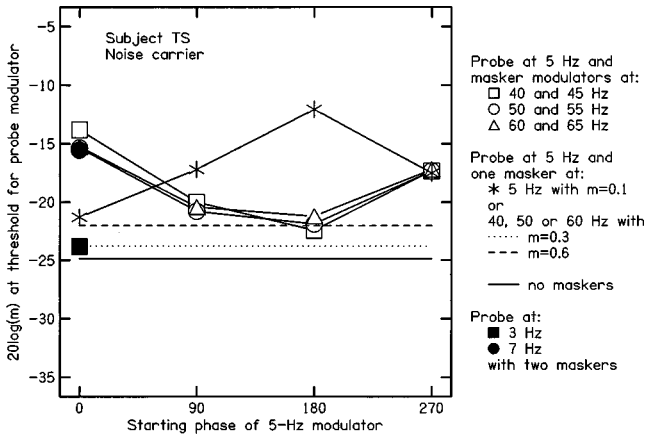

FIG. 5. As Fig. 2, but for the noise carrier.

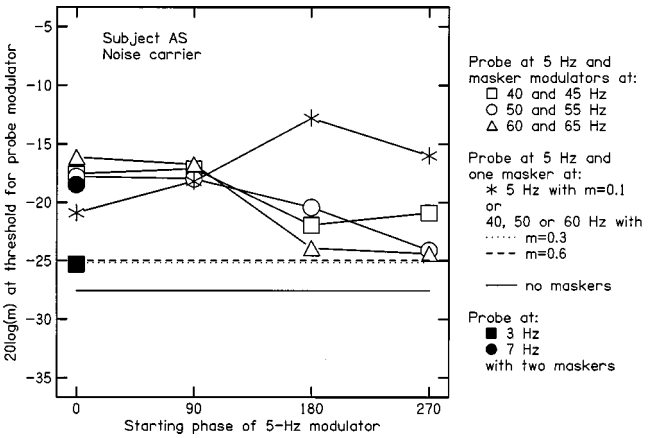

FIG. 7. As Fig. 5, but for subject AS.

lator. The results are consistent with the idea that the masking of the 5-Hz probe modulation by the two-component masker modulators was caused by a low-level 5-Hz distortion component in the internal representation of the masker envelope.

B. Noise carrier

The individual results for the noise carrier are shown in Figs. 5–7. The thresholds for detecting 5-Hz probe modulation in the absence of masker modulation (horizontal solid lines) are higher than those obtained using the sinusoidal carrier. This is consistent with the idea that the inherent random amplitude fluctuations in a narrow-band noise carrier make it harder to detect modulation of that carrier (Maiwald, 1967; Fleischer, 1982; Dau *et al.*, 1997a). For each subject, thresholds for detecting 5-Hz probe modulation in the presence of a single masker modulator component (40, 50, or 60 Hz) were almost the same for the three masker modulation rates used. The standard deviation of the thresholds across masker modulation rates was 0.5, 0.9, and 1.3 dB for subjects TS, RK, and AS, respectively. Therefore, these thresholds were averaged across masker modulation rate and are shown as the dotted line ($m=0.3$) and dashed line ($m=0.6$). Thresholds with $m=0.3$ were 1–3 dB higher than when no masker modulation was present, and those with $m=0.6$ were 3–4 dB higher. The single-component masker modulators had a smaller masking effect for the noise carrier than for the tone carrier, probably because thresholds in the absence of a masker modulator were higher for the noise carrier, as a result of the inherent fluctuations in the noise carrier (Dau *et al.*, 1997a). The modulation thresholds in the presence of the single-component masker modulators were only slightly higher for the noise carrier than for the sinusoidal carrier.

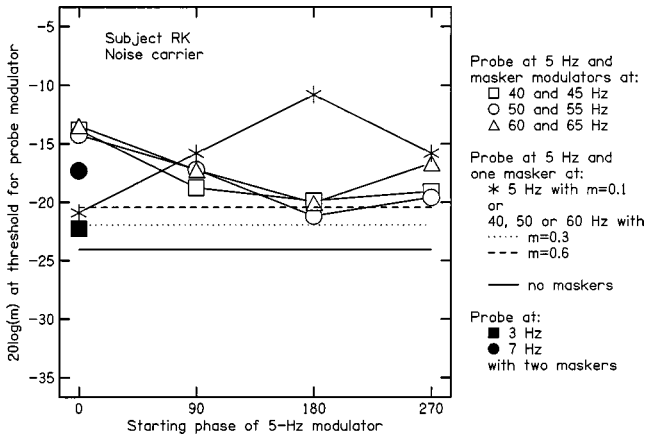

FIG. 6. As Fig. 5, but for subject RK.

The pattern of results with the two-component masker modulators and the noise carrier was similar to that found for the sinusoidal carrier. Thresholds for detecting 5-Hz probe modulation were highest for a phase of 0° for all three subjects. For this phase, thresholds were clearly higher than those found in the presence of the individual components of the maskers, with $m=0.3$ or 0.6. For the other phases, the pattern of results varied somewhat across subjects, but thresholds tended to be lowest for a phase of 180°.

Thresholds for detecting 3-Hz and 7-Hz probe modulation were similar for the three different masker modulator pairs, and the means across masker pairs are shown by the solid symbols in Figs. 5–7. The thresholds for 3-Hz probe modulation are clearly lower than those for 5-Hz probe modulation and are almost the same as the thresholds for detecting 5-Hz probe modulation in the absence of masker modulation. Thresholds for detecting 7-Hz probe modulation were only very slightly lower than for 5-Hz probe modulation. However, the thresholds for detecting the 7-Hz probe modulation in the absence of any masker modulation were higher than for the 3- and 5-Hz probe modulators; in fact, as for the 3-Hz probe, the two-component masker modulators did not raise the threshold for detecting 7-Hz probe modulation above that measured in the absence of masker modulation. Thus the masker modulator pairs produced more masking of the 5-Hz probe than of the 3- or 7-Hz probes.

The thresholds for detecting 5-Hz probe modulation in the presence of a single 5-Hz masker modulator showed a pattern very similar to that found with the sinusoidal carrier; thresholds were highest for the 180° phase and lowest for the 0° phase, the 90 and 270° phases giving intermediate thresholds. The change in modulation depth at threshold, averaged across phases, was 0.073, which is higher than found for the sinusoidal carrier, probably because the inherent fluctuations in the narrow-band noise carrier impaired performance. The

pattern of results for the 5-Hz masker modulator was similar to that for the two-component masker modulators, except that the phase giving the highest threshold was 180° different for the two cases. The results are consistent with the idea that the masking of the 5-Hz probe modulation by the two-component masker modulators was caused by a low-level 5-Hz distortion component in the internal representation of the masker envelope.

To assess the statistical significance of the phase effects, a within-subjects ANOVA was conducted with factors masker type (40 plus 45 Hz, 50 plus 55 Hz, 60 plus 65 Hz, and 5 Hz alone) and relative phase of the probe modulation. The main effect of masker type was significant; $F(3,6) = 9.08$, $p < 0.012$. The main effect of relative phase was not significant; $F(3,6) = 1.93$, $p = 0.226$. The interaction of masker type and phase was highly significant; $F(9,18) = 12.01$, $p < 0.001$. Post hoc tests, based on the least significant differences test (Snedecor and Cochran, 1967) showed that for each phase, results did not differ significantly for the three maskers consisting of pairs of modulators. However, for the relative phase of 0°, the 5-Hz masker modulator gave significantly lower thresholds than for all of the modulator pairs ($p < 0.001$), while for the relative phase of 180°, the 5-Hz masker modulator gave significantly higher thresholds than for all of the modulator pairs ($p < 0.001$).

III. MODELING THE RESULTS

We have compared two approaches to modeling the results. One is based on the concept of a sliding temporal integrator. The other is based on the concept of a modulation filter bank. We wanted to assess the extent to which simple models could account for the results. Since the results for the noise carrier were similar in form to those for the sinusoidal carrier, we modeled the results only for the sinusoidal carrier. Also, we did not explicitly model the effects of internal variability, i.e., fluctuations in the internal representation of the stimuli from one presentation to the next. Instead, we assumed that the threshold for detecting the probe modulation corresponded to a fixed difference in the internal representation of the masker modulation alone and the masker-plus-probe modulation.

A. Sliding temporal integrator

This model has the following stages:

(1) An array of bandpass filters (simulating the auditory filters). These are gammatone filters (Patterson *et al.*, 1995) with bandwidths as suggested by Glasberg and Moore (1990). As our stimuli were narrow band, we considered only the output of the auditory filter centered at the carrier frequency of 4 kHz.

(2) A nonlinearity. Initially the output was full-wave rectified. Then it was raised to a power less than 1, i.e., the nonlinearity was compressive, consistent with other studies (Oxenham and Moore, 1994, 1995; Moore *et al.*, 1996; Moore and Oxenham, 1998). We found that a good fit to the data could be obtained (as described below) by raising the rectified amplitude to the power 0.4. This is reasonably consistent with estimates of the amount of compression on the basilar membrane for mid-range levels (Ruggero *et al.*, 1997).

(3) A sliding temporal integrator with each side modeled as an exponential function, described by

$$W(-t) = \exp(-t/T_b), \quad t < 0, \tag{3}$$

and

$$W(t) = \exp(-t/T_a), \quad t > 0, \tag{4}$$

where t is time measured relative to the time at the peak of the function, and T_b and T_a are parameters determining the sharpness of the function for times before the peak and times after the peak, respectively. The equivalent rectangular duration (ERD) of this function is defined as $T_b + T_a$. We assumed that the asymmetry of the temporal integrator was similar to that measured in earlier studies (Oxenham and Moore, 1994); the value of T_b was assumed to be 0.63 times the value of T_a. The ERD was set to 7 ms, which is typical of the value estimated when a compressive nonlinearity is included in the model (Oxenham and Moore, 1994; Moore *et al.*, 1996). The exact value of the assumed ERD did not have a large effect on the outcome.

(4) A decision statistic. We considered various measures of the output of the temporal integrator that might be appropriate for predicting thresholds. In the past, modulation detection thresholds have been predicted based on various measures such as the mean output of the temporal integrator (Rodenburg, 1977), the variance of the output (Viemeister, 1979; Strickland and Viemeister, 1996), and the ratio of the highest sample value to the lowest sample value (Green and Forrest, 1988; Strickland and Viemeister, 1996). We found that our results were fitted best using the standard deviation (s.d.) of the output of the sliding temporal integrator, but all of the measures mentioned above gave good fits.

In initial evaluations of the model, we used as input to the model the masker modulator pairs alone (with $m = 0.3$ for each masker modulator), and the masker modulator pairs with 5-Hz probe modulation added at modulation depths corresponding to the mean measured thresholds for each starting phase; thresholds were averaged across subjects and across masker modulator pairs. Figure 8 shows the output of the sliding temporal integrator for the 40- and 45-Hz masker modulators. The top panel shows the output for the masker modulators alone. Note that the waveform is somewhat asymmetric about the mean value; this is a consequence of the compressive nonlinearity used in the model. The asymmetry indicates that there is a distortion component at the beat rate, and that the instantaneous amplitude of the distortion component is at its most negative value when the amplitude of the beats is at a maximum, e.g., at times 0.1, 0.3, and 0.5 ms. The next four panels show the outputs when threshold-level probe modulation was added with starting phases of 0, 90, 180, and 270°. The waveforms vary markedly with probe starting phase. However, the s.d.'s of the waveforms are almost constant across starting phase; the s.d.'s are 0.433, 0.426, 0.430, and 0.425 for starting phases

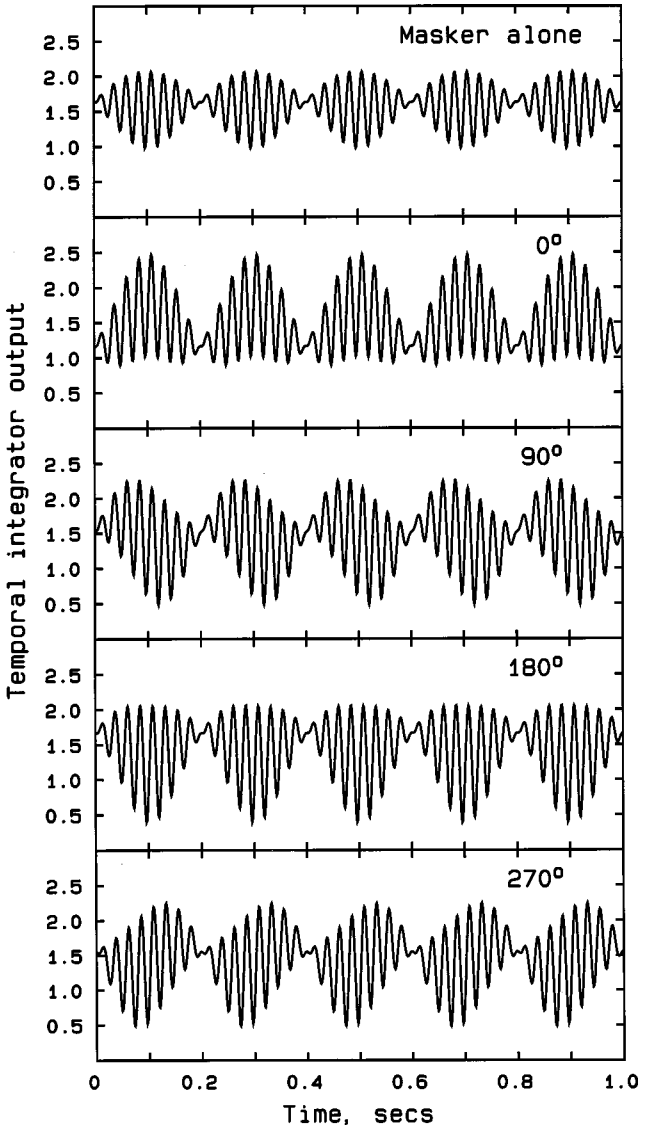

FIG. 8. The output of the sliding temporal integrator of the model for the 40- and 45-Hz masker modulator alone (top panel), and for the masker modulator with 5-Hz probe modulation added at four relative phases (panels 2–5). The amount of probe modulation corresponded to the mean measured threshold for each phase.

of 0, 90, 180, and 270°, respectively. The s.d. for the masker modulation alone is 0.273. Hence the change in s.d. between the masker alone and masker plus probe is 0.160, 0.153, 0.157, and 0.152 for starting phases of 0, 90, 180, and 270°, respectively. Similar results were found for the other masker modulator pairs; the change in s.d. of the waveforms at the output of the sliding temporal integrator produced by adding threshold-level probe modulation to the masker modulation was almost constant across starting phase.

To predict thresholds for each masker modulator pair, we adjusted the probe modulation depth for each starting phase so that the s.d. of the output was exactly equal to the mean value determined in the analysis above. For example, for the 40- and 45-Hz masker modulator pair, the probe modulation depth was adjusted to give an s.d. of 0.4285. The thresholds determined in this way were almost the same for the three masker modulator pairs, which is consistent with the experimental results. Figure 9 shows the mean obtained

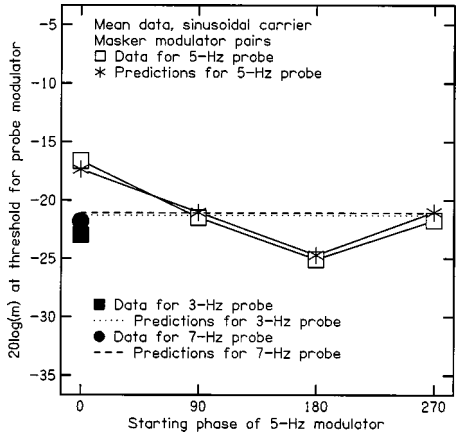

FIG. 9. Predictions of the model based on a sliding integrator for the masker-modulator pairs, compared with the mean obtained results.

thresholds (open squares) and the mean predicted thresholds (asterisks) for the 5-Hz probe modulation, plotted as a function of starting phase. There is an excellent correspondence between the obtained and predicted thresholds.

A similar method was used to predict thresholds for the 3- and 7-Hz probe modulators in the presence of the masker modulator pairs. The probe modulation depth was adjusted to give the same s.d. as for the 5-Hz modulation. For example, for the 40- and 45-Hz masker modulator pair, the probe modulation depth was adjusted to give an s.d. of 0.4285. The thresholds predicted in this way did not vary with probe modulation starting phase, and varied only very slightly across masker-modulator pairs, which is consistent with the experimental results. The mean predicted thresholds for the 3- and 7-Hz modulators are shown in Fig. 9 as the dotted and dashed lines, respectively. Again, there is an excellent correspondence between the obtained thresholds (solid symbols) and predicted thresholds.

We conclude that a model based on a sliding temporal integrator, and using the s.d. of the output of the integrator as a decision statistic, can account for the results very well.

B. Modulation filter bank

The first two stages of this model were the same as described above, namely a simulated auditory filter centered at 4000 Hz and a compressive nonlinearity implemented by raising the rectified output of the filter to the power 0.4. The output of the nonlinearity was passed through a sliding temporal integrator to extract the envelope. For this model, the ERD of the integrator was chosen to be 4 ms rather than 7 ms, so that the integrator would have a negligible smoothing effect on the representation of modulation components up to the highest value used (65 Hz); however, the exact value of the ERD did not markedly affect the results. The dc component of the output of the temporal integrator was removed, and the remaining ac component was fed to a modulation filter centered at the probe modulation frequency. The modulation filter was implemented as a fourth-order gammatone filter. Although the model described by Dau and co-workers (Dau, 1996; Dau *et al.*, 1997a, b) contains an array of modulation filters tuned to different modulation frequencies, we

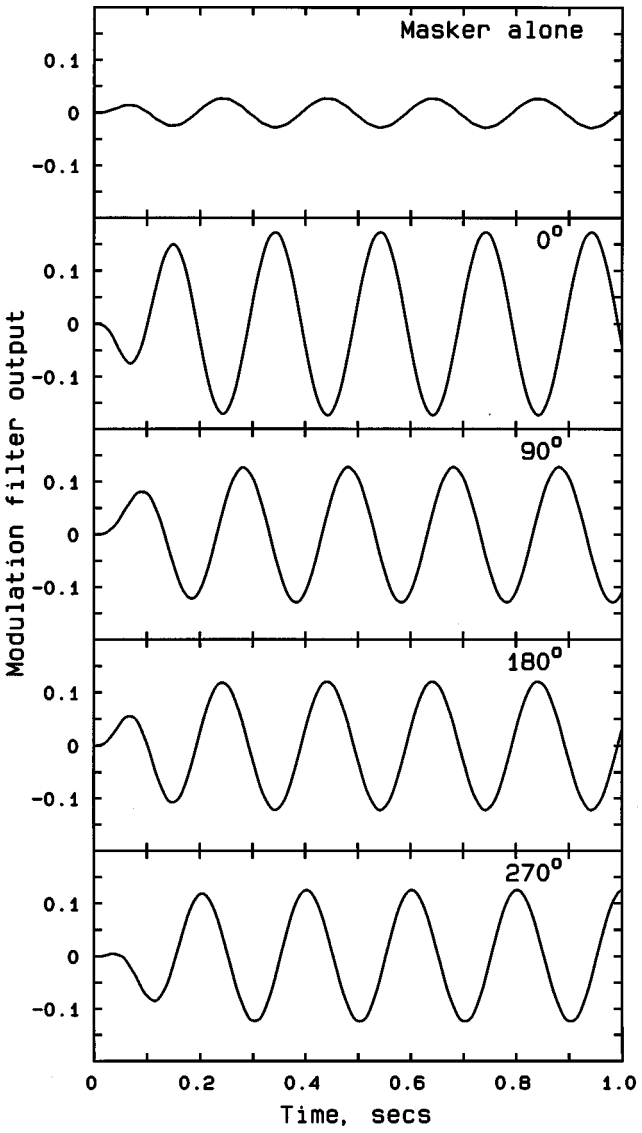

FIG. 10. The output of the modulation filter centered at 5 Hz for the 40- and 45-Hz masker modulator alone (top panel), and for the masker modulator with 5-Hz probe modulation added at four relative phases (panels 2–5). The amount of probe modulation corresponded to the mean measured threshold for each phase.

assumed that performance in our task would be mainly based on the output of the modulation filter centered at the probe modulation frequency. Consistent with their model, we assumed that the bandwidth of the modulation filter was 5 Hz.

The output of the modulation filter in response to the 40- and 45-Hz masker modulators is shown in the top panel of Fig. 10. The output is a 5-Hz sinusoid, confirming that the nonlinearity in the model introduces a 5-Hz distortion component in the internal representation of the envelope of the two-component masker; the primary masker modulation components at 40 and 45 Hz are almost entirely removed by the modulation filter, and are not visible. The magnitude of the 5-Hz distortion component is rather small. The input modulation depth of a 5-Hz modulator needed to match that magnitude is $m=0.027$ (-33.7 dB expressed as $20\log m$). In other words, the magnitude of the 5-Hz distortion component in the envelope of the two-component masker modulator is equivalent to that produced by a 5-Hz modulator with $m=0.0207$. This is below the detection threshold of 5-Hz modulation.

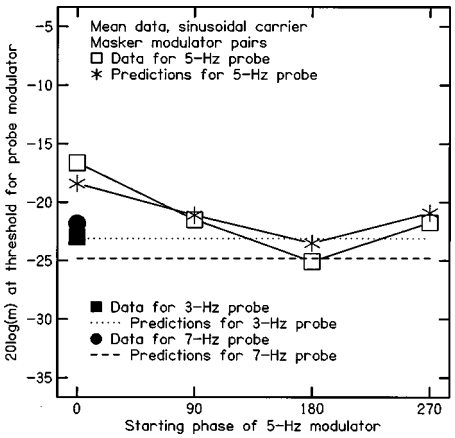

FIG. 11. Predictions of the model based on a modulation filter bank for the masker-modulator pairs, compared with the mean obtained results.

The lower four panels show the outputs of the modulation filter when threshold-level probe modulation was added with starting phases of 0, 90, 180, and 270°. Note that for the phase denoted as 0°, the probe modulation is actually 180° out of phase with the distortion component produced by the nonlinearity. The phase of the distortion component results from the fact that the nonlinearity in the model introduces an asymmetry in the internal representation of the envelope, as can be seen in the upper panel of Fig. 8; the distortion component has its minimum instantaneous amplitude when the beats are at a maximum. This can account, qualitatively, for the fact that thresholds were highest for the 0° phase condition. If the model were correct, the outputs of the modulation filter for the four different phases should all be the same in magnitude, this is roughly, but not exactly true; the s.d.'s of the outputs were 0.115, 0.086, 0.080, and 0.083 for phases of 0, 90, 180, and 270°, respectively.

To predict the thresholds for each masker modulator pair, we adjusted the probe modulation depth for each starting phase so that the s.d. of the output of the modulation filter was exactly equal to the mean value determined in the analysis above, i.e., 0.09. The thresholds determined in this way were almost the same for the three masker modulator pairs, which is consistent with the experimental results. Figure 11 shows the mean obtained thresholds (open squares) and the mean predicted thresholds (asterisks) for the 5-Hz probe modulation, plotted as a function of starting phase. The correspondence between the obtained and predicted thresholds is reasonable, but not quite as good as for the model based on the sliding temporal integrator. In particular, the model based on the modulation filter predicts less variation of thresholds with phase than was actually observed.

To predict thresholds for the 3- and 7-Hz probe modulators in the presence of the masker modulator pairs we used modulation filters centered at 3 and 7 Hz, respectively. As expected, the outputs of these filters in response to the two-component maskers alone were smaller than for the 5-Hz modulation filter; the mean output had an s.d. of 0.0142 for the 3-Hz modulation filter and 0.0116 for the 7-Hz modulation filter. To predict thresholds, the probe modulation depth

was chosen so that the ratio of the s.d. with the probe present to that with the masker alone was the same as the mean ratio for the 5-Hz probe. For example, for the 3-Hz probe, the probe modulation depth was adjusted to give an s.d. of 0.07. The thresholds predicted in this way did not vary with probe modulation starting phase, and varied only very slightly across masker-modulator pairs, which is consistent with the experimental results. The mean predicted thresholds for the 3- and 7-Hz modulators are shown in Fig. 11 as the dotted and dashed lines, respectively. There is a reasonable correspondence between the obtained thresholds (solid symbols) and predicted thresholds, although the latter lie a little below the former.

Overall, the model based on a modulation filter bank accounts for the data reasonably well, but not quite as well as the model based on a sliding temporal integrator. However, the accuracy of the predictions for the modulation filter model could be improved by incorporating greater nonlinearity before the modulation filter bank. In our version of the model, the only nonlinearity is a compressive nonlinearity simulating basilar-membrane compression. The model of Dau and co-workers (Dau, 1996; Dau *et al.*, 1997a, 1997b) incorporates ''adaptation loops'' to simulate adaptation processes, which introduce strong nonlinearity for low modulation rates. Other nonlinearities, such as those in the transduction process (Yates, 1990), may also play a role. The incorporation of such additional nonlinearities might well improve the predictions of the modulation filter model.

IV. DISCUSSION

Overall, the results of our experiment are inconclusive on one issue that it was originally intended to address, namely whether or not the auditory system contains a modulation filter bank. Our results suggest that, for the beating modulator that we used, nonlinearities in the auditory system introduce a distortion component at the beat rate in the internal representation of the envelope. The presence of this distortion component allows an explanation of the results either in terms of a sliding temporal integrator or in terms of a modulation filter bank. A distortion component of this type probably also influenced the results of Sheft and Yost (1997). Thus their results should not be taken as evidence against the concept of a modulation filter bank.

Our results differ from those of Dau *et al.* (1997a). As described in the introduction, they amplitude modulated a 5-kHz sinusoidal carrier with a masker that consisted of the third to seventh harmonics of a 30-Hz fundamental frequency. The task was to detect sinusoidal probe modulation in the range 20–120 Hz. There was no sign of a maximum in the masking function at 30 Hz, even though the temporal pattern of the masker and probe was similar at this frequency; both had the same repetition rate. In contrast, we found that, for a masker-modulator pair beating at 5 Hz, there was more masking at 5 Hz than at 3 or 7 Hz. The discrepancy may be connected with the probe modulation rate, which was much higher in the study of Dau *et al.* than in our study.

A role for modulation rate is suggested by the MDI data of Sheft and Yost (1997); note, however, that in their experiment the probe modulation was applied to a carrier frequency that was different from the carrier frequency or frequencies of the masker. They found that the interference effect of a beating two-component modulator on probe modulation at the beat rate was greater for a 4-Hz beat rate than for a 10-Hz rate. The reason why the effect was smaller at the higher rate is not clear. One possibility is that both the effect found in our experiment, and the MDI effect found by Sheft and Yost depend on the introduction of a distortion component at the masker beat rate in the internal representation of the envelope of the masker. If the nonlinearity was time varying, then the magnitude of the distortion component could vary with modulation rate. It is generally believed that the compression on the basilar membrane is fast acting, and would not vary with modulation rate over the range 5–30 Hz. However, the basilar-membrane compression might be influenced by more slow-acting efferent control processes (Russell and Murugasu, 1997); this could, in theory, increase the effective amount of compression for low modulation rates. Also, adaptation processes might result in greater effective nonlinearity for low modulation rates. The adaptation loops in the model of Dau *et al.* have this property. It should be noted, however, that the relatively slow envelope fluctuations at the beat rate were accompanied by much faster fluctuations corresponding to the component modulator frequencies. It is not clear whether the adaptation loops would result in greater nonlinearity for slow beat rates under such conditions.

V. CONCLUSIONS

The following conclusions can be drawn from this study:

(1) The threshold for detecting 5-Hz probe amplitude modulation of a 4-kHz sinusoidal or narrow-band noise carrier was affected (usually increased) by the presence of a pair of masker modulators beating at a 5-Hz rate (40 and .45 Hz, 50 and 55 Hz, or 60 and 65 Hz). The threshold was dependent on the phase of the probe modulation relative to the beat cycle of the masker modulators; most masking was produced when the peak amplitude of the probe modulation coincided with a peak in the beat cycle. We refer to this as 0° phase. The lowest thresholds were produced when the minimum amplitude of the probe modulation coincided with a peak in the beat cycle (180° phase).

(2) The threshold elevation of the 5-Hz probe produced by the beating masker modulators at 0° phase was greater than that produced by the individual components of the masker modulators.

(3) The threshold elevation produced by the beating masker modulators was usually greater for 5-Hz probe modulation at 0° phase than for 3- or 7-Hz probe modulation.

(4) The threshold for detecting 5-Hz probe modulation in the presence of 5-Hz masker modulation varied with the relative phase of the probe and masker modulation. The pattern of results was similar to that found with the beating two-component modulators, except that thresholds were highest when the masker and probe were 180° out of phase.

(5) The results cannot be explained in terms of the spectra of the envelopes of the *stimuli*, as the beating masker modulators did not produce a 5-Hz component in the spectra of the envelopes. However, the results are consistent with the idea that nonlinearities within the auditory system introduce distortion in the internal representation of the envelopes of the stimuli. In the case of two-component beating modulators, a weak component is introduced at the beat rate, and it has an amplitude minimum when the beat cycle is at its maximum.
(6) The results could be fitted well using two models, one based on the concept of a sliding temporal integrator and one based on the concept of a modulation filter bank.

ACKNOWLEDGMENTS

This work was supported by the Wellcome Trust and the Medical Research Council (U.K.). We thank Joost Festen, Torsten Dau, Wes Grantham, and an anonymous reviewer for helpful comments on an earlier version of this paper.

[1]For the 180° phase, subjects might, in principle, have achieved lower thresholds by choosing the interval with the lower modulation depth. For example, if the probe modulation depth was 0.15, the overall modulation depth in the probe interval would have been 0.05, less than the depth of 0.1 in the masker-alone interval. In pilot experiments, using a larger masker modulation depth ($m = 0.6$) we found that subjects did learn to identify the signal interval as the one with less modulation. However, with the masker modulation depth of 0.1, and with a high starting value for the probe modulation depth, the adaptive procedure usually did not lead to probe modulation depths less than 0.2. At this masker modulation depth subjects were not able to reverse their decision strategy during a run.

Bacon, S. P., and Grantham, D. W. (**1989**). ''Modulation masking: Effects of modulation frequency, depth, and phase,'' J. Acoust. Soc. Am. **85**, 2575–2580.
Dau, T. (**1996**). ''Modeling auditory processing of amplitude modulation,'' Ph. D. Thesis, University of Oldenburg.
Dau, T., Kollmeier, B., and Kohlrausch, A. (**1997a**). ''Modeling auditory processing of amplitude modulation: I. Detection and masking with narrowband carriers,'' J. Acoust. Soc. Am. **102**, 2892–2905.
Dau, T., Kollmeier, B., and Kohlrausch, A. (**1997b**). ''Modeling auditory processing of amplitude modulation: II. Spectral and temporal integration,'' J. Acoust. Soc. Am. **102**, 2906–2919.
Drullman, R., Festen, J. M., and Plomp, R. (**1994**). ''Effect of temporal envelope smearing on speech reception,'' J. Acoust. Soc. Am. **95**, 1053–1064.
Eddins, D. A. (**1993**). ''Amplitude modulation detection of narrow-band noise: Effects of absolute bandwidth and frequency region,'' J. Acoust. Soc. Am. **93**, 470–479.
Festen, J. M., and Plomp, R. (**1981**). ''Relations between auditory functions in normal hearing,'' J. Acoust. Soc. Am. **70**, 356–369.
Fleischer, H. (**1982**). ''Modulationsschwellen von Schmalbandrauschen,'' Acustica **51**, 154–161.
Glasberg, B. R., and Moore, B. C. J. (**1990**). ''Derivation of auditory filter shapes from notched-noise data,'' Hearing Res. **47**, 103–138.
Green, D. M., and Forrest, T. G. (**1988**). ''Detection of amplitude modulation and gaps in noise,'' in *Basic Issues in Hearing*, edited by H. Duifhuis, J. W. Horst, and H. P. Wit (Academic New York).
Greenberg, S., and Arai, T. (**1998**). ''Speech intelligibility is highly tolerant of cross-channel spectral asynchrony,'' J. Acoust. Soc. Am. **103**, 3057.
Houtgast, T. (**1989**). ''Frequency selectivity in amplitude-modulation detection,'' J. Acoust. Soc. Am. **85**, 1676–1680.
Kay, R. H. (**1982**). ''Hearing of modulation in sounds,'' Physiol. Rev. **62**, 894–975.
Lorenzi, C., Micheyl, C., and Berthommier, F. (**1995**). ''Neuronal correlates of perceptual amplitude-modulation detection,'' Hearing Res. **90**, 219–227.
Maiwald, D. (**1967**). ''Ein Funktionsschema des Gehörs zur Beschreibung der Erkennbarkeit kleiner Frequenz-und Amplitudenänderungen,'' Acustica **18**, 81–92.
Martens, J.-P. (**1982**). ''A new theory for multi-tone masking,'' J. Acoust. Soc. Am. **72**, 397–405.
Møller, A. R. (**1976**). ''Dynamic properties of primary auditory fibers compared with cells in the cochlear nucleus,'' Acta Physiol. Scand. **98**, 157–167.
Moore, B. C. J., Glasberg, B. R., Plack, C. J., and Biswas, A. K. (**1988**). ''The shape of the ear's temporal window,'' J. Acoust. Soc. Am. **83**, 1102–1116.
Moore, B. C. J., and Oxenham, A. J. (**1998**). ''Psychoacoustic consequences of compression in the peripheral auditory system,'' Psychol. Rev. **105**, 108–124.
Moore, B. C. J., Peters, R. W., and Glasberg, B. R. (**1996**). ''Detection of decrements and increments in sinusoids at high overall levels,'' J. Acoust. Soc. Am. **99**, 3669–3677.
Oxenham, A. J., and Moore, B. C. J. (**1994**). ''Modeling the additivity of nonsimultaneous masking,'' Hearing Res. **80**, 105–118.
Oxenham, A. J., and Moore, B. C. J. (**1995**). ''Additivity of masking in normally hearing and hearing-impaired subjects,'' J. Acoust. Soc. Am. **98**, 1921–1935.
Ozimek, E., and Sek, A. (**1988**). ''AM difference limens for noise bands,'' Acustica **66**, 153–160.
Palmer, A. R. (**1995**). ''Neural signal processing,'' in *Hearing*, edited by B. C. J. Moore (Academic, San Diego).
Patterson, R. D., Allerhand, M. H., and Giguère, C. (**1995**). ''Time-domain modeling of peripheral auditory processing: A modular architecture and a software platform,'' J. Acoust. Soc. Am. **98**, 1890–1894.
Plack, C. J., and Moore, B. C. J. (**1990**). ''Temporal window shape as a function of frequency and level,'' J. Acoust. Soc. Am. **87**, 2178–2187.
Plomp, R. (**1988**). ''The negative effect of amplitude compression in multichannel hearing aids in the light of the modulation-transfer function,'' J. Acoust. Soc. Am. **83**, 2322–2327.
Rees, A., and Møller, A. R. (**1983**). ''Responses of neurons in the inferior colliculus of the rat to AM and FM tones,'' Hearing Res. **10**, 301–310.
Rodenburg, M. (**1977**). ''Investigation of temporal effects with amplitude modulated signals,'' in *Psychophysics and Physiology of Hearing*, edited by E. F. Evans and J. P. Wilson (Academic, London).
Ruggero, M. A., Rich, N. C., Recio, A., Narayan, S. S., and Robles, L. (**1997**). ''Basilar-membrane responses to tones at the base of the chinchilla cochlea,'' J. Acoust. Soc. Am. **101**, 2151–2163.
Russell, I. J., and Murugasu, E. (**1997**). ''Medial efferent inhibition suppresses basilar membrane responses to near characteristic frequency tones of moderate to high intensities,'' J. Acoust. Soc. Am. **102**, 1734–1738.
Schöne, P. (**1979**). ''Messungen zur Schwankungsstärke von amplitudenmodulierten Sinustönen,'' Acustica **41**, 252–257.
Schreiner, C. E., and Langner, G. (**1988**). ''Coding of temporal patterns in the central auditory system,'' in *Auditory Function: Neurobiological Bases of Hearing*, edited by G. Edelman, W. Gall, and W. Cowan (Wiley, New York).
Sellick, P. M., Patuzzi, R., and Johnstone, B. M. (**1982**). ''Measurement of basilar membrane motion in the guinea pig using the Mössbauer technique,'' J. Acoust. Soc. Am. **72**, 131–141.
Sheft, S., and Yost, W. A. (**1997**). ''Modulation detection interference with two-component masker modulators,'' J. Acoust. Soc. Am. **102**, 1106–1112.
Shofner, S., Sheft, S., and Guzman, S. J. (**1996**). ''Responses of ventral cochlear nucleus units in the chinchilla to amplitude modulation by low-frequency, two-tone complexes,'' J. Acoust. Soc. Am. **99**, 3592–3605.
Snedecor, G. W., and Cochran, W. G. (**1967**). *Statistical Methods* (Iowa University Press, Ames, IA).
Strickland, E. A., and Viemeister, N. F. (**1996**).''Cues for discrimination of envelopes,'' J. Acoust. Soc. Am. **99**, 3638–3646.
Viemeister, N. F. (**1979**). ''Temporal modulation transfer functions based on modulation thresholds,'' J. Acoust. Soc. Am. **66**, 1364–1380.
Yates, G. K. (**1990**).''Basilar membrane nonlinearity and its influence on auditory nerve rate-intensity functions,'' Hearing Res. **50**, 145–162.

Correlational analysis of acoustic cues for the discrimination of auditory motion

Robert A. Lutfi and Wen Wang
Department of Communicative Disorders and Department of Psychology, University of Wisconsin, Madison, Wisconsin 53706

(Received 18 August 1997; revised 10 August 1998; accepted 21 April 1999)

The sound of a source moving in a straight path and passing directly in front of the listener on the azimuthal plane was synthesized over headphones to include three dynamic cues for motion: Doppler effect, overall intensity, and interaural time difference. Discriminability of a change in displacement, velocity, and acceleration of this source was measured using a standard two-interval, forced-choice procedure. In each case, the relative reliance or weight given to the three acoustic cues was estimated from correlations of the listener's response with small independent perturbations imposed on cues from trial to trial. Group estimates of threshold agreed well with results from past studies, while the obtained pattern of weights depended on the individual, starting velocity, and discrimination task. For the discrimination of displacement at moderate velocity (10 m/s), responses were most highly correlated with intensity or interaural time difference. For the discrimination of velocity and, to a lesser extent, acceleration, responses were most highly correlated with Doppler effect. At higher velocity (50 m/s) responses in all discrimination tasks were most strongly correlated with Doppler effect with few exceptions. Randomizing source spectrum or roving distance of the source from trial to trial did not significantly affect the pattern of results. The results suggest that motion perception is mutable, and not in all cases based on a single invariant acoustic cue. © *1999 Acoustical Society of America.* [S0001-4966(99)00508-1]

PACS numbers: 43.66.Fe, 43.66.Qp, 43.66.Sn [DWG]

INTRODUCTION

Although among the most basic of auditory abilities, the perception of auditory motion has only recently become an active area of research in the neuroscience community. One issue has dominated research in this area, and that is the question as to whether there is a specialized motion detection system in audition, such as is known to exist in the visual modality (e.g., Movshon, 1975; Andersen, 1997). The search for individual neural units specifically responsive to auditory motion has produced suggestive results (e.g., Sovijärvi and Hyvärinen, 1974; Ahissar *et al.*, 1992; Spitzer and Semple, 1991). However, parallel studies of auditory motion psychophysics have yet to provide convincing corroboratory evidence. Thresholds for a change in the angular displacement of a real moving source are found to not be significantly different from those of a stationary source (Harris and Sergeant, 1971; Harris, 1972; Perrott and Musicant, 1977; Perrott and Tucker, 1988; Chandler and Grantham, 1992), and motion aftereffects in audition, while reliable, are reported to be rather weak (Grantham, 1989, 1992).

Grantham (1986), in fact, has made a rather strong case against a specialized system for motion detection in audition. He measured differential thresholds for velocity using a technique to simulate motion. An impression of continuous auditory motion was produced by varying over time the relative intensity of a 500-Hz tone played over two loudspeakers situated in front and on opposite sides of the listener on the horizontal plane. Grantham found that thresholds for a change in velocity of the simulated motion corresponded roughly to a constant angular displacement independent of the duration of motion. He took this result to suggest that listeners infer velocity from total distance traveled, rather than appreciate velocity directly—an idea that is now known as the ''snapshot hypothesis.'' Others have since questioned this hypothesis. Perrott *et al.* (1993) used a spatial array of loudspeakers to simulate motion, and showed that listeners can discriminate between sounds traveling the same total distance in the same time, but accelerating differently throughout the trajectory. Wang and Lutfi (1994) also provided a test by comparing differential thresholds for displacement, velocity, and acceleration directly. They synthesized three dynamic cues for motion (Doppler, intensity, and interaural delay) over headphones to simulate linear motion in front of the listener on the horizontal plane. Their study failed to support the snapshot hypothesis inasmuch as displacements corresponding to differential thresholds for velocity and acceleration were typically smaller than differential thresholds for displacement. At present, the status of the snapshot hypothesis remains unclear. Opposing evidence is provided by these more recent studies, but the bulk of psychophysical data collected to date appear to be well summarized by a constant threshold for total displacement as the snapshot hypothesis would suggest.

In the present study we take a different approach to testing the snapshot hypothesis. To begin, we note that it is never possible to know with complete confidence that a given threshold reflects the detection of motion and not simply a static change in displacement, certainly not without some other convergent measure. The problem is that any change in motion must be accompanied by a change in displacement at some point in the trajectory. Hence, it is always possible that a listener may detect the static change in dis-

placement in lieu of the motion. For this reason we focus in our approach specifically on *how* listeners detect motion rather than on *how well* they detect motion. This is done by employing procedures to measure the relative reliance or weight listeners give to various acoustic cues for motion in different motion discrimination tasks. The snapshot hypothesis maintains that all motion thresholds are mediated by a constant change in total displacement. If so, then one might expect that all thresholds would be mediated by the same acoustic cue or cues related to the constant change in displacement. Evidence for qualitative differences in mediating cues for displacement and motion discrimination tasks could then be taken as evidence against the snapshot hypothesis.

To our knowledge, only one study to date has attempted to measure cue weights in the perception of auditory motion. Rosenblum *et al.* (1987) measured the relative importance listeners place on different acoustic cues for motion by placing these cues in conflict with one another within a single stimulus. The acoustic cues of Doppler, interaural delay, and overall intensity as the source approaches and recedes were synthesized over headphones for a sound source moving along a linear trajectory on the horizontal plane. The listener's task was to judge the point of closest approach of the sound where the different cues each indicated a different point of closest approach. For these conditions, Rosenblum *et al.* report that judgments were dominated by the intensity cue, with interaural delay and Doppler following in order. They interpret their results in terms of the generality of the intensity cue in everyday listening.

In the present study we adopt procedures similar to those of Rosenblum *et al.*, but take these a step further to provide a specific test of the snapshot hypothesis. We also improve on these procedures by providing a more realistic simulation of motion over headphones. Rosenblum *et al.* simulated motion by varying the frequency, amplitude, and ITD of steady-state tones in discrete one-half second steps. In the present study we vary these cues continuously according to principles of sound propagation from a moving source and sound diffraction about a spherical head (cf. Jenison and Lutfi, 1992; Jenison, 1997). Cue weights using these procedures are obtained in the discrimination of displacement, velocity, and acceleration. The prediction of the snapshot hypothesis is that cue weights will be the same for these tasks corresponding to a constant change in displacement.

I. GENERAL METHOD

A. Stimuli

Auditory motion was simulated over headphones using the principles of sound propagation from a moving source and sound diffraction about a spherical head. The source signal q was the first five harmonics of a 100-Hz tone of equal SPL. The source was simulated to move continuously in a linear trajectory, directly in front of the listener from left to right on the horizontal plane (see Fig. 1). The standard source in all conditions always began its trajectory at the same point, and traveled for a duration of 1 s at a velocity of $V=10$ m/s, and acceleration $A=0$ m/s^2. The point of closest approach for the standard occurred exactly halfway through the complete trajectory, at 5 m from the center of the listeners head. The comparison source traveled in the same trajectory as the standard for the same duration. In different conditions, the starting point, velocity, or acceleration of the comparison was changed relative to the standard (see Fig. 2). The change in values, ΔX, ΔV, and ΔA, was chosen for each listener to maintain discrimination performance within the range of 65–90 percent correct in a standard two-interval, forced-choice task. Our previous experience has indicated that performance levels outside this range can lead to unreliable estimates of cue weights.

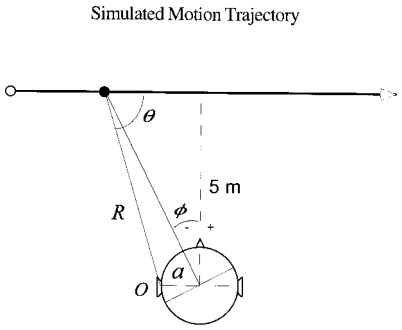

FIG. 1. Simulated motion trajectory used for the standard source. The standard always began its trajectory at the same point, and traveled from left to right for a duration of 1 s at a velocity of $V=10$ m/s (50 m/s in experiment 4), and acceleration $A=0$ m/s^2. The point of closest approach occurred halfway through the complete trajectory, at 5 m (variable distance in experiment 2) from the center of the listeners head.

The simulation of these conditions was undertaken in two parts. The first part specified the incident free-field pressure p at each ear (observation point O in Fig. 1). This is the sound-pressure wave measured at the ear in the absence of the head as an obstacle to the sound. The solution is given by Morse and Ingard (1968, p. 724). For source velocity V and source signal defined as the pressure waveform q,

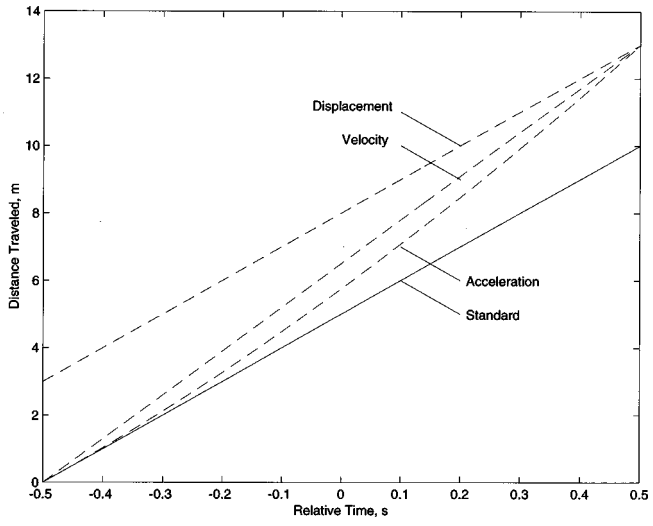

FIG. 2. Time course of the trajectory for the standard (continuous curve) and comparison (dashed curve) in the displacement, velocity, and acceleration discrimination tasks. In each case the endpoint of the trajectory for the comparison is displaced 3 m to the right of the endpoint for the standard. For displacement discrimination task the beginning point of the comparison is also displaced 3 m to the right.

$$p=\frac{1}{4\pi}\frac{q'(t-R/c)}{R(1-M\cos\theta)^2}+\frac{q}{4\pi}\frac{(\cos\theta-M)V}{R^2(1-M\cos\theta)^2}, \quad (1)$$

where q' is the time derivative of q, R is the distance of the source from O, θ is the angle between the direction of motion and the direction of R, $c=343$ m/s is the speed of sound in air, and $M=V/c$ is Mach number. There are two points to note about Eq. (1). First, unlike many natural sources for which sound radiation is directionally dependent, Eq. (1) assumes a monopole source with sound intensity radiating out equally in all directions. Second, there is no provision in Eq. (1) for energy loss due to air absorption. In actual practice, p is additionally attenuated by a factor $e^{-\alpha R}$, where the attenuation coefficient α is wavelength dependent and is determined by the viscosity and thermal relaxation of the propagation medium. At the low frequencies, low sound-pressure levels, and short distances used in the present experiments attenuation due to air absorption is not considered to be a significant factor (cf. Morse and Ingard, 1968, pp. 270–278).

In the second part of the simulation, we added the effects of sound diffraction by the head. Following Kuhn (1977), we assume the source to be harmonic plane wave and the head to be sphere with hard surface. We chose a radius of $a=8.5$ cm to correspond roughly to the average size of the human head. For these conditions Kuhn (1977) provides an approximation of the total complex pressure on the sphere normalized to the incident free-field pressure,

$$\left[\frac{p_i+p_s}{p}\right]\cong 1\pm i\frac{3}{2}ka\sin\phi, \quad (2)$$

where $k=2\pi f/c$ is the wave number, p_i and p_s are the sound pressures corresponding to the incident and scattered components of the pressure wave on the surface of the sphere, ϕ is the incident angle (as shown in Fig. 1), and the sin term is positive for the ear toward the source. The magnitude and phase of the normalized surface pressure were computed separately for each ear, and were used to scale the magnitude and shift the phase of the free-field incident pressure at each ear as computed from Eq. (1). All operations were performed digitally for final presentation over headphones. The final signals were 1 s in duration and were gated on and off with 10-ms cosine-squared ramps to eliminate transients. The signals for each ear were played over separate 16-bit DACs each at a 10-kHz sampling rate. The output of the DACs were low-pass filtered at a 8.5-kHz cutoff (120 dB/octave) and amplified before being delivered over Sennheiser HD-520 Kopfhorer headphones. Signal amplitude was calibrated using binaural loudness matching to a 500-Hz tone at the output of a TDH-49 headphone with known transfer function. At peak amplitude the signals were 75 dB SPL. All signals were presented to listeners seated individually in a double-walled, IAC sound-attenuation chamber.

B. Analysis of acoustic cues for motion

Figure 3 plots the time course of three cues for motion resulting from the stimulus synthesis. The continuous curve in each panel is for the standard traveling at 10 m/s, the dashed curved is for the comparison source traveling at 13 m/s. Corresponding curves for a change in displacement or acceleration are not shown, but are quite similar to those for the +3 m/s change in velocity. The time course of the overall intensity cue (not to be confused with the interaural intensity difference cue) is given in the first panel. Plotted on the ordinate is the dB surface intensity expressed relative to that of the standard at the point of closest approach. Specifically,

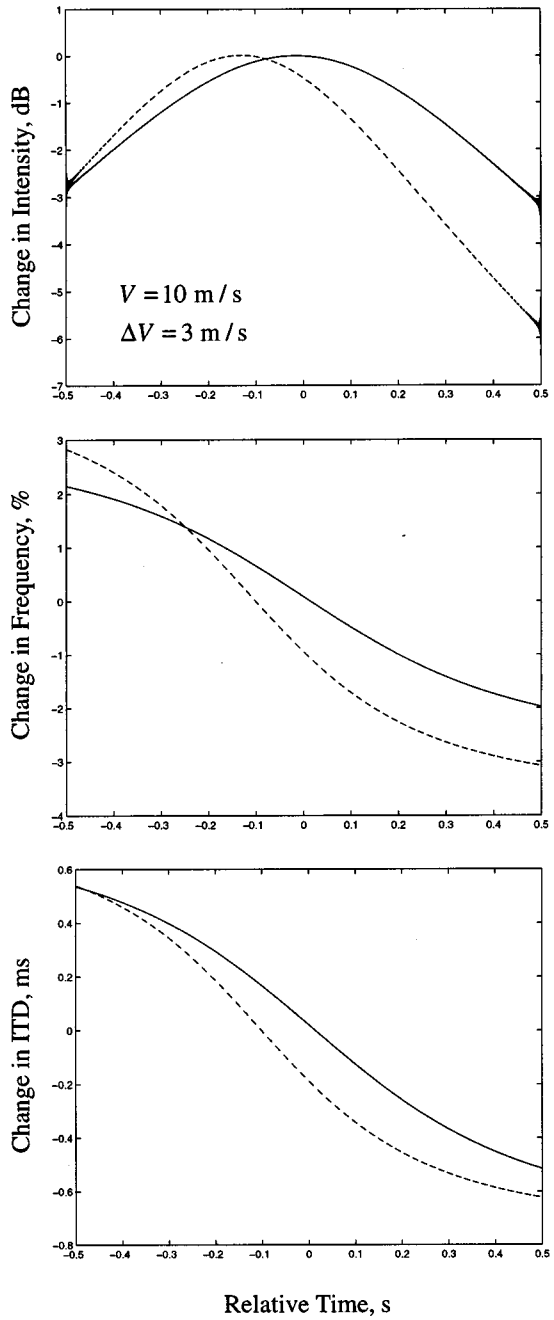

FIG. 3. Time course of the three acoustic cues for motion, intensity, Doppler effect, and ITD, for the standard traveling at 10 m/s (continuous curve), and for the comparison source traveling at 13 m/s (dashed curve). The change in values is expressed relative to the value at the point of closest approach (at time 0). Corresponding curves for a change in displacement or acceleration are not shown, but are quite similar to those for the change in velocity.

$$\frac{I}{I_0}\ \text{in dB}=20\log\left[\text{env}\left(\frac{p_i+p_s}{p_0}\right)\right], \quad (3)$$

where p_0 is the sound pressure at point of closest approach, and env(p) is the time envelope of p. Note that for the source in motion there is a slight departure from a strict inverse-square law such that the intensity is slightly greater for the approaching source than for the receding source. The Doppler cue is shown in the second panel. Here the frequency of the moving source is expressed relative to nominal frequency f_0 when the source is stationary. The exact expression is

$$\frac{f}{f_0} = \frac{1}{1 - M\cos\theta}, \tag{4}$$

and is derived by taking the time derivative of the phase $t - R/c$ of the harmonic source in Eq. (1). Note that in the limit from $t = -\infty$ to $t = +\infty$ the angle θ approachs 0 and π. The frequency f is therefore limited to values within the range between $f_0/(1-M)$ and $f_0/(1+M)$. Finally, the interaural time delay (ITD) cue is plotted in the third panel. It is obtained by taking the phase of Eq. (2) and normalizing with respect to frequency. The result depends on frequency except for low frequencies, $(ka)^2 \ll 1$. In this case, Kuhn (1977) provides an acceptable approximation which is used here:

$$\text{ITD} \approx 3(a/c)\sin\phi. \tag{5}$$

One cue not analyzed for in this study is the interaural intensity difference (IID) that results from the head acting as a barrier to the sound. For the low frequencies used in this study, both experiment and theory indicate that the IID would be a negligible cue for discriminating motion (Kuhn, 1977; Mills, 1958). Indeed, the maximum difference in intensity at the two ears in these conditions (for the source at the beginning of its trajectory) is estimated from Eqs. (1) to (3) to be less than 0.5 dB.

One might expect, based on the differences between the two curves in each panel, that any one or all three of the acoustic cues in Fig. 3 could be used to discriminate the +3 m/s change in velocity. The difference in intensity between the standard and comparison toward the end of the trajectory approaches 3 dB, well exceeding the just-noticeable difference of 1 dB at these moderate sound levels (Jesteadt *et al.*, 1977). The difference in frequency is as much as 1%, exceeding the just-noticeable difference of 0.3% (Wier *et al.*, 1977), and the difference in ITD near the point of closest approach is about 0.2 ms, greater than the just-noticeable difference of 0.02 ms for frequencies below 1.0 kHz (Durlach and Colburn, 1978). Our goal is to determine precisely how the listener makes use of these cues when discriminating the change in velocity. For this purpose we used a correlational procedure (see Richards and Zhu, 1994; Lutfi, 1995). In the standard two-interval, forced-choice trial, the listener judged which of two sounds traveled at the higher velocity. The sounds, however, were constructed in such a way that each of the three cues for motion indicated a slightly different velocity. For each cue the velocity was determined by adding an independent and random deviate $z_i\sigma_V$ to the nominal velocity V of the source. The three velocities, so selected, were then used individually in Eqs. (1)–(5) to synthesize a signal for that trial. The entire procedure was repeated anew for both the standard and comparison played on each trial.

By independently perturbing the motion cues in this way, it is possible to obtain an estimate of the relative reliance or weight listeners place on these cues when discriminating the change in velocity. Suppose, for example, we wish to measure the relative reliance the listener places on the Doppler cue. The difference in velocity indicated by this cue on a given trial is $\Delta V_f = (z_1 - z_2)_f \sigma_V \pm \Delta V$, where z_1 and z_2 are the standard deviates chosen for the first and second observation interval, and ΔV is positive or negative depending on whether the standard occurs in the first or second interval. The z-score difference in this case, $(z_1 - z_2)_f$, varies independently of the other cues. Hence by examining how the listener's response covaries with $(z_1 - z_2)_f$ it is possible to obtain an independent estimate of the weight placed on Doppler relative to the other cues. In practice, the weights are estimated from the regression equation,

$$R = \dot{r}_{R,I}\frac{\Delta V_l}{\sigma_V} + \dot{r}_{R,f}\frac{\Delta V_f}{\sigma_V} + \dot{r}_{R,\text{ITD}}\frac{\Delta V_{\text{ITD}}}{\sigma_V} + \epsilon, \tag{6}$$

where R is the listener's binary response, ϵ is the regression error, and $\dot{r}_{R,i}$ is the estimated weight corresponding to the partial point-biserial correlation (pbc) of the listener's response with ΔV_i. The partial pbc with a given cue is the correlation remaining after the relation to the other two cues has been accounted for (cf. Lutfi, 1995). Weights for the discrimination of displacement and acceleration were obtained in an identical fashion. The values of the perturbation parameter, σ, in each case were, 1 m for displacement, 1 m/s for velocity, and 1 m/s^2 for acceleration. These values were chosen to be large enough to produce reliable weights, but not so large as to produce a perceptible unnaturalness in the sounds.

A note about the pbc: Unlike the pearson-product moment correlation, the pbc maximum is less than 1.0. This results from the mapping of a continuous variable (e.g., frequency, intensity) onto a dichotomous response. However, the standard error of the pbc is equal to the reciprocal of the square-root of the number of trials. Thus small values of pbc are often significantly greater than 0 statistically (cf. Lutfi, 1995). In the present study, 98% of the values for the preferred acoustic dimension fell within the range of 0.2–0.8, more than 2.5 standard deviations from 0. The remaining 2%, which were less than 0.2, were within 2.5 standard deviations of 0.

C. Procedure

Within separate experimental conditions, listeners discriminated a positive change in displacement, velocity, or acceleration of the comparison signal relative to the standard. A two-interval, forced-choice procedure was used with sounds separated by 500 ms, and with correct feedback following each trial. Trials were run in blocks of 50 with short breaks between blocks. A total of 600 trials was run for each listener for each condition. During the first half of all trials, values of ΔX, ΔV, and ΔA, were selected for each listener

TABLE I. Values of Δ, $\Delta\phi$, percent correct $P(C)$, and d' from ''Experiment 1: Standard.''

Task	Experiment 1: Group averages			
	Δ	$\Delta\phi$	$P(C)$	d'
Displacement, X	3.8 m	15°	79	1.1
Velocity, V	2.4 m/s	11°	76	1.0
Acceleration, A	3.5 m/s^2	8°	80	1.2

to yield performance levels falling within the range of 65–90 percent correct. Starting values were 3 m, 3 m/s, and 3 m/s^2, respectively. If the desired performance level was not obtained after two trial blocks, the values were changed and an additional two blocks were run. The procedure was repeated until the desired performance level was obtained. These final values once determined were then fixed for the second half of all trials. Only the second half of trials was used in the analysis of weights.

A total of 11 listeners participated in the study, although not all listeners participated in each condition. Three of the listeners participated in the previous auditory motion study of Wang and Lutfi (1994). The others had no prior experience in auditory motion experiments. The listeners were students at the University of Wisconsin–Madison, and were between the ages of 20 and 37 years. All had normal hearing by standard audiometric tests, and all were paid an hourly rate for their participation. The listeners were told that on each trial they would hear two sounds traveling from left to right, and that in different conditions they were to indicate which of the two sounds was displaced farther to the right, traveled with greater velocity, or traveled with greater acceleration. They were instructed to use any cue or combination of cues they could so as to maximize the number of correct responses in the task, but they were not told what cues were available or how these cues differed for the standard and comparison.

II. RESULTS

A. Experiment 1: Discrimination of a change in displacement, velocity, and acceleration

Before analyzing the weights, we wish to check that our estimates of discrimination thresholds are reasonably within the range expected based on previous studies. Threshold estimates for individual listeners are not possible since data were obtained at only one value of Δ in each condition. However, by averaging over the data of listeners in each condition it is possible to obtain group estimates for the purpose of checking thresholds. The results are shown in Table I. To permit comparisons across studies and tasks, all thresholds are expressed as an equivalent change in incident angle ϕ over the total duration of the signal (see Fig. 1). For the source passing 5 m from the center of the listener's head at point of closest approach, the magnitude of the equivalent change in incident angle is

$$\Delta\phi = \tan^{-1}\left(\frac{5+\Delta X}{5}\right) - \frac{\pi}{4}, \tag{7}$$

where ΔX is the equivalent change in total displacement. Note that $\Delta\phi$ represents the change relative to an incident angle of $\phi = 45°$, where the standard has terminated its trajectory. In this case, $\Delta X = \Delta V \times 1$ s for a change in velocity, and $\Delta X = \frac{1}{2}\Delta A \times 1\ \text{s}^2$ for a change in acceleration.[1] Next to the estimated thresholds are given the corresponding values of percent correct and d' (cf. Macmillan and Creelman, 1991). The d' values differ slightly from one another but are close enough to 1.0 in each case to permit threshold comparisons with past studies.

Care must be taken in making these comparisons as there are significant procedural differences between this and past studies. In past studies listeners discriminated between a static and a moving source, whereas in the present study listeners discriminated between two moving sources. Also, in none of the previous studies for which thresholds are reported were the acoustic parameters randomly perturbed as in the present study. Either of these factors could be expected to yield higher thresholds in this study. Notwithstanding these differences our estimates of threshold agree reasonably well with those from most past studies. For the discrimination of displacement our estimate of threshold is 15°. Grantham (1986) reports displacement thresholds for the detection of movement ranging from 5° to 12° for individual listeners at an incident angle of 45°. Perrott and Musicant (1977) report a more divergent average estimate of 8°, but for very similar conditions, Chandler and Grantham (1992) report estimates ranging from 9° to 15° for individual listeners. Fewer data exist for the discrimination of velocity and acceleration, but again the agreement is not bad. Across conditions and listeners, Grantham (1986, experiment III) reports differential thresholds for velocity in the range from 2° to 10° equivalent angular displacement. The highest of these values is slightly smaller than the average 11° estimate obtained in this study. Wang and Lutfi (1994) report acceleration and velocity thresholds to be generally smaller than displacement thresholds obtained for the same listeners. Although procedural differences prevent direct comparisons with the thresholds of the present study, this observation appears consistent with the thresholds estimates given in Table I. Overall, we take these comparisons to substantiate the estimates of relative weights. With regard to the slightly higher thresholds reported in this study, it seems likely that procedural differences are responsible.

Figure 4 plots the relative weights given to each of the three acoustic cues for motion, in each of the three discrimination tasks. The relative weight in this case is defined as the proportional contribution of each correlation in Eq. (6) independent of its sign. It is computed by taking the absolute values of the correlations and then normalizing them to sum to one. Each symbol in Fig. 4 gives the relative weight for a single listener and task. The intersection point of the three lines in the center of the plot corresponds to the relative weight that would maximize percent correct, assuming equal sensitivity to each cue. These lines define the dominance region for each cue. Data falling in the lower right-hand region indicate a disproportionate weighting on intensity, data falling in the lower left-hand region indicate a disproportionate weighting on Doppler, and data falling in the up-

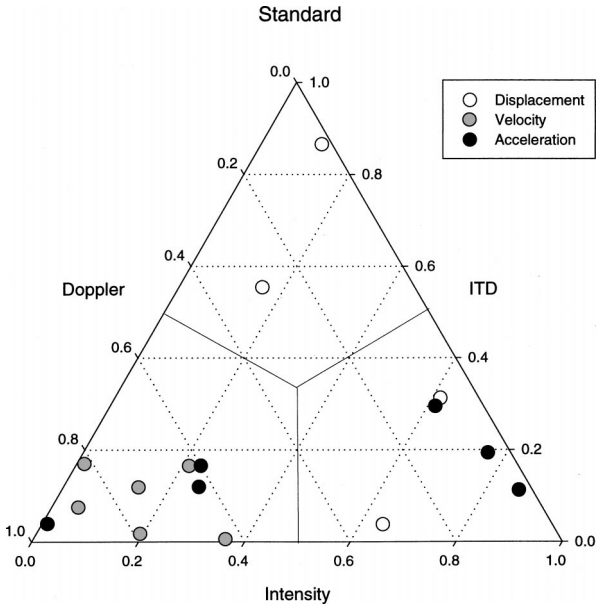

FIG. 4. Relative weights given to each of the three acoustic cues for motion, in each of the three discrimination tasks of experiment 1. Each symbol represents the relative weights for a single listener from a single task. The intersection point of the three lines in the center of the plot corresponds to the relative weight that would maximize percent correct, assuming equal sensitivity to each cue. These lines define the dominance region for each cue.

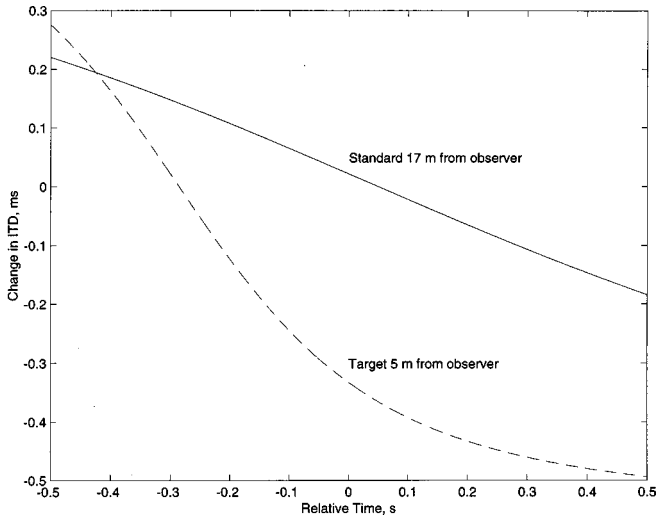

FIG. 5. Time course of the ITD cue for a randomly chosen standard and comparison in the roving distance condition of experiment 2. Standard (continuous curve) is 17 m and comparison (dashed curve) is 5 m from the point of closest approach. The comparison is displaced to the right by 3 m. Note that the ITD for the target at the start of the trajectory indicates a position to the left of the standard, while overall ITD places the target clearly to the right.

per region indicate a disproportionate weighting on ITD. The first point to note from this figure is that no listener weighs the three cues in a way that would maximize percent correct, that is, assuming equal sensitivity to each cue. The data generally tend to converge in one or the other corner of the plot. The second point to note is that there are differences both in individual preferences for the three cues, and in the preferred cues for each task. For the discrimination of displacement, two of the listeners prefer ITD, while the other two prefer intensity. For the discrimination of acceleration, three listeners prefer overall intensity, while the other three prefer Doppler. Only for the discrimination of velocity do all listeners show a common preference for Doppler. Individual differences in weights were observed even for listeners whose performance levels were quite similar for the same value of Δ.

B. Experiment 2: Effect of roving distance

While there were marked individual differences in cue weightings, the overall pattern of results from experiment 1 provides some evidence for a qualitative difference in cues used to detect a change in displacement, and those used to detect a change in velocity or acceleration. Unfortunately, there is a confounding in the displacement discrimination task of experiment 1 that clouds the interpretation of these results. As can be seen from Fig. 2, when the task is to detect a change in velocity or acceleration, the standard and target trajectories have identical starting points, but when the task is to detect a change in displacement the starting points of the standard and target are different. This difference could have, in part, been responsible for the qualitative difference in cues used in the displacement discrimination task. In particular the difference in ITD, intensity, or frequency measured at the starting points could have provided cues for detection of change in displacement that were not available when the task was to detect a change in velocity or acceleration.[2]

To test this possibility a followup experiment was conducted. In this experiment all acoustic cues at the starting points were made ambiguous by roving the distance of the source. All conditions were identical to those of experiment 1 except that on each presentation and for each discrimination task the distance of closest approach (constant at 5 m in experiment 1) was chosen at random with uniform probability over a range of 5–20 m. To produce acceptable levels of performance in this task the listener must resolve the ambiguity in motion cues introduced by the distance rove. This can be done effectively only by evaluating these cues over some course of the trajectory, not just at the start. Figure 5 demonstrates this point. The task is to detect a change in displacement (3 m), the figure shows the ITD functions for a randomly chosen standard at 17 m from the observer (continuous curve) and target at 5 m from the observer (dashed curve). Note that the ITD for the target at the start of the trajectory indicates a position to the left of the standard when, in fact, the target is displaced to the right. This happens frequently in this experiment, so a listener that based judgments only on the starting ITD would make frequent errors. Note, on the other hand, that ITD evaluated over the course of the trajectory clearly places the target to the right of the standard where it should be. This, in fact, will always be true for all three motion cues. Hence, to achieve acceptable performance in this task listeners must at least evaluate cues at some point other than the start. If this is what listeners were doing in experiment 1, then we should expect the results of the present experiment to replicate those of experiment 1.

Table II and Fig. 6 give the overall performance levels

TABLE II. Values of Δ, $\Delta\phi$, percent correct $P(C)$, and d' from ''Experiment 2: Roving Distance.''

	Experiment 2: Group averages			
Task	Δ	$\Delta\phi$	$P(C)$	d'
Displacement, X	2.7 m	12°	66	0.6
Velocity, V	3.5 m/s	14°	75	1.0
Acceleration, A	5.0 m/s^2	11°	70	0.7

TABLE III. Values of Δ, $\Delta\phi$, percent correct $P(C)$, and d' from ''Experiment 3: Random Spectra.''

	Experiment 3: Group averages			
Task	Δ	$\Delta\phi$	$P(C)$	d'
Displacement, X	2.9 m	13°	80	1.2
Velocity, V	3.3 m/s	14°	74	0.9
Acceleration, A	4.0 m/s^2	9°	83	1.3

and relative cue weights from this experiment. Overall performance levels are largely unchanged from those of experiment 1. In particular, for the discrimination of displacement a change of 12 degrees yields an average d' of 0.6. This compares favorably with the results of experiment 1 where a 14 degree displacement yielded an average d' of 1.0. The pattern of cue weights is also largely unchanged, with listeners equally divided in their preference for the ITD and intensity cue in the discrimination of displacement, but unanimous in their preference for the Doppler cue in the discrimination of velocity and acceleration. The results of experiment 2 suggest that the differences in cue preference observed in experiment 1 were not due to the confounding of starting positions in that experiment.

C. Experiment 3: Effect of random source spectrum

The results of experiments 1 and 2 appear to indicate a preference for the Doppler cue in discriminating velocity and, to a lesser extent, acceleration. However, there are at least two ways that the Doppler cue might have been used in these experiments. One strategy, which is clear from Fig. 3, is to discriminate a difference in the *rate of change* of frequency for each source; the faster the rate of change, the greater the velocity or acceleration. The second possible strategy, again from Fig. 3, is to discriminate a *simple difference* in the frequency of the two sources at a single point in time. A likely point would be at the termination of the source, since the difference in frequency is large at this point, and the termination provides an unambiguous mark in time. Experiment 3 was undertaken to test these two possibilities. The methods and procedure were identical to those of experiment 1 except that the fundamental frequency of the source spectrum was now chosen at random on each presentation. The fundamental frequencies were chosen from a normal distribution with a mean of 100 Hz and a standard deviation of 10 Hz. Randomizing the source spectrum in this way greatly disrupts the *simple difference* cue. The extent of the frequency variation is great enough in this case to cause performance to be near chance if based on this cue. In contrast, the frequency variation has no effect on the *rate of change* cue. The rate of change of frequency is expressed in Eq. (4) as a proportional change in frequency which is independent of the initial frequency, f_0, of the source. Therefore, varying source spectrum, as in this experiment, does not disrupt the rate of change cue.

The group estimates of thresholds from experiment 3 are presented in Table III and the relative weights are shown in Fig. 7. There are some differences in the pattern of results compared with experiments 1 and 2. The relative weights for displacement, which previously showed a divided preference between intensity and ITD, now show a unanimous preference for ITD. Also, for the one listener giving less weight to Doppler in the discrimination of acceleration, ITD is the pre-

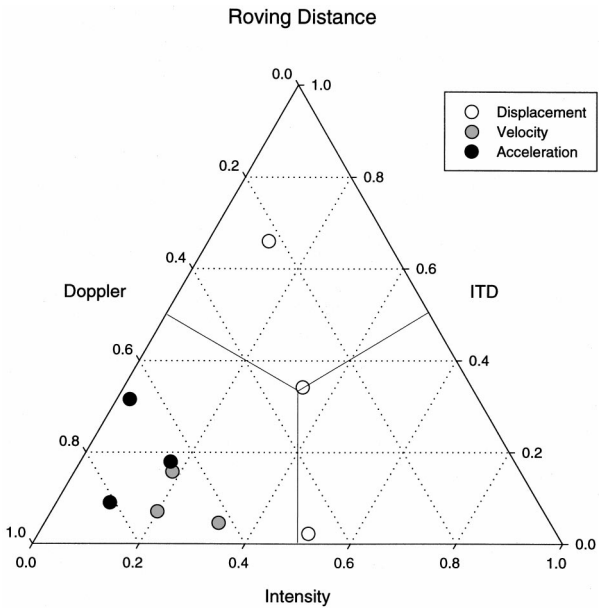

FIG. 6. Same as Fig. 4 except relative weights are from experiment 2, roving distance.

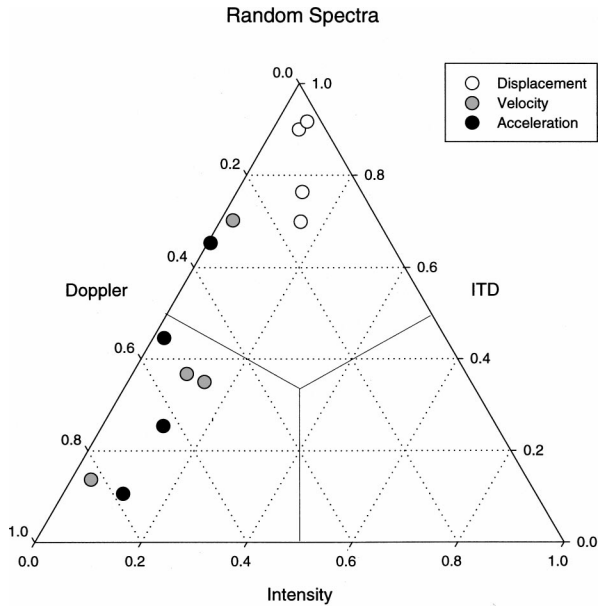

FIG. 7. Same as Fig. 4 except relative weights are from experiment 3, random spectra.

TABLE IV. Values of Δ, $\Delta\phi$, percent correct $P(C)$, and d' from ''Experiment 4: High Velocity.''

Task	Experiment 4: Group averages			
	Δ	$\Delta\phi$	$P(C)$	d'
Displacement, X	2.4 m	11°	69	0.7
Velocity, V	3.1 m/s	13°	71	1.0
Acceleration, A	4.2 m/s^2	10°	75	1.0

ferred alternative; previously for the listeners of experiment 1 it was intensity. It is difficult to interpret these differences inasmuch as a different group of listeners participated in experiment 3 than had participated in experiments 1 and 2. It is possible that the differences merely reflect individual differences in cue preference. Nevertheless, these comparisons do not significantly impact on the interpretation of the Doppler cue. In this regard, we note that the relative weights continue to show a clear preference for Doppler in the discrimination of velocity and acceleration. Moreover, the group estimates of threshold for velocity and acceleration differ across the three experiments no more than would be expected based on normal error variation. These results support the conclusion that the Doppler cue in these experiments reflects a discrimination based on the rate of change of frequency for each source, rather than a simple difference in frequency between the two sources at a single point in time.

D. Experiment 4: Discrimination at high velocity

In all preceding experiments the velocity of the standard source was selected to be 10 m/s, great enough to produce a perceptible Doppler effect. Since listeners prefer this cue in the discrimination of velocity and acceleration, the pattern of weights must inevitably change at lower velocities where the Doppler effect becomes imperceptible. An interesting question, however, is whether the pattern of weights would also change at velocities higher than 10 m/s where the Doppler effect becomes more salient. Note that, by comparison, both the ITD and intensity cue have an upper bound as velocity (distance) increases. In particular, the ITD can never exceed the maximum delay across the head, and the intensity at some distance becomes inaudible. An increase in salience of the Doppler effect might not be expected to strengthen the existing preference for Doppler in the discrimination of velocity and acceleration, but it might be expected to cause a shift in preference away from ITD or intensity in the discrimination of displacement. Experiment 4 was undertaken to test this possibility. All conditions were identical to those of experiment 1 except the velocity of the standard was changed to 50 m/s, just slightly greater than 100 mi/h. This value was chosen to be at the upper limit of everyday experience, for example, what one might experience passing oncoming traffic on a busy highway.

The results of experiment 4 are shown in Table IV and Fig. 8. Once again, the averaged thresholds are in good agreement with those from the previous experiments. The weights, however, now indicate a clear preference for the Doppler cue in all three discrimination tasks.

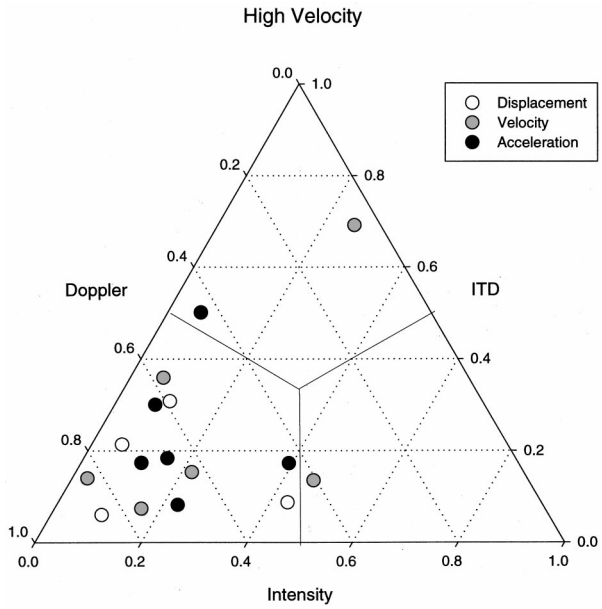

FIG. 8. Same as Fig. 4 except relative weights are from experiment 4, high velocity.

III. DISCUSSION

The results of the present series of experiments reveal both individual and task differences in the cues used to discriminate simple changes in motion. At a moderate velocity of 10 m/s, intensity and interaural time differences are most preferred for the discrimination of displacement, while the Doppler effect, as the rate of change of frequency, is preferred by most for the discrimination of velocity and acceleration. At a high velocity of 50 m/s there is a general preference for Doppler effect in all discrimination tasks with few exceptions.

It is of interest to compare these results to those of Rosenblum *et al.* (1987) who used a similar technique to measure relative preference for cues in judging the point of closest approach. Their experiment is most like our displacement discrimination task, inasmuch as velocity and acceleration were held constant for all conditions, and only displacement was changed to change the point of closest approach. Remarkably, at the moderate velocities used in both experiments, the relative preference for cues reported by Rosenblum *et al.* is similar to that observed for our displacement discrimination task; with intensity and ITD being the predominant cues followed by Doppler effect. There are many differences between these studies that might have been expected to yield a different result. Apart from the obvious difference in task, we simulated uninterrupted continuous motion, whereas Rosenblum *et al.* used a sequence of half-second, steady-state tones to simulate motion in discrete steps. The agreement of results despite these differences perhaps attests to the robustness of the relative preference for these cues in tasks involving judgments of displacement.

The present results also have implications for the snapshot hypothesis. Our data would seem to support this hypothesis inasmuch as the displacement, velocity, and acceleration thresholds in all conditions are quite similar to one another

when expressed as total angular displacement. In this regard our results replicate those of Grantham (1986). Analysis of cue preference, however, presents a very different picture. If in each case threshold is mediated by the same change in total displacement, then one might have expected that the acoustic cue or cues used to discriminate displacement would also be the same in each case. The present results show that this is not so, at least not at the moderate velocity. Although the preferred cues for the discrimination of velocity and acceleration are similar to one another, they are both qualitatively different from the preferred cues for the discrimination of displacement. The implication is that the perception of velocity and acceleration is mediated differently than the perception of simple displacement. This was also the conclusion reached by Wang and Lutfi (1994). These authors found that differential thresholds for velocity and acceleration were better related to each other by the equations for motion than either was related by these equations to the differential thresholds for displacement. Such results suggest that much might be learned by regularly examining the relation between cue weights and motion thresholds for each listener. The specific relation between cue weights and motion thresholds within a listener, and across various motion discrimination tasks, would likely allow for stronger statements regarding proposed theories of motion detection.

At present, we can only speculate regarding the reason for the observed qualitative differences in cue weights in these experiments. One possibility is that the cue weights reflect the relative discriminability of the cues in the different discrimination tasks. Our analysis of the acoustic cues in Sec. I B showed that, for particular points in the trajectory, the differences in frequency, intensity, and ITD are significantly greater than the just-noticeable difference for these cues measured under static listening conditions. This would suggest that differential sensitivity for these cues would not be a limiting factor in these experiments. However, such comparisons do not take into account the possible influence on sensitivity of the dynamic variation in these cues, or the potentially disruptive influence of one cue on another. Either of these factors could affect sensitivity by adding uncertainty or noise to the decision process. Moreover, either of these factors could cause one or another cue to become more or less discriminable as conditions change in the different discrimination tasks. In this sense, the observed pattern of weights, rather than diverging from the ideal, may in fact be optimized for motion detection within the measured limits of cue discriminability as they change from one condition to the next. Adequate treatment of this issue requires a careful examination of the relation between the individual cue discriminabilities and cue weights—a relation we hope to describe in a subsequent paper.

Finally, we conclude with a note regarding the stimulus synthesis technique. The technique undoubtedly represents an advance over past attempts to simulate auditory motion over headphones. However, it has its shortcomings. Most importantly, it did not include reflections of the incoming sound by the pinnae which occur naturally for a real moving source. Such reflections serve to filter the incoming sound differently depending on the direction of the source. Without them the sound image over headphones appears inside the head, clearly unlike that in everyday listening (Wightman and Kistler, 1993). It is impossible to say how the results of our experiments might have been affected by this factor. Techniques for simulating the dynamic effects of pinnae filtering for a moving source are available, but have yet to be tested experimentally (Jenison *et al.*, 1998). We hope to pursue this in a future study. In the meantime, we take the present results as evidence that auditory motion perception is both mutable and complex, and not likely to be described in all circumstances by simple models that assume a single detection strategy.

ACKNOWLEDGMENTS

The authors wish to thank Dr. Daniel Ashmead, Dr. D. Wesley Grantham, Dr. Lawrence D. Rosenblum, and an anonymous reviewer for comments on an earlier version of this manuscript. This research was supported by a grant from the NIDCD (R01 CD01262-08).

[1]Note that the displacement angle depends on the point in the trajectory at which it is measured. There is little evidence that listeners are differentially sensitive to changes in motion displacement between $\phi = 0 - 45°$ (Grantham, 1986). We have chosen, therefore, to measure at $\phi = 45°$ because the endpoint of the trajectory marks a likely place where listeners might be expected to detect a change in displacement, and is most consistent with a discrimination of total displacement as the snapshot hypothesis suggests.

[2]It is possible, of course, to control for the confounding in the displacement discrimination task by equating the starting points and changing the duration of the trajectory. This, however, merely creates a different and perhaps more serious confounding—that of a difference in stimulus duration between target and standard. It is for this reason that we chose to introduce the change in displacement in experiment 1 as we did.

Ahissar, M., Ahissar, E., Bergman, H., and Vaadia, E. (**1992**). ''Encoding of sound source location and movement: Activity of single neurons and interactions between adjacent neurons int he monkey auditory cortex,'' J. Neurophysiol. **67**, 203–215.

Andersen, R. A. (**1997**). ''Neural mechanisms of visual motion perception in primates'' Neuron **18**, 865–872.

Chandler, D. W., and Grantham, D. W. (**1992**). ''Minimum audible movement angle in the horizontal plane as a function of simulus frequency and bandwidth, source azimuth, and velocity,'' J. Acoust. Soc. Am. **91**, 1624–1636.

Durlach, N. I., and Colburn, H. S. (**1978**). ''Binaural phenomena,'' in *Handbook of Perception, Vol. IV, Hearing*, edited by E. C. Carterette and M. P. Friedman (Academic, New York), pp. 416–421.

Grantham, D. W. (**1986**). ''Detection and discrimination of simulated motion of auditory targets in the horizontal plane,'' J. Acoust. Soc. Am. **79**, 1939–1949.

Grantham, D. W. (**1989**). ''Motion aftereffects with horizontally moving sound sources in the free field,'' Percept. Psychophys. **45**, 129–136.

Grantham, D. W. (**1992**). ''Adaption to auditory motion in the horizontal plane: Effect of prior exposure to motion on motion detectability,'' Percept. Psychophys. **52**, 144–150.

Harris, J. D. (**1972**). ''A florilegium of experiments on directional hearing,'' Acta Oto-Laryngol. Suppl. **298**, .

Harris, J. D., and Sergeant, R. L. (**1971**). ''Monaural/binaural minimum audible angle for a moving sound source,'' J. Speech Hear. Res. **14**, 618–629.

Jenison, R. L. (**1997**). ''On acoustic information for motion,'' Ecol. Psychol. **9**, 131–151.

Jenison, R. L., and Lutfi, R. A. (**1992**). ''Kinematic synthesis of auditory motion,'' J. Acoust. Soc. Am. **92**, 2548.

Jenison, R. L., Neelon, M. F., Reale, R. A., and Brugge, J. F. (**1998**). ''Synthesis of virtual motion in 3D auditory space,'' IEEE Eng. Med. Bio. Mag. **20**, 1096–1100.

Jesteadt, W., Wier, C. C., and Green, D. M. (**1977**). ''Intensity discrimination as a function of frequency and sensation level,'' J. Acoust. Soc. Am. **61**, 169–177.
Kuhn, G. F. (**1977**). ''Model for the interaural time differences in the azimuthal plane,'' J. Acoust. Soc. Am. **62**, 157–167.
Lutfi, R. A. (**1995**). ''Correlation coefficients and correlation ratios as estimates of observer weights in multiple-observation tasks,'' J. Acoust. Soc. Am. **97**, 1333–1334.
Macmillan, N. A., and Creelman, C. D. (**1991**). *Detection Theory: A User's Guide* (Cambridge University Press, Cambridge, England).
Mills, A. W. (**1958**). ''On the minimum audible angle,'' J. Acoust. Soc. Am. **30**, 237–246.
Morse, P. M., and Ingard, K. U. (**1986**). *Theoretical Acoustics* (Princeton University Press, Princeton, NJ).
Movshon, J. A. (**1975**). ''The velocity tuning of single units in cat striate cortex,'' J. Physiol. (London) **249**, 445–468.
Perrott, D. R., Constantino, B., and Ball, J. (**1993**). ''Discrimination of moving events which accelerate or decelerate over the listening interval,'' J. Acoust. Soc. Am. **93**, 1053–1057.
Perrott, D. R., and Musicant, A. D. (**1977**). ''Minimum auditory movement angle: Binaural localization of moving sound sources,'' J. Acoust. Soc. Am. **62**, 1463–1466.
Perrott, D. R., and Tucker, J. (**1988**). ''Minimum audible movement angle as a function of signal frequency and the velocity of the source,'' J. Acoust. Soc. Am. **83**, 1522–1527.
Richards, V. M., and Zhu, S. (**1994**). ''Relative estimates of combination weights decision criteria, and internal noise hased on correlation coefficients,'' J. Acoust. Soc. Am. **95**, 424–434.
Rosenblum, L. D., Carello, C., and Pastore, R. E. (**1987**). ''Relative effectiveness of three stimulus variables for locating a moving sound source,'' Perception **16**, 175–186.
Sovijärvi, A. R. A., and Hyvärinen, J. (**1974**). ''Auditory cortical neurons in the cat sensitive to the direction of sound source movement,'' Brain Res. **73**, 455–471.
Spitzer, M. W., and Semple, M. N. (**1991**). ''Interaural phase coding in auditory midbrain: influence of dynamic stimulus features,'' Science **254**, 721–724.
Tanner, Jr., W. P., and Birdsall, T. G. (**1958**). ''Definitions of d' and η as psychophysical measures,'' J. Acoust. Soc. Am. **30**, 922–928.
Wang, W., and Lutfi, R. A. (**1994**). ''Thresholds for detection of a change in displacement, velocity, and acceleration of a synthesized sound-emitting source,'' J. Acoust. Soc. Am. **95**, 2897A.
Wier, C. C., Jesteadt, W., and Green, D. M. (**1977**). ''Frequency discrimination as a function of frequency and sensation level,'' J. Acoust. Soc. Am. **61**, 178–184.
Wightman, F. L., and Kistler, D. J. (**1993**). ''Sound localization,'' in *Human Psychophysics*, edited by R. Fay, A. Popper, and W. Yost (Springer-Verlag, New York).

Can macaques perceive place of articulation from formant transition information?

Joan M. Sinnott[a] and Trina L. Williamson
Comparative Hearing Laboratory, Psychology Department, University of South Alabama, Mobile, Alabama 36688

(Received 8 October 1998; revised 4 February 1999; accepted 5 April 1999)

An important problem in speech perception is to determine how humans extract the perceptually invariant place of articulation information in the speech wave across variable acoustic contexts. Although analyses have been developed that attempted to classify the voiced stops /b/ versus /d/ from stimulus onset information, most of the human perceptual research to date suggests that formant transition information is more important than onset information. The purpose of the present study was to determine if animal subjects, specifically Japanese macaque monkeys, are capable of categorizing /b/ versus /d/ in synthesized consonant–vowel (CV) syllables using only formant transition information. Three monkeys were trained to differentiate CV syllables with a ''go-left'' versus a ''go-right'' label. All monkeys first learned to differentiate a /zɑ/ versus /dɑ/ manner contrast and easily transferred to three new vowel contexts /ɔ, ɛ, ɪ/. Next, two of the three monkeys learned to differentiate a /bɑ/ versus /dɑ/ stop place contrast, but were unable to transfer it to the different vowel contexts. These results suggest that animals may not use the same mechanisms as humans do for classifying place contrasts, and call for further investigation of animal perception of formant transition information versus stimulus onset information in place contrasts. © *1999 Acoustical Society of America.* [S0001-4966(99)04007-2]

PACS numbers: 43.66.Gf, 43.71.Es [JH]

INTRODUCTION

A primary issue in speech perception research is to determine what kind of mechanism humans use to extract the perceptual invariance from the highly variable acoustic information that cues phonetic categories across different contexts. The invariance problem is most noticeable in differentiating the place of articulation contrast in stops, e.g., /b–d–g/ or /p–t–k/. For example, early research at the Haskins Laboratories during the 50's was relatively successful in discovering the relevant acoustic cues for voicing and various manner distinctions, but those for place remained elusive (see Liberman, 1996, for a review). Specifically, experimentation with burst frequencies, rising and falling $F2$ transitions, and $F2$ transition loci revealed that none of these cues was sufficient to differentiate all place categories in all vowel contexts, although some cues would sometimes work for one category in all vowel contexts, e.g., a noise burst with a center frequency above 3000 Hz cued a /t/ rather than a /p/ or /k/ (Liberman *et al.*, 1952); a rising $F2$ cued a /b/ rather than a /d/ or /g/ (Liberman *et al.*, 1954); an 1800-Hz locus cued a /d/ rather than a /b/ or a /g/ (Delattre *et al.*, 1955).

An interesting analysis to classify place was developed by Stevens and Blumstein (1978). They synthesized the voiced stops /b, d, g/ in CV syllables with the different vowels /a, i, u/, systematically manipulating the burst frequencies and formant transitions according to theoretical considerations concerning how sounds are generated in the vocal tract as place varies. They proposed that invariant place cues may reside, not so much in exact measures of burst and transition frequencies, but in a rather gross measure of the first 26 ms of the consonantal release. The onset spectrum showed a distinctive shape for each place: (1) a diffuse-falling spectrum for /b/, (2) a diffuse-rising spectrum for /d/, and (3) a prominent mid-frequency peak for /g/. These attributes were evident for stimuli containing transitions only, but were much enhanced by the presence of noise bursts at the onset.

Later refinements of this analysis were subsequently developed that incorporated time-varying features into the classification schemes. For example, Kewley-Port's (1983) running spectral displays derived from linear prediction analysis examined the initial 40 ms of natural CV syllables, and she reported improved classification of /g/, but not of /b/ and /d/. Lahiri *et al.* (1984) examined the change in the distribution of spectral energy from burst to voicing onset, rather than a static onset spectrum, and they reported success in classifying place contrasts in languages other than English.

However, while these analyses were focusing, for the most part, on onset spectra, perceptual research seemed to indicate that formant transition information was actually more important than onset phenomena in human classification of voiced place stops. For example, Stevens and Blumstein (1978) presented full and partial-cue (i.e., burst-only or transitions-only) stimuli to listeners and found that ''transitions-only'' stimuli were identified much better than ''burst-only'' stimuli (81% and 18% correct, respectively).

In a later ''conflicting-cue'' experiment, Blumstein *et al.* (1982) presented listeners with synthetic /b/ and /d/ stimuli that had appropriate formant transitions, but with onset spectra appropriate for either /b/ or /d/. They found that identification was determined primarily by the formant transitions,

[a]Electronic mail: jsinnott@jaguar1.usouthal.edu

although an inappropriate onset spectrum reduced performance somewhat. The authors conceded ''*although the invariant properties residing in the gross spectral shape of the onset spectrum may serve as a classificatory framework for the phonetic dimensions of natural language, they may not provide the primary perceptual attributes of place-of-articulation in ongoing speech processing*.'' Walley and Carrell (1983) also conducted a conflicting-cue study with both children and adults identifying /b,d,g/ and reported similar results indicating the perceptual primacy of formant transition information.

Most recently, Smits *et al.* (1996a, b) compared the perceptual relevance of bursts and transitions for /b/ and /d/ identification in Dutch voiced stops. For transitions-only stimuli, they found average rates of correct recognition to be 92% (/b/=96%; /d/=87%), much higher than those for burst-only stimuli (61%), leading them to conclude that formant transitions give a better account of perceptual data than gross onset cues such as global spectral tilt or its initial shape.

In fact, the only study to suggest that listeners might use stimulus onset over transitional information in classifying place in voiced stops comes from Lahiri *et al.* (1984), who conducted a conflicting-cue study in which /b/ and /d/ stimuli with normal transitional information were given conflicting time-varying onset spectra. Results showed that for /b/ stimuli, identification shifted to /d/ when a /d/ spectrum was added, but results were not clear for /d/ stimuli, where identification appeared to deteriorate to chance levels. Nevertheless, a replication of this study by Dorman and Loizou (1996), using different stimuli, led to the opposite result—that formant transition information was most important for listeners.

To summarize, most of the human perceptual studies that have compared stimulus-onset phenomena with formant transition information have shown the greater importance of transitions.

An important question is thus whether or not invariant place cues exist in the formant transitions, as opposed to the onset phenomena. Kewley-Port (1982) measured the formant transitions in natural speech tokens of /b,d,g/ in the context of eight vowels using linear prediction analysis in an attempt to find invariant acoustic loci. The only ones she found were for the alveolar stop /d/ ($F2=1797$ Hz; $F3=2581$ Hz), with her $F2$ locus at 1797 Hz very close to the 1800-Hz value first reported by Delattre *et al.* (1955). She did not find invariant acoustic loci for /b/ or /g/, however.

More recent work by Sussman *et al.* (1991) has focused new attention on formant transition information for place classification. They developed the concept of a ''locus equation'' as a source of *relational invariance* for place classification. A locus equation is a straight-line regression fit to data points formed by plotting $F2$ onsets as a function of $F2$ at the midvowel nuclei. They examined natural speech tokens of /b,d,g/ for 20 speakers in 10 vowel contexts, and found very linear regression functions characterized by distinct slopes and *y*-intercepts for each place. For example, /b/ had the steepest slope, /d/ had the flattest slope, and /g/ had two distinct slopes for velar and palatal articulation.

Further research by Fruchter and Sussman (1997) has shown good correspondence between locus equation acoustic data and identification frequencies, arguing for the perceptual relevance of these equations. However, some problems remain concerning locus equations: First, they are calculated using information from the midportion of the vowel accompanying the transition, yet studies have shown that /b,d,g/ can be fairly well identified from truncated CV syllables as short as 10–20 ms, clearly before the midpoint of the vowel (Blumstein and Stevens, 1980; Kewley-Port *et al.*, 1983). Second, Fowler (1994) has pointed out that the locus equations derived from stops are not the same as those derived from different manners of articulation (e.g., fricatives), so the equations are not as parsimonious as would be desired.

To summarize, although much has been learned about place classification from signal analysis and human perceptual studies, many questions remain concerning these rather elusive acoustic cues for place. Another important way in which the mechanisms of place perception in humans could be clarified is to examine the facility with which animal subjects can make these classifications. If animals can perceive these as effectively as humans, these results would provide evidence that the underlying mechanisms for place classification, in particular with regard to the invariance problem, can be explained by general auditory processes, and do not require extensive functional experience with human language in either the auditory or articulatory domain.

Two studies have used simple ''same–different'' discrimination procedures to examine monkey abilities to differentiate synthetic voiced place CV syllables with contrasting formant transitions and no bursts. Sinnott *et al.* (1976), used a ''repeating background procedure'' in which a monkey reported ''same'' by holding a response key during the background, and reported ''different'' by releasing the key when the background changed to a target stimulus. Monkeys easily discriminated /ba/ from /da/, and vice versa, although their difference limens along the /ba–da/ continuum were twice as high (320 Hz) as humans' (160 Hz).

Kuhl and Padden (1983) presented monkeys with same and different trials. In same trials, four identical stimuli were presented; in different trials, the last pair of stimuli was different from the first pair. A monkey was required to hold a response key for a same response, and to release it for a different response. The authors showed that monkeys could make two-step discriminations along a /b–d–g/ continuum, and exhibited phonetic boundaries in the regions of English place.

Basically, these two studies show that place contrasts consisting of formant transition differences are well discriminated by monkeys. An entirely different question, however, is the extent to which animals are capable of *categorizing* place contrasts. In a categorization task, stimuli to be differentiated are presented in variable contexts, and the subject must extract the relevant cues underlying each category and provide a ''label'' for each.

Only one experiment has been published examining animal categorization of place contrasts. Kluender *et al.* (1987) presented Japanese quail with natural speech CV tokens spoken by a male speaker. On any given trial, birds were pre-

sented with either /b/, /d/, or /g/ stimuli, and were intermittently reinforced for pecking in the presence of /d/ stimuli and for not pecking in the presence of /b/ or /g/ stimuli. Thus, birds applied a ''peck'' label for /d/ stimuli and a ''no-peck'' label for /b/ and /g/ stimuli. Birds were trained on four different vowels, all ending in /s/: /is/, /us/, /aes/ and /as/, and generalized to eight novel vowels /ls/, /Us/, /es/, /ʌs/, /e^{y}s/, /o^{w}s/, /o^{y}s/ and /ɜ˞s/. Birds had significantly higher pecking rates in the presence of the syllables beginning with /d/ compared to /b/ or /g/. The authors claimed that extensive acoustic analysis of the stimuli, in terms of voice-onset time, second formant onset transition, burst frequency, or burst amplitude, could not reveal any acoustic properties of the signals that totally differentiated the /d/ stimuli from the /b/ and /g/ stimuli. Hence, the authors claimed, the quail must have adopted a more complex strategy for mapping stimuli into categories, a strategy that current acoustic analyses could not uncover.

The evidence so far from the quail study suggests that animals may be sensitive, at least to some degree, to the invariance underlying natural place contrasts. The quail results seem to challenge theories of speech-sound categorization that posit uniquely human capacities in the extraction of invariance (e.g., Liberman *et al.*, 1967). However, even if human-specific mechanisms are not required to form place categories in natural speech, it still remains to be determined if in fact animals are using the same mechanisms as human use in this complex behavior.

One important way in which human and animal sensitivity to place categories could be further compared is to break the natural multidimensional speech stimuli down into simpler well-specified components by using synthetic speech. We could then determine if animals are responding to the same components in the stimuli as are humans. As discussed above, most of the perceptual research to date with humans has indicated that formant transitions are more important than stimulus-onset phenomena for place classification. Thus, our goal was to determine if monkeys could categorize the synthetic place contrast, /b/ versus /d/, based on formant transition information only. As control stimuli, we also presented the monkeys with the manner contrast, /z/ versus /d/ (fricative versus stop), for which there is a highly salient acoustic cue, i.e., the presence of noise in /z/ versus its absence in /d/.

I. METHOD

A. Subjects

The monkey subjects were three Japanese macaques (*Macaca fuscata*): Dart, Harry, and Port, all males about 12 years old. The human subjects were the two authors and three undergraduate students who worked in the lab. All monkey and human subjects had normal hearing, as measured by audiograms in our lab, and all had had some previous experience listening to synthetic speech sounds.

B. Apparatus

During testing, a monkey sat in a primate restraint chair. The chair was locked into position within a double-walled, IAC booth ($1.98\times1.82\times1.52$ m) padded with sound-insulating acoustic foam (Sonex Acoustical Products). Audio signals were presented through a Polk 10 loudspeaker, the distance between the speaker and a subject's head was 84 cm. The monkey responded by contacting a three-position lever mounted onto the chair and moving the lever in either a left or right position in response to the stimuli. The lever automatically reverted to a middle position upon release. A cue light was attached to the lever mounting and another was placed above the speaker. Next to the lever was a food cup attached to an automatic feeder (Gerbrands) located on the wall of the booth. The monkey earned 190-mg banana- or bacon-flavored food pellets for correct identification responses. Humans were tested similarly, seated in an ordinary chair with the lever apparatus mounted on a stand before them. Humans received auditory feedback from the feeder for correct identification responses. Stimulus delivery, experimental contingencies, and response recording were controlled by a Compaq computer. The analog-to-digital (A-D) converter, interfaces, 8000-Hz filter, and attenuators were all Tucker-Davis Technologies equipment. The amplifier was 3240DE NAD.

C. Stimuli

The CV stimuli were synthesized (10-kHz sampling rate) using the COMPUTERIZED SPEECH RESEARCH ENVIRONMENT (AVAAZ Innovations, Ontario, Canada), and consisted of the three consonants /z,d,b/, each coupled with the four vowels /ɑ,ɔ,ɛ,ɪ/. Specifications into the synthesizer were as follows: The steady-state portions of the vowels were always 270 ms long. $F0$ started at 120 Hz at vowel onset and ended at 80 Hz. The first three vowel formant frequencies ($F1-F3$), amplitudes ($A1-A3$), and bandwidths ($B1-B3$) are shown in Table I(a). $A4$, $A5$, and $A6$ remained constant at 20 dB, decreasing to 0 dB in the last 50 ms. Note that the two back vowels /ɑ/ and /ɔ/, have relatively low $F2$s, while the two front vowels /ɛ/ and /ɪ/, have higher $F2$s. These particular vowel formant frequencies were based on values presented in Petersen and Barney (1952).

The /z/ CV stimuli consisted of a 100-ms frication period (30-ms rise time), followed by a 30-ms formant transitional period, and the 270-ms steady-state vowel, resulting in a total duration of 400 ms. The overall voicing amplitude (AV) started at 0 dB, rose to 30 dB during the first 30 ms of frication, remained steady until 90 ms, rose to 55 dB at 100 ms (formant-transition onset), remained steady until 350 ms, and fell to 0 dB during the last 50 ms. $F1$ remained at 320 Hz during frication. $A1$ had a 10-ms rise time to 20 dB, remaining steady during frication. $A2$ and $A3$ were off during frication. $A4-A6$ were 20, 45, and 45 dB, respectively, with a 10-ms rise time. Frication amplitude (AF) was 45 dB. The formant onset frequencies are shown in Table I(b).

The /b/ and /d/ CVs each consisted of an initial 30-ms transition, coupled with a 270-ms vowel, resulting in a total duration of 300 ms. AV was set to 55 dB for 250 ms, with a 50-ms fall time. The formant onset frequencies are shown in Table I(b). Note that for /b/, $F2$ started 700 Hz in the back vowels /ɑ/ and /ɔ/, and at a higher frequency (1200 Hz) in

TABLE I. (a) Voicing amplitude (AV), formant frequencies ($F1$, $F2$, $F3$), amplitudes ($A1$, $A2$, $A3$) and bandwidths ($B1$, $B2$, $B3$) of the four steady-state vowel stimuli. (b) Formant frequencies at transition onset for /z/, /d/, and /b/ in the context of the four vowels.

(a)

	/ɑ/	/ɔ/	/ɛ/	/ɪ/
AV (dB)	55	55	55	55
$F1$ (Hz)	730	570	530	390
$F2$ (Hz)	1090	840	1840	1990
$F3$ (Hz)	2440	2410	2480	2550
$A1$ (dB)	50	49	47	50
$A2$ (dB)	46	47	43	40
$A3$ (dB)	27	20	42	41
$B1$ (Hz)	50	50	50	50
$B2$ (Hz)	70	70	70	70
$B3$ (Hz)	110	110	110	110

(b)

		/ɑ/	/ɔ/	/ɛ/	/ɪ/
z	$F1$ (Hz)	320	320	320	320
	$F2$ (Hz)	1700	1700	1800	1800
	$F3$ (Hz)	3000	3000	3000	3000
/d/	$F1$ (Hz)	400	150	150	150
	$F2$ (Hz)	1700	1700	1800	1800
	$F3$ (Hz)	3000	3000	3000	3000
/b/	$F1$ (Hz)	400	150	150	150
	$F2$ (Hz)	700	700	1200	1200
	$F3$ (Hz)	2000	2000	2000	2000

the front vowels /ɛ/, and /ɪ/. Nevertheless, all the /b/ CVs were ''invariant'' in that all contained rising $F2$ transitions. Also note that all the /d/ CVs were invariant in that they all contained nearly identical starting frequencies of either 1700 Hz (back vowels) or 1800 Hz (front vowels). These particular formant-onset frequencies were chosen by the authors as resulting in optimal perception of /b/ and /d/ for each vowel context. Figure 1 plots the frequency of $F2$ onset for our synthetic /b/ and /d/ CVs as a function of $F2$ of the four steady-state vowels. The data points resemble the ''locus equation'' analysis proposed by Sussman *et al.* (1991), in that /b/ has a steeper slope and lower intercept than /d/.

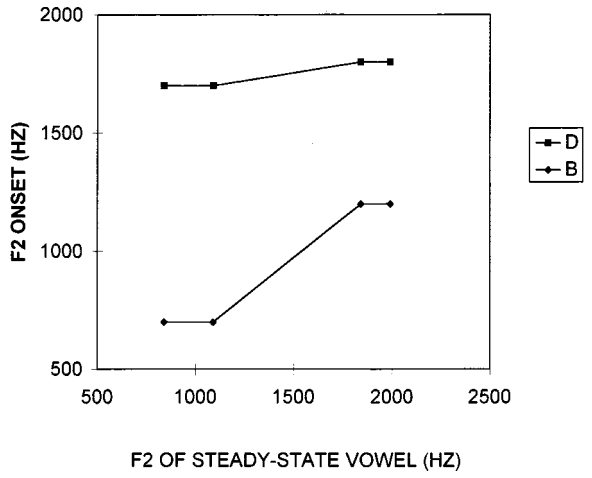

FIG. 1. Locus equation data points for the /b/ and /d/ stimuli in the context of four different vowels /ɑ,ɔ,ɛ,ɪ/. $F2$ onset is plotted as a function of vowel $F2$.

Note that the steady-state vowels for all CVs were 270 ms in duration. Thus, the overall durations of the /z/ CVs were 100 ms longer than the /b,d/ CVs. Nevertheless, these stimuli were perceived by the authors as more similar in duration than other /z/ stimuli that we synthesized in which overall syllable duration was held at 300 ms, resulting in a 170-ms vowel for /z/, and a 270-ms vowel for /b,d/. Thus, we elected to use stimuli that had equal vowel durations, rather than equal total durations.

All stimuli were presented at 60 dBA, which is approximately a 50-dB sensation level for human and monkey subjects tested in our free-field situation.

D. Procedure

To test the monkeys' speech-categorization abilities, we used a go-left/go-right procedure developed by Owren (1990). At the beginning of a trial, the flashing cue light signaled to the subject that a trial could be initiated by touching the lever. Upon contact, the cue light stopped flashing and remained bright. After a variable (1–2s) hold, a stimulus was presented, either a /z/ versus /d/ in condition 1, or a /b/ versus /d/ in condition 2. The /d/ stimulus always required pushing the lever to the right for reinforcement; the second stimulus, /z/ or /b/, always required a left response. The stimulus was continuously repeated until a response was made. If a subject released the lever before presentation of the sound, a prerelease error resulted. If the subject released after the sound was presented, or pushed the lever in the wrong direction, a miss resulted. Following misses or prereleases, the cue light extinguished for 8 s, during which the subject could not begin another trial. A correction procedure operated such that a missed stimulus was presented on subsequent trials until a correct response occurred. Responses from these trials were not counted in the data analysis; their purpose was to reduce left- or right-response biases in subjects. Monkeys worked for 150 rewards or 40 min; humans worked for 80 rewards or 15 min. Percent-correct responses to each stimulus were tabulated at the end of the session. Chance performance on the go-left/go-right procedure is 50% correct.

E. Monkey shaping

Prior to this experiment, the monkeys had never performed on a go-left/go-right procedure. Monkeys were shaped to move the key left or right in response to a stimulus while listening to a highly salient synthetic /i/ or /u/ stimulus. First, monkeys listened to a block of /i/ stimuli for all 150 trials. A lock was placed on the key so it only moved to the left. On alternating days, they listened to a block of /u/ stimuli, and the lock allowed movement only to the right. Once they had mastered this procedure, the lock was removed. When monkeys responded for 10 days with at least 85% correct for both the left and right stimuli, they were given 75 trials starting with /i/, switching to /u/ during the last 75 trials. The starting stimuli were alternated each day. After 5 days with at least 85% accuracy for both the left and

right sides, monkeys were moved to a block of 50 trials, then 25 trials, 10 trials, and finally 5 trials before being placed on the main testing experiment, in which both stimuli were presented randomly for all 150 trials. All monkeys learned to categorize /i/ and /u/ with greater than 90% accuracy for both the left- and right-side stimuli. This initial shaping required about 2–3 months for monkeys.

After initial training with the vowel stimuli, the monkeys were introduced to the CV syllables. In this process, a highly salient intensity cue (−15 dB) was added to the left-side stimulus (e.g., /zɑ/ or /bɑ/) , while the right side (/dɑ/) remained at 60 dBA SPL. Monkeys easily learned to respond to this highly salient intensity cue. When monkeys reached >=85% correct for both side stimuli at a given intensity level, the intensity of the left-side stimulus was increased by 1 dB per session until reaching 60 dBA. Monkeys typically required about 1–2 months to master the procedure using intensity shaping.

F. Methods of separate versus simultaneous presentation

We experimented with two methods of presenting stimuli to monkeys once they had learned to differentiate the manner and place contrasts using the single /ɑ/ vowel context. The *method of separate presentation* was used first. Here, the monkeys were first presented with the contrast in the context of the vowel /ɑ/. After performing for five consecutive daily sessions with >=85%-correct responses for both the left- and right-side stimuli at equal intensities for /ɑ/, they were then transferred to the /ɔ/ context for five sessions, then returned to /ɑ/ for five sessions, then transferred to the /ɛ/ context for five sessions, then returned to /ɑ/ for five sessions, and then finally transferred to the /ɪ/ context for five sessions. For monkeys, this method resulted in approximately 80 responses for each CV per session. Humans were not tested on this method.

If monkeys successfully transferred to new vowel contexts using the method of separate presentation, we then presented the stimuli according to the *method of simultaneous presentation*. Here, monkeys were presented with all four vowel contexts randomly presented together in each session for ten successive sessions. The purpose of this latter method was to determine if monkeys would become distracted by the varying vowel contexts presented simultaneously, possibly causing their performance to deteriorate. It is thus a more robust test of categorization than the method of separate presentation. For monkeys, this ''simultaneous'' method resulted in approximately 20 identifications per CV per session. Humans were tested for ten sessions using this method, resulting in about 10 responses per CV per session.

II. RESULTS

Since we tested only three monkeys, and because, to the best of our knowledge, speech-perception data have never been obtained from monkeys using a go-left/go-right procedure, we though it would be informative to readers to present each monkey's detailed response data on these tasks. These are shown in Appendix A–C.

A. Categorization of manner: /z/ versus /d/

In this condition, we asked if monkeys could learn to differentiate a manner (fricative versus stop) contrast /zɑ/ versus /dɑ/, and spontaneously transfer the distinction to the different vowels: /ɔ,ɛ,ɪ/.

Using the method of separate presentation, all three monkeys easily learned to differentiate the manner contrast in the /ɑ/ vowel context, performing at >=85% correct, averaged over the left and right side, for five successive test sessions. All monkeys also easily transferred to the new vowel contexts /ɔ,ɛ,ɪ/, where performance remained at >=85% correct, averaged over the five successive test sessions for each vowel context (see Appendix A).

All three monkeys also maintained the /z/ versus /d/ contrast when tested with the method of simultaneous presentation, in which vowel context varied randomly during the session. Each monkey's response scores, averaged over the left- and right-side stimuli, for the ten test sessions, remained at >=85% correct. For the most part, performance was even maintained at >=85% correct during the first five test sessions, except for two instances (Harry identifying /zɑ/ versus /dɑ/ (80% correct), and Port identifying /zɔ/ versus /dɔ/ (83% correct) (see Appendix B).

Human identification of /z/ versus /d/ was at 95%–100% correct for all vowel contexts, using the method of simultaneous presentation.

B. Categorization of place: /b/ versus /d/

In this condition, we asked if monkeys could learn to differentiate /bɑ/ versus /dɑ/ consisting of formant transition differences only and spontaneously transfer to the new vowels: /ɔ,ɛ,ɪ/.

One monkey (Port) was unable to learn to differentiate the initial training stimuli /bɑ/ versus /dɑ/ using the method of intensity shaping. He reached a level of −2 dB for /bɑ/ relative to /dɑ/, then performed for ten successive sessions at this level without reaching our criterion of >=85% correct. He was dropped from further experimentation. We did not attempt to train him with any other vowel context.

The two other monkeys, Dart and Harry, learned to differentiate /bɑ/ versus /dɑ/ at >=85% correct, and were transferred to the other vowel contexts using the method of separate presentation. However, neither monkey transferred to any other vowel context while maintaining >=85% correct, although Harry's performance for /bɔ/ versus /dɔ/ (83% correct) almost reached criterion (see Appendix C).

Figure 2 shows the performances of Dart and Harry on both the /z–d/ and the /b–d/ stimuli. Dart (top) clearly had no trouble with /z–d/, for either the separate or the simultaneous method of presentation. However, for /b–d/ (separate presentation) a different picture emerged. Although he learned /bɑ/ versus /dɑ/ to criterion, his performance did not approach criterion levels in the context of the next three vowels /ɔ,ɛ,ɪ/. Harry (bottom), also clearly had no trouble with /z–d/ in any conditions. Unlike Dart, Harry appeared to be able to transfer /b–d/ somewhat to the /ɔ/, vowel context, despite chance-level performance on the next two vowels /ɛ/ and /ɪ/. Due to their poor performance on the /b–d/ contrast

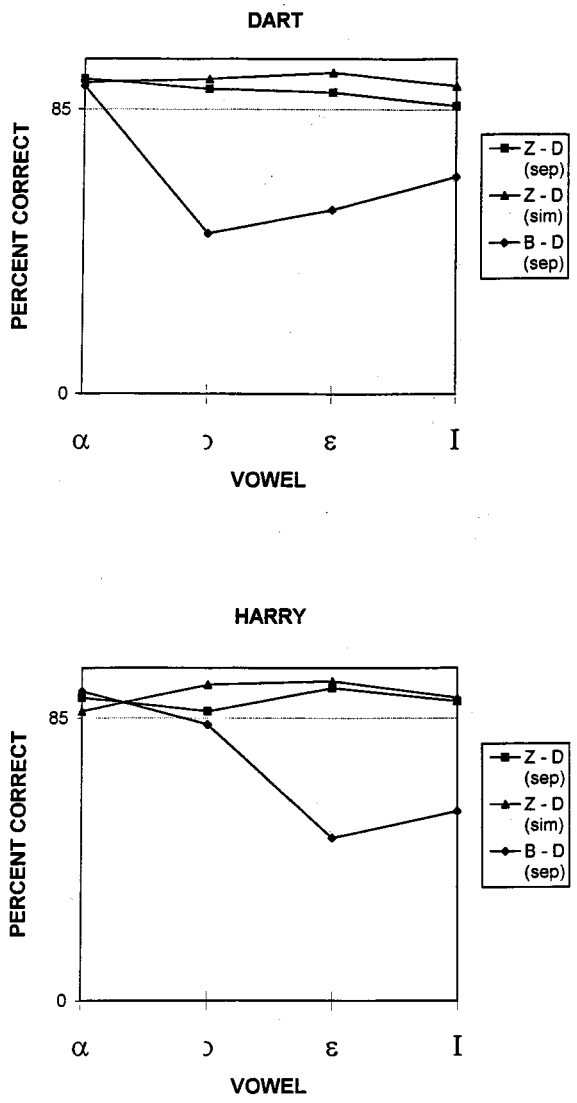

FIG. 2. Percent-correct identification of /z–d/ and /b–d/ in different vowel contexts by monkeys Dart and Harry (presentation methods: sep=separate; sim=simultaneous).

with the method of separate presentation, neither monkey was tested with the method of simultaneous presentation.

Human identification of /b/ versus /d/ was at 95%–100% correct for all vowel contexts, using the method of simultaneous presentation.

III. DISCUSSION

All three monkeys learned to reliably categorize the manner contrast /z–d/ in the context of the different vowels. However, all monkeys experienced various types of problems with the place contrast /b–d/.

One monkey (Port) was unable to differentiate /b/ from /d/ in our /ɑ/ training context. Therefore, the first question that arises is: How salient are the basic acoustic cues for differentiating /b/ from /d/ in an *identification*, as opposed to, a *discrimination* task? We know that monkeys can easily *discriminate* place contrasts (e.g., Sinnott *et al.*, 1976; Kuhl and Padden, 1983). However, some monkeys may not be as adept in differentiating place cues in the context of an identification procedure.

The second question is, given that monkeys can learn to differentiate a single place contrast using an identification procedure, can they extract the relevant cues that will allow them to transfer the contrast to other variable contexts? The answer may well be ''no.'' Dart, for example, learned to differentiate /bɑ/ versus /dɑ/ with no difficulty, but did not transfer to any other vowel context. Harry learned to identify /bɑ/ versus /dɑ/ and transferred somewhat to the /ɔ/ context, but not to the /ɛ/ and /ɪ/ contexts. Note that in the back vowels /ɑ/ and /ɔ/, $F2$ always rises for /b/ and always falls for /d/, whereas in the front vowels /ɛ/ and /ɪ/, $F2$ rises for both /b/ and /d/. Thus, $F2$ transition *direction* is a reliable cue for differentiating /b/ from /d/ in the back vowels, but not in the front vowels. Thus, Harry's performance suggests that he might have been basing his ''categorization'' on transition direction differences in $F2$.

As discussed earlier, all our /b/ stimuli were invariant with regard to the direction of $F2$, which rose for all the stimuli. In fact, a rising $F2$ transition was one of the first invariant /b/ cues discovered (Liberman *et al.*, 1954). Also, all our /d/ stimuli had nearly identical $F2$ onset frequencies in the region of 1700–1800 Hz, close to the /d/ $F2$ locus documented by others (Delattre *et al.*, 1955; Kewley-Port, 1982; Sussman *et al.*, 1991). Our monkeys, however, did not seem to hear these cues as invariants for either /b/ or /d/ in our set of stimuli.

Despite the present results showing our monkeys' inability to *spontaneously* form a perceptual category for the place contrast based on formant transitions, it is too early to assume that monkeys cannot *learn* to use transition cues in place classification. While transitions seem to be the major cues for highly experienced humans in categorizing /b–d/, the possibility cannot be ruled out that other types of information may be initially more important. Perhaps experience with onset phenomena (e.g., bursts) is necessary before the associated context-dependent transitional cues can be used effectively in identification (e.g., Stevens and Blumstein, 1978). Also, locus equations for place are derived by analyzing many different vowel contexts simultaneously (Sussman *et al.*, 1991). Thus, one obvious future experiment would be to use the Kluender *et al.* (1987) presentation paradigm to train monkeys to categorize place using natural speech stimuli with a variety of different vowels, right from the start of training. Perhaps in this way monkeys could *learn* to attend to the formant transition cues in classifying place, since they do not appear to attend to them spontaneously.

It is also possible that monkeys simply cannot use formant transition information effectively in place classification, no matter how they are trained. Perhaps their poorer (than humans') difference limens for formant-frequency onsets (Sinnott *et al.*, 1976) make it difficult for them to effectively process transitions at a purely sensory level. Perhaps Kluender *et al.*'s (1987) quail were using stimulus-onset phenomena (i.e., largely bursts) in categorization, rather than transitions. Perhaps the locus equations developed by Sussman *et al.* (1991), even if relevant for human perception, are too complicated for monkeys to learn.

In view of this latter possibility, the authors must add one introspective, anecdotal account to this discussion, which has been alluded to by others (e.g., Liberman *et al.*, 1967; Xu *et al.* (1997). When we humans categorized the present /b–d/ stimuli in the context of the different vowels (at essentially 100% correct), we were not aware that we were listening to different types of formant transitions (i.e., with rising, falling, high, or low frequency onsets) that we had *learned* to group into a particular place category, either via association with a stimulus-onset template or a locus equation. Rather, it was as if we were hearing (i.e., inputting at a very low sensory level) a simple *sensation* (rather than a complex *perception*) at stimulus onset. Put simply, all the /bV/ onsets sounded alike and all the /dV/ onsets sounded alike. It is very strange to think that our monkeys apparently did not experience these simple (for humans) sensations when they listened to these stimuli.

ACKNOWLEDGMENTS

This research was supported by NIH Grant No. PHS R01 DC 00541 to J.M.S. T.L.W. was the recipient of a Carol P. Sinnott Student Research Award and these data are based on her Senior Honors Thesis. We thank Kelly Mosteller, April Glenn, and Chris Williamson for participating as human subjects and for testing monkeys.

APPENDIX A

Percent-correct identification by three monkeys (Dart, Harry, Port) for the /z/ versus /d/ contrast in the context of four vowels over five consecutive testing sessions using the method of successive presentation. L=left; R=right. Boxed numbers are scores averaged over the right- and left-side stimuli for five successive test sessions.

	DAR			HAR			POR			
	L	R	L+R	L	R	L+R	L	R	L+R	
1	87	97	92	93	85	89	92	93	93	
2	93	97	95	96	92	94	85	88	87	
3	92	99	96	91	85	88	92	93	93	/ɑ/
4	88	99	94	93	89	91	85	91	88	
5	88	100	94	96	85	91	91	85	88	
Mean	90	98	94	94	87	91	89	90	90	
1	86	95	91	91	88	90	81	88	85	
2	83	96	90	85	88	87	87	85	86	
3	89	97	93	92	71	82	87	87	87	/ɔ/
4	89	100	95	91	80	86	86	78	82	
5	81	96	89	91	88	90	89	88	89	
Mean	86	97	91	90	83	87	86	85	86	
1	83	96	90	92	92	92	93	87	90	
2	81	95	88	92	99	96	88	91	90	
3	85	87	86	93	93	93	92	93	93	/ɛ/
4	89	92	91	95	95	95	93	93	93	
5	91	97	94	97	93	95	89	93	91	
Mean	86	93	90	94	94	94	91	91	91	
1	76	81	79	92	85	89	87	89	88	
2	89	92	91	93	86	90	88	88	88	
3	81	87	84	93	92	93	88	86	87	/ɪ/
4	85	87	86	88	88	88	91	92	92	
5	87	95	91	92	92	92	89	91	90	
Mean	84	88	86	92	89	90	89	89	89	

APPENDIX B

Percent-correct identification by three monkeys (Dart, Harry, Port) for the /z/ versus /d/ contrast in the context of four vowels over the first five and the last five testing sessions using the method of simultaneous presentation. L=left; R=right. Boxed numbers are scores averaged over the left- and right-side stimuli for ten successive sessions.

	DAR			HAR			POR			
	L	R	L+R	L	R	L+R	L	R	L+R	
sessions 1–5	93	90	92	64	97	80	87	91	89	
sessions 5–10	100	90	95	89	99	94	94	97	95	/ɑ/
Mean	96	90	93	76	98	87	91	94	92	
sessions 1–5	85	99	92	98	92	95	70	96	83	
sessions 5–10	92	100	96	99	93	96	89	97	93	/ɔ/
Mean	88	100	94	99	92	95	80	97	88	
sessions 1–5	90	99	95	98	94	96	91	89	90	
sessions 5–10	93	100	96	98	94	96	94	90	92	/ɛ/
Mean	92	100	96	98	94	96	93	90	91	
sessions 1–5	90	97	94	98	74	86	90	81	86	
sessions 5–10	81	98	90	98	94	96	97	83	90	/ɪ/
Mean	86	98	92	98	84	91	94	82	88	

APPENDIX C

Percent correct identification by two monkeys (Dart and Harry) for the /b/ versus /d/ contrast in the context of four vowels over five consecutive testing sessions using the method of successive presentation. L=left; R=right. Boxed numbers are scores averaged over the right- and left-side stimuli for five successive test sessions.

	DAR			HAR			
	L	R	L+R	L	R	L+R	
1	85	92	89	86	93	90	
2	89	92	91	96	92	94	
3	88	91	90	95	93	94	/ɑ/
4	88	99	94	92	93	93	
5	95	99	97	95	95	95	
Mean	89	95	92	93	93	93	
1	48	56	52	88	78	83	
2	48	52	50	77	93	85	
3	23	63	43	85	76	81	/ɔ/
4	6	88	47	88	77	83	
5	1	94	48	81	88	85	
Mean	25	71	48	84	82	83	
1	34	84	59	64	45	55	
2	20	81	51	44	31	38	
3	12	91	52	61	40	51	
4	24	91	58	58	30	44	/ɛ/
5	25	86	56	59	56	58	
Mean	23	87	55	57	40	49	
1	43	78	61	56	43	50	
2	35	86	61	55	55	55	
3	49	88	69	65	57	61	/ɪ
4	47	86	67	73	45	59	
5	55	83	69	69	56	63	
Mean	46	84	65	64	51	57	

Blumstein, S., Isaacs, E., and Mertus, J. (**1982**). ''The role of the gross spectral shape as a perceptual cue to place of articulation in initial stop consonants,'' J. Acoust. Soc. Am. **72**, 43–50.

Blumstein, S., and Stevens, K. (**1980**). ''Perceptual invariance and onset spectra for stop consonants in different vowel environments,'' J. Acoust. Soc. Am. **67**, 648–662.

Delattre, P., Liberman, A., and Cooper, F. (**1955**). ''Acoustic loci and transitional cues for consonants,'' J. Acoust. Soc. Am. **27**, 769–773.

Dorman, M., and Loizou, P. (**1996**). ''Relative spectral change and formant transitions as cues to labial and alveolar place of articulation,'' J. Acoust. Soc. Am. **100**, 3825–3830.

Fowler, C. (**1994**). ''Invariants, specifiers, cues: An investigation of locus equations as information for place of articulation,'' Percept. Psychophys. **55**, 597–610.

Fruchter, D., and Sussman, H. (**1997**). ''The perceptual relevance of locus equations,'' J. Acoust. Soc. Am. **102**, 2997–3008.

Kewley-Port, D. (**1982**). ''Measurements of formant transitions in naturally produced stop consonant–vowel syllables,'' J. Acoust. Soc. Am. **72**, 379–389.

Kewley-Port, D. (**1983**). ''Time varying features as correlates of place-of-articulation in stop consonants,'' J. Acoust. Soc. Am. **73**, 322–334.

Kewley-Port, D., Pisoni, D., and Studdert-Kennedy, M. (**1983**). ''Perception of static and dynamic acoustic cues to place of articulation in initial stop consonants,'' J. Acoust. Soc. Am. **73**, 1779–1793.

Kluender, K., Diehl, R., and Killeen, P. (**1987**). ''Japanese quail can learn phonetic categories,'' Science **237**, 1195–1197.

Kuhl, P., and Padden, D. (**1983**). ''Enhanced discrimination at the phonetic boundaries for the place feature in macaques,'' J. Acoust. Soc. Am. **73**, 1003–1010.

Lahiri, A., Gewirth, L., and Blumstein, S. (**1984**). ''A reconsideration of acoustic invariance for place of articulation in diffues stop consonants: Evidence from a cross-language study,'' J. Acoust. Soc. Am. **76**, 391–404.

Liberman, A. (**1996**). *Speech: A Special Code* (MIT Press, Cambridge, MA).

Liberman, A., Cooper, F., Shankweiler, D., and Studdert-Kennedy, M. (**1967**). ''Perception of the speech code,'' Psychol. Rev. **74**, 431–461.

Liberman, A., Delattre, P., and Cooper, F. (**1952**). ''The role of selected stimulus-variables in the perception of the unvoiced stop consonants,'' Am. J. Psychol. **65**, 497–516.

Liberman, A., Delattre, P., Cooper, F., and Gerstman, L. (**1954**). ''The role of consonant–vowel transitions in the perception of the stop and nasal consonants,'' Psych. Monog.: General and Applied **68**, 1–13.

Owren, M. (**1990**). ''Acoustic classification of alarm calls by vervet mon-

keys and humans I. Natural calls,'' J. Comp. Psych. **104**, 20–38.
Petersen, G., and Barney, H. (**1952**). ''Control methods used in a study of vowels,'' J. Acoust. Soc. Am. **24**, 175–184.
Sinnott, J. M., Beecher, M. D., Moody, D. B., and Stebbins, W. C. (**1976**). ''Speech sound discrimination by monkeys and humans,'' J. Acoust. Soc. Am. **60**, 687–695.
Smits, R., ten Bosch, L., and Collier, R. (**1996a**). ''Evaluation of various sets of acoustic cues for the perception of prevocalic stop consonants. I. Perception experiment,'' J. Acoust. Soc. Am. **100**, 3852–3864.
Smits, R., ten Bosch, L., and Collier, R. (**1996b**). ''Evaluation of various sets of acoustic cues for the perception of prevocalic stop consonants. II. Modeling and evaluation,'' J. Acoust. Soc. Am. **100**, 3865–3882.
Stevens, K., and Blumstein, S. (**1978**). ''Invariant cues for place of articulation in stop consonants,'' J. Acoust. Soc. Am. **64**, 1358–1368.
Sussman, H., McCaffrey, H., and Matthews, S. (**1991**). ''An investigation of locus equations as a source of relational invariance for stop place categorization,'' J. Acoust. Soc. Am. **90**, 1309–1325.
Walley, A., and Carrell, T. (**1983**). ''Onset spectra and formant transitions in the adult's and child's perception of place of articulation in stop consonants,'' J. Acoust. Soc. Am. **73**, 1011–1022.
Xu, Y., Liberman, A., and Whalen, D. (**1997**). ''On the immediacy of phonetic perception,'' Psych. Sci. **8**, 358–362.

The role of spectral and periodicity cues in auditory stream segregation, measured using a temporal discrimination task

Joyce Vliegen[a] and Brian C. J. Moore[b]
Department of Experimental Psychology, University of Cambridge, Downing Street, Cambridge CB2 3EB, United Kingdom

Andrew J. Oxenham[c]
Communication Research Laboratory (133 FR), Department of Speech-Language Pathology and Audiology, Northeastern University, Boston, Massachusetts 02115

(Received 2 October 1998; revised 20 March 1999; accepted 12 May 1999)

In a previous paper, it was shown that sequential stream segregation could be based on both spectral information and periodicity information, if listeners were encouraged to hear segregation [Vliegen and Oxenham, J. Acoust. Soc. Am. **105**, 339–346 (1999)]. The present paper investigates whether segregation based on periodicity information alone also occurs when the task requires *integration*. This addresses the question: Is segregation based on periodicity automatic and obligatory? A temporal discrimination task was used, as there is evidence that it is difficult to compare the timing of auditory events that are perceived as being in different perceptual streams. An ABA ABA ABA... sequence was used, in which tone B could be either exactly at the temporal midpoint between two successive tones A or slightly delayed. The tones A and B were of three types: (1) both pure tones; (2) both complex tones filtered through a fixed passband so as to contain only harmonics higher than the 10th, thereby eliminating detectable spectral differences, where only the fundamental frequency ($f0$) was varied between tones A and B; and (3) both complex tones with the same $f0$, but where the center frequency of the spectral passband varied between tones. Tone A had a fixed frequency of 300 Hz (when A and B were pure tones) or a fundamental frequency ($f0$) of 100 Hz (when A and B were complex tones). Five different intervals, ranging from 1 to 18 semitones, were used. The results for all three conditions showed that shift thresholds increased with increasing interval between tones A and B, but the effect was largest for the conditions where A and B differed in spectrum (i.e., the pure-tone and the variable-center-frequency conditions). The results suggest that spectral information is dominant in inducing (involuntary) segregation, but periodicity information can also play a role. [S0001-4966(99)04908-5]

PACS numbers: 43.66.Mk, 43.66.Hg [DWG]

INTRODUCTION

A rapid sequence of tones may be perceived in two ways: either as a single perceptual stream (called temporal coherence or integration), or as two or more perceptual streams, as if the sound were coming from two or more sources (called fission or segregation). Which of these occurs depends upon the frequency separation between successive tones and the presentation rate. In a rapid sequence of tones alternating between two frequencies, if the frequency difference between successive tones is increased from a small value, the sequence will at some point be perceived to split into two streams, one low and one high. Similarly, a tone sequence consisting of tones of different frequencies will be perceived as one coherent stream if the presentation rate is low, but will be perceived to segregate if the presentation rate is increased (Miller and Heise, 1950; van Noorden, 1975; Bregman, 1990). Another parameter that influences stream segregation is the attentional set of the listener (van Noorden, 1975). If listeners try to hear the sequence as a single stream, the integration boundary is measured: this is the largest frequency interval at which listeners are able to hear the sequence as a coherent whole. If listeners try to ''hear out'' one stream in a sequence, the segregation boundary is measured: this is the smallest frequency interval at which listeners can segregate the tones of a sequence. The segregation boundary lies below the integration boundary and seems to be relatively independent of the presentation rate of the tones, while the integration boundary decreases greatly with increasing presentation rate (van Noorden, 1975).

Recently, two models of auditory stream segregation have been proposed (Beauvois and Meddis, 1996; McCabe and Denham, 1997). They assume that segregation occurs if two tones are processed primarily through different auditory filters. Several experiments have shown that spectral information is very important in stream segregation. van Noorden (1975) found that listeners could not integrate a tone sequence if a pure tone was alternated with a complex tone, or if two complex tones with the same fundamental frequency ($f0$) but with different harmonics were alternated. He concluded that contiguity ''at the level of the cochlear hair

[a]Present address: Max Planck Institute for Psycholinguistics, Wundtlaan 1, P.O. Box 310, 6500 AH Nijmegen, The Netherlands.
[b]Author to whom correspondence should be addressed. Electronic mail: bcjm@cus.cam.ac.uk
[c]Present address: Research Laboratory of Electronics, Massachusetts Institute of Technology, Cambridge, MA 02139.

cells'' was a necessary (but not sufficient) condition for integration to occur. Hartmann and Johnson (1991) studied auditory stream segregation using interleaved melodies which were difficult to recognize unless they fell into different streams. They used both pure tones and complex tones with different harmonic structures. They found that conditions for which the most peripheral ''channeling'' could be expected (i.e., conditions where successive tones differed in spectrum) showed the largest effect of stream segregation. Therefore, they concluded that ''peripheral channeling is of paramount importance'' in determining stream segregation.

There is, however, some evidence that temporal parameters, such as amplitude envelope and fundamental frequency ($f0$), can contribute to stream segregation as well. Using edited samples of real instrument tones, Iverson (1995) found that tones with dissimilar amplitude envelopes received higher segregation ratings than tones with similar amplitude envelopes. Also, accuracy in an interleaved-melody recognition task increased when the target tones and the distracting tones had dissimilar amplitude envelopes. Singh and Bregman (1997) investigated the relative effect of amplitude envelope and number of harmonics on segregation. They measured the $f0$ interval at which segregation occurred as a function of each of the parameters. Their results showed that the $f0$ difference at the segregation boundary was largest if both parameters were the same for the tones of a sequence. When a dissimilarity in amplitude envelope alone was introduced, the $f0$ difference decreased significantly. It decreased even more, again significantly, with a difference in number of harmonics alone, and it was smallest if both parameters were dissimilar (but the $f0$ difference in this case was not significantly different from that when there was a difference in number of harmonics alone). This indicates that a dissimilarity in amplitude envelope can induce segregation, although its effect is not as strong as that of a dissimilarity in number of harmonics.

Singh (1987) and Bregman *et al.* (1990) both studied perceptual grouping using tone sequences where successive tones could differ either in spectral envelope, or in $f0$, or both. They found that $f0$ and spectral shape can contribute independently to stream segregation. But, as both experiments used tones consisting of resolved harmonics, it is possible that there were still some spectral cues present which influenced the results. Although the spectral envelope of the tones was held constant as $f0$ was varied, stream segregation could have been influenced by changes in place of excitation of individual harmonics. Vliegen and Oxenham (1999) used sequences of complex tones consisting of high, unresolved harmonics with a variable $f0$ difference between successive tones, while keeping the spectral envelope the same. A task requiring subjective judgments of segregation showed that listeners could segregate the tone sequences on the basis of $f0$ differences (presumably conveyed by temporal information alone), and that performance did not differ from that obtained with sequences of pure tones. In a melody recognition experiment, they showed that listeners could also use $f0$ differences to recognize a short atonal melody interleaved with random distracting tones if the melody was in an $f0$ range 11 semitones lower than that of the distracting tones.

In both of these experiments, listeners were encouraged to segregate the two streams; in the melody recognition experiment, it was assumed that segregation of successive tones would lead to better performance. An interesting question is whether stream segregation can occur in the absence of spectral cues, even when listeners try to perceive successive tones as belonging to one stream. In other words, is the segregation produced by $f0$ differences obligatory and automatic? One way of addressing this question is by obtaining judgments of the temporal order of tones in a sequence or judgments of the temporal displacement of one set of tones in a sequence with respect to the other tones. There is evidence that stream segregation can impede the perception of temporal relationships within a sequence. For instance, several studies have shown that listeners have difficulty in judging the order of sounds that are heard as coming from different streams (Broadbent and Ladefoged, 1959; Warren *et al.*, 1969; Bregman and Campbell, 1971). Also, gap detection and gap discrimination deteriorate with an increasing frequency difference between the tones surrounding the gap (Kinney, 1961; Williams and Perrott, 1972; Fitzgibbons *et al.*, 1974; Divenyi and Danner, 1977; Divenyi and Sachs, 1978; Williams *et al.*, 1978; Neff *et al.*, 1982; Formby *et al.*, 1998).

Most of these gap-detection/discrimination experiments used two-tone sequences. Very little research has been done for longer tone sequences. However, there is evidence that stream segregation builds up over time and is greater for longer sequences. The auditory system seems to begin with a bias towards integration, but gradually accumulates evidence which may cause streaming to occur (Bregman, 1978; Anstis and Saida, 1985). Hence, one might expect that the effect of frequency differences between successive tones on temporal discrimination would be greater for longer tone sequences. Kinney (1961) measured gap discrimination using six different sequences, among which were a basic two-tone sequence and that same sequence embedded in a sequence of seven tones. Listeners were required to discriminate a change in the temporal gap between the tones in the basic two-tone sequence. Each tone consisted of two adjacent harmonics of a 120-Hz fundamental presented simultaneously. The upper harmonic of the two tones surrounding the gap had frequencies of 1200 and 1440 Hz in the ''near'' condition, and 1200 and 3480 Hz in the ''far'' condition. For the basic two-tone pattern, gap-discrimination performance was better in the near condition than in the far condition. When the two-tone pattern was embedded in a longer sequence of tones (generated in the same way as those in the two-tone pattern) with frequencies close to that of the lower tone in the two-tone pattern, performance was impaired slightly in the near condition, but was impaired markedly in the far condition. This is consistent with an interpretation in terms of streaming; in the far condition, the lower tone in the two-tone pattern was ''captured'' by the surrounding sequence of tones with similar frequency, and the upper tone of the two-tone pattern was heard ''in isolation.'' This made it harder to detect the change in temporal gap between the two tones. However, some other results of Kinney are harder to interpret in terms of streaming. For example, when the basic two-tone pattern

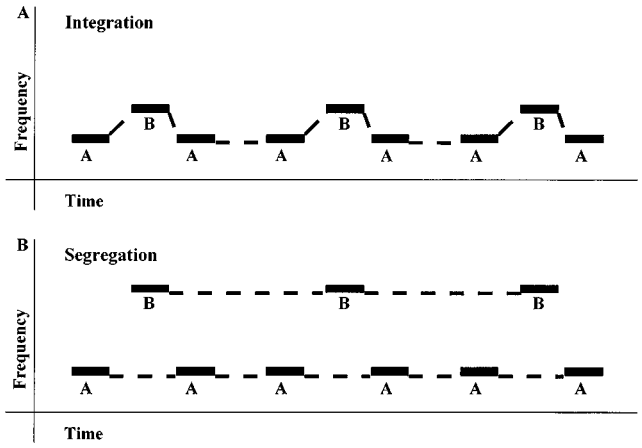

FIG. 1. Schematic illustration of the effect of perceptual streaming on temporal discrimination. If the two tones form one stream (integration—upper panel), the rhythm of the sequence becomes irregular if tone B is shifted in position. If the tones are perceived as two streams (segregation—lower panel), the rhythm within each of the streams remains unchanged and the temporal shift of tone B may be harder to detect.

was repeated two or four times (so that the altered gap duration could be heard two or four times), the difference between the near and far conditions was not greater for the longer sequences than for the short sequences. Possibly, performance for the repeated patterns was based on the initial two-tone pattern.

van Noorden (1975) investigated the detection of temporal displacement with two different long-tone sequences, ABAB... and ABA ABA ABA... (see Fig. 1) and with a three-tone sequence ABA. For both long-tone sequences, he found that the displacement of tone B that could just be detected increased with increasing frequency difference between the tones. Performance continued to deteriorate even beyond the frequency interval corresponding to the integration boundary. For the three-tone sequence, performance depended much less strongly on frequency interval than for the long-tone sequences. The effect of the length of the tone sequence is consistent with the idea that streaming builds up over time, and detection of temporal displacement is poorer between tones that are perceived in different streams.

Neff *et al.* (1982) examined the extent to which changes in gap detection and discrimination could be accounted for by stream segregation. They used tone sequences consisting of two 100-ms tones, four 100-ms tones, four 200-ms tones, eight 100-ms tones, and 16 50-ms tones. The four-tone sequence consisted of the basic two-tone pattern with a variable frequency interval (where the first tone was always higher than the second) with a tone added both before and after the basic pattern. The first tone was always 1/24 octave lower than the second tone, and the fourth tone was always 1/24 octave higher than the third tone. Each eight-tone sequence and 16-tone sequence was generated by repeating the four-tone sequence. The gap to be detected was present at only one of the possible positions (for example, between the second and third tones of a four-tone complex); the gap position was held constant within a block of trials but varied across blocks. They found that gap discrimination varied with frequency difference between successive tones, but they did not find an effect of number of tones, nor of tone duration. Gap discrimination did not change with presentation rate, in contrast to what happens for stream segregation. Therefore, they concluded that there is only an indirect relation between gap-discrimination performance and stream segregation judgments in that both are affected by the frequency separation between tones. However, the lack of an effect of presentation rate does not necessarily indicate that gap discrimination is unaffected by stream segregation. Münkner *et al.* (1996) used a sequence of noise pulses to measure gap-discrimination thresholds for different gap durations (silent intervals between pulses) while keeping the period constant by adjusting the pulse duration. They found that thresholds remained constant with changing gap duration. This suggests that the ''reference'' duration in a sequence of repeated sounds is the period, rather than gap duration itself. It may be that in the study of Neff *et al.*, the expected increase in gap thresholds with increasing presentation rate as a result of stream segregation was counterbalanced by the decreasing reference repetition period.

The purpose of the present study was to investigate if temporal discrimination for sequences of complex tones is adversely affected by a large $f0$ difference between the tones, when no detectable spectral differences are present. Detectable spectral differences were eliminated in some conditions by using complex tones consisting of a fixed passband of harmonics with harmonic numbers of 10 or higher. Plomp (1964) has shown that listeners are generally not capable of resolving harmonics higher than the fifth to the eighth, depending on the $f0$. It has nevertheless been shown that complexes consisting only of high, unresolved harmonics can induce a pitch sensation which can be used to identify melodies and discriminate musical intervals (Moore and Rosen, 1979; Houtsma and Smurzynski, 1990). If $f0$ differences produce an obligatory or involuntary segregation of successive tones when the differences are sufficiently large, then temporal discrimination should be impaired by a large $f0$ difference in the tones whose timing is to be compared. The tones were of three types: (1) pure tones; (2) complex tones filtered into a single frequency region, differing only in $f0$; and (3) complex tones with a fixed $f0$ but with spectral differences between successive tones. This last condition was added to compare the relative importance of spectral differences and $f0$ differences in producing stream segregation (and hence impaired temporal discrimination).

I. EXPERIMENT

Temporal discrimination performance was measured for alternating tone sequences, using three different conditions: pure tones; complex tones consisting of high, unresolved harmonics with a varying $f0$ and a fixed spectral shape (var$f0$); and complex tones consisting of high, unresolved harmonics with a fixed $f0$ and a varying spectral passband (varspec). The pure-tone condition was used as a baseline condition, since, as described above, temporal discrimination decreases with increasing frequency difference between successive pure tones (van Noorden, 1975). For convenience, the frequencies of the pure tones will also be described as $f0$s, even though these tones consisted of only a single fre-

TABLE I. Values of $f0$ for tone B in the var$f0$ condition and the pure-tone condition and −3-dB points of the passband for tone B in the varspec condition. Tone A had a fixed $f0$ of 100 Hz and −3-dB points of 1425 and 2485 Hz for both complex-tone conditions and an $f0$ of 300 Hz for the pure-tone condition.

Frequency interval (semitones)	$f0$ of tone B for the var$f0$ condition (Hz)	−3-dB points of the passband of tone B for the varspec condition (Hz)		$f0$ of tone B for the pure-tone condition (Hz)
1	105.95	1509	2633	317.85
4	125.99	1795	3130	377.97
8	158.74	2261	3944	476.22
13	211.89	3018	5265	635.67
18	282.84	4029	7028	848.52

quency component. Changes in the center frequency of the passband will be described in semitones, for comparison with the results of the first two conditions. The lowest $f0$ was fixed at 100 Hz and five different values for the $f0$ difference were used.

If it is mainly spectral information that determines auditory grouping, temporal discrimination performance should be similar for the pure-tone and the varspec conditions; for both these conditions it was expected that performance would deteriorate with an increasing frequency difference between the stimuli. For the var$f0$ condition, the effect of increasing $f0$ difference might be less than for the other two conditions. However, if a sufficiently large $f0$ difference results in automatic (involuntary) streaming, then some deterioration in performance should be observed for large $f0$ differences.

A. Stimuli

Each trial consisted of a sequence of tone triplets (ABA ABA ABA...) flanked by two triplets from which tone B was removed (A_A); the reason for using the flanking triplets will be described later. The frequency interval between tones A and B was varied randomly across runs, but fixed within a run, and could take the value of 1, 4, 8, 13, or 18 semitones; interval here refers to frequency for the pure tones, $f0$ for the var$f0$ tones, and center frequency of the spectral passband for the varspec tones. Each harmonic of the complex tones was generated separately, with components added in sine phase, and was scaled using a filter function that consisted of a flat bandpass region, flanked by two raised-cosine ramps in the linear frequency domain. This filter function was chosen so that no harmonics lower than the tenth would be present, so it could be assumed that all harmonics would be unresolved (Plomp, 1964). For the var$f0$ condition, the $f0$ of tone A was 100 Hz and the $f0$ of tone B varied from 105.95 to 282.84 Hz. As the highest $f0$ of tone B was 282.84 Hz, the start point of the filter function for the var$f0$ condition was set at 2828 Hz. The end point of the spectral ramp was set at 4714 Hz, and the start and end points of the second ramp were set at 5657 and 9428 Hz, respectively. This resulted in −3-dB points of 4029 and 7028 Hz. Filtering in this way made sure that the excitation pattern would hardly change with changes in $f0$; excitation patterns calculated using the method described by Glasberg and Moore (1990) showed only minimal changes (less than 0.5 dB) when the $f0$ was changed from 105.96 to 282.24 Hz, keeping the overall level constant.

For the varspec condition, both tone A and tone B had a fixed $f0$ of 100 Hz. The start point of the filter function of tone A was set at 1000 Hz and the ratios of the start and end points of the filter function were the same as for the var$f0$ condition. This resulted in −3-dB points of 1425 and 2485 Hz. For tone B, the −3-dB points were shifted according to the frequency interval between tones A and B. For example, for an interval of four semitones, the −3-dB points were shifted to 1795 and 3130 Hz. The harmonics were added in sine phase.

To derive frequencies for the pure-tone condition, the $f0$s of tones A and B in the var$f0$ condition were trebled. This was done to move the frequencies to the range where the pitches of the pure tones sounded clearer, and also to move the frequencies closer to the ranges used in previous experiments of this type (van Noorden, 1975; Neff *et al.*, 1982). The exact frequency values of the $f0$s and −3-dB points for tones A and B in all three conditions are shown in Table I.

The total duration of the tones was 90 ms, including 10-ms raised-cosine onset and offset ramps, with a silent interval after each of the tones of 30 ms, so that the tone repetition time (TRT, the time interval between the start of successive tones) was 120 ms. Each ABA triplet was separated by a silent interval of 120 ms. Each sequence consisted of four triplets ABA, flanked by two triplets from which tone B was removed (A_A). The initial A tones were introduced to encourage the perception of segregation. As the auditory system has a bias towards integration (Bregman, 1978; Anstis and Saida, 1985), a tone sequence will always initially be perceived as integrated. This would enable listeners to perform the task by only listening to the first one or two triplets of the tone sequence. In the reference stimulus, the position of tone B was exactly at the midpoint between two tones A. In the comparison stimulus, tone B was delayed, so that the galloping rhythm became irregular (see Fig. 1). The starting phase of the tones was randomized across trials.

The tones were presented at an overall level of 70 dB SPL. All stimuli were generated with a Tucker-Davis System II, using a TDT DD1 16-bit digital-to-analog converter (50-kHz sampling rate). Stimuli were then passed to a TDT PA4 programmable attenuator and a manual attenuator (Hatfield 2125) and were presented to the right ear over a Sennheiser HD414 headphone. There was no low-pass filter except for the filtering produced by the earphone. Spectral analysis of the output of the earphone (measured using a Bruel & Kjær

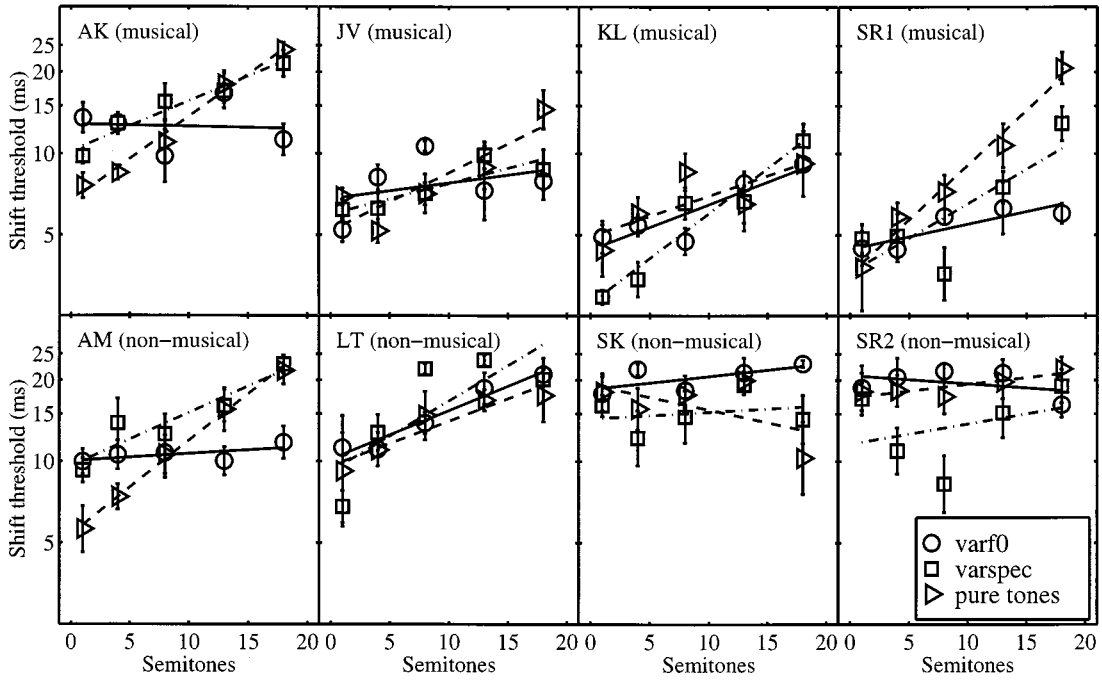

FIG. 2. Threshold values for the temporal shift of tone B in an alternating tone sequence ABA ABA ABA..., for $f0$ intervals of 1, 4, 8, 13, and 18 semitones. Shift-threshold values are plotted on a logarithmic axis. The straight lines are linear regression lines that were fitted to the data. The upper four panels show the results for the four musical listeners, while the lower four panels show the results for the nonmusical listeners. The stimuli were pure tones (right-pointing triangles and dashed lines), complex tones with fixed spectral passband and varying $f0$ (circles and solid lines), or complex tones with varying spectral passband and fixed $f0$ (squares and dash–dotted lines).

artificial ear type 4152) indicated that distortion and aliased components within the audible range (up to 15 kHz) were at least 60 dB lower in level than the primary components. Listeners were tested in an IAC sound-attenuating booth.

B. Listeners

The listeners were divided into two groups, consisting of four musical and four nonmusical listeners. Musical listeners may be expected to show better performance in a temporal discrimination task than nonmusical listeners. Listeners were considered musical if they had received at least 4 years of formal musical training. They were all between 18 and 30 years old and had absolute thresholds better than 20 dB HL at all audiometric frequencies. One of the listeners was author JV.

C. Procedure

A two-interval forced-choice (2-IFC) method with a two-down one-up adaptive procedure was used to measure temporal discrimination thresholds. This procedure estimates the 71%-correct point on the psychometric function. A trial consisted of a reference sequence in which the position of tone B was exactly at the midpoint between the two tones A, and a comparison sequence in which tone B was delayed, making the galloping rhythm irregular. The interval between two tones A in a triplet was kept the same, so that when the interval between tone A and tone B was increased by a certain amount, the interval between tone B and the second tone A was decreased by the same amount. The comparison sequence occurred randomly in either the first or the second interval. Listeners were asked to indicate in which interval tone B was shifted from the midpoint. After a response had been given, a light above the buttons indicated the interval containing the irregular sequence. The initial shift value was 28.18 ms; this was well above threshold for most listeners. This initial shift value was used as the upper limit of the shift value. The shift value was varied on a logarithmic scale. The initial logarithmic step size was 0.2 (corresponding to a change in shift by a factor of 1.58). After six turn points, the step size was reduced to a value of 0.05 (corresponding to a change in shift by a factor of 1.12). Then, it was held constant for another six turn points. Thresholds were defined as the median (log) value at the last six turn points. In each session, one measurement was taken for each of the 15 conditions. Each threshold reported is the mean of six such estimates. Each session took about 2 to 2.5 h to complete, including two breaks. Before the actual experiment started, listeners had six complete sessions of training to stabilize their performance.

D. Results

The results varied considerably across listeners. Therefore, Fig. 2 shows shift thresholds as a function of the frequency interval between tones A and B for each listener separately. Error bars represent ± 1 standard error of the mean across the six estimates. For all of the musical and two of the nonmusical listeners, there was an increase in shift thresholds with increasing frequency interval between tones A and B, at least for the pure tones and the varspec tones; the effect was not as clear for the var$f0$ tones. The other two nonmusical listeners had great difficulty with the task and showed high shift thresholds for all frequency intervals.

TABLE II. Values of the slopes of the regression lines (log of shift threshold in ms per semitone) for the six subjects who could perform the task reliably. Significance levels are indicated with an * for $p<0.05$ and ** for $p<0.01$.

Listener	Slope of the regression line for var$f0$ condition	Slope of the regression line for varspec condition	Slope of the regression line for pure-tone condition
AK	−0.0008	0.0183**	0.0311**
JV	0.0059	0.0114*	0.0215*
KL	0.0168*	0.0333**	0.0150
SR1	0.0093	0.0255	0.0404**
AM	0.0027	0.0197*	0.0346**
LT	0.0181**	0.0262	0.0168*

An analysis of variance (ANOVA) was performed on the raw data with shift threshold (in logarithmic units) as a dependent variable and frequency interval, spectral condition, and listener as independent variables, where listener was considered a random variable. The data were analyzed only for the six listeners who could perform the task reliably (AK, JV, KL, SR1, AM, and LT); these listeners all had shift thresholds for the smallest frequency interval of less than 15 ms in all conditions, while the remaining two listeners had shift thresholds greater than 15 ms. Of the main factors, frequency interval and listener had a significant effect [$F(4,20)=46.47$, $p<0.001$; $F(5,450)=91.26$, $p<0.001$], but the effect of spectral condition was not significant. The two-way interaction of spectral condition and listener was significant [$F(10,450)=3.58$, $p<0.001$], as was the two-way interaction of frequency interval and spectral condition [$F(8,40)=2.58$, $p=0.022$]. The latter interaction corresponds to the finding that increasing the frequency interval had a smaller average effect for the var$f0$ condition than for the other conditions. Finally, the three-way interaction of frequency interval, spectral condition, and listener was significant [$F(40,450)=2.22$, $p<0.001$]. To examine the effect of frequency interval more clearly, additional ANOVAs were performed on the raw data for each spectral condition separately, with shift threshold (in logarithmic units) as a dependent variable, and frequency interval and listener as independent variables. For all three spectral conditions, the effect of frequency interval was significant [$F(4,20)=3.04$, $p<0.05$ for the var$f0$ condition; $F(4,20)=12.51$, $p<0.001$ for the varspec condition, and $F(4,20)=24.48$, $p<0.001$ for the pure-tone condition].

Linear regression lines were fitted to the data for each listener and each condition; these lines are shown in Fig. 2. The values of the slopes of the regression lines for the six listeners who could do the task reliably are shown in Table II. For most listeners, the slopes of the regression lines differed significantly from zero for the varspec tones and the pure tones, but not for the var$f0$ tones.

To get a clearer picture of the results, shift thresholds as a function of the frequency interval between tones A and B were averaged (geometric means) over the six listeners who could do the task reliably. Results are shown in Fig. 3. Error bars represent ± one standard error of the mean across listeners. Regression lines were fitted to these data as well. For all three conditions the fit was very good. The slopes of the regression lines were significantly greater than zero (all $p<0.01$), indicating that shift thresholds increased significantly with increasing frequency interval. The slope was clearly smaller for the var$f0$ condition than for the other two conditions.

In summary, although the results varied across listeners, for the six listeners who could perform the task reliably there was an effect of frequency interval for all three conditions. The logarithm of the shift threshold increased roughly linearly with increasing frequency interval in semitones between tones A and B. There were no discontinuities in the performance function that could indicate an integration boundary. The effect of frequency interval was smallest for the var$f0$ condition, where the tones provided only periodicity information, and larger for the other two conditions, where there were detectable differences in spectrum. This implies that both a difference in spectrum and a difference in periodicity can have an adverse effect on temporal discrimination, but spectral differences have a larger effect.

II. DISCUSSION

The results of this experiment showed a clear effect of the frequency interval between the tones of a sequence on

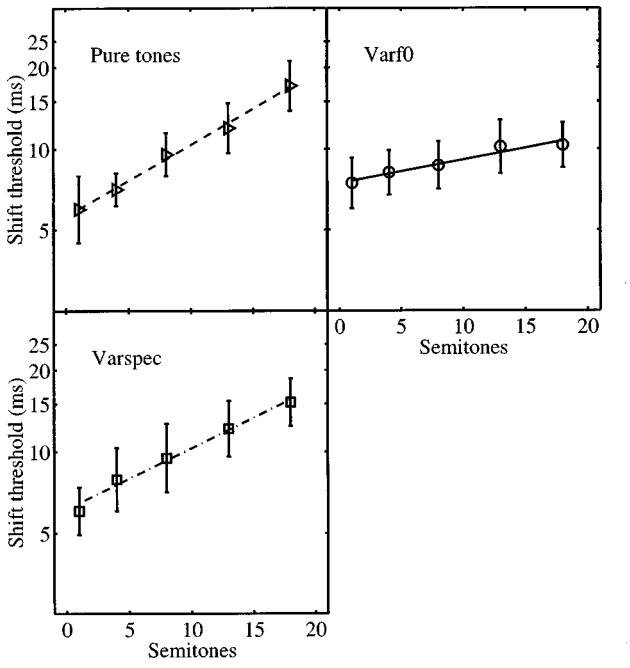

FIG. 3. Geometric mean results for the six listeners who could perform the task reliably. The straight lines are linear regression lines that were fitted to the data. Error bars represent ± one standard error of the mean across listeners.

temporal-shift discrimination. The effect was larger for the conditions where spectral information was available (pure tones and varspec tones), but it was statistically significant for all three conditions.

van Noorden (1975) and Neff *et al.* (1982) also measured temporal discrimination performance for pure tones. Van Noorden used two different tone sequences. For his ABAB... sequence with a TRT of 120 ms (with a tone duration of 40 ms), the displacement of tone B that could just be perceived ranged from about 10 ms for a frequency interval of 0 semitones to about 50 ms for a frequency interval of 25 semitones when tone B was delayed. For a frequency interval of 18 semitones, the just noticeable displacement was about 40 ms. If tone B was shifted forward, the value of the just noticeable displacement was much higher: 80 ms for a frequency interval of 25 semitones. For his ABA ABA ABA... sequence, he used a TRT of 100 ms and measured the forward displacement of tone B. Here, the just noticeable displacement ranged from about 10 ms for a frequency interval of 0 semitones to about 40 ms for a frequency interval of 7 semitones. Neff *et al.* (1982) used several tone sequences. The condition that resembled our stimuli most was their eight-tone sequence (with a tone duration of 100 ms and a silent interval between tones of 10 ms). For that, they found a gap-discrimination threshold that ranged from 7 ms for a frequency interval of 1/8 octave (1.5 semitone) to 35 ms for a frequency interval of 2.5 octaves (30 semitones). For a frequency interval of 18 semitones, the gap-discrimination threshold was about 30 ms.

The fact that thresholds were higher in these earlier experiments than in ours may be due to the much higher frequency of their stimuli (in van Noorden, 1975, the fixed tone had a frequency of 1000 Hz and in Neff *et al.*, 1982, the two tones had frequencies with a geometric mean of 1600 Hz) or, more likely, to the different tasks they used. Van Noorden (1975) used a tracking method, where tone B was shifted continuously within one trial and listeners had to press a button when they heard that the sequence was irregular. This might be more difficult for listeners than our 2-IFC method, where listeners had a reference stimulus and where the temporal shift of tone B stayed constant within one tone sequence of four ABA triplets. Neff *et al.* (1982) used a 2-IFC method, like we did, but in their sequences the gap was inserted only at one position in the tone sequence, whereas in our experiment tone B was shifted in all four ABA triplets.

There were no discontinuities in the performance function; performance deteriorated with increasing interval for all frequency intervals, so there was no indication of an integration boundary. This was also found by van Noorden (1975) and Neff *et al.* (1982). One possible explanation for this is that temporal discrimination performance is only indirectly connected with stream integration, in that they are both adversely affected by large frequency differences between successive tones. In a temporal discrimination task, large differences may distract the listener, thereby worsening performance. Another possible explanation is that there may not be a distinct and absolute boundary at which integration fails and segregation occurs. On each trial, when trying to hear integration, a listener may either succeed or fail in doing so. For very small differences between successive tones, integration will always be perceived, and for very large differences segregation will always be perceived. For intermediate differences, either percept can occur; the probability of perceiving integration decreases progressively with increasing differences. Also, it might be that streaming is perceived on a more or less continuous scale, with integration at the one end and segregation at the other. As differences between successive tones increase, the degree of perceived integration may decrease, while the degree of perceived segregation may increase. The progressive changes in performance with frequency interval found in our temporal discrimination task might reflect this continuous variation in the degrees of perceived integration and segregation.

Our results support the conclusion of Vliegen and Oxenham (1999) that listeners can segregate sounds into streams when successive sounds differ on *either* a spectral *or* a temporal dimension. They showed that stream segregation can be based solely on periodicity information in the absence of spectral cues. The present experiment shows that, for all three conditions, performance worsened with increasing frequency interval (either spectral or periodicity based). If the worse performance reflects stream segregation, this suggests that streaming on the basis of periodicity alone is at least partly involuntary; it takes place even if listeners try to hear the tone sequence as a coherent whole.

Our results differ from those of Vliegen and Oxenham (1999) in one important respect. They found very similar results for conditions in which only periodicity information was available (tones with high harmonics, similar to our var$f$0 condition), and conditions in which both periodicity information and spectral information were available (pure tones and complex tones with low harmonics). In contrast, we found a smaller effect for tones that differed in periodicity than for tones that differed in spectrum. The reason for the difference between the studies may lie in the nature of the tasks used. The tasks used by Vliegen and Oxenham (for example, the recognition of a short atonal melody interleaved with random distracting tones) were such that stream segregation would lead to better performance. In our task, stream segregation is assumed to lead to worse performance. It appears that periodicity differences can be as potent as spectral differences in promoting stream segregation, when segregation is advantageous, but periodicity differences are less potent than spectral differences in preventing segregation when integration is advantageous to the task at hand. It may be that, depending on the task, the available information is weighted differently. If it is more advantageous to integrate sounds, listeners will presumably try to ignore differences between the sounds and to focus on the similarities. It may be that periodicity differences are less potent than spectral differences and therefore easier to ignore. If, on the other hand, segregation is more advantageous, listeners will try to focus on whatever differences are available.

ACKNOWLEDGMENTS

We thank Thomas Baer, Brian Glasberg, Marina Rose, and Deborah Vickers for their help and technical assistance.

We also thank Hedwig Gockel and S. L. Denham for helpful comments on an earlier version of this paper.

Anstis, S., and Saida, S. (**1985**). ''Adaptation to auditory streaming of frequency-modulated tones,'' J. Exp. Psychol. **11**, 257–271.

Beauvois, M. W., and Meddis, R. (**1996**). ''Computer simulation of auditory stream segregation in alternating-tone sequences,'' J. Acoust. Soc. Am. **99**, 2270–2280.

Bregman, A. S. (**1978**). ''Auditory streaming is cumulative,'' J. Exp. Psychol. **4**, 380–387.

Bregman, A. S. (**1990**). *Auditory Scene Analysis: The Perceptual Organization of Sound* (Bradford Books, MIT Press, Cambridge, MA).

Bregman, A. S., and Campbell, J. (**1971**). ''Primary auditory stream segregation and perception of order in rapid sequences of tones,'' J. Exp. Psychol. **89**, 244–249.

Bregman, A. S., Liao, C., and Levitan, R. (**1990**). ''Auditory grouping based on fundamental frequency and formant peak frequency,'' Can. J. Psychol. **44**, 400–413.

Broadbent, D. E., and Ladefoged, P. (**1959**). ''Auditory perception of temporal order,'' J. Acoust. Soc. Am. **31**, 151–159.

Divenyi, P. L., and Danner, W. F. (**1977**). ''Discrimination of time intervals marked by brief acoustic pulses of various intensities and spectra,'' Percept. Psychophys. **21**, 125–142.

Divenyi, P. L., and Sachs, R. M. (**1978**). ''Discrimination of time intervals bounded by tone bursts,'' Percept. Psychophys. **24**, 429–436.

Fitzgibbons, P. J., Pollatsek, A., and Thomas, I. B. (**1974**). ''Detection of temporal gaps within and between perceptual tonal groups,'' Percept. Psychophys. **16**, 522–528.

Formby, C., Sherlock, L. P. and Li, S. (**1998**). ''Temporal gap detection measured with multiple sinusoidal markers: Effects of marker number, frequency, and temporal position,'' J. Acoust. Soc. Am. **104**, 984–998.

Glasberg, B. R., and Moore, B. C. J. (**1990**). ''Derivation of auditory filter shapes from notched-noise data,'' Hearing Res. **47**, 103–138.

Hartmann, W. M., and Johnson, D. (**1991**). ''Stream segregation and peripheral channeling,'' Music Percept. **9**, 155–184.

Houtsma, A. J. M., and Smurzynski, J. (**1990**). ''Pitch identification and discrimination for complex tones with many harmonics,'' J. Acoust. Soc. Am. **87**, 304–310.

Iverson, P. (**1995**). ''Auditory stream segregation by musical timbre: effects of static and dynamic acoustic attributes,'' J. Exp. Psychol. **21**, 751–763.

Kinney, J. A. S. (**1961**). ''Discrimination in auditory and visual patterns,'' Am. J. Psychol. **74**, 529–541.

McCabe, S. L., and Denham, M. J. (**1997**). ''A model of auditory streaming,'' J. Acoust. Soc. Am. **101**, 1611–1621.

Miller, G. A., and Heise, G. A. (**1950**). ''The trill threshold,'' J. Acoust. Soc. Am. **22**, 637–638.

Moore, B. C. J., and Rosen, S. M. (**1979**). ''Tune recognition with reduced pitch and interval information,'' Q. J. Exp. Psychol. **31**, 229–240.

Münkner, S., Kohlrausch, A., and Püschel, D. (**1996**). ''Influence of fine structure and envelope variability on gap-duration discrimination thresholds,'' J. Acoust. Soc. Am. **99**, 3126–3137.

Neff, D. L., Jesteadt, W., and Brown, E. L. (**1982**). ''The relation between gap discrimination and auditory stream segregation,'' Percept. Psychophys. **31**, 493–501.

Plomp, R. (**1964**). ''The ear as a frequency analyzer,'' J. Acoust. Soc. Am. **36**, 1628–1636.

Singh, P. G. (**1987**). ''Perceptual organization of complex-tone sequences: a trade off between pitch and timbre?,'' J. Acoust. Soc. Am. **82**, 886–895.

Singh, P. G., and Bregman, A. S. (**1997**). ''The influence of different timbre attributes on the perceptual segregation of complex-tone sequences,'' J. Acoust. Soc. Am. **102**, 1943–1952.

van Noorden, L. P. A. S. (**1975**). ''Temporal coherence in the perception of tone sequences,'' Ph.D. thesis, Eindhoven University of Technology.

Vliegen, J., and Oxenham, A. J. (**1999**). ''Sequential stream segregation in the absence of spectral cues,'' J. Acoust. Soc. Am. **105**, 339–346.

Warren, R. M., Obusek, C. J., Farmer, R. M., and Warren, R. P. (**1969**). ''Auditory sequence: confusion of patterns other than speech or music,'' Science **164**, 586–587.

Williams, K. N., Elfner, L. F., and Howse, W. R. (**1978**). ''Auditory temporal resolution: effects of sensation level,'' J. Audit. Research **18**, 265–270.

Williams, K. N., and Perrott, D. T. (**1972**). ''Temporal resolution of tonal pulses,'' J. Acoust. Soc. Am. **51**, 644–647.

Modulation gap detection: Effects of modulation rate, carrier separation, and mode of presentation

John H. Grose,[a] Joseph W. Hall III, and Emily Buss
Division of Otolaryngology/Head & Neck Surgery, University of North Carolina at Chapel Hill, Chapel Hill, North Carolina 27599-7070

(Received 25 September 1998; revised 22 February 1999; accepted 29 April 1999)

Modulation gap detection (MGD) is a procedure that measures the sensitivity to an interruption in the modulation pattern imposed upon one or more carrier frequencies. The MGD task was developed to test conditions where a temporal event traverses frequency, but without a concomitant interruption in the spectral continuity of the stimulus. This contrasts with across-frequency gap detection where there is an inherent spectral discontinuity associated with the temporal gap, and where there is a marked decline in performance when the markers of the temporal gap are widely separated in frequency. The purpose of this study was to test the hypothesis that a wideband temporal analysis will be facilitated if there exists a spectral continuity throughout the temporal event. Experiment 1 established the procedure of MGD and indicated that a modulation rate of 8 Hz was optimal for the task. Experiment 2 showed that performance declined markedly when the carrier frequencies of the modulation markers were widely separated in frequency. This finding indicates that spectral continuity across the temporal event is not a sufficient prerequisite for the auditory system to undertake a wideband temporal analysis. Experiment 3 revealed that dichotic MGD also results in poor performance, similar to that seen for widely separated carrier frequencies in the monaural case. This supports the hypothesis that the ''channels'' across which temporal events are poorly processed do not necessarily correspond to peripheral frequency channels. © *1999 Acoustical Society of America.* [S0001-4966(99)02808-8]

PACS numbers: 43.66.Mk [DWG]

INTRODUCTION

A common measure of temporal resolution in the auditory system is gap detection, a gauge of the sensitivity to a silent interval in an otherwise continuous stimulus. In gap-detection tasks, the silent interval is sometimes said to be ''marked'' by the two segments of the stimulus bounding it. Usually, the two segments—or markers—share similar frequency characteristics. However, several studies have investigated the effect of varying the frequencies of the two markers. The uniform finding is that gap detection is most acute when the marker prior to the gap has the same frequency as the marker following the gap and that, as the frequency separation between the two markers increases, performance declines (Kinney, 1961; Perrott and Williams, 1971; Collyer, 1974; Fitzgibbons *et al.*, 1974; Divenyi and Danner, 1977; Divenyi and Hirsh, 1978; Neff *et al.*, 1982; Formby *et al.*, 1996; Forrest and Formby, 1996; Grose and Hall, 1996; Formby *et al.*, 1997; Phillips *et al.*, 1997; Formby *et al.*, 1998). The rate of decline is most marked for frequency separations less than about two equivalent rectangular bandwidths (ERBs) and then approaches asymptote beyond this (Forrest and Formby, 1996). While a single-channel model can successfully account for this decline over a limited range of frequencies (Formby *et al.*, 1996), a multichannel—or across-frequency—model is necessary to account for the wider frequency separations (Heinz *et al.*, 1996). Work by Phillips *et al.* (1997) has suggested that the ''channels'' in the multichannel case may not necessarily relate to peripheral frequency channels. They found that gap-detection performance declined to the same level when two isofrequency markers were presented across the two ears as when two markers having widely separated frequencies were presented monaurally. They interpreted this as evidence that the channels may be more central in origin.

The general finding that performance declines when the temporal event (the gap) traverses frequency suggests that a wideband temporal analysis is not being undertaken by the auditory system. The concept of ''wideband temporal analysis'' is used here in the general sense that temporal information is integrated over several critical bands prior to the occurrence of a detection decision. No assumptions are implied as to where in a temporal processing scheme the spectral integration of information occurs. It could occur peripherally, yielding a broad effective—or internal—analysis bandwidth prior to a stage of ''envelope extraction'' as in the temporal processing models of Viemeister (1979) and Bacon and Viemeister (1985). On the other hand, it could occur more centrally, subsequent to a stage of envelope extraction within each frequency channel, as in the modulation filterbank model of Dau (1996). The failure to implement a wideband temporal analysis in across-frequency gap detection is notable because other gap-detection work indicates that the auditory system is adept at wideband temporal analysis. In particular, it is well able to integrate synchronous temporal gaps that are widely separated in frequency. For example, Hall *et al.* (1996) found that, relative to the case where a gap was imposed on a single narrow band of noise, gap-detection

[a]Electronic mail: jhg@med.unc.edu

performance improved when the gap was imposed synchronously on two narrow bands of noise. Importantly, this improvement was independent of the frequency separation between the two noisebands over a range of about 5 octaves. The finding that the auditory system adopts a wideband temporal analysis when the temporal event exists synchronously in different frequency channels but apparently does not when the temporal event to be detected traverses frequency was the point of departure for this investigation. A key difference between these two conditions is that, in the latter case of across-frequency gap detection, there is an inherent spectral discontinuity across the temporal event that does not exist in the synchronous gap case. That is, the auditory system must register the temporal event as existing between the offset of a marker in one frequency channel and the onset of the marker in a second—*previously inactive*—channel. In the case of multiple synchronous gaps, the complete temporal event exists within each frequency channel and the auditory system benefits from multiple simultaneous occurrences of the within-channel events. If there existed a sluggishness associated with the process of identifying and ''switching attention'' to the frequency channel containing the second marker in across-frequency gap detection, then detection thresholds would be expected to increase. This interpretation leads to the hypothesis that the processing of a temporal event that traverses frequency will be less adversely affected if there is spectral continuity in the spectral channels containing the markers of the temporal event; i.e., if the frequency channels across which the temporal event occur are continuously active. According to this hypothesis, a wideband temporal analysis will be facilitated if there exists a spectral continuity throughout the temporal event.

The purpose of this study was to test this hypothesis by devising a task where the temporal event to be detected traversed frequency while at the same time a spectral continuity was maintained throughout the stimulus. The paradigm of modulation gap detection (MGD) was developed to satisfy this stipulation. In MGD, the temporal event to be detected is an interruption, or gap, in the modulation pattern of a stimulus (see Fig. 1). The modulation gap is said to be marked by the modulator segment prior to the modulation gap (termed ''modulation marker 1'') and the modulator segment following the gap (termed ''modulation marker 2''). As will be described more fully in the second experiment, MGD allows for modulation marker 1 to be carried by a different frequency than modulation marker 2. Thus, it is possible to construct a stimulus where the modulation gap is marked by modulator segments carried by different frequencies, yet the carrier frequencies themselves are continuously present throughout the temporal event. Before advancing to this stage of experimentation, however, it was necessary to establish the procedure of MGD; in particular, it was necessary to determine the optimum rate of modulation for the modulation markers. This was undertaken in experiment 1 using a broadband noise carrier.

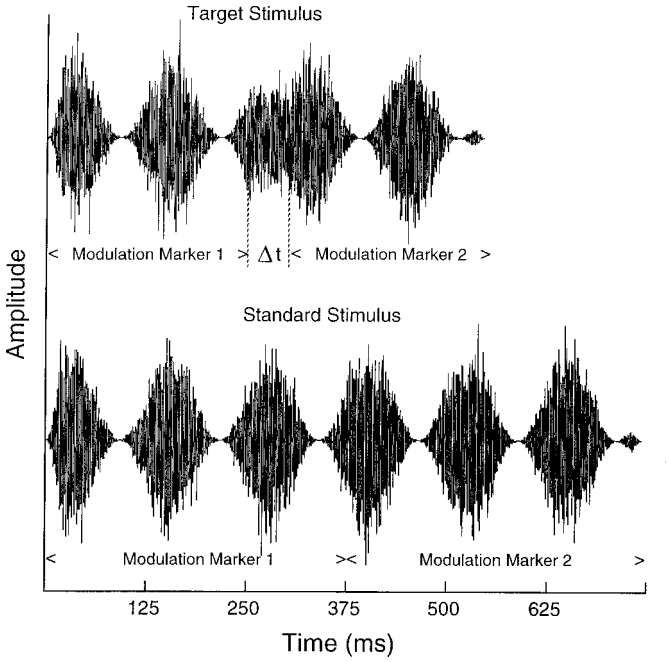

FIG. 1. Waveforms of sample stimuli from experiment 1 using an 8-Hz modulation rate. The target stimulus shows a modulation gap marked Δt bounded by two modulation markers. The modulated segment prior to the gap is referred to as modulation marker 1, and the modulated segment following the gap is referred to as modulation marker 2. The standard waveform has continuity of modulation between marker 1 and marker 2. Note that the number of modulation cycles per marker is randomly varied from interval to interval so that overall stimulus duration is not a viable cue for detection.

I. EXPERIMENT 1: MGD AS A FUNCTION OF MODULATION RATE FOR BROADBAND CARRIERS

The purpose of this experiment was to measure MGD as a function of modulation rate, with the particular intent being to select an appropriate rate for the later experiments. Because the spectral composition of a cosinusoidally modulated pure tone varies as a function of modulation rate, it was decided to undertake this experiment using a broadband noise as the carrier.

A. Method

1. Subjects

Four listeners with normal hearing participated in this experiment. All had pure-tone thresholds $\leqslant$20 dB HL across the audiometric frequencies (ANSI, 1989). Prior to data collection, training on the various conditions of the MGD task was undertaken until performance appeared stable. This period ranged from about 6 h for one listener to about 10 h for the remaining listeners.

2. Stimuli

The basic stimulus was a Gaussian noise modulated by a cosinusoidal modulator, as shown in Fig. 1. The independent variable was the frequency of the modulator, which was either 8, 16, 32, 64, 128, 256, or 512 Hz. The starting phase of the modulator was always $3\pi/2$ and the depth of modulation was 100%. This phase selection ensured that, following an integer number of modulation cycles, the amplitude of the waveform was essentially the same as that of the unmodu-

lated carrier. Thus, after an integer number of modulation cycles (i.e., after modulation marker 1) the carrier could be free of modulation for a variable duration (i.e., the modulation gap) before the modulation resumed at the $3\pi/2$ starting phase (i.e., the onset of modulation marker 2). The modulated segments were adjusted in amplitude to compensate for increases in level brought about by modulation, thus ensuring that the modulation gap could not be detected on the basis of a level change.[1] Because the imposition of the modulation gap would increase the overall stimulus duration if the modulation markers were of constant duration, it was necessary to vary the duration of the markers in a random fashion in order for overall stimulus duration to be an unreliable cue. The randomization of modulation marker duration was limited by the need for the markers to carry an integer number of modulation cycles. Therefore, in *each* interval of a 3-alternative forced-choice (3AFC) trial, the duration of the first modulation marker was equivalent to either two or three periods of an 8-Hz modulator, at random, while the duration of the second modulation marker was equivalent to either one, two, or three periods of an 8-Hz modulator, at random. Therefore, the stimulus duration in a standard interval could range from 375 to 750 ms, at random. A 15-ms cosine-squared shaping was imposed at the beginning and end of each waveform. All stimuli were generated digitally during the intertrial intervals using an array processor (TDT AP2). Following digital-to-analog conversion at a rate of 10 kHz (TDT PD1), the stimuli were low-pass filtered at 4 kHz (Stewart VBF 10M), attenuated (TDT PA4), and fed to the left earphone of a Sennheisser HD 580 headset via a headphone buffer (TDT HB6). The stimuli were presented at an overall level of 80 dB SPL.

3. Procedure

In each 3AFC trial, a stimulus containing a modulation gap was presented in one of the three observation intervals, at random. The interstimulus interval was 300 ms. A 3-down, 1-up adaptive stepping rule was incorporated which tracked the 79.4%-correct level. Following three correct responses, the duration of the modulation gap was reduced by a factor of 1.2; following one incorrect response, the gap duration was increased by the same factor. The transition between increasing and decreasing gap duration constituted a reversal. A threshold run continued until ten reversals had occurred and threshold was estimated as the geometric mean of the modulation gap durations for the final six reversals. At least three estimates of threshold were collected per condition, and final threshold for an individual was taken as the geometric mean of all estimates for that condition. The maximum gap duration tested was 250 ms. If a threshold track hit this ceiling at any point during the run, the run was rejected. For certain conditions where the MGD task proved to be very difficult, the threshold estimates were consistently rejected. In these conditions, a minimum of three attempts at obtaining a valid estimate of threshold was undertaken, after which threshold was tabulated as being in excess of 250 ms. The order of conditions was random across listeners. Listeners were tested in a double-walled, sound-attenuating booth and indicated their responses by means of a response box. Stimulus presentation and response collection were under the control of a Gateway 2000 computer.

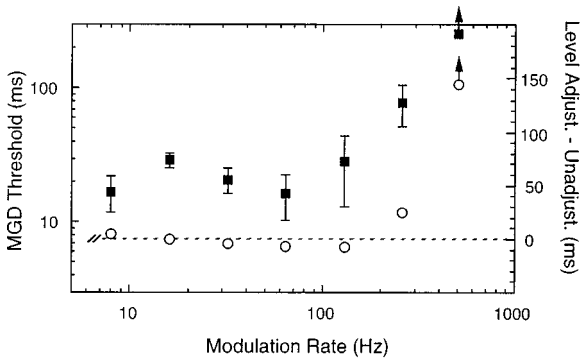

FIG. 2. Group mean MGD thresholds (solid squares referenced to left ordinate) for a Gaussian noise carrier plotted as a function of modulation frequency. Error bars indicate ±1 s.d. Datum point with upward-pointing arrow indicates thresholds in excess of 250-ms limit. Open circles referenced to right ordinate indicate differences in threshold between conditions employing level-compensated and uncompensated modulation segments (see the text).

B. Results and discussion

The pattern of results for the four listeners was similar and therefore the mean data are representative of the group. Figure 2 shows the MGD thresholds (solid squares referenced to left ordinate) plotted as a function of modulation rate. It can be seen that the function is nonmonotonic. Performance was best in the region of 8, 32, and 64 Hz with a slight elevation at 16 Hz. Performance declined markedly for the higher rates of modulation, and none of the listeners could detect the modulation gap for the highest rate of 512 Hz at the limits of the test. This pattern was confirmed by a one-factor repeated measures analysis of variance (ANOVA) which indicated a significant effect of modulation rate ($F_{5,15}=19.55$, $p<0.0001$). Note that the analysis was performed on the log transforms of the data because of the unequal variances in the various conditions. *Post hoc* contrasts confirmed that the slight decline in performance at 16 Hz relative to 8 Hz was significant ($F_{1,15}=9.53$, $p=0.008$), as was the improvement between 16 and 64 Hz ($F_{1,15}=10.88$; $p=0.005$).

The rapid decline in performance at the higher rates is not surprising, given the temporal modulation transfer function of human observers. For example, it is evident from the data of Viemeister (1979) that a modulation rate of 512 Hz approaches the limits of sensitivity to modulation of broadband noise in normal listeners. Thus, the listeners were unable to discriminate between the modulated and unmodulated segments of the stimuli. The reason for the slight elevation in threshold for a 16-Hz modulation rate is likely due to a transition in perceptual strategy in this region. At the low rate of 8 Hz, the modulation gap is perceived as an arrhythmia in an otherwise regular modulation pattern. At rates above about 32 Hz, the modulation gap is perceived as a ''smooth'' segment bounded by two ''rough'' segments; however, there is no salient percept of rhythm in the stimulus. Although per-

formance levels were similar at the 8- and 64-Hz rates, it was decided to undertake the second experiment using a modulation rate of 8 Hz since all listeners showed optimum MGD performance for this rate and the perceptual cue was uniform.

One factor which may be pertinent to consider in interpreting the findings of experiment 1 is the relation between a modulated sound and its loudness. Zhang and Zeng (1997) showed that a broadband stimulus modulated at a low rate can sound louder than an equal-rms unmodulated stimulus. The modulated segments of the stimuli in experiment 1 underwent level compensation to ensure constancy of level across the modulated and unmodulated segments. However, if a loudness difference remained between the modulated segments (the modulation markers) and the unmodulated segment (the modulation gap) despite the equivalence of level, then it is possible that the presence of the modulation gap was detected on the basis of a loudness change. Examination of the Zhang and Zeng (1997) findings suggests that this was probably not the case. They found that, for a 100% modulated broadband noise, the level difference between a modulated noise and an unmodulated noise that was required for equal loudness was less than 1 dB once the sinusoidally amplitude modulated noise level was 70 dB SPL. The stimuli in experiment 1 were presented at 80 dB SPL. To clarify the effect of imposing level compensation on the stimuli in the present experiment, subsidiary data were collected from two listeners where MGD thresholds were measured as a function of modulation rate under conditions where level compensation was imposed and conditions where level compensation was not imposed. Mean data from the two listeners are shown in Fig. 2 as open circles; the differences between thresholds in the compensated and uncompensated conditions (right-hand axis) are plotted as a function of modulation rate. The differences are negligible until the higher rates of modulation (256 and 512 Hz) where the sensitivity to modulation is poor and the modulation gap in the uncompensated conditions is perceived as an intensity decrement.

II. EXPERIMENT 2: MGD AS A FUNCTION OF CARRIER FREQUENCY SEPARATION

As noted earlier, the purpose of this experiment was to examine whether spectral continuity throughout a temporal event is sufficient for the auditory system to undertake a wideband temporal analysis. To this end, MGD was measured as a function of the frequency separation between the tonal carriers of the modulation markers. A single frequency region was selected for testing, since the study of Formby *et al.* (1996) suggests that the pattern of reduced performance for across-frequency gap detection is not restricted to any particular frequency region. The selected frequency region centered on 2500 Hz, where the ERB is about 295 Hz (Moore and Glasberg, 1987).

A. Method

1. Subjects

Five listeners with normal hearing participated in this experiment. Four had participated in experiment 1. The additional listener also had pure-tone thresholds ≤20 dB HL across the audiometric frequencies (ANSI, 1989) and received extensive training in MGD before data collection began.

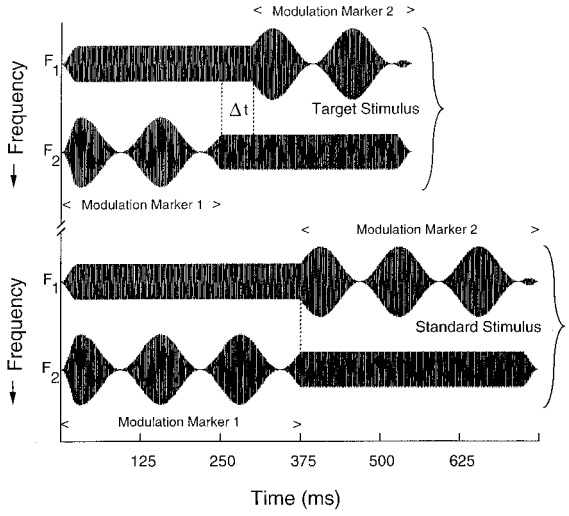

FIG. 3. Waveforms for sample stimuli for the two-frequency conditions of experiment 2. In the target stimulus (upper pair of traces), modulation marker 1 is imposed upon the higher-frequency carrier ($F2$); the lower-frequency carrier ($F1$) is unmodulated during this period. During the modulation gap, marked Δt, both carrier frequencies are unmodulated. Following the modulation gap, modulation marker 2 is carried by $F1$ while $F2$ continues unmodulated. The standard stimulus (lower pair of traces) is similar except that there is no interruption in the modulator cycle between the offset of modulation marker 1 (on $F2$) and the onset of modulation marker 2 (on $F1$). Note that both carrier frequencies are present throughout the interval, regardless of whether they are carrying the modulation marker or not. Note also that the durations of the modulation markers are randomly varied on an interval-by-interval basis to preclude overall stimulus duration as a viable cue for modulation gap detection.

2. Stimuli

In the baseline condition, both 8-Hz modulation markers were carried by a single 2500-Hz carrier. This provided a gauge of wholly within-channel performance. Four other monaural conditions were constructed which paired an 8-Hz modulation marker carried by a variable frequency with an 8-Hz modulation marker carried by 2500 Hz. In two of these conditions, the variable carrier was lower in frequency than 2500 Hz by 2 or 3 ERBs (1970 and 1745 Hz, respectively). In the remaining two conditions, the variable carrier was higher in frequency than 2500 Hz by 2 or 3 ERBs (3158 and 3545 Hz, respectively). These frequency separations were based on two considerations. First, it is apparent from the across-frequency gap-detection work of Formby *et al.* (1996) that such separations are wide enough to result in large changes in performance. Second, as expanded upon below, the need to mask aural distortion products generated by the intermodulations of the two carriers necessitated sufficient spectral separation to include a narrow-band masker which would not also mask the primary signals.

Sample stimuli for the two-frequency conditions are shown in Fig. 3. In the target stimulus, modulation marker 1 is imposed upon the higher-frequency carrier ($F2$); the lower-frequency carrier ($F1$) is unmodulated during this pe-

riod. During the modulation gap, marked Δt, both carrier frequencies are unmodulated. Following the modulation gap, modulation marker 2 is now carried by $F1$ while $F2$ continues unmodulated. The detection of the modulation gap therefore requires a comparison of the offset of modulation marker 1 carried by $F2$ with the onset of modulation marker 2 carried by $F1$. In the standard stimulus, modulation marker 1 is again imposed on $F2$ ($F1$ is unmodulated during this period) and modulation marker 2 is imposed on $F1$ ($F2$ is unmodulated during this period). However, there is no interruption in the modulator cycle between the offset of modulation marker 1 and the onset of modulation marker 2. The key point is that, for both target and standard stimuli, both carrier frequencies are present throughout the interval, regardless of whether or not they are carrying the modulation marker. Note also that the durations of the modulation markers varied randomly on an interval-by-interval basis as described in experiment 1. Thus, the overall stimulus duration was not a viable cue for modulation gap detection. In all conditions, the modulation marker prior to the modulation gap was carried by the higher-frequency carrier. The reverse order—i.e., modulation marker 1 being carried by the lower-frequency carrier—was not tested since findings from across-frequency gap detection suggest that a marker frequency order effect is not to be expected (Formby *et al.*, 1998). The stimuli were digitally generated on a trial-by-trial basis, with level compensation applied to the modulated segments. The presentation level of each carrier was 65 dB SPL.

In order to preclude any cues that might be based on aural distortion products, a continuous background noise was presented which was composed of two sources. The first source was a broadband background noise (0–3750 Hz) presented at a pressure spectrum level of 10 dB SPL. The upper cutoff was selected as being the upper boundary of an ERB centered on 3545 Hz—the highest frequency carrier employed. The second source of the background noise was a relatively narrow band of noise whose center frequency varied with the selection of the carrier-frequency pair. For each of the four carrier-frequency pairs, the narrow-band noise was centered on the $2f1-f2$ frequency and had a bandwidth set to the ERB of that frequency. This noise was presented at an overall level of 35 dB SPL since the work of Weber and Mellert (1975) indicates that, for the smallest $f2/f1$ ratio employed here (about 1.26), the $2f1-f2$ level is about 30 dB down from the level of the primaries. For the single-carrier baseline condition, where intermodulation distortion products are inherently absent, a narrow-band noise was also presented in order to make the background noise of this condition perceptually similar to the two-carrier conditions. Here, the narrow-band noise was centered on 1842 Hz, which is separated from 2500 Hz by the same number of ERBs as the smallest separation between the center frequency of the narrow-band noise and the lower carrier frequency in the two-carrier conditions.

3. Procedure

The same 3AFC procedure as described for experiment 1 was implemented. Again, at least three estimates of threshold were collected per condition, and final threshold for an individual was taken as the geometric mean of all estimates for that condition. Runs were rejected if the tracking procedure hit the maximum allowable gap duration of 250 ms at any point during the run. In these difficult conditions, a minimum of three attempts at obtaining a valid estimate of threshold was undertaken, after which threshold was tabulated as being in excess of 250 ms.

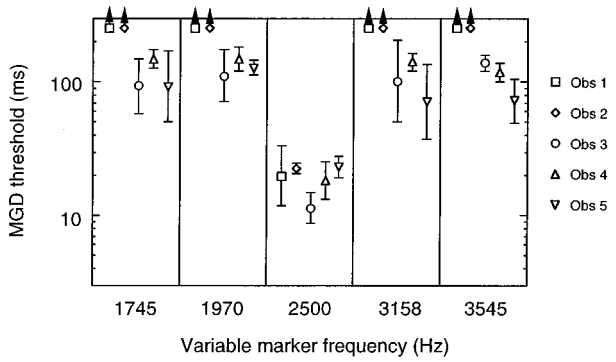

FIG. 4. Individual MGD thresholds for each carrier frequency pairing. The ordinate indicates only the variable marker frequency; the fixed marker frequency was always 2500 Hz. When the variable marker frequency was 2500 Hz (center panel), only a single carrier was present. Each panel shows the individual results from the five listeners. Error bars indicate ±1 s.d. Data points which exceeded the test limits of 250 ms are shown as upward-pointing arrows.

B. Results and discussion

The results from the five listeners showed some individual variation, and so the individual data are shown in Fig. 4. The overriding finding was that MGD performance was most acute in the baseline isofrequency condition and declined when the modulation gap traversed frequency. While three listeners were consistently able to provide valid thresholds in the across-frequency conditions (Obs 3, 4, and 5), the other two listeners were not (Obs 1 and 2). For the three listeners who provided complete sets of data, there was no apparent effect of carrier frequency separation in the across-frequency conditions.

The results of this experiment indicate that spectral continuity across the temporal event is not a sufficient prerequisite for the auditory system to undertake a wideband temporal analysis. Although the carrier frequencies were continuously present throughout the stimulus, MGD thresholds increased markedly compared to the isofrequency baseline. This pattern of results is similar to the across-frequency gap-detection results which indicate that gap detection worsens as a function of the frequency separation between markers (Kinney, 1961; Perrott and Williams, 1971; Collyer, 1974; Fitzgibbons *et al.*, 1974; Divenyi and Danner, 1977; Divenyi and Hirsh, 1978; Neff *et al.*, 1982; Formby *et al.*, 1996; Forrest and Formby, 1996; Grose and Hall, 1996; Formby *et al.*, 1997; Phillips *et al.*, 1997; Formby *et al.*, 1998).

III. EXPERIMENT 3: MGD FOR DICHOTIC PRESENTATION

Phillips *et al.* (1997) have shown that across-ear gap detection for isofrequency markers is as poor as monaural gap detection for markers widely separated in frequency. They interpret this as indicating that the channels across which the temporal judgments are being performed are central to at least the level of binaural integration. The purpose of this experiment was to determine whether a similar observation held for MGD performance. Here, the carrier of the modulation was presented diotically, but the first modulation marker was presented to one ear while the second modulation marker was presented to the opposite ear. Phillips *et al.* (1998) have also supported their contention that the channels across which the temporal judgments are being performed are central to at least the level of binaural integration by using a free-field gap-detection task using broadband noise markers. Although each ear presumably received some marker energy from both markers bounding the gap, irrespective of the position of the activated loudspeaker, the pattern of results was similar to that for dichotic conditions measured under headphones. A subsidiary condition was therefore included here in which a noise carrier was presented to both ears, but with an interaural level difference which changed during the stimulus presentation. The purpose of this condition was to create a binaural stimulus where the lateralized image moved during the presentation interval.

A. Method

1. Subjects

The same five listeners who participated in experiment 2 participated in the main condition of experiment 3. Only the four listeners who participated in experiment 1 undertook the subsidiary condition.

2. Stimuli

In the main condition of this experiment, a 2500-Hz carrier was presented diotically. The first 8-Hz modulation marker was applied to the carrier in the left ear while the second 8-Hz modulation marker was applied to the carrier in the right ear. In all other respects, the stimulus generation and presentation was the same as in previous experiments. In the subsidiary condition of this experiment, a broadband noise carrier was presented to the two ears. The noise at the two ears originated from a single noise generator and therefore was interaurally coherent. Each ear received both 8-Hz modulation markers. However, the waveform amplitude during the first modulation marker was 6 dB greater in the left ear than in the right ear, giving a lateralized image to the left side. During the modulation gap, the noise carrier was of equal level in the two ears, giving a centralized image. During the second modulation marker, the waveform amplitude was 6 dB greater in the right ear than in the left ear, giving a lateralized image to the right side. Although this stimulus resulted in abrupt level changes at two locations in the stimulus waveform during presentation, the percept was of a single noise whose apparent intracranial image moved from the left side of the head to the right during the modulation gap.

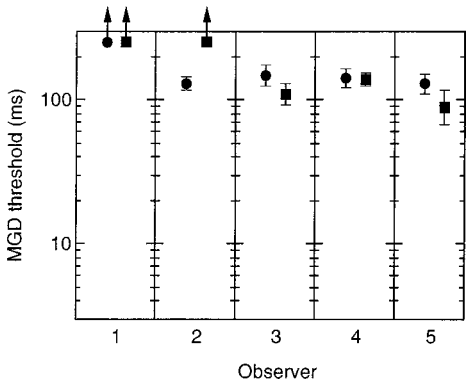

FIG. 5. Individual MGD thresholds for the dichotic isofrequency condition (circles). Also shown for comparison are the average monaural across-frequency MGD thresholds for the same listener (squares). Error bars indicate ±1 s.d. Data points with upward-pointing arrow indicate thresholds in excess of 250-ms limit.

3. Procedure

The procedure was the same as that used in the previous two experiments. At least three estimates of threshold were obtained from each listener for each condition.

B. Results and discussion

Figure 5 displays the results of the main condition. For each listener, the MGD threshold for the dichotic condition is displayed (circle) alongside the MGD threshold averaged across the four across-frequency conditions of experiment 2 (square). The general finding is that dichotic MGD yields roughly the same level of performance as the monaural across-frequency conditions. The exception to this trend was Observer 2, who was unable to perform across-frequency MGD but was able to provide a valid, albeit elevated, dichotic MGD threshold. The key demonstration, however, is that dichotic MGD for isofrequency carriers was markedly worse than for monaural isofrequency MGD. This is in line with the Phillips *et al.* (1997) gap-detection finding which suggested that the channels across which temporal events were poorly processed do not necessarily correspond to peripheral frequency channels; i.e., the channels may also be associated with different spatial locations (see also Phillips *et al.*, 1998).

While this interpretation is parsimonious, the two exemplars of ''across-channel'' temporal processing (monaural across-frequency and isofrequency across-ear) are dissimilar in terms of environmental realism. Naturally occurring sounds may incorporate temporal discontinuities across frequency (e.g., voiced stop consonants), but it is improbable that a sound source will switch instantaneously from one side of a listener's head to the other. Instead, there is usually a relative motion between a sound source and the listener that results in the perception of a moving image. The subsidiary condition of this experiment was a simple attempt to provide the listener with an illusory moving image in order to determine whether the auditory system is adept at processing tem-

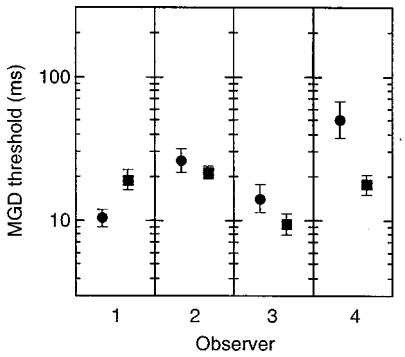

FIG. 6. Individual MGD thresholds for the dichotic broadband condition (circles). Also shown for comparison is the monaural broadband 8-Hz MGD threshold for the same listeners (squares). Error bars indicate ±1 s.d.

poral events which traverse spatial location in the strict sense but are nevertheless part of the same moving source. Four listeners participated in this condition, and the results are shown in Fig. 6. For each listener, the dichotic MGD threshold (circle) is compared to the monaural 8-Hz MGD threshold from experiment 1 (square). Three of the four listeners provided relatively similar thresholds in the two conditions, while Obs 4 provided a somewhat elevated threshold in the dichotic condition. Both parametric (paired *t*-test) and nonparametric (paired sign test) analysis found no reliable effect of condition. While this result is compatible with the suggestion that the auditory system is adept at processing temporal events in a moving sound source, the strength of the evidence is undermined by the fact that the modulation gap existed in its entirety in each ear, albeit with different levels of the modulation markers on either side of the gap. Thus, it is unclear whether performance in the dichotic condition was due to the listener undertaking a monaural analysis, although the reported percept was of a moving sound source.

IV. SUMMARY AND CONCLUSION

The primary purpose of this study was to determine whether the normal auditory system is generally poor at processing temporal events which traverse frequency or whether the poor performance seen for across-frequency gap detection is a result of the spectral discontinuity associated with the stimulus. The first experiment established the paradigm of MGD and indicated that performance was optimal for an 8-Hz modulator. The results of the second experiment indicated that spectral continuity was not sufficient to facilitate wideband analysis of temporal events which traversed frequency. The inability to make temporal judgments across channels appears to be a general property of the auditory system. This interpretation is compatible with findings in the area of stream segregation, which indicate that order/timing judgments among tones presented in sequences are disrupted if the sequences of tones are perceptually segregated into separate auditory streams (Bregman and Campbell, 1971; van Noorden, 1975). The results of the third experiment indicated that MGD performance across ears was as poor as MGD performance across frequency. This result supports the contention that the channels across which temporal events are poorly processed do not necessarily correspond to peripheral frequency channels.

ACKNOWLEDGMENTS

The helpful comments of Dr. Chris Plack and two other anonymous reviewers on an earlier version of this paper are gratefully acknowledged. This work was supported by the NIH NIDCD (Grant No. R01-DC01507).

[1]In order to compensate for increases in level brought about by modulation, the modulated segments were adjusted in amplitude by a factor of $1/\sqrt{1+m^2/2}$,

where the modulation index, m, was set equal to 1. The effect of this compensation on MGD performance for wideband noise stimuli is shown in Fig. 2.

ANSI (**1989**). ANSI 53.6-1989, NTIS (American National Standards Institute, New York).

Bacon, S. P., and Viemeister, N. F. (**1985**). ''Temporal modulation transfer functions in normal-hearing and hearing-impaired subjects,'' Audiology **24**, 117–134.

Bregman, A. S., and Campbell, J. (**1971**). ''Primary auditory stream segregation and perception of order in rapid sequences of tones,'' J. Exp. Psychol. **89**, 244–249.

Collyer, C. E. (**1974**). ''The detection of a temporal gap between two disparate stimuli,'' Percept. Psychophys. **16**, 96–100.

Dau, T. (**1996**). ''Modeling auditory processing of amplitude modulation,'' Doctoral dissertation, University of Oldenberg, Germany.

Divenyi, P. L., and Danner, W. F. (**1977**). ''Discrimination of time intervals marked by brief acoustic pulses of various intensities and spectra,'' Percept. Psychophys. **21**, 125–142.

Divenyi, P. L., and Hirsh, I. J. (**1978**). ''Some figural properties of auditory patterns,'' J. Acoust. Soc. Am. **64**, 1369–1385.

Fitzgibbons, P. J., Pollatsek, A., and Thomas, I. (**1974**). ''Detection of temporal gaps within and between perceptual tonal groups,'' Percept. Psychophys. **16**, 522–528.

Formby, C., Gerber, M. J., and Sherlock, L. P. (**1997**). ''Evidence for a simple two-channel model for asymptotic gap detection,'' J. Acoust. Soc. Am. **101**, 3150.

Formby, C., Sherlock, L. P., and Forrest, T. G. (**1996**). ''An asymmetric roex filter model for describing detection of silent temporal gaps in sinusoidal markers,'' Aud. Neurosci. **3**, 1–20.

Formby, C., Sherlock, L. P., and Li, S. (**1998**). ''Temporal gap detection measured with multiple sinusoidal markers: Effects of marker number, frequency, and temporal position,'' J. Acoust. Soc. Am. **104**, 984–998.

Forrest, T. G., and Formby, C. (**1996**). ''Detection of silent temporal gaps in sinusoidal markers simulated with a single-channel envelope detector model,'' Aud. Neurosci. **3**, 21–33.

Grose, J. H., and Hall, J. W. (**1996**). ''Perceptual organization of sequential stimuli in listeners with cochlear hearing loss,'' J. Speech Hear. Res. **39**, 1149–1158.

Hall, J. W., Grose, J. H., and Joy, S. (**1996**). ''Gap detection for pairs of noise bands: effects of stimulus level and frequency separation,'' J. Acoust. Soc. Am. **99**, 1091–1095.

Heinz, M. G., Goldstein, M. H., and Formby, C. (**1996**). ''Temporal gap detection thresholds in sinusoidal markers simulated with a multi-channel, multi-resolution model of the auditory periphery,'' Aud. Neurosci. **3**, 35–56.

Kinney, J. A. S. (**1961**). ''Discrimination ability in auditory and visual patterns,'' Am. J. Psychol. **74**, 529–541.

Moore, B. C. J., and Glasberg, B. R. (**1987**). ''Formulae describing frequency selectivity as a function of frequency and level and their use in calculating excitation patterns,'' Hearing Res. **28**, 209–225.

Neff, D. L., Jesteadt, W., and Brown, E. L. (**1982**). ''The relation between gap discimination and auditory stream segregation,'' Percept. Psychophys. **31**, 493–501.

Perrott, D. R., and Williams, K. L. (**1971**). ''Auditory temporal resolution: Gap detection as a function of interpulse frequency disparity,'' Psychon. Sci. **25**, 73–74.

Phillips, D. P., Hall, S. E., Harrington, I. A., and Taylor, T. L. (**1998**). ''Central auditory gap detection: a spatial case,'' J. Acoust. Soc. Am. **103**, 2064–2068.

Phillips, D. P., Taylor, T. L., Hall, S. E., Carr, M. M., and Mossop, J. E. (**1997**). ''Detection of silent intervals between noises activating different perceptual channels: Some properties of 'central' auditory gap detection,'' J. Acoust. Soc. Am. **101**, 3694–3705.

van Noorden, L. P. A. S. (**1975**). ''Temporal coherence in the perception of tone sequences,'' Ph.D. thesis, Eindhoven University of Technology.

Viemeister, N. F. (**1979**). ''Temporal modulation transfer functions based upon modulation thresholds,'' J. Acoust. Soc. Am. **66**, 1364–1380.

Weber, R., and Mellert, V. (**1975**). ''On the nonmonotonic behavior of cubic distortion products in the human ear,'' J. Acoust. Soc. Am. **57**, 207–214.

Zhang, C., and Zeng, F.-G. (**1997**). ''Loudness of dynamic stimuli in acoustic and electric hearing,'' J. Acoust. Soc. Am. **102**, 2925–2934.

Auditory temporal integration in the rhesus macaque (*Macaca mulatta*)

Kevin N. O'Connor, Phillip Barruel, Reza Hajalilou, and Mitchell L. Sutter
Center for Neuroscience, and the Department of Neurophysiology, Physiology and Behavior, University of California, Davis, California 95616

(Received 1 June 1998; revised 15 October 1998; accepted 11 May 1999)

Temporal integration for pure tones was examined in two rhesus macaques. The subjects were required to respond to a brief sound (a tone burst) that deviated from a previous series of sounds (noise bursts) on a trial (a deviant-stimulus detection paradigm). Psychometric functions and thresholds were determined from correct detections (hit proportions) alone, and from d' scores. Two models describing the decline in threshold as a function of stimulus duration, one a power function the other an exponential, were tested against the data. When the decline (slope) in threshold per log stimulus duration is used as a rate measure, our results yield a lower estimate of temporal integration rate in rhesus than did a previous study [Clack, J. Acoust. Soc. Am. **40**, 1140–1146 (1966)]. Both studies, however, gave slope estimates of integration rate that were higher than in most other species. Comparison of the models using data from several species, revealed that the exponential, but not the power model, could account for two sources of variation in threshold measurement. One source is due to the range across threshold as a function of duration (the linear rate component), and is described by the constant of proportionality I_k in the model. The other source of variation arises from the rate of decline *within* this range (the nonlinear rate component), and is described by the time constant τ. In terms of this model, differences in rate estimates between Clack's study and ours (and between rhesus and other species) are primarily due to the linear component. The nonlinear rate component was about equal for our study and Clack's ($\tau = \sim 150$ ms): a time constant that is just slightly larger (indicating a rate of temporal integration slightly slower) than for most other species examined. © *1999 Acoustical Society of America.* [S0001-4966(99)05108-5]

PACS numbers: 43.66.Mk, 43.66.Gf, 43.66.Ba [JWH]

INTRODUCTION

Complex natural sounds such as those used in acoustic communication tend to be dynamic, changing their spectra over time, rather than static. Physiological work in several species has revealed the existence of neurons that exhibit sensitivity to the spectrotemporal structure in vocalizations and other complex sounds. Many forebrain neurons in zebra finches, for example, are sensitive to combinations of two or more song elements presented in the appropriate order and at intervals of up to several hundred milliseconds (Margoliash, 1983; Margoliash and Fortune, 1992). Auditory cortical neurons in marmosets respond better to natural calls than temporally distorted synthetic variations or to reversed calls (Wang *et al.*, 1995). Neurons in cat auditory cortex show tuning to rate of amplitude (5–20 Hz; Schreiner and Urbas, 1986) and frequency modulation (Rauschecker, 1997), two prominent acoustic parameters found in vocalizations and other complex sounds. In humans, subsets of neurons in the lateral temporal lobe respond best to consonant/vowel combinations, or prefer compound to noncompound multisyllabic words (Creutzfeldt *et al.*, 1989). These studies suggest that one function of the auditory forebrain may be to temporally integrate acoustic information.

The precise neural circuitry underlying these forms of temporal integration is unknown. An ideal integrator would require sensitivity to rapid changes in spectrotemporal patterns, as well as the ability to integrate information regarding these changes over relatively long periods—at least several seconds for natural communication signals. It takes time, though, to resolve the frequency structure of signals, so an integrator (or more properly, a differentiator) that was sensitive to very fine-grained temporal structure or transients in signals, would not be able to recover much information regarding spectral structure—nor to summate over long periods because it lacks memory. And an integrator that focused on recovering the spectral information in signals would lose track of high-resolution temporal structure. The auditory system may have solved this dilemma by breaking the task into two stages—first responding primarily to changes from the steady state, then integrating the output in a second stage of processing, using a tonotopic, labeled-line strategy for extracting as much information from the frequency domain as possible. Alternatively, the problem might be tackled by a parallel system: one channel having high temporal resolution, responsive to fine-grained temporal structure, the other channel better tuned to frequency, with lower temporal resolution and able to integrate over longer periods.[1] In this last case, though, a final stage of integration or combining of information from the two channels would be necessary for their merger and coherence into a single percept.

In order to gain a full understanding of a specie's ability for processing the temporally complex information in signals, and to uncover the possible neural mechanisms underlying this ability, it is important to determine their capacity for integrating information over time. We are studying the auditory system of rhesus macaques for this purpose. This

species displays a rich vocal repertoire consisting of 25 to 30 different call types conveying social as well as ecological information (Hauser, 1991; Hauser and Marler, 1992). Their vocalizations exhibit considerable structural variation and vary in duration from about 0.1 s to almost 1 s in duration, depending on call type, and may contain distinct amplitude and/or frequency modulated components. If macaque call recognition depends on identification of individual call components, then there must exist neurons in the macaque brain sensitive to the temporal pattern of these components—neurons capable of integrating spectral information over relatively brief as well as longer intervals.

An organism's capacity for integrating information over time has traditionally been examined by measuring the threshold for detecting a sound, usually a pure tone, as a function of its duration. It has long been known that stimuli of near threshold intensity become more detectable with increasing duration (see, for reviews, Marks, 1974; Watson, 1986; Eddins and Green, 1995). In its simplest form this relationship has usually been expressed as

$$I\,t = k. \tag{1}$$

This equation (often referred to as ''Bloch's Law'') states that there is reciprocity between intensity (I) and duration (t) near threshold—in other words, that their product is a constant (k). Equation (1) implies perfect integration, in the sense that with each doubling in duration there is a doubling in effective intensity with a corresponding drop in threshold. There has been much work over the past half century exploring the accuracy of this very simple model for audition. In brief, two principle qualifications must be made. First, integration appears to proceed only up to some limiting duration (usually a few hundred milliseconds) beyond which threshold remains unaffected (Hughes, 1946; Garner and Miller, 1947). In other words, there exists some minimum threshold for a continuous stimulus. Second, the tradeoff between intensity and duration is usually less than perfect. With the addition of these caveats the relationship between threshold intensity and duration can be expressed as

$$I_T = I_k t^{-m} + I_\infty . \tag{2}$$

This equation expresses threshold intensity as a power function of signal duration, where m is a rate parameter [and is equal to one if Eq. (1) holds], I_∞ is a minimum-threshold intensity (threshold for a continuous stimulus, that is, as $t \rightarrow \infty$) below which energy is too low to be integrated, and I_k is a scaling parameter or constant of proportionality.

Intensity integration has also been described as a simple exponential function of signal duration, analogous to the charging of a capacitor through some resistance (Munson, 1947; Plomp and Bouman, 1959; Zwislocki, 1960). In terms of this model, threshold intensity can be expressed as

$$I_T = I_k \exp(-t/\tau) + I_\infty , \tag{3}$$

where τ is the time constant[2] for the rate of integration, and the remaining parameters are defined as for Eq. (2).

Use of threshold measurements to estimate integration of intensity permits the use of simple detection tasks, an advantage over more direct techniques (e.g., loudness scaling) of the intensity of suprathreshold stimuli, particularly with nonhuman subjects. The relationship in Eq. (1) has also held for the relationship between intensity and tone duration above threshold, such that loudness level is roughly proportional to the log of duration (Zwislocki, 1969), although there may be an increase in integration rate at high intensity levels (Miller, 1948; Zwislocki, 1969).

Equations (2) and (3) represent minimal models in the sense that omitting a parameter (such as I_∞) is likely to come at the expense of normalizing for individual subject differences. Most studies have used this approach in order to focus only on the rate of integration. The rate parameter in Eq. (2) has usually been found to be slightly less than unity (with negative sign) for human subjects (Garner, 1947; Gerken, *et al.*, 1983, 1990), while the time constant in Eq. (3) usually falls roughly near 200 ms (Plomp and Bowman, 1969; Watson and Gengel, 1969; Gerken, *et al.*, 1983; 1990). These estimates have also held for most auditory temporal integration studies using nonhuman subjects (for example, dolphins: Johnson, 1967; chinchillas: Henderson, 1969; mouse: Ehret, 1976; goldfish: Fay and Coombs, 1983; budgerigars: Dooling and Searcy, 1985; chickens: Saunders and Salvi, 1993). In a comparative study of humans and rhesus macaques, Clack (1966) found the rate of temporal integration in macaques to be close to that of humans for midrange pure-tone frequencies, but considerably higher at low (0.250–1 kHz) and high (8 kHz) frequencies.

Recently, there has been a spurt in growth in the number of laboratories doing behavioral and neurophysiological work on macaque audition. We thought a reexamination of the issue of temporal integration in macaques was timely, because of differences in Clack's methods and those currently employed by most investigators. Clack used a shock-avoidance paradigm, presenting a single acoustic stimulus on each trial. This procedure is quite different from the deviant-stimulus detection paradigm employing appetitive or positive reinforcement that has been widely adopted for auditory work in macaques and other monkey species (Moody *et al.*, 1976). Since Clack's paper appeared in 1966 there has been a great deal of work on the involvement of the ascending auditory system in aversive or fear-related conditioning, in which emotion-related responses such as behavioral ''freezing'' or changes in heart rate are observed (LeDoux, 1990). This work employs shock as the aversive (unconditioned) stimulus and pure tones as conditioned stimuli. It is now known that intact medial geniculate-amygdaloid circuitry (but not auditory cortex) is necessary for fear conditioning to auditory stimuli (LeDoux, 1990). Although most of this work has been done with rats, recent imaging studies confirm the involvement of the amygdala during fear conditioning in humans (LaBar *et al.*, 1998), as does a conditioning study with humans sustaining damage to the amygdaloid region (LaBar *et al.*, 1995). Clack's use of shock in training (in this case in an operant rather than classical conditioning paradigm) may have recruited the same or overlapping neuronal circuitry as that found in fear conditioning studies, including anatomical regions that may not necessarily be involved in auditory detection or discrimination tasks in the absence of aversive stimulation. The possibility that different neuronal

mechanisms may be engaged when using aversive rather than appetitive stimulation in training suggests that behavioral differences in detection may result that may in turn affect measurements of temporal integration.

Another significant point is that Clack tested and reported data on only two macaques. This is not at all unreasonable given the expense and time involved in behavioral work with this species—in fact, the present study reports data from just two subjects. In doing so, though, we double the number of rhesus monkeys tested on a temporal integration task, and provide the opportunity of confirming or disconfirming the previous findings.

Rather than employ a single stimulus per trial procedure to determine pure-tone thresholds, we used a technique in which a subject responds to a deviant sound (a tone burst) differing from a preceding series of repeated identical sounds (noise bursts). Use of this technique would permit more direct comparison to behavioral and neurophysiological studies of complex auditory discrimination that use the same method. It would be particularly useful for comparison with studies using the same method to examine neural correlates of auditory temporal integration.

We have also departed from the typical method of analysis. It has been traditional in the area of auditory temporal integration to mold threshold-intensity functions to linear form for further analysis. This has generally been accomplished by plotting threshold intensity in decibels as a function of stimulus duration on double-logarithmic coordinates. It should be pointed out that, because decibels are proportional to the logarithm of energy (or pressure) ratios, units of decibels have traditionally been plotted against the log of time. Thus although these graphs display a log–log scatterplot between energy and time, they actually depict a linear-log plot between units of sensation level, as measured in decibels and time. The slope of the best-fitting linear regression line to these points has then been used to estimate the rate of integration [m in Eq. (2) or the reciprocal of τ in Eq. (3)]. One problem with this technique is that large departures from linearity are often apparent (Dallos and Olsen, 1964), and in fact must be found if stimulus durations extend beyond the limits of integration. Solutions to this problem have included selecting only a linear portion of the data to fit, or subtracting a minimum asymptotic intensity value (threshold intensity at I_∞) before fitting (Garner and Miller, 1947; Dallos and Olsen, 1964). One or both of these methods have been adopted by most investigators. Both of these solutions are imperfect, of course, relying on arbitrary criteria to select and reject data, and so may not provide accurate estimates of integration times, nor stringent tests of a model. Rather than restrict our analysis to (quasi-) linear portions of the data set, we used nonlinear curve fits to examine threshold intensity across the entire domain of stimulus durations. In addition, in order to better compare our results against those from previous studies, the data were gauged against both models as described by Eqs. (2) and (3).

I. METHOD

A. Subjects

Two male rhesus monkeys (*Macaca mulatta*) undergoing water restriction were subjects. Subject Z was approximately 4.5 years, and subject Y approximately 4.0 years of age at the start of training.

B. Procedure, stimuli, and apparatus

All training and testing sessions were conducted in the ''free field,'' that is, in a sound-attenuated booth (IAC: 9.5 ft×10.5 ft×6.5 ft) foam lined to reduce echoes. Subjects sat in an ''acoustically transparent'' primate chair with a drinking tube in front of the mouth. A response lever (8×2.5 cm) extended inside the chair, positioned about 10 cm in front and center of the monkey's body. Water was held in a reservoir positioned approximately 0.5 m above and 0.5 m to the left of the subject, and was delivered via polyethylene tubing by opening a solenoid valve for 125 ms.

Subjects were initially trained to depress and release the lever for water using standard operant shaping techniques. Subjects were then trained to depress the lever (perform an observing response) to hear a 100-ms tone burst (either 1 or 4 kHz, randomly ordered). This tone burst occurred after a 100-ms silent delay (after microswitch closure), and a lever release after the tone resulted in water reinforcement. During subsequent sessions the pre-tone delay was gradually increased to 1 s, and a limit on response latency was imposed. The response limit (initially 10 s) was gradually decreased to 800 ms over the course of several sessions. Subsequently, two 100-ms broadband (''frozen'') noise bursts were introduced into the pre-tone interval (a 100-ms silent interstimulus interval (ISI) intervened between all sounds). This noise was ''faded-in,'' that is, gradually increased in intensity over the course of one session until equal in intensity to the tone stimulus. In the final phase of training, ISIs of 200, 400, or 800 ms replaced the fixed 100-ms ISI, and the number of possible pre-tone noise bursts was changed from two to either two, three, or four per trial (the new ISIs and additional noise bursts were introduced gradually over sessions). The primary purpose of the variable ISIs and noise repetitions was to make the tone temporally unpredictable: This was necessary because we found, during the early stages of training, that the subjects were able to time their responses to occur within the response window if it was temporally predictable, regardless of the stimulus presented. During training sessions all sound stimuli were presented well above threshold, at approximately 55 dB SPL, ±1.5 dB (Bruel & Kjaer 2231).

Threshold testing was essentially the same as training, with the exception of the introduction of noise-only trials. The subject was required to respond to a tone (target) which was presented after a preceding series of noise bursts (standards), and withhold responding on standard-only trials (a ''go/no-go'' task). Illumination of an LED directly below the speaker cued the start of each trial, and the subject initiated stimulus presentation by depressing the lever. The sound sequence consisted of two to four noise bursts followed by a pure-tone burst on target trials, and by a noise burst on non-

target trials. ISIs were either 200, 400, or 800 ms on a trial. An 800-ms response window immediately followed the final stimulus in the series. If the monkey released the lever following a target stimulus within this window (a hit) he was rewarded with water. False alarms were punished with a 12-s time out period—otherwise the next trial commenced after a 1.5-s intertrial interval. There were no consequences for either missing a target or correctly rejecting a nontarget stimulus. Responses made before onset of the response window were punished with a 5-s time-out followed by representation of the trial. Time-out periods were signaled by turning off a miniature incandescent lamp situated below the speaker. The proportion of target trials was approximately 0.90, and these were randomly interleaved with nontarget trials.

Thresholds for seven tone frequencies were examined: 0.5, 1, 2, 4, 6, 8, and 12 kHz. Only one target frequency was presented within a session which comprised 189 trials. The order of frequency presentation was randomized over sessions and was the same for both subjects. After one session at each frequency had been presented, the sessions were once again presented but in reversed order yielding a total of 378 trials at each frequency. Auditory stimuli were presented at six durations: 25, 50, 100, 200, 400, or 800 ms. Standard and target duration was kept constant within each trial. Tone and noise stimuli were delivered at six intensity levels: 45, 35, 25, 15, 5, or −5 dB at each duration. Stimulus duration and intensity levels were randomly ordered within a session. The subjects were permitted to work each day until sated, and typically completed 3–4 sessions (working 2–3 h) before stopping. Only completed sessions were included in the data analysis.

Acoustic signals were generated using a digital signal processor (AT&T DSP32O) with 16-bit output resolution and a digital-to-analog converter (TDT DA1), passed through a programmable attenuator (TDT PA4), and then through a passive attenuator (Leader LAT-45). The signal was then amplified (Radio Shack MPA-200) and delivered through a speaker (Radio Shack PA-110, 10-in. woofer and piezo horn tweeter, 38–27 000 Hz) positioned at ear level 1.5 m in front of the subject. All sounds were generated at a sampling rate of 50 kHz and were cosine-onset/-offset ramped (5-ms rise/fall time). All experimental timing and control functions were accomplished with a Pentium-based microcomputer controlling solid-state interface equipment (TDT Systems).

C. Curve fitting

Curve fits were performed using a Marquardt–Levenberg, least-squares technique (Marquardt, 1963). Psychometric functions were fitted with a three parameter sigmoid equation of the form

$$y = a/\{1+\exp[-(x-x_0)/b]\}. \quad (4)$$

The purpose of these curve fits was primarily to obtain the best estimate of a threshold point from each psychometric function (shown in Figs. 3 and 5). This equation was chosen for its utility, that is, because it provided good fits to the data points, and not on any theoretical grounds. Equations (2) and (3) were fitted to the threshold points (seen in Figs. 4 and 6) using the same technique, but in this case a weighted fit was employed. Each data point was weighted by the inverse of the norm of the residuals (the square root of the sum of squared residuals) obtained from the corresponding psychometric function and its fitted sigmoid curve. The r^2 statistic (representing the proportion of total variation accounted for by the fitted function) was then calculated, and an F statistic (the ratio between the variation from the dependent variable and the residual variation about the regression) was determined, giving the statistical significance of r^2 for each fitted threshold curve (Daniel and Wood, 1980).

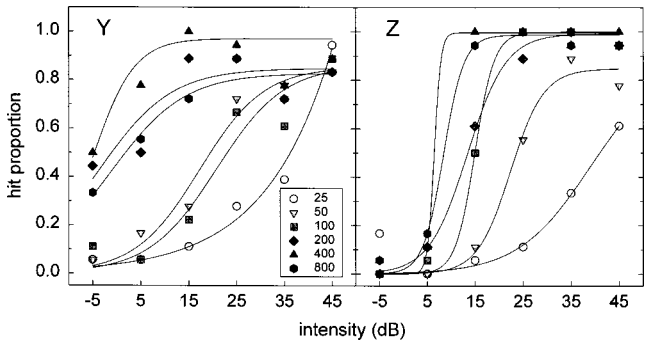

FIG. 1. Proportions of correct detections (hits) are plotted as a function of the intensity of 1-kHz tones for each stimulus duration (inset shows stimulus duration in milliseconds) for the two subjects (Y and Z). Solid lines represent best-fitting sigmoid curves (see footnote 1) to each set of data points.

II. RESULTS

The proportions of hits and false alarms were computed for each duration, intensity and frequency tested. The proportion of false alarms (subject Z: 0.027; subject Y: 0.060) was low—averaging less than two false alarm responses per session—or less than 0.10 for both subjects. Given this low false alarm rate, hit proportions were plotted against intensity to yield psychometric functions (Green and Swets, 1974). A set of such functions is plotted for 1 kHz in Fig. 1, together with the best-fitting sigmoid curves. Each point in this figure represents data from 18 trials. Threshold intensities, corresponding to the 0.50 hit proportion level at each duration, were then determined from the sigmoid curves for each frequency tested (subject *Z* failed to reach the 0.5 threshold criterion for the 25-ms duration at 0.5, 1, 4, and 12 kHz). Threshold values are plotted as a function of stimulus duration in Fig. 2. These plots show a strong nonlinear decrease in threshold intensity with increasing stimulus duration. A repeated measures ANOVA revealed a significant effect of duration on threshold [$F(1,5)=28.57$, $p<0.005$], but no significant effect of frequency [$F(1,6)=0.84$, $p>0.50$], nor a significant interaction between duration and frequency [$F(1,5,6)=1.18$, $p>0.34$]. Although subject Y's threshold values appear to decline to lower levels as a function of duration, the difference in subjects was not significant [$F(1)=3.13$, $p>0.10$]. The fact that we found no effect of frequency may seem unusual given that most studies have reported an inverse relationship between tone frequency and integration rate over the frequency ranges examined. However, some studies have failed to show this relationship

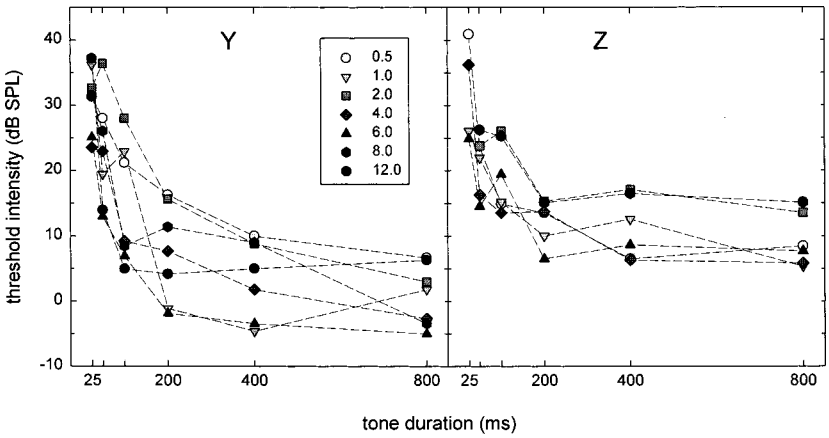

FIG. 2. Threshold intensities are plotted as a function of stimulus duration for each tone frequency tested (inset shows tone frequency in kHz).

(Hughes, 1946; Ehret, 1976), while others have reported an inverse-U-shaped relationship between frequency and integration rate (Clack, 1966; Johnson, 1968).

Given that there was no significant effect of tone frequency on threshold functions for the tested frequencies, hit proportions were collapsed over frequency and new psychometric functions calculated. These functions and the best-fitting sigmoid curves are plotted in Fig. 3. Thresholds were again determined and are displayed as a function of stimulus duration in Fig. 4, along with the best fits of Eqs. (2) and (3). Once again thresholds show a rapid nonlinear decline with increasing stimulus duration. Most of this decrease occurs by 200 ms, although there appears to be a continuing decline at a slower rate out to 800 ms. This represents a decline in threshold of 7.8 dB per doubling in duration for subject Y, and 6.8 dB/doubling for subject Z, during the first 200 ms of stimulus presentation. From 200 to 800 ms subjects Y's threshold decreases by 3.7 dB/doubling, and subject Z's threshold by 2.8 dB/doubling.

Parameter estimates from the fits are displayed in Table I. For both models the parameter estimates are congruent with those found in previous studies. The relationship between threshold and duration seems well described by both the power [Eq. (2)] and exponential [Eq. (3)] models, although the power function seems to provide a slightly better fit for subject Z's data as indicated by the higher significance level associated with r^2. This observation is supported by a paired *t*-test of the difference between the means of the absolute residuals for this fit ($t=3.64$, $df=5$, $p<0.05$).

It appears from Fig. 4 that the subjects differ. Subject Y declines to a threshold close to 0 dB by 800 ms. Subject Z shows a somewhat more modest decline in threshold reaching an asymptotic level of approximately 10 dB—this difference is reflected in the lower values of I_∞ obtained for subject Y. Subject differences are also apparent from inspection of Fig. 3. The psychometric functions of subject Y tend to be higher (shifted to the left) in comparison with those of subject Z, particularly at 5 and -5 dB. These observations are confirmed statistically: overall, subject Y exhibited better detection, that is, a greater number of hits, than did subject Z (subject Y: 2545; subject Z: 2145; $\chi^2=34.12$, $df=1$, $p<0.01$).

A more complete analysis of performance would take into account responses made to standard (nontarget) stimuli (false alarms). The higher level of detection by subject Y might be indicative of simply a greater readiness to respond to any stimulus, regardless of whether it was a target or standard, rather than to greater sensitivity. Although the overall number of false alarms was quite low, subject Y did, in fact, make significantly more false alarms over the course of the experiment than did subject Z (subject Y: 45; subject Z: 21; $\chi^2=8.73$, $df=1$, $p<0.01$). This difference is consistent with the notion that subject Y may have been slightly more responsive, rather than more sensitive, than subject Z.

We analyzed the data using signal detection theory (SDT) in order to address this issue. SDT permits the analysis of sensitivity independent of response bias (Peterson *et al.*, 1954; Green and Swets, 1974). To perform this analysis d' scores were computed from the proportions of hits and false alarms for each duration, at each intensity level.[3] Psy-

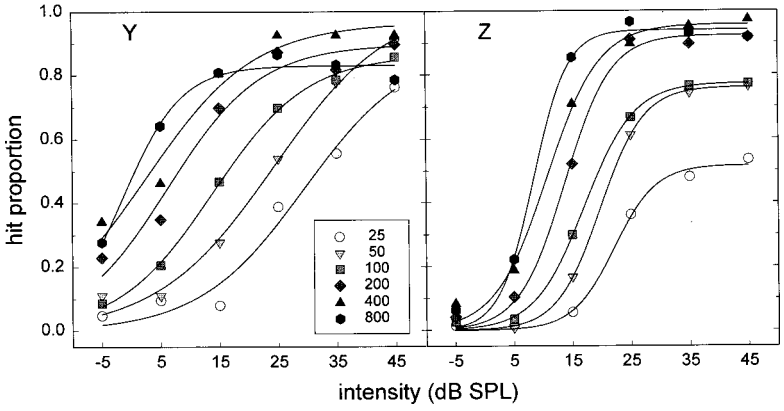

FIG. 3. Proportions of correct detections (hits) are plotted as a function of intensity for data are collapsed across tone frequency. Other details as in Fig. 1.

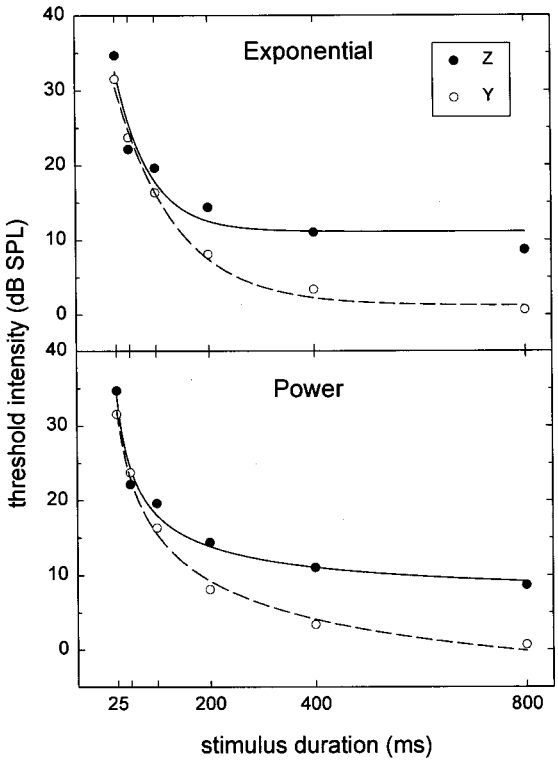

FIG. 4. Threshold intensities are plotted as a function of stimulus duration. Threshold values were determined from psychometric functions displayed in Fig. 3. The top panel shows the data points and curve fits for the exponential model [Eq. (3)]; the bottom panel the points and fits for the power model [Eq. (2)]. Solid circles represent thresholds from subject Z, open circles thresholds from subject Y.

chometric functions comprised of d' scores, and the best-fitting sigmoid curves, are shown in Fig. 5. Selection of a threshold point from a d' psychometric curve is somewhat arbitrary. Unlike such accuracy measures as hit proportion or percentage correct, the d' scale is unbounded (can take on any real value), so there is no *a priori* midway point between the extremes of performance. A reasonable threshold level, however, can be extracted from the data. For the curve fits in Fig. 5 [from Eq. (4)] a minimum d' value of zero was assumed to represent no detection. The asymptotic values of d' (obtained from the curve fits) were considered to represent maximum levels of performance on this task. The midway points between zero and asymptotic performance (averaged over duration) were 1.45 for subject Y and 1.49 for subject Z. We rounded up to $d'=1.50$ to obtain the threshold level actually used.

Figure 6 displays the threshold d' values for each stimulus duration, along with the best fits of Eqs. (2) and (3) which again appear reasonably good. The general form of the threshold curves appears similar to that depicted in Fig. 4. The d' measure seems to have somewhat lessened subject differences, particularly for shorter stimulus durations, although the two curves are still converging to different levels. With the d' threshold measure, the rates of integration appear somewhat lower, initially, than in the case of the threshold functions calculated using hit proportions. Subject Y's thresholds decline by 5.9 dB/doubling, and subject Z's by 3.7 dB/doubling, during the first 200 ms, followed by a decrease of 6.3 dB/doubling out to 800 ms for subject Y, and a 2.6 dB/doubling decline for subject Z.

Table II displays the parameters obtained from these fits. The rate parameters derived from using d' scores indicate slightly lower rates of integration than found using hit proportions [the time constants (τ) are larger, and values of m, smaller]. Once again the parameter estimates are within the range found in previous studies—with the exception of the power function fit to subject Y's data. In this case the rate parameter ($m=-0.06$) is quite a bit smaller than that typically found, much closer to zero than to one. The minimum-threshold parameter ($I_\infty=-127.74$) is also much lower than one would expect to find representing absolute threshold. To clarify this discrepancy, curve fits to subject Y's data were plotted using rate or minimum intensity parameters with values fixed within a more typical range (for example, $m=-0.5$; $I_\infty=-10$.) The resulting functions consistently overestimated threshold at 100 and 200 ms, and underestimated threshold at 800 ms, by 3–5 dB. This implies that subject Y exhibited a lower rate of integration and declined to a lower threshold in this case. In other words, this subject did not closely approach an asymptotic level for the durations tested.

The significance levels in Table II are higher for the power function for both subjects, indicating better curve fits, and suggesting that this model may provide a better formal description of the temporal integration function when measured by d' within the temporal range tested. This was not supported, however, by paired t-tests comparing differences between means of the absolute residuals (subject Y: $t=1.70$, $df=5$, $p>0.10$; subject Z: $t=0.61$, $df=5$, $p>0.50$).

III. DISCUSSION

Temporal integration was examined in two rhesus macaques using a deviant-detection procedure: The subjects were required to respond to a brief sound (a tone burst) that deviated from a previous series of sounds (noise bursts) on a trial. Two models describing the decline in threshold as a function of stimulus duration were tested against the data:

TABLE I. Shown are the best fitting parameter estimates for the power [Eq. (2)] and exponential [Eq. (3)] models for the threshold curves shown in Fig. 4, as well as the r^2 values for each fit. Superscripts denote significance levels: *<0.05, **<0.005, ***<0.0005.

	Power				Exponential			
Subject	m	I_∞	I_k	r^2	τ	I_∞	I_k	r^2
Y	−0.27	−20.56	126.61	0.995***	113.64	1.24	36.41	0.995***
Z	−0.60	5.66	193.93	0.981**	64.10	11.13	31.76	0.921*

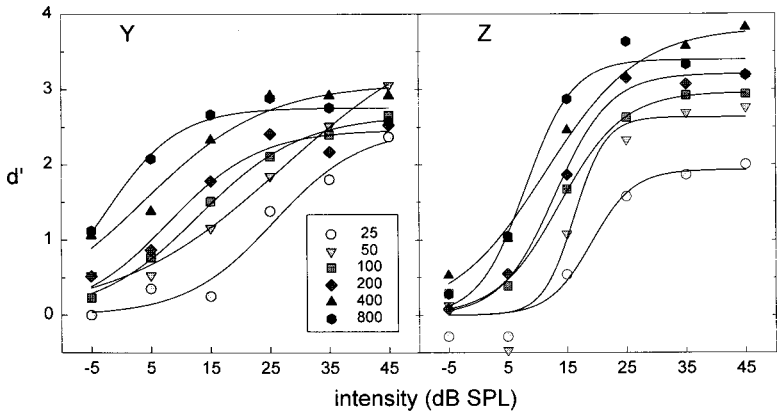

FIG. 5. Psychometric functions comprised of d' values plotted against intensity. d' values are calculated from hits and false alarm proportions collapsed across tone frequency. Other details as in Fig. 1.

one a power function [Eq. (2)], the other an exponential [Eq. (3)]. Both models provided reasonably good fits to the data, whether the thresholds were calculated from correct detections (hits) alone, or from d' scores. Rate parameter estimates for the power model were slightly less than one (with negative sign), and the time constants given by the exponential model were in the range of 60–200 ms. These estimated values are, for the most part, within the range previously found in human subjects as well as from some nonhuman species. The exception was the power function fit to subject Y's d' threshold data, in which the both the rate (m) and minimum-threshold parameters (I_∞) were found to be outside the typical range.

Our technique relied on presenting the target tone after an unpredictable number of standard noise bursts, with interstimulus intervals that varied from trial to trial. There was temporal uncertainty, then, associated with the precise occurrence of the target relative to the monkey's observing response. The presence of temporal uncertainty in determining threshold measurements might be a concern, because target unpredictability might be expected to lower target detection or hit responses, particularly for very short duration stimuli. It would also be expected, however, to decrease false alarms, and so leave the resulting threshold levels unaffected in a signal detection analysis—which we have employed here. We should also note that temporal uncertainty has been employed in studies of temporal integration in several nonhuman species by means of variable observing-response periods (Suthers and Summers, 1980; Costalupes, 1983; Brown and Maloney, 1986), and in human subjects using a forced-choice alternative interval test (Green *et al.*, 1957).

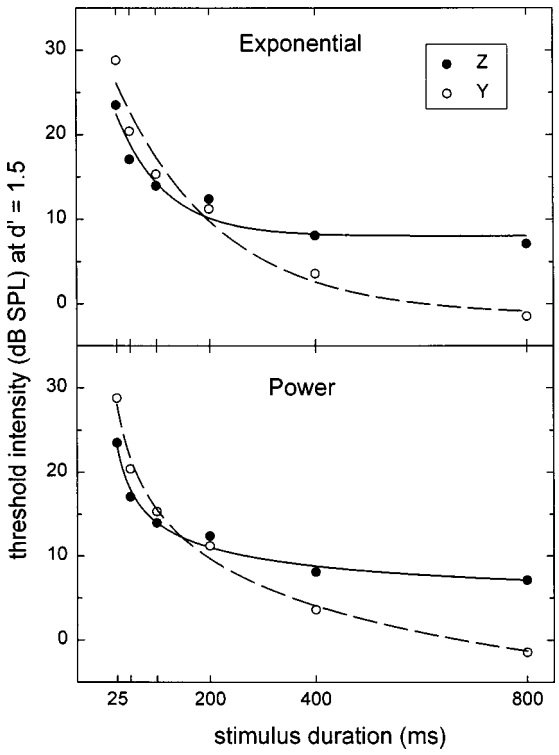

FIG. 6. Threshold intensities determined from the psychometric functions displayed in Fig. 5 (computed from d' scores) are plotted against stimulus duration. Other details as in Fig. 4.

As mentioned earlier, most investigators have quantified temporal integration by plotting threshold intensity in decibels as a function of log time over a particular interval, and then fitting a straight line to these points. The slope of this line is then used as an index of integration rate. For an exponential model, the inverse of the slope gives the time constant (τ)—for humans, time constants have ranged from about 100 ms (Plomp and Bouman, 1959; Gerken *et al.*, 1983) to almost 600 ms (Gerken *et al.*, 1990). Measurements from nonhuman subjects have yielded even larger ranges of τ, from 20 to 30 ms in dolphins (Johnson, 1967) and chickens (Saunders and Salvi, 1993), to values approaching 1 s in chickens (Saunders and Salvi, 1993). Our estimates of τ (60–200 ms) fall well within these ranges.

The slope in dB per log unit of time has usually been used as an estimate of the rate parameter or exponent (m) in tests of a power function model. The assumption is made that a slope of 10 dB/decade (or 3 dB/doubling) implies an exponent of (negative) one (Garner, 1947; Garner and Miller, 1947), in which case the change in threshold is exactly proportional to change in duration. Estimates of m in humans have ranged from about 0.5 (or 5 dB/decade) (Dallos and Olsen, 1964; Gerken et al., 1983)—implying that change in intensity is proportional to the square root of duration—to slightly greater than 1 (Gerken *et al.*, 1983, 1990). Most estimates from nonhuman subjects lie close to this range (Ehret, 1976; Dooling and Searcy, 1985; Saunders and Salvi, 1993), as do our own values of m derived from the nonlinear fits of Eq. (2) which fall approximately near 0.5 (but for the exception noted above). Our results, therefore, are consistent

TABLE II. The best-fitting parameter estimates are given for the threshold curves based on d' measurements shown in Fig. 6. Other details as in Table I.

	Power				Exponential			
Subject	m	I_∞	I_k	r^2	τ	I_∞	I_k	r^2
Y	−0.06	−127.74	189.25	0.992***	196.08	−1.36	34.31	0.971**
Z	−0.41	2.01	78.77	0.983**	90.91	8.05	19.04	0.950*

with a change in threshold intensity which is roughly proportional to the square root of time.

The slope values of Clack (1966) from the rhesus macaque are among the highest values reported. He found integration rates to be much faster at relatively high and low frequencies—at 0.25 and 0.5 kHz rates were roughly 30–40 dB/decade, and at 8 kHz rates were about 20–30 dB/decade. These rates, measured between 15 and 150 ms, are roughly equivalent to 10 dB/doubling and 8 dB/doubling of time, respectively, and are at least 2–3 times higher than those typically found in this time range. Our rates range between 6.8 and 7.8 dB per doubling for the hit proportion measure, and 3.7 and 5.9 dB/doubling for *d*' values. Although lower than Clack's estimates, these values are still higher than most reported rates of temporal integration.

It is difficult to compare integration rates across species because of the different models and measures used for analysis and reporting results. Therefore, in order to facilitate the quantitative comparison of our temporal integration estimates with Clack's results, and to permit a uniform comparison with other species, we made use of Fay's (1988) databook of vertebrate hearing. This volume presents a summary of thresholds as a function of stimulus duration (obtained from tables or figures in the original papers) for various species, including Clack's rhesus data. We performed linear regressions on threshold-log time functions from this work (for durations up to 200 ms), obtaining the slope for each line as the conventional measure of integration rate for several species.[4] We also determined the rate parameters of Eqs. (2) and (3) by fitting these equations over the range of durations tested for each species.[5]

Figure 7 summarizes the distributions for these parameters. The slope distribution [Fig. 7(A)] peaks at roughly 10 dB/decade, consistent with reports in the literature, although it shows a considerable range from about zero to a high of ~30 dB/decade. Of the species examined, the rhesus data of Clack and that of the horseshoe bat show the largest slopes with means (across subjects and frequency) of 22.3 and 26.7 dB/decade, respectively. Clack's mean value lies at about two standard deviations from the mean of the distribution (22.9). In contrast, our mean slope value of 15.7 dB/decade, though relatively high, lies at just less than one standard deviation from the mean (16.6).

The remaining graphs in Fig. 7 display the parameter distributions from the nonlinear curve fits of Eqs. (2) and (3). The distribution for the time constant (τ) in the exponential function [Fig. 7(E)] shows measures of central tendency near 100 ms, close to the values generally reported for this metric. The distribution for the rate exponent (m) in the power model [Fig. 7(C)] reveals a central tendency of roughly 0.3–0.4. This value of m is lower by about half than most estimates which, as noted above, are generally obtained by extrapolating from the slope of a linear regression fitted to threshold values plotted as a function of log time [as were the slopes in Fig. 7(A)]. Unlike most studies which claim a power exponent of about 1.0—from the assumption that a slope of 10 dB/decade is equivalent to an exponent of one and implying that intensity thresholds change precisely proportionally with duration—our estimate of m from Fay's summaries implies that thresholds decline at a slightly slower rate than (proportionally to) the square root of duration. On the basis of this same assumption, given that the slopes we calculated in Fig. 7(A) are distributed around 10 dB/decade, we would expect m values to cluster about 1.0—however, this is clearly not the case—and as we discuss below, results from the slope measure combining both the rate parameter m and constant of proportionality I_k.

In contrast to the slope rate measure, the mean rate parameters m and τ calculated for Clack's rhesus data ($m = 0.335$; $\tau = 141$ ms) lie considerably nearer the means of the distributions, well within one standard deviation (0.418 ± 0.305 and 107 ± 91 ms). Our rhesus values ($m = 0.216$; $\tau = 153$ ms) also fall well within this range. The results from the slope analysis seem to imply that the rate of auditory temporal integration for rhesus monkeys tends to lie above the species' mean. The rate parameter estimates we found for Eqs. (2) and (3), however, suggest that temporal integration rates in rhesus lie considerably closer to the means of the distributions. In the case of the time constant, values of τ from both studies are actually slightly higher than both measures of central tendency, indicating slightly *lower* rates of integration for rhesus than most other species. How can these discrepancies be resolved?

This apparent contradiction can be explained through careful consideration of the nonlinear models described by Eqs. (2) and (3). In these models, a change in threshold over an interval of time may be accounted for by either a rate parameter (m or τ), or by the scaling parameter I_k [the constants of proportionality displayed in Fig. 8(B),(D)]. The rate parameters affect the rate of change in a function by altering its shape—that is, by altering its concavity—over a particular interval of time. By decreasing the value of the exponent in the power model, or by increasing the time constant in the exponential model, the respective function will exhibit less concavity, that is, it will appear more nearly linear over this interval. The scaling parameter I_k, on the other hand, affects the range of the dependent variable, and therefore also the rate of change, by virtue of the fact that it is a multiplicative constant, that is, a constant of proportionality.

This relationship is illustrated in Fig. 8 which displays

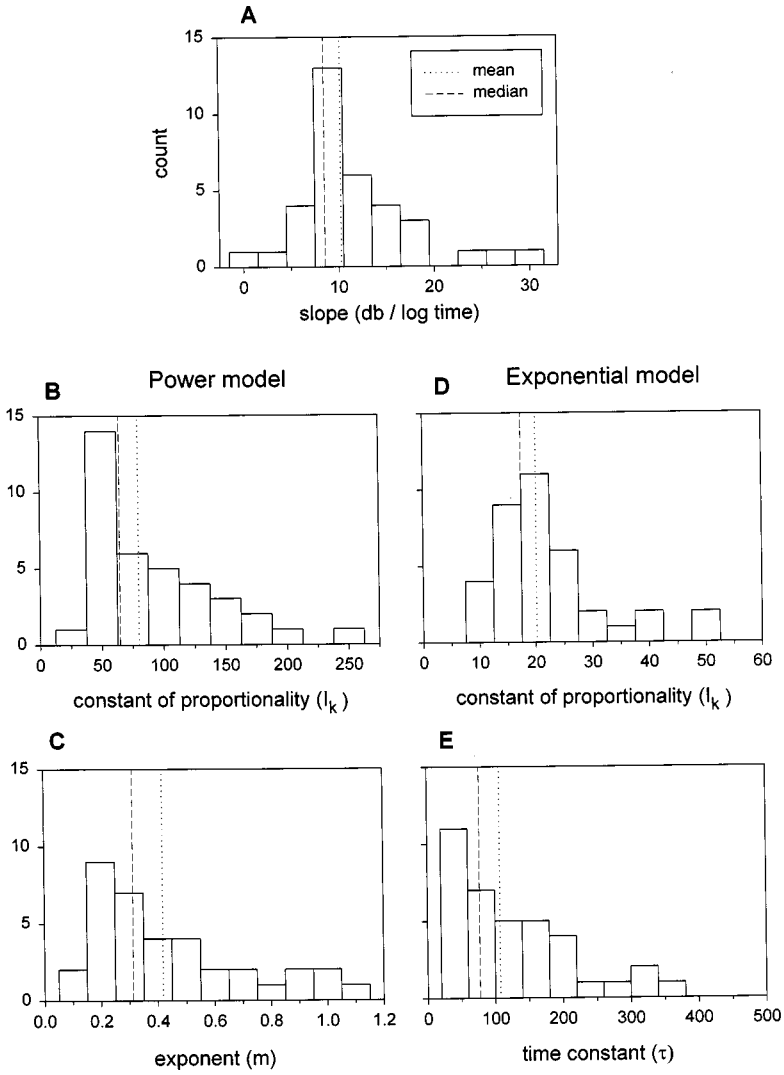

FIG. 7. Distributions of indices of temporal integration rate, computed from summaries compiled for several species (Fay, 1988; see footnotes 4 and 5 and text for discussion). (A) slopes (dB/log time) determined from linear regressions. (B,D) constants of proportionality (I_k) and (C,E) rate parameters (m and τ) from nonlinear curve fits of Eqs. (2) and (3). The dotted and dashed lines indicate the mean and median of each distribution, respectively.

scatterplots between parameter estimates and ranges of threshold measurement (the difference between thresholds at the shortest and longest durations for each frequency, for each species) obtained from Fay's summaries. As expected, the scatterplot in Fig. 8(A) displays a strong positive relationship ($r=0.862$, $df=36$, $p<0.01$) between the slope measure and threshold range. Neither rate parameter m or τ, however, is related to range of measurement (m: $r=-0.194$, $df=36$, $p>0.05$; τ: $r=-0.117$, $df=36$, $p>0.05$). The scaling parameter I_k, in the exponential model, though, shows a strong positive correlation ($r=0.857$, $df=36$, $p<0.01$), being roughly directly proportional to the range. In contrast, the scaling parameter in the power model shows no such relationship ($r=-0.168$, $df=36$, $p>0.05$).

The behavior of I_k in the exponential model, then, is consistent with the description above, and has an intuitive interpretation. That is, I_k accounts for variation in threshold due to the range of measurements in the studies examined—as mentioned, it is approximately proportional to the range—and its distribution extends from about 10 to 50 with a mean (and median) of roughly 20 [Fig. 7(D)]. Surprisingly, when this parameter is in the power model, it does not account for this variation—it appears unrelated to the range of measurements across studies, extending from about 50 to 250 [Fig. 7(B)]—and so lacks this intuitive interpretation. The rate parameters m and τ, on the other hand, describe the concavity or speed of decline of the functions. Inspection of Fay's plot summaries reveals that functions showing the greatest curvature, such as the human data of Watson and Gengel (1969), yield the smallest time constants and the largest values of m.

According to our analysis, then, the exponential model [Eq. (3)] is the most strongly descriptive of temporal integration because it separates two sources of variation in rate by means of two independent parameters. One source is due to the range of threshold measurement. It is the total decline in threshold as a function of duration and can be considered as the *linear* rate component, and is described by the constant of proportionality I_k. The other source of variation arises from the rate of decline *within* this range. It describes how quickly the lowest threshold is approached and can be considered to be the *nonlinear* rate component, and is described by the time constant τ. The differences in Clack's data and our own, then, can readily be interpreted in terms of the exponential model: Clack's data show a larger total decline in threshold, reflected in a larger I_k, or slope measure in dB per log time. The rates of decline within the ranges of measurement are about equivalent for the two studies, however,

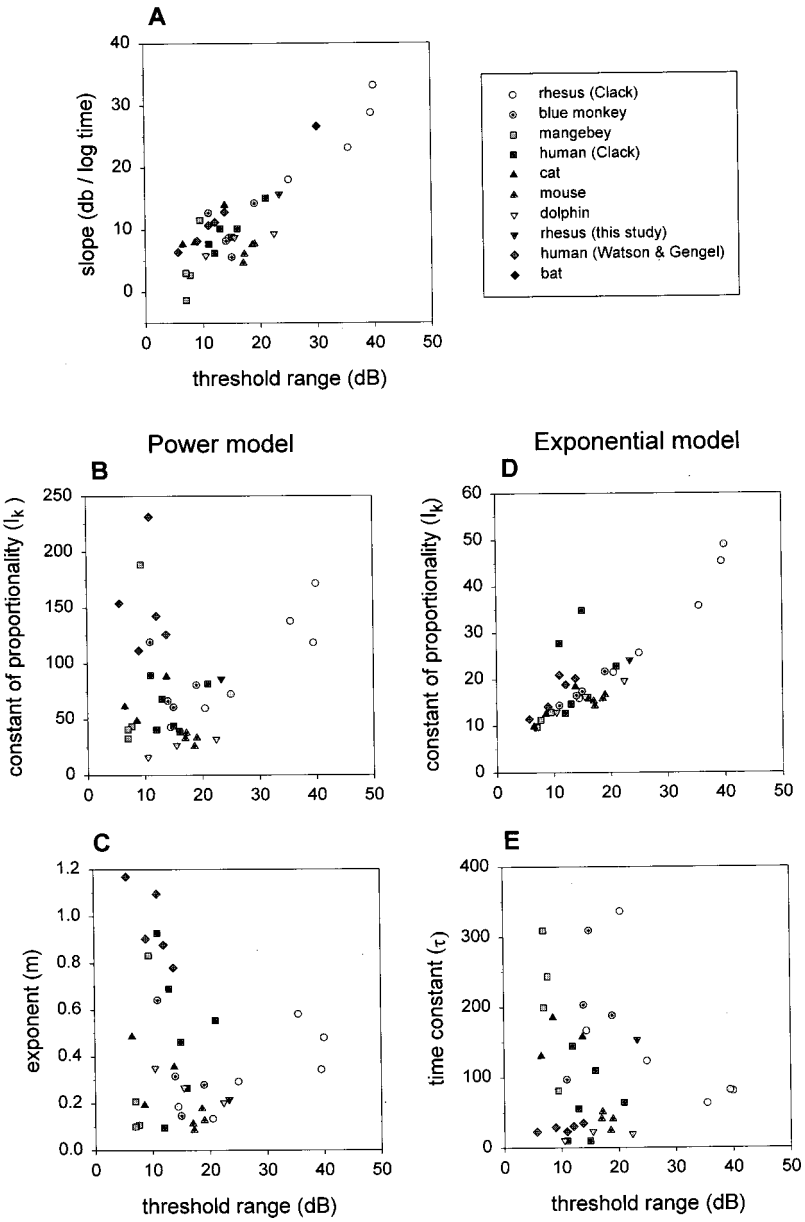

FIG. 8. Scatterplots showing the relationships between indices of integration rate and the range of threshold measurements for several species. See Fig. 7 and text for further details.

as reflected by the nearly equal time constants. In other words, Clack's study reveals larger linear components for the rate of integration (in comparison to our study and that of most other species), but the nonlinear rate component, or time constant, is more nearly equal to that of our data and that from other species. In other words, rhesus macaques show relatively larger overall changes in threshold as a function of duration, but a similar percentage or proportional increase in detectability as duration increases.

IV. SUMMARY AND CONCLUSIONS

Our results confirm the use of the deviant detection paradigm as a useful method for determining temporal integration functions for the rhesus macaque, and reveal temporal integration rates (measured by the slope in dB/log time) for this species to be closer to those found for other species than did a previous study (Clack, 1966). An analysis of temporal integration across studies and species revealed an exponential model to be superior to a power model, in so far as it successfully described two independent sources of variation in integration rate, while the power model did not. In terms of this model, differences in rate between the two rhesus studies (and between rhesus and other species) are due primarily to a linear rate component in the model. The nonlinear rate component, or time constant, was about equal for both studies ($\tau = \sim 150$ ms) indicating a rate of temporal integration slightly slower than for most other species examined.

If the parameters in these models are to have plausible psychophysical and neurophysiological interpretations, then these results argue in favor of the exponential model. This is an interesting result and carries implications for our understanding of the psychophysics and neurophysiological underpinnings of temporal integration. An important question, for example, concerns the causes of the two components of variation described by the exponential model, and whether one or both have neurophysiological underpinnings. Our results also argue for the importance of comparing fully de-

scriptive functions when evaluating models of temporal integration, rather than focusing on only a specific parameter in a model. These results underscore the importance of considering stimulus duration when assessing behavioral and/or physiological responses to acoustic stimuli, particularly when determining thresholds, in human and nonhuman auditory research.

ACKNOWLEDGMENTS

We thank Maiuyen Tran for assistance in training subjects. We also thank Christopher Plack and an anonymous reviewer for helpful comments on an earlier version of this manuscript. This research was supported by NIH Grant No. MH56649-01, NIDCD Grant No. DC02514-01A1, and the Sloan Foundation.

[1]Given that primary cortical (A1) neurons respond primarily with transient responses to changes in signal energy, this region may correspond to a first stage or channel of high temporal resolution processing (Creutzfeldt *et al.*, 1980).

[2]The time constant is the time required for a function to decline to $1/e$ ($\sim$0.37) of its initial value, or $1-1/e$ ($\sim$0.63) of its ultimate or limiting value.

[3]As is well known, d' is a measure of the difference between the means of the two distributions (the signal or target distribution and the noise or nontarget distribution) representing the likelihood of the sensory events assumed to underlie detection. In practice, d' is expressed as the difference between a pair of standardized (z) scores derived from hit and false alarm proportions that correspond to areas under the normal distribution. This calculation, therefore, assumes that the underlying sensory (or evidence) distributions are normal and have equal variance. In fact it is impossible to infer the form of these distributions with only a single pair of hit and false alarm proportions (in each condition), as is the case with our data. It is also impossible, therefore, to choose an ideal single metric of accuracy (Swets, 1996). The d' score has the advantages of being the best known, and most common measure of performance associated with detection theory, and so most readily permits comparisons with other studies.

[4]Threshold data summarized from the following eight studies and species were analyzed: (1) Clack's (1966) data from rhesus and humans (2) the blue monkey and gray-cheeked mangabey (Brown and Maloney, 1986) (3) cats (Costalupes, 1983) (4) the mouse (Ehret, 1976) (5) the bottlenosed dolphin (Johnson, 1968) (6) humans (Watson and Gengel, 1969) (7) the horseshoe bat (Ayrapet'yants and Konstantinov, 1974), and (8) this study on rhesus. All threshold values were available in tabular form in Fay's (1988) databook (pages 469–483), and were averaged over subjects at each frequency, with the exception of the human results from Clack. These we estimated using Fig. 2 from Clack (1969).

[5]Threshold values in Fay's databook are expressed relative to threshold at the longest duration tested for each species at each frequency, averaged over subject—in other words, the threshold at the longest duration was subtracted from each value, giving the longest duration in each case a threshold value of 0 dB. (For this cross-species comparison, we performed the same manipulation on our d' threshold values before fitting.) In terms of Eqs. (2) and (3), then, the assumption is made that the minimum threshold parameter (I_∞) is zero. When fitting Eqs. (2) and (3) to these data, however, I_∞ was retained as a ''free'' parameter (but constrained to lie above -20 dB), in order to assess the validity of this assumption (that is, $I_\infty = 0$) for each model. For the exponential model [Eq. (3)], estimates of I_∞ were quite close to zero—ranging from -0.5 to 2.7 dB—with a mean of 0.8 and standard deviation of 0.9 dB. In the case of the power model, the dispersion and error were larger, extending from 0.5 dB to the minimum constraint level of -20 dB, with mean and standard deviation (omitting the minimum constraint estimates) of -5.1 and 4.8 dB, respectively. The statistical significance of each regression was also determined. All of the linear regressions save two (94%) were significant (Pearson Product Moment, two-tailed, $p<0.05$). For each nonlinear regression [fits of Eqs. (2) and (3),] an r^2 and F statistic were determined (see Methods, Section C). Ninety-five percent of the r^2 values lay above 0.90 for both fitted equations. For the exponential model [Eq. (3)], 92% of the these fits were significant at the $p<0.05$ level; the power model [Eq. (2)] fared slightly less well with 84% of the fits significant. However, a paired t-test ($t=0.645$, $df=37$, $p>0.5$) did not reveal a significant difference in r^2 between the fitted equations.

Ayrapet'yants, E. Sh., and Konstantinov, A. I. (**1974**). ''Echolocation in Nature.'' An English translation of the National Technical Information service, Springfield, VA JPRS 63328-1 and -2.

Brown, C. H., and Maloney, C. G. (**1986**). ''Temporal integration in two species of Old World monkeys: Blue monkeys (*Cercopithecus mitis*) and grey-cheeked mangabeys (*Cercocebus albigena*),'' J. Acoust. Soc. Am. **79**, 1058–1064.

Clack, T. D. (**1966**). ''Effect of signal duration on the auditory sensitivity of humans and monkeys (*Macaca mulatta*),'' J. Acoust. Soc. Am. **40**, 1140–1146.

Costalupes, J. A. (**1983**). ''Temporal integration of pure tones in the cat,'' Hearing Res. **9**, 43–54.

Creutzfeldt, O., Hellweg, F. C., and Schreiner, C. (**1980**). ''Thalamocortical transformation of responses to complex auditory stimuli,'' Exp. Brain Res. **39**, 87–104.

Creutzfeldt, O., Ojeman, G., and Lettich, E. (**1989**). ''Neuronal activity in the human temporal lobe I. Responses to speech,'' Exp. Brain Res. **77**, 451–475.

Dallos, P. J., and Olsen, W. O. (**1964**). ''Integration of energy at threshold with gradual rise–fall tone pips,'' J. Acoust. Soc. Am. **36**, 743–751.

Daniel, C., and Wood, F. S. (**1980**). *Fitting Functions to Data* (Wiley, New York).

Dooling, R. J., and Searcy, M. H. (**1985**). ''Temporal integration of acoustic signals by the budgerigar (*Melopsittacus undulatus*),'' J. Acoust. Soc. Am. **77**, 1917–1920.

Eddins, D. A., and Green, D. M. (**1995**). ''Temporal integration and temporal resolution,'' in *Hearing*, edited by B. C. J. Moore (Academic, London).

Ehret, G. (**1976**). ''Temporal auditory summation for pure tones and white noise in the house mouse (*Mus musculus*),'' J. Acoust. Soc. Am. **59**, 1421–1427.

Fay, R. R. (**1988**). *Hearing in Vertebrates: A Psychophysics Databook* (Hill-Fay, Winnetka).

Fay, R. R., and Coombs, S. (**1983**). ''Neural mechanisms in sound detection and temporal summation,'' Hearing Res. **10**, 69–92.

Garner, W. R. (**1947**). ''The effect of frequency spectrum on temporal integration in the ear,'' J. Acoust. Soc. Am. **19**, 808–815.

Garner, W. R., and Miller, G. A. (**1947**). ''The masked threshold of pure tones as a function of duration,'' J. Exp. Psychol. **37**, 293–302.

Gerken, G. M., Bhat, V. K. H., and Hutchison-Clutter, M. (**1990**). ''Auditory temporal integration and the power function model,'' J. Acoust. Soc. Am. **88**, 767–778.

Gerken, G. M., Gunnarson, A. D., and Allen, C. M. (**1983**). ''Three models of temporal summation evaluated using normal hearing and hearing-impaired subjects,'' J. Speech Hear. Res. **26**, 256–262.

Green, D., and Swets, J. (**1974**). *Signal Detection Theory and Psychophysics* (Wiley, New York).

Green, D. M., Birshall, T. G., and Tanner, W. P. (**1957**). ''Signal detection as a function of signal intensity and duration,'' J. Acoust. Soc. Am. **29**, 523–531.

Hauser, M. D. (**1991**). ''Sources of acoustic variation in rhesus macaque (*Macaca mulatta*) vocalizations,'' Ethology **89**, 29–46.

Hauser, M. D., and Marler, P. (**1992**). ''Food-associated calls in rhesus macaques (*Macaca mulatta*): I. Sociological factors,'' Beh. Ecol. **4**, 194–205.

Henderson, D. (**1969**). ''Temporal summation of acoustic signals by the chinchilla,'' J. Acoust. Soc. Am. **46**, 474–475.

Hughes, J. W. (**1946**). ''The threshold of audition for short periods of stimulation,'' Proc. R. Soc. London, Ser. B **133**, 486–490.

Johnson, C. S. (**1966**). ''Relation between absolute threshold and duration of tone pulses in the bottlenosed porpoise,'' J. Acoust. Soc. Am. **43**, 757–763.

LaBar, K. S., LeDoux, J. E., Spencer, D. D., and Phelps, E. A. (**1995**). ''Impaired fear conditioning following unilateral temporal lobectomy in humans,'' J. Neurosci. **15**, 6846–6855.

LaBar, K. S., Gatenby, J. C., Gore, J. C., LeDoux, J. E., and Phelps, E. A. (**1998**). ''Human amygdala activation during conditioned fear acquisition and extinction: A mixed-trial fMRI study,'' Neuron **20**, 937–945.

Ledoux, J. E. (**1990**). ''Information flow from sensation to emotion: Plasticity in the neural computation of stimulus value,'' in *Learning and Computational Neuroscience: Foundations of Adaptive Networks*, edited by M. Gabriel and J. Moore (MIT, Cambridge, MA).
Margoliash, D. (**1983**). ''Acoustic parameters underlying the responses of song-specific neurons in the white-crowned sparrow,'' J. Neurosci. **3**, 1039–1057.
Margoliash, D., and Fortune, E. S. (**1992**). ''Temporal and harmonic combination-sensitive neurons in the zebra finch,'' J. Neurosci. **12**, 4309–4326.
Marquardt, D. W. (**1963**). ''An algorithm for least squares estimation of parameters,'' J. Soc. Ind. Appl. Math. **11**, 431–441.
Marks, L. E. (**1974**). *Sensory Processes: The New Psychophysics* (Academic, New York).
Miller, G. A. (**1948**). ''The perception of short bursts of noise,'' J. Acoust. Soc. Am. **20**, 160–170.
Moody, D. B., Beecher, M. D., and Stebbins, W. C. (**1976**). ''Behavioral methods in auditory research.'' in *Handbook of Auditory and Vestibular Research Methods*, edited by C. A. Smith and J. A. Vernon (Thomas, Springfield, IL).
Munson, W. A. (**1947**). ''The growth of auditory sensation,'' J. Acoust. Soc. Am. **55**, 584–591.
Peterson, W. W., Birdsall, T. G., and Fox, W. C. (**1954**). ''The theory of signal detectability,'' Trans. IRE Professional Group on Information Theory. **PGIT 2-4**, 171–212.
Plomp, R., and Bouman, M. A. (**1959**). ''Relation between hearing threshold and duration for tone pulses,'' J. Acoust. Soc. Am. **31**, 749–758.
Rauschecker, J. P. (**1997**). ''Processing of complex sounds in the auditory cortex of cat, monkey, and man,'' Acta Oto-Laryngol. Suppl. **532**, 34–38.
Saunders, S. S., and Salvi, R. J. (**1993**). ''Psychoacoustics of normal adult chickens: Thresholds and temporal integration,'' J. Acoust. Soc. Am. **94**, 83–90.
Schreiner, C. E., and Urbas, J. V. (**1986**). ''Representation of amplitude modulation in the auditory cortex of the cat. I. The anterior auditory field (AAF),'' Hearing Res. **21**, 227–241.
Suthers, R. A., and Summers, C. A. (**1980**). ''Behavioral audiogram and masked thresholds of the megachiropteran echolocating bat, *Rousettus*,'' J. Comp. Physiol. A **136**, 227–233.
Swets, J. A. (**1996**). *Signal Detection Theory and ROC Analysis in Psychology and Diagnostics* (Lawrence Erlbaum, Mahwah).
Wang, X., Merzenich, M. M., Beitel, R., and Schreiner, C. E. (**1995**). ''Representation of a species-specific vocalization in the primary auditory cortex of the common marmoset: temporal and spectral characteristics,'' J. Neurophysiol. **74**, 2685–2706.
Watson, A. (**1986**). ''Temporal sensitivity,'' in *Handbook of Perception and Human Performance*, Vol. I, edited by K. R. Boff, L. Kaufman, and J. P. Thomas (Wiley, New York).
Watson, C. S., and Gengel, R. W. (**1969**). ''Signal duration and frequency in relation to auditory sensitivity,'' J. Acoust. Soc. Am. **46**, 989–997.
Zwislocki, J. (**1960**). ''Theory of temporal auditory summation,'' J. Acoust. Soc. Am. **22**, 1046–1060.
Zwislocki, J. (**1969**). ''Temporal summation of loudness: An analysis,'' J. Acoust. Soc. Am. **46**, 431–441.

Psychometric functions for gap detection in noise measured from young and aged subjects

Ning-Ji He,[a] Amy R. Horwitz, Judy R. Dubno, and John H. Mills
Medical University of South Carolina, Charleston, South Carolina 29425-2242

(Received 4 September 1997; revised 25 June 1998; accepted 20 April 1999)

Psychometric functions for detection of temporal gaps in wideband noise were measured in a ''yes/no'' paradigm from normal-hearing young and aged subjects with closely matched audiograms. The effects of noise-burst duration, gap location, and uncertainty of gap location were tested. A typical psychometric function obtained in this study featured a steep slope, which was independent of most experimental conditions as well as age. However, gap thresholds were generally improved with increasing duration of the noise burst for both young and aged subjects. Gap location and uncertainty had no significant effects on the thresholds for the young subjects. For the aged subjects, whenever the gap was sufficiently away from the onset or offset of the noise burst, detectability was robust despite uncertainty about the gap location. Significant differences between young and aged subjects could be observed only when the gap was very close to the signal onset and offset. © *1999 Acoustical Society of America.* [S0001-4966(99)02408-X]

PACS numbers: 43.66.Mk, 43.66.Sr [JWH]

INTRODUCTION

Gap detection is used as one measure of the temporal resolving power of the auditory system, i.e., the ability to follow rapid changes over time. The typical threshold for detection of a gap in a wideband noise burst is 2 to 3 ms (Green, 1985). Plomp (1964) suggested that temporal resolution is limited by the decay of sensation produced by the first part of the stimulus, which would fill in the gap. In a recent study (Zhang *et al.*, 1990) measuring neural correlates of gap detection in eighth-nerve fibers from chinchilla, the decay in neural response was found to be inversely related to the characteristic frequency (CF) of the unit, about 1 ms for high-CF units and 5 ms for fibers with CF$<$1000 Hz. According to Zhang *et al.*, the neural representation of gap detection was characterized by a modulation of the firing rate in the peristimulus-time (PST) histogram with an abrupt drop followed by a sharp increase. The modulation was a function of gap length. As the gap length increased, the firing rate during the gap systematically decreased, and when the gap was 10 ms long the firing rate decreased to below the spontaneous rate of the unit. Also, the firing rate at the onset of the second part of the noise burst increased with increasing gap length. Thus, in some respects, the neural representations of gap detection resemble psychometric functions obtained in psychophysical measurements (Green and Forrest, 1989; Moore and Glasberg, 1988).

A distinctive feature of the psychometric function for gap detection is its steep slope, which, as suggested by Moore *et al.* (1992), would assure a high precision (or a low within-subject variability) in measurement of the gap-detection threshold. However, the steep slope does not guarantee good agreement among studies. Indeed, considerable controversy exists in the gap-detection literature regarding several factors, such as noise-burst duration, subject age, and gap location.

A. Effect of noise-burst duration

In many auditory perception tasks, performance decreases with decreasing stimulus duration (Garner and Miller, 1947; Moore, 1973; Hall and Fernandes, 1983; Florentine, 1986; Viemeister, 1979; Sheft and Yost, 1990; Lee, 1994; Lee and Bacon, 1997), thus suggesting a common underlying temporal integration process. However, reports of the noise-burst duration effect on gap detection are inconsistent. Forrest and Green (1987) found little difference ($<$1 ms) in gap threshold for noise-burst durations ranging from 5 to 400 ms with a minimum at 25 and 50 ms. For noise durations shorter than 25 ms, the trend was different than that reported by an earlier study (Penner, 1975), where the gap threshold progressively increased from 1 to 3 ms as the noise duration increased from 5 to 20 ms. Forrest and Green attributed the inconsistency to procedural differences. In their study, the overall duration of the noise burst was kept constant, whereas Penner used a pair of identical noise bursts so that the total duration varied with gap length. This duration cue became increasingly significant as the noise-burst duration decreased. In a large-sample study, Muchnik *et al.* (1985) showed that gap-detection thresholds of young, normally hearing subjects increased as noise burst duration decreased from 85 to 10 ms. A similar trend was observed for subjects in two other age groups (40–60 and 60–70 years) in the same study. There were age-related differences in the increment of gap thresholds when the noise-burst duration decreased; however, this potential age effect could be confounded by the subjects' hearing loss.

B. Effect of subject age

The effects of subject age on gap-detection ability are not clear. Schneider *et al.* (1994) reported that gap thresholds of elderly subjects were more variable and about twice as large as those from young subjects. Although Moore *et al.* (1992) also observed an age-related difference, these authors noted that the mean differences were mainly due to the data

[a]Electronic mail: hening@musc.edu

of a few elderly subjects who had markedly large gap thresholds, and that the majority of elderly subjects had gap thresholds within the range of young subjects. Although considerable overlap in gap thresholds between young and aged subjects was also reported by Snell (1997), her conclusion differed from that of Moore *et al.* in that mean gap thresholds were larger for aged subjects than for young subjects in all conditions studied. Analyses of individual data led Snell to conclude that the mean differences between age groups reflected shifts in the distributions of the aged subjects toward poorer temporal resolution.

A confounding factor in measuring temporal resolution for elderly subjects may be hearing loss, which is commonly associated with age. Numerous studies have reported degraded gap-detection ability associated with sensorineural hearing loss (Boothroyd, 1973; Fitzgibbons and Wightman, 1982; Irwin *et al.*, 1981; Florentine and Buus, 1984; Salvi and Arehole, 1985). In a large-scale study, Lutman (1991) found that gap detection deteriorated with hearing loss but not with age for three groups of subjects aged 50–59, 60–69, and 70–79 years. Recently, however, using a related paradigm, Fitzgibbons and Gordon-Salant (1995, 1996) measured difference limen for gaps from both young and aged subjects with or without hearing loss and reported that elderly listeners performed more poorly than young listeners, and that hearing loss had no systematic effect on gap detection.

C. Effects of location and uncertainty of gap as related to speech perception

Studies of the effects of age on temporal resolution are motivated, in part, by the search for auditory factors that contribute to difficulties in speech understanding experienced by elderly individuals (CHABA, 1988). Many studies (e.g., Humes and Christopherson, 1991; van Rooij and Plomp, 1990; Dubno *et al.*, 1984; Gordon-Salant, 1987) found that reduced audibility of the speech signal can account for a large portion of the differences between young and aged subjects. This conclusion is applicable to speech recognition with no temporal waveform distortion. However, there is a relatively large body of evidence showing age-related differences in the perception of temporally distorted speech. For example, in a series of studies on the relationship between temporal processing and speech perception (Gordon-Salant and Fitzgibbons, 1993; Fitzgibbons and Gordon-Salant, 1995), a robust aging effect was observed in recognition of speech stimuli modified by several temporal factors: speech rate, time compression, and/or reverberation. This aging effect was also found to be independent of and additive to the effect of hearing loss. Although these observations suggest that impaired temporal resolution may contribute to the diminished speech perception of aged subjects, a straightforward relationship between speech perception and temporal resolution has not been established (Tyler *et al.*, 1982; Glasberg and Moore, 1988; Strouse *et al.*, 1998).

Gap stimuli used in psychoacoustic studies are acoustically analogous to voice-onset time (VOT) for consonants in speech. However, unlike a conventional gap-detection paradigm, where the gaps are typically fixed at the center of a stimulus burst, the acoustic gaps in a continuous speech stream occur pseudorandomly at different locations. These differences in paradigm might explain the poor correlation between speech perception and gap detection noted in some studies, especially for aged subjects (e.g., Strouse *et al.*, 1998). In a recent report (Phillips *et al.*, 1997), gap detection was measured between a leading wideband noise burst and a 300-ms narrow-band noise burst as a function of the duration of the leading noise burst. When the leading noise burst was 5 to 10 ms, the threshold was about 30 ms for young, normally hearing subjects. This value is close to the VOT boundary that separates voiced and unvoiced consonants (Strouse *et al.*, 1998).

Few studies have examined the effect of the temporal location of the gap within a noise burst and the effect of randomness of the gap location. Forrest and Green (1987) measured gap thresholds with the gap fixed at 10, 30, 50, 70, or 90 ms after onset of a 100-ms noise burst. They found that the location had essentially no effect on gap threshold except for the location of 30 ms, where the detection threshold was slightly lower. However, an earlier study (Penner, 1977) showed that when the second noise-burst duration was kept constant (2 ms), the detectability of a gap between two noise bursts was decreased by increasing the duration of the first noise burst. In this paradigm, changing the duration of the first noise burst actually changed the relative location of the gap. Thus, the effect of varying the relative location of a temporal gap within a noise burst remains unclear.

In a later paper (Green and Forrest, 1989), the effect of uncertainty of gap location was investigated. When the gap threshold was measured with gaps located randomly from 6% to 94% of a 500-ms noise burst, the gap threshold averaged 1.4 times larger than with the gap fixed at the center of the noise burst. Because there were no comparisons of gap detection at specific locations between fixed and random presentations, it is not clear whether the observed differences were due to the effect of uncertainty, the effect of location, or a combination of both effects.

D. Purpose of this study

To further assess the psychophysical bases for the effects of age on speech perception, gap detection was measured here from young and aged subjects. Factors relevant to speech understanding, namely, the duration of noise bursts, gap location, and uncertainty were examined. Given that large variability exists in the literature regarding these effects on gap detection, a more comprehensive psychophysical paradigm, a constant stimuli procedure measuring the psychometric function, was applied in this study. Obtaining psychometric functions is more time-consuming than measuring thresholds using an adaptive procedure. However, the former can provide estimates not only of the threshold but also of the variability of the subject's performance in terms of the slope of the psychometric function. Green and Forrest (1989) measured psychometric functions for detection of partial and complete gaps, temporally centered in a 500-ms noise burst. They found that the function became progressively steeper as the gap changed from partially filled to complete silence. The present study was designed to assess the effects of noise-

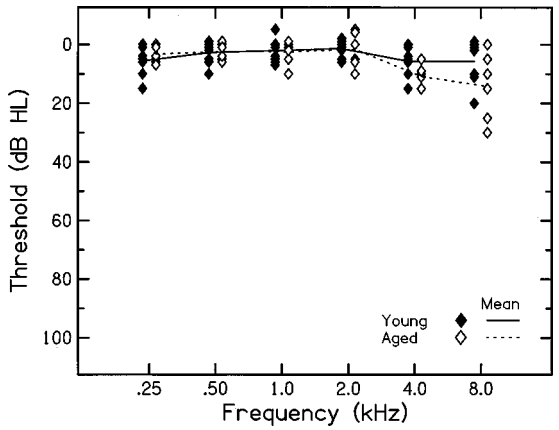

FIG. 1. Pure-tone thresholds (dB HL) for six aged and seven young subjects. Note the closely matched means of the two age groups.

burst duration, gap location, uncertainty in gap location, and subject age on the threshold and steepness of the psychometric function for gap detection.

I. GENERAL METHODS

Three experiments measuring gap detection from both young and aged subjects were conducted. In experiment 1, the effect of noise-burst duration was examined with the gap fixed at the temporal center of the noise burst. In experiment 2, the effect of uncertainty of gap location was examined. Comparisons were made between gap detection measured with the gap fixed at the middle of the noise burst and at random locations ranging from 15% to 85% of the total noise duration. Experiment 3 was designed to test simultaneously the effects of location and uncertainty by measuring gap detection for several gap locations in both fixed and random conditions.

A. Subjects

Six aged subjects (four female and two male) and seven young subjects (four female and three male) participated in this study. In each experiment, six subjects from each age group were tested. The average age was 31.9 years with a standard deviation (s.d.) of 8.1 for the young subjects, and 70.5 years with s.d. of 5.4 for the aged subjects. The subjects were recruited with the goal of matching audiograms between the two age groups, in addition to meeting the requirement of normal hearing (ANSI, 1989). Figure 1 shows individual pure-tone thresholds (dB HL) and group means for young subjects (solid symbols and line) and aged subjects (open symbols and dotted line). All subjects had pure-tone thresholds of 20 dB HL or better for frequencies from 0.25 to 8.0 kHz, except for two aged subjects (A1 and A5), whose pure-tone thresholds at 8.0 kHz were 30 and 25 dB HL, respectively. Differences in mean thresholds between the two groups were 5 dB or less, except at 8.0 kHz where the difference was 8.5 dB. Thus, the possible confounding effect of hearing loss was minimized in our data. Although some subjects had previous experience in other psychophysical experiments, such as intensity discrimination and frequency discrimination, none had previous experience with gap detection.

B. Stimuli

Low-pass filtered noise bursts with a cosine-squared rise/fall time of 5 ms were digitally generated by custom software. The cutoff frequency was 5 kHz with a roll-off slope of 80 dB/octave. The sampling frequency was 20 kHz, which also determined a 0.05-ms temporal accuracy for the stimuli. The noise bursts were either 100 or 400 ms in duration. In this study, duration is specified by the time between the zero-volt points at the onset and offset of the noise burst. Similarly, the 5-ms rise/fall refers to the time between the 0% and 100% points on the stimulus waveform. For each experimental condition, ten noise-burst samples were sequentially downloaded onto both channel 1 and 2 of a 16 $\times$16-bit waveform synthesizer (Pragmatic, 2201A). One of these noise bursts was randomly chosen during each stimulus presentation to prevent the subjects from becoming familiar with the characteristics of a single noise burst. The beginning portion of the chosen noise burst from channel 1 and the ending portion from channel 2 were assigned to a third channel, a carrier channel whose amplitude was zero across time. By specifying the length of each noise portion and its temporal location in the carrier channel, the output of the third channel was a noise burst with a silent gap of specific length and temporal location. The internal rise/fall time of the gap was 0 ms, and the noise was constrained to end and start at zero amplitude to minimize spectral energy spread. The spectra of the noise with and without a gap were essentially identical. The stimuli were then passed through an antialiasing filter (Krohn-Hite 3202R, low-passed at 5 kHz), attenuated (Hewlett-Packard, 350D), power-amplified (Yamaha, P2050), and delivered into the subject's ear canal through an insert earphone (Etymotic Research, ER-2). The overall level was 70 dB SPL. Stimulus timing and presentation, as well as collection of subjects' responses, were controlled by custom software implemented on a PC.

For all experiments, the total duration of the noise burst was kept constant during successive trials, a paradigm used by Forrest and Green (1987). All gap locations are referenced to the center of the gap. The minimum gap was zero (i.e., no gap). The maximum gap, hence the range, was predetermined to be 10 ms based on results from the literature (Green, 1985; Zhang *et al.*, 1990) as well as pilot data from both young and aged subjects. The range was further adjusted for each subject during practice (see below). Although in the more difficult random condition, shallower psychometric functions were sometimes observed, for fixed gap locations (i.e., 5%, 50%, or 95% of the 400-ms noise burst and 50% of the 100-ms noise burst), the 10-ms maximum gap provided a sufficient range for a psychometric function to cover the responses from 0% to 100%. However, two aged subjects required longer gaps in some conditions. For subject A4, the maximum gap had to be 15 ms when the noise burst was 100 ms. For subject A6, a 15-ms gap range was used when the gap occurred at the beginning or ending locations of the noise burst. Note that a gap of 15 ms was an upper limit in this study to prevent the gap from falling close to the rise/fall portion of the noise burst when the gap occurred at the edge locations.

C. Procedure

A constant-stimulus method with a yes/no task was used and psychometric functions for gap duration were measured under different conditions. These will be further described in later sections for individual experiments. For each subject, the maximum gap was evenly divided into ten intervals. Unless otherwise specified, each of the gap durations was presented 50 times in random order (50 repetitions), and each psychometric function resulted from 550 presentation trials (11 gap durations×50 repetitions). To minimize possible fatigue effects introduced by a large number of consecutive trials, the 550 trials were divided into five 110-trial blocks. Each block began with an orientation trial, during which a pair of noise bursts was repeatedly presented every 2 s with no gap in the first noise burst (gap=0 ms) and the maximum gap in the second noise burst. The orientation terminated when the subject pressed a button on a votebox. In each of the trials that followed, only one noise burst was presented. Subjects were instructed to push a button labeled ''yes'' if they heard a gap and a ''no'' button if they did not. Each block lasted about 3 to 4 min and a short pause was given at the end. Therefore, the time to collect a complete psychometric function was about 20 to 30 min.

The majority of the subjects (five young and six aged) participated in all three experiments. For each of these subjects, a total of ten psychometric functions was measured, four with fixed gap locations and six with varying gap locations. The data were collected in several sessions, each lasting 1 to 2 h.

D. Parameters of psychometric function and threshold

The measured psychometric functions were recast by a logistic function (Green, 1993),

$$P(\text{yes}) = \alpha + (1-\alpha)/(1+e^{-k(X-m)}), \quad (1)$$

where $P(\text{yes})$ is the probability of a yes response given to a specific gap, X and m are gap durations in ms (with m corresponding to the 50% point of the function and X as an independent variable), α is a false-alarm rate, which is the probability of a yes response given to the zero gap, and k is a factor defining the slope of the function. The parameters, α, k, and m were estimated in a curve-fitting procedure using a least-error method. Figure 2 shows an example of the curve fitting. The open squares represent raw data and the solid line represents fitted data. Given in the inset are estimated m, k, and α. Also presented is the rms difference between the raw and fitted data, indicating the goodness of fit. Note that the rms difference (0.02) was of the same order as the measurement resolution determined by the number of repetitions (1/50).

The parameter m could be used as the gap threshold. However, as shown in Eq. (1), m does not reflect the differences in α, the false-alarm rate. The false-alarm rate is related to the subject's decision criterion, which has been demonstrated to influence the threshold estimation (Gu and Green, 1994). Therefore, a threshold at $d'=1$ (Table I in the Appendix, Swets, 1964) was calculated based on each measured psychometric function. The resultant d' threshold is criterion-free because it is a function of false-alarm rate.

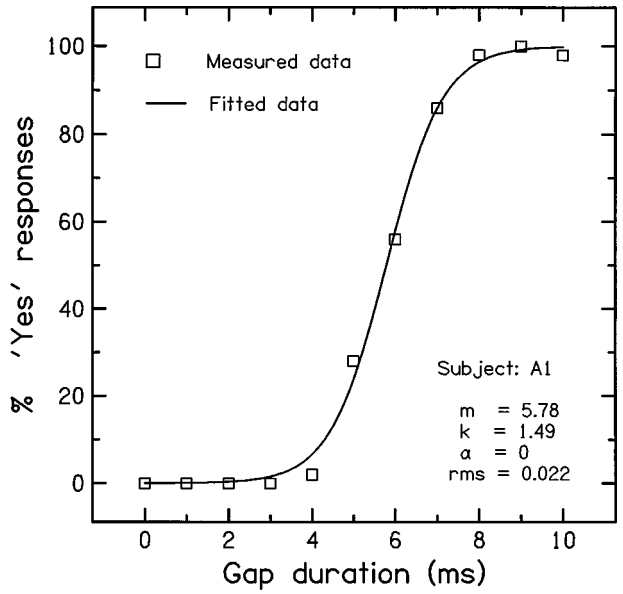

FIG. 2. An example of curve fitting of a logistic function to the measured psychometric function (Subject A1). Noise-burst duration was 100 ms. The estimated parameters: m (middlepoint)=5.78 ms, k (slope)=1.49; α (false-alarm rate)=0. The rms difference between fitted and measured data is 0.022.

E. Practice

For each experiment, practice was given to subjects prior to data collection. Three fixed gap locations for the 400-ms noise burst (5%, 50%, and 95%) and one fixed location for the 100-ms noise burst (50%) were practiced. During practice, psychometric functions were repeatedly measured in the same way described above, but with only ten repetitions per gap duration. There was no intention to improve subjects' thresholds through lengthy practice, but simply to assure that subjects were familiar with the stimuli and with the psychophysical procedure. The practice ended when ogive-shaped psychometric functions with reasonably steep slopes were obtained. All subjects met this criterion after about 30 min of practice for each condition. Extra practice time was provided to two aged subjects (A4) and (A6) when they experienced more difficulty than the others in detection of gaps occurring in the 100-ms noise burst or at edges of the 400-ms noise burst. The ranges of gap durations were adjusted for individual subjects during practice.

II. EXPERIMENT 1: EFFECT OF NOISE DURATION

A. Methods

For this experiment, the gap was always positioned at the temporal center of the noise burst. For each of six young and six aged subjects, psychometric functions for gap detection were measured for 100- and 400-ms noise bursts.

B. Results and discussion

Figure 3 shows psychometric functions measured from six young subjects (top two rows) and six aged subjects (bot-

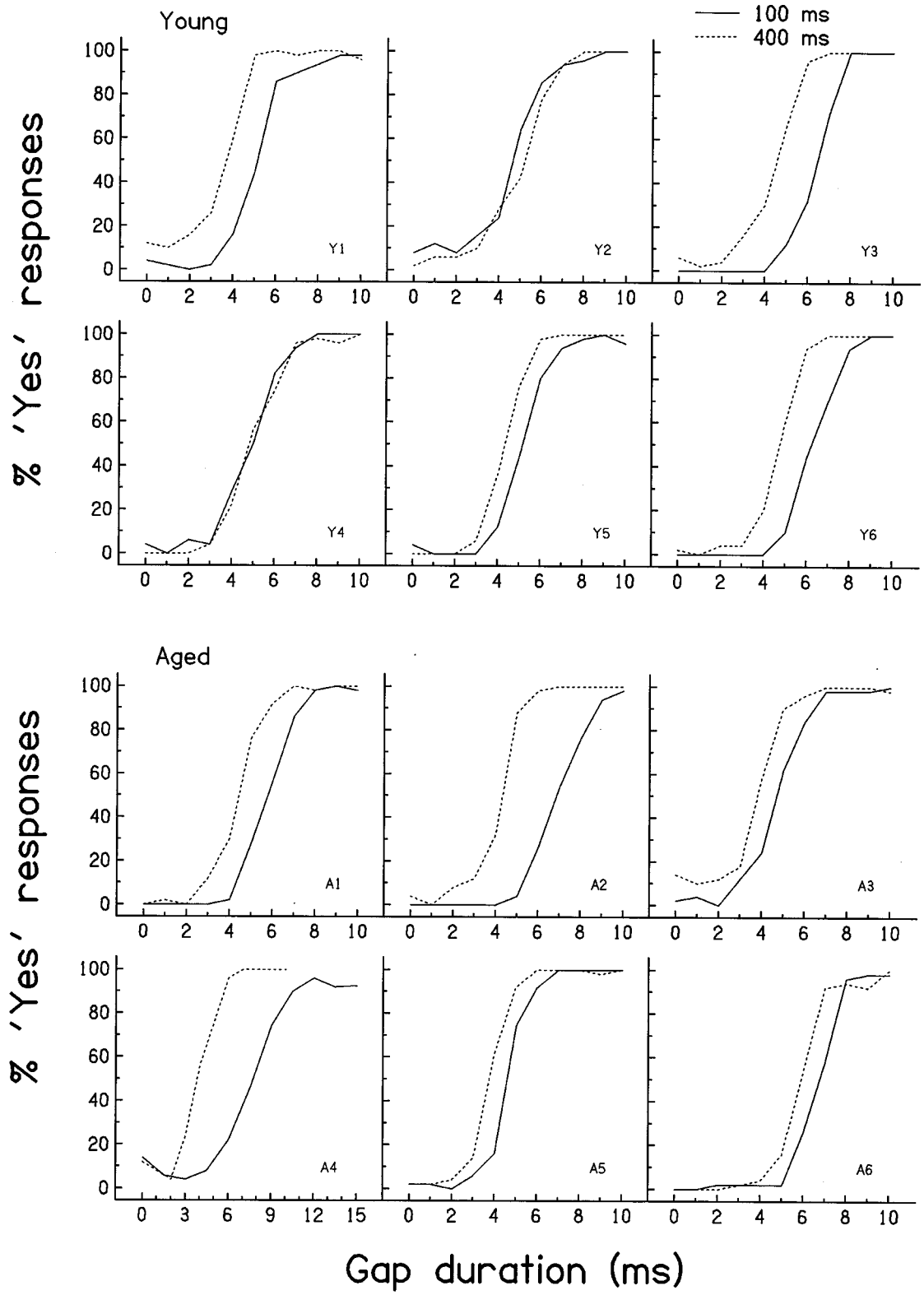

FIG. 3. Psychometric functions measured with 100-ms (solid lines) and 400-ms (dashed lines) noise bursts. Data of six young subjects are presented in the upper two rows and those of six aged subjects in the bottom two rows.

tom two rows). In each panel, the solid line represents data for 100-ms noise bursts, and the dashed line, 400-ms. All psychometric functions were sigmoidal in shape with steep slopes and reached >95% yes responses at the 10-ms gap value except for one (subject A4, 100 ms). For subject A4, the maximum gap was 15 ms for the 100-ms noise burst, with the 10-ms gap resulting in only about 80% yes responses.

Gap detection generally improved with the longer noise burst, especially for the aged subjects. For the aged subjects

(bottom rows), the psychometric functions for the longer stimulus shifted to smaller gap durations compared to the shorter stimulus. For the young subjects (top rows), the duration effect on gap threshold was not as clear as that for the aged subjects due to greater intersubject variability. While four of the young subjects showed sizable differences between 100-ms and 400-ms noise-burst durations, two (Y2 and Y4) did not.

The steepness of the functions does not appear to be influenced by the duration of the noise burst for either age group. For most subjects, the psychometric functions for 100- and 400-ms noise bursts were parallel, except for two aged subjects (A2 and A4), who showed shallower slopes for the shorter stimulus. The group mean k for the young subjects was 1.61 (s.d.=0.17) for the 100-ms burst and 1.71 (s.d.=0.40) for the 400-ms burst. For the aged subjects, the k averaged 1.58 (s.d.=0.59) and 2.05 (s.d.=0.44) for the 100- and 400-ms noise bursts, respectively. Thus, the mean slope for the 400-ms noise burst was slightly steeper than for the 100-ms noise burst for both age groups, but this trend was not consistent among individual subjects. A repeated-measures analysis of variance (ANOVA) on slope, k, with age as a grouping factor and the noise-burst duration (100 vs 400 ms) as the repeated measure, did not show significant effects of age [$F(1,10)=0.6618$, $p=0.4349$] or noise duration [$F(1,10)=3.4105$, $p=0.0945$]. Given that the slope was generally uniform, differences in gap detection can therefore be adequately described by a single parameter, namely the horizontal placement of the psychometric function, or gap threshold.

The average gap threshold ($d'=1$) for the young subjects was 4.14 (s.d.=0.60) ms for the 100-ms noise burst, and 3.46 (s.d.=0.29) ms for the 400-ms noise. For the aged subjects, the threshold averaged 4.78 ms (s.d.=1.20) for the 100-ms condition and 3.57 (s.d.=0.62) ms for the 400-ms condition. Although these gap thresholds (for both 100- and 400-ms noise bursts) were slightly larger than the 2 to 3 ms suggested by Green (1985), these differences could be attributed to procedural differences (yes/no vs forced choice). The duration-related differences observed in the present study averaged 0.68 ms for the young subjects and 1.21 ms for the aged subjects. Given the steepness of the psychometric function for gap detection, such differences can introduce large changes in subjects' performance. This was confirmed by a repeated-measures ANOVA on thresholds showing that the gap threshold for the 100-ms burst was significantly higher than the threshold for the 400-ms noise burst [$F(1,10)=12.2891$, $p=0.0057$]. However, gap thresholds for young and aged subjects were not significantly different [$F(1,10)=1.2426$, $p=0.2911$], a finding consistent with Moore *et al.* (1992), who argued against a robust age effect. Finally, threshold differences due to noise-burst duration were consistent for both age groups, as indicated by the nonsignificant age by duration interaction [$F(1,10)=0.9664$, $p=0.3488$].

This duration effect is contrary to the findings of some previous studies which showed either no change in gap detection (Penner, 1975) or small changes in the opposite direction from our results (Forrest and Green, 1987). Note that both of these previous studies used smaller sample sizes (two or three subjects). Furthermore, the trend was not consistent among subjects in Forrest and Green's study. Intersubject variability was also observed in our young subjects' data (Fig. 3), where two out of six subjects showed no shift of the psychometric function with increasing noise duration. Our findings regarding the duration effect were more similar to those of the young subjects in a large-sample study by Muchnik *et al.* (1985).

Improved detection with increasing stimulus duration has been observed in other temporal measurements, namely detection of amplitude modulation (AM) and beats (Viemeister, 1979; Sheft and Yost, 1990), as well as discrimination of AM rate and depth (Lee, 1994; Lee and Bacon, 1997). This suggests that a temporal integration process may be a fundamental property of auditory perception, including temporal resolution. This issue will be discussed further with the more comprehensive data of experiment 3.

III. EXPERIMENT 2: EFFECT OF VARYING GAP LOCATION

A. Methods

The paradigm used in this experiment was similar to that of Green and Forrest (1989) except that in this study the noise burst was 100 ms. For each trial, the gap occurred at a location randomly chosen from 15% to 85% of the total duration from the onset. The results were compared to those measured when the gap was fixed at the temporal center of the 100-ms noise burst (for most subjects, these data were from experiment 1).

B. Results and discussion

Figure 4 compares gap detection measured with fixed (solid lines) and random (dashed lines) gap locations. Six young subjects' data are plotted in individual panels in the top two rows, and six aged subjects' data in the bottom two rows. As shown in Fig. 4, the general placement of the psychometric function does not appear to be affected by the randomness of the gap location; for all subjects, the functions measured in fixed and random conditions generally overlap. The condition-related difference was smaller than the between-subject variability, indicating high reliability of individual subjects' performance. Below the 50% point (i.e., at the shorter-gap durations), differences between the two functions were minimal, which resulted in small differences in thresholds ($d'=1$). The most obvious difference was the reduced detectability at longer gap durations in some subjects, which resulted in shallower slopes of the functions for the random as compared to the fixed condition.

For both groups, the estimated $d'=1$ thresholds were similar for fixed and random conditions. For the young subjects, thresholds averaged 4.29 (s.d.=0.53) ms for the fixed condition and 3.92 (s.d.=0.54) ms for the random condition. For the aged subjects, the average thresholds were 4.88 (s.d.=1.27) and 5.00 (s.d.=2.08) for the fixed and random conditions, respectively. A repeated-measures ANOVA on $d'=1$ threshold with age as a grouping factor and a repeated measure on uncertainty (fixed vs random) did not find a significant effect of age [$F(1,10)=1.5025$, $p=0.2484$] or un-

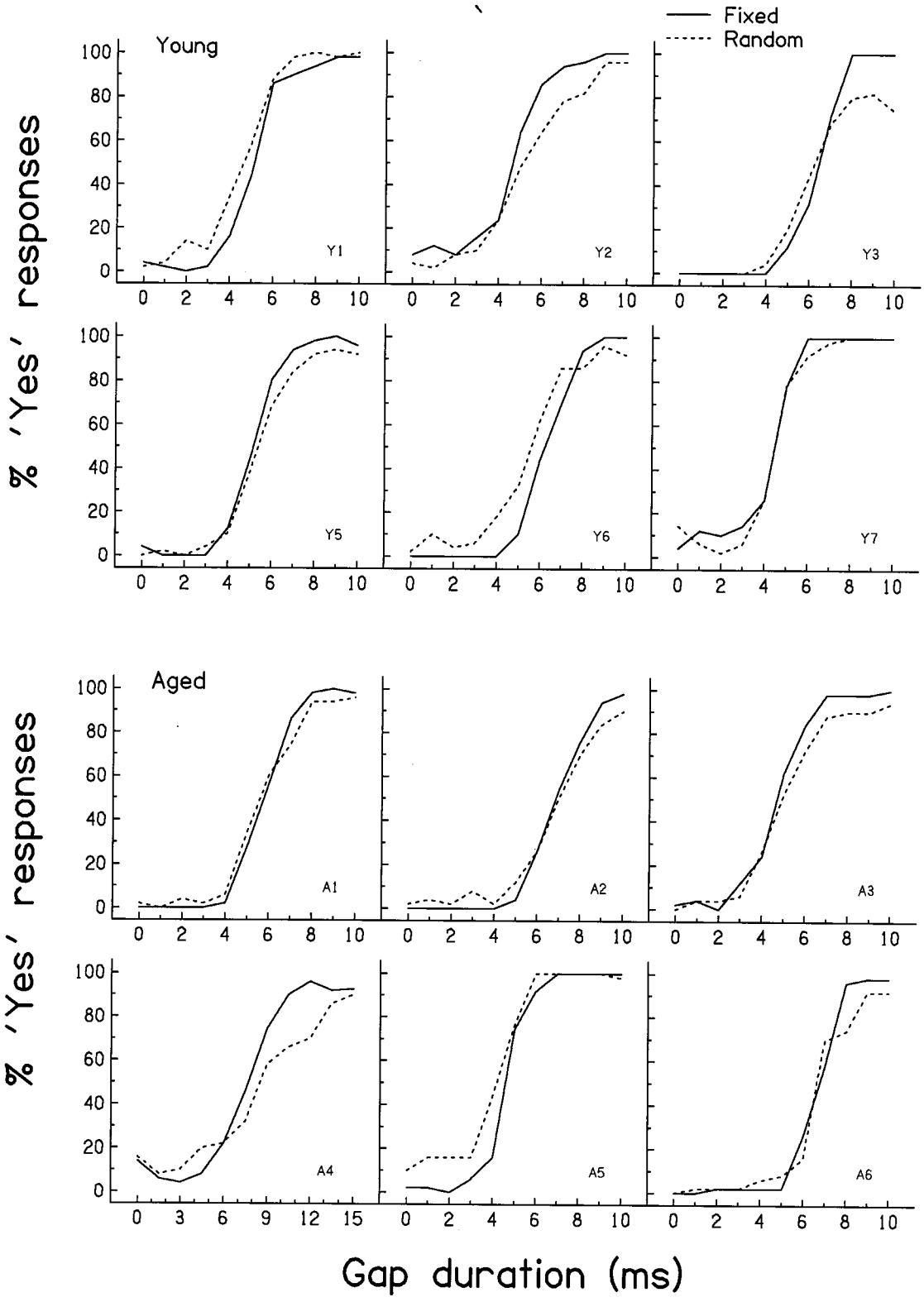

FIG. 4. Psychometric functions measured with gap position fixed at the temporal center of the noise burst (solid lines) or randomly varied over a range from 15% and 85% of the total duration from the onset (dashed lines). The total duration of the noise burst was 100 ms. Data of six young subjects are presented in the upper two rows, and those of six aged subjects in the bottom two rows.

certainty [$F(1,10)=0.7385$, $p=0.4103$], nor was their interaction significant [$F(1,10)=1.4475$, $p=0.2566$].

In contrast to the $d'=1$ thresholds, differences in the average slope (k) were sizable between the fixed and random condition for the young group [1.84 (s.d.=0.39) vs 1.42 (s.d. =0.55)] and the aged group [1.26 (s.d.=0.3) vs 0.85 (s.d. =0.3)]. This was confirmed by the ANOVA, which showed a significant main effect of uncertainty [$F(1,10)=56.2206$,

$p<0.001$]. However, there was no significant effect of age [$F(1,10)=0.9757$, $p=0.3466$], nor was the interaction of age and uncertainty significant [$F(1,10)=0.3062$, $p=0.5922$], indicating a consistent trend for both age groups.

Using a forced-choice adaptive procedure, Green and Forrest (1989) observed that gap thresholds with random gap locations were 1.3 to 1.5 times higher than those with a fixed gap location. A significant difference in thresholds was not observed in the present study, but the average slope for the fixed condition was 1.30 times larger than that for the random condition for the young subjects, and 1.48 times larger for the aged subjects. Because the variability of a subject's response is inversely related to the slope of the psychometric function (Green, 1993), the shallower slope of the psychometric function observed in this experiment may be an indication of increased variance of performance in the random condition.

Green and Forrest (1989) attributed the observed differences between random and fixed conditions in their study to the uncertainty of gap location. However, the result could also be affected by differences in gap location or a combination of both factors. The experimental design used in the Green and Forrest study and in the current experiment 2 was not sufficient to differentiate these two factors. A separate assessment of these factors requires the comparison of gap detection obtained at identical gap locations presented in both fixed and random conditions, as will be described in the next experiment.

IV. EXPERIMENT 3: EFFECT OF LOCATION VS UNCERTAINTY

A. Methods

The duration of the noise burst used in this experiment was 400 ms. Results of experiment 1, showing that gap detection was basically the same for young and aged subjects when the gap was fixed at the center of a 400-ms noise burst, provided a common baseline for both young and aged subjects to further assess effects of location and uncertainty of the gap. In this experiment, gap detection was measured under two conditions.

In condition 1, gap detection was measured in three runs of 50 repetitions for each gap duration. In each run, the gap was fixed at either 5%, 50%, or 95% of the total noise duration (one at the temporal center and the other two at the beginning and ending locations, i.e., 20 ms from the onset and offset of the noise burst, respectively).

In condition 2, gap detection was measured with gap location randomly chosen from five values: 5%, 27.5%, 50%, 72.5%, and 95% of the total duration. Each of these five locations was presented 50 times at each gap duration. Each combination of gap location and gap duration was presented to the subject in random order. For each subject, data were collected from a total of 2750 trials (5 locations×11 gap durations×50 repetitions), which were broken into 25 blocks, each with 110 trials. The data were then sorted according to the gap location and duration, resulting in five psychometric functions, each with 50 repetitions at each gap duration and each associated with a specific gap location (11 gap locations×50 repetitions=550 trials).

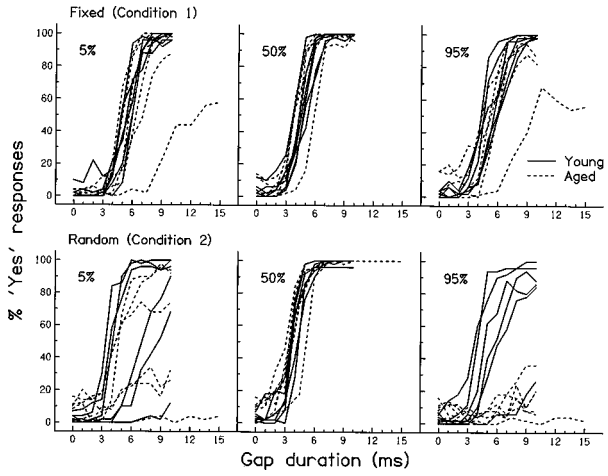

FIG. 5. Psychometric functions measured from both young (solid lines) and aged subjects (dashed lines) in experiment 3. Data in the top row were obtained in condition 1, where the gap was fixed from trial to trial at either 5%, 50%, or 95% of the total duration of the noise burst. Data in the bottom row were measured from condition 2 with the gap randomly occurring from trial to trial at one of five different locations: 5%, 27.5%, 50%, 72.5%, and 95%. For comparison with the fixed data, only data of three locations are presented. The total duration of the noise burst was 400 ms.

B. Results and discussion

1. Comparison of center location with 5% and 95% locations

Figure 5 shows psychometric functions measured with gaps occurring at the 5%, 50%, or 95% locations of the noise burst presented in fixed (top row) and in random conditions (bottom row). The solid lines represent data of the young subjects and the dashed lines, the aged subjects. When the gap was at the center of the noise burst (50%, middle panels), gap detection was independent of the uncertainty of gap location for both young and aged subjects. Furthermore, there was only a small difference in performance between the two age groups in either condition. The mean gap thresholds ($d'=1$) at the 50% location for the young subjects were 3.46 (s.d.=0.29) and 3.27 (s.d.=0.23) ms for the fixed and random conditions, respectively. For the aged subjects, the comparable values were 3.57 (s.d.=0.60) and 3.23 (s.d. =0.89) ms.

When the gap was located away from the center position to the two extreme end locations (5% and 95%), performance declined. In the fixed condition (top row), the functions for the 5% and 95% gap locations shifted toward larger gap durations, compared to the 50% location. The aged subjects also showed increased intersubject variability, mainly due to the extremely poor performance of one aged subject (A6). Also, at the fixed 95% location, there are data from only five elderly subjects because subject A4 was unable to perform this task. This was the same subject who required extended gap length for the 100-ms noise burst in experiments 1 and 2. For the young subjects, gap thresholds averaged 4.21 (s.d.=0.54) ms for the 5% location and 3.57 (s.d. =0.56) ms for the 95% location. For the aged subjects, the

mean thresholds were 5.07 (s.d.=1.63) ms and 4.80 (s.d. =0.78) ms for the 5% and 95% locations, respectively.

This location-related effect intensified when gap location was random (condition 2, bottom row). Significant intersubject variability was observed for both young and aged subjects at the 5% location, where half of the subjects from each group showed a large reduction in the percentage of yes responses. The gap-detection threshold averaged 5.03 (s.d. =2.68) ms for the young subjects and 7.40 (s.d.=4.81) ms for the aged subjects. Note that data of subject A6 were not included in the averages, because this subject's yes responses were <5% across gap durations. At the 95% location, all aged subjects performed below 50% for all gap durations tested. However, four of them (A1, A2, A3, and A5) still showed increased detectability with increasing gap duration which allowed parameters m, k, and α to be estimated. Based on these estimates, the psychometric function was reconstructed and extended so that the $d'=1$ threshold could be calculated. Certainly, the estimation of the slope was less accurate and the calculation of the threshold was somewhat artificial. Nevertheless, the resultant parameters reflected the general tendency as well as individual differences. The mean threshold at the 95% location for these four aged subjects was 12.35 (s.d.=4.22) ms. For the young subjects, the gap threshold averaged 4.41 (s.d.=1.99) ms.

A repeated-measures ANOVA on the $d'=1$ threshold with age as a grouping factor and repeated measures on gap location (5%, 50%, or 95%) and uncertainty (fixed vs random) revealed that all main effects and interactions were significant. In view of the significant second-order interaction of uncertainty by location by age [$F(2,16)=5.6625$, $p=0.0138$], the simple uncertainty by location interaction was analyzed for each age group. *Post hoc* tests of multiple comparisons were performed using A and C matrices from the multivariate general linear model (Morrison, 1976). The results showed that the interaction was significant for the aged subjects [$F(1,8)=22.9402$, $p=0.0014$] but not for the young subjects [$F(1,8)=1.1860$, $p=0.3079$]. That is, for aged subjects only, the location-related differences in gap thresholds were larger for the random condition than for the fixed condition.

For the significant first-order interaction of age by uncertainty [$F(1,8)=7.1886$, $p=0.0279$], the simple uncertainty effect was analyzed for each age group. Again, a significant uncertainty effect was observed for aged subjects [$F(1,8)=16.8890$, $p=0.0034$], but not for young subjects [$F(1,8)=0.63$, $p=0.4501$]. That is, for aged subjects only, thresholds in the random condition were higher than in the fixed condition. This also accounts for the significant main effect of uncertainty [$F(1,8)=13.5825$, $p=0.0062$].

For the significant first-order interaction of age by location [$F(2,16)=7.1679$, $p=0.0060$], as well as for the significant location main effect [$F(2,16)=10.2076$, $p=0.0014$], simple location effects were further examined for each age group and across three levels of gap locations. Significant differences in gap thresholds between the center location (50%) and the two end locations (5% and 95%) were observed for aged subjects [$F(1,8)=38.3903$, $p=0.0003$], but not for young subjects [$F(1,8)=3.6937$, $p=0.0908$]. Comparing gap detection for the 5% and 95% locations, again, the significant location effect was observed for aged subjects [$F(1,8)=6.3424$, $p=0.0359$], but not for young subjects [$F(1,8)=0.3767$, $p=0.5564$]. Thus, for aged subjects only, gap-detection thresholds were significantly lower at the middle location than at the end locations, and were significantly lower at the 5% location than at the 95% location. In summary, the significant main effect of age [$F(1,8)=8.3436$, $p=0.0202$] was due to the significantly higher gap thresholds of the aged subjects when the gap was at the end locations and was presented randomly.

The steepness of the psychometric functions changed considerably with gap location, as shown in Fig. 5. First, when the gap was at the 50% location (middle panels), there was little difference in the slopes of the functions between random and fixed conditions for both age groups. The slope (k) averaged 1.71 (s.d.=0.40) for the young subjects and 2.05 (s.d.=0.44) for the aged subjects in the fixed condition, and 2.45 (s.d.=0.69) and 2.04 (s.d.=0.58) for the young and aged groups, respectively, in the random condition. When the gap was positioned at the end locations (5% and 95%), the functions became shallower, especially for the random condition. For the fixed condition (top row, first and third panels), the average slopes for the young group were 1.70 (s.d.=0.67) for the 5% location and 1.47 (s.d.=0.52) for the 95% location, whereas for the aged subjects, the slopes averaged 1.41 (s.d.=0.68) and 1.09 (s.d.=0.54) for 5% and 95% locations, respectively. When the gap was presented randomly (condition 2, bottom row, first and third panels), the mean slopes for the 5% location were 1.62 (s.d.=0.73) and 0.82 (s.d.=0.77) for the young and aged subjects, respectively. The average slope for the 95% location in the random condition was 1.11 (s.d.=0.56) for the young subjects and 0.44 (s.d.=0.13) for the aged subjects.

The repeated-measures ANOVA on the slope (k) did not show a significant age effect [$F(1,8)=1.6138$, $p=0.2397$], nor were interactions of age by location [$F(2,16)=0.8554$, $p=0.4437$] or age by uncertainty [$F(1,8)=4.4856$, $p=0.0670$] significant. This suggested that although the thresholds were significantly different between the young and aged subjects in these conditions, the slope was generally consistent for the two age groups. Significant F ratios were obtained only on the main effect of location [$F(2,16)=15.8258$, $p=0.0002$] and the interaction of uncertainty by location [$F(2,16)=5.0274$, $p=0.0202$]. *Post hoc* tests confirmed that the slope at the 50% location was steeper than those at the 5% and 95% locations for both age groups [$F(1,8)=20.3973$, $p=0.0020$], and that the center/end location difference was larger in the random condition than in the fixed condition [$F(1,8)=33.1792$, $p=0.0004$].

2. Comparing the 50% location with the 27.5% and 72.5% locations

Two more gap locations, 27.5% and 72.5% of the total noise duration, were tested in the random condition. The relatively robust responses for the 50% location, despite uncertainty (Fig. 5), extended to these two locations. Figure 6 plots psychometric functions for these two locations, 27.5% and 72.5% (left and right panels, respectively), and the 50%

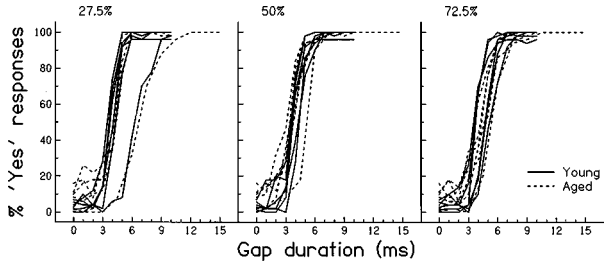

FIG. 6. Psychometric functions measured from both young (solid lines) and aged subjects (dashed lines) in the random condition of experiment 3 with the gap located at 27.5% (left panel), 50% (middle panel), and 72.5% (right panel) of the noise-burst duration (400 ms).

location (middle panel). The solid lines represent data for the young subjects and the dashed lines, the aged subjects. As shown in Fig. 6, the steepness and the overall placement were little affected by location, even though the gap was presented randomly. The intersubject variability was similar for both age groups and was generally constant across locations, except for the 27.5% location, where one subject from each group showed some departure from the rest of the group.

Gap thresholds for the young subjects averaged 3.53 (s.d.=0.83) ms for the 27.5% location and 3.58 (s.d.=0.43) ms for the 72.5% location. For the aged subjects, the mean thresholds were 3.88 (s.d.=0.49) ms and 3.85 (s.d.=0.46) ms. The values were symmetrical surrounding the thresholds at the 50% location, which were 3.27 ms for the young group and 3.23 ms for the aged group in the random condition. A repeated-measures ANOVA on the $d'=1$ thresholds obtained from condition 2 with age as the grouping factor and repeated measures on five levels of the gap location (5%, 27.5%, 50%, 72.5%, and 95%) showed significant effects of age [$F(1,8)=6.2221$, $p=0.0373$] and location [$F(4,32)=11.2857$, $p<0.0001$], as well as their interaction [$F(4,32)=7.1108$, $p=0.0003$]. This was expected because the analysis included the two end locations (5% and 95%), which were shown in the last section to significantly affect gap thresholds for the aged subjects. However, the main interest here was to compare the three central gap locations (27.5%, 50%, and 72.5%). The *post hoc* analysis revealed that the location-related difference (50% location vs 27.5% and 72.5% locations) was significant for the aged subjects [$F(1,8)=10.4325$, $p=0.0121$], but not for the young subjects [$F(1,8)=1.5241$, $p=0.2520$]. Nevertheless, even for the aged subjects, these differences ($\leqslant$0.65 ms) were about an order of magnitude smaller than the differences between the center location and the 5% and 95% locations (5 to 10 ms), as shown in Fig. 5.

The slopes (k) of the psychometric functions were generally constant across these locations for both young and aged subjects. The average slopes for the young group were 2.16 (s.d.=0.50) and 2.19 (s.d.=0.73) for the 27.5% and 72.5%, respectively, which is close to that for the 50% location (2.45). For the aged subjects, the slope averaged 2.48 (s.d.=1.10) for the 27.5% and 1.48 (s.d.=0.15) for the 72.5% locations, as compared to 2.04 for the 50% location. A repeated-measures ANOVA on the slope with age as the grouping factor and repeated measures on five levels of the location (5%, 27.5%, 50%, 72.5%, and 95%) found no significant effect of age [$F(1,8)=2.9897$, $p=0.1221$] but a significant effect of location [$F(4,32)=12.4157$, $p<0.0001$]. However, comparing only the 50% location with the 27.5% and 72.5% locations, the *post hoc* analysis revealed that the difference in slope was not significant for either young [$F(1,8)=1.1048$, $p=0.3239$] or aged subjects [$F(1,8)=0.0938$, $p=0.7672$].

3. Effect of signal onset and offset

In this experiment, effects of gap location and uncertainty were simultaneously examined. As shown in Fig. 5, the influence of gap location was more prominent than the influence of uncertainty. Both gap thresholds and the steepness of the psychometric functions were found to be affected by the gap location, especially for the aged subjects. For both age groups, the mean $d'=1$ threshold was lowest at the temporal center of the noise burst and increased as the gap moved away from the center, with the highest thresholds at the 5% and 95% locations. This trend suggested an influence of stimulus onset and offset, especially for the aged subjects. As shown in Fig. 6, when the gap was located sufficiently away from both ends of the noise burst (e.g., at 27.5% and 72.5%), perception was robust, regardless of the uncertainty about the gap location.

Now, a remaining question is whether this robust detection for the central gap locations is a function of the absolute duration of the noise burst or the proportion of the noise-burst duration. To answer this question, two aged subjects (A1 and A4) were further tested under condition 2 (random gap location) of experiment 3, with 100-ms noise duration and ten repetitions at each gap duration for each gap location. The resultant psychometric functions are presented in the left column of Fig. 7. The 400-ms data are included in the right column for comparison. Although the 100-ms functions obtained with ten repetitions (left) were not as smooth as the 400-ms data obtained with 50 repetitions (right), similarities between these two sets of data are obvious. In most cases, psychometric functions measured with the gap at central locations (32%, 50%, and 68% for the 100-ms noise burst, and 27.5%, 50%, and 72.5% for the 400-ms noise burst) can be differentiated from those obtained with the gap at end locations (14% and 86% for the 100-ms, 5% and 95% for the 400-ms noise burst). The full range of the psychometric function was consistently obtained for the three central gap locations for both the 100- and 400-ms noise bursts, despite large differences (in ms) in the absolute temporal locations of these gaps. On the other hand, for both 100- and 400-ms noise bursts, the gaps located near the onset and offset resulted in poor detection. These data confirmed that the effects of onset and offset are basically independent of noise-burst duration.

V. GENERAL DISCUSSION AND CONCLUSIONS

In this study, psychometric functions for gap detection were measured from six young and six aged subjects under several conditions. With pure-tone thresholds closely matched between subject groups, an aging effect could be

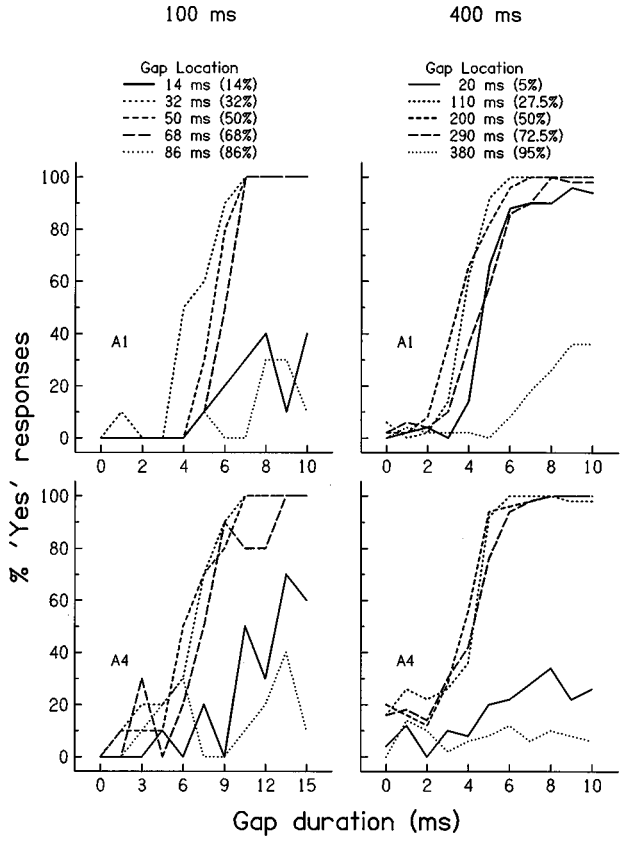

FIG. 7. Comparison of psychometric functions measured in the random condition of experiment 3 with 100-ms (left column) and 400-ms noise bursts (right column). Two aged subjects' data are presented. The parameter in each panel is gap location.

directly assessed. It should be pointed out that employing a small sample size may increase the possibility of missing some small- or medium-size effects. However, our data shared some features in common with other studies. Consistent with the reports by Moore *et al.* (1992) and Snell (1997), this study also observed a large overlap of data between the young and aged subjects.

The thresholds and the slopes of the psychometric function for gap detection were analyzed separately and were found to be differentially affected by age and by experimental conditions.

A. Slope of psychometric function for gap detection

In this study, a typical psychometric function for the detection of a temporal gap in a broadband noise burst was characterized by a steep slope with a k value between 1.5 and 2 (Fig. 2, as an example). Given this steepness, a change in detectability from 20% to 80% corresponded to a difference in gap duration of about 2 ms. This is consistent with the observation of Green and Forrest (1989), who found that the psychometric function for detecting a silent gap measured in a forced-choice paradigm covered a range of only 2 ms of gap duration over 50% to 100% correct responses. A steep function indicates high precision and low variability for detection of a gap within a noise burst. As can be calculated from Eq. (1), with k values greater than 1, differences in gap duration as small as 0.5 ms may change the percentage of yes responses by 15% to 25% and may be significant.

Reductions in the steepness of the functions were observed in this study under more difficult conditions, i.e., when the gap was located at the beginning and end of the noise bursts, especially in the random condition (Fig. 5). However, the shallower psychometric functions observed in these conditions may have been due to the limited maximum gap duration. If an extended range of gap durations were possible, detectability may have increased with a steeper slope. Therefore, when the gap was sufficiently removed from the onset and offset of a broadband noise burst, the slope of the psychometric function for gap detection was independent of age, noise-burst duration, and the position and uncertainty of gap location.

A uniform slope is desirable for the efficiency and accuracy of many adaptive procedures which estimate specific points on the psychometric function. For gap detection in a broadband noise, as in this study, a uniform slope was obtained by using a linear duration scale. However, in the case of gap detection in a tone burst or in a narrow-band noise carrier, where larger ranges of gap thresholds (in ms) were included, a logarithmic scale of gap duration should be used to obtain a uniform slope (Florentine, Buus, and Geng, 1998). Note that with different scales, the value of the slope (k) will change accordingly.

B. Factors that influence gap-detection thresholds

With a generally uniform slope of the psychometric function for gap detection across experimental conditions, effects of noise-burst duration, gap location, and uncertainty about gap location can be accessed by a single parameter, namely, the horizontal placement of the psychometric function, which determines the gap threshold. As demonstrated by the results of experiment 1 (Fig. 3), when the gap was located at the center of the noise burst, the noise-burst duration had a significant effect on the gap threshold, but the effect was not age related. For both young and aged subjects, gap threshold decreased with increasing stimulus duration.

According to previous studies (Forrest and Green, 1987; Green and Forrest, 1989), gap-detection threshold was not affected by the location of the gap within the noise burst, but by the randomness of gap location. Results of experiment 3 (Figs. 5 and 6), with control of both factors, showed that the effects differed with age. For the young subjects, neither location nor uncertainty had a statistically significant effect on gap-detection thresholds. These observations were consistent with previous studies on the location effect, but contradicted previous research on the uncertainty effect. The disparity was likely due to differences in experimental design. For the aged subjects, the detection threshold was affected by both the gap location and uncertainty, and furthermore, the effects were not independent. The uncertainty effect was location related. As shown in Fig. 5, significant differences between fixed and random conditions were observed when the gap was located near the onset and offset of the noise burst, but not when the gap was at the center of the stimulus. The effect of gap location was more prominent. There was a general tendency for the gap threshold to increase as the gap moved from the center to the two ends of the noise burst (Figs. 5

and 6). This age-related location effect was also independent of noise-burst duration (Fig. 7).

Earlier in this paper, temporal integration was suggested as a mechanism explaining the improvement in gap detection with increasing noise-burst duration, consistent with previous studies of other temporal resolution measures (Viemeister, 1979; Sheft and Yost, 1990; Lee, 1994; Lee and Bacon, 1997). Temporal cues do not exist in isolation, but rather are conveyed by intensity changes over time. As discussed by Plack and Moore (1990, 1991), the task of gap detection may require both temporal resolution and intensity resolution, as evidenced by the finding of a significant correlation between gap detection and intensity discrimination in hearing-impaired subjects (Glasberg and Moore, 1989). Given that intensity resolution is a function of stimulus duration (Florentine, 1986), the involvement of temporal integration in gap detection is a reasonable assumption.

Increased gap-detection thresholds for gaps near the onset and offset of the noise burst may also be related to the ''overshoot'' phenomenon (Bacon and Viemeister, 1985). Under certain conditions, the threshold of a brief tonal signal presented soon after the onset of a masker can be 10 to 20 dB higher than a tone presented several hundred ms later within the masker. The time course of the overshoot effect has been measured by Bacon and Viemeister (1985), who showed that the tone threshold was high at the masker onset, followed by a rapid decrease as the tone moved toward the center of the masker, reaching a minimum at the center. The threshold then increased again as the tone moved further toward the end of the masker. Furthermore, these onset and offset effects were consistent for both 300- and 800-ms maskers (their Fig. 1). Their data bear a similarity to the gap-detection data obtained in this study regarding onset and offset effects, as well as stimulus duration effects. In their study, the minimum masked threshold obtained with the tone at the temporal center of the masker was slightly higher for the 300-ms masker than for the 800-ms masker, similar to our observation of the effect of noise-burst duration on gap detection, as shown in Fig. 3 of this study. This suggests that detection of a gap in a noise burst and detection of a signal in a masker may share a common underlying mechanism.

Adaptation of eighth-nerve fibers has been suggested as a possible explanation for the overshoot effect. The improved detection threshold for the signal is thought to result from improved signal-to-noise ratios during the course of adaptation (Smith and Zwislocki, 1975; Smith, 1979). In the case of gap detection, when a gap moves away from stimulus onset, improved signal-to-noise ratios help listeners identify the gap, or, more generally, the intensity decrement. Adaptation may also explain the effect of noise-burst duration, because a gap at the center of a short noise burst is closer to the noise onset than is its counterpart in a longer noise burst.

Nevertheless, adaptation cannot account for the offset effect. According to the adaptation mechanism, progressively improved gap detection would be expected as the gap location moved away from the onset, with the poorest detection at the 5% location and the best at the 95% location for the 400-ms noise burst. Obviously, the stimulus offset produced an additional effect on gap detection. Because the ''off'' response is rarely observable in auditory-nerve fibers (Kiang *et al.*, 1965), the site for the offset effect may be located more centrally where many age-related alterations have been reported (e.g., Caspary *et al.*, 1995; Boettcher *et al.*, 1996; Walton *et al.*, 1998). This explanation is supported by the data obtained in this study where, as shown in Fig. 5, gap thresholds were influenced by the offset of the noise burst more for aged subjects than for young subjects. Furthermore, for aged subjects, thresholds near the noise offset were significantly elevated compared to those near the noise onset. This age-related onset/offset difference may be related to observations from studies of speech recognition. Consonants at the final position of a syllable are more difficult to identify than those at the initial position for both young and aged subjects (Dubno *et al.*, 1982; Gelfand *et al.*, 1986), and this initial/final difference increased with age in noise conditions (Gelfand *et al.*, 1986).

Throughout this study, a significant age effect was only observed when the gap was at the edge locations (5% and 95%) of the noise burst. This age-related edge location effect for gap detection should be considered when results are assessed in conjunction with age-related changes in speech recognition. Although both gap detection and speech recognition involve detection of temporal gaps, the location of the gap is quite different in the two situations. In gap-detection paradigms which position the gap at the center of the stimulus, the detection, as we know now, is robust. In consonant perception, however, the temporal gaps associated with consonants usually occur more randomly and often at the edges of syllables, making them more difficult to detect. Therefore, gap thresholds obtained with gaps located at the center of a stimulus may not be good predictors of speech recognition, especially for aged subjects.

ACKNOWLEDGMENTS

The authors are grateful to Chan F. Lam for assistance with signal generation, Fu-Shing Lee for advice on statistical analyses, and to Jayne B. Ahlstrom for help with preparation of figures and comments on the manuscript. The authors wish to thank Karen Snell and an anonymous reviewer whose valuable comments improved this manuscript. Thanks are also given to Mary Florentine, Soren Buus, and Flint Boettcher, who made valuable comments and suggestions. This work was supported (in part) by research Grant Nos. P50 DC00422 and R01 DC00184 from the National Institute on Deafness and Other Communication Disorders, National Institutes of Health.

ANSI (**1989**). ANSI S3.6-1989. ''Specifications for audiometers'' (American National Standards Institute, New York).

Bacon, S. P., and Viemeister, N. F. (**1985**). ''The time course of simultaneous tone-to-tone masking,'' J. Acoust. Soc. Am. **78**, 1231–1235.

Boettcher, F. A., Mills, J. H., Swerdloff, J. L., and Holley, B. L. (**1996**). ''Auditory evoked potentials in aged gerbils: responses elicited by noises separated by a silent gap,'' Hearing Res. **102**, 167–178.

Boothroyd, A. (**1973**). ''Detection of temporal gaps by deaf and hearing subjects,'' S.A.R.P. 12, Clarke School for Deaf, Northampton, MA.

Caspary, D. M., Milbrandt, J. C., and Helfert, R. H. (**1995**). ''Central auditory aging: GABA changes in the inferior colliculus,'' Exp. Gerontol. **30**, 349–360.

Committee on Hearing, Bioacoustics, and Biomechanics (CHABA) (**1988**). ''Speech understanding and aging,'' J. Acoust. Soc. Am. **83**, 859–895.
Dubno, J. R., Dirks, D. D., and Langhofer, L. R. (**1982**). ''Evaluation of hearing-impaired listeners using a nonsense-syllable test. II. Syllable recognition and consonant confusion patterns,'' J. Speech Hear. Res. **25**, 141–148.
Dubno, J. R., Dirks, D. D., and Morgan, D. E. (**1984**). ''Effects of age and mild hearing loss on speech perception in noise,'' J. Acoust. Soc. Am. **76**, 87–96.
Fitzgibbons, P. J., and Wightman, F. L. (**1982**). ''Temporal resolution in normal and hearing-impaired listeners,'' J. Acoust. Soc. Am. **72**, 761–765.
Fitzgibbons, P. J., and Gordon-Salant, S. (**1995**). ''Age effects on duration discrimination with simple and complex stimuli,'' J. Acoust. Soc. Am. **98**, 3140–3145.
Fitzgibbons, P. J., and Gordon-Salant, S. (**1996**). ''Auditory temporal processing in elderly listeners,'' J. Am. Acad. Audiol. **7**, 183–189.
Florentine, M. (**1986**). ''Level discrimination of tones as a function of duration,'' J. Acoust. Soc. Am. **79**, 792–798.
Florentine, M., and Buus, S. (**1984**). ''Temporal gap detection in sensorineural and simulated hearing impairments,'' J. Speech Hear. Res. **27**, 449–455.
Florentine, M., Buus, S., and Geng, W. (**1998**). ''Psychometric functions for gap detection,'' Proceedings of the 16th International Congress on Acoustics and the 135th Meeting of the Acoustical Society of America, pp. 881–882.
Forrest, T. G., and Green, D. (**1987**). ''Detection of partially filled gaps in noise and the temporal modulation transfer function,'' J. Acoust. Soc. Am. **82**, 1933–1943.
Garner, W. R., and Miller, G. A. (**1947**). ''The masked threshold of pure tones as a function of duration,'' J. Exp. Psychol. **37**, 293–303.
Gelfand, S. A., Piper, N., and Silman, S. (**1986**). ''Consonant recognition in quiet and in noise with aging among normal hearing listeners,'' J. Acoust. Soc. Am. **80**, 1589–1598.
Glasberg, B. R., and Moore, B. C. J. (**1988**). ''Psychoacoustic abilities of subjects with unilateral and bilateral cochlear hearing impairments and their relationship to the ability to understand speech,'' Scand. Audiol. Suppl. **32**, 1–25.
Glasberg, B. R., and Moore, B. C. J. (**1989**). ''Psychoacoustic abilities of subject with unilateral and bilateral cochlear hearing impairments and their relationship to understand speech,'' Scand. Audiol. Suppl. **32**, 1–25.
Gordon-Salant, S. (**1987**). ''Age-related differences in speech recognition performance as a function of test format and paradigm,'' Ear Hear. **8**, 277–282.
Gordon-Salant, S., and Fitzgibbons, P. J. (**1993**). ''Temporal factors and speech recognition performance in young and elderly listeners,'' J. Speech Hear. Res. **36**, 1276–1285.
Green, D. M. (**1985**). ''Temporal factors in psychoacoustics,'' in *Time Resolution in Auditory Systems*, edited by A. Michelsen (Springer, London), pp. 122–140.
Green, D. M. (**1993**). ''A maximum-likelihood method for estimating thresholds in a yes–no task,'' J. Acoust. Soc. Am. **93**, 2096–2105.
Green, D., and Forrest, T. G. (**1989**). ''Temporal gaps in noise and sinusoids,'' J. Acoust. Soc. Am. **86**, 961–970.
Gu, X., and Green, D. M. (**1994**). ''Further studies of a maximum-likelihood yes–no procedure,'' J. Acoust. Soc. Am. **96**, 93–101.
Hall, J. W., and Fernandes, M. A. (**1983**). ''Temporal integration, frequency resolution, and off-frequency listening in normal-hearing and cochlear-impaired listeners,'' J. Acoust. Soc. Am. **74**, 1172–1177.
Humes, L. E., and Christopherson, L. (**1991**). ''Speech identification difficulties of hearing-impaired elderly persons: The contributions of auditory processing deficits,'' J. Speech Hear. Res. **34**, 686–693.
Irwin, R. J., Hinchcliff, L. K., and Kemp, S. (**1981**). ''Temporal acuity in normal and hearing-impaired listeners,'' Audiology **20**, 234–243.
Kiang, N. Y. C. Watanabe, T., Thomas, C., and Clark, L. F. (**1965**). *Discharge Patterns of Single Fibers in the Cat's Auditory Nerve* (MIT Press, Cambridge, MA).
Lee, J. (**1994**). ''Amplitude modulation rate discrimination with sinusoidal carriers,'' J. Acoust. Soc. Am. **96**, 2140–2147.
Lee, J., and Bacon, S. P. (**1997**). ''Amplitude modulation depth discrimination of a sinusoidal carrier: effect of stimulus duration,'' J. Acoust. Soc. Am. **101**, 3688–3693.
Lutman, M. E. (**1991**). ''Degradations in frequency and temporal resolution with age and their impact on speech identification,'' Acta Oto-Laryngol. Suppl. **476**, 120–126.
Moore, B. C. J. (**1973**). ''Frequency difference limens for short-duration tones,'' J. Acoust. Soc. Am. **54**, 610–619.
Moore, B. C. J., and Glasberg, B. R. (**1988**). ''Gap detection with sinusoids and noise in normal, impaired and electrically stimulated ears,'' J. Acoust. Soc. Am. **83**, 1093–1101.
Moore, B. C. J., Peters, R. W., and Glasberg, B. R. (**1992**). ''Detection of temporal gaps in sinusoids by elderly subjects with and without hearing loss,'' J. Acoust. Soc. Am. **92**, 1923–1932.
Morrison, D. F. (**1976**). *Multivariate Statistical Methods*, 2nd ed. (McGraw-Hill, New York), pp. 197–204.
Muchnik, C., Hildesheimer, M., Rubinstein, M., Saden, M., Shegter, Y., and Shibolet, B. (**1985**). ''Minimal time interval in auditory temporal resolution,'' J. Aud. Res. **25**, 239–246.
Penner, M. J. (**1975**). ''Persistence and integration: Two consequences of a sliding integrator,'' Percept. Psychophys. **18**, 114–120.
Penner, M. J. (**1977**). ''Detection of temporal gaps in noise as a measure of the decay of auditory sensation,'' J. Acoust. Soc. Am. **61**, 552–557.
Phillips, D. P., Taylor, T. L., Hall, S. E., Carr, M. M., and Mossop, J. E. (**1997**). ''Detection of silent intervals between noises activating different perceptual channels: Some properties of 'central' auditory gap detection,'' J. Acoust. Soc. Am. **101**, 3694–3705.
Plack, C. J., and Moore, B. C. J. (**1990**). ''Temporal window shape as a function of frequency and level,'' J. Acoust. Soc. Am. **87**, 2178–2187.
Plack, C. J., and Moore, B. C. J. (**1991**). ''Decrement detection in normal and impaired ears,'' J. Acoust. Soc. Am. **90**, 3069–3076.
Plomp, R. (**1964**). ''Rate of decay of auditory sensation,'' J. Acoust. Soc. Am. **36**, 277–282.
Salvi, R. J., and Arehole, S. (**1985**). ''Gap detection in chinchillas with temporary high-frequency hearing loss,'' J. Acoust. Soc. Am. **77**, 1173–1177.
Schneider, B. A., Pichora-Fuller, M. K., Kowalchuck, D., and Lamb, M. (**1994**). ''Gap detection and the precedence effect in young and old adults,'' J. Acoust. Soc. Am. **95**, 980–991.
Sheft, S., and Yost, W. (**1990**). ''Temporal integration in amplitude modulation detection,'' J. Acoust. Soc. Am. **88**, 796–805.
Smith, R. L. (**1979**). ''Adaptation, saturation, and physiological masking in single auditory-nerve fibers,'' J. Acoust. Soc. Am. **65**, 166–178.
Smith, R. L., and Zwislocki, J. J. (**1975**). ''Short-term adaptation and incremental response of single auditory-nerve fibers,'' Biol. Cybern. **17**, 169–182.
Snell, K. B. (**1997**). ''Age-related changes in temporal gap detection,'' J. Acoust. Soc. Am. **101**, 2214–2220.
Strouse, A., Ashmead, D. H., Ohde, R. N., and Grantham, D. W. (**1998**). ''Temporal processing in the aging auditory system,'' J. Acoust. Soc. Am. **104**, 2385–2399.
Swets, J. A. (**1964**). *Signal Detection and Recognition by Human Observers* (Wiley, New York).
Tyler, R. S., Summerfield, Q., Wood, E. J., and Fernandes, M. A. (**1982**). ''Psychoacoustic and phonetic temporal processing in normal and hearing-impaired listeners,'' J. Acoust. Soc. Am. **72**, 740–752.
Van Rooji, J. C. G. M., and Plomp, R. (**1990**). ''Auditive and cognitive factors in speech perception by elderly listeners. II. Multivariate analyses,'' J. Acoust. Soc. Am. **88**, 2611–2624.
Viemeister, N. F. (**1979**). ''Temporal modulation transfer functions based upon modulation thresholds,'' J. Acoust. Soc. Am. **66**, 1364–1380.
Walton, J. P., Frisina, R. D., and O'Neill, W. E. (**1998**). ''Age-related alteration in processing of temporal sound features in the auditory midbrain of the CBA mouse,'' J. Neurosci. **18**, 2764–2776.
Zhang, W., Salvi, R. J., and Saunders, S. S. (**1990**). ''Neural correlates of gap detection in auditory nerve fibers of the chinchilla,'' Hearing Res. **46**, 181–200.

The contribution of static and dynamically varying ITDs and IIDs to binaural detection

Jeroen Breebaart and Steven van de Par
IPO Center for Research on User-System Interaction, P.O. Box 513, NL-5600 MB Eindhoven, The Netherlands

Armin Kohlrausch[a)]
IPO Center for Research on User-System Interaction, P.O. Box 513, NL-5600 MB Eindhoven, The Netherlands and Philips Research Laboratories Eindhoven, Prof. Holstlaan 4, NL-5656 AA Eindhoven, The Netherlands

(Received 10 December 1997; accepted for publication 4 May 1999)

This paper investigates the relative contribution of various interaural cues to binaural unmasking in conditions with an interaurally in-phase masker and an out-of-phase signal ($MoS\pi$). By using a modified version of multiplied noise as the masker and a sinusoid as the signal, conditions with only interaural intensity differences (IIDs), only interaural time differences (ITDs), or combinations of the two were realized. In addition, the experimental procedure allowed the presentation of specific combinations of static and dynamically varying interaural differences. In these conditions with multiplied noise as masker, the interaural differences have a bimodal distribution with a minimum at zero IID or ITD. Additionally, by using the sinusoid as masker and the multiplied noise as signal, a unimodal distribution of the interaural differences was realized. Through this variation in the shape of the distributions, the close correspondence between the change in the interaural cross correlation and the size of the interaural differences is no longer found, in contrast to the situation for a Gaussian-noise masker [Domnitz and Colburn, J. Acoust. Soc. Am. **59**, 598–601 (1976)]. When analyzing the mean thresholds across subjects, the experimental results could not be predicted from parameters of the distributions of the interaural differences (the mean, the standard deviation, or the root-mean-square value). A better description of the subjects' performance was given by the change in the interaural correlation, but this measure failed in conditions which produced a static interaural intensity difference. The data could best be described by using the energy of the difference signal as the decision variable, an approach similar to that of the equalization and cancellation model. [S0001-4966(99)03808-4]

PACS numbers: 43.66.Pn, 43.66.Ba, 43.66.Dc [DWG]

INTRODUCTION

Interaural time differences (ITDs) and interaural intensity differences (IIDs) are generally considered to be the primary cues underlying our ability to localize sounds in the horizontal plane. It has been shown that at low frequencies changes in either ITDs or IIDs affect the perceived locus of a sound source (Sayers, 1964; Hafter and Carrier, 1970; Yost, 1981). Besides mediating localization, it has been argued that the sensitivity to ITDs and IIDs of the auditory system is the principle basis of the occurrence of binaural masking level differences (BMLDs) (Jeffress *et al.*, 1962; McFadden *et al.*, 1971; Grantham and Robinson, 1977). When an interaurally out-of-phase sinusoid is added to an in-phase sinusoidal masker of the same frequency, i.e., a tone-on-tone condition, *static* IIDs and/or *static* ITDs are created, depending on the phase angle between masker and signal. These interaural differences result in lower detection thresholds for the out-of-phase signal compared to an in-phase signal (Yost, 1972a). In terms of the signal-to-masker ratio, subjects tend to be more sensitive to signals producing ITDs than to those producing IIDs (Yost, 1972a; Grantham and Robinson, 1977).

Besides sensitivity to static interaural differences, the binaural auditory system is also sensitive to dynamically varying ITDs (Grantham and Wightman, 1978) and IIDs (Grantham and Robinson, 1977; Grantham, 1984). As a consequence, BMLDs occur for stimuli with dynamically varying interaural differences. When an interaurally out-of-phase sinusoidal signal is added to an in-phase noise masker with the same (center) frequency, the detection threshold may be up to 25 dB lower than for an in-phase sinusoidal signal (Hirsh, 1948; Zurek and Durlach, 1987; Breebaart *et al.*, 1998). For such stimuli, both dynamically varying IIDs and ITDs are present (Zurek, 1991). Experiments which allow the separation of the sensitivity to IIDs and ITDs in a detection task with noise maskers were published by van de Par and Kohlrausch (1998b). They found that for multiplied-noise maskers, the thresholds for stimuli producing only IIDs or only ITDs are very similar.

These ''classical'' paradigms used in the investigation of the BMLD phenomenon with static and dynamically varying interaural differences exploited different perceptual phenomena. For the experiments that are performed with noise

a)Electronic mail: kohlraus@ipo.tue.nl

maskers, the average values of the IIDs and ITDs for a masker plus signal are zero, while the variances of these parameters are nonzero. The addition of an out-of-phase signal to a diotic noise masker (i.e., the production of time-varying interaural differences) is usually perceived as a widening of the sound image. For tone-on-tone masking conditions, however, a static interaural cue is introduced and detection is based on a change in the lateralization of the sound source. One notion which suggests that these situations differ from each other is that the binaural system is known to be sluggish, as has been shown by several studies (Perrott and Musicant, 1977; Grantham and Wightman, 1978, 1979; Grantham, 1984; Kollmeier and Gilkey, 1990; Holube, 1993; Holube *et al.*, 1998). These studies show that if the rate at which interaural cues fluctuate increases, the magnitude of the interaural differences at threshold increases also. It is often assumed that this reduction in sensitivity is the result of a longer time constant for the evaluation of binaural cues compared to the constant for monaural cues (Kollmeier and Gilkey, 1990; Culling and Summerfield, 1998). Another demonstration suggesting that the detection of static and dynamically varying interaural differences is different was given by Bernstein and Trahiotis (1997). They showed that roving of static IIDs and ITDs does not influence the detection of dynamically varying interaural differences, indicating that binaural detection of dynamically varying cues does not necessarily depend upon changes in laterality.

One of the proposed statistics for predicting binaural thresholds is the size of the change in the *mean* value of the interaural difference between the signal and no-signal intervals of the detection task. For example, studies by Webster (1951), Yost (1972a), Hafter (1971), and Zwicker and Henning (1985) argued that binaural masked thresholds could be described in terms of just-noticeable differences (jnd's) of the IID and ITD. For stimuli for which the mean interaural difference does not change by adding a test signal (e.g., in an MoSπ condition with Gaussian noise), it is often assumed that changes in the *width* (e.g., the standard deviation) of the distribution are used as a cue for detection (Zurek and Durlach, 1987; Zurek, 1991). The parameters of the distributions of the interaural differences are generally considered to be important properties for binaural detection. It is unknown, however, how the sensitivity for stimuli producing combinations of static and dynamically varying interaural differences can be described in terms of these parameters.

An attempt to describe the combined sensitivity to static and dynamically varying interaural differences was made by Grantham and Robinson (1977). They measured thresholds for stimuli producing static cues as well as dynamically varying cues.[1] They found that the thresholds for signals producing static cues only were very similar to thresholds for stimuli producing a fixed combination of static and dynamic cues. They discussed the data in terms of the mean interaural differences at threshold, which were very similar for the two conditions. Such an analysis does, however, ignore the contribution of dynamically varying cues for detection in those conditions where these cues are available in addition to static cues.

In the present study MoSπ stimuli will be used which contain either IIDs, ITDs, or combinations of both cues for which the ratio between the static and dynamic component will be varied over a wide range. This allows one to perform a critical assessment of whether detection data can be cast within a framework based on the IIDs and ITDs. A second point of interest of this study is related to an alternative theory that has become very popular for describing binaural detection which relies on the cross correlation of the signals arriving at both ears (cf. Osman, 1971; Colburn, 1977; Lindemann, 1986; Gaik, 1993; van de Par and Kohlrausch, 1995; Stern and Shear, 1996; van de Par and Kohlrausch, 1998a). In these models it is assumed that the change in the interaural correlation resulting from the addition of a signal to a masker is used as a decision variable. In fact, Domnitz and Colburn (1976) argued that for an interaurally out-of-phase tonal signal masked by a diotic Gaussian noise, a model based on the interaural correlation and a model based on the distribution of the interaural differences will yield essentially the same predictions of detection. Thus, theories based on the cross correlation are equivalent to models based on the *width* of the probability distribution functions of the interaural differences, as long as Gaussian-noise maskers and sinusoidal signals are used. However, this equivalence is not necessarily true in general. In the discussion it will be shown that the theories discussed above do not predict similar patterns of data for the stimuli used in the present experiments. Specifically, by producing stimuli with unimodal and bimodal distributions of the interaural cues, we can make a critical comparison between theories based on the IIDs and ITDs and theories based on the interaural cross correlation. Such a comparison is impossible for those MoSπ studies which employ Gaussian-noise maskers and sinusoidal signals.

In summary, this study has a twofold purpose. On the one hand, it intends to collect more data with stimuli producing combinations of static and dynamically varying cues. On the other hand, we wanted to collect data with stimuli producing different shapes of the distributions of the interaural differences. Specifically, the employed procedure enables the production of stimuli with both unimodal and bimodal distributions of the interaural differences. These data may supply considerable insight into how detection thresholds for combinations of static and dynamic cues can be described.

I. MULTIPLIED NOISE

Because of its specific properties, multiplied noise allows control of the fine-structure phase between a noise masker and a sinusoidal signal. As already mentioned by Jeffress and McFadden (1968), control of this phase angle allows the interaural phase and intensity difference between the signals arriving at both ears in an MoSπ condition to be specified. Multiplied noise is generated by multiplying a high-frequency sinusoidal carrier by a low-pass noise. The multiplication by the low-pass noise results in a band-pass noise with a center frequency that is equal to the frequency of the carrier and which has a symmetric spectrum that is twice the bandwidth of the initial low-pass noise. For our experiments, we modified this procedure by first adding a dc

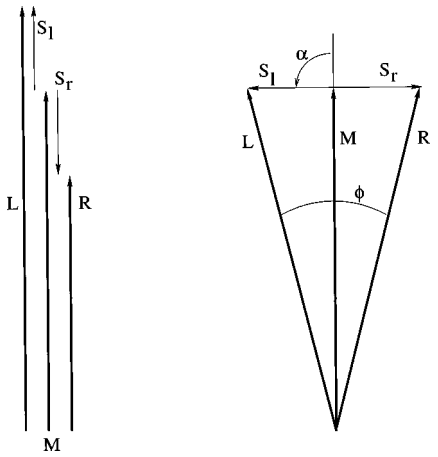

FIG. 1. Vector diagrams illustrating the addition of an interaurally out-of-phase signal (S_l and S_r) to an in-phase masker (M) for $\alpha=0$ (left panel) and $\alpha=\pi/2$ (right panel).

value to the Gaussian low-pass noise before multiplication with the carrier. The effect of using a noise with a nonzero mean is explained in the following section.

A. Multiplied noise as a masker

For the following description we assume an interaurally in-phase multiplied-noise masker and an interaurally out-of-phase sinusoidal signal (i.e., an MoSπ condition). An additional parameter is the phase angle α between the fine structures of noise and sinusoidal signal. If the frequency and phase of the signal that is added to the left ear are equal to those of the masker ($\alpha=0$), we can form a vector diagram of the stimulus as shown in the left panel of Fig. 1. Here, the vector **M** (the masker) rotates with a constant speed (the frequency of the carrier), while its length (i.e., the envelope of the multiplied noise) varies according to the instantaneous-value distribution of the low-pass noise. $\mathbf{S}_l$ and $\mathbf{S}_r$ denote the tonal signals added to the left and right ear, respectively, while **L** and **R** denote the total signals arriving at the left and right ears. Clearly, the vectors **L** and **R** differ only in length, thus only IIDs are present for this stimulus configuration.

If the fine-structure phase of the signal lags the fine-structure phase of the carrier by $\pi/2$ (i.e., $\alpha=\pi/2$), as shown in the right panel of Fig. 1, the resulting vectors **L** and **R** have the same length. However, **R** lags **L** by ϕ. Thus, only ITDs are produced. In a similar way, by adjusting the phase angle α to $\pi/4$ or $3\pi/4$, combinations of IIDs and ITDs can be produced.

Because the instantaneous value of the low-pass noise changes dynamically, the envelope of the multiplied noise constantly changes with a rate of fluctuation dependent on the bandwidth of the low-pass noise. The effect of the addition of a dc component to the low-pass noise before multiplication with the carrier can be visualized as follows. If no dc component is added, the instantaneous value of the low-pass noise has a Gaussian probability density function (PDF) with a zero mean and rms=1, as shown in the left panel of Fig. 2 by the solid line. If the instantaneous value of the low-pass noise is positive, and an Sπ signal with $\alpha=\pi/2$ is added to the multiplied-noise masker (see the right panel in

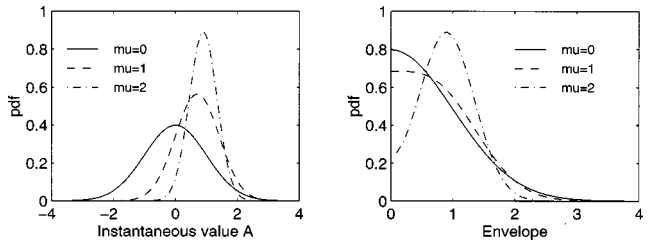

FIG. 2. Probability density functions of the instantaneous value of a Gaussian noise with a constant rms value of 1 (left panel) and the resulting multiplied-noise envelope (right panel). The three curves indicate different values of the static component of 0 (solid line), 1 (dashed line), and 2 (dash-dotted line).

Fig. 1), the fine-structure phase of the right ear lags the fine-structure phase of the left ear by ϕ. If, however, the instantaneous value of the low-pass noise is negative, and the same signal is added, the fine-structure phase of the left ear lags the fine-structure phase of the right ear by ϕ. Thus, the interaural phase difference has changed its sign. Due to symmetry around zero in the instantaneous-value probability density function of the low-pass noise, the probability for a certain positive interaural difference equals the probability for a negative interaural difference of the same amount. Therefore, the distribution of the interaural difference is symmetric with a mean of zero.

The static component μ is defined as the magnitude of the dc component added to the low-pass noise with a rms value of 1 and zero mean. For $\mu>0$, the mean of the low-pass noise shifts to a nonzero value (dashed and dash-dotted line of Fig. 2, for $\mu=1$ and $\mu=2$, respectively). If the rms value of the noise plus dc is held constant (i.e., set to 1), the width of the instantaneous-value probability density function of the low-pass noise becomes narrower with increasing μ.

The resulting envelope probability distribution of the multiplied noise is shown in the right panel of Fig. 2. For $\mu=0$ (solid line), the distribution function is half-Gaussian, while for increasing μ, the distribution becomes narrower; for μ approaching infinity, the envelope has a mean of one and a variance of zero.

The decreasing variance of the envelope probability distribution with increasing static component has a strong effect on the behavior of the interaural differences that occur when an Sπ signal is added. If, at a certain time, the noise envelope is large, the phase lag in the above example is relatively small. Adding the signal to a small masker envelope, however, results in a large interaural phase lag. Thus, the width of the masker envelope probability distribution determines the range over which the interaural phase difference fluctuates. A wide distribution implies large fluctuations in the interaural difference, while a very narrow distribution implies only small fluctuations. Because an increase of the static component results in a narrower envelope probability density function, the range over which the interaural difference fluctuates becomes smaller. Consequently, the dynamically varying part of the interaural difference decreases.

We also showed that for a zero mean of the low-pass noise, the overall probability of a positive interaural difference equals the probability of a negative interaural difference of the same magnitude. If a static component is introduced,

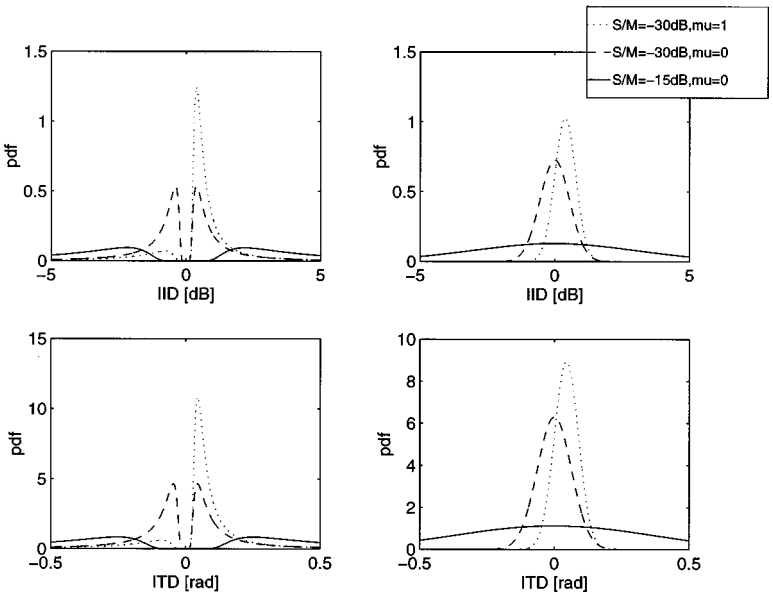

FIG. 3. Probability density functions for the interaural intensity difference for $\alpha=0$ (upper panels) and for the interaural phase difference for $\alpha=\pi/2$ (lower panels). Left panels: multiplied-noise masker, sinusoidal signal. Right panels: sinusoidal masker, multiplied-noise signal. Solid line: S/M$=-15$ dB, $\mu=0$. Dashed line: S/M $=-30$ dB, $\mu=0$. Dotted line: S/M$=-30$ dB, $\mu=1$.

however, the low-pass noise has a nonzero mean. Hence the probability of a positive interaural difference will be larger than the probability of a negative interaural difference. Consequently, an increase of the static component results in an increase in the mean interaural difference.

In summary, an increase of the static component of the multiplied-noise masker results for the MoSπ condition in an increase of the *mean* of the interaural difference and a decrease of the *range of fluctuations*. Thus, by controlling the value of the static component, binaural stimuli containing different combinations of static and time-varying interaural differences can be created in an MoSπ condition.

B. Multiplied noise as a signal

We now consider the situation where the roles of the multiplied noise and the sinusoid are reversed. The masker consists of an in-phase sinusoid, and the signal consists of an interaurally out-of-phase multiplied noise with a carrier having the same frequency as the sinusoidal masker. If the phase lag between the left-ear carrier and masker is zero ($\alpha=0$), this stimulus produces only IIDs. For $\alpha=\pi/2$, only ITDs are present. A phase lag of $\alpha=\pi/4$ results in IIDs and ITDs favoring the same ear, while a phase lag of $\alpha=3\pi/4$ results in IIDs and ITDs pointing in opposite directions. Again, by adding a static component to the low-pass noise, a mixture of static and dynamically varying interaural differences is achieved.

Two important differences exist between the stimulus described here (with a multiplied-noise *signal*) and the stimulus described in Sec. I A (with a multiplied-noise *masker*): (1) in the present condition, the envelope of the masker is flat, and besides interaural differences, the signal also produces fluctuations in the envelope of the waveforms arriving at both ears, and (2) an *increase* in the multiplied-noise signal envelope results in an *increase* in the interaural difference, while the opposite is true for the case with a multiplied-noise masker envelope. This reversed relation between multiplied-noise envelope and interaural difference has a strong effect on the probability density functions of the interaural differences that occur. This aspect will be discussed in the next section.

C. Probability density functions of the interaural cues

For a given phase angle α between sinusoid and masker carrier, a certain static component μ and a fixed signal-to-masker ratio S/M, the probability densities of the resulting IIDs and ITDs can be calculated as shown in Appendix A. In Fig. 3, the probability density functions for the interaural intensity difference are given for three values of μ and S/M for the two conditions that the masker consists of multiplied noise (left panels) and that the signal consists of multiplied noise (right panels). The upper panels show the IID probability density function for $\alpha=0$ (i.e., only IIDs), the lower panels show the ITD probability density function for $\alpha=\pi/2$ (i.e., only ITDs). The solid line represents no static component ($\mu=0$) and a signal-to-masker ratio of -15 dB, the dashed line represents $\mu=0$ and S/M$=-30$ dB, while the dotted line represents S/M$=-30$ dB but with a static component of $\mu=1$. Clearly, for $\mu=0$, the probability density functions are symmetric around zero. Furthermore, a smaller S/M ratio results in narrower distributions. Finally, we see that if the *masker* consists of multiplied noise and $\mu=0$, the probability density function has a *minimum* at zero (the distribution is bimodal), while for a multiplied noise *signal*, the probability density function shows a *maximum* at zero (the distribution is unimodal).

II. METHOD

A. Procedure

A three-interval three-alternative forced-choice procedure with adaptive signal-level adjustment was used to determine masked thresholds. Three masker intervals of 400-ms duration were separated by pauses of 300 ms. The subject's task was to indicate which of the three intervals contained the 300-ms interaurally out-of-phase signal. This

signal was temporally centered in the masker. Feedback was provided to the subject after each trial. In some experiments, the reference intervals contained an Mo masker alone, while in other experiments, an MoSo stimulus (i.e., both masker and signal interaurally in phase) was used. The rationale for these different procedures is explained in the next section.

The signal level was adjusted according to a two-down one-up rule (Levitt, 1971). The initial step size for adjusting the level was 8 dB. After each second reversal of the level track, the step size was halved until it reached 1 dB. The run was then continued for another eight reversals. From the level of these eight reversals, the median was calculated and used as a threshold value. At least four threshold values were obtained and averaged for each parameter setting and subject.

B. Stimuli

All stimuli were generated digitally and converted to analog signals with a two-channel, 16-bit D/A converter at a sampling rate of 32 kHz with no external filtering other than by the headphones. The maskers were presented to the subjects over Beyerdynamic DT990 headphones at a sound pressure level of 65 dB. The multiplied-noise samples were obtained by a random selection of a segment from a 2000-ms low-pass noise buffer with an appropriate dc component and a multiplication with a sinusoidal carrier. The low-pass noise buffer was created in the frequency domain by selecting the frequency range from a 2000-ms white-noise buffer after a Fourier transform. After an inverse Fourier transform, the addition of a dc component and rescaling the signal to the desired rms value, the noise buffer was obtained. All thresholds were determined at 500-Hz center frequency. In order to avoid spectral splatter, the signals and maskers were gated with 50-ms raised-cosine ramps. Thresholds are expressed as the signal-to-masker power ratio in decibels.

Thresholds were obtained by measuring the detectability of an interaurally out-of-phase signal in an in-phase masker (MoSπ) in the following four experiments:

(1) The masker consisted of in-phase multiplied noise, while the signal consisted of an interaurally out-of-phase sinusoid. In this experiment, the reference intervals contained only an Mo masker. Thresholds were obtained as a function of the static component (μ=0, 0.5, 1, 1.5, and 2) for α=0 and $\alpha=\pi/2$ and masker bandwidths of 10 and 80 Hz. The rationale for this experiment was to investigate binaural masked thresholds for combinations of static and dynamic interaural differences, for bimodal distributions of the interaural cues. Two bandwidths were applied; a narrow one in order to produce slowly varying interaural differences and a bandwidth corresponding to the equivalent rectangular bandwidth at 500 Hz (Glasberg and Moore, 1990), producing interaural cues which fluctuate faster. In this way the influence of the rate of fluctuations is investigated.

(2) The masker consisted of an in-phase sinusoid, while the signal consisted of interaurally out-of-phase multiplied noise. Thresholds were obtained for the same parameter settings as in experiment 1. This experiment served to study thresholds for unimodal distributions of the interaural differences. The reference intervals consisted of in-phase sinusoids combined with in-phase multiplied noise (i.e., MoSo). Thus, the task was to discriminate between MoSo and MoSπ, so that the subjects could not use the fluctuations in the envelope produced by the signal as a cue for detection.

(3) The masker consisted of an in-phase sinusoid, while the signal consisted of interaurally out-of-phase multiplied noise. For similar reasons as in experiment 2, the reference intervals consisted of in-phase sinusoids combined with in-phase multiplied noise. Thresholds were obtained as a function of the bandwidth (10, 20, 80, 160, 320, and 640 Hz) of the noise for μ=0 and α=0 and $\alpha=\pi/2$. This experiment served to check for possible effects of off-frequency listening in experiment 2. Because the noise bandwidth is larger than the bandwidth of the masker (the sinusoid), an auditory filter that is tuned to a frequency just above or below the masker frequency receives relatively more noise (signal) intensity than masker intensity. Furthermore, this difference increases with increasing signal bandwidth. It is therefore expected that for signal bandwidths beyond the critical band, off-frequency listening will result in lower thresholds compared with the case of a signal of subcritical bandwidth. If off-frequency listening influences the results in experiment 2, the parameters of the distributions of the interaural differences cannot be compared between experiments 1 and 2, since peripheral filtering would alter these parameters significantly. To investigate at which signal bandwidth this effect starts to play a role, we determined the bandwidth dependence of the thresholds for this stimulus configuration.

(4) Similar to experiment 1, the masker consisted of an in-phase multiplied noise, while the signal consisted of an interaurally out-of-phase sinusoid. The reference intervals contained an Mo masker alone. In this experiment, thresholds were obtained as a function of the fine-structure phase angle between masker and signal for α=0 (only IIDs), $\pi/4$ (IIDs and ITDs which favor the same ear), $\pi/2$ (only ITDs), and $3\pi/4$ (IIDs and ITDs pointing in opposite directions). No static component was present (μ=0). The masker had a bandwidth of 10 or 80 Hz. In addition, an in-phase sinusoid was used as a masker. This experiment served to investigate the effect of the phase angle α, for both dynamically varying and static interaural differences.

Table I shows a summary of the experimental conditions that were used.

III. RESULTS

A. Experiment 1: Multiplied noise as masker

In Fig. 4, the four lower panels show the detection thresholds for four subjects as a function of the static component for experiment 1. The upper panel shows the mean thresholds. The filled symbols denote the IID conditions (α =0), the open symbols denote the ITD conditions ($\alpha=\pi/2$). The upward triangles correspond to a masker bandwidth of

TABLE I. Table showing the experimental variables of experiments 1–4.

Experiment No.	Masker type	Signal type	Noise bandwidth (Hz)	Static component	α	Reference intervals
1	Multiplied noise	Sinusoid	10, 80	0, 0.5, 1, 1.5, 2	0, $\pi/2$	Mo
2	Sinusoid	Multiplied noise	10, 80	0, 0.5, 1, 1.5, 2	0, $\pi/2$	MoSo
3	Sinusoid	Multiplied noise	10, 20, 40, 80, 160, 320, 640	0	0, $\pi/2$	MoSo
4	Multiplied noise	Sinusoid	10, 80	0, infinity	0, $\pi/4$, $\pi/2$, $3\pi/4$	Mo

80 Hz, the downward triangles to 10 Hz. Most of the thresholds are in the range of −30 to −20 dB. Generally, we see that the mean thresholds (upper panel) show only small differences across bandwidth or physical nature of the cue (i.e., IIDs versus ITDs). Within subjects, however, some systematic differences are present. Subjects MV and JB show higher thresholds for the 80-Hz conditions than for the 10-Hz conditions, while for subject MD, the 80-Hz IID thresholds are lower than the 10-Hz IID data. Although within and across subjects thresholds vary by about 10 dB, the mean data do not show effects of that magnitude.

B. Experiment 2: Multiplied noise as signal

In Fig. 5, the detection thresholds for experiment 2 are shown as a function of the static component. The format is the same as in Fig. 4. The 80-Hz ITD data (open upward triangles) are systematically 4 to 5 dB lower than thresholds for the other stimulus configurations (especially for subjects MD and MV). For these subjects, the thresholds show an increase of up to 6 dB with increasing static component for the 80-Hz ITD condition. The other conditions show approximately constant thresholds for the mean data, independent of bandwidth and physical nature of the interaural cue.

Because of the small differences that were found in these two experiments, a multifactor analysis of variance (MANOVA) was performed for the results shown in Figs. 4 and 5 to determine the significance of the different experimental variables used in the experiments. The factors that were taken into account were (1) the multiplied-noise bandwidth, (2) the masker-signal phase angle α, (3) the static component μ, and (4) the masker type (multiplied noise as masker or signal). The p-values for the effects that were significant at a 5% level are shown in Table II.

Thus, significant factors are

(1) the masker-signal phase angle α: a change from $\alpha=0$ to $\pi/2$ results in a mean decrease in thresholds of 1.4 dB;

(2) the static component μ: an increase from $\mu=0$ to 2 results in an increase of the thresholds by 3 dB;

(3) the masker type: on average, conditions with a multiplied-noise masker have 2.2 dB lower thresholds than conditions with a multiplied-noise signal.

Significant interactions are

(1) the multiplied-noise bandwidth combined with α: an increase from 10- to 80-Hz bandwidth results in a decrease

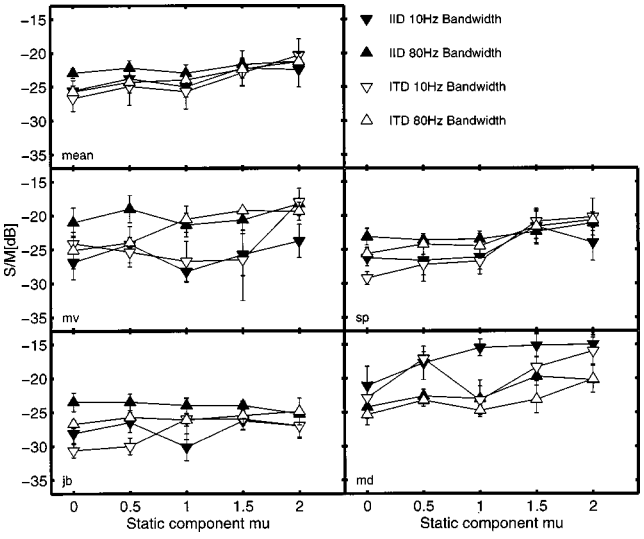

FIG. 4. Detection thresholds for an out-of-phase sinusoidal signal added to an in-phase multiplied-noise masker for $\alpha=0$, 10-Hz bandwidth (filled downward triangles); $\alpha=0$, 80-Hz bandwidth (filled upward triangles); $\alpha=\pi/2$, 10-Hz bandwidth (open downward triangles); and $\alpha=\pi/2$, 80-Hz bandwidth (open upward triangles). The four lower panels show thresholds for individual subjects, the upper panel represents the mean across four subjects. Error bars for the individual plots denote the standard error of the mean based on four trials of the same condition. The error bars in the upper panel denote the standard error of the mean across the mean data from the four subjects.

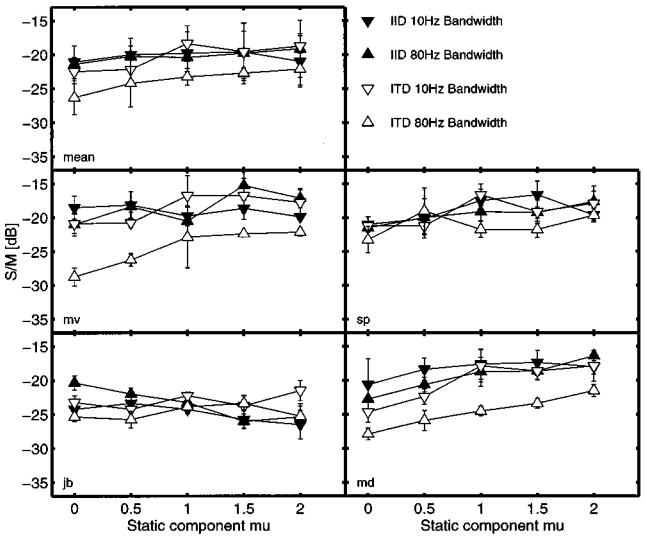

FIG. 5. Detection thresholds for an out-of-phase multiplied-noise signal added to a diotic sinusoidal masker as a function of the dc component μ. Same format as Fig. 4.

TABLE II. Factors and their significance levels according to a multifactor analysis of variance of the data shown in Figs. 4 and 5. Only those factors (upper three) and interactions (lower two) which are significant at a 5% level are given.

Effect	p value
Phase angle α	0.011 20
Static component	0.000 73
Masker type	0.000 01
Noise bandwidth and α	0.024 24
Noise bandwidth and masker type	0.006 42

of the thresholds by 5 dB for the ITD-only conditions, while the IID-only conditions are similar;

(2) the multiplied-noise bandwidth combined with the masker type: the above interaction is only seen for a multiplied-noise signal. For a multiplied-noise masker, the thresholds for $\alpha=0$ and $\alpha=\pi/2$ remain similar with changes in the masker bandwidth.

C. Experiment 3: Bandwidth dependence of a multiplied-noise signal

In this experiment, thresholds were determined as a function of the bandwidth of a multiplied-noise test signal added to a sinusoidal masker. Figure 6 shows the detection thresholds as a function of the bandwidth of the multiplied noise for $\alpha=0$ (IIDs, filled triangles) and $\alpha=\pi/2$ (ITDs, open triangles). Both for the ITD, and IID conditions, the thresholds remain approximately constant for bandwidths up to a bandwidth of 80 to 160 Hz, while for wider bandwidths, the thresholds decrease with a slope of 7 dB/oct of signal bandwidth. The measure of 80 Hz of the auditory filter bandwidth agrees with the monaural equivalent rectangular bandwidth estimates of 79 Hz at 500 Hz center frequency from Glasberg and Moore (1990). Furthermore, we see that, on average, the ITD thresholds are approximately 5 dB lower than the IID

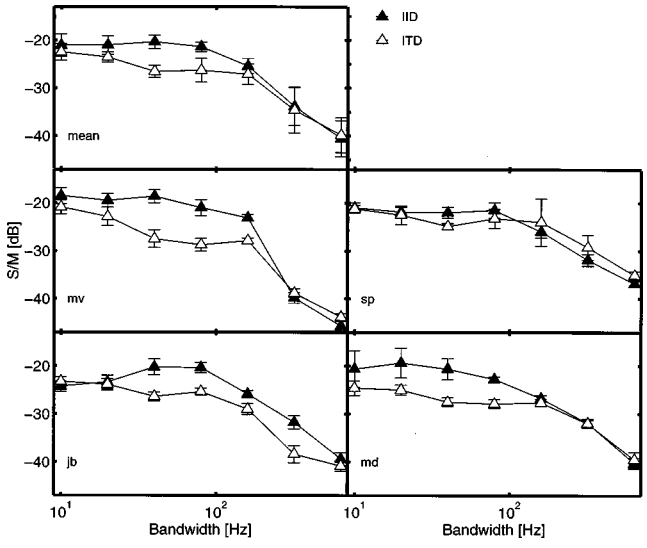

FIG. 6. Detection thresholds for an interaurally out-of-phase multiplied noise signal added to an in-phase sinusoidal masker as a function of the bandwidth of the noise for $\alpha=0$ (filled triangles) and $\alpha=\pi/2$ (open triangles). The upper panel shows the mean thresholds.

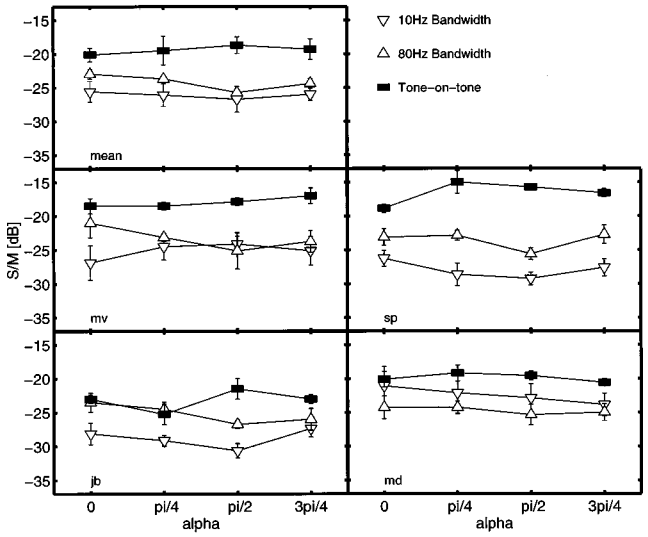

FIG. 7. Detection thresholds for an interaurally out-of-phase sinusoid added to an in-phase sinusoid (squares), a 10-Hz-wide multiplied noise (downward triangles), and an 80-Hz-wide multiplied noise (upward triangles) as a function of the fine-structure phase angle between signal and masker carrier. The lower four panels show thresholds for four subjects, the upper panel shows the mean thresholds.

thresholds for intermediate bandwidths (i.e., 40 and 80 Hz), which is consistent with the data from experiment 2.

D. Experiment 4: Dependence on α

Figure 7 shows thresholds for experiment 4 as a function of the phase angle between masker carrier and signal. The lower four panels show thresholds of four individual subjects, the upper panel shows the mean thresholds. The downward triangles refer to a masker bandwidth of 10 Hz, the upward triangles refer to a masker bandwidth of 80 Hz and the squares to the tone-on-tone condition. The latter has almost always the highest thresholds being 3 to 7 dB higher than thresholds for the noise maskers. Furthermore, a small decrease in thresholds is observed if α is increased from 0 to $\pi/2$ for the 80-Hz-wide condition. For the 10-Hz-wide and the tone-on-tone conditions, the thresholds are independent of α.

IV. DISCUSSION

A. Effect of α

If the overall means of the data presented in Figs. 4 and 5 are considered, the IID thresholds are on average 1.4 dB higher than the ITD thresholds. This value is roughly in line with the observed 3 dB found by van de Par and Kohlrausch (1998b). Furthermore, the data shown in Fig. 7 show a minor influence of the masker-signal phase α, for both static and dynamically varying interaural differences. Many studies have been published which present differences between ITD-only and IID-only conditions varying between -8 and $+6.5$ dB (Jeffress *et al.*, 1956; Hafter *et al.*, 1969; Wightman, 1969; Jeffress and McFadden, 1971; McFadden *et al.*, 1971; Wightman, 1971; Yost, 1972b; Yost *et al.*, 1974; Robinson *et al.*, 1974). Only one study reports differences that deviate

from these data with differences of up to 16 dB (Grantham and Robinson, 1977). We therefore conclude that our results are well within the range of other data, although there does not exist much consistency about the influence of α on detection thresholds.

If the thresholds for $\alpha=\pi/4$ and $\alpha=3\pi/4$ are compared, only small threshold differences of less than 3 dB are found. Grantham and Robinson (1977) reported differences varying between -5 and $+8$ dB across different subjects. Also studies of Robinson *et al.* (1974) and Hafter *et al.* (1969) report differences within that range.

Corresponding to results from other studies (cf. McFadden *et al.*, 1971; Jeffress and McFadden, 1971; Grantham and Robinson, 1977), large differences exist across subjects when the effect of α is concerned. Some subjects seem to be more sensitive to signals producing ITDs, and some to IIDs. Thus, one general model can never account for these interindividual differences. But since we are comparing theories and trying to model the general trend, we focus on the mean data knowing that individual differences are not taken into account.

If binaural detection were based on changes in laterality resulting from a combined time-intensity image, different thresholds would be expected for $\alpha=\pi/4$ and $\alpha=3\pi/4$. For $\alpha=\pi/4$, the interaural differences in time and intensity point in the same direction and the combined image would be lateralized more than for each cue separately, while for $\alpha=3\pi/4$, the ITDs and IIDs would (at least) partially cancel each other. The very similar threshold values suggest that detection is not based on changes in laterality resulting from a combined time-intensity image.

B. Binaural sluggishness

Several studies have provided evidence that the binaural auditory system is sluggish. We can classify these studies into two categories. The first category comprises experiments that determine the ability of human observers to detect interaural differences against a reference signal that contains no interaural differences. For example, if observers have to discriminate a binaural amplitude-modulated noise in which the modulating sinusoid is interaurally in-phase, from the same amplitude-modulated noise in which the modulator is interaurally out-of-phase, a substantial increase in the modulation depth at threshold is observed if the modulation frequency is increased from 0 to 50 Hz (Grantham, 1984). Similar results were found for dynamically varying ITDs (Grantham and Wightman, 1978). However, the time constant of processing dynamically varying ITDs seems to be longer than for IIDs. Estimates for these constants are approximately 200 and 50 ms, respectively (Grantham, 1984). Also many binaural masking conditions like MoSπ fall into this category of detection against a monaural reference signal (Zurek and Durlach, 1987). The second category comprises binaural detection experiments in which the masker has a time-varying correlation (cf. Grantham and Wightman, 1979; Kollmeier and Gilkey, 1990; Culling and Summerheld, 1998). These studies show that modulation rates of interaural correlation as low as 4 Hz result in large increases in detection thresholds.

The experiments performed in our study clearly belong to the first group, because the correlation of the masker is always one. The fact that our results do not show any difference between the 10- and 80-Hz-wide conditions runs counter to an expectation based on binaural sluggishness. If one tries to characterize the rate at which the interaural differences change from leading to lagging in each ear, one could take the expected number of zero-crossings of the low-pass noise used in generating the multiplied noise. Roughly, if the low-pass noise changes its sign, the resulting interaural difference in an MoSπ condition also changes its sign. Thus, the number of zero-crossings represents the number of changes per second in lateralization pointing to the left or right ear. For a 10-Hz-wide noise, the expected number of lateralization changes amounts to 5.8 per second, while for the conditions at 80-Hz bandwidth, the expected number is 46.2 (Rice, 1959). On the basis of the expected number of zero-crossings, assuming that the binaural system is sluggish in its processing of binaural cues, a difference in detection thresholds is expected between conditions at 10- and 80-Hz bandwidth. Furthermore, assuming that the time constant for processing ITDs is longer than for IIDs (Grantham, 1984), the ITD-only thresholds should be higher than than the IID-only thresholds for the 80-Hz-wide condition. The MANOVA analysis shows that the bandwidth of the multiplied noise is not a significant factor, indicating that the thresholds between the 10- and the 80-Hz-wide conditions are similar. Furthermore, the data do not show the expected difference between the IID-only and the ITD-only conditions for a bandwidth of 80 Hz. Thus, effects of sluggishness, although expected, were not found in this study.

C. Off-frequency listening

For bandwidths beyond 80 Hz using a multiplied-noise signal, the thresholds decrease with increasing bandwidth (see Fig. 6). This is probably caused by the fact that the signal bandwidth exceeds the equivalent rectangular bandwidth of the auditory filters. Thus, the signal-to-masker ratio within an auditory filter tuned to a frequency just below or just above the masker frequency will be larger than for an on-frequency filter, resulting in lower detection thresholds if off-frequency filters can be used for detection. These off-frequency effects start to play a role for a signal bandwidth of 160 Hz. This indicates that for the results of experiment 2, where the maximum employed bandwidth was 80 Hz, off-frequency listening is not likely to influence detection thresholds. Hence, the externally presented interaural differences are very similar to the differences after peripheral filtering for all experiments. Therefore, we can validly compare the parameters of the distributions of the interaural differences at threshold across experiments with multiplied noise as masker and as signal.

One noteworthy effect seen in the data which is a significant factor according to our statistical assessment is that the ITD-only thresholds for a multiplied-noise signal decrease by 5 dB when the bandwidth is increased from 10 to 80 Hz, while for a multiplied-noise masker, this decrease does not occur. It is not clear what causes this effect.

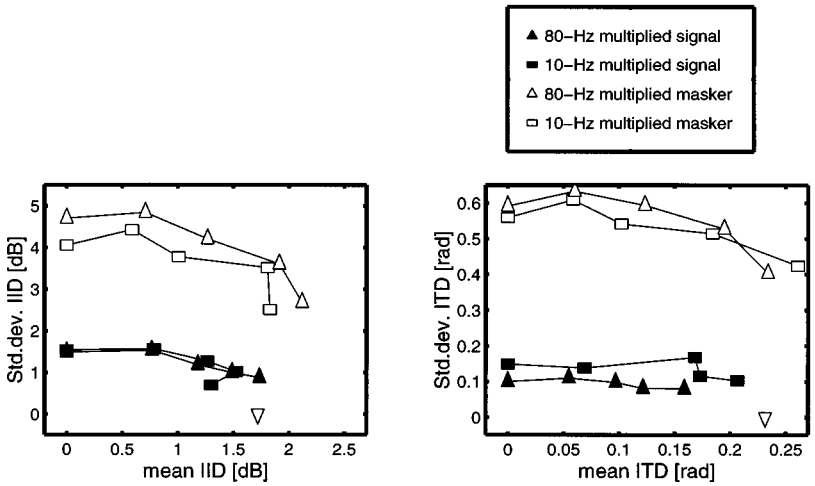

FIG. 8. Mean and standard deviation of the interaural cues at threshold level at 10-Hz bandwidth (squares) and 80-Hz bandwidth (upward triangles). The open symbols represent data for a diotic multiplied-noise masker (experiment 1), the filled symbols represent data for an interaurally out-of-phase multiplied noise signal (experiment 2). The downward triangles represent the data for the tone-on-tone conditions (experiment 4). The left panels shows data for the IID-only conditions, the right panel shows data for the ITD-only conditions.

D. Models based on the evaluation of IIDs and ITDs

In this section we analyze the contribution of static and dynamic cues to binaural detection. For this purpose we consider the mean, the standard deviation, and the rms of the probability density functions for IIDs and ITDs at threshold for the mean data shown in Figs. 4 and 5. The left panel of Fig. 8 shows the standard deviations of the probability density functions for IID-only conditions as a function of the mean IID, while the right panel shows the standard deviations of the ITD functions as a function of the mean ITD for the ITD-only conditions. The open symbols represent thresholds from experiment 1, the filled symbols represent thresholds from experiment 2. The squares represent the 10-Hz-wide noise, the upward triangles the 80-Hz-wide noise, and the downward triangles the tone-on-tone conditions. The data at the left side in each panel represent $\mu=0$, while from left to right, the static component increases. With increasing static component, the mean of the interaural difference at threshold level increases also, while the standard deviation shows a minor decrease.

Clearly, the mean interaural differences at $\mu=2$ for the conditions with multiplied noise (upward triangles and squares at the right side of each panel) are very similar to the tone-on-tone conditions (downward triangles). Furthermore, we see that points for 10-Hz bandwidth lie very close to points for 80-Hz bandwidth. This is expected, because these conditions have very similar detection thresholds. Because the mean and standard deviation of the interaural difference are independent of the bandwidth of the signals, similar thresholds result in similar statistics of the interaural differences.

The standard deviations for experiment 2 (filled symbols) are approximately four times smaller than for experiment 1 (open symbols). To end up with a similar standard deviation for IIDs at threshold for experiment 2 as in experiment 1, the signal-to-masker ratio must amount to -11 dB for $\mu=0$. However, the data show a threshold of -21 dB. Thus, the standard deviations of the interaural differences cannot be used to correctly predict binaural masked thresholds for both experiments.[2]

The only data available in the literature using comparable stimuli are those published by Grantham and Robinson (1977). Similar to our procedure, they used a noise stimulus with a certain dc offset and multiplied this noise with a sinusoidal carrier. The resulting bandpass noise (120 Hz wide) was used as a masker in an MoSπ condition. They did not vary the dc offset, however, but fixed it to a value that corresponds to $\mu=2.05$ in our framework. In addition, they in-

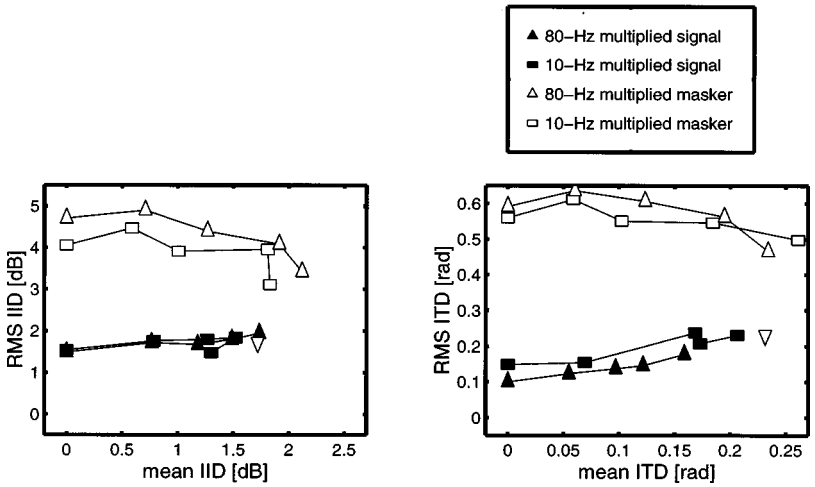

FIG. 9. Mean and rms value of the interaural cues at threshold level in the same format as Fig. 8.

cluded the tone-on-tone conditions in their experiment. Because of the fact that their IID data are relatively high and their ITD data are relatively low compared to our results, we focus on the relative difference between the conditions with noise maskers and tonal maskers. For IIDs only, Grantham and Robinson (1977) found a mean IID at threshold of 3.2 and 3.1 dB for tonal and noise maskers, respectively. For ITD-only conditions, these values amounted to 0.080 and 0.106 rad, respectively. Thus, in correspondence with our data, the mean interaural differences for the tonal masker are slightly lower than for the noise masker for $\alpha=\pi/2$. From our analysis based on PDFs, it is clear that the close correspondence between the mean values of the interaural cues found by Grantham and Robinson relies on their specific choice of μ. Had they chosen a lower value, then they probably would have found larger discrepancies: for $\mu=0$, the mean interaural cue is equal to zero at threshold, while for large values of μ, mean interaural differences of up to 4 dB or 0.1 rad may be found at threshold. Thus, the mean interaural difference cannot account for the complete set of data either.

A straightforward way to combine the sensitivity for static and dynamically varying interaural differences is to consider the rms value of the interaural differences. Figure 9 shows the rms values of the interaural cues of the mean data of experiments 1 and 2 as a function of the mean interaural cues. The format is the same as in Fig. 8. Within one experiment, the rms value remains fairly constant, although there is a tendency for the rms to decrease with increasing mean for the data with a multiplied-noise masker and to increase for the multiplied-noise signal. However, we can reject the rms as a valuable detection variable because for this measure, too, the values of the two experiments differ by a factor 2 to 4.

E. Models based on the interaural correlation

Another detection statistic that is often proposed to account for binaural masked thresholds is the interaural correlation. Domnitz and Colburn (1976) argued that for an out-of-phase sinusoidal signal combined with a diotic Gaussian-noise masker, models based on the PDFs of the interaural differences and models based on the interaural correlation

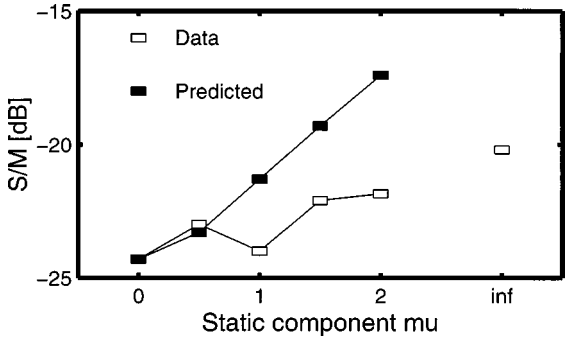

FIG. 10. Predicted values according to a simple interaural correlation model (filled symbols) and experimental data (open symbols) for an MoSπ condition with a multiplied-noise masker and $\alpha=0$ as a function of the static component.

are equivalent. We will now explore whether this statement also holds for our stimuli. For a diotic masker alone, the interaural correlation equals $+1$. The interaural correlation for the masker plus signal is given by (Durlach *et al.*, 1986):

$$\rho=\frac{1-\langle S^2\rangle/\langle M^2\rangle}{1+\langle S^2\rangle/\langle M^2\rangle}, \tag{1}$$

where $\langle S^2\rangle/\langle M^2\rangle$ denotes the signal-to-masker power ratio. This equation holds provided that masker and signal are statistically independent. For our stimuli, this is true provided that $\mu=0$ or $\alpha=\pi/2$. Thus, the correlation is only dependent on the signal-to-masker ratio and does not depend on the physical nature of the interaural difference (i.e., IIDs or ITDs). Furthermore, the correlation is not dependent on the shape of the PDFs of the interaural differences. Therefore, contrary to models based on the PDF of the interaural cues, a model based on the cross correlation will yield *equal* thresholds for experiments 1 and 2, on the condition that $\mu=0$ or $\alpha=\pi/2$ (i.e., masker and signal uncorrelated). This implies that the statement from Domnitz and Colburn (1976) cannot be generalized to our stimuli and that with our stimuli a valuable way to distinguish between cross-correlation models and binaural-cue-based models is available.

Equation (1) is, however, not applicable under conditions where $\alpha\neq\pi/2$ and $\mu>0$. For $\alpha=0$, the interaural correlation can be written as (see Appendix B)

$$\rho=\frac{\langle M^2\rangle-\langle S^2\rangle}{\sqrt{(\langle M^2\rangle+\langle S^2\rangle+\langle 2SM\mu\rangle/\sqrt{1+\mu^2})(\langle M^2\rangle+\langle S^2\rangle-\langle 2SM\mu\rangle/\sqrt{1+\mu^2})}}. \tag{2}$$

From the above equation, we see that the static component has a strong influence on the interaural correlation of an MoSπ stimulus. We therefore computed the predictions according to a simple interaural correlation model for an MoSπ condition with a multiplied-noise masker as a function of the static component μ. The overall mean signal-to-masker ratio at threshold for $\alpha=0$ and $\mu=0$ in our experiments was -24.3 dB, resulting in an interaural correlation of 0.9926. We therefore used a *decorrelation* of 0.0074 as a just noticeable difference (jnd) in the interaural correlation. From this correlation jnd, we computed the signal-to-masker ratios that produce the same amount of decorrelation as a function of the static component μ. The computed thresholds are shown by the filled squares in Fig. 10. The open symbols represent the mean experimental data from experiment 1 for $\alpha=0$. Clearly, the predicted values based on the change in the in-

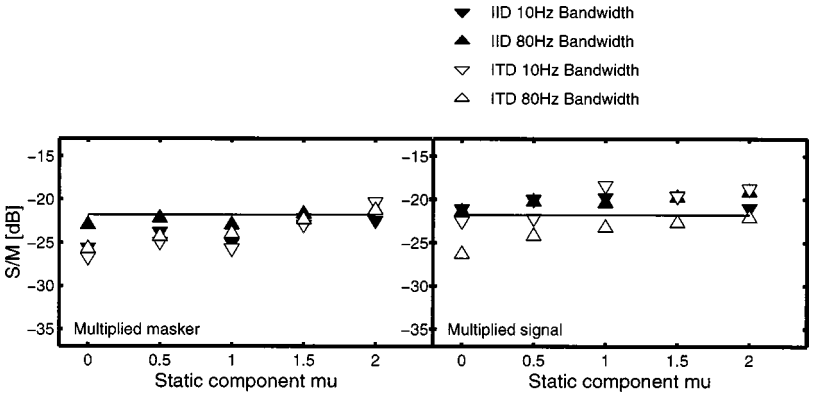

FIG. 11. Predicted values of experiments 1 and 2 according to an EC-like model (solid line) and experimental data (symbols, in the same format as in Fig. 4) for an MoSπ condition with a multiplied-noise masker (left panel) and a multiplied-noise signal (right panel) as a function of the static component.

teraural correlation show a large increase in threshold with increasing static component. This results from the insensitivity of the interaural correlation to static interaural intensity differences. This strong increase was not found in our experimental data, implying that a simple cross-correlation model without extensions for static interaural intensity differences cannot account for the data.

F. A new model

The question arises which other detection statistic can be used to characterize our data. Because the experimental data show approximately similar thresholds across all the experimental conditions, we propose that a model based on the *difference intensity* of the signals arriving at both ears could be a valid detection statistic. We define difference intensity as the intensity in the stimulus obtained when the waveforms to the two ears are equalized and differenced. This approach is related to Durlach's EC-theory (Durlach, 1963), but the two are not equivalent: the EC-theory predicts BMLDs, while this approach describes binaural thresholds directly. Such an approach also differs from a cross-correlation model for stimuli containing static IIDs. For tone-on-tone conditions with $\alpha=0$ (i.e., only static IIDs are present), a cross-correlation model fails to detect the static IID, while the present approach is sensitive to this cue, as will be explained below.

In our approach, an internal interaural delay and an internal interaural intensity difference are determined which tend to equalize the masking signal arriving at the two ears. These parameters can be obtained from the masker-alone intervals. For the signal interval, the *masker* is equalized and subsequently eliminated by a cancelation process. For signals producing interaural intensity differences, the amount of signal remaining after the described equalization process increases with an increasing interaural intensity difference; hence, static IIDs can be detected. For MoSπ stimuli, the masker-elimination process is simply performed by subtracting the waveforms at both ears, computing the power of the remaining signal and using this as a decision variable. If the signals arriving at the left and the right ears are denoted by $L(t)$ and $R(t)$, respectively, the difference intensity D is defined as

$$D=\int_0^T (L(t)-R(t))^2\,dt. \tag{3}$$

Here, T denotes the interval length. In fact, for an MoSπ condition, D is exactly equal to four times the energy of the out-of-phase signal. Hence a model based on this processing scheme would give equal thresholds for all subcritical conditions (i.e., with a noise bandwidth of 80 Hz or less), because the difference intensity D is directly proportional to the signal intensity. For all MoSπ conditions as presented in this study, the only limiting factor in the detection process will be the internal errors, since the masker can be cancelled completely. The magnitude of this internal error can, in principle, be set to any (fixed) value. We can therefore simply derive predictions for the experiments 1, 2, and 4. We adjusted this value to result in a signal-to-masker threshold value of -22 dB. The predictions according to this model are shown in Figs. 11 and 12. Figure 11 shows the thresholds for experiments 1 and 2 (left and right panels, respectively) in the same format as Fig. 4. The solid line represents the model predictions. Figure 12 shows the mean data of Fig. 7 (experiment 4) combined with the model predictions (solid line). We did not simulate the data for experiment 3, because modeling off-frequency effects needs a much more complicated model. We are in the process of describing such a model, but it is far beyond the scope of this paper to include it here.

The predictions match the experimental data quite well. There are, however, some differences between data and model predictions, which can be summarized as follows:

(i) The slight increase of thresholds with increasing static component (see Fig. 11) is not present in the model simulations.

(ii) The fact that the thresholds for a multiplied-noise

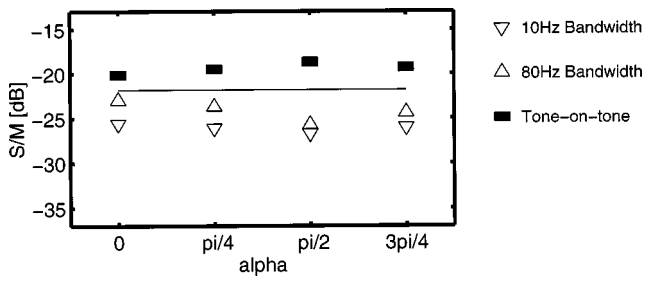

FIG. 12. Predicted values of experiment 4 according to an EC-like model (solid line) and experimental data (symbols, same format as in Fig. 7) for an MoSπ condition as a function of the masker-signal phase difference α.

masker are on average 2.2 dB lower than the data for a multiplied-noise signal is not represented in the model predictions.

(iii) The fact that the tone-on-tone conditions (filled symbols in Fig. 12) give higher thresholds than the multiplied-noise maskers (open symbols in Fig. 12) cannot be understood by this simple model.

(iv) The model's performance is independent of the masker-signal phase difference α, while the experimental data show an overall difference of 1.4 dB if α is changed from 0 to $\pi/2$.

However, some of these effects can be understood by considering the presence of nonlinearities in the peripheral auditory system. For example, we can qualitatively account for the fact that the ITD thresholds are 1.4 dB lower than the IID thresholds by assuming that peripheral compression at the level of the basilar membrane has an effect on binaural masked thresholds. This issue was already discussed by van de Par and Kohlrausch (1998c, 1999). Following their hypothesis, basilar membrane compression results in a decrease of the IIDs in the internal representation and has no effect on ITDs, resulting in higher IID thresholds if the difference intensity is used as a decision variable. Peripheral compression also has a strong effect on binaural masked thresholds with different masker-envelope statistics (van de Par and Kohlrausch, 1998b). Compression reduces interaural intensity differences most strongly for high envelope values. Because a sinusoidal masker has no valleys in the envelope and multiplied noise has many valleys in its envelope, it is expected that IID thresholds for a sinusoidal masker (see Fig. 5) are higher than for a multiplied noise masker (see Fig. 4), in line with the observed overall difference of 2.2 dB. This rationale also holds for the increase in thresholds with an increase of the static component. As described in Sec. I A, the static component has a strong influence on the envelope statistics of the stimuli, resulting in fewer valleys in the envelope if the static component is increased.

However, an EC-like model fails to account for the tone-on-tone data shown in Fig. 12. Here, the tone-on-tone conditions show distinctively higher thresholds than the conditions with a multiplied-noise masker, while an EC-like model without peripheral compression predicts equal thresholds. The inclusion of peripheral compression might account for the fact that the IID tone-on-tone thresholds are higher than the conditions with noise maskers. It is more difficult, however, to see how compression can explain the difference in threshold between tonal and noise maskers with ITDs only.

In summary, the binaural masked thresholds for MoSπ stimuli in the present study seem to be best described by a peripheral preprocessing stage followed by a differencing device that calculates the difference intensity of the signals from the left and right ears and uses this output as a detection variable. Although such an approach cannot account for all data presented here, it provides better predictions than a model based on the probability distributions of the interaural differences or a cross-correlation model *per se*.

ACKNOWLEDGMENTS

We would like to thank A. Houtsma, the associate editor D. W. Grantham, Q. Summerfield, and one anonymous reviewer for helpful comments on the manuscript. The investigations were (in part) supported by the Research Council for Earth and Lifesciences (ALW) with financial aid from the Netherlands Organization for Scientific Research (NWO).

APPENDIX A: DERIVATION OF THE DISTRIBUTIONS OF INTERAURAL DIFFERENCES

1. ITD probability density for a multiplied-noise masker

Figure 1 shows a vector diagram illustrating an interaurally out-of-phase signal $\mathbf{S}_l$ and $\mathbf{S}_r$, a noise masker $\mathbf{M}$, and the resulting signals $\mathbf{L}$ and $\mathbf{R}$ presented at the two ears. The phase angle between masker and signal fine structures is denoted by α, the phase angle between $\mathbf{L}$ and $\mathbf{R}$ by ϕ (with $-\pi<\phi\leqslant\pi$). For the interaural phase ϕ, a convenient expression relating the variables was given by Zurek (1991):

$$\phi=\frac{\pi}{2}-\arctan\frac{A\cos\alpha-S}{A\sin\alpha}-\arctan\frac{A\sin\alpha}{S+A\cos\alpha}. \quad \text{(A1)}$$

Here, A represents the instantaneous value of the low-pass noise. Note that A is defined as the sum of a dc component μ and a Gaussian noise with mean zero and rms=1, which is rescaled to have unit power. This results in a probability density function for A given by:

$$p(A)=\sqrt{\frac{1+\mu^2}{2\pi}}\exp\left(-1/2(-\mu+A\sqrt{1+\mu^2})^2\right). \quad \text{(A2)}$$

The phase probability density $p(\phi)$ can be written as the product of the probability density for $A(\phi)$, multiplied by the absolute derivative of A to ϕ:

$$p(\phi)=p(A(\phi))\left|\frac{dA(\phi)}{d\phi}\right|. \quad \text{(A3)}$$

Equation (A1) gives an expression for $\phi(A)$. However, to derive an expression for $p(\phi)$, an expression for $A(\phi)$ is needed. We have to study two distinct cases. We see from Fig. 1 that for $A\geqslant 0$, $\phi\geqslant 0$ and that for $A<0$, $\phi<0$. $A(\phi)$ can be derived by inverting Eq. (A1), resulting in a second-order polynomial equation which normally has two roots. However, according to the above restriction, the solution for $A(\phi)$ results in

$$A(\phi)=-S\sin\alpha\tan(\phi-\pi/2)+\beta S\sqrt{\sin^2\alpha\tan^2(\phi-\pi/2)+1}, \quad \text{(A4)}$$

where β equals 1 for $\phi\geqslant 0$ and -1 otherwise. The derivative of A to ϕ becomes

$$\frac{dA}{d\phi}=\frac{-S\sin\alpha}{\cos^2(\phi-\pi/2)}+\frac{\beta S\sin^2\alpha\tan(\phi-\pi/2)}{\cos^2(\phi-\pi/2)\sqrt{\sin^2\alpha\tan^2(\phi-\pi/2)+1}}. \quad \text{(A5)}$$

Now, all parameters for Eq. (A3) are known and $p(\phi)$ can be calculated.

2. IID probability density for a multiplied-noise masker

The probability density function for the IID can be derived in a very similar way as was done for the ITD. The interaural intensity difference λ is defined as

$$\lambda = 20 \log \frac{|R|}{|L|} = 10 \log \frac{A^2 + S^2 + 2AS \cos \alpha}{A^2 + S^2 - 2AS \cos \alpha}. \tag{A6}$$

Inverting the above equation results in

$$A(\lambda) = -S \cos \alpha \frac{1 + 10^{\lambda/10}}{1 - 10^{\lambda/10}} + \beta S \sqrt{-1 + \left(\frac{1 + 10^{\lambda/10}}{1 - 10^{\lambda/10}} \right)^2 \cos^2 \alpha}, \tag{A7}$$

for $\lambda \geqslant 0$, $A \geqslant 0$ and $\lambda < 0$, $A < 0$. Therefore, $\beta = 1$ for $\lambda \geqslant 0$ and -1 otherwise. The probability density function for λ is given by

$$p(\lambda) = p(A(\lambda)) \left| \frac{dA(\lambda)}{d\lambda} \right|. \tag{A8}$$

Equations (A2), (A7), and (A8) give all necessary parameters to calculate $p(\lambda)$.

3. ITD and IID probability density for a multiplied-noise signal

When exchanging the role of multiplied noise and sinusoid (i.e., the multiplied noise becomes an interaurally out-of-phase signal), we obtain a new relation between interaural phase ϕ and the instantaneous value of the low-pass noise A:

$$A(\phi) = S \sin \alpha \tan(\phi - \pi/2) + \beta S \sqrt{\sin^2 \alpha \tan^2(\phi - \pi/2) + 1}. \tag{A9}$$

Again, β equals one for $\phi \geqslant 1$ and -1 otherwise. The probability density function is then given by Eq. (A3), where $A(\phi)$ has to be taken from Eq. (A9).

The IID probability density function is given as in Eq. (A8), however, with

$$A(\lambda) = S \frac{1 + 10^{\lambda/10}}{1 - 10^{\lambda/10}} \cos \alpha + \beta S \sqrt{-1 + \left(\frac{1 + 10^{\lambda/10}}{1 - 10^{\lambda/10}} \right)^2 \cos^2 \alpha}, \tag{A10}$$

where $\beta = 1$ for $A \geqslant 0$ and -1 otherwise.

APPENDIX B: INTERAURAL CROSS CORRELATION FOR STIMULI WITH STATIC AND DYNAMICALLY VARYING IIDs

For a multiplied-noise masker combined with a sinusoidal test signal with $\alpha = 0$ in an MoSπ condition, the waveforms arriving at the left and right ears [$L(t)$ and $R(t)$, respectively] are given by

$$L(t) = M \sqrt{2} \frac{N(t) + \mu}{\sqrt{1 + \mu^2}} \sin(2\pi f t) + \sqrt{2} S \sin(2\pi f t), \tag{B1}$$

$$R(t) = M \sqrt{2} \frac{N(t) + \mu}{\sqrt{1 + \mu^2}} \sin(2\pi f t) - \sqrt{2} S \sin(2\pi f t). \tag{B2}$$

Here, M denotes the rms value of the masker, S the rms value of the signal, $N(t)$ denotes the low-pass noise that is used for generating the multiplied noise, μ denotes the static component, and f is the carrier frequency. The definition of the normalized interaural correlation is

$$\rho = \frac{\langle L.R \rangle}{\sqrt{\langle L^2 \rangle \langle R^2 \rangle}}, \tag{B3}$$

where $\langle . \rangle$ denotes the expected value. Combining Eqs. (B1) to (B3) results in

$$\rho = \frac{\langle M^2 \rangle - \langle S^2 \rangle}{\sqrt{(\langle M^2 \rangle + \langle S^2 \rangle + \langle 2SM\mu \rangle / \sqrt{1 + \mu^2})(\langle M^2 \rangle + \langle S^2 \rangle - \langle 2SM\mu \rangle / \sqrt{1 + \mu^2})}}. \tag{B4}$$

[1]The measure μ for expressing the relative amount of static and dynamically varying cues, which will be introduced in Sec. I A, was equal to 2.05 for the experiments performed by Grantham and Robinson.

[2]In addition, other moments of the PDFs of the interaural differences were evaluated at threshold level. These properties also resulted in significantly larger differences between the thresholds of experiments 1 and 2 than the observed difference of 2.2 dB.

Bernstein, L. R., and Trahiotis, C. (**1997**). ''The effects of randomizing values of interaural disparities on binaural detection and on discrimination of interaural correlation,'' J. Acoust. Soc. Am. **102**, 1113–1120.

Breebaart, J., van de Par, S., and Kohlrausch, A. (**1998**). ''Binaural signal detection with phase-shifted and time-delayed noise maskers,'' J. Acoust. Soc. Am. **103**, 2079–2083.

Colburn, H. S. (**1977**). ''Theory of binaural interaction based on auditory-nerve data. II. Detection of tones in noise,'' J. Acoust. Soc. Am. **61**, 525–533.

Culling, J. F., and Summerfield, Q. (**1998**). ''Measurements of the binaural temporal window using a detection task,'' J. Acoust. Soc. Am. **103**, 3540–3553.

Domnitz, R. H., and Colburn, H. S. (**1976**). ''Analysis of binaural detection models for dependence on interaural target parameters,'' J. Acoust. Soc. Am. **59**, 598–601.

Durlach, N. I. (**1963**). ''Equalization and cancellation theory of binaural masking-level differences,'' J. Acoust. Soc. Am. **35**, 1206–1218.

Durlach, N. I., Gabriel, K. J., Colburn, H. S., and Trahiotis, C. (**1986**). ''Interaural correlation discrimination: II. Relation to binaural unmasking,'' J. Acoust. Soc. Am. **79**, 1548–1557.

Gaik, W. (**1993**). ''Combined evaluation of interaural time and intensity differences: psychoacoustic results and computer modeling,'' J. Acoust. Soc. Am. **94**, 98–110.

Glasberg, B. R., and Moore, B. C. J. (**1990**). ''Derivation of auditory filter shapes from notched-noise data,'' Hearing Res. **47**, 103–138.
Grantham, D. W. (**1984**). ''Discrimination of dynamic interaural intensity differences,'' J. Acoust. Soc. Am. **76**, 71–76.
Grantham, D. W., and Robinson, D. E. (**1977**). ''Role of dynamic cues in monaural and binaural signal detection,'' J. Acoust. Soc. Am. **61**, 542–551.
Grantham, D. W., and Wightman, F. L. (**1978**). ''Detectability of varying interaural temporal differences,'' J. Acoust. Soc. Am. **63**, 511–523.
Grantham, D. W., and Wightman, F. L. (**1979**). ''Detectability of a pulsed tone in the presence of a masker with time-varying interaural correlation,'' J. Acoust. Soc. Am. **65**, 1509–1517.
Hafter, E. R. (**1971**). ''Quantitative evaluation of a lateralization model of masking-level differences,'' J. Acoust. Soc. Am. **50**, 1116–1122.
Hafter, E. R., and Carrier, S. C. (**1970**). ''Masking-level differences obtained with pulsed tonal maskers,'' J. Acoust. Soc. Am. **47**, 1041–1047.
Hafter, E. R., Bourbon, W. T., Blocker, A. S., and Tucker, A. (**1969**). ''A direct comparison between lateralization and detection under conditions of antiphasic masking,'' J. Acoust. Soc. Am. **46**, 1452–1457.
Hirsh, I. (**1948**). ''The influence of interaural phase on interaural summation and inhibition,'' J. Acoust. Soc. Am. **20**, 536–544.
Holube, I. (**1993**). ''Experimente und Modellvorstellungen zur Psychoakustik und zum Sprachverstehen bei Normal- und Schwerhörigen,'' Ph.D. thesis, Georg-August-Universität Göttingen, Göttingen.
Holube, I., Kinkel, M., and Kollmeier, B. (**1998**). ''Binaural and monaural auditory filter bandwidths and time constants in probe tone detection experiments,'' J. Acoust. Soc. Am. **104**, 2412–2425.
Jeffress, L. A., and McFadden, D. (**1968**). ''MLD's and the phase angle, alpha,'' J. Acoust. Soc. Am. **43**, 164.
Jeffress, L. A., and McFadden, D. (**1971**). ''Differences of interaural phase and level in detection and lateralization,'' J. Acoust. Soc. Am. **49**, 1169–1179.
Jeffress, L. A., Blodgett, H. C., and Deatherage, B. H. (**1962**). ''Masking and interaural phase. II. 167 cycles,'' J. Acoust. Soc. Am. **34**, 1124–1126.
Jeffress, L. A., Blodgett, H. C., Sandel, T. T., and Wood, C. L. (**1956**). ''Masking of tonal signals,'' J. Acoust. Soc. Am. **28**, 1416–1426.
Kollmeier, B., and Gilkey, R. H. (**1990**). ''Binaural forward and backward masking: evidence for sluggishness in binaural detection,'' J. Acoust. Soc. Am. **87**, 1709–1719.
Levitt, H. (**1971**). ''Transformed up-down methods in psychoacoustics,'' J. Acoust. Soc. Am. **49**, 467–477.
Lindemann, W. (**1986**). ''Extension of a binaural cross-correlation model by contralateral inhibition. I. Simulation of lateralization for stationary signals,'' J. Acoust. Soc. Am. **80**, 1608–1622.
McFadden, D., Jeffress, L. A., and Ermey, H. L. (**1971**). ''Difference in interaural phase and level in detection and lateralization: 250 Hz,'' J. Acoust. Soc. Am. **50**, 1484–1493.
Osman, E. (**1971**). ''A correlation model of binaural masking level differences,'' J. Acoust. Soc. Am. **50**, 1494–1511.
Perrott, D. R., and Musicant, A. D. (**1977**). ''Minimum auditory movement angle: binaural localization of moving sound sources,'' J. Acoust. Soc. Am. **62**, 1463–1466.
Rice, S. O. (**1959**). *Selected Papers on Noise and Stochastic Processes* (Dover, New York), Chap. Mathematical analysis of random noise.
Robinson, D. E., Langford, T. L., and Yost, W. A. (**1974**). ''Masking of tones by tones and of noise by noise,'' Percept. Psychophys. **15**, 159–167.
Sayers, B. M. (**1964**). ''Acoustic image lateralization judgments with binaural tones,'' J. Acoust. Soc. Am. **36**, 923–926.
Stern, R. M., and Shear, G. D. (**1996**). ''Lateralization and detection of low-frequency binaural stimuli: Effects of distribution of internal delay,'' J. Acoust. Soc. Am. **100**, 2278–2288.
van de Par, S., and Kohlrausch, A. (**1995**). ''Analytical expressions for the envelope correlation of certain narrow-band stimuli,'' J. Acoust. Soc. Am. **98**, 3157–3169.
van de Par, S., and Kohlrausch, A. (**1998a**). ''Analytical expressions for the envelope correlation of narrow-band stimuli used in CMR and BMLD research,'' J. Acoust. Soc. Am. **103**, 3605–3620.
van de Par, S., and Kohlrausch, A. (**1998b**). ''Diotic and dichotic detection using multiplied-noise maskers,'' J. Acoust. Soc. Am. **103**, 2100–2110.
van de Par, S., and Kohlrausch, A. (**1998c**). ''Further evidence for the influence of peripheral compression on binaural detection,'' in *Proceedings of the Joint Acoustical Society of America Meeting and the International Congress on Acoustics*, Seattle, June 1998, pp. 853–854.
van de Par, S., and Kohlrausch, A. (**1999**). ''The influence of basilar-membrane compression on binaural detection,'' J. Acoust. Soc. Am. (submitted for publication).
Webster, F. A. (**1951**). ''The influence of interaural phase on masked thresholds. I. The role of interaural time-deviation,'' J. Acoust. Soc. Am. **23**, 452–462.
Wightman, F. (**1969**). ''Binaural masking with sine-wave maskers,'' J. Acoust. Soc. Am. **45**, 71–78.
Wightman, F. (**1971**). ''Detection of binaural tones as a function of masker bandwidth,'' J. Acoust. Soc. Am. **50**, 623–636.
Yost, W. A. (**1972a**). ''Tone-in-tone masking for three binaural listening conditions,'' J. Acoust. Soc. Am. **52**, 1234–1237.
Yost, W. A. (**1972b**). ''Weber's fraction for the intensity of pure tones presented binaurally,'' Percept. Psychophys. **11**, 61–64.
Yost, W. A. (**1981**). ''Lateral position of sinusoids presented with interaural intensive and temporal differences,'' J. Acoust. Soc. Am. **70**, 397–409.
Yost, W. A., Nielsen, D. W., Tanis, D. C., and Bergert, B. (**1974**). ''Tone-on-tone binaural masking with an antiphasic masker,'' Percept. Psychophys. **15**, 233–237.
Zurek, P. M. (**1991**). ''Probability distributions of interaural phase and level differences in binaural detection stimuli,'' J. Acoust. Soc. Am. **90**, 1927–1932.
Zurek, P. M., and Durlach, N. I. (**1987**). ''Masker-bandwidth dependence in homophasic and antiphasic tone detection,'' J. Acoust. Soc. Am. **81**, 459–464.
Zwicker, E., and Henning, G. B. (**1985**). ''The four factors leading to binaural masking-level differences,'' Hearing Res. **19**, 29–47.

A comparison of monotic and dichotic complex-tone pitch perception in listeners with hearing loss

Kathryn Hoberg Arehart
Department of Speech, Language, and Hearing Sciences, University of Colorado at Boulder, Boulder, Colorado 80309-0409

Edward M. Burns
University of Washington, Seattle, Washington

(Received 13 November 1998; revised 7 April 1999; accepted 20 April 1999)

The perception of fundamental pitch for two-harmonic complex tones was examined in musically experienced listeners with cochlear-based high-frequency hearing loss. Performance in a musical interval identification task was measured as a function of the average rank of the lowest harmonic for both monotic and dichotic presentation of the harmonics at 14 dB Sensation Level. Listeners with hearing loss demonstrated excellent musical interval identification at low fundamental frequencies and low harmonic numbers, but abnormally poor identification at higher fundamental frequencies and higher average ranks. The upper frequency limit of performance in the listeners with hearing loss was similar in both monotic and dichotic conditions. These results suggest that something other than frequency resolution per se limits complex-tone pitch perception in listeners with hearing loss. © *1999 Acoustical Society of America.* [S0001-4966(99)02108-6]

PACS numbers: 43.66.Sr, 43.66.Hg [JWH]

INTRODUCTION

Listeners with normal hearing can derive a pitch corresponding to the missing fundamental frequency (F_0) of complex tones containing only two successive upper harmonics, regardless of whether the harmonics are presented to the same ear (monotic presentation) or to separate ears (dichotic presentation) (Houtsma and Goldstein, 1972). Performance in a musical interval identification task was perfect for harmonics presented monotically or dichotically when the harmonic number was below four, but deteriorated for higher harmonics; for example, for an F_0 of 200 Hz, performance dropped to chance at about harmonic number 10. The upper harmonic for which performance reached chance for various fundamental frequencies was consistent with the upper frequency limit found in other studies of the existence region of complex-tone fundamental pitch (e.g., Ritsma, 1962, 1963, 1967). This upper frequency limit also corresponds approximately to frequencies where individual harmonics of a complex tone are not resolvable (Plomp, 1964) because of interaction at the peripheral (basilar membrane) level. In this sense, the Houtsma and Goldstein results are compatible with the vast majority of results in the literature, which show that it is the lower, resolvable, harmonics which are most important for deriving the fundamental pitch of a complex tone (e.g., de Boer, 1976). However, the fact that listeners' performance was virtually identical for dichotic and monotic presentation of harmonics suggests that peripheral frequency resolution per se is not entirely responsible for limiting complex-tone fundamental pitch perception to lower harmonics.

Given the existence region data, most modern theories of complex-tone pitch perception require resolution of the lower harmonics. In so-called pattern-matching models (e.g., Wightman, 1973; Terhardt, 1972; Goldstein, 1973), this resolution is an absolute prerequisite as the pitch is derived exclusively from the frequencies (or pitches) of the resolved harmonics. In so-called spectro-temporal models (e.g., Moore, 1997; Meddis and Hewitt, 1992; Srulovicz and Goldstein, 1983), the frequency resolution serves to render less ambiguous the periodicity information from which the pitch is derived. The spectro-temporal models perform a cross-channel analysis on the periodicity information from individual auditory filters, and thus a limited degree of pitch information is available from unresolved harmonics.

The fact that listeners with hearing loss usually show larger-than-normal pure-tone frequency difference limens (reviewed in Moore, 1995) provides indirect evidence for degradation of the pitch of pure tones, while the exaggerated pure-tone pitch anomalies and highly variable musical interval adjustments in hearing-impaired listeners (e.g., Turner *et al.*, 1983; Burns and Turner, 1986) provide more direct evidence. For pattern-matching models of complex-tone pitch, a degradation of pure-tone pitch would, in turn, result in a degradation of complex-tone pitch. For spectro-temporal models, a degradation of pure- and complex-tone pitch would also be expected to be strongly correlated, since most of these models assume, either specifically or tacitly, that pure- and complex-tone pitch are coded by the same (temporal) mechanism. However, for both types of models, degradation due to impaired frequency resolution would be confounded with degradation due to degraded pitch information in normal listening situations.

Degraded complex-tone frequency discrimination in listeners with hearing loss has been documented by a number of authors (e.g., Moore, 1995; Arehart, 1994; Moore and Peters, 1992). As was the case for pure-tone frequency difference limens, these studies of complex-tone frequency discrimination provide only indirect evidence that complex-tone pitch perception is degraded. In addition, since these experi-

ments used either monaural or diotic signal presentation, degradation of pitch processing and degradation of frequency resolution were confounded.

The present study examines directly the extent to which complex-tone pitch perception is degraded in listeners with hearing loss and the role that decreased frequency selectivity plays in the degradation of complex-tone pitch perception. This study applies the monotic/dichotic musical interval identification paradigm of Houtsma and Goldstein (1972) to musically trained listeners with high-frequency hearing loss. If pitch perception is degraded in these listeners, they would be expected to perform poorly in the musical interval identification task. If this degraded pitch perception is in some measure due to degraded frequency resolution, the performance for conditions in which harmonics are in a region of hearing loss would be expected to be worse for monotic presentation of harmonics than for dichotic presentation.

I. METHOD

A. Listeners

The ability to identify musical intervals based on (a missing) fundamental frequency was measured in three listeners with high-frequency cochlear-based hearing loss (listeners L1, L2, and L3). The listeners demonstrated no air–bone gap, normal tympanometry, and absence of evoked otoacoustic emissions in regions of threshold loss. Using an adaptive, three-alternative, forced-choice procedure, detection thresholds in quiet were obtained for each listener for frequencies ranging from 100 Hz to 5000 Hz. These thresholds for the listeners with hearing loss are shown together with reference thresholds for normal-hearing listeners in Fig. 1. The listeners had extensive musical training (two were college music professors) and all could identify musical intervals conveyed by low-frequency pure and complex tones with 100% accuracy at the sensation levels used in this study. Listeners were tested individually in a double-walled booth in daily test sessions limited to 1 h. Listeners were paid $7/h for their participation.

B. Stimuli

Musical intervals were conveyed by two sequential complex tones. For a given block of trials, the missing F_0 of the first complex tone was either 100 Hz, 200 Hz, 300 Hz, 400 Hz, or 500 Hz. The missing F_0 of the second complex tone was such that the frequency ratio between the F_0's of the second and first tones defined one of the seven ascending musical intervals ranging from a minor second (frequency ratio of 1.059) through a fifth (frequency ratio of 1.498).[1]

Each of the complex tones contained two successive upper harmonics. The individual components of the two-harmonic complex tones were digitally generated with two 16-bit digital-to-analog (DA) converters at a sampling rate of 50 kHz. The tones were characterized by a 500-ms duration and 20-ms rise–fall times shaped by a raised cosine function. The delivery of the stimuli was controlled by a microprocessor that interfaced with signal conditioning equipment and a subject response box.

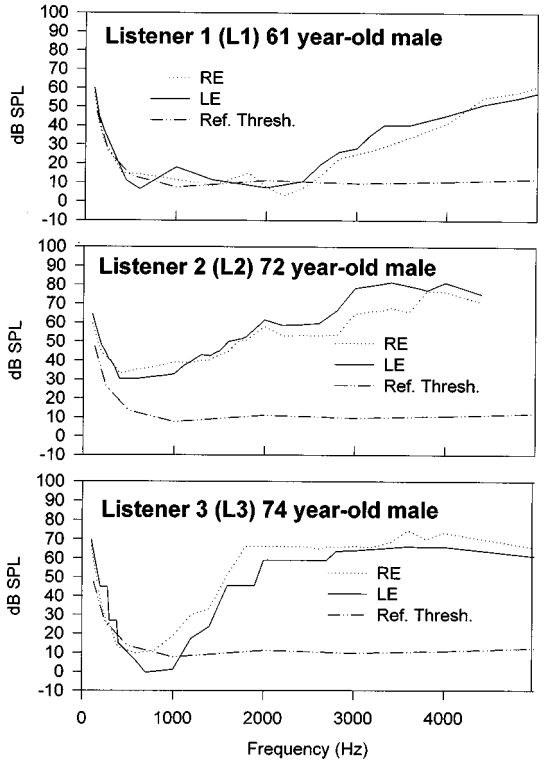

FIG. 1. Thresholds (in dB SPL) for listeners with hearing loss (L1, L2, and L3). Also shown are reference thresholds for normal hearing listeners (ANSI, 1989).

The two successive harmonics were presented either monotically or dichotically at 14 dB Sensation Level. This level was chosen because the goal of the study was to measure synthetic pitch and because synthetic pitch is most easily measured at low sensation levels (Houtmsa, 1979). The audibility of the pure-tone components was verified for each listener. Finally, to determine whether performance on the task changed at a higher sensation level, one listener (L3) was also tested at 24 dB SL.

In order to prevent subjects from basing their interval identifications on the pitch of individual harmonics rather than on the pitch corresponding to F_0, the rank of the lowest harmonic (N) was randomized for each tone over a range of three successive integers $(N-1,N,N+1)$. The harmonic rank was never the same for the two tones comprising an interval in a given trial. To eliminate the possible confounding effects of combination tones, a low-pass masking noise (spectrum level 10 dB/Hz; low-pass cutoff frequency 1/2 octave below the lowest component in the stimulus) was presented to a listener's test ear in the monotic condition. The stimuli were played out in the following way: the two harmonics of each complex tone were routed separately through low-pass filters (cutoff frequency=10 000 Hz) and programmable attenuators, combined in a mixer (for the monotic condition only) and then delivered to the listener's ears through TDH-49-P headphones.

C. Procedure

Percent correct performance on the musical interval identification task was measured as a function of the average rank (N) of the lowest harmonic for both monotic and di-

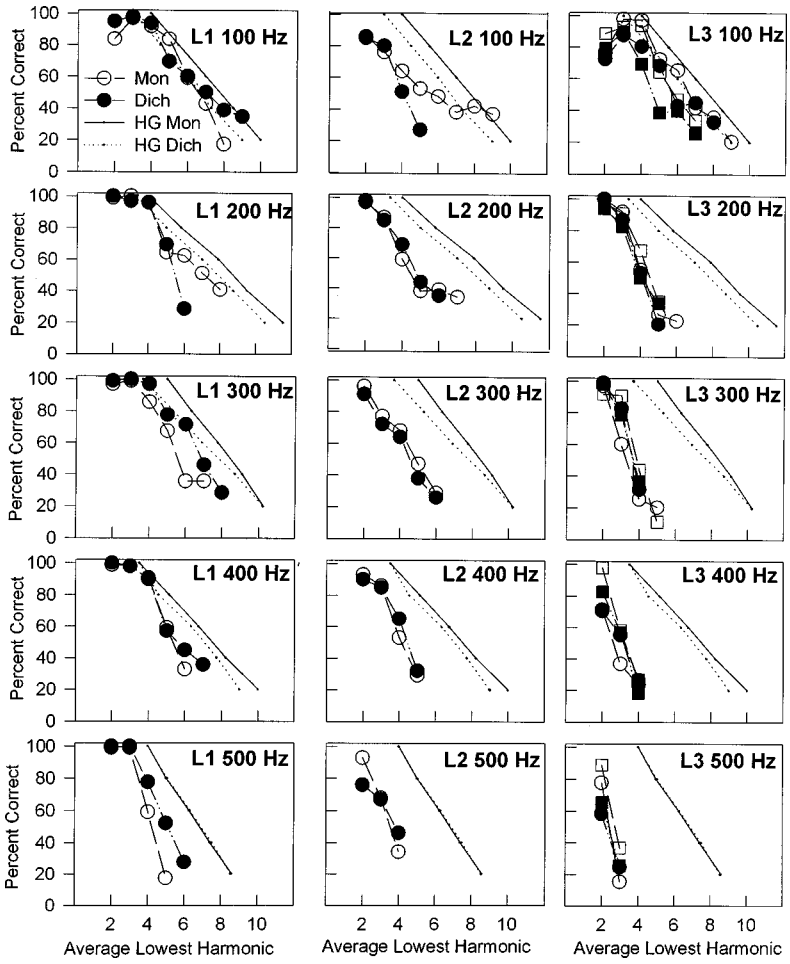

FIG. 2. Percent correct musical interval identification as a function of average lowest harmonic for monotic (unfilled circles) and dichotic presentation (filled circles) of harmonics for F_0 ranging from 100 Hz to 500 Hz for listeners L1, L2, and L3. Data shown are for 14 dB SL. Data for listener L3 at 24 dB SL are shown for monotic presentation (unfilled squares) and for dichotic presentation (filled squares) of harmonics. Also shown are the monotic (solid line) and dichotic (dashed line) results, averaged from the three normal-hearing musicians from Houtsma and Goldstein (1972).

chotic conditions. On each trial, listeners were presented two complex tones, separated by 500 ms, and were asked to identify which of seven musical intervals the pair of tones comprised. Listeners were provided feedback after each trial. Each run consisted of 49 trials (7 repetitions of each of the 7 musical intervals, played in random order). In each run of 49 trials, N and F_0 remained constant. F_0's were tested from low to high; monotic presentation was tested first, followed by dichotic presentation. For each F_0, the lowest value of N was tested first; sequentially higher values of N were then tested so as to obtain a range of N in which performance went from (near) perfect to (near) chance (14.3%). At each F_0/N combination, two blocks of trials were obtained, so that each data point for each listener is based on 98 trials.

II. RESULTS AND DISCUSSION

Figure 2 shows results for the three listeners with hearing loss in the monotic (unfilled circles) and dichotic (filled circles) conditions for missing F_0's ranging from 100 Hz to 500 Hz. Also shown are average results from the three normal-hearing musicians (solid and dashed lines) in Houtsma and Goldstein (1972). The results from the three listeners with cochlear-based hearing loss are similar to the results of the listeners from Houtsma and Goldstein (1972) in two ways. First, performance is very similar in the monotic and dichotic conditions. Second, the listeners with hearing loss show excellent musical interval identification at low harmonic numbers, but fall to chance performance at higher harmonic numbers. However, the decrease in performance with increasing N occurs at much lower harmonic numbers in the listeners with hearing loss than in listeners with normal hearing. The sharp falloff in the data of the listeners with hearing loss is most pronounced at higher F_0's. This indicates that the existence region for the fundamental pitch of two-harmonic complex tones in listeners with high-frequency hearing loss is confined to a lower range of frequencies than in normal-hearing listeners.

Figure 2 also shows the results for listener L3 for stimuli presented monotically (unfilled squares) and dichotically (filled squares) at 24 dB SL. Increasing the sensation level of the stimuli by 10 dB did not affect his performance on the musical interval identification task.

Figure 3 shows the upper frequency limit of performance for monotic and dichotic conditions for the same listeners. The upper frequency limit of performance is defined here as the average frequency of the second (higher) tone of the musical intervals at the average harmonic number for which performance falls to 40% correct. The average frequency ratio of the second to first tone was taken as the geometric mean of the range of frequency ratios: 350 cents, a ratio of 1.224/1. Thus by way of example, the upper frequency limit of performance for listener L2 at 200 Hz was calculated as follows: performance reached 40% at $N=5$, so that the upper frequency limit of performance was 200×5

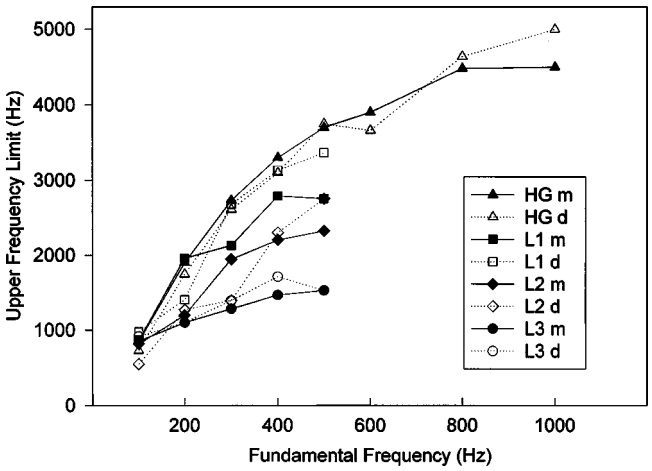

FIG. 3. Upper frequency limit of performance (where performance drops off to 40%) as a function of F_0 for monotic and dichotic conditions for listeners shown in Fig. 2.

$\times 1.224 = 1224$ Hz. Houtsma and Goldstein (1972) included eight musical intervals, four below the F_0 and four above the F_0, such that unison (the F_0) was the average higher interval. As such, the upper frequency limit of performance was simply the harmonic number corresponding to 40% performance multiplied by F_0.

As shown in Fig. 3, the upper frequency limit of performance is similar in monotic and dichotic conditions for all listeners. The upper frequency limit of performance in the normal-hearing listeners from Houtsma and Goldstein (1972) approaches 5000 Hz. The upper frequency limit of performance in the three listeners with hearing loss is lower and is related to the degree of high-frequency hearing loss. Listener L1 shows upper frequency limit between 2800 and 3300 Hz, which is consistent with his thresholds worsening at 3000 Hz and above. Listener L3 shows upper frequency limit at about 1500 Hz, which is consistent with his thresholds worsening between 1000 and 2000 Hz. The relationship between degree of loss and decreased ability to perceive a complex-tone pitch cannot be attributed to reduced audibility in the region of hearing loss, since all of the harmonics were presented at equal sensation level.

To further investigate the ability of listeners to process musical pitch information in regions of normal hearing and in regions of hearing loss, we tested the ability of two of the three listeners[2] to perform pure-tone octave judgments to reference frequencies of 125 Hz, 250 Hz, 500 Hz, 1000 Hz, and 2000 Hz. Both reference and comparison signals were 500-ms pure tones presented monotically at 14 dB SL. Shown in Table I, the results for L1 and L3 are based on five judgments by each listener at each reference frequency and are expressed in terms of cents above the reference frequency (1200 cents would correspond to a perfect octave match).

TABLE I. Means (in cents above reference frequency) and standard deviations (also expressed in cents) of octave matches by listeners L1 and L3.

Reference frequency	Listener L1	Listener L3
125 Hz	1293.3 (17.5)	1207.2 (18.5)
250 Hz	1229.8 (18.3)	1272.2 (45.8)
500 Hz	1212.1 (12.0)	1266.8 (2.0)
1000 Hz	1200.8 (14.8)	1294.3 (134.0)
2000 Hz	1349.1 (63.8)	1035.2 (150.9)

Normal-hearing musicians can make consistent octave matches for (upper) frequencies up to at least 5000 Hz, with standard deviations on the order of 5 to 20 cents (Ward, 1954). There is also a significant tendency to stretch the octave [i.e., to match to a value greater than 1200 cents, by up to a semitone (100 cents) at very low and very high frequencies]. In contrast to normal-hearing musicians, octave judgments by listeners L1 and L3 showed increased variability in the regions of hearing loss: above 2000 Hz for listener L1 and above 1000 Hz for listener L3 (although the variability of L3 was also high for matches relative to 250 Hz). These results further support the idea that something other than audibility decreases a listener's ability to process musical pitch information in regions of hearing loss.

III. GENERAL DISCUSSION

If performance by listeners with hearing loss is at all limited by peripheral frequency resolution, then a difference in performance for monotic and dichotic presentation of harmonics in the musical interval identification task would be expected. The similarity in dichotic and monotic performance indicates that peripheral frequency resolution per se is not limiting performance by listeners with hearing loss. This is consistent with the overall low correlation between complex-tone FDLs and psychophysical measures of frequency resolution in impaired listeners in other studies (Moore, 1995).

The fact that the upper frequency limit for dichotic complex-tone pitch in listeners with normal hearing corresponds roughly to frequencies where temporal synchrony in the auditory nerve is highly degraded (e.g., Palmer and Russell, 1986; Johnson, 1980) suggests that the upper frequency limit may be a consequence of a lack of temporal information. This, in turn, suggests that the poor performance of listeners with hearing loss when the harmonics are in a region of loss may be due to abnormally degraded temporal information from this region. Although the literature on neural synchrony in impaired ears is sparse, there is some evidence of reduced synchrony in neurons innervating regions of impairment (Woolf *et al.*, 1981). Some psychophysical studies also support the idea that reduced neural synchrony affects performance by listeners with hearing loss (e.g., Lacher-Fougere and Demany, 1998; Zurek and Formby, 1981; Moore, 1995).

The similarity between dichotic and monotic performance does not rule out the possibility that a degradation in tonotopic encoding underlies the degeneration of complex-tone pitch in regions of impairment. However, when combined with the low correlation between measures of frequency resolution and measures of both pure-tone and complex tone frequency discrimination in listeners with hearing loss (Moore, 1995), our results are more consistent with a degradation of temporal information as the underlying cause of impaired complex-tone pitch perception.

IV. CONCLUSION

The existence region for fundamental pitch engendered by monotic and dichotic two-harmonic complex tones in listeners with hearing loss is confined to a lower range of frequencies than in normal-hearing listeners and is related to the degree of high-frequency hearing loss. Neither reduced audibility nor reduced frequency resolution can explain this result. The result cannot unequivocally distinguish between degraded temporal information and degraded tonotopic information as the underlying cause of the degraded complex-tone pitch percept. However, when combined with the results of other studies the results reported here are more consistent with degraded temporal information as the cause of the degraded complex-tone pitch percept.

ACKNOWLEDGMENTS

Work supported by the Deafness Research Foundation and the Virginia Merrill Bloedel Research Center at the University of Washington. The authors would like to acknowledge the many hours of dedicated listening provided by the three musicians who participated in this study and would like to dedicate this paper to the memory of their colleague and fellow listener, Walter Collins, who passed away part way through this study.

[1]Although the intervals used in this study differ somewhat from the musical intervals used by Houtsma and Goldstein (1972), the results obtained in the two studies can be compared directly. The majority of intervals included in both studies were the same (minor second, major second, minor third, and major third). More importantly, as pointed out by Houtsma and Goldstein (1971), the set of musical intervals is not, in and of itself, a significant issue in the study of the pitch of complex tones containing two harmonics. Rather, the intervals provide a means by which musically trained listeners can describe the musical pitches that they hear.

[2]Listener L2 was unable to return for the octave matching experiment.

ANSI (**1989**). ANSI S3.6-1989, ''Specifications for Audiometers'' (American National Standards Institute, New York).

Arehart, K. H. (**1994**). ''Effects of harmonic content on complex tone fundamental frequency discrimination in hearing-impaired listeners,'' J. Acoust. Soc. Am. **95**, 3574–3583.

Burns, E. M., and Turner, C. (**1986**). ''Pure-tone pitch anomalies. II. Pitch-intensity effects and diplacusis in impaired ears,'' J. Acoust. Soc. Am. **79**, 1530–1540.

deBoer, E. G. (**1976**). ''On the 'residue' and auditory pitch perception,'' in *Handbook of Sensory Physiology*, edited by W. D. Kleidel and W. D. Neff (Springer, New York), Vol. 3.

Goldstein, J. L. (**1973**). ''An optimum processor theory for the central formation of the pitch of complex tones,'' J. Acoust. Soc. Am. **54**, 1496–1516.

Houtsma, A. J. M. (**1979**). ''Musical pitch of two-tone complexes and predictions by modern pitch theories,'' J. Acoust. Soc. Am. **66**, 87–99.

Houtsma, A. J. M., and Goldstein, J. L. (**1971**). ''Perception of musical intervals: Evidence for the central origin of the pitch of complex tones,'' MIT-RLE Tech. Rep. 484.

Houtsma, A. J. M., and Goldstein, J. L. (**1972**). ''The central origin of the pitch of complex tones: Evidence from musical interval recognition,'' J. Acoust. Soc. Am. **51**, 520–529.

Johnson, D. H. (**1980**). ''The relationship between spike rate and synchrony in responses of auditory-nerve fibers to single tones,'' J. Acoust. Soc. Am. **68**, 1115–1122.

Lacher-Fougere, S., and Demany, L. (**1998**). ''Modulation detection by normal and hearing-impaired listeners,'' Audiology **37**, 109–121.

Meddis, R., and Hewitt, M. J. (**1992**). ''Modeling the identification of concurrent vowels with different fundamental frequencies,'' J. Acoust. Soc. Am. **91**, 233–245.

Moore, B. C. J. (**1995**). *Perceptual Consequences of Cochlear Damage* (Oxford Medical Publications, New York).

Moore, B. C. J. (**1997**). *An Introduction to the Psychology of Hearing*, 4th ed. (Academic, London).

Moore, B. C. J., and Peters, R. W. (**1992**). ''Pitch discrimination and phase sensitivity in young and elderly subjects and its relationship to frequency selectivity,'' J. Acoust. Soc. Am. **91**, 2881–2893.

Palmer, A. R., and Russell, I. J. (**1986**). ''Phase-locking in the cochlear nerve of the guinea-pig and its relation to the receptor potential of inner hair cells,'' Hearing Res. **24**, 1–15.

Plomp, R. (**1964**). ''The ear as a frequency analyzer,'' J. Acoust. Soc. Am. **36**, 1628–1636.

Ritsma, R. J. (**1962**). ''Existence region of the tonal residue I.,'' J. Acoust. Soc. Am. **34**, 1224–1229.

Ritsma, R. J. (**1963**). ''Existence region of the tonal residue II.,'' J. Acoust. Soc. Am. **35**, 1241–1245.

Ritsma, R. J. (**1967**). ''Frequencies dominant in the perception of the pitch of complex sounds,'' J. Acoust. Soc. Am. **42**, 191–198.

Srulovicz, R., and Goldstein, J. L. (**1983**). ''A central spectrum model: A synthesis of auditory-nerve timing and place cues in monaural communication of frequency separation,'' J. Acoust. Soc. Am. **73**, 1266–1276.

Terhardt, E. (**1972**). ''Zur Tonhohenwahrnehmung von Klangen, II. Ein Funktionschema,'' Acustica **26**, 187–199.

Turner, C. W., Burns, E. M., and Nelson, D. A. (**1983**). ''Pure tone pitch perception and low-frequency hearing loss,'' J. Acoust. Soc. Am. **73**, 966–975.

Ward, W. D. (**1954**). ''Subjective musical pitch,'' J. Acoust. Soc. Am. **26**, 369–380.

Wightman, F. L. (**1973**). ''The pattern transformation model of pitch,'' J. Acoust. Soc. Am. **54**, 407–416.

Woolf, N. K., Ryan, R. F., and Bone, R. C. (**1981**). ''Neural phase-locking properties in the absence of outer hair cells,'' Hearing Res. **4**, 335–346.

Zurek, P. M., and Formby, C. (**1981**). ''Frequency-discrimination ability of hearing-impaired listeners,'' J. Speech Hear. Res. **46**, 108–112.

The perceptual effects of current pulse duration in electrical stimulation of the auditory nerve

Colette M. McKay and Hugh J. McDermott
The University of Melbourne, Department of Otolaryngology, Parkville, 3052, Australia

(Received 17 June 1998; revised 28 January 1999; accepted 6 May 1999)

In cochlear implants employing pulsatile stimulation, loudness is controlled by current amplitude and/or pulse duration. Five experiments were conducted with cochlear implantees to investigate the hypothesis that perceptual effects other than loudness result from changes in pulse duration for durations from 50 to 266 μs. In experiment 1, five subjects' ability to discriminate equally loud pulse trains employing differing pulse durations was measured at four electrode positions. In 11 of the 20 cases, subjects could significantly discriminate these stimuli. In experiments 2 and 3, discrimination was measured of dual-electrode stimuli which differed in overall temporal pattern but had an equal temporal pattern on each of the individual electrodes (separated by 0 to 9 mm). Discrimination was compared for stimuli employing short or long pulse durations and, in experiment 3, employing different pulse durations on each electrode. When the pulse duration was longer, six out of seven subjects could either combine temporal information across electrode positions at wider electrode separations (experiment 2) or had better discrimination at the same electrode separation (experiment 3). This result was consistent with the hypothesis that longer pulse durations result in a greater spread of excitation than equally loud stimuli using shorter pulse durations. In experiment 4, pulse rate discrimination was compared for stimuli with differing pulse durations, and in four out of five subjects, there was no effect of pulse duration. Finally, the dB change in current per doubling of pulse duration for threshold and equally loud stimuli was calculated for nine subjects (52 electrodes). Values ranged from -5.9 to -2.0 dB/doubling, and were significantly correlated with the absolute intensity of the stimulus. This result was hypothesized to be due to a relationship between the neural charging characteristics and the distance of the excited neural elements from the electrode. [S0001-4966(99)04708-6]

PACS numbers: 43.66.Ts, 43.66.Fe, 43.64.Me [JWH]

INTRODUCTION

For electrical stimulation of the acoustic nerve, the main parameter which controls the resultant loudness percept is the stimulus magnitude. In biphasic pulsatile stimulation, this is controlled by the current amplitude or duration of the pulses, with loudness being a monotonic function of both these parameters. In current speech processors for cochlear implants, either or both of these parameters are used to map the acoustic intensities to stimulus magnitude. Equivalent changes in these two electrical parameters (in terms of charge/phase) do not have equivalent effects on the activation of individual nerve fibers. If there were perfect integration of charge by the neural membrane over the duration of the pulse, then one would expect the threshold-current vs pulse duration curve of that neuron to have a slope of -6 dB/doubling of duration. However, measurements of single-fiber auditory nerve thresholds in monkeys (Parkins and Colombo, 1987) showed that doubling the pulse duration from 1 to 2 ms reduced the threshold current by an average of only 2.5 dB. That is, the longer pulse duration was less efficient at charging the neural membrane.

Psychophysical thresholds in monkeys (Pfingst *et al.*, 1991) are lower than the single-nerve electrophysiological thresholds, and psychophysical threshold-current vs pulse duration functions have steeper slopes. Pfingst *et al.* found that the average maximum slope ranged from -6.2 dB per doubling of pulse duration between 1 and 2 ms, to -2.6 dB/doubling above 5 to 10 ms, and -4.1 dB/doubling for shorter pulse durations (0.05 to 0.5 ms). The discrepancy between electrophysiological and psychophysical measures most likely arises from the psychophysical measures being the result of central processing of the auditory nerve activity. For example, the central processing system may be able to detect very low probability neural spikes by summing over multiple neurons or integrating over a short time window. In addition, if neural synchrony plays a role in psychophysical thresholds, the effects of pulse duration on thresholds may be contributed to by the increasing variance of spike initiation times with longer pulse duration, and variations of initiation times across fibers with different absolute thresholds (van den Honert and Stypulkowski, 1987; Parkins, 1989). Moon *et al.* (1993) made similar threshold-current vs pulse duration measurements in human subjects and found slopes significantly less than -6 dB/doubling and not constant across the pulse durations used.

Shannon (1985) measured loudness vs current functions in three implantees and showed that longer pulse durations (more than 1 ms) produced larger dynamic ranges due to a shallower growth of loudness at levels just above threshold. In one subject, loudness vs phase duration curves for stimuli with equal charge/phase converged for pulse durations from 100 to 500 μs, indicating a slower loudness growth with

stimulus intensity (charge/phase) for the longer pulse durations.

Zeng *et al.* (1998) also found wider dynamic range (or slower loudness growth) for longer pulse durations (over the range 10 to 4000 μs) in four implantees. Equal-loudness current vs pulse duration curves at threshold had an average slope of -4.2 dB/doubling [consistent with the data from monkeys of Pfingst *et al.* (1991)], whereas at maximum loudness, the equal-loudness curves had an average slope of -2.4 dB/doubling. It is also interesting to note that Zeng *et al.* used pulse durations up to 4000 μs, and that, in contrast to the data from monkeys (Pfingst *et al.*, 1991) cited above, the slope of the strength/duration curves was essentially constant over that range (at least for the data shown for one subject, and group data at 100 and 1000 Hz). It is possible that a species difference could explain the different results in these two studies.

Pfingst *et al.* (1996) have compared the effect of pulse separation (the time between the end of the first waveform and the onset of the next waveform) on thresholds of detection in human implantees, for short (500 μs) and long (2 ms) pulse durations. Pulse separation was varied in stimuli of fixed 500-ms duration (with rate and total number of stimulus pulses covarying), and in stimuli with a fixed number of pulses (with rate and stimulus duration covarying). They showed that the threshold vs rate function was monotonically decreasing for the short pulse duration, but was bowl-shaped for the long pulse duration. This result was consistent with previous data obtained with monkeys or humans (Shannon, 1985, 1989; Pfingst and Morris, 1993; Moon *et al.* 1993), except for a species difference in the pulse separation for which the threshold for the 2-ms pulse duration reached a minimum. The authors concluded that the actual pulse separation (rather than just rate per se, or number of stimulus pulses) contributed significantly to the shape of the threshold vs rate curves. They postulated that, in the case of long (2 ms) pulse durations, the nonmonotonic threshold vs rate functions were consistent with a neural inhibitory mechanism which operated for short time intervals after long duration pulses.

In current speech processing strategies which use sequential pulsatile stimulation, pulse durations are usually limited to durations shorter than 500 μs, since longer durations would impose an unacceptable limit on the rate of stimulation. Although the effects noted above for very long durations (more than 1 ms) are unlikely to occur in normal use of cochlear implants, it is still possible that different pulse durations in the range used in clinical practice may lead to differences in perception. For example, it is known that different sized fibers, or different sites on the same neuron, have different time constants for charging (Ranck, 1975). This results in different charging efficiency for equal-charge/phase stimuli of different pulse widths. For example, a neural membrane which loses charge quickly will be inefficiently charged by a longer pulse duration and lower current, compared to the same neuron charged by a higher current and shorter pulse duration, even if the total charge delivered is the same. Thus, if the activated neurons vary in size and type, nonidentical groups of neurons may be activated by stimulation with different pulse durations, even if the total number of neurons activated (or the resultant loudness) is the same.

Another pulse-duration-dependent effect on the stimulation of nerve fibers (for durations in the range of 10 to 500 μs) has been studied by Grill and Mortimer (1996). Their model simulation of neural threshold vs distance from the electrode for a single myelinated axon predicted a slower increase in threshold with distance for longer pulse durations. This would produce an improvement of spatial selectivity for shorter pulse durations. This effect in the model was due to the distribution of neural membrane potentials along the axon. For a constant pulse duration, the longitudinal spread of membrane potential is wider with increased distance from the stimulating electrode, leading to increased spike probability, and resulting in less increase in threshold with distance than predicted by the drop in stimulus amplitude. However, for shorter pulse durations, the spread of the neural membrane potential is smaller and the above effect is limited, resulting in a greater increase in threshold with distance than for long pulse durations. The model predictions were confirmed by measurements of muscle activation from electrical stimulation of sciatic nerves in cats. The shorter pulse durations allowed greater stimulus intensities and greater muscle response before ''spillover'' of activation to neighboring muscle areas, implying that the short pulse durations resulted in more place-specific stimulation.

The purpose of the psychophysical experiments reported below was to investigate the suprathreshold perceptual effects (other than loudness) of stimulating the auditory nerve using different pulse durations. Five experiments were undertaken. First, the ability of subjects to discriminate equally loud pulse trains with different pulse durations was determined. If subjects could discriminate these pulse trains, it would support the proposition that nonidentical neural populations are activated, or that there is a detectable difference in the temporal pattern of the neural responses.

Second, the ability of subjects to combine temporal information across different electrodes was measured using stimuli with two different pulse durations. McKay and McDermott (1996) showed that subjects could no longer combine temporal information across electrodes when the electrodes were farther apart than about 4 mm. At these larger separations, subjects perceived the temporal pattern applied to each individual electrode, rather than the temporal pattern associated with the combined stimulus pattern. The authors suggested that, at closer distances, the ability to combine temporal information from the two electrodes was probably facilitated by the overlapping of the areas of activated neurons. Thus, measurement of the ability to combine temporal information across separated electrodes may provide information about the place-specificity of the stimulation. Two experiments in the present study used a similar measurement procedure to that used in McKay and McDermott (1996) to determine whether equally loud stimuli using two different pulse durations may result in different sized regions of neural activation.

Third, rate discrimination was measured and compared for two different pulse durations. If different pulse durations

TABLE I. Details of the subjects who took part in the experiments.

Subject	Age (years)	Etiology	Implantation date	Length of profound deafness
1	56	Otosclerosis	October 1990	5 years
2	55	Meningitis	September 1990	39 years
3	47	Progressive/unknown	January 1986	1 year
4	65	Progressive/genetic	May 1986	30 years
5	35	Sudden onset/unknown	July 1989	5 months
6	51	Trauma	November 1988	17 years
7	41	Otosclerosis	November 1992	6 years
8	59	Otosclerosis	February 1992	14 years
9	49	Congenital/progressive	September 1996	20 years

result in changes in the synchrony of the neural responses, this may lead to differences in rate discrimination. Alternatively, if the spatial pattern of neural responses is altered for different pulse durations, this may in itself lead to differences in the ability of the central auditory system to extract information about rate from the peripheral responses.

Finally, the differences in charge/phase were investigated for different pulse durations at threshold and equally loud levels of stimulation. Effects of both absolute current level, and current relative to threshold, were investigated.

I. SUBJECTS AND EQUIPMENT

A total of nine subjects took part in the five experiments, with subsets of between four and nine subjects participating in individual experiments. All were postlingually deaf adults who have been implanted with the Mini System 22 implant, manufactured by Cochlear Ltd. In this implant, electrodes are spaced at distances of 0.75 mm, and can be activated in either a bipolar (BP+n) mode (where the current flows between two active electrode rings separated by n inactive rings), or the common ground (CG) mode (where there is a single active electrode ring and the remaining electrodes form a common current-return path). Where electrode positions are referred to in the data, they will be denoted by the two rings used in bipolar mode or the single active ring in CG mode. The rings are numbered from 1 to 22 in basal to apical direction. Details of the subjects' etiologies and histories of implant use are contained in Table I. During the experiments, an IBM-compatible PC was used to control the stimuli, and to record the subjects' responses. The PC was interfaced with a speech processor, which transmitted the encoded instructions defining each stimulus via a radio-frequency link to the implant.

II. EXPERIMENT 1: PULSE DURATION DISCRIMINATION

A. Methods 1

Subjects 2, 3, 4, 6, and 8 took part in this experiment. The stimuli were 100-Hz biphasic pulse trains (except for subject 6 where the rate was 200 Hz) delivered to a single electrode position, presented at a comfortably loud level with a total stimulus duration of 500 ms. BP+1 stimulation mode was used except for subjects 3 and 6, who normally use CG stimulation mode because of suspected electrode short-circuits. Two pulse durations were chosen for each subject: 266 μs, and the smallest duration (between 50 and 100 μs) which allowed comfortable loudness to be attained without the use of excessively high currents. For each subject, pulse duration discrimination was tested at four different cochlear locations which spanned the electrode array. The electrodes tested and the pulse durations compared are shown in Table II.

The stimuli containing the short and long pulse dura-

TABLE II. The results of experiment 1.

Subject (pulse durations) (μs)	Electrode (bipolar pair or CG)	No. of correct identifications out of 30 trials. Current variation in ± current steps: 0	1	2	4	Subject comments. Difference for 266 μs
2	[6,8]	8				don't know
[100,266]	[10,12]	28	**30**	**16**		higher pitch
	[14,16]	24	**15**	12		higher pitch
	[18,20]	28		**30**	**18**	lower pitch
3	6	23		23	**17**	higher? squeaky
[50,266]	12	22		**20**	**21**	lower pitch
	17	13		10		don't know
	21	14		**19**	12	lower pitch
4	[5,7]	30	11			lower pitch
[50,266]	[10,12]	6				don't know
	[14,16]	9				don't know
	[17,19]	10				don't know
6	7	15	8	11		don't know
[100,266]	10	26		**22**	**19**	lower pitch
	15	30		**26**	**26**	higher pitch
	20	26		**26**	**26**	lower pitch
8	[5,7]	17	16	8		lower pitch
[70,266]	[10,12]	29		23	**17**	lower pitch
	[12,14]	29		**27**	**20**	higher pitch
	[20,22]	13	8	6		higher pitch

tions were loudness balanced by adjusting the currents as follows. The two stimuli were presented continuously alternating with 500-ms silent intervals. The subjects adjusted the current of one stimulus using an unmarked rotary knob until they were satisfied that the two stimuli were equally loud. The current of the adjusted stimulus was then fixed at the value chosen by the subject, and the procedure was repeated with the other stimulus being adjusted. The two procedures were repeated, and the results of the four trials were averaged. This procedure was used for all loudness-balancing tasks in the five experiments.

The discrimination of the two pulse trains was then tested using a four-interval forced-choice procedure with 30 trials, in which one (random) interval in each set of four contained the stimulus with longer pulse duration. The subject was asked to identify the ''different'' interval. After completion of the measurements, the subjects were asked to describe the difference in percept that they were using to identify the ''different'' interval. To prevent identification based on any small residual loudness difference, the experiment was repeated with one or two ranges of random current variation applied to the stimuli in each interval. The maximum range of current variation was ± 4 current steps (a step is about 0.15 dB). If a chance-performance score was obtained with the first range of variation chosen, no wider ranges were tested.

B. Results 1

The results of experiment 1 are shown in Table II, where the number of correct identifications over 30 trials of the stimulus having the longer pulse duration is shown for each electrode position and current variation range. Scores of 13 or more out of 30 are significantly better than chance performance. The variability in the four loudness-balance trials for each discrimination task was determined by calculating the standard error of the estimated mean current difference for equal loudness. These standard errors ranged from 0.25 current steps to 1.2 current steps. Any current variation range which did not exceed two standard errors for that electrode was not considered sufficient to ensure that loudness was not being used as an identification cue. Each case which satisfied this criterion, and also resulted in a significant identification score, is marked by bold type in the table.

It can be seen from the table that, for four out of five subjects, there was a significant discrimination of pulse duration for at least two of the four electrode positions. There was a large variability in discrimination ability, both among subjects, and among different electrode positions for the same subject. Also shown in Table II are the comments of the subjects about what they thought was different about percept evoked by the test (long-pulse-duration) stimulus. In cases where there was a clear difference in percept between the two pulse durations, subjects described the difference as a pitch difference, but no subject consistently ranked the stimuli with long duration pulses as higher (or lower) in pitch than that with the short duration pulses. There was no correlation across subjects between the particular electrode regions (apical, middle, or basal) and the pulse-duration discriminability or direction of the pitch change.

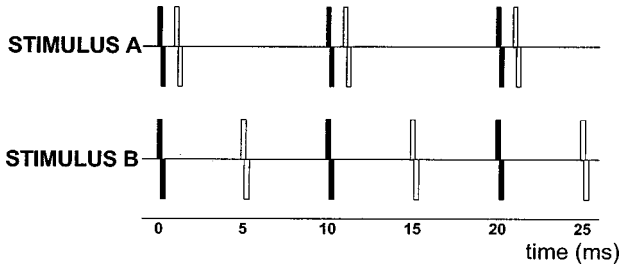

FIG. 1. Representative portions of the two dual-electrode stimulus waveforms used in experiments 2 and 3. The filled and unfilled pulses are presented to two different electrodes in the dual-electrode case, and to the same electrode in the single-electrode case, with a time offset of 1 (stimulus *A*) or 5 ms (stimulus *B*).

III. EXPERIMENT 2: TEMPORAL PATTERN DISCRIMINATION AND ELECTRODE SEPARATION

A. Methods 2

Subjects 1, 2, 3, and 5 took part in experiment 2. The stimuli were pulse trains of 500-ms duration (see Fig. 1). In each 10-ms period there were two biphasic pulses separated by either 1 (stimulus *A*) or 5 ms (stimulus *B*). These two biphasic pulses were either delivered to the same electrode, or alternated between two different electrodes. In the latter case, the stimuli were equivalent to two 100-Hz pulse trains, one on each electrode, with a time offset of 1 or 5 ms between the electrodes. These two dual-electrode stimuli are similar to the stimuli used by McKay and McDermott (1996), who investigated the perception of temporal patterns which were distributed across electrodes (see Introduction). It was expected that, in a similar fashion to the previous experiment, as electrode separation increased, there would be less integration of temporal information across the two electrodes, and the two stimuli (*A* and *B*) would become more difficult to discriminate. In the present case, two different pulse durations were used: a short duration of 50–100 μs; and a long duration of 266 μs. The experiment investigated whether the maximum electrode separation for effective integration of temporal information was dependent on pulse duration.

Equally loud stimuli were constructed using the following procedure. First, the threshold currents and equally loud currents at a comfortable loudness were determined for a series of adjacent electrode positions for 100-Hz pulse trains having the shorter pulse duration. The thresholds were determined using a modified Hughson–Westlake adaptive procedure (Carhart and Jerger, 1959). The equally loud currents were determined by the same loudness-balance procedure as described for experiment 1, using as the reference electrode the most basal of the series.

Each dual-electrode stimulus (*A* or *B*) was then constructed in the following way. Initially, all pulses in stimulus B were directed to the most basal electrode position (making, in effect, a 200-Hz pulse train on this electrode), with the current set to the comfortably loud level determined above. This stimulus (B_0) formed a loudness reference for the other *B* stimuli in the remainder of the experiment. Next, the dual-electrode stimulus B_1 was constructed using this electrode and the next electrode in the apical direction, using the

equally loud current levels determined above. This stimulus was then loudness-balanced to stimulus B_0. In this procedure, and all others involving dual-electrode stimuli, the separate currents on each electrode were adjusted by equal current steps to match the loudness. The corresponding dual-electrode stimulus A_1 (with the 1-ms interpulse interval) for the same pair of electrodes was constructed initially with the same currents as B_1, and then loudness balanced to that stimulus before being used in the discrimination task. Similarly, stimulus B_n, which used the first electrode and the electrode n positions in the apical direction, was constructed and loudness-balanced to stimulus B_0. Stimulus A_n was then loudness-balanced to stimulus B_n.

The discrimination task was a four-interval forced-choice task in which three intervals contained stimulus A_n, and one (random) interval contained stimulus B_n. The subject was asked to identify the different interval. Practice was provided initially using the loudness-balanced stimuli. Then, random current variation (up to ± 4 current steps) was introduced to limit the use of any residual loudness cues. The number of correct identifications of stimulus B out of 30 trials was determined at each electrode separation starting at zero separation, and for increasing distances until chance performance was obtained (12 or fewer correct).

A similar series of stimuli was then constructed as above using the longer pulse duration (266 μs). To ensure that these stimuli had the same overall loudness as the ones with shorter pulse duration, the new reference stimulus B_0' (with the longer pulse duration) was loudness-balanced with the previous reference stimulus B_0 (with the shorter pulse duration) before being used as the loudness reference for the new dual-electrode stimuli, B_n'. The ability of subjects to discriminate stimulus B_n' from stimulus A_n' was determined as above, with electrode separation increasing until chance performance was obtained. The effect of electrode separation on discrimination ability was then compared for the two pulse durations used for each subject.

In order to compare the results for different pulse durations, it was important to choose an equivalent amount of random current variation for the two conditions. It is difficult to know how to equalize the perceptual effect of current variation for different pulse durations. Although discrimination scores always decreased with increasing current variation, it is uncertain whether perceptual dimensions apart from loudness might have contributed to this effect. For example, pitch changes are also commonly associated with current changes in implantees, but these changes seem to be idiosyncratic. We chose to compare the results for the two pulse durations using current variation ranges which would be predicted to give approximately the same loudness variation. To achieve this goal, the current variation ranges for the two pulse durations were chosen to be as close as possible to equal proportions of the average dynamic range (in dB) across the electrodes used. For implantees using low-rate stimulation, the growth of loudness can be approximately described by either a power or exponential function of current. In practice, there is usually little difference between these two functions because of the small range of absolute currents within the perceptual dynamic range. Thus an equal

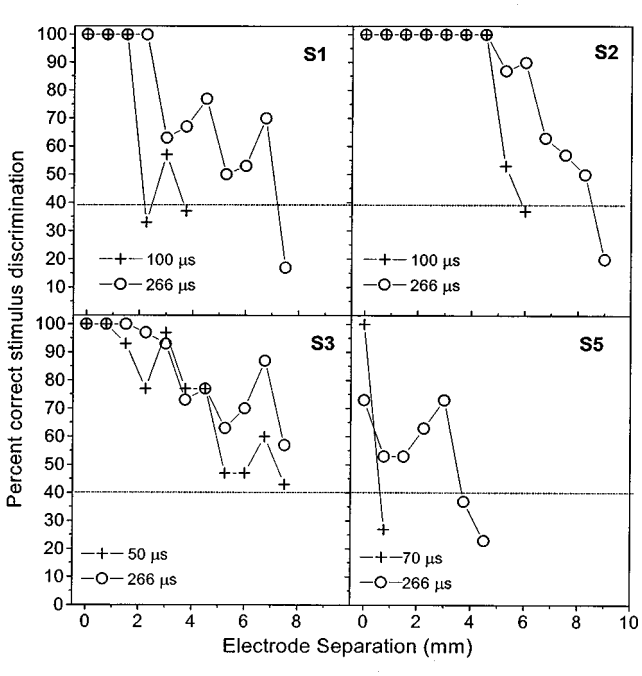

FIG. 2. The results of experiment 2 for four subjects. The vertical axes represent the percent correct discrimination of stimuli *A* and *B* for the dual-electrode stimuli shown in Fig. 1, with a random current variation of two current steps (i.e., about 0.3 dB) on either side of the loudness-balanced levels. The horizontal axes represent the separation of the two electrode positions used in the dual-electrode stimuli. The symbols represent the results for different pulse durations, as shown in the legends.

portion of the dynamic range (expressed in dB), should, on average, produce an approximately equal loudness variation. The average dynamic range was calculated from the thresholds and equally loud comfortable currents measured at the beginning of the experiment. These were averaged across the electrode positions used. The dB current change associated with a current step for currents at the comfortably loud level was obtained from the calibration table for each subject's implant, and then expressed as a proportion of the average dynamic range (in dB). In general, these proportions were nearly equal for the two pulse durations. Although the dynamic ranges tended to be slightly larger for the longer pulse duration (see below), this was largely offset by the fact that, at the lower current levels used for the long pulse duration, a current step produces a slightly larger dB change. The ratios representing the proportion of dynamic range (in dB) for a current step with long-pulse-duration stimuli, divided by the proportion with the short-pulse-duration stimuli, for the four subjects were as follows: *S*1, 0.875; *S*2, 0.97; *S*3, 1.43; *S*5, 1.23.

B. Results 2

The results of experiment 2 for the current variation range of ± 2 current steps are shown in Fig. 2. The results are consistent with those of McKay and McDermott (1996), in that the ability to discriminate the stimuli with different temporal patterns decreases with increasing electrode separation. When comparing the results for the short and long pulse durations, it can be seen that the longer pulse duration resulted in discrimination of the two stimuli at greater elec-

trode distances for three subjects (1, 2, and 5). Subject 3 could discriminate the stimuli with both pulse durations for larger separations than the other subjects, but her results are consistent with the other three subjects in that her discrimination ability is better for the longer pulse duration at the larger separations.

IV. EXPERIMENT 3: TEMPORAL PATTERN DISCRIMINATION WITH MIXED PULSE DURATIONS

A. Methods 3

Subjects 2, 6, 7, and 8 took part in experiment 3, which employed the same stimulus waveforms as experiment 2 (Fig. 1). In this case the discrimination of stimuli A_n and B_n was compared for a single electrode separation across three conditions: pulses on both electrodes with short pulse duration; pulses on both electrodes with long pulse duration; and pulses on one electrode with short duration and on the other with long duration.

To determine a suitable electrode separation that would not result in either perfect or chance discrimination, a pilot test was done for subjects 6, 7, and 8, in which the discrimination of A_n and B_n was tested for short pulse durations and varying electrode separation (as in experiment 2). A separation was chosen such that the discrimination score was between 40% and 70% correct. For subject 2, this separation (5.25 mm) was chosen from the results of experiment 2, and for the other three subjects it was 1.5 mm.

The currents for threshold and equal comfortable loudness were established for the two pulse durations with 100-Hz pulse trains on each of the two electrodes. For each subject, six dual-electrode stimuli were constructed using the two selected electrodes. These comprised two temporal patterns (*A* and *B*) for each of three pulse duration conditions (short, long, and mixed). Initially, the six stimuli were constructed using the equally loud currents determined above. The three stimuli *B* were loudness-balanced using as a reference the one with the short pulse duration. Each of the three *A* stimuli was then loudness-balanced with the corresponding *B* stimulus with the same pulse duration.

As in experiment 2, the proportions of the dynamic range represented by a current step for the two pulse durations and electrodes were calculated, and found to be similar, except for *S*7, where the long-duration current step was a larger proportion of the dynamic range. The ratios representing the proportion of dynamic range for a current step with long pulse duration, divided by the proportion with short pulse duration, for the four subjects were as follows: *S*2, 0.95; *S*6, 0.96; *S*7, 1.64; *S*8, 1.18. Therefore, the comparisons across the three pulse-duration conditions were performed using current variation over equal ranges of current steps (± 4 current steps for subjects 2 and 7, and ± 2 current steps for subjects 6 and 8).

The discrimination of stimuli *A* and *B* for the three pulse-duration conditions was measured using the same four-interval forced-choice procedure as in experiment 2. A total of 90 trials was presented in each condition. Each subject was tested in three sessions, in each of which 30 trials were completed in each condition. The order of testing of the three conditions was altered in the three sessions so that each condition was tested first, second, and third.

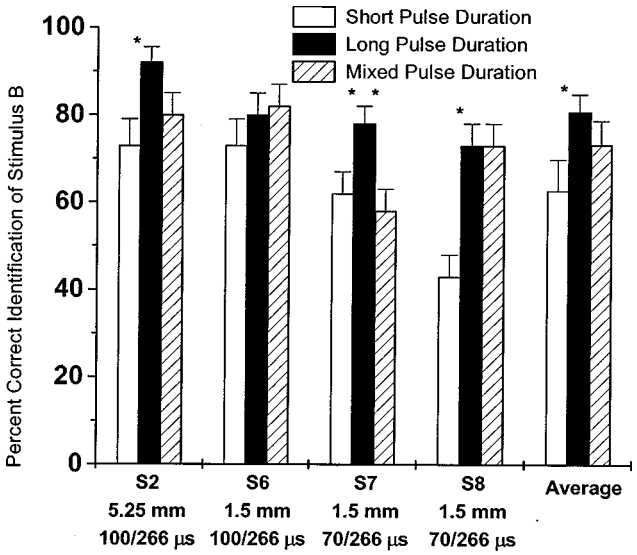

FIG. 3. The results of experiment 3 for four subjects. The vertical axis represents the percent correct discrimination of stimuli *A* and *B*. The scores for the three pulse-duration conditions are shown separately for each subject and the mean scores across subjects are shown by the last three bars. The error bars represent the sizes of the 95% confidence intervals, and asterisks above the boundary between two bars indicate scores which are significantly different ($p<0.05$). The pulse durations and electrode separations used are listed under the subject number.

B. Results 3

The results of experiment 3 are shown in Fig. 3. The mean correct identification score for stimulus *B*, along with the size of the 95% confidence interval calculated from binomial theory, is shown for each subject and condition. The differences in means for different pulse-duration conditions were compared for each subject using binomial theory. For three subjects (2, 7, and 8), the score for the long pulse duration was significantly higher ($p<0.05$) than the score for the short pulse duration. The score for mixed pulse durations was significantly higher than that for short pulse durations for subject 8, and for subject 6 was significantly lower than the score for long pulse durations. The significant differences are marked with asterisks in the figure.

The group means for the three pulse-duration conditions are also shown in Fig. 3. The group scores were analyzed with two-way analysis-of-variance, with subject and pulse-duration condition as factors. There was a significant condition effect [$F(2,9)=44.26$; $p<0.05$]. Further analysis with Tukey's critical distance test showed the long-pulse-duration condition to have significantly higher scores than the short-pulse-duration condition, consistent with the results of experiment 2. The condition with mixed pulse-duration gave scores intermediate to the other two conditions, and not significantly different from either of them.

V. EXPERIMENT 4: RATE DISCRIMINATION

A. Methods 4

Subjects 2, 3, 6, 8, and 9 took part in experiment 4. A single electrode was selected for each subject near the

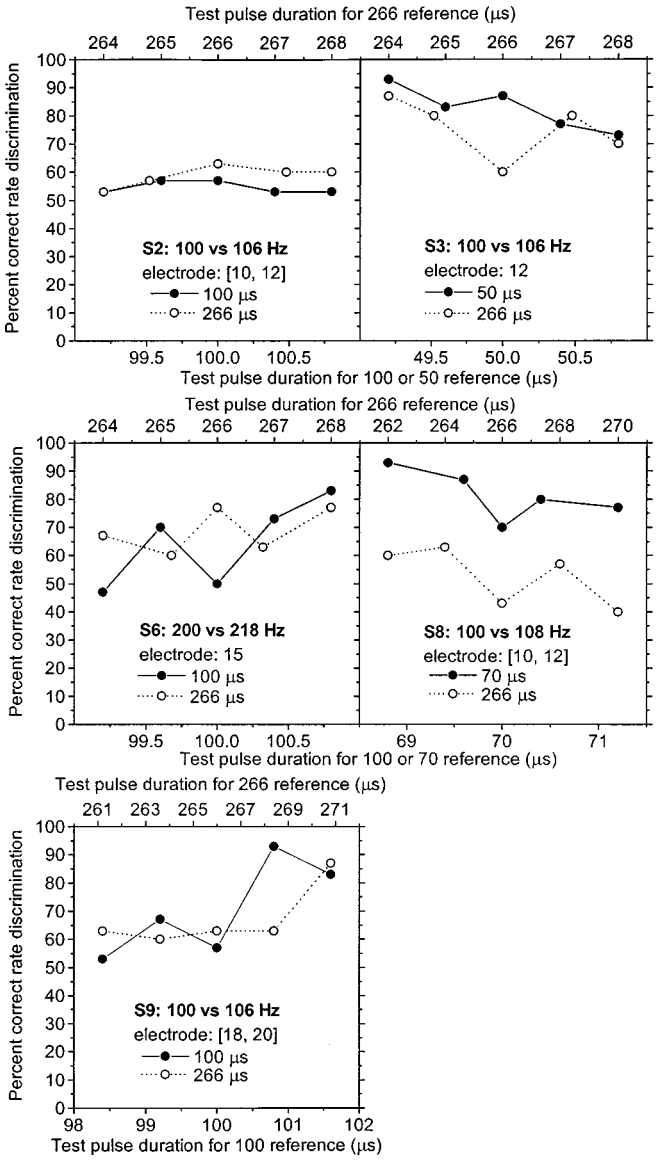

FIG. 4. The results of experiment 4 for five subjects. The vertical axes represent the percent correct rate discrimination for the two rates listed after the subject number. The lower horizontal axes represent the pulse duration of the test stimulus for the shorter-pulse-duration reference stimulus (filled circles). Similarly, the upper horizontal axes represent the pulse duration of the test stimulus for the reference stimulus with pulse duration of 266 μs. The electrode positions used for the experiment are also listed in each legend.

middle or apical half of the electrode array. The electrode position and pulse durations used are shown in Fig. 4. The reference stimuli for the discrimination experiments were 100 Hz (subjects 2, 3, 8, and 9) or 200 Hz (subject 6) pulse trains of 500-ms duration with short or long pulse duration, at a comfortably loud level. The reference stimuli were loudness-balanced.

Rate discrimination for each subject was measured using a four-interval forced-choice procedure in which one random interval contained a higher rate than the reference rate. A pilot study was conducted for each subject, in which a psychometric function was obtained to find the rate which was discriminated from the reference rate in the range 60%–80% correct. This rate, which we will term the test rate, was as follows for the five subjects: subjects 2, 3, and 9, 106 Hz; subject 6, 218 Hz; subject 8, 108 Hz. The test rate was then fixed for each subject, and used to compare rate discrimination for long and short pulse durations.

When measuring rate discrimination it is important to consider the way in which rate changes might affect the loudness of the stimuli. McKay and McDermott (1998) measured equal-loudness contours for rates between 20 and 750 Hz in four subjects at threshold and comfortable loudness. In all cases there was an increase in loudness for increasing rates above 100 Hz. At comfortable loudness, the loudness change with rate represented less than 1 dB current adjustment over a ten fold increase in rate (50 to 500 Hz). This implies that the expected loudness change over the 6%–9% increase in rates used in the present experiment would be much less than that resulting from a single current step (about 0.15 dB). This expectation was confirmed by loudness-balancing the reference and test rates; in each case the resulting currents were equal.

Since the precision of loudness-balancing the two rates was limited by the current step size available, four other test stimuli were constructed for each equal-current test stimulus, in which the pulse durations were adjusted in two small increments above and below the reference pulse duration. For each subject, the size of the pulse duration step was half the corresponding dB change in charge/phase than that of one current step. Thus for every reference stimulus, there were five test stimuli, all with the same test rate and with the same current value (equal to the reference current), but different pulse durations spanning a small range around the pulse duration of the reference stimulus. If identification of the ''different'' interval for any of these stimuli was aided by a perceivable loudness change, it would be expected that a minimum score would be obtained for the condition closest to equal-loudness [see Pfingst and Rai (1990), for example]. Based on our previous research (McKay and McDermott, 1998), this condition would be expected to be either the condition with the same pulse duration as the reference stimulus, or the condition with the nearest smaller pulse duration.

For each subject, rate discrimination was measured for ten test stimuli (five stimuli as described above, using the references with short and long pulse durations), using a four-interval forced-choice procedure over 30 trials. To minimize the influence of any learning effects during or across sessions, the following sequence was followed. Each of four sessions contained 75 trials with one reference pulse duration being tested in the first and fourth session and the other in the second and third session. Within each session, all five test stimuli were tested over 15 trials each. The 15 trials of a particular test stimulus were divided into five sets of three, and the order of testing of the five sets for the same stimulus was blocked across the five test stimuli.

B. Results 4

Before analysis for pulse duration effects, the scores for the same conditions in the initial and subsequent session were analyzed for learning effects for each subject using paired t-tests. For all five subjects there were no significant

differences between test sessions ($p>0.05$), and therefore the scores from the two sessions were combined.

The rate discrimination scores for the ten stimuli with each subject are shown in Fig. 4. It can be seen from the figure that only subject 8 showed a clear difference in rate discrimination for the two pulse durations, and for this subject, discrimination was better for the shorter pulse duration. The ten raw scores for each subject were analyzed in several ways. First, the effect of using the five slightly different test pulse durations was tested using one-way analysis of variance with the data pooled across subjects for each reference-pulse-duration. There was no significant effect of test pulse duration for the group over the range used ($p=0.792$ for short pulse duration, and $p=0.869$ for the long pulse duration). For each reference pulse duration, the lowest mean score was for the condition where the test pulse duration was equal to the reference pulse duration, which supported the expectation that the equal-loudness condition would be very close to this point. For some individual subjects, there appeared to be an overall tendency for scores to increase (subjects 6 and 9) or decrease (subjects 3 and 8) across the range of test pulse durations. This phenomenon will be addressed in the discussion below.

For the group statistical analysis, the five scores for the five test stimuli were treated as repeated measures for a two-way analysis of variance, with subject and reference pulse duration as variables. This resulted in a significant subject effect ($p<0.001$), and interaction of subject with reference-pulse-duration effect ($p=0.007$), but a nonsignificant effect of reference-pulse-duration ($p=0.069$). To investigate the interaction effect, the same analysis was repeated with subject 8's data removed. This resulted in no significant effect of reference-pulse-duration ($p=0.942$) and no interaction effect ($p=0.733$). *T*-tests were performed to compare the two reference-pulse-durations for each subject. For subject 8, there was a significant difference between reference-pulse-duration conditions ($p=0.0015$), with short pulse durations providing better rate discrimination. For subject 2 ($p=0.075$), subject 3 ($p=0.26$), subject 6 ($p=0.60$), and subject 9 ($p=0.719$), there were no significant differences between the two reference-pulse-duration conditions.

VI. EXPERIMENT 5: CURRENTS FOR THRESHOLD AND COMFORTABLE LOUDNESS

A. Methods 5

The threshold and equally loud currents measured across all four experiments reported above were converted to charge/phase measures for the two pulse durations used for each of the nine subjects. The differences in charge/phase for the two pulse durations at threshold and comfortable loudness were calculated. In order to normalize data across the different shorter pulse durations used, these data were converted to the dB change in current per doubling of pulse duration for threshold or equal comfortable loudness. These data were analyzed for any effects of absolute stimulus intensity and relative level (dB current above threshold).

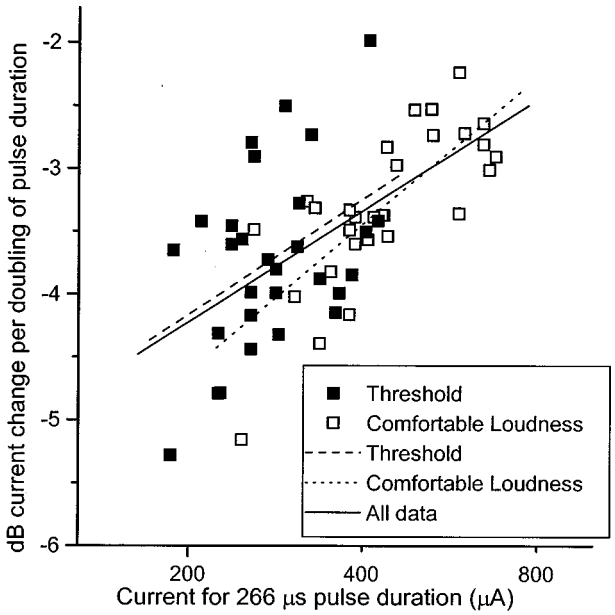

FIG. 5. The dB change in current per doubling of pulse duration for threshold (closed symbols) and equally loud comfortable loudness (open symbols) for each electrode for the six subjects in BP+1 mode. The horizontal axis represents the current for threshold or comfortable loudness with the 266-μs pulse duration. The three lines represent the best linear fits for the two sets of data, and the combined threshold and comfortably loud data.

B. Results 5

As discussed in the Introduction, in the hypothetical condition of perfect charge integration by the neural membrane, the charge/phase would be equal for two equally loud stimuli having different pulse durations, leading to a change of -6 dB in current per doubling of phase duration. In all 104 measurements, the current change for doubling of pulse duration was smaller than -6 dB, and varied over the range of -5.9 to -2.0 dB/doubling. This implies that the stimuli with longer pulse duration always required more charge/phase than those with shorter pulse duration to evoke an equally loud percept.

In order to investigate any effect of absolute stimulus intensity on this measure, the 58 measurements from the six subjects using BP+1 mode were plotted as a function of the current amplitude for the stimulus with 266-μs pulse duration (Fig. 5). Regression lines were fitted to the threshold data (closed symbols), the comfortable-loudness data (open symbols), and the full data set. These regression lines are also shown in Fig. 5. In all three cases, there was a significant relationship between the dB/doubling measure and the stimulus current, with the dB/doubling becoming smaller (closer to zero) for higher currents (threshold: $r=0.42$, $p=0.02$; comfortable loudness: $r=0.75$, $p<0.0001$; all data: $r=0.61$, $p<0.0001$). Furthermore, the slopes and intercepts of the three regression lines were not significantly different from each other ($p>0.05$), indicating that the effect of increasing current on the dB/doubling was independent of the level of the stimulus within these subjects' perceptual dynamic ranges. The regression line for all the data had a slope (and standard error of the slope) of 0.146 (0.025) dB/doubling per dB current amplitude. To investigate whether this effect of current amplitude also applied to current

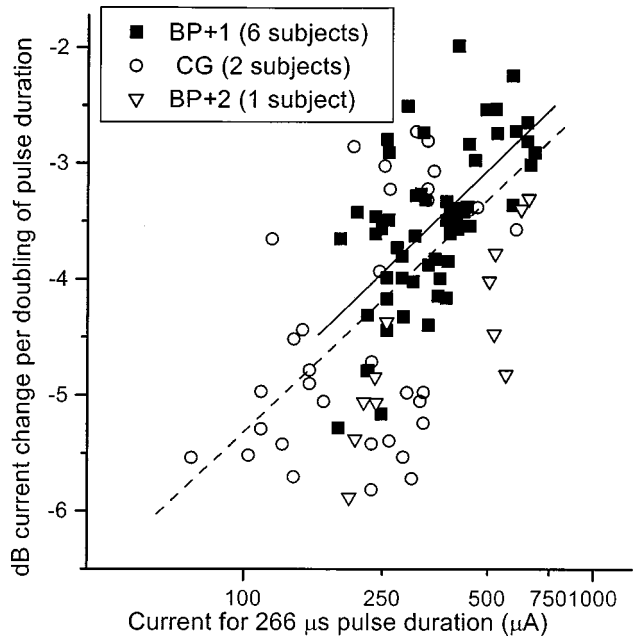

FIG. 6. The dB change in current for doubling of pulse duration at threshold and comfortable loudness for all subjects and electrodes (vertical axis) plotted against the current for the 266-μs pulse duration (horizontal axis). The three symbols represent data for three modes of stimulation as described in the legend. The dashed line is the best-fit linear regression for the whole data set and the solid line is that for only the BP+1 data (as in Fig. 5).

changes on individual electrodes, the change in dB/doubling from threshold to comfortable loudness was plotted against the current change (in dB) for the 29 electrodes, and a regression line fitted (restrained to go through the origin). This regression line had a slope (and error) of 0.131 (0.025), which is not significantly different from the slopes of the regression lines in Fig. 5, and there was a similar degree of correlation ($r=0.705$, $p=0.003$). Thus, for the subjects using the BP+1 mode and pulse durations in the range 50 to 266 μs, the regression line for all the data shown in Fig. 5 can predict the effect of absolute current magnitude on the dB current change per doubling of pulse duration both for different subjects and/or electrodes, and for different overall stimulus level on the same electrode.

The smaller data sets from the remaining three subjects (17 electrodes in CG mode, and 6 in BP+2 mode) were plotted on the same axes as the BP+1 data, to investigate the possible effect of using different electrode configurations on the relationship described above (Fig. 6). A regression line fitted to the whole data set (dashed line in Fig. 6) showed a significant correlation ($r=0.60$, $p<0.0001$). The slope (0.144) and intercept were not significantly different from those for the BP+1 data set (also shown in the figure for comparison). The inclusion of the extra data in BP+2 and CG modes did, however, increase the standard deviation of data points from the regression line (0.75 compared to 0.54 for the BP+1 group alone).

VII. DISCUSSION

The results of experiment 1 showed that two pulse trains with different pulse durations can be discriminable even when loudness cues are reduced by loudness balancing and random current variation. Although the perceptual difference which distinguished the pulse trains was described by the subjects as a pitch change, it should be noted that subjects may use the term ''pitch'' to describe either pitch or timbre changes. Given that potential loudness cues were controlled, this perceptual difference is likely to arise either from a change in the temporal pattern of neural responses, or from a change to the spatial distribution of neural responses.

Considering the variability in the amount and direction of the perceptual change reported by the subjects, it seems more likely that the change results from a spatial rather than temporal change in the neural responses. As discussed in the Introduction, if neurons are being activated which differ in size and/or site of activation, these neurons may have different charging time-constants, possibly leading to different spatial patterns of excitation for the two pulse durations. The distribution of size and site of neurons is likely to vary across subjects, and in different parts of the cochlea, due to differences in neural survival patterns. This would lead to subject- and electrode-dependent changes in pitch or timbre. Unfortunately, at present there is no means available to determine directly the pattern of neural survival in individual implantees.

The results of experiments 2 and 3 showed that using longer pulse durations enables better integration of temporal information across electrodes and/or a greater range of electrode separation over which temporal integration is possible. There are at least three possible explanations which may account for these results. First, it could be an artifact of the experimental method, if the current variation with longer pulse durations had a less detrimental effect on discrimination than the current variation with short pulse durations. However, this is unlikely if the effect of current variation was solely to vary the loudness. In the cases where the loudness variation was predicted to be most different for the two pulse durations (subjects 3 and 5 in experiment 2, and subject 7 in experiment 3), it was predicted to be greater for the long pulse duration. In spite of this potential disadvantage for discrimination with the long pulse duration, these subjects still showed higher scores for the longer pulse duration. If the current variation caused perceptual changes other than loudness (such as changes in place-pitch), then the results could be explained if the perceptual change was always greater with the shorter pulse duration. However, place-pitch changes with level have been reported to be variable and idiosyncratic. Thus they are unlikely to have caused the differences in results for the two pulse durations, since all seven subjects in these experiments gave results which were consistent with each other.

The second possible reason for the long-pulse-duration advantage in experiments 2 and 3 is that the temporal patterns in stimuli *A* and *B* were easier to distinguish with the longer pulse durations, independently of the effect of electrode separation. If temporal pattern discrimination were easier with long pulse durations, then it would be expected that rate discrimination would also be easier. The results of experiment 4 do not support this possibility, as rate discrimination was not better with the longer pulse duration for any subject.

A third, and more plausible, possible reason for the results of experiments 2 and 3 is that the area of excitation is wider for long pulse durations than for stimuli of the same loudness using short pulse durations. If so, it would lead to a wider overlapping area of neural excitation from the two electrodes, which may enable better integration of temporal information across the electrode positions. The implication that the stimulation is more spatially selective for shorter pulse durations (given equal loudness) is compatible with the observations of Grill and Mortimer (1996) which were discussed in the Introduction. Improved spatial selectivity, in our case, may be caused by similar effects of pulse duration on the relation between neural charging and distance from the stimulating electrode. In the experiment of Grill and Mortimer, shorter pulse durations elicited a more intense muscle response for a fixed spread of excitation. This would be analogous in our experiment to a greater neural response (and presumably greater loudness) for shorter pulse durations, for the same spatial spread of excitation in the auditory nerve. This implies a smaller spread of excitation for equally loud stimuli when using shorter pulse durations. It should be noted, however, that the Grill and Mortimer model and experiment assumed activation of myelinated axons. In cochlear implant subjects, myelinated axons are probably found only at sites central to the spiral ganglion cell bodies. It would have to be assumed that these fibers contributed significantly to the overall activation for the model to be applicable.

Given that different pulse durations probably activate nonidentical neural populations, it is interesting to question whether the use of different pulse durations on different electrodes might lead to increased independence of temporal perception on those electrodes. If integration of two temporal stimulation patterns depends on particular neurons responding to stimulation from both electrodes, then it might be that there are fewer such neurons for the mixed-pulse-duration condition in experiment 3 than for either of the same-pulse-duration conditions. If so, then one would expect lower scores for the mixed-pulse-duration condition than for either of the other two conditions. On the other hand, if the overall temporal pattern is deduced centrally by combining the peripheral neural responses from different neurons in the same region, then one would expect the scores to reflect the size of the area of overlapping stimulation. In this case one would expect the mixed-pulse-duration condition to produce scores intermediate to those for the two same-pulse-duration conditions. The data support the latter hypothesis, as the mixed-duration condition never produced a score significantly lower than that for the short-pulse-duration condition.

The results of experiment 4 imply that, for pulse durations in the range used by cochlear implant sound processors, there is unlikely to be any effect of pulse duration on rate discrimination that is of practical significance. In the one subject (8) who showed an effect of pulse duration, the results would represent an increase in rate difference limen of only 1–2 Hz (or 1%–2%) with a pulse duration increase of 11.6 dB.[1] The results are consistent with those of Baretto and Pfingst (1992), who measured rate discrimination in one implanted bonnet monkey, for pulse durations of 250, 800, and 2500 μs. Similarly to experiment 4, Baretto and Pfingst used a number of test stimulus intensities above and below that of the reference stimulus. However, the range of intensities used was an order of magnitude larger in their case, resulting in greatly improved discrimination (due presumably to loudness cues) when the intensities were most different. For 250- and 800-μs pulse durations, the minimum discrimination score was at the equal-stimulus-intensity point and showed no significant difference in rate difference limen for the two pulse durations, in accordance with our results in four subjects. However, for the very long pulse duration (2.5 ms), the rate difference limen (when judged from the minimum discrimination point) was about double that found for the shorter pulse durations.

The apparent asymmetry of the scores for some of our subjects about the equal-intensity (and presumable equal-loudness) points in Fig. 4 may be due to the effect of stimulus level on place-pitch (Townshend *et al.*, 1987; Pijl, 1997). For example, subjects 3 and 8 showed a trend for higher scores when the test amplitude was smaller. This may be due to the place-pitch increasing as the test intensity was reduced. If the subjects were listening for the interval with the higher pitch (the test stimulus always had a higher rate), then the place-pitch shift may have increased scores for lower intensities and decreased scores for higher intensities. Similarly, subjects 6 and 9 showed a tendency for higher scores for higher test intensities which may be explained by an increase in place-pitch with level in these subjects.

In another study, Aronson *et al.* (1994) found improved rate discrimination for shorter pulse durations in three users of the Cochlear Ltd. implant system (for pulse durations between 50 and 400 μs). To our knowledge, this is the only published investigation which reports the effects of pulse duration on rate discrimination in humans. However, it is difficult to assess the validity of their findings as there were only eight two-interval forced-choice trials per rate pair, and their reported difference limens (80%–100%) are an order of magnitude larger than others in the literature.

In summary, the results of experiment 4 indicate that, for most subjects, there is no significant effect of pulse duration on rate discrimination for durations in the range 50 to 266 μs. However, the result for our subject 8, and that for the pulse duration of 2.5 ms in Baretto and Pfingst (1992), suggest that in some situations, or some subjects, there may be an advantage for short pulse durations.

The results of experiment 5 confirm previous findings that more charge/phase is needed to attain threshold when using longer pulse durations, a finding also consistent with electrophysiological studies which show that longer pulse durations are less efficient at charging the neural membrane than shorter pulse durations. Our results show that the increase in charge/phase needed for longer pulse durations (at least in the range of pulse durations up to 266 μs) is predictable from the absolute current of the stimulus: if the stimulus has a higher amplitude, a relatively greater increase in charge/phase for doubling of pulse duration is necessary to achieve the same loudness. Subjects and/or electrodes exhibiting lower thresholds show less effect of pulse duration

changes on the charge/phase required for threshold or equally loud stimuli.

The same effect applies to different stimulus amplitudes on the same electrode: a greater increase in required charge/phase for longer pulse durations is seen at higher intensities than at lower intensities, leading to a wider dynamic range (in dB) for longer pulse durations. The wider dynamic range is consistent with the results of Zeng *et al.* (1998) in four implantees. The average slope of their measured current vs pulse duration curves at threshold and maximum loudness were broadly consistent with the values in Fig. 5 if their four subjects had thresholds and dynamic ranges similar to the averages of the nine subjects in this paper.

The relationship between absolute current amplitude and the dB current change per doubling of pulse duration accounted for 37% of the variability seen among subjects/electrodes using the same mode of stimulation (BP+1). This effect is unlikely to be due wholly to differences in the strength-duration curves of individual neurons at different levels in the neural dynamic range. If this were the case, then one would expect the dB/doubling measure to depend only on how high the current is above threshold, rather than depending on the absolute current value. One possible explanation is that the effect of pulse duration increases with the distance of the electrode from the excitable neurons. For subjects using the same mode of stimulation, higher currents will, in general, excite more distant neural elements. These more distant (or central) elements (such as cell bodies and more central axons) may have longer charging time-constants (Ranck, 1975) and their charging may show more dependence on pulse duration.

One subject-dependent factor which is likely to directly affect the amount of current spread at threshold is the density of surviving neural elements. In subjects with poorer nerve survival, a higher current will be needed to evoke the same overall neural activity. It is possible, then, that the dB/doubling measure at threshold is also correlated with the density of neural survival.

In a recent study (McKay and McDermott, 1998), the average spike probability across activated neurons for similar evoked loudness among individual implantees was also postulated to depend on the density of neural survival. In subjects with sparse neural survival, activated neurons may be driven at higher spike probabilities to achieve the same overall neural activity. In that study, a model of loudness integration was used to derive the average neural spike probability from equal loudness measurements in stimuli with variable interpulse intervals. Subjects 1 to 8 in the present study also participated in that study, and their derived spike probabilities (for a 50-Hz pulse train) ranged from 0.3 to 0.9. The possible relationship between the derived spike probabilities and density of neural survival was supported by a significant correlation of spike probability with the duration of profound deafness before implantation. Subjects who had a longer period of deafness were likely to have poorer nerve survival, and these subjects had higher spike probabilities.

If the derived spike probability at threshold from McKay and McDermott (1998) and the dB/doubling at threshold in this experiment are both correlated with the density of surviving neurons, then they should be correlated with each other when obtained from the same subjects. Figure 7 shows the relationship between these two psychophysically derived measures for subjects 1–8. It can be seen that there is a highly significant correlation ($r=0.94$, $p=0.0006$), with lower spike probabilities (greater implied neural density) associated with dB/doubling values closer to the equal charge/phase slope of -6 dB. This implies that subjects with good neural survival tend to have lower spike probabilities, and their activated neurons are more efficiently activated by longer pulse durations compared to subjects with poor neural survival. There was no apparent relationship between these measures and the results of experiments 1 to 3, however, indicating that those experiments were probably measuring independent effects of changes in pulse duration.

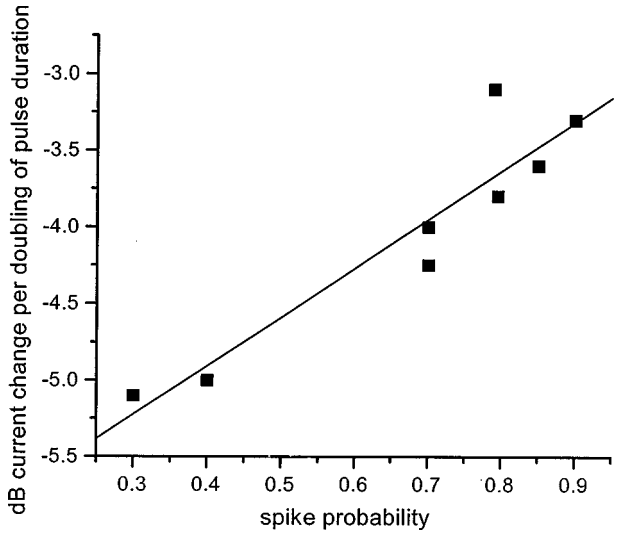

FIG. 7. The dB change in current for doubling of pulse duration at threshold, averaged across electrodes for subjects 1 to 8 (vertical axis), plotted against the derived average spike probability at threshold for a 50-Hz pulse train for the same subjects (data from McKay and McDermott, 1998). There is a significant correlation ($r=0.95$, $p=0.0006$) between these two measures.

The design of this experiment did not allow the effects of electrode configuration to be studied directly. This would require the effects related to electrode configuration to be studied for the same subject and cochlear location. However, it can be observed that including the CG and BP+2 data with the BP+1 data did not change the correlation between absolute stimulus amplitude and the dB/doubling value. It can be observed that some of these extra data points have somewhat lower dB/doubling values than predicted from the BP+1 data. It seems likely that if the relationship seen is dependent on the distance between activated neurons and the electrode, then a different electrode configuration may affect the outcome by changing the relationship between absolute amplitude and extent of current spread. However, the results suggest that, at least in terms of the slope of the regression line, the relationship between current and dB/doubling holds for all the electrode configurations measured.

VIII. CONCLUSIONS

The five experiments reported here have shown that percepts apart from loudness are affected by the pulse duration

used. A longer (266 μs) pulse duration resulted in a different timbre or pitch than a short pulse duration (50 to 100 μs) when other parameters (rate, electrode, loudness) were controlled. A longer pulse duration led to a greater perceptual interaction of temporal patterns on different electrodes, a result consistent with a larger spread of activation compared to that for short-pulse-duration stimuli of the same loudness. There was no effect on rate discrimination of different pulse durations for four out of five subjects, with a small advantage for short pulse durations in one subject. Finally, comparison of currents for threshold or equally loud stimulation at different pulse durations revealed a significant relationship between the absolute current amplitude and the dB change in current for doubling of pulse duration. This relationship was hypothesized to be due to a relationship between the neural charging characteristics and the distance of the excited neural elements from the stimulating electrode. Differences in this psychophysical measure among the subjects and electrode positions may be the result of differences in neural survival patterns.

The implications of these findings for speech perception with cochlear implants are not clear without further research. The fact that pulse duration variations can cause pitch or timbre changes may imply that a fixed pulse duration (i.e., using current alone to control loudness) may result in a more consistent place-pitch percept for subjects, and this may lead to improved speech perception. Furthermore, a more localized activation area for different electrodes may improve the place-specificity and hence the acoustic-frequency specificity of the stimulation patterns. If this leads to better speech perception, it would imply that shorter pulse durations may provide an advantage. The shortest pulse durations are attainable by using monopolar stimulation or wide bipolar stimulation modes. However, it has not been established how these electrode configurations might affect place-specificity in the absence of pulse duration changes. Further research should be directed at identifying the pulse-duration and stimulation mode combinations which optimize speech perception.

ACKNOWLEDGMENTS

This research was supported by the National Health and Medical Research Council of Australia project grant ''Speech perception by cochlear implantees: Perceptual and related psychophysical studies,'' the Human Communication Research Centre at the University of Melbourne, and the Co-operative Research Centre for Cochlear Implant, Speech and Hearing Research. We thank all the subjects who cheerfully took part in the experiments, and Professor Graeme Clark for his support.

[1]The pilot psychometric function determined for the longer pulse duration showed a chance score (37%) at 105 Hz and a score of 83% at 110 Hz.

Aronson, L., Rosenhouse, J., Podoshin, L., Rosenhouse, G., and Zanutto, S. (**1994**). ''Pitch perception in patients with a multi-channel cochlear implant using various pulse widths,'' Med. Prog. Technol. **20**, 43–51.

Baretto, R. L., and Pfingst, B. E. (**1992**). ''Electrical stimulation of the auditory nerve: Effects of pulse width on frequency discrimination,'' Hearing Res. **62**, 245–249.

Carhart, R., and Jerger, J. (**1959**). ''Preferred method for clinical determination of pure tone thresholds,'' J. Speech Hear. Disord. **24**, 330–345.

Grill, W. M., and Mortimer, J. T. (**1996**). ''The effect of stimulus pulse duration on selectivity of neural stimulation,'' IEEE Trans. Biomed. Eng. **43**, 161–166.

McKay, C. M., and McDermott, H. J. (**1996**). ''The perception of temporal patterns for electrical stimulation presented at one or two cochlear sites,'' J. Acoust. Soc. Am. **100**, 1081–1092.

McKay, C. M., and McDermott, H. J. (1998). ''Loudness perception with pulsatile electrical stimulation: The effect of interpulse intervals,'' J. Acoust. Soc. Am. **104**, 1061–1074.

Moon, A. K., Zwolan, T. A., and Pfingst, B. E. (**1993**). ''Effects of phase duration on detection of electrical stimulation of the human cochlea,'' Hearing Res. **67**, 166–178.

Parkins, C. W. (**1989**). ''Temporal response patterns of auditory nerve fibers to electrical stimulation in deafened squirrel monkeys,'' Hearing Res. **41**, 137–168.

Parkins, C. W., and Colombo, J. (**1987**). ''Auditory nerve single neuron thresholds to electrical stimulation from scala tympani electrodes,'' Hearing Res. **31**, 267–285.

Pfingst, B. E., and Morris, D. J. (**1993**). ''Stimulus features affecting psychophysical detection thresholds for electrical stimulation of the cochlea. II: Frequency and interpulse interval,'' J. Acoust. Soc. Am. **94**, 1287–1294.

Pfingst, B. E., and Rai, D. T. (**1990**). ''Effects of level on nonspectral frequency difference limens for electrical and acoustic stimuli,'' Hearing Res. **50**, 43–56.

Pfingst, B. E., de Haan, D. R., and Holloway, L. A. (**1991**). ''Stimulus features affecting psychophysical detection thresholds for electrical stimulation of the cochlea. I: Phase duration and stimulus duration,'' J. Acoust. Soc. Am. **90**, 1857–1866.

Pfingst, B. E., Holloway, L. A., and Razzaque, S. A. (**1996**). ''Effects of pulse separation on detection thresholds for electrical stimulation of the human cochlea,'' Hearing Res. **98**, 77–92.

Pijl, S. (**1997**). ''Pulse rate matching by cochlear implant patients: Effects of loudness randomization and electrode position,'' Ear Hear. **18**, 316–325.

Ranck, J. B. (**1975**). ''Which elements are excited in electrical stimulation of mammalian central nervous system: A review,'' Brain Res. **98**, 417–440.

Shannon, R. V. (**1985**). ''Threshold and loudness functions for pulsatile stimulation of cochlear implants,'' Hearing Res. **18**, 135–143.

Shannon, R. V. (**1989**). ''A model of threshold for pulsatile electrical stimulation of cochlear implants,'' Hearing Res. **40**, 197–204.

Townshend, B., Cotter, N., Van Compernolle, D., and White, R. L. (**1987**). ''Pitch perception by cochlear implant subjects,'' J. Acoust. Soc. Am. **82**, 106–115.

van den Honert, C., and Stypulkowski, P. H. (**1987**). ''Temporal response patterns of single auditory nerve fibers elicited by periodic electrical stimuli,'' Hearing Res. **29**, 207–222.

Zeng, F-G., Galvin III, J. J., and Zhang, C. (**1998**). ''Encoding loudness by electric stimulation of the auditory nerve,'' NeuroReport **9**, 1845–1848.

Constrained adaptation for feedback cancellation in hearing aids

James M. Kates
AudioLogic, 4870 Sterling Drive, Boulder, Colorado 80301

(Received 9 December 1998; revised 11 March 1999; accepted 11 May 1999)

In feedback cancellation in hearing aids, an adaptive filter is used to model the feedback path. The output of the adaptive filter is subtracted from the microphone signal to cancel the acoustic and mechanical feedback picked up by the microphone, thus allowing more gain in the hearing aid. In general, the feedback-cancellation filter adapts on the hearing-aid input signal, and signal cancellation and coloration artifacts can occur for a narrow-band input. In this paper, two procedures for LMS adaptation with a constraint on the magnitude of the adaptive weight vector are derived. The constraints greatly reduce the probability that the adaptive filter will cancel a narrow-band input. Simulation results are used to demonstrate the efficacy of the constrained adaptation. [S0001-4966(99)05308-4]

PACS numbers: 43.66.Ts, 43.60.Lq [JWH]

INTRODUCTION

Mechanical and acoustic feedback limits the maximum gain that can be achieved in most hearing aids (Lybarger, 1982). The acoustic feedback path includes the effects of the hearing-aid amplifier, receiver, and microphone as well as the acoustics of the vent or leak. System instability caused by feedback is sometimes audible as a continuous high-frequency tone or whistle emanating from the hearing aid. In most instruments, venting the earmold used with a behind-the-ear (BTE) hearing aid or venting the shell of an in-the-ear (ITE) hearing aid establishes an acoustic feedback path that limits the maximum possible gain to less than 40 dB for a small vent and even less for large vents (Kates, 1988).

In feedback cancellation, the feedback signal is estimated and subtracted from the microphone signal. The LMS adaptation algorithm (Widrow *et al.*, 1976) is generally used to adaptively estimate the feedback path in hearing aids, as opposed to more sophisticated adaptive algorithms, because of the limited processing power available in a battery-powered device. Computer simulations and prototype digital systems indicate that increases in gain of between 6 and 20 dB can be achieved in an adaptive system before the onset of oscillation, and no loss of high-frequency response is observed (Bustamante *et al.*, 1989; Engebretson *et al.*, 1990; Kates, 1991; Dyrlund and Bisgaard, 1991; Engebretson and French-St. George, 1993; Kaelin *et al.*, 1998). In laboratory tests of a wearable digital hearing aid (French-St. George *et al.*, 1993), a group of hearing-impaired subjects used an additional 4 dB of gain when adaptive feedback cancellation was engaged and showed significantly better speech recognition in quiet and in a background of speech babble. Field trials of a feedback-cancellation system built into a BTE hearing aid have shown increases of 8–10 dB in the gain used by severely impaired subjects (Bisgaard, 1993) and increases of 10–13 dB in the gain margin measured in real ears (Dyrlund *et al.*, 1994).

Feedback cancellation in hearing aids reduces the problems associated with acoustic feedback, but adaptive feedback-cancellation systems are, in turn, subject to signal cancellation and coloration artifacts that can occur for a narrow-band input signal. These problems are greatest for systems that do not inject a noise probe to assist in measuring the characteristics of the feedback path. This paper introduces a new approach to designing an adaptive feedback cancellation system when a probe signal is not used. The approach uses constraints applied to the adaptive filter coefficients to reduce the signal cancellation and coloration problems, and two different constraints are derived and evaluated.

One approach to adaptation for estimating the feedback path is to use a noise sequence continuously injected at a low level while the hearing aid is in normal operation (Engebretson *et al.*, 1990; Engebretson and French-St. George, 1993; Bisgaard, 1993). The weight update of the adaptive finite impulse response (FIR) filter proceeds on a continuous basis using the LMS algorithm. The difficulty with this approach is that the probe sequence reduces the signal-to-noise ratio (SNR) at the output of the hearing aid, thus compromising the sound quality. Adaptation using a probe signal injected during short intervals when the normal hearing-aid processing is turned off (Kates, 1991) would similarly degrade the sound quality by injecting noise and interrupting the audio output. Furthermore, the ability of such systems to cancel the feedback may be reduced by the presence of ambient noise or speech at the microphone input (Kates, 1991; Maxwell and Zurek, 1995).

Adaptive feedback cancellation without a probe signal is becoming the standard approach because it does not compromise the output noise level of the hearing aid. For a broadband input, such an adaptive system will generally converge to an accurate model of the feedback path. For a narrow-band input, however, the convergence behavior of the adaptive system will be severely compromised as a result of the large eigenvalue spread in the excitation correlation matrix (Haykin, 1996). The correlation between the input and output signals of the hearing aid for a narrow-band excitation leads to a bias in the adaptive solution unless adequate delay is provided in the hearing-aid processing (Bustamante *et al.*, 1989; Siqueira *et al.*, 1997). Frequency-domain adaptive al-

gorithms can also be used for feedback cancellation without a probe signal (Estermann and Kaelin, 1994; Knecht, 1997; Kaelin *et al.*, 1998). The block delay provided by frequency-domain processing using the short-time Fourier transform provides the input–output signal decorrelation needed for the convergence of the feedback cancellation in these systems. But for a sinusoidal input, even with a delay, feedback cancellation tends to minimize the error signal by canceling the input instead of modeling the feedback path.

The tendency for the feedback cancellation to cancel a sinusoidal input will, in general, cause a large mismatch between the adaptive feedback path model and the actual feedback path (Siqueira *et al.*, 1997). This mismatch is normally characterized by a large increase in the magnitude of the adaptive FIR filter coefficients. The excessively large filter coefficients, when combined with the hearing-aid gain function, can result in system instability or coloration of the output signal due to large undesired changes in the system frequency response.

One procedure to maintain system stability given a narrow-band input is to reduce the hearing-aid gain when a narrow-band input is detected. Kaelin *et al.* (1998) have proposed a block frequency-domain adaptive feedback-cancellation system that uses a metric similar to the block-to-block coherence of the input signal to control the hearing-aid gain. If the metric exceeds a threshold, the gain is reduced. This approach, however, reduces the hearing-aid gain even if the adaptive filter is not misbehaving, and can reduce the audibility of narrow-band sounds that the user may desire to hear.

An alternative approach to maintaining system stability for continuous adaptation without a probe signal is to limit the amount of mismatch that can occur between the physical feedback path and the adaptive model. In this paper, two procedures are derived for LMS adaptation with a constraint on the norm of the vector formed by the set of adaptive weights. The constraints greatly reduce the probability that the adaptive filter will cancel a narrow-band input.

The remainder of the paper presents an analysis of feedback cancellation in hearing aids and then shows the benefit of using the constrained adaptation for feedback cancellation. Steady-state analysis of the feedback-cancellation system illustrates the factors that can affect the accuracy of the adaptive filter and the filter convergence for systems adapting with or without a probe signal. The characteristics of the feedback path being modeled are then described. The two forms of constrained adaptation are then derived, and simulation results are used to give a comparison of the constrained adaptation with the conventional unconstrained approach for a system adapting without a probe signal.

I. STEADY-STATE ANALYSIS

A block diagram for a generic feedback-cancellation system is presented in Fig. 1. The system is assumed to be in steady state, with the adaptive filter weights having reached their asymptotic values; steady-state analysis does not depend on the procedure that was used to update the adaptive filter weights. The feedback cancellation is applied in an adaptive processing loop outside the hearing-aid processing

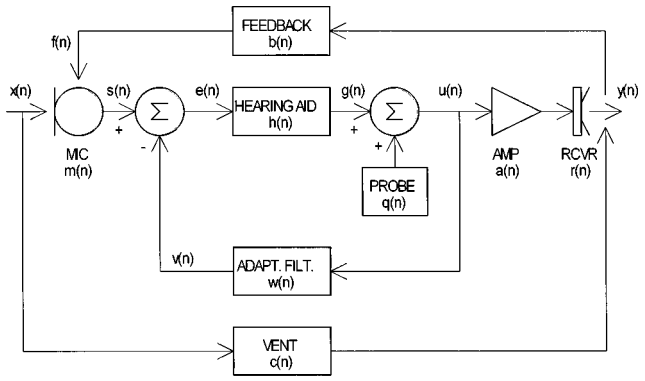

FIG. 1. Block diagram for a generic feedback-cancellation system in steady-state operation. The adaptive filter weights are assumed to have reached their asymptotic values.

$h(n)$ intended to ameliorate the hearing loss, and feedback cancellation has adapted to minimize the error signal $e(n)$. The probe signal used in some systems (Engebretson *et al.*, 1990; Engebretson and French-St. George, 1993; Bisgaard, 1993) is given by $q(n)$. Those systems that do not use a probe signal (Bustamante *et al.*, 1989; Estermann and Kaelin, 1994; Knecht, 1997; Siqueira *et al.*, 1997; Kaelin *et al.*, 1998) can be represented by setting $q(n)=0$ in the resultant system equations. The system of Kates (1991) that uses an intermittent probe signal can be represented by setting $q(n)=0$ during normal hearing-aid operation, and setting $h(n)=0$ during the time period when adaptation is performed.

The input to the hearing-aid processing is $s(n)$, which is the sum of the desired input signal $x(n)$ and the feedback signal $f(n)$. The processed hearing-aid signal is $g(n)$, which when combined with the optional probe signal gives the amplifier input signal $u(n)$. The amplifier impulse response is given by $a(n)$, the receiver impulse response by $r(n)$, and the microphone impulse response by $m(n)$. The adaptive filter weights are given by $w(n)$, and the signal in the ear canal is $y(n)$. The feedback path impulse response $b(n)$ includes both the acoustic and mechanical feedback, although acoustic feedback is assumed to dominate. The acoustic feedback path through the vent tends to have a high-pass behavior, and the acoustic feed-forward path $c(n)$ through the vent from the pinna to the ear canal tends to have a low-pass filter behavior (Macrae, 1985; Kates, 1988).

A steady-state analysis yields equations for the output signal $y(n)$, the microphone output signal $s(n)$, and the error signal $e(n)$. Details of the analysis are presented in the Appendix. Results of the analysis are presented in the frequency domain, denoted by uppercase variables, and the frequency variable ω is suppressed to save space. The output signal is given by

$$Y=\frac{QAR+X[C+H(WC+MAR)]}{(1-BC)-H[MARB-W(1-BC)]}. \tag{1}$$

Because C is a low-pass response and B is a high-pass response with reduced gain, one can safely assume that the product $|BC|\ll 1$. This assumption leads to a useful approximate solution:

$$Y \cong \frac{QAR + X[C + H(WC + MAR)]}{1 - H[MARB - W]}. \quad (2)$$

Thus the output consists of the probe signal (if used) filtered by the amplifier and receiver, plus the microphone input modified by the vent feed-forward path and the hearing-aid processing. The denominator of Eq. (2) shows that the system will be stable if either the gain of the hearing-aid processing H is low or if the feedback cancellation filter W comes close to canceling the feedback path $MARB$. Stability is guaranteed by the Nyquist criterion if

$$|H(MARB - W)| < 1. \quad (3)$$

The microphone output signal $s(n)$ is the combination of the microphone input and the feedback path output. The steady-state solution is given by

$$S = \frac{X[M(1 + WH)] + Q[MARB]}{(1 - BC) - H[MARB - W(1 - BC)]}. \quad (4)$$

The approximate solution for $|BC| \ll 1$ is given by

$$S \cong \frac{X[M(1 + WH)] + Q[MARB]}{1 - H[MARB - W]}. \quad (5)$$

Thus the signal input to the hearing-aid processing $h(n)$ can be colored by a mismatch between the feedback path and the filter modeling it in the denominator of Eq. (5), and can also be affected by the hearing-aid gain and the feedback path model if the product WH approaches unit magnitude.

The error signal used to control the feedback-cancellation filter adaptation is given by

$$E = \frac{XM + Q[MARB - W(1 - BC)]}{(1 - BC) - H[MARB - W(1 - BC)]}. \quad (6)$$

Again making the assumption that $|BC| \ll 1$ leads to

$$E \cong \frac{XM + Q[MARB - W]}{1 - H[MARB - W]}. \quad (7)$$

Exact feedback cancellation occurs when $W = MARB/(1 - BC)$, or approximately for $W \cong MARB$. System stability requires a very close match between the feedback path and the cancellation filter when the hearing-aid processing gain is high, and can tolerate poorer matches for low processing gains.

The error function given by Eq. (7) indicates how the system configuration will affect convergence of the adaptive filter. The best convergence will occur for an open-loop system (the hearing-aid processing is turned off by setting $H = 0$), such as the intermittent adaptation proposed by Kates (1991), because an open-loop system removes the effects of the denominator. Rapid adaptation in an open-loop system when using a probe signal requires $|Q| \gg |X|$, which is best achieved by injecting an intense probe signal in a quiet environment. Adapting in the presence of a stronger ambient signal, giving $|Q| \leqslant |X|$, will lead to slower convergence behavior because the error signal will be noisier, although the system will still tend to converge to the desired model of the feedback path. Thus the signal-to-noise ratio (SNR) that affects the convergence behavior in an open-loop system is the ratio of the probe signal power to that in the microphone input signal. The importance of the SNR in the performance of the adaptive system was observed by Kates (1991) and has also been discussed by Knecht (1997).

Despite the advantages of using a probe signal and adapting with the hearing-aid processing turned off, a practical hearing aid cannot use a probe and must adapt while in closed-loop operation. Adaptation during closed-loop operation without a probe signal (the probe is turned off by setting $Q = 0$) is problematical because the error can be minimized by either reducing the magnitude of the numerator or increasing the magnitude of the denominator of Eq. (7). For a sinusoidal input, the magnitude of the denominator can be driven large at the frequency of the sinusoid, converting Eq. (7) into a notch filter. This mode of operation can lead to cancellation of a sinusoidal input signal. Periodic input signals characterized by a limited number of spectral lines are also in danger of cancellation. The greater the number of coefficients in the adaptive FIR filter, the greater the number of sinusoidal components that can be canceled.

II. THE FEEDBACK PATH

The characteristics of the acoustic feedback path were measured for a ReSound BTE hearing aid attached to an AudioLogic Audallion processing unit containing a Motorola 56009 DSP with 12-bit A/D and 16-bit D/A converters. A white noise sequence was used to excite the receiver, and the response at the microphone was recorded. A sampling rate of 15.625 kHz was used. The feedback system impulse response was computed by cross-correlating the probe sequence with the microphone output. The frequency response was then computed by using an FFT of the windowed impulse response. The windowing involved removing the initial 60-sample system delay in the impulse response and then limiting the response to 256 samples using a window function that is unity for the first 128 samples followed by a half-cycle of a cosine to effect the transition from 1 to 0 over the second 128 samples.

Two sets of BTE vent test conditions were used. The conditions used the ''Eddi'' manikin (Earmold Design, Inc.) to simulate *in situ* BTE placement on the head and placement of the earmold in the ear canal. The dummy head has a pinna and ear canal but lacks an ear simulator to terminate the ear canal with the proper acoustic impedance. For the first condition, an unvented earmold was used, giving a tight fit in the ear canal. A telephone handset was then placed at varying distances from the side of the head. Responses were recorded for the handset removed, and in 1-cm increments from 5 cm from the ear to up against the ear. For the second condition a vented earmold was used.

The resulting frequency responses are shown in Figs. 2 and 3 for the two test conditions. The frequency response functions give the magnitude of the signal at the hearing-aid microphone relative to the magnitude of the digital probe signal sent to the amplifier. The measured feedback path includes the hearing-aid power amplifier, receiver, and microphone in addition to the acoustic and mechanical paths through and around the vent and earmold. The different head-mounted vent conditions give quite different transfer functions, although two or three peaks (2–3 complex pole

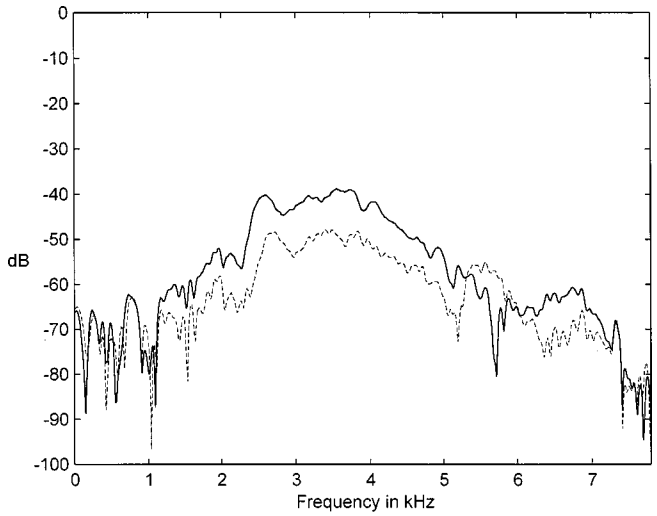

FIG. 2. Feedback path magnitude frequency response for a telephone handset removed (dashed line) and placed near the aided ear (solid line) for a behind-the-ear (BTE) hearing aid connected to an unvented earmold on a dummy head.

pairs) would be adequate to characterize the dominant shape for each of them. The magnitude of the transfer function for the vented earmold is about 30 dB greater than the transfer function for the unvented earmold, illustrating the increase in acoustic feedback that occurs when a vent is used. The response peak for the vented earmold occurs in the vicinity of 4–5 kHz, while the peak for the unvented earmold occurs in the vicinity of 2.5–4 kHz. These differences between the two earmolds illustrate the variety of possible feedback paths and the need to estimate the feedback path model parameters for each individual fitting.

Bringing the telephone handset up to the ear results in an increase of about 10 dB in the amplitude of the transfer functions independent of the type of earmold used. The shape of the transfer function in the vicinity of the peaks is essentially unchanged by the presence of the handset in these examples, but it is also possible that placing the handset close to the aided ear will create a resonant cavity that will cause substantial changes to the shape of the transfer function. The results for the intermediate handset positions (not shown) show many peaks and valleys in the responses caused by reflections between the head, handset, and the table top on which the dummy head was placed.

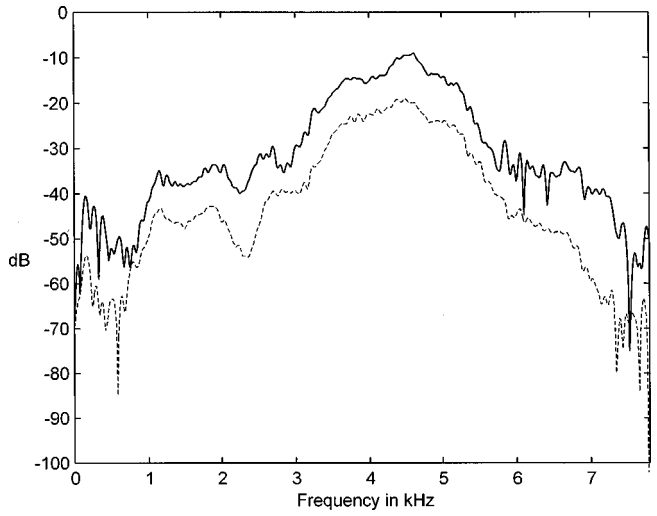

FIG. 3. Feedback path magnitude frequency response for a telephone handset removed (dashed line) and placed near the aided ear (solid line) for a behind-the-ear (BTE) hearing aid connected to a vented earmold on a dummy head.

III. CONSTRAINED ADAPTATION

The stability of the hearing aid will be maintained if the gain and feedback cancellation filter are constrained so that Eq. (3) is satisfied. This constraint requires that the physical feedback path transfer function be known at all times. However, the only information available during adaptation comprises the feedback-cancellation filter coefficients and the hearing-aid gain. Further information can be supplied by performing an initialization during the hearing-aid fitting; the initialization provides a reference set of adaptive filter coefficients obtained under controlled conditions. The reference set of coefficients can be determined by letting the system adapt in the presence of a white noise source until the adaptive filter coefficients reach steady state, or it can be determined using system identification procedures (Ljung, 1987). Even so, the information needed for an exact constraint is unavailable and approximate constraints must be derived instead.

Two approaches to constrained adaptation are derived in this section. Both approaches are designed to prevent the adaptive filter coefficients from deviating too far from the reference coefficients. In the first approach, the distance of the adaptive filter coefficients from the reference coefficients is determined, and the norm of the vector formed by the set of adaptive filter coefficients is clamped to prevent the distance from exceeding a pre-set threshold. In the second approach, a cost function is used in the adaptation to penalize excessive deviation of the adaptive filter coefficients from the reference coefficients.

A. Adaptation with clamp

The stability of the hearing aid will be maintained if the gain and feedback cancellation filter are constrained so that Eq. (3) is satisfied. The transfer function of the actual feedback path is not available, so the feedback path is approximated instead by the reference set of adaptive filter coefficients determined during initialization. This approximation leads to

$$|H(\omega,m)||W(\omega,m)-W(\omega,0)|\ll 1 \tag{8}$$

for block time-domain processing where $H(\omega,m)$ is the hearing-aid gain transfer function for block m, $W(\omega,m)$ is the adaptive filter transfer function for block m, and $W(\omega,0)$ is the transfer function for the reference adaptive filter coefficients. The less than sign in Eq. (3) has been replaced by very much less than in Eq. (8) for safety because the exact feedback path of Eq. (3) has been replaced by the approximate initial model fit to the feedback path. Starting with the definition of the discrete Fourier transform, one has

$$H(\omega,m)=\sum_{p=0}^{P-1} h_p(m)e^{-j\omega p}\ll \sum_{p=0}^{P-1}|h_p(m)| \tag{9}$$

and

$$W(\omega,m)-W(\omega,0)=\sum_{k=0}^{K-1}[w_k(m)-w_k(0)]e^{-j\omega k}$$
$$\leqslant\sum_{k=0}^{K-1}|w_k(m)-w_k(0)|,$$

where $h_p(m)$ are the P hearing-aid gain filter coefficients for block m, $w_k(m)$ are the K adaptive feedback-cancellation filter coefficients for block m, and $w_k(0)$ are the K reference adaptive feedback-cancellation filter coefficients. Thus the frequency-domain constraint of Eq. (8) can be rewritten in the time domain to get

$$\left[\sum_{p=0}^{P-1}|h_p(m)|\right]\left[\sum_{k=0}^{K-1}|w_k(m)-w_k(0)|\right]<\delta^2,$$

$$\text{where } \delta^2\ll 1. \quad (10)$$

The system stability can be maintained and coloration artifacts reduced by adjusting either the vector formed by the set of hearing-aid gain filter coefficients to have a reduced 1-norm, the difference between the adaptive and initial feedback filter coefficient vectors to have a reduced 1-norm, or by manipulating both sets of coefficients in combination.

In general, one wants the tightest bound on the adaptive filter coefficients that still allows the system to adapt to expected changes in the feedback path such as those caused by the presence of a telephone handset. The measurements of the feedback path indicate that the path response changes by about 10 dB in magnitude when a telephone handset is placed near the aided ear, and that this relative change is independent of the type of earmold used. The constraint on the norm of the adaptive filter coefficients can thus be expressed as

$$\frac{\sum_{k=0}^{K-1}|w_k(m)-w_k(0)|}{\sum_{k=0}^{K-1}|w_k(0)|}<\gamma, \quad (11)$$

where $\gamma\approx 2$ gives the desired 10-dB headroom above the reference condition.

The situation becomes more complicated when the hearing aid incorporates dynamic-range compression. Assume that the hearing-aid processing consists of a broadband compressor, giving a time-varying gain function $h(m)$. The stability constraint of Eq. (11) may be inadequate when the hearing aid is providing high gain at low signal levels, and a reduction in the gain may therefore be needed in addition to the constraint on the filter coefficients. The gain is to be reduced when instability is possible in the hearing aid, so an increase in the norm of the filter coefficients can be used to trigger the gain reduction. The resultant algorithm for the constraint after the adaptive weight update has been performed is given below:

0. Compute $\xi=\gamma\Sigma_{k=0}^{K-1}|w_k(0)|$.
1. If $\Sigma_{k=0}^{K-1}|w_k(m)-w_k(0)|<\xi$, set $\hat{\mathbf{w}}(m)=\mathbf{w}(m)$. Else $\hat{\mathbf{w}}(m)=\mathbf{w}(0)+[\mathbf{w}(m)-\mathbf{w}(0)]\xi/\Sigma_{k=0}^{K-1}|w_k(m)-w_k(0)|$.
2. If $\Sigma_{k=0}^{K-1}|w_k(m)-w_k(0)|\leqslant\alpha\Sigma_{k=0}^{K-1}|w_k(0)|$, set $\hat{h}(m)=h(m)$. Else $\hat{h}(m)$ is reduced monotonically as the norm of the coefficient difference increases.
3. Replace the adaptive filter coefficients $\mathbf{w}(m)$ with $\hat{\mathbf{w}}(m)$, and replace the compressor gain $h(m)$ with $\hat{h}(m)$.

Step 0 is performed at initialization, while steps 1–3 are performed for each block of data. Step 1 of the algorithm provides a clamp on the norm of the adaptive filter coefficient vector to prevent excessive vector growth and the associated coloration and stability problems. Step 2 reduces the hearing-aid gain to provide a further margin of stability if needed. The gain reduction in step 2 of the algorithm is purposefully left vague because the amount of gain reduction will depend on the hearing-aid compressor behavior and the audibility of the gain fluctuations introduced by the algorithm.

The algorithm for adaptation with a clamp given above is related to the scaled projection algorithm used in adaptive beamforming (Cox *et al.*, 1987). In the scaled projection algorithm, the weights for adaptive beamforming are divided into a nonadaptive set of weights that gives unit gain in the desired look direction plus an adaptive set of weights that adjusts to the spatial characteristics of the incoming signal. A projection matrix is used to remove any component of the adaptive weights that would lie parallel to the nonadaptive weights, thus minimizing cumulative roundoff errors, and the 2-norm of the adaptive weight vector is clamped to reduce the sensitivity of the adaptive system to correlated interference and errors in the assumed sensor locations. The clamp operation in the scaled projection algorithm prevents the cancellation of the signal when correlated interference is present at the sensor array, and thus serves the same function as the clamp on the adaptive weights in the hearing-aid feedback-cancellation algorithm. However, the derivation of the feedback-cancellation clamp is based on ensuring system stability, while the derivation of the clamp in the scaled projection algorithm is based on constraining the beamformer sensitivity to correlated measurement errors. Thus the clamp for the feedback-cancellation algorithm uses the 1-norm of the difference between the adaptive weight vector at any given time and the initial values, while the clamp for the scaled projection algorithm uses the 2-norm of the projection of the adaptive weight vector orthogonal to the look direction.

B. Adaptation with cost function

Feedback cancellation typically uses LMS adaptation to adjust the FIR filter that models the feedback path. The processing is most conveniently implemented in block form,

with the adaptive coefficients updated once for each block of data. Conventional LMS adaptation over the block of data minimizes the error signal given by

$$\epsilon(m)=\sum_{n=0}^{N-1} e_n^2(m)=\sum_{n=0}^{N-1}[s_n(m)-v_n(m)]^2, \tag{12}$$

where $s_n(m)$ is the microphone output signal and $v_n(m)$ is the output of the FIR filter for block m, and there are N samples per block. The new algorithm minimizes the error signal combined with a cost function based on the magnitude of the adaptive coefficient vector:

$$\epsilon(m)=\sum_{n=0}^{N-1}[s_n(m)-v_n(m)]^2+\beta\sum_{k=0}^{K-1}[w_k(m)-w_k(0)]^2, \tag{13}$$

where β is a weighting factor. The new constraint is intended to allow the feedback-cancellation filter to freely adapt near the initial coefficients, but to penalize coefficients that deviate too far from the initial values.

The LMS coefficient update for the new algorithm is given by

$$w_k(m+1)=w_k(m)-2\mu\beta[w_k(m)-w_k(0)]+2\mu\sum_{n=0}^{N-1} e_n(m)d_{n-k}(m), \tag{14}$$

where $d_{n-k}(m)$ is the input to the adaptive filter, delayed by k samples, for block m. The modified LMS adaptation uses the same cross-correlation operation as the conventional algorithm to update the coefficients, but combines the update with an exponential decay of the coefficients toward the initial values. At low input signal or cross-correlation levels the adaptive coefficients will tend to stay in the vicinity of the initial values. If the magnitude of the cross-correlation increases, the coefficients will adapt to new values that minimize the error as long as the magnitude of the adaptive coefficients does not grow too large. Adaptation that would require large changes in the adaptive filter coefficients, however, such as reacting to a sinusoid, will lead to incomplete reduction of the error. The exponential decay toward the initial values, which prevents the adaptive coefficients from becoming excessively large, also prevents the adaptive coefficients from reaching the optimum values for minimizing the error. In the case of the telephone handset the new algorithm may be less effective than the unconstrained approach given by Eq. (12). But in the case of a sinusoid or tonal input, the new algorithm greatly reduces the occurrence of processing artifacts because the artifacts are generally the result of unconstrained growth in the magnitude of the adaptive filter coefficients. Thus the adaptation with a cost function reduces coloration and improves system stability at the expense of a reduction in the ability to model large deviations from the initial feedback path.

IV. SIMULATION RESULTS

A feedback-cancellation system using closed-loop adaptation without a probe signal was simulated in MATLAB. The system block diagram is shown in Fig. 4. The adaptive

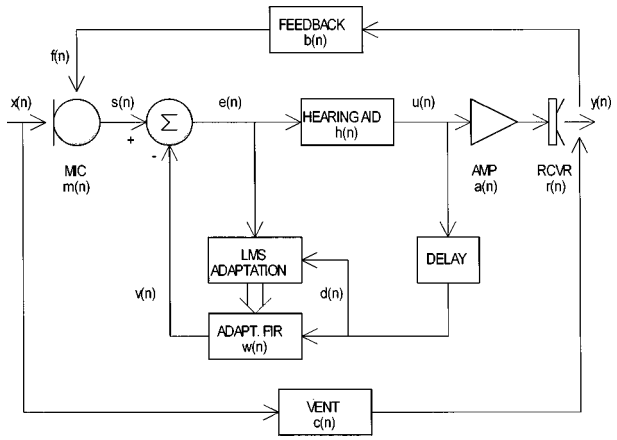

FIG. 4. Block diagram for the simulated feedback-cancellation system.

FIR filter modeling the feedback path used 16 taps. An ARX system identification procedure (Ljung, 1987) was used to determine the initial adaptive feedback-cancellation filter coefficients. It was assumed that there was no ambient noise present at the microphone during the initial parameter estimation. The feedback path used was the path measured for the vented earmold shown in Fig. 3 without the telephone handset present.

The magnitude frequency response of the feedback-cancellation filter after the initialization is shown in Fig. 5. The solid line is the measured feedback path, and the dashed line is the magnitude frequency response for the 16-tap FIR filter determined at the end of the initialization. The fit of the model to the actual data is quite good, and this system provides about 13 dB of additional hearing-aid gain when the feedback cancellation is engaged.

The adaptive system shown in Fig. 4 was then simulated. The hearing-aid processing consisted of a fixed 15-dB gain, and the feedback path was the one measured for the vented earmold without a telephone handset and presented in Fig. 3. The input signal was a 2-kHz sinusoid having unit amplitude, and the system sampling rate was 15.625 kHz. The adaptive system was run for the equivalent of 20 s in the

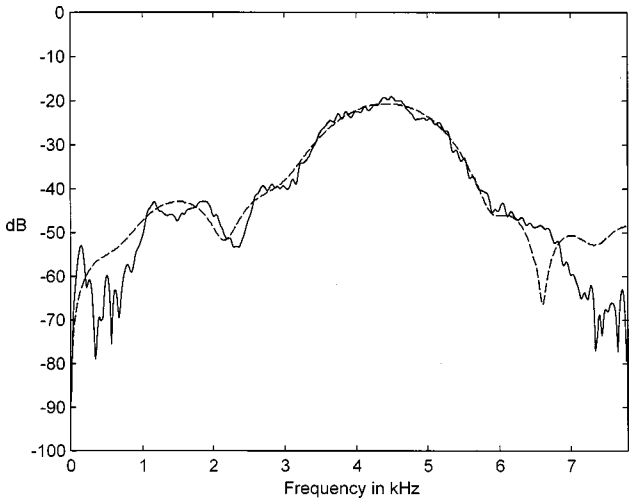

FIG. 5. Magnitude frequency response for the vented hearing-aid feedback path (solid line) and the 16-tap FIR model (dashed line) fit by the initial parameter estimation.

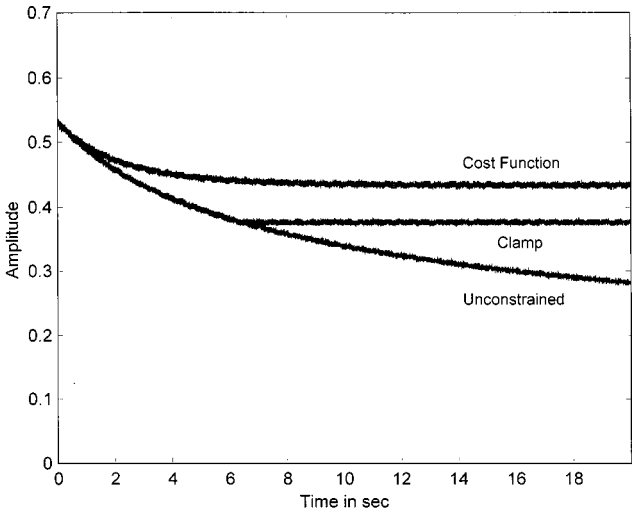

FIG. 6. Envelope of the hearing-aid output for the 2-kHz sinusoid for the unconstrained adaptation, clamped adaptation, and adaptation with the coefficient cost function.

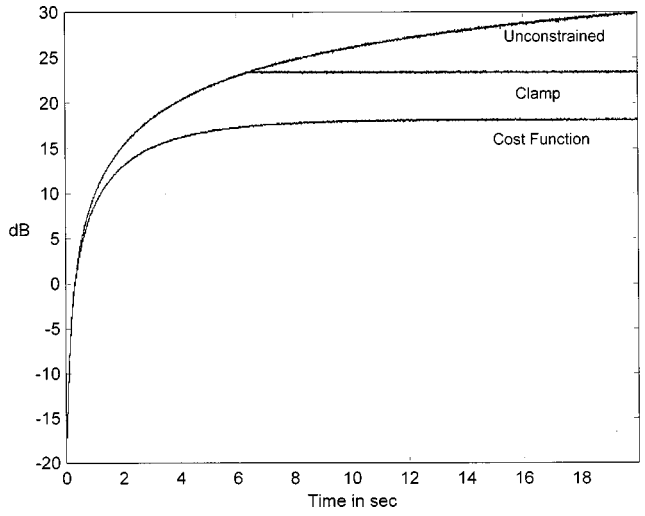

FIG. 7. Normalized signal for the difference between the feedback path model and the measured feedback path for the 2-kHz sinusoid for unconstrained adaptation, clamped adaptation, and adaptation with the coefficient cost function.

simulation time frame. This simulation time allowed the adaptive filter coefficients for the clamp and cost function approaches to essentially reach their asymptotic values.

The system was simulated for three versions of the block time-domain adaptive feedback cancellation. Unconstrained adaptation was used as the reference condition. The second test condition was the constrained adaptation of Eq. (11), with $\gamma=1.7$ chosen to give the tightest clamp that still allowed the system to adapt to a telephone handset brought up to the aided ear. The third test condition was the adaptation with the cost function given by Eq. (14). The adaptation exponential decay used $2\mu\beta=0.001$, and this value also allowed successful adaptive filter convergence for a telephone handset brought up to the aided ear. The adaptation used $\mu=10^{-7}$ and the data block size was 56 samples for all three algorithms tested. The time delay in the feedback path corresponded to one data block. Exciting the system with white noise resulted in the adaptive weights staying quite close to the values determined during initialization, indicating that the constrained adaptation has no deleterious effect on the system performance for a broadband input.

The excitation was then changed to the sinusoid, and the envelope of the hearing-aid output for the sinusoidal excitation is plotted in Fig. 6 for the three adaptation approaches. The feedback cancellation is working to minimize the error signal, which results in cancellation of the sinusoid. For the unconstrained adaptation, the sinusoid is multiplied by a decaying exponential gain function that will ultimately lead to complete cancellation of the output signal. The envelope for the clamped adaptation shows an initial decay similar to that for the unconstrained adaptation, but after the constraint on the 1-norm of the adaptive coefficient vector is engaged at approximately 6 s, the envelope decay ceases. The output signal intensity is reduced by about 2.9 dB, but further attenuation is prevented by the clamp constraint. The output signal envelope for the adaptation with the coefficient cost function shows the benefit of this approach to the adaptation. The signal is attenuated by only about 1.6 dB because the growth of the adaptive filter coefficients is constrained by the cost of becoming too large.

The normalized difference signal plotted in Fig. 7 is given by

$$z(n)=\frac{\langle|v(n)-f(n)|\rangle}{\langle|f(n)|\rangle}, \tag{15}$$

where $v(n)$ is the output of the adaptive filter modeling the feedback path and $f(n)$ is the output of the simulated feedback path, as shown in Fig. 4. The signal $z(n)$ gives the smoothed envelope of the difference between the modeled and measured feedback path signals, normalized by the envelope of the measured feedback path signal. A value of $z(n)$ less than 0 dB indicates that the model is converging to the measured feedback path. A value of $z(n)$ greater than 0 dB indicates that the model is diverging from the desired system even if the error signal $e(n)$ is being driven to zero by the adaptive filter. For a sinusoidal input, the minimum error will be obtained when the input signal is completely canceled and not when the adaptive system provides the best model of the feedback path.

The normalized difference plotted in Fig. 7 shows that the unconstrained adaptation starts at a reasonably close model of the measured feedback path, and then diverges from the desired model as the system attempts to cancel the 2-kHz sinusoid. The mismatch between the model and the actual feedback path for the unconstrained adaptation continues to grow with time as the signal cancellation shown in Fig. 6 becomes greater. The normalized difference signal for the clamped adaptation initially grows in a manner similar to that for the unconstrained adaptation. However, the mismatch gets clamped along with the adaptive coefficient vector once the 1-norm threshold of Eq. (11) is reached. The normalized difference signal for the adaptation with the coefficient cost constraint shows much less mismatch than for the coefficient vectors for the unconstrained or the clamped adaptation.

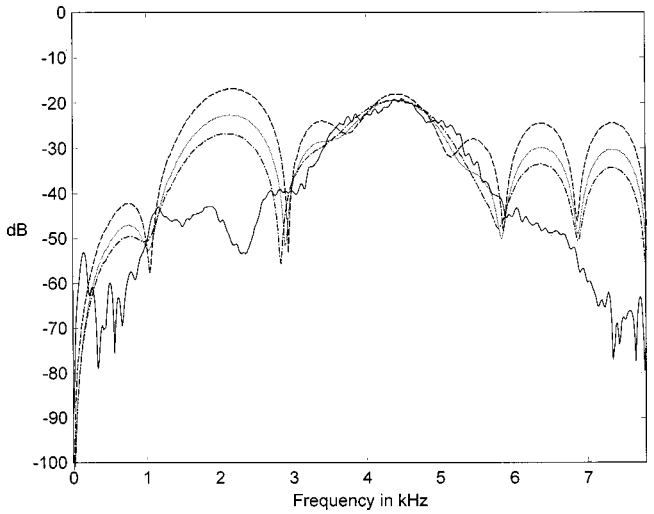

FIG. 8. Magnitude frequency response for the vented hearing-aid feedback path (solid line) and the FIR model after 20 s of adaptation. The response for the unconstrained adaptation is given by the dashed line, the response for the clamped adaptation is given by the dotted line, and the response for the adaptation with the coefficient cost function is given by the dot-dashed line.

The magnitude frequency response of the adaptive feedback path model at the end of the 20-s adaptation period is shown in Fig. 8. The mismatch between the measured and modeled feedback paths for the unconstrained adaptation is about 27 dB at 2 kHz, illustrating how the modeled feedback path is diverging from the desired transfer function. Continued unconstrained adaptation would result in even greater deviation of the model from the actual feedback path. Also note the increase in the unconstrained adaptive filter frequency response in the vicinity of 6.3 and 7.5 kHz, which increases the probability that the hearing aid will become unstable due to a violation of the Nyquist criterion at a frequency other than 2 kHz. The magnitude frequency response of the feedback path model for the clamped adaptation shows a slightly better match to the desired feedback path as the mismatch at 2 kHz is about 21 dB, and there is a corresponding reduction in the magnitude of the peaks at 6.3 and 7.5 kHz. The magnitude frequency response of the feedback path model for the adaptation with the coefficient cost function shows that the algorithm results in a feedback path model that stays closer to the measured feedback path than that resulting from unconstrained adaptation as the mismatch at 2 kHz has been reduced to about 17 dB.

V. DISCUSSION

Both the clamp and the cost factor approaches prevent the cancellation of an incoming sinusoid and the associated growth of the magnitude of the adaptive coefficient vector. Thus both approaches lead to better control of the stability problems and coloration artifacts associated with adaptive feedback cancellation in hearing aids while still allowing the system to track the expected changes in the feedback path. The approaches differ in the way the adaptive coefficients are constrained. The clamp allows free motion of the adaptive coefficient vector anywhere within a hypersphere centered on the tip of the reference coefficient vector, but prevents growth beyond the hypersphere boundary. Any point within the hypersphere that minimizes the error is equally valid, and the adaptive coefficient vector is free to wander within the hypersphere in response to changes in the input signal and feedback path. In the presence of a sinusoid or narrow-band input the adaptive coefficient vector will move to the hypersphere boundary, but there is nothing to force the adaptive coefficient vector to return to the vicinity of the reference vector once the narrow-band signal ends if it is followed by silence. Thus the choice of the scale factor that establishes the hypersphere radius is an important design decision because it involves a trade-off between the ability to adapt to a large change in the feedback path and the possibility that a large adaptive coefficient vector norm will lead to coloration artifacts or momentary instability.

The cost factor approach penalizes excessive growth in the norm of the difference between the adaptive and reference coefficient vectors. An analogy is that the tip of the adaptive coefficient vector is tied to an elastic band whose other end is fastened to the tip of the reference coefficient vector. The greater the separation between the two vectors, the greater the force to return the adaptive coefficients to the reference vector. Thus the cost factor approach replaces the hard boundary of the clamp with a soft boundary, but continuously pushes the adaptive coefficient vector toward the reference vector instead of allowing free motion within a bounded region. The factor that determines the distance that the adaptive coefficient vector is capable of moving away from the reference vector is the decay factor $2\mu\beta$ in Eq. (14), and this factor controls the trade-off between the ability to adapt to a large change in the feedback path as opposed to the possibility of causing coloration or momentary instability.

It is difficult to choose between the two approaches to constrained adaptation given the simulation results. To further investigate the processing, both forms of constrained adaptation were implemented in real time using a proprietary DSP chip in a behind-the-ear (BTE) hearing aid connected to a vented earmold fitted to the dummy head. Tests consisted of determining the maximum gain possible in the hearing aid before the onset of instability, determining the maximum gain when a telephone handset was placed close to the aided ear, and listening for processing artifacts when a tonal complex was used as the input signal as well as when the signal was suddenly stopped. The test results suggest that, at moderate hearing-aid gain levels, the clamp may be the more effective of the two approaches at allowing the system to adapt to the large changes in the feedback path associated with placing a telephone handset close to the aided ear. At high gain levels, the cost factor approach appears to be the more effective of the two approaches at reducing coloration artifacts. The differences between the two approaches depend on the adjustment of the parameters governing the adaptation constraints, and no one approach appears to be consistently superior.

VI. CONCLUSIONS

Feedback cancellation in hearing aids requires that the system track changes in the feedback path without any compromises in the sound quality of the instrument. The con-

cerns about sound quality preclude the use of a noise probe sequence since such a probe will reduce the SNR at the hearing-aid output. The feedback cancellation must therefore use the audio signal as the probe, with the result that adaptation during narrow-band or sinusoidal inputs must be accommodated. Feedback cancellation using unconstrained adaptation will lead to the cancellation of an incoming narrow-band signal instead of modeling the feedback path. As the adaptive feedback-cancellation filter deviates from the true feedback path, the tendency for the system to become unstable or for unwanted coloration to appear in the hearing-aid output greatly increases.

Two solutions to the problem of adapting in the presence of a sinusoid or narrow-band input were presented in this paper. The solutions involve constraining the adaptation, and use a reference filter coefficient vector determined during initialization. In the first approach, the adaptive feedback filter coefficient vector is constrained so that the 1-norm of the difference between the adaptive coefficient vector and the reference coefficient vector determined during initialization always stays below a threshold based on a scaled version of the 1-norm of the reference coefficient vector. In the second approach, a cost function is added to the adaptation, resulting in an adaptive coefficient update that incorporates an exponential decay of the coefficient vector toward the reference coefficient vector.

The simulation results presented in this paper have demonstrated the efficacy of the constrained adaptation algorithms. Both approaches prevent the cancellation of an incoming sinusoid and limit the mismatch between the adaptive feedback-cancellation coefficient vector and the reference coefficient vector. A real-time implementation indicates that both algorithms are effective in reducing coloration artifacts while still allowing the system to adapt to changes in the feedback path. Performance differences between the two approaches are subtle, however, and may depend on the specific implementation and feedback system being modeled.

The material presented in this paper is the subject of U.S. and international patent applications.

ACKNOWLEDGMENTS

The work reported in this paper was supported in part by ReSound Corporation and GN Danavox.

APPENDIX: DERIVATION OF THE STEADY-STATE SOLUTIONS

Working from left to right (input to output) in Fig. 1, the following signals can be defined:

$$F = YB, \tag{A1}$$

$$S = (X+F)M, \tag{A2}$$

$$E = (X+F)M - WU, \tag{A3}$$

$$U = (X+F)MH - UWH + Q, \tag{A4}$$

$$Y = UAR + (X+F)C. \tag{A5}$$

Solve Eq. (A4) for U, yielding

$$U = \frac{Q + (X+F)MH}{1+WH}. \tag{A6}$$

Substitute Eq. (A1) and Eq. (A6) into Eq. (A5) to then get

$$Y = \left[\frac{Q + (X+YB)MH}{1+WH}\right]AR + (X+YB)C. \tag{A7}$$

Solve Eq. (A7) for Y, yielding Eq. (1):

$$Y = \frac{QAR + X[C + H(WC + MAR)]}{(1-BC) - H[MARB - W(1-BC)]}. \tag{A8}$$

Equation (A8) and Eq. (A4) are then substituted into Eq. (A2) to give the solution for S of Eq. (4):

$$S = \frac{X[M(1+WH)] + Q[MARB]}{(1-BC) - H[MARB - W(1-BC)]}. \tag{A9}$$

To find the solution for E, start with the relationship from Fig. 1:

$$U = Q + HE. \tag{A10}$$

Substitute Eq. (A10) into Eq. (A3) to get

$$E = (X+F)M - W(Q+HE), \tag{A11}$$

which can be solved to yield

$$E = \frac{(X+F)M - WQ}{1+WH}. \tag{A12}$$

Substitute Eq. (A1) and Eq. (A8) into Eq. (A12) to give Eq. (6):

$$E = \frac{XM + Q[MARB - W(1-BC)]}{(1-BC) - H[MARB - W(1-BC)]}. \tag{A13}$$

Bisgaard, N. (**1993**). ''Digital feedback suppression: Clinical experiences with profoundly hearing impaired,'' in *Recent Developments in Hearing Instrument Technology: 15th Danavox Symposium*, edited by J. Beilin and G. R. Jensen (Kolding, Denmark), pp. 370–384.

Bustamante, D. K., Worrell, T. L., and Williamson, M. J. (**1989**). ''Measurement of adaptive suppression of acoustic feedback in hearing aids,'' Proc. 1989 Int. Conf. Acoust. Speech and Sig. Proc., Glasgow, pp. 2017–2020.

Cox, H., Zeskind, R. M., and Owen, M. M. (**1987**). ''Robust adaptive beamforming,'' IEEE Trans. Acoust., Speech, Signal Process. **ASSP-35**, 1365–1375.

Dyrlund, O., and Bisgaard, N. (**1991**). ''Acoustic feedback margin improvements in hearing instruments using a prototype DFS (digital feedback suppression) system,'' Scand. Audiol. **20**, 49–53.

Dyrlund, O., Henningsen, L. B., Bisgaard, N., and Jensen, J. H. (**1994**). ''Digital feedback suppression (DFS): Characterization of feedback-margin improvements in a DFS hearing instrument,'' Scand. Audiol. **23**, 135–138.

Engebretson, A. M., and French-St. George, M. (**1993**). ''Properties of an adaptive feedback equalization algorithm,'' J. Rehabil. Res. Dev. **30**, 8–16.

Engebretson, A. M., O'Connell, M. P., and Gong, F. (**1990**). ''An adaptive feedback equalization algorithm for the CID digital hearing aid,'' Proc. 12th Annual Int. Conf. of the IEEE Eng. in Medicine and Biology Soc., Part 5, Philadelphia, PA, pp. 2286–2287.

Estermann, P., and Kaelin, A. (**1994**). ''Feedback cancellation in hearing aids: Results from using frequency-domain adaptive filters,'' Proc. IEEE ISCAS, 1994, London, England.

French-St. George, M., Wood, D. J., and Engebretson, A. M. (**1993**). ''Behavioral assessment of adaptive feedback cancellation in a digital hearing aid,'' J. Rehabil. Res. Dev. **30**, 17–25.

Haykin, S. (**1996**). *Adaptive Filter Theory*, 3rd ed. (Prentice-Hall, Upper Saddle River, NJ).

Kaelin, A., Lindgren, A., and Wyrsch, S. (**1998**). ''A digital frequency-domain implementation of a very high gain hearing aid with compensation for recruitment of loudness and acoustic echo cancellation,'' Signal Process. **64**, 71–85.

Kates, J. M. (**1988**). ''A computer simulation of hearing aid response and the effects of ear canal size,'' J. Acoust. Soc. Am. **83**, 1952–1963.

Kates, J. M. (**1991**). ''Feedback cancellation in hearing aids: Results from a computer simulation,'' IEEE Trans. Signal Process. **39**, 553–562.

Knecht, W. G. (**1997**). ''Some notes on feedback suppression with adaptive filters in hearing aids,'' Proc. 1997 IEEE Workshop on Applications of Signal Processing to Audio and Acoustics, Mohonk Mountain House, New Paltz, NY, October 19–22, 1997, Session 2 paper 3.

Ljung, L. (**1987**). *System Identification: Theory for the User* (Prentice Hall, Englewood Cliffs, NJ).

Lybarger, S. F. (**1982**). ''Acoustic feedback control,'' in *The Vanderbilt Hearing-Aid Report*, edited by Studebaker and Bess (Monographs in Contemporary Audiology, Upper Darby, PA), pp. 87–90.

Macrae, J. (**1983**). ''Vents for high-powered hearing aids,'' The Hearing Journal, January 1983 , 13–16.

Maxwell, J. A., and Zurek, P. M. (**1995**). ''Reducing acoustic feedback in hearing aids,'' IEEE Trans. Speech Audio Process. **3**, 304–313.

Siqueira, M. G., Alwan, A., and Speece, R. (**1997**). ''Steady-state analysis of continuous adaptation systems in hearing aids,'' Proc. 1997 IEEE Workshop on Applications of Signal Processing to Audio and Acoustics, Mohonk Mountain House, New Paltz, NY, October 19–22, 1997, Session 2 paper 2.

Widrow, B., McCool, J. M., Larimore, M. G., and Johnson, Jr., C. R. (**1976**). ''Stationary and nonstationary learning characteristics of the LMS adaptive filter,'' Proc. IEEE **64**, 1151–1162.

On the lingual organization of the German vowel system

Philip Hoole
Institut für Phonetik und Sprachliche Kommunikation, Ludwig-Maximilians-Universität München, Schellingstrasse 3, D-80799 Munich, Germany

(Received 26 October 1998; revised 29 April 1999; accepted 3 May 1999)

A hybrid PARAFAC and principal-component model of tongue configuration in vowel production is presented, using a corpus of German vowels in multiple consonant contexts (fleshpoint data for seven speakers at two speech rates from electromagnetic articulography). The PARAFAC approach is attractive for explicitly separating speaker-independent and speaker-dependent effects within a parsimonious linear model. However, it proved impossible to derive a PARAFAC solution of the complete dataset (estimated to require three factors) due to complexities introduced by the consonant contexts. Accordingly, the final model was derived in two stages. First, a two-factor PARAFAC model was extracted. This succeeded; the result was treated as the basic vowel model. Second, the PARAFAC model error was subjected to a separate principal-component analysis for each subject. This revealed a further articulatory component mainly involving tongue-blade activity associated with the flanking consonants. However, the subject-specific details of the mapping from raw fleshpoint coordinates to this component were too complex to be consistent with the PARAFAC framework. The final model explained over 90% of the variance and gave a succinct and physiologically plausible articulatory representation of the German vowel space. © *1999 Acoustical Society of America.* [S0001-4966(99)03608-5]

PACS numbers: 43.70.Bk, 43.70.Kv, 43.70.Aj, 43.70.Jt [AL]

INTRODUCTION

A fundamental task in phonetic research is to arrive at a better understanding of how the set of contrasts required by a particular linguistic system on the one hand is implemented by the speech motor system on the other. The linguistic system with which we will be concerned here is the German vowel system, which can certainly be regarded as involving a rich set of contrasts.

The search to understand the motor implementation of such a system can lead in a number of different directions. For example, there is the major question of the interarticulatory coordination of different speech organs. Thus a phonologically defined contrast such as rounding proves to involve not only labial activity but also positioning of tongue and larynx (Wood, 1986; Hoole and Kroos, 1998). In a similar vein, there is the question of how lingual and mandibular activity are coordinated for vowel articulation (Johnson *et al.*, 1993; Hoole and Kühnert, 1996). A second important direction concerns the temporal organization of speech, for example, the way in which a contrast such as tense versus lax is reflected in the organization of elementary CV and VC movements for the production of complete syllables (Kroos *et al.*, 1997). In this paper we will be concentrating on a third important area, namely on the search for an efficient and hopefully revealing characterization of *resulting* tongue position in vowel production (i.e., we leave aside the question of separate lingual and mandibular contributions to resulting tongue position). This is a further crucial level, since tongue shape is largely responsible for vocal tract shape and thus for fundamental acoustic properties of the sounds produced (see Hoole, 1999, for preliminary analysis of articulatory-acoustic relations based on some of the speech material used in the present study).

We will explore a data-driven procedure for deriving a model of vowel articulation. This approach seems justified given that no complete concensus exists for the most appropriate articulatory characterization of vowels (Wood, 1975; Fischer-Jørgensen, 1985). Nonetheless, for the central technique to be used, the PARAFAC method of factor analysis, it has been claimed that it can uncover structures in the data that are not just convenient statistical constructs but actually have explanatory power.

Our question essentially boils down to determining how many dimensions underly the tongue shapes that can be observed for vowel articulation, and what their nature is. Thus it is inherently very unlikely that each of the many German vowels represents a unique way of configuring the tongue; rather, one would suspect that vowels scale a few common underlying patterns in slightly different ways. Indeed, given the fact that many descriptions of vowels use a two-dimensional framework (e.g., the traditional vowel chart; classification in terms of location, and width of the main constriction; $F1$ versus various combinations of the higher formants) it would be fairly surprising if the number of dimensions determined from direct measurement of tongue shape were substantially different from two. But precise number and nature remain an open empirical question and cannot be assumed *a priori.*

We can also consider the question of empirically uncovering the organizational principles underlying observable articulatory behavior from the point of view of the raw data available to articulatory analysis. We will be working with fleshpoint data from EMMA sensors. The raw data from such a sensor are not particularly revealing in themselves; the simple act of gluing a sensor to the tongue, however, carefully and systematically done, introduces an element of arbitrariness to the data. But it is a common problem in psychological research, and one of the motivations for the de-

velopment of factor analysis, that the underlying behavioral ''building blocks'' cannot be measured directly, but must be inferred from a multiplicity of (probably correlated) measures made on the behavioral surface. Similarly, direct measurements of the possible physiological building blocks of speech are very difficult to make, even with EMG (but see Maeda and Honda, 1994); nonetheless, measurements made on the tongue surface should systematically reflect these building blocks, and we may suspect that, due to the limited deformability of the tongue, their number is substantially less than the eight raw articulatory variables we have available in our data set (corresponding to two spatial dimensions measured at four sensor locations).

At the very least, such an endeavour should lead to a more readily apprehensible picture of the relation between vocal tract shape and linguistic structure, and ideally the results should be characterized by low dimensionality compared to the raw variables, phonetic interpretability, a potentially close relationship to the actual dimensions of organization employed by speakers, and finally by generalizability over speakers and perhaps languages.

We will here propose a hybrid PARAFAC and principal-component model of tongue position in German vowel production. The initial focus will be on the PARAFAC approach, which has given phonetically interesting results in a range of investigations (Harshman *et al.*, 1977; Jackson, 1988; most recently Nix *et al.*, 1996). PARAFAC is one of a class of three-mode analysis procedures, contrasting with standard principal-component and factor analyses, which are two-mode procedures. In the latter, the data to be analyzed are arranged in a two-dimensional array of observations (in our case the individual vowels) for a set of variables (in our case the fleshpoint coordinates). PARAFAC requires an inherently three-dimensional data structure, with the third dimension being represented in our case by the speakers (for a recent very extensive alternative approach to the analysis of multi-speaker datasets see Hashi *et al.*, 1998). The main advantage of PARAFAC over standard two-mode procedures is that it allows the problem of rotational indeterminacy in the orientation of the factor axes to be resolved, giving, it is claimed, greater explanatory power to the factors. A further related advantage, which is particularly important in the context of our current main goal of understanding the articulatory structure of a complete vowel system, is that the linguistic identity of the utterances analyzed is directly reflected in the way the data are structured for input to the PARAFAC algorithm. In other words, the data structure implicitly captures the investigator's knowledge as to what constitute linguistically equivalent observations for the different speakers. This contrasts with typical use of two-mode principal component or factor analyses (e.g., Maeda, 1990), where the aim is to sample the space of possible tongue shapes in some appropriate way, but without any particular reference to the linguistic identity of the selected observations.

Nonetheless, the PARAFAC model has a simple linear form:

Given measurements for nv vowels from na articulators for ns speakers, and assuming nf factors are extracted, then the results of the PARAFAC procedure are contained in three loading matrices **V**, **A**, and **S** (for vowels, articulators, and speakers) with dimensions $nv \times nf$, $na \times nf$, and $ns \times nf$, respectively.

For speaker k the complete dataset $\mathbf{Y}_k$ (dimension $na \times nv$) predicted by the model is then given by

$$\mathbf{Y}_k = \mathbf{A}\mathbf{S}_k\mathbf{V}^T, \tag{1}$$

where $\mathbf{S}_k$ is a matrix with the kth row of **S** on the main diagonal and zero elsewhere, and $\mathbf{V}^T$ is the transpose of **V**.

The articulators could be either a set of measurements along predefined gridlines or a set of fleshpoint x and y coordinates. Measurements for these articulators are assumed to be expressed as deviations from the mean for each speaker over all vowels (the formulation given here follows Jackson, 1988, p. 129. See Nix *et al.*, 1996, p. 3708 and Harshman *et al.*, 1977, p. 699, for alternative notations).

The simplicity of the model should be apparent from this formulation. Its potential for a parsimonious representation can be illustrated as follows: If two factors are enough to model a hypothetical dataset of ten vowels, ten speakers, and ten articulators, then the total size of the loading matrices is $2\times(10+10+10)=60$ compared to $(10\times10\times10)=1000$ elements in the raw dataset.

Nonetheless, finding a solution to the PARAFAC equation is mathematically more complex than the two-mode case and experimenter judgement plays a greater role.

In particular, the algorithm must be told in advance how many components to extract, whereas for principal-component analysis one can simply decide afterward how many components to retain for further consideration. In addition, the reliability of the solution must be assessed: Jackson (1988) discusses criteria for successful solutions under the headings convergence, uniqueness, degeneracy, generalizability, and goodness of fit (each of these criteria will be expanded on where appropriate below).

Moreover, there are also two sides to the simplicity of the model. On the one hand, it is very attractive that speaker-specific and speaker-independent effects are explicitly separated in the model; on the other hand, the model makes very strong assumptions about the form that these speaker-specific effects can take, i.e., each factor is simply scaled by a single speaker-specific weight for all vowels. As Harshman *et al.* (1977) put it:

''Thus if speaker A uses more of factor 1 than does speaker B for a particular vowel, then speaker A must use more of factor 1 than speaker B in all other vowels. The ratio of any two speakers' usage of a given factor must be the same for all vowels'' (p. 699).

Are these assumptions justified for human speech behavior? Interestingly, more recent work from UCLA (Johnson *et al.*, 1993) seems to have seen a turning away from this model and an emphasis on speaker-specific articulatory strategies that would not be compatible with the PARAFAC model. This kind of behavior emerged particularly from an analysis of patterns of *inter*articulator coordination (tongue, jaw) but the authors concede that the assumptions of the model may still hold for an examination of *resulting* tongue position. Nix *et al.* (1996) appear to concur with this view:

''the current claim is not that all speakers articulate the same vowels in exactly the same way; the claim made here is that two specific dimensions form an effective basis for the space of tongue shapes...'' (p. 3716).

Thus while one may even go as far as Nix *et al.* (1996) that the model is ''undoubtedly ultimately incorrect'' (p. 3708), it has nevertheless consistently given phonetically interesting characterizations of vowel systems. Moreover, by applying this attractively simple model we obtain the important benefit of a *quantitative* estimate of what might remain to be gained—at the price of greater complexity—from a more sophisticated model, and thus of how urgent the search for such a model really is. In addition to this quantitative benefit, it indeed turned out in the course of applying the model that we obtained improved *qualitative* insight as to where, in phonetic terms, speaker normalization by the simple PARAFAC linear scaling approach is too restrictive. Specifically, this mainly appeared to involve consonantal influences on vowel articulation, and led to the abovementioned hybrid modeling approach, in which the PARAFAC model was supplemented by a principal-component approach that retained as much as possible of the spirit of the PARAFAC approach, while incorporating a relaxation of the constraints on the possible form of speaker-specific effects.

I. SCOPE OF THE INVESTIGATION

The dataset to which we wished to apply the PARAFAC approach is richer in two main respects than those reported elsewhere in the literature. First, we had recorded data for seven speakers. This is a larger number than has previously been used for PARAFAC analyses of tongue configuration (though Linker, 1982, has analyzed lip configuration for eight speakers of multiple languages). More significantly, each speaker recorded the speech material at two different speech rates (normal and fast) in separate sessions. It has been clear since the investigation of Kuehn and Moll (1976) that speakers implement an increase in speech rate by different means. The main possibilities appear to be either a general scaling down of articulation, or a pattern in which there is little target undershoot, but in which temporal compression (not considered directly here; see Kroos *et al.*, 1997) is achieved by increasing velocity. Both these patterns represent consistent types of articulatory behavior, which should emerge as such in the speaker weights derived by the PARAFAC algorithm. For the present purposes the main interest is methodological: The claim that the PARAFAC algorithm allows us to capture underlying principles of articulatory organization would be seriously compromised if speaker weights varied haphazardly over sessions. This would suggest that the algorithm is unduly sensitive to incidental but unavoidable differences in recording conditions over sessions. In practice, for the purpose of running the algorithm the seven speakers×two sessions are simply treated as 14 different speakers. After running the algorithm the patterns in the speaker weights for the two sessions can then be compared.

Second, our speech material also included all vowels in three different consonantal contexts. Previous PARAFAC analyses have typically analyzed vowels in only one context (or at least only one token per vowel). Would it be possible to capture effects of consonantal context on vowel articulation in this kind of analysis? As we will see below, this task turned out to be not completely straightforward and required a departure from the basic PARAFAC model.

Application to data with carefully controlled consonantal contexts was also a necessary first step toward potentially being in a position to apply the PARAFAC approach to a further more natural corpus we have available for each speaker, in which each vowel is spoken in 15 different consonantal contexts.

A further difference between our work and earlier work lies in the use of fleshpoint data. Nix *et al.* (1996) suggested that the original PARAFAC work based on cineradiographic measurements made along anatomically defined grid lines may artificially constrain the possible solutions—i.e., there is no straightforward way of capturing horizontal movement of tongue tip/blade. In their reanalysis of Harshman *et al.*'s (1977) radiographic data (13 gridlines) they determined the x/y coordinates of 13 ''pseudo-pellets'' equally spaced on the tongue contour (*op. cit.*, p. 3711) and suggested that the resulting solution was more easily interpretable. Yet as far as we know, directly measured as opposed to reconstructed fleshpoint data has not yet been analyzed with the PARAFAC technique, so the above claim could clearly benefit from further substantiation. Measured fleshpoint data also have one clear disadvantage compared to radiographic data, which is that the pharyngeal region is typically not well represented. However, work by Kaburagi and Honda (1994) using simultaneous articulographic and ultrasound measurements of the tongue indicated that the tongue contour could be reconstructed quite well from electromagnetic sensors attached to the tongue at realistically accessible locations (see also Badin *et al.*, 1997).

In purely numerical terms we have 8 pieces of articulatory information available per utterance (4 sensors×2 coordinates), compared to 13 for the original Harshman *et al.* radiographic study.

A final minor point where our work supplements previous work is that the German vowel system has yet to be analyzed with this approach. The German vowel system differs both phonetically and phonologically quite substantially from the American English system. In particular, due to the presence of front rounded vowels (and leaving diphthongs out of consideration) there are 50% more vowels to be considered.

II. THE DATASET

A. Subjects

The speakers consisted of seven adults, six males and one female, all phonetically trained and experimentally experienced. Their dialects showed no marked regional characteristics but conformed to general High German.

B. Speech material

The speech sample consisted of all (15) monophthongal vowels of German. These can be grouped with one exception (ɛː) into tense–lax (long–short) pairs: /iː,ɪ/, /yː,ʏ/, /eː,ɛ/, /øː,œ/, /aː,a/, /oː,ɔ/, /uː,ʊ/.

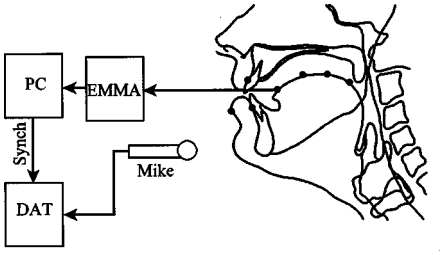

FIG. 1. Experimental setup showing approximate sensor locations (omitting reference sensor on bridge of nose).

The test utterances were formed by inserting the vowels into three different consonant contexts: /p_p/, /t_t/, and /k_k/. These contexts were chosen to give three strong and clearly defined directions of coarticulation with neighboring sounds. Each symmetric CVC sequence, in turn, was embedded in a carrier phrase of the structure *Ich habe geCVCe gesagt* (*I said* ____) with stress on the target vowel. The resulting test words are not lexical items in German but all conform to regular word formation rules. Spellings were devised using regular German spelling rules and the words were presented to the subjects in ordinary German orthography. The speakers read five repetitions of each of the CVC combinations at two different speaking rates, normal and fast.

C. Recordings

Articulatory movements were monitored by means of electromagnetic midsagittal articulography (AG100, Carstens Medizinelektronik). For a general overview of EMMA, see Perkell *et al.* (1992); for an evaluation of the AG100, see Hoole (1996).

In order to register tongue movements, four transducers were mounted on the midline of the tongue at roughly equidistant intervals from about 1 to 6 cm from the tongue tip. The main anatomical reference used was to locate the third coil in line with the rear edge of the lower second molars, with the tongue at rest in the mouth (normally roughly below the junction of the hard and soft palate). Jaw and lower-lip movement were also monitored, but will not be discussed further here. Two coils tracked head movement and were attached to the bridge of the nose and to the border of the upper incisors and gums. Finally, two additional reference coils mounted on a bite-plate were used to define the horizontal axis as the line from the lower edge of the upper central incisors to the lower edge of the upper second molars. Figure 1 shows typical locations of the transducers.

Movements were recorded with a sampling frequency of 250 Hz (low-pass filtered at 35 Hz). The audio signal was recorded on DAT tape, with synchronization pulses generated by the computer on the second channel. For a detailed description of system calibration and data preparation, see Hoole (1996).

D. Experimental procedure

The subjects were tested in two separate recording sessions, usually a few days apart, lasting about 1 h each. In the first recording session the speakers produced the utterances at normal speech rate, in the second recording at a fast speech rate. The consistency of the speech rate across an experimental session was controlled by regular presentations of taped example utterances which were determined for each subject individually in a previous pilot study.

During the recording sessions transducers were monitored with a set of online procedures for evidence of misalignment relative to the transmitter assembly (cf. Perkell *et al.*, 1992; Hoole, 1996).

In a separate session, a reference trace of the midsagittal contour of the subjects' hard palate was made from a dental impression.

For each vowel, one frame of articulatory data was extracted at the acoustically defined midpoint of the vowel. This was generally very close to the point that would be extracted by means of a minimum articulator velocity criterion, but avoided problems with a few systematic cases where minimum velocity was poorly defined, particularly back vowels in /k/-context.

The data were then averaged over the five repetitions of each vowel in each of the three consonantal contexts. This can be expected to improve the fit of the model to the data by removing some random variation and represents a slight departure from the procedure followed in earlier investigations in which individual vowel tokens were analyzed (in radiographic studies multiple repetitions have generally not been available). The use of averaged data appears justified since we are principally interested here in regularities in tongue configuration in the realization of the German vowel system. We have discussed patterns of token-to-token variability in vowel production elsewhere (Hoole and Kühnert, 1995).

After averaging over individual tokens the overall mean of each articulator position was then determined for each subject and subtracted from the data. The data seen by the subsequent algorithm thus consist of displacements from the average articulatory configuration of each subject.

III. ANALYSIS

This main section will trace out the steps required to arrive at a phonetically satisfying model of our dataset. The ride toward a PARAFAC model of vowel articulation turned out to be a bumpy one, and, as already mentioned above, a departure from the basic PARAFAC framework was ultimately required. Identifying in phonetic terms the sources of these difficulties effectively constitutes one of the results of this study.

The procedures followed and the results obtained will be given in the following four subsections: A. Development of the PARAFAC model; B. Discussion of the model; C. Extension of the model; D. Discussion of the extensions.

A. Development of the PARAFAC model

1. A false start

As already mentioned, for PARAFAC analysis it is necessary to choose the number of factors on which to base the model. A preliminary stage therefore involves assessing the number of factors likely to be appropriate to the data. One way of doing this is to apply a (two-mode) principal-component analysis to each speaker individually. If the speaker-specific differences are consistent with the

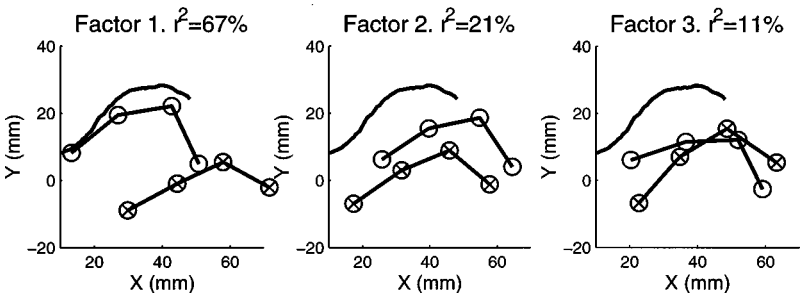

FIG. 2. Example for one speaker of tongue shapes related to the first three components of a principal-component analysis of vowel data. Each panel shows displacement from mean tongue position caused by setting each component in turn to ±2 standard deviations (positive deviation: unfilled circles; negative deviation: circles with crosses). More anterior locations are to the left. Percent variance explained is also indicated.

PARAFAC model, then PARAFAC should be able to model the complete data set using the number of factors typically appropriate for individual speakers in a principal-component analysis. For our data, the principal-component analyses consistently gave the picture that three factors captured the data well. The first two factors together usually accounted for about 85% of the variance and generally bore some resemblance to the factors referred to by Harshman *et al.* (1977) as ''front raising'' and ''back raising,'' respectively. The third factor, typically accounting for about 12% of the variance, captured the alternation between tongue-blade and tongue-dorsum raising for the (in our data) mutually exclusive consonantal contexts /t/ and /k/. An example of this analysis for one speaker is shown in Fig. 2.

It thus appeared warranted by the data to base the PARAFAC model on three factors. This figure also seemed plausible in phonetic terms, based on the expectation of a roughly two-dimensional vowel space, plus an additional dimension to capture nonvocalic behavior of the tongue-tip. The attempt proved unsuccessful, however. The algorithm failed to converge. This suggests that some aspects of the structure of the dataset are inconsistent with the PARAFAC model, and suspicion falls most obviously on the influence of consonantal context, as this represents the most substantial extension of our dataset compared with earlier, successful applications of the PARAFAC model. We will return again below to more precise consideration of the properties of the data inconsistent with the PARAFAC model.

Before attempting further analysis of the complete dataset it now appeared necessary to analyze the dataset separately for each consonantal context, first, in order simply to confirm that our data are amenable to analysis under conditions comparable to other reported investigations, and second, in order to provide a baseline against which to judge further attempts at getting to grips with the full data set.

2. Models for individual consonantal contexts

We present first the results for the vowels spoken in the /p_p/ context, as this can be regarded as the most neutral consonantal context with regard to lingual articulation.

Based on the results of the principal-component analysis and results from the literature mentioned above we would expect a two-factor solution to be appropriate for a dataset involving only one consonantal context. This indeed turned out to be the case. The two-factor solution was clearly reliable (whereas, as a cross-check, a three-factor solution again was not).

Here we should state more explicitly how reliability was assessed. For this stage of the analysis the following two criteria were used: first, the alternating least squares algorithm had to succeed in converging and giving the same solution when initiated from at least six different random starting points; second, acceptable values of a diagnostic for degeneracy had to be obtained. Following Nix *et al.* (in turn quoting Harshman and Lundy, 1984), this was based on the triple product (over the three modes) of the correlations between corresponding sets of weights for each pair of factors (in practice we never have more than one pair). Harshman suggested that triple products more negative than −0.3 are indicative of a degenerate model since the factors in the pair are simply tending to cancel each other out.[1]

For the two-factor solution of the /p/-context material the unexplained variance amounted to 7.7% and the rms error to 1.24 mm. This is very much par for the course: for example, Harshman *et al.* obtained 7.4% variance unexplained and an rms error of 1.74 mm.

As explained in the Introduction, the algorithm provides three sets of weights for each of the two factors: for the articulators (tongue *x* and *y* displacements), for the vowels and for the speakers. After deriving the final PARAFAC model we will look in detail below at the patterns to be observed in each of these sets of weights. Suffice it to say here, for this first analysis based on /p/-context only, that the first factor represents a contrast between high front and low back and the second factor mid front to high back. Particularly for the first factor this is not unlike Harshman *et al.*'s original two-factor solution.

For the /k/-context vowels a two-factor model was also successfully extracted. Both the modelling error (9% variance unexplained, 1.1-mm rms error) and the model itself were very similar to the /p/-context analysis. The latter aspect can be assessed by separately calculating for each factor the triple product of the correlation coefficients between corresponding sets of weights in the /p/-context model and the /k/-context model. Highly similar models would have triple products approaching +1.[2] For the two models compared here we obtained values of 0.84 for factor 1 and 0.69 for factor 2 (we note in passing that specifically for the correlation between the vowel weights we would expect a high but not perfect correlation since the two sets of vowels, i.e., those spoken in /p/-context and those spoken in /k/-context, are obviously in some sense different).

Surprisingly, the extraction of a two-factor model for the /t/-context vowels ran into problems. The algorithm took longer to converge than in the /p/- and /k/-contexts and the

resulting solution gave strong signs of being degenerate—the triple product was strongly negative: −0.56 (the amount of unexplained variance was also rather higher at 13%, although the rms error remained about the same: 1.2 mm). Moreover, the solution was substantially different from the /p/-case, especially for factor 2, the triple product of the correlation coefficients being 0.8 for factor 1 and −0.13 for factor 2.

One possible reason for a degenerate solution can be the extraction of too many factors from the data. At first sight it seems phonetically very implausible that this can be the case here, since it is unclear how one could model a vowel system such as German with just one factor. Indeed, checks made by extracting a one-factor solution for each of the three consonant contexts separately provided no evidence at all that the /t/-context data could be better modeled than the other two contexts with only one factor.

However, as we will see below, there remains a grain of truth in this possibility. A further situation that can lead to degeneracy is inconsistency of the data with the PARAFAC model. As we will also see below, it turns out that the way tongue tip/blade raising is captured by the front two EMMA sensors exhibits speaker-specific patterns that run contrary to the PARAFAC model. And clearly this problem is most relevant in the /t/-context.

These separate analyses of individual consonant contexts had indicated what the ideal result for a complete model might be (i.e., an rms modeling error in the region of 1.2 mm) and also enabled potential problems in the data to be localized. The aim was now to proceed back toward a model for the complete data set.

3. Models for multiple consonantal contexts

As a first step back we tested whether a successful two-factor model could be extracted when the data involving the two ''easy'' consonant contexts /p/ and /k/ were analyzed together. This proved to be the case. Compared to the previous independent analyses of the /p/- and /k/-context vowel material, the unexplained variance and the rms error deteriorated somewhat to 12% and 1.5 mm, respectively. The model for combined /p/- and /k/-context vowel material was very similar to the model extracted for /p/-context only, the triple product of the correlations between combined- and single-consonant models amounting to 0.97 and 0.98 for factors 1 and 2, respectively. The combined-consonant model was also similar to the model extracted for /k/-context only—the corresponding triple products being 0.94 and 0.78.[3]

Since this step had been successful we then restored the t-context material to the dataset and extracted a *two*-factor solution for the complete dataset. This was also successful in the sense that the algorithm converged readily to a reproducible solution, and no evidence of degeneracy was found. Not surprisingly, however, there was a further noticeable increase in model error. Unexplained variance now amounted to 20% and the rms error to 1.9 mm. In the subsection below on extending the model we will look in detail at the model error, in particular with regard to subject-specific and subject-independent patterns and with regard to the influence of consonantal coarticulatory effects. But first we will concentrate in the next subsection on discussing in detail the two-factor PARAFAC solution just extracted from the complete dataset. It seems justifiable to use this as our basic model of vowel articulation since the two-factor solution extracted from the complete dataset is still very similar to the solutions for the simple ''p-only'' or ''k-only'' data: triple products of 0.96 and 0.55 for factors 1 and 2, respectively (p-only comparison) and 0.93 and 0.88 (k-only comparison).

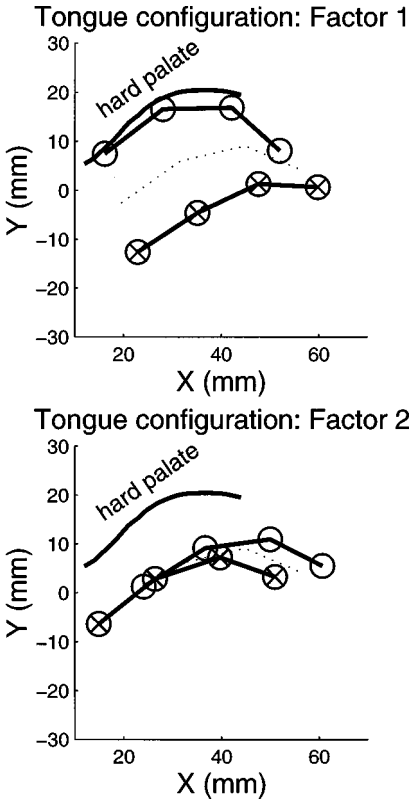

FIG. 3. Tongue shapes related to the factors of the two-factor PARAFAC model of the complete dataset. Each panel shows displacement using mean speaker weights from mean tongue position (shown by dotted line) caused by setting each factor in turn to ±2 standard deviations (positive deviation: unfilled circles; negative deviation: circles with crosses). More anterior locations are to the left. Palate contour is an average of overlapping portions of the palate contours of the seven speakers.

B. Discussion of the PARAFAC model

Detailed presentation of the two-factor model can proceed most conveniently by taking each of the three sets of weights in turn.

1. Articulator weights

The weights with respect to each factor for the eight articulator coordinates can be shown most vividly by plotting each factor as a pattern of tongue displacement around average tongue position using averaged speaker weights. The result is shown in the two panels of Fig. 3.

The first factor shape looks quite similar to the first factor derived by Harshman *et al.*, and referred to by them as ''front raising.'' In our Fig. 3 we see substantial raising (and some advancement) of the front part of the tongue, and advancement (with some raising) of the rear part of the tongue. Our second factor is less similar to their second one, how-

ever (referred to by them as ''back raising''). It would share with Harshman *et al.*'s factor the responsibility for forming a constriction in the velar region, but our factor 2 shows above all a pattern of advancement and retraction, which is hardly the case for the ''back raising'' factor.

Based on the rationale of Nix *et al.* that there may be advantages in interpretability in analyzing true *x*/*y* components of fleshpoint movement rather than displacements along a fixed set of gridlines, one might have expected that our result would be more similar to the Nix *et al.* reanalysis of the Harshman data. But this does not really seem to be the case. Our factor 1 is fairly similar to what (confusingly) emerges as factor 2 in their reanalysis (Nix *et al.*, 1996, Fig. 7b, p. 3715) but their factor does not involve much change in oral opening at the frontmost tongue location. Their factor 1 is similar to our factor 2 in mainly involving retraction versus advancement, but whereas our factor 2 couples slightly higher tongue position with retraction, with them the opposite is the case.

We will return in the concluding discussion to the differences between our solution and other solutions from the literature.

2. Vowel weights

We now turn to consideration of how the German vowel system is represented in the space of the first two factors. The three panels of Fig. 4 show the distribution of the vowels in this space separately for each of the three consonantal contexts.

Factor 1 has been allotted to the ordinate since it has the strongest tongue-raising component; however, since neither factor exclusively involves raising versus lowering, or advancement versus retraction, the vowel space mapped out by the two factors is rotated with respect to traditional phonetic representations of the vowel space. The extreme vowels for each factor are /i:/ and /o:/ for factor 1 and /ɛ:/ and /u:/ for factor 2.

Let us first discuss some further features of the vowel space that are similar over consonant context, before turning to some important differences.

We will look first at the contrast between tense and lax vowels. Here we need to consider front and back vowels separately. We find for the front vowels and /a/ that the lax variant takes on less extreme values (i.e., closer to zero) for factor 1.[4] However, a consistent pattern with respect to factor 2 is not discernible. For the back vowels /u/ and /o/ the situation is different since it is now factor 2 rather than factor 1 that shows the more consistent pattern: Lax vowels show less extreme values with respect to factor 2.

Comparing front unrounded and rounded vowels, it is clearly the case that the rounded cognates occupy less extreme positions with respect to factor 1. In fact, every front rounded vowel is actually closer on the factor 1 dimension not to its direct unrounded cognate, but to the phonologically next lowest unrounded vowel (/y:/ closer to /e:/ than to /i:/, etc.). The comparison between unrounded and rounded thus has similarities to that between tense and lax (see also Hoole and Kühnert, 1996). However, the unrounded–rounded contrast also involves slightly but consistently more negative values of factor 2 for unrounded (i.e., these show, roughly speaking, more fronting than the rounded vowels).

Let us now consider differences in the vowel space for the different consonantal contexts. Perhaps the most striking feature is the distribution of the vowels with respect to factor 2 for the /t/-context compared to the other two contexts. In /t/-context essentially all vowels except the tense back vowels /u:/ and /o:/ cluster close to zero; the range of variation along the factor 2 dimension is compressed, compared to the other two contexts. This probably provides part of the reason why we encountered difficulties in extracting a stable two-factor solution for /t/-context vowels on their own. Considering factor 2 primarily as an advancement-retraction dimension, the effect is thus essentially one of retraction of the front vowels (and /a/) in /t/-context. This is so substantial that there is no overlap in factor 2 values for front vowels in /t/-context with their values in the other two contexts. This is illustrated in terms of the complete fleshpoint data for one vowel of one speaker in the top panel of Fig. 5. The direction of this trend was absolutely consistent over all front vowels and all speakers. In terms of the raw data, the second tongue sensor from the front was located on average about 4 mm more posteriorily in /t/-context than in /k/-context, with generally larger effects for lax vowels than tense vowels and for the normal compared to fast-rate sessions.

A corollary of this finding is that the nominally front vowel /œ/ is located very close to the back vowels /ʊ/ and /ɔ/ in the /t/-context but is widely separated from them in the other two contexts. This is illustrated in terms of the raw fleshpoint data of one speaker in the bottom panel of Fig. 5.

It should be remarked that these strong coarticulatory

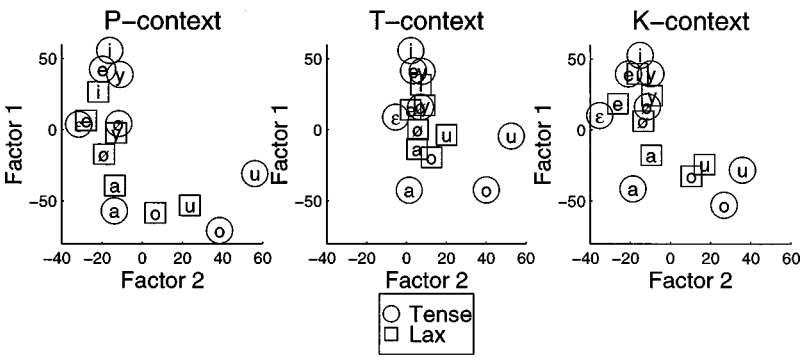

FIG. 4. Distribution of vowels in the factor 1/factor 2 space, shown separately for each of the three consonantal contexts. Lower-case letters i, y, e, ø, a, o, and u are used as generic symbols for the long/short (tense/lax) pairs /iː, ɪ/, /yː, ʏ/, /eː, ɛ/, /øː, œ/, /aː, a/, /oː, ɔ/, and /uː, ʊ/, respectively. The long member of each pair is enclosed in a circle, the short member in a square. ''ɛ'' with circular enclosure in the figure indicates the long vowel /ɛː/ (no short counterpart).

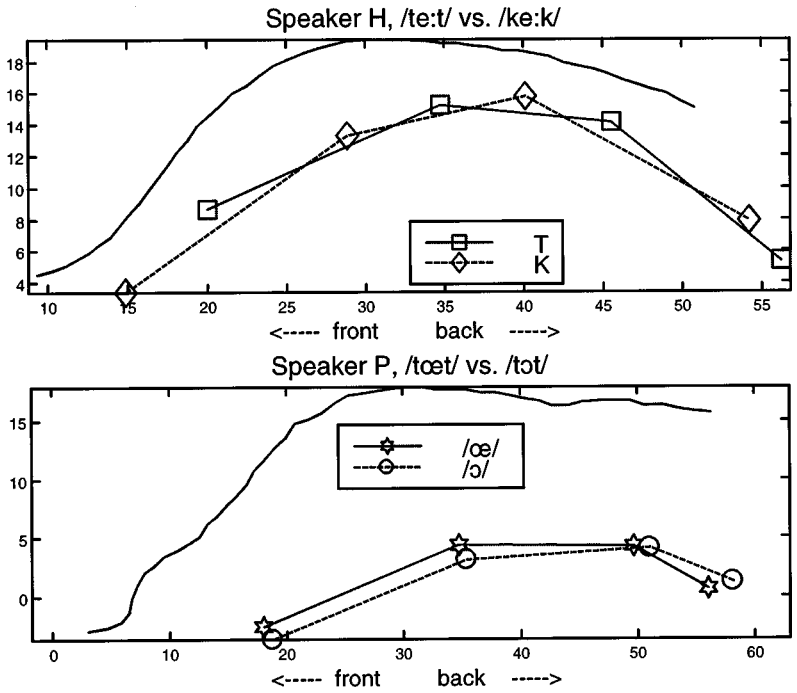

FIG. 5. Two examples of coarticulatory effects on tongue configuration of individual speakers. Top panel: Retraction of front vowel /e:/ in /t/ vs /k/ context. Bottom panel: Approximation of front vowel /œ/ and back vowel /ɔ/ in /t/-context.

effects captured by factor 2 involve advancement/retraction of the complete tongue; it is not until we extend the model below that we will be able to observe more localized coarticulatory contrasts in the region of the tongue-tip—which is where coarticulatory effects of /t/ might, *a priori*, have been expected to be most salient. In fact, as far as we are aware, this very simple yet basic finding that front vowels in /t/-context have a more retracted tongue-body position than in /k/-context has not yet been reported in the literature. Although it may seem counterintuitive at first blush, it is probably a natural strategy to provide the tongue-tip with room to elevate to form the alveolar closure.

A final, briefer observation related to coarticulatory effects remains to be made. The most neutral context /p/ shows very clearly an effect that has been known for almost 100 years, and has provoked much debate over the course of the century (Meyer, 1910; Wood, 1975; Fischer-Jørgensen, 1985), namely that /ɪ/, the lax cognate of /i:/, is substantially lower (here in terms of factor 1) than the next lowest tense vowel /e:/ (ceteris paribus for /y:/). However, when coarticulatory effects are taken into account this effect becomes blurred: In /k/-context /ɪ/ has about the same value as /e:/, and /ʏ/ is somewhat higher than /øː/. Again this is probably an easily explainable effect: /k/-context tends to elevate tongue-body position and does so relatively more for the lax vowels.

3. Subject weights

The subject weights are displayed in Fig. 6 with the same assignment of the factors to the *x* and *y* axes as used for the vowel space. From several points of view the pattern of the weights confirms that the extracted model is a satisfactory one. First of all, the sign of the weights is the same for all subjects. If, for a given factor, there were differences in the sign of the subject weights this would indicate that the factor itself is being used to capture subject-specific features. Such a situation would constitute a violation of the modeling assumption of capturing subject-specific effects in a simple scaling of subject-independent factors. Clearly this is not the case in our data.[5]

The relationship of the weights for session 1 (normal rate) versus session 2 (fast rate) is also intuitively satisfying. Essentially one of two patterns occurs: Either the weights for session 2 are located closer to the origin for both factors, indicating a rather straightforward scaling down of articulation (subjects B, C, M, S, and T), or the weights remain close together in the factor 1/factor 2 space, indicating that the subjects made only little change in movement amplitude, but

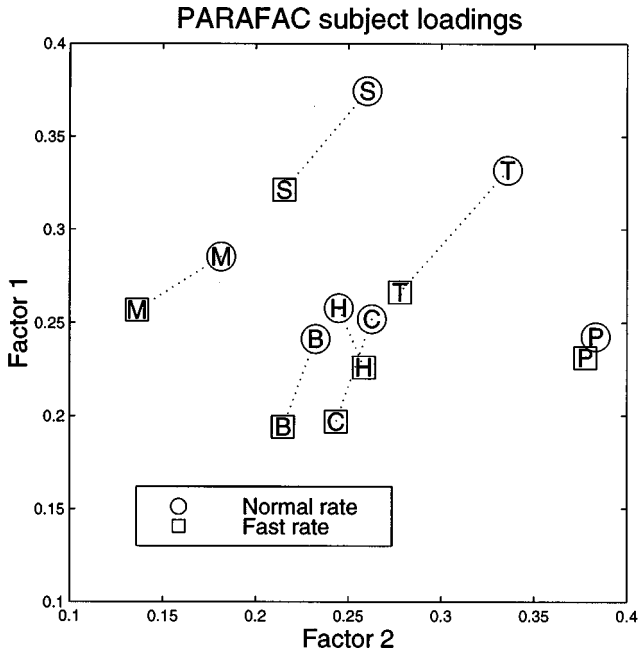

FIG. 6. Distribution of subject weights in the factor 1/factor 2 space. The subject initial is enclosed in a circle for the normal-rate session and in a square for the fast-rate session. The two sessions of each subject are joined by a dashed line.

importantly, remain consistent in their use of these two dimensions of tongue control: this applies to subject P and in slightly less obvious fashion to subject H. Subject P was in fact the subject who made least change in vowel duration over the two sessions. Subject H did have a substantial change in vowel duration; this reflects the simple fact (mentioned in Sec. I) that changes in tempo do not have to be accompanied by a reduction of movement amplitude.

As also discussed in Sec. I, it would have been disturbing if the subjects had shown unsystematic positioning of session 2 weights relative to session 1 weights in the factor space; this would probably have necessitated the conclusion that differences over sessions over which we do not have complete control, such as inevitable slight discrepancies (between subjects, and between the same subject in different sessions) in attachment of the sensors to the tongue, could have seriously deleterious effect on the interpretability of the results. Encouragingly, this does not occur, supporting the validity of this particular modeling approach on the basis of this particular kind of articulatory data.

The patterns in the speaker weights also make clear that a further prerequisite for successful application of the PARAFAC algorithm is met; in order to solve the problem of rotational indeterminacy of the factors, the PARAFAC algorithm requires the presence of differences in the *relative* importance of the factors over subjects (Harshman *et al.*, 1977, p. 699, draw an analogy to the solution of a system of simultaneous equations). Our subject population appears to fulfill this requirement. Although there is a subgroup of subjects quite close to a line with a gradient of 1, indicating fairly restricted differences in the relative importance of the two factors (subjects B, C, H, and T), taking the group as a whole (refer in particular to P, S, and M) a wide range in the relative contribution is covered.

Having made this point, it must be admitted that we now reach the limit of the interpretability of the weights. Thus while we can observe that, for example, speakers S and P represent the two extreme cases, the former making particularly heavy use of factor 1, the latter of factor 2, we can do no more than speculate as to what these differences reflect. Harshman *et al.* consider, for example, whether speaker weights can be related to anatomical features, such as oral cavity length, or relative length of pharynx and oral cavity, but results were rather inconclusive. The main anatomical information we currently have available for our subjects consists of tracings of the hard-palate contour, but these did not provide any obvious clue as to what might lie behind the different relative weight for S and P. Other systematic sources of influence on the speaker weights are certainly conceivable, such as slight differences in accent or in overall articulatory setting (Laver, 1980), but many more speakers would be required to achieve a balanced assessment of these issues.

C. Extending the model

Although the two-factor PARAFAC model discussed in the previous section appeared to give a consistent and revealing picture of vowel articulation per se, the process of extraction pointed to the presence of subject-specific effects, probably related to consonantal coarticulation, not able to be captured in the model. In the present section we outline the approach followed to try to come to terms with these problems and develop a model for the complete data set.

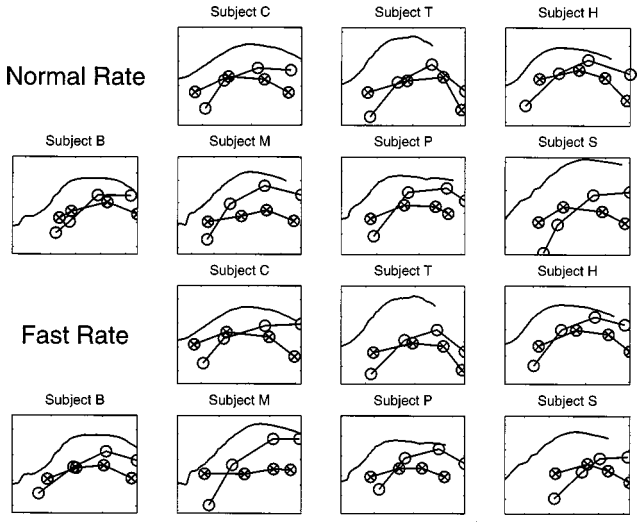

FIG. 7. Patterns of tongue displacement (around mean tongue position) associated with the first principal component of the PARAFAC model error (as in Fig. 3 configuration shown for ± 2 standard deviations). Patterns shown separately for each subject and session.

The approach essentially consists of examining the error of the two-factor PARAFAC model for systematic effects. Using the three sets of PARAFAC weights and Eq. (1) we can generate, for each subject separately, the articulatory data predicted by the model. Subtracting this from the original data (the input to the PARAFAC algorithm) gives the model error—for every vowel and for every articulatory coordinate. Note that these subject-specific error matrices still constitute a kind of data that is very similar to the original datasets; whereas these original datasets measure displacement of the tongue from the mean articulator position, the new error datasets measure the displacement of the tongue required to move it from its position predicted by the PARAFAC model to its actual position. Thus following the rationale underlying the whole of this paper, we can now employ procedures such as principal-component analysis to uncover typical pattern(s) of tongue displacement allowing us to succinctly capture a substantial proportion of the variance in the error data.

Carrying out separate principal-component analyses of the error data for each subject showed that the first principal component explained at least 37%, and on average 49%, of the variance in the data. It is revealing to plot the pattern of tongue displacement associated with the first principal component of the analyses. This can be done in a manner entirely analogous to the patterns of tongue displacement shown in Fig. 3 for the factors of the PARAFAC model. However, since there is a separate eigenvector for each subject, this must now be done in a subject-specific fashion. Figure 7 shows the results in this way.

Inspection of Fig. 7 suggests that conceptually this first principal component of the error captures rather similar articulatory behavior in each subject, namely the alternation

between tongue-tip/blade raising (presumably for vowels in /t/-context) and tongue-back raising (presumably for vowels in /k/-context). This is fortunate in terms of the aim, to which we still cling, of developing a reasonably parsimonious model of the complete dataset. If these articulatory patterns had shown little in common over subjects, it would have meant that the residuals after extraction of the PARAFAC model consisted of little more than idiosyncratic behavior. Nonetheless, it is important here to point out some clear differences in the patterns over subjects. Because this principal component represents an alternation between tip and back raising, there is an intersection of the tongue contour associated with strongly positive principal-component scores and the tongue contour associated with strongly negative ones. However, the point of intersection differs over subjects. This means that, particularly, the second tongue sensor from the front shows variability in whether it tends to raise or to lower for raised tongue-tip configuration (compare, e.g., subjects P and S, normal rate). The subjects also differ as to whether the raised tongue-tip configuration is associated with fronting (e.g., subject C, normal rate) or retraction (e.g., subject H, normal rate) of the tongue as a whole. These are precisely the kind of subject-specific differences that would be difficult to capture in the PARAFAC framework: It is not obvious how these individual tongue patterns could be generated by means of a simple subject-specific scaling of a subject-independent vector of articulator weights. Presumably we find here the explanation for the failed attempt to derive a three-factor PARAFAC model.

However, we have been assuming that the principal component extracted from the error data is conceptually very similar over subjects—and is readily interpretable phonetically. If this is accepted (and we will demonstrate more formally below that this does indeed seem to be justified) then it suggests that the analysis of consonantal aspects of articulation reacts more sensitively to the precise location of sensors on the tongue (a problem of experimental technique) and/or that the analysis must allow for subjects genuinely differing more as to the precise regions of the tongue involved in the realization of a phonetically defined task (cf. examples in Johnson *et al.*, 1993, p. 701). In other words, consonants are intrinsically less tractable objects for analysis of this kind than vowels (Jackson, 1988, p. 140, discusses why vowels should be particularly *well*-suited to this kind of analysis).

The least parsimonious approach to modeling the complete dataset would now be to retain separately for each subject both the eigenvector (length 8) defining the first principal component of the PARAFAC error, as well as each vowel's score on that component [i.e., 14 subjects $\times$ (15 vowels+8 articulator weights)]. Table I shows for each subject the rms error after application of the PARAFAC model (first column) together with the remaining rms error after incorporating the tongue displacements captured by the first principal component of the PARAFAC model error in the completely subject-specific manner just explained (second column). We will refer to the latter as the ideal error.

In the course of deriving the PARAFAC model in Sec. III A above, we suggested that a desirable goal would be to have a model of the complete dataset that has an error magnitude comparable to that found when models are set up for each consonant individually. In those terms our goal would be an rms error of about 1.2 mm. The second column of Table I shows that this aim could be comfortably achieved with a completely subject-specific modeling of the PARAFAC error. But can we still achieve this goal with a more parsimonious approach? Specifically, do we need a separate set of vowel scores on the first principal component of the PARAFAC error for each subject? If we assume—in the spirit of the PARAFAC approach—that this first principal component represents a similar underlying articulatory entity in each subject, and that the subjects employ this entity consistently over speech items, then this should not be necessary. To test this idea we computed a single set of vowel scores by simply averaging over subjects each vowel's score on the first principal component of the PARAFAC error (after first normalizing the scores of each subject to a standard deviation of 1). The resulting rms error is given in the first column of Table II for a model based on the two-factor PARAFAC solution plus averaged vowel scores from principal-component analysis, but with subject-specific eigenvectors from this analysis. The second column of this table gives the amount by which this falls short of the ''ideal'' result given in the second column of Table I.

TABLE I. Column 1: rms error (in mm) for PARAFAC two-factor solution; Column 2: Error after subject-specific principal-component analysis of model error (''ideal'').

Subject	PARAFAC	Ideal
	Normal rate	
C	1.6	1.1
T	1.7	1.0
H	2.0	0.9
B	1.4	0.9
M	2.3	1.5
P	1.9	1.2
S	1.9	1.1
	Fast rate	
C	1.9	1.1
T	1.5	0.9
H	1.7	0.9
B	1.4	1.0
M	2.3	1.2
P	2.2	1.3
S	1.8	1.1
Mean	1.8	1.1

As can be seen, the deterioration in accuracy is very small, amounting to just over 0.1 mm on average. This suggests that there is indeed justification for the PARAFAC-like assumptions just made with respect to this first principal component of the error. The main departure from the PARAFAC conception is the more complex mapping from the underlying articulatory entity to the actual fleshpoint displacements in individual subjects, captured in the subject-specific eigenvectors (articulator weights).

D. Discussion of the extended model

It will be recalled that our initial estimate was that a model consisting of three factors was likely to be appropriate

TABLE II. Column 1: Residual rms error (in mm); Column 2: Shortfall *re*: ideal error given in Table I.

Subject	Residual	Shortfall
	Normal rate	
C	1.2	0.09
T	1.2	0.16
H	1.2	0.28
B	1.1	0.16
M	1.7	0.16
P	1.2	0.04
S	1.3	0.19
	Fast rate	
C	1.1	0.07
T	1.0	0.12
H	1.0	0.07
B	1.0	0.07
M	1.3	0.13
P	1.5	0.14
S	1.2	0.04
Mean	1.2	0.12

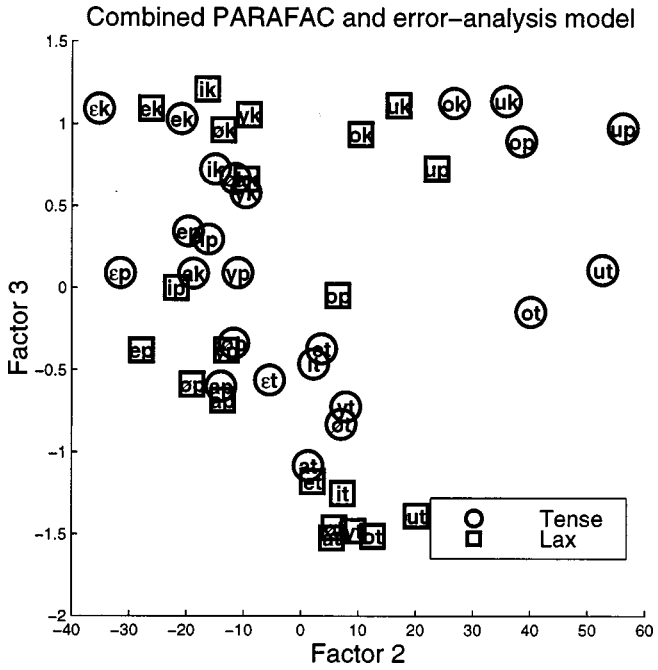

FIG. 8. Distribution of all vowel-consonant combinations in the factor 2/factor 3 space. Factor 2 is the PARAFAC factor also shown in Fig. 4 Factor 3 is derived from the first principal component of the analysis of the PARAFAC error. Same vowel-labeling conventions as in Fig. 4.

to the data. The result of the previous section was in effect to provide the third factor for our model (and we will now refer to it as ''factor 3''). Articulator and subject aspects of that factor have already been presented in some detail in that section. In the present section we look briefly at the remaining aspect, namely the vowel weights (i.e., the averaged principal-component scores). Since there appeared to be some justification for regarding these weights as an acceptably subject-independent representation, they can be plotted against the vowel weights from the PARAFAC analysis. The most interesting combination seems to be to plot our ''consonantal'' factor 3 against the second PARAFAC factor, which, as Fig. 4 has shown, incorporated clear contextual effects. This combination is shown in Fig. 8.

Factor 3 on its own separates the speech material with respect to consonantal context quite clearly, with /k/-context material at the positive end of this axis, /t/-context at the negative end, and /p/-context clustering around zero. /t/- and /k/-contexts show almost complete separation (the only exception is that tense /ka:k/ and /tu:t/ items have very similar values, near zero, for factor 3). /k/ and /p/, on the one hand, and /t/ and /p/, on the other hand, show slightly more overlap in terms of factor 3 alone, but taking the factor 2/factor 3 space overall, it is possible to delimit nonoverlapping regions for each consonantal context (/ka:k/ remains the only exception). Factor 3 clearly makes no contribution at all to characterizing individual vowel categories independently of consonantal context. The main regularity with regard to subcategories of vowels is that for /t/- and /k/-context the short lax cognates occupy the more extreme positions on the factor axis. This is very clear for /t/-context, slightly less so for /k/-context where the back vowels are an exception. The more extreme location of the lax vowels is readily understandable in terms of the lax vowels showing stronger consonantal coarticulatory effects at tongue-tip and tongue-back for /t/ and /k/, respectively.

IV. GENERAL DISCUSSION

This study confirms on the basis of a particularly large dataset that the control of the tongue for speech is organized around a small number of underlying components. Evidence for this has now accumulated from a number of studies. Investigations restricted to vocalic articulations (e.g., the PARAFAC investigations cited here) have typically extracted two factors;[6] this meshes in well with our study since the two factors from the PARAFAC-based part of our model gave a compact picture of the articulatory structure of the German vowel system. Investigations of both vocalic and consonantal articulation (connected speech) have typically required at least three factors for lingual articulation (e.g., Maeda, 1990; Sanguineti *et al.*, 1998; Badin *et al.*, 1997), one of these obviously being closely related to tongue-tip activity; again this is in close agreement with our result. Thus three components appear to capture much of the shaping of the tongue for speech. Nonetheless, there is a strong possibility that this may underestimate the number slightly. Our present corpus was not intended to capture all aspects of consonantal articulation, but rather to simply maximize the possibility for coarticulatory effects of consonants on vowels for a few important cases (major places of articulation). We will shortly be attempting to apply the techniques developed in this paper to vowel articulations in a richer set of consonantal contexts (and spoken in more natural sentences). The possibility that the number of components should be slightly higher appears all the stronger when it is recalled that our study, as well as many previous ones, has been restricted to mid-sagittal data. Stone and Lundberg (1996) investigated static vowels and consonants using a three-dimensional ultrasound technique and determined by inspection four characteristic ways of shaping the tongue. Yehia and Tiede

(1997) applied a principal-component analysis to vocal tract shapes of static vowels acquired by means of NMRI. Although analysis of the complete vocal tract introduces articulatory features that go considerably beyond the tongue by itself, they found that four basis functions would account for about 90% of the variance in the 3-D shape of the vocal tract, and in fact just taking the first two would already account for about 80% of the variance.

The above discussion relates to the number of components. Regarding the *nature* of the components, in Sec. III B 1 we went briefly into some similarities and differences between our results and earlier investigations. It is clear that in the PARAFAC procedure the nature of the factors into which observable tongue shapes can be decomposed is sensitive to the kind of data used. Nevertheless, the factor referred to by Harshman *et al.* as ''front raising,'' and emerging as our factor 1, appears to represent a family of tongue shapes that emerges with considerable consistency from very varied investigations.

Regarding our second factor, which mainly involves advancement versus retraction, the fact that such a factor emerged from our analysis (as it does in similar though by no means identical fashion in the ''pseudo-pellet'' analysis of Nix *et al.*) supports the latter authors' contention that use of a pre-defined grid system in radiographic analyses may artificially constrain the solutions that can be obtained. Nix *et al.* go further in contending that such a less constrained approach results in a more interpretable solution, specifically in the sense that the orientation of the vowels in the factor space more closely resembles a traditional vowel chart representation. It is indeed noteworthy that the distribution of the American English vowels in the factor space of Nix *et al.* shows very similar values of their factor 2 for front/back pairs such as i/u and e/o that have the same vowel height in traditional descriptions. However, this neat correspondence may be an artifact of the American vowels, which after all are not very cardinal in quality. Their ''pseudo-pellet'' analysis of the American English vowels involves, by and large, a rotation of the vowel space with respect to the result of the original gridline analysis. However, if a similar rotation is applied to the gridline style analysis they carried out on Jackson's Icelandic data, then a vowel system with a rather ''nontraditional'' orientation would result.[7] The Icelandic vowels would actually then be oriented in a manner not dissimilar to the German vowels in our factor space.

In fact, we see no particular problem in accepting that an empirically derived model may appear rotated with respect to traditional representations. Although empirically derived, we believe that our model is eminently interpretable. Indeed, of all the PARAFAC analyses presented to date, we feel that ours fits in most naturally with a plausible pattern of underlying muscle synergies. Specifically, Honda *et al.* (1993) have proposed a two-dimensional physiological space for vowel articulation in which one axis is formed by the agonist–antagonist pairing of Genioglossus Posterior with Hyoglossus, while the second axis is formed by the pairing of Genioglossus Anterior and Styloglossus (see also Maeda and Honda, 1994, especially Fig. 1). These two physiological axes match up very well with our factors 1 and 2, respectively. It is instructive to refer to Fig. 9 of Honda *et al.* (1993) where they display some point vowels in the two-dimensional physiological space defined by the aforementioned axes GGP-HG (ordinate) and GGA-SG (abscissa). In their figure, this coordinate system has been rotated by about 30 degrees, which would align the axes closer to the presumed main line of action of these muscles and in turn brings the physiological vowel space into close coincidence with a traditional vowel space, as they demonstrate by juxtaposing an $F1$ vs $F2$ plot of the vowels. Strikingly, a rotation of our factor space by the same amount (i.e., about 30 degrees) would be quite consistent with the main direction of action of the factors as shown in Fig. 3, and simultaneously would also orient the vowels along more traditional lines in the two-dimensional space (refer back to Fig. 4).

Here we ought to return to the question of the tongue shapes captured by our factors since Maeda and Honda relate the two physiological dimensions GGP-HG and GGA-SG to two of the parameters in the articulatory model that Maeda (1990) had previously derived by factor analysis, namely ''tongue-dorsal-position'' and ''tongue-dorsal-shape,'' respectively.

Our factor 1 appears to correspond quite well to the former of these two parameters[8] (involving advancement of the tongue root and raising of the front part of the tongue, cf. Maeda, 1990, Fig. 3b) but our factor 2 seems rather less similar to the Maeda ''tongue-dorsal-shape'' parameter, which involves a contrast between flat and arched shape. Currently, we are unclear what might explain this difference. Possibly, the different nature of the corpora analyzed may be an influence: Unlike the running-speech corpus of Maeda, our target sounds were restricted to vowels, and, in particular, did not include velar consonants. Functionally, however, Maeda's parameter and our factor 2 do appear reasonably similar, since they both clearly distinguish high back vowels from front vowels. The amount of variance explained by our factor 2, namely, about 20%, is also strikingly similar to that found by Maeda for his two subjects (23%).

Last of all, we return briefly to the question of vocalic versus consonantal aspects of articulation in this study. We believe that our first two factors are of some general validity, i.e., they capture a complete vowel system in a physiologically plausible manner. With respect to consonant articulation, the study was not aiming for the same level of generalizability. In fact, the important result was simply that these aspects of articulation were less amenable to the highly constrained PARAFAC model of speaker-specific effects. Interestingly, the factor we extracted as factor 3 (essentially by means of a major relaxation of the constraints) did seem compatible with the *spirit* of the PARAFAC approach of a basic articulatory component common to all speakers. Possibly some kind of preliminary transformation of the raw data could have made it feasible to work successfully within the basic PARAFAC framework throughout, even for this consonantal activity. However, this was beyond the scope of the present work, and, by itself, would still not resolve the general question of whether consonantal articulation requires a departure from the PARAFAC approach—simply because our corpus was not designed to give balanced coverage of

consonantal articulatory possibilities. This would be an interesting topic for future investigation.

ACKNOWLEDGMENTS

The experiments were performed in collaboration with Barbara Kühnert, Tine Mooshammer, and Christian Kroos, to all of whom thanks for numerous discussions are also due. Thanks also to one anonymous reviewer for incisive comments. For this work we used a MATLAB package developed by R. Bro (available online from http://newton.foodsci.kvl.dk/; see also Bro, 1997). We are grateful to M. Tiede for drawing our attention to this package. Work supported by DFG Ti 69/29-3.

[1]Here we should note in passing that PARAFAC factors are not constrained to be orthogonal, so triple products of exactly zero will not generally occur. Bro (1997) uses a diagnostic referred to as the triple cosine; this is not numerically identical, but is closely related, to the triple product measure used here.

[2]Numerically, the procedure is essentially the same as that outlined above to test for degeneracy, but whereas the degeneracy test considers different factors in the same model, the present test considers the same factors in different models.

[3]In order to be able to correlate the vowel weights, only those vowel weights from the combined model pertaining to the relevant single-consonant model were used, e.g., only p-context vowels from the /pk/-model when comparing to the /p/-only model.

[4]This regularity is least obvious for the pair /ø:/ vs /œ/ (both are located very close to 0 on factor 1); however, this difficulty would be resolved if we assume that neutral tongue position actually occurs at slightly negative values of factor 1. This is probably justified since the preponderance of mid to high front vowels in the German system may well displace average tongue position (i.e., zero on the factor axis) away from a neutral position.

[5]Nix *et al.* extracted a three-factor model for English, precisely in order to reinforce the potential for a subject-independent representation in terms of the first two factors; their third factor captured subject-specific behavior of a kind that presumably could not be captured directly in the subject weight matrix.

[6]Jackson extracted three factors for the Icelandic vowel system, but the reanalysis of Nix *et al.* suggested that two factors may actually be more appropriate. Nevertheless, we would not like to exclude the possibility that vowel systems may exist requiring more than two factors.

[7]This seems justified since Nix *et al.* found strikingly similar factors for the English and Icelandic data.

[8]In fact, it might be more correct to say that our factor 1 corresponds to a combination of the ''tongue-dorsum-position'' and ''jaw-position'' parameters in the Maeda model (and which we do not explicitly try to separate in this analysis). In his model these two parameters show considerable similarities. Interestingly, the amount of variance explained by our factor 1—about 57%—is practically identical to the cumulative variance explained by Maeda's jaw- and tongue-position parameters, namely 58% and 56% for his two speakers, respectively.

Badin, P., Baricchi, E., and Vilain, A. (**1997**). ''Determining tongue articulation: From discrete fleshpoints to continuous shadow,'' Proceedings of the European Conference on Speech, Communication, and Technology (Eurospeech 97, Rhodes, Greece), Vol. 1, pp. 47–50.

Bro, R. (**1997**). ''PARAFAC. Tutorial and applications,'' Chemom. Intell. Lab. Syst. **38**, 149ff.

Fischer-Jørgensen, E. (**1985**). ''Some basic vowel features, their articulatory correlates, and their explanatory power in phonology,'' in *Phonetic Linguistics, Essays in Honour of Peter Ladefoged*, edited by V. Fromkin (Academic, New York), pp. 79–99.

Harshman, R., and Lundy, M. (**1984**). ''The PARAFAC model for three-way factor analysis and multidimensional scaling,'' in *Research Methods for Multimode Data Analysis*, edited by H. G. Law, C. W. Snyder, J. A. Hattie, and R. P. MacDonald (Praeger, New York), pp. 122–215.

Harshman, R., Ladefoged, P., and Goldstein, L. (**1977**). ''Factor analysis of tongue shapes,'' J. Acoust. Soc. Am. **62**, 693–707.

Hashi, M., Westbury, J., and Honda, K. (**1998**). ''Vowel posture normalization,'' J. Acoust. Soc. Am. **104**, 2426–2437.

Honda, K., Hirai, H., and Kusakawa, N. (**1993**). ''Modeling vocal tract organs based on MRI and EMG observations and its implication on brain function,'' Annu. Bull. Res. Inst. Logopedics Phoniatrics, Tokyo **27**, 37–49.

Hoole, P. (**1996**). ''Issues in the acquisition, processing, reduction and parameterization of articulographic data,'' Forschungsberichte des Instituts für Phonetik und Sprachliche Kommunikation München (FIPKM) **34**, 158–173.

Hoole, P. (**1999**). ''Articulatory-acoustic relations in German vowels,'' Proc. 14th Int. Cong. Phon. Sci., San Francisco (in press).

Hoole, P., and Kroos, C. (**1998**). ''Control of larynx height in vowel production,'' Proc. 5th Int. Conf. Spoken Lang. Processing (Sydney, Australia) **2**, 531–534.

Hoole, P., and Kühnert, B. (**1995**). ''Patterns of lingual variability in German vowel production,'' Proceedings XIIIth Int. Conf. Phon. Sci., Stockholm **2**, 442–445.

Hoole, P., and Kühnert, B. (**1996**). ''Tongue-jaw coordination in German vowel production,'' Proceedings of the 1st ESCA tutorial and research workshop on Speech Production Modelling/4th Speech Production Seminar, Autrans, 1996, pp. 97–100.

Jackson, M. T. T. (**1988**). ''Analysis of tongue positions: Language-specific and cross-linguistic models,'' J. Acoust. Soc. Am. **84**, 124–143.

Johnson, K., Ladefoged, P., and Lindau, M. (**1993**). ''Individual differences in vowel production,'' J. Acoust. Soc. Am. **94**, 701–715.

Kaburagi, T., and Honda, M. (**1994**). ''Determination of sagittal tongue shape from the positions of points on the tongue surface,'' J. Acoust. Soc. Am. **96**, 1356–1366.

Kroos, C., Hoole, P., Kühnert, B., and Tillmann, H.-G. (**1997**). ''Phonetic evidence for the phonological status of the tense-lax distinction in German,'' Forschungsberichte des Instituts für Phonetik und Sprachliche Kommunikation München (FIPKM) **35**, 17–26.

Kuehn, D. P., and Moll, K. L. (**1976**). ''A cineradiographic study of VC and CV articulatory velocities,'' J. Phonetics **4**, 303–320.

Laver, J. (**1980**). *The Phonetic Description of Voice Quality* (Cambridge University Press, Cambridge).

Linker, W. (**1982**). ''Articulatory and acoustic correlates of labial activity in vowels: A cross-linguistic study,'' UCLA Working Papers in Phonetics **56**, 1–134.

Maeda, S. (**1990**). ''Compensatory articulation during speech; evidence from the analysis and synthesis of vocal-tract shapes using an articulatory model,'' in *Speech Production and Speech Modelling*, edited by W. Hardcastle and A. Marchal (Kluwer, Dordrecht), pp. 131–150.

Maeda, S., and Honda, K. (**1994**). ''From EMG to formant patterns of vowels: The implication of vowel spaces,'' Phonetica **51**, 17–29.

Meyer, E. A. (**1910**). ''Untersuchungen über Lautbildung,'' Die neueren Sprachen **18** (Ergänzungsband Festschrift Vietor), 166–248.

Nix, D. A., Papçun, G., Hogden, J., and Zlokarnik, I. (**1996**). ''Two cross-linguistic factors underlying tongue shapes for vowels,'' J. Acoust. Soc. Am. **99**, 3707–3718.

Perkell, J., Cohen, M., Svirsky, M., Matthies, M., Garabieta, I., and Jackson, M. (**1992**). ''Electromagnetic midsagittal articulometer (EMMA) systems for transducing speech articulatory movements,'' J. Acoust. Soc. Am. **92**, 3078–3096.

Sanguineti, V., Laboissière, R., and Ostry, D. J. (**1998**). ''A dynamic biomechanical model for neural control of speech production,'' J. Acoust. Soc. Am. **103**, 1615–1627.

Stone, M., and Lundberg, A. (**1996**). ''Three-dimensional tongue surface shapes of English consonants and vowels,'' J. Acoust. Soc. Am. **99**, 3728–3737.

Wood, S. (**1975**). ''The weaknesses of the tongue-arching model of vowel production,'' Phonetics Laboratory, Department of General Linguistics, Lund University, Working Papers **11**, 55–107.

Wood, S. (**1986**). ''The acoustical significance of tongue, lip and larynx maneuvers in rounded palatal vowels,'' J. Acoust. Soc. Am. **80**, 391–401.

Yehia, H., and Tiede, M. (**1997**). ''A parametric three-dimensional model of the vocal-tract based on MRI data,'' Proceedings of the International Conference on Acoustics, Speech, and Signal Processing (ICASSP97, Munich, Germany) **3**, 1619–1622.

Development of adaptive phonetic gestures in children: Evidence from vowel devoicing in two different dialects of Japanese

Satoshi Imaizumi
Speech and Cognitive Sciences, Graduate School of Medicine, University of Tokyo, 7-3-1 Hongo, Bunkyo-ku, Tokyo 113-0033, Japan

Kiyoko Fuwa
Faculty of Education, Saitama University, 255 Shimo-okubo, Urawa, Saitama, 338-0825, Japan

Hiroshi Hosoi
Department of Otorhinolaryngology, Nara Medical University, 840 Shijocho, Kashihara, Nara 634-8521, Japan

(Received 15 June 1998; revised 23 March 1999; accepted 20 April 1999)

High vowels between voiceless consonants are often devoiced in many languages, as well as in many dialects of Japanese. This phenomenon can be hypothesized to be a consequence of the adaptive organization of the laryngeal gestures to various conditions, including dialectal requirements. If this theory is correct, it may be possible to predict developmental changes in vowel devoicing based on the developmental improvement in the dialect-specific organization of the laryngeal gestures. To test this expectation, the developmental properties of vowel devoicing were investigated for 72 children of 4 and 5 years of age, and 37 adults in two dialects of Japanese. One was the Osaka dialect, with a low devoicing rate, and the other the Tokyo dialect, with a high devoicing rate. In the Tokyo dialect, the devoicing rate of children significantly increased and reached an adultlike level by the age of 5 years, whereas it remained low irrespective of age in Osaka. The vowel devoicing of 5-year-old children exhibited the same characteristics as that of the adults of their respective dialect. These results suggest that children growing up with the Tokyo dialect acquire the articulatory gestures which do not inhibit vowel devoicing by the age of 5 years, whereas children growing up with the Osaka dialect acquire those which inhibit the devoicing of vowels by the same age. The results fit in well with the predictions of the gestural account of vowel devoicing. It is also suggested that learning dialect-specific adaptive strategies to coordinate voicing and devoicing gestures as required to attain an adultlike vowel devoicing pattern is a long process: By the age of 5 years children have completed enough of this process to become members of their dialectal community. [S0001-4966(99)01008-5]

PACS numbers: 43.70.Ep, 43.70.Fq [AL]

INTRODUCTION

It is well known that high vowels between voiceless consonants are often devoiced in many languages such as Korean, English, French, and German (Jun and Beckman, 1993; Kondo, 1994), as well as in many Japanese dialects (Shibata, 1955; Han, 1962a, b; Hirose, 1971; Yoshioka, 1981; Beckman and Shoji, 1984). There has been a lively controversy, however, as to whether vowel devoicing should be described as allophonic variation (Hirose, 1971; Yoshioka, 1981) or as a lower-level coarticulatory effect (Jun and Beckman, 1993; Imaizumi *et al.*, 1995). This controversy results from the fact that the probability of such devoicing is dependent on phonological factors (Sakuma, 1929; Shibata, 1955; Han, 1962a, b; Sugito and Hirose, 1988), phonetic factors (Kuriyagawa and Sawashima, 1989; Jun and Beckman, 1993), pragmatic factors (Imaizumi *et al.*, 1995), and dialectal conditions (Sugito, 1969, 1988).

The present paper describes the development of vowel devoicing in childhood as an adaptive organization of the laryngeal gestures rather than a symbolic selection of allophones. The main issue tested is whether it is possible to predict developmental changes in vowel devoicing based on the natural improvement in the dialect-specific organization of the laryngeal gestures. For this purpose, two dialects of Japanese were analyzed: the Osaka dialect, which is known to have a low devoicing rate, and the Tokyo dialect, which is known to have a high devoicing rate (Sugito, 1969, 1988).

In several previous studies on vowel devoicing (Jun and Beckman, 1993; Imaizumi *et al.*, 1995), the concept of ''gesture'' has been adopted as formally defined in the articulatory phonology of Browman and Goldstein (e.g., 1986, 1989a, b, 1990, 1992). The degree of articulatory-acoustic variation due to the coproduction of gestures depends both on the extent to which overlapping gestures share articulators, and on the extent of their temporal overlap or blending. The gestural account of vowel devoicing explains this phenomenon as the articulatory-acoustic consequence of the voicing gestures for the intermediate vowel hidden by, or blended with, the devoicing gestures for any surrounding voiceless consonants (Jun and Beckman, 1993; Imaizumi *et al.*, 1995).

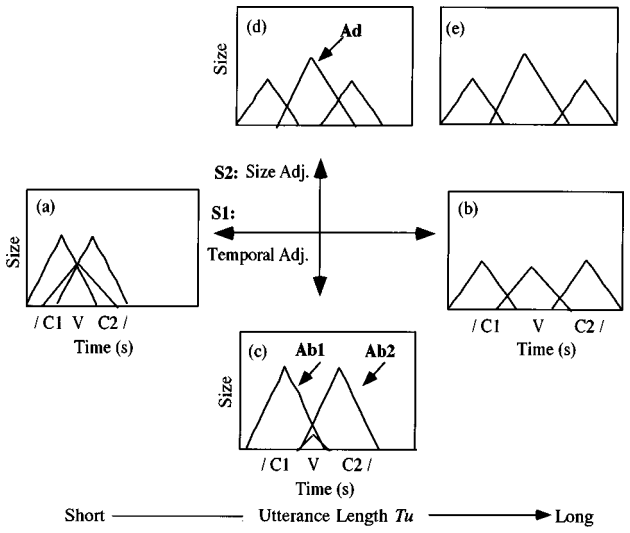

FIG. 1. Schematic representation of two different control strategies for vowel devoicing. Ab_1 and Ab_2 are the devoicing gestures for the unvoiced consonants C_1 and C_2, while A_d is the voicing gesture for the vowel V in the C_1VC_2 context. There are two component strategies to control vowel devoicing: Strategy 1 (S_1) simply involves lengthening or shortening the interval between successive devoicing gestures affecting utterance length—compare (a) vs (b). Strategy 2 (S_2) involves adjusting the size of the articulatory gestures independent of utterance length—compare (c) vs (d).

Based on acoustic analyses of listener-adaptive characteristics of vowel devoicing in Japanese dialogues, Imaizumi *et al.* (1995) suggested the hypothesis shown in Fig. 1, which schematically represents the possible laryngeal adjustments related to vowel devoicing. In Fig. 1, Ab_1 and Ab_2 represent the devoicing gestures of the laryngeal abductors, like the posterior cricoarytenoid, for the unvoiced consonants C_1 and C_2, and A_d represents the voicing gesture of the adductors, like the interarytenoid, for the vowel V in a C_1VC_2 context. Two different strategies can be suggested as possible controling vowel devoicing. Strategy 1 (S_1) simply involves a lengthening/shortening of the interval between the successive devoicing gestures, as represented by the arrow S_1 in Fig. 1. S_1 is dependent on the articulation speed. Strategy 2 (S_2) involves adjusting the size of the gestures and changing the relative size of the voicing and the devoicing gestures, as represented by the arrow S_2. This strategy could be independent of the articulation speed.

Strategy 1 would explain why vowel devoicing occurs more often for shorter, unaccented vowels at a faster speaking rate (Kuriyagawa and Sawashima, 1989; Jun and Beckman, 1993). Strategy 2 would explain physiological observations of the activity of the larynx which suggest that the glottal adjustments for devoicing require a positive effort to widen the larynx for the devoiced vowel segment (Sawashima, 1969, 1971; Hirose, 1971; Yoshioka, 1981; Yoshioka *et al.*, 1982). Furthermore, this model could explain certain listener-adaptive characteristics of vowel devoicing, such as those in which professional teachers of hearing-impaired children reduce their vowel devoicing, in order to improve their listeners' comprehension, not only by lengthening the interval of the successive voicing/devoicing gestures, but also by resizing their component gestures (Imaizumi *et al.*, 1995).

According to this hypothesis, vowel devoicing is a consequence of the adaptive organization of the articulatory gestures which reduce or permit gestural overlap and hiding. Since its probability of occurrence is dialect dependent, the organization of articulatory gestures should also be dialect dependent. When children become members of a particular dialectal community, they have to acquire this dialect-dependent organization of articulatory gestures, particularly in terms of size and timing. Children in Osaka have to learn the organization of articulatory gestures to inhibit devoicing, while those in Tokyo do not have to inhibit devoicing. When and how do children acquire such adaptive articulatory organizations? This is an important issue in the development of motor control for speech in children.

There is, however, a lively controversy concerning the putative differences in articulatory organization between young children and adults. Some investigators have reported that children's speech reveals less evidence of gestural overlap (or coarticulation) than adult speech (Katz *et al.*, 1991; Kent, 1983; Sereno *et al.*, 1987), while others have reported that children's articulatory gestures generally overlap more than those of adults (Goodell and Studdert-Kennedy, 1993; Nittrouer, 1993; Nittrouer *et al.*, 1989). A short review of the literature here will help to explain this controversy.

Standard accounts of speech production assume a linear sequence of phonemic segments produced one at a time, following articulatory plans uniquely associated with each successive phoneme or feature (e.g., Abercrombie, 1965). Such accounts have had to find ways of dealing with the fact that the acoustic and articulatory correlates of individual segments are influenced by nearby segments. Accordingly, models of ''coarticulation'' have been developed. That is, ideal canonical articulatory patterns are associated with each segment or its component features, but in actual speech these canonical patterns are adjusted to accommodate the patterns associated with neighboring segments or features (e.g., Daniloff and Hammarberg, 1973; Perkell, 1986). From this perspective on adult speech production, coarticulation could be viewed as a skill that children learn after they have mastered the articulation of individual segments. That is, children might learn the canonical patterns of production associated with each phoneme, and then learn how to make appropriate adjustments to accommodate neighboring segments (Katz *et al.*, 1991; Kent, 1983; Sereno *et al.*, 1987). From a developmental perspective, the acoustic and articulatory records of children's speech should reveal less evidence of coarticulation than adult records if this view is correct.

An alternative view of speech development assumes that the initial unit of linguistic contrast in child phonology is something larger than the phoneme, such as the word or formulaic phrase (e.g., Browman and Goldstein, 1989a, b; Ferguson and Farwell, 1975; Nittrouer *et al.*, 1989; Studdert-Kennedy, 1987; Vihman and Velleman, 1989; Menyuk *et al.*, 1986). From this perspective, smaller units of articulatory organization, whether consonants and vowels (Davis and MacNeilage, 1990) or the gestures that compose them (Studdert-Kennedy, 1987), gradually emerge as independently controllable units through the local differentiation of CV syllables into onset and nucleus (cf. Lindblom *et al.*,

1983). In this account, early phonological development involves the child gradually narrowing its minimal domain of articulatory organization from the syllable, or syllable string, to the segment (cf. Menn, 1983). If this is so, one might expect the spatiotemporal overlap of gestures to diminish as children become more able to segregate consonantal from vocalic gestures, and to coordinate them into the precise temporal patterns typical of adult speech.

To shed light on this controversy, the improvement in children's coordination of gestures across utterances has been examined by several investigators who have reached different conclusions. Some investigators have found evidence that children's articulatory gestures generally overlap more than those of adults (e.g., Goodell and Studdert-Kennedy, 1993; Nittrouer, 1993; Nittrouer *et al.*, 1989), possibly in order to allow adultlike syllabic timing in spite of children's slower articulatory movements. Other studies have reported that, at least by 3 years of age, children's speech production exhibits an intergestural coordination similar to that of adult speech (e.g., Katz *et al.*, 1991; Sereno *et al.*, 1987; Sereno and Liberman, 1987).

In the model of vowel devoicing shown in Fig. 1, the consonantal gestures were hypothesized to overlap and hide the vowel gestures, which is a reasonable way of explaining vowel devoicing in adult speech. However, there is no reason to avoid the reverse possibility, particularly for children's' speech, that the vowel gestures overlap and hide the consonantal gestures.

Some investigators have found evidence that vowel gestures are more prominent in children's speech than consonantal gestures. Based on acoustic analyses of consonant–vowel (CV) syllables, the place of stop closure (Davis and MacNeilage, 1990) and of fricative constriction (Nittrouer *et al.*, 1989; Nittrouer *et al.*, 1996) was reported to be more influenced by the place of vowel constriction for children than for adults. Nittrouer *et al.* (1989) also reported that children initiated their vowel gestures earlier in the syllable, and so coarticulated more extensively than adults, suggesting that it is the vowel that is influencing the consonant, and not the reverse.

From the above-mentioned perspectives, it is possible to assume the following three hypotheses. If children's production exhibits, at least by 3 years of age, a similar intergestural coordination as that of adult speech, we may assume H1: vowel devoicing in children 4 and 5 years of age should be the same as in adult speakers of the same dialects. However, if children's articulatory gestures generally overlap more than those of adults, and if the voicing gestures for the vowels are more prominent than the consonantal devoicing gestures, we may assume H2: vowel devoicing in children's speech should produce a shorter devoiced segment and a longer voiced segment than in adult speech, and it should approach the adult level in older children speaking the Tokyo dialect. Finally, if children's articulatory gestures generally overlap more than those of adults, and if the consonantal devoicing gestures are more prominent than the voicing gestures for vowels, we may assume H3: vowel devoicing should produce a longer devoiced segment and a shorter voiced segment than in adult speech, and it should approach the adult level in older children speaking the Osaka dialect.

TABLE I. Test words and their accent types denoted by LH.

Test word	Corresponding English	Tokyo dialect	Osaka dialect
/ki̥tsu̥tsu̥ki̥/	woodpecker	LHLL	LHLL
/haku̥tʃoo/	swan	LHHH	LHHH
/ki̥tsune/	fox	LHH	LLH
/hi̥tsudʒi/	sheep	LHH	LHH

The purpose of the present paper is to determine which of these hypotheses is valid by analyzing vowel devoicing in children 4 and 5 years of age and in adult speakers of two Japanese dialects: that of Osaka and that of Tokyo. No previous report has been made, as far as we know, on the acquisition of dialect-dependent vowel devoicing in Japanese. However, our preliminary analyses suggest that the articulation of syllables involving vowel devoicing is hard for children to acquire. Nakanishi *et al.* (1972) have also suggested that a long process is required for Japanese children to acquire the correct articulation of such syllables as /tsu/, for which the error rate was 23.3% among their 4-year-old subjects. Based on these findings, at least more than 75% of children between 4 and 5 years of age should be expected to be able to correctly articulate such syllables. In this paper, therefore, children between 4 and 5 years of age were analyzed compared to adult speakers.

I. METHOD

A. Materials

Two birds and two other animals were used to elicit utterances meeting the following three phonological conditions for inducing vowel devoicing: (P1) they contained one of high vowels /i/ and /u/; (P2) the vowel was positioned between voiceless consonants; and (P3) the syllable with the high vowel had a lack of accent (Sakuma, 1929; Shibata, 1955; Han, 1962a, b; Sugito and Hirose, 1988). The animals were familiar to the children so that they could say their names which consisted of target moras with the high vowel /i/ or /u/ surrounded by the voiceless consonants used for analysis. The mora is frequently used as a unit of temporal regulation in Japanese, which is known as the mora-based timing (Beckman, 1982; Kubozono, 1989; Otake *et al.*, 1993).

Table I shows the stimulus words with their surface pitch patterns in terms of an HL description, where H and L indicate a high or low surface pitch level, respectively (Haraguchi, 1977; Pierrehumbert and Beckman, 1988). The underlined vowel was the target of our analysis. The words had common accent types whether spoken in the Osaka or Tokyo dialect, except for /kitsune/ which is LHH in Tokyo but LLH in Osaka (Nippon Hoso Kyokai, 1966; Yoshihara, 1983). The accent was on the mora marked H followed by L. The second /tsu/ in /kitsutsuki/ was the only accented mora analyzed here. Most of the analyzed moras were marked L, and thus not accented. The only exception was the /ku/ which is marked H in /hakutʃoo/, and was not accented since it was followed by an H mora.

TABLE II. Profile of the participants from Osaka and Tokyo.

Dialect	Speaker group	No. subject	Mean age	
			Year	Month
Osaka	O4	25	4	4.4
	O5	18	5	5.9
	OA	19	22	2.2
Tokyo	T4	15	4	2.7
	T5	14	5	5.3
	TA	18	21	7.1

Among the analyzed moras, the accented second mora of /kitsutsuki/ is not usually devoiced in either dialect according to phonological condition P3. On the other hand, the first mora of /kitsutsuki/ and of /kitsune/, the third of /kitsutsuki/, the /ku/ of /hakutʃoo/ and the /hi/ of /hitsudʒi/, all of which are unaccented, are usually devoiced with a high probability only in the Tokyo dialect.

The four-mora word /kitsutsuki/, consisting of high vowels and voiceless consonants, was of particular interest. Based on phonological condition P3, the vowel /u/ of the second mora /tsu/ should be voiced, since it carried accent. The first and third moras, which were adjacent to this accented mora, should be devoiced, particularly in the Tokyo dialect. The last mora should be voiced following phonological condition P4—that is, devoicing in successive moras should be avoided in order to avoid a series of consonant clusters at the surface level which is not a favored structure in Japanese. This prediction, however, does not agree with phonological condition P5—that is, word-final high vowels following a voiceless consonant tend to be often devoiced in the Tokyo dialect (Sugito, 1988).

B. Subjects

Kindergarten children of 4 and 5 years of age growing up within the Osaka dialect (O4 and O5) and children within the Tokyo dialect (T4 and T5) participated as speakers in the test (Table II). Children whose parents were from the prescribed dialect group were selected based on reports made by kindergarten teachers who recorded their utterances of the names of the four familiar animals described above. Children who could not name any of the four names were excluded from further analyses. Although ten 3-year-old children also participated, only four of them could name all of the test words. Therefore, 3-year-old children were excluded from the analyses. Children older than 3 years of age, two 4-year-old and two 5-year-old children in Osaka and four 4-year-old and three 5-year-old children in Tokyo, were also excluded since they named an animal in an unexpected way such as /tori/ (a bird), /kitsuki/ (deletion of the third mora), or /kitsukitsu/ (mora metathesis) for /kitsutsuki/. Errors in accentuation such as LLH for LHH or in consonant articulation such as /tʃu/ for /tsu/ were carefully listed but not excluded from further analysis, since those errors are commonly found in children's speech (Nakanishi *et al.*, 1972). Thus, the children analyzed were 25 4-year-old and 18 5-year-old children in Osaka and 15 4-year-old and 14 5-year-old children in Tokyo. As controls, 19 adults speaking Osaka dialect (OA) and 18 speaking Tokyo dialect (TA) also participated. Those subjects were also classified as C4 (O4 and T4), C5 (O5 and T5), and AN (OA and TA) for age-related analyses.

C. Recording

Four pictures were prepared for the birds and other animals. Tape (digital audiotape) and video recordings were made in a soundproof testing room for each child. One microphone was placed about 20 cm from each child's mouth. Before each recording, the child was instructed to say the name of the pictures in the most normal way according to their dialect with the request ''Eno namae osiete (Tell me the name of the pictures).'' Presented each of the pictures in random order for recording, the child was encouraged to say its name. This procedure was used to avoid the possibility of the children adapting their speech to the dialect they heard so as to please the investigators.

D. Data analysis

A trained phonetician checked the accent type and phonetic quality for all of the utterances recorded. If an utterance of a speaker was judged to be an unexpected naming of a picture, for instance /tori/ (a bird) for /kitsutsuki/, the speaker was excluded from further analysis. Utterances with errors in accentuation such as LLH for LHH or in consonant articulation such as /tʃu/ for /tsu/ were listed but not excluded from further analysis, since those errors are commonly found in children's speech (Nakanishi *et al.*, 1972). Consonant clusters, potentially resulting from vowel devoicing, were also carefully evaluated.

The analysis method and parameters adopted were the same for the children's speech as for the adult speakers. As shown in Fig. 2, using an acoustic analysis system (Imaizumi *et al.*, 1993, 1994b, 1995) which generated a wideband sound spectrogram, the length of the unvoiced segment, U_m, and that of the voiced segment, V_m, and their sum, $L_m = U_m + V_m$, could be measured for each target mora, M_m. For the utterances of the four-mora word /kitsutsuki/, for instance, the boundaries between the unvoiced and voiced portions were marked by vertical lines, $t_{m1} - t_{m3}$, $m = 1-4$, as shown in Fig. 2. Segments with regularly repeated voice bars were determined as voiced, while those with noise components without any repeated voice bar were as unvoiced. For the *m*-th mora, the length of the unvoiced segment, $U_m = t_{m2} - t_{m1}$, and that of the voiced segment if any, $V_m = t_{m3} - t_{m2}$, were calculated. To monitor the articulation speed for an assessment of its possible influence on the devoicing rate, the word length, T_u, was also measured for each utterance *u*, as shown in Fig. 2. To measure the prominence of the voiced segment compared to the devoicied segment, the prominence P_m was calculated as $P_m = V_m - U_m$.

M_m was classified as ''devoiced'' if $V_m = 0$. The devoicing rate, *D*, was calculated as the percent of the number of moras classified as ''devoiced'' against the total number of moras analyzed for each word and each speaker group.

The devoicing rate was analyzed using the chi-square test for differences in the devoicing probabilities. To test the prominence of the devoicing gesture against the voicing ges-

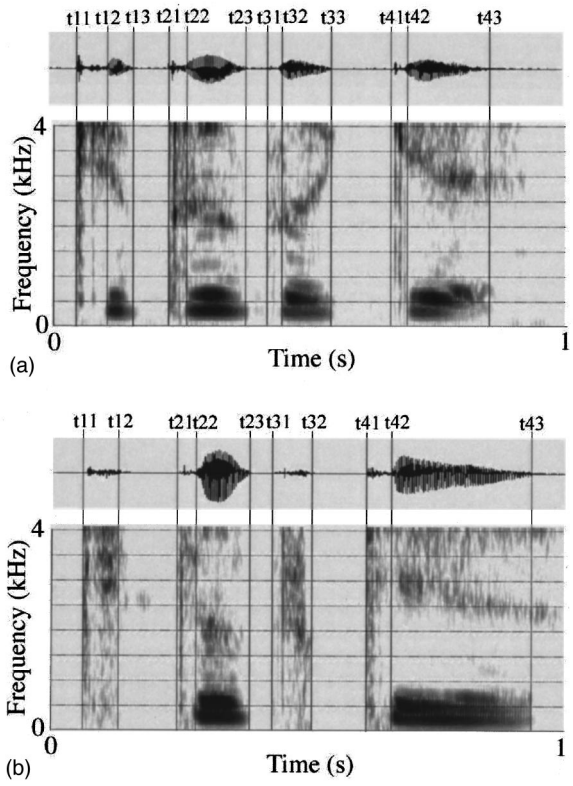

FIG. 2. Typical voice recordings showing the measurement of unvoiced and voiced segment length for /kitsutsuki/. (a) An example from a 5-year-old child in Osaka in which four vowels are voiced. (b) An example from a 5-year-old child in Tokyo in which the first and third vowels are devoiced. The upper panel is the speech waveform and the lower is its wideband sound spectrogram. The initial and final timing points of the unvoiced segment of the mth mora are marked by the vertical lines, t_{m1} and t_{m2}, and those of the voiced portion are marked by the vertical lines, t_{m2} and t_{m3}. Segments with regularly repeated voice bars are determined as voiced, while those with noise components without any repeated voice bar are as unvoiced. For the mth mora of the utterance of /ki tsu tsu ki/, the length of the unvoiced segment, $U_m = t_{m2} - t_{m1}$, and that of the voiced segment, $V_m = t_{m3} - t_{m2}$, were calculated. The utterance length, T_u, was calculated as $t_{43} - t_{11}$.

ture, P_m, U_m, and V_m were analyzed using a two-way analysis of variance with Fisher's protected, least-significant difference (PLSD) test for two factors: age (C4, C5, AN) and dialect (Osaka, Tokyo). U_m and V_m were also analyzed using a paired t-test. The length of the moras and that of the utterances were also analyzed using a two-way analysis of variance.

II. RESULTS

A. Error rate

The children tended to produce more errors than the adults both in accent type and in consonant articulation.

For tokens of /kitsutsuki/, which was supposed to be LHLL as shown in Table I, 16% of 4 year olds in Osaka (O4), 22% of 5 year olds in Osaka (O5), 27% of 4 year olds in Tokyo (T4) and 14% of 5 year olds in Tokyo (T5) were classified as LHHL with accent on the third mora /tsu/. Articulation errors substituting /tʃu/ for /tsu/, such as /kitʃutʃuki/ for /kitsutsuki/ were detected for 12% of O4, 17% of O5, 27% of T4, 7% of T5, but for none of the adult subjects in Osaka (OA) and those in Tokyo (TA). No tokens were assessed as having consonant clusters such as /kts/ or /tsk/.

TABLE III. Devoicing rate and utterance length of the four-mora word /kitsutsuki/.

Speaker group	Utterance length (ms)	Devoicing rate (%) /k̲itsutsuki/	/kitsu̲tsuki/	/kitsutsu̲ki/	/kitsutsuki̲/
O4	1037	22	0	14	9
O5	885	28	0	12	6
OA	635	36	15	40	0
T4	935	42	0	15	30
T5	807	62	0	54	15
TA	791	88	0	73	13

For tokens of /kitsune/, 64% of O4, 61% of O5, and 63% of OA were classified as LLH, which is the norm in the Osaka dialect, while 20% of O4, 28% of O5, and 37% of OA were classified as LHH which is the norm in the Tokyo dialect. The tokens of O4 were classified as HHL (8%), LHL (4%), and HHH (4%), and those of O5 as HHL (6%) and LHL (6%). Such accent types were not found in OA. On the other hand, 87% of T4, 100% of T5, and 83% of TA were classified as LHH, which is the correct form in the Tokyo dialect. Some of T4's tokens were classified as HHL (7%) and HHH (7%). Articulation errors substituting /tʃu/ for /tsu/ in /kitsune/ were detected for 12% of O4, 33% of T4, and 7% of T5, but not at all for O5, OA, or TA. No tokens were assessed to have the consonant cluster /kts/.

For tokens of /hitsudʒi/, LHL-type errors were detected for 24% of O4 and 7% of T4. HHH-type errors were detected for 13% of T4, 7% of T5, and 6% of TA, but for none of the Osaka subjects. Articulation errors substituting /tʃu/ for /tsu/ in /hitsudʒi/ were detected for 16% of O4, 17% of O5, 13% of T4, and 7% of T5, but not at all for OA or TA. No tokens were assessed to have the consonant cluster /hts/.

For tokens of /hakutʃoo/, 40% of O4, 17% of O5, 13% of T4, and 14% of T5 were judged neglecting the final mora /o/, resulting a three-mora word /hakutʃo/ with an accent type of LHH. This type of error was not found in the adult speakers. 56% of O4, 56% of O5, 67% of T4 and 71% of T5 articulated this word correct as LHHH. No tokens were assessed to have the consonant cluster /kts/.

B. Devoicing rate

With regards to the devoicing rates within the dialect groups for the first mora of /kitsutsuki/, as shown in Table III, the chi-square test revealed that those of 4 year olds (O4), 5 year olds (O5) and adults (OA) did not significantly differ from each other ($p > 0.43$) in Osaka. On the other hand, those of adults (TA) and 5 year olds (T5) were significantly higher than that of 4 year olds (T4) in Tokyo ($p = 0.038$). The devoicing rate tended to increase with age in both dialects, although significant differences were found only in the Tokyo dialect. With regards to the devoicing rates between the same age groups across dialects, those of O4 and T4 were low and showed no significant difference ($p = 0.22$), whereas those of T5 and TA were significantly

TABLE IV. Devoicing rate and utterance length of three test words.

Speaker group	/kitsune/		/hitsudʒi/		/hakutʃoo/	
	Length (ms)	Rate (%)	Length (ms)	Rate (%)	Length (ms)	Rate (%)
O4	830	12	830	12	831	0
O5	719	33	719	33	780	11
OA	573	30	573	30	685	32
T4	682	47	672	25	1147	27
T5	691	86	710	90	759	79
TA	620	81	702	73	827	75

higher than those of O5 and OA, respectively ($p<0.01$), but showed no significant difference between themselves ($p=0.11$).

A similar tendency, with some differences, was observed for the other tested moras which are supposed to be devoiced in the Tokyo dialect as summarized in Table IV. The devoicing rate tended to increase with age within each dialectal group. OA had a significantly higher devoicing rate than O4, but not O5, for the third mora /tsu/ of /kitsutsuki/ ($p=0.04$) and for /ku/ in /hakutʃoo/. For the other moras, there was no significant age-related difference within the Osaka group.

On the other hand, T5 and TA had significantly higher devoicing rates than T4 ($p<0.04$) for all the tested moras. The devoicing rates of T5 and TA were significantly higher than those of O5 and OA, respectively ($p<0.01$), but showed no significant difference between themselves ($p=0.28$). For /ki/ in /kitsune/ and /ku/ in /hakutʃoo/, the devoicing rate of T4 was significantly higher that that of O4 ($p=0.01$)

On the other hand, the devoicing rates for the second and the fourth moras of /kitsutsuki/, which are not supposed to be devoiced, were low irrespective of age and dialect. For the second mora of /kitsutsuki/, OA had a devoicing rate of 15%. For the last mora of /kitsutsuki/, the devoicing rate ranged between 13 and 30 for the Tokyo groups, which had higher rates than those of the Osaka groups, but the differences were not statistically significant ($p>0.08$).

In summary, 5-year-old children and adult subjects in Tokyo (T5 and TA) had a significantly higher devoicing rate than the other speakers for the tested moras which should be devoiced. There were some nonsignificant age-related increases in the devoicing rate in both dialect groups. There were no significant differences in the devoicing rate for the tested moras which should not be devoiced according to the phonological conditions triggering vowel devoicing.

C. Segment length

The devoiced segment length, U_m, and the voiced segment length, V_m, as shown in Fig. 3, varied depending on age and dialect. For most of the target moras, the devoiced segment was longer for the Tokyo speakers (filled bars in Fig. 3) than for the Osaka speakers (unfilled bars in Fig. 3) irrespective of age, whereas the voiced segment was significantly shorter for the older speakers than for the younger ones in both dialect groups and was significantly shorter in the Tokyo groups than in the Osaka groups—particularly so in 5 year olds (T5) and adults (TA) in Tokyo.

With regards to the dialect-related differences in U_m, the Tokyo group (T4, T5, and TA) had a significantly longer devoiced segment than the Osaka group (O4, O5, and OA) for /ku/ in /hakutʃoo/. The adults (TA) and 5 year olds (T5) in Tokyo had a significantly longer devoiced segment than those of adults (OA) and 5 year olds (O5) in Osaka ($p<0.01$) for the first /ki/ in /kitsutsuki/ and the /hi/ in /hitsudʒi/. TA had a significantly longer devoiced segment than OA for the third /tsu/ in /kitsutsuki/ and the last /ki/ in /kitsutsuki/.

There were also significant age-related differences in the U_m of some of the tested moras within each dialect group. T5 and TA had a U_m 46 ms longer than that of T4 for the /hi/ in /hitsudʒi/ ($p<0.01$). TA had a U_m 40 ms longer than T4 ($p<0.01$), for the third /tsu/ in /kitsutsuki/.

With regards to the dialect-related differences in V_m within the same age groups, TA had a significantly shorter V_m than OA: The significant difference in V_m was 32 ms for the first /ki/ in /kitsutsuki/ and 29 ms ($p=0.01$) for the /ki/ in /kitsune/. T5 had a significantly shorter V_m than O5: The significant difference in V_m was 51 ms ($p=0.01$) for the third /tsu/ in /kitsutsuki/, 48 ms ($p=0.03$) for the /ki/ in /kitsune/, 58 ms ($p=0.01$) for the /hi/ in /hitsudʒi/, and 69 ms ($p<0.01$) for the /ku/ in /hakutʃoo/.

In all the tested moras, significant decreases in V_m with age were found in each dialect group. For instance, the adults speakers had a significantly shorter V_m than the 4 and 5 year olds for the first /ki/ in /kitsutsuki/: These differences in V_m were 48 ms (O4–OA; $p<0.01$), 31 ms (O5–OA; $p=0.02$), 63 ms (T4–TA; $p<0.01$) and 33 ms (T5–TA; $P=0.025$). T5 had a significantly shorter V_m than T4: 65 ms ($p=0.01$) for the third /tsu/ in /kitsutsuki/, 62 ms ($p=0.01$) for the /hi/ in /hitsudʒi/, and 60 ms ($p=0.045$) for the /ku/ in /hakutʃoo/.

In summary, the devoiced segment was longer for the Tokyo speakers than the Osaka speakers, whereas the voiced segment was significantly shorter for the older speakers than for the younger ones in both dialects, but was significantly shorter in the Tokyo groups than the Osaka groups.

D. Prominence of the voiced segment

The prominence of the voiced segment compared to the devoiced segment, P_m, as shown in Table V, varied depending on age and dialect. P_m varied from a positive value to a negative value with age. For all the tested moras of 4 year

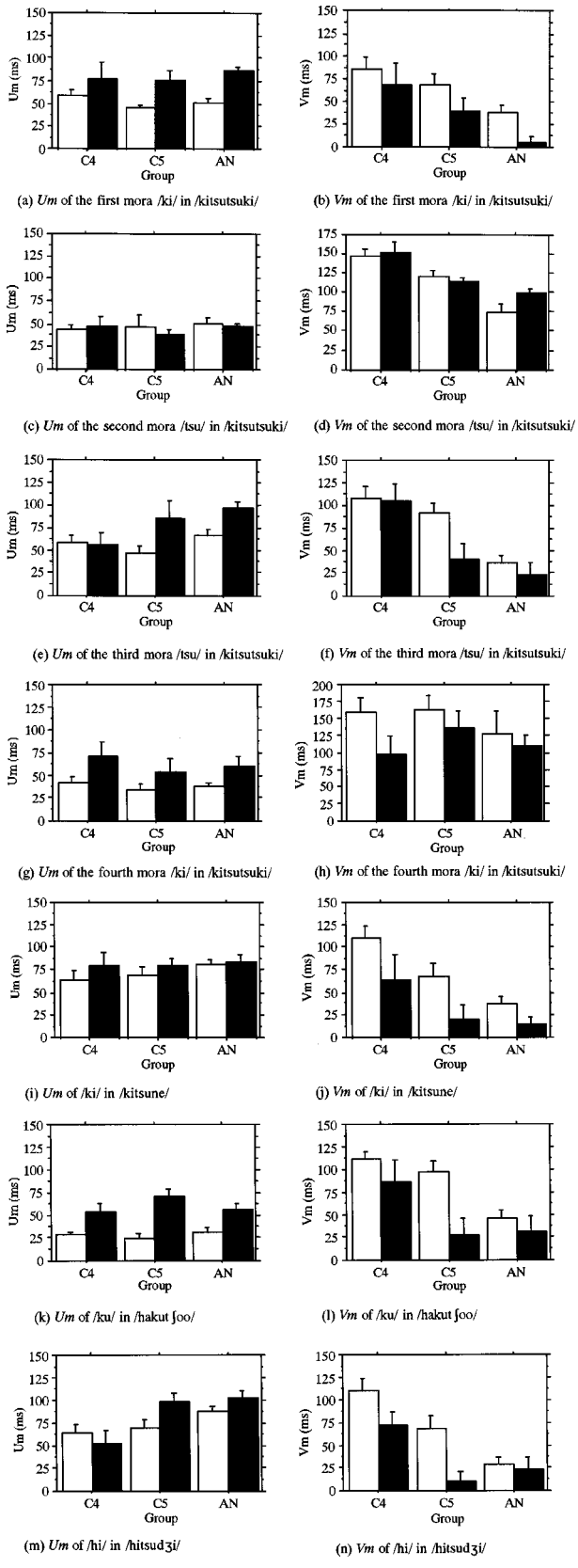

FIG. 3. The average length of the unvoiced segments and of the voiced segments for all the measured moras. C4 is 4-year-old children, C5 is 5-year-old children, and AN is adult subjects in Osaka and Tokyo. Filled bars are for the Tokyo speakers while unfilled bars are for the Osaka speakers.

olds (O4) and some of the 5 year olds (O5) in Osaka, P_m showed a large positive value, indicating that the voiced segment was significantly longer than the devoiced segment. On the other hand, for all the devoicable moras tested, P_m showed large negative values for the 5 year olds (T5) and adults (TA) in Tokyo, indicating that the devoiced segment was significantly longer than the voiced segment. The adult subjects in Osaka (OA) had negative values for P_m for all the devoicable moras, except for the /ku/ in /hakutʃoo/, which were larger than those of T5 and TA. In all the speaker groups, P_m was positive for the second and fourth moras of /kitsutsuki/, which should not be devoiced in either dialect.

A two-way analysis of variance with two factors, age (C4, C5, AN) and dialect (Osaka, Tokyo), revealed that the main effects of age and dialect were significant ($p<0.01$) for all the tested moras which should be devoiced, while their interaction was significant ($p=0.037$) only for the /ku/ in /hakutʃoo/.

Fisher's protected, least-significant difference (PLSD) test for the effect of dialect showed that the Tokyo speakers had a significantly smaller P_m than the Osaka speakers. This difference was 59 ms for the first /ki/ in /kitsutsuki/, 46 ms for the third /tsu/ in /kitsutsuki/, 56 ms for the /ki/ in /kitsune/, 57 for the /hi/ in /hitsudʒi/, and 68 ms for the /ku/ in hakutʃoo/. The *t*-test for P_m between the same age groups across dialects revealed that T4 had a significantly smaller P_m than O4 only for the /ku/ in /hakutʃoo/, for which the difference was 50 ms ($p=0.03$). T5 had a significantly smaller P_m than O5 for all the devoicable moras tested. The difference was 61 ms ($p=0.02$) for the /ki/ in /kitsutsuki/, 89 ms ($p=0.01$) for the third /tsu/ in /kitsutsuki/, 58 ms (0.026) for the /ki/ in /kitsune/, 87 ms ($p<0.01$) for the /hi/ in /hitsudʒi/, and 115 ms ($p<0.01$) for the /ku/ in /hakutʃoo/. TA had a significantly smaller P_m than OA for some of the devoicable moras tested except for the /ku/ in /hakutʃoo/. This difference was 68 ms ($p<0.01$) for the /ki/ in /kitsutsuki/, 42 ms ($p=0.03$) for the third /tsu/ in /kitsutsuki/, 34 ms ($p=0.05$) for the /ki/ in /kitsune/, and 45 ms ($p=0.026$) for the /hi/ in /hitsudʒi/.

In the Tokyo dialect, significant differences in P_m were found between T4 and T5 by the PLSD test for the third /tsu/ in /kitsutsuki/, the /hi/ in /hitsudʒi/ and the /ku/ in /hakutʃoo/. There were also significant differences in P_m between T4 and TA for all of the moras in /kitsutsuki/, except for the last, and for the /hi/ in /hitsudʒi/ and the /ku/ in /hakutʃoo/. There was, however, no significant difference in P_m between T5 and TA. In the Osaka dialect, significant differences in P_m were found between O4 and O5 for the /ki/ in /kitsune/ and the /hi/ in /hitsudʒi/. There were also significant differences in P_m for all of the moras tested—except for the last mora of /kitsutsuki/, between O4 and OA, and for the second and third moras of /kitsutsuki/ and the /ku/ of /hakutʃoo/ between O5 and OA.

In summary, the prominence of the voiced segment varied from a positive value to a negative value with age, suggesting that the voiced segment was more prominent than the devoiced segment for younger speakers, but that this relation

TABLE V. Prominence of voiced segments over devoiced segments, $P_m = V_m - U_m$, averaged across all productions and subjects in a given cell. The * indicates that the average P_m significantly differs from zero at 5% level and ** at 1% level.

	/kitsutsuki/				/kitsune/	/hitsudʒi/	/hakutʃoo/
	/ki/	/tsu/	/tsu/	/ki/	/ki/	/hi/	/ku/
O4	27	102**	48*	119**	46*	46*	83**
O5	24	73**	44*	129**	−1	−1	72**
OA	−12	25	−30*	90*	−35*	−35*	9
T4	−9	103**	49	29	−16	19	33
T5	−37	75**	−45	82*	−59**	−88**	−44
TA	−80**	51**	−73**	51*	−69**	−79**	−26

was reversed for the older speakers—particularly for 5-year-old children and adults subjects in Tokyo (T5 and TA). The Tokyo speakers showed significantly less prominence for the voiced segment than did the Osaka speakers.

E. Utterance length

For all the tested words except for /hakutʃoo/, the main effect of Age on utterance length, *Tu*, was significant ($p < 0.01$). The older speakers had significantly shorter *Tus* as shown in Table IV except for /hakutʃoo/. The main effect of dialect on *Tu* was not significant for any of the test words. The interaction between age and dialect ($p < 0.05$) was significant for all of the words tested, except /hakutʃoo/ and /kitsune/. This result was due to the tendency for adult subjects in Osaka (OA) to have a shorter *Tu* than the adult subjects in Tokyo (TA), although Osaka children (O4 and O5) had a longer *Tu* than Tokyo children (T4 and T5), respectively. OA had the shortest average *Tu* among the speaker groups for all the words.

III. DISCUSSION

The results can be summarized as follows:

(1) Although the children tended to produce more errors than the adults both in accentuation and consonant articulation, no tokens were assessed to have consonant clusters—such as /kts/, /tsk/, or /hts/—which are not permitted in Japanese.
(2) The adult subjects and 5-year-old children in Tokyo (TA and T5) had significantly higher devoicing rates than the other speakers for the devoicable moras tested, although there were some age-related increases in the devoicing rate in both dialect groups. There were no significant differences among the speaker groups in the devoicing rate for the tested moras which should not be devoiced.
(3) The devoiced segments were longer for the Tokyo speakers than the Osaka speakers, whereas the voiced segments were significantly shorter for the older speakers than the younger ones in both dialect, and were significantly shorter in the Tokyo groups than in the Osaka groups, particularly for T5 and TA.
(4) The prominence of the voiced segment varied from a positive value to a negative value with age, suggesting that the voiced segments were prominent over the devoiced segment for younger speakers, but that this relation was reversed for the older speakers, particularly for T5 and TA. The Tokyo speakers had a significantly smaller prominence for the voiced segments than the Osaka speakers.
(5) The older speakers had a significantly shorter utterance length than the younger speakers, without significant main effects of dialect.

Based on these results, the three hypotheses described in the Introduction can be evaluated. Hypothesis H1 predicted that the occurrence of vowel devoicing in children of 4 and 5 years of age should be the same as those of the adult speakers of their dialect. H1 is therefore not supported, because a significant difference in the devoicing rate was found between T4 and T5, but no such difference was between T5 and TA.

H3 predicted that vowel devoicing should occur more frequently in children's speech, with longer devoiced segments and shorter voiced segments than the adult speech. H3 also predicted that this should decrease approaching the adult level in older children speaking the Osaka dialect. However, H3 is not supported by our results, because vowel devoicing occurred less frequently in our children's speech than in the adult speech, and because the children's speech had shorter devoiced segments and longer voiced segments than in adult speech.

Finally, H2 assumed that the occurrence of vowel devoicing would be less frequent in children's speech with shorter devoiced segments and longer voiced segments than in adult speech, and that would increase approaching the adult level in older children speaking the Tokyo dialect. This hypothesis fits the results of our experiment as described above, suggesting that younger children's articulatory gestures generally overlap more than do those of older children or adults in such a way that the voicing gestures for vowels are more prominent than the consonantal devoicing gestures.

These results suggest that children growing up as speakers of the Tokyo dialect acquire articulatory gestures which permit vowel devoicing, whereas children growing up with the Osaka dialect acquire articulatory gestures which reduce vowel devoicing until the age of 5 years. Only adults (TA) and 5-year-old children (T5) of the Tokyo dialect showed a significantly higher devoicing rate than that of 4-year-old Tokyo children (T4) and all of the Osaka speakers (O4, O5, and OA) tested. Although utterance length decreased significantly with age in Osaka, the devoicing rate remained sig-

nificantly lower than in T5 and TA, irrespective of age. Therefore, the significant differences found in the devoicing rates of 5-year-old children and adult speakers between the two dialects cannot be accounted for by differences in utterance length or articulation speed.

Furthermore, it is important to note that the devoicing patterns of /kitsutsuki/ for T5 and O5 were the same as those of adult speakers of their respective dialects, suggesting that 5-year-old children have already acquired the normal pattern of devoicing of their dialect. This in turn suggests that learning dialect-specific adaptive strategies to coordinate voicing and devoicing gestures, as required for an adultlike vowel devoicing pattern is a long process, but is acquired by the age of 5 years, at which time children become indistinguishable members of their dialectal community in terms of those parameters.

To answer the question of exactly what articulatory gestures children must acquire to control their devoicing rate, both acoustical analyses and physiological studies of laryngeal adjustments in Japanese devoicing must be considered.

Yoshioka (1981) presents EMG data on the posterior cricoarytenoid (PCA), an abductor, and the interarytenoid (INT), an adductor, obtained from many tokens containing the word /hise:/, with mostly a voiceless first syllable. In the few tokens having a voiced [i], two distinct peaks occurred in the PCA signal for [h] and [s], while one peak occurred in the INT signal for the intervening [i]. In one token with a voiceless /hi/, however, a small peak appeared for the vowel in the INT signal, and two partially overlapping peaks for [h] and [s] appeared in the PCA signal. In contrast, other tokens with a voiceless /hi/ showed no peak in the INT signal, and their PCA signals showed either a large peak with a following shoulder or a single, broad peak.

Munhall and Löfqvist (1992) provide evidence of the temporal overlap of successive opening and closing gestures in the larynx from tokens of the phrase ''Kiss Ted'' spoken at many different tempi. At the slowest tempo, there were two distinct sets of opening and closing movements of the glottis for the two different voiceless consonants in the medial /st/ sequence. As the tempo was increased, these two gestures successively overlapped more and more, until they blended into each other: After this point, there was an apparent glottal opening gesture for only one voiceless consonant.

Referring to the work by Yoshioka (1981) and Munhall and Löfqvist (1992), Jun and Beckman (1993) suggested that vowel devoicing can be explained by the voicing gesture for vowel V in a C_1VC_2 context being overlapped and hidden by the devoicing/unvoicing gestures for the surrounding unvoiced consonants C_1 and C_2.

Based on acoustic analyses of the listener-adaptive characteristics of vowel devoicing in Japanese dialogue, Imaizumi *et al.* (1995) suggested the hypothesis that neural control, which takes into account gestural overlap and hiding, is responsible for vowel devoicing. Figures 1 and 4 show a schematic representation of their hypothesis describing the possible laryngeal adjustments related to vowel devoicing, where Ab_1 and Ab_2 are the devoicing gestures for the unvoiced consonants C_1 and C_2, and A_d is the voicing gesture for the vowel V in a C_1VC_2 context. In this sense, Ab_1 and Ab_2 schematically represent the separate peaks in the PCA signal for C_1 and C_2, while A_d is the peak in the INT signal for the intervening vowel.

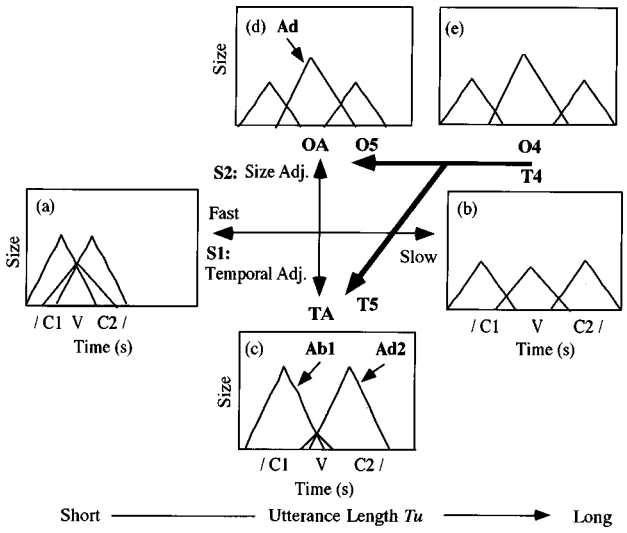

FIG. 4. Schematic representation of the development of vowel devoicing in children. The 4-year-old children acquire articulatory gestures at a slow articulation speed with clear voicing gestures as represented by panel (e). Articulation speed increases with age, and children exhibit dialect-specific strategies by the age of 5 years. Osaka children adopt articulatory gestures with increased voicing gestures, resulting in a low devoicing rate, as represented by panel (d). On the other hand, Tokyo children reduce their voicing gestures resulting in a high devoicing rate, as represented by panel (c).

If the timing and size of articulatory gestures are believed to affect devoicing, then at least two different strategies can be predicted as controlling it. Strategy 1 (S_1) simply involves lengthening or shortening of the interval between the successive devoicing gestures, as represented by the arrow S_1 in Fig. 1. S_1 is dependent on the articulation speed, which was monitored as utterance length in the present experiment. Strategy 2 (S_2) involves adjusting the size of the gestures and changing the relative sizes of the voicing and the unvoiced gestures, as represented by the arrow S_2. This strategy could be independent of articulation speed.

The 4-year-old children of both dialects in our study showed the longest utterance length, suggesting the slowest articulation speed, as well as the lowest devoicing rate among the speakers tested. This result suggests that children acquire articulatory gestures at a slow speed of articulation, with clear voicing gestures for the vowel, as represented by the panel (e) in Fig. 4. By the age of 5 years, children exhibit different characteristics. In the Osaka dialect, they decrease utterance length by reducing vowel length, while keeping their devoicing rate low. Therefore, they seem to acquire articulatory gestures at a fast articulation speed without significantly decreasing the voicing gesture for vowels, as represented by the panel (d) in Fig. 4. On the other hand, in the Tokyo dialect, children decrease utterance length by shortening the voiced segment while lengthening the devoiced segments which increases their devoicing rate. Therefore, they seem to acquire articulatory gestures at a fast articulation speed, with reduced voicing gestures for vowels and enhanced devoicing gestures for consonants, as represented by the panel (c) in Fig. 4. Lengthening the devoiced segment of

a devoiced mora is important for maintaining the mora-based timing structure of Japanese (Kubozono, 1989; Otake *et al.*, 1993). It should be noted that the 5-year-old children in Tokyo have already acquired vowel devoicing, which is not the same as vowel deletion. Vowel deletion generates undesirable consonant clusters and would destroy the Japanese mora-based timing. The vowel devoicing of T5 and TA did not result in such phonetic structures.

An intriguing question, then, arises as to why children clearly exhibit such adaptive articulatory gestures by the age of 5 years. Nittrouer (1993) has shown that children are able to differentiate intrasyllablic gestures as adults do when its consonants and vowel make use of articulators that have a greater anatomical independence from each other, such as when the jaw is the primary articulator for the consonant gesture and the tongue body is responsible for the vowel gesture. Nittrouer also suggested that one aspect of speech development may very well involve gaining a greater independence among gestures that use articulators of increasingly closer anatomical proximity. In that sense, vowel devoicing is a difficult task for children to acquire, and involves the coordination of devoicing and voicing gestures, both of which are mainly performed by a single articulator, that is, the larynx.

We should note that devoicing is a probabilistic phenomenon for which phonological conditions triggering vowel devoicing do not deterministically predict the actual devoicing rate. For instance, the second and the fourth moras of /kitsutsuki/ were devoiced by some speakers, although these moras are not supposed to be devoiced according to predictions drawn from phonological conditions. Osaka adults tested had a devoicing rate of 15% for the second mora of /kitsutsuki/ which carries accent. This result, however, is consistent with an interesting report suggesting that adult speakers of the Osaka dialect sometimes devoice accented high vowels without any accentual shift (Sugito and Hirose, 1988). It has also been reported that word-final high vowels following a voiceless consonant tend to be devoiced in the Tokyo dialect (Sugito, 1988), which is duplicated in the present study where the devoicing rate for the last mora of /kitsutsuki/ ranged between 13% and 30% in the Tokyo dialect. This mora should be voiced according to phonological condition P4, that is, devoicing in successive moras should be avoided so as not to create consonant clusters. This prediction conflicts with the generalization that word-final high vowels following a voiceless consonant tend to be devoiced in the Tokyo dialect (Sugito, 1988). This conflict may result in the low devoicing rate range we found in the Tokyo dialect.

Other previous studies have suggested that vowel devoicing is an optional selection of allophones made at a higher level than the phonetic with a probability dependent on various factors, including dialect. The optional selection of allophones, however, has to be represented as a corresponding gestural organization so as to produce the observed corresponding acoustic properties. In this sense, the gestural account of vowel devoicing includes the allphonic account and provides some important advantages.

In the gestural account, it is possible to describe developmental changes in the devoicing rate as well as in segmental prominence with age as a result of the improvement in the adaptive organization of the laryngeal gestures. It also clarifies dialect-specific organizations of the laryngeal gestures. The panels shown in Fig. 4 represent prototypical gestural organizations, which are most likely to be adopted by the respective speaker groups. As shown in Iamaizumi *et al.* (1995), adults can reorganize their articulatory gestures depending on dialectal situations. Such reorganizations, including token to token fluctuations, can be represented by variations around the prototypes. Without such prototypical gestural organizations, it would be difficult to explain certain regularities in vowel devoicing which have been clearly indicated by this article as well as others (Kuriyagawa and Sawashima, 1989; Imaizumi *et al.*, 1995; Sugito, 1969, 1988).

Several studies on the acquisition of American English dialects, such as vowel articulation by Philadelphia children (Roberts and Labov, 1995; Roberts, 1997), have suggested that children show an increasing adoption of community norms between the ages of 3 and 4. It has been reported that the precision of the temporal features of speech, such as the voice onset time for stop consonants, reaches adultlike values at 7 or 8 years of age (Eguchi and Hirsh, 1969; Kent, 1976). Although there has been no report on Japanese acquisition of dialect-dependent vowel devoicing, the present results suggest that it is acquired by the age of 5, which is late compared to the vowel acquisition by Philadelphia children, but is early compared to the precision of the voice onset time.

Articulatory development can be considered to vary depending on aspects of the target speech. As noted, Nittrouer (1993) suggests that speech development may very well involve gaining greater independence among gestures that use articulators of increasingly closer anatomical proximity. In this sense, vowel devoicing is a difficult task for children to acquire, because it involves the coordination of the devoicing and voicing gestures, both of which are mainly performed by a single articulator, the larynx. Furthermore, it is probably not easy for children to devoice vowel nuclei while maintaining mora-based timing without generating any undesirable consonant clusters.

There is at least one other factor which should be taken into account here. Vowel devoicing is important for understanding the emotional content of utterances as well as the dialectal background of speakers. For instance, our preliminary perceptual ratings of speech samples using adult Tokyo listeners (Imaizumi *et al.*, 1994a) showed that samples without devoicing were correspondingly ''slower,'' ''stronger,'' ''clearer,'' and more ''unnatural'' than those with devoicing. Child listeners in Tokyo rated the samples without devoicing as ''stranger'' but ''clearer'' than those with devoicing. It is possible, therefore, that children by this age become aware of the social meaning of utterances as cued by such subtle properties as devoicing. Since it has been reported that infants become to be able to recognize emotional expressions by the second half of the first year (Walker-Andrews, 1997), the above-mentioned expectation is highly feasible. By acquiring the cognitive and articulatory abilities to understand and ex-

press such subtle differences, children become full-fledged members of their dialect community.

IV. CONCLUSIONS

Based on the hypothesis that vowel devoicing is a consequence of the organization of articulatory gestures adapted to phonological, phonetic, and dialect-specific requirements, we tested when and how children acquire such an adaptive articulatory organization by analyzing vowel devoicing in two contrasting dialects of Japanese, those of Osaka and Tokyo. Tokyo adults and 5-year-old children showed a significantly higher devoicing rate than 4-year-old Tokyo children and all of the Osaka speaker groups tested. Although the length of utterance, moras, and voiced segments decreased significantly with age in both dialects, the devoicing rate of Osaka speakers remained significantly lower than the adult and 5-year-old speakers of the Tokyo dialect, irrespective of age. These results suggest that children growing up with the Tokyo dialect acquire the articulatory gestures which do not inhibit vowel devoicing by the age of 5 years, whereas children growing up with the Osaka dialect acquire those which inhibit the devoicing of vowels by the same age. Vowel devoicing is a difficult task for children to acquire, involving the coordination of the devoicing and voicing gestures, both of which are mainly performed by a single articulator, the larynx. The present results suggest that dialect-specific adaptive strategies to coordinate voicing and devoicing gestures as required to match the adult vowel devoicing pattern are acquired by the age of 5 years, when children become members of their dialect community.

ACKNOWLEDGMENT

This research was partially supported by a Grant-in-Aid for Scientific Research on the Priority Area of ''Development of Mind,'' Ministry of Education, Science and Culture, Japan.

Abercrombie, D. (**1965**). *Studies in Phonetics and Linguistics* (Oxford U.P., London).

Beckman, M. E. (**1982**). ''Segment duration and the 'Mora' in Japanese,'' Phonetica **39**, 113–135.

Beckman, M., and Shoji, A. (**1984**). ''Spectral and perceptual evidence for CV coarticulation in devoiced /si/ and /syu/ in Japanese,'' Phonetica **41**, 61–71.

Browman, C. P., and Goldstein, L. (1986). ''Towards an articulatory phonology,'' in *Phonology Yearbook 3*, edited by C. Ewan and J. Anderson (Cambridge U.P., Cambridge, UK), pp. 219–252.

Browman, C. P., and Goldstein, L. (**1989a**). ''Articulatory gestures as phonological units,'' Phonology **6**, 201–251.

Browman, C. P., and Goldstein, L. (**1989b**). ''Tiers in articulatory phonology, with some implications for casual speech,'' in *Papers in Laboratory Phonology I: Between the Grammer and the Physics of Speech*, edited by J. Kingston and M. E. Beckman (Cambridge U.P., Cambridge, UK), pp. 341–376.

Browman, C. P., and Goldstein, L. (**1990**). ''Gestural specification using dynamically-defined articulatory structures,'' J. Phonetics **18**, 299–320.

Browman, C. P., and Goldstein, L. (**1992**). ''Gestural structures and phonological patterns,'' in *Modularity and the Motor Theory of Speech Perception*, edited by I. G. Mattingly and M. Studdert-Kennedy (Erlbaum, Hillsdale, NJ).

Daniloff, R. D., and Hammarberg, R. E. (**1973**). ''On defining coarticulation,'' J. Phonetics **1**, 239–248.

Davis, R. D., and MacNeilage, P. F. (**1990**). ''Acquisition of correct vowel production: A quantitative case study,'' J. Speech Hear. Res. **33**, 16–27.

Eguchi, S., and Hirsh, I. J. (**1969**). ''Development of speech sounds in children,'' Acta Oto-Laryngol. Suppl. **257**, 307–356.

Ferguson, C. A., and Farwell, C. B. (**1975**). ''Words and sounds in early language acquisition,'' Language Acquisition **51**, 419–439.

Goodell, E. W., and Studdert-Kennedy, M. (**1993**). ''Acoustic evidence for the development of gestural coordination in the speech of 2-year-olds: a longitudinal study,'' J. Speech Hear. Res. **36**, 707–727.

Han, M. S. (**1962a**). *Japanese Phonology—An Analysis Based Upon Sound Spectrograms* (Kenkyusha, Tokyo).

Han, M. S. (**1962b**). ''Unvoicing of vowels in Japanese,'' The Study of Sounds, Phonetic Soc. Jpn. **10**, 81–100.

Haraguchi, S. (**1977**). *The Tone Pattern of Japanese: An Autosegmental Theory of Tonology* (Kaitakusha, Tokyo).

Hirose, H. (**1971**). ''The activity of the adductor laryngeal muscles in respect to vowel devoicing in Japanese,'' Phonetica **23**, 156–170.

Imaizumi, S., Hayashi, A., and Deguchi, T. (**1993**). ''Planning in speech production: Listener adaptive characteristics,'' Jpn. J. Logopedics and Phoniatrics **34**, 394–401 (in Japanese).

Imaizumi, S., Hayashi, A., and Deguchi, T. (**1994a**). ''Listener adaptive characteristics in dialogue speech—Effects of temporal adjustment on emotional aspects of speech,'' in *Proceedings of ICSLP 94*, Yokohama, Japan, September 1994, Acoust. Soc. Jpn. Vol. 4, pp. 1967–1970.

Imaizumi, S., Hayashi, A., and Deguchi, T. (**1995**). ''Listener adaptive characteristics of vowel devoicing in Japanese dialogue,'' J. Acoust. Soc. Am. **98**, 768–778.

Imaizumi, S., Hartono, A., Niimi, S., Hirose, H., Saida, H., and Shimura, Y. (**1994b**). ''Evaluation of vocal controllability by an object oriented acoustic analysis system,'' J. Acoust. Soc. Jpn. (E) **15**, 113–116.

Jun, S-A., and Beckman, M. (**1993**). ''A gestural-overlap analysis of vowel devoicing in Japanese and Korean,'' paper presented at the 1993 Annual Meeting of the Linguistic Society of America, Los Angeles, CA, January 1993.

Katz, W. F., Kripke, C., and Tallal, P. (**1991**). ''Anticipatory coarticulation in the speech of adults and young children: Acoustic, perceptual, and video data,'' J. Speech Hear. Res. **34**, 1222–1232.

Kent, R. D. (**1976**). ''Anatomical and neuromuscular maturation of the speech mechanism: Evidence from acoustic studies,'' J. Speech Hear. Res. **19**, 421–447.

Kent, R. D. (**1983**). ''The segmental organization of speech,'' in *The Production of Speech*, edited by P. MacNeilage (Springer-Verlag, New York), pp. 57–89.

Kondo, M. (**1994**). ''Mechanisms of vowel devoicing in Japanese,'' in *Proceedings of ICSLP 94*, Yokohama, Japan, September 1994, Acoust. Soc. Jpn., Vol. 1, pp. 61–64.

Kubozono, H. (**1989**). ''The mora and syllable structure in Japanese: Evidence from speech errors,'' Language and Speech **32**(3), 249–278.

Kuriyagawa, F., and Sawashima, M. (**1989**). ''Word accent, devoicing and duration of vowels in Japanese,'' Annual Bulletin (Research Institute of Logopedics and Phoniatrics, University of Tokyo, Japan), Vol. 23, pp. 85–108.

Lindblom, B., MacNeilage, P., and Studdert-Kennedy, M. (**1983**). ''Self-organizing processes and the explanation of language universals,'' in *Explanations for Language Universals*, edited by B. Butterworth, B. Comrie, and O. Dahl (Mouton, The Hague), pp. 181–203.

Menn, L. (**1983**). ''Development of articulatory, phonetic and phonological capabilities,'' in *Language Production*, edited by B. Butterworth (Academic, London), pp. 3–50.

Menyuk, P., Menn, L., and Silber, R. (**1986**). ''Early strategies for the perception and production of words and sounds,'' in *Language Acquisition*, 2nd ed., edited by P. Flecher and M. Garman (Cambridge U.P., Cambridge), pp. 223–239.

Munhall, K., and Löfqvist, A. (**1992**). ''Gestural aggregation in speech: Laryngeal gestures,'' J. Phonetics **20**, 111–126.

Nakanishi, Y., Owada, K., and Fujita, N. (**1972**). ''Koon kensa to sono kekka no kosatsu (Results and interpretation of articulation tests for children),'' RIEEC Report (Annual Report of Research Inst. Education of Exceptional Children, Tokyo Gakugei Univ.), Vol. 1, pp. 1–41.

Nippon Hoso Kyokai (**1966**). *Accent Dictionary* (NHK, Tokyo, Japan) (in Japanese).

Nittrouer, S. (**1993**). ''The emergence of mature gestural patterns is not uniform: Evidence from an acoustical study,'' J. Speech Hear. Res. **36**, 959–972.

Nittrouer, S., Studdert-Kennedy, M., and McGowan, R. S. (**1989**). ''The emergence of phonetic segments: evidence from the spectral structure of

fricative-vowel syllables spoken by children and adults,'' J. Speech Hear. Res. **32**, 120–132.
Nittrouer, S., Studdert-Kennedy, M., and Neely, S. T. (**1996**). ''How children learn to organize their speech gestures: Further evidence from fricative-vowel syllables,'' J. Speech Hear. Res. **39**, 379–389.
Otake, T., Hatano, G., Cutler, A., and Mehler, J. (**1993**). ''Mora or syllable? Speech segmentation in Japanese,'' J. Memory and Language **32**, 258–278.
Perkell, J. S. (**1986**). ''Coarticulation strategies: Prelininary implications of a detailed analysis of lower lip protrusion movements,'' Speech Commun. **5**, 47–68.
Pierrehumbert, J., and Beckman, M. (**1988**). *Japanese Tone Structure* (MIT, Cambridge, MA).
Roberts, J. (**1997**). ''Hitting a moving target: Acquisition of sound change in progress by Philadelphia children,'' Language Variation and Change **9**, 249–266.
Roberts, J., and Labov, W. (**1995**). ''Learning to talk Philadelphian: Acquisition of a short a by Philadelphia children,'' Language Variation and Change **7**, 101–112.
Sakuma, K. (**1929**). *Nihongo Onseigaku (Japanese Phonetics)* (Kyoubunsha, Tokyo, Japan), pp. 262–269 (in Japanese).
Sawashima, M. (**1969**). ''Devoiced syllables in Japanese—A preliminary study by photoelectric glottography,'' Annual Bulletin (Research Institute of Logopedics and Phoniatrics, University of Tokyo, Japan), Vol. 2, pp. 11–20.
Sawashima, M. (**1971**). ''Devoicing of vowels,'' Annual Bulletin (Research Institute of Logopedics and Phoniatrics, University of Tokyo, Japan), Vol. 5, pp. 7–14.
Sereno, J. A., and Lieberman, P. (**1987**). ''Developmental aspects of lingual coarticulation,'' J. Phonetics **15**, 247–257.
Sereno, J. A., Baum, S. R., Marean, G. C., and Lieberman, P. (**1987**). ''Acoustic analyses and perceptual data on anticipatory labial coarticulation in adults and children,'' J. Acoust. Soc. Am. **81**, 512–519.
Shibata, T. (**1955**). *''Museika,'' in Kokugogaku jiten* (''Devoicing,'' in Japanese Dictionary) (Kokugogaku Gakkai, Tokyo), p. 899 (in Japanese).
Studdert-Kennedy, M. (**1987**). ''The phoneme as a perceptomotor structure,'' in *Language Perception and Production*, edited by A. Allport, D. Mackay, W. Priuz, and E. Scheerer (Academic, London), pp. 67–84.
Sugito, M. (**1969**). ''Vowel devoicing in Tokyo and Osaka,'' The Study of Sounds, Phonetic Soc. Jpn. **14**, 1–4.
Sugito, M. (**1988**). ''Utterance of voiceless vowels by speakers in eight cities in Japan,'' Annual Reports (Osaka Shoin Women's College, Japan), Vol. 25, pp. 1–10.
Sugito, M., and Hirose, H. (**1988**). ''Production and perception of accented devoiced vowel in Japanese,'' Annual Bulletin (Research Institute of Logopedics and Phoniatrics, University of Tokyo, Japan), Vol. 22, pp. 19–37.
Vihman, M. M., and Velleman, S. L. (**1989**). ''Phonological reorganization: A case study,'' Language and Speech **32**, 149–170.
Walker-Andrews, A. S. (**1997**). ''Infants' perception of expressive behaviors: Differentiation of multimodal information,'' Psychol. Bull. **121**, 437–456.
Yoshihara, T. (**1983**). *Accent Dictionary of the Tokyo and Osaka Dialects* (Time, Tokyo) (in Japanese).
Yoshioka, H. (**1981**). ''Laryngeal adjustments in the production of the fricative consonants and devoiced vowels in Japanese,'' Phonetica **38**, 236–251.
Yoshioka, H., Löfqvist, A., and Hirose, H. (**1982**). ''Laryngeal adjustments in Japanese voiceless sound production,'' J. Phonetics **10**, 1–10.

Speech segment durations and quantity in Icelandic

Jörgen Pind
Department of Psychology, University of Iceland, Oddi, Reykjavík, IS-101 Iceland

(Received 19 October 1998; revised 26 April 1999; accepted 28 April 1999)

Icelandic has a phonologic contrast of quantity, distinguishing long and short vowels and consonants. Perceptual studies have shown that a major cue for quantity in perception is relational, involving the vowel-to-rhyme ratio. This cue is approximately invariant under transformations of rate, thus yielding a higher-order invariant for the perception of quantity in Icelandic. Recently it has, however, been shown that vowel spectra can also influence the perception of quantity. This holds for vowels which have different spectra in their long and short varieties. This finding raises the question of whether the durational contrast is less well articulated in those cases where vowel spectra provide another cue for quantity. To test this possibility, production measurements were carried out on vowels and consonants in words which were spoken by a number of speakers at different utterance rates in two experiments. A simple neural network was then trained on the production measurements. Using the network to classify the training stimuli shows that the durational distinctions between long and short phonemes are as clearly articulated whether or not there is a secondary, spectral, cue to quantity.
[S0001-4966(99)02508-4]

PACS numbers: 43.70.Fq [AL]

INTRODUCTION

Phonemic speech contrasts are signaled by a manifold of acoustic cues. These can be broadly split into two classes—spectral and temporal cues—although the distinction between the two classes is not always clear. One phonemic contrast which is usually associated with a clear temporal cue, i.e., acoustic duration, is that of vowel or consonant quantity, found in the distinction that some languages make between short and long phonemes (Lehiste, 1970; Rosner and Pickering, 1994).

Quantity distinctions, signaled by durational means, pose an interesting problem for the perceiver in that speech segment durations are highly susceptible to the influence of nonlinguistic context effects such as those caused by speech rate (Miller, 1987; Miller *et al.*, 1986; Pind, 1995), the number of syllables in the word (Klatt, 1976), and so on. Such contextual effects affect the very same durations that are used to signal the linguistically significant quantity. Some investigators have therefore surmised that listeners need to resort to some kind of normalization to disentangle the linguistic and nonlinguistic factors (e.g., Miller, 1987).

Icelandic contrasts long and short vowels and consonants in stressed syllables. The quantity distinction is such that a long vowel is either followed by one or no consonant, whereas a short vowel is followed by two or more consonants. An exception here is that a vowel is long if it precedes one of the phonemes /p,t,k,s/ followed by one of /v,j,r/. Complementary oppositions of vowel and consonant durations are found in syllables of the type V:C and VC:. In the former a long vowel is followed by a short consonant, in the latter a short vowel is followed by a long consonant. Examples of these contrasts are found in words such as *vina* [vɪ:na] ''female friend'' and *vinna* [vɪn:a] ''to work'' or *baka* [pa:ka] ''to bake'' and *bagga* [pak:a] ''burden, accusative.'' These are the word types considered in this paper. Further discussions of the phonology of quantity in Icelandic can be found in, e.g., Benediktsson (1963) and Árnason (1980).

A number of instrumental studies of Icelandic quantity have been conducted. The most important of these are an early study by Einarsson (1927) and more recent ones by Garnes (1973, 1976), Orešnik and Pétursson (1977), Pétursson (1976, 1978), and Pind (1982, 1995). To these may be added two studies that have only appeared in Icelandic (Indriðason *et al.*, 1991; Kristinsson *et al.*, 1985).

Einarsson's (1927) was the first instrumental phonetic study of Icelandic. He analyzed his own speech using kymographic records, using a corpus of over 500 words read in isolation. Einarsson's measurements of the duration of stressed monophthongs in two-syllable words showed long vowels averaging 207 ms, whereas the short ones were 106 ms on average. This corresponds to a long/short ratio of 1.95. As far as diphthongs are concerned, these averaged 240 ms when long and 136 ms when short, a ratio of 1.77.

Einarsson analyzes consonants in two-syllable words of the type V:C and VC: in some detail. In words of these types the long stops averaged 278 ms with the short stops being 151 ms on average. The long vowels averaged 190 ms and the short ones 91 ms. With these values it is possible to calculate the mean duration of the syllable rhymes[1] in V:C and VC: syllables, these, respectively, being 340 ms and 369 ms. These data accord reasonably well with the phonetic description of complementary vowel and consonant durations: A long vowel is followed by a short consonant and vice versa.

Another important early study is that of Bergsveinsson (1941) which looks into aspects of Icelandic ''sentence phonetics'' (Satzphonetik) within the phonometric tradition. A major thrust of the phonometric school was the importance attached to analyzing recordings of natural or quasi-natural

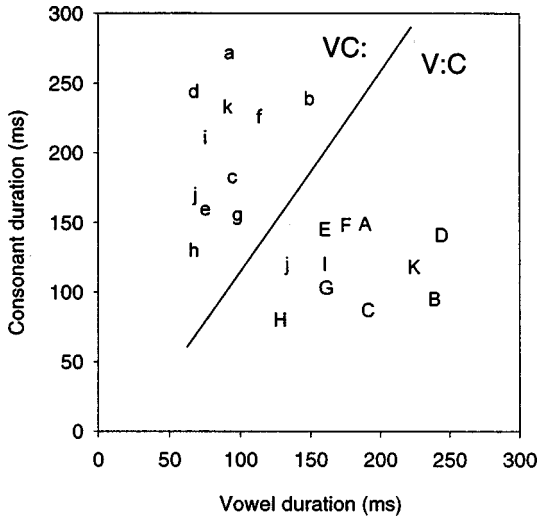

FIG. 1. This figure depicts a summary of findings from nine studies where measurements of vowel and consonant durations have been reported for disyllabic words in Icelandic. The upper case letters denote the average durations of vowels and consonants from words of V:C type, whereas the lower case letters denote the average durations from words of type VC:. The sources for the measurements are as follows: (A) Einarsson (1927); (B) Garnes (1976),—single words; (C) Garnes (1976)—words in sentence context; (D) Pétursson (1976); (E) Pétursson (1976)—northern dialect; (F) Pétursson (1978); (G) Pind (1982); (H) Kristinsson *et al.* (1985); (I) Indriðason *et al.* (1991); (J) Indriðason *et al.* (1991)—northern dialect; (K) Pind (1995).

speech. These studies can be seen as early attempts to come to grips with the variability of speech, an area of investigation which only received general interest much later with studies of automatic speech recognition where variability became a key issue.

Bergsveinsson's study involved analyzing two recorded passages, one being a short lecture on phonetics, the other an imitation of a telephone conversation. The first text, consisting of 417 words, lasted for 169 s of which pauses made up 37.2 s. The second text consisted of 390 words and lasted for 138 s, pauses amounting to 49.4 s. Bergsveinsson estimates the articulation rates for the first text as 0.17 s/syllable and as 0.15 s/syllable for the second text.

Bergsveinsson used his results to criticize the view of Einarsson (1927) that phonemically long and short segments are distinguished based on their different durations. He has a figure depicting the durations of all vowels he was able to measure in the first text (700 in all). This figure, Bergsveinsson points out, shows that, contrary to expectations, there do not emerge two modes in the distributions of vowel durations corresponding to two distinctive lengths. Rather, we just see one continuous distribution, where most of the values cluster around the shorter durations (the mean being 76 ms). This, according to Bergsveinsson, is ''proof that it is not possible to divide the durations into two classes based on absolute durations independently of other factors'' (Bergsveinsson, 1941, p. 99). While this is correct, Einarsson was also correct in pointing out that *average* durations of vowels and consonants do in fact distinguish short from long segments. This emerges from Fig. 1, which summarizes the findings from nine studies of Icelandic quantity, which have been published over the last 70 years. The figure shows the average durations of vowels and consonants, when it was possible to calculate these from the published papers (in all cases in disyllabic words). Most of the studies pertain to the southern, Reykjavík, dialect, but two studies report data for the northern dialect as well (details on Icelandic dialects can be found in Benediktsson, 1961). The figure does not indicate any difference between the dialects as regards vowel and consonant length. It can be seen that, in spite of considerable variability, the pattern of results corresponds, in general, to that found originally by Einarsson (1927) with the different syllable types, V:C and VC:, tending to cluster in distinct parts of the figure.

I have previously argued that the pattern of results emerging in Fig. 1 points to the existence of a relational invariant for quantity in Icelandic (Pind, 1986, 1995, 1996a; cf. also Port and Dalby, 1982). This invariant is expressed by the vowel-to-rhyme ratio and remains constant despite considerable variations in, e.g., speaking rate. Perception experiments have confirmed that listeners are indeed sensitive to a relational invariant (Pind, 1995). The importance of such a ratio had been surmised by Garnes (1976) in the first study of speech perception in Icelandic although she assigned the major importance to the vowel: ''The results show that vowel duration is the primary factor in determining responses but since consonant duration does influence the responses, it appears that a ratio of vowel: consonant durations affects the perception of quantity'' (Garnes, 1976, p. 141). It would now appear to be well established that the ratio is in fact the major cue to quantity (Pind, 1986, 1995).[2]

Two complications have, though, turned up in more recent research on the role of such a relational invariant. Perception experiments have shown that quantity can be perceived in syllables containing unreleased stops (Pind, 1996a). In those cases the listener should not be able to calculate the vowel/rhyme ratio since the end of the stop is indeterminate. Nevertheless, listeners will assign quantity to such syllables. Interestingly, in these cases, the vowel quantity becomes more susceptible to the influence of contextual speaking rate. Usually, surrounding speaking rate has a very limited effect on clearly articulated syllables, presumably because of the importance of the vowel/rhyme ratio (Pind, 1986). That the effect of surrounding context becomes more marked with indeterminate vowel/rhyme ratios is thus to be expected.

It has also turned out that the spectral difference between short and long vowels is sometimes so great that it will override the durational invariant. This holds, e.g., for the vowel [ɛ] in Icelandic, but not for a vowel such as [a] which has similar quality whether long or short. Table I reports vowel formants for the vowels [a] and [ɛ] from two studies. The first of these is the study by Svavarsdóttir *et al.* (1982) which is the most detailed study of Icelandic vowel formants available. The second one is a previous study by the present author (Pind, 1996b). It is clear from Table I that the long and short varieties of [ɛ] show much more extensive differences in the frequencies of the first and second formants than the two variants of the vowel [a]. These differences are well beyond the jnd's of 3%–5% for formant frequencies reported by Flanagan (1972). Pind (1996b) has furthermore shown

TABLE I. Average frequencies of the first three formants of the vowels [a] and [ɛ] in Icelandic. The data from the study by Svavarsdóttir *et al.* (1982) are averages for four male speakers; the data from Pind (1996b) are based on one male speaker. All values are in Hz.

		Vowel					
		[ɛ]			[a]		
Study	Quantity	*F*1	*F*2	*F*3	*F*1	*F*2	*F*3
Svavarsdóttir *et al.* (1982)	Long	470	1815	2690	695	1245	2430
	Short	510	1590	2540	665	1285	2480
Pind (1996b)	Long	435	1905	2445	805	1155	2515
	Short	510	1600	2425	805	1170	2480

that in the case of the vowel [ɛ] the spectral information is an important cue for the quantity of the vowel and can easily override the durational cue. Thus it was not possible, using a waveform editor, to shorten a phonemically long [ɛ] vowel to yield a short one or vice versa. This was, however, easy enough to accomplish with the vowel [a]. Thus it is clear that the spectral difference between long and short [ɛ] is of great importance for the perception of the vowel's quantity. This result has now been replicated with synthetic speech (Pind, 1998). Other investigators have noted the relationship between duration and spectrum (see Lehiste, 1970, pp. 30–33) and this has also been shown to affect the perception of quantity, e.g., in Swedish (Hadding-Koch and Abramson, 1964) and Thai (Abramson and Ren, 1990).

Lindblom (1990), in his H&H framework, has hypothesized that speakers are primarily guided by an effort to make themselves understood. Thus one should not expect that speakers always aim for idealized versions of speech segments but rather speak in order to make individual segments sufficiently different so that listeners will not have difficulty understanding their meaning. Such an approach leads to an interesting hypothesis as regards the quantity distinction in Icelandic, namely that the durational distinction will be less clearly demarcated in those cases where vowel spectra provide another cue for quantity, such as for the vowel [ɛ], than in those cases where this situation does not hold, e.g., for the vowel [a]. The primary purpose of this study is to compare how listeners articulate the durational distinctions depending on whether they have a secondary spectral cue or not. From Lindblom's theory it may be hypothesized that speakers would not articulate durational distinctions as clearly in those cases where quantity is signaled both by the duration and the spectrum of the vowel.

Measurements of vowel and consonant durations will be presented from two production experiments. Additionally, the production data will be fed to a simple neural network which will play the role of a hypothetical perceiver and the question will be posed whether any difference is to be observed in the behavior of the network depending on the identity of the stressed vowel. If the durational distinctions are less clearly articulated for the vowel [ɛ] than for the vowel [a], which would reveal itself by greater overlap of durational values for long and short [ɛ] tokens compared to [a] tokens, one can predict that the network will show more classification errors for words containing [ɛ] than for words containing [a], assuming it is only trained on the durational measurements.

I. EXPERIMENT 1

A. Method

1. Participants

Six undergraduate psychology majors at the University of Iceland, three female and three male, participated in this experiment for course credit. Participants were all native speakers of Icelandic.

2. Stimuli

The stimulus words chosen for this production experiment were the following: *saki* [sa:cɪ] ''to suffer (verb, 1st or 3rd pers. conj.),'' *saggi* [sac:ɪ] ''damp (noun, masc.sg. nom.),'' *seki* [sɛ:cɪ] ''guilty (adjective, masc.sg.nom.),'' *seggi* [sɛc:ɪ] ''men (noun, masc.acc.pl.).'' These two word pairs contrast in terms of quantity, the first word in each pair having a long vowel followed by a short consonant, the second word a short vowel followed by a long consonant.

3. Procedure

The stimulus words were embedded in sentence context ''Ég les orðið _____ núna'' (I read the word ____ now). A list of 40 such sentences, in randomized order, was made up containing 10 repetitions of each word. Participants read this list six times, twice at a normal rate, twice at a fast rate, and twice at a slow rate. All participants started by reading the list once at the normal rate; after that half the participants read the list once at the slow rate followed by one reading at the fast rate, the other half read at the fast rate followed by the slow rate. Following this, each participant read the list three times in the same order as originally. The procedure was explained to the participants before the readings started. They chose their own pace for the different utterance rates, and were free to take a break whenever they wanted. Ten tokens from each context were used for measurement purposes. These were usually the first ten tokens read in each condition, but misreadings, unnaturally hesitant readings, etc., were skipped.

The reading took place in a soundproof room (Industrial Acoustics) and was captured on digital audio tape using a Sony DAT recorder (model TCD-D7). The microphone used

was from Audio-Technica, model AT 813, placed on a table approximately 30 cm from the mouth of the participants. The readings were digitized onto a PC computer using the Sensimetrics SpeechStation at a frequency of 10 kHz. All duration measurements were carried out using the SpeechStation and its accompanying software.

Since there were six speakers in this experiment, with each speaker contributing ten readings of each target word at each of the three different speaking rates, the total number of tokens measured in this experiment was 720 (6 speakers $\times$4 words $\times$3 speaking rates $\times$10 readings).

The measurements were all made from the waveform display, aided by the spectrogram which the SpeechStation displays simultaneously with the waveform. The spectrographic display was especially useful in locating the end of the target words. Measurements of the vowel and closure durations were always based directly on the waveforms.[3] The following segments were labeled on the waveform: (A) The onset of the target word, marked by the beginning of the [s]. (B) The onset of the stressed vowel, [a] or [ɛ], this being located at the beginning of the first clear voiced pulse of the vowel. (C) The end of the vowel (beginning of closure). This was marked where the vowel pulses had faded away to the extent that clear periodicity in the waveform was no longer visible. (D) The end of closure, marked by the burst at the end of the closure. The onset of the second vowel [ɪ], again indicated by the onset of regular vowel pulses. (E) The end of the target word, taken to coincide with the end of the second vowel. When the end of the word was followed directly by the last word in the target sentence without a clear acoustic boundary, the boundary between the vowel [ɪ] and the following [n] (of the word ''núna'') was located in the middle of the [ɪ] to [n] formant transitions, as judged from the spectrographic displays.

All measurements were originally carried out by a research assistant according to the specifications above. Approximately five months later the author re-measured a random subset of 72 tokens (10% of the whole database). In the repeated measurements the same points were labeled as in the original measurements. In all cases these latter labels deviated on average less than 10 ms in their locations from the locations of original labels. The major interest in this paper focuses on the durations of the vowels and consonants of the stressed syllables. Deviations in the vowel onset locations averaged 2.7 ms, for the vowel offset location the average deviation amounted to 4.9 ms, but was only 0.9 ms for the location of the release of the closure.

B. Results and discussion

Word durations averaged 661 ms (s.d.=116 ms) at the fast rate, 791 ms (s.d.=170 ms) at the normal rate, and 1206 ms (s.d.=301 ms) at the slow rate. The words at the slow rate are thus, on average, almost twice as long as the words at the fast rate. Two of the speakers showed minimal differences between the fast and the normal rate. All speakers showed a clear difference in word duration at the normal and slow rate.

Table II shows the average vowel and consonant durations in all conditions of the present experiment. Overall the phonemically long vowels average 147 ms in duration with the following short consonant averaging 118 ms. The rhyme duration is thus 265 ms in the V:C syllables. For the VC: syllables the rhyme duration averages 266 ms with the short vowel being 77 ms on average and the long consonant 189 ms. Rhyme duration is therefore quite comparable between the two syllable types.

TABLE II. Average vowel and consonant durations in experiment 1. All values in ms. M=mean; s.d.=standard deviation.

			Syllable type			
			V:C		VC:	
	Rate		Vowel	Consonant	Vowel	Consonant
Vowel [a]	Fast	M	127	97	72	139
		s.d.	31	21	15	41
	Normal	M	150	112	78	166
		s.d.	26	19	14	35
	Slow	M	183	147	84	262
		s.d.	27	22	26	95
Vowel [ɛ]	Fast	M	114	91	70	138
		s.d.	31	16	13	40
	Normal	M	137	110	78	174
		s.d.	22	17	13	41
	Slow	M	170	149	80	253
		s.d.	30	21	18	85

It is clear that, on average, the phonemically long and short segments are separated by their durations. This, however, does not necessarily hold for individual tokens, as shown in Fig. 2, which shows the distribution of vowel and consonant durations for the long and short phonemes. Evidently there is considerable overlap in the durations of the long and short phonemes. This is natural enough, given that the segments are spoken at very different utterance rates. This shows that the duration of speech segments in Icelandic is at least controlled by two factors, the phonological quantity of the segments and by the utterance rate. The duration of an individual segment will therefore not uniquely specify the quantity of that segment. To arrive at that it is necessary to look at a longer stretch of the speech utterance. Previous research (Pind, 1986, 1995) has shown that this involves only a rather short window and that it is possible, in almost all cases, to arrive at a unique specification of quantity just by looking at the vowel and the following consonant simultaneously (rather than separately as done in Fig. 2).

This is illustrated in Fig. 3, showing scatter plots of all the vowel and consonant tokens measured in this experiment. This view of the data shows a clear separation of two clusters of data points, one containing the vowels and consonants in the V:C type syllables, the other containing the segments from the VC: type syllables. The data points show considerable dispersal, which can mainly be accounted for by the effects of differences in speaking rate. As speaking rate gets faster data points move closer to the origin of the graph. The main point of interest in the present study is, however, that the results for the vowels [a] and [ɛ] seem, at a first glance, quite comparable and do not indicate that the durational differences are less clearly demarcated for the vowel [ɛ] than

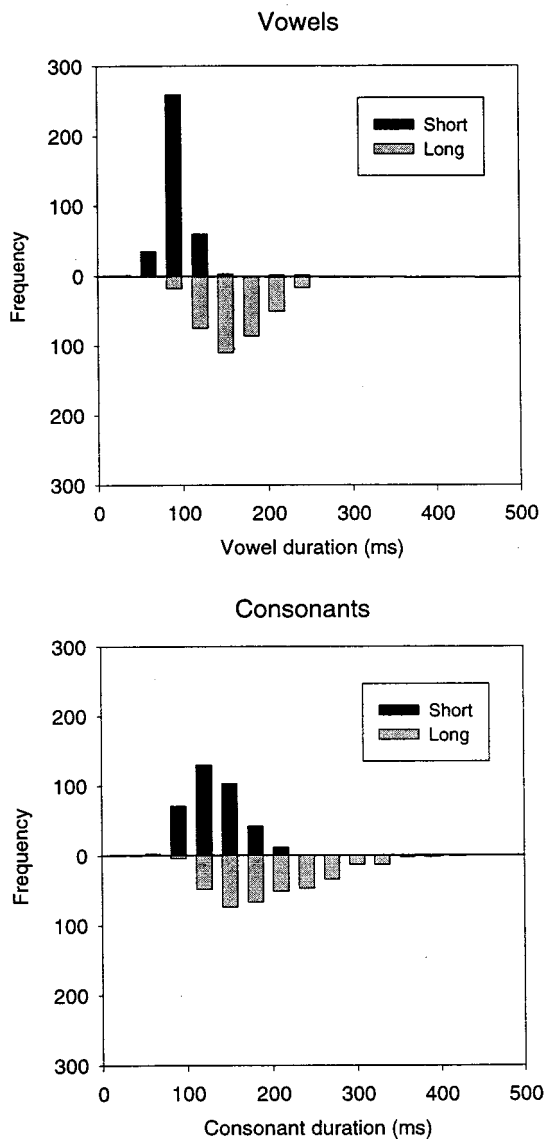

FIG. 2. Histograms showing the distribution of vowel and consonant durations in experiment 1. The individual bins are 30 ms wide ranging from 0 to 450 ms. There are four tokens with a long consonant which have consonant durations longer than 450 ms. These have been left out of this figure. Both figures have identical scaling to make it easier to compare the distribution of vowel and consonant durations. The legends ''Short'' and ''Long'' refer to the phonemic length of the segments.

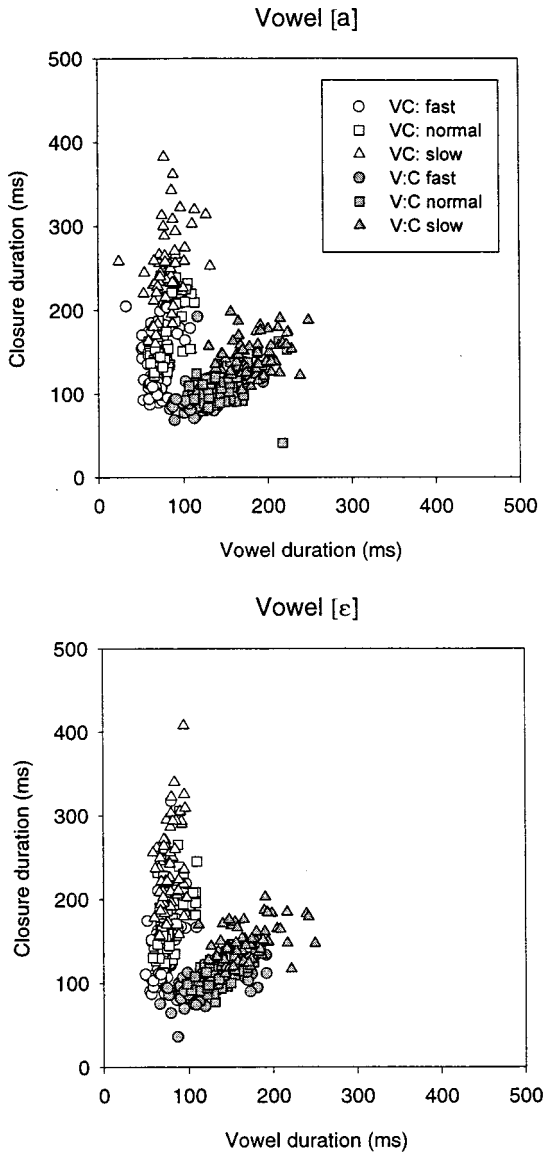

FIG. 3. Scatter plots showing the duration distributions of all vowels and consonants measured in experiment 1. The two plots show the results for the vowel [a] at top and [ɛ] below. Evidently the different syllable types (V:C with filled symbols, and VC: with open symbols) are pretty well separated when plotted in this manner.

for the vowel [a], an issue that will be considered in greater detail in Sec. III.[4]

II. EXPERIMENT 2

The previous experiment measured the duration of stressed vowels and consonants in disyllabic words embedded in fixed sentence frames. It is clear that this context is in some ways rather artificial and may lead to participants imposing a fixed accent pattern on the utterances which may perhaps not be representative of natural speech. For this reason it is of some interest if it is also possible to measure the durations of speech segments in somewhat more natural contexts. For this reason another production experiment was undertaken in which the four words used in experiment 1 were embedded in a longer, continuous text.

A. Method

1. Participants

Twenty-five undergraduate psychology majors at the University of Iceland, 15 female and 10 male, participated in this experiment for course credit. Participants were all native speakers of Icelandic.

2. Stimuli

The stimulus words were the same four words used in experiment 1, *saki, saggi, seki,* and *seggi*. These were now embedded in a 163 word long text made up of 25 sentences. The text was made up as a spelling exercise, very familiar to Icelandic students from their previous studies at the primary and secondary school levels. Such exercises contain a number of sentences, which are usually not thematically related (but all make good sense) and are used to test different as-

pects of Icelandic spelling. The four target words of interest here were in all cases found at the beginning of sentences, in word positions 18, 56, 111, and 144. This distance was kept between the words to minimize the likelihood that the participants would pay any special attention to these words. Most of the sentences were taken from published spelling exercises though the four sentences containing the target words were specifically made up for this experiment. The text is printed here as an Appendix.

3. Procedure

All participants read the text six times, two times at a normal utterance rate, two times at a fast rate, and two times at a slow rate. In all cases the participants read the text initially at the normal rate, and then half the participants read at the slow rate followed by the fast rate, for the other half the order was reversed. Participants chose their own pace for the different utterance rates and were free to take a break when they wished. The reading took place in a soundproof room (Industrial Acoustics) using the same setup as in experiment 1.

The readings were digitized onto a PC computer using the Sensimetrics SpeechStation at a frequency of 10 kHz. All duration measurements were carried out using the SpeechStation and its accompanying software. Since there were 25 speakers in this experiment with each speaker reading each target word 6 times the total number of tokens measured in this experiment amounts to 600 (25 speakers $\times 4$ words $\times 6$ readings). The measurements were carried out in the same manner as described for experiment 1.

After the original measurements had been made, the author re-measured a random subset of 60 tokens (10% of the whole dataset). These repeated measurements were obtained approximately 5 months after the original measurements had been carried out. In the repeated measurements the same points were labeled as in the original measurements. The average deviation for the onset of vowel amounted to 4.75 ms and the average deviation for the end of the vowel/beginning of closure was 9.35 ms. For the release of the closure the average deviation amounted to 1.08 ms.

B. Results and discussion

In this experiment the word durations averaged over all participants were 314 ms (s.d.=153 ms) at the fast rate, 406 ms (s.d.=55 ms) at the normal rate, and 573 ms (s.d.=69 ms) at the slow rate. These word durations are much shorter than in experiment 1. In fact the words spoken at the slowest rate in this experiment are shorter on average than the words at the fastest rate in experiment 1.

Table III shows average values for vowel and consonant durations in the present experiment, broken down by syllable type, speaking rate, and the identity of the vowel. In the V:C syllables the vowels averaged 122 ms and the consonants 88 ms. In the VC: syllables the average vowel duration was 71 ms while the average consonant duration was 152 ms. The average rhyme durations thus amount to 210 ms in the V:C syllables and 223 ms in the VC: syllables. Again the rhyme durations are comparable although on average about 50 ms shorter than in experiment 1.

TABLE III. Average durations of vowels and consonants in experiment 2. All values in ms. M=mean; s.d.=standard deviation.

			Syllable type			
			V:C		VC:	
	Rate		Vowel	Consonant	Vowel	Consonant
Vowel [a]	Fast	M	90	63	65	87
		s.d.	21	21	16	29
	Normal	M	119	83	73	139
		s.d.	20	18	15	37
	Slow	M	170	119	79	240
		s.d.	55	41	21	92
Vowel [ɛ]	Fast	M	79	62	60	90
		s.d.	20	14	15	27
	Normal	M	112	80	69	144
		s.d.	22	17	16	38
	Slow	M	164	119	80	213
		s.d.	62	45	23	64

The durations of the vowels [a] and [ɛ] are quite similar. At the fastest speaking rate the phonemically short vowels average 60–65 ms in duration, and about 80 ms at the slowest rate. This latter average duration is close to the average duration of the phonemically long vowels at the fastest speaking rate (79–90 ms). Naturally enough, at the slow rate the long vowels are much longer, around 164–170 ms on average. As has been previously found (Pind, 1995), the phonemically long vowels lengthen much more than the phonemically short vowels as speaking rate is slowed down. As for the consonants the phonemically long consonants increase in duration from around 90 to well over 200 ms as speaking rate decreases. For the short consonants the comparable lengthening is from roughly 60 ms to 120 ms. In general, it would seem that the consonants are somewhat more elastic than the vowels.

Figure 4 shows all measurements for the durations of vowels and consonants. The distribution of vowel and consonant durations is quite similar to that obtained in the previous experiment with the two syllable types again forming two clusters, one for V:C type words, one for VC: type words. This result holds irrespective of the quality of the stressed vowel, whether it is [ɛ] or [a]. Compared with experiment 1 (see Fig. 3) the only difference which emerges is that there is somewhat greater overlap between the two syllable categories in this experiment. This is to be expected given that many more speakers are involved and that speaking rate is in general faster in this experiment than in experiment 1 (the somewhat lower accuracy of the measurements in experiment 2 might also be a contributing factor).

III. GENERAL DISCUSSION

Do the data presented in Figs. 3 and 4 offer any suggestions as to what might be the most salient acoustic cue for the perception of quantity in Icelandic? The question of the relationship between speech acoustics and perception is a complex one (Lieberman *et al.*, 1967; Stevens, 1989;

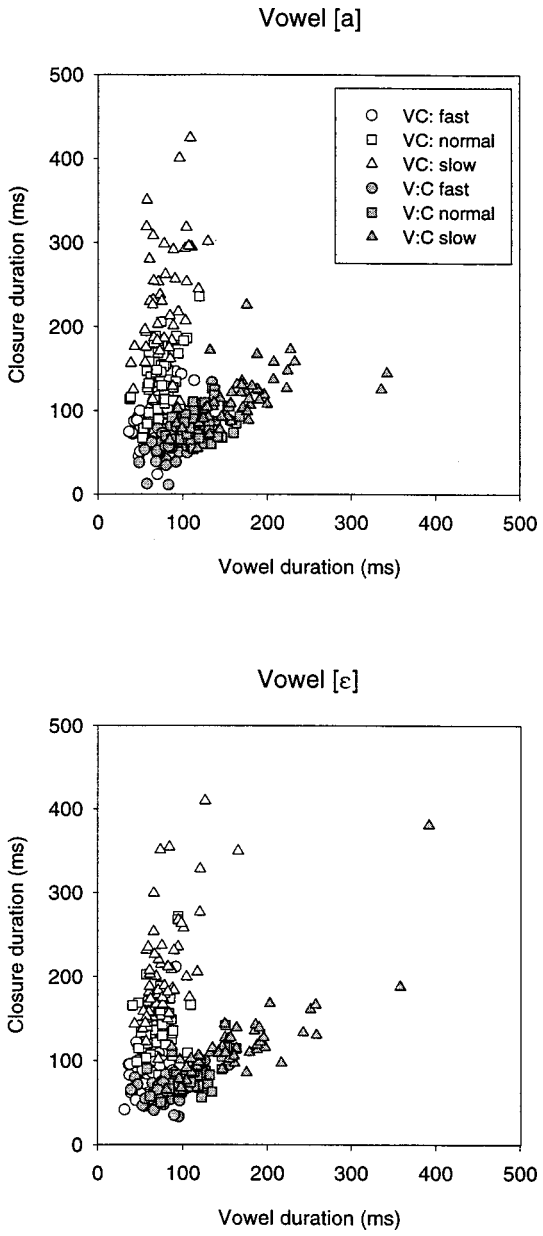

FIG. 4. Scatter plots showing the duration distributions of all vowels and consonants measured in experiment 2. The two plots show the results for the vowel [a] at top and [ε] below.

Stevens and Blumstein, 1981). It seems worthwhile to explore in some principled manner how a perceptual system would deal with the production data shown in Figs. 3 and 4, i.e., how it could assign the individual data points to the two classes of syllables, V:C and VC:. Intuitively, it would seem clear that a decision boundary forming an oblique line on the VC plane separating the two clusters of data point would form an ''optimal boundary'' correctly separating the production data into appropriate categories, cf. Fig. 1.

One way of predicting perceptual boundaries from production data was proposed by Miller *et al.* (1986). These authors introduced the notion of a ''variable optimal boundary'' for Voice Onset Time (VOT) measurements. This boundary was calculated by sorting VOTs measured at various utterance rates into 50-ms bins and calculating hypothetical phoneme boundaries that would optimally separate the two categories of unaspirated and aspirated stops for each bin. Miller *et al.* showed that this optimal boundary increased with slower utterance rates (as judged from the overall duration of the syllables) from 14 ms of VOT in 100–149 ms long syllables to 52.5 ms of VOT in 650–700 ms long syllables. Pind (1995) made use of this approach in a study comparing the perception of VOT and quantity in Icelandic, finding that such a boundary yielded a much closer fit of production and perception for quantity than for VOT.

Such decision boundaries can also be calculated by other methods. One is to feed the production data to a neural network and let the network find the decision boundary. This procedure has the advantage over the previous method of not needing the somewhat artificial division of individual data points into separate bins.

The data shown in Figs. 3 and 4 were accordingly fed to a simple neural network. The data presented in these figures indicate that the problem of finding an optimal boundary is linearly separable and so there is no need for hidden nodes in the network (Gurney, 1997). The network thus consists of two input units and one output unit connected in a feed forward fashion. The input units receive the vowel and consonant durations while the output unit responds by a number ranging from 0 to 1 indicating the strength of the V:C response. The network is trained with supervision, the teaching signal being 1 for those data points associated with a V:C type syllable and 0 for the data points associated with a VC: type syllable. All simulations were run using the publicly available ''tlearn'' simulator (Plunkett and Elman, 1997). In each case the network was trained for 100 epochs using a learning rate parameter of 0.5 and a momentum of 0.6. The network was trained randomly without replacement. Training the network in this manner leads to the weights of the network being set. After successful training the network will have partitioned the input space into two categories of syllables, V:C and VC:, in all cases finding an optimal boundary similar to that calculated by Miller *et al.* (1986) except that the boundaries here are in all cases linear since the network has no hidden units.

The network was trained twice on the data for each experiment, separately for the vowels [a] and [ε], in all cases using the parameters mentioned previously. After training, the network was in each case tested on the training data to see how many ''misperceptions'' it would yield. These will occur in those regions where there is overlap in the durational values of segments from V:C and VC: categories. If the vowel spectrum provides another cue for quantity, which may make speakers less careful in maintaining the durational differences of long and short segments, we would hypothesize that the network would show a greater frequency of misclassifications for the production data containing the vowel [ε] than for the vowel [a]. Table IV gives the results of the networks' classifications of the experimental data. It is clear that there is a notable difference between the overall percentage of misclassifications in the two experiments. There are only a negligible number of misclassified stimuli in experiment 1, while the percentage is appreciably higher for experiment 2. This is as expected since the tokens from experiment 2 were measured from connected speech,

TABLE IV. The number of misclassifications given by a simple neural network when trained on the production data from experiments 1 and 2. The directions of the misclassifications are also given. V:C→VC: thus denotes a syllable with a long vowel and a short consonant being misclassified as a syllable with a short vowel and long consonant.

	Vowel [a]		Vowel [ɛ]		Percentage wrongly classified
	V:C→VC:	VC:→V:C	V:C→VC:	VC:→V:C	
Experiment 1	1	1	3	0	0.7%
Experiment 2	3	14	6	12	5.8%

whereas those of experiment 1 were measured in a fixed sentence frame. Note, however, that there is no significant difference in the number of misclassifications depending on the identity of the vowel, $\chi^2(1)=0.129$, $p>0.10$. The results of these neural network simulations therefore show clearly that the addition of another cue for quantity in the case of the vowel [ɛ] does not lead to erosion of the durational distinction in speech. Speakers would appear to base their articulation on a relatively fixed temporal pattern for the production of V:C and VC: syllables in Icelandic rather than being guided by moment-to-moment considerations of intelligibility.

In conclusion it is thus clear that the existence of a secondary cue for quantity in words containing the vowel [ɛ] does not lessen the articulation of the temporal distinction by Icelandic speakers. The paper has additionally shown that simple neural networks can effectively be used to investigate the relationship between the production and perception of temporal speech cues.

ACKNOWLEDGMENTS

This research was supported by the Icelandic Science Foundation and by the Research Foundation of the University of Iceland. I am grateful to Margrét Dóra Ragnarsdóttir for help in carrying out the measurements reported here and to two anonymous reviewers for very helpful comments on an earlier version of the paper.

APPENDIX

The following text was used in experiment 2. The text is in Icelandic. The target words for the experiments have been italicized.

Drengurinn hrissti þykkan, úfinn hárlubbann. Enginn skyldi hneykslast þó að þráin brysti dirfsku til að klifa nípuna. *Saggi* getur verið æði hvimleiður. Ég býst við að Svava endurnýi miðann. Það er erfitt að hlíta þessum úrslitum. Bikkjan dróst áfram draghölt. Kofanum var hróflað upp. Hvar er eiðið mjóst? Viltu sjá hversu hryllilega pilturinn hefur meiðst. *Seki* maðurinn leit undan. Smalarnir hafa skipst á og annast fjárgæsluna á víxl. Sykurinn hefur stráðst um allt gólf. Hann þráinn flyst til bæjarians í næstu viku. Bókfærslukennsla Þorkels bar mikinn árangur. Ef Ingunn legði fylstu rækt við námið hlyti hún ávallt hæstu einkunnir í íslensku. Veistu um hvaða leyti presturinn ætlar að skíra drenginn? *Seggi* Sigurðar bónda langaði að fljúgast á. Búist er við því að bankinn rýi Skarphéðinn, heilsulítinn og útslitinn aumingjann, alveg inn að skyrtunni. Hvernig gastu fræðst um þessa nýjung? Kríurnar bitu tófuna miskunnarlaust. *Saki* konuna ekki getum við andað léttar. Umsækjendur lögðu fram ýmiss konar skírteini. Kristinn lyti lágt ef hann þægi bitlinginn.

[1]The syllable rhyme is defined as the syllable less any consonantal attack. In the experiments reported here the syllable rhyme consists of a vowel and a following consonant.

[2]The choice of the vowel/rhyme ratio as the proper invariant here was originally inspired by Bannert (1979). A different ratio such as V/C can equally well be used since for each vowel/rhyme ratio a V/C ratio can also be calculated. The former ratio highlights the fact the quantity is defined over the syllable rhyme in Icelandic.

[3]Both vowel and consonant are defined acoustically in this study. The vowel is equated with the voiced period of the waveforms following the initial [s] and preceding the silent gap of the closure. The consonant, in all cases a closure, is equated with the duration of the silent gap.

[4]The focus of this study is on the durational distinctions between long and short phonemes. Thus formant frequencies have not been measured since it would seem to be well established by earlier studies, as reviewed in the Introduction, that long and short varieties of [ɛ] are phonemically quite distinct while this does not hold for the vowel [a]. For comparison formant frequencies were measured in 36 word tokens by the three male speakers of this experiment, one from each word type at each of the three utterance rates. The average values for the first three formants were as follows (each average based on 9 tokens): 695, 1280, and 2550 Hz for [a]; 635, 1330, and 2375 Hz for [a]; 425, 1865, and 2540 Hz for [ɛ:], and finally 535, 1675, and 2520 Hz for [ɛ]. These values may be compared with those given in Table I. All these values were measured one-fourth of the way into the vowel, i.e., at the point where the steady state of the vowel had been reached. These values confirm that there are appreciable differences in $F1$ and $F2$ for the long and short varieties of the vowel [ɛ]. The differences are much smaller for the vowel [a].

Abramson, A. S., and Ren, N. (**1990**). ''Distinctive vowel length: duration vs. spectrum in Thai,'' J. Phonetics **18**, 79–92.

Árnason, K. (**1980**). *Quantity in Historical Phonology: Icelandic and Related Cases* (Cambridge University Press, Cambridge).

Bannert, R. (**1979**). ''The effect of sentence accent on quantity,'' in *Proceedings of the Ninth International Congress of Phonetic Sciences* (Institute of Phonetics, Copenhagen), Vol. II, pp. 253–259.

Benediktsson, H. (**1961**). ''Icelandic dialectology: Methods and results,'' Lingua Islandica-Íslenzk tunga **3**, 72–113.

Benediktsson, H. (**1963**). ''The non-uniqueness of phonemic solutions: Quantity and stress in Icelandic,'' Phonetica **10**, 133–153.

Bergsveinsson, S. (**1941**). *Grundfragen der isländischen Satzphonetik* (Munksgaard, Copenhagen).

Einarsson, S. (**1927**). *Beiträge zur Phonetik der Isländischen Sprache* (A. W. Brøgger, Oslo).

Flanagan, J. L. (**1972**). *Speech Analysis, Synthesis, and Perception* (Springer, New York).

Garnes, S. (**1973**). ''Phonetic evidence supporting a phonological analysis,'' J. Phonetics **1**, 273–283.

Garnes, S. (**1976**). *Quantity in Icelandic: Production and Perception* (Helmut Buske Verlag, Hamburg).

Gurney, K. (**1997**). *An Introduction to Neural Networks* (UCL Press, London).

Hadding-Koch, K., and Abramson, A. (**1964**). ''Duration versus spectrum in Swedish vowels: Some perceptual experiments,'' Studia Linguistica **18**, 94–107.

Indriðason, Þ, Eypórsson, A., Halldórsson, G. *et al.* (**1991**). ''Mál er að mæla: Um samhljóðalengd í íslensku [On consonant duration in Icelandic],'' Íslenskt mál og almenn málfræði [Icelandic language and general linguistics] **12–14**, 143–190.
Klatt, D. H. (**1976**). ''Linguistic uses of segmental duration in English: Acoustic and perceptual evidence,'' J. Acoust. Soc. Am. **59**, 1208–1221.
Kristinsson, A. P., Magnússon, F., Pálsdóttir, M., and Þorgeirsdóttir, S. (**1985**). ''Um andstæðuáherslu í íslensku [On contrastive stress in Icelandic],'' Íslenskt mál og almenn málfræði [Icelandic language and general linguistics] **7**, 7–47.
Lehiste, I. (**1970**). *Suprasegmentals* (MIT Press, Cambridge, MA).
Liberman, A. M., Cooper, F. S., Shankweiler, D. P., and Studdert-Kennedy, M. (**1967**). ''Perception of the speech code,'' Psychol. Rev. **74**, 431–461.
Lindblom, B. (**1990**). ''Explaining phonetic variation. A sketch of the H&H theory,'' in *Speech Production and Speech Modeling*, edited by W. Hardcastle and A. Marchal (Klüwer, Dordrecht), pp. 403–439.
Miller, J. L. (**1987**). ''Rate-dependent processing in speech perception,'' in *Progress in the Psychology of Language*, edited by A. W. Ellis (Lawrence Erlbaum Associates, London), Vol. III, pp. 119–157.
Miller, J. L., Green, K. P., and Reeves, A. (**1986**). ''Speaking rate and segments: A look at the relation between speech production and speech perception for the voicing contrast,'' Phonetica **43**, 106–115.
Orešnik, J., and Pétursson, M. (**1977**). ''Quantity in modern Icelandic,'' Arkiv för nordisk filologi **92**, 155–171.
Pétursson, M. (**1976**). ''Quantität und vokalische Klangfarbe im modernen Isländischen,'' Zeitschrift für Phonetik, Sprachwissenschaft und Kommunikationsforschung **29**, 49–63.
Pétursson, M. (**1978**). ''L'element temporel: Un problème de prononciation illustré par un example de l'islandais moderne, langue à quantité,'' Arkiv för nordisk filologi **93**, 174–181.
Pind, J. (**1982**). ''The perception of quantity and preaspiration in Icelandic,'' DPhil thesis, University of Sussex, U.K.
Pind, J. (**1986**). ''The perception of quantity in Icelandic,'' Phonetica **43**, 116–139.
Pind, J. (**1995**). ''Speaking rate, VOT and quantity: The search for higher-order invariants for two Icelandic speech cues,'' Percept. Psychophys. **57**, 291–304.
Pind, J. (**1996a**). ''Rate-dependent perception of quantity in released and unreleased syllables in Icelandic,'' Speech Commun. **19**, 295–306.
Pind, J. (**1996b**). ''Spectral factors in the perception of vowel quantity in Icelandic,'' Scand. J. Psychol. **37**, 121–131.
Pind, J. (**1998**). ''Auditory and linguistic factors in the perception of voice offset time as a cue for preaspiration,'' J. Acoust. Soc. Am. **103**, 2117–2127.
Plunkett, K., and Elman, J. L. (**1997**). *Exercises in Rethinking Innateness: A Handbook for Connectionist Simulations* (MIT Press, Cambridge, MA).
Port, R. F., and Dalby, J. (**1982**). ''Consonant/vowel ratio as a cue for voicing in English,'' Percept. Psychophys. **32**, 141–152.
Rosner, B. S., and Pickering, J. B. (**1994**). *Vowel Perception and Production* (Oxford, University Press, Oxford).
Stevens, K. N. (**1989**). ''On the quantal nature of speech,'' J. Phonetics **17**, 3–45.
Stevens, K. N., and Blumstein, S. E. (**1981**). ''The search for invariant acoustic correlates of acoustic features,'' in *Perspectives on the Study of Speech*, edited by P. D. Eimas and J. L. Miller (Lawrence Erlbaum Associates, Hillsdale, NJ), pp. 1–38.
Svavarsdóttir, Á., Sigurðsson, H. Á., Jónsson, S., and Konráðsson, S. (**1982**). ''Formendur íslenskra sérhljóða [The formants of Icelandic vowels],'' Íslenskt mál og almenn málfræði [Icelandic language and general linguistics] **4**, 63–85.

Acoustic correlates of talker sex and individual talker identity are present in a short vowel segment produced in running speech

Jo-Anne Bachorowski[a)]
Department of Psychology, Wilson Hall, Vanderbilt University, Nashville, Tennessee 37240

Michael J. Owren[b)]
Department of Psychology, Uris Hall, Cornell University, Ithaca, New York 14853

(Received 5 July 1998; revised 15 April 1999; accepted 28 April 1999)

Although listeners routinely perceive both the sex and individual identity of talkers from their speech, explanations of these abilities are incomplete. Here, variation in vocal production-related anatomy was assumed to affect vowel acoustics thought to be critical for indexical cueing. Integrating this approach with source-filter theory, patterns of acoustic parameters that should represent sex and identity were identified. Due to sexual dimorphism, the combination of fundamental frequency (F_0, reflecting larynx size) and vocal tract length cues (VTL, reflecting body size) was predicted to provide the strongest acoustic correlates of talker sex. Acoustic measures associated with presumed variations in supralaryngeal vocal tract-related anatomy occurring within sex were expected to be prominent in individual talker identity. These predictions were supported by results of analyses of 2500 tokens of the /ɛ/ phoneme, extracted from the naturally produced speech of 125 subjects. Classification by talker sex was virtually perfect when F_0 and VTL were used together, whereas talker classification depended primarily on the various acoustic parameters associated with vocal-tract filtering. © *1999 Acoustical Society of America.* [S0001-4966(99)02608-9]

PACS numbers: 43.70.Gr, 43.70.Bk [AL]

INTRODUCTION

Theorists have long proposed that speech utterances routinely include acoustic information concerning talker characteristics, in addition to their purely linguistic content. These personal or *indexical* parameters (e.g., Ladefoged and Broadbent, 1957; Ladefoged, 1967; Abercrombie, 1967) are studied in order to understand the nature of the information they convey (e.g., Scherer, 1986) and how linguistic information is recovered despite acoustic variability among talkers (e.g., Joos, 1948; Peters, 1954; Miller, 1989; cf. Goldinger, 1996; Pisoni, 1997). Although significant progress has been made, recent accounts highlight both the importance of indexical features and the general lack of knowledge about this topic (e.g., Goldinger, Pisoni, and Luce, 1996; Johnson and Mullenix, 1997).

Talker sex and individual identity are two notable aspects of indexical cueing in speech that are usually studied separately, although they are conceptually similar. For example, both vocal-fold action and vocal-tract transfer function characteristics are found to be important in each case in empirical studies. Vocal-fold action is often primarily characterized using the fundamental frequency of vibration (F_0), corresponding to perceived pitch. The transfer function (input–output relation) of the supralaryngeal vocal tract is usually described in terms of resonance (formant) characteristics. While considerable success has been achieved in classifying speech by sex using either F_0- or formant-related measures (e.g., Schwartz, 1968; Coleman, 1971, 1973, 1976; Sachs, 1975; Murry and Singh, 1980; Childers and Wu, 1991; Perry, 1997), some controversy exists over which kind of measure is the more reliable. Although classification by individual talker identity is typically less effective, both kinds of measures are also emphasized in such investigations (e.g., Bricker and Pruzansky, 1976; Kuwabara and Takagi, 1991; Tartter, 1991; Remez, Fellowes, and Rubin, 1997; Kreiman, 1997).

Indexical attributes of talker sex were extensively examined by Childers and Wu (1991; Wu and Childers, 1991), who successfully classified short, naturally recorded speech samples based on talker- and sex-specific templates. However, their approach was largely pragmatic and atheoretical, being primarily geared towards improving automated speech recognition. While achieving impressive results, this kind of approach has not led to an overarching theoretical framework for indexical cueing that specifies, for instance, why particular acoustic measures are either important or not important (Kreiman, 1997).

Here, we describe and test an approach to indexical cueing that involves an explicit application of biological principles concerning anatomical variation to the source-filter theory of vocal production (e.g., Stevens and House, 1955; Fant, 1960; Kent and Read, 1992; Lieberman and Blumstein, 1993; Titze, 1994). Aspects of this approach are implicit in many previous investigations, but an explicit consideration of how expected sex- and individual talker-based variation in vocal production anatomy interacts with source-filter principles is arguably more powerful. This approach allows

[a)]Electronic mail: j.a.bachorowski@vanderbilt.edu
[b)]Electronic mail: mjo9@cornell.edu

us to examine the acoustic correlates of both talker sex and individual identity within a single theoretical framework. Taking sexual dimorphism and likely individual variation into account, one can make specific predictions concerning which acoustic features and combinations of features should be the most important for sex- and individual-based classification. Several such predictions are nested in the current study. Our specific goals were to test predictions concerning indexical attributes by using segments of naturally produced speech in which the contributions of linguistic cues were minimized, but indexical variation would still be present. In order to test predictions concerning both talker sex and individual identity with the same data set, a large number of speech tokens were needed from each of an even larger number of talkers, both male and female. Practical considerations associated with analyzing such a large number of tokens constrained the set of acoustic parameters examined, but the basic approach was to emphasize measures related either to characteristics of the source, the vocal-tract transfer function, or a combination of the two. While the acoustic measurements made were therefore simple, readily made using commercially available software, they were also generally successful. The most important statistical comparisons involved discriminant classifications of talker sex and individual talker identity, and we did not have to use complex data transformations to achieve high classification rates.

Variation in vocal-production anatomy is highly likely to be important in indexical cueing, starting with the observation that humans show prominent sexual dimorphism in both the larynx and supralaryngeal vocal tract (reviewed by Fitch, 1994; Perry, 1997). On average, the vibrating segment of each vocal fold is 60% longer in males, resulting in F_0's that are 45% lower than in females (Titze, 1989, 1994). Supralarygeal vocal-tract length (VTL) is about 15% greater in males (Fant, 1966), producing characteristically lower formant frequencies.

However, these sex differences are average outcomes that may not distinguish particular talkers. In addition, features such as F_0 and formant characteristics are manipulated in running speech for linguistic and prosodic purposes. Overlap in speech acoustics between male and female talkers is therefore to be expected, depending both on the talker involved and the utterance being produced (e.g., Peterson and Barney, 1952; Maurer and Landis, 1996). Since listeners can nonetheless show highly accurate perception of talker sex, at least from small samples of talkers (e.g., Whiteside, 1998), disambiguating features must also be present. Noting that dimorphism occurs in both source and filter production components, we predicted that the *combination* of F_0 and acoustic indices of VTL would provide the best index of sex. While it has been claimed that these measures are either redundant or differentially weighted (Coleman, 1971; Childers and Wu, 1991; Wu and Childers, 1991), we expected these measures to provide a robust indicator of sex-based acoustic variation when considered together, but to be less reliable either in isolation or in combination with other features.

As vocal fold and supralaryngeal vocal-tract lengths are considered to be largely independent in adult talkers (discussed by Fitch, 1994, 1997), and because dimorphism exists in each case, moderately successful classification of talker sex should also occur for F_0 and VTL measures tested separately. This reasoning gave rise to two additional predictions concerning acoustic correlates of talker sex. First, both F_0 and VTL values were expected to be highly correlated across sex, but uncorrelated within sex. Second, a composite index of VTL derived from several formant frequencies should predict talker sex better than the individual variables used in its derivation.

Whereas human sexual dimorphism leads to the expectation that the combination of F_0 and VTL are especially powerful in classification of talker sex, neither can be expected to be primary markers of individual talker identity. Instead, differences in the size, shape, and tissue properties of vocal-production components found among talkers within sexes can all influence speech acoustics and therefore contribute to individual vocal uniqueness. Based on the source-filter perspective, however, one can nonetheless expect some measures to be inherently more robust and consistent than others.

Although little empirical evidence is available, a number of researchers have emphasized the importance of variation in the vocal-tract transfer function to indexical cueing (e.g., Fant, 1966), and some suggest that it may provide more stable, individually distinctive acoustic information than does variation in vocal-fold action (Carrell, 1984; Goldinger *et al.*, 1996; cf. Remez *et al.*, 1997). As detailed aspects of the transfer function are likely shaped by corresponding variation in anatomical characteristics, we expected that formant frequencies would be the most important for talker discrimination and that measures related to vocal-fold action would contribute less. Although vocal-fold characteristics differ among individuals, for instance, normative speech requires an individual to use a range of vibration rates. Further, aspects like F_0 and cycle-to-cycle variation in both the frequency (jitter) and amplitude (shimmer) of the source waveform can be affected by short-term changes in arousal or emotional state (e.g., Bachorowski and Owren, 1995; Protopapas and Lieberman, 1997). These measures were therefore specifically anticipated not to be especially useful in distinguishing among individual talkers.

Other readily measured aspects of speech included formant amplitudes and the duration of the vowel segment used for source-related measurements. As formant amplitudes likely reflect both source-energy properties and vocal-tract transfer function characteristics, clear predictions about how these measures might contribute to talker identity were more difficult to make. One possibility was that amplitude-related measures would improve talker classification when tested in conjunction with either source- or filter-related measures, but would not do well when tested alone. Similarly, vowel duration was not expected to be important when tested alone, but could arguably improve classification accuracies when tested as part of a variable cluster that might reflect a talker's global production ''style.''

For naturally occurring speech, predictions concerning indexical attributes can be tested most straightforwardly by statistical classification of identical linguistic utterances pro-

duced by many talkers. We therefore examined variation in the acoustic characteristics of a single vowel sound, a phoneme that occurred as part of a stock phrase produced by a large number of talkers who uttered it repeatedly while performing a behavioral distractor task. We have previously described the relationships between manipulations of emotional states and variation in F_0, jitter, and shimmer in this phoneme (Bachorowski and Owren, 1995). Here, data from these three variables were combined with formant frequencies and amplitudes, VTL, and vowel-segment duration in order to examine the relative contributions of source- and filter-related acoustic features in distinguishing talker sex and individual identity.

I. METHOD

A. Subjects

Participants were 50 male and 75 female undergraduate students who volunteered in exchange for credit toward an introductory psychology course requirement. Before testing, subjects provided oral and written informed consent to the experimental procedures and subsequent use of data. Next, they completed a background information form which included items concerning age and ethnic/racial status. Subject age varied more than is usually the case for undergraduate populations ($M = 22.2$ years, s.d. $= 5.7$, range 16–50), and the group was also ethnically diverse. Sixty-eight percent identified themselves as being Caucasian, 8% Black or African-American, 11.2% Hispanic, 8.0% Asian, and 1.6% Native American (1.6% chose ''Other'' and the remaining 1.6% declined to provide ethnicity information). Subjects were also queried about speech- and hearing-related anomalies, but no one reported notable problems.

B. Apparatus

Subjects performed a lexical-decision task via a microcomputer with a 15-in. monitor, using a modified Micro Experimental Laboratory program (Psychology Software Tools, Pittsburgh, PA). During testing, they were recorded on Ampex high-bias tape using a head-worn Audio Technica Pro 8 microphone (Stow, OH) and an NAD 6325 audio cassette deck (NAD Electronics, Boston, MA). Resulting speech samples were subsequently digitized using CSRE 4.0 software (Avaaz Innovations, London, Ontario), a DT2821 A/D board (Data Translation, Marborough, MA), a 16-channel audio interface, and a 30-band, 1/4-octave, 20-kHz equalizer used for antialias filtering. Both CSRE and CSPEECH Version 4 (Paul Milenkovic, Dept. of Electrical and Computer Engineering, University of Wisconsin-Madison) software were used in acoustic analysis. Statistical analyses were conducted using SPSS for Windows, version 6.1.2 (SPSS, Chicago, IL).

C. Design and procedure

Subjects were tested individually and began by completing several personality questionnaires (which are not relevant to the results described here). The remainder of the session was spent performing a 210-trial lexical-decision task. Participants were instructed to gaze steadily at a small cross that appeared on the monitor for 500 ms at the onset of each trial. Two letter strings were then displayed simultaneously above and below the cross. Using the keyboard number pad, participants pressed the ''1'' key if both letter strings were orthographically correct words, and the ''2'' key if either or both were nonwords. The brief, 100-ms displays made it difficult for participants to evaluate their performance.

Ten baseline and 20 on-task speech samples were recorded from each subject. Predetermined, noncontingent success and failure feedback displays were presented after each block of ten trials, with the relative proportion of each feedback type varying by condition (see Bachorowski and Owren, 1995). For each speech sample, participants read the phrase ''test *n* test,'' where *n* was the number of the baseline sample or next on-task trial block. During the task, speech samples were recorded after each feedback display. As baseline utterances were recitation-like, they were not included in the present analyses. Being primarily interested in acoustic correlates of sex and individual talker identity, we also do not describe feedback-related results. However, the findings were essentially identical when baseline trials were tested (both alone and in conjunction with on-task samples), and feedback conditions were found not to interact statistically with either sex or individual talker classification.

D. Acoustic analysis

The digitized /ɛ/ phoneme from the first test in each ''test *n* test'' was used in acoustic analysis. This sound was selected because it is a monophthong with stable acoustic characteristics and clear temporal boundaries (see Fig. 1). First, the beginning and ending points of each vowel were marked at corresponding zero crossings. To reduce the effects of onset and offset transitions, only the middle 60% of each vowel (''rounded'' to the nearest zero crossings) was used in source-related acoustic analysis. These vowel segments produced a duration variable (*60%* Dur) for use in statistical analyses. F_0, *jitter*, and *shimmer* were derived from waveforms digitized at 50 kHz and low-pass filtered at 25 kHz. As source-related measures require accurate identification of individual waveform cycles, automated marker placements were modified as necessary by hand. Source-related measures were obtained using CSRE 4.0, which calculates jitter factor (in percent) and shimmer (dB) measures described by Baken (1996).

Spectral measurements were made using CSPEECH. Each file was first low-pass filtered at 4.8 kHz and then downsampled to 10 kHz. These analyses were conducted using a single 512-point (51.2-ms) Blackman weighting window centered on the midpoint of the /ɛ/ segment. In each case, linear predictive coding (LPC) was used to derive the frequencies and amplitudes of the lowest three formants using 14 coefficients and full pre-emphasis. Each envelope was checked by overlaying it on a corresponding fast Fourier transform (FFT) of the waveform segment. In a small number of cases, the LPC function was recomputed with fewer coefficients (i.e., 10 or 12) to provide a more accurate match to the FFT spectrum. Both frequencies and amplitudes were measured from the LPC-based envelope using cursors, while a simultaneously displayed wideband spectrogram served as

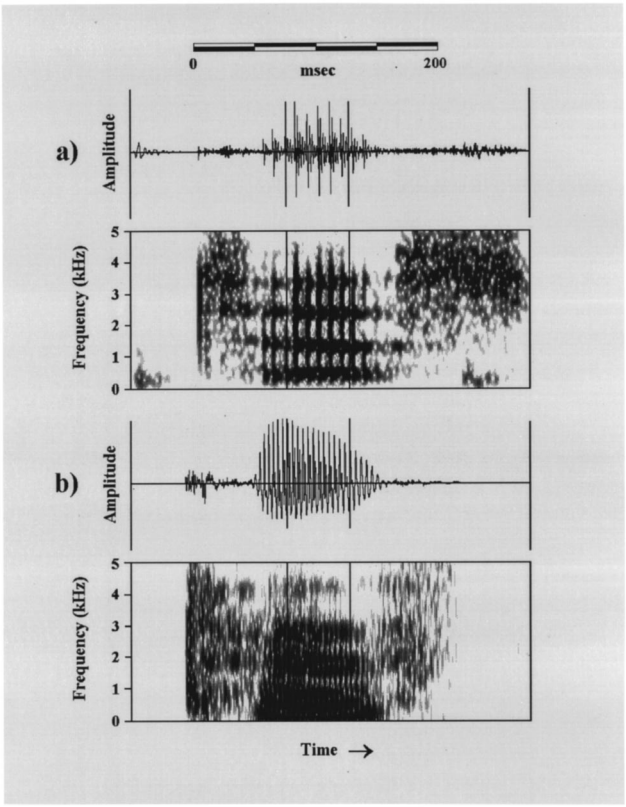

FIG. 1. Characteristic waveforms and spectograms of the word ''test'' from a male (a) and a female (b) talker, with parallel lines marking the middle 60% of the /ɛ/ phoneme in each case.

a reference. The resulting variables were $F1, F2$, and $F3$, and $A1, A2$, and $A3$, for frequencies and amplitudes, respectively. However, as absolute formant amplitude values fluctuate due to variation in production intensity, relative formant amplitudes were computed as the amplitude measures of primary interest (i.e., $A1-A2, A1-A3$, and $A2-A3$). In some cases, formant frequencies that fell outside the expected range of variation for the /ɛ/ phoneme (see Baken, 1996) were recorded as missing values and later replaced with the mean for that participant. Such substitutions were made for 50 of the 7500 formant frequency measurements used in statistical analysis.

VTL was estimated from formant frequency measurements using the following equation (adapted from Lieberman and Blumstein, 1993):

$$\mathrm{VTL}=\frac{(2k+1)c}{4F_{k+1}},$$

where $k=(0,1,2)$, F_{k+1} is the frequency of the formant of interest, and c is the speed of sound (34 400 cm/s). Separate calculations were made for each of the three formant frequencies, and the mean of these estimates provided the VTL value used in statistical analysis.

II. RESULTS

A. Characteristics of the speech sample

Descriptive summary statistics are shown in Table I. Coefficient-alpha values, which can range from 0 to 1.0, were computed as an index of reliability for the ten acoustic variables measured from the waveform and spectrum. These values all fell between 0.93 and 0.99, indicating that the acoustic measurements were highly reliable. As predictions for sex and talker classification involved the relative independence of F_0 and VTL, correlations between these two variables were examined first. The two were strongly correlated ($r=-0.77$) across sex, but only moderately associated within sex ($r=-0.23$ and $r=-0.17$ for males and females, respectively).

B. Factor analysis

Principal components analyses with varimax rotation were conducted in order to examine clustering among variables. These factor analyses were conducted separately for males and females because of the significant differences between the two sexes for most acoustic measures (see Table I). As relative formant amplitudes (i.e., $A1-A2, A1-A3$, and $A2-A3$) were interdependent, only the first two were entered. However, no substantive differences were noted when other pairings were used instead. Interpretation of the rotated solutions was facilitated by including only variables with factor-loading values of 0.4 or above, accounting for 16% or more of the overlap in variance between a variable and a factor. The resulting solutions (shown in Table II) accounted for 75.6% and 70.8% of the cumulative variance for males and females, respectively, indicating that these solutions effectively characterized the variance in these data sets (see Tabachnik and Fidell, 1996).

Solutions for both sexes were consistent and interpretable, with four factors appearing in each case. The first factor was related to formant frequencies, and consisted of $F1$, $F2$, $F3$, and VTL. This factor accounted for 33.4% and 26.7% of the variance for males and females, respectively. The second factor concerned vocal-fold action, included F_0, jitter, and shimmer, and accounted for 18.2% and 16.9% of the variance for the two sexes, respectively. The third factor consisted of the relative formant amplitudes, and accounted for 13.7% and 15.7% of the variance, respectively. The fourth factor was residual in nature, but accounted for 10.4% and 11.5% of the variance, respectively.

C. Classification of talker sex

Discriminant-function analyses were used to examine whether individual vowel segments could be classified by sex. Variables were entered in stepwise fashion using the Mahalanobis distance method, and the performance of the discriminant functions was validated through a split-sample approach (see Tabachnik and Fidell, 1996). Classification outcomes based on relevant individual variables and combinations of variables appear in Table III. The most inclusive analysis included all 11 acoustic measures, while other analyses involved correspondingly fewer variables, as indicated in Table III. In every case, measures from 15 of the 20 vowel segments from each individual were used to derive discriminant functions, and classification accuracy was then tested with the remaining five samples (a maximum of 20 625 and 6 875 measurements was thus available for deri-

TABLE I. Descriptive statistics for acoustic measures, where F_0 is fundamental frequency, $F1$, $F2$, $F3$, $A1$, $A2$, and $A3$ refer to the lowest three fundamental frequencies and amplitudes, respectively, VTL is vocal-tract length, and 60% Dur is the duration of the middle 60% of the vowel segment.

	Males			
Measure	*M*	s.d.	Minimum	Maximum
F_0 (Hz)	125	20	81	223
Jitter (%)	4.01	3.05	0.30	16.64
Shimmer (dB)	1.63	1.20	0.11	9.93
$F1$ (Hz)	582	52	400	762
$F2$ (Hz)	1604	111	1309	1914
$F3$ (Hz)	2573	140	2090	3135
$A1$ (dB)	−16.3	3.8	−33.0	−5.5
$A2$ (dB)	−23.9	5.1	−46.1	−9.3
$A3$ (dB)	−30.1	5.6	−47.7	−13.8
$A1–A2$ (dB)	7.58	4.8	−7.5	26.5
$A1–A3$ (dB)	13.83	5.8	−2.4	37.6
$A2–A3$ (dB)	6.25	4.7	−6.6	23.0
VTL (cm)	15.52	0.87	13.5	18.1
60% Dur (ms)	72.1	18.3	33.0	144.6
	Females			
Measure	*M*	s.d.	Minimum	Maximum
F_0 (Hz)	230	23	145	337
Jitter (%)	8.79	4.50	0.48	24.45
Shimmer (dB)	1.53	0.95	0.08	6.74
$F1$ (Hz)	716	75	469	977
$F2$ (Hz)	1900	149	1309	2771
$F3$ (Hz)	2981	238	1982	3594
$A1$ (dB)	−15.3	4.1	−29.2	−0.8
$A2$ (dB)	−23.3	5.6	−43.9	−5.7
$A3$ (dB)	−30.2	5.5	−48.1	−12.7
$A1–A2$ (dB)	8.0	4.8	−7.2	23.7
$A1–A3$ (dB)	15.0	5.3	−1.8	34.3
$A2–A3$ (dB)	6.9	5.2	−9.8	26.0
VTL (cm)	13.12	0.86	10.6	17.1
60% Dur (ms)	75.2	20.8	26.4	172.2

vation and test phases, respectively). Results shown are classification accuracies in derivation and test phases, as well as percent-error reduction associated with the former. This last metric takes into account the chance error rate, producing an unbiased measure of classification accuracy. On average, the discrepancy in classification accuracy for derivation and test phases was 0.1%.

Classification accuracy was 98.6% when the full complement of acoustic measures was used. However, entering only F_0 and VTL improved upon this outcome slightly. Moreover, this variable pair was found to perform better than any other combination of variables tested. Using F_0 and VTL together allowed nearly 100% correct classification of cases in both test and derivation phases, a level of accuracy associated with 97.6% error reduction. In all, 731 of 750 male cases (97.5%) and 1121 of 1125 female cases (99.6%) were correctly classified using this variable combination.

Classification rates were also very high when F_0 and

TABLE II. Rotated factor loadings for principal factors extraction with varimax rotation. A cutoff point of ±0.40 was used to include a variable in a factor, and variables meeting this criterion are noted in italics. Interpretive labels given to the four factor solutions are formant frequencies (factor I), vocal-fold action (factor II), relative formant amplitudes (factor III), and residual (factor IV).

	Males				Females			
Measure	Factor I	Factor II	Factor III	Factor IV	Factor I	Factor II	Factor III	Factor IV
F_0	0.19	*0.68*	−0.08	0.07	0.06	*0.45*	0.14	*0.53*
Jitter	0.08	*0.87*	−0.07	0.05	0.00	*0.83*	−0.08	−0.25
Shimmer	0.08	*0.79*	0.08	0.00	−0.06	*0.85*	0.04	0.15
60% Dur	0.03	0.05	−0.00	*0.94*	−0.04	−0.10	−0.03	*0.75*
$F1$	*0.65*	0.24	0.12	*0.40*	*0.42*	−0.02	−0.22	*0.61*
$F2$	*0.85*	0.15	−0.06	0.02	*0.80*	0.07	0.08	0.05
$F3$	*0.82*	0.01	0.13	−0.19	*0.88*	−0.08	0.04	−0.10
VTL	*−0.96*	−0.17	−0.09	−0.15	*−0.95*	0.03	0.04	−0.27
$A1–A2$	−0.05	−0.12	*0.89*	−0.09	−0.03	−0.11	*0.86*	−0.05
$A1–A3$	0.10	0.07	*0.90*	0.10	0.10	0.12	*0.84*	−0.02

TABLE III. Split-sample discriminant function results for classification by talker sex, including accuracy for functions derived from 15 vowel tokens from each talker (derivation accuracy), accuracy for functions using the remaining 5 tokens (test accuracy), and error reduction associated with the former. Variables used in discriminant functions are grouped by (A) comparisons of primary interest, and (B) comparisons of secondary interest. Chance classification accuracy was 50%. Error reduction was calculated as (((100−chance rate)−(100−observed rate))×100)/(100−chance rate).

		Derivation accuracy	Test accuracy	Error reduction
(A)	All measures	98.6	98.9	97.2
	F_0, VTL	98.8	98.7	97.6
	F_0	95.9	95.8	91.8
	VTL	92.4	92.3	84.9
(B)	F_0, jitter, shimmer	96.3	96.3	92.5
	F_0, jitter, shimmer, VTL	98.7	99.0	97.4
	F_0, jitter, shimmer, $A1-A2$, $A1-A3$, $A2-A3$	96.2	96.3	92.4
	$F1$, $F2$, $F3$	92.4	92.2	84.7
	$A1-A2$, $A1-A3$, $A2-A3$	56.0	54.9	12.0
	$F1$, $F2$, $F3$, $A1-A2$, $A1-A3$, $A2-A3$	92.8	92.5	85.6
	$F1$, $F2$, $F3$, $A1-A2$, $A1-A3$, $A2-A3$, VTL	92.8	92.2	85.5
	60% Dur	49.4	50.1	−1.1

VTL were entered separately, producing 95.9% and 92.4% correct classification, respectively. In fact, adding other variables to either of these did not markedly improve classification accuracy. Tested as a set, the three formant frequencies allowed 92.4% correct classification, an outcome that was identical to the classification accuracy obtained when VTL was entered alone. Variables $A1-A2$, $A1-A3$, $A2-A3$, and 60% Dur generally failed to contribute to classification of talker sex.

D. Classification of individual talker identity

Classification of vowel segments by talker identity was examined both across and within talker sex using the same split-sample, discriminant-function approach (see Table IV). As in classification by talker sex, the most inclusive analysis tested 11 acoustic measures for 15 tokens from each of the 125 talkers, whereas correspondingly fewer acoustic measurements were used in analyses that tested subsets of variables within each sex. Cross-validation again involved the remaining five vowel segments. Although talker classification accuracies were more variable than for sex, the discrepancy between derivation and test phases was again quite small, averaging 3.2% across the various test combinations.

Entering all 11 acoustic measures produced 75.6% correct classification, or 75.4% error reduction. Furthermore, filter-related measures were found to be considerably more important than source-related measures in sorting cases by individual talkers. For the former, classification accuracy and associated error reduction were 48.8% and 48.4%, respectively. In contrast, source-related parameters classified only 22.1% of observations, an error reduction of 21.5%. In marked contrast to outcomes for talker sex, the combination of F_0 and VTL was found to be unimportant in talker classification, producing only 24.9% correct classification.

Discriminant analyses were also conducted within talker sex, because the observed sex differences in acoustic parameters could be expected to yield distinct patterns of sorting accuracies. For males, the full variable set produced 79.1% correct classification and 78.6% error reduction. While no individual measures were found to provide such accurate classification, a number of combinations were relatively successful for male talkers. Variables related to the vocal-tract transfer function, especially formant frequencies, contributed more to talker classification than did measures characterizing vocal-fold action. For instance, 61.2% of cases were correctly classified using formant frequencies, relative formant amplitudes, and VTL. Tested as a set, the formant frequency variables correctly classified 42.7% of cases. In contrast, the combination of F_0, jitter, and shimmer resulted in correct classification of only 26.4% of cases.

Unlike their effectiveness in classification of talker sex, F_0 and VTL did not make disproportionate contributions to male talker discrimination. Here, each measure correctly classified only 13.3% of cases, which was comparable to the contributions made by relative formant amplitude variables and 60% Dur (13.9% and 9.7% correct classification, respectively). Whereas relative amplitudes and 60% Dur did not improve accuracy of sex-based classification, both did so here. Relative formant amplitudes were found to be important in combination with source-related measures, while 60% Dur contributed to classification accuracy when tested as part of a set of variables potentially related to talker-style differences (i.e., F_0, $F1$, $F2$, $F3$, and 60% Dur). This variable cluster resulted in very successful classification of male talkers. In fact, the 72.3% error reduction associated with this set of variables surpassed all other variable sets, and classified nearly as many cases as did the full complement of acoustic measures.

Results for females paralleled those described for males, but with consistently lower classification rates. The same outcomes occurred when data from two random subsets of 50 females each were tested in order to rule out an effect of sample size differences. For females, the full complement of acoustic measures allowed 64.8% correct classification, corresponding to 64.3% error reduction. When tested as a set, filter-related variables were more successful than measures

TABLE IV. Results of split-sample discriminant function analyses for talker classification using the full complement of acoustic cues and three theoretically derived groups of measures for (A) all subjects, (B) male subjects, and (C) female subjects. In (D) and (E), the results of classification tests using other variable clusters of potential interest are shown for male and female talkers, respectively. Depending on both the number of talkers and extent of missing data (see the text), chance classification accuracy rates ranged from 0.8% to 2.2%. Refer to Table III for a description of classification accuracy and error reduction.

	Derivation accuracy	Test accuracy	Error reduction
(A) All subjects			
All measures	75.6	70.5	75.4
$F1$, $F2$, $F3$, $A1-A2$, $A1-A3$, $A2-A3$, VTL	48.8	44.4	48.4
F_0, jitter, shimmer	22.1	20.1	21.5
F_0, VTL	24.9	25.7	24.2
(B) Males			
All measures	79.1	74.0	78.6
$F1$, $F2$, $F3$, $A1-A2$, $A1-A3$, $A2-A3$, VTL	61.2	55.2	60.4
F_0, jitter, shimmer	26.4	22.0	24.7
F_0, VTL	32.8	34.8	31.3
(C) Females			
All measures	64.8	60.3	64.3
$F1$, $F2$, $F3$, $A1-A2$, $A1-A3$, $A2-A3$, VTL	46.2	39.5	45.4
F_0, jitter, shimmer	19.5	16.5	18.3
F_0, VTL	19.2	20.8	18.1
(D) Males			
F_0	13.3	12.4	9.1
F_0, jitter, shimmer, $A1-A2$, $A1-A3$, $A2-A3$	42.0	36.8	40.7
VTL	13.3	13.6	11.5
$F1$, $F2$, $F3$	42.7	40.8	41.5
$A1-A2$, $A1-A3$, $A2-A3$	13.9	10.4	12.1
$F1$, $F2$, $F3$, $A1-A2$, $A1-A3$, $A2-A3$	61.7	56.8	60.9
F_0, $F1$, $F2$, $F3$, 60% Dur	72.9	68.8	72.3
60% Dur	9.7	9.6	7.7
(E) Females			
F_0	6.7	7.4	5.3
F_0, jitter, shimmer, $A1-A2$, $A1-A3$, $A2-A3$	31.7	27.7	30.8
VTL	6.5	5.6	5.3
$F1$, $F2$, $F3$	28.9	27.5	28.0
$A1-A2$, $A1-A3$, $A2-A3$	10.7	7.5	9.5
$F1$, $F2$, $F3$, $A1-A2$, $A1-A3$, $A2-A3$	46.8	38.9	46.1
F_0, $F1$, $F2$, $F3$, 60% Dur	49.0	45.9	48.3
60% Dur	6.7	8.3	5.3

of vocal-fold action, with the former correctly classifying 46.2%, but the latter classifying only 19.5% of cases. Although rather low classification accuracies resulted when either F_0, VTL, or the formant-amplitude variables were entered separately, each measure was important when tested in combination with other variables. As with male talkers, 60% Dur alone did not successfully distinguish female talkers but did contribute to classification success when tested as part of the talker-style variable cluster. The 48.3% error reduction obtained with these measures indicated moderately successful classification. However, this set did not produce better classification of female talkers than other combinations of filter-related measures, as it had for males.

III. DISCUSSION

Taken together, the results provide strong support for the proposal that individual vowel sounds routinely include acoustic correlates of talker sex and individual talker identity. While linguistic attributes such as dialect are components of indexical features of speech, the present findings are largely consistent with predictions made on the basis of variation in vocal-production anatomy. For example, the outcomes of factor analysis showed that statistical relationships among the various measurements were consistent with the tenets of the source-filter model—the two most important factors reflected aspects of source characteristics on the one hand, and characteristics associated with the vocal-tract transfer function on the other. A third factor that consisted of relative formant amplitudes arguably represents a combination of source and filter properties.

Overall, acoustic measures fell within previously reported ranges of variation (cf. Baken, 1996; Titze, 1994). F_0 and jitter values were slightly higher than the norm, but this outcome was expected as subjects were receiving success and failure feedback in a task designed to increase emotional arousal (see Bachorowski and Owren, 1995). Furthermore, as subjects were recorded on audiotape, jitter values may have overestimated the extent of vocal perturbation (Doherty and

Shipp, 1988). Formant-frequency outcomes were typical for $F1$ and $F3$, but $F2$ values were lower than reported elsewhere (Peterson and Barney, 1952; Childers and Wu, 1991; Hillenbrand *et al.*, 1995; Hagiwara, 1997). Both talker dialect (cf. Hagiwara, 1997) and rapid articulation were probably contributing factors to the latter outcome. The VTL estimates calculated from our data were comparable to analogous values that we could derive from mean /ɛ/ formant measurements reported in these other investigations (14.8 to 15 cm for males and 11.9 to 13.1 cm for females).

Effective sorting of /ɛ/ sounds by sex occurred using a variety of measures, with a number of variables and combinations of variables producing very high rates of classification. Nonetheless, the best classification outcomes resulted from combining F_0 and VTL, the two measures most closely associated with sexual dimorphism in the vocal folds and supralaryngeal vocal tract. Furthermore, as predicted from source-filter theory, these variables were strongly correlated when examined across sex. In contrast, F_0 and VTL made only modest contributions to individual talker classification and were only moderately correlated within sex. These outcomes indicate that for any given male or female talker, vocal-fold size and vocal-tract length are not strongly linked.

Our results are generally consistent with those of Childers and Wu (1991), who also found that a variety of measures contributed to successful sorting by talker sex and emphasized the importance of F_0 and formant characteristics. Given the differences in the approaches involved, the similarities in the results of this previous work and the current study are all the more noteworthy. However, sorting outcomes described by Childers and Wu were complex, and involved a variety of acoustic features, transformations of features, and classification techniques (see also Wu and Childers, 1991). In contrast, we found that effective classification by talker sex flowed straightforwardly from using the two variables most reliably associated with sexual dimorphism.

Our results are inconsistent with the findings reported by Lass *et al.* (1976). In their study, participants identified the sex of talkers from audiotapes of isolated vowels that were either voiced, whispered, or low-pass filtered. Identification was best with voiced sounds and corresponding low-pass-filtered versions, but significantly worse with whispered vowels. These investigators therefore concluded that F_0 was the most important acoustic correlate of talker sex for their listeners. More recent work by Eklund and Traünmuller (1997; see also Ingemann, 1968; Schwartz, 1968; Tartter, 1991) confirmed that accurate perceptual identification of talker sex is more difficult with whispered than with voiced vowels, but also found that phoneme identification was more difficult with whispered sounds. Thus, the noisiness of the source energy used in whispering may simply be decreasing the listener's ability to extract formant-related information in both cases. This discrepancy can best be resolved by directly testing perceptual sensitivity to formant characteristics of voiced and unvoiced speech sounds (e.g., Lyzenga and Wiebe Horst, 1997).

Classification rates for analyses in which vowel segments were sorted by talker were notably lower than in sex-based classification. However, this outcome was expected, due both to the large number of individuals involved in this study and to the inherently greater overlap in speech acoustics that occurs among talkers of the same sex than between sexes. In light of these factors, classification of individual talkers was surprisingly accurate.

Both across and within sex, individual talkers were best differentiated using the full complement of acoustic measures. Furthermore, as predicted, variables associated with the vocal-tract transfer function were found to be strong predictors of talker identity. Several other combinations of measures, including source-related variables, were comparatively ineffective. Whereas pairing the F_0 and VTL variables was the most powerful means of classifying talkers by sex, this combination did little when applied to sorting by individual talker identity. Thus, as expected, acoustic parameters associated with dimorphism did not have utility for distinguishing among individuals within sex.

Perception studies testing identity cueing using synthesized speech have also indicated that measures associated with the vocal-tract transfer function are more important than source characteristics. For instance, Kuwabara and Takagi (1991) used digital techniques to manipulate the F_0 and formant-frequency characteristics of naturally recorded speech. They found that listener identification of individual talkers was relatively undisturbed by F_0 changes, but was impaired when formant characteristics were altered by as little as 5% (see also Coleman, 1973; Carrell, 1984; Karlsson, 1991; Remez *et al.*, 1997). Important corroborative support for this general perspective comes from recent examinations of the vowel-like sounds produced by some nonhuman primate species, in which acoustic features likely produced by supralaryngeal vocal-tract filtering are important both in statistical sorting of calls by individual caller (e.g., Owren, Seyfarth, and Cheney, 1997) and in the behavioral responses of animals tested with call playbacks under natural conditions (e.g., Rendall, Owren, and Rodman, 1997).

Our theoretical approach did not lead us to predict the classification success observed for individual talkers when the variables $F0$, $F1$, $F2$, $F3$, and 60% Dur were combined. This set of measures is similar to clusters of variables denoted as speaker style, and was especially powerful for classifying male talkers. As has been widely noted (e.g., Labov, 1972, 1994; Pullum and Ladusaw, 1986; Byrd, 1992), cultural factors influence talkers to adopt particular speaking styles in order to indicate, for example, membership in particular social groups. Based on the relative flexibility of vocal-fold vibration rate and phonation duration, associated acoustic features (characterized here by F_0 and 60% Dur) are very likely to be modified in achieving a particular speaking style. Nonetheless, as formant frequencies are arguably linked to stable individual variation in supralaryngeal-vocal-tract anatomy, we expect formant-related characteristics to emerge as the most reliable source of cues to individual talker identity across linguistic contexts. However, as our results concern only a single, relatively static vowel sound, the most conservative conclusion is simply that empirical testing across a wider range of vowel sounds uttered in various linguistic contexts is needed to resolve this issue.

Whereas previous reports have suggested that different sets of acoustic attributes are used to distinguish among individual males than for individual females (e.g., Singh and Murry, 1978; Murry and Singh, 1980), our findings were very similar across sexes. In both cases, acoustic correlates of an individual's supralaryngeal transfer function were the most important in statistical classification. Finding that sorting accuracy was lower for female than for male talkers follows from this result, as the higher F_0 values characteristic of female voices are associated with more widely spaced harmonics than in male voices—producing requisitely less fine-grained resolution of vocal-tract filtering effects (discussed by Owren and Rendall, 1997). Perceptual testing has in fact shown that formant resolution in human listeners decreases with increases in either F_0 or formant frequency (e.g., Kewley-Port *et al.*, 1996).

As noted, the generality of these findings should be tested with a wider variety of vowel sounds and linguistic contexts. In light of suggestive evidence that the higher formants play an important role in indexical cueing (e.g., Fujisaki and Kawashima, 1968; Whalen and Sheffert, 1997), other extensions of the present work should test whether the higher formant frequencies (i.e., $F3$, $F4$, and $F5$) provide stable cues to individual talker identity, independent of articulatory gesture. More detailed measures of the source waveform (e.g., Carrell, 1984; Klatt and Klatt, 1990; Hanson, 1997) and corresponding perceptual tests are also needed. In the meantime, the present results provide strong support for a theoretical approach to indexical attributes in speech in which basic principles of human morphological variation are applied in the context of the source-filter model of vocal production.

ACKNOWLEDGMENTS

We thank Elizabeth Milligan, Bridget Sly, Rodrigo Araya, and Chris Linker for assistance with acoustic analysis, and Rosie Backes, Francesca Bonifazi, Rita Danna, Delores Ederer, Dorothy Hansen, Jodi Schneider, Pam Scooros, and Dani Thoreaux for testing research participants. We also appreciate the valuable suggestions made by reviewers regarding earlier versions of this article. This work was funded in part by NIMH B/START and NSF POWRE awards to Jo-Anne Bachorowski. Data were collected using the facilities of the Department of Psychology at the University of Colorado at Denver. Equipment and funding for acoustic analysis came from Vanderbilt University, the University of Colorado at Denver, the University of Otago, and Reed College. Work on portions of this manuscript was completed while the first author was hosted as a Visiting Scholar by the Department of Psychology, Cornell University. Portions of the current results were presented in November 1997, at the 134th meeting of the Acoustical Society of America in San Diego, CA.

Abercrombie, D. (**1967**). *Elements of General Phonetics* (Aldine, Chicago).

Bachorowski, J.-A., and Owren, M. J. (**1995**). ''Vocal expression of emotion: Acoustic properties of speech are associated with emotional intensity and context,'' Psych. Sci. **6**, 219–224.

Baken, R. J. (**1996**). *Clinical Measurement of Speech and Voice* (Singular, San Diego).

Bricker, P. D., and Pruzansky, S. (**1976**). ''Speaker recognition,'' in *Contemporary Issues in Experimental Phonetics*, edited by N. J. Lass (Academic, New York), pp. 295–326.

Byrd, D. (**1992**). ''Preliminary results on speaker-dependent variation in the TIMIT database,'' J. Acoust. Soc. Am. **92**, 593–596.

Carrell, T. D. (**1984**). ''Contributions of fundamental frequency, formant spacing, and glottal waveform to talker identification,'' Technical Report No. 5 (Speech Research Laboratory, Department of Psychology, Indiana University).

Childers, D. G., and Wu, K. (**1991**). ''Gender recognition from speech. Part II. Fine analysis,'' J. Acoust. Soc. Am. **90**, 1841–1856.

Coleman, R. O. (**1971**). ''Male and female voice quality and its relationship to vowel formant frequencies,'' J. Speech Hear. Res. **14**, 565–577.

Coleman, R. O. (**1973**). ''Speaker identification in the absence of inter-subject differences in glottal source characteristics,'' J. Acoust. Soc. Am. **53**, 1741–1743.

Coleman, R. O. (**1976**). ''A comparison of the contributions of two voice quality characteristics to the perception of maleness and femaleness of the voice,'' J. Speech Hear. Res. **19**, 168–180.

Doherty, E. T., and Shipp, T. (**1988**). Tape recorder effects on jitter and shimmer extraction. J. Speech Hear. Res. **31**, 485–490.

Eklund, I., and Traünmuller, H. (**1997**). ''Comparative study of male and female whispered and phonated versions of the long vowels of Swedish,'' Phonetica **54**, 1–21.

Fant, G. (**1960**). *Acoustic Theory of Speech Production* (Mouton, The Hague, Holland).

Fant, G. (**1966**). ''A note on vocal tract size factors and non-uniform *F*-pattern scaling,'' Speech Trans. Lab. Quart. Prog. and Status Report **4**, 22–30.

Fitch, W. T. S., III (**1994**). ''Vocal tract length perception and the evolution of language'' (Unpublished doctoral dissertation, Brown University).

Fitch, W. T. (**1997**). ''Vocal tract length and formant frequency dispersion correlate with body size in rhesus macaques,'' J. Acoust. Soc. Am. **102**, 1213–1222.

Fujisaki, H., and Kawashima, T. (**1968**). ''The role of pitch and higher formants in the perception of vowels,'' IEEE Trans. Audio Electroacoust. **AU-16**, 73–77.

Goldinger, S. D. (**1996**). ''Words and voices: Episodic traces in spoken word identification and recognition memory,'' J. Exp. Psy.: Learn., Mem., Cogn. **22**, 1166–1183.

Goldinger, S. D., Pisoni, D. B., and Luce, P. A. (**1996**). ''Speech perception and spoken word recognition: Research and theory,'' in *Principles of Experimental Phonetics*, edited by N. J. Lass (Mosby, St. Louis), pp. 277–327.

Hagiwara, R. (**1997**). ''Dialect variation and formant frequency: The American English vowels revisited,'' J. Acoust. Soc. Am. **102**, 655–658.

Hanson, H. M. (**1997**). ''Glottal characteristics of female speakers: Acoustic correlates,'' J. Acoust. Soc. Am. **101**, 466–481.

Hillenbrand, J., Getty, L. A., Clark, M. J., and Wheeler, K. (**1995**). ''Acoustic characteristics of American English vowels,'' J. Acoust. Soc. Am. **97**, 3099–3111.

Ingemann, F. (**1968**). ''Identification of the speaker's sex from voiceless fricatives,'' J. Acoust. Soc. Am. **44**, 1142–1145.

Johnson, K., and Mullenix, J. W., editors (**1997**). *Talker Variability in Speech Processing* (Academic, New York).

Joos, M. A. (**1948**). ''Acoustic phonetics,'' Lang. **24 (Suppl 2)**, 1–136.

Karlsson, I. (**1991**). ''Female voices in speech synthesis,'' J. Phonetics **19**, 111–120.

Kent, R. D., and Read, C. (**1992**). *The Acoustic Analysis of Speech* (Singular, San Diego).

Kewley-Port, D., Li, X., Zheng, Y., and Neal, A. T. (**1996**). ''Fundamental frequency effects on thresholds for vowel formant discrimination,'' J. Acoust. Soc. Am. **100**, 2462–2470.

Klatt, D. H., and Klatt, L. C. (**1990**). ''Analysis, synthesis, and perception of voice quality variations among female and male talkers,'' J. Acoust. Soc. Am. **87**, 820–857.

Kreiman, J. (**1997**). ''Listening to voices: Theory and practice in voice perception research,'' in *Talker Variability in Speech Processing*, edited by K. Johnson and J. W. Mullenix (Academic, New York), pp. 85–108.

Kuwabara, H., and Takagi, T. (**1991**). ''Acoustic parameters of voice individuality and voice-quality control by analysis-synthesis method,'' Speech Commun. **10**, 491–495.

Labov, W. (**1972**). *Sociolinguistic Patterns* (University of Pennsylvania, Philadelphia).

Labov, W. (**1994**). *Principles of Linguistic Change: Internal Factors* (Blackwell, Cambridge, MA).
Ladefoged, P. (**1967**). *Three Areas of Experimental Phonetics* (Cambridge University Press, Cambridge).
Ladefoged, P., and Broadbent, D. (**1957**). ''Information conveyed by vowels,'' J. Acoust. Soc. Am. **29**, 98–104.
Lass, N. J., Hughes, K. R., Bowyer, M. D., Waters, L. T., and Bourne, V. (**1976**). ''Speaker sex identification from voiced, whispered, and filtered isolated vowels,'' J. Acoust. Soc. Am. **59**, 675–678.
Lieberman, P., and Blumstein, S. E. (**1993**). *Speech Physiology, Speech Perception, and Acoustic Phonetics* (University Press, Cambridge, MA).
Lyzenga, J., and Wiebe Horst, J. (**1997**). ''Frequency discrimination of stylized synthetic vowels with a single formant,'' J. Acoust. Soc. Am. **102**, 1755–1767.
Maurer, D., and Landis, T. (**1996**). ''Intelligibility and spectral differences in high-pitched vowels,'' Folia Phoniatr. **48**, 1–10.
Miller, J. D. (**1989**). ''Auditory-perceptual interpretation of the vowel,'' J. Acoust. Soc. Am. **85**, 2114–2134.
Murry, T., and Singh, S. (**1980**). ''Multidimensional analysis of male and female voices,'' J. Acoust. Soc. Am. **68**, 1294–1300.
Owren, M. J., and Rendall, D. (**1997**). ''An affect-conditioning model of nonhuman primate vocal signaling,'' in *Perspectives in Ethology: Volume 12. Communication*, edited by D. H. Owings, M. D. Beecher, and N. S. Thompson (Plenum, New York), pp. 299–346.
Owren, M. J., Seyfarth, R. M., and Cheney, D. L. (**1997**). ''The acoustic features of vowel-like *grunt* calls in chacma baboons (*Papio cynocephalus ursinus*): Implications for production processes and functions,'' J. Acoust. Soc. Am. **101**, 2951–2962.
Perry, T. L. (**1997**). ''A developmental study of the acoustic and perceptual properties differentiating gender,'' Unpublished doctoral dissertation, Vanderbilt University.
Peters, R. W. (**1954**). ''The relative intelligibility of single-voice and multiple-voice messages under various conditions of noise,'' Joint Project Report No. 56, pp. 1–9 (U.S. Naval School of Aviation Medicine, Pensacola, FL).
Peterson, G. E., and Barney, H. L. (**1952**). ''Control methods used in a study of the identification of vowels,'' J. Acoust. Soc. Am. **24**, 175–184.
Pisoni, D. B. (**1997**). ''Some thoughts on 'normalization' in speech perception,'' in *Talker Variability in Speech Processing*, edited by K. Johnson and J. W. Mullenix (Academic, New York), pp. 9–32.
Protopapas, A., and Lieberman, P. (**1997**). ''Fundamental frequency of phonation and perceived emotional stress,'' J. Acoust. Soc. Am. **101**, 2267–2277.
Pullum, G. K., and Ladusaw, W. A. (**1996**). *Phonetic Symbol Guide* (University of Chicago Press, Chicago).
Remez, R. E., Fellowes, J. M., and Rubin, P. E. (**1997**). ''Talker identification based on phonetic information,'' J. Exp. Psy.: Human Percep. Perform. **23**, 651–666.
Rendall, D., Owren, M. J., and Rodman, P. S. (**1997**). ''The role of vocal tract filtering in identity cueing in rhesus monkey (*Macaca mulatta*) vocalizations,'' J. Acoust. Soc. Am. **103**, 602–614.
Sachs, J. (**1975**). ''Cues to the identification of sex in children's speech,'' in *Language and Sex: Difference and Dominance*, edited by B. Thorne and N. Henley (Newbury, Rowley, MA), pp. 152–171.
Scherer, K. R. (**1986**). ''Vocal affect expression: A review and model for future research,'' Psychol. Bull. **99**, 143–165.
Schwartz, M. F. (**1968**). ''Identification of speaker sex from isolated, voiceless fricatives,'' J. Acoust. Soc. Am. **43**, 1178–1179.
Singh, S., and Murry, T. (**1978**). ''Multidimensional classification of normal voice qualities,'' J. Acoust. Soc. Am. **64**, 81–87.
Stevens, K. N., and House, A. S. (**1955**). ''Development of a quantitative description of vowel articulation,'' J. Acoust. Soc. Am. **27**, 484–493.
Tabachnik, B. G., and Fidell, L. S. (**1996**). *Using Multivariate Statistics* (HarperCollins, New York).
Tartter, V. (**1991**). ''Identifiability of vowels and speakers from whispered syllables,'' Percept. Psychophys. **49**, 365–372.
Titze, I. R. (**1989**). ''Physiologic and acoustic differences between male and female voices,'' J. Acoust. Soc. Am. **85**, 1699–1707.
Titze, I. R. (**1994**). *Principles of Voice Production* (Prentice-Hall, Englewood Cliffs, NJ).
Whalen, D. H., and Sheffert, S. M. (**1997**). ''Normalization of vowels by breath sounds,'' in *Talker Variability in Speech Processing*, edited by K. Johnson and J. W. Mullenix (Academic, New York), pp. 133–144.
Whiteside, S. P. (**1998**). ''Identification of speaker's sex: A study of vowels,'' Percept. Mot. Skills **86**, 579–584.
Wu, K., and Childers, D. G. (**1991**). ''Gender recognition from speech. Part I. Coarse analysis,'' J. Acoust. Soc. Am. **90**, 1828–1840.

Glottal characteristics of male speakers: Acoustic correlates and comparison with female data[a)]

Helen M. Hanson[b)]
Sensimetrics Corporation, 48 Grove St., Suite 305, Somerville, Massachusetts 02144-2500

Erika S. Chuang
Department of Electrical Engineering, Stanford University, Stanford, California 94305-9505

(Received 18 June 1998; accepted for publication 18 May 1999)

Acoustic measurements believed to reflect glottal characteristics were made on recordings collected from 21 male speakers. The waveforms and spectra of three nonhigh vowels (/æ, ʌ, ɛ/) were analyzed to obtain acoustic parameters related to first-formant bandwidth, open quotient, spectral tilt, and aspiration noise. Comparisons were made with previous results obtained for 22 female speakers [H. M. Hanson, J. Acoust. Soc. Am. **101**, 466–481 (1997)]. While there is considerable overlap across gender, the male data show lower average values and less interspeaker variation for all measures. In particular, the amplitude of the first harmonic relative to that of the third formant is 9.6 dB lower for the male speakers than for the female speakers, suggesting that spectral tilt is an especially significant parameter for differentiating male and female speech. These findings are consistent with fiberscopic studies which have shown that males tend to have a more complete glottal closure, leading to less energy loss at the glottis and less spectral tilt. Observations of the speech waveforms and spectra suggest the presence of a second glottal excitation within a glottal period for some of the male speakers. Possible causes and acoustic consequences of these second excitations are discussed.
[S0001-4966(99)06208-6]

PACS numbers: 43.70.Gr, 43.70.Aj, 43.72.Ar [AL]

INTRODUCTION

The work reported in this paper focuses on individual variations in glottal configuration and glottal-source waveform characteristics. This research has relevance for several areas of speech research and applications. It adds to studies that seek to establish quantitative ranges of voice-source characteristics of normal speakers. Such studies are used to understand the production of normal voice and to evaluate pathological voice (Holmberg *et al.*, 1988). They may also be useful for modeling the variation among speakers encountered by speech recognition and speaker recognition systems. Likewise, it may be necessary to include models of such variations in voice in speech-synthesis systems.

In addition to individual variations, we address gender differences in voice production. In the past, much of the literature that described acoustic differences between male and female speech concentrated on differences in fundamental frequency and formant frequencies (for a review, see Karlsson, 1992b). These features can be used to automatically distinguish male speakers from female (Childers and Wu, 1991). However, it is noteworthy that while most speech-analysis tools and speech applications are also based on those features, they are generally more successful for male speech. A particular problem has been synthesis of female speech, which tends to sound less natural than synthesized male speech (Karlsson, 1992a). Thus, it would seem that features of the acoustic sound-pressure waveform other than fundamental frequency and formant frequencies contribute to gender characteristics of speech. Recent studies have looked more closely at female speech and the ways in which it differs from male speech, especially in regard to voice-source characteristics. (See, for example, Titze, 1989; Klatt and Klatt, 1990; Karlsson, 1992a.) Observation of the glottis during phonation has suggested that the presence of a posterior glottal opening that persists throughout a vibratory cycle is common for female speakers, but occurs much less frequently among male speakers (Södersten and Lindestad, 1990). Holmberg *et al.* (1988, 1989) have found differences in glottal-waveform characteristics that may affect perceived voice quality; for example, female speakers tended to have larger open quotients and more gradual rises and falls in glottal flow than male speakers. Klatt and Klatt (1990) and Hanson (1995b) have shown that careful control of glottal characteristics improves the naturalness of synthesized female speech. Thus, glottal configuration and its effects on voice-source characteristics may play a significant role in the perception of gender from speech.

Quantitative estimates of the characteristics of the glottal waveform are difficult to obtain. Inverse filtering of the acoustic sound pressure or oral-airflow signal are the most common methods of analysis, but both are sensitive to experimental error, and require strict conditions and special equipment during data acquisition. Thus, while voice-source characteristics may prove useful for improving applications such as speech synthesis, speech recognition, and speaker recognition, analysis techniques that are robust and easily

[a)]The work reported in this paper was completed while the authors were at the M.I.T. Research Laboratory of Electronics, Speech Communication Group.
[b)]Electronic mail: hanson@sens.com

automated are necessary in order to make their use practical.

One alternative to inverse filtering is to make measurements directly on the acoustic sound-pressure waveform and spectrum. These measurements require only simple microphone recordings, and have the potential to be easily automated. Such measures were described and used in a study of 22 female speakers (Hanson, 1995a, 1997). Preliminary evidence based on breathiness ratings and on fiberscopic images collected from a subset of the subjects suggested that the acoustic measures could be used to categorize the speakers by glottal configuration.

In the current paper, we describe an extension of the earlier work (Hanson, 1995a, 1997) to include male speakers. Acoustic data were collected from 21 males, interpreted in terms of the theoretical models presented in Hanson (1995a, 1997), and compared with the data from females. Based on previous research comparing glottal characteristics of males and females (see above), we expected that if these acoustic parameters did represent characteristics of the glottal source, we would find significant differences in the mean values for the two genders. In addition, because the size of a posterior glottal opening can be considered to provide an additional degree of variability in the acoustic parameters considered, and females are more likely than males to have these openings, we expected that we might find a smaller degree of interspeaker variation among males than among females. Note that there can be other factors that lead to variations among members of a gender group, and therefore gender differences in degree of variation are not necessarily due only to differences in posterior glottal openings.

The outline of the paper is as follows. Section I begins with a brief summary of the theoretical background of the acoustic measures and the results of the previous study. Expected means, maxima, and minima of some of the acoustic measurements are then calculated for male speakers. In Sec. II we describe the experimental procedure, and the methods of making the acoustic measures of the speech waveform and speech spectrum. Section III begins by describing the results of our analysis of the male data. The results are then compared to the female data.

I. THEORETICAL BACKGROUND AND PREDICTIONS

A. Summary of previous study with female speakers

During vowel production, the configuration of the vocal folds may vary in several ways. Four types of glottal configuration were considered by Hanson (1995a, 1997): (1) the arytenoids are approximated and the membranous part of the folds close abruptly; (2) the arytenoids are approximated, but the membranous folds close from front to back along the length of the folds; (3) there is a posterior glottal opening at the arytenoids that persists throughout the glottal cycle, and the folds close abruptly; (4) a posterior glottal opening extends into the membranous portion of the folds throughout the glottal cycle, forcing the folds to close from front to back. Theoretical background was given for the manner in which these various configurations affect the glottal vibration pattern and volume-velocity waveform, and how such effects are manifested in the speech spectrum or waveform. A set of acoustic descriptors was presented as possible correlates of different types of glottal configuration.

When there is complete glottal closure at some time during a cycle of vibration, the glottal waveform can show several kinds of differences. For example, there can be differences in the open quotient (OQ, expressed as a percent). In that case, if all else remains the same, the spectrum of the glottal source is only influenced at the low frequencies. Experiments have shown that changes in the relative amplitudes of the first and second harmonics reflect changes in the closed quotient (Holmberg *et al.*, 1995). (The closed quotient is 100–OQ.)

When the derivative of the glottal-airflow signal has a discontinuity at glottal closure, its spectrum drops off at 6 dB per octave at high frequencies (Stevens, 1998). Sometimes, however, the glottis closes nonsimultaneously; that is, the glottal closure begins at the anterior end of the vocal folds and proceeds back to the posterior end. This type of closure leads to a gradual, rather than abrupt, cutoff of glottal airflow, and thus the derivative of the glottal airflow does not have a discontinuity. As a result, the high-frequency content of the glottal waveform is reduced. If this gradual cutoff is approximated as an exponential, the closing time can be used to approximate the time constant of the effective low-pass filter, and thus the cutoff frequency. According to this model, the spectral tilt of the glottal source above the cutoff frequency increases from 6 to 12 dB per octave.

The presence of a posterior glottal opening (glottal chink) throughout a glottal cycle introduces additional modifications to the spectrum. First, formant bandwidths, particularly that of the first formant, are increased due to additional energy loss at the glottis. Given the size of the glottal chink, one can estimate the additional bandwidth introduced at the frequencies of the formants (Stevens, 1998). The second consequence of the glottal chink is the introduction of additional spectral tilt. This additional tilt is due to the fact that the airflow through the glottal chink cannot undergo a discontinuous change because of the acoustic mass of the moving air in the system. The change in airflow at glottal closure has a time constant which can be used to calculate the cutoff frequency of the effective low-pass filter. Above this frequency, the spectral tilt increases by 6 dB per octave. The third acoustic consequence of a glottal opening is the generation of turbulence noise in the vicinity of the glottis. When the glottal opening is large, the spectral amplitude of the noise becomes comparable to the spectral amplitude of the periodic source at high frequencies.

The following list summarizes the relevant acoustic measurements, made directly on the speech spectrum or waveform, that were used by Hanson (1995a, 1997). These measurements are illustrated by the speech waveforms and spectrum (collected from female speakers) shown in Fig. 1.

1. First-formant bandwidth (B1)

A formant oscillation can be modeled as a damped sinusoid of the form $e^{-\alpha_i t}\cos 2\pi f_i t$, where f_i is the frequency of the ith formant and the constant α_i is the exponential decay rate. By applying a bandpass filter to the speech waveform

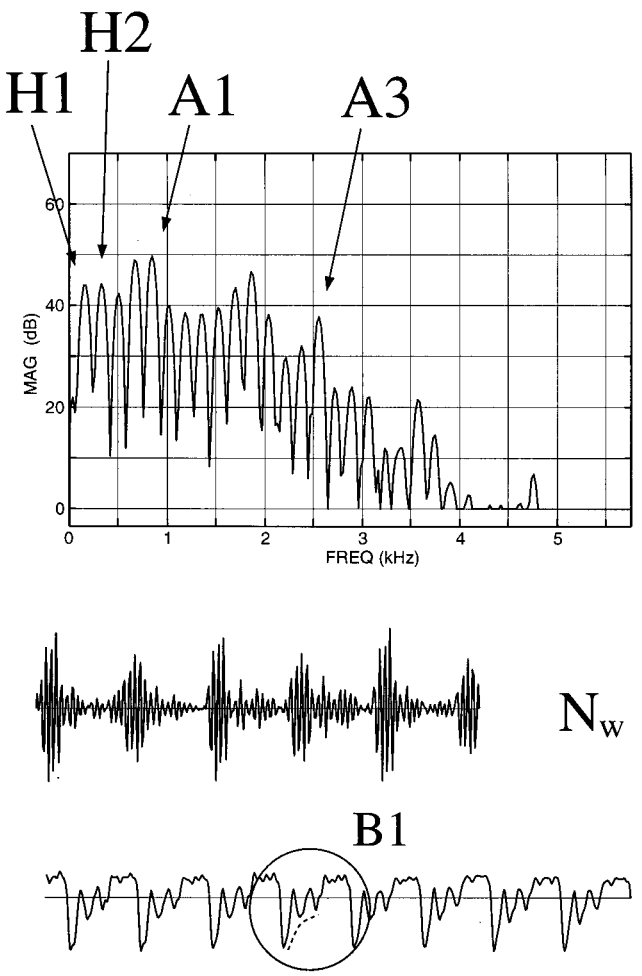

FIG. 1. Speech waveforms and a vowel spectrum produced by female speakers. The acoustic parameters labeled in the spectrum are the amplitudes of the first harmonic ($H1$), second harmonic ($H2$), first formant ($A1$), and third formant ($A3$). The top waveform, N_w, was obtained by bandpass filtering a sound-pressure waveform at the third-formant frequency region. The bottom waveform illustrates the decay of the first-formant oscillation, used to calculate an estimated bandwidth, $B1$. (Please note that each of these three examples is from a different speaker.)

centered at the first-formant frequency ($F1$) and measuring the decay rate of the resulting waveform (as shown in the waveform marked $B1$ in Fig. 1), the bandwidth of $F1$ can be approximated.

2. H1*–H2*

The amplitude of the first harmonic ($H1$) relative to that of the second ($H2$) is used as an indication of open quotient (OQ), the ratio of the open phase of the glottal cycle to the total period. The asterisks indicate that $H1$ and $H2$ have been corrected to remove the amount by which the vocal-tract transfer function, particularly the first formant, ''boosts'' the amplitudes of these harmonics. The effect of this correction is that the amplitudes of the harmonics more closely approximate those of the actual source spectrum. It is particularly important to make this correction when comparing this acoustic measure across vowels, for which the first-formant frequency can vary greatly. The correction factor used is given in Hanson (1997, footnote 5; 1995a, Appendix A). It assumes that the first-formant bandwidth is small. This assumption is valid unless the harmonic frequencies are too close to the first-formant frequency; that is, less than about 100 Hz away.

3. H1*–A1

The amplitude of the first harmonic ($H1$) relative to that of the first-formant prominence in the spectral domain ($A1$) reflects the bandwidth of $F1$, and may also be affected by source spectral tilt. Hence, this measure is an indication of the presence of a posterior glottal chink. Again, the asterisk indicates that H1 is corrected for the effect of the first formant.

4. H1*–A3*

The amplitude of the first harmonic ($H1$) relative to that of the third-formant spectral peak ($A3$) reflects the source spectral tilt. The mid- to high-frequency components are mostly influenced by how abruptly the flow is cut off when the glottis closes. $H1$ is corrected for the effect of the first formant (see above), and $A3$ is corrected for the contribution of the first and second formants on the amplitude of the third-formant prominence. As for the correction to $H1$ and $H2$, the correction to $A3$ is particularly important when comparing across vowels, for which the first two formant frequencies can vary greatly. This correction factor is given in Hanson (1997, footnote 6; 1995, Appendix A). It assumes that the bandwidths of the first two formants are small, which is valid as long as the third formant is not too close to the second. For the vowels considered in this study, the second and third formants are typically well separated.

5. Noise rating N_w

A posterior glottal opening that persists during phonation introduces an increase in turbulence noise generated in the vicinity of the glottis. The noise becomes prominent at the high-frequency range because of its increased amplitude, together with an increase in spectral tilt. Because the energy of the first and second formants is relatively strong, evidence of aspiration noise can usually not be seen when viewing the vowel waveform. Klatt and Klatt (1990) introduced a method of estimating degree of aspiration noise in a vowel waveform. Judgments of waveform irregularity are made on a four-point scale by viewing the vowel waveform after bandpass filtering at the third-formant frequency, where aspiration noise should be visible. An example of such a filtered waveform is given in Fig. 1.

Using acoustic models, Hanson (1995a, 1997) made estimates of maximum, minimum, and average values for some of the acoustic measures for female speakers. These predictions from models were based in part on analysis of the KL-GLOTT88 glottal-source model (Klatt and Klatt, 1990), together with minimum-airflow data collected during vowel production (Holmberg *et al.*, 1988). Data collected from 22 female speakers were in agreement with the model-based estimates, and substantial differences among individual speakers were found. There were strong correlations between several of the acoustic measures. In particular, the source

TABLE I. Average dimensions of the glottis, trachea, and vocal tract for male speakers.

Length of vocal tract	17 cm
Vertical length of glottis	0.4 cm
Length of trachea	12 cm
Cross-sectional area of vocal tract	4 cm^2
Cross-sectional area of trachea	2.5 cm^2

spectral tilt indicator ($H1^*-A3^*$) was found to be highly correlated with that of the first-formant prominence ($H1^*-A1$) and the noise judgment (N_w). According to the theoretical models, all three measurements are related to the existence and size of a glottal chink. Analysis of the acoustic measurements suggested that the subjects could be classified into two groups. Speakers having relatively low values of $H1^*-A3^*$ and $H1^*-A1$, indicating strong high-frequency content and prominent $F1$ spectral peaks, were classified as members of group 1. The noise ratings were also lower for this group, suggesting little aspiration noise in the vowels. Speakers in this group were hypothesized to have abrupt glottal closure, with posterior glottal chinks that vary in size (including zero). Speakers in group 2 had higher values of $H1^*-A3^*$ and $H1^*-A1$, indicating much less high-frequency energy and weaker $F1$ peaks. The higher noise ratings for these speakers suggested more aspiration noise in the speech. Therefore, speakers in this group were hypothesized to have relatively large posterior glottal chinks extending beyond the vocal processes, with nonsimultaneous glottal closure.

Preliminary results of fiberscopic images collected from four of the 22 subjects supported this hypothesis (Hanson, 1995a). Moreover, a listening test showed that group 2 speakers were perceived as having breathier voice quality than group 1 speakers, also suggesting that they had relatively large glottal chinks (cf. Södersten and Lindestad, 1990).

B. Current study

In the current study, we extended the earlier experiment to male speakers. Based on the theoretical models and the equations presented in Hanson (1995a, 1997), we calculated the contribution of a posterior glottal chink to the spectral tilt and the first-formant bandwidth, for a range of cross-sectional areas for the chink. For these calculations, we assumed a uniform vocal tract having the dimensions given in Table I. In addition, we assumed a subglottal pressure of 6300 dynes/cm^2 (6.4 cm H_2O), which is the average value for males found by Holmberg *et al.* (1988). For each cross-sectional area of the glottal chink A_{ch}, we also calculated U_{ch}, the minimum (dc) flow. The estimations are summarized in Table II. We see, for example, that a glottal chink of area 5 mm^2 would result in a first-formant bandwidth increase of 77 Hz and an additional tilt of 12 dB at 2500 Hz.

From analysis of the glottal-waveform model KLGLOTT88 (Klatt and Klatt, 1990) and experimentally measured formant bandwidths (Fant, 1972), we estimated minimum values for the measures $H1-A1$ and $H1-A3$. These calculations assumed a uniform vocal tract for which

TABLE II. Range of glottal chink areas (A_{ch}) and corresponding estimations of: glottal contribution to first formant (B_g); bandwidth of first formant ($B1$); flow through chink (U_{ch}); time constant (T) of flow cutoff; resulting increment in spectral tilt at 2500 Hz (Tilt). A subglottal pressure of 6300 dynes/cm^2 (6.4 cm H_2O) (Holmberg *et al.*, 1988) is assumed. Other assumed values include: vocal-tract, glottis, and trachea dimensions given in Table I, first-formant frequency of 500 Hz, and vocal-tract losses of 73 Hz for vowel /æ/ (House and Stevens, 1958).

A_{ch} (cm^2)	B_g (Hz)	$B1$ (Hz)	$20\log_{10} B1$ (dB)	U_{ch} (cm^3/s)	T (ms)	Tilt (dB)
0.00	0	73	37	0	0	0.0
0.01	15	88	39	33	0.13	7.3
0.02	31	104	40	66	0.16	8.8
0.03	46	119	42	100	0.17	10.0
0.04	62	135	43	133	0.20	11.1
0.05	77	150	44	166	0.23	12.1
0.06	93	166	44	199	0.25	13.0
0.07	108	181	45	232	0.28	13.8
0.08	124	197	46	265	0.30	14.5
0.09	139	212	47	299	0.32	15.2
0.10	155	228	47	332	0.35	15.8

$F1=500$ Hz, $F2=1500$ Hz, …, a fundamental frequency of 100 Hz, and an open quotient of 50%. For this hypothetical case, the formants are centered on harmonics, and measuring $H1-A1$ and $H1-A3$ directly from the synthesized spectra would give us estimates of the minimum *possible* values. However, because it is often the case that formant frequencies are not centered on harmonics, we estimated the minimum *expected* values by subtracting 3 dB from the amplitude of $A1$, and 2 dB from the amplitude of $A3$, to compensate. By matching the calculated minimum airflow (U_{ch}), shown in Table II, with measured minimum (dc) airflow data collected by Holmberg *et al.* (1988) and Perkell *et al.* (1994), we estimated the average and maximum expected areas of posterior glottal chinks (A_{ch}). From these values, the expected average and maximum first-formant bandwidths were obtained by calculating the contribution of the glottal chink to the first-formant bandwidth, using an equation given in Hanson (1997), and then adding that value to minimum bandwidths measured experimentally (Fant, 1972; House and Stevens, 1958). The average and maximum values of $H1-A1$ were estimated using the bandwidth estimates. The average and maximum values of $H1-A3$ were obtained from Table II using the average and maximum values of A_{ch}.

Table III summarizes these predicted values. Because

TABLE III. Predicted average, minimum, and maximum values of acoustic measures for male speakers, assuming an $F0$ of 100 Hz, an open quotient of 50 percent, and a uniform vocal tract with resonant frequencies at odd multiples of 500 Hz. $H1-A1$ and $H1-A3$ are given in dB, and $B1$ is given in Hz. The maximum estimated value of $H1-A3$, given in parentheses, is based on the assumption of simultaneous closure of the vocal folds, and therefore, measured values could be higher. See Sec. I B of the text for additional details of the calculations.

	$H1-A1$	$H1-A3$	$B1$
Average	−7.0	13.7	119
Minimum	−11.3	4.7	73
Maximum	−2.3	(19.7)	205

additional spectral tilt due to both a posterior glottal chink and nonsimultaneous glottal closure is difficult to estimate, our estimate of the maximum value of $H1-A3$ assumes a simultaneous glottal closure. Therefore, we expected that we might see even higher values in the human data. Predicted values for the females tended to be higher than those for the males; the maximum expected values of both $B1$ and $H1^*-A1$ were higher, as were both the minimum and maximum values of $H1^*-A3^*$.

We next describe experimental data collected from male speakers on which the acoustic measures described in Sec. I A were made. As described in the Introduction, earlier work by other researchers suggests that females are more likely to have posterior glottal chinks than are males. Therefore, theory predicts that there should be significant differences between the average values of the acoustical descriptors for male and female speakers. It is also possible that males will display a smaller degree of variation than females.

II. EXPERIMENT

A. Speakers and speech material

We collected data from 21 adult male speakers between the ages of 19 and 71. Most of these speakers were MIT students. Four of the subjects had significant experience participating in speech production experiments. The speakers appeared to have no signs of voice or hearing problems, and all were native speakers of American English. The microphone was positioned to be 20 cm from a speaker. Subjects were instructed to speak in their normal tone of voice, as naturally as was possible. There was otherwise no control of intensity. The utterances consisted of three nonhigh vowels, /æ, ɛ, ʌ/, embedded in the carrier phrase ''Say bVd again.'' These vowels were chosen because the first formant is well separated from the first harmonic, and the first and second formants are well separated from each other, thus simplifying the acoustic measures. Each utterance was repeated seven times, with the 21 sentences presented in random order. The first and last tokens of each vowel were discarded. The remaining 15 utterances were low-pass filtered at 4.5 kHz and digitized with a sampling rate of 10 kHz.

B. Measurements

The acoustic measurements described in Sec. I A were made in the following manner:

1. First formant bandwidth (B1)

Each repetition of the vowel /æ/ was bandpass filtered around its average $F1$ frequency using a four-pole digital Butterworth filter with a bandwidth of 600 Hz. The first-formant bandwidth was estimated from the rate of decay of the resulting waveform as determined by the peak-to-peak amplitude of the first two $F1$ oscillations. The vowel /æ/ was chosen because its $F1$ is usually high enough to allow at least two oscillations to take place during the closed part of the glottal cycle. Estimates were made on eight consecutive pitch periods during a stable section of each token. The 40 estimates were then averaged to obtain a mean value for each speaker.

2. H1−H2*, H1*−A1, H1*−A3**

Measurements were made for all repetitions of the three vowels. Spectra were obtained by applying a Hamming window to the speech signals, and computing the 512-point discrete Fourier transform (DFT). The length of the Hamming window was chosen such that a minimum of two complete pitch periods of the waveform were covered; it ranged from 32 to 50 ms, depending on the average pitch of each speaker. For the vowel /æ/, the window was centered at the initial part of the eight consecutive glottal cycles from which the first-formant bandwidth was estimated. For the vowels /ɛ/ and /ʌ/, the measurements were taken three times throughout each token at 20-ms intervals. Corrections were made to normalize transfer-function effects on the amplitude of the third formant. The effects of neighboring formants were removed, for which, on average, $A3$ was corrected by -7.8 dB for /æ/, -4.6 dB for /ɛ/, and $+2$ dB for /ʌ/. In addition, the amplitude $A3$ was further adjusted, because the average third-formant bandwidth varies by vowel. House and Stevens (1958) measured the $F3$ bandwidths for the vowels /æ, ʌ, ɛ/ at 103, 64, and 88 Hz, respectively. Thus, vowels /æ/ and /ɛ/ would, on average, have $F3$ amplitudes that are 4 and 3 dB lower, respectively, than that of the vowel /ʌ/. Because we are only interested in source effects on the amplitude of $F3$, we compensated by adding 4 dB to the measure $A3^*$ for /æ/, and 3 dB for /ɛ/.

3. Noise rating (N_w)

Each repetition of the three vowels was bandpass filtered around its average $F3$ frequency using a filter with a bandwidth of 600 Hz. Plots of the filtered waveforms were arranged randomly across vowel and speaker, and were rated on a four-point scale: (1) periodic, no visible noise; (2) periodic but occasional noise intrusion; (3) weakly periodic, clear evidence of noise excitation; (4) little or no periodicity, noise is predominant (Klatt and Klatt, 1990). The ratings were made independently by two judges, who did not know which waveforms corresponded to which speaker. Their ratings were well correlated ($r=0.77$), and the average difference in the two ratings for each token was only 0.36. Their two ratings were then averaged to obtain one noise rating for each token per speaker. Figure 2 shows typical waveforms corresponding to the four rating levels.

Despite the consistency of their ratings, the judges reported feeling somewhat uncertain about them because some of the waveforms had what appeared to be second pulses appearing about halfway through a pitch period. These extra pulses gave the appearance of noise, but did not really seem to be the random noise expected for aspiration. Hence, the judges were not convinced that high noise ratings actually reflected large degrees of aspiration noise. This effect is discussed further in Sec. III B.

III. RESULTS AND DISCUSSION

A. Statistical analysis and comparison with predicted values

The mean values of the acoustic parameters for each speaker are summarized by vowel in Tables IV–VI. Mini-

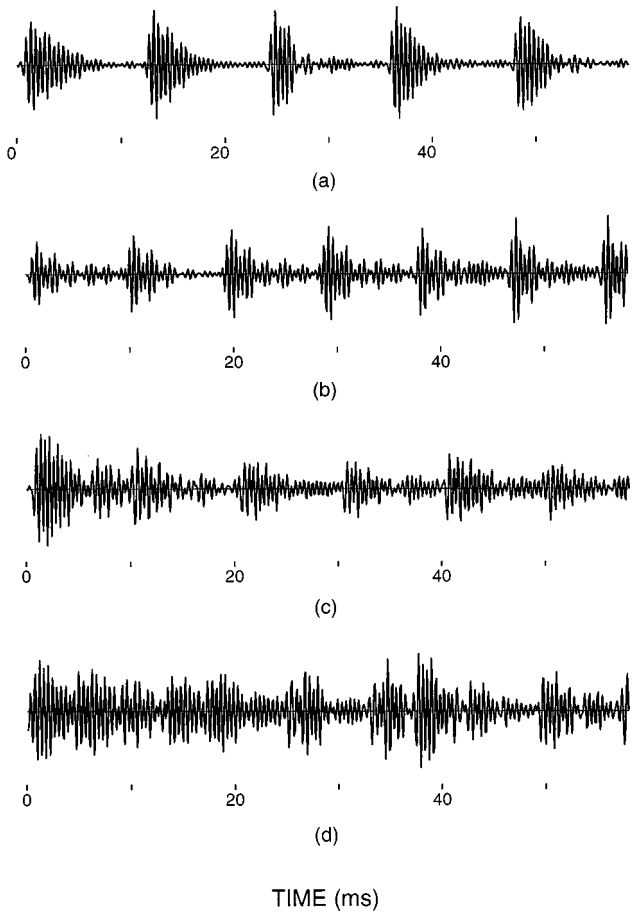

FIG. 2. Examples of the degree of aspiration noise ratings, N_w. The speech waveforms (vowel /æ/) have been bandpass filtered in the third-formant region, and their amplitudes have been scaled to fill the full available range. Ratings were made by two judges and averaged. Each example is from a different male speaker. (a) $N_w \approx 1$; periodic, little evidence of noise. (b) $N_w \approx 2$; periodic, occasional intrusion of noise. (c) $N_w \approx 3$; weakly periodic, clear evidence of noise. (d) $N_w \approx 4$; little or no periodicity, strong noise excitation.

TABLE IV. Average values of the acoustic parameters for the vowel /æ/, 21 male speakers, where $H1^*-H2^*$, $H1^*-A1$, and $H1^*-A3^*$ are given in dB, N_w is the waveform-based noise judgment, and $B1$ is the bandwidth of the first formant, given in Hz. Numbers in boldface represent maxima or minima for each measure across speakers. Parentheses around a noise judgment N_w indicate that a speaker was judged to consistently exhibit secondary pulses for the vowel (see Sec. III B for details). The mean value, the standard deviation, and the average standard deviation per each subject are also given for each measure.

Subject	$H1^*-H2^*$	$H1^*-A1$	$H1^*-A3^*$	N_w	$B1$
M1	3.7	−7.4	9.0	1.4	102
M2	−0.5	−8.0	**6.2**	(2.2)	115
M3	0.6	−6.4	20.6	1.9	103
M4	1.1	−1.2	22	1.9	213
M5	0.4	−2.3	14.6	**1.2**	65
M6	−0.2	−7.8	14.1	1.6	92
M7	−0.7	−8.6	15.8	(2.6)	101
M8	0.3	−2.3	11.1	1.3	127
M9	−0.3	−8.0	16.3	(2.3)	114
M10	−0.3	−7.7	12.6	1.7	80
M11	**−3.3**	−8.7	15.9	1.5	67
M12	0.4	−5.9	21.5	(2.8)	157
M13	−0.9	−5.5	12.7	1.4	147
M14	−0.9	−12.5	10.6	1.7	104
M15	−0.4	−10.3	16.6	1.5	178
M16	−1.3	−5.6	17.6	(2.9)	**58**
M17	−1.2	−5.5	15.2	1.6	**245**
M18	1.8	**0.4**	**24.1**	(**3.2**)	160
M19	**4.0**	−5.2	22.2	2.1	121
M20	−0.6	**−16.1**	11.1	1.8	63
M21	−0.6	−2.3	16.6	(2.2)	230
Mean	0.0	−6.5	15.5	1.9	126
s.d.	1.6	3.8	4.7	0.4	55
Mean s.d.	1.3	1.4	2.5	0.4	20.5

mum and maximum values for each measure are given in boldface, and mean values across speaker are shown at the bottom of each table. The standard deviations of the means are also given. To get some idea of the consistency of each speaker, standard deviations across token were computed for each measure. The average standard deviations across speaker are given at the bottom of Tables IV–VI. Comparing those with the range of values across speaker observed for each parameter, we can say that most speakers were generally quite consistent. However, there are only five tokens for each vowel, and it is not clear to what extent these measures of variability represent a larger sample size.

All measurements were subjected to repeated-measures analysis of variance (ANOVA) with vowel /æ, ʌ, ɛ/ as a within-subject factor (Table VII). Only $H1^*-A3^*$ showed a significant difference among vowels [$F(2,40)=11$, $p<0.01$]. Reference to Tables IV–VI shows that the mean for this measure is about 3.5 dB greater for the vowel /æ/ than for the other two vowels. Upon closer inspection, we found that for eight speakers $H1^*-A3^*$ is significantly larger for /æ/ than for /ɛ/ or /ʌ/, while for the remaining speakers there is little difference among the vowels. Recalling that /æ/ has a relatively large third-formant bandwidth because it is produced with a larger degree of mouth opening, it is possible that these speakers have particularly large third-formant bandwidths for this vowel. Although we attempted to remove filter effects, this result indicates that the measure might be sensitive to variations in articulation among speakers. However, given that the difference among vowels is due to a minority of speakers, and that compared with the total range of the measure, the difference is small, we do not consider each vowel separately in the following analysis.

The means, maxima, minima, and ranges of the measures are summarized in Table VIII, and compared with estimated values from Sec. I B where appropriate. As can be seen, there is considerable subject-to-subject variability in the measurements. For the most part, the measured values are quite close to the estimated values, in several cases within less than 1 decibel.

The minimum value of $H1^*-A1$ is about 5 dB less than that predicted, but this relatively large difference is only due to one speaker (M20) who has an unusually low first-harmonic amplitude ($H1$). It is likely that this speaker has an open quotient that is significantly lower than the 50% which was assumed for calculation of the predicted value. The prediction may also have been too conservative because we assumed that the first formant does not usually center on a harmonic, and therefore we reduced the estimated amplitude of the first-formant peak ($A1$) by 3 dB. In retrospect,

TABLE V. Average values of the acoustic parameters for the vowel /ʌ/, 21 male speakers, where $H1^*-H2^*$, $H1^*-A1$, and $H1^*-A3^*$ are given in dB, and N_w is the waveform-based noise judgment. Numbers in boldface represent maxima or minima for each measure across speakers. Parentheses around a noise judgment N_w indicate that a speaker was judged to consistently exhibit secondary pulses for the vowel (see Sec. III B for details). The mean value, the standard deviation, and the average standard deviation per each subject are also given for each measure.

Subject	$H1^*-H2^*$	$H1^*-A1$	$H1^*-A3^*$	N_w
M1	**4.2**	−4.9	10.3	1.5
M2	−0.2	−9.8	**4.8**	1.5
M3	1.9	−6.5	17.0	2.0
M4	0.8	−3.9	**22.8**	2.2
M5	2.5	−2.9	13.0	1.5
M6	−2.3	−9.8	11.1	1.7
M7	−0.1	−5.7	18.1	2.3
M8	0.4	−5.7	11.3	1.4
M9	−1.8	−11.1	8.8	(2.3)
M10	−2.3	−6.1	11.2	1.8
M11	**−2.7**	−9.4	14.8	2.0
M12	0.3	−6.6	15.4	2.3
M13	−1.8	−3.5	10.7	1.4
M14	−1.4	−11.2	9.7	1.3
M15	0.4	−6.0	15.4	1.6
M16	−1.9	−2.5	18.8	(2.5)
M17	1.2	−7.0	9.6	**1.2**
M18	2.0	**−2.2**	15.4	(2.5)
M19	−0.1	−8.5	18.4	**2.9**
M20	−2.3	**−14.9**	7.9	1.4
M21	−1.0	−7.5	10.9	1.5
Mean	−0.2	−6.9	13.1	1.8
s.d.	1.9	3.3	4.4	0.3
Mean s.d.	0.8	1.4	2.4	0.4

TABLE VI. Average values of the acoustic parameters for the vowel /ɛ/, 21 male speakers, where $H1^*-H2^*$, $H1^*-A1$, and $H1^*-A3^*$ are given in dB, and N_w is the waveform-based noise judgment. Numbers in boldface represent maxima or minima for each measure across speakers. Parentheses around a noise judgment N_w indicate that a speaker was judged to consistently exhibit secondary pulses for the vowel (see Sec. III B for details). The mean value, the standard deviation, and the average standard deviation per each subject are also given for each measure.

Subject	$H1^*-H2^*$	$H1^*-A1$	$H1^*-A3^*$	N_w
M1	**3.8**	−4.9	10.5	1.4
M2	1.2	−9.9	**5.7**	1.6
M3	0.8	−7.2	17.2	1.8
M4	−0.8	−5.9	18.8	2.1
M5	2.2	−3.7	13.5	1.4
M6	−2.3	−11.9	12.0	1.5
M7	−0.1	−7.0	12.7	1.8
M8	−0.2	−6.2	12.5	**1.3**
M9	−2.1	−12.3	7.8	(2.7)
M10	−2.3	−6.7	9.7	1.5
M11	**−3.2**	−9.6	11.7	1.7
M12	1.4	−5.1	**23.1**	(3.0)
M13	−0.7	−6.5	7.5	1.4
M14	−1.8	−12.7	8.2	1.8
M15	0.1	−7.3	15.6	1.7
M16	−1.5	−2.3	19.2	(2.8)
M17	2.6	−6.8	11.2	1.6
M18	3.5	**−1.2**	17.1	(**3.0**)
M19	3.1	−5.0	20.7	2.1
M20	−2.3	**−14.0**	6.4	1.5
M21	−0.7	−6.8	9.9	1.5
Mean	0.0	−7.3	12.9	1.9
s.d.	2.1	3.4	4.9	0.4
Mean s.d.	1.0	1.6	2.5	0.3

considering that the harmonics are closely spaced for most male speakers, perhaps we should not have made this adjustment.

The total range of $H1^*-A3^*$ is about 19 dB; that is, some speakers have strong high-frequency content in the vowel, while others do not. The maximum measured value of $H1^*-A3^*$ was 24.1 dB, about 4 dB larger than that expected for abrupt glottal closure, suggesting that some speakers may have nonsimultaneous glottal closure or relatively wide third-formant bandwidths.

The first-formant bandwidth $B1$, as estimated from the speech waveform, ranges widely from a minimum of 58 Hz to a maximum of 245 Hz, with an average of 126 Hz. The noise judgments ranged from 1.2 to 3.2, indicating that some of the speakers show little noise at high frequencies, while others show significant noise. This result is somewhat surprising because in Klatt and Klatt's (1990) male data, stressed syllables were not given noise ratings higher than 2.0. We discuss this result in more detail in the next section.

$H1^*-H2^*$ has a total range of about 7.5 dB. Holmberg *et al.* (1988) found that the open quotient for a group of 25 male subjects ranged from 46% to 77%. According to the KLGLOTT88 model (Klatt and Klatt, 1990), this range corresponds to an 8.6-dB change in the measure $H1^*-H2^*$, assuming that $F0$ is 100 Hz. Therefore, the range of $H1^*-H2^*$ found in the current experiment seems reasonable.

In Fig. 3 we compare spectra from two speakers, illustrating the variability among male speakers. Subject M20, in the upper panel, has strong harmonic structure at all frequencies, and sharp formant peaks. He has relatively little energy in the region of the first two harmonics. Subject M18, in the lower panel, has good harmonic structure only up to about 2 kHz; above that frequency, the spectrum appears noisy. His formant peaks are less well defined, especially the first. Energy in the region of the first and second harmonics is quite strong. The amplitudes of the formant peaks fall off more rapidly for M18 than for M20.

Table IX shows Pearson product moment correlation coefficients for the various measures. The correlations are moderate ($0.49 \leqslant r \leqslant 0.60$, $N=63$). One would expect that because degree of spectral tilt, high-frequency noise, and $H1^*-A1$ are related to the presence and size of a posterior glottal opening, higher correlations should be observed among these parameters. The correlation between $H1^*-A1$

TABLE VII. Results of repeated measures analyses of variance (ANOVA) performed to examine differences in the acoustic parameters across vowels. An asterisk (*) in the third column indicates statistical significance.

Measure	$F(2,40)$	p
$H1^*-H2^*$	0.4	>0.1
$H1^*-A1$	1.2	>0.1
$H1^*-A3^*$	11.0	<0.01*
Noise	0.8	>0.1

TABLE VIII. Mean, minimum, and maximum values of the measured (Meas.) acoustic parameters, compared, where appropriate, with the values estimated (Est.) in Sec. I B. $H1^*-H2^*$, $H1^*-A1$, and $H1^*-A3^*$ are given in dB, and $B1$ is given in Hz. The estimated maximum of $H1^*-A3^*$ is given in parentheses to indicate that it is a lower bound on the maximum (see the text and the caption for Table III for details).

	$H1^*-H2^*$	$H1^*-A1$		$H1^*-A3^*$		N_w	$B1$	
	Meas.	Meas.	Est.	Meas.	Est.	Meas.	Meas.	Est.
Mean	0	−6.9	−7.0	13.8	13.7	1.8	126	119
Minimum	−3.3	−16.1	−11.3	4.8	4.7	1.2	58	73
Maximum	4.2	0.4	−2.3	24.1	(19.7)	3.2	245	205
Range	7.5	16.5	13.6	19.3	15	2	187	132
s.d.	1.8	3.5	n.a.	4.8	n.a.	0.4	43	n.a.

and $B1$ is also low ($r=0.44$, $N=21$), given that A1 is mostly influenced by its bandwidth. However, other factors do influence A1, including decay rate during glottal opening and source spectral tilt. In addition, as we describe in the next section, the method of approximating the $F1$ bandwidth might have been inaccurate because of interference from a second excitation pulse.

B. Complicating factors

The analyses of the data were complicated by two factors not observed for female speakers. First, for a number of the male speakers, a second pulse during a glottal period was observed in the speech waveform. Such second pulses were rarely seen for the female subjects of Hanson (1995a, 1997). Figure 4(a) and (c) show vowel waveforms from subjects M9 and M16, in which examples of such pulses are indicated with arrows. As can be seen in Fig. 4(b) and (d), the pulses are more easily identified in the signals on which the noise judgments were made; that is, the speech waveform bandpass filtered at the third formant.

Given that the initial deflection for these pulses is in the same direction as the pulses at the beginning of a period, and that it occurs about halfway through a period, it is likely that it is the result of excitation of the vocal tract at the time of glottal opening. (Note that the change in the derivative of the glottal waveform is positive following both glottal opening and closure.) As a rough approximation, then, we can consider a second pulse to be a delayed, attenuated replica of the main pulse. By Fourier analysis, these second pulses should result in an attenuation of certain harmonics in the speech spectrum. The delay of the second excitation relative to the main excitation determines which harmonics are affected, with the effect being strongest when the second excitation is delayed by about 50% of the glottal cycle. Figure 5 is the spectrum of the waveform shown in Fig. 4(a), where the second excitations occur about halfway between the main pulses. As the model predicts, the amplitude of almost every other harmonic appears to be attenuated, resulting in a noisy-looking or irregular spectrum. Preliminary experiments with speech synthesis show similar changes in the speech spectrum. Note also that multipulse excitation has been found to improve the quality of speech synthesized according to the linear predictive coding (LPC) model (Atal and Remde, 1982). Therefore, our hypothesis that the secondary pulses are caused by excitation at glottal opening seems reasonable.

In Fig. 4(b) and (d), we see that the extra pulses interfere with the perceived regularity of the waveforms, and, in fact,

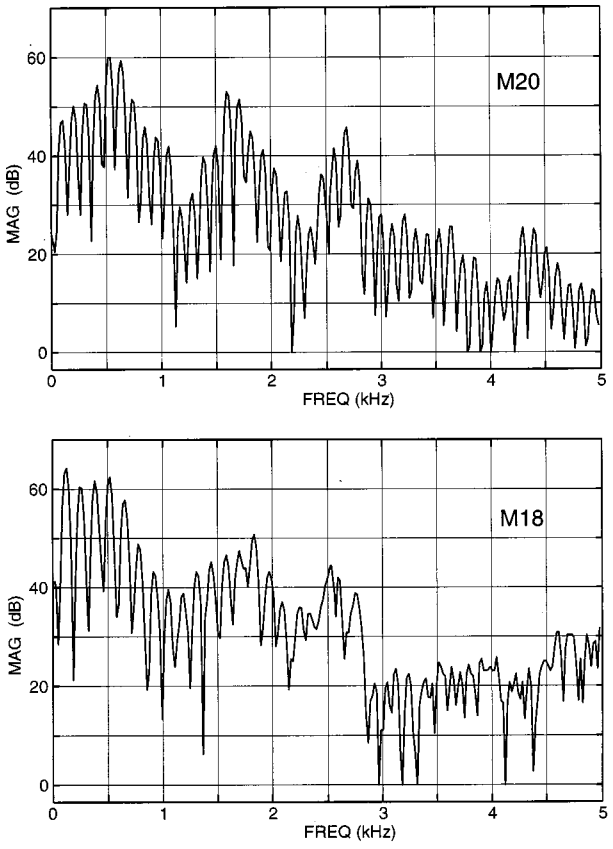

FIG. 3. Illustration of the range of spectral characteristics related to glottal configuration observed in male subjects. The vowel is /ɛ/. The spectrum for subject M18 (below) has greater spectral tilt, less well-defined formant peaks, a greater degree of noise at high frequencies, and a higher relative amplitude of the first harmonic, compared to the spectrum for subject M20 (above).

TABLE IX. Pearson product moment correlation coefficients for the acoustic parameters for the three vowels /æ, ʌ, ɛ/ combined. The notation n.s. indicates that a correlation was not significant. $N=63$, except for correlations with $B1$, for which $N=21$.

	$H1^*-H2^*$	$H1^*-A1$	$H1^*-A3^*$	N_w	$B1$ (/æ/)
$H1^*-H2^*$	1				
$H1^*-A1$	0.49	1			
$H1^*-A3^*$	n.s.	0.55	1		
N_w	n.s.	n.s.	0.60	1	
$B1$ (/æ/)	n.s.	0.44	0.33	n.s.	1

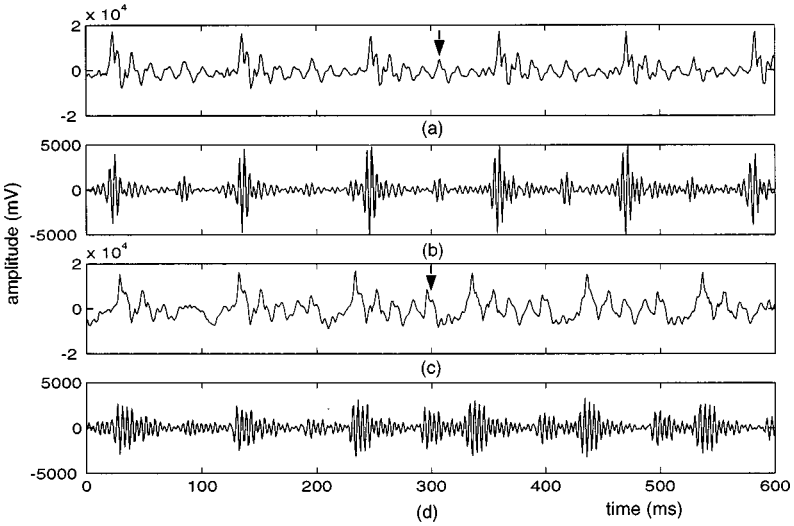

FIG. 4. Speech waveforms showing evidence of a second glottal excitation: (a) Speech waveform for vowel /æ/, subject M9. The arrow indicates an example of a second pulse; (b) The waveform of (a), following bandpass filtering in the $F3$ region. The second pulses are more easily seen. (c) Speech waveform for the vowel /ɛ/, subject M16; (d) The waveform of (c), following bandpass filtering in the $F3$ region. The second pulses show greater variation in amplitude than those of the waveform in (b), making this waveform appear relatively noisy.

we mentioned in Sec. II B that these pulses hampered the confidence of the judges in their noise ratings. To study this effect, the bandpass-filtered waveforms used for the noise judgments were presented to a third judge for evaluation of the existence of a second excitation. If extra pulses were consistently observed, that is, a second pulse was present in almost every glottal period in the waveform with the same amount of delay, the vowel token was judged to have a second excitation. If at least three out of the five tokens for a given vowel were found to have a second excitation, that vowel was labeled as having a second pulse; the remaining vowels were labeled as not having a second pulse. A plot of noise judgment (N_w) vs $H1^*-A3^*$ is shown in Fig. 6. The open circles represent vowel data judged to have a second excitation. Nearly all the vowel tokens given a noise rating much above 2 were also judged to show evidence of second pulses. Given that the male subjects of Klatt and Klatt (1990) did not have noise ratings greater than 2 for stressed syllables, this result suggests that for the group of data in question, the noise ratings do not accurately reflect the degree of aspiration noise in the signal. Although the ratings for this group of data are questionable, they are included in Tables IV–VI because this finding is the result of *post hoc* analysis and our hypothesis is not conclusive. The noise ratings that are in doubt are given in parentheses in those tables.

The question arises as to why we do not observe this phenomenon for all of the data. One possibility is that not every speaker has a second excitation at glottal opening. However, only three speakers were found to have second pulses in all three vowels, while one speaker had second pulses in two vowels and three showed second pulses only for /æ/. It seems unlikely that a speaker would have second pulses only for certain vowels. Hence, it is possible that excitation at glottal opening is common, but obvious only for vowel tokens in which the third-formant oscillations die out quickly. Evidence for the latter is that /æ/ usually has a relatively wide third-formant bandwidth and /æ/ tokens were much more likely to be judged to have a second pulse than the other two vowels.

One can also question why this problem arose for the male speakers and not for the female speakers. A possible explanation is that the lower fundamental frequency of males allows a longer time for the third formant to decay before glottal opening occurs, and thus a second excitation would be easier to see. It could also be that females are less likely to have second excitations for physiological reasons, such as less surface tension of the folds.

Details of the causes and consequences of these extra excitations will require further investigation. However, it is clear that this second excitation and its effects on the speech waveform and spectrum could have consequences for studies of male speech. As we have seen, the high-frequency noise judgments become more difficult, because the existence of the second pulses may make the filtered waveforms seem more irregular, as shown in Fig. 4(b) and (d). Spectrum-based noise measures could also be affected (Fig. 5).

A difficulty also arose for the estimation of the $F1$ bandwidth. For some speakers, the decay of the $F1$ oscillation did not appear to be exponential as expected. Some waveforms showed signs of an increase in the amplitude of the formant oscillation, possibly due to a second glottal excitation. In other cases, formant decay was truncated due to the opening of the glottis. Therefore, the accuracy of the bandwidth mea-

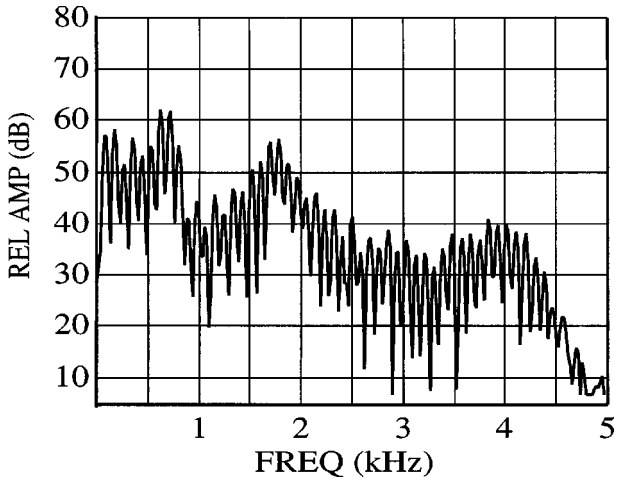

FIG. 5. Spectrum of the speech waveform in Fig. 4(a). The effect of the second pulse is evident in the attenuation of the alternating harmonics.

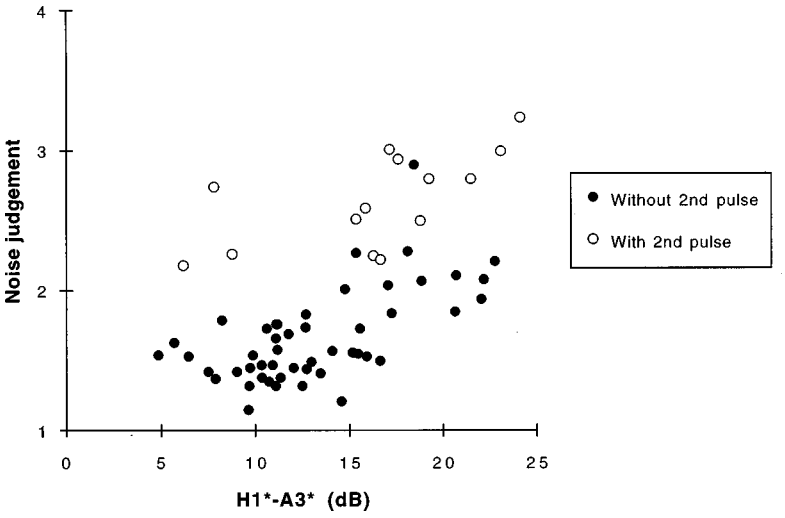

FIG. 6. Relation between the noise judgments, N_w, and the parameter $H1^*-A3^*$, for the male data. Each point represents data for one vowel of one speaker. The open circles indicate the cases that exhibited more evidence of second pulses.

surements is uncertain, which perhaps explains the low correlation between the measures $H1^*-A1$ and $B1$.

The complications described in this section suggest that the $F1$ bandwidth estimates and the waveform-based noise ratings must be interpreted with care for male speakers.

C. Comparison with female data

The acoustic measurements for male speakers were compared with the female data collected by Hanson (1995a, 1997). The maxima, minima, means, ranges, and average standard deviations of the acoustic parameters for male and female speakers are given in Table X. Histograms for each measure, illustrating the contrast between male and female speech, are shown in Fig. 7.

There are considerable differences between the mean values for female and male data for all measurements. The average $H1^*-H2^*$ for male and female speakers differs by about 3 dB. Previous studies which measured the relative amplitudes of $H1$ and $H2$ for both male and female speakers found somewhat greater differences. Klatt and Klatt (1990) found a difference of 5.7 dB between the genders, and Henton and Bladon (1985) also found that $H1-H2$ was about 6 dB greater for female speakers. However, the general trend is in agreement that female speakers have, on average, larger relative amplitudes of the first harmonic, suggesting that they have larger open quotients, as has been observed by Holmberg *et al.* (1988). Note that the range and standard deviation are also slightly larger for the female speakers, in agreement with previous data that females have a wider range of open quotient (Holmberg *et al.*, 1988). The histogram in Fig. 7(a) shows that the male and female data are fairly well separated, with only about a 4-dB overlap.

There is a highly significant difference between genders for $H1^*-A3^*$. The female speakers have an average of 23.4 dB, while the male speakers have an average of 13.8 dB, indicating that female speakers tend to have much weaker high-frequency content in the speech signal. This result is in agreement with the finding by Perkell *et al.* (1994) that males have a higher maximum flow declination rate (MFDR) than females. A 10-dB change in tilt is easily perceived, suggesting that spectral tilt may be an important parameter in differentiating male voice quality from female. In the histogram, Fig. 7(c), the female data are seen to be rather evenly spread throughout their range, while the male data are clustered around 8 to 12 dB.

For the measure $H1^*-A1$, the average difference between genders is around 3 dB, indicating that female speakers, on average, have a weaker $F1$ amplitude. In Fig. 7(b), the data are seen to be less well separated than those for $H1^*-H2^*$ and $H1^*-A3^*$. Out of a total range of 20 dB, significant overlap of the genders is about 10 dB. In Fig. 7(d), we see that females tend to have wider first-formant bandwidths than males, as was found experimentally by Fujimura and Lindqvist (1971). The male data are more tightly clustered than the female data.

The amount of aspiration noise is another acoustic cor-

TABLE X. Comparison of mean, maximum, and minimum values, and standard deviations of the acoustic parameters for male and female speakers. The measures $H1^*-H2^*$, $H1^*-A1$, and $H1^*-A3^*$ are given in dB and $B1$ is given in Hz. N_w is the waveform-based noise judgment. M indicates male data and F indicates female. [Female data from Hanson (1995a, 1997).]

	$H1^*-H2^*$		$H1^*-A1$		$H1^*-A3^*$		N_w		$B1$ (/æ/)	
	M	F	M	F	M	F	M	F	M	F
Mean	0.0	3.1	−6.9	−3.9	13.8	23.4	1.9	2.3	126	165
Minimum	−3.3	−2.6	−16.1	−12.4	4.8	8.6	1.2	1.1	53	53
Maximum	4.2	6.9	0.4	3.9	24.1	35.0	3.2	3.8	245	280
Range	7.5	9.5	16.5	16.3	19.3	26.4	2.0	2.7	192	227
s.d.	1.8	2.0	3.5	4.3	4.8	6.6	0.5	0.7	54	61

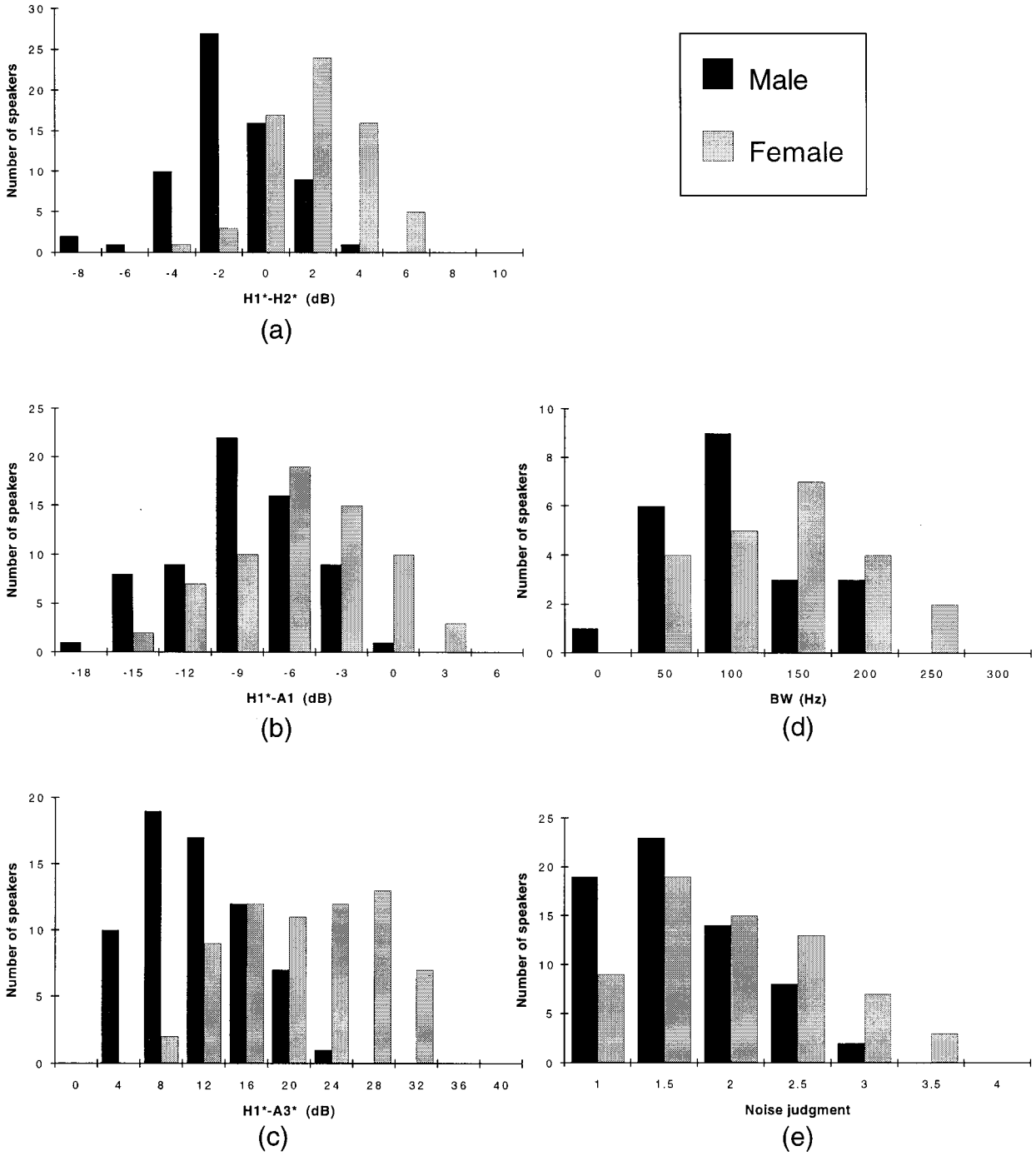

FIG. 7. Histograms of the acoustic measures for male and female speakers.

relate of the degree of breathiness of a vowel. Comparing the noise ratings of female and male speakers, we see that female speakers display more noise, on average, than male speakers, in the frequency range of the third formant. Although the average difference is not very large (1.9 for males vs 2.3 for females), as we discussed in Sec. III B it is likely that most male tokens given ratings of 2 or higher appeared to be noisy due to a second glottal excitation rather than to aspiration noise. In that case, the likelihood of females to have stronger aspiration noise than males is greater than is indicated by the data in Fig. 7(e) and Table X.

Figure 8 compares vowel spectra from male and female subjects having average values of the acoustic parameters. The gender differences discussed above are evident in these spectra: the female subject (upper plot) has less well-defined formants, steeper spectral tilt, more high-frequency noise, and a larger relative amplitude of the first harmonic.

Figure 9 plots the noise judgments against the measure $H1^*-A3^*$ for both male and female speakers. The data for the female speakers are divided in the two groups, group 1 and group 2, described in Sec. I A. The data of the male speakers are divided to indicate which tokens were judged to show evidence of having been produced with a second excitation. Most of the male data, with the exception of those given relatively higher noise ratings due to the second excitation, fall in the same range as the group 1 female data. This

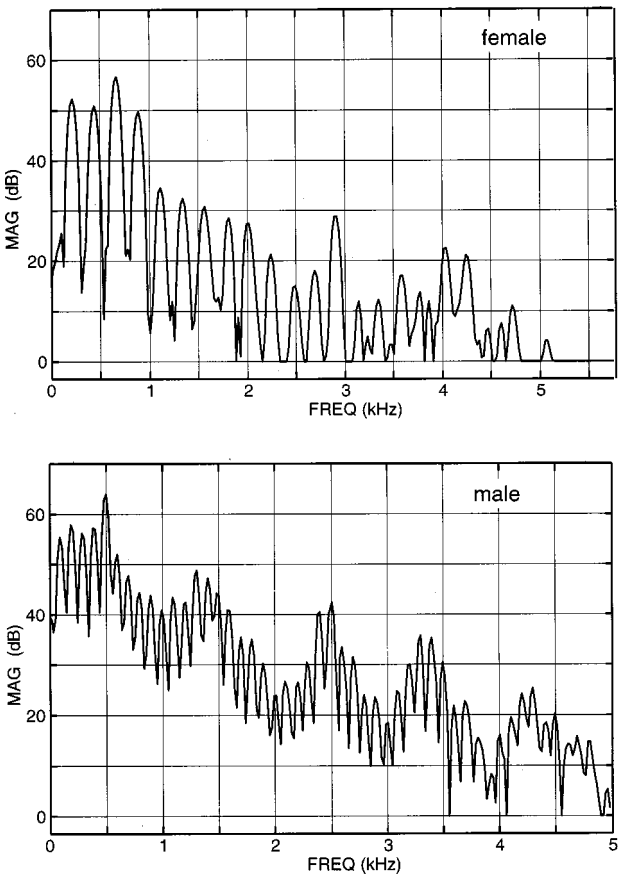

FIG. 8. Comparison of spectra of the vowel /ʌ/ for average female and male subjects. The female spectrum (upper plot) has greater spectral tilt, less well-defined formant peaks, a greater degree of noise at high frequencies, and a higher relative amplitude of the first harmonic, compared to the male speaker's vowel spectrum (lower plot).

result is not surprising if we recall that group 1 females were hypothesized to have abrupt glottal closure with relatively small posterior glottal chinks (Sec. I A). The male data that were marked by second excitations do not follow the trend set by the female data, providing further evidence that the high noise ratings for these vowel tokens do not truly reflect degree of aspiration noise.

Figure 10 shows the relationship between the measures $H1^*-A1$ and $H1^*-A3^*$. Most of the male data overlap with the group 1 female data. There is very little overlap of male data with the group 2 female data. This result agrees with the previous studies that the presence of a posterior glottal chink that persists throughout a glottal cycle is common for female speakers, while occurring much less frequently, or to a lesser degree, among male speakers (Södersten and Lindestad, 1990). Note also that, contrary to Fig. 9, the vowels judged to have been produced with a second excitation do not stand out in any way, but instead follow the trend set by the female data. This observation is further evidence that the noise judgments for these speakers are not representative of their glottal configurations.

It is well known that adult male speakers tend to have lower fundamental frequencies and formant frequencies than females. It is fair to ask how significantly these differences contributed to the gender differences reported. If the male formant frequencies are simply scaled versions of the female formants, the amplitudes of the peaks in the frequency response should remain the same. While that assumption is not entirely true, it is probably safe to assume that gender differences in formant frequencies have minimal effect on the acoustic measures considered here.

To analyze the effects of fundamental frequency differences, we consider the derivative of the glottal waveform, because that is the effective excitation; for simplicity we refer to this derivative as the source waveform $U(t)$. Let us first assume that the male source waveform $U_M(t)$ is simply the female source waveform $U_F(t)$ scaled in time, and therefore open quotient and waveform amplitude remain the same. On average, the pitch period of males is about twice that of females, and consequently we scale in time by a factor of 2, that is, $U_M(t)=U_F(t/2)$. In the frequency domain, $U_M(\omega)=2U_F(2\omega)$. There are two effects, then: a compression along the frequency axis and a scaling of spectrum amplitude. The compression in frequency and scaling in amplitude mean that a harmonic at 2500 Hz in the male spectrum will have the same amplitude as a harmonic at 5000 Hz in the female spectrum, plus 6 dB. At very low frequencies, where the source spectrum is relatively flat, the spectrum magnitude will be raised by 6 dB. At higher frequencies, the magnitude of the female spectrum falls off at 6 dB per octave; thus, at a given frequency ω,

$$20\log_{10}|U_M(\omega)| = 6 \text{ dB} + 20\log_{10}|U_F(2\omega)|$$

$$= 6 \text{ dB} + 20\log_{10}|U_F(\omega)| - 6 \text{ dB}.$$

The net effect of a simple waveform scaling, then, is that the lower-frequency harmonics increase in amplitude by 6 dB, but the amplitudes of the higher-frequency harmonics are unchanged. Therefore, all else being the same, the measure $H1^*-H2^*$ should be the same for males and females, but $H1^*-A1$ and $H1^*-A3^*$ should be 6 dB greater for males.

Our data suggest, however, that this model is not appropriate, and therefore the gender differences observed in our data are most likely due to details of the glottal configuration and waveform, and to vocal-tract losses, rather than to fundamental frequency and formant differences. In fact, we know from other experimental data that the male source waveform is not simply a time-scaled version of the female waveform. In particular, for male speakers the open quotient is smaller and the maximum flow declination rate (MFDR) is greater than for females (Holmberg *et al.*, 1988; Perkell *et al.*, 1994). Typical open quotients for males and females are 50% and 60%, respectively, leading to a gender difference of about 3 dB for the relative amplitudes of the first two harmonics, based on the KLGLOTT88 model of the glottal waveform (Klatt and Klatt, 1990). This difference is about the same as that found for our male and females subjects.

It is primarily the first harmonic that is affected by changes in open quotient, and therefore the predicted values of $H1^*-A1$ and $H1^*-A3^*$ for males relative to females are also reduced by about 3 dB. The MFDR, or negative peak of the flow derivative, mainly affects the spectrum well above the first harmonic (Fant, 1995). The higher MFDR of males should boost the amplitude of their formants, relative to those of females. Data reported in Perkell *et al.* (1994) pre-

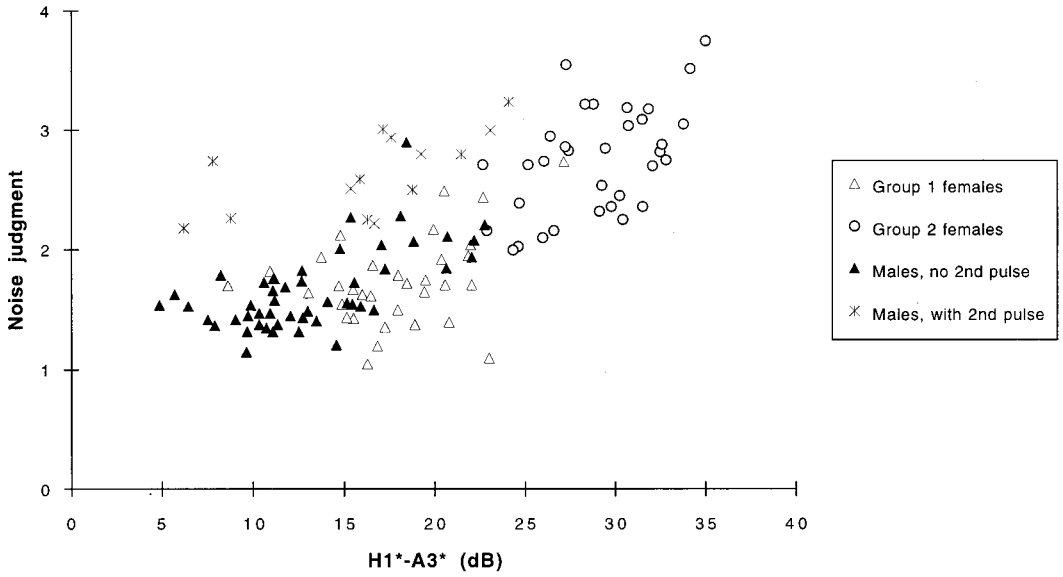

FIG. 9. Relation between noise judgment, N_w, and $H1^*-A3^*$ for the male and female data combined. Open triangles (△) represent group 1 female data, open circles (○) represent group 2 female data, filled triangles (▲) represent male data showing little evidence of second glottal excitations, and asterisks (*) represent male data showing significant evidence of second glottal excitations.

dict that the difference will be about 5.3 dB (for normal voice). The combination of the open quotient and MFDR effects with the time scaling, then, predicts that the measures $H1^*-A1$ and $H1^*-A3^*$ will be about 2.3 dB less for males than for females.

Our data show $H1^*-A1$ to be, on average, 3 dB less for males, and $H1^*-A3^*$ to be 9.6 dB less. Our first-formant bandwidth estimates (which include both glottal-chink and vocal-tract losses) would lead us to expect that $A1$ will be 2.3 dB higher for males than for females, in addition to the MFDR effect. The net effect is that $H1^*-A1$ should be 4.6 dB lower for males than for females, consistent with our finding. Third-formant bandwidth differences could increase the gender difference in $A3^*$ by 3 dB or so. It is reasonable to attribute the remaining 4.3-dB difference in the measure $H1^*-A3^*$ to the greater tendency for females to have posterior glottal chinks. Thus, we have shown that the observed gender differences are largely due to details of the glottal configuration and source waveform characteristics.

IV. SUMMARY

Vowel data were collected for 21 male speakers, and were analyzed using acoustic measures believed to reflect glottal configuration. Significant variations among the speakers were observed for all of the acoustic measures. The data were compared with female data collected in an earlier study. In agreement with predictions based on theoretical models

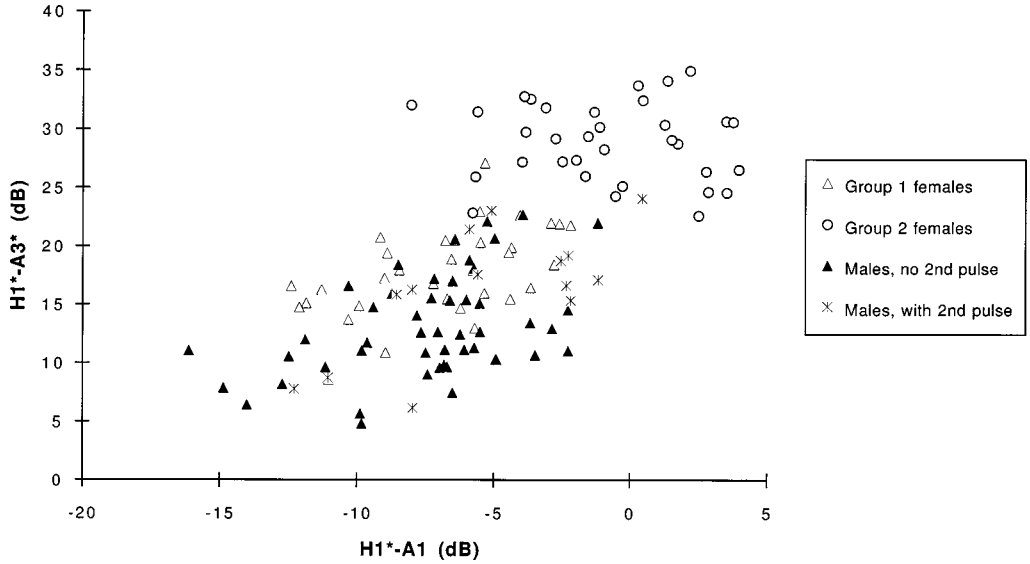

FIG. 10. Relation between $H1^*-A1$ and $H1^*-A3^*$ for the male and female data combined. Open triangles (△) represent group 1 female data, open circles (○) represent group 2 female data, filled triangles (▲) represent male data showing little evidence of second glottal excitations, and asterisks (*) represent male data showing significant evidence of second glottal excitations.

and previous reports of physiological and airflow data (Holmberg *et al.*, 1988; Södersten and Lindestad, 1990), we found that the group averages for all acoustic measures for the males were lower than those of the females. Although we found significant overlap of the male and female data, the male data tended to be more tightly clustered about the means. The greatest differences were observed for the measures $H1^*-H2^*$ and $H1^*-A3^*$, which reflect open quotient and source spectral tilt, respectively. Changes in tilt significantly affect perceived voice quality (see, for example, Klatt and Klatt, 1990), and therefore spectral tilt may greatly contribute to gender differences that we perceive in speech. Another gender difference that was observed in the speech waveforms is the presence of second excitation pulses for some of the male speakers. Such pulses were very rarely observed in the female data.

Some of the measures were found to be sensitive to second excitations during the glottal cycle, which were not apparent for all speakers. The ratings of high-frequency noise in the waveform in particular were affected, and the first-formant bandwidth estimates may also have been affected. The evidence for these secondary excitations on the speech waveform is hypothesized to be greatest for speakers with wide formant bandwidths. Therefore, some care must be taken when interpreting the acoustic measures.

Because the data illustrate normal variation of the source spectrum characteristics among individual speakers, and between males and females, they may be useful for applications such as speech synthesis, speech recognition, and speaker recognition. In addition, they may be used clinically, for example, to assess potential voice dysfunction or monitor remediation.

ACKNOWLEDGMENTS

This work was supported by Research Grants Nos. DC00075 and 1 F32 DC 00205-02 from the National Institute on Deafness and Other Communicative Disorders, National Institutes of Health. We are grateful to Kenneth N. Stevens and Eva Holmberg for their careful readings of an earlier version of the manuscript. Special thanks to Ken Stevens for help in working through the theoretical issues involved in comparing male and female acoustic measures. The comments and suggestions of Anders Löfqvist, Ronald C. Scherer, and an anonymous reviewer are also greatly appreciated.

Atal, B. S., and Remde, J. R. (**1982**). ''A new model of LPC excitation for producing natural-sounding speech at low bit rates,'' In Proceedings of the IEEE ICASSP '82, Paris, France, pp. 614–617.

Childers, D. G., and Wu, K. (**1991**). ''Gender recognition from speech. Part II: Fine analysis,'' J. Acoust. Soc. Am. **90**, 1841–1856.

Fant, G. (**1972**). ''Vocal tract wall effects, losses, and resonance bandwidths,'' Speech Trans. Lab. Q. Prog. Stat. Report 2–3, Royal Institute of Technology, Stockholm, pp. 28–52.

Fant, G. (**1995**). ''The LF-model revisited. Transformations and frequency domain analysis,'' Speech Trans. Lab. Q. Prog. Stat. Report 2–3, Royal Institute of Technology, Stockholm, pp. 119–156.

Fujimura, O., and Lindqvist, J. (**1971**). ''Sweep-tone measurements of vocal-tract characteristics,'' J. Acoust. Soc. Am. **49**, 541–558.

Hanson, H. M. (**1995a**). ''Glottal characteristics of female speakers,'' Ph.D. thesis, Harvard University, Cambridge, MA.

Hanson, H. M. (**1995b**). ''Synthesis of female speech using the Klatt synthesizer,'' Speech Communication Group Working Papers 10, Research Laboratory of Electronics, M.I.T., pp. 84–103.

Hanson, H. M. (**1997**). ''Glottal characteristics of female speakers: Acoustic correlates,'' J. Acoust. Soc. Am. **101**, 466–481.

Henton, C. G., and Bladon, R. A. W. (**1985**). ''Breathiness in normal female speech: Inefficiency versus desirability,'' Lang. Commun. **5**, 221–227.

Holmberg, E. B., Hillman, R. E., and Perkell, J. S. (**1988**). ''Glottal airflow and transglottal air pressure measurements for male and female speakers in soft, normal and loud voice,'' J. Acoust. Soc. Am. **84**, 511–529. Plus Erratum, *ibid.* **85**, 1787.

Holmberg, E. B., Hillman, R. E., and Perkell, J. S. (**1989**). ''Glottal airflow and transglottal air pressure measurements for male and female speakers in low, normal, and high pitch,'' J. Voice **4**, 294–305.

Holmberg, E. B., Hillman, R. E., Perkell, J. S., Guiod, P., and Goldman, S. L. (**1995**). ''Comparisons among aerodynamic, electroglottographic, and acoustic spectral measures of female voice,'' J. Speech Hear. Res. **38**, 1212–1223.

House, A. S., and Stevens, K. N. (**1958**). ''Estimation of formant band widths from measurements of transient response of the vocal tract,'' J. Speech Hear. Res. **1**, 309–315.

Karlsson, I. (**1992a**). ''Analysis and synthesis of different voices with emphasis on female speech,'' Ph.D. thesis, Royal Institute of Technology, Stockholm.

Karlsson, I. (**1992b**). ''Evaluations of acoustic differences between male and female voices: A pilot study,'' Speech Trans. Lab. Q. Prog. Stat. Report 1, Royal Institute of Technology, Stockholm, pp. 19–31.

Klatt, D., and Klatt, L. (**1990**). ''Analysis, synthesis, and perception of voice quality variations among female and male talkers,'' J. Acoust. Soc. Am. **87**, 820–857.

Perkell, J. S., Hillman, R. E., and Holmberg, E. B. (**1994**). ''Group differences in measures of voice production and revised values of maximum airflow declination rate,'' J. Acoust. Soc. Am. **96**, 695–698.

Södersten, M., and Lindestad, P.-Å. (**1990**). ''Glottal closure and perceived breathiness during phonation in normally speaking subjects,'' J. Speech Hear. Res. **33**, 601–611.

Stevens, K. N. (**1998**). *Acoustic Phonetics* (MIT Press, Cambridge, MA).

Titze, I. R., (**1989**). ''Physiologic and acoustic differences between male and female voices,'' J. Acoust. Soc. Am. **85**, 1699–1707.

Cortical auditory evoked potential correlates of categorical perception of voice-onset time

Anu Sharma[a] and Michael F. Dorman
Department of Speech and Hearing Science, Arizona State University, Tempe, Arizona 85287-0102

(Received 24 September 1998; revised 15 February 1999; accepted 6 April 1999)

The goal of this study was to examine the neural encoding of voice-onset time distinctions that indicate the phonetic categories /da/ and /ta/ for human listeners. Cortical Auditory Evoked Potentials (CAEP) were measured in conjunction with behavioral perception of a /da/-/ta/ continuum. Sixteen subjects participated in identification and discrimination experiments. A sharp category boundary was revealed between /da/ and /ta/ around the same location for all listeners. Subjects' discrimination of a VOT change of equal magnitude was significantly more accurate across the /da/-/ta/ categories than within the /ta/ category. Neurophysiologic correlates of VOT encoding were investigated using the N1 CAEP which reflects sensory encoding of stimulus features and the MMN CAEP which reflects sensory discrimination. The MMN elicited by the across-category pair was larger and more robust than the MMN which occurred in response to the within-category pair. Distinct changes in N1 morphology were related to VOT encoding. For stimuli that were behaviorally identified as /da/, a single negativity (N1) was apparent; however, for stimuli identified as /ta/, two distinct negativities (N1 and N1′) were apparent. Thus the enhanced MMN responses and the morphological discontinuity in N1 morphology observed in the region of the /da/-/ta/ phonetic boundary appear to provide neurophysiologic correlates of categorical perception for VOT. © *1999 Acoustical Society of America.* [S0001-4966(99)05407-7]

PACS numbers: 43.71.Es, 43.71.An, 43.64.Qh [JH]

INTRODUCTION

Many studies beginning with Liberman *et al.* (1961) have documented that when listeners are asked to identify and discriminate stimuli that vary in voice-onset time (VOT) the discrimination results can be predicted on the basis of the identification functions. That is, listeners are better able to discriminate between sounds which have been identified as belonging to different phonetic categories than between sounds which have been identified as belonging to the same phonetic category. This outcome has been labeled ''categorical perception.'' Early theoretical accounts of this nonmonotonic perceptual acuity suggested that it might be a unique capacity for the purpose of language processing (e.g., Studdert-Kennedy *et al.*, 1970; Studdert-Kennedy, 1982). However, subsequent psychophysical studies in humans (e.g., Pisoni, 1977; Soli, 1983; Kewley-Port *et al.*, 1988) and animals (e.g., Kuhl and Miller, 1975, 1978) have suggested that the nonmonotonic perceptual acuity may be a reflection of more general auditory processing capabilities of the mammalian auditory system.

Recent experiments have described the neural encoding of VOT. In a series of papers, Sinex and colleagues (Sinex and McDonald, 1989; Sinex *et al.*, 1991; Sinex, 1993; Sinex and Narayan, 1994) have reported extensively on the neural encoding of VOT by fibers in the auditory nerve of the chinchilla. For example, Sinex *et al.* (1991) measured, in auditory nerve fibers, discharge rates and response latencies elicited by stimuli from a /da/-/ta/ continuum. Responses elicited by stimuli with the shortest and longest VOTs (0–20 ms and 60–80 ms, respectively) were smaller and highly variable across groups of neurons with similar characteristic frequencies. On the other hand, for stimuli from the middle of the continuum, responses were larger and response latencies were more synchronous across the same group of neurons. That is, the magnitude and temporal variability of primary auditory nerve neurons varied nonmonotonically such that the neural encoding of acoustic features was more ''salient'' in the middle of the VOT continuum (i.e., in the region of the perceptual boundary between /da/ and /ta/ for human listeners). Sinex *et al.* (1991) suggested that the latencies were more synchronous for syllables from the middle of the continuum largely because the onset of voicing produced abrupt increases in amplitude which occurred at about the same time across several frequency bands. For shorter and longer VOTs, amplitude change was gradual and occurred at different times in different frequency bands; each of these factors increased the variability of the neural responses. Based on these findings, Sinex *et al.* (1991) proposed that variability across neurons is the equivalent of ''noise'' in the representation of the stimulus. Stimuli which elicit synchronous responses across a population of neurons are encoded with a greater ''signal-to-noise ratio,'' and may be recognized as an important event by the central nervous system than stimuli which elicit less synchronous responses across neural populations. Given this hypothesis, it is of interest to see whether the nonmonotonic neural representation of VOT reported by Sinex and colleagues at the level of the auditory nerve is observed at more central levels of the auditory system.

The purpose of this study was to examine neural correlates of VOT perception at the level of the auditory cortex in human listeners. We measured the N1 and MMN Cortical

[a]Electronic mail: anu.sharma@asu.edu

Auditory Evoked Potentials (CAEP) in conjunction with behavioral testing using the /da/-/ta/ continuum used by Sinex *et al.* (1991). The N1 is an obligatory evoked response which reflects *sensory encoding* of auditory stimulus attributes (Nätäänen and Picton, 1987), while the mismatch negativity (MMN) evoked response is elicited by acoustic changes and is a measure of *sensory discrimination* (Nätäänen, 1992). The N1 and MMN are considered indices of sensory or preattentive processing since they can be recorded without active participation from subjects, whose attention is actively directed away from the eliciting stimuli by having them read or watch a movie. Primary generator sites for the N1 and MMN include the auditory cortical and thalamic areas (Nätäänen and Picton, 1987; Csepe, 1995).

The MMN can be elicited in response to various attributes of the speech signal including changes in the starting frequencies and direction of second and third formant transitions and in steady state formant frequencies (Aaltonen *et al.*, 1987; Sams *et al.*, 1990; Sharma *et al.*, 1993; Maiste *et al.*, 1995). These studies have all demonstrated equally robust MMNs for within-category and across-category phonetic contrasts. In light of these data, and given the findings of Sinex *et al.* (1991) showing that neural encoding across VOT categories is enhanced relative to within a category, it is of interest to see if the MMN elicited by VOT contrasts will be equally robust within- and across-categories.

I. BEHAVIORAL EXPERIMENT

A. Method

1. Subjects

Sixteen adults (11 females and 5 males) ranging in age from 20 to 30 years (mean age 26 years) were paid $5/h for their participation in this experiment. All were native speakers of English, who reported no history of speech or hearing disorders.

2. Stimuli

The stimulus continuum was identical to the one used by Sinex *et al.* (1991). The continuum consisted of nine tokens varying from /da/ to /ta/. In each syllable, a brief (10-ms) burst of friction noise was present at syllable onset. From syllable onset to $F1$ onset, the higher formants ($F2$ to $F5$) were excited using aspiration noise. This aspirated interval corresponded to the VOT which was varied from 0 to 80 ms in 10-ms steps. The center frequency of $F1$ was 155 Hz for the first 10 ms of the syllable, increased to 270 Hz at 15 ms, and then increased linearly to its steady state value of 770 Hz at 65 ms. $F2$ and $F3$ decreased from 1550 to 1200 Hz and 3700 to 2200 Hz over a transition duration of 65 ms. Each syllable had a fundamental frequency of 114 Hz and an overall duration of 200 ms. The stimuli were equated in intensity and presented to the subjects at 75 dB SPL, binaurally through headphones.

3. Procedures

In the identification portion of the experiment, subjects were asked to listen to the sounds through headphones and to classify each sound either as a /da/ or a /ta/. Subjects were asked to indicate their responses by clicking with the mouse on panels marked DA and TA appearing on the computer screen. Each subject was given an initial practice session where he or she heard each stimulus along the continuum once. After that, ten repetitions of each of the nine stimuli were presented to the subject in a random order.

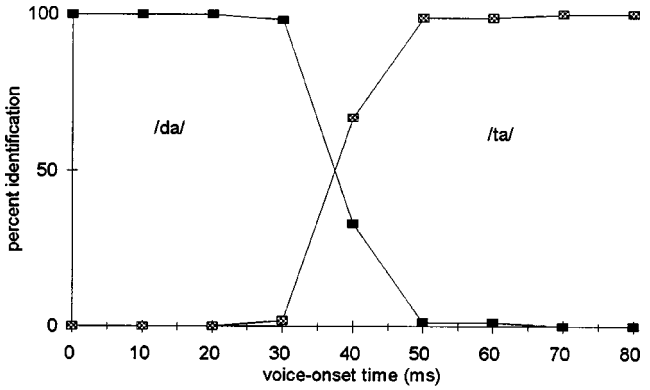

FIG. 1. Mean identification functions for the /da/-/ta/ continuum. Stimuli with VOTs of 0–30 ms were identified as /da/, while stimuli with VOTs of 60–80 ms were identified as /ta/. A sharp category boundary between /da/ and /ta/ was observed at VOT of 40 ms.

Following the identification task, subjects participated in a discrimination task. To anticipate the results of the identification experiment, the stimulus pairs in the discrimination task will be referred to as the across-category pair (30–50 ms VOT) and within-category pair (60–80 ms VOT), respectively. An AX discrimination task was employed. On each trial, subjects heard two stimuli with an interstimulus interval (ISI) of 500 ms. Subjects were asked to determine whether the stimuli in the pair were ''same'' or ''different.'' Subjects indicated their responses by clicking on panels labeled ''same'' or ''different'' on the computer screen. The presentation of stimulus pairs was randomized within the test and across subjects. To familiarize the subjects with the task, an initial practice session of 20 trials was presented (10 same and 10 different trials). The experimental session consisted of a total of 100 trials (50 same and 50 different) for each stimulus pair.

B. Results

For the behavioral identification experiment, responses to each of the nine tokens in the continuum were collapsed across subjects. The group means for each token are shown in Fig. 1. Stimuli with VOT of 0–30 ms were identified consistently as /da/ while stimuli with VOT of 50–80 ms were consistently identified as /ta/. The 40-ms VOT stimulus was identified as either sound approximately half of the time.

The mean discrimination scores for the 30–50 and 60–80 stimulus pairs are illustrated in Fig. 2. As expected, a paired *t*-test revealed that subjects' discrimination of the stimuli in the across-category stimulus (30–50) pair was significantly more accurate than their discrimination of stimuli in the within-category (60–80) pair ($t=20$; $df15$; $p<0.0001$). That is, subjects' discrimination of a VOT change of equal magnitude was better across the /da/-/ta/

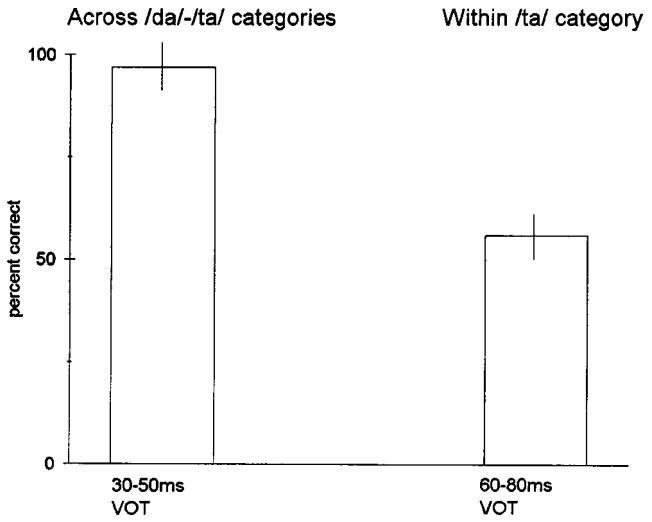

FIG. 2. Mean scores for the discrimination experiment. Subjects were significantly better at discriminating the 30–50 VOT pair compared to the 60–80 VOT pair ($p<0.0001$). Error bars indicate ± 1 standard error.

categories than within the /ta/ category. Overall, the identification and discrimination results are consistent with previous reports (see Harnad, 1987, for a review).

II. ELECTROPHYSIOLOGIC EXPERIMENT

A. Method

1. Subjects

MMN recordings were obtained in the same 16 subjects used in the behavioral experiment. Nine of those subjects (6 female and 3 male) ranging in age from 22 to 26 years (mean age 23 years) returned for a separate session of N1 recordings. During MMN and N1 recording sessions subjects' were seated comfortably in a sound booth. To control for arousal and to minimize subjects' attention to the test stimuli, subjects watched a videotaped movie of their choice. Videotape audio levels were kept below 40 dB SPL. Subjects were asked to ignore the stimuli that were presented through an insert earphones at 75 dB SPL in the right ear.

2. Stimuli

a. MMN. For the MMN recordings, the stimulus pairs were the same as those used in the behavioral discrimination experiment, i.e., the across-category (30–50 ms VOT) pair and the within-category (60–80 ms VOT) pair. The MMN was elicited using an oddball paradigm in which repetitive presentations of a ''standard'' stimulus were occasionally replaced with a ''deviant'' or ''target'' stimulus. The deviant stimulus had a probability of occurrence of 15%. For the across-category pair, the 30-ms VOT stimulus was the standard and the 50-ms VOT stimulus was the deviant. For the within-category pair, the 60-ms VOT stimulus was the standard and the 80-ms VOT stimulus was the deviant. The stimuli were presented at an offset-to-onset ISI of 510 ms. The order of the presentation of stimulus pairs was counterbalanced across subjects.

b. N1. The stimulus continuum was identical to the one used in the behavioral identification experiment. Repeated presentations of each stimulus separated by an onset-to-offset ISI of 800 ms were used to elicit the N1. The order of presentation of stimuli was counterbalanced across subjects.

3. Recording procedures

MMN and N1 evoked potentials were recorded using a NeuroScan Inc. data acquisition system. Silver-chloride electrodes were placed on the midline (Fz, Cz, and Pz). The reference electrode was placed on the right mastoid and the ground electrode was placed on the forehead. Eye movements were monitored with a bipolar electrode montage (supraorbital to lateral canthus). Averaging was suspended when the eye channel registered blinks. The recording window included a 100-ms pre-stimulus period and 500 ms of post-stimulus time. Evoked responses were bandpass filtered on-line from 0.1 to 100 Hz. Responses that were judged noisy or that were greater than 100 μV were rejected offline.

a. MMN. In the oddball paradigm, 2000 sweeps of the response to the standard and 300 sweeps of the response to the deviant stimulus were collected. By definition, the MMN is a response to stimulus change and occurs only when the deviant stimulus is presented in the context of a sequence of standard stimuli. A control condition was employed to en-

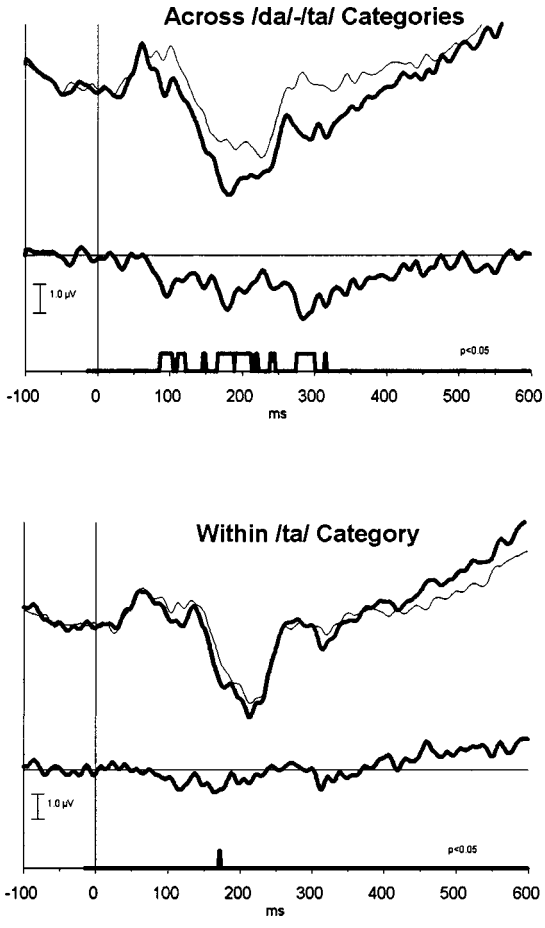

FIG. 3. Grand-averaged responses at the Fz scalp location in the across- and within-category stimulus conditions. The top thin line is the response to the deviant stimulus when it was presented alone. The thick line is the response to the deviant stimulus when it occurred in the mismatch condition. The MMN response is seen in the difference wave (lower thick line) as a negativity. The boxes on the *x*-axis indicate the region of a significant mismatch response ($p<0.05$).

sure that the response reflects a change as opposed to reflecting simply the stimulus difference between the standard stimulus and the deviant stimulus. In this condition, the response which occurred to the deviant stimulus in the oddball paradigm was compared to the response evoked by the same stimulus when it was presented alone. If a MMN is present, a relative negativity will be apparent only in the response elicited in the context of the oddball paradigm and not when the deviant stimulus was presented alone (Kraus *et al.*, 1995).

b. N1. For the N1 recordings, 300 sweeps elicited in response to each stimulus from the /da/-/ta/ continuum were collected.

4. Data analysis

a. MMN. For individual subjects, sweeps were averaged to compute an individual average waveform elicited by the deviant stimulus when it occurred in the context of the standard stimulus (i.e., in the oddball paradigm) and by the deviant stimulus when it was presented alone. A ''difference wave'' was computed by subtracting the response to the deviant stimulus from the deviant-alone stimulus presentation. In individual subjects, the morphologies of the alone, deviant, and difference waves were assessed relative to previously described morphologies of speech-evoked potentials (Kraus *et al.*, 1992). In individual subjects, the MMN was apparent in the difference waveform while the N1 was apparent in the alone and deviant waveforms. The MMN was identified visually as a relative negativity following the N1 peak. The point of maximum negativity of the MMN component was noted and the adjacent relative positive peaks were selected as the MMN onset and offset. To determine the area of the MMN, a line was drawn from the onset to the offset of the MMN in the difference wave. The area was defined as a summation of the point by point multiplication ($\text{ms}\times\mu\text{V}$) of the enclosed difference wave. The area of the MMN was computed for individual subjects from the Fz electrode since the most robust MMNs were observed at that electrode site.

Group averaged difference waves were computed by averaging individual subject difference waves. A point-to-point *t*-test of the values contributing to the group averaged difference waveform determined the period over which the grand averages were significantly different from zero at the $p<0.05$ level. A significant negativity in the mean difference wave was defined as the group MMN. The disadvantage of this analysis is that the number of *t*-tests performed and the high correlation between adjacent points on a waveform increases chances of spurious significant values. To counter this difficulty Gutherie and Buchwald (1991), based on multiple regression techniques on P300 waveforms, concluded that if a continuous interval of at least 12 sampling points shows significance then the power of the statistical test is sufficient. Because the A/D sampling rates and filter settings for the MMN are essentially similar to the P300, a similar significance interval should give appropriate statistical power (Kraus *et al.*, 1995; McGee *et al.*, 1997).

b. N1. For individual subjects, sweeps were averaged to compute an individual average waveform. All waveforms were digitally high pass filtered off-line at 4 Hz (filter slope 12 dB/octave). In the group mean waveforms, N1 was identified visually as a prominent negative peak within the first half of the time window. In order to aid in peak identification and measurement in data from individual subjects, response windows of +25 ms were created around the peak in the group mean waveforms. Peak latencies were detected based on the recordings from the electrode site Cz, where the response amplitudes were the largest in the group mean waveforms. The latency was typically marked at the center. When the waveform contained a double peak within the defined time frame (e.g., for waveforms of VOT 50–80 ms), the latency was measured at the center of each peak. Group averaged waveforms were computed by averaging across the individual average waveforms.

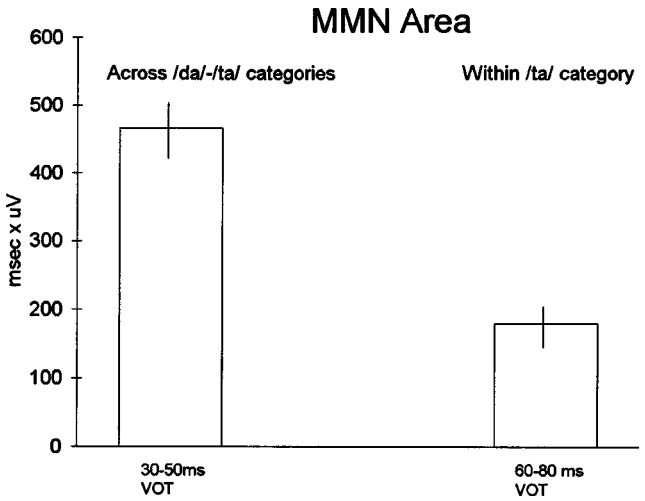

FIG. 4. Mean MMN area values. MMN area was significantly larger in the across-category condition compared to the within-category condition ($p<0.05$). Error bars indicate ± 1 standard error.

B. Results

1. MMN

The group averaged waveforms in the within- and across-category conditions are shown in Fig. 3. A robust MMN was obtained in the across-category condition. A minimal MMN was obtained in the within-category condition. Mean values for MMN area are shown in Fig. 4. A repeated-measures *t*-test revealed that MMN area was significantly larger in the across-category stimulus pair (i.e., 30–50 ms VOT) compared to the within-category stimulus pair (i.e., 60–80 ms VOT) ($t=4.06$, $df=15$; $p<0.001$).

Overall, the results obtained in the neurophysiologic discrimination (i.e., MMN) experiment complement the results of the behavioral discrimination experiment. That is, a significant MMN was elicited by the across-category stimulus pair, consistent with the excellent behavioral discrimination of the pair, while a significantly smaller MMN was elicited by the within-category stimulus contrast, consistent with its relatively poorer behavioral discrimination.

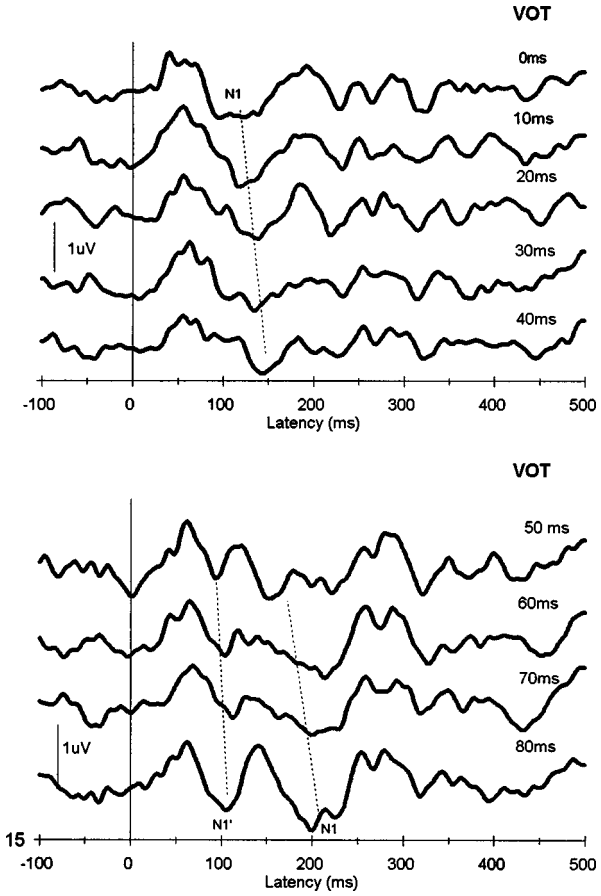

FIG. 5. Grand-averaged N1 responses elicited by stimuli in the /da/-/ta/ continuum. Stimuli with VOTs of less than 50 ms showed a single negativity (N1), while stimuli with VOTs of 50 ms and more showed two distinct negative components (N1′ and N1) indicated by the dashed lines.

2. N1

The group averaged waveforms elicited in response to stimuli from the VOT continuum are shown in Fig. 5. Distinct morphological changes related to encoding of VOT are seen in the AEP waveforms. For stimuli with short VOTs (0–30 ms), a single negativity was apparent. However, for stimuli with long VOTs (50–80 ms) two distinct negative components (N1′ and N1) were apparent. Thus stimuli that were behaviorally identified as /da/ were characterized by a single N1 component; in contrast, stimuli that were behaviorally identified as /ta/ were characterized by two distinct N1 components. These data demonstrate a discontinuity in morphology of the AEP waveform in the region of the boundary between perceptual categories /da/ and /ta/.

As pointed out in the stimulus description section, each stimulus began with a 10-ms burst. Given the time frame of the N1′ peak latency and given that it did not show a significant correlation with VOT ($r=0.03$; $p>0.8$), it would appear that this component occurred in response to the burst at syllable onset. On the other hand, the peak latency of the N1 component demonstrated a high positive correlation with VOT ($r=0.84$; $p<0.0001$), suggesting that this component occurs in response to the onset of voicing in the syllables.

III. GENERAL DISCUSSION

The results of the MMN experiment demonstrate a neurophysiologic correlate of the enhanced behavioral discrimination across the /da/-/ta/ phonetic boundary. That is, the MMN elicited by a 20-ms change in VOT was larger and more robust when the stimuli which elicited the MMN were identified as belonging to different phonetic categories (30 vs 50 ms VOT) than when the stimuli in the pair were identified as belonging to the same phonetic category (60 vs 80 ms VOT). It is useful to interpret these results in light of the results reported by Sinex *et al.* (1991) who examined in chinchillas the peripheral neural encoding of stimuli used in the present experiment. Sinex *et al.* (1991) found that stimuli with 30–50 ms VOTs elicited responses which were more synchronous than stimuli with VOTs between 60 and 80 ms. That is, there was less variability in the time of onset of neural discharges relative to the onset of voicing for stimuli with 30- and 50-ms VOTs than for stimuli with 60- and 80-ms VOTs. The better encoding of the time of onset for stimuli with 30- and 50-ms VOTs can account for the ease with which humans and chinchillas discriminate stimuli with 30- and 50-ms VOTs relative to stimuli with 60- and 80-ms VOTs. The finding from the present experiment, of a large MMN in response to a change from 30- to 50-ms VOT and a virtually nonexistent MMN to a change from 60- to 80-ms VOT, can be accommodated by the view that the more precise encoding of the 30- and 50-ms VOTs enables the thalamic and/or cortical ''comparitor mechanism'' which underlies the MMN to better see a difference between stimuli with 30- and 50-ms VOTs than between stimuli with 60- and 80-ms VOTs. Thus the relatively poor within-category discrimination for VOT arises at a sensory level of signal encoding.

The results of the present experiment stand in contrast to the results of other experiments in which the MMN has been recorded in response to across- and within-phonetic category changes in stimulation. Sams *et al.* (1990), Sharma *et al.* (1993), and Maiste *et al.* (1995) all reported that the MMN was as large to a within-category change of stimulation as to a between-category change of stimulation when the stimuli differed in place of articulation (i.e., the onset frequency and direction of $F2$ and $F3$ transitions). If we adopt the account taken in the previous paragraph, then we should suppose that, unlike VOT, differences in onset frequencies of $F2$ and $F3$ are equally well encoded by the peripheral auditory system and thus allow the thalamic and cortical ''comparitors'' to see, equally well, differences in between- and within-phonetic-category stimulation. The poor within category discrimination of stimuli which vary in $F2/F3$ onset frequency, therefore, arise from processes ''higher'' than sensory encoding.

The present study did not test contrasts on the short-lag end of the VOT continuum, where $F1$ typically varies to a greater extent than on the long-lag end of the continuum. It remains to be seen if the MMN elicited by within-category contrast on the short-lag end of a VOT continuum is more similar to the MMN elicited by within-category, long-lag contrasts, or to a MMN elicited by within-category changes in $F2/F3$ onset frequency.

The results of the N1 experiment revealed that sounds that were identified as belonging to different phonetic categories showed distinct waveform morphology. A single N1

component was observed for sounds that were behaviorally perceived as /da/. Two clearly defined components (N1′ and N1) were observed for stimuli perceived as /ta/. Latency of these components suggest that N1′ occurred in response to the burst at syllable onset, while N1 was elicited by onset of voicing. The two peaks were clearly apparent when the temporal spacing between the burst and voice-onset was 50 ms which is also the VOT value at which listeners' identification of sounds changed to /ta/. These data are consistent with previous reports of double-peaked responses (Kaukoranta *et al.*, 1987; Stienschnieder *et al.*, 1994, 1995; Eggermont *et al.*, 1995; McGee *et al.*, 1996) and other nonmonotonic evoked responses elicited by VOT stimuli (e.g., Molfese and Molfese, 1979; Adams *et al.*, 1987; Morse *et al.*, 1987). Examining multiple unit activity recorded from the auditory cortex of awake monkeys, Steinschnieder *et al.* (1994, 1995) found that /da/ syllables (VOT=0 and 20 ms) elicited essentially a ''single on'' response, while /ta/ syllables (VOT =40 and 60) elicited a clearly apparent ''double on'' response. McGee *et al.* (1996) examined averaged evoked potentials recordings from the scalp surface of anesthesized guinea pigs in response to /ba/ and /pa/ syllables. They found that the /ba/ syllable (VOT=10 ms) elicited a single-peaked component while the /pa/ syllables (VOTs=20,30,40) elicited double-peaked responses. Obviously any comparison of our results to results of these two studies is complicated by differences in recording methods, species, stimuli, and state. However, it is interesting to note that in those studies and in the present one, the appearance of a clearly apparent double-peaked response coincided with a stimulus identified as ''voiceless.'' Further studies are needed to determine if the change in AEP waveform from single- to double-peaked actually predicts a change in perceptual categories.

In conclusion, the enhanced MMN responses and the discontinuity in N1 morphology observed in the region of the /da/-/ta/ phonetic boundary appear to provide neurophysiologic correlates of the nonmonotonic perceptual acuity for VOT. Future studies will determine whether similar physiologic correlates exist for the categorical perception of other phonetic contrasts.

Aaltonen, O., Niemi, P., Nyrke, T., and Tuhkanen, M. (**1987**). ''Event-related brain potentials and the perception of a phonetic continuum,'' Biol. Psychol. **24**, 197–207.

Adams, C., Molfese, D., and Betz, J. (**1987**). ''Electrophysiological correlates of categorical speech perception for voicing contrasts in dogs,'' Dev. Neuropsychol, **3**, 175–189.

Csepe, V. (**1995**). ''On the origin and development of the Mismatch Negativity,'' Ear Hear. **16**, 91–104.

Eggermont, J. (**1995**). ''Representation of a voice-onset time continuum in primary auditory cortex of the cat.'' J. Acoust. Soc. Am. **98**, 911–920.

Gutherie, D., and Buchwald, J. (**1991**). ''Significance of testing difference potentials,'' Psychophysiology **28**, 240–244.

Harnad, S. (**1987**). *Categorical Perception* (Cambridge University Press, Cambridge).

Kaukaranta, E., Hari, R., and Lounasmaa, O. (**1987**). ''Responses of the human auditory cortex to vowel onset after fricative consonants,'' Exp. Brain Res. **69**, 19–23.

Kewley-Port, D., Watson, C., and Foyle, D. (**1988**). ''Auditory temporal acuity in relation to category boundaries: Speech and nonspeech stimuli,'' J. Acoust. Soc. Am. **69**, 1133–1145.

Kraus, N., McGee, T., Sharma, A., and Carrell, T. (**1995**). ''Neurophysiologic bases of speech discrimination,'' Ear Hear. **16**, 19–37.

Kraus, N., McGee, T., Sharma, A., Carrell, T., and Nicol, T. (**1992**). ''Mismatch negativity event-related potential elicited by speech stimuli,'' Ear Hear. **13**, 158–164.

Kuhl, P., and Miller, J. (**1975**). ''Speech perception by the chinchilla: Voiced–voiceless distinction in alveolar plosive consonants,'' Science **190**, 69–72.

Kuhl, P., and Miller, J. (**1978**). ''Speech perception by the chinchilla: Identification functions for synthetic VOT stimuli,'' J. Acoust. Soc. Am. **63**, 905–917.

Liberman, A. M., Harris, K. S., Kinney, J. A., and Lane, H. (**1961**). ''The discrimination of relative onset-time of components of certain speech and non-speech patterns,'' J. Exp. Psychol. **61**, 379.

Maiste, A., Wiens, A., Hunt, M., and Picton, T. (**1995**). ''Event-related potentials and the categorical perception of speech sounds,'' Ear Hear. **16**, 68–90.

McGee, T., Kraus, N., and Nicol, T. (**1997**). ''Is there really a mismatch negativity? An assessment of methods for determining response validity in individual subjects,'' Electroencephalogr. Clin. Neurophysiol. **104**, 359–368.

McGee, T., Kraus, N., Nicol, T., and Carrell, T. (**1996**). ''Acoustic elements of speech-like stimuli are reflected in surface recorded responses over the guinea pig temporal lobe,'' J. Acoust. Soc. Am. **99**, 3606–3614.

Mofese, D., and Molfese, V. (**1979**). ''VOT distinctions in infants: Learned or innate?,'' in *Studies in Neurolinguistics*, edited by H. A. Whitaker and H. Whitaker (Academic, New York).

Morse, P., Molfese, D., Burger-Judisch, L., and Hans, L. (**1987**). ''Categorical perception for voicing contrasts in normal and lead-treated Rhesus monkeys: Electrophysiological correlates,'' Brain. Lang. **30**, 63–80.

Nätäänen, R. (**1992**). *Attention and Brain Function* (Erlbaum, Hillsdale, NJ).

Nätäänen, R., and Picton, T. (**1987**). ''The N1 wave of the human electric and magnetic response to sound: A review and analysis of the component structure.'' Psychophysiology **24**, 375–425.

Pisoni, D. (**1977**). ''Identification and discrimination of the relative onset of two tone components: Implications for voicing perception in stops,'' J. Acoust. Soc. Am. **61**, 1352–1361.

Sams, M., Aulanko, R., Aaltonen, O., and Nätäänen, R. (**1990**). ''Event-related potentials to infrequent changes in synthesized phonetic stimuli,'' J. Cognitive Neuroscience **2**, 344–357.

Sharma, A., Kraus, N., McGee, T., Carrell, T., and Nicol, T. (**1993**). ''Acoustic versus phonetic representation of speech as reflected by the mismatch negativity event-related potential,'' Electroencephalogr. Clin. Neurophysiol. **88**, 64–71.

Sinex, D. (**1993**). ''Simulation of neural responses that underlie speech discrimination,'' in *Neural Systems: Analysis and Modeling*, edited by F. Eeckman (Kluwer Academic, Norwell, MA), pp. 307–313.

Sinex, D., and McDonald, L. (**1989**). ''Synchronized discharge rate representation of voice-onset time in the chinchilla auditory nerve,'' J. Acoust. Soc. Am. **85**, 1995–2004.

Sinex, D., and Narayan, S. (**1994**). ''Auditory-nerve fiber representation of temporal cues to voicing in word-medial stop consonants,'' J. Acoust. Soc. Am. **95**, 897–903.

Sinex, D., McDonald, L., and Mott, J. B. (**1991**). ''Neural correlates of nonmonotonic temporal acuity for voice-onset time,'' J. Acoust. Soc. Am. **90**, 2441–2449.

Soli, S. (**1983**). ''The role of spectral differences in the discrimination of voice-onset time differences,'' J. Acoust. Soc. Am. **73**, 2150–2165.

Steinschneider, M., Schroeder, C. E., Arezzo, J. C., and Vaughan, Jr., H. G. (**1994**). ''Speech-evoked activity in primary auditory cortex: Effects of voice onset time,'' Electroencephalogr. Clin. Neurophysiol. **92**, 30–43.

Steinschneider, M., Schroeder, C., Arezzo, J., and Vaughan, Jr., H. (**1995**). ''Physiological correlates of the voice onset time boundary in the primary auditory cortex (*A*1) of the awake monkey: Temporal response pattern,'' Brain. Lang. **48**, 326–340.

Studdert-Kennedy, M. (**1982**). ''On the dissociation of the auditory and phonetic perception,'' in *The Representation of Speech in the Peripheral Auditory System*, edited by R. Carlson and B. Granstrom (Elsevier, Amsterdam), pp. 9–26.

Studdert-Kennedy, M., Liberman, A., Harris, K. S., and Cooper, F. (**1970**). ''Motor theory of speech perception: A reply to Lane's critical review,'' Psychol. Rev. **77**, 234–249.

Acquisition of a tactile-alone vocabulary by normally hearing users of the Tickle Talker™

Karyn L. Galvin
CRC for Cochlear Implant, Speech and Hearing Research, and The Bionic Ear Institute, 384-388 Albert Street, East Melbourne 3002, Australia

Peter J. Blamey and Michael Oerlemans
Department of Otolaryngology, University of Melbourne, 2nd floor, RVEEH, 32 Gisborne Street, East Melbourne 3002, Australia

Robert S. C. Cowan and Graeme M. Clark
CRC for Cochlear Implant, Speech and Hearing Research, and The Bionic Ear Institute, 384-388 Albert Street and Department of Otolaryngology, University of Melbourne, 2nd floor, RVEEH, 32 Gisborne Street, East Melbourne 3002, Australia

(Received 15 August 1997; accepted for publication 8 February 1999)

Tactile-alone word recognition training was provided to six normally hearing users of the Tickle Talker™, an electrotactile speech perception device. A mean group tactile-alone vocabulary of 31 words was learned in 12 h of training. These results were comparable to, or superior to, those reported for other tactile devices and Tadoma. With increased training the group became faster at learning tactually new words, which were introduced in small training sets. However, as their tactile-alone vocabulary grew, subjects required more training time to reach the pass criterion when evaluated on their recognition of their whole vocabulary list. A maximum possible vocabulary size was not established. The application of tactile-alone training with hearing-impaired users of the device is discussed. © *1999 Acoustical Society of America.* [S0001-4966(99)01108-X]

PACS numbers: 43.71.Ma, 43.66.Ts, 43.66.Wv, 43.70.Lw [WS]

INTRODUCTION

Tactile devices have been developed to improve the communication of the hearing-impaired by presenting speech information to supplement auditory and visual information. Electrotactile devices present information to the user via electrocutaneous stimulation, while vibrotactile devices use vibrators to present information to the skin via transient tissue deformation or pressure change. In processing the input signal prior to presentation to the user, devices employ either a feature-extraction or bandpass filter approach. With the feature-extraction approach, particular features of the speech, considered important for speech understanding, are extracted from the signal and presented to the user. In the bandpass filter, or vocoder, approach, the input signal is filtered into a number of bands, with each band corresponding to a particular tactile transducer. The Tickle Talker™ is a wearable electrotactile device which implements a feature-extraction speech processing strategy. Results have been reported for adults and children who have used the device to supplement visual and auditory information (Cowan *et al.*, 1989a, 1990). Tactile-alone perception with the Tickle Talker™ has been given limited consideration, with evaluations confined to closed-set assessment of suprasegmental and segmental speech feature perception (Blamey *et al.*, 1988; Cowan *et al.*, 1989b). This emphasis on the provision of supplementary speech information is consistent with the focus of most other investigations of speech perception using tactile information. However, the Tadoma method of communication has provided evidence that speech can be understood using only tactile information (Reed, 1995). Tadoma users place their fingers across the lips and face of the talker to obtain information about such aspects of speech as breath flow, jaw movement, and voicing. Experienced deaf–blind users can track running speech at 30–40 words per min (Reed, 1995). Although no study has attempted to emulate this performance using a tactile device alone, a number of researchers have investigated the tactile-alone perception of isolated words and short sentences using various vibrotactile vocoders (Brooks, 1984; Brooks and Frost, 1983; Brooks *et al.*, 1985; Engelmann and Rosov, 1975; Lynch *et al.*, 1988, 1989). Table I presents details of these studies and the mean group results achieved.

Brooks and Frost (1983) trained tactile-alone word recognition to establish what speech information was provided by the Queen's University vocoder. One subject learned to recognize 70 words in 40.5 h of training. The second subject learned 150 words in the first 55 h of training, and a further 100 words in the next 25.5 h (Brooks *et al.*, 1985). Engelmann and Rosov's (1975) study aimed to demonstrate that extensive training and experience was required to make use of the tactile information provided by their vocoder. The two subjects with the most training, an average of 63.8 h, on a 60-word list achieved more than 90% on word-recognition tests. Lynch *et al.* (1988) examined the errors made during tactile-alone training with the Tacticon 1600 and the integration of auditory and tactile information in post-training word perception assessments. Using a similar procedure to Engelmann and Rosov, two hearing-impaired adults learned 50 words in an average of 44 h.

The aim of this initial study was to establish whether the provision of tactile-alone training to naive subjects would allow them to develop a vocabulary which they could recog-

TABLE I. Summary of tactile-alone word perception studies in the literature, with mean values calculated from individual results reported.

Authors	Device	Subjects	No. subjects	Mean hrs training[a]	Mean words learned
Brooks and Frost (1983)	16-channel Queen's University vocoder	n-h[b] adults	2	47.8	110
Brooks *et al.* (1985)	Queen's University vocoder	n-h adults	1	80.5	250
Brooks (1984)	modified Queen's vocoder	h-i[c] teenagers	2	26.3	50
Engelmann and Rosov (1975)	23-channel vocoder	n-h adults	2[d]	63.8	60
		h-i children	3	102.9	72.3
Lynch *et al.* (1988, 1989)	16-channel Tacticon 1600	h-i adults	2	44	50
	Tacticon 1600	h-i children[e]	6	5.6[f]	17.2
	2-channel Tactaid II	h-i children[e]	2	4.7	15

[a]Estimated from reported hours of total training for individuals; where a significant portion of training was not tactile-alone perception of words or trained words in sentences, an appropriate percentage of the reported total training time has been used.
[b]Normally hearing.
[c]Hearing-impaired.
[d]Words learned specified for only two of the four subjects in the study.
[e]Subjects had months of daily experience using the tactile devices.
[f]For four of the subjects, training of 5.6–5.9 h was reported; 5.6 h has been used in the calculation of the group mean.

nize using the Tickle Talker™ alone. A further aim was to measure the mean rate of word learning with the Tickle Talker™, and to compare this with rates achieved with Tadoma and other tactile devices.

I. METHOD

A. Design

Six normally hearing adults were provided with word-recognition training in the tactile-alone condition using the Tickle Talker™. Regular evaluations monitored the growth of each subject's tactile-alone vocabulary. The protocol followed was based on that of Brooks and Frost (1983).

B. Device

The Tickle Talker™ consists of a lapel microphone, a handset, and a speech processor. The handset has eight electrodes set into four rings and positioned to stimulate the digital nerve bundles on the sides of the fingers. The speech processor is based on an early processor previously used with the Nucleus 22-channel cochlear implant (Blamey, 1987). An updated speech processing strategy was implemented in the processors used in the present study (Cowan *et al.*, 1991). This strategy was designed to extract estimates of the fundamental frequency and the second formant frequency of speech, and to measure the overall amplitude of speech in the band up to 4 kHz and in a second band above 4 kHz. This information was then encoded as electrical stimulus parameters for presentation to the user through electrocutaneous stimulation of the digital nerve bundles.

C. Subjects and talkers

The subjects were six normally hearing adults, two females and four males, who ranged in age from 21 to 45 years. Subjects 1 (S1) to S5 had no prior experience of tactile speech perception. S6 had prior experience with the Tickle Talker™. As well as being a subject, S6 acted as talker 1, administering all training and evaluation of S1 to S5. He had also been the main investigator in previous vowel perception studies with the Tickle Talker™ (Oerlemans and Blamey, 1994), and was therefore aware of what speech information was provided by the device. Talker 2, a female, administered all training and evaluation of S6.

D. Experimental setup

During training and evaluation, the talker sat outside the soundproof booth, while the subject sat inside. There was no visual contact between the subject and the talker. Talker 1 wore a Tickle Talker™ so that he could feel the stimulus and response words and discuss the available tactile cues with the subject. Talker 2 did not wear a Tickle Talker™ during training as S6's prior experience made the discussion of available cues unnecessary.

The subject wore foam earplugs and received white noise via headphones. The intensity of the white noise was adjusted to ensure that the talker's speech could not be detected auditorily. The talker was able to override the presentation of white noise to converse with the subject. The subject was provided with a print-out of the current word list being trained and a television monitor for textual feedback. The subject's spoken responses were delivered to their own Tickle Talker™ to maximize their experience with the tactile signal.

E. Word set

The words used for training all subjects were from the word set of Brooks and Frost (1983). A variety of word forms were originally chosen by Brooks and Frost from *The Computational Analysis of Present-Day American English* (Kucera and Francis, 1967). The words were selected to contain the 40 phonemes of English and to be suitable for use in sentence construction. The 150 words were trained in random order by Brooks and Frost, and the same order was used in the present study. The first 20 words in the set can be found in Table II.

F. Training

Each subject attended an average of three half-hour training sessions per week, for between 6 and 17 weeks. The availability of the subjects to attend sessions determined the

TABLE II. The first five lists used during training with S1.[a] Tactually new words being introduced are italicized.

Vocabulary List 1 (10 words)	Training List 1 (10 words)	Vocabulary List 2 (15 words)	Training List 2 (10 words)	Vocabulary List 3 (20 words)
boy	giving	boy	giving	boy
house	go	house	little	house
put	little	put	put	put
show	thing	show	talking	show
we	boy	we	thing	we
go	*door*	go	*over*	go
giving	*paper*	giving	*radio*	giving
little	*speak*	little	*sing*	little
see	*talking*	see	*something*	see
thing	*they*	thing	*what*	thing
		door		door
		paper		paper
		speak		speak
		talking		talking
		they		they
				over
				radio
				sing
				something
				what

[a]The same words were trained with S2 to S6, although the exact compilation of the lists depended on the number of tactually new words introduced per list and the words each subject had difficulty recognizing.

number of sessions per week, and the number of weeks of training for each individual. Table III presents the number of weeks of training and the total number of hours of training for each subject. This training time excludes time spent on evaluations.

The aim of training was for subjects to feel the tactile presentation of each word as many times as possible, with maximized exposure to words the individual subject had difficulty recognizing. A software program was written by the second author to formulate the word lists, randomize the presentations, keep track of subject performance, and calculate the time spent training and evaluating. To familiarize the subject with the tactile pattern representing each word, the talker started each session by twice presenting each word in the appropriate word list, with accompanying textual presentation on the subject's monitor. Following this, the software program randomly selected a word from the list for presentation. The subject responded verbally from the print-out of the word list. The subject was able to compare the response with the talker's presentation on his own Tickle Talker™.

TABLE III. Final vocabulary sizes and hours of training received for each subject.

Subject	Training time		Final vocabulary
	Weeks	*Total hours*[a]	*Words*
S1	17	33.1	77
S2	13	17.8	46
S3	7	12.3	34
S4	11	17.7	27
S5	10.5	18.5	62
S6	6	12.5	52

[a]Hours of training excludes evaluation time.

The stimulus word and the response were then displayed on the subject's monitor. The talker repeated the stimulus word, allowing the subject to match the tactile pattern with the textual display. During training, the tactile cues available to clarify confusions were discussed.

To enable the talker to monitor progress and the confusions being made in each session, the software program displayed a running score of correct responses and, for each stimulus word, the number of presentations made, the number of correct responses and the last ten responses. If the subject was having difficulty with a particular word pair, the talker used an ABx presentation format to train the pair. In this presentation format, the two words were presented by the talker with accompanying textual display on the subject's monitor. One word was then repeated by the talker as the stimulus. As a step between the ABx presentation and the standard training procedure, the word pair was presented as a two-alternative forced choice. In this format, the two words of the pair were displayed on the monitor, but only one stimulus word was presented by the talker. If a larger number of words were being confused, a set of selected words could be trained or the talker could present the list of words with textual display. The talker decided when to use these alternative approaches to training based on the information provided by the program and feedback from the subject.

The selection of stimulus words was not completely random. Words which the subject was having difficulty recognizing were presented more often to focus training where it was most needed. To ensure that every word retained a chance of being presented and that no single word had too high a probability of being selected, the following formula was used to calculate the probability of selecting the ith word for presentation:

$$p(i)=\frac{\mathrm{MAX}(5-\mathrm{corr}[i],1)}{\Sigma_{j=1}^{n}A[j]},$$

where $\mathrm{corr}[i]$ is the number of correct responses given by the subject for the last ten presentations of the ith word, n is the total number of words in the list, i designates the specific word, and $A[j]=\mathrm{MAX}(5-\mathrm{corr}[j],1)$.

Figure 1 presents the training and evaluation protocol as a flow chart. As an example of the word lists used in training, Table II presents the first five lists used with S1. For all subjects, training began with *vocabulary list 1*, which consisted of the first 10 words from the 150-word list. This list was trained until the information from the program indicated that the subject was scoring at about 80% correct, or until the end of the session. The subject was then evaluated on the 10-word list, as described below. If the 80% criterion level of recognition was not achieved in the evaluation, training resumed with the same list. If the 80% criterion level was reached, the program compiled the next word list from the five words which the subject had the most difficulty recognizing in *vocabulary list 1*, and the next five words from the 150-word list. This 10-word list was *training list 1*. Training and subsequent evaluation then continued until the subject reached the 80% criterion level when evaluated on *training list 1*. The next list was then created by combining *training*

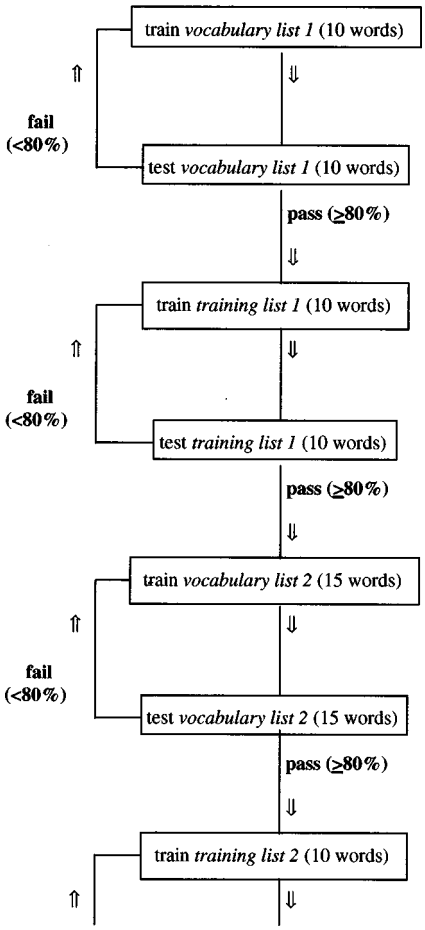

FIG. 1. Flow chart of training and evaluation protocol.

list 1 and *vocabulary list 1* to create a vocabulary list of 15 words, *vocabulary list 2*, which was then trained.

With this protocol, the subject was trained on a training list consisting of some difficult words which had already been trained and some tactually new words. Once this list was mastered it was added to the growing vocabulary list, which was then also trained and evaluated. This approach was designed to make learning to recognize tactually new words easier, as all words were introduced in a short training list before being incorporated into the growing vocabulary list. This approach also maximised exposure to difficult words.

Once S1 to S5 had passed *vocabulary list 3* and, therefore, had significant experience with the tactile signal, training lists were compiled from seven tactually new words and only three previously trained difficult words. This faster approach to word introduction was followed from the start of training for S6, as he was already an experienced user of the Tickle Talker™.

G. Evaluation

Subjects were evaluated when the information provided by the program suggested that they would reach the criterion level, and also at the end of each training session to ensure regular monitoring of progress. Prior to evaluation, the talker presented each word in the list with textual display. The talker then presented the words as randomly selected by the program. No visual or other feedback was provided to the subject during evaluation.

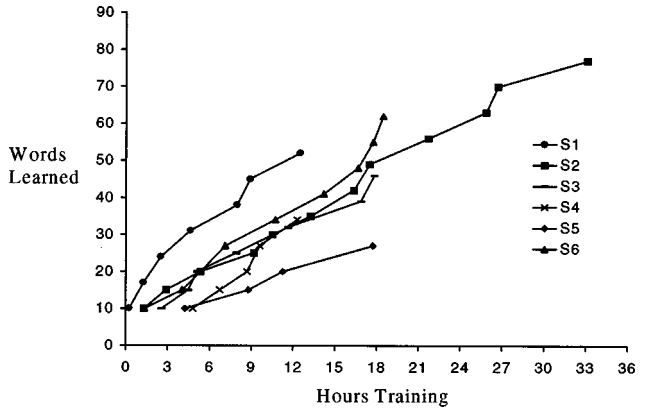

FIG. 2. Number of words learned by each subject as a function of hours of training.

Subjects were only available for a limited time each week, so the compilation of evaluation lists was a compromise between adequate evaluation and minimizing the time taken from the training session. For training lists of up to 35 words, the evaluation list consisted of two presentations of each word. For training lists of 36 words to 70 words, the evaluation list consisted of 70 randomly selected words, with each word presented at least once but no more than twice. For training lists longer than 70 words, the evaluation list consisted of 70 randomly selected words, with no word occurring more than once. Note that only S1 learned a vocabulary of more than 70 words.

The criterion for passing all training list evaluations was 80%. The criterion for passing vocabulary list evaluations was 80% up to *vocabulary list 3*. From then on, the criterion for the vocabulary lists was lowered to 70% to speed up the training process.

Although the training and evaluation procedures may appear complex, they provide more systematic rules for the introduction of tactually new words and the revision of tactually difficult words, and more rigorous evaluation than the procedure used by Brooks and Frost (1983). This is necessary for quantitative comparison of learning rates.

II. RESULTS

The total number of words learned by each subject is presented in Table III. Figure 2 presents the number of words learned by each subject as a function of the number of hours of training received. Only four of the subjects received more than 13 h of training. After 12 h of training the six subjects had learned an average of 31.3 words (s.d.=8.3).

The training time taken by each subject to pass each 10-word training list was entered into a General Linear Model (Minitab Reference Manual, 1995), which combined an Analysis of Variance (ANOVA) with a regression analysis. The categorical factors in the ANOVA were the number of tactually new words in each list and subject number. The analysis needed to account for the number of tactually new words as this varied between lists, being either five or seven words. A regression analysis, with the training list number as

the independent variable (covariate), was included as a linear relationship was expected between the time taken to pass each training list and the training list number. The results indicated that there was a significant decrease in training time of 9 min per list required to pass training lists as training progressed (slope $= -0.15$ h per list, $p = 0.003$).

The training time taken by each subject to pass each vocabulary list was entered into a General Linear Model. The model combined an ANOVA, with subject as the factor, and a regression analysis, with list length as the independent variable. The results indicated that there was a significant increase in training time of 1.8 min per word required to pass vocabulary lists with increasing list length (slope $= 0.03$ h per word, $p = 0.045$). Note that Fig. 2 shows an approximately linear relationship between tactual vocabulary size and total training time. This is compatible with the above results because the decrease in training time for the training lists was approximately balanced by the increase in training time for the vocabulary lists.

Anecdotal reports from the subjects indicated the tactile information that they were using to recognize the words. They reported identifying general aspects of the tactile signal, such as the direction of movement and stimulation on particular electrodes, and suprasegmental information in the signal, such as the amplitude of the tactile sensation and the syllabic pattern being conveyed. The subjects also reported identifying information about particular groups of phonemes, such as high frequency fricatives. Some words, which were particularly easy to identify, were recognized as whole units rather than at a phonemic level.

III. DISCUSSION

All subjects were able to learn to recognize a set of words using only tactile information. The decrease in time taken to pass training lists as the study progressed suggested that the ability of the subjects to identify and utilize the relevant tactile cues improved with further training. It is likely that more training time was required to pass longer lists because an increasing number of words would have been tactually similar. This would make it more difficult to recognize some words as whole units and also more difficult to identify cues which distinguished each word from all of the others. It is also possible that, in reviewing the longer vocabulary list, it was difficult for the subjects to retain the tactile pattern of the stimuli. Overall, it is likely that a trade-off occurred as tactile perceptual skills improved with training but the task became more difficult with increased list length.

The performance of the group compares well with that of groups in previous studies (Table I). Data extracted from individual results graphed in Brooks and Frost (1983) were used to calculate the mean group results. These results are compared with those of the present study in Fig. 3. The mean number of words learned for particular numbers of hours of training were surprisingly similar, particularly given the methodological differences between the studies. As shown in Table I, the present results were also similar to the group performance estimated from individual results for hearing-impaired teenagers (Brooks, 1984) and a group of children

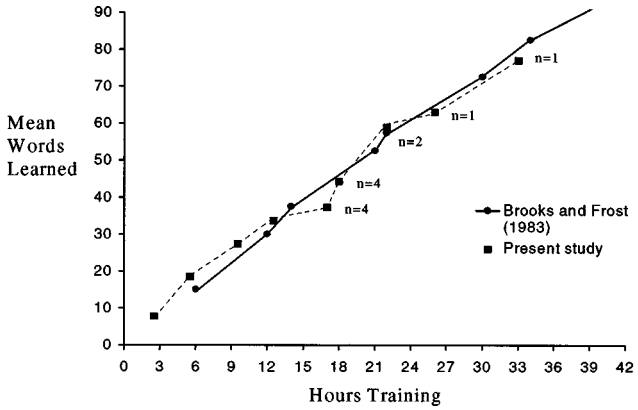

FIG. 3. Estimated mean number of words learned by Brooks and Frost's subject group ($n = 2$) as a function of hours of training. Data were extracted from individual results graphed in Brooks and Frost (1983). The dotted line represents mean group results from the present study for comparison ($n = 6$, unless otherwise specified).

who were experienced device users (Lynch *et al.*, 1989). The subjects of Engelmann and Rosov (1975) and the hearing-impaired adults in the study of Lynch *et al.* took longer than the present group to learn a comparable number of words. Differences in methodology and small subject samples make it impossible to establish whether the variation in results was due to differences in training, evaluation, subjects, or devices. However, the comparison between the present results and those of Brooks and Frost (1983) indicates that the differences in the number of channels and method of stimulation between the 16-channel vibrotactile vocoder and the 8-channel electrotactile Tickle Talker™ did not result in major performance differences.

Tadoma is the most successful method of tactile-alone communication, so it is relevant to compare the present tactile-alone results to those achieved by two normally hearing, normally sighted subjects learning Tadoma (Reed *et al.*, 1982). For the Tadoma subjects, new words were added when the most recently added words were being recognized with a similar accuracy to the rest of the vocabulary. The words were only presented in isolation a few times, and subsequently presented within sentences. Reed *et al.* reported that the subjects learned 43 words in 26 h of training, as compared with an average of 44 words being learned in 18 h in the present study and 38 words being learned in 15 h in the Brooks and Frost (1983) study. At least in the early stages of training, subjects did not gain more speech information from Tadoma than from the Tickle Talker™ or the Queen's vocoder. It has been hypothesized that the training and motivation of hearing-impaired users of Tadoma are crucial to their success (Reed *et al.*, 1989). The similar performance of novice users raises an old question—just how well would a tactile device user perform in the tactile-alone condition with the motivation and intensive, long-term training of a successful Tadoma user? So far, there is no answer to this important question, and the above comparison of naive subjects is simply an interesting point. Further research is required in which larger groups of naive users of tactile devices and Tadoma receive consistent training and evaluation. This will clarify the relative contributions of training and motivation, versus innate characteristics of the Tadoma

method, to successful tactile-alone communication.

In considering tactile-alone perception, maximum vocabulary size is perhaps as important as rate of learning. Engelmann and Rosov (1975) reported relatively slow progress for one hearing-impaired child, however, the 152-word vocabulary eventually learned by this child was impressive. Also impressive was the absence of a performance plateau for the subject of Brooks *et al.* (1985), who acquired a vocabulary of 250 words in 80.5 h. Unfortunately, no study has provided sufficient training to indicate if there is a limit to the vocabulary that can be learned with a tactile device. Although there is no plateau in performance in Fig. 2, the present group become slower at passing longer vocabulary lists, suggesting that there would be a vocabulary size for which they would be unable to recognize all of the words. In contrast, extensive research into the Tadoma method has not suggested a limit to potential vocabulary size (Reed, 1995). Chomsky's (1986) evaluation of the language skills of three experienced Tadoma users indicated that their vocabularies had developed well beyond what was possessed at the time of onset of their sensory disabilities. Chomsky was wary of concluding that an unlimited vocabulary would be possible for all Tadoma users, noting that individual characteristics may be important in developing the ability to perceive speech using touch alone, and it may not be possible for all individuals to learn this skill.

Given the results of the present subject group, the application of tactile-alone training with hearing-impaired users of the Tickle Talker™ should be reviewed. Previous trials of alternative training strategies with normally hearing subjects (Alcántara *et al.*, 1990a) and training studies with hearing-impaired device users (Cowan *et al.*, 1989a, 1990; Alcántara *et al.*, 1990b) led to the development of a training program which focused on combined modality training (Galvin *et al.*, 1993). In initial sessions, some basic detection and suprasegmental discrimination tasks were used to introduce the tactile signal, to allow the user to focus on the tactile information only and to develop an understanding that the tactile signal provided useful speech information. These aims would be well served through the provision of tactile-alone word recognition training. Whether this would result in an increase in the benefit gained from the tactile device in daily communication cannot be concluded from the results obtained to date.

IV. CONCLUSION

The provision of tactile-alone word recognition training enabled all subjects to learn to recognize a set of words using the Tickle Talker™ alone. It was not possible to establish if a maximum vocabulary size existed. The performance of the group was comparable with, or superior to, the performance shown with other tactile devices and by naive users of Tadoma. Whether the tactile-alone word recognition skills would be generalized to tasks more relevant to daily communication for the hearing-impaired is yet to be established. Further investigation should evaluate whether skills can be generalized to tactile-alone recognition of sentences and to improved combined-modality perception.

ACKNOWLEDGMENTS

The commitment of the subjects in this study to the difficult training program is greatly appreciated. Dr Andrew Faulkner and an anonymous reviewer provided very helpful reviews of the manuscript.

Alcántara, J. I., Cowan, R. S. C., Blamey, P. J., and Clark, G. M. (**1990a**). ''A comparison of two training strategies for speech recognition with an electrotactile speech processor,'' J. Speech Hear. Res. **33**, 195–204.

Alcántara, J. I., Whitford, L. A., Blamey, P. J., Cowan, R. S. C., and Clark, G. M. (**1990b**). ''Speech feature recognition by profoundly hearing-impaired children using a multiple-channel electrotactile speech processor and aided residual hearing,'' J. Acoust. Soc. Am. **88**, 1260–1273.

Blamey, P. J. (**1987**). ''Psychophysical and speech studies with an electrotactile speech processor,'' Ann. Otol. Rhinol. Laryngol. **1**, 87–89.

Blamey, P. J., Cowan, R. S. C., Alcántara, J. I., and Clark, G. M. (**1988**). ''Phonemic information transmitted by a multichannel electrotactile speech processor,'' J. Speech Hear. Res. **31**, 620–629.

Brooks, P. L. (**1984**). ''Comprehension of speech by profoundly deaf and normal-hearing subjects using the Queen's University tactile vocoder,'' Unpublished Doctoral thesis, Queen's University, Ontario.

Brooks, P. L., and Frost, B. J. (**1983**). ''Evaluation of a tactile vocoder for word recognition,'' J. Acoust. Soc. Am. **74**, 34–39.

Brooks, P. L., Frost, B. J., Mason, J. L., and Chung, K. (**1985**). ''Acquisition of a 250-word vocabulary through a tactile vocoder,'' J. Acoust. Soc. Am. **77**, 1576–1579.

Chomsky, C. (**1986**). ''Analytic study of the Tadoma method: Language abilities of three deaf-blind subjects,'' J. Speech Hear. Res. **29**, 332–347.

Cowan, R. S. C., Alcántara, J. I., Whitford, L. A., Blamey, P. J., and Clark, G. M. (**1989a**). ''Speech perception studies using a multichannel electrotactile speech processor, residual hearing, and lipreading,'' J. Acoust. Soc. Am. **85**, 2593–2607.

Cowan, R. S. C., Blamey, P. J., Alcántara, J. I., Whitford, L. A., and Clark, G. M. (**1989b**). ''Speech feature recognition with an electrotactile speech processor,'' Aust. J. Audiol. **11**, 57–72.

Cowan, R. S. C., Blamey, P. J., Sarant, J. Z., Galvin, K. L., and Clark, G. M. (**1991**). ''Perception of multiple electrode stimulus patterns: Implications for the design of an electrotactile speech processor,'' J. Acoust. Soc. Am. **89**, 360–368.

Cowan, R. S. C., Blamey, P. J., Galvin, K. L., Sarant, J. Z., Alcántara, J. I., and Clark, G. M. (**1990**). ''Perception of sentences, words and speech features by profoundly hearing-impaired children using a multichannel electrotactile speech processor,'' J. Acoust. Soc. Am. **88**, 1374–1384.

Engelmann, S., and Rosov, R. (**1975**). ''Tactual hearing experiment with deaf and hearing subjects,'' Exceptional Child **41**, 243–253.

Galvin, K. L., Cowan, R. S. C., Sarant, J. Z., Blamey, P. J., and Clark, G. M. (**1993**). ''Factors in the development of a training program for use with tactile devices,'' Ear Hear. **14**, 118–127.

Kucera, H., and Francis, W. N. (**1967**). *Computational Analysis of Present-Day American English* (Brown University Press, Rhode Island).

Lynch, M. P., Eilers, R. E., Oller, D. K., and Lavoie, L. L. (**1988**). ''Speech perception by congenitally deaf subjects using an electrocutaneous vocoder,'' J. Rehabil. Res. Dev. **25**, 41–50.

Lynch, M. P., Eilers, R. E., Oller, D. K., and Cobo-Lewis, A. (**1989**). ''Multisensory speech perception by profoundly hearing-impaired children,'' J. Speech Hear. Dis. **54**, 57–67.

Minitab Reference Manual (**1995**). (Minitab Inc., State College, PA).

Oerlemans, M., and Blamey, P. (**1994**). ''Multisensory speech perception: Integration of speech information,'' Proceedings of the Fifth Australian International Conference on Speech Science and Technology, Perth, Australia (December, 1994).

Reed, C. M. (**1995**). ''Tadoma: An overview of research,'' in *Profound Deafness and Speech Communication*, edited by G. Plant and K.-E. Spens (Whurr, London).

Reed, C. M., Doherty, M. J., Braida, L. D., and Durlach, N. I. (**1982**). ''Analytic study of the Tadoma method: Further experiments with inexperienced observers,'' J. Speech Hear. Res. **25**, 216–223.

Reed, C. M., Durlach, N. I., Delhorne, L. A., Rabinowitz, W. M., and Grant, K. W. (**1989**). ''Research on tactual communication of speech: Ideas, issues, and findings,'' Volta Rev. Monograph **97**, 65–78.

Vocal tract normalization for midsagittal articulatory recovery with analysis-by-synthesis

Richard S. McGowan and Steven Cushing
Sensimetrics Corporation, 48 Grove Street, Somerville, Massachusetts 02144

(Received 10 April 1998; revised 12 March 1999; accepted 10 May 1999)

A method is presented that accounts for differences in the acoustics of vowel production caused by human talkers' vocal-tract anatomies and postural settings. Such a method is needed by an analysis-by-synthesis procedure designed to recover midsagittal articulatory movement from speech acoustics because the procedure employs an articulatory model as an internal model. The normalization procedure involves the adjustment of parameters of the articulatory model that are not of interest for the midsagittal movement recovery procedure. These parameters are adjusted so that acoustic signals produced by the human and the articulatory model match as closely as possible over an initial set of pairs of corresponding human and model midsagittal shapes. Further, these initial midsagittal shape correspondences need to be generalized so that all midsagittal shapes of the human can be obtained from midsagittal shapes of the model. Once these procedures are complete, the midsagittal articulatory movement recovery algorithm can be used to derive model articulatory trajectories that, subsequently, can be transformed into human articulatory trajectories. In this paper the proposed normalization procedure is outlined and the results of experiments with data from two talkers contained in the X-ray Microbeam Speech Production Database are presented. It was found to be possible to characterize these vocal tracts during vowel production with the proposed procedure and to generalize the initial midsagittal correspondences over a set of vowels to other vowels. The procedure was also found to aid in midsagittal articulatory movement recovery from speech acoustics in a vowel-to-vowel production for the two subjects. [S0001-4966(99)05408-9]

PACS numbers: 43.72.Ct, 43.72.Ar, 43.70.Aj [JH]

INTRODUCTION

There are both anatomical/postural differences and motor control differences between talkers that result in inter-talker variability. This distinction in the types of inter-talker variability, important in its own right, is also important when designing a procedure that recovers articulatory movement, or motor behavior, from speech acoustics using analysis-by-synthesis with an articulatory model. Such a procedure, which could quantify articulatory movement differences between talkers, would necessarily be able to account for anatomical/postural differences between talkers, because articulatory analysis-by-synthesis employs anatomical/postural features to constrain the articulatory model.

The results presented here describe a method for characterizing, or extracting, a talker's anatomical/postural features that can be well-defined in a time-averaged way, such as average vocal tract length. This information is used to adjust, or normalize, the articulatory model employed in a procedure to recover articulatory movement from the acoustic speech signal. An articulatory movement recovery procedure is a computational procedure that is intended to infer the midsagittal position or movement of the supralaryngeal articulators, such as the tongue body, tongue blade or tip, and the lips, from the acoustic signal [see Schroeter and Sondhi (1994) for a review]. The computational recovery procedure used in conjunction with the normalization procedure presented here is essentially one of analysis-by-synthesis with an internal articulatory model in the form of an articulatory synthesizer. Previous work has shown that this procedure can recover midsagittal articulatory movement from speech acoustics when there is no mismatch between the data-producing articulatory model and the internal model (McGowan, 1994). Some experiments have tested the recovery procedure when there were limited mismatches between a data-producing speech production model and the internal model used for the recovery procedure (McGowan and Lee, 1996). To extend the proposed recovery procedure to the recovery of midsagittal movement for human subjects it is necessary to account for anatomical mismatches between the human subject's vocal tract and the vocal tract of the internal model itself, known here as the *standard vocal tract*. This requires normalization or adaptation of the anatomy/postural features of the standard vocal tract to that of the human vocal tract, because only with a good anatomical adaptation can an analysis-by-synthesis procedure attribute specific articulatory movements correctly to certain speech acoustic signals.

The proposed normalization procedure has two components: One is a mapping between midsagittal shapes of the human vocal tract and the standard vocal tract. The normalizing map, or NM, transforms midsagittal shapes or articulator positions of the human vocal tract to midsagittal shapes or articulator positions of the standard vocal tract. Thus the NM maps from the shape space of the human vocal tract in the midsagittal plane (the domain of the NM) into the shape space of the standard vocal tract in the midsagittal plane (the range of the NM). The human and standard vocal-tract shape spaces could be parameterized by the coordinates of the pellets of an articulatory tracking system and the articulator po-

sition coordinates of an articulatory synthesizer (e.g., Mermelstein, 1973; Rubin *et al.*, 1981), respectively. The movements of the pellet coordinates are what the articulatory recovery procedure is intended to recover. (In the procedure presented here, the inverse NM and not the NM will be constructed, because this is immediately useful in the midsagittal articulatory movement recovery procedure.) The other aspect of the normalization procedure is the adjustment, adaptation, or extraction of parameters of the standard vocal tract not affected by the NM. These parameters contain anatomical or postural features, such as average vocal tract length or average transverse pharyngeal dimension, that do not share in the parameterization of the range space of the NM (i.e., the midsagittal shapes or articulatory coordinates of the standard vocal tract). These parameters are called PONMs (Parameters Orthogonal to the range space of the NM). These parameters are adjusted so that shapes that are mapped to one another under the NM or its inverse produce very similar acoustic output [see Beautemps *et al.* (1995), and Badin *et al.* (1995)].

The procedure for constructing the inverse NM and extracting the PONM values is started by designating several pairs of midsagittal shapes of the human and standard vocal tracts to map to one another under the NM and the inverse NM. These pairs of shapes are known as *initial corresponding vocal tracts*, or as *initializing utterances*. The procedure for obtaining these pairs is a visual matching procedure that will be described below. Then PONM values of the standard vocal tract are extracted in an optimization (analysis-by-synthesis) procedure so that the acoustic output of the standard vocal tract closely matches that of the human's speech acoustics over the set of pairs of initializing utterances. If the pairs of midsagittal shapes that are designated to be initial corresponding vocal tracts match very closely, except for aspects of shape that have PONMs associated with them, and if the coverage of the initial set of equivalent midsagittal shapes in shape space is sufficient, then the standard vocal tract with adjusted PONM values obtained from the extraction procedure should be a good approximation to values of the corresponding anatomical/postural attributes of the human talker. The extracted PONM values should, therefore, generalize so that the acoustic output of the standard vocal tract closely matches the acoustic output of the human vocal tract for novel midsagittal shapes that are equivalent under the normalizing map and its inverse. This ability to generalize can work under less restrictive assumptions on the extracted PONM values. It is not required that each PONM accurately reflect a physical quantity, but only that they, as a group, sufficiently capture the acoustic consequences of time-invariant features of the talker. For instance, a PONM of vocal-tract length may also be related to some features of vocal-tract wall compliance because both affect the average formant frequencies. In this way, PONMs can still be useful for midsagittal movement recovery, even when they are not completely accurate in a physical sense. In summary, the standard vocal tract with the extracted PONM values can be used as a customized internal model in analysis-by-synthesis for midsagittal articulatory movement recovery. Assuming that the inverse NM between initial corresponding vocal tracts can be generalized to an inverse NM valid for all midsagittal shapes encountered in speech, the recovered midsagittal shapes of the standard vocal tract can be transformed into the shapes of the human vocal tract using the inverse NM.

This paper explores a particular procedure (with some variations) for obtaining PONM values and constructing the inverse NMs from human data. Experiments designed to test the validity of the procedure were performed on data from two subjects from the X-Ray Microbeam Speech Production Database (XRMB-SPD), which were collected and developed using the University of Wisconsin x-ray microbeam system (Westbury, 1994). We were interested in exploring the implementation and results of the normalization procedure in detail. The proposed normalization procedure allows for flexibility in its implementation, so fairly extensive numerical experiments were performed to find the best ways to implement the procedure, as well as explore relationships with fixed vocal-tract geometry. Further, both the acoustic and articulatory data extraction was done by hand. While this ensured that weaknesses in signal processing did not cause problems in the proposed normalization method, it did mean that data extraction was a labor-intensive process. As a consequence it was feasible to include only two subjects in this study. The standard vocal tract was provided by the Haskins Laboratories articulatory synthesizer, ASY (Mermelstein, 1973; Rubin *et al.*, 1981). The ASY vocal tract was used for the standard vocal tract because the articulatory movement recovery procedure currently employs the task-dynamic model for articulatory control (Saltzman and Munhall, 1989), and the task-dynamic model has been implemented using the ASY articulators as its end effectors. Other vocal tract models (e.g., Coker, 1976; Maeda, 1990) could, potentially, be used as the standard vocal tract.

In Sec. I, the general steps for normalization are presented, while in Sec. II a procedure for selecting initial corresponding vocal-tract pairs by visual matching is presented. In Sec. III the experiments on PONM extraction are presented, and in Sec. IV, the procedure and results for constructing inverse NM are given. Examples of midsagittal articulatory movement recovery employing the normalization procedure are presented in Sec. V. Concluding remarks are given in Sec. VI.

I. THE NORMALIZATION PROCEDURE

The steps of the normalization procedure are described, assuming that simultaneous articulatory and acoustic data are available for a selected set of initializing utterances (McGowan, 1997). After a step is described in general, the implementation of that step in these experiments is explained. In particular, it is assumed that articulatory point information, in terms of x-ray microbeam pellet data for the tongue, lips, and jaw, is simultaneously available with speech acoustic data for several vowels.

(1) Choose a representation, or coordinate system, in both the domain space (human vocal-tract midsagittal shape) and the range space (standard vocal-tract midsagittal shape) of the NM. This makes it possible to define the NM and its

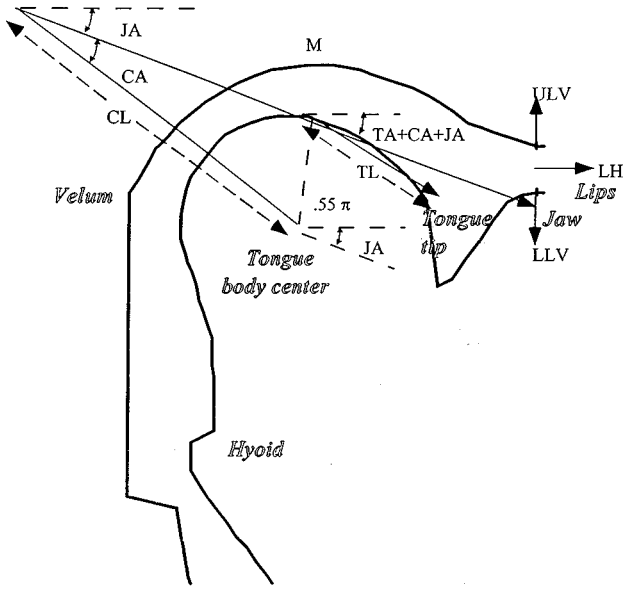

FIG. 1. The Haskins Laboratories articulatory synthesizer, ASY. The articulatory coordinates of interest are as follows. The jaw vector originates at the condyle and denotes the coordinate of the lower incisor. It has a fixed length and JA denotes the angle the jaw vector makes with the horizontal. CA is the angle of the tongue-body vector (originating at the condyle and terminating at the center of the tongue-body circle) with respect to JA. The length of the tongue-body vector is CL. The tongue-tip vector (originating on the surface of the tongue-body circle and terminating at the tongue tip) has angle TA, measured with respect to the sum of JA and CA. The length of the tongue-tip vector is TL. The upper lip's vertical coordinate is given by ULV and the lower lip's vertical coordinate (with respect to the jaw) is given by LLV. Both lips' horizontal coordinates are given by LH. Point *M* denotes the position of the highest point on the palate, but it is not an articulatory coordinate.

inverse as mathematical functions from one coordinate system to another. The problem of mapping midsagittal shapes becomes one of mapping coordinates.

In the experiments conducted here, the coordinate system for the standard vocal-tract midsagittal shape consisted of the articulatory coordinates of ASY (Fig. 1) and the coordinate system for the human vocal tract was the Cartesian coordinate system of the x-ray microbeam pellets [e.g., Fig. 2(a)].

(2) Choose a set of pairs of midsagittal shapes, one shape for the human vocal tract and another shape for the standard vocal tract, that are designated to map to one another under the NM and its inverse. These initial corresponding vocal tracts, or initializing utterances, represented in their respective coordinate systems, will initialize the NM or inverse NM, and will also be employed for extracting PONM values in an optimization procedure.

In the experiments conducted here, the initial corresponding vocal tracts were a subset of utterances for which there is available data from the XRMB-SPD. Vowels were the initializing utterances, and these are otherwise known as *initializing vowels*. For each initializing vowel, the midsagittal articulatory coordinates of ASY were adjusted so that there was a close visual match between the midsagittal outline of the ASY articulators and the pellet positions of the human utterance as described more fully in Sec. II below.

(3) Optimize for acoustic match over the set of initial corresponding vocal tracts by adjusting PONM values. The resulting optimum PONM values are know as *extracted* PONM values.

Here, the PONMs consisted of parameters such as nominal vocal-tract length, transverse pharyngeal dimensions, and the parameters used to convert midsagittal tongue-to-palate distances to cross-sectional areas. Two optimization criteria were used, each with the common property of least-squares matching in the first three formant frequencies, over all initial corresponding vocal tract or initializing vowel pairs simultaneously.

(4) Generalize the NM or inverse NM from the initial corresponding vocal tracts by using regression or interpolation.

The procedure for generalizing the inverse NM here employed neural networks with supervised learning over sets of initializing vowels.

II. METHOD FOR MATCHING STANDARD VOCAL TRACT (ASY) ARTICULATOR POSITIONS WITH HUMAN x-RAY MICROBEAM PELLET POSITIONS

The initial corresponding vocal tracts, or initializing vowels, were obtained from a set of nine test vowels, including /aa/, /uu/, /iy/, /ae/, /ey/, /ao/, /ih/, /eh/, and /ah/. The human midsagittal vocal-tract shapes corresponding to these vowels were from two subjects, JW16 (female) and JW40 (male), in the XRMB-SPD. A single frame of pellet data and the concurrent first three formant frequencies were extracted near the centers of these vowels. The x-ray microbeam data were from the midsagittal plane and included pellets on the tongue, lips, and teeth, a line representing the rear of the pharyngeal wall and a trace of the palate.

The visual matching for each subject and each vowel from the set of nine test vowels was performed. Visual matching was done instead of an automatic optimization procedure to gain experience fitting a human vocal-tract midsagittal shape with a model vocal tract possessing a large number of degrees of freedom. An automatic optimization procedure will become practical if it is constrained by previous experience in visual matching. A visual match was attained when the pellet data were as close to the midsagittal outlines of the ASY articulators as possible, under the constraints imposed by the ASY model and the steps outlined below. The general outline of steps used to attain the visual match is as follows. After plotting the pellet data, some initial adjustments were made to the raw pellet data to account for orientation differences between the human and ASY vocal tracts and to make some of the pellet positions more interpretable in terms of ASY landmarks. Then the ASY articulator coordinates were adjusted for good visual matching. Figure 2(a)–(e) provides illustrations of the following steps for vowel /ae/ of subject JW16.

(1) The first step was to plot the human data on graph paper [see Fig. 2(a)]. There were seven pellets that were plotted for each vowel, including four tongue pellets, the lower incisor pellet, and the upper and lower lip pellets. Quoting from the XRMB-SPD handbook: ''Four pellets [T1, T2, T3, and T4] were attached along the longitudinal sulcus

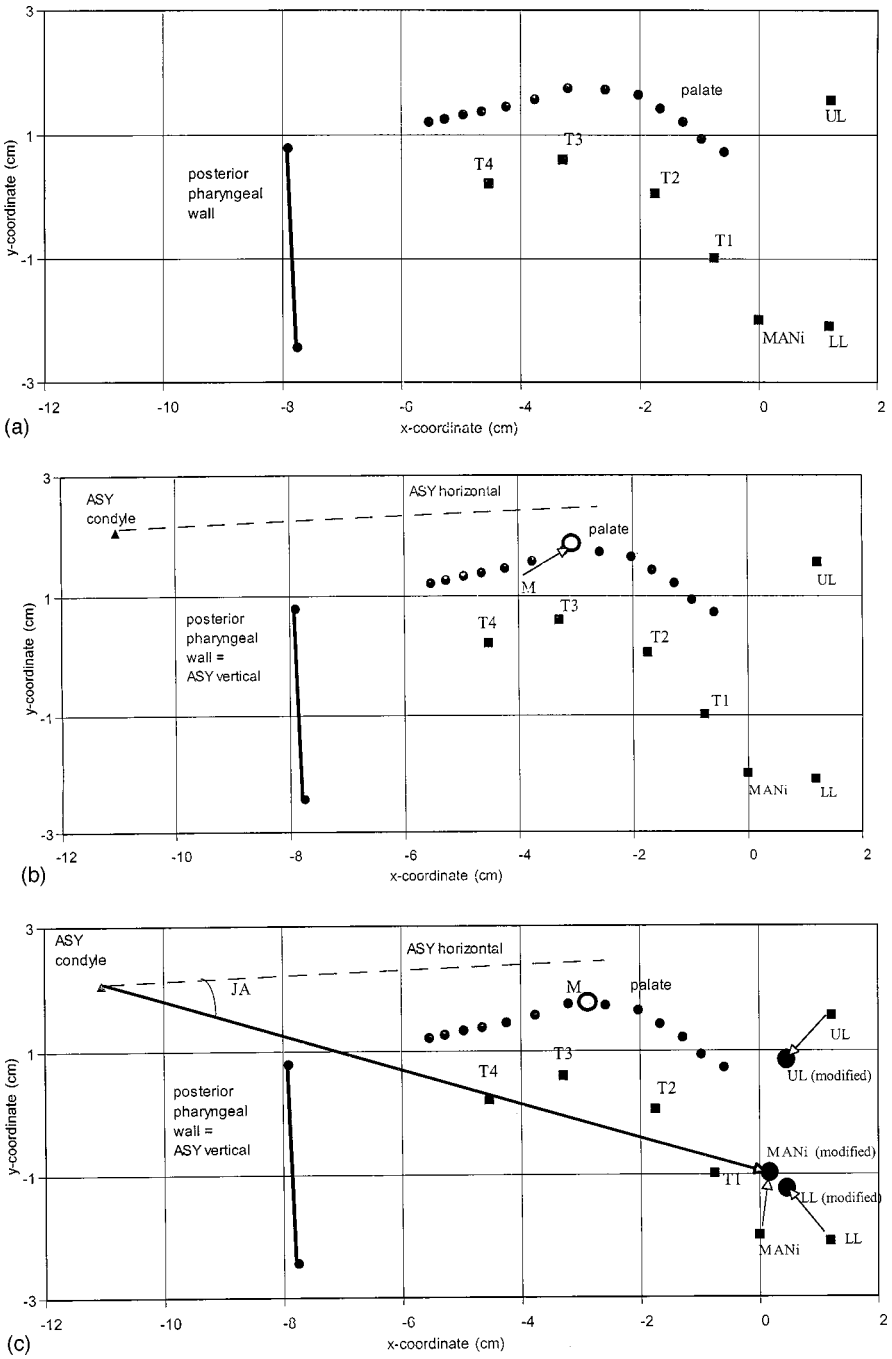

FIG. 2. (a) First step for midsagittal vocal tract matching, plotting x-ray microbeam data. Example from JW16 producing vowel /ae/. (b) Second step for midsagittal vocal tract matching, orienting ASY coordinate system and plotting ASY landmarks. Example from JW16 producing vowel /ae/. (c) Third step for midsagittal vocal tract matching, adjusting pellet positions and fitting jaw and lips. Example from JW16 producing /ae/. (d) Fourth step for midsagittal vocal tract matching, fitting the ASY tongue circle. Example from JW16 producing /ae/. (e) Fifth step for midsagittal vocal tract matching, fitting the ASY tongue tip. Example from JW16 producing /ae/.

of each speaker's tongue. The most ventral of these was typically placed in the vicinity of the so-called tongue ''blade,'' roughly 10-mm posterior to the apex of the extended tongue. The most dorsal was placed about 60-mm posterior to the apex, as far back as the speaker would tolerate without gagging, but always ventral to the circumvallate papillae. The medial pellets were placed so that the distance between the front most and rearmost pellets was divided into three roughly equal segments'' (p. 38, Westbury, 1994). There was a pellet attached to the lower teeth as well. From the same handbook: ''...one [mandibular pellet] (MANi) [was] glued to the buccal surface of the central incisors...in the pocket formed by the central diastema and the enamel-gingival border.'' (p. 38, Westbury, 1994). Also, ''One pellet each was attached to the upper (UL) and lower lip (LL), glued to the external surface at the vermillion border.'' (p. 39, Westbury, 1994). Palatal and posterior pharyngeal wall traces were most often obtained from averaging scans of a calibration bite plate and the others were obtained ''...by tracking the motion of a tracing pellet...drawn slowly down the midline'' (p. 46, Westbury, 1994). The Cartesian coordinate system used for the pellet data had its *x*-axis defined by the intersection of the occlusal plane and the midsagittal plane. The origin was placed at the tips of the central maxillary incisors (pp. 46–52, Westbury, 1994).

(2) The ASY coordinate system and some ASY landmarks were plotted on the graph paper with some adjustments for the relative orientation of the pellet coordinate system [Fig. 2(b)]. The origin of the ASY coordinate system corresponded with the origin of the pellet coordinate system.

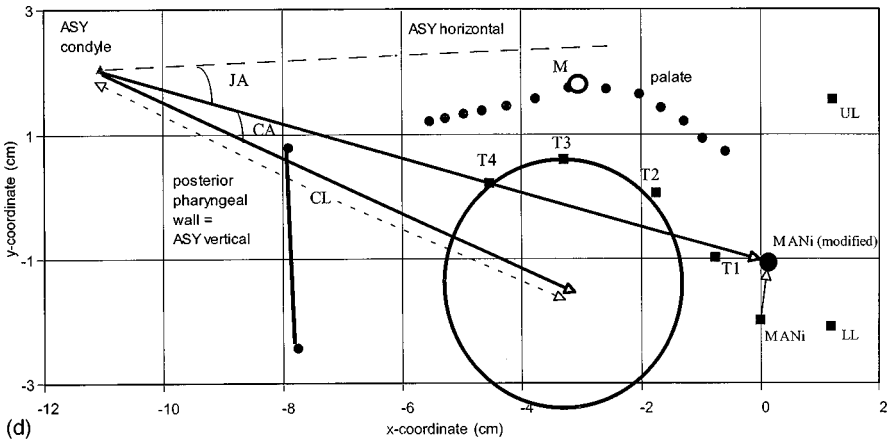

FIG. 2. (*Continued.*)

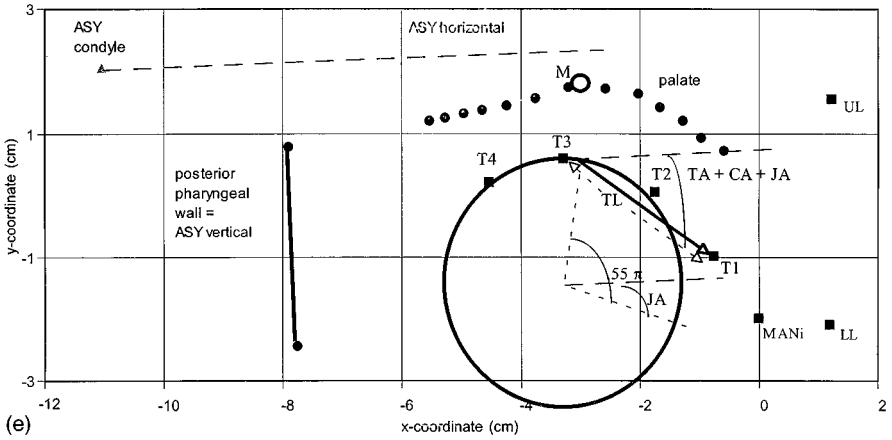

The ASY coordinate system was oriented with respect to the pellet coordinate system so that the ASY posterior pharyngeal wall was parallel to the same structure given by the x-ray microbeam pellet data. (Vertical in the ASY coordinate system is given by the posterior pharyngeal wall.) The position of the ASY condyle was computed to be 11.05 cm to the left and 2.05 cm up from the origin. Also, the highest point on the ASY palate, point *M*, was set to correspond to the highest point on the human palate. This was the only modification made to what is considered the fixed part of the outline of ASY.

(3) Adjustments were made to some of the raw pellet positions so that they would more closely correspond to ASY landmarks [Fig. 2(c)]. The MANi pellet position was shifted upward by 0.75 cm to more closely correspond to the positions of the ASY jaw vector. The upper lip pellet, UL, was shifted downward by 0.75 cm and to the left by 0.75 cm, and the lower lip pellet, LL, was shifted upward by 0.75 cm and to the left by 0.75 cm. These adjustments were made so that these pellet positions would correspond more closely to upper and lower lip positions (UL and LL) of ASY. The ASY jaw vector was drawn from the condyle to the modified MANi pellet position. A length scale which was defined to be the ratio of the length of this jaw vector to the default length of the ASY jaw vector (11.3 cm) was used to scale all further length measures. The ASY lip positions were set to match the adjusted lip pellet positions.

(4) A circle of radius 2 cm (scaled by the length scale derived above) was visually fit to the three rearmost tongue pellets, T2, T3, and T4, and the center of this circle marked as the center of the ASY tongue circle [Fig. 2(d)]. The tongue body vector was drawn from the condyle to the tongue body center.

(5) The intersection of the tongue blade line with the tongue body circle was determined to be the intersection of a line drawn from the tongue body center to the tongue ball at an angle of 0.55π radians with the jaw vector, as described in Mermelstein (1973). The tongue blade line was drawn from this point to the frontmost tongue pellet, T1 [Fig. 2(e)].

(6) The ASY hyoid coordinates were left at default values, and the nasal port was left closed.

When the matching procedure was completed for a test vowel, there was a set of pellets with two-dimensional Cartesian coordinates and an associated set of ASY articulatory coordinates, as well as the first three formant frequencies extracted from the acoustic signal of the human talker. The nine test vowels provided nine pairs of initial corresponding vocal tracts for each subject in the form of pellet coordinates and corresponding ASY coordinates. These pairs were used to initialize the inverse NM and to extract PONM values.

Even when great care was taken in matching midsagittal ASY articulator outlines to pellet positions, midsagittal mismatches between the human and the ASY vocal tract remained. For instance, palatal shape was not taken into account, other than for the location of the point of maximum height, and there was no corresponding PONM to adjust the ASY palatal shape. Also, the midsagittal tongue body never exactly matched a circle, the pellet T1 did not exactly corre-

TABLE I. PONM specifications for coding in the genetic algorithm.

PONM name	Minimum value	Maximum value	ASY default value	Number of bits	Resolution
vtln	0.800	1.314	1.000	8	0.002
trans_phar_inter	0.500	4.000	1.500	6	0.056
trans_phar_slope	0.000	4.000	0.500	6	0.063
soft_pal_pow	−2.000	3.000	0.500	6	0.079
soft_pal_coeff	0.000	4.000	2.667	6	0.063
hard_pal_pow	−2.000	3.000	0.500	6	0.079
hard_pal_coeff	0.000	4.000	2.000	6	0.063

spond to the tip end of the tongue, and the adjustments of the MANi, LL, and UL were rough. Further, there are inaccuracies in the algorithms ASY uses to convert midsagittal shapes to sound, such as the neglect of the compliance of the vocal-tract walls. The recovered values of the PONMs should, therefore, contain some of the effects of these mismatches and inaccuracies, and therefore not completely reflect the anatomical attributes of a talker. However, as long as the PONM values compensate for an inexact matching procedure, the procedure should be successful in characterizing the acoustic output of the human talker for any given midsagittal shape.

III. PONM EXTRACTION

A. Method

The experiments testing the extraction of PONM values were run with various sets of initializing vowels and different sets of PONMs. In any given condition, an optimization (analysis-by-synthesis) procedure was used to attain an optimal acoustic match in the first three formant frequencies over a set of initializing vowels drawn from the set of nine test vowels. At each analysis-by-synthesis step, the optimization procedure presented a candidate set of values for the PONMs. These were used, along with the ASY articulatory coordinates for the initializing vowels, to obtain synthetic output for each initializing vowel. The resulting output for each vowel could be compared to the first three formant frequencies of the same vowel produced by the human subject. The optimization procedure could then adjust the PONM values in further iterations, and, hopefully, improve the acoustic match.

The length of the ASY vocal tract and the parameters of formulas employed to convert midsagittal distances to cross-sectional areas served as PONMs. (Midsagittal distance denotes the distance between the anterior boundary, which includes the tongue and lower lip, and the posterior boundary, which includes the rear pharyngeal wall, soft and hard palates, and the upper lip. Midsagittal distance is a function of position along the center line of the vocal tract.) The length of the vocal tract was varied by using a multiplicative scaling factor for the formant frequencies. The reciprocal of this scaling factor equals the ratio of recovered vocal-tract length to the default vocal-tract length and this measure is called *vtln*. The cross sections in the pharyngeal region of the ASY vocal tract are modeled to be ellipses with the length of one axis equal to midsagittal distance, and the length of the transverse axis fixed. It is known that, for a human talker, the transverse axes are not fixed, but vary as the tongue changes position (Sundberg *et al.*, 1987; Baer *et al.*, 1991). Thus for our purposes, the transverse dimensions in ASY can be thought to represent a kind of average over all possible articulatory configurations attained in the speech of a given individual. For both the subjects tested in this work there were 13 pharyngeal sections. The default transverse lengths in these 13 sections in ASY are 2.0 cm for the lowest section, 2.5 cm for the next highest 3 sections, and 3.0 cm for the final 9 sections. For the purposes of the present experiments these three values were assumed to be the result of a linear fit, where the independent variable was equal to zero for the first section of the pharynx, one for the next three, and two for the final nine sections. The intercept and slope of a line connecting the three transverse pharyngeal dimension values were used as PONMs in some of the experiments. This intercept and this slope are known as *trans_phar_inter* and *trans_phar_slope*, respectively. In the soft palate and hard palate regions of ASY the cross-sectional areas are also modeled as ellipses with the transverse axis length being a parameterized function of the midsagittal distance. These functions are power functions so that ''transverse length $=\mathrm{COEFF}\times(\text{midsagittal distance})^{\mathrm{POW}}$'' and the parameters that appear in uppercase, for each the soft-palate and hard-palate region, were used as PONMs in some of the experiments. These parameters are known as *soft_pal_coeff* and *hard_pal_coeff* for COEFF, and *soft_pal_pow* and *hard_pal_pow* for POW.

The experiments were run with three different sets of PONMs. One set of PONMs, *PONM Set I*, consisted of *vtln* alone, another set, *PONM Set II*, consisted of *vtnl*, *trans_phar_inter*, and *trans_phar_slope*, and a third set, *PONM Set III*, consisted of *vtln*, *trans_phar_inter*, *trans_phar_slope*, *soft_pal_coeff*, *soft_pal_pow*, *hard_pal_coeff*, and *hard_pal_pow*.

An optimization procedure was used to extract the values of a given set of PONMs. The procedure provided an optimum match in the first three formant frequencies between the synthetic and natural vowels from initializing vowels chosen in subsets of the nine test vowels, whose midsagittal shapes had been matched visually. The optimization procedure that was employed in these experiments was the simple genetic algorithm (Goldberg, 1989). Each PONM was coded into strings of ones and zeros to form genes, and these genes were concatenated into longer strings called chromosomes. Table I shows the bounds, resolution, and the number of bits for each PONM gene.

One of two measures of fitness, which are defined below, was assigned to each chromosome. Fitness is a real number measure of acoustic match between the speech produced by ASY with specifications provided by the chromosomes and the speech produced by the human subject over the set of initializing vowels. A chromosome and its real number fitness constitute an individual. To start the simple genetic algorithm, a population of individuals is generated randomly. The algorithm progresses with the choice of including pairs of individuals into a subsequent generation made by fitness proportionate selection. To search the parameter space, mating, which swaps parts of chromosomes cut at a random point between pairs of individuals, and mutation of individual bits can also occur. For the experiments performed here optimization was run 32 times, each time with a population of 200 individuals for 100 generations. The probability of mating within pairs of chosen individuals was 0.6 and the probability of mutation was 0.001.

Two fitness functions were used in these experiments and two measures of goodness-of-fit were used to evaluate the results of these experiments. Intermediate definitions are helpful in defining these measures. For each synthetic test vowel, an individual sum of squared error, or individual SSE, can be computed, as the sum of squared differences between the first three synthetic formant frequencies and the corresponding formant frequencies of the data provided by the human utterance divided by the formant frequencies of the data. Thus the SSE is the sum of squared percent error in the first three formant frequencies,

$$\text{Individual SSE}=\text{SSE}_j=\left(\sum_{i=1}^{3}\left[(f_{ij}^{\text{syn}}-f_{ij}^{\text{data}})/f_{ij}^{\text{data}}\right]^2\right), \tag{1}$$

where $i=$formant number and $j=$test vowel. The fitness of an individual synthetic vowel can be defined as the reciprocal of the individual SSE,

$$\text{Individual Fitness}=\text{Fitness}_j=(\text{SSE}_j)^{-1}. \tag{2}$$

One fitness function used for PONM extraction was the reciprocal of the sum of individual SSEs over a set of initializing vowels, and this is known as the reciprocal of the sum of SSEs, or the RS_SSE fitness,

$$\text{RS\_SSE}=\left(\sum_{j\in\text{initializing vowels}}\text{SSE}_j\right)^{-1}. \tag{3}$$

(To obtain the root-mean-square error in percent of formant frequency, one takes the reciprocal of RS_SSE, and then divides by three times the number of initializing vowels, and then takes the square root.) In some experiments the fitness function was defined to be the minimum of the individual vowel fitness functions over the set of initializing vowels, which is known here as the minimum of the individual reciprocal SSE's, or the MIR_SSE fitness,

$$\text{MIR\_SSE}=\underset{j\in\text{initializing vowels}}{\text{MIN}}\ (\text{SSE}_j)^{-1}. \tag{4}$$

(To obtain the maximum individual root-mean-square error in percent formant frequency, one takes the reciprocal of MIR_SSE, divides by three, and then takes the square root.) The goodness-of-fit for PONM extractions was examined using either, or both, the RS_SSE fitness and MIR_SSE fitness over the entire set of nine test vowels. These are called, respectively, the RS_SSE and MIR_SSE goodness-of-fit measures.

Experiments consisted of a series of optimizations that extracted PONM values with growing sets of initializing vowels. First, PONM extraction was performed using three initializing vowels: the point vowels /iy/, /aa/, and /uu/. The resulting values of the PONMs obtained from the optimization were recorded and the vowel not among the initializing vowels, and with the smallest individual fitness, was chosen to be included in the set of initializing vowels with the original three for subsequent optimization. After another set of PONM values was extracted, the vowel remaining outside the set of initializing vowels with the smallest individual fitness was included into a new set of initializing vowels. This process was continued until all nine test vowels were included into the set of initializing vowels. In this way the evolution of PONM values and goodness-of-fit measures could be tracked as more information was added to the initialization set. Experiments were conducted with PONM Sets I, II, and III, using the RS_SSE fitness function, and they were conducted with the PONM Set III with the MIR_SSE fitness function. An extra experimental condition was added for subject JW16 to test the effect of changes in midsagittal palate height. In this series the modified palate was obtained by moving the highest point of the ''correct'' JW16 palate down by 0.5 cm. PONM Set III and MIR_SSE fitness were used in this series of experiments.

B. Results

The results in terms of goodness-of-fit measures are shown in Fig. 3(a)–(d). Figure 3(a) and (b) shows the RS_SSE and MIR_SSE goodness-of-fit measures, respectively, for subject JW16, and Fig. 3(c) and (d) shows the RS_SSE and MIR_SSE goodness-of-fit measures, respectively, for subject JW40. As more vowels were included into the set of initializing vowels, the goodness-of-fit measures increased overall. In the case of PONM Set III, both the optimization with the RS_SSE fitness criterion and the MIR_SSE fitness criterion were performed. Overall, when the RS_SSE fitness criterion was used for optimization, the RS_SSE goodness-of-fit measure increased faster than when the MIR_SSE fitness criterion was used for optimization. The reverse was also true, so that the MIR_SSE goodness-of-fit measure increased faster as a function of the number of initializing vowels when the MIR_SSE fitness criterion was employed in the optimization than when the RS_SSE fitness criterion was used. Also, optimizations with the PONM Set III, which contained the largest number of PONMs of all the sets, attained greater goodness-of-fit measures than did optimizations with PONM Sets I or II. Moreover, there was little improvement in the goodness-of-fit measures beyond those attained for the initial optimization over the set of three point vowels for the PONM Sets I and II compared to the improvements attained with PONM Set III. It should also be noted that JW16 had better goodness-of-fit measures than did JW40 for PONM Set III extractions. The goodness-of-fit measures for JW16 obtained with the modified palate and

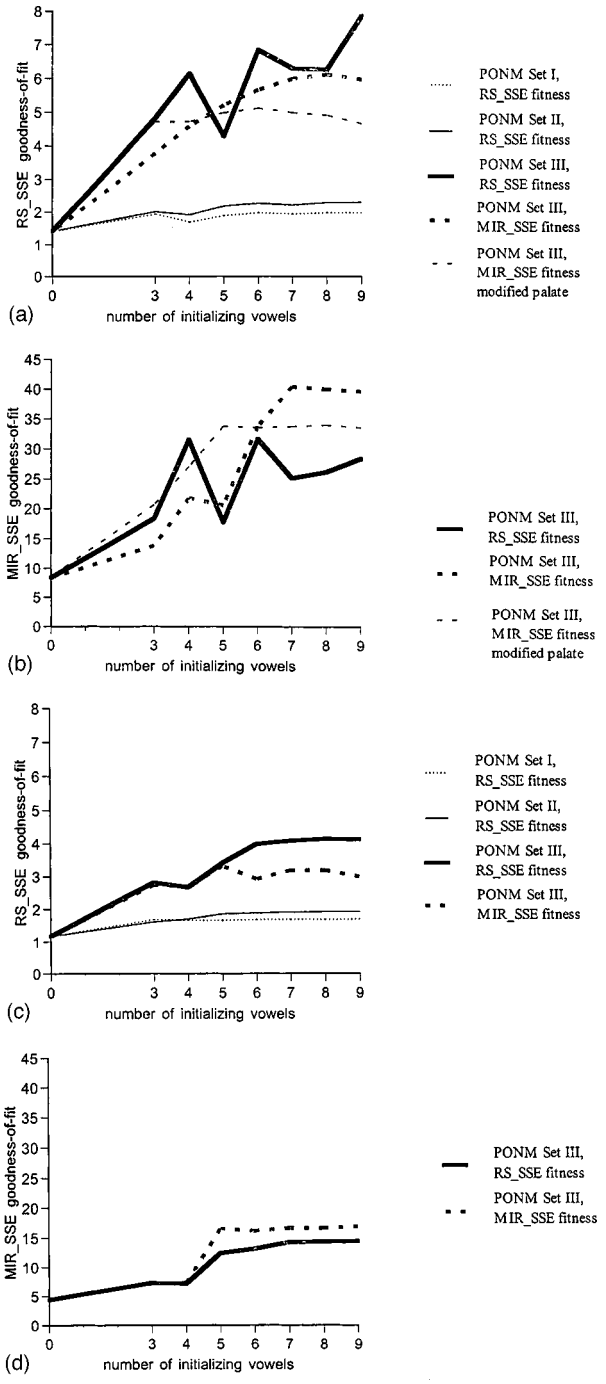

FIG. 3. (a) RS_SSE goodness-of-fit as a function of the number of initializing vowels for subject JW16. (b) MIR_SSE goodness-of-fit as a function of the number of initializing vowels for subject JW16. (c) RS_SSE goodness-of-fit as a function of the number of initializing vowels for subject JW40. (d) MIR_SSE goodness-of-fit as a function of the number of initializing vowels for subject JW40.

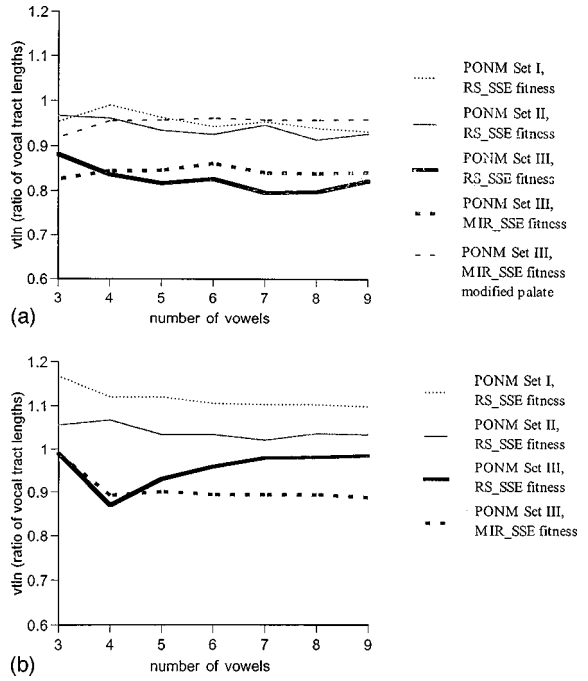

FIG. 4. (a) Ratio of recovered to default vocal tract length ($vtln$) for subject JW16. (b) Ratio of recovered to default vocal tract length ($vtln$) for subject JW40.

MIR_SSE fitness were not generally as large as the goodness-of-fit measures obtained with the correct palate.

The results for vocal-tract length extraction for the two talkers are shown in Fig. 4(a) (subject JW16) and 4(b) (subject JW40) as a ratio of extracted vocal-tract length to the default vocal-tract length ($vtln$) as a function of the number of initializing vowels. The estimates did not vary by more than 0.05 for initializing sets containing more than six vowels. For PONM Set III, optimization with the MIR_SSE criterion showed less variation as a function of the number of vowels than did optimization with the RS_SSE criterion. The PONM Set III extractions always produced vocal-tract lengths shorter than PONM Set I or II extractions did, except in the case of the modified palate for JW16. For comparable conditions, including number of initializing vowels, PONM set, and fitness criterion, the extracted $vtln$ for JW16 was less than that for JW40.

The algorithm extracted *trans_phar_inter* and *trans_phar_slope* values when PONM Set II or Set III were used. These parameters were used to compute the transverse pharyngeal lengths for each pharyngeal section, and these lengths, in turn, were summed over the 13 pharyngeal sections. The ratio of such a sum to the same sum taken for ASY default transverse lengths was called *stpl*. These are plotted against the number of initializing vowels in Fig. 5(a) (subject JW16) and 5(b) (subject JW40). For JW16 the PONM Set II extraction and the PONM Set III extraction with MIR_SSE fitness criterion showed little variation in *stpl* for initializing sets containing more than five vowels, compared to the PONM Set III optimization with the RS_SSE fitness criterion for both subjects. For JW40 $stpl$ varied little for both RS_SSE and MIR_SSE fitness beyond five initializing vowels. The pharyngeal dimension ratios for JW40 were greater than for JW16 for the same number of initializing vowels for PONM Set II and PONM Set III with MIR_SSE fitness. This relation reverses for PONM Set III with RS_SSE fitness with more than five initializing vowels.

For both subjects, the soft-palate power parameter, *soft_pal_pow*, exhibited large variation as a function of the number of vowels in the initialization set [Fig. 6(a) and (b)]. This is particularly true for subject JW16 under the RS_SSE fitness criterion. In all cases the soft-palate power parameter

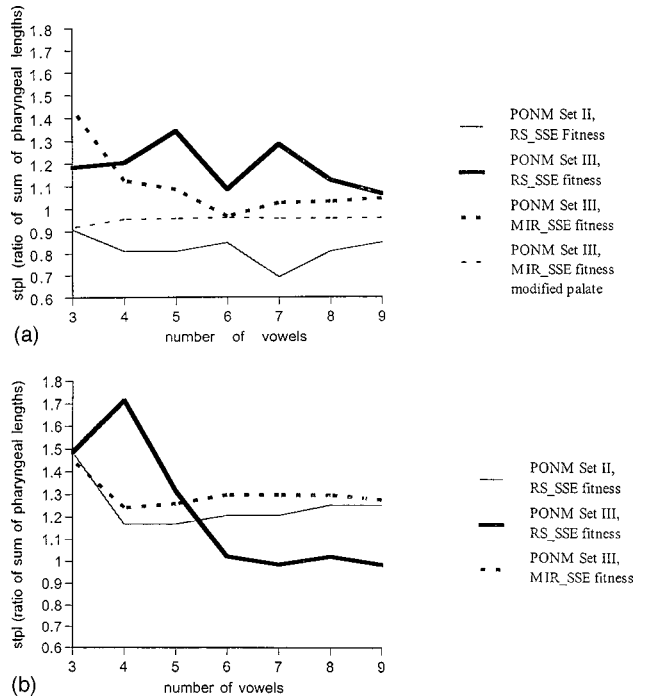

FIG. 5. (a) Ratio of the recovered to the default sums of transverse pharyngeal lengths (*stpl*) versus the number of initializing vowels for subject JW16. (b) Ratio of the recovered to the default sums of transverse pharyngeal lengths (*stpl*) versus the number of initializing vowels for subject JW40.

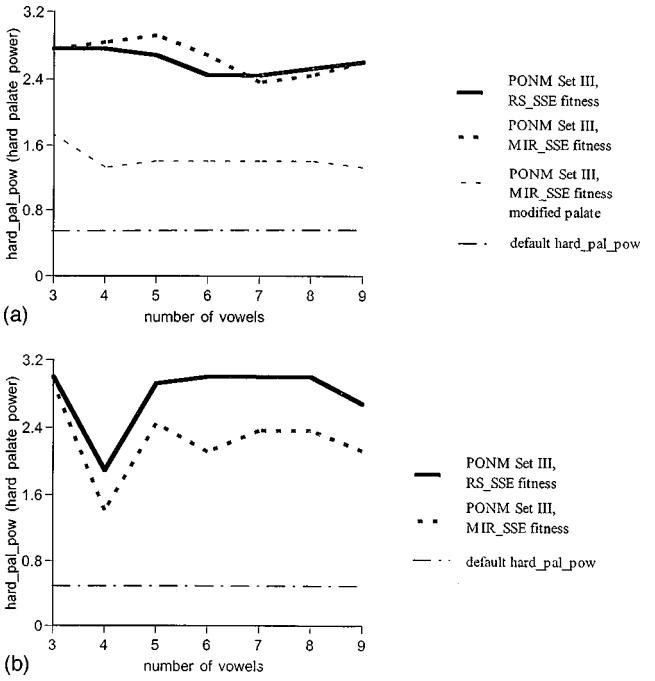

FIG. 7. (a) The power for the function that converts midsagittal distance to cross-sectional area in the hard-palate region (*hard_pal_pow*) versus the number of initializing vowels for subject JW16. (b) The power for the function that converts midsagittal distance to cross-sectional area in the hard-palate region (*hard_pal_pow*) versus the number of initializing vowels for subject JW40.

appeared to be well below the default value of 0.5 for more than five vowels in the initialization set. The results for the hard-palate power parameter, *hard_pal_pow*, are shown in Fig. 7(a) and (b). For both the *soft_pal_pow* and *hard_pal_pow* there was little variation for MIR_SSE fitness for five or more initialization vowels. Also, the recovered hard-palate parameter was always greater than the default value of 0.5.

These results do not completely resolve the issue of whether nine vowels are sufficient for the stable extraction of values for PONM Set III, where there are seven parameter values to be estimated. An example of the difficulty can be seen in Figs. 3(a) and 6(a), both of which illustrate PONM Set III recoveries for JW16 under the RS_SSE fitness criterion. The estimates of goodness-of-fit and *soft_pal_pow* did not approach an asymptote as the number of initializing vowels increased. On the other hand, goodness-of-fit and parameter values appeared to stabilize in the cases where MIR_SSE fitness was used.

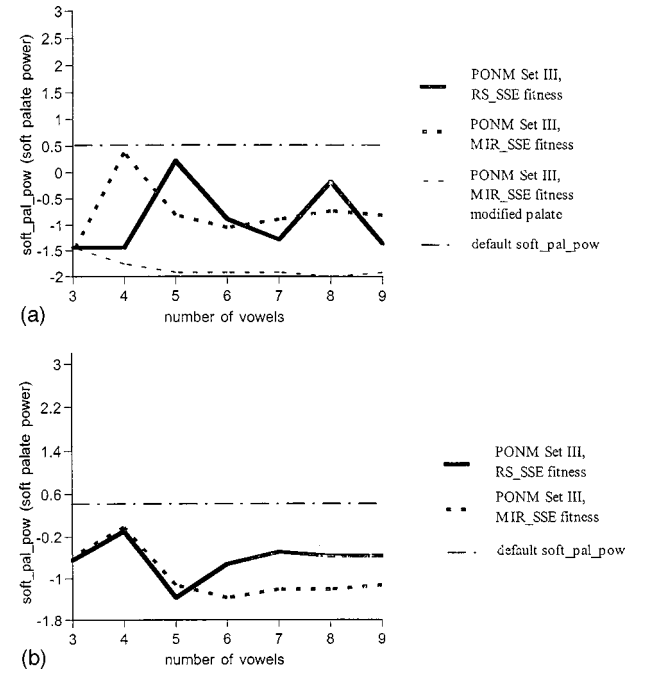

FIG. 6. (a) The power for the function that converts midsagittal distance to cross-sectional area in the soft-palate region (*soft_pal_pow*) versus the number of initializing vowels for subject JW16. (b) The power for the function that converts midsagittal distance to cross-sectional area in the soft-palate region (*soft_pal_pow*) versus the number of initializing vowels for subject JW40.

C. Discussion

The purpose of the experiments in extracting PONM values was to find whether these values were useful in making the standard vocal tract more like the talker's vocal tract. The sense of the phrase ''more like'' depends on the eventual application of this method. For purposes of recovering midsagittal articulatory movement in an analysis-by-synthesis procedure with the standard vocal tract as part of the internal model, it is important that the standard vocal tract produces acoustic output close to that of the human for midsagittal shapes that map to each other under the NM or its inverse. Therefore, an extraction of PONM values is deemed useful if it increases the acoustic match, or fitness, between the standard vocal tract and the human for shapes equivalent under the NM. Note that an extraction of PONM

values should generalize from the set of initializing utterance used to derive them to increase acoustic matching over all possible midsagittal shapes equivalent under the NM. In these experiments, the goodness-of-fit measures test some of this ability to generalize to novel utterances when the set of initializing vowels is a proper subset of the set of the nine test vowels. Therefore, an extraction of PONM values is useful for articulatory recovery purposes, if either one or both the RS_SSE and MIR_SSE goodness-of-fit measures increase as the number of initializing vowels increases.

The experimental results show that extracted PONM values could help to improve the standard vocal tract's ability to imitate the acoustic output of two human talkers. In general, this ability was enhanced as the number of initializing vowels and the number of PONMs increased [Fig. 3(a)–(d)]. This was particularly true when the goodness-of-fit measure used to quantify the match in acoustic output over all nine test vowels coincided with the fitness measure used to extract the PONM values (i.e., RS_SSE fitness and RS_SSE goodness-of-fit, and MIR_SSE fitness and MIR_SSE goodness-of-fit). Therefore the extractions of PONM values were successful according to the criterion of better simulating the acoustic output of two human talkers, with the largest set of PONMs producing the best results in terms of goodness-of-fit. Also, the values of the extracted parameters did not vary as much with the MIR_SSE fitness criterion as with the RS_SSE fitness criterion when more than five vowels were in the initialization set. The cause for this was discovered to be the fact that the individual fitnesses of all test vowels, whether they were in the initialization set or not, grew with the size of the initialization set. This meant that the minimum vowel fitness outside the initialization set was greater than the minimum vowel fitness in the initialization set, for large enough initialization sets. In such cases new vowels included into the initialization set were less likely to perturb the previous extracted PONM values under the MIR_SSE fitness criterion, while such new vowels were more likely to change the extracted PONM values under the RS_SSE fitness criterion. This also helps to explain the reason that parameter value estimates for PONM Set III stabilized with the MIR_SSE criterion and not necessarily for the RS_SSE criterion. These results for the MIR_SSE fitness criterion may only hold for the particular vowel set and particular talkers involved. More work will be necessary before these results can be generalized. Finally, while the correct palate performed better than the modified palate for JW16 for extractions with PONM Set III and MIR_SSE fitness, there were still substantial gains in goodness-of-fit with the modified palate.

Although it is not necessary that the PONM values reflect physical reality exactly for them to be useful, it is of interest to consider this aspect of the PONMs. The results regarding physical reality are difficult to evaluate, because we do not have direct physical measures of the quantities for the subjects involved. However, the physical appropriateness of the PONM values can be investigated indirectly by comparing extracted PONM values under different experimental conditions. Figures 4(a)–7(b) show that there was a large variation in the extracted PONM values depending on the number of vowels included into the initializing set and the PONM set used in the extraction. This sensitivity is an indication that the extracted PONM values do not possess physically realistic values in some conditions. Especially noteworthy were the changes in *vtln* and *stpl* between the various PONM sets, fitness criteria, and in the case of JW16, the height of the hard palate [Figs. 4(a)–5(b)], and, sometimes, the changes in the *soft_pal_pow* and *hard_pal_pow* as a function of the number of initializing vowels [Figs. 6(a), (b), and 7(b)]. It should be noted, however, with the MIR_SSE fitness criterion and the largest PONM set, Set III, that the values of the extracted parameter were stable as a function of the number of initializing vowels when five or more such vowels were employed. Further, when comparisons are made between the female (JW16) and male (JW40) subjects in extracted parameters under like experimental conditions, there were expected trends in *vtln* [Fig. 4(a) and (b)] with male $vtln >$ female $vtln$, and male $stpl >$ female $stpl$, except for PONM Set III with RS_SSE fitness. (For the purposes of these comparisons the modified palate condition for JW16 is excluded.) This exception may have been caused by the fact that the trading between *vtln* and *stpl* that appears to have gone in one direction for three out of four PONM Set III extractions for JW16 and JW40 went in the opposite direction in the experiments with PONM Set III with RS_SSE fitness for subject JW40, for more than five initializing vowels. The extra degrees of freedom provided by the soft- and hard-palate area functions parameters in PONM Set III appear to have allowed for such trading between vocal-tract length and the sum of pharyngeal transverse lengths. Even without the extra parameters, such a trading relation would be expected for the first formant frequency. The Helmholtz resonance frequency can be increased by decreasing pharyngeal volume, either by shortening the vocal-tract length or by decreasing the transverse pharyngeal lengths.

There are other reasons that the physical reality of the extracted PONM values are suspect, but these reasons can be accounted for after the extraction, or they may be obviated by improving the standard vocal tract as a model of the human vocal tract. For instance, the tongue circle was not always a good model for the shape of the tongue body. Instead of enumerating all such mismatches, a few will be illustrated here. The standard vocal tract did not account for wall compliance, which has a tendency to raise the formant frequencies, particularly the first formant frequency. This would lead to underestimates of *vtln* and *stpl* in the results obtained here. Another source of mismatch between the standard and human vocal tracts was in the midsagittal outline of the palate and the rear pharyngeal wall. A related mismatch was in the functional form of the standard vocal tract's conversion of midsagittal distance to transverse length, or, equivalently, mismatches in transverse outlines between the standard vocal tract and the human. As explained below, both of these mismatches should appear in the extracted values of *hard_pal_pow* and *soft_pal_pow*. Neglecting the modified palate condition for JW16, values of *soft_pal_pow* were well below the default value of 0.5 for both subjects [Fig. 6(a) and (b)] and the values of *hard_pal_pow* were well above the default value of 0.5 for both subjects [Fig. 7(a) and

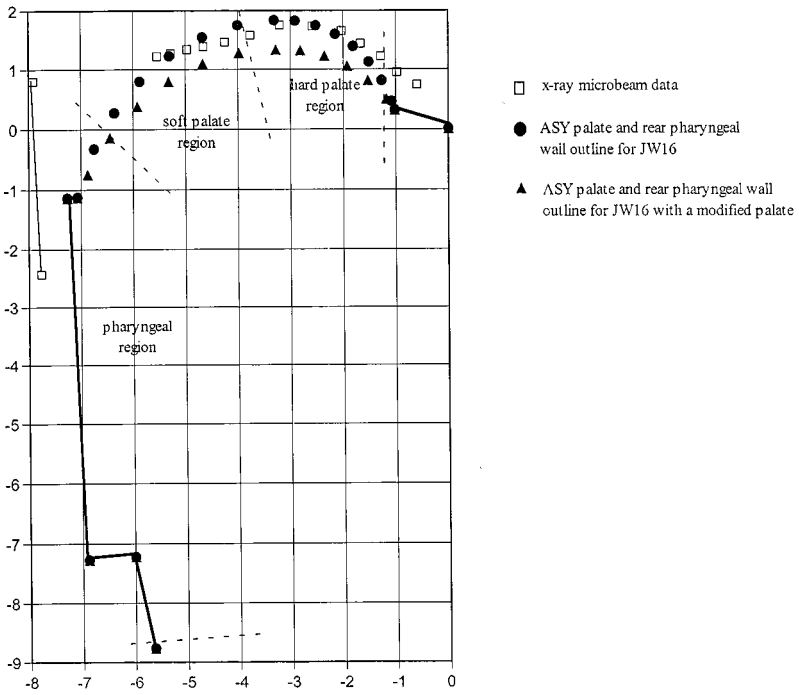

FIG. 8. Fixed midsagittal outlines for JW16.

(b)]. The two mismatches named above, a mismatch in midsagittal shape and in transverse outlines, could have been part of the cause of such discrepancies. One way that midsagittal shape of the standard vocal tract could have mismatched the human was in the average distance of the tongue from the hard and soft palates, where the average would be taken over the set of test vowels. If a midsagittal section of a wall in the standard vocal tract were placed farther from the tongue than it was for the human, on the average, then the power used in the conversion of midsagittal distance to transverse axis length and area would have been overestimated. This would have been in order to magnify area changes, and, therefore, formant frequency changes for tongue positions that were modeled to be too far from the wall. The opposite should have occurred, so that the power would have been underestimated, if the model wall in the midsagittal plane were closer to the tongue, on average, than the corresponding wall was for the human talker. The powers could have also compensated for transverse shape outline mismatches. The default behavior of the standard vocal tract is for the transverse axis length to grow as the square-root of the distance of the tongue from the hard or soft palates. If the human transverse outline had been triangular, then the corresponding transverse dimension would have been a linear function of midsagittal distance, and if it had been rectangular, then the corresponding transverse dimension would have been the zero power of midsagittal distance. Many power laws are possible, and they only reflect an average behavior.

The possibility of midsagittal shape mismatches is explored for subject JW16 in Fig. 8, which shows fixed points of the ASY outline corresponding to hard and soft palates and the rear pharyngeal wall for both the correct JW16 palate and the modified JW16 palate. These points and lines are overlayed onto the palate and rear pharyngeal wall traces from the x-ray microbeam data. The rear part of the JW16's palate trace and rear pharyngeal wall trace indicate that the ASY soft palate was closer to the tongue than it was for the human soft palate for the initializing vowels. This could have been the reason that $soft\_pal\_pow$ was consistently less than the default. In the hard-palate region the subject's midsagittal palate outline was close, or slightly inside the correct ASY palate for JW16. The ASY hard palate having been slightly outside the human palate could have been part of the cause of the relatively large value of the extracted $hard\_pal\_pow$. Also, mismatches in the transverse outline shapes in the hard-palate region cannot be ruled out. The power laws derived by Baer *et al.* (1991) show that a higher power than the ASY default may be reasonable in the hard-palate region where vertical cross sections are orthogonal to the vocal tract. The experiments with the modified palate for JW16 showed the expected trends in both $soft\_pal\_pow$ and $hard\_pal\_pow$. This modified palate brought the posterior and palate walls closer to the tongue in both the soft- and hard-palate regions, thus reducing the extracted values for both powers [Figs. 6(a) and 7(a)].

IV. CONSTRUCTING THE INVERSE NORMALIZING MAP (NM)

A. Method

The inverse NM maps the midsagittal shapes of the standard vocal tract to the midsagittal shapes of the human vocal tract. In these experiments the standard vocal tract was the ASY vocal tract, whose midsagittal shapes are determined by a set of articulatory coordinates (Fig. 1), and the midsagittal shape of the human vocal tract was equated with pellet positions in x-ray microbeam data. The ASY coordinates were the Cartesian coordinates of the hyoid, XP and YP (the values for these coordinates remained fixed), the tongue body vector length and angle, CL and CA, the tongue tip vector length and angle, TL and TA, the jaw angle, JA, the lips'

horizontal coordinate LH, and the lower and upper lip vertical positions, LLV and ULV. The pellet data consisted of the adjusted Cartesian coordinates of each of seven pellets: the four tongue pellets, T1, T2, T3, and T4, the upper and lower lip pellets, UL and LL, and the lower incisor pellet, MANi.

Subsets of the nine test vowels, whose vocal tract shapes had been visually matched with ASY midsagittal shapes, were used to initialize the construction of the complete inverse NM. The inverse NMs were generalized from the initializing vowels from the test set using artificial neural networks. The neural networks were multilayer perceptrons, designed with the MATLAB Neural Network Toolbox (Demuth and Beale, 1994) consisting of input nodes, a hidden layer, and an output layer. The input layer had ten nodes corresponding to each of the ASY articulator coordinates, with input values equal to scaled versions of these coordinates. The values of coordinates XP, YP, CL, and TL, normally given in units of 1/112 cm, were divided by 100. The values of coordinates LLV, ULV, and LH, also normally given in units of 1/112 cm, were divided by 10. These scalings had the effect of keeping the absolute values of these input parameters less than one. The remaining input parameters were in radians, and their absolute values were generally less than one. The input neurons were connected to neurons in the hidden layer using hyperbolic tangent weighting functions. The output layer had 14 neurons, a neuron for each adjusted Cartesian coordinate of each pellet position, producing two neurons for each pellet, one for the *x*-coordinate and the other for the *y*-coordinate. The output neurons were connected to the neurons in the hidden layer using linear weighting functions.

The purpose of the experimentation here was to find networks that would generalize to novel vowel articulations with the greatest possible accuracy. Two parameters were varied in the design of the networks to meet this goal. One was the number of neurons in the hidden layer and the other was the error criterion used for training the networks. The number of hidden neurons helped to determine the amount of variation allowed in the neural network's approximation to the functional mapping from the space of ASY articulator coordinates to the space of x-ray microbeam pellet coordinates. In applications of neural networks to regression problems if too few hidden neurons are used, then the approximate mapping will not allow for enough variation to do a good job of approximating the true mapping. If too many hidden neurons are used, then ''overfitting'' can occur with excess degrees-of-freedom allowing for a very tight fit to the mapping on the training data, but with extraneous variation. In either the case of too few or too many neurons the approximate neural net mapping will not generalize well to data outside its training set.

Training of the neural networks was done with backpropagation using the Levenberg–Marquadt algorithm (Press *et al.*, 1986). An error measure was used in both the training and test of the neural networks, and this was the sum of squared error in the pellet coordinates over all output neurons. Training was halted when the error in each initializing vowel used in the training fell below a training error criterion. The training error criterion was chosen by the experimenter in combination with the number of hidden neurons to produce the smallest possible maximum sum of squared error in each of the vowels not in the training or initializing set of three vowels, /aa/, /iy/, and /uu/. The vowel not in the initializing set and with the largest sum of square error was then included into the set of initializing vowels for training subsequent networks. This procedure continued until eight vowels were included in the initialization set. The number of neurons in the hidden layer was left unchanged until there was a failure to train a network, and then this number was adjusted upward.

TABLE II. Parameters for inverse NM neural nets for subjects JW16 and JW40.

Number of initializing vowels	Number of neurons in the hidden layer	Training error criterion
3	5	.001
4	5	.001
5	5	.001
6	5	.001
7	8	.001
8	8	.001

B. Results

The design parameters of the neural networks as a function of the number of initializing vowels are summarized in Table II. The design parameters were the same for both JW16 and JW40.

For each set of initializing vowels or neural network, the sum-of-squares (SSE) error predicted by the trained neural net and actual pellet positions for each vowel not included into the set of initializing vowels was computed. The maximum of these SSE's was plotted as a function of the number of vowels in the training set for each subject [Fig. 9(a) and (b)]. The overall trend was for this measure to decrease as more vowels were included into the training set for both subjects. For subject JW16, the SSE in the ninth vowel's pellet positions, based on the neural net trained on the other eight was 0.1859 cm^2, which corresponds to a root mean square error of 0.115 cm in each pellet coordinate. For subject JW40, the SSE error in the ninth vowel's pellet positions, based on the neural net trained on the other eight vowels, was 0.6184 cm^2, which corresponds to a root-mean-square error of 0.210 cm in each pellet coordinate. A comparison of Fig. 9(a) and (b) shows that the neural net mapping converged more quickly for JW16 than for JW40.

C. Discussion

If neural networks can be trained with initial corresponding vocal tracts in such a way that the mapping from standard vocal-tract coordinates to pellet coordinates improves for utterances not in the training set, then the generalization of the inverse normalizing map will have been successful. It was possible to train neural networks so that the pellet positions of one vowel could be predicted with less than 1-cm^2 SSE from the corresponding ASY coordinates of that vowel, when the training set contained seven or eight

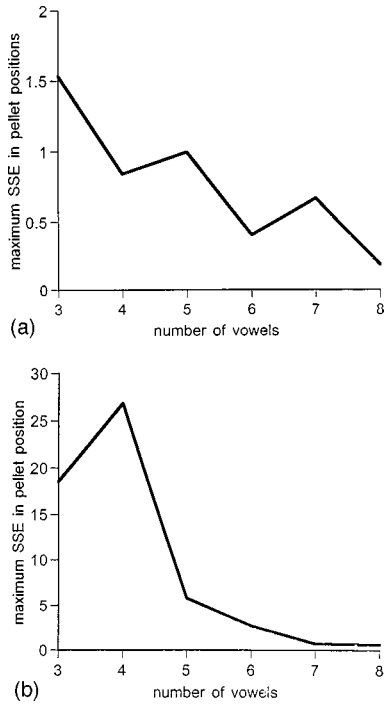

FIG. 9. (a) Maximum sum of squared errors in pellet position versus the number of vowels used to train a neural network in an inverse NM (ASY-to-pellet-position mapping) for subject JW16. (b) Maximum sum of squared errors in pellet position versus the number of vowels used to train a neural network in an inverse NM (ASY-to-pellet-position mapping) for subject JW40.

vowels. The data were examined to find the cause of the relatively slow convergence of the neural net mapping for JW40. It was found that the fourth vowel included into the training set, the vowel /ah/, was produced with a particularly flat tongue body (i.e., the pellets were in line). This meant that there was a large amount of uncertainty in determining the position of the tongue body center when the ASY articulatory coordinates were matched with the pellet positions. However, the neural network mappings for JW40 behaved well after the fifth vowel was included in the training set.

V. MIDSAGITTAL ARTICULATORY MOVEMENT RECOVERY WITH NORMALIZATION

A. Introduction

In this part of the investigation the normalization procedure was combined with the recovery of midsagittal articulatory movement from speech acoustics in a preliminary test of whether normalization aids in the recovery process. The test was performed on the vowel-to-vowel token /iy aa/ spoken by subjects JW16 and JW40 from the XRMB-SPD. The midsagittal articulatory movement recovery procedure was performed as described for previous experiments (McGowan, 1994; McGowan and Lee, 1996), using analysis-by-synthesis with the synthesis provided by the task-dynamic model, whose and effectors are the articulators of the ASY vocal tract (Saltzman and Munhall, 1989). A brief description of the task-dynamic model will now be given. The reader is referred to Saltzman and Munhall (1989) for a more complete description, and to McGowan (1994) and McGowan and Lee (1996) for its application to articulatory movement recovery.

The task-dynamic model specifies linear, second-order dynamics for constriction location and constriction degree pairs during activation intervals. In the experiments performed here, the location-degree pair employed was tongue body constriction location (TBCL) and the tongue body constriction degree (TBCD). The beginning and end activation times for these variables are assumed to be the same, as are the natural frequencies of their dynamics. The targets, or rest positions of the second-order systems, correspond to the place (TBCL) and degree (TBCD) of maximal constriction made with the tongue body. The task-dynamic model controls ASY, requiring that certain articulators move so that the trajectories of TBCL and TBCD are attained, as specified by the task-dynamic parameters. In the case of TBCL and TBCD, the tongue body vector (CL and CA) and the jaw angle (JA) can be recruited by task-dynamics for the TBCL and TBCD trajectories (see Fig. 1). To implement this, the linear, second-order systems of TBCL and TBCD are transformed into differential equations prescribing the evolution of the ASY articulators CL, CA, and JA using geometric transformations between the two coordinate systems. Because there are more ASY than task dynamic degrees-of-freedom, CL, CA, and JA can be recruited with various weightings. In the experiments performed here these weightings were equal. Thus in the implementation of task-dynamics the trajectories of ASY articulators are calculated in a numerical time-step extrapolation, providing time varying acoustic signals, which can be described in terms of formant frequency trajectories. These can be compared with formant frequency trajectories of speech data for subsequent adjustment of the task-dynamic parameters in an optimization procedure.

An optimization procedure was used to obtain the task-dynamic parameter values providing for an acoustic match with the data. For each subject, this recovery procedure was performed using the ASY default values of the PONMs and extracted values of PONMs. After each recovery of the task-dynamic parameters, the task-dynamic model was run to obtain the recovered ASY articulator trajectories, and these were converted into recovered pellet positions using appropriate inverse NMs. The recovered and measured pellet trajectories could then be compared to determine whether there was any improvement in midsagittal articulatory recovery using extracted PONM values compared to default PONM values.

B. Method

For both JW16 and JW40, and for the utterance /iy aa/ in the XRMB-SPD, the three rearmost tongue pellet (T2, T3, and T4) positions and the jaw pellet (MANi) positions were extracted at approximately 20-ms intervals, as were the first three formant frequencies. The task-dynamic recovery procedure was run for each subject under two conditions: one where default values of the Set III PONMs were used and the other where the values of the Set III PONMs were extracted with all nine initializing vowels with the MIR_SSE fitness

criterion. (In the case of JW16 the PONM values were re-extracted with the ASY default palate, because the task-dynamic model does not allow for variable palate shapes.) This new extraction was performed with nine initializing vowels with the MIR_SSE criterion. The resulting PONM values were nearly the same as those extractions described for JW16 with the modified palate discussed earlier. The MIR_SSE goodness-of-fit for the default palate extraction was 32.34 as opposed to 33.64 for the modified palate and 39.69 for the correct JW16 palate.)

The task-dynamic recovery was performed using a simple genetic algorithm with an elitist strategy, which required that the fittest individual of any generation be preserved into the subsequent generation. The individuals of the genetic algorithm consisted of chromosomes and fitnesses. The chromosomes specified task-dynamic parameters, which could be used for synthesis of a proposed utterance. The fitness of an individual was the reciprocal of the sum over frame number and the first three formant numbers of the squared percentage difference in formant frequency between the data and the proposed utterance:

$$\text{Fitness} = \left(\sum_{j} \sum_{i=1}^{3} \left[(f_{ij}^{\text{syn}} - f_{ij}^{\text{data}}) / f_{ij}^{\text{data}} \right]^2 \right)^{-1}, \tag{5}$$

where i = formant number and j = frame number. The genetic algorithm was started from an initial random assortment of 100 individuals for 100 generations. The probability of mutation was 0.001 and the probability of mating was 0.6.

The chromosomes were constrained to contain the specifications of two activations of the tongue body coordinates tongue body constriction location (TBCL) and tongue body constriction degree (TBCD). The parameters that were coded into the chromosomes were the initial and final times of the activations, the natural frequencies of the activations, and the targets of TBCL and TBCD for each of the activations. The first activation was intended to get the tongue into position for the steady state of the first vowel /iy/, and the second was intended to model the transition from the /iy/ to the /aa/. (The comparisons between proposed utterances and data took place after the first activation was finished to give the model time to attain the high-front vowel.) The dynamics of the each TBCL and TBCD were assumed to be critically damped.

In order to convert the recovered task-dynamic parameters and ASY articulatory trajectories to pellet trajectories, inverse NMs were constructed for JW16 and JW40. To ensure that statistical differences in neural networks did not affect the differences in the midsagittal recoveries' abilities to track pellet data, eight inverse NMs (eight neural nets trained from different random conditions) for each subject were constructed. These new mappings were specialized versions of the inverse NMs constructed earlier. Because TBCL and TBCD recruit only the jaw (JA) and the tongue body (CL and CA), these coordinates were used as inputs to the neural nets. The outputs were the coordinates of pellets T2, T3, T4, and MANi. The neural nets that generalized the inverse NM from the initializing vowels were trained with three input nodes corresponding to JA, CL, and CA and eight output nodes corresponding to the Cartesian coordinates of the pellets of interest. Each network had eight neurons in the hidden layer, and was trained to attain 0.05 error in the sum of square pellet positions over the training set of initializing vowels. The value of the error criterion in these experiments with a reduced set of articulators was increased from the values used in the experiments with a full set of articulators, because the pellet coordinates could not be predicted as well with this reduced set. For JW16 eight initializing vowels were used to design the neural networks that generalized the inverse NM, excluding the vowel /eh/ which was used for checking the trained networks. For JW40 seven initializing vowels, excluding /ah/ and /eh/, were used to train the neural networks inverse NM generalization. The vowel /ah/ for JW40 was excluded because, as noted previously, it typically had large errors on networks trained on other vowels.

C. Results

For both subjects, JW16 and JW40, the recovered task-dynamic parameter values for each recovery condition (with default PONM values and with extracted PONM values) were converted into trajectories of JA, CL, and CA. For each subject, eight inverse NMs were constructed according to the method described above. For each such network, the pellet coordinate trajectories were obtained from the ASY articulator trajectories corresponding to each the recovery with default PONM values and the recovery corresponding to extracted PONM values. To help quantify how well each type of recovery tracked the measured pellet positions, the root-mean-square error between predicted and measured pellet coordinates was calculated for each of the eight neural networks, where the mean was taken over the pellet coordinate and the time frame number. The time frames of interest spanned the part of the /iy aa/ utterance that corresponded to transition. For subject JW16 the comparison was over 200 ms or 10 frames of data, and for JW40 the comparison was over 300 ms or 15 frames of data.

Root-mean-square errors in the recovered versus measured pellet coordinates measure how well the midsagittal recovery procedure did with the extracted PONM values. The average, over the eight neural networks, of the root-mean-square error in the recovered pellet coordinates with extracted PONM values was 0.46 cm with a standard deviation of 0.02 cm for subject JW16. For subject JW40, this quantity was 0.55 cm with a standard deviation of 0.02 cm. These quantities can be compared to the root-mean-square error for the test vowel /eh/, averaged over the eight neural networks for each subject. For JW16 this quantity had an average value of 0.22 cm with a standard deviation of 0.02 cm, and for JW40 the average value was 0.23 cm with a standard deviation of 0.02 cm.

In both the case of JW16 and JW40, the recovery with extracted PONM values tracked the pellets more closely than did the recovery with default PONM values. Examples of recovery with default PONM values and extracted PONM values are given in Fig. 10(a) and (b), respectively. The results shown in these figures are for JW40 and for one neural network mapping from ASY articulator coordinates to pellet coordinates. In both figures the unfilled symbols are the po-

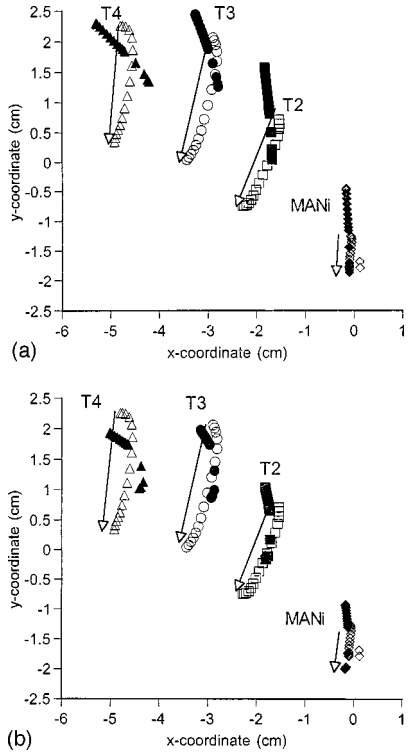

FIG. 10. (a) Result of articulatory recovery (including the mapping from ASY articulatory coordinates to pellet positions) without normalization. Pellet positions (T2, T3, T4, and MANi) for subject JW40 producing the vowel-to-vowel transition /iy/ to /aa/. The unfilled symbols are the pellet position data from the XRMB-D. The filled symbols are the recovered pellet positions recovered using default PONMs and a neural network mapping from ASY articulator coordinates and pellet coordinates. The arrows indicate the direction of motion. (b) Result of articulatory recovery (including the mapping from ASY articulatory coordinates to pellet positions) with normalization. Pellet positions (T2, T3, T4, and MANi) for subject JW40 producing the vowel-to-vowel transition /iy/ to /aa/. The unfilled symbols are the pellet position data from the XRMB-D. The filled symbols are the recovered pellet positions recovered using extracted PONMs and a neural network mapping from ASY articulator coordinates and pellet coordinates. The arrows indicate the direction of motion.

sitions of the T2, T3, T4, and MANi pellets taken from the XRMB-SPD at various times, and the filled symbols are the recovered pellet positions with default PONM values [Fig. 10(a)] and with extracted PONM values [Fig. 10(b)]. In this comparison the pellet positions recovered with extracted PONM values were closer to the pellet data than the pellet positions recovered with default PONM values. In quantitative terms, the mean difference in the root-mean-square errors over the eight neural networks between the recovery with extracted PONM values and the recovery with default PONM values was 10% with a standard deviation of 3% for subject JW16. For subject JW40 the mean difference was 25% with a standard deviation of 5%. Thus the extracted PONM values improved the recovery accuracy for both subjects.

D. Discussion

The results of this part of the experimentation, while encouraging, point to further research. In neither the case of JW16 or of JW40 did the root-mean-square error of the recovered pellet coordinate trajectories reach the root-mean-square error in the neural network test vowel /eh/. Also, the recovery exhibited in Fig. 10(b) is not completely satisfactory. One problem is the lack of flexibility in the circular tongue body. Also, the recoveries here were probably overconstrained because active tongue tip control was not allowed for in the task-dynamic recovery. Observations show that a pellet included in these experiments, T2, which was the second most forward tongue pellet, was a part of tongue blade motion. There were also many constraints on the task-dynamics parameters themselves, such as critically damped motion and particular articulator weighting schemes that might be loosened to improve the recovery results. The results for JW16 may be improved if the ASY palate shape used in the midsagittal recovery fit JW16 better.

VI. CONCLUSION

Detailed tests of a vocal-tract normalization procedure have been done on the data from two individuals contained in the X-ray Microbeam Speech Production Database. These experiments show that it was possible to extract PONM (Parameters Orthogonal to the range space of the NM) values for two human subjects that allowed for better acoustic imitation of the human's vowels by the standard vocal tract. The goodness-of-fit measures increased with the number of variable PONMs, and the goodness-of-fit measure was greatest in cases where the corresponding fitness measure was employed by the optimization procedure. Further, it was possible to construct inverse NMs (normalizing maps) for each of these two subjects, with good accuracy (i.e., better than 0.25-cm root-mean-square error in the pellet coordinates). However, the construction of the inverse NM can be hindered when there is a poor match between the midsagittal plane of the standard vocal tract and the midsagittal plane of the human vocal tract. This was the case for a vowel that was produced with a particularly flat tongue, because the standard vocal tract models the tongue body with a circle of fixed radius. An improvement in the control of the midsagittal outline of the articulatory synthesizer could alleviate such problems. Progress toward this end has been made with the Haskins Laboratories configurable articulatory synthesizer (CASY), where the tongue body is no longer restricted to be the shape of a fixed-radius circle (Rubin *et al.*, 1996). (CASY contains many other features which allows for a realistic modeling of midsagittal vocal-tract shape.) Further, the way to control a flexible model of the tongue is suggested by the statistical modeling of midsagittal tongue shape done, for example, by Harshman *et al.* (1977) and Maeda (1990). Maeda showed that four principle components could account 88% of the variance in tongue shape over 1000 digitized tracings from cineradiographic images of 10 French sentences produced by one talker. These components corresponded to the articulatory features of (1) jaw position, (2) tongue-dorsal position in terms of the front–back dimension, (3) tongue-dorsal shape in terms of flat versus arched shape, and (4) tongue-tip position in terms of raised versus lowered position. These coordinates could replace some or all of the ASY coordinates affecting tongue position and shape: JA, CL, CA, TL, and TA.

Whether, and under what conditions, the extracted PONM values correspond to physically accurate values is not completely known. Some expectations were met in terms of vocal-tract length differences between the female subject and the male subject for all experimental conditions. Also, the distance-to-area function parameters exhibited the expected changes with changes in the vocal-tract palate height. Overall the MIR_SSE fitness function produced PONM values that did not vary as a function of the number of initializing vowels as much as those extracted with the RS_SSE fitness function. This was the result of the fact that individual vowel fitness for each vowel in the test set tended to increase with the size of the vowel initialization set.

The midsagittal articulatory movement procedure was able to track pellet positions for a vowel-to-vowel utterance more closely when the standard vocal tract was adjusted with the results of the normalization procedure compared to when these adjustments were not made. However, more experimentation with the normalization and subsequent articulatory movement recovery will reveal the best way for combining these procedures. Future research will also explore ways to perform normalization without articulatory data for initialization and with different standard vocal-tract models and task-dynamic constraints.

ACKNOWLEDGMENTS

This work was supported by NIH Grant No. DC-01247 to Sensimetrics Corporation. The authors thank Philip Rubin, Ken Stevens, and Hani Yehia for providing very helpful comments on earlier versions of this paper.

Badin, P., Beautemps, D., Laboissière, R., and Schwartz, J. L. (**1995**). ''Recovery of vocal tract geometry from speech signal for vowels and fricative consonants using midsagittal-to-area function conversion model,'' J. Phonetics **23**, 221–229.

Baer, T., Gore, J. C., Gracco, L. C., and Nye, P. W. (**1991**). ''Analysis of vocal tract shape and dimensions using magnetic resonance imaging: Vowels,'' J. Acoust. Soc. Am. **90**, 799–828.

Beautemps, D., Badin, P., and Laboissière, R. (**1995**). ''Deriving vocal tract area functions from midsagittal profiles and formant frequencies: A new model for vowels and fricative consonants based on experimental data,'' Speech Commun. **16**, 27–47.

Coker, C. (**1976**). ''A model of articulatory dynamics and control,'' Proc. IEEE **64**, 452–460.

Demuth, H., and Beale, M. (**1994**). *Neural Network Toolbox User's Guide* (The MathWorks, Inc., Natick, MA).

Goldberg, D. E. (**1989**). *Genetic Algorithms in Search, Optimization, and Machine Learning* (Addison-Wesley, Reading, MA).

Harshman, R., Ladefoged, P., and Goldstein, L. (**1977**). ''Factor analysis of tongue shapes,'' J. Acoust. Soc. Am. **62**, 693–707.

McGowan, R. S. (**1994**). ''Recovering articulatory movement from formant frequency trajectories using task dynamics and a genetic algorithm: Preliminary studies,'' Speech Commun. **16**, 49–66.

McGowan, R. S. (**1997**). ''Vocal tract normalization for articulatory recovery and adaptation,'' in *Talker Variability in Speech Processing*, edited by Keith Johnson and John W. Mullennix (Academic, San Diego), pp. 211–226.

McGowan, R. S., and Lee, M. (**1996**). ''Task-dynamic and articulatory recovery of lip and velar approximations under model mismatch conditions,'' J. Acoust. Soc. Am. **99**, 595–608.

Maeda, S. (**1990**). ''Compensatory articulation during speech: Evidence from the analysis and synthesis of vocal-tract shapes using an articulatory model,'' in *Speech Production and Speech Modeling*, edited by W. J. Hardcastle and A. Marchal (Kluwer Academic, New York), pp. 131–149.

Mermelstein, P. (**1973**). ''Articulatory model for the study of speech production,'' J. Acoust. Soc. Am. **53**, 1070–1082.

Press, W. H., Flannery, B. P., Teukolsky, S. A., and Vetterling, W. T. (**1986**). *Numerical Recipes: The Art of Scientific Computing* (Cambridge University Press, Cambridge, England).

Rubin, P., Baer, T., and Mermelstein, P. (**1981**). ''An articulatory synthesizer for perceptual research,'' J. Acoust. Soc. Am. **70**, 321–328.

Rubin, P. E., Saltzman, E. S., Goldstein, L., McGowan, R. S., Tiede, M., and Browman, C. (**1996**). ''CASY Extensions to the Task Dynamic Model,'' in *Proceedings of the 4th Speech Production Seminar*, Grenoble, France, pp. 125–128.

Saltzman, E. L., and Munhall, K. G. (**1989**). ''A dynamic approach to gestural patterning in speech production,'' Ecological Psychology **14**, 333–382.

Schroeter, J., and Sondhi, M. M. (**1994**). ''Techniques for estimating vocal-tract shapes from the speech signal,'' IEEE Trans. Speech Audio Process. **2**, 133–150.

Sundberg, J., Johansson, C., Wilbrand, H., and Ytterbergh, C. (**1987**). ''From sagittal distance to area,'' Phonetica **44**, 76–90.

Westbury, J. R. (**1994**). *X-ray Microbeam Speech Production Database User's Handbook (Version 1.0)*. Waisman Center on Mental Retardation and Human Development, Madison, WI. Unpublished.

Acoustic properties of a reed (*Arundo donax* L.) used for the vibrating plate of a clarinet

E. Obataya
Institute of Agricultural and Forest Engineering, University of Tsukuba, Tsukuba, 305-8572, Japan

M. Norimoto
Wood Research Institute, Kyoto University, Uji, Kyoto, 611-0011, Japan

(Received 14 July 1998; accepted for publication 18 May 1999)

The effect of water-soluble extractives on the acoustic properties of a reed (*Arundo donax* L.) used for the vibrating plate of a clarinet was investigated at various relative humidities (RH). At low RH levels, the extractives enhanced the dynamic Young's modulus of the reed. This effect was reduced with increasing RH because of the deliquescence of extractives. It was suggested that the quality of the reed is improved by the extractives reinforcing its dry part. The extractives also increase the density and the internal friction of the reed remarkably. These might affect the frequency response of the reed to make the tone richer and softer. The tone quality of the reed lost by the removal of extractives was reproduced by impregnating the reed with glucose, which is the most abundant constituent of natural extractives. © *1999 Acoustical Society of America.*
[S0001-4966(99)06508-X]

PACS numbers: 43.75.Ef [WJS]

INTRODUCTION

A kind of reed, *Arundo donax* L., is used for the vibrating plate (reed) of woodwind instruments. Much attention is paid to the reed because its quality and shape influence the tone quality and performance of the instruments (Obataya, 1996a). The reed contains many water-soluble extractives mainly consisting of glucose, fructose, and sucrose. These extractives increase both the dynamic Young's modulus (E') and internal friction (Q^{-1}) of the reed along the grain in the dry state (Obataya *et al.*, 1999). Since the extractives are easily dissolved in water, they can hardly affect the acoustic properties of the reed when a reed is used in completely wet condition (Obataya, 1996b). In practice, however, the inner part of the reed is not always saturated with water unless it is soaked in water or used for a long period of time. Therefore, it is thought that the extractives can affect the quality of the reed in which some parts are still unsaturated with water. In this study, the acoustic properties of the reed over a frequency range of 0.3 to 10 kHz were measured at various levels of relative humidity (RH) to investigate the effects of extractives. In addition, an attempt was made to impregnate the reed with glucose to recover the acoustic properties reduced by the removal of extractives. The change of reed quality due to the water-extraction or glucose-impregnation was evaluated by professional clarinet players.

I. MATERIALS AND METHODS

A. Measurements of acoustic properties

In order to determine the acoustic properties of the reed, we used an internode of tubelike reed that had been harvested in Antibe (France) and selected for commercial clarinet reeds. The tube was separated in the fiber direction, and its inner parts were cut into the plates of 100 to $135\times10\times1.5$ mm, along the fiber, tangential, and radial direction, respectively. To remove the natural extractives, the reeds were soaked in water for 4 days, air-dried at room temperature and then steamed at 60 °C and 100% RH for 12 hours to recover the cells which collapsed during drying (Obataya, 1996b). To impregnate the reed with glucose, water-extracted reeds were soaked in 30% aqueous solution of glucose for 4 days with intermittent evacuation and ultrasonic vibration, then air-dried and steamed for 12 hours. It has been previously confirmed that the effects of steaming on the acoustic properties are smaller than those of water-extraction and glucose-impregnation.

The E' and Q^{-1} of these reed plates along the fiber direction were measured by using a free–free beam flexural vibration method (Hearmon, 1958). This method has been frequently used for measuring the acoustic properties of wooden beams. The measuring apparatus is schematically illustrated in Fig. 1. A thin piece of 3×10 mm iron was attached to the end of a reed plate. The plate, hung by silk threads, was vibrated by a magnetic driver, and the amplitude of vibration was detected using a B&K type 4145 microphone. The signal passed through the bandpass filter was observed by a fast fourier transform (FFT) analyzer, ADVANTEST TR9407. After the resonance frequency of the plate (f) was determined, the magnetic driver was switched off and the decrement of vibration was recorded. The E' value of the plate was calculated from f of the first to eighth modes, and its Q^{-1} value was calculated from the decay curve. The measurement was carried out in a closed box maintained at room temperature and 33%, 43%, 58%, 75%, 85%, or 92% RH.

B. Sensory evaluation test

The changes in the practical quality of commercial reeds due to water-extraction and glucose-impregnation were investigated with a sensory evaluation test by 32 Japanese professional clarinet players. First, the ''sonority (Nari, in Japanese),'' ''richness (Yutakasa),'' and ''softness

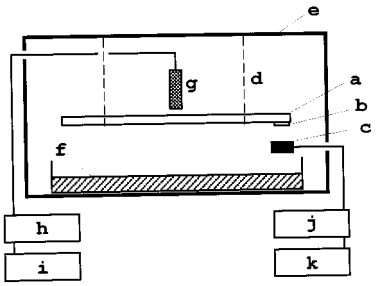

FIG. 1. Apparatus: (a) specimen; (b) iron piece; (c) magnetic driver; (d) silk thread; (e) conditioning box; (f) aqueous salt solution for maintaining relative humidity; (g) microphone; (h) power amplifier; (i) oscillator; (j) band-pass filter; (k) FFT analyzer.

(Yawarakasa)'' of tone, and ''ease of vibration (Shindo-shiyasusa)'' and ''response (Han-no no yosa)'' for ten commercial reeds were evaluated by each player in five steps. Next, four reeds were water-extracted, and two of them were subsequently impregnated with glucose. The qualities of the reeds were then evaluated again by the player in the same way. These quality factors are especially important in the grading of a reed (Obataya, 1996a). The condition of the evaluation depended on individual players' habits.

II. RESULTS AND DISCUSSION

A. The acoustic properties of the reed

In this study, the acoustic properties of reeds were determined by using the reed plates cut from a reed tube. Although these plates were not made from the clarinet reeds being used practically, their properties represent those of practical reeds because the reed tube had been selected for the commercial clarinet reeds. The contents of extractives or glucose (C), equilibrium moisture contents (M), and densities (ρ) of untreated and treated reeds at 25 °C and various RH levels are listed in Table I. The M values were higher for untreated than extracted reeds at all RH levels, and increased remarkably with an increase of RH. This was attributed to the high hygroscopicities of extractives (Obataya and Norimoto, 1995). The ρ values of the untreated reed were also higher than those of the extracted reed. This indicates that the extractives in the cell-lumens increase the weight of the reed without increasing its volume. Similar trends were observed in the glucose-impregnated reed.

TABLE I. The contents of extractives and glucose (C), equilibrium moisture contents (M), and densities (ρ) of untreated and treated reeds at 25 °C and various relative humidities (RH).

	RH(%)	Untreated	Water-extracted	Glucose-impregnated
C(%)		14.9[a]	0	37.1
	33	6.3	4.8	6.4
	43	7.2	5.6	7.5
M	58	8.8	7.5	10.7
(%)	75	12.1	10.3	16.6
	85	15.7	12.1	22.8
	92	23.8	15.6	40.8
	33	0.498	0.438	0.664
	43	0.501	0.440	0.670
ρ	58	0.509	0.447	0.690
(g/cm^3)	75	0.524	0.459	0.727
	85	0.540	0.466	0.764
	92	0.578	0.480	0.873

[a]Mainly consisting of glucose, fructose, and sucrose.

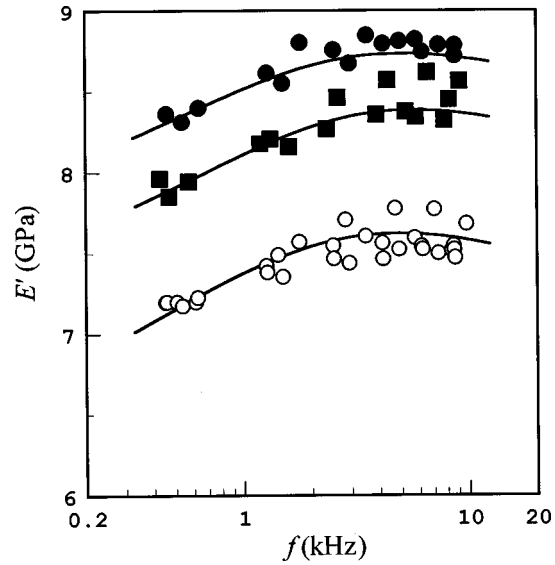

FIG. 2. Dynamic Young's modulus (E') of untreated (●), water-extracted (○), and glucose-impregnated (■) reed at 33% relative humidity (RH) plotted against frequency (f).

The E' values of untreated and treated reeds at 33% RH are plotted against f in Fig. 2. Similar shapes of $E'-f$ curves were observed in all reeds, although the E' values varied with the treatment methods. Irrespective of the treatment, the E' increased up to 5 kHz and then leveled off. The leveling off in E' above 5 kHz was due to shear deformation in bending (Hearmon, 1958; Ono and Kataoka 1979; Nakao *et al.*, 1985). Figure 3 shows the effect of RH on the E' of reeds under the first mode vibration whose frequency ranged from 0.3 to 0.6 kHz. The E' of the extracted reed was almost

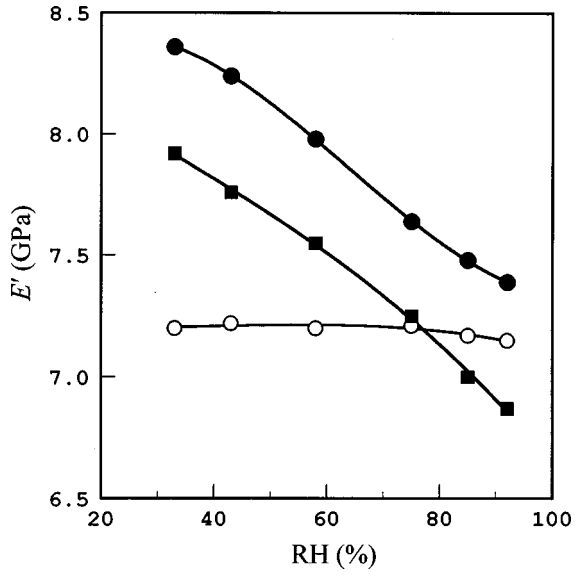

FIG. 3. Effect of relative humidity (RH) on the dynamic Young's modulus of reed (E') at the first mode vibration. Legends are the same as in Fig. 2.

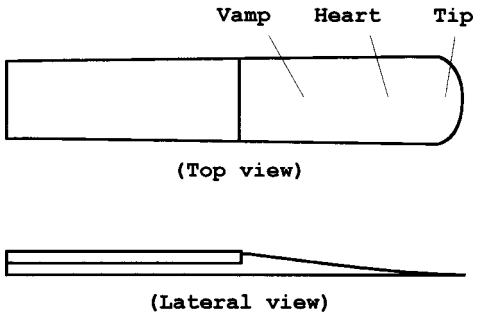

FIG. 4. Appearance of clarinet reed.

constant within the RH levels examined. The E' of the untreated reed was higher than that of the extracted one at low RH levels, but decreased remarkably with increasing RH. These results indicate that the extractives enhance E' at low RH levels, but have little effect on it at high RH levels with deliquescence. The glucose-impregnation treatment could enhance the E' of the reed reduced by the water-extraction. However, the E' of the glucose-impregnated reed was slightly lower than those of untreated reeds over the RH range examined. This might be caused by a distortion of the cell wall owing to the dry–wet cycle during the impregnation process, as well as the higher M values due to high glucose content.

Figure 4 depicts the appearance of a reed. Although the ''tip'' is completely wetted by the saliva of the player, the inner part of ''vamp'' and ''heart'' areas remains almost dry even if their surface becomes wet. Since the vamp and heart areas keep the reed opening against the strong force of the player's lower lip, these are thought to determine the controllability of frequency, amplitude, and the color of clarinet tone. Thus the extractives contribute to the reed quality by reinforcing the vamp and heart. The glucose-impregnation treatment seems effective in recovering the stiffness of the reed at limited low RH levels.

Figure 5 shows the Q^{-1} of the extracted reed at various RH levels with respect to f. Irrespective of RH level, Q^{-1} increased with increasing f. With increasing RH, Q^{-1} increased slightly over the frequency range examined. These trends were similar to those of wood. Although the Q^{-1} of wood along the grain is almost independent of f in this temperature-frequency range (Tonosaki *et al.*, 1983), the shear deformation in the bending gives higher Q^{-1} values at higher frequencies (Meinel, 1957, Ono and Kataoka 1979, Nakao *et al.*, 1985). Besides, the Q^{-1} of wood usually increases with RH because of the reduction of cohesive forces among the amorphous cell wall substances (Kollmann and Krech, 1960, Obataya *et al.*, 1998). Since the chemical components of the extracted reed are essentially the same as those of wood (Obataya, 1996b), its $Q^{-1}-f$ curve shows a similar trend to that of wood. Figure 6 shows the effect of RH on the Q^{-1} of the untreated reed over different f. The Q^{-1} of the untreated reed depended strongly on both RH and f. The Q^{-1} of the untreated reed was much higher than that of the extracted reed. In addition, the Q^{-1} of the untreated reed at low f range decreased with an increase of RH. This trend was evidently different from that of the extracted reed

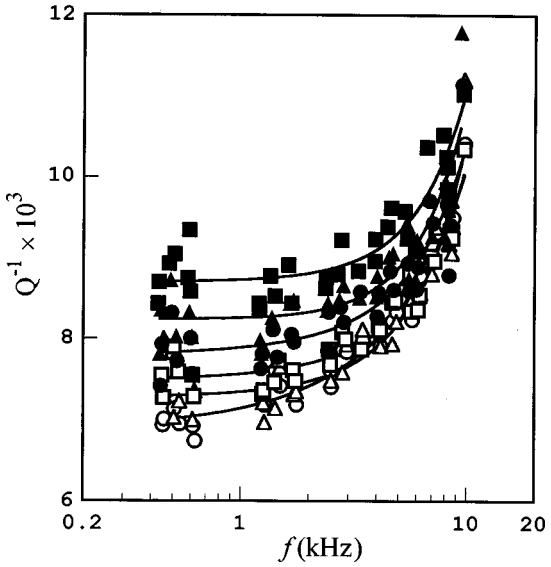

FIG. 5. Internal friction of water-extracted reed (Q^{-1}) at various relative humidities (RH) plotted against frequency (f). RH ○, 33%; △, 43%; □, 58%; ●, 75%; ▲, 85%; ■, 92%.

and wood. Figure 7 shows the frequency dependence of Q^{-1} of the glucose-impregnated reed at various RH. The $Q^{-1}-f$ curves of glucose-impregnated reed were similar to those of untreated reed, except for higher Q^{-1} values.

Here, the $Q^{-1}-f$ curves of various reeds were approximated with the quadratic function of f, and the effects of extractives or glucose on the Q^{-1} are expressed by $\Delta Q^{-1} = \log(Q_t^{-1}/Q_e^{-1})$, where Q_t^{-1} and Q_e^{-1} are the internal friction of treated and extracted reeds at the same frequency, respectively. The ''untreated reed'' in its natural state is regarded as ''treated'' with the natural extractives. The effect of extractives and glucose on the Q^{-1} at 33% and 58% RH are plotted against f in Fig. 8. At low RH levels, the ΔQ^{-1} values were very high at all frequencies examined. This indicates that the extractives and glucose damp the vibration of

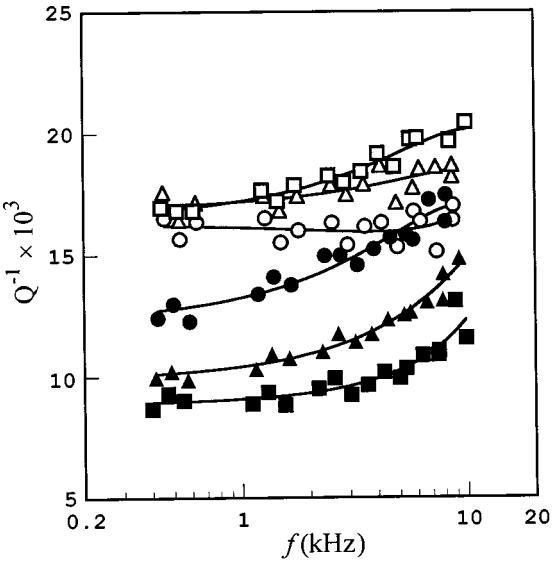

FIG. 6. Internal friction of untreated reed (Q^{-1}) at various relative humidities (RH) plotted against frequency (f). Legends are the same as in Fig. 5.

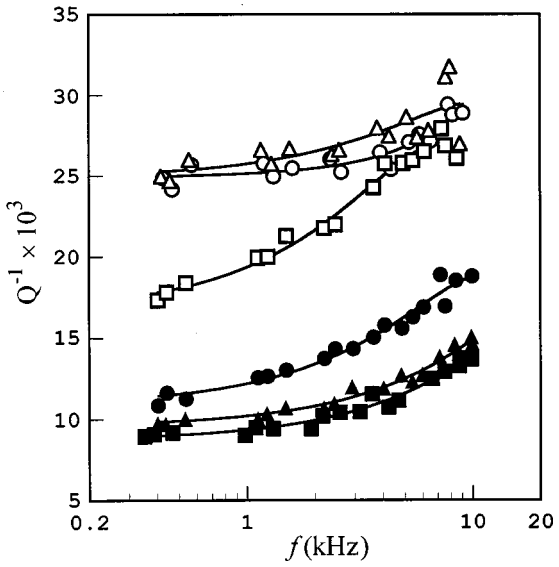

FIG. 7. Internal friction of glucose-impregnated reed (Q^{-1}) at various relative humidities (RH) plotted against frequency (f). Legends are the same as in Fig. 5.

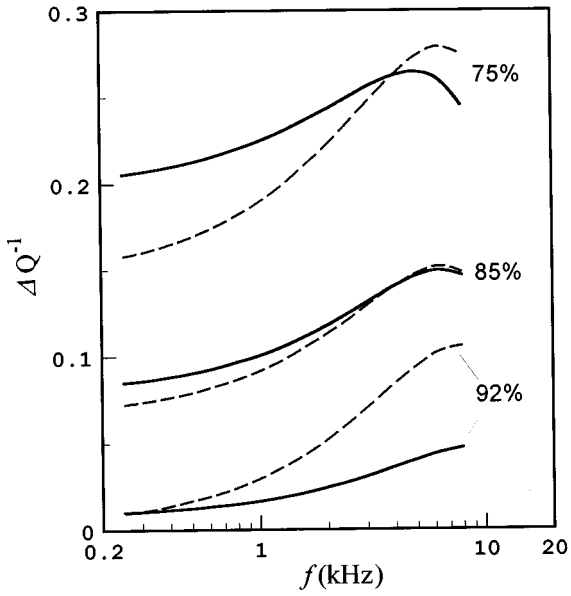

FIG. 9. Effects of extractives (solid line) and glucose (broken line) on the internal friction of reed (ΔQ^{-1}) at 75%, 85%, and 92% relative humidities plotted against frequency (f).

the reed over the range of clarinet sound. At 75% RH and above, the ΔQ^{-1} at low f decreased remarkably with increasing RH, as shown in Fig. 9. These $\Delta Q^{-1}-f$ curves indicate that the extractives and glucose especially damp the high-frequency vibration of the reed at higher RH levels.

Figures 8 and 9 show that the extractives and glucose enhance the Q^{-1} of the reed in a particular frequency range, and this range shifts to higher frequencies with increasing RH. We have found that various sugars in the reed induce mechanical relaxation processes at low frequencies and below 0 °C and the temperature locations of those processes shift to lower temperatures with increasing moisture content (Obataya and Norimoto, 1999). Thus the changes in $\Delta Q^{-1}-f$ curves with increasing RH can be explained by the relaxation processes due to sugar in the reed, whose relaxation time decreases with increasing moisture content.

B. Effect of extractives and glucose-impregnation treatment on the practical quality of the reed

The practical quality of the reed is frequently evaluated with respect to its tone quality, ease of vibration, and so on. Since these qualities are influenced by the shape of the reed and the preference of the player, in addition to the nature of the reed, it is difficult to account for the practical quality of the reed in terms of its acoustic properties. However, remark-

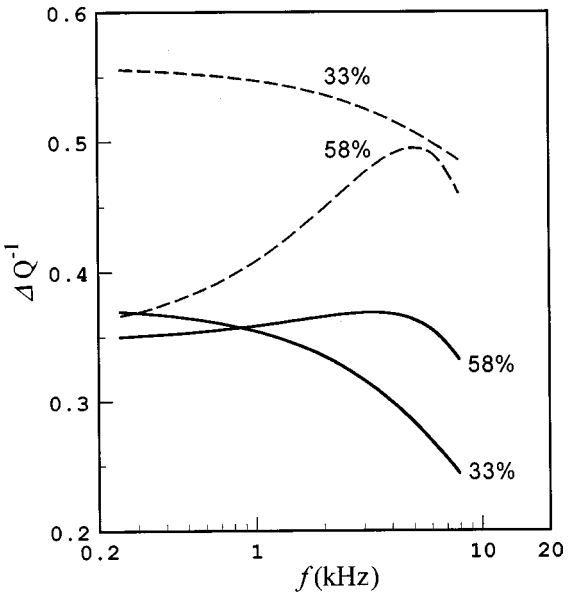

FIG. 8. Effects of extractives (solid line) and glucose (broken line) on the internal friction of reed (ΔQ^{-1}) at 33% and 58% relative humidities plotted against frequency (f).

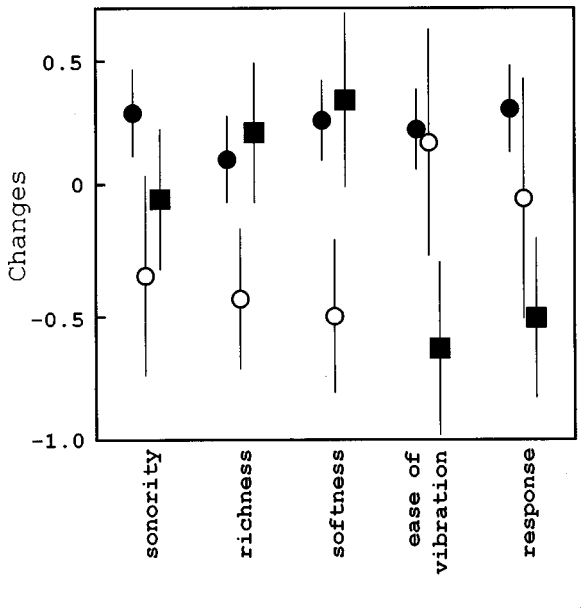

FIG. 10. Average changes of reed quality due to water-extraction and glucose-impregnation. ●, control; ○, water-extraction; ■, glucose-impregnation; bars, 95% confidence limit.

able change in acoustic properties due to water-extraction or glucose-impregnation should be reflected in reed quality.

To quantify the quality of the reeds tested, points from 1 (poor) to 5 (excellent) were given. Figure 10 exhibits the changes of reed quality due to water-extraction and glucose-impregnation. By water-extraction, the ''sonority,'' ''richness,'' and ''softness'' of tone were evidently reduced while the evaluations for the untreated reeds were almost unchanged. These qualities were recovered to their original levels by glucose-impregnation. The glucose-impregnation treatment seems useful to maintain or reproduce the tone of the reed, though it reduced the ''ease of vibration'' and ''response.''

These results indicate that both the extractives and glucose contribute to the sonority, richness, and softness of tone. These tone qualities are, in turn, thought to be dependent on the frequency response of the reed. It has been suggested that the appropriately tuned reed resonance increases the amplitude of corresponding harmonics to give the best tone quality (Thompson, 1979). With the removal of the extractives, the frequency of reed resonance shifts to higher frequencies as the ρ decreases at all RH levels. At the same time, the amplitude of harmonics corresponding to the reed resonance increases with decreasing Q^{-1} at high frequencies. Thus larger amplitude of harmonics might be produced at higher frequencies, making the tone poorer and harder.

On the other hand, Figs. 3 and 5 indicate that water-extracted reed has excellent stability in its acoustic properties against the changes in RH. Although the tone of the reed is degraded by the water-extraction, it is advisable for the players to remove extractives when the stability of acoustic properties is required.

III. CONCLUSION

The acoustic properties of the reed were markedly changed in the presence of water-soluble extractives consisting of glucose, fructose, and sucrose. The extractives enhanced the stiffness of the dry part of the reed and increased the internal friction at high frequencies under relatively high humidity. From the results of a sensory evaluation test, it was suggested that the extractives improved the tone quality of the reed. The tone quality, degraded with the removal of extractives, could be recovered by glucose-impregnation treatment, resulting in the recovery of acoustic properties.

ACKNOWLEDGMENTS

The authors express their gratitude to the clarinet players for their kind assistance in the sensory evaluation test. The authors also thank Ms. Wong Ee Ding, the research fellow of Wood Research Institute, Kyoto University, for her critical reading of this manuscript.

Hearmon, R. F. S. (**1958**). ''The influence of shear and rotatory inertia on the free flexual vibration of wooden beams,'' Br. J. Appl. Phys. **9**, 381–388.

Kollmann, F., and Krech, H. (**1960**). ''Dynamic measurement of damping capacity and elastic properties of wood,'' Holz als Roh-und Werkstoff **18**, 41–54.

Meinel, H. (**1957**). ''Regarding the sound quality of violins and a scientific basis for violin construction,'' J. Acoust. Soc. Am. **29(7)**, 817–822.

Nakao, T., Okano, T., and Asano, I. (**1985**). ''Theoretical and experimental analysis of flexual vibration of the viscoelastic Timoshenko beam,'' J. Appl. Mech. **52**, 728–731.

Obataya, E., and Norimoto, M. (**1995**). ''The water sorption isotherms of cane (Arundo donax L.) used for reeds of woodwind instruments,'' Mokuzai Gakkaishi **41(12)**, 1079–1085.

Obataya, E. (**1996a**). ''Importance of reed quality for the clarinet players,'' PIPERS **181**, 32–34.

Obataya, E. (**1996b**). ''Physical properties of cane used for clarinet reed,'' Wood Res. Tech. Notes **32**, 30–65.

Obataya, E., Gril, J., and Norimoto, M. (**1998**). ''The effects of adsorbed water on dynamic mechanical properties of wood,'' Polymer **39(14)**, 3059–3064.

Obataya, E., Umezawa, T., Nakatsubo, F., and Norimoto, M. (**1999**). ''The effects of water soluble extractives on the acoustic properties of reed (Arundo donax L.) used for woodwinds,'' Holzforschung **53(1)**, 63–67.

Obataya, E., and Norimoto, M. (**1999**). ''The mechanical relaxation processes due to sugars in cane (Arundo donax L.),'' J. Wood Sci. (in press).

Ono, T., and Kataoka, A. (**1979**). ''The frequency response of wood in the longitudinal direction,'' Mokuzai Gakkaishi **25(8)**, 535–542.

Thompson, S. C. (**1979**). ''The effect of the reed resonance on woodwind tone production,'' J. Acoust. Soc. Am. **66(5)**, 1299–1307.

Tonosaki, M. Okano, T., and Asano, I. (**1983**). ''Vibrational properties of Sitka spruce,'' Mokuzai Gakkaishi **29(9)**, 547–552.

An investigation of correlations between geometry, acoustic variables, and psychoacoustic parameters for French horn mouthpieces

George R. Plitnik
Department of Physics, Frostburg State University, Frostburg, Maryland 21532

Bruce A. Lawson
Lawson Brass Instrument, Inc., Boonsboro, Maryland 21713

(Received 18 February 1992; revised 10 December 1998; accepted 5 March 1999)

Because brass instrument mouthpieces are considered by musicians to be the single most important component of the instrument, a comparative investigation was made of seven French horn mouthpieces widely used by professional musicians. Acoustic parameters were obtained from both measured and computed impedance curves for the mouthpieces attached to a cylindrical tube with an overall length approximating that of the horn in B-flat. Hypothesized psychoacoustic correlates to these parameters were used by professional musicians to evaluate the mouthpieces by means of comparative testing. It was discovered that the peak amplitudes and *Q* values of the impedance peaks, as well as their respective variability, correlated well to the musicians' preference ratings. Based on the presented documented changes in the ratio of French horn mouthpiece cup length to throat plus backbore length throughout the twentieth century, the acoustical properties of modern designs to the older versions are compared. These results show that the average harmonics' peak amplitude has increased, while variability has simultaneously decreased, resulting in a more even envelope. Also, the impedance peak's average *Q*'s have increased, a probable explanation for musicians' expressed preference for mouthpieces which facilitate greater pitch control. © *1999 Acoustical Society of America.* [S0001-4966(99)02906-9]

PACS numbers: 43.75.Fg [WJS]

INTRODUCTION

Until recently musical instrument design has been predominantly a heuristic procedure, but certain basic characteristics have, nevertheless, evolved for all wind instruments. Foremost among these, perhaps, is that many of the input impedance peaks should be harmonically related for each playing configuration. Such a relationship is necessary for the musician to be able to produce clear, stable notes via the feedback from the instrument's bore to a nonlinear driver. When the higher bore resonances are aligned with the harmonics of the note being played, a strong cooperative feedback condition or ''regime of oscillation'' is established between the components of the sound spectrum and the bore resonances.[1] Given that a suitable set of resonances exist, the mouthpiece of a brass wind instrument is considered by musicians to be the single most crucial element regarding the performance of the entire horn.[2,3] Since a mouthpiece is not only an integral part of the instrument, but the section which interfaces the musician to the instrument, it is perhaps understandable that it should have a primary role in assisting the musician to generate favorable intonation. We have chosen to study the French horn mouthpiece in detail because, in addition to its importance to the French horn, it has measurable acoustic properties which can be considered to be relatively independent of the rest of the instrument, and it is an easily changeable component of a horn.

A French horn mouthpiece consists of four parts: the rim, the cup, the throat, and the backbore, as shown in Fig. 1. The art of mouthpiece design is to create the optimized relationship of the various mouthpiece dimensions, thus assisting a competent performer in achieving superior tone quality, attack clarity, flexibility, and a comfortable resistance. That different manufacturers have attempted to achieve this end by somewhat different means is apparent by inspecting Table I. This table is a compilation of accurate measurements on 61 French Horn mouthpieces by 37 designers and 15 different manufacturers ranging from late nineteenth century through contemporary companies. Although many mouthpiece manufacturers have, in the past, exhibited such astonishingly poor quality control that nominally identical mouthpieces have occasionally differed by amounts greater than the difference between models, no attempt was made to include this variable. Only one representative sample of each model was measured. The high standard deviation for some of the variables, particularly throat length, indicates that no consensus on mouthpiece design has been achieved, even considering that some of the differences may be accounted for by the varying requirements of different styles of horn. Nevertheless, despite design variation mandated by diverse horn models, styles of music, as well as the considerable variability of personal preference, certain regularities are apparent. Approximately half of the standard deviations are less than 6%, which indicates that many of the variables are standardized across a wide spectrum of designs. Most of the differences in mouthpiece design occur in cup length, throat length, and backbore length, which vary widely although the overall length is reasonably constant.

Table II(a) presents combinations of these ratios, as

 0001-4966/99/106(2)/1111/15/$15.00

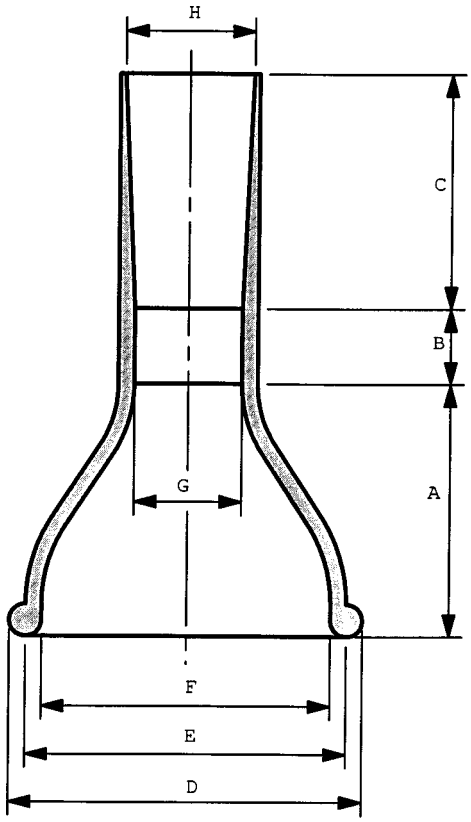

FIG. 1. The French horn mouthpiece. (A) cup length, (B) throat length, (C) backbore length, (D) cup rime o.d., (E) cup peak diameter, (F) rim inner diameter (grip), (G) throat diameter, (H) backbore end diameter.

well as several other ratios and products which have been regarded as important by manufacturers. Table II(b) shows the product-moment correlation coefficients of different combinations of the three important mouthpiece lengths and throat diameters. Note the strong negative correlations of cup versus throat length and throat versus backbore length. This may be interpreted as follows: when the throat is drilled out it becomes longer as well as wider, while the cup length and backbore length decrease by a corresponding amount. However, the negative correlation between cup and backbore length, where a positive correlation may reasonably have been expected, indicates that design procedures involve more complications than merely changing the throat diameter. This is also evidenced by the extremely strong negative correlation (-0.80) between cup length and throat plus backbore length, where a lesser correlation would be anticipated. The regularities apparent in Table I, as well as the considerable variation indicated by Tables II(a) and (b), have prompted us to attempt to determine optimum dimensions for a French horn mouthpiece which would be acceptable to professional musicians on a wide variety of contemporary horns.

Musical instrument manufacturers have long strived to produce instruments that satisfy their customers, but progress has been slow due to inherent difficulties in interpreting musicians' comments and the lack of accurate and economical methods of acoustical analysis. Although the recent introduction of computer modeling schemes has alleviated somewhat the analysis problem, there is still no firm consensus regarding the interpretation of the resultant data as they relate to musicians' preferences. Compounding the difficulty of the task is that musicians' preferences seem to have evolved or changed over the years.[4] Smithers *et al.*[5] have noted, for example, that the technical requirements of Baroque trumpeters and modern performers are not even remotely similar. More germane to the present study is the obvious evolution of

TABLE I. Mouthpiece measurements.

(Parentheticalletters refer to Fig. 1)	Number measured	Mean (cm)	Minimum (cm)	Maximum (cm)	Standard deviation	% Coeff. variation
Total length	53	6.5110	6.0198	7.2136	0.221	3.4%
Cup length (*A*) CL	43	2.9790	2.0960	4.5010	0.498	16.7%
Cup I.D. at screw joint (*F*)	28	1.6640	1.5950	1.7270	0.030	1.8%
Mouthpiece length w/o rim	45	6.1049	3.1750	6.9850	0.493	8.2%
Rim I.D. at joint (*F*)	37	1.6640	1.5950	1.7220	0.025	1.5%
Screw rim length	29	0.7520	0.5590	0.8050	0.084	11.2%
Rim face to joint depth	33	0.3250	0.2180	0.7060	0.124	38.2%
Rim O.D. (*D*)	58	2.4770	2.3500	2.6040	0.061	2.5%
Rim I.D.—grip	55	1.7400	1.6260	1.8160	0.041	2.4%
Rim full width	48	0.3530	0.2870	0.4570	0.046	13.0%
Rim peak diameter (*E*) *RPD*	43	2.0680	1.9810	2.1590	0.041	2.0%
Throat length (*B*) *THL*	43	1.0590	0.0000	4.0840	0.774	73.1%
Throat diameter (*G*) *THD*	60	0.4780	0.4090	0.5790	0.036	7.5%
Backbore end diam. (*H*) *BBED*	51	0.6350	0.5870	0.6600	0.018	2.8%
Backbore length (*C*) *BBL*	51	2.4710	0.9530	3.8100	0.543	22.0%

TABLE II. (a) Ratios of mouthpiece dimensions. (b) Product-moment correlation coefficients.

(a)	*RPD*/*CL*	*THD*/*THL*	THD_x/THL	THD^2/THL	*CL*/*BBL*	*CL*/(*THL*+*BBL*)
Number measured	39	41	42	42	41	41
Mean	0.710	0.695	0.497	0.230	1.385	0.882
Standard deviation	0.103	0.566	0.053	0.188	0.713	0.442
Coefficient variation (%)	15%	81%	69%	82%	52%	50%

(b)	
Number measured	41
Cup length versus Throat length	−0.51
Cup length versus Backbore length	−0.22
Throat length versus Backbore length	−0.58
Cup length versus Sum of throat and backbore length	−0.80
Throat diameter versus Throat length	+0.53

French horn mouthpiece designs during the course of this century, made apparent by Tables I and III. (Table III presents measurements taken on seven common mouthpieces used by musicians today; Table I is dominated by historic models currently out of favor.) This change is made even more obvious by an examination of contemporary musical compositions. Increasingly, wind instruments are being asked to perform over their entire frequency range, and sometimes even beyond the conventionally accepted compass. If a means of gauging and quantifying musicians' ''preferences'' and composers ''requirements'' could be discovered, future instruments could evolve more readily to meet these needs.

I. RATIONALE

A. Justification

In order to relate the geometry of a mouthpiece to a set of psychoacoustic variables which have meaning to a musician, it is first necessary to move from the realm of simple geometry to the acoustic domain. The air column from the entrance of the mouthpiece to the end of the bell can be regarded as a linear system whose role in tone generation may conveniently be characterized by a single function, the input impedance as a function of frequency. This function enables one to make accurate predictions about the playing characteristics of a brass instrument; the harmonics of a brass instrument's spectrum are the result of the nonlinear interaction between the player's lips and the input impedance function of the horn.[6] Oscillation is favored at a frequency where the input impedance is large and where there are several large values of impedance near integer multiples of this frequency. Thus because it is fundamental to the sound production mechanism and because it incorporates the instrument's internal geometry, the acoustic input impedance is the logical choice for objectively evaluating brass instrument mouthpieces.

To relate the input impedance to musicians' subjective evaluation, however, is considerably more difficult. It has been shown[7] that although the amplitudes and degree of harmonicity of impedance peaks are important, they are insufficient to account for the discrimination ability and strong preferences of professional musicians. It is also necessary to consider the *Q*'s of the impedance peaks and the overall shape of the impedance peak envelope. Since the instrument's spectrum is related to this shape, and since the spectrum influences the perceived timbre, the envelope is particularly important.

For our detailed study, we selected seven mouthpieces currently in wide use among professional musicians in the United States. The pertinent geometrical variables for these mouthpieces are listed in Table III, along with the labels used to identify them in this study. Comparing the mean values of the seven mouthpieces in current use (labeled AV-NEW in Table III) with those prevalent in the early twentieth century (the mean values from Table I, identified

TABLE III. Seven mouthpieces studied.

Manufacturer	Model	Total length (cm)	Cup length (*A*) (cm)	*THD* (*G*) (cm)	*THL* (*B*) (cm)	*BBL* (*B*) (cm)	*BB* diam (*H*) (cm)	Cup volume (cc)	Total volume (cc)
V. Bach	VB12	6.604	2.540	0.452	1.207	2.858	0.630	3.00	3.88
Giardinelli	C8	6.096	2.223	0.508	1.655	2.223	0.660	3.90	5.08
Giardinelli	S14	6.001	2.858	0.472	0.610	2.540	0.648	3.65	4.36
Holton	MC13	6.350	2.540	0.477	1.588	2.223	0.635	3.10	3.98
Holton	MDC	6.375	2.540	0.470	1.930	1.905	0.622	3.65	4.48
King	H2	6.350	2.858	0.470	0.953	2.540	0.648	3.80	4.61
Lawson	L5	6.383	2.540	0.488	1.778	2.065	0.622	3.20	4.01
AV-NEW		6.308	2.586	0.476	1.389	2.336	0.638	3.47	4.34
AV-OLD		6.511	2.979	0.478	1.059	2.471	0.635	3.65	4.37
AV NEW/OLD		0.969	0.868	0.996	1.312	0.945	1.005	0.951	0.993

in this study as AV-OLD) it is interesting to note that the geometric parameters exhibiting the greatest change are the cup and throat lengths, as summarized in the last row of Table III (the ratio of AV-NEW to AV-OLD). (The data of Table I include the mouthpieces of Table III but the predominance of older styles yields mean values more representative of a bygone era.) In general, cup lengths have decreased while throat lengths have increased.

B. Musician consensus

For our first experiment, we chose four mouthpieces in common use by professionals in the United States. Reproductions (accurate to one-thousandth of an in.) of these mouthpieces, each having the same rim and exterior, were sent to 34 performers in major symphony orchestras across the United States. The musicians were asked to play, on their own instrument, each mouthpiece in any order and any number of times. Based on this simple test, they were requested to separate the mouthpieces, by overall preference, into two categories: ''like'' or ''dislike.'' The results of this blind test appear in Table IV. Although the data make it apparent that there is considerable consensus on what is preferred and what is not, the test is not specific enough to correlate with acoustic variables.

C. Experimental model

Because of the importance of the input impedance, considerable effort has been devoted to determining this function for brass instruments.[8–10] In the present study, we have attempted to correlate the geometrical and acoustical parameters of French horn mouthpieces, as determined from the input impedance curves, to musicians' preferences for different designs. To limit the number of acoustic variables and to simplify the musical evaluation process, our experimental system consisted of a mouthpiece inserted into a standard 48-cm-long French horn leadpipe which was, in turn, inserted into a 1.19-cm, i.d. cylindrical tube, the entire system having a length approximating that of a B-flat French horn. Although it may seem as though a cylindrical tube is a rather poor imitation of a French horn, it has been recognized for some time[11–13] that the mouthpiece and leadpipe are the two most important sections of a French horn and their characteristics are reasonably independent of the remainder of the horn. Indeed, after the leadpipe, the balance of the horn serves mainly to fix intonation and to radiate the sound.[14] Some of the advantages of using a cylindrical tube to represent the body of a French horn are: (1) it considerably simplified the system while retaining the pertinent variables—a set of well-defined resonance peaks having approximately the same spacing as for the horn; (2) because of the small diameter, more peaks at high frequencies were present, giving the performer an extended playing range; (3) informal preliminary tests with 12 professional musicians indicated that they could consistently rank various mouthpieces by preference on the tube as well as on a horn, but the tube helped to exaggerate the pertinent differences between mouthpieces; (4) it is easier to model, it helps exaggerate the differences between mouthpieces, and musicians are better able to concentrate on properties of mouthpieces without being distracted by the French horn sound; (5) the plane wave model employed in the computer simulations to produce a calculated impedance curve is only accurate to about 600 Hz for a French horn because of the large bell while the model is accurate well beyond the frequency range of interest for the small diameter cylinder. (Figure 2 shows, for comparison, the input impedance function measured for a French Horn and for the cylindrical tube with the same mouthpiece installed.)

There is only one obvious disadvantage to replacing the bell flare by a cylindrical tube—harmonicity is compromised by the stretched partials. Since the advantages more than compensate for the disadvantage of stretched partials, our investigation was confined to a system consisting of a mouthpiece, leadpipe, and cylindrical tube.

TABLE IV. Mouthpiece preference by 34 professional musicians.

	C8	H2	MDC	L5
Number of times not liked	27	24	19	5
Number of times liked	4	4	13	27
Total number	31	28	32	32
% Preferred	12.9%	14.3%	40.6%	84.4%

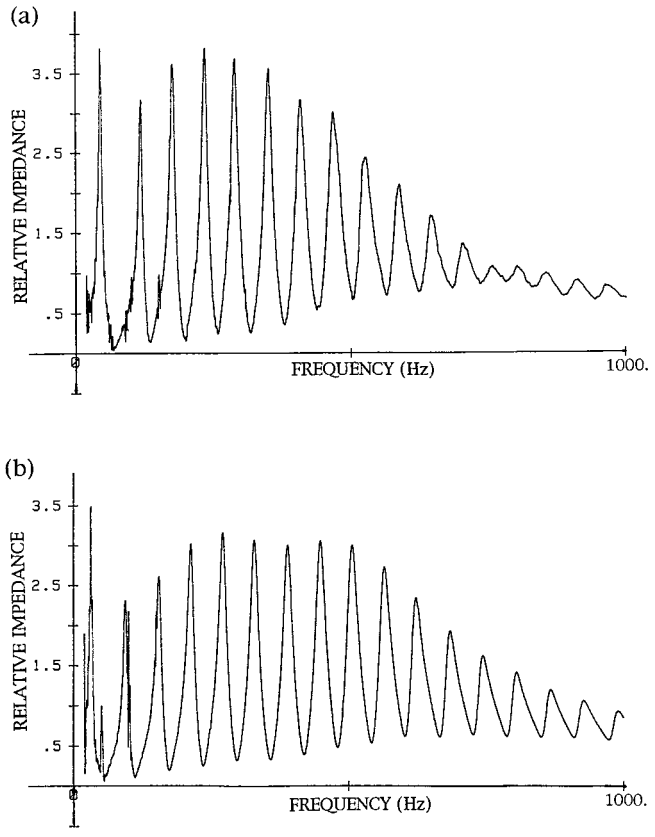

FIG. 2. Measured input impedance versus frequency for the L5 mouthpiece: (a) attached to a French horn: (b) attached to the cylindrical test instrument.

TABLE V. Mouthpiece analysis from measured data.

Manufact.	Model	Res. freq. (Hz)	Q of Res.	V_c/BBL $(\text{cm})^2$	% Deviation	$(f_r^{2x}V_c)/C$ $x\ S_{th}/L'$	% Diff. from Helmholtz	L_{e1}/L_{e2}	% Deviation	THD^2/V_c $(\text{cm})^{-1}$
V. Bach	VB12	602.3	7.74	1.05	26.1%	0.995	0.5%	4.51	9.5%	0.0675
Giardinell	C8	572.1	8.65	1.53	7.7%	1.175	17.5%	3.74	9.2%	0.0586
Giardinell	S14	593.1	7.27	1.28	9.9%	0.918	8.2%	4.20	2.0%	0.0610
Holton	MC13	617.0	7.72	1.22	14.1%	0.973	2.7%	4.43	7.6%	0.0737
Holton	MDC	585.3	6.63	1.43	0.7%	0.993	0.7%	4.14	0.5%	0.0605
King	H2	605.5	8.31	1.33	6.3%	1.015	1.5%	3.89	5.5%	0.0581
Lawson	L5	593.0	7.16	1.44	1.4%	0.730	27.0%	4.46	8.3%	0.0744

II. EXPERIMENTAL PROCEDURE

A. Acoustic input impedance

Input impedance curves were generated by two methods: direct measurement by means of the experimental apparatus of Bruneau,[15] and calculation from physical measurements via the computer model of Plitnik and Strong.[16] The resonance frequency of each mouthpiece alone, recorded in Table V, was measured by the Bruneau apparatus. For the computer calculations the interior dimensions of each mouthpiece were measured at 3.0-mm intervals to three significant figures. Accuracy was achieved in the cup by casting a mold of the interior with nonshrinking cerro base casting metal and measuring the cast cross section at 3.0-mm intervals. The interior volume of the cup, determined from the mass and density of its casting, is recorded in Table III.

The calculated input impedance curves were used to determine directly the following acoustic parameters: an overall spectral envelope defined by the impedance maxima, the ratio $Z_{\max}(n)/Z_{\text{min-av}}(n)$ as a function of harmonic number n, where $Z_{\max}(n)$ is the magnitude of the nth impedance peak and $Z_{\text{min-av}}(n)$ is the mean of the two impedance minima adjacent to each $Z_{\max}$, Q_n as a function of harmonic number n [where Q_n is defined as $Q_n=(f_n/n)*df$ and f_n is the frequency of the nth impedance peak and df is the bandwidth at the -3 dB points], and the harmonicity of the peaks as a function of n, where harmonicity was defined as $3(f_n/f_3)-n, f_3$ being the frequency of the third impedance peak (the third peak was used as a standard because the first two peaks are not as important as the third and because accurate data are somewhat more difficult to obtain at the lower frequencies). The input impedances are all relative to the characteristic impedance of air, $Z_0=\rho_0 c$. It has been shown[17] that every complicated acoustic system has a characteristic wave impedance related to the $Z_{\max}$ and $Z_{\min}$ of the system by the simple relationship $Z_{\max}*Z_{\min}=Z_c^2$. For simple ideal systems Z_c should be equivalent to Z_0 and constant across the impedance plot; our data clearly show that this is not the case. For our system Z_c changes with frequency for every mouthpiece and the changes are different for each mouthpiece. We therefore computed $Z_c^2(n)=Z_{\max}(n)*Z_{\min}(n)$ and defined an average Z_c for each mouthpiece as the mean Z_c for the 16 impedance maxima.

B. Psychoacoustic variables

Although horn playing is a highly subjective art, both musicians and researchers have attempted to identify significant parameters which could be used to assess instruments. Farkas[4] has identified three criteria which he considers paramount: proper response, characteristic tone, and good intonation, a somewhat vague and hardly exhaustive list. For a trombone, Pratt and Bowsher[18] assessed seven subjective features: dynamic range, intonation, responsiveness, resistance, stuffiness, timbre, and flexibility. The two most critical features were shown to be timbre and responsiveness, with intonation being of only secondary concern.

For our purposes, we attempted to identify the most important subjective qualities which would most likely be influenced by the French horn mouthpiece geometry. These psychoacoustic variables, which we wished to assess, were (1) *flexibility* (the ease with which the performer can slip from resonance peak to resonance peak), (2) *pitch control* (how well the pitch ''locks-in''), (3) *ease of playing* (the smoothness and consistency sensed by the player), (4) *intonation* (the facility of accurate pitch production), (5) *tonality* (the quality of the tone produced), (6) *dynamic range* (the range from the softest to the loudest tones possible, and (7) *attack clarity* (the smoothness and rapidity of the initial attack). As a preliminary test, the 7 mouthpieces were played on both the test pipe and on a French horn by 13 professional hornplayers in 3 major symphony orchestras, who were asked to comment on the above variables. (Pratt and Bowsher[18] have also shown the importance of using professional musicians in studies of this nature. While nonprofessional players had difficulty discriminating differences, a professional had no trouble quantifying his assessments of different instruments.) Typical responses were somewhat difficult to interpret, but the musicians were able to rate each mouthpiece on most of these factors, as well as assigning an overall rating. The musicians did not know which mouthpiece they were using and they were not allowed to inspect the mouthpieces. To ensure an unbiased evaluation, identical screw-on rims were used for each mouthpiece. Although only the i.d. of the rim affects mouthpiece acoustics, the size and shape of the outer elements most definitely affect the feel of a mouthpiece to a performer's lips. With the exception of intonation, the performer's comments about mouthpieces (for the other six factors) were completely consistent whether rated on a French horn or on the cylindrical tube. Confidence in using only the cylindrical tube for more detailed experiments was engendered by these preliminary trials.

We also asked the 13 musicians for an overall subjective evaluation of each mouthpiece as a means of ranking them from the most to the least preferred. In summary, we had two

TABLE VI. Mouthpiece preferences of P. Landgren.

	Like	Neutral	Dislike
Flexibility	L5, H2, MDC	C8, S14	S14, MC13, VB12
Pitch control	L5	MC13, MDC	H2, S14, C8, VB12
Ease of playing	MDC, L5	MC13, VB12	H2, S14, C8
Intonation	H2	MC13, MDC, L5	S14, C8, VB12
Tonality	L5	MC13, MDC	H2/S14, C8, VB12
Dynamic range	VB12, H2	MC13, MDC, L5	S14, C8
Attack clarity	L5	MC13, S14, MDC, C8, VB12	H2

TABLE VII. Psychoacoustic and acoustic correlates.

Psychoacoustic variable	Acoustic correlate
Flexibility	$Z_{\max}(n)/Z_{\min-\mathrm{av}}(n)$
Pitch control	$Q_n = f_n/n/Df$
Ease of playing	$Z_{\max}(n)/Z_{\min-\mathrm{av}}(n)/Q_n$
Intonation	harmonicity
Tonality	s.d. $\{Z_{\max}(n)\}_{\mathrm{av}}$
Dynamic range	$Z_{\max}(n)/Z_0$&harmonicity
Attack clarity	V_c/BBL

working hypotheses: although intonation is important, professional musicians will show preferences, even among mouthpieces having equivalent harmonicity, and musicians' subjective judgments of different aspects of various mouthpiece designs can be correlated to acoustic parameters derived from geometry or from the input impedance curves.

C. Mouthpiece preference

After the preliminary tests were completed, it was decided that it would be cumbersome to devise any detailed test which could clearly communicate the variables to be examined to a diverse group of musicians in various geographical locations. The preliminary tests showed that the mouthpiece ratings of one musician, Peter Landgren (associate principal of the Baltimore Symphony Orchestra), consistently agreed with the group consensus discussed in Sec. I B and the rankings discussed in Sec. II B. Furthermore, he is a reknowned performance teacher who is not only interested in and familiar with the psychoacoustic variables we are discussing, but someone who has been using similar terminology in his teaching. In other words, his mouthpiece rankings not only agreed with the consensus, but he understands the terminology and knows exactly what to listen for. We therefore decided to conduct the detailed analysis of the seven mouthpieces using only this one professional, Peter Landgren. He was asked to evaluate each of the seven mouthpieces according to the seven criteria listed above. He could select the unmarked mouthpieces in any order and he could return to any mouthpiece at any time in order to compare the same variable among different mouthpieces. Table VI is a summary of his comments, where for each of the seven criteria, the mouthpieces are listed in a ''like,'' ''neutral,'' or ''dislike'' column.

III. HYPOTHESIZED ACOUSTIC/PSYCHOACOUSTIC CORRELATES

Our operating assumption was that the seven psychoacoustic parameters might be identified with acoustic variables according to the scheme of Table VII. We assumed that a preferred rating for ''flexibility'' would relate to a low characteristic wave impedance Z_c, where $Z_c^2(n) = Z_{\max}(n) * Z_{\min}(n)$ over the playing range, since this should allow the performer to slip easily from one mode to the next. In conjunction with this, the ratio of $Z_{\max}/Z_{\text{min-av}}$ should be high so that the note sounds easily and seems focused.

The playing frequency is determined by the interaction between the lips and the regime of oscillation. If the impedance peaks are reasonably well tuned, ''pitch control'' should correlate with Q_n, since the narrower the resonances, the better a note ''locks in'' and the easier it is for the musician to hold the pitch.

To a musician, ''ease of playing'' implies the sound produced relative to the effort put into producing it; that is, how much effort is required to start a note and to sustain it. Within certain limits, a high value of $Z_{\max}/Z_{\text{min-av}}$ will yield a note which is easy to play. But a high amplitude ratio is usually accompanied by a high Q and the higher the Q the more difficult it becomes, during playing, to locate one particular impedance peak without accidentally finding its neighbors. We therefore hypothesized that ''ease of playing'' should correlate with $(Z_{\max}(n)/Z_{\text{min-av}}(n))/Q_n$, that is, the higher the ratio, the higher the preference rating should be. The higher $Z_{\max}$ increases efficiency, while a greater bandwidth (lower Q_n) helps the musician find the resonance of choice.

Obviously, ''intonation'' should correlate indirectly with the harmonicity of the impedance peaks. For an actual French horn, the shape of the instrument is carefully designed to yield as harmonic an intonation curve as feasible, particularly in the high frequency range. The leadpipe and straight tube, however, will produce a set of modes which are stretched considerably from their values on a French horn. Despite this effect, our musician (as well as a dozen others during preliminary tests) was able to make consistent musical judgments which separated mouthpieces by preference since the amount of harmonic spreading was different for each mouthpiece.

While there does not yet exist any consensus on a measure of ''tonality'' (tone quality),[19] it was assumed to correlate with the impedance peak amplitudes, i.e., with the spectral envelope. Pratt and Bowsher[7] have shown that the nature of the spectral envelope somehow correlates with the subjective evaluation of quality, but no causal link was hypothesized. Our assumption was that even envelopes (relatively constant across most of the playing range), would be preferred to erratic envelopes or envelopes which decreased rapidly at high frequencies. A more even envelope should yield more consistent dynamics across the playing range, and should therefore be preferred by musicians. In an effort to quantify the acoustic correlate, we will define ''evenness'' as the inverse of the median deviation of $Z_{\max}(n)/Z_0$, where $Z_0 = \rho_0 c$, for each mouthpiece's spectral envelope. Thus defined, the higher the evenness coefficient (a lower median

deviation), the more preferred the mouthpiece will be for its tonality.

''Dynamic range'' is the variation from the softest to the loudest sustainable tones. Two factors would appear to be important here—the ratio of $Z_{max}(n)/Z_0$, and the harmonicity of the peaks. Well-tuned peaks, in addition to higher peak impedances, allow for fortissimo playing.[20] Pianissimo playing is easier on small-bore instruments, which implies a higher characteristic impedance. Thus we hypothesize that the mouthpieces rated as having the best dynamic range will probably have a relatively low ratio of $Z_{max}(n)/Z_0$ which is compensated for by relatively well-tuned peaks.

The ''attack clarity,'' or comparative starting time of a note, is relatively easy for the musician to gauge, but considerably more difficult to relate to acoustic parameters. The player receives no feedback from the tube until the initial air pulse from his lips has traveled to the end of the system and back; the differing behavior of the performer's lips and the air column during this initial time period produces the French horn's easily identified and characteristic attack.[21] Different mouthpieces provide varying degrees of assistance in helping the musician to synchronize his lip vibration to the initially undeveloped standing wave ratio (SWR) determined by the input impedance. Indeed, it is believed[22] that brass instruments which do not start evenly are being adversely affected by premature reflections. Although the performer must rely upon his lip tension, mouth impedance, and innate sense of pitch in order to find the correct frequency without feedback, we believe that the geometry of the mouthpiece supplies some subtle aid in this endeavor. A rule of thumb long employed by French horn manufacturers is that the ratio of cup volume to the length of the backbore, V_c/BBL, is an important ratio for this purpose, and thus should be expected to remain approximately constant over a wide variety of mouthpieces. We were thus led to hypothesize that the musician's preference for attack clarity should correlate with the mean value of this ratio for all mouthpieces, and that any significant deviation from the mean would not be preferred. Although, strictly speaking, this ratio is a geometric parameter, not an acoustic correlate, we have included it in this list for completeness.

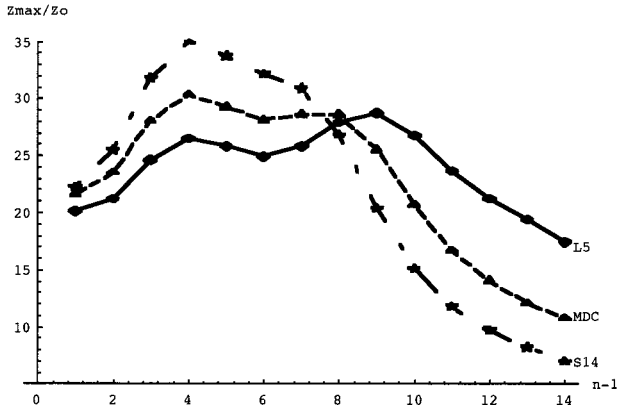

FIG. 3. Spectral envelopes of three mouthpieces.

IV. ACOUSTICAL MEASURES

The input impedance curves for the seven mouthpieces attached to the leadpipe and cylindrical tube were made using the Bruneau apparatus[15] and by computer model[16] based on accurate measurements of the system's geometry. Although the results were consistent, the somewhat idealized nature of the computer model (lack of noise) allowed a more accurate determination of the peak frequencies and bandwidths, thus allowing the data to be more easily separated when graphed. Since most of the computer generated data were used only in ratios, the idealized nature of these calculations was alleviated somewhat.

Figure 3, a graph of the spectral envelopes for several of the mouthpieces, shows that they are readily separable by this criterion. Table VIII tabulates the $Z_{max}(n)/Z_0$ vs n, determined from the computer model data, for the seven mouthpieces currently widely used in the United States.

Figure 4 is a graph of $Z_{max}(n)/Z_{min\text{-}av}(n)$ vs harmonic number n, constructed from the experimentally determined input impedance functions. For clarity, only three mouthpieces are plotted. In the middle register some obvious separation of the mouthpieces is apparent. Figure 5 is the Q_n vs n plot, constructed from the computer model data, for three

TABLE VIII. Impedance maxima for new mouthpieces.

n	L5	H2	MDC	MC13	S14	C8	VB12	AV-OLD	AV-NEW
1	29.16	33.15	30.60	31.97	30.37	30.60	29.65	30.61	31.14
2	20.08	23.40	21.51	22.55	22.20	21.97	20.71	21.67	21.98
3	21.17	25.67	23.47	24.77	25.44	24.81	22.36	23.95	24.13
4	24.54	30.62	28.00	29.88	31.76	30.49	26.58	28.83	29.04
5	26.45	32.77	30.31	32.91	35.01	33.26	29.18	30.89	31.73
6	25.73	31.02	29.19	32.40	33.68	31.87	28.83	29.05	30.88
7	24.86	29.31	28.06	31.91	32.09	30.44	28.50	27.25	30.03
8	25.76	29.21	28.53	33.23	30.84	29.94	30.13	26.71	30.84
9	27.87	28.43	28.56	33.74	26.76	27.32	32.19	25.22	30.84
10	28.68	24.69	25.48	30.07	20.33	21.77	31.09	21.10	27.17
11	26.70	19.74	20.63	24.15	15.06	16.50	26.70	16.50	21.73
12	23.60	15.91	16.65	19.36	11.78	13.01	22.21	13.15	17.41
13	21.16	13.41	13.99	16.15	9.72	10.79	18.97	11.04	14.55
14	19.35	11.56	12.01	13.71	8.20	9.14	16.43	9.46	12.40
15	17.40	9.90	10.73	11.55	6.94	7.73	13.98	8.69	10.49
16	15.08	8.42	8.65	–	5.93	–	11.69	7.39	9.10

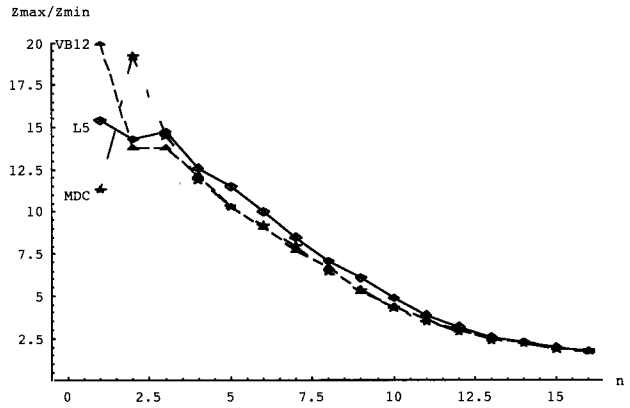

FIG. 4. Ratio of Z_{max} to $Z_{min\text{-}av}$ at each harmonic, n, for three mouthpieces, where $Z_{min\text{-}av}$ is the mean of the Z_{min}s on either side of each Z_{max} impedance peak.

mouthpieces. The Q_n plot shows some degree of separation between mouthpieces in the high range.

Figure 6 presents the harmonicity, defined relative to the third harmonic as $3(f_n/f_3)-n$ for three mouthpieces on the tube system and for a Lawson French horn for comparison. The extensive stretching of the harmonics of the experimental system compared to the French horn is quite obvious. More subtle, but readily discernible, are the variations among mouthpieces over the playing range of our system.

Figure 7 is $(Z_{max}(n)/Z_{min\text{-}av}(n))/Q_n$ vs n for three of the mouthpieces, constructed from computer model impedance graphs. Although it has been stated[17] that, for any peak, $Z_{max}=Z_0{*}Q$ and $Z_{min}=Z_0/Q$, which implies (Z_{max}/Z_{min}) is related to Q, it is overly simplistic to assume that this ratio is exactly equal to Q^2, even for uncomplicated high Q transmission lines. (The assumption behind the assertion of equivalence seems to be that since the maximum and minimum magnitude of impedance are directly related to the SWR defined by incident and reflected signals, and since Q is the ratio of the maximum energy to the energy dissipated, it should always equal to the SWR.) Although Z_{max}/Z_{min} and Q are both determined by internal geometry and system losses, Fig. 7 indicates that the precise manner in which they vary is somewhat different. (Since Fig. 7 is constructed from computer model data, other subtle effects, such as interior shape, smoothness, the number and magnitude of discontinuities, and wall material, which also might separately influence Z_{max}/Z_{min} and Q are not present.) We can further observe that this ratio shows considerable variation among mouthpieces.

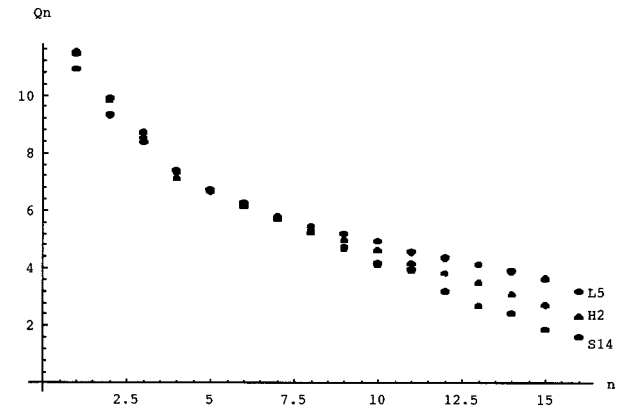

FIG. 5. Quality factor, Q_n, at each harmonic, n, for three mouthpieces.

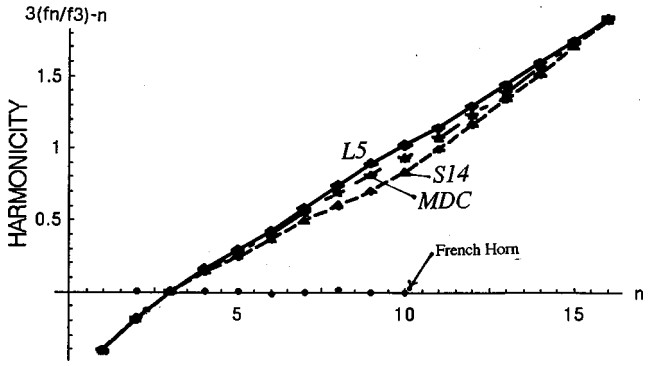

FIG. 6. Frequency deviation from integer values, defined by the third harmonic, for three mouthpieces. The points along the axis are the frequency deviations for the L5 when inserted into a French horn.

Table V lists the V_c/BBL and its percent deviation from the mean value for later consideration. Since it is widely assumed[23] that all brass instrument mouthpieces in isolation (when sealed at the rim), act as internally driven Helmholtz resonators, we calculated the following term:

$$f_r^2 = V_c/(C{*}S_{th}/L),$$

where f_r is the mouthpiece's measured[15] resonant frequency, V_c is the cup volume, S_{th} is the area of the throat, and (as a reasonable approximation) $L=THL+BBL+0.6a$, where $2a$ is the end diameter of the backbore (BBED), and C is a constant. For a Helmholtz resonator, the above term is equal to 1.00. Using data from Tables III and V, our results indicate that the mouthpieces show considerable deviation from the ideal Helmholtz resonator, as indicated by the percent differences, even though there is only a 10% variation in resonant frequency among the mouthpieces studied.

V. OBSERVED PSYCHOACOUSTIC/ACOUSTIC CORELATIONS

It has been asserted[20] that the qualities of ease of playing, clear speech, and good intonation for brass instrument

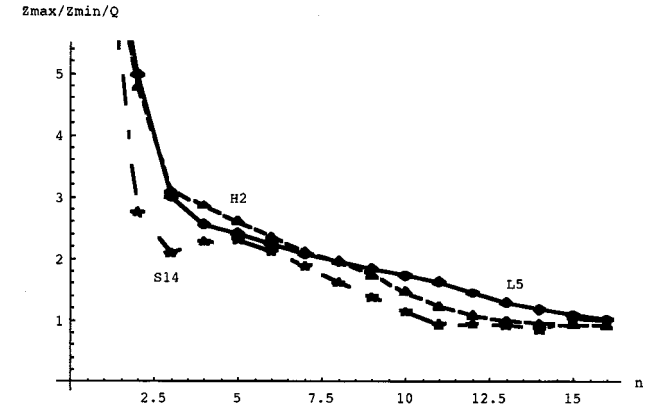

FIG. 7. Ratio of $Z_{max}(n)/Z_{min\text{-}av}(n)/Q_n$ at each harmonic, n, for three mouthpieces.

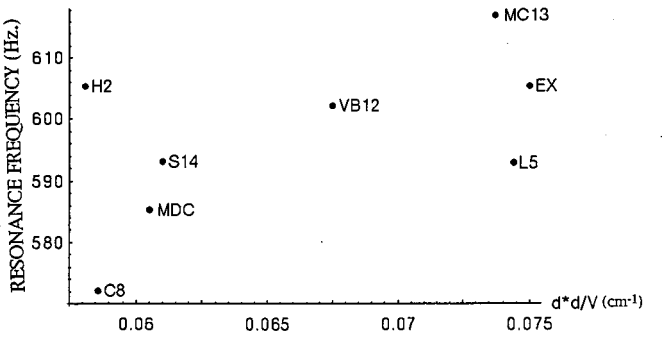

FIG. 8. Resonance frequency versus throat diameter squared divided by cup volume for eight mouthpieces.

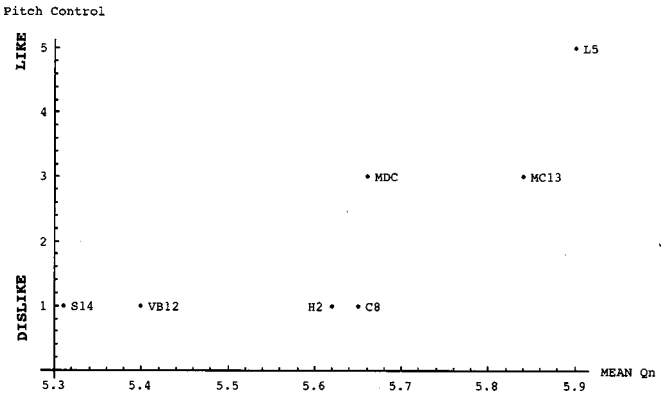

FIG. 10. Player preference for pitch control versus mean Q_n.

mouthpieces are all dominated by the relationship of total mouthpiece volume and resonance frequency. Defining a mouthpiece equivalent length at the resonance frequency as $L_{e1}=c/4*f_r$ and defining the low frequency equivalent length, L_{e2}, as that which matches the total volume of the mouthpiece, we might expect the ratio of L_{e1}/L_{e2} to be relatively constant for all French horn mouthpieces. Our tabulated results (Table V) indicate that this is not the case, although the deviations are not, for the most part, severe. It has also been widely reported[1,23] that mouthpiece resonance frequencies are carefully chosen by adjusting cup volume and throat diameter to match the mouthpiece impedance to the instrument. It would thus seem that the ratio of throat diameter squared to cup volume, V_c, if not constant, should, at least, correlate with the mouthpiece resonance frequency. Using the tabulated d^2/V_c and f_r of Table V, we constructed Fig. 8, which indicates no apparent correlation, although it does tend to separate the mouthpieces into groups.

Comparing Figs. 3–7 to Table VI we see that, although the mouthpieces can be separated, in this form correlations with criteria of Table VII are not immediately obvious, although subtle trends are apparent. For example, in Fig. 5, the mouthpiece most preferred for pitch control clearly has the highest Q_n values. Likewise, Fig. 7 suggests that the $(Z_{\max}(n)/Z_{\text{min-av}}(n))/Q_n$ correlates with ease of playing since the more preferred mouthpieces maintain a higher ratio throughout the mid-frequency range. Figure 6 is somewhat more difficult to relate to intonation as the preferred mouthpieces are those which appear toward the center of the deviations, i.e., those with partials not stretched too much or too little (considering that they are all severely stretched by this system).

The evenness of the spectral envelope of Fig. 3 should correlate to the preferred tonality. It is apparent that L5, having lower amplitude peaks at low frequencies and higher amplitude peaks at higher frequencies, is the most even, and consequently the most preferred, mouthpiece for this criterion, under this subjective evaluation. The MC13 and MDC, which were rated neutral, have similar spectral envelopes, which are lacking somewhat in the mid-frequency range. The least preferred mouthpieces are those with high amplitude peaks at low frequencies, but which fall off rapidly at high frequencies.

No obvious correlation for the player's preference for dynamic range and attack clarity could be found with the suggested physical correlates. Indeed, an examination of the V_c/BBL data of Table V indicates that this ratio is neither extremely important, nor particularly constant.

To better compare the acoustic and psycho-acoustic parameters, we next expressed the acoustic correlates in a more quantitative, but less easily visualized, form by averaging the appropriate variable over the impedance peaks of each mouthpiece. Although this procedure may gloss over some of the fine details, it is an effective way to rank the mouthpieces so that the acoustic correlates may be objectively related to the psychoacoustic variables. This has been presented as Figs. 9 through 14, where the preferences of Table VI have been plotted versus the appropriate correlate for six acoustic parameters. (We did not include ''attack clarity'' because of the obvious lack of correlation.) A brief discus-

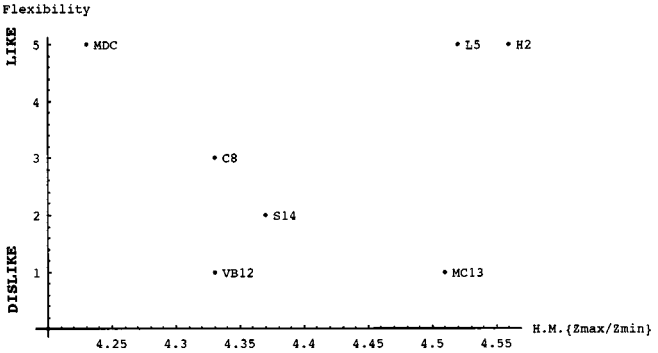

FIG. 9. Player preference for flexibility versus harmonic mean of $Z_{\max}/Z_{\min}$.

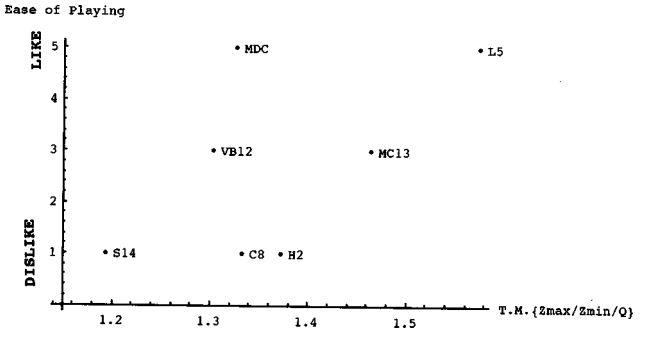

FIG. 11. Player preference for ease if playing versus trimmed mean of $Z_{\max}/Z_{\min}/Q_n$.

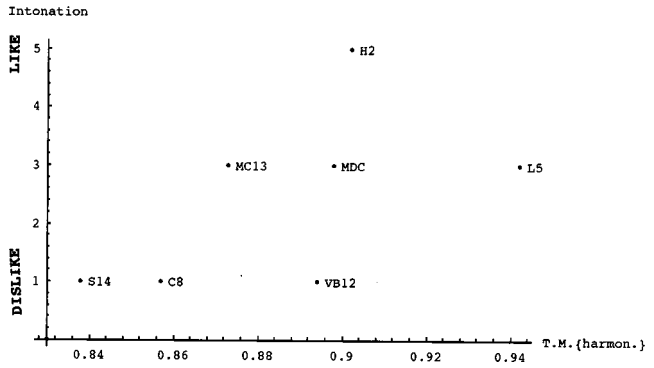

FIG. 12. Player preference for each of playing versus trimmed mean of harmonicity.

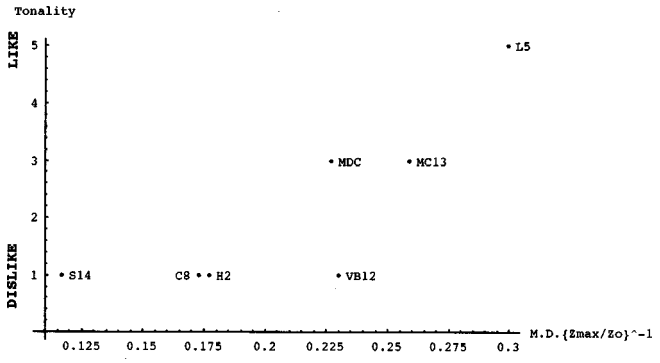

FIG. 13. Player preference for tonality versus median deviation of $\{Z/_{\max}/Z_0\}^{-1}$.

sion of these figures follows. Figure 9 indicates that the higher the ''harmonic mean'' of $Z_{\max}(n)/Z_{\text{min-av}}(n)$ for the partials of the experimentally determined impedance plot for each mouthpiece, the more the mouthpiece is liked for flexibility. Two notable exceptions are the MC13 which, despite its high numerical ranking was disliked, and the MDC which was liked even though its harmonic mean was quite low. For the MC13 this was undoubtedly due to its high mean characteristic impedance Z_c. (Since our data indicate that this quantity is somewhat frequency dependent, we have averaged it over all impedance peaks for each mouthpiece and recorded the results in Table IX.) The high mean Z_c indicates that it will be more difficult for the performer to slip between adjacent impedance peaks; consequently this mouthpiece will not be preferred despite the high mean $Z_{\max}(n)/Z_{\text{min-av}}(n)$. For a similar reason the VB12 is not preferred. The MDC, on the other hand, has quite a low mean Z_c, which tends to raise its flexibility preference even though the mean $Z_{\max}(n)/Z_{\text{min-av}}(n)$ is also relatively low.

Figure 10 demonstrates that although the mean Q_n ranks the mouthpieces in an approximately correct order, the correlation with ''pitch control'' shows a definite trend; mouthpieces with higher mean Q_n tend to be better liked. The correlation discrepancy for the pitch control parameter may be explained by considering that the perception of pitch as sensed by the player is not merely the aural feedback to his ear, but also includes how strongly the note ''locks in.'' It would seem, then, that three factors should be important: Q_n, $Z_{\max}$, and the s.d. of $Z_{\max}$ (which is related to ''tonality,'' i.e., the evenness of the spectral envelope). Since both the H2 and the C8 are mouthpieces with a relatively low $Z_{\max}$ and uneven spectral envelope, it is perhaps not unreasonable that they were rated poorly for ''pitch control'' despite their relatively high mean Q_n. If we consider, for each mouthpiece, the product of the mean Q_n and the inverse median deviation of $Z_{\max}/Z_0$ of Part E (which quantifies the unevenness of the spectral envelope), the mouthpieces are clearly ordered into three clusters which agree exactly with the ''pitch control'' grouping.

Figure 11 shows that ''ease of playing'' correlates reasonably well with the ''trimmed mean'' of $Z_{\max}(n)/Z_{\text{min-av}}(n)/Q_n$. (The trimmed mean is the mean of the above ratio with the first six harmonics deleted. This is desirable since the important variations between mouthpieces occur in the middle and upper frequency ranges.) That the MDC is more preferred than this ratio would indicate, and the H2 less preferred, is probably due to the surprisingly good start-up accuracy for the MDC and the unusually bad start-up accuracy exhibited by the H2.

Figure 12 indicates that the assumed correlation between ''intonation'' and ''trimmed mean harmonicity'' is less than perfect. (The trimmed mean harmonicity is the mean harmonicity without the first three or the last two partials, thus better emphasizing the differences between means.) Nevertheless, this acoustic variable orders the mouthpieces, with the exception of H2, into approximately the same basic arrangement as the preference test. Since the most preferred mouthpiece occupies an intermediate position in a harmonicity plot (such as Fig. 6), we next investigated the deviation from a least squares linear fit to the harmonicity versus mode number by calculating the rms deviation from the least squares fit for each mouthpiece. The data, incorporated into Table IX, indicate that, in general, the neutral mouthpieces show lower rms deviation while the deviation is greater for nonpreferred mouthpieces. Again, the obvious exception is the H2, with a fairly high rms deviation, but the most preferred mouthpiece for intonation. Perhaps this high deviation is offset by the decreased prominence of the higher mode peak amplitudes (see Table VIII).

Figure 13 shows that the inverse ''median deviation'' of $Z_{\max}(n)/Z_0$ correlates reasonably well with ''tonality.'' That is, the more preferred mouthpieces have the lowest deviation

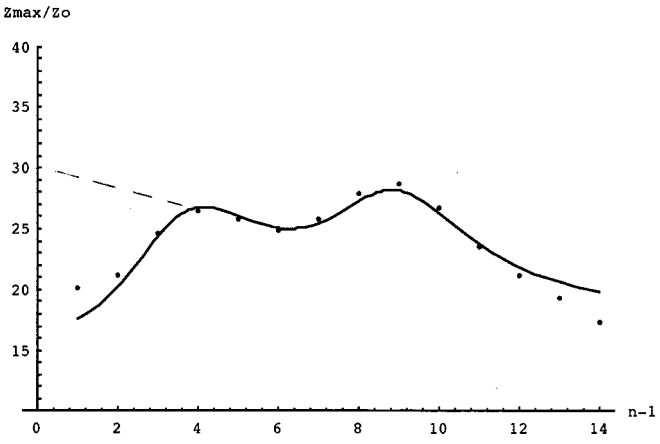

FIG. 14. Spectral envelope for L5.

TABLE IX. Computed quantities.

	L5	H2	MDC	MC13	S14	C8	VB12
Mean Z_c^2	59.59	54.73	53.32	72.03	54.40	54.07	71.53
Z_c^2 Stndrd. Deviat.	30.38	25.93	26.15	37.97	32.02	28.00	36.03
1.s. fit {harm}							
slope	0.148	0.150	0.147	0.140	0.143	0.141	0.143
y-inter.	−0.473	−0.509	−0.495	−0.461	−0.504	−0.482	−0.467
rms dev.	0.0282	0.0435	0.0392	0.0370	0.0584	0.0437	0.0352
Mean Z_{hi}	23.54	17.66	18.29	21.25	14.11	15.18	23.08
Mean Z_{lo}	24.72	29.39	27.46	29.95	30.21	29.17	26.99
Z_{hi}/Z_{lo}	0.952	0.601	0.666	0.710	0.467	0.521	0.855
C	16.78	13.50	12.17	12.69	8.67	9.91	14.91
$A(1)$	186.4	396.5	375.6	409.6	548.0	476.9	264.5
$A(2)$	176.4	115.7	153.7	237.6	126.5	133.0	242.2
$A(2)/A(1)$	0.943	0.292	0.410	0.581	0.231	0.279	0.917
Z-intercept	29.9	39.8	34.9	34.7	41.1	39.3	30.5
Q_n	5.90	5.62	5.66	5.84	5.31	5.65	5.40

and vice versa. The single exception is the VB12, which is seen to have relatively strong fifth and seventh harmonics. Since these harmonics are seriously out of tune on any natural system, they will add a strident quality to any tone played loudly. The VB12, which was rated poorly for harmonicity, is probably not preferred for tonality for precisely this reason. Table IX indicates that the mouthpieces may be similarly ordered by the ratio of the mean $Z_{\max}(n)/Z_0$ at high frequencies (impedance peaks 9–15) to the mean $Z_{\max}(n)/Z_0$ at low frequencies (the first eight impedance peaks). That is, the preferred mouthpieces have relatively high amplitude impedance peaks at high frequencies.

Following Pratt and Bowsher[5] we next investigated the nature of the spectral envelope in more detail in an attempt to identify other possible objective correlates to tonality. A visual inspection of the envelopes indicated that for most mouthpieces there seemed to be two formantlike peaks, one around the fifth partial, and one around the ninth or tenth partial. Consequently, a least squares analysis was performed to fit the impedance peaks of Table VIII by a curve having the form

$$Z(f)=C+A_1/[R+(f^2-f_1^2)^2 f^{-2}] + A_2/[R+(f^2-f_2^2)^2 f^{-2}],$$

where A_1, A_2, and C are constants determined by the least squares analysis, R is a resistance term, f is the frequency, and f_1 and f_2 are the first and second ''formant'' peak frequencies. Figures 14 through 20 present these curves for the seven mouthpieces studied (the first impedance peak has not been included in this analysis because it is severely out of tune and seldom used) in order of decreasing importance of the second ''formant.'' The constants A_1, A_2, and C, as determined for each mouthpiece, have been incorporated into Table IX. If the ''formant'' amplitude terms (A_1 and A_2) are divided, this ratio orders the mouthpieces correctly (with VB12 being the lone exception) for tonality from liked to disliked (compare Fig. 13), thus confirming the importance of the spectral envelope shape to tone quality.

To investigate the suggestion[7] that the impedance-axis intercept (defined by $n=1$ in this case) of the linear fit to the negative sloped portion of the spectral envelope (defined by peaks 5, 6, and 7, the mid-range of a horn) relates to tonality, we recorded this quantity in Table IX as the *Z*-intercept. Except for VB12, this quantity very clearly separates the mouthpieces into three groups. Preferred mouthpieces have an intercept value of about 30, neutral mouthpieces about 35, and unpreferred about 40. Figure 21 shows the strong corre-

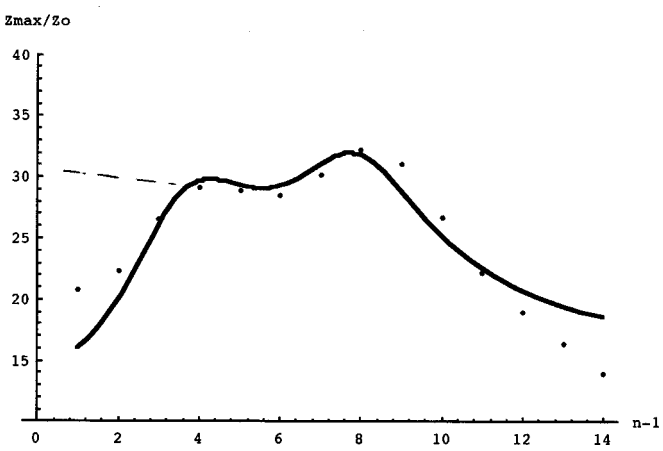

FIG. 15. Spectral envelope for VB12.

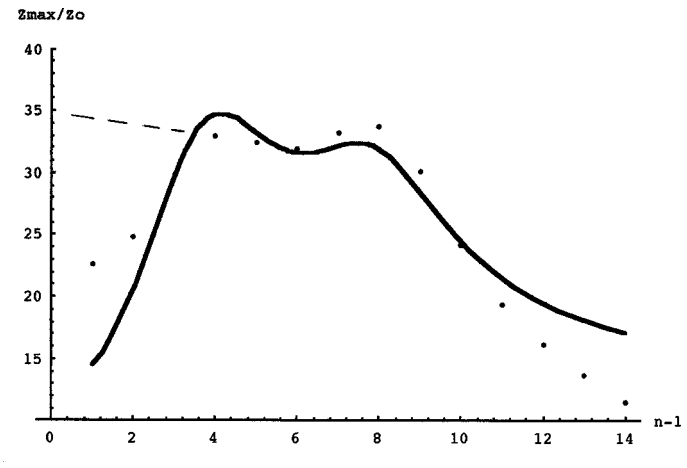

FIG. 16. Spectral envelope for MC13.

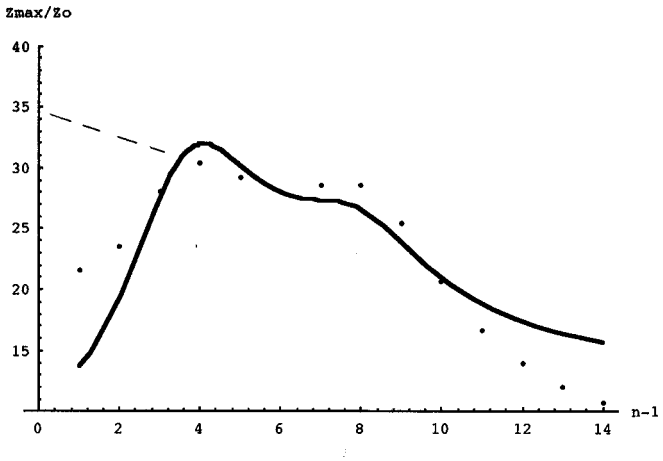

FIG. 17. Spectral envelope for MDC.

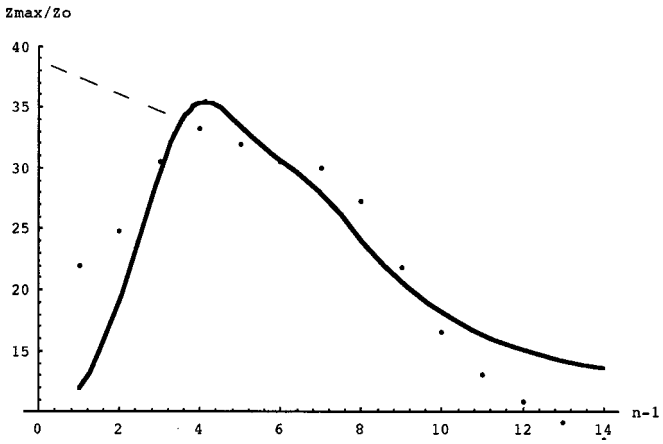

FIG. 19. Spectral envelope for C8.

lation between the *z*-intercept and musician's preference for tonality. Although the VB12 mouthpiece has a low *Z*-intercept, and therefore should have a high musician preference rating, it was disliked. This is most likely due to its strong fifth harmonic which is seriously out of tune; the ''bad'' intonation of one of the horn's most important harmonics ruins the otherwise excellent tonality.

Finally, the dynamic range, as summarized by the ''geometric mean'' of $Z_{\max}(n)/Z_0$, is presented in Fig. 22. (The geometric mean is preferred for this average because it tends to treat linear data logarithmically, which more closely approximates the manner in which this variable will be perceived.) Although the ''not-preferred'' mouthpieces are readily separated by their low ratio, the neutral and preferred ones cannot be separated by this variable alone. Including ''harmonicity,'' however, helps to explain some of the discrepancies. The rms of the deviation from a linear least squares fit to the harmonicity curve for each mouthpiece shows that the L5 is at the extreme low end (least deviation), while the S14 has the greatest deviation. The H2 plots at the mid-point of the range, thus confirming our suspicion that for the test system musicians, seem to prefer this design. Perhaps a greater stretching of the harmonics is preferred for tonality, but less support for fortissimo playing is then present, thus yielding a lower preference rating for dynamic range.

VI. CONSOLIDATED PSYCHO-ACOUSTIC PARAMETERS

Since the above results indicated that there is not a one-to-one correspondence between acoustic and psycho-acoustic variables, we next investigated correlations between one of the most significant variables, $Z_{\max}(n)$, and a consolidated set of psycho-acoustic parameters. Aside from intonation, which correlates with harmonicity, but which is difficult to access on our system, we redefined the psycho-acoustic variables as follows. ''*Playability*'' was defined as a combination of *dynamic range*, *ease of playing*, and *flexibility*, while ''*tonal responsiveness*'' was defined as a combination of *tonality*, *attack clarity*, and *pitch control*.[24] Mr. Landgren was then asked to order the mouthpieces by preference according to these two criteria only, a choice rendered considerably easier by the reduced number of variables. Two additional mouthpieces were also added for his consideration. These were specially constructed mouthpieces with respective physical dimensions of the mean of the 61 mouthpieces of Table I (called AV-OLD) and the mean of the seven mouthpieces of Table III widely used today (called AV-NEW). Geometrical data on these mouthpieces have been included in Table III and the last two columns of Table VIII list their $Z_{\max}/Z_0$.

In an attempt to correlate the psycho-acoustic data with the acoustical analysis, we next found the mean $Z_{\max}/Z_0$ over

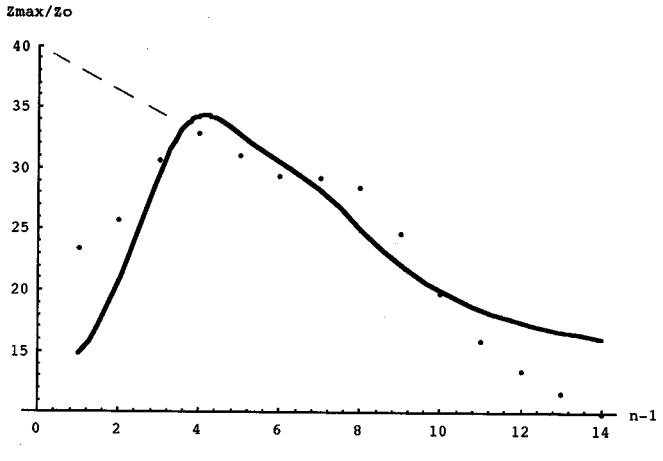

FIG. 18. Spectral envelope for H2.

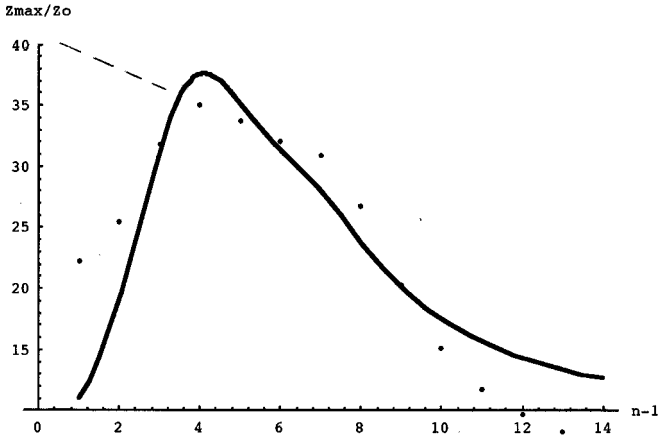

FIG. 20. Spectral envelope for S14.

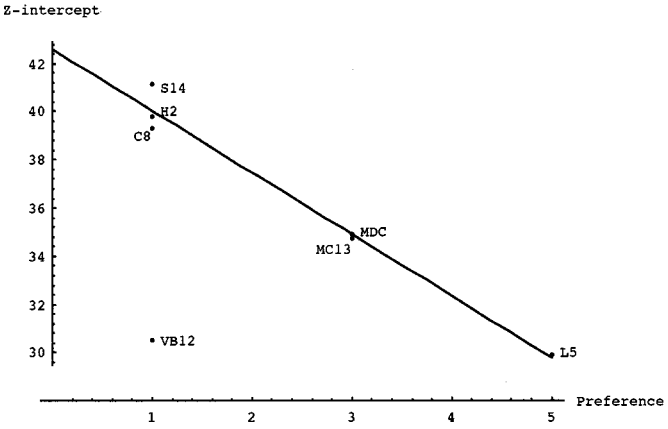

FIG. 21. Z-intercept versus musician preference for tonality.

16 harmonics, as well as the standard deviations, for each mouthpiece. A plot of the means versus standard deviations tends to separate the mouthpieces into different quadrants, as can be seen in Fig. 23, where the axes shown are the respective mean values for Z_{max}/Z_0 and the standard deviation. Each quadrant may be considered as a different psychoacoustic preference domain as indicated by plotting the mouthpieces according to the consolidated criteria of playability versus tonal responsiveness, as shown in Fig. 24. Comparing Figs. 23 and 24 we see that the ordering of the mouthpieces is similar and this two-dimensional representation is more informative. Perhaps an even more accurate correlation may be obtained if the vibrational characteristics of the player's lips were incorporated, since the input impedance function alone does not adequately represent the dynamics of a player sounding the instrument. Also, it is a generally accepted truth among performers that mouthpieces tend to perform differently at different dynamics levels.

The French Horn is part of a complicated ''input–output system'' which includes the player's buzzing lips (the input signal) and a transfer function which relates the input to the output signal.[25] We have documented many combinations of acoustic parameters which we had hoped would help define this transfer function as well as relate geometrical and acoustical parameters to musician's perceptions. While a reasonably good correlation between the consolidated parameters and the musician's ratings was obtained, it is still unknown exactly how these variables relate to the transfer function.

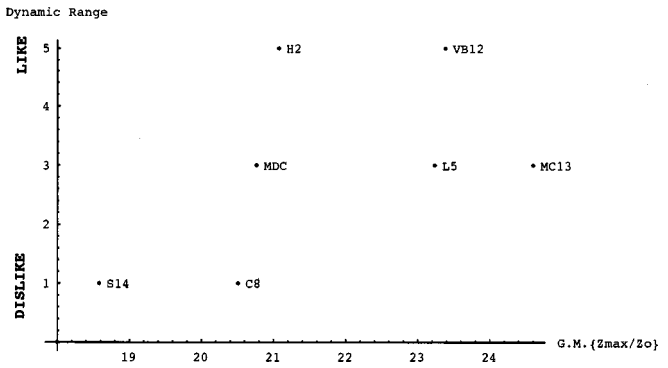

FIG. 22. Player preference for dynamic range versus geometric mean of $\{Z_{max}/Z_0\}$.

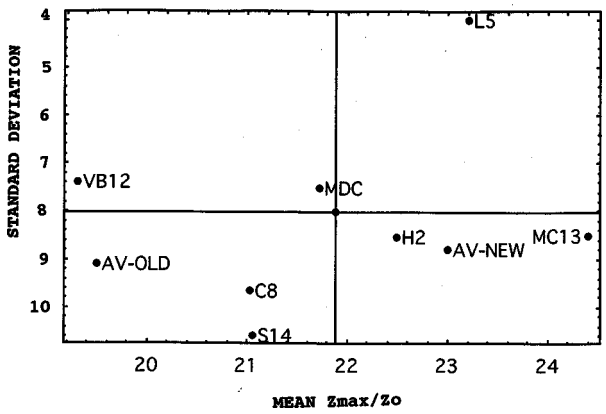

FIG. 23. Mean Z_{max}/Z_0 versus standard deviation for nine mouthpieces.

Once the input signal characteristics and its transform become known it should be obvious why many of the various combinations of the impedance curves did not correlate well. Therefore we believe that in order to derive a complete understanding of the entire IO mapping system once all parameters are known, all combinations will have to be included. Although the correlations of individual parameters were not as strong as expected, we discussed the correlations in some depth because we believe the data contain important information which may be useful to future researchers. Additionally, our complete and careful documentation of the relationships between the geometric and acoustic parameter correlations will insure that future improvements can be realized quickly and easily once the entire system is mapped.

VII. CONCLUSIONS

A fundamental acoustic characteristic of well-designed brass wind instruments is that as many of the input impedance peaks as feasible should be harmonically related. This characteristic, which is interpreted by musicians as the intonation of the instrument, can be easily gauged from the input impedance function. Our investigation of the French horn was predicated on the assumption that other psycho-acoustic parameters, at least as important as intonation, may correlate with acoustic data or geometric factors. Since the mouthpiece is considered by musicians to be the single most important component regarding how the entire horn performs,

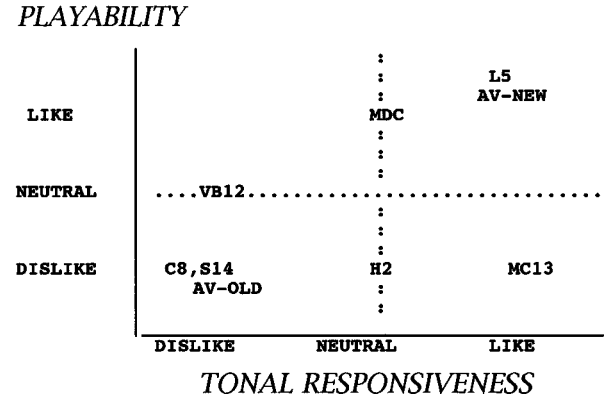

FIG. 24. Results of the two variable psychoacoustic criteria judgment test.

and because the mouthpiece is an easily changeable component of a wind instrument, our study was limited to a comparison of the acoustic and musical differences between various French horn mouthpiece designs attached to a ''simplified'' horn.

In addition to harmonicity, six other acoustic parameters, determined by geometry, were analyzed for possible correlations with psycho-acoustic factors measured by musicians' comparative evaluation testing. Although most of the correlations were reasonably good for the majority of the mouthpieces, the exceptions made it obvious that these parameters could not always be isolated and that searching for a one-to-one correspondence between psycho-acoustic and acoustic variables was counterproductive if not futile. The most important acoustic parameters seemed to be the impedance peak amplitudes, the Q_n and the overall shape of the spectral envelope. In an attempt to simplify the analysis and to include the cross correlations, we focused on the acoustic parameters $Z_{\max}(n)$. The psycho-acoustic variables were correspondingly condensed into two broad categories termed ''playability'' and ''tonal responsiveness.'' Plotting the mean $Z_{\max}$ (averaged over 16 harmonics) versus standard deviation for each of the eight mouthpieces separated them into different quadrants. This correlated reasonably well with psycho-acoustic preference domains defined by the two new variables used as coordinates. Players tended to prefer mouthpiece designs which had relatively high average peak amplitudes, but coincident low variability of harmonic peaks.

Based on our documented changes in the ratio of French horn mouthpiece cup length to throat plus backbore length during the course of the twentieth century, we compared the acoustical properties of modern designs to the older versions. Our results clearly show that the average harmonics' peak amplitude ($Z_{\max}$) has increased while variability has simultaneously decreased, resulting in a more even envelope. Also, the average values of Q_n have increased, a probable explanation for the longer measured decay times. The higher Q_n values may also be associated with musicians' expressed preference for greater pitch control.

Our experiments indicate that the equivalent length concept for brass mouthpieces is an outmoded notion which is too simplistic to be accurate or useful. It has also been widely assumed that brass instrument mouthpieces can be accurately represented as Helmholtz resonators, and that the performance of a given mouthpiece is dependent upon the cup volume and throat diameter, the shape being a much less important variable.[26] Our experimental results indicate that, for the French horn, the opposite is more nearly true. Although useful as a first approximation, the Helmholtz resonator description is clearly inadequate as an accurate characterization of French horn mouthpieces. We hypothesize that it will be an equally ineffectual representation for the mouthpieces of other members of the brass instrument family.

In so far as a ''consensus'' mouthpiece may be identified, the AV-NEW design comes closest to being acceptable for use on a wide variety of horns in different circumstances by professional musicians. It is also interesting to note that the one mouthpiece consistently chosen in most preference categories was the L5, whose dimensions are closer to those of AV-NEW than any of the other mouthpieces in common use today.

Although we have shown that subjective judgments may be correlated to acoustic parameters derived from geometry, further investigation is needed. Future research could be directed toward more elaborate and/or more extensive player sampling data and techniques. We have determined three acoustic variables, $Z_{\max}(n)/Z_0$, Q_n, and the spectral envelope, to be particularly relevant. It is interesting to note that an important attribute of well-trained singers is the ability to maintain a uniform spectrum over wide ranges of frequency and amplitude;[27] this corresponds to our observation that a uniform spectral envelope is one of the most important characteristics of the most highly rated French horn mouthpieces.

No attempt has been made to consider how the shape of the mouthpiece may influence musician's subjective evaluations or to include, as an objective parameter, turbulence and/or vorticity as a function of shape during performance. Although it is known[7] that dc airflow will reduce the Q's of impedance maxima, thus changing the input impedance under actual playing conditions, we did not consider this effect at this time. In addition, since the sensations perceived by a performer may change as the dynamic level is varied, the selected preference variable may deviate in a corresponding manner. Clearly, there is considerable work remaining to be enacted before the intricate association between subjective qualities and the geometry of brass instruments is fully comprehended.

ACKNOWLEDGMENTS

The authors wish to gratefully acknowledge Kendall Betts, Tom Cowan, and Walter Lawson for measuring and tabulating the mouthpiece data summarized in Table I. A special word of gratitude is also given to Michel Bruneau for being a perfect host and for making available the facilities of the Laboratoire d'Acoustique, Université du Maine, Lemans, France, where our experimental work was conducted. Shigeru Yoshikawa provided an extensive critical analysis of our pre-print which led to a significantly improved presentation. Last, but not least, we would like to thank the Faculty Development committee of Frostburg State University for partially supporting this effort.

[1] A. H. Benade, *Fundamentals of Musical Acoustics* (Oxford University Press, New York, 1976), p. 395.
[2] V. Bach, *The Search for the Perfect Mouthpiece* (Vincent Bach Corp., Elkhart, IN, 1968).
[3] J. Stork and P. Stork, *Understanding the Mouthpiece* (Editions Bim, 1989), p. 3.
[4] P. Farkas, *The Art of French Horn Playing* (Summy Birchard, 1956), pp. 11–13.
[5] D. Smithers, K. Wogram, and J. Bowsher, ''Playing the Baroque Trumpet,'' Sci. Am. April 1986, pp. 108–115.
[6] A. Benade and D. Gans, ''Sound production in wind instruments,'' Ann. (N.Y.) Acad. Sci. **155**, 247–263 (1968).
[7] R. Pratt and J. Bowsher, ''Objective assessment of trombone quality,'' J. Sound Vib. **65**, 521–547 (1979).
[8] J. Backus, ''Input impedance curves for the brass instruments,'' J. Acoust. Soc. Am. **60**, 470–480 (1976).
[9] R. L. Pratt, S. J. Elliott, and J. M. Bowsher, ''The measurement of the acoustic impedance of brass instruments,'' Acustica **38**, 236–246 (1977).
[10] R. Causse, J. Kergomard, and X. Lurton, ''Input impedance of brass mu-

sical instruments—Comparison between experiment and numerical models,'' J. Acoust. Soc. Am. **75**, 241–254 (1984).
[11] T. H. Long, ''The performance of cup mouthpiece instruments,'' J. Acoust. Soc. Am. **19**, 892–901 (1947).
[12] E. Kent, ''Wind instruments of the cup mouthpiece type,'' U.S. Patent No. 2987950 (1961).
[13] W. Cardwell, ''Cup mouthpiece wind instruments,'' U.S. Patent No. 3507181 (1970).
[14] R. W. Pyle, ''Effective length of horns,'' J. Acoust. Soc. Am. **57**, 1309–1317 (1975).
[15] A. M. Bruneau, ''An acoustic impedance sensor with two reciprocal transducers,'' J. Acoust. Soc. Am. **81**, 1168–1178 (1987).
[16] G. R. Plitnik and W. J. Strong, ''Numerical method for calculating input impedances of the oboe,'' J. Acoust. Soc. Am. **65**, 816–825 (1979).
[17] Reference 1, p. 400.
[18] R. Pratt and J. Bowsher, ''The subjective assessment of trombone quality,'' J. Sound Vib. **57**, 425–435 (1978).
[19] E. Zwicker and H. Fastl, *Psychoacoustics, Facts and Models* (Springer-Verlag, New York, 1990).
[20] Reference 1, pp. 418–425.
[21] D. Luce and M. Clark, ''Physical correlates of brass-instrument tones,'' J. Acoust. Soc. Am. **42**, 1232–1243 (1967).
[22] S. Elliott, J. Bowsher, and P. Watkinson, ''Input and transfer response of brass wind instruments,'' J. Acoust. Soc. Am. **72**, 1747–1760 (1982).
[23] N. Fletcher and T. Rossing, *The Physics of Musical Instruments* (Springer-Verlag, New York, 1991), p. 371.
[24] Reference 4, Chap. One.
[25] H. Kwakernaak, R. Sivan, and R. C. W. Strijbas, *Modern Signals and Systems* (Prentice-Hall, NJ, 1991), Chap. 3, pp. 65–157.
[26] Reference 23, p. 369.
[27] I. Titze, ''Singing: A story of training entrained oscillators,'' J. Acoust. Soc. Am. **97**, 704 (1995).

Nonlinear propagation effects on broadband attenuation measurements and its implications for ultrasonic tissue characterization

Jan D'hooge[a)]
Medical Image Computing, Department of Electrical Engineering, Katholieke Universiteit Leuven, Kardinaal Mercierlaan 94, B-3001 Heverlee, Belgium

Bart Bijnens
Department of Cardiology, Katholieke Universiteit Leuven, Herestraat 49, B-3000 Leuven, Belgium

Johan Nuyts
Department of Nuclear Medicine, Katholieke Universiteit Leuven, Herestraat 49, B-3000 Leuven, Belgium

Jean-Marie Gorce and Denis Friboulet
CREATIS, Unité de Recherche CNRS (UMR 5515), affiliée à l'INSERM, Lyon Insa 502, 69621 Villeurbanne Cedex, France

Jan Thoen
Laboratorium voor Akoestiek en Thermische Fysica, Departement Natuurkunde, Katholieke Universiteit Leuven, Celestijnenlaan 200 D, B-3001 Heverlee, Belgium

Frans Van de Werf
Department of Cardiology, Katholieke Universiteit Leuven, Herestraat 49, B-3000 Leuven, Belgium

Paul Suetens
Medical Image Computing, Department of Electrical Engineering, Katholieke Universiteit Leuven, Kardinaal Mercierlaan 94, B-3001 Heverlee, Belgium

(Received 2 January 1999; revised 17 March 1999; accepted 7 May 1999)

A study is presented in which the influence of the pressure amplitude of the incident pulse on the estimated frequency dependency of the attenuation coefficient is shown. First, the effect is demonstrated with a simple theoretical model for both transmission and reflection measurements. Simulations show that for both measurement techniques a high-amplitude incident pulse results in a biased estimate of the attenuation coefficient due to nonlinear interaction of the different frequency components of the incident pulse. It is shown that in transmission and reflection measurements the biases have opposite signs. The effect of bandwidth, central frequency, and phase of the incident pulse on this bias is investigated. Second, the effect is demonstrated both *in vitro*, using a broadband through-transmission substitution technique on a tissue mimicking gelatine phantom, and *in vivo*, using reflection measurements with standard clinical equipment. The experimental results agree well with the theoretical model. The relevance of this study for ultrasonic tissue characterization is shown. [S0001-4966(99)04608-1]

PACS numbers: 43.80.Ev, 43.80.Vj, 43.25.Ed [FD]

INTRODUCTION

The characterization of biological tissues based on the analysis of echographic images is receiving increased attention. It has been anticipated that the frequency dependency of the attenuation of tissues could be a good parameter for characterization since this parameter is independent of the reflection characteristics at tissue interfaces.[1] Therefore, the frequency dependency of the attenuation has been used in many studies trying to characterize different tissues *in vivo*.[2,3]

It has been shown that for both *in vitro* and *in vivo* measurements, diffraction effects can introduce a bias on the estimated attenuation coefficient. Therefore, a lot of work has been done on the compensation for diffraction errors (and hence focusing).[4–6] Less attention has been paid, however, on the influence of the pressure amplitude of the transmitted pulse on the attenuation estimate. However, it has been shown experimentally *in vitro* that in through-transmission substitution measurements (both narrow- and broadband), the attenuation coefficient is underestimated due to nonlinear propagation of finite-amplitude waves.[7–9] Since the acoustic power output of clinical scanners is high enough for nonlinear wave propagation in tissue,[10] it could be possible that *in vivo* estimates of the attenuation coefficient are biased as well. This hypothesis is further supported by the fact that there is a wide variation in published values for the attenuation coefficient of tissues measured *in vivo*.[11]

In order to investigate this further, a simple mathematical model for nonlinear wave propagation is used to predict the bias in the attenuation estimate, both in transmission and reflection experiments, and to investigate the influence of the

[a)]Author to whom correspondence should be addressed; Electronic mail: jan.dhooge@uz.kuleuven.ac.be

pulse characteristics (such as bandwidth and phase) on this bias. The model is validated by measuring the attenuation coefficient of both a tissue mimicking phantom *in vitro* and liver *in vivo* at several pressure amplitudes using transmission and reflection measurements, respectively. The relevance for attenuation measurements in a clinical situation for ultrasonic tissue characterization is shown.

I. SIMULATIONS

A. Methods

1. Theory

The most widely used model to study the combined effects of dissipation and nonlinearity on progressive plane finite-amplitude waves in a homogeneous, thermoviscous fluid, is the Burgers equation,[12]

$$\frac{\partial p}{\partial x}=\frac{\delta}{2c_0^3}\frac{\partial^2 p}{\partial \tau^2}+\frac{\beta p}{\rho_0 c_0^3}\frac{\partial p}{\partial \tau}, \tag{1}$$

where p is the sound pressure, x the coordinate along the axis of the beam, δ the diffusivity of sound, c_0 the sound speed of small-amplitude waves, β the nonlinearity parameter, ρ_0 the ambient density, and $\tau=t-x/c_0$ the retarded time. The first term on the right-hand side of the equation describes thermoviscous dissipation, while the second term describes the effect of nonlinearity. Several algorithms have been proposed to implement this equation and an excellent overview can be found in Ref. 12. Most algorithms are based on the operator-splitting principle, which assumes that if the discrete propagation steps Δx are sufficiently small, dissipative and nonlinear effects can be decoupled and will act independently. The combined effect on a wave propagating a distance Δx is then calculated by attenuating the wave over a distance Δx and subsequently nonlinearly distorting this attenuated pulse over the same distance Δx. It has been shown that the order in which the effects act is not important.[13]

In our simulator, attenuation was modeled in the frequency domain by defining a zero-phase transfer function $T(f,\Delta x)$ with amplitude,

$$|T(f,\Delta x)|=e^{-\alpha_0 f \Delta x}, \tag{2}$$

with α_0 the attenuation coefficient of the medium and f the frequency. Hence, the attenuation coefficient was modeled to be linearly dependent on the frequency, which is a good model for attenuation in biological tissues.[11]

Nonlinearity was modeled in the time domain as described in Ref. 13,

$$v_m^{n+1}=\begin{cases} v_m^n\left(1+\dfrac{\beta \Delta x_n f_s}{c_0^2}(v_{m+1}^n-v_m^n)\right), & \text{for } v_m^n \geqslant 0, \\ v_m^n\left(1+\dfrac{\beta \Delta x_n f_s}{c_0^2}(v_m^n-v_{m-1}^n)\right), & \text{for } v_m^n<0 \end{cases} \tag{3}$$

with f_s the sample frequency, v_m^n the m-th sample of the temporal velocity waveform at the distance $n\Delta x_n$, and

$$\Delta x_n < \frac{c_0^2/\beta f_s}{\max(v_m^n-v_{m-1}^n)} \tag{4}$$

a fraction of Δx in order to avoid multivalued solutions.

A parameter used to describe the nonlinear distortion process is the so-called shock parameter σ, which is defined as

$$\sigma=\frac{2\pi\beta f p_0 x}{\rho_0 c_0^3}, \tag{5}$$

where p_0 is the pressure amplitude of the wave. When this parameter reaches a value of 1, shocks start to form for sinusoidal waves. Although this is not necessarily true for broadband pulses, this parameter is still used to give a measure for the nonlinear distortion of a broadband pulse.

2. Transmission measurements

The simulation of a through-transmission substitution experiment was done in three steps:

(1) A reference measurement in water was simulated by propagating a wave through a nondissipative medium having $\alpha_0=0$ and $\beta=3.5$ over a distance of 11 cm (the position of the receiver).
(2) A transmission measurement was simulated assuming that attenuation in the substitution object is dominant over nonlinearity. Hence, the wave was propagated through water till the front of the object (positioned at 5 cm) as described in 1. Then the wave was propagated through the object (thickness 2 cm), modeled as a medium with $\alpha_0=0.5$ (dB/cm MHz) (a typical value for the attenuation coefficient of soft tissue) and $\beta=0$. Finally, the wave was propagated from the back of the object to the receiver as in 1.
(3) The attenuation coefficient was estimated by fitting a straight line to the difference of the logarithmic power spectra of the reference and the transmission measurement within the -6-dB bandwidth of the reference spectrum. The slope B of this curve relates to α_0 as: $\alpha_0=B/d$, with d the thickness of the object (see, e.g., Ref. 1 for a detailed explanation of the log-spectral difference method).

All waveforms were sampled at 1 GHz and were calculated at discrete propagation steps Δx of 5 mm. Moreover, since nonlinear distortion results in the transfer of energy to higher frequencies, aliasing was avoided by low-pass filtering the pulses after each propagation step by means of an eight-order Butterworth filter having its cutoff frequency at 90% of the Nyquist frequency (450 MHz).

Transmission measurements were simulated for a range of Gaussian pulses, modeled as a Gaussian multiplied with a cosine function, having zero-phase at the maximum of the Gaussian. Shock parameters from 0–1.5, center frequencies from 2.5–10 MHz, -6-dB bandwidths relative to the center frequency of 20%–100%, and phases of $-\pi$-$+\pi$ were simulated. Moreover, as a validation of the simulations, through-transmission experiments were performed *in vitro* (see Sec. II A). The low-amplitude reference measurements of these experiments were used as input of the simulator. The corresponding high-amplitude simulations were performed by using a scaled version of the low-amplitude pulse. This was done in such a way that the amplitude of the pulse used for

the high-amplitude simulation was the same as the one measured. The mean value of the low-amplitude measurements was used as the attenuation coefficient of the phantom.

3. Reflection measurements

To simulate the attenuation estimation from reflection measurements, a wave was propagated through an attenuating object as described in (2) of the previous paragraph. At each discrete propagation step of 5 mm between the source and receiver, a point reflector was positioned, resulting in a wave propagating back to the source. The assumption was made that the amplitude of the reflected wave was sufficiently small so that back-propagation could be modeled as a linear process ($\beta=0$). Reflections from behind the attenuating object were attenuated once more while traveling back through the object.

The attenuation coefficient was estimated as in (3) of the previous paragraph by taking a reflection from a shallow reflector (in front of the object) as the reference measurement and a reflection from a deep reflector (behind the object) as the transmission measurement, and by dividing the slope of the fitted straight line by $2d$ since the object was traversed twice. The reflection measurement was simulated for a Gaussian pulse with a center frequency of 3.5 MHz, relative bandwidth of 70%, and phase of $-\pi/2$, as a good representative of the pulse used by the clinical scanner in the experimental part of this study (see Sec. II A). The transmitted pressure amplitudes were chosen from 10 to 1000 kPa (since the waveforms have been attenuated by passing through the substitution object, the shock parameter could not be defined).

B. Results

1. Transmission measurements

The estimated attenuation coefficient as a function of shock parameter is shown in Figs. 1(a) and 1(b) for several bandwidths of zero-phase pulses having a center frequency of 2.5 and 10 MHz, respectively. The attenuation coefficient is estimated correctly at low-pressure amplitudes but decreases nonlinearly with increasing pressure amplitude, resulting in a negative bias at higher amplitudes. This result is almost independent of the relative bandwidth of the pulse. However, pulses having a higher center frequency show a smaller bias in the estimate at the same shock level.

Figure 2 shows the estimated attenuation coefficient as a function of shock parameter of the same pulses but having a phase of $-\pi/2$ (Fig. 3 gives an illustration of the 2.5 MHz, 60% relative bandwidth pulse of phase 0 and $-\pi/2$). At low bandwidths the behavior is similar to the zero-phase pulse. However, as the bandwidth increases, the negative bias at higher pressure amplitudes decreases and becomes positive, resulting in an overestimate of the attenuation coefficient. This effect is less pronounced for pulses with a higher center frequency.

The estimated attenuation coefficient at low- and high-amplitude measurement, using the experimentally measured pulses as input for the simulator, are shown in Table I. For all transducers, a decreased estimate of the attenuation coefficient is predicted for the corresponding high-amplitude measurement.

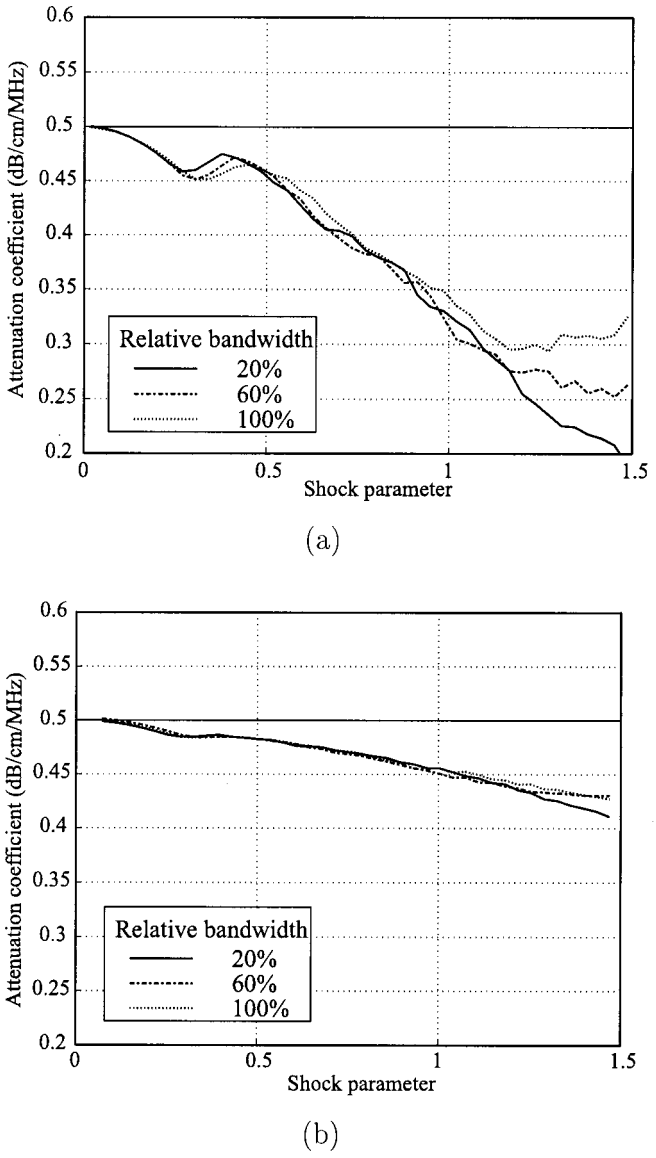

FIG. 1. Estimated attenuation coefficient as a function of shock parameter for zero-phase Gaussian pulses having relative bandwidths of 20%, 60%, and 100% and a center frequency of 2.5 (a) and 10 MHz (b).

2. Reflection measurements

Figure 4 shows the estimated attenuation coefficient as a function of the pressure amplitude of the emitted pulse for the reflection measurement. After an initial decrease in attenuation estimate, an increase is observed with increasing pressure amplitude.

II. EXPERIMENTS

A. Methods

1. In vitro

In order to make the attenuation coefficient for the *in vitro* measurements comparable to the *in vivo* situation (as described below), a tissue mimicking phantom was used for

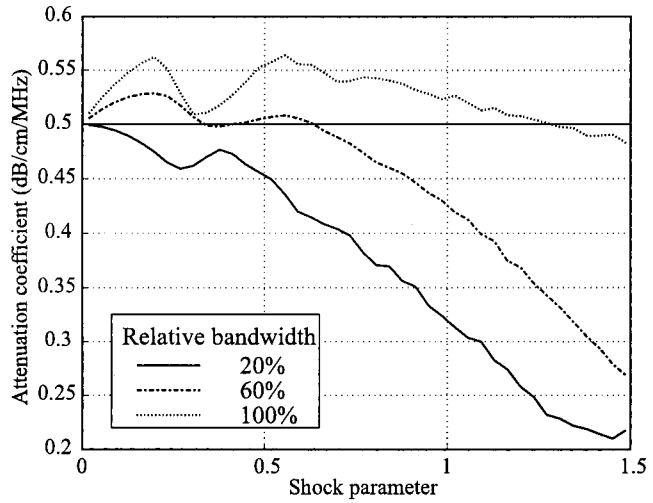

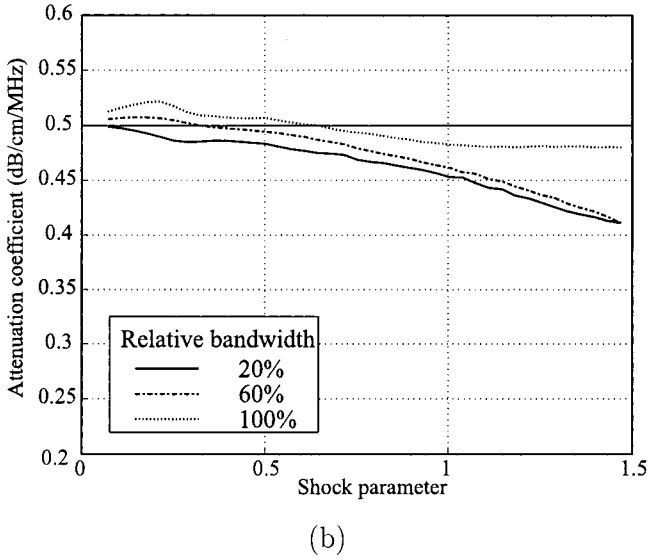

FIG. 2. Estimated attenuation coefficient as a function of shock parameter for Gaussian pulses having relative bandwidths of 20%, 60%, and 100% and a center frequency of 2.5 (a) and 10 MHz (b) and a phase of $-\pi/2$.

these measurements. The phantom was made of gelatine and graphite powder as described in Ref. 14. 100-ml distilled water was heated to a temperature of approximately 70 °C. While stirring (to avoid clotting), 10 gram powder, consisting of a mixture of 8 gram porcine gelatine (Sigma Chemicals, St. Louis) and 2 gram graphite with mean particle diameter of 3.3 μm (Timrex KS 6, Timcal $G+T$, Sins, Switzerland), was mixed. While setting, the phantom was continuously rotated in order to assure homogeneity. A cylindrical phantom was cut having a diameter of 4 cm and a height of approximately 2 cm similar to the attenuating object used for the simulations.

This phantom was used in a standard through-transmission substitution experiment in degassed tap water. Different broadband, circular, plane transducers (Panametrics, Inc.) having center frequencies of 2.25, 5, and 10 MHz with bandwidths of, respectively, 68%, 76%, and 60% of their center frequency at -6 dB, were used as acoustic sources and were excited by a standard pulser-receiver

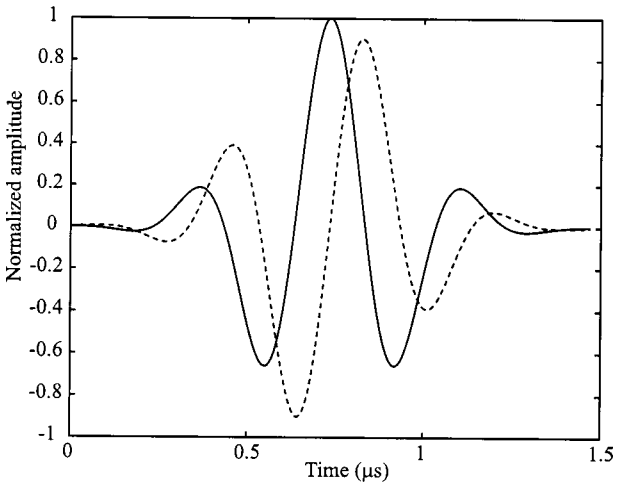

FIG. 3. Example of a zero-phase (solid) and $-\pi/2$-phase (dashed), 2.5-MHz Gaussian pulse having a relative bandwidth of 60%.

(Panametrics Sofranel model 5052PR). The radii of their active elements were respectively: 6.5, 5, and 3 mm. A 75-μm broadband PVDF needle hydrophone (Precision Acoustics, Dorchester, England) was used as a receiver. The position of the hydrophone with respect to the transducer was fixed by a frame and was kept at a distance larger than the last axial maximum of any of the transducers in order to stay in the far field. Since this maximum is positioned at a distance equal to a^2/λ, with a the radius of the transducer and λ the wavelength in the medium, an appropriate distance of 110 mm was taken (cf. position of the receiver in the simulations). The received signals were amplified by a 25-dB ''Booster amplifier'' (Precision Acoustics, Dorchester, England) and digitized by an oscilloscope (Lecroy 9410 dual 150 MHz, New York). The files were transferred to a computer to perform the analysis off-line. The phantom was positioned at a distance of approximately 50 mm from the transducer surface, as in the simulations.

For each transducer, 11 transmission signals were recorded at independent positions. At each position, four different pressure amplitudes of the emitted pulse were used, ranging from 77–384, 44–325, and 82–202 kPa, measured at the position of the hydrophone for the 2.25-, 5-, and 10-MHz pulse, respectively. These values corresponded to shock parameters within the range of 0.12–0.62, 0.16–1.16, and 0.59–1.45, respectively. Several independent measurements of the emitted pulse in water were made with the same four pressure amplitudes as the respective reference measurements.

TABLE I. Simulated and experimental estimate of the attenuation coefficient α for a low- and high-pressure amplitude measurement. The values are given in (dB/cm MHz).

		f_c (MHz)		
Amplitude		2.25	5	10
Low	experiment	0.47	0.52	0.57
	simulation	0.47	0.50	0.54
High	experiment	0.28	0.36	0.50
	simulation	0.35	0.34	0.45

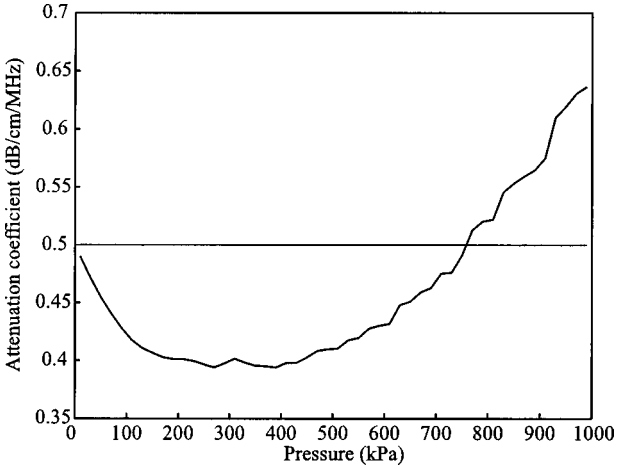

FIG. 4. Estimated attenuation coefficient from a reflection measurement as a function of pressure amplitude of the transmitted pulse. The transmitted pulse had a center frequency of 3.5 MHz, a relative bandwidth of 70%, and a phase of $-\pi/2$.

The frequency dependency of the attenuation was estimated as described in the simulation study above. The spectral estimates were made using standard fast Fourier transform (FFT). Since measurements at the same position but at different pressure amplitudes are paired, differences were shown to be statistically significant using a paired *t*-test. This test was necessary due to the inhomogeneous nature of the phantom, which resulted in a wide range of attenuation estimates (as in the *in vivo* situation).

2. In vivo experiments

To investigate the influence of the amplitude of the emitted pulse on the estimation of the attenuation coefficient *in vivo*, the livers of two young, healthy volunteers were imaged using a standard clinical echocardiographic scanner (VingMed System V, Horten, Norway). Five IQ data sets (in-phase quadrature sampled radio frequency data) from each volunteer were taken at high and low acoustic power output (indicated on the machine as 0 and -32 dB, respectively, equivalent to a mechanical index of 1.2 and $7.5e$-4) at independent positions. The images were taken in fundamental imaging mode at low frame rate (15 Hz), using a 3.5 MHz broadband phased array transducer focused at 20 cm. The acquisition was done at end-inspiration which was maintained during the acquisition of the high and low power data set in order to avoid as much as possible the motion of the image plane between the two data sets. Changing the power output of the scanner did not influence the aperture of the transducer.

The frequency dependency of the attenuation was calculated as described in the simulation of the reflection measurement above. However, since the backscattered signal is stochastic, a reliable estimate of the attenuation coefficient has to be made by averaging the estimates from several pairwise spectral comparisons.[15] Therefore, several spectral comparisons were made for each data set. Moreover, in order to improve the spectral estimate at a certain depth, the spectra (calculated using standard FFT on a window of 128 samples) of ten adjacent radio frequency (RF) lines were averaged.

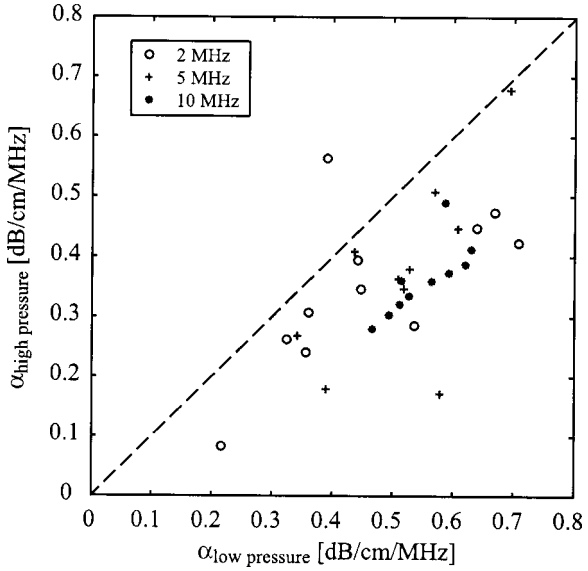

FIG. 5. A paired *t*-test shows that in a through-transmission measurement *in vitro* the lower estimate of the attenuation coefficient with increased amplitude of the emitted pulse is statistically significant.

These lines were extracted from the whole RF image in such a way that the traversed tissue was as homogeneous as possible. This was done based on a visual study of the *B*-scan images and allowed to keep hypo- or hyperechoic regions out of the study. In order to show the statistical significance of the results, a paired *t*-test was used as in the *in vitro* measurements.

B. Results

1. In vitro experiments

The paired estimates of the attenuation coefficient at the lowest versus the highest pressure amplitude are shown in Fig. 5. Measurements made with different transducers are indicated by different symbols. It can been observed that all estimates (except for one) are lower at higher pressure amplitude. Hence the paired-*t* test proved to be very significant ($p<1e$-5) for all transducers, indicating that the extracted attenuation coefficient was systematically estimated lower using higher amplitudes of the emitted pulse, independent of the transducer used. Two estimates were negative, suggesting a decrease of the attenuation coefficient with increasing frequency. These measurements were supposed to be erroneous and were excluded from the study.

The mean estimated attenuation coefficient at the lowest and highest pressure amplitude measurement is given in Table I for all transducers.

2. In vivo experiments

The paired *t*-test of the estimated attenuation coefficient of liver obtained at low and high acoustic power output is shown in Fig. 6. Each circle represents a paired estimate at low versus high acoustic power output. The mean value obtained at low acoustic pressure was 0.57 (dB/cm MHz), while this value increased to 0.69 (dB/cm MHz), at maximal acoustic pressure. A *p*-value of $2.9e$-8 was found, showing this difference to be statistically significant.

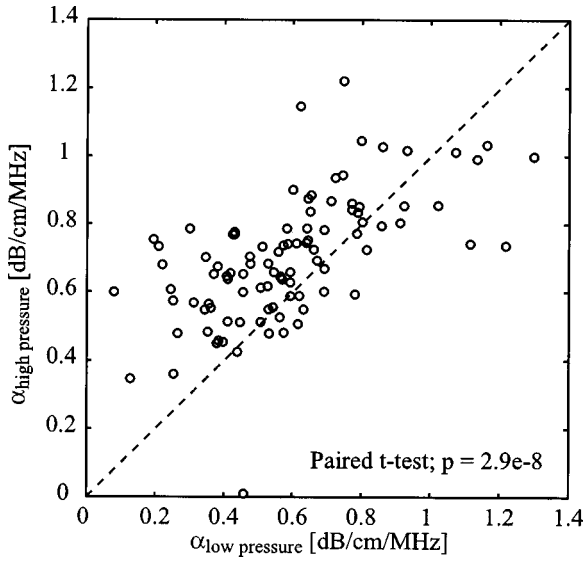

FIG. 6. Paired *t*-test of the estimates of the attenuation coefficient of liver *in vivo* at high versus low acoustic power output.

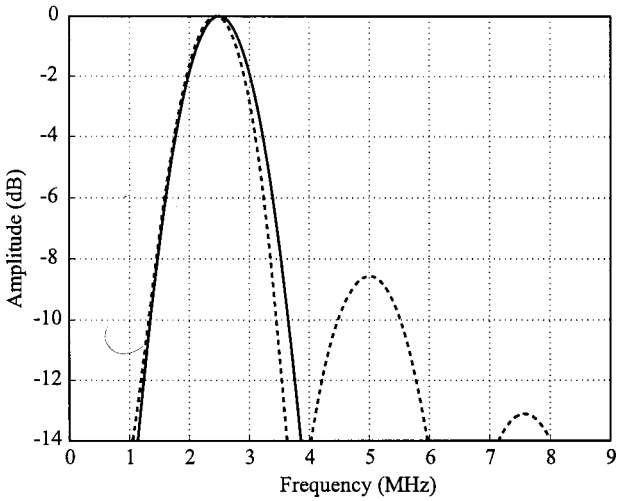

FIG. 7. Original spectrum (solid) and its simulated distorted version due to nonlinear propagation in water over a distance of 11 cm (dashed) of the zero-phase pulse shown in Fig. 3 having an amplitude of 830 kPa.

III. DISCUSSION

Figures 1 and 2 show that for narrow-band pulses in transmission measurements an increased pressure amplitude of the transmitted pulse results in a negative bias of the attenuation estimate. This is in agreement with the results found by Zeqiri.[8] Moreover, the simulations show that this result is almost independent of relative bandwidth or phase of the pulse and that a higher center frequency results in a smaller bias. However, when a broadband pulse is used for the attenuation measurement, the bias on the attenuation estimate becomes dependent on the phase of the transmitted pulse. When the phase lies between 0 and π, corresponding to initial compression followed by rarefaction, the bias is negative with increasing pressure amplitude as in the narrow-band situation. This is in agreement with the results published by Wu,[9] who used a pulse having a phase of approximately π. However, when the phase lies between 0 and $-\pi$, corresponding to initial rarefaction followed by compression, the bias is initially positive. The simulations show (data not presented) that the bandwidth limit where the phase of the pulse becomes important lies around 50% of the center frequency.

The origin of this biased estimate is the distortion of the reference measurement in water: since the attenuation in water is very small, the pressure amplitude will be significant and hence nonlinear distortion as well. On the other hand, the transmitted spectrum through the phantom is less nonlinearly distorted due to the lower amplitude, caused by phantom attenuation. The distortion of the reference is a result of the nonlinear interaction of different frequency components of the broadband incident pulse. This distortion is dependent on center frequency, bandwidth, and phase of the pulse. An example of the simulated distortion of the fundamental spectrum is given in Fig. 7, where the original spectrum of the zero-phase pulse, shown in Fig. 3 having an amplitude of 830 kPa, is plotted together with the spectrum obtained after 11 cm of propagation through water. Clearly, the result of nonlinear propagation is the narrowing of the fundamental spectrum.

Although low-pass filtering the distorted waveforms could result in an increased attenuation of the propagating wave, it seemed better in the context of this study to avoid aliasing as much as possible since this would have a direct influence on the shape of the fundamental spectrum and hence on the estimated attenuation coefficient.

As was already discussed in Sec. I A, the shock parameter is a measure for the nonlinear distortion of the wave and is in principle only meaningful for a narrow-band wave. This was emphasized by the simulation study, where the estimated attenuation coefficient and hence wave distortion were different for broadband pulses having different phases. As a consequence, the shock parameter does not describe quantitatively the amount of nonlinear distortion for broadband pulses.

Comparison of the experimental measured attenuation coefficients at low- and high-pressure amplitude with the simulated ones using the same pulse at the same pressure amplitudes, revealed a good agreement between experiment and theory (cf. Table I) notwithstanding the fact that the low-amplitude measurement, used as input for the simulations, was already inevitably (slightly) distorted. This showed that despite the simplicity of the theoretical model, the simulations were valid. The large variance observed in the attenuation estimates present in both the low- and the high-amplitude measurement (cf. Fig. 5) is a result of the inhomogeneous nature of the tissue phantom, which consists of a stochastic distribution of graphite particles.

In order to avoid the nonlinear distortion of the reference spectrum as much as possible, two possible solutions can be thought of: first, as was suggested theoretically by Zeqiri,[8] the phantom can be positioned as close as possible to the hydrophone. If the thickness of the phantom is small compared to the total propagation distance, both reference and transmission spectra will be (almost) equally distorted, resulting in an (almost) unbiased estimate. Second, if the transducer reacts linearly to the applied voltage and if the phan-

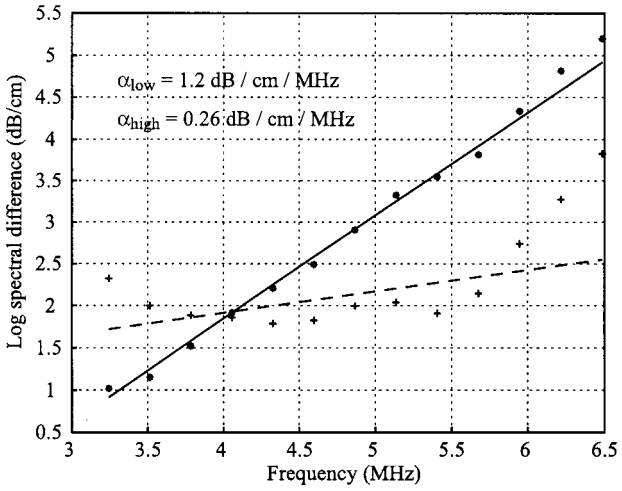

FIG. 8. Example of the log spectral differences and their linear fits of the spectra of a phantom acquired at high amplitude using a high-amplitude pulse (crosses; dashed line) or a (scaled) low-amplitude pulse (stars; solid line) as a reference.

tom is positioned not too far from the transducer, a low-amplitude pulse can be used as a reference of the high-amplitude transmission measurement if the amplitude is scaled to that of the high-amplitude pulse (since spectral information will remain the same). In this case, nonlinear propagation effects will be small for both the reference and transmission measurement, resulting in an (almost) unbiased estimate.

The log spectral difference of a high-amplitude transmission measurement with a (scaled) low-amplitude and high-amplitude reference is shown in Fig. 8 for the *in vitro* measurements. It is clear that there is a linear dependency of the attenuation coefficient on the frequency when using the nondistorted (low-amplitude) reference spectrum. However, this dependency seems parabolic like when using the distorted (high-amplitude) spectrum. This results in an underestimate of the attenuation coefficient. This phenomenon was observed in previous published data but was explained by the worse signal-to-noise ratio at these frequencies. However, decreasing the amplitude of the emitted pulse should further reduce the signal-to-noise ratio. Moreover, the decrease in attenuation coefficient estimate was found even when the useful bandwidth of the transducer was reduced.

The simulations of the reflection measurement showed the opposite effect: an increase of the estimate with increasing acoustic power output after an initial decrease (cf. Fig. 4). In this case the nonlinear effects act in a different manner. Indeed, the spectra from the deeper regions (attenuation measurement) are more distorted than the ones from the shallow regions (reference measurement), which is just the opposite of the distortion taking place in transmission measurements. This is schematically illustrated in Fig. 9.

The initial decrease in attenuation estimate is explained by the fact that the transmitted pulse had a phase of $-\pi/2$ [cf. the initial increase in Fig. 2(a)]. Hence, for the *in vivo* measurements on liver using a clinical scanner where pressure amplitudes are high (e.g., in water the pressure easily exceeds 1.5 MPa), we expect an opposite bias of the estimates when compared to the one in the substitution measure-

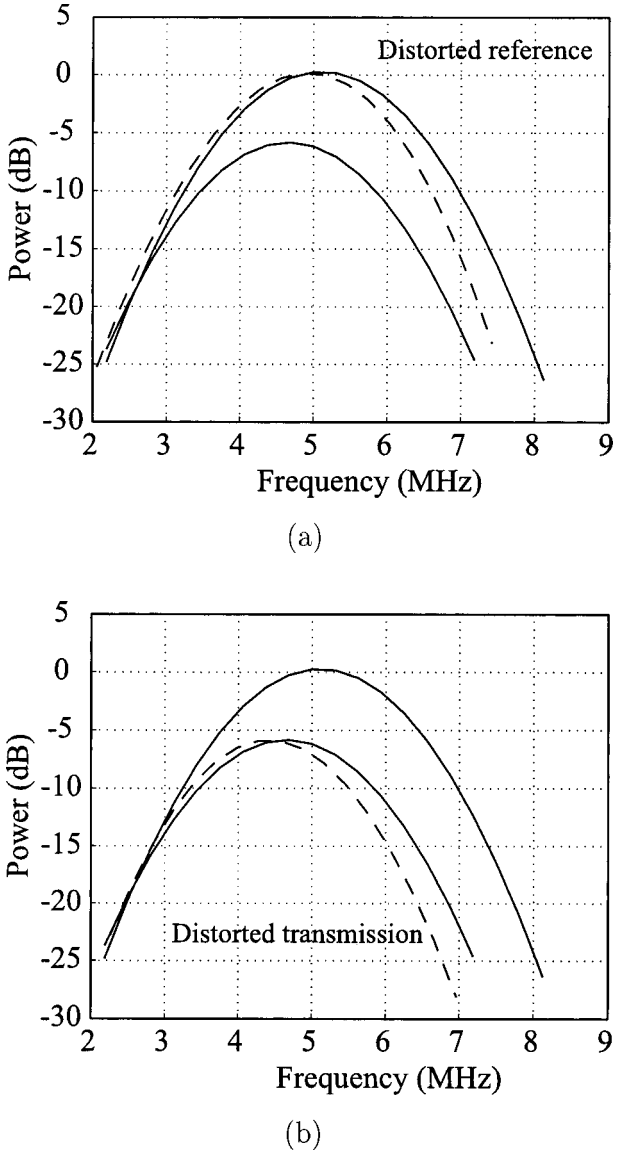

FIG. 9. In substitution experiments the reference spectrum will be distorted, resulting in a bias of the estimated attenuation coefficient (a), while in reflections measurements the reference spectra (from shallow regions) are less distorted (b) than the attenuated ones (from the deeper regions), resulting in an opposite bias.

ments. This was clearly observed in our *in vivo* data from the liver.

Despite the fact that the phased array transducer was focused, we did not attempt to compensate for diffraction effects. However, since similar regions were used for the analysis at low- and high-pressure amplitudes and since the aperture of the transducer did not change with changing power output, the diffraction pattern was the same and the possible effect should be equal on both measurements. Consequently, diffraction effects can be neglected in the *in vivo* measurements. This is further supported by the fact that the results were comparable to the simulations, which did not model diffraction.

Finally, remark that both for the *in vitro* and the *in vivo* measurements the variance between recordings was much larger than the influence of the bias due to the nonlinear effect. This means that for an individual measurement the

bias can probably be neglected, but in order to define the true attenuation coefficient of tissue *in vivo* (which is necessary for tissue characterization), the effect has to be taken into account.

IV. CONCLUSIONS

This study shows that nonlinear propagation effects of finite-amplitude waves bias the estimation of the frequency dependency of the attenuation coefficient. In substitution experiments (both in transmission and reflection), it results in a decreased estimate for narrow-band pulses. For broadband pulses it results in either an increased or a decreased estimate depending on the phase of the emitted pulse. In reflection measurements the opposite effect is expected. Both results were confirmed by experimental data, acquired both *in vitro* and *in vivo*. In order to avoid a biased estimate the center frequency should be chosen as high as possible since this minimizes the influence of nonlinear effects. Moreover, the amplitude of the emitted pulse should be as low as possible. Of course, a compromise with signal-to-noise ratio has to be made.

ACKNOWLEDGMENT

This work was supported by the Flemish Institute for the Improvement of the Scientific-Technological Research in the Industry (IWT).

[1] J. Ophir, T. H. Shawker, N. F. Maklad, J. G. Miller, S. W. Flax, P. A. Narayana, and J. P. Jones, ''Attenuation estimation in reflection: Progress and prospects,'' Ultrason. Imaging **6**(4), 349–95 (1984).
[2] B. S. Garra, M. F. Insana, T. H. Shawker, and M. A. Russel, ''Quantitative estimation of liver attenuation and echogenicity: Normal state versus diffuse liver disease,'' Radiology **162**, 61–67 (1987).
[3] K. J. Parker, M. S. Asztely, R. M. Lerner, E. A. Schenk, and R. C. Waag, ''In vivo measurements of ultrasound attenuation in normal or diseased liver,'' Ultrasound Med. Biol. **14**, 127–136 (1988).
[4] P. Laugier, G. Berger, M. Fink, and J. Perrin, ''Diffraction correction for focused transducers in attenuation measurements in vivo,'' Ultrason. Imaging **9**(4), 248–59 (1987).
[5] J. Ophir and D. Mehta, ''Elimination of diffraction error in acoustic attenuation estimation via axial beam translation,'' Ultrason. Imaging **10**, 139–152 (1988).
[6] X. Chen, D. Phillips, K. Q. Schwarz, J. G. Mottley, and K. J. Parker, ''The measurement of backscatter coefficient from a broadband pulse-echo system: A new formulation,'' IEEE Trans. Ultrason. Ferroelectr. Freq. Control **44**(2), 515–525 (1997).
[7] I. A. Akiyama, Y. Nishida, M. Nakajima, and S. Yuta, ''On the measurement of frequency dependent attenuation in biological tissues using broadband pulsed ultrasound,'' *IEEE Ultrasonics Symposium* (IEEE, New York), Vol. 1, pp. 800–805.
[8] B. Zeqiri, ''Errors in attenuation measurements due to nonlinear propagation effects,'' J. Acoust. Soc. Am. **91**(5), 2585–2593 (1992).
[9] J. Wu, ''Effects of nonlinear interaction on measurements of frequency-dependent attenuation coefficients,'' J. Acoust. Soc. Am. **99**(6), 3380–3384 (1996).
[10] M. Kornbluth, D. H. Liang, A. Paloma, and I. Schnittger, ''Native tissue harmonic imaging improves endocardial border definition and visualization of cardiac structures,'' J. Am. Soc. Echocardiography, **11**(7), 693–701 (1998).
[11] K. K. Shung and G. A. Thieme, *Ultrasonic Scattering in Biological Tissues* (CRC, Boca Raton, FL, 1992), pp. 372.
[12] M. F. Hamilton and D. T. Blackstock, *Nonlinear Acoustics* (Academic, San Diego, 1998), Chap. 11.
[13] Y. S. Lee and M. F. Hamilton, ''Time-domain modeling of pulsed finite-amplitude sound beams,'' J. Acoust. Soc. Am. **97**(2), 906–916 (1995).
[14] J. F. Greenleaf, *Tissue Characterization With Ultrasound* (CRC, Boca Raton, FL, 1986).
[15] K. J. Parker, ''Attenuation measurement uncertainties caused by speckle statistics,'' J. Acoust. Soc. Am. **80**, 727–734 (1986).

Killer whale (*Orcinus orca*) hearing: Auditory brainstem response and behavioral audiograms

Michael D. Szymanski[a)]
University of California Davis, Psychology Department, Davis, California 95616

David E. Bain
Marine World Foundation, Vallejo, California 94589

Kent Kiehl
University of British Columbia, Department of Psychiatry, 2255 Wesbrook Mall, Vancouver, British Columbia V6T 2A1, Canada

Scott Pennington, Scott Wong, and Kenneth R. Henry
University of California Davis, Psychology Department, Davis, California 95616

(Received 8 September 1998; revised 12 April 1999; accepted 5 May 1999)

Killer whale (*Orcinus orca*) audiograms were measured using behavioral responses and auditory evoked potentials (AEPs) from two trained adult females. The mean auditory brainstem response (ABR) audiogram to tones between 1 and 100 kHz was 12 dB (*re* 1 μPa) less sensitive than behavioral audiograms from the same individuals ($\pm$8 dB). The ABR and behavioral audiogram curves had shapes that were generally consistent and had the best threshold agreement (5 dB) in the most sensitive range 18–42 kHz, and the least (22 dB) at higher frequencies 60–100 kHz. The most sensitive frequency in the mean *Orcinus* audiogram was 20 kHz (36 dB), a frequency lower than many other odontocetes, but one that matches peak spectral energy reported for wild killer whale echolocation clicks. A previously reported audiogram of a male *Orcinus* had greatest sensitivity in this range (15 kHz, ~35 dB). Both whales reliably responded to 100-kHz tones (95 dB), and one whale to a 120-kHz tone, a variation from an earlier reported high-frequency limit of 32 kHz for a male *Orcinus*. Despite smaller amplitude ABRs than smaller delphinids, the results demonstrated that ABR audiometry can provide a useful suprathreshold estimate of hearing range in toothed whales. © *1999 Acoustical Society of America.* [S0001-4966(99)04408-2]

PACS numbers: 43.80.Lb, 43.80.Nd [WWLA]

INTRODUCTION

Members of the toothed whale family *delphinidae* have an auditory system with excellent high-frequency hearing, broad range, and high temporal resolution (rev. Au, 1993). Unusually sensitive high-frequency hearing to at least 100 kHz is a characteristic of most delphinids studied to date and can be explained in part by the selection for echolocation in these marine mammals. *Orcinus orca*, the largest delphinid species, echolocates (Diercks *et al.*, 1971), is cosmopolitan in distribution, and communicates with pulsed calls, whistles, and clicks (Dalheim and Awbrey, 1982; Ford, 1989; Barrett-Lennard, Ford, and Heise, 1996).

In a behavioral study of *Orcinus* hearing, Hall and Johnson (1972) found that a single male had a high frequency audiogram cutoff at 32 kHz, which is inconsistent with other odontocete audiograms that typically extend to 100 kHz and higher (rev. Au, 1993). More recent data from Orcinus indicated killer whales can respond to pure tones up to 120 kHz, although complete audiograms have not yet been reported (Bain, 1992; Bain and Dalheim, 1994; Szymanski *et al.*, 1995b).

Behavioral audiograms have been collected from nine odontocete species: bottlenose dolphin *Tursiops truncatus* (Johnson, 1967); harbor porpoise *Phocoena phocoena* (Anderson, 1970); common dolphin *Delphinus delphis* (Belkovich and Solntseva, 1970); *Orcinus* (Hall and Johnson, 1972); Amazon river dolphin *Inia geoffrensis* (Jacobs and Hall, 1972), beluga *Delphinapterus leucas* (White *et al.*, 1978; Awbrey *et al.*, 1988), false killer whale *Pseudorca crassidens* (Thomas *et al.*, 1988), tucuxi *Sotalia fluviatilis guianensis* (Sauerland and Dehnhardt, 1998), and Pacific white-sided dolphin *Lagenorhynchus obliquidens* (Remmel *et al.*, 1998). In these studies upper frequency limit ranges from 100 to 150 kHz, if Hall and Johnson's (1972) *Orcinus* data are not included. All species tested to date, including larger species such as *Delphinapterus* (White *et al.*, 1978) and *Pseudorca* (Thomas *et al.*, 1988), reportedly have high-frequency hearing to at least 100 kHz.

The auditory brainstem response (ABR) audiogram is an alternative to behavioral hearing tests and originally was examined in cetaceans by Bullock *et al.* (1968), Ladygina and Supin (1970), and Bullock and Ridgway (1972), all studies which used intracranial methods. Ridgway *et al.* (1981) demonstrated that dolphin ABRs could be recorded extracranially in awake, calmly behaving animals. The original noninvasive recording technique has been modified and extended (Popov and Supin, 1985, 1990a, 1990b; Dolphin *et al.*, 1995a,

a)Author to whom correspondence should be addressed; current address: University of California San Francisco, Department of Radiology, Biomagnetic Imaging Laboratory, S-362, 513 Parnassus Ave., San Francisco, CA 94143-0628.

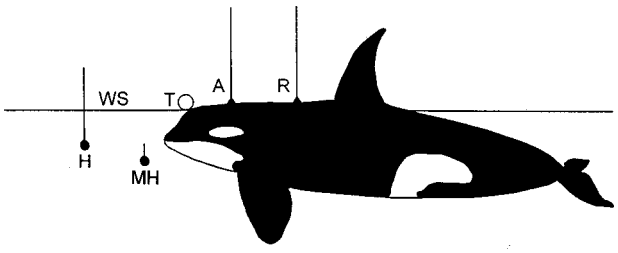

FIG. 1. The recording session position of the whale in the ABR audiogram paradigm. H—hydrophone, MH—monitoring hydrophone, WS—water surface, T—target, A—active electrode, R—reference electrode. Not to scale.

1995b; Szymanski *et al.*, 1995a, 1998). Odontocete ABRs have been recorded from six species, including: *Tursiops* (Bullock *et al.*, 1968), *Phocoena* (Bibikov, 1992), *Sotalia, Inia, Delphinapterus* (Popov and Supin, 1990b), and a neonatal sperm whale (Carder and Ridgway, 1991). Evoked potential audiograms have been collected mostly from smaller species.

Findings from ABR audiometry have been consistent with behavioral measures of hearing in toothed dolphins and whales. But there are not any published reports that have compared the evoked potential and behavioral audiograms from the same individuals. Recent recordings of the killer whale ABR (Szymanski *et al.*, 1998) suggested that ABR and behavioral audiograms could be compared in the same individual whales. Our study was conducted to compare the ABR and behavioral audiograms of two trained female killer whales.

I. MATERIAL AND METHODS

A. Subjects

Two adult female killer whales were tested, both had previously participated in behavioral (Bain and Dalheim, 1994) and evoked potential experiments (Szymanski *et al.*, 1995a, 1995b, 1998). One whale, ''Yaka,'' was 26–28 years old at the time of the study and originally was collected from the Northern resident A5 pod off the coast of British Columbia in 1969. The other whale, ''Vigga,'' was 16–18 years old during the study and was taken from lcelandic waters in 1980.

B. ABR experimental conditions

Evoked potential experiments were conducted at Marine World Africa USA, an oceanarium and animal park in Vallejo, California between 1995 and 1996. The test pool, filled with sea water, was about 4 m deep and 15 m in diameter. The whales were trained to remain stationary alongside the tank wall with the apex of the melon of their head at a target and their blowholes breaking the water surface. A transducer was submerged 1 m below the surface and 1 m from the whale's rostrum (Fig. 1). Slight movements occurred during testing, but if the whale moved off target more than 10 cm the trial was called off.

C. ABR stimuli

Cosine-gated tone bursts were digitally generated and attenuated with 12-bit resolution using Modular Instruments, Incorporated (MI^2) equipment. The projector was an International Transducer Corporation (ITC) spherical hydrophone model (ITC) 1042, 3.5 cm in diameter. Frequencies were tested in a random order at: 1, 2, 4, 8, 12, 16, 20, 32, 45, 60, 80, and 100 kHz. Tone burst duration was 1 ms at 1 and 2 kHz, and 0.5 ms at all other frequencies. The monitoring hydrophone was a Sea Systems model 1000r, which was positioned about 0.5 m lateral to the whale, 1 m below the surface, in line with the lower jaw at the approximate level of the pan bone, the presumed primary sound channel in delphinids (Fig. 1) (Brill *et al.*, 1988). Stimuli were calibrated daily at the frequencies being tested before the whale was in position. The monitoring hydrophone was placed at the approximate site where the whale's pan bone would be located and spectral content and intensity levels were measured. The signal level also was calibrated with the whale in position and found to fluctuate between 6–10 dB *re* 1 μPa (Fig. 2). In behavioral experiments, conducted in 1991–1993, an LC32 was used as a projecting hydrophone and a Brüel and Kjær 8105 as a monitoring hydrophone.

D. Stimuli presentation

A modified descending and ascending method of limits was used. Tone bursts were presented at 30/s, in blocks of 350 stimuli. Tone burst intensities ranged from 10 to 150 dB *re* 1 μPa, peak-to-peak, and in a given trial were first presented 40 to 60 dB above the previously measured behavioral threshold. The experimenter attenuated the tone burst in 10-dB steps until the ABR response was no longer visually detectable in two consecutive trials. Stimuli were then increased in 5-dB steps until the ABR reappeared. Threshold measures were taken at least two times for each whale at each frequency.

E. ABR threshold determination

Delphinid ABR wave IV (PIII-NIV) (Szymanski *et al.*, 1998), analogous to Jewett's wave V in humans (Ridgway *et al.*, 1981), was used as a dependent measure of threshold. Wave IV was chosen because it had the largest peak-to-peak amplitude and previously has been used for threshold measures in dolphins (Popov and Supin, 1990a, 1990b). Auditory threshold was defined as the minimum amount of stimulus power needed to evoke a response greater than background EEG noise (Elberling and Don, 1987). A peak-to-peak 350 nV PIII-NIV level was chosen because background, averaged EEG noise, on no-tone trials and prestimulus epochs, was about $\pm$150 nV (Fig. 3).

F. Evoked potential recording

When the whale was stationary, a trainer placed two gold Grass EEG electrodes embedded in suction cups on the animal's head. One suction cup electrode was affixed to a point about 17 cm caudal of the blowhole. The second electrode was placed near the dorsal fin about 75 cm caudal of

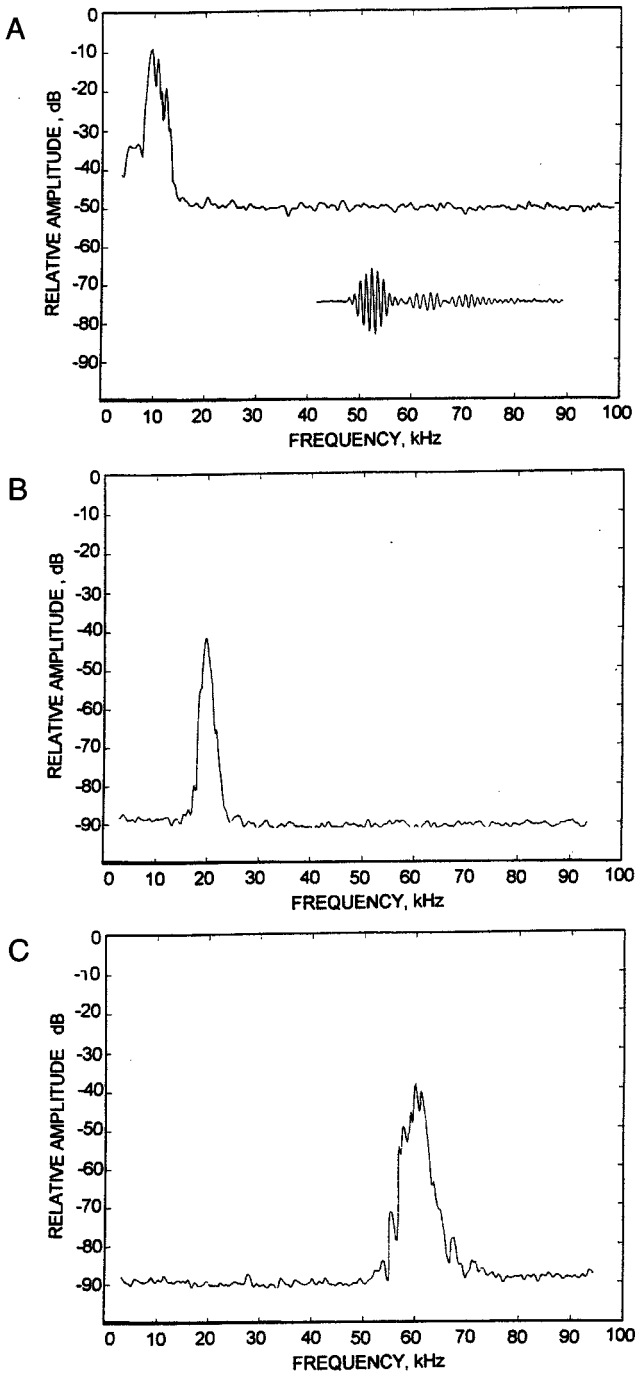

FIG. 2. Sample stimuli power spectrum at three frequencies (a) 10 kHz, (b) 20 kHz, (c) 60 kHz recorded near the whale's head at the lower jaw in approximate line with the pan bone. A 10-kHz stimulus waveform, recorded from the monitoring hydrophone, is shown in the top panel.

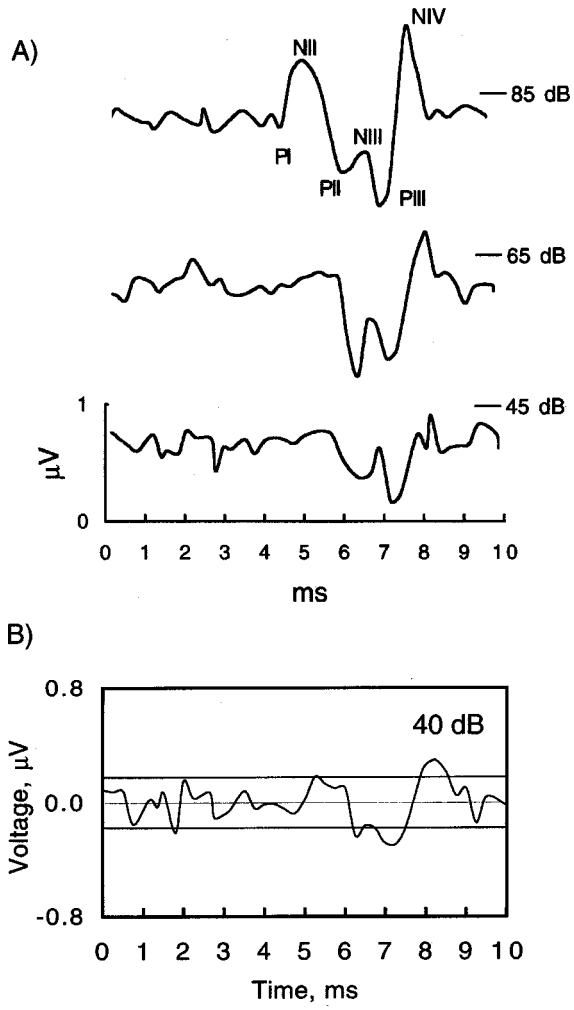

FIG. 3. (a) Representative *Orcinus* ABRs. Main response waves PI to NIV are labeled, negativity at active electrode plotted upward. Examples are *Orcinus* ABRs from ''Yaka'' to 32-kHz tones at three intensities, 85, 65, and 45 dB *re* 1 μPa. Acoustic levels are peak-to-peak measurements. (b) The horizontal lines at ± 0.175 μV illustrate the minimum ABR amplitude used as criteria for wave PII-NIV detection. Auditory threshold in this trial was 40 dB *re* 1 μPa, peak-to-peak.

the blowhole along the midline. Both electrodes were above the water surface, and their impedance varied between 0.5 and 3 kΩ.

The signal between the two electrodes was differentially amplified 100 000 times through two Grass P15 amplifiers and bandpass-filtered 100 Hz to 3 kHz. The AEPs were averaged in 30-ms epochs from 350 individual responses at 200-kHz sampling rate and stored for off-line analysis. On-line artifact rejection was used and amplitude swings >150 μV were excluded. A total of 350 artifact free traces were required for an average to be included. Each time the whale held a stationary position and the EEG electrodes were attached it was possible to collect two averaged waveforms, a procedure which lasted 2–3 min. Agreement between the two responses was not required. A response was judged acceptable, during later off-line analysis, if it corresponded with another trace collected at the same frequency and intensity in the same recording session.

Then the suction cups were removed, the whale was reinforced with fish and allowed to swim around the pool. Upon returning to the pool area near the trainer, the whale was typically instructed to perform one show or husbandry behavior, reinforced with fish, and then instructed to hold a stationary position for another ABR collection.

G. Behavioral methods

A go/no-go response paradigm was used to test the whales between 1991 and 1993. The whales were trained to station with the apex of the melon against a bar submerged 1 m below the water's surface. After the whale was stationed

underwater, a 2-sec tone randomly occurred between 1 to 10 sec and the whale had 4 sec to respond. A false alarm was scored if the whale responded prior to the tone onset, and the trial was repeated. A hit was scored if the whale responded within 4 sec after tone onset, after which the subject was reinforced with whole fish. A miss was scored if the whale responded later than 4 sec after tone onset. If the whale waited for the recall tone, which occurred after a tone presentation and a 4 sec response interval, the animal was reinforced. The reinforcement procedure used was the same as during the whale's husbandry and performance behavior, and food provided during research sessions typically constituted 20%–50% of the whale's daily diet.

There were two motivations for the behavioral paradigm: (1) to increase reinforcement on more than 50% of the trials; and (2) to minimize frustration in the animals. It is obvious that the whale could wait for the recall tone and get reinforced but the animals did not. More fish could be obtained by responding to the tone, i.e., the animal would be reinforced at least 3 sec earlier than if it waited for the recall tone. From an optimal foraging strategy perspective, this would be a better response because it would maximize fish intake.

H. Threshold determination for behavioral audiograms

Sound levels were reduced by 6–8 dB after signals were detected and increased by 6–8 dB after the whale failed to detect the tone. Threshold was defined as two detections at one intensity level, and two failures to detect the tone level below. Behavioral thresholds reported here are the averages of three determinations.

A variety of catch trials were employed. These included no signal presentation, very high or very low frequencies which the transducers could not produce, setting the signal level to 0 V, and disconnecting single components of the sound production system. Personnel were varied to ensure inadvertent cueing did not develop. Also, the whale's behavioral responses were judged by an observer who was blind to signal timing.

II. RESULTS

A. ABR data

Orcinus ABRs recorded to tone bursts resembled AEPs recorded to clicks from the same animals (Szymanski *et al.*, 1998). The waveform resembled the ABR in other delphinids and occurred within 10 ms of tone onset. The largest wave, PIII-NIV (Fig. 3), had a maximum peak-to-peak amplitude of about 1 μV and its maximum amplitude was greatest of the ABR waves. Response amplitude decreased as stimuli were attenuated, with smaller waves typically disappearing into background EEG noise before wave PIII-NIV. The ABR NIV peak latency also increased as stimuli were attenuated as shown in Szymanski *et al.* (1995a). The variability in ABR amplitude is shown in Fig. 4 as input-output function at 32 kHz.

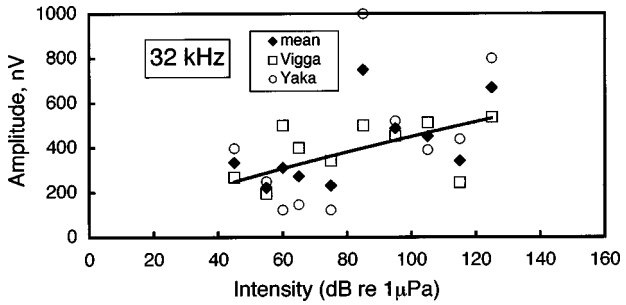

FIG. 4. A representative input-output function showing the relationship between acoustic intensity and ABR amplitude. The line of best fit represents a power function fitted to the mean. The acoustic level is peak-to-peak sound intensity in dB *re* 1 μPa. The output ABR amplitude in nanovolts (nV) is for wave PIII-NIV to 32-kHz tone bursts. Individual whale ABR amplitude data points are the mean of two responses at that intensity. The overall mean is based on four responses at that intensity, two ABR amplitudes from each whale.

B. Audiogram data

Both whales responded behaviorally and electrophysiologically to tones between 1 and 100 kHz. During behavioral trials, one whale responded to 120-kHz tones. The mean audiogram, computed from behavioral and ABR thresholds, was U-shaped and had its most sensitive frequency at 20 kHz (Fig. 5). The most sensitive range, herein defined as 10 dB from the most sensitive frequency (20 kHz at 36 dB [*re* 1 μ Pa]), was between 18 and 42 kHz. The ABR audiogram was about 5 dB less sensitive in this range, which was the area of best agreement between ABR and behavioral audiogram curves. The ABR audiogram was least sensitive at the highest frequencies tested (ABR threshold +41 dB at 100 kHz). In general, the ABR audiogram resembled the curve of the behavioral audiogram, but overall the behavioral audiogram was a mean of 12 dB more sensitive (Table I).

C. Behavioral responses

False alarm rates were less than 5% in catch trials for both whales. The whales' performance on trials that were 20 dB>threshold ($n=160$ trials) were analyzed. The whales did not make any false alarms when tones were 20 dB >threshold, and accuracy was 95% correct.

III. DISCUSSION

A. Audiogram comparisons

The killer whale audiogram resembles the hearing of other delphinids and extends to at least 120 kHz. The maximum sensitivity, +36 dB [*re* 1 μ Pa] at 20 kHz, is the greatest reported for odontocetes and is similar in sensitivity to that reported by Hall and Johnson (1972) (20 kHz, ~35 dB [*re* 1 μPa]). The nearly U-shaped audiogram resembles Hall and Johnson's (1972) data from a single male, except for their high-frequency cutoff of 32 kHz, and the current results of 120 kHz.

In light of Ridgway and Carder's (1993, 1997) findings that a sex difference in high-frequency hearing loss is associated with age in delphinids, it is necessary to consider whether presbycusis in the male *Orcinus* accounted for the current discrepancy in high-frequency hearing. Presbycusis

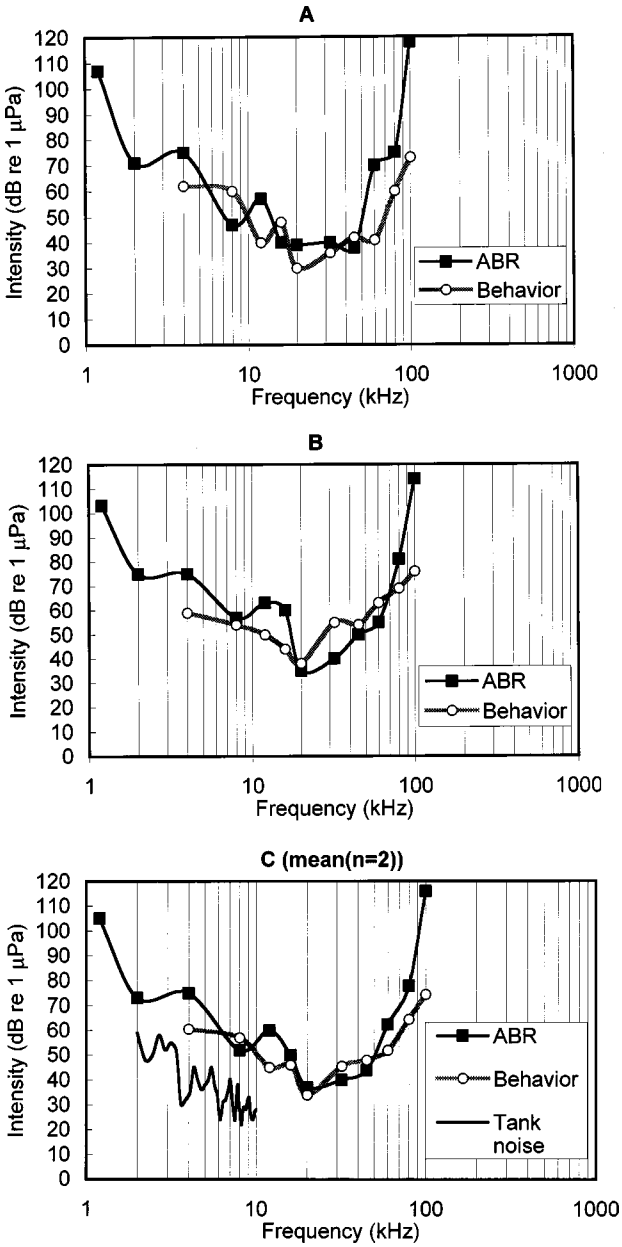

FIG. 5. The ABR and behavioral audiograms for (a) Yaka, and (b) Vigga. (c) Mean of both animals. Tank noise is plotted from a measurement made using an ITC 1042 hydrophone and a Hewlett Packard 3561 Dynamic Signal Analyzer bandwidth 238 Hz.

seems an unlikely explanation, however, because the male tested by Hall and Johnson (1972) was a subadult male captured three years prior to his audiogram measurement. While we can not rule out sex differences in hearing between a young male Orcinus and adult females, it seems unlikely because dramatic sexual dimorphisms in high-frequency audiograms have not been shown in other mammals or observed in other delphinid species.

Other factors that could alternatively explain a hearing loss include genetic and pathogenic disease, and ototoxic drug and noise exposure. It is worth noting, that noise has been used to herd wild marine mammals for capture, and that inner ear damage in wild marine mammals (Bohne *et al.*, 1985; Richardson *et al.*, 1991, 1995) and whales (Ketten, Lien, and Todd, 1993; Ketten *et al.*, 1998) has been attributed to anthropogenic noise from underwater explosive blasts. We were unable to determine whether the whale tested by Hall and Johnson (1972) was exposed to harmful levels of noise in its home range or during its capture. Of course it would be speculative to conclude that noise-induced hearing loss accounted for Hall and Johnson's (1972) subadult male *Orcinus* audiogram high-frequency cutoff of 32 kHz.

In captivity it is possible that hearing loss could be caused by animal husbandry factors including ototoxic antibiotic treatments and tank noise. Captive odontocetes commonly receive antibiotics, but there is no record that the whale tested by Hall and Johnson was given ototoxic drugs or exposed to damaging levels of tank noise (personal communication, Dan Odell, Sea World, Orlando, FL, 1994). When Hall and Johnson's (1972) audiogram is considered in light of the current data, their results are consistent with a sensorineural high-frequency hearing loss that could have been due to one or more of the above-mentioned factors.

TABLE I. Overall mean behavioral and ABR thresholds at each frequency tested. The acoustic level is based on peak-to-peak values. The ABR thresholds are based on four replications (two for each whale) of wave PIII-NIV at a minimum 350 nV peak-to-peak response amplitude.

Frequency in kHz	Behavioral threshold dB *re* 1 μPa RMS	Physiological (ABR) threshold dB *re* 1 μPa Peak-to-Peak
1	*	105
2	*	72
4	61	75
8	57	52
12	45	60
16	46	50
20	34	37
32	46	40
45	48	45
60	52	65
80	65	78
100	75	116

B. ABR and behavioral audiogram differences

The relationship between physiological and behavioral auditory thresholds is dependent upon organismal variables and stimuli characteristics, in addition to electrophysiological recording parameters. Elberling and Don (1987) suggested that the slope of the ABR amplitude function by stimulus intensity, and the magnitude of the averaged EEG background noise are the primary factors responsible for ABR detection and ABR audiogram thresholds. In killer whales, the background bioelectrical noise was greater and ABR signal magnitude less than in other odontocetes (Popov and Supin, 1990b). The small amplitude of the killer whale ABR is one factor that may account for some of the variability between the behavioral and ABR audiograms (Szymanski *et al.*, 1998). Two other contributing factors include: (1) natural variability in responsiveness, both behaviorally and physiologically, which can contribute to sensory threshold differences; and (2) variability in the received signal inten-

sity and signal spectrum near the whale's head and at the whale's acoustic pathway during the ABR experiment.

During ABR collection, the acoustic environment was variable because the whale was at the water surface, a reflective boundary, and near a wall without sound absorption materials. Second, the acoustic path to the delphinid inner ear is a controversial subject. Therefore the hydrophone may not have been in the optimal position (Au and Moore, 1984), and may also have been in the near field. In this experiment we assumed the acoustic path to be via the acoustic window of the mandible, although some researchers have maintained a sound path exists around the external auditory meatus, and further that high- and low-frequency pathways may differ.

A result that merits discussion is the threshold similarity found in ABR and behavioral audiograms to tones of different duration. Thresholds to 1-ms tones in the mean ABR audiogram overall are within 12 dB of behavioral thresholds to tones 2000 times as long, and in the most sensitive region (18–42 kHz) are within 6 dB. In Tursiops, Johnson (1968) found behavioral thresholds decreased 15 to 30 dB with increasing duration over this magnitude. Unfortunately, we did not determine behavioral thresholds to tones of different duration as Johnson did, rather we collected behavioral thresholds to 2-sec tones and ABR thresholds to 0.5- and 1-ms tones, therefore our duration-of-tone burst data are a comparison of behavioral thresholds to electrophysiological thresholds and should not be necessarily consistent with Johnson's findings, in part because the ABR response is primarily an onset response.

In mammals it is common for ABR thresholds to be about 10–30 dB greater than behavioral thresholds (Gorga *et al.*, 1988). But in dolphins, behavioral and ABR thresholds share a greater correspondence (Johnson, 1967; Bullock *et al.*, 1968; Popov and Supin, 1990b). In terrestrial mammals the increased sensitivity of behavioral compared to ABR audiograms can in part be attributed to temporal integration and effective stimuli differences. Effective stimuli for evoking the ABR are brief tone bursts (5–10 ms) with rapid onsets compared to the longer tones (1–2 s) and slower onsets commonly used in behavioral audiometry. Behavioral thresholds typically decrease inversely with tone duration up to about 200 ms, according to data from terrestrial mammals. It is worth noting that dolphins have short temporal integration, about 0.5 ms near threshold, according to behavioral (Moore *et al.*, 1984) and ABR studies (Popov and Supin, 1990a).

Because the ABR is an onset response it seems likely there is little effect of temporal integration on ABR audiogram threshold. Nonetheless, in light of known delphinid specializations for rapid temporal integration, it would be interesting to examine onset effects on ABR thresholds more carefully. When an ABR is generated, the auditory system is responding to a broad band component of the signal and therefore there is some frequency ambiguity. Furthermore, in regard to sensitivity, the ABR and behavioral audiograms here should only be considered an estimate of Orcinus hearing thresholds because the received intensity was likely variable between (6–10 dB). Thus in the current study the ABR audiogram only can provide a rough estimate of hearing sensitivity at a given frequency.

C. Odontocete ABR audiograms: Effects of body and head size

The ABR technique, though less sensitive than behavioral measures when collapsed over all frequencies, provides a reasonable suprathreshold estimate of hearing range in Orcinus (+5 dB in the most sensitive range 18–42 kHz, and +22 dB at higher frequencies 60–100 kHz). The ABR audiogram curve follows the behavioral audiogram and in general corresponds with the shapes of Popov and Supin's (1990b) ABR audiograms from four smaller odontocete species. Our maximum ABR peak-to-peak signal levels, however, were an order of magnitude smaller, 1.2 μV compared to a range of 10 to 20 μV in Popov and Supin's (1990b) results. This difference can be explained by the larger body size of *Orcinus*, which has a brain–body mass ratio of 1:1000, compared to 1:100 in dolphins (Ridgway and Brownson, 1984; Szymanski *et al.*, 1995a; Szymanski *et al.*, 1998). In odontocetes, because ABR amplitude seems to decrease with a lower brain–body mass ratio, these results suggest the ABR may be difficult to collect from larger cetaceans, such as baleen whales, which have a lower brain–body mass ratio than odontocetes.

The most sensitive frequency for Orcinus was 20 kHz, in both behavioral and ABR audiograms. This represents the lowest frequency of best sensitivity known among odontocetes, mean threshold 36 dB [*re* 1 μPa], which is consistent with general mammalian audiometric findings that larger species have more sensitive lower frequency audiograms (Heffner and Heffner, 1982). Among odontocete audiograms the most sensitive frequency varies as a function of species, but within a species the sensitive audiogram region typically corresponds to the typical peak energy in echolocation clicks, e.g., ~20 kHz in orcinus (Hall and Johnson, 1972; Awbrey *et al.*, 1982), ~30 kHz in delphinapterus (White *et al.*, 1978); ~64 kHz in pseudorea (Thomas *et al.*, 1988); ~65 kHz in tursiops (Johnson, 1967; Kamminga and Beitsma, 1990); and ~130 kHz in *phocoena* (Anderson, 1970; Dubrovsky, Krasnov and Titov, 1971; Popov and Supin, 1990a). The killer whale auditory system fits this trend, an obvious selective advantage when orienting or hunting with biosonar clicks and echoes.

Because *Orcinus* hearing has the lowest most sensitive frequency and one of the lowest high-frequency limits among odontocetes, it seems plausible that *Orcinus* auditory function has been constrained by body size, following general mammalian trends. But *Orcinus* also demonstrates remarkably good high-frequency hearing for an animal its size, which reflects its status as an echolocating odontocete in the family delphinidae. The upper limit of hearing, 100 kHz for Orcinus, is more similar to those of other toothed dolphins and whales than has been previously reported.

ACKNOWLEDGMENTS

Support was granted by the U.S. National Academy of Sciences Collaboration in Basic Science and Engineering

Grant to M.D.S. and D.E.B., and Russian Foundation for Basic Research Grant 97-04-48377 to Aleksander Ya. Supin. Support was provided by the Marine World Foundation, its staff, and trainers. The authors thank Dr. Aleksandar Ya. Supin, Dr. Sam H. Ridgway, and three anonymous reviewers for comments on the work. This report is based on Ph.D. research by the first author, and is dedicated to the memory of Yaka, trainer Sonny Allen, and Dr. Ken Norris.

Anderson, S. (**1970**). ''Auditory sensitivity of the harbor porpoise (*Phocoena phocoena*),'' in *Investigations on Cetacea*, edited by G. Pilleri (Bentili, AG Berne Bumpliz, Berne, Switzerland), Vol. 2, pp. 255–259.

Au, W. W. L. (**1993**). *The Sonar of Dolphins* (Springer Verlag, New York).

Au, W. W. L., and Moore, P. W. B. (**1984**). ''Receiving beam patterns and directivity indices of the Atlantic bottlenose dolphin *Tursiops truncatus*,'' J. Acoust. Soc. Am. **75**, 255–262.

Awbrey, R. T., Thomas, J. A., Evans, W. E., and Leatherwood, S. (**1982**). ''Ross Sea killer whale vocalizations: Preliminary description and comparison with those of some Northern Hemisphere killer whales,'' Rep. Int. Whal. Comm. **32**, 667–670.

Awbrey, F. T., Thomas, J. A., and Kastelein, R. A. (**1988**). ''Low frequency underwater hearing sensitivity in belugas (*Delphinapterus leucas*),'' J. Acoust. Soc. Am. **84**, 2273–2275.

Bain, D. E., and Dalheim, M. E. (**1994**). ''Effects of masking noise on detection thresholds of killer whales,'' in *Consequences of the Exxon Valdez Oil Spill*, edited by T. Loughlin (Academic, New York), pp. 243–256.

Bain, D. E. (**1992**). ''Hearing abilities of killer whales (*Orcinus orca*),'' National Marine Mammal Laboratory Contract Report #43ABNF00249 and #43ABNF002500, pp. 1–20.

Barrett-Lennard, L. G., Ford, J. K. B., and Heise, K. A. (**1996**). ''The mixed blessing of echolocation differences in sonar use by fish-eating and mammal-eating killer whales,'' Anim. Behav. **51**, 553–565.

Belkovich, V. M., and Solntseva, G. N. (**1970**). ''Anatomy and function of the ear in dolphins,'' J. Comparative Zoo. **2**, 275–282.

Bibikov, N. G. (**1992**). ''Auditory brainstem responses in the harbor porpoise (*Phocoena phocoena*),'' in *Marine Mammal Sensory Systems*, edited by J. Thomas, R. A. Kastelein, and A. Ya. Supin (Plenum, New York), pp. 197–211.

Bohne, B., Thomas, J., Yohe, E., and Stone, S. (**1985**). ''Examination of potential hearing damage in Weddell seals (*Leptonychotes weddelli*) in McMurdo Sound, Antarctica,'' Antarctic J. U.S. **20**, 174–176.

Brill, R. L., Sevenich, M. L., Sullivan, T. J., Sustmen, J. D., and Witt, R. E. (**1988**). ''Behavioral evidence for hearing through the lower jaw by an echolocating dolphin (*Tursiops truncatus*),'' Mar. Mam. Sci. **4**, 223–230.

Bullock, T. H., Grinnell, A. D., Ikezono, E., Kameda, K., Katsuki, Y., Nomoto, M., Sato, O., Suga, N., and Yanagisawa, K. (**1968**). ''Electrophysiological studies of central auditory mechanisms in cetaceans,'' J. Comp. Physiol. **59**, 117–156.

Bullock, T. H., and Ridgway, S. H. (**1972**). ''Evoked potentials in the central auditory system of alert porpoises to their own and artificial sounds,'' J. Neurobiol. **3**, 79–99.

Carder, D. A., and Ridgway, S. H. (**1991**). ''Auditory brainstem response in a neonatal sperm whale, Physeter spp.,'' J. Acoust. Soc. Am. Suppl. 1 **88**, S4.

Dalheim, M. E., and Awbrey, F. (**1982**). ''A classification and comparison of vocalizations of captive killer whales,'' J. Acoust. Soc. Am. **72**, 661–670.

Diercks, K. J., Trochta, R. T., Greenlaw, C. F., and Evans, W. E. (**1971**). ''Recording and analysis of dolphin echolocation signals,'' J. Acoust. Soc. Am. **49**, 1729–1732.

Dolphin, W. F. (**1995a**). ''The envelope following response in three species of cetaceans,'' in *Sensory Systems of Aquatic Mammals*, edited by R. A. Kastelein, J. A. Thomas, and P. E. Nachtigall (De Spil, Woerden, The Netherlands), pp. 197–211.

Dolphin, W. F., Au, W. W. L., and Nachtigall, P. (**1995b**). ''Modulation transfer function to low-frequency carriers in three species of cetaceans,'' J. Comp. Physiol. A **177**, 235–295.

Dubrovsky, N. A., Krasnov, P. S., and Titov, A. A. (**1971**). ''On the emission of echolocation signals by the Azov harbor porpoise,'' Sov. Phys. Acoust. **16**, 444–447.

Elberling, C., and Don, M. (**1987**). ''Threshold characteristics of the human auditory brain stem response,'' J. Acoust. Soc. Am. **81**, 115–121.

Ford, J. K. B. (**1989**). ''Acoustic behavior of resident killer whales (*orcinus orca*) off Vancouver Island, British Columbia,'' Can. J. Zoo. **67**, 727–745.

Gorga, M. P., Kaminski, J. R., Beauchaine, K. A., and Jesteadt, W. (**1988**). ''Auditory brainstem responses to tone bursts in normally hearing subjects,'' J. Speech Hear. Res. **31**, 87–97.

Hall, J. D., and Johnson, C. S. (**1972**). ''Auditory thresholds of a killer whale *Orcinus orca Linneaus*,'' J. Acoust. Soc. Am. **51**, 515–517.

Heffner, R. S., and Heffner, H. E. (**1982**). ''Hearing in the elephant (*Elphas Maximus*): Absolute sensitivity, frequency discrimination, and sound localization,'' J. Comp. Physiol. Psychol. **96**, 926–944.

Jacobs, D. W., and Hall, J. D. (**1972**). ''Auditory thresholds of a fresh water dolphin, *Inia geoffrensis* Blainville,'' J. Acoust. Soc. Am. **51**, 530–533.

Johnson, C. S. (**1968**). ''Relation between absolute threshold and duration-of-tone pulses in the bottlenosed porpoise,'' J. Acoust. Soc. Am. **43**, 757–763.

Johnson, C. S. (**1967**). ''Sound detection thresholds in marine mammals,'' in *Marine Bio-Acoustics*, edited by W. N. Tavolga (Pergamon, New York), Vol. 2, pp. 247–260.

Kamminga, C. A., and Beitsma, G. R. (**1990**). ''Investigations on cetacean sonar IX: Remarks on dominant sonar frequencies from *Tursiops truncatus*,'' Aquat. Mam. **16**, 14–20.

Ketten, D., Lien, J., and Todd, S. (**1993**). ''Blast injury in humpback whale ears: Evidence and implications,'' Invited paper, J. Acoust. Soc. Am. **94**, 1849–1850.

Ketten, D., Moore, P. W. B., Dankiewicz, L. A., Brill, R. A., and Van Bonn, W. (**1998**). ''The slippery slope of a Johnsonian ear: Natural variability versus natural loss,'' J. Acoust. Soc. Am. **102**, 3101.

Ladygina, T. F., and Supin A. Ya. (**1970**). ''The acoustic projection in the dolphin cerebral cortex,'' Fiz. Zh. SSSR **56**, 1554–1560.

Moore, P. W. B., Hall, R. W., Friedl, W. A., and Nachtigall, P. E. (**1984**). ''The critical interval in dolphin echolocation: What is it?'' J. Acoust. Soc. Am. **76**, 314–417.

Popov, V. V., and Supin, A. Ya. (**1985**). ''Determination of characteristics of dolphin hearing using brain stem evoked potentials,'' Dokl. Akad. Nauk SSSR **283**, 496–499.

Popov, V. V., and Supin, A. Ya. (**1990a**). ''Auditory brain stem responses in characterization of dolphin hearing,'' J. Comp. Physiol. A **166**, 385–393.

Popov, V. V., and Supin, A. Ya. (**1990b**). ''Electrophysiological studies of hearing in some cetaceans and manatee,'' in *Sensory Abilities of Cetaceans*, edited by J. A. Thomas and R. A. Kastelein (Plenum, New York), pp. 405–415.

Richardson, W. J., Greene, C. R., Jr., Malme, C. I., and Thomson, D. H. (**1991**). ''Effects of noise on marine mammals,'' USDI/MMA/OCS study 90-0093, LGL Ecological Research Assoc., Bryan, Texas.

Richardson, W. J., Greene, C. R., Jr., Malme, C. I., and Thomson, D. H. (**1995**). *Effects of Noise on Marine Mammals* (Academic, San Diego), pp. 576.

Ridgway, S. H., and Brownson, R. H. (**1984**). ''Relative brain sizes and cortical surface areas in odontocetes,'' J. Comparative Bio. **172**, 149–152.

Ridgway, S. H., Bullock, T. H., Carder, D. A., Seeley, R. L., Woods, D., and Galambos, R. (**1981**). ''Auditory brainstem response in dolphins,'' Proc. Natl. Acad. Sci. USA **78**, 1943–1947.

Ridgway, S. H., and Carder, D. A. (**1993**). ''High-frequency hearing loss in old (25+ years old) male dolphins,'' J. Acoust. Soc. Am. **94**, 1830.

Ridgway, S. H., and Carder, D. A. (**1997**). ''Hearing deficits measured in some *Tursiops truncatus*, and discovery of a deaf/mute dolphin,'' J. Acoust. Soc. Am. **101**, 590–594.

Sauerland, M., and Dehnhardt, G. (**1998**). ''Underwater audiogram of a tucuxi (*Sotalia fluviatilis guianensis*),'' J. Acoust. Soc. Am. **103**, 1199–1204.

Szymanski, M. D., Bain, D. E., and Henry, K. R. (**1995a**). ''Auditory evoked potentials of a killer whale (*Orcinus orca*),'' in *Sensory Systems of Aquatic Mammals*, edited by R. A. Kastelein, J. A. Thomas, and P. E. Nachtigall (De Spil, Woerden, The Netherlands), pp. 1–10.

Szymanski, M. D., Supin, A. Ya, Henry, K. R., and Bain, D. E. (**1995b**). ''The killer whale (*Orcinus orca*) auditory system assessed with evoked potentials: Click rates and audiograms,'' The 11th Biennial Conference on the Biology of Marine Mammals, Soc. Mar. Mam. Abstracts.

Szymanski, M. D., Supin, A. Ya., Bain, D. E., and Henry, K. R. (**1998**). ''Killer whale auditory evoked potentials to rhythmic clicks,'' Mar. Mam. Sci. **14**(4), 676–691.

Thomas, J., Chun, N., Au, W., and Pugh, K. (**1988**). ''Underwater audiogram of a false killer whale (*Pseudorca crassidens*),'' J. Acoust. Soc. Am. **84**, 936–940.

Tremmel, D. P., Thomas, J. A., Ramirez, K. T., Dye, G. S., Bachman, W. A., Orban, A. N., and Grim, K. K. (**1998**). ''Underwater hearing sensitivity of a Pacific white-sided dolphin *Lagenorhynchus obliquidens*,'' Aquat. Mam. **24**, 63–69.

White, M. J., Jr, Norris, J., Ljungblad, D., Baron, K., and di Sciara, G. (**1978**). ''Auditory thresholds of two beluga whales (*Delphinapterus leucas*),'' in HSWRI Tech. Rep. No. 78-109, Hubbs Marine Research Institute, San Diego, CA.

Underwater temporary threshold shift induced by octave-band noise in three species of pinniped

David Kastak, Ronald J. Schusterman, Brandon L. Southall, and Colleen J. Reichmuth
Long Marine Laboratory, University of California, 100 Shaffer Road, Santa Cruz, California 95060

(Received 11 November 1998; revised 4 April 1999; accepted 14 April 1999)

Pure-tone sound detection thresholds were obtained in water for one harbor seal (*Phoca vitulina*), two California sea lions (*Zalophus californianus*), and one northern elephant seal (*Mirounga angustirostris*) before and immediately following exposure to octave-band noise. Additional thresholds were obtained following a 24-h recovery period. Test frequencies ranged from 100 Hz to 2000 Hz and octave-band exposure levels were approximately 60–75 dB SL (sensation level at center frequency). Each subject was trained to dive into a noise field and remain stationed underwater during a noise-exposure period that lasted a total of 20–22 min. Following exposure, three of the subjects showed threshold shifts averaging 4.8 dB (*Phoca*), 4.9 dB (*Zalophus*), and 4.6 dB (*Mirounga*). Recovery to baseline threshold levels was observed in test sessions conducted within 24 h of noise exposure. Control sessions in which the subjects completed a simulated noise exposure produced shifts that were significantly smaller than those observed following noise exposure. These results indicate that noise of moderate intensity and duration is sufficient to induce TTS under water in these pinniped species.
[S0001-4966(99)05907-X]

PACS numbers: 43.80.Nd [WWLA]

INTRODUCTION

Noise-induced temporary threshold shift (TTS) is the reversible elevation in auditory threshold that may occur following overstimulation by a loud sound (see Ch. 14 in Yost, 1994, for a brief review). In mammals, noise-induced TTS involves structural and/or metabolic fatigue to the supporting, transducing, and processing elements within the peripheral and central auditory systems (Ward, 1997). The magnitude and duration of TTS are related to the level, duration, spectral distribution, and temporal pattern of the fatiguing stimulus. In addition, biological variables such as age, sex, and individual differences in auditory sensitivity may interact in complicated ways with these acoustic characteristics. Studies of TTS in nonhumans have generally been conducted on rodents, cats, and primates (Clark, 1991). These experiments, however, all involved airborne test and fatiguing stimuli; therefore, the few generalities developed from them may apply only to mammals with air-adapted hearing under conditions in which the fatiguing stimulus is also airborne. When human divers were tested underwater, for instance, the resultant levels of TTS were much higher than originally predicted (Smith and Wojtowicz, 1985). Thus the fatiguing effects of underwater noise on auditory sensitivity remain largely unexplored, particularly for animals adapted to hear in this medium.

The ears of marine mammals are modified from those of their terrestrial ancestors and are adapted to function in the naturally noisy environment of the ocean. Speculation that marine mammals have evolved a certain degree of protection from noise-induced hearing loss is consistent with a viewpoint that recognizes the evolution of these animals in such an acoustically challenging environment. If marine mammals do show diminished TTS susceptibility relative to terrestrial mammals, then concern about potential marine habitat degradation related to anthropogenic noise (Richardson *et al.*, 1995) may be exaggerated. If, however, the marine mammal ear is not particularly adapted to resist the damaging effects of noise, this concern is well placed. Thus an opposing viewpoint might consider marine mammals especially sensitive to acoustic overstimulation, given increasing levels of oceanic noise pollution. Considering the implications for conservation reflected by these two opposing viewpoints, it is extremely important to conduct studies of TTS in marine mammals.

Investigation into the effects of noise on marine animals, in terms of behavioral reactions to loud sounds and measurable losses in auditory sensitivity, may help to define zones of impact within which there may be significant immediate and/or short-term noise effects. Individual exposure events are not likely to have dramatic long-term or fitness consequences, except for cases of extremely high exposure level resulting in acoustic trauma. However, these events may result in short-term impairment in the ability to communicate, navigate, forage, and detect predators. Additionally, behavioral reactions to noise exposure such as startle responses or avoidance may interrupt ongoing behaviors, and have consequences as severe as mother–offspring separation.

Long-term noise effects, on the other hand, cannot be directly evaluated through TTS experiments. While permanent threshold shifts (PTS) may be caused by repeated temporary shifts over a long period of time, the magnitude of PTS cannot be predicted from the degree of TTS induced in single exposure events (Melnick, 1991; Yost, 1994). Exposure conditions with the potential to induce PTS are much more likely to compromise individual fitness, and, when viewed on a larger scale, affect the health of marine mammal populations. It will be necessary to develop new models or to expand upon current models in order to determine the rela-

tionships between frequent or numerous TTS events and PTS. These models can be invoked only when sufficient information regarding TTS in marine mammals is made available.

The experimental approach to TTS assessment involves the determination of a subject's auditory thresholds prior to and immediately following exposure to a fatiguing stimulus. Thresholds may be determined behaviorally (through classically or operantly conditioned responses to acoustic stimuli), or physiologically, by measuring evoked potentials (see Clark, 1991 for a review). Fatiguing stimuli can be pure tones, bands of noise, or impulsive sounds. Repeated threshold estimates over time provide an indication of the rate of recovery of TTS. Many of these procedures cannot be conducted with marine mammals because threshold determination, being largely voluntary, is time consuming, and large populations of test-sophisticated subjects do not exist.

Data on TTS have been obtained for two marine mammal species, the bottlenose dolphin (*Tursiops truncatus*) and harbor seal (*Phoca vitulina*). Threshold shift in bottlenose dolphins was examined following exposure to short-duration, intense, pure tones (Ridgway *et al.*, 1997). The harbor seal TTS data were obtained fortuitously, in air, and under somewhat uncontrolled conditions following long-term exposure to broadband noise (Kastak and Schusterman, 1996). The research reported herein was designed in part to replicate in water the earlier in-air harbor seal TTS. The primary goal of the current study was to determine minimum levels of continuous noise that would induce a measurable, recoverable shift in auditory threshold for one harbor seal (*Phoca vitulina*), two California sea lions (*Zalophus californianus*), and one northern elephant seal (*Mirounga angustirostris*) under water. In accordance with concern about anthropogenic noise (most of which is low frequency in nature), both the fatiguing stimuli and test tones used in this experiment were at or below 2000 Hz. Additionally, the duration of noise exposure was adjusted in such a way that fatiguing stimuli of moderate rather than high intensity could be used.

I. METHODS

A. Subjects

One male harbor seal (*Phoca vitulina*), age 10, two female California sea lions (*Zalophus californianus*) ages 12 and 21, and one female northern elephant seal (*Mirounga angustirostris*), age 4, were the subjects of these experiments. Subjects were housed at Long Marine Laboratory in Santa Cruz, California, in free-flow seawater tanks. All experiments were conducted with the approval of the University of California Chancellor's Animal Research Committee (CARC).

B. General procedure

We used a repeated measures design to compare auditory thresholds obtained in sessions prior to noise exposure (''baseline'' thresholds); immediately following noise exposure (''exposure'' thresholds); and following a recovery period of 24 h (''recovery'' thresholds). Subjects were usually tested over the course of two consecutive days to include all three conditions.

C. Threshold testing

The apparatus and design for threshold testing is described in detail elsewhere (Kastak and Schusterman, 1998). Testing took place in a 7.5-m diameter, 2.5-m deep concrete tank. The testing apparatus was a PVC platform mounted at one side of the tank. A chin-cup located at the base of the apparatus was the positioning point for the subject. A moveable opaque door served to delineate trials by opening to reveal a plastic response paddle. Pure-tone signals (500-ms duration, rise/fall times of 40 ms) were produced by a function generator, amplified, attenuated (in 4- or 2-dB increments) and manually triggered. Tones were projected through a J-9 underwater transducer positioned approximately 5 m behind the position of the subject's head. We used an up–down or staircase procedure in which an initial suprathreshold tone was attenuated by 4 dB following each correct detection (HIT), defined by the subject touching the response paddle with its nose. Following the first failure to detect (MISS), the signal level was increased by 2 dB. The 2-dB step size was used for the remainder of the test. The signal level was subsequently increased by one step following each MISS and decreased by one step following each HIT. Thresholds were defined by the signal level corresponding to 50% correct detections, according to the method outlined in Dixon and Mood (1948). Catch trials (signal absent trials) were incorporated into threshold sessions in order to obtain estimates of response bias. The proportion of catch trials was 0.5 for the harbor seal and sea lions, and was sufficient to maintain the percentage of false alarms (responses in the absence of a signal) at levels of 10%–20%. The elephant seal was relatively conservative with respect to reporting a signal, therefore the proportion of catch trials was occasionally decreased from 0.5 to 0.3 in order to attempt to maintain comparable false alarm rates between subjects.

D. Noise exposure regimes

Each subject was trained to submerge and place its muzzle into a plastic chin cup mounted on the front of a separate PVC platform, ensuring that no movement of the head would occur during noise exposure. Initially, the subjects dove into a noise field of low intensity, and this intensity was gradually increased as each subject became more tolerant of the noise. The chin cup was 51 cm from two University UW-30 underwater speakers mounted on the apparatus and positioned on either side of the animal's head. Gaussian white noise was first passed through a variable filter, with high and low pass cutoffs separated by one octave, and then projected from the University speakers. The sound field was uniform (i.e., did not change in level or spectral composition) in the area occupied by the subjects' heads, and was measured before and after exposure sessions with an H-56 hydrophone and PC-based spectral analysis software (SpectraPlus, Pioneer Hill). Because of transducer response and tank reverberation, noise spectra were not completely

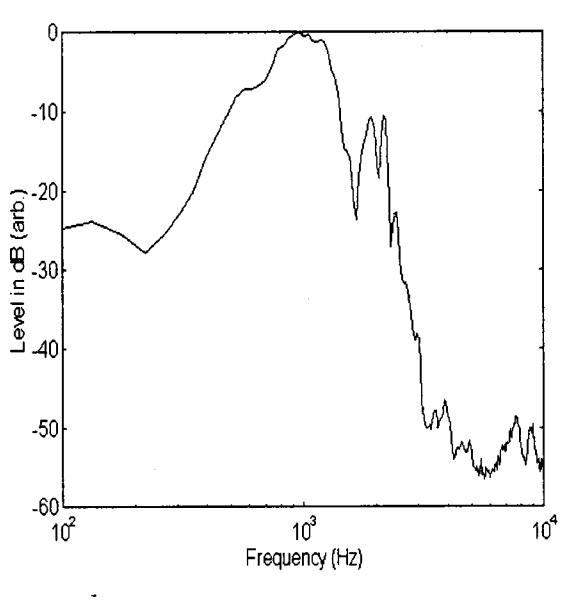

FIG. 1. Example of spectrum for 1000-Hz centered noise recorded at the position of the animal's head.

flat within the band of interest (see Fig. 1), and there was some spread of energy into adjacent octave bands. Only the noise level in the designated octave band was used for calibration.

The noise levels used for each noise-exposure period were referenced to sensation level, or the subject's baseline threshold. The harbor seal was exposed to octave-band noise (OBN) with center frequencies of 100 Hz (threshold testing at 100 Hz), 500 Hz (threshold testing at 500, 750, and 1000 Hz), and 1000 Hz (threshold testing at 1000 Hz). Center frequencies were 1000 Hz for corresponding threshold testing at 1000 Hz and 2000 Hz for threshold testing at 2000 Hz for the sea lions. The elephant seal was exposed to OBN with a center frequency of 1000 Hz with corresponding threshold testing at 1000 Hz. Exposure levels were approximately 60 dB SL (sensation level at center frequency) for the harbor seal, and ranged from approximately 55 to 65 dB SL for the sea lions. Because several preliminary exposures at levels of 55–65 dB SL failed to induce TTS in the elephant seal, the majority of noise exposures for this subject used levels of 70–75 dB SL. The duration of exposure was 20 min for the harbor seal and sea lions, and 22 min for the elephant seal.

During the diving regime, the subjects were intermittently reinforced with fish for remaining in the noise field. The subjects occasionally surfaced to breathe during the exposure period. These surface intervals were timed, and cumulative time spent at the surface was added to the total exposure time, so that the subjects were exposed to OBN for a net time of 20 or 22 min.

E. Control sessions

In order to ensure that physiological or behavioral changes associated with voluntary diving (as opposed to noise exposure) did not affect auditory thresholds, several control sessions were conducted. In the control procedure, an initial threshold was obtained in the usual manner, and then a simulated noise-exposure session was conducted, during which the subject stationed for a net time of 20 or 22 min at the noise apparatus with no fatiguing stimulus present. Following the mock exposure session, a ''recovery'' threshold was obtained in the same manner as in the experimental procedure.

Nine matched sets of baseline/noise/recovery thresholds were collected for the harbor seal, along with 11 control sets. There were 12 sets each of experimental and control thresholds collected for the older sea lion, and 11 experimental and 6 control sets collected for the elephant seal.

F. Analysis

Comparisons were made between thresholds obtained under baseline, exposure, and recovery conditions. These comparisons were based on thresholds pooled over all frequencies tested. Measures of threshold shift under exposure and recovery conditions are expressed relative to baseline thresholds, with positive values indicating a loss of sensitivity (i.e., TTS) and negative values indicating a sensitivity gain relative to the baseline condition. Statistical comparisons between the thresholds of each subject were conducted by using a one-way repeated measures ANOVA as a preliminary test for significant differences among the three conditions. When an overall difference was detected, a Student–Newman–Keuls test was performed on each pairwise comparison to detect differences between conditions (Glantz and Slinker, 1990). A Student's t-test was used to compare mean threshold shifts under test and control conditions.

We applied a signal detection analysis to the data collected from the harbor seal, primarily because of an apparent shift in response bias. This bias was evidenced by an elevated false alarm rate following noise exposure. The analysis was performed in the following way: indices of detectability (d') were calculated for pre-exposure threshold values, using a value of 0.5 (our definition of ''threshold'') for the probability of correct detection $P(y|sn)$, and the false alarm rate during the ''reversal'' or staircase phase of the session as $P(y|n)$. We subsequently determined the signal level which would be required to produce the same d' value during post-exposure sessions (i.e., how much more intense must a signal be *following exposure* to reach the same sensation level as a signal *before exposure*?). This was done by determining the post-exposure $P(y|sn)$ corresponding to the pre-exposure d' value, given the post-exposure $P(y|n)$. This is not a threshold correction for false alarms based on high threshold theory (Swets *et al.*, 1964); rather it is movement along an ROC curve corresponding to an assumed post-exposure change in response bias. We then determined the theoretical increase in signal level corresponding to the change in $P(y|sn)$ for exposure sessions versus baseline sessions, using psychometric functions obtained previously for this subject. Because the sea lion and elephant seal false alarm rates did not correlate with session type, this analysis was performed on the harbor seal data only.

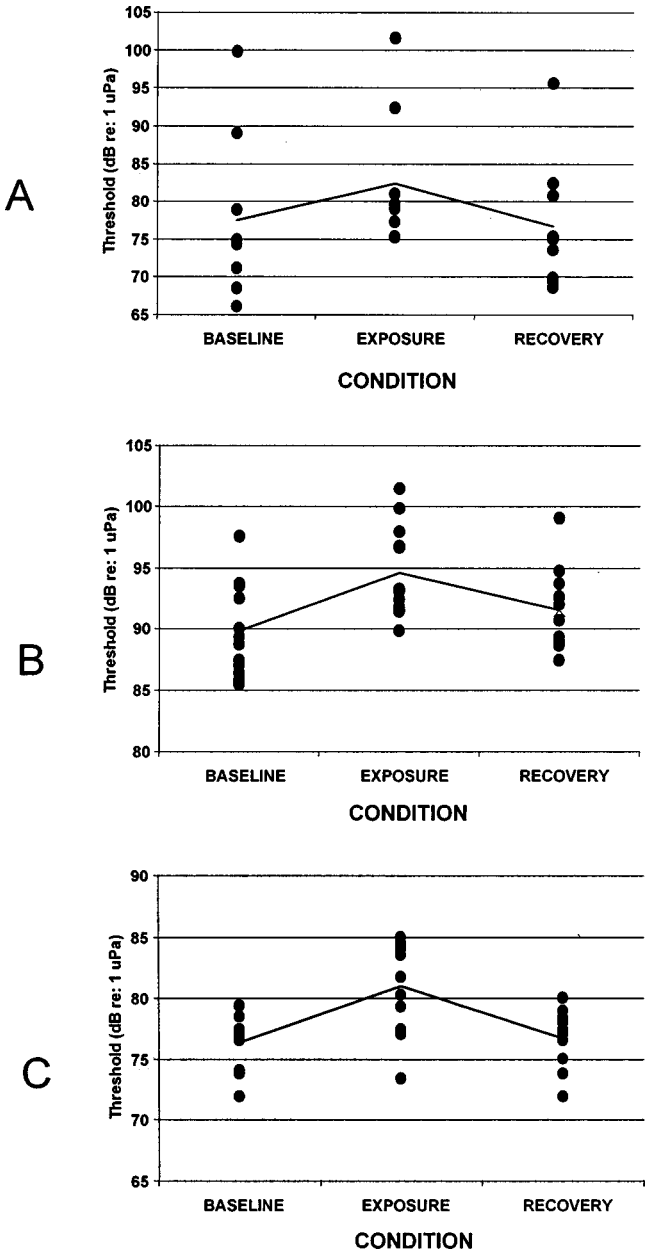

FIG. 2. Underwater pure-tone detection thresholds (in dB *re*: 1 μPa) for (A) the harbor seal (*Phoca vitulina*), (B) the California sea lion (*Zalophus californianus*), and (C) the northern elephant seal (*Mirounga angustirostris*), measured before noise exposure (baseline), immediately following noise exposure (exposure), and following a 24-h recovery period (recovery). The line connects mean thresholds for each condition. Note: test frequencies have been pooled for each condition (see text).

II. RESULTS

Thresholds for the harbor seal are shown in Fig. 2(A). The average threshold shift relative to baseline thresholds for this subject following noise exposure was 4.8 dB (range $=1.8$–9.2 dB) and the average shift following the recovery period was -0.8 dB. When the matched values for baseline, exposure, and recovery sessions were compared, there were significant differences between baseline and exposure thresholds ($q=5.98$; $p<0.01$), and between exposure and recovery thresholds ($q=6.93$; $p<0.01$). Baseline and recovery thresholds were not significantly different.

False alarm rates for the harbor seal were usually higher on exposure (0.28; range$=0.0$–0.64) vs both baseline (0.13; range$=0.0$–0.44) and recovery (0.16; range$=0.0$–0.56) sessions. Nine out of 11 individual exposure sessions (82%) showed an increase in false alarm responding over respective baseline sessions. In one post-noise session there was no change in false alarm rate, and in one exposure session the false alarm rate was lower than in the corresponding baseline session. For computational simplicity, $p(y|sn)$ values of 0.0 were changed to 0.01 before d' values were calculated (problems introduced by this adjustment will be addressed in Sec. III). The average d' for threshold signals in baseline sessions was 1.41 (range$=0.14$–2.33, s.d.$=0.67$). The average change in signal level required to match d' values for baseline and recovery sessions was about 3 dB, resulting in a mean corrected threshold shift of nearly 8 dB rather than the originally calculated value of nearly 5 dB. These adjustments assume an average psychometric function slope of about 0.25 normal deviate (probit) per dB. This number was obtained from prior psychoacoustic testing of the harbor seal using a method of constant stimuli.

Data for the harbor seal indicate that following similar dives without noise exposure, thresholds increased by an average of 1.0 dB for the harbor seal. Figure 3(A) shows that the degree of threshold shift on experimental sessions was significantly elevated compared to the control condition ($t_{18}=2.45$, $p<0.05$).

Threshold shifts relative to baseline thresholds for the older sea lion following noise exposure averaged 4.9 dB (range$=2.9$–6.7 dB). Thresholds obtained following the recovery period showed an average shift of 1.7 dB. A comparison of the matched values between the three experimental conditions [Fig. 2(B)] showed significant differences between baseline and exposure thresholds (Student–Neuman–Keuls $q=12.87$; $p<0.01$); between exposure and recovery thresholds ($q=8.25$; $p<0.01$); and between baseline and recovery thresholds ($q=4.64$; $p<0.05$).

On 12 control sessions, this sea lion showed an average threshold increase of 2.0 dB. The degree of threshold shift on experimental sessions was significantly elevated compared to the control condition [$t_{22}=3.04$; $p<0.01$; Fig. 3(B)].

The younger sea lion showed a marginal average threshold shift following noise exposure, but daily performance on exposure sessions was variable, and shifts were generally small and statistically unreliable. In addition, this subject did not complete a sufficient number of controls sessions to statistically compare performance with experimental sessions.

Figure 2(C) shows thresholds obtained under the three conditions for the elephant seal. Shifts following exposure averaged 4.6 dB (range$=-0.4$–12.3 dB), and shifts following recovery averaged -0.4 dB. Exposure thresholds were significantly higher than baseline thresholds ($q=6.37$; $p<0.01$) and recovery thresholds ($q=5.85$; $p<0.01$). There was no significant difference between baseline and recovery thresholds.

The mean threshold shift for the elephant seal was -2.1 on control sessions. As shown in Fig. 3(C), threshold shifts on test sessions were significantly elevated compared to shifts on control sessions ($t_{15}=3.38$; $p<0.01$).

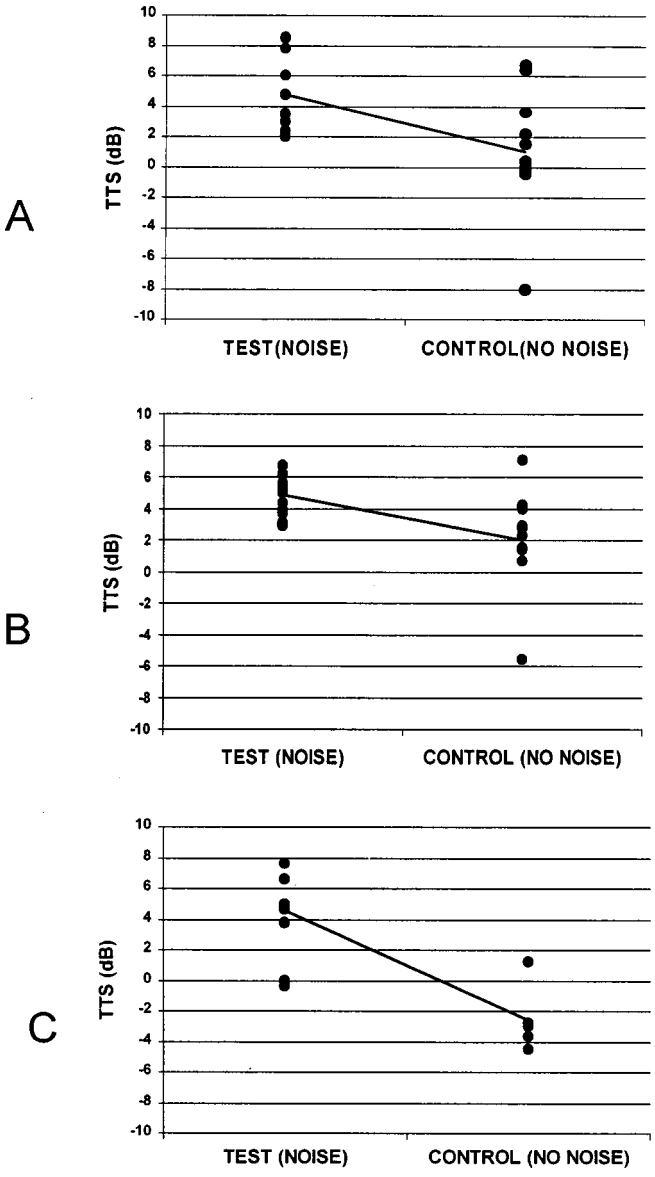

FIG. 3. Threshold shifts in experimental (diving with noise) and control (diving without noise) sessions for the harbor seal (A), sea lion (B), and elephant seal (C). The line connects mean shifts for experimental and control sessions.

III. DISCUSSION

This is the first report of underwater noise-induced temporary threshold shift in pinnipeds. Ridgway *et al.* (1997) reported TTS induced by intense tones in bottlenose dolphins (*Tursiops truncatus*); however, the methods differed significantly from those used in this study in the following ways: the fatiguing stimuli in the Ridgway *et al.* study were intense short-duration tones rather than bands of noise. Furthermore, the data obtained from dolphins (Ridgway *et al.*, 1997) represent shifts in masked thresholds rather than in absolute thresholds, because of high background noise levels in San Diego Bay, where the tests took place. While the effect (if any) of temporary hearing impairment on masked thresholds is not known for certain, some research has shown that the magnitude of measurable TTS decreases as the masker level increases (Parker *et al.*, 1976). Assessment of TTS under such circumstances is difficult because a noise masker decreases the *measured* level of TTS irrespective of whether temporary fatigue has occurred. Thus the underwater masked threshold shifts obtained by Ridgway *et al.* (1997) may underestimate the true threshold shifts (i.e., shift in absolute thresholds) and hence, the degree of fatigue to the dolphin auditory system that can potentially be induced by loud environmental noise.

It should also be noted that Ridgway *et al.* (1997) used a free operant psychophysical procedure (Egan *et al.*, 1964) that makes false alarm rates difficult to quantify, and therefore this approach is not particularly amenable to any sort of signal detection analysis. Shifts in response criteria, such as those shown by our harbor seal, cannot be evaluated without unambiguous estimates of false alarm responding.

Similar to the TTS study on dolphins (Ridgway *et al.*, 1997) we also found that the trained responses of our seals and sea lions were often disrupted by exposure to noise, especially during the early phases of the TTS experiments. These changes mirror those shown by one of the sea lions the harbor seal, and the elephant seal tested. The disruptions in pinniped behavior were reflected in hauling out, aggression directed at the apparatus and at the trainer, and refusal to station at the apparatus during noise exposure. These altered behaviors in the form of increased levels of aggression and/or avoidance of a location in which food had been received prior to noise exposure (bite plates or chin cups associated with acoustic testing) should be examined more closely in both lab and field settings. For instance, if marine mammals in the wild avoid breeding grounds or feeding locations following exposure to loud sounds (shipping noise, sonars, etc.), *regardless* of whether a temporary loss of hearing has occurred, there can be dramatic fitness effects (e.g., loss of reproductive output), especially if the animals become sensitized to the noxious stimuli (but see Perry *et al.*, 1998, for negative findings).

A second effect that may be considered separately from hearing loss in the classical sense is a change in response bias, for example, the increase in false alarm responding exhibited by the harbor seal in the present study. Marine mammals participating in psychophysical tasks are frequently trained to adopt a rather strict response criterion; that is, false alarm rates are typically very low (Schusterman, 1974). This was indeed the case for the harbor seal, whose average false alarm rate for absolute thresholds taken over a range of eight frequencies was 0.07 (Kastak and Schusterman, 1998), and whose baseline false alarm rate in this study averaged 0.13. The data from this study are also consistent with a previous increase in false alarm responding by the same subject following long-term exposure to airborne noise (Kastak and Schusterman, 1996). The cause of this animal's post-exposure change in responding is not clear. In the earlier study of hearing loss in air (Kastak and Schusterman, 1996), we hypothesized that the seal's anomalous responses were due to tinnitus; however, the requisite tests (for example, those described by Jastreboff, 1990) have not been conducted and would be methodologically taxing. An alternative explanation for the increase in false alarm rate is related to the testing procedure. The up–down psychophysical procedure that we used is designed to concentrate signal levels

around threshold. Following noise exposure, the sensation level of the tones presented on the first few trials would have been lower than expected by the subject because of the threshold shift. These weak signals may have led the seal to adopt a more liberal response criterion. The increased tendency to respond would have been reinforced if the subject responded fortuitously to signals that were actually below sensation level. Because signal levels in the up–down procedure are predictably weak (i.e., close to threshold), this method is particularly prone to such changes in response criterion. Regardless of the cause, criterional shifts could have dramatic consequences for free-ranging animals, in the form of responding inappropriately to conspecific signals, acoustic cues from potential predators and prey, or irrelevant, nonbiological sound.

The reader should keep in mind that the spread in thresholds depicted in Figs. 2 and 3 is partly a function of pooling thresholds of different frequencies. In addition, there was greater variability observed in baseline thresholds than was obtained in previous studies using the same subjects (Kastak and Schusterman, 1998). A probable cause of the increased threshold variance was a difference in psychophysical methods. In the Kastak and Schusterman (1998) study, most thresholds were estimated by the method of constants, while in this study, thresholds were always estimated using an abbreviated up–down staircase method, sometimes with a fairly large initial step size. The rationale for selecting the latter procedure was to obtain thresholds rapidly, before the onset of recovery.

We encountered one potential problem in the noise exposure regime directly related to the fact that noise exposure and threshold testing took place under water. The subjects surfaced to breathe, and generally returned to the noise apparatus immediately. However, each subject occasionally remained at the surface for a protracted interval, and it was clear that the noise could be avoided by adopting this strategy. Although surface intervals generally accounted for 20%–25% of the total exposure time, the duration and number of each surface interval varied dramatically both within and between individuals. The effects of this intermittence could theoretically range from none (consistent with an equal energy hypothesis) to reducing the TTS to 75%–80% of its value relative to 100% exposure time (consistent with an on-fraction hypothesis). The actual effect is likely to lie somewhere in between. There are several options for dealing with the complication of intermittence. One is to adjust the noise intensity and the dive durations so that the subjects are exposed to louder sounds for a continuous short period of time. We are currently working on this strategy with the northern elephant seal, which has been trained to submerge in a noise field for extended periods (12 min +) on a single breath. The second and perhaps more favorable strategy is to expose the subjects to noise in air, and obtain thresholds either in air or underwater. In this way the exposure could be better controlled, in that (1) reduced reverberation would allow easier manipulation of the fatiguing stimulus, and (2) the subjects would not have to withdraw from the sound field in order to breathe. Given that stimulus levels reaching the inner ear (in terms of sensation level) can be equated, data generated from airborne TTS studies should be comparable to those generated from studies taking place in water. Moreover, threshold shifts induced by aerial noise such as rocket flights, sonic booms, explosions, etc., have the potential to affect behavior the same way that TTS induced by underwater noise does. Indeed, temporary deafness caused by atmospheric noise can impact behavior under water as well as in air. It would be useful to quantify these effects in terms of ''safe'' exposure levels for airborne as well as underwater sound.

A second problem occurring during extended submersion has to do with behavioral changes in response to the dive *per se*, rather than to the noise exposure. These behavioral changes may be reflected in the small but statistically insignificant threshold shifts obtained for the pinniped subjects in the control procedures following mock noise exposures. We are unable at present to pinpoint the cause of these shifts, but can speculate that changes in motivational state following extended submersions may be at least partially responsible for threshold changes following dives.

Another difficulty in interpreting the pinniped TTS data lies in the timing between noise offset and threshold determination. Maximum TTS has been shown to occur approximately 2 min following exposure (TTS_2), yet it is difficult to precisely determine magnitudes of TTS_2 in nonhuman subjects (Yost, 1994). In this study, final threshold determination for all subjects occurred approximately 6–10 min following exposure, with the longest time intervals occurring for the elephant seal. Thus it is likely that we underestimated TTS in these subjects by up to several dB, when compared with standard TTS results.

Noise exposure criteria for marine mammals may be based on several different models that are based on both the characteristics of the noise and the auditory capabilities of the species of concern. The simplest of these criteria involves the zone of audibility, which is the area around a source within which the sound can be heard by a marine mammal. These zones can be estimated using propagation models or measurements in conjunction with estimated ambient noise levels and data on auditory thresholds and critical ratios. Audibility, however, does not imply dramatic behavioral change or auditory damage, so these models are of limited use in defining exposure criteria. In terms of behavioral changes, the zone of responsiveness is the area around a source within which an observable response to the noise occurs. This zone is likely to be smaller than the zone of audibility. Again, measures of behavioral responses are of limited use because of the potential for habituation or sensitization; lack of consistency in defining a behavioral response; and interactions of noise responses with other behavioral variables such as motivational state. Zones of hearing loss, within which auditory damage is likely to occur, can be calculated only by defining the parameters involved in TTS. These models will be more complicated, in that interactions between received sound levels and the duration of exposure will influence the degree of potential threshold shift at a given distance. For this reason, more detailed evaluations of intensity/duration interactions must be made.

The goal of these experiments was not to determine

''safe'' exposure levels for marine mammals to underwater sound. Rather, it was to demonstrate that TTS can be induced in pinnipeds on a repeatable and controlled basis. The threshold shifts obtained for our subjects were small in magnitude, but consistent and replicable. From these results we conclude that octave band noise levels below about 60 dB SL are unlikely to result in a measurable TTS, while moderate exposures of 65–75 dB SL reliably produce small amounts of TTS in three of the four experimental subjects. Clearly these animals do not have special mechanisms that protect against noise-induced hearing loss. We are currently developing modifications of the techniques used in this study to examine the role of intermittence and interactions between sound duration and intensity in inducing TTS. These techniques and results, as well as those of subsequent experiments, will ultimately play a role in defining anthropogenic noise-exposure criteria for pinnipeds and other marine animals.

ACKNOWLEDGMENTS

This work was financially supported by Grants Nos. N000149510936 and N000149910164 from the Office of Naval Research to Ronald Schusterman. The authors gratefully acknowledge the help of the Pinniped Research in Cognition and Sensory Systems group at Long Marine Laboratory, especially Jim Grayson who provided valuable assistance conducting experiments. Two anonymous reviewers provided thoughtful comments on an earlier version of this manuscript.

Clark, W. W. (**1991**). ''Recent studies of temporary threshold shift (TTS) and permanent threshold shift (PTS) in animals,'' J. Acoust. Soc. Am. **90**, 155–163.

Dixon, W. J., and Mood, A. M. (**1948**). ''A method for obtaining and analyzing sensitivity data,'' J. Am. Stat. Assoc. **43**, 109–126.

Egan, J. P., Greenberg, G. Z., and Schulman, A. I. (**1964**). ''Operating characteristics, signal detectability, and the method of free response,'' in *Signal Detection and Recognition by Human Observers*, edited by J. Swets (Wiley, New York), pp. 316–347.

Glantz, S. A., and Slinker, B. K. (**1990**). *Primer of Applied Regression and Analysis of Variance* (McGraw-Hill, New York).

Jastreboff, P. J. (**1990**). ''Phantom auditory perception (tinnitus): Mechanisms of generation and perception,'' Neurosci. Res. **8**, 221–254.

Kastak, D., and Schusterman, R. J. (**1996**). ''Temporary threshold shift in a harbor seal (*Phoca vitulina*),'' J. Acoust. Soc. Am. **100**, 1905–1908.

Kastak, D., and Schusterman, R. J. (**1998**). ''Low frequency amphibious hearing in pinnipeds: Methods, measurements, noise and ecology,'' J. Acoust. Soc. Am. **103**, 2216–2228.

Melnick, W. (**1991**). ''Human temporary threshold shift (TTS) and damage risk,'' J. Acoust. Soc. Am. **90**, 147–154.

Parker, D. E., Tubbs, R. L., Johnston, P. A., and Johnston, L. S. (**1976**). ''Influence of auditory fatigue on masked pure-tone thresholds,'' J. Acoust. Soc. Am. **60**, 881–885.

Perry, E. A., Boness, D. J., and Insley, S. J. (**1998**). ''A study of sonic boom effects on seals breeding on Sable Island, Canada,'' J. Acoust. Soc. Am. **104**, 1861.

Richardson, W. J., Greene, Jr., C. R., Malme, C. I., and Thomson, D. H. (**1995**). *Marine Mammals and Noise* (Academic, San Diego).

Ridgway, S. H., Carder, D. A., Smith, R. R., Kamolnick, T., Schlundt, C. E., and Elsberry, W. R. (**1997**). ''Behavioral Responses and Temporary Shift in Masked Hearing Threshold of Bottlenose Dolphins, Tursiops truncatus, to 1-second Tones of 141 to 201 dB *re* 1 μPa,'' Technical Report 1751, Revision 1, Naval Command, Control and Ocean Surveillance Center, RDT&E Division, San Diego.

Schusterman, R. J. (**1974**). ''Low false-alarm rates in signal detection by marine mammals,'' J. Acoust. Soc. Am. **55**, 845–848.

Smith, P. F., and Wojtowicz, J. (**1985**). ''Temporary auditory-threshold shifts induced by twenty-five-minute continuous exposures to intense tones in water,'' Report 1063, Naval Submarine Medical Center.

Swets, J. A., Tanner, Jr., W. P., and Birdsall, T. G. (**1964**). ''Decision processes in perception,'' in *Signal Detection and Recognition by Human Observers*, edited by J. Swets (Wiley, New York), pp. 3–57.

Ward (**1997**). ''Effects of high-intensity sound,'' in *Encyclopedia of Acoustics V. III*, edited by Malcolm Crocker (Wiley, New York), pp. 1497–1508.

Yost, W. A. (**1994**). *Fundamentals of Hearing: An Introduction*, 3rd ed. (Academic, San Diego).

Comparison of electrohydraulic lithotripters with rigid and pressure-release ellipsoidal reflectors. II. Cavitation fields

Michael R. Bailey
Applied Physics Laboratory, College of Ocean and Fishery Science, University of Washington, 1013 NE 40th St., Seattle, Washington 98105, Applied Research Laboratories, The University of Texas at Austin, P.O. Box 8029, Austin, Texas 78713-8029, and Department of Mechanical Engineering, The University of Texas at Austin, Austin, Texas 78712-1063

David T. Blackstock
Applied Research Laboratories, The University of Texas at Austin, P.O. Box 8029, Austin, Texas 78713-8029 and Department of Mechanical Engineering, The University of Texas at Austin, Austin, Texas 78712-1063

Robin O. Cleveland[a] and Lawrence A. Crum
Applied Physics Laboratory, College of Ocean and Fishery Science, University of Washington, 1013 NE 40th St., Seattle, Washington 98105

(Received 5 December 1998; revised 20 January 1999; accepted 3 May 1999)

Dramatically different cavitation was produced by two separate acoustic pulses that had different shapes but similar duration, frequency content, and peak positive and negative pressure. Both pulses were produced by a Dornier HM-3 style lithotripter: one pulse when the ellipsoidal reflector was rigid, the other when the reflector was pressure release. The cavitation, or bubble action, generated by the conventional rigid-reflector pulse was nearly 50 times longer lived and 3–13 times stronger than that produced by the pressure-release-reflector pulse. Cavitation durations measured by passive acoustic detection and high-speed video agreed with calculations based on the Gilmore equation. Cavitation intensity, or destructive potential, was judged (1) experimentally by the size of pits in aluminum foil detectors and (2) numerically by the calculated amplitude of the shock wave emitted by a collapsing bubble. The results indicate that the trailing positive spike in the pressure-release-reflector waveform stifles bubble growth and mitigates the collapse, whereas the trough after the positive spike in the rigid-reflector waveform triggers inertially driven growth and collapse. The two reflectors therefore provide a tool to compare effects in weakly and strongly cavitating fields and thereby help assess cavitation's role in lithotripsy. [S0001-4966(99)03708-X]

PACS numbers: 43.80.Sh, 43.25.Jh, 43.25.Yw [FD]

INTRODUCTION

In a companion paper, herein after referred to as Paper I,[1] we reported the use of a spark-source lithotripter to study the change in pulse produced when the ellipsoidal reflector was changed from rigid to pressure release. Although the pulses produced by the two reflectors are similar in amplitude, duration, and rise time, they are quite different in waveform. In particular, the pulse from a rigid reflector is a positive spike followed by a trough, whereas the order is reversed in the pulse produced by the pressure-release reflector (see Fig. 1). In the present paper, we demonstrate that the two pulses produce very different cavitation bubble dynamics and cavitation-induced injury to metal surfaces. Since cavitation is a mechanism of stone comminution or tissue damage shown to be highly sensitive to not only pressure amplitude but temporal pressure waveform,[2] the rigid and pressure-release reflectors provide a comparative way to isolate and to assess the role of cavitation in extracorporeal shock wave lithotripsy (ESWL). Better understanding of cavitation's role may lead to safer, more effective treatment of kidney stones by lithotripsy.

How does cavitation cause damage? The effect of the negative phase of the lithotripter pulse is to form and to expand bubbles in the fluid surrounding the stone or in or near the tissue.[3,4] Expansion of the cavitation bubbles can play a role in causing tissue damage[5,6] or breaking stones.[7] However, the violent collapse of the bubbles is generally considered to be more effective in producing damage. Bubble collapse can be sufficiently violent to erode the metal propellers on ships.[8] When bubbles collapse they create tiny but powerful jets of fluid,[9] radiate shock waves,[10,11] and even generate free radicals[12]—all of which have been shown to damage tissue or stones.

Many researchers[13–15] have observed the occurrence of cavitation in lithotripsy, but distinguishing the effect of cavitation from effects due to other mechanisms has been difficult. Three approaches have been taken: (1) replace the water bath with a liquid such as oil that inhibits cavitation,[16] (2) add or remove bubbles from the water,[16] and (3) pressurize the water.[17,18] All are efforts to reduce cavitation and measure a comparable change in biological effect. In all cases an

[a]Current address: Department of Aerospace and Mechanical Engineering, Boston University, 110 Cummington St., Boston, MA 02215.

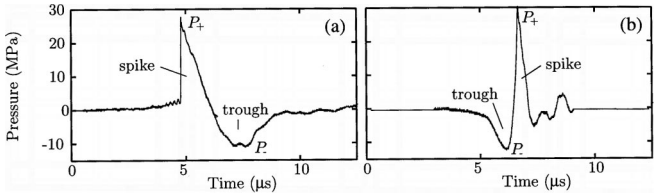

FIG. 1. Comparison of acoustic waveforms measured at the focus of (a) a rigid ellipsoidal reflector and (b) a pressure-release ellipsoidal reflector. Peak positive and negative pressures (P_+ and P_-), durations, and rise times are comparable, but the waveforms differ in shape. In (a) the spike comes before the trough, and in (b) the spike comes after the trough.

attempt is made to preserve the amplitude of the acoustic pulse. Castor oil is used, for example, because it is acoustically well matched to water. All three methods have disadvantages in that they affect the biological system being measured and make measurements in living systems difficult. For example, cells in castor oil may not be as healthy as cells in water.

A fourth approach is to change the conditions of the sound on the producing end so as to exploit cavitation's sensitivity to waveform. Short-pulse waveforms have previously been manipulated in bioeffects studies, and cavitation has been inferred as the affected mechanism of action. Bailey *et al.*[19] found that equal-amplitude positive and negative pressure pulses, anticipated respectively to excite and not to excite inertial cavitation, produced equal sized hemorrhages in bubble-rich tissue (e.g., lung). They concluded that the tissue studied constrained bubble expansion and that conventional growth and inertial collapse of the bubbles was not the mechanism of the observed damage. Tavakkoli *et al.*[20] compared two pulse shapes produced by a piezoceramic bowl and found differences in liver tissue ablation which they attributed to differences in cavitation. Instead of varying the individual pulses, Delius and Brendel[21] varied the time between lithotripter pulses. They found that a 15-Hz repetition rate caused more hemolysis *in vivo* than a 1-Hz rate and proposed that at the high repetition rate, the bubbles created by one pulse had not dissolved before the next pulse arrived and thus acted as cavitation seeds for the latter.

Waveform manipulation of cavitation has also been observed directly and calculated numerically. Müller's work[22] is of particular interest because he compared rigid and pressure-release ellipsoidal reflectors albeit in a different arrangement from that in ESWL. In schlieren images of the shock front produced by the pressure-release reflector, Müller observed bubble-created shock waves that were not present when the rigid reflector was used. He concluded that cavitation was greater with the pressure-release reflector. Our work and Müller's work are compared in Sec. III of this paper. A survey of clinical devices by Coleman and Saunders[23] showed one manufacturer had already electrically effected a change of waveform in its piezoceramic lithotripter, the EDAP LT-01. Using a code devised by Church,[11] Church and Crum[2] numerically calculated the radial response of a single bubble to various lithotripter pulses and found that the pressure amplitude of the shock radiated at bubble collapse was higher with the EDAP waveform than with the conventional rigid-reflector waveform. Ding and Gracewski[24] modified Church's code to investigate the effect of positive and negative pulses and sequences of pulses on constrained bubbles. Their results support the conclusions by Bailey *et al.*[19] and showed that a second pulse could intensify cavitation. Bailey[25] showed numerically and experimentally that a second pulse could be added during the growth phase of the bubbles to mitigate collapse or during the collapse phase to intensify collapse.

In this paper we compare the cavitation fields produced in water by a rigid reflector and a pressure-release reflector. Bubble radius and acoustic emission were calculated numerically as functions of time. Shock waves generated by bubble collapse were measured with a passive, focused hydrophone. The spatial field of collapsing bubbles was recorded as pits in aluminum foil, which were measured by a profilometer. By defining the cavitation fields produced by the rigid and pressure-release reflectors, this paper provides the groundwork for the comparative study of cavitation's role in biological effects.

I. METHODS

Relative cavitation intensity was assessed experimentally by the depth of pits in aluminum foil and numerically by the pressure radiated by a collapsing bubble. Bubble duration was measured by passive cavitation detection and calculated from radius versus time curves. The experimental and numerical methods are described in this section.

A. Sound source, water bath, and reflectors

The water bath, spark source, and reflectors are described in detail in Paper I.[1] In summary, an electrical spark was located underwater at the internal focus $F1$ of an ellipsoidal reflector, which was either rigid (brass) or pressure-release (polyurethane foam). See Fig. 2 in Paper I. The pressure-release reflectors, used here and in Paper I, showed no visible deterioration and produced no observable change in waveform after 2000 sparks at 18 kV, and none was used with more than 2000 sparks. The reflector dimensions (27.6- and 15.5-cm axes) and spark energy (18 kV, 80–100 nF) were the same as those in a Dornier HM-3 lithotripter. Refurbished Dornier electrodes (Service Trends, Kennesaw, GA) were used, and the water bath was 22 °C and degassed to 4 parts per million of oxygen by following Procedures B4.2 and B11.3 in IEEE Std. 790-1989.

Experimental measurements were made at the external focus $F2$ of the reflectors. Two techniques—passive acoustic detection and foil pitting—were used to map the cavitation field. In addition, cavitation was filmed with a high-speed digital camera and recorded on video tape.

B. Cavitation imaging by high-speed digital photography

Cavitation in the water tank was filmed with a Kodak Ektapro 4540 high-speed digital camera (Eastman Kodak Company, Rochester, NY) at a rate of 40 500 frames per second (i.e., each frame was exposed for 25 μs). We used a 150-mm lens with and without a 2×magnifying lens. The

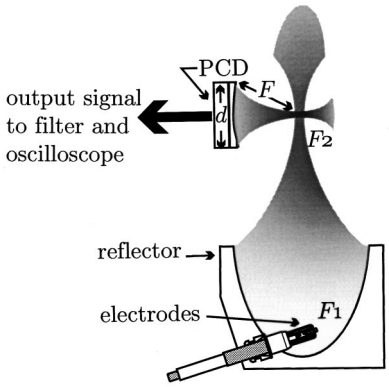

FIG. 2. Confocal arrangement of the spark/reflector lithotripter and the passive cavitation detector (PCD). The directive field of the PCD permits detection of acoustic emission from bubbles excited by the lithotripter. The focal spot of the PCD has a cigar shape 20 mm long and 4 mm across.

focal area was back lit with a 1000 W flood light and was filmed through the acrylic wall of the tank. The sensor had 256×256 pixels, and images were presented in 256 greyscale levels. The 10- or 20-mm-square images (30-mm depth of focus) captured the cloud of bubbles growing and collapsing along the lithotripter axis which ran from lower right to upper left in the image. Images were stored on VHS video tape.

C. Passive acoustic detection of cavitation

The passive (acoustic) cavitation detector (PCD)[15] recorded the shock waves emitted during bubble collapse.[13] Figure 2 shows the arrangement of the PCD for cavitation detection. The acoustic axes of the lithotripter and the PCD were perpendicular and confocal. The cavitation field of the lithotripter was mapped by scanning the focus of the PCD along and across the axis of the lithotripter.

The piezoceramic sensing element of our PCD was concave. Its radius of curvature F was 100 mm, its aperture diameter d was 100 mm, and its resonance frequency was 1.08 MHz. The PCD cable was connected to the oscilloscope via a Krohn-Hite model 3202 filter. The output signal was high-pass filtered (300 kHz) to remove noise (~20 kHz) created by excitation of a radial resonance of the sensing element.[13] A 1-V signal amplitude recorded by the filtered PCD corresponded to a shock wave pressure amplitude of 9.5 MPa 10 mm from the center of the cavitation bubble. The calibration method was devised and described by Cleveland *et al.*[15] They solved for the calibration value with the equation

$$\frac{P(r_0)}{V_{\text{peak}}} = \frac{F\tau_*}{2G_0 r_0 \tau(r_0)} = 9.5\,\text{MPa/V}, \tag{1}$$

where $P(r_0)$ is the peak pressure at $r_0 = 10$ mm from the bubble center, and V_{peak} is the peak voltage of the filtered PCD signal. The duration $\tau(r_0) = 35$ ns of the shock wave emission 10 mm from a bubble was obtained from measurements by Vogel and Lauterborn.[10] The decay constant $\tau_* = 7.4\,\mu$s of the PCD impulse response and the sensitivity ($G_0 = 111$ V/MPa) at the resonance frequency of the PCD were measured by Cleveland *et al.*[15]

Two spikes (and ringing due to the PCD) make up the PCD signature when a conventional lithotripter (rigid reflector) is used [look ahead to the left side of Fig. 8(b)]. The first spike occurs when the lithotripter pulse first interacts with any bubbles initially present in the focal region. The spike results from nonlinear scattering from bubbles (i.e., a combination of simple scattering and sound generated by the bubble motion), and bubbles are practically unavoidable in the large volume of water used, despite our efforts to degas the water.[26,27] The bubbles then grow and collapse. A second spike is emitted when the collapse halts. The time between the spikes is the bubble duration during which the bubble grows to its maximum radius and collapses. When the rigid reflector is used, longer bubble duration is correlated with stronger bubble collapse.[11] The time for bubbles to dissolve into solution is another issue not addressed in this paper, but conceivably bubbles that grow larger and take longer to collapse will dissolve more slowly and therefore be more likely to exist as cavitation seeds for subsequent lithotripter pulses.

D. Cavitation detection by pitting of aluminum foil

Cavitation was also detected by observing the pitting produced in aluminum foil. The PCD records bubble duration as described above; the foil records a relative measure of the intensity of bubble collapse. Pitting of aluminum foil is a well-documented,[3,28] highly sensitive method of detection; one pulse produced by our lithotripter charged to 18 kV creates visible pitting. In this investigation, one pulse was used per foil (unless otherwise stated), the foils were positioned along the acoustic beam on the axis of symmetry of the reflector, not perpendicular to it, and the pitted foils were imaged directly on a flatbed digital scanner. Positioning the foil along the beam, rather than perpendicular to it,[3,28] is new. High-speed video images (not shown) recorded no change in the growth and collapse of the cavitation cloud with and without the foil present, and PCD signals likewise were unchanged as reported in Sec. II B.

Figure 3 shows the foil-pitting arrangement. Kraft standard food service aluminum foil (Kraft Foodservices Inc., Dist., Glenview, IL), nominally 18 μm thick, was glued to a thin (0.165 cm thick) semicircular plastic frame (78 mm i.d. and 86 mm o.d.). The frame/foil packet was held in the water bath on a thin aluminum V-shaped mounting. The foil end facing the lithotripter was held taut by springs but otherwise left free, so as to minimize disturbance of the sound field.

The depth and size of the pits were measured with a Alpha Step 500 surface profiler (Tencor Instruments, Mountain View, CA). The exposed foil packet was taped to an aluminum plate and dipped in methanol. After cleaning the foil, the methanol evaporated, leaving the foil clinging flush to the flat plate. This process of getting the foil to meet flush with the plate minimized gross wrinkle on the foil without disturbing the pits caused by cavitation. The plate and foil were then placed in the profilometer. The profilometer scanned the foil in steps using a stylus. The stylus descended, sensed contact, recorded the height, ascended, made a horizontal step, and repeated the process. The stylus touched the foil but left no discernible impression. Repeated scans were identical. The vertical resolution was 2.5 nm, and

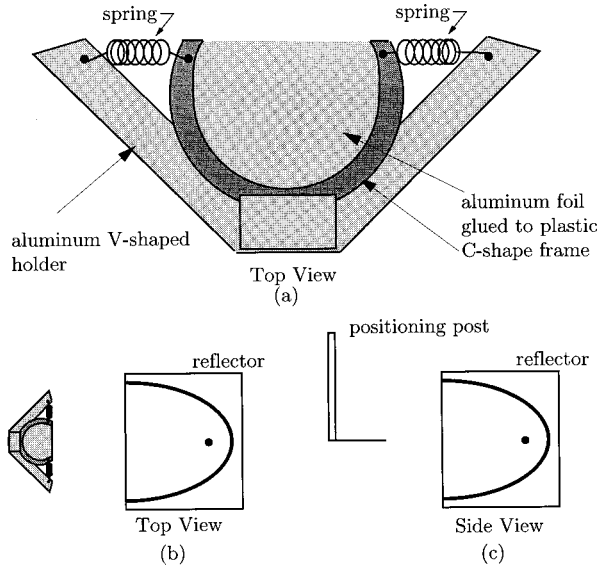

FIG. 3. (a) Top view of aluminum foil mounted on a plastic C-shaped frame that was attached to a V-shaped holder. (b) Top view of foil and holder positioned at $F2$ of the reflector. (c) Side view of foil and holder positioned at $F2$ of the reflector. Pitting of the foil by collapsing bubbles created a spatial map of the cavitation field produced by a single lithotripter shock wave.

the horizontal steps were 4 μm. Three linear scans (randomly chosen but within 10 mm of $F2$), each 1 cm long, were made across sections of three separate foils, and the average depth and width of measured pits was calculated.

E. Numerical prediction of cavitation

The radial response of a single spherical bubble driven by a lithotripter pulse and the acoustic pressure radiated by the excited bubble were found by numerical calculation. A single bubble is taken to be representative of the behavior of the bubble cloud excited in lithotripsy. Because our experiments were done in a large water bath, a free-field model was assumed. The Gilmore-Akulichev formulation was used as described by Church.[11]

1. The model

Fundamental assumptions of the model are as follows: a single bubble exists in an infinite medium; the bubble remains spherical at all times; the interior of the bubble is spatially uniform; the initial radius of the bubble R_0 is much less than the characteristic length of the acoustic excitation; body forces (e.g., gravity) have negligible effect on the bubble motion; bulk viscous effects can be ignored; the bubble is initially at equilibrium; gas content in the bubble is constant (i.e., no diffusion, mass transfer, or evaporation takes place across the bubble wall); the gas within the bubble behaves as an ideal gas; and flow in the liquid around the bubble is isentropic. Because dissipation is generally neglected, the model leads to an upper bound on the degree of radial bubble pulsation and the amplitude of the pressure wave radiated. Our goal was not to predict absolute amplitudes, but to investigate relative differences between the rigid and pressure-release reflectors.

The radial motion of the bubble is described by the Gilmore equation,[29]

$$R\left(1-\frac{U}{C}\right)\frac{dU}{dt}+\frac{3}{2}\left(1-\frac{U}{3C}\right)U^2 = \left(1+\frac{U}{C}\right)H+\frac{U}{C}\left(1-\frac{U}{C}\right)R\frac{dH}{dR}, \tag{2}$$

where R is the bubble radius, $U(=dR/dt)$ is the velocity of the bubble wall, C is the speed of sound in the water at the bubble wall, and H is the difference between the specific enthalpy in water at the bubble wall relative to the specific enthalpy in the water far from the bubble. The terms on the left side of Eq. (2) are inertial terms and those on the right side represent the work done by the difference in the pressure at the bubble and far from the bubble. Acoustic pressure, which drives the bubble, enters through C and H, which are functions of pressure.

Pressure p and density ρ of the water are related by a modified Tait equation[30,31]

$$p=A(\rho/\rho_0)^n-B, \tag{3}$$

where A, B, and n are empirical constants and ρ_0 is the equilibrium density of the liquid. (In calculations relevant to lithotripsy, the approximation is inaccurate for the short time periods in bubble collapse when pressure in the liquid exceeds 10^4 MPa.[11]) Given Eq. (3), the specific enthalpy is

$$H=\int_{p_\infty(t)}^{p(R,t)}\frac{dp}{\rho}=\frac{nA^{1/n}}{(n-1)\rho_0}\{[p(R,t)+B]^{(n-1)/n} -[p_\infty(t)+B]^{(n-1)/n}\}, \tag{4}$$

and sound speed is

$$C=\sqrt{\frac{dp}{d\rho}}=[c_0^2+(n-1)H]^{1/2}, \tag{5}$$

where $c_0=\sqrt{An/\rho_0}$ is the linear sound speed of the liquid, p_∞ is the pressure (hydrostatic and acoustic) of the liquid far from the bubble, and $p(R,t)$ is the pressure of the liquid at the bubble interface.

The sound wave P_r radiated by the pulsating bubble is calculated using an approximation made by Akulichev[32] and described by Church.[11] The approximation is

$$P_r=A\left\{\frac{2}{(n+1)}+\frac{(n-1)}{(n+1)}\left[1+\frac{G(n+1)}{rc_0^2}\right]^{1/2}\right\}^{2n/(n-1)}-B, \tag{6}$$

where r ($\geqslant R$) is the distance in the water from the center of the bubble and $G=R(H+\frac{1}{2}U^2)$. Calculations given in this paper were made for $r=10$ mm, because $r=10$ mm is near the bubble but not so near that the bubble grew beyond the calculation point. We use the peak radiated pressure $P_r^{\max}$ as a numerical measure of the intensity of collapse and compare it to the pit depth in the foil, which we consider to be an experimental measure of collapse intensity, or the destructive power of the bubble. The foil does, however, record many

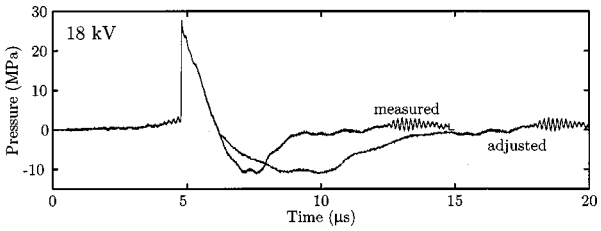

FIG. 4. Rigid-reflector waveform measured with an unshielded PVDF-membrane hydrophone and adjusted waveform with lengthened trough to correct for the shortening caused by the membrane hydrophone and measured by Staudenraus and Eisenmenger (Ref. 33).

pits from many bubbles, whereas only a single bubble is considered in the model.

2. Our implementation

The code used in the investigation reported here was written in MatLab (The Math Works, Inc., Natick, MA). The native fourth- and fifth-order Runga–Kutta routine with automatic time stepping was used to solve the Gilmore equation. Some physical constants appropriate for water and an ideal gas at 30 °C that were used in our code are $n=7$, $A=300.1$ MPa, $B=300$ MPa, $p_0=0.1$ MPa, $\rho_0=995.646$ kg/m^3, $c_0=1509.7$ m/s, viscosity $\mu_0=0.0008019$ Ns/m^2, surface tension $\sigma=0.071035$ N/m, and the ratio γ of specific heats of the gas equals 1.4.[24] Initial bubble radius was 2 μm. Our code can use either analytical or measured waveforms as forcing functions. For measured waveforms, linear interpolation was used to generate a waveform defined at each desired time step. The longest cases took nearly 3 hours to run on a 70-MHz Macintosh Power PC 7100 with 24 MB of RAM.

Since measured pulses vary because of random variation in strength, shape, and location of successive sparks (i.e., spark jitter), calculations were made using ten separate pulses measured with the same reflector and voltage. The calculated values of $P_r^{\max}$ and bubble duration t_c were averaged. Standard deviation in peak positive pressure P_+ of measured pulses was approximately 30%. Standard deviation in peak negative pressure P_- of measured pulses and in calculated values of $P_r^{\max}$ and t_c was approximately 15%.

3. An adjustment to PVDF-measured waveforms

Using a fiber-optic hydrophone, Staudenraus and Eisenmenger[33] measured waveforms at the focus of a Siemens Lithostar lithotripter and found that the trailing trough was 267% longer than that measured when using a hydrophone with an unshielded polyvinylidene difluoride (PVDF) membrane. By ''unshielded'' we mean not coated with metal electrical shielding. They proposed that under strong negative pressure, the water tore away from the metalized sensitive element of the membrane hydrophone and thus cut short the trough on the measured waveform. Because water–glass adhesion is much stronger (in fact stronger than water–water cohesion), they believe the fiber-optic hydrophone measured the full trough length. Recorded trough depth was the same for both hydrophones. Waveforms measured by Jöchle *et al.*[34] with a fiber-optic hydrophone corroborate Staudenraus and Eisenmenger's results. Based on Staudenraus and Eisenmenger's work, we propose lengthening the trough of membrane measured waves by 267%. The original and adjusted waves are shown in Fig. 4. Because Staudenraus and Eisenmenger and Jöchle *et al.* do not have data for a pressure-release ellipsoidal reflector, no adjustment of our pressure-release-reflector waveforms was attempted. However, because the waveforms of the pressure-release reflector end with a strong positive spike rather than a long shallow trough, no correction may be needed.

The correction to the duration of the trough of the pulse is new, and results with and without the correction are compared later in this paper. In defense of the correction, we note that, in his original paper describing the Gilmore code, Church[11] reported that a numerical analysis based on a pulse measured with a PVDF-membrane hydrophone yielded bubble durations t_c that were less than half as long as bubble durations that had been (or have been) measured.[35–37] Church did make a correction, but to the amplitude of the pulse. However, the pulse that he created to produce bubble durations comparable with measured bubble durations had a peak negative pressure P_- of -33 MPa. Negative 33 MPa is at least double the P_- that has been measured in a conventional lithotripter by either a PVDF-membrane or a fiber-optic hydrophone. The downside to our correction may be that the time integral of the pressure waveform is not necessarily zero. Church was careful to maintain a zero integral, but the zero integral was proven for spherical waves and does not have to hold for plane waves.[38] Whether or not focused lithotripter waves must yield a zero integral is not known, and, in fact, the time integral of the pressure waveform as measured is not necessarily zero either. In summary, we think the proposed correction to the length of the negative tail is preferable to correcting its amplitude.

II. RESULTS AND DISCUSSION

Cavitation produced by a rigid and a pressure-release reflector is compared here. Individual cavitation events and the cavitation field were investigated. In Sec. II A measurements of foil pits are compared with calculated values of $P_r^{\max}$. In Sec. II B bubble durations measured by PCD are compared to numerically calculated t_c. In Sec. II C t_c and $P_r^{\max}$ are compared for waveforms with artificially enlarged or reduced positive spikes. Finally, in Sec. II D the spatial extent of the cavitation fields is reported.

A. Pit depth and $P_r^{\max}$

Pitting produced by the rigid reflector (ten pulses) and by the pressure-release reflector (ten pulses) is shown in Fig. 5. The foil was positioned identically in both cases. The small, shallow pits produced by the pressure-release reflector are in strong contrast to the large, deep pits produced by the rigid reflector. Indeed ten pulses were necessary because a single pulse from the pressure-release reflector did not produce pitting sufficient to be observed by the unaided eye. Subsequent data reported here are for single shots.

Figure 6 compares the calculated $P_r^{\max}$ and measured pit depth for the rigid reflector and the pressure-release reflector. Figure 6(a) plots the peak acoustic amplitude $P_r^{\max}$ generated

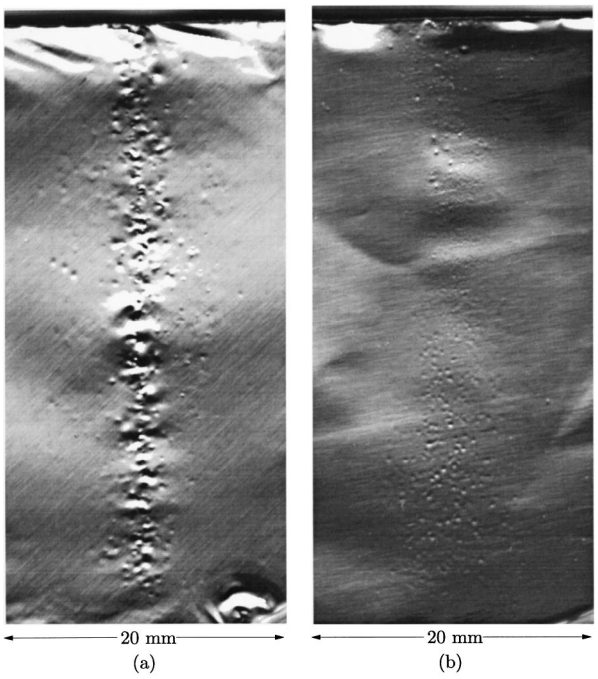

FIG. 5. Comparison of aluminum foil pitting by ten pulses produced by (a) a rigid reflector and (b) a pressure-release reflector. Bubbles pit the foil from both sides. No preferred direction is expected or observed. The foil edge at the top of the page was nearest to the reflector.

by a 2-μm bubble at $F2$, as calculated using Eq. (6). Calculations were made with each of ten separate measured waveforms produced by the rigid reflector and ten waveforms produced by the pressure-release reflector. Averages and sample standard deviations of $P_r^{\max}$ are reported. The rigid reflector produced $P_r^{\max}=85\pm10$ MPa, a value more than 13 times that for the pressure-release reflector. Although $P_r^{\max}$ was less (29 ± 5 MPa) when the rigid-reflector waveform was not adjusted as discussed in Sec. I E 2, it was still nearly five times the value (6 ± 2 MPa) calculated for the pressure-release reflector. Figure 6(b) and (c) shows the depth and width of bubble-induced pits in aluminum foil. Measurements in Fig. 6(b) and (c) were made from three separate scans on three separate foils. Each foil received one pulse from either the pressure-release reflector or the rigid reflector. Averages and sample standard deviations are shown. For the rigid reflector the pit depth was 24 ± 8 μm, the width 1.6 ± 0.4 mm. Corresponding values for the pressure-release reflector are 8 ± 2 μm and 0.2 ± 0.05 mm, respectively. Pits produced by the rigid reflector were three times deeper and eight times wider. Deeper pits correlate with the higher calculated $P_r^{\max}$.

B. Bubble duration

In Sec. II A we showed that cavitation produced by a rigid reflector produced larger pits and higher $P_r^{\max}$. In this section numerical calculations and PCD measurements were used to determine the length of time over which cavitation occurred. Pressure-release and rigid reflectors are again compared.

Each lithotripter pressure pulse acts as a forcing function for any bubble present at $F2$. Figure 7 shows the calculated

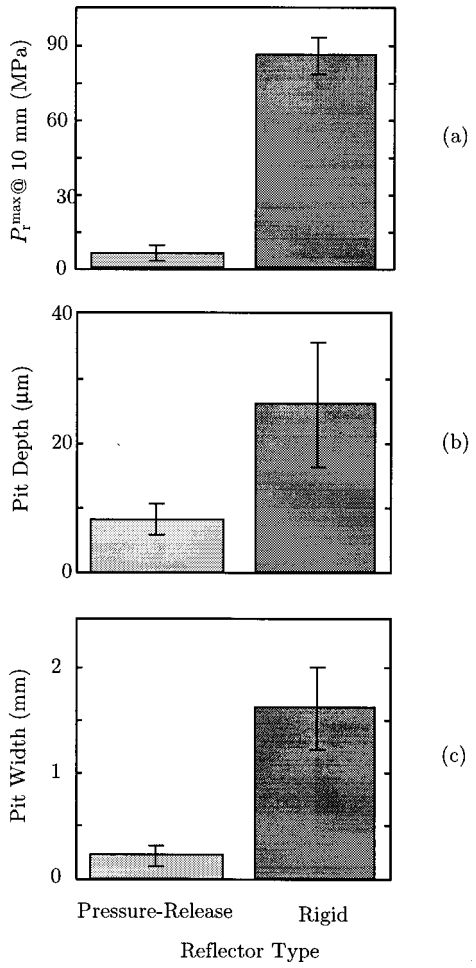

FIG. 6. Various measures of cavitation produced by a pressure-release reflector (left) and a rigid reflector (right): (a) calculated maximum amplitude $P_r^{\max}$ of the acoustic emission radiated by the collapsing model bubble, (b) measured depth of pits in aluminum foil, and (c) measured width of pits in aluminum foil.

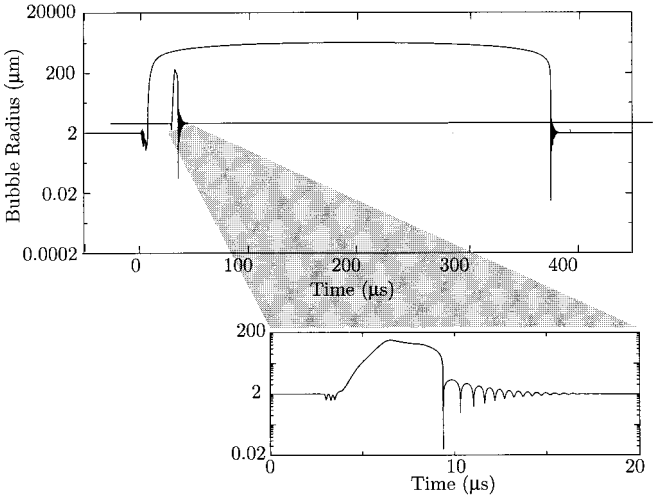

FIG. 7. Comparison of numerically calculated radius versus time curves due to the pressure pulses shown in Fig. 1. The curve for the pressure-release reflector was offset to distinguish the two curves, and an expanded version of the pressure-release-reflector curve is included.

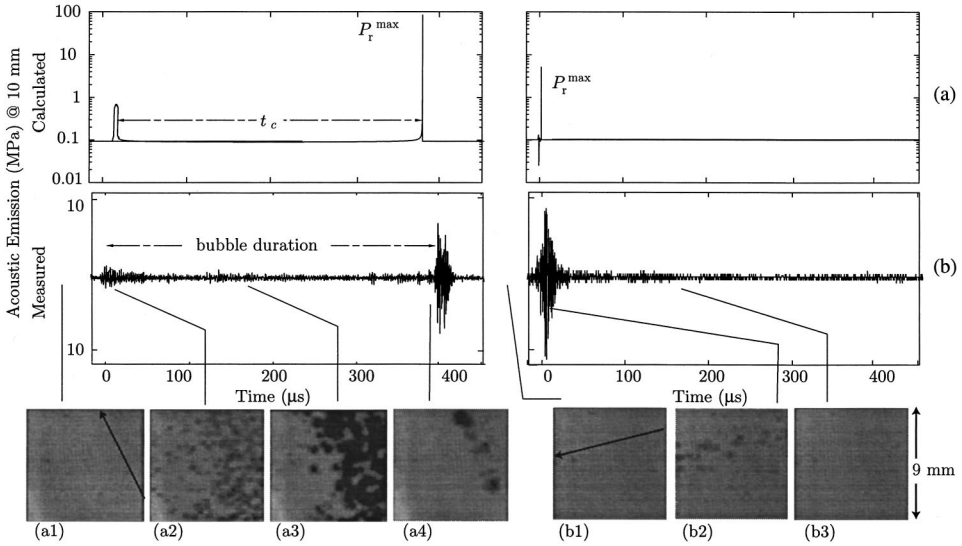

FIG. 8. Calculated (a) and measured (b) acoustic emissions produced by bubbles excited by the rigid reflector (left) and the pressure-release reflector (right). Two emission spaced nearly 400 μs apart are seen on the left, and one emission nearly coincident with the pulse arrival is seen on the right. High-speed video images (a1)–(a4) and (b1)–(b3) filmed simultaneously with the PCD recordings (b) show the growth and collapse of the bubble cloud over 400 μs on the left and within the resolution of a single frame (25 μs) on the right.

bubble response, in the form of a radius versus time ($r-t$) curve, for the lithotripter pulses shown in Fig. 1. The leading spike of the pulse produced by the rigid reflector initially crushes the bubble. Then the trailing trough triggers a growth-and-collapse cycle that lasts far longer than the driving acoustic pulse. The long growth and collapse phases are driven by the inertia of the water, and it is the pressure difference across the bubble interface that initiates or halts the bubble motion. The bubble grows very large before it implodes, and the tiny minimum radius achieved indicates the power of the collapse. The pulse from the pressure-release reflector initially causes the bubble to grow because of the leading pressure trough, but growth is quickly stifled by the trailing positive spike. An immediate collapse of the bubble ensues, but the collapse is weak because the bubble does not grow as large or collapse as small as the bubble forced by the rigid reflector pulse. The rigid-reflector pulse produces a growth-and-collapse cycle 380 μs long. The pressure-release reflector produces a growth-and-collapse cycle less than 7 μs long. The rigid-reflector cycle is more than 50 times longer.

Figure 8 compares calculated and measured acoustic emissions produced by bubbles excited by the rigid reflector and the pressure-release reflector. Pressure spikes which correspond to local minima in Fig. 7 are produced when the in-rushing water halts and is suddenly pushed outward again by the compressed gas in the bubble. The lithotripter pulse impinges on the bubbles at 0 μs and the time when the strongest emission spike appears is when the bubbles collapse. The time in between is the bubble duration.

When the rigid reflector is used, acoustic emissions are generated at 0 μs and much later at approximately 400 μs. The calculation shows only the two spikes, and the average t_c for ten such calculations is 380 ± 50 μs. The measurement also shows two signals, each a damped sinusoid and not a narrow spike because the PCD is narrowband and rings. The ringing is, however, accounted for in the impulse calibration technique,[15] and the average spacing between signals in ten successive measurements was 380 ± 40 μs. Agreement in bubble duration between theory and measurement is excellent.

When the pressure-release reflector is used, only one emission is generated. The single emission is nearly coincident with the arrival of the lithotripter pulse. Calculated and measured bubble durations agree to within the resolution of the PCD, and when the pressure-release reflector is used in place of the rigid reflector, the bubble durations are more than an order of magnitude shorter.

High-speed photographic frames (a1)–(a4) and (b1)–(b3) show the growth and collapse of the bubble cloud along the axis of the rigid and pressure-release reflectors, respectively. Arrows in (a1) and (b1) indicates the axes of the reflectors. Many small bubbles appear in (a2). The bubbles grow and the cloud consolidates on the axis in (a3). In (a4) the bubbles collapse. Frames (b1)–(b2) show that small disperse bubbles appear only briefly on the axis of the pressure-release reflector.

When the rigid reflector is used, agreement between the calculated and measured timing is excellent not only at 18 kV, but for a range of charging potentials as shown in Fig. 9. However, without the adjustment to the length of the negative tail, the cavitation cycle calculated for the rigid-reflector waveform at 18 kV is only 144 ± 15 μs which is nearly $\frac{1}{3}$ of the measured value. With or without the correction, t_c in-

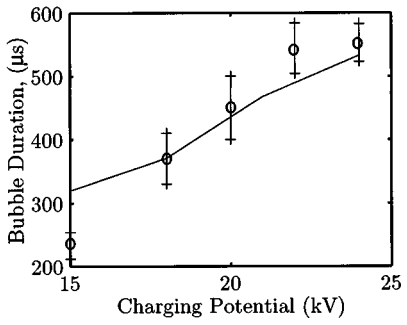

FIG. 9. Bubble duration calculated numerically with the Gilmore code (line) and measured with the PCD (circles). The PCD results are the mean of ten measurements, and the bars show the standard deviation. The calculations have a standard deviation of 15% which is due to the variation of waveforms that are measured and used as inputs.

creases with input potential, and $P_r^{\max}$ increases with t_c. When the pressure-release reflector is used, the measured and calculated signals appear within 40 μs of the arrival of the pulse regardless of the voltage. The ringing in the PCD inhibits finer resolution.

The peak absolute and relative amplitudes of the PCD signals are not in good agreement with the calculated $P_r^{\max}$ values. When the rigid reflector is used, measured pressures are approximately $\frac{1}{10}$ of calculated pressures. The factor of 10 is consistent with other works[10,15] and has been attributed to gas diffusing into the real bubble[11] and to natural asymmetries that arise in the collapse of the real bubble but that are not accounted for in the model. When the pressure-release reflector is used, the measured amplitude is nearly equal to that calculated; however, it is as large or larger than the pressure amplitude produced when the rigid reflector is used. The larger amplitude measured is in contradiction to the smaller pits measured and lower $P_r^{\max}$ calculated when comparing the pressure-release reflector to the rigid reflector. We speculate that most of the signal in right panel of Fig. 8(b) was not acoustic emission but rather scattering of the trailing spike of the incident shock wave by the bubbles that were grown by the leading trough. A test of a degassed rigid scatter placed at $F2$ reveals an equally strong initial signal in the rigid-reflector signature. We attribute these strong signals to scattering, not emission by cavitating bubbles. Note that no difference in the bubble duration or in the amplitude of the second signal was observed between the PCD recordings with and without foil at $F2$, which indicates that the presence of the foil did not alter the cavitation field.

C. Effect of the trailing positive spike.

Our contention is that bubble collapse pressures are mitigated by the trailing positive spike in the waveform generated by the pressure-release reflector. In this section, numerical results are presented to demonstrate the effect of a trailing positive spike on cavitation bubble dynamics. First the spike amplitude is set to zero and only the trough of the waveform in Fig. 1(b) is used to calculate t_c and $P_r^{\max}$. Then we increase the amplitude the spike trailing the trough in Fig. 1(b) and calculate $P_r^{\max}$. Finally, we calculate t_c and $P_r^{\max}$ produced by idealized pulses with equal troughs and different positive spikes.

Here a trough and a trough-then-spike pulse are compared. When the full waveform in Fig. 1(b) is used as the driving pulse in our code, $t_c=7\ \mu$s and $P_r^{\max}=12$ MPa. When the trough alone in Fig. 1(b) is used (e.g., when the spike is removed), $t_c=95\ \mu$s and $P_r^{\max}=37$ MPa. In other words, when the spike is present after the trough, t_c is $\frac{1}{13}$ as long, and $P_r^{\max}$ is $\frac{1}{3}$ as large.

However, the ratio of the area $\int p\,dt$ of the spike to the area of the trough may determine whether $P_r^{\max}$ is higher when the driving pulse contains a trailing spike or a trailing trough. We calculate a lower $P_r^{\max}$ when we use our trailing-spike pulse than when we use our trailing-trough pulse. In apparent agreement with our result, Tavakkoli *et al.*[20] saw less tissue damage which they attributed to weaker cavitation when they used a trailing-spike pulse than when they used a trailing-trough pulse. However, in contrast to our result, Church and Crum,[2] who included in their bubble simulation an approximation of gas diffusion into the bubble, calculated a higher $P_r^{\max}$ with a trailing-spike pulse than with the conventional trailing-trough pulse. Although we neglected diffusion, we suspect our different results stem from different area ratios

$$\mathrm{AR}=\frac{\int p_{\mathrm{spike}}\,dt}{\left|\int p_{\mathrm{trough}}\,dt\right|} \tag{7}$$

in our pulse and that of Church and Crum. Church and Crum's area ratio was approximately 10. Our trailing spike was relatively much weaker, AR$\approx$2.

In two numerical tests—one with the measured waveform in Fig. 1(b) and the other with idealized waveforms—the amplitude of the trailing spike and hence the area ratio was varied. The amplitude of the leading spike of a conventional lithotripsy pulse has been shown previously[24] to have negligible effect on t_c and $P_r^{\max}$; however, our hypothesis was that a strong (large area ratio) trailing spike can intensify bubble collapse and a weaker trailing spike like ours can mitigate collapse. In the first test, we multiply the amplitude of the trailing spike in Fig. 1(b) by five to obtain AR$\approx$10. We find that the $P_r^{\max}$ increases from 6 to 38 MPa and is greater than the 29 MPa produced by the conventional rigid-reflector pulse. These results agree with Church and Crum's findings. In the second test, the bubble response to idealized waveforms is considered. Three waveforms were constructed from triangular sections and are shown in Fig. 10 (left column). The waveforms consist of a -10-MPa trough followed by no spike, a $+15$-MPa spike, or a $+5$-MPa spike. Troughs and spikes are 1 μs in duration. When the trough alone (top left in Fig. 10) is used, $t_c=37\ \mu$s and $P_r^{\max}=6$ MPa (top right). When the trough with the $+15$-MPa trailing spike (middle left in Fig. 10) is used, t_c is shorter, but $P_r^{\max}$ is 1.5 times larger (9 MPa). When the trough with the $+5$-MPa trailing spike (bottom left in Fig. 10) is used, t_c is again shorter, but $P_r^{\max}$ is $\frac{1}{3}$ as large (2 MPa). Bubble duration t_c is not, in these cases, a reliable indicator of $P_r^{\max}$. The results corroborate the hypothesis that a strong positive spike after the pressure trough intensifies collapse, but a weak spike mitigates collapse.

D. Cavitation fields of the rigid and pressure-release reflectors

In this final results section, data are presented on the spatial extent of the cavitation fields produced by rigid and pressure-release reflectors. Both reflectors produce cavitation over a narrow area several centimeters long. The spatial mappings of the cavitation fields are reported here.

The cavitation field produced by the rigid reflector is very narrow. Three measures of the narrowness are shown in Fig. 11. A 1- to 2-mm-wide path is indicated by aluminum foil pits (a) and by the video frame (b) taken during bubble collapse. Figure 11(c), a plot of peak measured emission versus transverse position, has a 6-dB width of about 5 mm which is at the resolvable limit of the PCD. Each foil pitting and video photography measurement is the result of a single

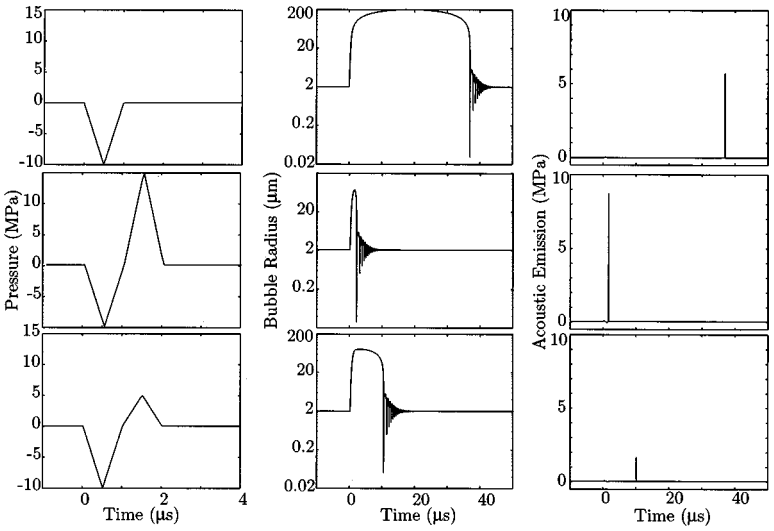

FIG. 10. Numerical calculation of the radial response (center) of a single bubble to the waveform (left) and the resulting acoustic emission (right). The waveforms have a −10-MPa trough followed by a 0 MPa (top), +15 MPa (middle), or +5 MPa (bottom) pressure spike. Troughs and spikes are 1 μs in duration.

lithotripter pulse. The PCD measurement is an average of ten pulses at each location. The amplitude of the measured acoustic emission dropped as the focus of the PCD was moved away from the lithotripter axis at $F2$. The amplitude decay and the observation that the recorded bubble duration was 350 ± 40 μs for all positions implies that off axis, weaker, earlier collapses were not detected, but rather that for each pulse the PCD detected a collapse on the lithotripter axis.

Figure 12 shows that the rigid reflector produced collapse emissions and pits in foil over an 80–90-mm length along the axis of the lithotripter. Figure 12(a) plots PCD-measured bubble duration versus axial position. The line connects the mean of ten measurements taken at each location. Bars show the standard deviation. The peak bubble duration is at $F2$, where the rigid reflector produces the maximum negative pressure,[1] and not at $z=+20$ mm, where the reflector produces the maximum positive pressure. Peak negative and positive pressure were determined by PVDF membrane hydrophone, and a spatial map of the pressure field was presented in Paper I. Figure 12(b) shows three foils, one pulse each, that were used to map the axial field. To obtain image (b), a foil was placed along the axis centered in front of $F2$, a spark was discharged, and the foil was removed. Then a foil was placed so that $F2$ was in the middle of the foil, a spark was discharged, and the foil was removed. The third foil was placed behind $F2$, and the procedure was repeated. In (b) the three foils are shown in their axial positions. The narrow streak of pits begins at $z=-40$ mm (40 mm in front of $F2$) and is well defined to $z=+30$ mm (30 mm beyond $F2$), where the pitting becomes weaker and the

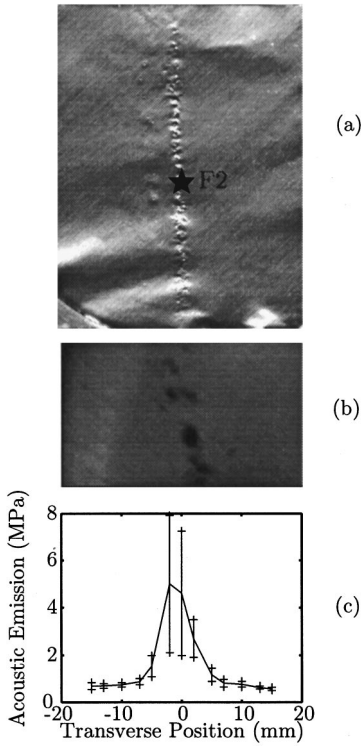

FIG. 11. Transverse cavitation field of the rigid reflector measured with (a) aluminum foil, (b) high-speed video camera, and (c) the passive cavitation detector (PCD). All are on the scale shown in (c).

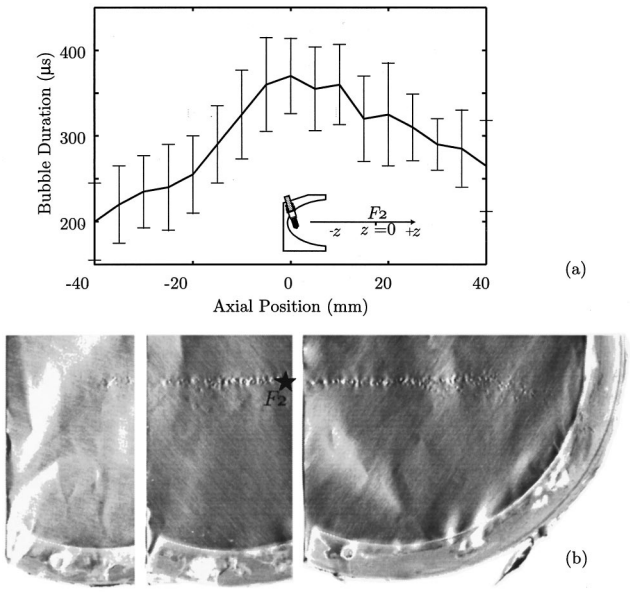

FIG. 12. Axial cavitation field of rigid reflector measured with (a) the PCD (ten pulse averages) and (b) aluminum foil (single pulse per foil). Positive z, along the outward normal axis of the reflector, has its origin at $F2$.

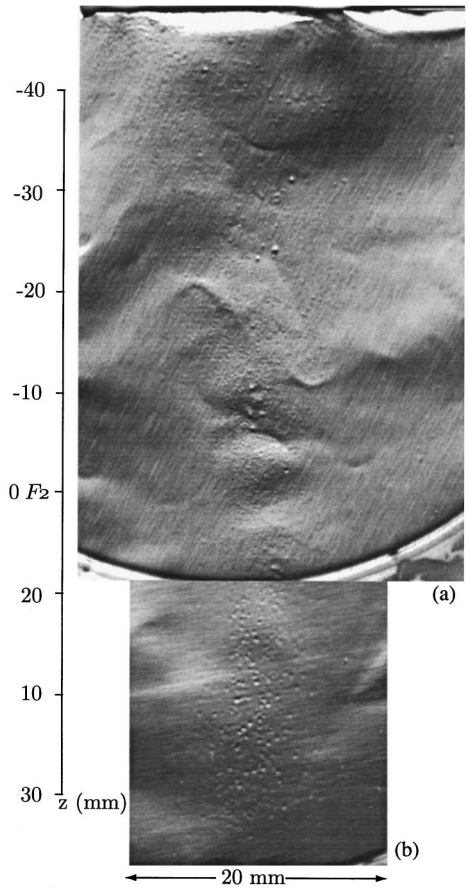

FIG. 13. Map of cavitation field produced by the pressure-release reflector. Foil (a) was centered at $z=-30$ mm and treated with ten pulses. Foil (b) was placed at $F2$ and treated with ten pulses.

streak diverges. After $z=+50$ mm no pitting is observed. The field was not investigated with the PCD beyond what is plotted.

A map of the cavitation field of the pressure-release reflector is presented in Fig. 13. Each foil was treated with ten pulses. The field is hourglass shaped. The width of the pit path is 15 mm at $z=-40$ mm, 2 mm at $F2$, and 9 mm at $z=30$ mm. The path is broader than that produced by the rigid reflector but has nearly the same length. It should be noted that when ten pulses produced by the rigid reflector are used (Fig. 5), spark jitter causes the rigid-reflector path to be broader ($\sim$10 mm) but not hourglass shaped. We propose that off-axis bubbles produced by the pressure-release reflector collapse before they can agglomerate along the reflector axis.

The size and density of the pits changes along the axis of the pressure-release reflector but not along the axis of the rigid reflector. For negative values of z, small, sparsely distributed pits are observed (Fig. 13). Tiny pits in a small dense cluster occur at $z=-10$ mm. For positive values of z, the pits are larger and again sparse. The acoustic waveform along the axis of the pressure-release reflector also changes, whereas that for the rigid reflector is more constant.[1] The pulse waveforms of the two reflectors are most similar for positive values of z, where the spike precedes the trough for both reflectors. Pits produced by the two reflectors also share the closest resemblance for positive values of z, where pits are large, smooth, and round.

The fine structure of the pits created at the focus of the pressure-release reflector may reveal evidence of bubble size and the shape of collapse. Coleman *et al.*[3] observed that pits produced by a rigid reflector have a toroidal shape that indicates asymmetric collapse. The structure of the pits recorded here was not studied under magnification and is beyond the scope of this paper.

III. SUMMARY AND CONCLUSIONS

Rigid and pressure-release reflectors produce different pulses that have equal amplitude.[1] In this paper, we have shown that the two pulses produce different cavitation. Cavitation-induced pits in aluminum foil are three times deeper and eight times wider when the rigid reflector is used. The calculated amplitude $P_r^{\max}$ of the shock wave radiated by the collapsing bubble is 13 times larger. Passive (acoustic) cavitation detection showed bubbles grow and collapse in 400 μs when the rigid reflector is used but in less than 40 μs when the pressure-release reflector is used. Calculated bubble durations are in excellent agreement with experimental results when the negative tail of the digitized, rigid-reflector waveform used as a numerical input is lengthened to correct for suspected misrepresentation by the PVDF membrane hydrophone. Cavitation is stronger and longer lived when the rigid reflector is used than when the pressure-release reflector is used.

The difference in cavitation is explained by a difference in the shape, not the amplitude, of the acoustic pulses produced by the two reflectors. The rigid reflector produces a positive-pressure spike followed by a negative-pressure trough; the pressure-release reflector reverses the order. When the spike comes first (rigid reflector), the spike crushes the bubble. The ensuing trough then triggers a growth-and-collapse cycle that is driven by the inertia of the surrounding water and lasts far longer than the pulse. The bubble grows very large before the pressure difference across the gas/water interface forces the bubble's violent collapse. When the trough comes first (pressure-release reflector), the bubble begins to grow, but growth is quickly stifled by the trailing positive spike. An immediate but weak collapse ensues.

Our measurements of the duration of cavitation events are in good agreement with previous studies based on schlieren measurements, which detect bubbles and the spherically diverging shock waves created when the bubbles collapse. Using a conventional lithotripter pulse, Carnell *et al.*[39] recorded an initial bubble collapse <5 μs after the shock wave and growing bubbles 5–100 μs after the shock wave. We anticipate images $\sim$400 μs after the passage of the shock wave would have recorded the primary inertial collapse of the bubbles. Müller,[22] using a pressure-release reflector, observed only cavitation collapse occurring 5–10 μs after the shock wave. Müller did not note cavitation activity with his rigid reflector perhaps because his arrangement was different from that used in lithotripsy (Müller recorded images at $F1$ with his spark source at $F2$) or, we propose, because the collapses occurred after the end of his imaging

period. Müller did observe that the acoustic emission of the bubble collapse propagated faster, and thus had higher amplitude, than the lithotripter pulse. We propose that in future schlieren studies, propagation speed be used as an aid to distinguish differences in bubble-collapse intensity.

In the study reported here, the size of pits created in aluminum foil and measured by profilometer have been used as a measure of bubble-collapse intensity. The foils were positioned along the axis of the reflector, not perpendicular to it, to allow mapping of the cavitation field produced by a single pulse. This arrangement also minimized the collection of bubbles that was created by successive pulses and propelled along the reflector's axis by radiation pressure. With foil positioned perpendicular to the reflector axis, radiation pressure yields a preferential pit direction (away from the reflector), as observed by Lifshitz *et al.*[28] Because our foils were placed along the axis, they show no preferential pit direction, and pits appear on both sides of the foil.

Next consider the width of the cavitation field produced by the rigid reflector. The data at first appear contradictory, some indicating a narrow field, some a wide field, Moreover, observations reported in the literature are also somewhat contradictory. The aluminum foil pattern produced in our single pulse measurements is a narrow strip 1 to 2 mm wide. The narrow pattern is in excellent agreement with our high-speed video measurements and also with stroboscopic photographs taken by Jöchle *et al.*[34] Our video sequence shows that the bubble cloud grew to a width of 10 mm and then narrowed to an axial streak 1 to 2 mm wide. We speculate that off-axis bubbles, which were only weakly excited, either collapsed earlier and more weakly (arguably not strong enough to pit the foil) or were engulfed by the larger axial bubbles. On the other hand, a much wider pattern is indicated by (1) the 6-dB beamwidth of the acoustic field, (2) our PCD measurements, and (3) the foil pitting observations of Coleman *et al.*[3] We believe that these measures show a wider pattern because they are based on averages of many pulses. Because of spark jitter, focal location and amplitude vary from pulse to pulse. The result is an average measure that is broader than any single measure in the average. Conclusions drawn from the foil measurements of Coleman *et al.* are further complicated because of the possibility that previous pulses created cavitation seeds that were acted on by subsequent pulses.

Our foil technique was also used to map the cavitation field produced by the pressure-release reflector. The pits produced by the pressure-release reflector were $\frac{1}{3}$ as deep and $\frac{1}{8}$ as wide as those produced by the rigid reflector. The field produced by the pressure-release reflector has an hourglass shape, perhaps because shorter bubble life prevents off-axis bubbles from being drawn to the axis before collapsing. The results also showed qualitatively that the pit size depends on waveform. Far from the reflector, the pressure-release-reflector waveform is similar to, although weaker than, the rigid-reflector focal waveform. This observation correlates with the fact that the pits are similar to, although weaker than, the pits produced by the rigid reflector.

ACKNOWLEDGMENTS

The authors thank Lewis A. Thompson and Dr. Robert L. Rogers, Applied Research Laboratories (ARL), University of Texas at Austin, for help with the spark-generating system and Don Artieschoufsky, Department of Mechanical Engineering, University of Texas at Austin, for cooperation and assistance in machining the reflectors. Dr. Andrew P. Evan is thanked for his help in editing the manuscript and Dr. Oleg A. Sapozhnikov and Jarred Swalwell for their help in taking data. Bailey appreciates the suggestion by Dr. E. Carr Everbach at Swarthmore College to quantify pit depth with a STM. The suggestion led to the profilometer measurements made possible by the cooperation of researchers at the University of Texas Microelectronics and Engineering Research Center. We gratefully acknowledge the support by the Office of Naval Research, the National Institutes for Health through Grant No. DK 43881, and ARL through the IR&D program.

[1] M. R. Bailey, D. T. Blackstock, R. O. Cleveland, and L. A. Crum, ''Comparison of electrohydraulic lithotripters with rigid and pressure-release ellipsoidal reflectors. I. Acoustic fields,'' J. Acoust. Soc. Am. **104**, 2517–2524 (1998).

[2] C. C. Church and L. A. Crum, ''A theoretical study of cavitation generated by four commercially available extracorporeal shock wave lithotripters,'' *Proceedings 12th International Symposium on Nonlinear Acoustics*, edited by M. F. Hamilton and D. T. Blackstock (Elsevier Applied Science, London, 1990), pp. 433–438.

[3] A. J. Coleman, J. E. Saunders, L. A. Crum, and M. Dyson, ''Acoustic cavitation generated by an extracorporeal shockwave lithotripter,'' Ultrasound Med. Biol. **13**, 69–76 (1987).

[4] L. A. Crum, ''Cavitation microjets as a contributory mechanism for renal calculi disintegration in ESWL,'' J. Urol. (Baltimore) **140**, 1587–1590 (1988).

[5] G. Delacrétaz, J. T. Walsh, Jr., and T. Asshauer, ''Dynamic polariscopic imaging of laser-induced strain in a tissue phantom,'' Appl. Phys. Lett. **70**, 3510–3512 (1997).

[6] E. L. Carstensen, D. S. Campbell, D. Hoffman, S. Z. Child, and E. J. Aymé-Bellagarda, ''Killing of *Drosophila* larvae by the fields of an electrohydraulic lithotripter,'' Ultrasound Med. Biol. **16**, 687–698 (1990).

[7] W. Sass, M. Bräunlich, H.-P. Dreyer, E. Matura, W. Folberth, H.-G. Priesmeyer, and J. Seifert, ''The mechanisms of stone disintegration by shock waves,'' Ultrasound Med. Biol. **17**, 239–243 (1991).

[8] Lord Rayleigh, ''On the pressure developed in a liquid during collapse of a spherical cavity,'' Philos. Mag. **34**, 94 (1917).

[9] L. A. Crum, ''Acoustic cavitation,'' Proc. Ultrasonics Symp. **1**, 1–11 (1982).

[10] A. Vogel and W. Lauterborn, ''Acoustic transient generation by laser-produced cavitation bubbles near solid boundaries,'' J. Acoust. Soc. Am. **84**, 719–731 (1988).

[11] C. C. Church, ''A theoretical study of cavitation generated by an extracorporeal shock wave lithotripter,'' J. Acoust. Soc. Am. **86**, 215–227 (1989).

[12] T. R. Morgan, V. P. Laudone, W. D. Heston, L. Zeitz, and W. R. Fair, ''Free radical production by high energy shock waves: Comparison with ionizing radiation,'' J. Urol. (Baltimore) **139**, 186–189 (1988).

[13] A. J. Coleman, M. J. Choi, J. E. Saunders, and T. G. Leighton, ''Acoustic emission and sonoluminescence due to cavitation at the beam focus of an electrohydraulic shock wave lithotripter,'' Ultrasound Med. Biol. **18**, 267–281 (1992).

[14] P. Zhong, I. Cioanta, F. H. Cocks, and G. M. Preminger, ''Inertial cavitation and associated acoustic emission produced during electrohydraulic shock wave lithotripsy,'' J. Acoust. Soc. Am. **101**, 2940–2950 (1997).

[15] R. O. Cleveland, O. A. Sapozhnikov, M. R. Bailey, and L. A. Crum, ''Localized detection of lithotripsy-induced cavitation *in vitro*,'' J. Acoust. Soc. Am. (submitted).

[16] N. Vakil, S. M. Gracewski, and E. C. Everbach, ''Relationship of model stone properties to fragmentation mechanisms during lithotripsy,'' J. Lithotripsy and Stone Disease **3**, 304–310 (1991).

[17] S. Gambihler, M. Delius, and W. Brendel, ''Biological effects of shock

waves: cell disruption, viability, and proliferation of L1210 cells exposed to shock waves *in vitro*,'' Ultrasound Med. Biol. **16**, 587–594 (1990).
[18] M. Delius, ''Minimal static pressure minimises the effect of extracorporeal shock waves on cells and reduces it on gallstones,'' Ultrasound Med. Biol. **23**, 611–617 (1997).
[19] M. R. Bailey, D. Dalecki, S. Z. Child, C. H. Raeman, D. P. Penney, D. T. Blackstock, and E. L. Carstensen, ''Bioeffects of positive and negative acoustic pressures *in vivo*,'' J. Acoust. Soc. Am. **100**, 3941–3946 (1996).
[20] J. Tavakkoli, A. Birer, A. Arefiev, F. Prat, J.-Y. Chapelon, and D. Cathignol, ''A piezocomposite shock wave generator with electronic focusing capability: Application for producing cavitation induced lesions in rabbit liver,'' Ultrasound Med. Biol. **23**, 107–115 (1997).
[21] M. Delius and W. Brendel, ''A model of extracorporeal shock wave action: Tandem action of shock waves,'' Ultrasound Med. Biol. **14**, 515–518 (1988).
[22] M. Müller, ''Experimental investigations on focusing of weak spherical shock waves in water by shallow ellipsoidal reflectors,'' Acustica **64**, 85–93 (1987).
[23] A. J. Coleman and J. E. Saunders, ''A survey of the acoustic output of commercial extracorporeal shock wave lithotripters,'' Ultrasound Med. Biol. **15**, 213–227 (1989).
[24] Z. Ding and S. M. Gracewski, ''Response of constrained and unconstrained bubbles to lithotripter shock wave pulses,'' J. Acoust. Soc. Am. **96**, 3636–3644 (1994).
[25] M. R. Bailey, ''Control of acoustic cavitation with application to lithotripsy,'' Ph.D. dissertation, The University of Texas at Austin, 1997. Also issued as Technical Report ARL-TR-97-1, Applied Research Laboratories, The University of Texas at Austin, Austin, Texas, March 1997.
[26] R. E. Apfel, ''The role of impurities in cavitation-threshold determination,'' J. Acoust. Soc. Am. **48**, 1179–1186 (1970).
[27] L. A. Crum, ''The tensile strength of water,'' Nature (London) **278**, 148 (1979).
[28] D. A. Lifshitz, J. C. Williams, Jr., B. Sturtevant, B. A. Conners, A. P. Evan, and J. A. McAteer, ''Quantization of shock wave cavitation damage *in vitro*,'' Ultrasound Med. Biol. **23**, 461–471 (1997).
[29] F. R. Gilmore, ''The growth or collapse of a spherical bubble in a viscous compressible liquid,'' Rep. 26-4, California Institute of Technology, Pasadena, California, 1952, pp. 1–40.
[30] P. A. Thompson, *Compressible-Fluid Dynamics* (Rensselaer Polytechnic Institute, Troy, NY, 1988), p. 102.
[31] D. A. Sullivan, ''Historical review of real-fluid isentropic flow models,'' J. Fluids Eng. **103**, 258–267 (1981).
[32] V. A. Akulichev, in *High-Intensity Ultrasonic Fields*, edited by L. D. Rozenberg (Plenum, New York, 1971), pp. 239–259.
[33] J. Staudenraus and W. Eisenmenger, ''Fibre-optic probe hydrophone for ultrasonic and shock-wave measurements in water,'' Ultrasonics **31**, 267–273 (1993).
[34] K. Jöchle, J. Debus, W. J. Lorenz, and P. Huber, ''A new method of quantitative cavitation assessment in the field of a lithotripter,'' Ultrasound Med. Biol. **22**, 329–338 (1996).
[35] P. T. Hunter, B. Finlayson, R. J. Hirko, W. C. Voreck, R. Walker, S. Walck, and M. Nasr, ''Measurement of shock wave pressures used for lithotripsy,'' J. Urol. (Baltimore) **136**, 733–738 (1986).
[36] M. E. Nasr, ''The Evolution in Dynamics of Spark Generated Shock Waves and Their Focusing by Ellipsoidal Reflectors in Lithotripsy,'' (Ph.D. dissertation, University of Florida, 1986).
[37] A. J. Coleman, M. Whitlock, T. Leighton, and J. E. Saunders, ''The spatial distribution of cavitation induced acoustic emission, sonoluminescence and cell lysis in the field of a shock wave lithotripter,'' Phys. Med. Biol. **38**, 1545–1560 (1993).
[38] L. D. Landau and E. M. Lifshitz, *Fluid Mechanics* (Pergamon, New York, 1959), p. 267.
[39] M. T. Carnell, R. D. Alcock, and D. C. Emmony, ''Optical imaging of shock waves produced by a high-energy electromagnetic transducer,'' Phys. Med. Biol. **38**, 1575–1588 (1993).

Uncertainties in estimates of lesion detectability in diagnostic ultrasound

Keith A. Wear, Robert M. Gagne, and Robert F. Wagner
U.S. Food and Drug Administration, Center for Devices and Radiological Health, HFZ-142, 12720 Twinbrook Parkway, Rockville, Maryland 20852

(Received 24 August 1998; revised 19 November 1998; accepted 20 April 1999)

Statistical properties of estimates of focal lesion detectability for medical ultrasonic imaging systems are investigated. Analytic forms for bias and variance of estimates of detectability of a lesion consisting of fully developed speckle embedded within a speckle background are derived. Bias and variance of estimates of detectability are investigated using a computer simulation and experiments on tissue-mimicking phantoms. This work offers a systematic methodology for interpreting measurements on phantoms in order to assess lesion detectability. In addition, it provides useful results which may be used to improve design of phantoms and experiments for imaging-system performance assessment. © *1999 Acoustical Society of America.* [S0001-4966(99)01208-4]

PACS numbers: 43.80.Vj, 43.80.Qf [FD]

TABLE OF VARIABLE DEFINITIONS

$\Delta\mu$	$\mu_1-\mu_2$
$\Delta\mu_a$	$\mu_{a1}-\mu_{a2}$
Δm	m_1-m_2
$\Gamma(\,)$	gamma function
λ	noncentrality parameter for the noncentral chi-square probability density function
μ_1,μ_2	mean pixel intensities for lesion and background, respectively
μ_{a1},μ_{a2}	mean pixel intensities averaged over lesion areas and equally-sized background areas
ν	number of degrees of freedom for a chi-square probability density function
σ_1,σ_2	standard deviations of pixel intensities within lesion and background, respectively
σ_{a1},σ_{a2}	standard deviations of mean intensities across lesion and background areas, respectively
a	mean intensity ratio, μ_2/μ_1
c	the effective number of degrees of freedom for the sum of two chi-square distributed random variables
C	lesion contrast
d'	detectability index
m_1,m_2	*estimated* mean pixel intensities across lesion and background areas, respectively
M	the number of independent samples contained within a lesion or background region
N	the number of lesion/background pairs analyzed
s_{m1},s_{m2}	standard deviations of the *estimates* of mean intensities across lesion and background areas, respectively
q	quotient$=u/v$
u	estimate for numerator of expression for lesion SNR, $u=(\Delta m)^2$
v	estimate for denominator of expression for lesion SNR, $v=(s_{m1}^2+s_{m2}^2)/2$
SNR	signal-to-noise ratio
$\mathrm{SNR}_1,\mathrm{SNR}_2$	point signal-to-noise ratios for region 1 (e.g., lesion) and region 2 (e.g., background)
X	noncentral chi-square distributed random variable $(\chi^2_{\nu,\lambda})$ with $\nu=1$ and $\lambda=N(d')^2/2$
Z	central chi-square distributed random variable with $\nu=c(N-1)$ degrees of freedom

INTRODUCTION

The performance of a medical ultrasonic imaging system is to some extent determined by its spatial resolution properties (axial, lateral, and elevational). These properties are functions of center frequency, bandwidth, transducer array geometry, focusing characteristics, and position in the field of view. Another important quantitative descriptor of imaging performance is focal lesion detectability. This refers to the ability of a system (in combination with a human or automated observer) to detect the presence of an object which differs somewhat in acoustic properties from the background. Lesion detectability is a complicated function of spatial resolution properties, statistical properties of the lesion and background signals, lesion contrast, and lesion size.

Several investigators have designed custom phantoms and evaluation methodologies for assessment of lesion detectability. Smith *et al.* have reported a phantom design consisting of low-contrast conical speckle targets embedded within a speckle background.[1] Using this phantom, Lopez and co-workers have compared clinical and computer-based observer evaluation methods and have concluded that the latter is more reliable and objective.[2] Lopez *et al.* subsequently reported a refined version of their computational observer.[3] Rownd and co-workers[4] have developed a phantom consisting of randomly distributed spherical simulated

lesions (all with the same diameter and contrast) scattered throughout a tissue-mimicking material. One advantage of their phantom compared with the conical design is that it can be used to evaluate system performance over a broad range of depths. In addition, while both phantom designs are sensitive to lateral and depth resolution properties of the imaging system, the spherical lesion phantom (unlike the conical target phantom) is sensitive to elevational resolution properties as well. The principal advantage of the conical phantom, on the other hand, is that it provides a wide range of contrasts and diameters that can be interrogated to generate a contrast-detail diagram.

The goal of the work reported here is to investigate accuracy and precision of measurements of lesion detectability using phantoms for medical ultrasonic imaging systems. Some descriptors of detectability include the lesion signal-to-noise ratio (SNR) and the area under the receiver-operating-characteristic (ROC) curve. In the model presented here, a lesion consisting of fully developed speckle embedded within a background consisting of fully developed speckle is considered. (Fully developed speckle corresponds to the situation in which the scatterers are sufficiently numerous and positioned sufficiently randomly such that the signal intensity obeys a chi-square probability density function with two degrees of freedom.[5]) Analytic forms are derived for the bias and variance of the estimate of the lesion SNR^2 as functions of (1) the expected number of speckles within the lesion, (2) the number of independent measurements performed, and (3) the ratio of mean pixel intensity of the lesion to that of the background. The theory is compared with results from computer simulation and experiments on tissue-mimicking phantoms. The experimental work was conducted on two macroscopically uniform phantoms, one representing lesion and the other background.

A question that needs to be addressed is the number of image samples necessary to achieve a given accuracy (low bias) and precision (low variance) in the measurement of lesion SNR. In general, it would be desirable to be able to solve this problem as a function of lesion size and for arbitrary lesion profile, e.g., cylindrical or pillbox, Gaussian, spherical, etc. This paper presents a first step toward this goal: a solution to the problem for the case where the lesion size is greater than several correlation cells (speckles), and for the special case of a pillbox profile.

Two methods for deriving the variance of the estimate of the square of the lesion SNR are presented. The first is based on an error propagation method which is valid in the regime of small statistical fluctuations. First-, second-, and third-order approximations are given. The first-order approximation is simpler and provides insight into the fundamental determinants of variance. The second- and third-order approximations are more complicated but often provide substantial improvement in accuracy. The second method assumes approximate forms for the probability density functions (PDFs) for the numerator and denominator of the expression for square of the lesion SNR, but is not limited to the realm of small statistical fluctuations. This method provides a formula to predict the bias in the estimate of the square of the lesion SNR. It is shown that the two methods yield similar results for a wide variety of common experimental situations. The conditions under which each method begins to lose validity are illustrated.

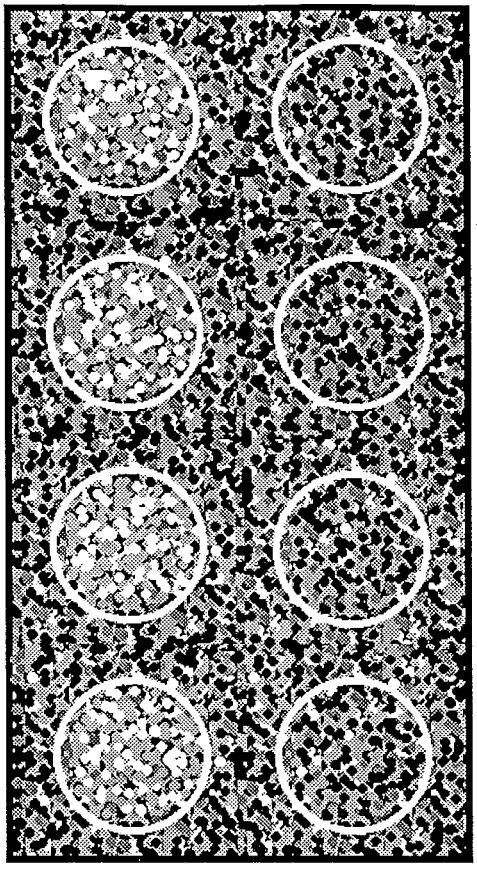

FIG. 1. Illustration of experiment with $N=4$ and $M=200$. The image shows four positive-contrast lesions vertically aligned along the left side. The mean intensity within each region of interest (ROI) is measured. The means and standard deviations of intensities in the lesions are compared with those in the background (four ROIs vertically aligned along the right side of the image) using Eq. (1).

I. THEORY

A. Preliminary considerations

The experiment which is considered here is as follows (see the illustration in Fig. 1). A phantom to be interrogated will contain a set of equally sized ''lesions'' (areas which are either brighter or darker on the average than the background). The signal intensity (the square or the *B*-mode or envelope) will be considered here rather than the envelope for algebraic simplicity (see below). The mean intensity over each lesion, which may be referred to as an ''area mean,'' will be measured. A set of N independent area means from the set of lesions will be collected. (N may be greater than the number of lesions if multiple independent measurements may be performed on each lesion.) Similarly, a set of N independent area means from equally sized background regions will be collected. The estimated means and standard deviations of the two sample distributions of area means will be compared in order to evaluate lesion detectability.

The means and standard deviations for the pixel intensities corresponding to the two media will be denoted by

μ_1, σ_1 (lesions), and μ_2, σ_2 (background). The corresponding area means will be denoted by μ_{a1} and μ_{a2}. The estimated sample mean intensities (averages of N estimated area means) will be denoted by random variables m_1 and m_2. Assuming stationarity and ergodicity so that area averages are equivalent to ensemble averages, the expected values of the sample mean intensities will be the same as the area means and the media means so that $\langle m_1 \rangle = \mu_{a1} = \mu_1$ and $\langle m_2 \rangle = \mu_{a2} = \mu_2$ where angular brackets denote the expectation operator. The variances of the area means will be denoted by σ_{a1}^2 and σ_{a2}^2. If the number of correlation cells or speckles contained within each lesion or background region is denoted by M, then the variances of the area means will be related to the media variances by $\sigma_{a1}^2 = \sigma_1^2/M$ and $\sigma_{a2}^2 = \sigma_2^2/M$ (i.e., each area contains M independent samples). The variances of the sample mean intensities, each obtained from N areas, will be given by $s_{m1}^2 = \sigma_{a1}^2/N = \sigma_1^2/NM$ and $s_{m2}^2 = \sigma_{a2}^2/N = \sigma_2^2/NM$.

The object of this paper is to consider uncertainties in the measurement of one particular figure of merit for lesion detection. The figure of merit is the square of the lesion SNR or detectability index (d'). This is denoted as d'^2 and defined by

$$(d')^2 = \frac{(\Delta \mu_a)^2}{\frac{1}{2}(\sigma_{a1}^2 + \sigma_{a2}^2)}, \tag{1}$$

where $\Delta \mu_a = \mu_{a1} - \mu_{a2}$. (The *lesion* SNR, of course, should not be confused with the *point* SNR, μ_i/σ_i where $i = 1$ or 2.) Alternatively, d' (without the square) could be used. However, the quantity d'^2 is more commonly used in studying model observer performance; the ratio of d'^2 for a model observer to d'^2 for the optimal observer is referred to as ''observer efficiency''—a concept directly related to that of statistical efficiency (see the Discussion section). Under conditions in which (1) the variances for the lesion (σ_{a1}^2) and the background (σ_{a2}^2) are comparable, and (2) the estimate of $\Delta \mu_a$ is normally distributed, sample values of the estimate of d'^2 follow a well-defined probability law called the noncentral t^2 distribution. (This is a straightforward extension of Student's t distribution; the multivariate generalization is Hotelling's T^2 distribution.[6]) The case of unequal variances has been considered by Behrens and Fisher.[7] In the following treatment, an approximate form for the uncertainties in the estimate of d'^2 using elementary methods of propagation of variance is derived. Subsequently, a second set of formulas based on assumed underlying statistical properties of the estimates of the numerator and denominator of Eq. (1) is derived. Both methods are shown to yield comparable results for a wide variety of circumstances.

B. Error propagation method

Here, the objective is to calculate the estimated uncertainty in the square of the lesion SNR. First the numerator is considered, then the denominator, and then the results are combined. In all of the analyses to follow, it is assumed that one is measuring signal intensity (the square of the *B*-scan or envelope). This problem can be treated in terms of the envelope variable, but the analysis is more complicated. However, as shown in the papers by Wagner *et al.*,[5] Wagner, Insana, and Smith,[8] and also Thijssen, Oosterveld, and Wagner,[9] the intensity analysis gives almost precisely the same results. The last reference shows that the results are rather insensitive to further nonlinear processing.

In order to analyze the propagation of error, it is convenient to make the following definitions regarding the estimate of the square of the lesion SNR:

$$(\hat{d}')^2 = q = \frac{u}{v}, \tag{2}$$

where u and v are the estimates of the numerator and denominator for the square of the lesion SNR,

$$u = (\Delta m)^2, \quad v = \tfrac{1}{2}(s_{m1}^2 + s_{m2}^2). \tag{3}$$

$\Delta m = m_1 - m_2$, and s_{m1}^2 and s_{m2}^2 are the sample variances of the mean intensities for the lesion and background. It is shown in Appendix A that, under the assumption of small statistical fluctuations, the third-order error propagation approximation for the relative variance in the quotient, q, is given by

$$\langle (\Delta q/\overline{q})^2 \rangle = \langle (\Delta u/\overline{u})^2 \rangle + \langle (\Delta v/\overline{v})^2 \rangle - 2\langle (\Delta v/\overline{v})^3 \rangle + 3\langle (\Delta u/\overline{u})^2 \rangle \langle (\Delta v/\overline{v})^2 \rangle + 3\langle (\Delta v/\overline{v})^4 \rangle + \ldots, \tag{4}$$

where bars denote mean values of variables, the Δ operator denotes excursions about mean values, and angular brackets denote the expectation operator.

The expected values of powers of excursions of a random variable about its mean [such as those appearing in Eq. (4)] are commonly referred to as the *central moments* of that random variable.[10] In order to obtain a practical form of Eq. (4), it is necessary to obtain forms for the normalized central moments of u and v in terms of the fundamental independent variables of the experiment.

First, the numerator of Eq. (2), (u), may be considered. The variance in the difference of the measurements of area-mean intensity from the numerator of Eq. (1) is the sum of the variances of the individual measurements (assuming that the measurements are independent of each other[11]).

$$\mathrm{var}[\Delta m] = s_{m1}^2 + s_{m2}^2 = \frac{1}{N}\left(\frac{\sigma_1^2}{M} + \frac{\sigma_2^2}{M}\right), \tag{5}$$

where the pixel variances are σ_1^2 and σ_2^2. The terms in parentheses correspond to the expected variances of mean signals averaged over areas that include M speckles. If one has N independent samples of these signals available to average together, there is a reduction in the variance of the estimate of Δm by a factor $1/N$. Equation (5) may be rewritten as follows:

$$\mathrm{var}[\Delta m] = \frac{1}{N}\left(\frac{\sigma_1^2}{M}\right)\left(1 + a^2 \frac{\mathrm{SNR}_1^2}{\mathrm{SNR}_2^2}\right), \tag{6}$$

where the mean intensity ratio $a = \mu_2/\mu_1$, and the point signal-to-noise ratio $\mathrm{SNR}_i = \mu_i/\sigma_i$ (where $i = 1$ or 2). The mean intensity ratio, a, may be related to lesion contrast $C = (\mu_1 - \mu_2)/[(\mu_1 + \mu_2)/2]$ by $a = (2 - C)/(2 + C)$.

The *relative variance* is obtained by normalizing this result by the square of the expected value of the mean-intensity difference or $\langle \Delta m \rangle^2 = (\langle m_1 \rangle - \langle m_2 \rangle)^2 = (\mu_1 - \mu_2)^2 = \mu_1^2 (1-a)^2$. Under the assumption that both the lesion and background contain fully developed speckle (intensity obeys a chi-squared distribution with two degrees of freedom, see Appendix B) so that $\mu_1^2 = \sigma_1^2$, $\mu_2^2 = \sigma_2^2$, and $\mathrm{SNR}_1^2 = \mathrm{SNR}_2^2 = 1$ (see Ref. 5),

$$\frac{\mathrm{var}[\Delta m]}{(\langle \Delta m \rangle)^2} = \frac{1}{NM} \frac{1+a^2}{(1-a)^2}. \tag{7}$$

The relative variance in the square of this quantity is equal to four times this result (see Ref. 11, chap. 4)

$$\langle (\Delta u/\overline{u})^2 \rangle = \frac{\mathrm{var}[(\Delta m)^2]}{(\langle \Delta m \rangle)^4} = \frac{4}{NM} \frac{1+a^2}{(1-a)^2}. \tag{8}$$

This equation may alternatively be expressed using the actual value (rather than the estimate) of the square of the lesion SNR as a parameter instead of the mean-intensity ratio

$$(d')^2 = \frac{(\Delta \mu_a)^2}{\frac{1}{2}(\sigma_{a1}^2 + \sigma_{a2}^2)} = \frac{(\mu_1 - \mu_2)^2}{\frac{1}{2M}(\sigma_1^2 + \sigma_2^2)} = 2M \frac{(1-a)^2}{1+a^2}. \tag{9}$$

Now, Eq. (8) may be rewritten as

$$\langle (\Delta u/\overline{u})^2 \rangle = \frac{8}{N(d')^2}. \tag{10}$$

Now, the estimate of the denominator of Eq. (1), (v), may be considered in order to calculate the remaining terms in Eq. (4). Thus, it is required to calculate

$$\langle (\Delta v/\overline{v})^k \rangle \quad \text{for} \quad k = 2,3,4. \tag{11}$$

The 2nd, 3rd, and 4th central moments of a sample variance are given in Appendix B. In order to obtain the 2nd, 3rd, and 4th central moments of the entire denominator, which is the weighted sum of two uncorrelated sample variance terms, it is necessary to take into account the following rules regarding central moments of a sum of two uncorrelated random variables. If $z = x + y$ and $\Delta z = \Delta x + \Delta y$, then

$$\begin{aligned}
\langle (\Delta z)^2 \rangle &= \langle (\Delta x)^2 \rangle + 2\langle (\Delta x) \rangle \langle (\Delta y) \rangle + \langle (\Delta y)^2 \rangle \\
&= \langle (\Delta x)^2 \rangle + \langle (\Delta y)^2 \rangle, \\
\langle (\Delta z)^3 \rangle &= \langle (\Delta x)^3 \rangle + 3\langle (\Delta x)^2 \rangle \langle (\Delta y) \rangle + 3\langle (\Delta x) \rangle \\
&\quad \times \langle (\Delta y)^2 \rangle + \langle (\Delta y)^3 \rangle = \langle (\Delta x)^3 \rangle + \langle (\Delta y)^3 \rangle, \\
\langle (\Delta z)^4 \rangle &= \langle (\Delta x)^4 \rangle + 4\langle (\Delta x)^3 \rangle \langle (\Delta y) \rangle + 6\langle (\Delta x)^2 \rangle \\
&\quad \times \langle (\Delta y)^2 \rangle + 4\langle (\Delta x) \rangle \langle (\Delta y)^3 \rangle + \langle (\Delta y)^4 \rangle \\
&= \langle (\Delta x)^4 \rangle + 6\langle (\Delta x)^2 \rangle \langle (\Delta y)^2 \rangle + \langle (\Delta y)^4 \rangle,
\end{aligned} \tag{12}$$

where Δx and Δy are uncorrelated zero-mean random variables. The second central moment of the denominator of the expression for square of the lesion SNR may now be calculated to be

$$\begin{aligned}
\langle (\Delta v)^2 \rangle &= \frac{1}{2(N-1)} \left(\frac{\sigma_1^2}{M} \right)^2 + \frac{1}{2(N-1)} \left(\frac{\sigma_2^2}{M} \right)^2 \\
&= \frac{1}{2(N-1)} \left(\frac{\sigma_1^2}{M} \right)^2 \left(1 + a^4 \frac{\mathrm{SNR}_1^4}{\mathrm{SNR}_2^4} \right),
\end{aligned} \tag{13}$$

where the variance (σ_x^2) from Appendix B has been replaced by σ_1^2/M in the first term and by σ_2^2/M in the second term. To express this as a relative variance, the normalization required is the squared expected value of the denominator. The result is found to be given by (again assuming fully developed speckle)

$$\langle (\Delta v/\overline{v})^2 \rangle = \frac{2}{(N-1)} \frac{1+a^4}{(1+a^2)^2}. \tag{14}$$

Similarly, it may be shown that

$$\langle (\Delta v/\overline{v})^3 \rangle = \frac{8}{(N-1)^2} \frac{1+a^6}{(1+a^2)^3}, \tag{15}$$

and

$$\begin{aligned}
\langle (\Delta v/\overline{v})^4 \rangle &= \frac{48 + 12(N-1)}{(N-1)^3} \frac{1+a^8}{(1+a^2)^4} \\
&\quad + \frac{3}{2(N-1)^2} \frac{a^4}{(1+a^2)^4}.
\end{aligned} \tag{16}$$

Note that in Eqs. (14)–(16), the ratios of polynomials in mean intensity ratio (a) possess the required property that they remain invariant under the transformation $a \rightarrow 1/a$. By combining Eqs. (4), (10), (14), (15), and (16), an expression for the relative variance in the estimate of square of the lesion SNR may be ascertained. The first-order approximation [the first two terms in Eq. (4)] is given by

$$\langle (\Delta q/\overline{q})^2 \rangle = \frac{\mathrm{var}[(\hat{d}')^2]}{(d')^4} = \frac{8}{N(d')^2} + \frac{2}{(N-1)} \frac{1+a^4}{(1+a^2)^2}. \tag{17}$$

As expected, the variance is approximately inversely proportional to the number of lesion–background pairs (N).

C. Approximate χ^2 method

In this section, analytic forms for the PDFs for the estimates of the numerator and denominator of Eq. (1) are derived. The mean and variance for the estimate of the square of the lesion SNR may then be obtained from the first and second moments of these PDFs. It is assumed that the estimates of the means (m_1 and m_2) are Gaussian-distributed random variables so that the estimate of the numerator obeys a noncentral chi-square PDF (see below). This assumption is valid, for example, when the number of speckle correlation cells per lesion (M) and/or the number of lesion/background pairs (N) is sufficiently large that the central limit theorem applies. In addition, an approximate form for the PDF of the denominator is assumed. In this analysis, unlike the error propagation treatment given above, the assumption of small statistical fluctuations in estimates is not made.

It can be shown that the numerator of the expression for the square of the lesion SNR [Eq. (1)] is proportional to a random variable that obeys a noncentral chi-square PDF (see Appendix B). This can be seen as follows. Suppose that the *estimates* of mean intensities (m_1 and m_2) may be expressed as the sums of the true mean intensities (μ_1 and μ_2) and zero-mean Gaussian (due to the central limit theorem) random error terms (δ_{m1} and δ_{m2}) so that $m_1=\mu_1+\delta_{m1}$ and $m_2=\mu_2+\delta_{m2}$. The variances of the error terms are given by $\text{var}(\delta_1)=\sigma_1^2/NM$ and $\text{var}(\delta_2)=\sigma_2^2/NM$. [Recall that these were the forms used for these variances in Eq. (5), even when underlying PDFs for m_1 and m_2 were not assumed.] Then

$$\begin{aligned}(\Delta m)^2&=(m_1-m_2)^2\\&=(\mu_1+\delta_{m1}-\mu_2-\delta_{m2})^2\\&=[\delta_{m1}-\delta_{m2}+\mu_1-\mu_2]^2\\&=\sigma_{\Delta\delta}^2\left[\frac{\delta_{m1}-\delta_{m2}}{\sigma_{\Delta\delta}}+\frac{\mu_1-\mu_2}{\sigma_{\Delta\delta}}\right]^2\\&=\left(\frac{\sigma_1^2+\sigma_2^2}{NM}\right)(x_1+\sqrt{\lambda})^2=\left(\frac{\sigma_1^2+\sigma_2^2}{NM}\right)\chi_{\nu,\lambda}^2,\end{aligned}\tag{18}$$

where $\sigma_{\Delta\delta}^2=(\sigma_1^2+\sigma_2^2)/NM$, x_1 is a standard normal random variable, $\chi_{\nu,\lambda}^2$ is noncentral chi-square distributed random variable (see Appendix B and Ref. 13) with $\nu=1$ degrees of freedom, and noncentrality parameter $\lambda=NM(\mu_1-\mu_2)^2/(\sigma_1^2+\sigma_2^2)$. From Eq. (9), it may be seen that $\lambda=N(d')^2/2$. It has been assumed [as was done for Eq. (5)] that m_1 and m_2 are independent so that the variance of the difference of the random error terms is equal to the sum of the individual variances [see Eq. (12)].

Now, attention may be turned to the PDF for the denominator of the expression of the square of the lesion SNR. As discussed in the previous section and in Appendix B, each sample variance term in the denominator of Eq. (1) is proportional to a random variable that obeys a central chi-square PDF with $N-1$ degrees of freedom:[12]

$$\frac{(N-1)s_{\text{mi}}^2}{\sigma_{\text{ai}}^2}=\frac{(N-1)s_{\text{mi}}^2}{\sigma_i^2/M}=\chi_{N-1}^2,\tag{19}$$

where s_{mi}^2 corresponds to the sample variance for the lesion or background mean and i equals 1 (e.g., lesion) or 2 (e.g., background). As shown in Appendix B, the PDF of the sum of the two sample variance terms may be approximated as a χ_ν^2PDF,

$$\frac{1}{2}(s_{m1}^2+s_{m2}^2)=\frac{\sigma_1^2}{2M(N-1)}\,\frac{1+a^4}{1+a^2}\,\chi_\nu^2,\tag{20}$$

where $\nu=c(N-1)$ degrees of freedom and

$$c=\frac{(1+\sigma_{a2}^2/\sigma_{a1}^2)^2}{1+(\sigma_{a2}^2/\sigma_{a1}^2)^2}=\frac{(1+a^2)^2}{1+a^4}.\tag{21}$$

Fully developed speckle has been assumed so that $\sigma_{a2}/\sigma_{a1}=[\sigma_2/M]/[\sigma_1/M]=\mu_2/\mu_1=a$. Note that $1\leqslant c\leqslant 2$. The low-contrast limit is represented by $a=1$ $(c=2)$. The high-contrast limit is represented by $a=0$ or $a=\infty$ $(c=1)$.

Combining Eqs. (1), (18), and (20), it may be shown that the estimate of d'^2 is given by

$$(\hat{d}')^2=\frac{2\nu}{N}\,\frac{X}{Z},\tag{22}$$

where X denotes a noncentral chi-square distributed random variable ($\chi_{\nu,\lambda}^2$) with $\nu=1$ and $\lambda=N(d')^2/2$ and Z denotes a central chi-square distributed random variable with $\nu=c(N-1)$ degrees of freedom. The first moment of the estimate of d'^2 is given by[14]

$$\langle(\hat{d}')^2\rangle=\frac{2\nu}{N}\langle X\rangle\langle Z^{-1}\rangle.\tag{23}$$

Using the formulas for the first moment of a noncentral chi-square distributed random variable and the first moment of the reciprocal of a central chi-square distributed random variable from Appendix B, it is found that

$$\begin{aligned}\langle(\hat{d}')^2\rangle&=\frac{2\nu}{N}\left[1+\frac{N(d')^2}{2}\right]\frac{1}{\nu-2}\\&=\frac{\nu}{\nu-2}\left[\frac{2}{N}+(d')^2\right]\quad(\nu>2),\end{aligned}\tag{24}$$

where the true lesion SNR^2 is $(d'^2)=2M(\Delta\mu)^2/(\sigma_1^2+\sigma_2^2)$ [see Eq. (9)]. Equation (24) shows that for small values of N, estimates of d'^2 will tend to be biased. This suggests an alternative unbiased estimator for d'^2

$$\langle(\hat{d}')^2\rangle_{\text{unbiased}}=\frac{\nu-2}{\nu}\langle(\hat{d}')^2\rangle-\frac{2}{N}\quad(\nu>2).\tag{25}$$

The second moment of the estimate of d'^2 is given by

$$\langle(\hat{d}')^4\rangle=\frac{4\nu^2}{N^2}\langle X^2\rangle\langle Z^{-2}\rangle.\tag{26}$$

The expected value of X^2 may be obtained from

$$\langle X^2\rangle=\sigma_X^2+\langle X\rangle^2=3+3N(d')^2+\tfrac{1}{4}N^2(d')^4.\tag{27}$$

Using this result and the second moment for the reciprocal of a χ^2 distributed random variable (see Appendix B), the variance of the estimate of d'^2 may be shown to be given by

$$\begin{aligned}\text{var}[(\hat{d}')^2]&=\langle(\hat{d}')^4\rangle-\langle(\hat{d}')^2\rangle^2\\&=\frac{4\nu^2}{N^2(\nu-2)^2(\nu-4)}\{(\nu-1)[2+2N(d')^2]\\&\quad+N^2(d')^4/2\}\quad(\nu>4).\end{aligned}\tag{28}$$

The square of the coefficient of variation for the estimate of d'^2 is then given by

$$\begin{aligned}\frac{\text{var}[(\hat{d}')^2]}{(d')^4}&=\frac{4\nu^2}{N^2(\nu-2)^2(\nu-4)}\{(\nu-1)[2/(d')^4\\&\quad+2N/(d')^2]+N^2/2\}\quad(\nu>4).\end{aligned}\tag{29}$$

The square of the coefficient of variation for the unbiased estimator of d'^2 [Eq. (25)] would be the same as Eq. 29 except reduced by a factor of $(\nu-2)^2/\nu^2$. In the limit where $N\gg 1$ (and therefore $\nu\gg 1$) and $N(d')^2\gg 1$, the square of the

TABLE I. Physical characteristics for both phantoms interrogated. The phantoms consisted of glass beads embedded in agar. Average scatterer number density refers to the average number of scatterer per unit volume. Average scatterers per resolution cell (J) refers to the average number of scatterer per system resolution cell in the focal region of the ATL system at 3.5 MHz (approximately 1.2 mm^3). The point intensity SNR is a function of J (Refs. 20, 21). Attenuation coefficients were measured in transmission substitution experiments over the range from 2 to 10 MHz. Power law fits are given in the table. The ratio of the backscatter coefficients yields a mean-intensity ratio of 0.73 and $C=0.31$.

	Phantom characteristics	
Phantom	A	B
Scatterer size range (μm)	75–90	90–106
Sound speed (m/s)	1556	1556
Backscatter coefficient at 3.5 MHz (cm^{-1} Sr^{-1})	0.0038	0.0052
Attenuation coefficient (cm^{-1})	$0.05f^{1.8}$	$0.05f^{1.9}$
Average scatterer number density (mm^{-3})	9.5	6.0
Average scatterers per resolution cell$=J$	11.4	7.2
Theoretical point SNR $=\mu/\sigma=[J/(J+1)]^{1/2}$	0.96	0.94
Measured point (SNR)	0.94$\pm$0.04	0.95$\pm$0.04

coefficient of variation of the estimate for d'^2 becomes

$$\frac{\mathrm{var}[(\hat{d}')^2]}{(d')^4}=\frac{8}{N(d')^2}+\frac{2}{\nu}=\frac{8}{N(d')^2}+\frac{2}{N}\frac{1+a^4}{(1+a^2)^2}, \tag{30}$$

which is identical to Eq. (17) (assuming $N\gg 1$).

II. METHODS

A. Simulation

A simulated experiment consisted of generating N lesion/background pairs, each containing M independent intensity samples. Each intensity sample was computed by using a Gaussian random-number generator to generate both the real and imaginary parts of the simulated radio frequency signal.[5] Intensity was computed as the sum of the squares of the real and imaginary parts. The lesion (or background) means were computed by averaging over all M independent samples throughout each simulated lesion (or background region) and then over all N lesions (or background regions). The variances were computed by taking the variance over each set of N lesion (or background) mean estimates. From the means and the variances of the estimates of the lesion and background means, a sample of d'^2 could be generated. This process was repeated many times (320/N) in order to generate many samples of d'^2. From the mean and variance of this set of samples of d'^2, the coefficient of variation could be estimated. (Ultimately, this entire process was repeated 200 times for each value of M, N, and mean-intensity ratio in order to obtain error bars for estimates of coefficient of variation.) The simulation was performed for many combinations of M, N, and mean-intensity ratio ($a=\mu_2/\mu_1$) where M ranged between 5 and 80, N ranged between 3 and 80, and a spanned a range from 0 to 1.

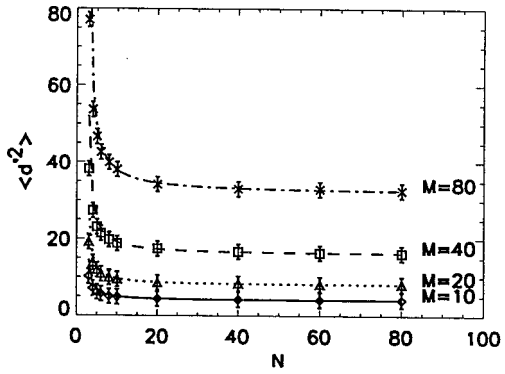

FIG. 2. Computer-simulated estimates of the square of the lesion SNR, d'^2, as functions of N (the number of lesion pairs) for four values of M (the number of independent samples per lesion). Results were generated for mean-intensity ratio $a=0.5$, corresponding to contrast level $C=0.67$. The curves correspond to the theoretical expected estimates of d'^2 from Eq. (24) (approximate chi-square method). Error bars denote standard deviations.

B. Experiment

An ATL Ultramark 8 with a 3.5-MHz annular array transducer was used. Radio frequency data were acquired with this system and digitized (11 bits) at 12 MHz, using a custom data-acquisition system provided by the manufacturer. Time gain compensation controls were held constant with depth. The 6-dB bandwidth was approximately 1.0 MHz. The resolution volume was approximately 1.2 mm^3.

Two phantoms were interrogated. They consisted of glass beads embedded in agar. The phantoms were constructed with average scatterer number densities of 6.0 and 9.5 mm^{-3}. (With a resolution volume equal to 1.2 mm^3 in the focal region, this led to 7.2 and 11.4 scatterers per resolution cell). The ratio of the backsetter coefficients yields a mean intensity ratio $a=0.73$. The sound speed for both phantoms was approximately 1556 m/s. The physical characteristics of the phantoms are summarized in Table I.

Nine regions of interest (ROIs) (1.5 cm in depth $\times$40 A-line segments or 3.5 cm wide) were acquired from each phantom. In order to investigate the dependence of estimates of d'^2 and relative coefficient of variation on N and M (computed using EQUATION C2), the ROIs were successively partitioned into $N=2$, 4, 5, 8, 10, 20, and 40 sub-ROIs. (Each sub-ROI was then 40/N A-line segments wide.) An estimate of average pixel intensity was computed for each sub-ROI. The mean and variance of this average pixel intensity was then computed for all sub-ROIs in each ROI. From the two means and two variances, one estimate of d'^2 could be computed. From the nine samples of d'^2 (from the nine ROIs), an average d'^2 and a relative coefficient of variation were computed (for each value of N investigated). Standard deviations of the estimates of relative coefficients of variation were estimated using the bootstrap method with 200 iterations.[15,16] (Unlike the simulation, the actual value of d'^2 depended on N. This was due to the decreasing size of the sub-ROI with N.)

III. RESULTS

Figure 2 shows means and standard deviations of estimates of d'^2 derived by simulation for four values of M and

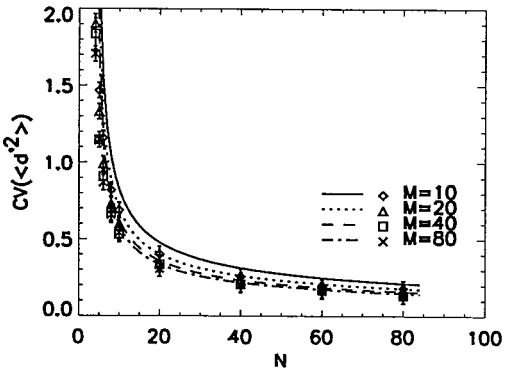

FIG. 3. Computer-simulated estimates of the coefficient of variation of the estimate of the square of the lesion SNR, d'^2, as functions of N (the number of lesion pairs) for four values of M (the number of independent samples per lesion). Results were generated for mean-intensity ratio $a=0.5$, corresponding to contrast levels $C=0.67$. The smooth curves denote the theoretical functions obtained using Eq. (29) (approximate chi-square method). Error bars denote standard deviations.

mean-intensity ratio=0.5. The curves correspond to the expected value of the estimate for d'^2 from Eq. (24). There is excellent agreement between theory and simulation. For sufficiently large N, the estimates are asymptotically unbiased. However, for small $N(N<10)$, estimates tend to be upward biased.

Figure 3 shows estimates of coefficient of variation of the estimate of d'^2 for four values of M and mean-intensity ratio=0.5. The curves correspond to the theoretically predicted function based on the approximate chi-square method [Eq. (29)]. Good agreement may be seen. The level of conformity between theory and simulation seems to increase with lesion size (M). This is probably due to the fact that the central limit theorem has increasing validity (in determining the statistical properties of the numerator of the expression for the square of the lesion SNR) as M is increased from 10 to 80.

Figure 4(a) shows a 3D plot of the magnitude of the error of the coefficient of variation of the estimate of the square of the lesion SNR associated with the third-order error propagation method as a function of number of lesion/background pairs and mean-intensity ratio for a lesion size (M) equal to 20 speckle correlation cells. Here, error is defined as the discrepancy between the theory and computer simulation. The error is quite low for a broad range of N and a. The theory begins to break down for small N and low contrast ($a\approx 1$). This is because in the low-contrast limit, d'^2 approaches 0 and causes the term arising from the numerator [Eq. (10)] to tend toward infinity and violate the small error assumption upon which the error propagation method is based.

Figure 4(b) gives the corresponding 3D plot for the approximate chi-square method. In this case, the theory breaks down at small N also. However, unlike the error propagation method, the main problem with the approximate chi-square method is at high ($a\ll 1$) rather than low ($a\approx 1$) contrast. Due to a limited regime of validity for the integral expression [Eq. (B13)] that was used in the derivation, the expression for coefficient of variation of square of the lesion SNR

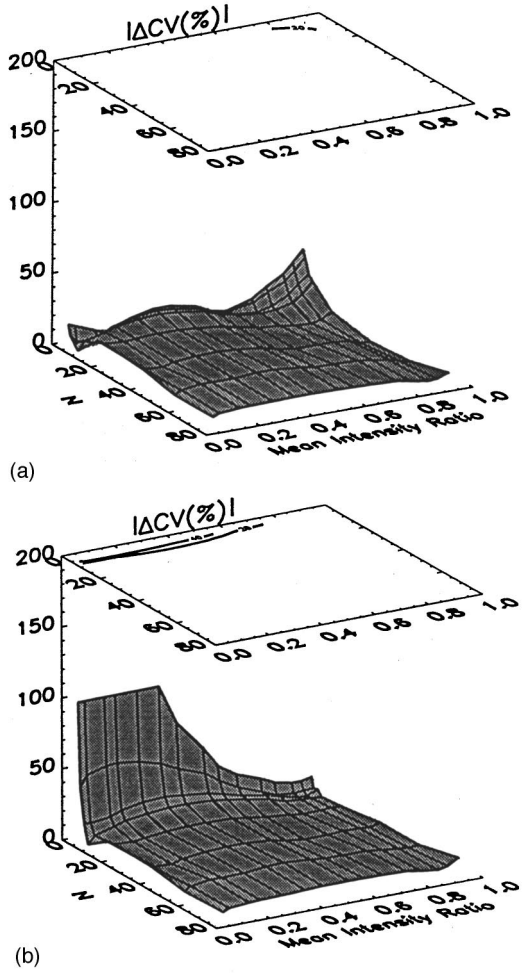

FIG. 4. 3D plots of the magnitude of the error of the coefficient of variation of the estimate of the square of the lesion SNR, d'^2, associated with the third-order error propagation method (a) and the approximate chi-square method (b) as a function of number of lesion/background pairs (N) and mean-intensity ratio (a) for a lesion size (M) equal to 20 speckle correlation cells. Here, error is defined as the discrepancy between the theory and computer simulation. See the Results section for explanation. Contours corresponding to 20% and 40% (if applicable) relative error are shown above. Error plots have been clipped at 100% for clarity of display.

is valid only for $\nu>4$. This condition places a more strict requirement on N at high contrast ($\nu=N-1>4$ or $N>5$) than at low contrast ($\nu=2N-2>4$ or $N>3$). Hence, in the 3D plot (which spans the range $5\leqslant N\leqslant 80$), limitations of theory are more apparent at high contrast.

Figure 5 illustrates in greater detail how the performance of the theories depends on N. The theoretical coefficient of variation of detectability index is shown as a function of mean-intensity ratio for the first-order approximation for the error propagation method (solid line), the third-order approximation for the error propagation method (dotted line), and the approximate chi-square method (dashed line) for a lesion size (M) of 20 speckle correlation cells. Three values of N shown are (a) 5, (b) 10, and (c) 20. The performances of the theoretical approaches may be evaluated by comparison with simulation results (asterisks with error bars) which are not based on limiting assumptions (e.g., small statistical fluctuations or assumed forms for the PDFs of the numerator and denominator for lesion detectability). As expected, errors de-

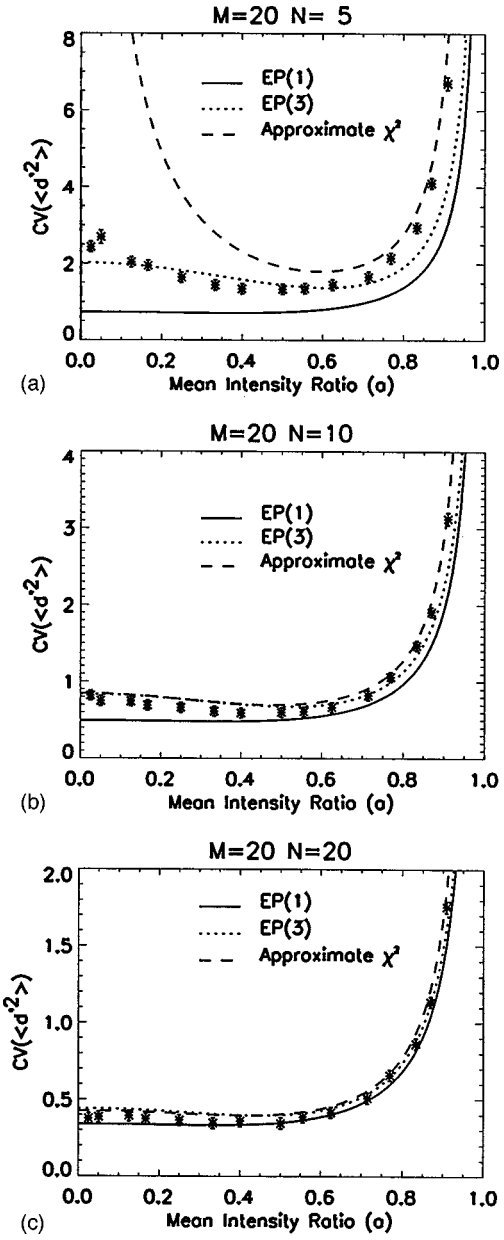

FIG. 5. Dependence of performance of theories on number of lesion/background pairs (N). The theoretical coefficient of variation is shown as a function of mean-intensity ratio for the first-order approximation for the error propagation method, EP(1), (solid line), the third-order approximation for the error propagation method, EP(3), (dotted line), and the approximate chi-square method (dashed line) for a lesion size (M) of 20 speckle correlation cells. Results from the simulation are also shown (asterisks). Three values of N are shown: (a) 5, (b) 10, and (c) 20. See the Results section for explanation.

crease with increasing N. At $N=5$, the high contrast ($a \ll 1$) limitations of the approximate chi-square method may be seen. The superior low-contrast ($a \approx 1$) performance (indicated by better conformity with simulation results) of the approximate chi-square method may be seen at $N=5$ and $N=10$. Finally, the improvement in performance of the third-order error propagation method compared with the first-order error propagation method, evident at $N=5$ and $N=10$, becomes less important for $N \geqslant 20$.

Figure 6 shows the experimental estimates of d'^2 from phantoms. The solid curve shows the value expected from

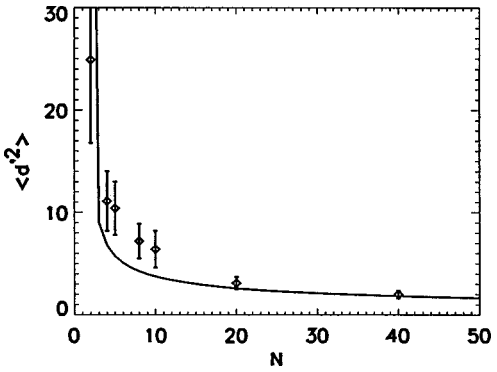

FIG. 6. Experimental estimates of the square of the lesion SNR, d'^2, as functions of N (the number of lesion pairs) from phantoms (see Table I). The solid curve denotes the theoretical functions obtained using the approximate chi-square method). Because a constant data set was successively partitioned to achieve different values of N, the effective value of M, and hence d'^2, varied with N. This is in contrast to the computer simulation in which M was held constant as N was varied. Hence, the actual value of d'^2 decreased with N. (See the Results section.) Error bars denote standard deviations.

Eq. (24) based on the mean-intensity ratio of the two phantoms and the effective number of speckles per region of interest (M) as a function of N. The mean-intensity ratio was measured experimentally as the ratio of the two average intensities of the backscatter data. Unlike the simulation, in which the actual value of d'^2 was independent of N, here d'^2 has a monotonically diminishing dependence on N. This is because in the experiment, N was increased by dividing data sets into progressively smaller units. So, although M was independent of N in the simulation, M was roughly proportional to $1/N$ in the experiment. [Equation (C2) gives the general formula for M as a function of ROI dimensions—i.e., lesion size—and system resolution cell size.] Fair agreement may be seen, especially for $N>10$.

Figure 7 shows the experimental estimates of coefficient of variation as a function of the number of lesion/background pairs, N. The theoretically predicted function, based on the third-order approximation for the error propagation method, is also shown. Deviations from perfect homogeneity of the phantoms, which would lead to increased variability of mea-

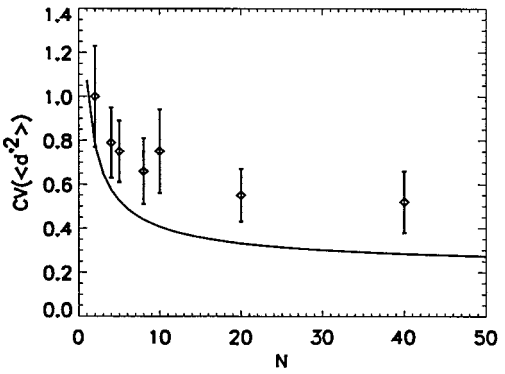

FIG. 7. Experimental estimates of the coefficient of variation of the estimate of the square of the lesion SNR, d'^2, as functions of N (the number of lesion pairs) for phantoms (see Table I). The solid curve denotes the theoretical function obtained from the error propagation method. Error bars denote standard deviations obtained using the bootstrap method.

TABLE II. Simple rules for choice for formula for coefficient of variation for the estimate of SNR^2. This table assumes lesions with between 10 and 80 speckle cells ($10 \leqslant M \leqslant 80$). The theories are abbreviated by EP(1) (first-order error propagation), EP(3) (third-order error propagation), and χ^2 (approximate chi-square). All three methods break down for $N<5$. This regime should be avoided anyway, as it is associated with unacceptably high values for coefficient of variation.

Preferred theoretical method for coefficient of variation of estimate of SNR^2		
Number of lesion/background pairs (N)	Mean-intensity ratio (a)	Preferred formula
<5	...	...
5	<0.75	EP(3)
	$\geqslant 0.75$	χ_2
6, 8, 10	<0.8	EP(3)
	$\geqslant 0.8$	χ^2
20	<0.9	EP(1), EP(3), or χ^2
	$\geqslant 0.9$	χ^2
$\geqslant 40$	all	EP(1), EP(3), or χ^2

surements, may partially or fully account for the discrepancy between theory and experimental results. When analyzing data from phantoms containing lesions embedded within a background, this problem may be mitigated somewhat by using more sophisticated templates which use data from the region immediately surrounding the lesion in order to perform some form of background subtraction.

IV. DISCUSSION

This work offers a methodology for interpreting measurements on phantoms in order to assess lesion detectability for ultrasonic imaging systems. Phantom measurements offer an economical and quantitative alternative or supplement to clinical images. Analytic forms for uncertainties in estimates of detectability of a lesion consisting of fully developed speckle embedded within a speckle background have been derived. The theory has been validated using a computer simulation and experiments on tissue-mimicking phantoms.

Two methods for predicting the coefficient of variation for the estimate of d'^2 have been presented. The regimes of validity for the two methods have been discussed in detail in the Results section and are illustrated in Figs. 2–5. To summarize: The methods have not been validated for extremely small lesions (fewer than $M=10$ speckle correlation cells). All methods break down for insufficiently sized data sets (fewer than $N=5$ lesion/background pairs). The error propagation method tends to have a comparative advantage at high contrasts, while the approximate chi-square method tends to have a comparative advantage at low contrasts. For small-to-moderate-sized data sets (fewer than $N=20$ lesion/background pairs), the third-order approximation for the error propagation method offers a substantial improvement over the first-order approximation. These characteristics are summarized in Table II.

The quantity d'^2 is more commonly used than the quantity d' in studying model observer performance; the ratio of d'^2 for a model observer to d'^2 for the optimal observer is referred to as ''observer efficiency''—a concept directly related to that of statistical efficiency.[17] (In most stochastic-noise-limited imaging applications outside of speckle-limited ultrasound, e.g., x-ray, CT, MRI, optics, d'^2 is directly proportional to some measure of exposure.)

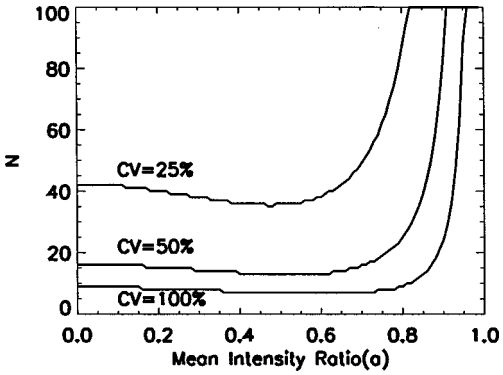

FIG. 8. Number of lesion/background pairs required to achieve coefficient of variation (CV) of the estimate of the lesion SNR, d'^2, equal to 25%, 50%, and 100% as a function of mean-intensity ratio (a). These curves are based on Eq. (29) and an assumed lesion size of $M=40$ speckle spots.

An important problem is how to design an economical phantom or set of phantoms which adequately tests the sensitivity of an imaging system. How should lesion contrast, size (M), and number (N) be chosen? The parameter most sensitively associated with phantom cost is the number of lesion/background pairs (N). Ideally, one would like to use as small a value as possible for N. For small data sets (N less than approximately 10), there exists the potential danger of overestimating system performance (as illustrated in Fig. 2). However, errors in estimates of d'^2 may be removed by using the unbiased estimator [Eq. (25)]. The more critical issue associated with the number of lesion/background pairs (N) is the variance of the estimate of d'^2. As depicted in Fig. 3, the coefficient of variation for the estimate of d'^2 diminishes rather rapidly with N for N less than approximately 20 or 30, and somewhat more gradually thereafter, suggesting the value in using at least 20 to 30 lesion/background pairs. This could be achieved either by manufacturing 20 to 30 lesion/background pairs or by manufacturing fewer lesion/background pairs, each of which could be accessed independently more than once (e.g., by altering the view angle or slice). In general, the best choice for N will also depend upon cost considerations and required precision.

The coefficient of variation of the estimate of d'^2 tends to increase dramatically at low contrasts. This may be seen in Fig. 5. (Recall that $a=0$ corresponds to high contrast and $a=1$ corresponds to low contrast). Thus, higher contrast lesions ($a \leqslant 0.5$) will tend to enable more precise assessment of the square of the lesion SNR and therefore better system performance assessment. This effect is also illustrated in Fig. 8.

Variance of the estimate of d'^2 decreases monotonically with M. This may be seen in Fig. 9. This may also be seen by inspecting Eqs. (17) and (29) and recalling from Eq. (9) that d'^2 is directly proportional to M. The sensitivity of the variance of the estimate of d'^2 to changes in M becomes more pronounced as the mean-intensity ratio approaches 1 (as contrast is reduced). Therefore, not surprisingly, precision may be enhanced through use of larger lesions.

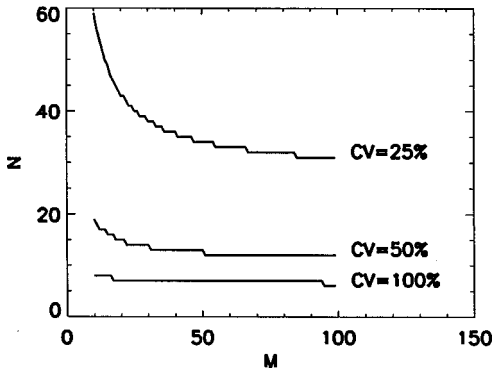

FIG. 9. Number of lesion/background pairs required to achieve coefficient of variation (CV) of the estimate of the lesion SNR, d'^2, equal to 25%, 50%, and 100% as a function of lesion size (measured by the number of speckle spots, M, contained within the lesion). These curves are based on Eq. (29) and an assumed mean-intensity ratio of 0.5 (3 dB).

Rather than using a single size and contrast, however, it may be desirable to have a set of sizes and contrasts so that the system may be evaluated over a range of difficulties of detection tasks.[1–4] For a fixed cost, increasing the number of sizes and contrasts would decrease the value of N for each individual size/contrast pair; this would lead to a corresponding increase in the coefficient of variation of the estimate of d'^2 for each size/contrast pair [see Eqs. (17) and (30)]. However, this increase may be mitigated somewhat by intelligently combining measurements. For example, it is known that d'^2 varies linearly with M [see Eq. (9)] and M varies linearly with lesion size, provided that the lesion is larger than about 10 speckles.[18] Therefore, a linear regression could be performed on estimates of d'^2 for a set of lesion sizes. The uncertainties in the parameters of the regression (i.e., slope and intercept) would reflect the total number of measurements performed (and their uncertainties), not just the number performed on each lesion size.

Any real phantom will exhibit some variability in contrast due to inconsistencies in the manufacturing process leading to a lack of complete homogeneity for all simulated lesions and background. This variability will add to the statistical variability described by the theory in this paper. This effect will become more pronounced as the size of the lesion decreases. This may partially or completely explain the discrepancy between experimental and theoretical coefficients of variation shown in Fig. 7.

The method outlined in the paper requires that the ROI corresponding to the lesion interior is free of contamination from signals emanating from outside the lesion. Partial volume effects have not been accounted for. Therefore, pixels close (within a resolution cell size) to the border of the lesion need to be avoided. This should not be a problem when analyzing data from two-dimensional (e.g., cylindrical) lesions. The application of this theory to three-dimensional (e.g., spherical) lesions may be more difficult as slice-thickness issues would need to be taken into account when delineating the ROI. This issue acquires increasing significance when the system resolution is challenged by the lesion size and whenever the system point-spread function has long-range tails due to either transducer geometry and apodization or the effects of aberrating media.

A potentially useful extension to this work would be to construct a template with which to multiply the image data in the lesion neighborhood. This template would consist of a positively weighted area corresponding to the lesion area surrounded by a negatively weighted ring that would coincide with the surrounding background. This modification would make a first-order correction for the variation in mean background level due to nonstationarity associated with trends from attenuation and/or imperfect time gain compensation. It is likely that when partial volume effects and nonstationarity are taken into account, the number of samples required for a specified level of accuracy and precision will increase over the numbers predicted in the present treatment.

Finally, it is instructive to review some of the assumptions underlying the theory presented above. The approximate chi-square method assumed specific forms for the PDFs of the numerator and denominator for the lesion detectability. These PDFs are generally valid in medical ultrasound (provided that the lesion contains a sufficient number of speckle cells that the central limit theorem ensures roughly Gaussian PDFs for the estimates of the means). Although its applicability is limited to the realm of small statistical fluctuations, the error propagation method may be more applicable to other problems as it makes no assumptions regarding underlying PDFs. In particular, it may perform better for predicting the statistical properties of estimates of detectability of small lesions ($M <$ approximately 10). In addition, although both formulations assume fully developed speckle (point SNR $= \mu_{pt}/\sigma_{pt} = 1$), it would be a straightforward, though potentially somewhat tedious, exercise to generalize the theory presented here for any diffusely scattering lesion and background for which the point SNR is known.

ACKNOWLEDGMENTS

The authors wish to thank Dr. Brian S. Garra, University of Vermont, for assistance in data acquisition, Hector Lopez, FDA, for helpful discussions, and Timothy Hall, University of Kansas, for constructing the phantoms used in the experiment. The mention of commercial products, their sources, or their use in connection with material reported herein is not to be construed as either an actual or implied endorsement of such products by the Food and Drug Administration.

APPENDIX A: RELATIVE VARIANCE OF A QUOTIENT OF RANDOM VARIABLES: THE THIRD-ORDER ERROR PROPAGATION APPROXIMATION

In this appendix, the third-order error propagation approximation for the relative variance of a quotient of random variables, q, defined by

$$q = \frac{u}{v}, \tag{A1}$$

is derived. First, denote q, u, and v as sums of their mean values and excursions from their mean values.

$$q = \bar{q} + \Delta q, \qquad u = \bar{u} + \Delta u, \qquad v = \bar{v} + \Delta v, \tag{A2}$$

where Δu, Δv, and Δq can be treated as zero-mean random variables. The quotient may be expressed as

$$\begin{aligned}\overline{q}+\Delta q &= \frac{\overline{u}+\Delta u}{\overline{v}+\Delta v} \\ &= \frac{\overline{u}}{\overline{v}}\frac{(1+\Delta u/\overline{u})}{(1+\Delta v/\overline{v})} \\ &= \overline{q}\{[1+(\Delta u/\overline{u})][1-(\Delta v/\overline{v})+(\Delta v/\overline{v})^2 \\ &\quad -(\Delta v/\overline{v})^3+\ldots]\}, \quad |\Delta v/\overline{v}|<1, \end{aligned} \tag{A3}$$

where a Taylor series expansion for the denominator has been used. The relative error in the quotient may now be expressed as

$$\begin{aligned}\Delta q/\overline{q} &= (\Delta u/\overline{u})-(\Delta v/\overline{v})-(\Delta u/\overline{u})(\Delta v/\overline{v})+(\Delta v/\overline{v})^2 \\ &\quad -(\Delta v/\overline{v})^3+(\Delta u/\overline{u})(\Delta v/\overline{v})^2+\ldots . \end{aligned} \tag{A4}$$

If this equation is squared, and the expectation operator (denoted by angular brackets) is subsequently applied, it is possible to obtain an expression for the relative variance of the quotient,

$$\begin{aligned}\langle(\Delta q/\overline{q})^2\rangle &= \langle(\Delta u/\overline{u})^2\rangle+\langle(\Delta v/\overline{v})^2\rangle-2\langle(\Delta v/\overline{v})^3\rangle \\ &\quad +3\langle(\Delta u/\overline{u})^2\rangle\langle(\Delta v/\overline{v})^2\rangle+3\langle(\Delta v/\overline{v})^4\rangle+\ldots . \end{aligned} \tag{A5}$$

Only terms up to fourth order in Δu and Δv have been retained. It has been assumed that Δu and Δv are independent and zero mean so that

$$\begin{aligned}\langle(\Delta u/\overline{u})^n(\Delta v/\overline{v})^m\rangle &= \langle(\Delta u/\overline{u})^n\rangle\langle(\Delta v/\overline{v})^m\rangle \\ &= 0 \quad \text{if } n=1 \text{ or } m=1. \end{aligned} \tag{A6}$$

[Strictly speaking, the sample mean and the sample variance of a normally distributed process are independent provided that the *maximum-likelihood* estimator for the sample variance is used.[19] Equation (A6) is only approximately true for the more commonly used *unbiased* estimator for the sample variance.] The first two terms in Eq. (A5) may be said to comprise the ''first-order'' error propagation solution. Addition of the third term, which is cubic in Δv, leads to the ''second-order'' error propagation solution. For a relatively symmetric PDF, this term can be quite small and therefore represent only a minor modification of the first-order solution. Therefore, it may be useful to incorporate the next two terms, resulting in the ''third-order'' error propagation solution.

APPENDIX B: PROPERTIES OF CHI-SQUARE PROBABILITY DENSITY FUNCTIONS

A. The central χ^2 PDF

The sample variance, s^2, estimated from N independent observations of a random variable x is given by

$$s^2=\frac{1}{N-1}\sum_{i=1}^{N}(x_i-\overline{x})^2. \tag{B1}$$

If x is a normal random variable with mean μ_x and standard deviation σ_x, it may be shown that the sample variance obeys a chi-square probability density function,[12]

$$\frac{(N-1)s^2}{\sigma_x^2}=\chi_\nu^2, \tag{B2}$$

where χ_ν^2 denotes a random variable which obeys a chi-square PDF with $\nu=N-1$ degrees of freedom and σ_x^2 is the actual variance of x. The chi-square PDF with ν degrees of freedom is defined by

$$p(\chi^2)=\frac{(\chi^2)^{\nu/2-1}e^{-\chi^2/2}}{\Gamma[\nu/2]2^{\nu/2}}, \quad \chi^2\geqslant 0, \tag{B3}$$

where $\Gamma()$ is the gamma function. (The chi-square PDF becomes fairly symmetric[12] for $N\geqslant 11$, thus providing incentive in this particular problem to go beyond the second-order error propagation solution and investigate the third-order error propagation solution as discussed in Appendix A.) The mean and the variance of the central chi-square PDF are given by

$$E(\chi_\nu^2)=\nu, \qquad \mathrm{Var}(\chi_\nu^2)=2\nu. \tag{B4}$$

Using the central moments of the chi-square PDF (see Table BI), the 2nd, 3rd, and 4th central moments of the sample variance may be obtained.

$$\begin{aligned}\langle(\Delta s)^2\rangle &= \frac{2\sigma_x^4}{N-1}, \\ \langle(\Delta s)^3\rangle &= \frac{8\sigma_x^6}{(N-1)^2}, \\ \langle(\Delta s)^4\rangle &= \frac{[48+12(N-1)]\sigma_x^8}{(N-1)^3}. \end{aligned} \tag{B5}$$

Note that the second moment is the variance of the sample variance.

TABLE BI. Central moments of the χ_ν^2 probability density function where ν corresponds to the number of degrees of freedom. The cumulants are calculated using the simple formula given in the second column above (Ref. 10, p. 940). Using the general relationship between the cumulants and the central moments of an arbitrary PDF $p(x)$ (third column, Ref. 10, p. 928), the central moments of the χ_ν^2 (fourth column) may be calculated. The mean and variance of the arbitrary PDF are denoted by μ and σ^2, respectively.

	Central moments of χ_ν^2 probability density function		
n	Cumulants of χ_ν^2 PDF $\kappa_n=2^{n-1}(n-1)!\,\nu$	Relationship between cumulants (κ_n) and central moments (α_n)	Central moments of χ_ν^2 (PDF) $\alpha_n=\int(x-m)^n p(x)dx$
1	$\kappa_1=\nu$	$\kappa_1=\mu$	0
2	$\kappa_2=2\nu$	$\kappa_2=\sigma^2=\alpha_2$	2ν
3	$\kappa_3=8\nu$	$\kappa_3=\alpha_3$	8ν
4	$\kappa_4=48\nu$	$\kappa_4=\alpha_4-3\alpha_2^2$	$48\nu+12\nu^2$

B. Approximate PDF of the sum of two independent central χ^2 distributed random variables

The denominator of the expression for the square of the lesion SNR has the form of the weighted sum of two sample variances,

$$\frac{1}{2}(s_1^2+s_2^2)=\frac{\sigma_1^2}{2(N-1)}\chi^2_{N-1}+\frac{\sigma_2^2}{2(N-1)}\chi^2_{N-1}. \quad \text{(B6)}$$

It is useful to obtain an approximate form for the PDF of this sum. This PDF is known in the limits of very low and very high contrast, but must be approximated otherwise. Under conditions of low contrast ($\sigma_1\approx\sigma_2$), the sum is proportional to the sum of equally weighted random variables, each of which obeys a χ^2_{N-1} PDF. The sum then obeys a $\chi^2_{2(N-1)}$ PDF. In the limit of very high contrast, one of the terms in the denominator is negligible and the sum simply obeys a χ^2_{N-1} PDF. In the general case, suppose that the PDF may be approximated as a χ^2_ν PDF with an effective value of number of degrees of freedom (ν) somewhere in between these two extremes so that

$$\tfrac{1}{2}(s_1^2+s_2^2)=B\chi^2_\nu. \quad \text{(B7)}$$

B and ν may be evaluated as follows. First, equate the expected value of the sum of sample variances to the mean of the scaled χ^2_ν PDF:

$$\langle \tfrac{1}{2}(s_1^2+s_2^2)\rangle=\tfrac{1}{2}(\sigma_1^2+\sigma_2^2)=B\nu. \quad \text{(B8)}$$

Next, equate the variance of the denominator to the variance of the scaled χ^2_ν PDF. Using Eq. (B5) for the variance of a sample variance and recalling that the variance of the sum of two independent random variables is the sum of their respective variances,

$$\mathrm{Var}\left[\frac{1}{2}(s_1^2+s_2^2)\right]=\frac{\sigma_1^4}{2(N-1)}+\frac{\sigma_2^4}{2(N-1)}=2B^2\nu. \quad \text{(B9)}$$

Dividing Eq. (B9) by Eq. (B8), it may be found that

$$B=\frac{1}{2(N-1)}\frac{\sigma_1^4+\sigma_2^4}{\sigma_1^2+\sigma_2^2}, \quad \text{(B10)}$$

and $\nu=c(N-1)$ degrees of freedom, where

$$c=\frac{(1+\sigma_2^2/\sigma_1^2)^2}{1+(\sigma_2^2/\sigma_1^2)^2}. \quad \text{(B11)}$$

Note that $1\leqslant c\leqslant 2$. The low-contrast limit ($\sigma_1\approx\sigma_2$) is represented by $c=2$. The high-contrast limit is represented by $c=1$.

C. Moments of the reciprocal of a central χ^2 distributed random variable

In order to obtain the moments of the first and second moments of the square of the lesion SNR, it is necessary to calculate the first and second moments of the reciprocal of a central χ^2 distributed random variable (denoted in this section by Z). Using the formula for the chi-squared probability density function, the expected value of Z^{-1} may be found from

$$\langle Z^{-1}\rangle=\int_0^\infty \frac{Z^{-1}Z^{\nu/2-1}e^{-z/2}}{\Gamma[\nu/2]2^{\nu/2}}dz, \quad \text{(B12)}$$

where $\Gamma()$ is the gamma function. Using the following two equations,

$$\int_0^\infty x^n e^{-cx}=\frac{\Gamma(n+1)}{c^{n+1}} \quad (n>0,c>0) \quad \text{(B13)}$$

and

$$\Gamma(n+1)=n\Gamma(n), \quad \text{(B14)}$$

it is possible to show that[14]

$$\langle Z^{-1}\rangle=\frac{1}{\nu-2} \quad (\nu>2). \quad \text{(B15)}$$

Similarly, the expected value of Z^{-2} may be shown to be given by

$$\langle Z^{-2}\rangle=\int_0^\infty \frac{Z^{-2}Z^{\nu/2-1}e^{-z/2}}{\Gamma(\nu/2)2^{\nu/2}}dz$$

$$=\frac{1}{(\nu-2)(\nu-4)} \quad (\nu>4). \quad \text{(B16)}$$

D. The noncentral χ^2 PDF

Consider a set of independent, standard, normally distributed random variables, x_i. Then the variable y, defined as

$$y=\sum_{i=1}^{\nu-1} x_i^2+(x_\nu+\sqrt{\lambda})^2 \quad (\nu>1)$$

$$=(x_1+\sqrt{\lambda})^2 \quad (\nu=1) \quad \text{(B17)}$$

obeys a noncentral chi-square distribution $\chi^2_{\nu,\lambda}$ with ν degrees of freedom and noncentrality parameter λ.[13] The noncentral chi-square distribution may be represented as a weighted sum of chi-square distributions.[10] The mean and variance are given by

$$E(\chi^2_{\nu,\lambda})=\nu+\lambda,$$
$$\mathrm{Var}(\chi^2_{\nu,\lambda})=2\nu+4\lambda. \quad \text{(B18)}$$

APPENDIX C: NUMBER OF INDEPENDENT SAMPLES PER LESION

The objective of this appendix is to describe how the number of independent samples per lesion (M) may be computed. Clearly, M is a function of both the speckle spot size (or ''correlation area''), S_c, and the lesion size, S_m. The correlation area, S_c, is given by[5]

$$S_c=\int_{-\infty}^{\infty}\int_{-\infty}^{\infty} d(\Delta x)d(\Delta z)\frac{C(\Delta x,\Delta z)}{C(0,0)}, \quad \text{(C1)}$$

where $C(\Delta x,\Delta z)$ is the two-dimensional correlation function. In the focal region, $C(\Delta x,\Delta z)$ is separable and S_c may be expressed as the product of a depth factor and a lateral factor so that $S_c=S_{cz}S_{cx}$ where $S_{cz}=0.685/\Delta f$, Δf is the system full width at half maximum (FWHM) in MHz, $S_{cx}=0.90\lambda z/D$, λ is the wavelength, z is the focal distance, and D is the aperture diameter (all in mm).

For lesions containing many speckle correlation areas, M is approximately equal to S_m/S_c, as expected, but for small lesions a more general expression must be used:[18]

$$M=\left\{\sqrt{\frac{S_c}{S_m}}\,\mathrm{erf}\left(\sqrt{\frac{\pi S_m}{S_c}}\right)-\left(\frac{S_c}{\pi S_m}\right)\times\left[1-\exp\left(-\frac{\pi S_m}{S_c}\right)\right]\right\}^{-2}, \tag{C2}$$

where

$$\mathrm{erf}(x)=\frac{2}{\sqrt{\pi}}\int_0^x e^{-z^2}dz. \tag{C3}$$

The minimum value that M can attain is 1. (This is reasonable, as it is impossible to have a fraction of an independent sample.)

[1] S. W. Smith, R. F. Wagner, J. M. Sandrik, and H. Lopez, ''Low contrast detectability and contrast/detail analysis in medical ultrasound,'' IEEE Trans. Sonics Ultrason. **30**, 164–173 (1983).

[2] H. Lopez, M. H. Loew, P. F. Butler, M. C. Hill, and R. M. Allman, ''Objective analysis of ultrasound images by use of a computational observer,'' Med. Phys. **17**, 48–57 (1990).

[3] H. Lopez, M. H. Loew, and D. J. Goodenough, ''Objective analysis of ultrasound images by use of a computational observer,'' IEEE Trans. Med. Imaging **11**, 496–506 (1992).

[4] J. J. Rownd, E. L. Madsen, J. A. Zagzebski, G. R. Frank, and F. Dong, ''Phantoms and automated system for testing the resolution of ultrasound scanners,'' Ultrasound Med. Biol. **23**, 245–260 (1997).

[5] R. F. Wagner, S. W. Smith, J. M. Sandrik, and H. Lopez, ''Statistics of speckle in ultrasound *B*-Scans,'' IEEE Trans. Sonics Ultrason. **30**, 156–163 (1983).

[6] R. A. Johnson and D. W. Wichern, *Applied Multivariate Statistical Analysis* (Prentice-Hall, Englewood Cliffs, NJ, 1982).

[7] R. A. Fisher, *Statistical Methods and Scientific Inference*, 3rd ed. (Oliver and Boyd, Hafner, NY, 1973).

[8] R. F. Wagner, M. F. Insana, and S. W. Smith, ''Fundamental correlation lengths of coherent speckle in medical ultrasonic images,'' IEEE Trans. Ultrason. Ferroelectr. Freq. Control **35**, 34–44 (1988).

[9] J. M. Thijssen, B. J. Oosterveld, and R. F. Wagner, ''Grey level transforms and lesion detectability in echographic images,'' Ultrason. Imaging **10**, 171–195 (1988).

[10] M. Abramowitz and I. A. Stegun, *Handbook of Mathematical Functions* (National Bureau of Standards Applied Mathematics Series 55, U.S. Government Printing Office, Washington, DC, 1972).

[11] P. R. Bevington, *Data Reduction and Error Analysis for the Physical Sciences* (McGraw-Hill, New York, 1969), Chap. 4.

[12] J. S. Bendat and A. G. Piersol, *Random Data: Analysis and Measurement Procedures* (Wiley-Interscience, New York, 1971), Chap. 4, pp. 119–122.

[13] D. M. Green and J. A. Swets, *Signal Detection Theory and Psychophysics* (Krieger, Huntington, NY, 1966), Appendix I.

[14] B. R. Frieden, *Probability, Statistical Optics, and Data Testing* (Springer, Berlin, 1983).

[15] B. Efron and B. Tibshirani, *An Introduction to the Bootstrap* (Chapman and Hall, New York, 1993).

[16] A. M. Zoubir and B. Boashash, ''The bootstrap and its application in signal processing,'' IEEE Signal Process. Mag. **15**, 56–76 (1998).

[17] D. G. Brown, M. F. Insana, and M. Tapiovaara, ''Detection performance of the ideal decision function and its McLaurin expansion: Signal position unknown,'' J. Acoust. Soc. Am. **97**, 379–398 (1995).

[18] J. W. Goodman, ''Statistical Properties of Laser Speckle Patterns,'' in *Laser Speckle and Related Phenomena*, edited by J. C. Dainty (Springer, Berlin, 1975).

[19] T. W. Anderson, *An Introduction to Multivariate Statistical Analysis*, 2nd ed. (Wiley, New York, 1984).

[20] E. Jakeman, ''Speckle statistics with a small number of scatterers,'' Opt. Eng. (Bellingham) **23**, 453–461 (1984).

[21] K. A. Wear, R. F. Wagner, D. G. Brown, and M. F. Insana, ''Statistical properties of estimates of scatterer number density,'' J. Acoust. Soc. Am. **102**, 635–641 (1997).

LETTERS TO THE EDITOR

Comments on "Mode coupling by internal waves for multimegameter acoustic propagation in the ocean" [J. Acoust. Soc. Am. 100, 3607–3620 (1996)]

Anatoly L. Virovlyansky
Institute of Applied Physics, Russian Academy of Science, 46 Ul'yanov Street, 603600 Nizhny Novgorod, Russia

(Received 7 October 1997; revised 13 February 1998; accepted 2 April 1999)

The results of numerical simulation presented in the subject paper shows that sound pulses carried by individual high modes in an underwater acoustic waveguide at ranges of a few thousand km are severely distorted due to inhomogeneities induced by random internal waves. At the same time, the total wave field reveals a rather coherent pattern, where raylike wavefronts are evident. Here, comment is made on this interesting result from the viewpoint of ray-mode relations in a waveguide with large-scale refractive index inhomogeneities. It is shown that when very distorted mode arrival patterns are synthesized together, the result is a much less distorted ray-arrival pattern. © *1999 Acoustical Society of America.* [S0001-4966(99)03107-0]

PACS numbers: 43.30.Bp, 43.30.Dr, 43.30.Cq [SAC-B]

INTRODUCTION

The authors of Ref. 1 have performed broadband parabolic-equation simulations of sound transmission (at a carrier frequency of 75 Hz with a bandwidth of 30 Hz) through a deep-water acoustic waveguide with inhomogeneities of refractive index induced by random internal waves. They have analyzed not only the total wave field but the contributions to it from individual modes as well. Here, we focus on one interesting result obtained in this paper.

It has turned out that, due to mode coupling, the arrival patterns for individual high modes at distances of a few thousand km change drastically as compared to the case of a range-independent environment. The pulses carried by individual high modes become several times longer and acquire irregular shapes. At the same time, the total wave field reveals a rather coherent pattern, where raylike wavefronts are evident. In particular, at a distance of 1000 km (the shortest range considered in the paper) the part of the received signal formed by high modes (early arrivals) looks rather similar to that in the unperturbed waveguide. The authors have come to the conclusion that ''while the high modes may be strongly affected by internal waves they are coherent enough that when they are synthesized together localized wave front results.''

Here, we offer a qualitative explanation to this effect on the basis of results obtained when studying ray-mode relationship in a range-independent waveguide[2–4] and in a waveguide with refractive index inhomogeneities.[5,6]

The main point which we want to clarify is how severely distorted pulses carried by individual modes, being put together, can produce much less distorted pulses coming to the receiver through individual ray paths.

I. RAY-MODE RELATIONS IN A RANGE-INDEPENDENT WAVEGUIDE

For simplicity, we consider a cylindrically symmetric problem. The mode representation of the continuous wave (cw) field, u, in a range-independent waveguide is[7]

$$u(r,z)=\frac{1}{\sqrt{r}}\sum_m B_m\varphi_m(z)e^{ik_m r}, \tag{1}$$

where z and r are the vertical and horizontal coordinates, respectively, $\varphi_m(z)$ is the eigenfunction for the mth mode, and k_m is the corresponding eigenvalue. The time factor $e^{-i\omega t}$ is omitted.

In the Wentzel–Kramers–Brilouin (WKB) approximation, the eigenfunction between its turning points can be represented as a superposition of the two terms:[7]

$$\varphi_m(z)=Q_m(z)(e^{i\Phi_m(z)}+e^{-i\Phi_m(z)}), \tag{2}$$

corresponding to two quasiplane waves (the so-called Brillouin waves) forming the mth mode.

Let us consider the case when the wave field is excited by a point source located at a depth $z=z_0$. Then, for the mode amplitude, B_m, we have

$$B_m = N_m \varphi_m(z_0) = N_m Q_m(z_0)(e^{i\Phi_m(z_0)} + e^{-i\Phi_m(z_0)}). \quad (3)$$

The explicit expressions for the amplitude, $Q_m(z)$, the phase, $\Phi_m(z)$, and the factor, N_m, depending on the source power, are simple and well-known (see, e.g., Ref. 7). According to Eqs. (2) and (3), each term in Eq. (1) can be split into four new ones, yielding

$$u(r,z) = \frac{1}{\sqrt{r}} \sum_{j=1}^{4} \sum_{m} N_m Q_m(z) Q_m(z_0) \times e^{i\alpha_j \Phi_m(z_0) + i\beta_j \Phi_m(z) + ik_m r}, \quad (4)$$

where the constants α_j and β_j are equal to ± 1.

The mode representation can be converted into the ray representation and vice versa using the Poisson sum formula.[3] However, there exists a much more detailed relationship between modes and rays. In particular, it can be shown that at not very large distances, the contribution to the total wave field from a single ray, $Ae^{ik\Psi}$, is approximately equal to the sum of Δm constructively interfering terms of the sum (4) with the same index j, i.e., with the same pair (α_j, β_j)

$$Ae^{ik\Psi} = \frac{1}{\sqrt{r}} \sum_{m=m_0-\Delta m/2}^{m_0+\Delta m/2} N_m Q_m(z) Q_m(z_0) \times e^{i\alpha_j \Phi_m(z_0) + i\beta_j \Phi_m(z) + ik_m r}, \quad (5)$$

where $1 \ll \Delta m \ll m_0$. The pair (α_j, β_j) defines the signs of the launch and arrival angles of the ray. The number m_0 corresponds to the mode formed by the Brillouin waves, one of which at the depth z_0 has the grazing angle most close to the launch angle of the ray, χ; that is,

$$n(z_0)\cos\chi = \frac{k_{m_0}}{k}, \quad (6)$$

where $n(z)$ is the refractive index profile, $k=\omega/c$, c is the sound speed corresponding to $n=1$. Excellent analysis of these issues has been done in Refs. 2–4.

Let us emphasize the two points which remain valid in an inhomogeneous waveguide considered below.

(i) The given mode constructively interferes with the neighboring modes along the trajectories of two rays, leaving the point source at the angles satisfying Eq. (6). We call them *mode rays*.

(ii) According to Eq. (3), the amplitude of the mode is a sum of two terms, but in Eq. (5) only one such term from each of Δm modes ''takes part.''

II. RAYS IN AN INHOMOGENEOUS WAVEGUIDE AS SUMS OF GROUPS OF CONSTRUCTIVELY INTERFERING MODES

Now, consider an inhomogeneous waveguide, where the unperturbed refractive index profile, $n(z)$, is replaced by $n(z)+\delta n(r,z)$ with $\delta n \ll n$. We assume that the small range-dependent component, $\delta n(r,z)$, is large-scaled as compared to the wavelength (otherwise the ray theory cannot be used), and restrict our consideration to not very long ranges where not only ray theory can be applied but ray trajectory deviations due to inhomogeneities can be neglected. This approximation yields a very simple formula for rays widely used in underwater acoustics:[8] the unperturbed cw ray field, $Ae^{ik\Psi}$, in presence of inhomogeneities changes to

$$Ae^{ik(\Psi+\delta\Psi)}, \quad \delta\Psi = \int_{\Gamma} \delta n \, ds, \quad (7)$$

where the integral runs along the unperturbed ray trajectory Γ, and ds is the arc length.

Under the same assumption, a quite similar formula can be derived for the mode amplitude variations with range.[5,6] According to it, Eq. (3) is replaced with

$$B_m(r) = N_m Q_m(z_0)(e^{i\Phi_m(z_0) + ikX_m^+} + e^{-i\Phi_m(z_0) + ikX_m^-}), \quad (8)$$

$$X_m^{\pm} = \int_{\Gamma_m^+} \delta n \, ds, \quad (9)$$

where the integrals run along the trajectories of mode rays $\Gamma_m^{\pm}$ in the unperturbed waveguide. The superscripts $\pm$ denote the signs of launch angles of the mode rays.

Note the important difference between Eq. (8) and its ray prototype, Eq. (7), which is crucial for our analysis. While the ray amplitude does not change due to inhomogeneities, the mode amplitude can change drastically when the phase shifts $kX_m^{\pm}$ exceed π. Moreover, since the ray-phase shift, $k\delta\Psi$, is proportional to frequency, inhomogeneities cause only shifts in ray travel times, and pulses coming to the receiver through different eigenrays have the shapes repeating, up to a multiplicative constant, the shape of the initially radiated pulse. In contrast, for the mode both the phase and the amplitude of $B_m(r)$ are very sensitive to inhomogeneities. Since the trajectories of two mode rays corresponding to the given mode leave the source at the grazing angles equal in absolute value and opposite in sign, these rays generally cross uncorrelated inhomogeneities and, hence, vary independently. This leads to significant distortions of the mode amplitude at such ranges where phase shifts along the ray trajectories become of order π. At frequencies of a few hundred Hz, such shifts induced by internal waves occur at ranges considerably less than 1000 km.[9] It is also clear that at the 1000-km range the mode-amplitude dependence on frequency also differs drastically from that in the unperturbed waveguide, yielding the distortions of mode arrival patterns demonstrated in Ref. 1.

Nevertheless, the raylike structure of clusters of constructively interfering modes remains even under these conditions. The contribution from a single ray to the total field is given by the analogous to Eq. (5) relation

$$A_1 e^{ik\Psi_1} = \frac{1}{\sqrt{r}} \sum_{m=m_0-\Delta m/2}^{m_0+\Delta m/2} N_m Q_m(z) Q_m(z_0) \times e^{i\alpha_j \Phi_m(z_0) + i\beta_j \Phi_m(z) + ik_m r + ikX_m}. \quad (10)$$

Here, the symbols X_m denote the phase shifts along the mode rays corresponding to different modes but having the *same*

signs of launch angles coinciding with the sign of the ray-launch angle. Since $\Delta m \ll m_0$, at not very long ranges the trajectories of these mode rays are close and pass through almost the same inhomogeneities. It means that all the phase shifts, kX_m, can be approximately replaced with kX_{m_0} (the value of kX_{m_0} itself can be greater than π). Factoring out the exponential $e^{ikX_{m_0}}$ and taking into account Eq. (5), we get

$$A_1 e^{ik\Psi_1} = A e^{ik(\Psi + X_{m_0})}. \tag{11}$$

Since the trajectory of the mode ray corresponding to the m_0th mode is very close to the unperturbed trajectory of the ray whose field is given in Eq. (11), the latter reduces to Eq. (7).

Taking into account small differences in the values of X_m for different m, we can get the small variations of ray amplitude due to inhomogeneities. The effects of diffraction can also be accounted for by modification of Eq. (10).[5,6] But, the discussion of these topics is beyond the scope of this paper.

For a signal with a finite bandwidth, the mode sum must include an integration over frequency. In Eq. (4) there are four terms corresponding to the given mode: they have the same index m and the different indices j. After the integration, these four terms give the four constituents forming the pulse carried by the mode (''mode'' pulse). On the other hand, the total signal at the observation point can be regarded as a sum of pulses arriving through different ray paths (''ray'' pulses). The shapes of these two types of pulses differ. The relationship between the two representations of the received signal, as the sums over ray and mode pulses, is similar to the ray-mode relations in the scope of cw theory. In particular, the ray pulse can be represented as a result of constructive interference of mode pulses. The detailed discussion of this topic is given in Refs. 10 and 11.

Here, we only note that an analog to the statement (ii), made at the end of the preceding section, can be formulated when considering the interference of a group of mode pulses producing a ray pulse. The latter, according to Eqs. (5) and (10), is formed by contributions from the constituents with the same index j. The random phase shifts corresponding to these constituents are approximately equal, and from the viewpoint of a ray-arrival pattern they yield only an additional time delay equal to $X_{m0}/c = \delta\Psi/c$. Other constituents (with, generally, other phase shifts) belonging to the same group of modes take part in forming other ray pulses.

When the characteristic spatial scales of inhomogeneities are so large that the adiabatic approximation can be used, the difference in phase shifts kX_m^+ and kX_m^- in Eq. (8) can be negligible, even if the values of kX_m^+ and kX_m^- are much greater than π. In such cases, the mode pulses will not be distorted. The relationship between mode and ray pulses under this condition is considered in Ref. 12.

III. CONCLUSION

The above considerations explain qualitatively how unstable, with respect to inhomogeneities, mode-arrival patterns form much more stable ray arrivals. According to the remark after Eqs. (8) and (9), significant distortions of mode-arrival patterns at carrier frequencies of a few hundred Hz can be expected at shorter ranges than 1000 km; that is, in those places where the ray arrival structures should look similar to that in the unperturbed waveguide.

Our approach is based on the WKB approximation, and therefore it cannot be used for low modes. On the other hand, we believe that it can be applied not only for qualitative analysis of high-mode arrival patterns, but for quantitative estimations as well. The validity region for results that will be obtained in this way is a subject for further investigations.

ACKNOWLEDGMENTS

This work was supported by the Russian Foundation for Fundamental Research (Grants No. 95-02-04565) and by the Grant U.S. Navy N 00014-97-1-0426. Most of the work has been done during my visit to the Courant Institute of Mathematical Sciences. I wish to thank Professor G. Zaslavsky for useful discussions and for the interest shown in these studies.

[1] J. A. Colosi and S. M. Flatte, ''Mode coupling by internal waves for multime-gameter acoustic propagation in the ocean,'' J. Acoust. Soc. Am. **100**, 3607–3620 (1996).
[2] C. T. Tindle and K. M. Guthrie, ''Rays as interfering modes in underwater acoustics,'' J. Sound Vib. **34**, 291–295 (1974).
[3] L. B. Felsen, ''Hybrid ray-mode fields in inhomogeneous waveguides and ducts,'' J. Acoust. Soc. Am. **69**, 352–361 (1981).
[4] T. Gao and E.-C. Shang, ''The transformation between the mode representation and the generalized ray representation of a sound field,'' J. Sound Vib. **80**(1), 105–115 (1982).
[5] A. L. Virovlyanskii and A. G. Kosterin, ''Method of smooth perturbation for the description of fields in multomode waveguides,'' Sov. Phys. Acoust. **33**(4), 351–354 (1987).
[6] A. L. Virovlyansky, V. V. Kurin, N. V. Pronchatov-Rubtsov, and S. I. Simdyankin, ''Fresnel zones for modes,'' J. Acoust. Soc. Am. **101**, 163–173 (1997).
[7] L. M. Brekhovskikh and Yu. Lysanov, *Fundamentals of Ocean Acoustics* (Springer, Berlin, 1991).
[8] S. M. Flatte, R. Dashen, W. Munk, K. M. Watson, and F. Zachariasen, *Sound Transmission Through a Fluctuating Ocean* (Cambridge University Press, Cambridge, 1979).
[9] A. L. Virovlyansky, A. G. Kosterin, and A. N. Malakhov, ''Mode fluctuations in a canonical underwater sound channel,'' Sov. Phys. Acoust. **35**, 229–235 (1989).
[10] K. M. Guthrie and C. T. Tindle, ''Ray effects in the normal mode approach to underwater acoustics,'' J. Sound Vib. **47**, 403–413 (1976).
[11] W. Munk and C. Wunsch, ''Ocean acoustic tomography: rays and modes,'' Rev. Geophys. Space Phys. **21**, 1–37 (1983).
[12] P. Traykovski, ''Travel-time perturbations due to internal waves: equivalence of modal and ray solutions,'' J. Acoust. Soc. Am. **99**, 822–830 (1996).

Verification of the HIC algorithm

John I. Dunlop
School of Physics, University of New South Wales, Sydney, Australia 2051

(Received 25 August 1998; accepted for publication 16 April 1999)

Computation of the Head Injury Criterion (HIC), specified in test standards for impact attenuation, involves an integrand maximization formula which should be verified in any system calibration. Two types of wave form—the translated triangle and half sine wave—are suggested as suitable for verifying the calibration of the test system and the validity of the computation algorithm. © *1999 Acoustical Society of America.* [S0001-4966(99)01808-1]

PACS numbers: 43.30.Ng [PJR]

The ASTM Standard F1292-93 ''Standard Specification for Impact Attenuation of Surface Systems Under and Around Playground Equipment'' uses the head injury criterion (HIC) for determination of the severity of an impact. This is defined by the formula

$$\mathrm{HIC}=(t_2-t_1)\left\{\frac{1}{t_2-t_1}\int_{t_1}^{t_2} a\ dt\right\}^{2.5},$$

where a is the instantaneous acceleration in units of G, and t_1 and t_2 are times within the impact duration chosen to maximize the value of the integrand.

A sample computation algorithm is given in the Standard together with a verification test. This test uses a translated square pulse of specified parameters to test the system and, while useful in the calibration of the system levels, is not particularly discriminating of the algorithm. For example, it will be satisfied by an algorithm using the start and stop times of the impact for t_1 and t_2. A more satisfactory test waveform is the translated triangular pulse for which an analytical value of HIC can be derived as follows.

Consider a half-triangular (sawtooth) pulse as in Fig. 1, of width W and height H. First evaluate the integrand I from an intermediate value t to the time W of the peak value viz.:

$$I=\left\{\frac{1}{w-t}\int_t^w\left(\frac{H}{W}\right)\ t\ dt\right\}^{2.5}(w-t)$$

$$=\left\{\frac{H}{2W}(w+t)\right\}^{2.5}(w-t).$$

The integrand is maximum when $dI/dt=0$. Then, $t=3W/7$ and the maximum value of the integrand is $(4W/7)\times\{5H/7\}^{2.5}$ with an integration width of $4W/7$.

The integrand and the evaluation of its maximum value correspond to the computation of HIC. Thus the waveform can be used to give a verification of the computation of HIC and also of the integration width which is required in some Standards (e.g., the Australian/New Zealand Standard ASNZS4422:1996).

A calibration check would be to use a translated triangle, either symmetric or asymmetric (sawtooth), of amplitude 200 G. A width of 7.17 ms yields a HIC of 1000; other widths giving proportionate values. If a suitable calibration source is not readily available, a single (translated) triangle can be obtained using a signal generator producing triangular waves. The dc offset can be used to move the bottom half of the wave form below the cutoff of the digital recorder leaving a single triangle. The digitized signal data must then be used to determine its width and height. Trials of the test on a typical system gave calibrations to within 2% (at HIC $=1000$), rounded tops on the triangles being the principal source of errors.

The translated half sine wave can be used to avoid the errors caused by the rounded top of the triangle, but then errors arise in defining the correct starting point of the sine wave if the offset is used to generate them. In this case the required relationships can be derived with a little more difficulty, the maximum value of the integrand being approximately $0.415\ H^{2.5}W$ with an integration width approximately $0.42W$. Trials of sample waveforms generated using the offset method gave calibrations to within 5% (at HIC around 1000) on a system algorithm.

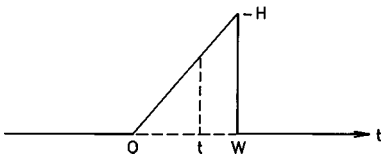

FIG. 1. Translated (half) triangular pulse of width W and height H.

Influence of visco-inertial effects on the ultrasonic properties of monodisperse silica suspensions

Norbert Herrmann and D. Julian McClements[a)]
Biopolymers and Colloids Research Laboratory, Department of Food Science, University of Massachusetts, Amherst, Massachusetts 01003

(Received 2 November 1998; revised 26 April 1999; accepted 6 May 1999)

The measured ultrasonic velocity and attenuation spectra (0.5–150 MHz) of colloidal suspensions containing monodisperse silica particles (ϕ=5%, r=190 nm) dispersed in a series of water–glycerol mixtures (0% to 80% glycerol) were in good agreement with predictions of multiple scattering theory. The major cause of excess attenuation and velocity dispersion was visco-inertial dissipation losses, which arose because of the density contrast between the silica particles and surrounding liquid. There was a maximum in the attenuation spectra that decreased in height and shifted to higher frequencies as the glycerol concentration was increased because of the reduction in density contrast and increase in continuous phase viscosity (1 to 60 mPa.s). These results suggest that ultrasound could be used to measure continuous phase viscosities in colloidal suspensions. [S0001-4966(99)04308-8]

PACS numbers: 43.35.Bf [HEB]

INTRODUCTION

In the long wavelength limit, the major cause of attenuation and velocity dispersion in colloidal suspensions containing particles that have a density similar to that of the surrounding liquid is thermal dissipation.[1–3] Thermal dissipation occurs because of the heat flow out of a particle as a result of the temperature gradients that arise at the particle interface in the presence of an ultrasonic wave.[4,5] Traditional multiple scattering theory provides an excellent description of the ultrasonic properties of dilute colloidal suspensions in which there is a low density-contrast between the particles and surrounding fluid.[3,6–9] Recently, it has been shown that this theory can be extended to concentrated colloidal suspensions by taking into account thermal overlap effects.[10]

The major cause of attenuation and velocity dispersion in colloidal dispersions in which there is a large density-contrast between the particles and surrounding liquid is visco-inertial dissipation.[4,5,11] In the presence of an ultrasonic wave, a particle oscillates backward and forward because it has a different density than the surrounding liquid. This oscillation is damped because of the viscosity of the fluid, and so some of the ultrasonic energy is converted to heat. As a result, the ultrasonic properties of this type of colloidal suspension depend on the density difference between particles and surrounding liquid, particle concentration, particle size, and continuous phase viscosity.[5] The viscosity of many fluids is frequency dependent because of various shear and volume relaxation processes.[12] This has important consequences for the application of ultrasonic techniques for the characterization of colloidal properties, such as particle size or concentration.[13–15] It is important to use a viscosity in the multiple scattering theory used to interpret ultrasonic spectra that is appropriate for the frequency range used in the experiments. On the other hand, if the particle size and concentration of a colloidal suspension are known then it should be possible to use ultrasonic spectrometry to provide valuable information about the rheological characteristics of the fluid surrounding the particles. Measurement of the shear rheology of liquids using the ultrasonic method may have advantages over alternative methods. For example, it may be possible to determine the viscosity of micro-regimes within a material by dispersing particles within them and examining the retardation of their oscillation at ultrasonic frequencies. At present, there are few experimental studies that have systematically examined the influence of visco-inertial effects on the ultrasonic spectra of colloidal suspensions. Recently, Schulitz *et al.* measured the ultrasonic properties of metal particles suspended in glycerol–water mixtures of varying viscosity.[15] They suggested that measurements of the ultrasonic attenuation spectra might prove useful for determining the viscosity of the suspending liquid. The purpose of the present study is to examine the influence of continuous phase viscosity (1–60 mPa.s) on the ultrasonic properties of well-characterized colloidal suspensions, and to assess whether ultrasonic spectrometry can be used to provide information about the rheology of suspending liquids.

I. MATERIALS AND METHODS

A. Preparation of colloidal suspensions

The colloidal suspensions used in this study were prepared from a 40 wt% monodisperse (radius=190 nm) silica-in-water suspension (MP-4540, Nissan Chemical Industries, Tarrytown, NY). The silica particles in these suspensions are nonporous, so their density does not depend on that of the continuous phase. This suspension was diluted with glycerol and water to obtain four samples with the same particle volume fraction (ϕ=0.05), but different glycerol concentrations in the continuous phase: 0%, 40%, 60%, and 80 wt% (Table

a)Author to whom correspondence should be addressed. Electronic mail: mcclements@foodsci.umass.edu.

TABLE I. Thermophysical properties of silica particles and water–glycerol mixtures at 20 °C.

	Silica	Water	40% glycerin	60% glycerin	80% glycerin
c (m s^{-1})	5960[a]	1486.0	1687.5	1792.0	1874.3
ρ (kg m^{-3})	2.20[a]	0.998[a,b]	1.0984[a,b]	1.1530[a,b]	1.2085[a,b]
β (K^{-1})	$1.56\cdot10^{-6}$	$2.13\cdot10^{-4}$[a]	$4.35\cdot10^{-4}$[b]	$5.45\cdot10^{-4}$[b]	$6.15\cdot10^{-4}$[b]
Cp (J kg^{-1} K^{-1})	730[a]	4182[a]	3697[d]	3365[d]	2920[d]
κ (W m^{-1} K^{-1})	1.36[a]	0.591[a]	0.447[b]	0.380[b]	0.326[b]
μ (kg m^{-1} s^{-2})	$3.13\cdot10^{10}$	...	...	...	...
η (kg m^{-1} s^{-1})	...	0.001[a,b]	0.003 65[a,b]	0.0107[a,b]	0.0598[a,b]
α (Np m^{-1})	$17\cdot10^{-17}\cdot f^2$	$24\cdot10^{-15}\cdot f^{2}$[c]	$23\cdot10^{-14}\cdot f^{1.92}$[c]	$59\cdot10^{-14}\cdot f^{1.91}$[c]	$124\cdot10^{-14}\cdot f^{1.94}$[c]

[a]Reference 20.
[b]Reference 21.
[c]Measured in the laboratory.
[d]Extrapolation from Ref. 22.
[e]Reference 23.

I). Glycerol–water mixtures were used in these studies because their physical properties are widely reported in the literature.[15] The volume fractions of the samples were calculated from knowledge of the density of silica particles ($\rho = 2200$ kg m^{-3}) and aqueous glycerol solutions (composition dependent). The samples were stored 24 hours prior to measurements to eliminate bubbles.

B. Ultrasonic measurements

Ultrasonic velocity and attenuation spectra were measured in the frequency range 0.5 to 150 MHz using a custom-built ultrasonic spectrometer whose principles have been described in detail elsewhere.[16] Briefly, a broadband pulse of ultrasound was propagated through a colloidal suspension and the time-of-flight and amplitude of the pulse were measured. The ultrasonic velocity was calculated from the time-of-flight and the attenuation coefficient from the amplitude. The frequency dependence of the ultrasonic properties was determined by carrying out a Fourier transform analysis of the ultrasonic pulse before and after it had traveled through the emulsion. The signal was averaged 400 times prior to analysis to improve the signal-to-noise ratio.

Two different measurement cells, and five different broadband ultrasonic transducers, were used to cover the whole frequency range. The first measurement cell was used for low-frequency measurements (0.4–7 MHz). It had a 5-mm plexiglass buffer rod (which separated the transducer from the sample), a 16-mm sample path-length, and required 25 ml of sample. The second measurement cell was used for high-frequency measurements (10–150 MHz). It had a 3-mm quartz delay line, a 2-mm sample path-length, and required 1 ml of sample. The delay line and reflector plate in the high-frequency cell were optically smooth and could be adjusted to make them parallel, thus minimizing errors caused by phase cancellation. Two transducers were used with the first measurement cell: (a) 1 MHz, 25-mm diameter (SLH 1-25, Baltaeu Sonatest); and (b) 3.5 MHz, 12.5-mm diameter (V682, Panametrics, Waltham, MA). Three transducers were used with the second measurement cell: (a) 20 MHz, 6 mm (V212BA, Panametrics); (b) 50 MHz, 6 mm (V214BA, Panametrics); and (c) 100 MHz, 3 mm (V2054, Panametrics). The velocity could be measured to within 1 ms^{-1} and the attenuation coefficient to within 5% using this technique. As the velocity and attenuation of highly viscous samples are temperature dependent, all measurements were carried out in a thermostated water bath at 20 ± 0.1 °C.

II. RESULTS AND DISCUSSION

Measurements of the ultrasonic velocity and attenuation spectra of a series of colloidal suspensions containing silica particles ($\phi=0.05$, $r=190$ nm) suspended in various glycerol–water mixtures (0% to 80 wt% glycerol) were compared with theoretical predictions made using ultrasonic scattering theory (Figs. 1 and 2). The scattering coefficients of the individual particles were calculated with the theory of Allegra and Hawley[5] using the known particle radius and thermophysical properties of the component phases (Table I). The ultrasonic velocity and attenuation coefficient of the colloidal suspensions were then computed using the multiple scattering theory of Lloyd and Berry[7,17] using the calculated scattering coefficients and the known particle volume fraction. There was good agreement between the theoretical predictions and experimental measurements (Figs. 1 and 2), which indicated that ultrasonic scattering theory could be used to describe the suspension properties. The observed discrepancies are probably due to experimental errors in the ultrasonic measurements and uncertainties about the exact density and elastic properties of the silica particles.

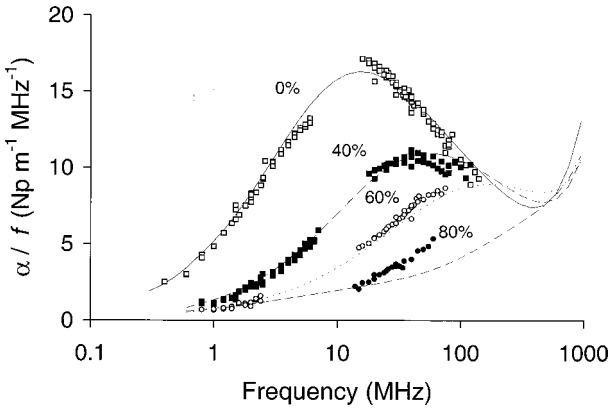

FIG. 1. Ultrasonic attenuation spectra of suspensions containing 5 vol% monodisperse silica particles dispersed in different glycerol–water mixtures. The theoretical curves were calculated using ultrasonic scattering theory (Refs. 5 and 17).

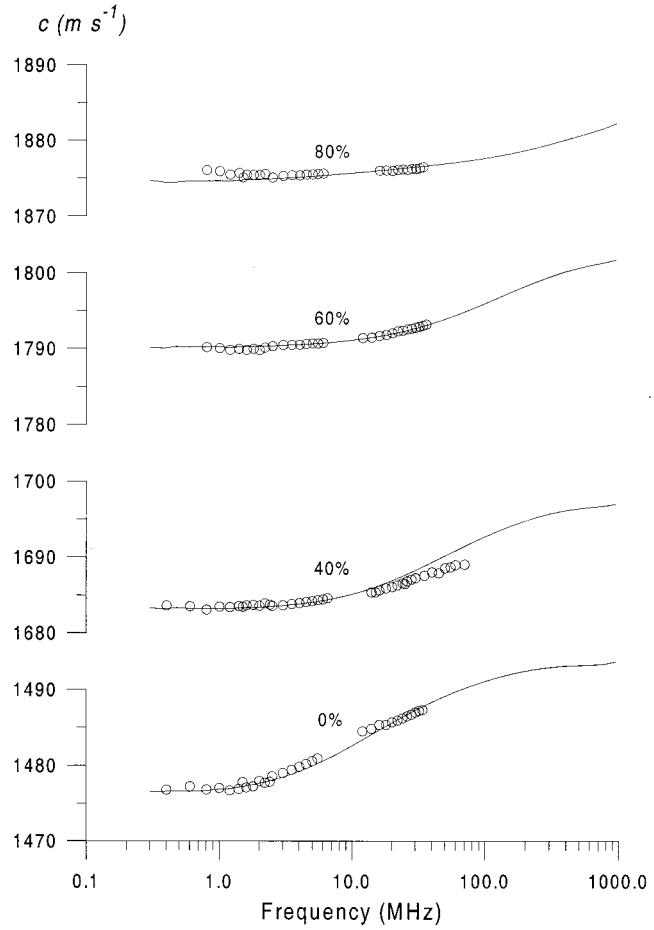

FIG. 2. Ultrasonic velocity spectra of suspensions containing 5 vol% monodisperse silica particles dispersed in different glycerol–water mixtures. The theoretical curves were calculated using ultrasonic scattering theory (Refs. 5 and 17).

In the absence of glycerol, there was a large maximum in the attenuation spectra around 10 MHz, which was due to visco-inertial dissipation losses.[1] As the glycerol concentration increased, the height of the maximum became smaller because the density contrast between the silica particles and surrounding liquid was reduced (Table I). In addition, the maximum shifted to higher frequencies because of the increase in viscosity of the surrounding liquid. In a high density-contrast colloidal dispersion, the maximum in the attenuation spectrum occurs when the particle radius is approximately equal to the viscous skin depth (δ_V),

$$r \approx \delta_V = \sqrt{\frac{2\eta_1}{\omega\rho_1}}, \tag{1}$$

where ω is the angular frequency ($=2\pi f$), f is the frequency, η_1 is the viscosity, and ρ_1 is the density of the continuous phase. Hence,

$$f_{\max} \approx \frac{\eta_1}{\pi r^2 \rho_1} \approx \frac{\upsilon_1}{\pi r^2}, \tag{2}$$

where $f_{\max}$ is the frequency at which the maximum in α/f occurs, and υ is the kinematic viscosity. This equation explains the shift in the maximum to higher frequencies that occurred when the viscosity of the continuous phase was increased (the relative change in density being small compared to that in viscosity).

For a Newtonian fluid, it should be possible to determine the viscosity of the liquid surrounding the particles by measuring the position of the maximum in the attenuation spectra (if the particle size is known). The range of viscosities that could be measured using this method depends on the size of the suspended particles [Eq. (2)]. For example, higher viscosity fluids could be analyzed by using particles with smaller sizes because then the maximum in the attenuation spectra would fall into the measurable frequency range (1–100 MHz) and there would be less interference from intrinsic absorption and scattering losses. For many applications, ultrasonic spectrometry may not be a practical means of determining the rheology of a liquid. Nevertheless, there may be certain specialized situations where it could be useful, e.g., if one wanted to probe the viscosity of a fluid within the pores of a matrix structure. The particles would be dispersed within the fluid (provided they were much smaller than the pore size) and then the attenuation spectra of the overall system would be measured. The attenuation spectra of the particles dispersed in the same fluid but in the absence of the matrix structure would also be measured. By comparing the spectra one could separate the contribution of the viscous interaction of the particles with the porous medium from that of the inherent viscous dissipation of the particles within the suspension. Another implication of our results is that it would be difficult to use ultrasonic spectrometry (at relatively low frequencies) to determine the size of particles suspended in highly viscous fluids because they would not oscillate in the ultrasonic field and therefore the attenuation due to viscous dissipation would be small.

The good agreement between the predictions of the ultrasonic scattering theory and the experimental attenuation spectra for the suspensions with the three lowest viscosities suggests that their continuous phases behave like Newtonian fluids at ultrasonic frequencies. On the other hand, the measured attenuation was significantly higher than the predicted attenuation for the suspension with the highest viscosity. This could have been because the viscosity of the continuous phase decreased at ultrasonic frequencies due to one or more relaxation processes.[12] Alternatively, it may be because the contribution of the visco-inertial effects is only about 5% of the overall attenuation of the suspension (the rest being thermal conduction, intrinsic absorption, and scattering losses), and so the technique is no longer sensitive to the continuous phase viscosity.

It should be noted that the shapes of the predicted attenuation spectra were sensitive to changes in thermal properties, such as specific heat, volume expansion coefficient, and thermal conductivity. This suggests that purely hydrodynamic models,[18,19] that ignore thermal effects may not give a good mathematical description of these systems.

III. CONCLUSIONS

The ultrasonic properties of relatively dilute colloidal suspensions containing monodisperse silica particles can be described using ultrasonic scattering theory. Ultrasonic spec-

trometry can be used to provide information about particle size and concentration if the thermophysical properties of the component phases are known. Alternatively, it can be used to provide information about the viscosity of the fluid surrounding the particles if the size and concentration of the particles are known. Nevertheless, it is important to take into account the fact that the viscosity of a fluid at ultrasonic frequencies may be different from that measured using conventional rheometry because of relaxation phenomena that occur at high frequencies. Our results suggest that it may be possible to use ultrasonic spectrometry to nondestructively measure the viscosity of fluids contained within pores in matrix systems. It may therefore be able to provide information that cannot be obtained using any other technique.

ACKNOWLEDGMENTS

The authors acknowledge support from the Cooperative State Research, Education and Extension Service, U.S. Department of Agriculture, under Agreement No. 97-35503-4371. The authors also thank Dr. Tonis Oja for his useful advice, the Nissan Company for providing the silica suspensions, and J. Candau for engineering the ultrasonic measurement cells.

[1] D. J. McClements, ''Ultrasonic characterization of emulsions and suspensions,'' Adv. Colloid Interface Sci. **37**, 33–72 (1991).
[2] M. J. W. Povey, *Ultrasonic Techniques for Fluid Characterization* (Academic, San Diego, 1997).
[3] A. S. Dukhin and P. J. Goetz, ''Acoustic spectroscopy for concentrated polydisperse colloids with low density contrast,'' Langmuir **12**, 4998–5008 (1996).
[4] P. S. Epstein and R. R. Carhart, ''The absorption of sound in suspensions and emulsions,'' J. Acoust. Soc. Am. **25**, 553–565 (1953).
[5] J. R. Allegra and S. A. Hawley, ''Attenuation of sound in suspensions and emulsions: Theory and experiments,'' J. Acoust. Soc. Am. **51**, 1545–1563 (1972).
[6] D. J. McClements, ''Comparison of multiple scattering theories with experimental measurements in emulsions,'' J. Acoust. Soc. Am. **91**, 849–853 (1992).
[7] D. J. McClements and M. J. W. Povey, ''Scattering of ultrasound by emulsions,'' J. Phys. D **22**, 38–47 (1989).
[8] N. Herrmann, P. Boltenhagen, and P. Lemarechal, ''Experimental study of sound attenuation in quasi-monodisperse emulsions,'' J. Phys. II **6**, 1389–1403 (1996).
[9] Y. Hemar, N. Herrmann, P. Lemarechal, R. Hocquart, and F. Lequeux, ''Effect medium model for ultrasonic attenuation due to the thermo-elastic effect in concentrated emulsions,'' J. Phys. II **7**, 637–647 (1997).
[10] D. J. McClements, Y. Hemar, and N. Herrmann, ''Incorporation of thermal overlap effects into multiple scattering theory,'' J. Acoust. Soc. Am. **105**, 915–918 (1999).
[11] A. S. Dukhin and P. J. Goetz, ''Acoustic spectroscopy for concentrated polydisperse colloids with high density contrast,'' Langmuir **12**, 4987–4997 (1996).
[12] A. B. Bhatia, *Ultrasonic Absorption* (Dover, New York, 1967).
[13] V. Hackely and J. Texter, *Handbook of Ultrasonic and Dielectric Characterization Techniques for Suspended Particulates* (The American Ceramic Society, Westerville, OH, 1998).
[14] D. J. McClements, ''Principles of ultrasonic droplet size determination,'' Langmuir **12**, 3454–3461 (1996).
[15] F. T. Schulitz, Y. Lu, and H. N. G. Wadley, ''Ultrasonic propagation in metal powder-viscous liquid suspensions,'' J. Acoust. Soc. Am. **103**, 1361–1369 (1998).
[16] D. J. McClements and P. Fairley, ''Ultrasonic pulse echo reflectometer,'' Ultrasonics **29**, 58–62 (1991).
[17] P. Lloyd and M. V. Berry, ''Wave propagation through an assembly of spheres: IV. Relations between different multiple scattering theories,'' Proc. Phys. Soc. London **91**, 678–688 (1967).
[18] A. H. Harker and J. A. G. Temple, ''Velocity and attenuation of ultrasound in suspensions of particles in fluids,'' J. Phys. D **21**, 1576–1588 (1988).
[19] J. M. Evans and K. Attenborough, ''Coupled phase theory for sound propagation in emulsions,'' J. Acoust. Soc. Am. **102**, 278–282 (1997).
[20] *Handbook of Chemistry and Physics*, 66th ed.
[21] A. A. Newman, *Glycerol* (CRC, Cleveland, 1968).
[22] F. T. Gucker and G. A. Marsh, ''Refrigerating capacity of two-component systems,'' Ind. Eng. Chem. **40**, 908–915 (1948).
[23] V. A. Del Grosso and C. W. Mader, ''Speed of sound in pure water,'' J. Acoust. Soc. Am. **52**, 5 (1972).

Comments on "Capped ceramic underwater sound projectors: The 'cymbal' transducer" [J. Acoust. Soc. Am. 105, 591–600 (1999)]

Jerome Goodman
Jerome Goodman and Associates, 11 Wooleys Lane-LE, Great Neck, New York 11023

(Received 18 February 1999; accepted for publication 21 April 1999)

The paper by Tressler, Newnham, and Hughes titled ''Capped ceramic underwater sound projector: The 'cymbal' transducer'' brought back some old memories. © *1999 Acoustical Society of America.* [S0001-4966(99)01408-3]

PACS numbers: 43.38.Fx, 43.30.Yj [SLE]

More than 40 years ago Dr. William J. Toulis was granted patents and published papers in *JASA* on flextensional projectors that became the basis of subsequent U.S. Navy investigations and developments. At North American Aviation, Inc. in Columbus, OH I worked with Dr. Toulis on the analysis, design, and construction of a flextensional variant that was called the ''watch fob'' transducer and that was very similar to the ''cymbal transducer.'' I do not think that this work appeared in the open literature.

Dr. Toulis also patented air-filled compliant tubes to act as underwater reflectors and as pressure release elements in U. S. Patent 3,021,504. A compliant tube was fabricated by sealing the ends of a copper tube and crushing the tube. About twenty years ago Dr. Richard V. Waterhouse of American University and Dr. Raymond Chuan of Brunswick Corporation proposed a variation by crushing hollow metal spheres. They termed this a ''crushed egg'' compliant element. An array of ''crushed egg'' elements was formed by potting a number of the ''crushed eggs'' to form a conformal pressure release surface.

Conformal hydrophone arrays of cymbal transducers proposed by Tressler, Newnham, and Hughes might exhibit enhanced performance, in some applications, by being mounted over an inertial signal conditioning plate and a conformal pressure release surface of the type proposed by Waterhouse and Chuan.

 0001-4966/99/106(2)/1182/1/$15.00

Love-theoretical analysis of periodic system of rods

B. Ravindra
Institut fur Mechanik II, Darmstadt University of Technology, Darmstadt D-64289, Germany

(Received 11 May 1998; revised 3 January 1999; accepted 28 April 1999)

Love-theoretical analysis of periodic system of rods is presented. It is shown that the proposed theory enables an extension of Snowdon's theory of vibration isolation. An example of a periodic vibration isolator, consisting of sandwiched rubber springs, is studied. © *1999 Acoustical Society of America.* [S0001-4966(99)02908-2]

PACS numbers: 43.40.Cw [CBB]

INTRODUCTION

The existence of localization in one-dimensional, random Schrodinger operators is established on a firm mathematical basis.[1] Similarity between the creation of localized modes for classical and electron waves has been recognized as early as Anderson.[2,3] However, there are important differences between the classical and the quantum situation.[3] In the quantum case, one needs to just perturb a homogeneous medium with a constant potential locally in order to cause localization. In the classical situation a localized mode cannot be generated by such a local perturbation when the medium is homogeneous. Even in the one-dimensional case (which is the most favored dimension for localization), the associated eigenvalue problem in the classical context cannot have square integrable solutions and hence implies no possibility for localization. A better understanding can be obtained if one thinks in terms of the spectral gap in the classical and quantum contexts. The edge of the spectral gap in a Schrodinger operator depends on the homogeneous medium and hence a perturbation can cause spectral expansion inside the gap, causing exponential localization of eigenmodes. But for classical waves the edge of the spectrum does not depend on the medium and hence local perturbations of the medium by a defect do not expand the spectrum into the gap. Thus in order to observe localization in the classical context, one needs to have a gap in the spectrum and the edge of the gap must depend on the medium. Common examples of classical media with spectral gaps are periodic structures. Wave motion in such periodic structures in the classical context has a rich historical heritage. Newton calculated the speed of sound using this approach. Numerous applications of interest to electrical engineers such as filters, transmission line networks, and their connection to the Floquet–Bloch theory well developed by physicists working on crystals and optics can be found in the classic work of Brillouin.[4] One of the first applications of these concepts to beamlike structures is due to Heckl[5] and extensive investigation into the context of structural vibrations has been carried out by Mead and co-workers.[6] The role of disorder has been considered by Bansal[7] and application to vibration isolation has been studied by Hodges and Woodhouse[8] and Kissel.[9] The Love-theoretical analysis of periodic system of rods[10–14] has not been considered so far in the literature.

The main objective of this work is to use the theory of periodic structures to analyze rodlike systems using Love's theory. It is shown that unlike Snowdon's four-pole parameter approach,[15] the proposed theory yields closed form analytical expressions and computational effort is independent of the number of elements in the periodic system. Furthermore, the proposed theory can be employed to extend Snowdon's theory of vibration isolation for periodic systems with an arbitrary number of elements and can be used to design sandwiched rubber springs and actuators.[16] These applications and the role of disorder in periodic rod-type systems and implications for design of practical systems of interest in engineering will be considered in future work.

I. SYSTEM DESCRIPTION

Consider a periodic system consisting of N rigid masses m connected serially by identical rods each of mass m_R and length L, as shown in Fig. 1. The mass m at the left end is subjected to a harmonic force $F_1=\mathbf{F}_1 e^{j\omega t}$ where $|\mathbf{F}_1|$ is the amplitude, ω is the frequency, and t denotes the time. The right end of the periodic system has fixed boundary conditions. The mass of the rod element is $m_R=\rho a L$; ρ is the density of the material, a is the cross section area of the rod, and L is the length of the rod element.

The harmonic velocity and forces (of frequency ω) at different locations of the three adjacent periodic rod elements (see Fig. 2) are denoted by $\mathbf{V}$ and $\mathbf{F}$, with appropriate subscripts and are related by the harmonic mobilities (denoted as β and to be defined in the next section) as

$$\mathbf{V}_k=\beta_{rl}\mathbf{F}_{k-1}+\beta_{rr}\mathbf{F}_k \tag{1}$$

and

$$\mathbf{V}_k=\beta_{lr}\mathbf{F}_{k+1}+\beta_{ll}\mathbf{F}_k\,. \tag{2}$$

The subscripts l and r refer, respectively, to the left and the right ends of the periodic element. The first subscript in βs denotes the location at which the velocity is measured, and the second subscript denotes the location at which the unit harmonic force is applied. The expressions for mobilities using the Love theory are outlined in the next section.

Love theory for evaluation of mobilities

Love theory accounts for the radial deformation of the plane cross sections of the rods caused by axial compression and extension. The approximation proposed by Love (and also a related method proposed by Rayleigh) has been employed in literature[10–14] while analyzing the vibration of un-

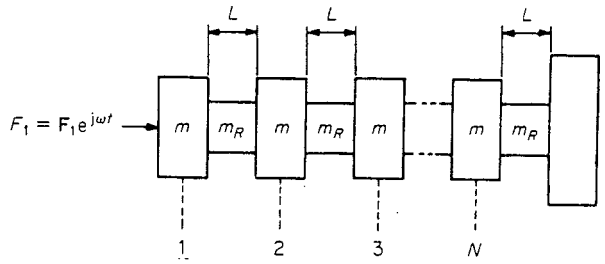

FIG. 1. Periodic system of rods.

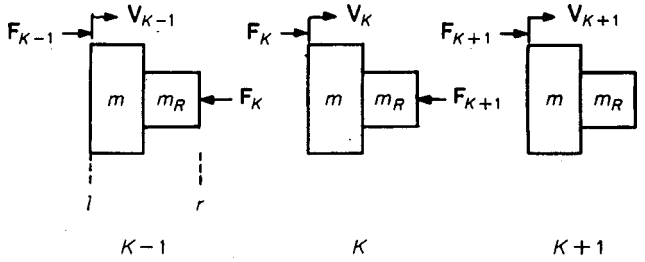

FIG. 2. Three adjacent periodic elements.

damped rods. It may be noted that there exists a theory (as opposed to the approximate theory of Love) referred to in literature as the Pochhammer–Chree theory which applies only to rods of infinite length or only to rods with lengths much greater than their diameters.

Consider one element of the periodic system of rods, as shown in Fig. 3. For sinusoidal excitation with frequency ω, the governing equation with Love's prescription can be written as

$$[1-(n\nu r)^2]\frac{\partial^2\zeta}{\partial x^2}+n^2\zeta=0, \tag{3}$$

where ν is Poisson's ratio and r is the radius of gyration of an elementary section of the rod about the x-axis. The parameter n is given in terms of the Young's modulus E and density ρ as

$$n=\omega\sqrt{\rho/E}. \tag{4}$$

The solution of the rod equation can be expressed as

$$\zeta=C\sin(Gx)+D\cos(Gx), \tag{5}$$

where C and D are evaluated from the boundary conditions and G is the term incorporating the Love approximation for lateral contraction (and/or expansion),

$$G=n\sqrt{1-(n\nu r)^2}. \tag{6}$$

Defining the mobilities as

$$\beta_{ll}=j\omega\zeta|_{x=0} \tag{7}$$

and

$$\beta_{rl}=j\omega\zeta|_{x=L}, \tag{8}$$

with a unit harmonic force at the left end (the right end being free), for which the boundary conditions are

$$\partial\zeta/\partial x=0|_{x=L}, \quad -m\omega^2\zeta=1-\mathbf{F}_1|_{x=0}, \tag{9}$$

where

$$\mathbf{F}_1=-aE\,\partial\zeta/\partial x=0|_{x=0}. \tag{10}$$

Solving for D and C from the above equations, one can find the mobilities as

$$\beta_{ll}=-j\omega\cos(GL)/aEG\theta \tag{11}$$

and

$$\beta_{rl}=-j\omega/aEG\theta, \tag{12}$$

where

$$\theta=\psi_1 GL\cos(GL)+\sin(GL), \tag{13}$$

with $\psi_1=m/m_R$. Similarly, the other mobilities are defined as

$$\beta_{rr}=j\omega\zeta|_{x=L} \tag{14}$$

and

$$\beta_{lr}=j\omega\zeta|_{x=0}, \tag{15}$$

with a unit harmonic force at the right end and the left end being free, for which the boundary conditions are

$$-aE\partial\zeta/\partial x|_{x=L}=1, \quad -m\omega^2\zeta=aE\partial\zeta/\partial x|_{x=0}. \tag{16}$$

Solving for D and C as before, one can obtain β_{rr} and β_{lr} as

$$\beta_{rr}=j\omega\eta/aEG\theta \tag{17}$$

and

$$\beta_{lr}=j\omega/aEG\theta, \tag{18}$$

where

$$\eta=-\psi_1 GL\sin(GL)+\cos(GL). \tag{19}$$

II. DERIVATION OF TRANSMISSIBILITY EXPRESSION

The objective in this section is to evaluate the performance of a periodic system of rods when used as an isolation system. Toward this end a performance measure, transmissibility, is defined as the ratio of the force transmitted from one end of the periodic system to the other,

$$T=|\mathbf{F}_{N+1}/\mathbf{F}_1|. \tag{20}$$

It may be observed that Snowdon's four-pole parameter method yields complicated expressions in terms of polynomials of various order and the coefficients of these polynomials have to be evaluated for each N. In this work an alternative based on the theory of periodic structures is proposed.[16] Using this method one can derive a general ex-

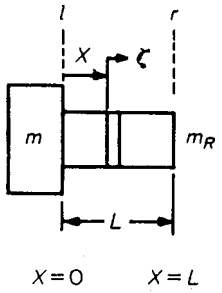

FIG. 3. Mobility calculation for a periodic element.

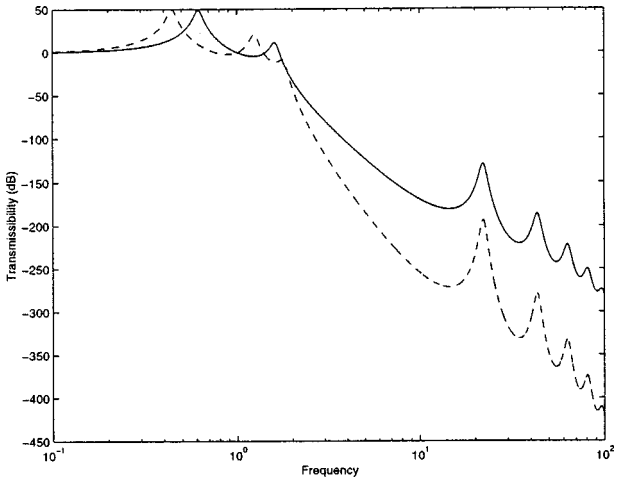

FIG. 4. Transmissibility for $L/d=5$, — $N=2$; - - - $N=3$.

pression for the transmissibility, valid for all values of N and hence resulting in computational efficiency.

Elimination of $\mathbf{V}_k$ from Eqs. (1) and (2) results in the difference equation,

$$\beta_{lr}\mathbf{F}_{k+1}+(\beta_{ll}-\beta_{rr})\mathbf{F}_k-\beta_{rl}\mathbf{F}_{k-1}=0. \tag{21}$$

The solution to the above equation can be expressed as

$$\mathbf{F}_{k+1}=\mathbf{F}_k\mu=\mathbf{F}_{k-1}\mu^2=\cdots. \tag{22}$$

The propagation constant used often in the theory of periodic systems is given by $ln(\mu)$. Re-arranging Eqs. (22) and (21) yields a quadratic equation for μ, whose two roots (corresponding to two oppositely traveling harmonic waves) can be written as

$$\mu^{(1),(2)}=[(\beta_{rr}-\beta_{ll})\mp\sqrt{(\beta_{ll}-\beta_{rr})^2+4\beta_{rl}\beta_{lr}}]/2\beta_{lr}. \tag{23}$$

Now expressing all the harmonic quantities as the superposition of two waves traveling in opposite directions, and using Eqs. (1), (2), and (22) one obtains the expression for the transmissibility after carrying out some algebraic manipulations:

$$T=|\mathbf{F}_{N+1}/\mathbf{F}_1|=\left|\frac{1+\lambda}{[\mu^{(2)}]^{-N}+\lambda[\mu^{(1)}]^{-N}}\right|, \tag{24}$$

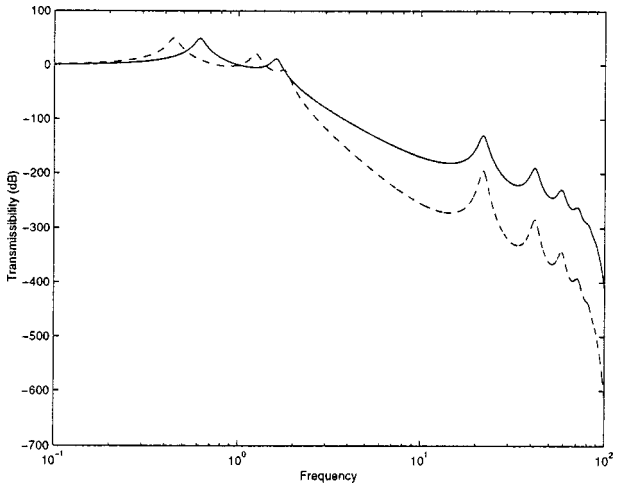

FIG. 5. Transmissibility for $L/d=3$, — $N=2$; - - - $N=3$.

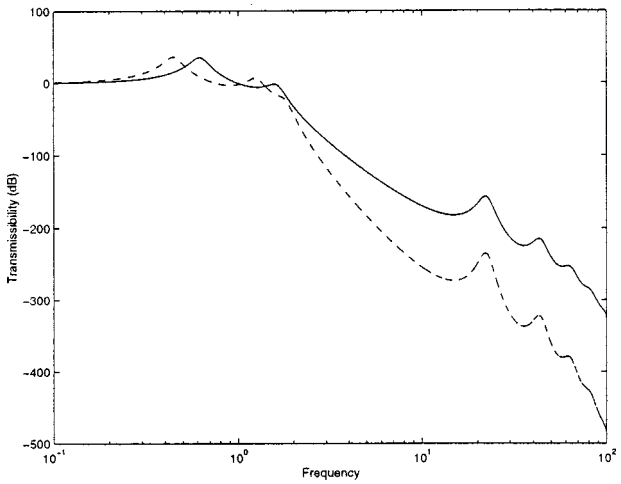

FIG. 6. Transmissibility for $L/d=5$, $\delta=0.2$, — $N=2$; - - - $N=3$.

where λ is given by

$$\lambda=\frac{\mathbf{F}_{N+1}^{(1)}}{\mathbf{F}_{N+1}^{(2)}}=-[-\beta_{rr}-(\beta_{rl}/\mu^{(2)})]/[-\beta_{rr}-(\beta_{rl}/\mu^{(1)})]. \tag{25}$$

The procedure outlined in this section can be extended to take care of internal damping of the rod element by using the complex modulus representation given by

$$E_c=E(1+j\,\delta), \tag{26}$$

where δ is the damping parameter. Now the expressions for n and G become complex. The transmissibility expression is still given by Eq. (24).

III. EXAMPLE

To illustrate the theory outlined, consider typical parameter values, $\delta=0.1$, $\psi_1=50$. Assuming a circular cross section of diameter d for the rod element, the radius of gyration $r=d/2\sqrt{2}$. The transmissibility values are calculated for different values of L/d to see the effect of the approximation incorporated using Love's theory. The solution obtained in the cases of $N=2$ and $N=3$ are shown in Figs. 4 and 5. It can be noted that, in both cases, a periodic system with

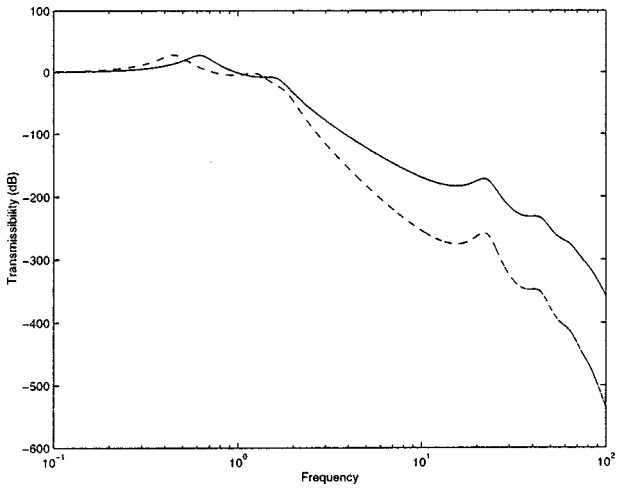

FIG. 7. Transmissibility for $L/d=5$, $\delta=0.3$, — $N=2$; - - - $N=3$.

$N=3$ yields lower values of transmissibility than with $N=2$ in the high frequency range of interest to vibration isolation applications. The wave resonances depend on the length-to-diameter (L/d) ratio. The lower the value of this ratio, the lower the value of transmissibility at the wave resonances. While these findings confirm the previous results of Snowdon,[15] the computational effort is independent of N in the present case. The effect of damping is presented in Figs. 6 and 7. It can be observed that the trasmissibility at the wave resonances decreases with increase in damping.

IV. CONCLUSIONS

A new formulation of periodic system of rods using Love theory is presented. The theory of periodic structures is shown to be effective in extending the classic work of Snowdon to analyze isolation systems with an arbitrary number of periodic elements. It is shown that a combination of Love theory and periodic structures can be effectively used in the design of isolators comprised of rod elements with internal damping.

ACKNOWLEDGMENTS

The author thanks the Alexander von Humboldt Foundation and Professor P. Hagedorn for their support, and Professor A. K. Mallik for valuable suggestions.

[1] W. G. Faris, ''Random waves and localization,'' Notices of the American Mathematical Society, **42**, 848 (1995).
[2] L. Pastur and A. Figotin, *Spectra of Random and almost-periodic operators, Grundlehren der mathematischen Wissenschaften 297* (Springer-Verlag, Berlin, 1992).
[3] P. W. Anderson, ''A question of classical localization, A theory of White paint,'' Philos. Mag. B **53**, 505 (1958).
[4] L. Brillouin, *Wave Propagation in Periodic Structures, Electric Filters and Crystal Lattices* (Dover, New York, 1953).
[5] M. A. Heckl, ''Investigations on the vibrations of grillages and other simple beam structures,'' J. Acoust. Soc. Am. **36**, 1335 (1964).
[6] D. J. Mead, ''A new method of analyzing wave propagation in periodic structures: applications to periodic Timoshenko beams and stiffened plates,'' J. Sound Vib. **104**, 9 (1986).
[7] A. S. Bansal, ''Free wave propagation through combinations of periodic and disordered system,'' J. Acoust. Soc. Am. **67**, 377 (1980).
[8] C. H. Hodges and J. Woodhouse, ''Vibration isolation from irregularity in a nearly periodic structure: Theory and measurements,'' J. Acoust. Soc. Am. **74**, 894 (1983).
[9] G. I. Kissel, ''Localization factor for multichannel disordered systems,'' Phys. Rev. A **44**, 1008 (1991).
[10] A. E. H. Love, *A Treatise on the Mathematical theory of Elasticity* (Dover, New York, 1944).
[11] Lord Rayleigh, *Theory of Sound* (Dover, New York, 1945).
[12] J. Zemanek, Jr. and I. Rudnick, J. Acoust. Soc. Am. **33**, 1283 (1961).
[13] H. Kolsky, *Stress Waves in Solids* (Dover, New York, 1963).
[14] H. N. Abramson, H. J. Plass, and E. A. Rippierger, ''Stress wave propagation in rods and beams,'' Adv. Appl. Mech. **5**, 111 (1958).
[15] J. C. Snowdon, ''Vibration isolation: Use and characterization,'' J. Acoust. Soc. Am. **66**, 1245 (1979).
[16] B. Ravindra and A. K. Mallik, ''Harmonic vibration isolation characteristics of periodic systems,'' J. Sound Vib. **154**, 249 (1992).

The fine structure of the recovering auditory detection threshold

Lance Nizami and Bruce A. Schneider
Department of Psychology, Erindale Campus, University of Toronto, 3359 Mississauga Road, Mississauga, Ontario L5L 1C6, Canada

(Received 15 June 1998; revised 29 March 1999; accepted 1 April 1999)

Detection thresholds were gathered for a 2 kHz Gaussian-shaped probe (standard deviation = 0.5 ms), centered at intervals of as little as half a millisecond over 0–30 ms following a 200 ms, 97 dB SPL, 2 kHz tone. Surprisingly, there were small, sudden rises and falls superimposed on each subject's generally smooth recovery. Even more obvious were nonmonotonicities in the standard deviation of the cumulative normal fitted to each threshold's psychometric function. © *1999 Acoustical Society of America.* [S0001-4966(99)04905-X]

PACS numbers: 43.66.Dc, 43.66.Mk, 43.66.Ba [RVS]

INTRODUCTION

The present experiment was an attempt to determine the fine structure of the recovery from an intense forward masker. To measure recovery, 2 kHz probe tones were presented at post-masker time gaps, t, separated by as little as $\frac{1}{2}$ ms. These probes were shaped by a very short Gaussian envelope, to ensure that the measured threshold reflected the state of recovery within a very narrow temporal window. Gaussian envelopes also ensure unambiguous masker-probe time-gaps t. In order to ensure a high degree of forward-masking, a 97 dB SPL, 200 ms, 2 kHz tone was used as masker. Masker-induced shifts in detection threshold should be profound, since 97 dB SPL is 10–30 dB higher than that of typical forward-masking studies. The 200 ms duration, which is more typical of the literature, is known to produce a large threshold shift for short probes of various durations (Fastl, 1979; Kidd and Feth, 1982; Zwicker, 1984; Carlyon, 1988).

I. METHODS

A. Subjects

All three subjects had normal audiometric thresholds (ANSI S3.6-1969) and were treated according to American Psychological Association guidelines. Subject LN (male, age 35), the first author, had no previous listening experience. Subject BAK (male, age 23), a paid undergraduate, had moderate listening experience in our laboratory. Subject JWC (female, age 38) was a research assistant with extensive experience in a variety of listening tasks.

B. Stimuli

The tone pip was formed by multiplying a 2 kHz pure tone by a Gaussian amplitude envelope whose standard deviation was 0.5 ms. Gaussian shaping provides the smallest amount of spectral spread for a given tone-pip duration (Gabor, 1946; see Schneider *et al.*, 1994), and the relative spectral density of the tone pip shows only a single relatively narrow lobe which spans 1517–2483 Hz at 10 dB below its maximum. The probe's intensity was specified in terms of the sound pressure level (SPL) of the pure-tone carrier. The 2 kHz, 200 ms (excluding ramps) forward-masker, fixed at 97 dB SPL, was formed by adding together 201 Gaussian pips spaced 1 ms apart following the procedure used in Schneider *et al.* (1994). The masker's on- and off-ramping was determined by the Gaussian envelope of its individual pips. The time gap, t, between forward-masker and tone pip is defined as the interval between the center of the last Gaussian in the masker, and the center of the pip. (Thus at $t=0$, for example, the masker and tone pip actually overlap.) Time-gap t was always an integer multiple of the period of the 2 kHz carrier, giving zero phase shift between masker and tone and thus eliminating a potential detection cue to which the human ear is quite sensitive (Rajcan, 1976).

Stimuli, digitized as voltages at 20 kHz sampling rate, were passed through a 16-bit digital-to-analog converter (TMS320C25 digital signal processing system) for actual presentation.

C. Apparatus

Subjects sat in a double-walled sound-attenuating chamber wearing a TDH-49 headset, with sound to the right ear only. The headphone was calibrated using a 6 cc coupler (Bruel and Kjaer 2209 sound level meter). All harmonics were at least 50 dB below the signal level. Tone-pip intensity was adjusted digitally over a 57 dB range; a Hewlett-Packard 350D passive attenuator was used to extend that range.

D. Procedure

Pip-detection thresholds were determined using a two-interval forced-choice (2IFC) procedure in which the subject initiated a trial by making contact with a silent sensor. In one of the intervals (randomly chosen), the masker was followed by a tone pip. In the other interval, the masker was presented alone. Each interval lasted 500 ms, with the masker starting 100 ms into the interval. A 1.5 s delay separated the two intervals. The literature suggests that 1 s is sufficient recovery time for typical forward-maskers (Samoilova, 1959, 20 ms probes; Weber and Moore, 1981, 5 ms probes).

The subject's task was to identify the interval containing the pip, by touching one of two silent sensors, with their choice being indicated as correct or incorrect by a visual signal. The pairs of forced-choices were given in blocks of 100 with both pip intensity and masker-pip time gap remaining constant within each block (the method of constant levels). To avoid any performance drop due to fatigue or attention loss (Zwislocki *et al.*, 1958), breaks were offered between blocks. The length of the break that followed each block of 100 trials was determined by the subject on each occasion. The typical break lasted 10–20 min. No subject was tested until ready; much longer breaks were given if requested, and subjects were free to request.

The order of time gaps was irregular. When each subject started at a new time gap, a new series of pip levels was chosen that was customized to each subject based on their performance at nearby time gaps. (For the first few time gaps, some trial-and-error was required.) The experimenter first chose a pip level just above that level at which $p(c)$ starts to drop below 1.0. Over successive blocks the pip level was lowered monotonically until the subject started making errors $[p(c)<1.0]$ and then further until performance approached chance $[p(c)=0.5]$. Such monotonic intensity changes proved easier for the participants to follow than the sudden large relative changes in level which occur when pip level is changed randomly from block to block over a range of dB. Randomizing intensity across blocks was tried initially and resulted in poorer performance.

Each day, enough data were gathered to assemble a psychometric function (percent correct vs intensity level). Over the first one or two days of testing at a particular time gap, a number of pip levels were presented in order to determine the approximate width of the psychometric function. Based on these preliminary observations, the number and spacing of the pip levels to be used in the final two days of testing was determined. In general, an attempt was made to cover the entire psychometric function with evenly spaced pip levels. The difference between any two adjacent pip levels never exceeded 2 dB and was never less than 1/4 dB. In general, the number of pip levels increased with the width of the psychometric function, ranging from 5 to 14 (median $=8$). Thus for a psychometric function spanning 10 dB, for example, there would be at least 5 pip levels spaced 2 dB apart, plus other levels inbetween.

After the number and spacing of the tone pips was determined, on successive days, psychometric functions were determined for a particular time gap until the subject's performance failed to show an improvement of more than a few percentage points relative to the previous day. A total of 3–5 experiment days were required (including the first one or two days during which the number and spacing of the pip levels were determined). The $p(c)$ scores from the last 2 days at each time gap were averaged at the common pip levels to get the final psychometric function. Nonmasked pip thresholds were determined at the end of the experiment; in the randomized 2IFC task, one of the intervals was silent, the other contained a pip located 390 ms into the interval.

The subjects had about 20 h of practice at the start of the experiment to familiarize themselves with the task. Due to the long hours required per day (2.5–8 per day; median $=4$), the test days were scheduled at the subject's convenience, averaging 2–3 per week. After finishing a particular time gap, subjects were sometimes absent for as much as several weeks; if so, when beginning at a new time gap, a larger number of days was often required before their psychometric function stabilized. All subjects maintained high morale despite the aggregate of hours (535 for BAK, $\sim$600 for JWC, $>$1,000 for LN). The subjects were free to offer self-evaluation. They soon became adept at self-assessment, recognizing those episodes where performance was substandard due to fatigue or attention lapses, even before seeing their scores. In such cases the subjects themselves always insisted on being re-tested, and were always re-tested, with the same block, after a suitable break. No more than one block was repeated per day per subject.

E. Data analysis

The psychometric threshold was estimated using probit analysis (McKee *et al.*, 1985) in which $p(c)$ scores are fitted to a cumulative normal distribution:

$$p(c|w)=\frac{1}{2}+\frac{1}{2}\frac{1}{\sqrt{2\pi\sigma^2}}\int_{-\infty}^{w} e^{-(x-\mu)^2/2\sigma^2}\,dx. \tag{1}$$

Thus $0.5\leqslant p(c|w)\leqslant 1$; multiplying by 100 gives actual percentages. Here x represents the sound intensity continuum in dB SPL, w is the stimulus intensity, and μ is the detection threshold such that $p(c|\mu)=0.75$. The fitted parameter σ (in dB) determines the slope of the psychometric function. In probit analysis, the values of μ and σ are selected which provide the best fit of Eq. (1). Confidence limits can be placed on threshold μ (see Finney, 1971). These limits remained quite small at all time gaps because the final psychometric function recorded at each time gap employed 200 trials at each probe level, with the number of levels increasing to compensate as the psychometric function becomes shallower.

II. RESULTS

Generally, pip-detection thresholds rise over the first couple of milliseconds and then decline (Fig. 1). Only one published study employed a fine enough time scale to provide enough data for comparison. Kohlrausch *et al.* (1992) employed an 80 dB SPL frozen noise with a rectangular envelope to forward-mask a 2 kHz tone shaped by a Hanning window. The general trend of their thresholds mirrors our own, showing a very steep recovery curve over the first 5 ms post-masker, followed by a relatively sharp transition to a much shallower, linear descent over 5–20 ms post-masker.

However, following the initial rise, the present threshold decline is by no means smooth (Fig. 1). For example, all three participants exhibit a very steep rise in threshold some 5.5 to 7 ms post-masker. Figure 1 reveals nonmonotonicities up to 17 ms. Previous forward-masking studies show very little evidence of nonmonotonicities. But earlier probes were considerably longer than our own, and did not sample the recovery curve very densely. For example, Kohlrausch

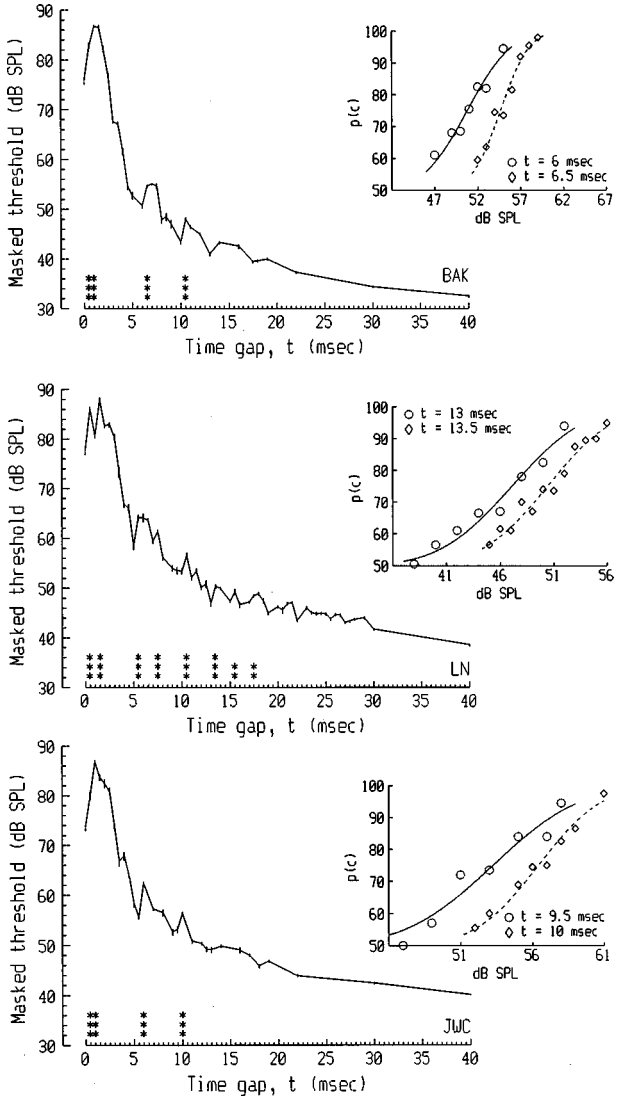

FIG. 1. Forward-masked thresholds with error bars indicating 95% confidence limits. The asterisks indicate times t at which the confidence limits at $t+\frac{1}{2}$ ms did not overlap with the corresponding confidence limits for t ms: ***, for 99.9% confidence limits; **, for 99% confidence limits. Inset panels: Percentage correct $p(c)$ vs the level of the Gaussian tone pip, along with the fitted psychometric functions, for some of the neighborhoods that show sudden increases in threshold.

et al.'s (1992) probe had an overall duration of 5 ms. Any oscillation occurring over $\frac{1}{2}$ ms increments would be averaged over, producing a much smoother and monotonic recovery function for each subject. (In the present case, the word ''oscillation'' refers only to nonmonotonicities, and does not imply actual periodicity.)

The departures from monotonicity become evident when examining selected pairs of psychometric functions (Fig. 1). BAK's psychometric function at 6.5 ms post-masker is to the right and steeper than his function at 6 ms post-masker (Fig. 1, top), LN's function at 13.5 ms is steeper and to the right of his function at 13 ms (Fig. 1, middle), and JWC's psychometric function at 10 ms is to the right and steeper than at 9.5 ms (Fig. 1, bottom). The lack of overlap in these pairs of functions reflects the lack of overlap of the 95% confidence limits for pairs of thresholds[1] in Fig. 1.

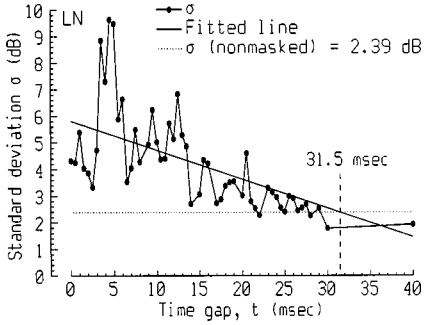

FIG. 2. The standard deviations σ of the psychometric function [Eq. (1)], for subject LN. The least-squares-fitted straight lines extrapolate the post-masker duration required for σ to return to its value for the nonmasked pip.

Inspection of all the psychometric functions suggests that an increase in threshold corresponds to an increase in the slope of the psychometric function (decrease in σ). In all but 2 of the 14 cases where the 99.9% confidence limits indicated a clear increase in threshold with a $\frac{1}{2}$ ms increase in masker-pip gap, there was also a decrease in σ, significant at $p<0.02$ (two-tail sign test). Furthermore, slope itself oscillates with t, for approximately 31 ms. Figure 2 shows σ for subject LN. For subjects BAK and JWC (figures omitted), the nonmasked σ and the extrapolated recovery times were {1.83 dB, 32.4 ms} and {1.64 dB, 29.1 ms}, respectively.

The other recovery time, that of detection threshold, was estimated for each subject by fitting A and B in $\text{Threshold (dB SPL)}=A/(B+\ln t)$ (see Xu *et al.*, 1995), for $t\geqslant 2.5$ ms. Setting $A/(B+\ln t)=\text{Threshold [nonmasked]}$ then gave recovery times of $t=434$, 475, and 1206 ms (BAK, LN, JWC; figures omitted). These are compatible with the literature for similar stimuli ($t\geqslant 400$ ms; Weber and Moore, 1981) and indicate that the 1.5 s inter-stimulus interval allowed full recovery from the forward-masker.

III. SUMMARY

Psychometric functions were obtained for detection of a brief Gaussian pip appearing within milliseconds of an intense tone. Derived detection thresholds show an oscillation superimposed on the general trend of recovery. The standard deviations of the psychometric functions also oscillate, for about 31 ms, much less than the time required for full recovery of the detection thresholds.

ACKNOWLEDGMENTS

Work supported in part by an NSERC grant to Bruce A. Schneider. Our special thanks to J. W. Carey and B. A. Kobilke. We thank Fan-Gang Zeng and William Rhode for comments on an earlier version of this manuscript and Suzanne P. McKee and Scott N. J. Watamaniuk for the probit analysis routine. Early results were reported in Nizami and Schneider (1994). Figures not shown in the text are available from the first author.

[1]We considered the possibility that threshold oscillation might result from interference between the probe pip and evoked otoacoustic emissions (OAEs), such that the emitted waves may partially cancel the incoming probe. OAE amplitudes are rarely above 20 dB SPL (Kemp, 1978; Zurek, 1981). A typical evoked emission of about 10 dB SPL (Veuillet *et al.*, 1991), if added to the pip, would not allow even a 1 dB change in pip level until the latter dropped below 30 dB SPL. For a 20 dB SPL emission, the relevant pip level is 38 dB SPL. It is unlikely that interference from evoked OAEs would significantly affect the probe's masked thresholds at short masker-probe delays.

ANSI (**1969**). ''ANSI S3.6-1969,'' Specifications for Audiometers (ANSI, New York).

Carlyon, R. P. (**1988**). ''The development and decline of forward masking,'' Hearing Res. **32**, 65–80.

Fastl, H. (**1979**). ''Temporal masking effects: III. Pure tone masker,'' Acustica **43**, 282–294.

Finney, D. J. (**1971**). *Probit Analysis* (Cambridge University Press, London).

Gabor, D. (**1946**). ''Theory of communication,'' J.I.E.E. London **93**, 429–457.

Kemp, D. T. (**1978**). ''Stimulated acoustic emissions from within the human auditory system,'' J. Acoust. Soc. Am. **64**, 1386–1391.

Kidd, Jr., G., and Feth, L. L. (**1982**). ''Effects of masker duration in pure-tone forward masking,'' J. Acoust. Soc. Am. **72**, 1384–1386.

Kohlrausch, A., Püschel, D., and Alphei, H. (**1992**). ''Temporal resolution and modulation analysis in models of the auditory system,'' in *Speech Research 10: The Auditory Processing of Speech,* edited by M. E. H. Schouten (Mouton de Gruyter, New York), pp. 85–98.

McKee, S. P., Klein, S. A., and Teller, D. A. (**1985**). ''Statistical properties of forced-choice psychometric functions: Implications of probit analysis,'' Percept. Psychophys. **37**, 286–298.

Nizami, L., and Schneider, B. A. (**1994**). ''Does recovery from forward masking reflect two or more neural channels?,'' J. Acoust. Soc. Am. **95**, 2943.

Rajcan, E. (**1976**). ''Auditory discrimination of the onset-offset phase of tone bursts,'' J. Acoust. Soc. Am. **59**, 1510–1512.

Samoilova, I. K. (**1959**). ''Masking of short tone signals as a function of the time interval between masked and masking sounds,'' Biophys. **4**, 44–52 (trans. of Biofizika).

Schneider, B. A., Pichora-Fuller, M. K., Kowalchuk, D., and Lamb, M. (**1994**). ''Gap detection and the precedence effect in young and old adults,'' J. Acoust. Soc. Am. **95**, 980–991.

Veuillet, E., Collet, L., and Duclaux, R. (**1991**). ''Effect of contralateral acoustic stimulation on active cochlear micromechanical properties in human subjects: dependence on stimulus variables,'' J. Neurophysiol. **65**, 724–735.

Weber, D. L., and Moore, B. C. J. (**1981**). ''Forward masking by sinusoidal and noise maskers,'' J. Acoust. Soc. Am. **69**, 1402–1409.

Xu, Z., Payne, J. R., and Nelson, M. E. (**1995**). ''Logarithmic time course of sensory adaptation in electro-sensory afferents of *Apteronotus leptorhynchus,*'' Soc. Neurosci. Abs. **25**, 185.

Zurek, P. M. (**1981**). ''Spontaneous narrow band acoustic signals emitted by human ears,'' J. Acoust. Soc. Am. **69**, 514–523.

Zwicker, E. (**1984**). ''Dependence of post-masking on masker duration and its relation to temporal effects in loudness,'' J. Acoust. Soc. Am. **75**, 219–223.

Zwislocki, J., Maire, F., Feldman, A. S., and Rubin, H. (**1958**). ''On the effect of practice and motivation on the threshold of audibility,'' J. Acoust. Soc. Am. **30**, 254–262.

Erratum: "Pitch accent in spoken-word recognition in Japanese" [J. Acoust. Soc. Am. 105, 1877–1888 (1999)]

Anne Cutler
Max-Planck-Institute for Psycholinguistics, Nijmegen, The Netherlands

Takashi Otake
Dokkyo University, Soka, Japan

(Received 15 April 1999; accepted for publication 27 April 1999)

[S0001-4966(99)05008-0]

PACS numbers: 43.71.Es, 43.71.Hw [JH]

This paper contains an error on p. 1884, involving the data reported in Sec. II D 3 and Fig. 3, which concern a sub-analysis (confidence ratings of guessed words) of experiment 2, perception of gated words. Mean confidence ratings are reported of 1.67 for correct-accent guesses and 0.5 for incorrect-accent guesses. The correct means are 1.84 and 1.65, respectively, and the difference is significant at fragment 4 only: 2.41 vs 1.87 $t[23]=8.3$, $p<0.001$. The error does not affect the overall conclusions of the paper, or the conclusions from experiment 2. However, the conclusion from this sub-analysis should be tempered: in the phrase ''listeners . . . are nevertheless significantly more confident in guesses which have the same accent pattern as the spoken word'' (p. 1884), the word ''significantly'' should be removed.

 0001-4966/99/106(2)/1191/1/$15.00